CODEN: 4966

THE JOURNAL of the Acoustical Society of America

Vol. 102, No. 1 July 1997

(Continued)

CONTENTS—*Continued from preceding page*

(Continued)

CONTENTS—*Continued from preceding page*

STRUCTURAL ACOUSTICS AND VIBRATION [40]

ACOUSTICAL MEASUREMENTS AND INSTRUMENTATION [58]

PHYSIOLOGICAL ACOUSTICS [64]

PSYCHOLOGICAL ACOUSTICS [66]

SPEECH PRODUCTION [70]

(Continued)

CONTENTS—*Continued from preceding page*

ACOUSTICAL NEWS—USA

Elaine Moran
Acoustical Society of America, 500 Sunnyside Boulevard, Woodbury, New York 11797

Editor's Note: *Deadline dates for news items and notices are 2 months prior to publication.*

New Fellows of the Acoustical Society of America

James F. Lynch—For contributions to shallow water acoustics and ocean acoustic tomography.

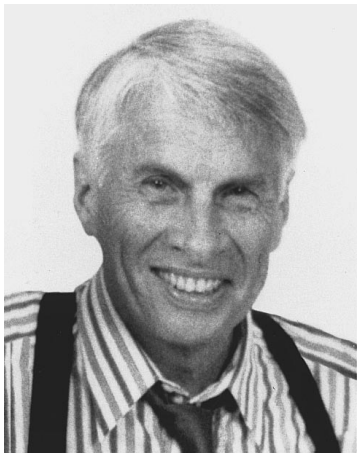

Thomas Shipp—For contributions to the understanding of laryngeal physiology.

Suk Wang Yoon—For contributions to the acoustics of bubble clouds in the ocean.

David L. Bradley succeeds James H. Miller as Associate Editor of the *Journal*

David L. Bradley

In January 1997 Professor David L. Bradley, now of the Applied Research Laboratory at Pennsylvania State University, became an Associate Editor of the *Journal* for papers in Underwater Sound (PACS 43.30). He succeeded Professor James H. Miller of the Department of Ocean Engineering at the University of Rhode Island. The Editor-in-Chief is happy to express his deep appreciation to Professor Miller who completed 4 years of faithful and effective service to the *Journal.*

David L. Bradley was born in Detroit, Michigan and received his B.S. degree in Physics from Michigan Technological University in 1960, and M.S. in Physics from Michigan State University in 1963. His Ph.D. in Mechanical Engineering (Applied Physics/Underwater Acoustics) was in 1970 from Catholic University, Washington, DC.

He has been a U.S. government employee since 1960, at the Naval Ordnance Laboratory until 1978; at NORD Activity until 1979; at OPNAV until 1982; and moved to the Office of Naval Research until 1985; then served as Superintendent, Acoustics Division, Naval Research Laboratory to 1993. He recently completed a three-year assignment as the Director of the SACLANT Undersea Research Center, La Spezia, Italy.

Dr. Bradley is a Fellow of the Society and has served on its Executive Council and as Chairman of the Underwater Acoustics Technical Committee. He is a member of the American Geophysical Union. He has authored or co-authored nearly 50 publications, and has received several Civilian Service Awards.

The Editor-in-Chief and his colleagues welcome Professor Bradley to membership on the Editorial Board.

DANIEL W. MARTIN
Editor-in-Chief

ASA members receive awards from the Society of Automotive Engineers (SAE)

ASA Fellow Emmanuel P. Papadakis, President of Quality Systems Concepts, Inc., has been recognized for the originality of his contribution to automotive engineering through authoring of an SAE paper. He is one of 43 recipients of the Arch T. Colwell Merit Award. Dr. Papadakis was honored for his paper ''An Ultrasonic Technique for Measuring the Elastic Constants of Small Samples'' presented at SAE's 1995 International Congress and Exposition.

ASA member Sean F. Wu, Associate Professor at Wayne State University, was selected to receive the 1997 SAE Ralph R. Teetor Education Award. Recipients of the Teetor Award are chosen on the basis of their academic training, contributions to teaching and research, and participation in extracurricular student involvement.

ASA member Pranab Saha, Secretary/Treasurer of Kolano and Saha Engineers, Inc., is the recipient of the 1997 Forest R. McFarland Award. The award, established in 1979, recognizes individuals who have rendered outstanding service in the organization of technical sessions and papers for SAE meetings and conferences.

USA Meetings Calendar

Listed below is a summary of meetings related to acoustics to be held in the U.S. in the near future. The month/year notation refers to the issue in which a complete meeting announcement appeared.

 0001-4966/97/102(1)/1/8/$10.00

1997

9–13 July	International Clarinet Association, Texas Tech Univ., Lubbock, TX [Keith Koons, Music Department, Univ. of Central Florida, P.O. Box 161354, Orlando, FL 23618-1354, Tel.: 407-823-5116; E-mail: kkoons@pegasus.cc.ucf.edu].
21–27 Aug.	1997 Conference on Implantable Auditory Prostheses, Pacific Grove, CA [Alena Wilson, Conference Coordinator, House Ear Inst., 2100 W. 3rd St., Los Angeles, CA 90057; Tel.: 213-353-7086; FAX: 213-413-0950; E-mail: alena@hei.org; WWW: http://www.rti.org/ciap97].
7–11 Sept.	American Academy of Otolaryngology—Head and Neck Surgery, San Francisco, CA [American Academy of Otolaryngology—Head and Neck Surgery, One Prince St., Alexandria, VA 22314; Tel.: 703-836-4444; FAX: 703-683-5100].
19–20 Sept.	Fifth Annual Conference on Management of the Tinnitus Patient, Iowa City, IA [Richard Tyler, Univ. of Iowa, Dept. of Otolaryngology—Head & Neck Surgery, 200 Hawkins Dr. C21-3GH, Iowa City, IA 52242-1078, Tel.: 319-356-2471; FAX: 319-353-7639; E-mail: rich-tyler@uiowa.edu].
22–24 Sept.	Second Biennial Hearing Aid Research and Development Conference, Bethesda, MD [National Institute of Deafness and Other Communication Disorders, 301-970-3844; FAX: 301-907-9666; E-mail: hearingaid@tascon.com]. Deadline for abstracts is 15 March.
1–5 Dec.	134th meeting of the Acoustical Society of America, San Diego, CA [ASA, 500 Sunnyside Blvd., Woodbury, NY 11797, Tel.: 516-576-2360; FAX: 516-576-2377; E-mail: asa@aip.org, WWW: http://asa.aip.org].

1998

22–26 June	135th meeting of the Acoustical Society of America/16th International Congress on Acoustics, Seattle, WA [ASA, 500 Sunnyside Blvd., Woodbury, NY 11797, Tel.: 516-576-2360; FAX: 516-576-2377; E-mail: asa@aip.org, WWW: http://asa.aip.org].
13–17 Sept.	American Academy of Otolaryngology—Head and Neck Surgery, San Francisco, CA [American Academy of Otolaryngology—Head and Neck Surgery, One Prince St., Alexandria, VA 22314; Tel.: 703-836-4444; FAX: 703-683-5100].
12–16 Oct.	136th meeting of the Acoustical Society of America, Norfolk, VA [ASA, 500 Sunnyside Blvd., Woodbury, NY 11797; Tel.: 516-576-2360; FAX: 516-576-2377; E-mail: asa@aip.org, WWW: http://asa.aip.org].

Revisions to Membership List

New Associates

Ahnert, Wolfgang, ADA Acoustic Design Ahnert, Gustav Meyer Allee 25, Berlin D-13355, Germany

Alwi, Hasan A. B., Dept. of Physics, Univ. of Kebangsaan Malaysia, Bangi 43600, Malaysia

Amirinia, Mohammad R., No. 17 Hammond House, Tiller Road, London E14 8PW, U.K.

Andruszkiewicz, Michael J., 30885 Crest Forest, Farmington Hills, MI 48331

Bean, Colin, R&D Dept., B&W Loudspeakers, Ltd., Elm Grove Lane, Steyning, West Sussex BN2 5JA, U.K.

Brunstrom, Jeff M., Psychology, Birmingham University, Birmingham B15 2TT, U.K.

Cheng, Chih-Chun, Dept. of Mechanical Engineering, National Chung Cheng Univ., 160 Sanhsing, Minghsium, Chia-Yi, Taiwan 621, R.O.C.

Dalsgaard, Paul, Grantoften 2, Aalborg DK-9210, Denmark

Deng, Cheri X., Biomedical Engineering Lab., Riverside Research Inst., 330 West 42nd Street, New York, NY 10036

Engel, Blake A., 18841 West Marian Drive, Lake Villa, IL 60046

Feleppa, Ernest J., Biomedical Engineering LAbs., Riverside Research Inst., 330 West 42nd Street, New York, NY 10036

Feves, Michael L., Earth Dynamics, 2284 NW Thurmon, Portland, OR 97210

Fortin, Christopher S., 43 Preston Drive, North Kingstown, RI 02852

Fox, Christopher G., Pacific Marine Environmental Lab., National Oceanic & Atmospheric Admin., 2115 SE OSU Drive, Newport, OR 97305

Fujiwara, Kyoji, Dept. of Acoustic Design, Kyushu Inst. or Design, Shiobaru 4-9-1, Minami, Fukuoka, 815 Japan

Gabrielsson, Alf G. H., Dept. of Psychology, Uppsala University, Box 1225, Uppsala S-751-42, Sweden

Garcia-Bonito, Juan, Inst. of Sound and Vibration, Univ. of Southampton, Southampton SO17 1BJ, U.K.

Gerard, Christian E., Av. Grecia #2541, Depto. 226, Nunoa, Santiago, Chile

Gruenhagen, Deborah A., 533A Frederick Street, Santa Cruz, CA 95062

Hall, Kristi D., Incredible Technologies, 4010 Winnetka Avenue, Rolling Meadows, IL 60008-1374

Hambric, Stephen A., Applied Research Lab., Pennsylvania State Univ., P.O. Box 30, State College, PA 16804

Harrison, Jonathan A., 68 Alfred Road, Dorchester, Dorset DT1 2DW, U.K.

Herr, Mary C., 7311 Coal Creek Parkway, Newcastle, WA 98059

Hindl, Dieter, Olgastrasse 36, Waiblingen 71332, Germany

Humphrey, Victor F., School of Physics, Univ. of Bath, Bath BA2 7AY, U.K.

Iah, Alur R., Civil Engineering, Indian Inst. of Technology Chennai, Chennai, Tamil Nadu 600036, India

Jaeger, Eric M., Research and Development, Symphonix Devices, Inc., 3047 Orchard Parkway, San Jose, CA 95134-2024

Jupiter, Tina, 20 West 86th Street, New York, NY 10024

Karlsson, Christer U., Kopmansvagen 21, Huddinge S-141 43, Sweden

Killeen, Peter R., Dept. of Psychology, ASU, Box 871104, Tempe, AZ 85287-1104

Kirkeby, Ole, Inst. of Sound and Vibration Research, Univ. of Southampton, Southampton, Highfield SO17 1BJ, U.K.

Krajewski, Chris A., Approvals, Ontario Ministry of Enviroment and Energy, 250 Davisville Avenue, Toronto, ON M4S 1H2, Canada

Krause, Nicholas D., 6086 Gary Place, San Luis Obispo, CA 93401

Kwolkoski, Jeffrey P., 818 West Geddes Circle, Littleton, CO 80120

Lakomyj, Alexander, 6040 Cipriano Road, Lanham, MD 20760

Lawson, Bill H., Robert Kahn, John Kahn & Assoc., Inc., 1601 Dove Street, Suite 290, Newport Beach, CA 92660

Leonard, John J., Dept. of Ocean Engineering, Massachusetts Inst. of Techology, Room 5-422, 77 Massachusetts Avenue, Cambridge, MA 02139

Lobkis, Oleg I., Center for NDE, Iowa State Univ., 1915 School Road, ASC II, Ames, IA 50011

Lohr, Bernard, Psychology, Univ. of Maryland, College Park, MD 20742

Luce, Paul A., Dept. of Psychology, Univ. at Buffalo, 365 Park Hall, Buffalo, NY 14260-4110

Mackey, Dermot, O., 208 Painter's Drive, Upper St. Clair, PA 15228

Madigan, Jeffrey M., Audiology, Howard Leight Industries, 7828 Waterville Road, San Diego, CA 92173

Marlin, Bruce E., Engineering, Atlas/Soundolier, 1859 Intertech Drive, Fenton, MO 63026

Maslov, Konstantin I., Aerospace Engineering, Texas A&M University, College Station, TX 77843-3141

Miyatake, Masanori, Sanyo North America Corporation, 453 Ravendale, Drive, Suite G, Mountain View, CA 94043

Morgan, Christopher D., Kumno Technical Center, 3500 Embassy Parkway, Akron, OH 44333

Nakamura, Isao, 1-33-25 Kokuryo, Chofu, Tokyo, 182 Japan

Nickols, David E., GECO-PRAKLA, DAPD, Schlumberger House, Buckingham Gate, Gatwick RH6 0NZ, U.K.

Nobili, Renato A., Dipt. di Fisica, Univ. Degli Studi di Padova, Via Marzolo 8, Padova 35131, Italy

Passechnik, Viktor I., Rostovskaya Nab. 1-97, Moscow 119121, Russia

Penesis, George K., 33-41 149th Place, Flushing, NY 11354

Popov, Anthony J., Research & Development, American Showa, Inc., 3342 State Route 28, Blanchester, OH 45107

Rama Rao, Kuchimanchi V. S., Physics, Indian Inst. of Technology, Chennai, Tamilnadi 600036, India

Rodgers, Eric G., 3M, OH & ESD, Insulation Products Project, 3M Center, Bldg. 260-4B-11, St. Paul, MN 55144-1000

Sakai, Masahiko, Development, Ono Sokki Co., Ltd., 1-16-1 Hakusan, Midori-ku, Yokohama City, 226 Japan

Salmento, John S., 713 Porter Street, Easton, PA 18042

Servosa, Roca J., Avbd. Sant Narcis 28, Gircona, Catalonia 17005, Spain
Shoykhet, Ilya, Roanwell Corporation, 80 Varick Street, 13th Floor, New York, NY 10014
Sivilotti, Massimo A., Tanner Labs., Tanner Research, Inc., 180 North Vinedo, Pasadena, CA 91107
Steffen, Gerald R., AFMETCAL Detachment 1, MLEE, 813 Irvingwick Drive, West, Suite 4M, Heath, OH 43056-6116
Su, Alvin W. Y., Computer Science & Info. Eng., Chung-Hwa Polytechnic Inst., No. 30, Tung-shiang, Hsin-chu, Taiwan
Sudo, Yasushi, 4-7-24-302 Hakusan, Bunkyo, Tokyo, 112 Japan
Susaki, Hironori, Research Lab., Furuno Electric Co., Ltd., 9-52 Ashihara-cho, Nishinomiya, Hyogo, 662 Japan
Taghipour, Farokh, 13274 Lasselle Street, Apt. 2025, Moreno Valley, CA 92553
Tomoki, Yokoyama, Dept. of Applied Physics, National Defense Academy, 1-10-20 Hashirimi-zu, Yokosuka-shi, Kanagawa-ken, 239 Japan
Van Doorn, Jan M., Nassauplein 5, Alkmaar 1015GM, The Netherlands
Veillette, Randy, 105 Hemlock Drive, Lunenburg, MA 01462
Vermiglio, Andrew J., Human Communication Sciences, and Devices, House Ear Institute, 2100 West Third Street, Los Angeles, CA 90057
Wright, Andrew B., Applied Science, Univ. of Arkansas at Little Rock, 2801 South University, ETAS 575, Little Rock, AZ 72204
Yu, Roger H., Physics Dept., Central Washington University, Ellensburg, WA 98926

New Students

Ali, Sherif F., Mechanical & Aerospace Eng., Arizona State Univ., Box 876106, Tempe, AZ 85287-6106
Anderson, Michael J., 148 Nichols Apt., Piscataway, NJ 08854
Baldridge, Minnie J., 28315 Lookout Road, Paola, KS 66071
Beiler, Todd R., 536 Vine Street, West Lafayette, IN 47906
Berchok, Catherine L., 801A West Aaron Drive, #6, State College, PA 16803
Billingsley, Stephen D., 10 University Village, Apt. F, Ames, IA 50010
Blomgren, Michael, 205 Vernon Avenue, #161, Vernon, CT 06066
Boudreau, Alex, 1136 Rue Auray, Apt. #13, Sherbrooke, PQ J1K 2C4, Canada
Carr, Scott A., 2023A Montreal Street, Victoria, BC V8V 1Z1, Canada
Chase, Lin L., 623 Ivy Street (Rear), Pittsburgh, PA 15232
Chi, Siu-Ling, Audiology, Univ. of Iowa, WJSHC Room 234F, Iowa City, IA 52242
Choudhri, Asim F., 100 Haven Avenue, #22G, New York, NY 10032
Coulter, Peter G., Power House Museum Sydney Austrialia, Exhibition Design, P.O. Box K346, Haymarket 2000, Australia
Debergue, Patricia C., Dept. Genie Mecanique, Univ. of Sherbrooke, 2500 Boulevard Universite, Sherbrooke, PQ J1H 2R1, Canada
De Lima, Washington J. N., 7201 Hart Lane, Apt. 1064, Austin, TX 78731
Derenburger, Corrie J., Mechanical Engineering, Ohio State Univ., 206 West 18th Avenue, Columbus, OH 43210
Di Mondo, Yannick, Chambre X520, 36 avenue Guy de Collongue, Ecully 69131, France
Dille, Marilyn F., Dept. of Speech and Hearing Sciences, Univ. of Washington, 1417 NE 42d, P.O. Box 354875, Seattle, WA 98195-4875
Doelman, Tobey L., 107 Cayuga Heights Road, Apt. 3, Ithaca, NY 14850
Doller, Andrew J., 600 East Pollock, Apt. 1304, State College, PA 16801
Dong, Fang, Medical Physics, Univ. of Wisconsin—Madison, Room 1530, 1300 University Avenue, Madison, WI 53706
Dutta, Debashree, CA-29, Salt Lake City, Calcutta, West Bengal 700064, India
Edson, Patrick L., 129 Chiswick Road, Apt. B, Brighton, MA 02135
Ehnert, Jesse J., 330 Arrowhead Boulevard, Apt. 63A, Jonesboro, Ga 30236
El Moutia, El Housain, 1025 93rd Street, #8, Bay Harbor, FL 33154
Figueiredo, Jamie M., 590 Country Club Lane, Nashville, TN 37205
Franck, Kevin H., 3635 Francis Avenue, North, #6, Seattle, WA 98103
Frivik, Svein A., Telecommunications, Norwegian Univ. of Science and Technology, O.S. Bragstadsplass 2B, Trondheim N-7034, Norway
Gabelman, Brian C., 7110 West 91st Street, Los Angeles, CA 90045
Garcia-Osuna, Fernando, Electrical & Computer Eng., Univ. of Texas at Austin, Engineering Science Bldg. #628, Austin, TX 78712-1084
Genot, Jean-Sebastien S., Dept. Genie Mecanique, Univ. Sherbrooke, 2500 Boulevard Universite, Sherbrooke, PQ J1H 2R1, Canada
Gentry, Cassandra A., 1042N University City Boulevard, Blacksburg, VA 24060
Gmeiner,Thomas, Im Egert 9, Ravensburg 88213, Germany
Gresham, Lisa C., Dept. of Electrical & Computer Eng., Duke University, 130 Hudson Hall, Box 90291, Durham, NC 27708-0291
Guertin, Louis, Genie Mecanique, Univ. Sherbrooke, Boulevard Universite, Sherbrooke, PQ J1K 2R1, Canada
Guiseppe, Vincente E., RR1, Box 1519, Mohnton, PA 19540
Honea, Mark S., 1900 Dartmouth, F-5, College Station, TX 7840
Horak, Jennifer R., 818 Shadwell, Garland, TX 75041
Houde, John F., Brain and Cognitive Sciences, MIT, E10-105B, Cambridge, MA 02139
Howard, Carl Q., Dept. of Mechanical Engineering, Univ. of Adelaide, North Terrace, Adelaide, SA 5005, Australia
Hula, William D., 707 White Cross Road, Chapel Hill, NC 27516
Jang, Hyunsook, 120H West Constitution, Norman, OK 73072
Jayachandran, Vijay, Mechanical Engineering, Univ. of Delaware, 126 Spencer Lab., Newark, DE 19716
Johnson, Dawn L., Zoology, Univ. of Texas at Austin, 141 Patterson Lab., Austin, TX 78712-1064
Johnson, Wayne M., Mechanical Engineering, Georgia Inst. of Technology, Atlanta, GA 30332
Jones, Megan M., 219 South Sparks Street, #5, State College, PA 16801
Kapodistrias, George, Applied Physics Lab., Univ. of Washington, 1013 NE 40th Street, Seattle, WA 98105
Kogan, Pablo, Angel Munoz 560, Valdivia, Chile
Kortenkamp, Peter S., 1761 West Market Street, Apt. C., Akron, OH 44313
Krishna, B. S., Neural Science, New York University, 4 Washington Place, Rm. 809, New York, NY 10003-6621
Lavoie, Lisa M., 1059 Danby Road, #2, Ithaca, NY 14850
Lee, Samson, 11701 Caplinger Road, Silver Spring, MD 20904
Lesniewski, Peter, School of Physics and Electronics, Systems Engineering, Univ. of South Australia, Warrendi Road, The Levels, SA 5095, Australia
Liddicoat, Craig A., Mechanical Engineering Dept., Univ. of Adelaide, North Terrace, Adelaide, SA 5005, Australia
Mann, Iain N., Dept. Electrical Engineering, Univ. of Edinburgh, King's Buildings, Mayfield Road, Edinburgh EH9 3JL, Scotland
Maruvada, Subha, Pennsylvania State Univ., Acoustics, 202 New ARL, University Park, PA 16802
Mielke, Michael M., P.O. Box 14912, Gainesville, FL 32604
Mitsuru, Henmi, 102 Honmura-cho, Asahi-ku, Yokohama-shi, Kanagawa-ken, 241 Japan
Munro, Andrew D., 2289 Smith Lane, Seaford, NY 11783
Neelon, Michael F., Psychology #427, Univ. of Wisconsin, Madison, 1202 West Johnson Street, Madison, WI 53706
Oboznenko, Elena I., General Delivery, Kiev-57 2520957, Ukraine
Okuno, Takatoshi, Information Engineering, Kogakuin Univ., 2665-1 Nakano-machi, Hachiouji, Tokyo 192 Japan
Parry, John J., Electrical and Computer Eng., Univ. of Wollongong, Northfields Avenue, Wollongong, NSW 2500, Australia
Patry, Benoit, Dept. Genie Mecanique, Univ. Sherbrooke, 2500 Boulevard Universite, Sherbrooke, PQ J1H 2R1, Canada
Pelser, Martin J. L., P.O. Box 7447, Stellenbosch, Cape Province 7599, South Africa
Raja, Muthupillai, Dept. of Biophysics & Physiology, MRI Research Lab., Mayo Clinic & Foundation, 200 1st Street, SW, Rochester, MN 55905
Ratle, Alain, Dept. Genie Mecanique, Univ. Sherbrooke, Sherbrooke, PQ J1H 2R1, Canada
Ratnam, Rama, Neuronal Pattern Analysis Group, Beckman Inst., 405 North Mathews Avenue, Ubana, IL 61801
Raymond, Jason L., 46 Park Vale Avenue, Apt. 2, Allston, MA 02134
Reeder, Angie S., Speech and Hearing Science, Psychoacoustic Lab., Arizona State Univ., P.O. Box 871908, Tempe, AZ 85287-1908
Renomeron, Richard J., Center for Computer Aids for Industrial Productivity, Rutgers University, Frelinghuysen Road, P.O. Box 1390, Piscataway, NJ 08855-1340
Richer, Max J., Genie Mecanique, Univ. de Sherbrooke, Science Appliquees, Sherbrook, PQ J1K 2R1, Canada
Roch, Marie A., 927 Sandusky Drive, Iowa City, IA 52240
Roche, Philippe-Emmanuel M., Ginzton Lab., Stanford University, Stanford, CA 94305-4085
Rose, Marina M., Experimental Psychology, Univ. of Cambridge, Downing Street, Cambridge LB2 3EB, England
Rosen, Kristin M., 1444 Bonneville, Laramie, WY 82070
Rosenberg, Eric J., 506 West 37th Street, #309, Austin, TX 78705
Ruiz, Grabriel, Rodrigo De Triana 1676, Valdivia, Chile
Shaw, Jennifer A., RR # 1, Box S-36, Astoria, IL 61501

Shoaf, Lisa C., 1095 Oxfordshire Drive, Columbus, OH 43228
Sinkevicius, Azuolas, 5445 North Sheridan Road, Apt. 1415, Chicago, IL 60640-1929
Sklanka, Bernard J., Pennsylvania State University, Acoustics, P.O. Box 30, University Park, PA 16804
Sundberg, Ulla, Dept. of Linguistics, Stockholm University, Universitetscagen 10, Stockholm S-10691, Sweden
Tooley-Young, Carolyn J., Speech and Hearing Sciences, Univ. of Washington, 1417 NE 42nd Street, JG-15, Seattle, WA 98105-6246
Tournour, Michel A., Dept. Genie Mecanique, Univ. Sherbrooke, 2500 Boulevard Universite, Sherbrooke, PQ J1H 2R1, Canada
Tsuchida, Ayako, 123 King Road East, #A3, Ithaca, NY 14850
Voix, Jeremie, Dept. Genie Mecanique, Univ. Sherbrooke, Sherbrooke, PQ J1H 2R1, Canada
Wayand, Joseph F., Psychology Dept., Kent State Univ., P.O. Box 5190, Kent, OH 44242
Williams, Gail M., 1549 Ryder Street, Brooklyn, NY 11234
Yang, Lening, School of Engineering Systems & Design, Southbank University, 103 Borough Road, London SE1 0AA, U.K.

Associates Elected Members

A. Abdou, D. R. Alach, N. Bi, K. A. Burgemeister, M. J. Choi, S. E. Crocker, M. H. Dunn, V. Dutt, S. Gatehouse, W. S. Fung, E. S. Ebbini, E. O. Bautista, C. E. Gelfer, S. J. Handel, J. R. Hauenstein, G. Hayward, S. Hirobayashi, J. J. Hoefler, M. K. Huffman, K. Th. Kalveram, R. A. Kennedy, R. T. Kessel, B-C. Kim, P. C. C. Lai, M. J. Lally, R. A. Lee, S-H. Lee, J. C. Lucero, G. G. Maze, H. J. McDermott, R. I. Odom, H. Pasterkamp, F. J. Patat, K. L. Peterman, R. E. Remez, E. Schonthal, D. Sen, S. Shaiman, M. Slaney, A. J. Szeri, K. K. Tjaden, J. D. Trout, P. K. Weber, E. M. Wenzel, P. Whistler, S. A. J. Wood, E. R. Writer, W. Yao, C. Y. Zhang

Students to Associates

V. P. Adamson, L. L. Auther, M. R. Bailey, F. Bitsie, D. K. Brown, J. R. Buck, A. M. Calabrese, J. R. Callister, J. E. Cates, I. Chitoran, W. D. Clarke, III, K. Corbin-Lewis, F. L. Degertekin, L. W. Dickey, J. F. Dorighi, P. A. Dorn, P. A. Elmore, J. W. A. Fackrell, S. Furukawa, S. D. Goldinger, C. A. Hargenrader, T. L. Hoffmann, K. J. Howell, D. A. Kastak, S. Krishnamurti, G. S. Madaras, R. S. McGuinn, V. Mehta, C. Micheyl, J. E. Moe, M. S. Ozyar, K. M. Rajana, J. Redner, C. L. Rogers, T. W. Simmermacher, P. S. Spoor, M. J. Swiergosz, B. D. Tinianow, Y-C. Tsao, M-P. Verger, Q. E. Wang, T. M. Whitney, S. R. Wood, L. Zhang

Associate to Student

Y. Mao

Reinstated

A. Cote—*Student*

Resigned

H. O. Berktay—*Fellow*

P. W. Alberti, A-P. Benguerel, S. P. Burke, A. G. Constam, D. F. Gingras, T. S. Graham, K. M. Guthrie, S-L. Hall, J. E. Hawkins, W. A. Hines, T. Koizumi, E. Y. T. Kuo, B. T. Oshika, J. W. Picone, D. E. Priest, G. E. Sheldon, M. D. Steer, M. Tanda, A. F. Wittenboro, M. E. Zakharia—*Members*

M. J. Altom, P. C. Baczewski, M. J. Campbell, C-P. Chen, T. R. Crain, M. H. De Leon, J. J. Eynck, P. Fausti, N. A. Gleiss, R. B. Jackson, S. Lefebvre, L. M. Lichtenstein, W. R. Naito, A. L. Pappas, L. P. Rybak, Q. T. Soon, B. E. Trimble, T. W. Vivyurka, G. Zaklan, P. Zuliani—*Associates*

J. P. Babish, C. W. Hodgson, J. Rao—*Students*

Deceased

R. Farrell, G. J. Thiessen, W. D. Ward—*Fellows*

A. R. Jones, R. E. Jones, J. A. Scrimger, W. Wathen-Dunn—*Members*

B. M. Hammond—*Student*

Drops

J. F. Brugge, C. R. Fuller, M. P. Haggard, S. K. Numrich, R. R. Rojas, H. L. Saxton, *Fellows*

A. Alippi, J. M. Aran, C. R. Arnold, S. E. Auyer, R. C. Baird, D. C. Barber, J. L. Becklehimer, I. A. Beresnev, I. M. Besieris, D. D. Bie, D. Boucher, B. E. Bowers, L. L. Boyer, H. Brandes, C. W. Brokish, C. H. Brown, C. Brunel, M. Burrill, F. J. Canals-Riera, R. F. Carlson, A. S. Chan, W. T. Chan, S-T. Chang, J. L. Christensen, R. J. Christian, J. P. Christopher, III, C. J. Dewdney, M. A. Dinno, A. M. K. Edee, F. J. Fahy, T. Y. Fung, F. G. Geil, C. R. Gerke, J. J. Godfrey, M. A. Gonzalez, L. C. Granger, J. J. Grannell, T. A. Graves, L. C. Gray, E. D. Haas, V. Hansen, M. E. Haran, H. W. Hehmann, J. C. Heine, T. L. Henderson, G. R. Hess, R. D. Hilliard, J-M. Ho, J. L. Hook, C-J. Hsu, P. D. Jackins, D. W. Johnson, J. B. Jones-Oliveira, P. K. Kasper, E. L. Kelsey, R. L. Kerlin, F. R. Kern, C-D. Kim, S. Kostek, S. Kishnamurthy, T. E. Landers, M. Lennig, N. D. Lewis, J. L. Locke Head, C. P. Loser, I. R. A. MacKay, P. H. Maedel, Jr., R. P. Maineri, J. B. Malosh, G. Margolis, R. L. Martin, D. J. McCarthy, R. J. McCauley, N. P. McKinney, J. R. Mendez y Suarez, H. L. Merck, C. R. Merz, R. E. Montgomery, K. J. Murphy, R. L. Nasoni, C. H. Norris, W. L. O'Neill, C. C. Oliver, C. W. Olson, E. R. Payne, M. T. Poldino, J. C. Preble, J. R. Prohs, B. Rafine, W. E. Robert, D. Roberti, L. M. Rowe, Jr., S. Ryan, S. Santi, D. J. Snow, A. G. Sotiropoulou, B. S. Spano, H. F. Stewart, J. M. Tattersall, R. Thorne, R. J. Thornhill, D. Thurmond, K. A. Tobin, M. D. Trudeau, K. M. Vandever, A. S. Victor, S. T. Walden, D. N. Washburn, J. M. Whitehead, R. J. Wilkes, J. M. Winey, N. K. Winsor, W. R. Woszczyk, E. A. A. Yaseen, Y. Yong, C. M. Young, *Members*

D. C. Anderson, M. A. Armstrong, S. M. Avanesyan, L. M. B. Baart de la Faille, D. G. Baize, S. M. Barlow, A. N. Bart, G. E. Bartuska, N. B. Bea, K. J. Becker, J. K. Bennighof, J. W. Benson, N. Bilaniuk, S. C. Bledsoe, Jr., G. J. Bock, S. M. Bott, J. R. Brazell, J. F. Bridger, R. L. Brill, W. R. Brink, Jr., D. E. Brown, M. L. Brown, B. S. Brubaker, S. K. Bui, R. C. Burkhardt, L. A. Busse, S. Candelaria de Ram, M. R. Cannon, E. Cavanaugh, F. W. Cazier, Jr., M. P. Chamness, H. A. Chandler, C. Chang, F. Charron, F. R. Chen, S-E. Chen, Y. Cho, G. F. Chollet, M. A. Clarkson, G. E. Clunis, E. S. Cole, D. S. Cooper, J-M. Cortambert, E. J. Crouchley, A. T. Culver, I. S. Curthoys, C. M. W. Daft, E. M. Daley J. A. Daniels, J. de Dios Exparza, X. M. de Gastines, D. T. Derbas, V. R. Desai, Y. Desaubies, M. B. Dev, M. DiPaolo, D. S. Dixon, L. A. Dorney, R. M. Dyas, J. M. Elliott, W. R. Evans, P. A. Ferlino, M. A. Fernandes, H. F. Fjerdingstad, J-F. Fluckinger, R. J. Gaillaard, A. Garcia, R. G. Gibson, D. Goldman, M. D. Good, F. J. Goodman, J. Gorchs, R. L. A. Gorling, G. Green, N. Grenie, M. Greska, C. Griffin, J. A. Gross, Y. Gu, M. Guirao, V. L. Hammen, S. Haran, R. W. Harris, D. R. Hatch, J. A. Henry, J-P. Hermand, R. E. Hillman, M. L. Hilton, A. Hofer, E. S. Holmes, K. D. Holton, S-Y. Hong, S. M. Howard, A. E. Hubbard, P. A. Hwang, K. C. Ireland, R. Jacks, B. M. Jagolinzer, S. K. Jain, P. E. James, R. B. Janisch, S. K. Lee, Z-Y. Jiang, M. S. Johansen, J. R. Johnstone, H. M. Jones, P. X. Joris, Y. Kadman, A. Kahraman, A. J. Kalinowski, K. V. Kamath, E. G. Keate, N. A. Kelly, R. C. Kemerait, R. H. Kemp, Jr., G. B. Kempster, Z. S. Kevanishvili, Issam Kheirallah, C. E. Klayman, K-L. Kong, L. J. J. Kopp, J. D. Krieger, F-M. Kuo, G. M. Kvistad, P. E. LaGasse, J-J. Laissus, R. W. Lally, J. H. LeClere, C. A. Ledoux, H. Y. Lee, S. Lee, S. Lee, T. Lee, K. A. Lenzo, K. D. LePage, T. D. Leroux, E. Lindemann, A. S. Lippa, B. Lisker, Y. Liu, M. F. Lopes, L. Louie, F-L. Lu, M. P. Lyons, C. C. Ma, J. C. Macie, K. K. M. Manabe, T. S. Margulies, J. B. Martinez, Jr., L. J. Marx, M. A. Mastroianni, N. P. McAngus, R. P. Meier, E. Mendez, T. J. Mermagen, J. A. Meyer, L. W. Middleditch, J. A. Miranda, M. A. Moehring, M. Mogilevsky, A. R. Mohanty, K. M. Mok, W. M. L. Morawitz, B. A. Morrongiello, D. C. Mountain, P. D. Mourad, J. W. Mullennix, H. Murakawa, A. Nadim, R. J. Nagem, R. Nici, J. C. Norris, S. Nowicki, B. L. O'Toole, J. F. Olsen, J. A. Ortiz Garcia, J. H. Park, B. J. Parker, S. I. Parks, M. T. Peet, J. J. Phelan, S. P. Pisciotta, R. Pitre, E. Pitts, III, T. D. Plemons, M. A. Plummer, D. K. Polican, A. J. Policastro, D. J. Powell, R. Priebe, J. O. Ramsay, K. J. Randolph, P. W. Rappold, M. A. Reed, D. R. Regan, J. A. Resnick, S. A. Rhodes, A. M. Richardson, K. M. Rittenmeyer, R. Robledo, C. A. Rogers, J. Roginsky, R. C. Rose, W. J. Rose, T. H. Rousseau, III, D. L. Rowley, E. Sabat Garibaldi, D. A. Sachs, S. Santiago, A. A. Sarkady, S. J. Saunders, A. Sauter, Jr., D. C. Savererbicr, P. R. Saxon, K. P. Scharnhorst, J. C. Schoppe, D. W. F. Schwarz, A. A. S. Sek, X. Serra, C. Sheris, K. A. Shipley, M. Simoni, L. Song, J. E. Spanier, M. W. Sprague, S. L. Staples, J. P. Stec, M. Stevenson, R. E. Sturz, J. A. Sullivan, S. Taherzadeh, T. Takanohashi, A. Tarraf, T. Tateno, A. J. Taylor, T. W. Taylor, S. A. Telenkov, L. F. M. Ten Bosch, R. Todd, S. K. Tomar, R. Torre, B. N. Tran, T. V. Tran, W. K. Trappe, L. Trevino, W. Tsoi, F. M. Tucker, J. S. Uhlman, S. A. Valderrabano, A. M. Vendetti, M. L. Vigilante, J. D. Vrieslander, J. M. Wagner, G. H. Wakefield, K. L. Warner, L. G. Weiss, J. A. Wilder, R. J. Williams, P. A. Wlodkowski, R. L. Woodcock, B. L. Wooley, K-T. Wu, D. D. X. Xiano, J. Yang, J. S. Yaruss, T. J. Yoder, A. Yonovitz, D. A. Zapala, R. L. Zimmerman, *Associates*

V. Aharonson, H. A. Akil, S. K. Alam, G. A. Alderman, M. Arsenault, R. A. Avery, J. Ball, S. R. Bar-Sela, M. G. Brandle, J. L. Brandt, S. R. Brunet, M.

P. Bryant, J. C. bulen, V. G. Burner, A. J. Burnette, J. P. Carneal, M. B. Carroll, C. M. Charlton, M. Chellappa, M. Y. Chen, J. E. Cisneros, K. B. Cohen, D. G. Cole, B. J. Collins, S. M. Cordry, D. L. Cosnowski, R. A. Coury, S. P. Crane, E. L. Da Costa, K. A. Denchfield, D. Distasio, S. S. Dodd, K. B. Doherty, M. Ebel, A. E. Ellis, B. Engers, C-H. Fang, D. L. Ferguson, B. H. Fitzgerald, E. J. Freeman, M. K. Gangala, L. Gavidia-Ceballos, L. J. Gelin, J. S. Gerber, S. D. Gogate, W. P. Goodwin, M. L. Grabb, R. Hagiwara, F. Hall, C. A. Harsin, H. He, K-A. Hegenwald, K. Heidenreich, M. A. Hennessy, S. R. Hensley, F. J. Herrmann, J. Herro, S. T. Ho, P-L. Hsiao, S. J. Hyun, E-E. Jan, T. K. Kapoor, A. Karali, D. E. Kayala, H-G. Kil, J-H. Kim, T. D. Kite, C. S. Kwiatkowski, Y-K. Kwon, T. Landgren, G. M. Lee, M. D. Lee, L. Levac, Y-F. Li, C. Lorenzi, T. M. J. Loucks, J. F. Madneil, E. S. Martin, C. Mattei, M. R. Mease, W. P. Meres, D. Y. Montoya, W-K. Moon, C. B. Moore, S. T. Myers, H. Nelisse, A. A. Nespor, L. Nguyen, M. N. Novaes, M. L. Oelze, G. W. Oliver, G. A. Owen, N. A. Ozluer, P. S. Palombi, J. A. Pavez Vidal, A. Pelletier, R. A. Peron, D. N. Peterson, H. Pham, M. Popovic, C. S. Post, M. J. Rametta, C. Rathinavelu, C. Remillat, J. Romero, H. H. Rump, T. J. Schwander, D. J. Sebald, M. L. Seltzer, T. M. Shaukat, J. W. Shen, R. K. Sherman, T. Shi, J-H. Shin, J. A. Shore, J. S. Sitter, M. A. Smith, A. B. Spalding, T. D. Sparks, K. J. Staub, W. F. Stewart, R. I. Sujith, J. B. Thoms, R. K. Thorburn, Y. Tian, E. L. Topps, J. D. Travis, S. A. Trent, Q. Wang, S. S. Wang, Z. Wang, T. J. Wardzala, J. M. Winograd, W. B. Wright, J. A. Yahner, L. J. York, J-D. Yu, G. Zhang, Q. Zhang, J. J. Zhou, *Students*

Fellows	789
Members	2674
Associates	2646
Students	801
	6910

REVIEWS OF ACOUSTICAL PATENTS

Daniel W. Martin
7349 Clough Pike, Cincinnati, Ohio 45244

The purpose of these acoustical patent reviews is to provide enough information for a Journal reader to decide whether to seek more information from the patent itself. Any opinions expressed here are those of reviewers as individuals and are not legal opinions. Printed copies of United States Patents may be ordered at $3.00 each from the Commissioner of Patents and Trademarks, Washington, DC 20231.

Reviewers for this issue:

GEORGE L. AUGSPURGER, *Perception Incorporated, Box 39536, Los Angeles, California 90039*
MAHLON D. BURKHARD, *31 Cloverdale Heights, Charles Town, West Virginia 25414*
JOHN ERDREICH, *Ostergaard Associates, 100 Executive Drive, West Orange, New Jersey 07052*
HARVEY H. HUBBARD, *325 Charleston Way, Newport News, Virginia 23606*
SAMUEL F. LYBARGER, *101 Oakwood Road, McMurray, Pennsylvania 15317*
D. LLOYD RICE, *11222 Flatiron Drive, Lafayette, Colorado 80026*
WILLIAM THOMPSON, JR., *The Pennsylvania State University, University Park, Pennsylvania 16802*
ERIC E. UNGAR, *Acentech Incorporated, 33 Moulton St., Cambridge, Massachusetts 02138*
ROBERT C. WAAG, *University of Rochester Medical Center, 601 Elmwood Avenue, Rochester, New York 14642*
ROBERT W. YOUNG, *1696 Los Altos Road, San Diego, California 92109*

5,455,475

43.20.Ye PIEZOELECTRIC RESONATOR SENSOR USING THE ACOUSTOELECTRIC EFFECT

Fabien J. Josse and Zack A. Shana, assignors to Marquette University
3 October 1995 (Class 310/316); filed 1 November 1993

''An AT cut quartz crystal resonator has an unbalanced electrode geometry to induce a particularly strong electrical field in a surface of the resonator adjacent a medium. The electrical field will interact with ions and dipoles in the medium and may be used to accurately and repeatably measure the electrical characteristics of the medium. Specific examples are provided illustrating the use of a sensor designed in accord with the invention in sensing dilute electrolytes, and other applications are contemplated.''—MDB

5,594,165

43.35.Yb METHOD AND APPARATUS FOR DETECTION OF PARTICLES IN ULTRA-PURE LIQUIDS USING ACOUSTIC SCATTERING AND CAVITATION

Sameer I. Madanshetty, assignor to Trustees of Boston
14 January 1997 (Class 73/61.75); filed 23 March 1996

In one apparatus of this patent for detecting very small particles in a liquid, an active transducer on one side of a tube, through which the liquid is flowing, generates at 30 MHz a peak negative focused sound pressure of 50 kilopascals that causes gas caps to form on the particles. Via a transducer on the other side of the tube, a 0.75-MHz 1.5-megapascal ''negative focused acoustic signal'' causes cavitation bubbles. Part of the first claim: ''...detecting an acoustic signature which comprises a reflection of said high frequency acoustic field or said low frequency, high tensile pressure pulsed cavitation filled off of said bubbles, whereby said acoustic signature indicates that the particles are present in the fluid.''—RWY

5,473,578

43.30.Lz SONAR AND CALIBRATION UTILIZING NONLINEAR ACOUSTIC RERADIATION

W. L. Conrad, assignor to the United States of America
5 December 1995 (Class 367/13); filed 14 March 1994

A radiated beam of sound impinges on a nonlinear reradiator which then returns sound waves of a different frequency to a hydrophone which is to be calibrated. This hydrophone is located proximate to the original source. The frequency and amplitude of the signal that is incident on the hydrophone can be controlled by varying the input to the original source. Since the original source and the hydrophone are near one another, the need for a wire communication link between operators at two distant sites is eliminated. In another application of the concept, a comparable effect is realized by having the original beam of sound interact with the cavitation produced by a ship's propeller.—WT

5,457,863

43.35.Zc METHOD OF MAKING A TWO DIMENSIONAL ULTRASONIC TRANSDUCER ARRAY

Lewis J. Thomas III and Lowell S. Smith, assignors to General Electric Company
17 October 1995 (Class 29/25.35); filed 22 March 1993

A relatively large transducer block comprises a rectangular piezoelectric body having two layers of backing material including an inner electrically conducting layer and an outer lossy backing layer. The transducer block is then cut or sawed in spaced parallel planes perpendicular to the layers to form a number of substantially identical elongated, relatively nar-

 0001-4966/97/102(1)/16/12/$10.00

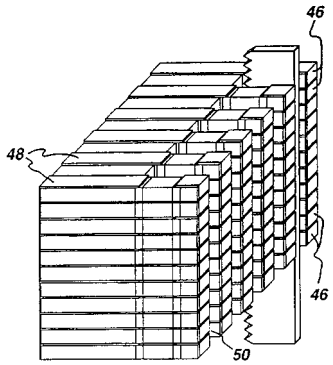

row transducer strips. Electrical connections to the front and back faces of the piezoelectric material are provided by metal films. After the conducting films are formed on the transducer strips, the strips are assembled into a block form, and grooves or kerfs are cut from the front face through the matching layers.—MDB

5,438,554

43.38.Fx TUNABLE ACOUSTIC RESONATOR FOR CLINICAL ULTRASONIC TRANSDUCERS

M. S. Seyed-Bolorforosh *et al.*, assignors to Hewlett-Packard Company
1 August 1995 (Class 367/140); filed 28 February 1994

A tunable ultrasonic probe comprises a number of pillars **102** of conventional piezoelectric ceramic such as lead zirconate titanate attached to similar pillars **103** of a relaxor ferroelectric ceramic such as lead magnesium niobate. The composite pillars sit on a base **104** of epoxy or other damping material. A suitable suite of electrodes allows 3–3 coupling to the longitu-

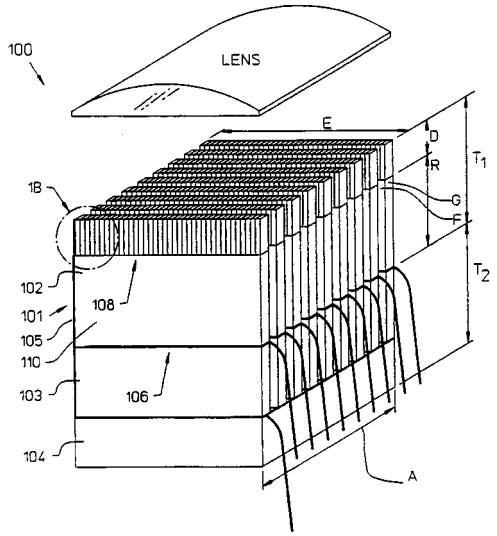

dinal vibrations of the composite pillars. Grooves are cut in the top portion **1B** of the lead zirconate titanate pillars to effect a better impedance match with the target medium (flesh). The polarization of the lead magnesium niobate material is variably controlled by an applied bias voltage, thereby controlling the resonance frequency of the structure.—WT

5,590,208

43.38.Ja SPEAKER SYSTEM

Shinji Koyano *et al.*, assignors to Pioneer Electronic Corporation
31 December 1996 (Class 381/154); filed in Japan 18 April 1994

It is difficult to know exactly what is patented here. The illustration depicts a variant of the 1951 R–J patent in which a duct is driven both by the front of a loudspeaker and by a vented rear chamber. The operating principle is rediscovered periodically, and the geometry shown has been

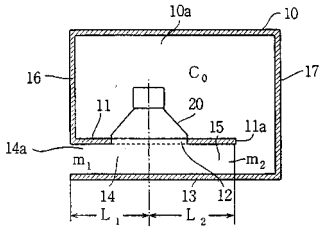

used by this reviewer in subwoofer designs for more than ten years. The patent text commendably emphasizes how interaction between the acoustic load and the frequency dividing network can be included in overall system design, but in the Claims section this is reduced to a generic filter ''...for eliminating a high frequency component contained in the drive signal.''—GLA

5,570,429

43.38.Ja AUDIO TRANSDUCER WITH FLEXIBLE FOAM ENCLOSURE

Paul W. Paddock, assignor to Lineaum Corporation
29 October 1996 (Class 381/202); filed 3 February 1995

Lineaum's previous patents describe a diaphragm shaped in cross section like a figure 3, clamped at its outer edges and driven at the center apex to create a generally dipolar radiation pattern. If instead the rear surface of the diaphragm works against a conforming block of elastic foam which fills a sealed cavity, then assembly is simplified and performance is improved.—GLA

5,444,790

43.38.Kb MICROPHONE WINDSCREEN MOUNTING

James H. Kogen, assignor to Shure Brothers, Incorporated
22 August 1995 (Class 381/168); filed 28 February 1994

The windscreen **12** slides over the microphone **13** and is secured to the

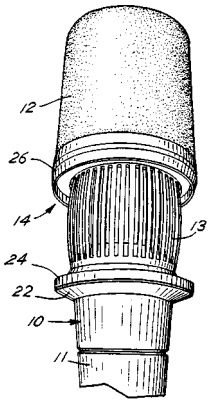

assembly by mating **26** with **24**. Ring **24** is preferably a permanent magnet material and ring **26** is ferrous material.—MDB

5,577,126

43.38.Lc OVERLOAD PROTECTION CIRCUIT FOR TRANSDUCER

Wolfgang Klippel, Dresden, Germany
19 November 1996 (Class 381/59); filed in Germany 27 October 1993

The patent describes a previous protection scheme based on a mirror filter plus a controllable high-pass filter. This improved circuit has a very short reaction time and minimizes audible changes in the input signal. It consists of a reference filter, a controller, a multiplier, and a summer. The reference filter serves both to provide a signal that can be used to indicate

overload, and to decrease the amplitude of those spectral components which cause the overload.—GLA

5,586,194

43.38.Lc AUGMENTATION AMPLIFIER

Jon M. Risch, assignor to Peavey Electronics Corporation
17 December 1996 (Class 381/120); filed 31 March 1994

Yes, power amplifiers can be connected in series. Solid-state amplifiers are commonly used in a bridge configuration with push–pull drive to the two inputs. However, a second unity-gain inverting amplifier can simply be driven from the output of the first amplifier. To the best of the reviewer's

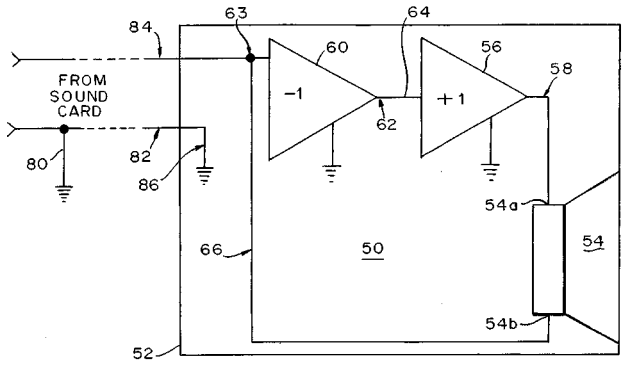

knowledge, this configuration was first used more than 20 years ago in special amplifiers supplied by JBL to Disney theme parks. The amplifier of this patent is intended primarily for use with computer audio systems and includes a clever provision for outboard equalization.—GLA

5,555,306

43.38.Md AUDIO SIGNAL PROCESSOR PROVIDING SIMULATED SOURCE DISTANCE CONTROL

Michael A. Gerzon, assignor to Trifield Productions Limited
10 September 1996 (Class 381/63); filed 27 June 1995

Audio processing applications such as computer gaming may require several program sources to be simultaneously and independently ''spatialized''. The patent discloses an interesting method for controlling the distance parameter.—GLA

5,561,737

43.38.Md VOICE ACTUATED SWITCHING SYSTEM

Donald J. Bowen, assignor to Lucent Technologies, Incorporated
1 October 1996 (Class 395/2.84); filed 9 May 1994

This conference microphone arrangement consists of a set of microphones facing outward in different directions from a central support stand. The angle covered by each microphone corresponds closely to the width of its directionality pattern as shown in the figure. A processor monitors all

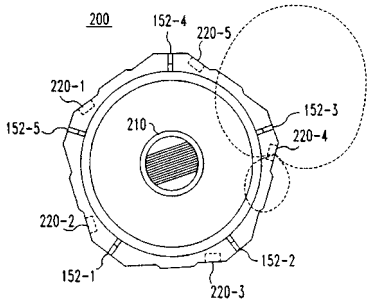

microphone channels for speech presence, selecting one or possibly mixing the signals from two active microphones for transmission. This offers a greatly reduced level of reverberation feedback signal as compared to that of a single microphone.—DLR

5,574,453

43.38.Md DIGITAL AUDIO RECORDING APPARATUS

Ayataka Nishio and Yasuhiro Ogura, assignors to Sony Corporation
12 November 1996 (Class 381/143); filed in Japan 3 March 1994

The patent document provides a good overview of the virtues of Sony's sigma-delta digital recording system. One object is to prevent a maximum-level noise burst if an abnormality occurs in the transmission system.—GLA

5,586,193

43.38.Md SIGNAL COMPRESSING AND TRANSMITTING APPARATUS

Atsushi Ichise and Kenji Inoue, assignors to Sony Corporation
17 December 1996 (Class 381/106); filed in Japan 27 February 1993

The process of decoding high-quality, perceptual encoded audio is time consuming. An in-flight entertainment system that employs such signal compressing means has a problem with announcements—the listener hears real-time audio from the overhead loudspeaker along with a delayed signal from his headset. The apparatus of this patent switches between two compression modes. ''By providing selectable compression time periods music can be enjoyed in high-quality sound, while the announcement of a message can be delivered satisfactorily without the loss of any information.''—GLA

5,467,322

43.38.Pf WATER HAMMER DRIVEN VIBRATOR

B. H. Walter, North Vancouver, British Columbia, Canada
14 November 1995 (Class 367/142); filed 26 October 1994

A vibrator for shaking structures, such as fluid agitators, shaking screens, conveyors, or the walls of bins with large amplitude vibrations, is discussed. The vibrations are generated by using water-hammer pressure pulses to shake the structures. Many versions of the hydraulic driving system and activator are discussed.—WT

5,590,213

43.38.Si HEADSET WITH ADJUSTABLE HEADPAD

Richard M. Urella and Glen A. Davis, assignors to David Clark Company
31 December 1996 (Class 381/183); filed 15 February 1995

The patent shows an adjustable cushioning headpad on a headband supporting earphones. Slide members on the leg portions of the headband

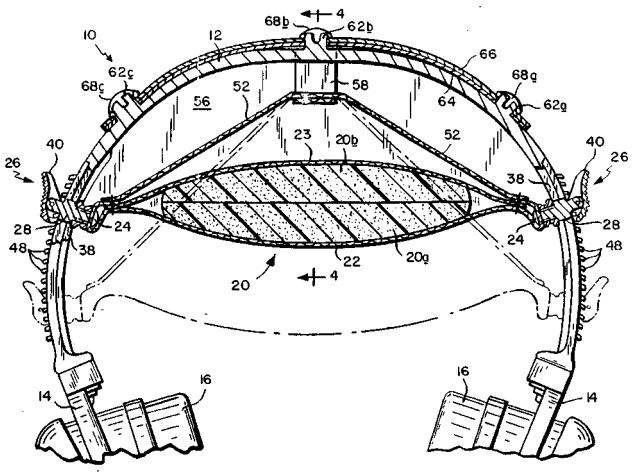

are adjustable to position the headpad in the desired location.—SFL

5,444,768

43.38.Si PORTABLE COMPUTER DEVICE FOR AUDIBLE PROCESSING OF REMOTELY STORED MESSAGES

Charles A. Lemaire *et al.*, assignors to International Business Machines Corporation
22 August 1995 (Class 379/68); filed 31 December 1991

The portable hand-held computer device connects to a remote central message facility through telephone systems. There is provided means for downloading the messages for local replay, and means for accessing through logic circuits the remote location. Local storage is either analog or digital in random access memory.—MDB

5,581,618

43.38.Vk SOUND-IMAGE POSITION CONTROL APPARATUS

Sekine Satoshi *et al.*, assignors to Yamaha Corporation
3 December 1996 (Class 381/17); filed in Japan 3 April 1992

This is yet another entry in the frantic field of computer game ''spatialization,'' in this case panning multiple sources between virtual loudspeakers. The patent abstract enthuses that ''...it is possible to obtain a brand-new live-audio effect, by which the point of producing the sounds corresponding to the animated image can be moved in accordance with the movement of the animated image which is moved by the player of the game.''—GLA

5,590,094

43.38.Vk SYSTEM AND METHOD FOR REPRODUCING SOUND

Kiyofumi Inanaga and Yuji Yamada, assignors to Sony Corporation
31 December 1996 (Class 369/4); filed in Japan 25 November 1991

The patent describes a many-channel recording system which is distributed through a large array of loudspeakers, allowing ''an actual audio image'' to be reproduced. A multiplexing scheme allows the audio signals, plus information about positions and dimensions, to be encoded within limits of practical signal processing and bandwidth.—GLA

5,574,962

43.38.Wl METHOD AND APPARATUS FOR AUTOMATICALLY IDENTIFYING A PROGRAM INCLUDING A SOUND SIGNAL

Michel Fardeau *et al.*, assignors to The Arbitron Company
12 November 1996 (Class 455/2); filed in France 30 September 1991

The object is to acoustically (but imperceptibly) tag radio or TV programs such that they can be identified when reproduced by an unmodified, commercial receiver. One or more narrow bands of frequencies within the overall range from 100–700 Hz are modulated by pulse-type encoding for short periods of time ''...so that the encoded message included in the sound signal is anaudible.''—GLA

5,574,963

43.38.Wl AUDIENCE MEASUREMENT DURING A MUTE MODE

Lee S. Weinblatt and Thomas Langer, assignors to Lee S. Weinblatt
12 November 1996 (Class 455/2); filed 31 July 1995

It is well known that broadcast ratings which state how many people are watching a certain TV program at a certain time are based on relatively few, carefully selected households. These viewers should be able to watch TV on standard receivers, yet have their program selections monitored automatically. One method is to inject specially coded, hopefully inaudible, signals into the audio portions of certain programs. These are detected and logged by small monitoring devices. But suppose the viewer presses the mute button? Now the monitoring device has no way of knowing what, if anything, is being watched. The patented circuit routes premute audio directly to the monitoring unit when the mute function is activated. This seems not only redundant but to contravene the requirement for unmodified TV sets.—GLA

5,394,378

43.38.Zp HYDROPHONE TRANSDUCTION MECHANISM

A. Dandridge *et al.*, assignors to the United States of America
28 February 1995 (Class 367/149); filed 21 June 1993

A planar array of interferometric fiber optic acoustic sensors is described. Each sensor comprises an optical fiber wound around a plurality of hollow compliant mandrels which are encapsulated in acoustically transparent material and mounted in a fixed planar relationship with respect to one another. The reference optical fiber is, of course, isolated from the incident pressure waves.—WT

5,537,688

43.40.Ng HAND COVERING WITH VIBRATION-REDUCING BLADDER

Douglas D. Reynolds and Thomas C. Jetzer, assignors to ErgoAir, Incorporated
23 July 1996 (Class 2/20); filed 30 December 1994

An air-bladder-based material from which gloves are fashioned is described. The material isolates vibrating sources such as pneumatic tools

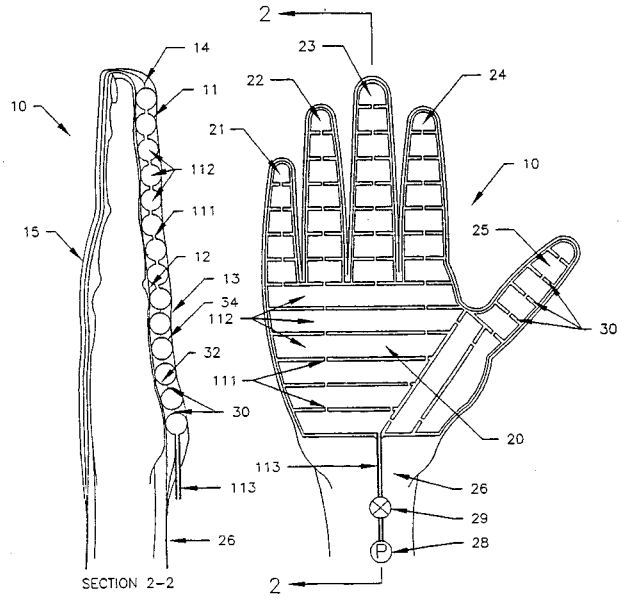

from the hand of the user.—JE

5,478,306

43.40.Ng APPARATUS AND METHOD TO SUPPORT CARPALS TO AID IN THE PREVENTION AND TREATMENT OF CARPAL TUNNEL SYNDROME AND RELATED CONDITIONS

L. Paul Stoner, Lititz, PA
26 December 1995 (Class 602/20); filed 12 October 1993

To ''aid in the prevention and treatment of carpal tunnel syndrome and related conditions,'' an adjustable band is described which fits around the wrist. Since carpal tunnel syndrome is caused by constriction of the space in the carpal tunnel, it is unclear how a device which further restricts this space can be beneficial.—JE

5,581,277

43.40.Ng ANTI-CARPAL TUNNEL DEVICE (ACTD) FOR COMPUTER OPERATORS

Akira Tajiri, Reedley, CA
3 December 1996 (Class 345/163); filed 6 March 1995

A device to position the wrist over a computer mouse in such a manner as to prevent hyper flexion is described. The device places a spacer in the form of a ball, attached to the top of the mouse by Velcro, between the hand

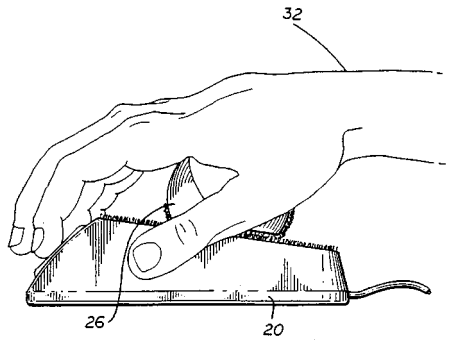

of the user and the device. The result is maintenance of a straight alignment from the fingers to the forearm.—JE

5,549,271

43.40.Tm VIBRATION CANCELER

Arno Hamaekers, assignor to Firma Carl Freudenberg
27 August 1996 (Class 73/669); filed in Germany 26 August 1993

This patent pertains to a simple tuned absorber that consists of a metal inertial mass and an elastomeric spring. The elastomeric spring has a metal clamping element at its end, and is configured to be easily inserted into a matching opening in the mass, so as to facilitate inexpensive assembly.—EEU

5,549,282

43.40.Tm VIBRATION PROOFING STRUCTURE

Masahiko Ikeda, assignor to Kiyoko Ikeda
27 August 1996 (Class 267/126); filed in Japan 24 May 1993

The device described in this patent is a vibration-attenuating support for a seat in a motor vehicle. The device basically consists of two stacked platforms that can slide horizontally; the lower platform can slide laterally relative to a base and the upper platform can slide axially relative to the lower platform. The platforms are interconnected via oil-filled piston dampers and include travel limiters.—EEU

5,550,335

43.40.Tm RESONANCE ABSORBER

Klaus Ermert *et al.*, assignors to Deutsche Aerospace AG
27 August 1996 (Class 181/207); filed in Germany 16 December 1993

This absorber for the attenuation of structure-borne sound essentially consists of an assembly of damped reeds of different lengths. The various reeds have different resonance frequencies; thus the assembly would attenuate vibrations of a body to which it is attached over a relatively wide range of frequencies. The reeds here are obtained by cutting parallel slots of different lengths into rectangular metal plates, which are stacked with a damping material between them and bolted to each other along a line.—EEU

5,444,324

43.40.Yq MECHANICALLY AMPLIFIED PIEZOELECTRIC ACOUSTIC TRANSDUCER

John F. Priest and Mathew G. Schmidt, assignors to Western Atlas International
22 August 1995 (Class 310/334); filed 25 July 1994

With applications to acoustic well logging, a piezoelectric actuator **6** consists of a single piezoelectric element. On application of a voltage the

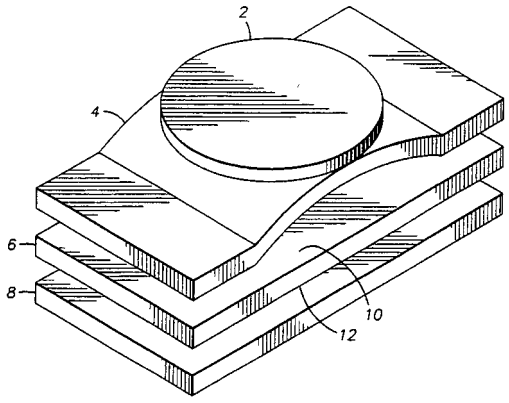

actuator elongates, causing movement of piston **2** which is in contact with the medium in the well.—MDB

5,456,111

43.40.Yq CAPACITIVE DRIVE VIBRATING BEAM ACCELEROMETER

Rand H. Huising II, assignor to Allied Signal, Incorporated
10 October 1995 (Class 73/514.32); filed 24 January 1994

The patent describes a micromachined vibrating beam accelerometer, of the type described in U.S. Patent 5,456,110, that has opposing surfaces within the structure coated with electrically conducting material so as to provide a capacitor. This capacitor may be driven by an external signal source as a method for reducing ''squeeze film damping'' when operated under nonvacuum environments.—MDB

5,456,110

43.40.Yq DUAL PENDULUM VIBRATING BEAM ACCELEROMETER

Rand H. Huising II, assignor to Allied Signal, Incorporated
10 October 1995 (Class 73/514.38); filed 12 November 1993

Two accelerometer elements are micro-machined into a rectangular piece of silicon. Each accelerometer element comprises a mass supported by

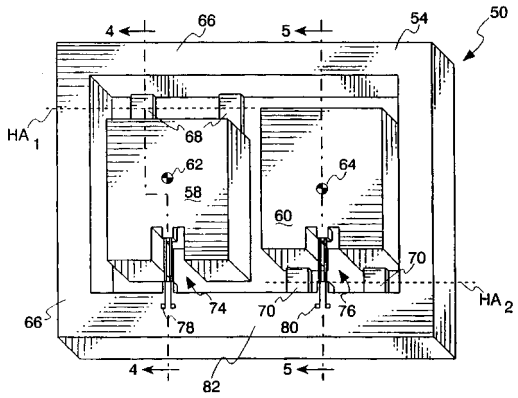

hinge elements connected to a frame. The two transducers are configured in a push–pull arrangement.—MDB

5,540,099

43.40.Yq VIBRATION DETECTING DEVICE AND VEHICULAR ROAD SIMULATOR EMPLOYING THE DEVICE

Shokichi Harashima, assignor to Honda Giken Kogyo Kabushiki Kaisha
30 July 1996 (Class 73/669); filed in Japan 19 November 1993

The detection device here consists of an accelerometer having its output fed to an integrator to produce a velocity signal so as to obtain better coverage of the low-frequency regime of importance in motor vehicles. The device is mounted near a vehicle's axis, and its output is used to record the vibrations that the vehicle experiences as it is being driven. The vibrations to which a test vehicle is subjected in a road simulator then are adjusted via a control system to correspond to those measured on the vehicle that was driven.—EEU

5,551,298

43.40.Yq IDENTIFICATION OF VIBRATION INDUCED NOISES IN VEHICLES

Kevin D. Rayment, assignor to Ford Motor Company
3 September 1996 (Class 73/669); filed in the United Kingdom 9 March 1994

In the approach described in this patent a vehicle is vibrated by means of a computer-controlled road simulator at frequencies that are changed slowly, while an observer notes the frequencies at which particular noises begin to appear and disappear. The frequency range in which a noise is present is compared then with stored data concerning the frequency ranges in which specific vibration-induced noises have been found previously.—EEU

5,461,777

43.50.Gf APPARATUS FOR MANUFACTURING A SILENCER

Tsukasa Ikeda and Akihiko Tamano, assignors to Sankei Giken Kogyo Kabushiki Kaisha
31 October 1995 (Class 29/890.08); filed in Japan 19 April 1993

This patent relates to a method of manufacturing a silencer for use in an internal combustion engine of an automobile and with the associated apparatus. Of particular interest is a silencer having a perforated inner tube, a solid surface outer tube, and with sound absorbing material filling the intervening cavity. Equipment is described for use in rapid assembly in order to fill the cavity uniformly and snugly without necessity for using a binding agent. The inner tube and wound absorbing material are rotated and shaped by leveling members, and are then inserted into the stationary outer tube for final assembly.—HHH

5,550,336

43.50.Gf TURBINE SOUND REDUCER

Joseph W. Kieffer, assignor to Wagner Spray Tech. Corporation
27 August 1996 (Class 181/230); filed 9 November 1994

This patent relates to control of bleed air associated with turbines used with air atomization assisted paint-spray guns. During those portions of the operating cycles for which air is bled from the turbine, it is routed into a discharge line and through an expansion chamber muffler which is built into the main equipment housing.—HHH

5,575,121

43.50.Gf SOUND BARRIER WALL CONSTRUCTION USING TIRE SECTIONS

Philippe LaJaunie, New York, NY
19 November 1996 (Class 52/144); filed 7 March 1995

This patent relates to the construction of sound barriers along highways and airport boundaries in order to shield adjacent residential areas from ground vehicle noise and aircraft generated ground run-up noises, respectively. A system is described for using half tire sections, stacked so that the open sides face the noise sources and are tilted to enhance drainage. Advantages cited are relatively low cost, durability and effective sound absorption.—HHH

5,577,888

43.50.Gf HIGH EFFICIENCY, LOW-NOISE AXIAL FAN ASSEMBLY

Hugo Capdevila *et al.*, assignors to Siemens Electric Limited
26 November 1996 (Class 415/210.2); filed 23 June 1995

This patent relates directly to the design of axial flow fans for generating air flows through automobile heat exchangers. A particular configuration having eight blades and 20 downstream guide vanes is described. Tapered and twisted blades and vanes are noted to have relatively high aerodynamic efficiency and low noise.—HHH

5,579,661

43.50.Gf NOISE AND VIBRATION DAMPENING CONNECTOR TO A TWO PIECE TRANSMISSION SHIFT LEVER ASSEMBLY

James A. Yarnell and Larry D. Stawinski, assignors to Dana Corporation
3 December 1996 (Class 74/473R); filed 2 September 1994

This patent relates to a device for reducing the vibration and noise from shifting lever assemblies for manually operated vehicle transmissions. An improved damping mechanism is provided in the shifting lever assembly to reduce vibrations and noise transmitted from the engine and transmission to the drive compartment. The damping mechanism is a cup-shaped isolator formed of resilient elastomeric material, and is located between the upper and lower shift lever members.—HHH

5,590,206

43.50.Ki NOISE CANCELER

Hyeong-keon An *et al.*, assignors to Samsung Electronics Company
31 December 1996 (Class 381/71); filed in Republic of Korea 9 April 1992

The text of this somewhat puzzling patent starts with the observation that ''...noise produced during the starting of an automobile or the overhead passage of an aircraft can result in the interruption of the normal operation of appliances.'' For example, the appliance might be some kind of audio recorder. When one uses the microphone input of a multi-media personal computer, then the resulting digital recording may be contaminated by noises of automobiles or aircraft. The remedy is to first digitally record a library of automobile, aircraft, and other noises. When you are ready to make a noise-free recording your computer first detects and identifies the background noise, then selects the appropriate library file and mixes inverted waveforms with the microphone output. It might be easier just to teach the computer how to identify unwanted noise and not record it at all.—GLA

5,594,174

43.58.Bh SYSTEM AND METHOD FOR MEASURING ACOUSTIC REFLECTANCE

Douglas H. Keefe, assignor to University of Washington
14 January 1997 (Class 73/585); filed 6 June 1994

Three phases of this system for measuring the linear and nonlinear acoustic reflectance of the human ear are stimulus activation, calibration, and activation. A computer calculates a custom-designed pulse for a driver at the closed end of a calibration tube 25–350 cm long; the tube fits into the ear canal. Reflections from the middle and inner ear back to a microphone at the closed end of the tube are interpreted by the computer as to the condition of the middle and inner ear. The system is usually calibrated for each patient. The system can be similarly attached to study the behavior of a musical instrument such as a trumpet.—RWY

5,467,321

43.58.Dj INSERTION ULTRASONIC TRANSDUCER WITH MODE CONVERSION AND METHOD FOR REDUCING MULTIPLE SIGNAL RECEPTION

J. Baumoel, assignor to Controlotron Corporation
14 November 1995 (Class 367/140); filed 26 September 1994

An insertion-type ultrasonic transducer for monitoring fluid flow rates in pipes consists of a longitudinally vibrating piezoceramic crystal **100** bonded to the end of a steel rod **120** which in turn is welded to a hole cut in the pipe wall **50**. The end **110** of the steel rod is cut at some angle (here indicated at 22°) to the rod axis. The primary beam of energy radiated by the transducer **115** is substantially converted from longitudinal waves to shear waves upon reflection at the rod wall at **122**. This beam of shear wave

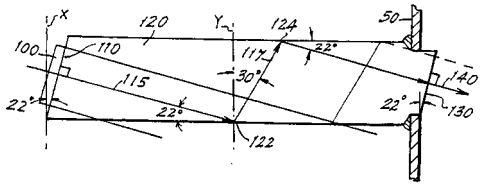

energy **117** (the indicated angle of 30° from the normal to the rod axis assumes a Poisson's ratio of 0.26) is then substantially reconverted to longitudinal waves after another reflection at the rod wall at **124**. Those longitudinal waves **140** exit the rod orthogonally to face **130** which is cut at the same 22° angle as the end **110**. The thesis here is that essentially all of the pulse of energy introduced into the rod experiences a well-defined emergent time, thereby avoiding a multplicity of modes which aberrate the received waveform and make a precise determination of the transmit time of the acoustic waves through the fluid very difficult to accomplish.—WT

5,563,953

43.58.Ry APPARATUS AND METHOD FOR EVALUATING AUDIO DISTORTING

Soon-Keon Kwon, assignor to Daewoo Electronics Company
8 October 1996 (Class 381/58); filed in Republic of Korea 25 August 1993

Measurement of the distortion in high-quality audio equipment has typically used physical signal parameters, such as total harmonic distortion (THD) and signal-to-noise ratio (SNR) to characterize the audio quality. The measurement method disclosed in this patent would use a masking threshold and spectral difference calculation to compute a perceptually weighted signal distortion rating (PWD?).—DLR

5,597,380

43.66.Ts SPECTRAL MAXIMA SOUND PROCESSOR

Hugh J. McDermott and Andrew E. Vandali, assignors to Cochlear Ltd.
28 January 1997 (Class 607/57); filed in Japan 2 July 1991

The patent shows a sound processor with particular application to cochlear implants. Received sound signals are channelized into at least ten analysis channels to produce amplitude signals for each channel. A predefined number—at least four—of channels with the largest amplitudes are used to modulate stimuli for the implanted array.—SFL

5,584,869

43.66.Ts FAILURE DETECTION IN AUDITORY RESPONSE STIMULATORS

Patrice L. Heck *et al.*, assignors to Advanced Bionics Corporation
17 December 1996 (Class 607/57); filed 13 February 1995

The method described utilizes a test signal at a low level to constantly monitor the functioning of the system. For a cochlear implant, this test signal might be comparable in magnitude to that produced when the implant

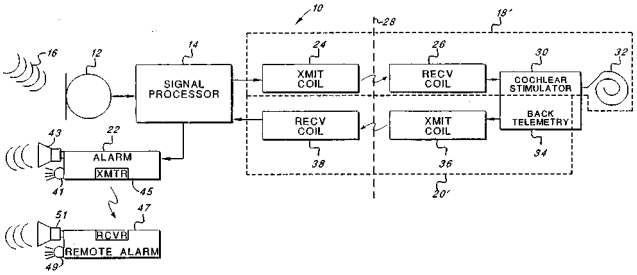

is being stimulated. If the output of the monitoring system drops significantly, an alarm is caused to function. The figure shows a block diagram of the device when used to monitor a cochlear implant. The arrangement shown requires transmission through the skin in both directions. The device appears to have limited application to cases where failure of a system would not be obvious to the wearer.—SFL

5,600,728

43.66.Ts MINIATURIZED HEARING AID CIRCUIT

Scot R. Satre, Concord, CA
4 February 1997 (Class 381/68.2); filed 12 December 1994

The patent shows a microelectronic circuit design with four sections to minimize size. One section contains ''normal use'' circuits, the second ''specialized circuits,'' the third ''for control,'' and a fourth section contains passive elements. The control circuit includes means for switching the passive elements of the fourth section between the first two sections. Several circuit diagrams are shown.—SFL

5,581,821

43.66.Vt REELABLE EAR PLUGS FOR CONSTRUCTION HELMETS

Steven A. Nakano, San Pedro, CA
10 December 1996 (Class 2/422); filed 26 June 1995

The patent shows a reel mounted on the back of a construction helmet that contains earplugs on the end of a flexible cord. The arrangement makes ear protection readily available when needed.—SFL

5,600,729

43.66.Vt EAR DEFENDERS EMPLOYING ACTIVE NOISE CONTROL

Paul Darlington and Gerald A. Powell, assignors to the Government of Great Britain and Northern Ireland
4 February 1997 (Class 381/71); filed in the United Kingdom 28 January 1993

The patent shows an active ear defender with a noise pickup microphone outside an earphone, and a small loudspeaker to deliver a noise-canceling signal inside the ear shell. A digital feedback controller generates a feedback signal derived from the microphone. An estimation means provides an approximation of the earshell transfer function.—SFL

5,555,272

43.72.Gy SIGNAL PROCESSING DEVICE USING SEVERAL DIFFERENT FILTERINGS, ESPECIALLY FOR AUDIO-FREQUENCY CODING OF VOICE SIGNALS

Freddy Balestro and Patrice Senn, assignors to France Telecom
10 September 1976 (Class 375/220); filed in France 16 April 1993

The patent text notes that current signal processing applications, such as cellular telephones and speaker phones, often use multiple analog and digital filters, many of which have similar passband and stopband characteristics. This patent promises cost reductions by applying methods of sharing hardware or software filter structures, either by time or frequency sharing or by specific design simplifications.—DLR

5,555,273

43.72.Gy AUDIO CODER

Toshiyuki Ishino, assignor to NEC Corporation
10 September 1996 (Class 375/244); filed in Japan 24 December 1993

This audio signal coder uses a combination of quantization step changes and Huffman coding to minimize the encoding bitrate. Two different quantizer step adjustment strategies are pursued simultaneously, routing both outcomes through the Huffman encoder. One of the two outputs is selected for transmission based on the resulting bitrates.—DLR

5,555,447

43.72.Gy METHOD AND APPARATUS FOR MITIGATING SPEECH LOSS IN A COMMUNICATION SYSTEM

Michael D. Kotzin and Gary W. Grube, assignors to Motorola, Incorporated
10 September 1996 (Class 455/72); filed 14 May 1993

This patent addresses a problem which arises in communications systems when a processing delay is imposed by hardware concerns. For example, portions of the equipment may have been shut down to conserve power. The user may, however, push a button and begin talking immediately. The incoming speech samples are stored, possibly compressed, in a FIFO buffer until the circuit is ready to operate. Once processing begins, samples from the buffer are processed with a slight sample rate speedup until the excess stored samples have been used. During this time, pitch correction may be applied to minimize effects of the speedup.—DLR

5,555,546

43.72.Gy APPARATUS FOR DECODING A DPCM ENCODED SIGNAL

Ichiro Matsumoto, assignor to Kokusai Electric Company
10 September 1996 (Class 315/244); filed in Japan 20 June 1994

In DPCM speech coders, it is advantageous to detect periods of silence so that portions of the circuitry can be shut down to minimize power loads. However, the transitions between active and quiet states can cause problems, particularly when a false ''active'' state change command is sent. In this case, the receiver stops producing the filler background noise signal and prepares to decode speech which does not arrive. The result is an annoying

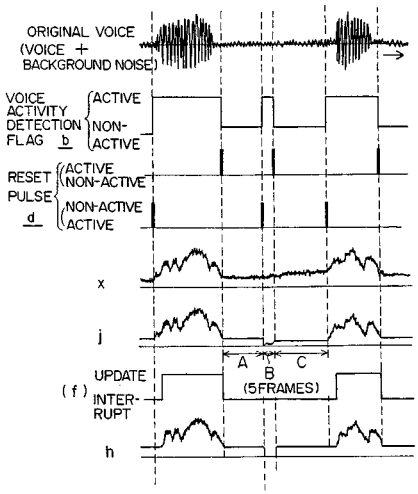

click as the background resumes. This apparatus inserts a five-frame holdover of the background sound until new activity is confirmed. The previous smoothed speech predictor values are also maintained to preset the decoder for the new activity.—DLR

5,557,705

43.72.Gy LOW BIT RATE SPEECH SIGNAL TRANSMITTING SYSTEM USING AN ANALYZER AND SYNTHESIZER

Tetsu Taguchi, assignor to NEC Corporation
17 September 1996 (Class 395/2.28); filed in Japan 3 December 1991

This multipulse vocoder uses a variety of techniques to reduce the transmission bitrate. With an 8K sample rate, frames of 256 samples are extrapolated for an additional 5 ms (negative overlap), lowering the frame rate to 27 per second. Perceptually weighted line spectral pair (LSP) parameters are computed for each frame. A separate impulse response is computed for each subframe of length 40 samples (5 ms). These are cross-correlated with the speech signal and also auto-correlated. From the correlations, a single positive or negative excitation pulse is placed at one of the 40 sample times of the subframe. The subframe pulse positions and polarities are transmitted along with the LSP parameters at the frame rate.—DLR

5,563,913

43.72.Gy HIGH EFFICIENCY ENCODING DEVICE AND A NOISE SPECTRUM MODIFYING DEVICE AND METHOD

Kenzo Akagiri and Makoto Akune, assignors to Sony Corporation
8 October 1996 (Class 375/243); filed in Japan 31 October 1992

This noise-reducing speech compression system provides a perceptually weighted background noise by using a fixed filter shaped like the hearing sensitivity curve to process the error signal. Sample-by-sample differences are observed over a block of samples to determine an appropriate compression constant. The compressed signal is transmitted and also fed back through a corresponding expander and subtracted from a block-length delayed copy of the input speech. The difference signal is passed through the fixed loudness curve filter and used to control the compression system.—DLR

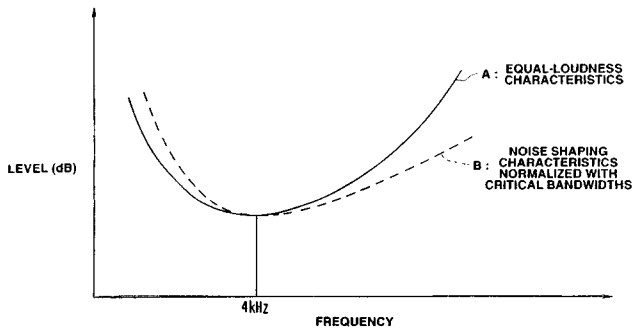

5,561,736

43.72.Ja THREE DIMENSIONAL SPEECH SYNTHESIS

Danial J. Moore and Peter W. Farrett, assignors to International Business Machines Corporation
1 October 1996 (Class 395/2.69); filed 4 June 1993

This text-to-speech synthesizer includes an additional system which generates stereophonic output channels corresponding to a specific, programmable spatial position for the reproduced talker. This is done by passing the synthesized speech signal through two transfer functions, one specific to each channel. The method for doing this is disclosed in prior U.S.

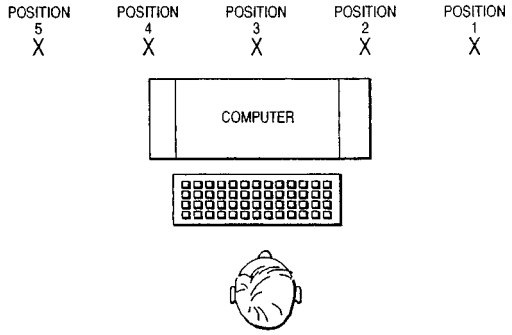

Patent No. 5,046,097. The synthesizer control structure allows separate spatial positions to be associated with each of several virtual talkers, each of which also has specific voice quality and accent or dialect parameters.—DLR

5,559,792

43.72.Kb SOUND MODIFICATION FOR USE IN SIMULTANEOUS VOICE AND DATA COMMUNICATIONS

Stanley Bottoms *et al.*, assignors to Lucent Technologies, Incorporated
24 September 1996 (Class 370/20); filed 20 April 1994

A simultaneous voice and data (SVD) modem is described which includes special features for applications in remote game playing. While transmitting the moves and other game progress information digitally, the modem also allows the user to alter the characteristics of the outgoing voice signal or that of the remote player. Various sound effects may also be added to the outgoing audio channel.—DLR

5,563,952

43.72.Kb AUTOMATIC DYNAMIC VOX CIRCUIT

Walter J. Mercer, assignor to Tandy Corporation
8 October 1996 (Class 381/56); filed 16 February 1994

The patent describes a hardware circuit for voice detection (VOX) intended for reliable, low-cost applications, such as an intercom system. A peak detector circuit operates in two modes, roughly following the smoothed incoming peak level when the system is in nonspeech state, and holding the previous peak level when the system is in speech state. The incoming speech

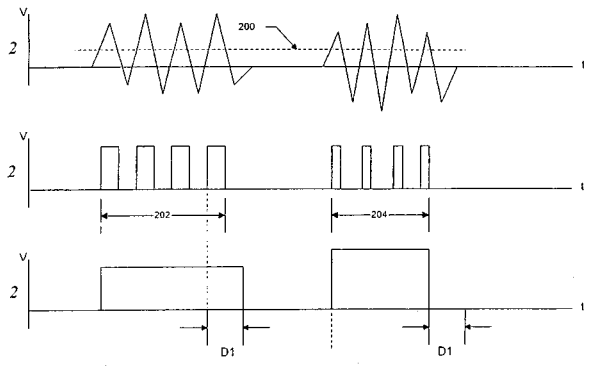

level is compared to the peak detector output. In nonspeech state, the comparator output provides the peak detector input signal. At all times, the comparator output drives a logic circuit which watches for comparator transitions within a duration range of 40 ms to 1 s. As long as transitions are seen in this duration range, the system stays in speech detection state.—DLR

5,553,119

43.72.Ne INTELLIGENT RECOGNITION OF SPEECH SIGNALS USING CALLER DEMOGRAPHICS

Alex McAllister and Laird Wise, assignors to Bell Atlantic Network Services, Incorporated

3 September 1996 (Class 379/67); filed 7 July 1994

This patent describes a method of combining existing technologies in an attempt to provide satisfactory speech recognition performance in a variety of telephone applications. Existing recognizers are notoriously temperamental in their need for narrow constraints; constraints on the speaker's voice, speaking style, and choice of phrases, to name only a few. In this system, information on the caller would first be obtained passively by number ID (ANI), caller ID, or other means. A database at the switching office would then supply demographics. The caller would be prompted for a specific response which would be analyzed to add to a growing information base on the caller. This information would be used to select one of multiple available recognition strategies most able to process the speech signal given the known information.—DLR

5,557,661

43.72.Ne SYSTEM FOR CODING AND DECODING MOVING PICTURES BASED ON THE RESULT OF SPEECH ANALYSIS

Yutaka Yokoyama, assignor to NEC Corporation

17 September 1996 (Class 379/96); filed in Japan 2 November 1993

This system would use information gathered from a voice channel to improve the naturalness of the image displayed on an associated video channel, especially when the video signal has been highly compressed, resulting in a reduced frame rate. A speech recognizer would process the audio signal and produce a sequence of phonetic symbols. These would be used to access a database of lip position information. Stored past video frames having the proper lip patterns would then be integrated with the incoming video frames to enhance the display. One wonders whether the patent term will expire before the technology is up to this task.—DLR

5,566,272

43.72.Ne AUTOMATIC SPEECH RECOGNITION (ASR) PROCESSING USING CONFIDENCE MEASURES

Douglas J. Brems and Max S. Schoeffler, assignors to Lucent Technologies, Incorporated

15 October 1996 (Class 395/2.4); filed 27 October 1993

Widespread public acceptance of speech recognition by machines will not take place before the machine appears to exhibit a modicum of intelligent behavior in its responses to the human. Even though the confidence measure described here may occasionally be faulty, the actions taken as a result of that measure will go a long way toward establishing a sense of ''communication'' in the user. As in many recognition systems, scores are obtained for multiple candidates in each recognition attempt. The difference between the top score and the first runner-up score gives the confidence measure. Based on that measure and a history of interactions, if any, with the present user, the system either uses the information as recognized, asks for confirmation, asks for repetition (saying the same thing in a different way), or tries to proceed using an alternative strategy.—DLR

5,468,906

43.75.Tv SOUND SYNTHESIS MODEL INCORPORATING SYMPATHETIC VIBRATION OF STRINGS

Bryan J. Colvin, Sr. and Perry R. Cook, assignors to Media Vision, Incorporated

21 November 1995 (Class 84/625); filed 2 September 1993

When a piano damper pedal is depressed, the undamped strings can respond sympathetically to vibrations they receive through the bridge from a struck string, creating tonal complexity. This patent describes the use of a bank of parallel single-string emulation circuits that can be connected to a digital electronic piano tone synthesizer for the addition of sympathetic string vibrations. Each single-string emulator can be in the form of a delay line loop containing a digital filter using ''waveguide synthesis,'' a method in which the circuit model is based on the physical structure of the instrument. From a practical standpoint, it is not necessary to provide an emulator for each string in the piano. Twelve emulators tuned to an octave of low tones is sufficient.—DWM

5,512,705

43.75.Tv MUSICAL TONE SYNTHESIZING APPARATUS

Kaoru Kobayashi, assignor to Yamaha Corporation

30 April 1996 (Class 84/622); filed in Japan 12 December 1989

In this digital piano tone synthesizer, closed-loop circuit **1**, which simulates the vibration of a piano string, includes delay circuits **3** and **7**, adder circuits **4** and **8**, filter circuits **5** and **9**, and phase-inversion circuits **6** and **10**. The inversion circuits correspond to the fixed ends of the string. The time period corresponding to excitation vibration traveling once around the closed-loop circuit defines the fundamental frequency of the string standing

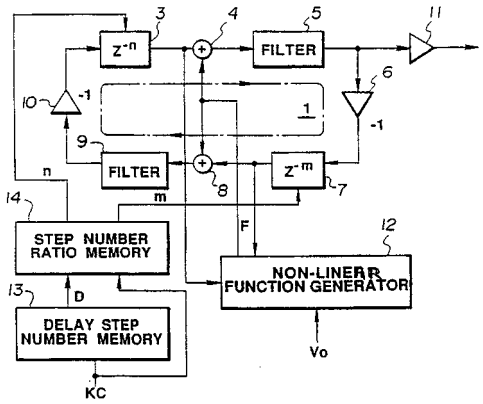

wave. The filters create more rapid decay for the higher partials. The playing key provides key code KC to memories **13** and **14** which control tone color. Input $\mathbf{V}_0$ is modified by nonlinear function generator **12** to provide the initial amplitude of the excitation signal. The delay step numbers **n** and **m** provide control of the hammer strike point along the string, depending upon the position of the note in the piano scale.—DWM

5,582,174

43.80.Qf ULTRASONIC DIAGNOSTIC SYSTEM

Takeshi Shirai, assignor to Fujitsu Limited
10 December 1996 (Class 128/661.01); filed in Japan 21 December 1994

In this system, a difference signal for flow velocity estimation is formed by subtracting from the received signal another received signal associated with the same scan line or a different scan line.—RCW

5,588,433

43.80.Qf ULTRASONIC DIAGNOSTIC APPARATUS

Takeshi Shirai *et al.*, assignors to Fujitsu Limited
31 December 1996 (Class 128/660.05); filed in Japan 12 December 1995

Color pixels that represent motion but appear in less than *n* (typically 1 or 2 or 3) continuous sets are replaced by data that represent the absence of displacement.—RCW

5,588,434

43.80.Qf ULTRASONIC DIAGNOSTIC APPARATUS PRESENTING CLOSELY CORRELATED ULTRASONIC IMAGE

Hiroshi Fujimoto, assignor to Olympus Optical Company
31 December 1996 (Class 128/660.07); filed 29 September 1995

A sequence of images produced by an intracavitary probe are stored sequentially as video frames in this apparatus that has a freeze frame capability. When a freeze frame operation is performed, the degree of coincidence between data obtained at the start of the scan and at the end of the scan is calculated, and the video with the highest coincidence is displayed as a frozen frame. This process reduces image artifacts caused by tissue motion when the first and last scan lines of an image are spatially adjacent.—RCW

5,582,588

43.80.Sh ULTRASONIC THERAPEUTIC APPARATUS

Tomohisa Sakurai *et al.*, assignors to Olympus Optical Company
10 December 1996 (Class 604/22); filed in Japan 19 April 1993

The distal end **14** of this apparatus vibrates ultrasonically to emulsify tissue. A sheath **15** forms a passage through which saline flows to cool the

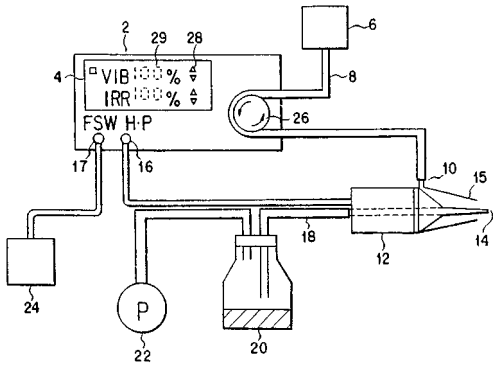

probe. Emulsified tissue is removed via a tube **18** into a bottle **20** via suction pump **22**. A foot switch **24** is used to turn the system on and off.—RCW

5,588,432

43.80.Sh CATHETERS FOR IMAGING, SENSING ELECTRICAL POTENTIALS, AND ABLATING TISSUE

Robert J. Crowley, assignor to Boston Scientific Corporation
31 December 1996 (Class 128/660.03); filed 10 July 1995

These catheters contain at their distal end an ultrasonic transducer and an electrode. The electrode makes electrical contact with the structure that is ablated chemically by delivery of a fluid or by mechanical vibration. A marker mounted on the catheter emits a sonic wave when excited and produces in an ultrasonic image an indication of the marker position.—RCW

5,582,173

43.80.Vj SYSTEM AND METHOD FOR 3-D MEDICAL IMAGING USING 2-D SCAN DATA

Ming Li, assignor to Siemens Medical Systems, Incorporated
10 December 1996 (Class 128/660.07); filed 18 September 1995

The correlation of speckle regions in a series of not necessarily parallel *b*-scan images is determined, and compared with a predetermined speckle correlation versus distance function to provide an estimate of the distance between frames. The reliability of distance estimates is improved and evaluated in various ways, for example, by comparing combinations of possible distances from end frames and by comparing calculated frame or subframe velocities with a known or estimated transducer velocity. Using estimates of distances between frames, a three-dimensional image is created.—RCW

5,582,176

43.80.Vj METHODS AND APPARATUS FOR AUTOMATICALLY DETERMINING EDGE FREQUENCY IN DOPPLER ULTRASOUND SIGNALS

Peter Swerling *et al.*, assignors to MedaSonics
10 December 1996 (Class 128/661.09); filed 15 August 1995

A maximum likelihood estimation process is used to distinguish between spectral power components arising from fluid flow and spectral power

components arising from background scattering and electronic noise.—RCW

5,582,177

43.80.Vj BROADBAND PHASED ARRAY TRANSDUCER DESIGN WITH FREQUENCY CONTROLLED TWO DIMENSION CAPABILITY AND METHODS FOR MANUFACTURE THEREOF

Amin M. Hanafy *et al.*, assignors to Acuson Corporation
10 December 1996 (Class 128/662.03); filed 3 March 1995

In this array, transducer elements have a thickness that gradually varies in elevation from a minimum at the center in the elevation direction to a maximum at the outer edges in the elevation direction. One or more matching layers may be used to improve bandwidth. Also, a two-crystal transducer element or a composite transducer structure may be employed.—RCW

5,582,178

43.80.Vj METHOD AND APPARATUS FOR INTRAVASCULAR ULTRASONOGRAPHY

Paul G. Yock, assignor to Cardiovascular Imaging Systems, Incorporated
10 December 1996 (Class 128/662.06); filed 6 June 1995

A catheter is employed to image vessel walls ultrasonically. The catheter includes a tube within which is a cable drive that rotates an ultrasonic probe to create a circumferential scan. Both the tube and the drive cable are sufficiently small and flexible to permit insertion into the vessel and advancement through the vessel to an imaging location.—RCW

5,584,294

43.80.Vj METHOD AND APPARATUS FOR ULTRASONIC BLOOD FLOW DISPLAY

Shinishi Amemiya *et al.*, assignors to GE Yokogawa Medical Systems
17 December 1996 (Class 128/660.05); filed 10 October 1995

This is an ultrasonic power Doppler blood flow display apparatus in which a change in the region selected for blood flow display is used to display a *b*-mode image in the blood flow display region, while the blood flow display region is moved, and to display the blood flow image in the blood flow display region when the motion is stopped.—RCW

5,585,546

43.80.Vj APPARATUS AND METHODS FOR CONTROLLING SENSITIVITY OF TRANSDUCERS

Turuvekere R. Gururaja *et al.*, assignors to Hewlett–Packard Company
17 December 1996 (Class 73/1 DV); filed 31 October 1994

Transducer element parameters such as temperature, acoustic pressure, input power, and a figure of merit determined from the dielectric constant and coupling coefficient are measured and stored. The stored data and model relations are used to monitor operational parameters during use. Feedback compensation is then determined and applied to maintain transducer sensitivity substantially constant.—RCW

5,588,435

43.80.Vj SYSTEM AND METHOD FOR AUTOMATIC MEASUREMENT OF BODY STRUCTURES

Lee Weng *et al.*, assignors to Siemens Medical Systems, Incorporated
31 December 1996 (Class 128/660.07); filed 22 November 1995

A user-designated geometric feature of an ultrasonic image frame is employed along with one or two reference points for the calculation of parameters that may be the circumference or diameter of the head or abdomen or the length of the humerus or femur. The image is then processed to calculate the parameter using a predetermined approximating function. The processing employs weighting, binarization, and morphologic filtering of the image before creating the approximating function.—RCW

5,588,436

43.80.Vj PULSED DOPPLER PROBE

Krishna Narayanan *et al.*, assignors to Cook Pacemaker Corporation
31 December 1996 (Class 128/662.03); filed 11 October 1995

This probe is designed to monitor blood flow within a vessel. The ultrasonic transducer **30** is positioned on the vessel with a mesh band **44** and thread **48** that passes through the band. The thread is enclosed in a sheath **17**

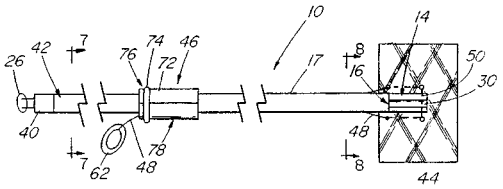

along with wires **26** connected to the ultrasonic transducer. to remove the probe, the thread is cut and the sheath along with transducer is withdrawn while the mesh band remains.—RCW

A study of temporal features and frequency characteristics in American English foreign accent[a)]

Levent M. Arslan and John H. L. Hansen[b)]
Robust Speech Processing Laboratory, Department of Electrical Engineering, Box 90291, Duke University, Durham, North Carolina 27708-0291

(Received 10 May 1996; revised 2 August 1996; accepted 27 November 1996)

In this paper, a detailed acoustic study of foreign accent is proposed using temporal features, intonation patterns, and frequency characteristics in American English. Using a database which consists of words uttered in isolation, temporal features such as voice onset time, word-final stop closure duration, and characteristics of duration are investigated. Accent differences for native-produced versus Mandarin, German, and Turkish accented English utterances are analyzed. Of the dimensions considered, the most important accent relayer is found to be word-final stop closure duration. Mandarin accented English utterances show significant differences in terms of this feature when compared to native speaker utterances. In addition, the intonation characteristics across a set of foreign accents in American English is investigated. It is shown that Mandarin speaker utterances possess a larger negative continuative intonation slope than native speaker utterances, and German speaker utterances had a more positive intonation slope when compared to native speaker utterances. Finally, a detailed frequency analysis of foreign accented speech is conducted. It is shown that the midfrequency range (1500–2500 Hz) is the most sensitive frequency band to non-native speaker pronunciation variations. Based on this knowledge a new frequency scale for the calculation of cepstrum coefficients is formulated which is shown to outperform the Mel-scale in terms of its ability to classify accent automatically among four accent classes. [S0001-4966(97)03804-6]

PACS numbers: 43.10.Ln, 43.72.Lc, 43.71.Hw [JS]

INTRODUCTION

Foreign accent can be defined as the change in pronunciation patterns of a non-native speaker due to his or her first language background. Speakers of a second language often exhibit varying degrees of foreign accent traits based on a number of factors such as the age of second language learning and the length of residence in the second language speaking country (Asher and Garcia, 1969; Leather, 1983; Flege, 1988; Flege and Fletcher, 1992b). An understanding of the causes and acoustic properties of foreign accent can be quite useful in several areas such as speech synthesis, speech coding, and speech recognition. Defining the acoustic norms of American English in terms of pronunciation patterns may lead to more natural sounding speech output from text-to-speech systems. In addition, for some applications it may be desirable to produce speech with a specific regional or foreign accent. On the other hand, improved speech recognition performance can be achieved by incorporating accent information as a means of adapting to speaker differences. In a recent study, Arslan and Hansen (1996) showed that incorporating accent information into an isolated word speech recognition system can lead to substantial improvement in recognizer performance. In a separate study, Brousseau and Fox (1992) showed that improvement in the continuous speech recognition rate can be achieved by retraining on European French as opposed to Canadian French, or British English as opposed to American English.

There has been considerable research directed at understanding the causes and acoustic characteristics of foreign accent in English. In the text by Chreist (1964), a brief overview of sound problems in foreign accent is presented, where the issue of accent is regarded as a speech pathology problem. An alternative was considered in a study by Wells (1982) where dialects in British English were examined from a linguistics point of view. From an historical perspective, these studies can be said to be more general in their treatment of accent. Recently, there have been more focused studies detailing the acoustic characteristics of foreign accent. For example, in a number of studies (Flege, 1980, 1984a; Flege and Hillenbrand, 1984b; Flege and Eefting, 1987; Flege, 1988; Flege *et al.*, 1992a, 1995; Port and Mitleb, 1983; Munro, 1993; Crowther and Mann, 1992; Bohn and Flege, 1992; Arslan and Hansen, 1996) specific language accents were investigated in terms of their acoustic characteristics. It was shown that the second formant (F_2) is statistically the most significant resonance frequency in discriminating French accent from American accent for the French syllables /tu/ ('tous') and /ty/ ('tu'). In another study, Arslan and Hansen (1996) compared computer algorithm performance with that of human listener performance in the detection and classification of foreign accent based on isolated words. It was shown that a hidden Markov model (HMM) based computer algorithm could both detect and classify accent better than the average human listener for isolated word based acoustic features derived from utterances of native and non-native speakers.

In this paper, we consider a study of temporal features, intonation patterns, and frequency characteristics of accented speech based on native-produced, Turkish, German, and

[a)]''Selected research articles'' are ones chosen occasionally by the Editor-in-Chief, that are judged (a) to have a subject of wide acoustical interest, and (b) to be written for understanding by broad acoustical readership.
[b)]Electronic mail: http://www.ee.duke.edu/Research/Speech

TABLE I. List of words and phrases that are included in the foreign accent database.

Foreign accent database				
Words				
aluminum	catch	line	student	thirty
bird	change	look	target	three
boy	communication	root	teeth	white
bringing	hear	south	there	would
Phrases				
This is my mother.				
He took my book.				
How old are you?				
Where are you going?				

Mandarin accents. In Sec. I, we describe the database that was established at Duke University for analysis of foreign accent. In Sec. II, an assessment of each temporal feature's ability to discriminate accent is made based on statistics generated from the accent database. The investigated features include voice onset time, word-final stop closure duration, average voicing, and average word duration. In Sec. III, the differences between intonation patterns of native and non-native speaker utterances are analyzed. In Sec. IV, we present an analysis to determine which frequency bands are more sensitive to foreign accent. In addition, the validity of using the Mel-scale in accent classification is questioned, and a more appropriate scale for accent classification is proposed. Finally, a discussion of the results and conclusions are drawn in Sec. V.

I. ACCENT DATABASE

Based on an extensive literature review of foreign accent problems in American English, a test vocabulary was selected which contained a rich collection of phoneme class to phoneme class transitions. Particular attention was paid to select the set of words that were identified to be more problematic for non-native speaker production (Chreist, 1964). The chosen vocabulary consists of 20 isolated words, and four test sentences. These words and phrases are listed in Table I. The data corpus was collected using a mixture of two environmental conditions including a head-mounted microphone in a quiet office environment and an on-line telephone interface (43 speakers used microphone input, 68 speakers used telephone input). The speakers were from the general Duke University community. All speech was sampled at 8 kHz and each vocabulary entry was repeated five times. Practice was not permitted before recording began. Available speech includes native-produced American English, and English under the following accents: German, Mandarin, Turkish, French, Persian, Spanish, Italian, Hindi, Rumanian, Japanese, Greek, and others. For the studies conducted here, the focus was on American English speech from 48 male[1] speakers between the ages of 20 and 40 across the following four accents: native-produced, Turkish, Mandarin, and German. In the evaluations, the microphone speech was bandpass filtered between 100 and 3800 Hz in order to simulate the same telephone channel response, and thereby provide consistency in the database.

II. TEMPORAL FEATURES

Studies have suggested that duration is an important suprasegmental feature in perception of foreign accent. A speaker often exhibits accent through hesitations, pauses, and the amount of time spent in producing or forming strings of different phonemes or phoneme classes. A number of studies have considered the analysis of temporal features in accented speech. For example, studies by Caramazza *et al.* (1973), Flege (1980), Flege and Hillenbrand (1984b), and Port and Mitleb (1983) showed that voice onset time is an important parameter in detecting the presence of French accent. Crowther and Mann (1992) investigated native language factors affecting use of vocalic cues to final consonant voicing. They found that Japanese and Mandarin speakers of English show less difference in F_1 offset frequencies in their tokens of *pod* compared to their tokens of *pot*. In another study, Byrd (1984) investigated the speaking-rate differences among eight regional dialects of American English in the TIMIT database.[2] Byrd found significant differences between the ''Army Brat''[3] group and ''South,'' and ''Army Brat'' and ''South Midland'' dialects. Part of the difference resulted from the frequency of pauses. Speakers from South Midland and South paused more often than expected, while speakers from the North Midland, West, and the ''Army Brat'' paused less often than expected given a random distribution.

In this study, we investigate voice onset time and word-final stop closure duration across native-produced, Turkish, Mandarin, and German accented English. Two of the language accents studied (Turkish, Mandarin) do not possess voiced stops at the word-final position. In addition, Mandarin does not have unvoiced stops at the word-final position. These facts led us to choose word-final stop closure duration as one variable in our study. Voice onset time has been investigated by many researchers (Caramazza *et al.*, 1973; Flege, 1980; Flege and Hillenbrand, 1984b) for the study of foreign accent, and therefore was chosen as the second variable to analyze. In addition, average voicing duration and average word duration are investigated which are found to be affected to a large extent by accent related factors based on time-frequency analysis of the accent database. The study here is by no means intended to cover all aspects of foreign accent in English; rather, we focus our analysis on a subset of acoustic features that we believe to be significant for the language accents considered here.

A. Word-final stop closure duration

Word-final stop closure duration has been investigated in several recent research studies. Port and Mitleb (1983), for example, showed that there are significant differences in consonant closure durations between word-final lax and tense stops produced by Arab and American speakers of English. In a separate study, Flege *et al.* (1992a), reported significantly longer closure durations in final stops produced by Mandarin and Spanish speakers when compared to native English speakers.

An extensive analysis of word-final stop closure duration was conducted using selected entries from the accent data corpus. This included the following words: *would, bird,*

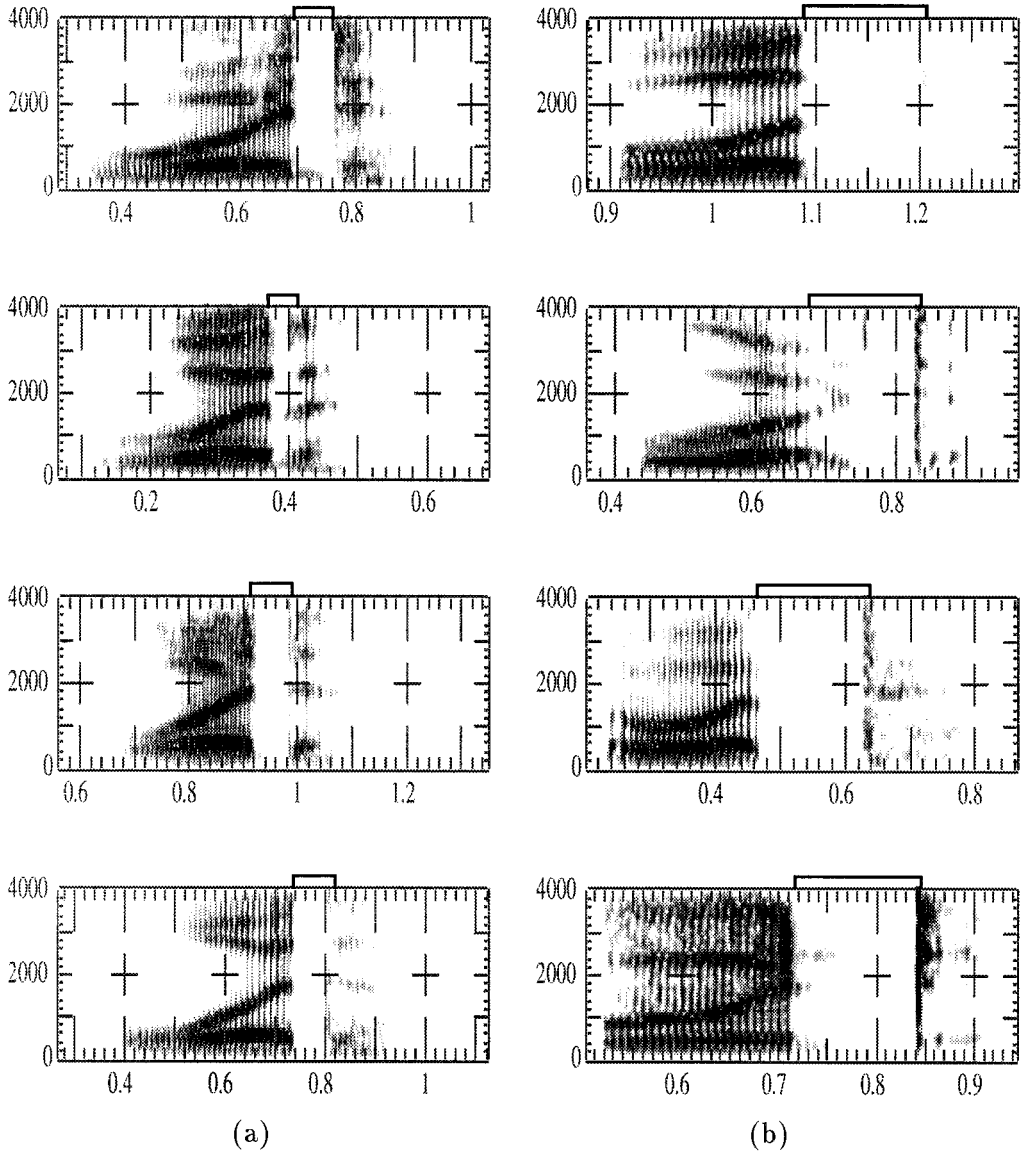

FIG. 1. Illustration of the change of stop closure durations (i.e., stop closure durations are indicated by solid bars above spectrograms) for the word ''would'' due to Mandarin accent. (a) Spectrograms of four native speaker utterances. (b) Spectrograms of four Mandarin speaker utterances.

target, look, root, white. In our analysis of time-frequency responses of native and non-native speaker utterances, we observed that the closure duration prior to the release of a stop consonant at the end of a word (word-final stop closure duration) is in general longer for non-native speakers than for native speakers. In Fig. 1, spectrograms of the English word ''would'' from eight different speakers are shown. The four spectrograms in Fig. 1(a) belong to American speakers, and the four spectrograms in Fig. 1(b) belong to Mandarin speakers. The closure before the release of the stop consonant /D/[4] is significantly longer in duration (+55 ms on average) for all Mandarin versus native speakers. This result complies with a previous study by Flege *et al.* (1992a) which indicates that Mandarin speakers produce the stop /D/ in *bVd* and *sVd* words 30–40 ms longer than American speakers. The small difference in the two studies may be due to different speaker population characteristics. Descriptive statistics of word-final stop closure durations are obtained across six words under the four accents (native-produced, Mandarin, German, and Turkish). In this analysis, a total of 12 male speakers from each accent group, and three tokens of each word from each speaker were used in estimating the statistics.[5] In order to assess the significance of differences among the four accent classes in terms of word-final stop closure duration, a one-way analysis of variance was performed. The results are summarized in Table II. The word-final stop closure duration for the word *would* was found to be highly dependent on speaker accent. However, it should be noted here that the largest contribution to statistical significance of differences across the four language accents comes from voiced stops produced by Mandarin speakers. Therefore, pairwise statistical significance tests were performed where native English closure durations were compared to Turkish, German, and Mandarin closure durations. The results of these tests are also summarized in Table II, with the superscript b indicating a ($p<0.05$) statistical sig-

TABLE II. A descriptive statistical analysis of word-final stop closure duration across accent groups. The mean and standard deviation (in parentheses) of word-final stop closure duration for each accent class across various words are listed. Null hypothesis represents the case where the averages of word-final stop closure durations are equal across four accents (native-produced, Turkish, German, Mandarin). ([a]: $p<0.01$). Pairwise ANOVA results comparing native-produced versus non-native accents are summarized as: [b]:$p<0.05$, [c]:$p<0.01$.

	Analysis of variance results for word-final stop closure duration (ms)				
Word	English	Mandarin	Turkish	German	$F(3,140)$
would	64.5 (13.7)	119.0 (34.1)[c]	85.5 (24.0)[c]	81.7 (31.1)[c]	27.8[a]
bird	64.1 (12.2)	104.0 (35.5)[c]	94.9 (30.3)[c]	76.2 (17.8)[c]	18.7[a]
target	89.8 (33.1)	118.3 (28.8)[c]	85.8 (15.7)	80.5 (25.1)	19.2[a]
look	124.4 (37.9)	138.0 (33.4)	111.5 (28.2)	108.2 (21.5)[b]	7.3[a]
root	104.7 (33.7)	138.1 (28.0)[c]	99.0 (16.9)	99.3 (30.7)	19.1[a]
white	102.6 (34.0)	128.1 (30.7)[c]	102.6 (14.5)	111.4 (29.0)	7.5[a]

nificance, and a superscript c indicating a ($p<0.01$) significance. Mandarin speakers had significantly longer stop closure durations for both word-final /T/ and /D/ sounds when compared to American speakers. However, for the /K/ sound in *look*, the differences were not statistically significant. Both Turkish and German speakers had significantly longer closure durations for the voiced stop /D/ when compared to native speakers. However, for unvoiced stops such as /T/ and /K/ the closure durations for Turkish and German speakers were not significantly different from American speakers. These results verify the presence of a direct influence from the first language background of the non-native speaker to his/her accent, since the Mandarin language does not allow voiced or unvoiced word-final stops, whereas Turkish does not allow voiced stops in word-final position.

Among the stop consonants, non-native speakers consistently used longer closure duration for the /D/ sound in *would* and *bird*. For the accents considered, Mandarin speakers were found to employ consistently longer closure duration for the investigated stop consonants.

In order to evaluate the discriminative power of word-final stop closure duration in terms of accent classification, the mean[6] and standard deviation are used to generate Gaussian probability density functions (PDF) for each word under each accent. Next, a maximum-likelihood classifier is developed which employs the PDF's in order to make a decision as to which accent PDF results in the closest match for an input set of data samples. Finally, the true accent classes and accent classes obtained after employing the maximum-likelihood classifier are compared to calculate the average accent classification rate based on the word-final stop closure duration. The closed set accent classification rate obtained following this approach is shown in Fig. 2. The average classification rate using only word-final stop closure duration is 44.9%, which is significantly higher than the chance rate (25% for four accents). Accent classification performance over several words with final stops are also summarized. Consistent classification results were obtained for both voiced and unvoiced stops. Here, it should be emphasized that the classification rate is based on closed test data, and should therefore be used only for the purposes of comparison as a relative confidence measure for the feature. The value of the classification rate here will take on further meaning when compared to the classification rates obtained from voice onset time and average voicing duration features in the following sections. Based on this average classification rate and the statistical significance test results, it can be concluded that word-final stop closure duration is a useful discriminator of accented speech.

B. Voice onset time

In this section, we consider voice onset time as a potential accent discriminator. Voice onset time (VOT) represents the interval between the release burst of a leading stop consonant and the onset of voicing for the following vowel.[7] Caramazza and Yeni-Komshian (1974) found that French talkers produced the /T/ phoneme with VOT values significantly longer than the VOT measured in French words produced by French monolinguals. However, in an experiment conducted by Flege (1984a), the /T/ edited from French speaker utterances of the /tu/ and /ti/ syllables were 30 and 15 ms shorter than that of native English speakers on the average. This result was also consistent with other studies on foreign accent (Caramazza *et al.*, 1973; Flege, 1980; Flege and Hillenbrand, 1984b).

In the present study, VOT values were investigated across four accents for a set of words which include a stop consonant in the initial position (*target, teeth, catch, commu-*

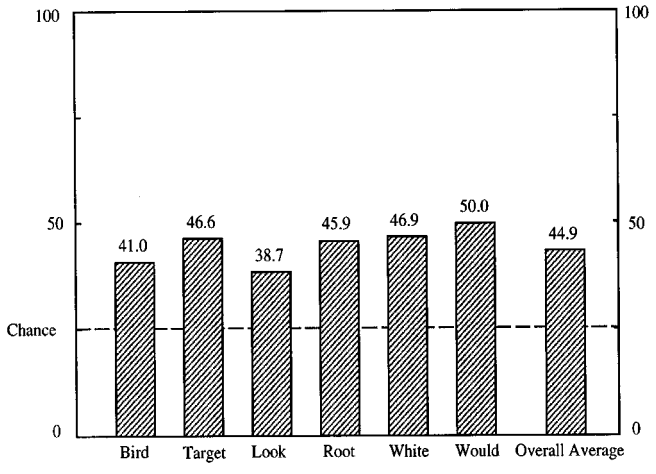

FIG. 2. Closed set accent classification rates among four accent classes (native-produced, Mandarin, Turkish, German) based on the maximum-likelihood estimate of word-final stop closure durations.

TABLE III. A descriptive statistical analysis of voice onset time across accent groups. Null hypothesis represents the case where the averages of voice onset times are equal across four accents (native-produced, Turkish, German, Mandarin). ([a]: $p<0.05$). Pairwise ANOVA results comparing native-produced versus non-native accents are summarized as: [b]:$p<0.05$, [c]: $p<0.01$.

	Analysis of variance results for voice onset time (ms)				
Word	English	Mandarin	Turkish	German	$F(3,140)$
target	69.2(20.1)	72.4(22.1)	57.4(16.3)[c]	73.0(28.5)	4.1[a]
teeth	76.1(18.4)	79.6(23.9)	72.7(23.1)	78.6(22.5)	0.7
catch	70.5(18.0)	73.1(16.4)	69.9(13.3)	80.6(28.8)	2.3
communication	65.4(19.1)	57.1(14.6)[b]	63.3(16.2)	69.3(15.2)	3.7[a]

nication). In general, Turkish speakers demonstrated shorter voice onset times, whereas Mandarin and German speakers had longer voice onset times when compared to American speakers. However, as shown in Table III, the statistics of VOT are not significantly different enough to discriminate reliably among the four accents. For the words *teeth* and *catch*, the average VOT differences across accent classes did not reach the minimum significance level ($p>0.05$). Pairwise statistical significance tests (also shown in Table III) verified that, in general, voice onset time is not a significant discriminator among the accent classes considered in this study. The VOT value for the unvoiced /T/ in *target* was found to be significantly shorter for Turkish speakers (57 ms) when compared with American speakers (69 ms). In addition, the VOT value for the /K/ sound in *communication* was found to be significantly shorter for Mandarin speakers (57 ms) when compared to American speakers (65 ms). As a result, when the maximum-likelihood classifier was employed for accent classification based on voice onset times for these words, an average classification rate of 32.0% was achieved in the closed set. The detailed classification results across the four words are shown in Fig. 3. Although this feature did not prove to be a strong indicator among the accent classes considered here, it may be more useful as a secondary feature in accent classification or potentially useful for other accent classes not considered here.

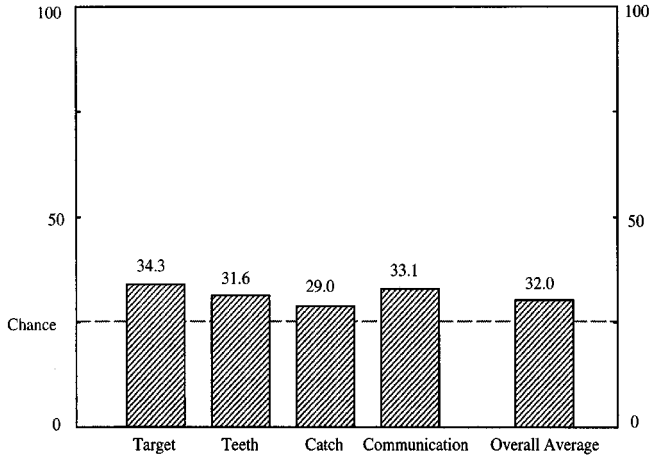

FIG. 3. Closed set accent classification rates among the four accents based on a maximum-likelihood classifier using voice onset time.

C. Average voicing duration

The third temporal feature investigated for accent discrimination is average voicing duration. There have been a number of studies on vowel duration as a perceptual cue to the voicing feature in word-final stops produced by native speakers of English (Raphael, 1972; Repp, 1978; Wardrip-Fruin, 1982; Hogan and Rozsypal, 1980; Port and Dalby, 1982). Voicing duration is measured from the first positive peak in the periodic portion of voiced speech until the point where voicing ends (i.e., the speech becomes unvoiced). The following eight words from the vocabulary set were selected for analysis: *bird, catch, change, hear, look, south, boy, teeth*. The statistics obtained here were based on the same speakers and accent classes as in the previous sections. Table IV summarizes the statistical analysis of average voicing duration. Excluding the word *change*, all words considered showed statistically significant differences among accent classes in terms of their average voicing duration. Accent classification rates across the eight words after employing the maximum-likelihood classifier are shown in Fig. 4. Again we see consistent performance, with an average classification rate of 37.0% which is clearly above the chance probability. In general, non-native speakers spent longer times in voiced speech sections. In particular, average voicing duration for Mandarin speakers was consistently longer than for native speakers.

D. Average word duration

Next, the average word duration is analyzed among the four accents as an indicator of the speaking rate. Using the same speaker and accent set, the average word duration and its standard deviation for the 20 words available in the database were obtained and tabulated in Table V. With the exception of the following three words (*bringing, change*, and *would*), the remainder of the 20 word vocabulary did reach statistically significant differences in average word duration for the accents considered. Mandarin speakers had significantly slower phoneme production rates when average word duration was chosen as the criterion. Average word duration for Mandarin speakers was 813 ms, whereas it was 741 ms for native speakers. In contrast with Mandarin speakers, Turkish speakers were found to be using shorter duration (725 ms) for the production of word utterances when compared to native speakers. One possible explanation for this

TABLE IV. A descriptive statistical analysis of average voicing duration across accent groups. Null hypothesis represents the case where the averages of average voicing duration are equal across four accents (native-produced, Turkish, German, Mandarin). ([a]: $p<0.05$.) Pairwise ANOVA results comparing native-produced versus non-native accents are summarized as: [b]: $p<0.05$, [c]: $p<0.01$.

	Analysis of variance results for average voicing duration (ms)				
Word	English	Mandarin	Turkish	German	$F(3,140)$
bird	233.5 (48.8)	283.7 (53.5)[c]	234.1 (46.2)	245.4 (43.8)	8.8[a]
catch	137.9 (25.5)	179.3 (40.0)[c]	148.6 (22.4)	150.5 (27.1)[b]	13.0[a]
change	306.2 (47.8)	325.3 (65.7)	303.1 (42.4)	316.3 (51.2)	1.4
hear	273.8 (60.0)	325.7 (55.0)[c]	259.4 (35.3)	325.3 (66.8)[c]	14.2[a]
look	194.8 (41.6)	220.0 (45.3)[b]	197.0 (43.0)	221.5 (45.2)[c]	4.1[a]
south	224.0 (39.2)	258.3 (48.1)[c]	229.6 (31.4)	255.0 (37.4)[c]	7.1[a]
boy	322.8 (67.9)	383.6 (73.0)[c]	318.7 (60.4)	346.6 (74.8)	6.7[a]
teeth	163.2 (23.1)	216.6 (64.6)[c]	205.0 (44.9)[c]	195.4 (42.6)[c]	9.0[a]

might be that Turkish speakers generally substitute shorter steady-state vowels for diphthongs in American English.

III. INTONATION

When a native speaker listens to foreign accented speech, it is quite common to perceive a change in the intonation patterns. The role of intonation in English and other languages has been studied extensively (Bolinger, 1958; Chomsky and Halle, 1991; Leon and Martin, 1980; Pilch, 1970). In general, each language shows different intonation patterns depending on syntax, semantics, and phonemic structure. An experiment by Grover *et al.* (1987) verified that French, English, and German speakers differ in the slopes (fundamental frequency divided by time) of their continuative intonation. In Fig. 5, the average intonation slopes among the four accents considered here are shown. The slopes are calculated based on the following delta parameter computation:

$$\Delta f_0(l)=\left[\sum_{k=-K}^{K} k f_0(l-k)\right]\cdot G, \quad 1\leqslant n\leqslant P, \tag{1}$$

where l is the frame index, and G is a gain term chosen to make the variances of $f_0(l)$ and $\Delta f_0(l)$ equal.[8] Here, $\pm K$ represents a 75-ms delta pitch analysis window. It should be noted that the slope calculation is based on words produced in isolation from the accent database using the previous set of 48 male speakers. The results discussed here should not be extended to continuous speech, since other suprasegmental issues must also be addressed. In fact, a study using continuous speech utterances could better represent intonation characteristics in a language accent. However, in this study the primary focus was on experiments using isolated speech utterances, and the results and conclusions of this study should be regarded in this context.

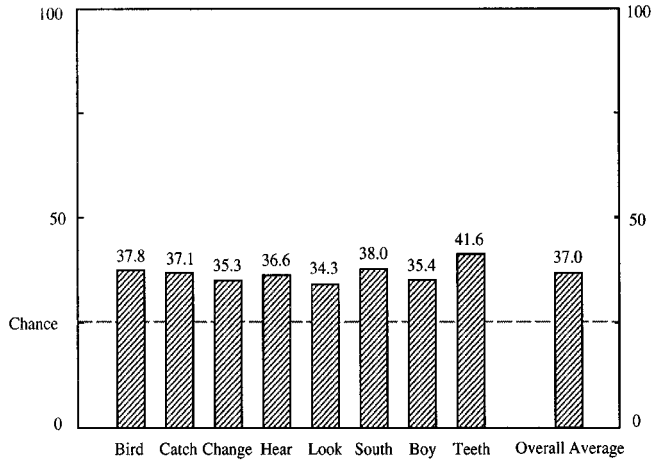

FIG. 4. Closed set accent classification rates among the four accents based on the maximum-likelihood estimate of average voicing duration.

Based on the average intonation slopes and their variation across speakers, three important conclusions can be drawn.

(1) German speakers consistently exhibited more positive continuative intonation slopes than American speakers.

(2) Mandarin speakers consistently exhibited more negative continuative intonation slopes than American speakers, which was due primarily to the sharp fall in pitch contour at the end of utterances.

(3) Turkish speakers showed much less variation in their intonation contours when compared to other accents.

The above results agree with previous findings that German speakers exhibit more positive intonation slope than American speakers, and that pitch information can be useful in determining the accent or language class of a speaker (Grover *et al.*, 1987). It should be noted that other factors also affect pitch characteristics such as a speaker's emotional state or the lexical stress across a word, phrase, or sentence. In general, the pitch variance across words is quite large as expected for a time-varying speech feature, which makes use of the maximum-likelihood classifier very difficult. Therefore, although pairwise accent classification (i.e., German versus English or Mandarin versus English) may benefit from pitch information, when a larger set of accent classes are employed it is not expected to provide a significant level of accent discrimination.

IV. FREQUENCY CHARACTERISTICS

In this next section, the focus for accent feature analysis shifts to frequency domain characteristics. Features that represent frequency characteristics of speech are commonly used in speech recognition systems. Although there has re-

TABLE V. Average word durations and standard deviations (in parentheses) across four accents for isolated words in the database. [a: statistically significant ($p<0.05$).]

Word	Statistics related to speaking rate differences among accents (in ms) Native-produced $\mu(\sigma)$	Mandarin $\mu(\sigma)$	Turkish $\mu(\sigma)$	German $\mu(\sigma)$	$F(3,143)$
aluminum	794(97)	894(123)	782(114)	867(102)	20.4[a]
bird	671(123)	744(194)	659(112)	676(99)	4.9[a]
boy	648(131)	727(120)	623(94)	662(101)	10.6[a]
bringing	753(156)	783(153)	756(117)	771(132)	2.1
catch	742(111)	794(119)	691(88)	763(75)	4.9[a]
change	828(106)	842(130)	763(97)	834(71)	2.3
communication	1047(118)	1133(155)	1092(144)	1134(94)	5.2[a]
hear	685(88)	773(124)	671(100)	754(84)	11.4[a]
line	755(143)	783(105)	692(121)	776(96)	2.9[a]
look	665(96)	702(139)	629(95)	714(93)	3.9[a]
root	680(129)	798(176)	721(112)	795(94)	12.4[a]
south	786(138)	814(140)	746(101)	814(87)	4.3[a]
student	895(150)	994(151)	913(115)	967(123)	4.7[a]
target	706(121)	874(158)	746(121)	790(101)	16.5[a]
teeth	719(124)	768(162)	691(110)	717(82)	2.9[a]
there	690(101)	776(172)	672(118)	732(112)	6.3[a]
thirty	668(126)	800(163)	679(97)	734(105)	20.0[a]
three	727(168)	762(156)	634(113)	723(89)	10.6[a]
white	671(142)	787(141)	682(101)	729(92)	10.6[a]
would	679(115)	704(165)	640(117)	680(83)	2.2
Avg.(ms)	741	813	725	782	

cently been significant improvement in speech recognition algorithm development, automatic speech recognition performance still lags far behind that achieved by humans. Therefore, in order to formulate better speech recognition algorithms, it may be beneficial to first consider aspects of the human auditory perception mechanism. Studies on psychoacoustic analysis of the human auditory perception mechanism have shown that the human ear responds differently to each acoustic tone based on their relative frequencies. Empirical evidence suggests that the human ear is more sensitive to low-frequency signals. After extensive experimental analysis, the Mel-scale was formulated for the sampling of the frequency axis based on perceptual criteria (Koenig, 1949). Speech features derived using the Mel-scale have also resulted in superior speech recognition performance when compared to parameters obtained from a linear scale (Davis and Mermelstein, 1980).

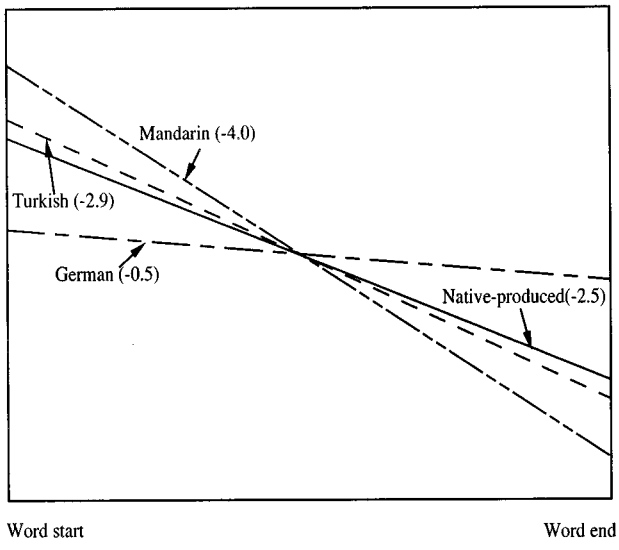

FIG. 5. Average intonation slopes across the four accents based on the 20-word accent database.

In this section, our main argument is that the problem of accent classification is different than that experienced in speech recognition. Therefore care must be taken when applying standard speech recognition parametrization techniques to the problem of accent classification (the same could also be said for speaker verification and language identification). It could be argued that a non-native speaker will focus his attention on speaking as close to an idealized native speech goal as possible based on ''perception'' of his own speech. As such, attempts would first be made to correct perceptually the most significant differences in pronunciation when compared to the native speaker pronunciation (e.g., what is typically done when students listen to teaching tapes of a new language). Therefore, a parameter set which is based on perceptual criteria for speech recognition may not be the optimal feature set for the problem of accent classification. In light of this argument, a series of experiments were conducted in order to assess the statistical significance of various resonant frequencies and frequency bands for both speech recognition and accent classification. The following sections will discuss the experimental framework and corresponding results.

A. Formant frequencies

In a previous study by Flege (1984a), the French syllables /tu/ ('tous') and /ty/ ('tu') produced in three speaking tasks by native speakers of American English and French talkers living in the United States were examined. Acoustic

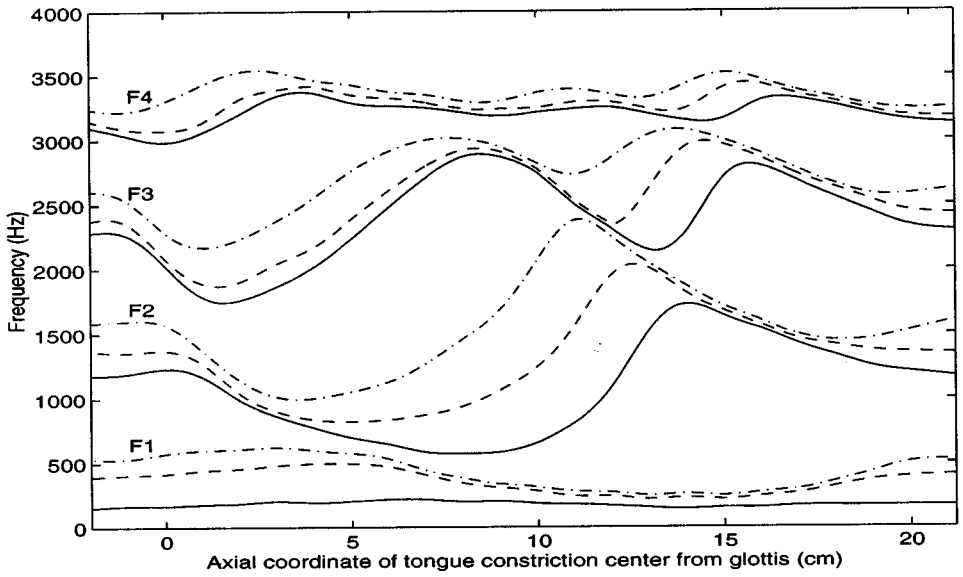

FIG. 6. The influence of the place of tongue constriction and constriction area on the formant frequencies. Each of the three curves for each formant frequency represent the contours corresponding to different cross-sectional areas at the place of constriction (dot-dashed line: $A=8.0\text{cm}^2$, dashed line: $A=2.0\ \text{cm}^2$, solid line: $A=0.16\ \text{cm}^2$). Adopted from Fant (1970).

analysis revealed that the American talkers produced the /U/ sound with significantly higher F_2 and F_3 formant frequency[9] locations than the French talkers. Fant (1970) performed a series of experiments in order to investigate the influence of the place of tongue constriction and the constriction area on formant frequencies. In Fig. 6, the measurements of formant frequencies based on an electrical line analog (LEA[10]) of the vocal tract model are plotted. In the graph, the horizontal axis corresponds to the axial coordinate of the tongue constriction center. Each of the three curves represent formant frequencies corresponding to the area of constriction values ranging between 0.16 and 8.0 cm^2. Based on these curves it can be stated that a very small change in the place of the center tongue constriction or the cross-sectional area at the tongue center constriction can lead to large shifts in F_2 and F_3, whereas the remaining formants follow a more gradual change. Large shifts in the frequency location of F_1 can only be observed when the overall shape of the vocal tract is changing (e.g., an increasing vocal tract area as in /AA/ versus a decreasing vocal tract area in /IY/). In general, non-native speakers do not produce the same tongue movements as native speakers, since they automatically produce different sounds based on learned tongue movements of their native language. Therefore, it is suggested that F_2 and F_3 will play a bigger role in the discrimination of foreign accent.

In our analysis of frequency across the accent database, F_2 and F_3 contours of native speaker utterances were observed to be significantly different from that of non-native speaker utterances. When time-frequency analysis of all words in the corpus was conducted for the four accents, we observed that the relative position of F_3 with respect to F_2 for the /ER/ sound was consistently different between native and non-native speakers. In Fig. 7, a comparison between the spectrograms of native and non-native speakers for the /ER/ sound in *bird* is illustrated. For American speakers, F_3 collapses into F_2 for the /ER/ sound [Fig. 7(a)] which suggests early oral cavity closure resulting from the tip of the tongue touching the hard palate and sliding back. However, for some non-native speakers the tongue does not touch the hard palate until the very last moment in the production of the /ER/ sound, which causes some degree of separation between these two formant frequencies [Fig. 7(b)].

A series of experiments were also performed in order to assess the relative significance of formant frequencies in the discrimination of accent. First, voiced sections of each word in the database were extracted. Next, the first four formant frequencies are estimated for each time frame. The formant frequency tracks were visually inspected and corrected after using a standard computer algorithm. For each formant frequency the derivative is estimated based on the delta parameter computation from Eq. (1). A hidden Markov model (HMM) is obtained for each word in the database for each accent using one formant with its derivative at a time (e.g., a HMM is formed based on F_1 and delta F_1 parameters of the word *thirty* from the Turkish training speaker set). It is important to note that when generating the HMM models, all the available data from speakers sharing the same first language background is used, and therefore no attempt is made to subjectively judge the level of accent exhibited by each utterance. Arslan and Hansen (1996b) attempted to address this issue by proposing a selective training algorithm to automatically detect any unreliable tokens[11] in the data and reduce their weights in the HMM model generation phase. Although improvements have been reported, this issue still poses an important problem in automatic accent model generation. Here, the HMM based accent recognizer employing formant location structure was evaluated. Open test accent classification results for the first four formant frequencies are shown in Fig. 8(a). Using the HMM set trained from Ameri-

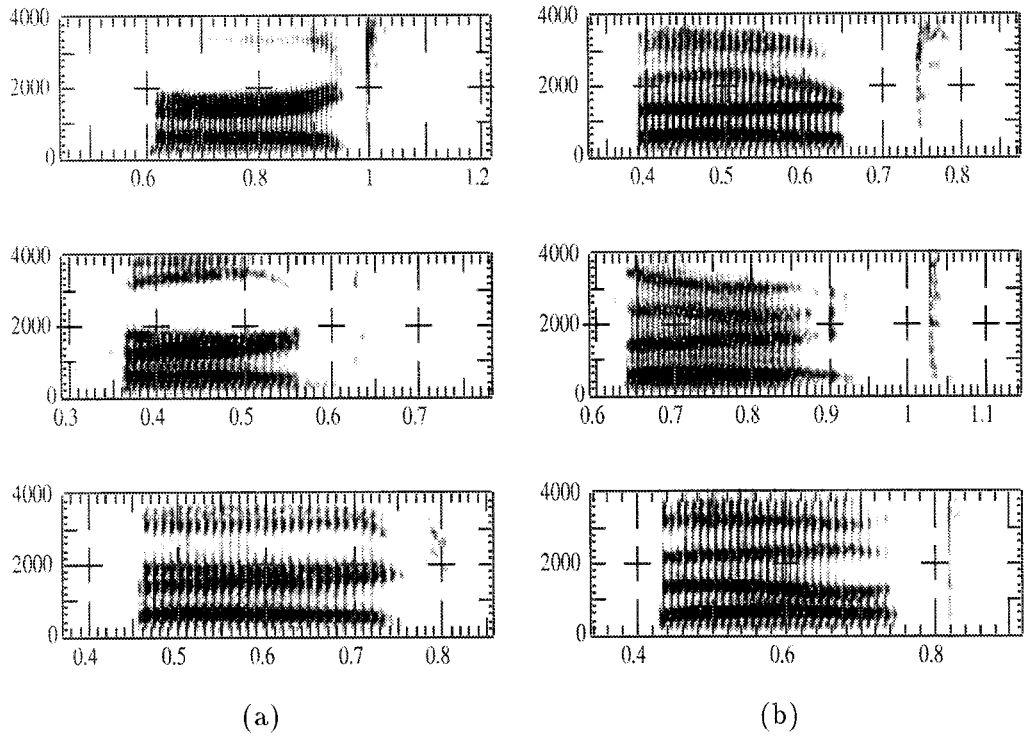

FIG. 7. Illustration of the influence of accent on F_2-F_3 separation in /ER/ sound in *bird*: (a) three native speakers (b) three non-native speakers (from top to bottom, Turkish, Mandarin, German).

can speakers, we evaluated speech recognition performance based on the 20-word vocabulary using a new (i.e., open) set of American speakers. In this case, the open test speech recognition performance for each formant is shown in Fig. 8(b). Here, speech recognition and accent classification evaluation is conducted for each formant. When accent classification and speech recognition performance are compared, F_2 is found to be the most significant resonant frequency contributing to correct classification for both problems. However, F_1 which is known to be important in speech recognition (and demonstrated here), was not found to be as useful as F_2 in accent classification. This result also supports our previous argument regarding the accented speech production mechanism, which states that previously developed percep-

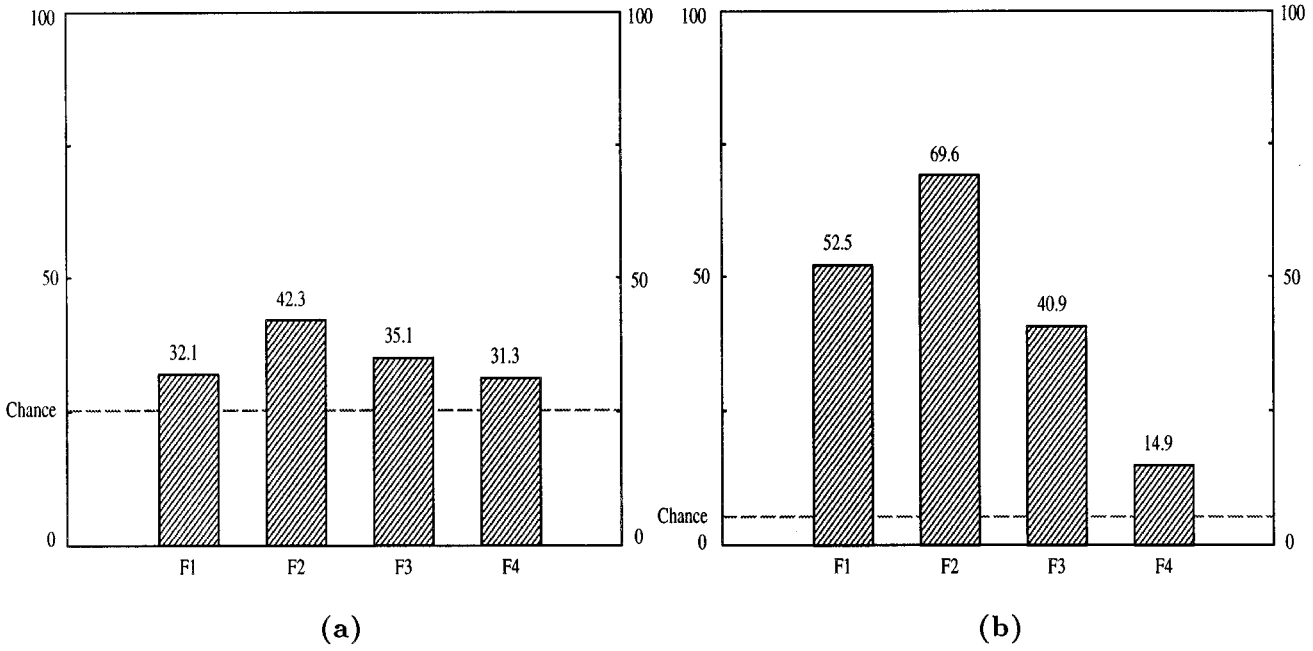

FIG. 8. The influence of formant frequencies on the performance of (a) accent classification and (b) speech recognition.

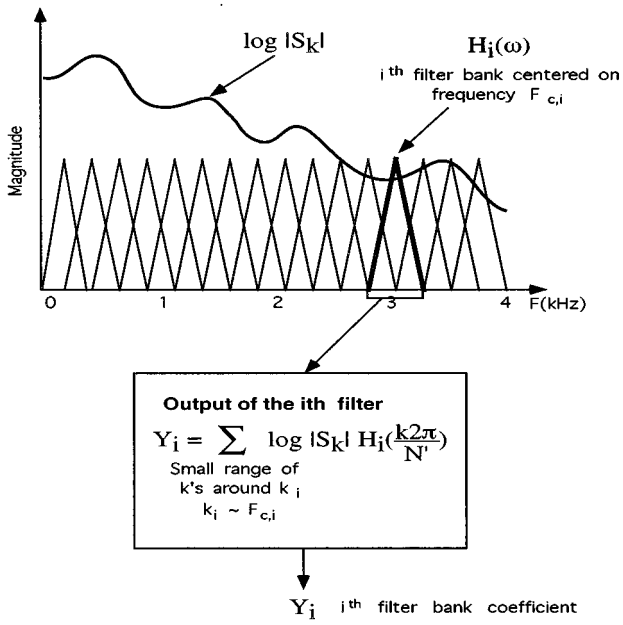

FIG. 9. The extraction of filter bank coefficients.

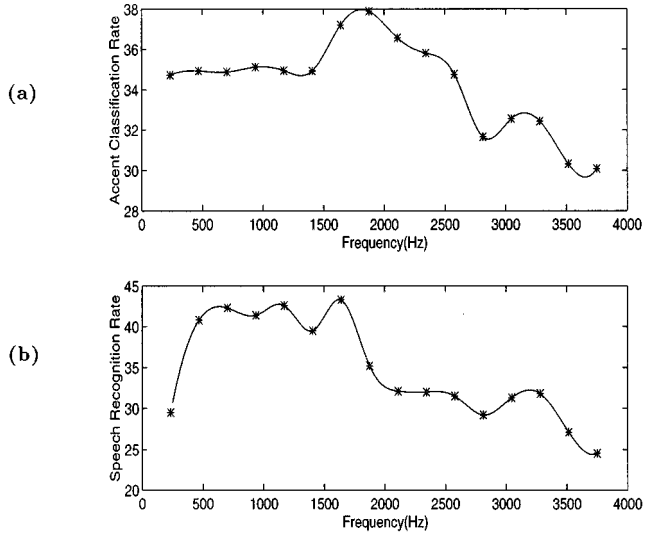

FIG. 10. Comparison of accent classification versus speech recognition performance based on the energy in each frequency band.

tual based critical frequency scales may not play such a significant role in differentiating between accent classes.

B. Filter banks

In automatic speech recognition systems, it is often difficult to work with formant frequencies as a standard parameter set because of the uncertainty involved with the estimation of these resonances. Moreover, the formant frequencies are not accurate representations of unvoiced sounds such as /F/ and /P/. Generally, a parameter set that represents the entire frequency band (e.g., filter bank coefficients or Mel-frequency cepstrum coefficients) is used in practice. In order to investigate the accent discrimination ability of various frequency bands, a series of experiments were performed. The frequency axis (0–4 kHz) was divided into 16 uniformly spaced frequency bands, as shown in Fig. 9. Energy in each frequency band is weighted with a triangular window. Next, the output of each filter is used as a single parameter in generating an HMM for each word across the four accent classes. Using a single filter bank output as the input parameter, isolated word HMM's for native-produced, Turkish, Mandarin, and German accented English were generated via the forward-backward training algorithm. The HMM topology was a left-to-right structure with no state skips allowed. The number of states for each word was between 7 and 21, and was set proportional to the duration of each word. In the training phase, 11 male speakers from each accent group were used as the closed set and 1 male speaker from each accent group was set aside for open speaker testing. In order to use all speakers in the open test evaluations, a round-robin training scenario was employed (i.e., the training simulations were repeated 12 times to test all 48 speakers under open test conditions).

In Fig. 10, plot (a) shows accent classification performance across the 16 frequency bands. In order to compare accent classification performance to speech recognition performance across frequency bands, a second experiment was performed. Using only HMM's trained with native-produced English utterances obtained in the previous experiment, open set American speaker utterances were tested to establish speech recognition performance on the 20-word vocabulary. The speech recognition performance as a function of frequency is shown in Fig. 10(b). From the graphs, it can be concluded that the impact of high frequencies on both speech recognition and accent classification performance is reduced. However, midrange frequencies (1500–2500 Hz) contribute to accent classification performance to a greater extent than for speech recognition, whereas low frequencies improve speech recognition performance more than for accent classification. These results are consistent with those obtained with individual formant frequencies, since the F_2-F_3 range which was shown to be significant in accent discrimination roughly corresponds to the 1500–2500 Hz frequency range, and F_1 which was shown not to be as significant in accent discrimination corresponds to lower frequencies in Fig. 10(a).

The Mel-scale which is approximately linear below 1 kHz and logarithmic above (Koenig, 1949), fits suitably with that of speech recognition performance across frequency bands. However, the results here suggest that it is not the most appropriate scale to use for accent classification. Therefore, a new frequency axis scale was formulated for accent classification which is shown in Fig. 11. Since a larger number of filter banks are concentrated in the midrange frequencies, the output coefficients are able to emphasize accent sensitive features better. The 16 center frequencies of the filter bank which range between 0–4 kHz are also given in Fig. 11.

While this new frequency scale will prove to be useful for accent, it could be argued that the frequency based results in Fig. 10 could be biased due to the chosen vocabulary or accent classes under consideration. Although this is a valid argument, the results presented here do show statistically significant performance improvement. Future studies may con-

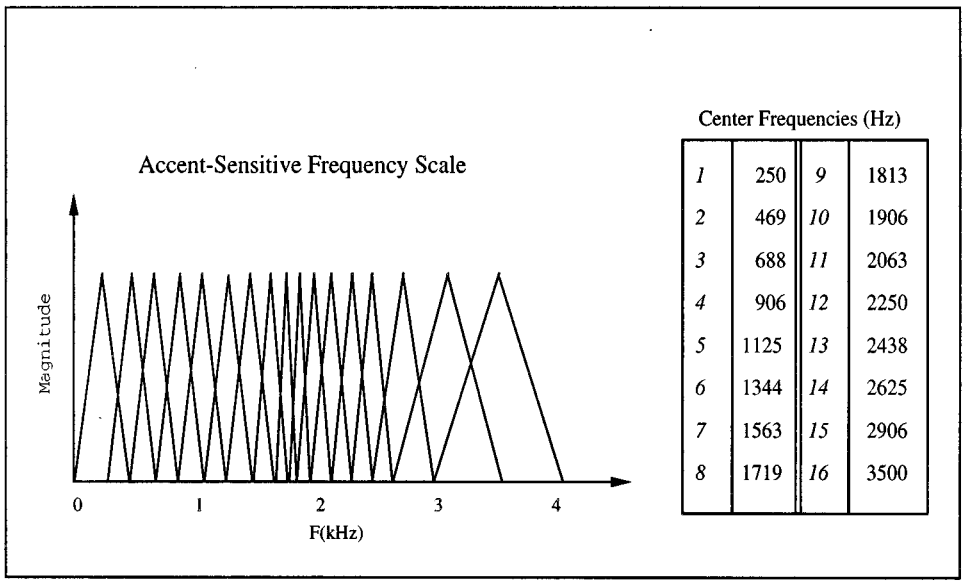

FIG. 11. A new sampling scheme for the filter banks which is more sensitive to accent characteristics.

sider larger databases or a wider range of accent classes. Unfortunately, at the present time, no extensive database is available (such as the OGI multilanguage or TIMIT available through LDC)[12] in order to perform more extensive analysis across a wider range of accents. However, the main goal in this section on frequency is to show that accent classification is a different problem than speech recognition. Since we have evaluated both accent classification and speech recognition performance on the same vocabulary set, respective rates based on each frequency band provide sufficient evidence to suggest that accent sensitive frequencies are somewhat different than perceptually motivated frequencies for recognition. The reason for the relatively poor accent classification rates at low frequencies can be explained by our previous hypothesis. Since the human auditory system is highly sensitive to low frequencies (Zwicker and Fastl, 1990), non-native speakers concentrate on correcting the low-frequency characteristics in their speech. On the other hand, the frequency response in midrange frequencies (1500–2500 Hz) differ from that of native speech, because the non-native speaker's auditory system is not as perceptually sensitive to changes in this frequency range. These frequencies (F_2-F_3 range) also represent detailed tongue movement which most non-native speakers have difficulty in adopting.

In order to compare the performance of the accent-sensitive frequency sampling scheme to that of the Mel-scale and linear scales, an accent classification experiment was performed on the accent database. The following three sets of cepstrum coefficients were extracted from the isolated word utterances across the four accents (native-produced, German, Turkish, Mandarin): (i) cepstrum coefficients derived from uniform sampling of the filter banks, (ii) Mel-frequency cepstrum coefficients, and (iii) cepstrum coefficients derived from accent-sensitive sampling of the filter banks. Using each parametrization approach, separate isolated word HMM's were generated using the forward-backward training algorithm. In order to reduce spectral bias, the long-term cepstral mean removal method is applied to each parameter set. The average accent classification rates for these parameter sets are shown in Table VI. The parameter set derived from the accent-sensitive scale resulted in the highest performance. It is also observed that the Mel-scale performed better than the linear scale for accent classification. When delta parameters as calculated using Eq. (1) are added to the feature set, an increase in accent classification rate is obtained across all three frequency scales, while the same ordering of performance among the three parameter sets is retained. The improved results after addition of delta parameters are also shown in Table VI. The results show that the use of an accent sensitive frequency scale in calculation of the cepstral parameters improves accent classification performance. The same frequency scale has also been tested for the related task of language classification, and significant improvement was achieved using the OGI multilanguage database (Arslan, 1996).

V. DISCUSSION AND CONCLUSION

In this study, a detailed acoustic feature analysis of foreign accent in American English has been considered using temporal features, intonation patterns, and frequency charac-

TABLE VI. Comparison of the linear scale, Mel-scale, and accent-sensitive scales in terms of their accent classification performance among native-produced, Mandarin, Turkish, and German accented English.

Comparison of different frequency scales in terms of accent classification performance	Linear scale	Mel-scale	Accent-sensitive
Accent classification %	55.4	57.1	58.3
With delta	60.0	60.7	61.9

teristics. First, it was shown that word-final stop closure duration is a significant indicator of accent. This was especially true for Mandarin speakers who could be identified reliably by their usage of long closures before the release of stop consonants at the end of word utterances. Voice onset time, on the other hand, was not found to be as useful in the discrimination of accented utterances for the set of accent classes considered. In general, durational parameters at the segmental and word level were found to be significant features in the study of foreign accent. The slope of the intonation contour differed among the four accent classes studied, namely native-produced, Mandarin, Turkish, and German. In general, Mandarin speaker utterances had a more negative intonation slope than native speaker utterances, and German speaker utterances had a more positive continuation slope than native speaker utterances.

In terms of frequency analysis of foreign accent, a number of significant results were obtained. The motivation for the study of frequency analysis was due to our belief that a parameter set designed based on perceptual criteria for speech recognition would not be the best parameter set for the problem of accent classification. This is because nonnative speakers concentrate their efforts highly on following native speaker pronunciation patterns, and in order to accomplish this they rely on feedback from their auditory system. The auditory perception mechanism, in turn, is highly sensitive to changes in low frequencies (perceptually significant frequencies). Therefore, speakers attempt to correct the low-frequency component of their utterances. With minor changes in their tongue movements, they can accomplish this correction to a large extent, but major tongue movements which are a learned habit through years of their first language experience are not as easy to modify. Therefore, the frequencies in the F_2-F_3 range should be the most sensitive frequencies to assess accent characteristics. In order to test this hypothesis, formant frequencies were first analyzed in terms of their ability in discriminating accented speech from native speech. In general, the second formant was found to be the most significant indicator of foreign accent characteristics. An additional experiment employing filter banks to identify accent sensitive frequency bands was also conducted, and similar results to that found in formant frequency analysis were obtained. The frequencies in the 1500–2500 Hz range were shown to be the most important frequencies based on accent classification performance. Finally, a new frequency sampling scheme was proposed and evaluated in the calculation of cepstrum coefficients in place of the commonly used Mel-scale. Consistent improvement over the Mel-scale was obtained through the use of the proposed accent-sensitive frequency scale with or without the inclusion of delta coefficients in the parameter set. We point out that future studies could consider integrating a measure of second language proficiency as part of the development of more advanced accent assessment methods. In conclusion, this study has shown that a variety of both temporal and frequency domain characteristics are modified when accent is present in American English, and that these issues can be used to formulate effective accent classification algorithms.

[1]In the analysis of frequency for this study, it was necessary to separate male and female speakers. Unfortunately, a sufficient number of female speakers for the accents under consideration were not available in the database in order to perform a similar acoustic analysis.

[2]Detailed information about the TIMIT database is available through the Linguistics Data Consortium (LDC) (URL address: *http://www.cis.upenn.edu/~ldc/home.html*). Details can be found in Fisher *et al.* (1986).

[3]The American English group ''Army Brat'' refers to a person who has moved frequently across the U.S., and therefore may possess less of a regional dialect. This term is derived from U.S. military personnel who are normally moved frequently across the U.S.

[4]In this study, uppercase ARPABET notation is used to describe phonemes for American English. See Deller, Proakis, and Hansen (1993), p. 118 for a summary.

[5]Three out of five tokens from each speaker, which were identified to have the most audible/visible release bursts for human operator labeling, were selected for statistical analysis.

[6]In order to better characterize the accented speech data, outliers in the data greater than 5σ were removed in the estimation of the mean.

[7]VOT is normally measured from the stop release to the instant of voicing. As such, VOT is positive for unvoiced stops, and negative for voiced stops. Here, only unvoiced stops were considered for accent classification.

[8]Obtaining similar variances between actual parameters and delta parameters are important in HMM training for most speech applications.

[9]In this discussion, the first, second, third, and fourth formants will be represented as F_1, F_2, F_3, and F_4, respectively.

[10]For a more complete description of the LEA speech synthesizer, see Fant (1970), p. 100.

[11]The term ''unreliable'' here, refers to speech which does not possess to the same degree, the typical accent sensitive feature variations.

[12]Databases such as the Oregon Graduate Institute Multilanguage Database, and TIMIT are available through the Linguistics Data Consortium (LDC) (see Footnote 2).

Asher, J., and Garcia, G. (**1969**). ''The optimal age to learn a foreign language,'' Modern Language J. **38**, 334–341.

Arslan, L.M. **(1996)**. ''Foreign Accent Classification in American English,'' Ph.D. thesis, Robust Speech Processing Laboratory, Dept. of Electrical Engineering, Duke University, Durham, NC.

Arslan, L.M., and Hansen, J.H.L. **(1996)**. ''Language Accent Classification in American English,'' Speech Commun. **18**, 353–367.

Arslan, L.M., and Hansen, J.H.L. **(1996b)**. ''Improved HMM Training and Scoring Strategies,'' IEEE Proc. ICASSP **2**, 589–592.

Bohn, O., and Flege, J.E. **(1992)**. ''The Production of New and Similar Vowels by Adult German Learners of English,'' Studies Second Language Acquisition **14**, 131–158.

Bolinger, D. **(1958)**. ''A theory of pitch accent in English,'' Word **14**, 109–149.

Brousseau, J., and Fox, S.A. **(1992)**. ''Dialect-dependent speech recognizers for Canadian and European French,'' in *Proceedings of the International Conference on Spoken Language Processing* (Univ. of Alberta, Alberta, Canada), pp. 1003–1006.

Byrd, D. **(1994)**. ''Relations of sex and dialect to reduction,'' Speech Commun. **15**, 39–54.

Caramazza, A., Yeni-Komshian, G., Zurif, E., and Carbone, E. (**1973**). ''The acquisition of a new phonological contrast: The case of stop consonants in French-English bilinguals,'' J. Acoust. Soc. Am. **54**, 421–428.

Caramazza, A., and Yeni-Komshian, G. **(1974)**. ''Voice onset time in two French dialects,'' J. Phonet. **2**, 239–245.

Chomsky, N., and Halle, M. **(1991)**. *The Sound Pattern of English* (MIT, Cambridge, MA).

Chreist, F. **(1964)**. *Foreign Accent* (Prentice-Hall, Englewood Cliffs, NJ).

Crowther, C. S., and Mann, V. (**1992**). ''Native language factors affecting use of vocalic cues to final consonant voicing in English,'' J. Acoust. Soc. Am. **92**, 711–723.

Davis, S., and Mermelstein, P. (**1980**). ''Comparison of parametric representations for monosyllabic word recognition in continuously spoken sentences,'' IEEE Trans. Acoust. Speech Signal Process. **ASSP-28,** 357–366.

Deller, J., Proakis, J., and Hansen, J.H.L. **(1993)**. *Discrete Time Processing of Speech Signals* (Macmillan Series for Prentice-Hall, New York).

Fant, G. (**1970**). *Acoustic Theory of Speech Production* (Mouton, Paris, France).

Fisher, W., Doddington, G., and Goudie-Marshall, K. **(1986)**. ''The DARPA speech recognition research database: Specifications and status,'' in *Proceedings of the DARPA Speech Recognition Workshop* (Morgan Kaufman, San Mateo, CA), pp. 93–99.
Flege, J.E. **(1980)**. ''Phonetic approximation in second language acquisition,'' Language Learning **30**, 117–134.
Flege, J. E. (**1984a**). ''The detection of French accent by American listeners,'' J. Acoust. Soc. Am. **76**, 692–707.
Flege, J. E. (**1988**). ''Factors affecting degree of perceived foreign accent in English sentences,'' J. Acoust. Soc. Am. **84**, 70–79.
Flege, J.E., and Eefting, W. **(1987)**. ''Cross-language switching in stop consonant perception and production by Dutch speakers of English,'' Speech Commun. **6**, 185–202.
Flege, J.E., and Hillenbrand, J. **(1984b)**. ''Limits on pronunciation accuracy in adult foreign language speech production,'' J. Acoust. Soc. Am. **76**, 708–721.
Flege, J. E., and Fletcher, K. L. (**1992b**). ''Talker and listener effects on degree of perceived foreign accent,'' J. Acoust. Soc. Am. **91**, 370–389.
Flege, J.E., Munro, M., and MacKay, I. **(1995)**. ''Effects of age of second-language learning on the production of English consonants,'' Speech Commun. **16**, 1–26.
Flege, J. E., Munro, M., and Skelton, L. (**1992a**). ''Production of the word-final English /t/-/d/ contrast by native speakers of English, Mandarin, and Spanish,'' J. Acoust. Soc. Am. **92**, 128–143.
Grover, C., Jamieson, D., and Dobrovolsky, M. **(1987)**. ''Intonation in English, French and German: Perception and production,'' Language and Speech **30**, 277–295.
Hogan, J., and Rozsypal, A. (**1980**). ''Evaluation of vowel duration as a cue for the voicing distinction in the following word-final consonant,'' J. Acoust. Soc. Am. **67**, 1764–1771.
Koenig, W. (**1949**). ''A new frequency scale for acoustic measurements,'' Bell Telephone Laboratory Record **27**, 299–301.
Leather, J. **(1983)**. ''Second language pronunciation and language teaching,'' Language Teaching Ab. **16**, 198–223.
Leon, P., and Martin, P. **(1980)**. *The Melody of a Language* (University Park, Baltimore), Chap. Des Accents, pp. 177–186.
Munro, M. J. **(1993)**. ''Productions of English Vowels by Native Speakers of Arabic: Acoustic Measurements and Accentedness Ratings,'' Language Speech **36**, 39–66.
Pilch, H. **(1970)**. ''The elementary intonation contour of English: A phonemic analysis,'' Phonetica **22**, 82–111.
Port, R., and Dalby, J. (**1982**). ''Consonant/vowel ratio as a cue for voicing in English,'' Percept. Psychophys. **32**, 141–152.
Port, R., and Mitleb, F. M. **(1983)**. ''Segmental Features and Implementation in Acquisition of English by Arabic Speakers,'' J. Phonetics **11**, 219–229.
Raphael, L. (**1972**). ''Preceding vowel duration as a cue to the perception of the voicing characteristic of word-final consonants in American English,'' J. Acoust. Soc. Am. **51**, 1296–1303.
Repp, B. (**1978**). ''Perceptual integration and differentiation cues for intervocalic stop consonants,'' Percept. Psychophys. **24**, 471–485.
Wardrip-Fruin, C. (**1982**). ''On the status of temporal cues to phonetic categories: Preceding vowel duration as a cue to voicing in final consonants,'' J. Acoust. Soc. Am. **71**, 187–195.
Wells, J. **(1982)**. *Accents of English* (Cambridge U. P., Cambridge, England).
Zwicker, E., and Fastl, H. **(1990)**. *Psychoacoustics: Facts and Models* (Springer-Verlag, Berlin).

Scattering of an obliquely incident plane wave from a circular clad rod

F. Honarvar and A. N. Sinclair
Department of Mechanical and Industrial Engineering, University of Toronto, 5 King's College Road, Toronto, Ontario M5S 3G8, Canada

(Received 12 September 1996; accepted for publication 11 February 1997)

The problem of scattering of an obliquely incident plane acoustic wave from an infinite solid elastic clad rod is formulated. Numerical calculations show the effects of the variations of the cladding thickness on both the backscattered pressure spectrum and individual normal modes. It is shown that various resonance frequencies have different levels of sensitivity to variations of the cladding thickness. Experimental measurements are also performed at both normal and oblique incident angles on a copper-clad aluminum rod; good agreement is observed between the calculated and the measured results. These results demonstrate the potential of acoustic resonance scattering procedures for application in nondestructive evaluation (NDE) of clad rods. © *1997 Acoustical Society of America.* [S0001-4966(97)01907-3]

PACS numbers: 43.20.Bi, 43.20.Fn, 43.20.Ks [ANN]

INTRODUCTION

There has been significant progress in both experimental and numerical studies of the scatter of acoustic waves from spheres and cylinders. There exists a potential for using these techniques in the field of nondestructive evaluation (NDE) of materials. This applies particularly to the NDE of long cylindrical components (such as rods, wires, tubes, etc.) which fall into the class of the few geometries for which the scattered pressure field has an explicit solution in the form of an infinite series. While studies on acoustic wave scattering from circular cylinders and shells are abundant in the literature, very little has been investigated about acoustic wave scattering from multi-layered cylinders. Particularly, the case of a plane acoustic wave obliquely incident on a two-layered cylinder (clad rod) has not been studied before. The study of the obliquely incident wave is important because, in practice, it is impossible to have a perfect normally incident plane wave, and traces of the obliquely incident components of the wave always show up in the backscattered pressure spectrum.

The physics of the scattering of an acoustic wave from an elastic target is a complicated phenomenon that involves the generation of different types of surface waves outside and inside the elastic target. Whenever an acoustic wave strikes the boundary of a cylinder, a specular reflection is returned. Waves are also launched from selected points on that boundary that circumnavigate the body in spiral or helical trajectories. These surface waves propagate near the boundary, either in the outer medium, or in the body of the scatterer.[1] The waves that propagate on the fluid side of the fluid-solid interface are Franz waves and Scholte–Stoneley waves (also called *creeping waves*).[2–4] When the cylinder is insonified by a normally incident plane acoustic wave, two distinct families of waves are generated inside the elastic cylinder. The first group are the *Rayleigh-type* (or more correctly pseudo-Rayleigh-type) waves and the other group are the *whispering gallery-type* (WG) waves.[1] It has been established that a close relationship exists between the resonances of an elastic scatterer and the circumferential waves which propagate along its periphery.[5] These surface waves and their relationship with the natural resonances of the scatterer have been extensively studied for the case of elastic cylinders. If the frequency of the incident wave coincides with one of the vibrational eigenfrequencies of the cylinder, surface waves match phases upon circumnavigation so as to build up to the resonance by constructive interference. When the wave is obliquely incident on the cylinder, additional types of waves are generated in the cylinder, and correspondingly additional resonance modes of the cylinder are excited. These additional (surface) waves are called *guided waves* (meaning *axially guided waves*)[6–8] and are mostly of a transverse nature. In the case of an obliquely incident wave, the travel path of all surface waves are helices. The angle of each helix depends on the phase velocity of the corresponding surface wave.[9]

Analytical and numerical studies of acoustic wave scattering from cylinders were initiated by Faran in 1951.[10] *Resonance scattering theory* (RST)[11] was one of the principal theoretical works in this area which presented a physical interpretation of the resonances generated in the body of the scatterer due to the constructive interference of the surface waves. RST also showed that the frequency spectrum of the backscattered echo is composed of a resonant part superimposed on a nonresonant spectrum, and that these two parts can be separated analytically. Flax *et al.*[12] formulated the problem of scattering of an obliquely incident plane wave from an infinite elastic cylinder. Surface waves generated by a plane acoustic wave obliquely incident on a cylinder were studied by Nagl *et al.*[9] based on RST and the Watson transformation. Veksler[13] computed the modal resonances for an aluminum cylinder insonified by an obliquely incident wave and showed their correspondence to the extrema of the backscattered spectrum. A geometrical interpretation of the phase matching of the helical surface waves was given by Conoir *et al.*,[14] who also showed that the resonances shift toward higher frequencies when the angle of incidence is increased.

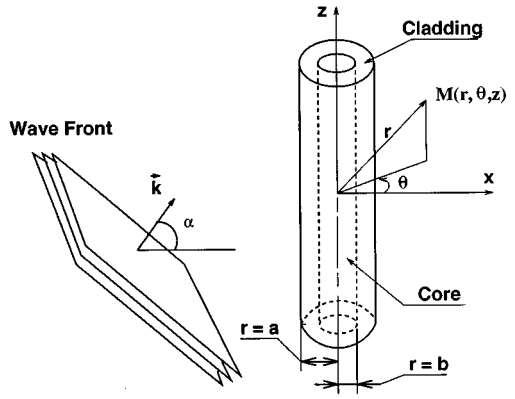

FIG. 1. Geometry of a plane wave obliquely incident on a submerged clad rod.

The major thrust in experimental work was made by the advent of the *Method of Isolation and Identification of Resonances* (MIIR) developed by French acousticians.[6,15] Using MIIR, the scattered spectrum, the resonance spectrum, and the mode shape of each resonance can be experimentally measured. Although tone bursts of long duration were used in early MIIR studies, it was later shown that short pulses can provide the same information.[16,17]

The problem of acoustic wave scattering from multilayered cylinders has also been considered by a few researchers. Flax and Neubauer[18] did the theoretical formulation and numerical evaluation of acoustic wave scattering from isotropic two-layered absorptive cylindrical shells. Sinclair and Addison[19] developed the equations of the scattering of a plane acoustic/elastic wave from a two-layered cylinder embedded in a solid or a fluid medium. The scattering of ultrasonic waves by two concentric fluid cylinders was investigated by Sinai and Wagg[20] and acoustic scattering from two eccentric cylinders was studied by Roumeliotis *et al.*[21] However, all of these works only consider the case of normally incident waves.

In this paper the detailed formulation for the scattering of an obliquely incident plane acoustic wave from a submerged clad rod is developed and the backscattered pressure spectrum of clad rods with various cladding thickness ratios are numerically evaluated. Experimental results, corresponding to small angles of incidence, are used to verify the mathematical calculations.

I. THEORY

Figure 1 shows an infinite plane acoustic wave of frequency $\omega/2\pi$ incident at an angle α on a submerged clad rod of infinite length, outer radius a, and core radius b. A cylindrical coordinate system (r,θ,z) is chosen with the z direction coincident with the axis of the cylinder. The pressure of the incident plane wave p_i at time t, external to the cylinder at an arbitrary point $M(r,\theta,z)$ is represented by,[12]

$$p_i = p_0 \sum_{n=0}^{\infty} \varepsilon_n i^n J_n(k_\perp r)\cos(n\theta)e^{i(k_z z-\omega t)}, \tag{1}$$

where

$$k_z = k\sin\alpha, \quad k_\perp = k\cos\alpha, \tag{2}$$

and $k=\omega/c$, c is the compressional wave velocity in the fluid medium outside the cylinder, ε_n is the Neumann factor $(\varepsilon_n = 2-\delta_{n0})$, p_0 is the incident pressure wave amplitude, and J_n are the Bessel functions of the first kind of order n. The outgoing scattered wave pressure p_s at point M must be symmetrical about $\theta=0$ and, therefore, of the form,

$$p_s = p_0 \sum_{n=0}^{\infty} \varepsilon_n i^n A_n H_n^{(1)}(k_\perp r)\cos(n\theta)e^{i(k_z z-\omega t)}, \tag{3}$$

where $H_n^{(1)}$ are the Hankel functions of the first kind of order n, and A_n are the unknown scattering coefficients. If the isotropic core and cladding media are designated by subscript $i=1,2$, respectively, then using Helmholtz displacement potential functions, ϕ_i (scalar) and $\boldsymbol{\psi}_i$ (vector), the Navier's equation for each medium can be written as

$$\boldsymbol{\nabla}\left((\lambda_i+2\mu_i)\nabla^2\phi_i-\rho_i\frac{\partial^2\phi_i}{\partial t^2}\right)+\boldsymbol{\nabla}\times\left(\mu_i\nabla^2\boldsymbol{\psi}_i-\rho_i\frac{\partial^2\boldsymbol{\psi}_i}{\partial t^2}\right) = 0, \quad i=1,2, \tag{4}$$

where λ_i and μ_i are the Lamé constants and ρ_i are the material densities. By expanding Eq. (4), four partial differential equations in terms of potential functions are obtained for each medium. In order to satisfy these partial differential equations, the potential functions should be of the following forms:

$$\begin{aligned}
\phi_1 &= \sum_{n=0}^{\infty} B_n J_n(k_{L_1} r)\cos(n\theta)e^{i(k_z z-\omega t)},\\
[\psi_1]_r &= \sum_{n=0}^{\infty} C_n J_{n+1}(k_{T_1} r)\sin(n\theta)e^{i(k_z z-\omega t)},\\
[\psi_1]_\theta &= \sum_{n=0}^{\infty} -C_n J_{n+1}(k_{T_1} r)\cos(n\theta)e^{i(k_z z-\omega t)},\\
[\psi_1]_z &= \sum_{n=0}^{\infty} D_n J_n(k_{T_1} r)\sin(n\theta)e^{i(k_z z-\omega t)},\\
\phi_2 &= \sum_{n=0}^{\infty} [E_n J_n(k_{L_2} r)+F_n Y_n(k_{L_2} r)]\cos(n\theta)e^{i(k_z z-\omega t)},\\
[\psi_2]_r &= \sum_{n=0}^{\infty} [K_n J_{n+1}(k_{T_2} r)\\
&\quad + L_n Y_{n+1}(k_{T_2} r)]\sin(n\theta)e^{i(k_z z-\omega t)},\\
[\psi_2]_\theta &= \sum_{n=0}^{\infty} [-K_{n+1} J_n(k_{T_2} r)\\
&\quad - L_n Y_{n+1}(k_{T_2} r)]\cos(n\theta)e^{i(k_z z-\omega t)},\\
[\psi_2]_z &= \sum_{n=0}^{\infty} [M_n J_n(k_{T_2} r)\\
&\quad + N_n Y_n(k_{T_2} r)]\sin(n\theta)e^{i(k_z z-\omega t)}
\end{aligned} \tag{5}$$

where

$$k_{L_i}=\left(\frac{\omega}{c_{L_i}}\right)^2-k_z^2,\quad k_{T_i}=\left(\frac{\omega}{c_{T_i}}\right)^2-k_z^2,\quad i=1,2. \tag{6}$$

c_{L_i} and c_{T_i} are the compressional and shear wave velocities respectively and $B_n, C_n, \ldots$ are unknown coefficients. By applying the boundary conditions at the core–cladding and fluid–cladding interfaces to Eqs. (5), the following system of linear algebraic equations is obtained,

$$[D_n^{(1)}]\{\mathscr{A}_n\}=\{\mathscr{B}_n\}, \tag{7}$$

where

$$\{\mathscr{A}_n\}=[A_n\ B_n\ C_n\ D_n\ E_n\ F_n\ K_n\ L_n\ M_n\ N_n]^T, \tag{8}$$

$$\{\mathscr{B}_n\}=[b_1\quad b_2\quad 0\quad 0\quad 0\quad 0\quad 0\quad 0\quad 0\quad 0]^T, \tag{9}$$

and $D_n^{(1)}$ is a 10×10 matrix.[22] Equation (7) could be solved for A_n at any given value of normalized frequency ka using Cramer's rule.

The scattered pressure field is usually evaluated in the far-field ($r\gg a$) at a fixed angle θ for a range of frequencies. The resulting normalized far-field amplitude spectrum, which is called the *form function*, is obtained from the following equation,[23]

$$f_\infty(\theta,ka)=\left(\frac{2r}{a}\right)^{1/2}\left(\frac{p_s}{p_0}\right)e^{-ik_\perp r}. \tag{10}$$

The form function can be decomposed into a sum of normal modes,

$$f_\infty(\theta,ka)=\sum_{n=0}^{\infty} f_n(\theta,ka), \tag{11}$$

where the individual normal modes are defined as:

$$f_n(\theta,ka)=\frac{2}{\sqrt{i\pi k_\perp a}}\varepsilon_n A_n\cos(n\theta). \tag{12}$$

For a cylindrical geometry, the nonresonant background scattering component (rigid background here) can be separated from the resonant part. For a rigid cylinder the scattering coefficients $A_n^{(\mathrm{rigid})}$ are given as:[23]

$$A_n^{(\mathrm{rigid})}(ka)=-\frac{J_n'(ka)}{H_n^{(1)'}(ka)}. \tag{13}$$

The resonant part of each mode can be obtained by subtracting the modal ($n=0,1,2,\ldots$) components of the rigid background $f_n^{(\mathrm{rigid})}(\theta,ka)$ from each of the normal mode components $f_n(\theta,ka)$ of the form function $f_\infty(\theta,ka)$ according to the following equation:

$$f_n^{(\mathrm{res})}(\theta,ka)=\frac{2}{\sqrt{i\pi k_\perp a}}\varepsilon_n[A_n-A_n^{(\mathrm{rigid})}]\cos(n\theta). \tag{14}$$

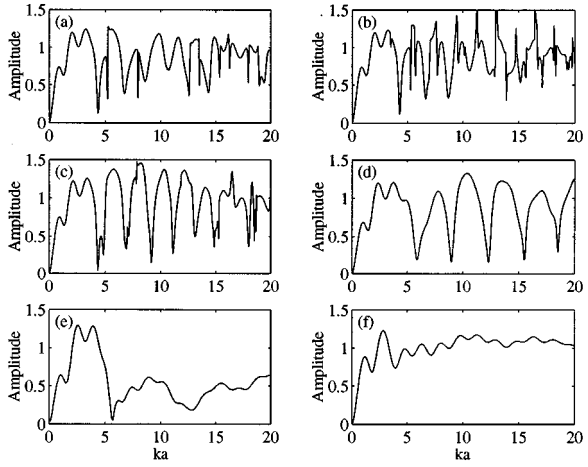

FIG. 2. Calculated form function of a copper-clad aluminum rod: (a) $\alpha=0°$; (b) $\alpha=5°$; (c) $\alpha=15°$; (d) $\alpha=30°$; (e) $\alpha=37°$; (f) $\alpha=45°$.

II. EVALUATION OF THE FORM FUNCTION AND RESONANCE SPECTRUM

Form functions of a copper-clad aluminum rod are calculated for various incident angles of the plane wave, see Fig. 2. Physical properties of the cladding and the core materials are given in Table I. The outer diameter of the clad rod is $a=9.15$ mm and its core diameter is $b=8.70$ mm. Similar to the case of an isotropic elastic cylinder,[12,14] when the incident angle is increased from $\alpha=0°$, initially new minima corresponding to the resonances associated with guided waves are observed on the form function, see Fig. 2(b). With further increase of α, all resonances (minima on the curve) shift to higher frequencies. Beyond the second critical angle, $\alpha=41.42°$, no elastic resonance can be detected on the form function and the form function becomes similar to that of a rigid cylinder.

The calculated form functions for a number of copper-clad aluminum rods with different cladding thickness ratios are shown in Fig. 3. The form functions are evaluated for $\alpha=3°$ and $0\leqslant ka\leqslant 20$. The cladding thickness ratio is defined as:

$$h=\frac{a-b}{a}. \tag{15}$$

Therefore $h=0$ refers to an aluminum cylinder with no cladding and $h=1$ is a simple copper cylinder. The common notation of designating the resonant modes by two indices (n,l) is used, where n is the mode number and l is the eigenfrequency label. $l=1$ corresponds to a Rayleigh-type wave and $l=2,3,\ldots$ corresponds to whispering gallery-type waves. Guided waves are designated as $\langle n,p\rangle$ where n is the mode number and p is the eigenfrequency label of the resonance.

From Fig. 3 it can be seen that with the increase of the cladding thickness from zero, the form function starts deviating from that of an aluminum cylinder ($h=0$) and gradu-

TABLE I. Physical properties of aluminum, copper, and tungsten.[22]

	ρ (kg/ m^3)	c_L (m/s)	c_T (m/s)
Aluminum	2694	6427	3112
Copper	8900	4600	2160
Tungsten	19 100	5460	2620

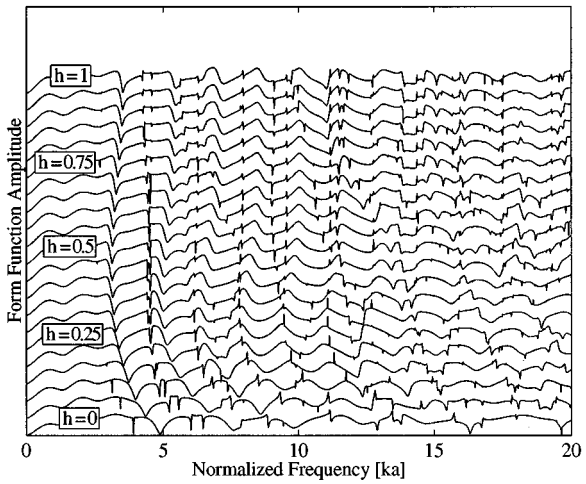

FIG. 3. Variation of the form function of the copper-clad aluminum rod with changes in cladding thickness at $\alpha=3°$.

ally approaches the form function of a simple copper cylinder ($h=1$). It can be observed that the resonance frequencies of the clad rod are significantly dependent on the thickness of the cladding.

Figure 4 shows the resonance spectra of the first three normal modes of the clad rod. These curves are evaluated from Eq. (14). The dependence of the resonance frequencies on cladding thickness can be observed more clearly with these resonance spectra than on the form functions of Fig. 3. Both the frequency and the quality of the resonances which are visible in these spectra vary with changes in h. Not many of the breathing mode ($n=0$) eigenfrequencies are excited in the frequency range considered and many of these resonances are so weak that they do not appear in the spectrum. The first two eigenfrequencies of the dipole mode ($n=1$) corresponding to the whispering gallery-type wave (1,2) and guided wave $\langle 1,1\rangle$ remain almost constant in the range $0.25\leqslant h\leqslant 1$. The first eigenfrequency of the Rayleigh-type wave (2,1) and guided wave $\langle 2,1\rangle$ of the quadrupole mode show a similar behavior for the range $0.5\leqslant h\leqslant 1$. This indicates that the surface waves corresponding to these eigenfrequencies do not penetrate deeply into the material and mostly propagate on the surface.

Resonances corresponding to higher values of l for all three modes show higher sensitivity to variations of the cladding thickness. This clearly indicates that high frequency resonances can be good indicators of the cladding thickness. The variations of the frequencies of these resonances with an increase in the value of h is not necessarily monotonic. This behavior can be correlated to the radial nodes of these resonances.[24] For a given mode number n, this nonmonotonic dependence of resonance frequencies on h becomes more severe with the increase of the eigenfrequency label l which corresponds to an increase in the number of radial nodes of the surface wave associated with that resonance.

It can also be shown that the nonmonotonic behavior of each resonance frequency with variations of h is consistent with the dependence of phase velocities of surface waves on h. The phase velocity of a helical surface wave is defined as[9]

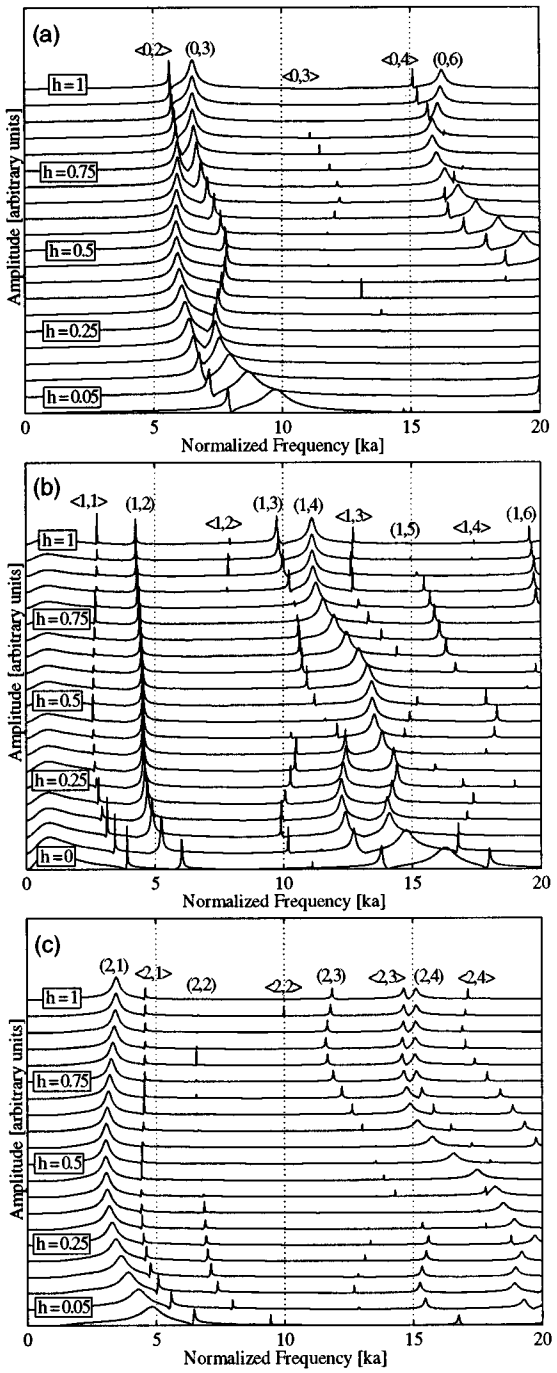

FIG. 4. Variation of the resonance spectra of the copper-clad aluminum rod with changes in cladding thickness at $\alpha=3°$: (a) breathing mode ($n=0$); (b) dipole mode ($n=1$); (c) quadrupole mode ($n=2$).

$$c_l^{ph}=c\{(n_l/ka)^2+\sin^2\alpha\}^{-1/2}, \tag{16}$$

where n_l is the mode number of the resonance and ka is its frequency. In Fig. 5(a) and (b), the phase velocities of the surface waves shown in Fig. 4(b) and (c) are plotted as a function of the cladding thickness ratio h. The behavior of the phase velocities of these surface waves is similar to that of their corresponding resonance frequencies in Fig. 4(b) and (c). This indicates that the primary reason for the nonmonotonic behavior observed in Fig. 4(a), (b), and (c) is the changes in the phase velocities of these surface waves.

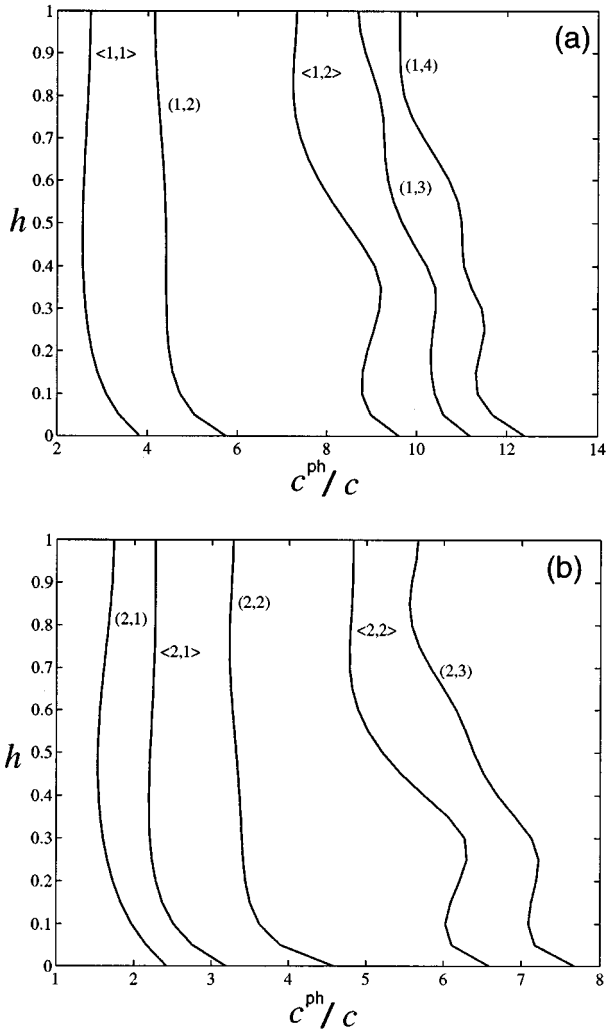

FIG. 5. Variation of the phase velocities of various surface waves with changes in cladding thickness of the copper clad aluminum rod: (a) dipole mode ($n=1$); (b) quadrupole mode ($n=2$).

Changes in the phase velocities of the surface waves are in turn due to the difference in the bulk wave velocities of the core and the cladding media.

III. EXPERIMENTS

A. Measurement of the backscattered pressure spectrum

A schematic diagram of the experimental setup for measuring the backscattered pressure field and the resonance spectrum using short pulses is shown in Fig. 6. The sample tested was a copper-clad aluminum rod. Physical properties of the cladding and the core metals are given in Table I and correspond to the numerical calculations of Section II. The velocity of sound in water was calculated from the water temperature according to the following equation,[25]

$$c_w=\sum_{n=0}^{5} g_n T^n, \tag{17}$$

where the coefficients g_n are listed in Table 3.3. of Reference 25 and T is the water temperature in °C. Two identical broadband ultrasonic transducers were used as transmitter

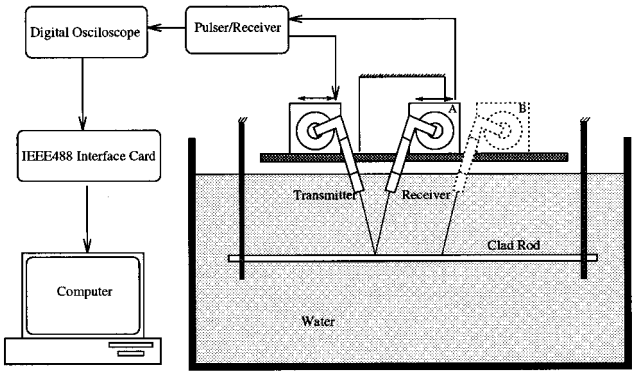

FIG. 6. Experimental setup for measuring the backscattered spectrum.

and receiver. Each transducer had a diameter of 1.125 in. and a nominal center frequency of 500 kHz. The useful frequency range of each transducer spanned from approximately 200 to 800 kHz. In all the experiments, the sampling frequency was 50 MHz. For the clad rod, $a=9.15$ mm and $b=8.70$ mm, and the length of the rod was 350 mm.

Frequency characteristics of the transmitting and receiving transducers were compensated by a deconvolution technique according to Reference 26. For this purpose a 0.25-mm-diam tungsten fiber was used to obtain a reference spectrum. Since the ka values for the tungsten fiber in the aforementioned frequency range are very small, none of the resonance frequencies of the tungsten fiber were excited and its frequency spectrum was smooth, see Fig. 7.

The frequency spectrum of the measured signal $S(\omega)$ for the copper-clad aluminum rod is a convolution of the cylinder transfer function $p_s(\omega)/p_0(\omega)$, and the frequency characteristics of the experimental system $G(\omega)$, i.e.,

$$|S(\omega)|=\left|G(\omega)\frac{p_s(\omega)}{p_0(\omega)}\right|. \tag{18}$$

A similar relationship exists for the tungsten fiber

$$|S'(\omega)|=\left|G(\omega)\frac{p_s'(\omega)}{p_0(\omega)}\right|, \tag{19}$$

where $S'(\omega)$ is the frequency spectrum of the measured signal and $p_s'(\omega)$ is the scattered pressure field for the tungsten fiber. The form function of the tungsten fiber is calculated from the following equation:

$$|f_\infty'|=\left(\frac{2r'}{a'}\right)^{1/2}\left|\frac{p_s'(\omega)}{p_0(\omega)}\right|e^{-ikr'\cos\alpha'}. \tag{20}$$

By substituting Eq. (20) into Eq. (19), one obtains

$$|G(\omega)|=\left|\frac{S'(\omega)}{f_\infty'}\right|\left(\frac{2r'}{a'}\right)^{1/2}e^{-ikr'\cos\alpha'}. \tag{21}$$

Moreover, substituting Eq. (10) into Eq. (18) results in

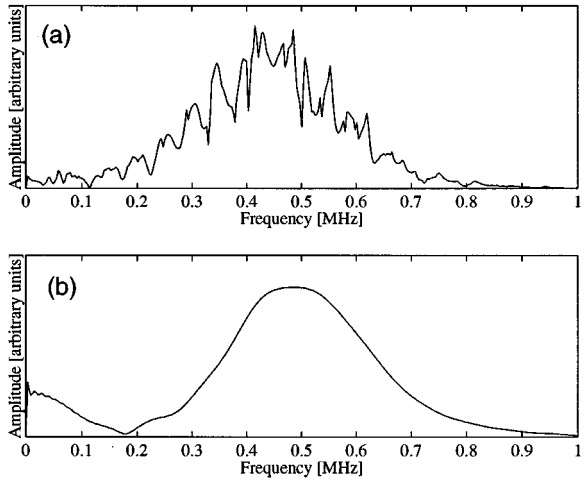

FIG. 7. Experimental frequency spectra of (a) copper-clad aluminum rod, (b) tungsten fiber.

$$|G(\omega)| = \left|\frac{S(\omega)}{f_\infty}\right| \left(\frac{2r}{a}\right)^{1/2} e^{-ikr\cos\alpha}. \tag{22}$$

Equating the right-hand sides of Eqs. (21) and (22) leads to the following equation:

$$|f_\infty| = \left|\frac{S(\omega)}{S'(\omega)}\right| \left(\frac{a'r}{ar'}\right)^{1/2} e^{ik(r'\cos\alpha' - r\cos\alpha)} |f'_\infty|. \tag{23}$$

For the case of Reference 26 where $r' = r\cos\alpha$ and $\alpha' = 0$, Eq. (23) reduces to the simpler expression of Eq. 27 of that paper. In Eq. (23) $S(\omega)$ and $S'(\omega)$ are measured experimentally and $|f'_\infty|$ is calculated numerically. The elastic properties of tungsten were obtained from Ref. 27 (Table A.1) see Table I. By measuring the backscattered echos from the sample rod and the tungsten fiber under similar conditions, one can obtain the form function of the rod from Eq. (23). Preliminary tests indicated that the best correspondence between measured and calculated form functions is obtained when $\alpha = \alpha'$.

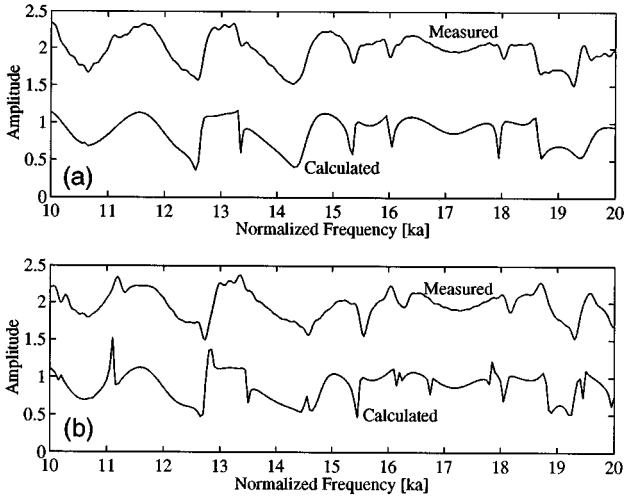

FIG. 8. Measured and calculated form functions for the copper-clad aluminum rod. (a) $\alpha = 0$ (normal incidence); (b) $\alpha = 3°$.

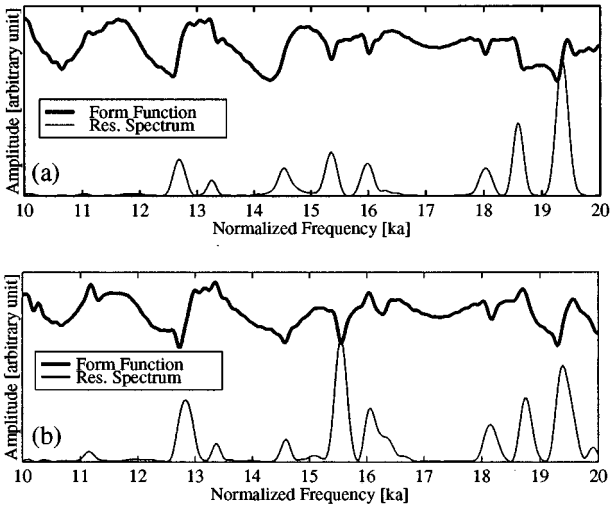

FIG. 9. Measured form functions and resonance spectra for the copper-clad aluminum rod. (a) $\alpha = 0$ (normal incidence); (b) $\alpha = 3°$.

It is impossible to insonify the cylinder at a normal angle with a truly infinite plane wave. General purpose NDE transducers cannot produce a completely normally incident wave because even when the surface of the transducer is exactly parallel to the axis of the cylinder (in a pulse-echo arrangement), some oblique components will still appear in the signal because of the nonplanar characteristics of the incident wave. The smaller the diameter of the receiver and the longer the distance between the probe and the cylinder, the less will be the effects of oblique components. In practice, there are limitations on the diameter of the probe. The maximum distance between the probe and the sample also depends on the energy of the signal and dimensions of the water tank. Moreover, the directivity pattern of a transducer restricts the measurements to small incident angles.[8,26]

Figure 8 shows the measured and calculated form functions for the clad rod sample. The numerically calculated and experimentally measured form functions are found to be consistent for both normally and obliquely incident waves. Figure 9 shows the measured form functions and the resonance

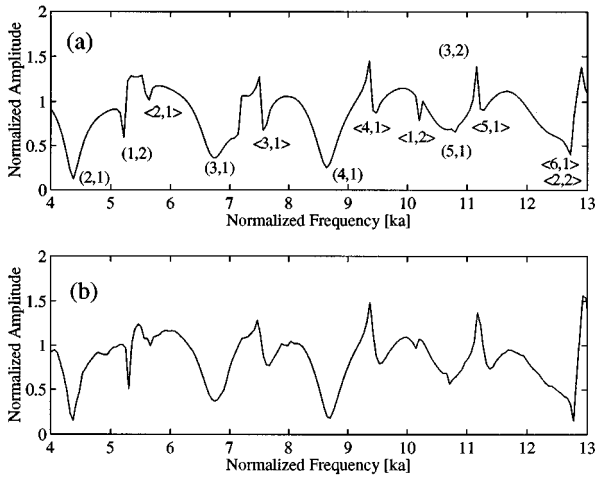

FIG. 10. Form functions for 8.026 mm diameter copper-clad aluminum rod at $\alpha = 3°$. (a) Calculated. (b) Measured.

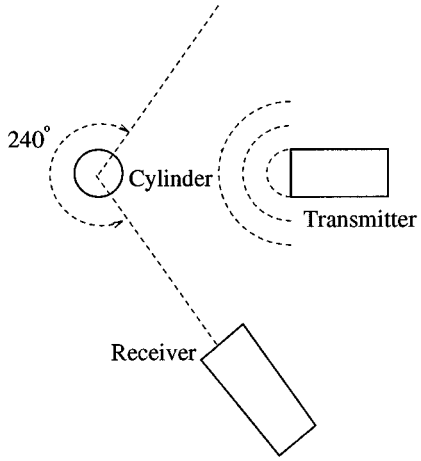

FIG. 11. Schematic diagram of the setup used for measuring the mode shape of the resonances.

spectra for the clad rod. The resonance spectra were obtained by removing the specular echo from the signal and then finding the power spectrum of the remaining echo. From these figures, it can be observed that when the cylinder is insonified at small oblique angles, the majority of the resonances that were visible at normal incidence are shifted to the left and additional resonances appear in the spectrum which are due to the axially guided waves. There is good agreement between experimental measurements and theoretical calculations.

Faint evidence of axially guided mode resonances (e.g., at $ka \approx 11$) can be observed in Figs. 8(a) and 9(a), corresponding to nominally zero degrees angle of incidence. This is due to the nonplanar characteristics of the incident wave as mentioned earlier.

B. Characterization of individual modes

Using short pulse MIIR,[17] the mode shapes of several resonances were measured at both normally and obliquely incident angles. The measurements were performed on a copper-clad aluminum rod with $2a = 8.026$ mm and $h = 0.05$. The frequency range for this sample was $4 \leqslant ka \leqslant 13$. The calculated and measured form functions for this sample are shown in Fig. 10.

Figure 11 shows the schematic diagram of the setup used for measuring the mode shapes. The transmitting transducer can insonify the cylinder at both normally and obliquely incident angles. The receiving transducer can be ro-

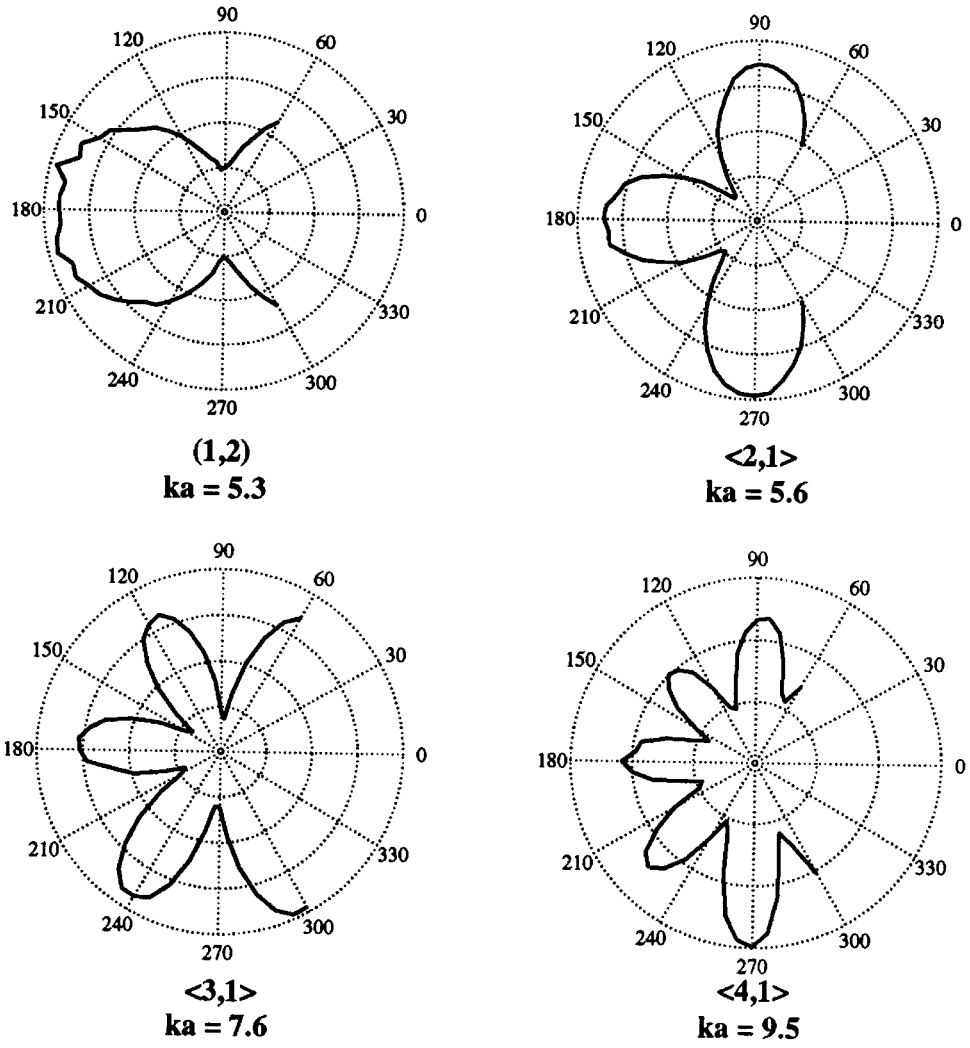

FIG. 12. Measured mode shapes of the copper-clad aluminum rod at incident angle of $\alpha = 3°$.

tated in a horizontal plane several centimeters along the cylinder axis z from that of the transmitting receiver. Thus, the resonances of the guided waves will be dominant in the acquired signal. In the measurements performed, the vertical distance (along the z axis) between the transmitter and the receiver was about 10 cm. The receiving transducer was swept through angles from 60° to 300° at 5° increments. Because of the symmetry of the cylinder, sweeping the receiving transducer through a range of at least 180° is sufficient for verification of the exact mode shape.[28] Figure 12 shows samples of the measured mode shapes of whispering gallery-type waves and guided waves for an incident angle of $\alpha = 3°$.

Measurement of the mode shape of a resonance is a practical means for identifying the mode number of that resonance. The mode number is simply half the number of nodes or antinodes around the cylinder.

IV. CONCLUSIONS

The problem of the scattering of an obliquely incident plane acoustic wave from a two-layered solid elastic cylinder (clad rod) has been formulated. Using RST, the dependence of resonance frequencies on the thickness of the cladding was evaluated. It is shown that different resonances react differently to the variations of the cladding thickness. Their sensitivity to these variations depends on the thickness of the cladding. In general, high frequency resonances are more sensitive than low frequency ones. Therefore, for NDE purposes, appropriate resonances can be selected to monitor or detect variations in cladding thickness.

The scattered pressure field from a copper-clad aluminum rod was measured using short pulses. The experimental measurements were consistent with numerical calculations and clearly showed the presence of all the predicted resonances.

The results explain one of the discrepancies between calculated and experimental diffraction spectra encountered in past studies of cylindrical components: At a nominal angle of incidence $\alpha = 0°$, the oblique components of the ultrasonic beam originating from non-planar characteristics of the wave generated by a finite-diameter transducer produce traces of guided-mode resonances not predicted by theory.

Using short pulse MIIR, the mode shapes of different resonances were measured experimentally for $\alpha = 3°$.

ACKNOWLEDGMENTS

This work was supported by a grant from the Manufacturing Research Corporation of Ontario (MRCO), and the National Science and Engineering Research Council (NSERC) of Canada. One of the authors (FH) acknowledges the financial support of the Ministry of Culture and Higher Education of Iran.

[1] H. Überall, ''Surface Waves in Acoustics,'' in *Physical Acoustics* (Academic, New York, 1973), Vol. 10, Chap. 1.
[2] W. Franz, Z. Naturforsch. **9a**, 705 (1954).
[3] G. V. Frisk, J. W. Dickey, and H. Überall, J. Acoust. Soc. Am. **58**, 996 (1975).
[4] J. W. Dickey, G. V. Frisk, and H. Überall, J. Acoust. Soc. Am. **59**, 1339 (1976).
[5] R. H. Vogt and W. G. Neubauer, J. Acoust. Soc. Am. **60**, 15 (1976).
[6] G. Maze, J. L. Izbicki, and J. Ripoche, J. Acoust. Soc. Am. **77**, 1352 (1985).
[7] J. L. Izbicki, G. Maze, and J. Ripoche, J. Acoust. Soc. Am. **80**, 1215 (1986).
[8] F. Léon, F. Lecroq, D. Décultot, and G. Maze, J. Acoust. Soc. Am. **91**, 1388 (1992).
[9] A. Nagl, H. Überall, P. P. Delsanto, J. D. Almar, and E. Rosario, Wave Motion **5**, 235 (1983).
[10] J. J. Faran, Jr., J. Acoust. Soc. Am. **23**, 405 (1951).
[11] L. Flax and W. G. Neubauer, J. Acoust. Soc. Am. **63**, 675 (1978).
[12] L. Flax, V. K. Varadan, and V. V. Varadan, J. Acoust. Soc. Am. **68**, 1832 (1980).
[13] N. D. Veksler, Acustica **71**, 111 (1990).
[14] J. M. Conoir, P. Rembert, O. Lenoir, and J. L. Izbicki, J. Acoust. Soc. Am. **93**, 1300 (1993).
[15] G. Maze, B. Taconet, and J. Ripoche, Phys. Lett. **84A**, 309 (1981).
[16] M. de Billy, J. Acoust. Soc. Am. **79**, 219 (1986).
[17] G. Quentin and A. Cand, Electron. Lett. **25**, 353 (1989).
[18] L. Flax and W. G. Neubauer, J. Acoust. Soc. Am. **61**, 307 (1977).
[19] A. N. Sinclair and R. C. Addison, Jr., J. Acoust. Soc. Am. **94**, 1126 (1993).
[20] J. Sinai and R. C. Waag, J. Acoust. Soc. Am. **83**, 1728 (1988).
[21] J. A. Roumeliotis and N. B. Kakoginnos, J. Acoust. Soc. Am. **97**, 2074 (1995).
[22] F. Honarvar, ''Nondestructive evaluation of cylindrical components by resonance acoustic spectroscopy,'' PhD thesis, University of Toronto, 1997.
[23] L. Flax, G. C. Gaunaurd, and H. Überall, ''Theory of Resonance Scattering,'' in Vol. 15 of *Physical Acoustics* (Academic, New York, 1981), Chap. 3, pp. 191–294.
[24] H. D. Dardy, L. Flax, and C. F. Gaumond, J. Acoust. Soc. Am. **82**, 1378 (1987).
[25] A. Briggs, *Acoustic Microscopy* (Oxford, New York, 1992).
[26] T. Li and M. Ueda, J. Acoust. Soc. Am. **86**, 2363 (1989).
[27] J. Krautkrämer and H. Krautkrämer, *Ultrasonic Testing of Materials* (Springer Verlag, New York, 1983), 3rd ed.
[28] H. Überall, *Acoustic Resonance Scattering* (Gordon and Breach Science, Philadelphia, 1992).

The resonances of finite-length elastic cylinders and elastic spheroids excited by sound scattering

X. L. Bao[a] and H. Überall[b]
Department of Physics, Catholic University of America, Washington, DC 20064

J. Niemiec
NSWC, Carderock Division, Carderock, Maryland 20817

D. Décultot, F. Lecroq, G. Maze, and J. Ripoche
LAUE, URA CNRS 1373, University of Le Havre, 76610 Le Havre, France

(Received 24 November 1995; accepted for publication 11 February 1997)

The predictions of resonance frequencies for elongated elastic cylinders and spheroids, based on various methods of approach, were discussed in a number of papers in recent years. In the present study, the regions of applicability of the phase matching method for surface waves and of the longitudinal bar wave approximation are examined by comparing the predicted results with the results of *T*-matrix calculations or with the results of scattering experiments. © *1997 Acoustical Society of America.* [S0001-4966(97)03606-0]

PACS numbers: 43.20.Fn, 43.20.Ks, 43.20.Px [ANN]

INTRODUCTION

In recent years, there appeared a series of papers[1–6] concerned with sound scattering and resonance predictions for elongated elastic cylinders and spheroids immersed in water. The *T*-matrix method was developed and became an effective method for numerical prediction of scattering acoustic fields for these types of objects. In the papers of Werby *et al.*[1–3] and Hackman *et al.*,[4–6] numerical results obtained using spherical-coordinate-based or spheroidal-coordinate-based *T*-matrix methods were presented for prolate spheroids and for cylinders with hemispherical end caps, for the case of end-on incidence, and a variety of aspect ratios and material properties. In these papers, the resonant responses of solid objects were obtained from the ''form function'' by subtracting the rigid scattering background. The phase matching principle, which is based on surface wave theory, has been used earlier by Flax *et al.*[7] to determine the average phase speed of a leaky Rayleigh wave propagating along a meridian of the spheroid. This method was used further on by Werby and Tango,[1] and has been refined by taking the effects of radius of curvature on phase velocity into account by Überall *et al.*,[8] while the previous studies had approximated the phase speed by a constant average. In Hackman's papers, which were mainly concerned with objects of higher aspect ratio, it was pointed out that in the low-ka region, the longitudinal resonance response of an elongated cylinder is closely related to a ''bar wave,'' so that the application of phase matching methods, based on surface waves, is limited here. Experimental results are presented in papers of Maze *et al.*[9,10] for solid and hollow cylinders with hemispherical end caps, and in our previous paper[11] for solid finite cylinders. The results of lake experiments by the David Taylor Research Center[12] (now Naval Surface Warfare Center, Carderock Division) also provided a series of data records for sound scattering from a thin, hollow, hemispherically end-capped steel cylinder with higher aspect ratio.

In this paper, the regions of applicability of the phase matching method for surface waves (PM), and of the longitudinal bar-wave approximation (LBW) are examined by comparing the predicted results with the results of *T*-matrix calculations or with the results of scattering experiments.

I. THE NATURE OF ELASTIC WAVES

A. The displacement distribution

In order to examine the nature of elastic excitations of the target, the interior elastic displacements of a steel prolate spheroid with aspect ratio $L/D=1.5$ at the resonant frequencies were presented in a paper by Hackman *et al.*[5] In that paper, the authors emphasized that the displacements and phase velocity, measured along the axis of the spheroid (or elongated object) are closely related to those of the lowest longitudinal modes of an elastic cylinder and resemble those of a ''bar wave'' at low frequencies.

In the following, the figures of Ref. 5 will be used to ascertain the existence of surface circumferential waves, even at lower frequencies. The vibrational state of a prolate spheroid with aspect ratio $L/D=1.5$ as shown in Fig. 1, can be viewed in different ways, either along the axial direction or around the meridian. The directions of surface displacements are marked by arrows, and the resonance modes n can be identified by the number of wavelengths around the meridian. The surface waves become stronger than the longitudinal waves along the axis when the normalized frequency $kL/2$ increases. Conversely, the longitudinal waves become stronger at low frequencies. But for a prolate spheroid with the small aspect ratio $L/D=1.5$, at the lowest mode $n=2$ [Fig. 1(a), $kL/2=6.35$ or $ka=4.23$], the surface wave is still strong enough and can be easily identified according to the

[a]Present address: Dept. of Mechanical Engineering, Auburn University, Auburn, AL 36849-5341.
[b]Also at LAUE, URA CNRS 1373, University of Le Havre, 76610 Le Havre, France.

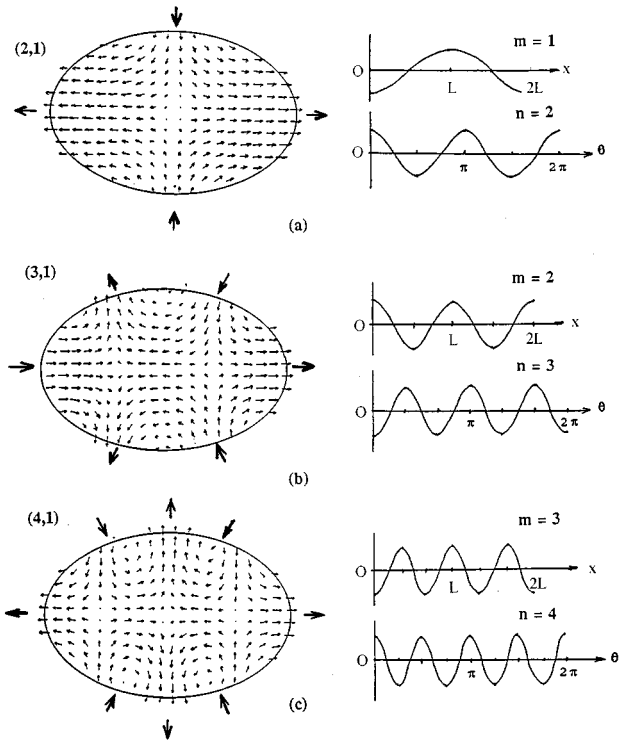

FIG. 1. Left: The interior elastic displacements of a prolate steel spheroid with aspect ratio $L/D=1.5$ for the resonance frequencies: (a) $kL/2=6.35$, (b) $kL/2=9.75$, (c) $kL/2=12.2$. Right: the amplitude of displacement along symmetry axis and meridian, respectively; n,m are the number of wavelengths around the closed paths.

surface displacements. So there exists a transitional frequency region, where both the surface wave and the longitudinal wave interpretation is applicable simultaneously.

B. The dispersion curves

A typical dispersion curve of the lowest axially propagating mode for an infinite solid steel cylinder is shown in Fig. 2. From this figure, the way in which the type of elastic wave transitions from one to the other mode can be seen clearly. At low frequencies ($ka<5$), the phase velocity is higher and approaches the phase velocity of a ''bar wave,'' [5]

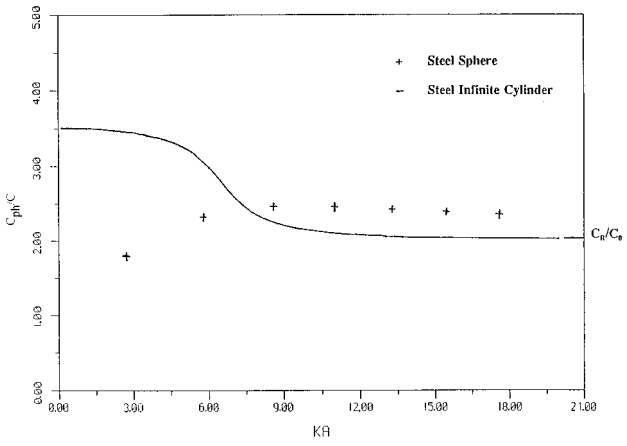

FIG. 2. Dispersion curves of the lowest axisymmetrical modes for an infinite solid steel cylinder and for a solid steel sphere.

and at higher frequencies ($ka>8$), the phase velocity is lower and tends to the limit of the Rayleigh wave. Between these regions, there is an intermediate region ($5<ka<8$), with the phase velocity varying rapidly from one level to the other level. This means that the sound energy will be uniformly distributed over the whole cross section, or be concentrated near the surface, for the cases of low ka or of higher ka, respectively. In the intermediate region, the phase matching method is applicable for $ka>5$, and the bar-wave approximation is applicable for $ka<8$.

II. PHASE VELOCITY AND RESONANCES

The phase matching condition based on the surface waves, as is well-known, can be written as:

$$\oint k_1 ds = 2\pi(n+1/2), \quad n=1,2,3,\ldots, \tag{1}$$

where k_1 is the wave number of the 1th surface wave type, and n is the number of wavelengths on the closed meridian path. The extra term 1/2 on the right-hand side of Eq. (1) originates from the fact that the meridian paths form a focal point at each apex of the end-capped cylinder or spheroid, at each of which a quarter-wavelength phase jump of the passing surface wave takes place.

According to the ''bar-wave'' approximation,[5] the longitudinal resonance condition is

$$\int_0^L k_1^b dx = \pi m, \quad m=1,2,3,\ldots, \tag{2}$$

where k_1^b is the wave number on the 1th longitudinal axisymmetrical wave for an infinite cylinder, and m is the number of half wavelengths along the whole length L of the scatterer. Physically, the condition of Eq. (2) expresses the fact that for any equal end conditions at the two ends, resonating standing waves form if half-wavelengths span the length L of the object.

At the resonant values of the frequency, the relation $n=m+1$ for the $l=1$ waves considered here is obtained immediately from Fig. 1, as shown there by the figures of displacements.[5] (In Fig. 1, the pictures on the left are distributions of displacement, and those on the right the corresponding amplitudes of displacement along the axis, or along the meridian of the prolate spheroid.) The resonant modes can be estimated by using Eqs. (1) or (2) depending on the situation of the objects, including aspect ratio and the frequency region considered.

In the resonance conditions as given by Eqs. (1) and (2), the wave numbers k_1 and k_1^b are dispersive and vary with position around the surface or along the axis of targets. The wave numbers usually are unknown for a general finite elastic cylinder, and can only be estimated approximately. In the paper of Überall *et al.*,[8] a simple ''tangent sphere'' model has been developed, where the known wave number on a sphere is used locally, the sphere being tangent to the object's surface along the propagation direction. This model is especially suitable for objects with low aspect ratio, or in the higher frequency region. But because only the local curvature along the propagation direction is matched by a tangent

sphere, errors are brought in where the effects of transverse curvature cannot be ignored. Both choices (the constant Rayleigh velocity, or the dispersive infinite-cylinder velocity) were used in the present example over the cylindrical portion of the body, and the results compared to each other, see below. A typical example is the cylindrical portion of a finite cylinder with hemispherical end caps. For an $1=1$ type surface wave along the axial direction, the constant phase velocity of the Rayleigh wave was often applied in terms of the ''tangent sphere'' model. But in this case, it is more reasonable to estimate the wave numbers (or phase velocities) by using the ''infinite cylinder'' model, where the known wave number on a infinite cylinder is used locally. An example of a dispersion curve for an infinite solid cylinder is shown in Fig. 2, it tends to the Rayleigh constant in the higher ka region. In this paper, the ''infinite cylinder'' model rather than the approximation of the Rayleigh speed limit is considered appropriate on the cylindrical portion of end-capped cylinders for estimating the wave number of surface waves, but the ''tangent sphere'' model is still applied on the terminal portions. For the prolate spheroid, a similar approach will be described below.

III. RESULTS AND DISCUSSION

In the following, the results for resonance modes of solid cylinders with hemispherical end caps and for solid prolate spheroids, estimated by the phase matching method and by the ''bar-wave'' approximation, are listed and compared to each other. Then these results are compared to the results obtained by T-matrix methods or by experiments.

A. Solid cylinders with hemispherical end caps

For a solid cylinder with low aspect ratio $L/D=2$, there are results from two sets of experiments, one performed in a water tank at the Catholic University of America for steel cylinders, the second one performed at the University of Le Havre, France for a tungsten carbide (WC) cylinder. For estimating the resonance modes, two methods based on phase matching of surface waves differ in using the ''Rayleigh limit'' model (PM-RL) or ''infinite cylinder'' model (PM-IC) on the cylinder portion, respectively. The other method is based on the longitudinal ''bar wave'' approximation (LBW); the equation used here is Eq. (2). The quantity $k_1^b(x)$ therein is a function of the local diameter $D(x)$ of the scatterer, the latter being calculated easily according to the geometrical shape of the spherically end-capped cylinder, or the prolate spheroid. Then, the dispersion curves of Fig. 2 are used to obtain $k_1^b(x)$.

Figures 3 and 4 show ''Regge trajectories'' (plots of ka resonance values versus mode number n) of the $1=1$ type wave, obtained from experiments and from predictions, for steel (material properties: compressional speed $c_L=5950$ m/s, shear speed $c_T=3240$ m/s, sound speed in water $c=1480$ m/s) and WC (material properties: $c_L=6940$ m/s, $c_T=4120$ m/c) cylinders with aspect ratio $L/D=2$, respectively. Correspondingly, the experimental curves of the resonant response are shown in Figs. 5 and 6, respectively. Resonances are labeled by $(n,1)$, where n = mode number, 1 = type of resonating wave.

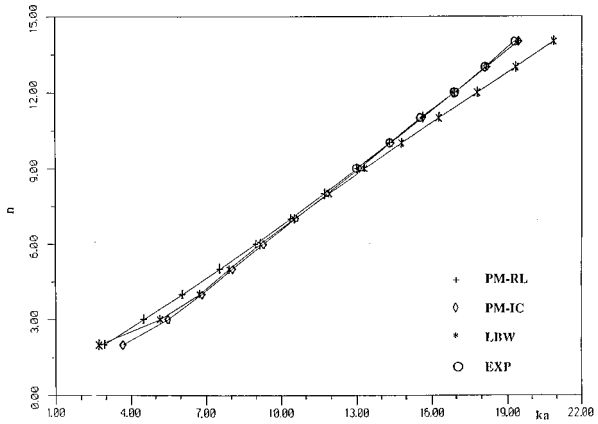

FIG. 3. Regge trajectory for a solid steel cylinder with hemispherical end caps with aspect ratio $L/D=2$ for the case of end-on incidence.

Figures 3 and 4 present similar physical quantities, but for different types of targets. The experimental results are available mainly in the relatively high ka region for the solid steel cylinder (as in Fig. 3), but mainly in the low ka region for the solid WC cylinder (as in Fig. 4). These two figures are complementary to each other, so we could obtain a complete comparison from these two figures taken together.

The results show that:

(a) In the high-ka region (see Fig. 3), there is almost no difference in using the prediction models PM-RL or PM-IC, but in the intermediate ka region ($ka=7-15$ for the WC cylinder, see Fig. 4), the PM-IC model is obviously better than the PM-RL model. This is easy to understand, because in the high ka region, the phase velocities used for the PM-IC model on the cylindrical section are near the Rayleigh limit C_R, which the PM-RL model uses. But in the intermediate ka region, the phase velocity changes rapidly for the infinite cylinder, the change being caused by the effect of transverse curvature. Thus PM-IC is better than PM-RL in the intermediate region because the effect of transverse curvature is considered in it.

(b) The phase matching (PM) method is better than the LBW approximation in the high-ka region (see Fig. 3). This is as expected because, as is physically clear, the surface

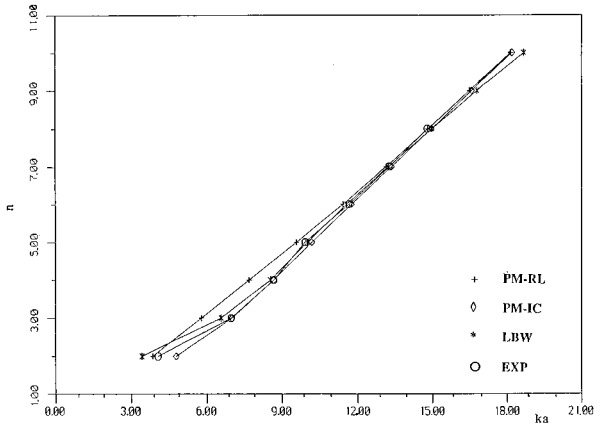

FIG. 4. Regge trajectory for a solid WC cylinder with hemispherical end caps with aspect ratio $L/D=2$, for the case of end-on incidence.

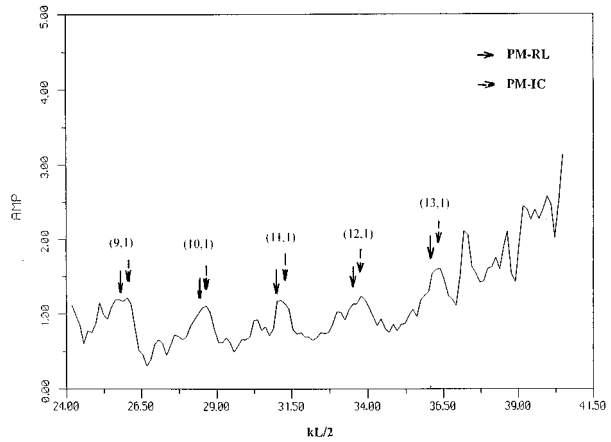

FIG. 5. Resonance responses obtained from experiments performed at Catholic University, for the same object as in Fig. 3. The predictions are being marked by arrows.

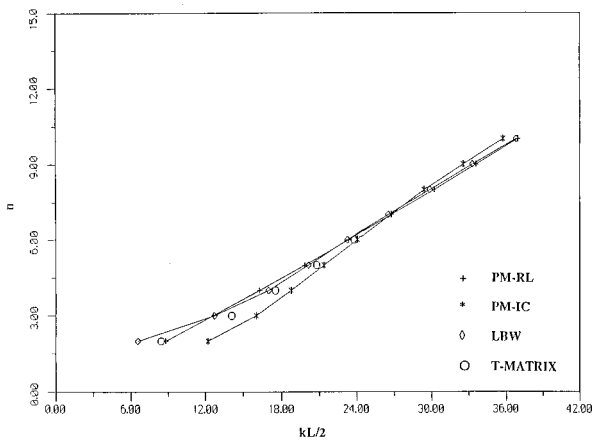

FIG. 7. The resonance modes obtained by T-matrix calculations compared with the results of the PM and LBW methods, for a solid prolate WC spheroid with $L/D=2$.

wave theory is suitable in the relatively higher frequency region and the bar-wave model is suitable in the relatively lower-frequency region.

(c) In the intermediate ka region ($k=7-15$ for the WC cylinder) both PM-IC and LBW methods coincide with each other and also with experiments (see Fig. 4). It is interesting that there exists a common region, in which the resonances could be predicted by both PM and LBW methods, based on the surface-wave and bar-wave viewpoint, respectively. As has been mentioned, in the intermediate region the wave property transits from ''bar-wave'' type to Rayleigh surface-wave type for the lowest axisymmetrical mode of the infinite cylinder (see Fig. 2).

(d) There is no clear answer for the low-ka region from the results. As shown in Fig. 4, both the predictions of PM-IC or of LBW do not coincide with experiment at the $n=2$ resonance mode.

It may be said in general that the bar-wave model can be expected, and indeed is seen to work at low frequency where the wavelength is close to the length of the target, and is still too long for being used for a surface wave picture; while the surface wave model works at high frequency where the wavelength is short enough to picture a distinct surface wave propagating over the target; with a transition region in between where either model can be used.

B. Solid prolate spheroids

Scattering by, and resonances of solid prolate spheroids are discussed in a number of papers.[2–5] Typical results obtained by using T-matrix methods are presented in the paper of Werby *et al.*[2] for WC spheroids with aspect ratio $L/D=1-4$, and in the paper of Williams *et al.*[4] for a steel spheroid with aspect ratio $L/D=10$.

In Figs. 7 and 8, the results of T-matrix calculations listed in previous papers are compared with the results of the PM method and the LBW approximation for $L/D=2$ and $L/D=10$ spheroids, respectively.

PM-IC model: We generally view the spheroid as a cylinder with a variable local diameter. According to the aspect ratio L/D, the length of the ''cylindrical portion'' is determined as $L_{cy}=(L/D-[1])\times D$. On the cylindrical portion, the ''infinite cylinder'' approximation is used. The local diameter of the cylinder is a function of the coordinate x. On the ''end caps'' the ''tangent sphere'' approximation is used,

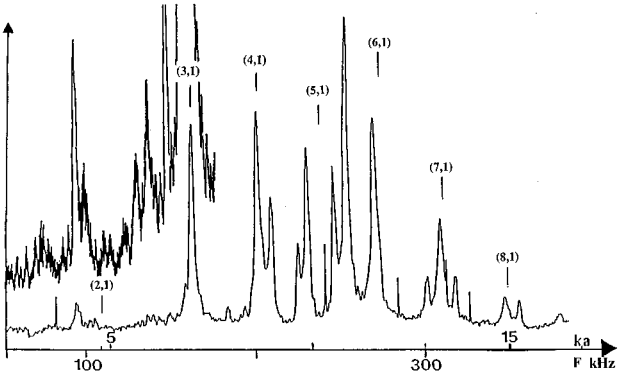

FIG. 6. Resonance response obtained from experiments performed at the University of Le Havre, France, for the same object as in Fig. 4. The predictions are marked by arrows.

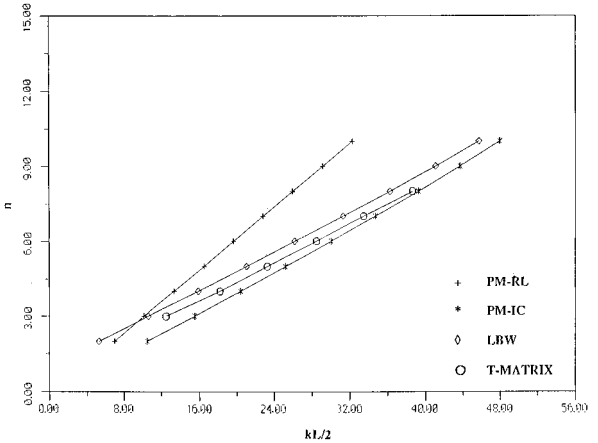

FIG. 8. Same as in Fig. 7, but for a steel spheroid with aspect ratio $L/D=10$.

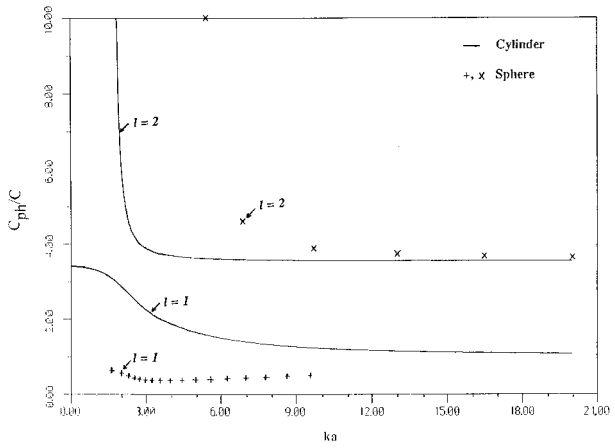

FIG. 9. Dispersion relations for a steel spherical shell and for an infinite cylindrical shell ($b/a=0.97$) for the $n=0$ mode.

the curvature being a function of position along the meridian. Then, Eq. (1) is used for searching the resonant modes.

LBW model: Equation (2) is used for the calculation. Again, the cylinder's local diameter changes along the cylinder axis. The local diameter can be determined from the equation of a prolate spheroid. Then the wave numbers are determined by using the corresponding dispersion relations.

PM-RL: The ''tangent sphere'' approximation is used along the meridian everywhere. Then, Eq. (1) is used for calculating the resonant modes.

The results are similar to the results for hemisperhically end-capped cylinders as shown above. We find that:

(a) For a prolate spheroid with relatively small aspect ratio $L/D=2$ (see Fig. 7), the PM model or LBW model predictions are close to the results of the T-matrix calculation, and the PM-IC approximation model is not obviously better than the PM-RL model in the intermediate ka region. The results of T-matrix calculations fall between both IC and RL predictions, because for this case, the middle portion of the prolate spheroid is neither like a sphere not like a cylinder, so that errors are brought in by both models. But for spheroids, the PM-RL model is better than for a cylinder with hemispherical end caps (compare Figs. 7 and 4).

(b) For a prolate spheroid with high aspect ratio $L/D=10$ (see Fig. 8), the results of T-matrix calculations are available only for the low-ka region ($ka=1.2-4.0$). The results fall between the predictions of LBW and PM-IC, and the PM-RL predictions are at fault in this region. This can be understood, because for a high aspect ratio, the spheroid's middle portion is more like a cylinder, so the PM-IC model is better than the PM-RL model.

C. Hollow cylinders with hemispherical end caps

The dispersion relations for a stainless-steel spherical shell and for an infinite cylindrical shell (with ratio of inner to outer radius $b/a=0.97$) at axial incidence, and the experimentally measured resonance response of a hollow stainless-steel hemispherically end-capped cylinder with aspect ratio $L/D=2$ performed at the University of Le Havre, are shown in Figs. 9 and 10, respectively. The experiment only shows the $1=2$ resonances since those of the $1=1$ (pseudo-

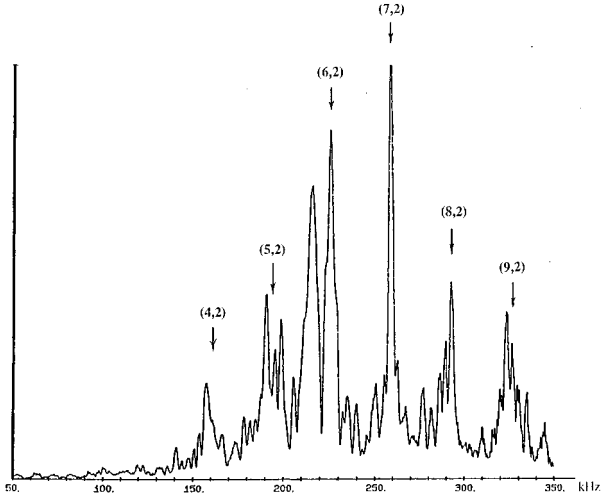

FIG. 10. The resonance response of a hollow steel cylinder with hemispherical end caps ($L/D=2$, $b/a=0.97$) for axial incidence. The arrows indicate the resonances from the PM-IC prediction.

Rayleigh) wave here are too wide to be visible. The phase matching method (PM-IC) based on surface paths is used for the resonance predictions. The predicted resonances marked by arrows in Fig. 10 which relate to the $1=2$ type of surface waves, are in good agreement with the peaks of the resonance response.

The results of a lake experiment for an $L/D=6.85$ end-capped hollow steel cylinder performed by NSWC Carderock are a set of amplitude responses of backscattered waves, i.e., the ''form functions.'' In Fig. 11, such ''form function'' curves are presented for the case of axial incidence. The ''form function'' curves are strongly affected by the specular wave and partly also by the waterborne creeping waves[4] (here, predominantly by the Scholte–Stoneley[13] wave). As shown in Fig. 11, the resonance modes marked by short lines are estimated by using the PM-IC method for the elastic surface wave, and those marked by solid dots are estimated as corresponding to creeping waves. Apart from one missing peak at 16 kHz, the dominant peaks largely coincide with the PM-IC predictions, while the frequency of

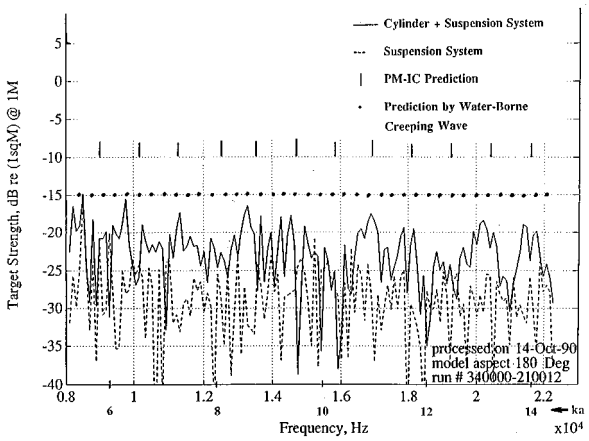

FIG. 11. The amplitude response (''form function'') of backscattering waves for a hollow steel cylinder with hemispherical end caps ($L/D=6.85$, $b/a=0.99$) at axial incidence.

the fluctuations agrees with the creeping-wave prediction, indicating here a superposition of both types of resonances.

IV. CONCLUSIONS

In this paper, problems regarding the resonance predictions for finite elastic cylinders in the case of end-on incidence are examined and discussed in some detail. By comparing the results of predictions with the results of experiments or *T*-matrix calculations, it is concluded that:

(a) Relatively speaking, the PM method is more suitable in the higher *ka* region for a solid finite cylinder. But the results also show that both methods merge in the intermediate region, where the resonances can be predicted either by the PM method or by the LBW method. This can be explained by inspecting the distribution of interior displacements of spheroids.

(b) It is important to obtain the local phase velocities accurately by using a suitable model, before the PM or LBW methods are applied. By using the ''infinite cylinder'' (PM-IC) model to replace the ''Rayleigh limit'' model on the cylinder portion of the target the PM method is improved in the intermediate *ka* region. In the high-*ka* region, both models are almost not different. The PM-IC model is also suitable for prolate spheroids in the case of relatively high aspect ratio.

(c) For the finite solid elastic cylinders, the range of the intermediate *ka* region is dependent on the acoustic parameters of the objects; it can be roughly determined in terms of the dispersion curves of infinite cylinders.

(d) For a hollow cylinder with hemispherical end caps, the phase matching method (PM-IC) results are in good agreement with the experiments for $1=2$ type waves.

[1] M. Werby and G. Tango, ''Numerical study of material properties of submerged elastic objects using resonance response,'' J. Acoust. Soc. Am. **79**, 1260–1268 (1986).

[2] M. Werby, J. Castillo, A. Nagl, R. Miller, J. D'Archangelo, J. Dickey, and H. Überall, ''Acoustic resonance spectroscopy for elastic spheroids of varying aspect ratios, and the level crossing phenomenon,'' J. Acoust. Soc. Am. **88**, 2822–2829 (1990).

[3] M. Werby and G. Gaunaurd, ''Resonance scattering from submerged elastic spheroids of high aspect ratios and its three-dimensional interpretation,'' J. Acoust. Soc. Am. **88**, 951–960 (1990).

[4] K. Williams, G. Sammelmann, D. Trivett, and R. Hackman, ''Transient response of an elastic spheroid—Surface wave and quasicylindrical modes,'' J. Acoust. Soc. Am. **85**, 2372–2377 (1989).

[5] R. Hackman, G. Sammelmann, K. Williams, and D. Trivett, ''A reanalysis of the acoustic scattering from elastic spheroids,'' J. Acoust. Soc. Am. **83**, 1255–1266 (1988).

[6] R. Hackman and D. Todoroff, ''An application of the spheroidal-coordinate-based transition matrix: The acoustic scattering from high aspect ratio solids,'' J. Acoust. Soc. Am. **78**, 1058–1071 (1985).

[7] L. Flax, L. Dragonette, V. K. Varadan, and V. V. Varadan, ''Analysis and computation of the acoustic scattering by an elastic prolate spheroid obtained from the *T* matrix formulation,'' J. Acoust. Soc. Am. **71**, 1077–1082 (1982).

[8] H. Überall, Y. Stoyanov, A. Nagl, M. Werby, S. Brown, J. Dickey, S. Numrich, and J. D'Archangelo, ''Resonance spectra of elongated elastic objects,'' J. Acoust. Soc. Am. **81**, 312–316 (1987).

[9] G. Maze, F. Lecroq, D. Décultot, J. Ripoche, S. Numrich, and H. Überall, ''Acoustic scattering from finite cylindrical elastic objects,'' J. Acoust. Soc. Am. **90**, 3271–3278 (1991).

[10] G. Maze, D. Décultot, F. Lecroq, J. Ripoche, X. L. Bao, and H. Überall, ''Resonance identification of a solid axisymmetric finite length target,'' J. Acoust. Soc. Am. **96**, 944–950 (1994).

[11] X. L. Bao and H. Überall, ''Acoustic resonances of elastic spheres and hemispherically endcapped cylinders,'' Proceedings of the Workshop on Integral and Field Equation Methods in Fluid-Structure Interactions, Dept. of Mechanical Sciences, University of Delaware, Tech. Rep. No. 90-1, 31–34 (1989).

[12] J. Niemiec (private communication).

[13] J. P. Sessarego, J. Sageloli, C. Gazanhes, and H. Überall, ''Two Scholte–Stoneley waves on doubly fluid-loaded plates and shells,'' J. Acoust. Soc. Am. **101**, 135–142 (1997).

Grazing incidence propagation over a soft rough surface

James P. Chambers, James M. Sabatier, and Richard Raspet
National Center for Physical Acoustics, University of Mississippi, University, Mississippi 38677

(Received 26 December 1995; accepted for publication 10 March 1997)

Attenborough has recently proposed [J. Acoust. Soc. Am. **98**, 1717–1722 (1995)] that the effects of surface roughness on an otherwise flat surface of finite acoustic admittance can be modeled as a smooth flat surface with an effective acoustic admittance β^*. This effective admittance is determined by the normalized admittance β_s and wave number k_s of the original smooth surface, as well as a surface roughness parameter σ_ν. Attenborough tested his theory by conducting excess attenuation measurements over plywood and Styrofoam surfaces with two-dimensional roughness elements. Specifically, he investigated the interference pattern between the direct and reflected signals over both smooth and rough surfaces. Experiments are conducted here with three-dimensional roughness elements at grazing incidence. Such a configuration is typical for outdoor sound propagation problems. The results presented here generally confirm Attenborough's model and open up the analogy to a broader class of problems. It was also found that placing the effective admittance plane at the top of the roughness elements rather than at the bottom yielded slightly better results for the higher acoustic frequencies investigated. © *1997 Acoustical Society of America.* [S0001-4966(97)01307-6]

PACS numbers: 43.20.Fn, 43.28.Fp, 43.30.Hw [LCS]

INTRODUCTION

The literature on the propagation of sound over hard rough surfaces is nearly as imposing as the literature on the propagation of sound over smooth surfaces of finite admittance (1/impedance). Less has been done on the combined problem of sound propagation over finite admittance rough surfaces although such surfaces are common in nature. Examples include agricultural fields and irregular ocean bottoms.

Howe[1] was among the first to suggest that surface roughness could be modeled as an effective admittance so that the problem could be solved as a standard flat smooth propagation problem. His analysis was for small scatterers that were sparsely packed. Tolstoy[2] as well as Medwin and D'Spain[3] analyzed the propagation of sound over flat rough surfaces at grazing incidence for steeply sloped roughness elements that were more densely packed. Their analysis was for impermeable surfaces or fluid–fluid interfaces. Attenborough[4] recently analyzed and combined all three of these works. He extended Howe's work by allowing for more arbitrary shapes than hemispherical bosses. He extended Tolstoy, Medwin, and D'Spain's work by incorporating complex impedance surfaces.

While Attenborough's work developed the model for propagation over two- and three-dimensional roughness elements, his experimental work was limited to two-dimensional surfaces such as semi-cylinders or triangular wedges. His work also had source and receiver heights of 14.5 cm with a separation of 1.0 m which yields an incidence angle of 16° from the ground. In the present work, the source is at a height of 3.5 cm and the receiver is at a height of 0.64 cm (1/4 in.) which yields incidence angles of 2° or lower for separation distances of 1.0–3.0 m. Additionally the problem investigated here is the propagation over three-dimensional rough surfaces. Both the smooth and rough surfaces investigated are made of the same material. Attenborough's model is used to determine the effective admittance of the rough surface. This effective admittance is then used in standard acoustic models for the propagation of sound over smooth finite admittance surfaces. This standard model is also used to predict the sound field over the smooth surface in these experiments. The relationship between roughness and admittance is presented in the first section, along with the model used to predict the propagation of sound over a smooth surface of finite admittance. The experimental configuration as well as a description of the relevant acoustic parameters is presented in the second section. The results are presented and analyzed in the third section.

I. THEORETICAL MODEL

For a rough finite admittance surface, Attenborough has shown that the effects of roughness can be incorporated into propagation models through the use of an effective admittance:

$$\beta_3^* = -ik_0\frac{\sigma_\nu}{2} + \beta_s(1 - ik_s\sigma_\nu), \tag{1}$$

where β_3^* is the effective admittance for a 3D roughness, k_0 is the wave number in the upper fluid, β_s is the normalized admittance, and k_s is the complex wave number of the smooth material. The roughness model was developed for protuberances, or bosses, projecting out of an otherwise smooth surface. The roughness parameter σ_ν is the volume of these roughness elements per unit area of the surface or the average height.[4]

Models for the propagation of sound over flat, smooth grounds of finite admittance have been reported extensively elsewhere.[5] A standard model for an extended reaction surface is repeated here for ease of reference. An $e^{-i\omega t}$ has been assumed and suppressed. The pressure is given as

$$\frac{p}{p_0 r_0} = \left(\frac{e^{ik_0 r_1}}{r_1} \right) + Q \left(\frac{e^{ik_0 r_2}}{r_2} \right), \tag{2}$$

where the spherical reflection factor Q is given as

$$Q = R_p + (1 - R_p) F(w), \tag{3}$$

the plane wave reflection coefficient R_p is

$$R_p = \frac{\cos(\theta) - \beta(1 - (k_0^2/k_s^2)\sin^2(\theta))^{1/2}}{\cos(\theta) + \beta(1 - (k_0^2/k_s^2)\sin^2(\theta))^{1/2}}, \tag{4}$$

the boundary loss factor $F(w)$ is

$$F(w) = 1 + i\pi^{1/2} w^{1/2} e^{-w} \operatorname{erfc}(-i\sqrt{w}), \tag{5}$$

and the numerical distance w is

$$w = \frac{i2k_0 r_2}{(1 - R_p)^2 \sin^2(\theta)} \beta^2 \left(1 - \frac{k_0^2}{k_s^2} \sin^2(\theta) \right). \tag{6}$$

In these equations, p_0 is the free-field reference pressure at a unit distance $r_0 = 1$ m for a monopole source. The path lengths r_1 and r_2 represent the direct and reflected signals, respectively, and θ is the incidence angle from the normal. In Eqs. (4) and (6), β is a dummy variable that represents the admittance of either the smooth or rough surface. Thus to solve for the propagation of sound over a rough finite impedance surface, it is necessary to determine the wave number, k_s, and admittance, β_s, for the original smooth surface, as well as the roughness parameter, σ_v. Equation (1) yields the effective admittance β_3^* which can be substituted for β in Eqs. (4) and (6) to solve for the pressure.

II. EXPERIMENTAL CONFIGURATION

In order to verify the applicability of Attenborough's model at grazing incidence over a soft surface, a set of experiments was conducted. These experiments were performed indoors in a well controlled environment to eliminate environmental factors such as wind noise and temperature gradients from the analysis. The acoustic pressure was measured for a variety of frequencies as a function of distance from the source. These experiments were conducted over smooth and rough surfaces of the same material in order to examine the combined effect of roughness and admittance as compared to the effects of the admittance alone.

The geometry of the experimental arrangement is presented in Fig. 1. The source used was an Altec driver with a horn diameter of 7.0 cm placed near the surface. A swept sine signal ranging from 500 Hz to 3.5 kHz was used as the signal. At the highest frequency the source had a nondimensional size, ka, of 2.2 which is low enough to be considered omnidirectional for the forward propagation considered here. The receiver was a 1.27-cm (1/2-in.) B&K condenser microphone. The signal was generated, received, and analyzed by an HP 35665 A signal analyzer. Measurements were made for source–receiver separations of 0.2–3.0 m in 0.2-m increments. For the smooth surface experiments the source was placed just above the surface and the receiver was laid on top of it. The center of the source was 3.5 cm above the smooth surface and the center of the receiver was at a height of 0.64 cm (1/4 in.) above the surface. For the rough surface experiments the source and receiver were at the same heights above the top of the roughness elements. These values will be used in the data prediction to follow.

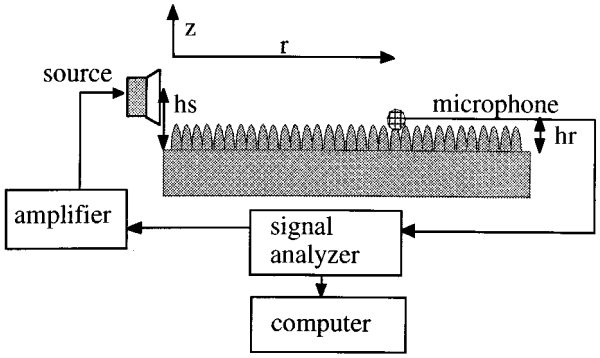

FIG. 1. Experimental configuration and geometry for the propagation of sound over smooth and rough surfaces of finite admittance.

Smooth and convoluted sheets of a partially closed cell, highly restrictive foam were used as the finite admittance surface. Two sheets of 5.1-cm (2.0-in.)-thick foam were placed on top of each other for the smooth surface experiments. A convoluted piece of foam was placed over one 5.1-cm piece of the smooth foam for the rough surface experiments. The convoluted piece had a base height of 2.5 cm and an overall height of 4.1 cm which yields a peak to trough height of 1.6 cm. The convoluted foam had semi-elliptical roughness elements and is of the type that is commonly found in shipping containers. It is also referred to as ''egg carton'' foam. The peak to trough height of 1.6 cm yields a value of 0.8 cm for the roughness parameter, σ_v. This value stems from the definition of the roughness parameter as the average volume of the roughness elements per unit area. If one were to cut the foam at a height of 0.8 cm above the bottom point the peaks would fill in the valleys.

It was found that due to its partially closed cell nature, material properties such as the flow resistivity and porosity did not yield useful measures of the acoustic impedance. Therefore, the normalized impedance of a sample of the smooth foam was determined with a B&K 4002 impedance tube by measuring the location and amplitude of the pressure maxima and minima. The samples had a diameter of either 10.5 or 3.0 cm depending on the frequency investigated. The results are presented in Fig. 2. Figure 2 also shows the predicted effective impedance of the rough surface based on Eq. 1. The real part of the effective impedance is lower than the original impedance over the entire range of frequencies. Furthermore, the reactance exceeds the resistivity which leads to the formation of a surface wave.

The acoustic wave number was calculated from the arrival of an acoustic tone burst at two microphones buried in the foam at depths of 5.1 cm (2 in.) and 10.2 cm (4 in.). The difference in the arrival times was used to evaluate the sound speed which was used to evaluate the real part of the wave number. The amplitude change was used to determine the attenuation which then determined the imaginary part of the wave number. The results of these measurements are presented in Table I. It should be recalled that the roughness parameter, σ_v, admittance, β_s, and wave number, k_s, are

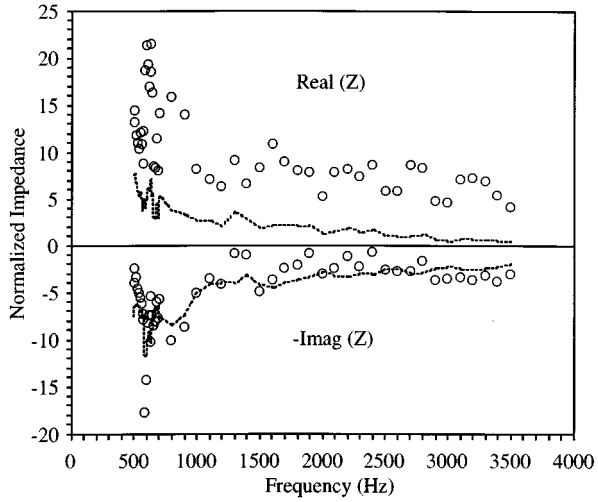

FIG. 2. Measured normalized impedance of the foam. The dotted line is the predicted effective impedance of the rough foam based on Eq. (1).

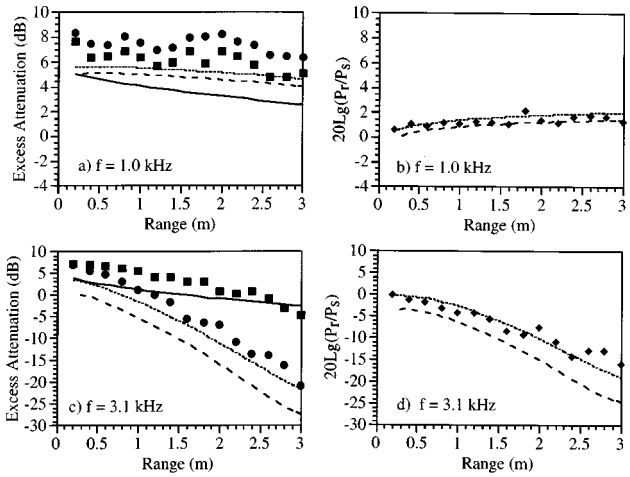

FIG. 3. Experimental data and theoretical predictions over the smooth and rough surfaces for $f=1.0$ kHz and 3.1 kHz. The data presented are the excess attenuation, (a) and (c), and a direct comparison of sound-pressure levels over the rough and smooth surfaces, (b) and (d). Solid line: smooth surface prediction ($hs=3.5$ cm and $hr=0.64$ cm). Dashed line: rough surface prediction with the admittance plane at the *bottom* of the roughness elements ($hs=5.1$ cm and $hr=2.24$ cm). Dotted line: rough surface prediction with the admittance plane at the *top* of the roughness elements ($hs=3.5$ cm and $hr=0.64$ cm). ■: Smooth surface data. ●: Rough surface data. ♦: $P_{\text{rough}}/P_{\text{smooth}}$ data.

necessary to determine the effective admittance, β_3^*, used in the propagation model.

The attenuation in the material was nominally 1 dB per cm in the frequency range of interest. This value translates into an attenuation of approximately 20 dB for any sound traveling through the material and back. Therefore it was assumed that the material was semi-infinite and the air backed bottom of the surface in the anechoic chamber was neglected. It should be noted that the foam samples used in the impedance tube were 10.2 cm thick and air backed which mimicked the experimental arrangement.

III. EXPERIMENTAL RESULTS

Figure 3(a) and (c) presents the excess attenuation over the smooth and rough surfaces for source–receiver separations from 0.2 to 3.0 m. The excess attenuation represents the propagation of sound over each surface as compared to the free-field sound-pressure level that would have existed in the absence of the surface. That is, the data have been normalized to account for spherical spreading such that the signal over a hard surface, from a source to a receiver on that surface, would consist of a straight line at 6 dB. A reference microphone at 1.0 m from the source was used before and after the experiments to capture the reference signal. Atmospheric attenuation can be neglected for the short ranges involved. Figure 3(b) and (d) shows the direct comparison of the sound-pressure level above the rough surface and the smooth surface.

In Fig. 3(a) there is little to no attenuation over the smooth surface. At a higher frequency as seen in Fig. 3(c), there is an increasing attenuation as a function of distance away from the source. Again, this attenuation is above and beyond spherical spreading and represents an excess attenuation of the signal caused by the surface. It should be noted that since the source and receiver are close to the surface, the path length differences are negligible with respect to a wavelength.

The trends in the data over the rough surface in Fig. 3(a) and (c) are similar to those in the smooth surface data. There is little to no attenuation at the lower frequency analyzed just as in the smooth surface data. In essence, the sound does not ''see'' the roughness since the wavelength is so much larger than the roughness elements. At 1.0 kHz the ratio of σ_v to λ is approximately 2%. At the higher frequency analyzed, the attenuation of the sound signal above the rough surface is greater than that above the smooth surface. At 3.1 kHz the ratio of σ_v to λ is approximately 7%. The difference in attenuation increases with increasing distance (up to approximately 15 dB in the data reported here). The attenuation can be attributed to scattering by the surface. As the propagation range increases, the sound interacts with more roughness elements which leads to greater attenuation.

Figure 3(b) illustrates that there is indeed little difference between the propagation over the rough and smooth surfaces at 1.0 kHz. There is a slight increase in the sound-pressure level over the rough surface as compared to the smooth surface which has been seen previously by Medwin *et al.*[6] and Medwin and D'Spain.[3] However, the gain here is 1 dB or less whereas the gain in the preceding works was 6 dB or more. A more significant finding is the added attenuation seen in Fig. 3(d). One can see that the presence of the roughness acts to increase the attenuation over the rough surface by as much as 15 dB.

The material parameters presented earlier have been

TABLE I. Measured wave number in foam.

Frequency, f (Hz)	Wave number, k_s (m^{-1})
600	$19.0+8.5i$
1000	$29.6+11.4i$
1500	$41.0+13.6i$
2000	$52.7+14.9i$
2500	$63.1+16.4i$
3000	$73.9+18.9i$

used in Eqs. (1)–(6) in order to predict the attenuation over the smooth and rough surfaces. These predictions are also presented in Fig. 3. The solid line is the predicted excess attenuation over the smooth surface. For propagation over the rough surface a slight subtlety arises which is where to locate the effective admittance surface. Howe[1] stated that for hemispherical bosses the effective boundary condition should be applied at a height of $\pi a^3/l^2$ above the plane containing the bosses where a is the radius of the boss and l is the center to center spacing. For the condition of sparse scatterers, which he assumed, $l \gg a$, which reduces to $\pi a^3/l^2 \approx 0$ or the bottom of the roughness elements. However, for a more closely packed configuration where, say, the bosses touch, one would have $l=2a$ and $\pi a^3/l^2 \approx a$ or the top of the roughness elements. In Fig. 3(a) and (c) the dashed line is the predicted excess attenuation for the rough surface if one assumes that the *bottom* of the roughness is the location of the admittance plane. This assumption is accomplished by adding the peak to trough height of 1.6 cm to the source and receiver heights. The dotted line is the prediction if one assumes that the *top* of the roughness is the location of the admittance plane. In Fig. 3(b) and (d) the dashed and dotted lines represent the predicted ratio of the sound-pressure levels above the rough and smooth surfaces with the same assumption concerning the location of the effective admittance plane. At the lower frequency examined it appears that placing the effective admittance surface at the bottom of the roughness yields a better fit to the data. At the higher frequency investigated it appears that a better fit is obtained by placing the effective admittance surface at the top of the roughness elements. It should be noted that if the differences in source and receiver heights associated with the location of the effective admittance plane are applied to the smooth surface prediction the effects are negligible. Therefore the differences noted are solely due to changes in the rough surface propagation.

The overall agreement between the theory and the data over the two surfaces is fairly good. The theory does not predict much attenuation over either surface at 1.0 kHz although there appears to be a consistent discrepancy between the data and the model. This discrepancy may be due to some property of the foam at grazing incidence which did not appear in the normal incidence impedance measurements. The direct comparison in Fig. 3(b), however, removes this discrepancy and yields a good agreement between the model and the data. At 3.1 kHz, the model predicts an increasing attenuation with distance for both surfaces and that the attenuation over the rough surface is greater than that over the smooth surface at long ranges. These findings are also in agreement with the data. Again there is a discrepancy between the data and the model in Fig. 3(c) which disappears when the direct comparison is made in Fig. 3(d).

Figure 4(a)–(d) presents experimental data and theoretical predictions as a function of frequency for two source–receiver separations. The symbols and line types are the same as those used in Fig. 3. The nonsmoothness of the theoretical predictions stems from the variability in the measured impedance. At lower frequencies, there is no significant difference between the propagation over smooth and rough surfaces. At higher frequencies, the sound field attenuates over both surfaces although it attenuates more markedly over the rough surface. The increasing difference between the propagation over rough and smooth surfaces occurs at lower frequencies as the range is increased. Again there is a consistent discrepancy between the data and the model for both surfaces principally centered around 2 kHz. This discrepancy disappears if one looks at the ratio of the rough to smooth surface sound pressure levels as seen in Fig. 4(b) and (d). It would appear that for the low- to mid-range frequencies, a better fit to the data is found by using the bottom of the roughness as the location of the effective admittance plane. At the higher frequencies investigated it would appear that the top of the roughness is a more suitable location for the admittance surface. This finding is somewhat clouded by the nonsmoothness of the model predictions and may be worthy of further study.

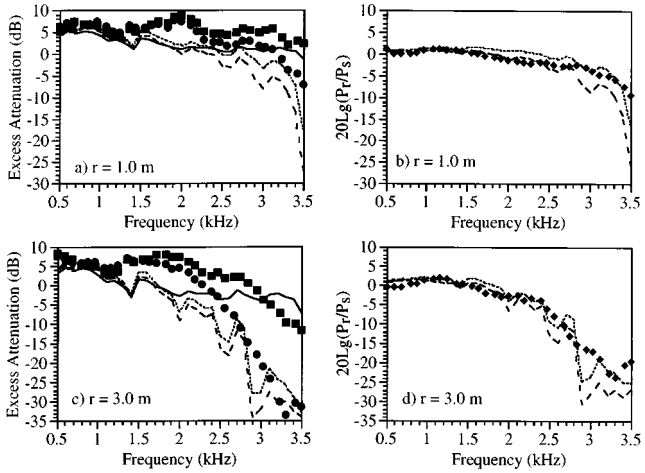

FIG. 4. Experimental data and theoretical predictions over the smooth and rough surfaces for $r=1.0$ m and 3.0 m. The data presented are the excess attenuation, (a) and (c), and a direct comparison of sound pressure-levels over the rough and smooth surfaces, (b) and (d). Solid line: smooth surface prediction ($hs=3.5$ cm and $hr=0.64$ cm). Dashed line: rough surface prediction with the admittance plane at the *bottom* of the roughness elements ($hs=5.1$ cm and $hr=2.24$ cm). Dotted line: rough surface prediction with the admittance plane at the *top* of the roughness elements ($hs=3.5$ cm and $hr=0.64$ cm). ■: Smooth surface data. ●: Rough surface data. ◆: $P_{\text{rough}}/P_{\text{smooth}}$ data.

IV. CONCLUSIONS

There is fairly good agreement between the data taken over a rough surface of finite admittance and the model proposed by Attenborough to treat the rough surface as a smooth surface with a modified surface admittance. Some discrepancies were found between the measured data and model predictions over both the smooth and rough surfaces examined. These discrepancies disappeared when the ratio of the sound-pressure level over the rough surface was compared directly to that over the smooth surface. The roughness causes an attenuation in the sound field that is greater than (or comparable to) that found over a smooth surface of the same material. This additional attenuation increases with increasing distance and/or frequency. A boundary wave that exceeds the amplitude of the direct wave by 6 dB or more, such as that found by Medwin and D'Spain[3] for hard sur-

faces, was not seen for this softer surface. At higher frequencies, there was better agreement between the model and the experimental data when the top of the roughness was defined as the location of the admittance plane rather than the bottom of the roughness as indicated by Attenborough.

The prospect that the analogy between roughness and admittance holds is quite appealing in terms of practical prediction routines. Existing models for predicting noise levels for outdoor sources, such as highways, could easily be extended to more realistic surfaces. A further extension of the work would be the inverse problem of determining the roughness scale from the acoustic signal. Such a procedure would have many useful applications ranging from agricultural research in erosion control to mineral nodule detection on the ocean floor.

ACKNOWLEDGMENTS

The authors would like to acknowledge financial support from the USDA-ARS National Sedimentation Laboratory. The authors would also like to thank Keith Attenborough, Craig Hickey, and Gordon Smith for their useful insights and help in determining material parameters.

[1] M. S. Howe, ''On the long range propagation of sound over irregular terrain,'' J. Sound Vib. **98**, 83–94 (1985).
[2] I. Tolstoy, ''Smoothed boundary conditions, coherent low-frequency scatter, and boundary modes,'' J. Acoust. Soc. Am. **75**, 1–22 (1984).
[3] H. Medwin and G. L. D'Spain, ''Near-grazing, low-frequency propagation over randomly rough, rigid surfaces,'' J. Acoust. Soc. Am. **79**, 657–665 (1986).
[4] K. Attenborough and S. Taherzadeh, ''Propagation from a point source over a rough finite impedance boundary,'' J. Acoust. Soc. Am. **98**, 1717–1722 (1995).
[5] T. F. W. Embleton, J. E. Piercy, and G. A. Daigle, ''Effective flow resistivity of ground surfaces determined by acoustical measurements,'' J. Acoust. Soc. Am. **74**, 1239–1244 (1983).
[6] H. Medwin, G. L. D'Spain, E. Childs, and S. J. Hollis, ''Low-frequency grazing propagation over periodic steep sloped rigid roughness elements,'' J. Acoust. Soc. Am. **76**, 1774–1790 (1984).

Acoustic scattering by nonmetallic and metallic cubes in the elastic resonance regime: Experimental measurements and combined finite element/boundary element modeling

Paul A. Chinnery,[a] Jingdong Zhang, and Victor F. Humphrey
School of Physics, University of Bath, Bath BA2 7AY, United Kingdom

(Received 11 November 1996; accepted 11 March 1997)

The acoustic backscattering behavior of both nonmetallic (glass) and metallic (steel) cubes has been investigated over a wide frequency range where elastic resonances are important in determining the acoustic response of the cubes. A laboratory system incorporating a parametric array was used to make measurements between 20 and 200 kHz using cubes of side (l) 20 mm, and a combined finite element/boundary element code was used to numerically model scattering by the cubes. The frequency range covered corresponds to ka values up to 10, where $a=l(3/4\pi)^{1/3}$ is a characteristic dimension of the cube. Results are presented for three scattering geometries involving incidence on to a face, an edge, and a corner. The backscattered form function differs greatly for the different geometries and is seen to depart significantly from that of a rigid cube when $ka>5$ due to the elastic resonances of the cube. The resonance contributions are clearly seen when the rigid background is subtracted from the elastic predictions.
[S0001-4966(97)01807-9]

PACS numbers: 43.20.Fn, 43.30.Gv, 43.30.Lz [ANN]

INTRODUCTION

Scattering of acoustic waves by discrete elastic objects is of interest in many fields and has been studied extensively for regular idealized targets such as spheres and cylinders. However, the more realistic scattering objects found in the marine environment are usually of a more complex geometry, often having facets, edges, and corners. Objects possessing such features include both irregularly shaped particles that occur naturally, and more regular, but nevertheless complex, manmade objects. The scattering by faceted objects is important in sedimentology where acoustic backscattering measurements are used to monitor the concentration and transport of suspended sediment in the marine environment.[1–5]

Analytical models are not generally capable of predicting the scattering characteristics of such complex targets, and so numerical methods must be used. The ever increasing power of computing facilities means that techniques such as finite element and boundary element methods can potentially provide detailed scattering information for very complicated geometries, and will increasingly be used to investigate fluid–structure interaction problems. Experimental validation of such models is therefore vitally important.

One relatively simple faceted geometry is the cube. In a previous paper[6] the low-frequency ($ka<5$) backscattering behavior of a metallic cube was investigated. At these frequencies the elastic behavior of the particle is not particularly significant and the cube could be modeled as a rigid body using a boundary element approach. The results, when averaged over a large number of cube orientations, indicated that the form function was very similar in appearance to that of a sphere, and also showed evidence for the propagation of surface waves around the cube. In this paper we deal with a higher-frequency regime (up to ka values of 10) where the elastic behavior of the body is important (manifesting itself as resonances) and significant differences exist between cubes of different materials. As sand is significant for sediment studies, a fused-silica glass cube was chosen as a suitable nonmetallic material to compare with a steel cube. A combined finite element/boundary element model has been used to predict the acoustic backscattering properties of the cubes and laboratory measurements have been made using a low-frequency parametric array facility. Results are presented for three different scattering geometries and the measurements are compared with numerical predictions of the backscattered form function for elastic and rigid cubes. The influence of the elastic resonances is isolated by subtracting the rigid predictions from those for the elastic cubes.

I. SCATTERING CONFIGURATIONS

The backscattering properties of both glass and steel cubes were studied using cubes of side (l) 20 mm, over the frequency range 20–200 kHz, corresponding to a ka range of approximately 1–10, where $a=l(3/4\pi)^{1/3}$ is a characteristic dimension of the cube (equaling the radius of a sphere having the same volume). Three scattering geometries were used, as illustrated in Fig. 1. For configuration (a) the cube was aligned so that the wavefield was normally incident on a face. For configuration (b) the cube was aligned so that the wavefield was normally and symmetrically incident on an edge. In the third configuration (c) the cube was aligned for incidence on a corner, the acoustic axis passing through a body diagonal. All three geometries can be realized by rotating the cube shown in Fig. 1(b) about a vertical axis passing

[a]Present address: Winfrith Technology Centre, Winfrith, Newburgh, Dorchester, Dorset DT2 8X5, UK.

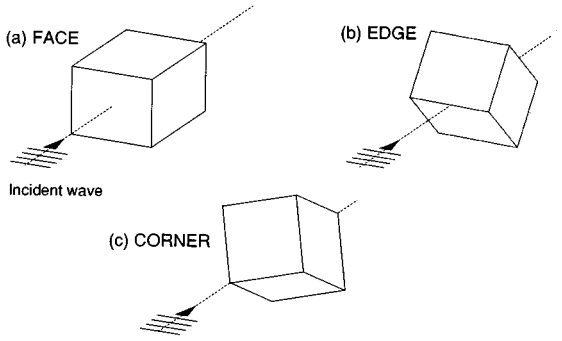

FIG. 1. Scattering geometries. Wave is incident normal to a face (a), an edge (b), and a corner (c).

through the centers of two opposite edges. In this case rotations of 0°, 35.26°, and 90° give edge, corner, and face incidence, respectively.

II. EXPERIMENTAL SYSTEM AND MEASUREMENT TECHNIQUE

A laboratory facility (Fig. 2) incorporating a parametric array[7] was used to make the experimental measurements. A conventional transducer generates high-amplitude high-frequency waves which propagate nonlinearly through the water and interact to produce additional low-frequency signals.[8,9] The nonlinear generation is a continuous process and the low-frequency waves can be considered to come from secondary sources distributed throughout the interaction region of the primary waves. The distributed nature of the secondary sources, and their phases, produces a behavior similar to that of an endfire array and results in an exceptionally narrow beam. The parametric source is used to generate a broadband pulse whose frequency content is easily varied by changing the primary frequencies transmitted by the transducer.

The use of such a source permits low ka measurements to be made on scattering targets of reasonably large size, over a broad frequency (ka) range, with a single transmitting transducer and a single target. Brief details of the measurement technique are given here; further details can be found in Refs. 6 and 7.

The parametric array was truncated by an acoustic filter in order to isolate a source-free region in the tank in which

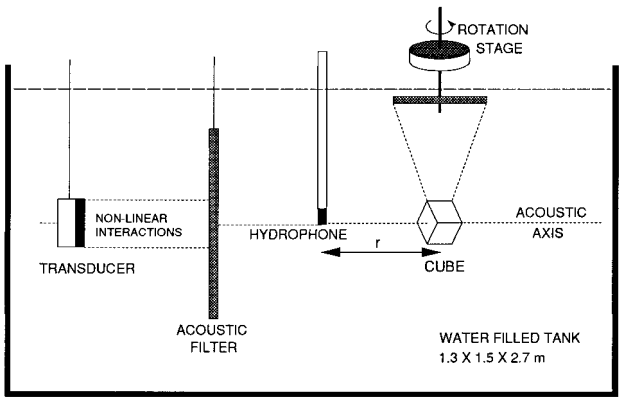

FIG. 2. Laboratory system incorporating parametric array.

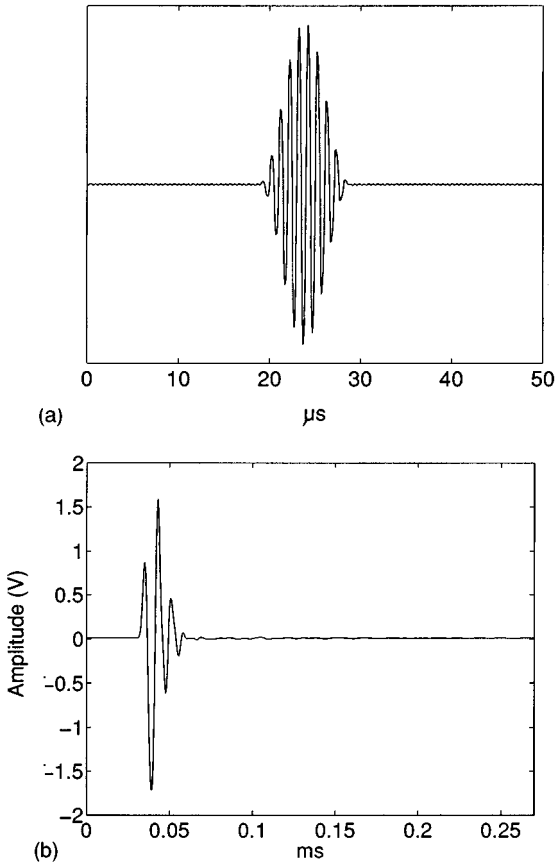

FIG. 3. Generation of the low-frequency pulse: (a) modulated tone burst applied to the transducer (raised cosine bell based on 100 kHz); (b) demodulated pulse after passage through receiving system.

measurements could be made without problems associated with the nonlinear response of the hydrophone or the interaction of the primary waves with the test cube itself. The transducer, acoustic filter, hydrophone, and test cube were all suspended from an optical bench aligned along the length of the tank and parallel to the acoustic axis of the transducer, allowing the positions of the components to be easily varied.

An amplitude modulated tone burst [Fig. 3(a)] was used to drive the transducer. The modulating envelope used in the present study was a ''raised cosine-bell,'' obtained by adding a dc offset to a single-cycle phase-shifted cosine wave. The resulting demodulated pulse generated by the parametric array has a spectrum which is easily altered by adjusting the length and shape of the modulating envelope, allowing an extended frequency range to be covered. An example of the resulting demodulated pulse (after passage through the receiving system) is shown in Fig. 3(b).

The signal detected by the hydrophone (Brüel & Kjær 8103) was passed through a passive low-pass (250-kHz) filter and a signal amplifier (Brookdeal 9452) before being digitized by a LeCroy 9310A digital oscilloscope. The frequency range 20–200 kHz of interest here was covered by using three pulses based on modulating envelopes of 20, 50, and 100 kHz.

The test cube was suspended from a rotation stage by nylon thread and careful adjustments of the vertical and horizontal position were used to orientate the cube accurately on

the acoustic axis. The hydrophone was placed at a distance (r) of 275 mm from the center of the test cube (see Fig. 2). The parametric array was truncated by the acoustic filter at a distance of 0.53 m from the transducer and the test cube was suspended at 1.02 m.

In order to make accurate measurements of the scattered field it was necessary to remove the effect of any coherent reverberation using the following technique. First the total field in the backscatter position was measured at a fixed distance (r) from the center of the test cube (Fig. 2). Then the cube was removed and the ''background'' reverberation signal measured with the hydrophone in the same position. This background signal was then subtracted from the total signal, leaving only the backscattered signal due to the cube. Finally, the incident (or ''reference'') signal was measured by moving the hydrophone to the position at the center of the cube (with the cube absent) and rotating the hydrophone by 180° to compensate for any directionality of the hydrophone.

The averaged signals were windowed to remove unwanted multiples, and Fourier transformed to obtain their spectra. The resulting backscattered spectrum (with background reverberation subtracted) and reference spectrum were used to calculate the normalized form function (Sec. IV).

III. NUMERICAL CALCULATIONS

At the frequencies considered in this paper it is not adequate to consider the cube to be rigid as its elastic response becomes significant. There are several analytical and numerical methods available for dealing with the problem of acoustic wave scattering from elastic fluid-immersed bodies. However, analytic solutions in terms of standard functions can be found only for a limited number of geometrical shapes such as spheres, infinite cylinders, and spheroids. Numerical methods must therefore be used to solve the problem of scattering from more complex geometries such as the cube. There are three popular methods capable of solving the scattering problem: the T-matrix method, the finite element method, and a combined finite element/boundary element method. The T-matrix is an efficient method for the scattering problem but it cannot easily deal with scatterers having corners, edges, or large aspect ratios, because of the poor convergence in such cases. A finite element model, where the cube and surrounding fluid are all modeled using finite elements, is not efficient for backscattering problems because such a method gives the solution for the whole field, not just at the points of interest. This is inefficient if only the backscattered pressure is required. Also, the wave reflected from the outer boundary of the fluid volume in the finite element model may give rise to errors because of the imperfect nature of the absorbing boundary condition.

A combined finite element and boundary element method is a very powerful method for scattering problems involving scatterers that have a size comparable with the acoustic wavelength, in an infinite fluid medium. In this case finite elements are used to describe the structural vibration, and boundary elements are used to describe the acoustic behavior of the infinite fluid. The commercial software package PAFEC[10] was used for this study as it is capable of dealing with the coupling between the elastic vibration of the structure and the acoustic fluid using such a combined finite element/boundary element approach.

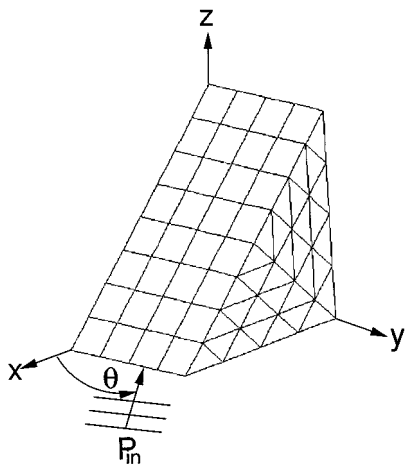

FIG. 4. Finite element meshing of an eighth of the elastic cube.

In order to construct the finite element mesh the three plane-wave scattering configurations shown in Fig. 1 were considered. As discussed in Sec. I, each of the three orientations can be obtained by aligning the cube as shown in Fig. 1(b) and changing the angle of the incident plane wave. Therefore it was only necessary to build a combined finite element/boundary element model for calculating the backscattered field for configuration (b) and rotate the incident plane wave to the three angles 0°, 35.26°, and 90°.

The accuracy of the calculated scattered pressure in such a model is largely dependent on the mesh density used. In practice, the maximum usable mesh size is limited by the wavelength in the fluid because the velocity of elastic waves in the solid are generally larger than those in the fluid. Using the PAFEC code, an acceptable accuracy was achieved by using five elements per wavelength if ten-noded triangle or twenty-noded quadratic elements were used. Although a nonuniform mesh (with a fine mesh near the surface of the structure and a coarse mesh inside) could reduce the number of elements, this was not easily achieved with PAFEC, and so a uniform mesh was used throughout the elastic structure. The upper frequency range of interest here is 200 kHz for a cube with a sidelength of 20 mm. In order to run the numerical model efficiently, the whole frequency range was divided into four subfrequency ranges. In each subfrequency range the numerical model was built using three elements per half-sidelength in the frequency range 3–60 kHz, four elements per half-sidelength in the range 62–100 kHz, five elements per half-sidelength in the range 102–160 kHz, and six elements per half-sidelength in the range 162–200 kHz. A frequency step of 2 kHz was used throughout. Although symmetry in the $z=0$ plane (Fig. 4) was exploited to halve the size of the numerical model, the calculations (on a PC) were still very computationally intensive as the frequency approached 200 kHz. By examining configuration (b) carefully [Figs. 1(b) and 4], it is noted that the cube itself is symmetrical about planes $x=0$, $y=0$, and $z=0$, but that the incident plane wave is only symmetrical about the $y=0$ and $z=0$

TABLE I. Symmetry of boundary conditions on the $x=0$ and $y=0$ planes for the eighth cube (see Fig. 4) used in the numerical model. The boundary condition on the $z=0$ plane is always symmetric.

Case	0°	35.26°	90°
1	$x=0$ symmetric $y=0$ symmetric	$x=0$ symmetric $y=0$ symmetric	$x=0$ symmetric $y=0$ symmetric
2	$x=0$ antisymmetric $y=0$ symmetric	$x=0$ antisymmetric $y=0$ symmetric	
3		$x=0$ symmetric $y=0$ antisymmetric	$x=0$ symmetric $y=0$ antisymmetric
4		$x=0$ antisymmetric $y=0$ antisymmetric	
Final result	1/2*(case 1+case 2)	1/4*(case 1+case 2 +case 3+case 4)	1/2*(case 1+case 3)

planes for an incident angle (θ) of 0°; symmetrical about $x=0$ and $z=0$ for 90° incidence, and about $z=0$ for an angle of 35.26°. Therefore it is only necessary to model an eighth of the cube, subject to a group of combining symmetric/antisymmetric conditions (see Fig. 4 and Table I). Using this approach the size of the numerical model was greatly reduced (from a half-cube to an eighth-cube) and the calculations were carried out efficiently on a pentium PC.

IV. FORM FUNCTION OF A CUBE

The field scattered by the cube is expressed in a normalized dimensionless form using the ''form function.'' The form function for spherical scatterers is a well known and much used expression in which the scattered pressure is normalized by the size of the sphere, the observation range, and the incident pressure.

From considerations involving the power in the incident wave intercepted by the cube and the scattered power the form function for a general three-dimensional scatterer can be defined as[6]

$$f(r,\theta,\phi)=\sqrt{\frac{4\pi r^2}{A}}\frac{P_{\mathrm{sc}}(r,\theta,\phi)}{P_{\mathrm{in}}}, \tag{1}$$

where P_{in} and P_{sc} are the incident and scattered signals, respectively, A is the projected cross-sectional area of the scatterer, and r is the distance from the particle to the observation point. For a sphere, the cross section does not vary with the orientation of the sphere ($A=\pi a^2$, where a is the sphere radius) and Eq. (1) reduces to

$$f(r,\theta)=\frac{2r}{a}\frac{P_{\mathrm{sc}}(r,\theta)}{P_{\mathrm{in}}}. \tag{2}$$

However, the projected cross section of a cube varies with orientation and so we must use the *average* cross section to normalize the form function (1). The average projected cross-sectional area ($\langle A\rangle$) of any body equals a quarter of the body's surface area. Thus for a cube of side l, $\langle A\rangle = 3l^2/2$ and the form function becomes

$$f(r,\theta,\phi)=\frac{2r}{l\sqrt{3/2\pi}}\frac{P_{\mathrm{sc}}(r,\theta,\phi)}{P_{\mathrm{in}}}, \tag{3}$$

which is equivalent to Eq. (2) with a value of a equal to $l\sqrt{(3/2\pi)}$, i.e., the radius of the sphere having the same *surface area* as the cube. Both the measured and predicted backscattered pressures are expressed using this normalized form function.

V. RESULTS

Experimental measurements and theoretical predictions were made using both fused-silica glass and steel cubes of side 20 mm; the material parameters used in the calculations are shown in Table II. In the calculations presented here, the backscattered field was evaluated at a distance of 0.2 m from the center of the cube. The incident plane wave was of unit amplitude.

For each of the three configurations illustrated in Fig. 1 measurements were made with pulses based on 20-, 50-, and 100-kHz envelopes. Examples of the scattered time waveforms obtained for the glass cube are shown in Fig. 5 for a 100-kHz incident pulse [Fig. 3(b)]. The strongest reflection is seen for configuration (a), the case of incidence normal to a cube face. Figure 5(b) and (c) shows the scattered time

TABLE II. Material parameters for the cubes and surrounding fluid. Young's modulus (E); Poisson's ratio (σ); density (ρ); compressional (c_l) and shear (c_t) wave velocities; loss (δ)—the ratio of real and imaginary parts of E. Data for fused–silica glass taken from Ref. 15 and steel from Ref. 16. Values of δ are estimates.

Material	E/(GPa)	σ	ρ/(kgm^{-3})	c_l/(m s^{-1})	c_t/(m s^{-1})	δ
Glass	72.9	0.17	2200	5968	3764	0.02
Steel	196.0	0.3	7910	5790	3100	0.01
Water			1000	1490		

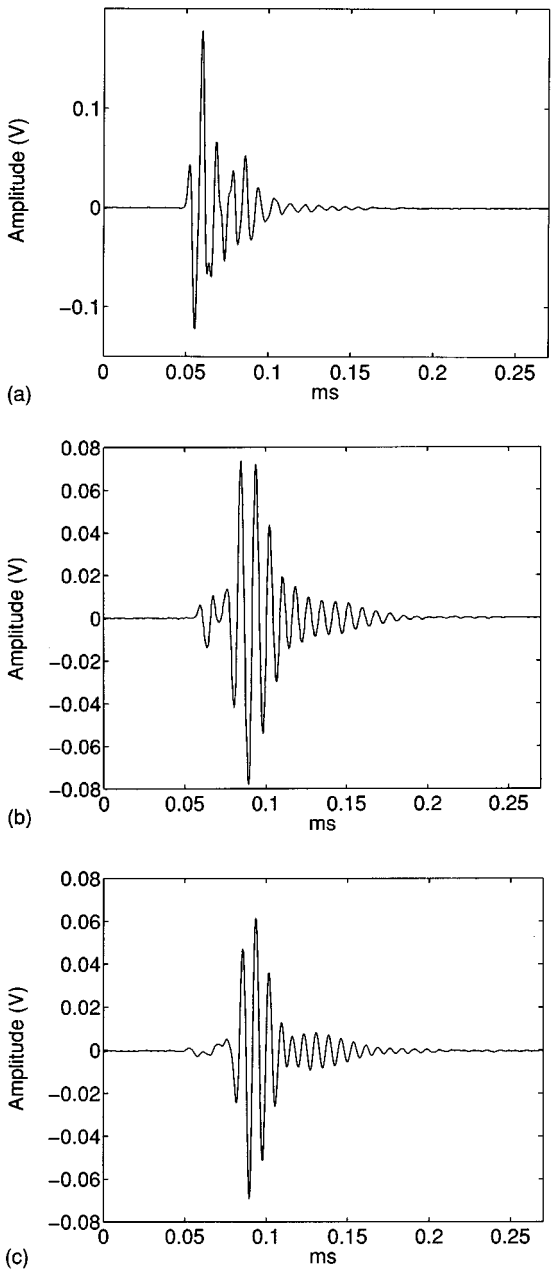

FIG. 5. Measured backscattered waveforms for a fused–silica glass cube of side 20 mm. Incidence normal to (a) face, (b) edge, and (c) corner. Incident pulse [shown in Fig. 3(b)] is based on a 100-kHz modulating envelope.

waveform when the wave is incident on a cube edge and a corner (note the change of vertical scale). Note also the apparent precursor in these cases.

These measured time waveforms were processed as described above and the form functions calculated. Results for the glass cube are presented in Fig. 6(a)–(c), which shows the variation of the form function with frequency for the three configurations shown in Fig. 1. The form function (y axis) is normalized using the average projected cross-sectional area of the cube [Eq. (3), Sec. IV] and the normalized frequency axis is ka, where a is the radius of the sphere having the same volume. Agreement is exceptionally good over all frequencies suggesting the elastic behavior is modeled correctly. The case of incidence normal to a face, shown in Fig. 6(a), exhibits a steady increase in backscattered pressure with frequency. The results for configurations (b) and (c) [Fig. 6(b) and (c)] show significantly different behavior, and, in general, lower backscatter.

Results for a stainless steel cube are shown in Fig. 7(a)–(c) for comparison. At low frequencies ($ka<5$) the steel cube behaves in a similar way to the glass cube. Above ka values of about 5 the resonance behavior is quite different, with the resonances notably narrower than those for glass.

VI. DISCUSSION

It is important to note the very good agreement obtained between experiment and theory. This indicates that the numerical model is able to cope with the elastic response of the cube, and more significantly, the boundary element approach accurately models the effects of the cube edges on the scattered wavefield. The agreement also indicates the power and precision of the experimental facility for making accurate scattering measurements in both the low and high ka regions.

At the highest frequencies considered the measurements appear to underestimate the scattered pressure, but only for configuration (a). This may well be a result of the incident field not being planar, an effect observed to affect scattering from other structures, or may result from slight errors in the orientation of the cube which is most significant for this configuration.

For the steel cube a number of elastic resonances are clearly visible for $ka>5$. Which resonances are important, and the extent to which they are excited appears to depend on the direction of incidence. Thus a pronounced resonance is observed in Fig. 7(b) at $ka=4.8$ that is not apparent in Fig. 7(a).

Many of the features observed in the form function of both the glass and steel cubes result from elastic resonances of the bodies. Resonance scattering theory[11] describes the backscattered field as being composed of a spectrum of resonances superimposed on a more gently varying background due to a rigid scatterer. In order to see the resonance contribution more clearly the rigid background can be subtracted, leaving just the elastic contribution. To do this the complex backscattered form function for a *rigid* cube was calculated using the boundary element technique, as described in Ref. 6. Results for both calculations and their difference are presented in Fig. 8 for glass (a) and steel (b) cubes insonified normal to a face.

For steel the rigid and elastic calculations give very similar results up to a ka of 5. This is to be expected from the high impedance of the cube. The subtraction shows a small broad peak centred on a ka of 1.5; this is attributed to the fact that the rigid calculation assumes that the cube is fixed while the elastic result allows the cube to be mobile. A similar difference is observed for spheres. Between $ka=5$ and $ka=10$ several distinct elastic resonances can be seen.

For the glass cube a slightly larger deviation from the rigid results is seen for low ka values, with the more mobile glass giving a higher difference around $ka=1.5$. In this case the resonances at higher ka are broader and not easily sepa-

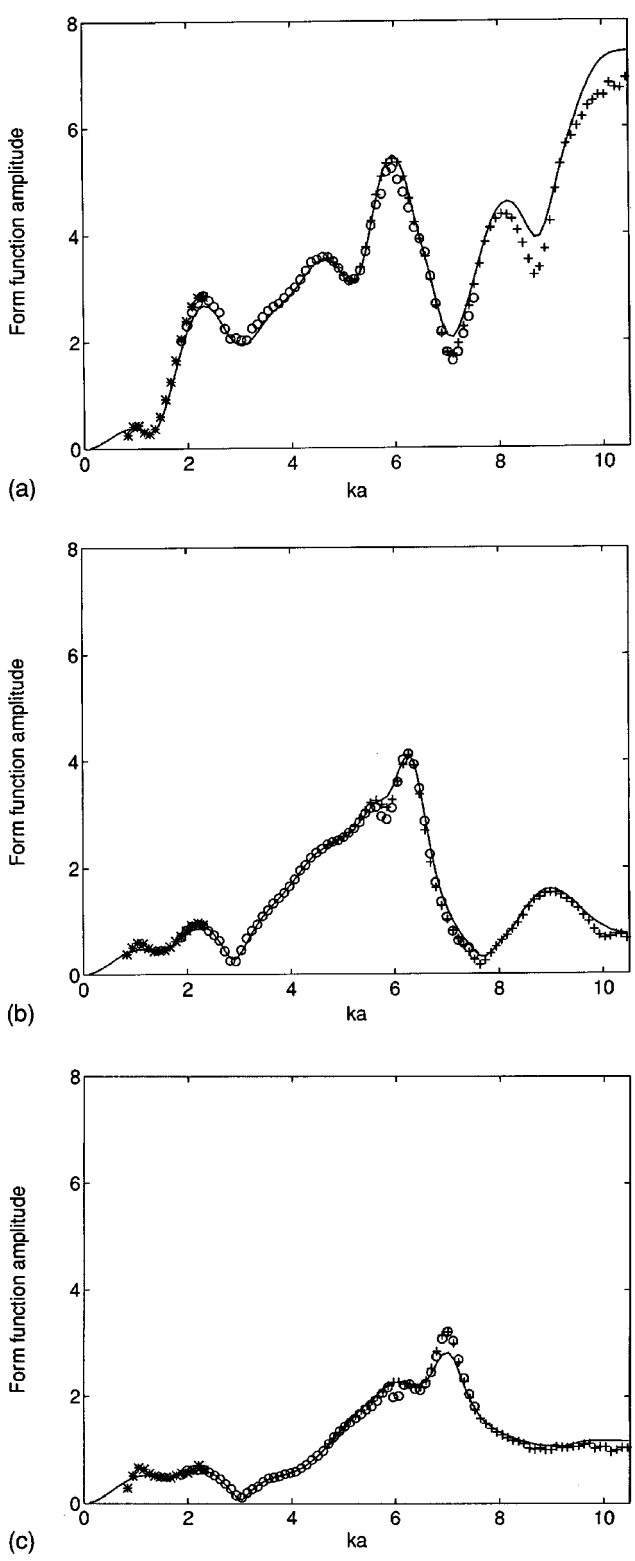

FIG. 6. Backscattered form function for a fused–silica glass cube insonified normal to a face (a), an edge (b), and a corner (c). Numerical predictions (line) and experimental measurements (points) obtained using pulses based on 20-kHz (*), 50-kHz (◦), and 100-kHz (+) envelopes.

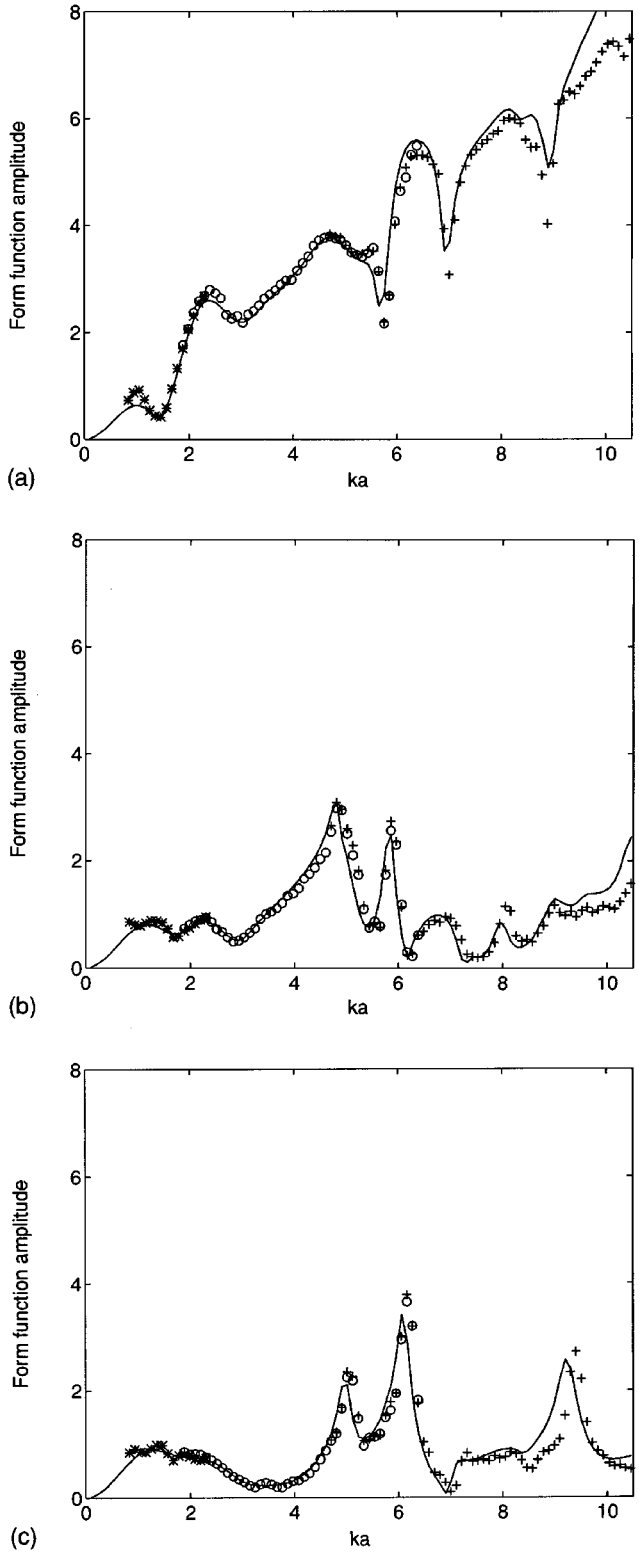

FIG. 7. Backscattered form function for a steel cube isonified normal to a face (a), an edge (b), and a corner (c). Numerical predictions (line) and experimental measurements (points) obtained using pulse based on 20-kHz (*), 50-kHz (◦), and 100-kHz (+) envelopes.

rated. This is presumably a result of the more significant water loading of the resonances for the glass cube.

The clear resonant structure observed in Fig. 8(b) suggests that it should be possible to associate this pattern with elastic resonances of the cube. A number of authors[12–14] have considered the free-vibrational modes of an elastic cube and produced results for the resonance mode shapes and frequencies. It is not, however, clear as to how these resonances will be affected by water loading. This, together with some variation in the predicted frequencies and the number of dif-

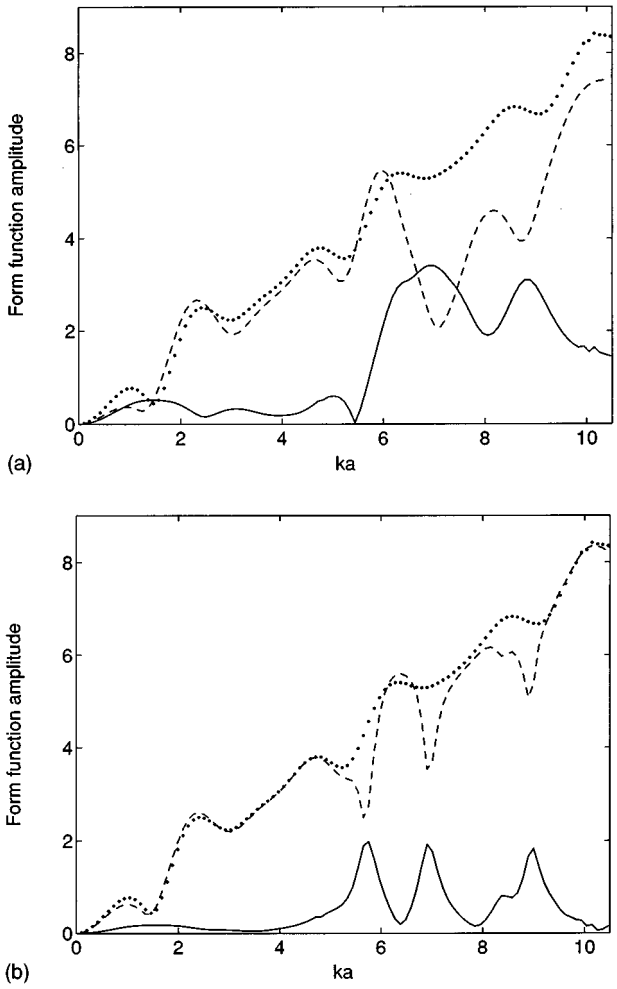

FIG. 8. Elastic resonance contribution to the backscattered form function for glass (a) and steel (b) cubes insonified normal to a face [Fig. 1(a)]. Rigid cube (.....); elastic cube (----); (complex) subtraction (———).

ferent modes possible, make it difficult to identify all of the resonances seen in Fig. 8(b) unambiguously. However, further calculations should help solve some of this uncertainty and help to explain the different strengths of the resonance peaks in Fig. 7(a)–(c).

VII. CONCLUSIONS

The backscattering properties of glass and steel cubes have been investigated both experimentally and theoretically over a ka range of 1–10. Results have been presented for several different orientations of the cube and good agreement between experiment and theory observed. At low frequencies ($ka<5$) the form functions for each orientation are very similar to those of a rigid cube[6] but at higher frequencies elastic resonances become important and significant deviations from rigid scattering behavior are observed. In this resonance dominated region the glass and steel cubes behave differently, the glass cube having resonances that are broader than those of the steel. The very good agreement obtained between measurements and numerical predictions validates the combined finite element/boundary element approach used and indicates the power of the experimental measurement technique.

ACKNOWLEDGMENTS

We would like to thank Peter Thorne of the Proudman Oceanographic Laboratory, Bidston Observatory, for many useful discussions having a bearing on this work, and for the interest shown in these studies. We are also grateful to PAFEC Ltd. for assistance in the provision of software for these calculations. This work was partially supported by the European Community under its MAST program, contract MAS3-CT95-0017 (TRIDISMA).

[1] J. Sheng and A. E. Hay, ''An examination of the spherical scatterer approximation in aqueous suspensions of sand,'' J. Acoust. Soc. Am. **83**, 598–610 (1988).
[2] A. M. Crawford and A. E. Hay, ''Determining suspended sand size and concentration from multifrequency acoustic backscatter,'' J. Acoust. Soc. Am. **94**, 3312–3324 (1993).
[3] P. D. Thorne, P. J. Hardcastle, and R. L. Soulsby, ''Analysis of acoustic measurements of suspended sediments,'' J. Geophys. Res. **98**, 899–910 (1993).
[4] P. D. Thorne, K. R. Waters, and T. J. Brudner, ''Acoustic measurements of scattering by objects of irregular shape,'' J. Acoust. Soc. Am. **97**, 242–251 (1995).
[5] P. D. Thorne, S. Sun, J. D. Zhang, I. Bjørnø, and T. Mazoyer, ''Measurements and analysis of acoustic backscattering by elastic cubes and irregular polyhedra,'' J. Acoust. Soc. Am. (submitted).
[6] P. A. Chinnery, V. F. Humphrey, and J. D. Zhang, ''Low-frequency acoustic scattering by a cube: Experimental measurements and theoretical prediction,'' J. Acoust. Soc. Am. **101**, 2571–2582 (1997).
[7] V. F. Humphrey, ''The measurement of acoustic properties of limited size panels by use of a parametric source,'' J. Sound Vib. **98**, 67–81 (1985).
[8] P. J. Westervelt, ''Parametric acoustic array,'' J. Acoust. Soc. Am. **35**, 535–537 (1963).
[9] H. O. Berktay, ''Possible exploitation of nonlinear acoustics in underwater transmitting applications,'' J. Sound Vib. **2**, 435–461 (1965).
[10] PAFEC VibroAcoustics, from Pafec Ltd., Strelley Hall, Nottingham N68 6PE, UK.
[11] N. D. Veksler, *Resonance Acoustic Spectroscopy* (Springer-Verlag, New York, 1993).
[12] K. M. Liew, K. C. Hung, and M. K. Lim, ''Free vibration studies on stress-free three-dimensional elastic solids,'' ASME J. Appl. Mech. **62**, 159–165 (1995).
[13] J. R. Hutchinson and S. D. Zillmer, ''Vibration of a free rectangular parallelepiped,'' J. Appl. Mech. **50**, 123–130 (1983). See also Errata **51**, 453.
[14] H. Ekstein and T. Schiffman, ''Free vibrations of isotropic cubes and nearly cubic parallelepipeds,'' J. Appl. Phys. **27**, 405–512 (1956).
[15] Kaye and Laby, *Tables of Physical and Chemical Constants* (Longman, London, 1986), 15th ed.
[16] *American Institute of Physics Handbook*, edited by D. E. Gray (McGraw-Hill, New York, 1972), 3rd ed.

On the derivation of boundary integral equations for scattering by an infinite one-dimensional rough surface

J. A. DeSanto and P. A. Martin[a)]
Department of Mathematical and Computer Sciences, Colorado School of Mines, Golden, Colorado 80401-1887

(Received 24 June 1996; revised 10 December 1996; accepted 29 January 1997)

A crucial ingredient in the formulation of boundary-value problems for acoustic scattering of time-harmonic waves is the radiation condition. This is well understood when the scatterer is a bounded obstacle. For plane-wave scattering by an infinite, rough, impenetrable surface S, the physics of the problem suggests that all scattered waves must travel away from (or along) the surface. This condition is used, together with Green's theorem and the free-space Green's function, to derive boundary integral equations over S. This requires careful consideration of certain integrals over a large semicircle of radius r; it is known that these integrals vanish as $r\to\infty$ if the scattered field satisfies the Sommerfeld radiation condition, but that is not the case here—reflected plane waves must be present. The integral equations obtained are Helmholtz integral equations; they must be modified for grazing incident waves. As such integral equations are often claimed to be exact, and are often used to generate benchmark numerical solutions, it seems worthwhile to establish their validity or otherwise. © *1997 Acoustical Society of America.* [S0001-4966(97)01406-9]

PACS numbers: 43.20.Fn, 43.30.Hw [ANN]

INTRODUCTION

Consider the scattering of a plane time-harmonic acoustic wave by a bounded obstacle. To fix ideas here, we consider a two-dimensional obstacle, with a smooth, sound-hard surface S. Mathematically, this is an exterior Neu mann problem for the Helmholtz equation. In order to have a well-posed problem, we impose the Sommerfeld radiation condition,

$$\sqrt{r}\left(\frac{\partial u}{\partial r}-iku\right)\to 0 \quad \text{as } r\to\infty, \tag{1}$$

uniformly in all directions. Here, u is the scattered field, r is a plane polar coordinate, k is the wave number, and we have assumed a time dependence of $e^{-i\omega t}$. Physically, the radiation condition ensures that the scattered waves propagate outwards, away from the obstacle. Mathematically, the radiation condition also yields uniqueness and existence for the boundary-value problem.

A familiar method for solving the above problem is to derive a boundary integral equation for the boundary values of u on S. In the derivation, Green's theorem is applied to u and a fundamental solution G, in the region bounded internally by S and externally by C_r, a large circle of radius r. It turns out that the radiation condition implies that the integral

$$I(u;C_r)\equiv\int_{C_r}\left(u\frac{\partial G}{\partial r}-G\frac{\partial u}{\partial r}\right)ds\to 0 \quad \text{as } r\to\infty, \tag{2}$$

and so only boundary integrals over S remain. Thus, the radiation condition is a crucial ingredient for two results: a well-posed boundary-value problem; and the vanishing of a standard integral over a large circle. See Colton and Kress (1983) for more information.

For a sound-hard surface S, the procedure described above leads to the following boundary integral equation:

$$u(p)-\int_S u(q)\frac{\partial G}{\partial n_q}(p,q)\,ds_q=\int_S\frac{\partial u_{\text{inc}}}{\partial n_q}G(p,q)\,ds_q, \qquad p\in S, \tag{3}$$

here, u_{inc} is the given incident wave. One can also derive an equation for the boundary values of the total field $u_{\text{tot}}=u_{\text{inc}}+u$; this boundary integral equation is

$$u_{\text{tot}}(p)-\int_S u_{\text{tot}}(q)\frac{\partial G}{\partial n_q}(p,q)\,ds_q=2u_{\text{inc}}(p), \quad p\in S. \tag{4}$$

We shall refer to (3) and (4) as *standard Helmholtz integral equations*. Similar equations can be derived for sound-soft surfaces (exterior Dirichlet problem, $u_{\text{tot}}=0$ on S).

Now, it is known that the waves scattered by a bounded two-dimensional obstacle have the form

$$u(r,\theta)=\frac{e^{ikr}}{\sqrt{r}}f(\theta)+O(r^{-3/2}) \quad \text{as } r\to\infty, \tag{5}$$

where (r,θ) are plane polar coordinates, and f is called the far-field pattern. Thus, apart from being outgoing (e^{ikr}), the waves decay with distance from the obstacle ($1/\sqrt{r}$). Indeed, the radiation condition implies that $u=O(r^{-1/2})$ as $r\to\infty$. As G also satisfies the radiation condition, we find that the integrand in (2) is

$$u\left(\frac{\partial G}{\partial r}-ikG\right)-G\left(\frac{\partial u}{\partial r}-iku\right)=o(r^{-1}) \quad \text{as } r\to\infty,$$

[a)]Permanent address: Department of Mathematics, University of Manchester, Manchester M13 9PL, United Kingdom.

whence $I(u;\mathscr{C})\to 0$ as $r\to\infty$, where $\mathscr{C}$ is any piece of C_r. This shows that the result (2) is due, essentially, to the decay of u (and G), not to any cancellation effects induced by the integration.

The description given above changes completely when the obstacle is *unbounded*. For example, suppose that S is an infinite, flat plane. Then, an incident plane wave will be scattered (reflected) specularly as a single propagating plane wave. More generally, suppose that S is an infinite corrugated surface; then, an incident plane wave will be scattered into a spectrum of plane waves. The specification of a ''radiation condition'' for such problems continues to attract attention (see, for example, Ramm, 1986); clearly, the Sommerfeld radiation condition is not appropriate, as it is not satisfied by a propagating plane wave. Nevertheless, it is customary to proceed, *assuming* that the scattered field can be represented in terms of plane waves, at least at some distance from S. Typically, this requires the discarding of an integral such as (2), but with the large circle C_r replaced by a large *semicircle* H_r. Can this step be justified? This paper began as an attempt to do this.

Another possible approach is to assume that u can be written as a surface distribution of sources or dipoles; see Sec. VI E. One might also invoke the limiting absorption principle, in which the wave number k is replaced by $k+i\varepsilon$, where ε is small and positive; the corresponding u is required to decay as $r\to\infty$. However, this is delicate (compared to scattering by a bounded obstacle) as the limits $\varepsilon\to 0$ and $z\to\infty$ for $\exp\{iz(k+i\varepsilon)\}$ do not commute.

The motivation behind the present work is the pervasive view that solving a boundary integral equation gives a rigorous, exact way (apart from numerical errors) of solving problems involving the scattering of plane waves by infinite rough surfaces. Indeed, one can find many books and papers setting out this view. (References to the literature will be given later.) However, very little attention has been given to the *derivation* of the boundary integral equations themselves, most writers being content to start by writing down a standard Helmholtz integral equation, (3) or (4). We will show that (3) is valid for plane-wave scattering by an infinite, one-dimensional, rough surface. We will also show that (4) is valid, except for grazing incident waves (in which case the right-hand side should be replaced by $u_{\rm inc}$).

The paper is organized as follows. Section I is devoted to formulating the problem, with some discussion on radiation conditions and some background on angular-spectrum representations and integral representations (using G). Estimation of integrals over the semicircle H_r is carried out in Secs. II, III, and IV. Thus, the method of stationary phase and an expansion method are used in Secs. II and III, respectively, but only for a single plane wave. Results for $I(u;H_r)$ are obtained in Sec. IV, and are then used in Sec. V to derive various boundary integral equations of Helmholtz type. Extensive discussion of the results is given in Sec. VI. For example, it is shown that the standard Helmholtz integral equations are valid for a finite patch of roughness and for finite incident beams.

I. FORMULATION

Consider the scattering of a plane wave by an infinite rough surface, S. In this paper, we assume that the surface is one-dimensional, so that it can be described by

$$z=s(x), \quad -\infty<x<\infty$$

with $-h<s(x)\leqslant 0$ and some constant $h\geqslant 0$. The acoustic medium occupies $z>s$ and, for definiteness, we assume that S is a smooth, sound-hard surface. Thus we can write the total field as

$$u_{\rm tot}=u_{\rm inc}+u,$$

where u is the scattered field and

$$u_{\rm inc}(r,\theta)=e^{-ikr\,\cos(\theta+\theta_i)}, \quad |\theta_i|\leqslant \tfrac{1}{2}\pi, \tag{6}$$

is the incident plane wave; θ_i is the angle of incidence (it is the angle between the direction of propagation and the negative z axis), and (r,θ) are plane polar coordinates: $x=r\,\sin\theta$ and $z=r\,\cos\theta$. All the fields $u_{\rm tot}$, $u_{\rm inc}$, and u satisfy the Helmholtz equation

$$(\nabla^2+k^2)u=0, \tag{7}$$

for $z>s$. The boundary condition is

$$\frac{\partial u_{\rm tot}}{\partial n}=0 \quad \text{on } S, \tag{8}$$

where $\partial/\partial n$ denotes normal differentiation *out* of the acoustic medium.

A. Reflection by a flat surface

If S is flat ($s=0$), the problem is trivial. Nevertheless, this problem can still teach us something. It is well known that the scattered field is

$$u(r,\theta)=e^{ikr\,\cos(\theta-\theta_i)} \quad \text{for } |\theta_i|<\tfrac{1}{2}\pi. \tag{9}$$

When $|\theta_i|=\frac{1}{2}\pi$ (''grazing incidence''), we have $u\equiv 0$: The incident wave satisfies the boundary condition on S.

Thus, for $|\theta_i|<\frac{1}{2}\pi$,

$$u_{\rm tot}=2\,e^{ikx\,\sin\theta_i}\,\cos(kz\,\cos\,\theta_i)$$

and

$$2\,e^{ikx\,\sin\theta_i}\,\cos(kz\cos\,\theta_i)+A_+e^{ikx}+A_-e^{-ikx}$$

both ''solve'' the problem, where A_+ and A_- are arbitrary constants. Of course, we disallow this second solution, unless $A_+=A_-=0$: but why? The answer is because of the radiation condition (which we have yet to specify). Physically, we want to exclude all ''incoming'' plane waves, apart from the incident wave. We will be more precise in Sec. I B.

B. Angular-spectrum representations

For any S, the scattered field above the corrugations, $z>0$, may be written using an angular-spectrum representation,

$$u(x,z)=\int_{-\infty}^{\infty}F(\mu)e^{ik(\mu x+mz)}\frac{d\mu}{m(\mu)} \tag{10}$$

$$=\int_{-\pi/2}^{\pi/2}A(\alpha)e^{ikr\cos(\theta-\alpha)}d\alpha$$

$$+\text{ evanescent terms.} \tag{11}$$

Here, $F(\mu)$ is the *spectral amplitude*, $A(\alpha)=F(\sin\alpha)$ and

$$m(\mu)=\begin{cases}\sqrt{1-\mu^2}, & |\mu|<1,\\ i\sqrt{\mu^2-1}, & |\mu|>1.\end{cases}$$

The integrals are superpositions of plane waves; they are propagating, homogeneous plane waves when $|\mu|<1$ and they are evanescent, inhomogeneous plane waves when $|\mu|>1$ In (11), we see the propagating plane waves explicitly: They propagate at an angle α to the positive z axis, with an (unknown) complex amplitude, $A(\alpha)$; the ''evanescent terms'' decay exponentially with z. For more information on angular-spectrum representations, see Clemmow (1966) and DeSanto and Martin (1996).

In general, the spectral amplitude must be considered as a generalized function, and not as a continuous or analytic function. This simple observation is motivated by known results for particular surfaces. Thus, for a flat surface we have

$$F(\mu)=\delta(\mu-\sin\,\theta_i)\cos\,\theta_i\,,\quad |\theta_i|<\tfrac{1}{2}\pi,$$

where δ is the Dirac delta function, whereas for a periodic surface F is a discrete sum of delta functions. So, we split the scattered field into three parts as

$$u=u_{\rm pr}+u_{\rm ev}+u_{\rm con}, \tag{12}$$

where

$$u_{\rm pr}(r,\theta)=\sum_{n=1}^{N}A_n v(r,\theta;\alpha_n),$$

$$u_{\rm ev}(r,\theta)=\sum_{m=1}^{M}B_m w(r,\theta;\mu_m), \tag{13}$$

$$u_{\rm con}(r,\theta)=\int_{-\infty}^{\infty}C(\mu)e^{ikr(\mu\,\sin\,\theta+m\,\cos\,\theta)}\frac{d\mu}{m(\mu)}, \tag{14}$$

$$v(r,\theta;\alpha)=e^{ikr\,\cos(\theta-\alpha)},\quad \text{with } |\alpha|\leqslant\tfrac{1}{2}\pi, \tag{15}$$

and

$$w(r,\theta;\mu)=e^{ikr\mu\,\sin\,\theta}e^{-kr\,\cos\,\theta\sqrt{\mu^2-1}}\quad \text{with } |\mu|>1. \tag{16}$$

The first term in (12) is a sum of propagating plane waves; the coefficients A_n and the angles α_n are unknown in general. The second term in (12) is a sum of evanescent waves; the coefficients B_m and μ_m are unknown in general. The third term in (12) is a continuous spectrum of plane waves; the unknown function C is continuous. Properties and consequences of the general representation (12) were investigated by DeSanto and Martin (1996).

Let us now return to the radiation condition. Having chosen an origin O, arbitrarily, we consider a large semicircle H_r, with radius r and center at O. We then require that all propagating plane-wave components $v(r,\theta;\alpha_n)$ in u propagate *outwards* through H_r, away from O. This is almost built into the decomposition (12): we have to be careful with grazing waves ($|\alpha_n|=\frac{1}{2}\pi$). For example, if $\alpha_n=\frac{1}{2}\pi$, $v=e^{ikx}$; this wave leaves the semicircle at $\theta=\frac{1}{2}\pi$ but enters at $\theta=-\frac{1}{2}\pi$. A simple way to impose our radiation condition without excluding grazing waves is to split the half-space $z>0$ and the semicircle H_r into two parts. Thus with

$$H_r^{\pm}=\{(r,\theta):0\leqslant\pm\theta\leqslant\tfrac{1}{2}\pi\} \tag{17}$$

being quarter-circles, we require that in the region $x\geqslant 0$, $z>0$, we use $0\leqslant\alpha_n\leqslant\frac{1}{2}\pi$, so that all plane waves propagate out through H_r^{+}. Similarly, in the region $x\leqslant 0$, $z>0$, we use $-\frac{1}{2}\pi\leqslant\alpha_n\leqslant 0$, so that all plane waves propagate out through H_r^{-}. This form of the radiation condition will be used to derive boundary integral equations.

C. Boundary integral equations

One way to determine the scattered field is to derive a boundary integral equation over the rough surface S. The appropriate fundamental solution is

$$G(P,Q)=G(\mathbf{y},\mathbf{x})=-\tfrac{1}{2}iH_0^{(1)}(k|\mathbf{x}-\mathbf{y}|),$$

where $\mathbf{x}$ and $\mathbf{y}$ are the position vectors of Q and P, respectively, with respect to the origin O, and $H_n^{(1)}$ is a Hankel function. Apply Green's theorem to u and G in the region D_r with boundary $\partial D_r=H_r\cup S_r\cup T_r$, where H_r is a large semicircle of radius r and center O,

$$S_r=\{(x,z):z=s(x),-r<x<r\}$$

is a truncated rough surface, and T_r consists of two line segments joining the ends of H_r and S_r. Then, as both u and G satisfy the Helmholtz equation (7) in D_r [apart from the singularity in $G(P,Q)$ at $P=Q$], we obtain

$$2u(P)=\int_{\partial D_r}\left\{u(q)\frac{\partial G}{\partial n_q}(P,q)-\frac{\partial u}{\partial n_q}G(P,q)\right\}ds_q,$$

where $P\in D_r$, $q\in\partial D_r$ and $\partial/\partial n_q$ denotes normal differentiation at q. Use of the boundary condition (8) yields

$$2u(P)=\int_{S_r}\left\{u(q)\frac{\partial G}{\partial n_q}(P,q)+\frac{\partial u_{\rm inc}}{\partial n_q}G(P,q)\right\}ds_q$$

$$+I(u;H_r)+I(u;T_r), \tag{18}$$

where

$$I(u;\mathscr{S})=\int_{\mathscr{S}}\left\{u(q)\frac{\partial G}{\partial n_q}(P,q)-\frac{\partial u}{\partial n_q}G(P,q)\right\}ds_q$$

and normal differentiation is taken in a direction away from the origin [so that $\partial/\partial n=\partial/\partial r$ on H_r, consistent with (2)].

The scattered field u and its derivative $\partial u/\partial x$ are bounded in the neighborhood of S. This assumption together with simple bounds and the large-argument asymptotic behavior of Hankel functions show that $I(u;T_r)=O(r^{-1/2})$ as $r\to\infty$, whence

$$I(u;T_r)\to 0\quad \text{as } r\to\infty. \tag{19}$$

Before estimating $I(u;H_r)$ for large r, using (12), we consider a single propagating plane-wave component in (12). Thus, we shall evaluate $I(v;H_r)$ as $r\to\infty$, where v is defined by (15). Indeed, we shall evaluate the limit using two different methods: the method of stationary phase (Sec. II) and an expansion method (Sec. III). We shall discuss the evaluation of $I(u;H_r)$ itself for large r in Sec. IV. Boundary integral equations will then be derived from (18) in Sec. V.

II. THE METHOD OF STATIONARY PHASE

We use the method of stationary phase to estimate $I(v;H_r)$. There are two cases, depending on the value of α, which can be smoothed together using a uniform approximation.

A. The method of stationary phase: $|\alpha|<\frac{1}{2}\pi$

We are interested in large values of $r=|\mathbf{x}|$ for fixed values of $\mathbf{y}$ and k. We have

$$G(P,q)\simeq\frac{B}{\sqrt{kr}}\exp\{ik(r-\mathbf{y}\cdot\hat{\mathbf{x}})\}$$

$$=\frac{B}{\sqrt{kr}}e^{ikr}e^{-ik\rho\cos(\theta-\varphi)}$$

as $r\to\infty$, where $\hat{\mathbf{x}}=\mathbf{x}/r$, $\mathbf{y}=(\rho\sin\varphi,\rho\cos\varphi)$ and

$$B=-\tfrac{1}{2}i\sqrt{(2/\pi)}e^{-i\pi/4}. \tag{20}$$

Hence, for large r,

$$v\frac{\partial G}{\partial r}-G\frac{\partial v}{\partial r}\simeq ik\frac{B}{\sqrt{kr}}[1-\cos(\theta-\alpha)]\times e^{ikr(1+\cos(\theta-\alpha))}e^{-ik\rho\cos(\theta-\varphi)}$$

and then

$$I(v;H_r)\simeq iBe^{ikr}L(kr), \tag{21}$$

where

$$L(\lambda)=\sqrt{\lambda}\int_{-\pi/2}^{\pi/2}g(\theta)e^{i\lambda F(\theta)}d\theta,$$

$$g(\theta)=[1-\cos(\theta-\alpha)]e^{-ik\rho\cos(\theta-\varphi)}$$

and

$$F(\theta)=\cos(\theta-\alpha).$$

For large $\lambda\equiv kr$, the dominant contribution to $L(\lambda)$ comes from those points c in the range of integration at which the phase F is stationary: $F'(c)=0$. As $F'(\theta)=\sin(\alpha-\theta)$ and $|\alpha|<\frac{1}{2}\pi$, the only stationary-phase point is at $\theta=\alpha$. Then (Bleistein and Handelsman, 1986, p. 220)

$$L(\lambda)\sim\mathscr{B}g(\alpha)e^{i\lambda F(\alpha)}\quad\text{as }\lambda\to\infty, \tag{22}$$

where

$$\mathscr{B}=\sqrt{\frac{2\pi}{|F''(\alpha)|}}\exp\left\{\frac{1}{4}i\pi\ \operatorname{sgn}F''(\alpha)\right\}=\sqrt{2\pi}e^{-i\pi/4}.$$

But $g(\alpha)=0$, and so $L(\lambda)=o(1)$ as $\lambda\to\infty$. In fact, an integration by parts gives

$$L(\lambda)=\frac{i}{\sqrt{\lambda}\cos\alpha}[(1-\sin\alpha)e^{i\Phi}+(1+\sin\alpha)e^{-i\Phi}]+O(\lambda^{-1})$$

as $\lambda\to\infty$, where $\Phi=\lambda\sin\alpha-k\rho\sin\varphi$. Hence, from (21), we obtain

$$I(v;H_r)=O((kr)^{-1/2})\quad\text{as }kr\to\infty,\text{ for }|\alpha|<\tfrac{1}{2}\pi. \tag{23}$$

B. The method of stationary phase: $|\alpha|=\frac{1}{2}\pi$

Suppose that $\alpha=\frac{1}{2}\pi$. In this case, $F(\theta)=\sin\theta$ is stationary at $\theta=\pm\frac{1}{2}\pi$, which are end points of the range of integration. We have

$$g(\tfrac{1}{2}\pi)=0\text{ and }g(-\tfrac{1}{2}\pi)=2e^{ik\rho\sin\varphi}.$$

It follows that

$$L(\lambda)\sim\sqrt{2\pi}e^{i\pi/4}e^{-i\lambda}e^{ik\rho\sin\varphi}\quad\text{as }\lambda\to\infty, \tag{24}$$

whence

$$I(v;H_r)=e^{ik\rho\sin\varphi}+O((kr)^{-1/2})\quad\text{as }kr\to\infty,\text{ for }\alpha=\tfrac{1}{2}\pi. \tag{25}$$

When $\alpha=-\frac{1}{2}\pi$, we obtain the same result except that φ is replaced by $-\varphi$. In this case, the relevant stationary-phase point is at $\theta=\frac{1}{2}\pi$.

When $\rho=0$, we can give an independent check of the result (24). In this case, we have

$$L(\lambda)=\sqrt{\lambda}\int_{-\pi/2}^{\pi/2}(1-\sin\theta)e^{i\lambda\sin\theta}d\theta$$

$$=\pi\sqrt{\lambda}\{J_0(\lambda)-iJ_1(\lambda)\},$$

where J_m is a Bessel function. The result follows from the well-known asymptotic approximation,

$$J_m(\lambda)\sim\sqrt{\frac{2}{\pi\lambda}}\cos\left(\lambda-\frac{1}{2}m\pi-\frac{1}{4}\pi\right)\quad\text{as }\lambda\to\infty. \tag{26}$$

C. Uniform asymptotics

We have seen that the results for $|\alpha|<\frac{1}{2}\pi$ and $|\alpha|=\frac{1}{2}\pi$ are different, that is, the asymptotic estimate of $I(v;H_r)$ is not uniform in the parameter α. However, we can obtain a uniform approximation (see Appendix A); for example, if α is near $\frac{1}{2}\pi$, we find that

$$I(v;H_r)\simeq\cos(\tfrac{1}{2}\delta)e^{ik\rho\sin\varphi}\operatorname{erfc}(\mu), \tag{27}$$

where

$$\operatorname{erfc}(\mu)=\frac{2}{\sqrt{\pi}}\int_{\mu}^{\infty}e^{-x^2}dx \tag{28}$$

is the complementary error function,

$$\mu=\sqrt{2\lambda}e^{-i\pi/4}\sin\tfrac{1}{2}\delta\text{ and }\delta=\tfrac{1}{2}\pi-\alpha.$$

Note that if $\alpha=\frac{1}{2}\pi$ ($\delta=0$), we recover (25). On the other hand, if $\alpha<\frac{1}{2}\pi$ ($\delta>0$), we recover (23), since $\mathrm{erfc}(\mu)\sim\pi^{-1/2}\mu^{-1}\exp(-\mu^2)$ as $\mu\to\infty$.

III. AN EXPANSION METHOD

The integral $I(v;H_r)$ is over a semicircle of radius r, between $\theta=-\frac{1}{2}\pi$ and $\theta=+\frac{1}{2}\pi$. We can evaluate this integral explicitly, using appropriate expansions of v and G. Thus

$$v(r,\theta;\alpha)=e^{ikr\cos(\theta-\alpha)}=\sum_{m=-\infty}^{\infty} i^m J_m(kr)e^{-im(\theta-\alpha)}, \tag{29}$$

henceforth, we suppress the limits when the summation is over all integers. Similarly,

$$G(P,q)=-\frac{1}{2}i\sum_n H_n(kr)J_n(k\rho)e^{in(\theta-\varphi)} \tag{30}$$

for $r>\rho$, where $H_n\equiv H_n^{(1)}$. Hence

$$I(v;H_r)=\sum_m\sum_n i^m J_n(k\rho)W_{mn}(kr)A_{mn}e^{i(m\alpha-n\varphi)},$$

where

$$W_{mn}(w)=-\tfrac{1}{2}i\pi w\{J_m(w)H_n'(w)-J_m'(w)H_n(w)\}$$

and

$$A_{mn}=\frac{1}{\pi}\int_{-\pi/2}^{\pi/2}e^{i(n-m)\theta}d\theta$$

$$=\begin{cases}1 & \text{if } m=n,\\ \dfrac{2(-1)^j}{(2j+1)\pi} & \text{if } m=n+2j+1,\\ 0 & \text{otherwise,}\end{cases}$$

here, j is an arbitrary integer. It follows that

$$I(v;H_r)=\sum_n i^n J_n(k\rho)\{W_{nn}(kr)-F_n(kr,\alpha)\}e^{in(\alpha-\varphi)},$$

where

$$F_n(kr,\alpha)=\frac{-2i}{\pi}\sum_j\frac{1}{2j+1}W_{n+2j+1,n}e^{i(2j+1)\alpha}. \tag{31}$$

We want to estimate $I(v;H_r)$ for large r. We can evaluate the first term in the braces exactly: W_{nn} is essentially a Wronskian, given by $W_{nn}=1$. For F_n, we have

$$W_{mn}(w)\sim\exp\{i(m-n)\pi/2\}$$

$$\text{as } w\to\infty, \text{ for fixed } m \text{ and } n. \tag{32}$$

We proceed formally, and use this approximation in (31). (This procedure can be justified; see Appendix B.) The result is

$$F_n(kr,\alpha)\sim\mathscr{G}(\alpha+\tfrac{1}{2}\pi)\quad \text{as } kr\to\infty,$$

independently of n, where

$$\mathscr{G}(\theta)=\frac{-2i}{\pi}\sum_j\frac{e^{i(2j+1)\theta}}{2j+1}=\frac{4}{\pi}\sum_{j=0}^{\infty}\frac{\sin(2j+1)\theta}{2j+1}, \tag{33}$$

this is a familiar Fourier series:

$$\mathscr{G}(\theta)=\begin{cases}1, & 0<\theta<\pi,\\ -1, & -\pi<\theta<0,\\ 0, & \theta=0,\pm\pi,\end{cases} \tag{34}$$

and is defined by periodicity for other values of θ. Hence, for large kr, $F_n\sim 1$ for $0\leqslant|\alpha|<\frac{1}{2}\pi$ but $F_n=o(1)$ for $|\alpha|=\frac{1}{2}\pi$. Thus we obtain the same (nonuniform) results as derived in Secs. II A and II B. The drawbacks with this method are that it does not yield results that are uniform in α for α near $\pm\frac{1}{2}\pi$, and it is very complicated to use for three-dimensional problems.

IV. ASYMPTOTIC BEHAVIOR OF $I(u;H_r)$

When a plane wave is reflected by a rough surface S, we can use the angular-spectrum representation (12) for the reflected field above the corrugations. Thus we have

$$I(u;H_r)=I(u_{\mathrm{pr}};H_r)+I(u_{\mathrm{ev}};H_r)+I(u_{\mathrm{con}};H_r).$$

For $I(u_{\mathrm{ev}};H_r)$, with u_{ev} defined by (13), we have

$$I(w;H_r)\simeq iB\sqrt{kr}e^{ikr}\int_{-\pi/2}^{\pi/2}g(\theta)e^{ikrF(\theta)}d\theta,$$

where w is defined by (16),

$$F(\theta)=\mu\sin\theta+i\sqrt{\mu^2-1}\cos\theta$$

and

$$g(\theta)=[1-F(\theta)]e^{-ik\rho\cos(\theta-\varphi)},$$

as $|\mu|>1$, integration by parts shows that

$$I(w;H_r)=O((kr)^{-1/2})\quad \text{as } kr\to\infty.$$

Hence, from (13),

$$I(u_{\mathrm{ev}};H_r)\to 0\quad \text{as } r\to\infty.$$

For u_{con}, we have

$$u_{\mathrm{con}}(r,\theta)\sim\sqrt{\frac{2\pi}{kr}}e^{i(kr-\pi/4)}C(\sin\theta)\quad \text{as } kr\to\infty.$$

This result makes essential use of the continuity of $C(\mu)$ (see Clemmow, 1966, Sec. 3.2). Thus, u_{con} satisfies the Sommerfeld radiation condition (1), whence

$$I(u_{\mathrm{con}};H_r)\to 0\quad \text{as } r\to\infty.$$

[A direct derivation of this result, based on (14) and the method of stationary phase, is given in Appendix C.]

Finally, consider $I(u_{\mathrm{pr}};H_r)$. If $|\alpha_n|<\frac{1}{2}\pi$, the results of the previous sections are immediately applicable, and show that $I(u_{\mathrm{pr}};H_r)\to 0$ as $r\to\infty$. Next, consider grazing waves, $|\alpha_n|=\frac{1}{2}\pi$, and write

$$v_{\pm}=v(r,\theta;\pm\tfrac{1}{2}\pi)=e^{\pm ikx}.$$

We have

$$I(u_{\mathrm{pr}};H_r)=I(u_{\mathrm{pr}};H_r^{+})+I(u_{\mathrm{pr}};H_r^{-}),$$

where $H_r^{\pm}$ are quarter-circles defined by (17); the radiation condition (all plane waves must propagate outwards through H_r, away from O) implies that we limit our attention to $I(v_{\pm};H_r^{\pm})$, as $v_{\pm}$ propagates inwards through $H_r^{\mp}$. So, from Sec. II A, we have

$$I(v_+;H_r^+)\simeq iBe^{i\lambda}\sqrt{\lambda}\int_0^{\pi/2}(1-\sin\theta)\times e^{-ik\rho\cos(\theta-\varphi)}e^{i\lambda\sin\theta}d\theta$$

for large $\lambda\equiv kr$. There is one point of stationary phase (cf. Sec. II B) at $\theta=\frac{1}{2}\pi$, but the integrand vanishes there whence $I(v_+;H_r^+)\to 0$ as $r\to\infty$. A similar argument succeeds for $I(v_-;H_r^-)$.

In summary, we find that our radiation condition ensures that

$$I(u;H_r)\to 0 \quad \text{as } r\to\infty. \tag{35}$$

V. BOUNDARY INTEGRAL EQUATIONS

In Sec. I, we used Green's theorem to obtain the integral representation

$$2u(P)=\int_{S_r}\left\{u(q)\frac{\partial G}{\partial n_q}(P,q)+\frac{\partial u_{\rm inc}}{\partial n_q}G(P,q)\right\}ds_q + I(u;H_r)+I(u;T_r)$$

when $P\in D_r$, the region bounded by the semicircle H_r, the truncated rough surface S_r, and the two line segments T_r. Note that the left-hand side of this equation does not depend on r, so that the right-hand side of the equation must have a limit as $r\to\infty$. Taking this limit, using (19) and (35), we obtain

$$2u(P)=\int_S\left\{u(q)\frac{\partial G}{\partial n_q}(P,q)+\frac{\partial u_{\rm inc}}{\partial n_q}G(P,q)\right\}ds_q, \quad P\in D_\infty, \tag{36}$$

where D_∞ is the unbounded region $z>s$ and

$$\int_S=\lim_{r\to\infty}\int_{S_r},$$

which is the standard definition of a principal-value integral at infinity. In fact, the integral over S exists as an ordinary improper integral; to see this, we note that the integrand behaves like

$$U(x)e^{ik|x|}|x|^{-1/2} \quad \text{as } |x|\to\infty,$$

where $U(x)$ is only required to be bounded.

We remark that Beckmann and Spizzichino (1963, p. 180) and Ogilvy (1991, p. 75) discard $I(u;H_r)$ by assuming erroneously that $u=0$ on H_r.

Letting $P\to p\in S$ in (36) gives

$$u(p)-\int_S u(q)\frac{\partial G}{\partial n_q}(p,q)ds_q=\int_S\frac{\partial u_{\rm inc}}{\partial n_q}G(p,q)ds_q, \quad p\in S. \tag{37}$$

This is (formally) the standard Helmholtz integral equation for the boundary values of u on S.

It is common to not work with (37) but with an integral equation for the total field, $u_{\rm tot}$. To obtain such an equation, we start by defining a region $\widetilde{D}_r$ with boundary $\partial\widetilde{D}_r$. Given r, let $\widetilde{H}_r$ denote the semicircle in $z\leqslant 0$, with radius r and center O; then, $\widetilde{D}_r$ is the bounded region in $z<s$ enclosed by $\widetilde{H}_r$ and the rough surface. The boundary $\partial\widetilde{D}_r$ consists of a piece of S_r, namely S_t with $t(r)<r$, and a piece of $\widetilde{H}_r$, namely $\widetilde{H}_r\setminus\widetilde{T}_r$ where $\widetilde{T}_r$ consists of two circular arcs joining the ends of $\widetilde{H}_r$ and the ends of S_t. Now, apply Green's theorem to $u_{\rm inc}$ and G in $\widetilde{D}_r$. As both fields satisfy (7) in $\widetilde{D}_r$, the result is

$$0=\int_{S_t}\left\{u_{\rm inc}(q)\frac{\partial G}{\partial n_q}(P,q)-\frac{\partial u_{\rm inc}}{\partial n_q}G(P,q)\right\}ds_q - I(u_{\rm inc};\widetilde{H}_r)+I(u_{\rm inc};\widetilde{T}_r) \tag{38}$$

when $P\in D_r$, taking into account the direction of the normal vector on S. As before, simple bounds show that $I(u_{\rm inc};\widetilde{T}_r)\to 0$ as $r\to\infty$. If $|\theta_i|<\frac{1}{2}\pi$, $u_{\rm inc}$ [given by (6)] is a plane wave propagating outwards through $\widetilde{H}_r$, whence

$$I(u_{\rm inc};\widetilde{H}_r)\to 0 \quad \text{as } r\to\infty(|\theta_i|<\tfrac{1}{2}\pi).$$

For grazing incidence, we have

$$I(u_{\rm inc};\widetilde{H}_r)=u_{\rm inc}(P)(|\theta_i|=\tfrac{1}{2}\pi).$$

We combine these formulas and write

$$I(u_{\rm inc};\widetilde{H}_r)\to\mathscr{U}_i(P) \quad \text{as } r\to\infty(|\theta_i|\leqslant\tfrac{1}{2}\pi). \tag{39}$$

Letting $r\to\infty$ in (38), and adding the result to (36), we obtain

$$2u(P)=\int_S u_{\rm tot}(q)\frac{\partial G}{\partial n_q}(P,q)ds_q-\mathscr{U}_i(P), \quad P\in D_\infty. \tag{40}$$

Then, letting $P\to p\in S$ gives

$$u_{\rm tot}(p)-\int_S u_{\rm tot}(q)\frac{\partial G}{\partial n_q}(p,q)ds_q=2u_{\rm inc}(p)-\mathscr{U}_i(p), \quad p\in S. \tag{41}$$

Now, the standard Helmholtz integral equation for the total field is

$$w(p)-\int_S w(q)\frac{\partial G}{\partial n_q}(p,q)ds_q=2u_{\rm inc}(p), \quad p\in S. \tag{42}$$

Thus, for nongrazing incident waves ($\mathscr{U}_i=0$), we see that $u_{\rm tot}$ does satisfy the standard Helmholtz integral equation. However, for grazing incident waves, $u_{\rm tot}$ does not satisfy the Helmholtz integral equation (42), but $2u_{\rm tot}$ does.

VI. DISCUSSION

A. Previous work: Helmholtz integral equations

The idea that a boundary integral equation may be used to solve the problem of plane-wave scattering by an infinite rough surface is familiar. It is discussed in books on such

problems; see for example Maystre and Dainty (1991), Ogilvy (1991, Secs. 4.1.1 and 6.3) and Voronovich (1994, Sec. 3.1). In particular, the standard Helmholtz integral equation (4) is equation (6.53) in Ogilvy's book and equation (3.1.37) in Voronovich's book.

Many recent authors refer to the paper by Holford (1981) on the scattering of a plane wave by a periodic sound-soft surface. He obtains the integral representation [his equation (20)]

$$u_{\rm tot}(P)=u_{\rm inc}(P)+\frac{1}{2}\int_S u_{\rm tot}(q)\,\frac{\partial G}{\partial n_q}(P,q)\,ds_q\,,$$

$$P\in D_\infty\,, \tag{43}$$

as in Sec. I C, by applying Green's theorem to $u_{\rm tot}$ and G in the semicircular region D_r [using our notation and the boundary condition (8)]. He claims that ''the term $u_{\rm inc}(P)$ is the contribution from the large semicircle'' H_r as $r\to\infty$. He does not prove this statement and, moreover, it is not true for grazing incident waves. To see this, we note that applying Green's theorem to $u_{\rm tot}$ and G in D_r gives

$$2u_{\rm tot}(P)=\int_{S_r} u_{\rm tot}(q)\,\frac{\partial G}{\partial n_q}(P,q)\,ds_q+I(u_{\rm tot};H_r)$$
$$+I(u_{\rm tot};T_r).$$

Now, $I(u_{\rm tot};T_r)\to 0$ as $r\to\infty$ and

$$I(u_{\rm tot};H_r)=I(u;H_r)+I(u_{\rm inc};H_r)$$
$$=I(u;H_r)+I(u_{\rm inc};C_r)-I(u_{\rm inc};\widetilde{H}_r),$$

where $C_r=H_r\cup\widetilde{H}_r$ is a large circle. But, for an incident plane wave,

$$I(u_{\rm inc};C_r)=2u_{\rm inc},$$

exactly, whence

$$I(u_{\rm tot};H_r)\to 2u_{\rm inc}-\mathscr{U}_i\quad\text{as } r\to\infty,$$

where $\mathscr{U}_i$ is defined by (39). Thus (43) is correct whenever $\mathscr{U}_i\equiv 0$.

Holford himself refers to earlier papers by Urosovskii (1960), who in turn refers to Lysanov (1956). For more recent work, we can cite Thorsos (1988), Bishop and Smith (1992) and McSharry *et al.* (1995). All these papers start from the Helmholtz integral equation for $u_{\rm tot}$, (4), or the analogous equation for a sound-soft surface. Moreover, all but one of these papers are concerned with plane-wave incidence, the exception being the paper by Thorsos (1988). He considers a 'tapered' plane wave; we will discuss beams of finite extent in Sec. VI D.

B. Far-field asymptotics

Care is needed when approximating the scattered field at large distances from an infinite surface. To illustrate this, consider the integral representation (40). Let $P\equiv(x,z)\in D_\infty$ and $q\equiv(\xi,s(\xi))\in S$ have position vectors $\mathbf{y}$ and $\mathbf{q}$, respectively. In the far field, $kR\gg 1$, where $R=|\mathbf{y}-\mathbf{q}|$, so that we can use the large-argument approximation for $H_1^{(1)}(kR)$. Thus, assuming for simplicity that $\mathscr{U}=\mathscr{U}_i=0$, (40) gives

$$2u(x,z)=\frac{ik}{2}\int_S u_{\rm tot}(q)\,\frac{H_1^{(1)}(kR)}{R}\,\mathbf{n}(q)\cdot(\mathbf{q}-\mathbf{y})\,ds_q$$
$$\sim iB\sqrt{k}\int_S u_{\rm tot}(q)\,\frac{e^{ikR}}{R^{3/2}}\,\mathbf{n}(q)\cdot(\mathbf{q}-\mathbf{y})\,ds_q \tag{44}$$

as $kz\to\infty$, where B is defined by (20) and $\mathbf{n}(q)$ is the unit normal vector at q pointing out of D_∞.

If $u_{\rm tot}(q)$ has a compact support (so that it vanishes for $|\mathbf{q}|>L$, say), or if S is finite (bounded scatterer), we can make a second approximation:

$$R=\{r^2-2\mathbf{y}\cdot\mathbf{q}+q^2\}^{1/2}=r-\hat{\mathbf{y}}\cdot\mathbf{q}+O(q^2/r)\quad\text{as } r\to\infty, \tag{45}$$

where $r=|\mathbf{y}|$, $\hat{\mathbf{y}}=\mathbf{y}/r$, and $q=|\mathbf{q}|$. (The notation used here differs from that used in Secs. I C and II A.) To the same order, we can also replace $(\mathbf{q}-\mathbf{y})$ in (44) by $(-\mathbf{y})$. Hence, we find that u is given by (5), where the far-field pattern is

$$f(\theta)=-\frac{iB\sqrt{k}}{2}\int_S u_{\rm tot}(q)\mathbf{n}(q)\cdot\hat{\mathbf{y}}\,\exp\{-ik\hat{\mathbf{y}}\cdot\mathbf{q}\}\,ds_q\,.$$

However, one cannot justify the use of the approximation (45) for plane-wave incidence and unbounded surfaces (see the discussion by Ogilvy, 1991, p. 78). This is immediately clear, because there must be a reflected plane wave, whereas (45) leads to a cylindrical wave. For explicit confirmation, consider the reflection of a plane wave by a flat surface, so that $u_{\rm tot}(q)=2\,\exp\{ik\xi\sin\theta_i\}$; the integral in (44) can then be estimated using the method of stationary phase [and yields the correct u, given by (9)], whereas the integral for $f(\theta)$ diverges.

C. A finite patch of roughness

Suppose that the infinite surface S is flat, apart from a finite patch of roughness, $S_{\rm patch}$, confined to $|x|<L$, say. A plane-wave incident on such a patch will generate a specular plane wave and a cylindrical wave. Thus, for nongrazing incidence, the standard Helmholtz integral equation for the total field, (4), is valid.

To see that the decomposition itself is valid, write

$$u_{\rm tot}=u_{\rm flat}+u_{\rm cyl},$$

where

$$u_{\rm flat}=e^{-ikr\cos(\theta+\theta_i)}+e^{ikr\,\cos(\theta-\theta_i)}\quad(|\theta_i|<\tfrac{1}{2}\pi)$$

is the total field for reflection by an infinite flat sound-hard surface. Thus

$$\frac{\partial u_{\rm cyl}}{\partial n}=-\frac{\partial u_{\rm flat}}{\partial n}\quad\text{on } S_{\rm patch}. \tag{46}$$

There are now three cases to consider, namely, ridges, grooves, and a combination thereof.

1. Ridges

Suppose that S_{patch} consists of a finite number of ridges (''bosses''), so that $s(x) \geqslant 0$. Then, the scattering problem is equivalent to the scattering of *two* plane waves, u_{flat}, by a finite bounded obstacle (a ''double-body'') with boundary $S_{\text{patch}} \cup S'_{\text{patch}}$, where S'_{patch} is the reflection of S_{patch} in the line $z=0$. Thus u_{cyl} is a cylindrical wave, satisfying the Sommerfeld radiation condition (1).

The use of bosses to model rough surfaces is well known (Ogilvy, 1991, Sec. 6.1). The use of images to treat scatterers near flat impenetrable boundaries is also well known; for a recent application, see Chao *et al.* (1996). Indeed, if we introduce the exact Green's function for the half-plane $z \geqslant 0$,

$$\begin{aligned} G^E(P,Q) &\equiv G^E(x,z;\xi,\zeta) \\ &= -\tfrac{1}{2} i \{ H_0^{(1)}(k\sqrt{(x-\xi)^2+(z-\zeta)^2}) \\ &\quad + H_0^{(1)}(k\sqrt{(x-\xi)^2+(z+\zeta)^2}) \}, \end{aligned}$$

we find that

$$2u_{\text{cyl}}(P) = \int_{S_{\text{ridge}}} \left\{ u_{\text{cyl}}(q) \frac{\partial G^E}{\partial n_q}(P,q) + \frac{\partial u_{\text{flat}}}{\partial n_q} G^E(P,q) \right\} ds_q, \quad P \in D_\infty,$$

where S_{ridge} is the union of all the ridge surfaces ($S_{\text{patch}} \setminus S_{\text{ridge}}$ is part of $z=0$). Letting $P \to p \in S_{\text{ridge}}$ yields a boundary integral equation for $u_{\text{cyl}}(p)$.

Alternatively, we can write

$$u_{\text{cyl}}(P) = \int_{S_{\text{ridge}}} \nu_1(q) G^E(P,q) ds_q, \quad P \in D_\infty, \tag{47}$$

where the boundary condition (46) implies that the source density ν_1 solves a Fredholm integral equation of the second kind over S_{ridge}.

2. Grooves

Suppose that S_{patch} consists of a finite number of grooves, so that $s(x) \leqslant 0$. Then, $\partial u_{\text{cyl}}/\partial z$ is known, in principle, for all x on $z=0$: It is zero except across the mouth of each groove. As there is a finite number of grooves, it follows that u_{cyl} is a cylindrical wave; it has an angular-spectrum representation with a continuous spectral amplitude.

Let S_{mouth} be the union of all the groove mouths; it is part of $z=0$. We can write

$$u_{\text{cyl}}(P) = \int_{S_{\text{mouth}}} \nu_2(q) G^E(P,q) ds_q, \quad P \equiv (x,z) \text{ and } z > 0. \tag{48}$$

To find the source density ν_2, we can apply Green's theorem inside each groove to u_{cyl} and G; we have the boundary condition (46) on the surface of each groove, and we have (transmission) conditions enforcing the continuity of u_{cyl} and $\partial u_{\text{cyl}}/\partial z$ across the mouth of each groove.

Note that we cannot use (48) inside the grooves because of the image singularities in G^E. This extra complication with grooves (compared to ridges) has given rise to more sophisticated methods for solving such problems, involving more complicated integral representations; see Willers (1987) and Asvestas and Kleinman (1994). Applications of G^E to rough-surface scattering were made by Berman and Perkins (1985) and by Shaw and Dougan (1995).

3. Ridges and grooves

From the discussion above, we see that if S_{patch} consists of a finite number of ridges and grooves, then u_{cyl} can be represented using

$$u_{\text{cyl}}(P) = \int_{S_+} \nu(q) G^E(P,q) ds_q,$$

where $S_+ = S_{\text{ridge}} \cup S_{\text{mouth}}$, $P \equiv (x,z)$ and $z > \max\{s(x),0\}$. The determination of ν on S_+ is complicated, although S_+ is a finite surface. If we use the Helmholtz integral equation for u_{tot}, which we know is legitimate, we have to solve an integral equation over an infinite surface. However, this can be reduced to an integral equation over S_{patch} as follows. Since $\partial G(p,q)/\partial n_q = 0$ when both p and q are on the flat part of S, $S_{\text{flat}} = S \setminus S_{\text{patch}}$, (4) gives

$$u_{\text{tot}}(p) = 2u_{\text{inc}}(p) + \int_{S_{\text{patch}}} u_{\text{tot}}(q) \frac{\partial G}{\partial n_q}(p,q) ds_q, \quad p \in S_{\text{flat}}.$$

This means that u_{tot} on the (infinite) flat part of S is known in terms of u_{tot} on the rough part of S. Hence, we can write (4) for $p \in S_{\text{patch}}$ as

$$u_{\text{tot}}(p) - \int_{S_{\text{patch}}} u_{\text{tot}}(q) K(p,q) ds_q = 2f(p), \quad p \in S_{\text{patch}},$$

where

$$K(p,q) = \frac{\partial G}{\partial n_q}(p,q) + \int_{S_{\text{flat}}} \frac{\partial G}{\partial n_l}(p,l) \frac{\partial G}{\partial n_q}(q,l) ds_l,$$

$$f(p) = u_{\text{inc}}(p) + \int_{S_{\text{flat}}} u_{\text{inc}}(q) \frac{\partial G}{\partial n_q}(p,q) ds_q.$$

D. Finite beams

So far we have taken the incident field to be a plane wave. However, for many applications, the incident field is a finite beam. To construct such a beam, we start by considering a single line-source at Q,

$$u_{\text{inc}}(P) = G(P,Q).$$

As u_{inc} satisfies the Sommerfeld radiation condition, an energy argument (DeSanto and Martin, 1996) shows that the scattered field cannot include any reflected plane waves. Thus, the standard Helmholtz integral equations, (3) and (4), are valid; see DeSanto and Brown (1986, Sec. 4.1).

Next, we distribute the line-sources over a finite curve $\mathcal{Q}$ (or a finite region), to give

$$u_{\text{inc}}(P) = \int_{\mathcal{Q}} \nu_{\text{inc}}(Q) G(P,Q) ds_Q,$$

where ν_{inc} is prescribed and can be adjusted to make u_{inc} beamlike. (If $\mathcal{Q}$ is far from S, the asymptotic approximations

described in Sec. VI B can be used.) It follows that the standard Helmholtz integral equations remain valid.

Another way to generate a beam is to use an angular-spectrum representation,

$$u_{\rm inc}(r,\theta)=\int_{-\pi/2}^{\pi/2} A_{\rm inc}(\alpha)e^{ikr\,\cos(\theta+\alpha)}d\alpha, \tag{49}$$

where $A_{\rm inc}$ is a prescribed continuous function, and is typically taken as a Gaussian (Saillard and Maystre, 1990). The standard Helmholtz integral equations are valid for incident fields of this type.

Thorsos (1988) uses a ''tapered'' plane wave. This incident field does not satisfy the Helmholtz equation, and so the derivation of the Helmholtz integral equation for $u_{\rm tot}$ fails. [The Helmholtz integral equation for u, (3), *is* valid without this qualification.] Nevertheless, as Thorsos points out, the tapered plane wave is an approximation to an actual wave field, constructed using (49); see Thorsos (1988, Sec. I B).

E. Other integral equations

An alternative way of solving scattering problems, touched on above, is to assume that the scattered field can be written as

$$u(P)=\int_S \gamma(q)G(P,q)ds_q, \quad P\in D,$$

where the source density γ is unknown. For sound-hard surfaces, the boundary condition (8) yields an integral equation for γ,

$$\gamma(p)-\int_S \gamma(q)\frac{\partial G}{\partial n_p}(p,q)ds_q=\frac{\partial u_{\rm inc}}{\partial n_p}, \quad p\in S.$$

For sound-soft surfaces, the corresponding integral equation is

$$\int_S \gamma(q)G(p,q)ds_q=-u_{\rm inc}(p), \quad p\in S;$$

this has been solved numerically by Lentz (1974), Rodríguez *et al.* (1992), and others.

Chandler-Wilde and Ross (1995, 1996) use a double-layer potential for sound-soft surfaces,

$$u(P)=\int_S \gamma(q)\frac{\partial G_1}{\partial n_q}(P,q)ds_q, \quad P\in D,$$

where G_1 satisfies an impedance condition on a line $z=-h_0$ $(h_0>h)$.

All of the formulations mentioned in this section are *indirect*, in that they assume that $u(P)$ can be represented in a specified form. Thus the radiation condition is implicit in the representation.

VII. CONCLUSIONS

We have seen that the use of standard Helmholtz integral equations for the scattering of a plane wave by an infinite, sound-hard, one-dimensional, rough surface is justified in most circumstances. In particular, the equation for the boundary values of the scattered field is always valid, whereas the integral equation for the boundary values of the total field is valid for nongrazing incident waves (a simple modification is required for grazing incident waves). These results underpin the use of these integral equations for numerical computations.

The standard Helmholtz integral equations are valid if the roughness is confined to a finite portion of an otherwise flat but infinite surface. They are also valid for incident beams of finite width.

Similar results may be obtained for sound-soft surfaces. Extension to electromagnetic and elastodynamic problems, and to penetrable interfaces, should be straightforward.

Finally, extension of these ideas to two-dimensional rough surfaces can also be made, although the analysis is more difficult and the results are different. Some of these aspects are currently under investigation.

ACKNOWLEDGMENTS

PAM acknowledges receipt of a Fulbright Scholarship Grant. He also thanks the Department of Mathematical and Computer Sciences, Colorado School of Mines, for its kind hospitality. Both authors are grateful to A.G. Voronovich for his perceptive remarks on an earlier version of the paper, which encouraged us to clarify the role of grazing waves.

APPENDIX A: UNIFORM ASYMPTOTICS

We derive a uniform approximation for $I(v;H_r)$, using a method discussed by Bleistein and Handelsman (1986, Sec 9.4). We start by focussing on the non-uniformity at $\alpha=\frac{1}{2}\pi$; the nonuniformity at $\alpha=-\frac{1}{2}\pi$ can be treated similarly. Write $L=L_1+L_2$ where

$$L_1(\lambda)=\sqrt{\lambda}\int_{-\pi/2}^{0} g(\theta)e^{i\lambda F(\theta)}d\theta$$

and $L_2=L-L_1$. We have $L_2=o(1)$ as $\lambda\to\infty$, uniformly in α, for α bounded away from $-\frac{1}{2}\pi$. For L_1 there is a point of stationary phase at $\theta=\alpha-\pi$ (outside the range of integration) which approaches the end point at $\theta=-\frac{1}{2}\pi$ as $\alpha\to\frac{1}{2}\pi$. Let us make a preliminary change of variables, mapping the end point to the origin: Put $\theta=x-\frac{1}{2}\pi$ and $\alpha=\frac{1}{2}\pi-\delta$ giving

$$L_1(\lambda)=\sqrt{\lambda}\int_0^{\pi/2} h(x)e^{i\lambda f(x;\delta)}dx$$

with

$$h(x)=[1+\cos(x+\delta)]e^{ik\rho\,\sin(\varphi-x)}$$

and

$$f(x;\delta)=-\cos(x+\delta).$$

Thus L_1 has a stationary-phase point at $x=-\delta$, which approaches the end-point $x=0$ as $\delta\to 0$. The prototype special function with this property is the complementary error function, defined by (28). In order to relate this function to L_1, we change the integration variable from x to t, using

$$f(x;\delta)-f(0;\delta)=\tfrac{1}{2}t^2+\gamma t,$$

requiring that $x=-\delta$ is mapped to $t=-\gamma$ gives $\gamma=2\times\sin\frac{1}{2}\delta$. Hence,

$$L_1(\lambda)=\sqrt{\lambda}e^{i\lambda f(0;\delta)}\int_0^T \tilde{h}(t)e^{i\lambda(1/2\,t^2+\gamma t)}dt,$$

where

$$\tilde{h}(t)=h(x(t))\frac{dx}{dt}\quad\text{and}\quad\frac{dx}{dt}=\frac{t+\gamma}{f'(x;\delta)}.$$

For the dominant contribution, we can set the upper limit $T=\infty$ and replace $\tilde{h}(t)$ by $\tilde{h}(0)$; this gives

$$L_1(\lambda)\simeq\sqrt{\lambda}e^{i\lambda f(0;\delta)}\frac{\gamma h(0)}{f'(0;\delta)}\int_0^\infty e^{i\lambda[(1/2)\,t^2+\gamma t]}dt.$$

Standard manipulations show that the integral can be expressed as

$$\sqrt{\frac{\pi}{2\lambda}}e^{i\pi/4}e^{-1/2i\lambda\gamma^2}\mathrm{erfc}(\mu)\quad\text{with}\quad\mu=\gamma\sqrt{\frac{1}{2}\lambda}e^{-i\pi/4}.$$

Substituting back, we obtain

$$L_1(\lambda)\simeq\sqrt{2\pi}\,\cos\tfrac{1}{2}\delta e^{i\pi/4}e^{-i\lambda}e^{ik\rho\,\sin\varphi}\mathrm{erfc}(\mu)$$

whence the final result (27) follows.

APPENDIX B: ASYMPTOTIC BEHAVIOR OF F_n

In order to estimate $F_n(kr,\alpha)$ for large kr, we substituted the asymptotic approximation (32) into (31). However, this requires some justification, as (32) presupposes that m and n are fixed. [A hint that nonuniform behavior might be expected comes from (29): The left-hand side is a plane wave whereas every term on the right-hand side is $O((kr)^{-1/2})$ as $kr\to\infty$.] We start by writing

$$F_n(w,\alpha)=w\{H_n'(w)\mathscr{F}_n(w,\alpha)-H_n(w)(\partial/\partial w)\mathscr{F}_n(w,\alpha)\},$$

where

$$\mathscr{F}_n(w,\alpha)=\sum_j\frac{1}{2j+1}J_{n+2j+1}(w)e^{i(2j+1)\alpha}.\tag{B1}$$

Next, we use a standard integral representation for Bessel functions,

$$J_m(w)=\frac{1}{2\pi}\int_{-\pi}^{\pi}e^{i(m\theta-w\,\sin\theta)}d\theta,$$

whence

$$\mathscr{F}_n(w,\alpha)=\frac{i}{4}\int_{-\pi}^{\pi}\mathscr{G}(\theta+\alpha)e^{i(n\theta-w\,\sin\theta)}d\theta\tag{B2}$$

where $\mathscr{G}(\theta)$ is defined by (33). Finally, we use the method of stationary phase to estimate (B2) for large w; there are stationary-phase points at $\theta=\pm\frac{1}{2}\pi$, whence (22) gives

$$\mathscr{F}_n(w,\alpha)=\sqrt{(\tfrac{1}{2}\pi/w)}\sin(w-\tfrac{1}{2}n\pi-\tfrac{1}{4}\pi)+O(w^{-1})$$

as $w\to\infty$, for $0\leqslant|\alpha|<\frac{1}{2}\pi$, whereas

$$\mathscr{F}_n(w,\pm\tfrac{1}{2}\pi)=O(w^{-1})\quad\text{as}\ w\to\infty.$$

These results are *exactly* the same as we would have obtained if we had replaced the Bessel function in (B1) by the leading term in its large-argument asymptotic expansion, namely (26).

APPENDIX C: ASYMPTOTIC BEHAVIOR OF $I(U_{\mathrm{con}};H_r)$

Disregarding the evanescent terms in (14), we can write u_{con} as the integral in (11), whence

$$I(u_{\mathrm{con}};H_r)=\int_{-\pi/2}^{\pi/2}A(\alpha)I(v;H_r)d\alpha\simeq iBe^{i\lambda}\sqrt{\lambda}\mathscr{D}(\lambda)$$

as $\lambda\equiv kr\to\infty$, where we have used (21), and

$$\begin{aligned}\mathscr{D}(\lambda)&=\int_{-\pi/2}^{\pi/2}A(\alpha)\int_{-\pi/2}^{\pi/2}[1-\cos(\theta-\alpha)]\\&\quad\times e^{-ik\rho\,\cos(\theta-\varphi)}e^{i\lambda\,\cos(\theta-\alpha)}d\theta d\alpha\\&=\int_{-\pi/2}^{\pi/2}A(\alpha)\int_{-\pi/2-\alpha}^{\pi/2-\alpha}(1-\cos\psi)\\&\quad\times e^{-ik\rho\,\cos(\psi+\alpha-\varphi)}e^{i\lambda\,\cos\psi}d\psi d\alpha.\end{aligned}$$

As A is a continuous function of α, we can change the order of integration to give

$$\mathscr{D}(\lambda)=\int_0^\pi(1-\cos\psi)Q(\psi)e^{i\lambda\,\cos\psi}d\psi,\tag{C1}$$

where

$$Q(\psi)=\int_{-\pi/2}^{\pi/2-\psi}\{A(\alpha)e^{-ik\rho\,\cos(\psi+\alpha-\varphi)}+A(-\alpha)e^{-ik\rho\,\cos(\psi+\alpha+\varphi)}\}d\alpha.$$

Now we can estimate $\mathscr{D}(\lambda)$ for large λ using the method of stationary phase. The stationary-phase points are $\psi=0$ and $\psi=\pi$. At $\psi=0$, $1-\cos\psi=0$, whereas $Q(\pi)=0$. Hence, the integrand in (C1) vanishes at both stationary-phase points, whence $\mathscr{D}(\lambda)=O(\lambda^{-1})$ as $\lambda\to\infty$. Thus, we deduce that $I(u_{\mathrm{con}};H_r)\to0$ as $r\to\infty$.

Asvestas, J. S., and Kleinman, R. E. (**1994**). ''Electromagnetic scattering by indented screens,'' IEEE Trans. **AP-42**, 22–30.

Beckmann, P., and Spizzichino, A. (**1963**). *The Scattering of Electromagnetic Waves from Rough Surfaces* (Pergamon, Oxford).

Berman, D. H., and Perkins, J. S. (**1985**). ''The Kirchhoff approximation and first-order perturbation theory for rough surface scattering,'' J. Acoust. Soc. Am. **78,** 1045–1051.

Bishop, G. C., and Smith, J. (**1992**). ''A scattering model for nondifferentiable periodic surface roughness,'' J. Acoust. Soc. Am. **91,** 744–770.

Bleistein, N., and Handelsman, R. A. (**1986**). *Asymptotic Expansions of Integrals* (Dover, New York).

Chandler-Wilde, S. N., and Ross, C. R. (**1995**). ''Scattering by one-dimensional rough surfaces,'' in *The 3rd International Conference on Mathematical and Numerical Aspects of Wave Propagation*, edited by G. Cohen, E. Bécache, P. Joly, and J. E. Roberts (SIAM, Philadelphia), pp. 208–215.

Chandler-Wilde, S. N., and Ross, C. R. (**1996**). ''Scattering by rough surfaces: the Dirichlet problem for the Helmholtz equation in a non-locally perturbed half-plane,'' Math. Methods Appl. Sci. **19**, 959–976.

Chao, J. C., Rizzo, F. J., El-Shafiey, I., Liu, Y. J., Udpa, L., and Martin, P. A. (**1996**). ''A general formulation for light scattering by a dielectric body near a perfectly conducting surface,'' J. Opt. Soc. Am. A **13,** 338–344.

Clemmow, P. C. (**1966**). *The Plane Wave Spectrum Representation of Electromagnetic Fields* (Pergamon, Oxford).
Colton, D., and Kress, R. (**1983**). *Integral Equation Methods in Scattering Theory* (Wiley, New York).
DeSanto, J. A., and Brown, G. S. (**1986**). ''Analytical techniques for multiple scattering from rough surfaces,'' in *Progress in Optics XXIII*, edited by E. Wolf (Elsevier, New York), pp. 1–62.
DeSanto, J. A., and Martin, P. A. (**1996**). ''On angular-spectrum representations for scattering by infinite rough surface,'' Wave Motion **24,** 421–433.
Holford, R. L. (**1981**). ''Scattering of sound waves at a periodic, pressure-release surface: An exact solution,'' J. Acoust. Soc. Am. **70,** 1116–1128.
Lentz, R. R. (**1974**). ''A numerical study of electromagnetic scattering from ocean-like surfaces,'' Radio Sci. **9,** 1139–1146.
Lysanov, Iu. P. (**1956**). ''One approximate solution for the problem of the scattering of acoustic waves by an uneven surface,'' Sov. Phys. Acoust. **2,** 190–197.
Maystre, D., and Dainty, J. C. (Eds.) (**1991**). *Modern Analysis of Scattering Phenomena* (Adam Hilger, Bristol).
McSharry, P. E., Moroney, D. T., and Cullen, P. J. (**1995**). ''Wave scattering by a two-dimensional pressure-release surface based on a perturbation of the Green's function,'' J. Acoust. Soc. Am. **98,** 1699–1716.
Ogilvy, J. A. (**1991**). *Theory of Wave Scattering from Random Rough Surfaces* (Adam Hilger, Bristol).
Ramm, A. G. (**1986**). *Scattering by Obstacles* (Reidel, Dordrecht).
Rodríguez, E., Kim, Y., and Durden, S. L. (**1992**). ''A numerical assessment of rough surface scattering theories: Horizontal polarization,'' Radio Sci. **27,** 497–513.
Saillard, M., and Maystre, D. (**1990**). ''Scattering from metallic and dielectric rough surfaces,'' J. Opt. Soc. Am. A **7,** 982–990.
Shaw, W. T., and Dougan, A. J. (**1995**). ''Half-space Green's functions and applications to scattering of electromagnetic waves from ocean-like surfaces,'' Waves Random Media **5,** 341–359.
Thorsos, E. I. (**1988**). ''The validity of the Kirchhoff approximation for rough surface scattering using a Gaussian roughness spectrum,'' J. Acoust. Soc. Am. **83,** 78–92.
Urosovskii, I. A. (**1960**). ''Sound scattering by a sinusoidally uneven surface characterized by normal acoustic conductivity,'' Sov. Phys. Acoust. **5,** 362–369.
Voronovich, A. G. (**1994**). *Wave Scattering from Rough Surfaces* (Springer-Verlag, Berlin).
Willers, A. (**1987**). ''The Helmholtz equation in disturbed half-spaces,'' Math. Methods Appl. Sci. **9**, 312–323.

The calculation of the transient near and far field of a baffled piston using low sampling frequencies

Jan D'hooge[a)]
Laboratory for Medical Imaging Research, Department of Electrical Engineering, Katholieke Universiteit Leuven, Kardinaal Mercierlaan 94, B-3001 Heverlee, Belgium

Johan Nuyts
Department of Nuclear Medicine, Katholieke Universiteit Leuven, Herestraat 49, B-3000 Leuven, Belgium

Bart Bijnens, Bruno De Man, and Paul Suetens
Laboratory for Medical Imaging Research, Department of Electrical Engineering, Katholieke Universiteit Leuven, Kardinaal Mercierlaan 94, B-3001 Heverlee, Belgium

Jan Thoen
Laboratorium voor Akoestiek en Thermische Fysica, Departement Natuurkunde, Katholieke Universiteit Leuven, Celestijnenlaan 200 D, B-3001 Heverlee, Belgium

Marie-Christine Herregods and Frans Van de Werf
Department of Cardiology, Katholieke Universiteit Leuven, Herestraat 49, B-3000 Leuven, Belgium

(Received 4 December 1996; accepted for publication 21 March 1997)

A method is presented to calculate the near- and far-field transient radiation of acoustical transducers using low sampling frequencies. The method is based on the classical impulse response approach and on the fact that in practical use the spectrum of the excitation function of a transducer is band limited. This makes it possible to use a smoothed version of the impulse response function. A simple expression to calculate this smoothed function, for a rectangular or circular transducer, is derived. The proposed solution allows accurate computation of pressure fields and backscatter signals, while avoiding high sampling frequencies in the far field of the transducers. Several examples illustrate the accuracy of this new solution and its use for spectral analysis of simulated reflected signals. © *1997 Acoustical Society of America.* [S0001-4966(97)05307-1]

PACS numbers: 43.20.Fn, 43.35.Wa, 43.20.Px [ANN]

INTRODUCTION

The characterization of biological tissues based on the analysis of echographic images is receiving increased attention. However, since biological tissue is a very complex propagation medium, it is not well understood which structures of the tissue cause scattering or contribute most to the backscattered signal. This knowledge would provide important feedback for developing signal processing techniques for ultrasonic tissue characterization. For this reason many investigators analyze simulated backscattered data from different tissue models to get a better understanding of the influence of tissue parameters (e.g., mean scatterer distance) on these signals.[1–3] However, in order to simulate reflected signals, the knowledge of the pressure field produced by the transducer is indispensable.

Several methods to calculate the transient pressure field of a planar transducer in an infinite rigid baffle have been proposed in the past. An excellent review of the theoretical approaches used is given by Harris.[4] A widely used method is the impulse response approach as described by Tupholme[5] and Stepanishen,[6,7] in which the pressure at a field point $\mathbf{r}$ is written as a convolution of the first time derivative of the normal velocity of the transducer surface with an impulse response function $h(\mathbf{r},t)$, which is dependent on the geometry of the piston. Analytic expressions of the impulse response function were proposed for different transducer geometries. Stepanishen[7] derived the response for a flat, circular aperture. An expression for a rectangular transducer was found by Lockwood and Willette.[8] The solution for a concave radiator was derived by Pentinnen and Luukkala[9] and recently an expression for a triangular transducer was proposed by Jensen.[10] However, in the far field of the transducers the impulse response function becomes very peaked. Hence, in order to calculate the exact impulse function numerically, high sampling frequencies are required, resulting in large computation times.

This paper presents a method to calculate the far field of transducers numerically using low sampling frequencies. The method is based on the fact that the spectrum of the excitation function of the transducer is band-limited, which means that the high-frequency information of the impulse response function is irrelevant. One way to reduce the high-frequency components is by smoothing the impulse response function. A simple expression for the impulse response function smoothed with a rectangular pulse is derived for both the circular and rectangular transducer. Plots of the normal and smoothed impulse response function will be presented. Spectrum analysis on reflected signals of simple scattering structures is performed. A comparison between the classical method and the proposed method is made.

[a)]Electronic mail: jan.dhooge@uz.kuleuven.ac.be

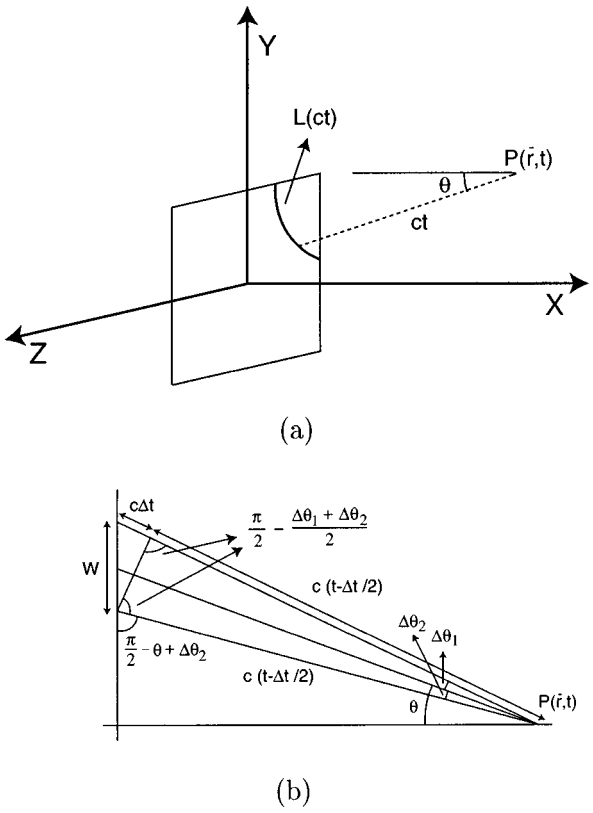

FIG. 1. Geometrical variables used to calculate the impulse response functions.

I. GENERAL THEORY

The excess pressure $p(\mathbf{r},t)$ generated by a planar source, vibrating with a uniform velocity distribution and surrounded by an infinite baffle, in a field point with coordinate vector $\mathbf{r}$ at a time instance t, can be written as[4]

$$p(\mathbf{r},t)=\rho\frac{\partial v(t)}{\partial t}*h(\mathbf{r},t), \tag{1}$$

where * denotes a convolution operation, ρ is the density of the medium, $v(t)$ is the velocity of a point on the transducer surface and the impulse response function h is defined as

$$h(\mathbf{r},t)=\int_S\frac{\delta(t-R/c)}{2\pi R}dS, \tag{2}$$

where δ is the Kronecker delta function, dS is an area element of the radiator, R is the distance from dS to the field point $\mathbf{r}$, and c is the velocity of sound inside the medium. Physically, Equation (2) means that the transducer surface can be represented by a collection of point sources, each emitting a spherical wavelet. Only these point sources on the surface that lie at the appropriate distance will contribute to the soundfield at time instance t.

This expression can also be written as[7]

$$h(\mathbf{r},t)=\frac{L(ct)}{2\pi t\ \sin\ \theta(ct)}, \tag{3}$$

where $L(ct)$ is the arc length of intersection of the piston with the surface of a sphere of radius ct centered at the field point $\mathbf{r}$. The circular intersection of this sphere with the transducer plane and the spatial point of interest $\mathbf{r}$ define a cone. The angle $\theta(ct)$ is half the top angle of this cone, as illustrated in Fig. 1(a).

The impulse response function can be calculated analytically for several transducer geometries,[7,8,10–12] for several transducer velocity profiles[13,14] and for curved transducers.[9,15]

II. SMOOTHED IMPULSE RESPONSE FUNCTION

In the far field of the transducer the impulse response function becomes very peaked and high sampling frequencies must be used.[15,16]

However, the Fourier transform of Equation (1) is

$$P(\mathbf{r},\omega)=i\omega\rho V(\omega)H(\mathbf{r},\omega). \tag{4}$$

In practical use the excitation function $V(\omega)$ of a transducer is band limited, which means that, in order to calculate the pressure field, all high-frequency information of the impulse response function is irrelevant, since these frequencies will be multiplied by zero. Hence, this function can be low pass filtered without losing any accuracy. In the time domain this means that the function can be smoothed.

In order to smooth the impulse response function with a rectangular pulse, $L(ct)$ in Equation (3) can be substituted by

$$L^*(ct)=\frac{1}{\Delta t}\int_{t-\Delta t/2}^{t+\Delta t/2}L(c\tau)d\tau$$

$$=\frac{O(c(t+\Delta t/2))-O(c(t-\Delta t/2))}{W(t)}, \tag{5}$$

where $O(ct)$ is the surface defined by the intersection of a solid sphere with radius ct around field point $\mathbf{r}$ and the transducer surface. Here, W is the difference in radius between the intersection of the transducer surface and the sphere with radius $c(t+\Delta t/2)$ and the smaller sphere with radius $c(t-\Delta t/2)$, as illustrated in Fig. 1(b). Using the notations as defined in Fig. 1(b) it can easily be derived that

$$W(t)=\frac{c\Delta t}{\sin(\theta+(\Delta\theta_1-\Delta\theta_2)/2)}\cos\frac{\Delta\theta_1+\Delta\theta_2}{2}. \tag{6}$$

However, in practical use is $c\Delta t\ll x$, which means that $(\Delta\theta_1+\Delta\theta_2)/2$ is very small. Hence, we can approximate the cosine term by one. If we assume that $(\Delta\theta_1-\Delta\theta_2)/2\ll\theta$ the second term of the argument of the sine function can be neglected. Hence, $L^*(ct)$ can be approximated by

$$L^*(ct)\approx\frac{O(c(t+\Delta t/2))-O(c(t-\Delta t/2))}{c\Delta t/\sin\ \theta(ct)}. \tag{7}$$

This means that the function $h(\mathbf{r},t)$ is smoothed with a rectangular pulse of width Δt. Notice that in order to keep the width of the pulse constant in the time domain, the width of the corresponding transducer area will decrease with time.

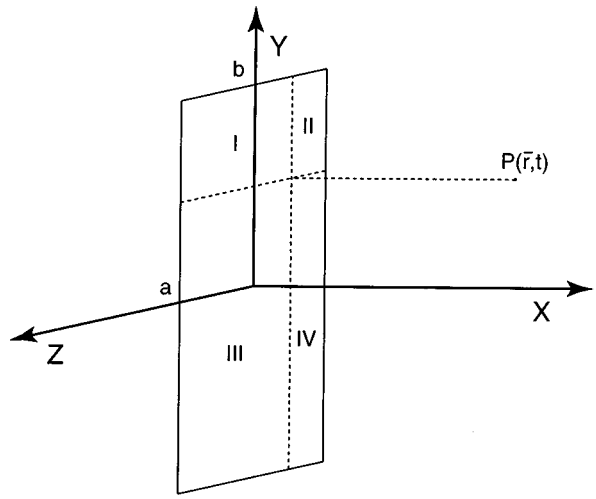

(a)

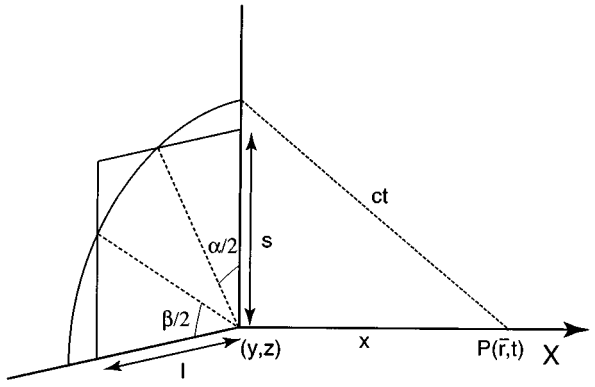

(b)

FIG. 2. General geometry for a field point in front of a rectangular transducer. The transducer is divided into four smaller rectangles, depending on the spatial position of the field point (a). Geometry for a field point in front of the corner of a rectangular element (b).

If we use the notations as illustrated in Fig. 2(b), an expression for $O(ct)$ for a field point in front of the corner of a rectangular transducer can easily be obtained (with $l \geqslant s$) :

$$O(ct)=\frac{(c^2t^2-x^2)}{4}\left\{(H_{ct}(x)-H_{ct}(\sqrt{x^2+s^2}))\pi \right.$$
$$+(H_{ct}(\sqrt{x^2+s^2})-H_{ct}(\sqrt{x^2+l^2}))(\pi-(\alpha-\sin\alpha))$$
$$+(H_{ct}(\sqrt{x^2+l^2})-H_{ct}(\sqrt{x^2+s^2+l^2}))$$
$$\times(\pi-[(\alpha-\sin\alpha)+(\beta-\sin\beta)])$$
$$\left.+H_{ct}(\sqrt{x^2+l^2+s^2})\left(\frac{4ls}{c^2t^2-x^2}\right)\right\},$$

where

$$H_{ct}(y)=\begin{cases}1, & ct \geqslant y,\\ 0, & ct<y,\end{cases} \tag{8}$$

$$\alpha=2\ \mathrm{Arccos}\frac{s}{\sqrt{c^2t^2-x^2}}, \tag{9}$$

and

$$\beta=2\ \mathrm{Arccos}\frac{l}{\sqrt{c^2t^2-x^2}}. \tag{10}$$

It is the area of a quarter of a circle with radius $\sqrt{c^2t^2-x^2}$ of which one or two half-circle segments, with area $[(c^2t^2-x^2)/4](\alpha-\sin\alpha)$ and $[(c^2t^2-x^2)/4](\beta-\sin\beta)$, are subtracted. The last term is the area of the entire rectangle. When the superposition method as described by Lockwood and Willette[8] and illustrated in Fig. 2(a) is used, the smoothed impulse response of a rectangular source in any field point can be calculated. Figure 3(a) illustrates the impulse response function for a rectangular transducer, smoothed by several rectangular pulses. A sampling frequency of 100 MHz was used.

However, by smoothing the impulse response function with a rectangular pulse, the spectrum of the original function is multiplied with a sinc-function. This is clearly illustrated in Fig. 3(b). As a consequence, not only the high-frequency components are reduced but also the low-frequency components are changed. In order to be able to reconstruct the correct spectrum, the spectrum of the smoothed impulse response function has to be divided by an appropriate sinc-function. This puts a constraint on how much the impulse response function can be smoothed without altering the results. The highest-frequency component of the excitation pulse has to be smaller than the first zero crossing of the sinc-function. Hence, we have the constraint that

$$f_{E\max}<\frac{1}{\Delta t}, \tag{11}$$

where $f_{E\max}$ is the highest-frequency component of the excitation pulse. Figure 3(b) clearly illustrates that in the non-smoothing case a sampling frequency of 50 MHz is well below the Nyquist frequency, which means that high-frequency information will be folded into the low-frequency band due to aliasing. This can alter the results significantly. However, since the spectrum of the smoothed impulse response function is multiplied with a sinc-function, the amount of energy folded into the low-frequency band will be much smaller.

Figure 4 shows the impulse response function and its smoothed version for different field points, sampled at 250 MHz. When the field point is located far off axis, its impulse function is smoother. Hence, smoothing is less important in these regions.

The same method can be used to find an expression for the smoothed impulse response function of a circular transducer. Using the notations in Fig. 5, $O(ct)$ can be expressed as

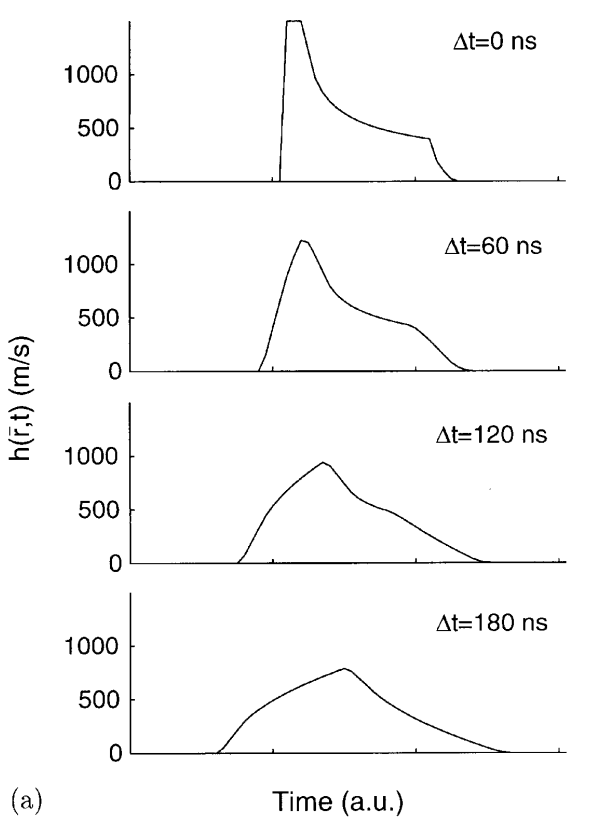

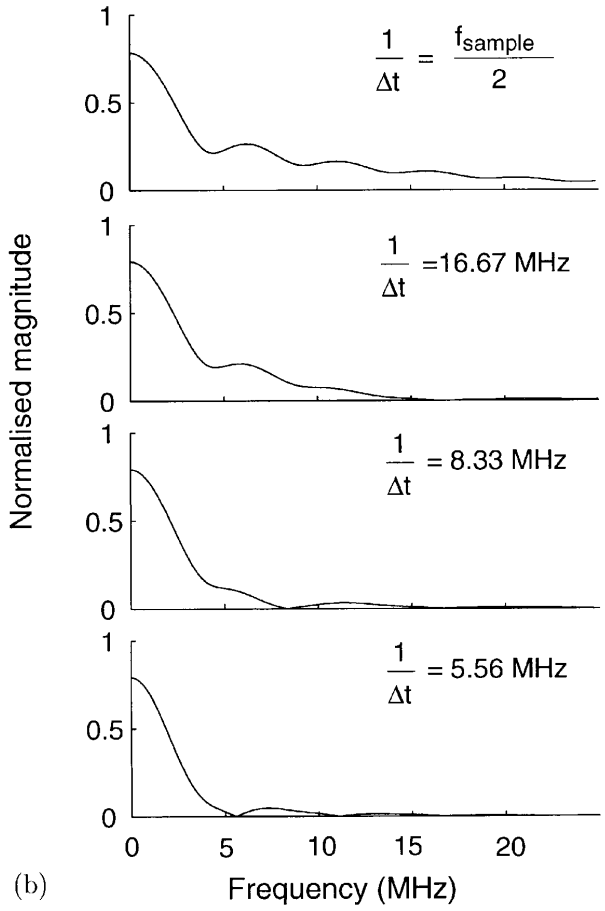

FIG. 3. The impulse response function of a rectangular transducer with $b/a=2.5$, smoothed with rectangular pulses of different width Δt (a) and their spectra (b). $x/a=20$, $y=0$ and $z=0$.

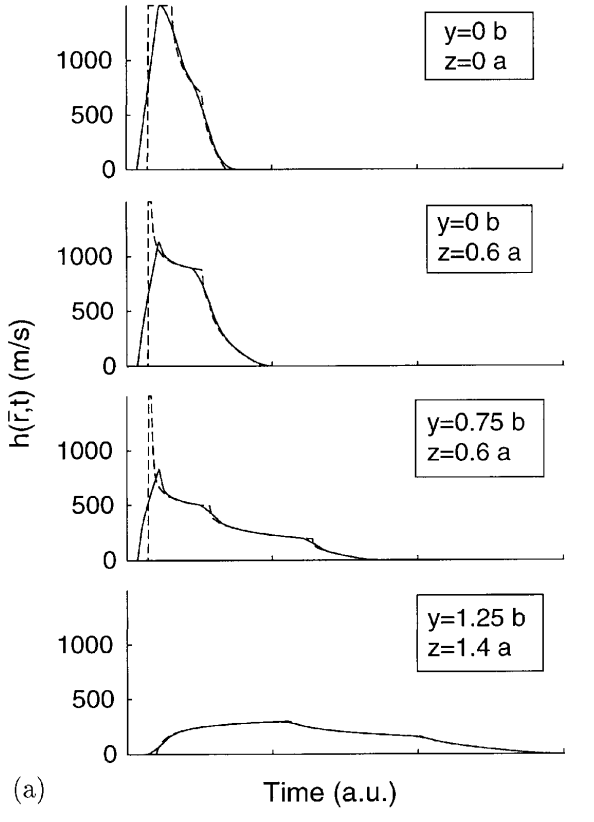

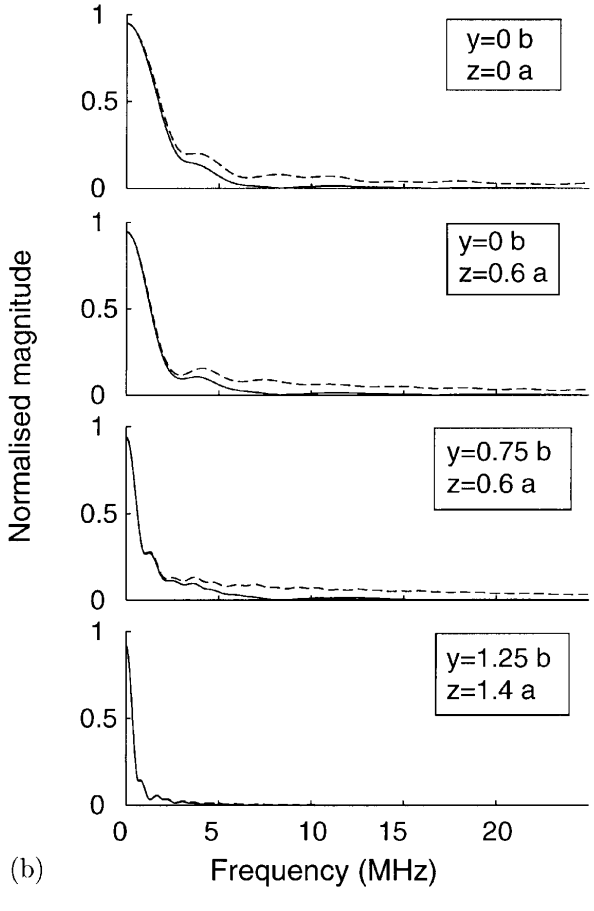

FIG. 4. The impulse response function of a rectangular transducer with $b/a=1.5$, at different field points without smoothing (dashed) and smoothed with a rectangular pulse of 120 ns (solid) (a) and their spectra (b). $x/a=10$.

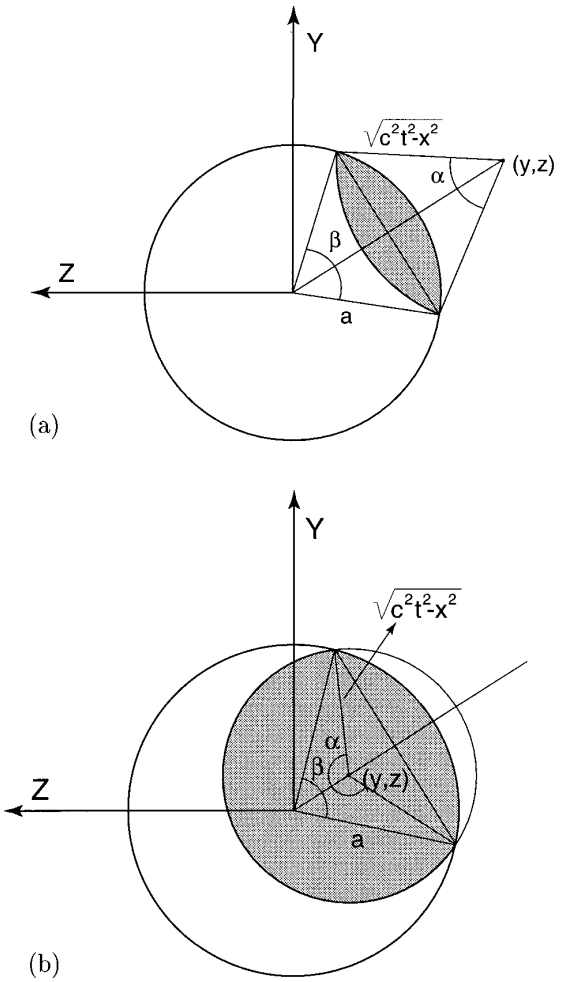

FIG. 5. Geometry for a field point in front of a circular transducer. The projection of the field point on the plane of the transducer lies outside (a) or inside (b) the transducer boundary.

$$\underline{\text{If } \sqrt{y^2+z^2} \geqslant a}$$

$$O(ct) = (H_{ct}(\sqrt{x^2+(\sqrt{y^2+z^2}-a)^2}) - H_{ct}(\sqrt{x^2+(\sqrt{y^2+z^2}+a)^2})) \times \left(\frac{c^2t^2-x^2}{2}(\alpha - \sin\alpha) + \frac{a^2}{2}(\beta - \sin\beta) \right) + (H_{ct}(\sqrt{x^2+(\sqrt{y^2+z^2}+a)^2}))(\pi a^2).$$

$$\underline{\text{If } \sqrt{y^2+z^2} < a}$$

$$O(ct) = (H_{ct}(x) - H_{ct}(\sqrt{x^2+(\sqrt{y^2+z^2}+a)^2})) \times (\pi(c^2t^2-x^2)) - (H_{ct}(\sqrt{x^2+(\sqrt{y^2+z^2}-a)^2}) - H_{ct}(\sqrt{x^2+(\sqrt{y^2+z^2}+a)^2})) \times \left(\frac{c^2t^2-x^2}{2}(2\pi - \alpha + \sin\alpha) - \frac{a^2}{2}(\beta - \sin\beta) \right) + (H_{ct}(\sqrt{x^2+(\sqrt{y^2+z^2}+a)^2})) \times (\pi a^2),$$

where

$$\alpha = 2\,\text{Arccos}\left(\frac{(c^2t^2-x^2)+(y^2+z^2)-a^2}{2\sqrt{(c^2t^2-x^2)(y^2+z^2)}} \right) \tag{12}$$

and

$$\beta = 2\,\text{Arccos}\left(\frac{a^2+(y^2+z^2)-(c^2t^2-x^2)}{2a\sqrt{y^2+z^2}} \right). \tag{13}$$

If $\sqrt{y^2+z^2} \geqslant a$ it is the sum of two circle segments with areas $(c^2t^2-x^2)/2(\alpha-\sin\alpha)$ and $(a^2/2)(\beta-\sin\beta)$, respectively. The last term is the area of the transducer surface. If $\sqrt{y^2+z^2} < a$ it is the area of a circle with radius $\sqrt{c^2t^2-x^2}$ of which one circle segment of area $[(c^2t^2-x^2)/2] \times (2\pi-\alpha+\sin\alpha)$ is subtracted. Because the subtracted area was too large, the area of a circle segment of area $(a^2/2) \times (\beta-\sin\beta)$ is added. Again, the last term is the area of the transducer surface.

An example of the smoothed impulse response function of a circular transducer for several field points is given in Fig. 6.

III. SIMULATIONS

Characterization of tissues by the analysis of echographic images is receiving increased attention. In order to evaluate new signal processing algorithms, many investigators use simulated reflected signals because they can be produced in a controllable environment. The theory of the impulse response can be extended to calculate the backscattered signal received from a point scatterer. However, since the scattering structures under investigation are located in the far field of the transducer, high sampling frequencies had to be used to assure the accuracy of the calculations. Since the assumption is made that the superposition principle holds, the total signal from a scattering structure is the sum of the reflections from the individual point scatterers. This means that computation time increases linearly with the number of scatterers.

Hence, a compromise had to be made between the amount of scatterers and the accuracy of the calculation, which depends on the sampling frequency. Two simulation examples illustrate that the proposed solution allows to produce accurate results using low sampling frequencies. This allows the simulation of large amounts of scatterers without losing accuracy.

However, by approximating Equation (6), an error, depending on several variables, is introduced in the calculations. In order to have an estimate of this error, the smoothed impulse response function calculated using the proposed method was compared with the normal impulse response function smoothed with a rectangular pulse in the time domain by normal convolution. According to Equation (5) this should give the same result. The latter function was computed numerically using very dense sampling. Hence, this function could be used as a reference. Figure 7 shows the

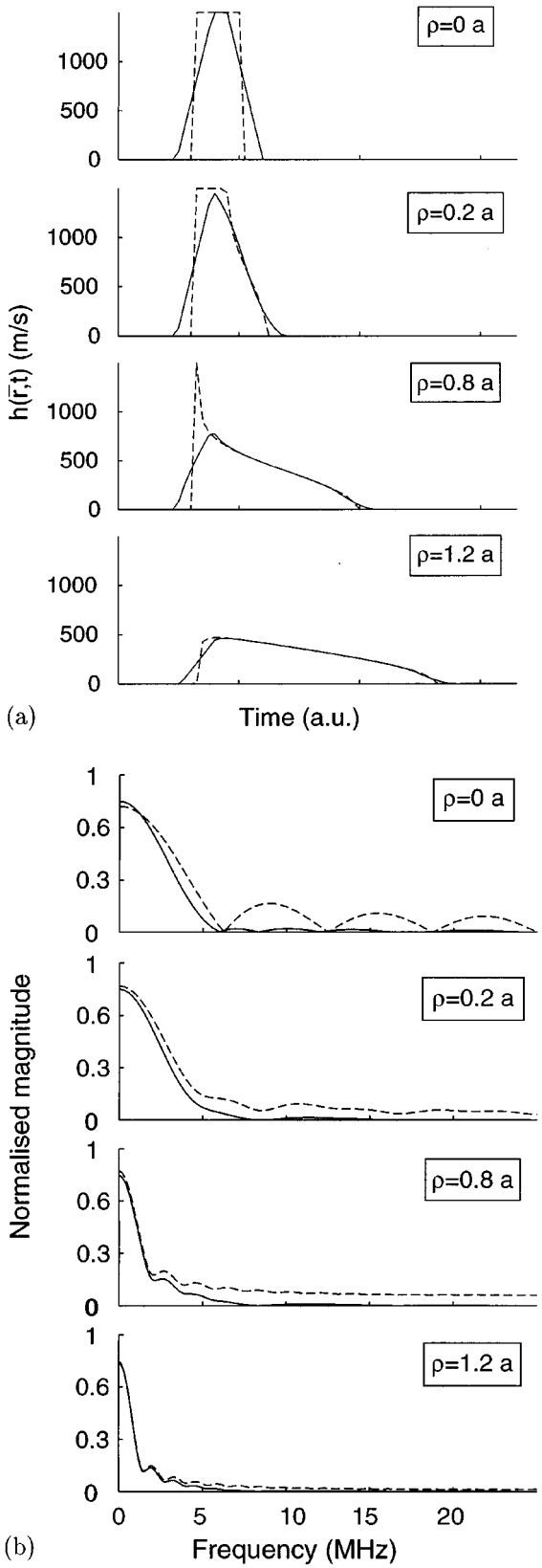

FIG. 6. The impulse response function (dashed) and its smoothed version (solid) of a circular transducer smoothed with a rectangular pulse of 120 ns (a) and their spectra (b). $x/a=10$, $\rho=\sqrt{y^2+z^2}$.

error of the impulse response smoothed by the proposed method relative to the mean value of the smoothed impulse response function for a practical situation. The error introduced is less than 0.6%.

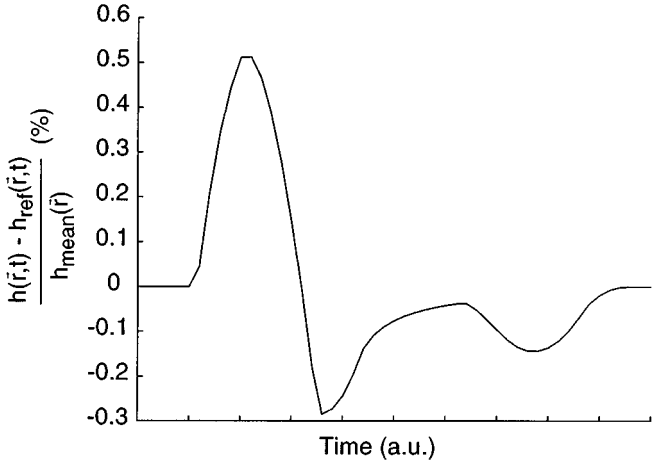

FIG. 7. The relative error of the smoothed impulse response function of a rectangular transducer with $b/a=2.5$, with a rectangular pulse of width $\Delta t=120$ ns. The sampling frequency was 100 MHz. $x/a=20$, $y=0$ and $z=0$. The smoothed impulse response function is shown is Fig. 3(a).

A. Transmit–receive echo from a distribution of point scatterers

In order to calculate the reflected signal from a rigid point scatterer, the theory outlined in Sec. I can be extended:[17]

$$E(t)=-\frac{k\rho}{2c}\left[\frac{\partial^2 v(t)}{\partial t^2}*h(\mathbf{r},t)*h(\mathbf{r},t)\right], \tag{14}$$

where $E(t)$ is the output voltage of the transducer at time instance t and k is a proportionality factor, depending on the characteristics of the scatterer and of the acousto-electrical transfer function of the transducer. This equation is valid for a transducer in transmit–receive mode. Remark that if the smoothed impulse function is used, the correct spectrum can be found by dividing the calculated spectrum by an appropriate sinc^2-function. Since a sinc-function has several zero crossings only the part before the first zero crossing is taken into account. The rest of the inverse sinc^2-function is set equal to zero. This means that we filter with the product of an inverse sinc^2-function and a rectangular window. Hence, the spectrum of the result is compensated for the multiplication with the sinc^2-function but the multiplication with a rectangular window is introduced. However, since relationship (11) holds, this will not have an influence on the results.

For a phased-array transducer receiving signals from a distribution of point scatterers, expression (14) becomes

$$E(t)=-\frac{k\rho}{2c}\sum_{j=1}^{N}\left[\frac{\partial^2 v(t)}{\partial t^2}*\left(\sum_{i=1}^{M} h_i(\mathbf{r}_j,t+\Delta t_i)\right)*\left(\sum_{i=1}^{M} h_i(\mathbf{r}_j,t)\right)\right], \tag{15}$$

with N the number of point scatterers, M the number of elements contained in the transducer, h_i the impulse response function of element i, and $\mathbf{r}_j$ the coordinate vector of scatterer j. Here, Δt_i is the time shift of the response from the ith element. This formula holds for a phased array that is focused in sending but unfocused while receiving (by intro-

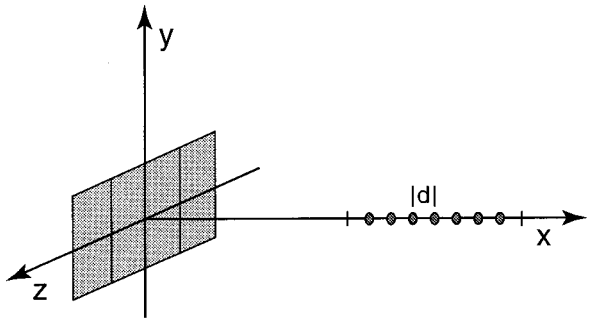

FIG. 8. Schematic representation of a phased-array transducer in a pulse-echo experiment, receiving reflections from a regular distribution of point scatterers.

ducing the phase shift Δt_i in the second impulse function as well, the transducer is also focused while receiving). Hence, the total reflected signal is the superposition of the signals of each individual scatterer.

B. Simulation I

Simulation I calculates the reflected signal, originating from a regular, one-dimensional distribution of scatterers, as illustrated in Fig. 8.

The phased-array transducer contained 64 elements and its size was 10 mm×8 mm. It was focused in the middle of the distribution of scatterers, which was located 55 mm from the transducer surface. The total length of the distribution was 20 mm. The emitted pulse had a mean frequency of 2.5 MHz and a Gaussian spectrum, which is illustrated in Fig. 9. Sampling frequencies of 50 MHz and 1.6 GHz were used. The distance between the scatterers was chosen equal to 400 μm. The width of the rectangular pulse to calculate the smoothed impulse response function was 120 ns.

C. Simulation II

Simulation II refers to the calculation of the reflected signal of a two-dimensional distribution of scatterers, contained within the xz plane. The scatterers were regularly positioned within a circle of radius 4.6 mm, with spacings of 500 μm in the x direction and 200 μm in the z direction. This distribution was rotated 10° perpendicular to the y axis. The transducer contained 64 elements and was excited with the same pulse as in simulation I. Sampling frequencies of 50 and 250 MHz were used. The same rectangular pulse as in simulation I was used to smooth the impulse function.

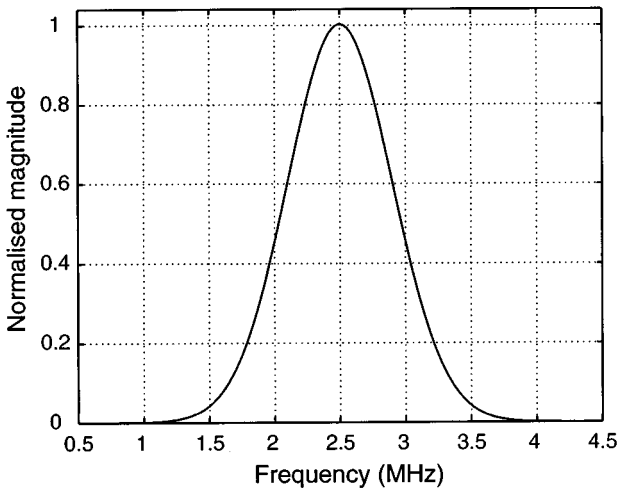

FIG. 9. Spectrum of the emitted pulse used in the simulation experiments.

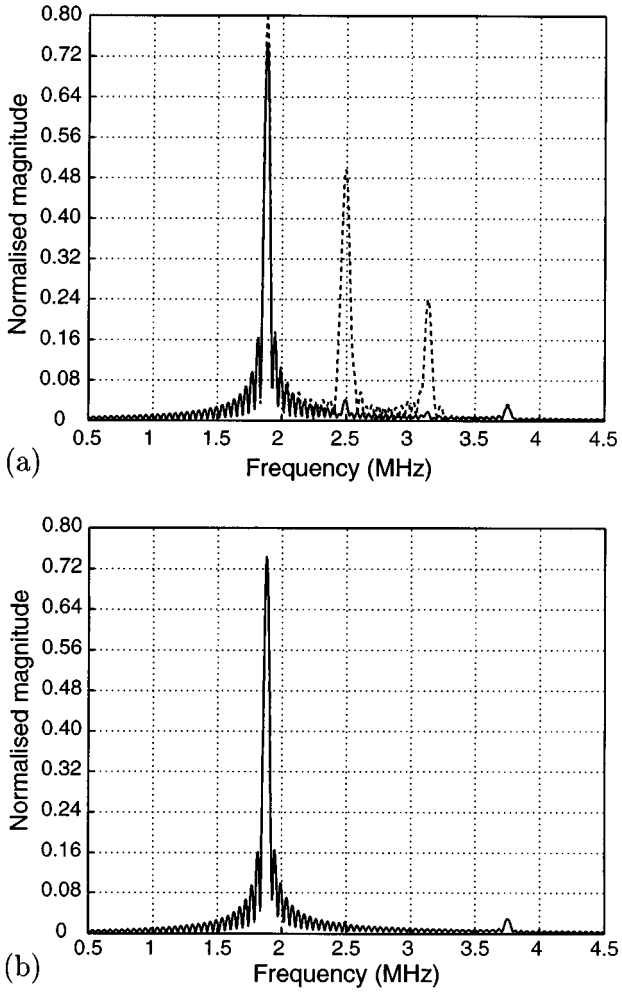

FIG. 10. Spectrum of the received backscattered signal originating from a regular distribution of scatterers using the impulse response method (dashed) and the smoothed impulse response method (solid). A phased-array transducer of 10 mm × 8 mm, containing 64 elements was simulated at a sampling frequency of 50 MHz (a) and 1.6 GHz (b).

D. Results

Figure 10 compares the spectra of the reflected signals for simulation I, calculated with the normal (dashed) and smoothed (solid) impulse response method, using a sampling frequency of 50 MHz (a) and 1.6 GHz (b). When the frequency f is equal to $c/2d$, with d the distance between the scatterers, constructive interference will occur. This means that we expect a peak in the spectrum at 1.875 MHz. However, the spectrum of the reflected signal calculated with the normal impulse response method at 50 MHz contains a large 2.5- and 3.1-MHz component. These peaks are suppressed

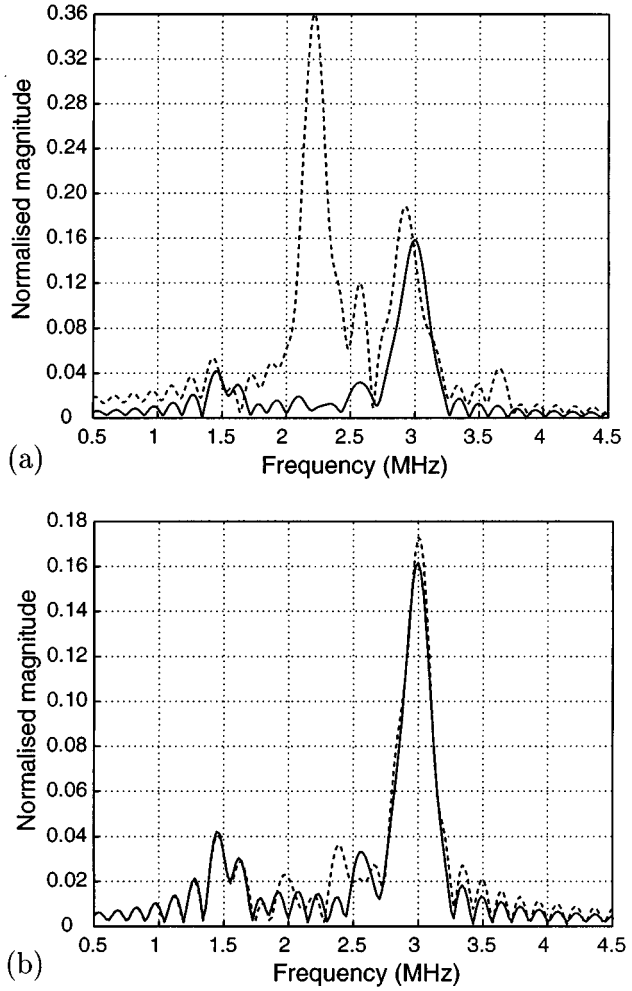

FIG. 11. Spectra of the reflected signals originating from a two-dimensional distribution of scatterers in the xz-plane using the normal method (dashed) and the smoothed method (solid) at 50 MHz (a) and 250 MHz (b). A phased-array transducer of 10 mm $\times$ 8 mm, containing 64 elements was simulated.

using the smoothed impulse response method. Remark that by both methods a peak appears at the second harmonic frequency, which will also constructively interfere.

Figure 11 compares the spectra of the reflected signals of simulation II, calculated with the normal (dashed) and the smoothed (solid) impulse response method at a sampling frequency of 50 MHz (a) and 250 MHz (b). The spectrum of the reflected signal calculated with the normal impulse response method at 50 MHz contains a large frequency component of 2.2 MHz. Moreover, a large contribution appears at 2.9 MHz. These contributions vanish when the sample frequency is increased to 250 MHz.

E. Discussion

Since the normal impulse response function has some abrupt changes, a high sampling frequency has to be used. Jensen[16] found out that a frequency of 1.6 GHz is adequate. This means that the results of simulation I, made at this sampling rate, can be used as a reference. When the normal impulse function is appropriately sampled, there is no difference between both methods, as was clearly illustrated in Fig. 10(b). However, when the sampling frequency decreases to 50 MHz, aliasing will become important and high-frequency information will be folded into the low-frequency band. This is the origin of the large peaks at 2.5 and 3.1 MHz for the normal impulse response method in Fig. 10(a). The spectrum calculated with the smoothed response also has a discrepancy at these frequencies but their energy content is much smaller. By smoothing the impulse response function with a rectangular pulse, the high-frequency components are suppressed (due to multiplication with a sinc-function) but not completely removed.

In this perspective it is clear that it would be better to smooth by a Hanning window, for instance. However, the construction used in this paper to find a solution for the smoothed impulse function cannot be used for these windows. In order to find an expression for, e.g., the Hanning-smoothed impulse function, the smoothing has to be done analytically. Unfortunally this results in solving a complex integral.

The results of simulation II clearly confirm the previous results: The difference between the two methods decreases if higher sampling frequencies are used. It is clear that the results using the smoothed impulse response function are much better but they are not exact. Since in practical use sampling frequencies of 50 MHz are often used, it is important to keep this in mind.

Both simulation examples clearly show that the error introduced by approximating Equation (6) and plotted in Fig. 7 for a practical situation, is negligible to the overall effect of the proposed method.

IV. CONCLUSIONS

A method has been presented to compute near- and far-field transient pressure fields of both circular and rectangular transducers using low sampling frequencies. The method is based on the impulse response approach but uses a smoothed version of the impulse response function. Closed form expressions to calculate this smoothed function were derived. Plots of the smoothed functions in comparison to the normal impulse functions were made for both transducer geometries.

A few simulation examples showed that reflected signals calculated with the normal impulse response function at low sampling frequencies, necessary in the past to simulate large amounts of scatterers, contain wrong frequency information due to aliasing. This makes the data inappropriate to evaluate new signal processing algorithms. The proposed solution solves this problem and can thus be valuable for further work in ultrasonic tissue characterization.

ACKNOWLEDGMENT

This work was supported by the Flemish Institute for the Improvement of the Scientific-Technological Research in the Industry (IWT).

[1] A. T. Kerr and J. W. Hunt, ''A method for computer simulation of ultrasound doppler color flow images—I. Theory and numerical method,'' Ultrasound Med. Biol. **18**, 861–872 (1992).
[2] R. F. Wagner, S. W. Smith, J. M. Sandrik, and H. Lopez, ''Statistics of

speckle in ultrasound *b*-scans,'' IEEE Trans. Sonics Ultrason. **30**, 156–163 (1983).
[3] J. T. M. Verhoeven, J. M. Thijssen, and A. G. Theeuwes, ''Improvement of lesion detection by echographic image processing: Signal-to-noise-ratio imaging,'' Ultrason. Imaging **13**, 238–251 (1991).
[4] G. R. Harris, ''Review of transient field theory for a baffled planar piston,'' J. Acoust. Soc. Am. **70**, 10–20 (1981).
[5] G. E. Tupholme, ''Generation of acoustic pulses by baffled plane pistons,'' Mathematika **16**, 209–224 (1969).
[6] P. R. Stepanishen, ''The time-dependent force and radiation impedance on a piston in a rigid infinite planar baffle,'' J. Acoust. Soc. Am. **49**, 841–849 (1971).
[7] P. R. Stepanishen, ''Transient radiation from pistons in an infinite planar baffle,'' J. Acoust. Soc. Am. **49**, 1629–1638 (1971).
[8] J. C. Lockwood and J. G. Willette, ''High-speed method for computing the exact solution for the pressure variations in the nearfield of a baffled piston,'' J. Acoust. Soc. Am. **53**, 735–741 (1973).
[9] A. Pentinnen and M. Luukkala, ''The impulse response and pressure nearfield of a curved ultrasonic radiator,'' J. Phys. D **9**, 1547–1557 (1976).
[10] J. A. Jensen, ''Ultrasound fields from triangular apertures,'' J. Acoust. Soc. Am. **100**, 2049–2056 (1996).
[11] J. L. San Emeterio and L. G. Ullate, ''Diffraction impulse response of rectangular transducers,'' J. Acoust. Soc. Am. **92**, 651–662 (1992).
[12] G. Scarano, N. Denisenko, M. Matteucci, and M. Pappalardo, ''A new approach to the derivation of the impulse response of a rectangular piston,'' J. Acoust. Soc. Am. **78**, 1109–1113 (1985).
[13] W. A. Verhoef, M. J. M. Cloostermans, and J. M. Thijssen, ''The impulse response of a focused source with an arbitrary axisymmetric surface velocity distribution,'' J. Acoust. Soc. Am. **75**, 1716–1721 (1984).
[14] H. Lasota, R. Salamon, and B. Delannoy, ''Acoustic diffraction analysis by the impulse response method: A line impulse response approach,'' J. Acoust. Soc. Am. **76**, 280–290 (1984).
[15] M. Arditi, F. S. Foster, and J. W. Hunt, ''Transient fields of concave annular arrays,'' Ultrason. Imaging **3**, 37–61 (1981).
[16] J. A. Jensen, ''A model for the propagation and scattering of ultrasound in tissue,'' J. Acoust. Soc. Am. **89**, 182–190 (1991).
[17] J. P. Weight and A. J. Hayman, ''Observations of the propagation of very short ultrasonic pulses and their reflection by small targets,'' J. Acoust. Soc. Am. **63**, 396–404 (1978).

Two-channel resonant scattering theory: Application to an absorbing elastic cylinder

H. Franklin, J.-M. Conoir, and J.-L. Izbicki
Laboratoire d'Acoustique Ultrasonore et d'Electronique, LAUE, URA 1373, Université du Havre, Place R. Schuman, 76610 Le Havre, France

(Received 28 May 1996; accepted for publication 13 March 1997)

The scattering of a plane sound wave normally incident on an absorbing elastic cylinder immersed in water is investigated theoretically. Because of the loss of acoustic energy due to absorption, the unitarity condition of the usual S matrix arising from the classical resonant scattering theory fails. However, it is shown that this unitarity condition can still be met by constructing a new S matrix which is nondiagonal. This construction is analogous to the multichannel scattering theory of particle physics. Computations are performed considering an absorbing elastic cylinder in order to check the validity of the theory. © *1997 Acoustical Society of America.* [S0001-4966(97)01607-X]

PACS numbers: 43.20.Fn [CBB]

INTRODUCTION

The scattering of a plane sound wave by infinite absorbing elastic cylinders or coated hollow cylinders has previously been studied by several investigators, both experimentally[1] and theoretically.[2–4] In the latter investigations, only the scattering cross sections or the form functions were examined extensively.

For nonabsorbing elastic materials, the resonance scattering theory[5,6] has given satisfactory results. However, it cannot be directly applied to absorbing media because the scattering matrix no longer satisfies the law of energy conservation, which is mathematically related to the unitarity condition of the S matrix. That is why we propose, in this paper, to extend the resonant scattering theory to absorbing media in light of the multichannel scattering theory developed in particle physics.[7,8] In the two-channel theory developed here, the scattering matrix is separated into elastic and absorbing parts and satisfies the unitarity condition. This presentation differs from previous works on scattering from absorbing elastic structures which concentrated only on the total pressure field scattered in the fluid, or on the form function. One of the advantages is that it allows us to decompose the resonance phenomenon into an elastic process (related to surface waves) and an absorbing process (related to energy absorbed by the scatterer). In Sec. I, the problem is described. Then, in Sec. II, a two-channel scattering theory is proposed that takes into account both the elastic and the absorbing processes. It is also briefly indicated how the theory can be applied to absorbing elastic bodies of arbitrary shapes. Section III is devoted to numerical computations.

I. DESCRIPTION OF THE PROBLEM

In this section, the results of the mathematical analysis of the scattering of a plane sound wave by infinite absorbing elastic cylinders are recalled. The absorption of acoustic energy in the cylinder is assumed to be small.

The material of the cylinder is assumed to be elastic, supporting longitudinal and transverse waves with velocities c_L and c_T, respectively, and immersed in a fluid of sound velocity c. If k is the incident wave number, the absorption can be included by introducing complex transverse and longitudinal wave numbers in the solid as[1]

$$k_L = k\,\frac{c}{c_L}\,(1-i\beta_L) \quad \text{and} \quad k_T = k\,\frac{c}{c_T}\,(1-i\beta_T), \tag{1}$$

where β_L and β_T are the absorption factors. Thus the purely elastic case is given by $\beta_L=\beta_T=0$.

For an acoustic plane wave normally incident on the cylinder, the pressure p_{scat} scattered by the cylinder is given by[5,6]

$$p_{\text{scat}} = p_0 \sum_{n=0}^{+\infty} \epsilon_n\,\frac{D_n^{[1]}(x)}{D_n(x)}\,H_n^{(1)}(kr)\cos n\theta, \tag{2}$$

where p_0 is the incident acoustic pressure, ϵ_n the Neumann factor, and $H_n^{(1)}$ the Hankel function of the first kind. The polar coordinates of the field point are r and θ, a is the cylinder radius, and $x=ka$ is the reduced frequency. The scattering coefficient usually denoted by $D_n^{[1]}/D_n$ is calculated from the boundary conditions.[5] Finally, as in the nonabsorbing case, the S^{abs} diagonal matrix is defined by the following relation:

$$S_n^{\text{abs}} = 1 + 2\,\frac{D_n^{[1]}}{D_n}, \tag{3}$$

where S_n^{abs} are the eigenvalues of S^{abs}. In the nonabsorbing case, the modulus of the eigenvalues is equal to one in agreement with the law of energy conservation, but that is no longer the case for the eigenvalues defined in Eq. (3) because of the loss of energy due to absorption. This fact leads us to call S^{abs} the operator of scattering and not the scattering ma-

 0001-4966/97/102(1)/87/9/$10.00

trix, the conservation of energy not being satisfied by S^{abs}. In what follows, we will write

$$S_n^{\mathrm{abs}} = \eta \overline{S_n}, \tag{4}$$

where η ($\eta \leqslant 1$) is the modulus of S_n^{abs} and $\overline{S_n}$ the phase term.

II. *S*-MATRIX THEORY FOR ABSORBING MEDIA

This section deals with an extension of the classical resonance scattering theory in order to analyze the resonances of absorbing elastic scatterers. If the absorption is small, then it is well known that the resonance frequencies are only slightly modified by absorption, whereas the widths of the resonances can be strongly modified by absorption. As a consequence, the absorption does not really affect the velocities of the surface waves propagating around the scatterer but mainly affects their reemission into the fluid surrounding the scatterer because of the loss of energy due to the absorption. Thus it is clear that the scattering process related to absorbing scatterers involves two different phenomena. The first one is related to the elasticity: This explains the propagation of the surface waves and the resonance frequencies. The second one is related to the absorption: This explains the difference in magnitude between the reemission of surface waves propagating around purely elastic scatterers and the reemission of surface waves propagating around absorbing scatterers, the difference being due to the absorption. As a consequence, we have to build a resonant scattering theory explaining the reemission of surface waves by assuming the existence of two channels, one for elastic and the other for absorbing effects. In terms of resonances, since the reemission of surface waves is linked to the width of resonances, we introduce two new widths of resonance related to the elastic and absorbing channels. In addition, because of the conservation of energy, the sum of these two widths has to be equal to the total widths of resonances, which are related to surface waves propagating around the absorbing scatterer.

Keeping in mind the results of nuclear physics,[7,8] the absorption can be taken into account by a scattering matrix but this matrix cannot be diagonal because of the law of energy conservation.

From this first analysis, it seems rather natural to build a scattering matrix S which is made up of 2×2 matrix blocks in order to describe the two channels (elastic and absorbing). The construction is based on the general multichannel scattering theory developed in particle physics. In fact, we will see that the multichannel theory is not directly appropriate, but the general frame of this theory can still be used. That is why this theory will be briefly developed in the first part of this section.

The two channels are denoted by 1 and 2 (in the following they correspond to the elastic and the absorbing channels, respectively). The multichannel theory serves to introduce a diagonal scattering matrix which is made up of blocks (2×2) having the following form:

$$\begin{bmatrix} S_{11}(n) & S_{12}(n) \\ S_{21}(n) & S_{22}(n) \end{bmatrix}, \tag{5}$$

where n denotes the nth mode vibration. In order to simplify the notations, the scattering matrix will be written:

$$S = \begin{bmatrix} S_{11} & S_{12} \\ S_{21} & S_{22} \end{bmatrix}, \tag{6}$$

and the law of energy conservation is then expressed as

$$SS^{T*} = 1, \tag{7}$$

where the transposition is denoted by T and the complex conjugate by $*$; 1 is the unity matrix. In this case, the usual way to analyze the resonances is first to remove the background from the global scattering and to diagonalize the resulting resonant scattering matrix. If the resonant scattering matrix is still denoted by S (in the following, we discuss only the resonant matrix S to minimize confusion), we obtain

$$S = R\Xi R^T, \tag{8}$$

where Ξ is the diagonal resonant scattering matrix defined by

$$\Xi = \begin{bmatrix} e^{2i\delta_1} & 0 \\ 0 & e^{2i\delta_2} \end{bmatrix}, \tag{9}$$

and R is an orthogonal matrix (because S is a unitary matrix) defined by

$$R = \begin{bmatrix} \cos\alpha & -\sin\alpha \\ \sin\alpha & \cos\alpha \end{bmatrix}. \tag{10}$$

In these matrices, the so-called eigenphases δ_i are real and α is called the mixing angle. Far from a resonance frequency, the eigenphases are equal to zero. One resonance corresponds to the case where the Breit–Wigner approximation is valid for one of the eigenphases, δ_1 for example. That is to say, δ_1 strongly varies around the resonance frequency $x^{(*)}$. If we neglect δ_2 in the vicinity of $x^{(*)}$, in a first approximation, the S-matrix takes the following form:

$$\begin{bmatrix} \cos^2\alpha\Xi_1 & \cos\alpha\sin\alpha\Xi_1 \\ \cos\alpha\sin\alpha\Xi_1 & \sin^2\alpha\Xi_1 \end{bmatrix} \tag{11}$$

with

$$\Xi_1 \approx \frac{x^{(*)} - x + i\Gamma/2}{x^{(*)} - x - i\Gamma/2}, \tag{12}$$

where $x^{(*)} - i\Gamma/2$ is the root of the equation $D_n(x) = 0$, $x^{(*)}$ being the resonance frequency and Γ the total width of the resonance. As a consequence, close to the resonance frequency $x^{(*)}$, the resonant transition matrix usually defined by

$$S = 1 + 2iT \tag{13}$$

will be approximated by

$$T=\begin{bmatrix} \cos^2\alpha\,\dfrac{\Gamma/2}{x^{(*)}-x-i\Gamma/2} & \cos\alpha\,\sin\alpha\,\dfrac{\Gamma/2}{x^{(*)}-x-i\Gamma/2} \\ \cos\alpha\,\sin\alpha\,\dfrac{\Gamma/2}{x^{(*)}-x-i\Gamma/2} & \sin^2\alpha\,\dfrac{\Gamma/2}{x^{(*)}-x-i\Gamma/2} \end{bmatrix}. \tag{14}$$

After that, it is convenient to define the partial width of resonance Γ_i as follows:

$$\cos\alpha\sqrt{\Gamma}=\sqrt{\Gamma_1} \quad \text{and} \quad \sin\alpha\sqrt{\Gamma}=\sqrt{\Gamma_2}, \tag{15}$$

so that the partial widths of resonance in each channel satisfy the law of energy conservation:

$$\Gamma_1+\Gamma_2=\Gamma, \tag{16}$$

and close to the resonance frequency $x^{(*)}$ the components of the resonant transition matrix take the form

$$T_{ij}\approx\frac{\sqrt{\Gamma_i\Gamma_j}/2}{x^{(*)}-x-i\Gamma/2}. \tag{17}$$

Relation (17) is known as the multichannel Breit–Wigner approximation.[7] It means that resonances appear in each component of the S- or T-matrices with an energy depending on the partial widths of resonance related to each other by Eq. (16). In addition, we have the useful relation

$$T_{ij}(x^{(*)})=i\,\frac{\sqrt{\Gamma_i\Gamma_j}}{\Gamma}. \tag{18}$$

An additional relation can be deduced from the multichannel theory useful to the acoustic scattering study. This relation is obtained by considering the multichannel Breit–Wigner approximation at the resonance frequency $x^{(*)}$ and Eq. (13). In this way we obtain

$$\frac{\Gamma_i}{\Gamma}=\frac{1}{2}\,(1\pm|S_{ii}(x^{(*)})|) \tag{19}$$

so that

$$|S_{ii}(x^{(*)})|=2\frac{\Gamma_i}{\Gamma}-1 \tag{20}$$

when $\Gamma_i/\Gamma\geqslant 1/2$, and

$$|S_{ii}(x^{(*)})|=1-2\frac{\Gamma_i}{\Gamma} \tag{21}$$

when $\Gamma_i/\Gamma\leqslant 1/2$.

Now the multichannel scattering theory will be adapted to acoustic scattering by absorbing scatterers. In order to do that, a convenient $S(2\times 2)$-matrix must be built where the first channel corresponds to the elastic channel, and the second one to the absorbing channel. First, it is obvious that the components of the S-matrix have to be related to the scattering operator $S^{\text{abs}}=\eta S$ describing the scattering by the absorbing cylinder. Then, the principle of the construction is based on the unitarity of S. Since $|S|=1$, we can write

$$\overline{S}=e^{2i\delta}, \tag{22}$$

where the phase δ is real. As a consequence, it is rather natural to consider that δ has to correspond to the eigenphase. Thus in the case of the scattering by absorbing scatterers, we have only one eigenphase δ, contrary to the cases usually considered in the classical multichannel theory. That is why the multichannel theory has to be adapted. The only way to build a matrix with two channels is to admit that $\delta_1+C_1=\delta_2+C_2=\delta$, where C_i are some constants. This hypothesis is realistic because the phase δ contains the whole resonant contribution of the scattering process as required by the multichannel theory.

From this analysis, we can build the Ξ resonant matrix by assuming that $\Xi=\Xi^+$ or $\Xi=\Xi^-$, where

$$\Xi^+=\begin{bmatrix} \overline{S} & 0 \\ 0 & -\overline{S} \end{bmatrix} \quad \text{and} \quad \Xi^-=\begin{bmatrix} -\overline{S} & 0 \\ 0 & \overline{S} \end{bmatrix}. \tag{23}$$

At this point of the scattering matrix construction, it is not possible to make a choice between Ξ^+ and Ξ^-. Equation (23) means that the S-matrix can take the following forms:

$$S=\begin{bmatrix} (\cos^2\alpha-\sin^2\alpha)\overline{S} & -2\cos\alpha\,\sin\alpha\overline{S} \\ -2\cos\alpha\,\sin\alpha\overline{S} & (\sin^2\alpha-\cos^2\alpha)\overline{S} \end{bmatrix} \tag{24a}$$

if $\Xi=\Xi^+$, or

$$S=\begin{bmatrix} -(\cos^2\alpha-\sin^2\alpha)\overline{S} & 2\cos\alpha\,\sin\alpha\overline{S} \\ 2\cos\alpha\,\sin\alpha\overline{S} & -(\sin^2\alpha-\cos^2\alpha)\overline{S} \end{bmatrix} \tag{24b}$$

if $\Xi=\Xi^-$.

These two matrices have several properties resulting from the general multichannel theory. First, it is obvious that S defined in Eqs. (24) satisfies Eq. (7); this result comes directly from the construction. Second, the resonant width corresponding to the elastic channel being denoted Γ_e, the resonant width corresponding to the absorbing channel being denoted Γ_a, and the total width of the resonance being denoted Γ, we have:

$$\cos\alpha\sqrt{\Gamma}=\sqrt{\Gamma_e} \quad \text{and} \quad \sin\alpha\sqrt{\Gamma}=\sqrt{\Gamma_a} \tag{25}$$

with

$$\Gamma_e+\Gamma_a=\Gamma. \tag{26}$$

The previous construction is up to now rather formal. First, we have implicitly decided that the first component of the scattering matrix was the elastic channel; the relations in Eq. (25) result from this choice. Second, we have not specified the sign used in the definition of Ξ. Third, the construction does not allow us to determine the mixing angle α. In order to solve these problems, we have to analyze more accurately the scattering operator S^{abs}. In fact, numerical calculations

performed in the following chapter will show that S^{abs} can be approximated using a Breit–Wigner approximation. More accurately, if we relate the resonant transition matrix T_e related to the elastic channel as

$$S^{\mathrm{abs}} = \eta\overline{S} = 1 + 2iT_e, \tag{27}$$

we can show that the resonant transition matrix T_e with a resonance frequency close to $x^{(*)}$ can be well approximated by the following Breit–Wigner function:

$$T_e \approx \frac{\Gamma_e/2}{x^{(*)} - x - i\Gamma/2}. \tag{28}$$

This approximation, which is numerically verified in the following, is a very important result because it allows us to determine the mixing angle α and to finish the construction of the scattering matrix S. As a matter of fact, using Eqs. (27) and (28), it is easy to show that

$$\eta = \left|1 - 2\frac{\Gamma_e}{\Gamma}\right| = \left|1 - 2\frac{\Gamma_a}{\Gamma}\right|. \tag{29}$$

As a consequence, by referring to Eq. (19) we can now write the relation

$$\cos\,\alpha = \sqrt{\frac{1 \pm \eta}{2}} \quad (\Gamma_e/\Gamma \geqslant \text{or} \leqslant 1/2). \tag{30}$$

Finally, because of the validity of the Breit–Wigner approximation applied to $\eta\overline{S}$, we are obliged to consider ηS as being the first component of the S-matrix corresponding to the elastic channel. That is the most important point of the construction. In this case, either $\Gamma_e/\Gamma \geqslant 1/2$ and we take $\Xi = \Xi^{+}$, or $\Gamma_e/\Gamma \leqslant 1/2$ and we take $\Xi = \Xi^{-}$. Thus in both cases the scattering matrix is then written

$$S = \begin{bmatrix} \eta\overline{S} & -\sqrt{1-\eta^2}\,\overline{S} \\ -\sqrt{1-\eta^2}\,\overline{S} & -\eta\overline{S} \end{bmatrix} \tag{31}$$

so that the elastic channel effectively corresponds to the first component of the S-matrix. This will be verified numerically in Sec. III.

It is now interesting to make some remarks about the absorbing S-matrix theory. First, the study of the resonant transition matrix does not only provide the value of the ratio Γ_e/Γ since [cf. Eq. (18)]

$$T_e(x^{(*)}) = i\frac{\Gamma_e}{\Gamma}, \tag{32}$$

but also the value of Γ by measuring the width of the curve defined by $|T_e|^2$ at the height $\Gamma_e{}^2/2\Gamma^2$. As a consequence, the theory enables us to determine both the resonance width Γ and the resonance width Γ_e in the elastic channel. The resonance width in the absorbing channel is then easily calculated by using Eq. (26). Another way to calculate the resonance width in the absorbing channel is to analyze the resonant transition matrix in the absorbing channel. As a matter of fact, this is defined according to the multichannel theory and Eq. (31) as

$$-\eta\overline{S} = 1 + 2iT_a. \tag{33}$$

Thus from Eq. (27) we obtain the following Breit–Wigner approximation (close to the resonance frequency $x^{(*)}$):

$$T_a \approx i\frac{x^{(*)} - x - i\Gamma_a/2}{x^{(*)} - x - i\Gamma/2} \tag{34}$$

so that

$$T_a(x^{(*)}) = i\frac{\Gamma_a}{\Gamma}, \tag{35}$$

as predicted by the multichannel theory. However, we have to note that the Breit–Wigner approximation given by Eq. (34) is different from that predicted by the multichannel theory which should have given by [cf. Eq. (17)]

$$T_a \approx \frac{\Gamma_a/2}{x^{(*)} - x - i\Gamma/2}. \tag{36}$$

This result is interesting because it shows that the absorbing scattering theory differs in fact from the classical multichannel theory. With the absorbing scattering theory, resonances appear naturally as Breit–Wigner peaks in the elastic channel and as Breit–Wigner troughs in the absorbing channel. This result is not surprising because the same behavior can be found again by studying the inelasticity parameter η. In the present case, this parameter is characteristic of the absorption and equal to 1 in the purely elastic case. Now η also has a Breit–Wigner behavior close to the resonance frequencies resulting from Eqs. (27) and (28):

$$\eta^2 \approx \frac{(x^{(*)} - x)^2 + ((\Gamma_e - \Gamma_a)/2)^2}{(x^{(*)} - x)^2 + (\Gamma/2)^2}. \tag{37}$$

Therefore we also observe a trough as

$$|T_a|^2 \approx \frac{(x^{(*)} - x)^2 + (\Gamma_a/2)^2}{(x^{(*)} - x)^2 + (\Gamma/2)^2}. \tag{38}$$

In conclusion, resonances appear in two different ways in the absorbing scattering theory—as Breit–Wigner peaks in the elastic channel and as Breit–Wigner troughs in the absorbing channel.

Another interesting question is that of the physical meaning of the scattering operator S. With the multichannel theory and using our construction, the scattering operator $\overline{S}$ corresponds to the operator that provides the eigenphases; close to the resonance frequencies, it is approximated by an expression similar to Eq. (12) where Γ is the total width of the resonance. In fact, the absorbing scattering theory still differs from the multichannel theory because S effectively has a Breit–Wigner form but not that required by the multichannel theory. First, two cases have to be analyzed according to $\Gamma_e/\Gamma \geqslant 1/2 \Leftrightarrow \Gamma_e \geqslant \Gamma_a$ or $\Gamma_e/\Gamma \leqslant 1/2 \Leftrightarrow \Gamma_e \leqslant \Gamma_a$. As a matter of fact, Eq. (27) gives either $\Gamma_e \geqslant \Gamma_a$ and $S(x^{(*)}) = -1$ or $\Gamma_e \leqslant \Gamma_a$ and $S(x^{(*)}) = +1$. As a consequence, the Breit–Wigner approximation given by Eq. (12) cannot be used because it is always equal to -1 at the resonance frequency. Once more, the fundamental relation given by Eq.

(27) is going to be used. From Eq. (27) with η defined by Eq. (29), we can show that S has a Breit–Wigner form (close to the resonance frequencies) given by

$$\overline{S} \approx \frac{x^{(*)} - x + i\gamma/2}{x^{(*)} - x - i\gamma/2} \tag{39}$$

with

$$\gamma = \Gamma \frac{\Gamma_e - \Gamma_a}{\Gamma_e}. \tag{40}$$

As a consequence, the study of the phases of the scattering operator S^{abs}, that is to say those of S, does not permit analysis of the resonances without precaution. Two cases have to be considered: either (1) $\Gamma_e \geqslant \Gamma_a$ and the resonance is detected when the half-phase of S^{abs} is equal to $\pi/2$ (*modulo* π), $\overline{S}(x^{(*)}) = -1$; or (2) $\Gamma_e \leqslant \Gamma_a$ and the resonance is detected when the half-phase of S^{abs} is equal to 0 (*modulo* π), $\overline{S}(x^{(*)}) = +1$. In these two cases, the width of the resonance is not given by Γ but by γ. The Breit–Wigner approximations of Eqs. (34) and (39) will be verified in the next section.

To conclude, it is necessary to distinguish the case where $\Gamma_e \geqslant \Gamma_a$ from the case where $\Gamma_e \leqslant \Gamma_a$. In the first case, the elastic channel is more prevalent than the absorbing channel and resonances are detected when $\delta = \pi/2$ as in the usual case corresponding to purely elastic scatterers; in the second case, the absorbing channel is prevalent and resonances are detected when $\delta = 0$. In addition, the resonance width γ is positive when $\Gamma_e \geqslant \Gamma_a$ as usually required but negative when $\Gamma_e \leqslant \Gamma_a$.

The extension of the theory to a target having a more complicated geometry than cylinders and spheres is possible as soon as we are able to construct the scattering matrix related to this target. For example, such a scattering matrix can be built using the formalism of the T-matrix developed by Waterman[9] and others.[10] In a general way, the scattering matrix, denoted by S is related to the T-matrix by relation (13) and the energy conservation when there is no absorption is expressed by Eq. (7). This last equation expresses the unitarity of the scattering matrix. In the case where the S-matrix is diagonal, one has $|S_n| = 1$ for each mode of vibration, that is to say for each eigenvalue S_n. As previously stated, the absorption introduces a loss of energy so that Eq. (7) is no longer verified. We now have $|S_n| < 1$ and can use the theory previously developed. In fact, this theory is viable as soon as the eigenvalues of the scattering operator are known. In the case where the S-matrix is not diagonal, the situation is numerically more complicated because we have to diagonalize the scattering matrix. However, from a theoretical point of view, there are no additional difficulties since it is always possible to diagonalize the scattering matrix because of the unitarity of this one.[11]

III. RESONANCE ANALYSIS

In order to test the theory developed in the preceding section, computations are performed by considering an absorbing aluminum cylinder immersed in water. One of the reasons is that the resonances and their effects on the acoustic scattering are well known.[12] Another is that the background to be removed is that of a rigid cylinder.[5,6] The values of the physical parameters used in the computations are for aluminum $\rho = 2700$ kg/m^3, $c_L = 6419.9$ m/s, and $c_T = 3039.9$ m/s. For water, $\rho_w = 1000$ kg/m^3 and $c = 1493$ m/s. The sound absorption is taken into account as indicated in the previous section. Here, the values of the aluminum absorption factors $\beta_L = -0.003\,48$ and $\beta_T = -0.005\,31$ are chosen arbitrarily with, however, the condition $|\beta_{L,T}| \ll 1$. The nonabsorbing case is obtained if $\beta_L = \beta_T = 0$. The exact values given in the text and in the tables have been computed by us.

A. Numerical calculations of the resonances from the characteristic equation

The resonances can be located by solving numerically the characteristic equation $D_n(x) = 0$. For each mode of vibration n there are several complex roots x_r lying in the half-plane $\text{Im}(x) < 0$. These roots are usually labeled (n,l), the integer l giving the order of emergence of the resonances. The real part $\text{Re}(x_r)$ gives the resonance frequency and will be denoted by $x^{(*)}$. The absolute value of the imaginary part $\text{Im}(x_r)$ is equal to $\Gamma/2$, where Γ is called the resonance width and is actually connected to the acoustic energy scattered into the water.

In the case of nonabsorbing scattering which corresponds to $\beta_L = \beta_T = 0$, some of the resonance frequencies $x_e^{(*)}$ and the widths labeled Γ_e are given in Table I. The results corresponding to absorption and to the partial width $\Gamma_a = \Gamma - \Gamma_e$ are also given in Table I. A comparison between the absorbing case and the nonabsorbing case shows that, for a given resonance (n,l), the values of $x^{(*)}$ and $x_e^{(*)}$ are practically the same, while for the widths one has $\Gamma_e < \Gamma$. Therefore, a first conclusion is that the absorption widens the resonance widths but has no significant influence on the resonance frequencies.

B. The Breit–Wigner approximation for the elastic channel

The method used in the previous section is a classical way to calculate the resonances. Its main advantage lies in the fact that it is not necessary to remove the background from the scattering. However, it is clear that the information given by this method is not precise enough for further exploration of the resonant scattering. A more complete method comes from the resonance scattering theory (RST) widely developed recently in order to compute the resonances.[7] The computation is possible if the background is well chosen. To remove the background, one must write $S^{\text{abs}} = S^{(0)} S^{(*)\text{abs}}$, where $S^{(0)}$ represents the background term and $S^{(*)\text{abs}}$ the purely resonant term. For the absorbing material considered here, it appears that the rigid background which was found to be well adapted in the case of the nonabsorbing aluminum is also a good approximation of the background in the case of absorbing aluminum. In the following it is implicit that the

TABLE I. Some of the resonance frequencies and half-widths of an aluminum cylinder in the nonabsorbing case (columns two and three) and in the absorbing case (columns four and five). Results obtained by solving the characteristic equation $D_n(x)=0$.

	Elastic case		Absorbing case			
(n,l)	$x_e^{(*)}=\mathrm{Re}(x_r)$	$\Gamma_e=-2\,\mathrm{Im}(x_r)$	$x^{(*)}=\mathrm{Re}(x_r)$	$\Gamma=-2\,\mathrm{Im}(x_r)$	$\Gamma_a=\Gamma-\Gamma_e$	
(2, 1)	4.731	0.751	4.731	0.802	0.051	$\Gamma_e>\Gamma_a$
(3, 1)	7.340	0.992	7.340	1.071	0.079	$\Gamma_e>\Gamma_a$
(5, 1)	11.766	1.329	11.766	1.453	0.124	$\Gamma_e>\Gamma_a$
(10, 1)	21.847	2.014	21.847	2.240	0.226	$\Gamma_e>\Gamma_a$
(1, 2)	5.870	0.027	5.870	0.086	0.059	$\Gamma_e<\Gamma_a$
(2, 2)	9.168	0.003	9.168	0.095	0.092	$\Gamma_e<\Gamma_a$
(3, 2)	12.525	0.079	12.525	0.205	0.126	$\Gamma_e<\Gamma_a$
(5, 2)	19.005	0.354	19.005	0.550	0.196	$\Gamma_e>\Gamma_a$
(10, 2)	32.862	0.734	32.861	1.082	0.348	$\Gamma_e>\Gamma_a$
(1, 3)	13.447	0.075	13.446	0.213	0.138	$\Gamma_e<\Gamma_a$
(2, 3)	16.315	0.044	16.314	0.212	0.168	$\Gamma_e<\Gamma_a$
(3, 3)	19.117	0.020	19.116	0.218	0.198	$\Gamma_e<\Gamma_a$
(5, 3)	24.717	0.002	24.717	0.256	0.254	$\Gamma_e<\Gamma_a$
(10, 3)	38.997	0.389	38.997	0.794	0.405	$\Gamma_e<\Gamma_a$
(1, 4)	16.004	0.755	16.004	0.868	0.113	$\Gamma_e>\Gamma_a$
(2, 4)	21.398	0.734	21.396	0.895	0.161	$\Gamma_e>\Gamma_a$
(3, 4)	25.417	0.302	25.411	0.542	0.240	$\Gamma_e>\Gamma_a$
(5, 4)	31.263	0.054	31.262	0.375	0.321	$\Gamma_e<\Gamma_a$
(10, 4)	45.042	0.042	45.042	0.507	0.465	$\Gamma_e<\Gamma_a$
(1, 5)	20.318	0.002	20.317	0.216	0.214	$\Gamma_e<\Gamma_a$
(2, 5)	23.547	0.087	23.548	0.326	0.239	$\Gamma_e<\Gamma_a$
(3, 5)	27.642	0.569	27.646	0.797	0.228	$\Gamma_e>\Gamma_a$
(5, 5)	36.671	0.635	36.667	0.943	0.308	$\Gamma_e>\Gamma_a$
(1, 7)	29.884	0.753	29.884	0.961	0.208	$\Gamma_e>\Gamma_a$
(2, 7)	35.663	0.552	35.652	0.836	0.284	$\Gamma_e>\Gamma_a$
(3, 7)	39.135	0.046	39.133	0.452	0.406	$\Gamma_e<\Gamma_a$

rigid background has been removed. Consequently, the subscript (*) will not be used, except for $x^{(*)}$ and finally the notations of the previous sections will be kept.

1. Study of the nonabsorbing case ($\beta_L=\beta_T=0$)

When the scatterer is nonabsorbing, $\eta=1$, and then $S^{\mathrm{abs}}=\overline{S}=S^{\mathrm{elast}}=e^{2i\delta_{\mathrm{elast}}}$, where δ_{elast} is a real phase. In addition, the transition term in the elastic channel verifies $T_e=T^{\mathrm{elast}}$ with

$$T^{\mathrm{elast}}=\frac{1}{2i}\,(S^{\mathrm{elast}}-1).$$

The function $|T^{\mathrm{elast}}(x)|^2$, plotted versus the frequencies (from $x=0$ to $x=20$) for the modes $n=1$ and 2, gives the resonance curves presented in Fig. 1. The resonances arise for the values of $x_e^{(*)}$ given in Table I. At these values one has $|T^{\mathrm{elast}}(x_e^{(*)})|^2=1$, which implies that $S^{\mathrm{elast}}=-1$ and then $\delta_{\mathrm{elast}}=p\pi/2$ where p is an odd integer. The half-width of each peak corresponds to the value of Γ_e given in Table I. Close to a resonance frequency $x_e^{(*)}$ the function $T^{\mathrm{elast}}(x)$ can be approximated as follows:

$$T^{\mathrm{elast}}(x)=\frac{\Gamma_e/2}{x_e^{(*)}-x-i\Gamma_e/2},$$

that is, the Breit–Wigner approximation for nonabsorbing resonant scattering, which is particularly accurate for small values of Γ_e.

2. Study of the absorbing case

When the scatterer is absorbing, $\eta<1$. Following Eq. (27), one can write for the elastic channel

$$T_e(x)=\frac{1}{2i}\,(\eta\overline{S}-1).$$

The function $|T_e(x)|^2$ plotted for modes $n=1$ and 2 shows resonances at the same frequencies as $|T^{\mathrm{elast}}(x)|^2$ (Fig. 2). As expected, this function never reaches the value 1. At a given resonance frequency $x^{(*)}$, one has $|T_e(x^{(*)})|^2<1$. In addition, the width of this resonance is equal to that calculated by the characteristic equation. One can easily verify that for the exact curves $|T_e(x^{(*)})|\approx\Gamma_e/\Gamma$, which corresponds effectively to the modulus of Eq. (32). The exactness of approximation Eq. (28) must be verified by comparing the exact curve with the approximate one. For instance, if we consider the resonance (2,1) for which $x^{(*)}=4.731$, the approximate curve close to this resonance shows excellent agreement with the exact curve as seen in Fig. 3. Relation (32) allows us to explain why, in the presence of absorption, some of the resonance heights are considerably shortened, as is the case for

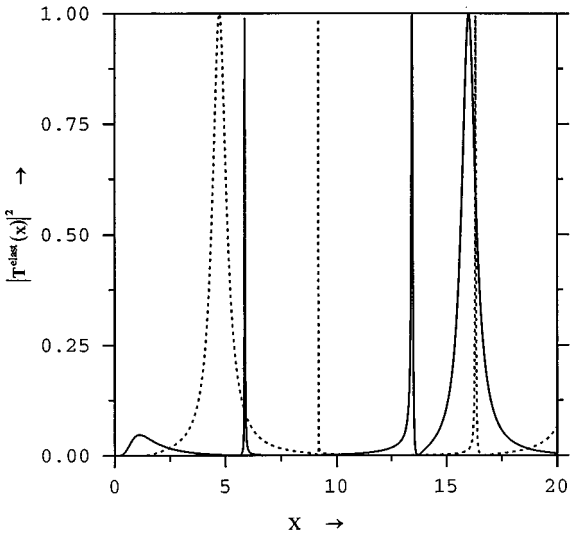

FIG. 1. Function $|T^{\text{elast}}(x)|^2$ plotted versus the frequency x for modes $n=1$ (solid line) and $n=2$ (dot line).

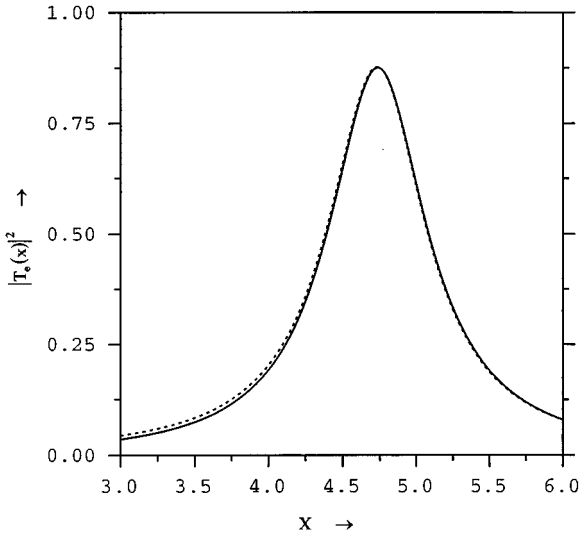

FIG. 3. Comparison between the exact (solid line) and the approximate (dot line) values of the function $|T_e(x)|^2$ near the resonance (2,1).

the resonance (2,2) for which $x^{(*)}=9.168$. This resonance has totally disappeared from the dotted curve in Fig. 2. With the values of $\Gamma_e=3\times10^{-3}$ and $\Gamma=9.5\times10^{-2}$, it is clear that $(\Gamma_e/\Gamma)^2\approx9.97\times10^{-4}$, which is very small in comparison to unity. This result is globally verified for sharp resonances. It can be concluded in this section that the amplitude of narrow resonances is more reduced by the absorption than the amplitude of broad resonances.

3. The absorption curves

The curves of the absorption coefficient $\eta(x)=|S^{\text{abs}}(x)|$ are presented in Fig. 4. They present a trough around each resonance frequency in agreement with the Breit–Wigner approximation given by Eq. (37). It results from Eq. (27) that $\overline{S}=e^{2i\delta}$, where δ is a real phase. At the resonance, one must have [from Eq. (28)] $T_e(x^{(*)})=i\Gamma_e/\Gamma$, which implies that $\text{Im}(\overline{S}(x^{(*)}))=0$ or $\delta=m\pi/2$, where m is an integer. It then follows from Eq. (27) that two families of resonances must be distinguished:

(i) The family corresponding to m even and $0<\Gamma_e/\Gamma\leqslant1/2$: In this case $\overline{S}(x^{(*)})=+1$ and $\eta=1-2\Gamma_e/\Gamma$. We recall that the coefficient η must be a positive number. The partial widths then satisfy the relation $\Gamma_e<\Gamma_a$. Some of the resonances related to this family (including the narrow resonances) are given in Table I. The parity of m is opposite to that of p defined in Sec. III B 1. It appears that the phase of this family of resonances has been strongly affected.

(ii) The family corresponding to m odd and $1/2\leqslant\Gamma_e/\Gamma\leqslant1$: In this case, $\overline{S}(x^{(*)})=-1$, $\eta=2\Gamma_e/\Gamma-1$, and it follows that the partial widths satisfy $\Gamma_e>\Gamma_a$. Some examples of these resonances (including the broad resonances) are also given in Table I. Here, the parity of m is that of p in Sec.

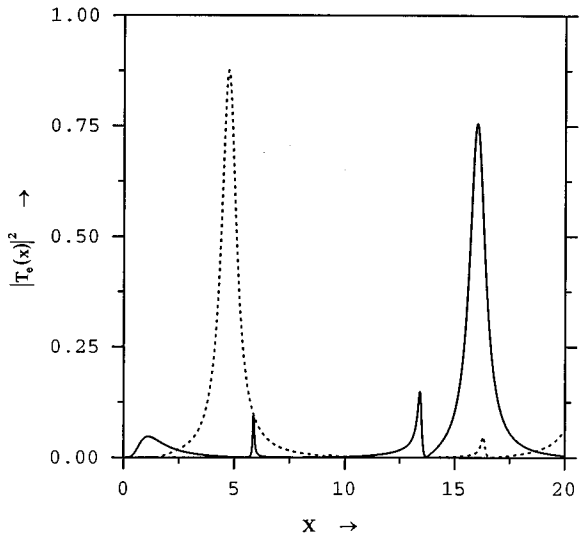

FIG. 2. Function $|T_e(x)|^2$ plotted versus the frequency x for modes $n=1$ (solid line) and $n=2$ (dot line).

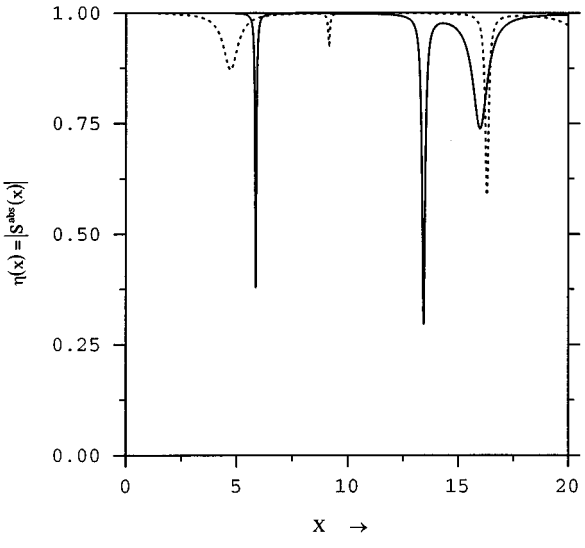

FIG. 4. Absorption coefficient $\eta(x)=|S^{\text{abs}}(x)|$ plotted versus the frequency for modes $n=1$ (solid line) and $n=2$ (dot line).

TABLE II. Comparisons between the exact values of $|T_e(x^{(*)})|$ and the ratios Γ_e/Γ (columns two and three) and between the exact values of $\eta(x^{(*)})$ and those given by the approximation $\eta=|1-2\Gamma_e/\Gamma|$ (columns four and five).

(n,l)	$\lvert T_e(x^{(*)})\rvert$	Γ_e/Γ	$\eta(x^{(*)})$	$\eta=\lvert 1-2\Gamma_e/\Gamma\rvert$
(2, 1)	0.936	0.936	0.871	0.872
(3, 1)	0.926	0.926	0.853	0.852
(1, 2)	0.312	0.314	0.378	0.372
(2, 2)	0.084	0.032	0.929	0.936
(3, 2)	0.392	0.385	0.238	0.230
(1, 3)	0.386	0.352	0.294	0.296
(2, 3)	0.218	0.208	0.587	0.584
(3, 3)	0.097	0.092	0.811	0.816

III B 1. The resonances of this family can be considered as unaffected in phase.

Generally speaking, at the resonance frequencies, the expression of η is simply related to the half-widths Γ_e and Γ and the values obtained are in good agreement with the exact values reported in Table II.

4. Sensitivity of the resonances to linearly varying absorption coefficients

The heights and the widths of the resonances depend strongly on the values of the absorption coefficients β_L and β_T. The fact that these coefficients are arbitrarily chosen leads us to present in this section numerical results in the particular case where the coefficients vary linearly, that is to say, when they are multiplied by the same factor ϵ. In Table III, at the resonance frequencies $x^{(*)}=4.731$ and $x^{(*)}=5.87$, values of the resonance widths Γ and of the partial widths Γ_a are given for several values of ϵ. First, one can see that the resonances widen out with an increase of ϵ. Second, the partial width Γ_a is proportional to $(\Gamma_a)_{\epsilon=1}$, which represents its value at $\epsilon=1$ [for the resonance $x^{(*)}=4{,}731$, $(\Gamma_a)_{\epsilon=1}=0.051$, and for the resonance $x^{(*)}=5.87$, $(\Gamma_a)_{\epsilon=1}=0.059$]. The partial widths are then simply given by the relation $\Gamma_a=\epsilon(\Gamma_a)_{\epsilon=1}$, and it follows immediately that the resonance widths Γ_a depend linearly on ϵ.

C. The Breit–Wigner approximation for the absorbing channel

The absorbing channel is defined by Eq. (33). The exact curves obtained by plotting the function $|T_a(x)|^2$ for modes $n=1$ and 2 are given in Fig. 5 and do not present the classical form of the Breit–Wigner resonance curves but look like the $\eta(x)$ curves, with a trough around the resonance frequencies. The result can be explained by the fact that, at the vicinity of a resonance, the approximate form of $T_a(x)$ is given by Eq. (34). At the resonances, we also satisfy the relation $|T_a(x^{(*)})|\approx\Gamma_a/\Gamma$. Additionally, one can verify that $|T_e(x^{(*)})+T_a(x^{(*)})|=1$, which is a consequence of the relation between the partial widths.

TABLE III. Sensitivity of the resonances to linearly varying absorption coefficients.

Absorption coefficients β_L,β_T multiplied by	Resonance (2,1): $x^{(*)}=4.73$		Resonance (1,2): $x^{(*)}=5.87$	
	Γ	$\Gamma_a=\Gamma-\Gamma_e$	Γ	$\Gamma_a=\Gamma-\Gamma_e$
$\epsilon=1/10$	0.756	0.005	0.033	0.006
$\epsilon=1/2$	0.776	0.025	0.056	0.029
$\epsilon=1$	0.802	0.051	0.086	0.059
$\epsilon=2$	0.854	0.103	0.145	0.118
$\epsilon=4$	0.957	0.206	0.263	0.236
$\epsilon=10$	1.265	0.514	0.615	0.588

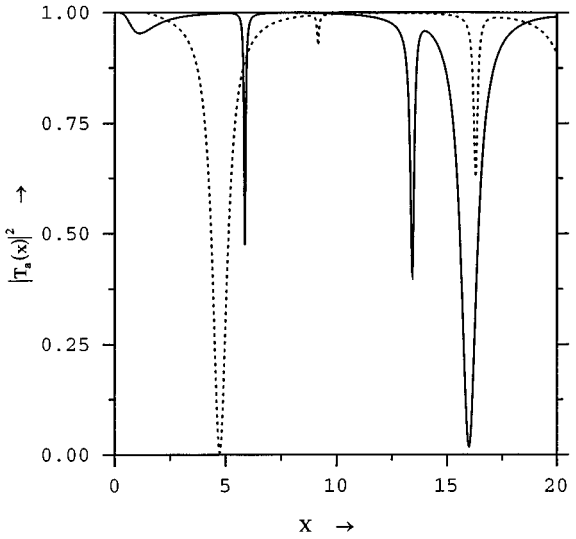

FIG. 5. Function $|T_a(x)|^2$ plotted versus the frequency for modes $n=1$ (solid line) and $n=2$ (dot line).

D. Study of the S^{abs} matrix phase

The S^{abs} matrix phase is given by the term $\overline{S}$ in Eq. (27). It has been shown, in Eq. (22), that this term can be written $\overline{S}=e^{2i\delta}$, where δ is a real phase. If we introduce the transition term T which is related to $\overline{S}$ by the relation $\overline{S}=1+2i\overline{T}$, there follows

$$\overline{T}(x)=\frac{1}{2i}\left(\frac{S^{\text{abs}}(x)}{\eta(x)}-1\right),$$

and if one considers the elastic channel, this relation becomes

$$\overline{T}(x)=e^{i\delta(x)}\sin(\delta(x)).$$

The curve of the function $|\overline{T}(x)|^2$ is plotted in Fig. 6 for the mode $n=1$. One must distinguish two families of resonances, according to Sec. III B 3:

(i) For the first family, the resonance curves reach the value 1 and the widths are given by Eq. (40). This family corresponds to $\overline{S}(x^{(*)})=-1$, e.g., to the phase $\delta=m\pi/2$ with m odd (see Sec. III B 3). The resonances of this family are of elastic type.

(ii) For the second family, the resonance curves seem to be those obtained previously by plotting $|T_e(x)|^2$ and they do not reach the value 0.5. A close-up of Fig. 6 shows that each of the resonances of this family now presents an oscillation, as can be seen in Fig. 7 for resonance (1,3). This family corresponds to $\overline{S}(x^{(*)})=+1$, e.g., to the phase $\delta=m\pi/2$ with m even. Then, $|\overline{T}(x^{(*)})|=0$ and the resonance

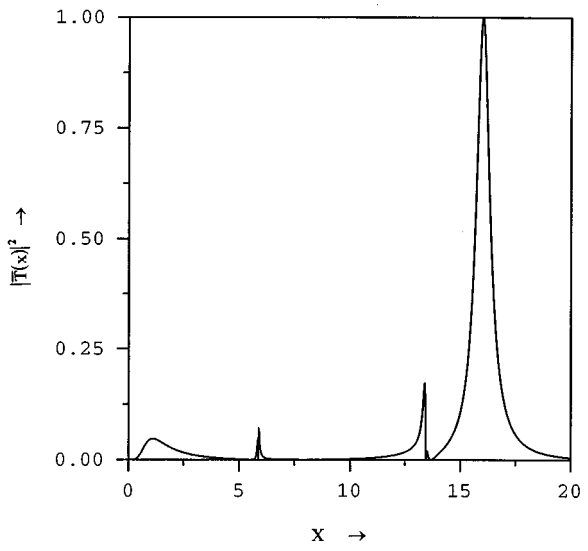

FIG. 6. Function $|\overline{T(x)}|^2$ plotted versus the frequency for mode $n=1$.

corresponds to a trough. That explains the presence of oscillations in the curves. These oscillating curves describe the strongly absorbed resonances.

It appears that the investigation of the phase term $\overline{S}$ brings an additional point of view to the general study of the resonances of absorbing scatterers. The phase term clearly shows that in the presence of absorption there are two families of resonances.

If one considers the absorbing channel, then

$$\overline{T(x)} = ie^{i\delta(x)} \cos(\delta(x)).$$

The situation is exactly contrary to the case encountered for the elastic channel. Now, the resonances of elastic type occur when $|\overline{T(x^{(*)})}|=0$ (the integer m is odd), and the absorbing ones when $|\overline{T(x^{(*)})}|=1$ (m is even).

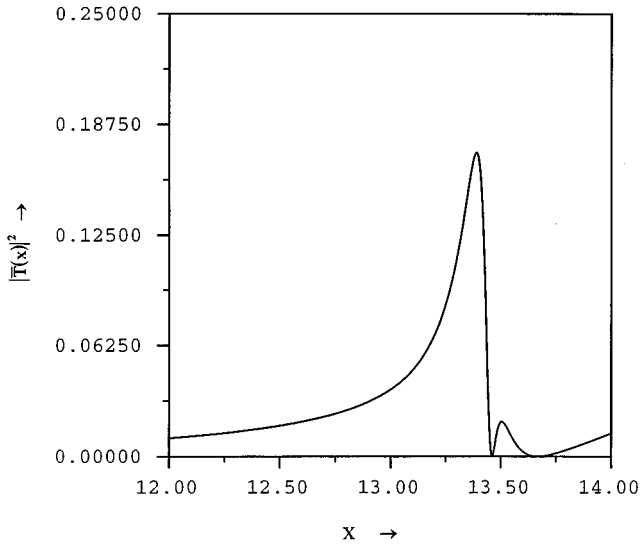

FIG. 7. Enlargement of the curve of Fig. 6 at the vicinity of resonance (1,3). The curve oscillates rapidly and $|\overline{T(x)}|^2=0$ at the resonance.

IV. CONCLUSION

The scattering process related to absorbing elastic scatterers involves two different phenomena. The first one is related to the elasticity, more specifically to the propagation of surface waves and to the resonance frequencies. The second is related to the absorption and explains the difference between the reemission of surface waves propagating around purely elastic scatterers and the reemission of surface waves propagating around absorbing scatterers. Consequently, a two-channel resonance scattering theory has been derived in order to explain the reemission of surface waves which are related to the widths Γ of the resonances. The law of energy conservation, expressed through the unitarity condition of the scattering matrix S^{abs} shows that, at a resonance frequency, $\Gamma=\Gamma_e+\Gamma_a$. Here, Γ_e is the elastic resonance width (when the scatterer is nonabsorbing) related to the elastic channel, and Γ_a the absorbing resonance width related to the absorbing channel.

At a resonance frequency, the absorption coefficient $\eta=|(\Gamma_e-\Gamma_a)/\Gamma|$ permits us to distinguish between two types of resonances: those for which $\Gamma_e>\Gamma_a$ (the elastic channel is prevalent over the absorbing one, so these resonances are of elastic type, e.g., they are weakly affected by absorption), and those for which $\Gamma_e<\Gamma_a$ (the absorbing channel is prevalent, so these resonances are strongly absorbed).

The theoretical developments have been tested numerically on an absorbing aluminum cylinder immersed in water. There is good agreement, especially in the vicinity of the resonances, between the results obtained by an exact computation and those stemming from the two-channel theory. At this stage, this theory can be considered as well adapted for further development and studies on absorbing resonance scattering.

[1] L. S. Schuetz and W. G. Neubauer, ''Acoustic reflexion from cylinders—Nonabsorbing and absorbing, '' J. Acoust. Soc. Am. **62**, 513–517 (1977).

[2] G. C. Gaunaurd, ''Sonar cross section of a coated hollow cylinder in water,'' J. Acoust. Soc. Am. **61**, 360–368 (1977).

[3] W. M. Ayres and G. C. Gaunaurd, ''Acoustic resonance scattering by viscoelastic objects,'' J. Acoust. Soc. Am. **81**, 301–311 (1978).

[4] C. M. Davis, L. R. Dragonette, and L. Flax, ''Acoustic scattering from silicone rubber cylinders and spheres,'' J. Acoust. Soc. Am. **63**, 1694–1697 (1978).

[5] H. Überall, *Acoustic Resonance Scattering* (Gordon and Breach, New York, 1992).

[6] A. Derem, ''Théorie de la matrice S et transformation de Sommerfeld–Watson dans la diffusion acoustique,'' in *La Diffusion Acoustique*, edited by N. Gespa, Vol. 9 (Cedocar, Paris, 1987), pp. 87–104.

[7] See, e.g., R. G. Newton, *Scattering Theory of Waves and Particles* (Springer-Verlag, New York, 1982), 2nd ed.; R. Omnès, *Introduction à l'étude des Particules Élémentaires* (Ediscience, Paris, 1970).

[8] R. H. Dalitz, ''Strange particle resonant states,'' Annu. Rev. Nucl. Sci. **13**, 339 (1963).

[9] P. C. Waterman, ''Matrix theory of elastic wave scattering,'' J. Acoust. Soc. Am. **60**, 567–580 (1976).

[10] See, e.g., A. Boström, ''Scattering of stationary acoustic waves by an elastic obstacle immersed in a fluid,'' J. Acoust. Soc. Am. **67**, 390–398 (1980); V. V. Varadan, ''Scattering matrix for elastic waves. II. Application to elliptic cylinders,'' J. Acoust. Soc. Am. **63**, 1014–1024 (1978).

[11] F. R. Gantmacher, *Théorie des Matrices* (Editions Jacques Gabay, Sceaux, 1990).

[12] N. D. Veksler, *Resonance Acoustic Spectroscopy* (Springer-Verlag, Berlin, 1993).

Boundary spectral method for acoustic scattering and radiation problems

W. S. Hwang
Department of Naval Architecture and Ocean Engineering, National Taiwan University, Taipei, Taiwan

(Received 27 September 1996; accepted for publication 9 March 1997)

The spectral method is considered in solving boundary integral equations. By subtracting known solutions from the Helmholtz integral equation, the singularities of the Helmholtz integral equation are removed. Therefore, any order of basis functions, used in spectral methods, that times nonsingular kernels in the modified Helmholtz integral equation can be integrated easily and efficiently. Instead of solving the variables at collocation points using conventional methods, the generalized Fourier coefficients are solved by the spectral method which reduces the number of unknowns and the storage of matrix elements in computation. Scattering and radiation problems from a sphere are used to illustrate the technique in the present paper. © *1997 Acoustical Society of America.* [S0001-4966(97)01707-4]

PACS numbers: 43.20.Fn [ANN]

INTRODUCTION

The prediction of acoustic fields from radiation or scattering is a problem of practical importance in many applications of engineering and science. Analytical solutions for such problems are generally limited to very special cases. Therefore, the boundary integral equation has gained popularity for solving such problems for bodies of arbitrary shape. The boundary integral equations contain both known and unknown boundary variables in the formulation. The unknown variables are obtained numerically by solving a system of algebraic equations which are discretized from the boundary integral equations. The discretization technique which is developed in finite element methods is commonly used and this approach is sometimes called the boundary element method. The boundary element method is one of the most important computational schemes in practice.

However, there is an essential difference between boundary integral formulations and finite element methods. In finite element methods, the interpolation functions, in general, are low-order polynomials which imply that the effect of interpolation functions is on the adjacent local elements only. The resultant system of algebraic equations is always banded or sparse, which also confirms the property that local variables can affect nearby elements only. On the other hand, boundary integral equations have completely different properties. The matrices formed from boundary integral methods are always full, and that means any local variables can affect the global behavior in boundary integral formulations. Therefore, the lower-order interpolation technique is not really fit for boundary integral formulations. A global approximation technique or higher-order interpolation functions should be more suitable for boundary integral formulation.

Spectral methods have been developed for solving partial differential equations since the early 1970s, especially in computationally intensive applications in meteorology and fluid dynamics.[1,2] Spectral methods generate algebraic equations with full matrices, which are more expensive to solve than banded matrices in the finite element methods, but in compensation the high order of the basis functions gives high accuracy for a given number of basis functions. Since full matrices are inevitable when boundary integral methods are used, it seems more reasonable to use the high-order interpolation function developed in spectral methods than the low-order interpolation function in finite element methods. Moreover, the boundary integral equation involves another difficulty in handling singular integrals, and special kinds of numerical treatment are needed for singular integrals to maintain the required accuracy in the conventional numerical methods. Usually, the accuracy of numerical quadrature depends on both the number of integration points and the order of interpolation functions. The higher-order interpolation function also gives higher accuracy. Again, this property is inherent in spectral methods.

Although spectral methods have these advantages and are successfully used in solving partial differential equations, they have not been applied in boundary integral equations until recently.[3,4] In acoustics, only a special geometry, the circular cylinder, has been evaluated by spectral methods for boundary integral equations.[5] In the present paper, this global approximation technique is applied to solve boundary integral equations for bodies of arbitrary shape instead of the local discretization schemes from finite element methods.

In the integral formulation of acoustic problems, the problem of nonuniqueness has been discussed frequently in the literature for a long time. The combined Helmholtz integral equation formulation (CHIEF) proposed by Schenck[6] or the combination of the Helmholtz integral equation and its normal derivative proposed by Burton and Miller[7] are widely used to solve this mathematical drawback.[8–16] In this paper, CHIEF is adopted because it is simple and easy to be programmed. In general, the spectral approach can also be applied in Burton and Miller's formulation, but the expressions are more complicated.

I. BOUNDARY INTEGRAL EQUATIONS

The standard Helmholtz integral equation for the exterior acoustic problem can be written as

$$\overline{\epsilon}\Phi(P)=\int_S\left[\Phi(Q)\,\frac{\partial G(P,Q)}{\partial n_Q}-G(P,Q)\,\frac{\partial\Phi}{\partial n_Q}\,(Q)\right]dS_Q+\Phi_{\text{in}}(P),\tag{1}$$

where P denotes the field point, Q the source point on the surface of body, n_Q the outward directed normal from surface S, and Φ_{in} the incident wave. Here, G is the free-space Green's function for the Helmholtz equation and can be written as

$$G(P,Q)=\frac{e^{ikr}}{4\pi r},\tag{2}$$

where k is the wave number and r the distance between points P and Q. The coefficient $\overline{\epsilon}$ is defined by the solid angle at P:

$$\overline{\epsilon}=1+\int_S\frac{\partial G_0}{\partial n_Q}\,dS_Q,\tag{3}$$

where $G_0=1/(4\pi r)$ is the free-space Green's function for the Laplace equation. The coefficient $\overline{\epsilon}$ has the value 0 for P inside surface S, the value 1 for P outside surface S, and the value 1/2 for P on the smooth part of surface S. An important property of the Laplace equation used in the following is the electrostatic capacitance or equipotential surface theorem. Using the existence theorem for interior Dirichlet problems of the Laplace equation, a source distribution $S(Q)$ on surface S, which generates a constant potential inside the domain and boundary, must satisfy the following equation:[17,18]

$$\int_S S(Q)\,\frac{\partial}{\partial n_p}\left(\frac{1}{2\pi r}\right)dS_Q=-S(P).\tag{4}$$

The value of potential Φ_e inside the domain and boundary corresponding to $S(Q)$ can be calculated, in which the integrand is never singular, by

$$\Phi_e=-\int_S\frac{S(Q)}{4\pi r}\,dS_q.\tag{5}$$

Since Eq. (1) is a singular integral equation, direct numerical integration methods are difficult to evaluate the integration efficiently and accurately. In the literature a polar coordinate transformation is frequently used to remove the weakly singular kernels. Although the polar coordinate transformation performs very successfully in local elements, it is inconvenient in general when a global approach is applied. A different kind of regularization process is used in the present study. By subtracting a known singular equation from Eq. (1), it turns out that new integrands are bounded but discontinuous. The main results are summarized in the following, and a detailed discussion can be found in Hwang.[19]

The first singularity term in the right-hand side integral of Eq. (1) can be removed by subtracting the relation Eq. (3) times $\Phi(P)$ when point P is on the smooth part of surface S:

$$\int_S\Phi(Q)\,\frac{\partial G}{\partial n_Q}\,dS_Q=\int_S\left[\Phi(Q)\,\frac{\partial G}{\partial n_Q}-\Phi(P)\,\frac{\partial G_0}{\partial n_Q}\right]dS_Q-\tfrac{1}{2}\,\Phi(P).\tag{6}$$

Multiplying Eq. (5) with a factor $[-1/S(P)](\partial\Phi/\partial n_P)$, and adding it to the second integral in the right-hand side of Eq. (1), we have another regularized integral when P is on surface S:

$$\int_S G\,\frac{\partial\Phi}{\partial n_Q}\,dS_Q=\int_S\left[G\,\frac{\partial\Phi}{\partial n_Q}-G_0\,\frac{\partial\Phi}{\partial n_P}\,\frac{S(Q)}{S(P)}\right]dS_Q-\frac{\Phi_e}{S(P)}\,\frac{\partial\Phi}{\partial n_P}.\tag{7}$$

II. SPECTRAL APPROXIMATION

Spectral methods are distinguished not only by the type of method, such as the Galerkin method, collocation method, or tau method, but also by the choice of basis functions.[1,2] The most frequently used basis functions are orthogonal functions such as trigonometric polynomials, Chebyshev polynomials, and Legendre polynomials.

The expansion of a function in terms of an infinite sequence of orthogonal functions underlies many numerical methods of approximation. The accuracy and the efficiency of those approximations influence the computational applicability of these methods. For periodic smooth functions, it is proven that Fourier series are the most efficient approximation functions in the root mean square sense. For nonperiodic functions the Chebyshev polynomials are frequently used as approximation functions, since the basic properties of Chebyshev polynomials are closely related to the Fourier series.

If the body is assumed to be rigid, the velocity potential on the body surface can be represented by a series involving basis functions, such that

$$\Phi(x,y,z)=\sum_{j=1}^{n}c_j\psi_j(x,y,z),\tag{8}$$

where $\Psi_j(x,y,z)$, $j=1,2,\ldots,n$, is the jth basis function. The unknown coefficients c_j, generalized Fourier coefficients, can be determined from Eq. (1). In the present paper, since only the axisymmetric cases are considered, Chebyshev polynomials are selected as basis functions along the x direction and defined as

$$T_n(x)=\cos(n\,\cos^{-1}x)\quad n\geqslant 1.\tag{9}$$

By substituting Eq. (8) into Eq. (1), one obtains approximate algebraic equations for scattering problems with the zero normal velocity at the body surface:

$$\sum_{j=1}^{n}\left[\frac{1}{2}\,\psi_j(P)-\int_S\psi_j(Q)\,\frac{\partial G}{\partial n_Q}\,dS_Q\right]c_j=\Phi_{\text{in}}(P).\tag{10}$$

If a radiation problem is considered, $\Phi_{\text{in}}(P)$ is simply replaced by $-\int_S G(\partial\Phi/\partial n_Q)dS_Q$, where $\partial\Phi/\partial n_Q$ represents the normal velocity on the body surface. As mentioned previously, several methods can be selected to solve the un-

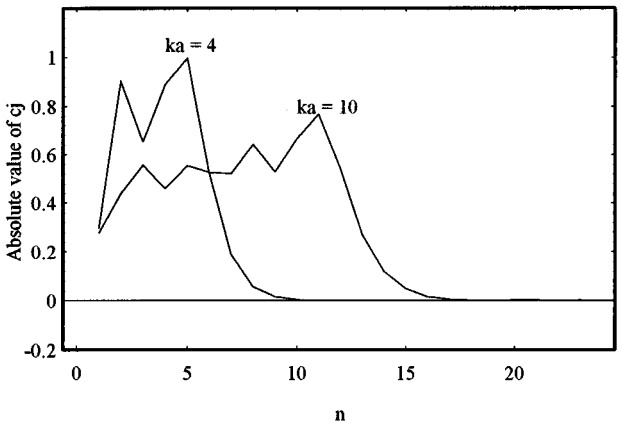

FIG. 1. Absolute values of generalized Fourier coefficients for scattering from a sphere for $ka=4$ and 10.

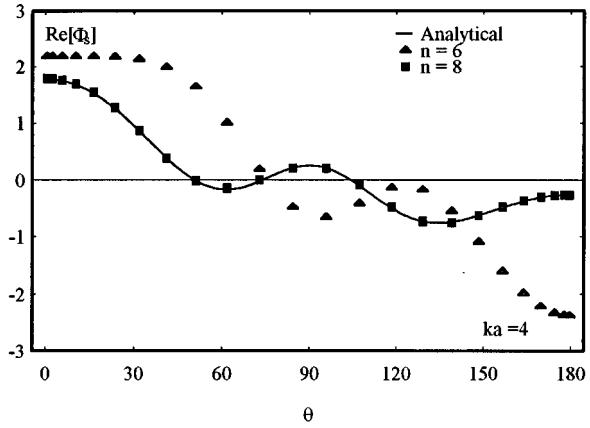

FIG. 2. Real parts of scattered velocity potentials on the surface of a sphere when $ka=4$.

known coefficient c_j by spectral methods. For simplicity, choosing the collocation method and carrying out the integration in Eq. (10), one obtains n simultaneous equations

$$[A]\{C\}=\{B\}. \tag{11}$$

The elements of matrix $[A]_{n\times n}$ and the column vector $\{B\}_n$ are, respectively,

$$a_{ij}=\frac{1}{2}\,\psi_j(P_i)-\int_S \psi_j(Q)\,\frac{\partial G}{\partial n_Q}\,dS_Q, \tag{12}$$

$$b_i=\Phi_{\text{in}}(P_i), \tag{13}$$

where P_i are collocation points. Assuming point P is on the smooth part of the surface, by utilizing Eqs. (3) and (6), the singularities of Eq. (12) can be removed, and the regularized forms can be written as

$$a_{ij}=\psi_j(P_i)-\int_S\left[\psi_j(Q)\,\frac{\partial G}{\partial n_Q}-\frac{\partial G_0}{\partial n_Q}\,\psi_j(P_i)\right]dS_Q. \tag{14}$$

For the radiation problem, b_i can be regularized by using Eq. (7):

$$b_i=-\int_S\left[G(P_i,Q)\,\frac{\partial\Phi}{\partial n_Q}-G_0(P_i,Q)\,\frac{\partial\Phi}{\partial n_P}\,\frac{S(Q)}{S(P_i)}\right]dS_Q + \frac{\Phi_e}{S(P_i)}\,\frac{\partial\Phi(P_i)}{\partial n_P}. \tag{15}$$

Because the integrands in (14) and (15) are bounded, many numerical quadrature methods are available for both integrals. In the present paper, trapezoidal rules are used to evaluate periodic functions and Gaussian quadrature formulas are applied for nonperiodic functions.

When the collocation method is applied to solve the unknown coefficients, the locations of collocation points will directly affect the accuracy of solutions, especially for high-order interpolation functions. From the error analysis of the approximation function theory in numerical textbooks, the uneven spacing of collocation points, dense near the ends, are preferred in order to avoid the Runge phenomenon[2] and reduce the maximal interpolation error. Detailed analysis of interpolation and approximation errors can be found in Refs. 2 and 20. Usually, the zeros of Chebyshev polynomials are chosen to be collocation points from the near-minmax approximation theory in the literature. However, in the present case, the locations of collocation points are chosen to be Gaussian points in order to reduce the computation time for numerical integration. Otherwise, if the zeros of Chebyshev polynomials are chosen to be collocation points, it takes much more computing time to redistribute integration nodes and to evaluate different nodal values for every integration while forming matrix A. Therefore, the chosen collocation points are not exactly the zeros of Chebyshev polynomials, but some Gaussian points close to them. In theory, this increases the interpolation error but saves much computation time. It turns out that the number of Gaussian points is not less than that of collocation points, and the distribution of collocation points is still uneven and dense near the ends after such a compromise.

Since the basis functions are orthogonal, the coefficient c_j is uniquely determined and is not dependent on the number of orthogonal functions we choose if the numerical integration is accurate enough. The convergence speed of the generalized Fourier series is easily shown from the variation of c_j. Therefore, the convergence of spectral methods can be

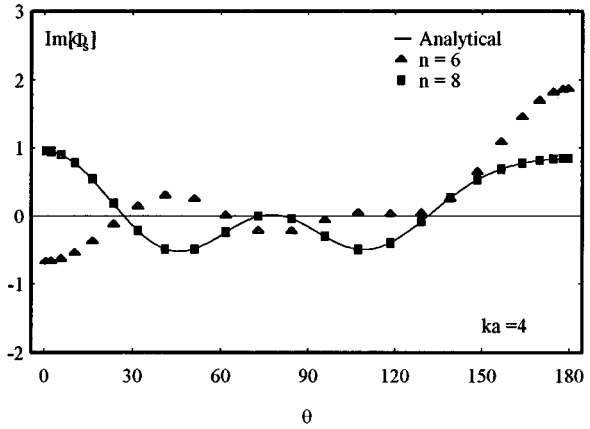

FIG. 3. Imaginary parts of scattered velocity potentials on the surface of a sphere when $ka=4$.

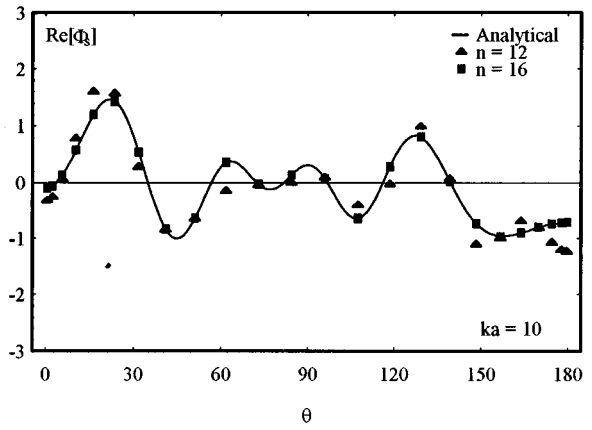

FIG. 4. Real parts of scattered velocity potentials on the surface of a sphere when $ka=10$.

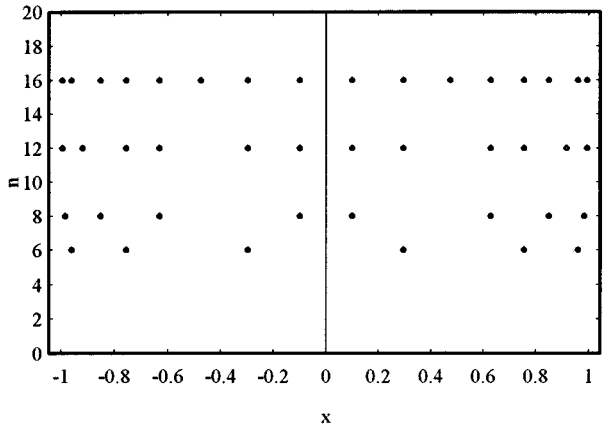

FIG. 6. Locations of collocation points at different numbers of orthogonal functions for a 24-point Gaussian formula.

estimated, while the conventional boundary element method cannot do so.

In practice, the surface may not be easy to be approximated by one single equation for irregular geometry. A surface discretization is needed, and the spectral approximation and the numerical integration can be directly applied on each discretized element. In conventional spectral methods, such an approach is called the spectral element method. In the present paper, only the spectral method on a whole element is considered.

A. Application to scattering from a sphere

For simplicity, a sphere is chosen for the demonstration, since its analytic solution of the scattering problem of a plane incident wave is well known and easy to compute. By utilizing the axisymmetric shape of sphere, the velocity potential can be treated as a one-dimensional case, and the Chebyshev polynomials are chosen to be the basis functions, although the analytic solution is known to be Legendre functions in the present case. The incoming unit plane wave travels to the right along the x axis and is described as $\Phi_{\text{in}}=\exp(ikx)$. For scattering from a sphere of radius a, the scattered velocity potential at a distance r from the center of sphere and an angle θ from the x axis is given by

$$\Phi_S(r,\theta)=\sum_{n=1}^{\infty} -\frac{i^n(2n+1)j_n'(ka)}{h_n'(ka)}P_n(\cos\,\theta)h_n(kr), \tag{16}$$

where $P_n(x)$ is the Legendre function of the first kind, $h_n(x)$ the spherical Hankel function of the first kind, and $j_n(x)$ the spherical Bessel function of the first kind.

Figure 1 shows the distribution of the absolute values of generalized Fourier coefficients for nondimensional wave numbers $ka=4$ and 10. A 24-point Gaussian formula is applied for the numerical integration in both cases. The variation of coefficients indicates the speed of convergence and one can determine the number of orthogonal functions for the required accuracy. Figures 2 and 3 show the comparison of analytical and numerical results for real and imaginary parts of scattered velocity potentials on the sphere surface for $ka=4$, respectively. As Fig. 1 shows, eight terms of Chebyshev polynomials for $ka=4$ are enough to approximate the analytic result. Figures 4 and 5 indicate the same comparison for an intermediately high nondimensional wave number $ka=10$. As Fig. 1 shows, a 16-term approximation is enough

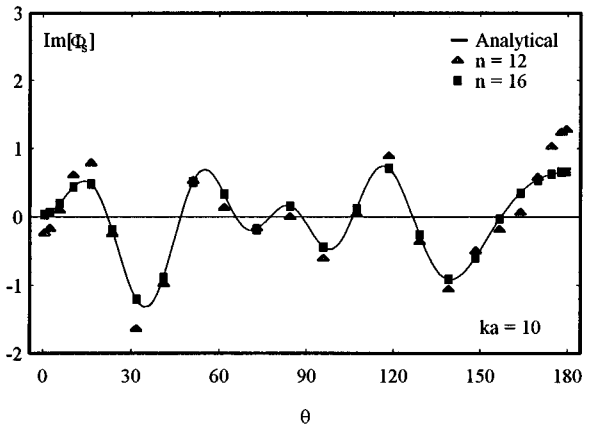

FIG. 5. Imaginary parts of scattered velocity potentials on a sphere surface when $ka=10$.

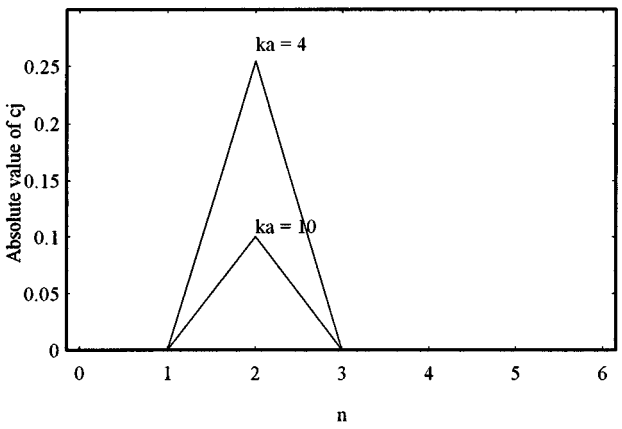

FIG. 7. Absolute values of generalized Fourier coefficients when radiation from a sphere for $ka=4$ and 10.

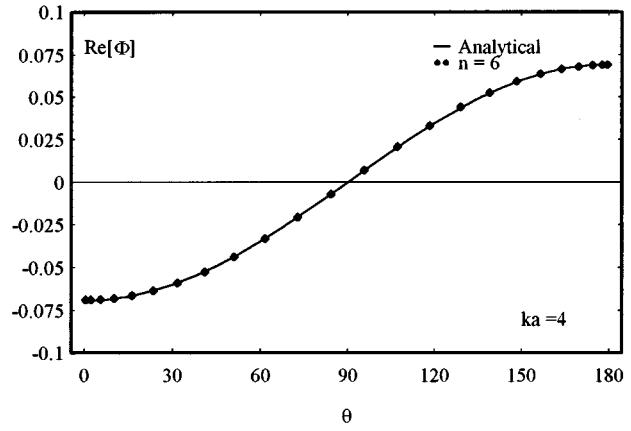

FIG. 8. Real part of the velocity potential on the surface of an oscillating sphere when $ka=4$.

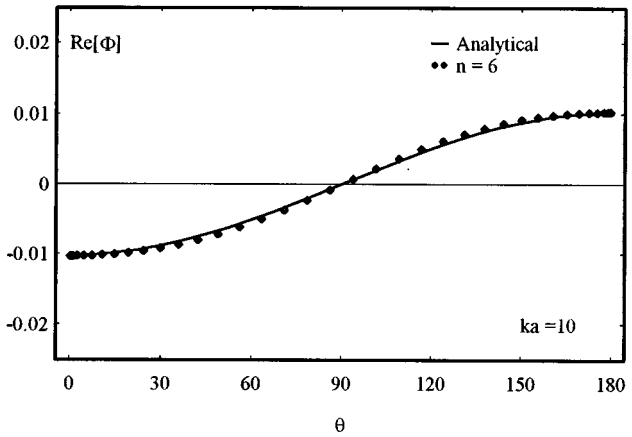

FIG. 10. Real part of the velocity potential on the surface of an oscillating sphere when $ka=10$.

for the convergence consideration when $ka=10$ and Figs. 4 and 5 also confirm these results. Different locations of collocation points used in the above cases for a 24-point Gaussian formula are shown in Fig. 6.

B. Application to radiation from a sphere

The analytical solution of the velocity potential for an oscillating sphere of radius a with a radial velocity $\cos\theta$ is given by

$$\Phi(P) = \left(\frac{a}{r}\right)^2 \cos\theta \, \frac{a(1-ikr)(k^2a^2-2-2ika)}{k^4a^4+4} \, e^{ik(r-a)}. \tag{17}$$

Equation (17) shows that the solution is a one-term polynomial when the velocity potential is on the sphere surface, $r=a$. Figure 7 indicates that the coefficient is at a peak when $n=2$ and almost zero when $n\neq 2$. In Figs. 8 and 9, a 24-point Gaussian formula is applied for the numerical integration and 6 terms of Chebyshev polynomials are selected. The comparison between analytical and numerical results is presented for real and imaginary parts of radiating velocity potentials on the sphere surface for $ka=4$, respectively. In Figs. 10 and 11, a 36-point Gaussian formula is chosen for the numerical integration and 6 terms of Chebyshev polynomial are used. The similar comparison of radiating velocity potentials is shown on the sphere surface for $ka=10$.

For these radiation examples, the variation of the velocity potential is linear in $\cos\theta$. Although a few terms of the basis functions are good enough for such approximations, it still needs many integration points to gain enough accuracy in the numerical quadrature. In boundary element methods, the number of collocation points is about the same as that of numerical integration points.[19] Consequently, a large matrix is constructed in conventional boundary element methods. Therefore, the spectral method needs much less collocation points than boundary element methods in the above cases.

III. CONCLUSION

The spectral method is developed in solving boundary integral equations. The new scheme presents orthogonal functions as basis functions for acoustic variables instead of low-order shape functions. The spectral method shows several advantages over conventional boundary element meth-

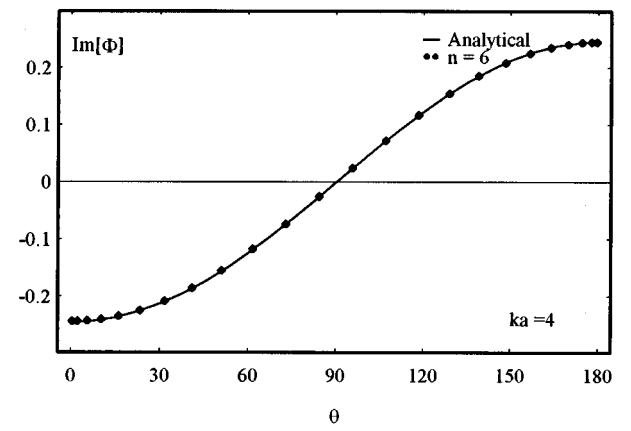

FIG. 9. Imaginary part of the velocity potential on the surface of an oscillating sphere when $ka=4$.

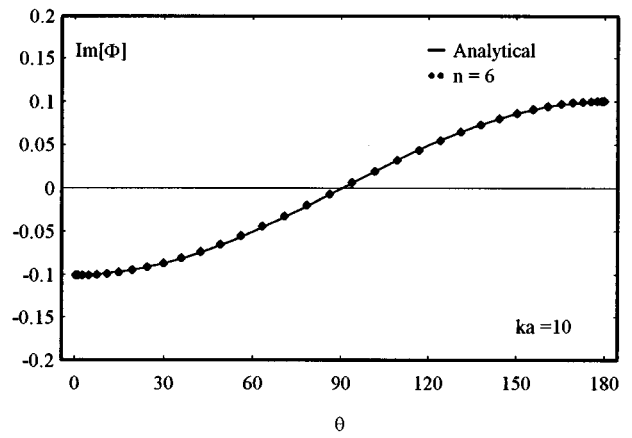

FIG. 11. Imaginary part of the velocity potential on the surface of an oscillating sphere when $ka=10$.

ods. The accuracy of spectral methods is high and can be estimated directly from the variation of generalized Fourier coefficients. If extremely high accuracy is required, spectral methods are even better than conventional boundary element methods. In general, the number of unknowns in the present method can be much less than that of conventional boundary element methods. Therefore, the present method saves a large amount of matrix storage and time when the matrix is solved.

[1] C. Canuto, M. Y. Hussaini, A. Quarteroni, and T. A. Zang, *Spectral Methods in Fluid Dynamics* (Springer-Verlag, Berlin, 1987).

[2] J. P. Boyd, *Chebyshev and Fourier Spectral Methods* (Springer-Verlag, Berlin, 1989).

[3] J. M. Occhialini, G. P. Muldowney, and J. J. L. Higdon, ''Boundary integral/spectral element approaches to the Navier–Stokes equations,'' Int. J. Numer. Methods Fluids **15**, 1361–1381 (1992).

[4] L. R. Hill and T. N. Farris, ''Fast Fourier transform of spectral boundary elements for transient heat conduction,'' Int. J. Numer. Methods Heat Fluid Flow **5**, 813–827 (1995).

[5] F. Q. Hu, ''A fast numerical solution of scattering by a cylinder: Spectral method for the boundary integral equations,'' J. Acoust. Soc. Am. **96**, 3693–3703 (1994).

[6] H. A. Schenck, ''Improved integral formulation for acoustic radiation problems,'' J. Acoust. Soc. Am. **44**, 41–58 (1968).

[7] A. J. Burton and G. F. Miller, ''The application of integral equation methods to the solution of some exterior boundary-value problems,'' Proc. R. Soc. London, Ser. A **323**, 201–210 (1971).

[8] A. F. Seybert and T. K. Rengarajan, ''The use of CHIEF to obtain unique solutions for acoustic radiation using boundary integral equations,'' J. Acoust. Soc. Am. **81**, 1299–1306 (1987).

[9] T. W. Wu and A. F. Seybert, ''Acoustic radiation and scattering,'' in *Advanced Boundary Element Methods in Acoustics*, edited by R. D. Ciskowski and C. A. Brebia (Computational Mechanics Publications, Southampton, U.K., 1991), Chap. 3.

[10] T. W. Wu and A. F. Seybert, ''A weighted residual formulation for the CHIEF method in acoustics,'' J. Acoust. Soc. Am. **90**, 1608–1614 (1991).

[11] D. J. Segalman and D. W. Lobitz, ''A method to overcome computational difficulties in the exterior acoustics problem,'' J. Acoust. Soc. Am. **91**, 1855–1861 (1992).

[12] Z. Reut, ''On the boundary integral methods for the exterior acoustic radiation problem,'' J. Sound Vib. **103**, 297–298 (1985).

[13] C. C. Chien, J. Rajiyah, and S. N. Atluri, ''An effective method for solving the hypersingular integral equations in 3-D acoustics,'' J. Acoust. Soc. Am. **88**, 918–937 (1990).

[14] G. Krishnasamy, L. W. Schmerr, T. J. Rudolphi, and F. J. Rizzo, ''Hypersingular boundary integral equations: Some applications in acoustic and elastic wave scattering,'' J. Appl. Mech. **57**, 404–414 (1990).

[15] T. W. Wu, A. F. Seybert, and G. C. Wan, ''On the numerical implementation of a cauchy principal value integral to insure a unique solution for acoustic radiation and scattering,'' J. Acoust. Soc. Am. **90**, 554–560 (1991).

[16] Y. Liu and F. J. Rizzo, ''A weakly singular form of the hypersingular boundary integral equation applied to 3-D acoustic wave problems,'' Comput. Methods Appl. Mech. Eng. **96**, 271–287 (1992).

[17] O. D. Kellogg, *Foundations of Potential Theory* (Dover, New York, 1954).

[18] M. A. Jaswon and G. T. Symm, *Integral Equation Methods in Potential Theory and Elastostatics* (Academic, London, 1977).

[19] W. S. Hwang, ''A boundary integral method for acoustic radiation and scattering,'' J. Acoust. Soc. Am. (1997) (to be published).

[20] K. E. Atkinson, *An Introduction to Numerical Analysis* (Wiley, New York, 1988).

Elastic waves in orthotropic incompressible materials and reflection from an interface

Sudhakar Nair and Dimitrios A. Sotiropoulos[a)]
Mechanical, Materials and Aerospace Engineering Department, Illinois Institute of Technology, Chicago, Illinois 60616

(Received 16 December 1996; accepted for publication 11 February 1997)

The propagation of elastic plane waves in orthotropic incompressible materials is examined under plane strain conditions in a plane of symmetry. The slowness surface is obtained by aligning a material axis of symmetry with the direction of minimum phase speed. The existence of incident homogeneous waves and reflected homogeneous and nonhomogeneous waves in the presence of a planar interface separating two half-spaces is subsequently examined. A surface which separates the range of existence of two homogeneous reflected waves from that of one homogeneous and one nonhomogeneous is obtained in terms of the angle of incidence, the orientation of the interface with respect to the material axis of symmetry, and one elastic parameter. The critical orientation beyond which there exist two homogeneous reflected waves is derived in explicit form in terms of the elastic parameter. Reflection coefficients are obtained and discussed when the interface is a free surface. Exclusion points are defined in the range of existence of the reflected waves as points for which only one reflected (homogeneous) wave exists. The analysis is complemented with numerical examples.
 [S0001-4966(97)05206-5]

PACS numbers: 43.20.Fn, 43.20.Gp [ANN]

INTRODUCTION

The propagation and reflection of elastic waves in anisotropic materials is a topic of research that finds applications in the areas of nondestructive evaluation, design, and seismology. For compressible elastic materials a number of papers have appeared recently in the technical literature both in the experimental[1,2] and in the theoretical[3] aspects to complement older theoretical papers, for example,[4,5] and the classical book on the subject by Fedorov.[6] In the theoretical papers the reflected waves were obtained numerically for specific anisotropic materials and wave motion.

The purpose of the present paper is to obtain explicit formulas for the range of existence of the different types of reflected waves in the presence of a bi-material interface. The prototype problem considered here deals with the propagation of a plane time-harmonic elastic wave in a homogeneous orthotropic incompressible material and its reflection from a planar interface separating the material from, in general, a different type of material. The assumption of incompressibility and orthotropy are applicable to several materials as, for example, polymer Kratons, thermoplastic elastomers, rubber composites when low frequency waves are considered to justify the assumption of material homogeneity, etc. The elastic motion considered in the present paper is such that plane strain conditions prevail in a plane of material symmetry. From a practical point of view, in a laboratory experiment, shear waves can be generated in materials by shear wave transducers. In materials which are nearly incompressible, since longitudinal waves are much faster than shear waves, upon reflection longitudinal waves play no role in the window for shear wave arrivals. When the incompressible material is isotropic, upon incidence of a homogeneous wave, there exist one homogeneous reflected wave and one nonhomogeneous interfacial wave for all angles of incidence except for 0, $\pi/4$ and $\pi/2$ rads for which there exists only a homogeneous wave. The effect of orthotropy introduces, for certain combinations of geometry and elastic parameters, a second homogeneous reflected wave. To know when this happens is important. For example, in nondestructive evaluation experiments it is advantageous to have only one homogeneous reflected wave. In Sections I and II the slowness surface is obtained and examined with reference to the existence of incident and reflected homogeneous waves. A surface which separates the range of existence of two homogeneous reflected waves from that of one homogeneous and one non-homogeneous is obtained in terms of the angle of incidence, the orientation of the interface with respect to the material axis of symmetry, and one elastic parameter. In Section III, a critical orientation of the interface beyond which there exist two homogeneous reflected waves is derived in explicit form in terms of the elastic parameter. In Section IV, the reflection coefficients are obtained and examined for a free surface. Exclusion points are found in the range of existence of reflected waves for which only one reflected (homogeneous) wave exists. In Section V, there is a summary of the conclusions.

I. HARMONIC WAVES IN ORTHOTROPIC INCOMPRESSIBLE MEDIA

For an orthotropic incompressible medium, let x_1, x_2, x_3 denote the three material axes of symmetry. With reference to these, the linear stress-strain relations for the material are

[a)]Permanent address: Department of Engineering Sciences, Technical University of Crete, Chania 73100, Greece.

$$\sigma_{11}=-p+C_{11}\epsilon_{11}+C_{12}\epsilon_{22}+C_{13}\epsilon_{33},$$
$$\sigma_{22}=-p+C_{12}\epsilon_{11}+C_{22}\epsilon_{22}+C_{23}\epsilon_{33},$$
$$\sigma_{33}=-p+C_{13}\epsilon_{11}+C_{23}\epsilon_{22}+C_{33}\epsilon_{33},$$
$$\sigma_{23}=2C_{44}\epsilon_{23},\qquad \sigma_{13}=2C_{55}\epsilon_{31},\qquad \sigma_{12}=2C_{66}\epsilon_{12}, \tag{1}$$

where σ's and ϵ's denote the stress and strain components, p the hydrostatic pressure and the C's the elastic constants. The strains are related to the displacement components, u_1, u_2 and u_3 through

$$\epsilon_{ij}=(u_{i,j}+u_{j,i})/2,\qquad i,j=1,2,3. \tag{2}$$

Assuming plane strain in the x_1,x_2-plane and incompressibility,

$$\epsilon_{13}=\epsilon_{23}=\epsilon_{33}=0,\qquad \epsilon_{11}+\epsilon_{22}=0, \tag{3}$$

the orthotropic stress-strain relations (1) reduce to

$$\sigma_{11}=-p+(C_{11}-C_{12})\epsilon_{11},$$
$$\sigma_{22}=-p+(C_{12}-C_{22})\epsilon_{11}, \tag{4}$$
$$\sigma_{12}=2C_{66}\epsilon_{12}.$$

For positive definite strain energy density function the elastic constants in Eqs. (4) must satisfy the inequalities

$$C_{66}\geqslant 0,\qquad C_{11}+C_{22}-2C_{12}\geqslant 0, \tag{5}$$

obtained directly by taking $\epsilon_{11}=0$ for the first and $\epsilon_{12}=0$ for the second.

It is to be noted that the incompressibility condition imposes three constraints on the six elastic constants in the normal stress-normal strain relations in Eqs. (1). As shown in the Appendix, the three constants C_{11}, C_{12}, and C_{22} can be viewed as independent constants.

The incompressibility condition in (3) is satisfied by introducing the displacement potential, ψ as

$$u_1=\psi_{,2},\qquad u_2=-\psi_{,1}. \tag{6}$$

Using Eqs. (6), (2), and (4) in the equations of motion,

$$\sigma_{11,1}+\sigma_{12,2}=\rho\ddot{u}_1,\quad \sigma_{12,1}+\sigma_{22,2}=\rho\ddot{u}_2, \tag{7}$$

where ρ is the mass density of the material and the dot denotes differentiation with respect to time, and eliminating the hydrostatic pressure, p, the displacement potential is seen to satisfy

$$\alpha[\Delta^2\psi+4\beta\psi_{,1122}]=\rho\Delta\ddot{\psi}, \tag{8}$$

where Δ is the two-dimensional Laplace operator and

$$\alpha=C_{66},\qquad \beta=\frac{C_{11}+C_{22}-2C_{12}}{C_{66}}-1. \tag{9}$$

The inequalities (5) required for the positive definiteness of the strain energy imply

$$\alpha\geqslant 0,\qquad \beta\geqslant -1. \tag{10}$$

The material parameter β plays a crucial role in characterizing the waves in this class of materials. For the range $-1\leqslant\beta\leqslant 0$, it is advantageous to choose a new material coordinate system, (x_1',x_2'), with the x_1'-axis at an angle $\pi/4$ from the x_1-axis. That is,

$$x_1'=(x_1+x_2)/\sqrt{2},\qquad x_2'=(x_2-x_1)/\sqrt{2}. \tag{11}$$

The Laplace operator Δ' in the new system is identical to Δ, but the mixed derivative in Eq. (8) is,

$$4\psi_{,1122}=(\Delta')^2\psi'-4\psi'_{,1122}, \tag{12}$$

where $\psi'=\psi(x_1',x_2')$.

Thus the governing equation (8) in the new coordinate system becomes

$$\alpha'[(\Delta')^2\psi'+4\beta'\psi'_{,1122}]=\rho\Delta\ddot{\psi}', \tag{13}$$

where

$$\alpha'=\alpha(1+\beta),\qquad \beta'=-\beta/(1+\beta). \tag{14}$$

If β is negative in the x_1,x_2-coordinate system, in the x_1',x_2'-system, β' will be positive. Thus, proper relabelling of the axes allows one to have $\beta\geqslant 0$.

For time-harmonic plane waves the displacement potential can be expressed as

$$\psi=Ae^{i\omega(\xi_1x_1+\xi_2x_2-t)}, \tag{15}$$

where A is the potential amplitude at the origin, taken to be small in accordance with the linearity assumption. Here, ω is the circular frequency, and ξ_1, ξ_2, the components of the slowness vector. The magnitude of the slowness vector, $\xi=\sqrt{\xi_1^2+\xi_2^2}$, represents the reciprocal of the wave speed, v.

Substituting the expression (15) in Eq. (8), the equation for the slowness curve is obtained as

$$\xi^4+4\beta\xi_1^2\xi_2^2-\rho\xi^2/\alpha=0. \tag{16}$$

For a wave propagating in the direction, θ, with respect to the x_1-axis, using

$$\xi_1=\cos\,\theta/v,\quad \xi_2=\sin\,\theta/v \tag{17}$$

in Eq. (16), it is seen that

$$v^2=\alpha(1+\beta\,\sin^2 2\theta)/\rho. \tag{18}$$

For materials with $\beta=0$, the speed v is independent of the propagation direction. In this group of materials are included transversely isotropic materials ($C_{11}=C_{22}$, $2C_{66}=C_{11}-C_{12}$) which cannot be distinguished, in this sense, from isotropic materials. The minimum and maximum values of v^2 are α/ρ and $\alpha(1+\beta)/\rho$ along the x_1-axis and along an axis $\pi/4$ radians from the x_1-axis, respectively. The conditions for real wave speeds, $\alpha\geqslant 0$, and $\beta\geqslant -1$, are identical to the inequalities (9) obtained from strain energy considerations. Since the extremum speeds are along directions $\pi/4$ radians apart, the choice of a system of material axes with $\beta\geqslant 0$ is equivalent to choosing a minimum speed direction as the x_1-axis.

Introducing nondimensional slowness vector components

$$m_1=\cos\,\theta/\hat{v},\qquad m_2=\sin\,\theta/\hat{v},\qquad \hat{v}=v/\sqrt{\alpha/\rho}, \tag{19}$$

and using Eq. (16), a slowness function Ω may be defined as

$$\Omega(m_1,m_2)=\tfrac{1}{2}[(m_1^2+m_2^2)^2+4\beta m_1^2m_2^2-m_1^2-m_2^2]=0. \tag{20}$$

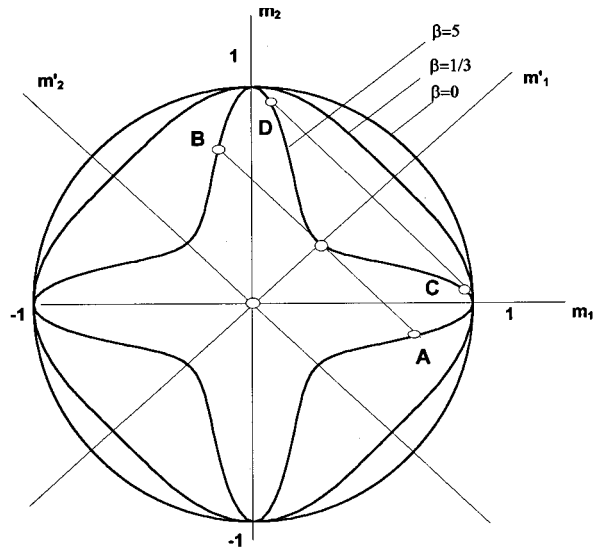

FIG. 1. The slowness curves for the orthotropic incompressible media for various values of the parameter β. The m_1-axis represents the direction of minimum wave speed and the $m_1{}'$-axis that of the maximum speed.

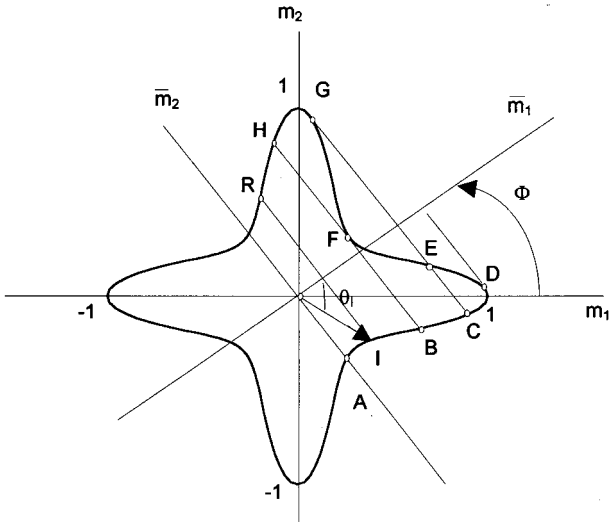

FIG. 2. The interface axes $(\overline{m_1},\overline{m_2})$ in relation to the material axes. The incident wave is represented by the point I on the curve.

The nondimensional energy flux vector associated with a wave propagating in the direction θ, coincides with the group velocity vector $\mathbf{V}_g$ which is given by the gradient of the slowness function, that is, normal to the slowness curve. Thus, the components of $\mathbf{V}_g$ are

$$V_{g1}=m_1[2(m_1^2+m_2^2)+4\beta m_2^2-1],$$
$$V_{g2}=m_2[2(m_1^2+m_2^2)+4\beta m_1^2-1]. \tag{21}$$

As indicated earlier, when $\beta=0$, Eq. (20) represents a circle of radius unity. As shown in Fig. 1, increasing the value of the parameter β, eventually leads to the loss of convexity of the slowness curve. This loss of convexity has interesting consequences in the context of the presence of interfaces in the media. In order to obtain a condition on the value of β for the transition from a convex slowness curve to a concave curve, it is convenient to use a rotated coordinate system according to Eq. (10). In this system, $\Omega=0$, gives

$$[(m_1')^2+(m_2')^2]^2-\frac{4\beta}{1+\beta}(m_1')^2(m_2')^2-(m_1')^2-(m_2')^2=0, \tag{22}$$

where, now, the nondimensional speed, $\hat{v}$ is defined using α' in accordance with Eqs. (19) and (14), to have the minimum slowness unity. When $m_1'=1$, Eq. (22) gives, as solutions for m_2',

$$m_2'=0,\pm\sqrt{\frac{3\beta-1}{\beta+1}}. \tag{23}$$

This result shows that when $\beta\leqslant 1/3$, $m_2'=0$ is the only real solution, confirming the convexity of the slowness curve. However, when $\beta>1/3$, two additional solutions appear, indicating a concave curve. There is a range of values for $m_1'>1$, in which each m_1' corresponds to four values of m_2'. This is qualitatively shown in Fig. 1 for $\beta=5$. When $m_1'=1$, the points A, B and $m_2'=0$ represent the three solutions of Eq. (23). When m_1' lies to the left of the line AB there are two real values of m_2' and when it lies to the right of AB there are four values for m_2'. Corresponding to the line CD which is tangent to the slowness curve, the two positive solutions and the two negative solutions for m_2' coalesce at C and D, respectively.

For interface problems, another aspect of the concave slowness curve, namely, the location of the inflection points is of interest. As seen in Fig. 1, these are eight in number, symmetrically located around the curve. Reverting to the original, m_1,m_2-system, these points are found by setting $d^2m_2/dm_1^2=0$ using Eq. (20). In the first quadrant, the inflection point closer to the m_1-axis is at the angle,

$$\theta_{in}=\frac{1}{2}\sin^{-1}\sqrt{\frac{\hat{v}_{in}^2-1}{\beta}}, \qquad \hat{v}_{in}^4=4(1+\beta)/3, \tag{24}$$

where $\hat{v}_{in}$ is the nondimensional wave speed corresponding to the inflection point.

Once the geometry of the slowness curve is understood, incident waves in the presence of an interface can be considered.

II. INCIDENT AND REFLECTED WAVES OF AN INTERFACE

Consider a linear interface separating the orthotropic incompressible medium from a second half-space. The interface is assumed to be at angle ϕ with the axis of symmetry, x_1, for which $\beta\geqslant 0$. Let $\overline{x_1}$, $\overline{x_2}$ represent a new system of coordinates parallel and perpendicular to the interface, respectively. The two systems are related as

$$\overline{x_1}=x_1\cos\phi+x_2\sin\phi, \qquad \overline{x_2}=x_2\cos\phi-x_1\sin\phi. \tag{25}$$

A plane shear wave is assumed to be incident on the interface from the side of the orthotropic medium, $\overline{x_2}>0$. With the angle of incidence θ_I, measured clockwise from the $\overline{x_1}$-axis, a generic point, I in Fig. 2 represents the incident wave on the slowness curve. The energy flux vector associated with the incident wave must obey

$$\overline{V_{g2}} = V_{g2} \cos\phi - V_{g2} \sin\phi < 0, \tag{26}$$

where V_{g1} and V_{g2} are given by (21).

The nondimensional slowness vector components (m_1, m_2) can be related to the corresponding components $(\overline{m_1}, \overline{m_2})$ in the interface coordinate system, $(\overline{x_1}, \overline{x_2})$, using the transformation law (25). The equation for the slowness curve in the interface coordinate system, using (20) becomes

$$\Omega(\overline{m_1}, \overline{m_2}) = \tfrac{1}{2}\{(\overline{m_1^2} + \overline{m_2^2})^2 + \beta[(\overline{m_2^2} - \overline{m_1^2})\sin 2\phi + 2\overline{m_1}\,\overline{m_2} \cos 2\phi]^2 - (\overline{m_1^2} + \overline{m_2^2})\} = 0. \tag{27}$$

The continuity of displacement and traction vectors at the interface is satisfied by introducing two reflected waves and two refracted waves and solving for their unknown amplitudes. The solutions require that the reflected and refracted waves have the same slowness vector component along the interface. Thus, for a given slowness component, $\overline{m_{1I}}$, of the incident slowness vector, the projections of the slowness vectors along $\overline{x_1}$ for the four excited waves must be $\overline{m_{1I}}$. Of course, the slowness vector for refracted waves lie on a different slowness curve depending on the properties of the second material. In the case of a free surface there are no continuity constraints on the displacement vector and in the case of a rigid second material there is no constraints on the traction vector. In all cases, to satisfy the interface conditions, two reflected waves are needed in general. The question regarding the existence of the solutions in the presence of an interface for arbitrary anisotropic materials has been addressed by Wright.[7] The slowness curve given by Eq. (27) has four solutions, $\overline{m_2}$ for a given $\overline{m_{1I}}$. One of these corresponds to the incident wave.

Letting

$$t = \overline{m_2}/\overline{m_{1I}}, \qquad \tau = \overline{m_{2I}}/\overline{m_{1I}}, \tag{28}$$

where $\tau = -\tan\theta_I$ is real and t, the unknown, may be complex in Eq. (27) and subtracting $\Omega(\overline{m_{1I}}, \overline{m_{2I}}) = 0$, it is seen that

$$(t-\tau)[a_1(t+\tau)^3 + a_2(t+\tau)^2 + a_3(t+\tau) + a_4] = 0, \tag{29}$$

where

$$\begin{aligned} a_1 &= a m_{1I}^2, \\ a_2 &= -2(a\tau - \beta \sin 4\phi)\overline{m_{1I}^2}, \\ a_3 &= 2[a(1+\tau^2) + 2\beta \cos 4\phi - \beta\tau \sin 4\phi]\overline{m_{1I}^2} - 1, \\ a_4 &= -2\beta(1-\tau^2)\sin 4\phi \overline{m_{1I}^2}, \\ a &= 1 + \beta \sin^2 2\phi. \end{aligned} \tag{30}$$

Discarding the solution $t = \tau$ corresponding to the incident wave, the cubic factor has three roots. These are, all real or one real and two complex, with the complex roots being complex conjugate of each other. The real roots represent homogeneous reflected waves, one of which is discarded on physical grounds as discussed below, the complex root with positive imaginary part represents a nonhomogeneous wave with amplitude decaying with increasing $\overline{x_2}$ and the complex root with negative imaginary part a nonhomogeneous wave with amplitude increasing with increasing $\overline{x_2}$. Waves with increasing amplitude are rejected as they are physically untenable. A reflected homogeneous wave with $t = -\tau$ corresponds to an angle of reflection equal to the angle of incidence. This is possible when $a_4 = 0$, i.e., when $\tau = 1$ or when $\phi = 0, \pm\pi/4$. Also when $\overline{m_{1I}} = 0$, the cubic degenerates into a linear equation with the solution $t = -\tau$. In Fig. 2, a generic incident wave is shown with slowness vector terminating at the point I on the slowness curve. When the incident wave is normal to the interface I moves to the point A. By constructing a tangent to the slowness curve at the point F, parallel to the $\overline{m_2}$-axis, the intersection points B and H are obtained. Another tangent at G gives the points C, E, and G. A third tangent is shown at D. Between the points A and B, there exists one homogeneous reflected wave corresponding to the point R and one acceptable nonhomogeneous wave. If I lies between B and C there are three homogeneous solutions for $\overline{m_2}$, one on the curve segment EF, one on FG and a third one on GH. The solution lying on the segment FG has its energy flux vector directed toward the interface and this solution is not acceptable as it corresponds to additional energy input into the medium at $\overline{x_2} \to \infty$ aside from that due to the incident wave. Thus, two physically acceptable solutions are always available to satisfy the boundary conditions. When I lies on the segment CD, again, there is only one homogeneous reflected wave with its slowness vector terminus on DE, and one acceptable nonhomogeneous reflected wave. The point I lying on the segment FG is also acceptable as its energy flux vector is pointing toward the interface.

The condition that the parameters, β, ϕ, and θ_I must satisfy for the existence of two homogeneous reflected waves is given, by considering the cubic factor in (29), as

$$q^3 + r^2 \leqslant 0, \tag{31}$$

where

$$q = \frac{1}{3}\frac{a_3}{a_1} - \frac{1}{9}\frac{a_2^2}{a_1^2}, \qquad r = \frac{a_2 a_3}{6a_1^2} - \frac{a_2^3}{27a_1^3}. \tag{32}$$

Outside the range defined by (31) there exists, in general, one homogeneous and one nonhomogeneous reflected wave. There are specific combinations of the three parameters as discussed in Sec. IV for which the amplitude of the nonhomogeneous wave vanishes. Without loss of generality, the incident waves can be considered with $\overline{m_1} \geqslant 0$ with the angle, ϕ, of the interface restricted to $-\pi/4 \leqslant \phi \leqslant \pi/4$.

The particularly simple cases of $\phi = 0$ and $\phi = \pi/4$ are now examined. When $\phi = 0$, the slowness curves appear as in Fig. 1 with the interface axis $\overline{x_1}$ coinciding with the material axis x_1. For this case the acceptable roots of the cubic of (29) which represent reflected waves become,

$$t = -\tau, \quad t = i\sqrt{1 + 4\beta \cos^2\theta_I}, \tag{33}$$

with the first root representing a homogeneous reflected wave with the angle of reflection equal to the angle of incidence, and the second an acceptable nonhomogeneous wave, it being a true interfacial wave with direction of propagation parallel to the interface. The quantity inside the square root symbol is positive for all values of θ_I.

When $\phi=\pi/4$, the slowness curve appears similar to that in Fig. 2 except that the point F lies on the $\overline{x_1}$-axis and the three points C, D, and E coalesce into a single point D. The nondimensional wave speed for any incidence angle θ_I is obtained from Eqs. (19) and (20), using $\theta=\pi/4-\theta_I$ as

$$\hat{v}^2=1+\beta\cos^2 2\theta_I. \tag{34}$$

With the notation $\gamma^4=(1+\beta)/4\beta$, the angle of incidence θ_I for the component of the slowness vector along the interface to be OF is given by $\cos\theta_I=\gamma^2$. As seen earlier, when $\beta<1/3$, the slowness curve is convex and the only solution for this equation is $\theta_I=0$. When $\beta\geqslant 1/3$, θ_I corresponding to the point B in Fig. 2 also represents an incident wave. Between the points B and D ($\cos\theta_I=\gamma$) there are two homogeneous reflected waves, one represented by a point on the segment DF and another on the segment GH. When the incident wave vector terminates at D the two reflected waves coalesce at G with the energy flux directed parallel to the interface.

It ought to be remarked here that inside the range of existence of the different types of reflected waves there is a finite number of *exclusion* points at which the energy flux of one of the reflected (homogeneous or nonhomogeneous) waves vanishes; a reflected nonhomogeneous wave cannot exist by itself as in such a case it would be a true interfacial wave—its energy flux being parallel to the interface—carrying negligible energy compared to that carried by the incident homogeneous reflected wave. The vanishing of the energy flux coincides with that of the wave amplitude so that exclusion points may be determined by the vanishing of the determinant formed by the coefficients of the wave amplitudes of the one incident, one reflected, and two refracted waves, involved in the four homogeneous equations representing the four continuity conditions. In Section IV exclusion points are determined for a free surface.

III. THE CRITICAL INTERFACE ORIENTATION

When $\phi=0$, as discussed above, there is only one homogeneous reflected wave. As ϕ increases, to represent different material symmetry orientations, there will be, for $\beta>1/3$, a critical value above which there will exist two homogeneous reflected waves for some angles of incidence. The range of such incident angles is, in general, not continuous. The critical angle, ϕ_{cr}, occurs when a tangent to the slowness surface first becomes normal to the interface as the angle ϕ in Fig. 2 is increased. This tangent is attained at the inflection point of the slowness surface of $\phi=0$ closest to the m_2-axis in the first quadrant. Using Eq. (24) for the location of the inflection point,

$$\phi_{cr}=\pi/2-\theta_{in}. \tag{35}$$

The necessary condition for the existence of two homogeneous reflected waves from the free surface of orthotropic materials with $\beta>1/3$ is

$$\phi>\phi_{cr}. \tag{36}$$

Thus, to satisfy (31) it is necessary to satisfy (36). Figure 3 shows the variation of the critical angle, ϕ_{cr} of (35) with β. Below the line in the figure there exists only one homogeneous reflected wave, whereas, above the line, as inequality (36) is satisfied, there can always be found angles of incidence for which two homogeneous reflected waves exist.

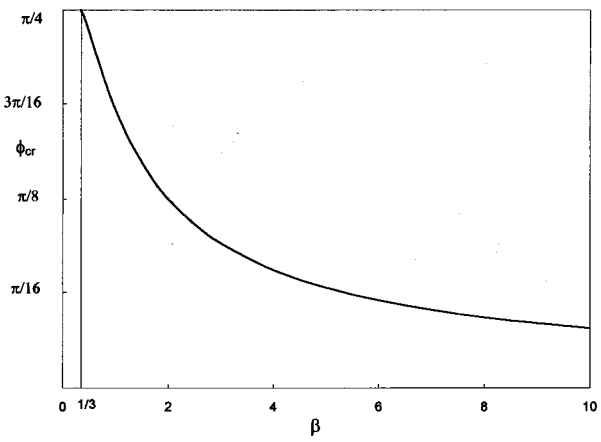

FIG. 3. The critical angle ϕ_{cr} of the interface with respect to the minimum speed axis x_1 for the existence of two homogeneous reflected waves, as a function of the elastic parameter, β.

IV. REFLECTION COEFFICIENTS FOR A FREE SURFACE

When the interface is a free surface, the amplitudes of the two reflected waves along with the amplitude of the incident wave combine to have zero traction components along the free surface. That is,

$$\overline{\sigma_{12}}=0, \qquad \overline{\sigma_{22}}=0 \ \text{ on } \ \overline{x_2}=0. \tag{37}$$

Using Eqs. (15), (4), and (7), the components of stress in the material coordinate system can be found as

$$\begin{aligned}
\sigma_{11}&=-2m_1m_2(1+2\beta\sin^2\theta)\rho\omega^2\psi,\\
\sigma_{22}&=2m_1m_2(1+2\beta\cos^2\theta)\rho\omega^2\psi,\\
\sigma_{12}&=(m_1^2-m_2^2)\rho\omega^2\psi.
\end{aligned} \tag{38}$$

For a free surface at an angle ϕ, the relevant stress components are

$$\begin{aligned}
\overline{\sigma_{12}}&=M\rho\omega^2\psi=\overline{m_1^2}\{1-t^2+\beta[(1-t^2)\sin^2 2\phi\\
&\qquad +t\sin 4\phi]\}\rho\omega^2\psi,\\
\overline{\sigma_{22}}&=N\rho\omega^2\psi=\overline{m_1^2}\left\{2t+\frac{\beta}{1+t^2}[(1-3t^2)\sin 4\phi\right.\\
&\qquad \left.+2t\cos 4\phi+2t^3\sin^2 2\phi]\right\}\rho\omega^2\psi,
\end{aligned} \tag{39}$$

where $t=\overline{m_2}/\overline{m_1}$.

At exclusion points, only one reflected wave exists, it being homogeneous and with a nonzero amplitude. The free surface boundary conditions (37) then yield

$$M_0A_0+M_1A_1=0, \qquad N_0A_0+N_1A_1=0, \tag{40}$$

where 0 and 1 refer to the incident and reflected waves and A to the wave amplitude. For Eq. (40) to be satisfied it is required that

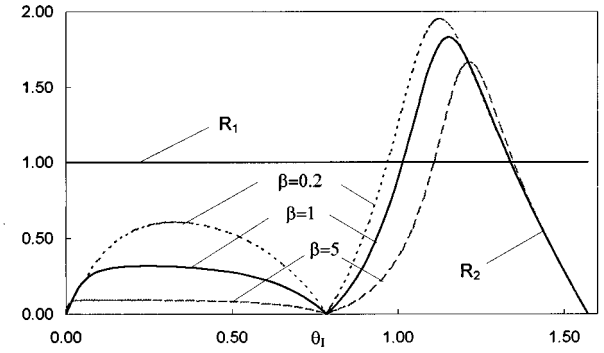

FIG. 4. The coefficients of reflection, R_1 and R_2, as function of the angle of incidence, θ_I, for various values of the parameter β when $\phi=0$.

$$M_0N_1-M_1N_0=0. \tag{41}$$

This equation defines exclusion points (ϕ,β,θ_I).

For the special case of transverse isotropy, $\beta=0$, and the stresses in Eq. (39) are independent of ϕ. Denoting the amplitude of the nonhomogeneous reflected wave by A_2, the reflection coefficients are defined as

$$R_1=|A_1/A_0|, \qquad R_2=|A_2/A_0|. \tag{42}$$

Using $t=\tau=-\tan\theta_I$, $t=-\tau$, and $t=i$, for the three waves, the values of the reflection coefficients are obtained explicitly as

$$R_1=1, \qquad R_2=2|\cos 2\theta_I|\tan\theta_I. \tag{43}$$

For $\theta_I=0,\pi/4$ the surface wave does not exist, i.e., $R_2=0$, thus these two points defining exclusion points.

When $\beta>0$, equations for the reflection coefficients will be presented for the two simple cases of $\phi=0$ and $\phi=\pi/4$. For the case, $\phi=0$, using the same notation for the amplitudes, the zero-traction boundary conditions give

$$\begin{aligned}&(1-t_1^2)A_1+(1-t_2^2)A_2=-(1-\tau^2)A_0,\\ &[1+2\beta/(1+t_1^2)]t_1A_1+[1+2\beta/(1+t_2^2)]t_2A_2\\ &\quad=-[1+2\beta/(1+\tau^2)]\tau A_0,\end{aligned} \tag{44}$$

where, in accordance with Eq. (33), $t_1=-\tau$ and $t_2=i\sqrt{1+4\beta\cos^2\theta_I}$.

Figure 4 shows a plot of the two reflection coefficients, R_1 and R_2 for $\beta=0.2$, $\beta=1$ and $\beta=5$, when the incident angle θ_I is varied from 0 to $\pi/2$. The maximum value of the reflection coefficient corresponding to the surface (nonhomogeneous) wave decreases with increasing values of β. It can also be seen that $\theta_I=0$, $\pi/4$, and $\pi/2$, are exclusion points inside the range of existence of the surface waves. The reflection coefficient for the homogeneous wave is unity for all values of β. This can also be seen from the system of equations (44) where the two coefficients of A_2 are one real and one imaginary. It is to be noted that the behavior of R_2 when $\beta=0$ is qualitatively different from it when $\beta>0$.

For the case $\phi=\pi/4$ the zero-traction boundary conditions give

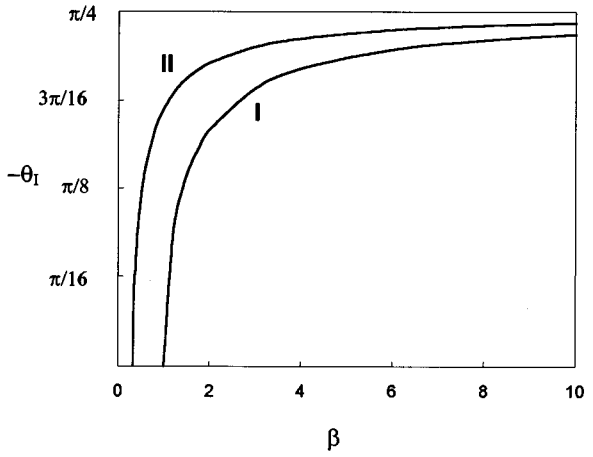

FIG. 5. Angles of incidence, θ_I, and material constants β for which, when $\phi=\pi/4$, there is only one reflected homogeneous wave: (I) angle of reflection equals angle of incidence, and (II) otherwise.

$$\begin{aligned}&(1-t_1^2)A_1+(1-t_2^2)A_2=-(1-\tau^2)A_0,\\ &\left[1-\beta\frac{1-t_1^2}{1+t_1^2}\right]t_1A_1+\left[1-\beta\frac{1-t_2^2}{1+t_2^2}\right]t_2A_2\\ &\quad=-\left[1-\beta\frac{1-\tau^2}{1+\tau^2}\right]\tau A_0,\end{aligned} \tag{45}$$

where $t_1=-\tau$ and $t_2=\sqrt{\gamma^{-4}\cos^2\theta_I-1}\,\mathrm{sgn}(\theta_I)$ with sgn being the *signum* function. When t_2 is imaginary, its imaginary part has to be positive. Here, A_1 represents the amplitude of the reflected wave with the angle reflection equal to the angle of incidence and A_2, the amplitude of the other homogeneous or nonhomogeneous wave.

When $\phi=\pi/4$, there are two sets of exclusion points. The first set corresponds to a nonzero amplitude homogeneous wave reflected at angle equal to the angle of incidence, whereas the second to one reflected at a different angle. The first set is found from Eq. (45) when $A_2=0$ as $\theta_I=\pi/4$ or $0,\pi/2,-0.5\cos^{-1}(1/\beta)$. Thus the exclusion points are independent of β for the first three angles of incidence and exist for the last angle only if $\beta>1$. It is noted that at $\theta_I=\pi/4$, the reflected wave which vanishes is nonhomogeneous when $\beta<1/3$ and homogeneous otherwise since this angle defines points on the segments BD.

The second set of exclusion points is found from Eq. (45) by setting $A_1=0$ and $t_2=\sqrt{\gamma^{-4}\cos^2\theta_I-1}\,\mathrm{sgn}(\theta_I)$ for $\beta>1/3$. These points correspond to the point G in Fig. 2. The two sets of exclusion points I and II, except the first three points of the first set, are shown in Fig. 5. It is observed that for large β, the exclusion points are defined by angles of incidence approaching $-\pi/4$ as the slowness curve degenerates into an $\times$-shape which bi-sects the four quadrants.

Figure 6(a) shows the dependence of the reflection coefficients on the angle of incidence, θ_I, when $\beta=0.2$. For this case, there is no inflection point on the slowness curve and t_2 is imaginary, representing a surface wave. The reflection coefficients, R_1 is unity and R_2 is similar to what is seen for $\phi=0$. The exclusion points are, again, at $\theta_I=0,\pi/4$ and at $\pi/2$.

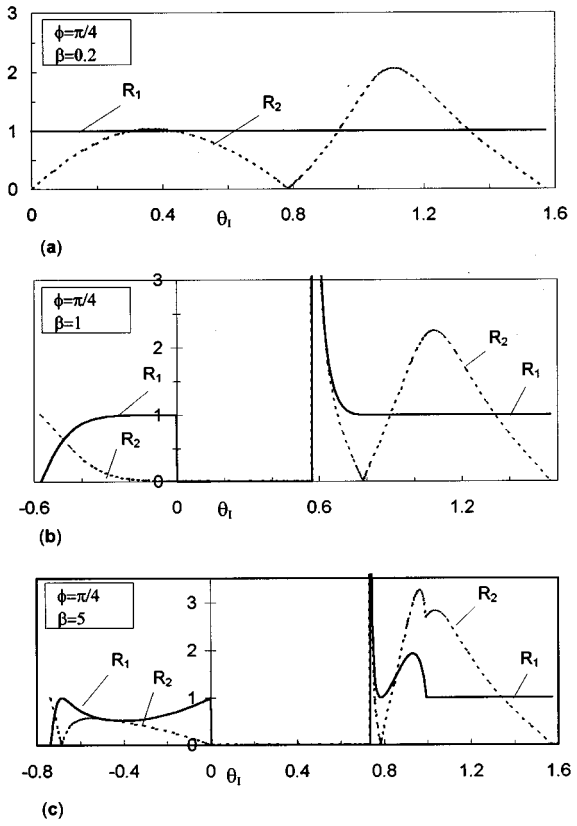

FIG. 6. The coefficients of reflection, R_1 and R_2, as functions of the angle of incidence, θ_I when $\phi=\pi/4$ and (a) $\beta=0.2$, (b) $\beta=1$, and (c) $\beta=5$. The domain for θ_I depends of the values of β.

When $\beta>1/3$, the slowness curve is as shown in Fig. 2, but now with $\phi=\pi/4$. Points on the segment GF are possible incident waves with energy flux vector directed toward the negative $\overline{x_2}$-direction. The angles of incidence are negative for this region. For the segment DF, the energy fluxes show that incident waves are not possible. This is a forbidden band in the range of incident angles. For the segment DB, there are two homogeneous reflected waves, one on DF and the other on GH. Finally, for the segment BA, there is a surface wave and a homogeneous wave.

Figure 6(b) and (c) show the reflection coefficients for $\beta=1$ and $\beta=5$. With the notation $\theta_G=\cos^{-1}(\gamma)$, the domains of these plots are $-\theta_G<\theta_I<\pi/2$, with the forbidden band $0<\theta_I<\theta_G$. Also, between $\theta_B=\cos^{-1}(\gamma^2)$ and $\pi/2$, there is a surface wave and the reflection coefficient for the homogeneous wave is unity. Corresponding to the point D in the slowness curve of Fig. 2, the incident energy flux is parallel to the free surface and the reflection coefficients are large. For $\beta=1$, the exclusion points of the set I are at 0, $\pi/4$ and $\pi/2$ and the exclusion point of the set II is at -0.5719. For $\beta=5$, set I consists of 0, $\pi/4$, $\pi/2$ and -0.6847 and set II is the single point at -0.7376. The point B in Fig. 2 where the transition from two homogeneous waves to one homogeneous and one nonhomogeneous wave occurs is at $\theta_I=0.9912$.

V. CONCLUSIONS

By choosing the material axis of symmetry of the orthotropic material to be the axis along which the phase speed is a minimum, the slowness curve is obtained and examined with reference to the existence of incident homogeneous and reflected homogeneous and nonhomogeneous waves in the presence of an interface the other side of which is occupied by, in general, a different type of material than the one considered. The surface which separates the range of existence of two homogeneous reflected waves from that of one homogeneous and one nonhomogeneous is obtained in explicit form in terms of the angle of incidence, θ_I, the orientation of the interface, ϕ, with respect to the material axis of symmetry, and one elastic parameter, β. It is shown that the elastic parameter β can be taken positive without loss of generality by an appropriate rotation of the coordinate system chosen. When $\beta>1/3$, there is a critical orientation, ϕ_{cr}, which is obtained in explicit form in terms of β, beyond which there exist angles of incidence for which two homogeneous reflected waves are possible. For a free surface, reflection coefficients were computed and exclusion points were determined as points for which only one reflected wave exists, it being homogeneous. The vanishing second reflected wave is either homogeneous or non-homogeneous depending on the parameters β and ϕ.

ACKNOWLEDGMENTS

The authors wish to thank two anonymous reviewers for their useful comments, and the Associate Editor A. N. Norris for pointing out and providing Ref. 7.

APPENDIX:

For compressible orthotropic materials the stress-strain relations are given by Eq. (1) with the hydrostatic pressure $p=0$. Inverting the normal stress-normal strain relations,

$$\begin{aligned}\epsilon_{11}&=D_{11}\sigma_{11}+D_{12}\sigma_{22}+D_{13}\sigma_{33},\\ \epsilon_{22}&=D_{12}\sigma_{11}+D_{22}\sigma_{22}+D_{23}\sigma_{33},\\ \epsilon_{33}&=D_{13}\sigma_{11}+D_{23}\sigma_{22}+D_{33}\sigma_{33},\end{aligned} \tag{A1}$$

where the matrix D is the inverse of the 3×3-leading minor of the C matrix.

The change in a unit volume is given by

$$\begin{aligned}\epsilon_{11}+\epsilon_{22}+\epsilon_{33}=&(D_{11}+D_{12}+D_{13})\sigma_{11}+(D_{12}+D_{22}\\ &+D_{23})\sigma_{22}+(D_{13}+D_{23}+D_{33})\sigma_{33}.\end{aligned} \tag{A2}$$

For this to be zero for all possible states of stress the coefficients of the normal stresses must independently vanish. Thus,

$$\begin{aligned}&D_{11}+D_{12}+D_{13}=0, \qquad D_{12}+D_{22}+D_{23}=0,\\ &D_{13}+D_{23}+D_{33}=0.\end{aligned} \tag{A3}$$

These three conditions can be used to obtain C_{i3} $(i=1,2,3)$ in terms of C_{11}, C_{12}, and C_{22}.

[1] A. G. Every and W. Sachse, ''Determination of the elastic constants of anisotropic solids from acoustic-wave group-velocity measurements,'' Phys. Rev. B **42**, 8196–8205 (1990).

[2] J. P. Wolfe, ''Acoustic wavefronts in crystalline solids,'' Phys. Today **48**, 34–40 (1995).
[3] J. J. Ditri and J. L. Rose, ''On the reflection of plane waves in transversely isotropic media,'' J. Acoust. Soc. Am. **92**, 3003–3006 (1992).
[4] E. G. Henneke II, ''Reflection-refraction of a stress wave at a plane boundary between anisotropic media,'' J. Acoust. Soc. Am. **51**, 210–217 (1972).
[5] S. I. Rokhlin, T. K. Bolland, and Laszlo Adler, ''Reflection and refraction of elastic waves on a plane interface between two generally anisotropic media,'' J. Acoust. Soc. Am. **79**, 906–918 (1986).
[6] F. I. Fedorov, *Theory of Elastic Waves in Crystals* (Plenum, New York, 1968).
[7] T. W. Wright, ''A note on oblique reflections in elastic crystals,'' Q. J. Mech. Appl. Math. **29**, 15–24 (1976).

Acoustic transient radiation and scattering from fluid-loaded elastic shells using convolution methods

Peter R. Stepanishen
Department of Ocean Engineering, University of Rhode Island, Narragansett, Rhode Island 02882

(Received 1 April 1996; revised 8 February 1997; accepted 13 February 1997)

A general time-domain approach is presented to address the acoustic transient radiation and scattering problem from fluid-loaded elastic shells. The approach is based on utilizing an *in-vacuo* eigenvector expansion with time-dependent coefficients for the velocity field of the shell. The time-dependent modal velocity coefficients of the shell are described by a universal set of coupled convolution integral equations. Substitution of the eigenvector expansion into the Kirchhoff integral solution leads to the external pressure field being expressed as a modal sum of convolution integrals of mode and space-dependent pressure impulse response functions with the modal velocity coefficients. Special cases which include an unbaffled finite plate and an arbitrarily shaped shell of revolution are addressed using the general approach. Simple closed-form expressions are presented for the pressure impulse response functions for the unbaffled finite plate and the on-axis response of a general shell of revolution. The characteristics of the mode and space-dependent far-field pressure impulse response functions for an unbaffled simply supported plate and a spherical shell are presented to illustrate the general characteristics of the impulse response functions. [S0001-4966(97)00307-X]

PACS numbers: 43.20.Fn, 43.20.Px, 43.20.Tb [JEG]

INTRODUCTION

Acoustic harmonic radiation and scattering from fluid-loaded shells continues to be an important subject of interest in both air and underwater acoustics. In the latter class of problems the effect of the fluid loading on the shell often leads to a considerable increase in the complexity of the problem; however, numerous analytical and numerical methods are presently available[1] for addressing the harmonic acoustic radiation and scattering from shells in both air and underwater environments. Although eigenfunction expansion methods can be used for the restricted class of geometries in which the reduced wave equation is separable, finite and boundary element methods[2,3] are often employed to address the general problem for nonseparable geometries.

The acoustic transient radiation and scattering problem has received considerably less attention as a result of its additional complexity. There is, however, an increasing interest in the solution of such problems for applications in noise control and system identification. In principle, the solution of the time-dependent problem can be obtained from the solution of the corresponding harmonic problem using Fourier synthesis methods. As an alternative, time-domain methods may be employed to address the general time-dependent fluid–solid interaction problem. In addition to providing more physical insight into the space–time properties of the field, such methods are becoming increasingly attractive as a result of the rapidly increasing computational power now available.

Considerable effort has been directed in the past to addressing various acoustic transient radiation and scattering problems from shells. These studies can be conveniently subdivided into two classes involving shells in which the external surface of the shell is or is not a constant coordinate surface in a coordinate system where the wave equation is separable. Not unexpectedly, there is a vast amount of literature for the class of separable problems relative to the more general nonseparable problem. Unlike the former class of separable problems which are amenable to a wide variety of analytical techniques, the latter nonseparable problems are of course much more formidable.

As a result of the separability of the wave equation in Cartesian coordinates the general planar problem in which a planar structure of interest is set in an infinite planar rigid baffle is among the simplest and has received much attention. Since the Green's function for the acoustic time-dependent Neumann boundary value problem is well-known,[1] integral equation methods are not required and the complexity of the fluid solid interaction problem is significantly reduced. Craggs[4] presented an analysis of a coupled plate-acoustic system using acoustic and plate finite elements. Stepanishen[5] and co-workers[6] used time-dependent eigenfunction expansion methods to address the transient vibratory response of fluid-loaded elastic membranes and plates to specified mechanical and/or acoustical excitations.

Perhaps the simplest of the separable time-dependent problems involving shells is the two-dimensional acoustic scattering problem of a planar shock pulse impinging onto a fluid-loaded cylindrical shell. As a result of the separability of the acoustic wave equation in cylindrical coordinates and the periodicity of the displacement field of the shell in the circumferential direction, modal solutions using trigonometric expansions are readily used to address the problem. Carrier,[7] Mindlin and Bleich,[8] Huang[9] and Geers[10] addressed the two-dimensional acoustic scattering problem using a variety of transform related methods since the Green's function for the acoustic harmonic Neumann boundary value problem is known.

Since the acoustic wave equation is separable in spheri-

cal coordinates the transient response of fluid-loaded spherical shells is also a very tractable problem and has thus been the focus of numerous past studies. Huang used a Laplace transform method to obtain a formally exact solution by transform inversion methods for the case of a single shell[11] and two concentric shells.[12] Menton and Magrab[13] also used a Laplace transform method to address the acoustic radiation problem. Most recently, Chen and Stepanishen[14] addressed the axisymmetric response of spherical shells using a general time-dependent eigenvector expansion method combined with a numerical evaluation of the Kirchhoff integral solution for the pressure field.

As a result of the additional complexity, the transient vibratory response of fluid-loaded elastic shells of arbitrary shape, including curved panels and closed shells, has received considerably less attention. Generally finite-element methods are used for the shell and boundary or finite-element methods may be used for the fluid. As an alternative to the use of boundary or finite-element methods for the fluid, various doubly asymptotic approximations (DAA)[15,16] have been previously developed and are presently being widely used in practice to approximate the fluid loading on shells. Since the approximations are strictly valid only in the high-frequency region where plane-wave relationships apply and in the low-frequency region where virtual mass approximations are applicable, the use of such approximations can lead to significant errors even for simple problems. Chen and Stepanishen[14] have also recently addressed the axisymmetric response of general shells of revolution using a time-dependent eigenvector expansion method.

In the present paper a formally exact approach is presented to evaluate the time-dependent shell response and associated pressure field of fluid-loaded shells which are excited by time-dependent mechanical forces or incident acoustic fields. The present approach is an extension of a recently developed approach[17] to evaluate the transient vibratory response of fluid-loaded shells using *in-vacuo* eigenvector expansion with time-dependent velocity coefficients which are described via a universal set of coupled convolution integral equations. Fluid loading on the shell is included via the use of convolution integrals involving the modal velocity coefficients and mode-dependent acoustic radiation impulse responses.[18] The external pressure field is expressed here using the retarded potential or Kirchhoff integral solution as a modal sum of convolution integrals of mode and space-dependent pressure impulse response functions and the modal velocity coefficients. Special cases which include a finite plate and an arbitrarily shaped shell of revolution are addressed using the approach and the general characteristics of the pressure impulse responses are noted from the results for a simply supported plate and a spherical shell.

I. THEORY

Consider an elastic shell of arbitrary shape which may be open or closed and is immersed in a fluid as indicated in Fig. 1. The basic acoustic radiation and scattering problem of interest here is to determine the time-dependent pressure field external to the structure which results from a specified time-dependent mechanical excitation and/or an incident

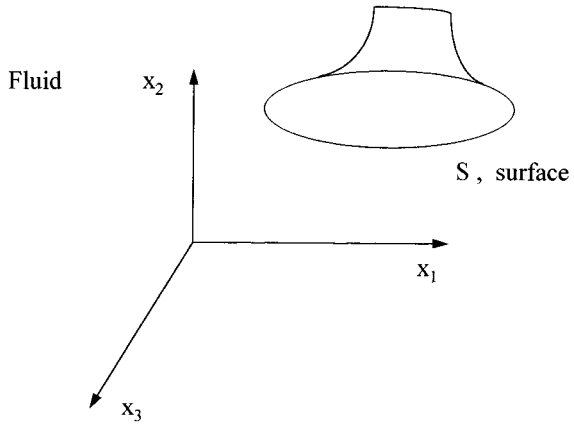

FIG. 1. A shell of arbitrary shape in a fluid.

acoustic excitation on the shell. All acoustical and mechanical field variables are normalized in the manner indicated in Table I and the shell is assumed to be thin for all time and length scales of interest. The latter assumptions are easily removed via the use of elasticity theory as opposed to the thin plate and shell theory used in the present development.

The normalized equations of motion for the thin shell when immersed in fluid can be expressed as follows:[19]

$$\begin{bmatrix} L_{11} & L_{12} & L_{13} \\ L_{21} & L_{22} & L_{23} \\ L_{13} & L_{32} & L_{33} \end{bmatrix} \begin{bmatrix} u(x_s,\tau) \\ v(x_s,\tau) \\ w(x_s,\tau) \end{bmatrix} + h \frac{\partial^2}{\partial \tau^2} \begin{bmatrix} u(x_s,\tau) \\ v(x_s,\tau) \\ w(x_s,\tau) \end{bmatrix}$$

$$= \begin{bmatrix} f^u(x_s,\tau) \\ f^v(x_s,\tau) \\ f^w(x_s,\tau) - p^b(x_s,\tau) \end{bmatrix} - \begin{bmatrix} 0 \\ 0 \\ p(x_s,\tau) \end{bmatrix}; \tag{1}$$

where $x_s = x_s(\alpha_1, \alpha_2)$ denotes a position vector to a point on the shell and α_1 and α_2 are orthogonal curvilinear surface coordinates. The L_{ij} represent partial differential operators in the curvilinear space-time coordinates, h is a normalized shell thickness, the $u(x_s,\tau)$ and $v(x_s,\tau)$ represent the orthogonal in-plane displacements and $w(x_s,\tau)$ represents the normal displacement of the neutral surface of the shell. The corresponding force density terms $f(x_s,\tau)$ in Eq. (1) represent the specified mechanical excitations on the shell whereas $p^b(x_s,\tau)$ represents the blocked pressure due to the incident acoustic excitation, i.e., the total acoustic pressure on the shell with zero normal velocity. Finally, $p(x_s,\tau)$ represents the acoustic pressure which acts on the shell as a result of the nonzero normal velocity of the shell.

TABLE I. Normalization factors for the variables.

Variable	Normalization factor
Length	L (characteristic length)
Velocity	c_p (plate wave velocity)
Time	L/c_p
Density	ρ_p (structural density)
Frequency	c_p/L
Pressure	$\rho_p c_p^2$

It is well–known that the total acoustic pressure field in the fluid external to the shell can be expressed as the following retarded potential or Kirchhoff surface integral solution:[20]

$$p^t(x,\tau)=p^i(x,\tau)+\frac{1}{4\pi}\int\int\left[\frac{\rho_0}{\rho_p}\frac{\partial^2}{\partial\tau^2}\frac{w(x_s,\tau-(c_p/c_0)R)}{R}+\hat{e}_R\cdot\hat{n}_s\left(\frac{c_p}{c_0}\frac{\partial}{\partial\tau}+\frac{1}{R}\right)\frac{p^t(x_s,\tau-(c_p/c_0)R)}{R}\right]dS, \quad (2)$$

where $p^i(x,\tau)$ is the incident pressure field, $p^t(x_s,\tau)$ is the total pressure field, $R=|x-x_s|$, $\hat{e}_R=(x-x_s)/R$, and $\hat{n}_s$ is the unit normal vector into the fluid. The occurrence of c_p/c_0, where c_0 is the acoustic wave speed in the fluid, is the result of selecting the characteristic time in Table I to be based on c_p the plate velocity for the shell material.

The difficulty of addressing the time-dependent acoustic radiation and scattering problem is apparent from Eqs. (1) and (2). In order to determine the external pressure field from Eq. (2) the normal displacement or velocity of the shell is required along with the surface pressure; however, the normal velocity is a function of the surface pressure on the shell as shown in Eq. (1). In contrast to the *in-vacuo* or lightly loaded structure where the above equations are uncoupled, the very nature of the in-fluid problem requires that both equations or their equivalent be simultaneously solved since the fluid provides important reaction forces to the motion of the shell which determines the pressure field.

In the following development it is useful to note that the total time-dependent pressure field of interest can be expressed as a sum of three components:

$$p^t(x,\tau)=p^i(x,\tau)+p^0(x,\tau)+p(x,\tau), \quad (3)$$

where $p^0(x,\tau)$ is the scattered pressure from the rigid shell and $p(x,\tau)$ is the pressure field resulting from the normal velocity of the shell. The blocked pressure in Eq. (1) can thus be expressed as

$$p^b(x_s,\tau)=p^i(x_s,\tau)+p^0(x_s,\tau) \quad (4)$$

and the total scattered pressure field is thus expressed as

$$p^s(x,\tau)=p^0(x,\tau)+p(x,\tau). \quad (5)$$

Since $p^0(x,\tau)$ can be expressed as the solution of a Neumann initial boundary value problem with a prescribed normal velocity distribution over the surface of the structure which is the negative of the incident field, the solution of the general time-dependent radiation problem is of paramount importance in addressing the general time-dependent scattering problem. The focus in the following paragraphs is thus on developing an approach to solve the general time-dependent acoustic radiation problem resulting from a known space and time-dependent blocked excitation.

The field variables associated with the fluid-loaded shell can be represented as *in-vacuo* eigenvector expansions[17] where $\boldsymbol{\phi}_{lmn}(x_s)$, the lmnth *in-vacuo* eigenvector of the shell, is defined as

$$\boldsymbol{\phi}_{lmn}(x_s)=\begin{bmatrix}\phi^u_{lmn}(x_s)\\ \phi^v_{lmn}(x_s)\\ \phi^w_{lmn}(x_s)\end{bmatrix}, \quad (6)$$

which must satisfy the following homogeneous equation:

$$[L]\boldsymbol{\phi}_{lmn}-\Omega^2_{lmn}h\boldsymbol{\phi}_{lmn}=0, \quad (7)$$

where Ω_{lmn} is the associated natural frequency and $[L]$ is the matrix of normalized partial differential operators L_{ij} in Eq. (1). The orthogonality property of the *in-vacuo* eigenvectors for a thin shell of constant thickness is noted as follows:

$$\int\int \boldsymbol{\phi}^T_{lmn}\boldsymbol{\phi}_{rst}dS=\begin{cases}0, & lmn\neq rst,\\ N_{lmn}, & lmn=rst.\end{cases} \quad (8)$$

It is also noted that a similar result for the more general three-dimensional problem including shells of variable thickness is available from elasticity theory where the integration is over the volume of the structure.

Equation (1) can now be expressed as:

$$[L]\mathbf{d}+h\frac{\partial^2}{\partial\tau^2}\mathbf{d}=\mathbf{f}-\mathbf{p}, \quad (9)$$

where

$$\mathbf{d}(x_s,\tau)=\begin{bmatrix}u(x_s,\tau)\\ v(x_s,\tau)\\ w(x_s,\tau)\end{bmatrix}=\sum_l\sum_m\sum_n d_{lmn}(\tau)\boldsymbol{\phi}_{lmn}(x_s).$$

It is then apparent that the normal velocity field of the shell may be expressed as[17]

$$\frac{\partial}{\partial\tau}w(x_s,\tau)=\sum_l\sum_m\sum_n v_{lmn}(\tau)\phi^w_{lmn}(x_s), \quad (10)$$

where $v_{lmn}(\tau)=d[d_{lmn}(\tau)]/d\tau$. The excitation force density vector $\mathbf{f}$ can be expressed as follows:

$$\mathbf{f}(x_s,\tau)=\begin{bmatrix}f^u(x_s,\tau)\\ f^v(x_s,\tau)\\ f^w(x_s,\tau)-p^b(x_s,\tau)\end{bmatrix}=\sum_l\sum_m\sum_n\frac{f_{lmn}(\tau)}{N_{lmn}}\boldsymbol{\phi}_{lmn}(x_s), \quad (11)$$

where $f_{lmn}(\tau)$ is the lmnth modal excitation force due to the specified blocked mechanical force density and acoustical excitations, and the fluid-loading vector $\mathbf{p}$ in Eq. (9) can be expressed as

$$\mathbf{p}(x_s,\tau)=\begin{bmatrix}0\\ 0\\ p(x_s,\tau)\end{bmatrix}=\sum_l\sum_m\sum_n p_{lmn}(\tau)\boldsymbol{\phi}_{lmn}(x_s). \quad (12)$$

It can then be shown via the general procedure presented in an earlier paper[17] that

$$M_{lmn}\frac{d}{d\tau}v_{lmn}(\tau)+K_{lmn}\int^\tau v_{lmn}(\tau')d\tau'=f_{lmn}(\tau)-f^a_{lmn}(\tau), \quad (13)$$

where M_{lmn} and K_{lmn} are the lmnth modal mass and stiffness for the *in-vacuo* shell, i.e.,

$$M_{lmn}=hN_{lmn}, \tag{14}$$

$$K_{lmn}=M_{lmn}\Omega_{lmn}^2. \tag{15}$$

The acoustical modal force $f_{lmn}^a(\tau)$, which provides the coupling among the velocity coefficients, is associated with the fluid loading on the shell and can be expressed as

$$f_{lmn}^a(\tau)=\int\int p(x_s,\tau)\phi_{lmn}^w(x_s)dS. \tag{16}$$

In light of earlier work,[18] a more useful form of $f_{lmn}^a(\tau)$ for the present analysis is

$$f_{lmn}^a(\tau)=\sum_r\sum_s\sum_t z_{lmn,rst}(\tau)\otimes v_{rst}(\tau), \tag{17}$$

where $\otimes$ denotes the convolution operator and the acoustic radiation impedance $z_{lmn,rst}(\tau)$ is expressed in the following general form.

$$z_{lmn,rst}(\tau)=B[N_{lmn,rst}^w\delta(\tau)+g_{lmn,rst}(\tau)], \tag{18}$$

where $B=\rho_0c_0/\rho_pc_p$ and $N_{lmn,rst}^w$ is defined as

$$N_{lmn,rst}^w=\int\int \phi_{lmn}^w(x)\phi_{rst}^w(x_s)dS. \tag{19}$$

It is noted that $N_{lmn,rst}^w$ is a measure of the similarity of the radial components of the lmnth and the rstth modes. The Dirac delta function $\delta(\tau)$ which is present in the normalized acoustic radiation modal impulse response $z_{lmn,rst}(\tau)$ accounts for the familiar high-frequency behavior in which the lmnth modal force and the rstth modal velocity are scaled replicas of one another whereas the $g_{lmn,rst}(\tau)$ accounts for the memory effect of the fluid which is associated with acoustic wave propagation over the surface of the structure.

The following set of coupled differential-integral equations for the modal velocities is then simply obtained from Eqs. (13), (17), and (18):

$$L_{lmn}v_{lmn}(\tau)=f_{lmn}(\tau)-B\sum_{r\neq l}\sum_{s\neq m}\sum_{t\neq n}N_{lmn,rst}^w v_{rst}(\tau)-B\sum_r\sum_s\sum_t g_{lmn,rst}(\tau)\otimes v_{rst}(\tau), \tag{20}$$

where the operator L_{lmn} is defined as follows:

$$L_{lmn}=M_{lmn}\frac{d}{d\tau}+R_{lmn}+K_{lmn}\int^\tau d\tau', \tag{21}$$

where $R_{lmn}=N_{lmn}^wB$. After introducing the modal admittance impulse response $y_{lmn}(\tau)$ such that

$$L_{lmn}y_{lmn}(\tau)=\delta(\tau) \tag{22}$$

and

$$y_{lmn}(\tau)=L_{lmn}^{-1}\delta(\tau) \tag{23}$$

it is easily shown[18] that the following set of coupled convolution integral equations for the modal velocities is readily obtained:

$$v_{lmn}(\tau)=y_{lmn}(\tau)\otimes f_{lmn}(\tau)-By_{lmn}(\tau)\otimes\sum_{r\neq l}\sum_{s\neq m}\sum_{t\neq n}N_{lmn,rst}^w v_{rst}(\tau)-B\sum_r\sum_s\sum_t j_{lmn,rst}(\tau)\otimes v_{rst}(\tau), \tag{24}$$

where closed-form expressions are available for $y_{lmn}(\tau)$ and

$$j_{lmn,rst}(\tau)=y_{lmn}(\tau)\otimes g_{lmn,rst}(\tau). \tag{25}$$

The modal velocities for the *in-vacuo* case are simply obtained by taking the limit as $B\to 0$ in Eq. (24) to obtain the following result

$$v_{lmn}(\tau)=\frac{1}{M_{lmn}}\cos(\Omega_{lmn}\tau)\otimes f_{lmn}(\tau). \tag{26}$$

As expected, the modal velocity coefficients for the *in-vacuo* case are uncoupled.

In order to evaluate the pressure field of interest using Eq. (2) it is noted that the normal surface velocity and the surface pressure of the shell are first required. The modal velocities can, however, be readily determined from the solution of Eq. (24) and the normal velocity field of the shell can then be obtained from Eq. (10). From Eqs. (8), (12), and (16) it follows that the modal components of the surface pressure can be expressed as

$$p_{lmn}(\tau)=f_{lmn}^a(\tau)/N_{lmn} \tag{27}$$

and the surface pressure can then be expressed as

$$p(x_s,\tau)=\sum_l\sum_m\sum_n f_{lmn}^a(\tau)\phi_{lmn}^w(x_s)/N_{lmn}. \tag{28}$$

After using Eq. (17) the surface pressure can then be expressed in terms of the modal velocities, i.e.,

$$p(x_s,\tau)=\sum_l\sum_m\sum_n\sum_r\sum_s\sum_t z_{lmn,rst}(\tau)\otimes v_{rst}(\tau)\phi_{lmn}^w(x_s)/N_{lmn}. \tag{29}$$

Consider now the case where the local surface pressure is assumed to be related to the local normal velocity of the surface, i.e.,

$$p(x_s,\tau)=B\frac{\partial}{\partial\tau}w(x_s,\tau). \tag{30}$$

In light of Eq. (12) it is apparent that

$$p_{lmn}(\tau)=\frac{\int\int p(x_s,\tau)\phi_{lmn}^w(x_s)dS}{N_{lmn}}. \tag{31}$$

After substituting Eq. (30) into (31) and using (10) it follows that

$$p_{lmn}(\tau)=\frac{B\Sigma_r\Sigma_s\Sigma_tN_{lmn,rst}^w v_{rst}(\tau)}{N_{lmn}}. \tag{32}$$

It then follows from Eq. (27) that the associated lmnth acoustic modal force can be expressed as

$$f^a_{lmn}(\tau)=B\sum_r\sum_s\sum_t N^w_{lmn,rst}v_{rst}(\tau). \tag{33}$$

Finally, it is then apparent that the plane-wave relationship for the surface loading in Eq. (27) corresponds to the special limiting case where the $g_{lmn,rst}(\tau)$ in Eq. (18) are neglected.

Although Eqs. (10) and (29) could be substituted into Eq. (2) and the resultant surface integral evaluated by numerical methods to determine the external pressure field, an alternative modal-based decomposition of the pressure field is now presented. In contrast to a numerical evaluation of the retarded potential or Kirchhoff surface integral solution via space-time quadrature methods, the individual modal contributions to the field pressures are more readily apparent via the modal-based approach. As noted earlier, the acoustic scattering problem is a special case of the general acoustic radiation problem; thus, the focus here is on developing a method for solving the latter problem.

The modal-based approach to determine the external pressure field is now developed by first noting that the Kirchhoff surface integral solution in Eq. (2) can be subdivided into a sum of two fields as follows:

$$p(x,\tau)=p_v(x,\tau)+p_p(x,\tau), \tag{34}$$

where $p_v(x,\tau)$ is the component associated with the normal surface velocity, i.e.,

$$p_v(x,\tau)=\frac{1}{4\pi}\frac{\rho_0}{\rho_p}\int\int\left[\frac{\partial}{\partial\tau}\frac{v(x_s,\tau-(c_p/c_0)R)}{R}\right]dS \tag{35}$$

and $p_p(x,\tau)$ is the component associated with the normal surface velocity, i.e.,

$$p_p(x,\tau)=\frac{1}{4\pi}\int\int\left[\hat{e}_R\cdot\hat{n}_s\left(\frac{c_p}{c_0}\frac{\partial}{\partial\tau}+\frac{1}{R}\right)\times\frac{p(x_s,\tau-(c_p/c_0)R)}{R}\right]dS, \tag{36}$$

where the surface integrations are required over the entire closed surface of the structure. In light of the sifting property of the Dirac delta function,[21] i.e.,

$$f\left(x,\tau-\frac{c_p}{c_0}R\right)=f(x,\tau)\otimes\delta\left(\tau-\frac{c_p}{c_0}R\right) \tag{37}$$

it then follows that $p_v(x,\tau)$ can be expressed as

$$p_v(x,\tau)=\frac{1}{4\pi}\frac{\rho_0}{\rho_p}\int\int\left[\frac{\partial}{\partial\tau}\frac{v(x_s,\tau)\otimes\delta(\tau-(c_p/c_0)R)}{R}\right]dS \tag{38}$$

and $p_p(x,\tau)$ can be expressed as

$$p_p(x,\tau)=\frac{1}{4\pi}\int\int\left[\hat{e}_R\cdot\hat{n}_s\left(\frac{c_p}{c_0}\frac{\partial}{\partial\tau}+\frac{1}{R}\right)\times\frac{p(x_s,\tau)\otimes\delta(\tau-(c_p/c_0)R)}{R}\right]dS. \tag{39}$$

It now follows from Eqs. (10) and (38) that $p_v(x,\tau)$ can be expressed as

$$p_v(x,\tau)=\sum_l\sum_m\sum_n\frac{\partial}{\partial\tau}v_{lmn}(\tau)\otimes h^v_{lmn}(x,\tau), \tag{40}$$

where the modal velocity/pressure impulse response $h^v_{lmn}(x,\tau)$ is defined as

$$h^v_{lmn}(x,\tau)\equiv\frac{1}{4\pi}\frac{\rho_0}{\rho_p}\int\int\frac{\delta(\tau-(c_p/c_0)R)}{R}\times\phi^w_{lmn}(x_s)dS. \tag{41}$$

Via a similar procedure it also follows that $p_p(x,\tau)$ can be expressed as

$$p_p(x,\tau)=\sum_l\sum_m\sum_n f_{lmn}(\tau)\otimes h^p_{lmn}(x,\tau)/N_{lmn}, \tag{42}$$

where the modal surface pressure/pressure impulse response $h^p_{lmn}(x,\tau)$ is defined as

$$h^p_{lmn}(x,\tau)\equiv\frac{1}{4\pi}\int\int\left[\hat{e}_R\cdot\hat{n}_s\left(\frac{c_p}{c_0}\frac{\partial}{\partial\tau}+\frac{1}{R}\right)\times\frac{\delta(\tau-(c_p/c_0)R)}{R}\phi^w_{lmn}(x_s)\right]dS. \tag{43}$$

Finally, in the far field at distances very large relative to the maximum dimension of the structure the usual far-field assumptions in the integrands for the impulse responses leads to the following expressions for the far-field impulse responses:

$$h^v_{lmn}(x,\tau)\equiv\frac{1}{4\pi R_0}\frac{\rho_0}{\rho_p}\int\int\delta\left(\tau-\frac{c_p}{c_0}R\right)\phi^w_{lmn}(x_s)dS \tag{44}$$

and

$$h^p_{lmn}(x,\tau)\equiv\frac{1}{4\pi R_0}\frac{c_p}{c_0}\frac{\partial}{\partial\tau}\int\int\left[\hat{e}_R\cdot\hat{n}_s\delta\left(\tau-\frac{c_p}{c_0}R\right)\times\phi^w_{lmn}(x_s)\right]dS, \tag{45}$$

where R_0 is a reference distance from x to a fixed reference point on the structure. As a result of the sifting property of the Dirac delta function the surface integrals can be further reduced to single integrals or evaluated in closed form for special cases as illustrated in the following section.

II. SPECIAL CASES

As noted earlier, the development in the preceding section is applicable to thin structures of arbitrary shape. Special geometries of interest which are addressed here are finite fluid-loaded plates and fluid-loaded shells of revolution. A brief review of analytical results for the vibratory response for each of these cases is presented along with more detailed analyses of the far-field modal velocity/pressure impulse response $h^v_{lmn}(x,\tau)$ and modal surface pressure/pressure impulse response $h^p_{lmn}(x,\tau)$ for these cases. Closed-form expressions for the far-field impulse responses for a finite fluid-loaded simply supported plate and fluid-loaded spherical shells are then simply obtained. These expressions illustrate

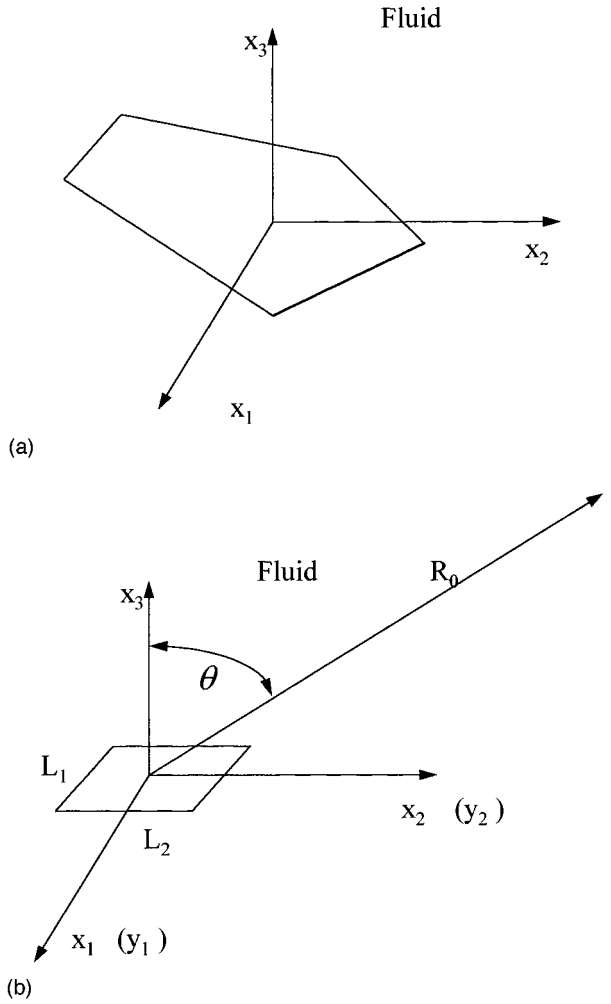

FIG. 2. A thin plate in a fluid. (a) A plate of arbrary shape. (b) A rectangular plate.

the general characteristics of the far-field impulse responses for the special problems and more general structures.

A. Finite plates

Consider now the case of a thin finite plate of arbitrary shape and constant thickness as illustrated in Fig. 2(a). The normalized equations of motion for the plate in a fluid can be expressed as shown in Eq. (1) where the in-plane displacements are decoupled from the normal displacement of the plate. The structural equation of interest then reduces to the single equation:

$$L_{33}w(x_s,\tau)+h\,\frac{\partial^2}{\partial\tau^2}\,w(x_s,\tau) = f^w(x_s,\tau)-p^b(x_s,\tau)-p(x_s,\tau). \tag{46}$$

Subject to the thin plate assumption noted earlier, the above equation describes the normal motion of the midsurface of the plate where it is explicitly noted that the blocked excitations represent the differences between the blocked mechanical excitation on the upper and lower surfaces of the plate, and $p(x_s,\tau)$ represent the difference between the velocity induced pressure on the upper and lower surfaces of the plate. Since the normal plate motion is antisymmetric about the midsurface, the associated surface pressure distribution is also antisymmetric and $p(x_s,\tau)$ is thus equivalent to twice the pressure on the upper or lower surface of the plate. In the midsurface plane external to the plate the pressure is noted to be zero.

The normal velocity of the plate which couples to the fluid can now be expressed as an eigenfunction expansion i.e.,

$$\frac{\partial}{\partial\tau}\,w(x_s,\tau)=\sum_m\sum_n\,v_{mn}(\tau)\phi^w_{mn}(x_s), \tag{47}$$

where the $\phi^w_{mn}(x_s)$ are the scalar eigenfunctions of the homogeneous plate equation of motion in Eq. (46) which now form a complete orthogonal set of functions where

$$\int\int\,\phi^w_{mn}\phi^w_{st}dS=\begin{cases}0, & mn\neq st,\\ N_{mn}, & mn=st.\end{cases} \tag{48}$$

Via the procedure presented in the preceding section the following set of coupled convolution equations are then simply obtained for the modal velocity coefficients:

$$v_{mn}(\tau)=y_{mn}(\tau)\otimes f_{mn}(\tau)-B\sum_s\sum_t\,j_{mn,st}(\tau)\otimes v_{st}(\tau), \tag{49}$$

where $y_{mn}(\tau)$ is the modal admittance impulse response of the mnth mode and

$$j_{mn,st}(\tau)=y_{mn}(\tau)\otimes g_{mn,st}(\tau). \tag{50}$$

As noted in the previous section the pressure field can be subdivided into a sum of two fields as follows:

$$p(x,\tau)=p_v(x,\tau)+p_p(x,\tau), \tag{51}$$

where $p_v(x,\tau)$ is the component associated with the normal surface velocity, i.e.,

$$p_v(x,\tau)=\frac{1}{4\pi}\,\frac{\rho_0}{\rho_p}\int\int\left[\frac{\partial}{\partial\tau}\,\frac{v(x_s,\tau-(c_p/c_0)R)}{R}\right]dS \tag{52}$$

and $p_p(x,\tau)$ is the component associated with the normal surface velocity, i.e.,

$$p_p(x,\tau)=\frac{1}{4\pi}\int\int\left[\hat{e}_R\cdot\hat{n}_s\left(\frac{c_p}{c_0}\,\frac{\partial}{\partial\tau}+\frac{1}{R}\right)\times\frac{p(x_s,\tau-(c_p/c_0)R)}{R}\right]dS \tag{53}$$

and where the surface integrations are required over the entire closed surface of the structure. In light of the antisymmetry of the normal surface velocity and associated pressure distribution it is apparent that useful approximations for thin plates are

$$p_v(x,\tau)=0 \tag{54}$$

and

$$p_p(x,\tau)=\frac{1}{2\pi}\int\int\left[\hat{e}_R\cdot\hat{n}_s\left(\frac{c_p}{c_0}\frac{\partial}{\partial\tau}+\frac{1}{R}\right)\times\frac{p(x_s,\tau-(c_p/c_0)R)}{R}\right]dS, \tag{55}$$

where the latter surface integration is only over the upper surface of the plate. It is then apparent that the pressure field from a finite plate is represented here as a field resulting from a finite planar time-dependent dipole distribution where the analysis in the preceding section connects the space- and time-dependent surface pressure or dipole density to the modal velocity coefficients. Such a result is to be expected from the well-known Rayleigh solution for the planar Dirichlet boundary value problem.[20]

From the development in the preceding section and Eq. (55) it is now noted that $p(x,\tau)$ can also be expressed as

$$p(x,\tau)=\sum_m\sum_n f_{mn}(\tau)\otimes h^p_{mn}(x,\tau)/N_{mn}, \tag{56}$$

where the modal surface pressure/pressure impulse response $h^p_{lmn}(x,\tau)$ is defined as

$$h^p_{mn}(x,\tau)=\frac{1}{2\pi}\int\int\left[\hat{e}_R\cdot\hat{n}_s\left(\frac{c_p}{c_0}\frac{\partial}{\partial\tau}+\frac{1}{R}\right)\times\frac{\delta(\tau-(c_p/c_0)R)}{R}\,\phi^w_{mn}(x_s)\right]dS. \tag{57}$$

In the far field the following expression for the modal surface pressure/pressure impulse response is then simply obtained:

$$h^p_{mn}(x,\tau)=\frac{\cos\theta}{2\pi R_0}\frac{c_p}{c_0}\frac{\partial}{\partial\tau}\int\int\left[\delta\left(\tau-\frac{c_p}{c_0}R\right)\phi^w_{mn}(x_s)\right]dS, \tag{58}$$

where R_0 is a reference distance from x to a fixed reference point on the plate and $\hat{e}_R\cdot\hat{n}_s=\cos\theta$.

In light of the Dirac delta function within the integrand of Eq. (58) the surface integral can be simply evaluated via the use of the sifting property of the delta function. Denoting the plate or source coordinates as $x_s=(y_1,y_2)$ it then follows that

$$h^p_{mn}(x,\tau)=\frac{\cos\theta}{2\pi R_0}\frac{c_p}{c_0}\frac{\partial}{\partial\tau}\int\int\left[\delta\left(\tau-\frac{c_p}{c_0}R\right)\times\phi^w_{mn}(y_1,y_2)\right]dy_1\,dy_2. \tag{59}$$

Since

$$R\approx R_0-y_2\sin\theta \tag{60}$$

then $h^p_{mn}(x,\tau)$ can be expressed, after performing the y_1 integration, as follows:

$$h^p_{mn}(x,\tau)=\frac{\cos\theta}{2\pi R_0}\frac{c_p}{c_0}\frac{\partial}{\partial\tau}\int\times\left[\delta\left(\tau-\frac{c_p}{c_0}(R_0-y_2\sin\theta)\right)\overline{\phi^w_{mn}}(y_2)\right]dy_2, \tag{61}$$

where $\overline{\phi^w_{mn}}(y_2)$ is defined as

$$\overline{\phi^w_{mn}}(y_2)=\int\phi^w_{mn}(y_1,y_2)dy_1. \tag{62}$$

The integral in Eq. (61) is then easily performed using the sifting property to obtain

$$h^p_{mn}(x,\tau)\equiv\frac{\cos\theta}{2\pi R_0}\frac{c_p}{c_0}\frac{\partial}{\partial\tau}\frac{1}{c_p/c_0\sin\theta}\times\overline{\phi^w_{mn}}\left[\frac{c_0}{c_p\sin\theta}\left(\tau-\frac{c_p}{c_0}R_0\right)\right], \tag{63}$$

which, after performing the differentiation, leads to

$$h^p_{mn}(x,\tau)\equiv-\frac{\cos\theta}{2\pi R_0}\frac{c_p}{c_0}\left(\frac{1}{c_p/c_0\sin\theta}\right)^2\times\overline{\phi^{w\prime}_{mn}}\left[\frac{c_0}{c_p\sin\theta}\left(\tau-\frac{c_p}{c_0}R_0\right)\right], \tag{64}$$

where $\overline{\phi^{w\prime}_{mn}}=d\overline{\phi^w_{mn}}(\alpha)/d\alpha$.

As a specific example of interest, consider now the case of an unbaffled rectangular plate with simply supported boundary conditions which is oriented as shown in Fig. 2(b). The eigenfunctions for the indicated geometry are simply expressed as:

$$\phi^w_{mn}(y_1,y_2)=\sin\left[\frac{m\pi}{L_1}\left(y_1+\frac{L_1}{2}\right)\right]\sin\left[\frac{n\pi}{L_2}\left(y_2+\frac{L_2}{2}\right)\right] \tag{65}$$

for $|y_1|\leqslant L_1/2$ and $|y_2|\leqslant L_2/2$. For points in the principal plane $y_1=0$ it readily follows from Eq. (62) that

$$\overline{\phi^w_{mn}}(y_2)=0,\quad m\ \text{even} \tag{66}$$

and thus

$$h^p_{mn}(x,\tau)=0,\quad m\ \text{even}. \tag{67}$$

For m odd it is apparent that

$$\overline{\phi^w_{mn}}(y_2)=\frac{2L_1}{m}\sin\left[\frac{n\pi}{L_2}\left(y_2+\frac{L_2}{2}\right)\right] \tag{68}$$

and

$$h^p_{mn}(x,\tau)\equiv-\frac{\cos\theta}{2\pi R_0}\frac{c_p}{c_0}\left(\frac{1}{c_p/c_0\sin\theta}\right)^2\frac{2L_1n\pi}{mL_2}\times\cos\left[\frac{m\pi}{L_1}\left(y_2+\frac{L_1}{2}\right)\right]_{y_2=[\tau-(c_p/c_0)R_0]/(c_p/c_0\sin\theta)}. \tag{69}$$

It is now apparent from Eq. (69) that the far-field modal surface pressure/pressure impulse response $h^p_{mn}(x,\tau)$ in the principal plane of a simply supported plate is a windowed cosine function with a normalized angular frequency $\Omega'=m\pi/(L_1(c_p/c_0)\sin\theta)$. In light of the convolution operation in Eq. (56) it is clear that the angular frequency component Ω' in the frequency spectrum of $f_{mn}(\tau)$ will clearly be a maximum in the the direction satisfying the above relationship. The far-field modal surface pressure/pressure impulse response $h^p_{mn}(x,\tau)$ can thus be viewed as the response of a

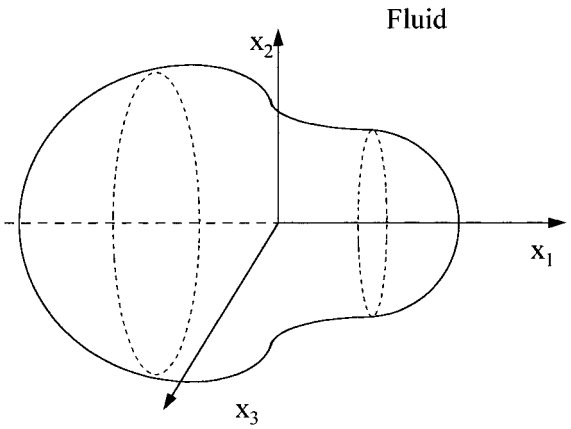

FIG. 3. A closed shell of revolution.

spatially varying matched filter[21] in which the output of the filter at a fixed angle θ is a maximum at a certain frequency. This relationship is in fact equivalent to the well-known coincidence angle relationship which is simply derived using spatial transforms or trace wavelength matching methods[17] for the harmonically excited simply supported plate in a rigid planar baffle. In contrast to the acoustic transient radiation or scattered pressure field case from a simply supported plate in a rigid planar baffle which is naturally addressed using a monopole planar source distribution and *in-vacuo* modal methods, it is apparent that the pressure field associated with a finite fluid-loaded unbaffled plate can be expressed as a dipole planar source distribution. However, in both cases the multipole strengths can be decomposed into various modal contributions all of which can be related back to the time-dependent velocity coefficients of the *in-vacuo* eigenvector expansion.

B. Shells of revolution

Consider now the case of a closed shell of revolution of arbitrary shape and constant thickness as illustrated in Fig. 3. Following the development in an earlier paper[17] on the vibratory response of the shell, with little loss in generality the mechanical excitations of the shell are considered here to be even functions of the circumferential coordinate. The velocity field of the shell may then be expressed as the following *in-vacuo* time-dependent eigenvector expansion:

$$\mathbf{v}(x_s,\tau)=\begin{bmatrix} u(x_s,\tau) \\ v(x_s,\tau) \\ w(x_s,\tau) \end{bmatrix}=\sum_l \sum_m \sum_n v_{lmn}(\tau)\boldsymbol{\phi}_{lmn}(x_s), \tag{70}$$

where $\boldsymbol{\phi}_{lmn}(x_s)$ can now be expressed as:

$$\boldsymbol{\phi}_{lmn}(x_s)=\begin{bmatrix} \cos(l\alpha_1)\phi^u_{mn}(\alpha_2) \\ \sin(l\alpha_1)\phi^v_{mn}(\alpha_2) \\ \cos(l\alpha_1)\phi^w_{mn}(\alpha_2) \end{bmatrix}, \tag{71}$$

where $x_s=(\alpha_1,\alpha_2)$ are the two-dimensional orthogonal curvilinear coordinates of the neutral surface and l now denotes the circumferential order of interest.

Referring to the earlier paper for details, it is obvious from symmetrical considerations that acoustical modal forces and thus modal velocities with different circumferential orders are uncoupled. The acoustical modal force $f^a_{lmn}(\tau)$ for the shell of revolution can then be related to the modal velocity components $v_{lst}(\tau)$ as follows:

$$f^a_{lmn}(\tau)=\sum_s \sum_t z_{lmn,lst}(\tau)\otimes v_{lst}(\tau), \tag{72}$$

where the normalized acoustic radiation impulse response $z_{lmn,lst}(\tau)$ is now expressed as

$$z_{lmn,rst}(\tau)=B[N^w_{lmn,rst}\delta(\tau)+g_{lmn,rst}(\tau)]\delta_{lr}. \tag{73}$$

The following set of coupled convolution integral equations for the modal velocities for each circumferential order l is thus simply obtained:

$$v_{lmn}(\tau)=y_{lmn}(\tau)\otimes f_{lmn}(\tau)-B\sum_{s\neq m}\sum_{t\neq n} N^w_{lmn,lst}v_{rst}(\tau) - B\sum_s \sum_t j_{lmn,lst}(\tau)\otimes v_{lst}(\tau), \tag{74}$$

where

$$j_{lmn,lst}(\tau)=y_{lmn}(\tau)\otimes g_{lmn,lst}(\tau). \tag{75}$$

For each circumferential order l the resulting set of equations is noted to be similar in form to the modal velocity equations for the plate.

As a general case of interest consider now the on-axis far-field pressure from a shell of revolution as illustrated in Fig. 3. It is clear from simple physical arguments that only the axisymmetric modes ($l=0$) contribute to the on-axis pressures. The pressure can thus be subdivided into a sum of two components as follows:

$$p(x,\tau)=p_v(x,\tau)+p_p(x,\tau), \tag{76}$$

where

$$p_v(x,\tau)=\sum_m \sum_n \frac{\partial}{\partial\tau} v_{0mn}(\tau)\otimes h^v_{0mn}(x,\tau) \tag{77}$$

and

$$p_p(x,\tau)=\sum_m \sum_n f_{0mn}(\tau)\otimes h^p_{0mn}(x,\tau)/N_{0mn}. \tag{78}$$

For points in the far field the modal velocity/pressure impulse response $h^v_{lmn}(x,\tau)$ is simply expressed as

$$h^v_{0mn}(x,\tau)\equiv\frac{1}{4\pi R_0}\frac{\rho_0}{\rho_p}\int\int \delta\left(\tau-\frac{c_p}{c_0}R\right)\phi^w_{0mn}(x_s)dS. \tag{79}$$

The far-field modal pressure/pressure impulse response $h^p_{lmn}(x,\tau)$ is simply expressed as follows:

$$h^p_{0mn}(x,\tau)\equiv\frac{1}{4\pi R_0}\frac{c_p}{c_0}\frac{\partial}{\partial\tau}\int\int\left[\hat{e}_R\cdot\hat{n}_s\delta\left(\tau-\frac{c_p}{c_0}R\right)\times\phi^w_{0mn}(x_s)\right]dS. \tag{80}$$

Simple closed-form expressions can be obtained for the far-field impulse responses by following a similar procedure as that followed for the plate problem. Since

$$R\approx R_0-z,\quad \text{for } |z|\leqslant L_s \tag{81}$$

then $h^v_{mn}(x,\tau)$ can be expressed as follows:

$$h^v_{0mn}(x,\tau)\equiv\frac{1}{4\pi R_0}\frac{\rho_0}{\rho_p}\int\int\delta\left(\tau-\frac{c_p}{c_0}(R_0-z)\right)\times\phi^w_{0mn}(x_s)2\pi x_s\sqrt{1+(x_s')^2}\,dz, \tag{82}$$

where $x_s=x_s(z)$ describes the generator for the surface and $x_s'=dx_s/dz$. Similarly, $h^p_{mn}(x,\tau)$ can be expressed as follows:

$$h^p_{mn}(x,\tau)\equiv\frac{1}{2\pi R_0}\frac{c_p}{c_0}\frac{\partial}{\partial\tau}\int\cos[\theta(z)]\delta\left(\tau-\frac{c_p}{c_0}(R_0-z)\right)\times\phi^w_{0mn}(x_s)2\pi x_s\sqrt{1+(x_s')^2}\,dz, \tag{83}$$

where $\cos[\theta(z)]=\hat{e}_R\cdot\hat{n}_s$. The preceding integrals are again easily evaluated using the sifting property of the delta function to obtain the following closed-form expressions for the far-field impulse responses

$$h^v_{0mn}(x,\tau)\equiv\frac{1}{2R_0}\frac{\rho_0}{\rho_p}\frac{c_0}{c_p}[\phi^w_{0mn}(x_s)x_s\times\sqrt{1+(x_s')^2}]_{z=[\tau-(c_p/c_0)R]/(c_p/c_0)} \tag{84}$$

and

$$h^p_{0mn}(x,\tau)\equiv\frac{1}{2R_0}\frac{c_p}{c_0}\frac{\partial}{\partial\tau}\cos[\theta(z)]\frac{c_0}{c_p}\times[\phi^w_{0mn}(x_s)x_s\sqrt{1+(x_s')^2}]_{z=[\tau-(c_p/c_0)R]/(c_p/c_0)}. \tag{85}$$

As a special case of the preceding development consider now a spherical elastic shell of radius a. It is easily shown that the radial components of the eigenvectors can be expressed as:

$$\phi^w_{0mn}(x_s(z))=P_n(z),\quad |z|\leqslant a, \tag{86}$$

where $P_n(z)$ is the nth-order Legendre polynomial. For a fixed n it is noted the radial components of the eigenfunctions are identical in shape on both branches of the eigenspectrum. Since $x_s=\sqrt{a^2-z^2}$, then

$$x_s\sqrt{1+(x_s')^2}=a, \tag{87}$$

and

$$h^v_{0mn}(x,\tau)\equiv\frac{a}{2R_0}\frac{\rho_0}{\rho_p}\frac{c_0}{c_p}[P_n(z)]_{z=[\tau-(c_p/c_0)R]/(c_p/c_0)}. \tag{88}$$

Noting that $\theta=\cos^{-1}(z/a)$ then $\cos[\theta(z)]=z/a$ and

$$h^p_{0mn}(x,\tau)\equiv\frac{1}{2R_0}\frac{\partial}{\partial\tau}[zP_n(z)]_{z=[\tau-(c_p/c_0)R]/(c_p/c_0)}. \tag{89}$$

In both cases the far-field impulse responses are time limited or finite impulse response functions whose oscillatory behavior increases with mode number in a manner similar to that observed from the analogous results for the plate.

III. SUMMARY AND CONCLUSIONS

A general time-domain approach has been presented to address the acoustic transient radiation and scattering problem from fluid-loaded elastic structures of arbitrary shape which are excited by general space and time-dependent mechanical and/or acoustical excitations. The structures of interest thus include both closed and open shells or plates as a limiting case. Since the scattering problem can be treated as a special type of radiation problem, the focus in the paper was on the radiation problem. The basic approach to addressing this latter problem consists of two steps: Evaluate the velocity response of the structure resulting from the known excitations, then evaluate the pressure field of interest.

The approach to evaluate the velocity response of the structure resulting from the known excitations is identical to that presented earlier[17] and is based on utilizing an *in-vacuo* eigenvector expansion with time-dependent coefficients to describe the velocity field of a structure. The time-dependent modal velocity coefficients of the structure are described by a universal set of coupled convolution integral equations. A key feature of the present approach is that fluid loading on the structure is described via the use of convolution integrals involving the modal velocity coefficients and mode-dependent acoustic radiation impulse responses. Since the numerical evaluation of the universal set of coupled convolution integral equations is readily performed by ''marching forward in time,'' the most formidable part of the approach is the evaluation of the mode-dependent acoustic radiation impulse responses.

The Kirchhoff integral solution, which relates the field pressure to the surface pressure and normal velocity fields, is used here as a starting point to evaluate the pressure field. Substitution of the eigenvector expansions for the surface loading and velocity fields into the Kirchhoff integral solution leads to the external pressure field being expressed as a modal sum of convolution integrals of mode- and space-dependent pressure impulse response functions with the modal velocity coefficients. In contrast to a direct numerical space-time integration via quadrature methods of the Kirchhoff integral solution, the external pressure field is thus decomposed here into its various modal contributions. Furthermore, for each mode, two types of modal impulse response functions are required. The two types provide information on the relative importance of the contributions from the modal surface pressure and modal velocity to the external pressure field.

Special cases which include an unbaffled finite plate and an arbitrarily shaped shell of revolution are addressed using the general approach. Results for the velocity fields for the structures are summarized from earlier work.[17] The mode-

and space-dependent pressure impulse response functions corresponding to the surface velocity contribution are shown to be zero for the case of thin plates. The external space- and time-dependent pressure field is not unexpectedly associated with the space- and time-dependent surface pressure distribution which is related to the modal velocity coefficients via convolution integral relationships involving the mode-dependent acoustic radiation impulse responses. Simple closed-form expressions are presented for the pressure impulse response functions for the unbaffled finite plate and the on-axis response of a general shell of revolution. The characteristics of the mode- and space-dependent far-field pressure impulse response functions for an unbaffled simply supported plate and a spherical shell are presented to illustrate the general characteristics of the impulse response functions.

[1] M. C. Junger and D. Feit, *Sound, Structures and their Interaction* (MIT, Cambridge, MA, 1986), 2nd ed.

[2] H. A. Schenck, ''Improved integral formulation for acoustic radiation problems,'' J. Acoust. Soc. Am. **44**, 41–58 (1968).

[3] A. J. Burton and G. F. Miller, ''The application of some integral equation methods to the numerical solution of some exterior boundary value problems,'' Proc. R. Soc. London, Ser. A **323**, 210–214 (1971).

[4] A. Craggs, ''The transient response of a coupled plate-acoustic system using plate and acoustic finite elements,'' J. Sound Vib. **15**, 509–528 (1971).

[5] P. R. Stepanishen and D. D. Ebenezer, ''An *in-vacuo* modal expansion to determine the transient response of fluid loaded planar vibrators,'' J. Acoust. Soc. Am. **153**, 453–472 (1992).

[6] D. D. Ebenezer and P. R. Stepanishen, ''Transient response of fluid loaded plates via an impulse response method,'' J. Acoust. Soc. Am. **82**, 659–666 (1987).

[7] G. F. Carrier, ''The interaction of an acoustic wave and an elastic cylindrical shell,'' Brown University Technical report, 1951.

[8] R. D. Mindlin and H. H. Bleich, ''Response of an elastic cylindrical shell to a transverse step shock wave,'' Trans. ASME **20**, 189–195 (1953).

[9] H. Huang, ''An exact analysis of the transient interaction of acoustic plane waves with a cylindrical shell,'' ASME J. Appl. Mech. **36**, 1091–1099 (1970).

[10] T. L. Geers, ''Excitation of an elastic cylindrical shell by a transient acoustic wave,'' ASME J. Appl. Mech. **35**, 459–469 (1969).

[11] H. Huang, ''Transient interaction of plane acoustic waves with a spherical elastic shell,'' J. Acoust. Soc. Am. **45**, 661–668 (1969).

[12] H. Huang, ''Transient response of two fluid-coupled spherical elastic shells to an incident pressure pulse,'' J. Acoust. Soc. Am. **65**, 881–887 (1979).

[13] R. T. Menton and E. B. Magrab, ''Farfield radiation of internally generated transient acoustic pulses transmitted through a spherical shell,'' J. Acoust. Soc. Am. **55**, 237–246 (1974).

[14] H. W. Chen and P. R. Stepanishen, ''Acoustic transient radiation from fluid loaded shells of revolution using time-dependent in-vacuo eigenvector expansions,'' J. Acoust. Soc. Am. **95**, 601–616 (1995).

[15] T. L. Geers, ''Residual potential and approximate methods for three dimensional fluid-structure interaction problems,'' J. Acoust. Soc. Am. **49**, 1505–1510 (1971).

[16] T. L. Geers, ''Doubly asymptotic approximations for transient motions of submerged strtuctures,'' J. Acoust. Soc. Am. **64**, 1500–1508 (1978).

[17] P. R. Stepanishen, ''Transient vibratory response of fluid-loaded structures using convolution integral equations,'' J. Acoust. Soc. Am. **101**, 1877–1889 (1997).

[18] P. R. Stepanishen and H. W. Chen, ''Acoustic time-dependent loading on elastic shells of revolution using the internal source density and single value decomposition method,'' J. Acoust. Soc. Am. **99**, 1913–1923 (1996).

[19] A. Leissa, *Vibration of Shells* (Acoustical Society of America, New York, 1973).

[20] A. D. Pierce, *Acoustics—An Introduction to Its Physical Principles and Applications* (Acoustical Society of America, New York, 1988).

[21] A. Papoulis, *Signal Analysis* (McGraw-Hill, New York, 1977), 1st ed.

Numerical investigation of fracture interface waves

Boliang Gu, Kurt T. Nihei, and Larry R. Myer
Earth Sciences Division, Lawrence Berkeley National Laboratory, One Cyclotron Road, MS 90-1116, Berkeley, California 94720

(Received 24 September 1995; revised 24 March 1997; accepted 31 March 1997)

Two-dimensional boundary element simulations are conducted to investigate the properties of Rayleigh-type fracture interface waves generated by a line source located near a single fracture. The fracture is modeled as a displacement–discontinuity boundary condition between two elastic half-spaces with identical properties. Numerical simulations are performed for different fracture stiffnesses, source polarizations, and source depths. Symmetric and antisymmetric fracture interface waves are observed with amplitudes and velocities that are controlled by the ratio of the fracture impedance to the half-space shear wave impedance, as predicted by plane-wave theory [Gu *et al.*, J. Geophys. Res. **101**, 827–835 (1996); Pyrak-Nolte and Cook, Geophys. Res. Lett. **14**, 1107–1110 (1987)]. When the source is located off the fracture, these waves develop at incidence angles that decrease with source depth. [S0001-4966(97)02207-8]

PACS numbers: 43.20.Gp, 43.20.Jr [JEG]

INTRODUCTION

Fractures in brittle materials such as rock and concrete are typically surfaces of irregular topography. Small amounts of relative motion between these surfaces can produce imperfect contact. Imperfect contact between the surfaces results in a thin, compliant interface of negligible thickness and density. Investigators in the fields of nondestructive evaluation and geophysics[1–4] have recognized that this additional compliance results in jumps in the normal and tangential displacements across the fracture that are proportional to the applied stress and compliance of the fracture. This work has established that the linear constitutive relations for a fracture can be described by a displacement–discontinuity boundary condition provided that the wavelength is long relative to the spacing between asperities of contact within the fracture.

Recent theoretical and experimental research has demonstrated that a single nonwelded interface, such as a fracture or an imperfect bond, can support Rayleigh-type interface waves which propagate along the fracture.[5–9] The amplitudes and velocities of these interface waves are sensitive to the magnitude of the shear and normal stiffnesses of the nonwelded interface, making these waves potentially useful for applications involving interface characterization.

Murty[7] examined the conditions for the existence of interface waves on a nonwelded interface with a discontinuity in the shear displacement across the interface. Pyrak-Nolte and Cook[6] extended Murty's analysis to the case where both normal and shear displacements are discontinuous across a nonwelded interface. Gu *et al.*[5] demonstrated that simple, closed-form dispersion equations for interface waves propagating along a single fracture could be obtained from the matrix equation developed by Pyrak-Nolte and Cook.[6] The basic form of these dispersion equations is similar to the classic Rayleigh equation for a surface wave on a half-space except that the symmetric and antisymmetric fracture interface waves are controlled by the fracture impedance ratio (i.e., ratio of the fracture impedance to the half-space shear wave impedance). For low values of the fracture impedance ratio, the dispersion equations for the symmetric and antisymmetric fracture interface waves degenerate to the classic nondispersive equation for Rayleigh waves on a half-space. For large values of the fracture impedance ratio, the symmetric wave reaches a cutoff value and ceases to exist as a normal mode, while the antisymmetric wave degenerates to a shear body wave propagating along the fracture. For intermediate values of the fracture impedance ratio, both waves are dispersive with the symmetric wave propagating faster than the antisymmetric wave for a given value of the fracture impedance ratio.

While the plane-wave analysis successfully predicts the velocities of fracture interface waves observed in laboratory measurements on fractures,[8] it does not provide information about the generation of these waves by a spatially localized source. In this paper, the generation of fracture interface waves from a line source is investigated using the boundary element method. The paper begins with a brief discussion of the boundary element method formulation for an elastic medium containing a single fracture. The following section describes techniques for generating symmetric and antisymmetric fracture interface waves and evaluates the effects of the fracture impedance ratio on wave amplitudes and velocities. The final section investigates the influence of source distance from the fracture on the generation of fracture interface waves.

I. BOUNDARY ELEMENT METHOD FOR FRACTURED MEDIA

The boundary element method is an accurate and computationally efficient numerical technique for modeling elastic wave propagation in a medium containing fractures.[10] Unlike the finite element and finite difference methods, which employ space-filling numerical meshes, the boundary element method only requires discretization of the fracture and employs the fundamental point source solution. Conse-

quently, the boundary element method is less susceptible to numerical dispersion for wave propagation problems.

An efficient two-dimensional boundary integral equation is developed by numerical integration of the three-dimensional boundary integral equations along the axis orthogonal to the plane of interest. The advantages of this approach are that the coefficient matrix for only the first time step needs to be assembled and solved, and that singularities of the Green's functions can be significantly reduced.[10,11]

For problems with zero initial conditions, the time-domain form of the three-dimensional boundary integral equation may be written as[11]

$$c_{ij}(\xi)u_i(\xi,t)=\int_\Gamma\{G_{ij}*\tau_i(\mathbf{x},t)-F_{ij}*u_i(\mathbf{x},t)\}d\Gamma + \rho\int_\Omega G_{ij}*b_i(\mathbf{x},t)d\Omega, \tag{1}$$

where $u_i(\xi,t)$ is the i component of the particle displacement observed at location ξ, $u_i(\mathbf{x},t)$ and $\tau_i(\mathbf{x},t)$ are the i component of the displacement and traction on the fracture surface Γ, G_{ij} is the three-dimensional Green's function for an unbounded elastic medium, F_{ij} is the traction derived from G_{ij} using Hooke's Law, $b_i(\mathbf{x},t)$ is a volumetric source acting in volume Ω, $*$ is the time convolution operator, c_{ij} is the *free-term* resulting from the singularity of F_{ij} as $\xi\rightarrow\mathbf{x}$, and $i,\ j=1,2$ for in-plane problems.

To solve the boundary integral equation for boundary displacements and tractions, the fracture surfaces are divided into boundary elements and the boundary variables are discretized in both the space and time. The discretization here is completed using quadratic shape functions and the Heaviside function for the spatial coordinate along the fracture,

$$x_i=M_\alpha X_{i\alpha}, \tag{2}$$

and the displacement and traction along the fracture,[11]

$$u_i(\xi,t)=\sum_{n=1}^{N} M_\alpha U_{i\alpha}^n\Phi^n(t),$$
$$\tau_i(\xi,t)=\sum_{n=1}^{N} M_\alpha T_{i\alpha}^n\Phi^n(t), \tag{3}$$

where $X_{i\alpha}$ is the nodal coordinate of the element, $U_{i\alpha}^n$ and $T_{i\alpha}^n$ are the nodal displacement and traction, respectively, M_α is a quadratic shape function, $\Phi^n(t)=H[t-(n-1)\Delta t]-H[t-n\Delta t]$, where $H[\cdot]$ is the Heaviside function, $n=1,2,3,\ldots,N$ is the time step, and $\alpha=1$, 2, and 3 represents the nodal points on a single boundary element.

In the numerical model, the fracture is modeled as a displacement–discontinuity boundary condition between two elastic half-spaces.[2] Across such a discontinuity, stresses are continuous and particle displacements are discontinuous. For in-plane motion, the displacement–discontinuity boundary conditions are

$$u_i^a-u_i^b=\tau_{i2}^a/k_i,\quad \tau_{i2}^a=\tau_{i2}^b, \tag{4}$$

where superscripts a and b denote the half-space above and below the fracture, respectively, k_i is the fracture stiffness in the i direction, and $i=1,2$ (see Fig. 1). As $k_i\rightarrow\infty$, the interface becomes welded and the particle displacements across the fracture are continuous. As $k_i\rightarrow 0$, the two surfaces of the fracture become two traction-free surfaces.

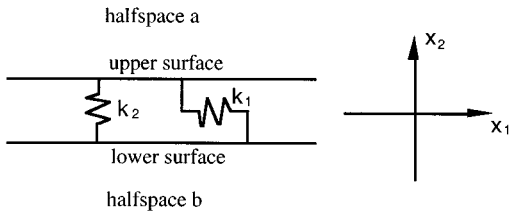

FIG. 1. Displacement–discontinuity fracture model. k_1 and k_2 are the tangential and normal fracture stiffnesses.

For elastic wave transmission across a single natural fracture in granite, the ultrasonic measurements of Pyrak-Nolte *et al.*[3] were found to exhibit frequency-dependent amplitude reductions that are well predicted by plane-wave transmission coefficients derived using the displacement-discontinuity boundary conditions given in Eq. (4). The displacement–discontinuity model has also been used extensively by researchers in nondestructive evaluation of welds and adhesive bonds[4] with considerable success.

The boundary integral equation given in Eq. (1) can be assembled to form a system of the discretized boundary integral equations for a medium containing a fracture using Eqs. (1), (2), and (3) and applying the displacement-discontinuity boundary condition of Eq. (4). The resulting linear system of such discretized equations has the following form:[10]

$$\begin{bmatrix} F_{11}^a+k_1G_{11}^a & F_{12}^a+k_2G_{12}^a & -k_1G_{11}^a & -k_2G_{12}^a \\ F_{21}^a+k_1G_{21}^a & F_{22}^a+k_2G_{22}^a & -k_1G_{21}^a & -k_2G_{22}^a \\ -k_1G_{11}^b & -k_2G_{12}^b & F_{11}^b+k_1G_{11}^b & F_{12}^b+k_2G_{12}^b \\ -k_1G_{21}^b & -k_2G_{22}^b & F_{21}^b+k_1G_{21}^b & F_{22}^b+k_2G_{22}^b \end{bmatrix} \times \begin{Bmatrix} U_1^a \\ U_2^a \\ U_1^b \\ U_2^b \end{Bmatrix}^n = \begin{Bmatrix} B_1^a \\ B_2^a \\ B_1^b \\ B_2^b \end{Bmatrix}^n, \tag{5}$$

where $\{B\}^n$ is the accumulated boundary displacements from time step 1 to $n-1$, and $[\cdot]^1$ is the coefficient matrix for the first time step. Since all quantities in $\{B\}^n$ and $[\cdot]^1$ are known, the displacements $\{U\}^n$ on the fracture surfaces at a time step n can be obtained by the numerical solution of Eq. (5). Interior displacements can be obtained by direct numerical integration of Eq. (1) once the displacements and tractions on the surfaces of the fracture are known.

II. FRACTURE INTERFACE WAVES

The analyses of Pyrak-Nolte and Cook[6] and Gu *et al.*[5] and laboratory measurements of Pyrak-Nolte *et al.*[8] demonstrate that a fracture can support dispersive symmetric (i.e., extensional mode) and antisymmetric (i.e., flexural mode) interface waves that propagate between the Rayleigh wave

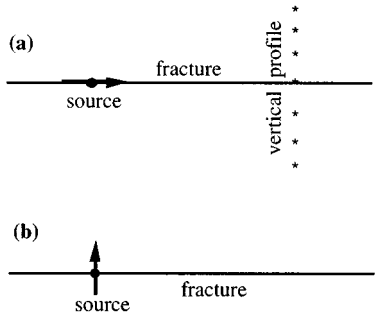

FIG. 2. Simulation geometry used to generate (a) symmetric and (b) antisymmetric fracture interface waves.

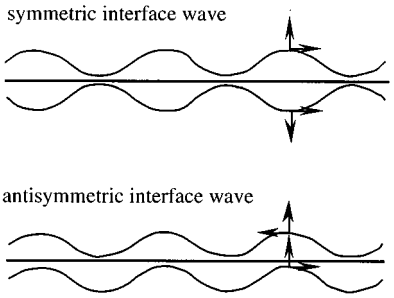

FIG. 3. Schematic illustration of the particle displacements of the symmetric and antisymmetric fracture interface waves.

and shear wave velocities. The dispersion equations for symmetric and antisymmetric fracture interface waves (Fig. 3) are[5]

$$(1-2\xi^2)^2-4\xi^2\sqrt{\xi^2-\zeta^2}\sqrt{\xi^2-1}-2\overline{k_2}\sqrt{\xi^2-\zeta^2}=0, \quad \text{symmetric wave} \tag{6}$$

$$(1-2\xi^2)^2-4\xi^2\sqrt{\xi^2-\zeta^2}\sqrt{\xi^2-1}-2\overline{k_1}\sqrt{\xi^2-1}=0, \quad \text{antisymmetric wave.} \tag{7}$$

In Eqs. (6) and (7), $\xi=c_s/c$ is the ratio of shear wave velocity to the interface wave velocity, $\zeta=c_s/c_p$ is the ratio of the shear wave velocity to the compressional wave velocity, and $\overline{k_1}=(k_1/\omega)/z_s$ and $\overline{k_2}=(k_2/\omega)/z_s$ are the nondimensional fracture impedance ratios, where (k_i/ω) is the fracture impedance (fracture stiffness divided by the angular frequency) and z_s is the shear wave impedance (density multiplied by the shear wave velocity).

Equations (6) and (7) reveal that the velocities of the two interface waves are functions of the nondimensional fracture impedance ratios $\overline{k_1}$ and $\overline{k_2}$, and the Poisson's ratio of the half-spaces $\nu=0.5[(\zeta^{-2}-2)/(\zeta^{-2}-1)]$. Numerical solution of Eqs. (6) and (7) shows that with increasing the fracture impedance ratios, the velocities of the symmetric and antisymmetric interface waves increase from the Rayleigh wave velocity to the shear wave velocity.[5,6] The particle motions of both waves are elliptical retrograde near the fracture, reversing to prograde at less than a wavelength away from the fracture.

For the horizontal source configuration of Fig. 2(a), source–fracture symmetry requires that the shear stresses on the upper and lower surfaces vanish and the horizontal displacements on the upper and lower surfaces be equal,

$$\tau_{12}^a=\tau_{12}^b=0, \quad u_1^a=u_1^b. \tag{8}$$

Equations (8) reveal that the displacement–discontinuity boundary condition for the fracture, $u_1^b-u_1^a=\tau_{12}^a/k_1$, is always satisfied. This indicates that the tangential fracture stiffness has no effect on the symmetric fracture interface wave. Similarly, it can also be demonstrated that the normal fracture stiffness has no effect on the antisymmetric fracture interface wave (Fig. 3). The dependence of the symmetric and antisymmetric fracture interface waves on the fracture stiffness is consistent with that predicted by Eqs. (6) and (7).

A. Effect of fracture stiffness

To evaluate the effects of fracture stiffness on fracture interface waves generated by a line source, a series of two-dimensional boundary element simulations were performed. The half-spaces were assigned properties typical of granite: compressional and shear wave velocities $c_p=5800$ m/s and $c_s=3800$ m/s, and density $\rho=2600$ kg/m^3. The two-dimensional fracture consisted of a line 76.0 m in length which was discretized into 100 quadratic elements. The source wavelet was a broadband three-loop wavelet with a central frequency of 800 Hz. The computation was carried out to 20.1 ms in 310 time steps.

Snapshots of the horizontal displacement at 10.37 ms are displayed for a completely welded fracture ($k_1=k_2=\infty$) and a nonwelded fracture ($k_2=5\times10^9$ Pa/m) in Figs. 4 and 5 for the two source configurations shown in Fig. 2. Figures 4 and 5 provide visual evidence that a compliant fracture concentrates wave energy along the fracture in the form of Rayleigh

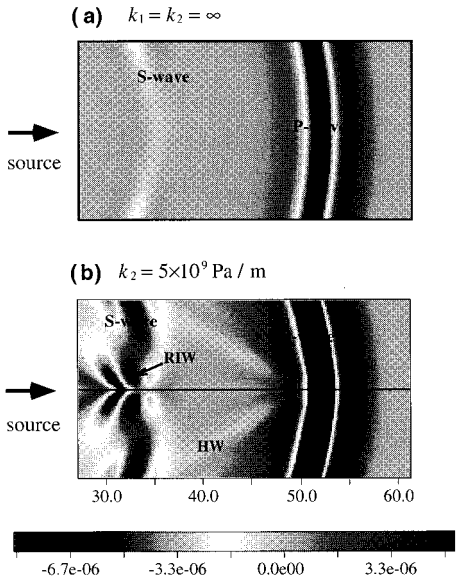

FIG. 4. Horizontal displacements near a fracture of (a) $k_1=k_2=\infty$ (an infinite space) and (b) $k_2=5\times10^9$ Pa/m for the source–fracture configuration shown in Fig. 2(a). A Rayleigh-type interface wave RIW and a head wave HW are present on the finite stiffness fracture in addition to the body compressional and shear waves.

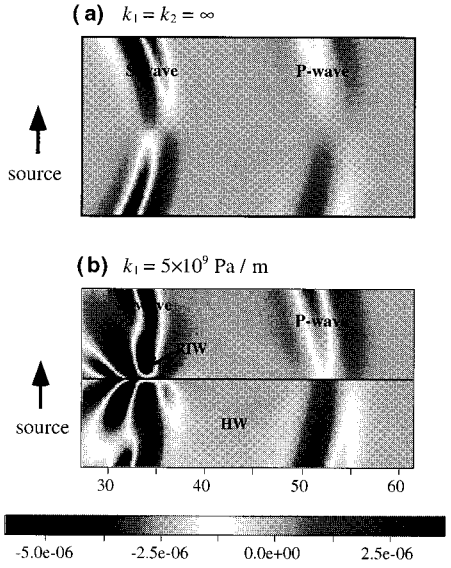

FIG. 5. Horizontal displacements near a fracture of (a) $k_1=k_2=\infty$ (an infinite space) and (b) $k_1=5\times10^9$ Pa/m for the source–fracture configuration shown in Fig. 2(b). A Rayleigh-type interface wave RIW and a head wave HW are observed to exist on the finite stiffness fracture in addition to the body compressional and shear waves.

fracture interface waves (labeled RIW). A compliant fracture also supports a compressional head wave (labeled HW) which propagates along the fracture while continuously radiating energy into the half-spaces.

Particle displacement waveforms for a receiver located on the lower surface of the fracture at a distance of 45.79 m from the source are displayed for a range of fracture stiffnesses in Figs. 6 and 7 for the horizontally and vertically

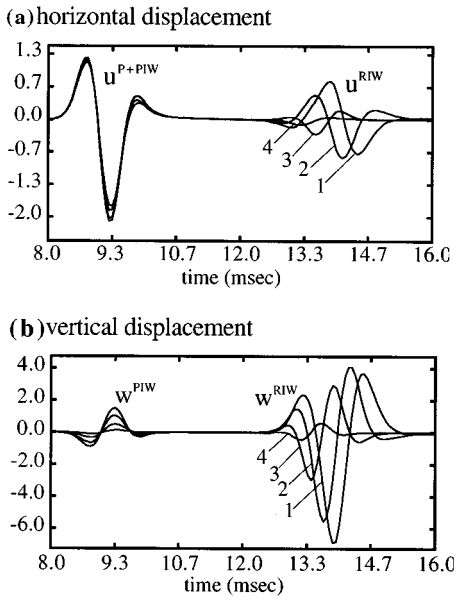

FIG. 6. Waveforms on the lower surface of the fracture at a distance of 45.79 m from the source for the model shown in Fig. 2(a). The fracture is assigned stiffness values of (1) $k_2=10^9$, (2) $k_2=5\times10^9$, (3) $k_2=2.5\times10^{10}$, and (4) $k_2=10^{11}$ Pa/m.

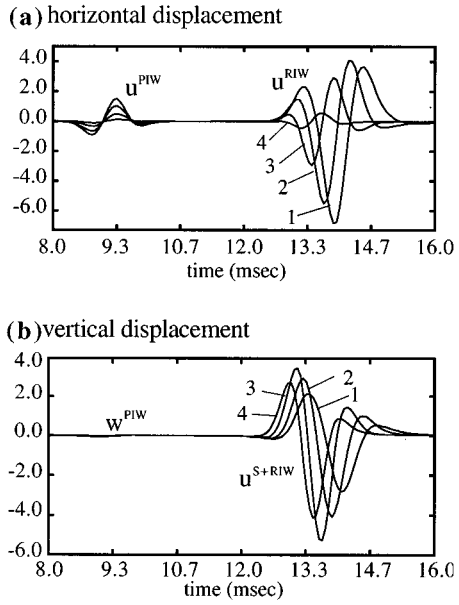

FIG. 7. Waveforms on the lower surface of the fracture at a distance of 45.79 m from the source for the simulation configuration shown in Fig. 2(b). The fracture is assigned stiffness values of (1) $k_1=5\times10^9$, (2) $k_1=10^{10}$, (3) $k_1=2.5\times10^{10}$, and (4) $k_1=10^{11}$ Pa/m.

polarized sources (Fig. 2). Four waves are present and are denoted by the superscripts PIW and RIW to indicate compressional and Rayleigh interface waves, P+PIW to denote a mixture of a compressional body wave and PIW, and S+RIW to denote a mixture of shear body wave and RIW. The mixing of RIW and the shear wave resulted because computational limitations prevented the use of a fracture long enough to allow the two waves to separate from each other.

A horizontally polarized source located on a welded fracture (i.e., whole space) produces only a compressional

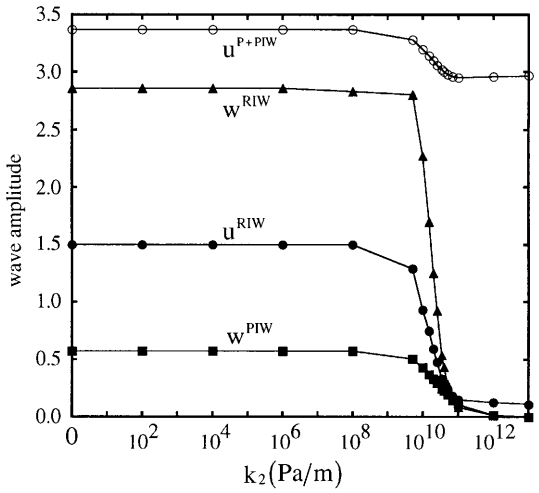

FIG. 8. Displacements on the fracture surface at a distance of 45.79 m from the source as a function of fracture stiffness for the model shown in Fig. 2(a).

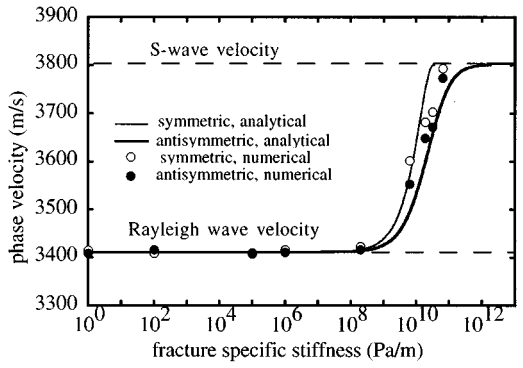

FIG. 9. Phase velocities of the symmetric and antisymmetric fracture interface waves as a function of fracture stiffness.

wave with horizontal displacement [Fig. 4(a)]. Therefore, w^{PIW}, u^{RIW}, and w^{RIW} shown in Figs. 4(a) and 6 exist solely due to the finite stiffness of the fracture, and hence are fracture interface waves. Because of the symmetry of the source–fracture configuration, w^{PIW}, u^{RIW}, and w^{RIW} must be symmetric about the fracture, that is, they are symmetric waves. Similarly, u^{PIW}, w^{PIW}, and u^{RIW} displayed in Figs. 5(b) and 7 for a vertically polarized source are antisymmetric about the fracture and are antisymmetric waves.

The displacements on the fracture surface, at a distance of 45.79 m from the source, are displayed in Fig. 8 as a function of fracture stiffnesses for a horizontally polarized source [Fig. 2(a)]. For the source spectrum and seismic properties of the half-spaces used in this simulation, a tangential fracture stiffness of $k_2=10^8$ Pa/m is the threshold value above which the displacements of all the waves traveling along the fracture start to decrease with increasing fracture stiffness. The decrease of $u^{\mathrm{P+PIW}}$, w^{PIW}, u^{RIW}, and w^{RIW} results because the stiffness of the fracture is too large to result in localization of compressional and shear waves along the fracture. When the fracture stiffness increases above 10^{11} Pa/m (nearly welded condition), the small-amplitude u^{RIW} is the near-field term traveling directly from the source,[12] and the large-amplitude $u^{\mathrm{P+PIW}}$ is the compressional body wave.

The phase velocities of the symmetric and antisymmetric RIW interface waves are shown in Fig. 9 for a range of fracture stiffnesses. The analytic phase velocities were computed by numerical solution of the dispersion equations given in Eqs. (6) and (7). The numerical phase velocities were obtained from the RIW by calculating $L/(\Delta\Theta/\omega)$, where L is the distance between two receiver locations 29.83 m and 44.65 m from the source, $\Delta\Theta$ is the phase difference between the interface waves at the two locations, and ω is the angular frequency. The phase velocities displayed in Fig. 9 indicate that the interface waves supported by a fracture are dispersive despite the zero thickness of the fracture. The numerical and analytic velocities show general agreement.

B. Effect of half-space impedance

To investigate the effects of the acoustic impedance of the half-spaces on fracture interface waves, a series of boundary element simulations were performed using the horizontal source [Fig. 2(a)] located on a 46.0-m-long fracture with a stiffness $k_2=10^9$ Pa/m. Both the upper and lower surfaces of the fracture were discretized into 201 nodes using 100 quadratic elements 0.46 m in length. The computation was carried out to 18.2 m in 460 time steps. The compressional wave impedance and density of the half-spaces are $z_p=15\,080\,000$ m/s kg/m^3 and $\rho=2600$ kg/m^3 while the shear wave impedance was varied from $z_s=9\,880\,000$ to $z_s=6\,634\,420$ m/s kg/m^3, as listed in Table I. The compressional and shear wave velocities and Poisson's ratios calculated from z_p, z_s, and ρ are also given in Table I.

The waveforms recorded on the lower surface of the fracture at a distance of 23.12 m from the source are displayed in Fig. 10. $u^{\mathrm{P+PIW}}$, w^{PIW}, u^{RIW}, and w^{RIW} waves have different shapes and amplitudes for different values of the shear wave impedance. Figure 11 displays the displacements as a function of the shear wave impedance. As z_s increases, interface waves w^{PIW}, u^{RIW}, and w^{RIW} increase, and $u^{\mathrm{P+PIW}}$ decreases. These variations in displacement indicate that more seismic energy is partitioned from the body wave part of $u^{\mathrm{P+PIW}}$ into w^{PIW}, u^{RIW}, and w^{RIW} with increasing z_s.

C. Particle motions

Particle motions recorded along a vertical profile [Fig. 2(a)] are displayed in Fig. 12. A horizontally polarized source was applied on the lower surface of the fracture with stiffnesses $k_1=5\times10^9$ and $k_2=10^9$ Pa/m. The particle motion of the S+RIW wave reverses from retrograde to prograde at a depth of $0.17\lambda_s$ (λ_s is the wavelength of the shear wave). The particle motion of the P+PIW wave reverses from prograde near the fracture to retrograde at a depth of $0.17\lambda_p$ (λ_p indicates the wavelength of the compressional wave). The vertical component of the P+PIW wave and the horizontal component of the S+RIW wave pass through zero

TABLE I. Properties of the half-spaces.

Z_P m/s kg/m^3	Z_S m/s kg/m^3	ρ kg/m^3	C_P m/s	C_S m/s	ν
15 080 000	9 880 000	2 600	5 800	3 800.0	0.12
15 080 000	9 508 720	2 600	5 800	3 657.2	0.17
15 080 000	9 035 000	2 600	5 800	3 475.0	0.22
15 080 000	8 464 560	2 600	5 800	3 255.6	0.27
15 080 000	7 596 160	2 600	5 800	2 921.6	0.33
15 080 000	6 634 420	2 600	5 800	2 551.7	0.38

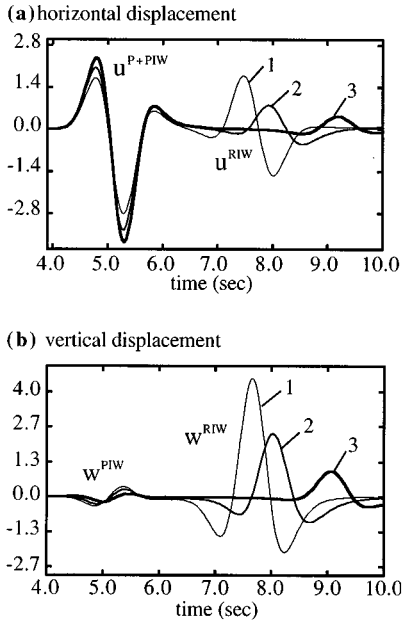

FIG. 10. Waveforms on the lower fracture surface at a distance of 23.12 m from the source for the model shown in Fig. 2(a). The fracture stiffness is $k_2=10^9$ Pa/m, the compressional wave impedance is $z_P=15\,080\,000$ m/s kg/m^3, and the shear wave impedance is: (1) $z_S=9\,880\,000$, (2) $z_S=9\,035\,000$, and (3) $z_S=7\,596\,160$ m/s kg/m^3.

at depths of $0.17\lambda_p$ and $0.17\lambda_s$, respectively. The vertical displacement of the P+PIW wave reaches a maximum at approximately $0.06\lambda_p$ away from the fracture. Figure 12 also displays particle motions of the P+PIW and S+RIW waves which become less elliptically and more linearly polarized at depths greater than $1.18\lambda_s$, and particle trajectories that are smaller on the upper half-space than the lower half-space.

Elliptical particle motions which decay exponentially away from the fracture while changing from retrograde to prograde are characteristic of Rayleigh fracture interface waves,[5,6] which can be viewed as stiffness-coupled free-surface Rayleigh waves on the upper and lower fracture surfaces. The particle motions of Fig. 12 indicate that fracture interface waves are localized to within $1.2\lambda_s$ of the fracture, and that beyond this depth compressional and shear body waves dominate. Smaller particle trajectories in the upper half-space results because seismic energy is not completely transmitted from the lower half-space to the upper half-space because of the finite stiffness of the fracture. The particle motion of the PIW interface wave is consistent with that of water surface waves on water.

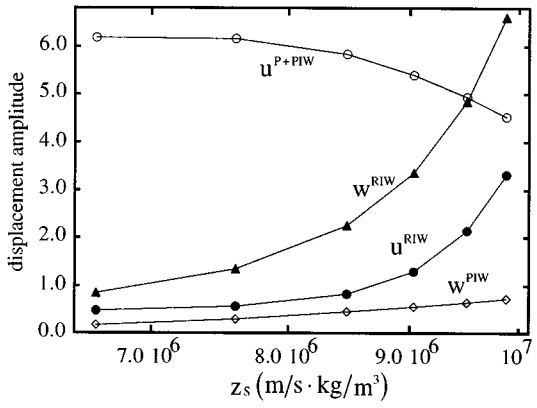

FIG. 11. Displacements on the fracture surface at a distance of 23.12 m from the source as a function of the shear wave impedance of the halfspaces for the simulation configuration shown in Fig. 2(a).

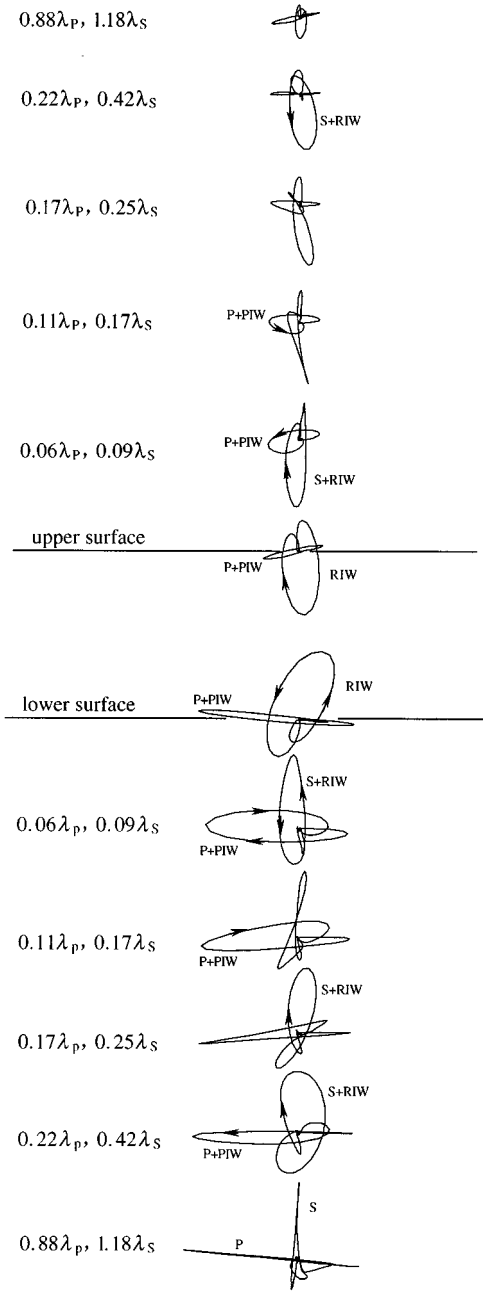

FIG. 12. Particle motions of waves recorded along the vertical profile in Fig. 2(a). The fracture stiffnesses are $k_1=10^9$ and $k_2=5\times10^9$ Pa/m.

D. Generation by an off-fracture source

The effects of source depth on the generation of fracture interface waves is examined using the model geometry shown in Fig. 13 (see Table II). The 76.0-m-long fracture

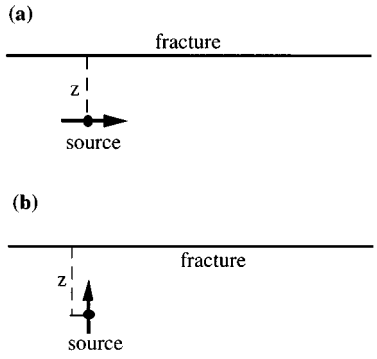

FIG. 13. Model used to examine the effects of source depth on the generation of fracture interface waves.

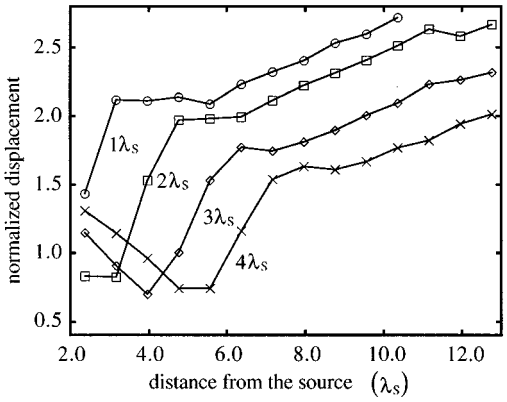

FIG. 14. Normalized horizontal displacements of the RIW interface wave on the lower fracture surface as a function of distance from the source along the fracture for the model shown in Fig. 13(a). The numbers labeled on the curves are the source depths. Symbol λ_S denotes the shear wave wavelength.

was assigned stiffnesses of $k_1 = k_2 = 2.5 \times 10^{10}$ Pa/m. The two half-spaces were assigned compressional and shear wave velocities $c_p = 5800$ m/s and $c_s = 3800$ m/s, and a density $\rho = 2600$ kg/m^3. The fracture was discretized into 100 quadratic elements, and the computation was carried out to 20.1 ms in 310 time steps. The source depth was varied from $1\lambda_s$ to $4\lambda_s$.

Because of the geometric spreading, body waves at the fracture become smaller as the source moves deeper. The variation of the incidence body wave will produce changes in amplitude of the generated interface waves. In the analysis, the fracture interface waves recorded on the fracture surfaces are normalized by the amplitude of the incidence body wave. Figure 14 displays normalized horizontal displacements of the RIW interface wave recorded on the lower fracture surface as a function of distance from the source along the fracture for the simulation configuration shown in Fig. 13(a). The numbers labeled on the curves are source depths in terms of shear wave wavelengths.

For discussion convenience, the curve for source depth $z = 3\lambda_s$ in Fig. 14 is replotted in Fig. 15. The variation of the normalized displacement can be explained as follows. From E and A, the main mechanism is the reflection of the incident body wave. The reflected wave decreases with increasing incidence angle θ. At location A, a critical incidence angle for the generation of the RIW interface wave is reached. As the wave travels from A to B, the RIW interface wave is developing, resulting in a continuous increase of the RIW interface wave. After location B, the persisting but slower increase of the normalized displacement with propagation distance may be due to the decrease of the incident body wave instead of the growth of the RIW interface wave. In other words, the RIW interface wave may be already fully developed at point B.

The angle θ defined in Fig. 15 are listed in Tables II and III for the horizontally and vertically polarized sources, respectively [see Fig. 13(a) and (b)]. It is found from Tables II and III that as source depth increases from $1\lambda_s$ to $4\lambda_s$, and θ decreases from around 72.5 to 63 degrees.

TABLE II. Critical angles for the generation of the Rayleigh fracture interface waves (RIW) for the source–fracture configuration shown in Fig. 13(a).

Source depth (λ_s)	1	2	3	4
θ (degree)	72.6	67.4	64.9	63.4

III. SUMMARY AND CONCLUSIONS

This paper has used boundary element simulations to examine the properties of fracture interface waves generated by a line source located near a single fracture. The fracture was modeled as a displacement–discontinuity boundary condition between two elastic half-spaces. The effects of fracture stiffness and the seismic impedance of the half-spaces on the fracture interface waves and the influences of the source depth on the generation of the fracture interface waves were examined.

The numerical simulations reveal that symmetric and antisymmetric Rayleigh fracture interface waves can be generated by a directional source located on or near the fracture and polarized in the tangential and orthogonal directions with respect to the fracture, respectively. The symmetric interface wave is supported by the normal fracture stiffness, and the antisymmetric fracture interface wave is supported by the tangential fracture stiffness. The velocity and ampli-

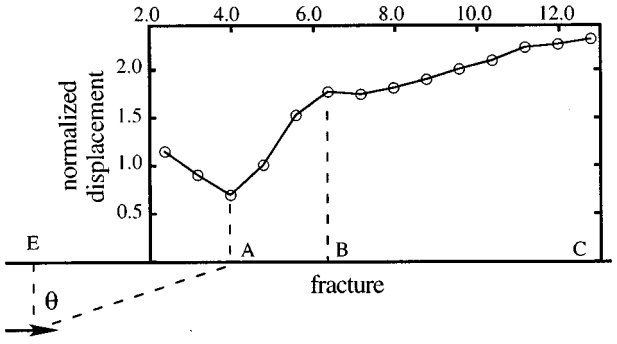

FIG. 15. Normalized displacement on the fracture surface as a function of the critical angle θ for the generation of RIW interface waves.

TABLE III. Critical angles for the generation of RIW interface waves for the source-fracture configuration shown in Fig. 13(b).

Source depth (λ_s)	1	2	3	4
θ (degree)	72.4	67.2	64.7	63.3

tude of the interface waves are functions of the ratio of the fracture impedance to the half-space impedance. There is a threshold value of the fracture stiffness above which the fracture interface waves start to decrease in amplitude with increasing fracture stiffness. The interface waves also increase as the shear wave acoustic impedance increases. With increasing fracture stiffness from the threshold to infinity, the phase velocity of the RIW interface waves increase from the free-surface Rayleigh wave velocity to the shear wave velocity. The symmetric interface wave propagates faster than the antisymmetric interface wave for a given value of the fracture stiffness and the half-space impedance.

The PIW and RIW waves exhibit elliptical particle motion because of the existence of a phase shift between two displacement components. Particle motion ellipse of the PIW wave is polarized largely in the horizontal direction while that of the RIW wave is polarized more vertically than horizontally. The direction of the particle motion of the RIW wave is retrograde near the fracture and reverses to prograde at a depth of less than a wavelength, while the particle motion of the PIW wave changes from prograde near the fracture to retrograde. The particle motion of the PIW and RIW interface waves are consistent, respectively, with that of water surface waves and the free-surface Rayleigh wave. In addition to the two fracture interface waves, a head wave is also observed to exist on a finite stiffness fracture.

These results may find direct applications to seismic detection and characterization of fractures in the rock. For example, the leaky nature of the fracture head wave may allow fractures to be detected by receivers located off the fracture. The sensitivities of the symmetric and antisymmetric interface waves to the normal and tangential fracture stiffnesses, respectively, may allow separate estimates of these properties from the velocities of fracture interface waves.

ACKNOWLEDGMENTS

This work resulted from discussions with Neville G. W. Cook. We would like to thank Neville for sharing his insights on the mechanics of fractures. This work was conducted with support from the Director, Office of Energy Research, Office of Basic Energy Sciences under U.S. Department of Energy Contract No. DE-AC03-76SF00098.

[1] K. Kendall and D. Tabor, ''An ultrasonic study of the area of contact between stationary and sliding surfaces,'' Proc. R. Soc. London, Ser. A **323**, 321–340 (1971).
[2] M. Schoenberg, ''Elastic wave behavior across linear slip interfaces,'' J. Acoust. Soc. Am. **68**, 1516–1521 (1980).
[3] L. J. Pyrak-Nolte, L. R. Myer, and N. G. W. Cook, ''Transmission of seismic waves across natural fractures,'' J. Geophys. Res. **95**, 8617–8638 (1990).
[4] S. I. Rokhlin and Y. J. Wang, ''Analysis of boundary conditions for elastic wave interaction with an interface between two solids,'' J. Acoust. Soc. Am. **89**, 503–515 (1991).
[5] B. Gu, K. T. Nihei, and L. R. Myer, ''Fracture interface waves,'' J. Geophys. Res. **101**, 827–835 (1996).
[6] L. J. Pyrak-Nolte and N. G. W. Cook, ''Elastic interface waves along a fracture,'' Geophys. Res. Lett. **14**, 1107–1110 (1987).
[7] G. S. Murty, ''A theoretical model for the attenuation and dispersion of Stoneley waves at the loosely bonded interface of an elastic half-space,'' Phys. Earth Planet. Interiors **11**, 65–79 (1975).
[8] L. J. Pyrak-Nolte, J. Xu, and G. M. Haley, ''Elastic interface waves propagating in a fracture,'' Phys. Rev. Lett. **68**, 3650–3653 (1992).
[9] P. B. Nagy and L. Adler, ''New ultrasonic techniques to evaluate interfaces,'' in *Elastic Waves and Ultrasonic Nondestructive Evaluation*, edited by A. K. Datta, J. D. Achenbach, and Y. J. Rajapaske (North-Holland, New York, 1990), pp. 229–239.
[10] B. Gu, K. T. Nihei, L. R. Myer, and L. J. Pyrak-Nolte, ''Numerical simulation of elastic wave propagation in fractured rock with the boundary integral equation method,'' J. Geophys. Res. **101**, 15 933–15 943 (1996).
[11] G. D. Manolis and D. E. Beskos, *Boundary Element Methods in Elastodynamics* (Unwin Hyman, Boston, 1988).
[12] K. Aki and P. G. Richards, *Quantitative Seismology* (Freeman, New York, 1980), Vol. 1, p. 87.

Measurements of two types of dilatational waves in an air-filled unconsolidated sand

Craig J. Hickey and James M. Sabatier
National Center for Physical Acoustics and Department of Physics and Astronomy, University of Mississippi, University, Mississippi 38677

(Received 13 August 1996; accepted for publication 31 March 1997)

This study consists of laboratory measurements of dilatational waves propagating through an air-filled unconsolidated sand. One excitation technique consists of a loudspeaker suspended in the air above the packing of sand. A second excitation technique uses a mechanical shaker in contact with the sand. The transmitted signals are received using microphones and geophones located at various depths within the sand. An interpretation based on measured phase speeds indicates that the transmitted energy from the suspended loudspeaker source is partitioned primarily but not exclusively into the type-II dilatational wave. This wave attenuates rapidly and is only detected at depths of less than about 15 cm for this particular sample. At the deeper depths the detected signal is associated with the type-I dilatational wave. The mechanical shaker produces only a type-I dilatational wave. Both the geophone and microphone sensors can detect both types of dilatational waves. [S0001-4966(97)06507-7]

PACS numbers: 43.20.Gp, 43.20.Jr [JEG]

INTRODUCTION

Theories[1–11] describing wave propagation through deformable porous materials predict the existence of two dilatational and one (or two) rotational waves. The dilatational waves are usually referred to as the fast or type-I waves and the slow or type-II waves. For an air-filled sand or sandstone, these theories predict that the fast or type-I wave usually has the larger phase speed and smaller attenuation. It deforms both the solid and fluid constituents by approximately the same amount and the deformations are approximately in phase. The slow or type-II wave has the lower phase speed and larger attenuation. Both phase speed and attenuation are strongly frequency dependent. The deformation associated with the type-II wave consists of primarily fluid component deformation and a very small deformation of the solid component. The deformation of the components is almost out of phase. It should be noted, however, that the phase speed and deformation characteristics of the waves are not mutually inclusive for all materials and frequencies.[12,13] For example, it has been predicted[13] that if the rigidity of an air-filled soil is sufficiently small the type-II dilatational wave has a higher phase speed than the type-I dilatational wave at the higher frequencies.

Laboratory measurements, on an air-filled unconsolidated packing of sand, are carried out using microphones and geophones located at various depths within the sand. Two sources are employed: a loudspeaker suspended in the air above the sand and a mechanical shaker on the surface of the sand. In the context of this paper the waves are characterized solely by their values of phase speed. The fast or type-I wave is the wave with the larger phase speed and lower attenuation whereas the slow or type-II wave is the wave of lower phase speed and higher attenuation. The slow wave is also dispersive. The difference or similarity in phase speeds calculated using the microphones and geophones, at the various depths, will determine what wave these sensors can detect.

Further characterization of these waves might be carried out based on the ratio of solid to fluid deformation, i.e., fluid pressure to solid velocity, associated with each wave type at a particular depth. At present there are unresolved problems concerning the calibration of microphones inserted in sands as well as the ''particle velocity'' measured by geophones. These problems will be addressed in future publications.

In Sec. I relevant theoretical models are reviewed. A review of existing literature pertaining to the predictions of these models and actual detection of the type-I and type-II dilatational waves is carried out. The reasoning behind the use of the various sources and receivers in the current experiment is explained. Section II describes the physical characteristics of the sand sample and the geometrical configuration of the experimental setup. The use of continuous wave signals is discussed. The use of pulses for acquiring the time-of-flight measurements and peak to peak amplitudes for the calculation of phase speed and attenuation are outlined. The measurements are presented in Sec. III. A discussion of these measurements and observations with respect to predictions of existing theories is also included in this section. Section IV presents concluding remarks of this work.

I. THEORETICAL MODELS AND PREVIOUS WORK

The elastic theory of wave propagation predicts one dilatational wave and one shear wave. The waves are nondispersive and no attenuation is present at low frequencies if adiabatic deformations are assumed. The associated physical properties of the medium are the density, the bulk modulus, and the shear modulus. Attenuation has been incorporated into the single continuum models through a simplified viscoelastic approach in which bulk and shear moduli of the medium are allowed to be frequency dependent and complex valued.[14–16] However, this approach does not make an association between the measured attenuation, quantified by the value of the imaginary part of moduli, and the actual physi-

cal mechanism responsible. Since most earth materials are porous or cracked and filled with multiple fluids then the single continuum theory cannot fully account for the interaction of the solid and fluids. It clearly cannot predict the existence of two distinct dilatational waves which are the focus of the study presented in this paper. Theoretical models for wave propagation which involve two coupled and interacting continua are required and are referred to here as ''dual wave models.''

Dual wave models are unique in that they predict the existence of two dilatational waves as well as the shear waves. The most popular dual wave model for wave propagation through porous media was developed by Biot.[1–4] The Biot model is characterized by two coupled differential vector equations. The macroscopic ''effective'' parameters in Biot's constitutive relations are related to quasistatic measurements in the work of Biot and Willis.[5] The model predicts the existence of one shear wave.

Other dual wave models[6–11] have been obtained by applying various homogenization schemes to the governing equations at the pore scale. This approach utilizes the well-established single continuum equations as the foundation for the theoretical development in lieu of the more axiomatic approach of Biot. In the work of de la Cruz and Spanos,[6,7] the macroscopic continuum equations that describe wave propagation in a fluid-filled porous medium have been constructed by using volume averaging. The porous medium consists of an elastic matrix whose pores are interconnected and are completely filled with a viscous compressible fluid. The medium is assumed to be macroscopically homogenous and isotropic. The model predicts two dilatational and two shear waves. Generalizations of the de la Cruz and Spanos model as well as relations between macroscopic elastic parameters and quasistatic compressibilities were presented by Hickey *et al.*[8] Subtle fundamental differences between the Biot model and the de la Cruz and Spanos model have also been discussed.

The description of porous materials as a single continuum has had some success. Rigid frame theories have been used extensively to model sound absorbing materials.[17–20] In this limit the porous material is treated as an effective fluid having complex material parameters. The viscous effects are incorporated into a complex frequency-dependent density whereas the thermal effects are incorporated into a complex frequency-dependent bulk modulus. These frequency-dependent material parameters are functions of the tortuosity, flow resistivity, porosity, and the properties of the air. Expressions for the complex density and bulk modulus are deduced from the solutions for the fluid-flow and thermal fields in capillary tubes or between parallel plates.

The classical theory for a rigid porous material has been used almost exclusively to interpret the interaction of airborne sound with the ground.[21–25] In this model the ground allows the transmission of only one wave and therefore it can be characterized by a single complex valued characteristic impedance. Ground parameters are currently being deduced, via the rigid frame model, by means of reflection experiments.[26]

A comparison between the classical theory for a rigid porous material and the dual wave theory of Biot has been presented.[27,28] The rigid frame limit of the Biot theory for dilatation motion[27–29] was obtained by assuming that the scalar potential associated with the solid displacement is zero. It was shown that the wave described in this limit was the type II or slow dilatational wave. Both descriptions, the rigid frame limit of the Biot theory and classical theory of rigid porous materials, are equivalent and describe the type-II dilatational wave.

The rigid frame model appears adequate for describing the reflection of airborne sound from the surface of the sand.[26] This is because the sand surface is composed of pores filled with air and the sand grains. The air just above the surface induces motion of the air within the pores due to their similar inertial characteristics. The solid grains, however, have a much higher density and bulk modulus and are therefore only slightly deformed. The deformation induced into the sand by the impinging sound wave is one in which the motion is primarily that of the fluid constituent. This type of deformation is characteristic of the type-II dilatational wave. Numerical models[12,30] for an air-filled half space overlying an air-filled sand, based on a dual wave theory, shows that a majority of the transmitted energy is partitioned into the type-II dilatational wave. Hence, this source configuration is a good way to selectively excite type-II dilatational waves in an air-filled porous material.

Measurements of the air pressure associated with the transmitted waves, from a suspended loudspeaker source, were obtained using a probe microphone.[13,31,32] Measurements at various depths and over a range in frequency enables the calculation of a complex valued propagation constant. Material properties are deduced by way of the rigid frame limit of the Biot theory or the classical theory for a rigid porous material. The deduced material properties are associated with the hydrodynamic characteristics of the porous material. For most cases the data at the deeper depths do not fit the model.

Several authors[12,33–35] have observed that an airborne acoustic wave incident on a ground surface could couple energy into the ground as seismic motion, i.e., type I dilatational wave. These observations were based on measurements using geophones. Since the geophones are sensors which respond to the ''particle'' velocity of the medium this signal was interpreted as being associated with the type-I dilatational wave.

Mechanical sources placed in contact with the surface of the ground are used extensively in exploration seismology. The assumption is that they produce one dilatational wave, one shear wave (isotropic media), and surface waves. Richart *et al.*[36] have calculated the distribution of displacement waves from a circular footing on a homogeneous, isotropic, elastic half space. In order to obtain a signal from a vertical component geophone that is associated dominantly with the dilatational wave and not the shear or Rayleigh waves, the source must be placed directly above the vertical component geophone.

For a mechanical source in contact with a porous material it would appear that the normal component of the solid

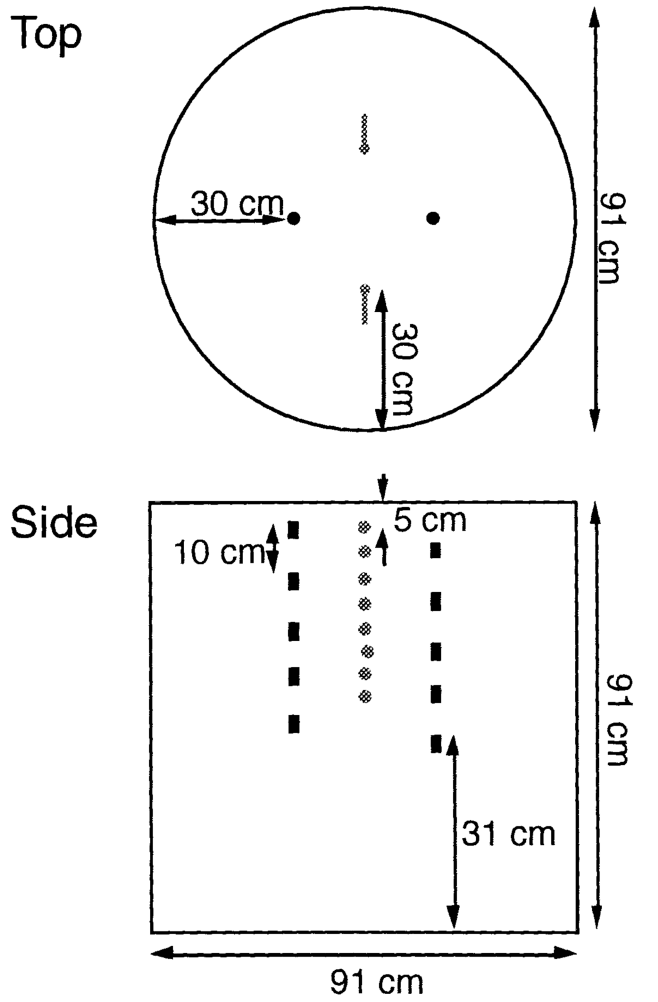

FIG. 1. Schematic of experimental setup for the acoustic wave transmission experiment. The black symbols (■, ●) represent vertical component geophones and the grey symbols (※ , ⟿) represent microphones. The probe microphone was inserted in the center of the container.

and fluid displacements of the sand at the surface should be in phase. Such in-phase motion of material components is usually associated with the type-I dilatational wave at low frequencies. Geertsma and Smit[29] have studied the case of an elastic wave passing through an interface separating an elastic solid and a fluid-filled permeable porous material. They concluded that no second wave is generated at an interface of two media of which one is impermeable.

Based on these previous works it appears that the shaker generates significantly more type-I dilatational wave energy than type-II dilatational wave energy. Whereas a suspended loudspeaker emitting an acoustic wave which impinges on the surface of the sand should be a good source for the transmission of type-II dilatational wave energy into the sand sample. However, both types of dilatation waves might be detectible when the loudspeaker is used as the source.

II. EXPERIMENTAL SETUP AND PROCEDURES

A schematic of the experimental setup with the sensor configuration is shown in Fig. 1. A cylindrical container measuring 91 cm (36 in.) in diameter and 91 cm (36 in.) deep was used to hold sandblasting sand. The container was filled in 10-cm increments. The sand was manually leveled out and lightly tamped for each increment. This was repeated until the container was filled to 50 cm from the top. At that point, the deepest vertical component geophone (uncased Marks Products L-410) was placed in the container. The geophone was placed 30 cm from the wall of the container. The deepest microphone was placed 30 cm from the wall and 40 cm from the top of the container. The microphone consisted of a Panasonic electret condenser microphone cartridge glued into brass cylinders with a diameter of 0.7 cm and lengths varying from 8 to 20 cm. More sand was added and additional sensors were placed, in a staggered fashion, at 5-cm depth intervals with an accuracy of about ± 0.2 cm. A total of ten vertical component geophones and eight microphones were buried. This configuration allowed for measurements to be taken with both microphones and vertical component geophones at 5-cm depth intervals.

Two separate sources were used. A loudspeaker, consisting of an Altec Lansing 902-8b driver with a conical horn 8 cm long and a mouth diameter of 6 cm. The loudspeaker source was suspended about 2 m directly above the sand surface in order to satisfy the assumption of a normal incident plane wave. As previously discussed, this source configuration is a good way to selectively excite a type-II dilatational wave in an air-filled porous material. The other source was a mechanical shaker, Ling Dynamic Systems model V203, placed in contact with the surface of the sand. This mechanical shaker has a circular base with a diameter of 7.5 cm. As discussed earlier, in order to obtain a signal from a vertical component geophone that is associated dominantly with the dilatational wave the source must be placed directly above the geophone. For the sensor configuration shown in Fig. 1 the mechanical source was moved four times in order to obtain a complete set of data.

The condition for a point source is $ka \ll 1$, where k is the wave number of the disturbance and a is the radius of the source. At a frequency of 1 kHz and assuming a speed of 250 m/s, typical for sand, the ka for the shaker is 0.9. The condition for far field is $kr \gg 1$, where r is the source to receiver distance. For a frequency of 1 kHz and a speed of 250 m/s, $kr = 1.3$ at the nearest sensor which was 5 cm away. Hence the conditions for a point source as well as the ''far-field'' condition are only weakly satisfied. Therefore, no correction is applied to the amplitude data collected with the shaker. The attenuation derived from the amplitude data is the total attenuation incorporating intrinsic attenuation as well as geometric spreading.

The source signals were either continuous waves (cw) signals or five cycle tone burst. The signal to the loudspeaker was amplified using a Techron 5515 power supply whereas the signal to the shaker was amplified using its own power oscillator.

The continuous wave technique using a probe microscope has been published.[31,32] In short, the continuous wave technique consists of measuring transfer functions between a reference, usually a microphone on the surface, and the probe microphone at a known depth in the sand. In this experiment an HP 35665A dynamic signal analyzer was used

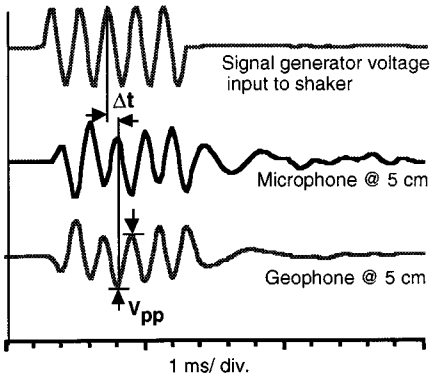

FIG. 2. Procedure for the determination of transit time interval Δt and peak to peak voltage V_{pp} from five cycle tone bursts. This figure is to illustrate which cycle of the pulse is used for the measurements, but this actual time scale was never actually used to obtain the travel time. The source was moved above the appropriate column for the geophone and microphone data. Note that the geophone signal is opposite polarity to the microphone, as expected.

to measure the magnitude and phase of the transfer function. The source signal from 250 Hz to 3.6 kHz was generated using the HP 35665A in swept sine mode at 801 points per sweep. The signal was averaged over 40 cycles with a settle time of 40 cycles between frequency increments.

Continuous wave signals make it quite convenient to calculate phase speed and attenuation over a range of frequencies. However, due to the finite size of the sample used, reflections from the walls and bottom of the container may interfere with the direct wave causing maximums and minimums in the transfer function. Other possible sources of ''noise'' include resonances of the room (low frequency) and the container. It will be shown later that the cw signal, at the greater depths, exhibits large fluctuations in magnitude and phase as a function of frequency even though the mean signal was well above the noise floor. These fluctuations could be attributed to the interaction of the type I and type II waves.

A pulse transmission technique was used to measure the phase velocity and attenuation of the sand. The ''pulse'' consisted of five cycle tone bursts generated by an HP 3314A signal generator. Three different bursts of 750 Hz, 1 kHz, and 1.5 kHz were used. The received pulses were amplified and bandpass filtered (10 Hz–10 kHz) using a Tektronix TM506 and then displayed on an HP 54520A (500 MS a/s) digitizing oscilloscope. The signals were averaged 100 times. Figure 2 shows three typical time traces and indicates how the travel time and peak to peak voltages were measured. The first break arrival times and the peak to peak amplitudes were measured using the third cycle of the tone burst. The first break arrival times were measured with reference to the signal generator input voltage, to ± 0.002 ms, by expanding the traces on the oscilloscope. The time base shown in Fig. 2 was never used for travel time measurements. The peak-to-peak voltages were obviously dependent on the amplifier gains. These gains were held constant for all measurements at one frequency. The error in measuring the peak to peak amplitude was about 2%.

Knowing the spatial separation between the sensors and the difference in arrival times the wave speed can be determined. Several receivers at known locations were used to determine phase speed and attenuation. The slopes of the travel time versus sensor location were used to find the wave speed. Amplitude versus sensor location was used to determine the attenuation. This method uses the data from all receivers rather than just one but requires that the material be homogeneous over the spread of the receivers.

The measurements were carried out in the following sequence. Phase speed and attenuation measurements using the cw technique were obtained first. Then the speed and attenuation using the probe microphone and loudspeaker were determined using a five cycle tone burst at frequencies of 750 Hz, 1 kHz, and 1.5 kHz. The measurements from the pulse transmission technique were compared to the cw measurements to check the validity of the pulse transmission technique. The pulse transmission technique was then used to obtain measurements at greater depths. The loudspeaker was used as a source and the *in-situ* microphones and geophones as receivers. Finally, the mechanical shaker was used as the source and the *in-situ* microphones and geophones as receivers.

III. RESULTS AND DISCUSSION

Acoustic transmission measurements were obtained indoors on a container of sandblasting sand. Sandblasting sand is a commercially available dry sand and is ideal if the effect of water content are to be minimized. The sand grains are subangular in shape and composed primarily of quartz. The bulk density of the sand was measured to be 1680 kg/m^3. Assuming a solid grain density of quartz (2650 kg/m^3) the porosity of the small sample used for the density measurement was 37%.

Probe microphone measurements were obtained at one centimeter intervals down to a depth of 20 cm and over the frequency range of 250 Hz–3.6 kHz using continuous waves. The phase difference and relative magnitude between the reference microphone, placed at the soil surface near the probe, and the probe microphone are shown in Fig. 3(a) and (b), respectively. The figure shows data to a depth of 12 cm in 2-cm intervals. The magnitude and phase of the probe microphone decreases somewhat systematically with depth to about 10 cm. The change in magnitude and phase per unit depth becomes larger with increasing frequency. Calculations of the phase speed and attenuation, over the depth intervals of 1–6 cm and 3–8 cm, are shown in Fig. 4(a) and (d), respectively. Lines representing best fit polynomial regressions using KaleidaGraph™ are superposed onto the data. The attenuation and phase speed increase with increasing frequency but remain fairly constant as a function of depth. There is about a 10% ''variation'' in phase velocity and attenuation as a direct consequence of fluctuations in the phase and magnitude. However, the general feature of increasing phase velocity and attenuation proportional to the square root of the frequency is typical of the type-II wave and it is therefore inferred that these signals, at shallow depths, are dominated by only one wave, namely the type II wave. This interpretation of the data is not new and has been discussed extensively in the literature.[12,13,27,28,30–32]

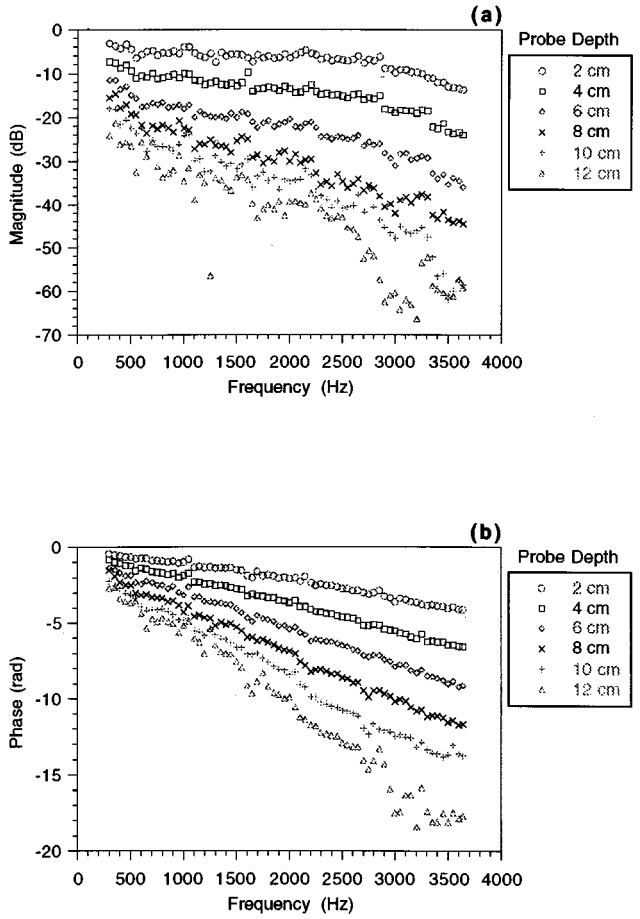

FIG. 3. Measured (a) relative magnitude and (b) phase difference between the probe microphone at various depths and a reference microphone located on the surface of the sand. The source is a loudspeaker transmitting a continuous wave signal.

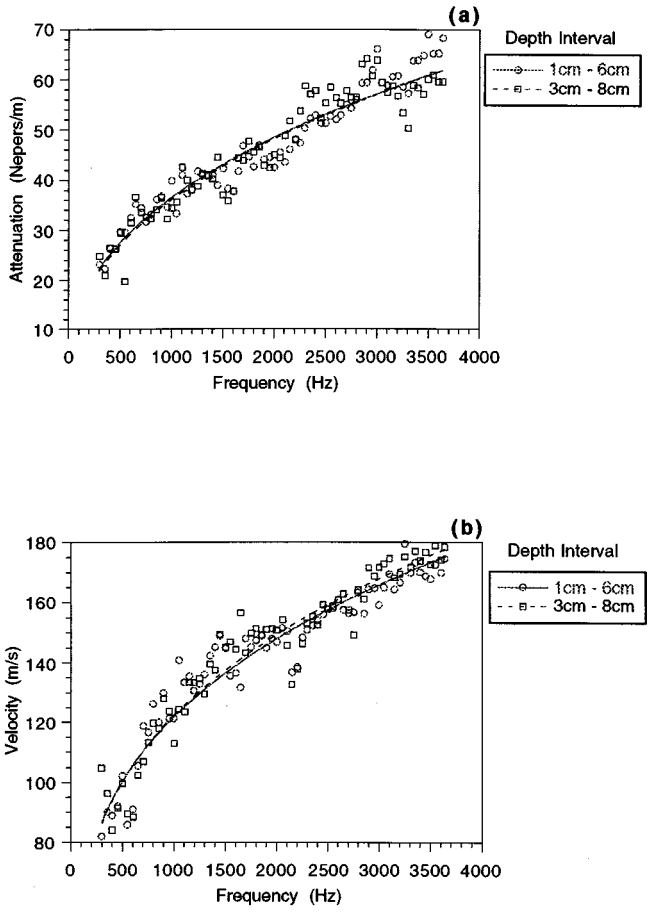

FIG. 4. Calculated (a) phase speed and (b) attenuation using the data in Fig. 3 over two different depth intervals.

The fluctuations in magnitude and phase present in the data are more prominent at the higher frequencies for the 10- and 12-cm depths. These fluctuations in the data extend to the lower frequencies with increasing probe depth. The signal-to-noise ratio was measured with the probe at a depth of 25 cm. The ratio of the probe voltage measured with the source on and off was 20 dB. Fluctuations in the transfer function have also been observed in data which were collected outdoors.[31,32] This suggests that these fluctuations are not solely a consequence of performing this experiment indoors on a finite size sample.

In the studies of soils using the probe microphone, Sabatier *et al.*[31,32] attribute the most significant source of error in probe measurements to inaccuracy in determining the depth of the probe. The error in phase speed and attenuation using measurements over a 5-cm depth interval and assuming an accuracy of ± 0.002 m in probe position is about 8%. Although this type of error could account for differences in phase velocity and attenuation determined over different depth intervals it clearly cannot account for the variations in velocity and attenuation as a function of frequency displayed in Fig. 4. This is because the probe positions were held constant for the measurements over the sweep in frequency.

Other studies of granular materials have also shown these fluctuations in frequency response. Lui and Nagel[37] have studied these fluctuations in glass beads which were excited by a buried aluminum disk connected to an external speaker by a horizontal rigid rod. They showed that these fluctuations exhibit a power-law behavior and were independent of the driving frequency. They were, however, dependent on the amplitude of the source including the low-

TABLE I. Phase speed and attenuation for three selected frequencies as calculated from the measurements using the probe microphone and a continuous wave signal shown in Fig. 4. The error in phase velocity and attenuation due to probe placement is 8%.

Depth interval (cm)	Phase velocity (m/s)			Attenuation (Np/m)		
	750 Hz	1 kHz	1.5 kHz	750 Hz	1 kHz	1.5 kHz
1–6	112	122	137	32	36	43
3–8	113	123	139	32	36	43

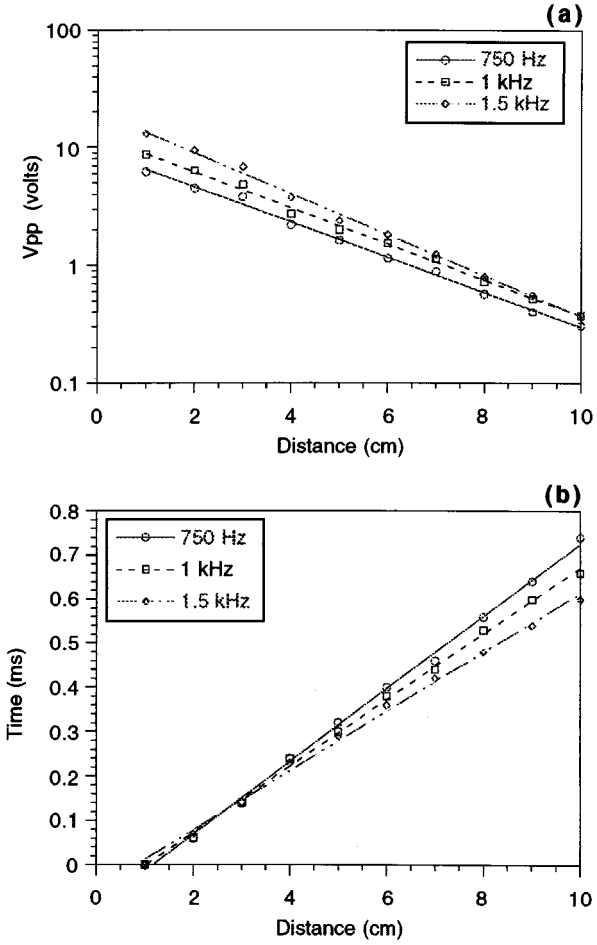

FIG. 5. Pulse transmission measurements using the probe microphone apparatus. Measured (a) peak to peak voltage versus probe depth and (b) arrival time versus probe depth of five cycle tone burst at frequencies of 750 Hz, 1 kHz, and 1.5 kHz.

amplitude regime. They suggested that the fluctuations in the response were due to rearrangements in the material due to the vibration of the wave. It is clear that the mechanism responsible is just one of many unique features of granular materials which are of current research interest.[38]

Values of the phase speeds and attenuation shown in Fig. 4 for frequencies of 750 Kz, 1 kHz, and 1.5 kHz are presented in Table I. The phase speeds are well within the 8% error associated with probe placement. The attenuations are the same within the accuracy of the measurements. The close agreement in values over different depth intervals supports the assumption of a homogeneous sample with depth. This assumption is required for calculation of phase velocities and attenuations from pulse transmission data.

TABLE II. Phase speed and attenuation calculated from the best-fit linear regression lines to the data collected [Fig. 5(a) and (b)] with the probe microphone using five cycle tone bursts.

Frequency (Hz)	Phase speed (m/s)	Cor. coef.	Attenuation (Np/m)	Cor. coef.
750	122	0.9990	34	0.9945
1000	134	0.9990	35	0.9970
1500	149	0.9984	40	0.9966

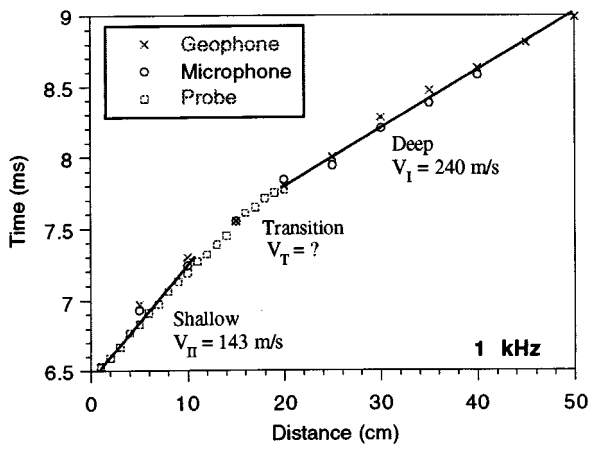

FIG. 6. Travel time versus receiver depth measured by pulse transmission. A loudspeaker transmitting a 1-kHz five cycle toneburst is the source and the probe microphone, *in-situ* geophone, and *in-situ* microphone are used as receivers.

The probe microphone was used to record five cycle tone bursts emitted by the loudspeaker at frequencies of 750 Hz, 1 kHz, and 1.5 kHz. Measurements with the probe were taken at 1-cm intervals down to 20 cm. The peak to peak voltage and the arrival time for ''shallow'' depths (<10 cm) are shown in Fig. 5(a) and (b), respectively. In Fig. 5(b) the times were referenced to the time recorded by the probe at a 1-cm depth. The phase velocities and attenuations, determined from the slopes of the linear regression lines, are presented in Table II along with the correlation coefficient. Both velocity and attenuation increase with increasing frequency. The speeds are consistently larger than the speeds obtaining using cw presented in Table I but are within the 8% error associated with probe positioning. The attenuation coefficients are similar whether pulses or continuous waves were used. The slight difference in values determined using cw and the pulses might also be attributed to the dispersive character of the type-II wave. The dispersive nature and high attenuation of the observed signal suggests that the mode responsible was the type-II dilatational wave.

Arrival times were measured from the loudspeaker tone bursts down to much greater depths using the *in-situ* vertical component geophones and *in-situ* microphones. Figure 6 shows the arrival times versus the relative depth to the sensors for a 1-kHz tone burst. The *in-situ* microphones were at every 5 cm down to a depth of 40 cm and the geophones were at every 5 cm down to a depth of 50 cm. The probe microphone measurements to a depth of 20 cm are also shown. Time measurements from the *in-situ* microphones and geophones were corrected to the time measured by the probe at the 15-cm depth.

The travel time curve shown in Fig. 6 is divided into three regimes: a shallow regime in the range 0–10 cm, a deep regime comprising depths greater than about 20 cm, and an intermediate ''transistion'' regime. It was argued above that the signal in the shallow regime was due to the type-II wave. The data shows that the geophones at 5 and 10 cm respond to the same disturbance as do the microphones and the probe. This infers that the geophones are capable of

detecting the type-II dilatational wave even though most of its deformation is associated with the air. The average phase speed determined, using the 1 kHz tone burst, from all sensors in the shallow regime is 143 m/s. This speed is slightly larger than the speed of the type-II dilatational wave measured at 1 kHz using the probe and a cw signal. This may be because the data at the 10-cm depth, which is approaching the transition region, was used in the calculation or to the dispersive character of the type-II wave. At deeper depths (>20 cm) the speed is calculated to be 240 m/s. It will be shown later that this speed is similar to the speed determined using the mechanical shaker source and is associated with the type-I dilatational wave.

Although there is about 100 m/s difference in phase velocity, at 1 kHz, the two waves cannot be separated in time at these low frequencies. For example, an ideal five cycle 1-kHz tone burst has a time duration of 5 ms. This would require a propagation distance of about 45 cm before the five cycles of the type-I wave arrive before the initial cycle of the type-II wave. Given the high attenuation of the type-II wave, ~3 dB/cm at 1 kHz, the type-II wave would not be detectable at this depth.

The transition regime is where both the type-I and type-II waves are of similar magnitude. Within the transition region the signal is therefore a superposition of both the type-I and the type-II waves. The difference in arrival times between the type-I and type-II waves at the center of the transition region, say at 15 cm experiment, is about 0.5 ms. The ability to detect the presence of an individual wave at the front or back of the superposed pulse might be masked by the distortion of the transducer turning on and off. The spatial ''width'' of the transition region depends on the relative attenuation of the waves. For example, the signal amplitudes, at 1 kHz, are within a factor of 10 for a depth interval of about 13 cm if the attenuation of the type-I wave is neglected. Although data is presented in a transition region of Fig. 6, choosing the third peak of the tone burst is questionable and the time measured is not easily interpreted since there exists a superposition of two pulses. Therefore, although data within the transition is presented in Fig. 6 it is not very meaningful. A refinement of the experimental apparatus is required to further examine this transition region.

In order to explain the two speeds displayed in Fig. 6, a possible scenario is that the loudspeaker transmits primarily type-II dilatational wave energy into the soil, but also a small amount of type-I dilatational wave. Since the type-II wave is strongly attenuated, its energy can only penetrate to a shallow depth after which the type-I dilatational wave dominates the signal.

In order to study the properties of the type-I dilatational wave a mechanical shaker was used as a source. The receivers used were the *in-situ* microphones and geophones. The probe was not used in conjunction with this mechanical shaker. The source was placed in contact with the surface of the sand. As mentioned earlier, a circular footing in contact with an elastic solid produces a dilatation wave, shear wave, and a Rayleigh wave. In order to obtain a signal from a vertical component geophone that was associated predominantly with the dilatational wave and not the shear of Rayleigh waves, the source was placed directly above the column of sensors. Therefore, to obtain measurements from all geophones and microphones the source was moved four times. Moving the source might cause different source amplitudes due to a change in coupling between the source and the sand. However, it appears that the source coupling was quite reproducible since no significant amplitude differences were observed between columns of sensors.

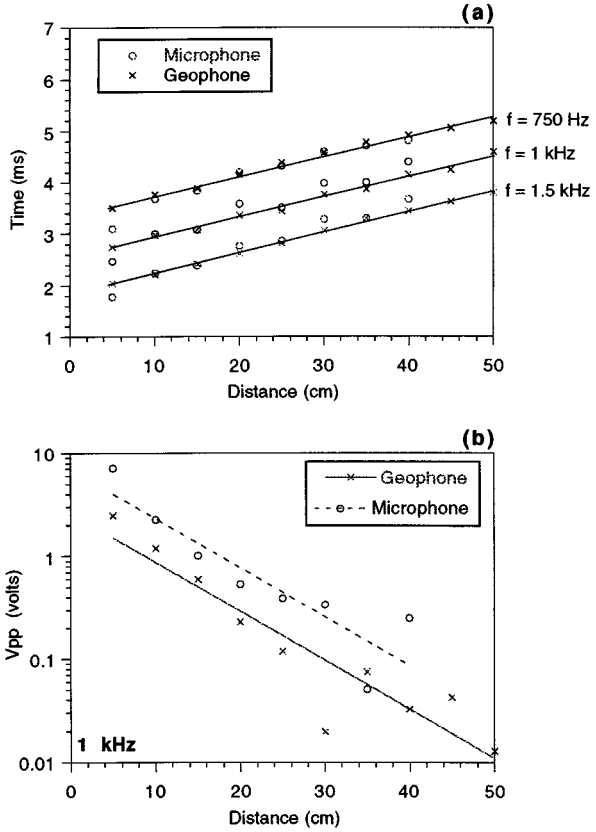

FIG. 7. Using a mechanical shaker source at a frequency of 1 kHz; (a) travel time versus receiver depth and (b) peak to peak voltage versus receiver depth are measured by pulse transmission. *In-situ* microphones and geophones are used as receivers.

Figure 7(a) shows the pulse arrival times recorded using geophones and microphones as a function of depth. The offset in the time direction for different frequencies is due to measuring the transit time using the electronic trigger and the third peak of the tone burst. Linear regression best fit lines are superposed onto the data. The graph shows only one slope suggesting the presence of only one wave as opposed to what was seen in Fig. 6. Values of phase speeds (inverse of the slope) with their respective correlation coefficients are

TABLE III. Phase speed and total attenuation calculated from the slopes of the best-fit linear regression lines to the data collected (Fig. 7) with the *in-situ* microphones and geophones using a five cycle tone burst signal from a mechanical shaker source.

Frequency (Hz)	Phase speed (m/s)	Cor. coef.	Attenuation (Np/m)	Cor. coef.
750	260	0.9953	11	0.9732
1000	251	0.9953	10	0.9569
1500	248	0.9991	10	0.9719

presented in Table III. The three speeds are equal within the 8% experimental error associated with the sensor placement. This suggests that the wave responsible has little dispersion over this frequency range. The measured speed of 251 m/s at 1 kHz is quite close to the value of 240 m/s measured in the ''deep region'' using the loudspeaker source. This similarity in velocity supports the notion that the signal transmitted into the sand from the loudspeaker source is indeed dominated by the type-I wave at greater depths.

The peak to peak voltage versus depth for 1-kHz tone burst is shown in Fig. 7(b). No corrections for geometric spreading have been applied to the amplitudes because the radiation pattern of the source is unknown. The large scatter in the data might be due to being in the near field of a finite size source, scattering off of clusters of grains, or variation in coupling of the receivers.

Values of total attenuation with their respective correlation coefficients are presented in Table III. The correlation of the data used for the determination of the total attenuation is poor and therefore values obtained have errors greater than 8%. It is interesting to note, however, that the total attenuation measured with the shaker source is still about three times less than the attenuation of a type-II wave presented in Tables I and II.

From Fig. 7 it appears that the microphones are as good as geophones for the detection of the type-I dilatational wave. Microphones respond to changes in pressure of the fluid component. Therefore, such signals must be sensitive to fluid deformations. There can also be some information about the matrix deformation in microphone measurements. This comes about through a porosity change associated with the matrix deformation which creates an induced pore pressure. Such induced pore pressure has been observed in quasistatic experiments.[39–41] The use of microphones to detect the type-I wave could prove quite useful given their frequency response and physical size.

IV. CONCLUSIONS

Acoustic signals generated by a loudspeaker suspended in the air above the sand surface and a mechanical shaker in contact with the sand surface can be detected by both buried geophones and microphones. Using the observed signals, at various depths, the phase speed and attenuation are calculated assuming that the sand is homogeneous. Characterization of the type-I and type-II dilatational waves is based on these values.

The observed signals from the loudspeaker source are interpreted as being associated with the type-II dilatational wave at shallow depths. The signals are detected using both the microphones and geophones although most of its deformation is associated with the air. The signals are believed to be associated with the type-II dilatational wave because the measured phase speed and attenuation increase with increasing frequency. Measurements of phase speed and attenuation in the shallow region using the pulse and continuous wave signals are also in agreement. At the deep depths, the type-II dilatational wave is believed to have decayed away and the signal is now due to the type-I dilatational wave. This interpretation is supported by measurements using a mechanical shaker.

The mechanical shaker source is interpreted as producing only type-I dilatational wave because of its in-phase deformation. The phase speed (no dispersion) and attenuation measured using the shaker source are about the same as that obtained from the loudspeaker source in the deep region. The determined phase speed, ~240 m/s is about an order of magnitude less than what is reported for consolidated sandstone. However, it is similar to published values for sand.[42] The signals from the shaker source can be detected using both the microphones and geophones. Using microphones for the detection of the type-I dilatational wave could be advantageous. Since, in general, microphones have a higher frequency response and can be built with smaller physical dimensions.

A study of the transition region, where the type-I and type-II dilatational waves are of the same magnitude using a loudspeaker source requires further investigation.

ACKNOWLEDGMENTS

This work is supported jointly by the Office of Naval Research and the USDA-ARS National Sedimentation Laboratory.

[1] M. A. Biot, ''Theory of propagation of elastic waves in a fluid-saturated porous solid. I. Low frequency range,'' J. Acoust. Soc. Am. **28**, 168–178 (1956).
[2] M. A. Biot, ''Theory of propagation of elastic waves in a fluid-saturated porous solid. II. Higher frequency range,'' J. Acoust. Soc. Am. **28**, 179–191 (1956).
[3] M. A. Biot, ''Mechanics of deformation and acoustic propagation in porous media,'' J. Appl. Phys. **33**, 1482–1498 (1962).
[4] M. A. Biot, ''Generalized theory of acoustic propagation in porous dissipative media,'' J. Acoust. Soc. Am. **34**, 1254–1264 (1962).
[5] M. A. Biot and D. G. Willis, ''The elastic coefficients of the theory of consolidation,'' J. Appl. Mech. **24**, 594–601 (1957).
[6] V. de la Cruz and T. J. T. Spanos, ''Seismic wave propagation in porous media,'' Geophysics **50**, 1556–1565 (1985).
[7] V. de la Cruz and T. J. T. Spanos, ''Thermomechanical coupling during seismic wave propagation in a porous medium,'' J. Geophys. Res. **94**, 637–642 (1989).
[8] C. J. Hickey, T. J. T. Spanos, and V. de la Cruz, ''Deformation parameters of porous media,'' Geophys. J. Int. **121**, 359–370 (1995).
[9] R. Burridge and J. B. Keller, ''Poroelasticity equations derived from microstructure,'' J. Acoust. Soc. Am. **70**, 1140–1146 (1981).
[10] N. Katsube and M. M. Carroll, ''The modified theory for fluid-filled porous materials: Theory,'' J. Appl. Mech. **54**, 35–40 (1987).
[11] C. C. Mei and J.-L. Auriault, ''Mechanics of heterogeneous porous media with several spatial scales,'' Proc. R. Soc. London, Ser. A **380**, 305–331 (1989).
[12] D. G. Albert, ''A comparison between wave propagation in water-saturated and air-saturated porous materials,'' J. Appl. Phys. **73**, 28–36 (1993).
[13] K. Attenborough, J. M. Sabatier, H. E. Bass, and L. N. Bolen, ''The acoustic transfer function at the surface of a layered poroelastic soil,'' J. Acoust. Soc. Am. **79**, 1353–1358 (1986).
[14] J. W. Spencer, Jr., ''Bulk and shear attenuation in berea sandstone: The effects of pore fluids,'' J. Geophys. Res. **84**, 7521–7523 (1979).
[15] R. J. O'Connell and B. Budiansky, ''Viscoelastic properties of fluid-saturated cracked solids,'' J. Geophys. Res. **82**, 5719–5735 (1977).
[16] R. J. O'Connell and R. Budiansky, ''Measures of dissipation in viscoelastic media,'' Geophys. Res. Lett. **5**, 5–8 (1978).
[17] C. Zwicker and C. W. Kosten, *Sound Absorbing Materials* (Elsevier, Amsterdam, 1949).
[18] R. W. Morse, ''Acoustic propagation in granular media,'' J. Acoust. Soc. Am. **24**, 696–700 (1952).

[19] P. M. Morse, *Vibration and Sound* (Acoustical Society of America, New York, 1981).
[20] A. D. Pierce, *Acoustics: An Introduction to its Physical Principles and Applications* (Acoustical Society of America, New York, 1989).
[21] H. E. Bass and L. N. Bolen, ''Coupling of airborne sound into the earth frequency dependence,'' J. Acoust. Soc. Am. **67**, 1502–1506 (1980).
[22] K. Attenborough, ''Acoustical impedance models for outdoor ground surfaces,''J. Sound Vib. **99**, 521–544 (1985).
[23] T. F. W. Embleton, J. E. Piercy, and N. Olson, ''Outdoor sound propagation over ground of finite impedance,'' J. Acoust. Soc. Am. **59**, 267–277 (1976).
[24] T. F. W. Embleton, J. E. Piercy, and G. A. Daigle, ''Effective flow resistivity of ground surfaces by acoustical measurements,'' J. Acoust. Soc. Am. **74**, 1239–1244 (1983).
[25] Y. Champoux and M. R. Stinson, ''On acoustical models for sound propagation in rigid frame porous materials and the influence of shape factors,'' J. Acoust. Soc. Am. **92**, 1120–1131 (1992).
[26] J. M. Sabatier, R. Raspet, and C. K. Frederickson, ''An improved procedure for the determination of ground parameters using level difference measurements,'' J. Acoust. Soc. Am. **94**, 396–399 (1993).
[27] K. Attenborough, ''Acoustical characteristics of rigid fibrous absorbents and granular materials,'' J. Acoust. Soc. Am. **73**, 785–799 (1983).
[28] K. Attenborough, ''On the acoustic slow wave in air-filled granular media,'' J. Acoust. Soc. Am. **81**, 93–102 (1987).
[29] J. Geertsma and D. C. Smit, ''Some aspects of elastic wave propagation in fluid-saturated porous solids,'' Geophysics **26**, 169–181 (1961).
[30] J. M. Sabatier, H. E. Bass, L. N. Bolen, K. Attenborough, and V. V. S. S. Sastry, ''The interaction of airborne sound with the porous ground: The theoretical formulation,'' J. Acoust. Soc. Am. **79**, 1345–1352 (1986).
[31] J. M. Sabatier, H. Hess, W. P. Arnott, K. Attenborough, M. J. M. Robekens, and E. H. Grissinger, ''*In-situ* measurements of soil physical properties by acoustical techniques,'' Soil Sci. Soc. Am. J. **54**, 658–672 (1990).
[32] J. M. Sabatier, D. C. Sokol, C. K. Frederickson, M. J. M. Romkens, E. H. Grissenger, and J. C. Shipps, ''Probe microphone instrumentation for determining soil physical properties: Testing in model porous materials,'' Soil Technol. **8**, 259–274 (1996).
[33] D. G. Albert and J. A. Orcutt, ''Acoustic pulse propagation above grassland and snow: Comparison of theoretical and experimental waveforms,'' J. Acoust. Soc. Am. **87**, 93–100 (1990).
[34] D. G. Albert and J. A. Orcutt, ''Observation of low frequency acoustic-to-seismic coupling in the summer and winter,'' J. Acoust. Soc. Am. **86**, 352–359 (1989).
[35] J. M. Sabatier, H. E. Bass, L. N. Bolen, and K. Attenborough, ''Acoustically induced seismic waves,'' J. Acoust. Soc. Am. **80**, 646–649 (1986).
[36] F. E. Richart, J. R. Hall, and R. D. Woods, *Vibration of Soils and Foundations* (Prentice-Hall, Englewood Cliffs, NJ, 1970).
[37] C.-h. Liu and S. R. Nagel, ''Sound in sand,'' Phys. Rev. Lett. **68**, 2301–2304 (1992).
[38] H. M. Jaeger, S. R. Nagel, and R. P. Behringer, ''The physics of granular material,'' Phys. Today **49**(4), 32–38 (1996).
[39] A. W. Skempton, ''The pore-pressure coefficients A and B,'' Geotechnique **4**, 143–147 (1954).
[40] J. R. Rice and M. P. Cleary, ''Some basic stress diffusion solutions for fluid saturated elastic porous media with compressible constituents,'' Rev. Geophys. Space Phys. **14**, 227–241 (1976).
[41] D. H. Green and H. F. Wang, ''Fluid pressure response to undrained compression in saturated sedimentary rock,'' Geophysics **51**, 948–956 (1986).
[42] F. Press, ''Seismic velocities,'' *Handbook of Physical Constants* (Geological Society of America, New York, 1966).

Acoustic/elastic stop-band interaction in waveguides involving two periodicities

Muhammad A. Hawwa
Seagate Technology, Advanced Platform Development Group, 5898 Condor Drive, Moorpark, California 93021

(Received 15 July 1996; revised 10 February 1997; accepted 13 February 1997)

A structure with two periodicities can couple up to six modes under a case of simultaneous resonance resulting in a stop-band interaction. The method of multiple scales is employed to analyze the modal coupling in a two-dimensional acoustic duct with rigid periodically undulated walls as well as in an elastic plate having periodically corrugated outerfaces, leading to the coupled-mode equations. The comparison between the three possible cases of interaction under simultaneous resonance are given in terms of the power reflection coefficient spectrum as a function of frequency. The strength of the stop-band interaction is found to be strongly related to the number of direct couplings between the incident and reflected modes. © *1997 Acoustical Society of America.* [S0001-4966(97)00207-5]

PACS numbers: 43.20.Mv, 43.20.Gp, 43.20.Jr [JEG]

INTRODUCTION

Wave motion in periodic structures has been a subject of special interest to many researchers. This stems from the fact that propagating modes interact with a structural periodicity in different manners. The interaction could be constructive leading to the generation of a new mode, or destructive resulting in the filtration of a mode. Understanding the nature of the modal interaction is of great help for the design of wave processing devices such as mode couplers, filters, or resonators.

Acoustic wave propagation in two-dimensional waveguides with sinusoidal walls was first studied by Salant.[1] The regular perturbation expansion used in Salant's study was not uniform in the vicinity of resonance. Nayfeh[2] employed the method of multiple scales to find a uniform expansion near resonance, and found that neither of the resonating modes could occur without generating the other. Later, Nayfeh[3] extended his work to account for the mean flow carried by the waveguide. Nayfeh and Asfar[4] considered the parallel problem of electromagnetic waves propagating within sinusoidally corrugated perfectly conducting surfaces. Sandstrom[5] used the null-field method to find the stop-band structure of a two-dimensional waveguide with symmetric, antisymmetric, or one-sided sinusoidal corrugations. Hawwa and Asfar[6] studied SH waves in an elastic plate whose free outerfaces are nonuniformly sinusoidal, and designed an ultrasonic filter with enhanced characteristics.

In all of the prementioned investigations, a single structural periodicity was involved. In his exhaustive review on the state-of-the-art of the field of wave propagation in periodic systems, Elachi[7] called for more investigations to structures having multiperiodicity. Asfar and Nayfeh[8] analyzed the coupling between two as well as three TM modes propagating in a parallel plate waveguide having two wall periodicities, and they presented the transition curves separating passbands from stop bands.

Having more than one periodicity in a system leads to various possibilities of mode coupling under a case of simultaneous resonance. It is the aim of this study to focus on the stop-band interaction of six acoustic/elastic modes in a structure involving two periodicities. The wave propagation in two-dimensional waveguides having two periodicities is analyzed using the method of multiple scales. Simultaneous resonance is found to occur by satisfying the following conditions in three different combinations: (i) the codirectional coupling of two modes, (ii) the contradirectional coupling of two modes, and (iii) the Bragg condition. The comparison between different cases is given in terms of the power reflection coefficient spectrum as a function of frequency. The study aims to serve the design of acoustic/ultrasonic filters in multimode environments.

I. PROBLEM FORMULATION

Figure 1 could represent either an acoustic duct having rigid sinusoidally undulated walls or an elastic plate with sinusoidally corrugated outerfaces. The undulations (corrugations) can be described in a Cartesian coordinate system $(\hat{x},\hat{y},\hat{z})$ by $\hat{z}=\hat{h}\epsilon\ \sin(\hat{k}_1\hat{x})$, and $\hat{z}=\hat{h}[1+\epsilon\alpha\ \sin(\hat{k}_2\hat{x})]$, where $\hat{k}_1$ and $\hat{k}_2$ are the wave numbers of the walls (outerfaces), $\hat{h}$ is the average width of the duct (average thickness of the plate), ϵ is a small dimensionless parameter equal to the ratio of the amplitude of the lower wall undulation (bottom outerface corrugation) to $\hat{h}$, and α is a constant allowing for a different undulation (corrugation) amplitude at the upper wall (outerface).

We assume that the motion of the fluid inside the acoustic duct is inviscid and irrotational (the motion in the elastic plate is of the horizontally polarized type). The propagating waves are assumed to have a temporal variation in the form $\exp(-i\hat{\omega}\hat{t})$, where $\hat{\omega}$ is the frequency of oscillation, and $\hat{t}$ is the time coordinate. Then, the governing equation of motion takes the form

$$\frac{\partial^2\phi}{\partial x^2}+\frac{\partial^2\phi}{\partial z^2}+k^2\phi=0, \tag{1}$$

where $\phi(x,z)$ is the acoustic pressure inside the duct (the y component of displacement in the plate), $k=\hat{\omega}\hat{h}/c$ repre-

 0001-4966/97/102(1)/137/6/$10.00

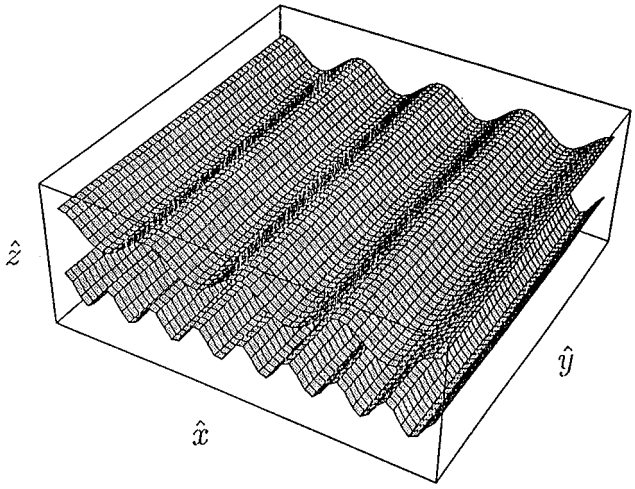

FIG. 1. Waveguide geometry.

sents the wave number of a bulk wave, and c is the speed of sound in the fluid (in the elastic solid). Note that dimensionless quantities (without the carets) have been used by introducing $\hat{\omega}$ and $\hat{h}$ as reference quantities.

The boundary conditions are the vanishing of the velocity component normal to the walls of the duct (the vanishing of traction at the outerfaces of the plate), i.e.,

$$\frac{\partial \phi}{\partial x}\, n_x + \frac{\partial \phi}{\partial z}\, n_z = 0 \quad \text{at} \quad z = \epsilon \sin(k_1 x), \quad \text{and} \quad z = 1 + \epsilon\alpha \sin(k_2 x), \tag{2}$$

where n_x and n_z are the components of the local outward-pointing unit normal.

In order to determine the resonance conditions, a solution of the system (1) and (2) in the form of a first-order straightforward asymptotic expansion is sought. The expansion is found to break down when

$$k_m \mp k_n \approx k_{1,2}, \tag{3}$$

where k_m and k_n are the wave numbers of two interacting modes. The $+$ sign corresponds to a contradirectional mode coupling, while the $-$ sign indicates a codirectional mode coupling. When $m=n$, relation (3) becomes the well-known Bragg resonance condition ($2k_m \approx k_{1,2}$), where an incident mode interacts destructively with its reflected counterpart.

In the sequel, uniformly valid asymptotic expansions in the neighborhood of resonance will be obtained by using the method of multiple scales (Nayfeh).[9]

We seek a first-order perturbation expansion for ϕ in powers of ϵ in the form

$$\phi(x,z) = \phi_0(z, X_0, X_1) + \epsilon \phi_0(z, X_0, X_1) + \cdots, \tag{4}$$

where $X_0 = x$ is a short scale of the order of the wavelength in the guide and $X_1 = \epsilon x$ is a long scale which characterizes the amplitude and phase modulations due to the surface undulation (corrugation). Using the chain rule, we can write the derivatives with respect to x in terms of X_0 and X_1 as

$$\frac{\partial}{\partial x} = \frac{\partial}{\partial X_0} + \epsilon \frac{\partial}{\partial X_1} + \cdots, \tag{5}$$

$$\frac{\partial^2}{\partial x^2} = \frac{\partial^2}{\partial X_0^2} + 2\epsilon \frac{\partial^2}{\partial X_0\, \partial X_1} + \cdots. \tag{6}$$

Substituting (4)–(6) into (1) and (2), expanding ϕ at $z = \epsilon \sin(k_1 X_0)$ in a Taylor series around $z=0$, ϕ at $z = 1 + \epsilon\alpha \sin(k_2 X_0)$ around $z=1$, and equating the coefficients of ϵ^0 and ϵ^1 on both sides, we have two sets of problems. They are the zeroth-order and the first-order problems.

$O(1)$

$$\frac{\partial^2 \phi_0}{\partial z^2} + \frac{\partial^2 \phi_0}{\partial X_0^2} + k^2 \phi_0 = 0, \tag{7}$$

$$\frac{\partial \phi_0}{\partial z} = 0, \quad \text{at} \quad z = 0, \tag{8}$$

$$\frac{\partial \phi_0}{\partial z} = 0, \quad \text{at} \quad z = 1. \tag{9}$$

$O(\epsilon)$

$$\frac{\partial^2 \phi_1}{\partial z^2} + \frac{\partial^2 \phi_1}{\partial X_0^2} + k^2 \phi_1 = -2 \frac{\partial^2 \phi_0}{\partial X_0\, \partial X_1}, \tag{10}$$

$$\frac{\partial \phi_1}{\partial z} = k_1 \cos(k_1 X_0) \frac{\partial \phi_0}{\partial X_0} - \sin(k_1 X_0) \frac{\partial^2 \phi_0}{\partial z^2}, \quad \text{at} \quad z = 0, \tag{11}$$

$$\frac{\partial \phi_1}{\partial z} = \alpha k_2 \cos(k_2 X_0) \frac{\partial \phi_0}{\partial X_0} - \alpha \sin(k_2 X_0) \frac{\partial^2 \phi_0}{\partial z^2}, \quad \text{at} \quad z = 1. \tag{12}$$

II. SIMULTANEOUS RESONANCE

The stop-band interaction of four modes with a single periodicity under simultaneous resonance was considered earlier by Hawwa and Asfar.[5] When a system has two structural periodicities, up to six modes can interact destructively with the structural periodicities under different cases of simultaneous resonance. By investigating the different possibilities of mode coupling, one could conclude that there are three cases of simultaneous resonance which produce a stop band. These are

(i) Two conditions on the codirectional modes p and q, and p and r, and a Bragg condition on the r modes

$$k_p - k_q = k_1 + \epsilon\sigma_1, \tag{13a}$$

$$k_p - k_r = k_2 + \epsilon\sigma_2, \tag{13b}$$

$$2k_r = k_2 + \epsilon\sigma_3. \tag{13c}$$

(ii) A condition on the contradirectional modes p and q, another on the codirectional modes p and r, and a Bragg condition on the r modes

$$k_p + k_q = k_1 + \epsilon\sigma_1, \tag{14a}$$

$$k_p - k_r = k_2 + \epsilon\sigma_2, \tag{14b}$$

$$2k_r = k_2 + \epsilon\sigma_3. \tag{14c}$$

(iii) A Bragg condition on the q modes, a condition on the codirectional modes p and r, and another Bragg condition on the r modes

$$2k_q = k_1 + \epsilon\sigma_1, \tag{15a}$$

$$k_p - k_r = k_2 + \epsilon\sigma_2, \tag{15b}$$

$$2k_r = k_2 + \epsilon\sigma_3. \tag{15c}$$

Note that σ's are detuning parameters introduced to quantitatively describe the nearness to resonance. It is also worth noticing that the second and the third conditions in all cases correspond to the coupling of four modes with the structural wave number k_2.

III. COUPLED-MODE ANALYSIS

Equation (7) admits a solution in the form of a linear combination of incident and reflected modes; i.e.,

$$\phi_0 = \sum_j \cos(\beta_j z)[A_j^+(X_1)e^{ik_jX_0} + A_j^-(X_1)e^{-ik_jX_0}], \tag{16}$$

where $\beta_j = j\pi$, the superscript "+" ("−") indicates an incident (reflected) mode, and $A_j^{\mp}(X_1)$ are unknown functions at this level of approximation. They are determined by imposing the appropriate solvability condition at the next level of approximation. Substitution of (16) into the boundary conditions given by (8) and (9) leads to the dispersion relation of guided modes.

$$k_j^2 = k^2 - \beta_j^2. \tag{17}$$

Since the homogeneous part of the first-order problem has a nontrivial solution, then the inhomogeneous first-order problem has a solution if, and only if, a solvability (consistency) condition is satisfied. To determine this condition, let us seek a particular solution for ϕ_1 in the form

$$\phi_1 = \sum_{j=p,q,r} [\Psi_j^+(z)e^{ik_jX_0} + \Psi_j^-(z)e^{-ik_jX_0}]. \tag{18}$$

Substituting (16) together with (18) into the governing equation (10), and equating the coefficients of $\exp(\mp ik_jX_0)$ on both sides, we obtain

$$\left[\frac{d^2}{dz^2} + \beta_j^2\right]\Psi_j^{\mp} = \pm 2ik_j \frac{dA_j^{\mp}}{dX_1}\cos(\beta_j z). \tag{19}$$

We multiply (19) by $\cos(\beta_j z)$ and integrate by parts from $z=0$ to $z=1$. This leads to the equations

$$\Psi_j^{\mp\prime}(1)\cos(\beta_j) - \Psi_j^{\mp\prime}(0) = \pm ik_j \frac{dA_j^{\mp}}{dX_1}, \tag{20}$$

where primes indicate derivatives with respect to the arguments.

To this end, we substitute the solutions (16) and (18) into the boundary conditions (11) and (12), express $\cos(k_{1,2}X_0)$ and $\sin(k_{1,2}X_0)$ in polar form to get

$$\begin{aligned}\Sigma_j[\Phi_j^{+\prime}(0)e^{ik_jX_0} + \Phi_j^{-\prime}(0)e^{-ik_jX_0}] &= \Sigma_j i\{(-k_1k_j - \beta_j^2/2)A_j^+ e^{i(k_j+k_1)X_0} + (-k_1k_j \\ &+ \beta_j^2/2)A_j^+ e^{i(k_j-k_1)X_0} + (k_1k_j - \beta_j^2/2)A_j^- e^{-i(k_j-k_1)X_0} \\ &+ (k_1k_j + \beta_j^2/2)A_j^- e^{-i(k_j+k_1)X_0}\},\end{aligned} \tag{21}$$

$$\begin{aligned}\Sigma_j[\Phi_j^{+\prime}(1)e^{ik_jX_0} + \Phi_j^{-\prime}(1)e^{-ik_jX_1}] &= \Sigma_j i\alpha\cos\beta_j\{(-k_2k_j - \beta_j^2/2)A_j^+ e^{i(k_j+k_2)X_0} + (-k_2k_j \\ &+ \beta_j^2/2)A_j^+ e^{i(k_j-k_2)X_0} + (k_2k_j - \beta_j^2/2)A_j^- e^{-i(k_j-k_2)X_0} \\ &+ (k_2k_j + \beta_j^2/2)A_j^- e^{-i(k_j+k_2)X_0}\}.\end{aligned} \tag{22}$$

Invoking the resonance conditions (13), (14), or (15) into (21) and (22), equating the coefficients of $\exp(\mp ik_jX_0)$ on both sides, and substituting the result into (20) leads to the following three sets of coupled-mode equations:

(i) For the first case

$$\frac{dA_p^+}{dX_1} = B_{pq}A_q^+ e^{-i\sigma_1X_1} + B_{pr}A_r^+ e^{i\sigma_2X_1}, \tag{23}$$

$$\frac{dA_q^+}{dX_1} = B_{qp}A_p^+ e^{i\sigma_1X_1}, \tag{24}$$

$$\frac{dA_r^+}{dX_1} = B_{rp}A_p^+ e^{i\sigma_2X_1} + B_{rr}A_r^- e^{-i\sigma_3X_1}, \tag{25}$$

$$\frac{dA_p^-}{dX_1} = B_{pq}A_q^- e^{i\sigma_1X_1} + B_{pr}A_r^- e^{-i\sigma_2X_1}, \tag{26}$$

$$\frac{dA_q^-}{dX_1} = B_{qp}A_p^- e^{-i\sigma_1X_1}, \tag{27}$$

$$\frac{dA_r^-}{dX_1} = B_{rp}A_p^- e^{-i\sigma_2X_1} + B_{rr}A_r^+ e^{i\sigma_3X_1}, \tag{28}$$

where B_{pq}, B_{pr}, B_{qp}, B_{rp}, and B_{rr} are given in the Appendix.

(ii) For the second case

$$\frac{dA_p^+}{dX_1} = C_{pq}A_q^- e^{-i\sigma_1X_1} + C_{pr}A_r^+ e^{-i\sigma_2X_1}, \tag{29}$$

$$\frac{dA_q^+}{dX_1} = C_{qp}A_p^- e^{-i\sigma_1X_1}, \tag{30}$$

$$\frac{dA_r^+}{dX_1} = C_{rp}A_p^+ e^{i\sigma_2X_1} + C_{rr}A_r^- e^{-i\sigma_3X_1}, \tag{31}$$

$$\frac{dA_p^-}{dX_1} = C_{pq}A_q^+ e^{i\sigma_1X_1} + C_{pr}A_r^- e^{i\sigma_2X_1}, \tag{32}$$

$$\frac{dA_q^-}{dX_1} = C_{qp}A_p^+ e^{i\sigma_1X_1}, \tag{33}$$

$$\frac{dA_r^-}{dX_1} = C_{rp}A_p^- e^{-i\sigma_2X_1} + C_{rr}A_r^+ e^{i\sigma_3X_1}, \tag{34}$$

where C_{pq}, C_{pr}, C_{qp}, C_{rp}, and C_{rr} are given in the Appendix.

(iii) For the third case

$$\frac{dA_p^+}{dX_1} = D_{pr}A_r^+ e^{-i\sigma_2X_1}, \tag{35}$$

$$\frac{dA_q^+}{dX_1} = D_{qq}A_q^- e^{-i\sigma_1X_1}, \tag{36}$$

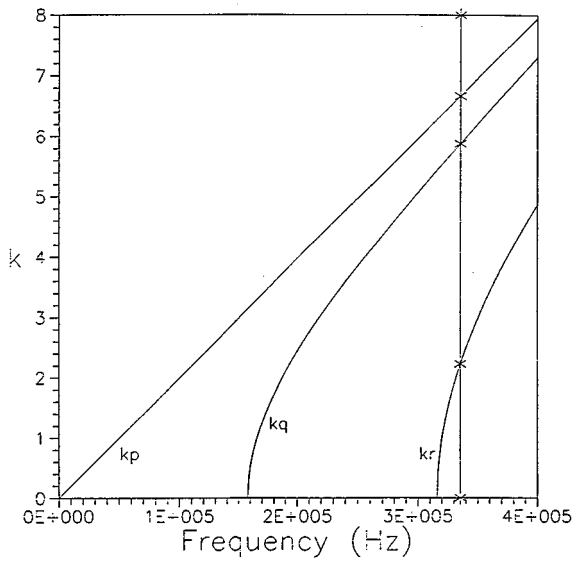

FIG. 2. Dispersion curves with simultaneous resonance location.

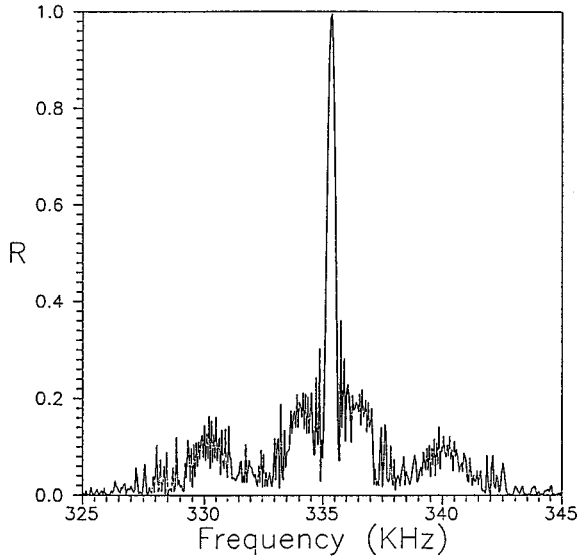

FIG. 3. Power reflection coefficient versus frequency for case (i).

$$\frac{dA_r^+}{dX_1} = D_{rp}A_p^+ e^{i\sigma_2 X_1} + D_{rr}A_r^- e^{-i\sigma_3 X_1}, \tag{37}$$

$$\frac{dA_p^-}{dX_1} = D_{pr}A_r^- e^{i\sigma_2 X_1}, \tag{38}$$

$$\frac{dA_q^-}{dX_1} = D_{qq}A_q^+ e^{i\sigma_1 X_1}, \tag{39}$$

$$\frac{dA_r^-}{dX_1} = D_{rp}A_p^- e^{-i\sigma_2 X_1} + D_{rr}A_r^+ e^{i\sigma_3 X_1}, \tag{40}$$

where D_{pq}, D_{pr}, D_{qp}, D_{rp}, and D_{rr} are given in the Appendix.

IV. NUMERICAL RESULTS

Since both of the acoustic and the elastic problems are mathematically equivalent, representative examples will only be given for SH waves propagating in a plate which is made of an elastic material with $c=10^3$ m/s. The thickness of the plate is $\hat{h}=10^{-3}$ m, and $\epsilon=0.1$. Dispersion curves for the $p=0$, $q=1$, and $r=2$ modes are shown in Fig. 2. To determine the resonance frequency one has to satisfy the relation $k_p \approx 3k_r$ required by all of the sets of simultaneous resonance conditions. This occurs at 335.4 kHz, at which $k_p=6.664$, $k_q=5.877$, and $k_r=2.221$. Hence, the outerface wave numbers will be as follows: For case (i) $k_1=0.787$; for case (ii) $k_1=12.641$, and for case (iii) $k_1=11.754$, while $k_2=4.442$ for all cases.

To quantitatively evaluate the performance of the periodic waveguide, the power reflection coefficient is used as an indicator. This coefficient can be calculated after solving the coupled-mode equations in the range $0<X_1<L$, where L is the length of the periodic section, together with relevant endpoint conditions. These are, for the p^+ incidence, given as

$$A_p^+=1, \quad A_q^+=0, \quad A_r^+=0 \quad \text{at } X_1=0 \tag{41}$$

and

$$A_p^-=0, \quad A_q^-=0, \quad A_r^-=0 \quad \text{at } X_1=L. \tag{42}$$

Note that $A_j^-=0$, since reflection vanishes at the end of the periodic section $X_1=L$. A sensible way is to take the length of the periodic section to be a multiple of both wavelengths of the guide. Let $L=4\lambda_1\lambda_2$, where λ_1 and λ_2 are the wavelengths corresponding to k_1 and k_2, respectively.

The coupled-mode equations with the boundary conditions (41) and (42) form a typical two-point boundary-value problem. This is solved numerically using a code based on the fundamental matrix method (Asfar and Hussein).[10] The power reflection coefficient can be calculated from

$$R=\frac{\Sigma_j k_j[A_j^-(X_1=0)]^2}{\Sigma_j k_j[A_j^+(X_1=0)]^2}. \tag{43}$$

Figures 3, 4, and 5 show the power reflection coefficient as a function of frequency for the cases (i), (ii), and (iii),

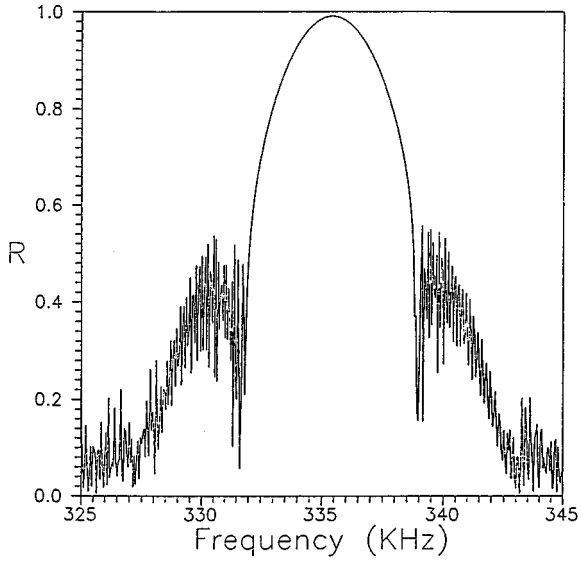

FIG. 4. Power reflection coefficient versus frequency for case (ii).

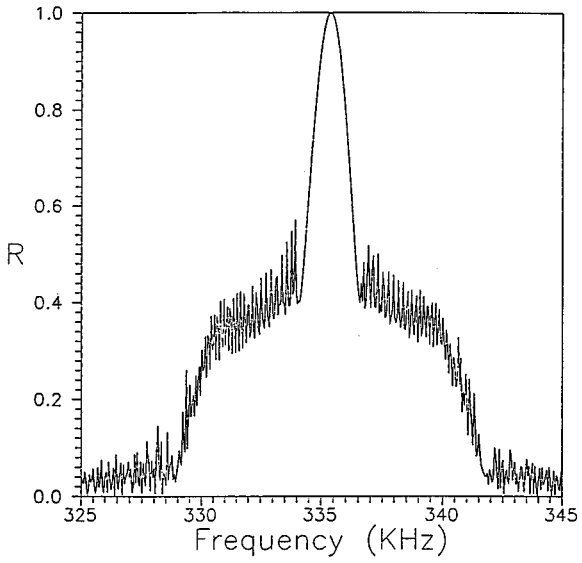

FIG. 5. Power reflection coefficient versus frequency for case (iii).

respectively. Each figure reflects a stop-band interaction with different strength. Total reflection is realized at the resonance frequency in all of the cases, however, the width of the stop band and the levels of the side ripples are different from one case to another. Figure 3 represents the weakest filter action, while Fig. 4 represents the strongest. In order to physically explain the nature of interaction in the three cases, a schematic plot for types of the modal coupling in the three cases is depicted in Fig. 6. In case (i), there is one direct coupling between the incident and reflected r modes, while the p and q modes are indirectly coupled. In case (ii), three direct couplings between the incident and reflected modes are noticed. In case (iii), the incident and reflected q and r modes are directly coupled to each other. Hence, one can draw a conclusion that, the strength of the stop-band interaction is directly proportional to the number of direct couplings between the incident and reflected modes. It remains to mention that the choice of the simultaneous resonance conditions depends on the type of application in which the filter is to be employed.

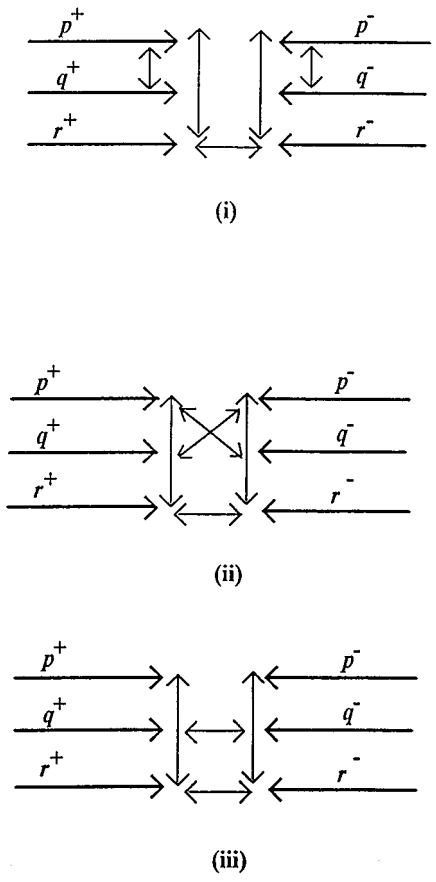

FIG. 6. Schematic plot for type of mode coupling.

V. CONCLUSION

The stop-band interaction of six modes in an acoustic/elastic waveguide having two structural periodicities has been considered under three different cases of simultaneous resonance. Analytical treatment of the problem using the method of multiple scales led to the derivation of the coupled-mode equations. The power reflection coefficient has been used as a measure to the strength of the modal interactions. It is found that the strength of the interaction depends on the number of direct couplings between the incident and reflected modes.

APPENDIX

$$B_{pq}=(k_1k_q-\beta_q^2/2)/k_p,$$

$$B_{pr}=(-k_2k_r+\beta_r^2/2)\alpha\cos\beta_p\cos\beta_r/k_p,$$

$$B_{qp}=(k_1k_p+\beta_p^2/2)/k_q,$$

$$B_{rp}=(-k_2k_p-\beta_p^2/2)\alpha\cos\beta_p\cos\beta_r/k_r,$$

$$B_{rr}=(k_2k_r+\beta_r^2/2)\alpha\cos^2\beta_r/k_r,$$

$$C_{pq}=(-k_1k_q-\beta_q^2/2)/k_p,$$

$$C_{pr}=(-k_2k_r+\beta_r^2/2)\alpha\cos\beta_p\cos\beta_r/k_p,$$

$$C_{qp}=(-k_1k_p-\beta_p^2/2)/k_q,$$

$$C_{rp}=(-k_2k_p-\beta_p^2/2)\alpha\cos\beta_p\cos\beta_r/k_r,$$

$$C_{rr}=(k_2k_r+\beta_r^2/2)\alpha\cos^2\beta_r/k_r,$$

$$D_{pr}=(-k_2k_r+\beta_r^2/2)\alpha\cos\beta_p\cos\beta_r/k_p,$$

$$D_{qq}=(-k_1k_q-\beta_q^2/2)/k_q,$$

$$D_{rp}=(-k_2k_p-\beta_p^2/2)\alpha\cos\beta_p\cos\beta_r/k_r,$$

$$D_{rr}=(k_2k_r+\beta_r^2/2)\alpha\cos^2\beta_r/k_r.$$

[1] R. F. Salant, ''Acoustic propagation in waveguides with sinusoidal walls,'' J. Acoust. Soc. Am. **53**, 504–507 (1971).
[2] A. H. Nayfeh, ''Sound waves in two-dimensional ducts with sinusoidal walls,'' J. Acoust. Soc. Am. **56**, 768–770 (1974).
[3] A. H. Nayfeh, ''Acoustic waves in ducts with sinusoidally perturbed walls and mean flow,'' J. Acoust. Soc. Am. **57**, 1036–1039 (1975).
[4] A. H. Nayfeh and O. R. Asfar, ''Parallel Plate Waveguide with Sinusoidally Perturbed Boundaries,'' J. Appl. Phys. **45**, 4797–4800 (1974).
[5] M. A. Hawwa and O. R. Asfar, ''Mechanical-Wave Filtering in a Periodi-

cally Corrugated Elastic Plate,'' Trans. ASME, J. Vib. Acoust. **117**, 16–20 (1996).
[6] O. R. Asfar and A. H. Nayfeh, ''Stopbands of the First-Order Bragg Interaction in a Parallel Plate Waveguide Having Multiperiodic Wall Corrugations,'' IEEE Trans. Microwave Theory Tech. **MTT-28**, 1187–1191 (1980).
[7] C. E. Sandstrom, ''Stopbands in a corrugated parallel plate waveguide,'' J. Acoust. Soc. Am. **79**, 1293–1298 (1984).
[8] C. Elachi, ''Waves in Active and Passive Periodic Structures: A Review,'' Proc. IEEE **64**, 1666–1698 (1976).
[9] A. H. Nayfeh, *Introduction to Perturbation Techniques* (Wiley, New York, 1981).
[10] O. R. Asfar and A. M. Hussein, ''Numerical Solution of Linear Two-Point Boundary-Value Problems Via the Fundamental Matrix Method,'' Int. J. Numer. Methods Eng. **28**, 1205–1216 (1989).

Elastic guided waves in plates with surface roughness. I. Model calculation

O. I. Lobkis
Center For Nondestructive Evaluation, Iowa State University, Ames, Iowa 50011-3020

D. E. Chimenti[a)]
Center For Nondestructive Evaluation and Aerospace Engineering and Engineering Mechanics Department, Iowa State University, Ames, Iowa 50011-3020

(Received 3 February 1997; accepted for publication 26 March 1997)

This paper reports analytical research on the effect of surface roughness on ultrasonic guided waves in plates. The theoretical model is constructed by exploiting the phase-screen assumption that takes advantage of the Kirchhoff approximation, where, on a local scale, the roughness degrades only the signal phase. The effect of the rough surface on the guided wave is treated by decomposing the wave modes into their constituent partial waves and considering individually the effect of the roughness on the partial wave components as they reflect from the plate surfaces. An approximate dispersion relation is derived for the traction-free rough waveguide that is formally identical to the conventional Lamb wave equation, but incorporating the roughness parameter as a complex plate thickness. A more accurate version of the model calculation is generalized to fluid-immersed plates having only a single rough surface either on the same, or opposite, side of the plate as the incident ultrasonic field. Calculations of the reflection coefficients in the presence of roughness serve to illustrate the phenomena for the case of the guided waves.
[S0001-4966(97)05907-9]

PACS numbers: 43.20.Mv, 43.20.Gp [ANN]

INTRODUCTION

One of the earliest effects of pitting or pillowing corrosion is the roughening of corroded surfaces. This roughening can therefore be an excellent indication of incipient corrosion and the attendant reduction in structural integrity. When a guided wave propagates in a plate-like structure, its constituent partial waves scatter repeatedly from the surfaces of the guiding medium. This process, central to the propagation of guided waves, is also quite sensitive to the condition of the guiding surfaces. Thus, guided wave ultrasonics can provide an early warning for the incipient formation of hidden corrosion, and this is the problem we address in this article.

Sound wave interaction with rough surfaces has attracted much attention in recent years, both theoretically and experimentally, owing to its significance in several fields. Scattering from wavy surfaces, seabeds and surface ice in ocean acoustics has been extensively dealt with, and here we can only hint at this literature.[1–3] Moreover, rough surface scattering in dielectric waveguides, such as optical fibers, has also been widely researched. In either of these problems the fields can be assumed to be represented by a single scalar potential. The problem we consider here concerns the propagation of guided elastic waves in a planar solid waveguide having rough surfaces, with compressional and shear potentials that are coupled at each interface.

Most of the treatments of the acoustic rough-surface problem fall into two main categories: mean field integral transform methods[1,2] and perturbation methods.[4–8] There have also been studies of specific kinds of roughness, namely wave scattering at periodic surfaces.[9–11] Elements of wave scattering in a rough elastic layer have been treated in Ref. 12, but there is no consideration of guided waves. Each of the major approaches has its advantages and drawbacks. Those which are accurate under a broad range of conditions also typically involve complicated calculations. Those that are easier to manipulate analytically may not give such accurate results for all wave components or in all parameter limits. There is, however, a simple approximate result for scattering from a randomly rough fluid–solid interface that can be conveniently expressed as a product of the zeroeth order (smooth surface) reflection coefficient and a simple function dependent on the wavelength and the roughness parameters. We will demonstrate that this approximate expression is, in fact, entirely sufficient as a basis from which to derive an initial estimate of scattering amplitude in guided elastic wave propagation.

Such an approximation was first introduced by Eckhart,[13] in which the scattered field is taken to be composed of a random, incoherent component, owing to the rough-surface scattering, and a residual coherent component. This approach, termed the phase-screen approximation (PSA), ignores any amplitude effects of the scattering and instead considers all the influence of the rough surface to be felt in the signal phase. Strictly speaking, the PSA is valid only in the Kirchhoff limit, when both the rms roughness height h and the fluid wavelength are much less than the roughness correlation length L $(h,\lambda_f \ll L)$. This expression has also been derived by Ogilvy[14] and Nagy and Adler[15] from the Kirchhoff integral and has been discussed by Nagy and Rose,[16] Ogilvy,[2] and Dacol.[17] Using the PSA, comparisons to experimental measurements of fluid–solid rough-

[a)]Electronic mail: chimenti@ameslab.gov

surface ultrasonic scattering, in both transmission and reflection, have shown excellent agreement.[15,16]

The interaction can also be modeled using brute-force techniques such as the boundary integral equation method (BIE).[18] Also, Nagy and Rose[16] have examined the detection of flaws located under a rough surface, as have Rose *et al.*[19] Other effects such as the correlation length, rms height, and incident angle have also received attention.[14–20] However, the phase-screen approximation obtained from the Kirchhoff integral seems, in many applications, to perform well enough to warrant the full investigation of its potential and limits of applicability before reaching for more complicated methods. In fact, as a tool in nondestructive evaluation, its simplicity makes it that much more attractive, as long as we can demonstrate that it has sufficient accuracy under conditions relevant to the problem of roughness characterization with guided waves.

There has been little work, however, on the effect of rough surfaces on elastic guided waves. Significant efforts have been directed towards rough acoustic guides (fluid medium with solid boundaries) for ocean engineering[17,2] and toward dielectric waveguides,[21–25] where in each case only a single wave potential is sufficient to describe wave behavior in the guiding medium. In elastic solids the situation is much more complicated, since there are two wave potentials, and these are coupled to each other at every material interface. A preliminary and highly abbreviated version of this work appears elsewhere.[26]

I. THEORETICAL DEVELOPMENT

We begin with a description of our theoretical approach and the derivation of a rough-surface waveguide dispersion relation. In the second half of the section this approach is generalized to obtain a rough-surface reflection coefficient for a plate having either one or two rough surfaces and immersed in liquid. We also demonstrate some properties of the solutions. Finally, we suggest in which directions the model must be extended to form the basis of an attack on practical inspection problems.

A. Rough-surface waveguide dispersion relation

In elastic waveguide problems it is well known[27] that the guided wave mode can be decomposed into propagating or evanescent compressional and shear partial waves. In an earlier report[26] we presented a calculation of the dispersion relation for an elastic waveguide with two rough traction-free surfaces, proceeding from the assumption that we may use the phase-screen approximation to model the interaction of the partial waves with the rough surfaces and that this interaction is the principal mechanism by which the rough surface damps the guided wave. To derive a free rough-surface plate wave dispersion relation, we exploited the transverse resonance method,[27] which naturally incorporates the partial wave reflection coefficients at the traction-free guide surfaces. In the geometry assumed throughout, the center of the infinite plate lies at the origin, the guided waves propagate in the x_1 direction, and the x_3 direction is normal to the plate surface. No field variable depends on x_2.

The secular determinant of the resulting system of linear equations yields,

$$1 \mp \epsilon\Gamma_{pp}e^{i\kappa_p d} \pm \delta\Gamma_{pp}e^{i\kappa_s d} - \lambda^2 e^{i(\kappa_p+\kappa_s)d} - (\epsilon\delta-\lambda^2)\Gamma_{pp}^2 e^{i(\kappa_p+\kappa_s)d} = 0, \tag{1}$$

where the $\pm$ selects the symmetric (upper sign) or antisymmetric (lower sign) guided wave modes. The quantities Γ_{ab} ($a=\{p,s\}$, $b=\{p,s\}$) are the solid–vacuum, smooth-surface reflection coefficients for an incident a-type wave and reflected b-type wave, where p refers to compressional and s to shear waves. The relations $\Gamma_{ss}=-\Gamma_{pp}$ and $\Gamma_{ps}\Gamma_{sp}=(1-\Gamma_{pp}^2)$ (Ref. 27) have been used to obtain Eq. (1). The plate thickness is d and the transverse (x_3-projection) wave vector components κ_p (compressional) and κ_s (shear) are given by $\kappa_{p,s}=(k_{p,s}^2-\xi^2)^{1/2}$, respectively. Here $k_{p,s}(=\omega/V_{p,s})$ are the compressional and shear wave numbers, ω is the angular frequency, $V_{p,s}$ are the two pure mode wavespeeds, and ξ is the wave number of the propagating guided wave.

The PSA contributions are

$$\epsilon = e^{-2h^2\kappa_p^2}, \quad \delta = e^{-2h^2\kappa_s^2}, \quad \lambda = e^{-h^2(\kappa_p+\kappa_s)^2/2}. \tag{2}$$

Rigorously speaking, the PSA model is valid only for propagating partial waves with real $\kappa_{p,s}$, and in this treatment we truncate the PSA to avoid the unphysical situation of negative attenuation for evanescent partial waves ($k_{p,s}<\xi$), which propagate parallel to the plate surface. This realization implies that we should take only the real parts of $\kappa_{p,s}$ in the expressions for ϵ, δ, and λ. Otherwise, evanescent wave amplitudes could increase after interaction with the rough surfaces. For most practical cases, however, when the plate thickness d is much larger than the rms roughness h, this restriction is not important. If $d \gg |\kappa_{p,s}|h^2$, the amplitudes of evanescent partial waves at the opposite plate surface would be negligible anyway, since they decay as $\exp\{-|\kappa_{p,s}|(d-|\kappa_{p,s}|h^2)\}$.

Equation (1) is the dispersion relation for a rough-surface waveguide using the PSA scattering model to treat the effective attenuation of guided mode partial waves as they interact with the surface. A further interesting simplification of this expression is possible if we can assume that the shear contribution is large enough to consider the compressional one negligible. For materials where the Poisson ratio is greater than about 0.3 this approximation is not so unreasonable, since the rough-surface losses scale geometrically as $(\kappa h)^2$. Then, let us take $\lambda^2 \approx \epsilon\delta$, with which Eq. (1) becomes

$$1 \mp \Gamma_{pp}e^{i\kappa_p d - 2\kappa_p^2 h^2} \pm \Gamma_{pp}e^{i\kappa_s d - 2\kappa_s^2 h^2} - e^{i(\kappa_p+\kappa_s)d - 2(\kappa_p^2+\kappa_s^2)h^2} = 0, \tag{3}$$

after substituting for ϵ and δ from the expressions given above. With one further step we can now incorporate the terms $2h^2\kappa_p$ and $2h^2\kappa_s$ into effective complex thicknesses d_p and d_s, whose imaginary parts introduce the lossy rough-

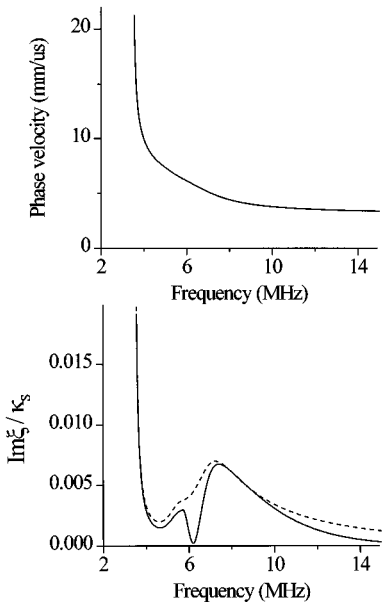

FIG. 1. Real and imaginary solutions for the A_4 antisymmetric mode in a 2.3-mm aluminum plate with Eq. (1) (solid curve) and the approximate Eq. (4) (dashed curve). Upper frame shows mode phase velocity, which differs almost not at all from the ordinary Lamb wave; lower frame shows rough-surface damping loss plotted as $\Im(\xi)/k_s$ for the two approximations.

surface contribution. Using the explicit form of Γ_{pp}, from Ref. 27 for example, Eq. (3) may be expressed as

$$(k_s^2-2\xi^2)^2\frac{\cot(\kappa_p d_p/2)}{\tan(\kappa_p d_p/2)}+4\xi^2\kappa_p\kappa_s\frac{\cot(\kappa_s d_s/2)}{\tan(\kappa_s d_s/2)}=0. \quad (4)$$

Equations (4) are formally identical to the conventional smooth-surface symmetrical (upper terms) and antisymmetrical (lower terms) Lamb wave dispersion relations, but with complex thickness parameters. As expected, if the rms roughness parameter h vanishes, we recover the ordinary Lamb wave equations. The complex thicknesses are given by

$$d_p=d+2i\kappa_p h^2, \quad d_s=d+2i\kappa_s h^2. \quad (5)$$

By way of example, the simple dispersion relation in Eqs. (4) allows us to estimate quickly the damping of a 100-kHz S_0 Lamb wave mode propagating in 0.5-in thick steel plate having a rms roughness of 200 μm. We easily obtain a value of 5.4 dB/100 m, and a value of 82 dB/100 m for the same conditions, but at 150 kHz. Using Eqs. (4) this estimate required no more complication than that of solving the conventional Lamb wave equation. The rapid increase in RS loss in this calculation illustrates not only the $\exp[f^2]$ damping dependence, but also the significant partial wave reconfiguration between these two frequencies. The large increase in transverse partial wave motion at 150 kHz accounts for the majority of the change in damping. In fact, this situation is similar to the case of fluid-loaded smooth plates, where the leaky component of the S_0 mode at low fd depends strongly on out-of-plane motion at the surface.

Despite the apparently gross nature of this approximation, we find in fact that it represents the more accurate approximation in Eq. (1) rather well in most regions of the wave dispersion. A comparison of the solutions of these two equations is shown in Fig. 1 for the A_4 mode. The real part of the solution is plotted as phase velocity in the upper frame for Eq. (1) (solid) and Eqs. (4) (dashed); the imaginary solution is plotted as normalized guided wave number ξ/k_s in the lower frame, each as a function of frequency f. If the sample had a smooth surface the imaginary solution would vanish altogether, in the absence of other material losses.

Several features of Fig. 1 deserve mention. First, the real solution is changed from the smooth-surface result almost not at all by the introduction of surface roughness, and the two approximations give essentially identical results for any roughness. In the lower frame the large increase in imaginary wave number at the mode cutoff near 4 MHz has a clearly intuitive explanation. As the mode approaches cutoff, both the partial wave vectors propagate nearly normal to the plate surface, implying many reflections per wavelength and leading to a large increase in surface-induced losses. As frequency increases, the imaginary solutions fall, increase, and decrease again towards zero at high frequency.

We explain the minimum in the solid curve near 6 MHz by noting that it occurs close to the compressional critical angle β_p. Near this branch point of the function in Eq. (1) conversion of compressional to shear wave energy is at a minimum, and therefore the lower attenuation of the compressional wave dominates at this point. After the critical angle the p wave eventually ceases to be a factor, and the s-wave damping increases as f^2. At even higher frequency, the s partial wave vector makes progressively larger angles with the plate normal as it approaches its critical value k_s, and the partial wave interaction with the rough surface is predicted to decrease. The dashed approximation is less accurate as either critical angle is approached. At the p-wave critical angle (near 6 MHz) the decrease predicted in the solid curve is entirely absent, owing to a lack of detailed cancellation of terms in Eqs. (4). This situation occurs again past 12 MHz for the s-wave component, as it approaches its critical angle. In the regions where the partial-wave dynamics dominate the losses, however, the solution of Eqs. (4) is quite accurate. In fact, as we shall see below and again in Part II of this work, the prediction of the solid curve near 6 MHz is neither physically reasonable nor in agreement with experimental results.

The vanishing of roughness-induced damping at large internal angles is not entirely realistic, although both the PSA and the guided mode decomposition into partial waves lead to this conclusion. The model assumptions imply that the partial waves contribute to the surface-induced losses only to the extent that their ray paths bring them into contact with the rough surface. If this behavior does not occur, as in the case of the evanescent compressional wave, or occurs only rarely, as for the shear wave near the Lamb mode limiting velocity, then the model predicts a strong reduction of rough-surface damping. It is well known that the PSA is not valid near the critical angles, where the partial waves strike the plate surfaces at grazing incidence.[16,17] Moreover, it is also just at this point where the partial wave intersections with the surface occur least frequently. One consolation is that operation near the limiting values of κ_p or κ_s is seldom useful for materials inspection with plate waves because of

the simultaneous reduction in wave coupling to a contacting ideal fluid.

Among the limitations of the phase-screen model are its independence of the correlation length L and its assumption of a random roughness distribution. Our calculation further assumes the random roughness distribution is Gaussian. While the incoherently reflected signal can also be predicted by the PSA model, it is mostly applied to model only the coherent component. Yet, for our purposes reliance on this model still makes good sense and may explain why relatively little work on rough elastic waveguides exists in the literature. For ultrasonic NDE measurements the usual transmitter or receiver is a baffled piston radiator several wavelengths or more in diameter. The directivity and phase sensitivity afforded by the finite transducer radius and its uniform piezoelectric vibrational mode may be added to the wave number/frequency selectivity of the guided wave modes themselves. Together, these effects strongly militate against a latent sensitivity, under almost any conditions, to the incoherent component of the scattered field. Therefore, we may confidently ignore the incoherent field in favor of the one typically modeled in the PSA, the coherent field. This is a great advantage and significantly simplifies the modeling.

B. Generalized scattering coefficients for RS plates

To apply our model, based on the PSA, to immersion reflection measurements it is essential to have a generalized model of plane wave interaction with RS plates. Considering our experimental samples and the kinds of measurements we have made, the expression in Eq. (1) will only be useful if recast into the form of scattering (reflection and transmission) coefficients. With samples having roughness on one side only, a different dispersion relation is needed, and the collateral reflection coefficient must differentiate between the RS facing toward the transducers and facing away from them. The difference in the immersion measurements is substantial. The reflected wave amplitude consists of two rather distinct contributions. One comes from the wave reflected at the upper plate surface, essentially a specular reflection, and the other is the leaky guided wave that suffers reradiation as it propagates. Both components will be affected by the roughness, but each in a different way.

The specular signal reflected back into the fluid medium where the wavelength is small (owing to the low fluid compressional wavespeed), is substantially reduced by interaction with the rough surface, whereas the guided wave interacts in the way described earlier. One additional complication is that for the RS facing upward, the guided wave must reradiate through this surface, additionally complicating the signal. With the RS on the lower surface (on the side opposite the incident wave), only the guided wave signal experiences the influence of the roughness.

To construct a plate reflection coefficient (RC) from the half-space RS reflection coefficients, we begin with an expression derived for the plate RC using joined half-space scattering coefficients,[28]

$$R = R_h + \frac{T_p(\tau_{pf}(1-\tau_{ss})+\tau_{sf}\tau_{ps}) + T_s(\tau_{sf}(1-\tau_{pp})+\tau_{pf}\tau_{sp})}{(1-\tau_{pp})(1-\tau_{ss})-\tau_{ps}\tau_{sp}}, \tag{6}$$

where R_h and T_p and T_s are the joined half-space reflection and compressional and shear transmission coefficients for a fluid–solid interface (see the Appendix). We have used R and T here instead of Γ from the earlier section to distinguish between a half-space RC, where the material interfaces to a vacuum, and the joined half-space RC, where two acoustic media meet at a planar interface, in this case fluid and solid. The term in Eq. (6) $\tau_{\alpha\beta}$ refers to the following RC products,

$$\tau_{\alpha\beta} = R^{\mathrm{II}}_{\alpha p} R^{\mathrm{I}}_{p\alpha} + R^{\mathrm{II}}_{\alpha s} R^{\mathrm{I}}_{s\beta}, \tag{7}$$

with $\alpha=\{p,s\}$ and $\beta=\{f,p,s\}$ (f: fluid), as before; $R^{\mathrm{I,II}}_{\alpha\beta}$ are smooth-surface reflection and transmission coefficients on solid–fluid interfaces I and II (see the Appendix).

The six coefficients $\tau_{\alpha\beta}$ represent two successive reflections and transmissions of an incident plane wave of type α on interface II. Thus, after two further reflections from interfaces II and I, this wave again yields an incident plane wave of type β at interface II. In other words, these coefficients provide two possibilities for obtaining a wave of type α from a wave of type β, as illustrated in Fig. 2 of Ref. 28.

We also establish the terminology that $\hat{R}_h$ and $\hat{T}_{p,s}$ are the rough-surface equivalents in the phase-screen approximation to their counterparts in the absence of roughness, presented above. The explicit rough-surface dependence is given by

$$\begin{aligned}
&\hat{R}_h = R_h e^{-2h^2\kappa_f^2},\\
&\hat{T}_p = T_p e^{-h^2(\kappa_p-\kappa_f)^2/2}, \quad \hat{T}_s = T_s e^{-h^2(\kappa_s-\kappa_f)^2/2},\\
&\hat{R}^{\mathrm{I,II}}_{\alpha\beta} = R^{\mathrm{I,II}}_{\alpha\beta} e^{-h^2(\kappa_\alpha+\kappa_\beta)^2/2}, \quad \text{if } \beta \neq f,\\
&\hat{R}^{\mathrm{I,II}}_{\alpha f} = R^{\mathrm{I,II}}_{\alpha f} e^{-h^2(\kappa_\alpha-\kappa_f)^2/2}.
\end{aligned} \tag{8}$$

To accommodate the rough upper or rough lower fluid-loaded plate surfaces independently, the appropriate RS reflection $\hat{R}$ and transmission $\hat{T}$ coefficients are inserted in Eqs. (6) and (7) in place of their smooth-surface counterparts.

The denominator in Eq. (6), $(1-\tau_{pp})(1-\tau_{ss})-\tau_{ps}\tau_{sp}$ forms the characteristic equation of the fluid-loaded rough plate, where one or both surfaces may be rough or fluid-loaded. Further, if we were to assume the approximation leading to Eqs. (4) above, an equivalent simplified dispersion equation for the doubly rough plate could also be derived. The advantage of the denominator in Eq. (6) is that it is completely general and can accommodate roughness or fluid-loading on either or both plate surfaces.

II. NUMERICAL RESULTS

The most direct way to see the effect of rough guiding surfaces on the behavior of plate waves is to examine the reflection coefficient. This quantity contains all the material property information, including surface condition, pertaining

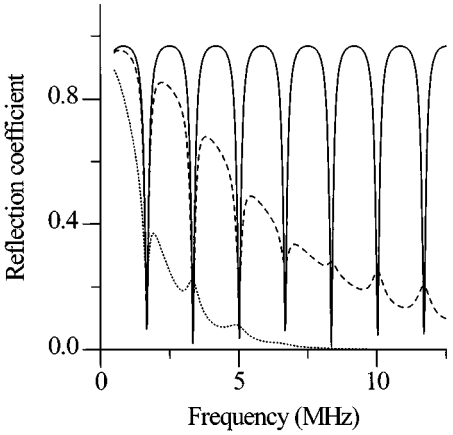

FIG. 2. Plane wave reflection coefficient magnitude for progressively increasing roughness on the upper plate surface (toward incident wave); rms roughness $h=0$ μm (solid curve), $h=30$ μm (dashed), and $h=100$ μm (dotted). Plate thickness is 1.37 mm and incident angle is 20°.

to the plate. The measured signal can, of course, differ sharply from the RC, owing to the effects of diffraction and experimental geometry. This critical point is the essence of the analysis presented in Ref. 29 and discussed further in Part II. For now, let us look at two reflection coefficients, one for roughness on the upper plate surface, Fig. 2, and the other for roughness on the lower surface, Fig. 3.

In Fig. 2 the effect of the roughness is very pronounced since both specular and reradiated components of the signal interact with it. For $h=30$ μm the RC magnitude has characteristic minima at low frequencies where propagating guided modes exist. These interfere coherently with the specular component and lead to RC minima. At higher frequencies the minima are less deep, and finally above 8 MHz they become small but growing peaks. Why is this? The roughness on the upper surface becomes a much stronger influence at high frequency, severely attenuating the specular wave (proportional to $\exp[-2\kappa_f^2 h^2]$, where $\kappa_f > \kappa_{p,s}$ is always satisfied), so that the additive influence of the resonant guided wave is now seen as an *increase* in reflected energy.

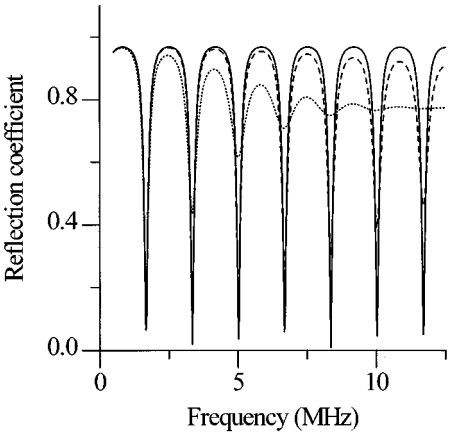

FIG. 3. Plane wave reflection coefficient magnitude for progressively increasing roughness on the lower plate surface (opposite incident wave); rms roughness $h=0$ μm (solid curve), $h=30$ μm (dashed), and $h=100$ μm (dotted). Plate thickness is 1.37 mm and incident angle is 20°.

At $h=100$ μm this behavior is very well developed, and only a single minimum near 2 MHz can be discerned. Beyond 7 MHz, the damping of the plate resonances and dephasing of the specular signal are so strong that virtually no energy at all is reflected.

Very different behavior is seen for roughness on the bottom surface in Fig. 3; the $h=0$ μm curve is repeated for comparison. At $h=30$ μm both the depth of the minima and the intervening maxima are reduced as the frequency grows. With roughness on the lower surface, only the reradiated guided wave can feel its influence. So, the roughness acts in this case only to broaden the plate acoustic resonances. The natural effect of this resonance broadening will be the imperfect phase cancellation and reinforcement of the unaffected specular signal at the minima and maxima, respectively. This effect explains why the resonance minima are progressively less deep and why the maxima no longer reach all the way to unity. Eventually, for $h=100$ μm, the roughness spoils the quality factor or ''Q'' of the acoustic resonances so badly that above 8 MHz only the constant specular component remains. The rest of the acoustic energy is dissipated (dephased in the PSA) in one or two interactions with the lower (rough) plate surface.

This last plot, especially, illustrates the importance of examining guided wave behavior to elucidate roughness on hidden surfaces. When the roughness is exposed, as in Fig. 2, its effect on the ultrasonic signal is strong and obvious, as found by Nagy and Rose.[16] But, practically speaking, roughness in this case can be detected by visual examination. When, however, the roughness is hidden, as in Fig. 3, straightforward ultrasonic reflection measurements, exemplified by the RC behavior, are hardly sufficient to detect any but the grossest roughness ($h=100$ μm). Even then, the average difference between the smooth and rough surface is only about 20% in the absolute RC magnitude, hardly an unequivocal indicator of roughness. By contrast, the guided waves demonstrate a *much* larger effect from the roughness, as we will see below. This happens because the guided mode partial waves interact many times with the surface as they propagate, giving them a greater sensitivity to roughness in plate-like structures than virtually any other ultrasonic wave type.

A different way of looking at these calculated reflection coefficients is seen in Figs. 4 and 5. In Fig. 4 the reflection coefficient for roughness on only the *lower* plate surface, opposite the incident wave, is shown as a function of angle at 8 MHz instead of frequency for three different rms roughnesses, $h=0$, 30, 100 μm. Recalling the behavior of the guided mode shown in Fig. 1, the greatest losses occur near 15°, where the curves have the shallowest minima and the lowest maxima. As the angle increases toward the shear critical angle of 28.6°, the RS damping contribution vanishes. Past 29° there is no predicted RS effect. This plot illustrates most clearly, perhaps, the one unrealistic aspect of the PSA-based guided wave RS model: Damping ceases when the wave becomes evanescent. For guided plate waves, this may not be too serious, since the shear partial wave remains and contributes to wave losses past the compressional critical angle. And as we pointed out earlier, Lamb waves are sel-

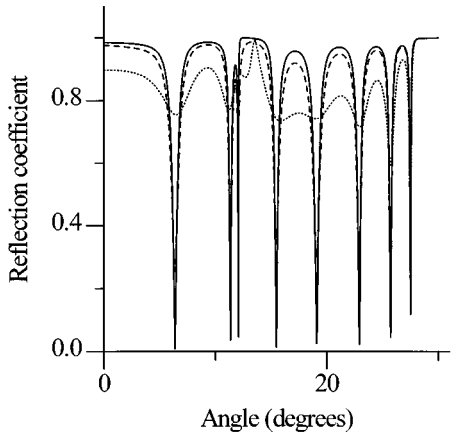

FIG. 4. Plane wave reflection coefficient magnitude for progressively increasing roughness on the lower plate surface (opposite incident wave); rms roughness $h=0$ μm (solid curve), $h=30$ μm (dashed), and $h=100$ μm (dotted). Plate thickness is 1.37 mm and fixed frequency is 8 MHz.

dom used near the shear limiting wavespeed, because all modes pile up at this accumulation velocity, and distinguishing among them can be difficult. The problem comes in consideration of the A_0 mode, whose entire dispersion branch lies in the region where both partial waves are evanescent. This proviso pertains also to Rayleigh surface waves, whose partial waves are both evanescent.

The corresponding plot for the rough surface on the same side as the incident plane wave is shown in Fig. 5 for rms roughnesses $h=0$, 15, 30 μm. The upper rough surface dephases the specular wave, and the roughness effect is much more pronounced for much smaller rms values. These data further amplify the importance and utility of guided wave measurements to elucidate roughness parameters in plate-like structures. The frequency is again 8 MHz. The reduction in the specular reflection is strong enough at $h=30$ μm that the guided wave resonances again appear as peaks in the calculated RC. With upper surface roughness the RS contribution does not vanish past the internal shear critical angle. As the incident angle increases, however, the magnitude of the RC does approach unity.

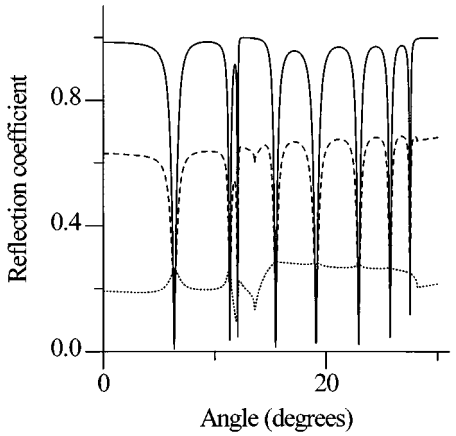

FIG. 5. Plane wave reflection coefficient magnitude for progressively increasing roughness on the upper plate surface (toward incident wave); rms roughness $h=0$ μm (solid curve), $h=15$ μm (dashed), and $h=30$ μm (dotted). Plate thickness is 1.37 mm and fixed frequency is 8 MHz.

III. SUMMARY AND CONCLUSIONS

In this article we have developed a simple, easily calculated model of rough surface guided wave dispersion and reflection showing many of the important features of the damping effects of rough guiding surfaces. The model incorporates the straightforward, yet powerful, phase-screen approximation by suitable modifications to the partial wave reflections at each guiding surface. A simple approximate characteristic equation is derived that is formally identical to the conventional Lamb wave dispersion relation. An extension of these ideas to fluid-loaded plates is accomplished by application of a reflection series expression. Our result isolates individual halfspace scattering coefficients, enabling us to treat one-sided roughness and roughness in the presence of one- or two-sided fluid-loading using the same partial wave approach.

In Part II these concepts are examined experimentally to study the limits of applicability of the model and areas in which it might be improved.

ACKNOWLEDGMENTS

This work was supported by the Aerospace Sciences Directorate, Air Force Office of Scientific Research under Grant F49620-95-1-0294. We would like to acknowledge helpful discussions with J. H. Rose of Iowa State University.

APPENDIX: REFLECTION COEFFICIENT FOR A SOLID-LIQUID INTERFACE

The reflection and transmission coefficients $R_{\alpha\beta}^{(\mathrm{I,II})}$ (α is an incident wave and β is a reflected or transmitted wave) for the solid–fluid interfaces I and II are[27]

$$R_{pf}^{\mathrm{I,II}}(\xi)=\frac{2\kappa_p k_s^2(k_s^2-2\xi^2)}{\kappa_f D}e^{i\varphi_p},$$

$$R_{ps}^{\mathrm{I,II}}(\xi)=-\frac{4\xi\kappa_p(k_s^2-2\xi^2)}{D}e^{i(\varphi_p+\varphi_s)},$$

$$R_{pp}^{\mathrm{I,II}}(\xi)=\frac{-(k_s^2-2\xi^2)^2+4\xi^2\kappa_p\kappa_s+Y}{D}e^{2i\varphi_p},$$

$$R_{sf}^{\mathrm{I,II}}(\xi)=\frac{4\xi\kappa_p\kappa_s k_s^2}{\kappa_f D}e^{i\varphi_s},$$

$$R_{sp}^{\mathrm{I,II}}(\xi)=-\frac{4\xi\kappa_s(k_s^2-2\xi^2)}{D}e^{i(\varphi_p+\varphi_s)},$$

$$R_{ss}^{\mathrm{I,II}}(\xi)=\frac{(k_s^2-2\xi^2)^2-4\xi^2\kappa_p\kappa_s+Y}{D}e^{2i\varphi_s},$$

$$R_h(\xi)=\frac{(k_s^2-2\xi^2)^2+4\xi^2\kappa_p\kappa_s-Y}{D},$$

$$T_p(\xi)=\frac{2\rho k_s^2(k_s^2-2\xi^2)}{D}e^{i\varphi_p},\quad T_s(\xi)=\frac{4\xi k_s^2\kappa_p}{D}e^{i\varphi_s}.$$

Here,

$$D=(k_s^2-2\xi^2)^2+4\xi^2\kappa_p\kappa_s+Y$$

is the denominator of each of the RC expressions above, $\varphi_{p,s}=\kappa_{p,s}d/2$ are the compressional and shear wave propagators, and Y is the fluid term given by

$$Y=\left(\frac{\rho_f}{\rho}\right)\frac{k_s^4\kappa_p}{\kappa_f},$$

where κ_f is the x_3 wave vector projection in the fluid, and ρ_f and ρ are the fluid and solid material densities.

[1] F. G. Bass and I. M. Fuks, *Wave Scattering from Statistically Rough Surfaces* (Pergamon, Oxford, 1979).
[2] J. A. Ogilvy, *Theory of Wave Scattering from Random Rough Surfaces* (Adam Hilger, London, 1991).
[3] A. G. Voronovich, *Wave Scattering from Rough Surfaces* (Springer-Verlag, Berlin, 1994).
[4] D. K. Dacol and D. H. Berman, ''Sound scattering from a randomly rough fluid-solid interface,'' J. Acoust. Soc. Am. **84**, 292–302 (1988).
[5] D. H. Berman, ''Effective reflection coefficients for the mean acoustic field between two rough interfaces,'' J. Acoust. Soc. Am. **96**, 417–426 (1994).
[6] F. M. Labianca and E. Y. Harper, ''Connection between various small waveheight solutions of the problem of scattering from the ocean surface,'' J. Acoust. Soc. Am. **62**, 1144–1157 (1977).
[7] W. A. Kuperman and H. Schmidt, ''Self-consistent perturbation approach to rough surface scattering in stratified elastic media,'' J. Acoust. Soc. Am. **86**, 1511–1522 (1989).
[8] H. Schmidt and W. A. Kuperman, ''Spectral representations of rough interface reverberation in stratified ocean waveguides,'' J. Acoust. Soc. Am. **97**, 2199–2209 (1995).
[9] J. T. Fokkema, ''Reflection and transmission of elastic waves by the spatially periodic interface between two solids (numerical results for the sinusoidal interface),'' Wave Motion **3**, 33–48 (1981).
[10] A. Lakhtakia, V. K. Varadan, and V. V. Varadan, ''Scalar scattering characteristics of a periodic, impenetrable surface: Effect of surface modeling errors,'' J. Appl. Phys. **60**, 4090–4094 (1986).
[11] A. El-Bahrawy, '''Guided modes in a layered elastic half-space with doubly corrugated surfaces,'' J. Acoust. Soc. Am. **96**, 3155–3166 (1994).
[12] J. D. Sheard and M. Spivak, ''Wave scattering in a rough elastic layer adjoining a fluid half-space,'' J. Acoust. Soc. Am. **97**, 72–83 (1995).
[13] C. Eckhart, ''The scattering of sound from the sea surface,'' J. Acoust. Soc. Am. **25**, 566–570 (1953).
[14] J. A. Ogilvy, ''Theoretical comparison of ultrasonic signal amplitudes from smooth and rough defects,'' NDT Intern. **19**, 371–385 (1986).
[15] P. B. Nagy and L. Adler, ''Surface roughness induced attenuation of reflected and transmitted ultrasonic waves,'' J. Acoust. Soc. Am. **82**, 193–197 (1987).
[16] P. B. Nagy and J. H. Rose, ''Surface roughness and the ultrasonic detection of subsurface scatterers,'' J. Appl. Phys. **73**, 566–580 (1993).
[17] D. K. Dacol, ''The Kirchhoff approximation for acoustic scattering from a rough fluid-elastic solid interface,'' J. Acoust. Soc. Am. **88**, 978–983 (1990).
[18] P. P. Goswami, T. J. Rudolphi, F. J. Rizzo, and D. J. Shippy, ''A boundary element method for acoustic-elastic interaction with applications in ultrasonic NDE,'' J. Nondestruct. Eval. **9**, 101–112 (1990).
[19] J. H. Rose, M. Bilgen, and P. B. Nagy, ''Acoustic double-reflection and transmission at a rough water-solid interface,'' J. Acoust. Soc. Am. **95**, 3242–3251 (1994).
[20] M. DeBilly and G. Quentin, ''Backscattering of acoustic waves by randomly rough surfaces of elastic solids immersed in water,'' J. Acoust. Soc. Am. **72**, 591–601 (1982).
[21] S. L. Broschat, E. I. Thorsos, and A. Ishimaru, ''The phase perturbation technique vs. an exact numerical method for random rough surface scattering,'' J. Electromag. Waves Appl. **3**, 237–256 (1989).
[22] E. I. Thorsos, ''The validity of the Kirchhoff approximation for rough surface scattering using Gaussian roughness spectrum,'' J. Acoust. Soc. Am. **83**, 78–92 (1988).
[23] E. I. Thorsos and D. R. Jackson, ''The validity of the perturbation approximation for rough surface scattering using a Gaussian roughness spectrum,'' J. Acoust. Soc. Am. **86**, 261–277 (1989).
[24] Y. A. Kravtsov and A. I. Saichev, ''Effects of double passage of waves in randomly inhomogeneous media,'' Sov. Phys. Usp. **25**, 494–508 (1982).
[25] E. Jakeman, ''Enhanced backscattering through a deep random phase screen,'' J. Opt. Soc. Am. A **5**, 1638–1548 (1988).
[26] O. I. Lobkis and D. E. Chimenti, ''Elastic guided waves in plates with rough surfaces,'' Appl. Phys. Lett. **69**, 3486–3488 (1996).
[27] B. A. Auld, *Acoustic Waves and Fields in Solids* (Krieger, Malabar, FL, 1990), 2nd ed.
[28] M. Deschamps and C.-W. Cao, ''Reflection /refraction of a solid layer by Debye's series expansion,'' Ultrasonics **29**, 288–296 (1991).
[29] O. I. Lobkis, A. Safaeinili, and D. E. Chimenti, ''Precision ultrasonic reflection studies in fluid-coupled plates,'' J. Acoust. Soc. Am. **99**, 2727–2736 (1996).

Elastic guided waves in plates with surface roughness. II. Experiments

O. I. Lobkis
Center for Nondestructive Evaluation, Iowa State Univeristy, Ames, Iowa 50011-3020

D. E. Chimenti[a)]
Center for Nondestructive Evaluation and Aerospace Engineering and Enginnering Mechanics Department, Iowa State University, Ames, Iowa 50011-3020

(Received 3 February 1997; accepted for publication 26 March 1997)

In this artice are reported fundamental experimental measurements on guided waves in plates with surface roughness; the experimental data are critically compared to theoretical calculations presented in Part I. All experiments, in either immersion or contact coupling mode, are modeled by the theory developed in I that exploits the phase-screen approximation. In this theory the effect of the rough surface on the received signal, on a local scale, is assumed to be restricted to the signal phase. The comparisons between experiment and predictions show good agreement in most regimes, despite the rather simplifying approximations contained in the calculation. The model is shown to fail only when the guided wave vector is close to a branch point, that is when the guided wave phase velocity approaches the compressional or shear wavespeeds of the plate. Near these values the internal partial waves comprising the guided wave strike the surfaces at grazing incidence or are evanescent, and a simple phase-screen model cannot account for this behavior. Elsewhere in the guided wave spectrum, agreement is quite good. Of practical significance is the finding that the rough-surface damping contrast can be maximized by configuring the experimental conditions to measure just below and well above the compressional critical angle. Aluminum samples, prepared by indenting or sandblasting and independently profiled to determine rms roughness, are measured in immersion and in contact transduction, the latter with wedge couplers and line sources. The influence of the roughness in immersion experiments is strongly affected by whether the upper or lower plate surface is rough, but only in the interaction zone between specular and nonspecular reflection components. [S0001-4966(97)06007-9]

PACS numbers: 43.20.Mv, 43.20.Gp [ANN]

INTRODUCTION

From a practical standpoint, guided wave propagation in the presence of rough surfaces can be considered an effective model for several problems of interest in applied science. The progressive effect of pitting or pillowing corrosion is the roughening of corroded surfaces, which can be an excellent indication of incipient corrosion and the consequent reduction in structural integrity. Another case is the propagation of sound in layers of sea ice,[1] which generally have rough surfaces. A third might be related to materials processing of various films or protective layers.

In all these cases a guided wave propagating in a plate-like structure can be thought of in terms of its partial waves components that scatter repeatedly from the surfaces of the guiding medium. This surface scattering is clearly quite sensitive to the condition of the guiding surfaces. Thus, guided wave ultrasonics can provide a means to assess the roughness, whether exposed or hidden, in a layer. In this Part II we present extensive experimental data, all accompanied by detailed comparisons to the theory developed in Part I. We will find that the model calculations are surprisingly accurate, despite the rather gross approximations inherent in the phase-screen approximation.[2,3] Only when propagation occurs near a critical angle does the model substantially underestimate the effect of the roughness.

A review of the theoretical literature on this extensively researched topic is given in Part I. The interaction of waves at rough fluid–solid interfaces has also been studied experimentally. These studies have focused on the attenuation and in some cases enhancement of the scattered wave. Nagy and Adler[2] have presented results on the attenuation of the transmitted and reflected wave for rough surfaces. They considered a reflection/transmission problem for a water/aluminum interface. They found that the transmitted wave is much less attenuated than the reflected wave. Furthermore, they noticed that the reflection from the back surface of the plate is less attenuated than the front-wall reflection. This phenomenon is due to higher velocity in aluminum. This observation raises an important issue since this fact may suggest that for the plate application, one can reduce the effect of surface roughness conditions by exciting the wave on a smooth part of the surface. Once the wave is in the faster medium it is not affected as severely by the roughness, compared with a case where the wave is excited through a slower couplant on the rough surface (RS).

Recently, Nagy and Rose[4] have examined the problem of detection of flaws located under a rough surface. They found that rough surfaces can cause serious degradation in the flaw signal-to-noise ratio, to the point where flaw detec-

[a)]Electronic mail: chimenti@iastate.edu

tion is problematic. Bilgen and Rose[5] have studied the effects of focusing and flaw location in detection of flaws located under the rough surface. The influence of other parameters is well known;[1–7] these include the dependence of the transmission and reflection coefficients on the incident angle, and on the roughness characteristics, such as correlation length and rms height.

We begin with an exposition of the experimental procedure, including sample preparation and independent roughness determination. Then, we present results of immersion measurements in which several significant experimental parameters are varied over the full range available in the measurements. We also report contact measurements in which the experiments are performed both with shoe-type coupling wedges and with more reliable line source wedges. Each series of measurements is compared to calculations and interpreted. A preliminary and highly abbreviated version of this work appears elsewhere.[8]

I. EXPERIMENTAL TECHNIQUE

Many experiments have been performed in this work to elucidate the rough-surface damping phenomena in plates and to examine the potential of the analysis to make accurate predictions of guided wave propagation for potential usage in deducing roughness from ultrasonic measurements. We show here processed spectra and coordinate scans, where the frequency dependent transducer characteristics and effects of diffraction have been removed. Data are collected as either video-detected tone burst amplitudes or full time-domain sampled tone bursts. Only at the highest frequency and the largest transducer offset is the signal-to-noise ratio ever less than 20 dB.

A. Measurement procedure

Broadband piezoelectric piston transducers are excited with tone burst rf signals 50 μs in length, with or without power amplification. The acoustic wave generated in this way interacts with the plate and is reradiated into the fluid, where it is detected by a second, nominally identical device. This detected signal is amplified and either envelope-detected by an rf receiver or captured on a digital oscilloscope for analysis. The time-domain signal is Fourier transformed numerically in order to isolate a particular frequency component from the narrow, but finite bandwidth burst. This operation is nominally equivalent to video envelope detection of the burst followed by boxcar integration and dc sampling. The transform method, although more time-consuming, results in a cleaner signal, less influenced by out-of-band energy. But, the two methods have been shown to yield essentially equivalent results. Using one of these two methods, both the frequency and the spatial dependence of the received voltage are measured in separate experiments.

Two fundamentally different kinds of measurements have been made in this work. One kind is done in contact mode, either with polystyrene wedges or with knife-edge (line-source) couplers; the other is done in immersion. In the immersion testing, transducers (9.5 mm diameter) are aligned by observing the amplitude of signals reflected from sample surfaces and by precise mechanical measurements of

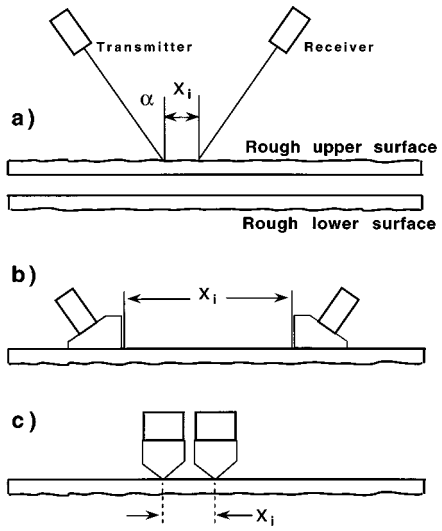

FIG. 1. Schematic diagram of contact and immersion experiments showing the deployment of the transducers and the parameters varied.

transducer spatial relationships. Incident angles are accurately selected ($<0.01°$) using optical rotation stages. We perform measurements with the mechanical scanner and all instruments operating under computer control. In contact mode, transducers (12.5 mm diameter) are aligned using signal amplitude, and a miniature precision scan apparatus is used to make transducer position adjustments at the 10-μm scale level. While every effort is made to suppress the disturbing effect of variable contact efficiency, the plate fabrication methods left some surfaces not quite flat, further complicating the measurements. For these reasons, many averages are made to lessen the influence of variable contact. Contact force, couplant thickness, and other geometrical parameters are controlled as far as possible. However, some variability remains. Data acquisition is rapid and precise, even allowing for some averaging of the digitized signal, in order to minimize the effects of gain variation, temperature fluctuations, or instrument drift.

In the immersion measurements the samples are oriented with their rough surfaces either toward or away from the transducers. Generally speaking, averages of several measurements made at different positions are used to obtain as representative a sampling of the surface roughness as possible. A schematic diagram of the immersion experimental setup is shown in Fig. 1(a), the shoe-contact measurement geometry is illustrated in Fig. 1(b), and the knife-edge schematic is shown in Fig. 1(c).

B. Sample preparation

Samples for this study have been fabricated in one of two ways. The phase-screen approximation can model surface roughness as a random distribution of surface height with a well defined mean and variance. For our investigation we seek samples with a nearly Gaussian distribution of roughness. This goal can be accomplished either with a chaotic bombardment of small abrasive particles, such as sandblasting, or with pseudorandom indentation, where careful deterministic calculations are performed to construct an ap-

proximately Gaussian random surface roughness. All samples are fabricated from 2024 aluminum (physical properties: $V_p = 6.37$ km/s, $V_s = 3.13$ km/s, $\rho = 2720$ kg/m^3). These samples have been selected from a series of 9-mm thick plates used in a previous study.[4] They have been independently characterized by acoustic profilometry.[9] From the set of nine samples we have selected a smooth plate, a mid-size roughness, and a high-roughness plate for use in the current study. While no independent measurements of the correlation length L have been made on our specimens, acoustic scattering studies on other samples in the same set[6] indicate a correlation length of between 500 μm and 1000 μm, which is typical of rough surfaces made in this manner. For our work the only significant aspect of L is that it is much larger than the rms roughness h.

To render these thick plates (effectively halfspaces) useful for our purposes, each sandblasted sample has been milled from the back surface, opposite the roughness, until a desired smaller thickness is attained. Then, to relieve any residual stresses that might warp the plates, each plate (2.3 or 1.4 mm) is annealed at 500 °F under static pressure and slowly cooled to room temperature. After this treatment, the flatness of the plates is tested on a reference surface. In most cases no residual warping can be detected.

II. RESULTS AND DISCUSSION

In this section we present data and calculations on the three types of measurements performed in this study: immersion, contact, and knife-edge. Because of the coupling variability in the contact measurements most of the critical comparisons between experiment and prediction and most of the exploration of rough-surface phenomenology has centered on experimental investigations using reliable immersion coupling methods. In most cases we show superimposed results, experiment and theory, to illustrate the effect of rough surfaces on guided waves in plates and how this effect can change with different wave propagation conditions. Accompanying each plot of experimental data is a corresponding prediction of the approximate model discussed above. As we will see, in most cases the RS model predicts the experimental behavior very well, both the character of the phenomena and its quantitative expression.

A. Immersion experiments

For the immersion measurements, one additional element must be added to the results of Part I and Eqs. (5) through (8) therein. This is the transducer voltage calculation mentioned earlier.[10] The result of that prior analysis, including three-dimensional transducer effects of both transmitter and receiver and realistic beam directivity functions, is

$$V(x_i,f) = \frac{ik_f}{4\pi^2}\int_0^{2\pi} d\phi \int_0^{\pi/2-i\infty} \hat{R}(\theta,f) D_T(\theta,\phi) \times D_R(\theta,\phi)\sin\theta\, d\theta, \tag{1}$$

where $D_R(\theta,\phi)$ and $D_T(\theta,\phi)$ are the receiver and transmitter directivity functions, respectively, and contain the dependence on x_i, the relative transducer position shown in Fig. 1. Here, k_f is the incident wave number in the fluid, f is the frequency, $\hat{R}(\theta,f)$ is the reflection coefficient for a RS plate [see Eq. (6) of Part I], and θ and ϕ are the polar and azimuthal angles. For simplicity we have omitted the explicit dependence of the transducers on frequency and several other constant prefactors before the integrals in Eq. (1). The integral is expressed in terms of angles instead of wave numbers to emphasize the 3-D nature of the calculation. A major result of our earlier work[10] is that the voltage is quite insensitive to the exact form of the directivity functions D_T and D_R, as long as only the *product* $D_T D_R$ appears in Eq. (1), and that Gaussian beams model the experiment fully as well as Bessel functions, which are more appropriate for baffled piston radiators.

Substituting Gaussian beams for the directivity functions D_T and D_R of the transducers yields an expression which can be integrated numerically to give the receiver voltage for any experimental conditions. Alternatively, the integral in Eq. (1) can be reduced analytically by uniform asymptotics[11,10] to yield an expression containing the pole and zero of the reflection coefficient as the only intrinsic plate parameters. If we restrict incidence to the phase matching angle only, we can write

$$V(x_i,f) \approx \mathscr{K}\{\exp[i\Phi_S - (x_i/x_\ell)^2] - \sqrt{\pi\kappa_f\rho/2}(\theta''_{\mathscr{P}} - \theta''_{\mathscr{Z}}) \times \exp[i\Phi_L - k_f\theta''_{\mathscr{P}}x_i]\}, \tag{2}$$

where the multiplicative term $\mathscr{K}$ contains geometrical constants and the transducer frequency dependence, Φ_S and Φ_L, are the phases of the specular and leaky components, x_ℓ is the beam localization parameter (equal to the beam projection on the plate surface), and ρ is the total distance between the transducer centers.[10] The complex guided wave pole $\theta_{\mathscr{P}}$ is given by $\theta_{\mathscr{P}} = \theta'_{\mathscr{P}} + i\theta''_{\mathscr{P}}$, and $\theta_{\mathscr{Z}} = \theta'_{\mathscr{Z}} + i\theta''_{\mathscr{Z}}$ is the corresponding zero, so that the resonance form of the reflection coefficient near a mode is $\hat{R}(\theta) = (\theta - \theta_{\mathscr{Z}})/(\theta - \theta_{\mathscr{P}})$.[12] Equation (2) represents the voltage intuitively as the sum of two contributions, the specular term and the leaky wave term. For the phase matching conditions the real parts of the pole and zero are nearly equal $\theta'_{\mathscr{P}} \approx \theta'_{\mathscr{Z}} = \alpha$, where α is the transducer incidence angle, as shown in Fig. 1.

In the case of a smooth plate without material losses $\theta''_{\mathscr{Z}} \approx 0$, and $k_f\theta''_{\mathscr{P}}$ is the damping constant for reradiation of guided wave energy into the surrounding fluid. For a rough plate both $\theta''_{\mathscr{Z}}$ and $\theta''_{\mathscr{P}}$ increase with increasing roughness, but at different rates, to produce additional guided wave attenuation through scattering at the rough plate surfaces, as seen in the amplitude factor of the second term in Eq. (2). At the same time, the real parts of the pole and zero change proportionately almost not at all with variations in h, the rms roughness height.

In order to isolate the effects of roughness and provide the basis of a reliable inspection method, it is essential to eliminate all geometric influences on the signal, such as those arising from diffraction and transducer placement. Equations (1) and (2) allow us to do this, and all subsequent immersion results have been calculated by incorporating the RS reflection coefficient into the above integral expression, or into its asymptotic analytical form.

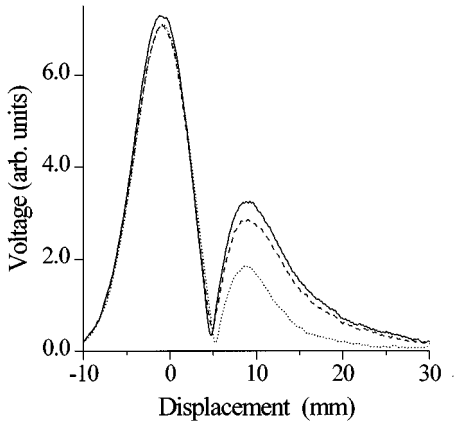

FIG. 2. Experimental dependence of receiver voltage on displacement x_i for smooth (solid) and *lower* rough plate surfaces with $h=13$ μm (dashed) and $h=26$ μm (dotted); incident angle is 20° for the S_5 mode at 11 MHz.

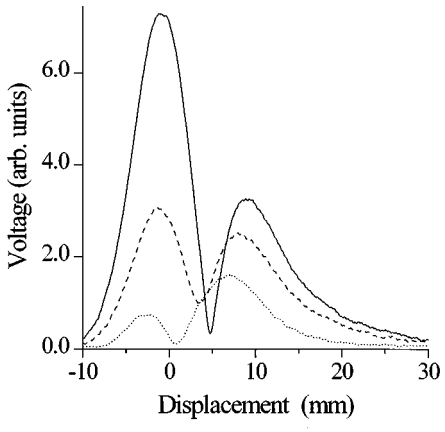

FIG. 3. Experimental dependence of receiver voltage for the same conditions as in Fig. 2, but for *upper* rough plate surface.

In preparation for the spectral plots presented below, we first examine the coordinate-dependent behavior of the receiving transducer voltage when the incident beam interacts with roughness on first the lower and then the upper plate surfaces. These experimental results portray the same behavior as the spectral data, but from a different standpoint. Figure 2 shows a coordinate scan for the S_5 Lamb wave mode with *lower* surface roughness at a 20° incident angle and at a fixed frequency of 11 MHz. The influence of the rough surface is at once apparent in the progressive reduction of the nonspecular peak ($x_i>5$ mm) following the large specular reflection, in which there is no roughness information. To put the results on a more concrete footing, the values of the wave number roughness product kh for the fluid, solid compressional, and solid shear waves are $k_fh=0.6$, $k_ph=0.15$, and $k_sh=0.3$, respectively for the 13-μm plate. Inside the plate, the internal angles dictate very different values of κh, and these values control the RS damping of the guided wave. The sharp decline in receiver amplitude in Fig. 2 at $x_i=5$ mm is the result of phase cancellation of the remnant specular reflection and the developing leaky guided wave. The guided wave dominates thereafter, and the decreasing amplitude in the dashed (13 μm) and dotted curves (26 μm) shows the damping effect of progressive roughness.

Under the same experimental conditions, but with roughness on the *upper* surface, the data have a very different appearance. The solid curve in Fig. 3 for the smooth plate is identical, but for 13-μm and 26-μm plates the specular reflection has decreased substantially, as expected, and the minima have consequently shifted to the left. With upper surface roughness the specular amplitudes are much more strongly affected by the roughness than in Fig. 2. Away from the specular beam ($x_i>8$ mm) the decaying leaky wave fields are almost identical between Figs. 2 and 3. The only small difference arises from the fact that with upper surface roughness the guided wave must leak through the rough surface.

We continue with a series of plots for which the roughness is on the *lower* plate surface only to emphasize the effect of the roughness on the guided wave. Ultrasonic scattering from the interface of a rough half-space has been extensively studied.[2,4–6] As we showed in Part I, our model works best well away from critical angles where partial waves make grazing incidence on the plate surfaces. In the following plots we therefore investigate the performance of the model under three different conditions: well below the compressional critical angle β_p, near β_p, and well above β_p. In Fig. 4 with an incident angle of 20° and a transducer separation of $x_i=0$ (see Fig. 1), we are beyond the compressional critical angle, and only shear partial waves are propagating in the plate. For this circumstance, we expect our model to function quite well. With zero transducer separation, on the other hand, there should be little RS contribution to the attenuation, in fact at any incident angle.

In this and each of the following cases, the upper frame shows the measurement (solid curve) and theoretical predic-

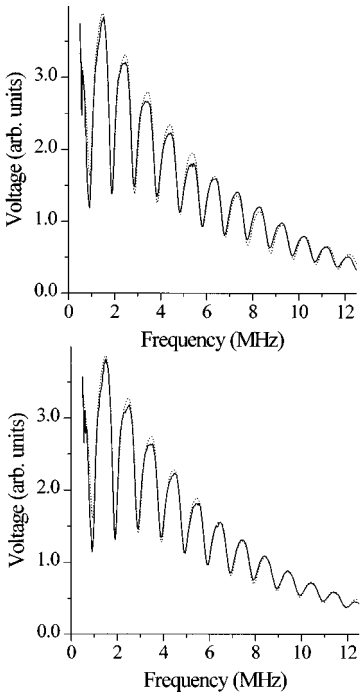

FIG. 4. Experimental (solid) and theoretical (dashed) frequency dependence of receiver voltage for smooth (upper frame) and lower rough (lower frame) plate surfaces with $h=26$ μm, $x_i=0$ mm, and incidence at 20°.

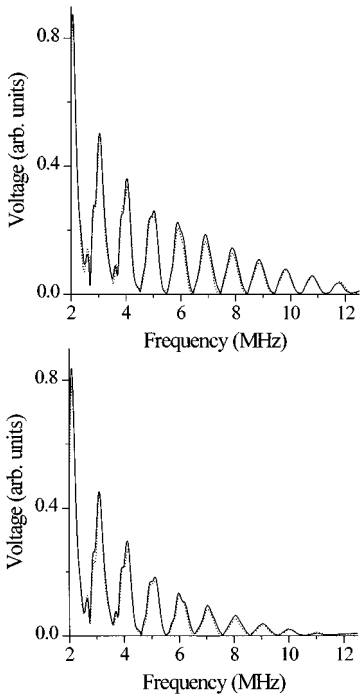

FIG. 5. Experimental (solid) and theoretical (dashed) frequency dependence of receiver voltage for smooth (upper frame) and lower rough (lower frame) plate surfaces with $h=26$ μm, $x_i=20$ mm, and incidence at 20°.

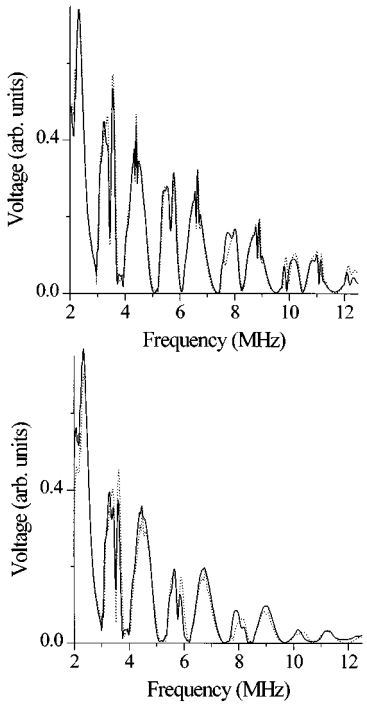

FIG. 6. Experimental (solid) and theoretical (dashed) frequency dependence of receiver voltage for smooth (upper frame) and lower rough (lower frame) plate surfaces with $h=26$ μm, $x_i=20$ mm, but for incidence at 10°.

tion (dashed curve) for a smooth plate (0-μm rms roughness) as a function of frequency from 2 to 12.5 MHz. The lower frame shows the corresponding rough-surface (26-μm rms roughness) data for the same experimental conditions. The regular oscillations in the signal mark the excitation of guided wave modes of varying order and symmetry in the plate. (These results may be compared with Figs. 2–5 of Part I.) Indeed, there is little difference between the two frames in Fig. 4, owing to the small effective signal path on the rough surface. This observation squares perfectly with the analysis presented in Part I in conjunction with the discussion on the reflection coefficient. Simple plate reflection measurements cannot probe subtle hidden-surface roughness with high sensitivity. The prediction is in good agreement with the data, both with and without roughness, confirming the accuracy of the receiver voltage model as expressed in Eq. (1). There are features to note in this and the following plots. First, there is a small difference ($\sim 2\%$) in plate thickness from the smooth to the 26-μm rms roughness plate. To eliminate any apparent difference in the experimental data, the results have all been scaled to a common value of plate thickness, equivalent to plotting the data versus fd. Second, to obtain a closer fit to the data, the theory curves have all been calculated for a rms roughness of 28 μm. This disparity is explained below.

A rather different situation is seen in Fig. 5, where the transducer separation $x_i=20$ mm is now sufficient to remove almost all directly reflected rays (except at the very lowest frequencies) from the received signal. Here, the peaks mark the guided wave excitations, and the effect of the roughness is pronounced. At low frequency there is almost no difference between the two frames, growing to about 8 dB difference at 8 MHz, and almost complete signal loss above 12 MHz. This strong frequency behavior is to be expected, since the losses are climbing as $\exp(f^2)$. Again, the agreement between prediction and measurement is quite good in both frames.

The character of the loss observed in the data at $\alpha=10°$ and $x_i=20$ mm demonstrates another aspect of the roughness. With both partial waves propagating and the internal shear partial wave vector close to the normal, the mode damping is larger and can depend on factors other than frequency, as seen in Fig. 6. For example, the pair of modes near 9 MHz has relatively little shear wave energy, and so is more weakly damped than the A_7 and S_7 modes near 8 MHz that are composed mostly of shear deformations. In fact, at this incident angle the behavior described above repeats for every two pairs of even- and odd-order modes of opposite symmetry.

The change in shape from Fig. 4 and the rapid variations near the peaks in Fig. 6 arise since at this incident angle there are several modes very close in frequency and contained in the spatial bandwidth of the transducers. Most of the unusual signal excursions in Fig. 6 are in fact predictable consequences of mode interaction and experimental geometry. These interacting modes give rise to interference effects that can be seen in the spectra, making this a useful test case for the model. Larger diameter transducers would reduce this effect by concentrating acoustic energy in a narrower range of angles about the transducer central ray. By contrast at 20° the modes are widely separated in frequency, and the influence of one mode on another is negligible. All these beam diffraction and mode coupling effects are well modeled by the prediction. As the incident beam and receiver are

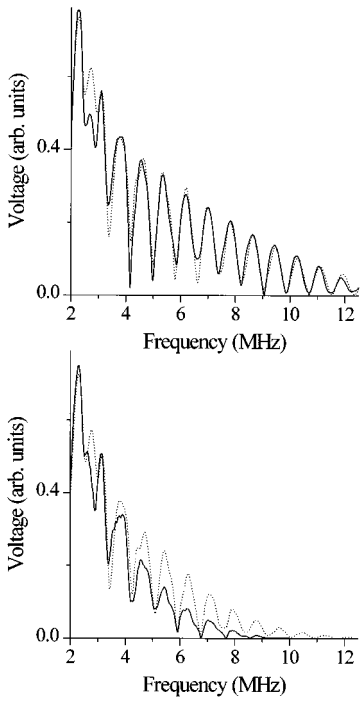

FIG. 7. Experimental (solid) and theoretical (dashed) frequency dependence of receiver voltage for smooth (upper frame) and lower rough (lower frame) plate surfaces with $h=26$ μm, $x_i=20$ mm, but incidence at 15°, near compressional critical angle.

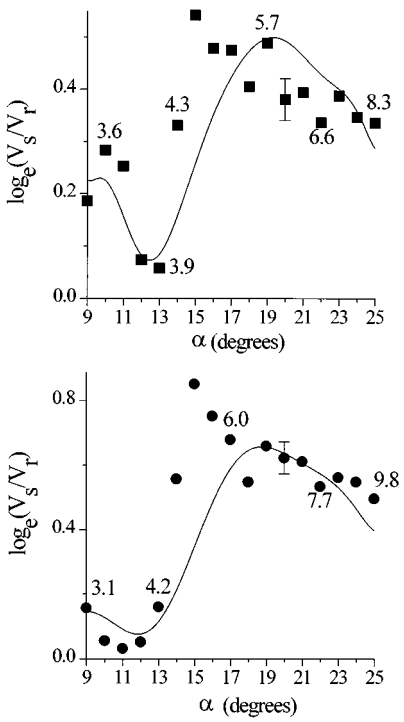

FIG. 8. Collected experimental (discrete points) and theoretical (solid curves) voltage ratio V_s for the smooth surface over V_r for the rough surface as a function of incident angle α. The plate has a lower rough surface, and the plot shows the A_3 Lamb mode (upper frame) and S_3 Lamb mode (lower frame) with $h=26$ μm and $x_i=20$ mm. The numbers attached to data points show the frequency in MHz at which the respective mode occurs at that angle.

separated and the frequency increases, the receiver intercepts less and less energy from the specular component. Consequently, the guided wave minima of Fig. 4 transform into maxima. The model calculation using 28-μm rms roughness is in very good detailed agreement with the data.

At incidence near the compressional and shear critical angles, grazing incidence behavior of the partial waves renders the model less accurate. This effect is amply illustrated by data in Fig. 7 taken at 15° for a transducer separation of $x_i=20$ mm. The smooth surface data in the upper frame are well modeled in the calculation, but the experimental curve lies well below the prediction for the RS plate in the lower frame. By 8 MHz the predicted peak is about three times as large as the measurement. Most of the various assumptions that motivate the model are not valid when the partial waves strike the plate surfaces at nearly 90° from the normal. Furthermore, since the transit path across the plate for grazing partial waves is long, the predicted RS loss vanishes at this point, leading to the substantial underestimate of the damping seen in Fig. 7. Past the critical angle the compressional evanescent partial wave is ignored, since it contributes little to the signal.

As mentioned above, in the calculations for the preceding plots there are no adjustable parameters, only the geometrical variables and the rms roughness height h. However, since the samples we are working with have been sectioned from a larger piece of material, we have found that the best comparison with the data is achieved by assuming a slightly different rms roughness ($h=28$ μm) for the coarser of the two specimens. We have made no further attempt to perfect the comparisons, and predictions reported here for the sand-blasted plates have been calculated with the 13-μm or 28-μm estimates. The reason for this variation in the coarser sample is likely genuine. In the schematic of Fig. 1 the only transducer rays that make a significant contribution to the voltage are those contained in the plane of incidence. Therefore, although the beam path is 9 mm or more wide, we sample only rays traveling parallel to the incident plane. This situation leads to a more restricted sampling than the acoustic microscopy[4] used to infer the rms roughness independently from our measurements. It is not too surprising, therefore, that we may observe fluctuations of 10% or so from the mean. It is our conjecture that such fluctuations account almost entirely for any differences between the model prediction and the experimental data shown in Figs. 4 through 7, as long as we are far from a critical angle.

In the upper frame of Fig. 8 are shown the collected data and predictions for the A_3 guided wave mode in the 26-μm plate as a function of angle. The experimental points are obtained from the spectra (such as Figs. 4 to 7) by estimating the voltage amplitude ratio for the smooth and rough surface at the frequency of the A_3 mode occurrence. A typical experimental uncertainty, consisting of run-to-run variation at different sample positions, is illustrated by the error bar. The electronic noise is very small and not a factor at all, except at the highest frequency. Any disparity between prediction and measurement is likely caused by systematic error, such as residual bowing of the plates. Since the dependence of RS damping on angle is dominated by the loss factor $-k_f\theta''_{\mathscr{S}}x_i$

in the second term of Eq. (2), we plot the log of the smooth-to-rough-surface ratio. The solid curve in Fig. 8 is the prediction of Eq. (2) for the same conditions. Considering the variability of the random rough surface and the nature of the approximations leading to Eq. (2), the agreement is actually quite good. From the compressional critical angle β_p to about 16°, however, we measure a much larger RS-induced loss than the model predicts, as noted above. This region is just the vicinity of $\beta_p(=13.7°)$. The large increase in damping just after β_p is a consequence of the strong p to s mode conversion, as predicted in Fig. 1 of Part I.

Excluding this behavior, which is beyond the simple model to treat, the theory is remarkably accurate. The observed drop in RS damping leading up to β_p, the large difference in damping between β_p and 18°, and the subsequent reduction toward the shear critical angle β_s are all well reproduced in the model calculation. The numbers recorded near some of the individual data points are the values of frequency in MHz at which measurements are made. A second example of this dependence for a symmetric mode is shown in the lower frame of Fig. 8 for the S_3 mode in the 26-μm plate. All other conditions are the same as in the upper frame. Again, the region from 9° to 13° is well described, as is the region above 16°. Only near β_p does the model seriously underestimate the roughness. But, these two plots also illustrate an important practical conclusion: If one can make RS measurements near 11°, then above 17°, the highest possible contrast will be achieved, possibly eliminating the need for a smooth-surface calibration. In general, experimental conditions can be chosen to satisfy these requirements. This result is a major conclusion of this work.

Further insight into the variation of RS guided wave damping as the propagation conditions change is seen in Fig. 9, where only the experimental results at $\alpha=13°$ for a smooth surface (solid) and lower rough surface (dashed) are shown. The complicated nature of the spectrum owes to the strong interaction of higher order modes within the spatial bandwidth of the transducers. The resulting mode overlap and interference gives the spectrum an irregular appearance. We can see, though, that the RS damping at this point is not at all large, as depicted in Fig. 8 near 12°. The RS curve lacks the structure of the smooth plate data because of the signal phase averaging of the rough surface. In the lower frame of Fig. 9 similar data for incidence at 24° are shown. Here, the RS losses are apparent, but not as large as the case for propagation just beyond $\alpha=\beta_p$. The spectrum is regular again, since the modes are well separated.

These data complete the presentation of results from immersion testing on smooth and rough aluminum plates. Immersion has been chosen for comparative experimental measurements because the reliability of ultrasonic coupling permits the predictions of our rough-surface plate-wave model to receive the most critical examination.

B. Contact measurements

Many measurements have also been made in contact mode, using polystyrene wedges in place of a couplant fluid. The wedge angles (there are two sets of wedges) have been calculated to produce waves with phase velocities in the aluminum plate centered on 4.7 km/s and 3.2 km/s. Most of the experiments have been performed with the 3.2-km/s wedge (wedge angle $=45°$). The notorious difficulty of attaining a reliable, consistent contact in this mode of operation has been a problem in these studies as well. We have attempted to circumvent these difficulties by making measurements at many physical locations and performing appropriate averages to reduce any bias introduced by inconsistent contacts. The major effect of a changing contact is the variation in signal amplitude. There is generally little effect on the shape of the signal spectrum. Since we are principally interested in relative amplitudes within a spectrum, the contact problem is not as severe as it might be for a purely amplitude-based measurement.

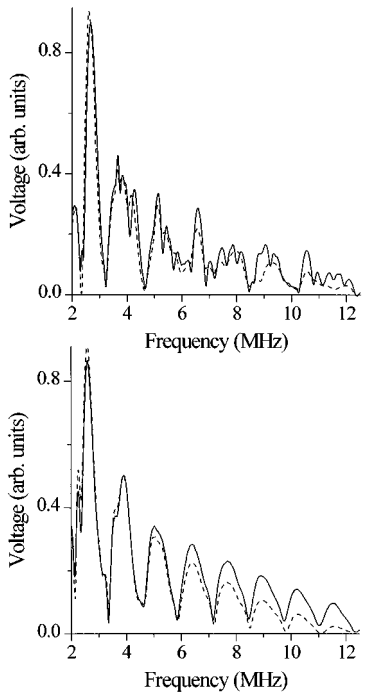

FIG. 9. Experimental frequency dependence of receiver voltage for smooth (solid) and lower rough (dashed) plate surfaces with $h=26$ μm for $x_i=20$ mm, and incidence at 13° (upper frame), just before compressional critical angle and incidence at 24°, well past p-wave critical angle.

Experimental data obtained with this procedure are shown in Fig. 10. Here, the results of many measurements performed on different portions of the plate are averaged and presented as signal amplitude versus frequency. The thinner plate (1.4 mm) is shown in the upper frame and the thicker one (2.3 mm), having more modes in the same bandwidth, is shown in the lower one. The three different curves in each frame relate to different separations of the transducer axis intersection x_i, as shown schematically in Fig. 1(b); the three curves are solid ($x_i=20$ mm), dashed ($x_i=30$ mm), and dotted ($x_i=40$ mm). For the thinner sample in the upper frame fewer modes are produced within the transducer bandwidth, but the effect of increasing separation is more pronounced from mode to mode. The S_0 mode in either case is very little affected since the phase velocity and frequency lie at a point where $\mathrm{Im}(\xi)$ is small, as shown in Fig. 1 of Part I. In addition, its frequency is well below that of the next

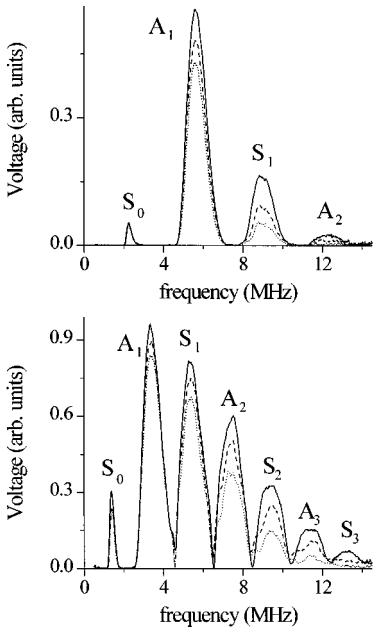

FIG. 10. Experimental shoe-contact signal from sandblasted rough aluminum plates ($h=26$ μm) for three different transducer separations x_i (solid: $x_i=20$ mm; dashed: 30 mm; dotted: 40 mm); upper frame is thin plate (1.4 mm) and lower frame is thick plate (2.3 mm).

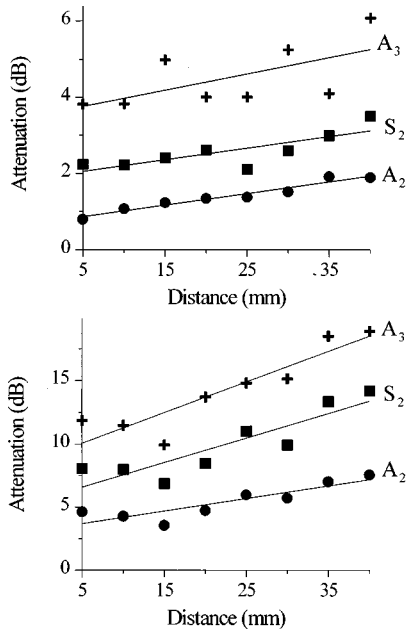

FIG. 11. Collected experimental amplitude data for rough aluminum plates as a function of transducer separations x_i; three modes are illustrated for each of the two rms roughnesses, $h=13$ μm and $h=26$ μm. Solid lines are best-fit curves from which rough-surface attenuation is inferred.

higher mode. Another effect is at work here: The S_0 mode is particularly susceptible to damping caused by wave leakage back into the transmitting coupling wedge. For this reason it is also much smaller than the higher order modes and contains less roughness information. In the lower frame of Fig. 10 more modes are generated in the thicker plate, showing the progressive effects of both increasing frequency and transducer separation.

To analyze the behavior in Fig. 10 for comparison to our model, the mode amplitude data are accumulated in Fig. 11. In the upper frame are the results for the 13-μm RS plate, while the 26-μm RS plate data and calculations are reported in the lower frame. Each experimental curve is denoted by a different plotting symbol, (+) for the A_3 mode, (■) for the S_2 mode, and (●) for the A_2 mode, referring to the different modes from Fig. 10. Each mode occurs at a fixed frequency determined by the wedge angle, which is a constant for the experiment. Despite difficulties with the contact, the normalized amplitude data fall on, or close to, the expected straight line. A typical experimental uncertainty estimated from the observed measurement variability is about three times the size of the plotting symbol. Moreover, there is a small oscillatory component visible in nearly every data set, which we attribute to the residual plate curvature. Although good compensation schemes exist to suppress the effects of contact variations,[13] in our case these would not have been of much help, since we can sample only the transmitted signal. When analyzing the scattering from discrete defects these compensation methods give excellent results.

The slopes are higher for the 26-μm roughness than for the smaller h, and we expect this behavior. The solid lines through the data in each case are best-fit curves from which attenuation values can be deduced. The theoretical estimates for the slopes are calculated using Eq. (1) of Part I, and we find a ratio between the square roots of the slopes of the experimental curves that is entirely consistent with the roughness ratio of the mode occurrences. The root slope ratio is given by

$$\mathscr{R}_{h_1/h_2}=\sqrt{\frac{\mathscr{M}(A_1;h_1)}{\mathscr{M}(A_1;h_2)}}, \tag{3}$$

where $\mathscr{M}(A_1;h_1)$ is the slope of the A_1 mode for a RS plate with $h=h_1$ rms roughness. For the slopes of the curves in Fig. 11 we calculate a roughness root slope ratio $\mathscr{R}_{h_1/h_2}$ of 2.2, whereas we expect a ratio of 2 ($=26$ μm/13 μm). This comparison is very favorable considering the inconsistencies in the contact, and it demonstrates the relative lack of sensitivity to the disturbing influence of contact variations.

C. Knife-edge contact coupling

We have also explored, in a limited number of measurements, the character of data obtained using knife-edge type coupling wedges. These devices are also fabricated from polystyrene and are brought to a relatively narrow strip ($\sim$1 mm) that makes contact with the specimen. With this line contact, a broader range of spatial frequencies is generated than we could obtain with conventional contact coupling, which would extend over 10 mm or more. The knife-edge is the spatial/wave number domain equivalent of a broadband transducer in the time/frequency domain. The knife-edge generates elastic energy at many wave numbers. By contrast, the planar piston transducer we normally use has a fairly narrow directivity function, and generates an elastic far field reasonably sharply peaked about the transducer central ray. Like the piston radiator, however, the finite knife-edge too will have a sharper directivity function as frequency increases.

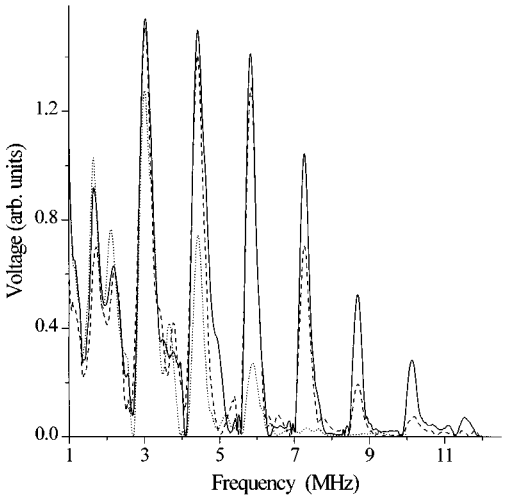

FIG. 12. Knife-edge contact experimental signals from smooth (solid) and rough (dashed: $h=13$ μm), (dotted: $h=26$ μm) aluminum plates for a transducer separation $x_i=22$ mm. Sharp decrease in received signal from the 26-μm rms plate between 3 and 8 MHz illustrates effect of narrowing spatial bandwidth.

Results for the knife-edge are displayed in Fig. 12, where three curves are shown for a knife-edge contact separation of 22 mm. The solid curve is for a smooth surface, the dashed curve is 13-μm roughness, and the dotted curve is the 26-μm sample. All curves have been normalized to remove both transducer frequency and polystyrene damping effects. With the knife-edge wedges we have found the expected behavior, namely that the sensitivity of the signal to contact force is very much reduced. Therefore, contact problems are much less bothersome with knife-edge coupling than with conventional shoe-type contact wedges.

Even with the relatively small roughness path of 22 mm, we find an interesting effect. The signals for the 26-μm roughness plate almost disappear in a frequency range from 3 to 8 MHz. The spatial bandwidth of the knife-edges decreases as the frequency approaches midband (4–8 MHz), and most of the acoustic energy is concentrated in a relatively narrow range about $\alpha=0°$. This result makes sense for a contact width a of 1 mm, where the k_pa at 5 MHz is about 5. For a very broad spatial radiator k_pa should be much less than 1.

But, the current choice of contact width may have an unforeseen advantage. The concentration of energy about $\alpha=0°$ permits only the higher order modes near cutoff to be generated. From Fig. 1 of Part I this region (near mode cutoff) is the one most sensitive to roughness. When frequency and spatial bandwidth are suitably chosen, the signal contrast between smooth and rough surfaces should be strongly enhanced. This is exactly the circumstance we find with the 26-μm rough surface shown in Fig. 12 as the dotted curve, where the signal nearly vanishes above 6 MHz. The dashed curve for 13-μm roughness in Fig. 12 only begins the steep drop (compared to the smooth surface) after 6 MHz. But because the angles near cutoff are favored, each peak in Fig. 12 will likely include contributions from one or more individual modes. From $\alpha=0°$ to $\sim 10°$ ($V_{\text{phase}}=\infty$ to 12.7 km/s) the symmetric and antisymmetric modes are crossing each other and close modal approaches are possible. The magnitude of each mode's contribution to peaks in Fig. 12 depends on the strength of mode excitation, and this value is related to the coupling strength of elastic wave energy at the polystyrene–aluminum interface.

III. SUMMARY AND CONCLUSIONS

In this article we have examined the behavior of guided elastic waves in the presence of rough surfaces. These investigations have led to a broader understanding of the phenomenology of rough-surface interactions with elastic guided waves. Extensive measurements in immersion, contact mode, and with a knife-edge coupler demonstrate the wide range of physical behavior of elastic guided waves and their dependence on the condition of the guiding surfaces.

Comparisons between predictions of the simple rough-surface plate wave model and experimental data demonstrate surprisingly good agreement in most of the parameter space we have investigated, except in the vicinity of the critical angles. We have found how to configure experimental conditions to maximize the rough-surface damping contrast, by measuring below and above the compressional critical angle. As well, we have seen that conventional testing methods would be of little use in developing procedures to reveal the presence of weak, hidden roughness (corrosion) in plate-like structures. For contact mode coupling, we have demonstrated that accurate quantitative results can be deduced from the data and that these results agree rather well with the predictions of our simple model in all technologically significant regimes of the phenomenon.

One principal shortcoming of the model is the absence of its dependence on the roughness correlation length L. The influence of this parameter should grow as the plate thickness d decreases, as suggested by some recent work.[14] These additional effects are not included in the phase-screen approximation, and the influence of these parameters on guided wave propagation in rough plates needs yet to be studied.

ACKNOWLEDGMENTS

This work was supported by the Aerospace Sciences Directorate, Air Force Office of Scientific Research under Grant No. F49620-95-1-0294. The experimental work has benefitted from the generous loan of characterized rough-surface samples made available by P. B. Nagy of the University of Cincinnati. In the early stages of the project A. Safaeinili also made substantial contributions to the work.

[1] J. A. Ogilvy, *Theory of Wave Scattering from Random Rough Surfaces* (Adam Hilger, London, 1991).
[2] P. B. Nagy and L. Adler, ''Surface roughness induced attenuation of reflected and transmitted ultrasonic waves,'' J. Acoust. Soc. Am. **82**, 193–197 (1987).
[3] E. I. Thorsos, ''The validity of the Kirchhoff approximation for rough surface scattering using Gaussian roughness spectrum,'' J. Acoust. Soc. Am. **83**, 78–92 (1988).
[4] P. B. Nagy and J. H. Rose, ''Surface roughness and the ultrasonic detection of subsurface scatterers,'' J. Appl. Phys. **73**, 566–580 (1993).
[5] M. Bilgen and J. H. Rose, ''Effects of one-dimensional random rough surfaces on ultrasonic backscatter: Utility of phase-screen and Fresnel approximations,'' J. Acoust. Soc. Am. **96**, 2849–2855 (1994).
[6] J. H. Rose, M. Bilgen, and P. B. Nagy, ''Acoustic double-reflection and

transmission at a rough water-solid interface,'' J. Acoust. Soc. Am. **95**, 3242–3251 (1994).
[7] M. DeBilly and G. Quentin, ''Backscattering of acoustic waves by randomly rough surfaces of elastic solids immersed in water,'' J. Acoust. Soc. Am. **72**, 591–601 (1982).
[8] O. I. Lobkis and D. E. Chimenti, ''Elastic guided waves in plates with rough surfaces,'' Appl. Phys. Lett. **69**, 3486–3488 (1996).
[9] P. B. Nagy (private communication).
[10] O. I. Lobkis, A. Safaeinili, and D. E. Chimenti, ''Precision ultrasonic reflection studies in fluid-coupled plates,'' J. Acoust. Soc. Am. **99**, 2727–2736 (1996).
[11] L. B. Felsen and N. Marcuvitz, *Radiation and Scattering of Waves* (Prentice-Hall, Englewood Cliffs, NJ, 1973).
[12] L. E. Pitts, T. J. Plona, and W. G. Mayer, ''Theory of nonspecular reflection effects for an ultrasonic beam incident on a solid plate in a liquid,'' IEEE Trans. Sonics Ultrason. **SU-24**, 101–109 (1977).
[13] J. D. Achenbach, I. N. Komsky, Y. C. Lee, and Y. C. Angel, ''Self-calibrating ultrasonic technique for R/T and T/R measurements,'' in *Review of Progress in Quantitative NDE*, Vol. 11A, edited by D. O. Thompson and D. E. Chimenti (Plenum, New York, 1992), pp. 1035–1042.
[14] J. D. Sheard and M. Spivak, ''Wave scattering in a rough elastic layer adjoining a fluid half-space,'' J. Acoust. Soc. Am. **97**, 72–83 (1995).

A perturbation method for the modes of cylindrical acoustic waveguides in the presence of temperature gradients

Brian J. McCartin
Applied Mathematics, GMI Engineering & Management Institute, 1700 West Third Avenue, Flint, Michigan 48504-4898

(Received 15 May 1996; revised 4 February 1997; accepted 13 February 1997)

This paper concerns itself with how the cut-off frequencies and modal shapes of cylindrical acoustic waveguides are altered by the presence of temperature gradients induced by an applied temperature distribution along the duct walls. A physical model is first formulated which incorporates an inhomogeneous sound speed as well as a density gradient. The associated mathematical model is then a generalized eigenproblem. This is then discretized via the control region approximation (a finite difference scheme) yielding a generalized matrix eigenproblem. Under the assumption that the boundary temperature distribution is nearly constant, we apply a procedure of Schrödinger to express the propagation constants and modal functions as perturbation series whose successive terms can be generated recursively. The case of a rectangular duct with temperature variations in the cross section is considered in detail. All numerical computations are performed using MATLAB©.
 [S0001-4966(97)00507-9]

PACS numbers: 43.20.Mv [JEG]

INTRODUCTION

The modal propagation characteristics of cylindrical acoustic waveguides at constant temperature have been investigated analytically for canonical duct cross sections such as rectangular and circular[1] and numerically for general simply connected cross sections.[2] However, if there is a temperature variation across the duct, then these analyses are inadequate. This is due to the inhomogeneous sound speed and density gradient induced by such a temperature distribution.

Such temperature variations occur in the exhaust systems of vehicles where the bottom portion of the waveguide is in direct contact with the ambient atmosphere while the upper portion is either near or in contact with the body of the vehicle which is, of course, at a different temperature. As we shall show by our subsequent analysis, such an induced temperature perturbation across the waveguide can significantly alter the modal characteristics of the exhaust system with a consequent reduction in its overall effectiveness at suppressing selected acoustic frequencies.

In ocean acoustics,[3] both depth- and range-dependent sound speeds are typically considered. Density gradients are usually ignored since the spatial scale of such variations is much larger than the wavelength of the acoustic disturbance. The same situation obtains in atmospheric propagation.[4] Unlike such ocean and atmospheric waveguides, the ducts under consideration in this paper are fully enclosed and hence density gradients must be accounted for.

The present study will commence with the formulation of a physical model which includes both an inhomogeneous sound speed and a density gradient across the duct. We will confine our attention to small perturbations of an isothermal ambient state.

The corresponding mathematical model will involve a generalized Helmholtz operator whose eigenvalues (related to the cut-off frequencies) and eigenfunctions (modal shapes) are to be determined. This continuous problem is discretized via the control region approximation[5] (a finite difference procedure) resulting in a generalized matrix eigenvalue problem.

A perturbation procedure, originally developed by Schrödinger[6] and previously applied to uniform waveguides,[7] is invoked to produce perturbation expansions for the aforementioned eigenvalues and eigenvectors. In turn, this permits the development of *analytical* expressions for dispersion curves and cut-off frequencies.

This procedure is illustrated for the case of a rectangular duct with an applied parabolic temperature profile along its lower wall. All numerical computations were performed using MATLAB©.

I. FORMULATION

With reference to Fig. 1, we consider the acoustic field within an infinitely long, hard-walled, cylindrical tube of general cross section, Ω. The analysis of the propagation characteristics of such an acoustical waveguide typically proceeds by assuming a constant temperature throughout the undisturbed fluid.

However, in the present study, we permit a small temperature perturbation about the average cross-sectional temperature

$$\hat{T}(x,y;\epsilon)=\hat{T}_0[1+\epsilon f(x,y)], \tag{1}$$

where $\int\int_\Omega f(x,y)\,dA=0$ and ϵ is small.

This temperature perturbation is due to an applied temperature distribution along the walls of the duct

$$\Delta\hat{T}=0 \ \text{ in } \ \Omega, \quad \hat{T}=T_{\text{applied}} \ \text{ on } \ \partial\Omega, \tag{2}$$

where, here as well as in the ensuing analysis, all differential operators are transverse to the longitudinal axis of the waveguide. Consequently, $\nabla(f^n)=nf^{n-1}(\nabla f)$ and $\Delta(f^n)=n(n-1)f^{n-2}(\nabla f\cdot\nabla f)$.

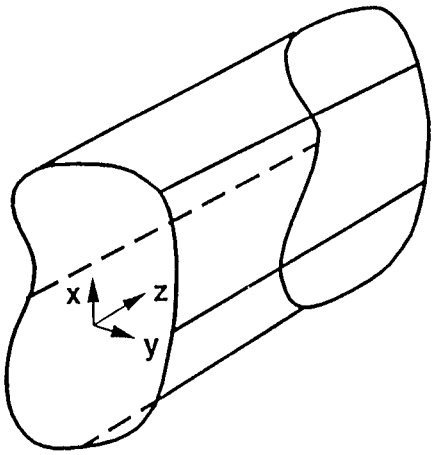

FIG. 1. Waveguide cross section.

This small temperature variation across the duct will produce inhomogeneities in the background fluid density

$$\hat{\rho}(x,y;\epsilon)=\frac{1}{R}\cdot\frac{\hat{p}(\epsilon)}{\hat{T}(x,y;\epsilon)}=\frac{1}{R\hat{T}_0}\cdot\frac{\hat{p}(\epsilon)}{[1+\epsilon f(x,y)]} \tag{3}$$

and sound speed

$$c^2=R\hat{T}(x,y;\epsilon)=c_0^2[1+\epsilon f(x,y)]. \tag{4}$$

The self-consistent governing equation for the acoustic pressure p with frequency ω and propagation constant β is[8]

$$\nabla\cdot\left(\frac{\hat{\rho}_0}{\hat{\rho}}\nabla p\right)+\frac{\hat{\rho}_0}{\hat{\rho}}\left(\frac{\omega^2}{c^2}-\beta^2\right)p-\frac{\hat{\rho}_0}{\hat{\rho}}\nabla\cdot\left(\frac{1}{\hat{\rho}}\nabla\hat{\rho}\right)p$$

$$=0\ \text{ in }\ \Omega,\quad \frac{\partial p}{\partial n}=0\ \text{ on }\ \partial\Omega \tag{5}$$

assuming that the fluid is at rest (the cut-off frequencies are unaltered by uniform flow down the tube).[15] In what follows, it is important to preserve the self-adjointness of this equation.

II. PERTURBATION PROCEDURE

We now expand the pressure in a perturbation series in the small parameter ϵ

$$\hat{p}(\epsilon)=\sum_{n=0}^{\infty}\epsilon^n\hat{p}_n, \tag{6}$$

which induces a corresponding perturbation expansion for the density

$$\hat{\rho}=\hat{\rho}_0[1+\epsilon(A_1-f\ )+\epsilon^2(A_2-A_1f+f^2)$$
$$+\epsilon^3(A_3-A_2f+A_1f^2-f^3)+\cdots], \tag{7}$$

where $\hat{\rho}_0:=\hat{p}_0/(R\hat{T}_0)$ and $A_n:=\hat{p}_n/\hat{p}_0$.

By invoking conservation of mass, $M:=\int\int_\Omega\hat{\rho}(x,y;\epsilon)\times dA$ must be independent of ϵ which together with $\int\int_\Omega f\,dA=0$ implies that $A_1=0$, $A_2=-(\int\int_\Omega f^2\,dA)/A_\Omega$, $A_3=(\int\int_\Omega f^3\,dA)/A_\Omega$. Thus

$$\hat{\rho}=\hat{\rho}_0[1-\epsilon f+\epsilon^2(A_2+f^2)+\epsilon^3(A_3-A_2f-f^3)+\cdots], \tag{8}$$

$$\frac{1}{\hat{\rho}}=\frac{1}{\hat{\rho}_0}[1+\epsilon f-\epsilon^2A_2-\epsilon^3(A_2+A_3)+\cdots], \tag{9}$$

$$\nabla\hat{\rho}=\hat{\rho}_0[-\epsilon+\epsilon^2(2f\ )+\epsilon^3(-A_2-3f^2)+\cdots]\nabla f, \tag{10}$$

$$\frac{1}{c^2}=\frac{1}{c_0^2}[1-\epsilon f+\epsilon^2f^2-\epsilon^3f^3+\cdots]. \tag{11}$$

Inserting these expansions into Eq. (5) results in

$$\Delta p+\epsilon\nabla\cdot(f\nabla p)+\epsilon^2[\alpha_2(\Delta p+k_0^2p)-(\nabla f\cdot\nabla f\ )p]$$
$$+\epsilon^3[\alpha_3(\Delta p+k_0^2p)+\alpha_2\nabla\cdot(f\nabla p)+(f\nabla f\cdot\nabla f\ )p]$$
$$+\cdots=\lambda p, \tag{12}$$

where the wave number is $k_0^2:=\omega^2/c_0^2$ and $\lambda:=\beta^2-k_0^2$, $\alpha_2:=A_2$, $\alpha_3=-A_3$. It is interesting to note that the 2nd and 3rd terms of Eq. (5) make no $O(\epsilon)$ contribution and thus are of ''higher order'' than the 1st term of that equation.

If we discretize Eq. (12) using the control region approximation[5] (finite differences), we obtain the matrix generalized eigenvalue problem

$$Ap+\epsilon Cp+\epsilon^2[\alpha_2(A+k_0^2B)+D_1]p+\epsilon^3[\alpha_3(A+k_0^2B)$$
$$+\alpha_2C+D_2]p=\lambda Bp, \tag{13}$$

where A is symmetric and nonpositive-definite, C is symmetric, B is positive and diagonal, and both D_1 and D_2 are diagonal.

We next apply the perturbation procedure of Schrödinger[6] to construct expansions

$$\lambda(\epsilon)=\sum_{n=0}^{\infty}\epsilon^n\lambda_n,\quad p(\epsilon)=\sum_{n=0}^{\infty}\epsilon^np_n, \tag{14}$$

the convergence of which are studied in Ref. 9.

Here we assume that λ_0 is a simple eigenvalue with corresponding eigenvector p_0 for the unperturbed problem

$$Ap_0=\lambda_0Bp_0 \tag{15}$$

which can be determined by the procedure of Ref. 2. An eigenvalue of multiplicity m would entail an expansion in $\epsilon^{1/m}$.[10] As will be evident in what follows, our approximation scheme is greatly enhanced by the symmetry of A.[11]

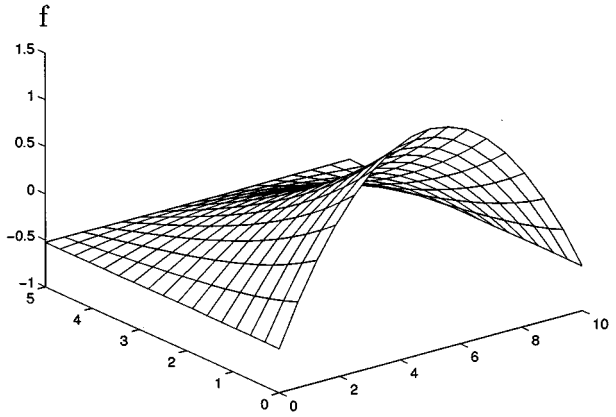

FIG. 2. Temperature perturbation profile.

TABLE I. Computed modal eigenvalue corrections.

Mode	λ_0	λ_1	$\hat{\lambda}_2$	$\hat{\lambda}_3$
(1,0)	−0.0987	−0.0166	−0.1359	−0.1359
(0,1)	−0.3948	0.0126	−0.1941	0.1077
(1,1)	−0.4935	0.0552	−0.2192	0.0568

Inserting the expansions, Eq. (14), into the eigenproblem, Eq. (13), collecting terms, and equating coefficients of like powers of ϵ results in

$$(A-\lambda_0 B)p_0=0, \tag{16}$$

$$(A-\lambda_0 B)p_1=\lambda_1 Bp_0-Cp_0, \tag{17}$$

$$(A-\lambda_0 B)p_2=\lambda_2 Bp_0+\lambda_1 Bp_1-Cp_1 -[\alpha_2(A+k_0^2 B)+D_1]p_0, \tag{18}$$

$$(A-\lambda_0 B)p_3=\lambda_3 Bp_0+\lambda_2 Bp_1+\lambda_1 Bp_2-Cp_2 -[\alpha_2(A+k_0^2 B)+D_1]p_1-[\alpha_3(A+k_0^2 B) +\alpha_2 C+D_2]p_0, \tag{19}$$

and so forth. Alternatively, we could have inserted the expansions, Eq. (14), into the continuous Eq. (12) and then discretized via the control region approximation with the same end result, Eqs. (16)–(19).

Equation (16) together with the normalization $\langle p_0, Bp_0\rangle=1$ yields $\lambda_0=\langle p_0, Ap_0\rangle$. Note that $(A-\lambda_0 B)$ is singular (in fact, its nullity is one by assumption) and that the symmetry of A implies that the right-hand side of Eq. (17) must be orthogonal to p_0 producing

$$\lambda_1=\langle p_0, Cp_0\rangle. \tag{20}$$

Thus the symmetry of A has produced λ_1 *without* calculating p_1. Note that this first-order correction is independent of the frequency. Since C is indefinite, λ_1 may be either positive or negative. As a result, this perturbation procedure provides neither lower nor upper bounds on the eigenvalues.

However, in order to proceed any further, we must calculate p_1 from Eq. (17) by performing the QR factorization of $(A-\lambda_0 B)$ and then employ it to produce the minimum-norm least-squares solution, q, to this rank-deficient system.[12] We then define $p_1 := q-\langle q, Bp_0\rangle p_0$ producing $\langle p_1, Bp_0\rangle=0$ which simplifies subsequent computations.

The knowledge of p_1, together with the symmetry of A, permits the computation of *both* λ_2 and λ_3:

$$\lambda_2=\alpha_2 k_0^2+\hat{\lambda}_2, \quad \lambda_3=\alpha_3 k_0^2+\hat{\lambda}_3, \tag{21}$$

$$\hat{\lambda}_2=\langle p_0, Cp_1+(\alpha_2 A+D_1)p_0\rangle, \tag{22}$$

$$\hat{\lambda}_3=\langle p_1, (C-\lambda_1 B)p_1\rangle+\langle p_0, 2(\alpha_2 A+D_1)p_1 +(\alpha_3 A+\alpha_2 C+D_2)p_0\rangle. \tag{23}$$

In evaluating the required inner products, we benefit greatly from the sparsity of A and C and the diagonality of B, D_1, and D_2.

We can continue indefinitely in this fashion, with each succeeding term in the expansion for p producing the next *two* terms in the expansion for λ. If we had reduced this to a standard eigenvalue problem through multiplication of Eq. (13) by B^{-1}, we would have destroyed the symmetry of the operators and sacrificed this substantial economy of computation. Also, note that only a single QR factorization is required to produce *all* of the modal corrections, p_n.

III. EXAMPLE

We now apply the above perturbation procedure to an analysis of the modal characteristics of a 10×5 rectangular

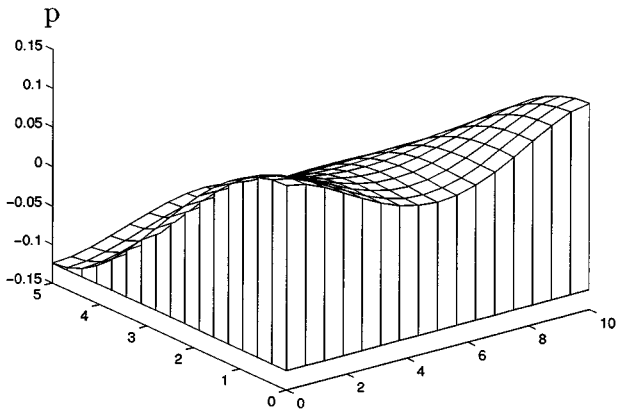

FIG. 4. $\epsilon=+1$ (heated wall).

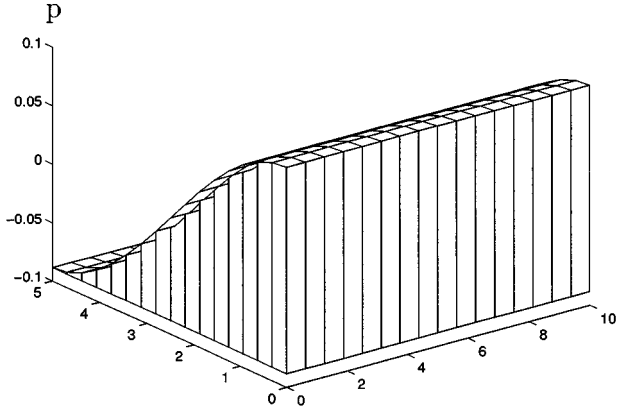

FIG. 3. (0,1)-mode (hard wall).

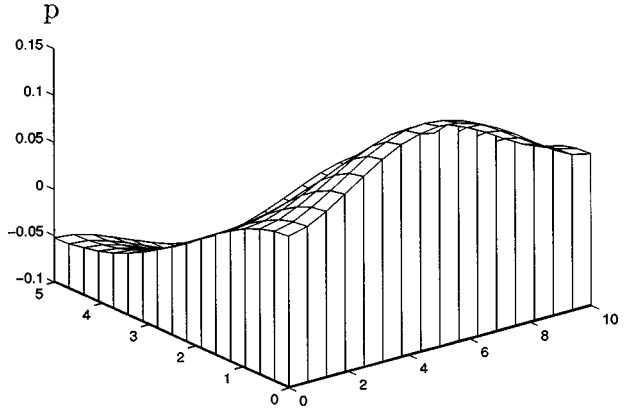

FIG. 5. $\epsilon=-1$ (cooled wall).

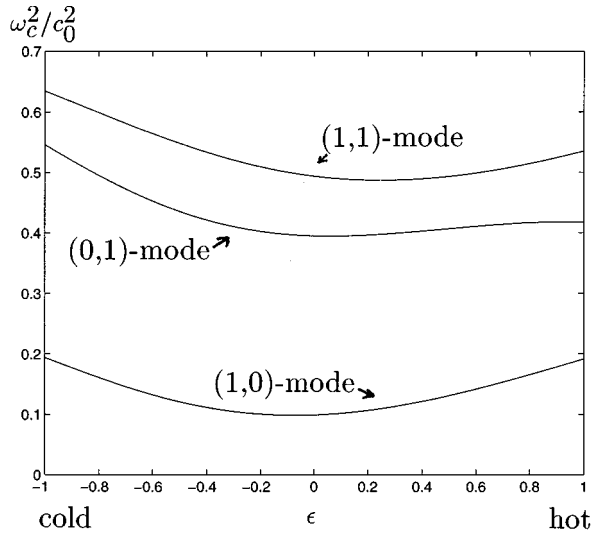

FIG. 6. Cut-off frequencies.

duct (for which the unperturbed eigenvalues and eigenvectors are available[13]) with the lower wall subjected to the parabolic temperature profile

$$T_b = 1 + 16\left(\frac{x}{10}\right)\left(1 - \frac{x}{10}\right) \tag{24}$$

while the other three walls are set to $T_b = 1$. We then solve $\Delta T = 0$ subject to this boundary condition, calculate T_{avg}, and define

$$f(x,y) = \frac{T(x,y)}{T_{\text{avg}}} - 1, \tag{25}$$

which is displayed in Fig. 2.

This yields $\alpha_2 = 0.2108$ and $\alpha_3 = -0.08813$. In this and subsequent computations, which were performed using MATLAB©, a coarse 9×9 mesh and a fine 17×17 mesh were employed. These results were then enhanced using Richardson extrapolation.[14]

We compute the cut-off frequencies by setting to zero the expression for the dispersion curves, $\beta^2 = k_0^2 + \lambda$, producing

$$\frac{\omega_c^2}{c_0^2} = -\frac{\lambda_0 + \epsilon\lambda_1 + \epsilon^2\hat{\lambda}_2 + \epsilon^3\hat{\lambda}_3 + O(\epsilon^4)}{1 + \epsilon^2\alpha_2 + \epsilon^3\alpha_3 + O(\epsilon^4)}. \tag{26}$$

Note that the denominator [corresponding to the frequency-dependent portion of $\lambda(\epsilon)$] is independent of the mode number.

Table I displays the computed eigenvalue corrections for the three lowest-order modes. Figure 3 shows the unperturbed (0,1) mode while Figs. 4 and 5 show this same mode with a heated/cooled lower wall, respectively. Figure 6 displays the cut-off frequencies for these same modes as ϵ varies.

IV. CONCLUSION

In the preceding sections, we have presented a perturbation procedure for the modal characteristics of cylindrical acoustic waveguides in the presence of temperature gradients induced by an applied temperature distribution along the walls of the duct. Rather than simply making the sound speed spatially varying, as is done in atmospheric propagation and underwater acoustics, we have been careful to utilize a self-consistent physical model since we have dealt here with a fluid fully confined to a narrow region.

We have also taken great pains to preserve the self-adjointness inherent in our governing wave equation. This in turn leads to a symmetric generalized eigenvalue problem. As a consequence of this special care, we have been able to produce a *third-order* expression for the cut-off frequencies while only requiring a *first-order* correction to the modes.

We have presented a detailed numerical example intended to intimate the broad possibilities offered by the resulting analytical expressions for cut-off frequencies and modal shapes. These include shifting of cut-off frequencies and shaping of modes. In point of fact, one could now pose the inverse problem: What boundary temperature distribution would produce prescribed cut-off frequencies?

[1] D. S. Jones, *Acoustic and Electromagnetic Waves* (Oxford U.P., New York, 1986).
[2] B. J. McCartin, ''Numerical Computation of Guided Electromagnetic Waves,'' *Proceedings of the 12th Annual Conference on Applied Mathematics* (University Central Oklahoma, Edmond, OK, 1996).
[3] L. M. Brekhovskikh and Yu. P. Lyasov, *Fundamentals of Ocean Acoustics* (Springer-Verlag, Berlin, 1991), 2nd ed.
[4] L. Brekhovskikh and V. Goncharov, *Mechanics of Continua and Wave Dynamics* (Springer-Verlag, Berlin, 1985).
[5] B. J. McCartin, ''Control Region Approximation for Electromagnetic Scattering Computations,'' *Proceedings of Workshop on Computational Wave Propagation*, edited by B. Engquist and G. A. Kriegsmann (Institute for Mathematics and Its Applications, Springer-Verlag, Berlin, 1996).
[6] F. W. Byron, Jr. and R. W. Fuller, *Mathematics of Classical and Quantum Physics* (Dover, New York, 1992).
[7] B. J. McCartin, ''A Perturbation Procedure for Nearly-Rectangular, Homogeneously-Filled, Cylindrical Waveguides,'' IEEE Trans. Microwave Guided Wave Lett. **6**(10), 354–356 (1996).
[8] J. A. DeSanto, *Scalar Wave Theory* (Springer-Verlag, Berlin, 1992).
[9] K. O. Friedrichs, *Perturbation of Spectra in Hilbert Space* (American Mathematical Society, Providence, 1965).
[10] J. H. Wilkinson, *The Algebraic Eigenvalue Problem* (Oxford U.P., New York, 1965).
[11] T. Kato, *Perturbation Theory for Linear Operators* (Springer-Verlag, Berlin, 1980), 2nd ed.
[12] B. Noble and J. W. Daniel, *Applied Linear Algebra* (Prentice-Hall, Englewood Cliffs, NJ, 1988), 3rd ed.
[13] F. B. Hildebrand, *Finite-Difference Equations and Simulations* (Prentice-Hall, Englewood Cliffs, NJ, 1968).
[14] S. D. Conte and C. de Boor, *Elementary Numerical Analysis* (McGraw-Hill, New York, 1980), 3rd ed.
[15] P. M. Morse and K. U. Ingard, ''Linear Acoustic Theory,'' *Handbuch der Physik, Vol. XI/1, Acoustics I*, edited by S. Flügge (Springer-Verlag, Berlin, 1961).

Modified Herschel–Quincke tube: Attenuation and resonance for *n*-duct configuration

A. Selamet and V. Easwaran
The Ohio State University, Department of Mechanical Engineering and Center for Automotive Research, 206 West 18th Avenue, Columbus, Ohio 43210

(Received 8 September 1996; revised 9 February 1997; accepted 13 February 1997)

The classical two-duct Herschel–Quincke tube is generalized to an n-duct configuration. A closed-form expression is developed for the transmission loss characteristics, as well as for the resonance locations. While the results are illustrated in the present study in terms of three-duct configurations alone and in comparison with the two-duct arrangements, the developed expressions hold for any number of ducts and cross-sectional area combination. © *1997 Acoustical Society of America.* [S0001-4966(97)00107-0]

PACS numbers: 43.20.Mv, 43.50.Gf [JEG]

LIST OF SYMBOLS

A	area
c	speed of sound
i	imaginary unit, $\sqrt{-1}$
k	wave number, ω/c_0
l	length
n	number of parallel ducts
p	acoustic pressure
T	transfer matrix
TL	transmission loss
v	acoustic volume velocity

Greek symbols

ρ	density
ω	angular frequency

Subscripts

d	downstream of a duct
j	duct index
o	outlet
u	upstream of a duct
0	mean value

INTRODUCTION

The classical Herschel–Quincke tube consists of a parallel connection of two pipes. While the origin dates back to Herschel (1833) and Quincke (1866), the working mechanism was quantitatively described first by Stewart (1928) and later by Stewart and Lindsay (1930). Rayleigh's interpretation of this classical configuration is as follows (1945): ''Other examples of the absorption of sound by resonators are afforded by certain modifications of Herschel's interference tube used by Quincke to stop tones of definite pitch from reaching the air.'' Later a referral is made by Davis *et al.* (1954) and a presentation by Hixson and Kahlbau (1963). Recently, a study by Selamet *et al.* (1994) presented an analytical expression for the transmission loss and resonance behavior for the classical configuration, and compared the predictions to computational and experimental results. Since the appearance of this recent work, somewhat related studies have been brought to the attention of the present authors. These include the interesting works of Fuller and Bies (1978, 1979); DePollier *et al.* (1990); and Chen and Hastings (1994). In the first publication, Fuller and Bies investigated the effect of a crescent shaped center-body fitted into a right-angled bend in a duct system. This attenuator works based on the principle of relative mean path difference, which clearly resembles the classical Herschel–Quincke tube. In the second paper, they introduced the effect of flow. DePollier *et al.* attacked the wave propagation in 2-D lattices. Chen and Hastings investigated a variation to the Herschel–Quincke tube, where a half-wavelength flexible tube (tuning cable) inside the hydraulic line replaced the external side branch. They examined the ability of this design to reduce fluid-borne noise in power steering hydraulic transmission lines. Numerous works also deserve to be further credited for referrals to or brief explanations on the classical design, including Stewart's brief article supplemented by H. S. Uhler (1945) which was overlooked by the authors earlier; Luxton (1968) and Rostafinski (1991).

The classical configuration and its modifications have also been suggested by numerous inventors to suppress the exhaust noise from internal combustion engines. The resulting patents include the variations proposed by Holmes (1926), Brice (1929), and Smith (1935) earlier, and Ohashi (1981), Sun (1987), and Feuling (1991) more recently. These patents were intuitively based on the original concept of Herschel, which was to blend two out of phase sounds at the same frequency. While some suggested two ducts, patents also included three, four, six (and more) parallel duct combinations, and a pair of two ducts.

While the basic attenuation and resonance behavior of two duct combination is now well-established analytically, the need exists to extend this treatment to multiple ducts—more than two, and if possible, to ''n'' number of ducts, where n may be an arbitrarily large number. The objective of the present study is to generalize the classical two-duct Herschel–Quincke treatment to an n-duct configuration. A closed-form expression is developed for the transmission

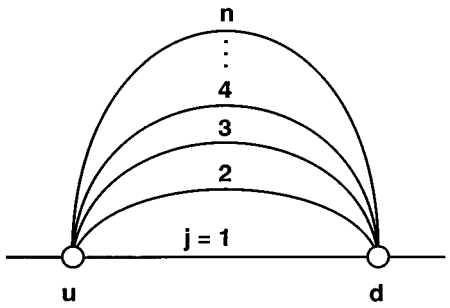

FIG. 1. Schematic of modified Herschel–Quincke tube with n ducts.

loss characteristics and the resonance locations of this generalized silencer. These expressions are expected to eliminate the guesswork in determining the acoustic performance of the Herschel–Quincke-like configurations with an arbitrary number of parallel pipes.

The study consists of four sections: Following this Introduction, the closed-form expression for transmission loss of a Herschel–Quincke tube generalized for n arbitrary ducts is developed, in combination with a new expression for the resonance locations. Then, the predictions are illustrated in terms of three-duct configurations and in comparison with the two-duct arrangements. The study is concluded with some final remarks.

I. THEORY

The modified Herschel–Quincke tube has ''n'' parallel ducts connecting the inlet and the outlet ports (see Fig. 1). Assuming plane-wave propagation, the state variables upstream of the inlet junction and the state variables downstream of the outlet junction are related by

$$\begin{Bmatrix} p_u \\ v_u \end{Bmatrix} = [\mathbf{T}] \begin{Bmatrix} p_d \\ v_d \end{Bmatrix}, \tag{1}$$

where p is the acoustic pressure, v is the acoustic volume velocity, $\mathbf{T}$ is the transfer matrix, and subscripts ''u'' and ''d'' denote, respectively, the junctions upstream and downstream of the n-pipe modified Herschel–Quincke tube. Similarly, the state variables at the two ends of each duct are related by

$$\begin{Bmatrix} p_{ju} \\ v_{ju} \end{Bmatrix} = \begin{bmatrix} \cos kl_j & i\,\dfrac{\rho_0 c_0}{A_j}\sin kl_j \\ i\,\dfrac{A_j}{\rho_0 c_0}\sin kl_j & \cos kl_j \end{bmatrix} \begin{Bmatrix} p_{jd} \\ v_{jd} \end{Bmatrix}, \quad j=1,2,3,\ldots,n, \tag{2}$$

where $k=\omega/c_0$ is the wave number, ω is the angular frequency, ρ_0 is the density, c_0 is the speed of sound, and l_j and A_j are the length and the cross-sectional area, respectively, of duct j. Here, ''ju'' and ''jd'' denote the two ends of duct j (see Fig. 1).

Conditions of pressure equilibrium and conservation of volume velocity (assuming uniform density) at junction ''u'' and ''d'' yield

$$p_u = p_{1u} = p_{2u} = p_{3u} \cdots = p_{nu}, \tag{3}$$

and

$$v_u = v_{1u} + v_{2u} + v_{3u} + \cdots v_{nu} \tag{4}$$

for junction ''u,'' and

$$p_d = p_{1d} = p_{2d} = p_{3d} \cdots = p_{nd} \tag{5}$$

and

$$v_d = v_{1d} + v_{2d} + v_{3d} + \cdots v_{nd} \tag{6}$$

for junction ''d.'' Combining Eqs. (2) and (3) results in

$$v_{jd} = -i\,\frac{A_j}{\rho_0 c_0}\left(\frac{\cos kl_1 - \cos kl_j}{\sin kl_j}\right) p_d + \frac{A_j}{A_1}\left(\frac{\sin kl_1}{\sin kl_j}\right) v_{1d}, \quad j=2,3,\ldots,n. \tag{7}$$

Substituting Eq. (7) into Eq. (6) gives

$$v_d = -\frac{i}{\rho_0 c_0}\left[\sum_{j=2}^{n} \frac{A_j(\cos kl_1 - \cos kl_j)}{\sin kl_j}\right] p_d + \frac{\sin kl_1}{A_1}\left(\sum_{j=1}^{n} \frac{A_j}{\sin kl_j}\right) v_{1d}. \tag{8}$$

In view of Eqs. (2), (3), and (5),

$$p_u = (\cos kl_1) p_d + i\,\frac{\rho_0 c_0}{A_1}(\sin kl_1) v_{1d}. \tag{9}$$

Eliminating v_{1d} from Eqs. (8) and (9) results in

$$p_u = T_{11} p_d + T_{12} v_d, \tag{10}$$

where

$$T_{11} = \frac{\Sigma_{j=1}^{n} A_j(\cos kl_j / \sin kl_j)}{\Sigma_{j=1}^{n}(A_j / \sin kl_j)}, \tag{11}$$

and

$$T_{12} = \frac{i\rho_0 c_0}{\Sigma_{j=1}^{n}(A_j / \sin kl_j)}, \tag{12}$$

which are two of the four matrix elements needed in Eq. (1). The remaining two matrix elements may be obtained similarly. Thus, from Eqs. (2), (4), (7), and (8),

$$v_u = T_{21} p_d + T_{22} v_d, \tag{13}$$

where

$$T_{21} = \frac{i}{\rho_0 c_0}\sum_{j=1}^{n} A_j \sin kl_j - \frac{i}{\rho_0 c_0}\sum_{j=2}^{n} A_j \frac{\cos kl_j}{\sin kl_j}(\cos kl_1 - \cos kl_j) + \frac{i}{\rho_0 c_0}\frac{\Sigma_{j=1}^{n} A_j(\cos kl_j / \sin kl_j)}{\Sigma_{j=1}^{n}(A_j / \sin kl_j)} \times \left(\sum_{j=2}^{n} \frac{A_j(\cos kl_1 - \cos kl_j)}{\sin kl_j}\right), \tag{14}$$

and

$$T_{22}=\frac{\Sigma_{j=1}^{n}A_j(\cos kl_j/\sin kl_j)}{\Sigma_{j=1}^{n}(A_j/\sin kl_j)}. \tag{15}$$

Equation (14) may be rearranged further as

$$T_{21}=\frac{i}{\rho_0 c_0}\sum_{j=1}^{n}\frac{A_j}{\sin kl_j}-\frac{i}{\rho_0 c_0}\times\left(\frac{\Sigma_{j=1}^{n}A_j(\cos kl_j/\sin kl_j)}{\Sigma_{j=1}^{n}(A_j/\sin kl_j)}\right)\sum_{j=1}^{n}\frac{A_j\cos kl_j}{\sin kl_j}. \tag{16}$$

Now all four components of the overall transfer matrix defined by Eq. (1) are expressed in closed form by Eqs. (11), (12), (15), and (16).

The expression for the transmission loss (TL) in terms of the transfer matrix elements T_{ij}'s is given by

$$\mathrm{TL}=20\log_{10}\left|\frac{1}{2}\left(T_{11}+\frac{A_d}{\rho_0 c_0}T_{12}+\frac{\rho_0 c_0}{A_u}T_{21}+\frac{A_d}{A_u}T_{22}\right)\sqrt{\frac{A_u}{A_d}}\right|. \tag{17}$$

If the areas of the inlet and outlet ducts are the same, i.e., $A_u=A_d$, the following expression for the transmission loss can be deduced from Eqs. (11), (12), (15), (16), and (17):

$$\mathrm{TL}=20\log_{10}\left|\frac{i}{2A_u}\left[\sum_{j=1}^{n}\frac{A_j}{\sin kl_j}+\frac{(A_u-i\Sigma_{j=1}^{n}A_j\cos kl_j/\sin kl_j)^2}{\Sigma_{j=1}^{n}A_j/\sin kl_j}\right]\right| \tag{18}$$

with resonances occurring when

$$\sum_{j=1}^{n}\frac{A_j}{\sin kl_j}=0. \tag{19}$$

Stewart (1945) reported a similar resonance criterion for a two-duct system. A formal proof for the two-duct system was later presented by Selamet *et al.* (1994).[1]

For the two-duct configuration, Eq. (18) can be shown to be identical to Eq. (8) of Selamet *et al.* (1994) if the following substitution is made:

$$\alpha_j=\frac{e^{-ikl_j}}{1-e^{-2ikl_j}},\quad \phi_j=\frac{1+e^{-2ikl_j}}{1-e^{-2ikl_j}},\quad n=2. \tag{20}$$

For the special case of equal l_j's, that is, $l_1=l_2=l_3=\cdots=l_n=l$, the expression for transmission loss, Eq. (18), reduces to

$$\mathrm{TL}=10\log_{10}[1+\tfrac{1}{4}(m-1/m)\sin^2 kl], \tag{21}$$

where the area ratio $m=\Sigma_{j=1}^{n}A_j/A_u$. This expression is identical, as expected, to that of the simple expansion chamber by Davis *et al.* (1954). The next section provides illustrative examples from a three-duct Herschel–Quincke tube, coupled with some comparisons to two-duct classical configuration.

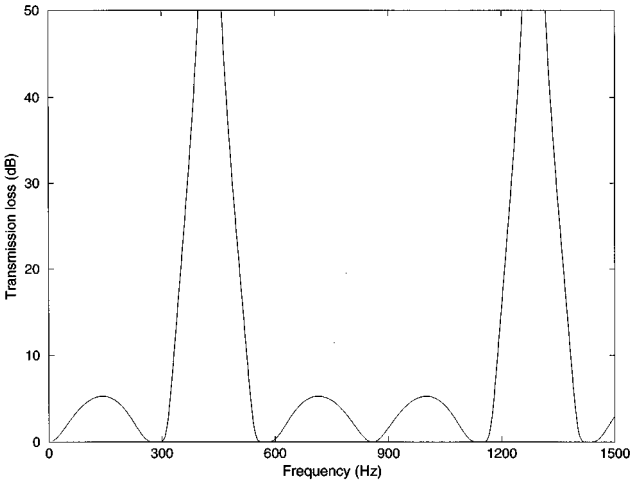

FIG. 2. Transmission loss characteristics of a three-duct Herschel–Quincke tube ($d_1=d_2=d_3=0.05$ m, $l_1=0.4$ m, and $l_2=l_3=0.8$ m).

II. RESULTS

The presence of numerous resonances, as dictated by Eq. (19), complicates the attenuation behavior of even the two-duct classical Herschel–Quincke tube. The increasing number of ducts will clearly lead to more complex attenuation patterns. As a result, it becomes more difficult to choose a combination of duct dimensions to illustrate the overall characteristics of modified Herschel–Quincke structures with n ducts, and to arrive at general conclusions. The objective of the present section is to select some interesting combination of dimensions and point out some of the typical behavior. In view of practically infinite possibilities and variations with the dimensions and the number of ducts, the present study confines the illustration to three-duct structures with some discrete duct lengths and diameters. Nevertheless, the analytical expressions developed in this study, including Eqs. (17) or (18), coupled with Eq. (19), are expected to enable the reader to perform calculations for any arbitrary configuration.

For all the figures illustrated in this paper the diameter of the ducts upstream of the inlet junction and downstream of the outlet junction are, respectively, $d_u=0.05$ m and $d_d=0.05$ m. Also, the following default values are used for various parameters: $d_1=d_2=d_3=0.05$ m, $l_1=0.4$ m, and $l_2=l_3=0.8$ m. Thus while holding all diameters the same, the lengths of the second and third ducts are specified as twice the length of the first duct. The variation of transmission loss as a function of frequency for a three-duct modified Herschel–Quincke tube with the default dimensions is shown in Fig. 2. This configuration exhibits frequency bands where the transmission loss is high. The corresponding resonance frequencies may be determined from Eq. (19) as 428.75 and 1286.25 Hz, for the first and second peaks, respectively. Secondary peaks associated with a broadband transmission loss behavior may also be observed in the same figure. The width of the attenuation bands near resonances is considerable, which may prove to be useful in noise control. This particular plot is superimposed in a number of

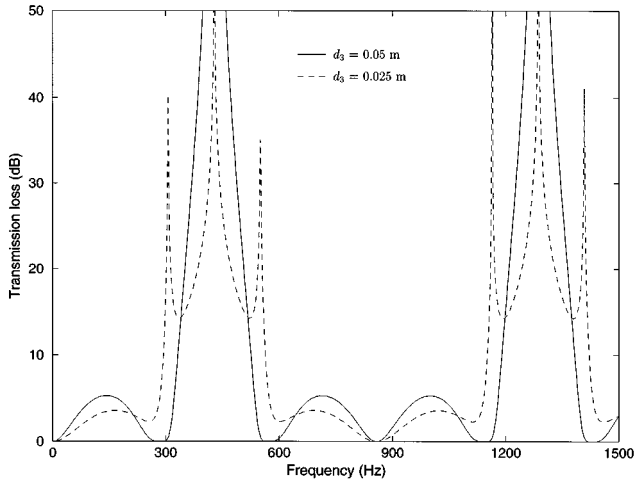

FIG. 3. Effect of duct diameter on transmission loss ($d_1=d_2=0.05$ m, $l_1=0.4$ m, and $l_2=l_3=0.8$ m).

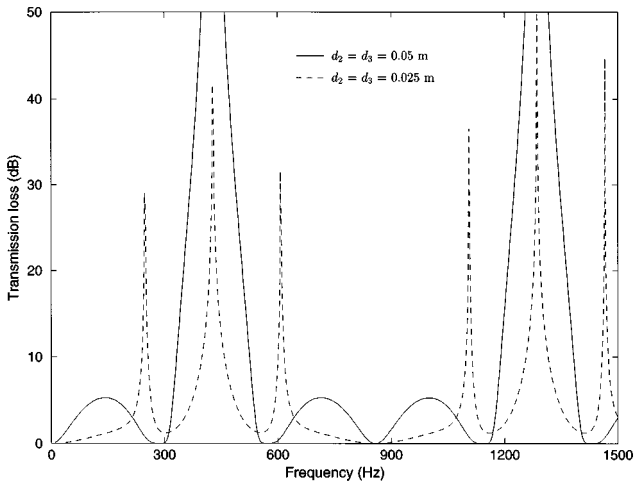

FIG. 5. Effect of changing the diameter of two ducts on the transmission loss ($d_1=0.05$ m, $l_1=0.4$ m, and $l_2=l_3=0.8$ m).

figures that follow to provide a common basis for comparison.

The TL characteristics of the three-duct Herschel–Quincke tube is shown in Fig. 3 for two different values of the diameter of one of the ducts, that is, for $d_3=0.025$ m and $d_3=0.05$ m. Note that the curve represented by the solid line is identical to that shown in Fig. 2, as indicated earlier. Lowering the diameter broadens the resonant frequency band and introduces local TL minima in the neighborhood of resonance. Increasing the duct diameter increases the TL of the secondary peaks. The effect of varying the length of one of the ducts, say l_3, from its default value of 0.8 to 1.0 m, on the TL behavior, is shown in Fig. 4. Increasing the length of the duct shifts the peaks and introduces secondary resonances.

Figure 5 illustrates the effect of changing the diameter of two ducts, say d_2 and d_3, from their default values of $d_2=d_3=0.05$ m to $d_2=d_3=0.025$ m, on the TL characteristics. Increasing the duct dimensions significantly enhances the transmission loss. Similarly, the effect of changing the length of two ducts, that is, l_2 and l_3 from their default values to $l_2=l_3=0.4$ m and $l_2=l_3=1.0$ m, on the TL behavior is depicted in Fig. 6. The dashed line corresponds to the TL of an expansion chamber [see Eq. (21)]. The expansion chamber can be seen to be inferior in overall performance to the modified Herschel–Quincke tube.

Figures 7 and 8 compare the attenuation and resonance behavior of the foregoing three-duct arrangement to that of the classical two-duct Herschel–Quincke tube for two different values of the diameter of duct 2, that is, for $d_2=0.05$ m (default) and $d_2=0.025$ m, respectively. The difference in the performance of the two-duct and three-duct Herschel–Quincke tubes is significant. However, this difference seems to decrease with increasing duct diameter. The comparison of the attenuation and resonance behavior of the three-duct and the classical Herschel–Quincke tube in Fig. 9 for $l_2=1.0$ m to that of Fig. 7 for $l_2=0.8$ m illustrates the increasing complexity and the differences with changing length.

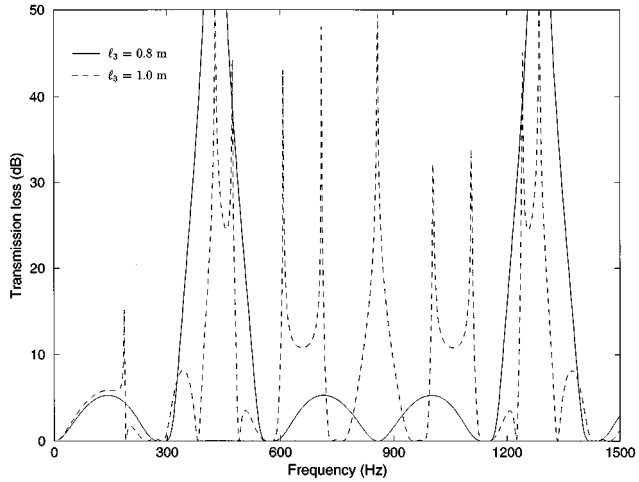

FIG. 4. Effect of duct length on transmission loss ($d_1=d_2=d_3=0.05$ m, $l_1=0.4$ m and $l_2=0.8$ m).

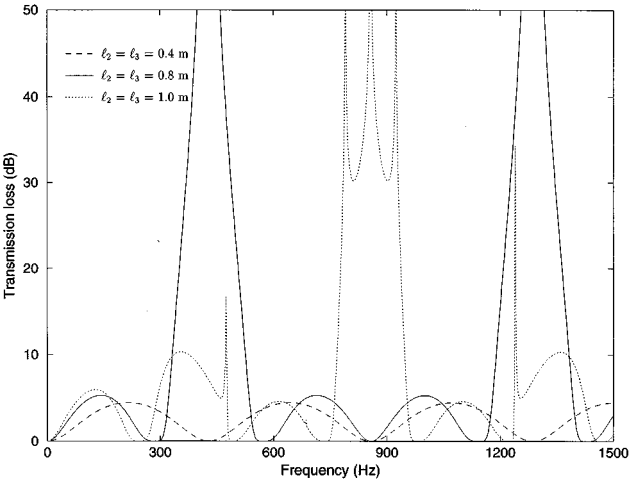

FIG. 6. Effect of changing the length of two ducts on the transmission loss ($d_1=d_2=d_3=0.05$ m and $l_1=0.4$ m).

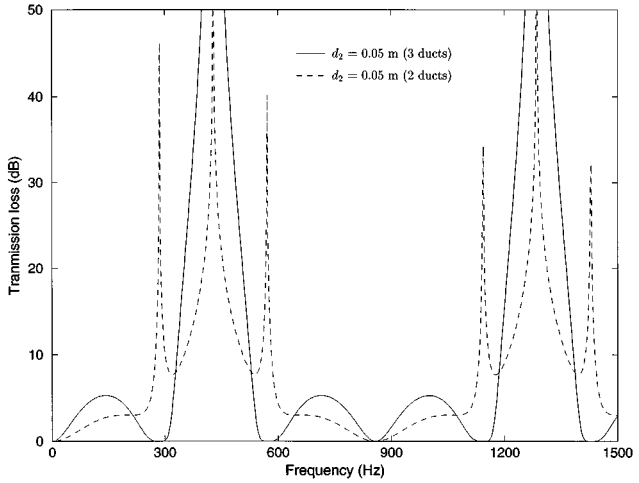

FIG. 7. Comparison of the transmission loss of a three-duct modified and the two-duct classical Herschel–Quincke tubes ($d_1 = d_3 = 0.05$ m, $l_1 = 0.4$ m, and $l_2 = l_3 = 0.8$ m).

III. CONCLUDING REMARKS

The present study has generalized the treatment of the classical two-duct Herschel–Quincke tube to an n-duct configuration. A closed-form expression has been developed for the transmission loss characteristics, as well as for the resonance locations. Due to a prohibitive number of variations, the results are illustrated only in terms of three-duct arrangements, along with a comparison to two-duct configurations. However, the expressions developed in the study are valid for any number of ducts and cross-sectional area combination, including that of inlet and outlet ducts. Thus, the methodology and the equations derived in this paper are expected to be useful in examining the attenuation behavior of these structures in noise control applications.

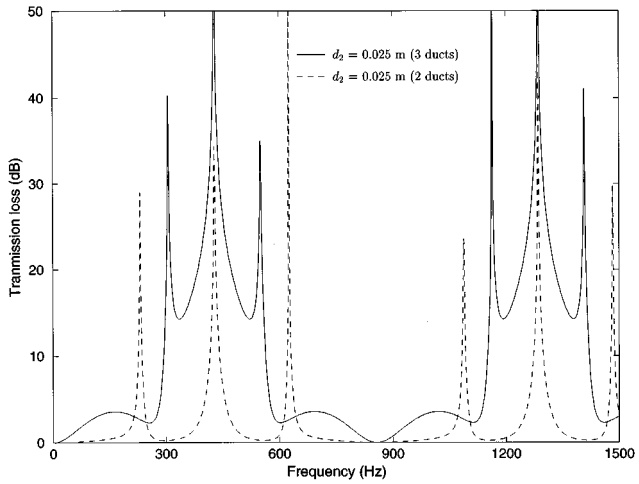

FIG. 8. Comparison of the transmission loss of a three-duct modified and the two-duct classical Herschel–Quincke tubes ($d_1 = d_3 = 0.05$ m, $l_1 = 0.4$ m, and $l_2 = l_3 = 0.8$ m).

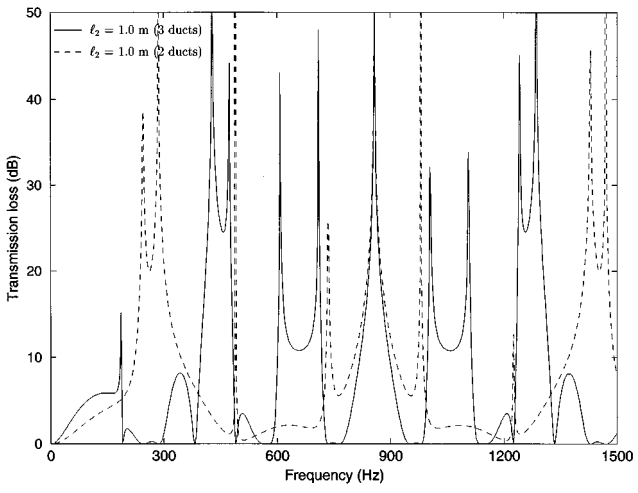

FIG. 9. Comparison of the transmission loss of a three-duct modified and the two-duct classical Herschel–Quincke tubes ($d_1 = d_2 = d_3 = 0.05$ m, $l_1 = 0.4$ m, and $l_3 = 0.8$ m).

ACKNOWLEDGMENTS

We wish to thank Professor C. R. Fuller of the Virginia Polytechnic Institute and Professor J. Kergomard of Université du Maine, who kindly brought their own published works in the related areas to our attention. Professor Kergomard also pointed out Stewart's brief, yet useful article published in 1945 in the *Journal of the Acoustical Society of America*.

[1]Let, for example, $\sin kl_m \to 0$ (for $j = m$). The resonance may then appear to be occurring in view of a brief look at the first term in Eq. (18). In reality, for such a condition, the terms with $\sin kl_m$ may be shown to cancel out in Eq. (18), leaving Eq. (19) as the only proper relationship to describe resonances.

Brice, C. H. (**1929**). ''Exhaust silencer for internal-combustion engines,'' U.S. Patent No. 1,740,805.

Chen, C. C., and Hastings, M. C. (**1994**). ''Half-wavelength tuning cables for passive noise control in automotive power steering systems,'' Act. Control Vib. Noise, ASME Proc. **DE-75**, 355–361.

Davis, D. D., Jr., Stokes, G. M., Moore, D., and Stevens, G. L., Jr. (**1954**). ''Theoretical and experimental investigation of mufflers with comments on engine-exhaust muffler design,'' National Advisory Committee for Aeronautics Report No. 1192.

Depollier, C., Kergomard, J., and Lesueur, J. C. (**1990**). ''Propagation of low frequency acoustic waves in periodic 2-D lattices of tubes,'' J. Sound Vib. **142,** 153–170.

Feuling, J. J. (**1991**). ''Muffler for an internal combustion engine,'' U.S. Patent No. 5,033,581.

Fuller, C. R., and Bies, D. A. (**1978**). ''A reactive acoustic attenuator,'' J. Sound Vib. **56,** 45–59.

Fuller, C. R., and Bies, D. A. (**1979**). ''The effects of flow on the performance of a reactive acoustic attenuator,'' J. Sound Vib. **62,** 73–92.

Herschel, J. F. W. (**1833**). ''On the absorption of sound by coloured media, viewed in connection with undulatory theory,'' Philos. Mag. **3,** 401–412.

Hixson, E. L., and Kahlbau, J. V. (**1963**). ''Quincke-tube acoustic filter for fluid ducts,'' J. Acoust. Soc. Am. **35,** 1895.

Holmes, W. H. (**1926**). ''Hydrocarbon motor,'' U.S. Patent No. 1,591,088.

Luxton, R. E. (**1968**). ''A low pressure loss attenuating bend for air flow ducts,'' Presented at the 6th International Congress on Acoustics, Tokyo (unpublished).

Ohashi, Y. (**1981**). ''Exhaust device for internal combustion engines,'' U.K. Patent No. 2,056,555.

Quincke, G. (**1866**). ''Ueber interferenzapparate für schallwellen,'' Ann. Phys. Chem. **128**, 177–192.

Rayleigh, B. (**1945**). *The Theory of Sound* (Dover, New York).
Rostafinski, W. J. (**1991**). ''Monograph of Sound Waves in Curved Ducts,'' NASA Ref. Pub No. 1248.
Selamet, A., Dickey, N. S., and Novak, J. M. (**1994**). ''The Herschel–Quincke tube: A theoretical, computational, and experimental investigation,'' J. Acoust. Soc. Am. **96,** 3177–3185.
Smith, B. (**1935**). ''Exhaust silencer for internal combustion engines,'' U.S. Patent No. 2,019,697.
Stewart, G. W. (**1928**). ''The theory of Herschel–Quincke tube,'' Phys. Rev. **31,** 696–698.
Stewart, G. W., and Lindsay, R. B. (**1930**). *Acoustics* (Van Nostrand, Princeton, NJ).
Stewart, G. W. (**1945**). ''The theory of Herschel–Quincke tube,'' J. Acoust. Soc. Am. **17,** 107–108.
Sun, Y. (**1987**). ''Exhaust silencer for internal combustion engines,'' U.S. Patent No. 4,712,644.

Vorticity and entropy boundary conditions for acoustical finite-difference time-domain simulations

D. Botteldooren
Department of Information Technology, University of Gent, St. Pietersnieuwstraat 41, 9000 Gent, Belgium

(Received 7 February 1997; revised 15 March 1997; accepted 31 March 1997)

In this paper a time-domain numerical model for describing the presence of vorticity and entropy boundary layers is introduced. The boundary model can be inserted in acoustic time-domain models such as the finite-difference time-domain (FDTD) model for studying the acoustic behavior of high-quality resonator structures. The main focus in deriving the model is on numerical efficiency. Boundary layer theory is reviewed to obtain a three-dimensional formulation of its influence on FDTD equations that must be applied in boundary discretization cells. The $\sqrt{\omega}$ dependence that is encountered is approximated in time domain in such a way that no numerical convolution is required. Although this approximation is rather inaccurate, it is sufficient for most applications and introduces almost no extra computational effort. Several numerical examples illustrate the applicability of the model. © *1997 Acoustical Society of America.* [S0001-4966(97)05507-0]

PACS numbers: 43.20.Px, 43.20.Mv, 43.30.Gv [JEG]

INTRODUCTION

In highly resonant acoustic structures such as Helmholtz resonators, long hard ducts, strongly resonant enclosures, etc., absorption caused by the medium itself becomes important. In free air, molecular relaxation, viscosity and heat flux are important. In the presence of hard boundaries, absorption is often dominated by very thin layers near this boundary, called vorticity and entropy layers.[1] These layers are naturally incorporated in the solution of the wave equations that include viscosity and heat flux if appropriate boundary conditions are imposed. Solving the equations numerically leads to serious discretization problems because length scales of acoustic effects are typically several orders of magnitude larger than the boundary layer thickness. Using grid refinement near the boundary can solve the problem to some extent, but numerical cost remains considerable. In this paper it is therefore assumed that the boundary layer is much thinner than the typical grid cell required for the acoustic simulation, and a special boundary cell numerical model is introduced to take into account the influence of both vorticity and entropy layers.

First, boundary layer theory is reviewed. The mathematical theory starts from a formulation of the equations of linear acoustics in terms of acoustic pressure fluctuation p, acoustic density fluctuation ρ, and acoustic particle velocity $\mathbf{v}$. The equations include viscosity, heat flux, molecular rotational relaxation and molecular vibrational relaxation. It is preferred to stick with pressure and density to describe the absorption effects rather than to switch to the more usual entropy formulation for compatibility with linear acoustic studies in lossless media. When the boundary layer assumption is introduced in the derivation of the numerical model that can be applied in a boundary cell, a full three-dimensional description of boundary layer absorption emerges naturally.

The equations for the boundary cells have an important drawback. They include a $\sqrt{\omega}$ frequency dependence. An accurate transformation of this frequency dependence to time domain introduces a convolution. In general, this convolution must be evaluated numerically for each time step. This introduces an important calculation overhead. Recent papers in the field of electromagnetics[2,3] give some ideas on how to approximately solve the problem. Here the $\sqrt{\omega}$ frequency dependence is approximated by a combination of frequency domain functions that transform back to time-domain expressions that can more easily be evaluated numerically. The result is a numerical model for the boundary layer that requires only a very limited amount of additional CPU time.

The examples given at the end of this paper are mainly chosen to demonstrate the accuracy and applicability of the new boundary layer numerical formulation.

I. MATHEMATICAL MODEL

A. Equations of linear acoustics

To study the influence of vorticity and entropy boundary layers on the absorption of sound, an accurate free-field mathematical model must be used as a starting point. It is assumed that all boundaries of the acoustic environment that are studied are acoustically hard and that no material other than air is present in the simulation region. The frequency range of interest corresponds approximately to the audible frequency range. To cover this broad range several absorption mechanisms must be taken into account: fluid viscosity, heat flux, molecular rotational relaxation and molecular vibrational relaxation. Fluid viscosity μ influences the linearized Euler equation only.[1,4] It now reads

$$\rho_0 \frac{\partial \mathbf{v}}{\partial t} = -\nabla p + \frac{\mu}{3}\nabla(\nabla\cdot\mathbf{v}) + \mu\nabla^2\mathbf{v}, \tag{1}$$

where no static fluid flow is assumed, $\mathbf{v}$ is the acoustical particle velocity, p is the acoustic pressure, and ρ_0 is the density of air. Pierce[1] proves that the small departure of translational and rotational molecular kinetic energy from mutual thermodynamic equilibrium can be taken into account up to first order in acoustical quantities by introducing a bulk viscosity μ_B in Eq. (1). This gives

$$\rho_0 \frac{\partial \mathbf{v}}{\partial t} = -\nabla p + \left(\mu_B + \frac{\mu}{3}\right)\nabla(\nabla\cdot) + \mu\nabla^2\mathbf{v}. \tag{2}$$

The linearized conservation of mass equation is not changed by introducing the absorption mechanisms that are under consideration:

$$\frac{\partial \rho}{\partial t} = -\rho_0 \nabla\cdot\mathbf{v}. \tag{3}$$

To take into account sound absorption by heat conduction in the acoustic wave, nonadiabatic sound propagation must to be studied. This is often done by introducing acoustic entropy and temperature change as new variables.[1] Because sound pressure is much more often used for studying linear sound propagation, the energy conservation equation was transformed to a pressure equation that includes both the heat conduction and vibrational molecular relaxation terms in Ref. 4. In its linearized form the pressure equation reads

$$\frac{\partial p}{\partial t} = -\gamma p_0 \nabla\cdot\mathbf{v} + (\gamma-1)\kappa\nabla^2 T - (\gamma-1)\sum_i \frac{\rho_0 c_{vi}}{\tau_i} \times\left\{ T - \int^t T \exp\left(\frac{\tau - t}{\tau_i}\right)\frac{d\tau}{\tau_i}\right\}, \tag{4}$$

where γ is the ratio of specific heats, p_0 is the atmospheric pressure, κ is the coefficient of thermal conductivity, and T is the gas temperature (with vibrational molecular states frozen). The summation is over all types of molecules i present in the air gas mixture. The vibrational specific heat c_{vi} and the vibrational relaxation time τ_i can be obtained from absorption measurements and are found in literature. Since propagation Eqs. (3) and (4) for acoustic density and pressure are now different, acoustic density change will no longer be proportional to acoustic pressure change. Using the ideal gas law and the relation $\gamma p_0 = \rho_0 c^2$ between equilibrium pressure and equilibrium density, the gas temperature can be calculated in first order approximation as

$$T = \frac{p + p_0}{R(\rho + \rho_0)} \approx \frac{c^2}{\gamma R} + \frac{\gamma p - \rho c^2}{\gamma R \rho_0}. \tag{5}$$

Introducing this approximate value for T in Eq. (4) gives

$$\frac{\partial p}{\partial t} = -\gamma p_0 \nabla\cdot\mathbf{v} + \frac{(\gamma-1)}{\gamma R\rho_0}\kappa\nabla^2(\gamma p - \rho c^2) - \frac{(\gamma-1)}{\gamma R}\sum_i \frac{c_{vi}}{\tau_i}\left\{\gamma p - \rho c^2 - \int^t (\gamma p - \rho c^2) \times\exp\left(\frac{\tau - t}{\tau_i}\right)\frac{d\tau}{\tau_i}\right\}. \tag{6}$$

Since the absorption terms in Eq. (4) are small in free field and since ρ only influences the sound propagation through T, it is safe to assume $p = \rho c^2$ with first-order accuracy in the acoustic quantities, away from any boundaries. This approximation will easily be verified numerically in Sec. III. Introducing this approximation in Eq. (6) results in

$$\frac{\partial p}{\partial t} = -\gamma p_0 \nabla\cdot\mathbf{v} + \frac{(\gamma-1)^2}{\gamma R\rho_0}\kappa\nabla^2 p - \frac{(\gamma-1)^2}{\gamma R}\sum_i \frac{c_{vi}}{\tau_i}\left\{ p - \int^t p \exp\left(\frac{\tau - t}{\tau_i}\right)\frac{d\tau}{\tau_i}\right\}. \tag{7}$$

The set of equations (2) and (7) is sufficient to calculate sound propagation in free field, including all absorption mechanisms mentioned above and contains only $\mathbf{v}$ and p as unknown quantities. The numerical effort required to solve the set of equations is reduced considerably by this last approximation.

B. Vorticity and entropy boundary layer formulation

For simulations in linear acoustics it is sufficient to impose $\mathbf{v}\cdot\mathbf{n} = 0$ as a boundary condition when no absorption mechanisms are taken into account in Eqs. (2) and (6), where $\mathbf{n}$ is orthogonal on the surface. When viscosity and heat conduction terms are added to the equations for linear acoustics, assumptions must be made concerning tangential particle velocity and fluid temperature on the hard boundary. Three strategies can be considered:

(i) Real microscopic boundary conditions on a perfectly hard and heat conducting boundary imply that the tangential component of particle velocity is zero and the temperature near the boundary is equal to the constant surface material temperature. This approach implies that boundary layers are fully calculated and requires a very important numerical effort.

(ii) On the scale of acoustic wavelengths, boundary effects due to viscosity and heat conduction span only a very small region. Therefore, they are neglected in many circumstances. A corresponding boundary condition is

$$\frac{\partial \mathbf{v}_t}{\partial n} = 0 \quad \text{and} \quad \frac{\partial T}{\partial n} = 0, \tag{8}$$

where $\mathbf{v}_t$ is the tangential component of particle velocity. This approximation neglects all boundary absorption, which is the major sound absorption mechanism for highly resonant structures.

(iii) An analytical approach can be used for describing the vorticity and entropy boundary layers. The boundary condition for the acoustic simulation that is derived from this analytical approximation is the main subject of this paper.

The acoustic boundary layer theory[1] is based on the assumption that the solution of the full set of linear wave equations near a solid surface can be written as a superposition of an acoustic mode, an entropy mode and a vorticity mode. A solution for each of these fields is then found in the form of a plane wave: $\mathrm{Re}(\psi \exp(-j\omega t + j\mathbf{k}\cdot\mathbf{r}))$, where ω is the pulsation, $\mathbf{k}$ is the wave vector, and $\mathbf{r}$ is the spatial coordinate. For the vorticity and entropy part of the solution, the imaginary part of $\mathbf{k}$ is known to be quite large compared to the acoustic wave number in air. This means that vorticity and entropy fields must be localized near interfaces, surfaces and sources.

Based on this traditional theory it is assumed in this work that the total sound field very close to a flat acoustically hard surface only changes considerably in the direction n, which is orthogonal to this surface. As long as the boundary

layer is very thin compared to the wavelength of the sound and as long as the surface is flat on the same length scale, this is a good approximation. It is the only initial assumption that is made. The tangential velocity $\mathbf{v}_t$ at the boundary can be calculated by introducing this hypothesis in Eq. (2). This gives

$$\rho_0 \frac{\partial \mathbf{v}_t(n)}{\partial t} = \mu \frac{\partial^2 \mathbf{v}_t(n)}{\partial n^2}; \tag{9}$$

and the corresponding plane wave solution has the dispersion relation

$$k_n^2 = j\omega \frac{\rho_0}{\mu}, \tag{10}$$

where k_n is the orthogonal component of the wave vector $\mathbf{k}$. This dispersion relation, together with the condition that $\mathbf{v}_t = 0$ on the hard surface, completely describes the vorticity boundary field near the hard surface and will by used to obtain a special boundary cell in the numerical model.

To find a similar relation for the other acoustic quantities, the assumption that fields only change considerably in the n-direction is introduced in Eqs. (3) and (6) and in Eq. (2) for the v_n component only. Remark that Eq. (7) cannot be used since the assumption $p = \rho c^2$ is not valid in the boundary region. The resulting set of equations can be written in matrix form, where molecular relaxation effects have been omitted for simplicity since they do not contribute substantially to the boundary layer formation:

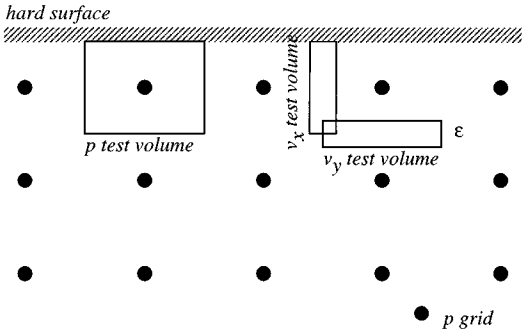

FIG. 1. Test volumes related to the unit cell that can be used to derive the FDTD equations.

$$\begin{pmatrix} \rho_0 \dfrac{\partial}{\partial t} - \left(\mu_B + \dfrac{4\mu}{3}\right)\dfrac{\partial^2}{\partial n^2} & \dfrac{\partial}{\partial n} & 0 \\ \gamma p_0 \dfrac{\partial}{\partial n} & \dfrac{\partial}{\partial t} - \dfrac{(\gamma-1)}{R\rho_0}\kappa\dfrac{\partial^2}{\partial n^2} & \dfrac{(\gamma-1)c^2}{\gamma R\rho_0}\kappa\dfrac{\partial^2}{\partial n^2} \\ \rho_0 \dfrac{\partial}{\partial n} & 0 & \dfrac{\partial}{\partial t} \end{pmatrix} \begin{pmatrix} v_n \\ p \\ \rho \end{pmatrix} = \begin{pmatrix} 0 \\ 0 \\ 0 \end{pmatrix}. \tag{11}$$

This set of equations has a nonzero solution only if the determinant of the first matrix is zero. After replacing the time derivative by $-j\omega$ and the spatial derivative by jk_n, a dispersion relation can be obtained that is of fourth order in k_n and of third order in ω. This equation can be solved for k_n^2 but the result is a rather complex function of ω. Taking into account the fact that μ, μ_B and κ are very small in air, two approximate solutions are found:

$$k_n^2 \approx \frac{\omega^2}{c^2} \quad \text{and} \quad k_n^2 \approx j\omega \frac{\gamma R \rho_0}{(\gamma-1)\kappa}. \tag{12}$$

The first relation describes the acoustic mode. Introducing this relation in Eq. (11) approximately gives the plane wave equations of linear acoustics with absorption neglected. The second dispersion relation describes the entropy field. From this relation and Eq. (11), it can be concluded that the entropy part of p must be very small. All field components v_n, p, and ρ show the same exponential behavior determined by this k_n in the entropy boundary region and so do all linear combinations of these fields. Of particular interest for the derivation of the numerical model is the combination $\gamma p - \rho c^2$ which is proportional to the change in temperature due to the sound wave as can be seen in Eq. (5). If the temperature of the hard surface can be assumed constant (and equal to the equilibrium temperature), then the quantity $\gamma p - \rho c^2$ is also zero on the surface. This completely describes the entropy boundary field.

II. NUMERICAL MODEL

A. General formulation

The numerical approximation to Eqs. (2) and (7) away from any boundary is based on a finite-difference time-domain (FDTD) discretization in a staggered grid.[5,6] In this paper the numerical approximation will be given in a Cartesian grid only. There is no fundamental problem in extending the implementation to a more general grid. The grid is described by the spatial steps δx, δy, and δz and the time step δt. In the following, a general spatial step is noted as $\delta\alpha$ and a spatial step orthogonal to a surface is noted as δn. Pressure p is discretized in locations given by integer multiples of the grid step; components of particle velocity are discretized in three staggered grids obtained by shifting this grid in the direction of the component that is considered, by half a grid step. Discretized pressure and particle velocity are determined at intermediate time, $t = \ell\,\delta t$ and $t = (\ell + 0.5)\,\delta t$, respectively.

The FDTD equations can be obtained by approximating all derivatives in Eqs. (2) and (7) by finite differences using a central difference scheme. An interesting alternative consists in integrating the analytic equations over well-chosen test volumes around the discretization locations. Suitable test volumes for pressure and particle velocity are shown in Fig. 1. Each approach leads to the set of FDTD equations

$$v_\alpha^{[\ell+0.5]}(\alpha+\tfrac{1}{2}) = v_\alpha^{[\ell-0.5]}\left(\alpha+\frac{1}{2}\right) - \frac{\delta t}{\rho_0\,\delta\alpha}(p^{[\ell]}(\alpha+1)-p^{[\ell]}) + \frac{\delta t(\mu_B+\mu/3)}{\rho_0\,\delta\alpha}(\psi^{[\ell]}(\alpha+1)-\psi^{[\ell]}) + \frac{\mu\,\delta t}{\rho_0}\chi_\alpha^{[\ell]}\left(\alpha+\frac{1}{2}\right), \tag{13}$$

and

$$p^{[\ell+1]} = p^{[\ell]} - \gamma p_0\ \delta t\ \psi^{[\ell+0.5]} + \frac{\kappa(\gamma-1)^2\ \delta t}{\gamma R\rho_0} \times \sum_\alpha \frac{p^{[\ell+0.5]}(\alpha+1)+p^{[\ell+0.5]}(\alpha-1)-2p^{[\ell+0.5]}}{\delta\alpha^2} - \frac{(\gamma-1)^2\delta t}{\gamma R\rho_0}\sum_i \frac{c_{vi}}{\tau_i}\{p^{[\ell+0.5]}-I_{\tau_i}^{[\ell+0.5]}\}, \tag{14}$$

with

$$\psi^{[\ell+0.5]} = \sum_\alpha \frac{v_\alpha^{[\ell+0.5]}(\alpha+\frac{1}{2})-v_\alpha^{[\ell+0.5]}(\alpha-\frac{1}{2})}{\delta\alpha}, \tag{15}$$

$$\chi_\alpha^{[\ell+0.5]}(\alpha+\tfrac{1}{2}) = \sum_{\alpha'} \frac{v_\alpha^{[\ell+0.5]}(\alpha+\frac{1}{2},\alpha'+1)+v_\alpha^{[\ell+0.5]}(\alpha+\frac{1}{2},\alpha'-1)-2v_\alpha^{[\ell+0.5]}(\alpha+\frac{1}{2})}{\delta\alpha'^2}, \tag{16}$$

where the index ℓ in square brackets is used for time discretization and where the spatial indices for the central pressure discretization location are omitted and spatial translation in the α-direction over $\delta\alpha/2$ is indicated as $(\alpha+\frac{1}{2})$. Summations over α run over the three Cartesian indices. A new variable I_{τ_i}, that contains the time integration up to now, is introduced. It can be calculated from the pressure p and its previous value at each time step as will be shown in Eq. (22). It is well known that a central difference approximation matches the staggered grid discretization completely for linear lossless sound propagation. Absorption terms in Eqs. (13) and (14) conserve the spatial match but introduce a time discretization mismatch; some quantities are needed at a moment in time where the are not calculated. An accurate and stable way to resolve this mismatch consists in interpolating linearly between the previously calculated value and the value that is calculated in the current time step. The drawback of this approach is that it interrelates the FDTD equations at different spatial locations. This increases the computational effort needed to solve the system of equations at each time step considerably. Since the terms involved are much smaller than the major terms in the FDTD equations, a less accurate approach seems sufficient. Two alternatives, which have comparable numerical accuracy, were tested. The first one consists in assuming that the unknown values are the same as the value $\delta t/2$ ago, which is known. The second one consists in extrapolating linearly to the future. The latter approach requires an increase in storage by about 50% but calculation time remains practically unchanged. Mainly because of the storage requirement, the first approximation is preferred. Stability analyses cannot be performed analytically. The approach is not unconditionally stable but since constants involved in the additional terms in the stability condition are always small, it can be assumed that the stability condition for lossless sound propagation $c\,\delta t < (1/\delta x + 1/\delta y + 1/\delta z)^{-1/2}$ is sufficient. This assumption is validated experimentally.

B. Special boundary cell formulation

In FDTD simulation, grid cells typically have a diameter that is about one tenth of the wavelength of the highest frequency of interest. In air, vorticity and entropy boundary effects typically span only a much smaller range even for the highest frequencies of interest. Therefore it is useful to try to incorporate the influence of the whole boundary layer on sound propagation in a single layer of special boundary cells. The derivation of the special FDTD equations for the boundary cell starts from Eqs. (2) and (6). These equations include first and second order derivatives of the unknown quantities. Only the derivatives orthogonal to the boundary are important if the boundary layer conditions stated in Sec. I B are fulfilled. The treatment of all field quantities is very similar. Therefore a description for a general field Ξ is given first. The field is assumed to be zero on the surface and to increase approximately exponentially away from the surface, so in the frequency domain

$$\Xi(n) \approx \Xi_0(1-e^{jk_n n}), \tag{17}$$

where k_n is the appropriate root from Eq. (10) or (12) and Ξ_0 is a constant. The discrete fields introduced in the previous section are easily interpreted as average values over the volume or surface of an elementary cell. Since Ξ is assumed to be constant in a plane parallel to the boundary, only an average over the n-direction will be important. If δn is the grid step in the n-direction this leads to

$$\frac{1}{\delta n}\int_0^{\delta n}\Xi(n)dn \approx \Xi_0\left(1-\frac{1}{jk_n\delta n}(e^{jk_n\delta n}-1)\right)\approx \Xi_0,$$

$$\frac{1}{\delta n}\int_0^{\delta n}\frac{\partial\Xi(n)}{\partial n}dn \approx -\frac{\Xi_0}{\delta n}(e^{jk_n\delta n}-1)\approx \frac{\Xi_0}{\delta n}, \tag{18}$$

$$\frac{1}{\delta n}\int_0^{\delta n}\frac{\partial^2\Xi(n)}{\partial n^2}dn \approx -\frac{jk_n\Xi_0}{\delta n}(e^{jk_n\delta n}-1)\approx \frac{jk_n\Xi_0}{\delta n},$$

where the last approximations are based on the assumption that $jk_n\delta n$ has a very large negative real part. This is the case if the grid cell is much larger than the boundary layer thickness. The first two relations in Eq. (18) can very easily be transformed back into time domain. The third relation poses a problem since both entropy layer and vorticity layer dispersion relations introduce a $\sqrt{\omega}$ frequency dependence through k_n.

Transforming this frequency dependence back to time domain is not an easy task. Recently Szabo[7] obtained a parabolic wave equation for lossy media obeying a general frequency power law. For the special case studied here (power $\frac{1}{2}$), his result requires a convolution in time domain with $t^{-3/2}$. The numerical implementation of this convolution requires a serious calculation effort at each time step and an important amount of additional storage. A less accurate, but more efficient approximation is required.

A time-domain approximation corresponding to the $\sqrt{\omega}$ dependence is obtained as a combination of a number of functions that can easily be implemented in time domain. In general the time-domain simulation is used to study signals that have a limited frequency content. Typically a frequency range of about one octave around a known central frequency f_0 is sufficient. Furthermore it is imposed that the absorption part of the approximation should not drop to zero at higher frequencies. High frequencies are not modeled accurately and some nonphysical absorption that eliminates them is appreciated. This is especially true if nonlinear effects are taken into account. Finally, the phase part can be approximated less accurately than the absorption part.

Frequency dependence that is easily implemented in time-domain models are low order integer powers of $j\omega$ or $1/j\omega$, and $1/(a-j\omega)$ which correspond to time derivatives, time integrations and a convolution with an exponential decay function in time domain, respectively. A comparison of different linear combinations of these basis functions learns that

$$-j\sqrt{j\omega}\approx C\frac{j\omega}{j\omega-1/\tau_0} \tag{19}$$

is a reasonable choice. In this approximation τ_0 is a relaxation parameter and C is a multiplier that can be used to tune the approximation. Figure 2(a) shows real and imaginary parts of the approximate frequency dependence for a fitted parameter set $\tau_0=1.2/\omega_0$ and $C=1.2\sqrt{\omega_0}$. The stars on the ω axes of this figure are the limits of the octave band around ω_0. For comparison a similar accuracy estimate is shown in Fig. 2(b) for Szabo's approach. A not sophisticated numerical integration based on the last 128 and 16 samples is used to evaluate the convolution. If sufficient samples are used this approximation becomes very accurate as can be expected.

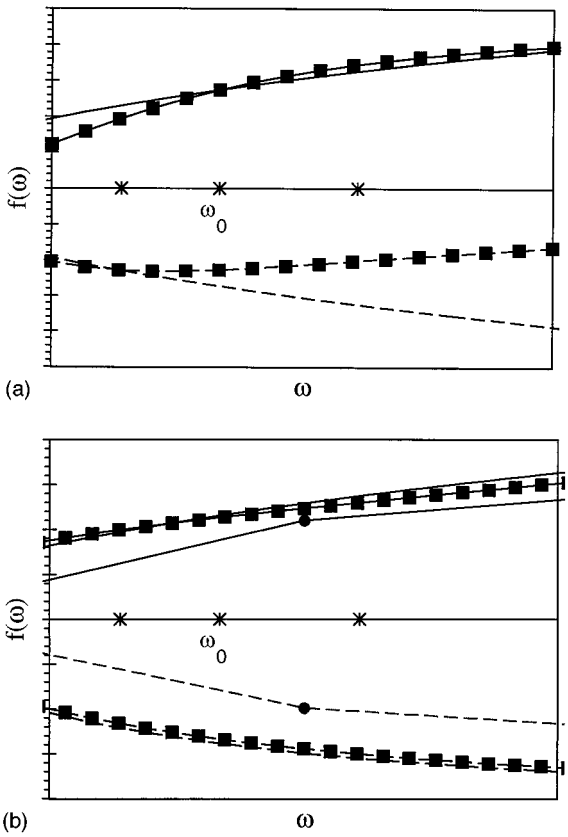

FIG. 2. Approximated frequency dependence (a) for the approximation used in this work (squares), (b) for the convolution approach using 128 (squares) and 16 (circles) past values; full line shows real part, dashed line shows imaginary part; stars limit one octave band

Based on the above approximation, the last equation of (18) can now be transformed back to time domain. Using the vorticity dispersion relation in Eq. (10) this leads to

$$\frac{1}{\delta n}\int_0^{\delta n}\frac{\partial^2\xi(n,t)}{\partial n^2}dn \approx -\frac{C}{\delta n}\sqrt{\frac{\rho_0}{\mu}}\left(\xi_0(t) - \frac{1}{\tau_o}\int_{-\infty}^{t}\xi_0(\tau)e^{(\tau-t)/\tau_0}\,d\tau\right), \tag{20}$$

where $\xi(n,t)$ and $\xi_0(t)$ are the time domain equivalents of $\Xi(n)$ and Ξ_0. To calculate the time integration numerically, a recursion formula can be found from

$$\frac{1}{\tau_o}\int_{-\infty}^{t+\delta t}\xi_0(\tau)e^{(\tau-(t+\delta t))/\tau_0}\,d\tau \approx \xi_0\left(t+\frac{\delta t}{2}\right)(1-e^{-\delta t/\tau_0}) + e^{-\delta t/\tau_0}/\tau_o\int_{-\infty}^{t}\xi_0(\tau)e^{(\tau-t)/\tau_0}\,d\tau, \tag{21}$$

where ξ_0 was assumed constant over a time interval δt. If the value of the integration up to $t=\ell\,\delta t$ is stored in the variable $I_{\tau_0}^{[\ell]}$ then the discrete form of Eq. (21) can be written as

$$I_{\tau_0}^{[\ell+1]} = \xi_0^{[\ell+1/2]}(1-e^{-\delta t/\tau_0}) + e^{-\delta t/\tau_0} I_{\tau_0}^{[\ell]}. \tag{22}$$

Special boundary cell FDTD equations can now be derived from Eqs. (2) and (6). Relevant changes to the FDTD Eqs. (14) and (13) can most easily be found by integrating (or averaging) the relevant acoustic equation over a well-chosen test volume. For the pressure equation (6) this test volume is the beam with dimensions δx, δy, and δz spanned around the discretization point (Fig. 1). At the left hand side of this equation, the pressure is averaged over the test volume. Equation (18) learns that this average is approximately equal to the value away from the boundary layer. The first term on the right hand side contains an integration of $\boldsymbol{\nabla}\cdot\mathbf{v}$, which can be transformed to an integration of the orthogonal component of $\mathbf{v}$ over the closed surface of the test volume. On the different flat sub-surfaces this integration equals the unknown components of the particle velocity, which include entropy and vorticity fields. In particular on the hard surface $v_n = 0$ can be used to first order. The summation over molecular vibration resonances contains only averaging of p and ρ over the test volume. They can be approximated as shown in Eq. (18) by the value away from the boundary. Therefore it is also possible to calculate ρ in this part of the equation by using the relation $p = \rho c^2$. The second term on the right-hand side contains an average of $\nabla^2(\gamma p - \rho c^2)$ over the test volume. As was argued in Section I B, $(\gamma p - \rho c^2)$ changes primarily in the direction orthogonal to the boundary so the derivatives parallel to this boundary can safely be neglected compared to the orthogonal derivative. The average of the second order derivative orthogonal to the boundary of $(\gamma p - \rho c^2)$ can be calculated by substituting $\xi(n,t)$ by $(\gamma p - \rho c^2)$ in the equivalent of Eq. (20) for the entropy layer. The quantity $\xi_0(t)$ now corresponds to the value of $(\gamma p - \rho c^2)$ away from the boundary, which is equal to $(\gamma - 1)p$. Taking into account these remarks a first FDTD equation for a boundary cell is obtained

$$\begin{aligned} p^{[\ell+1]} = p^{[\ell]} &- \gamma p_0 \ \delta t \ \psi^{[\ell+0.5]} \\ &- \frac{(\gamma-1)C}{\delta n}\sqrt{\frac{(\gamma-1)\kappa}{\gamma R \rho_0}}(p^{[\ell+0.5]} - I_{\tau_0}^{[\ell+0.5]}) \\ &- \frac{(\gamma-1)^2}{\gamma R \rho_0}\sum_i \frac{c_{vi}}{\tau_i}\{p^{[\ell+0.5]} - I_{\tau_i}^{[\ell+0.5]}\}, \end{aligned} \tag{23}$$

where Eq. (21) with ξ_0 replaced by p is used to update $I_{\tau_0}^{[\ell+0.5]}$ and $I_{\tau_i}^{[\ell+0.5]}$ every time step and ψ is defined in Eq. (15).

Equation (2) must be studied separately for the orthogonal and for the parallel component of the particle velocity. A flat test volume of height ϵ located around each surface of the test volume used to derive the pressure equation can be used (Fig. 1). All terms in Eq. (2) applied to one component of the particle velocity are integrated over the appropriate test volume. The time derivative on the left-hand side reduces to the time derivative of the discretized unknown velocity: the orthogonal component averaged over a surface of the pressure test volume. The volume integration of the first and second term on the right-hand side can be transformed to an integration over the surface surrounding the test volume.

TABLE I. Absorption (/m) in a long duct for different spatial discretization steps.

$\delta\alpha$	FDTD simulation	Analytical	Relative difference
$\lambda/14$	2.22×10^{-4}	2.47×10^{-4}	9.97%
$\lambda/28$	2.34×10^{-4}	2.47×10^{-4}	5.22%
$\lambda/56$	2.41×10^{-4}	2.47×10^{-4}	2.46%

The contribution of the small sides of the test volume is zero since these surfaces are orthogonal to the velocity component that is considered. The integration over the two larger surfaces introduces a gradient of p and $\boldsymbol{\nabla}\cdot\mathbf{v}$. Both can be calculated from the assumption that p and $\boldsymbol{\nabla}\cdot\mathbf{v}$ vary linearly between known values in the center of the adjacent pressure test volumes. Boundary layers only influence these terms indirectly through p and $\boldsymbol{\nabla}\cdot\mathbf{v}$. The last term on the right-hand side must be studied more carefully. For a parallel component of particle velocity v_α the test volume clearly crosses the boundary layer. The average of the second order derivative orthogonal to the boundary can be calculated by substituting $\xi(n,t)$ by v_α in Eq. (20), since v_α is zero on the boundary and decays according to dispersion relation (10) as explained in Sec. I B. The quantity $\xi_0(t)$ now corresponds to the value of v_α away from the boundary. Second-order derivatives parallel with the surface are neglected since they are much smaller than the orthogonal derivative. Taking into account these remarks, the FDTD equation for a component v_α parallel with the surface, in a boundary cell is obtained

$$\begin{aligned} v_\alpha^{[\ell+0.5]}(\alpha+\tfrac{1}{2}) = v_\alpha^{[\ell-0.5]}(\alpha+\tfrac{1}{2}) &- \frac{\delta t}{\rho_0 \ \delta\alpha}(p^{[\ell]}(\alpha-1) - p^{[\ell]}) \\ &+ \frac{\delta t\left(\mu_B + \dfrac{\mu}{3}\right)}{\rho_0 \ \delta\alpha}(\psi^{[\ell]}(\alpha+1) - \psi^{[\ell]}) \\ &+ \frac{C \ \delta t}{\delta n}\sqrt{\frac{\mu}{\rho_0}}(v_\alpha^{[\ell]} - J_{\tau_0}^{[\ell]}), \end{aligned} \tag{24}$$

where Eq. (21) with ξ_0 replaced by v_α is used to update $J_{\tau_0}^{[\ell]}$ every time-step and ψ is defined in Eq. (15).

The orthogonal component v_n is zero on the surface so no time stepping is required. To calculate the discretized component of v_n at a distance δn from the surface, the standard FDTD equation (13) can be used. The discretized approximation of the second order derivative uses the surface value of v_n, which is assumed to be zero. Although this is a very poor approximation for the second order derivative in this case, the error on viscous damping that this approxima-

TABLE II. Absorption (/m) in a long duct for different values of the central frequency in the narrow-band excitation.

f	FDTD simulation	Analytical	Relative difference
$f_0/2$	0.92×10^{-4}	1.64×10^{-4}	43.9%
f_0	2.34×10^{-4}	2.47×10^{-4}	5.22%
$2f_0$	4.43×10^{-4}	3.81×10^{-4}	−16.5%

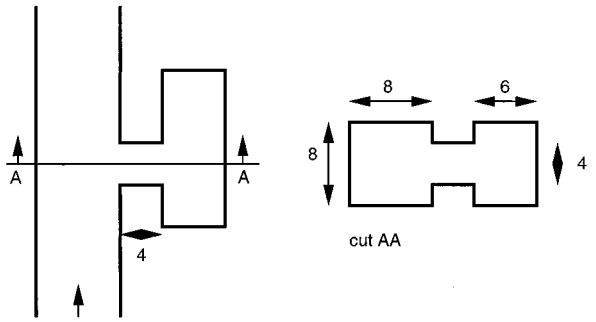

FIG. 3. Structure of the Helmholtz resonator on a duct used in the example (sizes in cm).

tion introduces is always small compared to the large damping that is present in the adjacent boundary pressure cell. Therefore it can safely be used.

In Eqs. (23) and (24) all spatial inconsistencies are resolved. Inconsistency in time discretization is again approximately resolved by linear extrapolation.

III. NUMERICAL RESULTS

A. One-dimensional test cases

To evaluate the accuracy of the numerical model that is described in this paper, sound propagation in a long, quasi one-dimensional duct is studied numerically and compared to known analytical results.[1] Since these analytical results are based on a number of approximations, they cannot be considered as an absolute reference. All numerical simulations described in this section will be performed with a test signal that is limited both in frequency content and in time

$$g(t)=A\ \sin(2\pi f(t-t_0))e^{-(t-t_0)^2/\sigma^2}, \tag{25}$$

where A is the amplitude, f is the central frequency, t_0 is some initial delay, and σ determines both bandwidth and signal duration. For the simulations in this section $\sigma=1.6/f$. A typical frequency of interest f_0 is chosen and boundary layer approximations are based on this frequency. The diameter of the duct that is studied is $\lambda_0/3.4$ and its length is $4.5\lambda_0$ where λ_0 is the wavelength corresponding to the frequency f_0. The duct is terminated with perfectly reflecting boundaries at both ends.

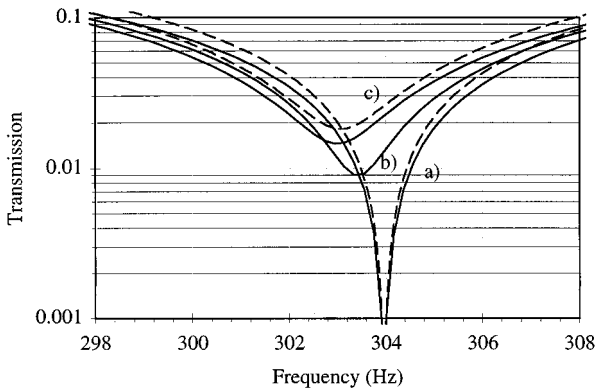

FIG. 4. Resonance peak in the transmission corresponding to the lowest order resonance of the resonator; (a) no boundary layer; (b) vorticity layer included; (c) vorticity and entropy layer included; dashed lines are results of the analytical model.

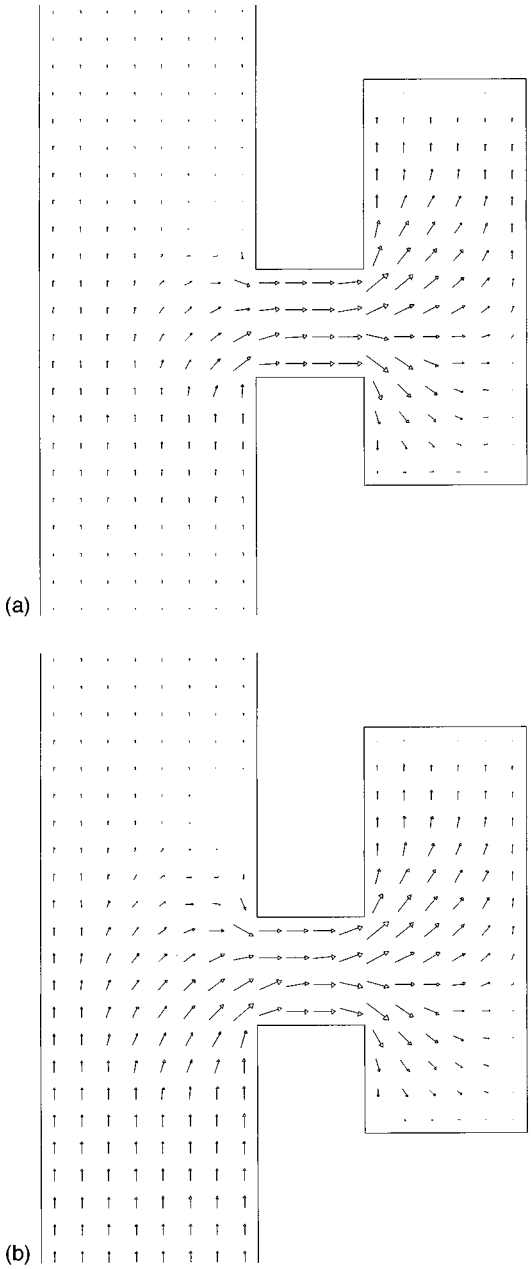

FIG. 5. Vector sound intensity in the plane of the resonator; (a) without boundary layer effects; (b) with boundary layer effects included.

First the inaccuracy introduced by the assumption $p=\rho c^2$ is investigated. This is done by comparing simulation results of the model presented in this paper to results obtained with a model that discretizes Eqs. (2), (3), and (6). The relative difference between both simulation results remains within 0.5% for simulated time up to 10 seconds or corresponding propagation distance of 3.4 km. This is clearly sufficient. Moreover such a small difference can easily be due to different numerical error in both implementations.

A strong point of the vorticity and entropy boundary layer formulation that is introduced in this paper is its numerical efficiency. An increase of 6.5% in CPU-time requirement for boundary cells was observed after introducing

the new boundary formulation. Since boundary cells normally occupy less than 10% of the simulation region, this is indeed an insignificant increase in CPU-requirements.

FDTD results for a bandlimited signal with central frequency f are compared to analytical predictions for a single frequency corresponding to f for different spatial discretization steps ($\delta x = \delta y = \delta z$) in Table I. Absorption was measured by calculating the rms value of the finite length time signal at different instances near one end of the duct. The simulation was done for $f = f_0 = 50$ Hz so the boundary layer thickness can have no influence on the results in the table. The relative difference in absorption coefficients decreases approximately linear with spatial discretization step and is typically below 5%. The same behavior was observed for frequencies up to 20 kHz. Considering the fact that several minor effects such as finite duct length and finite bandwidth were neglected in the analytical model, this result is quite promising.

The previous numerical test does not measure the accuracy of the approximate frequency dependence of the boundary layer effect that is introduced in Eq. (19). Keeping f_0 and spatial discretization fixed, the central frequency f of the excitation was detuned. In Table II numerical results are again compared to analytical approximations. Away from f_0 numerical error increases. As can be expected from Fig. 2, the error is much more important for lower frequencies. This limitation of the model should be kept in mind. Fortunately in practical situations where vorticity and entropy boundary layers are important, the frequency band of interest is rather small since highly resonant structures are studied.

B. High quality resonator

The second simulation example is a high quality resonator placed on a duct. Two resonator modes are investigated: the traditional lowest-order resonance and a first-order mode in the resonator, parallel to the duct. The structure is shown in Fig. 3. Frequency-domain transmission change is found by FFT transform of the time-domain response for a wavelet excitation. For the lowest-order resonance an approximate analytical model is available.[8] One of the parameters in the model is the neck end correction. Since this parameter cannot be calculated analytically for the structure that is modeled here, it is fitted in order to match the resonance frequency obtained with the FDTD model to that obtained with the analytical model, for the lossless case. Figure 4 shows the lowest order resonance in the transmission change simulated with the FDTD model if no boundary layers are included, if only the vorticity layer is included and if both vorticity and entropy layer are included. FDTD results are obtained with $f_0 = 300$ Hz. The dashed line is the transmission change calculated with the analytical model with and without absorption effects. FDTD results and analytical results correspond quite well. Remember however that the resonator neck end correction that was used in the analytical model is a fitted parameter. The model presented here can be used to determine this parameter for several resonator configurations.

Interesting distributions of acoustical quantities can be displayed to analyze the influence of the boundary layer absorption in greater detail. Vector sound intensity averaged over 50 periods in the plane of the resonator is shown in Fig. 5. The duct is excited with a pure tone tuned exactly to the resonance frequency of the resonator. If boundary layer effects are neglected, there is no difference between duct energy flux before and after the resonator. If boundary absorption is included a clear energy transport from the source to the resonator is observed.

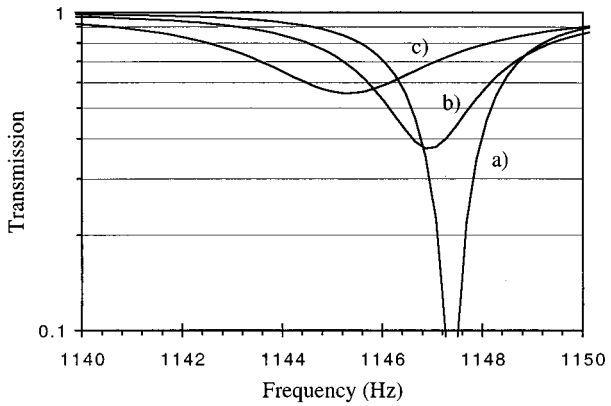

FIG. 6. Resonance peak in the transmission corresponding to the first longitudinal resonance in the resonator; (a) no boundary layer; (b) vorticity layer included; (c) vorticity and entropy layer included.

The first longitudinal resonance of the resonator occurs at a frequency of 1150 Hz. The corresponding resonance in the transmission change is shown in Fig. 6 as obtained by the FDTD simulation. For these simulations $f_0 = 1200$ Hz. Three situations are again compared: no boundary layer, vorticity layer only, and both vorticity and entropy layer. The influence of the boundary layers on the resonance peak is slightly different than in the previous case. The reason for this difference can be found in the fact that the absorption caused by the vorticity and the entropy boundary layer depend in a different way on the direction of incidence of the acoustic wave. Absorption by the vorticity layer is larger for shear sound propagation while absorption by the entropy layer is independent on direction of the sound propagation.

IV. CONCLUSIONS

A new numerical time-domain model that describes the influence of vorticity and entropy boundary layers on sound propagation is introduced. The model can very efficiently be included in a finite-difference time-domain simulation of acoustic problems. The computational overhead is very small. Numerical accuracy is sufficient for the problems that require the use of such a model.

ACKNOWLEDGMENT

The author is a senior research assistant with the Belgian National Fund for Scientific Research.

[1] A. D. Pierce, *Acoustics* (McGraw-Hill, New York, 1981).

[2] F. Torres, P. Vaudon, and B. Jecko, ''Application of fractional derivatives to the FDTD modeling of pulse propagation in a Cole–Cole dispersive medium,'' Microw. Opt. Technol. Lett. **13**, 300–304 (1996).

[3] R. J. Luebbers and F. Hunsberger, ''FDTD for *n*th-order dispersive media,'' IEEE Trans. Antennas Propag. **40**, 1297–1301 (1992).

[4] D. Botteldooren, ''Numerical model for moderately non-linear sound propagation in three dimensional structures,'' J. Acoust. Soc. Am. **100**, 1357–1367 (1996).
[5] K. S. Kunz and R. J. Luebbers, *The Finite Difference Time Domain Method for Electromagnetics* (CRC, Boca Raton, 1993).
[6] A. Taflove, *Computational Electrodynamics: The Finite-Difference Time-Domain Method* (Artech House, Boston, MA, 1995).
[7] T. L. Szabo, ''Time domain wave equations for lossy media obeying a frequency power law,'' J. Acoust. Soc. Am. **96**, 491–500 (1994).
[8] F. P. Mechel and I. L. Vér, ''Sound-absorbing materials and sound absorbers,'' in *Noise Control*, edited by L. L. Beranek and I. L. Vér (Wiley, New York, 1992).

Numerical implementation of the lumped parameter model for the acoustic power output of a vibrating structure

John B. Fahnline and Gary H. Koopmann
Center for Acoustics and Vibration, 157 Hammond Building, The Pennsylvania State University, University Park, Pennsylvania 16802

(Received 19 August 1996; revised 27 February 1997; accepted 31 March 1997)

In a previous paper, a lumped parameter model for the acoustic radiation from a vibrating structure was defined by dividing the surface of the structure into elements, expanding the acoustic field from each of the elements in a multipole expansion, and truncating all but the lowest-order terms in the expansion. Here, the lumped parameter model is implemented numerically by requiring the boundary condition for the normal surface velocity to be satisfied in a lumped parameter sense. This alleviates the difficulties typically encountered in enforcing the boundary condition, leading to a relatively simple numerical solution with well-defined convergence properties. The basis functions for the numerical analysis are taken as the acoustic fields of discrete simple, dipole, and tripole sources located at the geometrical centers of the surface elements. The different source types are used to represent the radiation from different kinds of surface elements: simple sources for elements in the plane of an infinite baffle, dipole sources for very thin structures which deform only in bending, and tripole sources for elements associated with parts of a structure enclosing a finite volume. The convergence of the numerical solution for the power output as a function of both frequency and element size is demonstrated through several example problems. [S0001-4966(97)05707-X]

PACS numbers: 43.20.Tb, 43.20.Rz, 43.40.Rj [JEG]

INTRODUCTION

This is the second in a series of three papers concerned with assessing the sound power radiated by a vibrating structure. In the first paper,[1] a lumped parameter model for the acoustic radiation from a vibrating structure was defined by dividing the surface of the structure into elements, expanding the acoustic field from each of the elements in a multipole expansion, and truncating all but the lowest-order terms in the expansion. The analytical model requires a solution for the imaginary component of the Green's function of the second kind, which is only available for a few simple boundary surface geometries. In this paper, we investigate the possibility of constructing an approximate solution for the imaginary component of the Green's function numerically, with the ultimate goal of computing the acoustic power output of the vibrating structure. Because we are only interested in computing the power output, several results derived in the previous paper can be used to simplify the analysis.

First, the theoretical analysis showed that as long as the element size is small compared to both the acoustic and structural wavelengths, any two surface velocity profiles with the same elemental volume velocity distribution produce nearly the same acoustic power output. This allows us to generate an approximate solution for the Green's function by satisfying the boundary condition for the normal component of the surface velocity in a lumped parameter sense rather than on a point-by-point basis. Thus we generate the Green's function by specifying unit volume velocity over one element and zero volume velocity over the remaining elements. Second, we note that the calculation of the power output requires the knowledge of the Green's function at the points on the boundary surface only, not at the field points within the solution domain. This means that we only have to store $N \times N$ numbers to fully characterize the acoustic power output at a particular frequency (where N is the number of surface elements).

Even with these simplifications, the task of generating a suitable solution for the Green's function is not straightforward. In general, all of the problems associated with numerical solutions of integral equations can occur in the solution procedure, including nonuniqueness, nonexistence, singular and hypersingular integrands, numerical instability, etc. We will endeavor to show that all of these problems can be overcome by taking advantage of the relaxed requirements for the functional representation of the acoustic field afforded by only satisfying the boundary condition in a lumped parameter sense. In particular, the basis functions used to represent the acoustic field can be chosen from a much broader class of functions, allowing the use of relatively simple functional representation for the acoustic field, with an accompanying reduction in both the difficulty and computational cost of the numerical calculations. In the first section of the paper we will describe our numerical solution procedure, emphasizing each of the procedure's potential difficulties and the method used to overcome them.

I. APPROXIMATE SOLUTION FOR THE ACOUSTIC FIELD

The numerical procedure described in this paper is classified as a boundary method. Excellent discussions of boundary methods can be found in the texts by Collatz,[2] Hildebrand,[3] and Crandall[4] and a relatively recent listing of related research in the area of acoustics is given in the book edited by Ciskowski and Brebbia.[5] The basic idea of all

boundary methods is to assume a solution of the boundary value problem as a series summation of basis functions satisfying the governing partial differential equation everywhere in the solution domain. The basis functions are weighted by undetermined coefficients, which are determined in the solution process such that the numerical solution approximately satisfies the specified boundary condition. Specializing to the acoustic radiation problem, the approximate solution for the acoustic pressure at the field point $\mathbf{x}$ (approximate quantities are denoted by an overbar) takes the form

$$\hat{\bar{p}}(\mathbf{x}) = \sum_{\nu=1}^{N} \hat{s}_\nu P_\nu(\mathbf{x}), \tag{1}$$

where the $P_\nu(\mathbf{x})$ are functions satisfying both the Helmholtz equation in the solution domain V and the Sommerfeld radiation condition. The caret notation indicates the complex amplitude of a time-harmonic function, as discussed in the previous paper.[1] The undetermined coefficients $\hat{s}_\nu$ are determined in the solution process such that boundary condition for the normal velocity is approximately satisfied. To enforce the boundary condition, we first use Euler's equation to rewrite Eq. (1) in terms of the particle velocity at the field point as

$$\hat{\bar{v}}_n(\mathbf{x}) = \frac{1}{ik\rho c} \sum_{\nu=1}^{N} \hat{s}_\nu \nabla P_\nu(\mathbf{x}) \cdot \mathbf{n}. \tag{2}$$

We now want to force $\hat{\bar{v}}_n(\mathbf{x})$ to mimic the specified boundary condition, where the difference in the boundary conditions is typically used as a measure of the solution accuracy; the error being zero if the boundary condition is matched exactly.

The degree to which the boundary condition can be enforced depends primarily on how well the basis functions can represent the specified boundary condition. If possible, they should be chosen such that they can represent any possible boundary condition, ensuring that they can also represent any possible acoustic field. Unfortunately, this is easier said than done, especially considering that the basis functions are typically generated from the acoustic fields of point sources and are thus singular. The following analysis is directed toward revising the boundary method to alleviate some of the most bothersome difficulties of the conventional solution procedure.

A. Lumped parameter form of the boundary condition

The key step to resolving the difficulties in enforcing the specified boundary condition is to focus on determining an accurate solution for the acoustic power output rather than surface pressure. This allows us to simplify the boundary condition by dividing the boundary surface into elements and replacing the actual boundary condition by its lumped parameter equivalent. For the acoustic radiation problem, we thus replace the actual boundary condition for the normal surface velocity at each point on the boundary surface by the lumped parameter form of the boundary condition as

$$\hat{u}_\mu = \int\int_{S_\mu} \hat{v}_n(\mathbf{x}) dS(\mathbf{x}), \quad \nu = 1,\ldots,N, \tag{3}$$

where N is the number of surface elements, and S_μ and $\hat{u}_\mu$ are the surface area and volume velocity of element μ, respectively. As was shown in the first paper of this series,[1] the validity of replacing the actual boundary condition by its lumped parameter equivalent depends primarily on the size of the elements in comparison to both the acoustic and structural wavelengths, with the error in the solution for the power output diminishing as the element size is reduced. With this knowledge, we now want to reformulate the boundary method to take advantage of the unique properties of the volume velocity matching scheme. In particular, because the volume velocity matching scheme does not require the basis functions to reproduce the specified boundary condition on a point-by-point basis, the functional representation of the acoustic field can be simplified considerably, as is discussed in more detail in the next section.

The interelated subject of solution validation is also of considerable importance. Traditionally, the error in a numerical solution generated using a boundary method is measured as the difference between the boundary condition satisfied by the numerical solution and the specified boundary condition, as demonstrated by Collatz,[2] Zielinski and Herrera,[6] and Fahnline.[7] This method works well for simple problems, but is difficult to apply to problems with geometrically complicated boundary surfaces, primarily because it is difficult to find a numerical solution which closely matches the boundary condition. When the boundary condition is enforced in a lumped parameter sense, we instead validate our numerical solution by checking the convergence of the solution for the acoustic power output as a function of the element size, where we know that the solution must eventually converge to the correct solution. In this form, the process of validating the solution is straightforward because satisfying the boundary condition is no longer a major difficulty. Thus enforcing the boundary condition in a lumped parameter sense eases the difficulties in assessing the accuracy of the numerical solution.

The calculation of the elemental volume velocity distribution in Eq. (3) requires the knowledge of the specified normal surface velocity distribution, which is generally determined either through experimental measurements or a finite element analysis of the structural displacements. The finite element analysis typically ignores fluid loading, thus assuming that the displacements of the surface of the structure are not influenced by the acoustic pressure field. This assumption is generally not valid if the acoustic medium is water, or if the vibrating structure is made of lightweight components. The finite element analysis works well as a precursor to the acoustic analysis because solutions generated using the finite element method are also validated through mesh refinement. Thus both the finite element analysis and the acoustic analysis can be validated at the same time, with the solution error measured by the convergence of the solution for the acoustic power output. Determining the boundary condition for the normal surface velocity by direct measurement is less amenable to the process of refining the surface element mesh, especially when the boundary surface is geometrically complex. We anticipate that scanning laser vibrometers will eventually be able to perform this measurement

with relative ease, but presently, experimentally measuring the surface velocity distribution for even a simple boundary surface is an arduous task.

B. Definition of the basis functions

The overall goal in the following analysis is to determine a set of basis functions which satisfy the Helmholtz equation everywhere in the solution domain and are able to represent any possible *volume velocity* distribution over the boundary surface. In the following discussion, we demonstrate why the conventional choice for the basis functions leads to difficulties in enforcing the boundary condition, and suggest an alternate set of basis functions to alleviate the difficulties. The discussion is somewhat lengthy, but relevant, since the choice of basis functions is critical to the success of the numerical solution.

To find a suitable set of basis functions for the acoustic radiation problem, most researchers have sought guidance from the Kirchhoff–Helmholtz equation, which is an exact solution of the boundary value problem in the form of an integral equation. Derivations of the Kirchhoff-Helmholtz equation can be found in the texts by Pierce,[8] Junger and Feit,[9] Morse and Ingard,[10] and Temkin.[11] The Kirchhoff–Helmholtz equation can be viewed as an integral equation because the unknown surface pressure appears as a weighting function of a surface integral. The normal component of the surface velocity also appears as a weighting function of a surface integral, but it is a known function because it is specified as the boundary condition. The acoustic fields of simple and dipole sources distributed over the boundary surface of the radiating structure are superposed in the Kirchhoff–Helmholtz equation to give the solution of the boundary value problem. These functions satisfy the governing partial differential equation everywhere in the solution domain; that is, everywhere *outside* the boundary surface. If viewed from the context of boundary methods, the acoustic fields of the simple and dipole sources are the basis functions and the normal component of the surface velocity and the surface pressure are the exact solutions for their weighting functions, respectively. Thus most researchers have tried to imitate the Kirchhoff–Helmholtz equation, using simple and/or dipole sources distributed over the boundary surface as basis functions with approximate representations of the surface pressure and normal surface velocity as weighting functions. Typical formulations can be found in the articles by Chen and Schweikert,[12] Chertock,[13] Copley,[14] and Engbloom and Nelson.[15]

The basic problem with this idea is that the acoustic pressure fields of simple and dipole sources are weakly singular and strongly singular functions, respectively. Mathematically, this means that the pressure field of a simple source goes to infinity as $1/R$ as the distance between the source and field points R goes to zero and that of a dipole source goes to infinity as $1/R^2$. The acoustical particle velocity is obtained by taking the gradient of the acoustic pressure field, resulting in strongly singular functions for simple sources and hypersingular functions (which depend on $1/R^3$ near the source point) for dipole sources. Discussions of weakly singular, strongly singular and hypersingular functions can be found in the articles by Krishnasamy *et al.*,[16] Gray and San Soucie,[17] Liu and Rizzo,[18] and Jawson and Symm.[19] To enforce the boundary condition for the normal surface velocity, the acoustic particle velocity due to the distributions of simple and dipole sources is evaluated. When the field point is not near the boundary surface, the surface integrals can be easily evaluated using Gaussian integration techniques, but when the field point approaches the boundary surface, the evaluation of the surface integrals becomes increasingly difficult due to the singularity in the acoustic field of the sources. Unfortunately, we must be able to accurately compute the acoustic particle velocity created by the sources if we are to enforce the specified boundary condition, and as a result, it is nearly impossible to judge how well the numerical solution satisfies the specified boundary condition. This problem is exacerbated near edges and corners where the outward surface normal is discontinuous and the specified boundary condition may possibly be discontinuous, as discussed by Krishnasamy *et al.*[16,20] and Gray and Lutz.[21] In general, then, when simple and dipole sources distributed continuously over the boundary surface are used as basis functions, the accuracy of the numerical solution is unknown because it is very difficult to assess how well the numerical solution satisfies the specified boundary condition.

A great number of researchers have tried to alleviate this difficulty using a variety of schemes. One possibility is to move the source distributions off of the boundary surface (into the volume enclosed by the boundary surface), so that the basis functions are no longer singular. Some recent examples of this method are given by Han and Olson,[22] Fahnline and Koopmann,[23] Huang and Chang,[24] and Bobrovnitskii and Tomilina.[25] When the sources were on the boundary surface, we could show that in the limit as the number of basis functions went to infinity an exact solution for the weighting function of the surface integral always existed. However, when the sources are moved off of the boundary surface, it may not be possible to exactly represent the acoustic field of the vibrating structure, no matter how many sources are used to represent the field. The numerical solution derived from these basis functions is then typically unstable, such that a small change in the solution for the undetermined coefficients causes a very large change in the numerical solution, as discussed by Miller,[26] Baker,[27] and Smithies.[28] The integral equation associated with the numerical solution is then classified as an integral equation of the first kind, which is generally ill-posed; in contrast to the Kirchhoff–Helmholtz equation, which is well-posed. We thus conclude that moving the sources off the boundary surface gives satisfactory results when the surface is relatively simple in shape, but is unsuitable for surfaces with edges and corners where the numerical procedure yields increasingly unstable solutions. Examples of this instability are given by Fahnline.[6]

Another way to alleviate the difficulty is to develop a method for accurately computing the acoustic field near the boundary surface. In particular, the acoustic particle velocity due to a distribution of dipole sources is very difficult to calculate in the vicinity of the sources, especially near edges and corners. Progress is being made by a number of re-

TABLE I. Values of the constants α and β for the various surface elements.

Description of the surface elements	Source type	α	β
In the plane of an infinite baffle	simple	1	0
Part of a surface enclosing no volume	dipole	0	i/k
Part of a surface enclosing a finite volume	tripole	1	i/k

searchers (see Refs. 16–21), but it may be some time before a truly accurate reconstruction of the acoustic field near the boundary surface is demonstrated. Reiterating, without an accurate reconstruction of the acoustic field on the boundary surface, the boundary condition satisfied by the numerical solution and the solution accuracy are unknown.

Ideally, it is preferable to use continuous distributions of sources on the boundary surface as basis functions, but because of the difficulties in evaluating the acoustic field of the sources, we have adopted an alternative approach. In our numerical solution, we avoid the difficulties involved in the integration process by simply using discrete sources as basis functions instead of continuous distributions of sources, with the sources located very near the boundary surface to ensure the stability of the matrix inversion. This becomes possible only after replacing the boundary condition for the normal surface velocity by its lumped parameter equivalent, allowing us to use a much broader class of functions as basis functions. These functions are inappropriate as basis functions when the boundary condition is to be satisfied exactly, but are permissible when the boundary condition is to be satisfied in a lumped parameter sense. Because it is relatively easy to evaluate the acoustic field of a discrete source, the *volume velocity* boundary condition can be enforced with great accuracy. Ultimately, using the acoustic fields of discrete point sources as basis functions allows us to eliminate the difficulties in enforcing the boundary condition so that the solution process can proceed in a straightforward manner.

Having chosen to use discrete sources instead of continuous distributions of sources, there can still be problems with the numerical solution if the basis functions are not chosen properly. In particular, if only simple or dipole sources are used to represent the acoustic field radiated from a surface enclosing a finite volume, it is easy to demonstrate that nonexistence difficulties cause the numerical solution to become unstable at certain discrete frequencies, resulting in very high amplitude oscillations in the normal surface velocity distribution over each element. General discussions of the nonuniqueness and nonexistence difficulties can be found in the articles by Copley[29] and Schenck.[30] The truncated terms of the multipole expansion for the acoustic power output then grow dramatically in comparison to the monopole terms [see Eq. (24) of Ref. 1], resulting in a loss of accuracy in the numerical solution at a set of discrete frequencies. This problem can be eliminated by choosing the basis functions as a combination of both simple and dipole source fields with their amplitudes related through a purely imaginary constant, as discussed by Huang and Chang,[24] Burton and Miller,[31] Fillipi,[32] Terai,[33] and Kress and Spassov.[34] We will refer to a coincidentally located simple and dipole source with an imaginary coupling coefficient as a ''tripole source.'' The tripole sources are associated with parts of the structure enclosing a finite volume, where the nonexistence and nonuniqueness difficulties may occur. A more complete explanation of the tripole source basis function is given in the Appendix.

Simple and dipole sources are used to model the radiation from the other types of structural components, with simple sources representing the radiation from elements lying in the plane of an infinite baffle, and dipole sources representing the radiation from very thin elements which deform only in bending. The idea of using dipole sources to represent the radiation from very thin elements originated with Fillipi.[32] In this model, the radiation from any small source with negligible volume velocity is approximated as equivalent to that of a point dipole source. Thus because the very thin elements deform primarily in bending, their overall volume velocity is negligible (summing the volume velocities from both faces of the thin structure) and the radiation from each of the elements is approximately equivalent to that of a point dipole source. Confirmation of the validity of using simple and dipole sources as basis functions can readily be obtained from the Kirchhoff–Helmholtz equation, as given in the Appendix.

With that as an introduction, we now define the basis functions in general terms as

$$P_\nu(\mathbf{x}) = \alpha \hat{g}(\mathbf{x}, \mathbf{q}_\nu) + \beta [\nabla_q \hat{g}(\mathbf{x}, \mathbf{q}) \cdot \mathbf{n}_q]_{\mathbf{q}=\mathbf{q}_\nu}. \tag{4}$$

In Eq. (4) the lower case $\hat{g}$ indicates the free-space Green's function

$$\hat{g}(\mathbf{x}, \mathbf{q}) = \frac{1}{R} e^{ikR}, \tag{5}$$

where $R = |\mathbf{x} - \mathbf{q}|$, and $\mathbf{q}_\nu$ is the location of source ν in Cartesian coordinates. The constants α and β dictate the relative amplitudes of the simple and dipole sources, respectively. Higher-order sources such as quadrupoles and octupoles are not included in the representation because their acoustic fields are relatively difficult to calculate, and because a general representation of any acoustic field can be determined without them. The values for the constants α and β are chosen such that the radiation from each part of the structure is correctly represented in terms of simple, dipole, or tripole sources. Table I lists the values of the constants for each of the source types. In choosing the locations for the sources, we have tried to make the numerical solution as stable as possible. We thus locate the sources just inside the boundary surface, such that the associated integral equation is well-posed, as discussed previously. To keep the equation system square, we take one source per element, with the source lo-

cated at the geometrical center of the element. Also, we align the dipole sources in the direction of the outward normal to the surface at the geometrical center of the element, which is taken as $\mathbf{n}_\nu$.

C. Solution for the source amplitudes

Based on the analysis of the previous section we now take the approximate solution for the acoustic pressure field as

$$\hat{\tilde{p}}(\mathbf{x}) = \sum_{\nu=1}^{N} \hat{s}_\nu \{\alpha_\nu \hat{g}(\mathbf{x},\mathbf{q}_\nu) + \beta_\nu [\nabla_q \hat{g}(\mathbf{x},\mathbf{q}) \cdot \mathbf{n}_q]_{\mathbf{q}=\mathbf{q}_\nu}\}, \quad (6)$$

where the α_ν and β_ν are known constants, chosen such that the radiation from each element of the structure is correctly represented in terms of simple, dipole, or tripole sources. Using Euler's equation, Eq. (6) can be rewritten in terms of the velocity in the direction $\mathbf{n}$ at the field point $\mathbf{x}$ as

$$\hat{\tilde{v}}_n(\mathbf{x}) = \frac{1}{ik\rho c} \sum_{\nu=1}^{N} \hat{s}_\nu \nabla \{\alpha_\nu \hat{g}(\mathbf{x},\mathbf{q}_\nu) + \beta_\nu [\nabla_q \hat{g}(\mathbf{x},\mathbf{q}) \cdot \mathbf{n}_q]_{\mathbf{q}=\mathbf{q}_\nu}\} \cdot \mathbf{n}. \quad (7)$$

The volume velocity over element μ of the boundary surface is determined by integrating Eq. (7) over the element surface as

$$\begin{aligned} \hat{\tilde{u}}_\mu &= \int\int_{S_\mu} \hat{\tilde{v}}_n(\mathbf{x}) dS(\mathbf{x}) \\ &= \frac{1}{ik\rho c} \sum_{\nu=1}^{N} \hat{s}_\nu \int\int_{S_\mu} \nabla \{\alpha_\nu \hat{g}(\mathbf{x},\mathbf{q}_\nu) + \beta_\nu [\nabla_q \hat{g}(\mathbf{x},\mathbf{q}) \cdot \mathbf{n}_q]_{\mathbf{q}=\mathbf{q}_\nu}\} \cdot \mathbf{n}\, dS(\mathbf{x}), \end{aligned} \quad (8)$$

for $\mu = 1,\ldots,N$. The system of equations given in Eq. (8) can be written in matrix form as

$$\mathbf{u} = \mathbf{U}\mathbf{s}, \quad (9)$$

where the individual terms of the matrix $\mathbf{U}$ then become

$$U_{\mu\nu} = \frac{1}{ik\rho c} \int\int_{S_\mu} \nabla \{\alpha_\nu \hat{g}(\mathbf{x},\mathbf{q}_\nu) + \beta_\nu [\nabla_q \hat{g}(\mathbf{x},\mathbf{q}) \cdot \mathbf{n}_q]_{\mathbf{q}=\mathbf{q}_\nu}\} \cdot \mathbf{n}\, dS(\mathbf{x}). \quad (10)$$

Once the element discretization is defined, the matrix $\mathbf{U}$ can be explicitly calculated.

To calculate the individual elements of $\mathbf{U}$, the volume velocity of simple, dipole, and tripole sources over the element surfaces are determined, as shown in Fig. 1 for a triangular element. First, consider the evaluation of the volume velocity of a source over a triangular surface element. When the source is not near the integration surface, standard Gauss quadrature can be used to integrate the normal velocity created by the source over the surface S_μ. A listing of the abscissas and weights for 4-, 7-, and 13-point integrations over triangular regions can be found in the article by Cowper.[35] As the source approaches the surface of the triangle, the velocity field of the source becomes more concentrated near the source location, and more Gauss points are necessary to evaluate the volume velocity. When the source is very close to the element surface, even the 13-point Gaussian integration formula does not yield accurate results for the volume velocity of the source. A semi-analytical integration scheme, similar to that given by Duong,[36] has been devised for this circumstance. The scheme yields very accurate results for the volume velocity of a source near a surface element, but does not yield accurate results when the source is far from the element. Details are omitted in this paper because of the complexity of the integration scheme.

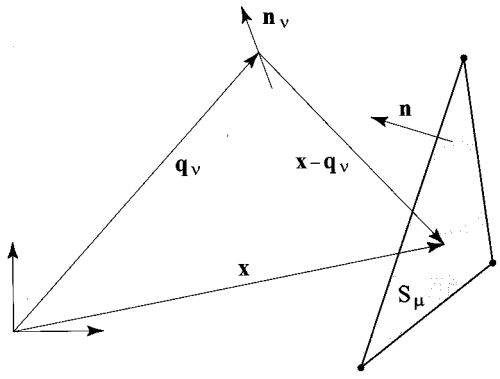

FIG. 1. Illustration of the geometrical relationship between the source at $\mathbf{q}_\nu$ and the field point on S_μ.

Similar results can also be derived for planar, quadrilateral elements. Typically, the Gaussian quadrature routines are developed as generalizations of the one-dimensional quadrature formulas, examples of which can be found in the text by Cook *et al.*[37] The semi-analytical integration routine devised for triangular elements can easily be generalized for planar quadrilateral elements, but it is difficult to extend the routine to nonplanar quadrilateral elements. To avoid the resulting difficulties in evaluating the volume velocity of a source over a nonplanar quadrilateral, these elements are first broken into two triangles, and the volume velocity over each of the triangles is evaluated separately. The overall volume velocity is then calculated as the summation of the volume velocities over the two triangles. Clearly this methodology can be generalized, such that a number of surface elements can be grouped together as a single acoustic element, as discussed in a recent paper by Fahnline.[38] After an extensive analysis of the integration routines, we have determined that the volume velocity is enforced to within 0.1%. We will subsequently demonstrate that in the general case this limits the maximum possible accuracy of the numerical solution for the power output to 0.1%.

Once the matrix $\mathbf{U}$ has been calculated, the sources amplitudes producing the specified volume velocity distribution can be determined as

$$\mathbf{s} = \mathbf{U}^{-1}\mathbf{u}. \quad (11)$$

The solution for the pressure field is then determined by substituting the source amplitudes back into Eq. (6). After determining the source amplitudes which give the correct volume velocity distribution over the boundary surface, the next step in the analysis is to determine the acoustic power output of the sources.

II. COMPUTING THE ACOUSTIC POWER OUTPUT

Knowing the solution for the source amplitudes, we next want to calculate the acoustic power output. Two different methods are used to calculate the power output. The first method is based on an analytical expression for the acoustic power output of a number of simple, dipole, and tripole sources. As such, the power output predicted using this formula is very nearly exact. The second method is based on a numerical integration of the acoustic intensity over a spherical surface a surrounding the vibrating structure. A direct comparison of the two results is used to verify the accuracy of the calculations.

A. Analytical solution for the power output

The acoustic power output of a number of simple, dipole, and tripole sources can be determined by extending the derivation given by Levine.[39] A similar derivation is given by Nelson and Elliott[40] for a slightly different choice of the source amplitudes. The analysis is derived by mathematically manipulating the inhomogeneous form of the Helmholtz equation. The extension of Levine's derivation is relatively straightforward but tedious, and will only be outlined.

The partial differential equation governing the acoustic field of a number of simple, dipole, and tripole sources submerged in an infinite fluid medium can be written as

$$\nabla^2\hat{p}(\mathbf{x})+k^2\hat{p}(\mathbf{x})=-4\pi\sum_{\nu=1}^{N}\hat{s}_\nu\{\alpha_\nu\delta(\mathbf{x}-\mathbf{q}_\nu)+\beta_\nu\mathbf{n}_\nu\cdot[\nabla_q\delta(\mathbf{x}-\mathbf{q})]_{\mathbf{q}=\mathbf{q}_\nu}\}. \tag{12}$$

Following the steps in Levine's derivation, the power output can eventually be written in terms of the pressure at the locations of the sources as

$$\Pi_{\mathrm{av}}=\frac{2\pi}{k\rho c}\sum_{\nu=1}^{N}\mathrm{Re}\{i\hat{s}_\nu\alpha_\nu\hat{p}^*(\mathbf{x}_\nu)+i\hat{s}_\nu\beta_\nu\mathbf{n}_\nu\cdot[\nabla\hat{p}^*(\mathbf{x})]_{\mathbf{x}=\mathbf{x}_\nu}\}. \tag{13}$$

Substituting for the pressure at the source locations from Eq. (1) gives

$$\Pi_{\mathrm{av}}=\frac{2\pi}{k\rho c}\sum_{\mu=1}^{N}\sum_{\nu=1}^{N}\mathrm{Re}\{i\hat{s}_\mu^*\hat{s}_\nu\alpha_\nu P_\mu^*(\mathbf{x}_\nu)+i\hat{s}_\mu^*\hat{s}_\nu\beta_\nu\mathbf{n}_\nu\cdot[\nabla P_\mu^*(\mathbf{x})]_{\mathbf{x}=\mathbf{x}_\nu}\}. \tag{14}$$

The final step is to substitute for the acoustic field of the simple, dipole, and tripole sources and carry through the differentiations. After a considerable amount of algebra, the power output can be written in the form

$$\Pi_{\mathrm{av}}=\Pi_{\mathrm{av},s}+\Pi_{\mathrm{av},c}+\Pi_{\mathrm{av},d}, \tag{15}$$

where

$$\Pi_{\mathrm{av},s}=\frac{2\pi}{\rho c}\sum_{\mu=1}^{N}\sum_{\nu=1}^{N}\alpha_\mu^*\alpha_\nu\hat{s}_\mu^*\hat{s}_\nu j_0(kR_{\mu\nu}), \tag{16}$$

$$\Pi_{\mathrm{av},c}=\frac{2\pi ik}{\rho c}\sum_{\mu=1}^{N}\sum_{\nu=1}^{N}\alpha_\mu^*\beta_\nu\hat{s}_\mu^*\hat{s}_\nu\times\frac{(\mathbf{x}_\mu-\mathbf{x}_\nu)\cdot(\mathbf{n}_\mu+\mathbf{n}_\nu)}{R_{\mu\nu}}j_1(kR_{\mu\nu}), \tag{17}$$

$$\Pi_{\mathrm{av},d}=\frac{2\pi k^2}{3\rho c}\sum_{\mu=1}^{N}\sum_{\nu=1}^{N}\beta_\mu^*\beta_\nu\hat{s}_\mu^*\hat{s}_\nu\left\{\frac{3}{kR_{\mu\nu}}j_1(kR_{\mu\nu})\mathbf{n}_\mu\cdot\mathbf{n}_\nu-3\frac{(\mathbf{x}_\mu-\mathbf{x}_\nu)\cdot\mathbf{n}_\mu}{R_{\mu\nu}}\frac{(\mathbf{x}_\mu-\mathbf{x}_\nu)\cdot\mathbf{n}_\nu}{R_{\mu\nu}}j_2(kR_{\mu\nu})\right\}, \tag{18}$$

where j_n is the nth-order spherical Bessel function of the first kind[41] and $R_{\mu\nu}=|\mathbf{x}_\mu-\mathbf{x}_\nu|$. Each of the quantities on the right-hand side of Eq. (15) are real numbers, as can be demonstrated by performing the computations for a particular example problem. Equations (15)–(18) can be written in matrix form as

$$\Pi_{\mathrm{av}}=\tfrac{1}{2}\mathbf{s}^H\mathbf{S}\cdot\mathbf{s}, \tag{19}$$

where the superscript H denotes the Hermitian transpose (i.e., transpose and conjugation) and $\mathbf{S}$ is a Hermitian matrix. The power output of the tripole sources can now be calculated directly from Eq. (19) knowing the solution for the source amplitudes.

B. Numerical integration of the far-field intensity

As a check on the accuracy of Eq. (19), the power output can also be determined by integrating the far-field intensity of the sources over a large spherical surface of radius R. Writing the power output as an integral of the normal component of the intensity over the surface of the sphere and substituting the plane-wave approximation for the normal component of the particle velocity on the surface of the large sphere, the time-averaged power output becomes

$$\Pi_{\mathrm{av}}=\frac{1}{2}\int_0^{2\pi}\int_0^{\pi}\mathrm{Re}\{\hat{p}^*(\mathbf{x})[\hat{p}(\mathbf{x})/\rho c]\}R^2\sin\theta\,d\theta\,d\phi=\frac{R^2}{2\rho c}\int_0^{2\pi}\int_0^{\pi}|\hat{p}(\mathbf{x})|^2\sin\theta\,d\theta\,d\phi. \tag{20}$$

The accuracy of Eq. (19) can now be checked by computing the power output using Eq. (20) and verifying that both methods for computing the power output give very nearly the same result.

C. Definition of the resistance matrix

It is also useful to define the power output in terms of the specified volume velocity distribution instead of the source amplitudes. Substituting for $\mathbf{s}$ from Eq. (11) into Eq. (19) gives

$$\Pi_{\mathrm{av}}=\tfrac{1}{2}\mathbf{u}^H\mathbf{U}^{-H}\mathbf{S}\mathbf{U}^{-1}\mathbf{u}, \tag{21}$$

where the superscript $-H$ denotes the Hermitian transpose of the inverse. Taking

$$\mathbf{H}=\mathbf{U}^{-H}\mathbf{S}\mathbf{U}^{-1}, \tag{22}$$

the final result for the power output is

$$\Pi_{\mathrm{av}} = \tfrac{1}{2}\mathbf{u}^H \mathbf{H}\mathbf{u}. \tag{23}$$

The matrix **H** in Eq. (23) must be Hermitian because **S** is Hermitian and because the power output is a positive definite quantity.

In our previous paper,[1] the power output of a vibrating structure was determined by dividing the boundary surface into elements and substituting a separate Taylor series expansion for the imaginary component of the Green's function for each combination of the source and field elements. The resulting equation for the power output was determined as

$$\Pi_{\mathrm{av}} = \tfrac{1}{2}\mathbf{u}^H \mathfrak{R}\mathbf{u}. \tag{24}$$

Simply comparing Eqs. (23) and (24), one expects that **H** should be a good approximation for $\mathfrak{R}$ as long as the numerical solution gives accurate predictions for the overall power output of the radiator. As an example to show that the individual terms of the matrices must be nearly equal, consider the power output of a vibrating structure having the volume velocity distribution $\mathbf{u}^T = \{1,0,0,\ldots,0\}$. The power output is then

$$\Pi_{\mathrm{av}} = \tfrac{1}{2}\mathfrak{R}_{11} \approx \tfrac{1}{2}H_{11}, \tag{25}$$

and thus if the numerical solution for the power output is accurate, H_{11} must be a good approximation for $\mathfrak{R}_{11}$. A similar argument can be used to show that each of the individual terms of the matrices must be nearly equal if the overall power output is to be nearly the same for any arbitrary volume velocity distribution.

In the Introduction we said that we wanted to compute the imaginary component of the Green's function of the second kind numerically. The matrix **H** gives the numerical approximation for the imaginary component of the Green's function, where the relationship between the Green's function of the second kind and the resistance matrix is the same as defined in Eq. (24) of Ref. 1. Because the calculation of the resistance matrix requires a full matrix inversion and several matrix multiplications, it is impractical to calculate and store the numerical approximation for the resistance matrix at each frequency. In general, it is much more practical to simply solve the system of equations for the source amplitudes and compute the power output using Eq. (19).

III. NUMERICAL EXAMPLE PROBLEMS

In this section, our method is used to compute the power output from vibrating structures with relatively simple, but not trivial, boundary surfaces. Four examples will be given: (1) a block with one face vibrating as a piston; (2) a rectangular plate above a baffled simple source; (3) an open, thin-walled cylinder attached to a cylindrical driver; and (4) a transversely oscillating unbaffled circular disk. These examples were chosen primarily because they can be described fairly easily and because the surface element meshes can be continuously refined, providing a check of the solution's convergence. We are especially interested to see if the solution for the power output converges uniformly to the correct solution as the element mesh is refined. All of the numerical results were computed using the FORTRAN program POWER written by John Fahnline.

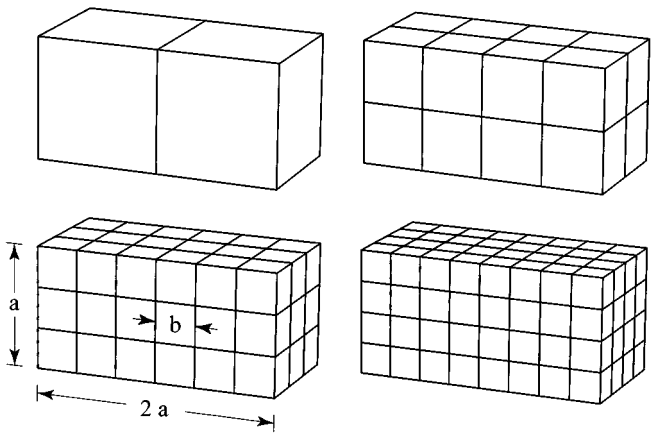

FIG. 2. The four surface element meshes for the block radiator.

A. Block with one face vibrating as a piston

The numerical implementation of the lumped parameter model is ideally suited to problems where the overall volume velocity of the vibrating structure is nonzero. As an example of a boundary value problem with nonzero volume velocity, consider the acoustic power output from a boundary surface in the shape of a block with one face vibrating as a piston. The four surface element meshes used in the numerical analysis are shown in Fig. 2. The square sides of the block are of length a, and the longer dimension of the rectangular sides of the block are of length $2\,a$. Each of the surface elements are square with sidelength b. The convergence of the predicted power output as a function of the element size is used to judge the accuracy of the approximate solutions.

The boundary condition for the surface velocity is taken as $\hat{\mathbf{v}}_n(\mathbf{x}) = 1$ m/s on one of the square faces of the block and $\hat{\mathbf{v}}_n(\mathbf{x}) = 0$ on the other faces. This velocity distribution could be physically realized by driving one face of the block as a piston, as shown in Fig. 3. The specified volume velocity distribution for the block is thus given as $\hat{u}_\nu = b^2$ for the elements on the vibrating face of the block and $\hat{u}_\nu = 0$ for the elements on the other faces. Figure 4 gives the predicted power level of the block as a function of ka for each of the surface element grids, where the power level is defined as $L_P = 10\log(\Pi_{\mathrm{av}}/\Pi_{\mathrm{ref}})$ with $\Pi_{\mathrm{ref}} = 10^{-12}$ W. The power level was evaluated in ka increments of 0.05 for each of the curves plotted in Fig. 4. The low-frequency approximation for the power output from a vibrating structure can be determined as $\Pi_{\mathrm{av}} = k^2\rho c|\hat{u}|^2/8\pi$ where $\hat{u}$ is the structure's overall volume velocity. For values of ka below 0.5 (not shown),

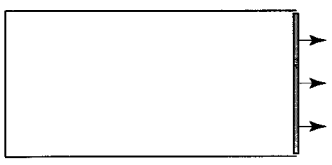

FIG. 3. Block with one face moving as a piston.

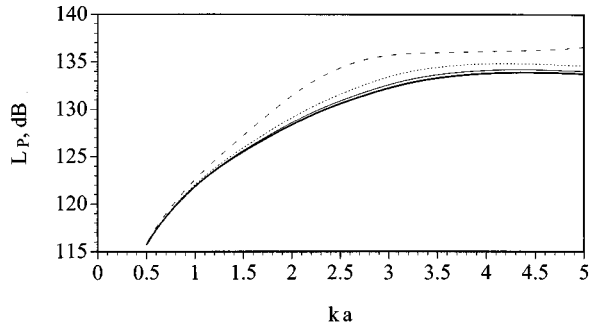

FIG. 4. Power level of the block as a function of ka where $a=0.3048$ m (1 ft) (-- $N=10$, ------ $N=40$, ——— $N=90$, ——— $N=160$).

the numerical results all compare well with the low-frequency approximation. In general, the solution accuracy is very good, agreeing to within a decibel for the two finest element meshes over almost all of the frequency range shown in the figure.

To illustrate the convergence properties of the numerical solution, a very refined mesh with 490 elements was used as a very nearly exact solution, and the previous results were compared to the power output predicted for the refined mesh. As a measure the error in the approximate solution, we define the quantity

$$E=(\overline{\Pi}_{\mathrm{av}}-\Pi_{\mathrm{av}})/\Pi_{\mathrm{av}}, \tag{26}$$

where $\overline{\Pi}_{\mathrm{av}}$ is the approximate solution for the power output, and thus E represents the relative error in the predicted power output. To provide reference points on the scale, a 10% error in the power output corresponds to $|E|=0.1$ (≈ 0.5 dB) and a 1% error in the power output corresponds to $|E|=0.01(\approx 0.05$ dB). Figure 5 shows a plot of the logarithm of the magnitude of the relative error as a function of ka for each of the various surface element meshes. The results show that the convergence is uniform as the element mesh is refined and that the solution converges to the correct solution at low frequency. The slopes of the curves can be used to determine the dependence of the solution error on the nondimensional wave number. The line marked REFERENCE in Fig. 5 shows a curve whose slope is proportional to $(ka)^2$. Because the slopes of the curves for $\log(|E|)$ are somewhat greater than the reference line, we conclude that

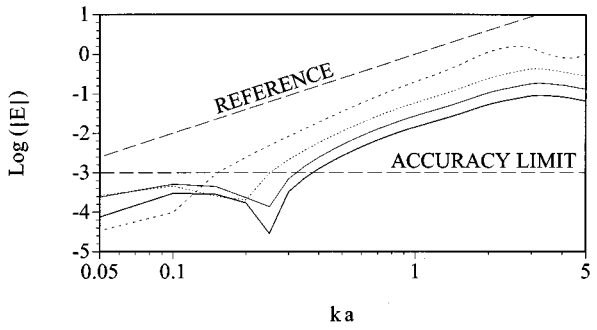

FIG. 5. Variation in the logarithm of the magnitude of the relative error as a function of ka for each of the surface element meshes (-- $N=10$, ------ $N=40$, ——— $N=90$, ——— $N=160$).

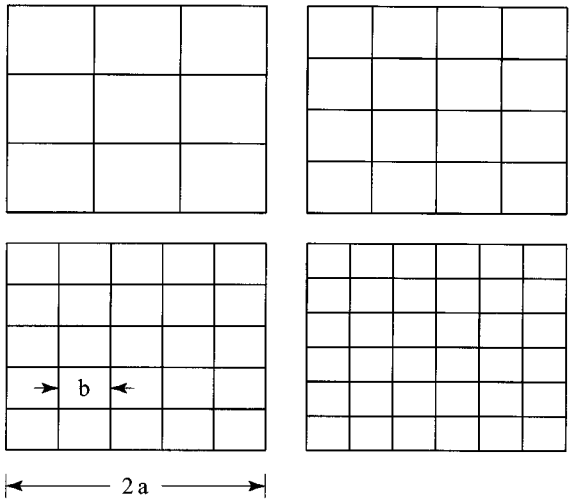

FIG. 6. The four surface element meshes for the rectangular plate.

the ka dependence is faster than $(ka)^2$, which is at least as good as expected. The line marked ACCURACY LIMIT in Fig. 5 shows the specified accuracy limit for the numerical integration schemes (0.1%). When $\log(|E|)$ is less than -3, the difference between the power outputs of the exact and approximate solution is less than 0.1%, and we expect that random errors in the numerical integration scheme will begin to dominate the overall solution error. The results shown in the figure tend to verify this conclusion, and we thus conclude that in the general case the maximum possible solution accuracy is approximately 0.1%.

The results in Fig. 5 also show that the convergence is uniform as a function of the element size at a particular frequency; that is, the solution for the power output is always more accurate for a smaller element size. This example problem is not typical of all radiation problems though, because the acoustic field exhibits no resonance phenomena. The effect of acoustic resonances on the convergence of the numerical solution is examined in the next two example problems.

B. Rectangular plate above a baffled simple source

The second example problem was inspired by a recent paper by Lee and Ih[42] where they sought to determine how the power output of a baffled loudspeaker was effected by mounting a circular plate directly above it. Their results demonstrated that the plate causes the frequency response of the loudspeaker to exhibit a series of well-defined acoustic resonances. We will perform a similar analysis, except we replace the loudspeaker by a simple source and use a rectangular plate instead of a circular plate. The plate is assumed to be infinitely rigid, such that the pressure field of the simple source does not cause the plate to vibrate. Thus each of the elements representing the surface of the plate is given zero volume velocity. Because the plate is thin, we model only one side of the plate and represent the radiation from the plate using dipole sources only. The four surface element meshes used in the numerical analysis are shown in Fig. 6. The dimensions of the plate were arbitrarily taken to be

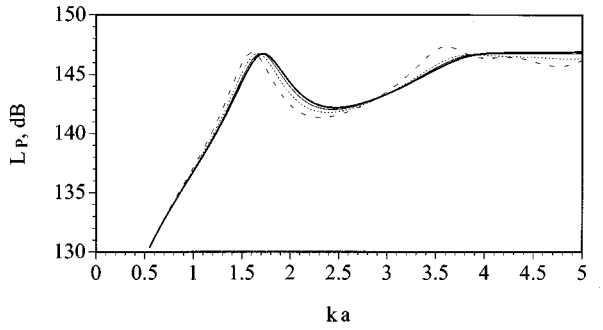

FIG. 7. Power level of the baffled simple source as a function of ka where $a=1$ m (-- $N=9$, ------ $N=16$, ——— $N=25$, ——— $N=36$).

1.6 m by 2 m, and the plate is located 0.5 m above the plane of the baffle, with the simple source located directly below the center of the plate. The element size b is equal to $(2\,a)$ divided by the number of elements in the direction of the longer side of the plate.

To compute the frequency response of the baffled simple source, we give the simple source a unit volume velocity ($1\ \mathrm{m}^3/\mathrm{s}$), and compute the power out at a series of discrete frequencies. Figure 7 gives the predicted power level of the simple source as a function of ka for each of the surface element grids. The power level was evaluated in ka increments of 0.05 for each of the curves plotted in Fig. 7. In this case, the low-frequency approximation for the power output from a vibrating structure can be determined as $\Pi_{\mathrm{av}}=k^2\rho c|\hat{u}|^2/4\pi$, where $\hat{u}$ is the volume velocity of the simple source. Again, for values of ka below 0.5, the numerical results all compare well with the low-frequency approximation.

To illustrate the convergence properties of the numerical solution, a very refined mesh with 144 elements was used as a very nearly exact solution, and the previous results were compared to the power output predicted for the refined mesh. Figure 8 shows a plot of the logarithm of the magnitude of the relative error as a function of ka for each of the various surface element meshes. In contrast to the previous example, the convergence of the solution for the power output is not necessarily uniform as a function of the element size, i.e., frequency ranges exist where the accuracy in the predicted power output decreases when the element mesh is refined.

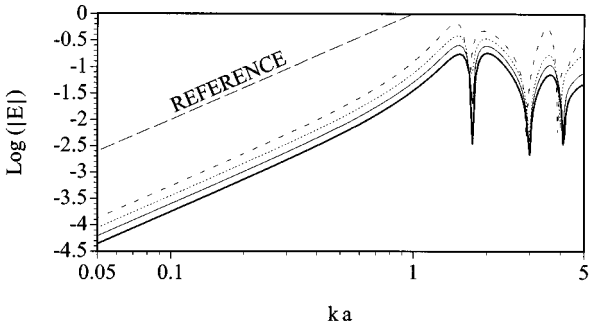

FIG. 8. Variation in the logarithm of the magnitude of the relative error as a function of ka for each of the surface element meshes (-- $N=9$, ------ $N=16$, ——— $N=25$, ——— $N=36$).

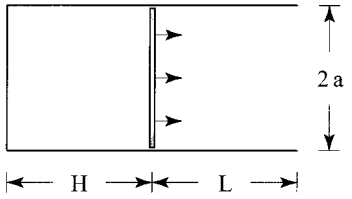

FIG. 9. An open thin-walled cylinder attached to a cylindrical driver.

This phenomenon is especially prevalent near acoustic resonances, where the nonuniform convergence is primarily due to the error in the prediction of the resonance frequency, not in the prediction in the amplitude of the acoustic power output near the resonances. Still, the overall accuracy in the predicted power output is very good, and the convergence, although nonuniform over some frequency ranges, is fairly rapid. The fact that the error does not become random for values of E smaller than the 0.001 is probably due to the configuration of the boundary surface. Because all of the surface elements occupy the same plane, the random errors in the calculation of $\mathbf{U}$ are minimized, which then increases the overall solution accuracy.

C. Open thin-walled cylinder attached to a cylindrical driver

In the previous two examples, the elemental volume velocities were matched exactly by the numerical solution. In this example, the effect of small errors in the specified volume velocity distribution are examined. Consider the calculation of the power output of an open thin-walled cylinder attached to a cylindrical driver; a cross-sectional view of which is shown in Fig. 9.

The cylindrical driver is of radius a and height H, and the open cylinder is of radius a and length L. This problem is notable because it is very difficult to analyze using a conventional boundary element formulation as discussed by Martinez,[43] although Wu[44] has recently made an attempt to extend the conventional boundary element formulation to address this type of problem. In our formulation, the presence of the thin-walled cylinder causes no difficulties because we can represent the radiation from the elements associated with the cylinder using dipole sources. The normal velocity of the speaker diaphragm of the cylindrical driver is taken to be $\hat{\mathbf{v}}_n(\mathbf{x})=1$ m/s and all the other components of the structure are assumed to be stationary. Four different models are used to compute the radiated sound power, as shown in Fig. 10.

Predictions for the power level as a function of frequency for each of the four models are shown in Fig. 11, where the geometrical parameters were taken as $a=1$ m, $L=1$ m, and $H=1$ m, and the ka increment was taken as 0.025. The refined frequency increment was necessary to resolve the peak in the power level near $ka=1$. Each of the models accurately predicts the large increase in the power output near the resonances of the open cylinder, although there are slight variations in the predicted resonance frequencies.

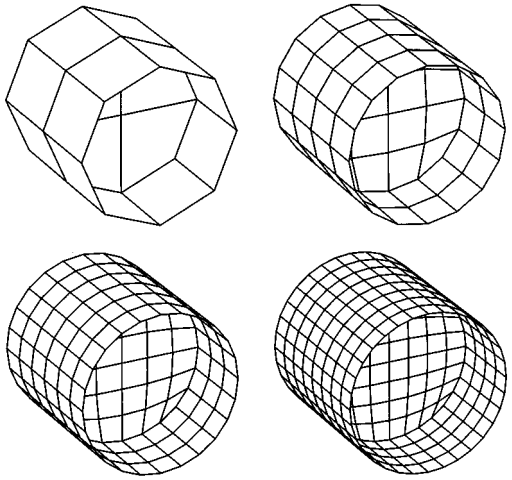

FIG. 10. Four surface element meshes for the open thin-walled cylinder attached to a cylindrical driver.

As in the previous examples, we want to determine the convergence of the solution as a function of frequency and the element size. For this problem the nearly exact solution required a large number of elements (600) because the vibrating structure is made up of a number of individual parts. Figure 12 shows a plot of the logarithm of the magnitude of the relative error as a function of ka for each of the various surface element meshes. Again, the convergence of the solution for the power output is not necessarily uniform, especially near the frequencies where acoustic resonances occur.

A comparison of Figs. 5, 8, and 12 shows that at low frequency the convergence properties of the solution for the power output of the short cylinder are quite different from the convergence properties of the solutions for either the block or the shield. More specifically, the slopes of the curves in Fig. 12 are very nearly zero at low frequency, indicating that the solution does not converge as a function of frequency at low frequency. The lack of convergence is due to inaccuracies in the representation of the overall volume velocity of the structure, caused by discretizing the surface area of the diaphragm. For example, Fig. 13 shows a comparison of the actual size of the diaphragm and the coarsest discretization of the diaphragm. The figure shows that all of the area of the diaphragm is not accounted for in the

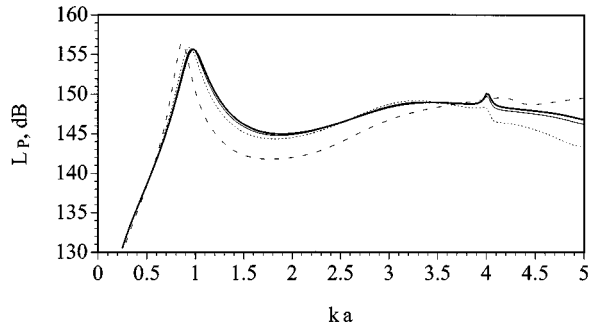

FIG. 11. Power level of the open thin-walled cylinder attatched to a cylindrical driver as a function of ka (–– $N=24$, ------ $N=96$, ——— $N=216$, ——— $N=384$).

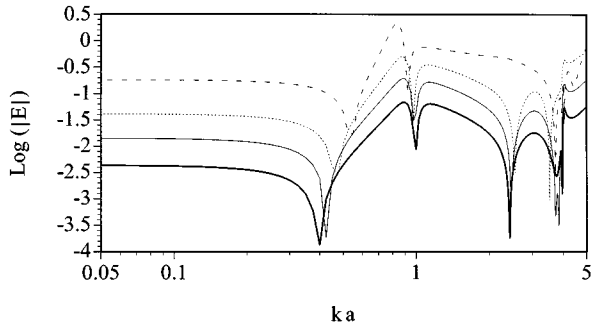

FIG. 12. Variation in the logarithm of the magnitude of the relative error as a function of ka for each of the surface element meshes (–– $N=24$, ------ $N=96$, ——— $N=216$, ——— $N=384$).

element discretization. Assuming that each point of the diaphragm has a normal surface velocity of 1 m/s then leads to a slight underestimation of the overall volume velocity of the structure. As the element mesh is refined, more of the surface area of the diaphragm is accounted for, and thus the error in the solution decreases. Still, there is always a slight inaccuracy in the overall volume velocity, so that using this discretization, the solution will never converge as a function of frequency at low frequency. In general, most problems will suffer from this difficulty due to slight errors in the specified surface velocity and discretization errors, and thus the results shown in Fig. 12 must then be considered typical, rather than exceptional. In practice, this simply means that the predicted power output for a given surface element mesh is not necessarily more accurate at low frequencies than at intermediate frequencies.

D. Transversely oscillating unbaffled circular disk

As a more difficult example problem, the power output from a transversely oscillating disk is analyzed. The problem is more difficult because the overall volume velocity of the disk is zero. Our previous analysis[1] predicts that error in the approximate solution should decrease as the element mesh is refined, but should not decrease as the frequency decreases for a particular element mesh. The main goal of the analysis is to verify this prediction. The amplitude of the vibration is taken to be unity such that the normal velocity is specified as

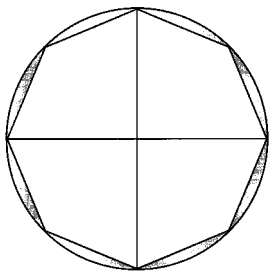

FIG. 13. Comparison of the actual size of the diaphragm and the coarsest discretization of the diaphragm.

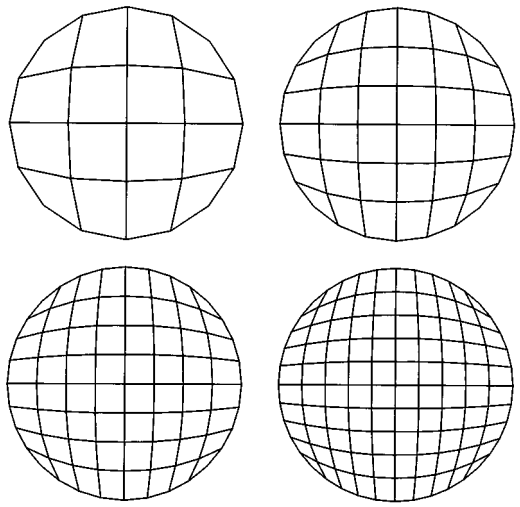

FIG. 14. Surface element meshes for the transversely vibrating disk.

$\hat{\mathbf{v}}_n(\mathbf{x})=1$ m/s on the front face of the disk, and $\hat{\mathbf{v}}_n(\mathbf{x})=-1$ m/s on the back face of the disk. Again, we only model the centerplane of the disk and represent the radiation from the disk using dipole sources only. Four element meshes were analyzed, as shown in Fig. 14.

Figure 15 gives the predicted power level of a transversely oscillating disk of radius 1 m as a function of ka for each of the surface element grids. Because each of the curves shown in Fig. 15 are very closely spaced, we are tempted to conclude (wrongly) that the lumped parameter model converges very quickly to the correct solution, perhaps even more quickly than in the previous examples. To correctly interpret the results, however, we must compare the predicted power output to an exact solution for the power output, as given by Bouwkamp.[45] Figure 16 shows a plot of the logarithm of the magnitude of the relative error as a function of ka for each of the various surface element meshes. The results show that the solution converges as a function of element size, but not as a function of frequency, as predicted. The results also show that the convergence is relatively slow, accounting for the relatively small change in the predicted power output as a function of the element mesh density. In this problem, the small errors in the representation of the surface of the disk do not result in errors in the predicted power output because the numerical model correctly represents the overall volume velocity of the disk as zero. If the model incorrectly represented the overall volume velocity of the disk, the error in the predicted power output would become very large.

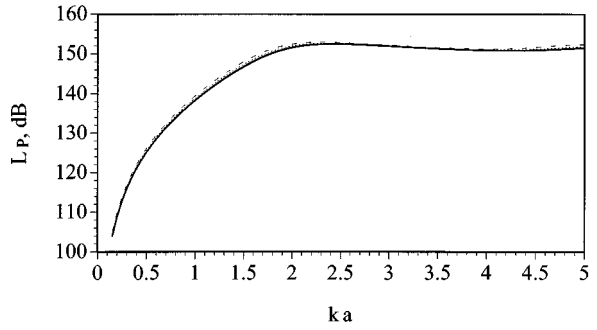

FIG. 15. Power level of the disk as a function of ka, with $a=1$ m (–– $N=16$, ------ $N=36$, ——— $N=64$, ——— $N=100$).

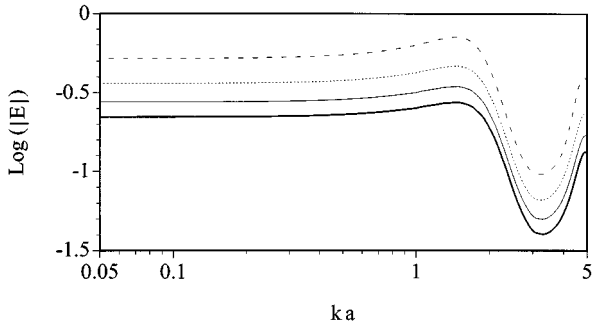

FIG. 16. Variation in the logarithm of the magnitude of the relative error as a function of ka for each of the surface element meshes (–– $N=16$, ------ $N=36$, ——— $N=64$, ——— $N=100$).

IV. CONCLUSIONS

A method has been developed for numerically computing the sound power radiated by a vibrating structure. The method differs from previous boundary methods primarily in the way the boundary condition is enforced. By satisfying the boundary condition in a lumped parameter sense, rather than on a point-to-point basis, the requirements on the basis functions for the acoustic field are relaxed significantly. This allows the use of discrete sources instead of continuous distributions of sources as basis functions, alleviating the difficulties in enforcing the boundary condition and leading to a solution with well-defined convergence properties.

The theoretical analysis in our previous paper (Ref. 1) predicted that the resulting solution for the acoustic power output of the structure must converge to the correct solution as the element mesh is refined at a particular frequency. To test this prediction, four example problems were examined. The results of the numerical analysis show that the solution does converge to the correct solution, but that the convergence may not be uniform as a function of the mesh density over some frequency ranges; that is, the error in the solution for the acoustic power output may possibly increase as the element size decreases. Still, the overall convergence of the numerical solution is excellent, with the error in the predicted power output smaller than a few decibels over a broad frequency range for even the coarsest surface element meshes.

The main drawback of the method is the computational cost of solving the system of equations for the source amplitudes. A method to alleviate this difficulty has been given recently by Fahnline[38] (written after the first edition of this paper, but already in print). The article shows how a very dense structural mesh can be condensed into a much coarser acoustic element mesh, resulting in a much smaller number of equations to solve for the source amplitudes. This step essentially eliminates the time required to solve the system

of equations, which previously required most of the time in the solution process (when the number of equations exceeds about 1000 elements). We presume that using this condensation, our numerical solution is now at least as fast as a typical finite element solution,[46] but no direct comparisons of the solution speeds have been attempted.

APPENDIX

In the following derivation, we show that the radiation from different parts of a structure are best represented by a particular source type. Consider a boundary surface made up of three distinct areas, as shown in Fig. A1. To simplify the analysis, we use image sources to automatically enforce the boundary condition on the infinite baffle. For each source location on the boundary surface, we place an image source at the reflection of the source point about the infinite plane, as illustrated in Fig. A2. We now want to use the Kirchhoff–Helmholtz equation to determine the source type which is appropriate for each of the three components of the boundary surface. To start, we write the pressure field as a summation of three surface integrals as

$$\hat{p}(\mathbf{x}) = I_1 + I_2 + I_3, \tag{A1}$$

where the individual terms represent the integrations over each of the three surfaces making up the boundary surface.

Starting with the surface S_1, we now proceed to evaluate the contribution of each of the surfaces to the overall acoustic field. Using primes to denote quantities associated with the image sources, the integral I_1 becomes

$$I_1 = -\frac{1}{4\pi}\int\int_{S_1}\{ik\rho c\hat{g}(\mathbf{x},\mathbf{q})\hat{v}_n(\mathbf{q}) - \hat{p}(\mathbf{q})\nabla_q\hat{g}(\mathbf{x},\mathbf{q})\cdot\mathbf{n}_q\} \times dS(\mathbf{q}) - \frac{1}{4\pi}\int\int_{S_1'}\{ik\rho c\hat{g}(\mathbf{x},\mathbf{q})\hat{v}_n(\mathbf{q}) - \hat{p}(\mathbf{q})\nabla_q\hat{g}(\mathbf{x},\mathbf{q})\cdot\mathbf{n}_q'\}dS(\mathbf{q}), \tag{A2}$$

where the lower case $\hat{g}$ indicates the free-space Green's function,

$$\hat{g}(\mathbf{x},\mathbf{q}) = \frac{1}{R}e^{ikR}, \tag{A3}$$

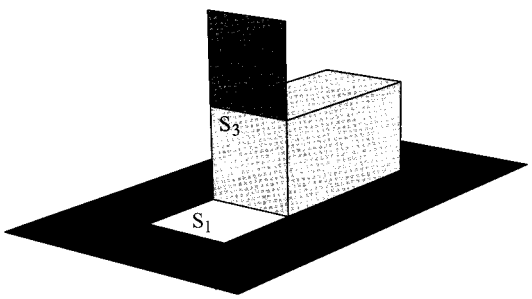

FIG. A1. Boundary surface made up of three areas: S_1 which is in the plane of an infinite baffle, S_2 which is very thin and encloses negligible volume, and S_3 which encloses a finite volume.

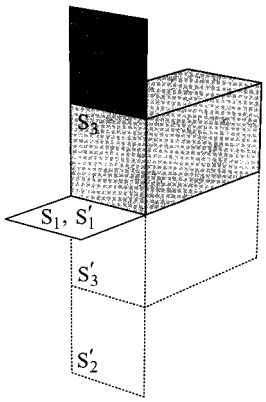

FIG. A2. Illustration of the image of the boundary surface.

with $R=|\mathbf{x}-\mathbf{q}|$. Because the surface area S_1 is in the plane of the baffle, $S_1'=S_1$ and $\mathbf{n}_q'=-\mathbf{n}_q$. Equation (A2) can now be simplified as

$$I_1 = -\frac{ik\rho c}{2\pi}\int\int_{S_1}\hat{g}(\mathbf{x},\mathbf{q})\hat{v}_n(\mathbf{q})dS(\mathbf{q}), \tag{A4}$$

so that the radiation from the elements in the plane of the infinite baffle can be represented in terms of simple sources only.

To evaluate the Kirchoff–Helmhotz equation over the surface S_2, we must include both the ''front'' and ''back'' faces of the surface because both are in contact with the acoustic medium. Denoting the front and back faces with a superscript + and − sign, respectively, the contribution of the very thin surface to the overall acoustic pressure field becomes

$$I_2 = -\frac{1}{4\pi}\int\int_{S_2^+}\{ik\rho c\hat{g}(\mathbf{x},\mathbf{q})\hat{v}_n(\mathbf{q}) - \hat{p}(\mathbf{q})\nabla_q\hat{g}(\mathbf{x},\mathbf{q})\cdot\mathbf{n}_q^+\} \times dS(\mathbf{q}) - \frac{1}{4\pi}\int\int_{S_2^-}\{ik\rho c\hat{g}(\mathbf{x},\mathbf{q})\hat{v}_n(\mathbf{q}) - \hat{p}(\mathbf{q})\nabla_q\hat{g}(\mathbf{x},\mathbf{q})\cdot\mathbf{n}_q^-\}dS(\mathbf{q}) + I_2', \tag{A5}$$

where I_2' is the contribution from the image sources. Because S_2 is very thin and deforms only in bending, the surface normal and normal surface velocity on the two faces of the structure are exact opposites of each other, and thus Eq. (A5) reduces to

$$I_2 = \frac{1}{4\pi}\int\int_{S_2}[\hat{p}(\mathbf{q}^+) - \hat{p}(\mathbf{q}^-)]\nabla_q\hat{g}(\mathbf{x},\mathbf{q})\cdot\mathbf{n}_q^+\, dS(\mathbf{q}) + I_2'. \tag{A6}$$

The function $\nabla_q\hat{g}(\mathbf{x},\mathbf{q})\cdot\mathbf{n}_q^+$ represents the acoustic field of a dipole source aligned in the direction $\mathbf{n}_q^+$ at the point $\mathbf{q}$, so that the radiation from the very thin structure can be represented by dipole sources only. We can now replace the pressure difference on the two sides of the surface by a dipole source amplitude, which is then determined by enforcing the boundary condition for the normal surface velocity. We only have to enforce the boundary condition over one face of S_2 because the normal surface velocity on the other face must

be its exact opposite, as is easily proven by explicitly writing the normal surface velocity on either side of the surface. A related discussion is given by Martinez.[43]

Finally, we evaluate the integral over the surface S_3 as

$$I_3 = -\frac{1}{4\pi}\int\int_{S_3}\{ik\rho c\hat{g}(\mathbf{x},\mathbf{q})\hat{v}_n(\mathbf{q}) - \hat{p}(\mathbf{q})\nabla_q\hat{g}(\mathbf{x},\mathbf{q})\cdot\mathbf{n}_q\} \times dS(\mathbf{q}) + I_3', \tag{A7}$$

where I_3' is the contribution from the image sources. In Eq. (A7), the radiation includes contributions from both simple and dipole sources, with the relative size of their contributions depending both on the frequency and the source location. We can get an idea of the relative sizes by examining the low- and high-frequency limits for the integral. Because we are primarily interested in computing the acoustic power output, we assume that the field point $\mathbf{x}$ is located a great distance from the surface of the structure. At low frequency, the dipole sources do not radiate nearly as efficiently as the simple sources, and we can then approximate the integral as

$$I_3 = -\frac{ik\rho c}{4\pi}\int\int_{S_3}\hat{g}(\mathbf{x},\mathbf{q})\hat{v}_n(\mathbf{q})dS(\mathbf{q}) + I_3'. \tag{A8}$$

At high frequency, the surface pressure is approximately given as[9]

$$\hat{p}(\mathbf{q}) = \rho c\hat{v}_n(\mathbf{q}), \tag{A9}$$

so that Eq. (A7) becomes

$$I_3 = -\frac{\rho c}{4\pi}\int\int_{S_3}\{ik\hat{g}(\mathbf{x},\mathbf{q}) - \nabla_q\hat{g}(\mathbf{x},\mathbf{q})\cdot\mathbf{n}_q\}\hat{v}_n(\mathbf{q})dS(\mathbf{q}) + I_3'. \tag{A10}$$

Thus in the high-frequency limit the contributions from the two source types are directly related, with the difference in the source amplitudes proportional to ik, as for a ''tripole source.''

At this point, we have two possible choices for the basis functions. One possibility is to assume the weighting function for the simple sources is known, and to try to determine the pressure field as the weighting function for the dipole sources. This method is probably the most logical, simply because the normal surface velocity is specified and the surface pressure is unknown. Unfortunately, this set of basis functions will suffer from nonuniqueness difficulties at a set of discrete frequencies. Another possibility is to assume the source amplitudes of the simple and dipole sources are related through a complex constant, as in the high-frequency limit given in Eq. (A10). Clearly, the pressure and normal surface velocity on the boundary surface are not generally related through a single complex constant, and thus an exact solution for the acoustic field cannot be determined using this assumption. However, we seek only to enforce the boundary condition in a lumped parameter sense, and thus the nonexistence of an exact solution for the acoustic field is not a problem. Because this method guarantees the elimination of the nonexistence and nonuniqueness difficulties, we chose the tripole sources as basis functions for surfaces enclosing a finite volume.

[1] J. B. Fahnline and G. H. Koopmann, ''A lumped parameter model for the acoustic power output from a vibrating structure,'' J. Acoust. Soc. Am. **100**, 3539–3547 (1996).
[2] L. Collatz, *The Numerical Treatment of Differential Equations*, translated by P. G. Williams (Springer-Verlag, New York, 1960), 3rd ed.
[3] F. B. Hildebrand, *Methods of Applied Mathematics* (Dover, New York, 1965), 2nd ed.
[4] S. H. Crandall, *Engineering Analysis: A Survey of Numerical Procedures* (McGraw-Hill, New York, 1956).
[5] R. D. Ciskowski and C. A. Brebbia, *Boundary Element Methods in Acoustics* (Computational Mechanics, New York, 1991).
[6] A. P. Zielinski and I. Herrera, ''Trefftz method: Fitting boundary conditions,'' Int. J. Numer. Methods Eng. **24**, 871–891 (1987).
[7] J. B. Fahnline, ''The generalized inverse source method for the computation of acoustic fields,'' Ph.D. thesis, The Pennsylvania State University, University Park, 1993.
[8] A. D. Pierce, *Acoustics: An Introduction to its Physical Principles and Applications* (Acoustical Society of America, New York, 1989).
[9] M. C. Junger and D. Feit, *Sound Structures and Their Interaction* (Acoustical Society of America, New York, 1993).
[10] P. M. Morse and K. U. Ingard, *Theoretical Acoustics* (Princeton U. P., Princeton, NJ, 1968).
[11] S. Temkin, *Elements of Acoustics* (Wiley, New York, 1968).
[12] L. H. Chen and D. G. Schweikert, ''Sound radiation from an arbitrary body,'' J. Acoust. Soc. Am. **35**, 1626–1632 (1963).
[13] G. Chertock, ''Sound radiation from vibrating surfaces,'' J. Acoust. Soc. Am. **36**, 1305–1313 (1964).
[14] L. G. Copley, ''Integral equation method for radiation from vibrating bodies,'' J. Acoust. Soc. Am. **41**, 807–816 (1967).
[15] J. J. Engbloom and R. B. Nelson, ''Consistent formulation of sound radiation from arbitrary structures,'' J. Appl. Mech. **42**, 295–300 (1975).
[16] G. Krishnasamy, F. J. Rizzo, and T. J. Rudolphi, ''Continuity requirements for density functions in the boundary integral equation method,'' Comput. Mech. **9**, 267–284 (1992).
[17] L. J. Gray and C. San Soucie, ''A hermite interpolation algorithm for hypersingular boundary integrals,'' Int. J. Numer. Methods Eng. **36**, 2357–2367 (1993).
[18] Y. Liu and F. J. Rizzo, ''A weakly singular form of the hypersingular boundary integral equation applied to 3-D acoustic wave problems,'' Comput. Methods Appl. Mech. Eng. **96**, 271–287 (1992).
[19] M. A. Jawson and G. T. Symm, *Integral Equation Methods in Potential Theory and Elastostatics* (Academic, London, 1977).
[20] G. Krishnasamy, F. J. Rizzo, and T. J. Rudolphi, ''Hypersingular boundary integral equations: Their occurrence, interpretation, regularization and computation,'' in *Advanced Dynamic Analysis by Boundary Element Methods*, edited by P. K. Bannerjee and S. Kobayashi (Elsevier Applied Science, New York, 1992).
[21] L. J. Gray and E. Lutz, ''On the treatment of corners in the boundary element method,'' J. Comput. Appl. Math. **32**, 369–386 (1990).
[22] P. S. Han and M. D. Olson, ''An adaptive boundary element method,'' Int. J. Numer. Methods Eng. **24**, 1187–1202 (1987).
[23] J. B. Fahnline and G. H. Koopmann, ''A numerical solution for the general radiation problem based on the combined methods of superposition and singular-value decomposition,'' J. Acoust. Soc. Am. **90**, 2808–2819 (1991).
[24] J. Y. Hwang and S. C. Chang, ''A retracted boundary integral equation for exterior acoustic problems with unique solution for all wave numbers,'' J. Acoust. Soc. Am. **90**, 1167–1180 (1991).
[25] Y. I. Bobrovnitskii and T. M. Tomilina, ''General properties and fundamental errors of the method of equivalent sources,'' Acoust. Phys. **41**, 649–660 (1995).
[26] G. F. Miller, ''Fredholm equations of the first kind,'' in *Numerical Solution of Integral Equations*, edited by L. M. Delves and J. Walsh (Clarendon, Oxford, 1974).
[27] C. T. H. Baker, *Numerical Treatment of Integral Equations* (Clarendon, Oxford, 1977).
[28] F. Smithies, *Integral Equations* (Cambridge U. P., Cambridge, 1977).
[29] L. G. Copley, ''Fundamental results concerning integral representations in acoustic radiation,'' J. Acoust. Soc. Am. **44**, 28–32 (1968).
[30] H. A. Schenck, ''Improved integral formulation for acoustic radiation problems,'' J. Acoust. Soc. Am. **44**, 41–58 (1968).
[31] A. J. Burton and G. F. Miller, ''The application of integral equation methods to the numerical solution of some exterior boundary-value problems,'' Proc. R. Soc. London, Ser. A **323**, 201–210 (1971).

[32] P. J. T. Filippi, ''Layer potentials and acoustic diffraction,'' J. Sound Vib. **54**, 473–500 (1978).
[33] T. Terai, ''On calculation of sound fields around three-dimensional objects by integral equations,'' J. Sound Vib. **69**, 71–100 (1980).
[34] R. Kress and W. T. Spassov, ''On the condition number of boundary integral operators for the exterior Dirichlet problem for the Helmholtz equation,'' Numer. Math. **42**, 77–95 (1983).
[35] G. R. Cowper, ''Gaussian quadrature formulas for triangles,'' Int. J. Numer. Methods Eng. **7**, 405–408 (1973).
[36] T. H. Duong, ''A finite element method for the double-layer potential solutions of the Neumann exterior problem,'' Math. Methods Appl. Sci. **2**, 191–208 (1980).
[37] R. D. Cook, D. S. Malkus, and M. E. Plesha, *Concepts and Applications of Finite Element Analysis* (Wiley, New York, 1989), 3rd ed.
[38] J. B. Fahnline, ''Condensing Structural Finite Element Meshes into Coarser Acoustic Element Meshes,'' DE-Vol. 84-2, Proceedings of the 1995 Design Engineering Technical Conferences, Vol. 3–Part B, ASME, pp. 641–646 (1995).
[39] H. Levine, ''Output of acoustical sources,'' J. Acoust. Soc. Am. **67**, 1935–1946 (1980).
[40] P. A. Nelson and S. J. Elliott, *Active Control of Sound* (Academic, New York, 1992).
[41] M. Abromowitz and I. A. Stegun, *Handbook of Mathematical Functions* (Dover, New York, 1965).
[42] J. Lee and J. Ih, ''Reactive characteristics of partial screens for a sound source mounted in an infinite baffle,'' J. Acoust. Soc. Am. **98**, 1008–1016 (1995).
[43] R. Martinez, ''The thin-shape breakdown (TSB) of the Helmholtz integral equation,'' J. Acoust. Soc. Am. **90**, 2728–2738 (1991).
[44] T. W. Wu, ''A direct boundary element method for acoustic radiation and scattering from mixed regular and thin bodies,'' J. Acoust. Soc. Am. **97**, 84–91 (1995).
[45] C. Bouwkamp, ''Theoretical and numerical treatment of diffraction through a circular aperture,'' IEEE Trans. Antennas Propagat. **18**, 152–176 (1970).
[46] D. S. Burnett, ''A three-dimensional acoustic infinite element based on a prolate spheroidal multipole expansion,'' J. Acoust. Soc. Am. **96**, 2798–2816 (1994).

Determination of the second- and third-order elastic constants in Al from the natural frequencies

V. Chiroiu
Institute of Solid Mechanics, Romanian Academy, Bucharest, Romania

P. P. Delsanto
INFM, Dipartimento di Fisica del Politecnico di Torino, Torino, Italy

L. Munteanu and C. Rugina
Institute of Solid Mechanics, Romanian Academy, Bucharest, Romania

M. Scalerandi
INFM, Dipartimento di Fisica del Politecnico di Torino, Torino, Italy

(Received 30 July 1996; revised 15 February 1997; accepted 27 February 1997)

The Hamiltonian approach to the calculation of vibrational modes of elastic cubic objects is exploited, including the effect of higher-order elastic constants. A technique is presented for solving the inverse problem, i.e., the determination of second- and third-order elastic constants for face cubic centered crystals by inversion of natural frequencies data. An unconstrained minimization algorithm, using gradient methods, is used to numerically solve the inverse problem. The method is applied to the case of Al alloys, since they are particularly suitable for applications of the acoustoelastic effect, which requires a knowledge of the third-order elastic constants. The efficiency and the accuracy of the method and the influence of measurement errors are discussed. © *1997 Acoustical Society of America.* [S0001-4966(97)05306-X]

PACS numbers: 43.25.−x, 43.35.Cg [MAB]

INTRODUCTION

The reconstruction of the physical properties of a system by means of natural frequencies data inversion is an old problem. Holland[1] and Demarest[2] observed that a very simple variational principle can be used for deriving an eigenvalue equation for the normal-mode frequencies of an elastic body with free boundaries. Ohno[3] applied the method to the resonant ultrasonic determination of the elastic constants of materials by using small rectangular parallelepipedal single-crystal samples. Simple specimen geometries (sphere, cylinder, cube, etc.) have been frequently used in the literature,[4,5] for both analytical studies and experimental measurements.

The analytical results have contributed to the development of resonant ultrasound spectroscopy (RUS)[6,7] techniques for the experimental determination of natural frequencies (NF), which are useful for the solution of inversion problems. RUS has been most extensively applied in geophysics (for the measurement of thermodynamic properties) and for the determination of second-order elastic constants.[8–10] Great success has recently been achieved in the study of phase transition for high-temperature superconductors,[8] for the determination of relaxation effects in some complex systems,[9] and in the anisotropy determination for quasicrystals.[10]

The purpose of the present article is to present in a compact form a RUS method for the determination of both the second- and third-order elastic constants from the natural frequencies of a cube of an Al alloy. A quantitative knowledge of the third-order elastic constants is essential for the study and application of the acoustoelastic effect (AE).[11,12] Since Al alloys are particularly suitable for AE applications (e.g., to the determination of applied and residual stress fields),[13,14] the proposed method is applied to the case of Al alloys. Another important example of the relevance of third- (or higher-) order elastic constants is in the proximity of internal defects. In fact, linear elasticity predicts that stresses and strains vary as the inverse first power of the distance from the defect and, therefore, are unbounded as this distance goes to zero. Close to the defects, nonlinear effects must clearly be taken into account and the knowledge of higher-order elastic constants becomes a prerequisite.

In Sec. I, the direct problem of obtaining the natural frequencies from the elastic constants is formulated and discussed. By means of the Rayleigh–Ritz method the expressions for the NFs of a cube specimen of a face cubic centered (fcc) material, such as Al, are obtained. Section II presents the inverse problem and its solution. Also, some properties related to the accuracy of the inversion scheme are discussed. In Sec. III the determination of the third-order elastic constants for aluminum is performed and the computed values are compared with the experimental values found in the literature.

I. THE FORWARD PROBLEM

Let us consider a rectangular parallelepiped (for brevity we shall call it ''cell'') with dimensions $2a, 2b, 2c$, made of a material with face centered cubic symmetry (fcc). Let Σ be its free surface, surrounding a volume V. The Lagrangian of the system may be written as

$$L=\int_V (K-W)dV, \tag{1}$$

where K is the kinetic energy density

$$K=\tfrac{1}{2}\rho\omega^2(u_1^2+u_2^2+u_3^3), \tag{2}$$

and W the potential energy density; $\overline{u}$ the displacement vector and ω the angular frequency of the displacement wave.

In order to take into account nonlinear phenomena, such as acoustoelasticity in elastic materials, we must include the lower-order nonlinear terms in the expression of W.[11] Correspondingly, the stress tensor is defined as

$$\begin{aligned}\sigma_{kl}=&C_{klmn}\eta_{mn}(1-\eta_{pp})+C_{plmn}H_{kp}\eta_{mn}\\&+C_{kpmn}H_{lp}\eta_{mn}+\tfrac{1}{2}C_{klmn}H_{pm}H_{pn}\\&+\tfrac{1}{2}C_{klmnrs}\eta_{mn}\eta_{rs},\end{aligned} \tag{3}$$

where C_{ijkl} and $C_{ijk\underline{lmn}}$ are the second- and third-order elastic constants, resp., $H=\nabla\overline{u}$ and η is the Lagrangian linear strain tensor

$$\eta_{ij}=\frac{1}{2}\left(\frac{\partial u_i}{\partial x_j}+\frac{\partial u_j}{\partial x_i}\right).$$

By using Voigt's notation

$$(i,j)\rightarrow i\,\delta_{i,j}+(9-i-j)(1-\delta_{ij})$$

and Brugger's notation

$$\sigma_{kl}\rightarrow\sigma_k,\quad \eta_{kl}\rightarrow\tfrac{1}{2}(1+\delta_{kl})\eta_k,$$

we may write the potential energy density as

$$W=\tfrac{1}{2}C_{ij}\eta_i\eta_j+\tfrac{1}{6}C_{ijk}\eta_i\eta_j\eta_k\quad(i,j,k=1...6), \tag{4}$$

where it has been assumed that no initial elastic potential is present.

For fcc crystals, Eq. (4) may be written in the form

$$\begin{aligned}W=&\tfrac{1}{2}[C_{11}I_1^2+2(C_{12}-C_{11})I_2+C_{44}I_3]+\tfrac{1}{6}[C_{111}I_1^3\\&+3(C_{112}-C_{111})I_1I_2+3(C_{111}-3C_{112}+2C_{123})I_4\\&+6C_{456}I_5+3(C_{144}-3C_{155})I_6-3C_{144}I_1I_3],\end{aligned} \tag{5}$$

where the scalar invariants

$$\begin{aligned}&I_1=tr\,\eta=\eta_1+\eta_2+\eta_3,\\&I_2=\eta_1\eta_2+\eta_2\eta_3+\eta_1\eta_3,\\&I_3=\eta_4^2+\eta_5^2+\eta_6^2,\\&I_4=\eta_1\eta_2\eta_3,\quad I_5=\eta_4\eta_5\eta_6,\\&I_6=(\eta_2+\eta_3)\eta_4^2+(\eta_1+\eta_3)\eta_5^2+(\eta_2+\eta_1)\eta_6^2\end{aligned}$$

have been used.

The equations of motion are obtained by applying Hamilton's principle

$$\int_{t_1}^{t_2}\delta L\;dt=0. \tag{6}$$

For free vibrations, the displacement field of the cell may be expressed as

$$u(x,y,z,t)=U(x,y,z)e^{i\omega t}, \tag{7}$$

and we may write

$$K=\frac{1}{2}\int_V\rho\omega^2(U_1^2+U_2^2+U_3^2)dV \tag{8}$$

and

$$\begin{aligned}&\eta_1=U_{1,x},\quad \eta_2=U_{2,y},\quad \eta_3=U_{3,z},\\&\eta_4=U_{2,z}+U_{3,y},\quad \eta_5=U_{1,z}+U_{3,x},\quad \eta_6=U_{2,x}+U_{1,y},\end{aligned}$$

where a subscript after the comma means a spatial differentiation with respect to the corresponding coordinate.

An approximative solution for the natural frequencies is obtained by using the Rayleigh–Ritz method. The first step is to fix a complete system of coordinate displacement functions satisfying the homogeneous form of the boundary conditions and such that any linear combination of a finite number of functions is an admissible comparison function for the variational problem.

Visscher *et al.*[5] proposed for the linear case a choice of basis functions in the simple form $x^l y^m z^n$, showing that the choice of basis in terms of Legendre polynomials is not advantageous. However, in the nonlinear case Visscher basis functions do not allow a proper rearrangement of terms to obtain a linear homogeneous system. On the other hand, the choice of Legendre polynomials as a complete orthogonal set is more efficient, since it allows a grouping according to known mode shapes and adds a physical insight into the type of vibrational modes associated with a given frequency.

Considering the nondimensional variables

$$\xi=\frac{x}{a},\quad \chi=\frac{y}{b},\quad \zeta=\frac{z}{c},$$

we choose the following functions for the displacement field

$$\begin{aligned}&U_1(\xi,\chi,\zeta)=S_0(\xi)S_b(\chi)S_c(\zeta),\\&U_2(\xi,\chi,\zeta)=S_a(\xi)S_0(\chi)S_c(\zeta),\\&U_3(\xi,\chi,\zeta)=S_a(\xi)S_b(\chi)S_0(\zeta),\end{aligned} \tag{9}$$

where

$$\begin{aligned}&S_0(x)=\sum_{i=1}^{N}p_i(x),\quad S_a(x)=\sum_{i=1}^{N}a_ip_i(x),\\&S_b(x)=\sum_{i=1}^{N}b_ip_i(x),\quad S_c(x)=\sum_{i=1}^{N}c_ip_i(x).\end{aligned} \tag{10}$$

The functions p_i are the normalized Legendre polynomials, defined as functions of the Legendre polynomials P_i, up to a given order N

$$p_i=\left(\frac{2i+1}{2}\right)^{0.5}P_i,\quad i=1...N.$$

The variation of Eq. (6) with respect to the coefficients $x_i=(a_i,b_i,c_i)$, with $i=1\cdots N$, yields a homogeneous nonlinear system of equations. After a proper rearrangement of terms, we obtain a linear homogeneous system in the 12 unknowns

$$S_1=\sum_{i=1}^{N} x_i^2, \quad S_2=\sum_{i=1}^{N} x_i^3, \quad S_3=\sum_{i=1}^{N} x_i^4, \quad S_4=\sum_{i=1}^{N} x_i^5,$$

$$S_5=\sum_{i,j=1}^{N} x_i x_j, \quad S_6=\sum_{i,j,k=1}^{N} x_i x_j x_k,$$

$$S_7=\sum_{i,j,k,l=1}^{N} x_i x_j x_k x_l, \quad S_8=\sum_{i,j=1}^{N} x_i^2 x_j, \tag{11}$$

$$S_9=\sum_{i,j=1}^{N} x_i^3 x_j, \quad S_{10}=\sum_{i,j=1}^{N} x_i^2 x_j^2,$$

$$S_{11}=\sum_{i,j=1}^{N} x_i^2 x_j^3, \quad S_{12}=\sum_{i,j=1}^{N} x_i^4 x_j.$$

This system can be written in the form of a classical eigenvalues problem as

$$(K-\omega M)S=0, \tag{12}$$

where K is the stiffness matrix, $M=\rho I$ is the mass matrix, and S the vector of the unknown solutions of the system.

The eigenfrequencies of the cell are obtained from the solution of the corresponding secular equation

$$\det(K-\omega M)=0. \tag{13}$$

The submatrix elements of K in the case $N=4$ are reported in the Appendix.

We remark that, for the linear case, $N=4$ is a completely inadequate polynomial order for the solution of the inverse problem. In fact, comparing the results for $N=4$, $N=6$, and $N=7$ in the solution of the inverse problem, we found differences in the predictions of the elastic moduli of the order of up to about 10%. However, in the nonlinear case, a corresponding calculation led to differences of the order of up to 0.01%. Therefore, $N=4$ is a totally adequate order in the nonlinear case.

A detailed analysis of the function $\omega(C)$, where C is the set of elastic constants, points out to a strong and complex dependence of the NFs on the elastic moduli. Numerical calculations (see Sec. V) show a large perturbation of NFs even if only one elastic constant is modified. Therefore, since many false minima may appear in the solution of the inverse problem, an accurate technique for the inversion is introduced in the next section.

II. THE INVERSE PROBLEM

We now consider the reconstruction of the physical properties of a cube by assuming that its dimensions and the NFs are known. We determine the second- and third-order elastic constants, which minimize the least-squares ''distance'' between computed and measured NFs. This ''distance,'' called in the following objective function, is defined as

$$J=\sum_{i=1}^{p} R_i^2=\sum_{i=1}^{p} w_i(\tilde{\omega}_i-\omega_i(C))^2, \tag{14}$$

where $\tilde{\omega}_i$ and $\omega_i(C)$ are the measured and computed NFs, respectively. C represents a set of elastic moduli in the parameter space (or search space). The integer p is the number of measured NFs, which must be larger than the number of unknown parameters (dimension of the parameter space). The R_i are the residuals and w_i are properly chosen weights.

When the objective function J is differentiable with respect to the parameters (in our case the elastic constants), the nonlinear minimization problem can be solved by using a gradient method, such as the quasi-Newton method.[15,16] The analytical formulation of the direct problem, given in Sec. I, is expected in fact to improve the accuracy and computational efficiency of the method.

By defining $J^*=J(C^*)$ as the minimum value of J for the optimal set of parameters C^*, the ϵ-indifference region can be defined as the region in the parameter space in which

$$|J(C)-J^*|\leq\epsilon. \tag{15}$$

In such a region, J can be expressed by means of a second-order Taylor expansion as

$$J(C)=J^*+0.5\delta C^T H^* \delta C, \tag{16}$$

where $\delta C=C-C^*$ and H is the Hessian of J in C^*

$$H_{ij}^*=2\sum_{k=1}^{p} w_k \frac{\partial\omega_k}{\partial C_i^*}\frac{\partial\omega_k}{\partial C_j^*}. \tag{17}$$

By using Eq. (16), the ϵ-indifference region is defined as a nine-dimensional ellipsoid given by

$$\delta C^T H^* \delta C\leq 2\epsilon. \tag{18}$$

The estimation matrix is therefore approximated by[17]

$$V_C=2m^2H^{-1}, \tag{19}$$

where the constant m is given by

$$m^2=\sum_{i=1}^{p} {R_i^*}^2. \tag{20}$$

The confidence region is chosen so that it coincides with the ϵ-indifference region of the objective function.

The eigenvalues decomposition of H^* is given by

$$H^*=Q\Lambda Q^T, \tag{21}$$

where Λ is the diagonal matrix of eigenvalues λ_i of H^*, and Q is a unitary matrix with columns given by the eigenvectors forming the nine principal axes of the ellipsoid. The lengths of the principal axes are inversely proportional to the square roots of the eigenvalues. The longest axis defines the worst-determined direction in C space, and the shortest axis defines the best-determined direction. The eigenvectors contained in Q introduce a new set of principal components that are linear combinations of original parameters. Equation (19) implies that the standard deviation π_i of the estimates is given by

$$\pi_i=m\left(\frac{2}{\lambda_i}\right)^{0.5}. \tag{22}$$

III. NUMERICAL RESULTS

Numerical studies show that an acceptable accuracy (with errors up to 10%–15%) may be obtained considering Legendre polynomials up to the third order ($N=4$) in Eq.

TABLE I. The measured and computed natural frequencies and their residuals.

NF number	Experimental (MHz)	Predicted (MHz)	Residuals $\epsilon=0$	Residuals $\epsilon=0.01$	Residuals $\epsilon=0.1$
1	91.7	91	0.006	0.009	0.037
2	122.6	122	0.005	0.008	0.035
3	124.9	125	−0.006	−0.010	−0.037
4	150.8	149	−0.025	−0.028	−0.060
5	153.5	154	0.068	0.075	0.099
6	175.8	175	−0.008	−0.012	−0.039
7	222.7	225	0.073	0.077	0.104
8	242.4	235	−0.032	−0.035	−0.063
9	252.5	250	−0.172	−0.176	−0.204
10	268.1	275	0.069	0.073	0.114
11	299.3	290	−0.219	−0.224	−0.249
12	282.5	311	0.053	0.059	0.084

(13). The first 12 experimental NFs (measured by a pulse-echo technique) for an Al alloy cube with $a=b=c=15.7$ mm and $\rho=2697$ kg/m^3 are used for solving the inverse problem. By coding the C vector with the following ordering

$$C=(C_{11},C_{12},C_{44},C_{111},C_{112},C_{123},C_{144},C_{155},C_{456})^T, \tag{23}$$

the elastic constants are given (in GPa units) by[18,19]

$$C=(106.43,\ 60.35,\ 28.21,-1076,-315,\ 36,-23,\ -340,-30). \tag{24}$$

The first 12 measured and predicted values of the NFs (MHz) are reported in Table I, together with the corresponding residuals in the column $\epsilon=0$. Table I shows that the reliability of the method is very good, with errors generally less than 3%, except for the highest frequency.

As already mentioned, each frequency is strongly dependent on the choice of the elastic constants set C. A detailed numerical analysis has been performed, but, it is not easy to give a reliable prediction of the dependence of each mode on each elastic constant, due to the many factors involved.

The gradient quasi-Newton method has been used for the inversion. Three different initial guesses have been used, to guarantee convergence independently from the initial choice. The three initial sets are randomly selected

$$\begin{aligned}\widetilde{C}_1&=(0,150,15,0,30,-30,\ 0,300,\ 40)^T,\\ \widetilde{C}_2&=(50,\ 100,\ 20,-500,\ 0,0,10,0,0)^T,\\ \widetilde{C}_3&=(100,\ 50,\ 30,-1000,-300,\ 30,\ 20,\ -300,\ -40)^T.\end{aligned} \tag{25}$$

In Fig. 1 the objective function and its gradient are plotted vs the number of iterations n. The plots show a good and fast convergence for all three choices of initial conditions.

In Fig. 2 the iteration history for nine elastic constants obtained from the third initial set ($\widetilde{C}_3$) is displayed. Similar results have also been obtained for the other choices of initial sets.

The final values of the elastic constants, obtained by inverting the NFs data reported in Table I, are (in GPa units)

$$C_f=(106.9,61.75,30.12,-1077.9,-335.4,35.3,-25.5,\ -353.8,-33.5), \tag{26}$$

with a marginal confidence interval $\pm 0.85\%$. Comparing the results of Eq. (26) with Eq. (24) we find a very good overall agreement.

In order to analyze the effect of noise in the experimental data acquisition, the NFs data ω_i have been multiplied by $(1+r_i)$, where r_i are random numbers uniformly distributed in a given interval $[-\epsilon,\epsilon]$, with $\epsilon=0$, 0.01, 0.1. The final values J_{fin} of the objective function after 15 iterations for the three initial choices are reported in Table II. It is found that the residuals (see Table I) vary linearly and J_{fin} quadratically

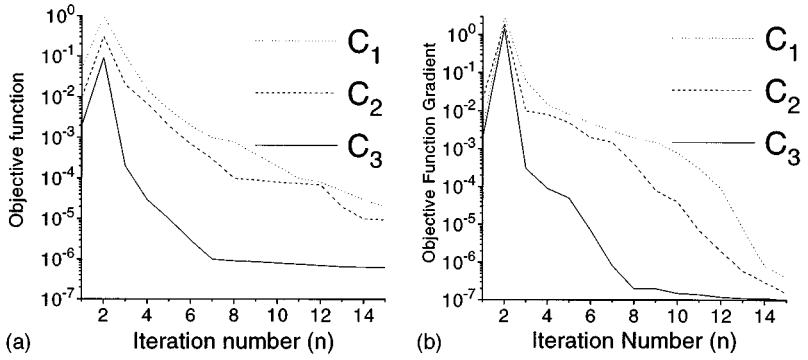

FIG. 1. Evolution of (a) the objective function and (b) its gradient for the three initial guesses of Eq. (25).

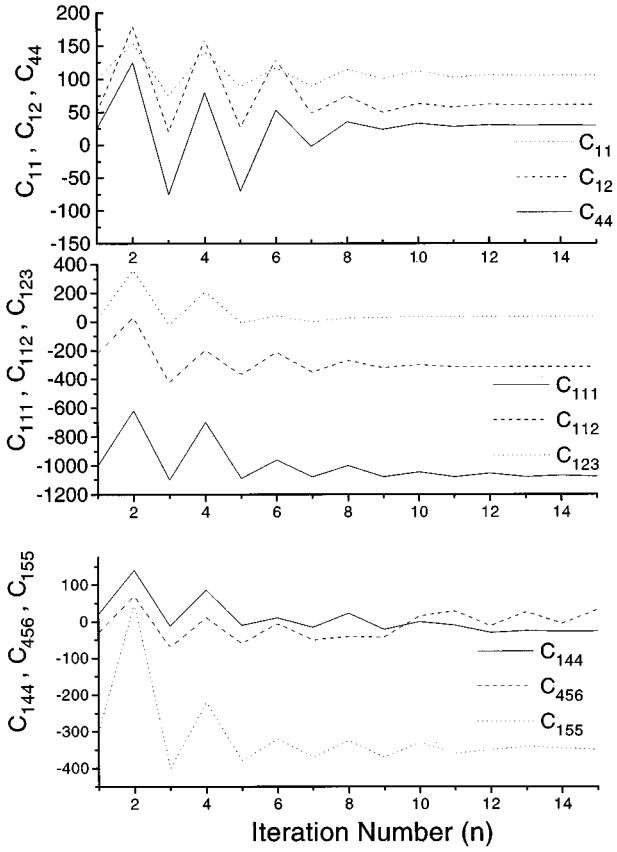

FIG. 2. Iteration history of the nine elastic constants for the initial guess $\tilde{C}_3$.

with respect to ϵ. This means that highly accurate measurements for the NFs, such as provided by RUS techniques, are required to obtain good predictions for the elastic constants. Even small perturbations in the experimental frequencies can lead to erroneous estimates.

IV. CONCLUSIONS

We have presented a method for the solution of the direct problem of obtaining the natural frequencies of a cube of a fcc crystal from its elastic constants and of the inverse problem of determining the elastic constants from the NFs. Both second- and third-order elastic constants can be determined. The method has been applied to the case of Al alloys, due to the importance of the third-order elastic constants in Al for applications of the acoustoelastic effect.

In the application of the method to the forward problem, the NFs are obtained with a good accuracy (generally better than 3%, except for the highest ones). Likewise the application to the inverse problem yields very good predictions for the second-order elastic constants and satisfactory results for the third-order elastic constants. The iteration history of the elastic constants and the evolution of the objective function and its gradient show that a small number (10–15) of iterations is sufficient for good convergence. Several (3) randomly selected initial guesses of the elastic moduli are considered, with the conclusion that the algorithm does not depend strongly on the initial guesses. A numerical simulation of measurement noise by multiplications of the NFs data by random factors shows, however, that accurate measurements of the NFs are required, with even small perturbations in the experimental NFs leading to erroneous estimates of the elastic moduli.

TABLE II. Numerical values of J_{fin} after 15 iterations for the three initial guesses.

	$\epsilon=0$	$\epsilon=0.01$	$\epsilon=0.1$
C_1	8.6910^{-4}	1.7910^{-2}	9.8110^{-1}
C_2	1.4010^{-5}	8.8410^{-3}	4.3310^{-2}
C_3	6.4510^{-6}	3.3510^{-4}	5.4910^{-2}

ACKNOWLEDGMENTS

This research was supported by the EC Program Copernicus Contract No. ER BCIPA CT 940132, 1995.

APPENDIX

In Eq. (12) the 12×12 matrix K can be written in terms of four 9×9 submatrices K_{ij}, given, for $N=4$ by

$$K_{11}^{kl}=\int_V\left[\frac{1}{a^2}(C_{11}-3C_{44}+2C_{111}+3C_{112})V_{km,\xi}^{(1)}V_{ml,\xi}^{(1)}+\frac{1}{b^2}(3C_{44}+3C_{144}+2C_{155})V_{km,\chi}^{(1)}V_{ml,\chi}^{(1)}+\frac{1}{c^2}(3C_{11}+2C_{144}+3C_{155})V_{km,\zeta}^{(1)}V_{ml,\zeta}^{(1)}\right]dV,$$

$$K_{22}^{kl}=\int_V\left[\frac{1}{b^2}(C_{11}-3C_{44}+2C_{111}+3C_{112})V_{km,\chi}^{(2)}V_{ml,\chi}^{(2)}+\frac{1}{a^2}(3C_{44}+3C_{144}+2C_{155})V_{km,\xi}^{(2)}V_{ml,\xi}^{(2)}+\frac{1}{c^2}(3C_{11}+2C_{144}+3C_{155})V_{km,\zeta}^{(2)}V_{ml,\zeta}^{(2)}\right]dV,$$

$$K_{33}^{kl}=\int_V\left[\frac{1}{c^2}(C_{11}-3C_{44}+2C_{111}+3C_{112})V_{km,\zeta}^{(3)}V_{ml,\zeta}^{(3)}+\frac{1}{a^2}(3C_{44}+3C_{144}+2C_{155})V_{km,\xi}^{(3)}V_{ml,\xi}^{(3)}+\frac{1}{c^2}(3C_{11}+2C_{144}+3C_{155})V_{km,\chi}^{(3)}V_{ml,\chi}^{(3)}\right]dV,$$

$$K_{12}^{kl}=K_{21}^{kl}=\int_V\frac{1}{ab}[(C_{12}+2C_{112}+3C_{123})V_{km,\xi}^{(1)}V_{ml,\chi}^{(2)}+2C_{144}(V_{km,\xi}^{(1)}V_{ml,\chi}^{(3)}+2V_{km,\xi}^{(3)}V_{ml,\chi}^{(2)}+V_{km,\xi}^{(2)}V_{ml,\chi}^{(1)})+3C_{155}(2V_{km,\xi}^{(1)}V_{ml,\chi}^{(1)}+V_{km,\xi}^{(2)}V_{ml,\chi}^{(1)})+2C_{456}(2V_{km,\xi}^{(3)}V_{ml,\chi}^{(1)}+2V_{km,\xi}^{(2)}V_{ml,\chi}^{(3)}+V_{km,\xi}^{(3)}V_{ml,\chi}^{(3)})]dV,$$

$$K_{13}^{kl}=K_{31}^{kl}=\int_V \frac{1}{ac}\,[(C_{12}+2C_{112}+3C_{123})V_{km,\xi}^{(1)}V_{ml,\zeta}^{(3)}$$
$$+2C_{144}(V_{km,\xi}^{(1)}V_{ml,\zeta}^{(2)}+2V_{km,\xi}^{(2)}V_{ml,\zeta}^{(3)}+V_{km,\xi}^{(3)}V_{ml,\zeta}^{(1)})$$
$$+3C_{155}(2V_{km,\xi}^{(1)}V_{ml,\zeta}^{(1)}+V_{km,\xi}^{(3)}V_{ml,\zeta}^{(1)})$$
$$+2C_{456}(2V_{km,\xi}^{(2)}V_{ml,\zeta}^{(1)}+2V_{km,\xi}^{(3)}V_{ml,\zeta}^{(2)}$$
$$+V_{km,\xi}^{(2)}V_{ml,\zeta}^{(2)})]dV,$$

$$K_{23}^{kl}=K_{32}^{kl}=\int_V \frac{1}{bc}\,[(C_{12}+2C_{112}+3C_{123})V_{km,\chi}^{(2)}V_{ml,\zeta}^{(3)}$$
$$+2C_{144}(V_{km,\chi}^{(2)}V_{ml,\zeta}^{(1)}+2V_{km,\chi}^{(1)}V_{ml,\zeta}^{(3)}+V_{km,\chi}^{(3)}V_{ml,\zeta}^{(2)})$$
$$+3C_{155}(2V_{km,\chi}^{(2)}V_{ml,\zeta}^{(2)}+V_{km,\chi}^{(3)}V_{ml,\zeta}^{(2)})$$
$$+2C_{456}(2V_{km,\chi}^{(1)}V_{ml,\zeta}^{(2)}+2V_{km,\chi}^{(3)}V_{ml,\zeta}^{(1)}$$
$$+V_{km,\chi}^{(1)}V_{ml,\zeta}^{(1)})]dV,$$

where

$$V_{km}^{(1)}=p_k(\chi)p_m(\zeta)S_0(\xi),$$
$$V_{km}^{(2)}=p_k(\xi)p_m(\zeta)S_0(\chi),$$
$$V_{km}^{(3)}=p_k(\xi)p_m(\chi)S_0(\zeta),$$
$$klmn=1\cdots4.$$

[1] R. Holland, J. Acoust. Soc. Am. **43**, 988 (1968).
[2] H. H. Demarest, Jr., J. Acoust. Soc. Am. **49**, 768 (1971).
[3] I. Ohno, J. Phys. Hearth **24**, 355 (1976).
[4] A. Migliori *et al.*, Phys. Rev. B **41**, 2098 (1990).
[5] W. M. Visscher, A. Migliori, T. M. Bell, and R. A. Reinert, J. Acoust. Soc. Am. **90**, 2154 (1991).
[6] J. D. Maynard, J. Acoust. Soc. Am. **91**, 1754 (1992).
[7] J. D. Maynard, Phys. Today **49**(1), 26 (1996).
[8] A. Migliori *et al.*, Phys. Rev. Lett. **64**, 2408 (1990).
[9] F. Willis, R. G. Leisure, and I. Jacob, Phys. Rev. B **50**, 13 792 (1994).
[10] P. S. Spoor, J. D. Maynard, and A. R. Kortan, Phys. Rev. Lett. **75**, 3462 (1995).
[11] T. Berruti, P. P. Delsanto, M. Gola, and M. Scalerandi, *A Microscopic Model for Acoustoelasticity*, Proceedings of the Conference Euromat '94, edited by B. Vosatz and E. Szoke (Ombke, Budapest, 1994), p. 251.
[12] P. P. Delsanto, ''Acoustoelasticity and Applications,'' in *Evaluation of Materials and Structures by Quantitative Ultrasonics*, edited by J. D. Achenbach (Springer-Verlag, Berlin, 1993), p. 301.
[13] P. P. Delsanto and A. V. Clark, J. Acoust. Soc. Am. **81**, 952 (1987).
[14] P. P. Delsanto, A. V. Clark, and R. B. Mignogna, J. Acoust. Soc. Am. **87**, 215 (1990).
[15] D. G. Luenberger, *Linear and Non-Linear Programming* (Addison-Wesley, Reading, MA, 1984).
[16] J. E. Dennis, G. M. Gay, and R. E. Welsch, ''Algorithm 573 NL2SOL—An Adaptive Nonlinear Least-Squares Algorithm,'' in TOMS v. 7 (1981), p. 365.
[17] P. S. Frederiksen, *Estimation of Elastic Moduli in Thick Composite Plates by Inversion of Mechanical Systems*, edited by Bui Tanaka *et al.* (Balkema, Rotterdam, 1994).
[18] R. Bechmann, R. F. S. Hearmon, and J. K. Kurtz, ''Elastic Piezoelectric and Related Constants of Crystals,'' in *Landolt-Bornstein Tables* (1969), Vol. 2.
[19] M. J. P. Musgrave, *Crystal Acoustics* (Holden Day, San Francisco, CA, 1970), p. 279.
[20] C. Teodosiu, *Elastic Models of Crystal Defects* (Academy, Bucharest, 1982).
[21] H. Popescu and V. Chiroiu, *Optimum Design of Structures* (in Romanian) (Academy, Bucharest, 1981).

Increased off-axis energy deposition due to diffraction and nonlinear propagation of ultrasound from rectangular sources

Mark D. Cahill[a] and Andrew C. Baker
School of Physics, University of Bath, Bath BA2 7AY, United Kingdom

(Received 30 September 1996; accepted for publication 19 March 1997)

An existing model, the Bergen code, is used to simulate the propagation of ultrasonic beams of finite amplitude, due to rectangular and square sources. It is found that the edges of the source give rise to peaks in the diffraction pattern at the fundamental frequency, which can cause the strongest shockwaves to form off-axis. These tend to be sharply bounded, causing rapid variation in heat deposition and streaming pressure across even an unfocused beam, and suppressing axial maxima in the pressure field. © *1997 Acoustical Society of America.* [S0001-4966(97)03207-4]

PACS numbers: 43.25.Jh [MAB]

INTRODUCTION

It is increasingly becoming clear that nonlinearities in the propagation of ultrasound have a significant effect on beams used for medical purposes,[1,2] for example in the heating of the medium through which the beam travels, and that such nonlinearities should be considered in the design and calibration of transducers. While beams due to circular transducers have been studied in some detail (see, for example, Refs. 3–8), it is only recently that models have been developed,[9,10] that are capable of predicting the nonlinear evolution of beams lacking cylindrical symmetry, partly due to the demands they place on the computer, and partly to the need for reliable algorithms.[11] Yet real ultrasound scanners now usually involve a rectangular phased array of rectangular elements. With such arrays in mind, the present study considers idealized beams of finite amplitude due to rectangular sources, propagating through water, and a subsequent paper will consider a real medical scanner.

We use here the Bergen code,[9,12] which implements the transformed beam equation (TBE),[13] and which has successfully been compared with experiment in two studies, by Berg *et al.*,[9] and by Baker *et al.*[12] The TBE has also been compared with experiment in air for rectangular sources by Kamakura *et al.*[10,14] with excellent results. All of these studies, however, concentrated on variations along the axis of symmetry, as has been the practice for circular sources, and also on beam profiles (the distribution of pressure in a plane perpendicular to the direction of propagation) near or beyond the last axial maximum. This study considers off-axis effects in the near field of rectangular sources, and the distribution of loss of energy and momentum to the medium.

I. THEORY

The Khokhlov–Zabolotskaya–Kuznetsov equation[15] can be written as

$$\frac{\partial^2 p'}{\partial\sigma\,\partial\tau}=\alpha r_0\,\frac{\partial^3 p'}{\partial\tau^3}+\frac{1}{4}\,\nabla_\perp^2 p'+\frac{r_0}{2l_d}\,\frac{\partial^2 p'^2}{\partial\tau^2}, \tag{1}$$

which describes the propagation of sound of finite amplitude, in the ''parabolic'' limit; that is, the limit in which the variation of the instantaneous pressure in one direction (taken to be the z direction) is far greater than that in a perpendicular direction. One such system is a beam with characteristic wavelength λ propagating from a source or aperture of characteristic scale a, provided[16]

$$2\pi a/\lambda\equiv ka\gg 1 \tag{2}$$

and

$$z\gtrsim a(ka)^{1/3}. \tag{3}$$

Here p' is a dimensionless measure of the overpressure, $p'\equiv(P-p_0)/P_0$, where P is the pressure, p_0 is the ambient pressure, and P_0 is a characteristic pressure of the system (e.g., the average acoustic pressure at the source), r_0 is the Rayleigh distance $r_0=\pi a^2/\lambda$, α is the attenuation coefficient of a wave with wavelength λ, frequency f, given by $\alpha=\alpha_0 f^2$, $\alpha_0=2.5\times10^{-14}$ Np m^{-1} Hz^{-2} in water, l_d is the ''discontinuity length''

$$l_d=\frac{c^2\rho_0}{3.5kP_0}$$

in water (c is the speed of sound, ρ_0 the ambient density of the medium), σ is a dimensionless coordinate in the direction of propagation $\sigma=z/r_0$, τ is a dimensionless retarded time

$$\tau=\omega t-kz$$

($\omega=2\pi f$), and

$$\nabla_\perp^2=a^2\left(\frac{\partial^2}{\partial x^2}+\frac{\partial^2}{\partial y^2}\right).$$

The fields considered here will be those due to a plane wave impinging on an aperture, but for $z\gg\lambda$, which is 0.66 mm in the examples considered here, these approximate to those due to a uniform velocity source. The TBE transforms this equation into coordinates appropriate to a spreading beam;

$$\xi=\frac{(x,y)}{a(1+\sigma)}, \tag{4}$$

[a]Current address: Medical Physics Directorate, St. Thomas' Hospital, Lambeth Palace Road, London SE1 7EH, UK.

$$\tau_s = \left(\tau - k \frac{x^2+y^2}{2(r_0+z)} \right) \Big/ \nu, \tag{5}$$

$$p = (1+\sigma)p', \tag{6}$$

see Ref. 12. The factor of ν introduced to the definition of τ_s is the ratio of the carrier frequency of a pulse f, to the pulse repetition frequency (PRF), f_{PRF}. It is unity for a continuous wave. Finally, the Bergen code decomposes the field into its temporal Fourier spectrum, by

$$p(\tau_s) = \sum_{n=1}^{N} (g_n \sin(n\tau_s) + h_n \cos(n\tau_s)), \tag{7}$$

$$= \frac{1}{2i} \sum_{n=-N}^{N} p_n \exp(in\tau_s), \tag{8}$$

where $p_n = g_n + ih_n$, $p_{-n} = -p_n^*$, and N is a number large enough to represent the spectrum of the wave. In order to prevent the buildup of energy in the highest harmonics, it is necessary to increase artificially the attenuation of a few modes, specifically those with $n \geqslant N - 3.5\nu$ by a factor b_n smoothly varying from 1 to 4.5.

Hitherto, the nonlinear term in Eq. (1), $(r_0/2l_d) \times (\partial^2 p'^2/\partial\tau^2)$ has usually been calculated as a sum of Fourier modes,[11] but this process is quadratic in the number of harmonics, N, and the degree of shock to be considered in this paper requires such a large number of modes (particularly for pulsed beams) that the calculation of this term is performed in the time domain, by means of a fast Fourier transform. Care must be taken to ensure that the true spectrum of the nonlinear term does not overlap that of its image, which appears translated by M modes up and down in frequency, where the representation in the time domain has M points. Since only N harmonics are to be retained, and the image of the nonlinear term has a half-width of $2N$, $M > 3N$ to avoid distortion of the wave.

This device produces code which is faster than the quadratic algorithm for $N > 54$ on a Convex C3860 computer, and $N > 10$ on a DEC Alpha 8400, and which thereafter is effectively of order $N \log N$.

A. Heating

In calculating the deposition of heat and the streaming pressure (the pressure applied to the medium due to loss of momentum by the acoustic beam), we use the plane-wave approximation for intensity which is valid when the parabolic approximation is used,[17] and write

$$I_z = \frac{1}{2\pi\rho_0 c} \int_0^{2\pi} (P_0 p'(\tau))^2 \, d\tau \tag{9}$$

$$\approx \frac{P_0^2}{2\rho_0 c} \sum_{n=1}^{N} \frac{|p_n|^2}{(1+\sigma)^2}, \tag{10}$$

and

$$\frac{\partial p_{n,a}}{\partial z} = -\alpha \frac{n^2}{\nu^2} b_n p_n, \tag{11}$$

where $\partial p_{n,a}/\partial z$ is the variation in p_n due to attenuation by the medium, assumed to be dominated by absorption of energy. We include a taper function (b_n) in order to correctly represent the loss of energy by the modeled wave, since it stands in for the attenuation of harmonics of higher frequency than are included in the model.[18] The effectiveness of the taper function was assessed by comparison with calculations using more harmonics but no taper function.

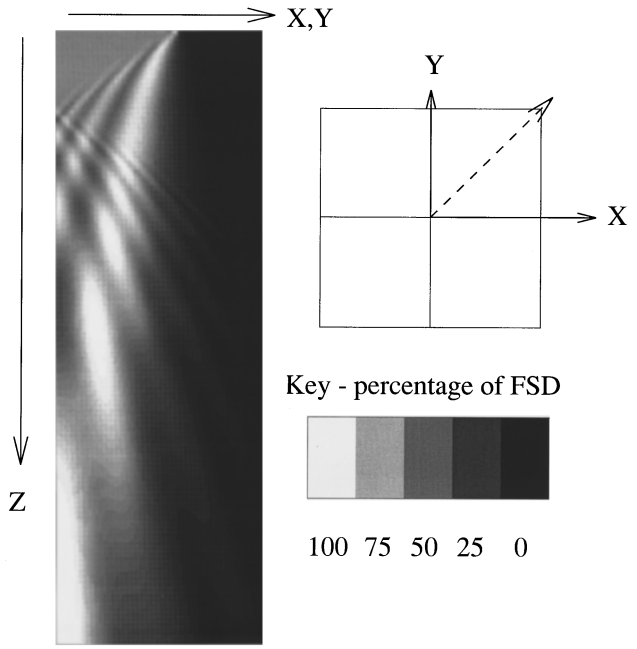

FIG. 1. Amplitude plot of linear propagation (down the page) over 20 cm, from a square aperture of side 2 cm. Plane of image cuts the source along a diagonal as shown. Full scale deflection (FSD) is $1.4P_0$.

We then have for the rate of loss of intensity due to attenuation,

$$\frac{\partial I_{z,a}}{\partial z} = \frac{-P_0^2}{\rho_0 c} \sum_{n=1}^{N} \alpha_0 f^2 \frac{n^2}{\nu^2} b_n \frac{|p_n|^2}{(1+\sigma)^2}, \tag{12}$$

which we assume to be converted largely into heat. A similar approximation[19] leads to the expression for the streaming pressure per unit length,

$$F \approx \frac{1}{c} \frac{\partial I_{z,a}}{\partial z}. \tag{13}$$

II. FRESNEL DIFFRACTION

As is well known, any sharp edge in a source, or in an aperture exposed to a plane wave, will produce spatial oscillations in amplitude and phase of the propagated wave, approximated by the Fresnel functions. It is these oscillations which are responsible for the axial variation in the field of a circular piston source, and also for the changes in the waveform, such as the asymmetry of the shockwave in the far field.[20] Figure 1 illustrates the amplitude of the field due to a low-amplitude plane wave of frequency 2.25 MHz impinging on a square aperture with sides of 2 cm, in water. At the top is the aperture, the beam propagating downward for 20 cm (all images have been stretched laterally), and in order to accentuate the Fresnel diffraction, the plane of the image is taken across a diagonal of the square aperture, as shown. The

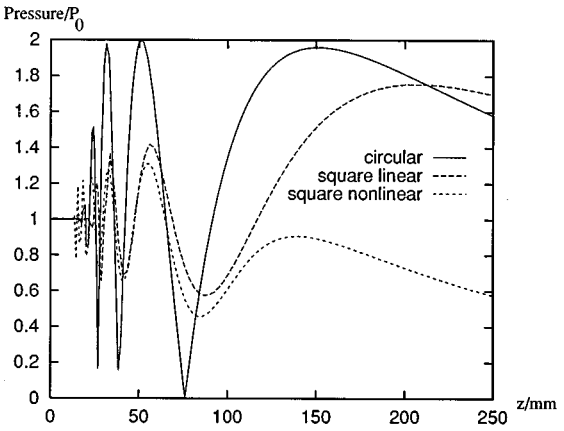

FIG. 2. Axial amplitude of linear propagation from circular and square apertures.

peak amplitude of each fringe is thus 37% more than the initial amplitude of the wave, rather than the 17% which we would see in a simple cross section. The calculation was performed on a 256 by 256 grid. Taking the characteristic length a as 1 cm, Eq. (2) is easily satisfied, and Eq. (3) gives

$$z \gtrsim 4.6 \text{ cm}.$$

Figure 2 shows the axial amplitude of the square aperture, and compares it with that of a circular aperture of diameter 2 cm. Note that not only is the last axial maximum weaker for the square aperture, but all other maxima and minima are much less marked. This is readily attributable to the tendency of the circular edge to concentrate its fringes at the axis, while those due to a straight edge propagate away from the edge unenhanced. As a result of this, the fringes of a straight-edged aperture vary only in transverse width and position, not in amplitude, as they propagate. (Attenuation at this frequency is weak.)

Figure 3(a) shows the amplitude of the fundamental mode of a beam with amplitude 1 MPa (60 harmonics were used in the calculation). Otherwise it is identical to Fig. 1, and it is immediately apparent that the beam has been disproportionately attenuated toward the last axial maximum. Figure 3(b) and (c) show the amplitudes of the 2nd and 10th harmonics, respectively, normalized to the values found in a pure sawtooth shockwave. Notable features of these higher harmonics are their relative freedom from structures due to higher-order fringes, and the extremely sharp inner edges, also clearly visible in the beam profile for the 10th harmonic (Fig. 4). What seems to be happening is that the shock due to the central wave meets the fringe and rapidly converts it to energy at higher frequencies. One consequence of this is that the principal fringe, responsible for the last axial maximum, is attenuated, and the ratio of the maximum to its preceding minimum is diminished, as seen in Fig. 2. Furthermore, this attenuation is stronger on the side of the fringe away from the source, which will tend to move the axial maxima toward the source. It will also move the maximum in beam profiles, inward before the fringe has crossed the axis, and outward after. This may be a cause of the ''defocusing'' noted by other researchers,[18,6] since in the focal plane of a focused

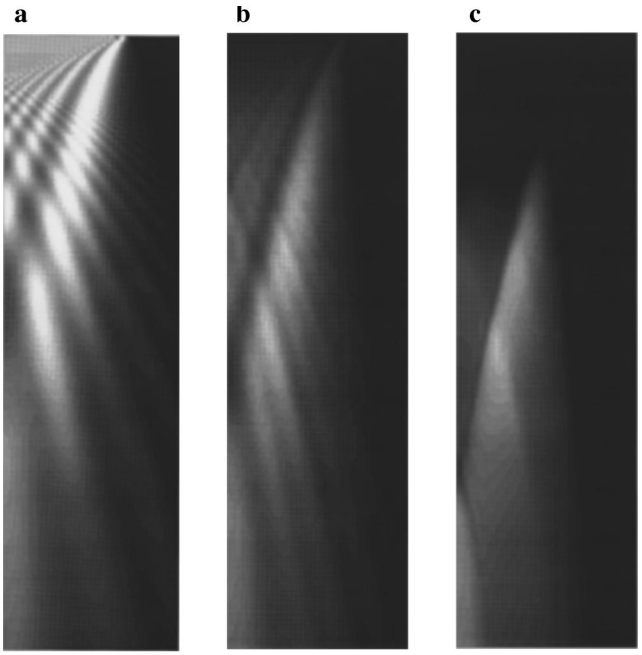

FIG. 3. Amplitude plots of nonlinear propagation over 20 cm, of a beam of initial amplitude 1 MPa, from a square aperture, showing three harmonics; (a) first harmonic, FSD=1.2 MPa; (b) second harmonic, FSD=0.6 MPa; (c) 10th harmonic, FSD=0.12 MPa.

source, the decreasing of the amplitude at the center would appear as a broadening of the central lobe. Figure 5 shows the beam profiles in the XZ-plane for the square aperture at 300 mm, and the broadening of the central lobe is clear. Incidentally, Fig. 3(b) clearly shows the generation of ''fingers,''[21] or subsidiary fringes located between the fringes of the fundamental.

The accentuation of the higher frequencies off-axis is startling; it was necessary to run the model with increments in z of less than 0.4 mm in order for the algorithm to converge, due to the large nonlinear term far off-axis. A more significant indication of its magnitude is seen in Figs. 6(a) and 7, which show the power lost per unit volume, under the assumption of continuous wave operation; because attenuation is proportional to the square of frequency, the higher

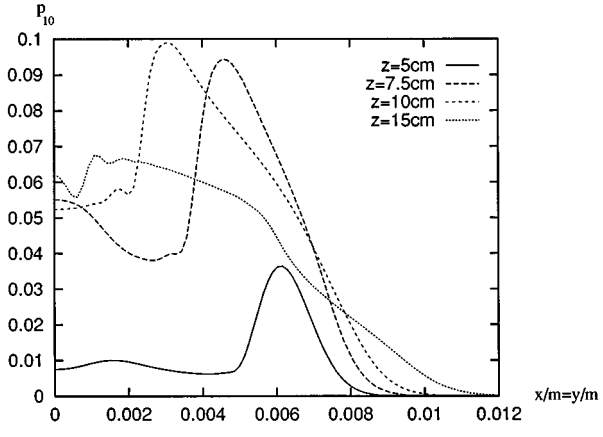

FIG. 4. Diagonal beam profiles ($x=y$) at different values of z, for the tenth harmonic of the continuous-wave nonlinear beam. Compare with Fig. 3(c).

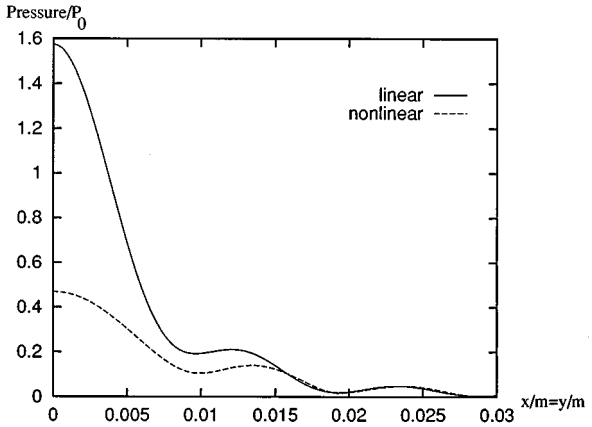

FIG. 5. Diagonal beam profiles ($x=y$) at $z=30$ cm, for the first harmonic of linear and nonlinear beams.

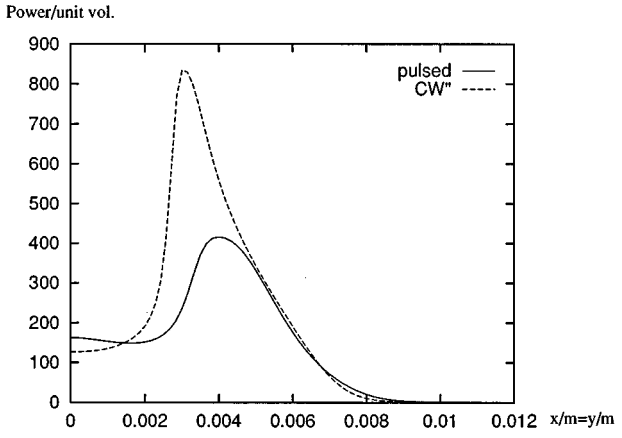

FIG. 7. Diagonal profiles of heat generation ($x=y$) at $z=10$ cm, for nonlinear beams. Units are 10^4 W/m^3 for the continuous wave, and 10^3 W/m^3 for the pulsed wave, with PRF 225 kHz.

harmonics contribute greatly to the dissipation of energy. Note also that far less power is lost at the last axial maximum than off-axis, due to the attenuation of the fringe.

Figures 6(b) and 7 also show results for a pulsed run. Because the beam is represented by a Fourier series, it is impractical to model the low PRFs used in real scanners, rather one must ignore structure near the source, which is influenced by the interference of consecutive pulses, and divide the power of the beam by the ratio of the model PRF (here, 225 kHz) and the real PRF, typically around 4 kHz. The waveform used here is taken from a large circular transducer, transposed so that its modal frequency is that of the continuous wave and normalized to a peak positive on-source pressure of 1 MPa, and has approximately two cycles. The calculation used 335 harmonics, with $\nu=10$. Despite the broadening of the fringe, to be expected from a short pulse, we see that the corner fringe dissipates some three times as much power as the center of the beam at 10 cm, although this is 3% less than the axial maximum, which coincides with the bottom of the image [Fig. 6(b)].

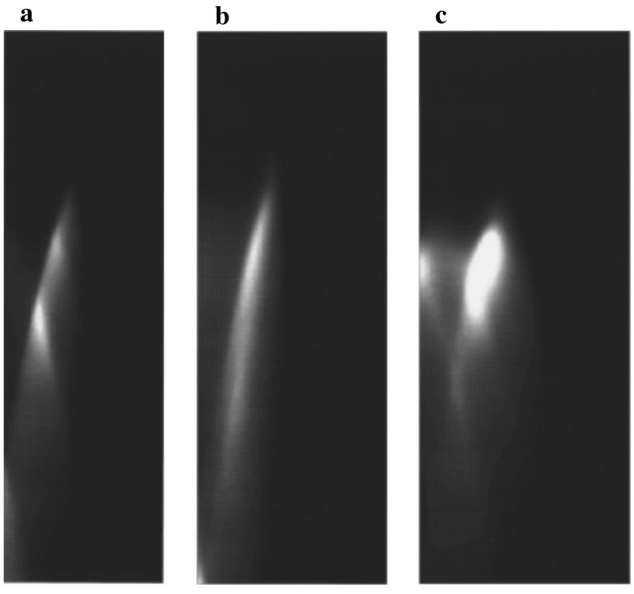

FIG. 6. Plots of heat generation in the medium by nonlinear beams; (a) diagonal plot of continuous wave from square source, FSD=9×10^6 W/m^3; (b) diagonal plot of wave pulsed at 225 kHz from square source, FSD=5×10^5 W/m^3; (c) plot of continuous wave from a rectangular source (see text), FSD=9×10^6 W/m^3.

In view of Eq. (13), the peak streaming pressure is also much greater at the edge of the beam, reaching 5.6 Pa/m at 7 cm (assuming a PRF of 4 kHz), but more interesting is that it varies by half of that value in 1 mm. It should be noted that while Eqs. (12) and (13) assume a plane wave, this is still a reasonable approximation, despite the characteristic (longitudinal) wavelength of the system being 0.66 mm, and the heating and streaming pressure varying over a transverse distance of that order. This is because the variation is due to components with a higher frequency and shorter wavelength, as is exemplified by Fig. 4, which shows the 10th harmonic of the continuous wave varying by a factor of 2 within 1 mm, which is still more than 10 wavelengths of that mode.

While the examples presented so far have all had square sources, this has largely been for simplicity of presentation. The suppression of the axial maximum and defocusing, for example, are due to attenuation of fringes from each edge, and so are seen in beams from rectangular sources which possess different fringe systems in each plane of symmetry. The enhancement of off-axis heating and streaming pressure is exaggerated by considering a diagonal, but is present in sections in other planes. Rather more extreme enhancement is seen, for example, from a rectangular source [Fig. 7(c)] which differs from the square continuous-wave case only in having a source of dimensions 1.1 cm by 2.3 cm (the calculation was performed to 20 harmonics on a 256 by 256 grid). The image is taken in the plane of the long axis, and the enhancement can be attributed to three principal fringes coinciding, two from the long edges, and one from a short edge. An identical ''eye'' appears on the other side of the axis.

III. CONCLUSION

Examples have been given of the interaction of near-field Fresnel diffraction with nonlinear propagation in ideal-

ized systems, which show how interactions away from the axis of an acoustic beam can significantly affect the axial behavior, by suppressing axial maxima in the amplitude of pressure and the dissipation of power, and also by increasing these maxima off-axis. Such effects are more pronounced in fields whose sources contain straight edges than in those due to circular sources, and the off-axis enhancement is further exacerbated when the edges meet at a point.

It is appropriate to consider how these results might be applied to real situations. The edges of the transducers in medical scanners will cause enhanced generation of shocks in fringes, moving inward from the edge of the beam as it propagates forward, and this might be missed in a calibration procedure which concentrates on axial behavior. A worst case might involve the measurement of an unrepresentatively low amplitude on-axis, while missing unwelcome ''hot-spots'' closer to the scanner head, and to the side.

Not only will longer pulses, as used in modes which measure Doppler shifts, cause greater generation of heat and streaming pressure, by virtue of their greater time-averaged power, but they will produce greater shear stresses than short pulses, because their narrower spectra cause better-defined fringes.

Effects which would tend to decrease the severity of the problem are focusing in the scanner head, defocusing *in vivo*, and the higher coefficient of attenuation of tissues. Focusing in the scanner has less effect on the edge shocks than at the axis, so a moderately strong focal power might ensure that the shock at the focus is significantly greater than that off-axis. Irregularities in the tissues or other media through which the beam is transmitted may defocus the effective edges enough, not only to lessen the transverse gradient of streaming pressure, but also to decrease the maximum amplitude of the carrier frequency, which drives the growth of the shock. These effects of course also limit the resolution of the scanner.

The higher coefficient of attenuation of tissues, and to a lesser extent of body fluids, will have a significant effect on the behavior of the beam. The shock will tend to build up to a lower peak, but will also dissipate more power than in water, and if the beam passes from a fluid to tissue it is known that shocks built up in the fluid can cause enhanced heating in the tissue.[18] It seems that further research into the near-field behavior of ultrasonic beams in biological media is indicated.

ACKNOWLEDGMENTS

The authors are grateful to Professors S. Tjøtta, J. Naze Tjøtta, and J. Berntsen for the use of the Bergen code. This research was funded by Engineering and Physical Sciences Research Council Grant No. GR/K28022.

[1] P. K. Verma, V. F. Humphrey, and H. C. Starritt, ''Enhanced absorption due to nonlinear propagation in diagnostic ultrasound,'' in *Proceedings of the 13th ISNA*, edited by H. Hobæk (World Scientific, Singapore, 1993), pp. 297–302.

[2] H. C. Starritt, F. A. Duck, and V. F. Humphrey, ''Forces acting in the direction of propagation in pulsed ultrasound fields,'' Phys. Med. Biol. **36**, 1465–1474 (1991).

[3] A. C. Baker, ''Prediction of nonlinear propagation in water due to diagnostic medical ultrasound equipment,'' Phys. Med. Biol. **36**, 1457–1464 (1991).

[4] A. C. Baker and V. F. Humphrey, ''Distortion and high-frequency generation due to nonlinear propagation of short ultrasonic pulses from a plane circular piston,'' J. Acoust. Soc. Am. **92**, 1699–1705 (1992).

[5] C. J. Veccio and P. A. Lewin, ''Finite amplitude acoustic propagation modeling using the extended angular spectrum method,'' J. Acoust. Soc. Am. **95**, 2399–2408 (1994).

[6] S. Nachef, D. Cathignol, J. Naze Tjøtta, A. M. Berg, and S. Tjøtta, ''Investigation of a high-intensity sound beam from a plane transducer—Experimental and theoretical results,'' J. Acoust. Soc. Am. **98**, 2303–2323 (1995).

[7] M. A. Averkiou and M. F. Hamilton, ''Measurements of harmonic generation in a focused finite-amplitude sound beam,'' J. Acoust. Soc. Am. **98**, 3439–3442 (1995).

[8] J. A. TenCate, ''An experimental investigation of the nonlinear pressure field produced by a plane circular piston,'' J. Acoust. Soc. Am. **94**, 1084–1089 (1993).

[9] A. M. Berg and J. Naze Tjøtta, ''Numeric simulation of the sound pressure field from finite amplitude, plane or focusing, rectangular apertures,'' in *Proceedings of the 13th ISNA*, edited by H. Hobæk (World Scientific, Singapore, 1993), pp. 309–314.

[10] T. Kamakura, M. Tani, Y. Kuamoto, and K. Ueda, ''Harmonic generation in finite amplitude sound beams from a rectangular aperture source,'' J. Acoust. Soc. Am. **91**, 3144–3151 (1992).

[11] J. Berntsen, ''Numerical calculation of finite amplitude sound beams,'' in *Frontiers of Nonlinear Acoustics: Proceedings of the 12th ISNA*, edited by M. F. Hamilton and D. T. Blackstock (Elsevier Science, New York, 1990), pp. 191–196.

[12] A. C. Baker, A. M. Berg, A. Sahin, and J. Naze Tjøtta, ''The nonlinear pressure field of plane, rectangular apertures: Experimental and theoretical results,'' J. Acoust. Soc. Am. **97**, 3510–3517 (1995).

[13] S. I. Aanonsen, T. Barkve, J. Naze Tjøtta, and S. Tjøtta, ''Distortion and harmonic generation in the near field of a finite amplitude sound beam,'' J. Acoust. Soc. Am. **75**, 749–768 (1984).

[14] T. Kamakura, M. Tani, Y. Kumamoto, and M. A. Breazeale, ''Parametric sound radiation from a rectangular aperture source,'' Acustica **80**, 332–338 (1994).

[15] V. P. Kuznetsov, ''Equations of nonlinear acoustics,'' Sov. Phys. Acoust. **16**, 467–470 (1971).

[16] J. Naze Tjøtta, S. Tjøtta, and E. H. Vefring, ''Effects of focusing on the nonlinear interaction between two collinear finite amplitude sound beams,'' J. Acoust. Soc. Am. **89**, 1017–1027 (1991).

[17] J. Naze Tjøtta and S. Tjøtta, ''Nonlinear equations of acoustics,'' in *Frontiers of Nonlinear Acoustics: Proceedings of the 12th ISNA*, edited by M. F. Hamilton and D. T. Blackstock (Elsevier Science, New York, 1990), pp. 80–97.

[18] P. T. Christopher and K. J. Parker, ''New approaches to nonlinear diffractive field propagation,'' J. Acoust. Soc. Am. **90**, 488–499 (1991).

[19] H. Mitome, T. Kozuka, and T. Tuziuti, ''Effects of nonlinearity in development of acoustic streaming,'' Jpn. J. Appl. Phys. 1 **34**, 2584–2589 (1995).

[20] V. F. Humphrey, M. Burgess, and M. Sampson, ''Harmonic generation due to nonlinear propagation in a focused ultrasonic field,'' Proc. Inst. Acoust. **8**, 47–54 (1986).

[21] J. Berntsen, J. Naze Tjøtta, and S. Tjøtta, ''Near field of a large acoustic transducer. Part IV: Second harmonic and sum frequency radiation,'' J. Acoust. Soc. Am. **75**, 1383–1391 (1984).

Sound amplification by stimulated emission of radiation in nonlinear mode

S. T. Zavtrak and I. V. Volkov
The Institute of Nuclear Problems, Bobruiskaya 11, 220050 Minsk, Republic of Belarus

(Received 3 January 1996; accepted for publication 18 February 1997)

The operation of the sound amplification by stimulated emission of radiation in the nonlinear mode is considered. Liquid with gas bubbles serves as an active medium. Pumping is produced by alternating electric field. The amplification of the useful wave in the plane resonator is investigated analytically. © *1997 Acoustical Society of America.* [S0001-4966(97)04006-X]

PACS numbers: 43.25.Ts [MAB]

INTRODUCTION

Recently the theoretical scheme of an acoustic analog of a free-electron laser, which will be referred to below as SASER (sound amplification by stimulated emission of radiation), was introduced by Zavtrak.[1,2] Liquid dielectric with dispersed particles (e.g., distilled water with gas bubbles, which can be obtained by electrolysis) was selected for an active medium. Pumping was produced in the active medium enclosed in plane resonator. Initially a bubble distribution had been spatially homogeneous and the summary radiation of bubbles had been equal to zero, but then they began to bunch due to acoustic radiation forces. This led to self-synchronization of the wiggling particles and amplification of the useful wave.

The scheme of saser with pumping by electric field was considered in Ref. 1. The process of the gas bubbles self-synchronization in the early stage of the saser operation and the generation conditions were investigated in Ref. 2. It was shown that two types of losses must be overcome. The first type is caused by energy dissipation in the active medium, the second one is caused by the radiation losses on the faces of the resonator. In the above mentioned papers the deviation of the spatial distribution of bubbles was assumed to be small when compared with the initial distribution. Besides, we considered an initial stage of operation so that the useful wave was less than the pumping pressure. In the present paper we relax these assumptions, considering saser operation for all time.

I. BASIC FORMULAS

The scheme of saser with electric pumping is shown in Fig. 1. The active medium is placed between two planes. The radiation propagates along z axis, L is the length of resonator in this direction. For simplicity we will assume all bubbles to be equal in radii.

The dynamics of the gas–liquid mixture is described by the following set of equations:[1,2]

$$\Delta P' - \frac{1}{c_l^2}\frac{\partial^2 P'}{\partial t^2} - (\alpha + i\beta)P' = (\alpha + i\beta)P_E \exp(i\omega t), \tag{1}$$

$$\gamma \mathbf{U} = -\alpha_0 \nabla |P|^2 + i\beta_0 (P^* \nabla P - P \nabla P^*), \tag{2}$$

$$\frac{\partial n}{\partial t} + \operatorname{div}(n\mathbf{U}) = 0. \tag{3}$$

In these equations c_l is the velocity of sound in pure liquid, P_E is the amplitude of pumping, ω is the pumping frequency, P' is the pressure of useful wave, $P = P_E \exp(i\omega t) + P'$ is the resulting pressure (static pressure is skipped) acting on the bubbles; in this case P_E does not depend on spatial coordinates.[1,2]

The quantity $n(\mathbf{r}, R_0, t)$ is a function of spatial distribution of the bubbles by radii (n is equal to the number of bubbles with mean radii from R_0 to $R_0 + dR_0$ in a unit of volume in the vicinity of the point $\mathbf{r}$); $\mathbf{U}$ is the translational velocity of a bubble under the acoustic radiation forces. In the case of equal bubbles the quantities α and β are described by the following expressions:

$$\alpha = -4\pi \operatorname{Re}(A) n, \quad \beta = -4\pi \operatorname{Im}(A) n, \tag{4}$$

where

$$A = \frac{R_0}{(\omega_0^2/\omega^2) - 1 + i\delta} \tag{5}$$

is the scattering amplitude of sound on a bubble, ω_0 is the resonance angular frequency of a bubble, and δ is the absorption constant. In initial moment ($t = 0$) $n = n_0$, $\alpha = \alpha_0$, and $\beta = \beta_0$. At last, $\gamma = 16\pi\mu_l R_0 \rho_l \omega^2 n_0$, where μ_l and ρ_l are viscosity and density of the pure liquid, respectively.

Let us represent pressure P' as $P' = \overline{P} \exp(i\omega t)$ and assume that concentration n and useful wave P' depend only on the z coordinate. Substituting (2) and (3) and applying the Bogolubov–Mitropol'sky's averaging method[3] over high-frequency component $\exp(i\omega t)$, one can obtain

$$\left(\frac{\omega^2}{c_l^2} - \frac{2i\omega}{c_l^2}\frac{\partial}{\partial t} + \Delta\right)\overline{P} + 4\pi n A \overline{P} = -4\pi n A P_E, \tag{6}$$

$$\frac{\partial n}{\partial t} = \frac{\alpha_0}{\gamma}\frac{\partial}{\partial z}\left(n \frac{\partial}{\partial z}\left[(\overline{P} + \overline{P^*})P_E + \overline{P P^*}\right]\right). \tag{7}$$

On derivation of these equations it was assumed that the energy dissipation in the active medium was small and all the bubbles were far from the resonance, i.e., $\beta_0 \ll \alpha_0$.

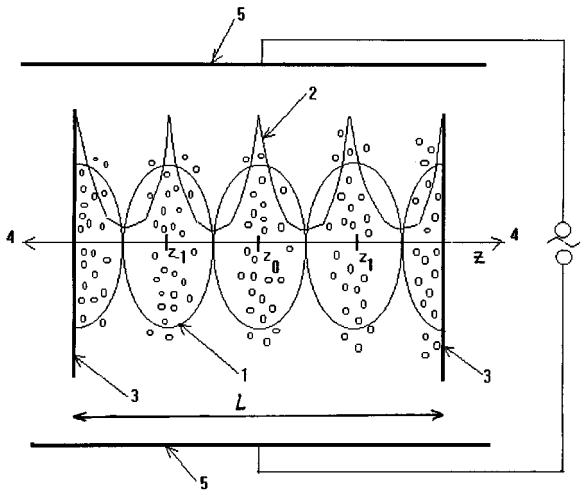

FIG. 1. The scheme of a saser with electric pumping: (1) the useful standing wave; (2) the spatial distribution of gas bubbles; (3) the walls of plane resonator; (4) the saser's emission; (5) electric pumping.

II. ANALYSIS OF EQUATIONS IN THE INITIAL STAGE OF GENERATION

In the initial stage of generation (at small t) we will seek the solution of (6) and (7) in the form of standing wave:[2]

$$\overline{P}(z,t)=P_0(t)\cos k_L z, \tag{8}$$

$$n=n_0+n' \tag{9}$$

with $k_L=\pi m/L$, $m=1,2,\ldots$, and $|n'|\ll n_0$, $|\overline{P_0}|\ll|\overline{P_E}|$. Then Eqs. (6) and (7) give the following:

$$\left(\frac{\omega^2}{c_l^2}-k_L^2-\frac{2i\omega}{c_l^2}\frac{\partial}{\partial t}-\alpha_0-i\beta_0\right)P_0(t)$$

$$=-\frac{\alpha_0^2P_E^2k_L^2}{\gamma}\int_0^t(P_0(t')+P_0^*(t'))dt'. \tag{10}$$

Let us represent the solution of this equation as

$$P_0(t)=A^+\exp(i\omega' t)+A^-\exp(-i\omega'^* t),$$

where ω' is the complex quantity. Then, with the proviso that $|A^-|\ll|A^+|$, it is easy to find that

$$\mathrm{Re}(\omega')\approx-\frac{c_l^2}{2\omega}\left[\left(\frac{\omega^2}{c_l^2}-\alpha_0\right)-k_L^2\right]\equiv-\frac{\delta_L\omega}{2}, \tag{11}$$

$$\mathrm{Im}(\omega')\approx\frac{c_l^2}{2\omega}\left(\beta_0+\frac{\alpha_0^2k_L^2P_E^2}{\gamma\,\mathrm{Re}(\omega')}\right). \tag{12}$$

The real part of ω' defines the frequency shift between pumping frequency ω and resonance frequency $\omega_L=c_l\sqrt{k_L^2+\alpha_0}$; the imaginary component defines the increment of useful wave amplification. One can seen from (12) that the generation takes place when $\delta_L>0$ and

$$P_E>P_{st}=\frac{\sqrt{\beta_0\gamma\delta_L\omega/2}}{|\alpha_0|k_L}. \tag{13}$$

The quantity P_{st} defines the starting (threshold) pumping pressure for the beginning of generation.[2] The right side of (13) involves only the term associated with the sound energy dissipation in the active medium but not the term attributed to the radiation losses on the faces of the resonator. This comes as no surprise because, for simplicity, the useful wave was chosen in the form of standing wave corresponding to the perfectly rigid reflecting walls of the resonator. A more general case was considered by Zavtral.[2]

It should be noted that the threshold conditions for the generation of fractional harmonics in the resonant fluid-filled cavity was observed experimentally by Adler and Breazeale;[4] in this case the problem associated with the nonlinear effects under resonator wall vibrations was considered.

III. SASER OPERATION IN NONLINEAR MODE

Now, let us analyze (6) and (7) for all time. The time- and z-dependence of pressure is given by (8). Multiplying (6) on $\cos k_L z$ and averaging over spatial coordinate one can find:

$$\left(\frac{\omega^2}{c_l^2}-\frac{2i\omega}{c_l^2}\frac{d}{dt}-k_L^2\right)P_0(t)+8\pi AP_0(t)n_2=$$

$$-8\pi AP_En_1, \tag{14}$$

$$n_1=n_1(t)=\langle n(z,t)\cos k_L z\rangle, \tag{15}$$

$$n_2=n_2(t)=\langle n(z,t)\cos^2 k_L z\rangle, \tag{16}$$

$$\ldots$$

$$n_i=n_i(t)=\langle n(z,t)\cos^i k_L z\rangle. \tag{17}$$

The substitution of (8) in (7) and multiplication of (7) by $\cos k_L z$, $\cos^2 k_L z$,..., and so on sequentially, give us an infinite set of equations (like Bogolubov–Green–Kirkwood–Ivon's chain in statistical physics[5]):

$$\frac{\partial n_1}{\partial t}=-\frac{\alpha_0k_L^2}{\gamma}((P_0+P_0^*)P_E(n_0-n_2)$$

$$+2P_0P_0^*(n_1-n_3)), \tag{18}$$

$$\frac{\partial n_2}{\partial t}=-\frac{2\alpha_0k_L^2}{\gamma}((P_0+P_0^*)P_E(n_1-n_3)$$

$$+2P_0P_0^*(n_2-n_4)), \tag{19}$$

$$\ldots.$$

We must make some approximations to analyze this set. Usually, the chain is cut at definite number. As a first approximation, let us replace quantity $\cos^2 k_L z$ with 1/2 in the expressions for n_2 and n_3. Then $n_2\approx n_0/2$, $n_3\approx n_1/2$. As a result, one can approximately find instead of (18):

$$\frac{\partial n_1}{\partial t}+\frac{\alpha_0k_L^2}{\gamma}P_0P_0^*n_1=-\frac{\alpha_0k_L^2}{2\gamma}(P_0+P_0^*)P_En_0. \tag{20}$$

The pressure $P_0(t)$ may be represented as

$$P_0(t)=\exp(i\omega' t)\Phi_0(t), \tag{21}$$

where ω' is the frequency shift which will be defined below. The substitution of (21) in (20) and averaging (20) over $\phi=\omega' t$ yields

$$n_1=a\exp(i\omega' t)+a^*\exp(-i\omega'^* t), \tag{22}$$

where

$$a=\frac{i\alpha_0 k_L^2 n_0 \Phi_0 P_E}{2\gamma\omega'[1+(i\alpha_0 k_L^2 \Phi_0 \Phi_0^*/\gamma\omega')]}. \tag{23}$$

Substituting (21)–(23) in (14) and averaging it over phase $\phi=\omega' t$ which is slow when compared with ωt one can obtain the expressions for the frequency shift and for growth of the useful wave:

$$\frac{\omega^2}{c_l^2}+\frac{2\omega\omega'}{c_l^2}-k_L^2-\alpha_0 = \frac{\alpha_0^2 k_L^2 P_E^2}{\gamma\omega'}\frac{[(\alpha_0 k_L^2/\gamma\omega')\Phi_0\Phi_0^*]}{1+[(\alpha_0 k_L^2/\gamma\omega')\Phi_0\Phi_0^*]^2}, \tag{24}$$

$$\frac{d\Phi_0}{dt}=-\frac{\beta_0 c_l^2}{2\omega}\times\left(1+\frac{\alpha_0^2 k_L^2 P_E^2}{\gamma\omega'\beta_0\{1+[(\alpha_0 k_L^2/\gamma\omega')\Phi_0\Phi_0^*]^2\}}\right)\Phi_0. \tag{25}$$

In the initial stage of generation (when Φ_0 is small) Eqs. (24) and (25) turn to the following ones:

$$\omega'=-\delta_L\omega/2, \tag{26}$$

$$\frac{d\Phi_0}{dt}=-\frac{\beta_0 c_l^2}{2\omega}\left(1-\frac{P_E^2}{P_{st}^2}\right)\Phi_0. \tag{27}$$

Formula (26) makes it clear that resulting angular frequency $\omega+\omega'$ of saser radiation at the beginning of generation is determined by the proper propagation constant of the resonator. As the useful wave increases, the nonlinear terms from the right-hand side of (24) begin to play a more important role. This leads to the additional shift of ω'.

As mentioned above, in the case of $P_E>P_{st}$, Eq. (25) describes growth of the useful wave amplitude, up to values which reduce the right-hand side to zero. So we can estimate the maximal value of the useful wave:

$$|P_{0_{\max}}|=P_E\left(\frac{P_E^2}{P_{st}^2}-1\right)^{1/4}\left(\frac{|\alpha_0|}{\beta_0}\right)^{1/2}. \tag{28}$$

Because $|\alpha_0|/\beta_0\sim 1/\delta$, expression (28) may be written in the form

$$|P_{0_{\max}}|=P_E\left(\frac{P_E^2}{P_{st}^2}-1\right)^{1/4}\delta^{-1/2}. \tag{29}$$

In ordinary conditions $\delta\sim 10^{-2}$ for air bubbles in water.[6] Hence, the maximal pressure amplitude of the useful wave can exceed pumping pressure P_E by approximately one order of magnitude. As is shown in the previous papers,[1,2] the value of P_{st} is about a few units of kPa.

The function n_1 describes nonuniformity of the spatial distributive density of bubbles. The expression (22) shows that the density oscillates with angular frequency ω'.

IV. CONCLUSIONS

By this means during the operation the saser emission goes to saturation. This effect is analogous to that in the free-electron lasers theory. In the experimental process the amplification will take place on frequency $\omega+\omega'$.

ACKNOWLEDGMENTS

The research described in this publication was made possible for S. T. Zavtrak in part by Grant No. U9Y000 from the International Science Foundation.

[1] S. T. Zavtrak, ''Acoustic laser with dispersed particles as an analog of free-electron laser,'' Phys. Rev. E **51**, 2480–2484 (1995).
[2] S. T. Zavtrak, ''Generation conditions for an acoustic laser,'' Phys. Rev. E **51**, 3767–3769 (1995).
[3] N. N. Bogolubov and Yu. A. Mitropol'sky, *Asymptotic Methods in the Theory of Nonlinear Oscillations* (Gos.izd.fiz.math.lit., Moscow, 1958).
[4] L. Adler and M. A. Breazeale, ''Generation of fractional harmonics in a resonant ultrasonic wave system,'' J. Acoust. Soc. Am. **48**(5), 1077–1083 (1970).
[5] A. Isihara, *Statistical Physics* (Academic, New York, 1971).
[6] K. Klei and G. Medvin, *Acoustic Oceanography* (Mir, Moscow, 1980).

Aircraft flight parameter estimation based on passive acoustic techniques using the polynomial Wigner–Ville distribution

David C. Reid,[a] Abdelhak M. Zoubir, and Boualem Boashash
Signal Processing Research Centre, Queensland University of Technology, G.P.O. Box 2434, Brisbane, Queensland 4001, Australia

(Received 15 May 1995; revised 25 January 1997; accepted 4 March 1997)

The acoustic signal from an overflying aircraft, as heard by a stationary observer, is used to estimate an aircraft's constant height, ground speed, range, and acoustic frequency. Central to the success of this flight parameter estimation scheme is the need for an accurate estimate of the instantaneous frequency of the observed acoustic signal. In this paper, the polynomial Wigner–Ville distribution is used in this application as the instantaneous frequency estimator. Its performance and the issue of the optimal time domain window length are addressed. © *1997 Acoustical Society of America.* [S0001-4966(97)06106-7]

PACS numbers: 43.28.Tc, 43.60.Gk [LCS]

INTRODUCTION

Ground-based radar systems are commonly used in military applications and general aviation to provide an estimate of an aircraft's height, ground speed, and range. In this paper we consider aspects of an alternative approach based on passive acoustic techniques which provide a simple, portable, easily implemented, covert, and biologically safe estimation scheme. In this scheme, the acoustic signal from an overflying aircraft is recorded by a single ground-based microphone. An estimate of the aircraft's flight parameters (constant height, constant ground speed, constant acoustic frequency, and range) can then be made by estimating the form of the time varying Doppler shift of the received acoustic signal.

The Doppler effect describes the perceived change in frequency of an acoustic source which is moving relative to an observer. The observed sound of an overflying aircraft provides a good example of this phenomenon. From experience, a stationary observer is able to make some useful judgement about the velocity and height of the overflying aircraft based on the observed time varying frequency of the narrow-band acoustic signal from the aircraft's engines or propellers. For example, a rapid transition in the acoustic frequency, as an aircraft passes overhead, would indicate to a stationary observer that the aircraft was either flying fast or low, or both. Ferguson[1] formalized this concept by proposing an observer frequency model which, based on a number of assumptions, relates the acoustic frequency of the observed signal to the aircraft flight parameters. The application of this model was demonstrated in Refs. 1 and 2 where it was shown that, given an estimate of the time varying acoustic frequency from a single microphone recording, the observer frequency model could be used to provide a meaningful estimate of the aircraft flight parameters. Central to the success of this passive acoustic parameter estimation scheme is the need for an accurate estimate of the aircraft's time varying acoustic frequency. In Ref. 3 it is shown that this acoustic frequency is the instantaneous frequency of the observed passive acoustic signal.

In Sec. I we discuss the use of time–frequency representations (TFRs) as instantaneous frequency estimators. In particular we briefly compare the use of the polynomial Wigner–Ville distribution and the Wigner–Ville distribution.[4,2,5] Other estimation schemes have been proposed based on spectral phase,[1,6] central finite difference and signal phase estimators,[3,7] and frequency and signal amplitude.[8] Bootstrap statistical techniques have been employed to determine confidence bounds for the aircraft parameters given a single acoustic recording.[9,7] A general discussion of the aircraft flight parameter estimation scheme is presented in Sec. II where examples of the passive acoustic instantaneous frequency and its relationship to the flight parameters is given. In Sec. III it is shown that a trade-off between the bias and variance of the polynomial Wigner–Ville and Wigner–Ville based instantaneous frequency estimators can be controlled by using a time domain window. Comparative examples of this trade-off are given for these time–frequency representations and analytical expressions for the instantaneous frequency estimator bias and variance and optimal window length are derived. These theoretical results are supported by computer simulations in Sec. IV and the strengths and limitations of the polynomial Wigner–Ville distribution in the passive acoustic application are demonstrated.

I. INSTANTANEOUS FREQUENCY ESTIMATION

The acoustic signal from a propeller driven aircraft is narrow-band with the dominant frequency given by the propeller blade rate which is defined as the product of the engine rotational speed and the number of propeller blades.[1] The aircraft acoustic signal, as heard by a stationary observer is nonstationary in the sense that the spectral content varies with time due to the Doppler effect. Consideration of the frequency of such acoustic signals, at a particular time instant, leads to the concept of instantaneous frequency (see Ref. 10 for a detailed discussion of instantaneous frequency). One particular method of instantaneous frequency estimation

[a]Commonwealth Scientific and Industrial Research Organisation, Exploration and Mining, Queensland Centre for Advanced Technologies, P.O. Box 883, Kenmore, Queensland 4069, Australia.

is based on the signal's time–frequency representation. The time–frequency representation is a two-dimensional function which attempts to show the distribution of the signal energy in a joint time–frequency plane. Ideally we would like all the energy concentrated at the instantaneous frequency, denoted $f_i(t)$, so as to yield the ideal time–frequency representation

$$\mathcal{T}(t,f) \propto (\delta[f - f_i(t)]), \tag{1}$$

where $\delta(.)$ is the Dirac delta and $\propto$ indicates proportionality. It follows that the peak of (1) would describe $f_i(t)$ exactly. In practice, due to finite data lengths, noisy observations, and the particular characteristics of the time–frequency representation being used, we only obtain an approximation to (1). For a particular signal, some time–frequency representations will provide a better approximation than others. For example, the Wigner–Ville distribution is optimal for the analysis of deterministic signals having a linearly time varying instantaneous frequency law.

For this class of signals, the peak of the Wigner–Ville distribution, with respect to time, describes exactly the instantaneous frequency. In a similar manner, the peak of a class of time–frequency representations known as polynomial Wigner–Ville distributions provide an optimal instantaneous frequency estimate for deterministic signals having an instantaneous frequency not exceeding a given polynomial order.[11]

II. THE AIRCRAFT FLIGHT PARAMETER ESTIMATION SCHEME

A. The observer frequency model

The passive acoustic observer frequency model proposed in Ref. 1 is based on the assumptions that, throughout the observation period: (1) the aircraft is flying at a constant altitude and subsonic ground speed, (2) the wind velocity is constant in both space and time, and (3) the acoustic source frequency is constant. These assumptions only need to hold throughout the observation period (typically about 30 s). Under these assumptions, the observer frequency model, $f_0(t)$, is given by

$$f_0(t) = \frac{f_a(c + v_m \cos\ \gamma(t))}{(c + v_m \cos\ \gamma(t) \pm v_a \cos\ \gamma(t))}, \tag{2}$$

where f_a is the source acoustic frequency, c is the speed of sound in the medium, v_m is the velocity of the wind, and v_a is the velocity of the aircraft, where each velocity represents the component along the aircraft flight path. Furthermore, $\gamma(t)$ is the angle of depression of the observer from the aircraft such that

$$\cos\ \gamma(t) = \frac{r(t)}{\sqrt{h^2 + r^2(t)}}, \tag{3}$$

where h is the distance between the aircraft and the observer at the point of closest approach, and $r(t)$ is the horizontal range of the aircraft from the observer when it generates the sound that reaches the observer later at time t, which is defined to be

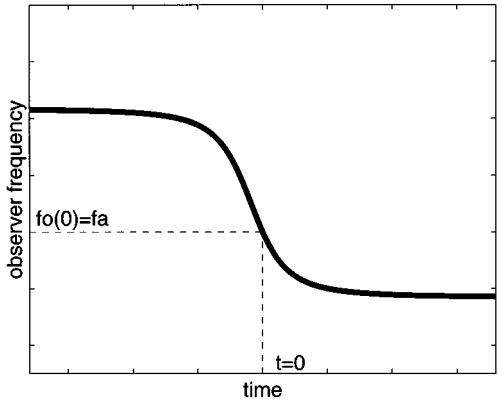

FIG. 1. The general form of the passive acoustic instantaneous frequency as described by the observer frequency model. The intersection of the dashed lines indicates the time in the instantaneous frequency where the acoustic signal from the directly overhead aircraft is subsequently heard by the observer.

$$t = \frac{\pm r(t)}{v_a} + \frac{\sqrt{(h^2 + r^2(t))} - h}{c}. \tag{4}$$

If the flight path of the aircraft is directly over the observer (i.e., overflying), h is the constant height of the aircraft above the observer. Experimental results with real aircraft acoustic data, collected under accurately monitored conditions, have confirmed the veracity and practical usefulness of the observer frequency model.[3]

The general form of the observer frequency model $f_0(t)$ is shown qualitatively in Fig. 1. The intersection of the dashed lines is the value of the instantaneous frequency where the acoustic signal from the aircraft at the point of closest approach (i.e., no Doppler shift) is subsequently heard by the observer. At this point $t=0$, $r(0)=0$, and $f_0(0)=f_a$. A more detailed description of this model can be found in Ref. 1. Given v_m and c, the aircraft flight parameters which are to be estimated, v_a, h, $r(t)$, and f_a are uniquely related to $f_0(t)$ by (2). It is for this reason that we now turn our attention to the estimation of $f_0(t)$.

B. Passive acoustic instantaneous frequency estimation

In Refs. 2 and 4 the Wigner–Ville distribution was used in the aircraft flight parameter estimation application. An example of this technique is given in Fig. 2 which shows the Wigner–Ville distribution of an acoustic recording of an overlying propeller-driven light aircraft being flown under controlled conditions. The form of the instantaneous frequency is graphically evident and indicates that the peak of this time–frequency representation provides an estimate of the instantaneous frequency. Such an estimate is given in Fig. 3.

The polynomial Wigner–Ville distribution, which will be defined and described in detail in Sec. III, is a class of time–frequency representations which include and extend the Wigner–Ville distribution to higher polynomial orders. For the purpose of comparison, Fig. 4 shows the fourth-order polynomial Wigner–Ville distribution of the same acoustic

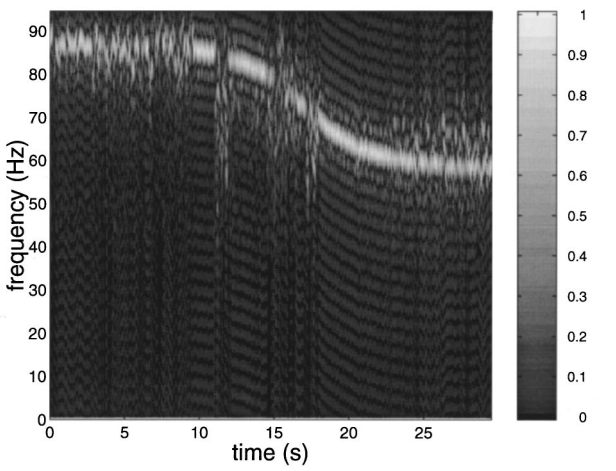

FIG. 2. A Wigner–Ville time–frequency representation of a typical acoustic recording of an overflying aircraft.

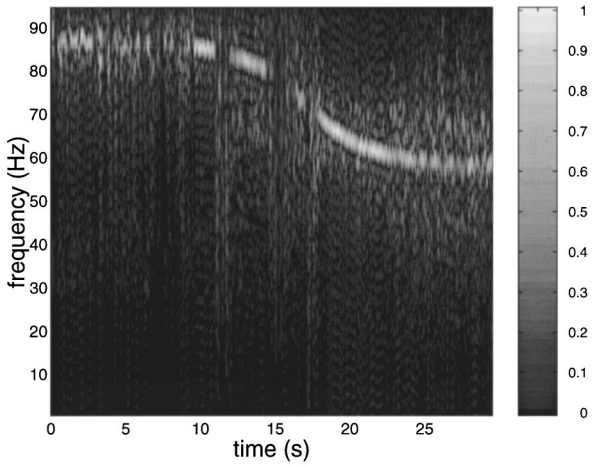

FIG. 4. A fourth-order polynomial Wigner–Ville time–frequency representation of the same acoustic recording as used in Fig. 2.

signal as used in Fig. 2 and the corresponding instantaneous frequency estimate is shown in Fig. 5. It is apparent that the Wigner–Ville- and polynomial Wigner–Ville-based instantaneous frequency estimates of Fig. 3 and 5 differ from each other. The noticeable differences are that the polynomial Wigner–Ville-based estimator has higher variance at the extremities which corresponds to the distant aircraft and consequently is the region of low signal-to-noise ratio. Also the Wigner–Ville-based estimator performs poorly in the central transitional region where the coefficients of the higher-order derivatives of instantaneous frequency, with respect to time, are greatest. These observations are significant as it will be shown in later sections that the choice between the Wigner–Ville and polynomial Wigner–Ville as an instantaneous frequency estimator is, in general, very much dependent on the signal-to-noise ratio and the higher-order derivatives present in the instantaneous frequency law.

In this particular application, the aircraft flight parameters being estimated are a nonlinear function of the instantaneous frequency. Each of the parameters depend, to a varying extent, on different temporal regions or characteristics of the observer frequency model. For example, the height parameter is particularly sensitive to the form of the central transitional region of the frequency model, whereas the source frequency parameter is largely dependent on the flat extremities, and by comparison with the height parameter, is far less sensitive. This dependence is demonstrated graphically in Fig. 6 where the solid line represents $f_0(t)$ for typical parameters: $h=304.8$ m (1000 ft), $v_a=102.9$ m/s (200 kn), $f_a=100$ Hz, and at an arbitrarily chosen time reference, $r=1.646$ km. For the instantaneous frequency described by the dashed line, the relatively small change in the central transitional region results from a 50% reduction in the value of the height parameter with the other parameters remaining unchanged. On the other hand, the instantaneous frequency described by the dotted line results from only a 5% reduction in the source frequency parameter with the other parameters remaining unchanged.

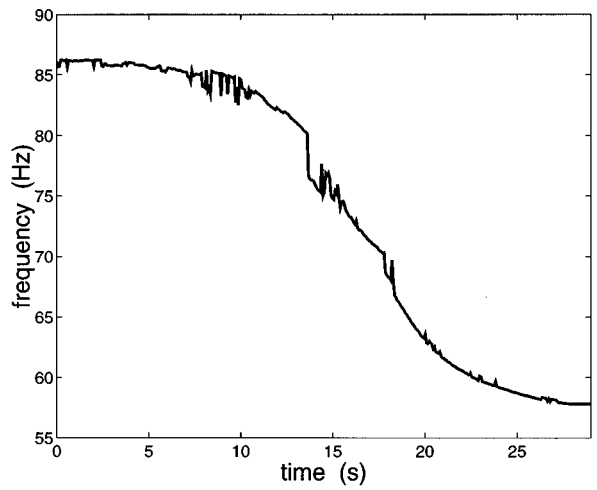

FIG. 3. An instantaneous frequency estimate given by the peak, with respect to time, of the Wigner–Ville time–frequency representation of Fig. 2.

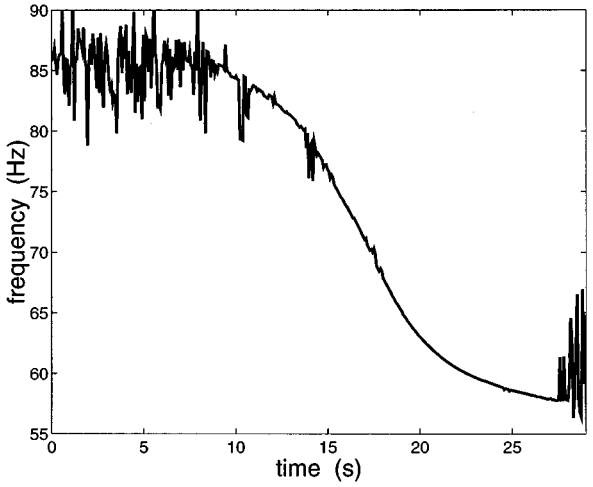

FIG. 5. An instantaneous frequency estimate given by the peak, with respect to time, of the fourth-order polynomial Wigner–Ville time–frequency representation of Fig. 4.

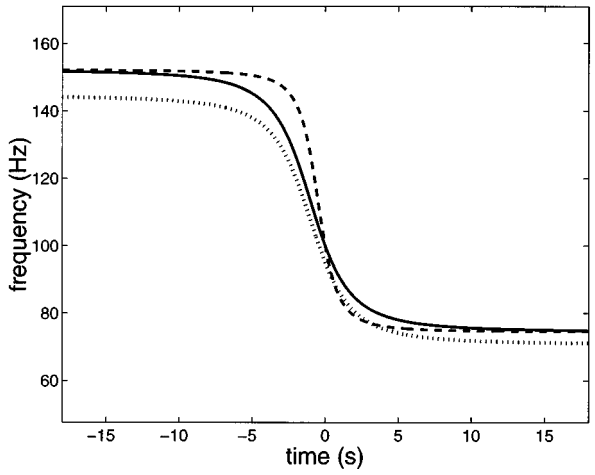

FIG. 6. A comparison of the instantaneous frequency, as described by the observer frequency model, for varying values of the height and source frequency parameter. The aircraft flight parameters associated with the solid line are $h=304.8$ m (1000 ft), $v_a=102.9$ m/s (200 kn), $f_a=100$ Hz and range=1.646 km. The dashed line is the instantaneous frequency where the height parameter alone has been reduced by 50% and the dotted line is the instantaneous frequency where the source frequency parameter alone has been reduced by 5%.

C. Aircraft flight parameter estimates

In the final step in this flight parameter estimation scheme we extract the parameters by fitting the instantaneous frequency estimate to the observer frequency model in a minimum least-squares sense. Using this approach, the aircraft parameter estimates, based on the Wigner–Ville and fourth-order polynomial Wigner–Ville derived instantaneous frequency estimates of Figs. 3 and 5, respectively, are shown in Table I (for this example we have used $c=339$ m/s, $v_m=0$ and have calculated the range corresponding to $t=0$ s).

In the remaining sections we consider the use of the Wigner–Ville distribution and polynomial Wigner–Ville distribution as estimators of higher polynomial order instantaneous frequency laws (such as the passive acoustic instantaneous frequency).

III. THE POLYNOMIAL WIGNER–VILLE DISTRIBUTION

A desirable property of a time–frequency representation is that it provides good concentration by localizing the signal energy in both time and frequency. Numerous time–frequency representations have been proposed that exhibit this property for particular classes of signals, achieving both good time and frequency concentration simultaneously.[12] Significant among these is the Wigner–Ville distribution which is known, for linear frequency modulated signals (i.e., linear instantaneous frequency), to be an ideal time–frequency representation in that it provides maximum localization of the signal energy about the true instantaneous frequency. The instantaneous frequency $f_i(t)$ of a real valued signal $x(t)$ can be expressed as

$$f_i(t)=\frac{1}{2\pi}\frac{d\theta(t)}{dt}, \tag{5}$$

where $\theta(t)$ is the phase of the analytic signal associated with $x(t)$.[10] From (5), it follows that a linear or first-order polynomial frequency law corresponds to a second-order polynomial phase law. For polynomial phase laws greater than two, the Wigner–Ville distribution will become distorted and the peak of the time–frequency representation will no longer exactly describe the instantaneous frequency.[13] Polynomial Wigner–Ville distributions are a higher order extension of the Wigner–Ville distribution and are designed to properly localize, in time and frequency, signals having higher-order instantaneous frequency laws.[11] The qth-order polynomial Wigner–Ville distribution (which we abbreviate as PWVD$_q$) will provide an optimal time–frequency representation of a signal having phase law of polynomial order $\leqslant q$, in which case we say that the polynomial Wigner–Ville distribution and the signal are matched (the Wigner–Ville distribution is the second-order polynomial Wigner–Ville distribution).

TABLE I. Comparison of aircraft flight parameter estimates using the Wigner–Ville and polynomial Wigner–Ville distribution.

	Height (m)	Velocity (m/s)	Range (km)	Source freq. (Hz)
WVD	404	73.3	1.30	68.4
PWVD	309	68.7	1.21	68.9

A. Definitions

The qth-order polynomial Wigner–Ville distribution, denoted as $W_q(t,f)$, is defined in terms of the Fourier transform of a qth-order kernel function $K_q(t,f)$. With the inclusion of a time domain window, which controls the trade-off between estimator bias and variance, the qth-order polynomial Wigner–Ville distribution is defined as[14]

$$W_q(t,f)\triangleq\int_{-\infty}^{\infty}h(\tau)K_q(t,\tau)e^{-j2\pi f\tau}\,d\tau, \tag{6}$$

where

$$K_q(t,\tau)\triangleq\prod_{k=0}^{q/2}z(t+c_k\tau)^{b_k}z^*(t+c_{-k}\tau)^{-b_{-k}}, \tag{7}$$

$z(t)$ is the analytic signal associated with $x(t)$ and, for our purposes, we choose $h(\tau)$ to be a centered rectangular window function of length T. In the ''integer power'' implementation of the polynomial Wigner–Ville distribution[15] that we are considering, b_k is an integer, $b_k=-b_{-k}$, $q/2$ is a positive integer, c_k is a real number, and $c_k=-c_{-k}$. As discussed in Refs. 15 and 11, the values of b_k and c_k are chosen so that for each time increment, the kernel $K_q(t,\tau)$ attempts to demodulate $z(t)$ into a complex sinusoid with frequency equal to the instantaneous frequency. If this is achieved (and as T increases) the resulting time–frequency representation $W_q(t,f)$ approaches $\mathcal{T}(t,f)$ by exhibiting impulses in the time–frequency plane at coordinates corresponding to the true instantaneous frequency. The set of b_k coefficients are uniquely specified by further requiring that $\Sigma_k|b_k|$ be minimized. This requirement minimizes the number of multiplicative terms, and therefore the multilinearity, of the kernel.

For the specific case of the fourth-order polynomial Wigner–Ville, the kernel parameters are[15]

$$b_2=-b_{-2}=1, \quad b_1=-b_{-1}=2, \quad b_0=0, \tag{8}$$

$$c_1=-c_{-1}=\frac{1}{2(2-2^{1/3})}\approx 0.675, \quad c_2=-c_{-2}=-2^{1/3}c_1\approx -0.85. \tag{9}$$

For $k=0$, $z(t+c_{\pm 0})=1$ for all values of $c_{\pm 0}$ so that c_0 or $-c_{-0}$ need not be specified.

These parameter values yield the fourth-order kernel

$$K_4(t,\tau)=[z(t+0.675\tau)z^*(t-0.675\tau)]^2 \times z^*(t+0.85\tau)z(t-0.85\tau). \tag{10}$$

Similarly, for the second-order case,

$$b_1=-b_{-1}=1, \quad b_0=0, \tag{11}$$

$$c_1=-c_{-1}=0.5 \tag{12}$$

yielding the second-order kernel

$$K_2(t,\tau)=z(t+0.5\tau)z^*(t-0.5\tau) \tag{13}$$

which results in the Wigner–Ville distribution.

The purpose of the window function $h(\tau)$ is discussed next.

B. Time domain window effect on instantaneous frequency estimator error

In the absence of noise, exact instantaneous frequency estimates up to polynomial order $(q-1)$ can be obtained from the peak of the qth-order polynomial Wigner–Ville distribution, however, error in the instantaneous frequency estimates occurs when analyzing signals having polynomial phase laws of order greater than q. Furthermore, it will be shown that, for a given polynomial phase law of order p such that $p>q$, this instantaneous frequency error will increase as q decreases. It is this error, which manifests itself in the absence of noise, that we will refer to as systematic bias. This systematic bias may be minimized by using a time domain window to provide a region of time support where the signal's polynomial phase law can be locally approximated as qth order. It will be shown that the systematic bias *decreases* with decreasing window length.

In the presence of noise, there is also an error due to the variance of the estimator. It will be shown that the variance, which of course increases with decreasing signal-to-noise ratio, also *decreases* with increasing window length. Thus the two instantaneous frequency error factors behave in a counterdependent manner over window length. The effect of the time domain window is illustrated below by example using simulated signals.

In the following examples we use the discrete fourth-order polynomial Wigner–Ville distribution and Wigner–Ville distribution to analyze a seventh-order polynomial phase test signal $z(t)$. This test signal is intentionally chosen to be of higher polynomial order than the time–frequency representations so as to ensure that the signal is mismatched and that the effects of time domain windowing can be observed. The test signal is given by

$$z(t)=e^{j2\pi\phi(t)}+n(t), \quad t=-N/2+1,\ldots,N/2-1, \tag{14}$$

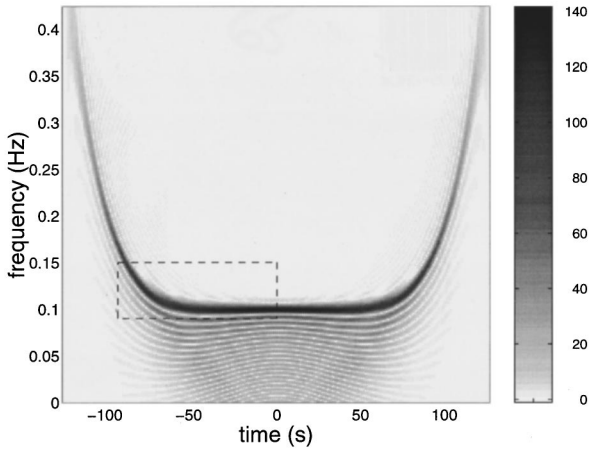

FIG. 7. A fourth-order polynomial Wigner–Ville distribution of a seventh-order polynomial phase test signal at 40-dB signal-to-noise ratio, where a long window (100% of data length) has been used. The dashed rectangular box marks the region in which the instantaneous frequency estimate comparison of Fig. 9 is made.

$$\phi(t)=0.1t+0.4t^7/(7(N/2)^6), \tag{15}$$

t is an integer, $n(t)$ is a complex white Gaussian stationary noise process, and $N=256$. By the definition of instantaneous frequency in (5), $z(t)$ represents a sixth-order frequency modulated signal with a maximum and a minimum frequency of 0.5 and 0.1 Hz, respectively.

1. Example 1

The fourth-order polynomial Wigner–Ville distribution and Wigner–Ville distribution of $z(t)$ at 40-dB signal-to-noise ratio, where a long window (100% of data length) has been used, are shown in Figs. 7 and 8, respectively. An instantaneous frequency estimate, based on the clearly distinguishable peaks of these time-frequency representations, will exhibit low variance but will be distorted away from the true instantaneous frequency. This distortion, which is due to the systematic bias, is shown in Fig. 9 where an enlarged portion

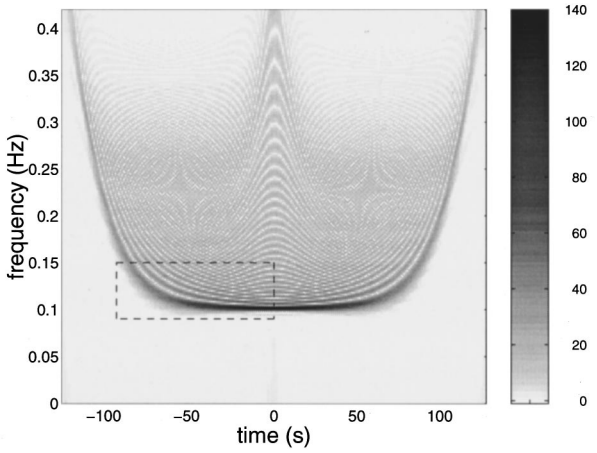

FIG. 8. A Wigner–Ville distribution (second-order polynomial Wigner–Ville distribution) of a seventh-order polynomial phase test signal at 40-dB signal-to-noise ratio, where a long window (100% of data length) has been used. The dashed rectangular box marks the region in which the instantaneous frequency estimate comparison of Fig. 9 is made.

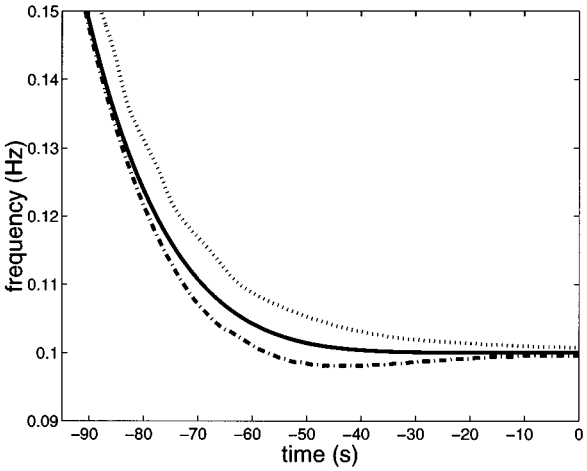

FIG. 9. An enlarged portion of the true instantaneous frequency (solid line) is compared to the instantaneous frequency estimates based on the peak of the fourth-order polynomial Wigner–Ville distribution (dashed line) of Fig. 7 and the Wigner–Ville distribution (dotted line) of Fig. 8 in the regions marked by the dashed rectangular boxes. The maximum systematic error occurs in this portion of the instantaneous frequency estimate. The mean-square error of the fourth-order polynomial Wigner–Ville-based estimate is approximately one-tenth that of the Wigner–Ville based estimate.

of the true instantaneous frequency (solid line) is compared to the instantaneous frequency estimates based on the peak of the fourth-order polynomial Wigner–Ville distribution (dashed line) and Wigner–Ville distribution (dotted line) of Figs. 7 and 8, respectively, in the region marked by the dashed rectangular box. In this case, the instantaneous frequency estimator mean-square error is essentially that associated with the systematic bias. Furthermore, the mean-square error of the fourth-order polynomial Wigner–Ville based estimate (which for this realization is estimated to be 4.2×10^{-6} Hz^2) is much less than for the Wigner–Ville based estimate (which is estimated for this realization to be 3.5×10^{-5} Hz^2). For a short window (3% of data length), the fourth-order polynomial Wigner–Ville and Wigner–Ville distribution, as shown in Figs. 10 and 11, respectively, are smeared in frequency and the peaks are of lower amplitude and are not so clearly distinguishable. However, the systematic bias has been reduced, as shown in Fig. 12, where the true instantaneous frequency and the estimates are practically coincident, and the mean-square error associated with the systematic bias of both estimates is negligible. In the high signal-to-noise ratio case, the short window estimate of Fig. 12 will give the more accurate instantaneous frequency estimate for both the polynomial Wigner–Ville distribution and the Wigner–Ville distribution, even though the peaks of both time-frequency representations are indistinct and of a much lower amplitude than for the large window time–frequency representations of Figs. 7 and 8.

2. Example 2

We now consider the same instantaneous frequency estimates of example 1 in the presence of noise at 10-dB signal-to-noise ratio. Figures 13 and 14 show the fourth-order polynomial Wigner–Ville distribution and Wigner–Ville distribution, respectively, of the noisy signal when a

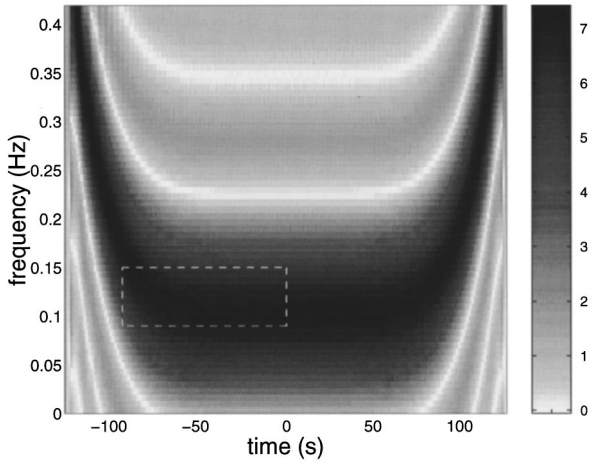

FIG. 10. A fourth-order polynomial Wigner–Ville distribution of a seventh-order polynomial phase test signal at 40-dB signal-to-noise ratio, where a short window (3% of data length) has been used. The dashed rectangular box marks the region in which the instantaneous frequency estimate comparison of Fig. 12 is made.

full length window is used. It appears that the peak of both time–frequency representations are still clearly distinguishable and that the overall instantaneous frequency estimator mean-square error will still essentially be that associated with the systematic bias. This is confirmed in Fig. 15 which shows a comparison of the true instantaneous frequency (solid line) and instantaneous frequency estimates based on the fourth-order polynomial Wigner–Ville distribution (dashed line) and Wigner–Ville distribution (dotted line) of Figs. 13 and 14, respectively, in the region marked by the dashed rectangular box. The mean-square error for the fourth-order polynomial Wigner-Ville- and Wigner–Ville-based estimates are 4.5×10^{-6} Hz^2 and 4.2×10^{-5} Hz^2, respectively, and are essentially the same as for the high signal-to-noise ratio example of Fig. 9. Figures 16 and 17 show the fourth-order polynomial Wigner–Ville and Wigner–Ville distribution of the noisy signal when the short

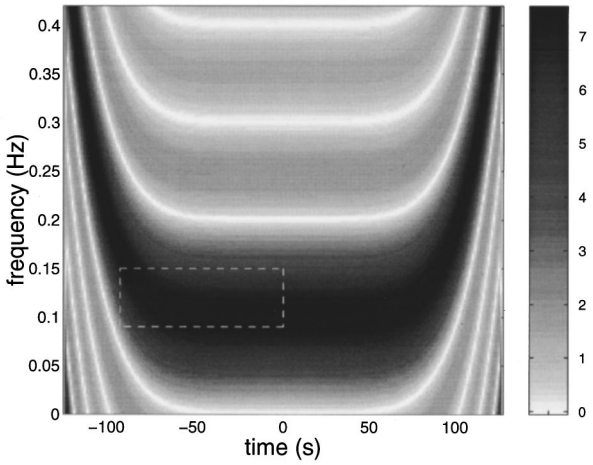

FIG. 11. A Wigner–Ville distribution (second-order polynomial Wigner–Ville distribution) of a seventh-order polynomial phase test signal at 40-dB signal-to-noise ratio, where a short window (3% of data length) has been used. The dashed rectangular box marks the region in which the instantaneous frequency estimate comparison of Fig. 12 is made.

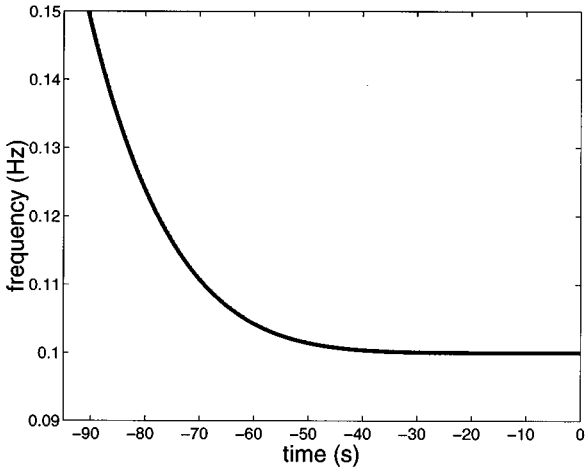

FIG. 12. An enlarged portion of the true instantaneous frequency (solid line) is compared to the instantaneous frequency estimates based on the peak of the fourth-order polynomial Wigner–Ville distribution of Fig. 10 and the Wigner–Ville distribution of Fig. 11 in the regions marked by the dashed rectangular boxes. In this plot, the three lines are coincident and the systematic error, which is maximum in this region, is negligible for both time–frequency representations.

window is used. Figure 18 shows the comparison of the true instantaneous frequency (heavy solid line), fourth-order polynomial Wigner–Ville-based estimate (broken line) and Wigner–Ville-based estimate (finer solid line) for a single realization. It is apparent that the mean-square error of the fourth-order polynomial Wigner–Ville-based estimator (calculated for this realization to be 3.3×10^{-5} Hz^2) will be greater than the Wigner–Ville-based estimator (calculated for this realization to be 9.3×10^{-6} Hz^2). It is also apparent that the mean-square error for both of these estimators, which are dominated by the estimator variance, may be greater than for the long window case of Fig. 15.

These simple examples demonstrate the relationship between instantaneous frequency estimator error, signal-to-noise ratio, window length, and the polynomial phase order

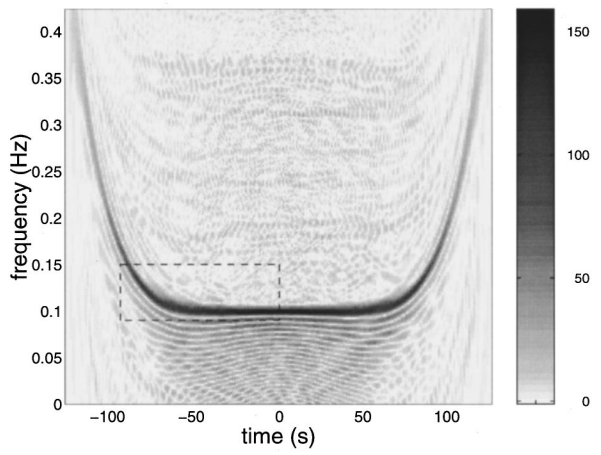

FIG. 13. A fourth-order polynomial Wigner–Ville distribution of a seventh-order polynomial phase test signal at 10-dB signal-to-noise ratio, where a long window (100% of data length) has been used. The dashed rectangular box marks the region in which the instantaneous frequency estimate comparison of Fig. 15 is made.

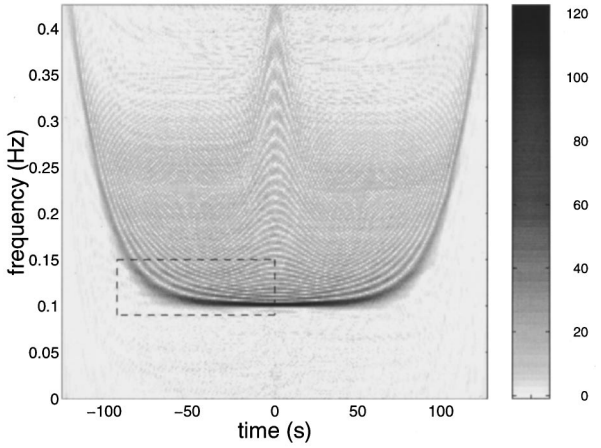

FIG. 14. A Wigner–Ville distribution (second-order polynomial Wigner–Ville distribution) of a seventh-order polynomial phase test signal at 10-dB signal-to-noise ratio, where a long window (100% of data length) has been used. The dashed rectangular box marks the region in which the instantaneous frequency estimate comparison of Fig. 15 is made.

of the signal. In the following sections we formalize these relationships by deriving expressions for the bias and variance of the polynomial Wigner–Ville-based instantaneous frequency estimator as functions, amongst other things, of the time domain window length. An expression for the optimal window length for the qth-order polynomial Wigner–Ville distribution is then derived where the criterion of optimality is the instantaneous frequency estimator minimum mean-square error. The derivations presented in the paper extend and generalize the fourth-order results previously presented in Ref. 16.

C. Polynomial Wigner–Ville-based instantaneous frequency estimator bias

We first consider the bias of the polynomial Wigner–Ville-based instantaneous frequency estimator which is com-

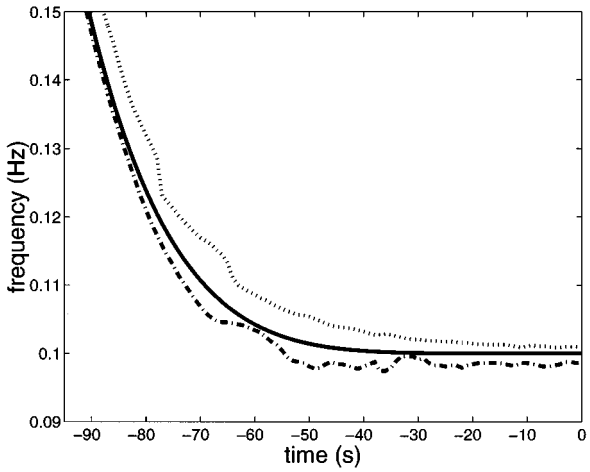

FIG. 15. An enlarged portion of the true instantaneous frequency (solid line) is compared to the instantaneous frequency estimates based on the peak of the fourth-order polynomial Wigner–Ville distribution (dashed line) of Fig. 13 and the Wigner–Ville distribution (dotted line) of Fig. 14 in the regions marked by the dashed rectangular boxes. The maximum systematic error occurs in this portion of the instantaneous frequency estimate.

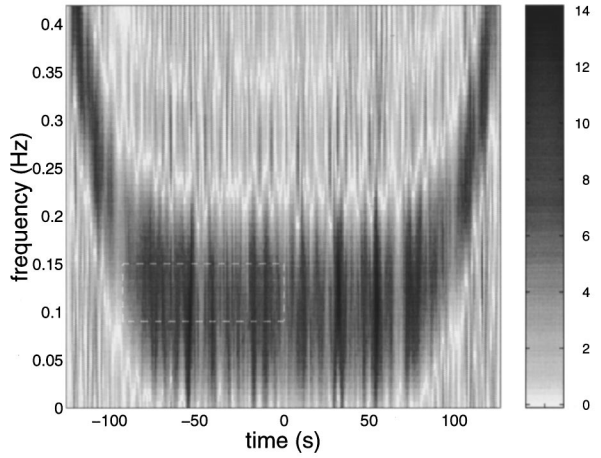

FIG. 16. A fourth-order polynomial Wigner–Ville distribution of a seventh-order polynomial phase test signal at 10-dB signal-to-noise ratio, where a short window (3% of data length) has been used. The dashed rectangular box marks the region in which the instantaneous frequency estimate comparison of Fig. 18 is made.

posed of two parts: the statistical bias (due to random effects), and the systematic bias (due to model mismatch). For the high signal-to-noise ratio case, which we consider in the following derivation, the statistical bias is considered to be negligible[17] and only the systematic bias, which results solely from the mismatched polynomial order of the polynomial Wigner–Ville distribution and the signal phase law, is of concern. An expression for the bias of the qth-order polynomial Wigner–Ville distribution can be derived as follows.

Consider a complex signal of the form

$$s(t)=Ae^{j2\pi\phi(t)}, \tag{16}$$

where t is a real number and where $\phi(t)$ is described, at least within some observation window, by a polynomial phase law of arbitrary order p. Expanding the qth-order kernel in (7) for this signal results in the phase terms

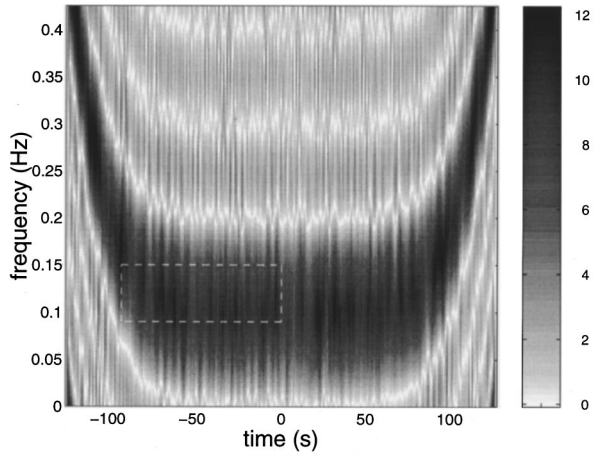

FIG. 17. A Wigner–Ville distribution (second-order polynomial Wigner–Ville distribution) of a seventh-order polynomial phase test signal at 10-dB signal-to-noise ratio, where a short window (3% of data length) has been used. The dashed rectangular box marks the region in which the instantaneous frequency estimate comparison of Fig. 18 is made.

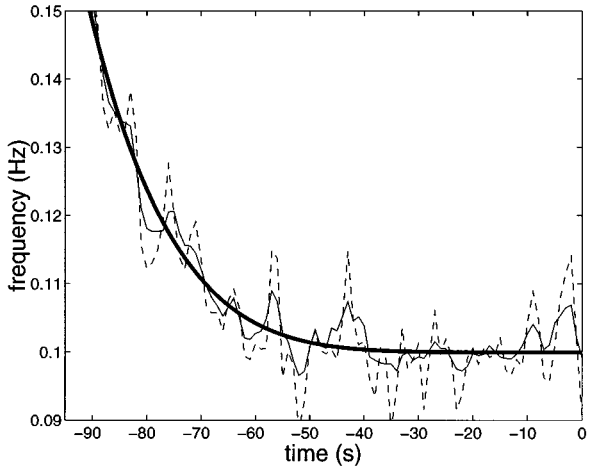

FIG. 18. An enlarged portion of the true instantaneous frequency (heavy solid line) is compared to the instantaneous frequency estimates based on the peak of the fourth-order polynomial Wigner–Ville distribution (dashed line) of Fig. 16 and Wigner–Ville distribution (finer solid line) of Fig. 17 in the regions marked by the dashed rectangular boxes. The mean-square error of both estimates is dominated by the estimator variance. The mean-square error of the fourth-order polynomial Wigner–Ville based estimate is approximately three times that of the Wigner–Ville based estimate.

$$\arg K_q[s(t)]=2\pi\sum_{k=-q/2}^{q/2} b_k\phi(t+c_k\tau). \tag{17}$$

By Taylor series expansion about an arbitrary point t, an exact expression for the kernel phase of $s(t)$ is:

$$\begin{aligned}
&\arg K_q[s(t)]\\
&=2\pi\Bigg[\frac{d\phi(t)}{dt}\,\tau+\frac{\tau^{(q+1)}}{(q+1)!}\,\frac{d^{(q+1)}\phi(t)}{dt^{(q+1)}}\sum_{k=-q/2}^{q/2} b_k c_k^{(q+1)}\\
&\quad+\frac{\tau^{(q+3)}}{(q+3)!}\,\frac{d^{(q+3)}\phi(t)}{dt^{(q+3)}}\\
&\quad\times\sum_{k=-q/2}^{q/2} b_k c_k^{(q+3)}+\cdots+\frac{\tau^p}{p!}\,\frac{d^p\phi(t)}{dt^p}\sum_{k=-q/2}^{q/2} b_k c_k^p\Bigg]\\
&=2\pi\Bigg[\frac{d\phi(t)}{dt}\,\tau+\sum_{l=q/2}^{(p-1)/2}\frac{\tau^{(2l+1)}}{(2l+1)!}\,\frac{d^{(2l+1)}\phi(t)}{dt^{(2l+1)}}\\
&\quad\times\sum_{k=-q/2}^{q/2} b_k c_k^{(2l+1)}\Bigg]\\
&=2\pi\Bigg[\frac{d\phi(t)}{dt}\,\tau+\xi(t,\tau)\Bigg],
\end{aligned} \tag{18}$$

where

$$\xi(t,\tau)=\sum_{l=q/2}^{(p-1)/2}\frac{\tau^{(2l+1)}}{(2l+1)!}\,\frac{d^{(2l+1)}\phi(t)}{dt^{(2l+1)}}\sum_{k=-q/2}^{q/2} b_k c_k^{(2l+1)}. \tag{19}$$

In the above expansion we have made use of the fact that the c_k and b_k coefficients of the qth-order polynomial Wigner–Ville kernel are chosen such that the coefficients of $[d^n\phi(t)/dt^n]\tau^n$ are zero for $1<n<q$ and unity for $n=1$.[15]

Using the above kernel expansion, the qth-order polynomial Wigner–Ville distribution (6) can be expressed as

$$W_q(t,f) = \int_{-\infty}^{\infty} h(\tau)\exp\left\{ j2\pi\left[\left(\frac{d\phi(t)}{dt} - f\right)\tau + \xi(t,\tau)\right]\right\} d\tau$$
$$= \int_{-T/2}^{T/2} \exp\left\{ j2\pi\left[\left(\frac{d\phi(t)}{dt} - f\right)\tau + \xi(t,\tau)\right]\right\} d\tau \tag{20}$$

with a rectangular window $h(\tau)$ of length T.

The instantaneous frequency estimate $\hat{f}_i(t)$ is then determined by the peak of (20) so that

$$\hat{f}_i(t) \triangleq \underset{f}{\text{argmax}}\{|W_q(t,f)|\}, \tag{21}$$

where f is an element of the set of real numbers. By the stationary phase principal,[18] the abscissa(s) of the frequency peak(s) of the polynomial Wigner–Ville distribution are approximately given by the values of f, at each instant of time, for which the phase of the integrand of (20) is stationary, or equivalently, where the first derivative of the kernel phase, with respect to τ, is zero.

$$\frac{\partial}{\partial\tau}\left[\left(\frac{d\phi(t)}{dt} - \hat{f}_i(t)\right)\tau + \xi(t,\tau)\right] \equiv 0. \tag{22}$$

Thus for the polynomial Wigner–Ville peak-based instantaneous frequency estimator,

$$\hat{f}_i(t) = \frac{d\phi(t)}{dt} = \frac{\partial\xi(t,\tau)}{\partial\tau}. \tag{23}$$

From (5), $d\phi(t)/dt$ is defined as the true instantaneous frequency $f_i(t)$ of the signal $s(t)$ and so the systematic bias $\epsilon(t)$ can be explicitly written as

$$\epsilon(t) = \hat{f}_i(t) - f_i(t)$$
$$= \frac{\partial\xi(t,\tau)}{\partial\tau}$$
$$= \sum_{l=q/2}^{(p=1)/2} \frac{\tau^{2l}}{(2l)!}\frac{d^{(2l+1)}\phi(t)}{dt^{(2l+1)}}\sum_{k=-q/2}^{q/2} b_k c_k^{(2l+1)} \tag{24}$$

with the maximum value of $\tau = T/2$. Equivalently, for the discrete time polynomial Wigner–Ville distribution with rectangular window of length L and sampling frequency f_s, the maximum value of $\tau = L/(2f_s)$. From (24) it can be seen that the higher-order derivatives of the signal phase in (18) (i.e., $d^n\phi/dt^n$, $n > q$) will generally introduce an error in the instantaneous frequency estimator. These higher-order components are due solely to the phase order mismatch between the signal and the polynomial Wigner–Ville kernel. In practice, due to the factorial denominator in (24) and the often decreasing value of higher-order phase derivatives, $\epsilon(t)$ may be dominated by the first term in the summation in l. In this case, and by making the substitution $\tau = L/(2f_s)$, the maximum systematic bias is approximately

$$\epsilon(t) \approx \frac{L^q}{(2f_s)^q q!}\frac{d^{(q+1)}\phi(t)}{dt^{(q+1)}}\sum_{k=-q/2}^{q/2} b_k c_k^{(q+1)}. \tag{25}$$

This result confirms our previous observation that the systematic bias can be controlled via the length of the window function $h(\tau)$ by effectively restricting the possible excursion on τ in (18). As we may expect, in considering only the systematic bias of the unmatched polynomial Wigner–Ville distribution, the window length should be chosen as small as possible so as to reduce the effect of the error term $\epsilon(t)$. Equation (24) [or (25), as appropriate] provides the first step in deriving an expression for the mean-square error of the polynomial Wigner–Ville-based instantaneous frequency estimator. We next require an expression for the estimator variance.

D. Polynomial Wigner–Ville-based instantaneous frequency estimator variance

The polynomial Wigner–Ville distribution, as defined by (6) is the Fourier transform of the kernel function $K(t,\tau)$. As previously discussed, this kernel function attempts to resolve a nonstationary signal, at each time instant, into a sinusoid having frequency given by the instantaneous frequency. Thus, in considering the usual discrete time implementation, the analysis of variance of $\hat{f}_i(t)$ reduces to that associated with estimating the frequency of a discrete noisy sinusoid from the peak of the magnitude of the discrete Fourier transform (DFT). The point to note here is that, due to the multilinear nature of $K(t,\tau)$, the signal-to-noise ratio (denoted $\mathscr{S}_K$) of the noisy kernel sinusoid will be less than the signal-to-noise ratio of the original signal under analysis. In this section we derive an expression for $\mathscr{S}_K$ leading to an expression for the variance of $\hat{f}_i(t)$.

For the case of the peak of the magnitude of the discrete Fourier transform of a discrete noisy sinusoid of length N with constant scale A, unknown initial phase, and for sufficiently high signal-to-noise ratio (specifically, above a threshold value to be described in Sec. III D 1) and for all but very small values of N, the frequency estimator variance $\text{var}_{\text{DFT}}(\hat{f})$ closely approximates the Cramér–Rao lower bound.[17,19]

$$\text{var}_{\text{DFT}}(\hat{f}) = \frac{12 f_s^2}{(2\pi)^2 \mathscr{S}(N^2-1)N}, \tag{26}$$

where

$$\mathscr{S} = A^2/\sigma^2 \tag{27}$$

and σ^2 is the variance of the real noise. Based on this result, to determine the variance of the polynomial Wigner–Ville peak-based instantaneous frequency estimator, it only remains to determine the signal-to-noise ratio of the polynomial Wigner–Ville kernel. Consider the complex signal

$$z(t) = s(t) + n(t), \tag{28}$$

where $s(t)$ has been previously defined in (16) and $n(t)$ is a zero-mean, complex independent white Gaussian stationary noise process with variance $\text{var}[n(t)] = \text{var}[n_{\mathscr{R}}(t)] + \text{var}[n_{\mathscr{I}}(t)] = \sigma^2 + \sigma^2 = 2\sigma^2$, where $n_{\mathscr{R}}(t)$ and $n_{\mathscr{I}}(t)$ are the real and imaginary noise components, respectively.

To formulate an expression for the kernel signal-to-noise ratio we begin by considering the expansion of the qth-order polynomial Wigner–Ville kernel (7) for the signal $z(t)$.

$$
\begin{aligned}
&K_q(t,\tau)\\
&\quad=\prod_{k=1}^{q/2}\,[s(t+c_k\tau)+n(t+c_k\tau)]^{b_k}\\
&\qquad\times[s^*(t+c_{-k}\tau)+n^*(t+c_{-k}\tau)]^{b_k}\\
&\quad=\prod_{k=1}^{q/2}\left\{\left[\sum_{j=0}^{b_k}\binom{b_k}{j}n^j(t+c_k\tau)s^{b_k-j}(t+c_k\tau)\right]\right.\\
&\qquad\left.\times\left[\sum_{m=0}^{b_k}\binom{b_k}{m}n^{*m}(t+c_{-k}\tau)s^{*(b_k-m)}(t+c_{-k}\tau)\right]\right\}\\
&\quad=\prod_{k=1}^{q/2}\{[s^{b_k}(t+c_k\tau)+b_ks^{b_k-1}(t+c_k\tau)n(t+c_k\tau)+\cdots]\\
&\qquad\times[s^{*b_k}(t+c_{-k}\tau)+b_ks^{*(b_k-1)}(t+c_{-k}\tau)\\
&\qquad\times n^*(t+c_{-k}\tau)+\cdots]\},
\end{aligned}
\tag{29}
$$

and finally

$$
\begin{aligned}
K_q(t,\tau)=&\prod_{k=1}^{q/2}\,s^{b_k}(t+c_k\tau)s^{*b_k}(t+c_{-k}\tau)\\
&+\left[\prod_{k=1}^{q/2}\,s^{b_k}(t+c_k\tau)s^{*b_k}(t+c_{-k}\tau)\right]\\
&\times\left\{\sum_{j=1}^{q/2}\,b_j[s^{-1}(t+c_j\tau)n(t+c_j\tau)\right.\\
&\left.+s^{*-1}(t+c_{-j}\tau)n^*(t+c_{-j}\tau)]+\cdots\right\}\\
&+\prod_{k=1}^{q/2}\,n^{b_k}(t+c_k\tau)n^{*b_k}(t+c_{-k}\tau),
\end{aligned}
\tag{30}
$$

where the asterisk denotes complex conjugation. This results generalizes the result in Ref. 20.

This expansion reveals three types of terms: a signal self-term [first line of (30)], a noise self-term [last line of (30)], and signal–noise cross terms [the remaining terms in (30)]. First, the term containing only signal terms is simply the expression for the qth-order PWVD kernel of the noiseless signal $s(t)$. The amplitude of this term is A^{b_Σ}, where

$$
b_\Sigma=\sum_{k=-q/2}^{q/2}|b_k|=2\sum_{k=1}^{q/2}|b_k| \tag{31}
$$

and consequently has power

$$
P_S=A^{2b_\Sigma}. \tag{32}
$$

Second, the term containing only noise terms has power

$$
P_{\mathrm{N}}=\begin{cases}\Pi_{k=0}^{q/2}\mathbb{U}_{2b_k} & \text{if } \tau\neq 0,\\ \mathbb{U}_{2b_\Sigma} & \text{if } \tau=0,\end{cases} \tag{33}
$$

where $\mathbb{U}_p$ is the pth moment of $|n(t)|$

$$
\begin{aligned}
\mathbb{U}_p&=E(|n(t)|^p)\\
&=E[(n_{\mathscr{R}}(t)^2+n_{\mathscr{I}}(t)^2)^{p/2}]\\
&=\sum_{i=0}^{p/2}\binom{p/2}{i}E(n_{\mathscr{R}}(t)^{(p-2i)})E(n_{\mathscr{I}}(t)^{(2i)})\\
&=\sum_{i=0}^{p/2}\binom{p/2}{i}\mu_{(p-2i)}\mu_{2i},
\end{aligned}
\tag{34}
$$

where $\mu_n=1\cdot3\cdot5\cdot\cdots\cdot(n-1)\sigma^n$ and $E(\cdot)$ is the expectation operator.

Third, at high signal-to-noise ratio, the signal–noise cross terms are dominated by the terms in the expansion which are a product of a single-noise term and $(b_\Sigma-1)$ signal terms. Consequently the cross terms indicated as $+\cdots$ in (30) will be neglected.

For each $j=1\cdots q/2$, the power of the cross terms is

$$
(b_jA^{b_\Sigma-1})^2 2\sigma^2=2b_j^2A^{2(b_\Sigma-1)}\sigma^2 \tag{35}
$$

and the total cross term power can be approximated as

$$
P_{\mathrm{SN}}\approx 2\sum\,b^2A^{2(b_\Sigma-1)}\sigma^2, \tag{36}
$$

where

$$
\sum\,b^2=\sum_{k=-q/2}^{q/2}b_k^2. \tag{37}
$$

Comparing P_{N} and P_{SN} at high signal-to-noise ratio, it can be seen that the total noise power $(P_{\mathrm{N}}+P_{\mathrm{SN}})$ will be dominated by the P_{SN} term. We can therefore conclude that the signal-to-noise ratio of the polynomial Wigner–Ville kernel will be lower than the signal-to-noise ratio of $z(t)$ due to the signal–noise cross terms generated by the multilinear kernel. The kernel signal-to-noise ratio is approximately:

$$
\mathscr{S}_K\approx\frac{P_{\mathrm{S}}}{P_{\mathrm{SN}}}=\frac{A^2}{2\Sigma b^2\sigma^2}=\frac{\mathscr{S}}{2\Sigma b^2}. \tag{38}
$$

In addition, the effective length of the signal is reduced by the conjugate symmetry of the kernel such that $N=L/2$.[21] Thus from (26), the polynomial Wigner–Ville-based instantaneous frequency estimator variance is approximately given by

$$
\mathrm{var}_{\mathrm{PWVD}}(\hat{f}\,)\approx\frac{12\Sigma b^2\sigma^2f_s^2}{(2\pi)^2A^2[(L^2/4)-1]L/2}. \tag{39}
$$

This result confirms that the longer the window length L at a given signal-to-noise ratio, the lower the variance of the instantaneous frequency estimator. As we may expect, in considering variance stability alone, the window length should be as long as possible. Equation (39) provides the variance

term in the expression for the mean-square error of the polynomial Wigner–Ville-based instantaneous frequency estimator. In deriving expressions for both the bias (24) and variance (39) we have assumed high signal-to-noise ratio. We show in the next section that the polynomial Wigner–Ville-based instantaneous frequency estimator is subject to a signal-to-noise ratio threshold beyond which the estimator variance increases dramatically. In practice therefore, the polynomial Wigner–Ville distribution (including the Wigner–Ville distribution) is used at signal-to-noise ratio levels above the threshold and thus the high signal-to-noise ratio assumption is reasonable.

1. Polynomial Wigner–Ville-based instantaneous frequency estimator variance threshold

The derivation of the variance of the polynomial Wigner–Ville-based instantaneous frequency estimator (39) was based on the result for the variance of the frequency estimator based on the peak of the magnitude of the discrete Fourier transform under the assumption of high signal-to-noise ratio. For fixed data length N and decreasing signal-to-noise ratio, or for fixed signal-to-noise ratio and decreasing data length, the variance is known to reach a threshold $\mathscr{S}_{\mathrm{THRES}}$ beyond which the variance increases dramatically.[19] This result can be directly applied to the polynomial Wigner–Ville distribution which is the discrete Fourier transform of the kernel $K(t,\tau)$ in the variable τ. Quinn and Kootsookos[19] showed that the signal-to-noise ratio at which this threshold occurs can be approximated (quite accurately) as

$$\psi_D = 10\log_{10}\{[6\log(N)+2\log(\log(N))+4\log(\pi) - 2\log(6)]/(N-1)\}\ \text{dB}. \tag{40}$$

From (38), $\mathscr{S}\approx\mathscr{S}_K 2\Sigma b^2$ and rearranging in terms of the original signal-to-noise ratio $\mathscr{S}=A^2/\sigma^2$, and making the substitution $N=L/2$ yields

$$\mathscr{S}_{\mathrm{THRES}} = 10\log_{10}\left\{\frac{2\Sigma b^2}{(L/2-1)}\,[6\log(L/2) + 2\log(\log(L/2))+4\log(\pi) - 2\log(6)]\right\}\ \text{dB}, \tag{41}$$

which provides a lower signal-to-noise ratio bound for the approximation in (39). From (41) it can be seen that the $\mathscr{S}_{\mathrm{THRES}}$ for the Wigner–Ville distribution ($\Sigma b^2=2$) will be approximately 7 dB lower than for the fourth-order polynomial Wigner–Ville distribution ($\Sigma b^2=10$). For this reason the use of the polynomial Wigner–Ville distribution is restricted to applications having sufficiently high signal-to-noise ratio.

E. Polynomial Wigner–Ville optimal window length

Using the expression for the bias (24) and variance (39), the mean-square error $\lambda(L)$ of the qth-order polynomial Wigner–Ville-based instantaneous frequency estimator at a given signal-to-noise ratio (above the threshold) can be expressed as

$$\lambda(L) = \frac{12\Sigma b^2 f_s^2}{(2\pi)^2\mathscr{S}[(L^2/4)-1]L/2} + \left[\sum_{l=q/2}^{(p-1)/2} \frac{L^{2l}}{(2f_s)^{2l}(2l)!}\frac{d^{(2l+1)}\phi(t)}{dt^{(2l+1)}} \times \sum_{k=-q/2}^{q/2} b_k c_k^{(2l+1)}\right]^2 \tag{42}$$

and by using the simplified bias expression of (25), $\lambda(L)$ can, where appropriate, be approximated as

$$\lambda(L) \approx \frac{12\Sigma b^2 f_s^2}{(2\pi)^2\mathscr{S}[(L^2/4)-1]L/2} + L^{2q}\left[\frac{1}{(2f_s)^q q!}\frac{d^{(q+1)}\phi(t)}{dt^{(q+1)}}\sum_{k=-q/2}^{q/2} b_k c_k^{(q+1)}\right]^2. \tag{43}$$

A minimum mean-square error, assuming one exists, can be found by setting

$$\frac{\partial\lambda(L)}{\partial L}=0, \tag{44}$$

which yields

$$a\,\frac{(3L^2-4)}{(L^3-4L)^2} = L^{(2q-1)}b, \tag{45}$$

where

$$a = \frac{96\Sigma b^2 f_s^2}{(2\pi)^2\mathscr{S}}, \tag{46}$$

$$b = 2^{2q}\left(\frac{1}{(2f_s)^q q!}\frac{d^{(q+1)}\phi(t)}{dt^{(q+1)}}\sum_{k=-q/2}^{q/2} b_k c_k^{(q+1)}\right)^2. \tag{47}$$

Rearranging yields

$$L^{2q-1}(L^6-4L^4+16L^2) = (3L^2-4)a/b \tag{48}$$

for which an approximate solution, for $L\gg 1$, is given by

$$L\approx\left(\frac{3a}{b}\right)^{1/(2q+3)}. \tag{49}$$

Thus in (49) we have achieved the objective of this section to derive an expression for the window length L which minimizes the mean-square error of the qth-order polynomial Wigner–Ville-based instantaneous frequency estimator. In deriving this result, a number of simplifying assumptions have been made and it is not readily apparent what combined effect this has on the result. In the next section we establish the practical usefulness of (49) by applying the optimal window theory to simulated data.[3]

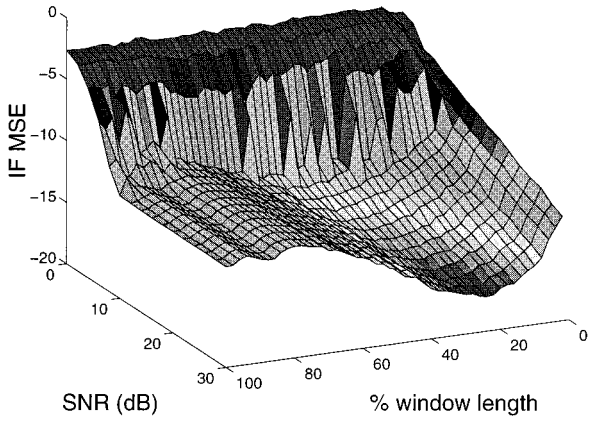

FIG. 19. Instantaneous frequency estimator mean-square error for a fifth-order polynomial phase signal for varying signal-to-noise ratio and window length. The instantaneous frequency was estimated from the peak of the fourth-order polynomial Wigner–Ville distribution calculated at the central time instant ($t=0$).

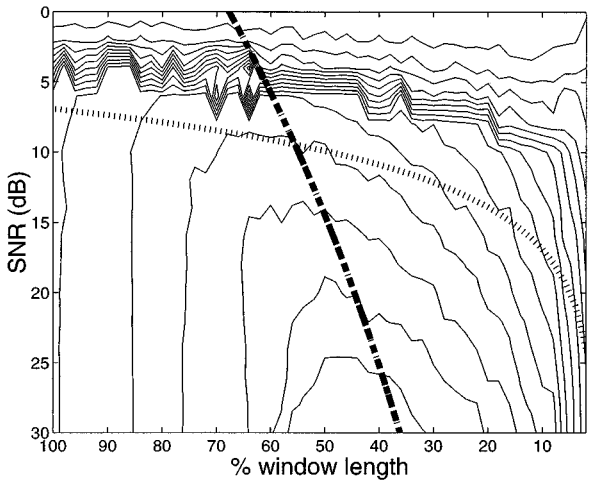

FIG. 20. A contour plot of the mean-square error surface of Fig. 19. The heavy dashed line represents the theoretical line of minimum mean-square error calculated using Eq. (49). The finer broken line represents the theoretical variance threshold calculated using Eq. (41).

IV. EXAMPLES

A. Instantaneous frequency estimator minimum mean-square error

In the previous section we derived an expression for the polynomial Wigner–Ville window length which yielded the instantaneous frequency estimator minimum mean-square error. This result is now verified by computer simulation.

In these examples we estimate the instantaneous frequency of a fifth-order polynomial phase test signal using the fourth-order polynomial Wigner–Ville distribution. The polynomial order of the test signal is intentionally chosen to be higher than that of the time–frequency representation so that the optimal window theory can be applied. The test signal $z(t)$ is of the form (28).

1. Example 1

In the first simulation the phase of $z(t)$ is chosen to be

$$\phi(t)=0.25t+\frac{0.25t^5}{5(64^4)},$$

$$t=-N/2+1,\ldots,N/2-1, \quad N=128. \tag{50}$$

Using the fourth-order polynomial Wigner–Ville distribution, the instantaneous frequency was estimated for signal-to-noise ratio values of 0,2,4,...,30 dB and window length $L=2,4,6,\ldots,100$ as a percentage of the total data length. The estimator mean-square error was then computed from 200 realizations. So that the full range of window lengths could be used, it was necessary to calculate the mean-square error at the central time instant (i.e., $t=0$) as this is the only point where a full length window could be applied. The mean-square error surface for this experiment is shown in Fig. 19 where a *valley* of minimum mean-square error can be clearly seen. Figure 20 shows a contour plot of the same mean-square error surface. The heavy dashed line represents the theoretical line of minimum mean-square error calculated from (49) and is closely aligned with the empirical result. The variance threshold effect, as discussed in Sec. III D 1, is also apparent in Fig. 20 where the finer broken line represents the theoretical variance threshold as predicted by (41).

2. Example 2

In this second simulation, the phase of $z(t)$ (50) is modified so as to reduce the coefficient of the fifth derivative of phase.

$$\phi(t)=\frac{0.5t^5}{5(128^4)}, \quad t=0,1,2,\ldots,N-1, \quad N=128. \tag{51}$$

The mean-square error surface for this experiment, calculated at the central time instant $t=64$, is shown in Fig. 21. It can be seen that, due to the lower value of the fifth derivative, the minimum mean-square error occurs for larger window lengths than for example 1. The theoretical minimum mean-square error, calculated from (49), is shown in the contour plot of Fig. 22 and again it is closely aligned with the

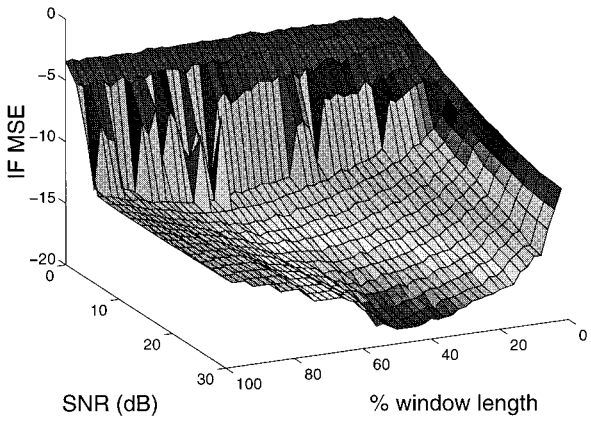

FIG. 21. Instantaneous frequency estimator mean-square error for a fifth-order polynomial phase signal for varying signal-to-noise ratio and window length. For the test signal used in this example, the fifth derivative of phase is less than for the test signal used in Fig. 19. The instantaneous frequency was estimated from the peak of the fourth-order polynomial Wigner–Ville distribution calculated at the central time instant ($t=64$).

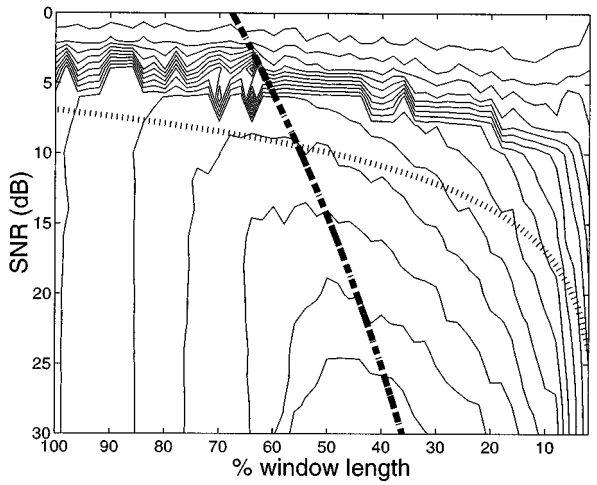

FIG. 22. A contour plot of the mean-square error surface of Fig. 21. The heavy dashed line represents the theoretical line of minimum mean-square error calculated using Eq. (49). The finer broken line represents the theoretical variance threshold calculated using (41).

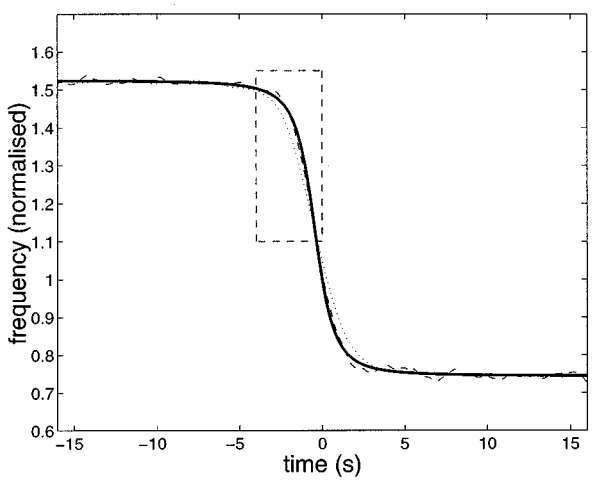

FIG. 23. A comparison of the Wigner–Ville (dotted line) and polynomial Wigner–Ville (dashed line) based instantaneous frequency estimates of a simulated passive acoustic signal at 20-dB signal-to-noise ratio. The true instantaneous frequency (solid line) represents an aircraft with the following parameters: $h=152.4$ m (500 ft), $v=30.8$ m/s (60 kn), $r=1.837$ km and normalized source frequency.

empirical result. The finer broken line represents the theoretical variance threshold as predicted by (41) and, as this threshold is not signal dependent, is unchanged from the previous example.

B. Passive acoustic parameter estimation

We now return to our original focus of passive acoustic parameter estimation. In the first experiment we use a real passive acoustic recording to demonstrate the importance of using the correct window length in estimating the aircraft flight parameters. In experiments 2–4 passive acoustic signals are synthesized using the observer frequency model (2) with chosen parameters and with additive stationary, white Gaussian noise. The sample mean and variance for the Wigner–Ville- and fourth-order polynomial Wigner–Ville-based estimators are then computed over multiple realizations so as to evaluate the relative performance of these two estimation schemes. These examples demonstrate that, by using the optimal window, the fourth-order polynomial Wigner–Ville distribution will yield flight parameter estimates having lower mean-square error than for the Wigner–Ville distribution (second-order polynomial Wigner–Ville distribution) in the high signal-to-noise ratio case.

1. Experiment 1

In Sec. II C a recording of an overflying aircraft was analyzed separately using the Wigner–Ville distribution and fourth-order polynomial Wigner–Ville distribution to estimate the aircraft's physical parameters. The time–frequency representations, and the resulting aircraft parameter estimates of Table I, were calculated using a 30% window. To demonstrate the influence of the window length, the aircraft parameters are recalculated in Table II using a larger window (50%) and shorter window (15%) and are compared to those estimated in Table I (30% window).

In this example the estimates were based on a single recording and so it is not possible to draw any conclusions as to the relative merit of each of the estimators. However, it does serve to demonstrate the importance of choosing the correct window length when applying the polynomial Wigner–Ville distribution (thus including the Wigner–Ville distribution) to the passive acoustic problem. More quantitative results are provided using synthesized passive acoustic data in the following examples.

2. Experiment 2

In this example we use a synthesized signal (144 data points, sampling frequency $f_s=4$ Hz) representative of an overflying aircraft at 20-dB signal-to-noise ratio with the following parameters: $h=152.4$ m (500 ft), $v_a=30.8$ m/s (60 kn), $r=1.837$ km, and normalized source frequency. The observer frequency model for this signal, which is shown in Fig. 23 (solid line), exhibits a sharp transition between the maximum and minimum Doppler shifted frequencies. The

TABLE II. Comparison of aircraft flight parameter estimates from real passive acoustic data using the Wigner–Ville and fourth-order polynomial Wigner–Ville distribution where a 50% (bold face), 15% (italicized), and 30% (bracketed) window length has been used.

	Height (m)	Velocity (m/s)	Range (km)	Source freq. (Hz)
WVD	**897** *334* (404)	**87.8** *71.0* (73.3)	**1.70** *1.25* (1.30)	**66.2** *68.6* (68.4)
PWVD	**383** *301* (309)	**71.0** *67.6* (68.7)	**1.26** *1.17* (1.21)	**68.5** *69.0* (68.9)

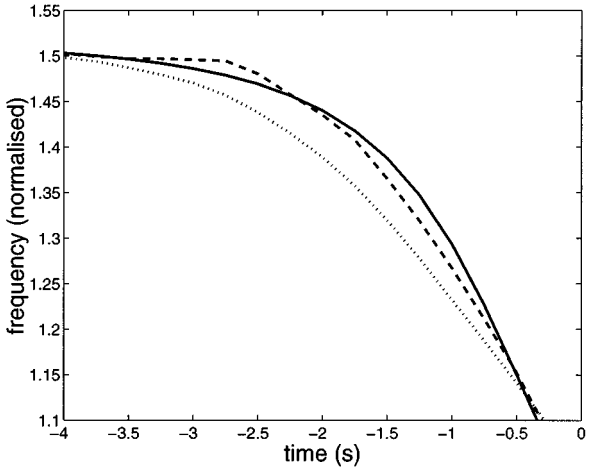

FIG. 24. An enlarged portion of Fig. 23 (in the region marked by the dashed rectangular box) which shows, for a typical realization, the departure of the Wigner–Ville-based (dotted line) and polynomial Wigner–Ville-based (dashed line) instantaneous frequency estimates from the true instantaneous frequency (solid line).

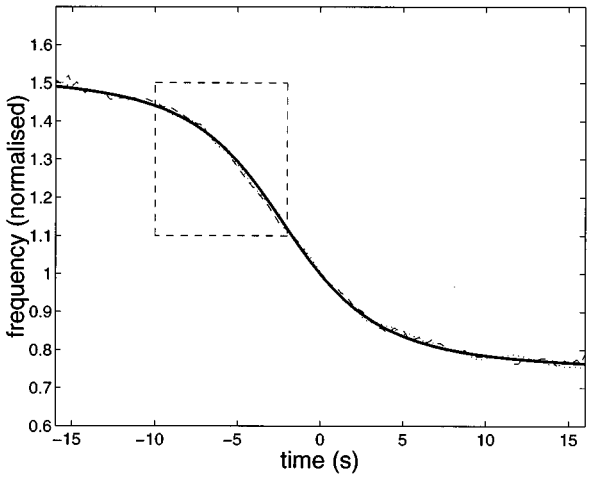

FIG. 25. A comparison of Wigner–Ville-based (dotted line) and polynomial Wigner–Ville-based (dashed line) instantaneous frequency estimates of a simulated passive acoustic signal at 12-dB signal-to-noise ratio. The true instantaneous frequency (solid line) represents an aircraft with the following parameters: $h=762.0$ m (2500 ft), $v=30.8$ m/s (60 kn), $r=1.837$ km and normalized source frequency.

coefficients of $d^3\phi(t)/dt^3$ and $d^5\phi(t)/dt^5$ for this instantaneous frequency law were estimated to be -0.07 and -9.3×10^{-4} and the optimal window length for the Wigner–Ville distribution and fourth-order polynomial Wigner–Ville distribution were computed using (49) to be 10% and 25%, respectively. From (43) the instantaneous frequency estimator mean-square error is predicted to be smaller for the fourth-order polynomial Wigner–Ville than for the Wigner–Ville distribution.

The Wigner–Ville and fourth-order polynomial Wigner–Ville-based instantaneous frequency estimates for this signal are also shown in Fig. 23 (dotted line for Wigner–Ville and dashed line for polynomial Wigner–Ville) and more clearly in Fig. 24 for the region marked by the dashed rectangular box in Fig. 23. The sample mean, variance, and mean-square error of the aircraft flight parameter estimates, based on 50 realizations of this signal, are given in Table III.

Considering the estimator mean-square error in Table III, these results demonstrate the superior performance of the fourth-order polynomial Wigner–Ville-based flight parameter estimation method for the particular case where there is a rapid transition in the instantaneous frequency (corresponding to a high velocity and/or low altitude aircraft) and where the signal-to-noise ratio is above the threshold (41).

3. Experiment 3

In this example, the signal is the same as in example 2 except that the signal-to-noise ratio is reduced to 12 dB and the height parameter is increased to 762.0 m (2500 ft). This increase in height is reflected in a more gradually varying observer frequency model as shown in Fig. 25 (solid line). The coefficients of $d^3\phi(t)/dt^3$ and $d^5\phi(t)dt^5$ for this instantaneous frequency law were estimated to be -0.01 and -1.9×10^{-4} and the optimal window length for the Wigner–Ville and fourth-order polynomial Wigner–Ville distribution were computed using (49) to be 19% and 39%, respectively. From (43) the instantaneous frequency estimator mean-square error is predicted to be larger for the fourth-order polynomial Wigner–Ville than for the Wigner–Ville distribution.

Typical instantaneous frequency estimates for this signal are also shown in Fig. 25 (dotted line for the Wigner–Ville and dashed line for polynomial Wigner–Ville distribution).

TABLE III. Comparison of the actual aircraft flight parameter values with the sample mean and variance of the Wigner–Ville- and fourth-order polynomial Wigner–Ville-based flight parameter estimators. The deterministic instantaneous frequency law for this simulated signal is shown in Fig. 23. These statistics were computed from 50 realizations using simulated passive acoustic data at 20-dB signal-to-noise ratio.

	Height (m)		Velocity (m/s)		Range (km)		Source freq. (norm)	
	mean	variance	mean	variance	mean	variance	mean	variance
Actual	152.4		30.8		1.837		1	
WVD	227.3	7.08	31.3	0.001	1.889	9.31×10^{-6}	0.996	1.718×10^{-7}
$PWVD_4$	154.3	20.26	31.1	0.003	1.854	3.14×10^{-5}	0.998	7.442×10^{-7}
	Estimated MSE		Estimated MSE		Estimated MSE		Estimated MSE	
WVD	5617		0.250		27.13×10^{-4}		16.17×10^{-6}	
$PWVD_4$	23.87		0.092		3.20×10^{-4}		4.74×10^{-6}	

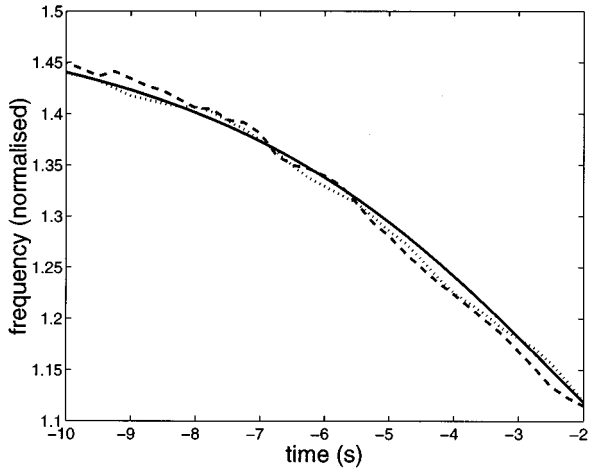

FIG. 26. An enlarged portion of Fig. 25 (in the region marked by the dashed rectangular box) which shows, for a typical realization, the departure of the Wigner–Ville-based (dotted line) and polynomial Wigner–Ville-based (dashed line) instantaneous frequency estimates from the true instantaneous frequency (solid line).

The region of Fig. 25 indicated by the dashed rectangular box is shown more clearly in the enlarged view of Fig. 26. The aircraft flight parameter estimator sample mean, variance, and mean-square error, base on 50 realizations of this signal, are given in Table IV.

It is clear from Table IV that the Wigner–Ville distribution has performed better than the fourth-order polynomial Wigner–Ville distribution. This result is predicted by (43) and demonstrates that, while the bias of the polynomial Wigner–Ville-based estimator is always less than that of the Wigner–Ville distribution, the greater variance of the polynomial Wigner–Ville distribution, at reduced signal-to-noise ratio, may result in higher estimator mean-square error.

4. Experiment 4

In our final example, the aircraft flight parameters are unchanged from example 3 and the signal-to-noise ratio is increased to 20 dB. The optimal window length for the Wigner–Ville and fourth-order polynomial Wigner–Ville distribution were computed using (49) to be 13% and 22%, respectively. The flight parameter estimator sample mean, variance, and mean-square error, based on 50 realizations of this signal, are given in Table V. In this example, where the signal-to-noise ratio is high, the polynomial Wigner–Ville-based estimator has performed better than the Wigner–Ville distribution. As predicted by (43), the improvement is not as great as in the first example (Table III) where the coefficient of $d^3\phi(t)/dt^3$ was higher.

5. Discussion of results

The previous four experiments demonstrated the following points. Experiment 1 showed that the flight parameter estimates are very much dependent on the chosen window length. The optimal window theory allows us to find the best (in the minimum mean-square error sense) estimators. Experiment 2 demonstrated that the flight parameter estimator based on the fourth-order polynomial Wigner–Ville distribution is better (again in the minimum mean-square error sense) than that based on the Wigner–Ville distribution when the signal-to-noise ratio is above the threshold. The more rapid the transition in the instantaneous frequency [in particular, the higher the coefficient of $d^3\phi(t)/dt^3$] the better the performance of the polynomial Wigner–Ville relative to the Wigner–Ville distribution [see Eq. (42)]. In experiment 3, the relative performance of the polynomial Wigner–Ville distribution is reduced by two factors; first, the instantaneous frequency is slowly varying, and second the signal-to-noise ratio has been reduced. The result is that, under these conditions, the Wigner–Ville distribution has performed better than the polynomial Wigner–Ville distribution. However, example 4 shows that even for a slowly varying instantaneous frequency, the fourth-order polynomial Wigner–Ville distribution performs better than the Wigner–Ville distribution at high signal-to-noise ratio.

In this paper, we have considered a frequency model which assumes straight, level, and constant velocity flight throughout the observation period. Other more complex models may be proposed. For example, it has been suggested[22] that the observer frequency model for an aircraft in a distant (not directly overhead) circular flight path would be of an oscillatory form and therefore highly nonlinear. Because such a flight parameter estimation scheme would necessitate the estimation of higher-order instantaneous frequency laws, the use of the polynomial Wigner–Ville may be particularly appropriate.

TABLE IV. Comparison of the actual aircraft flight parameter values with the sample mean and variance of the Wigner–Ville- and fourth-order polynomial Wigner–Ville-based flight parameter estimators. The deterministic instantaneous frequency law for this simulated signal is shown in Fig. 25. These statistics were computed from 50 realizations using simulated passive acoustic data at 12-dB signal-to-noise ratio.

	Height (m)		Velocity (m/s)		Range (km)		Source freq. (norm)	
	mean	variance	mean	variance	mean	variance	mean	variance
Actual	762.0		30.8		1.837		1	
WVD	790.3	1040	31.0	0.098	1.854	7.46×10^{-4}	0.999	6.27×10^{-6}
$PWVD_4$	792.5	3140	31.1	0.312	1.867	3.35×10^{-3}	0.997	3.04×10^{-5}
	Estimated MSE		Estimated MSE		Estimated MSE		Estimated MSE	
WVD	1841		0.14		1.03×10^{-3}		7.3×10^{-6}	
$PWVD_4$	4070		0.40		4.25×10^{-3}		39.4×10^{-6}	

TABLE V. Comparison of the actual aircraft flight parameter values with the sample mean and variance of the Wigner–Ville- and fourth-order polynomial Wigner–Ville-based flight parameter estimators. The deterministic instantaneous frequency law for this simulated signal is shown in Fig. 25. These statistics were computed from 50 realizations using simulated passive acoustic data at 20-dB signal-to-noise ratio.

	Height (m)		Velocity (m/s)		Range (km)		Source freq. (norm)	
	mean	variance	mean	variance	mean	variance	mean	variance
Actual	762.0		30.8		1.837		1	
WVD	774.8	125.4	30.9	0.026	1.845	1.05×10^{-4}	0.9995	9.39×10^{-7}
$PWVD_4$	765.6	129.1	30.9	0.026	1.841	1.09×10^{-4}	0.9997	1.04×10^{-6}
	Estimated MSE		Estimated MSE		Estimated MSE		Estimated MSE	
WVD	289.2		0.036		3.94×10^{-4}		1.19×10^{-6}	
$PWVD_4$	142.0		0.036		1.25×10^{-4}		1.13×10^{-6}	

V. CONCLUSION

The sound from an overflying aircraft, as heard by a stationary observer, can be used to estimate the aircraft's flight parameters. This passive acoustic approach is demonstrated using an observer frequency model to describe the time varying acoustic Doppler shift. Central to the success of this frequency-based passive acoustic flight parameter estimation scheme is the need for an accurate estimate of the time varying instantaneous frequency. We have considered the Wigner–Ville distribution (second-order polynomial Wigner–Ville distribution) and the generalized qth-order polynomial Wigner–Ville distribution in this application. We have shown that instantaneous frequency estimators based on the peak of the windowed polynomial Wigner–Ville distribution are subject to two error factors which behave in a counterdependent manner over the time domain window length. The first, which is due to the systematic bias, is a result of a mismatch between the polynomial order of the polynomial Wigner–Ville distribution and the phase of the signal under analysis. The second error is due to the variance of the estimator.

An expression is derived for the window length which minimizes the estimator mean-square error, as a function of signal-to-noise ratio and the coefficients of the higher-order derivatives of the signal phase. This general theoretical result is then applied to the passive acoustic aircraft flight parameter estimation problem where it was shown, using computer simulations, that the fourth-order polynomial Wigner–Ville-based estimator can provide a lower mean-square error than the more commonly used Wigner–Ville distribution. This is particularly the case for signals at high signal-to-noise ratio having rapidly changing instantaneous frequency such as occur for aircrafts at low altitude. For signals at low signal-to-noise ratio having slowly changing instantaneous frequency such as occur for high altitude aircraft, the polynomial Wigner–Ville distribution may provide little or no improvement.

The observer frequency model employed in this paper assumes that the aircraft flight parameters are constant throughout the observation period. Other more complex models could be considered in future research. Such models may necessitate the estimation of higher-order instantaneous frequency laws and the use of the polynomial Wigner–Ville distribution may therefore be particularly appropriate.

ACKNOWLEDGMENTS

The authors acknowledge Jonathon Ralston for his earlier contribution to this work.[16] The authors would like to thank the anonymous reviewers for their helpful comments, and the Australian Research Council for partial funding of this research through its mechanism B.

[1] B. Ferguson, ''A ground based narrow-band passive acoustic technique for estimating the altitude and speed of a propeller driven aircraft,'' J. Acoust. Soc. Am. **92**, 1403–1407 (1992).
[2] B. G. Ferguson and G. C. Speechley, ''Time-varying spectral analysis and spatial array processing of acoustic data from a microphone array,'' in *Proceedings of the 3rd IASTED International Symposium on Signal Processing and its Applications, ISSPA 92,* edited by B. Boashash and D. A. Gray (Gold Coast, Australia, 1992), pp. 408–411.
[3] D. C. Reid, ''Improved Aircraft Flight Parameter Estimation based on Passive Acoustic Techniques using Time-Frequency Analysis,'' Ph.D. thesis, Queensland University of Technology, 1997.
[4] B. G. Ferguson and B. G. Quinn, ''Application of the short-time Fourier transform and the Wigner–Ville distribution to the acoustic localization of aircraft,'' J. Acoust. Soc. Am. **96**, 821–827 (1994).
[5] B. G. Ferguson, R. C. Trider, and J. L. Hanlon, ''Acoustic detection, recognition, and localization of propellor-driven aircraft and helicopters,'' in *Proceedings of the Fourth International Conference on Signal Processing Applications and Technology* (Defence Science and Technology Organization, Sydney, Australia, 1993), Vol. 2, pp. 1578–1583.
[6] B. G. Ferguson, ''Doppler effect for sound emitted by a moving airborne source and received by acoustic sensors located above and below the sea surface,'' J. Acoust. Soc. Am. **94**, 3244–3247 (1993).
[7] D. C. Reid, ''The bootstrap applied to passive acoustic aircraft flight parameter estimation,'' in *Proceedings of the IEEE International Conference on Acoustics, Speech and Signal Processing, ICASSP 96, Atlanta,* 1996 (IEEE, New York, 1996).
[8] B. Quinn, ''Doppler speed and range estimation using frequency and amplitude estimates,'' J. Acoust. Soc. Am. **98**, 2560–2566 (1995).
[9] A. M. Zoubir and B. Boashash, ''The Bootstrap: Signal Processing Applications,'' IEEE Signal Process. Mag. (to appear).
[10] B. Boashash, ''Interpreting and estimating the instantaneous frequency of a signal—Part I: Fundamentals; Part II: Algorithms,'' Proc. IEEE **80**(4), 519–569 (1992).
[11] B. Boashash and P. J. O'Shea, ''Polynomial Wigner–Ville distributions and their relationship to time-varying higher order spectra,'' IEEE Trans. Signal Process **42**, (1994).
[12] L. Cohen, ''Introduction: A primer on time-frequency distributions,'' in *Time-Frequency Signal Analysis: Methods and Applications,* edited by B. Boashash (Longman, Cheshire, 1992), Chap. 1, pp. 3–42.

[13] B. Boashash and G. Jones, ''Instantaneous frequency and time-frequency distributions,'' in *Time-Frequency Signal Analysis: Methods and Applications*, edited by B. Boashash (Longman, Cheshire, 1992), Chap. 2, pp. 43–73.
[14] B. Boashash, ''Time-frequency signal analysis,'' in *Advances in Spectrum Analysis and Array Processing*, edited by S. Haykin (Prentice-Hall, Englewood Cliffs, NJ, 1991), Vol. 1, Chap. 9, pp. 418–517.
[15] B. Ristic and B. Boashash, ''Use of cross Polynomial Wigner-Ville distribution for instantaneous frequency estimation of non-linear FM signals,'' in *Proc. IEEE-SP International Symposium on Time-Frequency and Time-Scale Analysis*, Philadelphia 1994, pp. 252–255.
[16] D. C. Reid and J. C. Ralston, ''An optimum window length for the PWVD with application to passive acoustic parameter estimation,'' in *Proceedings of the IEEE International Conference on Acoustics, Speech and Signal Processing, ICASSP 94*, Vol. IV, Adelaide, Australia (IEEE, New York, 1994), pp. 313–316.
[17] D. C. Rife and R. R. Boorstyn, ''Single tone parameter estimation from discrete-time observations,'' IEEE Trans. Inf. Theory **20**, 591–598 (1974).
[18] R. Wong, *Asymptotic Approximations of Integrals* (Academic, New York, 1989).
[19] B. Quinn and P. Kootsookos, ''Threshold behavior of the maximum likelihood estimator of frequency,'' IEEE Trans. Signal Process **42**, 3291–3294 (1994).
[20] P. O'Shea, ''Detection and estimation methods for non-stationary signals,'' Ph.D. thesis, University of Queensland, 1991.
[21] P. Rao and F. J. Taylor, ''Estimation of instantaneous frequency using the Wigner distribution,'' Electron. Lett. **26**, 246–248 (1990).
[22] Anonymous (1995). A helpful suggestion from an anonymous reviewer.

Nonlinear wide-angle paraxial acoustic propagation in shallow-water channels

Rahul S. Kulkarni and William L. Siegmann
Rensselaer Polytechnic Institute, Troy, New York 12180-3590

Michael D. Collins
Naval Research Laboratory, Code 7140, Washington, DC 20375-5320

(Received 25 June 1996; accepted for publication 6 December 1996)

A time-domain model that describes wide-angle paraxial propagation of acoustic pulses in shallow water is developed. This model incorporates weak nonlinear effects and depth variability in both ambient density and sound speed. Derivations of paraxial approximations are based on an iterative approach, in which the wide-angle approximation is obtained by using a narrow-angle equation to approximate the second range derivative in the two-way equation. Scaling arguments are used to obtain a more tractable simplification of the equation. The wide-angle equation is solved numerically by splitting into components representing distinct physical processes and using a modified version of the time-domain parabolic equation (TDPE) code [M. D. Collins, J. Acoust. Soc. Am. **84**, 2114–2125 (1988)]. A high-order upwind flux-correction method is modified to handle the nonlinear component. Numerical results are presented for adiabatic propagation in a shallow, isospeed channel. It is demonstrated that nonlinear effects are significant, even at small ranges, if the peak source pressure is high enough. Both nonlinear and wide-angle effects are illustrated, and their differences are discussed. [S0001-4966(97)03406-1]

PACS numbers: 43.30.Dr, 43.30.Lz [MBP]

INTRODUCTION

The paraxial approximation method, otherwise known as the parabolic equation (PE) method, has evolved greatly since its first application to underwater acoustics.[1] It has successfully modeled high-angle propagation in a variety of environments.[2,3] Recent extensions emphasize capabilities for shallow-water propagation,[4–6] where the occurrence of many vertical modes is handled by high-angle, range-dependent models. Most current work is based on frequency-domain propagation, so that Fourier synthesis can be used to recover the time-domain signal from a broadband source. A difficulty associated with this approach is that the effects of nonlinear terms can be significant for sufficiently strong pulses, particularly when sediment interactions are important. Consequently, it is appropriate to develop efficient time-domain models for shallow channels which incorporate nonlinear effects.

A number of previous theoretical developments exist for general nonlinear acoustics, and these can be traced back to work by Westervelt.[7] They have been chronicled and summarized by Hamilton,[8] Blackstock,[9] and Tjotta.[10] One significant development was formulation of the parabolic Khokhlov–Zabolotskaya–Kuznetsov (KZK) equation.[11,12]

In underwater acoustics, nonlinear propagation modeling with the PE method was first investigated using the nonlinear progressive wave equation (NPE).[13,14] One advantage of this time-domain technique is that it involves separate terms for refraction, diffraction, and nonlinear steepening. Each of these mechanisms is treated to first-order accuracy in the original NPE, which is sufficient for many problems in ocean acoustics. The NPE involves marching the solution forward in time. In order to avoid stability problems associated with incoming waves, wide-angle corrections for refraction and diffraction were developed using a related technique, the time-domain parabolic equation (TDPE),[15] which marches the field outward in range. The TDPE also includes terms that account for density variations, attenuation, and sediment dispersion. It is related to the frequency-domain PE, which also marches in range, via the Fourier transform. Other investigations of the TDPE developed high-angle terms for the linear case[2] and examined its stability properties and extensions.[16,17]

The primary objective of this paper is to develop a new propagation equation which simultaneously treats nonlinear and wide-angle effects. It is based on the TDPE and includes nonlinear terms as well as a higher-order diffraction term to account for wide-angle propagation. In Sec. I, a two-way equation which incorporates spatial dependence in ambient density and sound speed is derived, starting from the fundamental equations of adiabatic, inviscid fluid motion. In Sec. II, the wide-angle paraxial approximation of the nonlinear two-way equation is developed by a novel iterative approach, which uses a narrow-angle equation to approximate the range derivative in the two-way equation. Scaling arguments are then used to obtain a more tractable simplification of the wide-angle equation. The iterative procedure can be continued to obtain higher-angle approximations. In Sec. III, the special case of an isospeed channel is considered for initial numerical implementation, and an efficient computational strategy based on extension of the operator splitting method is described. Numerical results that illustrate both nonlinear and wide-angle effects are displayed and discussed. It is demonstrated that nonlinear effects are significant if the

peak source pressure is high enough and that coupling between the nonlinearity and propagation angle can be negligible.

I. DERIVATION OF THE TWO-WAY EQUATION

The acoustic fluctuations are assumed to occur in an ocean model governed by the following momentum, continuity, and state equations:

$$\rho \frac{D\mathbf{v}}{Dt} + \nabla p = 0, \tag{1}$$

$$\frac{D\rho}{Dt} + \rho \nabla \cdot \mathbf{v} = 0, \tag{2}$$

$$\frac{Dp}{Dt} = c^2 \frac{D\rho}{Dt}, \tag{3}$$

where $D/Dt \equiv \partial/\partial t + \mathbf{v}\cdot\nabla$ is the material derivative and $c^2 = c^2(\rho,p)$ is the square of the sound speed. Pressure and density are denoted by p and ρ, respectively, and $\mathbf{v}=(v_1,v_2,v_3)$ is the fluid velocity. Gravitational body forces are neglected, as any conceivable influence of gravity on acoustic propagation is negligible except at very low frequencies.[18] For simplicity the propagation process is assumed adiabatic, and dissipative mechanisms are neglected. Equations (1), (2), and (3) form a closed system for p, ρ, and $\mathbf{v}$, respectively.

The acoustic disturbance is a perturbation of the field variables about a motionless, time-independent mean state,

$$[p,\rho,\mathbf{v}](\mathbf{x},t) = [p_0,\overline{\rho(\mathbf{x})},\mathbf{0}] + [p',\rho',\mathbf{v}'](\mathbf{x},t), \tag{4}$$

where $\mathbf{x}$ represents Cartesian coordinates (x,y,z). Spatial dependence is permitted in the mean density, while Eq. (1) requires that the mean pressure is constant. In this section, magnitudes of quantities are taken to refer to their sizes relative to some appropriately chosen reference values. With this understanding, acoustic fluctuations ρ', p', and v_i' are assumed to be small enough to ignore cubic and higher order terms, as is typical in nonlinear acoustics.[10,12,19–22] Equations for the disturbance fields are obtained by substituting Eq. (4) into Eqs. (1)–(3) and expanding $c^2(\rho,p)$ about the mean state $(\overline{\rho},p_0)$.

Applying the operator $\overline{\rho}\nabla\cdot(1/\overline{\rho})$ to the approximation of Eq. (1), subtracting a time derivative of the approximation of Eq. (2), and dropping primes leads to

$$\overline{\rho}\,\nabla\cdot\frac{1}{\overline{\rho}}\nabla p - \left(\frac{\partial^2\rho}{\partial t^2} + \nabla\overline{\rho}\cdot\frac{\partial\mathbf{v}}{\partial t}\right) = \frac{\partial}{\partial t}(\nabla\cdot\rho\mathbf{v}) - \overline{\rho}\nabla\cdot\frac{1}{\overline{\rho}}\left\{\rho\frac{\partial\mathbf{v}}{\partial t} + \overline{\rho}(\mathbf{v}\cdot\nabla)\mathbf{v}\right\}. \tag{5}$$

The linear terms in parentheses on the left side of Eq. (5) are replaced by the first time derivative of the following second-order approximation of Eq. (3),

$$\frac{\partial^2\rho}{\partial t^2} + \nabla\overline{\rho}\cdot\frac{\partial\mathbf{v}}{\partial t} = \frac{1}{\overline{c^2}}\frac{\partial}{\partial t}\left\{\frac{\partial p}{\partial t} + \mathbf{v}\cdot\nabla p - \overline{c^2}\mathbf{v}\cdot\nabla\rho - (\beta_1\rho+\beta_2 p)\left(\frac{\partial\rho}{\partial t} + \mathbf{v}\cdot\nabla\overline{\rho}\right)\right\}, \tag{6}$$

where

$$\beta_1 \equiv \left.\frac{\partial c^2}{\partial\rho}\right|_{(\overline{\rho},p_0)}, \quad \beta_2 \equiv \left.\frac{\partial c^2}{\partial p}\right|_{(\overline{\rho},p_0)}. \tag{7}$$

After substituting Eq. (6) into Eq. (5), $\mathbf{v}$ and ρ appear only in the nonlinear terms and can be expressed in terms of p using the first-order approximations of Eqs. (1) and (3),

$$\mathbf{v} = -\frac{1}{\overline{\rho}}\nabla\int_{t_1}^{t} p(\mathbf{x},\tau)\,d\tau \equiv -\frac{1}{\overline{\rho}}\nabla I p, \tag{8}$$

$$\rho = \frac{1}{\overline{c^2}}\,p - \nabla\overline{\rho}\cdot I\mathbf{v}, \tag{9}$$

where t_1 is before the onset of the acoustic fluctuations. Without any additional assumptions, we simplify the resulting nonlinear terms using the first-order approximation of Eq. (2),

$$\nabla\cdot\mathbf{v} = -\frac{1}{\overline{\rho}}\left(\frac{\partial\rho}{\partial t} + \mathbf{v}\cdot\nabla\overline{\rho}\right), \tag{10}$$

and the zeroth-order relation

$$\nabla\overline{c^2} = \beta_1\nabla\overline{\rho}, \tag{11}$$

obtained from $\overline{c^2} = \overline{c^2}(\overline{\rho},p_0)$. This leads to the two-way equation for the pressure field,

$$\begin{aligned}\overline{\rho}\,\nabla\cdot\frac{1}{\overline{\rho}}\nabla p - \frac{1}{\overline{c^2}}\frac{\partial^2 p}{\partial t^2} &= -\frac{\beta}{\overline{\rho c^4}}\frac{\partial^2 p^2}{\partial t^2} - \left[\overline{\rho}\nabla\cdot(\mathbf{v}\cdot\nabla)\mathbf{v} - \overline{\rho}\,\nabla\cdot\frac{1}{\overline{\rho^2}}\left\{\frac{1}{2\overline{c^2}}\nabla p^2 - (\nabla\overline{\rho}\cdot I\mathbf{v})\nabla p\right\}\right] \\ &\quad - \frac{1}{\overline{c^2}}\frac{\partial}{\partial t}\left[\frac{\partial}{\partial t}\left\{\frac{\overline{\rho}|\mathbf{v}|^2}{2} - \frac{p^2}{2\overline{\rho c^2}}\right\} - \frac{1}{\overline{\rho c^2}}\{\nabla(\overline{\rho c^2})\cdot I\mathbf{v}\}\frac{\partial p}{\partial t}\right],\end{aligned} \tag{12}$$

where $\beta \equiv 1 + (\overline{\rho}/2\overline{c^2})(\beta_1 + \overline{c^2}\beta_2)$ is the parameter of nonlinearity.[20,23,24]

Equation (12) incorporates quadratic nonlinearities as well as spatial variability in the ambient density and sound speed, and is completely general for adiabatic propagation in an inviscid fluid. It reduces to the linear wave equation for inhomogeneous media when nonlinear terms are dropped. If $\overline{\rho}$ and $\overline{c}$ are constant, Eq. (12) reduces to the nondissipative form of Westervelt's equation,[7] from which the nondissipative forms of Burgers' and KZK equations appear in appropriate limits.[19]

II. DERIVATION OF WIDE-ANGLE PARAXIAL APPROXIMATIONS

Wide-angle paraxial approximations of the nonlinear two-way Eq. (12) are conveniently obtained using a novel iterative approach combined with scaling arguments.

Equation (12) is written in cylindrical coordinates (r,θ,z), variations with θ are ignored, and the substitution $q=p\sqrt{r}$ is introduced to account for cylindrical spreading. As is typical in PE applications,[1,25] a far-field approximation is made. This assumes that $r \gg L$, where L is some characteristic length associated with the pulse, so that spreading terms of order L^2/r^2 are negligibly small. For simplicity we also make the usual assumption for PE methods, that locally range-independent segments of the environment are treated,[2,3] so that $\overline{\rho}=\overline{\rho}(z)$ and $\overline{c}=\overline{c}(z)$ and the resulting equation is

$$\frac{1}{\sqrt{r}}\left[\frac{\partial^2 q}{\partial r^2}+\overline{\rho}\frac{\partial}{\partial z}\frac{1}{\overline{\rho}}\frac{\partial q}{\partial z}-\frac{1}{\overline{c}^2}\frac{\partial^2 q}{\partial t^2}\right]-F(q)=0, \tag{13}$$

where $F(q)$ is a nonlinear function of q. With the notation $\nabla \equiv \hat{i}_z(\partial/\partial z)+\hat{i}_r(\partial/\partial r)$,

$$\begin{aligned}F(q)\equiv\frac{1}{r}\Bigg[&-\frac{\beta}{\overline{\rho c^4}}\frac{\partial^2 q^2}{\partial t^2}-\overline{\rho}\overline{\nabla}\cdot\left\{\left(\frac{1}{\overline{\rho}}\overline{\nabla I q}\cdot\overline{\nabla}\right)\frac{1}{\overline{\rho}}\overline{\nabla I q}\right.\\&\left.-\frac{1}{2\overline{\rho^2 c^2}}\overline{\nabla q}^2-\frac{1}{\overline{\rho}^3}(\overline{\nabla\overline{\rho}\cdot\nabla I^2 q})\overline{\nabla q}\right\}\\&-\frac{1}{2\overline{\rho c^2}}\frac{\partial^2}{\partial t^2}\left\{\overline{\nabla(Iq)}\cdot\overline{\nabla Iq}-\frac{1}{\overline{c}^2}q^2\right\}\\&-\frac{1}{\overline{\rho}^2\overline{c}^4}\frac{\partial}{\partial t}\{\overline{\nabla(\overline{\rho c^2})}\cdot\overline{\nabla I^2 q}\}\frac{\partial q}{\partial t}\Bigg],\end{aligned} \tag{14}$$

where $I^2 q \equiv \int_{t_1}^{t}\int_{t_1}^{\tau} q(r,z,\tilde{\tau})\,d\tilde{\tau}\,d\tau$. Range-dependent environments can be handled by an appropriate interface condition at the boundaries of the segments.

A reference sound speed c_0 is chosen and Eq. (13) is transformed to pulse-tracking coordinates $q(r,z,t) \rightarrow u(r,z,t-r/c_0)$, so that $(\partial/\partial r \rightarrow \partial/\partial r - c_0^{-1}\partial/\partial t)$. Consequently, u satisfies

$$\frac{1}{\sqrt{r}}\left[\frac{\partial^2 u}{\partial r^2}-\frac{2}{c_0}\frac{\partial^2 u}{\partial r\,\partial t}-\left(\frac{1}{\overline{c}^2}-\frac{1}{c_0^2}\right)\frac{\partial^2 u}{\partial t^2}+\overline{\rho}\frac{\partial}{\partial z}\frac{1}{\overline{\rho}}\frac{\partial u}{\partial z}\right]-\hat{F}(u)=0, \tag{15}$$

where $\hat{F}(u)$ represents the transformation of $F(q)$ to the pulse-tracking reference frame. The narrow-angle paraxial approximation of Eq. (15) is obtained by neglecting the second range derivative and retaining only leading-order nonlinear terms. The wide-angle approximation is then obtained conveniently by iteration, using the narrow-angle equation to approximate the second range derivative in Eq. (15). The combined procedure involving scaling arguments and iteration is described next.

The parameter $\epsilon = 1/f^2 \ll 1$ is introduced, where f is chosen depending on the environment under consideration.[25] One choice[1] of f suitable for many applications is the channel f number, $f=\sqrt{c_0/\Delta c}$, where Δc is a spatially averaged deviation of sound speed from c_0. For environments such as an isospeed waveguide, an appropriate choice[26] is $f=R/H$, where R is the maximum range of interest and H is the waveguide depth. In any case, the scaling arguments here are independent of the specific choice of f. With $k_0=\omega_0/c_0$ as the reference wave number, the scaled variables $\tilde{r}=\epsilon k_0 r$, $\tilde{z}=\sqrt{\epsilon}k_0 z$, and $\tilde{t}=\omega_0 t$ are introduced. It is assumed that the dimensionless pressure $\tilde{p}=p/p_s$, where p_s is the peak source pressure given by $p_s=\delta\rho_0 c_0^2$, with ρ_0 as a reference density and δ as a dimensionless source strength parameter. The dimensionless far-field pressure is then $\tilde{u}=u/u_s$, where $u_s=p_s/\sqrt{k_0}$. We regard the independent parameters δ and ϵ as having comparably small values, which physically permits nonlinear effects caused by the source amplitude to be roughly as significant as propagation angle effects.

The narrow-angle approximation retains $O(\epsilon\delta)$ and $O(\delta^2)$ terms and, when written in terms of dimensional independent variables r, z, t, and the dimensionless far-field pressure $\tilde{u}$, is

$$\begin{aligned}\frac{1}{c_0^2}\frac{\partial^2\tilde{u}}{\partial r\,\partial t}=\frac{1}{2c_0}\Bigg[&-\left(\frac{1}{\overline{c}^2}-\frac{1}{c_0^2}\right)\frac{\partial^2\tilde{u}}{\partial t^2}+\overline{\rho}\frac{\partial}{\partial z}\frac{1}{\overline{\rho}}\frac{\partial\tilde{u}}{\partial z}\\&+\frac{\beta u_s}{\overline{\rho c_0^4}\sqrt{r}}\frac{\partial^2\tilde{u}^2}{\partial t^2}\Bigg].\end{aligned} \tag{16}$$

Note that the NPE[13] is accurate to the same order as Eq. (16) and is therefore valid only for narrow propagation angles. For comparison with the NPE, we integrate Eq. (16) with respect to t,

$$\begin{aligned}\frac{\partial\tilde{u}}{\partial r}=\frac{\partial}{\partial t}\Bigg[&-\frac{c_0}{2}\left(\frac{1}{\overline{c}^2}-\frac{1}{c_0^2}\right)\tilde{u}+\frac{\beta u_s}{2\overline{\rho c_0^3}\sqrt{r}}\tilde{u}^2\Bigg]\\&+\frac{c_0}{2}\int_{t_1}^{t}\overline{\rho}\frac{\partial}{\partial z}\frac{1}{\overline{\rho}}\frac{\partial\tilde{u}}{\partial z}\,dt.\end{aligned} \tag{17}$$

The NPE is

$$\frac{\partial R}{\partial t}=-\frac{\partial}{\partial r}\left(c_1 R+\frac{c_0}{2}\beta R^2\right)-\frac{c_0}{2}\int_{r_1}^{r}\frac{\partial^2 R}{\partial z^2}\,dr-\frac{c_0}{2r}R, \tag{18}$$

where $R=\rho/\rho_0$, c_1 is a sound-speed perturbation, ρ_0 is a reference density, and r_1 is in the quiescent medium ahead of the pulse. In both Eqs. (17) and (18), the first three terms on the right represent physically the effects of refraction, nonlinearity, and diffraction, respectively. The NPE has an additional spreading term on the right; this type of term is absent in Eq. (17) because of the dependent-variable transformation $q=p\sqrt{r}$. The NPE marches the solution in time, whereas Eq. (17) marches the solution in range.

A wide-angle equation is obtained from Eq. (15) by using Eq. (17) to approximate the second range derivative term as well as the range derivatives in $\hat{F}(u)$. Terms which are asymptotically $O(\epsilon\delta)$, $O(\delta^2)$, $O(\epsilon^2\delta)$, and $O(\epsilon\delta^2)$ are retained. The resulting equation is

$$\left[\frac{1}{c_0^2}+\underbrace{\frac{1}{4}\left(\frac{1}{\bar{c}^2}-\frac{1}{c_0^2}\right)}_{A}\right]\frac{\partial^2}{\partial t^2}\frac{\partial\tilde{u}}{\partial r}-\underbrace{\frac{\bar{\rho}}{4}\frac{\partial}{\partial z}\frac{1}{\bar{\rho}}\frac{\partial}{\partial z}\frac{\partial\tilde{u}}{\partial r}}_{B}=-\frac{1}{2c_0}\left[\left(\frac{1}{\bar{c}^2}-\frac{1}{c_0^2}\right)\frac{\partial^2}{\partial t^2}-\bar{\rho}\frac{\partial}{\partial z}\frac{1}{\bar{\rho}}\frac{\partial}{\partial z}\right]\frac{\partial\tilde{u}}{\partial t}+\frac{\beta u_s}{2c_0\bar{\rho}\bar{c}^4\sqrt{r}}\frac{\partial^3\tilde{u}^2}{\partial t^3}+\underbrace{G(\tilde{u})}_{C}, \tag{19}$$

where

$$G(\tilde{u})=O(\epsilon\delta^2). \tag{20}$$

Equation (19) describes weakly nonlinear wide-angle paraxial propagation in a waveguide in which density and sound speed vary continuously with depth. Terms (A) and (B), which are both $O(\epsilon^2\delta)$, and term (C) are not present in the narrow-angle Eq. (16). Physically, (A) and (B) represent second-order refraction and diffraction, respectively, and (C) represents coupling of nonlinear and wide-angle effects.

Higher-order approximations of Eq. (15) can be obtained by continuing the iterative procedure. For example, the next improvement can be found by using the wide-angle Eq. (19) to approximate the second range derivative in Eq. (15). Note that for the linear TDPE model, all orders in ϵ of paraxial approximations are obtained easily by an operator formalism.[27] This formalism is inapplicable when nonlinear terms are present, necessitating a different procedure such as our iterative scheme.

The tilde notation on $\tilde{u}$ is now dropped for simplicity, with the understanding that u is now dimensionless and r, z, and t are dimensional. An extension[28] of the operator splitting method[27] is applied so that the approximate solution of Eq. (19) involves solution of the following component equations at each range step:

$$\frac{\partial u}{\partial r}=-\frac{1}{2c_0\gamma}\left(\frac{1}{\bar{c}^2}-\frac{1}{c_0^2}\right)\frac{\partial u}{\partial t}, \tag{21}$$

$$L\,\frac{\partial u}{\partial r}=-\left[\left\{-\frac{1}{2c_0}+\frac{1}{8c_0\gamma}\left(\frac{1}{\bar{c}^2}-\frac{1}{c_0^2}\right)\right\}\bar{\rho}\frac{\partial}{\partial z}\frac{1}{\bar{\rho}}\frac{\partial}{\partial z}\right]\frac{\partial u}{\partial t}, \tag{22}$$

$$L\,\frac{\partial u}{\partial r}=\frac{\beta u_s}{2\bar{\rho}\bar{c}_0^5\sqrt{r}}\frac{\partial^3 u^2}{\partial t^3}+G(u), \tag{23}$$

where

$$\gamma\equiv\frac{1}{c_0^2}+\frac{1}{4}\left(\frac{1}{\bar{c}^2}-\frac{1}{c_0^2}\right),\quad L\equiv\gamma\frac{\partial^2}{\partial t^2}-\frac{\bar{\rho}}{4}\frac{\partial}{\partial z}\frac{1}{\bar{\rho}}\frac{\partial}{\partial z}. \tag{24}$$

Equations (21), (22), and (23) represent the effects of leading-order refraction, diffraction, and nonlinearity, respectively. Not only are these equations more amenable to numerical solution than Eq. (19), but also it is intuitively appealing to have distinct physical effects in separate component equations. To solve Eqs. (21)–(23), the boundary conditions $u=\partial u/\partial t=0$ are used at $t=t_1$, before the signal is detected by the observer, and it is assumed that the surface and absolute bottom of the waveguide are pressure-release boundaries. The pressure field is initialized by the image solution[34] generated at a specified range from the source. Convergence and accuracy of operator splitting methods such as the one used to obtain Eqs. (21)–(23) are discussed by Yanenko.[28]

III. NUMERICAL IMPLEMENTATION FOR AN ISOSPEED CHANNEL

We first discuss a numerical implementation using Eqs. (21), (22), and a simplified form of (23), and then describe what happens when this simplification is relaxed. For both cases the implementation here does not incorporate energy-conserving conditions[29] at interfaces in the r direction, and consequently it is applicable only for stratified and weakly range-dependent environments. This does not interfere with our main objectives, which are to study effects of weak nonlinearity on wide-angle propagation and differences between narrow- and wide-angle nonlinear cases. The specific example of an isospeed channel is used here, with more realistic shallow-water environments considered subsequently.[30]

The initial simplification of Eq. (23) is that only the leading-order terms are retained and the $O(\epsilon^2\delta)$ and $O(\epsilon\delta^2)$ terms are dropped, so that Eq. (23) reduces to

$$\underbrace{\frac{1}{c_0^2}\frac{\partial^2}{\partial t^2}\frac{\partial u}{\partial r}}_{O(\epsilon\delta)}=\underbrace{\frac{\beta u_s}{2c_0\bar{\rho}\bar{c}^4\sqrt{r}}\frac{\partial^3 u^2}{\partial t^3}}_{O(\delta^2)}. \tag{25}$$

Physically, this is equivalent to ignoring locally the coupling between wide-angle and nonlinear effects. Wide-angle effects are still present in Eqs. (21) and (22). We note that if operator splitting is applied to the narrow-angle Eq. (16), then the isospeed component equations are the same as Eqs. (21), (22), and (25), except with $L=\gamma\partial^2/\partial t^2$ and $\gamma=1/c_0^2$. Hence, the numerical solution for the nonlinear narrow-angle case is conveniently obtained from the same computer code as the one used for Eqs. (21), (22), and (25).

A modification of the linear TDPE code in Ref. 2 is used for the actual implementation. A range-marching scheme is employed, in which the solution over each range step consists of predicting u using Eq. (21) and correcting it to account for diffraction and nonlinearity by Eqs. (22) and (25) successively. Equation (21) is a first-order hyperbolic equation and is solved with the Lax–Wendroff scheme.[31] To discretize depth dependence in Eq. (22), a Galerkin's method[2] is used which facilitates treatment of horizontally stratified environments. The resulting equation is solved with Crank–Nicolson integration in r, using upwind centered differences[31] in t while sweeping from $t=t_1$ to $t=t_2$. The boundary conditions $u=\partial u/\partial t=0$ are imposed at $t=t_1$, before the signal is detected by the observer. The other bound-

ary $t=t_2$ is chosen so that the window $t_1 \leqslant t \leqslant t_2$ captures the times of interest for the pulse $u(r,z,t)$ for all r,z.

To solve the nonlinear Eq. (25), it is integrated twice in time using the boundary conditions $u=\partial u/\partial t=0$ at $t=t_1$. The transformation $x=2\sqrt{r}$ then results in

$$\frac{\partial u}{\partial x}+\frac{\partial}{\partial t}[\phi(u)]=0, \tag{26}$$

where

$$\phi(u)=-\frac{\beta u_s}{2\overline{\rho c_0^3}}u^2. \tag{27}$$

Equation (26) has the same form as the inviscid Burgers' equation, expressed in conservation form with flux $\phi(u)$, but with the roles of t and x reversed. Its numerical solution is obtained by using a high-order upwind flux-correction method developed for hyperbolic conservation laws.[32] The reasons for this approach, along with some implementation details, are briefly described in the Appendix.

The original TDPE implementation assumes that a pulsed source $f(t)$ is located at $r=0$ and depth $z=z_0$ and that in the near-field, pressure p satisfies the wave equation

$$\frac{\partial^2 p}{\partial r^2}+\frac{1}{r}\frac{\partial p}{\partial r}+\frac{\partial^2 p}{\partial z^2}=\frac{1}{c_0^2}\frac{\partial^2 p}{\partial t^2}-\frac{2f(t)}{r}\delta(r)\delta(z-z_0), \tag{28}$$

with the fundamental solution $p(r,z,t)=f(t-r/c_0)/R$, where $R=\sqrt{r^2+(z-z_0)^2}$. The near-field here refers to time scales too short for medium inhomogeneities to have a significant effect. To circumvent the singularity at $R=0$, the homogeneous half-space field[33] generated from this solution is used to produce, at a specified range r_0, a starting field $u(r_0,z,t)$, $t_1 \leqslant t \leqslant t_2$, in the pulse-tracking reference frame. This starting field should be used only when the waveguide is sufficiently deep and possesses a lossy sediment layer so that bottom reflections are insignificant. For the present case of a shallow isospeed channel, more terms in the image solution[34] are needed to produce an accurate starting field, to account for multiple reflections from the surface and bottom of the waveguide (the number depends on the width of the time window). Our modified implementation takes this into account, while assuming that nonlinear effects are not significant over the time scales for which Eq. (28) holds. The starting field is propagated in range by predicting the solution at each successive range step by Eq. (21) and correcting it by Eqs. (22) and (25).

An isospeed channel of depth 200 m, with sound speed $\overline{c(z)}=c_0=1500$ m/s and water density $\overline{\rho(z)}=\rho_0=1000$ kg/m^3 is considered. The source is assumed to be a Gaussian, $f(t)=e^{-(t/\tau)^2}$ where $\tau=6.7$ ms, and is located at a depth of 50 m. The starting field is generated at range $r_0=50$ m from the source. The magnitude of the source strength parameter, chosen to be $\delta=0.5$, does not qualitatively affect the linear solution [which is obtained by setting the right side of Eq. (25) to zero], but does determine the intensity of nonlinear effects. Figure 1 is a field plot of the dimensionless starting field as a function of relative time and depth. This is a sequence of waveforms in depth recorded by a vertical receiving array placed 50 m away from the source. Traversing the figure from left to right at any depth gives the time evolution of the pulse. Figure 2 shows these waveforms at five depth locations. The receivers start recording before the signal can reach them, at $t_1=-20$ ms.

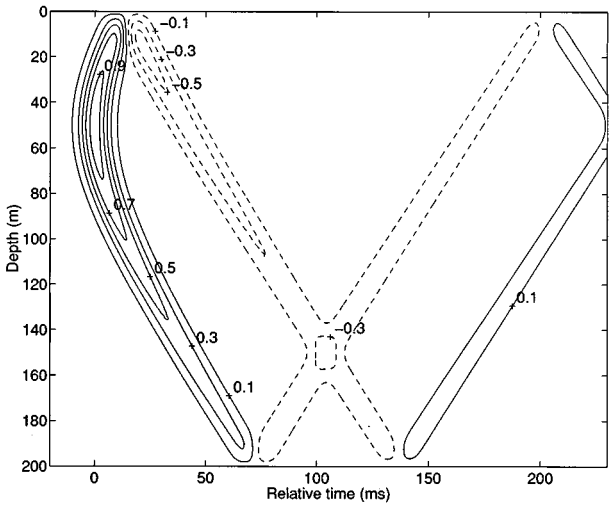

FIG. 1. Field plot of the starting field versus relative time and depth, normalized with respect to its maximum amplitude. Environment is an isospeed channel 200-m deep, and the field is generated at range 50 m from a Gaussian source at depth 50 m.

To appraise whether or not nonlinear effects are significant, some measure of the deviation between linear (L) and nonlinear (NL) results is needed. Possible characteristics that could be measured and compared are the waveform distortion, peak amplitude, arrival time of peak amplitude, and spectrum. Here we measure the first two by regarding nonlinear effects as ''significant at range r'' if

$$\alpha(r)\equiv\frac{\max_{z,t}|u_{\mathrm{NL}}-u_{\mathrm{L}}|}{\max_{z,t}|u_{\mathrm{L}}|}\geqslant 5\%. \tag{29}$$

This measure of differences between the linear and nonlinear solutions might be misleading if the two solutions differed only in phase. However, as is borne out by subsequent re-

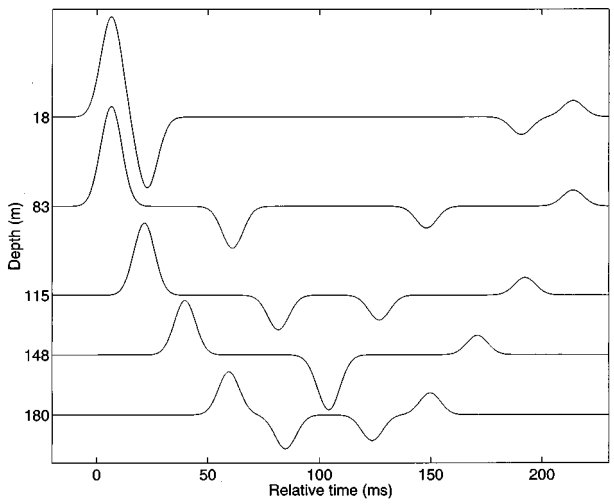

FIG. 2. Time-series waveforms at five depths of the starting field from Fig. 1.

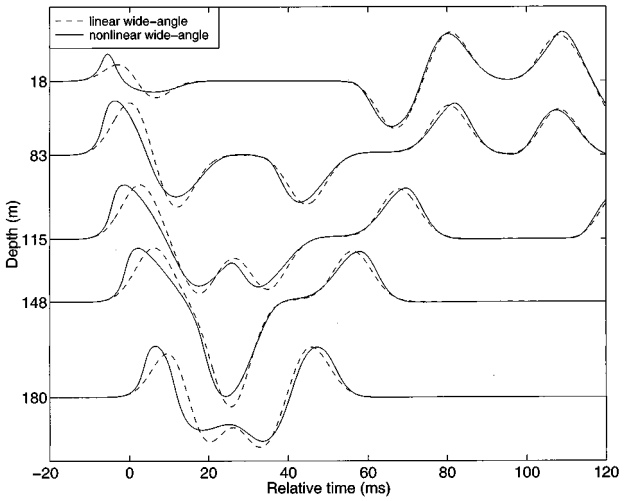

FIG. 3. Linear (dashed) and nonlinear (solid) wide-angle solutions at range 500 m and five depths for the environment of Fig. 1. Nonlinear steepening effects are evident, especially for earlier arrivals at the left.

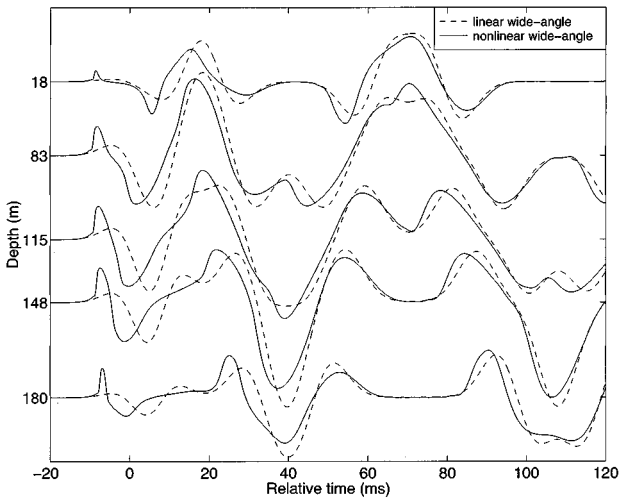

FIG. 5. Linear (dashed) and nonlinear (solid) wide-angle solutions at range 3 km and five depths for the environment of Fig. 1.

sults, this is not the situation in our simulations. For instance, it is found that for the source function and environment used, $\alpha(500\text{ m}) \geqslant 5\%$ if $\delta \geqslant 0.07$, which says that nonlinear effects are significant at $r = 500$ m for a peak source pressure $p_s \geqslant 0.1575 \times 10^9$ Pa (≈ 1550 atm).

Figures 3–7 illustrate differences between linear and nonlinear wide-angle propagation for $\delta = 0.5$. Figures 3, 4, and 5 show the waveforms at ranges 500 m, 1.5 km, and 3.0 km, respectively. They demonstrate significant nonlinear steepening effects; the computed values for $\alpha(r)$ at these ranges are 33%, 54%, and 48% respectively. At any range, the nonlinear distortions are most pronounced for the earlier arrivals. The distortions begin to accumulate with range, as is apparent from the results at 500 m and 1.5 km. Differences in the intensities of the nonlinear distortions at ranges 1.5 and 3.0 km are less apparent, because the cylindrical spreading factor $\sqrt{r}$ tends to reduce the influence of the nonlinear term with range. Figures 6 and 7 are field plots of the linear and nonlinear wide-angle solutions, respectively, at range 3 km. The steepening effects produced by the nonlinearity are clearly visible.

To examine differences in narrow- and wide-angle propagation, we consider the corresponding linear and nonlinear solutions at $r = 500$ m. Figure 8 shows the narrow- and wide-angle linear solutions plotted with the exact image solution. The narrow-angle model accurately captures the earlier arrivals but develops substantial amplitude and phase errors in time. The wide-angle solution is clearly more accurate, especially for the later arrivals. Figure 9 shows the corresponding narrow- and wide-angle nonlinear solutions. The differences between the curves here are similar to those in the linear case. It appears that the propagation angle does not qualitatively affect the nonlinear distortions, possibly because coupling between the two effects in Eq. (23) was not taken into account. To test this hypothesis, we obtain results when the leading-order coupling term in Eq. (23) is retained.

We return to Eq. (19) and assume that nonlinear effects are not as important as propagation angle effects, so that

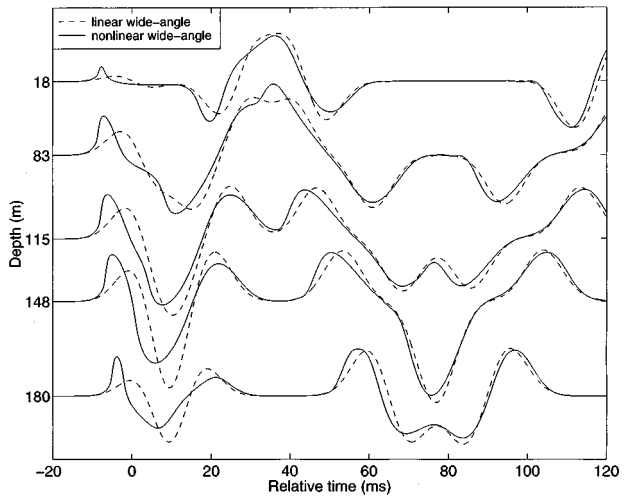

FIG. 4. Linear (dashed) and nonlinear (solid) wide-angle solutions at range 1.5 km and five depths for the environment of Fig. 1.

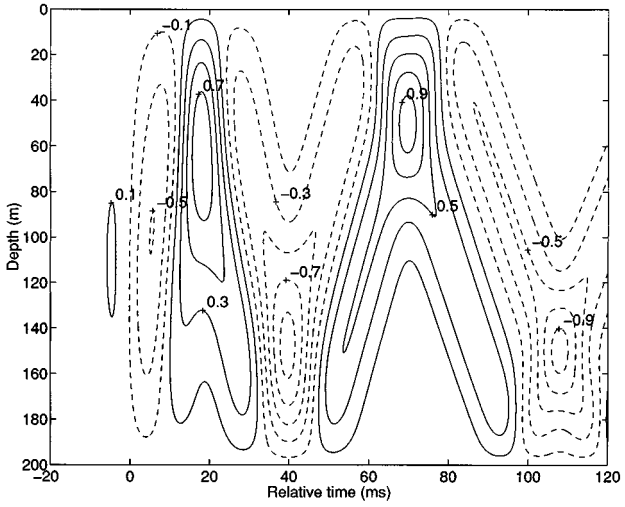

FIG. 6. Field plot of linear wide-angle solutions at range 3 km for the environment of Fig. 1, showing multiple reflections from waveguide surface and bottom.

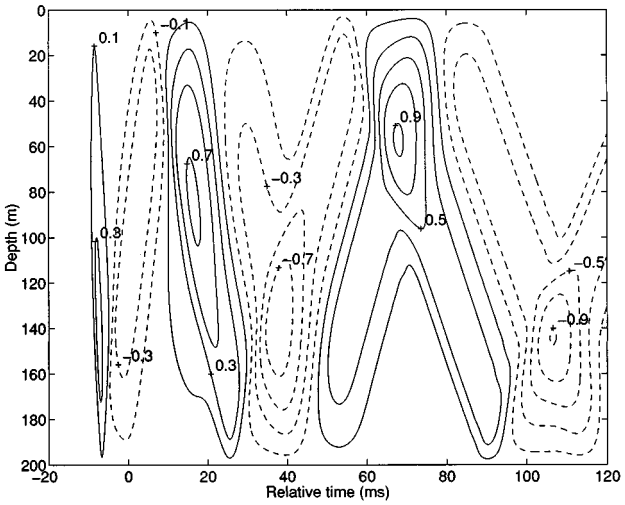

FIG. 7. Field plot of nonlinear wide-angle solutions at range 3 km for the environment of Fig. 1. In comparison with Fig. 6, significant nonlinear steepening effects are visible.

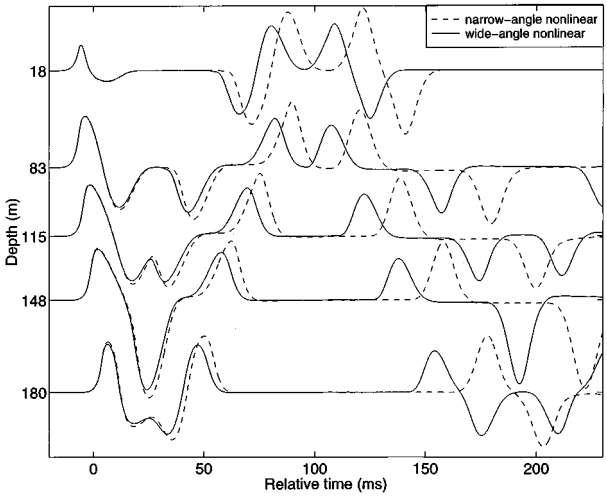

FIG. 9. Narrow-angle (dashed) and wide-angle (solid) nonlinear solutions at range 500 m and five depths for the environment of Fig. 1. Differences between curves are similar to those in Fig. 8.

$\delta < \epsilon$. The $O(\epsilon\delta^2)$ terms, marked (C), are thus neglected in comparison with $O(\epsilon^2\delta)$ terms, marked (A) and (B). As before, operator splitting results in Eqs. (21), (22), and (23) but without the term $G(u)$. The nonlinear equation after time integration can be written as

$$\frac{\partial}{\partial x}\left[u - \frac{1}{4\gamma}\int_{t_1}^{t}\int_{t_1}^{\tau_1} \rho \frac{\partial}{\partial z}\frac{1}{\rho}\frac{\partial u}{\partial z}(x,z,\tau_2)\,d\tau_2\,d\tau_1\right] + \frac{\partial}{\partial t}\left[\frac{\phi(u)}{c_0^2\gamma}\right] = 0. \tag{30}$$

The revised implementation solves Eqs. (21), (22), and (30) in place of (25). The double-integral term in Eq. (30) represents the leading-order coupling between nonlinearity and second-order diffraction. The high-order flux correction method which was used to solve Eq. (26) is modified to accommodate the double-integral term in Eq. (30), as described in the Appendix.

The results for our test environment are found to be visually indistinguishable from those with the coupling neglected. We conclude that in this problem, the coupling between the nonlinearity and propagation angle is insignificant as compared to their individual effects. Although we cannot generalize this conclusion to all cases, experience suggests that it may be true for many cases of interest. It is more efficient to compute without the coupling term, and to include it only when an appraisal of its importance is needed.

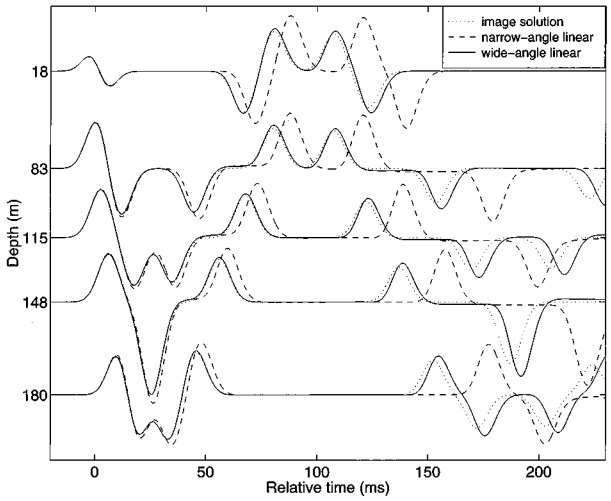

FIG. 8. Narrow-angle (dashed) and wide-angle (solid) linear solutions at range 500 m and five depths for the environment of Fig. 1, plotted with the exact image solution (dotted). Wide-angle solutions more accurately represent the pulse amplitude and phase, especially after multiple reflections.

IV. SUMMARY

A two-way nonlinear wave equation for adiabatic propagation that incorporates spatial dependence in the ambient density and sound speed is derived from the fundamental fluid equations. A wide-angle paraxial approximation of this equation is then derived using an iterative procedure combined with scaling arguments. This method can be extended to obtain higher-order approximations. Numerical results are presented for a shallow, isospeed channel.

The primary objective of the numerical simulations is to illustrate differences between linear and nonlinear wide-angle propagation. These differences depend on the strength of the acoustic source. For a Gaussian-shaped pulse, nonlinear distortions are found to be significant even at small ranges, for sufficiently strong peak source pressure. The distortions accumulate with range, but the rate at which they do so diminishes due to cylindrical spreading.

The other objective of the simulations is to investigate differences between narrow-angle and wide-angle nonlinear propagation. The results indicate that these differences are similar to those in the corresponding linear case, and that coupling between the nonlinearity and propagation angle may be insignificant as compared to their individual effects. As in the linear case, the wide-angle model more accurately represents the amplitude and phase of the signal, especially

after multiple reflections from the boundaries of the waveguide.

A numerical implementation is being developed[30] for wide-angle nonlinear propagation in more realistic shallow-water environments. A primary objective is to investigate the effects of both nonlinearity and sediment dispersion on wide-angle propagation.

ACKNOWLEDGMENTS

This work was supported by Grant No. N00014-J-91-1033 from Code 3210A, Office of Naval Research. It is part of a thesis to be submitted by Rahul S. Kulkarni in partial fulfilment of the requirements for the degree of Doctor of Philosophy in the Department of Mathematical Sciences at Rensselaer Polytechnic Institute. We thank Dr. B. Edward McDonald for his assistance, and Professor Mark F. Hamilton for supplying material on nonlinear acoustics. We also wish to thank a reviewer for helpful comments.

APPENDIX: HIGH-ORDER UPWIND FLUX CORRECTION METHOD

The high-order upwind flux-correction procedure was developed by McDonald and Ambrosiano[32] to obtain an accurate numerical solution of first-order hyperbolic equations such as Eq. (26). Here we summarize the motivation for their method, their implementation applied to Eq. (26), and our modification for handling Eq. (30).

Any straightforward discretization scheme for Eq. (26) results in spurious artifacts in its solution. This known difficulty[32,35] arises from the differencing scheme used for the time derivative of the flux ϕ. A first-order upwind difference scheme has the advantage of being monotonic,[35] but suffers from numerical dissipation because of its low accuracy. On the other hand, a more accurate second-order scheme is not monotonic and therefore tends to produce dispersive ripples near steep gradients in the solution. A hybrid scheme which combines the desirable aspects of both is used. The idea is to add to a first-order monotone solution a limited amount of the difference between the second-order and first-order fluxes. This difference, the antidifusive flux, is filtered to remove the excessive dissipation of the first-order scheme without creating unwanted oscillations due to the second-order scheme, a process called flux correction. A simple Euler discretization is used for the x derivative.

For application to Eq. (26), the first-order scheme

$$u_i^* = u_i^n - \frac{\Delta x}{\Delta t}\,(\phi_{i+1/2}^n - \phi_{i-1/2}^n), \tag{A1}$$

where i represents a time step, is first used to predict the solution u_i^* at range step (in the x direction) $n+1$. The fluxes $\phi_{i\pm 1/2}^n$ are defined so that the time derivative is one sided, with its direction based on a local estimate of the sign of a characteristic speed. The relationship

$$\frac{\partial \phi}{\partial x} = \frac{\partial \phi}{\partial u}\frac{\partial u}{\partial x} = \frac{\partial \phi}{\partial u}\left(-\frac{\partial}{\partial t}[\phi(u)]\right) = \frac{\beta u_s}{\overline{\rho} c_0^3}\frac{\partial}{\partial t}[\phi(u)] \tag{A2}$$

is then used to estimate the second-order fluxes $\phi_{i\pm 1/2}^{n+1/2}$ at range step $n+1/2$, with a second-order one-sided differencing of the time derivative. Each antidiffusive flux such as

$$\Delta\phi_{i+1/2} = \phi_{i+1/2}^{n+1/2} - \phi_{i+1/2}^n \tag{A3}$$

is filtered by replacing it with the quantity

$$\begin{aligned}\tilde{\Delta}\phi_{i+1/2} = {} & \mathrm{sgn}(\Delta\phi_{i+1/2}) \\ & \cdot \max[0, \min\{|\Delta\phi_{i+1/2}|, \mathrm{sgn}(\Delta\phi_{i+1/2})(u_{i+2}^* \\ & - u_{i+1}^*), \mathrm{sgn}(\Delta\phi_{i+1/2})(u_i^* - u_{i-1}^*)\}].\end{aligned} \tag{A4}$$

The high-order upwind flux-corrected solution at range step $n+1$ is given by

$$u_i^{n+1} = u_i^* - \frac{\Delta x}{\Delta t}\,(\tilde{\Delta}\phi_{i+1/2} - \tilde{\Delta}\phi_{i-1/2}). \tag{A5}$$

For implementation of Eq. (30), the composite open Newton–Cotes formula[36]

$$\begin{aligned}\int_{y_1}^{y_N} f(y)\,dy \approx \Delta y\Big(\frac{3}{2}f_2 + f_3 + f_4 + \cdots + f_{N-2} \\ + \frac{3}{2}f_{N-1}\Big),\end{aligned} \tag{A6}$$

where $f_i \equiv f(y_1 + (i-1)\Delta y)$, is used to discretize the double integral. This step is incorporated into the calculation of the intermediate solution u_i^* in Eq. (A1) and the fluxes $\phi_{i\pm 1/2}^{n+1/2}$ in Eq. (A2). An open integration formula retains the explicit nature of these calculations, permitting the sweep from $t = t_1$ to $t = t_2$.

[1] F. D. Tappert, ''The parabolic approximation method,'' in *Wave Propagation in Underwater Acoustics*, edited by J. B. Keller and J. S. Papadakis (Springer-Verlag, New York, 1977), pp. 224–287.
[2] M. D. Collins, ''Applications and time-domain solution of higher-order parabolic equations in underwater acoustics,'' J. Acoust. Soc. Am. **86**, 1097–1102 (1989).
[3] M. D. Collins, ''A higher-order parabolic equation for wave propagation in an ocean overlying an elastic bottom,'' J. Acoust. Soc. Am. **86**, 1459–1464 (1989).
[4] M. D. Collins, ''An energy-conserving parabolic equation for elastic media,'' J. Acoust. Soc. Am. **94**, 975–982 (1993).
[5] M. D. Collins and R. B. Evans, ''A two-way parabolic equation for acoustic backscattering in the ocean,'' J. Acoust. Soc. Am. **91**, 1357–1368 (1992).
[6] M. D. Collins, W. L. Siegmann, and W. A. Kuperman, ''A parabolic equation for poro-elastic media,'' J. Acoust. Soc. Am. **98**, 1645–1656 (1995).
[7] P. J. Westervelt, ''Parametric acoustic array,'' J. Acoust. Soc. Am. **35**, 535–537 (1963).
[8] M. F. Hamilton, ''Fundamentals and applications of nonlinear acoustics,'' in *Nonlinear Wave Propagation in Mechanics*, edited by T. W. Wright (American Society of Mechanical Engineers, New York, 1986).
[9] D. T. Blackstock, ''History of nonlinear acoustics and a survey of Burgers' and related equations,'' in *Nonlinear Acoustics, Proceedings of the Symposium held at Applied Research Laboratories*, edited by T. G. Muir (University of Texas at Austin, Austin, 1969), pp. 1–27.
[10] J. N. Tjotta and S. Tjotta, ''Nonlinear equations of acoustics,'' in *Frontiers of Nonlinear Acoustics: Proceedings of 12th ISNA*, edited by M. F. Hamilton and D. T. Blackstock (Elsevier, London, England, 1990), pp. 80–97.
[11] E. A. Zabolotskaya and R. V. Khokhlov, ''Quasi-plane waves in the nonlinear acoustics of confined beams,'' Sov. Phys. Acoust. **15**, 35–40 (1969).

[12] V. P. Kuznetsov, ''Equations of nonlinear acoustics,'' Sov. Phys. Acoust. **16**, 467–470 (1971).
[13] B. E. McDonald and W. A. Kuperman, ''Time domain formulation for pulse propagation including nonlinear behaviour at a caustic,'' J. Acoust. Soc. Am. **81**, 1406–1417 (1987).
[14] J. J. Ambrosiano, D. R. Plante, B. E. McDonald, and W. A. Kuperman, ''Nonlinear propagation in an ocean acoustic waveguide,'' J. Acoust. Soc. Am. **87**, 1473–1481 (1990).
[15] M. D. Collins, ''The time-domain solution of the wide-angle parabolic equation including the effects of sediment dispersion,'' J. Acoust. Soc. Am. **84**, 2114–2125 (1988).
[16] B. J. Orchard, W. L. Siegmann, and M. J. Jacobson, ''Three-dimensional time-domain paraxial approximations for ocean acoustic wave propagation,'' J. Acoust. Soc. Am. **91**, 788–801 (1991).
[17] B. J. Orchard, W. L. Siegmann, G. J. Habetler, and M. J. Jacobson, ''Stability analysis of higher-order time-domain paraxial equations,'' J. Acoust. Soc. Am. **93**, 1335–1346 (1992).
[18] M. J. Lighthill, *Waves in Fluids* (Cambridge University Press, Cambridge, England, 1978).
[19] M. F. Hamilton, ''Model equations of nonlinear acoustics'' (private communication).
[20] B. K. Novikov, O. V. Rudenko, and V. L. Timoshenko, *Nonlinear Underwater Acoustics* (Sudostrooenie, Leningrad, Russia, 1981).
[21] S. I. Aanonsen, T. Barkve, J. N. Tjotta, and S. Tjotta, ''Distortion and harmonic generation in the nearfield of a finite amplitude sound beam,'' J. Acoust. Soc. Am. **75**, 749–768 (1983).
[22] V. W. Sparrow, ''Time-domain computations in nonlinear acoustics without one-way assumptions,'' in *Computational Acoustics*, edited by R. L. Lau, D. Lee, and A. R. Robinson (Elsevier, North-Holland, Amsterdam, 1993), pp. 359–369.
[23] R. T. Beyer, ''Nonlinear acoustics in fluids,'' in *Benchmark Papers in Acoustics, Vol. 18* (Van Nostrand Reinhold, New York, 1984).
[24] R. T. Beyer, ''Parameter of nonlinearity of fluids,'' J. Acoust. Soc. Am. **32**, 719–721 (1960).
[25] W. L. Siegmann, G. A. Kriegsmann, and D. Lee, ''A wide-angle three-dimensional parabolic wave equation,'' J. Acoust. Soc. Am. **78**, 659–664 (1985).
[26] G. A. Kriegsmann, ''A multiscale derivation of a new parabolic equation which includes density variations,'' Comput. Math. Appl. **11**, 817–821 (1985).
[27] M. D. Collins, ''Time-domain solution of higher-order parabolic equations,'' in *Computational Acoustics*, edited by D. Lee, A. Cakmak, and R. Vichnevetsky (Elsevier, North-Holland, Amsterdam, 1990), pp. 261–273.
[28] N. N. Yanenko, *The Method of Fractional Steps* (Springer-Verlag, New York, 1971).
[29] M. D. Collins and E. K. Westwood, ''A higher-order energy-conserving parabolic equation for range-dependent ocean depth, sound speed, and density,'' J. Acoust. Soc. Am. **89**, 1068–1075 (1991).
[30] R. S. Kulkarni, W. L. Siegmann, M. D. Collins, and B. E. McDonald, ''Nonlinear pulse propagation in shallow-water environments with attenuating and dispersive sediments'' (in preparation).
[31] A. R. Mitchell and D. F. Griffiths, *The Finite Difference Method in Partial Differential Equations* (Wiley, New York, 1980).
[32] B. E. McDonald and J. Ambrosiano, ''High-order upwind flux correction methods for hyperbolic conservation laws,'' J. Comp. Phys. **56**, 448–460 (1984).
[33] M. D. Collins, ''A nearfield asymptotic analysis for underwater acoustics,'' J. Acoust. Soc. Am. **85**, 1107–1114 (1989).
[34] G. V. Frisk, *Ocean and Seabed Acoustics: A Theory of Wave Propagation* (Prentice-Hall, Englewood Cliffs, NJ, 1994).
[35] C. Hirsch, *Numerical Computation of Internal and External Flows* (Wiley, New York, 1988), Vol. 2.
[36] W. H. Press, S. A. Teukolski, W. T. Vetterling, and B. P. Flannery, *Numerical Recipes in FORTRAN: The Art of Scientific Computing*, 2nd ed. (Cambridge University Press, Cambridge, England, 1992).

The coupled mode parabolic equation

Ahmad T. Abawi[a] and W. A. Kuperman
Scripps Institution of Oceanography, La Jolla, California 92093

Michael D. Collins
Naval Research Laboratory, Washington, DC 20375

(Received 3 September 1996; accepted for publication 4 February 1997)

The coupled mode parabolic equation (PE) is a generalization of the adiabatic mode PE that includes mode coupling terms. It is practical to apply this approach to large-scale problems involving coupling of energy between both modes and azimuths. The solution is expressed in terms of the normal modes and mode coefficients, which satisfy coupled horizontal wave equations. The coupled mode PE may be solved efficiently with the splitting method. The first step is equivalent to solving the adiabatic mode PE over one range step. The second step involves the integration of the coupling term. The coupling mode PE solution conserves energy, which is an important aspect of a range-dependent propagation model. The derivation of the coupled mode PE, which involves completing the square of an operator, is related to the derivation of an adiabatic mode PE that accounts for ambient flow. Examples are presented to illustrate the accuracy of the coupled mode PE. © *1997 Acoustical Society of America.* [S0001-4966(97)05406-4]

PACS numbers: 43.30.Bp, 43.30.Dr [SAC-B]

INTRODUCTION

The Perth–Bermuda[1–3] and Heard Island[4–7] experiments have stimulated interest in global-scale ocean acoustics. It is very difficult to solve global-scale problems due to the size and complexity of the medium and the coupling of energy between both modes and azimuths. The global-scale results that have been generated[2,3,5–8] neglect one type of coupling and are based on adiabatic mode,[9–12] parabolic equation (PE),[13–16] and ray approximations. There are indications that both types of coupling occur for some global-scale problems.[5] Three-dimensional PE models[17,18] handle both types of coupling but are only practical for small-scale problems. In this paper, we derive and test a generalization of the adiabatic mode PE[19] that includes coupling terms. It is practical to apply the coupled mode PE to large-scale problems and possibly even global-scale problems at low frequencies.

The adiabatic mode solution is based on the assumption that energy does not couple between the modes (or eigenfunctions) of the depth separated wave equation. The acoustic field is represented locally in terms of the modes, and the mode coefficients satisfy horizontal wave equations. In some cases, it is possible to obtain useful information by solving for only a fraction of the mode coefficients. The horizontal wave equations may be solved efficiently with the PE method,[19] which handles caustics and horizontal variations in the properties of the medium. At low frequencies, it is practical to solve global-scale problems with the adiabatic mode PE.[8] This approach is more efficient than three-dimensional PE models because the number of propagating modes is usually much smaller than the number of grid points that are required in a finite-difference treatment of the depth operator.

The coupled mode PE is obtained by including coupling terms[20–29] in the horizontal wave equations. Mode coupling may also be treated using vertical interface conditions.[30] The splitting solution[31] of the coupled mode PE involves the numerical solution of the adiabatic mode PE (which does not involve coupled equations) and the integration of a mode coupling term (which does not involve azimuthal coupling). The coupled mode PE solution conserves energy, which is an important property of a range-dependent propagation model.[32–34] The derivation of the coupled mode PE involves completing the square of an operator and is similar to the derivation of the windy PE,[35] which is a generalization of the adiabatic mode PE that accounts for ambient flow. The derivation of the coupled mode PE is presented in Sec. I. Examples are presented in Sec. II to illustrate the accuracy of the coupled mode PE.

I. DERIVATION

We derive the coupled mode PE in this section. To simplify the derivation, we work in Cartesian coordinates and neglect attenuation. We later convert to cylindrical coordinates and include the effects of attenuation as a perturbation by allowing the modal eigenvalues to be complex.[30] The sound speed c and density ρ may vary arbitrarily with the depth z but are assumed to vary gradually with the range x and cross range y. We place a time-harmonic point source of circular frequency ω on the z axis and remove the factor $\exp(-i\omega t)$ from the complex pressure P.

In order to handle density variations efficiently we work with the reduced pressure $p = \rho^{-1/2}P$, which satisfies the Helmholtz equation,

$$\nabla_\perp^2 p + \frac{\partial^2 p}{\partial z^2} + \tilde{k}^2 p = 0, \tag{1}$$

[a]Present address: Naval Command Control, Ocean Survey Center, San Diego, CA 92152.

 0001-4966/97/102(1)/233/6/$10.00

$$\tilde{k}^2 = k^2 + \frac{1}{2}\frac{\partial^2 \gamma}{\partial z^2} - \frac{1}{4}\left(\frac{\partial \gamma}{\partial z}\right)^2, \tag{2}$$

where $k=\omega/c$ is the wave number, $\gamma=\log \rho$, and $\nabla_\perp^2$ is the horizontal component of the Laplacian. The solution of Eq. (1) is expressed in terms of the local normal modes as

$$p(x,y,z) = \sum_j p_j(x,y)\,\phi_j(z;x,y), \tag{3}$$

where p_j is the jth mode coefficient and the jth mode ϕ_j and eigenvalue $k_j^2(x,y)$ satisfy

$$\frac{\partial^2 \phi_j}{\partial z^2} + \tilde{k}^2 \phi_j = k_j^2 \phi_j, \tag{4}$$

$$\int \phi_i \phi_j \, dz = \delta_{ij}. \tag{5}$$

The semicolon in the argument of ϕ_j indicates slow variation with respect to the horizontal coordinates. To obtain a leading-order mode coupling correction in the limit of gradual horizontal variations in c and ρ, we retain only the first horizontal derivatives of ϕ_j. We later account for horizontal variations in k_j by including an energy-conservation correction.

Substituting the normal mode representation into Eq. (1), we obtain

$$\sum_j \phi_j(\nabla_\perp^2 p_j + k_j^2 p_j) \sim -2\sum_j \left(\frac{\partial \phi_j}{\partial x}\frac{\partial p_j}{\partial x} + \frac{\partial \phi_j}{\partial y}\frac{\partial p_j}{\partial y}\right). \tag{6}$$

Multiplying Eq. (6) by ϕ_i, integrating over depth, and using Eq. (5), we obtain the horizontal wave equations,

$$\nabla_\perp^2 p_i + k_i^2 p_i \sim -2\sum_j \left(A_{x,i,j}\frac{\partial p_j}{\partial x} + A_{y,i,j}\frac{\partial p_j}{\partial y}\right), \tag{7}$$

where the coupling coefficients $A_{x,i,j}$ and $A_{y,i,j}$ are defined by

$$A_{x,i,j} = \int \phi_i \frac{\partial \phi_j}{\partial x}\, dz, \tag{8}$$

$$A_{y,i,j} = \int \phi_i \frac{\partial \phi_j}{\partial y}\, dz. \tag{9}$$

The adiabatic mode solution is recovered by neglecting the terms on the right side of Eq. (7). Placing the mode coefficients into the vector $\mathbf{p}$, the coupling coefficients into the matrices A_x and A_y, and the eigenvalues into the diagonal matrix K^2, we obtain

$$\frac{\partial^2 \mathbf{p}}{\partial x^2} + \frac{\partial^2 \mathbf{p}}{\partial y^2} + K^2\mathbf{p} + 2A_x\frac{\partial \mathbf{p}}{\partial x} + 2A_y\frac{\partial \mathbf{p}}{\partial y} = \mathbf{0}. \tag{10}$$

It follows from Eq. (5) that the coupling matrices $A_x = -A_x^t$ and $A_y = -A_y^t$ are antisymmetric. We refer to solutions of Eq. (10) as continuous coupled mode solutions as opposed to the stepwise coupled mode solutions of Ref. 30.

Completing the square of the range operator in Eq. (10) and neglecting a higher-order coupling term, we obtain

$$\left(\frac{\partial}{\partial x} + A_x\right)^2 \mathbf{p} + \frac{\partial^2 \mathbf{p}}{\partial y^2} + 2A_y\frac{\partial \mathbf{p}}{\partial y} + K^2\mathbf{p} = \mathbf{0}. \tag{11}$$

Factoring the operator in Eq. (11) under the assumption of gradual range dependence, we obtain

$$\left[\frac{\partial}{\partial x} + A_x - i\left(\frac{\partial^2}{\partial y^2} + 2A_y\frac{\partial}{\partial y} + K^2\right)^{1/2}\right] \times \left[\frac{\partial}{\partial x} + A_x + i\left(\frac{\partial^2}{\partial y^2} + 2A_y\frac{\partial}{\partial y} + K^2\right)^{1/2}\right]\mathbf{p} = \mathbf{0}. \tag{12}$$

This approach for factoring Eq. (10) was used to derive the windy PE from a similar horizontal wave equation in which advection terms play the role of the coupling terms.[35] Assuming that outgoing energy dominates backscattered energy, we obtain the outgoing wave equation:

$$\frac{\partial \mathbf{p}}{\partial x} = -A_x\mathbf{p} + i\left(\frac{\partial^2}{\partial y^2} + 2A_y\frac{\partial}{\partial y} + K^2\right)^{1/2}\mathbf{p}. \tag{13}$$

In cylindrical geometry, we remove the spreading factor $r^{-1/2}$ from $\mathbf{p}$ and obtain the following counterpart to Eq. (13):

$$\frac{\partial \mathbf{p}}{\partial r} = -A_r\mathbf{p} + i\left(\frac{1}{r^2}\frac{\partial^2}{\partial \theta^2} + 2A_\theta\frac{1}{r}\frac{\partial}{\partial \theta} + K^2\right)^{1/2}\mathbf{p}, \tag{14}$$

where the entries of A_r and A_θ are defined by

$$A_{r,i,j} = \int \phi_i \frac{\partial \phi_j}{\partial r}\, dz, \tag{15}$$

$$A_{\theta,i,j} = \int \phi_i \frac{1}{r}\frac{\partial \phi_j}{\partial \theta}\, dz. \tag{16}$$

When acoustic energy propagates from a point source in a medium with gradual horizontal variations, azimuthal terms are usually dominated by other terms in the wave equation. For many problems, it is possible to ignore azimuthal terms altogether and apply the uncoupled azimuth approximation.[36] Even when azimuthal coupling is significant, the azimuthal terms tend to be less important than other terms (e.g., the three-dimensional PE models of Refs. 17 and 18 are based on a narrow-angle expansion in the azimuth term but a wide-angle expansion in the depth term). We use this fact and observations of solutions of the windy PE to motivate a useful simplification of Eq. (14). The windy PE is based on the following outgoing wave equation that is similar to Eq. (14):

$$\frac{\partial p_j}{\partial r} = -ik_jU_{jr}p_j + i\left(\frac{1}{r^2}\frac{\partial^2}{\partial \theta^2} + 2ik_jU_{j\theta}\frac{1}{r}\frac{\partial}{\partial \theta} + k_j^2\right)^{1/2}p_j, \tag{17}$$

where U_{jr} and $U_{j\theta}$ are defined in terms of the wind velocity.[35] We have found that the cross term in Eq. (17), which involves the product of a flow operator and an azimuthal coupling operator, tends to be dominated by the other terms. In particular, the solutions of the equation

$$\frac{\partial p_j}{\partial r} = -ik_jU_{jr}p_j + i\left(\frac{1}{r^2}\frac{\partial^2}{\partial \theta^2} + k_j^2\right)^{1/2}p_j \tag{18}$$

are nearly identical to the solutions of Eq. (17) for the examples presented in Ref. 35.

Neglecting the cross term in Eq. (14), we obtain the coupled mode PE,

$$\frac{\partial \mathbf{p}}{\partial r} = -A_r \mathbf{p} + i\left(\frac{1}{r^2}\frac{\partial^2}{\partial \theta^2} + K^2\right)^{1/2} \mathbf{p}. \tag{19}$$

The first term on the right side of Eq. (19) accounts for mode coupling in the radial direction. The second term accounts for azimuthal coupling and refraction. Neglecting the cross term to obtain Eq. (18) does not provide a significant advantage for the windy PE. Neglecting the cross term to obtain Eq. (19) leads to a significant simplification of the numerical solution of the coupled mode PE because it permits the use of alternating directions. Neglecting the cross term can be justified by an asymptotic argument. We regard azimuthal coupling as a perturbation and retain only the leading order mode coupling correction to the adiabatic mode PE. Since $A_r\mathbf{p}$ and $A_\theta\mathbf{p}$ are of the same order, it follows that

$$\left|K^{-1}A_\theta \frac{1}{r}\frac{\partial \mathbf{p}}{\partial \theta}\right| \ll |A_r \mathbf{p}|. \tag{20}$$

In other words, the first term on the right side of Eq. (14) dominates the cross term.

The solution of Eq. (19) does not conserve energy. One approach for deriving a coupled mode PE that conserves energy would be to perform a WKB analysis that includes horizontal derivatives of the environmental parameters. An easier approach is to incorporate previous results and then verify that energy is conserved. Energy-conserving solutions can be obtained by defining a new dependent variable that is related to the energy-flux density. The dependent variable in Eq. (19) is missing the correction factor $k_j^{1/2}$ that occurs in the complete energy conservation correction.[34] Applying this correction as described in Ref. 19, we define $u_j = k_j^{1/2} p_j$ and obtain the energy-conserving coupled mode PE solution,

$$p(r,\theta,z) = r^{-1/2} \sum_j [k_j(r,\theta)]^{-1/2} u_j(r,\theta)\phi_j(z;r,\theta), \tag{21}$$

$$\frac{\partial \mathbf{u}}{\partial r} = -A_r \mathbf{u} + i\left(\frac{1}{r^2}\frac{\partial^2}{\partial \theta^2} + K^2\right)^{1/2} \mathbf{u}, \tag{22}$$

where u_j is the j th entry of $\mathbf{u}$. The initial condition corresponding to a point source at $z = z_0$ is

$$u_j(0,\theta) = \phi_j(z_0;0,\theta). \tag{23}$$

The second term on the right side of Eq. (22) conserves energy because the adiabatic mode PE conserves energy.[19] The coupling term produces a rotation of $\mathbf{u}$ and conserves energy because

$$\frac{dE}{dr} = \mathbf{u}^* \frac{\partial \mathbf{u}}{\partial r} + \frac{\partial \mathbf{u}^*}{\partial r}\mathbf{u} = -\mathbf{u}^* A_r \mathbf{u} - \mathbf{u}^* A_r^t \mathbf{u} = 0, \tag{24}$$

where $E = |\mathbf{u}|^2$ is the energy flux. The third equal sign in Eq. (24) follows from the antisymmetry of A_r.

We solve Eq. (22) with the splitting method,[31] which involves numerical solutions of the equations

$$\frac{\partial \mathbf{u}}{\partial r} = i\left(\frac{1}{r^2}\frac{\partial^2}{\partial \theta^2} + K^2\right)^{1/2} \mathbf{u}, \tag{25}$$

$$\frac{\partial \mathbf{u}}{\partial r} = -A_r \mathbf{u}. \tag{26}$$

Since K^2 is diagonal and the cross term in Eq. (14) was dropped, Eq. (25) is an uncoupled system that reduces to the horizontal wave equations involved in the adiabatic mode PE solution. We therefore solve Eq. (25) over a range step using the approach described in Ref. 19. The operator square root is approximated using a rational function expansion about the representative horizontal wave number k_0. Crank–Nicolson integration is used for the range discretization. The azimuth discretization involves a tridiagonal matrix modified with entries in the upper right and lower left corners to account for periodicity. The numerical solution of Eq. (26) is obtained using Crank–Nicolson integration.

There are several possible ways to extend or improve the coupled mode PE. When coupling is mostly into neighboring modes, it is possible to improve efficiency by approximating A_r with a banded matrix.[12] The coupled mode PE can be modified to account for energy loss due to coupling into the nonpropagating or nontrapped modes by including positive entries along the main diagonal of the coupling matrix. It should be possible to include the effects of coupling with the stepwise approach of Ref. 30 as an alternative to using the coupling term in Eq. (19). With this approach, the medium is approximated by a sequence of range-independent regions and the transmitted fields across vertical interfaces are approximated with the energy-conserving condition described in Ref. 34. This approach includes higher-order coupling terms and is a generalization of the step-wise coupled mode solution to three dimensions.

II. IMPLEMENTATION AND EXAMPLES

In this section, we present examples to illustrate and test solutions of the coupled mode PE. Although several papers have been published on continuous coupled modes, there apparently has not been any benchmark testing to confirm that this technique actually works. The implementation of the coupled mode PE involves the solution of the eigenvalue problem throughout the region of interest. Once the eigenvalues, eigenfunctions, and coupling coefficients are obtained and stored, the coupled mode PE solution may be obtained efficiently for different combinations of source and receiver locations. For the adiabatic case, this precalculation approach[12] has been used to solve problems in matched-field processing[37,38] that require replica fields for large numbers of source and receiver locations[39]

Example A is a two-dimensional problem involving a 25-Hz source at $z = 50$ m in a 200-m-thick waveguide that is lossless and of constant density. The waveguide consists of two layers that are divided by an interface at

$$z = \begin{cases} d_0 & \text{for } r < 1 \text{ km} \\ d_0 + \alpha \sin\left(\dfrac{2\pi r}{\lambda}\right) & \text{for } r > 1 \text{ km}, \end{cases} \tag{27}$$

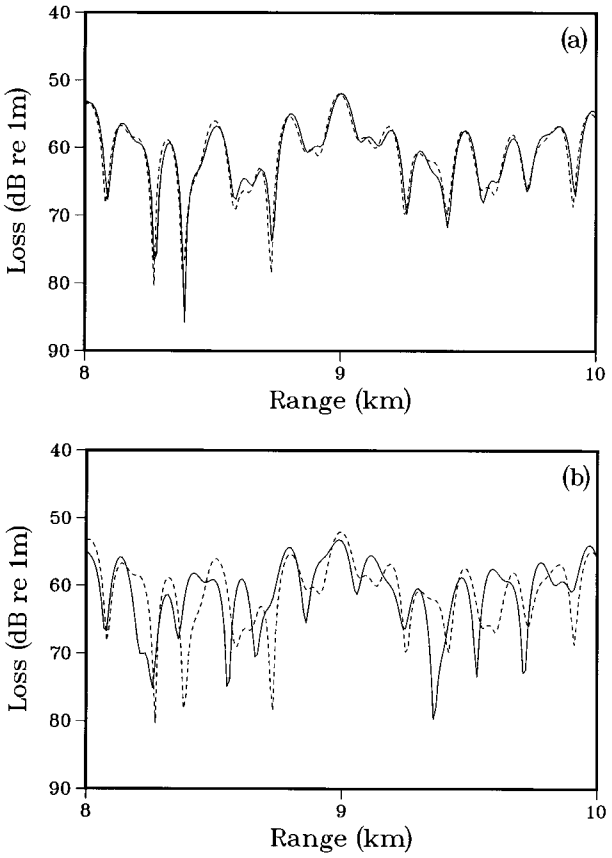

FIG. 1. Transmission loss at $z=30$ m for example A, which is a two-dimensional problem that involves a sinusoidal interface between two homogeneous layers. The solid curves correspond to (a) the coupled mode PE solution and (b) the adiabatic mode solution. The dashed curves correspond to the energy-conserving PE solution.

where $d_0=100$ m, $\alpha=5$ m, and $\lambda=200$ m. The speed of sound is 1500 m/s in the upper layer and 1600 m/s in the lower layer. The purpose of this example is to show that the coupling term accurately handles extensive mode coupling. The waveguide supports six modes corresponding to horizontal phase speeds that range between about 1538 and 4190 m/s. Results for example A appear in Fig. 1. The coupled mode PE solution is in agreement with a reference solution that was generated using a finite-difference PE model based on the complete energy-conservation correction.[34] The adiabatic mode solution breaks down for this problem.

Example B is identical to example A, with the exception that the interface is at

$$z=d_0+\alpha\,\sin\left(\frac{2\pi x}{\lambda}\right). \tag{28}$$

We were motivated to consider this problem because corrugated interfaces can cause azimuthal coupling by channeling energy in the y direction.[17] To handle the wide range of horizontal phase speeds, we take $\omega/k_0=2000$ m/s and approximate the operator square root in Eq. (22) with an eight-term rational function. We use range and azimuthal grid spacings of 10 m and 0.25°. Results for example B appear in Fig. 2. Since both types of coupling are important for this problem, there are significant differences between the coupled mode PE solution and the solutions that neglect one type of coupling. Comparing the left and center columns, we observe that azimuthal coupling is strongest near the y axis, where the corrugations cause channeling. Comparing the left and right columns, we observe that mode coupling is strongest near the x axis, where range dependence is greatest.

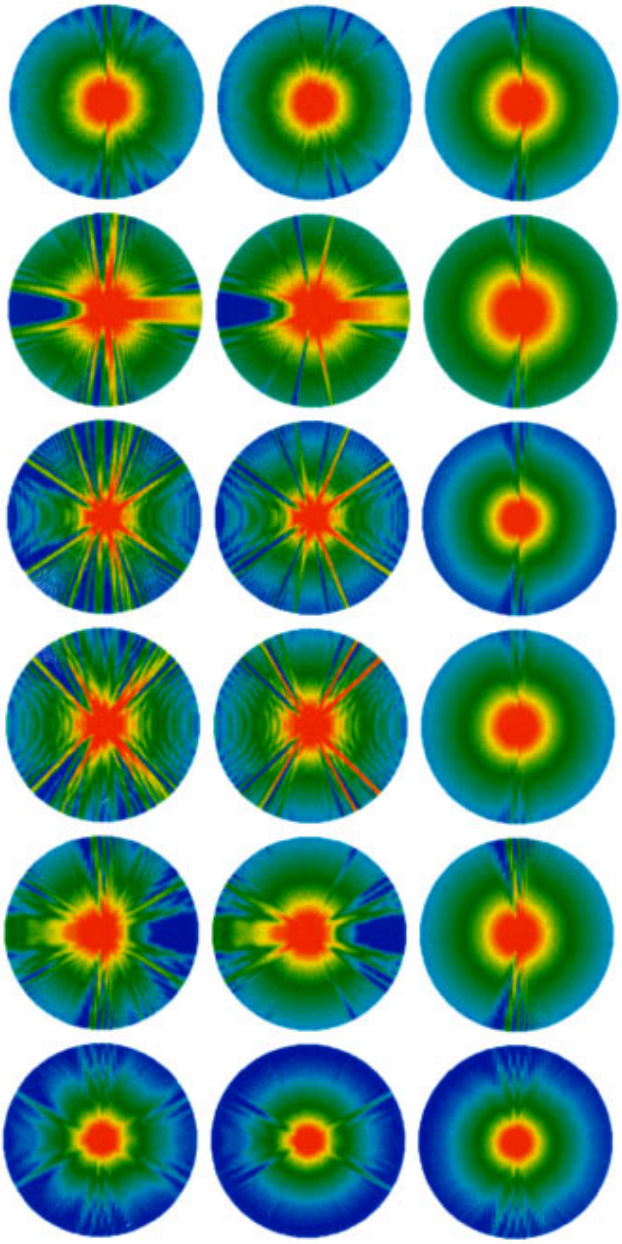

FIG. 2. The mode coefficients for example B, which is a three-dimensional problem that involves a corrugated interface between two homogeneous layers. The maximum range is 5 km, the positive x direction is to the right, and the positive y direction is to the top. The left column contains the coupled mode PE solutions, the center column contains the uncoupled azimuth solution, and the right column contains the adiabatic mode PE solution. The modes are shown in increasing order going downward in each column. The dynamic range is 10 dB, with red corresponding to the highest intensities.

Example C involves a 25-Hz source at $z=180$ m in a shallow water ocean environment. The sound speed is 1500 m/s in the water column and 1700 m/s in the sediment. The density of the sediment is 1.5 times the density of the water. The attenuation in the sediment is 0.5 dB/λ. The ocean depth

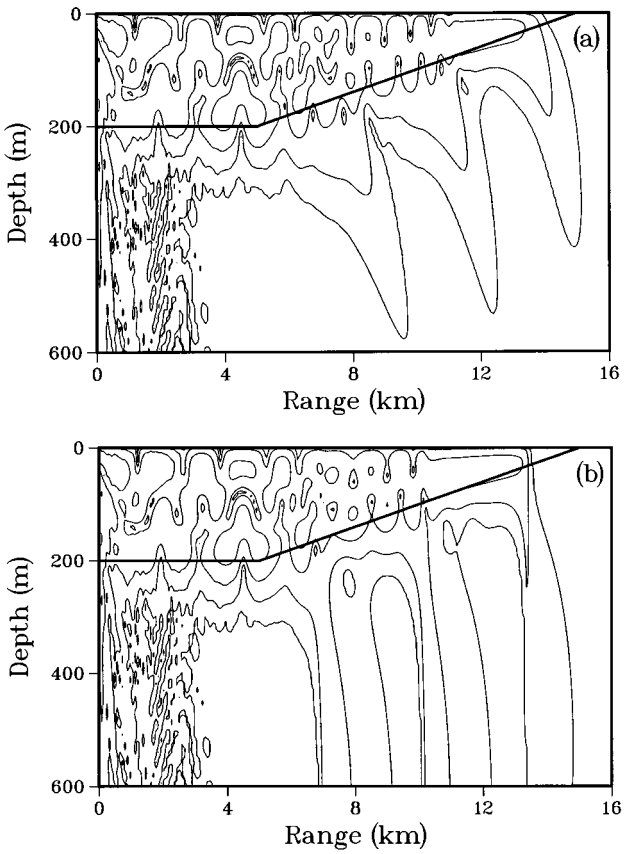

FIG. 3. Transmission loss contours for example C, which involves a sloping ocean bottom and mode cutoff. (a) The coupled mode PE solution. (b) The adiabatic mode solution.

is 200 m for $r<5$ km and linearly decreases to an apex at $r=15$ km. In the upslope region, the three trapped modes cut off and couple into beams in the sediment.[40] The purpose of this example is to illustrate the coupled mode PE for a realistic example and to illustrate coupling between trapped and nontrapped modes. We truncate the domain at $z=1200$ m and use 36 modes in the coupled mode PE calculation. Contour plots for example C appear in Fig. 3. The adiabatic mode solution breaks down in the sediment (the beams are not correct). The coupled mode PE solution is accurate in the sediment (the beams are correct).

III. CONCLUSION

The coupled mode PE was derived by including a coupling term in the adiabatic mode PE. This technique is efficient for solving acoustic propagation problems that involve both mode and azimuthal coupling. The coupled mode PE is simplified by neglecting a higher-order cross term that involves a product of mode and azimuthal coupling operators. Tests involving a similar cross term in the windy PE suggest that this approximation is robust. The numerical solution is based on standard techniques such as splitting and Crank–Nicolson integration. The coupled mode PE conserves energy because the adiabatic mode PE conserves energy and the coupling matrix is antisymmetric. The accuracy of the coupled mode PE was demonstrated for benchmark problems. The coupled mode PE was also applied to solve a three-dimensional problem.

ACKNOWLEDGMENTS

This work was supported by the Office of Naval Research, Code 321OA, and DARPA Grant No. MDA972-93-1-0003.

[1] R. C. Shockley, J. Northrop, P. G. Hansen, and C. Hartdegen, ''SOFAR propagation paths from Australia to Bermuda: Comparison of signal speed algorithms and experiments,'' J. Acoust. Soc. Am. **71**, 51–60 (1982).
[2] W. C. O'Reilly, W. H. Munk, and J. L. Reid, ''Australia–Bermuda sound transmission experiment (1960) revised,'' J. Phys. Oceanogr. **18**, 1878–1898 (1988).
[3] K. D. Heaney, W. A. Kuperman, and B. E. McDonald, ''Perth–Bermuda sound propagation (1960): Adiabatic mode interpretation,'' J. Acoust. Soc. Am. **90**, 2586–2594 (1991).
[4] W. H. Munk, R. C. Spindel, A. Baggeroer, and T. G. Birdsall, ''The Heard Island feasibility test,'' J. Acoust. Soc. Am. **96**, 2330–2342 (1994).
[5] B. E. McDonald, M. D. Collins, W. A. Kuperman, and K. D. Heaney, ''Comparison of data and model predictions for Heard Island acoustic transmissions,'' J. Acoust. Soc. Am. **96**, 2357–2370 (1994).
[6] E. C. Shang, Y. Y. Wang, and T. M. Georges, ''Dispersion and repopulation of the Heard–Ascension modes,'' J. Acoust. Soc. Am. **96**, 2371–2379 (1994).
[7] C. S. Chiu, A. J. Semtner, C. M. Ort, J. H. Miller, and L. L. Ehret, ''A ray variability analysis of sound transmission from Heard Island to California,'' J. Acoust. Soc. Am. **96**, 2380–2388 (1994).
[8] M. D. Collins, B. E. McDonald, K. D. Heaney, and W. A. Kuperman, ''Three-dimensional effects in global acoustics,'' J. Acoust. Soc. Am. **97**, 1567–1575 (1995).
[9] A. D. Pierce, ''Extension of the method of normal modes to sound propagation in an almost-stratified medium,'' J. Acoust. Soc. Am. **37**, 19–27 (1965).
[10] D. M. Milder, ''Ray and wave invariants for SOFAR channel propagation,'' J. Acoust. Soc. Am. **46**, 1259–1263 (1969).
[11] H. Weinberg and R. Burridge, ''Horizontal ray theory for ocean acoustics,'' J. Acoust. Soc. Am. **55**, 63–79 (1974).
[12] W. A. Kuperman, M. B. Porter, J. S. Perkins, and R. B. Evans, ''Rapid computation of acoustic fields in three-dimensional ocean environments,'' J. Acoust. Soc. Am. **89**, 125–133 (1991).
[13] M. A. Leontovich and V. A. Fock, ''Solution of the problem of propagation of electromagnetic waves along the earth's surface by the method of parabolic equation,'' J. Exp. Theor. Phys. **16**, 557–573 (1946).
[14] V. A. Fock, *Electromagnetic Diffraction and Propagation Problems* (Pergamon, New York, 1965), pp. 213–234.
[15] F. D. Tappert, ''The parabolic approximation method,'' in *Wave Propagation and Underwater Acoustics*, edited by J. B. Keller and J. S. Papadakis, Lecture Notes in Physics 70 (Springer-Verlag, New York, 1977).
[16] F. B. Jensen, W. A. Kuperman, M. B. Porter, and H. Schmidt, *Computational Ocean Acoustics* (American Institute of Physics, New York, 1994), pp. 343–412.
[17] M. D. Collins and S. A. Chin-Bing, ''A three-dimensional parabolic equation model that includes the effects of rough boundaries,'' J. Acoust. Soc. Am. **87**, 1104–1109 (1990).
[18] D. Lee, G. Botseas, and W. L. Siegmann, ''Examination of three-dimensional effects using a propagation model with azimuth-coupling capability (FOR3D),'' J. Acoust. Soc. Am. **91**, 3192–3202 (1992).
[19] M. D. Collins, ''The adiabatic mode parabolic equation,'' J. Acoust. Soc. Am. **94**, 2269–2278 (1993).
[20] R. D. Graves, A. Nagl, H. Überall, and G. L. Zarur, ''Range-dependent normal modes in underwater sound propagation: Application to the wedge-shaped ocean,'' J. Acoust. Soc. Am. **58**, 1171–1177 (1975).
[21] S. R. Rutherford, ''An examination of coupled mode theory as applied to underwater sound propagation,'' Rep. No. APL-TR-79-44 (Applied Research Laboratories, Austin, TX, 1979).
[22] S. R. Rutherford and K. E. Hawker, ''Consistent coupled mode theory of sound propagation for a class of nonseparable problems,'' J. Acoust. Soc. Am. **70**, 554–564 (1981).

[23] S. T. McDaniel, ''Mode coupling due to interaction with the seabed,'' J. Acoust. Soc. Am. **72**, 916–923 (1982).
[24] C. A. Boyles, ''Coupled mode solution for a cylindrically symmetric oceanic waveguide with a range and depth dependent refractive index and a time varying rough sea surface,'' J. Acoust. Soc. Am. **73**, 800–805 (1983).
[25] J. A. Fawcett, ''A derivation of the differential equations of coupled-mode propagation,'' J. Acoust. Soc. Am. **92**, 290–295 (1992).
[26] G. Gillette, ''Coupled modes in a waveguide with a range-dependent rigid basement,'' J. Acoust. Soc. Am. **95**, 187–200 (1994).
[27] D. P. Knobles, ''Solutions of coupled-mode equations with a large dimension in underwater acoustics,'' J. Acoust. Soc. Am. **96**, 1741–1747 (1994).
[28] Y. Desaubies and K. Dysthe, ''Normal-mode propagation in slowly varying ocean waveguides,'' J. Acoust. Soc. Am. **97**, 933–946 (1995).
[29] B. E. McDonald, ''Bathymetric and volumetric contributions in ocean acoustic mode coupling,'' J. Acoust. Soc. Am. **100**, 219–224 (1996).
[30] R. B. Evans, ''A coupled mode solution for acoustic propagation in a waveguide with stepwise depth variations of a penetrable bottom,'' J. Acoust. Soc. Am. **74**, 188–195 (1983).
[31] A. R. Mitchell and D. F. Griffiths, *The Finite Difference Method in Partial Differential Equations* (Wiley, New York, 1980), pp. 59–70.
[32] M. B. Porter, F. B. Jensen, and C. M. Ferla, ''The problem of energy conservation in one-way models,'' J. Acoust. Soc. Am. **89**, 1058–1067 (1991).
[33] M. D. Collins and E. K. Westwood, ''A higher-order energy-conserving parabolic equation for range-dependent ocean depth, sound speed, and density,'' J. Acoust. Soc. Am. **89**, 1068–1075 (1991).
[34] M. D. Collins, ''An energy-conserving parabolic equation for elastic media,'' J. Acoust. Soc. Am. **94**, 975–982 (1993).
[35] M. D. Collins, B. E. McDonald, W. A. Kuperman, and W. L. Siegmann, ''Jovian acoustics and Comet Shoemaker–Levy 9,'' J. Acoust. Soc. Am. **97**, 2147–2158 (1995).
[36] J. S. Perkins and R. N. Baer, ''An approximation to the three-dimensional parabolic-equation method for acoustic propagation,'' J. Acoust. Soc. Am. **72**, 515–522 (1982).
[37] H. P. Bucker, ''Use of calculated sound fields and matched-field detection to locate sound sources in shallow water,'' J. Acoust. Soc. Am. **59**, 368–373 (1976).
[38] A. B. Baggeroer, W. A. Kuperman, and P. N. Mikhalevsky, ''An overview of matched field methods in ocean acoustics,'' IEEE J. Ocean Eng. **18**, 401–424 (1993).
[39] J. S. Perkins and W. A. Kuperman, ''Environmental signal processing: Three-dimensional matched-field processing with a vertical array,'' J. Acoust. Soc. Am. **87**, 1553–1556 (1990).
[40] F. B. Jensen and W. A. Kuperman, ''Sound propagation in a wedge-shaped ocean with a penetrable bottom,'' J. Acoust. Soc. Am. **67**, 1564–1566 (1980).

Wavefront folding, chaos, and diffraction for sound propagation through ocean internal waves

Jeffrey Simmen, Stanley M. Flatté, and Guang-Yu Wang
Physics Department and Institute of Tectonics, University of California at Santa Cruz, Santa Cruz, California 95064

(Received 27 November 1995; revised 4 December 1996; accepted 5 January 1997)

This work presents an analysis of the effects of ocean internal waves on long-range acoustic pulse propagation from the geometrical-optics point of view. The chaotic behavior of rays and the microfolding of timefronts are investigated. The extent of the region of the timefront in which strongly chaotic rays appear, and the strength of the rays' sensitivity to initial conditions, are found to depend on the average (range-independent) sound-speed profile, on the range from the source to the receiver, and on the internal-wave spectral model, but not on the specific realization of the internal waves. For a particular experiment (SLICE89), it is concluded that the observed depth diffusion of energy in the late-arriving portion of the timefront is a result of refraction (of geometrical-optics rays), not diffraction. It is found that internal-wave effects cause an upper turning point of a ray to be spread to the extent of 10 km horizontally and 100 m vertically, which affects the resolution of ocean-acoustic tomography. The validity and usefulness of ray-based, semi-classical (WKB) waveforms to represent received arrivals are evaluated by comparing with waveforms generated with multifrequency, parabolic-equation simulations. Center frequencies of 250 Hz and 1000 Hz with 100-Hz bandwidth are used. The semi-classical waveforms reproduce the correct arrival time and temporal shape of almost all arrivals, even those that are made of dozens of microrays induced by the internal waves. The overall intensities of the 1000-Hz arrivals are reasonably accurate, while the 250-Hz intensities show differences of order 5 dB. [S0001-4966(97)04707-3]

PACS numbers: 43.30.Cq [JHM]

INTRODUCTION

Interest has grown in recent years in the use of sound propagation as a tomographic means to study and monitor the ocean.[1,2] So far, pulse travel time has been the principal signal characteristic from which inversions have been performed to reconstruct ocean sound-speed (or temperature) structure. However, for propagation over long ranges (exceeding several hundred km) it has been noted that pulse timefront arrivals sometimes become so smeared together due to internal waves that they cannot be used for travel-time measurements.[3,4] As a result, considerable effort has been expended in investigating the use of modal travel times as an alternative set of observables on which to base a tomographic inversion (e.g., Voronovich and Shang,[5] and Colosi and Flatté[6]).

In the study of pulse propagation, it becomes useful to work with the asymptotic behavior (e.g., the WKB approximation) of the wave equation. The linear wave equation then reduces to the ''geometric'' Eikonal equation describing pulse travel time and the transport equation describing pulse amplitude. If the Eikonal equation is decomposed into a nonlinear system of ordinary differential equations that give the travel time along ray trajectories, then the coupled equations for the ray trajectories form a Hamiltonian system. When the ocean medium through which the acoustic pulse propagates contains range-dependent structure, such as that due to internal waves and mesoscale fluctuations, then this Hamiltonian system is nonintegrable and can exhibit notable sensitivity to initial conditions or environmental perturbations. Palmer *et al.*[7] initiated the study of this chaotic behavior in ocean acoustics. Smith *et al.*[8] further suggested that the partial breakdown in identifying isolated and resolved arrivals from pulses transmitted over long ranges is due to ray chaos induced by range-dependent ocean structure. Their ocean sound-speed model consisted of a range-independent canonical sound channel perturbed by a single periodic disturbance. The results of their analysis, based on numerically calculated Lyapunov exponents and Poincaré maps, indicated the potential for ray-chaotic behavior in the ocean but did not compare well with experimental findings, due to their simple ocean model. Attempting to attribute the breakdown in identifying isolated pulse arrivals to ocean mesoscale, follow-on work[9] was aimed at studying the effect on ray sensitivity of mesocale perturbations, where the mesoscale behavior was defined by several modes. More recently, by comparing experimental data and model results, Colosi *et al.*[4] have shown through parabolic-equation (PE) simulations that ocean internal waves are the likely candidate responsible for the inability to distinguish separate arrivals when pulses are transmitted over a 1000-km range. The extent to which other ocean phenomena (e.g., mesoscale) affect transmissions at longer ranges and lower frequencies, or at other ocean locations, remains to be determined.

The emphasis in this paper is on the *ray-based* view of long-range sound propagation through ocean *internal waves*. Our goal is not to precisely quantify acoustic fluctuations due to internal waves but rather to show that a ray-based description of sound propagation through internal waves accurately

captures the important characteristics of the acoustic arrivals. In Sec. I we define the ocean model (including our model internal-wave field) through which pulse propagation is simulated. In Secs. II and III the equations that govern the acoustic propagation and the numerical methods used to solve these equations are presented, respectively. In Sec. IV the numerical results are provided and include: (i) the sensitivity to initial conditions of acoustical ray trajectories, and the geometric character of the resultant timefront, as well as the dependence of this behavior on the average sound-speed profile and particular realizations of the ocean internal-wave field; (ii) the level of diffraction due to internal waves, or equivalently, the accuracy of the asymptotic description (WKB) for pulse propagation through internal waves; and (iii) the diffusion in space of multiple ray paths (or ''ray-tubes'') that contribute to a single arriving peak and that diffusion's impact on the resolution of acoustic tomography. Finally, in Sec. V the results of this work are summarized.

I. OCEAN MODEL

We shall assume that the ocean sound speed $c(r,z,t)$ consists of an average sound-speed profile $\overline{c(z)}$, dependent only on depth coordinate z, and a small perturbation, $\delta c(r,z,t)$, dependent on range r, depth coordinate z, and time t:

$$c(r,z,t)=\overline{c(z)}+\delta c(r,z,t). \tag{1}$$

The source is at $r=0$ and the maximum range for most of our calculations is 1000 km. The vertical position z varies from $z=0$ at the ocean surface to $z=-D$ $(D>0)$ at the ocean bottom. The second horizontal spatial coordinate has been omitted since for our choice of δc the cross-range gradients of the sound speed are typically two orders of magnitude smaller than the vertical gradients, and so the sound propagation is believed to be sufficiently well described as two dimensional (having no out-of-plane scattering). (However, see Voronovich and Shang;[5] and Grabb *et al.*[10] for other points of view.)

The quantity δc will represent the sound-speed perturbation due to a field of internal waves. Typically in the ocean, $\delta c/c\approx 10^{-4}$ for a depth of 1 km (near the sound axis) and $\delta c/c\approx 5\times 10^{-4}$ near the surface.[11] For our numerical experiments, δc is constructed from a superposition of linear internal waves, constrained by the following assumptions: the ocean depth is range independent at $D=4$ km and the buoyancy profile $N(z)$ is a canonical exponential:

$$N(z)=N_0 e^{z/B}, \tag{2}$$

where $B=1$ km and $N_0=3$ cyc/h. This buoyancy profile is always assumed, independent of the average sound-speed profile.

Neglecting the small effects due to internal-wave currents, we describe the sound-speed perturbation due to internal waves by[11]

$$\delta c(r,z,t)/\overline{c(z)}\approx G N^2(z)\zeta(r,z,t), \tag{3}$$

where ζ is the vertical water displacement due to the internal waves, and G, assumed constant here, has the value 3.0 s^2/m.

We have chosen to construct the displacement ζ from the superposition of a subset field of linear internal waves traveling only along the source–receiver direction. For linear (small amplitude) waves in a flat bottom ocean, the wave displacement ζ is given by

$$\zeta(r,z,t)=\mathrm{Re}[\hat{\zeta}(z)\exp\, i(\kappa r-\omega t)], \tag{4}$$

where $\hat{\zeta}$ satisfies

$$(\omega^2-\omega_i^2)\frac{d^2\hat{\zeta}}{dz^2}+(N^2(z)-\omega^2)\kappa^2\hat{\zeta}=0, \tag{5}$$

$$\hat{\zeta}=0 \quad \text{at} \quad z=0, \tag{6}$$

$$\hat{\zeta}=0 \quad \text{at} \quad z=-D. \tag{7}$$

Here the inertial frequency ω_i is taken to be 1 cycle/day, corresponding to a latitude of 30°. Given the wave frequency ω there can be found a sequence of modes $\hat{\zeta}_j(z)$ and corresponding wave numbers κ_j, $j=1,\ldots,\infty$, satisfying the equations above. These modes form an orthogonal set so that

$$\int_{-D}^{0}(N^2(z)-\omega_i^2)\hat{\zeta}_m(z)\hat{\zeta}_n(z)dz=\gamma\delta_{mn}, \tag{8}$$

where γ is any arbitrary normalization constant independent of m and n; for later convenience γ is taken to be $2/(B*N_0^2)$.

To simplify the description of our sound-speed perturbation and simultaneously enhance the speed of calculation in our simulation we choose a single ω, $\omega=2\pi/12.5$ rad h^{-1}, corresponding to the semi-diurnal tide. Summing over the first ten modes or the first 40 modes associated with that tidal frequency produces our model internal-wave field, or more specifically, an internal-tide field. Individually, modes 1–40 introduce ocean structure with horizontal wavelengths ranging from nearly 100 km down to 2 km, and with vertical scales ranging from a few kilometers down to roughly 100 m. For modes up to ten only, horizontal wavelengths extend down to about 8 km and vertical scales range down to about a few hundred meters. We choose to construct sound-speed perturbations using modes up to 40, although typically (due to computational demands) we use only modes 1–10. It has been shown that in a typical 1000-km experiment, for acoustic frequencies of 200–300 Hz, modes above approximately 40 have a very small influence on the received field, while modes above 10 also have small effects on many aspects (e.g., broadband and wander variances) of the received field.[4]

After summing, the internal-wave displacement is given by

$$\zeta(r,z,t)=\mathrm{Re}\left[\sum_{j=1}^{N}A_j\hat{\zeta}_j(z)\exp\, i(\kappa_j r-\omega t+\lambda_j)\right], \tag{9}$$

where $N=10$ or 40, $\omega=2\pi/12.5$ rad h^{-1}, κ_j and $\hat{\zeta}_j(z)$ are determined from Eqs. (5) to (7), and λ_j are random phases. $A_j e^{i\lambda_j}$ is a complex random variable with A_j weighted according to

$$\langle A_j^2\rangle=a(j^2+j_*^2)^{-1}, \tag{10}$$

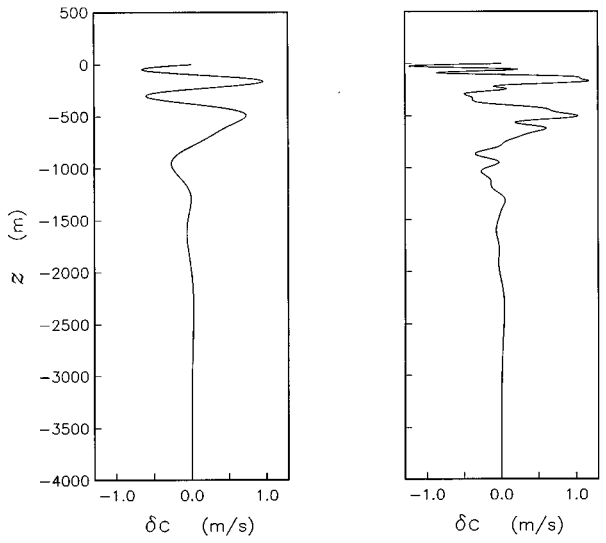

FIG. 1. Sound-speed perturbation versus depth for one fixed range. The plots show the sound-speed perturbation for one realization of our 10-mode (left) and 40-mode (right) internal-wave field.

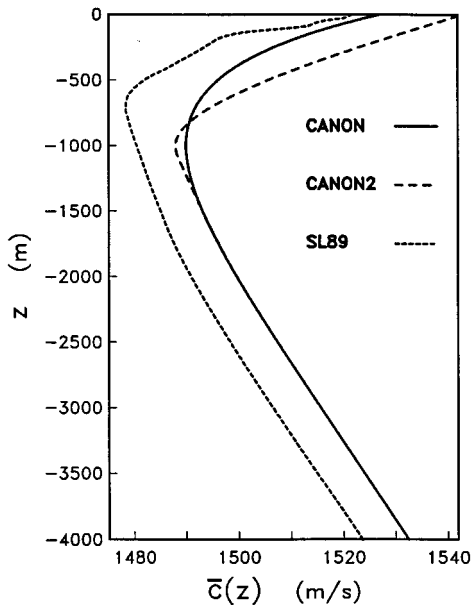

FIG. 2. Average sound-speed profiles for the three selected cases: the Munk canonical profile identified as CANON, a second smooth profile identified as CANON2, and the profile from the SLICE89 experiment.

where $j_* = 3$. If the Garrett–Munk[12] spectral density, a function of mode number and wave number, is integrated over wave number κ, then the remaining dependence on mode number j is as above. Therefore, this mode-number weighting is chosen to resemble Garrett–Munk behavior in some average sense, even though internal tides are likely to have a mode-number dependence of their own. Our primary goal here is to construct a simple ocean model which has realistic range dependence: We want structure and spatial scales similar to those exhibited by internal waves in the real ocean.

So that the internal-wave displacement is realistic in magnitude, a is chosen to force $\zeta_{\rm rms}$, when extrapolated to the surface, to be 7.3 m.[11] When sums over 10 modes are extended to 40 modes by adding on higher modes, the internal-wave energy increases slightly, but to a fair approximation perturbations with 10 or 40 modes have nearly the same energy, although the extent of their spatial scales is different.

For any realization of A_j and λ_j, $j=1,\ldots,N$, substituting the displacement given by (9) into (3) gives a characterization of the sound-speed perturbation. Figure 1 shows the vertical profile of the perturbation for one realization of 10 modes and for the extended 40-mode case. Given the perturbation δc and the average sound-speed profile $\overline{c(z)}$, the total sound-speed field is given by (1).

The average sound-speed profile is selected from a set of three profiles: the profile from the SLICE89 experiment,[3] the Munk canonical profile[13] identified as CANON, and a second smooth profile identified as CANON2. As Fig. 2 shows, the two canonical profiles have their minimum sound speeds at a depth of 1000 m, while the SLICE89 profile has its minimum at 800 m depth. The curvatures at the sound-channel axes of the two canonical profiles are different.

II. ACOUSTIC PROPAGATION

Since in the ocean the speed of sound is so much greater than the phase speed of internal waves, the ocean medium is assumed *frozen* for the acoustical simulations; i.e., during the time a sound impulse is transmitted from the source to the receiver the sound-speed dependence on time can be neglected and $c(r,z,t)$ can be replaced by $c(r,z)$, the pulse-to-pulse dependence of sound speed on time being implicit.

Our emphasis is on studying the geometric (ray-based) description of impulse propagation through ocean internal waves. It is therefore natural to solve the Eikonal and transport equations that are derived from the full wave equation. Section A below describes our approach to solving those equations.

To study diffraction, however, we need to solve a wave equation, and it is prohibitive to solve the full wave equation over 1000 km for ocean-acoustic frequencies of interest. Therefore, in addition to solving the full-wave Eikonal and transport equations, we also solve the standard parabolic equation (PE), and its WKB counterpart: the Eikonal and transport equations that correspond to this parabolic approximation. [Efficient and accurate marching algorithms exist for solving the parabolic equation. The standard PE is chosen over other parabolic approximations because of the simple, uncoupled form of its transport equation (29).] An implicit assumption driving this approach is that diffractive effects for the PE will be similar in nature and magnitude to those of the full wave equation. Comparison between the results of the PE and the corresponding WKB calculations then reveals the role of diffraction. The WKB calculations (and the semiclassical approximation) for the standard PE are discussed in Section B below.

A. Full wave equation

In the limit of high frequency, if $S(t)$ is a ''positive-band'' signal at the source and $\phi(r,z,t)$ is the signal away from the source, then

$$\phi(r,z,t) \sim A(r,z) S(t-\tau(r,z)), \tag{11}$$

where the travel time (arrival time, or time delay) τ and the amplitude A satisfy the Eikonal and transport equations:

$$c^2 \nabla\tau \cdot \nabla\tau = 1, \tag{12}$$

$$\nabla \cdot (A^2 \nabla\tau) = 0. \tag{13}$$

These are the lowest-order equations describing the asymptotic behavior (WKB) of the acoustic pressure field, given by the real part of ϕ.

Equation (11) holds for a ''positive-band'' source signal, characterized by having a Fourier transform $(\hat{S}(\omega))$ whose energy contribution from all negative frequencies $(\int_{-\infty}^{0} |\hat{S}(\omega)|^2 d\omega)$ is zero (or relatively small); such source signals include those numerically generated for Sec. IV B of this paper, as well as those precisely of the form $\exp(-t^2/2\sigma_t^2) * \exp(-i\omega_0 t)$ so long as $\omega_0 * \sigma_t$ is sufficiently greater than unity. [For a more general source signal, Eq. (11) should also include a term involving the Hilbert transform of $S(t)$.]

By the method of characteristics, Eikonal equation (12) can be written as a coupled system of ordinary differential equations. The 2-D (one-way) ray trajectories are described by

$$\frac{dz}{dr} = \frac{\partial H}{\partial p}, \tag{14}$$

$$\frac{dp}{dr} = -\frac{\partial H}{\partial z}, \tag{15}$$

where $H = -(c^{-2} - p^2)^{1/2}$. The travel time along a ray trajectory is given by

$$\frac{d\tau}{dr} = c^{-1}(1 - (pc)^2)^{-1/2}. \tag{16}$$

The first two coupled equations describing the ray trajectories comprise a Hamiltonian system with Hamiltonian H. The variables z and p are related to the depth and slope of the ray, respectively. Specifically, $p = \sin(\theta)/c$, where θ is the angle the local ray tangent makes with the horizontal. To trace a ray trajectory emanating from the sound source (at $r = 0$) out to some range r_f, Eqs. (14) and (15) need to be solved out to $r = r_f$ with the initial conditions

$$z(0) = z_{\mathrm{so}}, \tag{17}$$

$$p(0) = \sin\,\theta_0 / c_{\mathrm{so}}, \tag{18}$$

where z_{so} and c_{so} are the z coordinate and sound speed, respectively, at the source, and θ_0 is the ray's *launch* angle with respect to the horizontal. Additionally, solving Eq. (16) out to $r = r_f$ with the initial condition

$$\tau(0) = 0 \tag{19}$$

gives the travel time of that ray. By incrementing the ray launch angle θ_0, and plotting for each such angle the travel time τ and depth coordinate z of the corresponding ray after it traverses some fixed range r_f, a *timefront* is constructed. A timefront shows the expected travel time of a pulse as a function of depth after traveling a fixed horizontal distance. There is a well-known analogy between acoustic (or optical) rays and the trajectories of particles moving in one dimension. In that analogy, the range becomes time and the ray angle, or better, p, becomes speed or momentum.[11] We will be investigating ray behavior with plots of p vs z as initial launch angle θ_0 is varied; these plots are called phase diagrams.[14,15]

B. Parabolic equation (PE)

In addition to understanding the geometric behavior of rays, one of the goals of this work is also to describe the accuracy of the WKB approximation, or ray-based waveforms, for sound propagation through an ocean having small-scale range-dependent structure (i.e., internal waves). We will use the word ''diffraction'' to mean the difference between solutions to the wave equation and its low-order WKB approximation.

We first transform to the frequency domain by defining ψ by the relation $\phi(r,z,t) = \psi(r,z)e^{-i\omega t}$. The wave function ψ then satisfies the Helmholtz equation. In the limit of small-angle propagation, the 2-D Helmholtz equation for ψ can be approximated by the parabolic equation for Ψ,

$$\frac{i}{k_0}\frac{\partial \Psi}{\partial r} = -\frac{1}{2k_0^2}\frac{\partial^2 \Psi}{\partial z^2} + \frac{1}{2}\left(1 - \frac{c_0^2}{c^2}\right)\Psi, \tag{20}$$

where $\psi = \Psi e^{ik_0 r}$, $k_0 = \omega/c_0$, and c_0 is a reference sound speed, in this case taken to be the value of the sound speed at the source. For boundary conditions, the ocean surface is modeled as a perfect reflector, and the bottom is modeled as an absorbing boundary. Solutions to (20) are computed for each frequency and then the impulse response is generated by integrating over the frequency band with the appropriate weighting, as set by the impulse signal at the source.

In the WKB approximation to the PE, the Eikonal and transport equations are, letting $s = c_0\tau - r$,

$$\frac{\partial s}{\partial r} + \frac{1}{2}\left(\frac{\partial s}{\partial z}\right)^2 + \frac{1}{2}\left(1 - \frac{c_0^2}{c^2}\right) = 0, \tag{21}$$

$$\frac{\partial A}{\partial r} + \frac{\partial A}{\partial z}\frac{\partial s}{\partial z} + A\frac{\partial^2 s}{\partial z^2} = 0. \tag{22}$$

In order to compare the WKB approximate solutions to the solutions of the parabolic equation, we need to solve both the Eikonal and transport equations. Rewriting the Eikonal equation, via the method of characteristics, yields the ordinary differential equations describing the ray trajectories and the travel-time τ along them:

$$\frac{dz}{dr} = \frac{\partial H}{\partial p}, \tag{23}$$

$$\frac{dp}{dr} = -\frac{\partial H}{\partial z}, \tag{24}$$

$$\frac{d\tau}{dr} = \frac{1}{2c_0}(1 + p^2 + c_0^2/c^2), \tag{25}$$

where $H = \frac{1}{2}p^2 - \frac{1}{2}c_0^2/c^2$ and $\tau = (r+s)/c_0$. Note that we are using the same symbol τ for the travel time in the PE approximation as we did for the full wave equation. There should be no confusion if it is kept in mind that when we are

investigating geometric behavior we use the ray equations that correspond to the full wave equation, and when we are investigating diffraction we use those corresponding to the PE approximation.

The appropriate initial conditions are

$$z(0)=z_{so}, \tag{26}$$

$$p(0)=\tan\ \theta_0, \tag{27}$$

$$\tau(0)=0, \tag{28}$$

where z_{so} is the z coordinate of the source and θ_0 is the ray's launch angle. If $J=1/A^2$, the Transport equation can also be rewritten along a ray as a second-order differential equation:

$$\frac{d^2J}{dr^2}+J\left[c\ \frac{\partial^2 c}{\partial z^2}-3\left(\frac{\partial c}{\partial z}\right)^2\right]\frac{c_0^2}{c^4}=0. \tag{29}$$

The initial conditions are

$$J(0)=0, \tag{30}$$

$$\frac{dJ}{dr}\,(0)=\delta(\theta_0)\sec^2\ \theta_0, \tag{31}$$

where $\delta(\theta_0)$ is a frequency-dependent correction chosen to make the point source here mimic the slightly nonuniform point source that is inherent when numerically solving the PE equation. Note that the intensities of the different rays are therefore in different ratios for different frequencies because of this point-source correction.

To determine by WKB the signal $\phi(r,z,t)$ away from the source (whose emitted signal $S(t)$ is ''positive-band''), the ''semi-classical'' sum over all ray paths connecting the source to the receiver is computed according to

$$\phi\sim\sum_j\ \alpha_j S(t-\tau_j)e^{-i(\pi/2)m_j} \tag{32}$$

where for the jth ray, τ_j is the travel time given by (25), $\alpha_j=1/\sqrt{|J_j|}$, where J_j is given by Eqs. (29)–(31), and m_j is the Maslov index, or the integral number of times along the ray that J_j takes on the value zero. Along ray j, A_j from the transport equation has been rewritten as $A_j=\alpha_j e^{-i(\pi/2)m_j}$ where α_j is real. Each time the ray passes a caustic (where there is a square-root branch-cut singularity) a phase shift of $\pi/2$ occurs.

III. NUMERICAL METHODS

All numerical computations were done in double precision to insure minimal effects of roundoff; in most cases, especially where numerical solutions to the PE equation were compared to their semi-classical counterparts, accuracy of the computations was extremely important. Because of the lengthy computation time necessary to satisfy accuracy requirements, calculations of sound propagation were primarily done on a 4K-processor MasPar MP-2 parallel computer.

A. Internal-wave modes

Internal-wave modes are determined by the boundary value problem defined by (5)–(7); numerical solutions to this set of equations are easily constructed by using a standard shooting method.[16] The vertical dependence of sound speed is then known numerically, although only at discrete depths. [As Eq. (4) indicates, the ocean's sound-speed dependence on range r is described analytically rather than numerically.] Since for the acoustical computations it is necessary to know the sound speed at all depths, values between grid points are given by (natural) cubic spline interpolation.[16]

B. Ray-based computations

All ray-based systems of ODEs [Eqs. (14)–(16), (23)–(25), and (29)] derived from the Eikonal and transport equations are solved using fourth-order Runge–Kutta methods on a set of gridpoints uniformly spaced in range. Parallelization is done with ray launch angle, so that each processor solves the equations along one ray, giving 4096 ray computations per run. Gridpoint spacing is continually halved until convergence is realized and changes in the dependent variables become insignificant. For propagation out to 1000 km the number of range steps depends on the sound-speed profile and varies between 50 000 and 1 600 000; but for all rays (except strongly chaotic ones) the final grid spacing is chosen to insure that arrival depth and time are accurate to within a fraction of 1 m and 1 ms, respectively. Table I shows the convergence of the numerical solution as a function of the number of range grid points for three different ocean realizations.

In order to make comparisons between the PE solutions and their semi-classical counterparts it is necessary to find the rays emanating from the sound source that pass through some prescribed depth at some given range. We solve this boundary value problem sufficiently easily by shooting as ray launch angle is varied, where the final launch angle is found iteratively by a Newton–Raphson scheme. For strongly chaotic rays, one may wish to resort to a relaxation method rather than shooting,[17] but relaxation methods alone can fail to find all eigenrays. For profiles that generate strongly chaotic rays, the computational effort necessary to find all eigenrays can become prohibitive. This in fact happens to us for late arrivals in the SLICE89 environment. To investigate that case completely will require significantly more computational effort than we have expended up until now.

C. PE computations

To solve the PE we use a split-step marching algorithm (see, for example, Tappert[18]). To simulate a point source the initial pulse at $r=0$ is given the following form in the frequency domain:

$$\tilde{\Psi}(z,r=0,\omega)=\exp\left(\frac{-(\omega-\omega_0)^2\sigma_t^2}{2}\right)\exp\left(\frac{-(z-z_{so})^2}{2\sigma_z^2}\right), \tag{33}$$

where ω_0 is the center frequency, σ_t is the pulse width in time, σ_z is initial pulse width in depth, and z_{so} is the location of the source.

Wave functions for each frequency then propagate through the internal-wave environment using a standard split-step PE method. At a given range r_f, the simulated

TABLE I. Convergence of the numerical solution as a function of grid size (range step). For propagation through the three different average sound-speed profiles in the presence of internal waves, the variations in ray arrival (time and depth) are compared as the number of range gridpoints is doubled. The travel time and depth of each of 4096 rays, after traveling 1000 kilometers, is differenced with that for the same ray calculated on the finest grid, taken to be ground truth; then the rms and maximum differences are tabulated. Note that for the CANON profile, travel time and depth for the arriving rays seem to be given very accurately even for a grid of 25,000 points. Because the late-arriving rays for the SLICE89 profile are very chaotic, the time and depth of only the early arrivals is numerically accurate and convergent.

Grid	t (rms)	z (rms)	t (max)	z (max)
		CANON case: (4096 rays) Difference with 200 K		
025 K	0.000 430 ms	0.004 50 m	0.0100 ms	0.1200 m
050 K	0.000 073 ms	0.000 75 m	0.0012 ms	0.0170 m
100 K	0.000 018 ms	0.000 13 m	0.0003 ms	0.0037 m
		CANON2 case: (4096 rays) Difference with 400 K		
050 K	0.4400 ms	8.90 m	24.0 ms	400.0 m
100 K	0.0600 ms	1.30 m	3.50 ms	69.00 m
200 K	0.0032 ms	0.076 m	0.130 ms	2.800 m
		SLICE89 case: (4096 rays) Difference with 1600 K		
100 K	21.0 ms	160 m	220 ms	1300 m
200 K	16.0 ms	130 m	200 ms	1400 m
400 K	10.0 ms	110 m	120 ms	0850 m
800 K	07.0 ms	073 m	110 ms	0920 m
		SLICE89—Early arrivals: (2513 rays arriving before 675.9 s)		
100 K	0.8800 ms	20.0 m	38.0 ms	760.0 m
200 K	0.3900 ms	8.60 m	17.0 ms	380.0 m
400 K	0.0470 ms	0.920 m	1.90 ms	33.00 m
800 K	0.0067 ms	0.120 m	0.33 ms	15.700 m

wave functions $\tilde{\Psi}(z,r_f,\omega)$ are Fourier recombined to get the pulse shape, where the integration in frequency is done over the range $\omega_0-\Delta$ to $\omega_0+\Delta$ and Δ is chosen so that $\Delta\cdot\sigma_t = O(1)$ and $\omega_0-\Delta$ is positive. We have used $\Delta=50$ Hz in all cases in this article.

In our simulation, an absorbing boundary condition is used for the ocean bottom. The boundary condition at the ocean surface is $\Psi(0,r,t)=0$ which is enforced in the simulation by using a mirror image of the ocean. The vertical extent of the ocean is discretized by 2048 gridpoints (which translates into 4096 gridpoints to represent the true ocean plus its mirror image). In most of our simulations, 512 and 1024 frequencies are used to span the frequency window covering $\omega_0-\Delta$ to $\omega_0+\Delta$. Vertical grid spacing and range stepping are halved to verify the convergence and accuracy of the computed solution. Parallelization is done in the frequency domain; for example, with 512 frequencies, 8 processors are used to simulate each frequency.

IV. NUMERICAL RESULTS

In this section we present numerical results describing the geometric behavior of sound propagation through realizations of our model internal-wave field. We examine the behavior, as a function of propagation range and average sound-speed profile, of both the individual rays and the more relevant timefronts. To test the validity or accuracy of ray-based methods, or equivalently, to measure diffraction, we also compare the semi-classical solution (based on WKB) to the wave solution of the parabolic equation (PE). Finally, we relate the arrival of an increasing number of multipaths (due to microfolding) to a broadening of the effective ray tube connecting the source with a fixed receiver point.

A. Rays and timefronts

Figure 3 shows the timefront computed for 1000-km propagation through a range-independent ocean described by the CANON average sound-speed profile (Fig. 2), as well as the timefronts for similar propagation through a range-

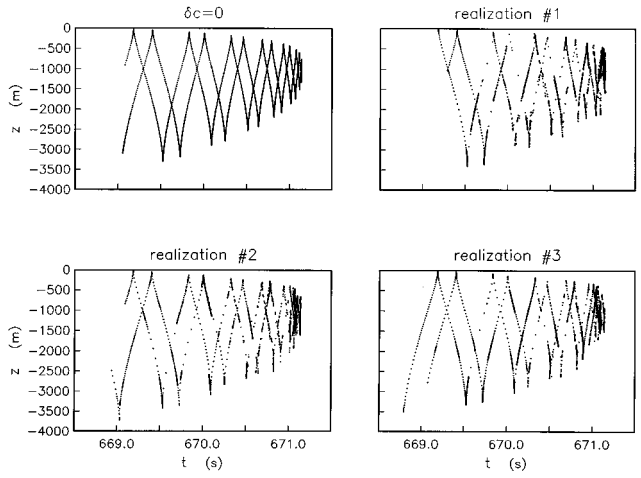

FIG. 3. Timefronts for 1000-km propagation through an ocean described by the CANON average sound-speed profile with and without internal waves present. The figure in the upper left is the result for the case of no internal waves, and the remaining three figures are the results for three different realizations of the 10-mode internal-wave field. Each point on the timefronts represents the arrival of one ray, and there are 4096 ray arrivals having uniformly incremented launch angles.

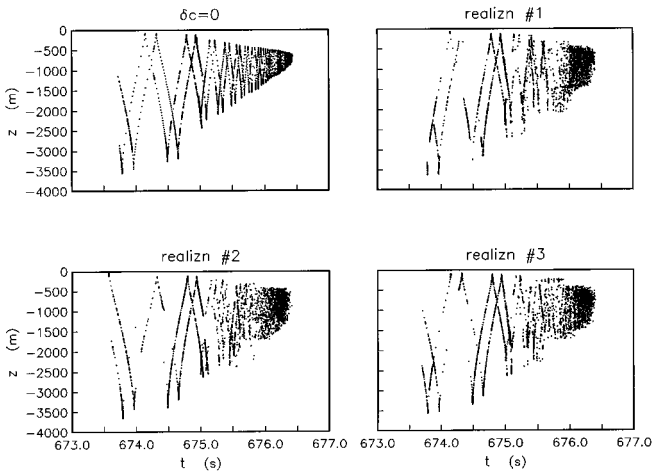

FIG. 4. Timefronts for 1000-km propagation through an ocean described by the SLICE89 average sound-speed profile with and without internal waves present. The figure in the upper left is the result for the case of no internal waves, and the remaining three figures are the results for three different realizations of the 10-mode internal-wave field. Each point on the timefronts represents the arrival of one ray, and there are 4096 ray arrivals having uniformly incremented launch angles.

dependent ocean described by this same average sound-speed profile perturbed by different realizations of a ten-mode internal-wave subfield. Every point on each of the timefronts represents the arrival of one ray, and there are 4096 ray arrivals with uniformly incremented launch angles that image the timefront. Launch angles corresponding to rays that interact with the ocean surface or bottom are omitted since their attenuation over long propagation ranges would be substantial. For these calculations the sound source was set at the sound-channel axis, at a depth of 1000 m.

When internal waves are absent, the timefront has the folded accordion shape due to refraction, as in Fig. 3, and the ray arrivals are spread in a smooth and predictable way. Without internal waves a smooth increase in intensity is suggested as the caustics (i.e., fold vertices) are approached. (Recall from geometric theory that away from caustics, the vertical distance between neighboring timefront points is approximately inversely proportional to the local intensity.) In the presence of internal waves, however, there is an apparent grouping and nonuniformity of ray arrivals along the folded fronts, suggesting a significant variation in intensity. Increasing the resolution by adding more ray arrivals to this timefront picture, and then zooming in on accumulations of arrivals, would reveal the presence of smaller folds, or microfolds, along the long segments that make up the macroscopic folded timefront. This will be discussed in more detail later.

Figure 4 is the analog to Fig. 3 but with the average sound-speed profile given by the SLICE89 profile. Here the source depth is 800 m, corresponding to the depth of the sound channel axis for the SLICE89 experiment. Due to roughness of the SLICE89 average sound-speed profile, even in the absence of internal waves the distribution of ray arrivals along the timefront shows some nonuniformity, suggesting smaller folds on the legs of the bigger folds. There are, however, outstanding differences between the SLICE89 timefronts for propagation with and without internal waves:

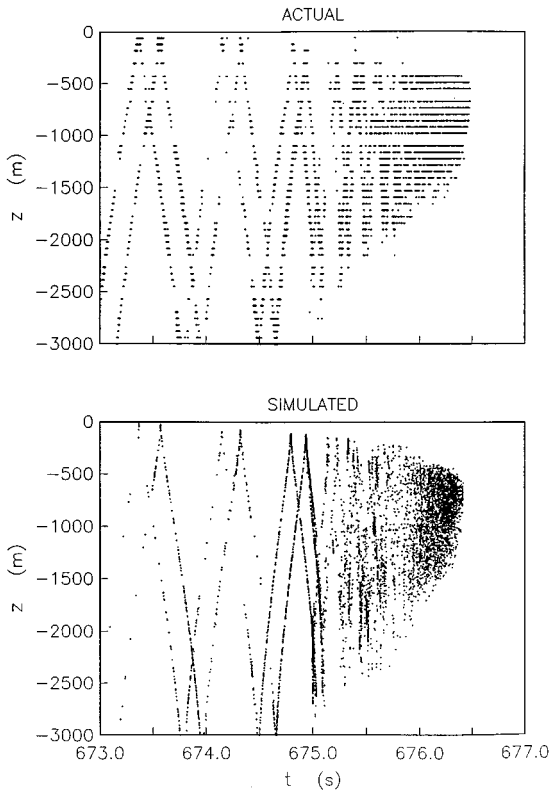

FIG. 5. Comparison of simulation and actual timefront for SLICE89. The upper figure shows reconstructed arrivals (above some threshold intensity) for a single pulse during the actual SLICE89 experiment. The lower figure shows the superposition of ray arrivals for three separate realizations of the interval-wave field. The distinguished, early-arriving, timefront segments, the smearing of timefront segments in the rear of the pulse, and the envelope of arriving energy in the rear of the pulse compare well between simulation and actual case. This shows that ray *refraction* can account for the observed scattering in the rear of the pulse.

In the presence of internal waves the late-arriving folds of the SLICE89 timefront no longer appear distinguishable, as they do when internal waves are absent; furthermore, these late arrivals appear diffuse and more spread in depth.[4] The addition of internal waves to a scenario results in the near axial final cutoff occurring about 10–15 ms earlier, in agreement with the simulations of Colosi *et al.*[4] On the other hand, the early-arriving segments of the timefront remain intact and distinguishable, even when internal waves are present. Figure 5 shows the superposition of ray arrivals for all three realizations with internal waves and compares it to a reconstructed timefront from the actual SLICE89 experiment.[19,3,20] A similar comparison was made by Colosi *et al.*[4] between timefronts from the experiment and from parabolic-equation full wave simulations through internal waves. That comparison identified internal waves as the likely cause of the diffusion of energy in depth in the late-arriving portion of the timefront, but they did not identify exactly how the internal waves caused the depth diffusion. Our results from following geometrical-optics rays, shown in Fig. 5, have no effects of diffraction in them, yet the depth diffusion has occurred and is quantitatively in agreement with the experiment. This agreement strongly suggests that the indistinguishable and diffuse pattern of arrivals in the rear of the SLICE89 pulses are primarily due to *refractive*

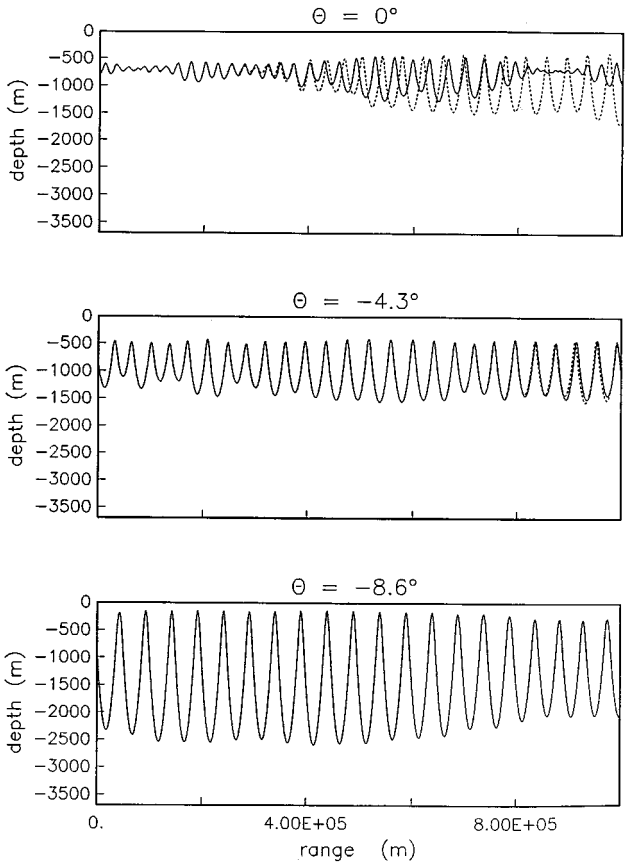

FIG. 6. Ray traces for the SLICE89 profile in the presence of a 10-mode internal-wave field. Each figure shows the ray traces for two slightly different launch angles (although in the bottom figure the two ray traces overlay). The solid and dotted curves, respectively, are rays for the original and slightly perturbed launch angles: The original angles are (top) 0°, (middle) $-4.3°$, and (bottom) $-8.6°$. The perturbed ray and the original ray differ by an angle of 10^{-7} rads.

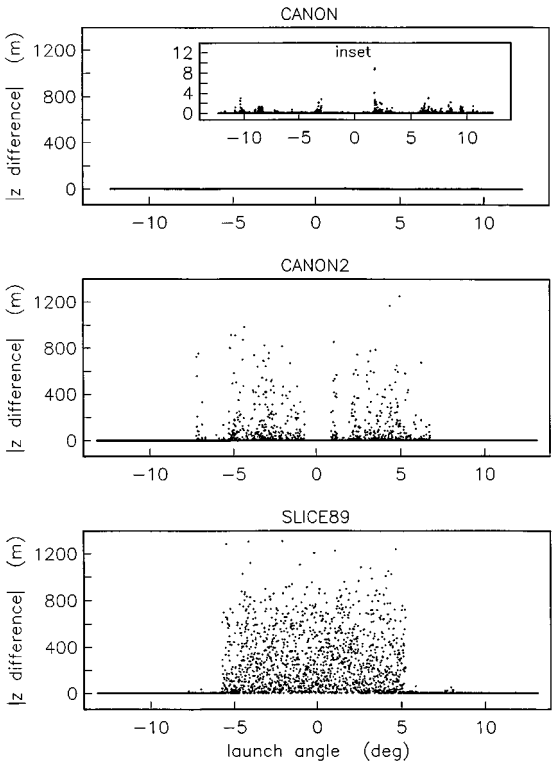

FIG. 7. Bubble plot corresponding to 1000-km propagation for each of the three average sound-speed profiles in the presence of a 10-mode internal-wave field. Each point represents for a given launch angle the absolute difference in arrival depth for two rays: a ray with the original launch angle and one with a the slightly perturbed launch angle (which is the original angle plus 10^{-7} rads). To construct this plot 4096 pairs of rays were used. There is a clear dependence of the global picture of ray sensitivity on the average sound-speed profile. Note the CANON inset with the vertical axis rescaled to 1% of the original.

(not *diffractive*) effects of internal waves. The distinguished, early-arriving frontal segments of the actual and simulated pulses also agree well between our ray simulations and the experiment.

In order to understand the incoherent behavior in the late-arriving portion of the SLICE89 pulse propagating through internal waves, it is useful to look at the dynamics of the ray trajectories. Figure 6 shows rays with three different launch angles (corresponding to an early, middle, and late arrival) traced through one of the internal-wave realizations. Also shown in this figure are the ray trajectories corresponding to these same launch angles perturbed a very tiny amount. For the early arrival, the trajectories of the ray and its perturbed companion appear identical over the 1000-km propagation. For the late arrival, the two companion trajectories exponentially diverge to the point of being very different after 1000 km. For the middle arrival, the pair of trajectories also exponentially separate, although at a slower pace than for the late-arriving ray. This suggests that the late-arriving rays in the SLICE89 profile are more ''chaotic'' than the early-arriving ones after propagating through an internal-wave field, and that this (sensitivity to initial conditions) is the driving mechanism behind the incoherent behavior (or, as illustrated later, the extreme folding of the timefront) in the rear of the arriving pulse.

In order to identify regions of ray instability along the timefront, rays having launch angles that differ only infinitesimally were compared, as a function of launch angle. Each plot of Fig. 7 shows the absolute difference in arrival depth for two rays with slightly different launch angles, as a function of launch angle, and after propagating 1000 km. Each of these ''bubble'' plots is a global descriptor of ray stability as a function of launch angle. For example, the plot corresponding to the SLICE89 profile shows that rays with angles steeper than 5° are much less sensitive to launch angle perturbations than rays between about $-5°$ and $+5°$. The regime of launch angles between $-5°$ and $+5°$ corresponds to the late arrivals that are scattered in the rear of the timefront.

It is useful to have a systematic understanding of how the sensitivity to initial conditions depends on the propagation conditions. First, consider changes in the sound-speed profile. There is a strong dependence of global ray sensitivity or instability on average sound-speed profile. In the case of the canonical profile CANON (see Fig. 7) all rays appear insensitive to slight launch angle perturbations. The inset in the CANON plot shows the z difference on a factor-of-100 smaller scale, and shows that there are small pockets of sensitivity for the CANON profile, although this sensitivity is quite weak in comparison to that of the SLICE89 profile. The

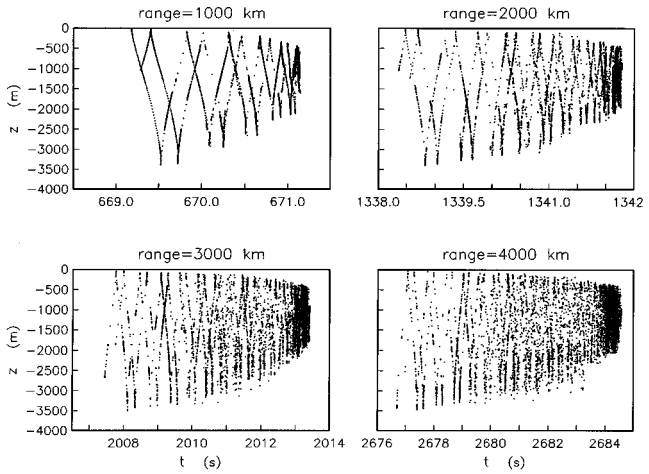

FIG. 8. Timefronts for propagation through an ocean described by the CANON average sound-speed profile in the presence of a 10-mode internal-wave field. Cases are shown for propagation ranges of 1000, 2000, 3000, and 4000 km. Each point on the timefront represents the arrival of one ray, and there are 8191 ray arrivals (having uniformly incremented launch angles). At 4000 km, early-arriving timefront segments are still distinguishable, but the energy in the rear of the pulse shows substantial fluctuation in arrival time and depth.

CANON2 profile shows (again see Fig. 7) a sensitivity of ray arrivals in the rear of the timefront similar to that of SLICE89. Since CANON2 is just the smooth CANON profile with more curvature at the sound-speed minimum, it appears that the curvature at the sound-speed axis strongly influences the character of the ray behavior. Duda and Bowlin[21] argue that a normalized sound-speed curvature strongly controls caustic formation.

We find that the bubble-plot global behavior is qualitatively similar for different realizations of the internal-wave field, when absolute difference in arrival depth is replaced by absolute difference in travel time, or when 40 instead of 10 internal-wave modes are summed.

These bubble plots describe the cumulative separation of rays out to the exact range of interest. There is a strong dependence of behavior on transmission range, as well as on the average sound-speed profile. It should be noted, for example, that the relatively well-behaved timefront associated with the CANON profile for 1000-km propagation (in the presence of internal waves) becomes more ill-behaved at longer ranges. Figure 8 shows that as transmission range approaches 4000 km the CANON timefront begins to resemble the SLICE89 timefront at 1000 km in that it shows very scattered and diffuse late arrivals.

Difference in arrival depth can be related to a Lyapunov exponent, defined to quantitatively measure chaotic behavior.[7–9] The Lyapunov exponent λ arises from the expectation that, for large r,

$$\frac{1}{r}\ln\left[\frac{d(r)}{d_0}\right)\sim\lambda(\lambda \ \text{constant}), \tag{34}$$

where $d(r)$ is the depth difference plotted in Fig. 7 (for $r=1000$ km) and d_0 is a reference separation near $r=0$. There are many subtleties associated with finding a numerical value for λ: for example, how to define d_0, how large r should be where λ is evaluated, and how to deal with the fact that two rays from a common point and with a small launch angle difference are actually affected by two λ's, one positive and one negative. For the purpose of characterizing 1000-km acoustic propagation we can avoid these problems by calculating an effective *difference* in Lyapunov exponents between two propagations under different conditions: for example, between propagation through the SLICE89 and CANON profiles. Then, for large r,

$$\lambda_{\mathrm{S89}}-\lambda_{\mathrm{CAN}}\sim\frac{1}{r}\ln\left[\frac{d_{\mathrm{S89}}}{d_{\mathrm{CAN}}}\right], \tag{35}$$

and d_0 disappears from the calculation. From late-arriving rays in Fig. 7, we take $d_{\mathrm{S89}}=500$ m, $d_{\mathrm{CAN}}=1$ m, and $r=1000$ km, resulting in

$$\lambda_{\mathrm{S89}}-\lambda_{\mathrm{CAN}}\approx 0.01 \ \mathrm{km}^{-1}. \tag{36}$$

This value is positive, implying that the rays traveling in the SLICE89 profile are more strongly ''chaotic'' than those traveling in the CANON profile. Furthermore, the magnitude of the difference, 0.01 km^{-1}, is of the same order of magnitude as λ's previously calculated from the effects of the mesoscale-like range-dependent sound-speed structure.[8,9]

It has been shown that in the late-arriving portion of the pulse where strong scattering has occurred, arriving rays are most sensitive to initial conditions. Although at first glance these ray arrivals appear to be scattered about almost randomly, we know that the points must lie on a continuous timefront curve; thus this curve is full of frontal microstructure: Extreme microfolding is evident when the timefront is resolved by a much tighter fan of launched rays. In Fig. 9 the effect of internal waves superimposed on the SLICE89 profile is shown for propagation to 500 km. Macroscopic examination of the rear of the timefront reveals strong scattering and unresolved structure. However, if the timefront is more minutely examined by tracing out a tight fan of 8191 rays with launch angles between -2.3×10^{-5} and $+2.3\times10^{-5}$ rads, then a highly folded structure emerges. The individual ray arrivals that describe the complex timefront structure in the rear of the pulse are very chaotic, moving (vertically and temporally) with leaps and bounds from tiny perturbations in launch angle (as Fig. 9 illustrates). Since the rays are confined to fall on a continuous curve, their chaotic behavior gives way to a timefront that folds extensively (back and forth) across the region. It is the behavior of the timefront, controlled by the rays that define it, that directly relates to the behavior of the received acoustic pulse. It may be that even though the individual rays can be very chaotic, the folded timefront defined by them is more stable and less sensitive to perturbation (in the ocean medium, for example); this is an area requiring further investigation and quantification. At greater ranges, the microstructure in the rear of the pulse is even richer, the number of microfolds growing exponentially with range.[8]

Timefront microfolds are more easily identified from a phase diagram than from the timefront, where these structures are relatively minute. A phase diagram can be defined as a scatter plot of p vs z, for a fixed propagation range, with each point representing a different ray launch angle.[14] Figure 10 shows the phase diagram for propagation out to 1000 km

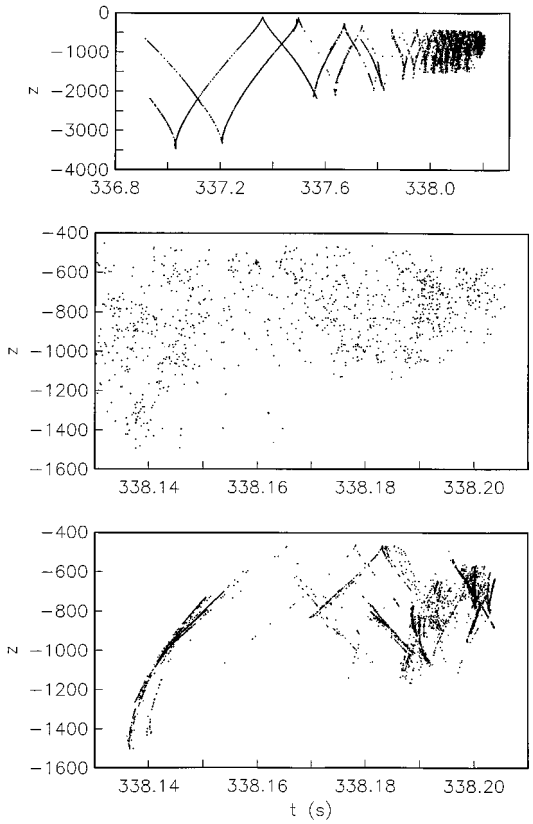

FIG. 9. Timefront for 500-km propagation through an ocean described by the SLICE89 average sound-speed profile in the presence of a 10-mode internal-wave field. The figure at the top shows the timefront determined by all refracted rays. Each point on this timefront represents the arrival of one ray, and there are 8191 ray arrivals. The middle figure shows a magnified view of the rear of the pulse taken directly from the top figure. The bottom figure shows, for the same ocean and propagation range, the timefront structure traced out by a fan of 8191 rays whose launch angles uniformly span the small sector -2.3×10^{-5} to $+2.3\times10^{-5}$ rads. Note how the trace of this very small sector of launch angles still extends across the region that a sector approximately three orders of magnitude larger maps out (middle figure); traces of other ray fans spanning very small sectors would likewise extend across this region, filling it over and over again with folded timefronts.

for the CANON profile with no internal waves. It is very useful to consider the set of individual points on a phase diagram as forming a continuous curve that smoothly connects adjacent launch angles. Each point on the curve that

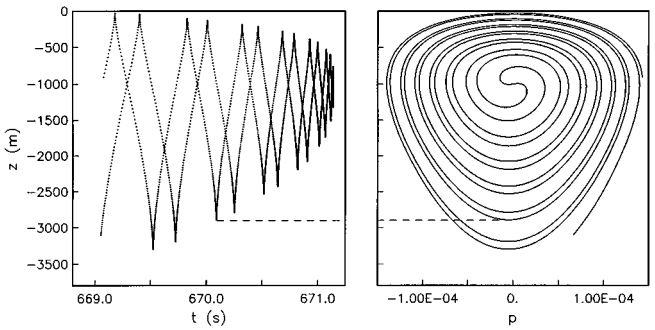

FIG. 10. Timefront and phase diagram for 1000-km propagation through the range-independent (without internal waves) ocean described by the CANON sound-speed profile. Horizontal tangents in the phase diagram (at right) correspond to caustics in the timefront (at left), as shown by the example (dotted line).

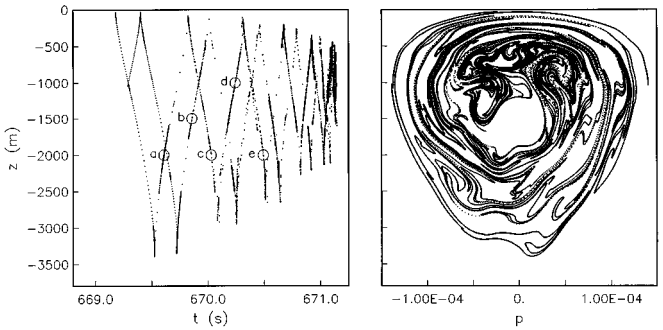

FIG. 11. Timefront and phase diagram for the same scenario in Fig. 10 but with the added presence of a 10-mode internal-wave field. Each point on the phase diagram represents the arrival of one ray, and 163,801 rays were used to adequately map out the phase diagram. When internal waves are present, the phase diagram has numerous windings and intricate structure, indicating the presence of microcaustics and microfolds; this is not so evident from a macroscopic view of the timefront. The regions of the timefront marked by circles will be described in more detail in later figures.

has a horizontal tangent (where $dz/dp=0$) corresponds to a caustic, or, therefore, the beginning of a fold on the timefront. Detecting caustics or folds on the timefront is equivalent to detecting horizontal tangents on the phase diagram. In Fig. 10 the phase diagram is a rather simple spiral, and the horizontal tangents on the spiral equate to the primary caustics on the timefront: There are no microcaustics or microfolds. Figure 11 has the analogous phase diagram for propagation in the presence of internal waves. This phase diagram is complex, with intricate windings and numerous bends: The numerous horizontal tangents, especially near the center of the curve (corresponding to the rear of the timefront), indicate the existence of many microcaustics and microfolds. Microscopic examination is required for these microfolds to be detected amid the macroscopic folds of the timefront.

B. Diffraction

The validity of the geometric approximation comes into question for sound propagating over long ranges through internal waves. Presumably in much the same way that classical mechanics fails to exactly represent quantum behavior,[22] geometric acoustics should fail to describe the wave equation. In acoustics it might be expected that as acoustic timefront folds multiply and produce numerous caustics (as evidenced in the chaotic rear of the timefront), ray-based or semi-classical methods will fail; however, there has not been any accurate characterization or quantification of the failure of the semi-classical approximation in ocean acoustics. In attempting to bridge between classical and quantum mechanics, semi-classical descriptors have been studied[23–27] and shown to be much more robust than expected for chaotic physical systems. Here we will study the accuracy of ray-based acoustics for 1000-km propagation through an internal-wave subfield superimposed on the CANON average sound-speed profile. Our interest is in that portion of the sound field that is refracted only and does not interact with (reflect from) the ocean boundaries.

To study diffraction, or equivalently, to study the accuracy of the semi-classical approximation, we shall compare

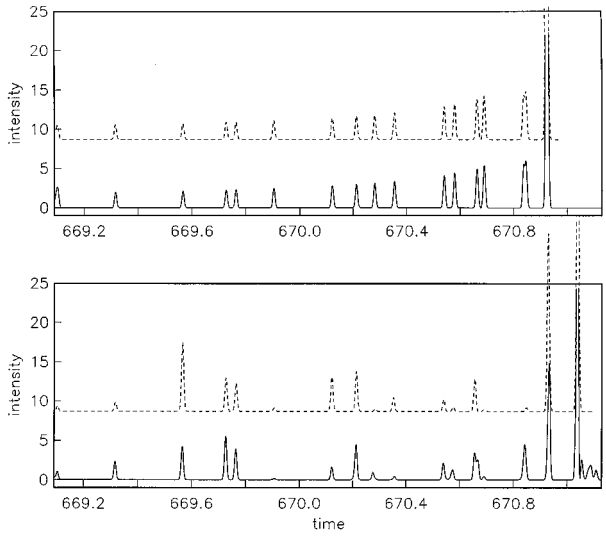

FIG. 12. Comparison of semi-classical (dashed) and PE (solid) solutions for 1000-km propagation through the CANON profile, for cases without (upper plot) and with (lower plot) internal waves. Time series correspond to the received intensity as a function of time for a receiver at a depth of 2000 m. (Figure 13, examined at $z=-2000$ m, shows that 17 semi-classical peaks are expected.) The center frequency of the source signal is 250 Hz. When internal waves are absent the PE and semi-classical solutions are in excellent agreement. In the presence of internal waves, arrival times of PE and semi-classical intensity peaks agree to within ms, but the corresponding peak intensities are often a few dB in error. Note that in the presence of internal waves the PE solution has some very late arriving peaks that are nonexistent in the semi-classical approximation; these are peaks due to energy emanating from the shadow side of caustics above (see Fig. 13).

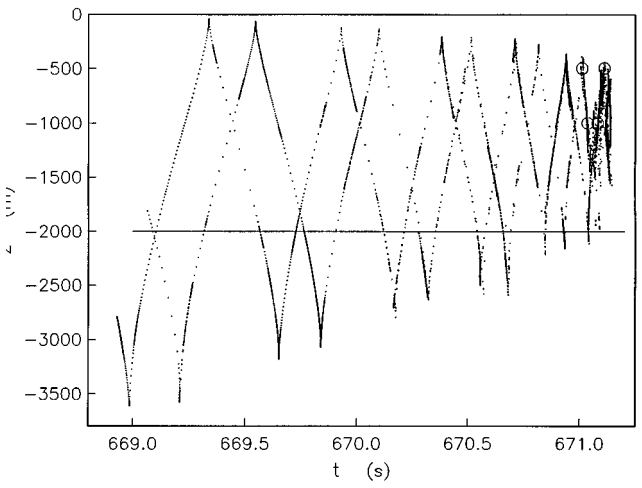

FIG. 13. Timefront for standard PE corresponding to 1000-km propagation through a 10-mode internal wave field superimposed on the CANON average sound-speed profile. The timefront is described by 8191 ray arrivals. Note the similarity to the ''full wave'' timefront presented in Fig. 11 for the same ocean. The regions of the timefront marked by circles will be described in more detail in later figures. At $z=2000$ m, given by the horizontal line, an intensity time series is shown in the previous figure.

solutions to the standard parabolic equation (PE) and its WKB counterpart. Numerical solutions to the PE, found by the method described in Sec. III C, are compared to the semi-classical sum over all ray paths, given by Eq. (32). So as to guarantee that any differences between the PE and its ray-based counterpart are real and not numerical, all grid spacings and range-step sizes are continually halved until convergence within the required accuracy is obtained.

To insure that we emphasize diffractive effects due to sound-speed variability (internal waves) and not due to the presence of the ocean boundaries, we smoothly extend our simulated ocean when solving the PE so that the ocean surface is 1 km higher. Except for the earliest arriving portion of the timefront, whose rays have turning points close to the original ocean surface, the effect of moving this boundary is small.

It is crucial in the semi-classical approximation that all ray paths connecting the source to the receiving point are identified, and the phase diagram is useful in this regard. The phase diagram for the geometric approximation to the PE at a transmission range of 1000 km for propagation through a 10-mode internal-wave field superimposed on the CANON sound-speed profile is very similar to that presented in Fig. 11. All intersections of the phase curve with any line prescribing a fixed depth z indicate ray paths connecting the source and receiver at that depth z. Since the phase curve is discretized (points on it are given for discrete values of ray launch angle), intersections of the phase curve and the constant-depth line are initially calculated by interpolation, and refined later by successive iteration. Once all launch angles corresponding to the eigenrays are identified, Eqs. (29)–(31) are integrated along each separate ray path, providing α_j and m_j in Eq. (32).

We simulate the transmission of a finite-frequency pulse from the source by setting the pulse width at about 10 ms ($2\Delta=100$ Hz) and the center frequency at either 250 Hz or 1000 Hz. Figure 12 presents, for a prescribed depth, the received intensity as a function of time for the PE solution and the semi-classical approximation. (The word ''intensity'' is used in the cases that follow to mean the square of the magnitude of the wave function; e.g., $|\phi|^2$ for the semi-classical approximation.) It shows a comparison with and without internal waves for the received intensity versus time at a depth and range of 2000 m and 1000 km, respectively, and for a center frequency of 250 Hz. We note here that, in all cases that we have investigated, the comparison between the PE solution and the semi-classical approximation is excellent when internal waves are absent. When internal waves are present there are slight differences in peak arrival time and significant differences in peak intensity between the PE and semi-classical solutions, as Fig. 12 indicates. By comparing 76 peaks from the PE and semi-classical time series at depths of 500, 1000, 1500, and 2000 m, we found that in the presence of internal waves the average and variance of the peak-arrival-time difference is 0.17 ms and 5.1 ms^2, respectively, for a 250-Hz center frequency. Peak arrival times for PE and semi-classical solutions, then, commonly lie within 2 ms of each other. Likewise, for the same 76 peaks the average and variance of $\log_{10}(I_{SC}/I_{PE})$, where I_{SC}/I_{PE} is the ratio of peak intensities, is -0.036 and 0.26, respectively, indicating that the two intensities commonly agree to within 5 dB. (Sometimes there are, as noted in Fig. 12, PE peaks corresponding to caustic ''tails'' that do not have a semi-classical analog and so are not represented in this comparison.)

Figure 13 shows the PE timefront corresponding to the 1000-km propagation for which the previous statistical com-

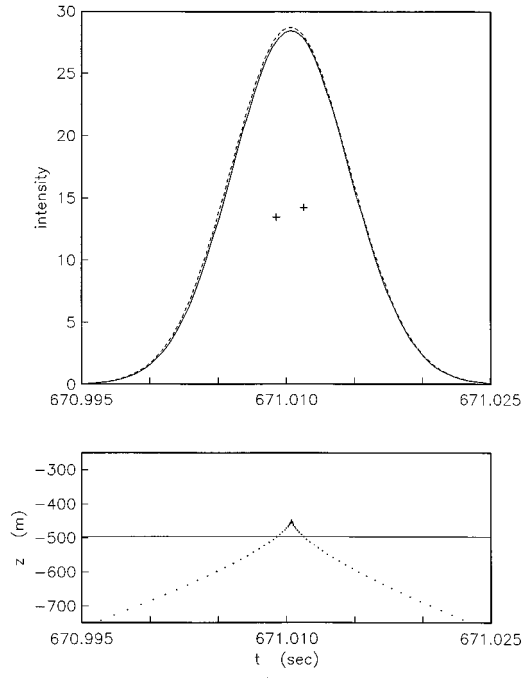

FIG. 14. Comparison of semi-classical and PE solutions for the case of no internal waves. The point of comparison corresponds to the selected circle in Fig. 13 having depth near 500 m and arrival time near 671.01 s. The simulated source signal has 250-Hz center frequency. The top figure shows intensity versus time for both the semi-classical solution (dashed) and the PE solution (solid). The agreement between PE and semi-classical is excellent in the absence of internal waves. Two ray arrivals (indicated by the two crosses in the upper figure) interfere to produce the single peak in intensity. The bottom figure indicates the presence of a primary caustic near the prescribed depth, which is marked by the horizontal line. This line intersects the local timefront at the two ray arrival times indicated by the two crosses in the upper figure.

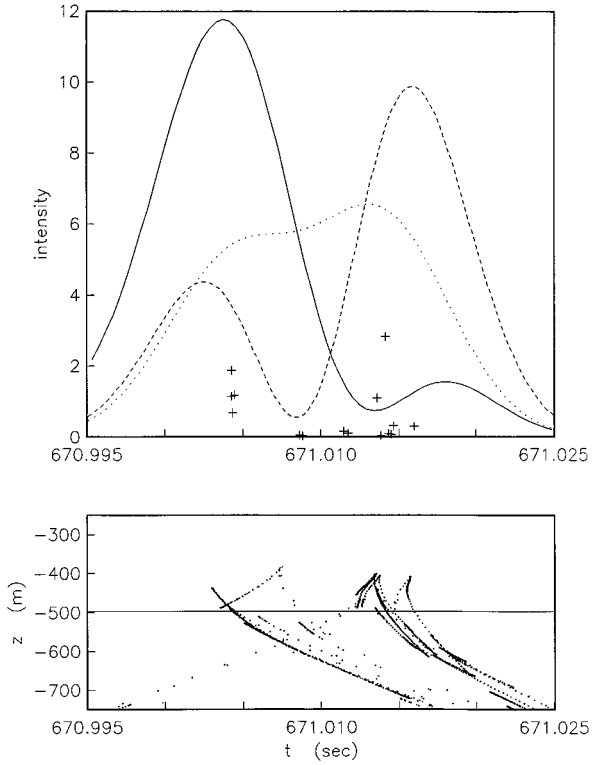

FIG. 15. Comparison of semi-classical and PE solutions for the case of a 10-mode internal-wave field. The point of comparison corresponds to the same point selected in Fig. 14, and the simulated source signal again has 250-Hz center frequency. The top figure shows intensity versus time for both the semi-classical solution (dashed) and the PE solution (solid). The intensity calculated from an incoherent sum of ray arrivals (dotted) shows the error incurred if phase information is excluded from the semi-classical sum. The 15 crosses in the top figure show the arrival time and intensity of the 15 individual ray arrivals that contribute to the two peaks in intensity. The bottom figure reveals the presence of microfolds and microcaustics that give rise to the 15 multipath arrivals at a depth near 500 m (given by the horizontal line). In the vicinity of so many microcaustics, there is still good agreement between PE and semi-classical waveform shapes and peak arrival times.

parison of peak intensities and arrival times was done; microfolds, corresponding to multipaths, are not easily visible at this scale. In the remainder of this section, portions of this timefront at the circles indicated in Fig. 13 are magnified in order to highlight microfolds, and the intensity time series for the PE solution and the semi-classical approximation at these points are more closely examined. These timefront locations are chosen because they exhibit significant microfolding so that the semi-classical sum has a contribution from many rays. In some cases we compare the propagation information at the selected timefront point for both the 250-Hz and 1000-Hz center frequencies, or at the corresponding point when no internal waves are present. (Without consequence, the intensities in Figs. 14–20 are normalized differently for the 250-Hz and 1000-Hz cases.)

The results for the earliest of the selected points for 250-Hz propagation are shown in Fig. 14 (no internal waves) and Fig. 15 (with internal waves). In Fig. 15, 15 multipath arrivals sum to produce 2 peaks within a few milliseconds of the peaks given by the PE. Multipath interference seems to accurately account for the received signal in this range-dependent propagation. If ray arrivals are *incoherently* summed the intensity pattern is significantly different, clearly showing the importance of phase interference. In the absence of internal waves, as noted in Fig. 14, the semi-classical sum approximates the PE superbly: in this case at a point within about 50 m of a primary caustic. Note that a single timefront caustic, for propagation in the absence of internal waves, is replaced by several microcaustics (displaced by several ms) when internal waves are present.

Figures 16 and 17 involve comparisons at a point on the timefront that exhibits severe microfolding. At the higher frequency (1000 Hz: Fig. 17) the comparison is better, for both travel time and intensity, although at the lower frequency (250 Hz: Fig. 16) the peaks still arrive within a few ms of each other. A comparison to the case of no internal waves would show that internal waves cause microfolding of a single timefront segment and a shift in the location of the peak intensity of several ms.

Figure 18 shows how almost 200 multipath arrivals, spread in time over more than a pulsewidth, interfere at 250 Hz to produce one dominant peak in intensity. The number of nonnegligible arrivals is large; about one-third of them have amplitudes that are at least one-third of the largest amplitude. Figure 19 shows how at a higher frequency (1000 Hz) the same multipaths sum to produce two peaks. In both cases the PE and the semi-classical approximation agree remarkably well in shape and arrival time. Since the ray-based

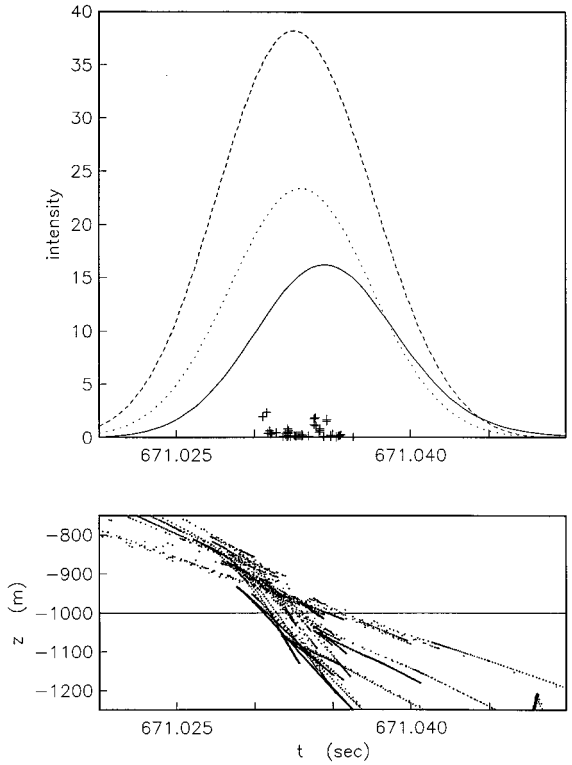

FIG. 16. Comparison of semi-classical and PE solutions for the case of a 10-mode internal-wave field. The point of comparison corresponds to the selected circle in Fig. 13 having depth at 1000 m and arrival time near 671.04 s. The simulated source signal has 250-Hz center frequency. The top figure shows intensity versus time for the semi-classical solution (dashed), the incoherent semi-classical sum (dotted), and the PE solution (solid). The numerous crosses in the top figure show the arrival time and intensity of the many individual ray arrivals that contribute to the single peak in intensity. The PE and semi-classical intensity peaks arrive within a couple of milliseconds of one another. The peak intensities, however, differ noticeably, because the (semi-classical) Transport equation overestimates the intensity on the timefront in the vicinity of a strong caustic. The bottom figure reveals the presence of severe microfolding, along what would have been a single diagonal timefront segment in the absence of internal waves. It also shows that the horizontal line at $z=-1000$ m intersects the timefront near a strong caustic (at left).

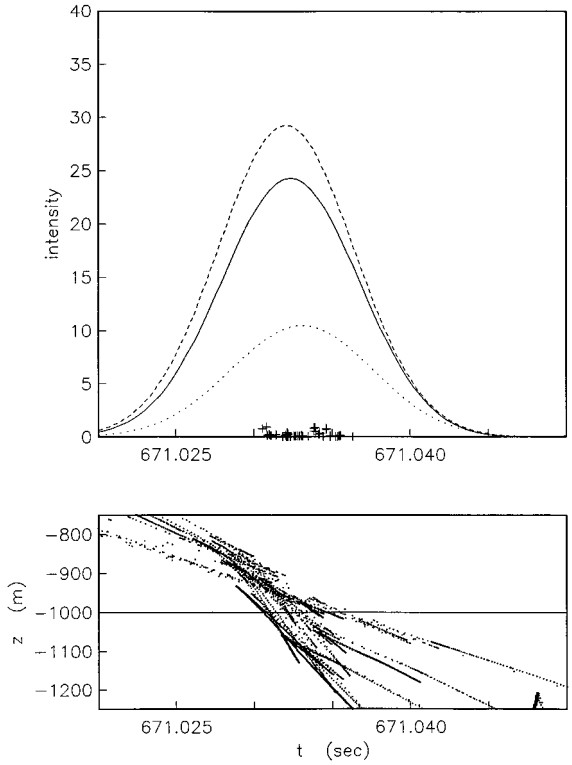

FIG. 17. Comparison of semi-classical and PE solutions for the case of a 10-mode internal-wave field when the simulated source signal has 1000-Hz center frequency. The point of comparison corresponds to the same point selected in Fig. 16. The top figure shows intensity versus time for the semi-classical solution (dashed), the incoherent semi-classical sum (dotted), and the PE solution (solid). The comparison between the semi-classical and PE solutions is better at 1000 Hz than at 250 Hz (Fig. 16). The horizontal line at $z=-1000$ m in the bottom figure intersects the local timefront structure at the many ray arrival times indicated by crosses in the upper figure.

approximation is an asymptotic description in the limit of high frequency, as expected, the PE solution and its semi-classical counterpart match more closely in intensity at higher frequencies. In Fig. 19 the incoherent sum of ray arrivals differs significantly from the standard (coherent) semi-classical sum.

Figure 20 shows that when the semi-classical approximation fails to account for any contribution from the shadow side of significant caustics, agreement between the PE and this ray-based approximation is poor. In the same figure, however, the other PE peak is very accurately approximated by the semi-classical sum.

It appears that the semi-classical approximation is fairly robust for propagation over 1000 km through our 10-mode internal-wave field. Even in the cases of extreme microfolding, this ray-based approximation describes qualitative behavior well: Its number of peaks and travel times agree closely (within a ms or two) to those given by the corresponding wave equation, and the intensities agree to within 5 dB. Only on the shadow side of strong caustics does the geometric approximation seem to fail considerably in its description. (Presumably a better approximation in the vicinity of caustics, such as that from the use of complex rays, or a Maslov integral representation,[28] could improve the semi-classical approach.)

The number of microfolds (and microcaustics) in the late-arriving portion of the SLICE89 pulse (after propagating through internal waves) is much greater than for the CANON pulse. Although it may be impractical to identify all multipaths in the SLICE89 case, the semi-classical approximation may still perform well there. There would be an exponentially large number of microcaustics there, and diffractive effects are normally associated with regions nearby caustics; however, because these caustics would be weak,[29] it might be that ray-based acoustics would still sufficiently describe the behavior there, but this is clearly an area requiring further investigation and computation.

C. Tomographic resolution

In the absence of internal waves, a single intensity peak in the received signal is usually associated with a single eigenray from source to receiver. That same arrival, when internal waves are present, was shown in Secs. IV A and IV B to consist of contributions from numerous new eigenrays that are induced by the internal waves. Figure 21 shows

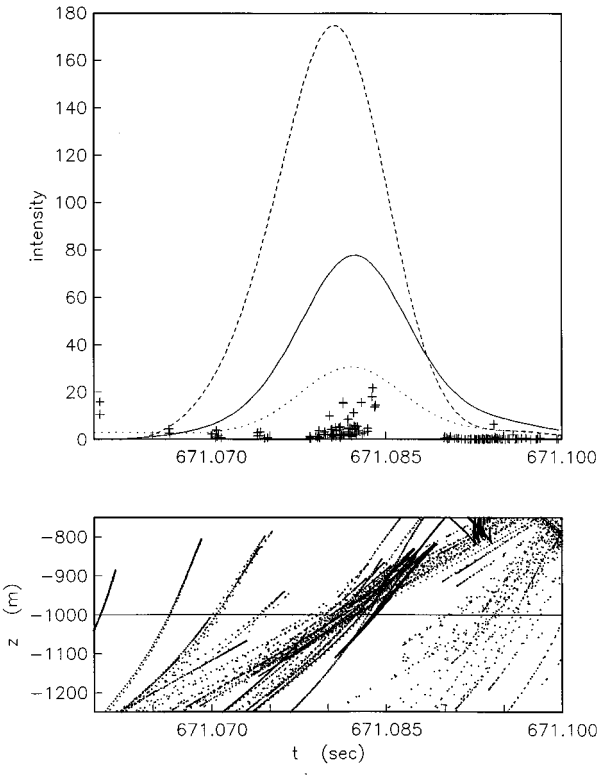

FIG. 18. Comparison of semi-classical and PE solutions for the case of a 10-mode internal-wave field. The point of comparison corresponds to the selected circle in Fig. 13 having depth at 1000 m and arrival time near 671.08 s. The simulated source signal has 250-Hz center frequency. The top figure shows intensity versus time for the semi-classical solution (dashed), the incoherent semi-classical sum (dotted), and the PE solution (solid). Almost 200 individual ray arrivals contribute to the single peak in intensity. (The crosses in the top figure have had their intensities rescaled by a factor of 10 so as to make the arrivals more visible.) The bottom figure reveals the presence of severe microfolding. In the vicinity of so many microcaustics, there is still remarkable agreement between PE and semi-classical for the pulse shape and arrival time.

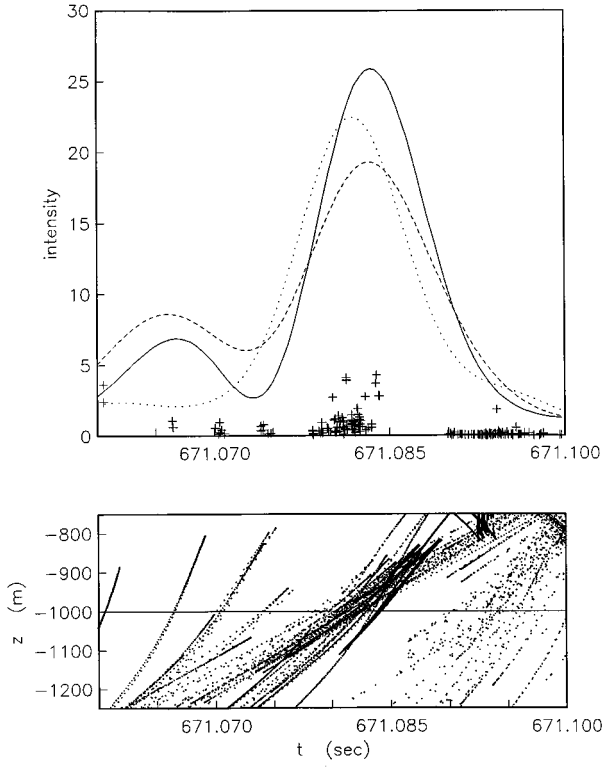

FIG. 19. Comparison of semi-classical and PE solutions for the case of a 10-mode internal-wave field when the simulated source signal has 1000-Hz center frequency. The point of comparison corresponds to the same point selected in Fig. 18. The top figure shows intensity versus time for both the semi-classical solution (dashed) and the PE solution (solid). The intensity calculated from an incoherent sum of ray arrivals (dotted) shows the error incurred if phase information is excluded from the semi-classical sum. At this higher frequency multipaths interfere to produce two peaks rather than one (Fig. 18). (The crosses in the top figure have had their intensities rescaled by a factor of 3 so as to make the arrivals more visible.) Note that the intensities of different ray arrivals are in different ratios for the 250-Hz (Fig. 18) and 1000-Hz frequencies because of the point-source correction needed when comparing to PE.

the internal-wave-induced eigenrays corresponding to the single intensity peak graphed in Figs. 16 and 17. Since the contributions (amplitudes) of most of these rays are significant, and these rays sample slightly different parts of the ocean, any tomography scheme ought to associate the single intensity peak with a ''raytube,'' identified by the tube of rays illustrated.

The width of the raytube is a measure of the resolution one obtains from travel-time tomography. We should measure the raytube width at points along the eigenray that are important for the specific tomography experiment that we have in mind. For example, if mesoscale structure in the upper 500 m of the ocean is being measured, or if internal-wave strength, which is confined mainly to the upper 500 m of the ocean, is being measured, then the important places along the eigenray to measure the raytube width are the upper turning points. We therefore define measures of raytube width by considering the behavior of the upper turning points of the set of internal-wave-induced eigenrays. Consider one specific upper turning point on the single ray in the absence of internal waves. Each of the multiple eigenrays induced by the internal-wave field has a corresponding upper turning point. The distribution in horizontal and vertical position of the set of corresponding upper turning points measures the raytube extent at that particular upper turning point. We have calculated the maximum extents in both horizontal and vertical for every upper turning point of the raytube in Fig. 21, and the results are also shown in that figure. The typical horizontal and vertical maximum extents are 10 km and 100 m, respectively.

In studying the character of raytubes, there is no need to assume a parabolic approximation, and one can work with the standard (one-way) ray equations (14)–(16) corresponding to the full wave equation. Figure 11 shows the timefront corresponding to the standard Eikonal equation for propagation over 1000 km through internal waves. The circles identify selected timefront arrivals for which raytube extents are presented in Fig. 22. Figure 22 shows that raytube extent does vary along the timefront; for the cases shown, the maximum horizontal extent varies from 6 to 16 km, while the maximum vertical extent varies from 50 to 100 m. The raytubes in Fig. 22 all correspond to early-to-middle arrivals in the (CANON) timefront; a late arrival in the SLICE89 timefront is expected to have a raytube with much greater extent (poorer resolution).

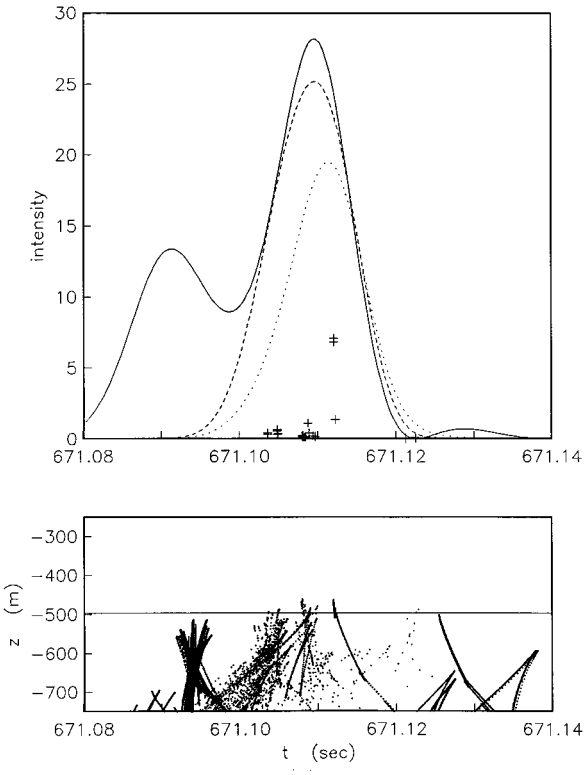

FIG. 20. Comparison of semi-classical and PE solutions for the case of a 10-mode internal-wave field. The point of comparison corresponds to the latest selected circle in Fig. 13, having depth near 500 m and arrival time near 671.11 s. The simulated source signal has 250-Hz center frequency. The top figure shows intensity versus time for both the semi-classical solution (dashed) and the PE solution (solid). The intensity calculated from an incoherent sum of ray arrivals (dotted) shows the error incurred if phase information is excluded from the semi-classical sum. The semi-classical solution, which does not account for any contribution from the shadow side of caustics, fails to pick up the first PE peak. The bottom figure reveals the presence of numerous micro-caustics; the horizontal line marks the depth of comparison and shows that the semi-classical sum slightly misses contributions from the dark mass of microcaustics on the left.

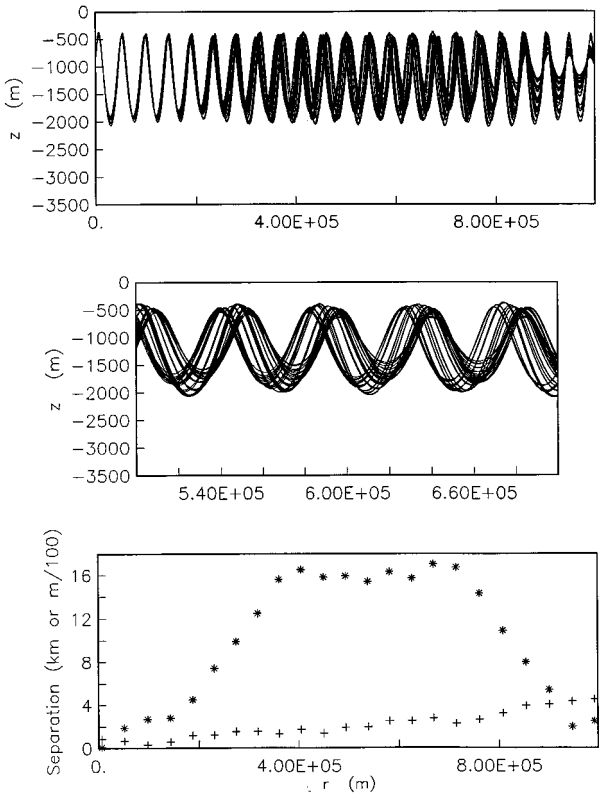

FIG. 21. Eigenrays that contribute to the single peak in intensity graphed in Figs. 16 and 17. The top figure shows the eigenray traces from the source to the receiving point 1000 km away at a depth of 1000 m. The middle figure magnifies a portion of the eigenray traces. The bottom figure describes the extent of the raytube as a function of range in two ways: the asterisks and the crosses give the maximum horizontal distance and vertical distance, respectively, between corresponding ray upper turning points within the raytube. The units of the vertical axis are km and m/100 for the asterisks and crosses, respectively. In this instance, horizontal resolution increases (i.e., raytube horizontal extent decreases) while vertical resolution decreases (i.e., vertical extent increases), as the raytube nears the receiver.

We also note here that use of an internal-wave field with 40 modes instead of 10 does not qualitatively change any of the above plots or conclusions.

V. SUMMARY

Through numerical simulation we have studied the transmission of sound impulses through a model field of ocean internal waves for propagation ranges of order 1000 km. The simulated internal-wave field was constructed from the superposition of either 10 or 40 modes of linear internal waves, traveling only in the source–receiver direction, and having amplitudes weighted to resemble the Garrett–Munk spectrum. The acoustic propagation was simulated in two different ways. First, geometrical-optics rays were followed using a Hamiltonian formulation and various numerical schemes for integrating ordinary differential equations; then acoustic waveforms were calculated semi-classically from the WKB approximation. Second, for comparison, the parabolic wave equation was solved by the split-step Fourier algorithm. Pulses were synthesized at center frequencies of 250 and 1000 Hz, with a bandwidth of 100 Hz. Thus the lowest frequency in our simulations was 200 Hz. The emphasis of this work has been on understanding the geometrical, or ray-based, behavior of the sound propagation, and at the same time investigating the accuracy of ray-based (WKB) waveforms for propagation through small-scale sound-speed structure in the ocean. We have considered three different deterministic (range-independent) sound-speed profiles: two canonical, smooth profiles, and one profile from the SLICE89 experiment.

The ray-based description of acoustic propagation starts from the impulse-response arrival at long range, expressed as a timefront. This timefront in the absence of internal waves has many accordion-shaped folds and covers the depth of the ocean, but is smooth. It has been shown that by introducing range-dependent, internal-wavelike structure on to an otherwise range-independent (or average) sound-speed profile, timefronts develop smaller microfolds on top of the larger folds resulting from range-independent propagation alone. Furthermore, it has been shown that at sufficiently long range, and for the later-arriving portions of the timefront, these microfolds become too numerous to resolve. We have introduced ''bubble'' plots as a suitable means to present the sensitivity of rays to initial conditions for the propagation

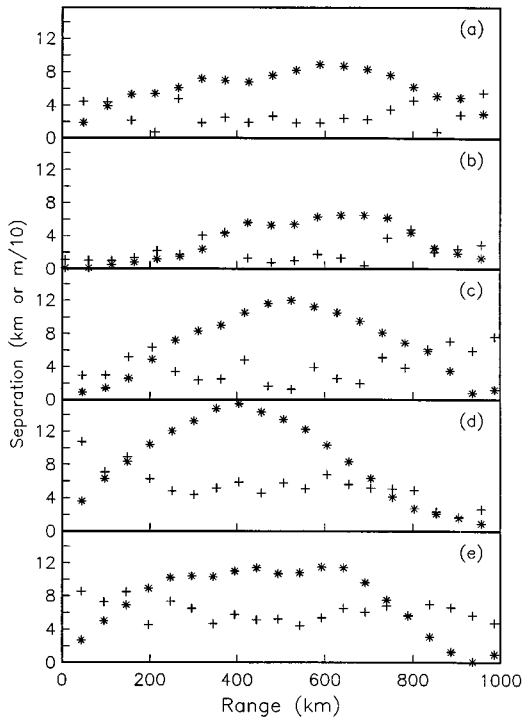

FIG. 22. Raytube extent as a function of range for 1000-km propagation through internal waves superimposed on the CANON average sound-speed profile. The plots are in order of arrival time, for each of five selected arrivals in Fig. 11. The asterisks and the crosses give the maximum horizontal distance and vertical distance, respectively, between corresponding ray upper turning points within the raytube. The units of the vertical axis are km and m/10 for the asterisks and crosses, respectively.

ranges of interest. Our simulations have made it very plausible that in the SLICE89 case the chaotic behavior of later-arriving rays is responsible for extreme timefront folding, which in turn, is responsible for the indistinguishable and diffused late arrivals observed in the actual experimental data. We conclude that for frequencies as low as 200 Hz *refraction* rather than *diffraction* accounts for most of the fluctuation in sound energy in the late-arriving part of the pulse.

We have found that the region of launch angle (or equivalently the region of arrival time) for which rays are chaotic depends on the internal-wave model. For example, earlier work that used a one-mode model of range-dependent sound-speed perturbation found strong chaotic behavior for steep rays, but not for rays with near-horizontal launch angles.[8] In contrast, our results for 10-mode and 40-mode internal-wave models, and other multimode models,[9] show the opposite: strong chaotic behavior for near-horizontal launch angles, but not for steep rays. We have also found that given a specific, parameterized, internal-wave model, the regions of chaotic behavior do not depend on the specific realization of the internal waves.

We have found that the region of launch angle for which internal waves induce chaotic rays depends on the average (range-independent) sound-speed profile. At 1000-km range we have studied three profiles: for the Munk canonical profile (CANON), all rays show stability or only a very weak sensitivity to initial conditions; for another canonical profile with a larger second derivative at the sound-channel axis there does exist a significant late-arriving portion of the timefront in which the rays are chaotic; and, finally, for the SLICE89 experimental sound-speed profile there is a very substantial chaotic region in the latest-arriving portion of the timefront.

We have found that there is a strong dependence of global ray and timefront behavior on transmission range. For the Munk canonical profile (CANON), ray arrivals are insensitive to slight launch perturbations and a relatively well-behaved timefront emerges at 1000 km, while the timefront shows very scattered and diffuse late arrivals at 4000 km.

It was shown that internal waves induce multiple rays for an arrival that came from a single ray in the absence of internal waves. The raytube comprised of these multiple rays has an extent that defines the resolution of ocean acoustic tomography. For 1000-km propagation, a measure of this resolution is the typical spread of upper-turning-point depths: 10 km in the horizontal and 100 m in the vertical.

We have compared semi-classical (WKB) waveforms with waveforms from calculations using the parabolic-equation approximation. We have found that the semi-classical expansion is fairly robust, describing accurately the shape and peak travel time of arriving signals, except possibly on the shadow side of strong caustics or groups of caustics. We summed semi-classically over all multipaths in a number of regions of the pulse in which many arrivals occurred, and even when there were nearly a hundred or so multipath arrivals, semi-classical and PE solutions were amazingly similar. As the ray behavior becomes more strongly chaotic, the computer effort necessary to find all eigenrays becomes large. In our calculations, it was prohibitive to calculate all the necessary rays in the late-arriving portion of the SLICE89 timefront with the computer resources we had available. More powerful computers that will be available soon will have to be used in order to evaluate semi-classical waveforms and determine their accuracy for the very late arrivals in SLICE89.

The main failure in the semi-classical waveform estimates is in the overall intensity of an arrival; for the 1000-Hz comparisons the differences from the PE calculated intensity were generally small, but for the 250-Hz comparisons we found differences of order 5 dB.

ACKNOWLEDGMENTS

This research was supported in part by the U.S. Office of Naval Research Ocean Acoustics Program. We are grateful for a grant from the W. M. Keck Foundation. This is Contribution Number 289 of the Institute of Tectonics.

[1] W. H. Munk and C. Wunsch, ''Ocean acoustic tomography: A scheme for large-scale monitoring,'' Deep-Sea Res. **26A**, 123–161 (1979).
[2] W. Munk, P. Worcester, and C. Wunsch, *Ocean Acoustic Tomography* (Cambridge U. P., London, 1995).
[3] T. F. Duda, S. M. Flatté, J. A. Colosi, B. D. Cornuelle, J. A. Hildebrand, W. S. Hodgkiss, Jr., P. F. Worcester, B. M. Howe, J. A. Mercer, and R. C. Spindel, ''Measured wavefront fluctuations in 1000-km pulse propagation in the Pacific Ocean,'' J. Acoust. Soc. Am. **92**, 939–955 (1992).
[4] J. A. Colosi, S. M. Flatté, and C. Bracher, ''Internal-wave effects on 1000-km oceanic acoustic pulse propagation: Simulation and comparison with experiment,'' J. Acoust. Soc. Am. **96**, 452–468 (1994).

[5] A. G. Voronovich and E. C. Shang, ''A note on horizontal-refraction-modal tomography,'' J. Acoust. Soc. Am. **98**, 2708–2716 (1995).
[6] J. Colosi and S. M. Flatté, ''Mode coupling by internal waves for multi-megameter acoustic propagation in the ocean,'' J. Acoust. Soc. Am. **100**, 3607–3620 (1996).
[7] D. R. Palmer, M. G. Brown, F. D. Tappert, and H. F. Bezdek, ''Classical chaos in nonseparable wave propagation problems,'' Geophys. Res. Lett. **15**, 569–572 (1988).
[8] K. B. Smith, M. G. Brown, and F. D. Tappert, ''Ray chaos in underwater acoustics,'' J. Acoust. Soc. Am. **91**, 1939–1949 (1992).
[9] K. B. Smith, M. G. Brown, and F. D. Tappert, ''Acoustic ray chaos induced by mesoscale ocean structure,'' J. Acoust. Soc. Am. **91**, 1950–1959 (1992).
[10] M. L. Grabb, S. Wang, and T. G. Birdsall, ''Deterministic, three-dimensional analysis of long-range sound propagation through internal-wave fields,'' J. Ocean Eng. **21**, 260–272 (1996).
[11] S. M. Flatté, R. Dashen, W. M. Munk, K. M. Watson, and F. Zachariasen, *Sound Transmission Through a Fluctuating Ocean* (Cambridge U. P., London, 1979).
[12] C. Garrett and W. H. Munk, ''Spacetime scales of internal waves: A progress report,'' J. Geophys. Res. **80**, 291–297 (1975).
[13] W. H. Munk, ''Sound channel in an exponentially stratified ocean, with application to SOFAR,'' J. Acoust. Soc. Am. **55**, 220–226 (1974).
[14] S. M. Flatté, ''An angle-depth diagram for underwater acoustics,'' J. Acoust. Soc. Am. **60**, 1020–1023 (1976).
[15] H. Cox, ''The approximate ray-angle diagram,'' J. Acoust. Soc. Am. **61**, 353–359 (1977).
[16] W. H. Press, B. P. Flannery, S. A. Teukolsky, and W. T. Vetterling, *Numerical Recipes* (Cambridge U. P., Cambridge, 1986).
[17] M. D. Collins and W. A. Kuperman, ''Overcoming ray chaos,'' J. Acoust. Soc. Am. **95**, 3167–3170 (1994).
[18] F. D. Tappert, ''The parabolic approximation method,'' in *Wave Propagation and Underwater Acoustics*, edited by J. B. Keller and J. S. Papadakis, Topics in Current Physics, Volume 8 (Springer-Verlag, Berlin, 1977).
[19] B. M. Howe, J. A. Mercer, R. C. Spindel, P. F. Worcester, J. A. Hildebrand, W. S. Hodgkiss, Jr., T. F. Duda, and S. M. Flatté, ''SLICE89: A single-slice tomography experiment,'' in *Ocean Variability and Acoustic Propagation*, edited by J. Potter and A. Warn-Varnas (Kluwer Academic, New York, 1991), pp. 81–86.
[20] B. D. Cornuelle, P. F. Worcester, J. A. Hildebrand, W. S. Hodgkiss, Jr., T. F. Duda, J. Boyd, B. M. Howe, J. A. Mercer, and R. C. Spindel, ''Ocean acoustic tomography at 1000-km range using wavefronts measured with a large-aperture vertical array,'' J. Geophys. Res. **98**, 16 365–16 377 (1993).
[21] T. F. Duda and J. B. Bowlin, ''Ray-acoustic caustic formation and timing effects from ocean sound-speed relative curvature,'' J. Acoust. Soc. Am. **96**, 1033–1046 (1994).
[22] M. C. Gutzwiller, *Chaos in Classical and Quantum Mechanics, Interdisciplinary Applied Mathematics* (Springer-Verlag, New York, 1990), Vol. 1.
[23] E. J. Heller, ''The role of interference in the semiclassical approximation to chaotic motion,'' Prog. Theor. Phys. Suppl. **N116**, 45–58 (1994).
[24] S. Tomsovic and E. J. Heller, ''Semiclassical dynamics of chaos—The stadium billiard,'' Phys. Rev. E **47**, 282–299 (1993).
[25] S. Tomsovic and E. J. Heller, ''Semiclassical construction of chaotic eigenstates,'' Phys. Rev. Lett. **70**, 1405–1408 (1993).
[26] P. W. O'Connor, S. Tomsovic, and E. J. Heller, ''Accuracy of semiclassical dynamics in the presence of chaos,'' J. Stat. Phys. **68**, 131–152 (1992).
[27] M. A. Sepulveda, S. Tomsovic, and E. J. Heller, ''Semiclassical propagation—How long can it last?'' Phys. Rev. Lett. **69**, 402–405 (1992).
[28] M. G. Brown, ''A Maslov–Chapman wavefield representation for wide-angle one-way propagation,'' Geophys. J. Int. **116**, 513–526 (1994).
[29] A. Draganov and J. Spiesberger, ''Diffraction and pulse delay in a structured ocean,'' J. Acoust. Soc. Am. **98**, 1065–1074 (1995).

Acoustic scattering from a three-dimensional protuberance on a thin, infinite, submerged elastic plate

Tarun K. Kapoor and Henrik Schmidt
Massachusetts Institute of Technology, 77 Massachusetts Avenue, Cambridge, Massachusetts 02139

(Received 27 June 1995; accepted for publication 22 June 1996)

Scattering of sound from an infinite plate is significantly altered by the presence of an impedance discontinuity. Here, an approximate analytical solution is developed for the scattering of sound from a three-dimensional protuberance on a thin, infinite, submerged elastic plate. The protuberance is modeled as a solid elastic sphere of dimensions comparable to the incident acoustic wave [$ka \sim O(1)$], and is attached to the plate along its equatorial plane. The plate is modeled using thin plate theory and supports the lowest-order flexural, compressional, and horizontally polarized shear (SH) modes, while the solid sphere is modeled with the full three-dimensional elastodynamic equations of motion. This idealized environmental model provides an understanding of the underlying physics of 3-D scattering, which is shown to be strongly frequency dependent. The analysis demonstrates that the attachment of the plate manifests itself in the scattered field in a frequency selective manner, and that the resonances of the elastic modes in the sphere leave their imprint on the elastic waves coupled into the plate. It is also shown that since the attached plate primarily restrains the motions of the sphere in the horizontal plane, the dominant contribution to the scattered field arises from the in-plane coupling forces. [S0001-4966(97)00606-1]

PACS numbers: 43.30.Gv, 43.30.Ma, 43.20.Tb, 43.40.Rj [JHM]

INTRODUCTION

The problem of scattering from irregular boundaries plays a significant role in many acoustic disciplines. For example, in structural acoustics, while the scattering of sound from ideal spherical and cylindrical shells are well understood, real world structures have attached sub-structures like stiffeners, bulkheads, etc. Similarly, the Arctic ice cover is often treated as a homogeneous elastic flat plate, and has been studied extensively.[1–5] However, real ice has keels and leads. A canonical model representing the fundamental properties of such scattering problems is an infinite elastic plate with protuberances. There have been numerous efforts in the past to model scattering from a ribbed plate,[6,7] where the size of the rib was assumed to be small compared to the wavelength of the incident acoustic wave. More recently, Guo[8] addressed the problem of scattering from an infinite elastic plate loaded with fluid on one side and a semi-infinite plate on the other. These two-dimensional studies revealed that an impedance discontinuity in the canonical geometry of a flat plate produces significant scattering into the fluid by both supersonic and subsonic waves in the plate. Additionally, subsonic waves couple into the plate by interaction of the acoustic wave with the impedance discontinuity.

The complexity of this problem may be augmented by increasing the dimensionality of the problem, i.e., by considering scattering from a three-dimensional feature. There have been attempts in the past to model scattering from hemispherical bumps on an infinite plane. However, in the work presented here, we consider scattering from an infinite, submerged elastic plate with a three-dimensional protuberance whose dimensions are comparable with the wavelength of the incident acoustic waves. The impedance discontinuity is not compact ($ka \ll 1$) but can support elastic waves which can resonate and additionally radiate into the surrounding fluid. It is possible to model this problem by using finite difference[9] or boundary element approaches.[10] However, these methods are computationally intensive for three-dimensional scattering scenarios. Therefore, in this paper we formulate the scattering problem analytically using the Eulerian approach.[11,12]

Our interest in this problem stems from the consideration of the scattering of acoustic waves from the three-dimensional features under the rough ice in the Arctic Ocean. Previous analyses[13,14] have modeled these, for example, as impenetrable hemispherical protuberances on an infinite plane. Even though the idealized environmental model presented here does not represent the real scattering scenario, it is more complete than such earlier representations in terms of the fundamental scattering mechanisms involved. For example, it allows analysis of whether scattering into in-plane (shear and compressional) waves in the plate plays an important role in defining the beampattern of the scattered field. That this is the case will become evident from our model which allows for excitation of the in-plane motions of the plate. In a later paper,[15] where we analyze the acoustic scattering from an isolated protuberance under the Arctic ice sheet, we will draw upon the analysis presented here.

We begin by parametrizing the various wave phenomena involved in the scattering process in Sec. I. Section II formulates the exact scattering problem using the Eulerian approach. In Sec. III, we solve the decoupled constituent problems of the free submerged sphere, the elastic plate, and the sphere excited by ring coupling forces and bending moment. Section IV contains the final results from our analysis where we evaluate the attachment ring kinematics, the backscat-

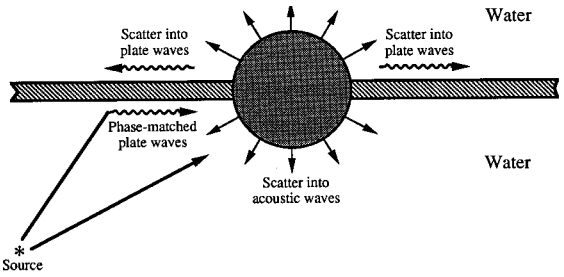

FIG. 1. Schematic representation of source, plate, and sphere geometry. The incident field excites waves inside both the sphere and the plate, which then couple back into the surrounding acoustic medium.

tered pressure, and the bistatic scattering pattern for scatter from the three-dimensional protuberance.

I. PARAMETRIZATION OF THE PROBLEM

Before formulating the problem of three-dimensional scatter, we begin by parametrizing the wave phenomena involved in the scattering process. Figure 1 shows the interaction between the incident sound field due to a point source and the plate–sphere coupled structure. The incident field excites elastic modes in the plate by phase-matching.[16] In general, assuming the plate to be thin, both compressional and flexural waves could be excited in the plate. With our plate parameters and frequencies of interest, only the lowest-order plate modes are excited. These plate waves then travel towards the plate–sphere junction while radiating back into the fluid by phase-matched leakage. At the junction, they interact with the sphere and are (i) partially reflected back, (ii) partially converted into plate waves of other types, (iii) excite elastic waves in the sphere, and (iv) diffract into the fluid by scattering at the junction. Simultaneously, the incident acoustic field excites the shear and compressional modes in the solid sphere, which then (i) radiate back into the fluid, (ii) excite structural waves in the plate, and (iii) diffract into the fluid by scattering at the junction. The total displacement components of the plate (subscripted with p) and sphere (subscripted with s) at the attachment ring can therefore be expressed as a sum of two components—one due to excitation by the acoustic wave (subscripted with a) and the other contribution due to the excitation by coupling forces and bending moment (subscripted with c) at that attachment ring, i.e.,

$$\mathbf{u}_{p,t}=\mathbf{u}_{p,a}+\mathbf{u}_{p,c}\,, \qquad \mathbf{u}_{s,t}=\mathbf{u}_{s,a}+\mathbf{u}_{s,c}\,, \tag{1}$$

where $\mathbf{u}_{p,t}$ and $\mathbf{u}_{s,t}$ represent the total displacements of the plate and sphere, respectively, at the attachment ring.

Having identified all the wave constituents that enter into the scattering scenario, we then proceed to synthesize the total scattered field at the observer in terms of the contributions arising from the plate waves and those due to the elastic waves in the sphere. The contributions from the plate waves excited by the incident field consist of (i) direct leakage of plate waves into the fluid by phase-matching, and (ii) diffraction of plate waves at the plate–sphere junction into the fluid. Similarly the elastic modes in the solid sphere contribute to the scattered field by (i) radiating back into the fluid, and (ii) diffracting into the fluid at the junction. The direct leakage of the plate waves and the radiation of the sphere modes can be easily computed by solving the canonical problems of an infinite submerged plate and the solid elastic sphere fully submerged under water. The solutions to both these constituent problems is well known and will not be discussed in detail here; only the significant results will be presented. Finally, just as we expressed the displacements in terms of two components, we express the total scattered pressure (p_t) in the fluid as a sum of the contributions from the plate and sphere excited by the acoustic wave, and the coupling forces as

$$p_t=p_{s,a}+p_{s,c}+p_{p,a}+p_{p,c}\,. \tag{2}$$

It must be pointed out that in the formulation above we have neglected the contribution due to the specular reflection from the side of the plate which may easily be added.

II. COUPLING FORMULATION

The formulation for scattering from coupled elastic structures has been previously studied in great detail[11,12] using the Eulerian formulation to decompose the coupled structure into its decoupled constituents, with their interactions being accounted for by coupling forces and moments at the attachments. It was shown that when the size of the attachments is small compared to wavelength, the junction could be approximated as a point or ring junction as appropriate to the problem under consideration. If the attachment area is larger, then this may be viewed as a first-order approximation to the exact solution.

The methodology of this approach is as follows. First, one must solve for the dynamics of the decoupled constituents independently. However, one needs to add some unknown source terms to account for the coupling at the attachment. In general, one expands these source terms in terms of coupling forces and moments depending on the characteristics of the attachment junctions. For example, if we have a pinned joint we need to retain only forces, whereas for a clamped joint, the analysis must include both forces and moments. These are in turn then determined by matching the kinematics of the constituent structures at the attachment junction, for example, displacements and slopes. This yields a set of algebraic equations which can then be solved for the unknown coupling forces and moments.

At this juncture, it is worthwhile to point out that for an arbitrary attachment between two structures, three components of stress and three displacement components must be matched at that junction. This is a complex problem to solve since the stress distribution at the junction is not known *a priori.* A possible solution procedure would involve making assumptions regarding the form of the stress distribution in terms of some unknown coefficients, and then solving the boundary conditions for those unknown constants. Thus, in our model, where the thickness of the plate is small but not negligible compared to wavelength, we should match stresses at the plate–sphere junction. However, we choose to make the analysis more tractable by matching equivalent forces and moments (or integrated stresses) at the junction modeled as a ring of zero width. This is also consistent with

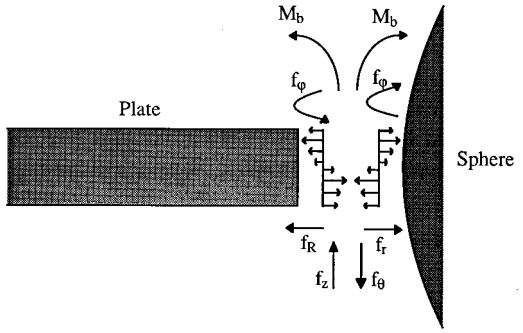

FIG. 2. Coupling forces and bending moments involved in characterization of the attachment ring. The forces and moments for the plate are shown in their positive sense.

the use of thin plate theory for the plate. Moreover, structural continuity requirements will be satisfied since we constrain the displacements and slopes at the junction.

The dynamics of the plate at the attachment junction are characterized by in-plane and out-of-plane motions. Out-of-plane displacements are produced by including a vertical shear force (f_z) and a bending moment (M_b) while in-plane displacements are obtained by including the radial (f_R) and circumferential (f_φ) in-plane forces in the analysis. Figure 2 shows the junction between the plate and the sphere with the various coupling forces and moments. Also shown in the figure is the unknown stress distribution that exists at the coupling junction.

The displacements of the sphere due to the incident acoustic wave ($\mathbf{u}_{s,a}$) will be found in Sec. III A, and may be expressed as

$$\mathbf{u}_{s,a}=\sum_{m=-\infty}^{\infty}\underbrace{\left\{\sum_{n=|m|}^{\infty}G_n^m\tilde{\mathbf{u}}_{s,a}\right\}}_{\hat{\mathbf{Y}}_s}e^{im\varphi}, \tag{3}$$

where $\tilde{\mathbf{u}}_{s,a}$ are the displacements of polar order n and azimuthal order m, and G_n^m is defined later in Eq. (17). Here the ''hat'' notation is used to denote dependence on the azimuthal order m only. Similarly, the plate displacements due to the incident acoustic wave may be expressed in the form

$$\mathbf{u}_{p,a}=\sum_{m=-\infty}^{\infty}\hat{\mathbf{Y}}_p e^{im\varphi}. \tag{4}$$

From the analysis of the governing equations of motion of the elastic plate (see Sec. III B), we may write the displacements of the plate due to the ring forces and bending moments as

$$\mathbf{u}_{p,c}=\sum_{m=-\infty}^{\infty}\hat{\mathbf{\Lambda}}_p\hat{\mathbf{f}}_p e^{im\varphi}, \tag{5}$$

where $\hat{\mathbf{\Lambda}}_p=\hat{\mathbf{Z}}_p/2\pi$ and $\hat{\mathbf{f}}$ denotes the Fourier transform of the vector of coupling forces and is a function of the Fourier (azimuthal) order m only. $\hat{\mathbf{Z}}_p$ is the *influence matrix* for the plate and is given by

$$\begin{Bmatrix}\hat{v}_R\\ \hat{v}_\varphi\\ \hat{w}\\ \partial\hat{w}/\partial R\end{Bmatrix}=\begin{bmatrix}\hat{P}_{11}&\hat{P}_{12}&0&0\\ \hat{P}_{21}&\hat{P}_{22}&0&0\\ 0&0&\hat{P}_{33}&\hat{P}_{34}\\ 0&0&\hat{P}_{43}&\hat{P}_{44}\end{bmatrix}\begin{Bmatrix}\hat{f}_R\\ \hat{f}_\varphi\\ \hat{f}_z\\ \hat{M}_b\end{Bmatrix}. \tag{6}$$

The upper-right and lower-left quarters of the influence matrix are 0 since the in-plane motions are decoupled from the out-of-plane motions in thin plate theory, as shown later. For the sphere, the resultants act in the opposite direction, and we will have

$$\mathbf{u}_{s,c}=\sum_{m=-\infty}^{\infty}\underbrace{\left\{\frac{1}{2\pi}\sum_{n=|m|}^{\infty}a_{mn}\tilde{\mathbf{Z}}_s\right\}}_{\hat{\mathbf{\Lambda}}_s}\hat{\mathbf{f}}_s e^{im\varphi}, \tag{7}$$

where

$$a_{mn}=\frac{2n+1}{2}\frac{(n-m)!}{(n+m)!},$$

and $\mathbf{u}_{s,c}$ is the displacement of the sphere due to the ring forces and bending moments. Note that we have implicitly assumed that $\hat{f}_s$ acts in an opposite sense to $\hat{f}_p$. $\tilde{\mathbf{Z}}_s$ is the *influence matrix* for the sphere (derived in Sec. III C), and is given by

$$\begin{Bmatrix}\tilde{u}_r\\ \tilde{u}_\varphi\\ \tilde{u}_\theta\\ \partial\tilde{u}_r/r\partial\theta\end{Bmatrix}=\begin{bmatrix}\tilde{S}_{11}&\tilde{S}_{12}&\tilde{S}_{13}&\tilde{S}_{14}\\ \tilde{S}_{21}&\tilde{S}_{22}&\tilde{S}_{23}&\tilde{S}_{24}\\ \tilde{S}_{31}&\tilde{S}_{32}&\tilde{S}_{33}&\tilde{S}_{34}\\ \tilde{S}_{41}&\tilde{S}_{42}&\tilde{S}_{43}&\tilde{S}_{44}\end{bmatrix}\begin{Bmatrix}\hat{f}_r\\ \hat{f}_\varphi\\ \hat{f}_\theta\\ \hat{M}_b\end{Bmatrix}. \tag{8}$$

Here the ''tilde'' notation is used to denote dependence on both the polar order n and the azimuthal order m. Matching displacements at the attachment ring yields

$$\mathbf{u}_{p,a}+\mathbf{u}_{p,c}=\mathbf{T}[\mathbf{u}_{s,a}+\mathbf{u}_{s,c}]$$

or

$$\mathbf{u}_{s,a}-\mathbf{T}^{-1}\mathbf{u}_{p,a}=\mathbf{T}^{-1}\mathbf{u}_{p,c}-\mathbf{u}_{s,c}, \tag{9}$$

where $\mathbf{T}$ is the transformation matrix from spherical to cylindrical coordinates for both displacements and forces, and is given by

$$\begin{Bmatrix}\hat{f}_R\\ \hat{f}_\varphi\\ \hat{f}_z\\ \hat{M}_b\end{Bmatrix}=\begin{bmatrix}\sin\gamma&0&\cos\gamma&0\\ 0&1&0&0\\ \cos\gamma&0&-\sin\gamma&0\\ 0&0&0&1\end{bmatrix}\begin{Bmatrix}\hat{f}_r\\ \hat{f}_\varphi\\ \hat{f}_\theta\\ \hat{M}_b\end{Bmatrix}. \tag{10}$$

Here γ is the polar angle at the junction ring. Inserting Eqs. (5) and (7) into Eq. (9), we can write

$$\hat{\mathbf{Y}}_s-\mathbf{T}^{-1}\hat{\mathbf{Y}}_p=\mathbf{T}^{-1}\hat{\mathbf{\Lambda}}_p\hat{\mathbf{f}}_p-\hat{\mathbf{\Lambda}}_s\hat{\mathbf{f}}_s. \tag{11}$$

Now inserting $\hat{\mathbf{f}}_p=\mathbf{T}\hat{\mathbf{f}}_s$ into Eq. (11), we have

$$\hat{\mathbf{Y}}_s-\mathbf{T}^{-1}\hat{\mathbf{Y}}_p=[\mathbf{T}^{-1}\hat{\mathbf{\Lambda}}_p\mathbf{T}-\hat{\mathbf{\Lambda}}_s]\hat{\mathbf{f}}_s,$$

and therefore, the coupling forces are found to be

$$\hat{\mathbf{f}}_s=[\mathbf{T}^{-1}\hat{\mathbf{\Lambda}}_p\mathbf{T}-\hat{\mathbf{\Lambda}}_s]^{-1}[\hat{\mathbf{Y}}_s-\mathbf{T}^{-1}\hat{\mathbf{Y}}_p]. \tag{12}$$

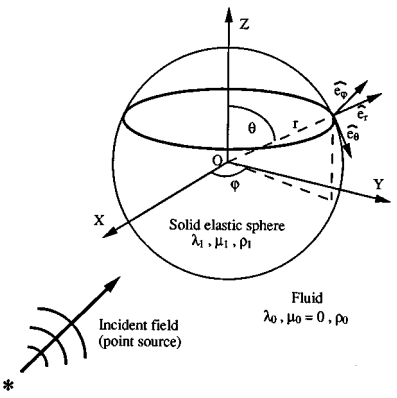

FIG. 3. Geometry for scattering from a submerged solid elastic sphere due to an incident point source field.

Then using Eqs. (5) and (7), we can finally solve for the displacements $\mathbf{u}_{s,c}$ and $\mathbf{u}_{p,c}$.

III. THE DECOUPLED CONSTITUENT PROBLEMS

In our formulation, we need to determine the kinematics of the plate and sphere at the attachment ring. This is done by solving each of the decoupled constituent problems separately. In the following sections, we shall determine the displacement of the sphere at the coupling junction due to the incident acoustic wave ($\mathbf{u}_{s,a}$) in Sec. III A, and the influence matrices for the plate ($\hat{\mathbf{Z}}_p$) and the sphere ($\tilde{\mathbf{Z}}_s$) in Secs. III B and III C, respectively. The total scattered field is then synthesized in Sec. III D.

A. The free submerged sphere

Scattering of acoustic waves by a solid elastic sphere submerged in a fluid is well understood.[17–20] However, previous analyses were limited to plane waves incident along one of the coordinate axes, or axisymmetric point source loadings,[21] which simplified the algebra considerably. In our case, we need to compute the scattered field and displacement fields along a ring on the sphere due to a point source located at an arbitrary position (r_0, θ_0, φ_0) as shown in Fig. 3. The sphere is assumed to have material properties (λ_1, μ_1, ρ_1) and is of radius a while the surrounding fluid medium has material properties (λ_0, $\mu_0=0$, ρ_0), where λ and μ are Lamé constants, and ρ is the density of the material. The equations governing the motions of a homogeneous isotropic elastic solid are given by

$$(\lambda_1+2\mu_1)\boldsymbol{\nabla}\boldsymbol{\nabla}\cdot\mathbf{u}-\mu_1\boldsymbol{\nabla}\times\boldsymbol{\nabla}\times\mathbf{u}+\rho_1\mathbf{f}=\rho_1\frac{\partial^2\mathbf{u}}{\partial t^2}, \tag{13}$$

where $\mathbf{u}$ is the displacement vector and $\mathbf{f}$ is the body force per unit mass of material. Following Ref. 22, we write the displacement potential in terms of three scalar fields, ϕ, ψ, and $\check{\chi}$, i.e.,

$$\mathbf{u}=\boldsymbol{\nabla}\phi+\boldsymbol{\nabla}\times(\hat{e}_r r\psi)+\boldsymbol{\nabla}\times\boldsymbol{\nabla}\times(\hat{e}_r r\check{\chi}), \tag{14}$$

where $\hat{e}_r$ is a unit vector in the radial direction, the first term is the longitudinal part of the solution, and the other two are the transverse parts. We have retained both transverse components to fully represent the displacement field in the most general case of asymmetric excitation. Assuming an $\exp(-i\omega t)$ harmonic time dependence (suppressed henceforth), the potentials may be shown to satisfy the following Helmholtz equations:

$$(\nabla^2+\alpha_1^2)\phi=0,\quad (\nabla^2+\beta_1^2)\psi=0,\quad (\nabla^2+\beta_1^2)\chi=0, \tag{15}$$

where $\alpha_1=\omega/c_\alpha$ and $\beta_1=\omega/c_\beta$ denote the wave numbers for the compressional and shear waves, respectively, and c_α and c_β are compressional and shear wave speeds, respectively, with

$$c_\alpha=\sqrt{\frac{\lambda_1+2\mu_1}{\rho_1}},\quad c_\beta=\sqrt{\frac{\mu_1}{\rho_1}}.$$

Also, we have normalized the potential $\check{\chi}$ by the shear wave number β as $\chi=\beta\check{\chi}$ so that the dimensions of ϕ, $r\psi$, and $r\chi$ are the same. Expanding the potential functions which satisfy (15) in terms of spherical Bessel functions in r, associated Legendre functions in θ, and Fourier series in φ, we can find the resulting stress and displacement components. However, as discussed in Refs. 23 and 24, these stresses and displacements contain a mixed dependence on the order of the associated Legendre functions $P_n^m(\cos\theta)$ and $P_{n-1}^m(\cos\theta)$. Therefore, following Ref. 24, we shall instead satisfy the boundary conditions with transformed stress and displacement components which decouple in order n.

We begin by expanding the Helmholtz potentials for the incident, scattered, and interior fields in terms of spherical waves as

$$\begin{aligned}
\phi_i&=\sum_{m=-\infty}^{\infty}\sum_{n=|m|}^{\infty}G_n^m j_n(\alpha_0 r)P_n^m(\cos\theta)e^{im\varphi},\\
\phi_s&=\sum_{m=-\infty}^{\infty}\sum_{n=|m|}^{\infty}A_{mn}G_n^m h_n(\alpha_0 r)P_n^m(\cos\theta)e^{im\varphi},\\
\phi_r&=\sum_{m=-\infty}^{\infty}\sum_{n=|m|}^{\infty}B_{mn}G_n^m j_n(\alpha_1 r)P_n^m(\cos\theta)e^{im\varphi},\\
\psi_r&=\sum_{m=-\infty}^{\infty}\sum_{n=|m|}^{\infty}C_{mn}G_n^m j_n(\beta_1 r)P_n^m(\cos\theta)e^{im\varphi},\\
\chi_r&=\sum_{m=-\infty}^{\infty}\sum_{n=|m|}^{\infty}D_{mn}G_n^m j_n(\beta_1 r)P_n^m(\cos\theta)e^{im\varphi},
\end{aligned} \tag{16}$$

where we have used the compact notation $h_n^{(1)}\equiv h_n$ to denote spherical Hankel functions of the first kind. The subscripts i and s denote the incident and scattered fields, respectively, and r denotes the field inside the solid, and

$$G_n^m=i2\alpha_0\frac{p_0}{\rho_0\omega^2}a_{mn}h_n(\alpha_0 r_0)P_n^m(\cos\theta_0)e^{-im\varphi_0}. \tag{17}$$

Here p_0 is the amplitude of the incident pressure at the surface of the sphere and a_{mn} was defined earlier. The scattered pressure is given by $p_{s,a}=\rho_0\omega^2\phi_s$, and our notation for negative orders m for the associated Legendre functions P_n^{-m} is as follows:

$$P_n^{-m}(\cos\theta)=(-1)^m\frac{(n-m)!}{(n+m)!}P_n^m(\cos\theta).$$

Following Ref. 25, four boundary conditions need to be satisfied at the fluid–solid interface: (i) continuity of normal displacement, (ii) continuity of normal stress (pressure), (iii) vanishing of the shear stress $\tau_{r\theta}$ at the boundary, and (iv) vanishing of the shear stress $\tau_{r\varphi}$ at the surface of the sphere. The tangential stresses $\tau_{r\theta}$ and $\tau_{r\phi}$ are coupled in the polar order n and the azimuthal order m. Since both must vanish at the surface of the sphere, any linear combination of these stresses must also be identically zero there. As described in Ref. 24, we can alternatively prescribe the vanishing on the transformed stress components which are decoupled between the orders n and m. Then, using (16) and the expressions for displacements and stresses from Ref. 24, the boundary conditions yield a system of equations which can be solved for the four unknown constants A_{mn}, B_{mn}, C_{mn}, and D_{mn} (see Kapoor[23] for details). Finally, we can write the displacement components $\tilde{\mathbf{u}}_{s,a}$ at the attachment ring, $r=a$ and $\theta=\gamma$, on the free submerged sphere due to the incident acoustic wave as

$$\begin{aligned}
\tilde{u}_r&=\frac{1}{a}\Bigg[B_{mn}\{nj_n(\alpha_1 a)-\alpha_1 a j_{n+1}(\alpha_1 a)\}\\
&\quad+D_{mn}\frac{n(n+1)}{\beta_1}j_n(\beta_1 a)\Bigg]P_n^m(\cos\gamma),\\
\tilde{u}_\theta&=\frac{1}{a}\Bigg[B_{mn}j_n(\alpha_1 a)+D_{mn}\frac{1}{\beta_1}\{(n+1)j_n(\beta_1 a)\\
&\quad-\beta_1 a j_{n+1}(\beta_1 a)\}\Bigg]\left[\frac{d}{d\theta}P_n^m(\cos\theta)\right]_{\theta=\gamma}\\
&\quad+C_{mn}j_n(\beta_1 a)\frac{im}{\sin\gamma}P_n^m(\cos\gamma),\\
\tilde{u}_\varphi&=\frac{1}{a}\Bigg[B_{mn}j_n(\alpha_1 a)+D_{mn}\frac{1}{\beta_1}\{(n+1)j_n(\beta_1 a)\\
&\quad-\beta_1 a j_{n+1}(\beta_1 a)\}\Bigg]\frac{im}{\sin\gamma}P_n^m(\cos\gamma)\\
&\quad-C_{mn}j_n(\beta_1 a)\left[\frac{d}{d\theta}P_n^m(\cos\theta)\right]_{\theta=\gamma},
\end{aligned}\tag{18}$$

$$\frac{1}{r}\frac{\partial\tilde{u}_r}{\partial\theta}=\frac{1}{a^2}\Bigg[B_{mn}\{nj_n(\alpha_1 a)-\alpha_1 a j_{n+1}(\alpha_1 a)\}+D_{mn}\frac{n(n+1)}{\beta_1}j_n(\beta_1 a)\Bigg]\left[\frac{d}{d\theta}P_n^m(\cos\theta)\right]_{\theta=\gamma},$$

where

$$\left[\frac{d}{d\theta}P_n^m(\cos\theta)\right]_{\theta=\gamma}=n\cot\gamma P_n^m(\cos\gamma)-\frac{n+m}{\sin\gamma}P_{n-1}^m(\cos\gamma).$$

B. Thin elastic plate vibrations

Consider a thin infinite circular elastic plate of thickness h with an interior annulus of radius $b=a\sin\gamma$, as shown in Fig. 4, and completely submerged in fluid. Here γ is the polar angle on the sphere at which the sphere is attached to the plate and a is the radius of the sphere. The elastic plate is assumed to have material properties $(\lambda_2,\ \mu_2,\ \rho_2)$ which could possibly be the same as those of the attached sphere $(\lambda_1,\ \mu_1,\ \rho_1)$ while, as before, the fluid medium has material properties $(\lambda_0,\ \mu_0=0,\ \rho_0)$. We assume the plate to be thin so that its flexural motions are decoupled from its extensional and shear motions. Moreover, using thin plate theory is consistent with our model of the plate–sphere ring attachment junction where we apply equivalent coupling forces and bending moments. Also, assuming a 3.0-m-thick ice sheet, thin plate theory is applicable for frequencies less than about 100 Hz (see Ref. 5). It must also be pointed out here that the exact decoupled problem required to be solved as per our formulation is that of an annular plate completely submerged in water. For low frequencies, we assume that the fluid filling the annulus of the plate will not significantly alter the results of the analysis of plate vibrations presented in the following sections.

1. In-plane (compressional and shear) motions

The extensional and shear motions of the plate can be formulated in terms of the in-plane displacement components, v_R and v_φ, in the radial and azimuthal directions, respectively, which in turn can be expressed in terms of two potential functions Γ and Ω[26,27] which satisfy the wave equations

$$\nabla^2\Gamma+\kappa^2\Gamma=0,\quad \nabla^2\Omega+\eta^2\Omega=0\cdot\tag{19}$$

Here $\kappa=\omega/c_\kappa$, $\eta=\omega/c_\eta$ are the wave numbers of the compressional and shear waves, respectively, c_κ and c_η are the compressional and shear wave speeds,

$$c_\kappa=\sqrt{\frac{\lambda_2+2\mu_2}{\rho_2}},\quad c_\eta=\sqrt{\frac{\mu_2}{\rho_2}}.\tag{20}$$

The in-plane displacements can then be expressed in terms of the two displacement potential functions as

$$v_R=\frac{\partial\Gamma}{\partial R}+\frac{1}{R}\frac{\partial\Omega}{\partial\varphi},\tag{21}$$

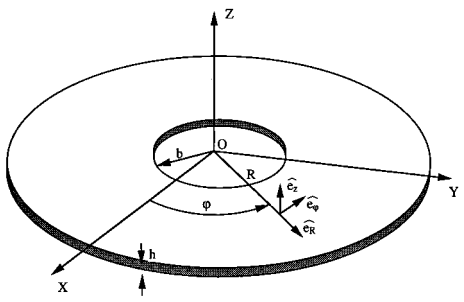

FIG. 4. Geometry for a fluid-loaded elastic plate of thickness h excited by ring forces and bending moment at the interior annulus of radius b.

$$v_\varphi = \frac{1}{R}\frac{\partial \Gamma}{\partial \varphi} - \frac{\partial \Omega}{\partial R}.$$

Note that there is no z dependence in these expressions since the plate is assumed to be thin. For $R \geqslant a$, the solutions are

$$\Gamma(R,\varphi) = \frac{1}{2\pi}\sum_{m=-\infty}^{\infty} \hat{C}_1 H_m(\kappa R) e^{im\varphi},$$
$$\Omega(R,\varphi) = \frac{1}{2\pi}\sum_{m=-\infty}^{\infty} \hat{C}_2 H_m(\eta R) e^{im\varphi}, \tag{22}$$

where we have used the compact notation $H_m^{(1)} \equiv H_m$ to denote cylindrical Hankel functions of the first kind. The two unknown coefficients $\hat{C}_1$ and $\hat{C}_2$ are determined from the boundary conditions at $R=b$. Assuming the stresses τ_{RR} and $\tau_{R\varphi}$ are uniformly distributed over the inner circular edge of the plate, force equilibrium yields

$$-\frac{f_R}{2\pi b h} = (\lambda_2 + 2\mu_2)\frac{\partial v_R}{\partial R} + \frac{\lambda_2}{R}\left[v_R + \frac{\partial v_\varphi}{\partial \varphi}\right],$$
$$-\frac{f_\varphi}{2\pi b h} = \mu_2\left[\frac{\partial v_\varphi}{\partial R} - \frac{v_\varphi}{R} + \frac{1}{R}\frac{\partial v_R}{\partial \varphi}\right]. \tag{23}$$

Substituting for v_R and v_φ from Eqs. (21) and (22), and on taking the Fourier transform, we can solve for the constants $\hat{C}_1$ and $\hat{C}_2$, and therefore for the elements P_{ij} $(i,j=1,2)$ of the plate influence matrix. Details of this analysis and appropriate results may be found in Ref. 23.

2. Out-of-plane (flexural) motions

The transverse displacement $w(R,\varphi)$, of the fully submerged plate satisfy the PDE[1,5]

$$\nabla^4 w - k_f^4 w = -\frac{1}{D}[p_2|_{z=h/2} - p_1|_{z=-h/2}], \tag{24}$$

where p_1 and p_2 are the acoustic fields in the lower and upper semi-infinite media, respectively. $k_f = (\rho_s h \omega^2/D)^{1/4}$ is the flexural wave number of the free plate in vacuum, h is the thickness of the plate, $D = Eh^3/12(1-\nu^2)$, and E and ν are the Young's modulus and Poisson's ratio respectively. As in the case of in-plane motions, we begin by decomposing the φ dependence into angular harmonics, and then solve Eq. (24) in terms of cylindrical Hankel functions and modified Bessel functions as

$$w(R,\varphi) = \frac{1}{2\pi}\sum_{m=-\infty}^{\infty}[\hat{C}_3 H_m(\xi_f R) + \hat{C}_4 K_m(\xi_f R)] e^{im\varphi}. \tag{25}$$

ξ_f is the flexural wave number in the submerged plate in the low-frequency limit approximated by[3,5]

$$\xi_f \sim k_f\left[1 + \frac{2\rho_0}{\rho_2 h\sqrt{k_f^2 - k_0^2}}\right]^{1/4}. \tag{26}$$

We account for the coupling forces and bending moments via the boundary conditions at $R=b$. From Ref. 28, the boundary conditions are given by

$$-\frac{M_b}{2\pi b} = -D\left[\frac{\partial^2 w}{\partial R^2} + \nu\left(\frac{1}{R}\frac{\partial w}{\partial R} + \frac{1}{R^2}\frac{\partial^2 w}{\partial \varphi^2}\right)\right]_{R=b},$$
$$-\frac{f_z}{2\pi b} = -D\left[\frac{\partial(\nabla^2 w)}{\partial R} + \frac{(1-\nu)}{R^2}\frac{\partial^2}{\partial \varphi^2}\left(\frac{\partial w}{\partial R} - \frac{w}{R}\right)\right]_{R=b}. \tag{27}$$

Matching these at the inner annulus of the plate, yields another set of equations for the constants $\hat{C}_3$ and $\hat{C}_4$, and therefore for the elements P_{ij} $(i,j=3,4)$ of the plate influence matrix. Details of this analysis may also be found in Ref. 23.

For the sake of completeness of our analytical formulation, we need to evaluate the displacement components in the plate due to the incident acoustic field due to a point source in the fluid. In general, the components of $\hat{\mathbf{Y}}_p$ may be found by carrying out an analysis similar to the one described in the previous sections. We can expand the incident and scattered fields, as well as the plate displacement components, in terms of cylindrical waves. In general, at low frequencies, both compressional and flexural modes can be excited in the infinite submerged plate, with the supersonic compressional wave being excited due to Poisson's effect. In-plane shear modes are not excited as their motions do not couple into the fluid. The flexural modes are subsonic in this frequency regime and do not radiate from the plate by phase-matching[29] but create only an evanescent wave field near the surface of the plate. The Fourier coefficients corresponding to the flexural and compressional can then be found by matching the boundary conditions at the fluid–elastic interface. However, as shown by Kapoor,[23] the displacement components at the attachment ring due to these acoustically excited modes is extremely small compared to those due to the coupling forces and moments. Therefore, we can set the plate displacement vector $\mathbf{u}_{p,a}$ to be identically *zero* and Eq. (12) simplifies to

$$\hat{\mathbf{f}}_s = [\mathbf{T}^{-1}\hat{\mathbf{\Lambda}}_p\mathbf{T} - \hat{\mathbf{\Lambda}}_s]^{-1}\hat{\mathbf{Y}}_s. \tag{28}$$

C. Solid elastic sphere kinematics

In developing the solutions for the displacement components on the sphere excited by surface ring tractions, we will follow the approach detailed in Ref. 23 by first eliminating the mixed dependence of the tractions and displacements on terms containing P_n^m and P_{n-1}^m using the linear transformation described there. Next we expand the radiated and interior Helmholtz potentials in terms of spherical harmonic waves (SHW) as

$$\widetilde{\phi_s} = I_{mn} h_n(\alpha_0 r), \quad \widetilde{\phi_r} = J_{mn} j_n(\alpha_1 r),$$
$$\widetilde{\psi_r} = K_{mn} j_n(\beta_1 r), \quad \widetilde{\chi_r} = L_{mn} j_n(\beta_1 r), \tag{29}$$

where the SHW decomposition is defined as

$$\tilde{g}(n,m) = \int_{-\pi}^{\pi} e^{-im\varphi} d\varphi \int_0^{\pi} g(\theta,\varphi) P_n^m(\cos\theta)\sin\theta\, d\theta,$$

$$g(\theta,\varphi) = \frac{1}{2\pi}\sum_{m=-\infty}^{\infty} e^{im\varphi}\sum_{n=|m|}^{\infty} a_{mn}\tilde{g}(n,m) P_n^m(\cos\theta).$$

The coefficients I_{mn}, J_{mn}, K_{mn}, and L_{mn} for the ring traction loads $\mathbf{f}_s$, with components $(f_r, f_\theta, f_\varphi, M_b)$, are found by matching the stresses at the attachment ring $(r=a,\ \theta=\gamma)$ for each constituent traction load individually. The traction loads at the attachment ring can be represented as

$$\tau_s^0(a,\theta,\varphi)=\mathbf{f}_s(\varphi)\frac{\delta(\theta-\gamma)}{2\pi a^2 \sin\theta}. \tag{30}$$

Expanding both sides in terms of SHW and balancing tractions yields expressions for the amplitudes of the potentials I_{mn}, J_{mn}, K_{mn}, and L_{mn}. The details of this analysis and appropriate results have also been presented in Ref. 23.

D. Total scattered pressure

As discussed earlier, the total scattered pressure is the sum of two contributions—one due to the incident acoustic wave, and the other due to the forced motions of the sphere. The flexural modes are subsonic in this frequency regime and produce an evanescent field in the fluid. Therefore, assuming the receiver to be further than a few wavelengths from the plate, the contribution due to the latter can be neglected. The compressional modes are coupled to the fluid; however, their contribution to the total scattered field is small compared to that due to the sphere modes. Therefore, ignoring the radiated field due to the plate modes, the contributions from the plate due to $p_{p,a}$ and $p_{p,c}$ can be identically set to $zero$. The contributions from the sphere consist of the component due to the acoustic field $(p_{s,a})$, which was found earlier, and that due to excitation by the coupling forces and bending moment which is computed as

$$p_{s,c}=\frac{1}{2\pi}\sum_{m=-\infty}^{\infty}\sum_{n=|m|}^{\infty} a_{mn}I_{mn}h_n(\alpha_0 r)P_n^m(\cos\theta)e^{im\varphi}, \tag{31}$$

where

$$I_{mn}=\rho_0\omega^2[I_{mn}|_{\hat{f}_r}+I_{mn}|_{\hat{f}_\varphi}+I_{mn}|_{\hat{f}_\theta}+I_{mn}|_{\hat{M}_b}]. \tag{32}$$

IV. RESULTS

In this section, we present the results from our model of scattering from the three-dimensional protuberance on the thin, infinite, submerged elastic plate. For the purpose of illustration, the material for the model is chosen to be solid ice of density $\rho_1=\rho_2=910$ kg/m^3, compressional wave speed $C_p=3500$ m s^{-1}, and shear wave speed $C_s=1600$ m s^{-1}. The ice plate is assumed to be 3.0 m thick and attached to a sphere of radius 10.0 m along its equator $(\gamma=90.0°)$. The coupled structure is completely submerged in water of density 1000 kg/m^3 and sound speed 1460 ms^{-1}. The sphere is placed at the origin of the coordinate system and the point source is positioned at $r=780$ m, $\theta_0=130.0°$ 40.0° grazing) and $\varphi=0.0°$ which corresponds to $X=-600$ m, $Y=0$ m, $Z=-500$ m in Cartesian coordinates.

Figure 5 shows the coupling forces and bending moment at the point $(\varphi=0.0°)$ on the attachment ring $(\gamma=90.0°)$ as a function of the nondimensional frequency parameter ka, where k is the acoustic wavelength in water and a is the radius of the sphere. Examination of the figure reveals that

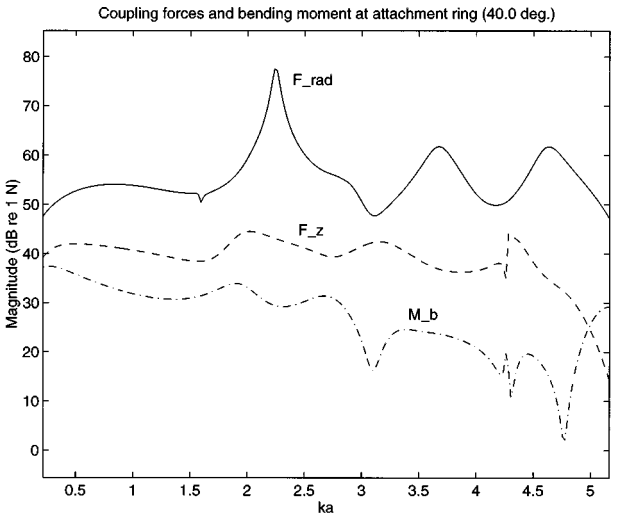

FIG. 5. Coupling forces and bending moment at the attachment ring for $\theta_0=130.0°$. The solid line represents f_R, the dashed line f_z, while the dashed-dotted line denotes M_b (re: 1 Nm).

the radial in-plane force f_R has resonances at ka values of 2.3, 3.7, and 4.6. It is more strongly excited compared to the vertical force f_z and the bending moment M_b because the attached plate primarily constrains the motions of the sphere in the horizontal plane. The azimuthal force f_φ has a node at this point, and therefore its magnitude is extremely small and does not appear in this plot.

The displacement components of the plate at the same point on the attachment ring are shown in Fig. 6. Once again we observe the resonances in the radial displacement component v_R at ka of 2.3, 3.7, and 4.6. At low frequencies $(ka<0.6)$ the out-of-plane displacements are higher in magnitude than the in-plane displacements. However, as the impedance of the plate to vertical motions increases with frequency, we observe the roll-off in amplitude of the out-of-plane motions. Once again, the azimuthal displacement

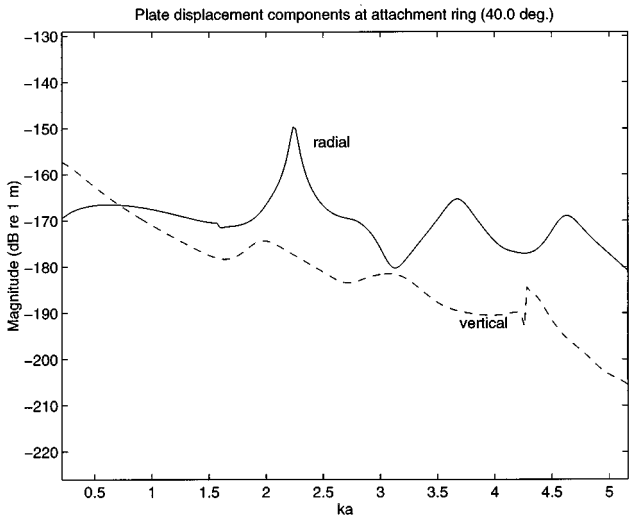

FIG. 6. Plate displacement components at attachment ring for $\theta_0=130.0°$. The solid line represents v_R, the dashed line represents v_z. v_φ has a node at this point, and therefore being extremely small is not shown here.

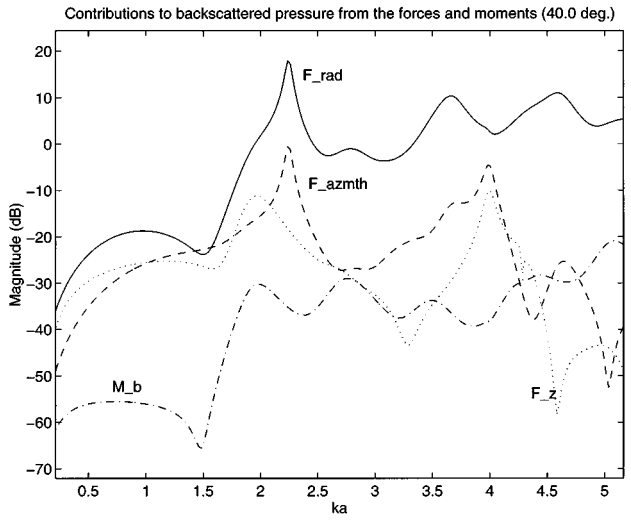

FIG. 7. Individual contributions to backscattered pressure from the coupling forces and bending moment. The solid line represents the contribution due to f_R, the dashed line due to f_φ, while the dotted line corresponds to f_z, and the dashed-dotted line represents that due to M_b.

component v_φ has a node at this location and therefore does not appear in this plot.

The individual contributions to the backscattered pressure resulting from the excitations by the coupling forces and bending moment are shown in Fig. 7. The figure reveals that for $ka<2$, the contributions from all the forces are comparable in magnitude. However, for $ka>2$, the dominant contribution arises from the in-plane forces (f_R and f_φ), and is higher than that from the vertical force (f_z). The contribution from the bending moment is the weakest being about 30 dB lower than the radial force f_R at most frequencies. Note that even though the azimuthal components of force and displacement have a node at this point, the radiated field, being

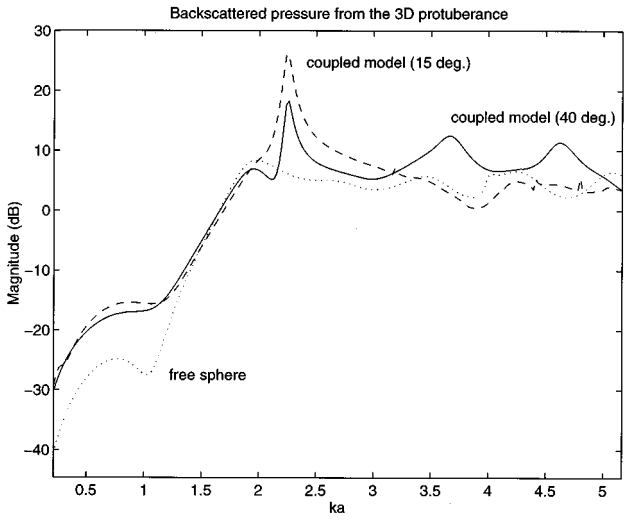

FIG. 8. Backscattered pressure from the three-dimensional protuberance for source located at grazing angles of 15.0° and 40.0°. The continuous line represents the backscattered pressure from the coupled model for the source at 40.0° while the dashed line is that due to the source at 15.0° grazing. The dotted line represents the backscattered pressure from the fully submerged sphere only.

a summation over all Fourier orders m, is still dominated by the contributions from the azimuthal components.

Figure 8 shows the total backscattered pressure from the three-dimensional protuberance, the solid line being the sum of the contributions from the free submerged sphere and all the forces and the bending moment, whereas the background field due to the fully submerged elastic sphere only is represented by the dotted line. As the radial force is the dominant contributor, we observe its characteristic structure in the total backscattered field. Note that the attachment of the plate to the sphere results in a modulation of the form function of the free sphere by the kinematics of the sphere at the attachment ring. The resonance structure is due to standing waves set up inside the sphere when excited by the coupling forces and bending moment.[23] An important conclusion from this figure is that the attachment of the plate to the sphere is a frequency selective process and is manifested in the scattered field at certain frequencies only.

The dashed line in Fig. 8 shows the total backscattered pressure for a shallower grazing angle of incidence ($\theta_0=105.0°$ or 15.0° grazing). Comparison between these results with those for the case $\theta_0=130.0°$ reveals that for small frequencies ($ka<3.0$) there is almost no difference between the results for the two different grazing angles of incidence. At higher frequencies, the resonances observed in the 40.0° incidence case are not as prominent here. The conclusion then is that for low frequencies the backscattered pressure is not qualitatively affected by changing the angle of incidence.

The next step is to evaluate the bistatic scattering pattern from the protuberance. We shall compute the scattering pattern for a fixed source and receiver geometry. The source is assumed to be positioned, as before, at $X=-600$ m, $Y=0$ m, $Z=-500$ m, i.e., a grazing angle of incidence roughly corresponding to 40.0°, while the sphere is located at the origin of the coordinate system. We will investigate the field in a plane located 500 m below the plate, i.e., at the depth corresponding to the depth of the source. We shall compute the scattering pattern at four distinct values of ka, i.e., at $ka=0.5$, 2.3, 3.7, 4.6. The first frequency $ka=0.5$, is a typical low frequency value, whereas the other three are the locations of the resonances of the in-plane radial motions as observed in Fig. 6.

In Fig. 9, we have plotted the bistatic scattering pattern for a ka value of 0.5. The pressure levels have been corrected for the transmission loss from source to scatterer, and from scatterer to receiver corresponding to *target strength*. We observe very high scatter in the backward direction, and very low levels in the forward direction. This arises from the fact that at this frequency, the contributions from the coupling forces and bending moment are comparable with that from the direct scatter from the sphere resulting in an interference pattern that produces a deep null in the forward direction. However, as we move away from this frequency to $ka=2.3$, as shown in Fig. 10, we observe deep null regions at angles of 45° from the source-sphere axis. These nulls are caused by the interference between the compressional and shear modes in the sphere, as is also evident by the strong radial component of motion of the sphere. At this frequency,

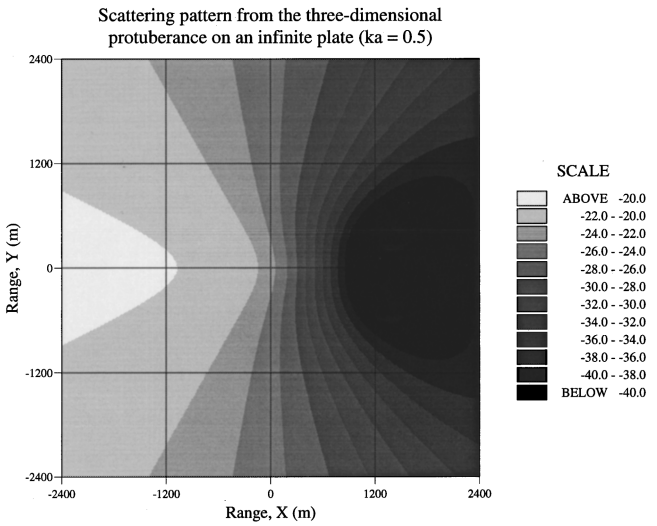

FIG. 9. Scattering pattern from the 3-D protuberance on the elastic plate for ka of 0.5. The source is located at $(-600,0)$ and at a depth of 500 m, the receiver plane is also located at a depth of 500 m, while the spherical protuberance is centered at the origin.

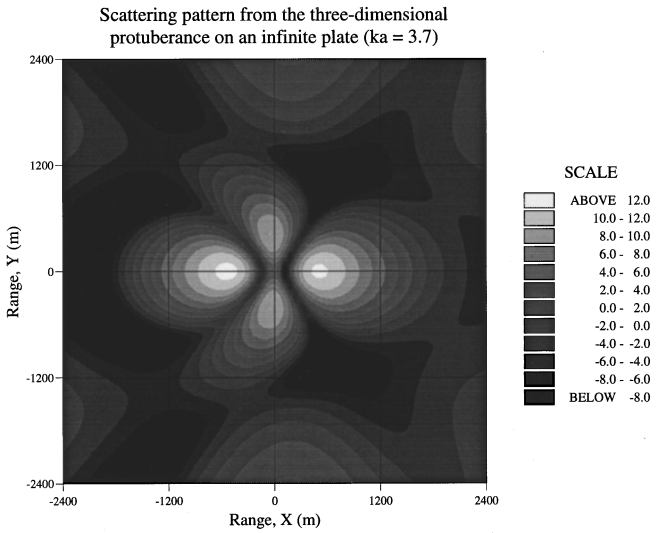

FIG. 11. Scattering pattern from the 3-D protuberance on the elastic plate for ka of 3.7. The source is located at $(-600,0)$ and at a depth of 500 m, the receiver plane is also located at a depth of 500 m, while the spherical protuberance is centered at the origin.

the predominant mode of vibration of the sphere is like a quadrupole, where the sphere expands along the X axis, and simultaneously contracts in the Y direction, and vice versa. This multilobar nature of the radial motion of the free sphere has previously been referred to as the *football resonance*.[30]

Next, we compute the scattering pattern for $ka=3.7$ as shown in Fig. 11. At this frequency, the acoustic wavelength is almost equal to the diameter of the sphere and causes a global resonance in the sphere. The bright spots correspond to direct forward and backscatter. Note the multilobar structure of the beampattern. We observe regions of deep null beyond the lobes of the beampattern. At $ka=4.6$, as shown in Fig. 12, we observe a similar field except for the presence of additional lobes of high scatter. This interesting lobar nature of the beampattern arises from the constructive and destructive interference between the elastic modes in the sphere. Also, at these frequencies, the primary motion of the sphere is in the horizontal plane, with constraints from the attached plate. As we go higher in frequency, we expect to see more and more lobes in the pattern. An essential outcome of these results is to demonstrate the three-dimensional nature of the scattering pattern from plate protuberances.

V. SUMMARY

We have developed an analytical model for the analysis of scattering from a three-dimensional protuberance on a thin, infinite, submerged elastic plate. The protuberance was modeled as a solid elastic sphere attached to the plate along its equatorial plane. The three-dimensional analytical model allows the inclusion of horizontally polarized shear plate

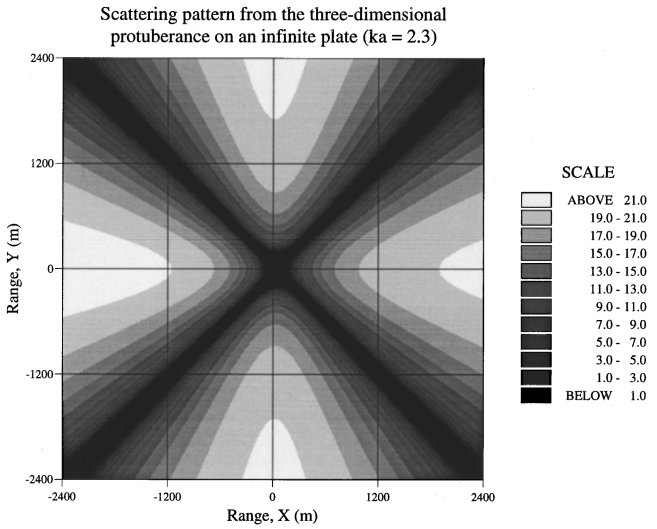

FIG. 10. Scattering pattern from the 3-D protuberance on the elastic plate for ka of 2.3. The source is located at $(-600,0)$ and at a depth of 500 m, the receiver plane is also located at a depth of 500 m, while the spherical protuberance is centered at the origin.

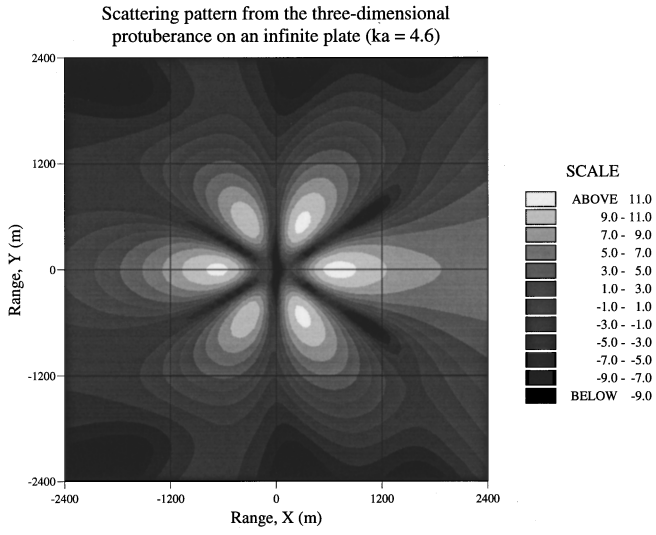

FIG. 12. Scattering pattern from the 3-D protuberance on the elastic plate for ka of 4.6. The source is located at $(-600,0)$ and at a depth of 500 m, the receiver plane is also located at a depth of 500 m, while the spherical protuberance is centered at the origin.

(*SH*) modes. Our results demonstrate that excitation of the in-plane shear and compressional modes dominates the dynamics of the plate, and that the attached plate manifests itself in the scattered field on a frequency selective basis corresponding to the resonances of the sphere excited by the coupling forces. This is significant in the context of three-dimensional scattering from Arctic ice. Lepage[31] has shown that the excitation of the *SH* modes in the ice play a role in the low-frequency loss observed in the Arctic ice propagation environment. Our results have demonstrated that the contributions from these *SH* modes can be significant, which therefore necessitates their inclusion in any realistic model of the three-dimensional scattering scenario. In a forthcoming publication,[15] we will use the analytical model developed here to guide us in the experimental evaluation of the scattering characteristics of discrete large-scale features under the Arctic ice canopy.

ACKNOWLEDGMENTS

This work was supported by the Office of Naval Research (High Latitude Program). The authors are grateful to Dr. Yueping Guo for some illuminating discussions.

[1] L. M. Lyamshev, ''Reflection of sound from a moving thin plate,'' Sov. Phys. Acoust. **6**, 505–507 (1961).
[2] L. M. Brekhovskikh, *Waves in Layered Media* (Academic, New York, 1980), 2nd ed., pp. 76–80.
[3] A. J. Langley, ''The sound fields of an infinite, fluid-loaded plate excited by a point force,'' J. Acoust. Soc. Am. **83**, 1360–1365 (1988).
[4] D. G. Crighton, ''The 1988 Rayleigh Medal Lecture: Fluid loading–the interaction between sound and vibration,'' J. Sound Vib. **133**, 1–27 (1989).
[5] M. C. Junger and D. Feit, *Sound, Structures, and their Interaction* (Acoustical Society of America, Woodbury, NY, 1993), pp. 237–239.
[6] G. Maidanik, A. J. Tucker, and W. H. Vogel, ''Transmission of free waves across a rib on a panel,'' J. Sound Vib. **49**, 445–452 (1976).
[7] D. G. Crighton and G. Maidanik, ''Acoustic and vibration fields generated by ribs on a fluid-loaded panel, I: Plane-wave problems for a single rib,'' J. Sound Vib. **75**, 437–452 (1981).
[8] Y. P. Guo, ''Effect of structural joints on sound scattering,'' J. Acoust. Soc. Am. **93**, 857–863 (1993).
[9] J. R. Fricke, ''Acoustic Scattering from Elastic Ice: A Finite Difference Solution,'' Ph.D. thesis, WHOI-MIT, 1991.
[10] P. Gerstoft and H. Schmidt, ''A boundary element approach to ocean seismoacoustic facet reverberation,'' J. Acoust. Soc. Am. **89**, 1629–1642 (1991).
[11] Y. P. Guo, ''Sound scattering by bulkheads in cylindrical shells,'' J. Acoust. Soc. Am. **95**, 2250–2559 (1994).
[12] J. D. Achenbach, J. Bjarnason, and T. Igusa, ''Effect of vibrating substructure on acoustic radiation from a cylindrical shell,'' J. Vib. Acoust. **114**, 312–318 (1992).
[13] V. Twersky, ''On scattering and reflection of sound by rough surfaces,'' J. Acoust. Soc. Am. **29**, 209–255 (1957).
[14] J. E. Burke and V. Twersky, ''On scattering and reflection by elliptically straited surfaces,'' J. Acoust. Soc. Am. **40**, 883–895 (1966).
[15] T. Kapoor and H. Schmidt, ''Matched-field evaluation of low-frequency acoustic scattering from rough Arctic ice,'' J. Acoust. Soc. Am. **98**, 2783–2791 (1995).
[16] T. Kapoor and L. B. Felsen, ''Hybrid ray-mode analysis of acoustic scattering from a finite, fluid-loaded plate,'' Wave Motion **22**, 109–131 (1995).
[17] P. M. Morse and K. U. Ingard, *Theoretical Acoustics* (Princeton U.P., Princeton, NJ, 1986), pp. 418–440.
[18] J. J. Faran, Jr., ''Sound scattering by solid cylinders and spheres,'' J. Acoust. Soc. Am. **23**, 405–418 (1951).
[19] R. Hickling, ''Analysis of echoes from a solid elastic sphere in water,'' J. Acoust. Soc. Am. **34**, 1582–1591 (1962).
[20] Y. H. Pao and C. C. Mow, ''Scattering of plane compressional waves by a spherical obstacle,'' J. Appl. Phys. **34**, 493–499 (1963).
[21] H. Schmidt, ''Numerically stable global matrix approach to radiation and scattering from spherically stratified shells,'' J. Acoust. Soc. Am. **94**, 2420–2430 (1993).
[22] P. M. Morse and H. Feshbach, *Methods of Theoretical Physics* (McGraw-Hill, New York, 1953), pp. 1762–1766, 1462–1466.
[23] T. K. Kapoor, ''Three-dimensional acoustic scattering from Arctic ice protuberances,'' Ph.D. thesis, MIT, 1995.
[24] T. Kapoor and H. Schmidt, ''Spherical coordinate Green's functions for ring tractions in a solid unbounded elastic medium,'' J. Acoust. Soc. Am. **98**, 2783–2791 (1995).
[25] H. Schmidt, ''SAFARI: User's Guide,'' SR 113, SACLANT ASW Research Center, La Spezia, Italy, 1987.
[26] K. F. Graff, *Wave Motion in Elastic Solids* (Dover, New York, 1991).
[27] J. D. Achenback, *Wave Propagation in Elastic Solids* (North-Holland, Amsterdam, 1984).
[28] A. L. Leissa, ''Vibration of Plates,'' NASA SP-160, Washington, DC, 1969, pp. 1, 2.
[29] L. Cremer and M. Heckl, *Structure-Borne Sound* (Springer-Verlag, Berlin, 1988), 2nd ed., pp. 502–505.
[30] A. Ben-Menahem and S. J. Singh, *Seismic Waves and Sources* (Springer-Verlag, New York, 1981), pp. 347.
[31] K. D. LePage, ''Elastic scattering in oceanic waveguides,'' Ph.D. thesis, MIT, 1992.

Finite correlation and coherent propagation effects in the normal-mode description of bottom reverberation

J. E. LeMond and Robert A. Koch
Applied Research Laboratories, The University of Texas at Austin, P.O. Box 8029, Austin, Texas 78713-8029

(Received 7 December 1995; revised 8 July 1996; accepted 15 October 1996)

A normal-mode scattering formulation that assumes a finite spatial correlation length in the distribution of scattering features is used to compute single-frequency bottom reverberation for bistatic and monostatic scattering geometries in a shallow water and deep water environment. Spatial correlation of the scattering features allows the superposition of modes scattered within each spatially correlated region and produces diffraction in the scattered field that is not predicted in the limit of a zero spatial correlation length (point scattering). For bistatic scattering geometries, the scattered field computed as a function of scattering location in the horizontal plane exhibits a pattern of diffractive maxima and minima for nonzero spatial correlation lengths. The spatial details of the diffraction pattern and its influence on the scattered energy depend on the frequency and spatial correlation length and can result in a significant reduction in the predicted levels of received reverberation. The greatest sensitivity to finite correlation effects occurs for monostatic scattering geometries because the strongest diffractive effects occur in the backscattering direction. The effects of including modal interference in the incident and scattered field propagation are also examined in this paper. The inclusion of modal interference in the propagating fields imposes an interference pattern on the spatial structure of the scattered field in the horizontal plane, and can cause the temporal dependence of the reverberated return to oscillate about the levels of return predicted when modal interference in the propagating fields is neglected. In agreement with previously published results for bottom backscattering, the effects of including modal interference in the propagating fields were found to be significant for deep water environments that exhibit convergent zone propagation and to be of limited importance for shallow water environments in which the energy incident on the bottom is characterized by a large number of multipaths. The present work includes results which show that the effects of including modal interference in the propagating fields can be important for shallow water environments that exhibit significant bottom penetration. [S0001-4966(97)04807-8]

PACS numbers: 43.30.Gv, 43.30.Bp, 43.20.Fn [JHM]

INTRODUCTION

Normal-mode scattering formulations have been developed as a practical approach for predicting shallow water bottom reverberation.[1–4] This paper examines the importance of retaining two sources of modal interference in the normal-mode description of bottom scattering. The first interference effect is introduced by using a finite spatial correlation length in the distribution of the bottom scattering features;[4] the second is caused by including the constructive and destructive interference of modes in the propagation of the incident and scattered fields.[1]

The distribution of scatterers within a volume of scattering elements affects the spatial structure of the scattered field. In the limit of infinite spatial correlation, corresponding to a periodic distribution of scattering elements, the scattered field exhibits a highly structured diffraction pattern (Bragg scattering) caused by modal superposition occurring throughout the scattering region. In the opposite limit of zero correlation length, corresponding to statistically independent scattering elements, the scattered field exhibits no interference structure and is represented exactly by a point scattering formulation. It is therefore plausible that the scattered field will exhibit some degree of diffractive effects for scattering element distributions that have a finite spatial correlation length.

In normal-mode formulations of acoustic scattering caused by random fluctuations in the bottom boundary, reverberation is typically computed by averaging the scattered energy over the bottom (i.e., the point-scattering limit), thereby neglecting possibly significant diffractive effects for environments with bottom fluctuations that exhibit a finite spatial correlation.[1–3] However, scattering coefficients for a spatially correlated rough bottom in a isovelocity shallow water environment have been previously published.[4] Consistent with this previous work, the normal-mode expression used in the present paper for the field scattered from each region on the bottom is an average over an area of finite size that is determined by the spatial correlation length. Bottom scattering results presented herein show that the inclusion of a finite spatial correlation length imposes a diffraction pattern on the spatial structure of the scattered return in the horizontal plane that is not predicted in the point-scattering limit. It is also shown that the inclusion of the finite correlation induced diffractive effects can result in a significant reduction in the levels of reverberated return as a function of time. An examination of the diffractive effects caused by

spatial correlation of the bottom scattering features, and the dependence of these effects on environment, frequency, and spatial correlation length are the focus of the present paper. The scattering coefficients used in numerical calculations to illustrate the presence and important of the diffractive effects are given by a combination of Lambert and MacKenzie scattering.[5]

Modal interference in the incident and scattered field propagation can also affect the received scattered energy. The normal-mode equation for the complex field is a sum of mode terms comprised of both an amplitude and a phase. The received energy, determined by the square of the complex field, is therefore a double mode summation and includes cross terms. These cross terms describe the constructive and destructive interference of modes which can have a significant influence on the spatial dependence of the received energy (termed ''coherent propagation''), and predicts behavior such as convergence zone propagation. A computationally less intensive expression that is often used for the received energy neglects the cross terms in the double mode sum (termed ''incoherent propagation''), and the remaining sum of squared mode amplitudes represents an average of the received energy over the variations produced by modal interference.

The incoherent approximation of propagation for the incident and scattered fields is commonly used in normal-mode formulations of bottom scattering.[1–4] However, because the strength of the acoustic field at a given depth is determined by the constructive and destructive interference of propagating modes, it is reasonable to expect smaller contributions to the scattered energy from regions for which there is destructive interference in the field incident on the bottom at the scattering location. A recent normal-mode treatment of bottom backscattering concluded that in deep water environments, which exhibit convergence zone propagation, coherent propagation effects could not be neglected.[1] Results presented in the present paper show that a similar effect can occur for shallow water environments in which the field incident on the bottom exhibits significant penetration into the sediment.

In Sec. I, the expression for the field scattered from a distribution of bottom scattering elements that exhibit a finite spatial correlation length is cast in terms of a normal-mode expansion.[4] The scattered energy, computed by either a coherent or incoherent mode sum, is separated into terms that isolate the effects of including a finite correlation length. Model results for monostatic and bistatic scattering geometries in a shallow water and a deep water range-invariant environment are presented and discussed in Sec. II.

I. FORMULATION

The scattering of normal modes can be described using a transition or mode-coupling function derivable by boundary-integral or perturbative methods for a given realization of the bottom description.[6–11] For the purpose of the present study, the Bass perturbation theory is used to determine the field scattered by spatially dependent random fluctuations in the bottom boundary;[11] the Green's formula is used to obtain an integral expression for the scattered field which is cast in terms of the normal-mode solutions of the (nonisospeed) waveguide in the absence of scattering.[4,6] The scattering process is denoted by scattering functions S_{mn}, and the received scattered field is written as a sum over the incoming and outgoing modes

$$p_s(\mathbf{r}|\mathbf{r}_0)=\sum_m \sum_n \Phi_m(z)S_{mn}(|\boldsymbol{\rho}-\boldsymbol{\rho}_0|)\Phi_n(z_0), \tag{1}$$

where the receiver position $\mathbf{r}=(\boldsymbol{\rho},z)$ and source position $\mathbf{r}_0=(\boldsymbol{\rho}_0,z_0)$ are specified in circular cylindrical coordinates, and the Φ_m are the eigenfunctions of the waveguide with the unperturbed bottom boundary condition. The form of the scattering function element S_{mn} is given by

$$S_{mn}(|\boldsymbol{\rho}-\boldsymbol{\rho}_0|)=\int d\sigma' \Phi_m(z')g_m(|\boldsymbol{\rho}-\boldsymbol{\rho}'|)T_{mn}(|\boldsymbol{\rho}'-\boldsymbol{\rho}_0|) \times\Phi_n(z')g_n(|\boldsymbol{\rho}'-\boldsymbol{\rho}_0|), \tag{2}$$

where the area integral extends over the entire scattering region (bottom boundary). The conversion of energy from each incident mode into all available modes, which may be interpreted as the excitation of secondary sources along the bottom, is described by a transition or mode conversion matrix $\mathbf{T}$. The radial Green's functions g_m and g_n describe horizontal propagation of the incoming and outgoing modes in the waveguide with the unperturbed bottom boundary.

The scattering operators, T_{mn}, represent an expansion of the bottom boundary condition to first order in the random perturbation. This technique can be used to describe scattering caused by random impedance fluctuations or surface irregularities.[11] Because the focus of the current study is to examine finite correlation effects, independent of the precise details of the scattering process, a specific form will not be assumed for the scattering coefficients T_{mn}.

The bottom can be divided into a set of nonoverlapping regions, $\{\sigma_i\}$, with center coordinates $\mathbf{r}_i=(\boldsymbol{\rho}_i,z_i)$, which span the entire bottom boundary. The area integral in Eq. (2) is written as a sum over the integrals for each region, expressed in terms of the center coordinates $\boldsymbol{\rho}_i=\boldsymbol{\rho}'-\mathbf{x}$:

$$S_{mn}(|\boldsymbol{\rho}-\boldsymbol{\rho}_0|)=\sum_i \int_{\sigma_i} d\sigma\ \Phi_m(z_i)g_m(|\boldsymbol{\rho}-\boldsymbol{\rho}_i-\mathbf{x}|) \times T_{mn}(|\boldsymbol{\rho}_i-\boldsymbol{\rho}_{0+\mathbf{x}|})\Phi_n(z_i)g_n(|\boldsymbol{\rho}_i-\boldsymbol{\rho}_0+\mathbf{x}|). \tag{3}$$

The bistatic scattering geometry is shown in Fig. 1 for a single (circular) scattering region.

Approximation of the radial Green's functions by the asymptotic expansion for the outgoing Hankel function results in

$$g_m(|\boldsymbol{\rho}_2-\boldsymbol{\rho}_1|)\approx\frac{C\ \exp[ik_m|\boldsymbol{\rho}_2-\boldsymbol{\rho}_1|]}{\sqrt{k_m|\boldsymbol{\rho}_2-\boldsymbol{\rho}_1|}},$$

where $C=i\sqrt{2\pi}e^{-i\pi/4}$. The scattering region is assumed to be in the far field of both source and receiver; expansion of the radial phase functions to first order in $\mathbf{x}/|\boldsymbol{\rho}-\boldsymbol{\rho}_i|$ and $\mathbf{x}/|\boldsymbol{\rho}_i-\boldsymbol{\rho}_0|$ gives

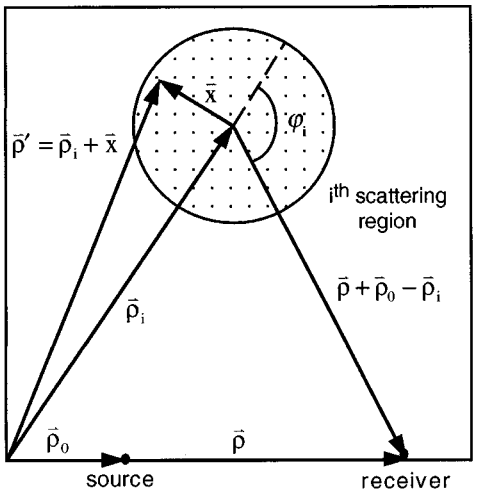

FIG. 1. Bistatic scattering geometry in horizontal plane. Omnidirectional point source is located at $\boldsymbol{\rho}_0$ and receiver at $\boldsymbol{\rho}$.

$$g_m(|\boldsymbol{\rho}-\boldsymbol{\rho}_i-\mathbf{x}|)\approx g_m(|\boldsymbol{\rho}-\boldsymbol{\rho}_i|)\exp\left[\frac{-ik_m(\boldsymbol{\rho}-\boldsymbol{\rho}_i)\cdot\mathbf{x}}{|\boldsymbol{\rho}-\boldsymbol{\rho}_i|}\right],$$

$$g_n(|\boldsymbol{\rho}_i-\boldsymbol{\rho}_0+\mathbf{x}|)\approx g_n(|\boldsymbol{\rho}_i-\boldsymbol{\rho}_0|)\exp\left[\frac{ik_n(\boldsymbol{\rho}_i-\boldsymbol{\rho}_0)\cdot\mathbf{x}}{|\boldsymbol{\rho}_i-\boldsymbol{\rho}_0|}\right],$$

and the area integral of Eq. (3) becomes

$$S_{mn}(|\boldsymbol{\rho}-\boldsymbol{\rho}_0|)=\sum_i \Phi_m(z_i)g_m(|\boldsymbol{\rho}-\boldsymbol{\rho}_i|)\Phi_n(z_i)g_n(|\boldsymbol{\rho}_i-\boldsymbol{\rho}_0|)\times\int_{\sigma_i} d\sigma\ \exp[i\boldsymbol{\alpha}_{mn}(\boldsymbol{\rho}|\boldsymbol{\rho}_i|\boldsymbol{\rho}_0)\cdot\mathbf{x}]\times T_{mn}(|\boldsymbol{\rho}_i+\mathbf{x}|), \tag{4}$$

where

$$\boldsymbol{\alpha}_{mn}(\boldsymbol{\rho}|\boldsymbol{\rho}_i|\boldsymbol{\rho}_0)\equiv\frac{k_n(\boldsymbol{\rho}_i-\boldsymbol{\rho}_0)}{|\boldsymbol{\rho}_i-\boldsymbol{\rho}_0|}-\frac{k_m(\boldsymbol{\rho}-\boldsymbol{\rho}_i)}{|\boldsymbol{\rho}-\boldsymbol{\rho}_i|}.$$

Finally, combining Eqs. (1) and (4), the reverberated return from the ith patch can be written as

$$p_i(\mathbf{r}|\mathbf{r}_i|\mathbf{r}_0)=\sum_m\sum_n \Phi_m(z)g_m(|\boldsymbol{\rho}-\boldsymbol{\rho}_i|)\times\Phi_m(z_i)\Phi_n(z_i)g_n(|\boldsymbol{\rho}_i-\boldsymbol{\rho}_0|)\Phi_n(z_0)\times\int_{\sigma_i} d\sigma\ \exp[i\boldsymbol{\alpha}_{mn}(\boldsymbol{\rho}|\boldsymbol{\rho}_i|\boldsymbol{\rho}_0)\cdot\mathbf{x}]\times T_{mn}(|\boldsymbol{\rho}_i+\mathbf{x}|).$$

The scattering coefficients are expressed in the general form,

$$T_{mn}(\boldsymbol{\rho}_i+\mathbf{x})\equiv\mu_{mn}(\boldsymbol{\rho}_i)f[\epsilon(\boldsymbol{\rho}_i+\mathbf{x})],$$

with

$$\langle T_{mn}(\boldsymbol{\rho}_i+\mathbf{x})T^*_{sq}(\boldsymbol{\rho}_i+\mathbf{x}')\rangle\equiv\mu_{mn}(\boldsymbol{\rho}_i)\mu^*_{sq}(\boldsymbol{\rho}_i)\,\eta^2\varpi(\mathbf{x}-\mathbf{x}')\equiv\tau_{mn}(\boldsymbol{\rho}_i)\tau^*_{sq}(\boldsymbol{\rho}_i)\varpi(\mathbf{x}-\mathbf{x}'),$$

where $\epsilon(\boldsymbol{\rho}_i+\mathbf{x})$ is a statistically homogeneous random variable. For the purpose of this investigation, the correlation function, $\varpi(\mathbf{x}-\mathbf{x}')$, is assumed to have a value of unity within each spatially correlated scattering region (patch), with the fields scattered from different patches being uncorrelated; thus the energy scattered from the ith patch is given by

$$\langle|p_i(\mathbf{r}|\mathbf{r}_i|\mathbf{r}_0)|^2\rangle=\left|\sum_m\sum_n \Phi_m(z)\Phi_m(z_i)g_m(|\boldsymbol{\rho}-\boldsymbol{\rho}_i|)\times\sigma_i\tau_{mn}(\boldsymbol{\rho}_i)I_{mn}(\boldsymbol{\rho}_i)g_n(|\boldsymbol{\rho}_i-\boldsymbol{\rho}_0|)\times\Phi_n(z_i)\Phi_n(z_0)\right|^2,$$

where

$$I_{mn}(\boldsymbol{\rho}_i)\equiv(\sigma_i)^{-1}\int_{\sigma_i} d\sigma\ \exp[i\boldsymbol{\alpha}_{mn}(\boldsymbol{\rho}|\boldsymbol{\rho}_i|\boldsymbol{\rho}_0)\cdot\mathbf{x}]. \tag{5}$$

This integral [cf. Eq. (3)] is a spatial correlation (over the scattering region) of the modal phase portions of the incoming and scattered fields, and its maximum value, unity, is attained in the point-scattering limit [cf. Ref. 11, pp. 108–109].

With the definition

$$P_{mn}(\mathbf{r}_i)\equiv\Phi_m(z)\Phi_m(z_i)g_m(|\boldsymbol{\rho}-\boldsymbol{\rho}_i|)\sigma_i\tau_{mn}(\boldsymbol{\rho}_i)\times g_n(|\boldsymbol{\rho}_i-\boldsymbol{\rho}_0|)\Phi_n(z_i)\Phi_n(z_0), \tag{6}$$

the root mean square value of the field scattered from the ith patch is given by

$$\overline{p_i}(\mathbf{r}|\mathbf{r}_i|\mathbf{r}_0)=\sqrt{\langle\overline{p_i}(\mathbf{r}|\mathbf{r}_i|\mathbf{r}_0)|^2\rangle}=\left|\sum_m\sum_n P_{mn}(\mathbf{r}_i)I_{mn}(\boldsymbol{\rho}_i)\right|. \tag{7}$$

Each modal field term $P_{mn}I_{mn}$ describes the scattering of incoming mode n into outgoing mode m. The coefficient I_{mn}, an integral of a mode-dependent phase function, describes the averaged effect of the superposition of modes n and m over the region for which the bottom features are spatially correlated. In the limit of a zero spatial correlation length, the phase integral I_{mn} is unity, and Eq. (7) reduces to the expression for the point scattering of normal modes.[1–3]

Evaluation of the finite correlation phase integral for a circular scattering region of radius $a/2$, where a is the spatial correlation length of the bottom distribution, gives

$$I_{mn}(\boldsymbol{\rho}_i)=(\pi a^2/4)^{-1}\int_0^{a/2} x\,dx\int_0^{2\pi} d\varphi\times\exp[i|\boldsymbol{\alpha}_{mn}(\boldsymbol{\rho}|\boldsymbol{\rho}_i|\boldsymbol{\rho}_0)|x\cos\varphi],$$
$$=2J_1(x_{mn})/x_{mn}, \tag{8a}$$

where

$$x_{mn}\equiv\sqrt{(\pi a/\Lambda_{mn})^2+k_mk_na^2\sin^2(\varphi_i/2)},\qquad \Lambda_{mn}\equiv 2\pi/|k_m-k_n|. \tag{8b}$$

The J_1 is a Bessel function of the first kind; φ_i is the azimuthal scattering angle (see Fig. 1), and Λ_{mn} is the beat

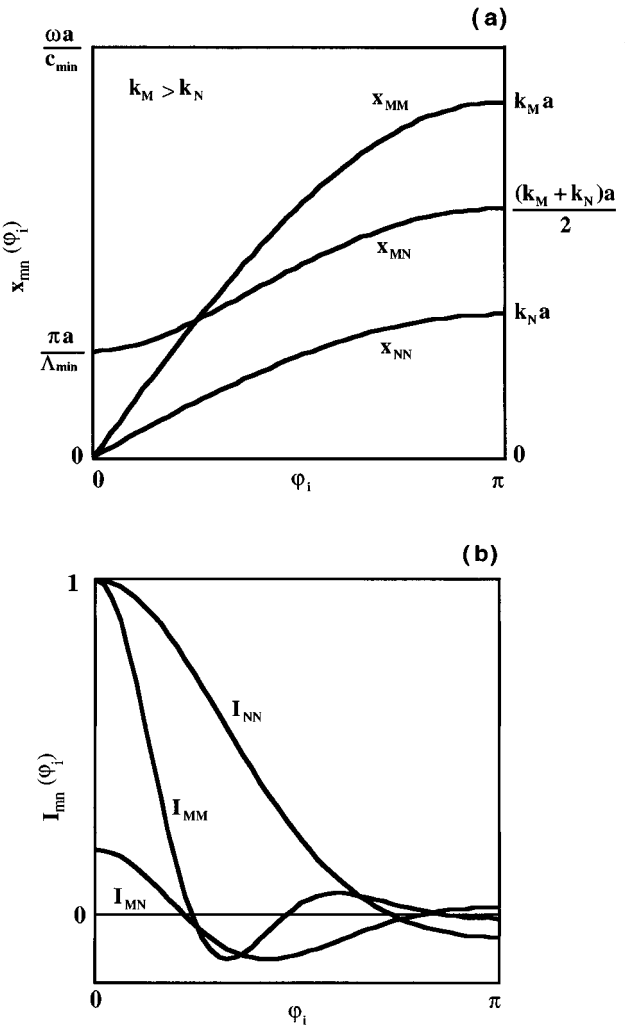

FIG. 2. For two modes such that $k_M > k_N$, the azimuthal dependence of: (a) x_{mn} from Eq. (8b); and (b) I_{mn} from Eq. (8a).

distance (spatial period) of the interference pattern of modes n and m. The function $x_{mn}(\varphi_i)$ increases monotonically on $[0,\pi]$, and $2J_1(x)/x$ is oscillatory with decreasing amplitude as $|x|$ increases. In the limit $x_{mn}=0$, $I_{mn}=1$, and Eq. (7) reduces to the normal-mode expression for point scattering.

The behavior of x_{mn} and I_{mn} as a function of the azimuthal scattering angle φ_i is shown in Fig. 2(a)–(b) for modes M and N such that $k_M > k_N$. The function x_{MN} increases continuously with azimuthal scattering angle, from a minimum value $\pi a/\Lambda_{mn}$ at $\varphi_i=0$ to a maximum value $(k_M+k_N)a/2$ at $\varphi_i=\pi$, and the finite correlation phase integral, I_{mn}, thus progresses through a series of diffractive maxima and minima. The order and significance of the diffractive effects depends on the parameter $k_1 a$, where k_1 is the largest horizontal wave number. The lowest-order diffraction corresponds to scattering in the forward direction ($\varphi_i=0$), and the highest-order diffractive effects occur for scattering in the back direction ($\varphi_i=\pi$). Therefore, the expression for the scattered field [Eq. (7)] derived using a finite spatial correlation length includes a directional dependence such that the envelope of the diffraction pattern produces a scattered intensity that is largest in the forward direction (central diffractive maximum) and is most reduced in the back direction (highest-order diffraction).

In the forward direction $x_{MM}=x_{NN}=0$ ($I_{MM}=I_{NN}=1$), so that scattering between identical modes exhibits no reduction in the scattered intensity due to finite correlation induced diffraction. The largest value of x_{MN} in the forward direction occurs for the smallest value of Λ_{MN}; thus the strongest diffractive effects occur for scattering between modes with the largest difference in vertical angle.

The significance of the diffractive effects for scattering in the back direction increases with increasing $(k_M+k_N)a/2$. Therefore, the reduction in the scattered energy caused by finite correlation induced diffraction is least significant in the back direction for the mode with the largest vertical angle. The greatest reduction of scattered intensity occurs for the mode with the smallest vertical angle.

For a given environment, the frequency $f_{\min}$, below which finite correlation diffraction can be ignored, depends on the spatial correlation length and the minimum beat distance. At frequencies below $f_{\min}$, for which $k_1 a \approx 1$, there is a single diffractive lobe, and the scattered energy is well represented by the point-scattering limit. The number of diffractive lobes increases with frequency so that finite correlation induced level reduction, which initially affects scattering in the back direction, becomes increasingly important for smaller azimuthal scattering angles. At frequencies for which $\pi a/\Lambda_{\min} \approx 1$, diffractive effects become important for scattering in the forward direction.

The scattered energy received from the ith patch is determined by the square of the field given in Eq. (7); performing a coherent mode sum gives

$$E=\left|\sum_m \sum_n P_{mn} I_{mn}\right|^2. \tag{9}$$

This result includes diffractive effects caused by the superposition of modes scattered within a correlated bottom region and also includes the constructive and destructive interference of modes propagating to and from the scattering region. Retaining finite correlation effects but neglecting coherent propagation gives

$$E_{\text{inc}}=\sum_m \sum_n |P_{mn} I_{mn}|^2. \tag{10}$$

The scattered energy given by Eqs. (9) and (10) will be compared in Sec. II to the values computed in the limit of a zero spatial correlation length ($I_{mn}=1$).

The expression in Eq. (10) can be separated into two terms:

$$E_{\text{inc}}=\sum_m \sum_n |P_{mn}|^2 - \sum_m \sum_n |P_{mn}|^2(1-|I_{mn}|^2) \equiv E_0 - E_1,$$

with

$$E_0 \equiv \sum_m \sum_n |P_{mn}|^2, \tag{11a}$$

$$E_1 \equiv \sum_m \sum_n |P_{mn}|^2(1-|I_{mn}|^2). \tag{11b}$$

The term E_0 represents the average of the received scattered energy over a single scattering area (i.e., point scattering) with an incoherent treatment of the propagation. The term E_1, which also neglects coherent propagation effects, contains the finite correlation phase integral I_{mn} and therefore introduces diffraction into the expression for the scattered energy. Because the maximum magnitude of I_{mn} is unity, the decomposition of E_{inc} in terms of E_0 and E_1 directly shows that consideration of a finite spatial correlation length results in a reduction in the predicted level of received reverberation from each correlated scattering region.

The expression for the scattered energy given in Eq. (9) includes both finite correlation and coherent propagation and, in terms of E_0 and E_1, can also be written

$$E = E_0 - E_1 + E_2,$$

with

$$E_2 \equiv \sum_m \sum_{s \neq m} \sum_n \sum_{q \neq n} P_{mn} P_{sq}^* I_{mn} I_{sq}^* . \tag{12}$$

For $I_{mn} = 1$,

$$E = E_0 + E_2 = \left| \sum_m \sum_n P_{mn} \right|^2 , \tag{13}$$

which represents the scattered energy computed using coherent propagation in the point-scattering limit.

The effects of finite spatial correlation and coherent propagation are combined in the term E_2. Because this term may be either positive or negative, it can either increase or decrease the scattered energy received from each location relative to the scattered energy computed using incoherent propagation.

II. MODEL RESULTS AND DISCUSSION

The normal-mode computations used to calculate the scattered fields were performed with the ARL:UT model MODELAB.[12] A combination of Lambert's law and the MacKenzie scattering coefficient were used to evaluate the local value of the transition matrix,

$$\tau_{mn}(\overline{\rho_i}) = \mu \sin \vartheta_m \sin \vartheta_n ,$$

where $10 \log \mu = -27$ dB, and ϑ_m is the grazing angle of the mth mode.[5]

Model calculations were performed for monostatic and bistatic scattering geometries in a shallow water and deep water range-invariant environment. The profiles are shown in Fig. 3(a) and (b). Figure 4(a) shows the modal interference pattern at 15 Hz for propagation of unscattered energy in the shallow water environment. There are only two trapped modes producing a beat pattern with a period of approximately 1.7 km. The deep water environment has a surface duct and a convergence zone; propagation of unscattered energy at 50 Hz is shown in Fig. 4(b). Because the field computation included only discrete modes (i.e., the continuum was neglected), high-angle energy is absent at short ranges.

In the following, scattering results are displayed as an image of the received scattered energy as a function of the patch location in the horizontal plane. For a given frequency and spatial correlation length, the scattered energy received from each patch was computed using both the coherent mode sum of Eq. (9) and the incoherent sum of Eq. (10). The source depth is 30 m, and the receiver depth is 90 m. In the bistatic calculations, the separation between the source and receiver is 30 km. The level of received reverberation as a function of time (using approach 2 of Ref. 1) is also computed using both an incoherent and coherent mode sum, and comparisons are made with predictions of the point-scattering limit.

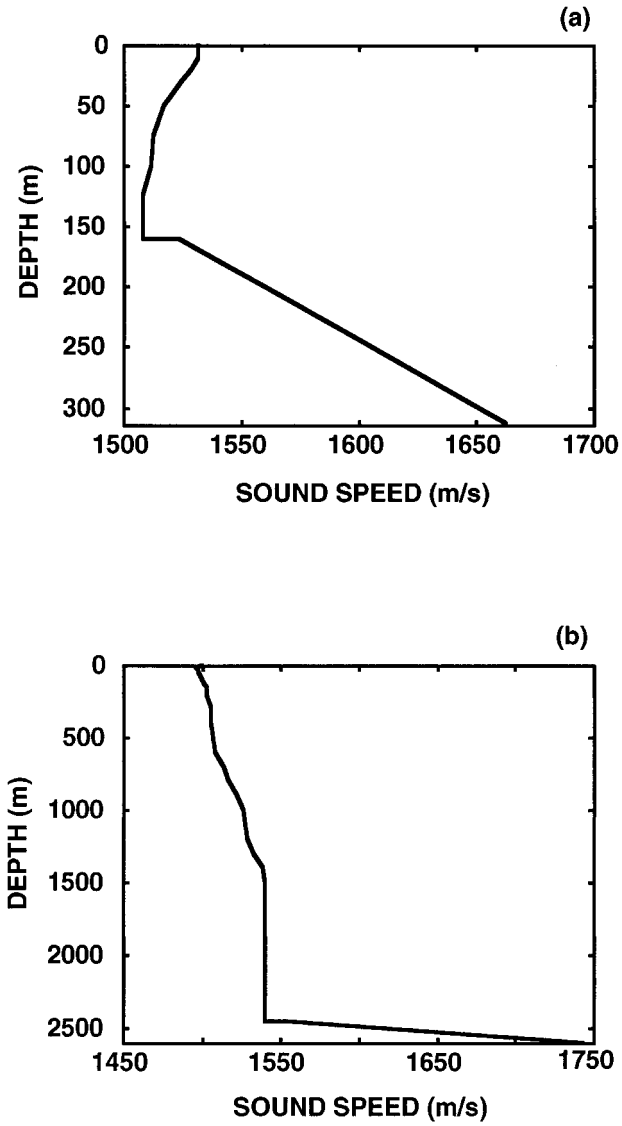

FIG. 3. Sound velocity profiles of environments used in model calculations: (a) downward refracting shallow water environment, water depth is 160 m; (b) upward refracting deep water environment, water depth is 2456 m.

A. Bistatic geometry

Predictions that show the spatial behavior of the received scattered energy, computed in the point-scattering limit at 15 Hz for a bistatic scattering geometry in the shallow water environment, are presented in Fig. 5(a) and (b). The received scattered energy computed using an incoherent mode sum [E_0 from Eq. (11a)] is shown in Fig. 5(a). There is no spatial interference structure, and the largest contributions

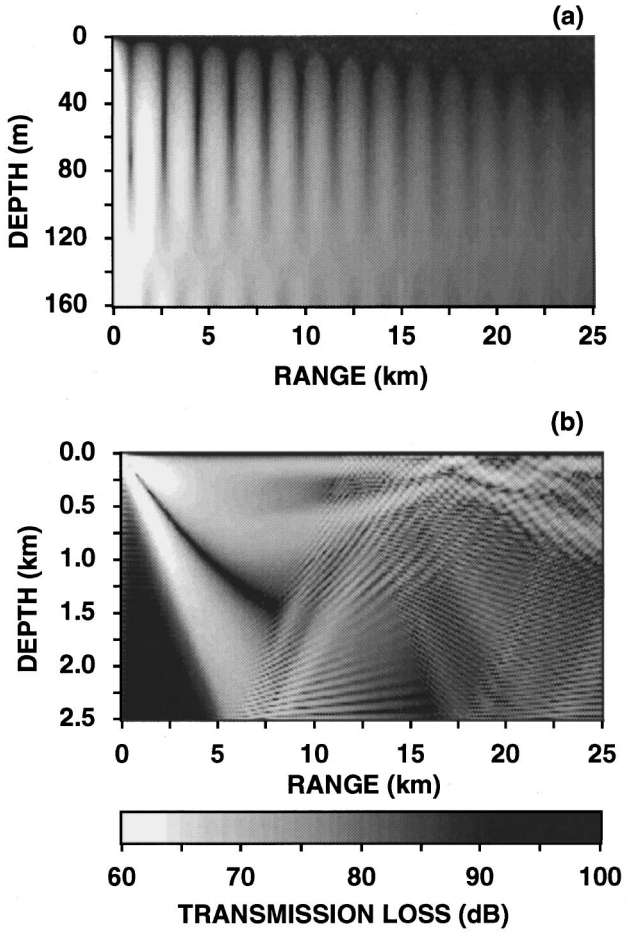

FIG. 4. Range and depth dependence of propagation loss in environments used in model calculations. Source depth is 30 m and receiver depth is 90 m: (a) shallow water environment of Fig. 3(a) at 15 Hz (interference distance is approximately 1.7 km); (b) deep water environment of Fig. 3(b) at 50 Hz.

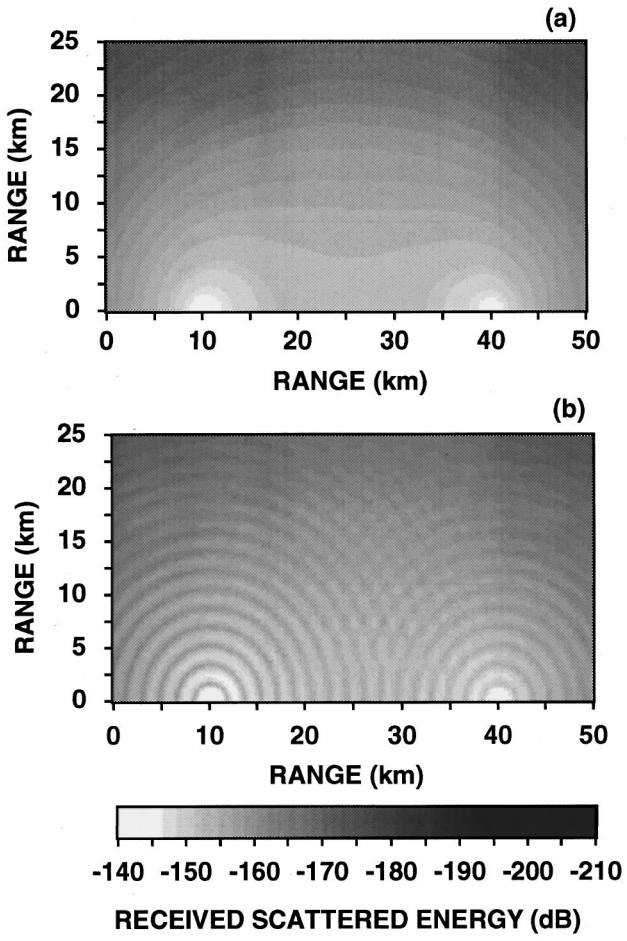

FIG. 5. Dependence of received scattered energy on location of scattering region in the horizontal plane, computed at 15 Hz in the point-scattering limit for a bistatic scattering geometry. Source range is 10 km and source depth is 30 m. Receiver range is 40 km and receiver depth is 90 m: (a) using incoherent propagation, E_0 from Eq. (11a); (b) using coherent propagation, E from Eq. (13).

are received from patches located near the source or receiver. Contributions to the received scattered energy decrease with increased separation of the patch from either source or receiver because of attenuation and spreading loss.

Point-scattering results that include coherent propagation are presented in Fig. 5(b). Coherent propagation of the incoming and outgoing fields imposes an interference structure on the received scattered energy, as evidenced by the circular beat patterns centered on both source and receiver. Scattering areas for which modal interference is destructive, either in the field incident from the source or the field scattered to the receiver, contribute significantly less scattered energy than those areas for which the interference is constructive. As in the case of E_0 [Fig. 5(a)], the received scattered energy decreases with increased separation of the patch from either source or receiver because of spreading and attenuation losses.

The spatial structure of the received scattered energy, computed using a finite spatial correlation length ($a = 250$ m) and using incoherent and coherent propagation, is shown in Fig. 6(a) and (b), respectively, for the bistatic scattering geometry. The series of bands radiating outward from the source and receiver locations in Fig. 6(a) represent the succession of diffractive lobes and nulls discussed in Sec. I. The dominance of forward scattering, which corresponds to the central diffractive lobe, is evidenced by the intense band in the received scattered energy that stretches between the source and receiver. Contributions to the received scattered energy decrease with increasing lobe order as predicted by the $\sin^2(\varphi_i/2)$ term in Eq. (8b). As expected, the most significant reduction occurs for scattering from patches in the backscattering direction, which corresponds to the highest-order diffractive lobe.

The combined effects of coherent propagation and a finite spatial correlation length on the spatial structure of the received scattered energy are presented in Fig. 6(b). These results show the beat pattern caused by coherent propagation of the incident and scattered fields superimposed with the diffractive lobes and nulls induced by the finite spatial correlation length.

The effects of the spatial structure in the scattered fields on the predicted levels of received reverberation as a function of time are shown in Fig. 7 for the bistatic scattering geometry. The upper pair of curves represent the point-scattering limit, and the lower pair of curves include finite correlation effects. Each pair of curves gives the level of

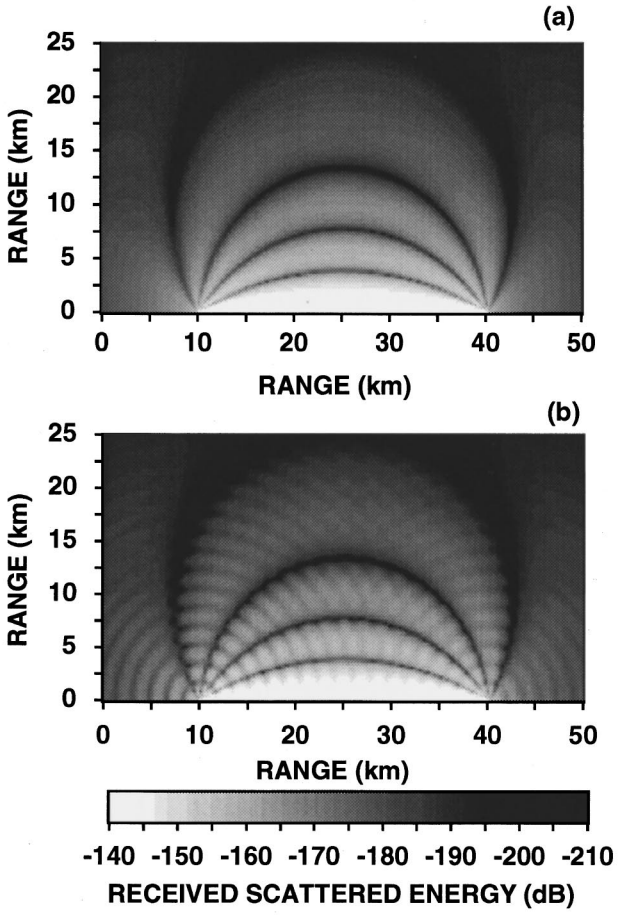

FIG. 6. Dependence of received scattered energy on location of scattering region in the horizontal plane, computed at 15 Hz for a bistatic scattering geometry with a finite spatial correlation length $a=250$ m. Source range is 10 km and source depth is 30 m. Receiver range is 40 km and receiver depth is 90 m: (a) using incoherent propagation, E_{inc} from Eq. (10); (b) using coherent propagation, E from Eq. (9).

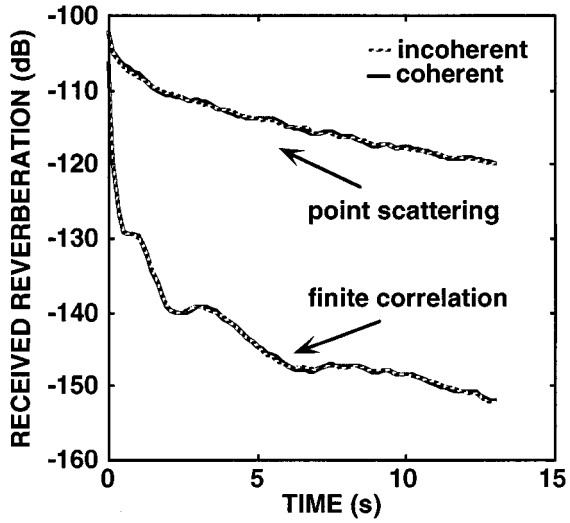

FIG. 7. Temporal dependence of levels of received reverberation for bistatic scattering geometry in shallow water environment at 15 Hz. Finite correlation results computed using $a=250$ m. Source range is 10 km and source depth is 30 m. Receiver range is 40 km and receiver depth is 90 m.

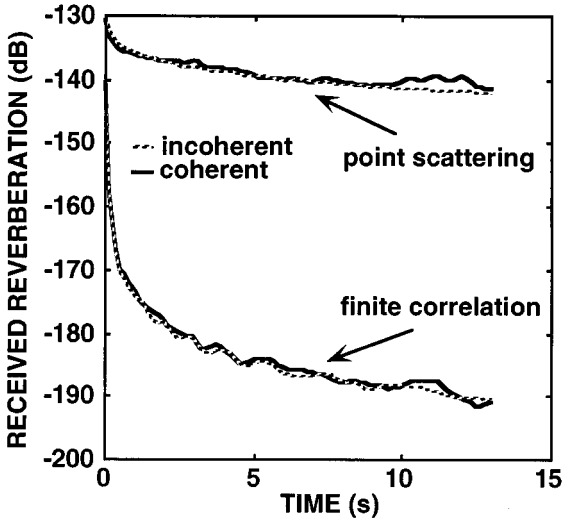

FIG. 8. Temporal dependence of levels of received reverberation for bistatic scattering geometry in deep water environment at 50 Hz. Finite correlation results computed using $a=250$ m. Source range is 10 km and source depth is 30 m. Receiver range is 40 km and receiver depth is 90 m.

received reverberation computed with and without coherent propagation.[1] These results indicate that, independent of coherent propagation effects, diffraction induced by a finite spatial correlation length can cause a significant reduction in the level of received reverberation, as predicted by the addition of the nonpositive term E_1 in Eq. (13). The presence of the diffractive lobes and nulls in the received scattered energy is apparent in the pattern of peaks and lows observed in the predicted level of received reverberation computed using a finite spatial correlation length.

The complicated spatial structure imposed by the combined interference patterns of the incident and scattered fields for the bistatic scattering geometry [Fig. 6(b)] caused only a small oscillation in the levels of received reverberation about those predicted using the incoherent approximation of the propagating fields. Thus for bistatic scattering geometries and range-invariant environments, the effects caused by coherent propagation of the incident and scattered fields appear to be negligible.

Computations were performed in the deep water environment at 50 Hz for the bistatic scattering geometry, and predicted levels of received reverberation are presented in Fig. 8. With the exception of having additional diffractive lobes and nulls, the spatial behavior of the received scattered energy for the deep water environment is analogous to that shown in Fig. 6(a) and (b) for the shallow water environment and is not shown here. As in the case of the shallow water environment, results computed using a finite spatial correlation length show a substantial reduction in the levels of received reverberation. The increased frequency of peaks and lows observed in the levels of received reverberation computed using a finite spatial correlation length (lower pair of curves) is evidence of the increased number of diffractive lobes and nulls in the spatial structure of the received scattered energy for the deep water environment. Although this environment exhibited convergent zone propagation, the oscillation caused by coherent propagation effects remains small for the bistatic scattering configuration. This provides

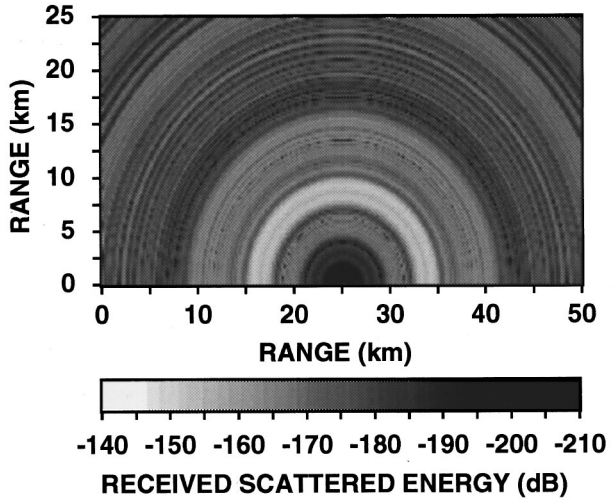

FIG. 9. Dependence of received scattered energy on location of scattering region in the horizontal plane, computed in the point-scattering limit at 50 Hz for a monostatic scattering geometry in a deep water environment assuming coherent propagation. Source range is 10 km and source depth is 30 m. Receiver range is 40 km and receiver depth is 90 m.

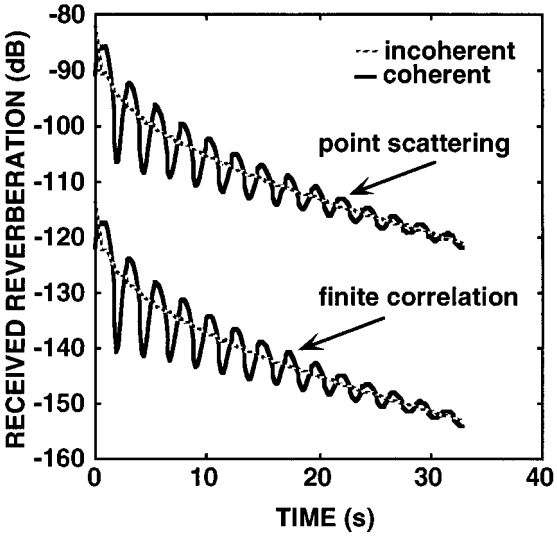

FIG. 10. Temporal dependence of levels of received reverberation for monostatic scattering geometry in shallow water environment at 15 Hz. Finite correlation results computed using $a=250$ m. Source range is 10 km and source depth is 30 m. Receiver range is 40 km and receiver depth is 90 m.

further evidence that the complicated interference pattern caused by coherent propagation of the incident and scattered fields tends to average out for bistatic scattering geometries and produces a small net effect in the levels of received reverberation for range-invariant environments.

B. Monostatic geometry

The spatial structure imposed by coherent propagation for a monostatic scattering geometry is shown in Fig. 9. Computations were performed in the deep water environment at 50 Hz. The beat patterns of the incident and scattered fields appear as concentric rings centered on the source and receiver location. No diffraction pattern is imposed on the received scattered energy computed including a finite spatial correlation length because a monostatic scattering geometry corresponds to scattering in the back direction; thus results computed including both a finite spatial correlation length and coherent propagation have the same interference pattern as shown in Fig. 9 and are not presented. There is however a large difference between the levels of received scattered energy predicted by the point-scattering and finite correlation methods because diffractive effects induced by a finite spatial correlation length are strongest for scattering in the back direction.

The predicted levels of received reverberation computed in the shallow water environment at 15 Hz are shown in Fig. 10 for a monostatic scattering geometry. As expected, the level reduction caused by the finite correlation induced diffraction is much larger for the monostatic (back scattering) configuration (cf. Fig. 7). Coherent propagation effects also show an increased significance for the monostatic scattering geometry because the interference patterns of the incident and scattered field propagation are identical and are reinforced by their superposition.

Previously published results have shown that coherent propagation of the incident and scattered fields induces a rapid oscillation in the predicted level of received reverberation for a monostatic scattering geometry in a shallow water environment with little bottom penetration.[1] Computations performed using the present method in shallow water environments with hard sediment layers are in agreement with the prior results and are not presented. However, the results presented in Fig. 10 show that a relatively slow oscillation in the received levels of reverberation are introduced by including coherent propagation. Therefore, it appears that coherent propagation effects may be important for monostatic scattering geometries in shallow water environments that exhibit significant bottom penetration.

The received levels of reverberation, computed in the deep water environment at 50 Hz for a monostatic scattering geometry are presented in Fig. 11. Consistent with the shallow water predictions, results computed in the deep water environment for the monostatic geometry show a greater finite correlation induced reduction in level (cf. Fig. 8). Furthermore, the inclusion of coherent propagation has a significant effect on predicted levels of received reverberation for the deep water environment, again in agreement with previous results.[1] At short times, the reverberation levels predicted assuming coherent propagation show a large null; this is due to the absence of high-angle energy at short ranges because the field computations included only discrete modes.

C. Frequency dependence

The magnitude of diffractive effects predicted by Eqs. (8a)–(8b) increases with increasing ratio of the spatial correlation length to the interference distance, a/Λ_{mn}. Because the minimum value of Λ_{mn} decreases with increasing frequency for a discrete wave number spectrum, diffractive effects for a given correlation length should increase with frequency (Sec. I). To illustrate this effect, the received scattered energy was computed in the shallow water environ-

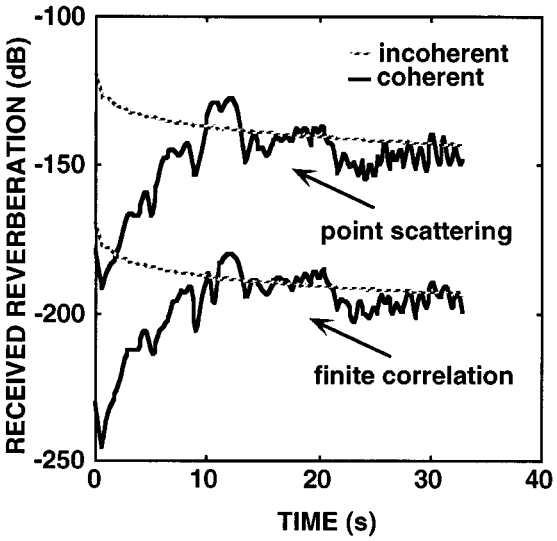

FIG. 11. Temporal dependence of levels of received reverberation for monostatic scattering geometry in deep water environment at 50 Hz. Finite correlation results computed using $a=250$ m. Source range is 10 km and source depth is 30 m. Receiver range is 40 km and receiver depth is 90 m.

ment for a bistatic scattering geometry at a frequency of 50 Hz, using the same spatial correlation length of 250 m [cf. Fig. 6(a)] and is presented in Fig. 12. In comparison with the calculations performed at 15 Hz, predictions at 50 Hz show a substantial increase in the number of diffractive lobes and nulls, which should result in a further reduction in the levels of received reverberation. The predicted increase in level reduction is verified in Fig. 13, which shows the levels of received reverberation computed at 50 Hz in the shallow water environment. Coherent propagation effects remain insignificant for the bistatic scattering geometry.

The dependence of the strength of the diffractive effects on the ratio a/Λ_{mn} also indicates that, for a given spatial correlation length, there is a minimum frequency below which diffraction caused by the finite correlation length can be neglected. This predicted decrease in finite correlation effects with decreasing frequency is verified in Figs. 14 and 15, which show results computed for a bistatic scattering geometry in the shallow water environment using a 50-m spatial correlation length. The received scattered energy computed at 50 Hz using $a=50$ m (Fig. 14) has fewer diffractive lobes and nulls than that computed using $a=250$ m (cf. Fig. 12). The levels of received reverberation computed at 50 Hz using $a=50$ m are shown in Fig. 15(a). As expected, the decreased number of diffractive lobes and nulls in the spatial structure of the received scattered energy results in a smaller reduction in the level of received reverberation computed using a finite spatial correlation length. The received scattered energy computed at 15 Hz using $a=50$ m is shown in Fig. 15(b). At 15 Hz, no diffractive nulls are apparent as evidenced by the absence of the pattern of peaks and valleys in the levels of received reverberation computed using a finite spatial correlation length. Furthermore, the level reduction caused by finite correlation effects is significantly smaller than at 50 Hz, indicating that for a 50-m correlation length in the shallow water environment, 15 Hz is

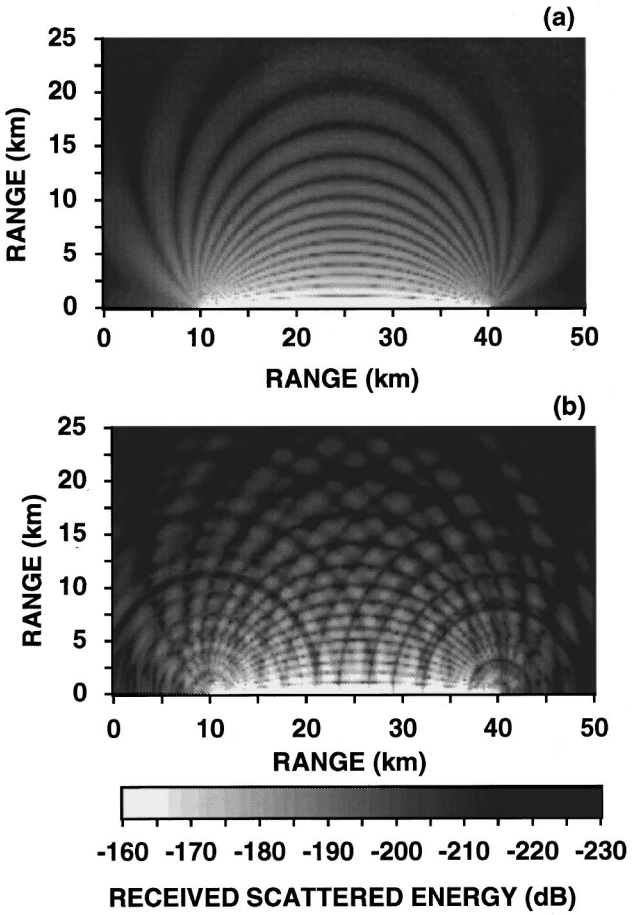

FIG. 12. Dependence of received scattered energy on location of scattering region in the horizontal plane, computed at 50 Hz for a bistatic scattering geometry in shallow water environment with a finite spatial correlation length $a=250$ m. Source range is 10 km and source depth is 30 m. Receiver range is 40 km and receiver depth is 90 m: (a) using incoherent propagation, E_{inc} from Eq. (10); (b) using coherent propagation, E from Eq. (9).

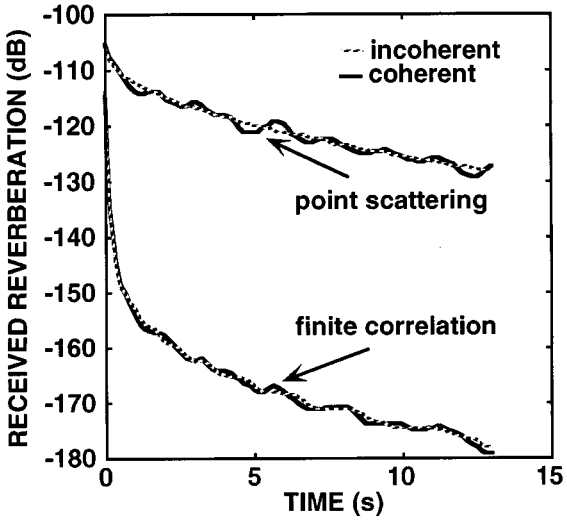

FIG. 13. Temporal dependence of levels of received reverberation for bistatic scattering geometry in shallow water environment at 50 Hz. Finite correlation results computed using $a=250$ m. Source range is 10 km and source depth is 30 m. Receiver range is 40 km and receiver depth is 90 m.

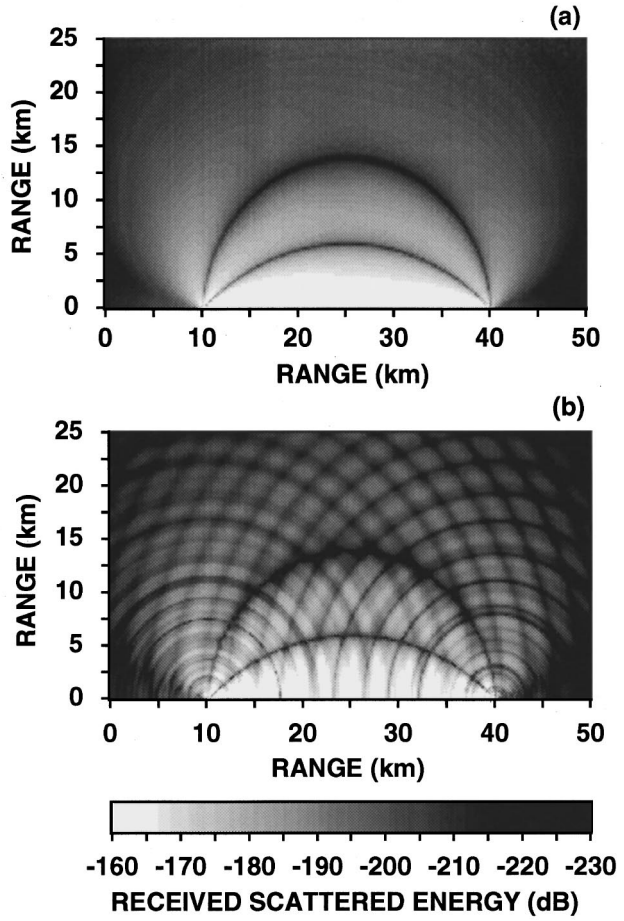

FIG. 14. Dependence of received scattered energy on location of scattering region in the horizontal plane, computed at 50 Hz for a bistatic scattering geometry in shallow water environment with a finite spatial correlation length $a=50$ m. Source range is 10 km and source depth is 30 m. Receiver range is 40 km and receiver depth is 90 m: (a) using incoherent propagation, E_{inc} from Eq. (10); (b) using coherent propagation, E from Eq. (9).

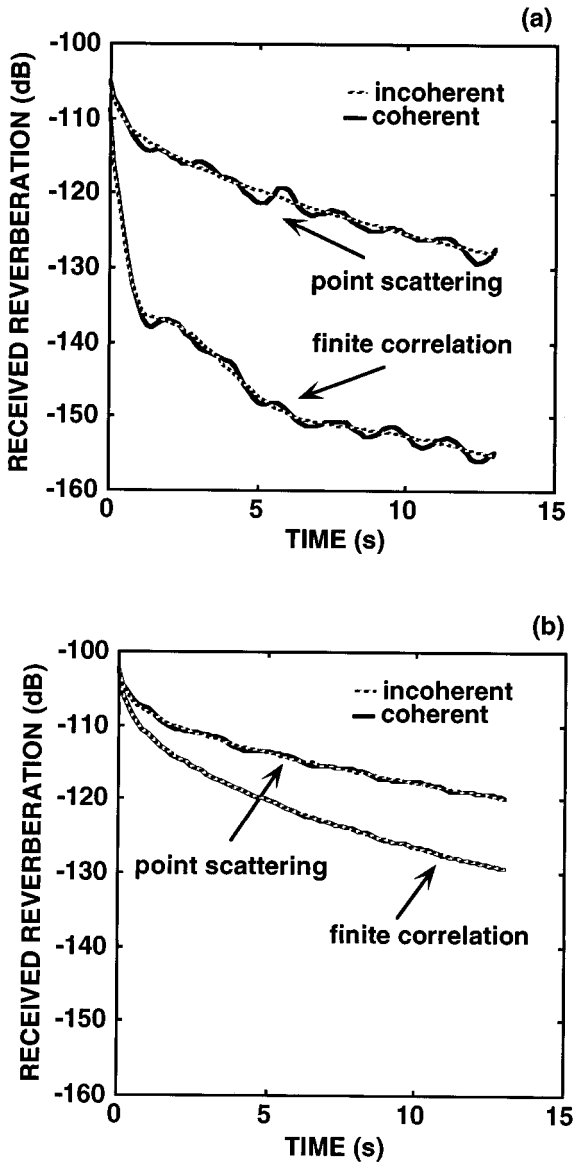

FIG. 15. Temporal dependence of levels of received reverberation for bistatic scattering geometry in shallow water environment. Finite correlation results computed using $a=50$ m. Source range is 10 km and source depth is 30 m. Receiver range is 40 km and receiver depth is 90 m: (a) $f=50$ Hz; (b) $f=15$ Hz.

approaching the minimum frequency below which diffractive effects can be ignored.

D. Environmental dependence

Scattering results for a shallow water environment with a soft sediment layer were presented in the previous sections, and the agreement between previously published results[1] and results obtained in this work for a downward refracting shallow water environment with a hard sediment layer was discussed. To investigate the dependence of finite correlation and coherent propagation effects on the sound velocity profile and sediment properties of shallow water environments, computations were also performed for bistatic and monostatic scattering geometries in shallow water environments with an upward refracting sound velocity profile and either a hard or soft sediment layer. Model predictions for the upward refracting environment are consistent with those obtained for the downward refracting environment, and will not be presented.

Model predictions for the upward refracting environments, computed at 15 and 50 Hz using finite spatial correlation lengths $a=250$ m and $a=50$ m show that the inclusion of a finite spatial correlation length produces diffraction in the scattered field that is not predicted in the point-scattering limit, and that the details and strength of the diffractive effects are determined by the frequency, spatial correlation length, and interference distances of propagation. In addition, results that included modal interference in the propagating fields show that, as in the case of the downward refracting environment, the spatial structure of the scattered field in the horizontal plane is determined by a superposition of the interference patterns of the incident and scattered fields. The temporal dependence of the reverberated energy appears largely unaffected by coherent propagation of the bistatic scattering geometry and for a monostatic geometry; the reverberated return computed including modal interference in the propagating fields oscillates about the levels computed using the incoherent approximation of the propagated energy. For the hard sediment environment, the oscillation

induced by coherent propagation is rapid and irregular, whereas a slow periodicity is observed for the environment with a soft sediment.

It appears that, although the sound velocity profile is important to determining the energy incident on the bottom, scattering predictions which include a finite spatial correlation length can be significantly different from those predicted in the point-scattering limit and that the strength of the diffractive effects relative to point-scattering predictions are not highly sensitive to the shape of the water sound velocity profile. Furthermore, backscattering results show that coherent propagation effects are highly dependent on the sediment properties. In an environment for which there is little bottom penetration, the persistence of high-angle energy, even at long ranges, results in a large number of multipaths and the temporal dependence of the reverberated return therefore exhibits a rapid oscillation about the return computed using the incoherent approximation. In an environment which allows significant bottom penetration, the high-angle energy that is incident on the bottom is quickly attenuated and reverberation is dominated beyond short ranges by the scattering of a relatively small number of low-order modes; thus the temporal dependence of the reverberated return computed including modal interference in the propagating fields exhibits a slow periodicity which could be important to bottom backscattering predictions.

III. CONCLUSIONS

The importance of two independent sources of modal interference effects in the normal-mode treatment of bottom scattering have been investigated. Model computations were performed for monostatic and bistatic scattering geometries in both a shallow water and deep water range-invariant environment. The first interference effect involves the superposition of modes scattered within a region over which the distribution of bottom scattering elements exhibits a finite spatial correlation. For the bistatic scattering geometry, modal superposition over each finite scattering region imposes a diffraction pattern on the spatial structure of the received scattered energy that is not predicted in the point-scattering limit. The azimuthal directionality of the diffractive lobes and nulls for the bistatic geometry strongly favors forward scattering, which corresponds to the central diffractive maximum. The least significant diffractive effects in the forward direction occur for scattering between identical or adjacent modes. The diffractive order increases with azimuthal scattering angle, and the strongest diffractive effects therefore occur for scattering in the back direction, with scattering between low-order modes the most affected.

The diffraction pattern imposed on the received scattered energy by a finite spatial correlation length causes a net reduction in the predicted levels of received reverberation. In addition, the levels computed using a finite spatial correlation length exhibit a pattern of peaks and nulls which correspond to the diffractive lobes and nulls in the spatial structure of the received scattered field. For a given environment and frequency, the largest finite correlation induced reduction in level occurs for monostatic scattering geometries because finite correlation induced diffractive effects are greatest for scattering in the back direction.

The significance of the diffractive effects induced by a finite spatial correlation increases with the ratio of the spatial correlation length to the interference distance, a/Λ_{mn}. The number of diffractive lobes and nulls in the spatial structure of the received scattered energy, and the corresponding reduction in the levels of received reverberation, increases with both frequency and spatial correlation length. For a given spatial correlation length, there exists a minimum frequency below which diffractive effects can be ignored.

An experimental measurement of finite correlation induced diffractive effects would require a horizontal line array to observe azimuthal variations in the measured levels of reverberation. Furthermore, such a measurement would be required if the correlation length and scattering strength were to be determined independently. Results presented in this paper suggest that there may be a significant difference between point-scattering and finite correlation reverberation levels; neglecting this difference in a determination of scattering strength from measurements of single receiver time series could give a significantly smaller result.

The second type of modal interference examined in this paper is due to the constructive and destructive interference of modes in the incident and scattered field propagation. Predictions of the received scattered energy as a function of scattering location for a bistatic scattering geometry show that, as expected, there is little contribution from scattering areas for which there is destructive interference either in the incident field on the bottom or the scattered field at the receiver. However, the predicted levels of received reverberation computed in both the shallow water and deep water environment indicate that coherent propagation effects are small for bistatic scattering configurations and range-invariant environments.

For a monostatic scattering geometry, the inclusion of modal interference in the propagating fields introduces an oscillation in the levels of received reverberation about those predicted using an incoherent approximation of the propagating fields. Consistent with previously published work,[1] coherent propagation effects were found to be significant in the deep water environment and of limited importance for shallow water environments with hard sediment layers. However, coherent effects for monostatic scattering geometries were found to be substantial for shallow water environments which exhibit significant bottom penetration.

ACKNOWLEDGMENT

This work was supported under Contract no. N00039-91-C-0082 by the Advanced Surveillance and Prediction System (ASAPS) Program of the Space and Naval Warfare Systems Command (SPAWAR, PMW 181-16).

[1] D. D. Ellis, ''A shallow-water normal-mode reverberation model,'' J. Acoust. Soc. Am. **97**, 2804–2814 (1995), and references therein.
[2] D. M. Fromm, B. J. Orchard, and S. N. Wolfe, ''Range-dependent, normal-mode reverberation model for bistatic geometries,'' in *Ocean Reverberation*, edited by D. D. Ellis, J. R. Preston, and H. G. Urban (Kluwer, Dordrecht, The Netherlands, 1993), pp. 155–160.
[3] K. J. McCann, ''A full-wave treatment of acoustic reverberation,'' The

Johns Hopkins University Applied Physics Laboratory, Laurel, MD, STD-R-1903 (1990).
[4] E. C. Shang, ''Some new challenges in shallow water acoustics,'' in *Progress in Underwater Acoustics*, edited by Harold M. Merklinger (Plenum, New York, 1986), pp. 461–471.
[5] K. V. MacKenzie, ''Long range shallow water bottom reverberation,'' J. Acoust. Soc. Am. **34**, 62–66 (1962).
[6] T. Udagawa and D. P. Knobles, ''Scattering of acoustic waves from a rigid spherical target in a stratified waveguide'' (unpublished).
[7] J. A. Fawcett, ''A derivation of the differential equations of coupled-mode propagation,'' J. Acoust. Soc. Am. **92**, 290–295 (1992).
[8] F. Ingenito, ''Scattering from an object in a stratified medium,'' J. Acoust. Soc. Am. **82**, 2051–2059 (1987).
[9] P. C. Waterford, ''New formulation of acoustic scattering,'' J. Acoust. Soc. Am. **45**, 1417–1429 (1969).
[10] A. Ishimaru, *Wave Propagation and Scattering in Random Media* (Academic, New York, 1978), Vol. II, Chap. 21.
[11] F. G. Bass and I. M. Fuks, *Wave Scattering from Statistically Rough Surfaces* (Pergamon, New York, 1979).
[12] S. J. Levinson, E. K. Westwood, R. A. Koch, S. K. Mitchell, and C. V. Sheppard, ''An efficient and robust method for underwater acoustic normal mode computations,'' J. Acoust. Soc. Am. **97**, 1576–1585 (1995).

Coupled phase theory for sound propagation in emulsions

J. M. Evans and K. Attenborough
Faculty of Technology, The Open University, Milton Keynes MK7 6AA, United Kingdom

(Received 5 August 1996; accepted for publication 3 April 1997)

The coupled phase approach is extended to model sound propagation in an emulsion of two compressible, thermoviscous liquids. This provides an alternative to scattering theory for modeling sound propagation in emulsions in the low-acoustic radius regime. Predictions of the new theory are compared with predictions of multiple-scattering theory and experimental results for ultrasonic velocity and attenuation in an emulsion. For the particular set of experimental data used here, the coupled phase theory gives predictions close to the scattering theory predictions, and a better prediction of the dependence of the attenuation on volume fraction. A similar difference between the two theoretical approaches has been found in earlier work on coupled phase models for sound propagation in suspensions. © *1997 Acoustical Society of America.* [S0001-4966(97)06607-1]

PACS numbers: 43.35.Bf [HEB]

LIST OF SYMBOLS

a	radius of particles
C, C_p	specific heat at constant volume and constant pressure
k	complex wave number
k_2	thermal wave number
K	k/ω
p	pressure$=p^0+p'\exp[i(kz-\omega t)]$
S, S_h	frequency dependent momentum and heat transfer terms
T	temperature$=T_0+T'\exp[i(kz-\omega t)]$
u	velocity$=u'\exp[i(kz-\omega t)]$
α	$1-\phi^0$
β	coefficient of thermal (volume) expansion
γ	ratio of specific heats
δ, δ_h	viscous and thermal boundary layer thickness
ϕ	volume fraction$=\phi^0+\phi'\exp[i(kz-\omega t)]$
κ	adiabatic compressibility
μ	dynamic viscosity
ρ	density$=\rho^0+\rho'\exp[i(kz-\omega t)]$
τ	thermal conductivity
ω	angular frequency

Subscripts

f	continuous phase
s	particulate phase

INTRODUCTION

Coupled phase theory has proved successful as an alternative to scattering theory for modeling sound propagation in suspensions in the low-acoustic radius, or continuum, regime. The main difference between the coupled phase and scattering approaches is that coupled phase theory is self-consistent. The self-consistency is generated by the use of volume averaged field variables.[1,2] The coupled phase approach can be extended to model various phenomena which would be difficult to include in scattering theory, such as: viscous and thermal wave interactions, particle nonsphericity, chemical reactions, and mass transfer.

Previous coupled phase theories have been of two forms. The first (Gumerov *et al.*[3] and Margulies and Schwartz[1]) assumes an incompressible particular phase and allows for heat transfer between the phases. The second, which has been derived by Harker and Temple,[4] Gibson and Toksoz,[5] and Atkinson and Kytomaa,[6] allows for a compressible particulate phase but neglects heat transfer. Both include coupling due to the viscous, inertial, and buoyancy forces.

Urick[7] and Hampton[8] have measured the ultrasonic attenuation and velocity for suspensions at high-volume fractions and low $k_f a$. Strout[9] compared coupled phase theory and multiple-scattering theory predictions with the experimental data of Urick. The coupled phase theory used a momentum transfer term modified to account for hydrodynamic interactions between the particles at high-volume fractions. This theory gave a better prediction of the volume fraction dependence of the attenuation than the scattering theory. Gibson and Toksoz[5] and Ogushwitz[10] compared predictions of Biot's porous media theory[11] with the Hampton data. The Biot theory predictions were closer to the experimental data than predictions of coupled phase theory. However, The Biot theory requires the use of an adjustable parameter.

To model sound propagation in emulsions at high-volume fractions, the Harker and Temple theory has been extended to include irreversible heat transfer between the phases. This paper outlines the new coupled phase theory, which includes heat transfer *and* a compressible particulate phase. The set of equations determining the complex wave number are solved numerically. Predictions of the new theory and predictions of scattering theory are compared with experimental results for sound propagation in an emulsion obtained by McClements and Povey.[12] For this experiment, heat transfer and compressibility in the particulate phase are important influences on the sound propagation. The comparison shows the difference between the predictions of the two theoretical approaches at high-volume fractions.

I. THEORY

For sound propagation in the z direction, the linearized, volume averaged equations for conservation of mass, momentum, and energy for the two liquids are

$$\phi^0 \frac{\partial \rho_s}{\partial t} + \rho_s^0 \frac{\partial \phi}{\partial t} + \phi^0 \rho_s^0 \frac{\partial u_s}{\partial z} = 0, \tag{1}$$

$$\alpha \frac{\partial \rho_f}{\partial t} - \rho_f^0 \frac{\partial \phi}{\partial t} + \alpha \rho_f^0 \frac{\partial u_f}{\partial z} = 0, \tag{2}$$

$$\rho_s^0 \frac{\partial u_s}{\partial t} = -i\omega \rho_f^0 S(u_f - u_s) - \frac{\partial p}{\partial z}, \tag{3}$$

$$\rho_f^0 \frac{\partial u_f}{\partial t} = i\omega \frac{\phi^0}{\alpha} \rho_f^0 S(u_f - u_s) - \frac{\partial p}{\partial z}, \tag{4}$$

$$\rho_s^0 C_s \frac{\partial T_s}{\partial t} + \frac{\rho_s^0 (\gamma_s - 1) C_s}{\beta_s} \frac{\partial u_s}{\partial z} = -i\omega \rho_f^0 S_h (T_f - T_s), \tag{5}$$

$$\rho_f^0 C_f \frac{\partial T_f}{\partial t} + \frac{\rho_f^0 (\gamma_f - 1) C_f}{\beta_f} \frac{\partial u_f}{\partial z} = i\omega \frac{\phi^0}{\alpha} \rho_f^0 S_h (T_f - T_s). \tag{6}$$

Here the superscript zero indicates the constant equilibrium component of the variable. Equations (1)–(4) are the same as those of Harker and Temple.[4] The energy equations (5) and (6) are derived from the usual energy equation for a liquid. This has been volume averaged for the particulate and continuous phases, respectively, and the heat transfer term added. The momentum transfer term S is given by[4]

$$\frac{9}{4} i \frac{\delta^2}{a^2} + \frac{9}{4}(1+i)\frac{\delta}{a} + \frac{1+2\phi^0}{2\alpha}, \qquad \delta = \sqrt{\frac{2\mu_f}{\rho_f^0 \omega}},$$

and the heat transfer term S_h is given by[3]

$$\frac{-3\tau_f}{i\omega a^2 \rho_f^0} \left[\frac{1}{1 - i k_{2f} a} - \frac{\tau_f}{\tau_s} \frac{\tan(k_{2s}a) + 2/(k_{2s}a) - 3\tan(k_{2s}a)/(k_{2s}a)^2}{\tan(k_{2s}a) - k_{2s}a} \right]^{-1},$$

$$k_{2f} = \frac{1+i}{\delta_{hf}}, \qquad \delta_{hf} = \sqrt{\frac{2\tau_f}{\rho_f^0 C_{pf} \omega}}.$$

Particle size distributions can be incorporated into the theory by using momentum and heat transfer terms summed or integrated over the range of particle radii, weighted with the volume fraction as a function of radius.[1] The more rigorous approach of Harker *et al.*[13] included a number of particle sizes from the beginning, in the conservation equations. A coupled phase theory extended following this approach will be subject of a future paper.

The thermodynamic equations of state for the two liquids, in terms of the magnitudes of the fluctuating parts of the field variables (indicted by a prime) are

$$\rho_s' + \rho_s^0 \beta_s T_s' - \gamma_s \rho_s^0 \kappa_s p' = 0, \tag{7}$$

$$\rho_f' + \rho_f^0 \beta_f T_f' - \gamma_f \rho_f^0 \kappa_f p' = 0. \tag{8}$$

The fluctuating parts of the field variables vary as $\exp[i(kz - \omega t)]$. Replacing the field variables by the sum of their steady state and fluctuating components in Eqs. (1)–(8) and using the transformations $\partial/\partial t / \rightarrow -i\omega$ and $\partial/\partial z \rightarrow ik$ leads to the matrix equation

$$\mathbf{A}\mathbf{x} = 0, \tag{9}$$

where

$$\mathbf{x} = (\rho_f' \rho_s' u_f' u_s' T_f' T_s' p' \phi')^T$$

and

$$\mathbf{A} = \begin{pmatrix}
0 & \phi & 0 & -K\phi\rho_s & 0 & 0 & 0 & \rho_s \\
-\alpha & 0 & K\alpha\rho_f & 0 & 0 & 0 & 0 & \rho_f \\
0 & 0 & \rho_f S & -(\rho_s + \rho_f S) & 0 & 0 & K & 0 \\
0 & 0 & -\rho_f(\alpha + \phi S) & \phi\rho_f S & 0 & 0 & \alpha K & 0 \\
0 & 0 & 0 & K\dfrac{\rho_s C_s(\gamma_s - 1)}{\beta_s} & \rho_f S_h & -(\rho_s C_s + \rho_f S_h) & 0 & 0 \\
0 & 0 & K\dfrac{\alpha\rho_f C_f(\gamma_f - 1)}{\beta_f} & 0 & -\rho_f[\alpha C_f + \phi S_h] & \phi\rho_f S_h & 0 & 0 \\
0 & 1 & 0 & 0 & 0 & \rho_s\beta_s & -\gamma_s\rho_s\kappa_s & 0 \\
1 & 0 & 0 & 0 & \rho_f\beta_f & 0 & -\gamma_f\rho_f\kappa_f & 0
\end{pmatrix}.$$

In the matrix and the following work the superscript zeros have been omitted: The equilibrium components of the field variables are understood.

$\mathbf{x}$ has a nontrivial solution if and only if

$$\det \mathbf{A} = 0. \tag{10}$$

Equation (10) was solved numerically using Mathematica to obtain the sound speed and attenuation. The physical constants and the values of S and S_h at a single value of a and ω are entered in the matrix $\mathbf{A}$, leaving ϕ, and K which is unknown. Using the ''solve'' and ''det'' functions, Eq. (10) is then solved to give an equation for k in terms of the volume fraction ϕ. The imaginary part of k gives the attenuation and the ratio of ω to the real part of k gives the sound speed.

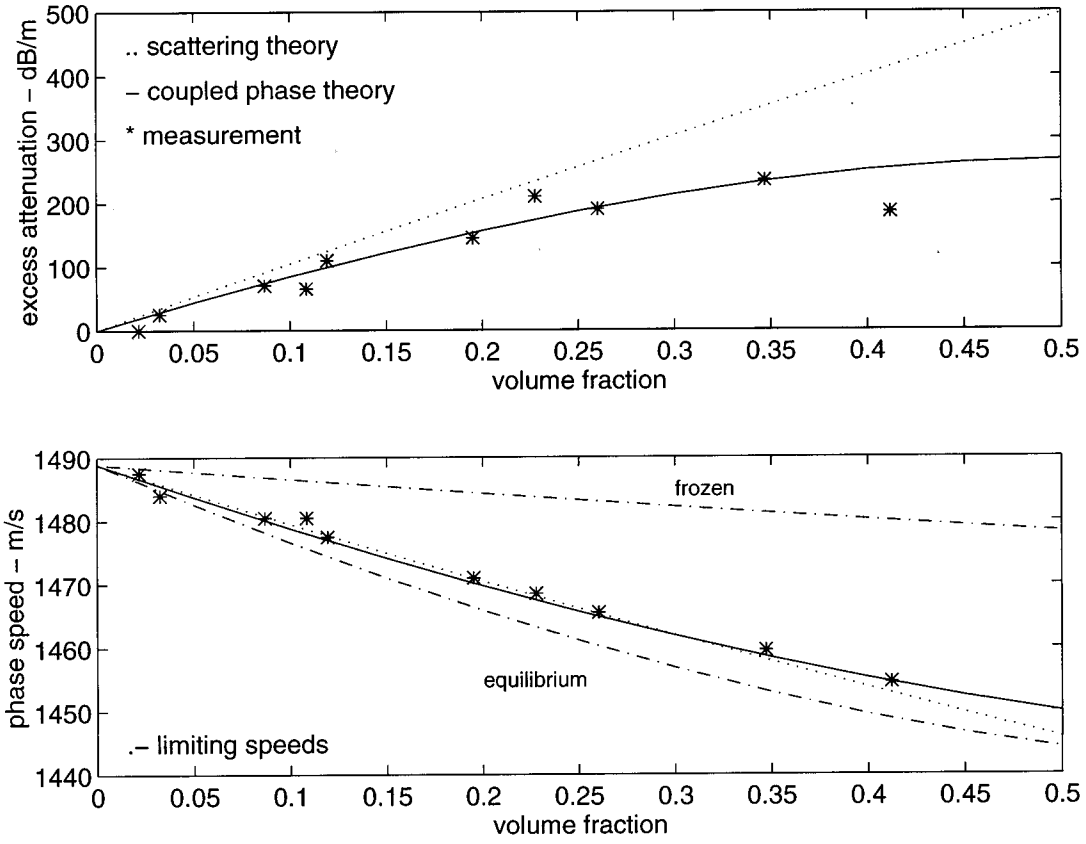

FIG. 1. Excess attenuation in dB m^{-1} and ultrasonic velocity at 1.25 MHz versus oil volume fraction for a sunflower oil in water emulsion with mean particle radius 0.27 μm. Comparison of data of McClements and Povey and predictions of coupled phase theory and multiple-scattering theory. Also shown are the limiting sound speeds.

Because intrinsic losses in the liquids have been neglected here, the attenuation given by k is the excess attenuation.

A. High-frequency limit

Explicit expressions for k can be obtained by neglecting either momentum transfer or heat transfer.

1. No heat transfer

In the limit $\omega\to\infty$, $S_h\to 0$, i.e., no heat transfer. Putting $S_h=0$ in Eq. (10), the solution for K is

$$\left(\frac{k}{\omega}\right)^2=\frac{(\kappa\gamma)_{\rm va}(S\rho_{\rm va}+\rho_s\alpha)}{S\gamma_{\rm va}+\rho_s\alpha\rho_\infty}, \tag{11}$$

where

$$\rho_\infty=\left(\frac{\gamma}{\rho}\right)_{\rm va}=\frac{\alpha\gamma_f}{\rho_f}+\frac{\phi\gamma_s}{\rho_s}.$$

The subscript va indicates volume averaging, e.g., $(x)_{\rm va}=\alpha x_f+\phi x_s$. If $\gamma_f=\gamma_s=1$ (11) is identical to the result obtained by Harker and Temple[4] [Eq. (2.25)].

2. No momentum transfer

The high-frequency limit of the S term is

$$S=\frac{1+2\phi}{2\alpha},$$

which is the induced mass term. For simplicity, however, it is assumed that $S\to 0$ in the high-frequency limit, i.e., there is no momentum transfer. Putting $S=0$ in Eq. (10), the solution for K is

$$\left(\frac{k}{\omega}\right)^2=\frac{(\kappa\gamma)_{\rm va}(S_h(\rho C)_{\rm va}+C_fC_s\rho_s\alpha)}{S_hA+C_fC_s\rho_s\alpha\rho_\infty}, \tag{12}$$

$$A=\phi\alpha\left[C_f\left(\frac{\rho_f}{\rho_s}+(\gamma_f-1)\frac{\beta_s}{\beta_f}+\gamma_f\frac{\alpha}{\phi}\right)+C_s\left(\frac{\rho_s}{\rho_f}+(\gamma_s-1)\frac{\beta_f}{\beta_s}+\gamma_s\frac{\phi}{\alpha}\right)\right].$$

This equation is a useful approximation for sound propagation in emulsions in which irreversible heat transfer is the dominant loss mechanism. In the limit $S\to 0$ Eq. (11) gives the ''frozen'' sound speed[3]

$$c_\infty^{-2}=\frac{(\kappa\gamma)_{\rm va}}{\rho_\infty}, \tag{13}$$

which is also given by Eq. (12) in the limit $S_h\to 0$.

B. Low-frequency limit

After assuming harmonic time and z dependence, the momentum equations (3) and (4) can be arranged to give

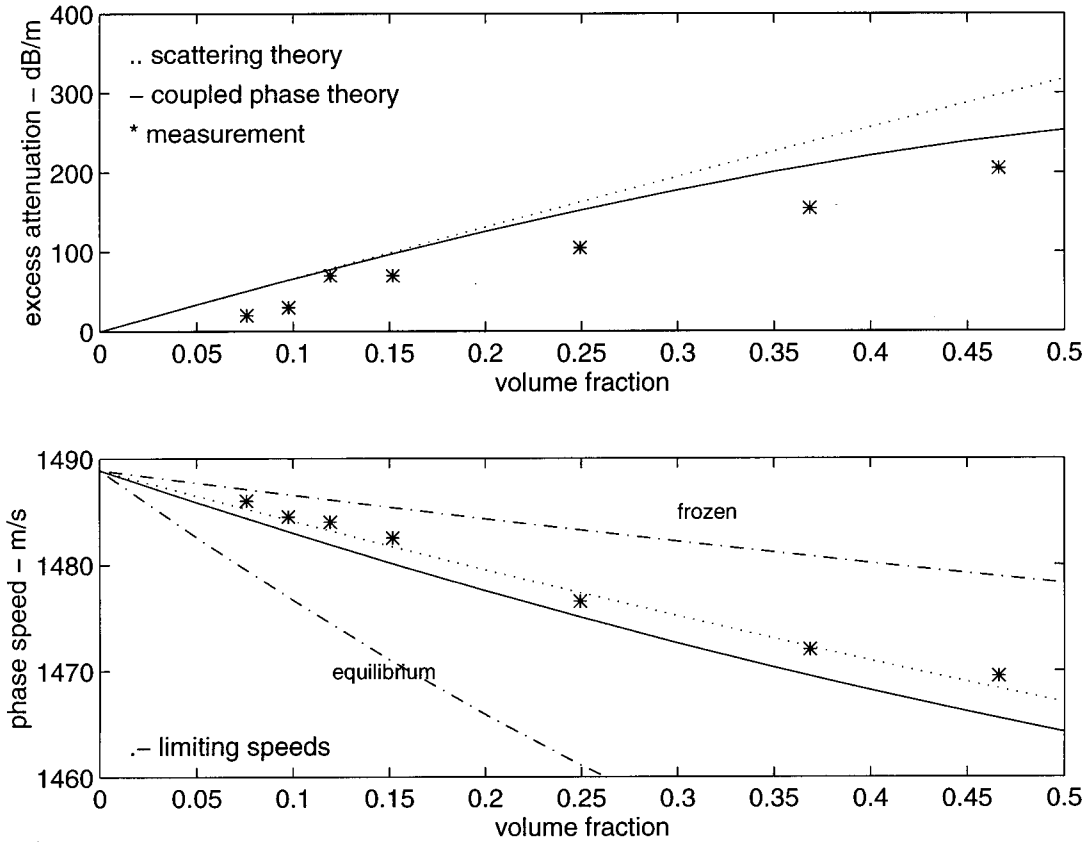

FIG. 2. Excess attenuation in dB m^{-1} and ultrasonic velocity at 1.25 MHz versus oil volume fraction for a sunflower oil in water emulsion with mean particle radius 0.74 μm. Comparison of data of McClements and Povey and predictions of coupled phase theory and multiple-scattering theory. Also shown are the limiting sound speeds.

$$u_s' = \frac{kp'}{\omega} \frac{\rho_f + S(\rho_f/\alpha)}{\rho_f \rho_s + S(\rho_f/\alpha)\rho_{va}}$$

and

$$u_f' = \frac{kp'}{\omega} \frac{\rho_s + S(\rho_f/\alpha)}{\rho_f \rho_s + S(\rho_f/\alpha)\rho_{va}}.$$

In the limit $\omega \to 0$, $S \to \infty$ and so

$$u_s' \alpha u_f' \to \frac{kp'}{\omega \rho_{va}}. \tag{14}$$

Using Eqs. (14) in (10) gives

$$\left(\frac{k}{\omega}\right)^2 = \frac{(\kappa\gamma)_{va}\rho_{va}(S_h(\rho C)_{va} + C_f C_s \rho_s \alpha)}{S_h A_{eq} + C_f C_s \rho_s \alpha \gamma_{va}}, \tag{15}$$

$$A_{eq} = \phi\alpha\left[\rho_f C_f\left(1 + (\gamma_f - 1)\frac{\beta_s}{\beta_f} + \gamma_f \frac{\alpha}{\phi}\right) + \rho_s C_s\left(1 + (\gamma_s - 1)\frac{\beta_f}{\beta_s} + \gamma_s \frac{\phi}{\alpha}\right)\right].$$

In the limit $\omega \to 0$, $S_h \to \infty$, and Eq. (15) gives for the equilibrium sound speed c_{eq}

$$c_{eq}^{-2} = \frac{(\kappa\gamma)_{va}\rho_{va}(\rho C)_{va}}{A_{eq}}. \tag{16}$$

II. COMPARISON WITH SCATTERING THEORY AND EXPERIMENT

McClements and Povey[12] measured the ultrasonic attenuation and velocity for a sunflower oil in water emulsion. The frequency range was 1.25–10 MHz, the particle radius range was 0.14–0.74 μm, and the volume fraction range was 0–0.5. Figures 1 and 2 compare the measurements with predictions of Eq. (10) and multiple-scattering theory. Also shown are the frozen sound speed from Eq. (13) and the equilibrium sound speed from Eq. (16). The experimental error was estimated at $\pm 0.05\%$ for the velocity and ± 30 dB m^{-1} for the attenuation.

The scattering theory uses the Waterman and Truell equation and the low-frequency limit of the first two Allegra and Hawley scattering coefficients. The details can be found in McClements,[14] the theory is given by Eqs. (1), (2), (8), and (9) in Ref. 14. Predictions of the $S=0$ theory [Eq. (12)] were compared to this experimental data in Ref. 15.

The particle radius values used for the predictions shown in Figs. 1 and 2 are mean values because the emulsions had polydisperse size distributions. As was discussed in Ref. 12, polydispersity will have a significant effect on the complex wave number and should be taken account of in theoretical work. For scattering theory this has been done by McClements.[14,16] A coupled phase theory including polydispersity is the subject of current work and a future paper will compare predictions of this theory with experimental data.

The predictions of the two theories and the measurements agree at low-volume fractions. At the higher-volume fractions the coupled phase theory predicts a smaller attenuation which agrees more closely with the measurements than the scattering theory. For the larger particle radius, the velocity prediction of the coupled phase theory is slightly less close to the measurements than that of the scattering theory.

The comparison suggests that the coupled phase theory is a good alternative to scattering theory for modeling sound propagation in emulsions in the low-acoustic radius regime. The coupled phase theory may be a better model for the dependence of the attenuation on volume fraction.

McClements[14] compared predictions of multiple-scattering theory with measurements of sound propagation in hexadecane emulsions. Here too, scattering theory was found to overpredict the attenuation at high-volume fractions.

III. CONCLUSIONS

A new coupled phase theory has been derived which includes heat transfer between the phases and compressibility in the particulate phase. Predictions of the theory have been compared with multiple-scattering theory predictions and measurements of sound propagation in an emulsion of compressible thermoviscous liquids. At low-volume fractions (<0.1), the predictions of the new theory agree well with the measurements and the scattering theory predictions. At higher-volume fractions (>0.1), the coupled phase theory predicts a lower attenuation than the scattering theory and agrees more closely with the measured data. The comparison suggests that the coupled phase theory is a good alternative to scattering theory for modeling sound propagation in emulsions in the low-acoustic radius regime. The coupled phase theory may be a better model for the dependence of the attenuation on volume fraction, although further comparisons with a wide range of experimental data will be necessary to determine which is a satisfactory theory.

ACKNOWLEDGMENT

This work is supported by the Engineering and Physical Sciences Research Council (UK).

[1] T. S. Margulies and W. H. Schwartz, ''A multiphase continuum theory for sound wave propagation through dilute suspensions of particles,'' J. Acoust. Soc. Am. **96**, 319–331 (1994).
[2] H. W. Schwartz and T. S. Margulies, ''Sound wave propagation through emulsions, colloids, and suspensions using a generalized Fick's law,'' J. Acoust. Soc. Am. **90**, 3209–3217 (1991).
[3] N. A. Gumerov, A. I. Ivandaev, and R. I. Nigmatulin, ''Sound waves in monodisperse gas-particle or vapour-droplet mixtures,'' J. Fluid Mech. **193**, 53–74 (1988).
[4] A. H. Harker and J. A. G. Temple, ''Velocity and attenuation of ultrasound in suspensions of particles in fluids,'' J. Phys. D **21**, 1576–1588 (1988).
[5] R. L. Gibson and M. N. Toksoz, ''Viscous attenuation of acoustic waves in suspensions,'' J. Acoust. Soc. Am. **85**, 1925–1934 (1989).
[6] C. M. Atkinson and H. K. Kytomaa, ''Acoustic wave speed and attenuation in suspensions,'' Int. J. Multiphase Flow **18**, 577–592 (1992).
[7] R. J. Urick, ''The absorption of sound in suspensions of irregular particles,'' J. Acoust. Soc. Am. **20**, 283–289 (1948).
[8] L. D. Hampton, ''Acoustic properties of sediments,'' J. Acoust. Soc. Am. **42**, 882–890 (1967).
[9] T. A. Strout, ''Attenuation of sound in high-concentration suspensions: Development and application of an oscillatory cell model,'' Ph.D. thesis, University of Maine, 1991.
[10] P. R. Ogushwitz, ''Applicability of the Biot theory. II. Suspensions,'' J. Acoust. Soc. Am. **77**, 441–452 (1985).
[11] J. F. Allard, *Sound Propagation in Porous Media: Modelling Sound Absorbing Materials* (Elsevier, New York, 1993).
[12] D. J. McClements and M. J W. Povey, ''Scattering of ultrasound by emulsions,'' J. Phys. D **22**, 38–47 (1989).
[13] A. H. Harker, P. Schofield, B. P. Stimpson, R. G. Taylor, and J. A. G. Temple, ''Ultrasonic propagation in slurries,'' Ultrasonics **29**, 427–438 (1991).
[14] D. J. McClements, ''Comparison of multiple scattering theories with experimental measurements in emulsions,'' J. Acoust. Soc. Am. **91**, 849–853 (1992).
[15] J. M. Evans and K. Attenborough, ''A coupled phase theory for sound propagation in an emulsion of heat-conducting, compressible liquids,'' in *Proceedings of the 15th International Congress on Acoustics*, edited by M. Newman (Acoustical Society of Norway, Trondheim, Norway, 1995), Vol 1, pp. 345–348.
[16] D. J. McClements, ''Ultrasonic characterization of emulsions and suspensions,'' Adv. Colloid Interface Sci. **37**, 33–72 (1991).

Leaky waves and the elastic wave resonance reflection on a crystal–thin solid layer interface

A. N. Darinskii[a)]
Institute of Crystallography, Academy of Sciences of Russia, Leninskii pr. 59, Moscow 117333, Russia

(Received 10 July 1996; accepted for publication 18 March 1997)

When a Rayleigh wave becomes ''supersonic'' for a given geometry of propagation, a thin solid layer coated on the surface of the medium can bring about the transformation of this wave into a leaky wave. In such a case in the sagittal plane there emerges a narrow interval of angles of incidence within which the phase of the reflection coefficient suffers abrupt changes, and the reflection is accompanied by excitation of surface vibrations with amplitudes greatly exceeding the amplitude of the incident wave. The effect is due to the resonance excitation of the leaky wave. The critical angle of incidence and the width of the resonance interval are determined by the real and imaginary parts of the leaky wave speed. Approximate expressions for the leaky wave speed and for the coefficients of plane wave conversion are derived and analyzed without any assumptions about the crystallographic symmetry of both the substrate and the layer. © *1997 Acoustical Society of America.* [S0001-4966(97)02107-3]

PACS numbers: 43.35.Cg [HEB]

INTRODUCTION

Deposition of additional layers as a method of governing reflection properties of an interface is well-known and widely applied in many areas of technics. The idea is that the waves reflected from, or transmitted through, a sequence of parallel interfaces add up with different phases and amplitudes in the bulk of the medium, so that interference amplification or extinguishing or specific phase shift dependencies can occur for certain directions of propagation or frequency ranges, see, e.g., Refs. 1 and 2.

Accounting for only the aforementioned effect of a purely interference nature one could suggest that a layer coated on the surface affects strongly the reflection of elastic waves, providing its thickness is at least of order of a sound wavelength. If the thickness-to-wavelength ratio is small, the difference between the reflection from the crystal–layer interface and from the mechanically free surface should not be appreciable, unless, of course, material parameters of the film and the crystal differ significantly. However, this is not always the case. In this paper, we shall discuss the case in which a thin layer modifies appreciably the behavior of the coefficients of mode conversion for a narrow interval of the angles of incidence.

This phenomenon is related to the resonance excitation of a leaky wave originating in the presence of a layer from a ''supersonic'' Rayleigh wave. The latter is a surface wave, the phase velocity of which appears to be larger than that of a bulk wave for certain directions of propagation, or even for any direction, confined to the sagittal plane (the plane spanned by the normal to the boundary of the medium and the direction of propagation of this surface wave). It a simple matter to realize that such a situation can take place only in an anisotropic medium. ''Supersonic'' Rayleigh waves appear most commonly in the case when the sagittal plane is a plane of crystallographic symmetry of the medium. A great deal of examples of crystals where the speed of such ''symmetric'' Rayleigh waves in fact turns out to be larger than the phase speed of the shear horizontal polarized bulk waves is listed in Ref. 3. However, examples of ''supersonic'' surface solutions at generic orientations of the sagittal plane and the direction of propagation are known too.[4,5]

A particular case of the problem, the reflection of shear waves incident in the plane of transverse isotropy of a hexagonal crystal, was studied in Ref. 6. In the present work, the resonance reflection will be investigated without any assumptions about the symmetry of both the crystal and the layer. We shall obtain approximate expressions for the leaky wave speed, the real and imaginary parts of which determine the value of the resonant angle of incidence and the width of the resonance interval of angles of incidence, respectively, as well as expressions for the coefficients of mode conversion themselves.

Note that other situations in which the presence of a thin layer in a medium leads to the appearance of a leaky wave and thereby to the reflection of a resonance type were still under consideration in other papers.[7,8] In Ref. 7 a study was made of the resonance reflection from a thin layer immersed in a uniform crystal. The leaky wave arises from a bulk wave with the group velocity parallel to the plane which becomes later the interface between the halves of the crystal and the layer. In Ref. 8 the authors investigated the case in which a thin solid layer is sandwiched between two piezoelectrics with contrarily directed polar axes. The leaky wave originates then from the shear interfacial wave which exists in this ''domain'' structure in the absence of the layer.[9,10]

I. PRELIMINARY REMARKS

We discuss briefly some general relations to be frequently used in this paper. Let a half-infinite anisotropic medium be characterized by the elastic constants C_{ijkl} and the

a)Electronic mail: adar@mechan.incr.msk.su

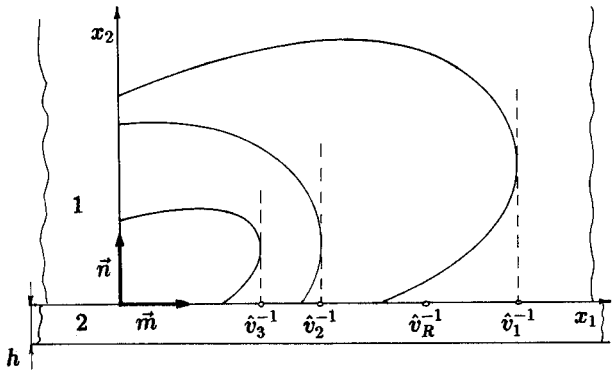

FIG. 1. Geometry of the problem; 1—crystal, 2—layer. Cross sections (one fourth) of the slowness surfaces of bulk modes in the crystal are shown. Dashed lines are vertical tangents to slowness curves; $\hat{v}_1^{-1}$, $\hat{v}_2^{-1}$, and $\hat{v}_3^{-1}$ are the inverses of the limiting speeds of the slow, intermediate, and fast bulk waves, v_R^{-1} is the inverse of the Rayleigh wave speed.

density ρ. We are concerned with solutions of the boundary-value problem constructed in the form of linear superpositions of plane modes

$$\mathbf{u}_\alpha(\mathbf{r},t)=\mathbf{A}_\alpha e^{ik[x_1+p_\alpha x_2-vt]} \tag{1}$$

which obey the elastodynamic equation of motion

$$\rho\frac{\partial^2 u_i}{\partial t^2}=C_{ijkl}\frac{\partial^2 u_k}{\partial x_j \partial x_l}. \tag{2}$$

In (1) $\mathbf{A}_\alpha$ is the polarization vector of mode α, k is the component of the wave vector along the unit vector $\mathbf{m}$, which lies in the surface specified by the unit inner normal $\mathbf{n}$ (Fig. 1), and v is the trace speed defined as the ratio of the frequency ω to k. The parameter p_α defines the normal component of the wave vector and it can occur either complex (inhomogeneous mode) or real (bulk homogeneous mode) depending on the value of v. Each of the modes in (1) produces on the unit area of the surface $x_2=$const a traction with amplitude $\mathbf{F}_\alpha=-ik\mathbf{L}_\alpha e^{ikp_\alpha x_2}$, where

$$\mathbf{L}_\alpha=-[(nm)+p_\alpha(nn)]\mathbf{A}_\alpha, \tag{3}$$

where the symbols $(nm),(nn)$, etc. denote 3×3 real matrices formed following the convention that for a pair of three-component vectors $\mathbf{a}$ and $\mathbf{b}$ the symbol (ab) designates the matrix with elements

$$(ab)_{ik}=a_j C_{ijkl} b_l, \quad i,j,k,l=1,2,3. \tag{4}$$

By substituting (1) into (2) one can obtain the equation

$$[p_\alpha^2(nn)+p_\alpha\{(nm)+(mn)\}+(mm)-\rho v^2 I]\mathbf{A}_\alpha=0, \tag{5}$$

where $\hat{I}$ is the 3×3 unit matrix. Combining (3) and (5) yields the relation[11,12]

$$\hat{N}\boldsymbol{\xi}_\alpha=p_\alpha\boldsymbol{\xi}_\alpha, \quad \alpha=1,\ldots,6. \tag{6}$$

Here $\hat{N}$ is a 6×6 real matrix,

$$\hat{N}=-\begin{Bmatrix} (nn)^{-1}(nm) & (nn)^{-1} \\ (mn)(nn)^{-1}(nm)-(mm)+\rho v^2\hat{I} & (mn)(nn)^{-1} \end{Bmatrix}, \tag{7}$$

$\boldsymbol{\xi}_\alpha$ is a six-component vector,

$$\boldsymbol{\xi}_\alpha=\begin{pmatrix}\mathbf{A}_\alpha\\ \mathbf{L}_\alpha\end{pmatrix}. \tag{8}$$

Since the matrix $\hat{N}$ satisfies the equality

$$(\hat{T}\hat{N})^t=\hat{T}\hat{N}, \tag{9}$$

where the superscript t means the transposition,

$$\hat{T}=\begin{pmatrix}\hat{O} & \hat{I}\\ \hat{I} & \hat{O}\end{pmatrix}, \tag{10}$$

and $\hat{O}$ is the 3×3 zero matrix, the eigenvectors $\boldsymbol{\xi}_\alpha$ can be introduced in such a way that

$$\boldsymbol{\xi}_\alpha\hat{T}\boldsymbol{\xi}_\beta=\mathbf{A}_\alpha\mathbf{L}_\beta+\mathbf{L}_\alpha\mathbf{A}_\beta=\delta_{\alpha\beta}, \quad \alpha,\beta=1,\ldots,6. \tag{11}$$

Then due to the completeness of the set $\boldsymbol{\xi}_\alpha$, $\alpha=1,\ldots,6$,

$$\sum_{\alpha=1}^{6}\boldsymbol{\xi}_\alpha\otimes\hat{T}\boldsymbol{\xi}_\alpha=\begin{pmatrix}\hat{I} & \hat{O}\\ \hat{O} & \hat{I}\end{pmatrix}, \tag{12}$$

where $\otimes$ signifies dyadic multiplication.[12] For further use we write out an identity which follows straightforward from Eq. (12),

$$\sum_{\alpha=1}^{6}\mathbf{L}_\alpha\otimes\mathbf{L}_\alpha=\hat{O}. \tag{13}$$

We shall consider the first intersonic interval, $\hat{v}_2^{-1}<v^{-1}<\hat{v}_1^{-1}$ in Fig. 1. The limiting speed $\hat{v}_1$ bounds from above the velocity interval where all partial modes (1) occur inhomogeneous. The limiting speed $\hat{v}_2$ is the lower border of the region in which there are at least four bulk partial modes. A ''supersonic'' Rayleigh wave exists only in the first intersonic interval and normally it involves two inhomogeneous modes (see Ref. 13 and also Refs. 3–5). Exclusions, i.e., one-component surface waves, can arise, but under very specific conditions.[14] These special cases demand a separate discussion which is out of the scope of the present paper.

Within the range $\hat{v}_1<v<\hat{v}_2$ there are two bulk partial solutions of Eq. (2) to which we assign the subscripts $\alpha=i$ (incident) and $\alpha=r$ (reflected) and four inhomogeneous ones, $\alpha=2,3,5,6$. The parameters p_α, $\alpha=2,3,5,6$, occur in complex conjugate pairs and we set

$$p_{\alpha+3}=p_\alpha^*, \quad \mathrm{Im}(p_\alpha)>0, \quad \boldsymbol{\xi}_{\alpha+3}=\boldsymbol{\xi}_\alpha^*, \quad \alpha=2,3. \tag{14}$$

The asterisk means complex conjugation. All the vectors $\boldsymbol{\xi}_\alpha$, $\alpha=i,r,2,3,5,6$, are assumed to satisfy Eq. (11). The vectors $\boldsymbol{\xi}_i$ and $\boldsymbol{\xi}_r$ turn out then to be purely real and imaginary, respectively,[13]

$$\boldsymbol{\xi}_i=\boldsymbol{\xi}_i^*, \quad \boldsymbol{\xi}_r=-\boldsymbol{\xi}_r^*. \tag{15}$$

Consider a number of relations in which the tractions $\mathbf{L}_\alpha$ can satisfy. Generally only four three-component vectors $\mathbf{L}_\alpha$, $\alpha=i,r,2,3$, are linearly dependent,

$$\sum_{\alpha=r,2,3}b_\alpha(v)\mathbf{L}_\alpha+f_R(v)\mathbf{L}_i=0, \tag{16}$$

$$f_R(v)=[\mathbf{L}_r\mathbf{L}_2\mathbf{L}_3], \tag{17}$$

$$b_r(v)=[\mathbf{L}_i\mathbf{L}_3\mathbf{L}_2],\quad b_2(v)=[\mathbf{L}_r\mathbf{L}_3\mathbf{L}_i],$$
$$b_3(v)=[\mathbf{L}_r\mathbf{L}_i\mathbf{L}_2], \tag{18}$$

and the brackets $[\ldots]$ denote the scalar triple product of the enclosed vectors. Accordingly, the linear superposition of the modes $\alpha=i,r,2,3$ with coefficients (17) and (18) represents the general solution of the reflection problem on the free surface. Meanwhile, employing Eqs. (11), (13)–(15) one can prove that at a real velocity v_R, $\hat{v}_1<v_R<\hat{v}_2$, satisfying the equation

$$f_R(v)=0, \tag{19}$$

$\mathbf{L}_2,\mathbf{L}_3$ and $\mathbf{L}_i,\mathbf{L}_r$ become pairwise collinear and then the relations

$$\mathbf{L}_2+B_S\mathbf{L}_3=0,\quad B_S=\pm i, \tag{20}$$

$$\mathbf{L}_i+B_r\mathbf{L}_r=0,\quad B_r=\pm i \tag{21}$$

are valid.[13] Equations (20) and (21) show that at $v=v_R$ there emerges a ''supersonic'' Rayleigh solution, which involves modes $\alpha=2,3$, and that, in parallel, there is a two-partial solution of the reflection problem (the simple reflection) at the same speed.[13,15] The signs of B_S, B_r depend on common signs of $\mathbf{A}_\alpha$, $\mathbf{L}_\alpha$, which are not determined by the normalization condition (11), so that B_S and B_r need not be equal.

Let us multiply Eq. (13) by the vector $\mathbf{L}_r\times\mathbf{L}_3^*$, where the symbol $\times$ designates the vector product. Due to (14) and (15) we obtain a useful relation,

$$\sum_{\alpha=i,2,3} d_\alpha(v)\mathbf{L}_\alpha+f_R^*(v)\mathbf{L}_2^*=0, \tag{22}$$

$$d_\alpha(v)=[\mathbf{L}_r\mathbf{L}_3^*\mathbf{L}_\alpha],\quad \alpha=i,2,3. \tag{23}$$

Note that in view of (21) $d_i(v_R)=0$ while, as can be proved with the help of Eq. (11), $d_\alpha(v_R)$, $\alpha=2,3$, are not ever equal to zero.

In subsequent evaluations the necessity of computing derivatives of a number of functions, of $f_R(v)$ (17) in particular, with respect to the speed v at the point $v=v_R$ arises. In deriving the required expressions it is expedient to represent the derivatives $\partial^n\boldsymbol{\xi}_\alpha/\partial v^n$ and $\partial^n\mathbf{L}_\alpha/\partial v^n$ as follows:

$$\frac{\partial^n\boldsymbol{\xi}_\alpha}{\partial v^n}=\hat{D}^{(n)}\boldsymbol{\xi}_\alpha=\sum_{\beta=1}^{6}(\hat{D}^{(n)})_{\beta\alpha}\boldsymbol{\xi}_\beta,$$
$$\frac{\partial^n\mathbf{L}_\alpha}{\partial v^n}=\sum_{\beta=1}^{6}(\hat{D}^{(n)})_{\beta\alpha}\mathbf{L}_\beta, \tag{24}$$

where $\hat{D}^{(n)}$ are real matrices (see Appendix A) and, because of Eq. (11),

$$\hat{D}^{(n)}=\sum_{\alpha,\beta=1}^{6}(\hat{D}^{(n)})_{\beta\alpha}\boldsymbol{\xi}_\beta\otimes\hat{T}\boldsymbol{\xi}_\alpha,$$
$$(\hat{D}^{(n)})_{\beta\alpha}=(\boldsymbol{\xi}_\beta\hat{T}\hat{D}^{(n)}\boldsymbol{\xi}_\alpha). \tag{25}$$

We remark here that the following notations will be used henceforth: $(\hat{Q})_{\alpha\beta}$ signifies the contraction of a 6×6 matrix $\hat{Q}$ being multiplied from the right-hand side by matrix $\hat{T}$ (10) with vectors $\boldsymbol{\xi}_\alpha$, $\boldsymbol{\xi}_\beta$; the symbol $(\hat{Q})_{AB}$ with capital Latin letters as subscripts denotes the contraction of $\hat{T}\hat{Q}$ with vectors $\mathbf{A}$, $\mathbf{B}$,

$$(\hat{Q})_{\alpha\beta}=(\boldsymbol{\xi}_\alpha\hat{T}\hat{Q}\boldsymbol{\xi}_\beta),\quad (\hat{Q})_{AB}=(\mathbf{A}\hat{T}\hat{Q}\mathbf{B}). \tag{26}$$

The symbols of type $(\hat{Q})_{\alpha^*\beta}$, $(\hat{Q})_{A^*B}$ stand for contractions (26) in which vectors $\boldsymbol{\xi}_\alpha^*$, $\mathbf{A}^*$ are involved, respectively.

In view of Eqs. (24), (14)–(23), and (A1) the expressions for the derivatives $\partial f_R/\partial v_R$ and $\partial^2 f_R/\partial v_R^2$ of function (17) at the point $v=v_R$ become

$$\frac{\partial f_R}{\partial v_R}=d_2^*(v_R)(\hat{D}^{(1)})_{S^*S}, \tag{27}$$

$$\frac{\partial^2 f_R}{\partial v_R^2}=d_2^*(v_R)\{\Xi^{(2)}-2B_r(\hat{D}^{(1)})_{ir}(\hat{D}^{(1)})_{S^*S}\}, \tag{28}$$

where

$$\Xi^{(2)}=(\hat{D}^{(2)})_{S^*S}-(\hat{D}^{(2)})_{SS^*}+0.5[(\hat{D}^{(1)})_{SR}(\hat{D}^{(1)})_{S^*P}$$
$$-(\hat{D}^{(1)})_{S^*R}(\hat{D}^{(1)})_{SP}]$$
$$-\sum_{\alpha=2,3}[(\hat{D}^{(1)})_{S^*\alpha^*}(\hat{D}^{(1)})_{S\alpha^*}$$
$$-(\hat{D}^{(1)})_{S^*\alpha}(\hat{D}^{(1)})_{S\alpha}]-|(\hat{D}^{(1)})_{SR}|^2. \tag{29}$$

Vectors $\mathbf{S}$, $\mathbf{R}$, and $\mathbf{P}$ involved in the contractions are introduced as follows:

$$\mathbf{S}=\boldsymbol{\xi}_2+B_S\boldsymbol{\xi}_3=\begin{pmatrix}\mathbf{A}_S\\ \mathbf{0}\end{pmatrix},\quad \mathbf{R}=\boldsymbol{\xi}_i+B_r\boldsymbol{\xi}_r=\begin{pmatrix}\mathbf{A}_R\\ \mathbf{0}\end{pmatrix},$$
$$\mathbf{P}=\boldsymbol{\xi}_i-B_r\boldsymbol{\xi}_r. \tag{30}$$

Here $\mathbf{A}_S$ and $\mathbf{A}_R$ are the polarization vectors of the wave fields associated with the Rayleigh wave and with the simple reflection at the point $v=v_R$, respectively. Note that generally neither the ''polarization'' nor ''traction'' parts of vector $\mathbf{P}$ are equal to zero and also that due to Eq. (15) vectors $\mathbf{R}$, $\mathbf{P}$ are real. Explicit expressions for contractions $(\hat{D}^{(1)})_{\alpha\beta}$ and $(\hat{D}^{(2)})_{\alpha\beta}$ as well as for derivatives of some other functions are given in Appendix A.

II. THE LEAKY WAVE AND RESONANCE FEATURES OF REFLECTION

We assume that a solid layer is placed on the surface of a crystal and perfect rigid contact between them is provided (Fig. 1). The second face of the layer, $x_2=-h$, remains mechanically free. Both the crystal and the layer are taken to have arbitrary anisotropy. Bear in mind that on the mechanically free surface of the crystal there exists a ''supersonic'' Rayleigh wave propagating along $\mathbf{m}$ with speed v_R.

As will be seen below, generally a ''supersonic'' Rayleigh wave transforms into a leaky wave in the presence of a foreign layer on the surface. The wave field associated with the leaky solution in the crystal is constructed from the inhomogeneous modes $\alpha=2,3$ and the reflected mode $\alpha=r$. The energy flux of the latter is directed into the bulk of the

crystal so that the leaky solution attenuates because of the radiation and accordingly its speed v_l turns out to be complex,

$$v_l = v_l' - iv_l'', \quad v_l'' > 0, \tag{31}$$

the imaginary component v_l'' and the difference $v_l' - v_R$ being controlled by the parameter $k_R h$, where $k_R = \omega / v_R$ is the wave number of the Rayleigh wave.

In what follows, in the course of solving the reflection problem we shall derive an equation defining the leaky wave speed v_l and, letting the parameter $k_R h$ be small, $k_R h \ll 1$, approximately find v_l as well as the amplitudes of the modes involved in the leaky wave in the crystal. Afterward, we shall turn back to the reflection problem and analyze the behavior of the coefficients of mode conversion at the angles of incidence which provide closeness of the trace speed v of the incident wave to the real part v_l' of the leaky wave speed.

Consider reflection of the wave $\alpha = i$ from the crystal–layer interface. The wave fields in the crystal, $\mathbf{u}(\mathbf{r},t)$, and in the layer, $\mathbf{u}^{(f)}(\mathbf{r},t)$, are sought in the form

$$\mathbf{u}(\mathbf{r},t) = \sum_{\alpha = i,r,2,3} b_\alpha' \mathbf{A}_\alpha e^{ik[x_1 + p_\alpha x_2 - vt]}, \tag{32}$$

$$\mathbf{u}^{(f)}(\mathbf{r},t) = \sum_{\alpha=1}^{6} b_\alpha^{(f)} \mathbf{A}_\alpha^{(f)} e^{ik[x_1 + p_\alpha^{(f)} x_2 - vt]} \tag{33}$$

subject to the boundary conditions

$$\sum_{\alpha=1}^{6} b_\alpha^{(f)} \boldsymbol{\xi}_\alpha^{(f)} = \sum_{\alpha = i,r,2,3} b_\alpha' \boldsymbol{\xi}_\alpha, \quad x_2 = 0, \tag{34}$$

$$\sum_{\alpha=1}^{6} b_\alpha^{(f)} \mathbf{L}_\alpha^{(f)} e^{-ikp_\alpha^{(f)} h} = 0, \quad x_2 = -h, \tag{35}$$

where b_α', $b_\alpha^{(f)}$ are the coefficients to be found and the superscript (f) is assigned to the parameters of the partial modes in the film. Notice that the equation upon the leaky wave speed is

$$b_i'(v,h) = 0 \tag{36}$$

because (36) is none other than the condition for the incident wave to be excluded from a solution of the boundary-value problem. Hence, to find v_l, one should first of all derive a general expression for $b_i'(v,h)$.

Equation (35) implies that the ''traction'' components of the vector

$$\boldsymbol{\xi}^{(f)}(-h) = \sum_{\alpha=1}^{6} b_\alpha^{(f)} \boldsymbol{\xi}_\alpha^{(f)} e^{-ikp_\alpha^{(f)} h}, \tag{37}$$

vanish. Due to Eq. (34) and the relation $\hat{N}^{(f)} \boldsymbol{\xi}_\alpha^{(f)} = p_\alpha^{(f)} \boldsymbol{\xi}_\alpha^{(f)}$, $\alpha = 1, \ldots, 6$, where $\hat{N}^{(f)}$ is the matrix (7) for the layer, $\boldsymbol{\xi}^{(f)}(-h)$ is equal to

$$\boldsymbol{\xi}^{(f)}(-h) = e^{-ikh\hat{N}^{(f)}} \left(\sum_{\alpha=1}^{6} b_\alpha^{(f)} \boldsymbol{\xi}_\alpha^{(f)} \right) = \sum_{\alpha = i,r,2,3} b_\alpha' \boldsymbol{\xi}_\alpha', \tag{38}$$

$$\boldsymbol{\xi}_\alpha' = e^{-ikh\hat{N}^{(f)}} \boldsymbol{\xi}_\alpha, \quad \alpha = i,r,2,3. \tag{39}$$

Hence, Eq. (35) reduces to the condition

$$\sum_{\alpha = i,r,2,3} b_\alpha' \mathbf{L}_\alpha' = 0, \tag{40}$$

where $\mathbf{L}_\alpha'$ is the traction ''part'' of the vector $\boldsymbol{\xi}_\alpha'$, and we find to within an ambiguity of a common constant $b_i'(v,h)$ and, in parallel, $b_\alpha'(v,h)$, $\alpha = r,2,3$,

$$b_i'(v,h) = [\mathbf{L}_r' \mathbf{L}_2' \mathbf{L}_3'], \tag{41}$$

$$b_r'(v,h) = [\mathbf{L}_i' \mathbf{L}_3' \mathbf{L}_2'], \quad b_2'(v,h) = [\mathbf{L}_r' \mathbf{L}_3' \mathbf{L}_i'], \quad b_3'(v,h) = [\mathbf{L}_r' \mathbf{L}_i' \mathbf{L}_2']. \tag{42}$$

We now estimate the leaky wave speed v_l and let $k_R h \ll 1$. It is natural to look for v_l in the form of an expansion in powers of $k_R h$, the zero-order term being v_R because $b_i'(v,0) \equiv f_R(v)$. In calculations allowance will be made for the linear and quadratic terms in $k_R h$ since it appears that the imaginary component v_l'' has the order $(k_R h)^2$.

As a starting point we derive an appropriate approximate expression for $b_i'(v,h)$. Equation (11) enables one to represent the vectors $\boldsymbol{\xi}_\alpha'$ in the form

$$\boldsymbol{\xi}_\alpha' = \sum_\beta \left(e^{-ikh\hat{N}^{(f)}} \right)_{\beta\alpha} \boldsymbol{\xi}_\beta = \boldsymbol{\xi}_\alpha - ikh\boldsymbol{\xi}_\alpha^{(1)} - 0.5(kh)^2 \boldsymbol{\xi}_\alpha^{(2)} + \ldots, \tag{43}$$

$$\boldsymbol{\xi}_\alpha^{(n)} = \sum_\beta \left(\{\hat{N}^{(f)}\}^n \right)_{\beta\alpha} \boldsymbol{\xi}_\beta, \quad n = 1,2, \ldots, \tag{44}$$

and then

$$\mathbf{L}_\alpha' = \mathbf{L}_\alpha - ikh\mathbf{L}_\alpha^{(1)} - 0.5(kh)^2 \mathbf{L}_\alpha^{(2)} + \ldots, \tag{45}$$

$$\mathbf{L}_\alpha^{(n)} = \sum_\beta \left(\{\hat{N}^{(f)}\}^n \right)_{\beta\alpha} \mathbf{L}_\beta, \quad n = 1,2, \ldots . \tag{46}$$

Summation is carried out over $\beta = i,r,2,3,5,6$. The symbol $\{\hat{N}^{(f)}\}^n$ stands for the matrix $\hat{N}^{(f)}$ in power n.

After substitution of Eq. (45) in $b_i'(v,h)$ (36) one obtains

$$b_i'(v,h) \approx f_R(v) - ikh f_1'(v) - (k_R h)^2 f_2'(v_R), \tag{47}$$

where $f_R(v)$ is the function (17),

$$f_1'(v) = [\mathbf{L}_r^{(1)} \mathbf{L}_2 \mathbf{L}_3] + [\mathbf{L}_r \mathbf{L}_2^{(1)} \mathbf{L}_3] + [\mathbf{L}_r \mathbf{L}_2 \mathbf{L}_3^{(1)}], \tag{48}$$

$$f_2'(v_R) = [\mathbf{L}_r^{(1)} \mathbf{L}_2^{(1)} \mathbf{L}_3] + [\mathbf{L}_r^{(1)} \mathbf{L}_2 \mathbf{L}_3^{(1)}] + [\mathbf{L}_r \mathbf{L}_2^{(1)} \mathbf{L}_3^{(1)}] + 0.5\{[\mathbf{L}_r \mathbf{L}_2^{(2)} \mathbf{L}_3] + [\mathbf{L}_r \mathbf{L}_2 \mathbf{L}_3^{(2)}]\}. \tag{49}$$

The velocity dependence is kept in $khf_1'(v)$ while we have set $v = v_R$ in the third term in Eq. (47).

The function $f_1'(v)$ can be simplified by eliminating a number of terms which yield the contribution of an order higher than $(k_R h)^2$ in v_l. Replacing the $\mathbf{L}_\alpha^{(1)}$'s in (48) by (46) and using Eqs. (14)–(23) provides

$$f_1'(v) = f_1(v) + \Xi'(v) f_R(v) + \Delta(v). \tag{50}$$

In (50) $f_1(v) = (\hat{N}^{(f)})_{J*J} / d_2(v)$, the vector $\mathbf{J}(v)$ is defined in Appendix A,

$$\Xi'(v)=\sum_{\alpha=r,2,3}(\hat{N}^{(f)})_{\alpha\alpha}-\frac{b_r(v)}{f_R(v)}(\hat{N}^{(f)})_{ir}+\frac{1}{d_2(v)}\left\{\frac{d_i^*(v)}{f_R(v)}(\hat{N}^{(f)})_{iJ}+\frac{d_i(v)}{f_R(v)}\times[a_2(v)(\hat{N}^{(f)})_{2*r}+a_3(v)(\hat{N}^{(f)})_{3*r}]\right\}, \quad (51)$$

where $a_\alpha(v)=[\mathbf{L}_i\mathbf{L}_\alpha^*\mathbf{L}_3]$, $\alpha=2,3$, and

$$\Delta(v)=\frac{1}{d_2(v)}\{[(\hat{N}^{(f)})_{3*r}a(v)-(\hat{N}^{(f)})_{i3}b_3^*(v)]f_R^*(v)-(\hat{N}^{(f)})_{2*3}b_3^*(v)d_i(v)+(\hat{N}^{(f)})_{3*3}\times[d_i^2(v)+[f_R^*(v)]^2]\} \quad (52)$$

with $a(v)=[\mathbf{L}_3\mathbf{L}_2^*\mathbf{L}_3^*]$. In view of Eqs. (20) and (21) $d_i(v_R)=b_3(v_R)=a(v_R)=0$ while $d_2(v_R)\neq 0$ so that near v_R the function $\Delta(v)$ behaves as $(v-v_R)^2$. Disregarding $\Delta(v)$ and setting $v=v_R$ in $\Xi'(v)$ we obtain

$$f_1'(v)\approx f_1(v)+\Xi'(v_R)f_R(v), \quad (53)$$

where, accounting for the relation $a_\alpha(v_R)=-B_rd_\alpha^*(v_R)$ and Eq. (A9),

$$\Xi'(v_R)=\sum_{\alpha=r,2,3}(\hat{N}^{(f)})_{\alpha\alpha}-B_r(\hat{N}^{(f)})_{ir}+\frac{1}{(\hat{D}^{(1)})_{S*S}}\{(\hat{D}^{(1)})_{S*R}(\hat{N}^{(f)})_{iS}-B_r(\hat{D}^{(1)})_{SR}(\hat{N}^{(f)})_{S*r}\}. \quad (54)$$

Further, we substitute (53) for $f_1'(v)$ in Eq. (47) and retain in (47) only the terms which will yield the corrections of order k_Rh and $(k_Rh)^2$ to v_R. The result is

$$b_i'(v,h)\approx\frac{\partial f_R}{\partial v_R}(v-v_R)-ik_Rhf_1(v_R)+0.5\frac{\partial^2 f_R}{\partial v_R^2}\times(v-v_R)^2+ik_Rh\left\{\frac{f_1(v_R)}{v_R}-\frac{\partial f_1}{\partial v_R}\right\}(v-v_R)-(k_Rh)^2f_2(v_R), \quad (55)$$

where

$$f_1(v_R)=d_2^*(v_R)(\hat{N}^{(f)})_{S*S}, \quad (56)$$

since in view of Eqs. (20), (21), (23), and (30) $\mathbf{J}(v_R)=d_2(v_R)\mathbf{S}$, and $f_2(v_R)=f_2'(v_R)-f_1(v_R)\Xi'(v_R)$. To calculate $f_2(v_R)$, we evaluate first $f_2'(v_R)$ (49) with the aid of Eqs. (46), (20), (21), and the relations

$$(\hat{N}^{(f)})_{\alpha\beta}=(\hat{N}^{(f)})_{\beta\alpha}, \quad (57)$$

$$(\{\hat{N}^{(f)}\}^2)_{\alpha\beta}=\sum_{\gamma=i,r,2,3,5,6}(\hat{N}^{(f)})_{\alpha\gamma}(\hat{N}^{(f)})_{\gamma\beta} \quad (58)$$

which follow from (9) and (12). Taking into account Eqs. (54) and (56) and grouping addends lead then to

$$f_2(v_R)=0.5d_2^*(v_R)\left\{|(\hat{N}^{(f)})_{SR}|^2+0.5[(\hat{N}^{(f)})_{S*R}(\hat{N}^{(f)})_{SP}-(\hat{N}^{(f)})_{SR}(\hat{N}^{(f)})_{S*P}]-\frac{2(\hat{N}^{(f)})_{S*S}}{(\hat{D}^{(1)})_{S*S}}\{(\hat{D}^{(1)})_{S*R}(\hat{N}^{(f)})_{iS}-B_r(\hat{D}^{(1)})_{SR}(\hat{N}^{(f)})_{S*r}\}+\sum_{\alpha=2,3}[(\hat{N}^{(f)})_{S*\alpha*}\times(\hat{N}^{(f)})_{S\alpha*}-(\hat{N}^{(f)})_{S*\alpha}(\hat{N}^{(f)})_{S\alpha}]\right\}. \quad (59)$$

Thus one has an approximate equation, Eq. (55), which allows the root of Eq. (36) to be found with accuracy $(k_Rh)^2$. We substitute

$$v=v_l\approx v_R+(k_Rh)v_1+(k_Rh)^2v_2 \quad (60)$$

into (55) and, on equating the coefficients at k_Rh and $(k_Rh)^2$ to zero, we get

$$v_1=i\frac{f_1(v_R)}{\partial f_R/\partial v_R}, \quad (61)$$

$$v_2=\frac{1}{\partial f_R/\partial v_R}\left\{iv_1\frac{\partial f_1}{\partial v_R}-v_1^2\left[0.5\frac{\partial^2 f_R}{\partial v_R^2}+\frac{1}{v_R}\frac{\partial f_R}{\partial v_R}\right]+f_2(v_R)\right\}. \quad (62)$$

It remains to introduce Eqs. (27), (28), (56), (59), and (A10) into (61) and (62) and again group addends. Manipulations yield

$$v_1=\frac{i(\hat{N}^{(f)})_{S*S}}{(\hat{D}^{(1)})_{S*S}}, \quad v_2=\Xi+\frac{|(\hat{N}_g)_{SR}|^2}{2(\hat{D}^{(1)})_{S*S}}, \quad (63)$$

where

$$\Xi=-\frac{v_1^2}{v_R}+\frac{1}{2(\hat{D}^{(1)})_{S*S}}\left\{v_1[(\hat{D}_g)_{S*S}-(\hat{D}_g^*)_{SS*}-4i\rho^{(f)}v_R|\mathbf{A}_S|^2]+0.5[(\hat{N}_g^*)_{S*R}(\hat{N}_g)_{SP}-(\hat{N}_g)_{SR}(\hat{N}_g^*)_{S*P}]+\sum_{\alpha=2,3}[(\hat{N}_g^*)_{S*\alpha*}(\hat{N}_g^*)_{\alpha*S}-(\hat{N}_g)_{S\alpha}(\hat{N}_g)_{\alpha S*}]\right\}, \quad (64)$$

and $\hat{N}_g=\hat{N}^{(f)}-iv_1\hat{D}^{(1)}$, $\hat{D}_g=i\hat{N}^{(f)}\hat{D}^{(1)}-v_1\hat{D}^{(2)}$, the matrices $\hat{N}_g^*$, $\hat{D}_g^*$ are complex conjugates of the matrices $\hat{N}_g$, $\hat{D}_g$ respectively, $\rho^{(f)}$ is the density of the layer, and $\mathbf{A}_S$ is the ''polarization'' part of the vector $\mathbf{S}$ (30).

To separate the real and imaginary parts of v_l, we use Eqs. (A6) and (57). By (A6) the value of $(\hat{D}^{(1)})_{S*S}$ is purely imaginary while due to (57) $(\hat{N}^{(f)})_{S*S}$ has a purely real value. Therefore the linear correction v_1 is purely real. In contrast, v_2 occurs complex. The first term in v_2 is real and

the second one is imaginary. To summarize, the real part v_l' and the imaginary component v_l'' of the leaky wave speed v_l (31) take on the form

$$v_l' \approx v_R + (k_R h) v_1 + (k_R h)^2 \Xi, \quad v_l'' \approx \frac{i|(\hat{N}_g)_{SR}|^2}{2(\hat{D}^{(1)})_{S*S}} (k_R h)^2. \tag{65}$$

Using (A6), the value of $i/(\hat{D}^{(1)})_{S*S}$ is positive definite and, hence, as it should be, $v_l'' \neq 0$ always occurs positive.

From Eq. (30) it follows that the contraction $(\hat{N}_g)_{SR}$ is of the form

$$(\hat{N}_g)_{SR} = (\mathbf{A}_S \hat{X}^{(f)} \mathbf{A}_R) - i v_1 (\mathbf{A}_S \hat{D}_{21}^{(1)} \mathbf{A}_R), \tag{66}$$

where $\hat{X}^{(f)}$ is the 3×3 bottom left-hand block of the matrix (7) of the layer and $\hat{D}_{21}^{(1)}$ is the 3×3 bottom left-hand block of the matrix $\hat{D}^{(1)}$. Accordingly, with regard to (66) one can say that the leakage, $v_l'' \neq 0$, arises owing to the ''mixing'' of the displacements associated with the Rayleigh wave, $\mathbf{A}_S$, and with the simple reflection, $\mathbf{A}_R$, see (30). The examination of Eq. (66) allows one to conjecture that if the plane $(\mathbf{n},\mathbf{m})$ has a generic orientation (the case of a ''nonsymmetric'' Rayleigh wave), then the presence of any foreign layer, whether anisotropic or isotropic, generally should result in the transformation of a purely surface wave into a leaky one.

A different situation takes place if the plane $(\mathbf{n},\mathbf{m})$ is a plane of symmetry of the crystal. In this case the inhomogeneous modes $\alpha = 2,3$ from which the ''supersonic'' surface wave is constructed are in-plane polarized while the bulk modes $\alpha = i,r$ are out-of-plane polarized (shear horizontal polarized modes), i.e. $\mathbf{A}_2$, $\mathbf{A}_3 \perp \mathbf{A}_i$, $\mathbf{A}_r$. From (A2) it follows that $(\hat{D}^{(1)})_{SR} = 0$ and then $(\hat{N}_g)_{SR} = (\mathbf{A}_S \hat{X}^{(f)} \mathbf{A}_R)$ so that the magnitude of v_l'' is determined only by those elements of $\hat{N}^{(f)}$ which couple in-plane and out-of -plane vibrations in the film. Therefore we conclude that a ''symmetric'' Rayleigh wave transforms into a leaky wave, providing the layer first is anisotropic and second is positioned such that its plane of symmetry does not coincide with the sagittal plane of the Rayleigh wave. Note also that if the layer and the crystal are identical, $\hat{N}^{(f)} \equiv \hat{N}$, i.e. the boundary of the crystal is ''moved'' to the distance h, then via Eq. (11) we naturally obtain $v_1 = v_2 = 0$.

Let us find the amplitudes of modes $\alpha = r,2,3$ with which they are incorporated in the leaky wave. It can be shown (see Appendix B) that function $b_r'(v,h)$ (42) vanishes at $v = v_l^*$. Therefore, due to (27)

$$b_r'(v,h) \approx \frac{\partial b_r'}{\partial v}(v - v_l^*) \approx \frac{\partial b_r}{\partial v_R}(v - v_l^*) = d_2^*(v_R) B_r (\hat{D}^{(1)})_{S*S} (v - v_l^*), \tag{67}$$

since by virtue of (17) and (21) $\partial b_r / \partial v_R = B_r \partial f_R / \partial v_R$, and then

$$b_r'(v_l,h) \approx -2 i v_l'' d_2^*(v_R) B_r (\hat{D}^{(1)})_{S*S} \approx d_2^*(v_R) B_r |(\hat{N}^{(f)})_{SR}|^2 (k_R h)^2. \tag{68}$$

Note that Eq. (67) can also be derived through calculations of types (47)–(63). Further, one can approximate $b_\alpha'(v,h)$, $\alpha = 2,3$, (42) in the neighborhood of v_R of order $k_R h$ as

$$b_\alpha'(v,h) \approx \frac{\partial b_\alpha'}{\partial v_R}(v - v_R) + \frac{\partial b_\alpha'}{\partial (k_R h)} k_R h, \quad \alpha = 2,3. \tag{69}$$

Using Eqs. (24) and (45) to find derivatives of $b_\alpha'(v,h)$ we obtain

$$\frac{\partial b_2'}{\partial v_R} = -B_S \frac{\partial b_3'}{\partial v_R} = -d_2^*(v_R)(\hat{D}^{(1)})_{S*R}, \quad \frac{\partial b_2'}{\partial (k_R h)} = -B_S \frac{\partial b_3'}{\partial (k_R h)} = -d_2^*(v_R)(\hat{N}^{(f)})_{S*R}, \tag{70}$$

so that

$$b_2'(v,h) \approx -B_S b_3'(v,h) \approx -d_2^*(v_R)\{(\hat{D}^{(1)})_{S*R}(v - v_R) + (\hat{N}^{(f)})_{S*R} k_R h\} \approx -d_2^*(v_R)\{(\hat{D}^{(1)})_{S*R}(v - v_l) + (\hat{N}_g)_{S*R} k_R h\}. \tag{71}$$

Accordingly, at $v = v_l$

$$b_2'(v_l,h) \approx -B_S b_3'(v_l,h) \approx -d_2^*(v_R)(\hat{N}_g)_{S*R} k_R h \tag{72}$$

and omitting a common multiplier in (68) and (72) we have

$$b_2'(v_l,h) \approx 1, \quad b_3'(v_l,h) \approx B_S, \quad b_r'(v_l,h) \approx -B_r (\hat{N}_g)_{SR} k_R h. \tag{73}$$

It is seen that within the accuracy used the leaky wave represents the Rayleigh wave to which the reflected mode $\alpha = r$ is added with small amplitude.

Consider now the behavior of the reflection coefficient $R(v,h)$ and the coefficients of excitation of modes $\alpha = 2,3$, $T_\alpha(v,h)$ at v close to the real part v_l' of the leaky wave speed. Since $b_i'(v_l,h) = 0$,

$$b_i'(v,h) \approx \frac{\partial b_i'}{\partial v}(v - v_l) \approx \frac{\partial f_R}{\partial v_R}(v - v_l) = d_2^*(v_R)(\hat{D}^{(1)})_{S*S}(v - v_l). \tag{74}$$

Correspondingly, by virtue of (67) and (71) in the region of our concern

$$R(v,h) = \frac{b_r'(v,h)}{b_i'(v,h)} \approx B_r \frac{v - v_l^*}{v - v_l}, \quad T_2(v,h) = \frac{b_2'(v,h)}{b_i'(v,h)} \approx -\frac{(\hat{D}^{(1)})_{S*R}}{(\hat{D}^{(1)})_{S*S}} - T^R(v,h), \quad T_3(v,h) = \frac{b_3'(v,h)}{b_i'(v,h)} \approx B_S T_2(v,h), \tag{75}$$

where

$$T^R(v,h)\approx\frac{(\hat{N}_g)_{S*R}k_Rh}{(\hat{D}^{(1)})_{S*S}(v-v_l)}. \tag{76}$$

One sees that the phase

$$\psi_r(v)=2\,\mathrm{cotan}^{-1}\left(\frac{v-v_l'}{v_l''}\right) \tag{77}$$

of coefficient $R(v,h)$ changes by 2π within the interval

$$|v-v_l'|\propto v_l''. \tag{78}$$

The alternating part of the phase of the coefficients $T_\alpha(v,h)$, i.e. the phase of $T^R(v,h)$ equal to $0.5\psi_r(v)$, changes by π and, besides, the magnitude of $T_\alpha(v,h)$ increases abruptly and at $v=v_l'$ reaches the maximum

$$|T_\alpha(v_l',h)|\approx|T^R(v_l',h)|\approx\frac{2}{|(\hat{N}_g)_{SR}|k_Rh}\gg 1, \tag{79}$$

whereas $|T_\alpha(v,h)|\propto 1$ outside the velocity range (78). The value of $|R(v,h)|$ is equal to unity independent of v which is consistent with the law of energy conservation. The latter results in such an identity provided the vectors $\boldsymbol{\xi}_i$, $\boldsymbol{\xi}_r$ obey Eq. (11), see Appendix B.

Accounting for (75) and (76) one can represent the wave field $\mathbf{u}(\mathbf{r},t)$ in the crystal, which corresponds to the reflection of the wave $\alpha=i$ incident with a given amplitude C, as follows:

$$\mathbf{u}(\mathbf{r},t)\approx C\{\mathbf{u}_0(\mathbf{r},t)-T^R(v,h)\mathbf{u}_l(\mathbf{r},t)\}, \tag{80}$$

where

$$\mathbf{u}_0(\mathbf{r},t)=\mathbf{u}_0^B(\mathbf{r},t)-\frac{(\hat{D}^{(1)})_{S*R}}{(\hat{D}^{(1)})_{S*S}}\mathbf{u}_0^S(\mathbf{r},t) \tag{81}$$

with

$$\begin{aligned}\mathbf{u}_0^B(\mathbf{r},t)&=\mathbf{u}_i(\mathbf{r},t)+B_r\mathbf{u}_r(\mathbf{r},t),\\ \mathbf{u}_0^S(\mathbf{r},t)&=\mathbf{u}_2(\mathbf{r},t)+B_S\mathbf{u}_3(\mathbf{r},t)\end{aligned} \tag{82}$$

corresponds to the reflection from the free surface of the crystal in the vicinity of v_R and

$$\mathbf{u}_l(\mathbf{r},t)=\sum_{\alpha=r,2,3}b_\alpha'(v_l,h)\mathbf{u}_\alpha(\mathbf{r},t), \tag{83}$$

where $b_\alpha'(v_l,h)$ are the partial amplitudes (73), almost exactly reproduces the leaky wave and enters $\mathbf{u}(\mathbf{r},t)$ with coefficient $T^R(v,h)$ (76) which exhibits the dependence of a resonance type on v. Hence, a strong difference between, on the one hand, reflection on the free surface as well as on the interface crystal-thin layer outside interval (78) and, on the other hand, reflection within region (78) can be interpreted as a consequence of the resonance excitation of the leaky wave.

Note that the wave $\mathbf{u}_0(\mathbf{r},t)$ is an exact solution of the reflection problem on the free surface at $v=v_R$. It incorporates two-partial combinations, $\mathbf{u}_0^B(\mathbf{r},t)$ and $\mathbf{u}_0^S(\mathbf{r},t)$, both satisfying the boundary conditions, see (20) and (21). In principle any superposition of $\mathbf{u}_0^B(\mathbf{r},t)$ and $\mathbf{u}_0^S(\mathbf{r},t)$ can be treated as a solution of the reflection problem at $v=v_R$ but it is the combination (81) which provides the continuity of $\mathbf{u}_0(\mathbf{r},t)$ at the point $v=v_R$. It should be underlined that in spite of $\mathbf{u}_0^S(\mathbf{r},t)$ describing the Rayleigh wave the reflection on the free surface of the crystal at $v=v_R$ is not of a resonance type and the modes $\alpha=2,3$ just play a role of so-called accompanied surface vibrations as it takes place at an arbitrary v, see, e.g., Ref. 16.

From physical reasons it follows that the interval of values of k_Rh within which Eqs. (75) and (76) are applicable is bounded from below by condition $v_l''\gg v_R''$, where v_R'' is the imaginary component of the speed of the Rayleigh wave which describes its dissipative attenuation. To allow for such losses, it is possible to replace the real quantity v_R by the complex one $v_R=v_R'-iv_R''$ in Eqs. (75) and (76); note that v_l^* in the numerator of $R(v,h)$ becomes $v_l^*=v_l'-i(v_R''-v_l'')$. Then it is seen in particular that because of the absorption of surface vibrations the modulus $|R(v,h)|$ can have a deep narrow minimum and even vanish at $v=v_l'$ provided $v_l''=v_R''$. Besides, with k_Rh decreasing, the resonance magnitude of the coefficients $T_\alpha(v,h)$, $|T_\alpha(v_l',h)|$ increases not up to infinity but up to $[|(\hat{D}^{(1)})_{S*S}|/2v_R'']^{1/2}$ at $v_l''=v_R''$ and afterward it goes down to zero at $k_Rh=0$. Apparently, on the condition that $v_R''\gg v_l''$ the resonance phenomena do not show up.

III. CONCLUSION

The presence of a thin solid layer on the surface of an anisotropic medium can result in the transformation of a ''supersonic'' Rayleigh wave, which exists on the free surface of this medium in the absence of the coating, into a leaky wave. Then in the sagittal plane of such a Rayleigh solution a narrow interval of angles of incidence emerges in which the phase of the reflection coefficient changes abruptly. Moreover, reflection is accompanied by excitation of surface vibrations with amplitudes greatly exceeding the amplitude of the incident wave. The phenomenon appears to be of a resonance nature and is related to the excitation of a leaky intrinsic solution in the crystal–layer structure. The resonant value of the angle of incidence is found from the condition of the equality of the trace speed of the incident wave to the real part v_l' of the leaky wave speed v_l. The width of the resonance interval of the angles of incidence is determined by the value of the imaginary part v_l'' of v_l, v_l'' being small as long as $(k_Rh)^2$ is small. With k_Rh diminishing, the resonance peculiarities of the coefficients of mode conversion become more pronounced but the range of permissible values of k_Rh is bounded from below by the dissipative damping of surface modes. At the same time, weak dissipation results in additional features in the behavior of the coefficients of mode conversion.

Similar resonance effects can also occur on the free surface of the anisotropic media, providing the plane of incidence is deflected from the sagittal plane of the Rayleigh wave.[13,17] The leaky wave arises due to the coupling between inhomogeneous and bulk modes brought about by the characteristic anisotropy of the crystal as long as the angle of deviation is small. Besides, one should mention a well-known situation, which is the reflection of a sound wave incident on an interface liquid–solid from the liquid at the so-called Rayleigh angle, see, e.g., Refs. 1 and 18. However,

the latter is not a complete analog because in this case surface vibrations cannot be excited with amplitudes much greater than the amplitude of the incident wave due to the requirement of continuity of the normal components of the displacements and the law of energy conservation.

Expressions deduced in the present paper allow one to find the leaky wave speed with accuracy $(k_R h)^2$ in terms of parameters of the modes in the crystal and elastic moduli of the coating. Their employment becomes especially convenient for ''symmetric'' Rayleigh waves in crystals of symmetry $m3m$, 432, $m3$, $6mm$, $6/m$, $4/mmm$, $4/m$, mmm, since then there are fairly concise analytical expressions for all involved physical quantities. At the same time the leakage appears only if the layer is elastically anisotropic and oriented ''non-symmetrically.'' If the plane of symmetry of the layer coincides with the sagittal plane of the Rayleigh wave, the latter remains purely localized solution but now its phase speed turns out to be frequency dependent. Equation (65) enables one to find then the surface wave speed to within second-order corrections. As to ''supersonic'' Rayleigh waves of the generic type, generally they should transform into leaky waves in the presence of an arbitrary coating.

The dependence of the resonant angle of incidence on frequency allows one to control the effect by varying the frequency of the incident wave. In particular an acoustic pulse incident on the interface can suffer a significant distortion. The peculiarities of the coefficients of mode conversion result also in strong nonspecular reflection of an acoustic bounded beam. Under resonance conditions there emerges a lateral shift of the reflected beam over a distance of the same order as its width accompanied by considerable distortion of the shape and by a specific distribution of the amplitude of the wave field on the surface.[18–20] Meanwhile the fact that in practice one always deals not with plane waves but with acoustic bounded beams implies one more constraint on the values of $k_R h$. It is simple to understand that the relative width of the resonance interval, v_l''/v_l', should not be much smaller than the angle of divergence of the incident beam, i.e., than $1/k_R W$, where W is the beam width. Otherwise the wave will not ''feel'' the peculiarities of the coefficients of mode conversion, since then only a small portion of the peckium of incident plane waves is discovered to be under resonance conditions.

ACKNOWLEDGMENTS

A. N. Darinskii is grateful to V. I. Alshits and A. L. Shuvalov for fruitful discussions. The work is supported in part by the Fundamental Research Foundation of Russia (Grant No. 95-02-03921-a).

APPENDIX A

Let us prove that matrices $\hat{D}^{(n)}$ (25) are real. As the complex eigenvectors of matrix $\hat{N}$ (7) occur in complex conjugate pairs, by Eq. (24) $\hat{D}^{(n)}\boldsymbol{\xi}_\alpha = \hat{D}^{(n)*}\boldsymbol{\xi}_\alpha$ for any of the six vectors $\boldsymbol{\xi}_\alpha$. Let $\hat{D}^{(n)} \neq \hat{D}^{(n)*}$. Multiplying both sides of Eq. (12) by $\hat{D}^{(n)} - \hat{D}^{(n)*}$ yields then $\hat{O} = \hat{D}^{(n)} - \hat{D}^{(n)*}$; here $\hat{O}$ is the 6×6 zero matrix. Hence, $\hat{D}^{(n)} = \hat{D}^{(n)*}$.

Consider a number of properties of matrices $\hat{D}^{(1)}$ and $\hat{D}^{(2)}$. In view of (11) these matrices obey the equalities

$$(\hat{T}\hat{D}^{(1)})^t = -\hat{T}\hat{D}^{(1)}, \quad (\hat{T}\hat{D}^{(2)})^t + \hat{T}\hat{D}^{(2)} = \hat{T}\{\hat{D}^{(1)}\}^2. \tag{A1}$$

The symbol $\{\hat{D}^{(1)}\}^2$ designates the square of the matrix $\hat{D}^{(1)}$. Applying the perturbation theory to the eigenvalue problem (6) results in the following expressions for the contractions $(\hat{D}^{(1)})_{\alpha\beta}$, $(\hat{D}^{(2)})_{\alpha\beta}$:

$$(\hat{D}^{(1)})_{\alpha\beta} = 2\rho v \frac{\mathbf{A}_\alpha \mathbf{A}_\beta}{p_\alpha - p_\beta}, \quad \beta \neq \alpha, \quad (\hat{D}^{(1)})_{\alpha\alpha} = 0; \tag{A2}$$

$$(\hat{D}^{(2)})_{\alpha\beta} = \frac{2\rho v}{p_\alpha - p_\beta}\left\{ \sum_\gamma \mathbf{A}_\alpha \mathbf{A}_\gamma (\hat{D}^{(1)})_{\gamma\beta} - \mathbf{A}_\beta^2 (\hat{D}^{(1)})_{\alpha\beta} \right\} + \frac{(\hat{D}^{(1)})_{\alpha\beta}}{v}, \quad \beta \neq \alpha, \tag{A3}$$

$$(\hat{D}^{(2)})_{\alpha\alpha} = -0.5 \sum_\gamma (\hat{D}^{(1)})_{\alpha\gamma}^2.$$

By virtue of (A2) and (30) the contraction $(\hat{D}^{(1)})_{S*S}$ takes on the form

$$(\hat{D}^{(1)})_{S*S} = 2\rho v_R \left\{ \frac{|\mathbf{A}_2|^2}{p_2^* - p_2} + \frac{|\mathbf{A}_3|^2}{p_3^* - p_3} + B_S \left[\frac{\mathbf{A}_2^* \mathbf{A}_3}{p_2^* - p_3} - \frac{\mathbf{A}_3^* \mathbf{A}_2}{p_3^* - p_2} \right] \right\}. \tag{A4}$$

On the other hand, Eq. (A4) can be written as

$$(\hat{D}^{(1)})_{S*S} = -\frac{2\rho\omega}{i} \int_0^\infty |\mathbf{A}_2 e^{ikp_2 x_2} + B_S \mathbf{A}_3 e^{ikp_3 x_2}|^2 \, dx_2, \tag{A5}$$

where it is seen that $(\hat{D}^{(1)})_{S*S}$ is a purely imaginary quantity, its imaginary part being positive definite,

$$[(\hat{D}^{(1)})_{S*S}]^* = -(\hat{D}^{(1)})_{S*S}, \qquad \mathrm{Im}[(\hat{D}^{(1)})_{S*S}] = \frac{(\hat{D}^{(1)})_{S*S}}{i} > 0. \tag{A6}$$

One can make use of Eqs. (24) and (14)–(23) to find the fist derivatives of functions $d_\alpha(v)$ (23) at $v = v_R$,

$$\frac{\partial d_i}{\partial v_R} = d_2(v_R)(\hat{D}^{(1)})_{SR}, \tag{A7}$$

$$\frac{\partial d_\alpha}{\partial v_R} = d_\alpha(v_R)\{B_S[(\hat{D}^{(1)})_{2*3*} - (\hat{D}^{(1)})_{23}] - B_r(\hat{D}^{(1)})_{ir}\}, \quad \alpha = 2,3. \tag{A8}$$

In deriving Eq. (55) it is necessary to compute the values of the functions $b_r(v)/f_R(v)$, $d_r(v)/f_R(v)$, and $d_r^*(v)/f_R(v)$ at $v = v_R$. Since $b_r(v_R) = d_r(v_R) = f_R(v_R) = 0$, due to Eqs. (A7) and (27) and the relation $\partial b_r/\partial v_R = B_r \partial f_R/\partial v_R$ we obtain

$$\frac{b_r(v_R)}{f_R(v_R)}=B_r,\quad \frac{d_i(v_R)}{f_R(v_R)}=\frac{d_2(v_R)}{d_2^*(v_R)}\frac{(\hat{D}^{(1)})_{SR}}{(\hat{D}^{(1)})_{S*S}},$$
$$\frac{d_i^*(v_R)}{f_R(v_R)}=\frac{(\hat{D}^{(1)})_{S*R}}{(\hat{D}^{(1)})_{S*S}}. \tag{A9}$$

Let us write out an expression for the derivative $\partial\mathbf{J}/\partial v_R$ the vector $\mathbf{J}(v)=d_2(v)\boldsymbol{\xi}_2(v)+d_3(v)\boldsymbol{\xi}_3(v)$. Taking into account (A8) and the relation $\mathbf{J}(v_R)=d_2(v_R)\mathbf{S}$ yields $\partial\mathbf{J}/\partial v_R=(\partial d_2/\partial v_R)\mathbf{S}+d_2(v_R)\hat{D}^{(1)}\mathbf{S}$. Then, employing Eqs. (A8) and (7), (30), (A1), one can represent the derivative $\partial f_1/\partial v_R$ of the function $f_1(v)$ in (50) as follows:

$$\frac{\partial f_1}{\partial v_R}=\frac{\partial d_2^*}{\partial v_R}(\hat{N}^{(f)})_{S*S}+d_2^*(v_R)\{(\hat{N}^{(f)}\hat{D}^{(1)})_{S*S}$$
$$+(\hat{N}^{(f)}\hat{D}^{(1)})_{SS*}-2\rho^{(f)}v_R|\mathbf{A}_S|^2\}. \tag{A10}$$

APPENDIX B

Here we prove that $b_r'(v_l^*,h)=0$. To this end we introduce vectors $\boldsymbol{\xi}_\alpha'$ (39) and $\boldsymbol{\xi}_\alpha''=e^{ikh\hat{N}^{(f)}}\boldsymbol{\xi}_\alpha$, $\alpha=i,r,2,3,5,6$. It follows from (12) that

$$\sum_{\alpha=i,r,2,3,5,6}\boldsymbol{\xi}_\alpha'\otimes\hat{T}\boldsymbol{\xi}_\alpha''=\begin{pmatrix}\hat{I} & \hat{O}\\ \hat{O} & \hat{I}\end{pmatrix} \tag{B1}$$

and, hence, identity (13) is replaced by

$$\sum_{\alpha=i,r,2,3,5,6}\mathbf{L}_\alpha'\otimes\mathbf{L}_\alpha''=\hat{O}, \tag{B2}$$

where $\mathbf{L}_\alpha''$ is the traction part of the vector $\boldsymbol{\xi}_\alpha''$. Due to (14) and (15) for real v

$$(\mathbf{L}_\alpha'')^*=\mathbf{L}_{\alpha+3}',\quad (\mathbf{L}_\alpha')^*=\mathbf{L}_{\alpha+3}'',\quad \alpha=2,3,$$
$$(\mathbf{L}_i')^*=\mathbf{L}_i'',\quad (\mathbf{L}_r')^*=-\mathbf{L}_r''. \tag{B3}$$

Multiplying (B2) by the vector $\mathbf{L}_r'\times\mathbf{L}_3'$ from the left we obtain at $v=v_l$

$$\sum_{\alpha=i,5,6}[\mathbf{L}_r'\mathbf{L}_3'\mathbf{L}_\alpha']\mathbf{L}_\alpha''=0. \tag{B4}$$

Since $[\mathbf{L}_r'\mathbf{L}_3'\mathbf{L}_\alpha']$, $\alpha=5,6$, at $k_Rh=0$, $v=v_R$ are equal to $-d_\alpha^*(v_R)$, $\alpha=2,3$, Eq. (23), and accordingly do not vanish, by virtue of the continuity of the vectors $\mathbf{L}_\alpha'$ as functions of k_Rh and v, these determinants cannot turn into zero at $v=v_l$ which slightly differs from v_R as long as k_Rh is small. Therefore $\mathbf{L}_\alpha''$, $\alpha=i,5,6$, are linearly dependent at $v=v_l$ and then, by (B3), the vectors $\mathbf{L}_\alpha'$, $\alpha=i,2,3$, fall into linear dependence at $v=v_l^*$, i.e. v_l^* is a root of the equation $b_r'(v,h)=0$. Note that in fact $[\mathbf{L}_r'\mathbf{L}_3'\mathbf{L}_i']$ in (B4) cannot also be equal to zero if v_l is known to be complex. One can show that its vanishing would entail the value of v_l be real and then v_l would correspond not to a leaky but to a purely localized interfacial wave.

Consider that v is real. We can multiply (B2) from the left by the vector $\mathbf{L}_2'\times\mathbf{L}_3'$ and from the right by $\mathbf{L}_5''\times\mathbf{L}_6''$ to obtain

$$[\mathbf{L}_r'\mathbf{L}_2'\mathbf{L}_3'][\mathbf{L}_r''\mathbf{L}_5''\mathbf{L}_6'']+[\mathbf{L}_i'\mathbf{L}_2'\mathbf{L}_3'][\mathbf{L}_i''\mathbf{L}_5''\mathbf{L}_6'']=0. \tag{B5}$$

Accounting for (B3), (41), and (42) we conclude that

$$|b_i'(v,h)|=|b_r'(v,h)| \tag{B6}$$

and, hence, the magnitude of the coefficient of reflection is identically equal to unity. The same takes place on the mechanically free surface.[13] It is of interest to note that (B6) also follows from the law of energy conservation. Indeed, the time averaged normal component $E_{n\alpha}$ of the energy flux of a bulk mode with amplitude b_α' is expressed in terms of vectors (8) as $E_{n\alpha}=-\omega k|b_\alpha'|^2\boldsymbol{\xi}_\alpha\hat{T}\boldsymbol{\xi}_\alpha^*/4$. Due to Eqs. (11) and (15) the equality $E_{ni}+E_{nr}=0$ yields relation (B6).

[1] L. M. Brekhovskikh, *Waves in Layered Media* (Academic, New York, 1980), 2nd ed.
[2] M. Born and E. Wolf, *Principles of Optics* (Macmillan, New York, 1964).
[3] G. W. Farnell, ''Properties of elastic surface waves,'' in *Physical Acoustics*, edited by W. P. Mason and R. N. Thurston (Academic, New York, 1970), pp. 109–166.
[4] S. A. Gundersen, L. Wang, and J. Lothe, ''Secluded supersonic elastic surface waves,'' Wave Motion **14**, 129–143 (1991).
[5] A. A. Maznev and A. G. Every, ''Secluded supersonic surface waves in germanium,'' Phys. Lett. A **197**, 423–427 (1995).
[6] A. N. Darinskii, ''Resonance phenomena in the reflection of an elastic wave at the boundary between a hexagonal crystal and an anisotropic film,'' Zh. Eksp. Teor. Fiz. **107**, 585–598 (1995).
[7] A. N. Darinskii and G. A. Maugin, ''The elastic wave resonance reflection from a thin solid layer in a crystal,'' Wave Motion **23**, 363–385 (1995).
[8] A. N. Darinskii and G. A. Maugin, ''Features of elastic wave reflection in the piezoelectric—thin solid layer—piezoelectric structure,'' Acta Acustica (in press).
[9] C. Maerfield and P. Tournois, ''Pure shear wave guided by the interface of to semi-infinite media,'' Appl. Phys. Lett. **19**, 117–118 (1971).
[10] G. G. Kessenikh, V. N. Lyubimov, and D. G. Sannikov, ''Surface elastopolarization waves at a domain boundaries in a ferroelectric,'' Kristallografiya **17**, 591–594 (1972) [English transl.: Sov. Phys. Crystallogr. **17**, 512–514 (1972)].
[11] A. N. Stroh, ''Steady state problems in anisotropic elasticity,'' J. Math. Phys. (N.Y.) **41**, 77–103 (1962).
[12] P. Chadwick and G. D. Smith, ''Foundation of the theory of surface waves in anisotropic elastic media,'' *Advances Applied Mechanics 17*, edited by C.-S. Yih (Academic, New York, 1977), pp. 303–376.
[13] V. I. Alshits and J. Lothe, ''Comments on the relation between surface wave theory and the theory of reflections,'' Wave Motion **3**, 297–310 (1981).
[14] D. M. Barnett, P. Chadwick, and J. Lothe, ''The behavior of elastic surface waves polarized in a plane of material symmetry. Addendum to part 1,'' Proc. R. Soc. London, Ser. A **433**, 699 (1991).
[15] L. Wang and J. Lothe, ''Simple reflection in anisotropic elastic media and its relation to exceptional waves and supersonic surface waves,'' Wave Motion **16**, 89–112 (1992).
[16] M. K. Balakirev and I. A. Gilinskii, ''Waves in piezoelectrics,'' Novosibirsk: Nauka (1982) (in Russian).
[17] A. N. Darinskii, ''On the theory of leaky waves in crystals,'' Wave Motion **25**, 35–49 (1997).
[18] H. I. Bertoni and T. Tamir, ''Unified theory of Rayleigh-angle phenomena for acoustic beams at liquid–solid interface,'' J. Appl. Phys. **2**, 157–172 (1973).
[19] V. I. Alshits, A. N. Darinskii, R. K. Kotowski, and A. L. Shuvalov, ''Analog of School effect in reflection of acoustic beams from free boundaries of a crystal,'' Kristallografiya **33**, 541–553 (1988) [English transl.: Sov. Phys. Crystallogr. **33**, 318–325 (1988)].
[20] V. I. Alshits, A. N. Darinskii, and A. L. Shuvalov, ''Resonant reflection of 'three-dimensional' acoustic beam from the free boundary of a crystal,'' Kristallografiya **35**, 812–815 (1990).

Lamb waves generated by complex harmonic inhomogeneous plane waves

O. Poncelet and M. Deschamps
Laboratoire de Mécanique Physique, Université Bordeaux I, URA C.N.R.S. No. 867.
351, Cours de la Libération, 33405 Talence Cedex, France

(Received 28 June 1996; accepted for publication 13 February 1997)

This paper presents a theoretical investigation of the generation of Lamb waves inside an immersed plate by complex harmonic inhomogeneous plane waves. Whereas free modes of a fluid-loaded plate are classically assumed to be formed by inhomogeneous plane waves with real frequency (leaky waves), the nature of Lamb waves is searched in this study in terms of combinations of transient inhomogeneous plane waves characterized by a complex slowness vector and a complex frequency. It is shown that dispersion curves of transient Lamb waves (only the frequency is complex) can be very different from the dispersion curves of permanent leaky waves (only the slowness is complex), especially for the A_0 and S_0 modes for which there exists a cut-off frequency beyond which these modes do not exist. In the general case, when both the frequency and the slowness are complex, connections between modes clearly appear from the calculation of dispersion curves. © *1997 Acoustical Society of America.* [S0001-4966(97)03006-3]

PACS numbers: 43.35.Cg [HEB]

INTRODUCTION

Study of guided elastic waves in layered media is of fundamental importance in many areas. The associated basic problem is the plate in vacuum, first inspected by Lamb.[1] Free modes are then characterized by the dispersion curves relating phase velocity of waves within the plate to the frequency. In such a case, the solutions deriving from the resolution of the dispersion equation are real. However, for a plate bounded by media on both sides, the dispersion equation generally exhibits complex solutions.

Free-modes properties of fluid-loaded plates have been studied theoretically in terms of plane waves[2–4] and also in the context of reflection and transmission of bounded beams.[5–7] In those problems, frequency is assumed to be real and wave number to be complex. Resolution of the dispersion equation requires Lamb modes to be a combination of inhomogeneous plane waves. Consequently, the Lamb waves inside a fluid-loaded plate are necessarily generated by an inhomogeneous plane wave if the frequency is real. For an inhomogeneous plane wave incident on an immersed plate, the reflection and transmission coefficients are then infinite for the conditions of Lamb wave generation.[7,8] In acoustics, most investigations on Lamb waves have been carried out considering real frequency and complex wave number, in order to account for attenuating wave modes during their propagation. This decision was often taken in accordance with specific ultrasonics applications[9] inherent in a space leakage of energy. A good review and ample references to this choice and generally to the literature on Lamb waves may be found in Ref. 10.

In a general way, Lamb wave generation is not only due to spatial effects. In geophysics many problems are related to excitation of free modes in stratified waveguides owing to a point-source explosion. In this case, leaky modes can be also transient modes because of the shortness of the source. Then two approaches have been considered on the structure of plane waves forming free modes[11–13] according to whether spatial or time effects must be investigated. On the one hand, when attenuation of leaky modes is seen as a function of distance of propagation, the velocity is assumed to be complex and the frequency to be real. On the other hand, when interest is focused on time solution rather than on space, complex frequency must be considered even though the velocity is real. This is a transient approach in the time domain of the problem of free modes propagation in waveguides. Those transient states have been studied in detail by Burvingt *et al.*[14,15] for the acoustic responses backscattered by cylinders.

In acoustics it seems that particular attention has been paid to the spatial problem whereas the time problem has not been treated in detail, in terms of propagating plane waves. The purpose of this paper is then to analyze all the different physical natures of Lamb waves that can propagate along immersed plates by finding the solutions of the dispersion equation of Lamb waves for inhomogeneous plane waves with complex frequency.

First the structure of the inhomogeneous plane wave with complex frequency, which is the most general representation of a plane wave, is presented within the context of propagation in an infinite medium. Next the dispersion equations of Lamb waves are analyzed in terms of homogeneous plane waves with complex frequency. The dispersion curves are calculated and the structure of this type of Lamb waves is discussed. Particular attention will be paid to the A_0 and S_0 modes for which the behavior of their dispersion curves is absolutely different from the case of a plate in vacuum. Afterward, the most general Lamb waves are presented. Then both the slowness vector and the frequency are assumed to be complex, which includes space and time phenomena at the same time. Finally, influence of the fluid loading on dispersion curve is inspected when the Lamb modes are transient.

I. THE COMPLEX HARMONIC INHOMOGENEOUS PLANE WAVE

The solution of the linear wave equation for an absorbing solid is searched for the complex harmonic inhomogeneous plane wave. This more general plane wave is defined, at any point space **M**, and time t by the following acoustic displacement:[16–20]

$$\mathbf{d}=\mathrm{Re}\{{}^*a\,{}^*\mathbf{P}\ \exp\ i({}^*\omega t-{}^*\mathbf{K}\cdot\mathbf{M})\}. \tag{1}$$

In the above expression, ${}^*a$ is the complex amplitude, ${}^*\mathbf{K}=\mathbf{K}'-i\mathbf{K}''$ denotes the complex wave vector that is the so-called wave bivector,[21] ${}^*\mathbf{P}$ represents the normalized polarization vector, and ${}^*\omega=\omega'+i\omega''$ is the complex angular frequency. The notation Re{ } stands for the real part. The superscript indexes * on the left-hand side indicate that the quantities are complex. All the others parameters will be real.

The propagation vector is noted $\mathbf{K}'$ and the attenuation (or damping) vector is represented by $\mathbf{K}''$. The real positive scalar ω' stands for the angular frequency. The parameter ω'' is the extinction coefficient (with $\omega''>0$) or the switching on of the source coefficient (with $\omega''<0$). This coefficient describes the time dependent exponentially transient part of the wave.

In a recent paper,[20] for complex harmonic inhomogeneous plane waves, it was shown that it is necessary to differentiate both the slowness and the wave bivectors. As a matter of fact, the energy velocity of these waves is oriented following the real part of the slowness bivector ${}^*\mathbf{S}$, which is really the propagation direction of these waves, while the real part of the wave bivector ${}^*\mathbf{K}$ does not always represent this direction. These two bivectors are related by

$${}^*\mathbf{K}={}^*\omega\,{}^*\mathbf{S}, \tag{2}$$

where ${}^*\mathbf{S}=\mathbf{S}'-i\mathbf{S}''$.

Although the computation of Lamb wave dispersion curves does not make use of any assumption about media, for simplicity they are assumed to be nonabsorbing. The dispersion equation for an infinite medium is then given by the following relation:

$${}^*\mathbf{S}\cdot{}^*\mathbf{S}=S^2, \tag{3}$$

where $S=c_0^{-1}$ in which c_0 is the homogeneous wave velocity for an ideal medium.

From a given slowness bivector ${}^*\mathbf{S}$, the real and imaginary parts of ${}^*\mathbf{K}$ are expressed, respectively, by

$$\mathbf{K}'=\omega'\mathbf{S}'+\omega''\mathbf{S}'', \tag{4}$$

$$\mathbf{K}''=\omega'\mathbf{S}''-\omega''\mathbf{S}'. \tag{5}$$

Let us now give more details concerning the complex slowness vector ${}^*\mathbf{S}$. Figure 1 shows the relation between ${}^*\mathbf{S}$ and ${}^*\mathbf{K}$ for nonabsorbing medium. The solid and dashed lines correspond to the complex wave vector associated to $\omega''<0$ and $\omega''>0$, respectively. Notice that for nonabsorbing media [cf. Eq. (3)] the vector $\mathbf{S}''$ is, if it is nonzero, necessarily orthogonal to the vector $\mathbf{S}'$. Depending on the complex frequency, the damping and propagation vectors, $\mathbf{K}''$ and $\mathbf{K}'$, are not necessarily orthogonal. For transient plane waves, the relative directions of these two vectors are not directly related to the wave structural behavior. Indeed, for real harmonic plane waves, i.e., $\omega''=0$, $\mathbf{S}'$ and $\mathbf{S}''$ are, respectively, colinear to $\mathbf{K}'$ and $\mathbf{K}''$. A more detailed discussion regarding this result should be found in Refs. 21 and 22.

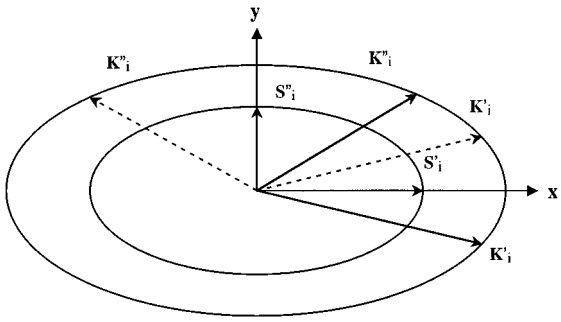

FIG. 1. Relation between the bivectors ${}^*\mathbf{S}$ and ${}^*\mathbf{K}$ for nonabsorbing medium: $\omega''<0$ (solid lines); $\omega''>0$ (dashed lines).

II. DISPERSION EQUATION OF LAMB WAVES

It is the purpose of this chapter to write briefly the dispersion equation of Lamb waves. Consider an inhomogeneous complex harmonic plane wave incident on an immersed solid layer. Suppose that the solid is an isotropic medium. Consequently, there is no loss of generality in assuming all vectors to be expressed in the two-dimensional coordinate system (**x**,**y**). The y axis is normal to the interfaces, which are located at $y=\pm d/2$, where d is the thickness of the plate.

The characteristic equation for the vibrations of a plate in vacuum, which can be solved for the dispersion curves of the phase velocities of the Lamb modes A_n and S_n, is given in textbooks such as Ref. 23. For the more general case of a plate immersed in a fluid, it is given by the transcendental equation of the implicit form:[24]

$$S({}^*\omega,{}^*S_x)A({}^*\omega,{}^*S_x)=0, \tag{6}$$

with

$$S({}^*\omega,{}^*S_x)=4\,{}^*S_x^2\,{}^*\varphi\,{}^*\psi\ \mathrm{cotan}({}^*\omega\,{}^*\varphi h)+(S_T^2-2\,{}^*S_x^2)^2\ \mathrm{cotan}({}^*\omega\,{}^*\psi h)+i\,{}^*\tau, \tag{7}$$

where

$${}^*\psi=\sqrt{S_L^2-{}^*S_x^2},\quad {}^*\varphi=\sqrt{S_T^2-{}^*S_x^2},$$

$${}^*\tau=\frac{\rho_f\,{}^*\psi S_T^4}{\rho_s\,{}^*S_{iy}},\quad \text{and}\ h=\frac{d}{2}.$$

The function $A({}^*\omega,{}^*S_x)$ originates from $S({}^*\omega,{}^*S_x)$ by replacing every cotan by tan and by changing the sign of ${}^*\tau$. The variables ρ_f and ρ_s represent the densities of fluid and solid, respectively. The dispersion equations of each longitudinal ($n=L$) and transversal ($n=T$) modes in the plate and of each wave in the fluid ($n=i$) are such that ${}^*\mathbf{S}_n\cdot{}^*\mathbf{S}_n=S_n^2=c_n^{-2}$, where c_L and c_T are the elastic-wave velocities in the solid and c_i is the bulk wave velocity in the fluid. The quantity ${}^*S_x$ stands for the x component of the complex slowness vector of each wave, in agreement with the gener-

alized Snell's laws.[25] These laws are given by: $^*\omega_n = {}^*\omega$ and $^*S_{xn} = {}^*S_x$, for $n = L, T, i$, and consequently $^*S_{iy}^2 = c_i^{-2} - {}^*S_x^2$.

Solving the characteristic equation (6) is complicated and generally requires numerical analysis. The solutions classically give the symmetric and antisymmertric modes for, respectively, $S(^*\omega, {}^*S_x) = 0$ and $A(^*\omega, {}^*S_x) = 0$. Note that owing to the fluid coupling the resulting solutions are complex. As a consequence, this equation can be satisfied either if the incident wave is inhomogeneous and harmonic (only $^*S_x$ is complex) or if it is transient and homogeneous (only $^*\omega$ is complex) or if, of course, it is transient and inhomogeneous.

The interest of the formulation (2) lies in the fact that both the frequency and the slowness are two independent quantities, contrary to $^*\omega$ and $^*\mathbf{K}$. Accordingly, the solutions for $^*S_x$ cannot *a priori* provide the solutions for $^*\omega$, and *vice versa*. Thus there exists an infinite number of dispersion curves for a fixed A_n (or S_n) mode. It is then immediately apparent that the problem can be solved by two different approaches. On the one hand, by setting the frequency, one can search the slowness, on the other hand, by setting the slowness the solution may be obtained for frequency. In view of these results it is made clear that the way for obtaining the dispersion curves of Lamb waves has an important physical consequence that will be explored fully in the remainder of this paper.

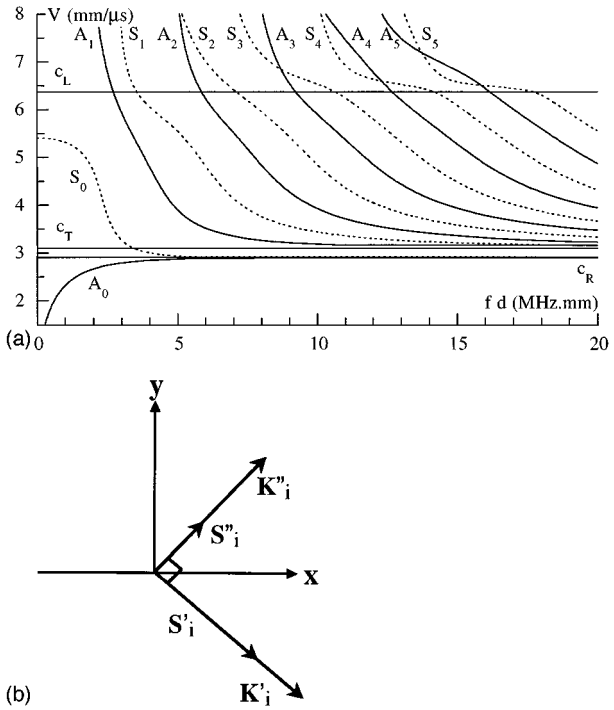

FIG. 2. Dispersion curves for complex slowness solutions $^*S_x$. (a) Antisymmetric modes (solid lines); symmetric modes (dashed lines). (b) Associated incident plane wave for Lamb modes with real frequency.

III. RESULTS AND DISCUSSION

This chapter reports numerical results for the prediction of the dispersion curves for plate waves. From a theoretical point of view, any point on the dispersion curves represents conditions of complex frequency and complex slowness couples for which the characteristic equation yields a zero value. From a numerical point of view, such a point is found by using a Newton–Raphson method that simultaneously provides a good value of zeros of the dispersion equation and a robust search algorithm.

The characteristics of the material and the fluid are chosen as: $c_i = 1.5$ mm/μs, $c_L = 6.37$ mm/μs, $c_T = 3.1$ mm/μs, $\rho_f = 1$, and $\rho_s = 2.8$. The corresponding Rayleigh wave velocity is $c_R = 2.908$ mm/μs for a fluid/solid interface and $c_R = 2.896$ mm/μs for a vacuum/solid interface. This velocity difference is due to the attenuation along the interface issued from the leakage.

As pointed out above, the transcendental equation (6) for any fixed values of the complex frequency $^*\omega$ (or complex slowness $^*S_x$) yields an infinite number of solutions for the complex slowness $^*S_x$ (or complex frequency $^*\omega$). In other words, by changing, for instance, the complex slowness, there exists an infinite number of each given S_n and A_n modes.

With loss of generality, both the complex frequency and the slowness x component can be associated to an incident inhomogeneous plane wave with complex frequency. It is then immediately apparent that both the reflection and refraction coefficients tend to infinity simultaneously, revealing the generation of leaky Lamb waves.[7,8,26] This link, although not absolutely necessary, is made to orient further discussions on the specific case of the generation of a Lamb wave by an acoustic beam incident on a plate, without loss of generality on the dispersion curves presented. To fix ideas, three typical situations are analyzed in comparison with the usual case. First, the incident wave is assumed to be homogeneous ($^*S_x$ is real) and the solutions are searched for complex frequencies $^*\omega$. Second, the spatial incident field is a fixed inhomogenous wave ($^*S_x$ is complex) and the generation of dispersion curves is otained for complex frequencies $^*\omega$. Finally, the incident wave is a fixed transient wave (ω''/ω' is constant) and the solutions are, in this case, searched in terms of complex slowness $^*S_x$. In what follows, calculations are limited to Lamb wave velocities greater than the sound velocity in water. Stoneley waves are therefore not inspected.

The velocities $V = [\mathrm{Re}\{^*S_x\}]^{-1}$ of the full set of Lamb modes are plotted versus the product real frequency thickness $fd = (\omega'/2\pi)d$. Depending on the incident wave, either the dimensionless factor $\Omega = \omega''/\omega'$ or the dimensionless factor $\Sigma = \pm|\mathbf{S}_i''|/|\mathbf{S}_i'|$, which correspond to the imaginary part of solutions, is plotted versus the product fd as well. The choice of the sign of Σ is such that, for $\Sigma > 0$, the damping vector $\mathbf{S}''$ of the incident wave is oriented toward the interface and for $\Sigma < 0$ the reverse.

In order to compare with the classical dispersion curves,[3] the results obtained by searching the complex slowness $^*S_x$ with a real frequency are shown in Fig. 2(a). From these curves, it can be drawn that the fluid loading does not sensibly affect the shape of the curves. For instance, the two S_0 and A_0 modes exist at all frequencies and, at very high frequency, their phase velocities converge towards the leaky

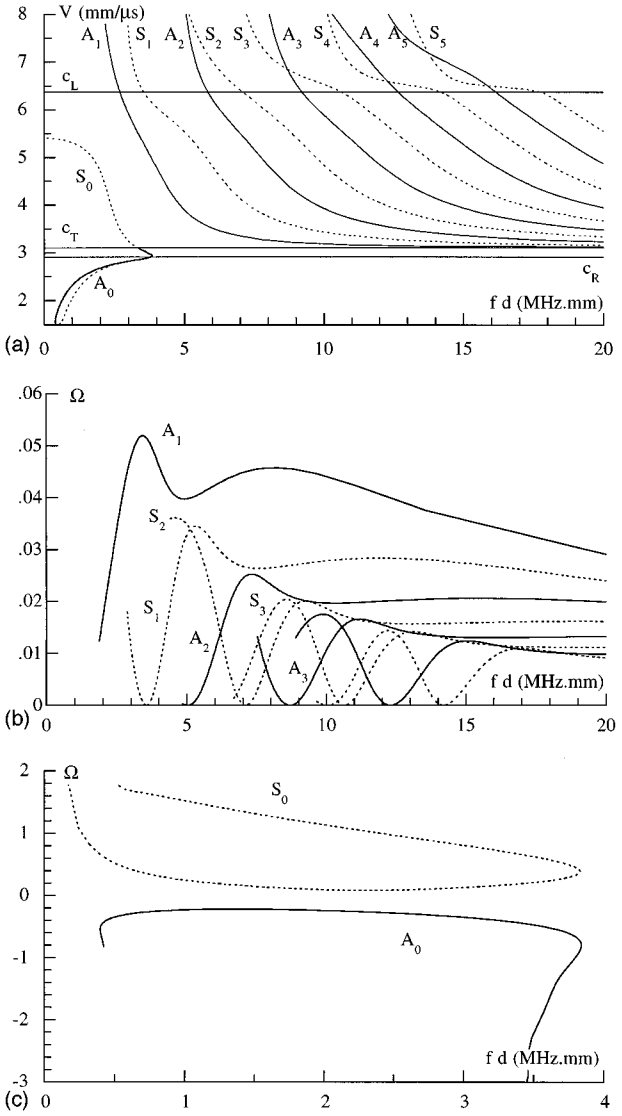

FIG. 3. Dispersion curves for complex frequency solutions $^*\omega$: antisymmetric modes (solid lines); symmetric modes (dashed lines). (a) Real part fd. (b) Imaginary part Ω. (c) Imaginary part Ω for the S_0 and A_0 modes only.

Rayleigh wave velocity. The full set of the Lamb modes are leaky waves, for which the amplitude decreases when they propagate along the plate.[4] The incident wave associated is then such that both x components of $\mathbf{S}_i'$ and $\mathbf{S}_i''$ have the same sign and consequently $\mathbf{K}_i'$ and $\mathbf{K}_i''$, see Fig. 2(b). This result is in agreement with the classical Lamb wave solution (see, for example, Refs. 4 and 5). Owing to the nature of the incident wave, the following results presented in this paper will be different.

A. Incident homogeneous plane wave with complex frequency

In the first instance, the solutions are searched in terms of complex frequencies and the slowness $^*S_x$ is assume to be real. There are some new observations that can be drawn by comparing Figs. 2 and 3.

Beyond the evident difference due to the different nature of the incident wave, it is made clear that the Lamb wave dispersion curves are different when the solutions are searched for complex frequencies or for complex slownesses. The greater the angle of incidence is, the greater the difference between both approaches. Accordingly, the largest differences are visible on both S_0 and A_0 modes and on the other modes in the vicinity of the shear velocity. On the other hand, the dispersion curves of A_n and S_n modes, for $n \neq 0$, are not strongly affected, except close to the shear velocity.

Another interesting result is the observation of the limit behavior of the velocity of these two modes. In fact, these velocities do not tend to the Rayleigh wave velocity as the frequency increases. Mathematically, for large values of the real frequency the transcendental equation (6) tends to the Rayleigh equation.[3] For the fluid–solid interface, it is well known that only complex solutions $^*S_x$ satisfy this equation. Setting $^*S_x$ strictly real and searching complex frequency solutions for Lamb waves, logically these solutions cannot tend to the Rayleigh wave solution. This is because the Rayleigh wave generation at a plane interface is a purely spatial phenomenon. However, when searching complex solutions $^*S_x$ the velocities of the S_0 and A_0 modes tend to the Rayleigh wave velocity as the frequency increases; refer to Fig. 2. Consequently, if the value of the complex slowness component $^*S_x$ of the incident wave corresponds approximately to the condition of Rayleigh wave generation, the solutions exhibit this asymptotic behavior for large real values of the complex frequency, as will be seen later on (see Figs. 7 and 8).

The major consequence is that, for incident homogeneous plane waves, there exists a cut-off frequency beyond which the S_0 and A_0 modes disappear simultaneously. Moreover, in contrast to the case of the evanescent plane wave incident (cf. Fig. 2) the A_0 mode exists for velocities larger than the Rayleigh wave velocity and lower than the shear wave velocity. Similarly, the S_0 mode can be excited with velocities lower than that of the Rayleigh wave. The different behavior of the solutions searched for complex frequencies or complex slownesses shows the nonduality between time and space.

In addition to these remarks, it should be mentioned that the dispersion curves for complex frequencies correspond very well to the minima of the reflection coefficient calculated for an incident harmonic homogeneous plane wave, in contrast to the dispersion curves calculated for the solutions with complex slownesses. A detailed discussion concerning the difference between the reflection coefficients and the dispersion curves of Lamb waves for immersed layers is presented in Ref. 27. From this point of view, since no sensible difference is visible, the use of complex frequencies is considerably more attractive.

We now turn our attention to the limit behavior of the A_0 mode, as illustrated by Fig. 4. Numerically, it can be observed that this mode tends sinusoidally to the shear velocity with a quasi-period which tends to zero as the limit is reached. It seems therefore that the solution exhibits the same behavior as the function $\sin(1/x)$ when x tends to zero.

At this stage it is instructive to examine in detail the structure of the incident waves that generate the Lamb

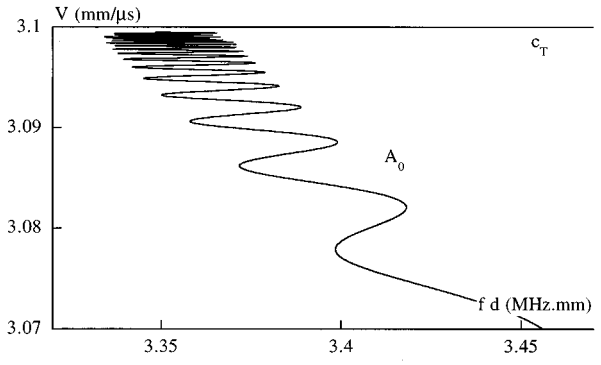

FIG. 4. Dispersion curve for complex frequency solutions $^*\omega$: limit behaviour of the A_0 mode near the shear velocity.

modes. To this end, let us inspect the imaginary part of the solutions. The resulting Lamb waves are issued from two types of source. Apart from the A_0 mode ($\Omega<0$), the envelope of the incident waveform decreases exponentially with time in accordance with $\Omega>0$. The associated wave bivector is shown in Fig. 5(a), where, in agreement with Eq. (2), it can be seen that the wave amplitude increases exponentially with increasing distance in the propagation direction $\mathbf{K}'$. At first sight this result seems surprising but it must be remembered that the damping vector $\mathbf{K}_i''$ is, in this case, given by $\mathbf{K}_i''=-\omega''\mathbf{S}_i'$. Hence, the amplitude increase corresponds only to a time effect. An opposite behavior, i.e., temporal increase and spatial decay, is observed for the A_0 since $\Omega<0$; see Fig. 5(b). Particular attention will be then focused on this mode.

In addition, it is important to note that although the imaginary x component K_x'' of the wave bivector is nonzero, the Lamb wave generated is not a leaky Lamb wave, in the sense that its amplitude does not decrease along the plate

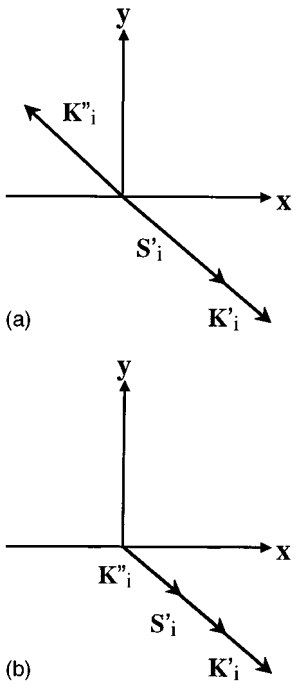

FIG. 5. Relation between the bivectors $^*\mathbf{S}_i$ and $^*\mathbf{K}_i$ for different solutions Ω. (a) $\Omega>0$. (b) $\Omega<0$.

when following its propagation. This comes from the fact that the imaginary x component S_x'' of the slowness bivector is always zero, which was not the case for the wave shown in Fig. 2(b). This amplitude decay cannot then be associated to spatial re-emission of these Lamb waves. Here is an example of the nonduality between time and space for the inhomogeneous plane wave with complex frequency. On the contrary, for an elastic plate in vacuum since the solutions of Lamb waves are real the time approach and the space approach are dual.

In the resonance scattering theory (RST)[24,28] the frequency resonances of sound reflection and transmission from a fluid-loaded elastic plate are defined by a frequency position and a width. Even if in the RST the frequency width of resonance can be related to the time exponential decay of the final transient state of the back scattered signal, it seems to be incorrect to physically link up this width with a spatial leakage of energy of Lamb waves during their propagation. However, from a numerical point of view, subject to some hypotheses, there exists relationships between time and space decays associated to the resonances.[29] From a physical point of view, it is made clear from the present study that care must be exercised in the interpretation of the link between a frequency resonance and the spatial re-emission of the associated Lamb wave. In other words, the damping vector $\mathbf{K}''$ cannot be, at the same time, issued from $\mathbf{S}''$ and from ω''.

In this context the question naturally arises as to what is the signification of different solutions of each A_n and S_n modes. The answer appears when remarking that the Lamb waves can be generated in immersed plate only by spatial or temporal limited beams. For any experimental situations, i.e., any transducer apertures (symbolized by S_x'') or any time dependence of the source (described by ω''), it is then not surprising that different possibilities exist to generate these waves. Accordingly, there is no difficulty in interpreting these different dispersion curves of Lamb waves, so long as the physical meaning of the evanescent plane wave with complex frequency is kept clearly in mind. In other words, in the same manner that bounded beam effects can generate Lamb waves,[6,7] temporal limited sources may contribute to excite these waves,[11] which, of course, exhibit in such a circumstance different dispersion curves.

B. Incident inhomogeneous plane wave with complex frequency

It should be emphasized that between these two limit cases, corresponding to harmonic inhomogeneous plane waves or transient homogeneous plane waves, there exists an infinite amount of Lamb wave dispersion curves. All that remains to be done is then to investigate the network of the solutions for some specific modes when the spatial form of the excitation has been fixed (as seen on the intermediate situations presented in Figs. 7 and 8).

Before turning to an investigation of an incident evanescent plane wave, let us attempt to obtain an exact idea as to the number of the solutions below the shear velocity for the case presented in Fig. 3 where the incident wave is assumed to be homogeneous. In this area, both the shear and the lon-

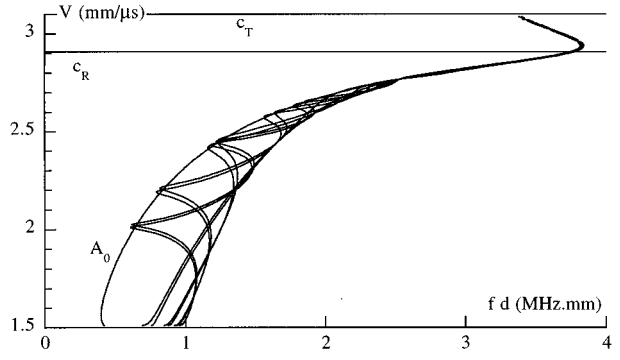

FIG. 6. Dispersion curves for complex frequency solutions $*\omega$ when $*S_x$ is real. Multisolutions of the A_0 mode.

gitudinal waves within the plate are evanescent surface waves and the functions $S(*\omega,*S_x)$ and $A(*\omega,*S_x)$ are quasi-periodic in terms of ω'' since $*\psi$ and $*\varphi$ are purely imaginary. As a result, in addition to the S_0 and A_0 modes there exists in fact an infinity of other modes identified by S_0^n and A_0^n, for which the real frequency is *almost* the same as for the S_0 and A_0 modes. Figure 6 shows the dispersion curves of these additional modes for the anti symmetric cases. For convenience, the imaginary part of the solution is not plotted. To label it the sign of n is chosen identical to the sign of Ω and $n=0$ corresponds to the lowest absolute value of Ω. Note that the greater value of n corresponds to the greater imaginary part of frequency. Consequently, these additional modes will be particularly difficult to excite.

Return now to the problem of incident evanescent plane waves characterized by the relative heterogeneity coefficient $\Sigma=\pm|\mathbf{S}_i''|/|\mathbf{S}_i'|$. The solutions are searched for complex frequencies. Comparisons between homogeneous and inhomogeneous incident waves reveal that the Lamb wave numbering does not hold good for inhomogeneous incident waves, as outlined in Figs. 7 and 8.

Let us first of all inspect the example illustrated in Fig. 7(a). It is clear that the mode, classically labeled S_3 for homogeneous waves with complex frequency (or inhomogeneous with real frequency), becomes the S_0 mode, as the Lamb wave velocities decrease. The S_1 mode is transformed in the S_0^1 mode. Similar and more complex connections can be visible on the other modes. For instance, the S_4 mode becomes the S_3 mode to finally finish as the S_0^3 mode beyond the Rayleigh velocity. The same relation subsists between (S_7,S_6,S_0^6), between (S_8,S_7,S_0^7). Examination of both S_6 and S_9 modes reveals other kinds of properties. Starting from specific modes they vary continuously, without following a particular classic dispersion curve, to solutions with a negative real part of the frequency. In this area these modes are connected to the periodic additional modes presented in Fig. 6 that exist also for negative frequencies.

These paths depend, of course, on the heterogeneity of the incident wave. For a different value of this, the mode connection can be different. For instance, the link between the S_7 and S_6 modes previously observed does not hold for a negative relative heterogeneity coefficient Σ, as shown in Fig. 7(b).

Comparison of symmetric and antisymmetric dispersion

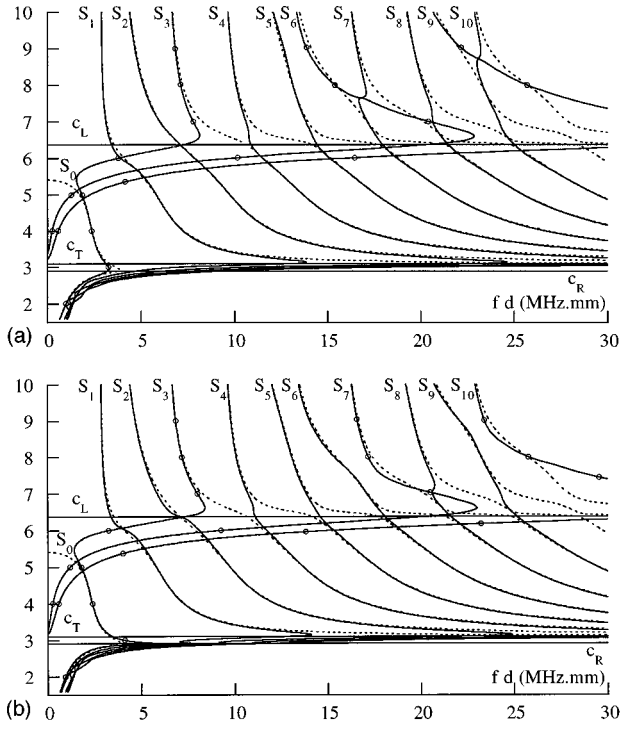

FIG. 7. Dispersion curves of the symmetric modes for complex frequency solutions $*\omega$: inhomogeneous incident plane wave (solid lines); homogeneous incident plane wave (dashed lines). (a) $\Sigma=2/3\times10^{-3}$. (b) $\Sigma=-2/3\times10^{-3}$.

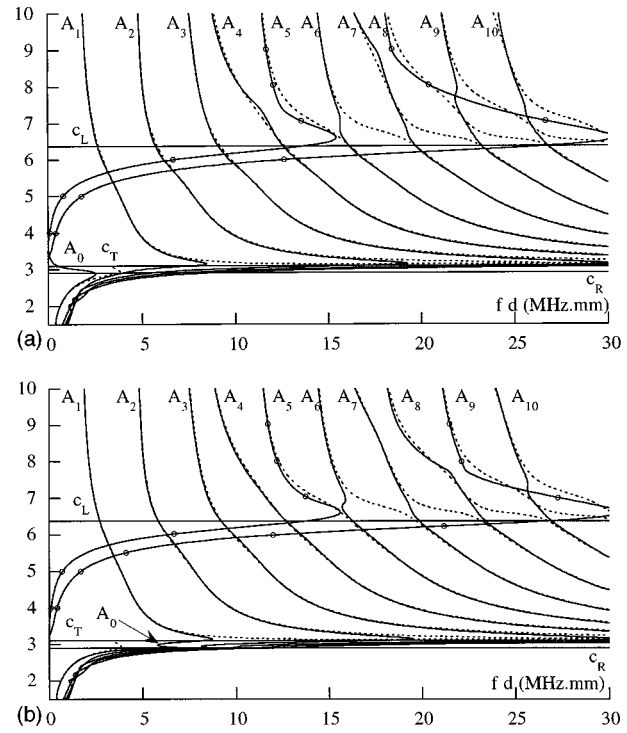

FIG. 8. Dispersion curves of the antisymmetric modes for complex frequency solutions $*\omega$: inhomogeneous incident plane wave (solid lines); homogeneous incident plane wave (dashed lines). (a) $\Sigma=2/3\times10^{-3}$. (b) $\Sigma=-2/3\times10^{-3}$.

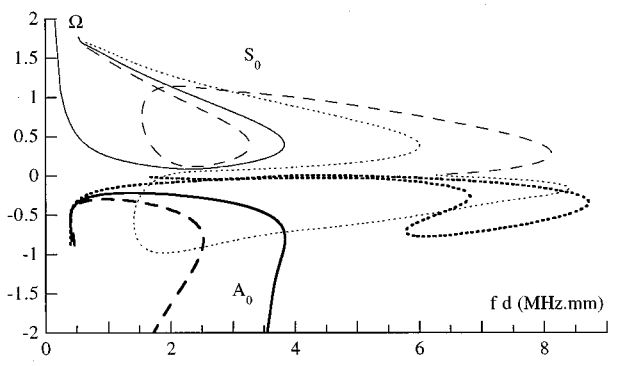

FIG. 9. Imaginary part Ω of the S_0 and A_0 modes for the cases presented in Figs. 7 and 8: $\Sigma=0$ (solid lines); $\Sigma=-2/3\times10^{-3}$ (dotted lines); $\Sigma=2/3\times10^{-3}$ (dashed lines); thick line A_0; thin line S_0.

curves indicates that no special dependence exists between both sets of connections for an identical incident wave. As an example, the S_3 mode and the A_3 mode are differently transformed; compare Figs. 7 and 8.

Moreover from a general point of view, the S_0 mode does not tend, as usual, to the limit velocity of the nondispersive mode issued from plane stress boundary conditions, i.e., $\omega^* d\rightarrow 0$. This is consistent with the fact that this limit velocity is real. From a zeroth-order approximation of Eq. (6), it is easy to show that the solution of $A(0,{}^*S_x)=A(0,S_x)=0$, in terms of slowness, is purely real. In a sense, the complex solutions cannot tend to a limit which is real. Similar properties have previously been observed on the Rayleigh wave velocity, which was not attained as expected.

For brevity the imaginary parts of solutions are not systematically plotted. For inspection purpose the observation are only reported in Fig. 9 for the S_0 and A_0 modes. Let us examine the sign of the relative parameter Ω. If for a homogeneous incident wave this parameter is systematically positive for all modes, except for the A_0 mode for which it is negative, for an inhomogeneous incident wave, depending on the value of the heterogeneity Σ and on the angle of incidence, this parameter may be either positive or negative. Accordingly, the corresponding bivectors ${}^*\mathbf{S}_i$ and ${}^*\mathbf{K}_i$ of the incident wave, are visualized graphically in Fig. 10, for four different situations which can exist. As a matter of fact, depending on relative values between the heterogeneity Σ and the parameter Ω the full set of Lamb waves can be one of them. At the first sight, these solutions seem to be not all physically acceptable. First, the phase velocity direction can change considerably for different complex frequencies, and consequently, the generated wave inside the plate. Second, since for $\Sigma<0$ the energy of the incident wave increases toward the interface. Nevertheless, it has been shown in Ref. 20 that the energy velocity of the inhomogeneous plane wave with a complex frequency is not oriented following the phase velocity direction but always following the real slowness direction. On the other hand, for both positive and negative heterogeneities, for real frequencies, a very good agreement between the theoretically calculated coefficients of the plate and the measurements has been obtained in Refs. 25 and 26.

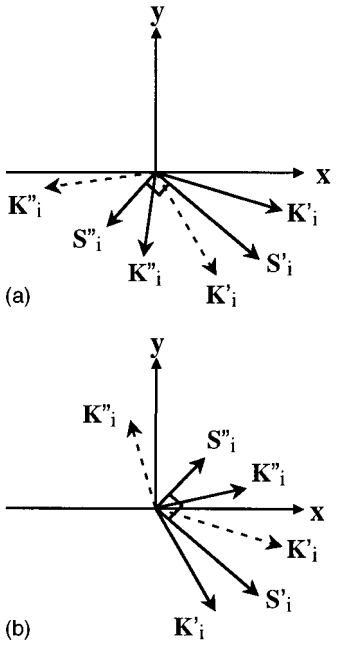

FIG. 10. Relation between the bivectors ${}^*\mathbf{S}_i$ and ${}^*\mathbf{K}_i$ for different heterogeneities Σ. (a) $\Sigma>0$. (b) $\Sigma<0$. $\Omega<0$ (solid lines); $\Omega>0$ (dashed lines).

C. Incident inhomogeneous plane wave with complex frequency: Solution for complex slownesses

An investigation of complex slowness search at various fixed complex frequencies is now conducted. Particular attention is paid on the A_0 and S_0 modes for which peculiar behaviors of their dispersion curves has been already observed.

For a fixed transient incident wave (i.e., Ω fixed), the dispersion equation is solved for ${}^*S_x$. Figures 11 and 12 show the real and imaginary parts of complex slowness versus real frequency (product fd). Concerning the A_0 mode, as the frequency increases, both the real and imaginary parts of slowness tend to the values corresponding to the complex Rayleigh wave velocity predicted by the theory when two semi-infinite media are considered (see Fig. 11). Moreover it can be observed that, depending on the value of Ω, the dispersion curves can be quite different from each other at low frequency, however they have the same shape.

As regards the symmetric mode, it seems that the trajectory of the S_0 mode, defined for $\Omega=0$ (long-dashed line in Fig. 12), can be followed by two different modes having the same Ω. For instance, let us inspect this for $\Omega=-0.2$. First, at low frequencies, this trajectory is followed by a mode which finally tends to constant values of velocity and Σ. Second, at higher frequencies, it is another mode that describes the end of this trajectory up to the Rayleigh wave properties. Depending on the imaginary part Ω of the complex frequency, this path can be more or less well-described, see the curves for $\Omega=+0.2$. From a general point of view, it is noticeable that these two different branches exist only above a limit value of the imaginary part of the complex frequency and that analysis of the solution becomes difficult when all the variables are complex.

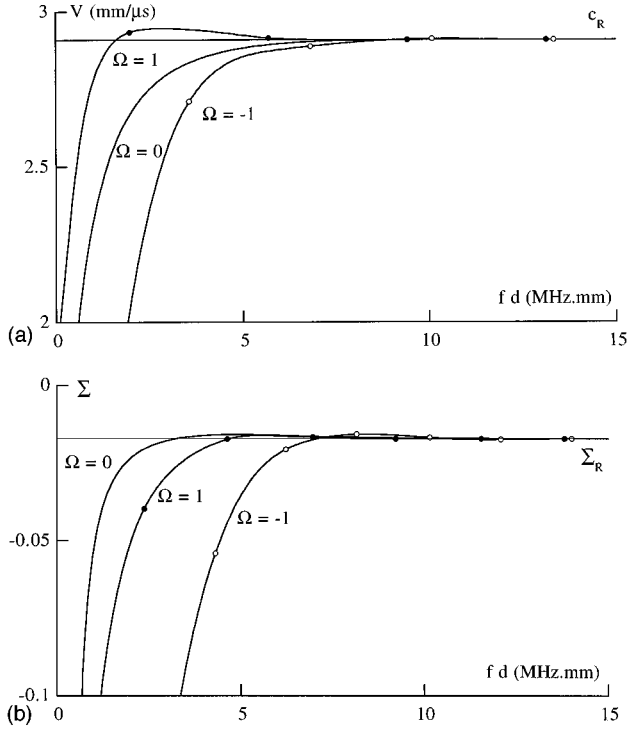

FIG. 11. Dispersion curves for complex slowness solutions $*S_x$ of the A_0 mode for various complex frequencies. (a) Real part (velocity V). (b) Imaginary part Σ.

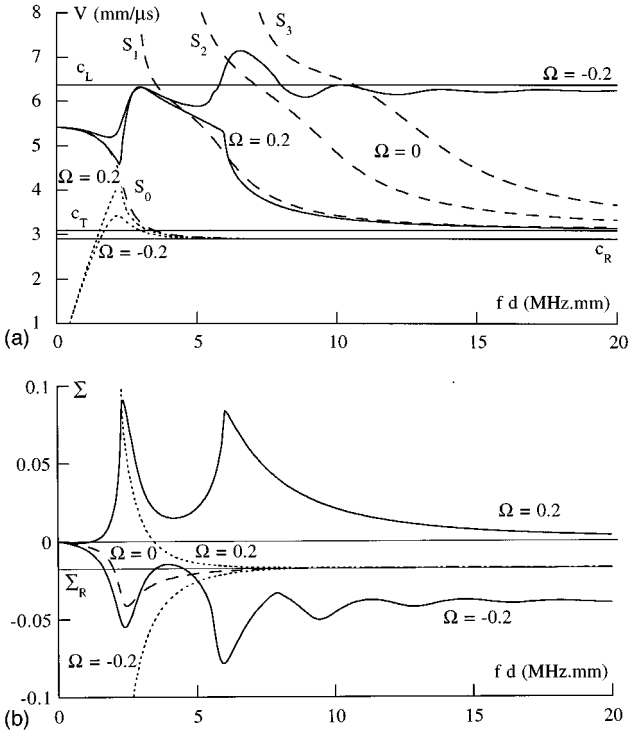

FIG. 12. Dispersion curves for complex slowness solutions $*S_x$ of the S_0 mode for various complex frequencies. $\Omega=-0.2$ (solid line); $\Omega=+0.2$ (dashed line); $\Omega=0$ (long-dashed line); (a) Real part (velocity V). (b) Imaginary part Σ.

D. Influence of the fluid density

Before closing this section, a final set of predictions shows the influence of the fluid density on the dispersion curves. The interest is more specifically focused on the A_0 mode, since as has already been seen the effects under investigation are greater for this mode that usually exists at low frequencies.

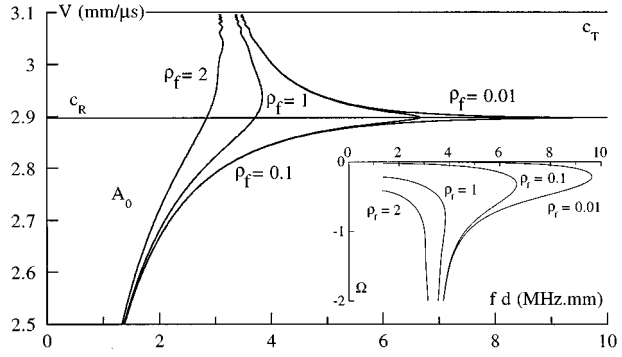

FIG. 13. Dispersion curves for complex frequency solutions $*\omega$ of the A_0 mode for various densities: real part in the main plot and imaginary part in the second plot.

Considering a homogeneous incident plane wave, the dispersion equation is solved for complex frequencies (Fig. 13). As pointed out before, the dispersion curve of the A_0 mode does not tend to the Rayleigh wave velocity at high frequencies which is the main consequence of the fluid loading when complex frequencies of transient Lamb waves are searched. Figure 13 shows that when the fluid density ρ_f approaches zero, the velocity (and heterogeneity) of the A_0 mode tends, as expected, to the velocity (and heterogeneity) of the Rayleigh wave that propagates along the vacuum/solid interface. This result appears to be quite natural. However, note that the part of the curves located between the shear velocity and the Rayleigh wave velocity exists even for the limit case: $\rho_f=0$. For a free plate, these solutions are not usually calculated in view of large values of the imaginary part of frequencies, for which any physical meaning is lost.

IV. CONCLUSION

Two different basic ways to solve the dispersion equation of Lamb waves in an immersed plate have been analyzed in this paper. From this study different interesting observations may be drawn.

Among these, one may mention first the case when only a dependence in space is assumed for Lamb waves. Those waves are permanent waves, i.e., real frequency, and are described by complex slownesses related to the decreasing of their amplitude during their propagation, i.e., the well-known leaky Lamb waves.

In another way, Lamb waves can be transient waves. In this case, the slownesses are real and the time dependence is described by complex frequencies. The dispersion curves of transient Lamb waves are different from the case of a plate in vacuum especially for the A_0 and S_0 modes. For these modes, which are usually defined as Rayleigh-type waves, there is a cut-off frequency beyond which they do not propagate. Then branches associated to the A_0 and S_0 modes do not tend to the Rayleigh wave velocity as in the case of plate in vacuum. Furthermore the imaginary part of the complex

frequency of the A_0 mode is negative, contrary to all the other ones, which corresponds to an exponential increasing signal with respect to time.

Between these two basic points of view (either the slowness is complex or the frequency) there exists an infinite number of possibility for those quantities. Both of them can be complex and then free modes, which are transient leaky Lamb waves, are related to temporal and spatial effects at once. In this case many specific behaviors can exist as the connection of branches of A_n and S_n with the ones of A_0 and S_0.

All the cases treated in this paper illustrate clearly that it is difficult to separate an analysis on the structure of Lamb waves from the way they have been generated. Then one must keep in mind that limiting oneself to the extreme cases, Lamb waves are excited either by bounded beams or by transient sources and there is no physical relation between those two types of Lamb waves since they represent two different phenomena. For example, when analyzing the reflection coefficient in the specular direction the temporal complexity dominates the Lamb wave generation. Nevertheless, when inspecting the reflected field along the plate by scanning the receiver, the spatial complexity dominates the Lamb wave generation, since in such a case the emitter must necessary be considered as limited.

Several studies are under consideration at present, such as the asymptotic behavior of Lamb waves for subsonic plate waves. Moreover, influence of plate anisotropy on Lamb waves propagation will be investigated, as well as multilayered immersed structures. It is clear that the phenomena described in this paper will be present in these situations.

ACKNOWLEDGMENT

This work was supported by D.R.E.T. Contract No. 94/088.

[1] H. Lamb, ''On waves in an elastic plate,'' Proc. R. Soc. London, Ser. A **93**, 114–128 (1917).
[2] M. F. M. Osborne and S. D. Hart, ''Transmission, reflection and guiding of an exponential pulse by a steel plate in water. I. Theory,'' J. Acoust. Soc. Am. **17**, 1–18 (1945).
[3] L. E. Pitts, T. J. Plona, and W. G. Mayer, ''Theoretical similarities of Rayleigh and Lamb modes of vibration,'' J. Acoust. Soc. Am. **60**, 374–377 (1976).
[4] L. G. Merkulov, ''Damping of normal modes in a plate immersed in a liquid,'' Sov. Phys. Acoust. **10**, 169–173 (1964).
[5] G. Mott, ''Reflection and refraction coefficients at a fluid-solid interface,'' J. Acoust. Soc. Am. **50**, 819–829 (1971).
[6] T. J. Plona, L. E. Pitts, and W. G. Mayer, ''Ultrasonic bounded beam reflection and transmission effects at a liquid/solid-plate/liquid interface,'' J. Acoust. Soc. Am. **59**, 1324–1328 (1976).
[7] K. V. D. Abeele and O. Leroy, ''On the influence of frequency and width of an ultrasonic bounded beam in the investigation of materials: Study in terms of heterogeneous plane waves,'' J. Acoust. Soc. Am. **93**, 2688–2699 (1993).
[8] M. Deschamps, in *Acoustic Interaction with Submerged Elastic Structures*, Part I, edited by A. Guran, J. Ripoche, and F. Ziegler (World Scientific, Singapore, 1996), pp. 164–206.
[9] A. H. Nayfeh and D. E. Chimenti, ''Propagation of guided waves in fluid-coupled plates of fiber-reinforced composite,'' J. Acoust. Soc. Am. **83**, 1736–1743 (1988).
[10] M. J. S. Lowe, ''Matrix techniques for modeling ultrasonic waves in multilayered media,'' IEEE Trans. Ultrason. Ferroelectr. Freq. Control **42,** 525–542 (1995).
[11] J. H. Rosenbaum, ''The long-time response of a layered elastic medium to explosive sound,'' J. Geophys. Res. **65**, 1577–1613 (1960).
[12] L. E. Alsop, ''The leaky-mode period equation. A plane-wave approach,'' Bull. Seismol. Soc. Am. **60**, 1989–1998 (1970).
[13] F. Gilbert, ''Propagation of transient leaking modes in a stratified elastic waveguide,'' Rev. Geophys. **2**, 123–153 (1964).
[14] R. Burvingt, ''Response to a long acoustic transient signal,'' Wave Motion **8**, 349–369 (1986).
[15] R. Burvingt, J. L. Rousselot, A. Derem, G. Maze, and J. Ripoche, ''Réponse résonnante de cylindres élastiques,'' Rev. Cethedec **78**, 73–93 (1984).
[16] M. Warenghem, ''Contribution à l'étude de l'extension complexe du quadrivecteur d'onde des ondes planes,'' thesis of the Université des sciences et techniques de Lille (1976).
[17] H. C. Ko, ''On the relativistic invariance of the complex phase of plane waves,'' Radio Sci. **12**, 151–155 (1977).
[18] P. Borejko, ''Inhomogeneous plane waves in a constrained elastic body,'' Q. J. Mech. Appl. Math. **40**, 71–87 (1987).
[19] B. Poirée, in *Symposium on Physical Acoustics: Fundamentals and Applications*, edited by O. Leroy and M. Breazeale (Plenum, New York, 1990), pp. 99–117.
[20] M. Deschamps, B. Poirée, and O. Poncelet, ''Energy velocity of complex harmonic plane waves in viscous fluids,'' Wave Motion **25,** 51–60 (1997).
[21] M. Hayes, ''Inhomogeneous plane waves,'' Arch. Ration. Mech. Anal. **85**, 41–79 (1984).
[22] M. Hayes, ''Inhomogeneous electromagnetic plane waves in crystals,'' Arch. Ration. Mech. Anal. **97**, 221–260 (1987).
[23] L. M. Brekhovskikh, *Waves in Layered Media* (Academic, New York, 1980), 2nd ed.
[24] R. Fiorito, W. Madigosky, and H. Überall, ''Resonance theory of acoustic waves interacting with an elastic plate,'' J. Acoust. Soc. Am. **66**, 1857–1866 (1979).
[25] M. Deschamps, ''Reflection and refraction of the evanescent plane wave on plane interfaces,'' J. Acoust. Soc. Am. **96**, 2841–2848 (1994).
[26] M. Deschamps and P. Chevée, ''Reflection and refraction of a heterogeneous plane wave by a solid layer,'' Wave Motion **15**, 61–75 (1992).
[27] D. E. Chimenti and S. I. Rokhlin, ''Relationship between leaky Lamb modes and reflection coefficient zeroes for a fluid-coupled elastic layer,'' J. Acoust. Soc. Am. **88**, 1603–1611 (1990).
[28] L. Flax, L. R. Dragonette, and H. Überall, ''Theory of elastic resonance excitation by sound scattering,'' J. Acoust. Soc. Am. **63**, 723–731 (1978).
[29] O. Lenoir, J. Duclos, J. M. Conoir, and J. L. Izbicki, ''Study of Lamb waves based upon the frequency and angular derivatives of the phase of the reflection coefficient,'' J. Acoust. Soc. Am. **94**, 330–343 (1993).

Wave propagation in a pyroelectric cylinder of inner and outer arbitrary shape

H. S. Paul[a] and Vazhapadi K. Nelson[b]
Department of Mathematics, Indian Institute of Technology, Madras-600 036, India

(Received 20 October 1995; accepted for publication 20 February 1997)

The wave propagation in a long pyroelectric cylinder of crystal class 6 with inner and outer irregular shape is considered. The frequency equation has been derived for the traction free, earth connected, and thermally insulated surfaces. The boundary conditions at the arbitrarily shaped boundaries are satisfied using the Fourier series expansion collocation method. The longitudinal and flexural vibrations of barium titanate ceramic, which belongs to the (6 mm) class, have been analyzed numerically. The numerical results in the case of elliptical and cardioidal cross sections with an elliptical cavity are tabulated and are presented graphically. © *1997 Acoustical Society of America.* [S0001-4966(97)03906-4]

PACS numbers: 43.38.Ar, 43.38.Fx [SLE]

LIST OF SYMBOLS

r,θ,z	cylindrical polar coordinates
$(T_{qq})_i$	
$(T_{qs})_i$	
$(T_{qz})_i$	normal and shearing stresses at the ith segment of curved boundaries of arbitrary shape
$(\ )_i$	denotes the value at the ith segment of the boundary
q,s	coordinate normal and tangential at the ith boundary (Fig. 1)
γ_i	angle between the normal to ith segment and the reference axis (Fig. 1)
u,v,w	radial, circumferential, and axial displacements
e_{mn}	piezoelectric constants; c_{ij} elastic constants
ϵ_{kl}^s	dielectric constants; p_m^s pyroelectric constants
$\tilde{\theta}_0$	reference temperature; $\tilde{\theta}$ temperature
ρ	mass density; t time
k	wave number; ω angular frequency
V	electric potential
c_v	specific heat capacity constants
β_j	thermal stress coefficients
k_{ij}	heat conduction coefficients
J_n	Bessel function of first kind and order n
Y_n	Bessel function of second kind and order n

INTRODUCTION

Wave propagation in long piezoelectric and pyroelectric cylinders with circular cross section have been reported in the literature.[1–7] Nagaya[8–11] has developed the Fourier expansion collocation method to study the vibrations of membranes, plates, and cylinders. This method has been extended by Paul and Venkatesan[12–14] to study some wave propagation problems of piezoelectric cylinders with inner regular and outer arbitrary or both inner and outer arbitrary cross sections. Paul and Raman[15] have considered the vibration of a pyroelectric cylinder with an irregular outer boundary. In most of the engineering applications, piezoelectric or pyroelectric materials are used. Hence the study of pyroelectric materials with regular and irregular shape and size are required in instrumentation. The pyroelectric materials are used in vidicons, thermal imaging instruments, hydrophones, and infrared detectors. Sullivan and Powers[16] and Ricketts[17] have used PVF_2 polymers in the construction of the flexural disk hydrophones and cylindrical hydrophones, respectively. $BaTiO_3$ ceramic dosimeters are used in the detection of high-intensity, short-duration bremsstrahlung pulses. In review articles, Dokmeci[18] and Lang[19,20] have discussed the applications of piezoelectric and pyroelectric materials in the area of defense and space research.

In this paper, wave propagation in a piezoelectric bone of arbitrary cross section[14] is extended to a pyroelectric cylinder of both inner and outer arbitrary cross sections. The frequency equations obtained for traction free, earth connected, and thermally insulated surfaces of the infinite cylinder are applicable for any general cross sections. As all the material constants of crystal class 6 are not available, the material constants of barium titanate, which belongs to the (6 mm) class, are taken for numerical computation. Numerical calculations are carried out for a $BaTiO_3$ ceramic cylinder of elliptical cavity with elliptical and cardioidal outer boundary. Results for both symmetric and antisymmetric modes of vibration are tabulated and are also presented graphically.

I. METHOD OF ANALYSIS

The governing equations for pyroelectric materials of class 6 are given by Mindlin.[21] The equations of motion, Gauss's equation, and the entropy equation in cylindrical polar coordinates (r,θ,z) for class 6 are given in Ref. 15 as

[a]Present address: 47/20 First Main Road, Gandhi Nagar, Adyar, Chennai-600 020, India.
[b]Present address: Department of Mathematics, Government College of Engineering, Salem-636 011, India.

 0001-4966/97/102(1)/301/7/$10.00

$$c_{11}(u_{,rr}+r^{-1}u_{,r}-r^{-2}u)+c_{66}r^{-2}u_{,\theta\theta}+c_{44}u_{,zz}+(c_{66}+c_{12})r^{-1}v_{,r\theta}-(c_{66}+c_{11})r^{-2}v_{,\theta}+(c_{44}+c_{13})w_{,rz}+(e_{31}+e_{15})V_{,rz}-e_{14}r^{-1}V_{,\theta z}-\beta_1\tilde{\theta}_{,r}=\rho u_{,tt}, \tag{1.1}$$

$$(c_{66}+c_{12})r^{-1}u_{,r\theta}+(c_{66}+c_{11})r^{-2}u_{,\theta}+c_{66}(v_{,rr}+r^{-1}v_{,r}-r^{-2}v)+c_{11}r^{-2}v_{,\theta\theta}+c_{44}v_{,zz}+(c_{44}+c_{13})r^{-1}w_{,\theta z}+e_{14}V_{,rz}+(e_{31}+e_{15})r^{-1}V_{,\theta z}-r^{-1}\beta_1\tilde{\theta}_{,\theta}=\rho v_{,tt}, \tag{1.2}$$

$$(c_{44}+c_{13})(u_{,rz}+r^{-1}u_{,z}+r^{-1}v_{,\theta z})+c_{44}(w_{,rr}+r^{-1}w_{,r}+r^{-2}w_{,\theta\theta})+c_{33}w_{,zz}+e_{15}(V_{,rr}+r^{-1}V_{,r}+r^{-2}V_{,\theta\theta})+e_{33}V_{,zz}-\beta_3\tilde{\theta}_{,z}=\rho w_{,tt}, \tag{1.3}$$

$$\epsilon_{11}^s(V_{,rr}+r^{-1}V_{,r}+r^{-2}V_{,\theta\theta})+\epsilon_{33}^sV_{,zz}-(\epsilon_{31}+e_{15})(u_{,rz}+r^{-1}u_{,z}+r^{-1}v_{,\theta z})+e_{14}[r^{-1}(u_{,\theta z}-v_{,z})-v_{,rz}]-e_{15}(w_{,rr}+r^{-1}w_{,r}+r^{-2}w_{,\theta\theta})-e_{33}w_{,zz}-p_3^s\tilde{\theta}_{,z}=0, \tag{1.4}$$

$$k_{11}(\tilde{\theta}_{,rr}+r^{-1}\tilde{\theta}_{,r}+r^{-2}\tilde{\theta}_{,\theta\theta})+k_{33}\tilde{\theta}_{,zz}-\tilde{\theta}_0\tilde{d}\tilde{\theta}_{,t}=\tilde{\theta}_0[\beta_1(u_{,rt}+r^{-1}(u_{,t}+v_{,\theta t})+\beta_3w_{,zt}-p_3^sV_{,zt}], \tag{1.5}$$

where $\tilde{d}=\rho c_v/\tilde{\theta}_0$.

With z axis as the axis of symmetry, the solutions of Eqs. (1) can be taken for an infinitely long cylinder as

$$u(r,\theta,z,t)=\sum_{n=0}^{\infty}\epsilon_n(\phi_{n,r}+r^{-1}\psi_{n,\theta})e^{i(kz+\omega t)}, \tag{2.1}$$

$$v(r,\theta,z,t)=\sum_{n=0}^{\infty}\epsilon_n(r^{-1}\phi_{n,\theta}-\psi_{n,r})e^{i(kz+\omega t)}, \tag{2.2}$$

$$w(r,\theta,z,t)=\left(\frac{i}{d}\right)\sum_{n=0}^{\infty}\epsilon_nW_ne^{i(kz+\omega t)}, \tag{2.3}$$

$$V(r,\theta,z,t)=i\left(\frac{c_{44}}{e_{33}d}\right)\sum_{n=0}^{\infty}\epsilon_nV_ne^{i(kz+\omega t)}, \tag{2.4}$$

$$\tilde{\theta}(r,\theta,z,t)=\left(\frac{c_{44}}{\beta_3d^2}\right)\sum_{n=0}^{\infty}\epsilon_n\tilde{\theta}_ne^{i(kz+\omega t)}. \tag{2.5}$$

Here $i=\sqrt{-1}$ and

$$\epsilon_n=\begin{cases}1/2 & \text{for } n=0\\ 1 & \text{for } n\geqslant 1,\end{cases}$$

where ϕ_n, ψ_n, W_n, V_n, and $\tilde{\theta}_n$ are functions of r and θ only, k is the wave number, and ω is the angular frequency. The inner radius d of the circular cross section in Ref. 15 is defined here as a characteristic length and is suitably modified for the particular shape of the cross section.

Substituting Eqs. (2) in Eqs. (1), the transformed equations can be written as[15]

$$\left(\frac{\partial}{\partial\overline{r}}\right)\{[\overline{c}_{11}\nabla^2+(cd)^2-\epsilon^2]\Phi_n-(1+\overline{c}_{13})\epsilon W_n-(\overline{e}_{31}+\overline{e}_{15})\epsilon V_n-\overline{\beta}\tilde{\theta}_n\}+\left(\frac{1}{\overline{r}}\right)\left(\frac{\partial}{\partial\theta}\right)\{(\overline{c}_{66}\nabla^2+(cd)^2-\epsilon^2)\Psi_n+\overline{e}_{14}\epsilon V_n\}=0, \tag{3.1}$$

$$\left(\frac{1}{\overline{r}}\right)\left(\frac{\partial}{\partial\theta}\right)\{[\overline{c}_{11}\nabla^2+(cd)^2-\epsilon^2]\Phi_n-(1+\overline{c}_{13})\epsilon W_n-(\overline{e}_{31}+\overline{e}_{15})\epsilon V_n-\overline{\beta}\tilde{\theta}_n\}-\left(\frac{\partial}{\partial\overline{r}}\right)\{(\overline{c}_{66}\nabla^2+(cd)^2-\epsilon^2)\times\Psi_n+\overline{e}_{14}\epsilon V_n\}=0, \tag{3.2}$$

$$(1+\overline{c}_{13})\epsilon\nabla^2\Phi_n+[\nabla^2-\overline{c}_{33}\epsilon^2+(cd)^2]W_n+(\overline{e}_{15}\nabla^2-\epsilon^2)V_n-\epsilon\tilde{\theta}_n=0, \tag{3.3}$$

$$(\overline{e}_{31}+\overline{e}_{15})\epsilon\nabla^2\Phi_n+(\overline{e}_{15}\nabla^2-\epsilon^2)W_n-(k_{13}^{-2}\nabla^2-k_{33}^{-2}\epsilon^2)V_n-\overline{e}_{14}\epsilon\nabla^2\Psi_n+\overline{p}\epsilon\tilde{\theta}_n=0. \tag{3.4}$$

$$\overline{\beta}\nabla^2\Phi_n-\epsilon W_n+\overline{p}\epsilon V_n+(\overline{d}-i\overline{k}_3\epsilon^2+i\overline{k}_1\nabla^2)\tilde{\theta}_n=0, \tag{3.5}$$

where

$$\nabla^2=(\partial^2/\partial\overline{r}^{-2})+\overline{r}^{-1}(\partial/\partial\overline{r})+\overline{r}^{-2}(\partial^2/\partial\theta^2),$$

$$\overline{r}=r/d,\quad \overline{c}_{ij}=c_{ij}/c_{44},$$

$$\overline{e}_{ij}=e_{ij}/e_{33},\quad \overline{d}=(\rho c_Vc_{44})/(\beta_3^2\tilde{\theta}_0),\quad \overline{\beta}=\beta_1/\beta_3,$$

$$\overline{p}=(p_3^sc_{44})/(e_{33}\beta_3),$$

$$k_{i3}^2=e_{33}^2/(\epsilon_{ii}^sc_{44}),\quad \epsilon=kd,\quad c^2=\rho\omega^2/c_{44},$$

and

$$\overline{k}_i=\sqrt{\rho c_{44}}k_{ii}/(\beta^2cd^2\tilde{\theta}_0).$$

Equations (3.1) and (3.2) can be expressed as

$$[\overline{c}_{11}\nabla^2+(cd)^2-\epsilon^2]\Phi_n-(1+\overline{c}_{13})\epsilon W_n-(\overline{e}_{31}+\overline{e}_{15})\epsilon V_n-\overline{\beta}\tilde{\theta}_n=0, \tag{4.1}$$

$$[\overline{c}_{66}\nabla^2+(cd)^2-\epsilon^2]\Psi_n+\overline{e}_{14}\epsilon V_n=0. \tag{4.2}$$

In assuming the solutions of Eqs. (1) in the form of Eqs. (2), the order of the differential equations in Eqs. (1) is increased. Taking Eqs. (3.1) and (3.2) in the form of Eqs. (4.1) and (4.2), the order of the differential equations in Eqs. (1) is decreased. Therefore additional boundary conditions are not required. Hence the system is consistent. The above assumptions for displacements are superior to the Helmholtz function[22] ($\overline{u}=\nabla\overline{\phi}+\overline{\nabla}\times\overline{\psi}$) as these do not require the additional equation ($\nabla\cdot\psi=0$). The present choice of displacements is valid for isotropic and transversely isotropic materials whereas the Helmholtz function is valid only for isotropic material. It is also observed that solutions, obtained by the Helmholtz function method cannot be derived from present method, as the present method does not use $\overline{\nabla\cdot\psi}=0$. However, the two solutions of a problem in isotropic material are numerically equal.

The solutions of Eqs. (3.3)–(3.5) and the transformed Eqs. (4.1) and (4.2) can be taken as

$$\Phi_n=\sum_{l=1}^{5}(A_{ln}J_n(\alpha_l r)+B_{ln}Y_n(\alpha_l r))e^{(in\theta)},$$

$$\Psi_n=-i\sum_{l=1}^{5}c_l(A_{ln}J_n(\alpha_l r)+B_{ln}Y_n(\alpha_l r))e^{(in\theta)},$$

$$W_n=\sum_{l=1}^{5}d_l(A_{ln}J_n(\alpha_l r)+B_{ln}Y_n(\alpha_l r))e^{(in\Theta)},$$

$$V_n=\sum_{l=1}^{5}e_l(A_{ln}J_n(\alpha_l r)+B_{ln}Y_n(\alpha_l r))e^{(in\theta)},$$

$$\tilde{\theta}_n=\sum_{l=1}^{5}h_l(A_{ln}J_n(\alpha_l r)+B_{ln}Y_n(\alpha_l r))e^{(in\theta)},$$

where $(\alpha_l d)^2$ are the five nonzero roots of the equation

$$|D(i,j)|=0, \quad i,j=1,2,3,4,5. \tag{5}$$

The elements of $D(i,j)$, $(i,j=1,2,3,4,5)$ are given by

$$D(1,1)=\overline{c_{11}}(\alpha_l d)^2+\epsilon^2-(cd)^2,$$

$$D(1,3)=(1+\overline{c_{13}})\epsilon,$$

$$D(1,4)=(\overline{e_{31}}+\overline{e_{15}})\epsilon, \quad D(1,5)=\overline{\beta},$$

$$D(2,2)=\overline{c_{66}}(\alpha_l d)^2+\epsilon^2-(cd)^2, \quad D(2,4)=-\overline{e_{14}}\epsilon,$$

$$D(3,1)=(1+\overline{c_{13}})\epsilon(\alpha_l d)^2,$$

$$D(3,3)=(\alpha_l d)^2+\overline{c_{33}}\epsilon^2-(cd)^2,$$

$$D(3,4)=\overline{e_{15}}(\alpha_l d)^2+\epsilon^2, \quad D(3,5)=\epsilon,$$

$$D(4,1)=(\overline{e_{15}}+\overline{e_{31}})\epsilon(\alpha_l d)^2, \quad D(4,2)=-\overline{e_{14}}\epsilon(\alpha_l d)^2,$$

$$D(4,3)=\overline{e_{15}}(\alpha_l d)^2+\epsilon^2,$$

$$D(4,4)=-[k_{13}^{-2}(\alpha_l d)^2+k_{33}^{-2}\epsilon^2],$$

$$D(4,5)=-\overline{p\epsilon}, \quad D(5,1)=\overline{\beta}(\alpha_l d)^2,$$

$$D(5,3)=\epsilon, \quad D(5,4)=-\overline{p\epsilon},$$

$$D(5,5)=i\overline{k_1}(\alpha_l d)^2+i\overline{k_3}\epsilon^2-\overline{d}$$

and

$$D(1,2)=D(2,1)=D(2,3)=D(2,5)=D(3,2)=D(5,2)=0.$$

The constants c_l, d_l, e_l, h_l can be obtained from the following relations:

$$[\overline{c_{11}}(\alpha_l d)^2+\epsilon^2-(cd)^2]+(1+\overline{c_{13}})\epsilon d_l+(\overline{e_{31}}+\overline{e_{15}})\epsilon e_l+\overline{\beta}h_l=0,$$

$$[\overline{c_{66}}(\alpha_l d)^2+\epsilon^2-(cd)^2]c_l-\overline{e_{14}}\epsilon e_l=0,$$

$$(1+\overline{c_{13}})\epsilon(\alpha_l d)^2+[(\alpha_l d)^2+\overline{c_{33}}\epsilon^2-(cd)^2]d_l+[\overline{e_{15}}(\alpha_l d)^2+\epsilon^2]e_l+\epsilon h_l=0$$

$$-(\overline{e_{15}}+\overline{e_{31}})\epsilon(\alpha_l d)^2+\overline{e_{14}}\epsilon(\alpha_l d)^2 c_l-[\overline{e_{15}}(\alpha_l d)^2+\epsilon^2]d_l+[k_{13}^{-2}(\alpha_l d)^2+k_{33}^{-2}\epsilon^2]e_l+\overline{p\epsilon}h_l=0.$$

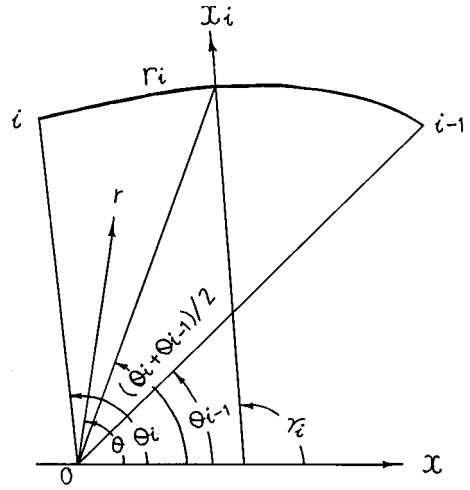

FIG. 1. Geometry of the ith segment of curved boundaries of arbitrary shape.

II. BOUNDARY CONDITIONS

The inner and outer irregular surfaces of the infinite cylinder are traction free, earth connected, and thermally insulated. Hence the boundary conditions at the ith segment of the curved boundaries of arbitrary shape are

(i) Mechanical boundary conditions:
$(T_{qq})_i=(T_{qs})_i=(T_{qz})_i=0.$

(i) Electrical boundary condition:
$(V)_i=0.$

(i) Thermal boundary condition:
$(\tilde{\theta},q)_i=0.$

Since both the inner and outer boundary are arbitrary surfaces, it is difficult to satisfy boundary conditions as in Ref. 15. To satisfy boundary conditions, the Fourier expansion is performed on the inner and outer boundary lines of the cross section. For this purpose the assumptions made by Nagaya[8–11] are extended to the pyroelectric case. Taking the angle γ_i (Fig. 1) between the normal to be the segment and the reference axis to be constant, the transformed expressions of the stresses are

$$T_{qq}=(c_{11}\cos^2\overline{\theta}+c_{12}\sin^2\overline{\theta})u_{,r}+(c_{11}\sin^2\overline{\theta}+c_{12}\cos^2\overline{\theta})r^{-1}(u+v_{,\theta})-c_{66}[v_{,r}+r^{-1}\times(u_{,\theta}-v)]\sin 2\overline{\theta}+c_{13}w_{,z}+e_{31}V_{,z}-\beta_1 T, \tag{6.1}$$

$$T_{qs}=c_{66}\{[(u_{,r}-r^{-1}(u+v_{,\theta})]\sin 2\overline{\theta}+[v_{,r}+r^{-1}\times(u_{,\theta}-v)]\cos 2\overline{\theta}\}, \tag{6.2}$$

$$T_{qz}=c_{44}[(u_{,z}+w_{,r})\cos\overline{\theta}-(v_{,z}+r^{-1}w_{,\theta})\sin\overline{\theta}]+e_{15}[V_{,r}\cos\overline{\theta}-r^{-1}V_{,\theta}\sin\overline{\theta}]-e_{14}[V_{,r}\sin\overline{\theta}+r^{-1}V_{,\theta}\cos\overline{\theta}], \tag{6.3}$$

where $\overline{\theta}=(\theta-\gamma_i)$.

Substituting Eqs. (2) in Eqs. (6) and nondimensionalizing, we get

$$\sum_{n=0}^{\infty}\sum_{l=1}^{5}(A_{ln}c_{1n}^{l}+B_{ln}c_{2n}^{l})=0,$$

$$\sum_{n=0}^{\infty}\sum_{l=1}^{5}(A_{ln}d_{1n}^{l}+B_{ln}d_{2n}^{l})=0,$$

$$\sum_{n=0}^{\infty}\sum_{l=1}^{5}(A_{ln}e_{1n}^{l}+B_{ln}e_{2n}^{l})=0,$$

$$\sum_{n=0}^{\infty}\sum_{l=1}^{5}(A_{ln}f_{1n}^{l}+B_{ln}f_{2n}^{l})=0,$$

$$\sum_{n=0}^{\infty}\sum_{l=1}^{5}(A_{ln}g_{1n}^{l}+B_{ln}g_{2n}^{l})=0,$$

where A_{ln} and B_{ln} are arbitrary constants and

$$c_{1n}^{l}=e_lJ_n(\alpha_lr)e^{(in\theta)},$$

$$d_{1n}^{l}=(\{2\overline{c_{66}}\cos 2\overline{\theta}[(\alpha_lr)(1-nc_l)j_{n+1}(\alpha_lr)+(1+c_l)n(n-1)J_n(\alpha_lr)]-[(\alpha_lr)^2(\overline{c_{11}}\cos^2\overline{\theta}+\overline{c_{12}}\sin^2\overline{\theta})$$
$$+\epsilon(\overline{c_{13}}d_l+\overline{e_{31}}e_l)+\overline{\beta h_l}]J_n(\alpha_lr)\}+i\overline{c_{66}}\sin 2\overline{\theta}\{2(\alpha_lr)(n-c_l)J_{n+1}(\alpha_lr)+[c_l((\alpha_lr)^2-2n(n-1))$$
$$-2n(n-1)]J_n(\alpha_lr)\})e^{(in\theta)},$$

$$e_{1n}^{l}=(\{2(\alpha_lr)(1-nc_l)J_{n+1}(\alpha_lr)-[(\alpha_lr)^2-2n(n-1)(1+c_l)]J_n(\alpha_lr)\}\sin 2\overline{\theta}-i\{2(\alpha_lr)(n-c_l)J_{n+1}(\alpha_lr)$$
$$+[c_l((\alpha_lr)^2-2n(n-1))-2n(n-1)]J_n(\alpha_lr)\}\cos 2\overline{\theta})e^{(in\theta)},$$

$$f_{1n}^{l}=[\epsilon+d_l+\overline{e_{15}}e_l][nJ_n(\alpha_lr)e^{i(n\theta-\overline{\theta})}-(\alpha_lr)J_{n+1}(\alpha_lr)e^{(in\theta)}\cos\overline{\theta}]+\epsilon c_l[nJ_n(\alpha_lr)e^{i(n\theta-\overline{\theta})}$$
$$+i(\alpha_lr)J_{n+1}(\alpha_lr)e^{(in\theta)}\sin\overline{\theta}]+\overline{e_{14}}e_l[-inJ_n(\alpha_lr)e^{i(n\theta-\overline{\theta})}+(\alpha_lr)J_{n+1}(\alpha_lr)e^{(in\theta)}\sin\overline{\theta}],$$

$$g_{1n}^{l}=h_l[nJ_n(\alpha_lr)-(\alpha_lr)J_{n+1}(\alpha_lr)]\cos 2\overline{\theta}e^{(in\theta)}.$$

The expressions for c_{2n}^{l}, d_{2n}^{l}, e_{2n}^{l}, f_{2n}^{l}, and g_{2n}^{l} can be obtained from the above expressions by replacing J_n, J_{n+1} by Y_n, Y_{n+1}, respectively.

The boundary conditions along the whole range of inner and outer boundary lines cannot be satisfied directly. Hence, to satisfy boundary conditions, the Fourier series expansion is performed on the boundary conditions along the inner as well as the outer boundary lines. Here one straight line is considered to be one segment and one curved line is divided into many segments according to the convergence of the solutions.[8–15] The Fourier coefficients are therefore obtained by additions of these for separately considered boundaries. When the cross section is symmetric about an axis, the analysis can be separated into symmetric and antisymmetric cases. Hence choosing the coordinate θ from an axis of symmetry, the boundary conditions are expanded into the following Fourier series:

$$\sum_{m=0}^{\infty}\epsilon_m\{A_{10}C_{1m0}^{1}+B_{10}C_{2m0}^{1}+A_{20}C_{1m0}^{2}+B_{20}C_{2m0}^{2}+A_{30}C_{1m0}^{3}+B_{30}C_{2m0}^{3}+A_{40}C_{1m0}^{4}+B_{40}C_{2m0}^{4}$$
$$+\sum_{n=1}^{\infty}[A_{1n}C_{1mn}^{1}+B_{1n}C_{2mn}^{1}+A_{2n}C_{1mn}^{2}+B_{2n}C_{2mn}^{2}+A_{3n}C_{1mn}^{3}+B_{3n}C_{2mn}^{3}+A_{4n}C_{1mn}^{4}+B_{4n}C_{2mn}^{4}]\}\cos\theta=0, \tag{7.1}$$

$$\sum_{m=0}^{\infty}\epsilon_m\Big\{A_{10}D_{1m0}^{1}+B_{10}D_{2m0}^{1}+A_{20}D_{1m0}^{2}+B_{20}D_{2m0}^{2}+A_{30}D_{1m0}^{3}+B_{30}D_{2m0}^{3}+A_{40}D_{1m0}^{4}+B_{40}D_{2m0}^{4}$$
$$+\sum_{n=1}^{\infty}[A_{1n}D_{1mn}^{1}+B_{1n}D_{2mn}^{1}+A_{2n}D_{1mn}^{2}+B_{2n}D_{2mn}^{2}+A_{3n}D_{1mn}^{3}+B_{3n}D_{2mn}^{3}+A_{4n}D_{1mn}^{4}+B_{4n}D_{2mn}^{4}+A_{5n}D_{1mn}^{5}$$
$$+B_{5n}D_{2mn}^{5}]\Big\}\cos m\theta=0, \tag{7.2}$$

$$\sum_{m=1}^{\infty}\Big\{A_{10}E_{1m0}^{1}+B_{10}E_{2m0}^{1}+A_{20}E_{1m0}^{2}+B_{20}E_{2m0}^{2}+A_{30}E_{1m0}^{3}+B_{30}E_{2m0}^{3}+A_{40}E_{1m0}^{4}+B_{40}E_{2m0}^{4}+\sum_{n=1}^{\infty}[A_{1n}E_{1mn}^{1}+B_{1n}E_{2mn}^{1}$$
$$+A_{2n}E_{1mn}^{2}+B_{2n}E_{2mn}^{2}+A_{3n}E_{1mn}^{3}+B_{3n}E_{2mn}^{3}+A_{4n}E_{1mn}^{4}+B_{4n}E_{2mn}^{4}+A_{5n}E_{1mn}^{5}+B_{5n}E_{2mn}^{5}]\}\sin m\theta=0, \tag{7.3}$$

$$\sum_{m=0}^{\infty} \epsilon_m \Big\{ A_{10}F^1_{1m0}+B_{10}F^1_{2m0}+A_{20}F^2_{1m0}+B_{20}F^2_{2m0}+A_{30}F^3_{1m0}+B_{30}F^3_{2m0}+A_{40}F^4_{1m0}+B_{40}F^4_{2m0}+\sum_{n=1}^{\infty}[A_{1n}F^1_{1mn}+B_{1n}F^1_{2mn}$$

$$+A_{2n}F^2_{1mn}+B_{2n}F^2_{2mn}+A_{3n}F^3_{1mn}+B_{3n}F^3_{2mn}+A_{4n}F^4_{1mn}+B_{4n}F^4_{2mn}+A_{5n}F^5_{1mn}+B_{5n}F^5_{2mn}]\Big\}\cos\, m\theta=0, \tag{7.4}$$

$$\sum_{m=0}^{\infty} \epsilon_m \Big\{ A_{10}G^1_{1m0}+B_{10}G^1_{2m0}+A_{20}G^2_{1m0}+B_{20}G^2_{2m0}+A_{30}G^3_{1m0}+B_{30}G^3_{2m0}+A_{40}G^4_{1m0}+B_{40}G^4_{2m0}+\sum_{n=1}^{\infty}[A_{1n}G^1_{1mn}+B_{1n}G^1_{2mn}$$

$$+A_{2n}G^2_{1mn}+B_{2n}G^2_{2mn}+A_{3n}G^3_{1mn}+B_{3n}G^3_{2mn}+A_{4n}G^4_{1mn}+B_{4n}G^4_{2mn}]\Big\}\cos\, m\theta=0, \tag{7.5}$$

where

$$C^l_{jmn}=(2\epsilon_n/\pi)\sum_{i=1}^{I}\int_{\theta_{i-1}}^{\theta i} c^l_{jn}(R_i,\theta)\cos\, m\theta\, d\theta,$$

$$D^l_{jmn}=(2\epsilon_n/\pi)\sum_{i=1}^{I}\int_{\theta_{i-1}}^{\theta i} d^l_{jn}(R_i,\theta)\cos\, m\theta\, d\theta,$$

$$E^l_{jmn}=(2\epsilon_n/\pi)\sum_{i=1}^{I}\int_{\theta_{i-1}}^{\theta i} e^l_{jn}(R_i,\theta)\sin\, m\theta\, d\theta,$$

$$F^l_{jmn}=(2\epsilon_n/\pi)\sum_{i=1}^{I}\int_{\theta_{i-1}}^{\theta i} f^l_{jn}(R_i,\theta)\cos\, m\theta\, d\theta,$$

$$G^l_{jmn}=(2\epsilon_n/\pi)\sum_{i=1}^{I}\int_{\theta_{i-1}}^{\theta i} g^l_{jn}(R_i,\theta)\cos\, m\theta\, d\theta.$$

Here l takes values 1–5, j takes values 1 and 2, $\epsilon_m=1/2$ for $m=0$, and $\epsilon_m=1$ for $m\geqslant 1$. I is the number of segments including the straight line boundaries and R_i is the coordinate r at the ith segment which is expressed as a function of θ. The frequency equations can be obtained by equating the determinant of the coefficients of the amplitudes A_{ln} and B_{ln} to zero from Eqs. (7).

III. NUMERICAL RESULTS

Since the heat conduction coefficient and specific heat capacity of crystal class 6 are not available, the frequency equation for crystal class (6 mm) are analyzed numerically. An infinite cylindrical bar of barium titanate ceramic is considered with an elliptical cavity and outer elliptical as well as cardioidal cross sections. The convergence of the solution is good when each of the inner and outer irregular boundaries is divided into 20 segments. The numerical computation is proceeded with four Fourier components. The elastic, piezoelectric, and pyroelectric constants of $BaTiO_3$ ceramic[23] (class 6 mm) are

$c_{11}=15.0\times10^{10}$ N/m^2, $c_{12}=6.60\times10^{10}$ N/m^2,

$c_{13}=6.60\times10^{10}$ N/m^2, $c_{33}=14.6\times10^{10}$ N/m^2,

$c_{44}=4.40\times10^{10}$ N/m^2, $c_{66}=4.20\times10^{10}$ N/m^2,

$e_{31}=-4.35$ C/m^2, $e_{33}=17.50$ C/m^2,

$e_{15}=11.40$ C/m^2, $p_3=2.135\times10^{-4}$ C/(m^2 °C),

$\epsilon^s_{11}=128.325\times10^{-10}$ F/m, $\epsilon^s_{33}=111.51\times10^{-10}$ F/m,

$\rho=5700$ kg/m^3.

The geometric relation for elliptic cross section[9] is

$$R_1/b_2=(b_1/b_2)(a_1/b_1)/[\cos^2\theta+(a_1/b_1)^2\sin^2\theta]^{1/2},$$

$$R_2/b_2=(a_2/b_2)/[\cos^2\theta+(a_2/b_2)^2\sin^2\theta]^{1/2},$$

$$\gamma_i=\pi/2-\tan^{-1}[(b_1/a_1)^2/\tan\theta^*_i] \quad \text{for } \theta^*<\pi/2,$$

$$\gamma_i=\pi/2 \quad \text{for } \theta^*=\pi/2,$$

$$\gamma_i=\pi/2+\tan^{-1}[(b_1/a_1)^2/|\tan\theta^*_i|] \quad \text{for } \pi/2<\theta<\pi,$$

where $\theta^*_i=(\theta_{i-1}+\theta_i)/2$ and the angle θ_i is chosen from the major axis and the lengths of semimajor and minor axis of inner and outer elliptical boundary are taken as a_1, a_2 and b_1, b_2. The numerical calculations are carried out for the longitudinal and the flexural mode. The characteristic length

TABLE I. Values of ϵ for different values of dimensionless frequency (cb_2) for elliptical cross section with elliptical cavity for longitudinal vibration with aspect ratio $a_1/b_1=a_2/b_2=1$ and $b_1/b_2=0.5$.

cb_2	Nondimensional wave no. (ϵ) Symmetric case
0.50	0.07500+i0.250E-02
1.00	0.18872+i0.510E-02
1.50	0.27032+i0.525E-02
2.00	0.43354+i0.255E-03
2.50	0.57656+i0.510E-04
3.00	0.73245+i0.151E-03
3.50	0.94455+i0.424E-03
4.00	1.02535+i0.252E-04

TABLE II. Values of ϵ for different values of dimensionless frequency (cb_2) for elliptical cross section with elliptical cavity for flexural vibration with aspect ratio $a_1/b_1 = a_2/b_2 = 1.5$ and $b_1/b_2 = 0.5$.

	Nondimensional wave number (ϵ)	
cb_2	Symmetric case	Antisymmetric case
0.50	0.07395+i0.408E-03	0.07585+i0.404E-02
1.00	0.17675+i0.101E-02	0.15760+i0.204E-01
1.50	0.28057+i0.000E-00	0.28409+i0.204E-03
2.00	0.42385+i0.612E-03	0.40248+i0.404E-03
2.50	0.68175+i0.404E-04	0.68528+i0.252E-02
3.00	0.87112+i0.505E-03	0.88697+i0.102E-02
3.50	0.93425+i0.505E-03	0.93677+i0.252E-03
4.00	1.02250+i0.500E-03	1.03550+i0.450E-03

d is taken as the length of the semiminor axis b_2 of the outer elliptical cross section.

The displacements due to longitudinal vibrations are symmetrical about both the x and the y axis. The frequency equation for this set of modes is obtained from Eqs. (7) by taking $n,m = 0,2,4,6,\ldots$. The results are evaluated for the aspect ratio $a_1/b_1 = a_2/b_2 = 1.5$ and $b_1/b_2 = 0.5$ and are presented in Table I.

For flexural motion, the displacements are symmetrical about the y axis and antisymmetrical about the x axis. By taking $n,m = 1,3,5,\ldots$, the frequency equation is obtained from Eqs. (7). The results are given in Table II for both symmetrical and antisymmetrical modes of vibration for $a_1/b_1 = a_2/b_2 = 1.5$ and $b_1/b_2 = 0.5$. The dispersion curves are drawn by fixing the eigenfrequency and varying wave number for the aspect ratio $a_1/b_1 = a_2/b_2 = 1.2$ and $b_1/b_2 = 0.5$. In Fig. 2 the dispersion curves are drawn for both longitudinal and flexural motion. In Fig. 3 the curves in both symmetric and asymmetric modes are compared. Comparing the corresponding dispersion curves in Figs. 1 and 2 of Ref. 15, the curves in Figs. 2 and 3 are more oscillatory in nature.

The geometric relations for a cardioidal cross section[10] are:

$$R_2/b_2 = (1+s^2+2s\cos\theta^*)^{1/2}/(1+s),$$

$$G(\theta^*) = (\cos\theta^* + 2s\cos\theta^*)/(\sin\theta^* + 2s\sin\theta^*),$$

$$\gamma_i = \pi/2 - \tan^{-1}[G(\theta_i^*)] \quad \text{for } G(\theta_i^*) < 0,$$

$$\gamma_i = \pi/2 \quad \text{for } G(\theta_i^*) = 0,$$

$$\gamma_i = \pi/2 + \tan^{-1}[G(\theta_i^*)] \quad \text{for } G(\theta_i^*) > 0.$$

Here the characteristic length $d = b_2$ is the radius of the circumscribing circle for the cardioid and $\theta_i^* = (\theta_{i-1} + \theta_i)/2$. In the case of a cardioidal cross section the displacements are antisymmetrical about the y axis. The frequency equation is obtained by choosing $n,m = 1,2,3,\ldots$. The results evaluated at $a_1/b_1 = 1.5$ and $s = 0.3$ are presented in Table III. The dispersion curves in Fig. 4 are drawn for the ratio $a_1/b_1 = 1.2$ and $s = 0.3$.

IV. CONCLUSION

The frequency equation for an infinitely long pyroelectric cylinder of inner and outer arbitrary cross section of class 6 is obtained by using a Fourier expansion collocation method. The frequency equation in the case of an elliptical

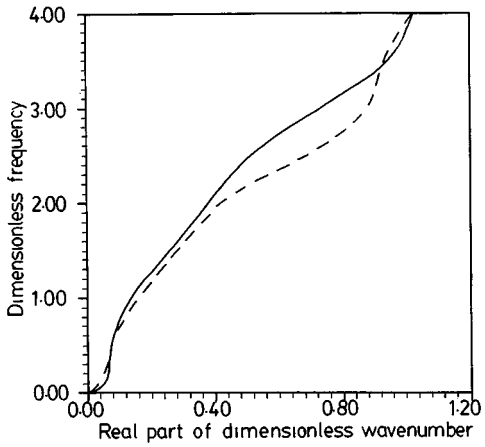

FIG. 2. Dispersion curves for the inner and outer elliptical cross sections for the symmetric case with aspect ratios of $a_1/b_1 = a_2/b_2 = 1.2$ and $b_1/b_2 = 0.5$; —, longitudinal mode; -----, flexural mode.

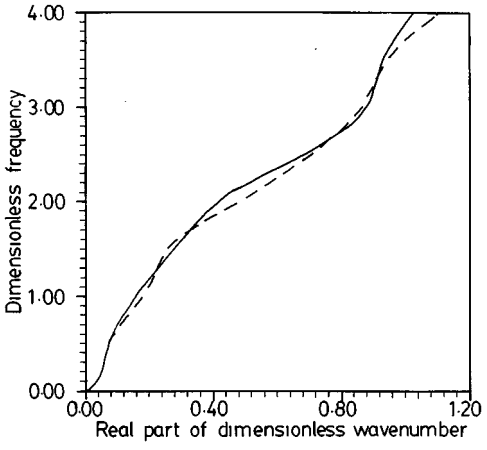

FIG. 3. Dispersion curves for the inner and outer elliptical cross sections for both the symmetric and antisymmetric cases with aspect ratios of $a_1/b_1 = a_2/b_2 = 1.2$ and $b_1/b_2 = 0.5$; —, symmetric case; -----, antisymmetric case.

TABLE III. Values of ϵ for different values of dimensionless frequency for cardioidal (cb_2) cross section with elliptical cavity for flexural vibration with aspect ratio $a_1/b_1 = 1.5$ and $s = 0.3$.

cb_2	Nondimensional wave no. (ϵ)
0.50	0.07423+i0.121E-02
1.00	0.17018+i0.505E-03
1.50	0.28734+i0.202E-04
2.00	0.42066+i0.103E-02
2.50	0.59176+i0.204E-04
3.00	0.88546+i0.121E-03
3.50	0.96144+i0.663E-03
4.00	1.14506+i0.775E-03

cavity with elliptical and cardioidal outer boundary has been analyzed numerically. Analysis provided in the present paper can be extended to nonconvex boundaries like star shape. The same problem in piezoelectric material has been studied by Paul and Venkatesan.[14] In the present case, besides the thermal field, the entropy equation comes into play which makes the problem more complicated to solve analytically.

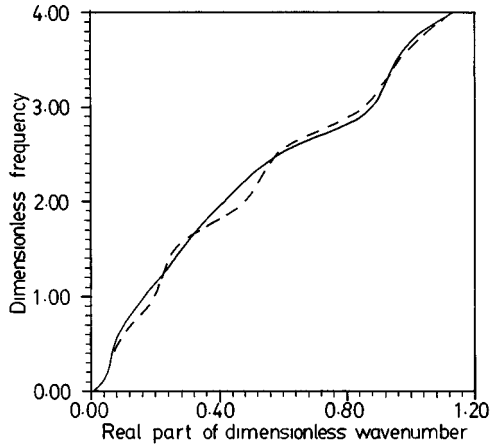

FIG. 4. Dispersion curves for a cardioidal cross section with elliptical cavity with aspect ratios of $a_1/b_1 = 1.2$ and $s = 0.3$; —, symmetric case; -----, antisymmetric case.

Results presented for symmetric and antisymmetric modes are the lowest modes of vibration. As the lowest mode gives the maximum resonance, the other modes of vibration from the transcendental frequency equation are not provided. However, tables are different from dispersion curves drawn in figures as the aspect ratio is not the same. It may not be out of point to state again that the limiting case of this problem is not applicable to either the piezoelectric case or the elastic case as there are additional governing equations. For the same reason, solutions of the Helmholtz function method cannot be derived from our method. When the segment is divided into 20 parts, four Fourier components are sufficient to get good convergence of the series.

ACKNOWLEDGMENTS

The authors wish to express their grateful thanks to the reviewers for their valuable suggestions to improve the presentation.

[1] H. S. Paul, Archiwum Mechaniki Stosowanej. **4**, 14 (1962).
[2] H. S. Paul, J. Acoust. Soc. Am. **40**, 1077 (1966).
[3] N. Guzelsu and S. Saha, J. Biomech. **14**, 19 (1981).
[4] H. S. Paul and D. P. Raju, J. Acoust. Soc. Am. **77**, 255 (1982).
[5] H. S. Paul and M. Venkatesan, J. Acoust. Soc. Am. **82**, 952 (1987).
[6] H. S. Paul and G. V. Raman, Acta Mech. **87**, 37 (1991).
[7] H. S. Paul and G. V. Raman, Proc. INSA, Pt. A **57**, 585 (1991).
[8] K. Nagaya, J. Acoust. Soc. Am. **70**, 763 (1981).
[9] K. Nagaya, J. Appl. Mech. **49**, 157 (1982).
[10] K. Nagaya, J. Vib. Acoust. Stress. Rel. Design **105**, 132 (1983).
[11] K. Nagaya and T. Watanabe, J. Acoust. Soc. Am. **75**, 834 (1984).
[12] H. S. Paul and M. Venkatesan, Int. J. Eng. Sci. **27**, 847 (1989).
[13] H. S. Paul and M. Venkatesan, J. Acoust. Soc. Am. **89**, 196 (1991).
[14] H. S. Paul and M. Venkatesan, Int. J. Eng. Sci. **29**, 1601 (1991).
[15] H. S. Paul and G. V. Raman, J. Acoust. Soc. Am. **93**, 1175 (1993).
[16] T. D. Sullivan and J. M. Powers, J. Acoust. Soc. Am. **63**, 1396 (1978).
[17] D. Ricketts, J. Acoust. Soc. Am. **68**, 1025 (1980).
[18] M. C. Dokmeci, Int. J. Eng. Sci. **18**, 431 (1980).
[19] S. B. Lang, Ferroelectrics **142**, 3–4, 263 (1993).
[20] S. B. Lang, Ferroelectrics **146**, 1–4, 153 (1993).
[21] R. D. Mindlin, *Problems in Continuum Mechanics* (SIAM, Philadelphia, 1961), p. 282.
[22] H. S. Paul and K. Natrajan, J. Acoust. Soc. Am. **99**, 373 (1996).
[23] D. A. Berlincourt, D. R. Curran, and H. Jaffe, *Physical Acoustics* (Academic, New York, 1964), Vol. 1, Pt. A, p. 204.

A low-frequency directional flextensional transducer and line array[a)]

Stephen C. Butler
Naval Undersea Warfare Center, Newport, Rhode Island 02841

John L. Butler and Alexander L. Butler
Image Acoustics, Incorporated, 97 Elm Street, Cohasset, Massachusetts 02025

George H. Cavanagh
Massa Products Corporation, 280 Lincoln Street, Hingham, Massachusetts 02043

(Received 14 August 1996; accepted for publication 20 February 1997)

A unique low-frequency (900 Hz) class IV flextensional transducer that produces an enhanced far-field pressure on one side and canceled far-field pressure on the other side has been developed. The transducer radiating surface consists of a thick-walled elliptical aluminum shell and a U.S. Navy type III piezoelectric stack along its major axis with two active sections and one inactive section. The directionality is achieved by simultaneously exciting the shell into an omnidirectional and dipole operation by driving stack into both extensional and bending modes. Both measurements and modeling on this device show a front to back pressure ratio of more than 30 dB, producing cardioid-type radiation patterns over an octave band, for a single transducer element. The transducers measured mechanical Q is 8, coupling coefficient is 0.25, and electroacoustic efficiency is 80% and produced a source level of 215 dB *re:* 1 μPa at 1 m when driven at a field limit of 394 kV/m (10 kV/in.) at resonance. The uniqueness of this transducer is its directional beam patterns (directivity index=3.4 dB) and high acoustic output power from a small (less than a third of a wavelength) single element. Six of these transducers were placed in a closely packed line array two-wavelengths long. The array successfully produced narrow directional sound beams (directivity index=8.7 dB) with a front to back ratio greater than 30 dB and a source level of 225 dB *re:* 1 μPa at 1 m. [S0001-4966(97)03806-X]

PACS numbers: 43.38.Fx, 43.30.Yj, 43.30.Yj [SLE]

INTRODUCTION

Flextensional transducers are used for low-frequency, high-power sound sources in underwater applications. Standard class IV flextensional transducers[1] contain an elliptical shell of inert material such as aluminum or fiberglass, with a drive motor stack of piezoelectric ceramics mounted along the major axis. When the motor is driven the displacement of the sides of the shell are typically much larger than the displacement of the ceramic stack itself, thus producing the large amplitudes necessary for high-power, low-frequency, underwater sound generation.

Since flextensional transducers are small compared to the wavelength of sound at resonance, and because the majority of the surface area of the shell moves in phase, the acoustic radiating patterns from the transducers are nearly omnidirectional. This creates a significant problem in designing arrays that are to radiate in only one direction. At the present time, such arrays must be fabricated utilizing large baffles or rows of transducers spaced and phased to give directional patterns. This requirement for massive, expensive baffles or multiple lines can be eliminated by using a flextensional transducer which radiates in only one direction.

This development is an extension of the previous work on a 3.25-kHz directional flextensional transducer.[2] The original directional flextensional transducer was designed so that the frequencies of both the omnidirectional mode of vibration, which is also called the quadrupole mode, and the bending mode of vibration exist close to each other. (Here the quadrupole mode refers to the four nodes of a class IV flextensional transducer shell, rather than the radiation beam pattern type. The quadrupole mode produces a nearly omnidirectional radiation beam pattern since the majority of the surface area of the shell moves in phase and also these transducers are generally smaller than a half wavelength.) During operation, both of these modes were excited simultaneously, resulting in one side of the shell remaining relatively stationary, while the other side moves in and out, thus producing a flextensional transducer operating in a directional mode.[3]

During this development, the method of driving the transducer was improved thereby allowing higher sound power levels and an optimized front to back ratio. Lower-frequency 900-Hz transducers were fabricated,[4] tested, and installed into a six-element line array. Both measurements and modeling on this device show a front to back pressure ratio of more than 30 dB, producing cardioid type radiation patterns for a single element and narrow-beam radiation patterns for the six-element line array (see Fig. 1) of over an octave frequency bandwidth.

[a)]Portions of this paper were presented at the 3rd Joint (132nd) Meeting of the Acoustical Societies of America and Japan, Honolulu, HI [J. Acoust. Soc. Am. **100**, 2730(A) (1996)].

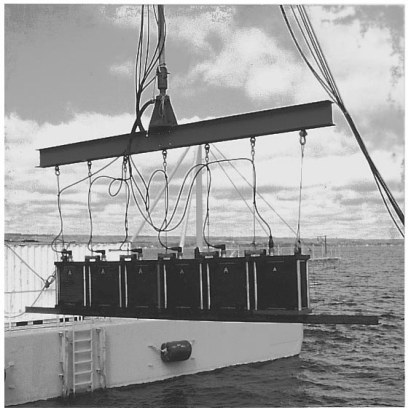

FIG. 1. Photograph of the 900-Hz directional flextensional six-element two-wavelength long line array prior to testing, showing side A.

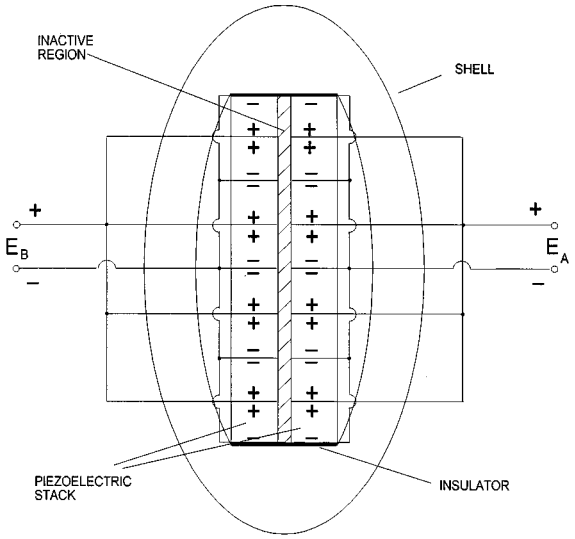

FIG. 2. Example of an electrical drive arrangement for the simultaneous excitation of the quadrupole and dipole modes leading to the creation of the directional mode.

I. THEORY OF OPERATION AND MODELING

We present here the theory of operation of two methods of drive which can be used to achieve directionality in class IV flextensional transducers under either array or single-element applications, respectively.[4] We first review the condition for displacement drive directionality and then introduce the condition for pressure field directionality.

The directional flextensional transducer achieves directionality by simultaneously combining the shell quadrupole mode with a shell/stack dipole mode. In one means of excitation the two modes are driven together to create a displacement reduction on one surface and enhancement on the opposite surface. This case allows potentially unidirectional operation from planar arrays and modest directional operation for a single element. In the second means of excitation the two modes are driven to create a pressure reduction in one direction and a pressure enhancement in the other direction. This second case allows unidirectional operation from a single element or a line array of elements.

The unidirectional mode is achieved by simultaneously exciting the flextensional transducer into its fundamental quadrupole mode (which is essentially omnidirectional) and also into its fundamental dipole mode. The excitation of the dipole mode is accomplished by driving the piezoelectric stack into a bending mode which causes the shell to move in an oscillatory way as a reaction to the stack bending motion. The stack bending mode is excited by dividing the stack into two separate electrical parts and driving them out of phase to cause bending. The conventional omnidirectional quadrupole mode is excited by driving the two sides of the stack in phase. The combined directional results are canceled motion on one side and enhanced motion on the other side.[3]

The drive scheme is illustrated in Fig. 2 showing two halves of a drive stack assembly. To excite the quadrupole mode we put equal polarity values $+E_q$ on side A and $+E_q$ on side B of the stack. To excite the dipole mode we put opposite polarity values such as $+E_d$ on the left and $-E_d$ on the right side. We sum both of these modes to obtain the directional mode. In this case with E_A the total voltage on side A and E_B the total voltage on side B we would have

$$E_{\mathrm{A}}=E_q+E_d \quad \text{and} \quad E_{\mathrm{B}}=E_q-E_d. \tag{1}$$

For the simple case where E_d is set equal to E_q we have $E_{\mathrm{A}}=2E_q$ and $E_{\mathrm{B}}=0$. In this case only one half of the ceramic stack would be driven. This assumes that equal drives yield equal displacement amplitudes. If the displacement of the dipole mode were twice as much at resonance due to a higher mechanical Q, the dipole drive voltage should be reduced to $E_d=E_q/2$ yielding the drive condition $E_{\mathrm{A}}=(3/2)E_q$ and $E_{\mathrm{B}}=E_q/2$ or the ratio condition $E_{\mathrm{A}}/E_{\mathrm{B}}=3$.

For the most effective operation the directional flextensional transducer is designed so that the transducer dipole mode resonates in the vicinity of the transducer quadrupole mode resonances. Since the dipole and quadrupole amplitudes and phase may not be the same at the desired operating frequency, the dipole mode may require a different amplitude and phase drive condition to attain reduced motion on one surface. Moreover, if the desire is to attain a deep pressure null on one side an additional 90° phase shift may be required to compensate for the quadrature related radiation characteristics of the dipole and monopole sources.

If planar array operation is desired, then the cancellation of the displacement on one surface (say the back surface) should be the goal. However, for a single element or line array stationary motion on one surface may not be sufficient for directionality since the front surface radiation may be diffracted around to the back as a result of the small size of the element. In this case the goal should be the cancellation of the pressure in the back direction.

The cancellation of the pressure in one direction can be understood by considering the case of an ideal spherical radiator, of radius a, operating in both an omnidirectional (pulsating) and a dipole (oscillating) mode of vibration. First let p_o and v_o be the pressure and velocity in the omnidirectional mode and p_d and v_d be the pressure and velocity in the dipole mode. Then with k the wave number, $2\pi/\lambda$, it can be shown that the dipole pressure can be written in terms of the omnidirectional pressure as

$$p_d=p_o\cos(\theta)(v_d/v_o)jka/(1+jka), \tag{2}$$

where θ is the angle from the direction of the maximum output of the dipole mode and $j=\sqrt{(-1)}$. With the sphere operating in both modes with corresponding modal velocities v_o and v_d the total pressure $p_t=p_o+p_d$ is then

$$p_t=p_o[1+\cos(\theta)(v_d/v_o)jka/(1+jka)]. \tag{3}$$

In the high-frequency range we get the approximation

$$p_t\cong p_o[1+\cos(\theta)(v_d/v_o)], \quad ka\gg 1 \tag{4}$$

while in the low-frequency range we get

$$p_t\cong p_o[1+jka\ \cos(\theta)(v_d/v_o)], \quad ka\ll 1. \tag{5}$$

The intermediate frequency range is generally located just above the quadrupole resonance for a class IV transducer.

We see that in the high-frequency range we get a cardioid type $[1+\cos(\theta)]$ condition for velocity cancellation on one side. This condition should also apply to the case of an array that is large compared to wavelength of sound. In the lower frequency range it can be seen that there must also be a 90° phase shift and frequency dependence between the velocities in order to arrive at $jka(v_d/v_o)=1$ and achieve the cardioid pressure function $[1+\cos(\theta)]$. That is, for a cardioid function we would need to electrically drive the dipole mode so that the dipole velocity $v_d=v_o/jka$.

The cardioid function may be obtained over a broad frequency range if the dipole velocity follows the relation

$$v_d=v_o(1+1/jka), \tag{6}$$

as may be seen from Eq. (3). The 90° phase difference at low frequency and the zero phase difference at high frequencies between the two modes can be generalized and applied to most transducers including the class IV flextensional. The combined use of monopole and dipole operation of a spherical transducer has been described by Ehrlich.[5]

At high frequencies we would not expect to need a phase shift between the quadrupole and dipole modes while at low frequencies an additional 90° phase shift on the dipole mode would be needed to accomplish the desired results. If in addition to this, the dipole mode operates with twice the output at resonance (e.g., due to a higher mechanical Q as a result of the lower radiation loading) the drive condition for pressure cancellation would be $E_d=jE_q/2$ yielding $E_{\mathrm{A}}=E_q(1+j/2)$ and $E_{\mathrm{B}}=E_q(1-j/2)$ or $E_{\mathrm{A}}/E_{\mathrm{B}}=3/5+j4/5$ yielding an amplitude ratio of unity and phase angle difference between stack sides A and B given by 53°. The corresponding condition for displacement cancellation was shown earlier to be a less favorable amplitude ratio of three with no phase difference between the two sides.

The transducer was modeled using the ANSYS[6] finite element program which contains structural, piezoelectric, and acoustical fluid elements. Our ANSYS results were limited to a 2-D model which under fluid loading conditions corresponds to the results for a long line array rather than a short single element.

In Fig. 3 we show computed ANSYS results for both displacement and pressure cancellation for the 900-Hz design. The top figure is for the case of displacement cancellation showing a smaller front to back ratio below resonance due to back diffraction. However, because of self-baffling, there is an improved ratio above resonance. Here the quadrupole is driven at one volt and the dipole mode is driven at one-half volt to compensate for the higher Q of this mode. One part of the stack is driven at 1.5 V and the other part is driven at 0.5 V. The lower illustration is for the same mechanical Q conditions but with the dipole additionally phase shifted by 90°. This yields identical stack sectional voltage magnitudes and a phase shift of 53° as discussed earlier. This condition yields greater output and an improved front to back ratio below resonance. A reduction in phase difference above resonance yields improved front to back ratios above resonance.

The ANSYS theoretical predictions for velocity or pressure cancellation were based on a given drive condition between the quadrupole and dipole modes. One would expect that an optimized frequency-dependent amplitude and phase drive condition could yield a large front to back ratio over a broad range of frequencies. From the above discussion of the ideal spherical radiator we would expect that the required wideband dipole velocity response should follow Eq. (6), with v_o replaced by v_q yielding

$$v_d\cong v_q(1+1/jka). \tag{7}$$

However, because the two modes may have different resonant frequencies and a class IV flextensional is not an ideal sphere, this relation between v_d and v_o is an over simplification.

In practice we usually have direct control of the input voltages rather than the modal velocities. Accordingly, an accurate model of the transducer in both the nearly omnidirectional quadrupole and dipole modes is needed. Although ANSYS yields reasonably good predictions, it is not accurate enough to predict deep nulls in the back radiation where a near exact prediction of the separate omnidirectional and dipole pressure amplitudes and phases are needed. Another approach is to separately measure the on-axis omnidirectional (quadrupole) and dipole amplitude and phase responses of the transducer or array of transducers for a given voltage input. From this information the dipole input voltage amplitude may be adjusted so that the on-axis pressure amplitudes and phases match that of the quadrupole mode. Since the dipole mode has two lobes of opposite phase, one lobe will add to the quadrupole (omnidirectional) mode and the other will cancel yielding a null on one side and a pressure increase on the other side.

This method may be described mathematically through Eq. (1) written as

$$E_{\mathrm{B}}/E_{\mathrm{A}}=(1-R)/(1+R), \quad \text{where} \quad R=E_d/E_q. \tag{8}$$

Thus given the desired complex ratio R of dipole and quadrupole drives we can determine the corresponding complex voltage ratio for sides A and B of the piezoelectric stack.

In order to relate this to the pressure response levels let the transmitting voltage response (TVR) for the dipole p_d and quadrupole p_q mode pressures be

$$\mathrm{TVR}_d=p_d/E_d \quad \text{and} \quad \mathrm{TVR}_q=p_q/E_q. \tag{9}$$

For a null in one direction the pressures should be equal; i.e., $p_d=p_q$, leading to the required condition $E_d=p_q/\mathrm{TVR}_d$ so

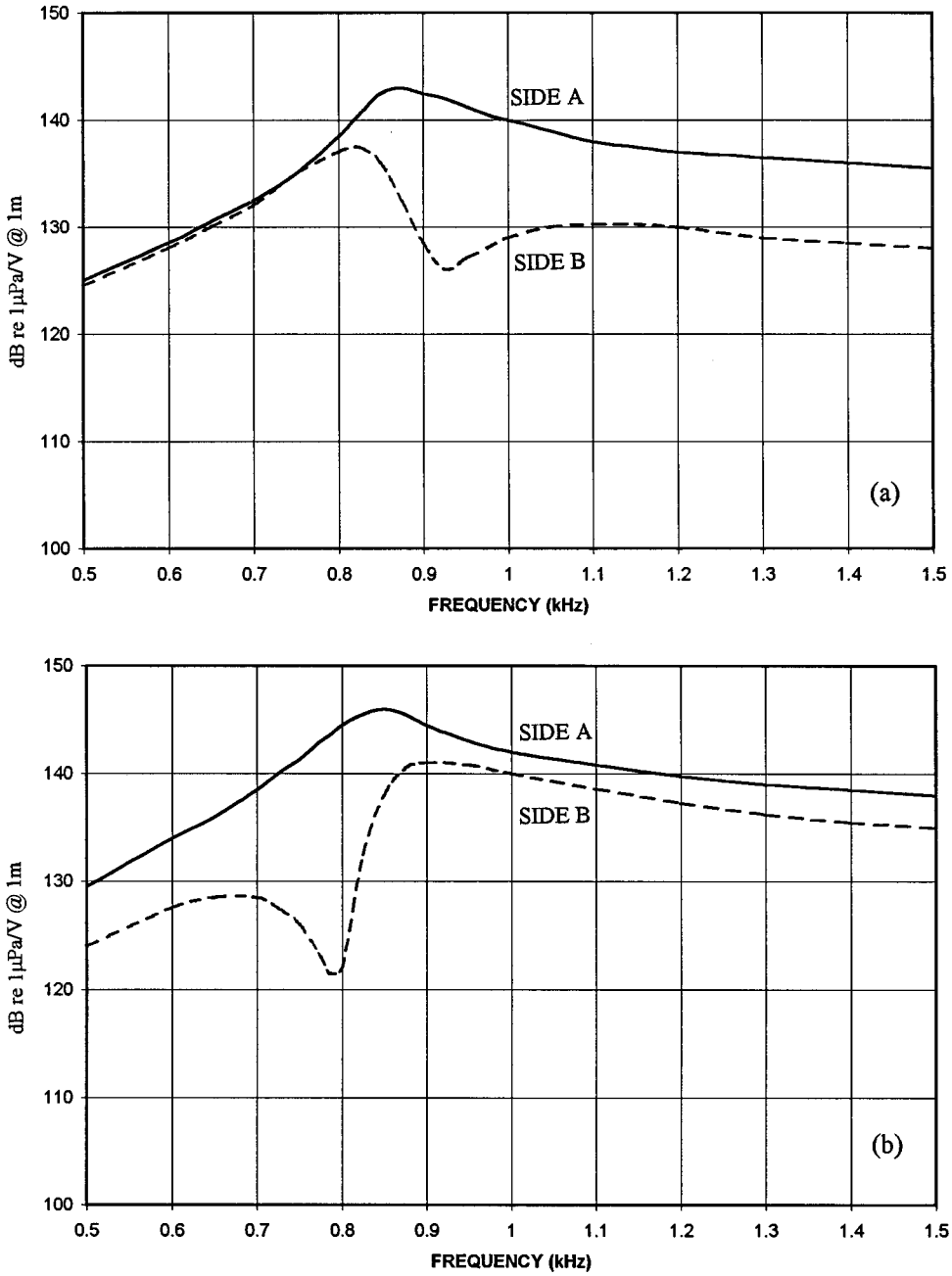

FIG. 3. ANSYS finite-element modeled transmitting voltage response operating in the directional (a) displacement mode, $E_A=1.5$ and $E_B=0.5$ ($E_q=1$, $E_d=0.5$) and (b) pressure mode, $E_A=1$ and $E_B=1$ at 53° ($E_q=1$, $E_d=0.5$ at 90°).

that for this case R, which is equal to E_d/E_q, is given by

$$R=\mathrm{TVR}_q/\mathrm{TVR}_d. \tag{10}$$

Thus, the complex quantity R is determined by the complex ratio of the quadrupole and dipole constant voltage transmitting responses yielding the desired complex ratio of the voltages on each side of the stack through the equation

$$E_B/E_A=(1-R)/(1+R). \tag{11}$$

This expression, which is written in complex quantities, may also be written in terms of amplitude and phase quantities for ease in measured data reduction and voltage drive application.

II. THE PHYSICAL MODEL AND MEASURED RESULTS

The transducer is composed of two elliptical aluminum shells each 7.5-in. (19.05-cm) high, a wall thickness of 1.2 in. (3.05 cm), and semimajor and semiminor axes radii of 8.1 in. (20.57 cm) and 3.1 in. (7.87 cm), respectively. A piezoelectric ceramic stack is inserted along the major axis of the shell. Each ceramic stack is 13-in. (33.02-cm) long, 6-in. (15.24-cm) high, 3-in. (7.62-cm) thick, and composed of 52 U.S. Navy type III 1/4-in. (6.35-mm) thick ceramic plates stacked in series. The ceramic plates were manufactured with an inactive central margin, by removing 1/4 in. (6.35-mm) of silver electrodes from the surface on both the top and bottom of the plates. All of the electrodes on each side of the stack

TABLE I. Measured transmit response of omnidirectional and dipole mode used to determine the drive condition for a directional mode at 900 Hz.

	TVR_q		TVR_d		R		E_B/E_A (volts)		Measured
	Level	Phase	Level	Phase	Level	Phase	Magnitude	Phase	Front/Back
Single element	141.4 dB	70.6°	151.2 dB	−67.8°	−9.8 dB	238.4°	0.728	−31.6°	55 dB
Array	154.4 dB	−74.4°	161.9 dB	−123.9°	−7.5 dB	49.5°	1.66	38.0°	62 dB

are electrically connected in parallel permitting each side of the stack to be independently driven for the excitation of the stack bending modes. The shells were pinned together to form the complete transducer and enclosed with a bonded rubber boot banded to two aluminum end plates separated by four stainless-steel rods, giving the transducer overall dimensions of 19.4-in. (49.3-cm) long, 9.5-in. (24.1-cm) wide, 20.3-in (51.6-cm) high, and an in-air weight of 350 lb (147.4 kg). Six of these transducers were fabricated and separately acoustically tested then assembled into a six-element horizontal line array (see Fig. 1) two-wavelengths long with a 20-in. (50.8-cm) center to center spacing. The testing was conducted in a free-field open-water environment at a depth of 308 feet (94 m) to avoid unwanted reflections and cavitation.

The method in Sec. I which describes a mathematical procedure to determine the electrical drive condition for obtaining a large front to back ratio, was used during the testing of the transducer in order to create directional beams. This method requires the measurement of the complex pressure response (magnitude and phase) of the transducer or array in the omnidirectional and dipole modes [see Eq. (9)]. For a pressure null on one side to exist the omnidirectional and dipole pressures must be equal, leading to Eq. (10). This complex quantity R was calculated for both the single transducer element and the array, so that complex drive ratios of E_B/E_A of Eq. (11) could be determined. Table I lists the results at 900 Hz for both the single element and array. This method was used over a wide frequency band and fine adjustments were made with hydrophones placed on opposite sides A and B to obtain the largest front to back ratio as possible.

Each element was tested in the omnidirectional, dipole, and directional mode. In the single element omnidirectional mode, the transducer elements produced a sound-pressure level (SPL) of 211 dB *re:* 1 μPa at 1 m referenced to the flat side of the transducer. The directional mode yielded an increased SPL of approximately 215 dB *re:* 1 μPa at 1 m when driven at the full power field limit of 394 kV/m (10 kV/in). The power based electroacoustic efficiency, measured during the tests, was approximately 80% in both modes. The measured directivity index (DI) of the directional mode at 900 Hz is 3.4 dB and −1.8 dB for omnidirectional mode when referenced to the sides of the shell. The omnidirectional mode mechanical Q is 4 (typical for flextensional transducers), the mechanical Q in the dipole mode is 13 and in the directional mode the mechanical Q is 8. Figure 4 shows the measured omnidirectional, dipole, and directional (cardioid) beam patterns. In Fig. 5 we show the single-element transducer measured transmitting voltage response driven in the fundamental omnidirectional mode (both stack sections A and B driven electrically in phase with the same amplitude), the dipole mode (A and B driven electrically 180° out of phase from each other with the same amplitude), and the directional mode of operation with the phase and amplitude adjusted to obtain a maximum front to back ratio over that frequency band. It is interesting to note that the mechanical Q and transmitting voltage response of the directional mode is approximately the average of the omnidirectional and dipole modes.

In the array configuration all of the side A drive leads were connected in parallel and all of side B drive leads were connected in parallel with each side driven by separate waveform generators and power amplifiers. The six-element line array produced a SPL of 225 dB *re:* 1 μPa at 1 m in the directional mode with a measured operating electroacoustic efficiency of over 80% and a mechanical Q of 4. Radiation patterns yielded back reductions of 53 to 75 dB between 600 and 1400 Hz in a single line of six elements. The array maximum response axis is easily changed by reversing the drive signals producing an array capable of projecting in either the forward or backward directions. The radiation pat-

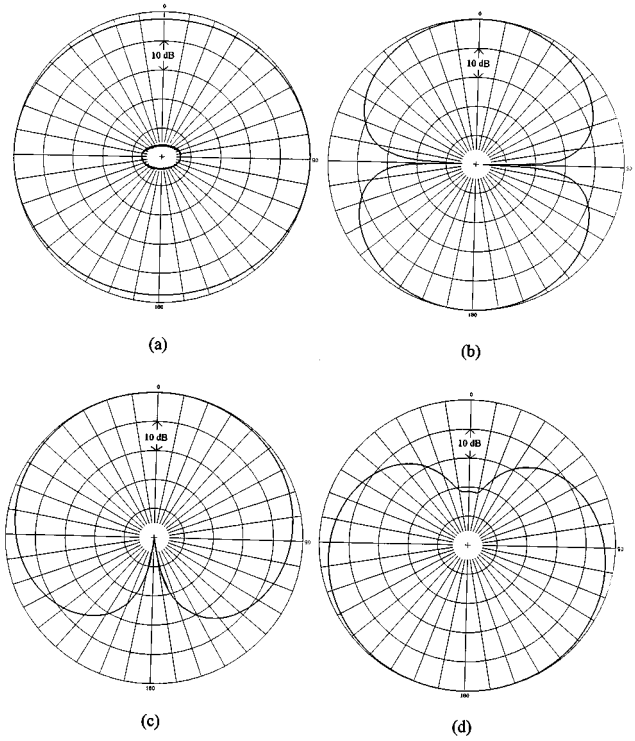

FIG. 4. Measured single-element 900-Hz radiation patterns operating in the (a) quadrupole mode, $E_A = E_B$, (b) dipole mode $E_A = -E_B$, (c) directional mode $E_A/E_B = 0.73$ at 31.6°, and (d) directional mode drive leads reversed.

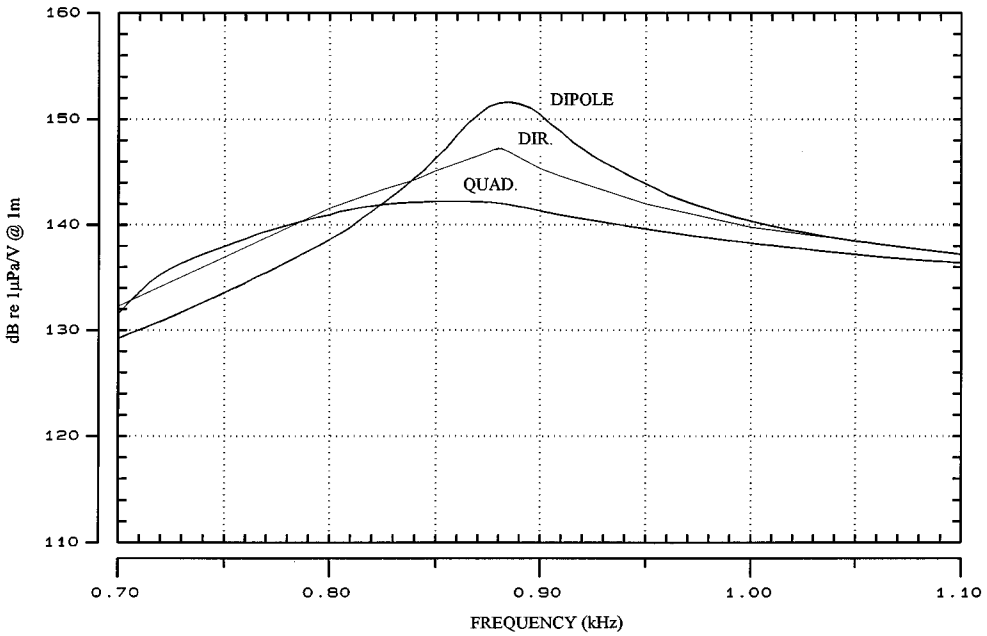

FIG. 5. Measured single-element transmitting voltage response driven in quadrupole, dipole, and directional modes.

terns for the six-element line array are shown in Fig. 6 for the array steered in both the forward and backward directions at 900 Hz. The measured beamwidth is 27.4° which is close to that of an ideal two-wavelength line with a calculated beamwidth of 27.8°. Another method of presenting directional array performance is through a plot of the TVR across the operating band in the forward and backward direction. In the upper plot of Fig. 7, the top trace is the TVR measured on side A of the array, while the lower trace is the B side or back side TVR. The vertical scale is 20 dB/division to allow the significant front to back ratios to be displayed. The lower plot of Fig. 7 is identical to the upper plot, but the A and B drive leads of the array have been reversed, thereby reversing the direction of radiation.

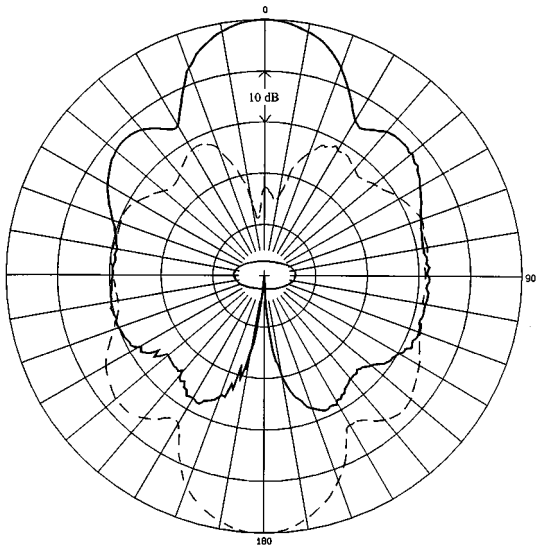

FIG. 6. Measured 900-Hz radiation patterns for the six-element line array operating in the directional mode (—) and with the drive leads reversed (------).

III. SUMMARY AND CONCLUSIONS

We have presented a directional class IV flextensional transducer which can be operated in either displacement or field pressure canceling modes. The transducer uses both the conventional quadrupole mode which is excited by the extensional motion of the piezoelectric stack and a body dipole mode which is excited by the inextensional bending mode of the stack. The piezoelectric stack is separated into two sides so that both sides may be separately energized to excite both modes. The displacement drive condition is the preferred choice for unidirectional planar array applications. The phase shifted pressure drive condition is the choice for single-element or line array applications. This choice yields not only a large front to back ratio but also an increase in source level and greater power capacity since both sides of the stack are simultaneously driven. This method also allows the optimization of the front to back ratio at all frequencies by use of the phase and amplitude transmitting voltage response values of the quadrupole and dipole mode to obtain the required input voltage amplitude and phase for each side of the piezoelectric stack.

The phase shifted pressure drive condition significantly improves operation by providing increased SPL and back reductions of up to 75 dB with both single elements or line arrays. Measured results revealed a directional transducer which operated efficiently in both the normal (omnidirectional) and directional mode. A six-element line array of directional flextensional transducers produced a SPL of over 225 dB *re:* 1 μPa at 1 m with an operating efficiency of over 80%.

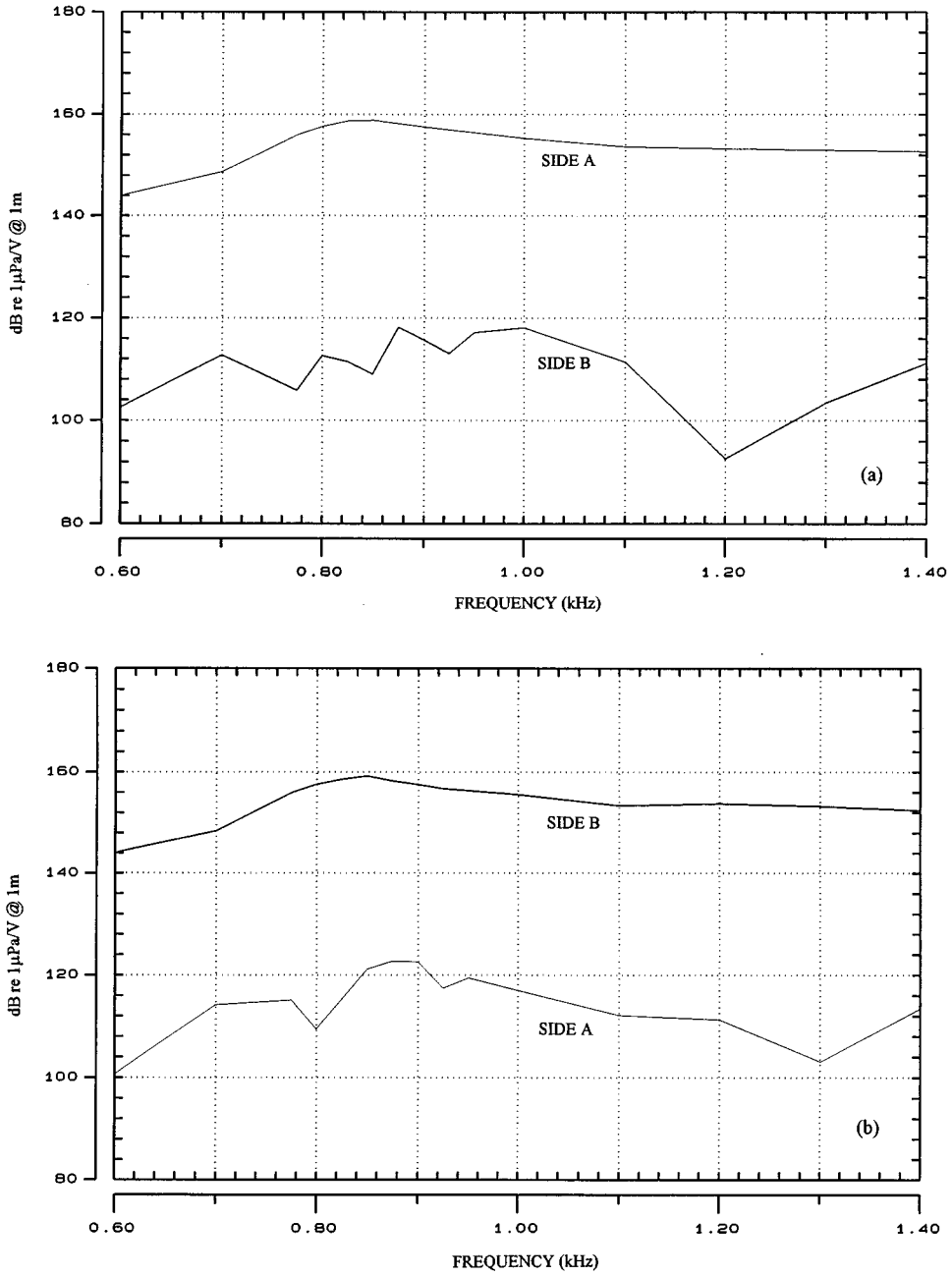

FIG. 7. Measured transmitting voltage responses for the six-element line array operating in the directional mode in the (a) forward (side A) and backward (side B) directions and (b) with the drive leads reversed, forward (side B) and backward (side A).

ACKNOWLEDGMENTS

The authors would like to thank Jan F. Lindberg of the Naval Undersea Warfare Center (NUWC), Newport, RI for his support on this project. Work was performed in a joint venture by Massa Products Corporation and Image Acoustics, Inc., with support, in part through a U. S. Navy SBIR contract.

[1] K. D. Rolt, ''History of flextensional electroacoustic transducers,'' J. Acoust. Soc. Am. **87**, 1340–1349 (1990).

[2] S. C. Butler, A. L. Butler, and J. L. Butler, ''Directional flextensional transducer,'' J. Acoust. Soc. Am. **92**, 2977–2979 (1992).

[3] J. L. Butler, ''Directional Flextensional Transducer,'' US Patent No. 4,754,441 (28 June 1988).

[4] J. L. Butler, A. L. Butler, and G. H. Cavanagh, ''A Unidirectional Flextensional Transducer for Single Element and Array Application,'' Proc. Inst. Acoust. **17**, Part 3, 189–199 (1995).

[5] S. L. Ehrlich, ''Spherical Acoustic Transducer,'' US Patent No. 3,732,535 (8 May 1973). See also, S.-H. Ko, G. A. Brigham, and J. L. Butler, ''Multimode Spherical Hydrophone,'' J. Acoust. Soc. Am. **56**, 1890–1898 (1974); J. L. Butler and S. L. Ehrlich, ''Superdirective Spherical Radiator,'' J. Acoust. Soc. Am. **61**, 1427–1431 (1977).

[6] ANSYS, Inc., 210 Johnson Road, Houston, PA 15342.

Dynamic response and power flow in three-dimensional coupled beam structures. I. Analytical modeling

N. H. Farag and J. Pan
Department of Mechanical and Materials Engineering, University of Western Australia, Nedlands, Western Australia 6907, Australia

(Received 16 September 1996; accepted for publication 7 February 1997)

This paper deals with the prediction of the dynamic response and vibrational power flow in general three-dimensional coupled beam structures. An arbitrary loading condition is assumed and flexural waves in two perpendicular planes and longitudinal and torsional waves, may be excited simultaneously in each beam. The interaction of different wave types at the coupling boundaries is therefore expected. Suitable for the low- and medium-frequency range, the modal receptance method used here allows the prediction of the detailed structural response and power flow components carried by the different wave types through joint boundaries and at any cross section of the beam structure. The mathematical description of the three-dimensional beam structure and the manipulation of receptance matrices are presented in such a form that the vibration of any complex beam structure may be described systematically and with clear physical interpretations. The prediction of the input and output power for each component beam quantifies the energy dissipation in the beam, which may be taken as a measure of the spatial average response level of the beam. Computational examples of the power flow components at the joint boundaries of the component beams in coupled three-dimensional structures are used to illustrate the significance of the theoretical results. [S0001-4966(97)02806-3]

PACS numbers: 43.40.Cw [CBB]

INTRODUCTION

The prediction of the dynamic response and vibrational power flow characteristics of three-dimensional coupled beam structures is the concern of this paper. In their previous work,[1] the authors presented a method to predict the power flow in coupled beam structures. However, their formulation was limited to the case of in-plane structures under in-plane loads and as a consequence only longitudinal and in-plane flexural vibrations were considered.

The present work is a natural extension to the previous one. It presents a formulation describing the dynamic response of general multiple beam structures in the three-dimensional space under general loading conditions. Within this type of structure, flexural waves in two perpendicular planes, and longitudinal and torsional waves, can be excited simultaneously. The prediction of dynamic response includes the calculation of vibrational velocities, internal forces, and then power flow at any location of the beam structure.

Two methods are now widely used for the prediction of the dynamic response of coupled structures. They are finite element analysis (FEA) and the statistical energy analysis (SEA). Other methods have also been developed to encounter the problem, especially in the medium-frequency range where both FEA and SEA have their own limitations. It is observed that the majority of these methods employed the wave solution to the basic equations of vibration in their formulation and little work can be found in the literature that adopts the modal analysis approach. Yong and Lin[2] used a wave scattering matrix formulation for the dynamic response of truss-type structural networks. Langley[3] used a dynamic stiffness approach to analyze power flow in beams and frameworks. Mead[4] used wave receptance functions in his analysis of the free and forced response of the periodic structures. Miller and Flotow[5] used a transfer matrix approach and recently Beale and Accorsi[6] used a matrix method and the wave approach to solve the problem of two- and three-dimensional frame structures. Their model can accept only forces at the joints and they investigated the total power flow rather than the components.

Among the researchers using the modal solutions, Cuschieri[7,8] used a mobility approach for periodic structures and L-shaped plates. Guyader *et al.*[9] developed a modal formulation for coupled plates (which can be equally adapted to coupled beams) but in their formulation they used the modal properties of the coupled structure rather than that of the components. Very recently Miccoli *et al.*[10] presented a modal receptance approach to the case of beam-stiffened plates representing an idealized aircraft wing. It should also be stated in this quick survey that Bishop and Johnson[11] discussed the use of receptance approach in single and coupled beam structures. Also Soedel[12] applied the receptance technique to the coupled structures of shells and plates.

In the present analysis, the modal receptance approach is adopted because it allows convenient estimation of band-limited power flow as demonstrated for acoustical–structural coupling problems by Pope and Wilby.[13] Because the boundary conditions of the component beams are included when the resonance frequencies and mode shapes are selected in the first stages of the solution, the approach presented in this paper leads to simplification of the subsequent mathematical manipulation. Furthermore, the modal properties of the component beams are already available in the literature and they are used directly to obtain the characteristics of the coupled structure. Different damping values for different modes or

for different frequency bands can be conveniently used in the model for the estimation of the response of real structures. As will be shown, the receptance matrix for a component beam is a 6×6 matrix for general loading conditions. It can be easily used as the building block for modeling the response of complex three-dimensional beam structures. This leads, in the very general case, to a maximum number of degrees of freedom which is six times the number of beam ends terminating at intermediate joints of the coupled beam structure. Consequently, the size of the characteristic matrix to be inverted for the response can be determined. The computational effort may be easily assessed from the size of the characteristic matrix and the number of modes participating in synthesising the coupled response.

In the previous work,[1] the modal receptance approach was defined and explained and the basic relations were derived for the special case of in-plane coupled beams under in-plane loading where only in-plane flexural and longitudinal vibrations were considered. In this paper, the basic relations are written for the general case of loading of the three-dimensional structures of coupled beams, the receptance matrix is developed for the general case of loading. The basic equations for multibeam, multijoint structures are derived and their practical applications discussed. The formulation is also extended to the prediction of the internal forces, the displacement vector, and the power flow total and components at an arbitrary cross section. Computational examples are used to illustrate the results of the analysis. In a companion paper,[14] experimental measurements are used to compare with the computational results from the present method and from the finite element method for assessing and verifying the accuracy of the method.

I. POWER FLOW IN COUPLED BEAMS CARRYING FOUR WAVE TYPES

Three-dimensional coupled beam structures under the general case of loading will carry flexural waves in two perpendicular planes, longitudinal and torsional waves. The force and displacement components at a cross section of the ith component beam at position x of the local beam coordinates (X_i, Y_i, Z_i) are presented in Fig. 1. The force vector at x is defined as

$$\mathbf{F}_i(x)=[N_x, N_y, N_z, M_x, M_y, M_z]^T, \tag{1}$$

where T denotes the transpose of the matrix. The elements of the force vector are, respectively, longitudinal force in the X_i direction, shear in the Y_i direction, shear in the Z_i direction, moment about X_i axis (torsion), bending moment about the Y_i axis, and bending moment about the Z_i axis. The displacement vector is defined as

$$\mathbf{S}_i(x)=[u, v, w, \theta_x, \theta_y, \theta_z]^T. \tag{2}$$

The elements of this displacement vector are respectively the linear displacements along the X_i, Y_i, and Z_i axes and the angular rotations about the X_i, Y_i, and Z_i axes.

For steady-state harmonic vibrations, the numerical values of the components of the force and displacement vectors are the complex amplitudes, and the time variation takes the form $e^{-j\omega t}$, where ω is the angular frequency. The velocity vector at position x can be written as

$$\dot{\mathbf{S}}_i(x)=-j\omega\mathbf{S}_i(x). \tag{3}$$

The time-averaged total power flow at position x is given by

$$P_t(x)=\tfrac{1}{2}\,\mathrm{Re}[\mathbf{F}_i^T(x)\dot{\mathbf{S}}_i^*(x)], \tag{4}$$

where * denotes the complex conjugate. If we define a diagonal force matrix $\mathbf{F}_d^{(i)}(x)$, where the components of the force vector are the main diagonal elements and all the off-diagonal elements are zeros, the components of the power flow can be obtained:

$$\begin{aligned} P_c(x)&=[P_{N_x}, P_{N_y}, P_{N_z}, P_{M_x}, P_{M_y}, P_{M_z}]\\ &=\tfrac{1}{2}\,\mathrm{Re}[\mathbf{F}_d^{(i)}(x)\dot{\mathbf{S}}_i^*(x)]. \end{aligned} \tag{5}$$

II. FORCE-DISPLACEMENT RELATIONSHIPS FOR COMPONENT BEAMS

For coupled beam structures under general loading condition, each component beam will carry four wave types (flexural waves in two perpendicular planes, longitudinal and torsional waves). To describe the four wave types, six degrees of freedom have to be considered at each cross section of a beam. The displacement vector $\mathbf{S}_i(x_1)$ at position x_1 is related to the force vector $\mathbf{F}_i(x_2)$ at position x_2 of beam i via a receptance matrix $\mathbf{R}_i(x_1, x_2)$ by the relation

$$\mathbf{S_i}(x_1)=\mathbf{R_i}(x_1, x_2)\mathbf{F_i}(x_2), \tag{6}$$

where

$$\mathbf{R}(x_1, x_2)=\begin{bmatrix} R_{uN_x}(x_1,x_2) & 0 & 0 & 0 & 0 & 0\\ 0 & R_{vN_y}(x_1,x_2) & 0 & 0 & 0 & R_{vM_z}(x_1,x_2)\\ 0 & 0 & R_{wN_z}(x_1,x_2) & 0 & R_{wM_y}(x_1,x_2) & 0\\ 0 & 0 & 0 & R_{\theta_xM_x}(x_1,x_2) & 0 & 0\\ 0 & 0 & R_{\theta_yN_z}(x_1,x_2) & 0 & R_{\theta_yM_y}(x_1,x_2) & 0\\ 0 & R_{\theta_zN_y}(x_1,x_2) & 0 & 0 & 0 & R_{\theta_zM_z}(x_1,x_2) \end{bmatrix}. \tag{7}$$

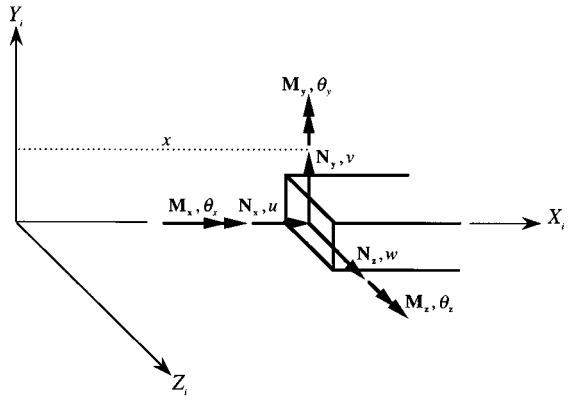

FIG. 1. Positive directions of force and displacement components in the general case of loading.

The above receptance matrix may be partitioned as follows:

$$\mathbf{R}(x_1,x_2)=\begin{bmatrix}\mathbf{R}_{11}(x_1x,_2) & \mathbf{R}_{12}(x_1,x_2)\\ \mathbf{R}_{21}(x_1,x_2) & \mathbf{R}_{22}(x_1,x_2)\end{bmatrix}, \tag{8}$$

where $\mathbf{R}_{11}(x_1,x_2)$, $\mathbf{R}_{12}(x_1,x_2)$, $\mathbf{R}_{21}(x_1,x_2)$, and $\mathbf{R}_{22}(x_1,x_2)$ are 3×3 matrices representing, respectively, translational displacements due to forces and moments, angular displacements due to forces, and moments. The elements of the receptance matrix are the receptance functions where the first subscript refers to the displacement component (translation or rotation), the second subscript refers to the component force (or moment), and the two coordinates (x_1,x_2) are, respectively, the positions of the response displacement and the excitation force components in the local coordinates of the beam. General expressions for the receptance functions constituting the receptance matrix $\mathbf{R}(x_1,x_2)$ are listed in Ref. 1 for flexural vibration in one plane and longitudinal vibration. The flexural receptance can be adapted to the flexural vibration in the perpendicular plane. The torsional receptance can be obtained in a similar way to that for the longitudinal receptance functions shown in Ref. 1 and expressed as

$$R_{\theta_x M_x}(x_1,x_2)=\frac{1}{\rho J}\sum_{t=1}^{\infty}\frac{\varphi_t(x_1)\varphi_t(x_2)}{(\overline{\omega_t}^2-\omega^2)},$$

where J is the polar moment of inertia of the cross section, and $\overline{\omega_t}=(t\pi/L)\sqrt{D/\rho J}$ is the complex eigenfrequency of a free–free component beam for torsional vibrations. D is the complex torsional rigidity ($D=D_0(1-j\eta_t)$, where η_t is the structural damping coefficient for torsional vibration, and L is the length of the component beam. The mode shape $\varphi_t(x)$ used for the torsional receptance is identical to that for the longitudinal receptance for the same boundary conditions.

Three observations on the receptance matrix [Eq. (7)] are worth mentioning. First, the reciprocity principle usually leads to reduction in the number of receptance functions to be computed. Second, the zero elements in the receptance matrix are due to the assumption that the only coupling between the forces and displacements at a specific cross section are between the two components of flexural vibration (shear and moment) about a specific axis (Y_i or Z_i). Should any other type of coupling occurs, the relevant element of the receptance matrix will be nonzero. Third, the present model is based on the Euler–Bernoulli beam theory which implies an upper frequency limit to its accurate predictions.

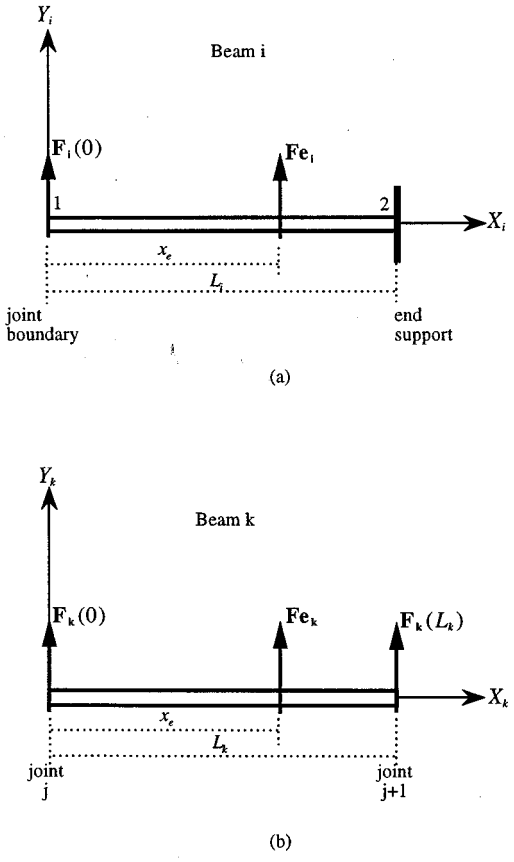

FIG. 2. (a) Component beam connecting a joint to an end support. (b) Component beam connecting two joints.

Damping is introduced in the receptance functions by using the complex resonance frequencies for all the wave types in the beam structure. It is possible to introduce different values for the structural damping loss factor for the different vibrational modes and for the different frequency bands.

In general the grounding supports may be located at coupling joints or at the ends of some component beams. Therefore, the component beams may be classified into two groups:

(1) Component beams terminating at a joint from one end and at a support from the other are shown in Fig. 2(a). By superposition, a force-displacement relation can be written for the ith beam as

$$\mathbf{S_i}(0)=\mathbf{R_i}(0,0)\mathbf{F_i}(0)+\mathbf{R_i}(0,x_e)\mathbf{F_{ei}}(x_e). \tag{9}$$

(2) Component beams terminating at joints from both ends are shown in Fig. 2(b). Similar relations for the kth beam are

$$\mathbf{S_k}(0)=\mathbf{R_k}(0,0)\mathbf{F_k}(0)+\mathbf{R_k}(0,l_k)\mathbf{F_k}(l_k)+\mathbf{R_k}(0,x_e)\mathbf{F_{ek}}(x_e), \tag{10a}$$

$$\mathbf{S_k}(l_k)=\mathbf{R_k}(l_k,0)\mathbf{F_k}(0)+\mathbf{R_k}(l_k,l_k)\mathbf{F_k}(l_k)$$
$$+\mathbf{R_k}(l_k,x_e)\mathbf{F_{ek}}(x_e), \tag{10b}$$

where x_e is the position of the excitation vector $\mathbf{F_e}$ in the local beam coordinates. Multiple excitation vectors may be included in the force-displacement expressions of any component beam.

The force and displacement vectors at any beam cross section can be transformed from the beam local coordinate system $(X_iY_iZ_i)$ to a global coordinate system for the coupled structure (X_0,Y_0,Z_0) via a transformation matrix T_i. For the component beam i, the transformations are

$$\mathbf{S_0}=\mathbf{T_i}\mathbf{S_i}, \tag{11a}$$

$$\mathbf{F_0}=\mathbf{T_i}\mathbf{F_i}. \tag{11b}$$

The transformation matrix is an orthogonal matrix[15] with the property of

$$\mathbf{T}_i^{-1}=\mathbf{T}_i^T. \tag{12}$$

This property is used in Eqs. (11) to transform the force and displacement vectors from the global back to the local coordinates without any need for matrix inversion, i.e.,

$$\mathbf{S}_i=\mathbf{T}_i^T\mathbf{S}_0, \tag{13a}$$

$$\mathbf{F}_i=\mathbf{T}_i^T\mathbf{F_0}. \tag{13b}$$

For details of the transformation matrix, see Ref. 6 or 15.

III. DYNAMIC RESPONSE OF 3-D COUPLED BEAM STRUCTURES

A. Rigid joint of *m* beams

In this section, a coupled structure with m beams rigidly connected at one joint is considered. The other ends of the beams may be described by any standard support condition such as simply supported, clamped, or free boundary conditions. The force and displacement vectors at the joint end of each beam are transformed from the local coordinates of each beam to the global frame of reference as per Eqs. (11). The force equilibrium at the joint (in the global coordinate system) is expressed as

$$\sum_{i=1}^{m}\mathbf{T}_i\mathbf{F}_i=\mathbf{0}_{6\times1}, \tag{14}$$

where $\mathbf{0}_{6\times1}$ is a 6×1 vector of zero elements. The displacement compatibility at the joint are:

$$\mathbf{T_i}\mathbf{S_i}=\mathbf{T_{i+1}}\mathbf{S_{i+1}}, \quad i=1,2,\ldots,(m-1). \tag{15}$$

The force-displacement relations of Eq. (9) are written for the component beams to form, together with Eqs. (14) and (15), $2m$ sets of equations in the force and displacement vectors at the rigid joint of the component beams. A solution of these equations for the displacement vector at the joint in the global coordinates can be obtained using the orthogonality property of the transformation matrix [Eq. (12)] as detailed in the previous work:[1]

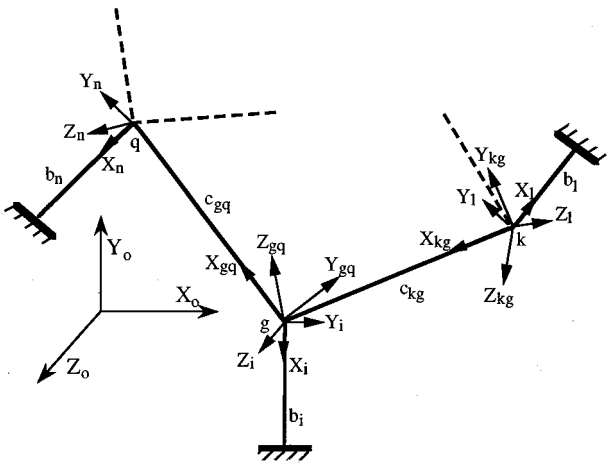

FIG. 3. Coupled beam structure of ''n'' beams connected at ''J'' joints.

$$\mathbf{S_0}(0)=\left[\sum_{\mathbf{i}=1}^{\mathbf{m}}\mathbf{T_i}\mathbf{R_i^{-1}}(0,0)\mathbf{T_i^T}\right]^{-1}\left\{\sum_{\mathbf{i}=1}^{\mathbf{m}}[\mathbf{T_i}\mathbf{R_i^{-1}}(0,0)\mathbf{T_i^T}]\right.$$
$$\left.\times[\mathbf{T_i}\mathbf{R_i}(0,\mathbf{x_e})\mathbf{F_{ei}}(\mathbf{x_e})]\right\}. \tag{16}$$

Equation (13a) can now be used to transform the displacement vector from the global to the local coordinates of each beam. Substituting the resulting local displacement vector into Eq. (9) leads to the determination of the force vector at the joint boundary in the local coordinates of each component beam. Having determined $\mathbf{S_i}$ and $\mathbf{F_i}$ for each component beam, the power flow can be computed using Eqs. (4) and (5). The physical and mathematical explanations of Eq. (16) were given in a previous paper.[1]

B. Coupled structures with multiple beam/multiple joint

The coupled structure with multiple beam/multiple joint in three-dimensional space and under general loading conditions is considered here. The coupled structure is consisted of n component beams. If n_1 is the number of beams connected to boundary supports as shown in Fig. 2(a), and n_2 is the number of beams connecting two intermediate joints as shown in Fig. 2(b), then $n=n_1+n_2$. The number of unknown force vectors at the intermediate joints of the component beams is n_1+2n_2. At each joint, it is possible to write one force equilibrium equation and a number of compatibility relations which is less by one than the number of beams connected at this specific joint. It follows that for a coupled structure with J joints, J force equilibrium equations and n_1+2n_2-J compatibility relations can be written leading to a total number of equations equal to the total number of unknown force vectors. It should be noted here that each of these equations is a matrix equation including six equations for the six degrees of freedom at the joint of a component beam. We now consider the gth joint connecting two beams

c_{kg} and c_{gq} which terminate in their other ends at joints k and q, respectively, as shown in Fig. 3. The joint ''g'' is also connected to beam b_i which terminates at an end support. The force equilibrium at ''g'' is

$$\mathbf{T}_{b_i}\mathbf{F}_{b_i}(0)+\mathbf{T}_{gq}\mathbf{F}_{gq}(0)+\mathbf{T}_{kg}\mathbf{F}_{kg}(L_{kg})=\mathbf{0}_{6\times 1}, \tag{17}$$

and the displacement compatibility relations may be written as follows:

$$\mathbf{T}_{kg}\mathbf{S}_{kg}(L_{kg})=\mathbf{T}_{b_i}\mathbf{S}_{b_i}(0), \tag{18}$$

$$\mathbf{T}_{b_i}\mathbf{S}_{b_i}(0)=\mathbf{T}_{gq}\mathbf{S}_{gq}(0). \tag{19}$$

Expressions for $\mathbf{S}_{gq}(0)$ and $\mathbf{S}_{kg}(L_{kg})$ as functions of the external excitation vectors and boundary force vectors (not shown in Fig. 3) are obtained utilizing Eq. (10). Similarly, expression for $\mathbf{S}_{b_i}(0)$ is obtained from Eq. (9). Repeating the same procedure for joints k and q of Fig. 3 and considering only the beams drawn in solid lines, the resulting equations may be written in the following matrix form:

$$\left[\begin{array}{cc:ccc:ccc}
\mathbf{T}_{b_1} & \mathbf{T}_{kg} & & & & & & \\
-\mathbf{T}_{b_1}\mathbf{R}_{b_1}(0,0) & \mathbf{T}_{kg}\mathbf{R}_{kg}(0,0) & \mathbf{T}_{kg}\mathbf{R}_{kg}(0,1) & & & & & \\
\hdashline
 & & \mathbf{T}_{kg} & \mathbf{T}_{b_i} & \mathbf{T}_{gq} & & & \\
 & \mathbf{T}_{kg}\mathbf{R}_{kg}(1,0) & \mathbf{T}_{kg}\mathbf{R}_{kg}(1,1) & -\mathbf{T}_{b_i}\mathbf{R}_{b_i}(0,0) & & & & \\
 & & & -\mathbf{T}_{b_i}\mathbf{R}_{b_i}(0,0) & \mathbf{T}_{gq}\mathbf{R}_{gq}(0,0) & \mathbf{T}_{gq}\mathbf{R}_{gq}(0,1) & & \\
\hdashline
 & & & & & \mathbf{T}_{gq} & \mathbf{T}_{b_n} & \\
 & & & & \mathbf{T}_{gq}\mathbf{R}_{gq}(1,0) & \mathbf{T}_{gq}\mathbf{R}_{gq}(1,1) & -\mathbf{T}_{b_n}\mathbf{R}_{b_n}(0,0) &
\end{array}\right]
\left[\begin{array}{c}
\mathbf{F}_{b_1}(0) \\
\mathbf{F}_{kg}(0) \\
\hdashline
\mathbf{F}_{kg}(1) \\
\mathbf{F}_{b_i}(0) \\
\mathbf{F}_{gq}(0) \\
\hdashline
\mathbf{F}_{gq}(1) \\
\mathbf{F}_{b_n}(0)
\end{array}\right]$$

$$=\left[\begin{array}{c}
\mathbf{0}_{6\times 1} \\
\mathbf{T}_{b_1}\mathbf{R}_{b_1}(0,x_e)\mathbf{F}\mathbf{e}_{b_1}-\mathbf{T}_{kg}\mathbf{R}_{kg}(0,x_e)\mathbf{F}\mathbf{e}_{kg} \\
\hdashline
\mathbf{0}_{6\times 1} \\
\mathbf{T}_{b_i}\mathbf{R}_{b_i}(0,x_e)\mathbf{F}\mathbf{e}_{b_i}-\mathbf{T}_{kg}\mathbf{R}_{kg}(1,x_e)\mathbf{F}\mathbf{e}_{kg} \\
\mathbf{T}_{b_i}\mathbf{R}_{b_i}(0,x_e)\mathbf{F}\mathbf{e}_{b_i}-\mathbf{T}_{gq}\mathbf{R}_{gq}(0,x_e)\mathbf{F}\mathbf{e}_{gq} \\
\hdashline
\mathbf{0}_{6\times 1} \\
\mathbf{T}_{b_n}\mathbf{R}_{b_n}(0,x_e)\mathbf{F}\mathbf{e}_{b_n}-\mathbf{T}_{gq}\mathbf{R}_{gq}(1,x_e)\mathbf{F}\mathbf{e}_{gq}
\end{array}\right], \tag{20}$$

or briefly,

$$[\mathbf{R_G}][\mathbf{F_G}]=[\mathbf{S_G}], \tag{21}$$

where each nonfilled element of $[\mathbf{R_G}]$ is a 6×6 matrix with zero elements.

Equation (20) presents the governing equations for the three-dimensional coupled beam structure drawn in solid lines in Fig. 3. This matrix equation can be solved for the force vectors at the joint boundaries of the component beams, and consequently the displacement vectors and power flow can be determined as detailed in the previous section. The solution of these equations involves the inversion of one sparse matrix of the order $6(n_1+2n_2)$ which equals the total number of force components at the intermediate joints of all the component beams of the coupled structure. It is a straight forward exercise to expand Eq. (20) for a more general case of multiple beam/multiple joint and of arbitrary number of beams connected at each joint. More than one excitation force vector may be considered for each beam.

The modal receptance solution for the dynamic response of coupled beam structures, as represented by Eqs. (20) and (21) has the following characteristics:

(1) $[\mathbf{R_G}]$ is a ''global receptance matrix'' including the transformation matrices of the component beams and their receptance matrices relating the displacement and the force vectors at the joint boundaries. The matrix is divided into groups of rows separated by dashed lines. Each group is related to one joint. Each element in $[\mathbf{R_G}]$ is a 6×6 matrix. The nonzero elements are concentrated in the main diagonal band. Elements related to one joint are mainly occupying a square submatrix in the main diagonal band. The few elements outside that submatrix represent the remote ends of the beams coupled to other joints.
(2) $[\mathbf{F_G}]$ is a ''total force vector'' including all the force vectors at the joint boundaries of the component beams.
(3) $[\mathbf{S_G}]$ is a ''global vector of joint displacements due to external excitations.'' Those displacements are resolved

into the global frame of reference as it is clear from examining the nonzero terms in this matrix. It is clear that more than one excitation vector at different positions may apply to any component beam.

(4) Equation (20) may be read as follows: Each group of lines represents the governing equations for one joint. The first equation in a group is the force equilibrium relation. The subsequent equations in the group are the displacement compatibility relations written for each pair of beams at a time. All the forces and displacements are resolved into the global axes.

(5) It follows from the abovementioned characteristics that Eq. (20) can be written directly for any coupled beam structure under general loading conditions.

C. Components of power flow at arbitrary cross section

The components of the force vector [see Eq. (1) and Fig. 1] at a cross section x along any component beam may be computed from the spatial derivatives of the components of the displacement vector—Eq. (2)—using the relations:

$$N_x = -EA\,\frac{\partial u}{\partial x}, \tag{22a}$$

$$N_y = EI_z\,\frac{\partial^3 v}{\partial x^3}, \tag{22b}$$

$$N_z = EI_y\,\frac{\partial^3 w}{\partial x^3}, \tag{22c}$$

$$M_x = -GJ\,\frac{\partial \theta_x}{\partial x}, \tag{22d}$$

$$M_y = EI_y\,\frac{\partial^2 w}{\partial x^2}, \tag{22e}$$

$$M_z = -EI_z\,\frac{\partial^2 v}{\partial x^2}. \tag{22f}$$

The above equations may be written in a matrix form:

$$\mathbf{F}(x) = [\mathbf{P}]\mathbf{D}(x), \tag{23}$$

where $[\mathbf{P}]$ is a 6×6 diagonal matrix of the material and cross sectional properties appearing in the right-hand sides of Eqs. (22). $\mathbf{D}(x)$ is the vector whose components are, respectively, the derivatives of the displacement components.

For linear vibration, the displacement vector at a cross section x along a component beam k connecting two joints [see Fig. 2(b)] may be expressed as:

$$\mathbf{S}_k(x) = \mathbf{R}_k(x,0)\mathbf{F}_k(0) + \mathbf{R}_k(x,1_k)\mathbf{F}_k(1_k) + \mathbf{R}_k(x,x_e)\mathbf{Fe}_k(x_e). \tag{24}$$

Consequently, the vector of the displacement derivatives is:

$$\mathbf{D}_k(x) = \mathbf{R}_k^D(x,0)\mathbf{F}_k(0) + \mathbf{R}_k^D(x,1_k)\mathbf{F}_k(1_k) + \mathbf{R}_k^D(x,x_e)\mathbf{Fe}_k(x_e), \tag{25}$$

where $\mathbf{R}_k^D(x,x_l)$ is a 6×6 ''matrix of receptance derivatives'' at x of beam k due to unit loads at x_l:

$$\mathbf{R}_k^D(x,x_l) = \begin{bmatrix} -\frac{\partial}{\partial x}R_{uN_x} & 0 & 0 & 0 & 0 & 0 \\ 0 & \frac{\partial^3}{\partial x^3}R_{vN_y} & 0 & 0 & 0 & \frac{\partial^3}{\partial x^3}R_{vM_z} \\ 0 & 0 & \frac{\partial^3}{\partial x^3}R_{wN_z} & 0 & -\frac{\partial^3}{\partial x^3}R_{wM_y} & 0 \\ 0 & 0 & 0 & -\frac{\partial}{\partial x}R_{\theta_x M_x} & 0 & 0 \\ 0 & 0 & \frac{\partial^2}{\partial x^2}R_{wN_z} & 0 & -\frac{\partial^2}{\partial x^2}R_{wM_y} & 0 \\ 0 & -\frac{\partial^2}{\partial x^2}R_{vN_y} & 0 & 0 & 0 & -\frac{\partial^2}{\partial x^2}R_{vM_z} \end{bmatrix}, \tag{26}$$

where the response and excitation positions (x,x_l) are removed from the nonzero elements of the matrix. It is worth mentioning that the signs in Eqs. (22) and (26) are adjusted to be compatible with the sign convention of Fig. 1 and that the derivatives are always evaluated at the response position x.

Having obtained the displacement vector at position x from Eq. (24) and the internal force vector at the same cross section from combining Eqs. (25) and (23), the total power flow and its components at position x can be obtained employing Eqs. (4) and (5). The input power at an excitation point can be estimated in a similar way by first estimating the

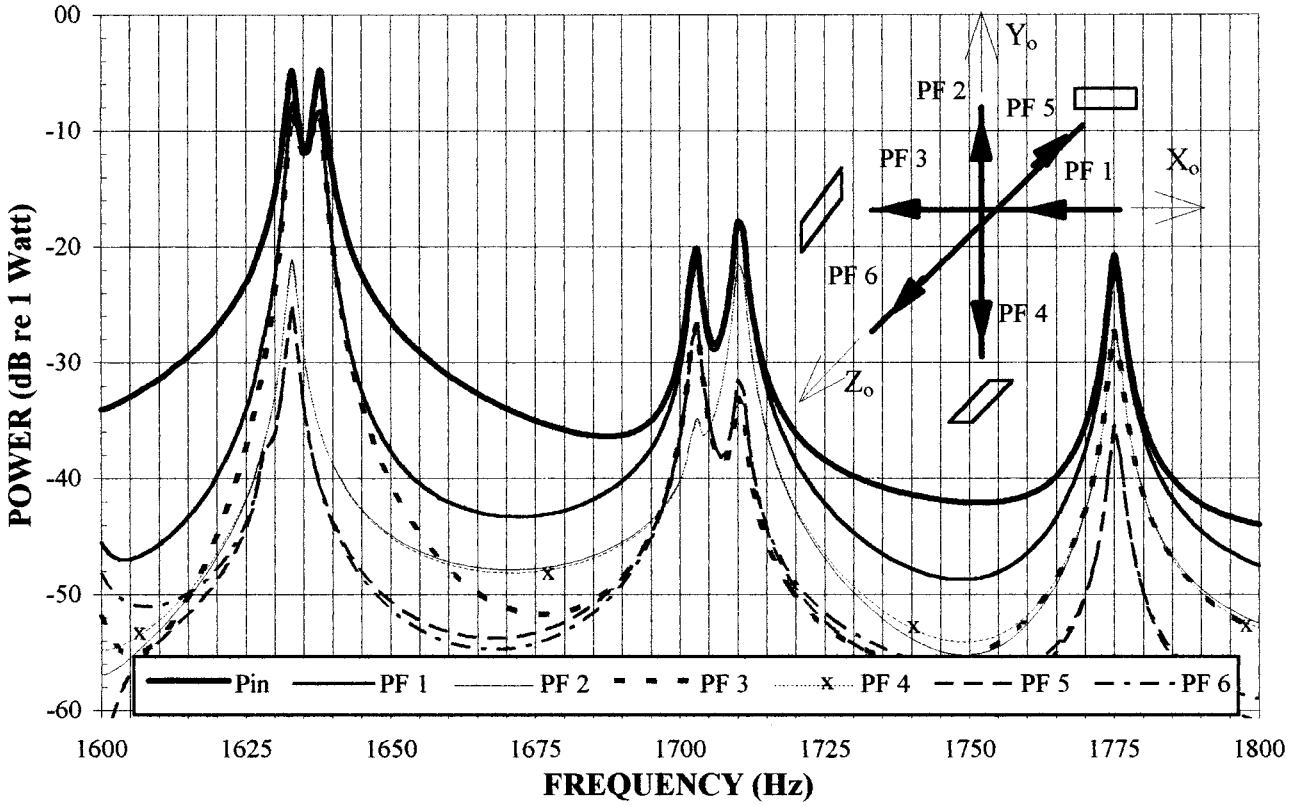

FIG. 4. Power flow at the rigid joint of six coupled beams in the frequency band of torsional resonance.

response displacement vector at the excitation position employing Eq. (24) and the appropriate receptance functions. The response displacement vector and the excitation vector are then used to compute the total and components of the input power using Eqs. (4) and (5). The prediction of the spectrum of the components of the input power due to the corresponding components of the excitation force vector leads directly to an evaluation of the capability of the different components of the excitation force vector to inject power into the structure. As a consequence, manufacturing and assembly tolerances may be used at the design stage to prevent some force components from injecting excessive power into the structure in some frequency bands.

The evaluation of the internal force vectors employing the receptance derivatives as formulated in this section is usually not causing numerical or convergence problems as long as the number of flexural modes are within about 100 modes for the practical beams' configurations. This number of modes is sufficient for accurate results. If higher number of modes are used, some special numerical manipulation will be required to avoid numerical over flow. However, it was observed from the numerical examples that the predictions of the internal forces in the vicinity of the boundaries are less accurate due to the spatial fluctuations in the modal predictions near the boundaries as demonstrated in Ref. 16. Away from the boundaries and discontinuity the predictions are accurate as shown in the second example (and Fig. 6 in the next section).

D. Summary of the general procedure

It is useful at this stage to summarize a general procedure for the dynamic response prediction of any three-dimensional coupled beam structure. The dimensional and material properties of the constituent beams as well as the idealized supporting conditions have to first be defined. Modal properties of each component beam have to be obtained. Orientations of the local coordinate axes of each beam with respect to a global frame of reference have to be defined and the transformation matrix has to be calculated for each component beam. The excitation force vectors have to be defined.

Having completed the above preparatory work, the governing equations can now be written similar to Eq. (20) and solved for the force vectors at the coupling joints. The displacement vectors at the joints can then be obtained using one of the force displacement relations described by Eqs. (9) and (10). The force and displacement vectors at the coupling joints of each beam will be sufficient to define completely the dynamic response at each frequency and to subsequently calculate any response quantity at any cross section as detailed before.

IV. COMPUTATIONAL EXAMPLES

A. Power flow through a rigid joint of six beams

Six beams connected rigidly at one joint and clamped at the other ends are shown schematically in Fig. 4. The beams are chosen to be in the positive and negative directions of the

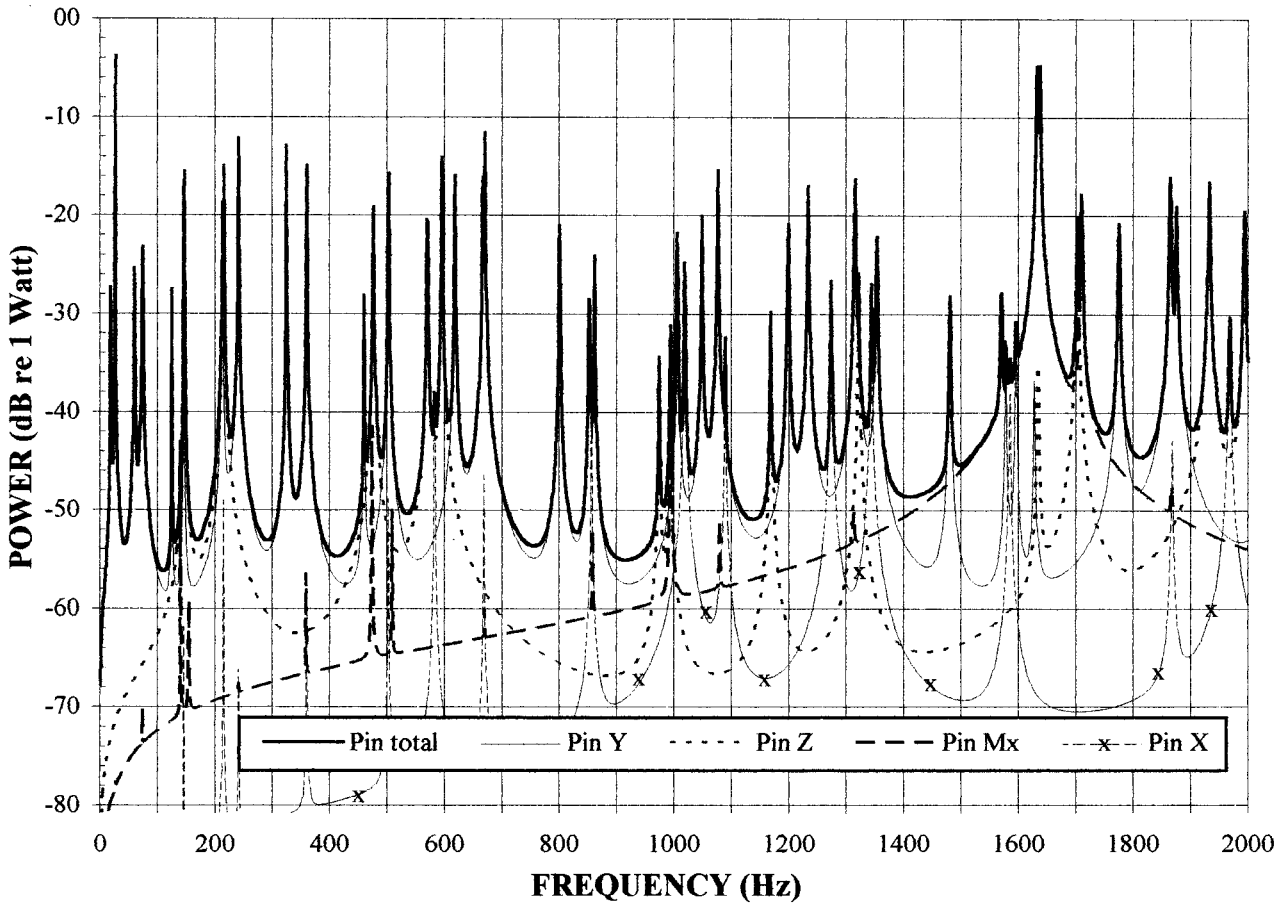

FIG. 5. Total and components of input power to six rigidly coupled beams due to an excitation force vector [1, 1, 1, 0.01, 0, 0].

global system of axes so that the interpretation of the wave interactions at the joint becomes obvious. The coupled beam structure is assumed to be manufactured from steel of Young's modulus 210×10^9 N/m^2, density 7800 kg/m^3, Poisson ratio 0.28, and a structural damping coefficient of 0.001. The cross sections are 0.005×0.04 m^2 in the directions indicated in Fig. 4 and the length is 1.0 m for all beams. Beam 1 is excited at position $x_e=0.37$ m by a force vector $\mathbf{F}_e$ = [1, 1, 1, 0.01, 0.0, 0.0] where the components are, respectively, the three force components along the directions of the global axes in Newtons and the moments about these axes in Nm. This loading is representative of a practical case where, for example, a force is transmitted through a machine mount to one of the supporting beams in such a direction that three force components are created and the components of moment are due to the eccentricity from the center of the cross section. Zero moment components about *Y* and *Z* axes are considered in this specific loading for simplicity and due to the fact that the linear force components are sufficient to excite the flexural modes in the two perpendicular directions (when the excitation position does not coincide with a node). It is also found from the computational results that the components of input power due to these moment components exhibit the same pattern of behavior as the input power components due to the linear forces, although at different levels according to the excitation position relative to the neighboring nodes or antinodes of the dominating modes.

The modal receptance method described in the previous sections for three-dimensional coupled beams was used to predict the spectrum of the total input power and the components of input power due to the different components of the excitation force as presented in Fig. 5 for the frequency band 0–2000 Hz. It can be seen from these plots that the relative contributions of the different components of the excitation force vector to the input power are frequency dependant. The predictions show clearly the components of the excitation force vector which must be reduced to the minimum possible should the vibration excitation be controlled to a minimum.

In the input power spectrums the peaks correspond to the resonance frequencies of the different modes of vibration. At any resonance frequency, the corresponding input power is at a peak value. One can classify the modes according to the type of vibration which dominates the input power. Some modes, such as the mode at 146 Hz in the example shown in Fig. 5, are characterized by peaks, although at different levels, in the input power spectrums for all wave types. This type of vibrational mode is expected to happen more frequently as the flexural stiffness of the cross section of the excited beam in the two perpendicular planes become close to each other. Other modes are dominated by only one wave type like the mode at 801 Hz.

The input power spectrums at only one point are suffi-

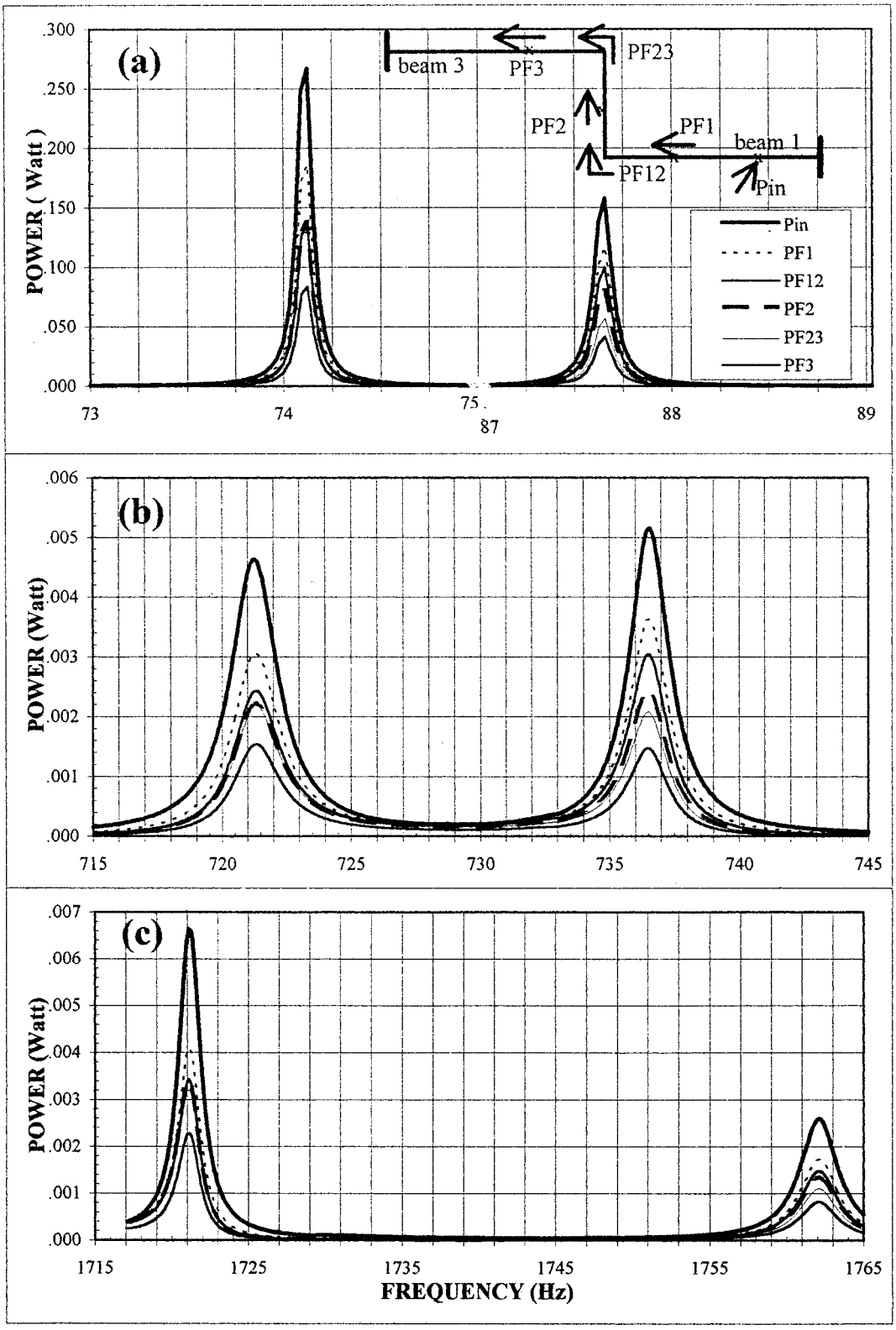

FIG. 6. Predictions of total power flow at different cross sections of a three-beam/two-joint structure excited by an out-of-plane force of 1 N in three frequency bands: (a) 73–89, (b) 715–745, and (c) 1715–1765 Hz.

cient to identify all the resonance frequencies of the coupled structure as long as the excitation force vector used in the prediction consists of all six components (three force and three moment components). If the excitation point coincides with a nodal point for a flexural wave, the input power spectrum due to the moment component will still show a peak due to the fact that the rotational velocity component is a maximum although the linear velocity component at the node is zero. When the structure is excited at a nodal point of longitudinal or torsional wave, the flexural waves will still

show a peak at resonance due to the coupling of waves in the three-dimensional structure.

Figure 5 also shows a very strong torsional resonance at 1638 Hz in which the input power is at the highest level as compared to other peaks in the frequency range 50–2000 Hz. At this resonance, the power input is mainly due to the 0.01 Nm twisting moment which may arise from a 10 N resultant linear force shifted by 1 mm from the shear center of the cross section in any practical structure. In this situation, very tight tolerances may be necessary to avoid the creation of such a moment component if excessive input power is to be avoided. The input power due to the axial force component is always at very low levels in this frequency range. It is also evident from Fig. 5 that although the input power due to the force component in the Z direction is very low at off resonances, which may be attributed to the higher stiffness of the structure in this direction, it is still very high at the resonance frequencies.

The distribution of the vibrational power at the joint of the six beams in the frequency band including a torsional resonance (1625–1800 Hz) is shown in Fig. 4. Although most of the power leaving beam 1 goes to beam 3 in the two resonances at 1633 and 1638 Hz, which may intuitively be expected, the distribution of power is completely different at 1703, 1710, and 1775 Hz where the input power is dominated respectively by $F_Z^{(e)}$, $F_{Mx}^{(e)}$, and $F_Y^{(e)}$ components of the excitation force as demonstrated by Fig. 5. It is also possible to examine the components of the input power to each beam at the joint or at any cross section away from the boundaries. This will be presented in the companion paper.[14]

B. Power flow at different cross sections in three coupled beams

The structure presented schematically in Fig. 6(a) consists of three in-plane beams connected rigidly at two joints and clamped at the remote ends. The beams are, respectively, 1.65, 0.985, and 1.65 m in length, 0.016×0.016 m^2 cross sections, and of the same material properties as that in the previous example. Beam 1 is excited by a force component of 1 N in a direction perpendicular to the plane of the beams at 0.555 m from the clamped end. Thus flexural waves in planes perpendicular to the plane of the beams in addition to torsional and longitudinal waves are excited and coupled at the excitation position and at the joints. The modal receptance method was used to predict the input power and the total power flow through the joints. Power flow through three intermediate cross sections (0.5 m from the joints) is also computed using the receptance derivatives formulation. The predictions are presented in Fig. 6(a)–(c) for three different frequency bands. The resonance locations and magnitudes in all the calculated power flows clearly show the consistency of the predictions.

V. CONCLUSIONS

A mathematical model is presented for the prediction of the dynamic response of three-dimensional coupled beam structures using a modal receptance formulation. It is shown that matrix equation (21) governing the dynamic behavior of the coupled structure has a clear physical meaning and may be written directly for any multiple beam/multiple joint structure given the physical and modal characteristics of the component beams and the excitations of the structure. The formulation is such that the force vectors at the intermediate joints are obtained directly from the solution of the governing equations. Displacement vectors at the joints are subsequently computed employing the force-displacement relations. The internal force vectors and displacement vectors may also be computed at any cross section of a component beam. Components of input power due to different components of the excitation force vector and components of power flow at the joints or at any cross section may also be predicted. The difference between the input and the output power for any given beam can be used as a measure of the average response level at any frequency.

This model fills the gap between the FEA and SEA in the medium-frequency range where each method has its own limitations. The model is based only on the basics of structural and vibrational analysis. It is computationally efficient in the prediction of the resonant behavior of coupled beam structures in the medium-frequency range. It can be further developed for more general case of arbitrary beam's cross sections, nonrigidly connected beams or nonstandard end conditions for the component beams.

Assessment of the accuracy of predictions from the present method and its limitations are the subject of part 3 of the present series of papers.[14] It is shown by comparing the measured and predicted values of power that the best agreement can be achieved in the medium-frequency range. At low frequencies (below $\sim$100 Hz), although the predictions are accurate, measurement of power flow is usually difficult, if not impossible, not accurate and time consuming. On the other hand, at high frequencies (above $\sim$1000 Hz), the accuracy of the predictions starts to decline due to the effect of shear deformation and rotary inertia neglected by Euler–Bernoulli beam theory, the limited number of modes used in synthesizing the coupled response, and due to uncertainties in material properties.

ACKNOWLEDGMENTS

Support for this work from the Australian Research Council, Transfield Australia Shipbuilding Industry, and Engineering Foundation of Western Australia is gratefully acknowledged.

[1] N. H. Farag and J. Pan, ''Dynamic response and power flow in two dimensional coupled beam structures under in-plane loading,'' J. Acoust. Soc. Am. **99**, 2930–2937 (1996).
[2] Y. Yong and Y. K. Lin, ''Dynamic response analysis of truss-type structural networks: A wave propagation approach,'' J. Sound Vib. **156**, 27–45 (1992).
[3] R. S. Langley, ''Analysis of power flow in beams and frameworks using the direct-dynamic stiffness method,'' J. Sound Vib. **136**, 439–452 (1990).
[4] D. J. Mead, ''A new method of analyzing wave propagation in periodic structures; applications to periodic Timoshenko beams and stiffened plates,'' J. Sound Vib. **104**, 9–27 (1986).
[5] D. W. Miller and A. Von Flotow, ''A traveling wave approach to power flow in structural networks,'' J. Sound Vib. **128**, 145–162 (1989).
[6] L. S. Beale and M. L. Accorsi, ''Power flow in two- and three-dimensional frame structures,'' J. Sound Vib. **185**, 685–702 (1995).

[7] J. M. Cuschieri, ''Vibration transmission through periodic structures using mobility power flow approach,'' J. Sound Vib. **143**, 65–74 (1990).
[8] J. M. Cuschieri, ''Structural power flow analysis using a mobility approach of an L-shaped plate,'' J. Acoust. Soc. Am. **87**, 1159–1165 (1990).
[9] J. L. Guyader, C. Boisson, and C. Lesueur, ''Energy transmission in finite coupled plates, Part I: Theory,'' J. Sound Vib. **81**, 81–92 (1982).
[10] G. Miccoli, A. Jacob, D. Allaei, and D. Tarnowski, ''An efficient modelling technique for vibration analysis of composite and complex structures,'' IMAC, 338–344 (1995).
[11] R. E. D. Bishop and D. C. Johnson, *The Mechanics of Vibration* (Cambridge U.P., Cambridge, MA, 1960).
[12] W. Soedel, *Vibrations of Shells and Plates* (Marcel Dekker, New York, 1981).
[13] L. D. Pope and J. F. Wilby, ''Band-limited power flow into enclosures,'' J. Acoust. Soc. Am. **62**, 906–911 (1977).
[14] N. H. Farag and J. Pan, ''Dynamic response and power flow in three-dimensional coupled beam structures. III. Experimental assessment of the theory,'' J. Acoust. Soc. Am. (submitted).
[15] J. M. Gere and W. Weaver, Jr., *Matrix Algebra for Engineers* (Van Nostrand Reinhold, New York, 1965).
[16] J. Pan and J. Q. Pan, ''A comparison of modal expansion and travelling wave methods for prediction of structural intensity,'' J. Sound Vib. (submitted).

Flexural vibration of an infinite wedge

Rajendra Gunda, Sandeep M. Vijayakar, and Rajendra Singh[a)]
Acoustics and Dynamics Laboratory, Department of Mechanical Engineering, The Ohio State University, 206 West 18th Avenue, Columbus, Ohio 43210-1107

(Received 17 July 1996; accepted for publication 23 January 1997)

A new solution to the problem of flexural vibration of an infinite wedge excited by a point harmonic load is obtained via a superposition of the geometric and diffraction fields, for simply supported and roller boundary conditions along the edges. The diffraction integrals are evaluated both in closed form in terms of the Faddeeva function and also as an asymptotic series using the steepest descent method. An eigensolution is also derived by expanding eigenfunctions in the angular direction and propagation terms in the radial direction. These two representations of the solution are compared numerically for accuracy and spatial distribution in different frequency regimes. The relative contribution of the geometric and diffraction fields to the overall solution is examined. This result is then compared to the second-order Helmholtz wave equation solution in order to demonstrate the near-field effects arising due to the fourth-order biharmonic formulation. The authors' motivation for obtaining the solution for a wedge-shaped infinite plate is that it is an essential step toward devising numerical models for the vibration of arbitrary polygonal plates. By combining the contribution from diffraction at the vertices of a polygonal plate with the geometrical solution obtained by the method of images, the authors expect to obtain better predictions at mid and high frequencies than is possible by other available methods. [S0001-4966(97)00406-2]

PACS numbers: 43.40.Dx, 43.40.At [CBB]

INTRODUCTION

The diffraction effects arising from wedge-shaped geometries are of interest in several disciplines including acoustics, optics, geophysics, and electromagnetics.[1–7] For those wedge angles β which are submultiples of π, any process of isotropic symmetry can be solved by applying the *method of images*.[8] This technique was generalized by Bromwich[2] for noninteger wedge indices by using a complex integral representation of the image series.[9] For instance, Bowman and Senior[4] have generated solutions for E and H polarized electric fields in noninteger wedges with various source excitations. The diffraction effects for the flexural vibration of thin wedge-shaped plates have not been analyzed before to the best of our knowledge. Previous investigations have been confined to phenomena governed by the classical wave equation, where as in plate vibrations a biharmonic formulation is required. In this article, the arbitrary structural wedge problem is formulated and the diffraction integral is evaluated in closed form by using an asymptotic expansion of Hankel functions for large arguments. The diffraction integral is also evaluated by the method of steepest descent, a high-frequency approximation, that is equivalent to the geometric theory of diffraction as introduced by Keller.[10]

The region enclosed by the wedge of Fig. 1 is given in cylindrical polar coordinates as

$$\mathbf{r} \equiv (\rho, \phi) \in [0, \infty) \times [0, \beta]. \tag{1}$$

The wedge index (ν) is defined in terms of wedge angle (β) as $\nu = \pi/\beta$. The thickness of the plate is denoted by h. Wedges are classified as integer wedges if ν is an integer and as noninteger wedges if ν is not an integer.

According to the classical thin plate theory,[11] the equation governing the flexural motion of an isotropic, homogeneous plate of constant thickness h is expressed in terms of transverse displacement $w(\mathbf{r},t)$ as

$$D\nabla^4 w(\mathbf{r},t) + \rho_m h \frac{\partial^2 w(\mathbf{r},t)}{\partial t^2} = p(\mathbf{r},t), \tag{2}$$

where $D = Eh^3/12(1-\nu^2)$ is the flexural rigidity of the plate; further, ∇^4, t, E, ρ_m, p, and ν are the biharmonic operator, time, Young's modulus, density, lateral force per unit area, and Poisson's ratio, respectively. For harmonic excitation at a frequency ω, $p(\mathbf{r},t) = F(\mathbf{r})\exp(-i\omega t)$, the response w is given by $w(\mathbf{r},t) = u(\mathbf{r})\exp(-i\omega t)$. From this point on, the analysis is carried out in spectral domain in terms of $u(\mathbf{r})$ and $F(\mathbf{r})$, and the $\exp(-i\omega t)$ time dependence is dropped from expressions for the sake of brevity. The governing equation is expressed in terms of the bending wave number γ as

$$(\nabla^4 - \gamma^4) u(\mathbf{r}) = F(\mathbf{r})/D, \quad \gamma^4 = \rho_m h \omega^2 / D. \tag{3}$$

Structural damping behavior is incorporated in the formulation by replacing D in Eq. (3) with $D = D(1 + i\eta)$ where η is the material loss factor. We consider a unit harmonic point load at the source point $S(\rho_s, \phi_s)$ as depicted in Fig. 1. The force distribution, for this case, is the Dirac delta function, $\delta(\mathbf{r} - \mathbf{r}_s)$.

a)Corresponding author.

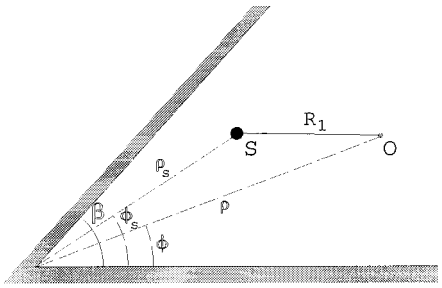

FIG. 1. The infinite wedge geometry with source at S, response or observation at O.

I. BOUNDARY CONDITIONS AND FUNDAMENTAL SOLUTION

In addition to satisfying the Eq. (3) inside the domain, the solution to the wedge vibration problem must satisfy certain boundary conditions. Assume that along the edges $\phi=0$ and $\phi=\beta$, either of the following conditions are satisfied.

$$\text{Simple supports:} \quad M_n(u)=0, \quad u=0,$$
$$\text{``Roller'':} \quad V_n(u)=0, \quad \frac{\partial u}{\partial \phi}=0. \tag{4}$$

Far away from the vertex along ρ, the Sommerfeld radiation or free-field condition must be satisfied, i.e., only outward propagating waves are assumed to exist:

$$\lim_{\rho\to\infty}\left\{\rho^{1/2}\left(\frac{\partial u}{\partial \rho}-i\gamma u\right)\right\}=0. \tag{5}$$

The fundamental solution to Eq. (3), $U(R(\phi-\phi_s);\gamma)$, represents the transverse deflection at a point $\mathbf{r}$ in an infinite plate due to a unit point load of frequency ω at $\mathbf{r}_s$. Let $R_1=R(\phi-\phi_s)=|\mathbf{r}-\mathbf{r}_s|$ be the distance between the source and observation points. The fundamental solution is given from[12,13] as

$$U(R(\phi-\phi_s);\gamma)=-\frac{i}{8\gamma^2 D}\left[H_0^{(1)}(\gamma R_1)-H_0^{(1)}(i\gamma R_1)\right], \tag{6}$$

where $H_0^{(1)}$ is the zeroth-order Hankel function of the first kind. Since we use the Hankel function of the first kind only, the superscript (1) is dropped from now on. For high-frequency excitation ($\gamma R_1 \gg 1$), a simplified form of Eq. (6) is obtained by using an asymptotic expansion of Hankel functions for large argument:[14]

$$H_0(z)\approx\sqrt{\frac{2}{\pi z}}\exp\left\{i\left(z-\frac{\pi}{4}\right)\right\}, \quad -\pi<\arg(z)<2\pi. \tag{7}$$

Hence, the fundamental solution (6) is simplified for $\gamma R_1 \gg 1$ as

$$\begin{aligned}U(R(\phi-\phi_s);\gamma)\approx&-\frac{i}{8\gamma^2 D}\sqrt{\frac{2}{\pi\gamma R_1}}\\&\times\left[\exp\left\{i\left(\gamma R_1-\frac{\pi}{4}\right)\right\}+i\exp(-\gamma R_1)\right]\\=&K_p\left[\exp\left\{i\left(\gamma R_1-\frac{\pi}{4}\right)\right\}\right]\\&+K_p[i\exp(-\gamma R_1)],\end{aligned} \tag{8}$$

where

$$K_p=-\frac{i}{8\gamma^2 D}\sqrt{\frac{2}{\pi\gamma R_1}}.$$

II. ARBITRARY WEDGES

A. Integer wedges

In Fig. 1, $S(\rho_s,\phi_s)$ is the location of the excitation point and $O(\rho,\phi)$ is the observation point. For an integer wedge index, the solution at O can be constructed using the method of images.[8,15] The solution has contributions from the source at S and $2\nu-1$ images suitably placed to ensure the boundary conditions are satisfied:

$$\begin{aligned}u(\mathbf{r})=&\sum_{m=0}^{\nu-1}U\left[R\left(\frac{2m\pi}{\nu}+\phi_s-\phi\right);\gamma\right]\\&\mp U\left[R\left(\frac{2m\pi}{\nu}-\phi_s-\phi\right);\gamma\right].\end{aligned} \tag{9}$$

Each term in the series represents an ''image'' seen at the observation point O. Each image simulates waves reflected from boundaries and represents a ray path connecting S and O. It should be noted that, in this particular case of integer wedges, all the images are visible at any observation point, irrespective of its location within the domain. In Eq. (9), the negative sign gives the solution for simply supported boundary conditions while the positive sign is the solution for roller boundary conditions, as defined earlier by Eq. (4).

B. Noninteger wedges

A function $R(s)$ representing the distance between the observation and source/image points as a function of their relative angular positions is given by $R(s)=\{\rho^2+\rho_s^2-2\rho\rho_s\cos(s)\}^{1/2}$. For real s, we take the positive square root of $R(s)$. In order to solve the arbitrary wedge problem, it is convenient to let the argument s of the function $R(s)$ to become complex valued.[2,15] For complex s, we need to stay on the branch of the square root which has a positive real part. If we want to evaluate the contour integrals in the s plane, the contours should not cross a branch cut that is appropriately defined. The location of the branch points is given by

$$s=2l\pi\pm iq$$
$$\text{where} \quad l=0,\pm1,\pm2,\ldots, \quad q=\cosh^{-1}\frac{\rho^2+\rho_s^2}{2\rho\rho_s}. \tag{10}$$

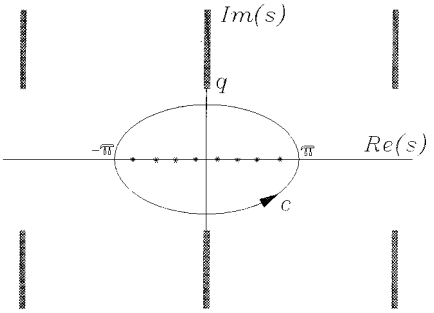

FIG. 2. Integration contour in s plane for integer ν. Poles of $h(s+\phi-\phi_s)$ and $h(s+\phi+\phi_s)$ are designated by an asterisk.

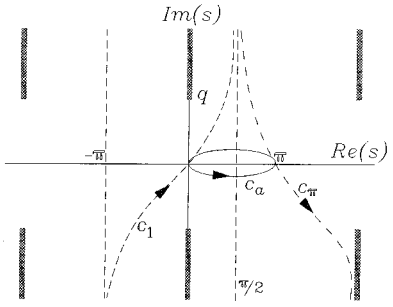

FIG. 3. Modified integration contour.

The branch cuts for $R(s)$ are vertical lines passing through the branch points and extending to $\pm\infty$. We like to replace Eq. (9) which is valid for integer ν by one of the form.

$$u(\mathbf{r})=\frac{1}{2\pi i}\oint_c U(R(s);\gamma)[h(s+\phi-\phi_s) \mp h(s+\phi+\phi_s)]ds. \tag{11}$$

The function $h(s)=\nu/2\cot(\nu s/2)$ is periodic in s with a period 2π, has poles at $s=2m\pi/\nu$ with a residue of unity at each pole. Note that $U(R(s);\gamma)$ has no poles in the s plane. The contour c is any simple loop which cuts the $\Re(s)$ axis at two points, 2π apart, as shown in Fig. 2. The representations for u as given by Eqs. (9) and (11) are equivalent from Cauchy's residue theorem. Thus, we have replaced Eq. (9) which is valid only for integer ν by Eq. (11) which holds for any ν.[2] Adjacent poles of $h(s)$ are $2\pi/\nu$ apart. Therefore, for integer ν, the contour c always encloses ν poles each of both $h(s+\phi-\phi_s)$ and $h(s+\phi+\phi_s)$. Hence, the solution given by Eq. (11) is continuous. For noninteger ν, the number of poles enclosed by the contour c is no longer fixed but varies depending on the location of the source and observation points. Hence, Eq. (11) gives a solution which is a discontinuous function of the position of the observation point. Therefore, the contour c has to be replaced by an equivalent contour which does not intersect the $\Re(s)$ axis. After a series of simplifications using contour deformations, symmetry and asymmetry properties of the integrand,[15] one arrives at the following representation for u:

$$u(\mathbf{r})=\frac{1}{2\pi i}\int_{c_1+c_a+c_\pi} U(R(s);\gamma)\sum h\, ds, \tag{12}$$

where

$$\sum h=[h(s+\phi-\phi_s)+h(s-\phi+\phi_s)] \mp[h(s+\phi+\phi_s)+h(s-\phi-\phi_s)]. \tag{13}$$

The contours c_1, c_a, and c_π are depicted in Fig. 3. The integral over c_1 is zero since c_1 is an inversion of itself and the integrand is odd. The integral over c_a is the geometric field and c_π is the diffracted field. The total field, at any point $u=u_g+u_d$ is composed of the geometric field u_g and diffraction field u_d. The poles of Σh occur when $\sin[(\pi/2\beta)(s\pm\phi\pm\phi_s)]$ vanishes or $s_p=2\beta l\pm\phi\pm\phi_s$. Only poles $0<s_p<\pi$ are enclosed by c_a and have to be taken into account when evaluating the geometric field. Therefore,

$$u_g(\mathbf{r})=\sum_l [U(R(2\beta l+\phi_s-\phi);\gamma) \mp U(R(2\beta l-\phi_s-\phi);\gamma)]. \tag{14}$$

The sum in Eq. (14) extends over all values of l for which the argument of R lies in the interval $(-\pi,\pi)$ corresponding to contributions of the images which are *visible* at the observation point.

III. THE DIFFRACTION INTEGRAL

The diffraction integral is evaluated by deforming the contour c_π to coincide with the line $\Re(s)=\pi$.

$$u_d(\mathbf{r})=\frac{1}{2\pi i}\int_{\pi+i\infty}^{\pi-i\infty} U(R(s);\gamma)\sum h\, ds. \tag{15}$$

Substituting $s=\pi-iz$ in Eq. (15) and simplifying gives

$$u_d(\mathbf{r})=\frac{-1}{4\beta}\int_{-\infty}^{\infty} U(R(\pi-iz);\gamma)[B_\nu(z,\phi-\phi_s) \mp B_\nu(z,\phi+\phi_s)]\, dz, \tag{16}$$

where

$$B_\nu(z,\phi)=\frac{-2\sin\nu\pi[(\cos\nu\pi-\cos\nu\phi)-(\cosh\nu z-1)\cos\nu\phi]}{(\cosh\nu z-1)^2+2(\cosh\nu z-1)(1-\cos\nu\pi\cos\nu\phi)+(\cos\nu\pi-\cos\nu\phi)^2}. \tag{17}$$

Equation (16) can be rewritten as

$$u_d(\mathbf{r}) = \frac{\sin\ \nu\pi}{2\beta} \int_{-\infty}^{\infty} U(R(\pi - iz);\gamma)[F_\nu(z, \phi - \phi_s) \mp F_\nu(z, \phi + \phi_s)]\ dz, \tag{18}$$

where

$$B_\nu(z,\phi) = -2 \sin\ \nu\pi F_\nu(z,\phi). \tag{19}$$

Equation (18) explicitly shows the dependence of u_d on the wedge index ν. Hence for integer wedges, as expected, there is no diffraction field ($\sin\ \nu\pi = 0$) and the geometric field is the total solution. To find an approximate closed-form integral for Eq. (18), we need to study the behavior of the integrand for different values of z, as z goes from $-\infty$ to $+\infty$ along the $\Re(z)$ axis. Consider the part $F_\nu(z, \phi - \phi_s)$ and $F_\nu(z, \phi + \phi_s)$. Note that $F_\nu(z,\phi)$ has no singularities while z is on the real axis, as long as $z \neq 0$. If $z = 0$, the denominator can become zero if $\cos\ \nu\pi = \cos\ \nu\phi$. Next examine $R(\pi - iz)$:

$$R(\pi - iz) = \{\rho^2 + \rho_s^2 + 2\rho\rho_s\ \cosh\ z\}^{1/2}. \tag{20}$$

Here, $R(\pi - iz)$ is positive and real for all $\Re(z)$ and has a minimum value at $z = 0$. As z moves away from 0, along the real axis, $R(\pi - iz)$ stays real, but increases rapidly. This implies that the major contribution to the integral u_d comes from the region $z \approx 0$. Thus we may expand the integrand as a Taylor series around $z = 0$ without losing much accuracy:

$$R(\pi - iz) \approx L\left\{1 + \frac{\rho\rho_s z^2}{2L^2}\right\} \quad \text{where} \quad L = (\rho + \rho_s). \tag{21}$$

Now consider the $F_\nu(z,\phi)$ terms. Using $\cosh z \approx 1 + z^2/2$ and neglecting z^4 terms in the denominator in comparison to z^2 terms, we get

$$F_\nu(z,\phi) \approx \frac{1}{2\nu\sqrt{1 - \cos\ \nu\pi\ \cos\ \nu\phi}} \left\{\frac{2M_\nu(\phi)}{z^2 + M_\nu(\phi)}\right\} = \frac{1}{2\nu\sqrt{1 - \cos\ \nu\pi\ \cos\ \nu\phi}} \left\{\frac{1}{M_\nu(\phi) + iz} + \frac{1}{M_\nu(\phi) - iz}\right\}, \tag{22}$$

where

$$M_\nu(\phi) = \frac{\cos\ \nu\pi - \cos\ \nu\phi}{\nu\sqrt{1 - \cos\ \nu\pi\ \cos\ \nu\phi}}. \tag{23}$$

Let $\Gamma = \sqrt{\gamma\rho\rho_s/\pi L}$. Then $\gamma R(\pi - iz) = \gamma L + \pi\Gamma^2 z^2/2$. Equation (8) can be rewritten as

$$U(R(\pi - iz);\gamma) = K_p e^{i(\gamma L - \pi/4)} e^{i\pi\Gamma^2 z^2/2} + K_p i e^{-\gamma L} e^{-\pi\Gamma^2 z^2/2}. \tag{24}$$

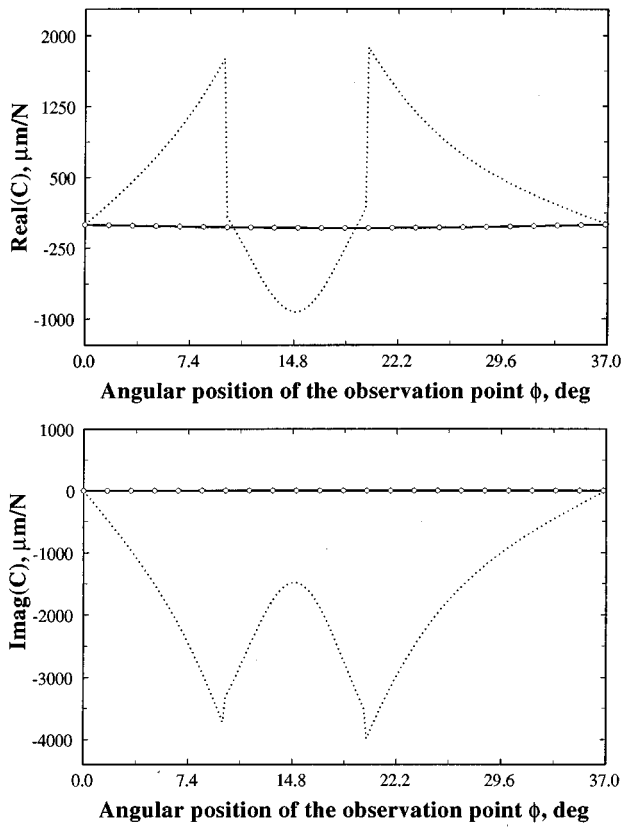

FIG. 4. Comparison of the closed-form solution with the eigenseries solution for $\gamma\rho\rho_s/2L = 0.1$ for simply supported boundary conditions along the edges. Key: ·····, $u_g(\mathbf{r}) + u_d(\mathbf{r})$; —○—, eigensolution.

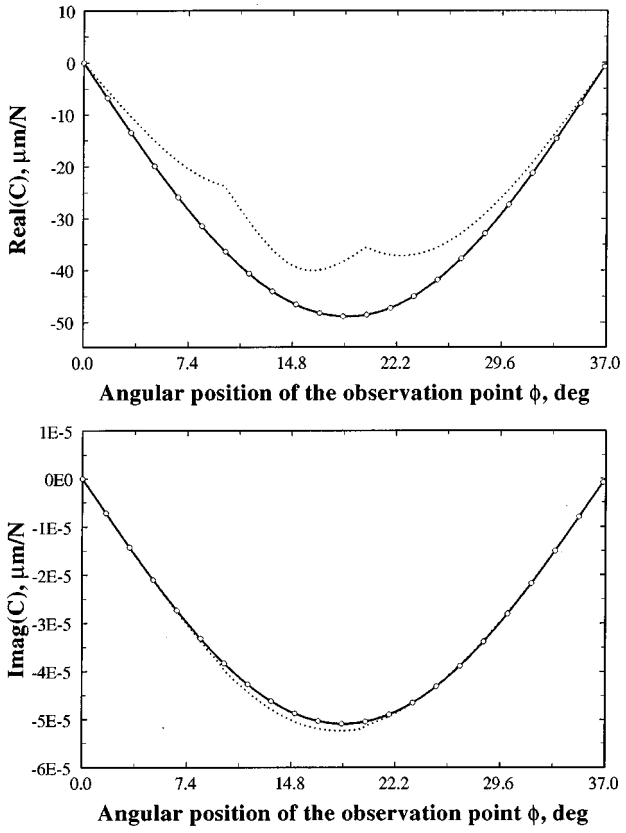

FIG. 5. Comparison of the closed-form solution with the eigenseries solution for $\gamma\rho\rho_s/2L = 1$ for simply supported boundary conditions along the edges. Key: ·····, $u_g(\mathbf{r}) + u_d(\mathbf{r})$; —○—, eigensolution.

An integral representation for the Faddeeva function $w(z) = \exp(-z^2)\mathrm{erfc}(-iz)$ is given by Eq. (25), where $\mathrm{erfc}(z)$ is the complementary error function:[16]

$$w(z) = \frac{i}{\pi} \int_{-\infty}^{\infty} \frac{\exp(-t^2)}{z-t}\, dt = \frac{i}{\pi} \int_{-\infty}^{\infty} \frac{\exp(-t^2)}{z+t}\, dt; \quad \Im(z) > 0. \tag{25}$$

Let

$$V_{1\nu}(\phi) = \int_{-\infty}^{\infty} \frac{e^{i\pi\Gamma^2 z^2/2}}{M_\nu(\phi) - iz}\, dz = i \int_{-\infty}^{\infty} \frac{e^{-u^2}}{M_\nu(\phi) e^{i\pi/4}\sqrt{\pi/2}\Gamma + u}\, du = \pi\ \mathrm{sgn}(M_\nu(\phi)) w\left(|M_\nu(\phi)| e^{i\pi/4} \sqrt{\frac{\pi}{2}}\, \Gamma \right). \tag{26}$$

Similarly,

$$V_{2\nu}(\phi) = \int_{-\infty}^{\infty} \frac{e^{-\pi\Gamma^2 z^2/2}}{M_\nu(\phi) - iz}\, dz = i \int_{-\infty}^{\infty} \frac{e^{-u^2}}{M_\nu(\phi) i\sqrt{\pi/2}\Gamma + u}\, du = \pi\ \mathrm{sgn}(M_\nu(\phi)) w(i|M_\nu(\phi)|\sqrt{\pi/2}\Gamma). \tag{27}$$

Let

$$C_\nu(\phi) = K_p \{ e^{i(\gamma L - \pi/4)} V_{1\nu}(\phi) + i e^{-\gamma L} V_{2\nu}(\phi) \} \frac{1}{\sqrt{1 - \cos\ \nu\pi\ \cos\ \nu\phi}}. \tag{28}$$

Equation (18) is therefore written as

$$u_d(\mathbf{r}) = \frac{\sin\ \nu\pi}{2\pi} (C_\nu(\phi - \phi_s) \mp C_\nu(\phi + \phi_s)). \tag{29}$$

This is the closed-form representation for the diffraction field u_d, valid when $\gamma\rho\rho_s/2L \gg 1$. It can be deduced that $V_{2\nu}(\phi)$ is purely real from the fact that it is represented as a Faddeeva function of a purely imaginary argument and $w(z)$ satisfies the following property:[16] $w(z) = \overline{w(-\bar{z})}$.

IV. METHOD OF STEEPEST DESCENT

For high-frequency excitation, one can use uniform asymptotic expansions to reduce $V_{1\nu}(\phi)$ and $V_{2\nu}(\phi)$ into canonical forms, which are simpler to evaluate but contain the same essential features as the original integrals. This form of the solution may reveal certain features that are not quite evident in the closed-form integrals. Consider $V_{1\nu}(\phi)$:

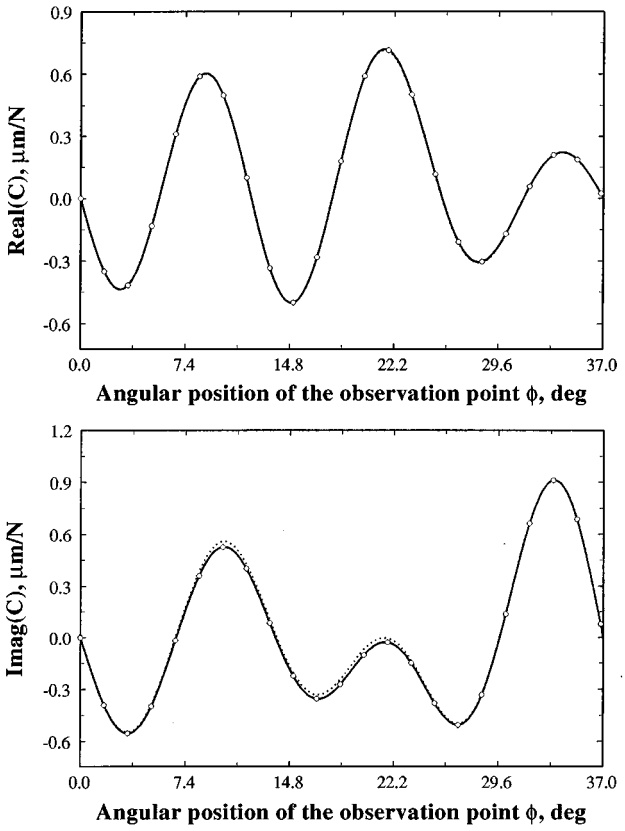

FIG. 6. Comparison of the closed-form solution with the eigenseries solution for $\gamma\rho\rho_s/2L = 10$ for simply supported boundary conditions along the edges. Key: ·····, $u_g(\mathbf{r}) + u_d(\mathbf{r})$; —○—, eigensolution.

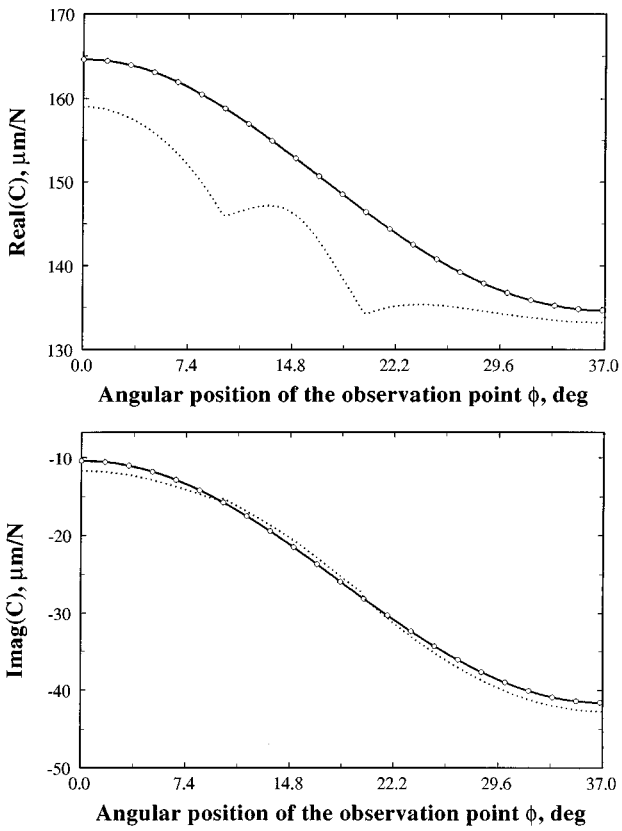

FIG. 7. Comparison of the closed-form solution with the eigenseries solution for $\gamma\rho\rho_s/2L = 1$ for roller boundary condition along the edges. Key: ·····, $u_g(\mathbf{r}) + u_d(\mathbf{r})$; —○——, eigensolution.

$$V_{1\nu}(\phi)=\int_{-\infty}^{\infty}\frac{e^{k(iz^2)}}{M_\nu(\phi)-iz}\,dz,\quad k=\pi\Gamma^2/2, \tag{30}$$

$z_s=0$ is the saddle point. On the steepest descent path through z_s, C_{sdp}, $|e^{k(iz^2)}|$ decreases most rapidly. This path makes an angle of $\pi/4$ with the $\Re(z)$ line. A variable transformation $\xi=ze^{-i\pi/4}$ causes C_{sdp} to coincide with the $\Re(\xi)$ line. Thus $V_{1\nu}(\phi)$ simplifies to

$$\begin{aligned}V_{1\nu}(\phi)&=\frac{1}{a}\int_{-\infty}^{\infty}\frac{e^{-k\xi^2}}{1-i\xi/a}\,d\xi,\\&=\frac{1}{a}\int_{-\infty}^{\infty}e^{-k\xi^2}\sum_{l=0}^{\infty}\left(\frac{i\xi}{a}\right)^l d\xi\\&=\frac{1}{a}\sum_{l=0}^{\infty}\int_{-\infty}^{\infty}e^{-k\xi^2}\left(\frac{i\xi}{a}\right)^l d\xi\\&=\frac{1}{a}\sum_{l=0}^{\infty}\frac{(-1)^l\Gamma((2l+1)/2)}{k^{(2l+1)/2}a^{2l}}\quad\text{if } M_\nu(\phi)\neq 0,\\&\qquad a=M_\nu(\phi)e^{-i\pi/4}.\end{aligned} \tag{31}$$

Similarly consider $V_{2\nu}(\phi)$:

$$V_{2\nu}(\phi)=\int_{-\infty}^{\infty}\frac{e^{-kz^2}}{M_\nu(\phi)-iz}\,dz. \tag{32}$$

The path of integration, $\Re(z)$ line, is the steepest descent path. Hence, no contour deformations are required. The integral for $V_{2\nu}(\phi)$ can be evaluated directly as

$$V_{2\nu}(\phi)=\frac{1}{b}\sum_{l=0}^{\infty}\frac{(-1)^l\Gamma((2l+1)/2)}{k^{(2l+1)/2}b^{2l}}$$
$$\text{if } M_\nu(\phi)\neq 0,\ b=M_\nu(\phi). \tag{33}$$

From the expressions (31) and (33), it is observed that, as the excitation frequency increases, $V_{1\nu}(\phi)$ and $V_{2\nu}(\phi)$ decrease due to the frequency related term k in the denominator, showing explicitly that diffraction is a low-frequency phenomenon. At high frequencies, the total solution is adequately represented by the geometric solution alone.

V. EIGENSERIES EXPANSION

Eigenseries representation for $u(\mathbf{r})$ is derived using eigenfunctions in the angular direction and propagation terms along the radial coordinate. This technique is similar to Macdonald's approach[17] for solving the Helmholtz equation in a wedge for a line source:

$$(\nabla^4-\gamma^4)u(\mathbf{r})=\frac{\delta(\rho-\rho_s)\,\delta(\phi-\phi_s)}{\rho D}. \tag{34}$$

Let us consider the simply supported boundary conditions first. Assume a solution of the form

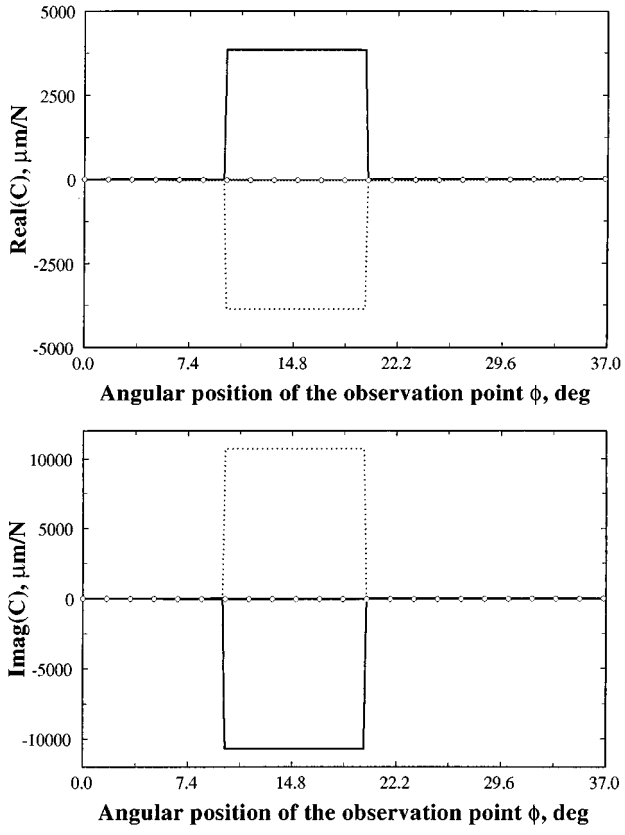

FIG. 8. Comparison of the geometric field with diffraction field for $\gamma\rho\rho_s/2L=0.1$ for simply supported boundary conditions along the edges. Key: ———, $u_g(\mathbf{r})$; ·····, $u_d(\mathbf{r})$; —○—, $u(\mathbf{r})$.

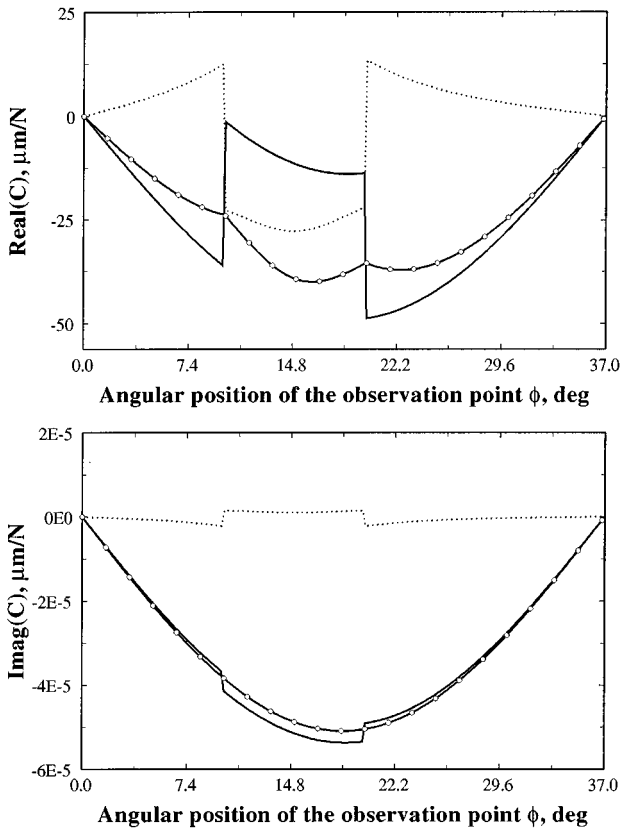

FIG. 9. Comparison of the geometric field with diffraction field for $\gamma\rho\rho_s/2L=1$ for simply supported boundary conditions along the edges. Key: ———, $u_g(\mathbf{r})$; ·····, $u_d(\mathbf{r})$; —○—, $u(\mathbf{r})$.

$$u(\mathbf{r})=\sum_{n=1}^{\infty} R_n(\rho)\sin(n\nu\phi). \tag{35}$$

Substituting Eq. (35) in Eq. (34), we get

$$\sum_{n=1}^{\infty} (\nabla^4-\gamma^4)R_n(\rho)\sin(n\nu\phi)=\frac{\delta(\rho-\rho_s)\delta(\phi-\phi_s)}{\rho D}. \tag{36}$$

Utilizing the orthogonality of the angular eigenfunctions, the radial solution $R_n(\rho)$ is obtained as

$$\begin{aligned} R_n(\rho)&=A_nJ_{n\nu}(\gamma\rho)+B_nH_{n\nu}(\gamma\rho)+C_nJ_{n\nu}(i\gamma\rho)\\ &\quad+D_nH_{n\nu}(i\gamma\rho), \quad \rho<\rho_s\\ &=W_nJ_{n\nu}(\gamma\rho)+X_nH_{n\nu}(\gamma\rho)+P_nJ_{n\nu}(i\gamma\rho)\\ &\quad+Q_nH_{n\nu}(i\gamma\rho), \quad \rho>\rho_s. \end{aligned} \tag{37}$$

The solution $u(\mathbf{r})$ satisfies zero displacement at the origin and the radiation condition at infinity, reducing the number of undetermined coefficients from eight to four.

$$\begin{aligned} R_n(\rho)&=A_nJ_{n\nu}(\gamma\rho)+C_nJ_{n\nu}(i\gamma\rho), \quad \rho<\rho_s\\ &=P_nH_{n\nu}(\gamma\rho)+Q_nH_{n\nu}(i\gamma\rho), \quad \rho>\rho_s. \end{aligned} \tag{38}$$

Across $\rho=\rho_s$, the displacement, slope, and bending moment are continuous. Matching the solutions at $\rho=\rho_s^-$ for displacement, slope, and bending moment with the corresponding quantities at $\rho=\rho_s^+$ results in the following relations between the coefficients. In Eq. (39), the prime stands for differentiation with respect to the variable ρ'.

$$\begin{bmatrix} J_{n\nu}(\gamma\rho_s) & J_{n\nu}(i\gamma\rho_s) & -H_{n\nu}(\gamma\rho_s) & -H_{n\nu}(i\gamma\rho_s)\\ J'_{n\nu}(\gamma\rho_s) & J'_{n\nu}(i\gamma\rho_s) & -H'_{n\nu}(\gamma\rho_s) & -H'_{n\nu}(i\gamma\rho_s)\\ J''_{n\nu}(\gamma\rho_s) & J''_{n\nu}(i\gamma\rho_s) & -H''_{n\nu}(\gamma\rho_s) & -H''_{n\nu}(i\gamma\rho_s) \end{bmatrix} \times \begin{Bmatrix} A_n\\ C_n\\ P_n\\ Q_n \end{Bmatrix} = \begin{Bmatrix} 0\\ 0\\ 0\\ 0 \end{Bmatrix}. \tag{39}$$

By using the following Wronskians of Bessel functions:[14]

$$\mathscr{W}(J_\nu(z),H_\nu(z))=\frac{2i}{\pi z},$$

$$J_\nu(z)H''_\nu(z)-J''_\nu(z)H_\nu(z)=\mathscr{W}(J_\nu(z),H_\nu(z))'=\frac{-2i}{\pi z^2}, \tag{40}$$

we find the solution to Eq. (39) as

$$\begin{Bmatrix} A_n\\ C_n\\ F_n\\ H_n \end{Bmatrix} = E_n \begin{Bmatrix} H_{n\nu}(\gamma\rho_s)\\ -H_{n\nu}(i\gamma\rho_s)\\ J_{n\nu}(\gamma\rho_s)\\ -J_{n\nu}(i\gamma\rho_s) \end{Bmatrix}. \tag{41}$$

Thus we are left with one undetermined coefficient, E_n, which is calculated by equating the transverse radial shear

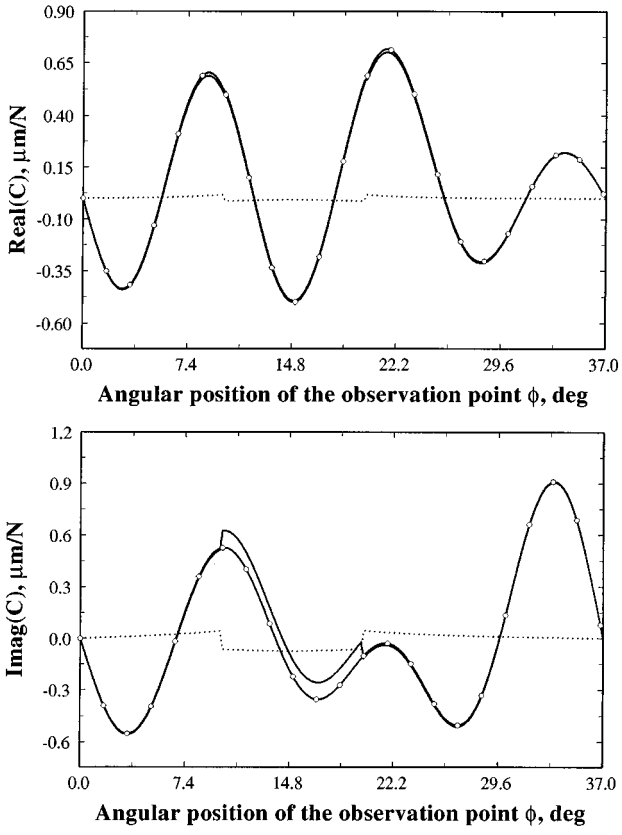

FIG. 10. Comparison of the geometric field with diffraction field for $\gamma\rho\rho_s/2L=10$ for simply supported boundary conditions along the edges. Key: ———, $u_g(\mathbf{r})$; ·····, $u_d(\mathbf{r})$; —○—, $u(\mathbf{r})$.

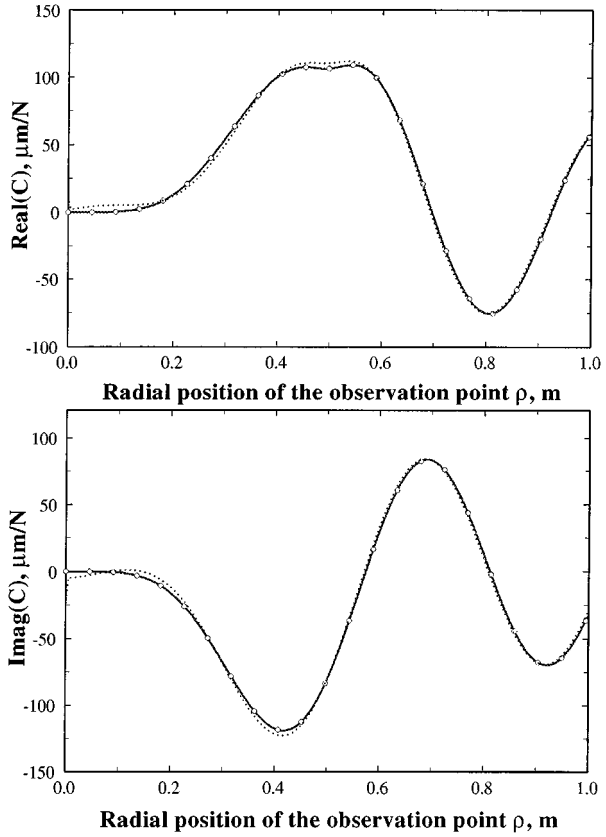

FIG. 11. Comparison of the closed-form solution with the eigenseries solution along a radial line for simply supported boundary conditions along the edges. Key: ·····, $u_g(\mathbf{r})+u_d(\mathbf{r})$; —○—, eigensolution.

force difference $V_r(\rho_s^+)-V_r(\rho_s^-)$ given by Eqs. (42) and (43) to the angular load distribution at ρ_s given in this case by $\delta(\phi-\phi_s)/\rho_s$:

$$V_r(\rho_s^+)=\gamma^2 D\sum_{n=1}^{\infty} E_n \sin n\nu\phi[J_{n\nu}(\gamma\rho_s)H'_{n\nu}(\gamma\rho_s) + J_{n\nu}(i\gamma\rho_s)H'_{n\nu}(i\gamma\rho_s)], \tag{42}$$

$$V_r(\rho_s^-)=\gamma^2 D\sum_{n=1}^{\infty} E_n \sin n\nu\phi[J'_{n\nu}(\gamma\rho_s)H_{n\nu}(\gamma\rho_s) + J'_{n\nu}(i\gamma\rho_s)H_{n\nu}(i\gamma\rho_s)]. \tag{43}$$

Here E_n is given by $-\nu i\epsilon_n \sin n\nu\phi_s/4\gamma^2 D$. The complete expression for $u(\mathbf{r})$ for simply supported boundary conditions is given by

$$u(\mathbf{r})=\frac{-\nu i}{4\gamma^2 D}\sum_{n=0}^{\infty}\epsilon_n \sin n\nu\phi \sin n\nu\phi_s \times\{J_{n\nu}(\gamma\rho^<)H_{n\nu}(\gamma\rho^>)-J_{n\nu}(i\gamma\rho^<)H_{n\nu}(i\gamma\rho^>)\}, \tag{44}$$

where

$$\rho^<\equiv\min(\rho,\rho_s),\quad \rho^>\equiv\max(\rho,\rho_s),\quad \epsilon_n=\begin{cases}1, & n=0\\ 2, & n\geqslant 1.\end{cases} \tag{45}$$

Similarly, the solution for roller boundary conditions is given by

$$u(\mathbf{r})=\frac{-\nu i}{4\gamma^2 D}\sum_{n=0}^{\infty}\epsilon_n \cos n\nu\phi \cos n\nu\phi_s \times\{J_{n\nu}(\gamma\rho^<)H_{n\nu}(\gamma\rho^>)-J_{n\nu}(i\gamma\rho^<)H_{n\nu}(i\gamma\rho^>)\}. \tag{46}$$

VI. RESULTS

In this section the relative contribution of the geometric $u_g(\mathbf{r})$ and the diffraction fields $u_d(\mathbf{r})$ to the overall solution $u(\mathbf{r})$ is examined at different frequencies. Also, their spatial properties along ρ and ϕ are studied using a specific example case for three different frequency regimes. Finally, the near-field effects, as induced by the biharmonic formulation, are examined.

A steel wedge with $\beta=37°$, $E=210$ GPa, $\rho_m=7800$ kg/m^3, $\nu=0.3$, and thickness of $h=0.762$ mm is used as the primary example. The Faddeeva function is computed using the algorithm developed by Poppe and Wijers.[18] The force excitation point S is kept fixed at $\rho_s=0.5$ m and $\phi_s=22°$ and the angular position ϕ of the observation point O is varied between $[0,\beta]$ at a radial distance of $\rho=0.3$ m. The closed-form solution $u_g(\mathbf{r})+u_d(\mathbf{r})$ is compared with the eigensolution for $\gamma\rho\rho_s/2L=0.1$, 1 and 10. The results are plotted in terms of the cross-point dynamic compliance spectrum $C(\omega;\mathbf{r},\mathbf{r}_s)=u(\mathbf{r})/F(\mathbf{r}_s)$ over the range of interest as shown in Figs. 4–6 for the simply supported boundary conditions along the edges. Observe that the closed-form solu-

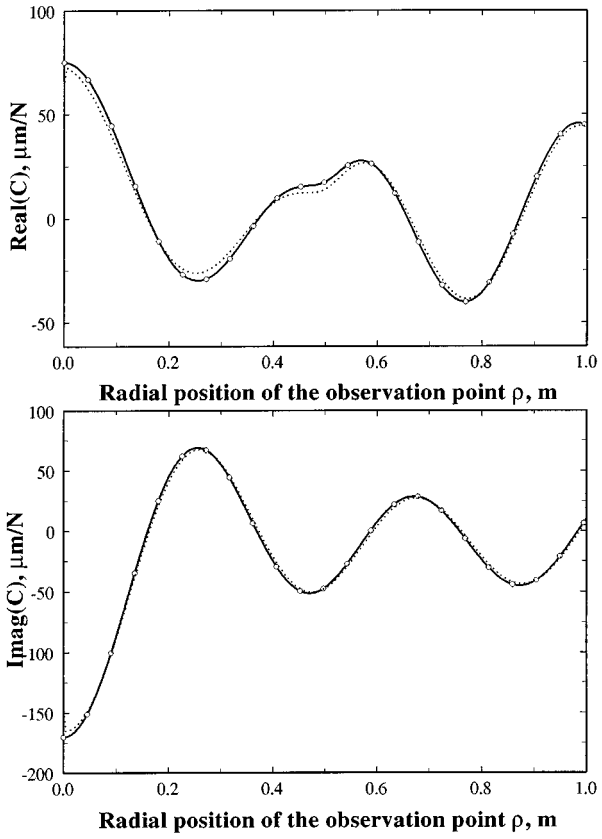

FIG. 12. Comparison of the closed-form solution with the eigenseries solution along a radial line for roller boundary conditions along the edges. Key: ·····, $u_g(\mathbf{r})+u_d(\mathbf{r})$; —○—, eigensolution.

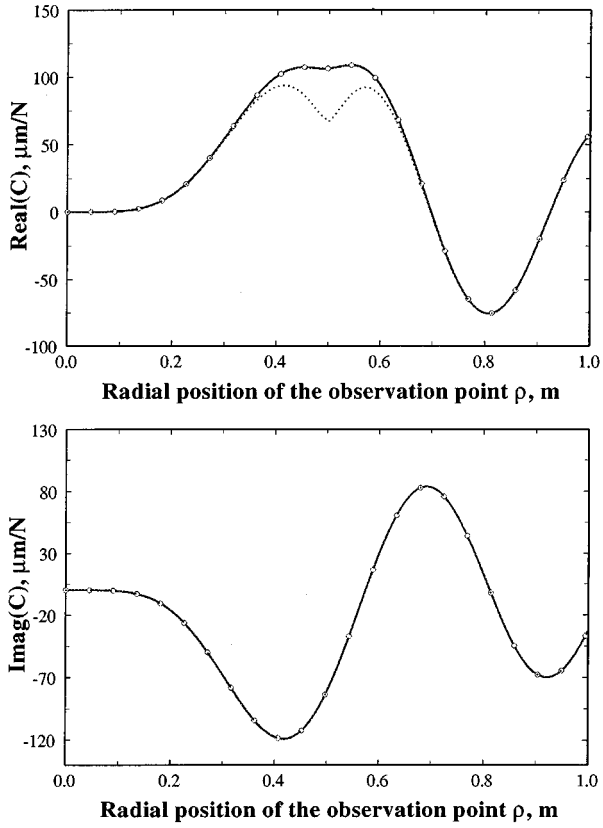

FIG. 13. Comparison of biharmonic solution with the classical wave equation solution along a radial line for simply supported boundary conditions along the edges. Key: —○—, biharmonic solution; ·····, classical wave equation solution.

tion is not very accurate for $\gamma\rho\rho_s/2L \leqslant O(0.1)$. It is expected since this was one of the assumptions involved in the derivation of the closed-form solution. Therefore, in order to calculate the the diffraction field $u_d(\mathbf{r})$ for small values of $\gamma\rho\rho_s/2L$, we must subtract the geometric field $u_g(\mathbf{r})$ from the total field $u(\mathbf{r})$ as given by the eigenseries expansion. Sample results for the roller boundary conditions along the edges are shown in Fig. 7 for $\gamma\rho\rho_s/2L=1$ from which similar conclusions can be drawn.

For the same example with simple supports, the geometric and the diffracted fields, $u_g(\mathbf{r})$ and $u_d(\mathbf{r})$ are plotted in Figs. 8–10. From these results, it is evident that the contribution of the diffraction field $u_d(\mathbf{r})$ to the total displacement field $u(\mathbf{r})$ is not as important as the geometric field $u_g(\mathbf{r})$ at higher frequencies as predicted by the steepest descent technique in Sec. IV. Therefore, we conclude that diffraction is basically a low-frequency phenomenon for the biharmonic problem, like the classical wave equation theory.[4,10] Next, the force excitation is located at $\rho_s=0.5$ m and $\phi_s=22°$ and the observation point is moved along a radial line at $\phi=18°$ from $\rho=0$ to $\rho=1$. Excellent agreement is seen between the closed-form solution and the eigensolution as evident from Fig. 11 (simply supported) and Fig. 12 (roller).

The first term of the fundamental solution (6) to the biharmonic equation satisfies the Helmholtz wave equation given by Eq. (47). By the ''Helmholtz wave equation solution,'' we refer to the solution of the following equation for the wedge geometry with Dirichlet or Neumann boundary conditions along the edges.[4]

$$(\nabla^2+\gamma^2)u(\mathbf{r})=\frac{1}{2\gamma^2 D}\,\delta(\mathbf{r}-\mathbf{r}_s). \tag{47}$$

Comparison of the fourth-order biharmonic with the second-order Helmholtz wave equation reveals that both yield similar solutions in most of the spatial domain except for small regions near the source and the boundary edges. This near-field effect is illustrated in Fig. 13.

VII. CONCLUSION

The chief contribution of this paper is the evaluation of the diffraction integral in a closed-form in terms of Faddeeva functions. Using the steepest descent method, it is analytically shown and numerically verified that the diffraction effects are important only at low frequencies. Near-field effects are significant only when the observation point is close to the edges or the excitation location. Finally, the eigenseries expansion converges rapidly at lower frequencies while $u_g(\mathbf{r})+u_d(\mathbf{r})$ predicts accurate high-frequency responses. Following the approach used in the derivation of eigenseries expansion, the solution to other excitations such as angularly distributed line load can be obtained. The solutions developed here will be used to address the problem of obtaining spectral characteristics of arbitrary finite polygonal plates with medium to high modal density for which there are no satisfactory techniques available at present. Future research will also examine other boundary conditions.

ACKNOWLEDGMENTS

This work has been supported by the U. S. Army Research Office (URI Grant No. DAAL-03-92-G-0120; Project Monitor: Dr. T. L. Doligalski).

[1] J. L. Graeme, *Geometric Theory of Diffraction for Electromagnetic Waves* (Institution of Electric Engineers, New York, 1986).
[2] T. J. I.'A. Bromwich, ''Diffraction of waves by a wedge, '' Proc. Math. Soc. London **14**, 450–463 (1915).
[3] A. A. Tuzhilin, ''New representations of diffraction fields in wedge-shaped regions with ideal boundaries,'' Sov. Phys. Acoust. **9**(2), 168–172 (1963).
[4] J. J. Bowman and T. B. A. Senior, ''The Wedge,'' in *Electromagnetic and Acoustic Scattering by Simple Shapes*, edited by J. J. Bowman, T. B. A. Senior, and P. L. E. Uslenghi (Hemisphere, New York, 1987), Chap. 6, pp. 252–283.
[5] F. J. W. Whipple, ''Diffraction by wedge and kindred problems,'' Proc. Math. Soc. London **16**, 481–500 (1915).
[6] M. A. Biot and I. Tolstoy, ''Formulation of wave propagation in infinite media by normal coordinates with an application to diffraction,'' J. Acoust. Soc. Am. **29**, 381–391 (1957).
[7] H. M. Macdonald, ''A class of diffraction problems,'' Proc. Math. Soc. London **14**, 410–427 (1915).
[8] A. Sommerfeld, *Partial Differential Equations in Physics* (Academic, New York, 1964).
[9] P. M. Morse and H. Feshbach, *Methods of Theoretical Physics* (McGraw-Hill, New York, 1953), Vol. 1.
[10] J. B. Keller, ''Geometrical theory of diffraction,'' J. Opt. Soc. Am. **52**(2), 116–130 (1961).
[11] A. W. Leissa, *Vibration of Plates* (NASA SP-160, NASA Special Publication, 1969).
[12] D. Feit and M. C. Junger, *Sound, Structures, and their Interaction* (MIT, Cambridge, MA, 1972), pp. 210–213.
[13] Y. Niwa, S. Kobayashi, and M. Kitahara, ''Eigen frequency analysis of a plate by the integral equation method,'' Theor. Appl. Mech. **29**, 287–367 (1981).
[14] G. N. Watson, *A Treatise on the Theory of Bessel Functions* (Cambridge U. P., Cambridge, England, 1944), pp. 196–200.
[15] A. D. Pierce, *Acoustics—An Introduction to its Physical Principles and Applications* (Acoustical Society of America, Woodbury, NY, 1989), pp. 481–500.
[16] M. Abramowitz and I. A. Stegun, *Handbook of Mathematical Functions with Formulas, Graphs, and Mathematical Tables* (Wiley, New York, 1972).
[17] H. M. Macdonald, *Electric Waves* (Cambridge U.P., Cambridge, England, 1902).
[18] G. P. M. Poppe and C. M. J. Wijers, ''Algorithm 680: Evaluation of the complex error function,''ACM Trans. Math. Softw. **16**(1), 47 (1990).

Structural intensity of acoustically excited waves in a fluid-loaded elastic plate

Steven L. Means[a] and Ralph R. Goodman
Applied Research Laboratory, Penn State University, P.O. Box 30, State College, Pennsylvania 16801

(Received 10 April 1996; accepted for publication 10 March 1997)

When an acoustic plane wave is incident on an elastic plate, energy propagates within the plate, as well as being reflected from and transmitted through the plate. The present study determines the structural intensity as a function of incident angle at different depths along the cross section. It is found that most peaks, but not all, in the structural intensity may be identified as free waves of the fluid–plate system yielding a form of ''numerical spectroscopy.'' It is also found that for particular frequencies and angles of incidence the direction of the structural intensity parallel to the plane of the plate is opposite than what would normally be expected. Various studies are performed to gain physical insight into this phenomenon. © *1997 Acoustical Society of America.*
[S0001-4966(97)00607-3]

PACS numbers: 43.40.Dx, 43.40.At [CBB]

INTRODUCTION

There have been numerous studies both theoretical and experimental of elastic wave propagation in fluid-loaded elastic plates.[1–4] Most of these studies were principally concerned with the reflection and transmission of acoustic waves incident on the plate. However, in the active control of fluid-loaded structures exposed to acoustic fields[5] and in the study of scattering of sound from elastic structures[6,7] there is an interest in the energy flow within the structure. The present study applies the exact theory of elasticity to model the wave motion in plates, irrespective of their thickness, to determine the energy flow (structural intensity) within the thickness of the structure. A similar study has been performed, by one of the current authors, on the energy flow within a semi-infinite elastic medium due to an incident acoustic wave.[6]

The analytic study of energy flow is complicated by the presence of both compressional and shear waves within the plate. Further complicating matters is that generally neither of the wave types acting alone can satisfy the boundary conditions at the interfaces. Due to these complications, an exact analytic study has not been undertaken until now. The present study incorporates the use of symbolic mathematical software to aid in the algebraic manipulations of the rather large analytic expressions. Once the expressions have been obtained they may be used to study how the energy flows within the structure for incident waves of various frequencies and angles of incidence.

I. MATHEMATICAL DEVELOPMENT

A plane acoustic wave is incident on a fluid-immersed elastic plate at an angle θ_0 with respect to the normal of the plate's surface which is horizontally oriented (see Fig. 1). The fluid is considered to be homogeneous, having a density ρ_0 and a bulk modulus of elasticity λ_0. The plate is considered to be infinite in length, having a thickness h, Lamé constants of λ and μ, and a density of ρ.

The incident wave may be represented in the form of a scalar potential[2]

$$\phi_{\text{inc}} = e^{-ik_0 \cos\theta_0 x} e^{i(\omega t - k_0 \sin\theta_0 y)} \tag{1}$$

and the potentials above, inside, and beneath the plate may be expressed as

$$\begin{aligned}
\phi_0 &= [e^{-ik_0 \cos\theta_0 x} + Ae^{ik_0 \cos\theta_0 x}] e^{i(\omega t - k_0 \sin\theta_0 y)}, \\
\phi &= [Be^{-ik_l \cos\theta_l x} + Ce^{ik_l \cos\theta_l x}] e^{i(\omega t - k_l \sin\theta_l y)}, \\
\psi &= [De^{-ik_t \cos\theta_t x} + Ee^{ik_t \cos\theta_t x}] e^{i(\omega t - k_t \sin\theta_t y)}, \\
\phi_T &= Fe^{-ik_0 \cos\theta_0 x} e^{i(\omega t - k_0 \sin\theta_0 y)}.
\end{aligned} \tag{2}$$

In the above expressions, the fact that shear horizontal waves are not excited, since tangential stresses at the surfaces must vanish,[8] has been used. Thus the vector potential $\boldsymbol{\psi}$ within the plate is $(0,0,\psi)$. One can determine, from Snell's law, that

$$k_0 \sin\theta_0 = k_l \sin\theta_l = k_t \sin\theta_t \equiv \beta. \tag{3}$$

The displacements and strains within the plate may be determined from the potentials by

$$\begin{Bmatrix} u_x \\ u_y \end{Bmatrix} = \begin{Bmatrix} \dfrac{\partial\phi}{\partial x} + \dfrac{\partial\psi}{\partial y} \\ \dfrac{\partial\phi}{\partial y} - \dfrac{\partial\psi}{\partial x} \end{Bmatrix} \quad \text{and} \quad \epsilon_{ij} = \frac{1}{2}\left(\frac{\partial u_i}{\partial x_j} + \frac{\partial u_j}{\partial x_i}\right). \tag{4}$$

The stresses may be obtained by using the relationship between stress and strain given by

$$\sigma_{ij} = \lambda \delta_{ij} \epsilon_{\alpha\alpha} + 2\mu \epsilon_{ij}. \tag{5}$$

The boundary conditions that the potentials must satisfy on both surfaces of the plate are

(a) continuity of displacement,
(b) no shear stresses, and
(c) continuity of normal stress (pressure).

[a]Present address: Naval Research Laboratory, Code 7121, Washington, DC 20375.

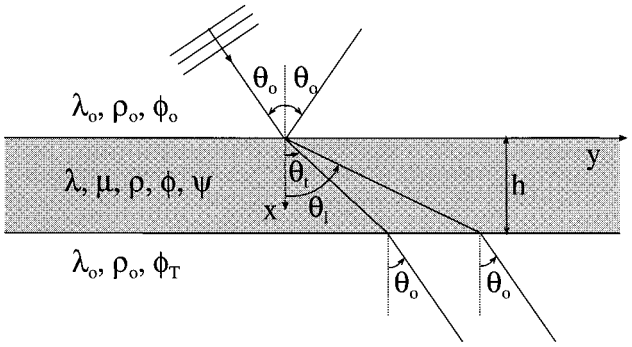

FIG. 1. Coordinate system and nomenclature used in discussion of a plane acoustic wave incident on a submerged elastic plate.

The amplitude coefficients for the potentials may be determined from the system of equations obtained by applying the boundary conditions to Eqs. (2), which yields

$$
\begin{aligned}
&A+\frac{\alpha_l}{\alpha_0}(B-C)+\frac{\beta}{\alpha_0}(D+E)=1,\\
&-\alpha_l\beta(B-C)+\tfrac{1}{2}(\alpha_t^2-\beta^2)(D+E)=0,\\
&A+\frac{\rho}{\rho_0}\left[\left(\frac{2\beta^2}{k_t^2}-1\right)(B+C)-\frac{2\alpha_t\beta}{k_t^2}(D-E)\right]=-1,\\
&\frac{\alpha_l}{\alpha_0}(Be^{-i\alpha_l h}-Ce^{i\alpha_l h})+\frac{\beta}{\alpha_0}(De^{-i\alpha_t h}+Ee^{i\alpha_t h})\\
&\qquad -Fe^{-i\alpha_0 h}=0,\\
&-\alpha_l\beta(Be^{-i\alpha_l h}-Ce^{i\alpha_l h})+\tfrac{1}{2}(\alpha_t^2-\beta^2)\\
&\qquad \times(De^{-i\alpha_t h}+Ee^{i\alpha_t h})=0,\\
&\frac{\rho}{\rho_0}\left[\left(1-\frac{2\beta^2}{k_t^2}\right)(Be^{-i\alpha_l h}+Ce^{i\alpha_l h})+\frac{2\alpha_t\beta}{k_t^2}\right.\\
&\qquad \left.\times(De^{-i\alpha_l h}-Ee^{i\alpha_t h})-Fe^{-i\alpha_0 h}=0,\right.
\end{aligned}
\tag{6}
$$

where $\alpha_m \equiv k_m \cos\theta_m$.

Although straightforward in concept, it is impractical to attempt solving the above system of equations in written form. However, with the use of symbolic mathematical computer packages it is possible to obtain exact analytic expressions for the above coefficients. This task has been performed, however, due to space considerations these expressions are not shown.

II. DISPERSION RELATIONS FOR FREE WAVES

The aim of this paper is to investigate the structural intensity within the acoustically excited plate. When the trace velocity of the incident wave matches the phase velocity of a free wave of the system the free wave will be excited.[9] These excited free waves are expected to produce peaks in the time-averaged intensity for various angles of incidence and frequencies of excitation. Therefore, it is constructive to consider the free waves of a fluid-loaded plate. The familiar equations of motion for an elastic plate in a vacuum were originally derived by Rayleigh in 1889.[10] (A derivation of these equations may be found in a text by Ewing *et al.*[8]) A dispersion relation may be obtained from these equations of motion and may be expressed as

$$
\frac{\tanh((h/2)(k^2-\omega^2/c_l^2)^{1/2})}{\tanh((h/2)(k^2-\omega^2/c_t^2)^{1/2})}
=\left[\frac{(2k^2-\omega^2/c_t^2)^2}{4k^2(k^2-\omega^2/c_t^2)^{1/2}(k^2-\omega^2/c_l^2)^{1/2}}\right]^{\pm 1},
\tag{7}
$$

where the plus sign is for symmetric waves and the minus sign is for antisymmetric waves. Similar expressions may be obtained for the symmetric and antisymmetric vibrations of a fluid-loaded elastic plate. They are

$$
\begin{aligned}
&\frac{\tanh((h/2)(k^2-\omega^2/c_l^2)^{1/2})}{\tanh((h/2)(k^2-\omega^2/c_t^2)^{1/2})}\\
&\quad=\frac{(2k^2-\omega^2/c_t^2)^2}{4k^2(k^2-\omega^2/c_t^2)^{1/2}(k^2-\omega^2/c_l^2)^{1/2}}\\
&\qquad+\frac{\rho_0\omega^4\tanh((h/2)(k^2-\omega^2/c_l^2)^{1/2})}{4\rho k^2c_t^4(k^2-\omega^2/c_0^2)^{1/2}(k^2-\omega^2/c_t^2)^{1/2}}
\end{aligned}
\tag{8}
$$

for symmetric waves and

$$
\begin{aligned}
&\frac{\tanh((h/2)(k^2-\omega^2/c_l^2)^{1/2})}{\tanh((h/2)(k^2-\omega^2/c_t^2)^{1/2})}\\
&\quad=\frac{4k^2(k^2-\omega^2/c_t^2)^{1/2}(k^2-\omega^2/c_l^2)^{1/2}}{(2k^2-\omega^2/c_t^2)^2}\\
&\qquad-\frac{\rho_0\omega^4(k^2-\omega^2/c_l^2)^{1/2}\coth((h/2)(k^2-\omega^2/c_t^2)^{1/2})}{\rho c_t^4(k^2-\omega^2/c_0^2)^{1/2}(2k^2-\omega^2/c_t^2)^2}
\end{aligned}
\tag{9}
$$

for antisymmetric waves. These expressions will allow one to identify some of the peaks in the time-averaged intensity plots. However, it will later be found that not all peaks correspond to the excitation of free waves.

III. TIME-AVERAGED STRUCTURAL INTENSITY

The field intensity of elastic waves is given in tensor notation in the text of Morse and Feshbach.[11] From their expression, one may obtain the time-averaged intensity in the ith direction in terms of particle displacement and strain components as

$$
I_i=\tfrac{1}{4}[\lambda(\dot{u}_i^*\epsilon_{\alpha\alpha}+\dot{u}_i\epsilon_{\alpha\alpha}^*)+2\mu(\dot{u}_\alpha^*\epsilon_{\alpha i}+\dot{u}_\alpha\epsilon_{\alpha i}^*)],
\tag{10}
$$

where repeated indices imply a summation and the asterisk implies the complex conjugate.

The interest in this section is to determine the distribution of energy that flows parallel to the axis of the plate. The

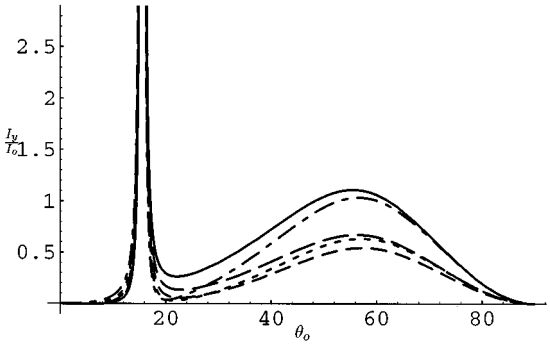

FIG. 2. Time-averaged intensity in the y direction normalized by the incident intensity at $k_0h \approx 1.0$ for various values of x: (——), $0.0h$; (— —), $0.25h$; (– – –), $0.5h$; (----), $0.75h$; and (— - —), $1.0h$.

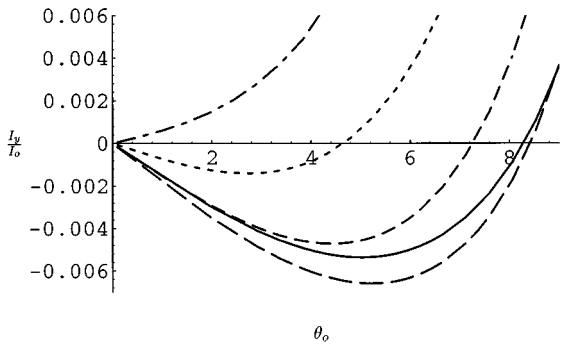

FIG. 3. An expansion of the previous plot for small angles of incidence.

intensity in the y direction may be determined by using Eqs. (2) and (4) in Eq. (10). One then obtains

$$\frac{2I_y}{\rho\omega^3} = \beta\left[1+\frac{2}{k_t^2}(\beta^2+\alpha_l\alpha_l^*-k_l^2)\right]\phi\phi^* + \frac{2\beta}{k_t^2}\left[\alpha_t\alpha_t^* - \frac{\alpha_t^2-\beta^2}{2}\right]\psi\psi^* + \frac{1}{k_t^2}\left[-4\beta(\alpha_l\alpha_l^*\Phi+\alpha_t\alpha_t^*\Psi) + \left(2\beta^2-k_l^2+\frac{k_t^2}{2}\right)(\alpha_t\phi^*(\psi_\uparrow-\psi_\downarrow) + \alpha_t^*\phi(\psi_\uparrow^*-\psi_\downarrow^*)) - \left(2\beta^2-\frac{k_t^2}{2}\right)(\alpha_l\psi^*(\phi_\uparrow-\phi_\downarrow) + \alpha_l^*\psi(\phi_\uparrow^*-\phi_\downarrow^*))\right], \tag{11}$$

where the following variables are defined as

$$2\Phi \equiv \phi\phi^* - (\phi_\uparrow-\phi_\downarrow)(\phi_\uparrow^*-\phi_\downarrow^*),$$

$$2\Psi \equiv \psi\psi^* - (\psi_\uparrow-\psi_\downarrow)(\psi_\uparrow^*-\psi_\downarrow^*).$$

The symbols $\uparrow$ and $\downarrow$ identify the portion of the potentials which correspond to upward and downward propagating waves.

The above expression for I_y, normalized by the incident intensity I_0, has been plotted in Fig. 2 as a function of incident angle θ_0 and for five different depths into the thickness of the plate at a frequency such that $k_0h \approx 1.0$. The properties of the plate and fluid used in this paper are given in Table I. It should be noted here that at the scale of the plots within this paper some peaks appear infinite, however, they are indeed finite. The two distinctive peaks at θ_0 of 15.5° and 55.5° may be explained by considering the free waves of a fluid-loaded elastic plate. The trace velocity of the wave incident at $\theta_0 = 15.5$ is equal to the phase velocity of a free longitudinal wave on the fluid-loaded plate. Thus, one determines that the peak at $\theta_0 = 15.5°$ corresponds to an excited longitudinal plate wave. The peak at $\theta_0 = 55.5°$ corresponds to an excited flexural wave. If the region near normal incidence is expanded, as in Fig. 3, one notices that there is a negative time-averaged intensity, i.e., there is energy flowing in the negative y direction. Since Lamb waves (some of which are known to have negative group velocities[12]) are not excited at frequencies this low, the phenomenon cannot be attributed to their presence.

TABLE I. Plate and fluid properties.

Property	Aluminum	Water
Lamé-λ	5.6372×10^{10} Pa	2.146×10^{9} Pa
Lamé-μ	2.752×10^{10} Pa	…
density	2770 kg/m^3	1000 kg/m^3

In Figs. 4, 5, and 6 the normalized time-averaged intensity I_y/I_0 at the upper surface of the plate has been plotted for various frequencies. Examining first the series of plots in Fig. 4, one notices that the peak corresponding to the longitudinal plate wave is fixed at $\theta_0 = 15.5°$. This is due to the nature of longitudinal plate waves being nondispersive. It is seen, however, that the peak corresponding to flexural waves is excited at smaller angles of incidence as the frequency is increased. This is due to the dispersive nature of flexural plate waves, that is, as frequency increases the phase velocity increases.

When one considers a higher range of frequencies, as in Fig. 5, it is noticed that there is an additional peak in the time-averaged plot at a low angle of incidence for $k_0h = 6.83$. This peak corresponds to an excited Lamb wave. It also shows, by its being excited at larger angles of incidence, that this wave decreases in phase velocity as frequency is increased. Within this range of frequencies, it is also noticed that the peak corresponding to the longitudinal plate wave decreases in magnitude until it is negligible at $k_0h = 9.42$. However, it reforms into another longitudinal wave having different characteristics. Namely, it is now dispersive, decreasing in phase velocity at higher frequencies. At higher frequencies within this range, additional peaks in the intensity plots are formed. These correspond to the excitation of other Lamb waves. In studying the time-averaged intensity in this manner, it may be thought of as a form of ''numerical spectroscopy'' for the elastic structure. As one increases the frequency one sees additional free waves being excited.

At higher frequencies still, as in Fig. 6, one sees as before that additional waves have been excited. Of particular interest in this range of plots is the merging of the peaks corresponding to the longitudinal wave and the flexural wave. As known previously, the combination of a longitudinal wave and a flexural wave forms a Rayleigh wave.[13] Ray-

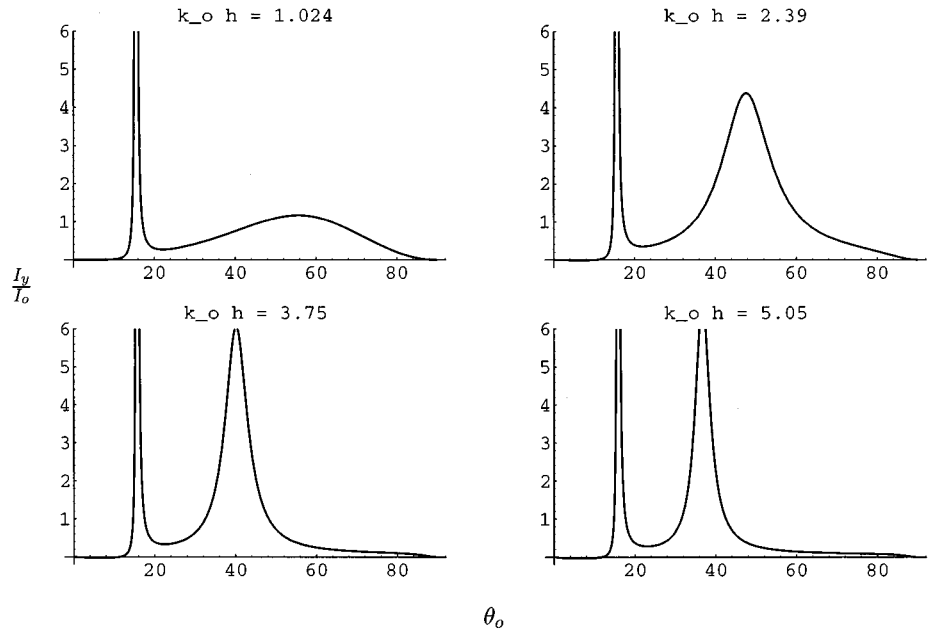

FIG. 4. Normalized axial time-averaged intensity at the upper surface for various angles of incidence and a range of k_0h values. The first peak from the left corresponds to longitudinal plate waves. The second peak corresponds to flexural waves. The dispersive nature of the flexural waves is seen in the apparent movement of the peak toward the left as one views the individual plots from left to right.

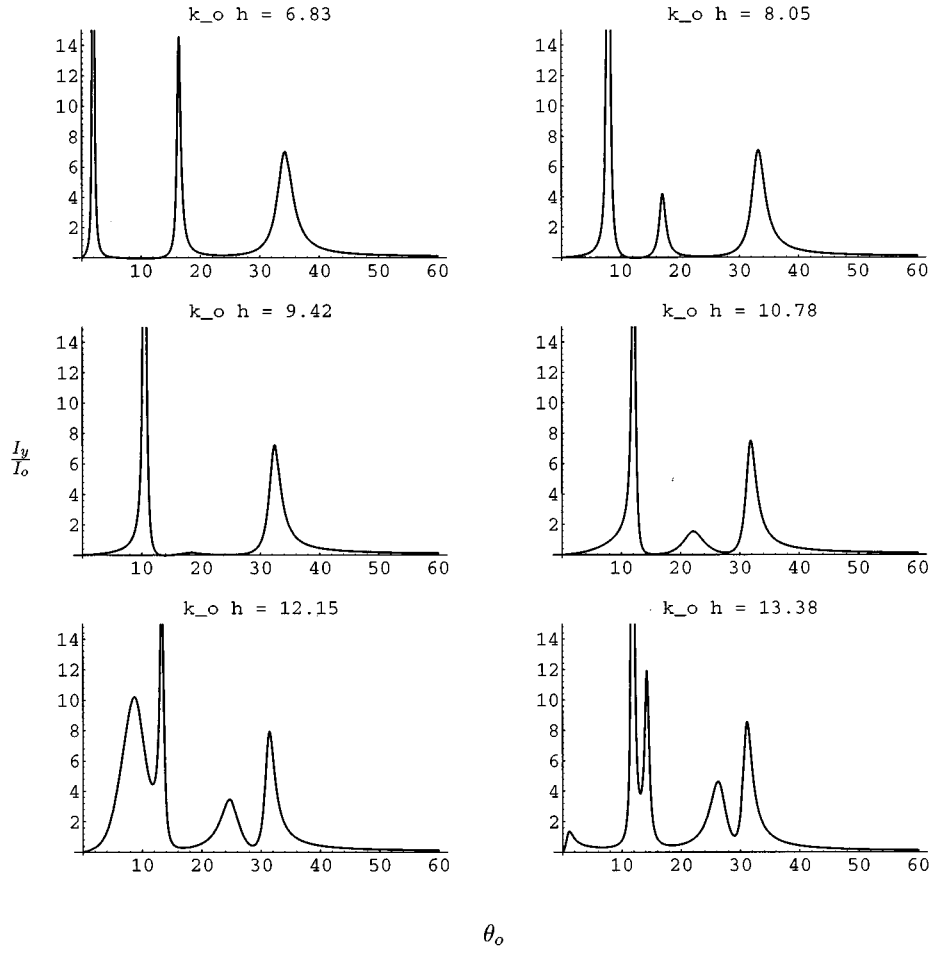

FIG. 5. Normalized axial time-averaged intensity at the upper surface for various angles of incidence and a range of k_0h values.

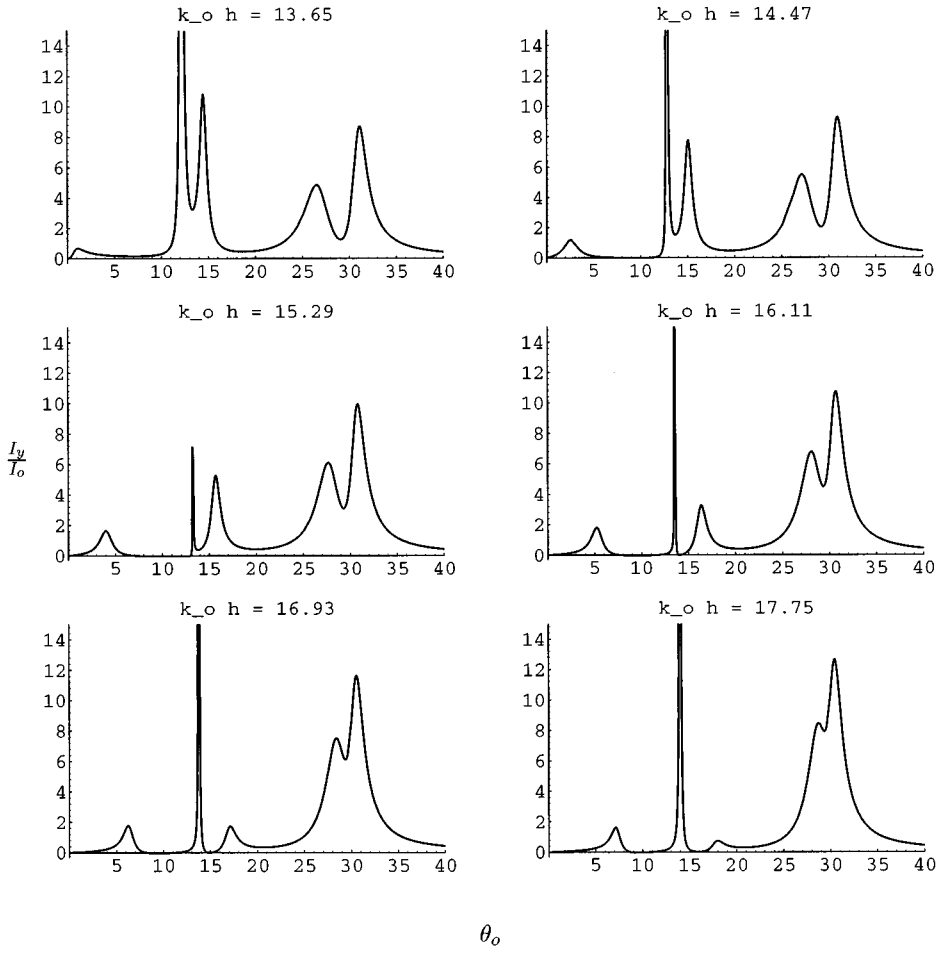

FIG. 6. Normalized axial time-averaged intensity at the upper surface for various angles of incidence and a range of k_0h values.

leigh waves are normally thought to propagate on the surface of semi-infinite elastic media. However, at high frequencies, quasi-Rayleigh waves can propagate on the surfaces of a plate.

To determine how the time-averaged intensity varies with depth into the plate, a series of plots has been made at a frequency such that $k_0h=27.3$, see Fig. 7. This frequency is chosen as a moderate value of k_0h. In this series of plots, the peak corresponding to the quasi-Rayleigh wave ($\theta_0\approx30°$) is seen to decay as the depth from the surface increases, as expected. Although much lower in amplitude than at the top surface, there is a noticeable peak due to a quasi-Rayleigh wave at the bottom surface.

The other peak of interest is at $\theta_0\approx14°$. In observing this peak for different depths into the plate, one notices that the intensity changes direction. At depths of $x/h=0.25$, 0.5, and 0.75 the intensity pointed in the negative y direction. Although not illustrated in this figure, the intensity changes back to positive in the regions between $x/h=0.25$ and 0.5 and $x/h=0.5$ and 0.75 (see Fig. 12). Similar phenomena have been observed previously by others[7,14,15] and may be attributed to excited free waves. However, this peak does not correspond to a free wave, i.e., it does not satisfy either Eq. (8) or Eq. (9). It does, however, satisfy the imaginary part of Eq. (9). Properties of this peak will be discussed in more detail in a later section.

IV. INSTANTANEOUS STRUCTURAL INTENSITY

The excitation of the free waves may be seen more clearly by examining the instantaneous intensity through the depth of the plate for specific frequencies and angles of incidence. The components of instantaneous intensity[11] may be expressed in terms of strains and displacements as

$$I_i^{\text{inst}}=-\tfrac{1}{2}[\lambda\dot{u}_i\epsilon_{\alpha\alpha}+2\mu\dot{u}_\alpha\epsilon_{\alpha i}]. \tag{12}$$

If the x and y components of intensity are calculated, one may plot a vector field through the depth of the plate. This has been done for several frequencies and for specific angles of incidence. In Fig. 8 an instantaneous intensity vector field has been plotted at the frequency and angle of incidence such that a longitudinal plate wave is excited. It is seen that essentially all of the energy is flowing parallel to the axis of the plate. Although not apparent from this figure, there is a small amount propagating along the vertical direction corresponding to transmission into the lower fluid. In Figs. 9 and 10 similar plots have been made at frequencies and angles of incidence such that a flexural and quasi-Rayleigh wave are excited, respectively. As one would expect, the circular rotation is evident in the vector field of the flexural wave (see Fig. 9). The magnitude of the intensity field is seen to decay exponentially away from the upper surface for the quasi-Rayleigh wave. Although not evident in this figure, there is

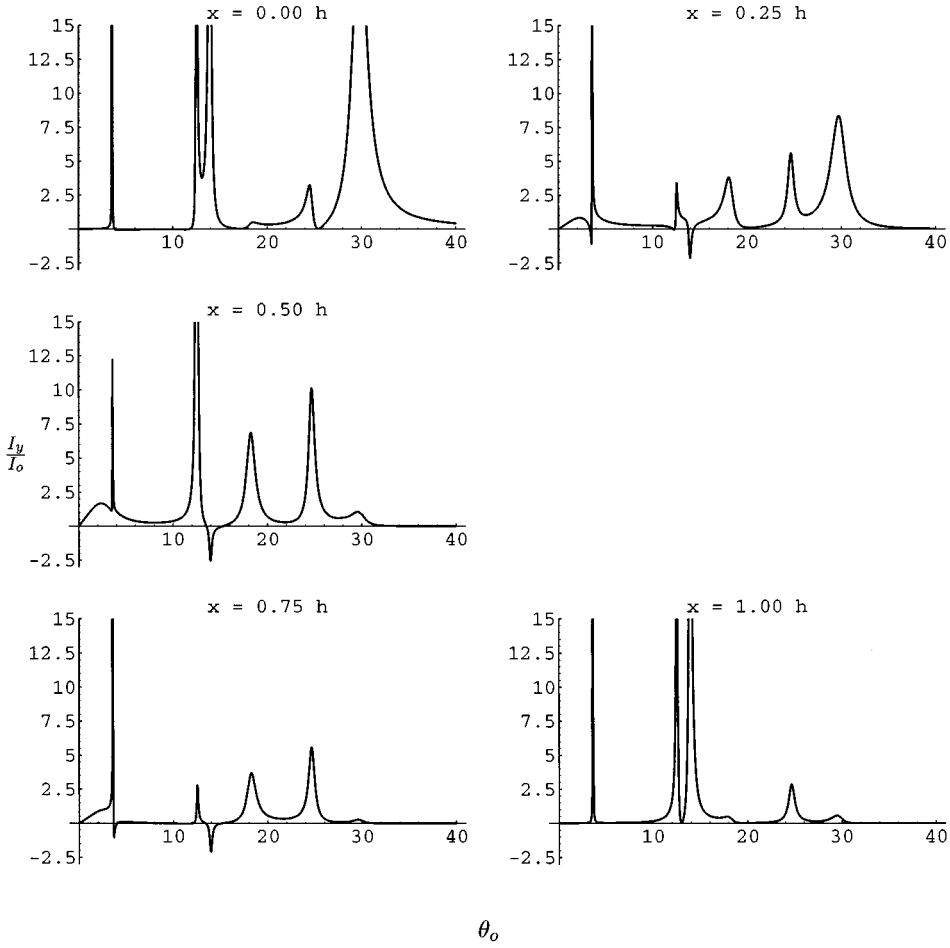

FIG. 7. Normalized axial time-averaged intensity at the upper surface for various angles of incidence and a range of depths into the plate.

also an exponential decay away from the lower surface (see Fig. 7). For comparison, a similar plot (Fig. 11) has been made for the instantaneous vector field corresponding to the peak at $\theta_0 \approx 14°$ in the time-averaged intensity plots in Fig. 7. One should remember that this excitation does not correspond to any excited free wave.

V. ANALYSIS OF NEGATIVE INTENSITY

To gain physical insight into this phenomenon, it is convenient to consider the separate components of the time-averaged intensity. Since the time-averaged structural intensity, Eq. (11), consists of the products of ϕ's and ψ's and their complex conjugates, the longitudinal component (I_{long}) may be obtained by setting C and D to zero. Similarly, the shear component (I_{shear}) is obtained by setting A and B to zero. There is also a third component (I_{int}), due to the interaction of the longitudinal and shear waves at the boundaries, which is obtained by setting all but the cross terms (i.e., AC, BC, AD, and BD) to zero. One should remember that the coefficients are not independent, they are

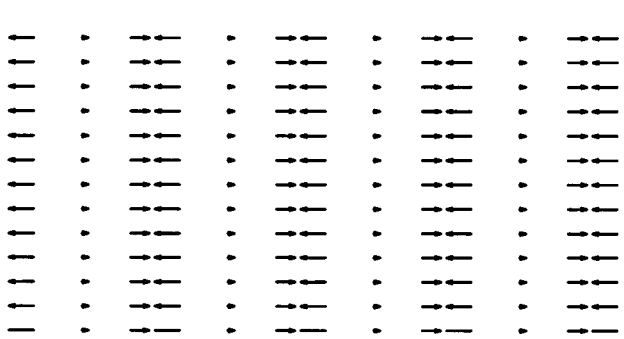

FIG. 8. Instantaneous intensity of a free longitudinal plate wave excited by an incident acoustic wave.

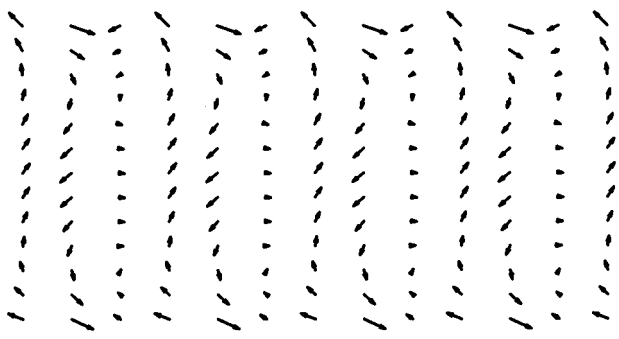

FIG. 9. Instantaneous intensity of a free flexural wave excited by an incident acoustic wave.

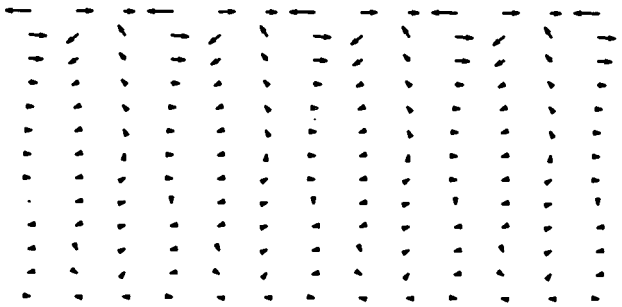

FIG. 10. Instantaneous intensity of a free quasi-Rayleigh wave excited by an incident acoustic wave.

related through the boundary conditions. Therefore the axial time-averaged intensity, Eq. (11), may be separated into the three components as

$$I_y = I_y[A,B,C,D]|_{C,D=0} \quad \} I_{\text{long}} + I_y[A,B,C,D]|_{A,B=0} \quad \} I_{\text{shear}} + I_y[A,B,C,D]|_{\text{cross terms}\neq 0} \quad \} I_{\text{int}}. \tag{13}$$

The three components of the axial time-averaged intensity, I_{long}, I_{shear}, and I_{int} have been plotted in Fig. 12. It is seen that the negative portion of the total time-averaged intensity halfway through the thickness of the plate is due to the I_{shear} component. The negative portions at $0.25x/h$ and $0.75x/h$ are due to both I_{shear} and I_{int}.

VI. SUMMARY

The structural intensity within an elastic fluid-loaded plate due to incident acoustic plane wave has been investigated using the exact theory of elasticity. With the aid of symbolic mathematical software, symbolic expressions for time-averaged and instantaneous structural intensities have been obtained. These expressions allow one to plot the structural intensity as a function of the angle of incidence at various frequencies. From these plots, one can then identify many of the excited free waves or modes of the elastic plate as they appear as peaks in the structural intensity. This capability is essentially a form of ''numerical spectroscopy.'' It has been determined that for certain angles of incidence and frequency of excitation that there is power flow in the opposite direction from the axial component of the incident

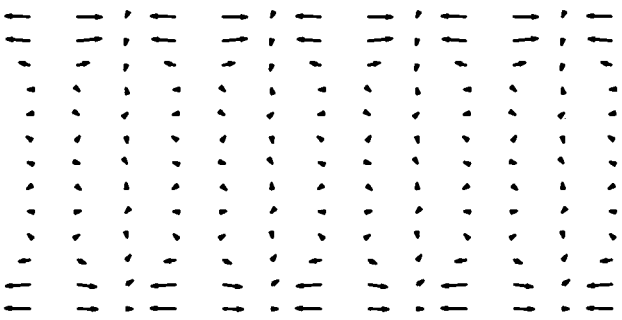

FIG. 11. Instantaneous intensity in plate corresponding to peak in time-averaged intensity at $\theta_0 \approx 14°$.

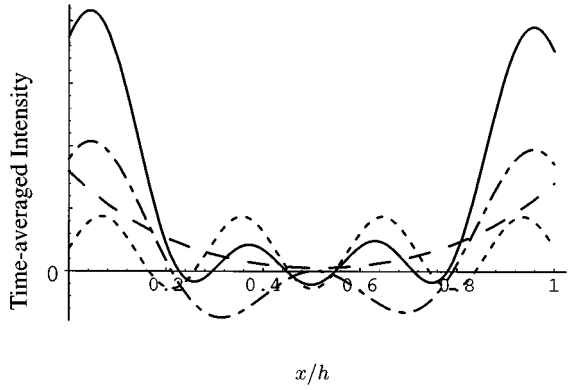

FIG. 12. Normalized axial time-averaged intensity through the thickness of the plate. The individual curves represent the following: (———) for the total and (— - —) for I_{int}, (— — —) for I_{long}, and (---) for I_{shear}.

acoustic wave at certain depths within the elastic plate. It has been shown that some of these phenomena can be attributed to the coupling of the longitudinal and shear waves at the boundaries of the plate.

ACKNOWLEDGMENTS

The authors wish to acknowledge the contribution that was made to this work by the late Dr. Robert Bunney. It was he who first observed, mathematically, the reversal of the intensity. One of the authors (RRG) cherishes the close association and friendship that he had with Bob.

[1] H. Reissner, ''Der senkrechte und schräge Durchtritt einer in einem flüssigen Medium erzeugten ebenen Dilatations Welle durch eine in diesem Medium befindliche plan-parallelle feste Platte,'' Helv. Phys. Acta **11**, 140–155 (1938).
[2] M. F. Osborne and S. D. Hart, ''Transmission, reflection, and guiding of an exponential pulse by a steel plate in water. I. Theory,'' J. Acoust. Soc. Am. **17**, 1–18 (1945).
[3] R. D. Fay and O. V. Fortier, ''Transmission of sound through steel plates immersed in water,'' J. Acoust. Soc. Am. **23**, 339–346 (1951).
[4] R. D. Fay, ''Notes on the transmission of sound through plates,'' J. Acoust. Soc. Am. **25**, 220–223 (1953).
[5] N. Tanaka, S. D. Snyder, Y. Kikushima, and M. Kuroda, ''Vortex structural power flow in a thin plate and the influence of the acoustic field,'' J. Acoust. Soc. Am. **96**, 1563–1574 (1994).
[6] R. E. Bunney and R. R. Goodman, ''Energy of the acoustically excited surface wave on a flat semi-infinite elastic medium,'' J. Acoust. Soc. Am. **53**, 1658–1662 (1973).
[7] G. Kaduchak, D. Hughes, and P. Marston, ''Enhancement of the backscattering of high-frequency tone bursts by thin spherical shells associated with a backwards wave: Observations and ray approximation,'' J. Acoust. Soc. Am. **96**, 3704–3714 (1994).
[8] I. A. Ewing, W. S. Jardetzky, and F. Press, *Elastic Waves in Layered Media* (McGraw-Hill, New York, 1957).
[9] A. D. Pierce, *Acoustics: An Introduction to Its Physical Principles and Applications* (Acoustical Society of America, Woodbury, NY, 1989), p. 124.
[10] J. W. S. Rayleigh, ''On the Free Vibrations of an Infinite Plate of Homogeneous Isotropic Elastic Matter,'' Proc. London Math. Soc. **20**, 225 (1889).
[11] P. M. Morse and H. Feshbach, *Methods of Theoretical Physics* (McGraw-Hill, New York, 1953), Vol. 1, p. 345.
[12] I. Tolstoy and E. Usdin, ''Wave propagation in elastic plates: Low and high mode dispersion,'' J. Acoust. Soc. Am. **29**, 37–42 (1957).
[13] W. M. Viktorov, *Rayleigh and Lamb Waves: Physical Theory and Applications* (Plenum, New York, 1967), p. 3.
[14] A. Meitzler, ''Backward-wave transmission of stress pulses in elastic cylinders and plates,'' J. Acoust. Soc. Am. **38**, 835–842 (1965).
[15] K. Negishi, ''Negative group velocities of lamb waves,'' J. Acoust. Soc. Am. Suppl. 1 **64**, S63 (1978).

Modification of Skudrzyk's mean-value theory parameters to predict fluid-loaded plate vibration

Rendell R. Torres,[a] Victor W. Sparrow, and Alan D. Stuart
Graduate Program in Acoustics, The Pennsylvania State University, P.O. Box 30, State College, Pennsylvania 16804

(Received 26 March 1996; revised 4 March 1997; accepted 21 March 1997)

The geometric-mean drive-point admittance (or ''mobility'') of a complex structure is given by the admittance of the corresponding infinite structure (i.e., the ''characteristic admittance,'' Y_c). The frequency response of an infinite plate, for example, coincides with the geometric-mean response of a finite one. Eugen Skudrzyk's ''mean-value theorem'' was derived and experimentally verified without consideration of fluid loading. This paper shows that Skudrzyk's method can be applied to fluid-loaded plates well below the coincidence frequency. Skudrzyk's general mathematical expression allows simplified modifications that account for fluid loading and result in an approximate fluid-loaded characteristic admittance that differs only by a small multiplicative factor (< 2 dB) from a correct analytical expression derived by Crighton. © *1997 Acoustical Society of America.* [S0001-4966(97)04107-6]

PACS numbers: 43.40.Dx, 43.20.Tb [CBB]

INTRODUCTION

The vibration of complex structures is often impractical to model using classical theory or even modern computational power and techniques. Fortunately, other methods have developed. Statistical theories, such as those developed by Lyon and Maidanik,[1] form one approach. Heckl's work[2] is representative of theories that use mathematical approximations when classical theory becomes unwieldy.

A third powerful method of analysis is based on electrical network theory: the ''mean-value theory,'' developed by Eugen Skudrzyk.[3–6] Using simple mathematical expressions, one can predict the mean admittance of the frequency response for any vibrating structure, as well as the values of the extrema above and below this mean. The computations are simple, accurate, and thus extremely useful. In addition, the computations are based on familiar quantities: the modal masses and the density of the resonances. Neither a statistical nor asymptotic theory, it applies for the entire frequency spectrum above the structure's first resonance.

Skudrzyk's foundation for his mean-value theory was that a forced infinite structure has a characteristic velocity (and admittance) that corresponds simply to the amplitude of an outgoing wave. Since the resonances and antiresonances of a finite structure coalesce to the characteristic admittance with increasing modal overlap, the characteristic response of a finite structure may be used to predict the mean line between the extrema of its actual response.

Skudrzyk utilized orthogonal mode summations to derive a general expression for the geometric-mean drive-point admittance (see Ref. 7). This general expression relies on only a few properties of a given structure, i.e., its density, modal spacing (inverse of modal density), mode functions, the force source, and the location of the observation (receiver) point.

Skudrzyk's mathematics, however, do not account for heavy fluid loading, as such modes are not orthogonal. Nevertheless, it will be shown that the characteristic response of a point-driven rectangular plate, in the presence of fluid loading on both sides and well below the critical (or coincidence) frequency, accurately predicts the geometric mean line. Similar to the *in vacuo* plate, when the structural damping is increased in the fluid-loaded plate, the extrema of its frequency response coalesce to the fluid-loaded characteristic response. A frequency-dependent expression for the fluid-loaded drive-point admittance of an infinite plate has previously been derived by Crighton[8,9] via a wave approach. His expression is modified for the case considered here and is used to predict the mean line. In Sec. III, Skudrzyk's mathematical parameters are modified to account for heavy fluid loading well below the coincidence frequency (with some small but expected error when compared to Crighton's expression). It is also shown that the boundary conditions have negligible effect on predicting the mean line.

I. PREVIOUS WORK

For the case of fluid-loaded rectangular plates, Davies[10] presented a low-frequency analysis (well below the coincidence frequency and based on the *in vacuo* modes of a plate and its ''intermodal'' coupling coefficients) that yielded an approximate solution for a plate's velocity in terms of its *in vacuo* modal admittances. He found that the apparent internal damping added to the plate was determined by the amount of modal coupling, in turn related to modal overlap and structural damping. Davies concluded, therefore, that for light to zero structural damping there was no power flow between modes because there was no overlap between resonance peaks. He also found in his analysis that the total effect of the reactive *coupling* term is considerably less than the modal *inertia* term. This will be demonstrated here when

[a]Current address: Department of Applied Acoustics, Chalmers University of Technology, S-412 96 Gothenburg, Sweden, Electronic mail: rendell@ta.chalmers.se

Skudrzyk's general expression is modified to account for only gross fluid-loading effects (neglecting modal coupling) and still compares well to Crighton's expression. Although a modal method can become unwieldy, Davies' approach provides a physical picture of modal interactions. Mkhitarov[11] also presented a similar analysis in terms of a radiation impedance that coupled the pressure distribution of one mode to the structural velocity of another.

In Refs. 8 and 9, Crighton derived the line and point admittance of an infinite thin elastic plate with fluid loading on one side. These expressions are most useful in the lowest-frequency range, well below coincidence, where coupling effects are greatest and where the mathematics also simplify significantly, although Crighton also wrote that Heckl found the expressions accurate even beyond their strict frequency limits.

Graham[12] investigated the vibration and acoustic radiation at higher frequencies (above coincidence) for a fluid-loaded, simply supported plate excited by a random pressure field. He derived asymptotic expressions for high-frequency modal coupling coefficients, which allow the solution of full coupled modal equations.

II. THEORY: *IN VACUO* AND FLUID-LOADED CHARACTERISTIC ADMITTANCES

Skudrzyk's general expression for the *in vacuo* characteristic admittance is the following:

$$G_c = \frac{\pi}{2\epsilon_n M_n}, \tag{1}$$

where ϵ_n is the modal spacing of a structure and M_n denotes the modal mass of the structure (Refs. 1–5). Skudrzyk mathematically defines the parameters ϵ_n and M_n as

$$\epsilon_n \equiv \frac{\partial \omega_n}{\partial n}, \tag{2}$$

$$M_n \equiv \frac{M\langle \xi_n^2 \rangle}{\kappa_n \xi_n^2(A)}, \tag{3}$$

where n is mode number, ω_n is the nth modal frequency, M is the total mass, $\langle \xi_n^2 \rangle$ represents the spatial average of the eigenfunctions ξ_n,(A) denotes the coordinates of the receiver, and

$$\kappa_n \equiv \int \frac{F\xi_n(x,y)}{F_0 \xi_n(A)}\, d\sigma \tag{4}$$

is a ''mode excitation constant'' that describes the contribution of the total force ($F_0 = \int F\, d\sigma$) to the excitation of the nth mode. As shown in pp. 267–268 of Ref. 4, at the drive point $\kappa_n = 1$, and Eq. (3) becomes

$$M_n = \frac{M}{4} \tag{5}$$

for a rectangular plate, with the exception of one-dimensional modes, for which $M_n = M/2$. For an *in vacuo* plate Eq. (1) becomes the following well-known expression for the characteristic admittance (Refs. 4–7):

$$G_c = \frac{1}{8(D\rho_s h)^{1/2}}, \tag{6}$$

where $D = Eh^3/12(1 - \nu_P^2)$ is bending stiffness, ρ_s is the plate's density, and h is the thickness of the plate.

Equation (1) will always yield the real part G_c of the characteristic admittance ($Y_c = G_c + jB_c$), which typically has no imaginary part except for cases such as beams (having frequency-dependent modal spacing). Thus when Eq. (1) is modified in Sec. III to include fluid-loading effects, it will be compared to the real part of Crighton's analytical expression.

Crighton's low-frequency expression, modified in Ref. 7 to account for fluid loading on two sides, is

$$Y_c' = 0.8 Y_c \left(\frac{1}{2\rho_0} \left(\frac{m^5 \omega^2}{D} \right)^{1/4} \right)^{2/5} \left(1 + j \tan \frac{\pi}{10} \right), \tag{7}$$

where $m = \rho_s h$ is specific mass, $Y_c = G_c$ [i.e., from Eq. (6) above] for an *in vacuo* plate, and the prime notation, henceforth, denotes fluid loading. The magnitude of this expression is the following:

$$\begin{aligned} |Y_c'| &= 0.8 Y_c \left(\frac{1}{2\rho_0} \left(\frac{m^5 \omega^2}{D} \right)^{1/4} \right)^{2/5} \left(1 + \tan^2 \left(\frac{\pi}{10} \right) \right)^{1/2} \\ &= 0.8 Y_c \left(\frac{1}{2\rho_0} \left(\frac{m^5 \omega^2}{D} \right)^{1/4} \right)^{2/5} (1.05). \end{aligned} \tag{8}$$

Skudrzyk's expression, Eq. (6), is used to predict the mean line through the frequency response curve for the *in vacuo* case. Equation (8) is used to predict the mean line for the corresponding fluid-loaded case. When using the magnitude of Crighton's expression to predict the mean line, one may observe that the small effect of the imaginary part (i.e., about 5%) is included.

The coincidence frequency is given by

$$\omega_c = c_0^2 \left(\frac{\rho_s h}{D} \right)^{1/2}. \tag{9}$$

III. MODIFICATION OF SKUDRZYK'S PARAMETERS TO INCLUDE FLUID LOADING

Skudrzyk's mode parameters ϵ_n and M_n can be modified to account for the gross effects of fluid loading, i.e., incorporating the added entrained fluid mass and neglecting smaller modal coupling effects. The fluid mass loading for mode (p,q) of a *finite* rectangular plate is known to be ρ_0/k_{pq} (Ref. 13, p. 135), which has the units of specific mass (i.e., per unit area) and where $k_{pq} = [(p\pi/a)^2 + (q\pi/b)^2]^{1/2}$ is the plate modal wave number. One may hypothesize that the effective specific mass added to a fluid-loaded *infinite* plate is ρ_0/k_b', where k_b' is the fluid-loaded wave number.

First, an approximate expression for k_b' may be found (Ref. 13). Well below coincidence, heavy fluid loading decreases the structural phase speed, thus increasing the *in vacuo* free-bending wave number $k_p = (\omega^2 m/D)^{1/4}$, which becomes the *fluid-loaded* free-bending wave number $k_b' \gg k_0$. The imaginary fluid wave impedance becomes

$$\tilde{Z}_{wf} \approx j\omega \frac{2\rho_0}{k_b'}.$$

For free-wave propagation, the total wave impedance is set equal to zero, so that

$$0=\tilde{Z}_{wp}+\tilde{Z}_{wf},$$

$$0=\frac{-j(Ds^4-m\omega^2)}{\omega}+j\omega\,\frac{2\rho_0}{k_b'},$$

where $\tilde{Z}_{wp}$ is the wave impedance of the plate, D is the bending stiffness, $m=\rho_s h$ is the specific mass, and s is the plate wave number. With zero input force, $s\rightarrow k_b'$ so that

$$0=D(k_b')^4-\omega^2\left(m+\frac{2\rho_0}{k_b'}\right).$$

For the *in vacuo* case, $Dk_p^4=\omega^2 m$. With fluid loading, k_p increases and becomes the fluid-loaded wave number k_b' such that $k_p^4\rightarrow(k_b')^4$ and $D(k_b')^4\gg\omega^2 m$. Thus

$$k_b'\approx\left(\frac{2\rho_0\omega^2}{D}\right)^{1/5}. \tag{10}$$

It should be remembered that above approximations are valid for frequencies such that $k_b'\gg k_p$. (The condition for the aluminum plate in Sec. IV is $f\ll 28.7$ kHz.)

Two parameters may now be redefined (the detailed derivation given in Ref. 7): $M_n\rightarrow M_n'$ and $\epsilon_n\rightarrow\epsilon_n'$, where $()'$ again denotes fluid loading. These redefined parameters can be used in Eq. (1), and the resulting expression may then be compared to $\mathrm{Re}(Y_c')$ to determine its applicability to the fluid-loaded plate.

For an infinite plate, one may approximate the fluid-loaded value M_n' by adding an effective surface mass-loading $2\rho_0/k_b'$. This results in

$$M_n'=M_n\left(1+\frac{2\rho_0}{mk_b}\right). \tag{11}$$

The modification of the frequency spacing ϵ_n is less obvious. First, one can consider the shifting of resonances lower in frequency; each resonance decreases by some proportion, so the spacing between them also decreases by a related proportion. If a given resonance is modeled as an equivalent mass–spring system, one finds the following:

$$\omega_n'=\sqrt{\frac{s_e}{m_e'}}$$

$$=\sqrt{\frac{s_e}{m_e(1+2\rho_0/mk_{pq})}}$$

$$=\omega_n\,\frac{1}{\sqrt{1+2\rho_0/mk_{pq}}}$$

$$=\omega_n\Phi_n, \tag{12}$$

where ω_n' is a fluid-loaded resonance frequency, s_e is the effective stiffness, m_e is the effective surface mass per unit area, and the definition $\Phi_n\equiv(1+2\rho_0/mk_{pq})^{-1/2}$ is a ''shift factor'' for each resonance of the finite plate. The spacing between resonances is

$$\Delta\omega_{n+1,n}'=\Phi_{n+1}\omega_{n+1}-\Phi_n\omega_n. \tag{13}$$

As the plate dimensions approach infinity, the spacing decreases between resonances, such that

$$\Delta\omega_{n+1,n}'\approx\Phi_b'\omega_{n+1}-\Phi_b'\omega_n$$

$$\approx\Phi_b'(\omega_{n+1}-\omega_n),$$

so that for an infinite plate

$$d\omega_n'=\Phi_b'\,d\omega_n, \tag{14}$$

where the shift factor assumes a form Φ_b' appropriate for an *infinite* plate, i.e.,

$$\Phi_n\rightarrow\Phi_b'\equiv(1+2\rho_0/mk_b')^{-1/2}, \tag{15}$$

and is assumed constant over the infinitesimal interval between resonances. Now one may define the parameter ϵ_n' which accounts for fluid loading. For an infinite plate,

$$\frac{\Delta\omega_n'}{\Delta n}\rightarrow\frac{d\omega_n'}{dn}=\epsilon_n',$$

which, using Eq. (14), may also be written as

$$\frac{\partial\omega_n'}{\partial n}=\Phi_b'\,\frac{\partial\omega_n}{\partial n}.$$

Thus

$$\epsilon_n'=\Phi_b'\epsilon_n$$

$$=\frac{\epsilon_n}{\sqrt{1+(2\rho_0/mk_b')}}. \tag{16}$$

Now these modified parameters ϵ_n' and M_n' are used in Skudrzyk's expression G_c, i.e., Eq. (1), so that $G_c\rightarrow G_c'$:

$$G_c=\frac{\pi}{2\epsilon_n'M_n'}$$

$$=\frac{\pi}{2\epsilon_n M_n}\left(\frac{\sqrt{1+(2\rho_0/mk_b')}}{1+(2\rho_0/mk_b')}\right)$$

$$=Y_c\sqrt{\frac{\Upsilon}{\Upsilon+1}}\left\{\frac{1}{2\rho_0}\left(\frac{m^5\omega^2}{D}\right)^{1/4}\right\}^{2/5}, \tag{17}$$

where the frequency-dependent parameter

$$\Upsilon=\left\{2\rho_0\left(\frac{D}{m^5\omega^2}\right)^{1/4}\right\}^{4/5} \tag{18}$$

assumes values, for the sample plate in Sec. IV, such as 22 (for 13 Hz) to 6 (for 300 Hz) to 1.8 (for 16.7 kHz). (To be conservative, it will not be assumed that $\Upsilon\gg 1$.) This corresponds to values for $\sqrt{\Upsilon/(\Upsilon+1)}$ of 0.98 (for 13 Hz) to 0.8 (for 16.7 kHz).

Since Skudrzyk's mean-value admittance G_c is used to find the real part of the characteristic admittance, the final form[14] of Eq. (17) should be compared to the real part of Crighton's expression Eq. (7):

$$\mathrm{Re}(Y_c')=0.8Y_c\left\{\frac{1}{2\rho_0}\left(\frac{m^5\omega^2}{D}\right)^{1/4}\right\}^{2/5}. \tag{19}$$

The results are the same, except for a slowly varying multiplicative factor $\sqrt{\Upsilon/(\Upsilon+1)}$ in G_c'. This helps confirm

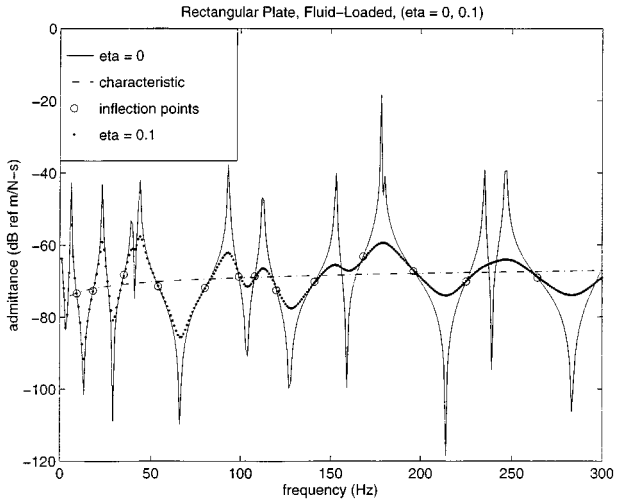

FIG. 1. In this computational experiment, the fluid-loaded characteristic response Y_c' passes reasonably well through the inflection points and predicts the mean line. The plate is point driven at its center.

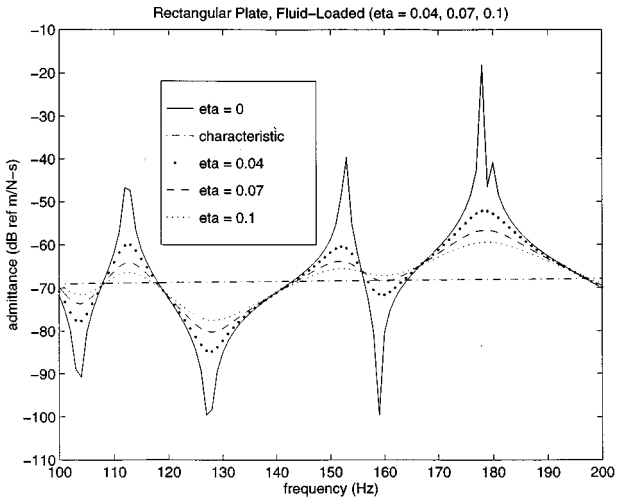

FIG. 2. As the structural damping is incrementally increased ($\eta = 0-0.1$), the extrema of the fluid-loaded plate's frequency response approach the characteristic admittance, as Skudrzyk's theory predicts for the *in vacuo* case.

why Crighton's expression works to predict the mean line. [Note that the term in the braces in Eq. (17) is not obtained if the effective surface mass is taken to be $(m + 2\rho_0/k_{pq})$ instead of $(m + 2\rho_0/k_b')$.] For the modified expression G_c' to accurately approximate Eq. (19), comparison implies that $\sqrt{\Upsilon/(\Upsilon+1)} = 0.8$. In the frequency range of the computational experiments performed here (0–300 Hz), $\sqrt{\Upsilon/(\Upsilon+1)} \approx 0.95$, which corresponds to a value of G_c' that is only 1–2 dB greater than Eq. (19). The final expression matches Crighton's except for a small factor, and it is expected that G_c' will not be entirely precise, as it has its roots in the original expression G_c, which is based on orthogonal modes. The slight discrepancy between the factors (0.8) and $\sqrt{\Upsilon/(\Upsilon+1)} \approx (0.95)$ in Eqs. (19) and (17) likely stems from accounting for the inertial fluid loading but neglecting intermodal fluid coupling effects, deemed relatively small by Davies. Thus although a direct use of Skudrzyk's theory does not appear possible, these modifications to ϵ_n and M_n seem the most straightforward while maintaining good accuracy in the low wave number region.

IV. COMPUTATIONAL RESULTS

A combined finite element/boundary element computational model is validated in Ref. 7 via comparison to Williams' *in vacuo* physical experiments on a point-driven, aluminum rectangular plate with ''free''-boundary conditions.[15] Typical material values are used: $\nu\rho = 0.33$ is Poisson's ratio, $E = 7.1 \times 10^{10}$ N/m^2 is the elastic modulus, and $\rho_s = 2700$ kg/m^3. The plate's dimensions are the same as Williams': 24 in.$\times$42 in.$\times\frac{3}{16}$ in. (0.61 m$\times$1.07 m$\times$0.0048 m). Its coincidence frequency is 48 kHz in water.[16]

The effect of heavy fluid loading (i.e., water) is then included in the computations, with a point force again at the center of the plate. The resulting frequency response curve is plotted in Fig. 1 with the fluid-loaded characteristic admittance, i.e., Eq. (8). (The figures show the frequency ranges where the computational models are accurate.)

Two approaches are used to check whether the characteristic admittance does, in fact, predict the mean line. First, for the case of zero to light damping (e.g., $\eta = 0.01$), one can examine whether the characteristic admittance passes through the inflection points of the frequency response. Second, one can examine whether the extrema approach the mean as the structural damping increases (e.g., from $\eta = 0.04-0.1$), as presented in Fig. 2.

It is evident from the plots that the characteristic response passes reasonably well through the inflection points. The fact that the response approaches Y_c' as η increases in Fig. 2 also confirms that the fluid-loaded driven plate has a mean response which coincides with the characteristic response. Thus the mean value can be predicted from the response of the *fluid-loaded infinite structure*. (Figure 2 shows that not all of the ''undamped'' extrema are computed at their exact resonance frequencies. In such cases, the inflection points more accurately indicate the mean line than the extrema.)

Finally, the boundary conditions are changed to simply supported, and results are shown in Fig. 3. Again, the fluid-loaded plate has a mean response which coincides with the characteristic response. Similar to the mean-value theory *in vacuo*, the boundary conditions of the fluid-loaded plate do not affect the prediction of the mean line.

The characteristic admittances $G_c = Y_c$ (*in vacuo*) and Y_c' (fluid loaded) are plotted in Fig. 4. Only slightly offset from Y_c', the modified G_c' from Sec. III is plotted between the two. As Skudrzyk's theory itself is only accurate to within 2–3 dB, G_c' forms a reasonably good approximation to Crighton's analytical expression, i.e., Eq. (8).

V. CONCLUSIONS

It is shown that the characteristic response of a fluid-loaded plate can be used as a measure of its geometric-mean response. It is only assumed that the driving force is at an inner point of the plate and that, to use Crighton's final ex-

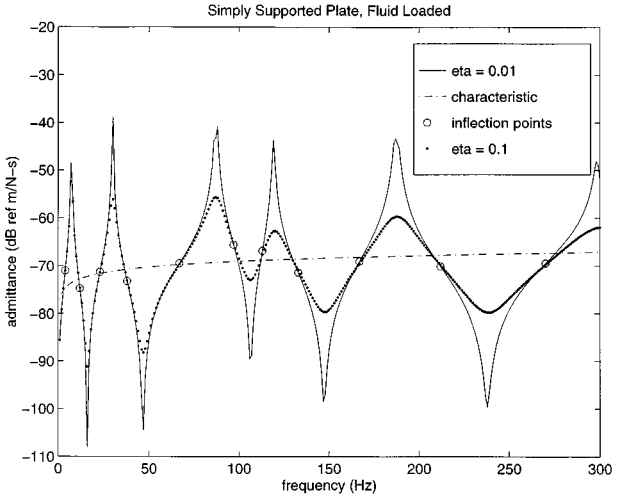

FIG. 3. For changed boundary conditions (i.e., simply supported), the fluid-loaded plate again has a mean response that coincides with Y_c'.

pression, the excitation is well below the coincidence frequency, where fluid-loading effects are greatest. The boundary conditions are also shown to have negligible effect on the predictive ability of the fluid-loaded characteristic admittance. This may suggest that ''near-field'' fluid effects from the edges are not seen by the driving point.

When Skudrzyk's parameters ϵ_n and M_n are modified to account for heavy fluid loading on a plate below its critical frequency, the correct analytical expression is obtained, except for a small and slowly varying multiplicative factor. This differs by less than 2 dB from Crighton's rigorous expression and offers a reasonably good approximation with less effort. For greater precision, Skudrzyk's characteristic admittance cannot be used without sacrificing one of its greatest attractions, its utility. The modal spacing parameter ϵ_n loses its simplicity, and expressions for resonance frequencies that account for fluid coupling become much more involved—at best only semi-analytical, as shown by Lomas and Hayek.[17]

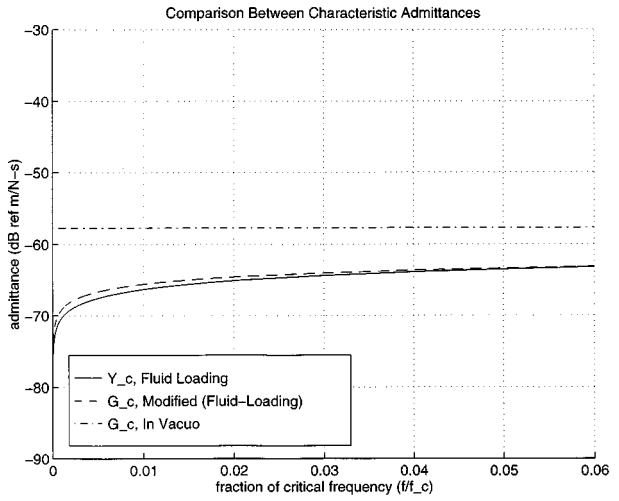

FIG. 4. The characteristic admittances $G_c = Y_c$ (*in vacuo*) and Y_c' (fluid-loaded) are plotted above. Slightly offset from Y_c', the modified admittance G_c' from Sec. III is plotted between the two. The horizontal axis corresponds to the frequency interval 0 Hz–3 kHz for the plate in Sec. IV.

Neither Skudrzyk's modal mass nor modal spacing parameters are inclined toward exactly accounting for fluid coupling; they are inherently based on an *in vacuo* modal analysis. As emphasized in Ref. 6, however, Skudrzyk's theory is based in essence on the interaction of progressive wave fields, which is conceptually compatible with the wave approach used by Crighton in analyzing infinite fluid-loaded structures. This can explain the similarity between Eqs. (17) and (19). The small difference between the two presumably results from neglecting the small coupling effects in the first expression (and only including inertial loading).

Skudrzyk's general theory is applicable in a larger sense. His concept of using the infinite-structure response works well in predicting the mean line. Although no general expression for the drive-point admittance of fluid-loaded structures has yet been derived in terms of the basic structural parameters discussed in the Introduction, the characteristic admittances for various fluid-loaded geometries *have* already been found. Such results can be practically used to predict the mean response of fluid-loaded structures. Finally, the methodology of Sec. III for modifying Skudrzyk's parameters may also be employed in achieving relatively accurate expressions with reasonable effort.

ACKNOWLEDGMENTS

The authors would like to acknowledge the financial support of the Applied Research Laboratory. The second author was supported by the Office of Naval Research during this study. Several suggestions from the reviewers were also appreciated.

[1] R. H. Lyon and C. Maidanik, ''Power flow between linearly coupled oscillators,'' J. Acoust. Soc. Am. **34**, 623–639 (1962).
[2] L. Cremer, M. Heckl, and E. E. Ungar, *Structure-Borne Sound* (Springer-Verlag, Berlin, 1988).
[3] E. J. Skudrzyk, ''Vibrations and sound radiation of complex vibratory systems,'' in *Underwater Acoustics, Volume 2*, edited by V. Albers, Proc. of an Institute Sponsored by the Scientific Affairs Committee of NATO and Conducted by Penn State at the Technical Univ. of Denmark, July 25–August 5, 1966 (Plenum, New York, 1967), pp. 297–350.
[4] E. J. Skudrzyk, *Simple and Complex Vibratory Systems*, second printing (1981) (The Pennsylvania State University, University Park, PA, 1968), pp. 217–240, 263–287.
[5] E. J. Skudrzyk, ''The mean-value method of predicting the dynamic response of complex vibrators,'' J. Acoust. Soc. Am. **67**, 1105–1135 (1980).
[6] E. J. Skudrzyk, ''Understanding the dynamic behavior of complex vibrators,'' Acustica **64**, 123–147 (1987).
[7] R. R. Torres, ''Application of Skudrzyk's mean-value theory toward predicting the vibration of fluid-loaded plates,'' M.S. thesis, The Pennsylvania State University, December 1995.
[8] D. G. Crighton, ''Point admittance of an infinite thin elastic plate under fluid loading,'' J. Sound Vib. **54**, 389–391 (1977).
[9] D. G. Crighton, ''Force and moment admittance of plates under arbitrary fluid loading,'' J. Sound Vib. **20**, 209–218 (1972).
[10] H. G. Davies, ''Low-frequency random excitation of water-loaded rectangular plates,'' J. Sound Vib. **15**, 107–126 (1971).
[11] R. A. Mkhitarov, ''Interaction of the vibrational modes of a thin bounded plate in a liquid,'' Sov. Phys. Acoust. **18**, 123–126 (1972).
[12] W. R. Graham, ''High-frequency vibration and acoustic radiation of fluid-loaded plates,'' Philos. Trans. R. Soc. London **352**, 1–43 (1995).
[13] F. Fahy, *Sound and Structural Vibration*, second printing (1993) (Academic, London, 1985), pp. 126–141.

[14] The parameter G_c' may also be written in terms of the *in vacuo* free-bending wave number k_p which, interestingly, appears in this fluid-loading analysis. (No approximation was made such that $k_p \approx k_b$.) Thus

$$G_c' = Y_c \sqrt{\frac{\Upsilon}{\Upsilon + 1}} \left\{ \frac{k_p}{2\rho_0 / m} \right\}^{2/5}.$$

[15] E. G. Williams, ''Vibration of plates of various geometries,'' Ph.D. thesis, The Pennsylvania State University, July 1979.

[16] For water the speed of sound is taken as $c_0 = 1500$ m/s and the ambient density as $\rho_0 = 1000$ kg/m^3.

[17] N. S. Lomas and S. I. Hayek, ''Vibration and acoustic radiation of elastically supported rectangular plates,'' J. Sound Vib. **52**, 1–25 (1977).

Acoustics of a fluid-loaded plate with attached oscillators. Part I. Feynman rules

Douglas M. Photiadis
Naval Research Laboratory, Washington, DC 20375-5000

(Received 11 November 1996; revised 28 February 1997; accepted 6 March 1997)

The ''fuzzy structure'' paradigm developed by Soize and others provides a framework within which the acoustic properties of systems with complex internal structure can be explored. In this two part paper, the acoustic properties of one of the simplest such systems, a fluid-loaded plate with attached internal oscillators, are explored. In Part I, the theoretical tools needed in this investigation, the representation of the Neumann series in terms of Feynman diagrams, is presented. In most ways, the formal aspects of this development are identical to similar results from other disciplines, but the presence of damping in the system, either internal or due to radiation into the fluid, requires one to make some modifications to existing theories. The rules for evaluating averaged quantities such as $G\cdots GG^*\cdots G^*$ involving higher-order products of the Green's function are given. These quantities are necessary to determine a number of relevant properties of the system including the scattering cross section and the size of typical fluctuations. The Feynman rules, detailed mathematical expressions which enable averaged quantities to be evaluated for particular systems, are explicitly given for the case in which the internals are simple oscillators distributed uniformly and independently in both space and frequency. In Part II of this paper, the theoretical approach will be applied to predict a number of acoustic properties of the system. [S0001-4966(97)01007-2]

PACS numbers: 43.40.Hb, 43.40.Dx, 43.40.At [CBB]

INTRODUCTION

The effects of complex internal structure on the acoustic behavior of large elastic systems has long been of interest to those seeking to understand and control the acoustic behavior of real world systems. The main issue confronting us is this: How should one account for the effects of complex internal structure on the behavior of ''simple'' elastic systems without needing to understand in detail the behavior of the internals? The simplest nontrivial answer to this question is that the internals can be accounted for simply by modifying the parameters of the elastic structure to which they are attached; i.e., a mean-field theory. Recent results due to Strasburg and Feit[1] and Pierce *et al.*[2] have provided some guidance of this sort, giving formulas for the effective added mass and damping resulting from internals described by simple oscillators. But the approaches employed by these researchers do not address the more fundamental issue of when, and in what context, complex internals can be accounted for in this manner.

Soize introduced[3] a systematic approach to this problem. Within this approach, the impedance of the system is split into two pieces, a ''simple'' deterministic piece Z_0 referred to as the base structure, and a stochastic piece Z_{fuzzy} denoted the ''structural fuzzy.'' The structural fuzzy is assumed to be small in some sense and a Neumann expansion in powers of Z_{fuzzy} is performed to obtain the Green's functions of the system;

$$G=Z^{-1}=Z_0^{-1}-Z_0^{-1}Z_{\text{fuzzy}}Z_0^{-1}+\cdots . \tag{1}$$

Averages over the structural fuzzy are then performed and in this way mean values of various quantities are obtained. The aspect we consider here is the way in which the above program of computation is to be carried out. Following work in other areas,[4–6] we introduce Feynman diagrams as a tool to employ in this effort. Rybak[7] and Turner and Weaver[8] have considered problems of this type but rather than developing the diagramatic perturbation theory they have directly examined the integral equations which govern the mean Green's functions to leading order.

The basic idea of the approach we propose is to carry out the averaging over the structural fuzzy as soon as the formal perturbation theory is written down for a quantity of interest, but not in the equations of motion themselves. This produces great simplifications of the calculations provided the average structure possesses more symmetry than the actual structure, usually the case. By delaying the averaging until the equations of motion are formally solved, increased control over the approximations involved in the averaging procedure is obtained. In particular, certain quantities, such as the increased fluid loading due to the randomness of the internals, can never be evaluated if the averaging is performed directly in the equations of motion.

The mathematical averaging process generates a series of terms which can be represented as Feynman diagrams. We explicitly give the Feynman rules which enable the evaluation of these diagrams for the simple case of a large fluid-loaded plate. The Feynman rules, detailed analytical expressions which give a mathematical meaning to the diagrams or graphs, are given both in real space and in wave-number space. The perturbation series generated in this way is an expansion in the deviation of internal structure from its mean value. One does not require that the total mass of the internal structure be small; it may in fact be larger than that of the

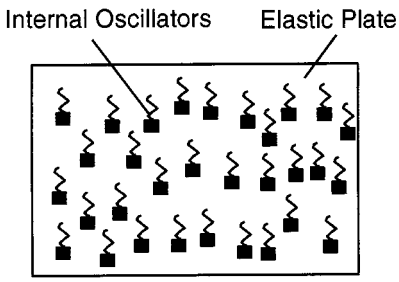

FIG. 1. A depiction of the flat plate with attached oscillators.

base structure. Instead one requires that the fluctuations of the impedance in some sense be small.

At first sight, one might question what has been gained by recasting the Neumann series into a series of Feynman graphs. The answer is that the evaluation of the Neumann series is quite formidable, and the recasting of the perturbation theory into Feynman graphs enables one to discern patterns in the expansion based on the topological character of the graphs. In this way, one may determine which classes of higher-order terms in the expansion must be taken into account, and which may give rise to divergences in the perturbative expansion. In addition, the Feynman graphs admit a natural interpretation in terms of scattering processes and so enhance one's physical intuition. Finally, once the Feynman rules have been derived and verified, the evaluation of individual terms becomes a much more straightforward and systematic task. In fact, this last practical issue, while seemingly modest, has been of great importance in obtaining predictions in other contexts.

The outline of this paper is as follows. The basic model is presented in Sec. I. The principal goal of this section is to clearly define the mathematical decomposition of the system into deterministic and stochastic pieces. In Sec. II, the real space Feynman rules for evaluating the average Green's function of the system are derived. Enroute to this result, the relationship of this approach to that of Strasburg and Feit[1] and Pierce *et al.*[2] is examined. In Sec. III, the wave-number space Feynman rules are derived; this is typically the preferred method of calculation. The additional rules needed to calculated averages of higher-order quantities such as $\langle GG\rangle$ or $\langle GG^*\rangle$ are derived in Sec. IV. In conclusion, we summarize the main results.

I. THE BASIC MODEL

The prototype system is shown in Fig. 1, a flat plate with some attached internal oscillators immersed in a fluid. We shall focus in this paper on the flexural vibration of the plate. Nevertheless, the principal result of this section, a formal definition of the decomposition of the impedance operator into deterministic and stochastic parts, is independent of the geometry. One may just as easily interpret the operators appearing in the main result, Eq. (7), as applying to a cylindrical shell or some more complex nonseparable geometry. Of course, in doing so, the vector nature of the displacements may become important so that the operators appearing in Eq. (7) would need to be reinterpreted as matrices. This poses no fundamental difficulties.

The internal structure is imagined to be attached at discrete points or lines along the plate. At frequency ω, the equation of motion for the normal velocity field of the plate subject to an arbitrary pressure f is

$$Z_t v(x) = (Z_p + Z_f + Z_{\text{int}}) v(x) = f. \tag{2}$$

The fluid impedance operator Z_f and the plate impedance operator Z_p are given in wave-number space[9] for a flat plate geometry by

$$\begin{aligned} Z_f(k) &= \rho_0 c_0 (1 - k^2/k_0^2)^{1/2}, \\ Z_p(k) &= -i\omega m(1 - (k/k_f)^4). \end{aligned} \tag{3}$$

Here, ρ_0 is the density of the fluid, c_0 and k_0 are the wave speed and wave number of acoustic waves in the fluid, while m is the mass/area of the plate and k_f is the wave number of flexural waves in the plate. The treatment of in-plane compression or shear is quite similar to that which we give here, but the vector nature of the motion makes the problem more complicated if the various components are coupled.

The quantity $Z_{\text{int}} v(x)$ yields the forces and torques acting upon the plate which arise from the internal structure. We consider the simple case for which the operator Z_{int} is given by

$$Z_{\text{int}} v(x) = \sum_i Z_i \delta^d(x - \xi_i) v(x). \tag{4}$$

The attachment points ξ_i and/or the input impedances Z_i are considered to vary in a fairly complex and irregular manner. The ξ_i and associated δ functions are d-dimensional ($d = 1,2$) depending on the nature of the attached scatterers (lines, points). We shall omit the dependence on d when the dimension is clear by context.

The Z_i are taken to be given by

$$Z_i \approx \frac{i M_i \omega_i^2 \omega}{\omega^2 - \omega_i^2 + 2i\zeta_i \omega_i \omega} \tag{5}$$

as appropriate for a simple oscillator attached normally to the plate by its spring. Here M_i and κ_i are the effective mass and stiffness of the oscillator, ω_i is its resonance frequency, and ζ_i its damping factor scaled to the critical damping factor $\zeta_c = 2M\omega_i$. For line scatterers, Z_i is an impedance per unit length and one should interpret M_i as mass/length, etc. This formula gives an effective damping at resonance in proportion to the mass of the oscillator, the key result for the fuzzy structure theories.[1,2]

A particular system is described by some definite set of quantities ξ_i and Z_i, and given appropriate computational ability could be numerically simulated. An ensemble of such systems is generated by taking the attachments points ξ_i and input impedances Z_i to be described by a probability density $P\{\xi_i, Z_i\}$ within a large group of similar systems. Then $[\Pi_j\, d\xi_j\, dZ_j]\, P\{\xi_i, Z_i\}$ is the probability that a single system has the specific set of parameters $\{\xi_i, Z_i\}$. Averages of any function depending on the internal impedances, and in particular of the Green's functions are obtained simply as

$$\langle f\rangle = \left[\prod_j \int d\xi_j\, dZ_j\right] P\{\xi_i, Z_i\} f\{\xi_i, Z_i\}. \tag{6}$$

To complete the specification of the basic equations of motion, rewrite Eq. (2) as a sum of a deterministic and stochastic part,

$$Z_t v(x) = (Z_0 + V) v(x) = f, \tag{7}$$

where

$$Z_0 = \langle Z_t \rangle \quad \text{and} \quad V = Z_t - \langle Z_t \rangle. \tag{8}$$

The fluctuations contained within the operator V are spatial, depending on the specific positions and impedances of the internal structure. The action of the operator V upon the function $v(x)$ is simply multiplication by a stochastic function $V(x)$. The decomposition of Z_t into a deterministic and fluctuating part, Eq. (7) (given also by Soize[3]), is the basis for our formulation.

II. REAL SPACE FEYNMAN RULES

A. Deriving the formal rules

The derivation of the formal real-space Feynman rules for the calculation of ensemble averaged quantities is similar for a wide range of systems which have been treated in this way; systems ranging from quantum mechanical systems of elementary particles or excitations in solids,[4] to classical waves propagating in random elastic or optical media.[5,6] As in the previous section, to make these considerations concrete, the system at hand is taken to be an infinite flat plate with an array of attached oscillators with varying properties and positions. But the results are in fact applicable to a wide range of systems merely by using the appropriate Green's functions. In the case of a vector system, the results are formally identical to the results we give here, but care must be taken to obtain the proper ordering of the operators.

The fundamental quantities of interest are most often the average Green's function $\langle G(x,x') \rangle$ or various powers of the Green's function, $\langle G(x_1,x_1') G(x_2,x_2') \rangle$. Define the Green's functions $G(x,x')$ and $G_0(x,x')$ by

$$\begin{aligned} &Z_t G(x,x') = -\delta(x-x') \\ &\text{and} \\ &Z_0 G_0(x,x') = -\delta(x-x'). \end{aligned} \tag{9}$$

Perturbative expansions for the ensemble averaged quantities are obtained from the Neumann series as

$$\langle G(x,x') \rangle = G_0(x,x') + \int dx_1\, dx_2\, G_0(x,x_1) G_0(x_1,x_2) \times G_0(x_2,x') \langle V(x_1) V(x_2) \rangle + \cdots \tag{10}$$

and so forth. By construction, the first-order term involving $\langle V \rangle$ vanishes. Evidently, the nth-order term is given by

$$\int \prod d^d x_i\, G_0(x,x_1) G_0(x_1,x_2) \cdots G_0(x_n,x') \times \langle V(x_1) \cdots V(x_n) \rangle \tag{11}$$

and involves the n-point average $\langle V(x_1) \cdots V(x_n) \rangle$. The integrals above are of the dimensionality of the scatterers; 1-D for line attachments, 2-D for point attachments.

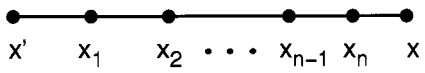

FIG. 2. A diagrammatic representation of an nth-order term in a Neumann series.

A diagrammatic representation of the nth-order term in the Neumann series prior to carrying out the averaging is given in Fig. 2, where each solid line with end points (x,y) is to be replaced by a Green's function $G_0(x,y)$, each ''dot'' specified by x_i with the function $V(x_i)$, and all internal coordinates are to be integrated. Such a diagram is clearly just a shorthand for the above expression and not all that useful since writing down the associated term in the perturbative expansion is so simple; the value of the diagrammatic approach is in handling the averaging.

The average $\langle V(x_1) \cdots V(x_n) \rangle$ can be evaluated interactively as a cluster expansion[10]

$$\begin{aligned} &\langle V(x_1) V(x_2) \rangle = \Gamma_2(x_1,x_2), \\ &\langle V(x_1) V(x_2) V(x_3) \rangle = \Gamma_3(x_1,x_2,x_3), \\ &\langle V(x_1) \cdots V(x_4) \rangle = \sum_{\text{pairs}} \Gamma_2(x_{i_1},x_{i_2}) \Gamma_2(x_{i_3},x_{i_4}) + \Gamma_4(x_1,\ldots,x_4), \\ &\langle V(x_1) \cdots V(x_n) \rangle = \sum_{\text{partitions}} \Gamma_\alpha(x_{i_1},\ldots,x_{i_\alpha}) \times \Gamma_\beta(x_{j_1},\ldots,x_{j_\beta}) \cdots , \end{aligned} \tag{12}$$

where the indicated sum (pairs or partitions) is over all possible partitions of the n points into clusters of more than one point (because $\langle V(x) \rangle = 0$). Algebraically, such sums are awkward to write down, but diagrammatically, it is quite simple; simply connect the dots in Fig. 2 in all topologically distinct ways. This procedure automatically generates all possible partitions of n points into clusters. Diagrams of this sort are called Feynman diagrams. Some fourth-order diagrams are given in Fig. 3. The diagram shown in Fig. 3(a) has the value

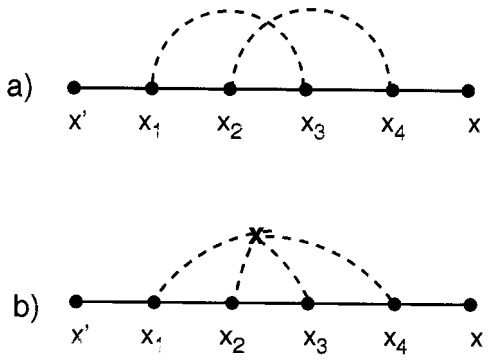

FIG. 3. Some fourth-order Feynman diagrams for the average Green's function in real space.

$$\int \prod dx_i \; G_0(x,x_4)G_0(x_4,x_3)G_0(x_3,x_2)$$
$$\times G_0(x_2,x_1)G_0(x_1,x')\Gamma_2(x_3,x_1)\Gamma_2(x_4,x_2) \tag{13}$$

while the diagram in Fig. 3(b) is given by

$$\int \prod dx_i \; G_0(x,x_4)G_0(x_4,x_3)G_0(x_3,x_2)$$
$$\times G_0(x_2,x_1)G_0(x_1,x')\Gamma_4(x_1,x_2,x_3,x_4). \tag{14}$$

The order of the arguments of $G_0(x,x')$ is actually not important because of reciprocity, but it makes it easier to understand the formulas if one consistently interprets the first argument as the observation point and the second as the source point, particularly as we transform to wave-number space.

The rules by which the nth-order contributions to $\langle G\rangle$ are constructed are simple in a formal sense.

(1) Draw a single solid line connecting points x and x'.
(2) Label n internal dots on this line $(x_1,\ldots,x_n)$.
(3) Connect the n internal dots together by dotted lines in all topologically distinct ways.
(4) More than 2 points may be joined together by a cluster of dotted lines which join together at a cross.

The Feynman rules which enable the evaluation of a particular diagram are also simple in a formal sense.

(1) Replace each solid line connecting the points (x,y) by the Green's function $G_0(x,y)$.
(2) Replace each dotted line cluster connecting the points $(x_1,\ldots,x_j)$ by the function $\Gamma_j(x_1,\ldots,x_j)$.
(3) Integrate over all internal coordinates.
(4) Evaluate and sum all diagrams.

One must perform n d-dimensional integrals to evaluate a general nth-order diagram. While the evaluation of a particular higher-order diagram will involve a multiple integral and may be difficult to evaluate, at least the organization of the calculation is relatively straightforward. The same formal Feynman rules obtain for a wide variety of systems, more detailed and extensive discussions may be found in a number of texts and review articles.[4–6]

B. Feynman rules for a fluid-loaded plate with uniformly attached oscillators

In order to actually compute anything, one must explicitly specify the Feynman rules, that is, supply expressions for the Green's function $G_0(x,y)$ and the various correlation functions Γ_j. It is hence necessary to make some statistical assumptions. We shall assume:

(1) The spatial and frequency distributions of the oscillators are independent, $P\{\xi_i,Z_i\}=P_x\{\xi_i\}P_\omega\{\omega_i\}$;
(2) The oscillators are distributed independently and in a spatially uniform manner; that is

$$P_x\{\xi_i\}=\prod_i p_x(\xi_i)=\prod_i (1/L^d),$$

and

$$P_\omega\{\omega_i\}=\prod_i n(\omega_i)/N, \tag{15}$$

where $d=1,2$ depending on whether the scatterers are lines or points. Here $n(\omega_i)$ is the average density of internal oscillator states; we leave this function arbitrary because it is likely to vary depending on the system of interest.

(3) The masses m_i and damping factors ζ_i of the oscillators are constant. We therefore let $Z_i\to Z(\omega_i)$ and freely interchange dependence on Z_i with dependence on ω_i.

The first two of these assumptions afford great simplifications, implying that the oscillators are uncorrelated with one another in frequency and in space. This produces a change in the sort of calculations required, collapsing integrals, etc. The third assumption is not crucial and produces only simpler formulas, a reasonable goal nevertheless.

1. The zeroth-order Green's functions G_0

The Green's function $G_0(x,x')$ is defined by Eqs. (7)–(9), which specify the decomposition of the equations of motion into a deterministic and fluctuating part, and Eqs. (3)–(5), which define the detailed operators appropriate to a fluid-loaded plate with point or line attachments. We recall

$$Z_0G_0(x,x')=-\delta(x-x'),$$
$$Z_0=\langle Z_t\rangle=Z_p+Z_f+\langle Z_{\rm int}\rangle. \tag{16}$$

It is therefore necessary to have in hand the ensemble averaged impedance before G_0 can be determined. Consider then the ensemble average [see Eq. (6)],

$$\langle Z_{\rm int}\rangle=\left[\prod_j \int d\xi_j\, dZ_j\right]P\{\xi_i,Z_i\}Z_{\rm int}(\xi_i,Z_i). \tag{17}$$

Proceeding, we find using the above expressions for $P\{\xi_i,Z_i\}$

$$\langle Z_{\rm int}\rangle=\left[\prod_j \int d\xi_j\; p_x(\xi_j)\right]$$
$$\times\left[\prod_j \int d\omega_j\,\frac{n(\omega_j)}{N}\right]\sum_i Z(\omega_i)\,\delta(x-\xi_i)$$
$$=\sum_i\left[\prod_j \int d\xi_j\; p_x(\xi_j)\,\delta(x-\xi_i)\right]$$
$$\times\left[\prod_j \int d\omega_j\,\frac{n(\omega_j)}{N}\,Z(\omega_i)\right]$$
$$=\sum_i\left[\int \frac{d\xi_i}{L^d}\,\delta(x-\xi_i)\right]\left[\int d\omega_i\,\frac{n(\omega_i)}{N}\,Z(\omega_i)\right], \tag{18}$$

where we have first merely substituted appropriate expressions for the probability distribution, and then exploited the statistical independence, the simple product form for $P\{\xi_i,Z_i\}$. In the final step, we note that any term in the product with $j\neq i$ integrates to one by definition, hence the appearance only of the index i. The result is therefore

$$\langle Z_{\rm int}\rangle=\frac{N}{L^d}\langle Z\rangle_f, \tag{19}$$

where the impedance Z is averaged over resonance frequency weighted by the average density of states. This average is precisely of the sort that has been considered by Strasburg and Feit[1] and Pierce *et al.*[2] for some simple systems. Pierce *et al.* give in the limit of small damping the effective damping and added mass due to the internal oscillators

$$M_{\rm int}=Pr\left\{\int_0^\infty \frac{d\overline{m_f}}{d\Omega}\,\frac{\Omega^2}{\Omega^2-\omega^2}\right\},\quad R_{\rm int}=\frac{\pi\omega^2}{2}\,\frac{d\overline{m_f}}{d\omega},\quad (20)$$

where $\overline{m_f}(\omega)$ is the mass of the internal oscillators with natural frequencies on average less than ω. In the case of a uniform distribution of oscillator frequencies,

$$\frac{n(\omega_j)}{N}=\begin{cases}1/\Delta\omega, & \omega\in[\omega_-,\omega_+],\\ 0, & \text{otherwise.}\end{cases}\quad (21)$$

The expressions above may be worked out to find

$$M_{\rm int}=m_0\left(1-\frac{\omega}{2\Delta\omega}\ln\frac{|\omega^2-\omega_+\omega_-+\omega\Delta\omega|}{|\omega^2-\omega_+\omega_--\omega\Delta\omega|}\right),$$
$$R_{\rm int}=m_0\,\frac{\pi\omega^2}{2\Delta\omega},\quad (22)$$

where $m_0=(N/L^d)M$ is the mass density of the internal structure. The added damping given here is in agreement with Strasburg and Feit.[1] Soize in his earlier paper[3] gave similar formulas for these quantities.

The appropriate Green's functions are therefore found from solving

$$\langle Z_t\rangle G_0(x,x')=(Z_p+Z_f+R_{\rm int}-i\omega M_{\rm int})G_0(x,x')$$
$$=-\delta(x-x')\quad (23)$$

and are hence those of a fluid-loaded plate with an added frequency-dependent mass and intrinsic damping. Exact expressions are complicated but known, as are a number of approximate results. We refer the reader interested in detailed expressions for these quantities in coordinate space to the literature.[11–13] Note that in the case of a more complex geometry, the zeroth-order Green's functions will still be given by the solution for the idealized deterministic system with added mass and damping, and thus can be found by employing conventional tools for the study of canonical systems.

2. The correlation functions Γ_n

The other pieces which need to be specified in detail are the correlation functions Γ_n. These quantities are once again computed via the average

$$\langle V(x_1)\cdots V(x_n)\rangle$$
$$=\left[\prod_j\int d\xi_j\,dZ_j\right]P\{\xi_i,Z_i\}V(x_1)\cdots V(x_n),\quad (24)$$

where the implicit dependence of the stochastic field V on the ξ_i and Z_i has been omitted, and recall that $V=Z_{\rm int}-\langle Z_{\rm int}\rangle$.

Consider first the two-point function

$$\Gamma_2(x_1,x_2)=\left[\int\prod_i\frac{d\xi_i}{L^d}\right]\left[\int\prod_i d\omega_i\,\frac{n(\omega_i)}{N}\right]\sum_j\delta(x_1-\xi_j)Z(\omega_j)\sum_k\delta(x_2-\xi_k)Z(\omega_k)-\langle Z_{\rm int}\rangle^2.\quad (25)$$

The terms with $j\neq k$ give the result $\langle Z_{\rm int}\rangle^2$ up to corrections of order L^{-d} because of the statistical independence of the internal structure. Ignoring the small contributions associated with the boundaries, we find the simple result

$$\Gamma_2(x_1,x_2)=\sum_j\left[\int\prod_i\frac{d\xi_i}{L^d}\,\delta(x_1-\xi_j)\delta(x_2-\xi_j)\right]\times\left[\int\prod_i d\omega_i\,\frac{n(\omega_i)}{N}\,Z^2(\omega_j)\right]$$
$$=\frac{N\delta(x_1-x_2)}{L^d}\,\langle Z^2\rangle_f,\quad (26)$$

where the average $\langle Z^2\rangle_f$ is over the resonant frequencies of the oscillators, just as for $\langle Z\rangle_f$. This extremely simple result obtains from the complete lack of correlation of the internal structure, in some cases, perhaps not a bad approximation.

The three-point function is given by

$$\langle V(x_1)V(x_2)V(x_3)\rangle=\langle Z_{\rm int}(x_1)Z_{\rm int}(x_2)Z_{\rm int}(x_3)\rangle-\langle Z_{\rm int}\rangle\sum_{\rm pairs}\Gamma(x_i,x_j)-\langle Z_{\rm int}\rangle^3.\quad (27)$$

When all three points x_i are distinct, one simply obtains $\langle Z_{\rm int}\rangle^3$, cancelling the last term in this equation, while if any two of the points coincide, one will find terms cancelling the appropriate piece of the second term (up to terms of order L^{-d} again). And therefore the triple sum indicated in the above average collapses to a single sum to yield the result

$$\Gamma_3(x_1,x_2,x_3)=\sum_j\left[\int\prod_i\frac{d\xi_i}{L^d}\,\delta(x_1-\xi_j)\times\delta(x_2-\xi_j)\delta(x_3-\xi_j)\right]\times\left[\int\prod_i d\omega_i\,\frac{n(\omega_i)}{N}\,Z^3(\omega_j)\right]$$
$$=\frac{N\delta(x_1-x_2)\delta(x_1-x_3)}{L^d}\,\langle Z^3\rangle_f.\quad (28)$$

By similar arguments, one may show that the n-point correlation function is given by

$$\Gamma_n(x_1,\ldots,x_n)=\frac{N\delta(x_1-x_2)\cdots\delta(x_{n-1}-x_n)}{L^d}\,\langle Z^n\rangle_f.\quad (29)$$

The specification of the real-space Feynman rules is now complete. Let us begin to evaluate the 4th-order diagram in Fig. 3(a). The result is

$$(3a)=\left(\frac{N}{L^d}\langle Z^2\rangle_f\right)^2\int dx_1\ dx_2$$
$$\cdot G_0(x,x_2)G_0^3(x_2,x_1)G_0(x_1,x'). \tag{30}$$

To obtain a ''real'' answer one still must carry out the indicated integrations involving the nontrivial functions $G_0(x,x')$.

III. WAVE-NUMBER SPACE FEYNMAN RULES

For systems which are uniform in an average sense, wave-number space is very convenient because on average, wave number is conserved. Average uniformity means that average correlation or response functions depend only on the spacing of the points in question, not their absolute position on the structure.

One proceeds by Fourier transforming the above real space diagrams. It is convenient to define the Fourier transform of $G(x,x')$ (or for that matter of any two-point response function) by the rule

$$G(k_1,k_2)=\int dx_1\ dx_2\ \exp(-ik_1x_1+ik_2x_2)G(x_1,x_2) \tag{31}$$

because k_1 then corresponds to the normally defined wave number (by our convention) of the response, while k_2 represents the wave number of the excitation spectrum. Since $G_0(x_1,x_2)=G_0(x_1-x_2)$ one quickly finds

$$G_0(k_1,k_2)=2\pi\delta(k_1-k_2)G_0(k_1),$$
$$G_0(x_1-x_2)=\int dx\ e^{ik(x_1-x_2)}G_0(k). \tag{32}$$

And a similar expression holds for the two-point correlation function because of the assumed average translation invariance of the system;

$$\Gamma_2(k_1,k_2)=2\pi\delta(k_1-k_2)\Gamma_2(k_1),$$
$$\Gamma_2(x_1,x_2)=\Gamma_2(x_1-x_2)=\int dx\ e^{ik(x_1-x_2)}\Gamma_2(k). \tag{33}$$

Consider the Fourier transform of the diagram of Fig. 3(a). We have

$$\mathrm{FT}(3a)=\int dx\ dx'\ \exp(-ikx+ik'x')$$
$$\times\prod dx_i\left[\prod\frac{dk_i}{2\pi}G_0(k_i)\right]$$
$$\times\left[\prod\frac{dl_i}{2\pi}\Gamma_2(l_i)\right]\exp\{ik_5(x-x_4)+k_4(x_4-x_3)$$
$$+k_3(x_3-x_2)+k_2(x_2-x_1)+k_1(x_1-x')\}$$
$$\times\exp\{il_1(x_3-x_1)+l_2(x_4-x_2)\}$$
$$=G_0(k)G_0(k')\int\left[\prod_{2,\ldots,4}\frac{d^dk_i}{(2\pi)^d}G_0(k_i)\right]$$
$$\times\left[\prod_{1,2}\frac{d^dl_i}{(2\pi)^d}\Gamma_2(l_i)\right]2\pi\delta(k_2-k'+l_1)$$

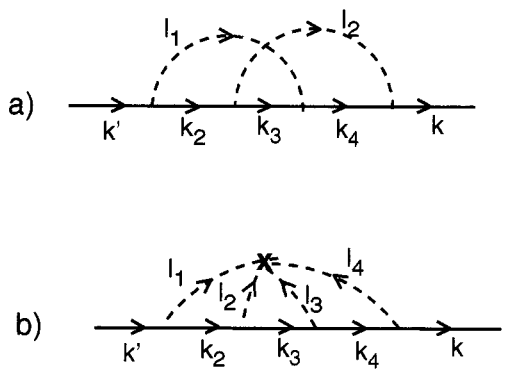

FIG. 4. Some fourth-order Feynman diagrams for the average Green's function in wave-number space.

$$\times 2\pi\delta(k_3-k_2+l_2)2\pi\delta(k_4-k_3-l_1)$$
$$\times 2\pi\delta(k-k_4-l_2), \tag{34}$$

where the integration over each coordinate has produced a wave-number conservation rule because of the translation invariance of the system.

It is easy to understand the role of the various delta functions if we draw a wave-number space diagram corresponding to Fig. 3(a). This is shown in Fig. 4(a). One simply insists upon wave-number conservation at each vertex. This is a consequence of the average translational invariance of the system. For example, examine the vertex involving k_2, k_3, and l_2 (corresponding to the point x_2 in real space diagram). The delta functions imply that $k_2=k_3+l_2$, an aspect which is obvious from the diagram. After integrating over the δ functions, one obtains for the diagram in Fig. 4(a),

$$(4\mathrm{a})=2\pi\delta(k-k')G_0(k')$$
$$\times\left[\frac{N}{L^d}\langle Z^2\rangle_f\right]^2\int\frac{dl_1}{2\pi}\frac{dl_2}{2\pi}G_0(k'-l_1)$$
$$\times G_0(k'-l_1-l_2)G_0(k'-l_1)G_0(k), \tag{35}$$

a result which is almost trivial to find using the wave-number conservation rules. In obtaining this fairly explicit result we have used the fact that

$$\Gamma_2(k)=\frac{N}{L^d}\langle Z^2\rangle_f \tag{36}$$

an expression easily derived by Fourier transforming the coordinate space correlation function given in Eq. (28).

The generalization of this specific example to an arbitrary diagram is carried out in the following section in which higher-order quantities are considered. The result is that the simple rules obtained in the above example do indeed apply to any diagram. For now, let us simply state the wave-number space Feynman rules. The procedure for drawing the wave-number space diagrams is exactly the same as the procedure for coordinate space diagrams, but the labeling and Feynman rules are changed. One draws a diagram with wave number (momentum) flowing from the input wave number to the output wave number. The direction of the flow is indi-

cated by an arrow. The n points are no longer labeled by position; instead the lines are labeled by wave number. The Feynman rules are

(1) Replace each solid line with a wave-number space Green's function $G_0(k)$.
(2) Replace each dotted line with the Fourier transform of the two-point correlation function $\Gamma_2(k)$.
(3) For each vertex, include a wave-number conserving δ function, $\delta(\Sigma k_{\text{in}} - \Sigma k_{\text{out}})$.
(4) Integrate over all internal wave numbers, $\int d^d k/(2\pi)^d$.

A general nth-order diagram involving only the two-point correlation function will have $(n-1)$ internal wave numbers associated with Green's functions, $n/2$ internal wave numbers associated with correlation functions, and n wave-number conserving δ functions. One of the δ functions must provide overall wave-number conservation and therefore evaluation of this diagram will involve only $(n/2)$ d-dimensional integrals (as opposed n in coordinate space). In practice, the evaluation of the various δ functions is done graphically: As one writes down the diagrams, one ensures wave-number conservation at each vertex.

The rules for the higher-order correlation functions are derived in a similar fashion. Translational invariance no longer implies a simple expression such as Eq. (33) for the two-point function, but rather, we have

$$\tilde{\Gamma}_n(k_1,\ldots,k_n) = \int \prod\, dx_i \, \exp\left(i \sum k_i x_i\right) \Gamma_n(x_1,\ldots,x_n) \tag{37}$$

with

$$\tilde{\Gamma}_n(k_1,\ldots,k_n) = 2\pi\delta\left(\sum\, k_i\right) \Gamma_n(k_2,\ldots,k_n). \tag{38}$$

Translational invariance forces the net wave number entering the n-point correlation function to vanish. The sign convention in the Fourier transform corresponds to that for a source and therefore the wave number is pointing away from the vertices and towards the center of the cluster. To allow this case, one more Feynman rule must be added:

(5) For an n-point correlation function, assign each dotted line entering the cluster a wave number pointing towards the center of the cluster (the cross), and assign the cluster the value $2\pi\delta(\Sigma k_i)\Gamma_n(k_2,\ldots,k_n)$.

Notice that this formula reduces to that of the two-point function when $n=2$. Shown in Fig. 4(b) is the diagram corresponding to Fig. 3(b) involving a four-point correlation function. This diagram is given by

$$\begin{aligned}(4\text{a}) = {} & 2\pi\delta(k-k') \\ & \times G_0(k') \frac{N}{L^d} \langle Z^4 \rangle_f \int \frac{dl_1}{2\pi} \frac{dl_2}{2\pi} \frac{dl_3}{2\pi} G_0(k'-l_1) \\ & \times G_0(k'-l_1-l_2) G_0(k'-l_1-l_2-l_3) G_0(k).\end{aligned} \tag{39}$$

Notice how simple this diagram is to work out by first doing the l_3 integral, next the l_2 integral, etc., yielding the result

$$(4\text{a}) = 2\pi\delta(k-k') G_0(k') \frac{N}{L^d} \langle Z^4 \rangle_f [G_0(x=0)]^3 G_0(k). \tag{40}$$

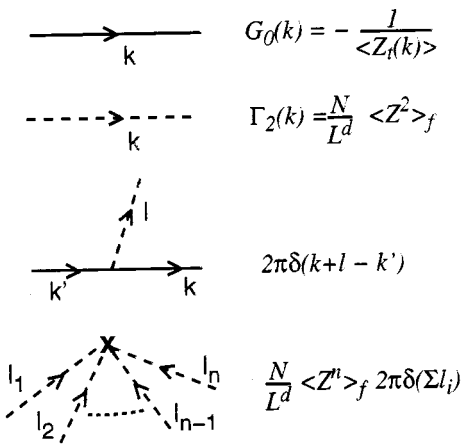

FIG. 5. Feynman rules for a fluid-loaded plate with attached oscillators.

Just as was the case for the coordinate space Feynman rules, these same rules obtain for a wide variety of systems. We are, however, now in a position to write down the specific wave-number space Feynman rules which may be used to evaluate averaged Green's functions for a fluid-loaded plate with internal oscillators. The rules for drawing the diagrams have been discussed in this and the previous sections. In Fig. 5, the wave-number space Feynman rules are presented. The expression for the n-point correlation function given in the figure can be verified by Fourier transforming the coordinate space correlation function given in Eq. (28).

IV. HIGHER-ORDER AVERAGES: CUT DIAGRAMS

It is often useful to consider higher-order averages when one seeks to focus on energy quantities or magnitudes of fluctuations. The evaluation of such quantities is very similar to that given above for $\langle G \rangle$. However, in this case, because of the explicit appearance of damping, the obtained Feynman rules differ somewhat from the usual expressions.

Consider the quadradic quantity $\langle G(x,x')G(y,y') \rangle$. Expanding both Green's functions in a Neumann series and averaging, it is not difficult to show that the nth-order terms are generated by drawing two solid lines (one for each Green's function) connecting (x,x') and (y,y'), respectively, selecting n total points as ''scattering'' centers, and connecting the points in all possible ways with dashed lines. The Feynman rules for the diagrams so generated are identical to the real space rules given in Sec. III. Perturbation expansions for yet higher-order averages, $\langle GGG \rangle$, etc., are constructed in the same way. An example of a fourth-order diagram is given in Fig. 6(a).

Also interesting are quantities such as $\langle G(x,x')G^*(y,y') \rangle$ which are directly related to energy densities and the scattering cross section. It is clear that the series for this quantity will be exactly the same as for the above case, except that all quantities associated with the y coordinates will be complex conjugates. This can be indicated pictorially using a cut diagram.[14] A cut diagram in real space is shown in Fig. 6(b). The additional rule for the cut diagram is that quantities above the cut are to be complex conjugated. This is quite simple to carry out for the Green's

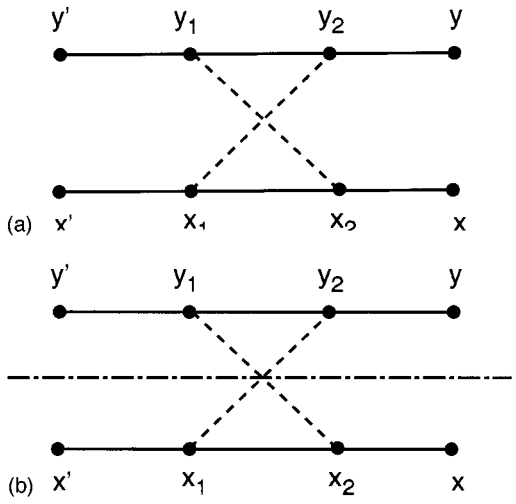

FIG. 6. Fourth-order Feynman diagrams for the real-space calculation of: (a) $\langle GG\rangle$, (b) $\langle GG^*\rangle$, a cut real-space diagram.

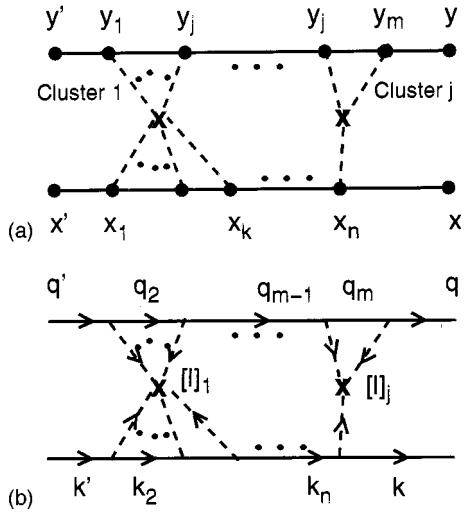

FIG. 7. Feynman diagrams for the calculation of $\langle GG\rangle$ to arbitrary order: (a) a general real-space diagram, (b) the corresponding wave-number space diagram.

functions $G_0(x,x')$ but does introduce a small complication in our notation for the correlation functions. Let

$$\Gamma_i^j(x_1,\ldots,x_i,y_1,\ldots,y_j)$$
$$=\langle V(x_1)\cdots V(x_i)V^*(y_1)^*V^*(y_j)\rangle$$
$$=\frac{(i+j)}{L^d}\,\delta(x_1-x_2)\cdots\delta(x_{i-1}-x_i)\,\delta(x_i-y_1)\cdots$$
$$\delta(y_{j-1}-y_j)\langle(Z)^i(Z^*)^j\rangle_f. \tag{41}$$

The additional Feynman rules for cut diagrams in real space are:

1) Replace solid lines above the cut with $G_0^*(x,y)$
2) Replace dotted line clusters with i points below the cut and j points above the cut with $\Gamma_i^j(x_1,\ldots,x_i,y_1,\ldots,y_j)$.

In wave-number space, we proceed as in the previous section. In this case, we consider a general coordinate space diagram contributing to the quantity $\langle GG\rangle$ as shown in Fig. 7(a). The Fourier transform of this diagram is given by

$$\mathrm{FT(7a)}=\int dx\,dx'\,\exp(-ikx+ik'x')\int dy\,dy'\,\exp(-iqy+iq'y')\prod dx_i\left[\prod\frac{dk_i}{2\pi}G_0(k_i)\right]\left[\prod\frac{dq_i}{2\pi}G_0(q_i)\right]$$
$$\times\left[\prod_j\frac{[dl]}{2\pi}\tilde{\Gamma}_{n_j}([l]_j)\right]\exp(ik_{n+1}(x-x_n))\left(\prod_{i=2}^{n}\exp(ik_i(x_i-x_{i-1}))\right)\exp(ik_1(x_1-x'))\exp(iq_{m+1}(y-y_m))$$
$$\times\left(\prod_{i=2}^{m}\exp(iq_i(y_i-y_{i-1}))\right)\exp(iq_1(y_1-y'))\left(\prod_j\exp(-i[l]_j\cdot\{[x]_j,[y]_j\})\right), \tag{42}$$

where the quantities $[l]_j$ and $\{[x]_j,[y]_j\}$ correspond to clusters involving n_j points. The abstract inner product involving the clusters is given by

$$[l]_j\cdot\{[x]_j,[y]_j\}=\sum_{x_{j_i}\in j\text{th cluster}}l_{x_{j_i}}\cdot x_{j_i}+\sum_{y_{j_i}\in j\text{th cluster}}l_{y_{j_i}}\cdot y_{j_i}, \tag{43}$$

where $l_{x_{j_i}}$ is the wave number entering the jth cluster from the point x_{j_i} and similarly $l_{y_{j_i}}$ is associated with point y_{j_i}.

The expression above is lengthy but simple to analyze. Every coordinate integration leads to a wave-number space delta function. The integrations over the external points x,x',y,y' yield $2\pi\delta(k_{n+1}-k)$, $2\pi\delta(k_1-k')$, etc. While the integration over any internal point x_i (or y_i) gives $2\pi\delta(k_i-l_{x_i}-k_{i+1})$ [or $2\pi\delta(q_i-l_{y_i}-q_{i+1})$]. Therefore, the wave-number space diagram is obtained by orienting the wave-number flow of the two lines corresponding to the two Green's functions in the same direction, and employing the same wave-number space rules as before. Notice that since each cluster conserves wave number, there will be an overall wave-number conserving delta function $2\pi\delta((k+q)-(k'+q'))$, left over in the end.

Consider now the important case $\langle GG^*\rangle$. The Fourier transform of the cut diagram shown in Fig. 8(a) is given by a similar expression,

$$\text{FT(8a)}=\int dx\ dx'\ \exp(-ikx+ik'x')\int dy\ dy'\ \exp(iqy-iq'y')\prod dx_i\left[\prod \frac{dk_i}{2\pi}\,G_0(k_i)\right]$$
$$\times\left[\prod \frac{dq_i}{2\pi}\,G_0^*(q_i)\right]\left[\prod_j \frac{[dl]}{2\pi}\,\tilde{\Gamma}^{n_{yj}}_{n_{xj}}([l]_j)\right]\exp(ik_{n+1}(x-x_n))\left(\prod_{i=2}^{i=n}\exp(ik_i(x_i-x_{i-1}))\right)\exp(ik_1(x_1-x'))$$
$$\times\exp(-iq_{m+1}(y-y_m))\left(\prod_{i=2}^{i=m}\exp(-iq_i(y_i-y_{i-1}))\right)\exp(-iq_1(y_1-y'))\left(\prod_j\exp(-i[l]_j\cdot\{[x]_j,-[y]_j\})\right). \tag{44}$$

Here, we have defined the Fourier transform of the correlation functions via

$$\tilde{\Gamma}^{n_{yj}}_{n_{xj}}([l]_j)=\int\prod dx_i\ \exp(i[l]_j\cdot\{[x]_j,-[y]_j\})\tilde{\Gamma}^{n_{yj}}_{n_{xj}}(x_1,\ldots,x_{n_{xj}},y_1,\ldots,y_{n_{yj}}) \tag{45}$$

following the convention that wave number occuring in the Fourier transform of a complex conjugate quantity should be negative. Notice that translational invariance implies in this case the constraint,

$$\tilde{\Gamma}^{n_{yj}}_{n_{xj}}([l]_j)=2\pi\delta\left(\sum l_{x_{j_i}}-\sum l_{y_{j_i}}\right)\Gamma^{n_{yj}}_{n_{xj}}([l]_j), \tag{46}$$

i.e., we should regard the wave numbers above the cut as outgoing for the conservation rules to make pictorial sense at a cluster. We have shown this in Fig. 8(b).

Consider now the effects of integrating out the various coordinates. Once again, the end-point integrations over (x,x',y,y') are trivial yielding $\delta(k-k_{n+1})$, $\delta(k'-k_1)$, $\delta(q-q_{m+1})$, and $\delta(q'-q_1)$. The integration over interior points is also simple, giving $2\pi\delta(k_i-l_i-k_{i+1})$ for vertices below the cut and similarly $2\pi\delta(q_i-l_i-q_{i+1})$ for vertices above the cut. The difference in the cut diagram versus the uncut case in Fig. 7(b) is merely the direction of the wave number $l_{y_{j_i}}$ above the cut. In order to have this conservation rule make pictorial sense, we must therefore reverse the direction of all the q_i; that is, the wave-number flow in lines above the cut is reversed. Once again, this is shown in Fig. 8(b). And therefore, the wave-number space rules for constructing cut diagrams corresponding to averages of the sort $\langle GG^*\rangle$ are just as before with the additional rules:

(1) reverse the wave-number flow in lines above the cut;
(2) replace solid lines above the cut with complex conjugates of the Green's functions;
(3) replace the correlation function with $n_{xj}+n_{yj}$ points with the quantity $\tilde{\Gamma}^{n_{yj}}_{n_{xj}}([l]_j)$.

While the algebra above may have been a bit complicated, the final result is very simple.

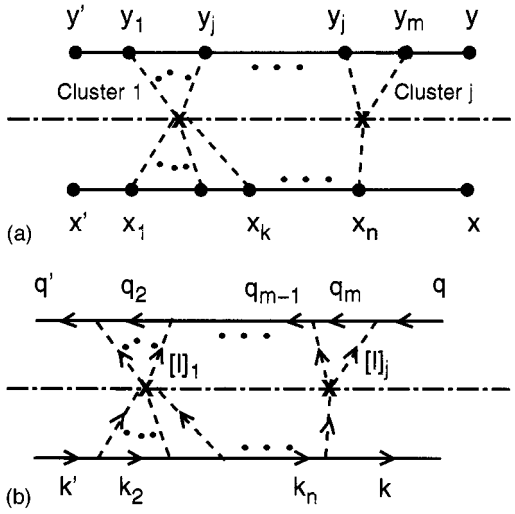

FIG. 8. Feynman diagrams for the calculation of $\langle GG^*\rangle$ to arbitrary order: (a) a general real-space cut diagram, (b) the corresponding wave-number space cut diagram.

V. CONCLUSION

The ''fuzzy structure'' approach proposed by Soize[3] for the analysis of the effects of complex internal structure has been formulated in terms of Feynman diagrams for the case of a large fluid-loaded plate. The Feynman rules to write down and evaluate the diagrams have been derived both in real space and wave-number space for a highly idealized form of internal structure; we have assumed that the internal oscillators are attached via normal forces and are distributed independently and in a spatially uniform manner. The method we have employed is, however, quite general[4–6] and similar rules could be derived for different and more complicated systems.

The Feynman rules enable the evaluation of the mean scattering properties due to the internal structure, an issue of great recent interest in structural acoustics, and is an extension of the study of the damping effects of the internals.[1,2] We defer the application of these techniques to a particular system to Part II of this paper.

ACKNOWLEDGMENTS

This research was supported by the Office of Naval Research.

[1] M. Strasburg and D. Feit, ''Vibration damping of large structures induced by attached small resonant structures,'' J. Acoust. Soc. Am. **99**, 335–344 (1996).
[2] A. D. Pierce, V. W. Sparrow, and D. A. Russell, ''Fundamental structural acoustic idealizations for structures with fuzzy internals,'' Trans. ASME, J. Vib. Acoust. **117**, 339–348 (1995).

[3] C. Soize, ''Probabilistic structural modeling in linear dynamic analysis of complex mechanical systems I. Theoretical elements,'' J. Recherche Aerospat. ONERA (France) **5**, 23–48 (1986).
[4] A. A. Abrikosov, L. P. Gorkov, and I. E. Dzhyaloshinskii, *Methods of Quantum Field Theory in Statistical Physics* (Prentice-Hall, Englewood Cliffs, NJ, 1963).
[5] U. Frisch, ''Wave propagation in random media,'' in *Probabilistic Methods in Applied Mathematics*, edited by A. T. Bharucha-Reid (Academic, New York, 1968), Vol. 1, pp. 75–198.
[6] A. Ishimaru, *Wave Propagation and Scattering in Random Media* (Academic, New York, 1978), Vol. 1, pp. 75–198.
[7] S. A. Rybak, ''Waves in a plate containing random inhomogeneities,'' Sov. Phys. Acoust. **17**, 345–349 (1972).
[8] J. A. Turner and R. L. Weaver, ''Coupling and attenuation of waves in plates by randomly distributed attached impedances,'' J. Acoust. Soc. Am. **99**, 2167–2175 (1996).
[9] M. Junger and D. Feit, *Sound, Structures, and Their Interaction* (MIT, Cambridge, MA, 1972) 2nd ed., pp. 235–272.
[10] R. Kubo, ''Stochastic Liouville Equation,'' J. Math. Phys. (N.Y.) **4**, 174–183 (1963).
[11] D. G. Crighton, ''The free and forced waves on a fluid-loaded elastic plate,'' J. Sound Vib. **63**, 225–235 (1979).
[12] D. M. Photiadis, ''Approximations for the two-dimensional Green's function of a fluid-loaded plate,'' J. Acoust. Soc. Am. **93**, 42–47 (1993).
[13] C. Serrin and S. Hayek, ''Acoustic radiation from an insonified elastic plate with a line discontinuity,'' J. Acoust. Soc. Am. **86**, 195–209 (1989).
[14] This definition is similar to, but not quite the same as the definition of the Cutkosky rules in quantum field theory. The resulting diagrams are also sometimes referred to as cut diagrams. See for example, C. Itzykson and J. Zuber, *Quantum Field Theory* (McGraw-Hill, New York, 1980), p. 315.

Approximate meridional leaky ray amplitudes for tilted cylinders: End-backscattering enhancements and comparisons with exact theory for infinite solid cylinders

Philip L. Marston
Department of Physics, Washington State University, Pullman, Washington 99164-2814

(Received 31 October 1996; revised 15 March 1997; accepted 24 March 1997)

Leaky waves propagating on cylinders in (or close to) a meridional plane have been found to significantly enhance the high-frequency acoustic visibility of the ends of tilted cylinders [G. Kaduchak *et al.*, J. Acoust. Soc. Am. **100**, 64–71 (1996)]. The meridian of interest is in the plane containing the incident wave vector and the cylinder's axis. A ray model for this enhancement is developed along with a ray model for a canonical test case: scattering by an infinite circular cylinder. To isolate a single high-frequency leaky wave contribution, numerical examples are shown for generalized Rayleigh waves on a solid circular cylinder. Partial wave series (PWS) calculations show that the meridional Rayleigh wave contribution is maximized when the tilt angle is close to the flat-surface coupling angle. The ray model approximates the superposition of leaky waves excited by the incident acoustic wave as a simple integral that accounts for the phase shift and attenuation for propagation from each illuminated surface point to a surface point of interest. While the model gives the spatial evolution of the leaky wave amplitude as would be measured by acoustic imaging, it also approximates the far-field amplitude. Important features of the canonical PWS calculation are reproduced by the model. The far-field magnitude of the end contribution can be larger than for reflection off a rigid sphere having the same radius as the cylinder. The end is assumed to be flat and perpendicular to the cylinder's axis.
[S0001-4966(97)05407-6]

PACS numbers: 43.40.Rj, 43.20.Fn, 43.30.Vh [CBB]

INTRODUCTION AND MOTIVATION

High-frequency sonar images of truncated cylindrical shells show evidence of scattering enhancements that can greatly improve the visibility of the ends of the shell.[1,2] The enhancements are manifested when the tilt angle γ for the cylinder shown in Fig. 1 is close to a leaky wave coupling angle $\theta_l = \sin^{-1}(c/c_l)$, where c_l is the phase velocity of the leaky wave and c is the speed of sound in the surrounding water. The conditions and arrival time for the enhancements indicate that a major contribution results from the reflection of a meridional leaky ray from the end of the cylinder and the radiation of sound by the leaky ray subsequent to its reflection. This ray is described as a meridional ray since it is confined to the plane defined by the direction of the incident wave vector and the axis of the cylinder. This is a meridional plane of the cylinder, and similar terminology is used to distinguish optical rays guided by cylindrical glass fibers that are confined to a meridional plane from those which follow a helical trajectory.[3] As demonstrated in Ref. 1, for a water-filled shell there is also a family of meridional rays which cross the interior of the shell an even number of times prior to giving strong backscattering contributions. While it is anticipated that such contributions could be approximated by an extension of the analysis given here, the analysis of such contributions is beyond the scope of the present paper. If a denotes the radius of the cylinder and k the acoustic wave number in water, the typical ka of interest are in the range of 50–150.

A meridional ray can also be a major contributor to the canonical problem shown in Fig. 2 for which an exact partial-wave series solution exists.[4,5] A plane wave is incident on an infinite tilted solid or hollow cylinder. The tilt angle γ is adjusted to be the leaky wave coupling angle θ_l. The observation point is taken to lie in the meridional plane on the illuminated side of the cylinder so that, as shown in Fig. 2, radiation from the meridional leaky ray propagates to the observer without reflecting or propagating around the back side of the cylinder. While the meridional ray shown in Fig. 2 is relevant to the interpretation of bistatic scattering data, the scattering is analyzed in the present paper since the resulting ray approximation may be compared directly with partial wave series results. For the applications of interest as illustrated in Fig. 1, the response of the elastic scatterer would not be correctly described by thin shell theories typically used in the formulation of ray methods[6–9] since the frequency is significantly above the coincidence frequency of the shells of interest.[1] Consequently the ray theory is formulated so as to avoid specialization to a specific model for the elastic response of the scatterer, except in the final numerical evaluation of the amplitudes.

Depending on the classification of the leaky meridional ray contribution under consideration, the tilt angle γ may be such that helical waves due to other types of leaky waves are also excited, which contribute to the scattering for the situations considered in Figs. 1 and 2. The interference from helical wave contributions is avoided in the comparison between partial wave and ray theory, given here by showing only the case of high-frequency scattering by an infinite solid cylinder. In that case there is only a single class of leaky

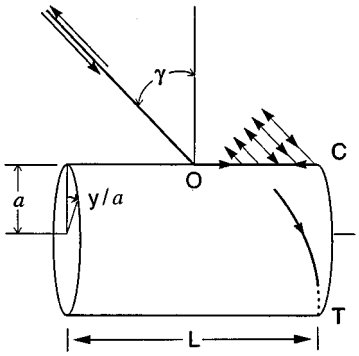

FIG. 1. The leaky wave process considered is the ray lying in the meridional plane. That plane is defined by the incident wave vector and the cylinder's axis. Reflection of this surface ray at C results in a radiated wavefront directed back to the source when the tilt angle γ is equal to the leaky wave radiation angle θ_l as in this figure. In the meridional plane, the wavefront's Gaussian curvature vanishes and its amplitude decays transversely because of the decaying amplitude of the surface wave. This process was demonstrated by Kaduchak *et al.*[1] to significantly enhance the visibility of the end of a cylinder viewed with high-frequency sonar. The process is analyzed using a surface integral which approximates the leaky wave excitation. Another backscattering process is the launching of helical rays which can reflect at T in the meridional plane as shown by the solid and dashed arcs.

wave excited: the leaky generalized Rayleigh wave. As demonstrated in Appendix A for ka in the region of interest, the phase velocity c_l and spatial damping rate α are only weakly affected by the curvature of the cylinder. Consideration of the solid cylinder case is also of intrinsic value because the physical interpretation of the scattering with the tilt angle equal to the Rayleigh angle, given originally by Flax *et al.*,[4] is re-examined here to achieve the proper flat-surface limit. The situation shown in Fig. 2 is also relevant to the understanding of the high-frequency sonar inspection of solid elastic rods in water and to certain problems in ultrasonic nondestructive testing such as the detection of flaws in pipes. Relevant partial wave series computations are presented in Sec. I.

The ray formulation used here is based on an extension[10] of earlier two-dimensional formulations[11,12] to approximate

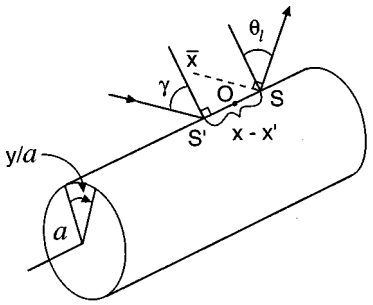

FIG. 2. A meridional leaky ray can be a major contributor to the scattering in the meridional plane of an infinite cylinder, a section of which is shown here. The surface points S' and S are shown to lie on the meridian (the x axis) where the surface intersects the meridional plane. The orthogonal coordinate of the unwrapped surface is denoted by y. The axis $\bar{x}$ in Sec. V lies in the meridional plane and is perpendicular to the outgoing wave vector. Synchronous excitation of a meridional leaky ray occurs when $\gamma = \theta_l$ and the leaky wave contribution to the scattering in the meridional plane is strongly enhanced [see discussion of Fig. 5(b)]. There is also a reflected ray at S.

out-going leaky wave amplitudes for weakly curved three-dimensional scatterers. The application to the tilted infinite cylinder is introduced in Sec. II. The leaky wave amplitude is approximated by a surface integral which includes path contributions outside of the Fermat path for the process of interest. In Sec. III the Fresnel coupling patch is examined so as to motivate certain approximations which greatly simplify the evaluation of the surface integral. Previous studies have found that identification of Fresnel coupling patches is helpful for understanding the excitation or subsequent radiation of leaky waves.[10,12,13] The patch shape for meridional rays is found to have unusual features. Section IV discusses the approximation of the resulting integral when the surface point S in Fig. 2 lies in the meridional plane. The formulation allows for possible axial variations of the incident wave amplitude, as in the case of illumination by a two-dimensional acoustic beam, although the final evaluation is only given for uniform plane-wave incidence. To improve the estimate of the resulting far-field amplitude, it is necessary to approximate the curvature of the wavefront radiated by the leaky wave. The curvature is found by considering in Sec. V the leaky wave amplitude at a surface point adjacent to the meridional plane. The far-field amplitude and comparison to PWS results for an infinite stainless steel cylinder are given in Sec. VI.

Section VII discusses the approximation of the near- and far-field meridional ray amplitude for the situation illustrated in Fig. 1. It is assumed that the coefficient of leaky wave reflection off the end of the cylinder is known and that the coefficient varies only slowly with the angle of incidence near the Fermat path of interest. For the case of high ka reflection of leaky Rayleigh waves off of the end of a solid stainless steel cylinder, the effects of fluid loading and curvature should be sufficiently weak that the reflection coefficient may be estimated from computations by Gautesen[14,15] and others[16] of the reflection of a Rayleigh wave from the traction-free edge of an elastic quarter space. These computations show that for near-normal reflection of the Rayleigh wave (corresponding to the meridional ray shown in Fig. 1), the phase and amplitude depend only weakly on the angle of incidence. The approximation of the far-field amplitudes given in Sec. VII shows that for a wide range of leaky wave parameters, the far-field backscattering magnitude due to end-reflected meridional leaky waves can exceed the specular reflection amplitude from a fixed rigid sphere having the same *radius* as the cylinder.

End-reflection of helical leaky waves can also result in backscattering enhancements as discussed, e.g., by Bao[17] for a truncated elastic cylinder; an approximation for the outgoing amplitude at the cylinder's surface is given in Ref. 10. Helical leaky waves on infinite solid cylinders[4,17–20] and thick cylindrical shells[5] have been related to resonances in the bistatic scattering. As illustrated by the observations in Ref. 1, the meridional ray mechanisms can be distinguished from helical mechanisms and they appear more important in certain situations. Helical wave contributions are outside the scope of the present paper.

TABLE I. Material properties used in the example.

	Density (g/cm^3)	c or c_L (m/s)	c_T (m/s)
Water	0.998	1483	
Stainless steel 304[a]	7.57	5675	3141

[a]Poisson's ratio=0.2792.

I. PARTIAL WAVE SERIES PREDICTIONS FOR RAYLEIGH ANGLE SCATTERING

The exact partial wave series (PWS) solution for scattering by an infinite circular cylinder[4,5] relates the scattered pressure p_{sca} at a far-field point having cylindrical coordinates (r,ϕ,x) with the incident wave amplitude p_{i0} at (0,0,0) in the absence of the cylinder; ϕ is measured from the meridional plane. The relationship between p_{sca} and p_{i0} is

$$p_{\mathrm{sca}}=p_{i0}(a/2r)^{1/2}f\ \exp(ik_x x+ik_r r), \tag{1}$$

where $k_x=k\ \sin\gamma$, $k_r=k\ \cos\gamma$, γ is the tilt angle as in Fig. 2, f is a dimensionless form function, and a factor $\exp(-i\omega t)$ is not shown. For observation points in the meridional plane on the illuminated side of the cylinder, the PWS for f may be put in the form

$$f=[-2\exp(-i\pi/4)/(\pi k_r a)^{1/2}]\sum_{n=0}^{N}(-1)^n\epsilon_n(B_n/D_n), \tag{2}$$

where $\epsilon_n=1$ for $n=0$ and $\epsilon_n=2$ for $n>0$, and $N>ka$ is selected to give proper convergence. For a solid elastic cylinder,[4,18–20] B_n and D_n are 4×4 determinants which depend on the tilt angle γ (see Appendix A). The details of the derivation are a special case of the more general analysis given in Ref. 21. The normalization in Eq. (2) is such that geometrically calculated specular reflection into the meridional plane from a fixed-rigid infinite cylinder gives $|f|=1$. Relevant computations of f discussed below were carried out for a stainless steel 304 cylinder in water with the material properties listed in Table I. The flat-surface leaky wave pole of the reflection coefficient was evaluated as summarized in Appendix A, giving the coupling angle $\theta_l=\sin^{-1}(k_l/k)=30.703°$, where k_l denotes the real part of the surface wave number at the pole.

In the first pair of PWS calculations, the tilt angle γ was set equal to the flat surface θ_l. The solid curve in Fig. 3 shows $|f|$ from Eq. (2), while the dashed curves are ray approximations having different levels of complexity as explained in Sec. VI. Above $ka\approx20$, the structure evident in $|f|$ for smaller ka is replaced by a smooth monotonic increase. This is to be expected since as $ka\to\infty$ the normalization is such that $|f|$ should approach the magnitude of the flat-surface reflection coefficient $|R|$ evaluated at θ_l. Since θ_l exceeds the shear critical angle, $|R|=1$ and the expected limit of $|f|$ is unity as $ka\to\infty$ (see Sec. VI).

To assist in the testing of the ray approximations, it is helpful to subtract a background contribution from f. Following the usual approach of resonance scattering theory[22] for the present case of a solid metallic cylinder, the background is approximated by the form function $f^{(r)}$ for a rigid cylinder at the same tilt angle. [Computations for other materials such as polymer cylinders in water indicate that while this choice of a rigid background is not universally applicable for solid cylinders, the rigid choice is useful for solid metallic cylinders for distinguishing certain features the elastic response; $f^{(r)}$ is evaluated from (2) with appropriate choices for B_n and D_n.] The solid curve in Fig. 4 shows $|f-f^{(r)}|$ evaluated with $\gamma=\theta_l$ as explained above. Above $ka\approx20$, the curve increases smoothly with increasing ka and it levels off as $ka\to\infty$. The dashed curves are Rayleigh wave contributions to the scattering calculated with different levels of complexity, as explained in Secs. IV and VI.

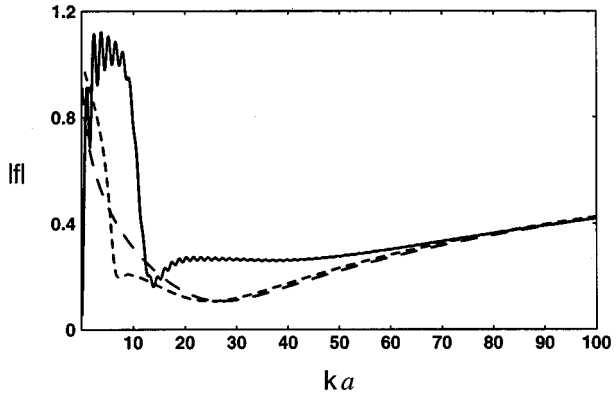

FIG. 3. The solid curve shows the form function $|f|$ in the meridional plane as computed by the partial wave series for an infinite stainless steel cylinder in water. The tilt angle γ is equal to the flat-surface coupling angle for a Rayleigh wave. The curve with the long dashes is the ray approximation, Eq. (25), evaluated using the flat-surface parameters. The curve with short dashes is also from Eq. (25) but the damping ratio α/k is varied as shown in Fig. A1 in the evaluation of Eq. (24).

To assist in interpreting Figs. 3 and 4, the corresponding PWS are shown in Fig. 5(a) as a function of tilt angle γ for $ka=50$ and 100. The solid curve shows $|f|$ and the dashed curve with the longest dashes shows $|f-f^{(r)}|$, both for $ka=100$. In each case the dependence is locally flat near $\gamma=\theta_l$; for example, the minimum in $|f|$ is offset from θ_l by

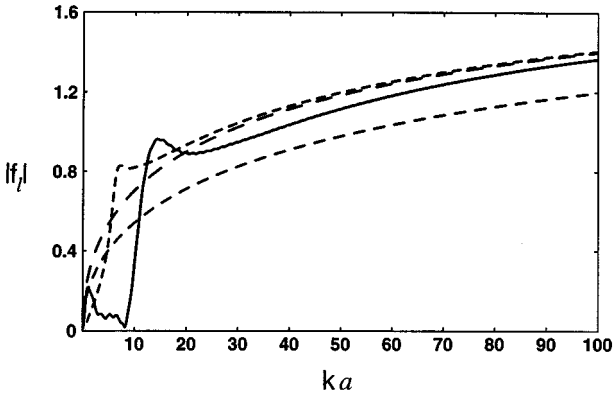

FIG. 4. Approximations for the Rayleigh wave contribution to f are shown for the tilted cylinder considered in Fig. 3. The solid curve is the partial wave series result for $|f-f^{(r)}|$, where f and $f^{(r)}$ are the exact elastic and rigid form functions. The curves with the longest and shortest dashes are ray approximations from Eq. (24) with the parameters chosen as in Fig. 3. The curve with intermediate length dashes is the approximation $|f_l|\approx2F(\mu)$ discussed in Sec. IV. It neglects the wavefront curvature correction given in Sec. V.

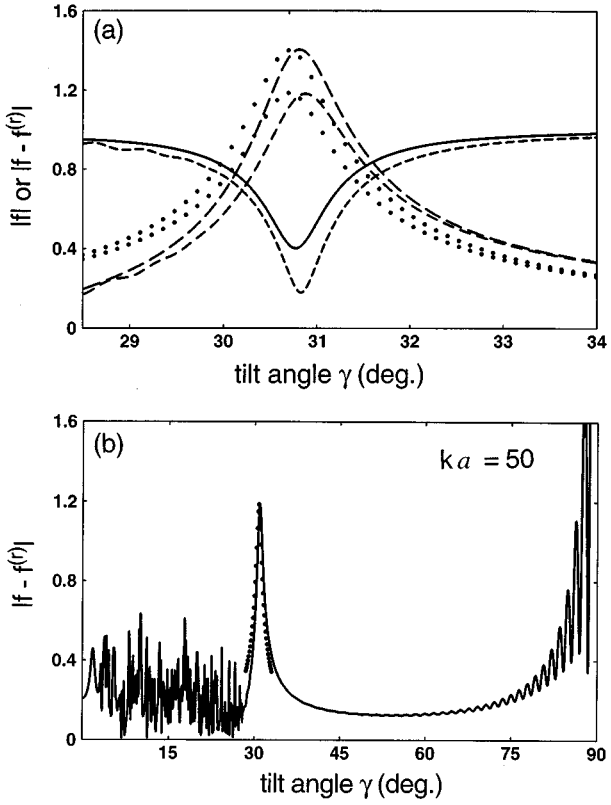

FIG. 5. (a) The solid and dashed curves with the central dip show $|f|$ from the partial wave series for ka of 100 and 50, respectively. The peaked curves with long and short dashes are the corresponding plots of $|f-f^{(r)}|$ and are a measure of the Rayleigh wave contribution to the meridional plane scattering. The extreme of both sets of curves lie close to the flat surface coupling angle $\theta_l=30.703°$ marked on the upper abscissa. The width of the Rayleigh wave feature indicates that the PWS plots in Figs. 3 and 4 are not highly dependent on γ. (b) The solid curve is the PWS for $|f-f^{(r)}|$ evaluated between 0° and 89°. The Rayleigh wave peak dominates the elastic response below 80°. The dotted curves in (a) and (b) are the ray approximation for that peak, Eq. (26).

only 0.08°. Small changes in γ from the value used in Figs. 3 and 4 cause only minor shifts in the PWS results plotted in the region of interest above $ka=50$. Since it is shown in Appendix A that c_l/c varies only slowly with ka in the region of interest, for the purpose of comparisons with the ray theory to be discussed, the tilt angle γ may be fixed at the asymptotic value of θ_l in the evaluation of the PWS as was done in Figs. 3 and 4. Another plot of $|f-f^{(r)}|$ was computed over the angular range from 0 to 89° in tilt to investigate the global behavior. *The Rayleigh peak shown in Fig. 5(b) is the only broad prominent peak* well separated from the diffractive structure at large γ. Consequently, the ray model developed here primarily concerns this mechanism and its contribution to the end-enhancement shown in Fig. 1. Helical wave contributions appear to be relatively weak for this cylinder.

II. INTEGRAL APPROXIMATION OF THE LEAKY WAVE SURFACE AMPLITUDE

The leaky wave surface amplitude for two-dimensional situations, where the local incident amplitude p_i varies only along one dimension, has been previously approximated as a

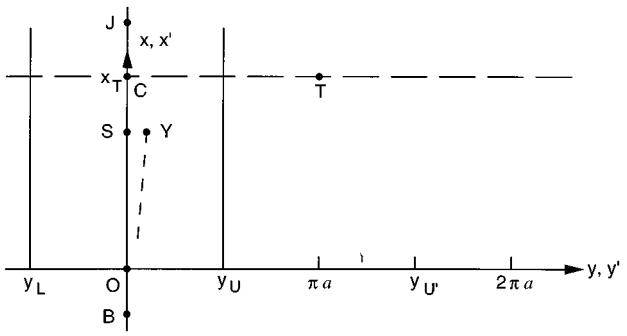

FIG. 6. Unwrapped Cartesian coordinates which cover the cylinder where the x axis is the meridian in the section of interest as in Fig. 2. That section is illuminated between the lateral coordinate y' of $-\pi a/2$ and $\pi a/2$. The launching points B are degenerate for S on the x axis when $\gamma=\theta_l$; B lies on the axis below S since the projection of the incident acoustic wave vector is taken to be vertical. Helical rays are excited for $\gamma<\theta_l$ as illustrated by the dashed line to a point Y displaced from the axis. In Sec. VII, the cylinder is taken to be truncated at x_T and the downward-directed leaky wave amplitude at S is approximated by considering the image J reflected about the truncation. $y_{U'}$ denotes the image of $y_U=\pi a/2$ reflected about the line at $y=\pi a$ where the dark side of the cylinder intersects the meridional plane. It denotes the left boundary of an illuminated strip, but the leaky wave excitation in that strip is unimportant near $y=0$ when $\gamma\approx\theta_l$.

one-dimensional convolution of p_i with a one-sided line response function.[11,12] Bertoni's analysis[11] is used in scanning acoustic microscopy to explain signatures for flat surfaces,[23] while the incorporation of the effects of weak curvature along the propagation direction[12] has facilitated the recovery of the coupling coefficient for leaky wave contributions to the scattering by cylinders[6–10,24–26] except for certain weak $O(1/k)$ phase corrections. For the situations shown in Figs. 1 and 2, it is necessary to incorporate the effect of *lateral curvature*. The following approximation[10] for the outgoing leaky wave surface amplitude p_l accounts for the leading effects of lateral curvature while recovering the previous results[11,12] in the absence of lateral curvature:

$$p_l(x,y)\approx\kappa\int_{-\infty}^{x}dx'\int_{-\infty}^{\infty}dy'\;p_i(x',y')H_0^{(1)}(k_p s), \qquad (3)$$

where s is the geodesic arc length between (x',y') and the surface point of interest (x,y), the phase of the local incident amplitude $p_i(x',y')$ depends on tilt and lateral curvature, and $k_p=k_l+i\alpha$ is the leaky wave pole of interest (see Appendix A). The surface coordinates (x,y) are the unwrapped cartesian coordinates which cover the cylinder as shown in Fig. 6 so that $s=[(x-x')^2+(y-y')^2]^{1/2}$. The domain of integration is restricted in (3) so as to approximate the physically relevant component of p_l for the situations of interest in Fig. 2: the leaky wave component propagating in the direction of increasing x. For the case of a solid cylinder or an evacuated shell, the coefficient may be approximated as[10]

$$\kappa\approx-\alpha k_l\exp(i\varphi_{bl}), \qquad (4)$$

where the background phase φ_{bl} is discussed in Appendices A and B. (For a sufficiently thin water-filled cylinder, where the fluid loading on each surface is symmetric, the magnitude of κ is decreased by one-half.[10,12] This is approximately the situation in Refs. 1 and 2.) Surface anisotropy of the

leaky wave phase velocity and damping rate are neglected in this formulation;[10] however, these corrections are anticipated to be small in the present application because of the dominant effect of the axially propagating component and because of the weak dependence on curvature discussed in Appendix A.

For plane-wave incidence on a tilted circular cylinder

$$p_i(x',y')=p_O e^{i\varphi_i},$$
$$\varphi_i=ka[1-\cos(y'/a)]\cos\ \gamma+kx'\ \sin\ \gamma,\quad y_L<y'<y_U, \tag{5}$$

where the origin O lies on the cylinder's surface in the meridional plane and $y_{U,L}=\pm\pi a/2$ denote the shadow boundaries of the illuminated strip shown in Fig. 6. There are other periodically illuminated strips having their symmetry axis shifted in y by integer multiples of $2\pi a$; however, phase considerations summarized in Sec. III indicate that those strips do not significantly contribute to the outgoing *meridional ray* amplitudes.

The limit of no lateral curvature corresponds to $ka\to\infty$ for the cylinder problems under consideration and p_i depends only on x'. The integration over y' may then be carried out using the integral[27]

$$\frac{i}{2}\int_{-\infty}^{\infty}H_0^{(1)}[k_p((x-x')^2+y'^2)^{1/2}]e^{i\xi y'}\,dy'$$
$$=(\xi^2-k_p^2)^{-1/2}e^{-(\xi^2-k_p^2)^{1/2}|x-x'|}, \tag{6}$$

with $-\alpha<\mathrm{Im}(\xi)<\alpha$. Application of (6) with $\xi=0$ and branches chosen as discussed in Ref. 27 reduces (3) to the previous[11,12] one-dimensional convolution.

It is helpful to identify regions of the integrand contributing significantly to (3) by replacing the Hankel function by its large argument form which gives

$$p_l(x,y)\approx\kappa(2/\pi)^{1/2}e^{-i\pi/4}p_O$$
$$\times\int_{-\infty}^{x}dx'\int_{y_L}^{y_U}dy'(k_ps)^{-1/2}e^{-\alpha s}e^{i(k_ls+\varphi_i)}. \tag{7}$$

For the situations of interest, $\alpha\ll k_l$. The Fermat paths correspond to $S'\equiv(x',y')$ for which the phase $k_ls+\varphi_i$ is stationary for a given surface point $S\equiv(x,y)$. Let such points S' be denoted by B. The path through B to S represents a ray to S. For the case of a cylinder tilted with $\gamma=\theta_l$ with S in the meridional plane so that $y=0$, the Fermat paths are degenerate and includes all $x'<x$ with $y'=0$. The integrals in (3) and (7) include the effect of the defective paths that are displaced from the Fermat path by superposing the leaky waves excited on the illuminated surface.

III. FRESNEL COUPLING PATCH FOR *S* IN THE MERIDIONAL PLANE

The Fresnel patch is bounded by the locus of defective paths where the phase defect in (7) has a magnitude of π relative to the ray (or set of rays) of interest.[13] The phase of the integrand varies relatively slowly for (x',y') within this patch so that identification of this patch is useful for identifying the regions which contribute significantly to $p_l(x,y)$ except in certain special cases.[10,12] Consider the situation of interest where the cylinder is tilted with $\gamma=\theta_l$ and S is in the meridional plane. The Fresnel patch is bounded by the locus: $k_ls+\varphi_i-k_l(x-x')-kx'\ \sin\ \gamma=\pi$. Figure 7 shows the numerical solutions of this locus. Figure 7 also shows the flat surface limit:[10] the parabola opening to the left given by the solid curve. For convenience, $x=0$ and a single value of $\theta_l=30°$ is used so as to illustrate the behavior typical of Rayleigh waves on solid metal cylinders. Figure 7 also shows two circular arcs having radii of k_l/α where Rayleigh waves on a stainless steel surface in contact with water gives the large circle and the small circle is for aluminum. The arcs are centered on (0,0) and they show the locus of coupling paths beyond which surface propagation to S attenuates the amplitude in excess of e^{-1}. Both Fermat paths and defective paths through surface points to the left of the respective arcs contribute relatively weakly to p_l because of attenuation.

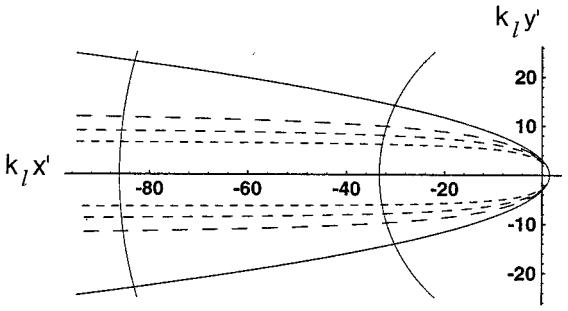

FIG. 7. The dashed curves show the boundaries of the Fresnel patches for a surface point at the origin on the meridional axis. The curves are for $ka=25$, 50, and 100 beginning in the order of increasing dash length. The cylinder has a tilt angle γ equal to the coupling angle θ_l (assumed for the purpose of this figure to be 30°) and the patches extend to infinity on the left. The left facing parabola is the flat surface ($ka=\infty$) limit of the Fresnel boundary. The comparison shows that decreasing ka causes the leaky wave excitation to be more localized near the meridional axis in the normalized units of this plot. The circular arcs have radii k_l/α of 85.8 and 33, corresponding to the parameters for stainless steel and aluminum cylinders in water. The radiation damping for points outside these arcs is appreciable for propagation to the origin. Consequently the physically significant coupling region is not determined entirely from the phase defect, and the region is smaller for aluminum than for stainless steel. Both metals have θ_l near 30°.

Figure 7 shows that as ka decreases, the Fresnel patch is confined to a strip around the meridian that grows narrow in the units shown. Furthermore, the boundaries of the illuminated region at $y'=y_{U,L}=\pm\pi a/2$ lie far outside the patches shown for all ka of interest. In the units of Fig. 7, these boundaries are at $k_ly_{U,L}=\pm\pi ka/4$ when $\theta_l=30°$. While the largest ka shown has $ka=100$, in the limit of $ka\to\infty$, the loci approach the parabola. For all cases shown, the loci are virtually unchanged if $[1-\cos(y'/a)]$ is replaced in φ_i by $(y'/a)^2/2$; the effect of this replacement is greatest for small ka.

The phase defect grows especially rapidly for meridional points to the right of the Fresnel loci in Fig. 7. This observation supports the truncation of the x' integration at x in (3) in the present case of a laterally curved surface. This limit of integration was derived for the flat surface case in Refs. 11 and 12 by contour methods.

The dashed line in Fig. 6 shows a section of a helical ray

to a point Y displaced from the meridional axis. Helical rays for a leaky wave of class l are present if $\gamma<\theta_l$, and they are excited in a Fresnel patch of finite area A_f. The calculation of A_f given in Ref. 10 shows that A_f diverges as γ approaches θ_l, which is to be expected since the area is infinite for the meridional ray patches shown in Fig. 7. The approximation for helical wave amplitudes given in Ref. 10 breaks down when the long dimension of the Fresnel patch greatly exceeds the attenuation distance α^{-1}. Therefore, the separate analysis of the meridional ray case given here is needed. It may also be shown that the illuminated regions shifted by integer multiples of $2\pi a$ from the meridional plane do not contribute significantly to the *meridional ray* amplitude at S though for $\gamma<\theta_l$ the shifted regions contribute to helical ray amplitudes not considered here.[10]

IV. APPROXIMATION OF THE LEAKY WAVE AMPLITUDE IN THE MERIDIONAL PLANE

The narrowness of the Fresnel patches shown in Fig. 7 indicates that the dominant contributions to p_l are from regions where the *paraxial approximation* $s\approx(x-x')[1+(y-y')^2/2(x-x')^2]$ may be used in the phase factor in (7). This is the approach shown here because the analysis is greatly simplified and may be modified to consider other cases. It is important to note, however, that the intermediate result, Eq. (10) below, has also been obtained by spectral methods directly from (3) and (5) by using (6) and the Fourier transform convolution theorem. (That method avoids the paraxial approximation but is longer.) In addition to the aforementioned paraxial phase approximation, the spreading factor $s^{-1/2}$ in (7) is replaced by $(x-x')^{-1/2}$. For future reference, $p_i(x',y')$ is generalized to allow for an x-dependent aperture or beam shading. These may be included in a factor $p'(x')$ so that $p_i(x',y')\approx p'(x')\exp(iky'^2/2a)$ where the phase dependence parabolic in y' is used as discussed in Sec. III. For the principal case of tilted plane-wave illumination $p'(x')=p_O\times\exp(ikx'\sin\gamma)$. In the paraxial approximation (7) becomes

$$p_l(x,y)\approx\kappa(2/\pi)^{1/2}e^{-i\pi/4}\int_{-\infty}^{x}p'(x')e^{ik_p(x-x')}I_y\,dx', \tag{8}$$

$$I_y=[k_p(x-x')]^{-1/2}e^{i(k/2a)(\cos\gamma)y^2}\times\int_{y''_L}^{y''_U}e^{-A_1y''^2}e^{iA_2y''^2}e^{iA_3y''}\,dy'', \tag{9a}$$

$$A_1=\frac{\alpha}{2(x-x')},\quad A_2=\frac{k\cos\gamma}{2a}+\frac{k_l}{2(x-x')}, \tag{9b}$$

where $A_3=(ky/a)\cos\gamma$ and $y''=y'-y$. Without loss of generality, the condition $y\geqslant 0$ may be assumed because of the symmetry about the meridional plane. Consequently, the coefficients A_j are real and non-negative. The limits of integration are $y''_{U,L}=y_{U,L}-y$. Inspection of (9) shows that the integral does not diverge if $y''_{U,L}$ are replaced by $\pm\infty$ as in the asymptotic evaluation summarized below. Evaluation of I_y with these modified limits by the following methods gives the same result: (i) stationary phase with a rotated contour of integration;[28] (ii) steepest decent,[29] (iii) application of tables.[28] In (iii), the asymptotic form of the complementary error function erfc is used.[28] The result is

$$I_y\approx e^{i\pi/4}e^{[iy^2k_p/2(\beta+x-x')]}\left[\frac{2\pi a/(k_pk\cos\gamma)}{\beta+x-x'}\right]^{1/2}, \tag{10}$$

$$\beta=k_pa/(k\cos\gamma)=(k_l+i\alpha)a/(k\cos\gamma). \tag{11}$$

In the case of uniform plane-wave illumination, (8) becomes

$$p_l(x,y)\approx\kappa(a/kk_p\cos\gamma)^{1/2}p_Oe^{ikx\sin\gamma}I, \tag{12}$$

$$I(\nu,\beta,\tau)=\int_0^\infty\{(\beta+q)^{-1/2}e^{-\tau/(\beta+q)}\}e^{-\nu q}\,dq, \tag{13}$$

$$\nu=\alpha+i(k\sin\gamma-k_l), \tag{14a}$$

$$\tau=y^2(\alpha-ik_l)/2, \tag{14b}$$

where $q=x-x'$ and I has the form of a Laplace transform of the quantity in brackets. For points in the meridional plane $y=0$ and I is evaluated with the substitution $u^2=\nu(\beta+q)$ provided $\alpha>0$ and $|\arg\beta|<\pi$, as in this problem. The result agrees with tables and is[30]

$$I(\nu,\beta,0)=(\pi/\nu)^{1/2}e^{\beta\nu}\,\mathrm{erfc}[(\beta\nu)^{1/2}],\qquad \mathrm{erfc}(w)=(2/\pi)^{1/2}\int_w^\infty e^{-u^2}\,du. \tag{15}$$

Consider the case where $\gamma=\theta_l$ so that $\nu=\alpha$. If (4) is used and $O(\alpha/k_l)$ phase corrections are omitted (which are weak for the applications of interest), (12) and (15) give

$$p_l(0,0)\approx-2p_Oe^{i\varphi_{bl}}F(\mu'), \tag{16a}$$

$$F(\mu')=(\pi\mu')^{1/2}e^{\mu'}\,\mathrm{erfc}(\mu'^{1/2}); \tag{16b}$$

$$\mu'=\mu(1+i\alpha/k_l), \tag{17a}$$

$$\mu=\alpha a\tan\theta_l. \tag{17b}$$

While the parameter μ is not large for high-frequency sonar applications of interest (e.g., $\mu\approx 0.18$ for stainless steel in water with $ka=50$), the asymptotic form of erfc is such that $|F|\to 1$ and $\mathrm{Arg}(F)\to 0$ as $\mu\to\infty$. For leaky Rayleigh waves, this gives the expected flat-surface limit for p_l which becomes the difference of the reflected and background amplitudes: $p_O[R(k_l)-\exp(i\varphi_{bl})]\approx-2p_O\exp(i\varphi_{bl})$. Here $R(k_l)$ is the reflection coefficient (see Appendix A) when the angle of incidence is θ_l and, from Eq. (A3) of Ref. 10, $R(k_l)\approx-\exp(i\varphi_{bl})$ when an $O(\alpha/k_l)$ phase correction is neglected. Numerical evaluation of $F(\mu')$ throughout the expected range of complex μ' shows that the errors in amplitude and phase are negligible if μ' is replaced by μ for typical leaky wave parameters of interest. For example, for a leaky Rayleigh wave on stainless steel, the magnitude error introduced is $<0.5\%$ while the phase error is $<0.000\,13$ rad. Figure 8 shows how the resulting simplified amplitude factor $F(\mu)$ approaches unity as μ increases. Replacing μ' by μ in F is equivalent to neglecting the term $i\alpha a/k\cos\gamma$ in (11).

The above approximation to $p_l(0,0)$ is for the outgoing leaky wave amplitude at the surface of the infinite cylinder shown in Fig. 2. To calculate the magnitude of the leaky

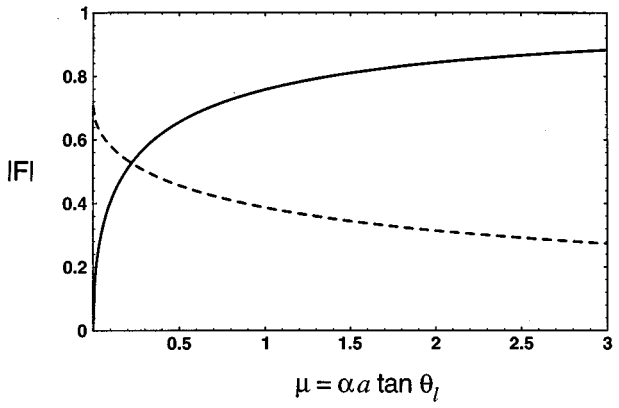

FIG. 8. The solid curve is the local surface amplitude factor $F(\mu)$ for points on the meridian of an infinite tilted cylinder. F is real, being proportional to a complementary error function of real argument, Eq. (16b). The abscissa μ is approximately linear in frequency for Rayleigh waves on cylinders since α/k is nearly constant in the ka range of interest. The dashed curve is the end-contribution backscattering-amplitude factor $F_e(\mu)$ used in the farfield calculation, Eq. (34).

wave contribution f_l to the form function f, a geometric spreading factor is introduced which depends on the curvature of the radiated leaky wavefront. While the analysis of that curvature is considered in Sec. V, a first approximation which recovers the appropriate flat surface limit is to approximate the curvature of the radiated leaky wavefront by that for a specularly reflected wave off of a rigid cylinder of radius a. Using that curvature (see Sec. VI) gives the approximation $|f_l| \approx 2F(\mu)$ which is plotted in Fig. 4 as the smooth dashed curve that is offset below the solid curve at large ka. The solid curve showing $|f-f^{(r)}|$ is expected to be a good approximation of the leaky wave contribution, so the comparison indicates that an improved approximation of the wavefront curvature is needed.

V. LEAKY WAVE AMPLITUDE ADJACENT TO THE MERIDIONAL PLANE

To find the curvature of the radiated leaky wavefront, the shift in the phase of the surface amplitude $p_l(x,y)$ is approximated for an infinitesimal displacement of y from zero. The required Laplace transform (13) is evaluated by first making the substitution $u^2=\nu(\beta+q)$ giving

$$I(\nu,\beta,\tau)=2\nu^{-1/2}e^{\beta\nu}\int_{(\beta\nu)^{1/2}}^{\infty}e^{-\tau\nu/u^2}e^{-u^2}\,du. \tag{18}$$

The substitution $u'=u+u^{-1}(\tau\nu)^{1/2}$ yields the following result in agreement with Eq. (7.4.33) of Ref. 28:

$$I=(\pi/\nu)^{1/2}e^{\beta\nu}[e^{2\sqrt{\tau\nu}}\ \mathrm{erfc}(\sqrt{\beta\nu}+\sqrt{\tau/\beta}) + e^{-2\sqrt{\tau\nu}}\ \mathrm{erfc}(\sqrt{\beta\nu}-\sqrt{\tau/\beta})]/2. \tag{19}$$

The effect of displacing the surface point S from the meridional plane was found by a Taylor expansion of I about $y=0$. The leading order terms were confirmed by symbolic manipulation with the programming language MATHEMATICA (®Wolfram Research, Inc.) with the following result:

$$I(\nu,\beta,\tau)/I(\nu,\beta,0)\approx 1-2\tau\nu[(1/F(\beta\nu))-1], \tag{20}$$

where F is evaluated with μ' in (16b) replaced by $\beta\nu$. For small y, the effects of this displacement may be approximated as an amplitude and phase factor $\exp(i\chi y^2)\approx 1+i\chi y^2$. Comparison with (14a) and (20) yields the following complex coefficient: $\chi(\nu,\beta,k_p)=k_p\nu[(1/F(\beta\nu))-1]$.

Consider the situation where the cylinder is tilted with $\gamma=\theta_l$. Inspection of the PWS plots of $|f-f^{(r)}|$ in Fig. 5 shows that the Rayleigh wave contribution to the scattering appears to be maximized at (or very near) this tilt. This is to be expected since the axial component of the incident wave vector matches the Rayleigh value in the limit of large ka. In Eq. (14a), $\nu=\alpha$, and χ is nearly real, being well approximated by $\chi(\alpha,a\ \tan\theta_l,k_l)=k_l\alpha[(1/F(\mu))-1]$ with μ given by (17b). Since this χ is positive definite, the phase fronts of the leaky wave on the cylinder at locations adjacent to the meridional plane are delayed relative to their meridional locations. While χ accounts for the wavefront curvature on the cylinder, there is an additional propagation contribution to the curvature of the radiated wavefront because of the lateral curvature of the radiating surface. A geometric construction summarized in Appendix B shows that there is an additional phase shift in a reference plane $(\overline{x,y})$ tangent to the radiated wavefront at the meridional plane. This propagation phase shift introduces the phase factor $\exp(ik\overline{y}^2\cos\theta_l/2a)$, where $\overline{y}$ denotes the displacement in this orthogonal reference plane from the intersection with the meridional plane. Combining this with the phase dependence on the cylinder gives the following curvature of the radiated acoustic wavefront:

$$\rho_l^{-1}=(\cos\ \theta_l)\{1+2\mu[(1/F(\mu))-1]\}/a, \tag{21}$$

where ρ_l is the radius of curvature of the radiated wavefront at the cylinder's surface and the combined aforementioned phase factor is $\exp(ik\overline{y}^2/2\rho_l)$.

VI. SYNTHESIZED FORM FUNCTION OF THE INFINITE CYLINDER AND DISCUSSION

Let ρ_S denote the radius of the wavefront specularly reflected from a cylinder and evaluated in the meridional plane at the surface of the cylinder. Geometry [e.g., Appendix B and Eq. (67) of Ref. 25] gives

$$\rho_S(\gamma)=a/(2\cos\ \gamma), \tag{22}$$

where γ denotes the cylinder's tilt angle. In the limit $\mu\to\infty$, ρ_l from (21) approaches $\rho_S(\theta_l)$. The resulting form function contribution in this limit was noted in Sec. IV in the discussion of Eq. (16). As shown in Fig. 2, the outgoing leaky wave is radiated at an angle θ_l in the meridional plane. The spreading factor for far-field propagation is calculated as discussed, e.g., in Ref. 25 with the result that the contribution to the form function f in (1) is related to the pressure p_l of the outgoing wavefront by

$$|f_l|=|p_l(0,0)/p_O|(2\rho_l\cos\ \theta_l/a)^{1/2}, \tag{23}$$

where p_{i0} in (1) and p_O in (5) and (23) differ only by a geometric phase factor. Combined with (16) and (21), the contribution for $\gamma=\theta_l$ becomes

$$|f_l(\gamma=\theta_l)|\approx 2^{3/2}F(\mu)\{1+2\mu[(1/F(\mu))-1]\}^{-1/2}. \tag{24}$$

The curve with the longest dashes in Fig. 4 shows the resulting $|f_l|$ where μ is calculated from (17b) with α and θ_l fixed at the asymptotic values noted in Appendix A. The agreement with the PWS result is improved in comparison with the approximation $|f_l| \approx 2F(\mu)$ discussed below Eq. (16) where in (23), ρ_l is replaced by the specular value $\rho_S(\theta_l)$. The curve with the shortest dashes in Fig. 4 is given by (24) where in the evaluation of μ the value of α/k is varied with ka (as shown in Fig. A1) for the axisymmetric leaky mode. α/k is peaked near $ka=6$ (as shown in Fig. A1). The resulting modified structure parallels the PWS results with an offset. The comparison on the left is only qualitative, however, because at low ka the rigid background assumed in $|f - f^{(r)}|$ may not adequately describe the background contribution. Both of the results based on (24) recover the general behavior of $|f-f^{(r)}|$ in the ka region of interest for high-frequency sonar applications.

The ray approximation to f is given by including the specular background contribution f_S and approximating the phase as discussed in Appendix B. The geometric approximation of $|f_S|$ is calculated as in (23) with the result $|f_S| \approx 1$. The combined result gives the magnitude

$$|f_{\text{ray}}| \approx |[1-|f_l|\exp(i\varphi_{bl})]|, \tag{25}$$

where $\varphi_{bl} \approx 0.106$ rad as found in Appendix A from the stainless steel/water flat interface limit. The curves with long and short dashes in Fig. 3 show $|f_{\text{ray}}|$ with α fixed or variable in the evaluation of μ in (24) as discussed for Fig. 4. The comparison confirms that both approaches capture the smooth rise of $|f|$ in the high-frequency region. The result for variable α/k, the curve with short dashes, has an abrupt rise near ka of 10 which parallels a corresponding feature in the exact $|f|$. For the purpose of evaluating the leaky wave approximation, the comparison on the left is again only qualitative because of the geometric approximation used for f_S. The comparison suggests, however, that a peak in the radiation damping contributes to the broad peak in $|f|$ by suppressing the destructive interference of the Rayleigh wave contribution.

Approximations (24) and (25) appear to remain accurate *beyond the highest ka of interest in sonar applications*. At $ka=200$ they differ by less than 0.7% and 1% from the PWS values, respectively, where the PWS values are $|f|=0.60$ and $|f-f^{(r)}|=1.58$.

While a uniform analysis of the dependence of $|f_l|$ on the tilt γ is outside the scope of this paper, a combination of results from Secs. IV and V gives a simple approximation. In this result the wavefront curvature is approximated by the value for $\gamma=\theta_l$ from (21), while the amplitude factor is given by replacing $I(\alpha,k_la/(k\cos\theta_l),0)$ by $I(\nu,k_la/(k\times\cos\gamma),0)$. The result is

$$|f_l(\gamma)| \approx 2^{3/2}|(\alpha/\nu)F(\mu'')|\{1+2\mu[(1/F(\mu))-1]\}^{-1/2}, \tag{26a}$$

$$\mu'' = \mu(\cos\theta_l/\cos\gamma)[1+i(k\sin\gamma - k_l)/\alpha], \tag{26b}$$

and gives the curves plotted as points in Fig. 5 for ka of 50 and 100. The values for α/k and θ_l used in (14a) and (17b) are the flat-surface values. This simplified ray model is seen to predict the approximate location and width of the peak in the PWS for $|f-f^{(r)}|$. When $\gamma \neq \theta_l$, ν and μ'' become complex because of the dephasing of the leaky wave relative to the incident wave.

Comparisons between PWS results and the ray approximation for the ka dependence of $|f|$ and $|f-f^{(r)}|$ similar to Figs. 3 and 4 were evaluated for an aluminum cylinder in water. The PWS result for $|f|$ reproduced the corresponding plot in Fig. 3 of Ref. 4 and was evaluated up to $ka=400$ from the maximum ka of 15 shown in Ref. 4. Since the agreement with ray theory is similar to the results shown here for stainless steel in water, it is appropriate to comment on a point of interpretation noted in Ref. 4. The values obtained for $|f|$ were small (generally <0.2) for ka from 11 to the maximum ka shown in Ref. 4. (This feature corresponds roughly to the minimum in $|f|$ near ka of 13 in Fig. 3 of the present paper.) Flax *et al.* interpreted that feature the small value of $|f|$ as extending to large ka ''as consistent with a backscattered field made up of the destructive interference between specular reflection and radiation from an axially generated Rayleigh surface wave.'' While the assertion that leaky wave and specular contributions interfere destructively is correct, as evident, e.g., in the form of Eq. (25), the proper limit as $ka \to \infty$ is that $|f| \approx 1$ when $\gamma = \theta_l$. This limit is consistent with the $ka \to \infty$ limit for the total outgoing amplitude at the interface of $p_O R(k_l)$ [where R is the reflectivity as noted below Eq. (17)]. Note that $|R(k_l)|=1$ because the angle of incidence exceeds the shear wave critical angle. It is anticipated that for very large ka there is a phase offset in the specular contribution which would cancel the $\exp(i\varphi_{bl})$ factor in (25) such that $|f| \to 1$. Taking φ_{bl} as a constant in (25) while neglecting any specular phase offset is an approximation. See also the discussion of phase in Appendix B. The specular interference is not important in the application considered below.

VII. MERIDIONAL BACKSCATTERING ENHANCEMENTS FROM ENDS AND TRUNCATIONS

While the agreement is not perfect between PWS and ray theory comparisons shown in Figs. 3–5, the accuracy of the ray theory in the ka region of high-frequency sonar systems is adequate for the purpose of estimating the strength of echoes due to leaky waves. A natural extension of the analysis given in Secs. IV and V that illustrates the simplicity of applying this formulation is the *reflected* meridional ray shown in Fig. 1. The goal of this section is to estimate the far-field scattering amplitude of such contributions when the cylinder is tilted at θ_l and the contribution is isolated from other mechanisms. The existence of such dominant isolated contributions is consistent with the high-frequency experimental[1] and computational[2] results for thick shells. The numerical results given here are limited to the case of a stainless steel cylinder with the end cut at right angles relative to the axis as shown in Fig. 1. An important result is that the meridional leaky wave backscattering can significantly exceed the magnitude of the specular reflection from a rigid *sphere* having the same radius as the cylinder.

In the approximation given below of the leaky wave amplitude from the right end in Fig. 1, it is assumed that the length L of the cylinder is sufficiently large that the cylinder

can be modeled as semi-infinite. This assumption is applicable if $\alpha L \gg 1$ where α is the leaky wave attenuation rate. While only the case of steady-state scattering is modeled, for weakly dispersive leaky waves the analysis may be easily modified to approximate the evolution of the scattering amplitude for an incident tone burst of finite duration. For many high-frequency sonar applications, the value of α found for leaky Lamb or Rayleigh waves of interest can be sufficiently large that the assumption $\alpha L \gg 1$ does not overly restrict L in situations where the assumption $\alpha/k_l \ll 1$ remains applicable. The assumption $\alpha L \gg 1$ may be relaxed by truncating the upper limit of integration in Eq. (27), which has the effect of introducing a second term if only the lowest-order end correction is required. If αL is not large, it may be necessary to sum the infinite series of repeated contributions of the leaky wave reflections from each end.

The amplitude of the reflected leaky wave is approximated by modifying the analysis in Sec. IV and by introducing a effective end-reflection coefficient. The end of the cylinder is shown as the dashed line at x_T in Fig. 6, and the point J beyond the end on the meridional axis corresponds to an image of the surface point of interest S. Upward-directed meridional rays in the image space correspond to the downward-directed waves in the physical space that radiate back toward the source as shown in Fig. 1. Consider first the unphysical situation where the end reflection introduces no reduction in amplitude or shift in phase. The image amplitude at $x_J > x_T$ is given by (8) with the upper limit of integration replaced by x_T. This reduces to (12) with $I(\nu,\beta,\tau)$ replaced by

$$K(\nu,\beta,\tau,\eta) = \int_\eta^\infty \{(\beta+q)^{-1/2} e^{-\tau/(\beta+q)}\} e^{-\nu q}\, dq = e^{-\nu\eta} I(\nu,\beta+\eta,\tau), \tag{27}$$

where $\eta = x_J - x_T \geqslant 0$ and y in (14b) becomes the displacement of J from the meridional axis. The second expression follows by substituting $q = u + \eta$ in the integral. Consequently, (15) and (19) with β replaced by $\beta+\eta$ may be used in the evaluation of K. The dependence on y that follows from (20) is

$$K(\nu,\beta,\tau,\eta)/K(\nu,\beta,0,\eta) \approx 1 - 2\tau\nu[(1/F(\beta\nu+\eta\nu)) - 1], \tag{28}$$

and the χ coefficient is replaced by $\chi(\nu,\beta+\eta,k_p)$. Restricting attention to the case $\gamma = \theta_l$ gives $\nu = \alpha$ and the curvature of the radiated acoustic wavefront, Eq. (21), becomes

$$\rho_l^{-1}(\eta) = (\cos\,\theta_l)\{1 + 2\mu[(1/F(\mu+\alpha\eta)) - 1]\}/a. \tag{29}$$

The amplitude p_l of the outgoing wave on the surface of the cylinder is approximated by introducing a leaky wave reflection coefficient B evaluated at normal incidence. The leaky waves that expand from an illuminated surface point and reflect from the edge do not all have the same angle of incidence; however, in the modified Eq. (9), the reflection coefficient is taken to be a slowly varying function in the paraxial approximation such that it may be evaluated at the stationary phase condition which, for $y = 0$, corresponds to perpendicular incidence. The edge contribution which replaces (16) is

$$p_l(\eta,y) \approx -2Bp_C e^{i\varphi_{bl}} e^{ik_l\eta} e^{i\chi y^2} (\pi\mu)^{1/2} e^{\mu} \times \mathrm{erfc}[(\mu+\alpha\eta)^{1/2}] H(\eta), \tag{30}$$

with $\chi = \chi(\alpha, \eta + a\,\tan\theta_l, k_l)$ as defined below (20) and p_C is the incident amplitude phase referenced to the intersection of the meridional axis with the cylinder's end at point C in Figs. 1 and 6. The step function $H(\eta)$ vanishes for $\eta < 0$ and is unity for $\eta \geqslant 0$. Any contribution to χ resulting from the dependence of the phase of B on the angle of incidence of a surface wave is assumed to be negligible. The amplitude in a reference plane $(\overline{x,y})$ now tangential to the *cylinder* at C is approximated as in the discussion of (21) to be

$$\overline{p_l}(\overline{x},\overline{y}) \approx -2Bp_C e^{i\varphi_{bl}} e^{ik_l\overline{x}} e^{ik\overline{y}^2/2\rho_l} (\pi\mu)^{1/2} e^{\mu} \times \mathrm{erfc}[(\mu+\alpha\overline{x})^{1/2}] H(\overline{x}), \tag{31}$$

where $\overline{x} = \eta$, $\overline{y}$ is the displacement perpendicular to the meridional plane, and the $\overline{z}$ axis is perpendicular to the meridian; the effective aperture due to the end of the cylinder is approximated to lie on the $\overline{y}$ axis. As $\overline{x}$ increases, $|\overline{p_l}(\overline{x},0)|$ decreases because the surface wave decays in amplitude after reflection at C. In the meridional plane $\overline{y} = 0$ and the Gaussian curvature of the radiated wavefront vanishes, which enhances the farfield amplitude.[25] The far-field backscattering amplitude at a distance R_C from C becomes [see, e.g., Eq. (6) of Ref. 25]

$$p_{l\mathrm{sca}} \approx -ik\,\frac{e^{ikR_C}}{2\pi R_C}\cos\gamma \int_0^\infty d\overline{x} \int_{-\infty}^\infty d\overline{y}\,\overline{p_l}(\overline{x},\overline{y}) \times \exp(-ik\overline{x}\sin\gamma). \tag{32}$$

Since $\gamma = \theta_l$, the integral is proportional to:

$$I_{\overline{xy}} = \int_0^\infty d\overline{x} \int_{-\infty}^\infty d\overline{y}\, e^{ik\overline{y}^2/2\rho_l}\,\mathrm{erfc}[(\mu+\alpha\overline{x})^{1/2}], \tag{33}$$

where ρ_l depends on $\overline{x} = \eta$ as noted above. Though this integral does not appear reducible, the following approximation simplifies its evaluation. Numerical evaluation of the curvature $\rho_l^{-1}(\eta)$ in (29) shows that the curvature decreases slowly with the distance η of the launching point from the end of the cylinder. For example, $\rho_l^{-1}(\eta)/\rho_l^{-1}(0) \approx 0.80$ and 0.70 for $\eta = \alpha^{-1}$ and $10\,\alpha^{-1}$, respectively. Consequently replacing $\rho_l(\eta)$ by the result in (21), $\rho_l(0)$, gives an approximation for $I_{\overline{xy}}$ that should be sufficiently accurate for most sonar applications. The approximated $|I_{\overline{xy}}|$ is less than the true magnitude. The resulting integral may be factored as $I_{\overline{x}} I_{\overline{y}}$ where $I_{\overline{y}}$ is evaluated by a stationary phase integration over $\overline{y}$ and $I_{\overline{x}}$ is evaluated by numerical integration. The final result for $p_{l\mathrm{sca}}$ may be expressed in terms of a form function f_{ls} for backscattering by a *sphere* of radius a at a distance R_c through the usual normalization[25] $p_{\mathrm{sca}} = (p_C f_{ls} a/2R_C)\,\exp(ikR_C)$. The result is

$$f_{ls} \approx -e^{-i\pi/4} e^{i\varphi_{bl}} [2B(k_l/\alpha)^{1/2}]\, F_e, \tag{34}$$

$$F_e(\mu) = F_\rho e^{\mu} \int_\mu^\infty \mathrm{erfc}(\sqrt{w})\, dw, \tag{35a}$$

$$F_\rho(\mu) = (\rho_l(0)/\rho_S)^{1/2} = \{[\mu/F(\mu)] - \mu + 1/2\}^{-1/2}, \tag{35b}$$

where $\rho_S = a/(2\cos\theta_l)$ and F_ρ corresponds to a curvature correction to the scattering amplitude that is typically only slightly greater than unity; $F_\rho(\infty)=1$. Figure 8 includes a plot of the edge contribution factor $F_e(\mu)$ obtained by numerical evaluation of the integral.

The bracketed factors in (34) are estimated to give 6.3 for the case of Rayleigh waves on a stainless steel cylinder so that $|f_{ls}|$ is significantly larger than unity over a broad range of ka. For example, $ka=50$ and 100 give $|f_{ls}|\approx 3.4$ and 3.1, respectively, with $|f_{ls}|$ decreasing slowly with increasing ka (and hence with increasing μ) according to Fig. 8. In this estimate the flat surface values for α and k_l were used giving $(k_l/\alpha)^{1/2}=9.3$. The approximation $|B|\approx 0.34$ is used from Gautesen's analysis[14] for normally incident reflection of a Rayleigh wave from an elastic corner in a vacuum, so that any effects of fluid loading on $|B|$ have been neglected. The loading correction is expected to be small at high ka because of the relatively large density of the solid. For normal incidence Gautesen's analysis gives $\arg(B)\approx 0.8$ rad.

The elastic scattering contribution of the leaky Rayleigh wave that is transmitted around the corner at point C in Fig. 1 has been neglected. Depending on the specific properties of the end of the cylinder, that transmitted wave may propagate across the end and partially reflect from the corner at T. The resulting partially reflected wave will be partially transmitted around the corner at C, giving rise to a radiated wavefront that is directed back toward the source as in the primary mechanism under consideration. At high ka, that backscattering contribution will be significantly reduced in magnitude for several reasons including: (i) the partial transmission and reflection at each corner; (ii) a propagation loss $\approx\exp(-4\alpha a)$ due to crossing the diameter twice; and (iii) curvature of the wavefront of the Rayleigh wave introduced upon reflection or transmission from each curved corner that contributes additional curvature to the final radiated acoustic wavefront. Of course there is an infinite series of contributions due to the repeated reverberations across the end between points C and T in Fig. 1, but the terms are complicated by combined propagation and spreading factors as in the case of reverberation across the thickness of a shell (Sec. 4.11 of Ref. 25). Other elastic contributions which have been neglected in this analysis include: (i) the partial mode conversion of Rayleigh waves to elastic longitudinal and shear waves upon reflection at the corner;[14–16] and (ii) radiation from any pistonlike motion at the end of the cylinder excited by the elastic waves propagating to the end of the cylinder.[31] It may be argued that both of these mechanisms should give *insignificant backscattering* contributions at high ka for an obliquely tilted cylinder in comparison to the mechanism in Fig. 1 when $\gamma\approx\theta_l$. Acoustic illumination of the edge at the cylinder's end can also excite leaky waves as discussed for example in Ref. 10 for the case of edge-excited helical waves. That mechanism has been neglected in the above analysis and is anticipated to be weaker than the meridional ray mechanism considered for backscattering for the geometry under consideration.

For the case of the elastic response of a hollow circular cylinder due to the high-frequency generalization of leaky Lamb waves,[1,2] the coefficient in brackets in Eq. (34) should also be sufficiently large for the resulting backscattering contribution diagrammed in Fig. 1 to be of significant magnitude. If the cylinder is filled with water and is sufficiently thin that the fluid loading on each side is symmetric, then the expression for $|\kappa|$ is reduced by a factor of 2 as noted below Eq. (4) and the factor in brackets in (34) is also reduced by a factor of 2. For both the solid and hollow cylinder cases, the meridional ray backscattering enhancement is significantly localized in tilt angle γ near the θ_l of the relevant leaky wave. This qualitative experimental result from Ref. 1 is consistent with the quantitative results for the Rayleigh meridional ray amplitude from an infinite cylinder shown in Fig. 5. The corresponding end contribution, predicted to have a peak magnitude given by (34), should be *at least as localized in angle* because of a similar angular dependence of the excitation factor, Eq. (27), as well as a related angular dependence of a reradiation factor expected from reciprocity. Minor modifications of (34) make it feasible to approximate reductions in f_{ls} due to structural damping. In both the solid and hollow cylinder cases, the meridional ray mechanism considered here is significantly stronger for $\gamma\approx\theta_l$ than are the end-contributions to high ka backscattering estimated for an obliquely tilted *rigid* cylinder as predicted, e.g., by GTD or other methods (e.g., Sec. 2.12 of Ref. 25, Ref. 32, and references cited therein). The rigid cylinder form function contribution for this geometry may be shown to decrease as $(ka)^{-1/2}$, where the normalization noted above Eq. (34) is used for the scaling of the far-field amplitude.

ACKNOWLEDGMENTS

This research was supported by the Office of Naval Research. I am grateful for M. J. Marr-Lyon for assisting with the very high-frequency PWS calculation for an aluminum cylinder mentioned in Sec. VI.

APPENDIX A: LEAKY RAYLEIGH WAVE PROPERTIES AND THE PWS

Let R denote the acoustic amplitude reflectance considered as a function of the complex horizontal component of the incident wave vector k_x for an isotropic elastic half-space as given, e.g., by Bertoni.[11] The Rayleigh wave pole of $R(k_x)$ at $k_x=k_l+i\alpha$ was determined numerically giving the following limiting values for a flat interface: $k_l/k=0.5106$, $\alpha/k=0.005\,92$, and $\alpha/k_l=0.0116$. The coefficient κ in (4) also depends on[10] $\varphi_{bl}=\arg(R_0(k_l))$, where R_0 is related to R by[10]

$$R_0(k_l)=-R(k_l)\left(\frac{2k_l+i\alpha}{2k_l-i\alpha}\right)=-R(k_l)e^{i2\tan^{-1}(\alpha/2k_l)}. \tag{A1}$$

Numerical evaluation gives $\varphi_{bl}=0.106$ rad for the leaky Rayleigh pole for the system shown in Table I.

The weak dependence of the leaky Rayleigh wave parameters on curvature for the ka region of interest was confirmed as follows. The denominator D_n of the nth partial wave of the series in Eq. (2) may be written as a function of the axial wave number k_x by defining

$$x_r=[(ka)^2-(k_xa)^2]^{1/2} \tag{A2a}$$

$$x_L=[(k_xa)^2-(kac/c_L)^2]^{1/2}, \tag{A2b}$$

$$x_T=[(kac/c_T)^2-(k_xa)]^{1/2}, \tag{A2c}$$

$x_x = k_xa$, and taking $D_n(ka,k_xa)$ to be the determinant of d_{ij} where $d_{ij}=0$ except for

$$\begin{aligned}
&d_{11}=\rho(kac/c_T)^2H_n^{(1)}(x_r), \quad d_{21}=-\rho_E x_r H_n^{(1)\prime}(x_r),\\
&d_{12}=[(kac/c_T)^2-2x_x^2-2n^2]I_n(x_L)+2x_LI_n'(x_L),\\
&d_{22}=-x_LI_n'(x_L), \quad d_{32}=2n[x_LI_n'(x_L)-I_n(x_L)],\\
&d_{42}=-2x_x^2x_LI_n'(x_L), \quad d_{23}=x_TJ_n'(x_T),\\
&d_{13}=2[-x_T^2J_n(x_T)+n^2J_n(x_T)-x_TJ_n'(x_T)],\\
&d_{33}=2n[-x_TJ_n'(x_T)+J_n(x_T)],\\
&d_{43}=x_T[-x_T^2J_n'(x_T)+(k_xa)^2J_n'(x_T)],\\
&d_{14}=2n[x_TJ_n'(x_T)-J_n(x_T)], \quad d_{24}=nJ_n(x_T),\\
&d_{34}=x_T^2J_n(x_T)-2n^2J_n(x_T)+2x_TJ_n'(x_T),\\
&d_{44}=n(k_xa)^2J_n(x_T),
\end{aligned} \tag{A3}$$

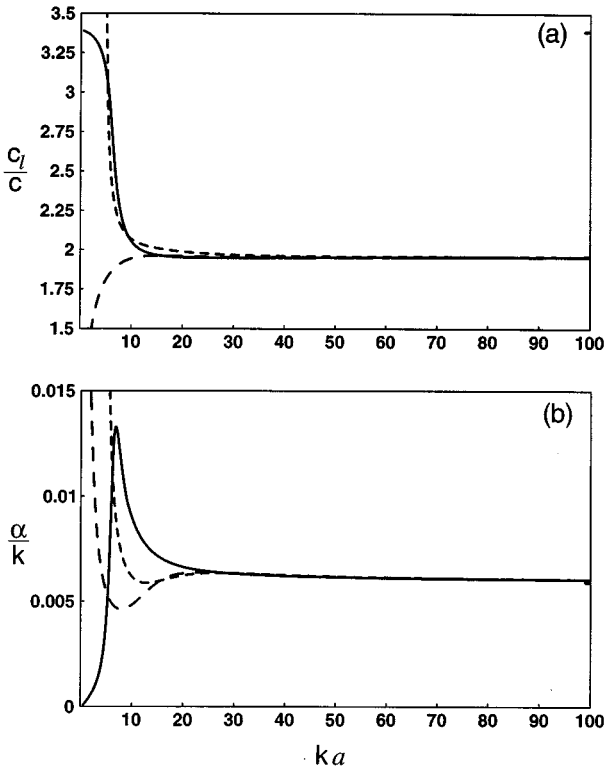

FIG. A1. (a) Phase velocity ratio c_l/c and (b) ratio of the axial damping rate to the acoustic wave number are shown for the fundamental $n=0,1$, and 2 modes of a stainless steel cylinder in water as the solid, medium-dashed, and short-dashed curves, respectively. A lower tick mark on the left of (a) meets the curves and shows the Rayleigh wave velocity ratio $c_R/c=1.958$ for a flat surface in contact with water. The upper-left tick mark in (a) at $c_l/c=3.39$ corresponds to the bar wave velocity c_b. The tick mark on the left of (b), slightly below the curve, shows α/k for a flat surface. Notice that throughout the ka region of interest (which typically exceeds $ka=50$), α/k and c_l/c are nearly constant, and they are similar for the different modes. The $n=1$ mode is a bending mode of the cylinder so that c_l decreases at low frequencies.

where ρ and ρ_E are the densities of water and the elastic solid, respectively, and c_L and c_T denote longitudinal and transverse velocities of the elastic material. Here I_n denotes the modified Bessel function and primes denote differentiation with respect to the indicated argument. In the evaluation of the PWS in (2), $k_x=k\sin\gamma$ and the d_{ij} are shown for the case $c/c_L<\sin\gamma<c/c_T$. Outside this range the expressions are modified as has been noted by others.[19,20] If $\sin\gamma>c/c_T$, the $J_n(x_T)$ and $J_n'(x_T)$ are replaced by $I_n(x_T)$ and $I_n'(x_T)$ except in the leftmost terms of d_{13}, d_{43}, and d_{34} where the replacements $-I_n(x_T)$ and $-I_n'(x_T)$ are used. To evaluate the leaky mode properties for the fluid loaded cylinder, a simpler procedure is used. The leaky mode properties are given by solving $D_n(ka,k_xa)=0$ for k_xa where ka is given and the index n describes the azimuthal deformation of the mode. The resulting $k_x=k_l+i\alpha$ gives the leaky mode properties k_l and α. The sequence is to first determine k_l and α when ka is large (typically 100) by using the flat interface Rayleigh pole as an initial estimate for k_x. The evolution of the root is followed by decreasing ka where the k_x root from the adjacent ka value is used as an estimate. Figure A1 shows the resulting values of $c_l/c=k/k_l$ and α/k for the fundamental $n=0$, 1, and 2 modes. At $ka=100$, c_l/c and α/k are close to the flat surface values. As $ka\to0$, c_l for the $n=0$ mode, the axisymmetric mode, approaches the bar wave phase velocity $c_b=(E/\rho_E)^{1/2}$, where E is Young's modulus. As $ka\to\infty$, c_l for $n=0$ approaches the flat surface leaky Rayleigh value from below since there is a shallow minimum near $ka=28.3$ for this system. This minimum is known to be present even in the absence of fluid loading.[33] The c_l/c curves are similar to ones shown by Hackman[31] for an aluminum cylinder, where the modes are designated $L(0,1)$, $F(1,1)$, and $F(2,1)$ for the $n=0$, 1, and 2 cases shown. The behavior of α/k has not been investigated as often by others. The meridional *leaky wave* excited as described in Secs. IV–VII is actually a *superposition of leaky cylinder modes* having different values of n but similar c_l/c and α. This similarity and the weak dependence on ka support the assumption of *isotropic leaky wave properties* implicit in the form of Eq. (3). At small values of ka the properties cease to be similar which contributes to the breakdown of the ray analysis when ka is not large. The effects of lateral curvature appear to be weaker than for curvature along the propagation direction.[34]

In the evaluation of Eq. (2), B_n is the determinant of b_{ij} where

$$b_{11}=\rho(kac/c_T)^2J_n(x_r), \quad b_{21}=-\rho_E x_rJ_n'(x_r),$$

and the other b_{ij} are the d_{ij} as explained above.

APPENDIX B: PROPAGATION PHASE SHIFTS AND SPECULAR REFLECTION

The purpose of this Appendix is to explain some of the phase shifts introduced in Secs. V–VII and to give mutual phase factors in the synthesis that may be needed for other purposes. Consider first the case of specular reflection from a rigid cylinder. From Eq. (5) the phase at surface points with $x'=0$ is $\varphi_i\approx ky'^2\cos\gamma/2a$. Consider a reference plane tangent to the reflected wavefront at the meridian. The addi-

tional propagation phase shift to reach that plane from a surface point at y' is φ_i to $O(y'^2)$. If $\overline{y}$ denotes the transverse coordinate, the amplitude of the reflected wave in this plane, the $(\overline{x},\overline{y})$ plane in Fig. 2, becomes $\overline{p}_{\text{rigid}} \approx p_O \exp(ik\overline{y}^2/2\rho_S)$, where ρ_S is given by (22). The spreading factor and phase shift for propagation to a far-field observer in the meridional plane are calculated geometrically since it assumed that $k\rho_S \gg 1$. When the result is compared with (1) and the phase difference between p_O (on the surface) and p_{io} (on the cylinder's axis) is accounted for, the geometrically approximated rigid cylinder form function in the meridional plane is given as

$$f_g^{(r)}(\gamma) \approx e^{i\varphi_r}, \tag{B1a}$$

$$\varphi_r(\gamma) = -2ka\cos\gamma. \tag{B1b}$$

This was confirmed by evaluating the PWS for a rigid cylinder for large ka for the case of interest which is $\gamma = \theta_l$. It was found that (B1) has an $O(1/ka)$ phase error that may be neglected in the ka region of interest. Repeating this procedure for the leaky wave contribution for an infinite cylinder with $\gamma = \theta_l$ gives the phase factors in Eqs. (24) and (25) with the result: $f_l \approx -|f_l|\exp[i\varphi_{bl} + i\varphi_r(\theta_l)]$ and $f_{\text{ray}} \approx f_g^{(r)}(\theta_l) + f_l$. Order $(1/ka)$ phase corrections have been neglected.

In the ka region of interest between 50 and 100, there is computational evidence that the specular contribution is better approximated by (B1) than if it includes an additional background phase shift φ_{bl} as expected for the flat surface limit.[10] The following magnitudes are computed from the PWS: $|f|$, $|f - f^{(r)}|$, and $|f^{(r)}|$. While $|f^{(r)}|$ is always very close to unity, it is found that $(|f| + |f^{(r)}|) > |f - f^{(r)}|$. Consequently, it is not possible to have $f = f^{(r)} + f_l$ with f_l having a π phase shift relative to $f^{(r)}$. The extra phase increment inferred is close to the magnitude of φ_{bl} used in the evaluation of (25) that was found in Appendix A. The flat-surface limit for the sum of the leaky and specular amplitudes, evaluated as described below Eq. (17), is consistent with the corresponding wide beam limit from Ref. 35.

[1] G. Kaduchak, C. M. Wassmuth, and C. M. Loeffler, ''Elastic wave contributions in high resolution acoustic images of fluid-filled finite cylindrical shells in water,'' J. Acoust. Soc. Am. **100**, 64–71 (1996).

[2] S. S. Dodd, ''Sonar imaging of elastic fluid-filled cylindrical shells,'' Ph.D. thesis, University of Texas at Austin, 1995.

[3] D. Marcuse, *Principles of Optical Fiber Measurements* (Academic, New York, 1981).

[4] L. Flax, V. K. Varadan, and V. V. Varadan, ''Scattering of an obliquely incident acoustic wave by an infinite cylinder,'' J. Acoust. Soc. Am. **68**, 1823–1835 (1980).

[5] F. Léon, F. Lecroq, D. Décultot, and G. Maze, ''Scattering of an obliquely incident acoustic wave by an infinite hollow cylindrical shell,'' J. Acoust. Soc. Am. **91**, 1388–1397 (1992).

[6] L. B. Felsen, J. M. Ho, and I. T. Lu, ''Three-dimensional Green's function for fluid-loaded thin elastic cylindrical shell: Alternative representations and ray acoustic forms,'' J. Acoust. Soc. Am. **87**, 554–569 (1990); **89**, 1463–1464 (1991).

[7] J. M. Ho, ''Acoustic scattering by submerged elastic cylindrical shells: Uniform ray asymptotics,'' J. Acoust. Soc. Am. **94**, 2936–2946 (1993).

[8] M. L. Rumerman, ''Application of the Sommerfeld–Watson transformation to scattering of acoustic waves obliquely incident upon cylindrical shells,'' J. Acoust. Soc. Am. **91**, 2503–2509 (1992).

[9] A. N. Norris and D. A. Rebinsky, ''Acoustic coupling to membrane waves on elastic shells,'' J. Acoust. Soc. Am. **95**, 1809–1829 (1994).

[10] P. L. Marston, ''Spatial approximation of leaky wave surface amplitudes for three-dimensional high-frequency scattering: Fresnel patches and application to edge-excited and regular helical waves on cylinders,'' J. Acoust. Soc. Am. (to be published).

[11] H. L. Bertoni, ''Ray-Optical Evaluation of $V(z)$ in the Reflection Acoustic Microscope,'' IEEE Trans. Sonics Ultrason. **SU-31**, 105–116 (1984).

[12] P. L. Marston, ''Leaky waves on weakly curved scatterers. II. Convolution formulation for two-dimensional high-frequency scattering,'' J. Acoust. Soc. Am. **97**, 34–41 (1995).

[13] P. L. Marston, ''Leaky waves on curved scatterers. I. Fresnel width of coupling regions and elliptical Fresnel patches,'' J. Acoust. Soc. Am. **96**, 1893–1898 (1994).

[14] A. K. Gautesen, ''Scattering of a Rayleigh wave by an elastic quarterspace,'' J. Appl. Mech. **52**, 664–668 (1985).

[15] A. K. Gautesen, ''Scattering of an obliquely incident Rayleigh wave in an elastic quarterspace,'' Wave Motion **8**, 27–41 (1986).

[16] Z. L. Li, J. D. Achenbach, I. Komsky, and Y. C. Lee, ''Reflection and transmission of obliquely incident surface waves by an edge of a quarter space: Theory and experiment,'' J. Appl. Mech. **59**, 349–355 (1992).

[17] X. L. Bao, ''Echoes and helical surface waves on a finite elastic cylinder excited by sound pulses in water,'' J. Acoust. Soc. Am. **94**, 1461–1466 (1993).

[18] X. L. Bao, H. Cao, and H. Überall, ''Resonances and surface waves in the scattering of an obliquely incident acoustic field by an infinite elastic cylinder,'' J. Acoust. Soc. Am. **87**, 106–110 (1990).

[19] J. M. Conoir, P. Rembert, O. Lenoir, and J. L. Izbicki, ''Relation between surface helical waves and elastic cylinder resonances,'' J. Acoust. Soc. Am. **93**, 1300–1307 (1993).

[20] N. D. Veksler, ''Scattering of a plane acoustic wave obliquely incident on a solid elastic cylinder,'' Acustica **71**, 111–120 (1990).

[21] F. Honarvar and A. N. Sinclair, ''Acoustic wave scattering from transversely isotropic cylinders,'' J. Acoust. Soc. Am. **100**, 57–63 (1996).

[22] L. Flax, L. R. Dragonette, and H. Überall, ''Theory of elastic resonance excitation by sound scattering,'' J. Acoust. Soc. Am. **63**, 723–731 (1978).

[23] Z. Yu and S. Boseck, ''Scanning acoustic microscopy and its applications to material characterization,'' Rev. Mod. Phys. **67**, 863–891 (1995).

[24] P. L. Marston, ''GTD for backscattering from elastic spheres and cylinders in water and the coupling of surface elastic waves with the acoustic field,'' J. Acoust. Soc. Am. **83**, 25–37 (1988).

[25] P. L. Marston, ''Geometrical and catastrophe optics methods in scattering,'' in *Physical Acoustics*, edited by R. N. Thurston and A. D. Pierce (Academic, Boston, 1992), Vol. 21, pp. 1–234.

[26] P. L. Marston, ''Variable phase coupling coefficient for leaky waves on spheres and cylinders from resonance scattering theory,'' Wave Motion **22**, 65–74 (1995).

[27] B. Noble, *Methods Based on the Wiener–Hopf Technique for the Solution of Partial Differential Equations* (Chelsea, New York, 1988), Sec. 2.5.

[28] M. Abramowitz and I. A. Stegun, *Handbook of Mathematical Functions* (Dover, New York, 1965), Chap. 7 and Eq. (7.4.32).

[29] E. T. Copson, *Asymptotic Expansions* (Cambridge U. P., Cambridge, 1965).

[30] I. S. Gradshteyn and I. M. Ryzhik, *Table of Integrals, Series, and Products* (Academic, New York, 1980), p. 315, Eq. (3.362-2).

[31] R. H. Hackman, ''Acoustic scattering from elastic solids,'' in *Physical Acoustics*, edited by A. D. Pierce and R. N. Thurston (Academic, Boston, 1992), Vol. 22, pp. 1–194.

[32] P. Y. Ufimtsev, ''Theory of acoustical edge waves,'' J. Acoust. Soc. Am. **86**, 463–474 (1989).

[33] D. Bancroft, ''The velocity of longitudinal waves in cylindrical bars,'' Phys. Rev. **59**, 588–593 (1941).

[34] G. V. Frisk, J. W. Dickey, and H. Überall, ''Surface wave modes on elastic cylinders,'' J. Acoust. Soc. Am. **58**, 996–1008 (1975).

[35] M. Rousseau and Ph. Gatignol, ''Short wave analysis for the reflection of bounded acoustic beams onto liquid–solid interfaces at the Rayleigh incidences,'' J. Acoust. Soc. Am. **78**, 1859–1867 (1985).

Active control of structurally radiated sound from plates

Chia-Chi Sung and C. T. Jan[a)]
Department of Naval Architecture and Ocean Engineering, National Taiwan University, Taipei, Taiwan, Republic of China

(Received 23 December 1996; accepted for publication 14 April 1997)

Active control of sound radiation from a clamped rectangular plate by piezoelectric moments is investigated both analytically and experimentally. A new theoretical derivation for the dynamic response of a plate excited by steady-state harmonic point forces, couples, and piezomoments is presented. Four point moments, simulating a piezoceramic patch bonded directly on the surface of the plate, are used to achieve the control. Control gain is obtained by minimizing the sound radiation power. The sound radiation measurement is conducted in a reverberation room equipped with an anechoic chamber. The results indicate that this research not only provides an accurate and efficient approach to theoretically predict the response of a clamped rectangular plate subjected to piezomoment excitation but also achieves effective global attenuation of sound radiation power. The highest reduction of the total power radiated from the plate was approximately 24 dB. © *1997 Acoustical Society of America.* [S0001-4966(97)06907-5]

PACS numbers: 43.40.Vn, 43.40.Dx [PJR]

INTRODUCTION

For sounds of medium and high frequencies the attenuation of radiation power is usually achieved by placing energy absorbing materials on the surfaces of structures. However, this technique is very inefficient for low-frequency sounds because the scale of the absorbing material must increase with decreasing frequency. Active noise control is suggested where destructive interference is employed to reduce the sound-pressure field. A number of successful active noise control techniques have been demonstrated and summarized in Refs. 1 and 2. Even for a simple source, e.g., monopole, many acoustic sources will be necessary to obtain global control of sound when the control sources are located more than a quarter of a wavelength away from the noise.[3] For structurally radiated noise the situation of active control is further exacerbated because most structural noise sources are complex or distributed. Recent research work suggests that structurally radiated noise might be better controlled by applying vibrational forces directly to the radiating structure.[4]

The present work is concerned with the application of this technique to the problem of control of sound radiating from vibrating plates. The calculation of the control inputs is simplified if all the necessary information for control can be obtained from the plate itself. Therefore the prediction of plate response becomes important. Much research has been devoted to the derivation of plate responses with various boundary conditions. For simply supported plates the solution is easier to obtain.[5] However, for plates which are not simply supported, e.g., clamped–clamped, clamped–elastically supported and clamped–simply supported, etc., the solution becomes much more complex. Either the Ritz[6] or the superposition method[7] must be employed to solve high-order simultaneous equations or high-order matrices making the calculation of structural sound radiation power even more difficult.

Based on Galerkin's method Vlasov proposed a solution[8] for a clamped or simply supported rectangular plate under static loading in 1949. In the present work, the dynamic response of a clamped or elastically supported plate subjected to various excitations, point forces, couples, and point moments, is predicted. The Rayleigh integral formula[9] is then employed to obtain the sound-pressure distribution and the sound radiation power. Optimal control forces are determined by minimizing the sound radiation power.

A 40-×40-cm clamped steel plate with 2-mm thickness is employed in the experiment. The response of the plate is measured using an electromagnetic shaker and piezoceramics as excitors, respectively. The weight of the piezoceramic patches which are bonded directly to the plate surface is 6.3 g and thus negligible compared to the weight of a steel plate.[10–12] The linearity of the piezoceramic excitors and the bonding layer is experimentally verified through the testing frequency range. The measurement of sound radiation power before and after control is conducted in the reverberation room with an anechoic chamber to simulate a semi-infinite space. The calculated and measured sound power results agree with each other after the acoustic absorbing conditions are improved for the opening of the anechoic chamber. The results show that the response prediction of the plate is accurate and the control performance is efficient.

I. SOLUTION OF THE FORCED VIBRATION RESPONSE FOR A CLAMPED PLATE

For an undamped thin plate under the external excitation force $P_e(x,y,t)$, Fig. 1, the governing equation of bending vibration is given by

$$D\left(\frac{\partial^4}{\partial x^4}+2\frac{\partial^4}{\partial x^2\partial y^2}+\frac{\partial^4}{\partial y^4}\right)w(x,y,t)+\rho_s h\frac{\partial^2 w(x,y,t)}{\partial t^2}=p_e(x,y,t), \tag{1}$$

[a)]Present address: Mechanical Research Laboratories, Industrial Technology Research Institute, Hsinchu, Taiwan, Republic of China.

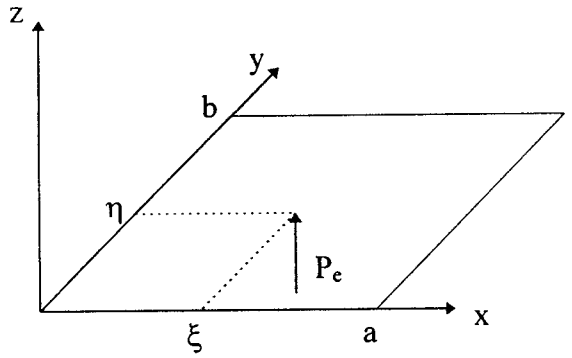

FIG. 1. Coordinate system of the plate.

where $w(x,y,t)$ is the displacement along the z direction at the point (x,y), $D=Eh^3/12(1-\nu^2)$, E is the Young's modules, h is the plate thickness, ν is the Poison's ratio, and ρ_s is the density of the plate.

Considering the external point force P_e to be harmonic with frequency ω and acting on the point (ξ,η), along the positive z axis and letting

$$w(x,y,t)=W(x,y)\cdot e^{i\omega t},$$
$$p_e(x,y,t)=P(x,y)\cdot e^{i\omega t} \tag{2}$$

the governing equation can be simplified as

$$D\left(\frac{\partial^4}{\partial x^4}+2\frac{\partial^4}{\partial x^2\partial y^2}+\frac{\partial^4}{\partial y^4}\right)W(x,y)-\overline{m}\omega^2W(x,y)$$
$$-P(x,y)=0, \tag{3}$$

where $\overline{m}=\rho_s h$ is the area density of the plate.

Expand $W(x,y)$ and $P(x,y)$ as a superposition of adequate shape functions[8]

$$W(x,y)=\sum_{m=1}^{\infty}\sum_{n=1}^{\infty}W_{mn}\phi_{mn}(x,y), \tag{4a}$$

$$P(x,y)=\sum_{m=1}^{\infty}\sum_{n=1}^{\infty}P_{mn}\phi_{mn}(x,y), \tag{4b}$$

choose $X_m(x)$ and $Y_n(y)$ which satisfy the required boundary conditions of the plateas as the shape functions and decompose the shape functions ϕ_{mn} as

$$\phi_{mn}(x,y)=X_m(x)\cdot Y_n(y). \tag{5}$$

Equation (4b) becomes the Fourier series expansion of $P(x,y)$. Because of the orthogonality of the shape functions $X_m(x)$ and $Y_n(y)$, P_{mn} can be expressed as

$$P_{mn}=\frac{\int_0^b\int_0^a P(x,y)X_m(x)Y_n(y)dx\ dy}{\int_0^b\int_0^a X_m^2(x)Y_n^2(y)dx\ dy}. \tag{6}$$

Utilizing the Virtual Work Principle we have

$$\int_0^b\int_0^a[D\nabla^2\nabla^2W(x,y)-\overline{m}\omega^2W(x,y)-P(x,y)]$$
$$\times(\delta W)dx\ dy=0, \tag{7}$$

where the virtual displacement δW is written as

$$\delta W=\sum_{i=1}^{\infty}\sum_{k=1}^{\infty}\delta W_{ik}\cdot\phi_{ik}(x,y).$$

Substitute Eq. (4) into Eq. (7) and apply the orthogonality of the shape functions $X_m(x)$, $Y_n(y)$ and $X_i(x)$, $Y_k(y)$, i.e.,

$$\left.\begin{aligned}\int_0^a X_p(x)X_q(x)dx=\int_0^a X_p''(x)X_q''(x)dx=0\\ \int_0^b Y_p(y)Y_q(y)dy=\int_0^b Y_p''(y)Y_q''(y)dy=0\end{aligned}\right\}\quad \text{if } p\neq q.$$

Equation (7) can be converted to

$$D\sum_m\sum_n W_{mn}(I_1I_2+2I_3I_4+I_5I_6)-\overline{m}\omega^2\sum_m\sum_n W_{mn}I_2I_6$$
$$=\sum_m\sum_n\int_0^b\int_0^a P(x,y)X_mY_n\,dx\,dy, \tag{8}$$

where

$$I_1=\int_0^a X_m^{(4)}X_m\,dx,\quad I_4=\int_0^b Y_n''Y_n\,dy,$$
$$I_2=\int_0^b Y_n^2\,dy,\quad I_5=\int_0^b Y_n^{(4)}Y_n\,dy,$$
$$I_3=\int_0^a X_m''X_m\,dx,\quad I_6=\int_0^a X_m^2\,dx.$$

Considering a specific set of m, n values and for a concentrated load $P(x,y)=\underline{P}\,\delta(x-\xi)\,\delta(y-\eta)$, Eq. (8) can be reduced to

$$W_{mn}=\frac{\underline{P}X_m(\xi)Y_n(\eta)}{D(I_1I_2+2I_3I_4+I_5I_6)-\overline{m}\omega^2I_2I_6}, \tag{9}$$

where $\delta(x)$ is the dirac delta function. The dynamic response $W(x,y)$ of a plate subjected to a harmonic point force can thus be expressed as

$$W(x,y)=\sum_m\sum_n\frac{\underline{P}X_m(\xi)Y_n(\eta)}{D(I_1I_2+2I_3I_4+I_5I_6)-\overline{m}\omega^2I_2I_6}\cdot X_m(x)Y_n(y). \tag{10}$$

The shape functions $X_m(x)$ and $Y_n(y)$ can be chosen arbitrarily as long as they are quasiorthogonal and satisfy the required boundary conditions.[13] For the clamped plate, $X_m(x)$ and $Y_n(y)$ are chosen as

$$X_m(x)=J\left(\frac{\lambda_m x}{a}\right)-\frac{J(\lambda_m)}{H(\lambda_m)}H\left(\frac{\lambda_m x}{a}\right)$$

and

$$Y_n(y)=J\left(\frac{\lambda_n y}{b}\right)-\frac{J(\lambda_n)}{H(\lambda_n)}H\left(\frac{\lambda_n y}{b}\right),$$

where

$$J(u)=\cosh(u)-\cos(u)$$
$$H(u)=\sinh(u)-\sin(u)$$

and λ_m and λ_n satisfy $\cosh(\lambda_m)\cos(\lambda_m)=1$.

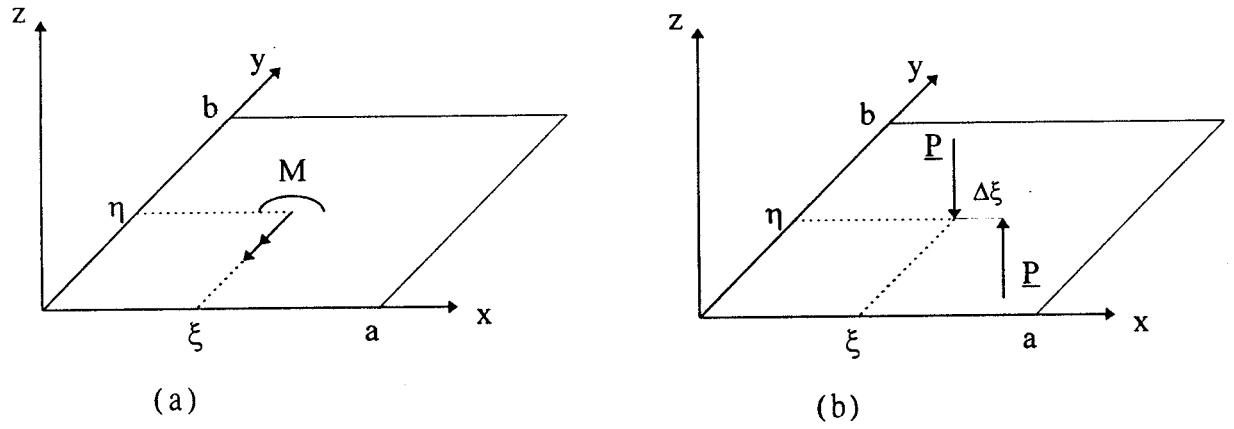

FIG. 2. Plate under the excitation of (a) a single concentrated moment, (b) two concentrated forces to simulate a single concentrated moment.

The natural frequencies ω_{mn} can be found by setting the denominator of Eq. (9) to be zero. Thus

$$\omega_{mn}=\sqrt{\frac{D(I_1I_2+2I_3I_4+I_5I_6)}{\overline{m}I_2I_6}}. \tag{11}$$

A point moment can be treated as two point forces with the same magnitude, separated by a distance $\Delta\xi$ and oriented along opposite direction with respect to each other.[6] Consider a point moment M acting on the plate at point (ξ,η), as shown in Fig. 2(a), we represent M as

$$M=\underline{M}\,\delta(x-\xi)\,\delta(y-\eta)e^{i\omega t}, \tag{12}$$

where $\underline{M}$ is the magnitude of M.

When the point moment $\underline{M}$ is substituted with a couple and we set $\underline{M}=\underline{P}(\Delta\xi)$ [Fig. 2(b)], the total response of the plate becomes the superposition of the responses induced by the two point forces.

$$W(x,y)=\underline{P}\left[\lim_{\Delta\xi\to 0} f(\xi+\Delta\xi,\eta,x,y)-f(\xi,\eta,x,y)\right], \tag{13}$$

where $f(\xi,\eta)$ and $f(\xi+\Delta\xi,\eta)$ represent the responses induced by the two unit point forces located at (ξ,η) and $(\xi+\Delta\xi,\eta)$, respectively.

If we let $\Delta\xi$ approach zero and keep $\underline{M}=\underline{P}\cdot(\Delta\xi)$ constant $\underline{P}$ will approach infinity and Eq. (13) becomes

$$W(x,y)=\underline{M}\left[\lim_{\Delta\xi\to 0}\frac{f(\xi+\Delta\xi,\eta,x,y)-f(\xi,\eta,x,y)}{\Delta\xi}\right]. \tag{14}$$

With Eq. (14), Eq. (10) can be rewritten as

$$W(x,y)=\sum_m\sum_n\left[\frac{\underline{M}X_m(x)Y_n(y)Y_n(\eta)}{D(I_1I_2+2I_3I_4+I_5I_6)-\overline{m}\omega^2I_2I_6}\cdot\frac{\partial X_m(\xi)}{\partial\xi}\right]. \tag{15}$$

Equation (15) represents the response of the plate due to the excitation of the point moment acting along negative y direction. Similarly, when the moment is applied along the x direction, the plate response is obtained as

$$W(x,y)=\sum_m\sum_n\left[\frac{\underline{M}X_m(x)Y_n(y)X_m(\xi)}{D(I_1I_2+2I_3I_4+I_5I_6)-\overline{m}\omega^2I_2I_6}\cdot\frac{\partial Y_n(\eta)}{\partial\eta}\right]. \tag{16}$$

Consider a square piezoceramic excitor with length l on each side perfectly bonded on the plate. When an alternating electric field is applied to the piezoceramic actuator along the z direction, the induced strain along the x and y directions will cause the plate to vibrate. The excitation can be treated as four point moments concentrated, respectively, on the midpoints of the four edges of the piezoceramic actuator.

From Eqs. (15) and (16), the plate response induced by the piezoceramic actuator is the superposition of the responses induced by four point moments, respectively.

$$\begin{aligned}W(x,y)=\sum_m\sum_n\ &\frac{\underline{M}X_m(x)Y_n(y)}{D(I_1I_2+2I_3I_4+I_5I_6)-\overline{m}\omega^2I_2I_6}\\ &\times\left[Y_n(\eta_0)\cdot\left.\frac{\partial X_m(\xi)}{\partial\xi}\right|_{\xi=\xi_0-1/2}\right.\\ &-Y_n(\eta_0)\cdot\left.\frac{\partial X_m(\xi)}{\partial\xi}\right|_{\xi=\xi_0+1/2}\\ &+X_m(\xi_0)\cdot\left.\frac{\partial Y_n(\eta)}{\partial\eta}\right|_{\eta=\eta_0-1/2}\\ &-X_m(\xi_0)\cdot\left.\frac{\partial Y_n(\eta)}{\partial\eta}\right|_{\eta=\eta_0+1/2}\Bigg].\end{aligned} \tag{17}$$

The bonding layer between the piezoceramic patch and the plate is assumed to be linear. The relation between the piezomoment $\underline{M}$ and the applied voltage ϵ_{PZT} is then assumed to be

$$\underline{M}=k_0\epsilon_{\mathrm{PZT}}, \tag{18}$$

where k_0 is the proportionality between the generated piezomoment $\underline{M}$ and the applied voltage ϵ_{PZT} to the piezoceramic excitor.

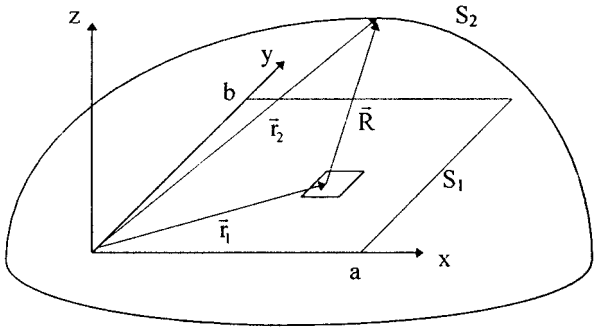

FIG. 3. Integration areas S_1 and S_2 used in the calculation of plate radiation power.

II. CALCULATION OF THE SOUND RADIATION POWER FROM THE PLATE

In Fig. 4, when the plate vibrates, the acoustic pressure $P(\mathbf{r}_2)$ at $\mathbf{r}_2$ exists and can be obtained by Rayleigh's integral

$$P(\mathbf{r}_2)=\frac{\omega\rho_f}{2\pi}\int_{S_1}\nu(\mathbf{r}_1)\,\frac{e^{-ikR}}{R}\,dS_1, \tag{19}$$

where ω is the angular frequency of the plate, k is the wave number, ρ_f is the density of the air, $\nu(\mathbf{r}_1)$ is the normal velocity of the plate at $\mathbf{r}_1$, $R=|\mathbf{r}_1-\mathbf{r}_2|$, and S_1 is the area of the plate.

The acoustic intensity $I(\mathbf{r}_2)$ can be expressed as

$$I(\mathbf{r}_2)=\tfrac{1}{2}\mathrm{Re}\{P(\mathbf{r}_2)\cdot\nu^*(\mathbf{r}_2)\}, \tag{20}$$

where $\nu(\mathbf{r}_2)$ is the normal velocity of the acoustic medium at $\mathbf{r}_2$ and the asterisk denotes the complex conjugate of the function $\nu(\mathbf{r})$.

The sound power $\overline{W_P}$ radiating into the half-space above the plate is

$$\overline{W_P}=\int_{S_2} I(\mathbf{r}_2)dS_2, \tag{21}$$

where S_2 is an arbitrary surface which covers area S_1 and $\mathbf{r}_2$ is the position vector of S_2 (Fig. 3).

From Eqs. (19) and (20), we can set $S_2=S_1$ such that $\mathbf{r}_1$ and $\mathbf{r}_2$ become two arbitrary position vectors on the surface of the plate (Fig. 4).[14] Due to the reciprocity relationship between the source at $\mathbf{r}_1$ and the receiver at $\mathbf{r}_2$, and for an arbitrary complex function C, $\mathrm{Re}\{C\}=(C+C^*)/2$, the radiation power of the plate then becomes

$$\overline{W_P}=\frac{\omega\rho_f}{4\pi}\int_0^b\int_0^a\left[\int_0^b\int_0^a\nu(\mathbf{r}_1)\cdot\left(\frac{\sin(kR)}{R}\right)\cdot\nu^*(\mathbf{r}_2)dx_1\,dy_1\right]dx_2\,dy_2. \tag{22}$$

Suppose the rectangular plate is divided into N elements of area ΔS (Fig. 4). We can then approximate Eq. (22) as the finite series

$$\overline{W_P}\cong\frac{\omega\rho_f}{4\pi}\sum_J\sum_l\frac{\sin(kR)}{R}\,\nu(\mathbf{r}_l)\cdot\nu^*(\mathbf{r}_J)(\Delta S)\cdot(\Delta S), \tag{23}$$

where $\mathbf{r}_l$ and $\mathbf{r}_J$ are the position vectors of the center point of two arbitrary elements, respectively.

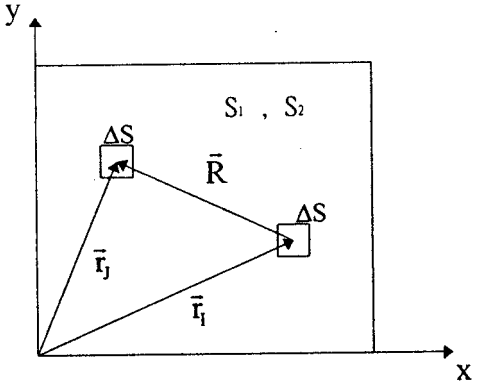

FIG. 4. Discretization of plate area.

III. CALCULATION OF THE OPTIMAL CONTROL MOMENTS

Assume two piezoceramic patches are bonded to the surface of the plate. One patch serves as the vibration input or excitor and the other as the vibration reduction controller. The center locations of the excitor and the controller are (ξ_e,η_e) and (ξ_c,η_c), respectively.

Rewriting Eq. (17) in a simpler form we have

$$W(x,y)=\underline{M}G(\xi_0,\eta_0,x,y), \tag{24}$$

where

$$G(\xi_0,\eta_0,x,y)=\sum_m\sum_n\frac{X_m(x)Y_n(y)}{D(I_1I_2+2I_3I_4+I_5I_6)-\overline{m}\omega^2I_2I_6}\times\left[Y_n(\eta_0)\cdot\left.\frac{\partial X_m(\xi)}{\partial\xi}\right|_{\xi=\xi_0-1/2}-Y_n(\eta_0)\cdot\left.\frac{\partial X_m(\xi)}{\partial\xi}\right|_{\xi=\xi_0+1/2}+X_m(\xi_0)\cdot\left.\frac{\partial Y_n(\eta)}{\partial\eta}\right|_{\eta=\eta_0-1/2}-X_m(\xi_0)\cdot\left.\frac{\partial Y_n(\eta)}{\partial\eta}\right|_{\eta=\eta_0+1/2}\right]$$

and (ξ_0,η_0) is the center location of either the excitor or controller piezoceramic.

When the excitor and controller are activated simultaneously the plate response can be expressed as

$$W(x,y)=\underline{M}_eG(\xi_e,\eta_e,x,y)+\underline{M}_cG(\xi_c,\eta_c,x,y), \tag{25}$$

where $\underline{M}_e$ and $\underline{M}_c$ are the amplitudes of the four point moments from the excitor and controller to the plate, respectively.

The velocity amplitude of the plate $V(x,y)$ becomes

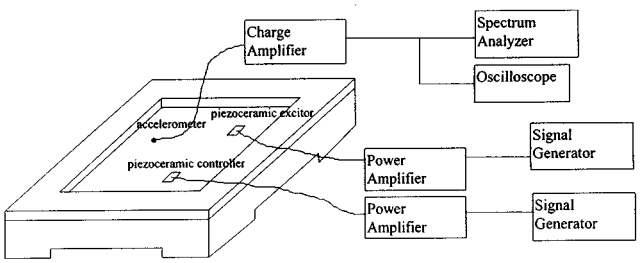

FIG. 5. Equipment layout of plate response measurement.

$$V(x,y)=\omega[\underline{M}_e G(\xi_e,\eta_e,x,y)+\underline{M}_c G(\xi_c,\eta_c,x,y)]$$
$$=\underline{M}_e\Phi_e+\underline{M}_c\Phi_c, \tag{26}$$

where $\Phi_e=\omega G(\xi_e,\eta_e,x,y)$ and $\Phi_c=\omega G(\xi_c,\eta_c,x,y)$, and the sound radiation power in Eq. (23) becomes

$$\overline{W_p}=\frac{\omega\rho_f(\Delta S)^2}{4\pi}\sum_I\sum_J\frac{\sin(kR)}{R}(\underline{M}_e\Phi_{el}+\underline{M}_c\Phi_{cl})$$
$$\times(\underline{M}_e\Phi_{eJ}+\underline{M}_c\Phi_{cJ})$$
$$=\frac{\omega\rho_f(\Delta S)^2}{4\pi}(\Gamma_1\underline{M}_c^2+\Gamma_2\underline{M}_e\underline{M}_c+\Gamma_3\underline{M}_e^2), \tag{27}$$

where $\Phi_{el}=\omega G(\xi_e,\eta_e,x_l,y_I)$, $\Phi_{eJ}=\omega G(\xi_e,\eta_e,x_J,y_J)$, $\Phi_{cl}=\omega G(\xi_c,\eta_c,x_l,y_I)$, $\Phi_{cJ}=\omega G(\xi_c,\eta_c,x_J,y_J)$, $\Gamma_1=\Sigma_l\times\Sigma_J\sin(kR)/R(\Phi_{cl}\Phi_{cJ})$, $\Gamma_2=\Sigma_l\Sigma_J\sin(kR)/R(\Phi_{el}\Phi_{cl}+\Phi_{el}\Phi_{cJ})$, and $\Gamma_3=\Sigma_l\Sigma_J\sin(kR)/R(\Phi_{el}\Phi_{eJ})$.

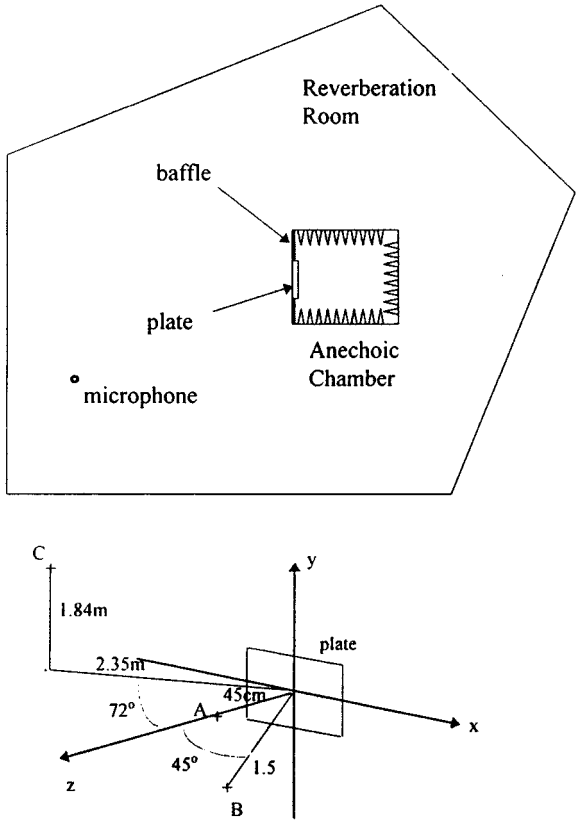

FIG. 6. The experimental setup for the measurement of plate radiation power in a reverberation room equipped with an anechoic chamber.

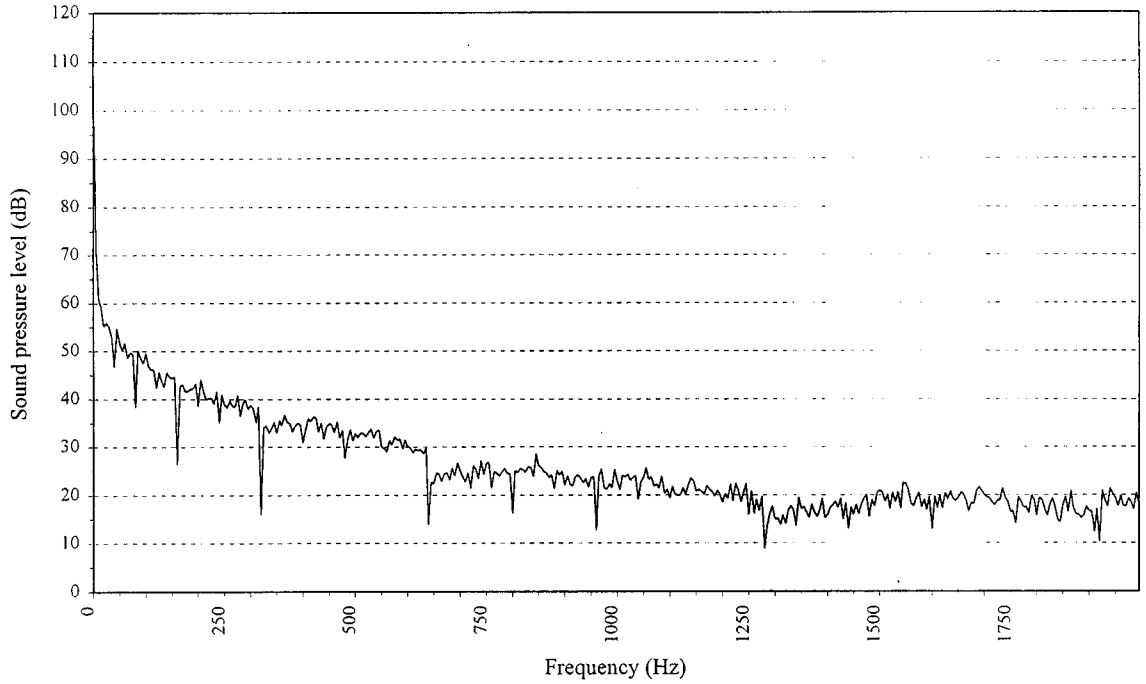

FIG. 7. Background noise of the reverberation room.

To minimize the sound radiation power $\overline{W_p}$ the control moment $\underline{M}_c$ must satisfy

$$\frac{\partial \overline{W_p}}{\partial \underline{M}_c} = 0. \tag{28}$$

Therefore, the control moment $\underline{M}_c$ must be

$$\underline{M}_c = \frac{-\Gamma_2}{2\Gamma_1}\,\underline{M}_e \tag{29}$$

and the minimum radiation power will be

$$(\overline{W_p})_{\min} = \frac{\omega \rho_f (\Delta S)^2}{4\pi}\left[\Gamma_3 - \frac{3\Gamma_2^2}{4\Gamma_1}\right]\underline{M}_e^2. \tag{30}$$

IV. CONTROL OF SOUND RADIATION POWER FROM A PLATE IN A REVERBERATION ROOM

The experiment was performed on a $400\times400\times2$-mm rectangular steel plate. The plate boundary was a rectangular steel frame. The plate was clamped to the frame with four 2-cm thick steel bars with screws spaced every 5 cm in between. The total weight of the frame and four bars was 40 kg.

Piezoceramic patches numbered 1 and 2 were bonded on the upper surface at locations (8.7, 11.5)cm, (11.3, 31)cm, respectively. Numbers 3 and 4 piezoceramic patches were bonded on the lower surface at locations (13.8, 11)cm, (26.4, 26.1)cm, respectively. Piezoceramic number 1 was used as an excitor. An accelerometer (B&K 4393) was used as a sensor for measuring the vibration responses. For sound radiation control, the number 1 piezoceramic is used as the excitor and one of the number 2, number 3, and number 4 piezoceramics were used as the controller. The harmonic amplitude of the excitation voltage is 141.4 V. Each piezoceramic patch measured $25\times25\times1$ mm and weighed 6.3 g. The accelerometer weight was 2.2 g. Figure 5 shows the electronic circuit setup.

In the previous calculation of sound radiation power, only the upper semi-infinite space is taken into consideration. Therefore, the plate was baffled and placed on the opening of the anechoic chamber (Fig. 6). The radiation power from the back of the plate can be completely absorbed in such an arrangement. In the first measurement, the original baffle of the plate on the opening of the anechoic chamber was about 1.0-cm-thick plywood. In the second measurement, the original baffle was replaced by 2-cm plywood to prevent part of the sound power from penetrating into the anechoic chamber from the reverberation room. All the gaps were well sealed with acoustic absorbing material. The fundamental data of the reverberation room refers Ref. 15. The background noise of the reverberation room is shown in Fig. 7. The procedure for measuring the sound radiation power in the reverberation room followed ANSI-S1.21-1972.[16]

V. RESULTS AND COMPARISONS

The calculated and measured resonant frequencies for the first six modes are compared to those from the Rayleigh–Ritz method and listed in Table I. The comparison shows that the presented method is accurate and efficient. The fixed boundary in the experimental setup is perfect and the influence of the attached piezoceramic patches is almost negligible.

TABLE I. Comparisons of the natural frequencies for the clamped plate bonded by four piezoceramic patches.

	Natural frequencies (Hz) of			
Mode	Rayleigh–Ritz method	Present method	Experimental measurements for plate bonded by four PZT patchers	Error between columns (2) and (3) (%)
1	106.88	107.24	106	1.2
2	217.98	219.20	214.45	2.2
3	321.42	324.29	319	1.7
4	390.81	396.37	389	1.9
5	392.66	396.37	390.8	1.4
6	490.07	502.13	489	2.7

From Eq. (24) it can be shown that the plate displacement $W(x,y)$ is proportional to the applied moment $\underline{M}$ and the velocity amplitude is also proportional to the input moment as

$$V(x,y) = \omega \underline{M} G(\xi_0, \eta_0, x, y). \tag{31}$$

To verify the proportionality of the relationship $\underline{M} = k_0 \epsilon_{\mathrm{PZT}}$, we applied harmonic input voltages of 25, 50, 75, and 100 V at the frequency of each mode to the number 1 piezoceramic and measured the response of each voltage. The velocity amplitudes at three different locations $A(12, 14.6)$ cm, $B(5.8, 26.7)$ cm, and $C(32.1, 27.4)$ cm were measured and plotted in Fig. 8. Figure 8 demonstrates the proportionality for each individual mode and thus the validity of the relationship $\underline{M} = k_0 \epsilon_{\mathrm{PZT}}$. The coupling coefficient k_0 can be determined by using Eq. (31) and the value of the measured velocity amplitude on the plate. Choose the number 1 piezoceramic as the excitor and let $\underline{M} = 1$ Newton-meter the velocity amplitude V_1 of the plate for various mode can be calculated. By applying $\epsilon_{\mathrm{PZT}} = 141.4$ V to the number 1 piezoceramic with the corresponding frequency and measuring the velocity amplitude V_2 at the same location on the plate, k_0 is obtained as

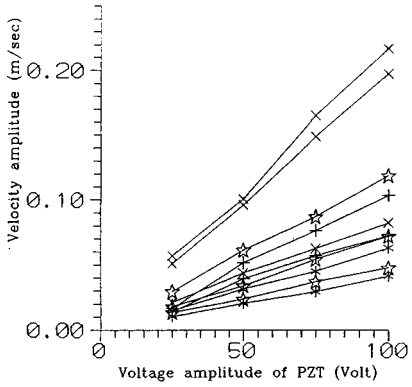

FIG. 8. The proportionality of plate velocity amplitude and the piezoactuator excitation voltage ϵ_c.

TABLE II. Coupling coefficient k_0 for the piezoceramics at various frequencies.

Mode (frequency)	1 (106)	2 (214.45)	3 (319)	4 (389)	5 (489)
Coupling coefficient k_0 (Newton-meter/V)$\times 10^{-4}$	7.199	30.31	35.99	28.75	27.56

$$k_0 = \frac{V_2}{141.4 \times V_1}. \tag{32}$$

Table II exhibits the coupling coefficient k_0 for the first five modes. Figure 9 shows the calculated and measured responses. The responses are calculated by applying $\underline{M} = 1$ Newton-meter as an excitation moment to the number 1 piezoceramic. The measurements are obtained by applying $\epsilon_{\mathrm{PZT}} = 141.4$ V to the same piezoceramic.

From Eq. (29) and the proportionality between the input voltage and output moment of the piezocerami, the optimal control voltage ϵ_c can be expressed as

$$\epsilon_c = \frac{-\Gamma_2}{2\Gamma_1}\,\epsilon_{\mathrm{PZT}}.$$

Figures 10–13 show the spectrum of sound-pressure level (SPL) at three, as examples, of all the required measurement locations for the calculation of radiation power for each mode. Table III summarizes the results of calculated and measured sound radiation power before and after control. The analytical results are obtained from Eq. (25) by giving the number 1 piezoceramic a 141.4-V harmonic excitation voltage.

VI. DISCUSSION AND CONCLUSIONS

A method has been presented for the analysis of the response and sound radiation power of a clamped rectangular plate. Instead of solving a high-order matrix, this method provides a more efficient approach to obtain the plate responses under various boundary conditions. This approach is of particular value when the simulation of piezo-moment as controller and/or optimal control forces for radiated sound power are needed.

Based on the minimization of the total radiated sound power, a strategy for reducing the sound power radiated from a plate structure subjected to a harmonic excitation and control piezo-moments has been presented. The analysis has been verified experimentally. The experimental measure-

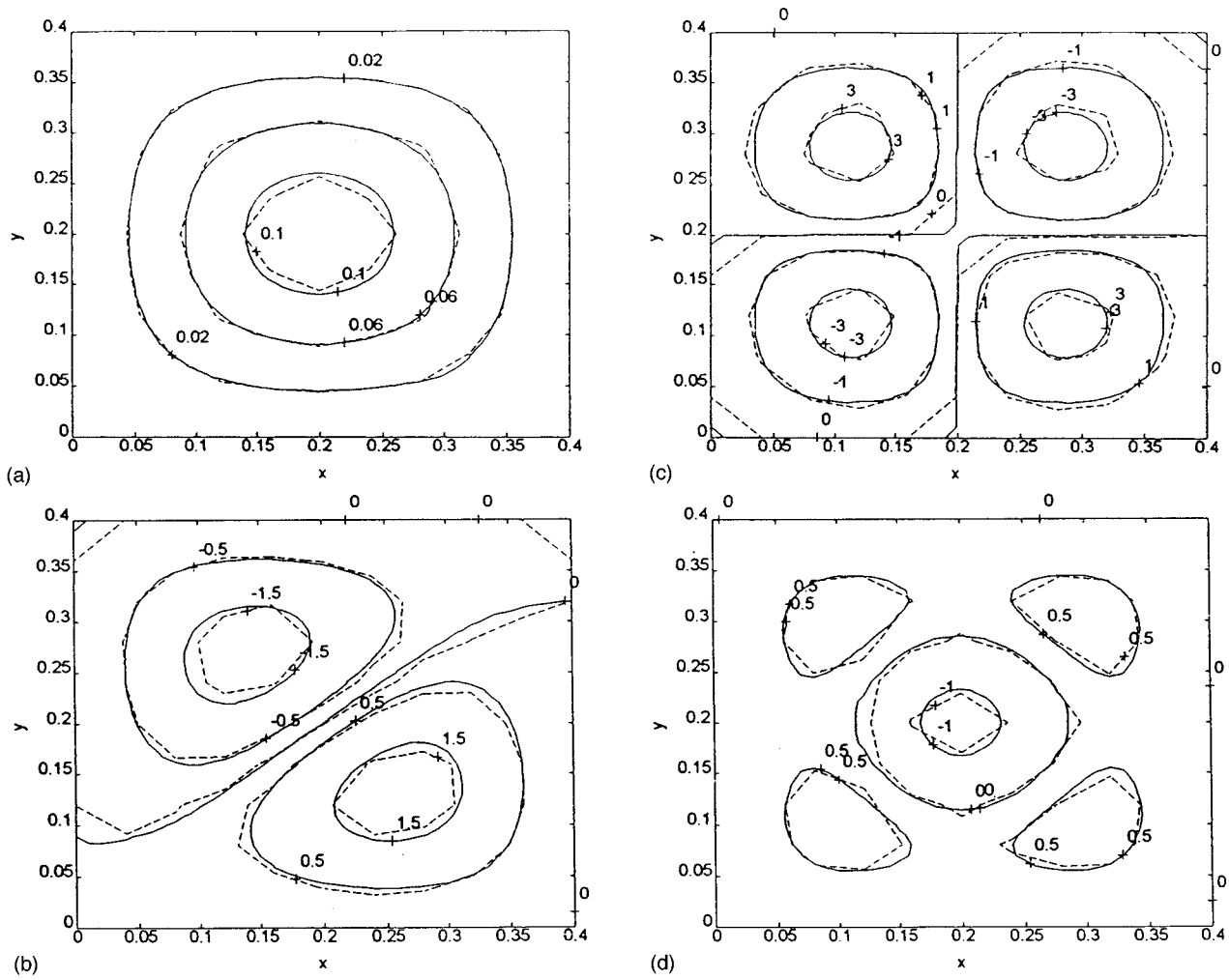

FIG. 9. Calculation and experimental measurements of plate responses (m/s^2) under the excitation of no. 1 piezoceramic (——— calculated data, ----- experimental data), (a) first mode (106 Hz), (b) second mode (214.45 Hz), (c) fourth mode (319 Hz), (d) fifth mode (389 Hz).

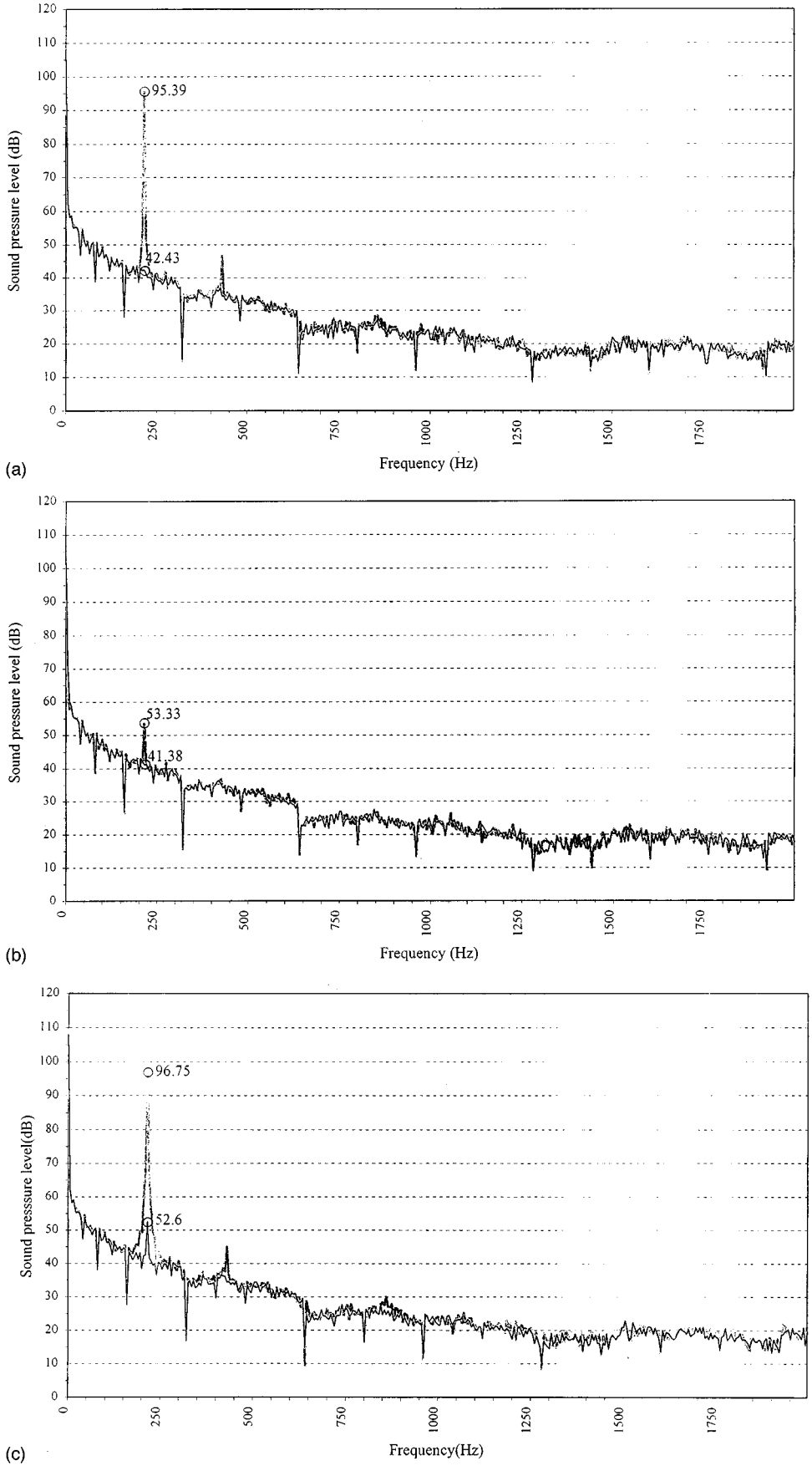

FIG. 10. Sound-pressure level before (gray line) and after (black line) control for the 2nd mode (214.45 Hz), (a) measured at location A, (b) measured at location B, (c) measured at location C.

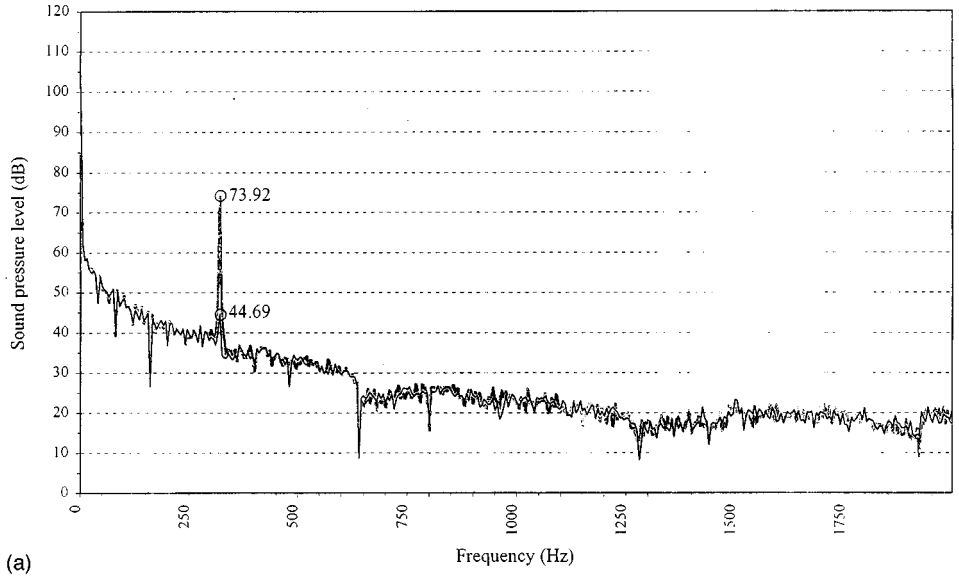

(a)

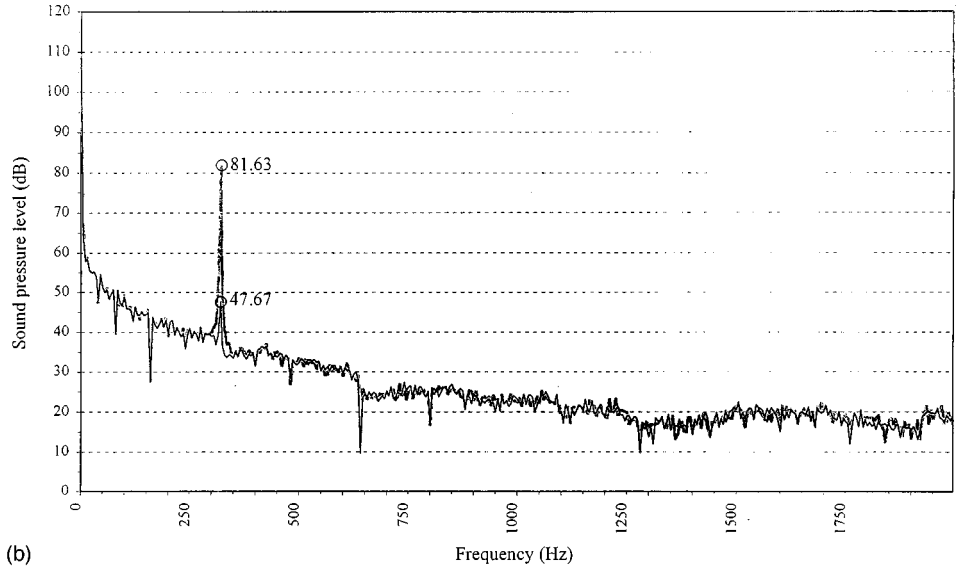

(b)

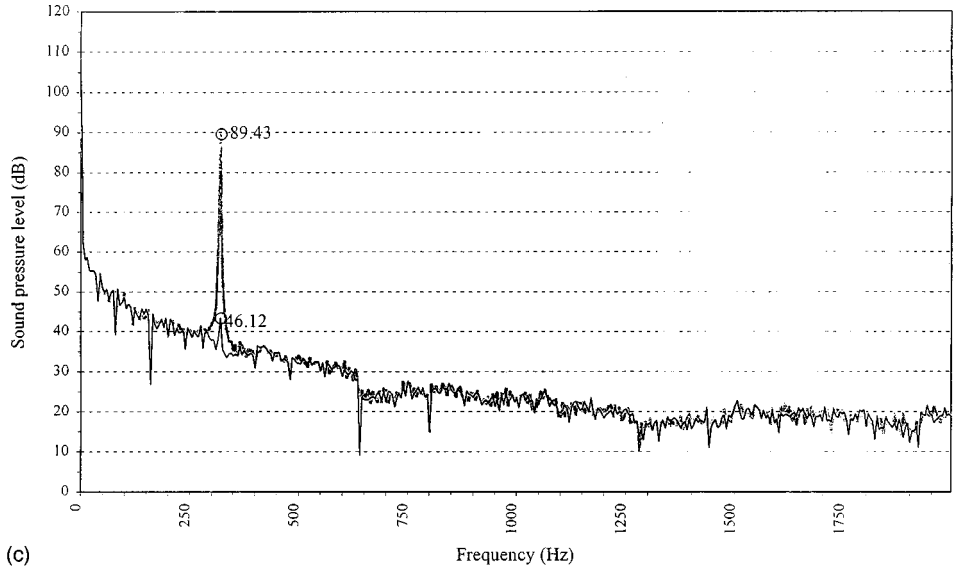

(c)

FIG. 11. Sound-pressure level before (gray line) and after (black line) control for the 3rd mode (319 Hz), (a) measured at location A, (b) measured at location B, (c) measured at location C.

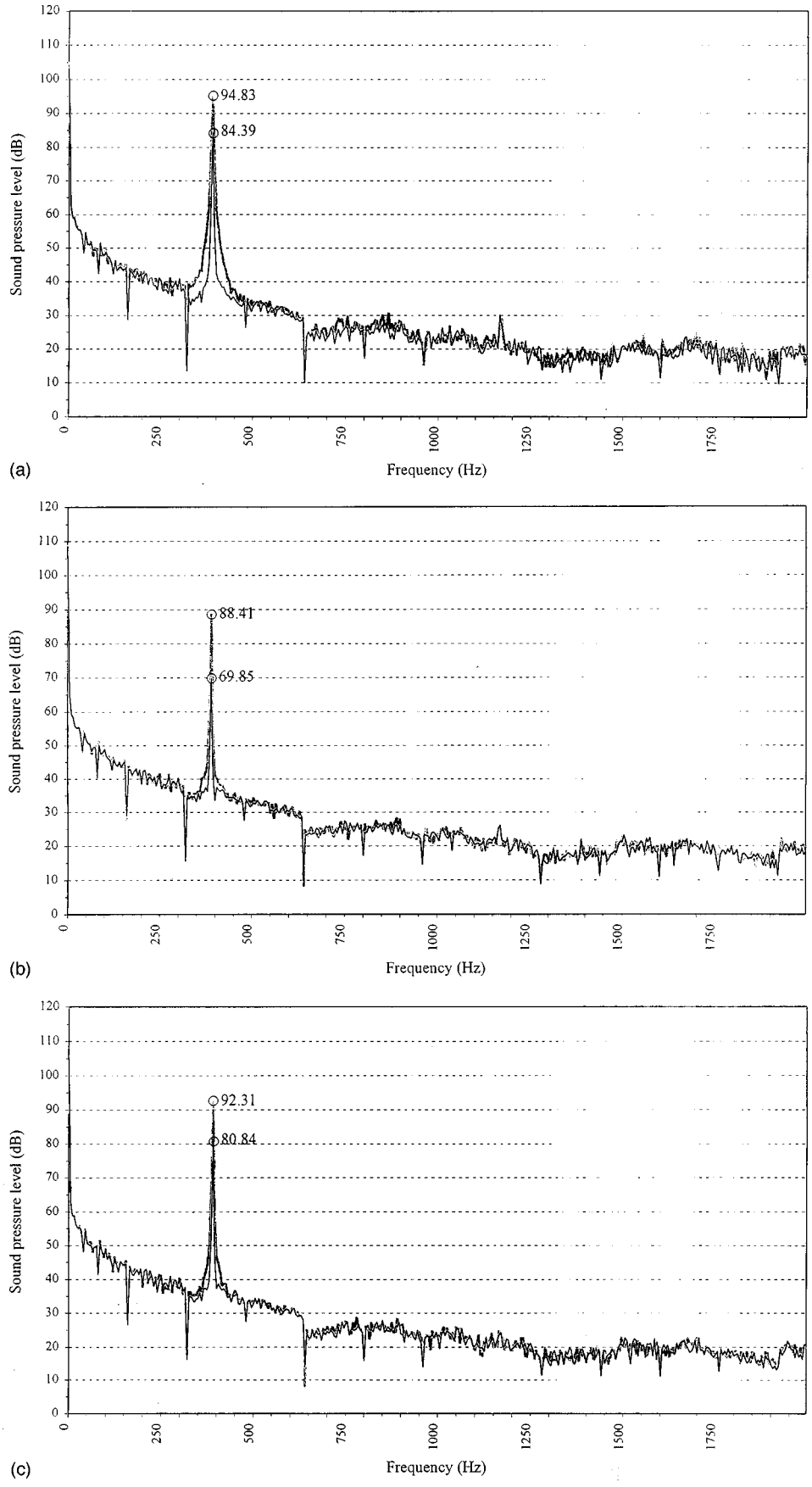

FIG. 12. Sound-pressure level before (gray line) and after (black line) control for the 4th mode (389 Hz), (a) measured at location A, (b) measured at location B, (c) measured at location C.

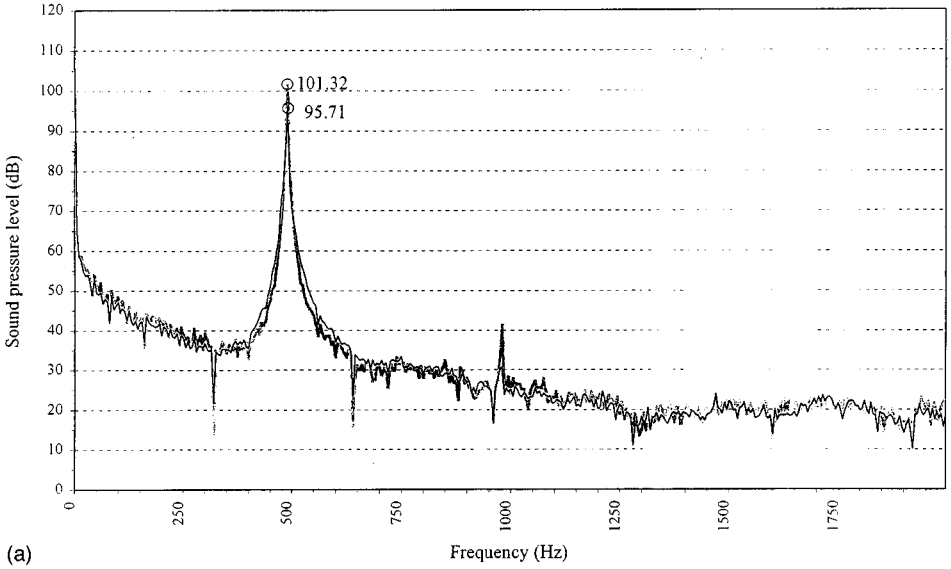

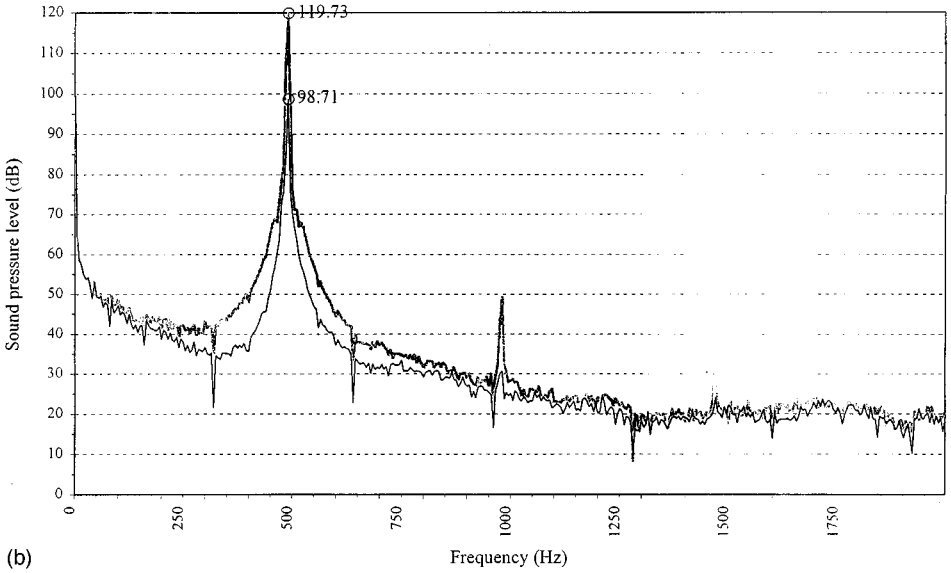

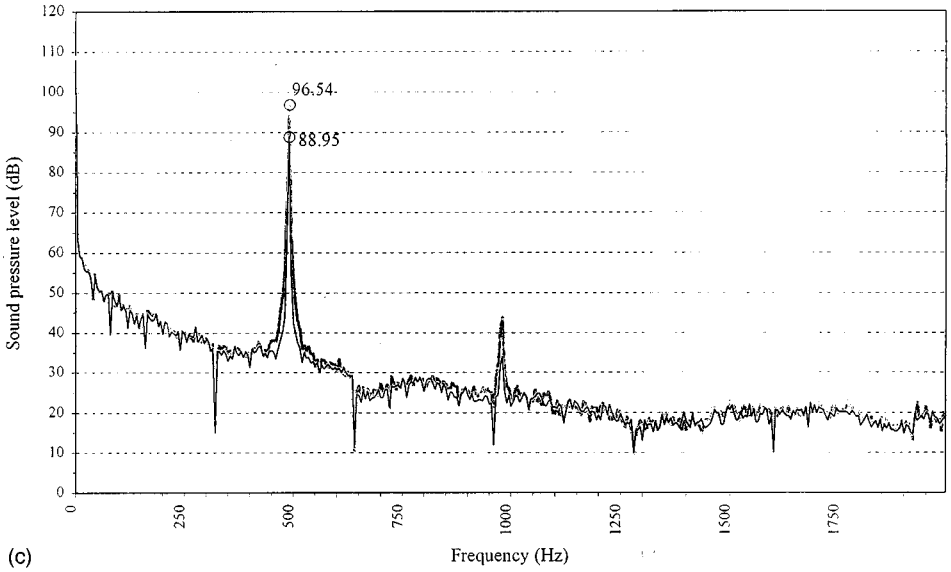

FIG. 13. Sound-pressure level before (gray line) and after (black line) control for the 5th mode (489 Hz), (a) measured at location A, (b) measured at location B, (c) measured at location C.

TABLE III. Comparisons of calculated and measured sound radiation power before and after control.

Mode no.	Excitor		Controller		Radiated sound power (dB) uncontrolled		Radiated sound power (dB) controlled		Sound power reduction (dB)	
(freqs.)	ϵ_e	$\underline{M}_e$	ϵ_c	$\underline{M}_c$	calculated	measured	calculated	measured	calculated	measured
2 (214.45)	141.4	0.429	−80.6	−0.244	90.4	88.6	77.3	65.1	13.1	23.5
3 (319)	141.4	0.509	93.3	0.336	91.5	85.8	75.8	67.2	15.7	18.6
4 (389)	141.4	0.406	−137.2	−0.394	107.5	100.7	83.5	86.5	24.0	14.2
6 (489)	141.4	0.389	125.8	0.347	104.9	98.3	86.4	88.2	18.5	10.1

ments were conducted in the reverberation room equipped with an anechoic chamber. The results demonstrate that for low frequencies, large global reductions of radiated sound power can be achieved with a single piezo-actuator. The highest reduction of the total power radiated from the plate was approximately 24 dB.

ACKNOWLEDGMENTS

The authors would like to acknowledge the National Science Council, Taiwan, Republic of China for the partial-funding support under project No. NSC 83-0209-E-002-010.

[1] G. E. Warnaka, ''Active attenuation of noise—The state of art,'' Noise Control Eng. J. **18**, 100–110 (1982).
[2] M. J. Ffowcs-Williams, ''Anti-sound,'' Proc. R. Soc. London, Ser. A **395**, 63–88 (1984).
[3] P. A. Nelson, A. R. D. Curtis, S. J. Elliott, and A. J. Bullmore, ''The minimum of free field point sources and the active control of sound,'' J. Sound Vib. **116**, 397–414 (1987).
[4] C. R. Fuller, ''Apparatus and method for global noise reduction,'' U.S. Patent No. 4,715,599 (1987).
[5] G. B. Warbuton, ''The Vibration of Rectangular Plates,'' Proc. Inst. Mech. Eng. London **168**, 371–381 (1954).
[6] R. Szilard, *Theory and Analysis of Plates, Classical and Numerical Methods* (Prentice-Hall, Englewood Cliffs, NJ, 1966), p. 435.
[7] N. Li, ''Forced vibration analysis of the clamped orthotropic rectangular plate by the superposition method,'' J. Sound Vib. **158**, 307–316 (1992).
[8] V. Z. Vlasov, ''Some new problems on shell and thin structures,'' Natl. Adv. Comm. Aeron., Naca Tech. Memo, No. 1204 (1949).
[9] J. W. S. Rayleigh, *The Theory of Sound* (Dover, New York, 1945).
[10] E. F. Crawley and J. de Luis, ''Use of piezoelectric actuators as element of intelligent structures,'' AIAA J. **25**, 1373–1385 (1987).
[11] R. L. Clark, C. R. Fuller, and A. Wicks, ''Characterization of multiple piezoelectric actuators for structural excitation,'' J. Acoust. Soc. Am. **90**, 346–357 (1991).
[12] K. Naghshineh and G. H. Koopmann, ''A design method for achieving weak radiator structures using active vibration control,'' J. Acoust. Soc. Am. **92**, 856–870 (1992).
[13] W. Flugge, *Handbook of Engineering Mechanics* (McGraw-Hill, New York, 1962).
[14] K. Naghshineh and G. H. Koopmann, ''Material tailoring of structures to achieve a minimum radiation condition,'' J. Acoust. Soc. Am. **92**, 841–855 (1992).
[15] *Introduction of Noise and Acoustic Laboratory* (Department of Naval Architecture and Ocean Engineering (National Taiwan University, Taipei, Taiwan, Republic of China, 1988).
[16] ANSI-S1.21-1972, ''Methods for the determination of sound power level of small sources in reverberation rooms'' (American National Standards Institute, New York, 1972).

Vibration monitoring of slotted beams using an analytical model

XiuTing C. Man and Robert D. Finch
Department of Mechanical Engineering, University of Houston, Houston, Texas 77204-4792

Ben H. Jansen
Department of Electrical Engineering, University of Houston, Houston, Texas 77204-4793

(Received 6 July 1995; revised 27 November 1996; accepted 25 March 1997)

This paper reports part of a research program aimed at developing the scientific basis for vibration monitoring in rapid and automatic global inspection of structures for faults. Slotted steel beams in various conditions were used as experimental samples. A mathematical model of the slotted beam's vibration was solved using a perturbation method. Relationships between the defect parameters and the vibration signature showed a strong dependence of the modal frequency on the slot characteristics, including location and size. The method is computationally efficient, robust and could be used for on-line signal processing. The experimental modal parameters were determined from the mobility function calculated from the excitation and response signals. The modal frequencies and their shifts were then used to quantify the slot. A test of 11 beams with various conditions demonstrated that the slot can be characterized inversely. Frequency shift contours which were numerically calculated from the analytical model were used to do this. The slot locations were assessed with great accuracy, although the slot depths were estimated to be larger than the actual values, due to the limitation of the perturbation method. © *1997 Acoustical Society of America.* [S0001-4966(97)03807-1]

PACS numbers: 43.58.Kr, 43.60.Lq, 43.40.At, 43.35.Cg [SLE]

LIST OF SYMBOLS

E	Young's modulus
ρ	density
a	location of left slot edge from left end of the beam
c	slot width
ds	slot depth
h	beam height
l	beam length
ds/h	relative slot depth
$I(x)$	moment of inertia, in general, a function of spatial coordinate x
$A(x)$	cross-sectional area, in general, a function of spatial coordinate x
$\alpha=I'/I_0$	ratio of moment of inertia with and without a slot
$\gamma=A'/A_0$	ratio of cross-sectional area with and without a slot
$\delta_{mn}=1, \quad m=n,$ $=0, \quad m\neq n$	Kronecker delta
$\kappa=1/\alpha-1$	slot depth factor related to moment of inertia
$\mu=1/\gamma-1$	slot depth factor related to cross-sectional area
$v(x,t)$	displacement
$V_n(x)$	nth mode shape
ω_n	nth modal frequency
$V_{n1}(x)$	first-order perturbation of nth mode shape
ω_{n1}	first-order perturbation of nth modal frequency
$V_{n2}(x)$	second-order perturbation of nth mode shape
ω_{n2}	second-order perturbation of nth modal frequency
$u(x-a)$	unit step function, $u(x-a)=1$ for $x>a$ and 0 elsewhere

INTRODUCTION

As we pointed out in an earlier paper,[1] there is a great motivation to develop techniques for rapid, global inspection of structures. That paper also contained an extensive literature survey which will not be repeated here. Most earlier work employed standard signal processing techniques which do not include any model to make account of the nature of the test object. The purpose of our research program is to develop the scientific understanding necessary to make monitoring effective and thus our first step was the development of a mathematical model of a defective test article. It was pointed out in the previous paper[1] that the limitation of the method is the effect on the signal of harmless uncertainties such as coatings, flexible end conditions, and wear. The use of a model potentially might allow the effects of these uncertainties to be separated from the changes due to a harmful defect. We chose a beam as the test body since it is a basic component of most structures and used a slot as a simulated defect.

Solution of the mathematical model of the slotted beam using a Laplace transform method as presented in the previous publication[1] led to a complicated frequency equation

which had to be solved numerically. It was therefore not suitable for on-line use. As the main purpose of having a model is to program it into the data processing, a more computationally efficient technique was desirable. In this paper therefore, a perturbation method is adapted to solve the same mathematical model more efficiently. The formulas resulting from the perturbation method could be incorporated in real-time data processing. The perturbation method has the added advantage that the process using it is invertible, so that the defect characteristics can be determined solely from the measured vibration response of the system. Finite element methods are not suited for this application because high-frequency responses are required necessitating small elements and prohibitively long computation time.

I. ANALYTICAL MODEL

A. First-order perturbation

The Euler–Bernoulli theory for vibration of a beam with varying moment of inertia and cross-sectional area leads to the equation

$$\frac{\partial^2}{\partial x^2}\left(EI(x)\,\frac{\partial^2 v}{\partial x^2}\right)+m\,\frac{\partial^2 v}{\partial t^2}=0. \tag{1}$$

For a nonslotted uniform beam, the vibration equation may be written in terms of the nth mode shape $V_{n0}(x)$ and the nth modal frequency ω_{n0} of the uniform beam, thus

$$EI_0\,\frac{\partial^4 V_{n0}(x)}{\partial x^4}-\rho A_0\omega_{n0}^2 V_{n0}(x)=0. \tag{2}$$

The modal frequency of such a beam is determined by the boundary conditions. For example, the nth modal frequency of a cantilever is given by

$$1+\cosh(\beta_n l)\cos(\beta_n l)=0, \tag{3}$$

where

$$\beta_{n0}^4=\frac{\rho A_0\omega_{n0}^2}{EI_0}. \tag{4}$$

For a slotted beam, Eq. (1) becomes

$$\frac{\partial^2}{\partial x^2}\left(EI(x)\,\frac{\partial^2 V_n(x)}{\partial x^2}\right)-\rho A\omega_n^2 V_n(x)=0, \tag{5}$$

where ω_n and $V_n(x)$ are the nth modal frequency and nth mode shape of the slotted beam. The presence of the slot causes the moment of inertia and the cross-sectional area to be reduced at the slot location, thus increasing the local flexibility which will tend to decrease the modal frequency and change the mode shape. On the other hand, the presence of the slot implies that there is mass reduction and thus the modal frequency tends to increase. The parameters of the slotted beam are shown in Fig. 1. The changes in the moment of inertia and the cross-sectional area are directly related to the slot depth, slot width, and location and can be described by

$$I(x)=I_0-I_1(x)=I_0-\kappa I_0[u(x-a)-u(x-a-c)], \tag{6}$$

and

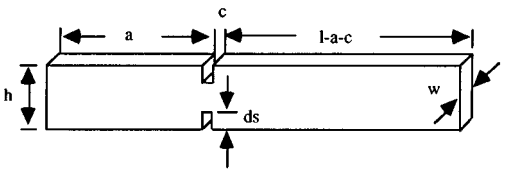

FIG. 1. Parameters for a beam with a symmetric slot of width c, and depth ds from top and bottom of the beam. The slot is located at $x=a$ from the left end. The beam is l by h by w.

$$A(x)=A_0-A_1(x)=A_0-\mu A_0[u(x-a)-u(x-a-c)]. \tag{7}$$

In the case of small slots, $I_1(x)$ and $A_1(x)$ can be taken as the perturbation introduced by the slot. The parameters κ and μ depend on the relative slot depth. Both of them are zero for uniform beams.

We assume that the modal parameters have a small perturbation $V_{n1}(x)$ due to the defect given by the form

$$V_n(x)=V_{n0}(x)+V_{n1}(x)=V_{n0}(x)+\sum_{\substack{j=1,\\ j\neq n}}^{N}\epsilon_{nj}V_{j0}(x). \tag{8}$$

Since the eigenvalue depends on the square of the frequency, we assume the perturbation in the nth modal frequency is given by

$$\omega_n^2=\omega_{n0}^2-\omega_{n1}^2. \tag{9}$$

Solving Eq. (5) using the assumed perturbations (see Appendix) yields

$$\frac{1}{N_{mn}}\sum_{\substack{j=1,\\ j\neq n}}^{N}\epsilon_{nj}(\omega_{j0}^2-\omega_{n0}^2)N_{mj}\delta_{mj}-\kappa\omega_{n0}^2A_{nm}+\mu\omega_{n0}^2B_{nm}+\omega_{n1}^2\delta_{mn}=0, \tag{10}$$

where

$$\int_0^l V_{m0}(x)V_{n0}(x)\,dx=N_{nm}\delta_{mn}, \tag{11}$$

$$\frac{EI_0}{N_{nn}\rho A_0\omega_{n0}^2}\int_a^{a+c}\frac{\partial^2 V_{n0}}{\partial x^2}\,\frac{\partial^2 V_{j0}}{\partial x^2}\,dx=A_{nj}, \tag{12}$$

and

$$\frac{1}{N_{nn}}\int_a^{a+c}V_{n0}V_{j0}\,dx=B_{nj}. \tag{13}$$

Thus we have for the nth modal frequency of the slotted beam

$$\omega_n^2=\omega_{n0}^2-\omega_{n1}^2=\omega_{n0}^2-\omega_{n0}^2[\kappa A_{nn}-\mu B_{nn}], \tag{14}$$

and the nth mode shape is

$$V_n(x)=V_{n0}(x)+\sum_{\substack{m=1\\ m\neq n}}^{N}\left[\frac{\kappa A_{mn}\omega_{m0}^2-\mu\omega_{n0}^2B_{mn}}{\omega_{m0}^2-\omega_{n0}^2}\right]V_{m0}(x). \tag{15}$$

If the slot depth $ds=0$, i.e., $\kappa=\mu=0$, Eqs. (14) and (15) reduce to those of the uniform beam. If the slot width $c=0$, and then $A_{mn}=B_{mn}=0$, Eqs. (14) and (15) reduce to those of the uniform beam. Equations (14) and (15) are valid

for relatively small slot depth because they include only the first-order perturbation, although no assumption is made on the slot width to derive Eqs. (14) and (15). To validate the model, another special case is considered. When the slot width is the same as the beam length, the ''slotted beam'' is actually a beam with reduced overall height, or in other words, it is another uniform beam. In this case, we have

$$A_{mn}=\delta_{mn}, \tag{16}$$

$$B_{mn}=\delta_{mn}, \tag{17}$$

and therefore Eqs. (14) and (15) reduce to

$$\omega_n^2=\omega_{n0}^2[1-\kappa+\mu] \tag{18}$$

and

$$V_n(x)=V_{n0}(x). \tag{19}$$

Equation (19) states that the slotted beam with a slot width equal to the beam length has the same mode shape as the original uniform beam, which is definitely true. The effects of changing slot width can be discussed using Eq. (18). When the mass reduction overwhelms the decrease of moment of inertia ($\mu \geqslant \kappa$), the perturbation term ω_{n1} is imaginary and the natural frequency of the slotted beam actually increases as can be seen from Eq. (18). This model does not apply to the case of a large slot or for the beam being cut through ($ds/h \rightarrow 1$) because the fundamental assumption of the perturbation method is that the perturbation terms are very small which implies $ds/h \ll 1$.

B. Second-order perturbation

Including only the first-order perturbation in computing the modal frequency and mode shape implies that the second- and higher-order perturbations are negligible. This has to be justified. The following discussion applies to all possible cases and should better justify the neglect of higher-order terms.

To obtain the second-order perturbation, we assume

$$V_n=V_{n0}+V_{n1}+V_{n2} \tag{20}$$

and

$$\omega_n^2=\omega_{n0}^2-\omega_{n1}^2-\omega_{n2}^2. \tag{21}$$

Here ω_{n2} and $V_{n2}(x)$ are the second-order perturbations in the nth modal frequency and the nth mode shape, respectively. Substituting Eqs. (20) and (21) into Eq. (7), and following the same procedures used to solve for the first-order perturbation, we obtain the nth modal frequency and mode shape:

$$\omega_{n2}^2=\mu\omega_{n1}^2B_{nn}+\omega_{n0}^2\sum_{j\neq n}[\kappa\epsilon_{nj}A_{nj}-\mu\epsilon_{nj}B_{nj}]. \tag{22}$$

$$V_{n2}(x)=\sum_{\substack{m=1\\ m\neq n}}^{N}\gamma_{nm}V_{m0}(x), \tag{23}$$

where

$$\gamma_{nm}=\frac{\{\kappa\omega_{m0}^2(\delta_{nl}+\Sigma_{l=1,l\neq n}\epsilon_{nl})A_{m1}-[(\omega_{n0}^2-\omega_{n1}^2)\delta_{nl}+\omega_{n0}^2\Sigma_{l=1,l\neq n}\epsilon_{nl}]B_{m1}-(\omega_{m0}^2-\omega_{n0}^2+\omega_{n1}^2)\epsilon_{nm}\}}{(\omega_{m0}^2-\omega_{n0}^2)}. \tag{24}$$

There are two limiting cases which are apparent. When the slot width c is zero, both the first- and the second-order perturbations in the modal frequency vanish. For the other limiting case when the slot width is the same as the beam length, we have, for small slot depth,

$$\omega_{n2}^2=\mu\omega_{n1}^2 \ll \omega_{n1}^2. \tag{25}$$

For the intermediate case when the slot width is nonzero, and much smaller than the beam length, we have to demonstrate that the second-order perturbation is negligibly small compared to the first-order one.

We know from Eq. (8) that

$$V_{n0}(x) \gg V_{n1}(x)=\sum_{j\neq n}\epsilon_{nj}V_{j0}(x), \tag{26}$$

therefore we have

$$A_{nn}=\frac{EI_0}{N_{nn}\rho A_0\omega_{n0}^2}\int_a^{a+c}\left[\frac{\partial^2V_{n0}}{\partial x^2}\right]^2dx \geqslant \frac{EI_0}{N_{nn}\rho A_0\omega_{n0}^2}\int_a^{a+c}\frac{\partial^2V_{n0}}{\partial x^2}\frac{\partial^2V_{n1}}{\partial x^2}dx=\sum_{j\neq n}\epsilon_{nj}A_{nj} \tag{27}$$

and

$$B_{nn}=\frac{1}{N_{nn}}\int_a^{a+c}V_{n0}^2dx \gg \frac{1}{N_{nn}}\int_a^{a+c}V_{n0}V_{n1}\,dx = \sum_{j\neq n}\epsilon_{nj}B_{nj}. \tag{28}$$

We also have

$$0<A_{nn}\approx\frac{c}{l}\ll 1, \tag{29}$$

$$0<B_{nn}\approx\frac{c}{l}\ll 1. \tag{30}$$

To compare the first- and second-order perturbations in the modal frequency, their ratio is used:

$$\frac{\omega_{n2}^2}{\omega_{n1}^2} = \mu B_{nn} + \frac{\kappa \Sigma_{j\neq n} \epsilon_{nj} A_{nj} - \mu \Sigma_{j\neq n} \epsilon_{nj} B_{nj}}{\omega_{n1}^2}\, \omega_{n0}^2$$

$$= \mu B_{nn} + \frac{\kappa \Sigma_{j\neq n} \epsilon_{nj} A_{nj} - \mu \Sigma_{j\neq n} \epsilon_{nj} B_{nj}}{\kappa A_{nn} - \mu B_{nn}}$$

$$= \mu B_{nn} + \frac{\Sigma_{j\neq n} \epsilon_{nj} A_{nj}}{A_{nn}} \frac{1 - (\mu \Sigma_{j\neq n} \epsilon_{nj} B_{nj} / \kappa \Sigma_{j\neq n} \epsilon_{nj} A_{nj})}{(1 - \mu B_{nn} / \kappa A_{nn})}. \quad (31)$$

Because

$$\frac{1 - (\mu/\kappa)(\Sigma_{j\neq n} \epsilon_{nj} B_{nj} / \Sigma_{j\neq n} \epsilon_{nj} A_{nj})}{1 - (\mu B_{nn} / \kappa A_{nn})} \approx \frac{1 - (\mu/\kappa)}{1 - (\mu/\kappa)} = 1, \quad (32)$$

and

$$A_{nn} \gg \sum_{j\neq n} \epsilon_{nj} A_{nj} \quad (33)$$

we have

$$\frac{\Sigma_{j\neq n} \epsilon_{nj} A_{nj}}{A_{nn}} \frac{(1 - \mu \Sigma_{j\neq n} \epsilon_{nj} B_{nj} / \kappa \Sigma_{j\neq n} \epsilon_{nj} A_{nj})}{(1 - \mu B_{nn} / \kappa A_{nn})} \ll 1. \quad (34)$$

We also have

$$\mu B_{nn} \ll 1, \quad (35)$$

and therefore Eq. (31) yields

$$\omega_{n2}^2 \ll \omega_{n1}^2. \quad (36)$$

In other words, the second-order perturbation in the modal frequency is much smaller than the first-order perturbation for all $0 < c \ll l$. Similarly it can be shown that the second-order perturbation in the mode shape is much smaller than the first-order perturbation for all $0 < c \ll l$. Thus including only the first-order perturbation is sufficient to compute the modal frequency and mode shape for most cases in which $0 < c \ll l$ is well satisfied.

Solving the first-order perturbation of the natural frequency using Eq. (14) involves only computation of two coefficients A_{nn} and B_{nn}, while the addition of the second order using Eq. (22) would increase computation effort dramatically as all the cross coefficients A_{nj} and B_{nj} are required as well. The computation of the mode shape in both cases requires at least all the cross coefficients and thus would not be efficient for on-line processing.

As the method proposed uses only the modal frequency, it is more computationally efficient than the complete perturbation solution including both mode shapes and modal frequencies. Although the first-order perturbation method is of limited accuracy, it can serve to check for computer errors when solving not only by the previous analytical method[1] but also finite element models.

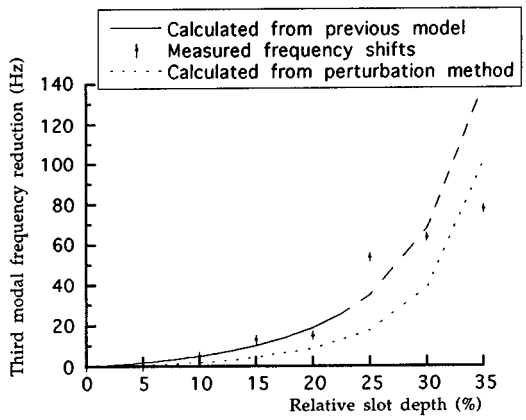

FIG. 2. Comparison of results from the previous model and the present perturbation method with measured data. The beam is a clamped-clamped beam of 36 by 2 by 0.75 in.

II. NUMERICAL RESULTS

A clamped-clamped steel beam was used to compare the results from the previous model[1] and the perturbation method along with the appropriate measured data as shown in Fig. 2. The beam is 36 by 2 by 0.75 in. with a slot centrally located. The frequency resolution for the measured data is about 5 Hz. As expected, the perturbation method predicted smaller frequency reductions when compared to those from the previous model. When the slot is about 20% of the beam height, the previous model predicts a frequency shift with about 7.5% discrepancy from the measured value while the perturbation method has a discrepancy of about 30%. The previous model provides a better match to the measured frequency reduction although it is less efficient in computation than the perturbation method. Neither model is expected to work very well for slots larger than 20%. The calculated results from the perturbation method have the same trend as those calculated from the previous model as well as the measured data.

The perturbation model can also be used to predict the modal frequency for a beam as a function of slot parameters. For example, the third modal frequency for a slotted cantilever (18 by 2 by 0.75 in.) was calculated for different slot locations and depths as shown in Fig. 3. It can be seen that at a given location, the larger the slot depth, the larger the frequency reduction. The third modal frequency shift versus slot location resembles the shape of the third mode. A reduction in the cross-sectional area is related to the removal of mass, which therefore tends to increase the modal frequency. A reduction in the moment of inertia is related to a decrease in stiffness, and therefore leads to a reduction of the modal frequency. Close to the clamped end, the effect due to the reduction in the moment of inertia dominates, and thus the modal frequency then has a large reduction. Alternatively the effect may be viewed as a transition in the boundary condition to a pinned end. Close to the free-free end, the effect due to the reduction in the cross-sectional area dominates, and actually results in an increase in the modal frequency. This is equivalent to shortening the beam.

For any assumed slot characteristics, including the slot depth, width, and location, the first several modal frequen-

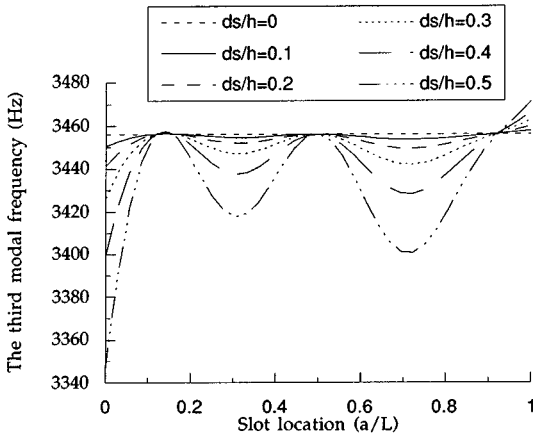

FIG. 3. The third modal frequency versus relative slot location (a/L) for six different slot depths ($ds/h=0$ to 0.5). Slot width c is constant 0.04 in. The cantilever beam is 18 by 2 by 0.75 in. and is clamped at $x=0$.

cies can be computed from Eqs. (16) and (17). For example, using a constant slot width, frequency contours are shown for the first, second, and third modes of a cantilever in Figs. 4, 5, and 6, respectively. Each point located on one of these frequency contours represents a combination of slot depth and location which will produce a resonance for the given mode at the given frequency. Figure 7 illustrates how frequency contours may be used inversely to determine the slot characteristics. Suppose there was a slot in the beam with $ds/h=0.6$ and $a/L=0.3$, then the first mode contour passing through (0.3,0.6) is at a frequency of 195 Hz, the second mode contour a frequency of 1230 Hz, and the third mode contour a frequency of 3410 Hz. Thus in the inverse process, if the modal frequencies are known to be at 195, 1230, and 3410 Hz then the slot parameters can be determined by finding the points at which the contours for these frequencies intersect.

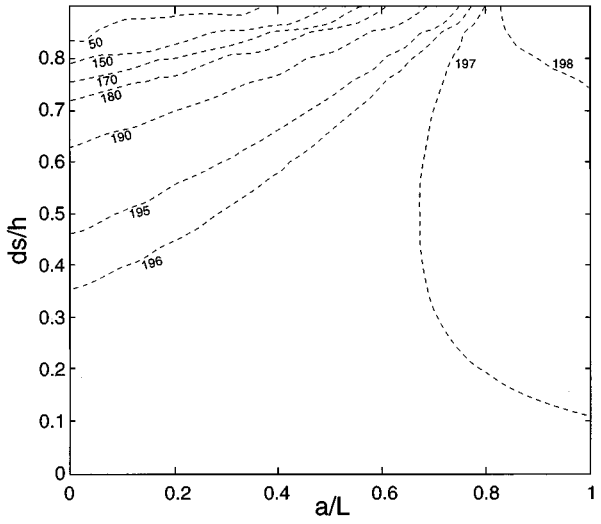

FIG. 4. Contour plot for the first modal frequency (Hz) versus slot location (a/L) and slot depth (ds/h). The cantilever beam is 18 by 2 by 0.75 in. The slot width remains constant at 0.04 in.

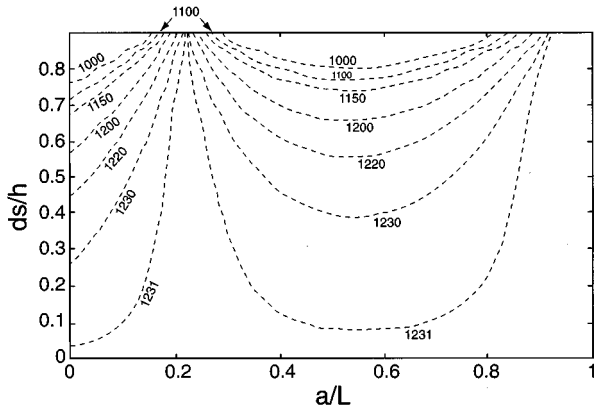

FIG. 5. Contour plot for the second modal frequency (Hz) versus slot location (a/L) and slot depth (ds/h). The cantilever beam is 18 by 2 by 0.75 in. The slot width remains constant at 0.04 in.

III. EXPERIMENTAL RESULTS

Steel beams were tested on a fixture described previously.[1] The vibration was excited using an impact hammer. The vibration response signals were recorded with an accelerometer. Low-pass filters with a cutoff frequency of 10 kHz were used. The signal was sampled using an analog to digital conversion board controlled by a Compudyne microcomputer. The sampling frequency was set at 20 kHz. A frequency transfer function in terms of a mobility function was computed from the excitation and response signals. As the signals are nonstationary,[2] no smoothing was done in estimation of the amplitude spectra of the signals. The final mobility function was obtained by averaging over those from ten repeated impacts to reduce the estimation error. The modal parameters were then determined from the mobility function using modal analysis techniques.[3]

A cantilever beam (18 by 2 by 0.75 in.) was cut with a slot whose depth was increased in increments from 0 to 0.7 in. final total depth. For each slot depth, the cantilever beam was placed on the fixture. The third mode frequency reduction versus the slot depth for the cantilever beam are shown in Fig. 8, with a 0.04-in.-wide slot located at 5 in. from the clamped end. Because the cantiliver beams have a slender-

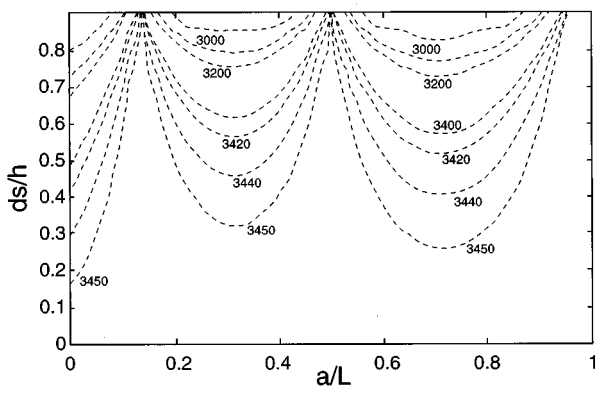

FIG. 6. Contour plot for the third modal frequency (Hz) versus slot location (a/L) and slot depth (ds/h). The cantilever beam is 18 by 2 by 0.75 in. The slot width remains constant at 0.04 in.

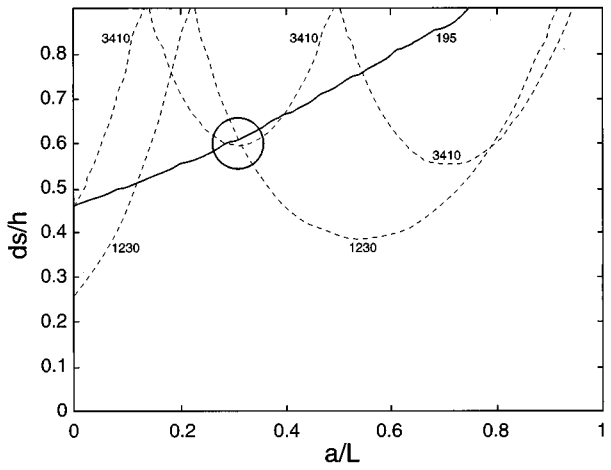

FIG. 7. Determination of the slot location (a/L) and slot depth (ds/h) from the first three modal frequency contours and three assumed modal frequency values. The cantilever beam is 18 by 2 by 0.75 in. The slot width is 0.04 in. The intersection point (0.3, 0.6) determines the beam parameters.

ness of only 0.032, the Timoshenko correction[4–6] is included. Slenderness is defined as the ratio of the radius of gyration and the beam length. As can be seen from Fig. 8, the perturbation method predicted the third modal frequency with acceptable accuracy for slots with depth less than 20% of the beam. The discrepancy between the experimental modal frequency and the calculated values becomes large as the slot depth increases, as shown in Fig. 1, and thus the applicability of this model is limited to slots of relatively small depth.

Eleven steel beams (seven slotted and four uniform) were used as a test population. As a first exercise, the defective beams were separated from the nondefective ones using the measured modal frequency of each. A defectiveness index was defined by

$$\text{defectiveness index (DI)} = \sum_{i=1}^{n} \frac{|f_i^{\text{cal}} - f_i^{\text{est}}|}{f_i^{\text{est}}} \times 100\%. \qquad (37)$$

Here f_i^{est} is the experimentally estimated ith modal frequency and f_i^{cal} is the value calculated from Euler–Bernoulli beam theory. In addition, for greater accuracy, corrections are included in the model from Timoshenko beam theory, and for slight flexibility in the end conditions. The DI values are significantly different between the defective beams and the nondefective ones as shown in Table I. Here c stands for clamped, f, for free, and p for pinned. The beam with a DI larger than a certain threshold is determined to be defective. A threshold of 5% is sufficient to discriminate the defective beams from the nondefective ones. No false decision occurred for all 11 specimens.

TABLE I. Defectiveness of the beam specimens.

	End condition	Defectiveness index (%)	Defective? Yes/No	Decision correctness
Beam 1	c-f	27.58	Yes	Correct
Beam 2	c-f	18.84	Yes	Correct
Beam 3	c-c	10.83	Yes	Correct
Beam 4	c-c	0.94	No	Correct
Beam 5	c-c	0.61	No	Correct
Beam 6	f-f	0.65	No	Correct
Beam 7	f-f	54.04	Yes	Correct
Beam 8	f-f	54.04	Yes	Correct
Beam 9	f-f	51.57	Yes	Correct
Beam 11	p-p	26.25	Yes	Correct
Beam 12	p-p	1.6	No	Correct

Once the defective beams are separated from the nondefective ones, the next objective was to identify the defect size and location. Each defective beam has a slot of the same width, but different depth and location. Equation (16) was used to compute the numerical frequency shifts for several modes. Frequency shift contours were obtained, and thus the size of the slot was assessed.

As an example, the first defective beam measured had frequency shifts of 18.0, 19.8, and 420.5 Hz in the first three modes. The corresponding contours for these three modal frequency shifts were recalled from a data base calculated using Eq. (14) and are shown in Fig. 9. The relative slot depth and location were found from Fig. 9 to be those corresponding to the intersection of the three contours. As the modal frequency was always estimated within a range of

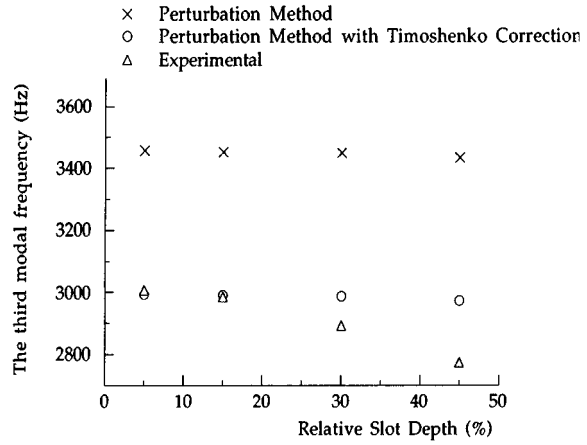

FIG. 8. The third modal frequency versus relative slot depth for a cantilever beam of 18 by 2 by 0.75 in. Slot width $c = 0.04$ in., and slot location $a = 5$ in.

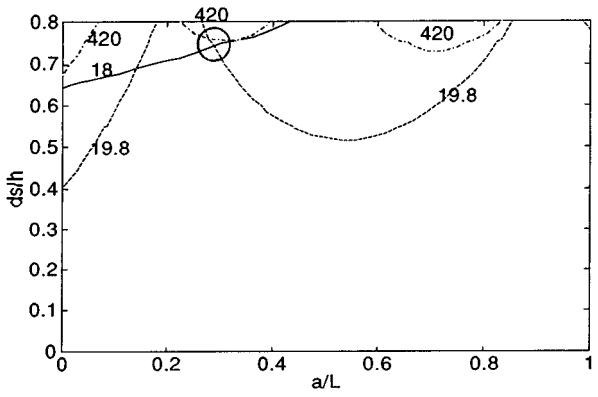

FIG. 9. The first three frequency shift contours for the first defective beam versus the relative slot location and depth. The solid, dot-dashed, and dashed contours are for the *measured* frequency shifts in the first, second, and third modes, respectively.

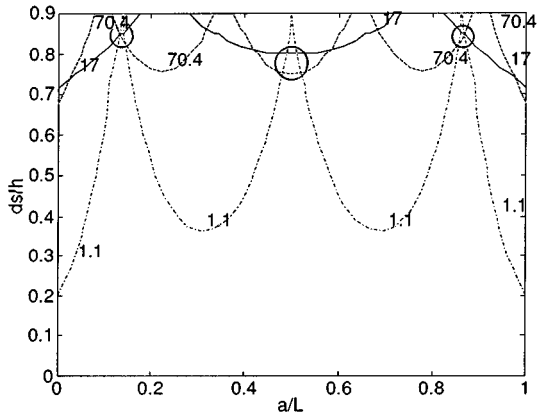

FIG. 10. The first three frequency shift contours for the first defective beam versus the relative slot location and depth. The solid, dot-dashed, and dashed contours are for the *measured* frequency shifts in the first, second, and third modes, respectively.

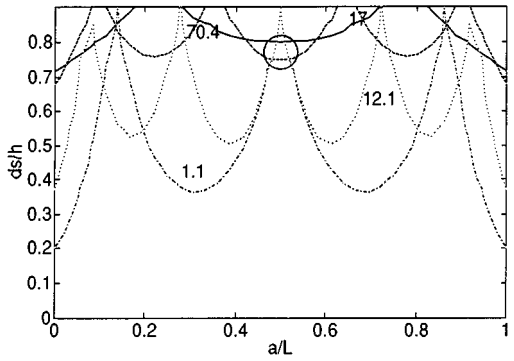

FIG. 11. Quantification of the slot parameters of the third defective beam using the first four frequency shift contours. The solid, dot-dashed, dashed, and dotted contours are for the *measured* frequency shifts in the first, second, third, and fourth modes, respectively.

uncertainty, the ''intersection'' was an area of overlap which determines the range of the slot depth and location. For this beam, the slot was determined to have a relative depth of about 0.75 and a relative location of about 0.27, i.e., a depth of 1.5 in. and location at 4.9 in. from the fixed end. The actual slot was 0.7 in. deep at 5.0 in. from the fixed end. The discrepancy in estimation of the slot depth is over 100% but less than 5% in identification of the slot location. The reason for this is discussed later.

If we had only one modal frequency shift to use, the slot depth and location could be any of an infinite number of possible combinations. If two modal frequency shifts are available, the possible slot location and depth combinations are those at the intersections of the two frequency shift contours. If there is more than one combination found from the two frequency contours, then the frequency shift for another mode has to be employed. Using more modes eventually leads to a unique determination of the slot depth and location. To illustrate this, the first three modal frequency shifts of a clamped-clamped slotted beam were used. These have the frequency shift contours shown in Fig. 10. Three possible combinations of the slot location and depth were found here. The slot might be at the relative slot locations at 0.15, 0.5, and 0.85 with corresponding relative depth of 0.8, 0.85, and 0.85. Of these, the first and the third combinations are virtually the same as the beam is symmetric about its center.

To be able to determine the real slot depth and location, the fourth modal frequency shift of 12.1 Hz was added as shown in Fig. 11. Only a slot located at the middle of the beam (i.e., the relative location $a/L=0.5$, $a=18$ in.) with a slot depth 1.6 in. (i.e., the relative slot depth $ds/h=0.8$) was left. The actual slot was located at the middle of the beam with a slot depth of 0.7 in. The discrepancy in the slot depth estimation is over 120% for this large slot ($ds/h=35\%$). Once again the slot depth is estimated larger than the actual value.

The test results for all seven slotted beams are summarized in Table II. The slot locations were estimated with great accuracy while the slot depths were always assessed much larger than the actual values. The reason for this is that the perturbation method tends to predict smaller frequency shifts than the actual values (see Figs. 2 and 3), and when used inversely, reports larger slot depths. Even though the perturbation model used is much less accurate in modeling the effect of the slot depth, it is encouraging how well it does identify slot location. As discussed before, the discrepancy between the natural frequency reduction as measured and predicted was small when the previous analytical method was used (about 7.5% error when $ds/h=20\%$), but is large when the perturbation method is used as shown in Fig. 2. The large error when using the perturbation method to estimate slot depth is expected but is compensated by the great improvement in the computation efficiency which it produces.

IV. DISCUSSION AND CONCLUSIONS

The main conclusion of this paper is that by including a model in the data processing, the characteristics of a slot can be quantified inversely from the vibration response of the beam. The mathematical model of the slotted beam solved by a perturbation method leads to direct relationships between the defect parameters and the modal properties. The resulting equations clearly show the dependence of modal frequency reductions upon the slot characteristics, including location and size. Laboratory investigations with beams of increasing slot depths agreed with the results calculated from the model for slots of depth less than 20% of the beam height. As only the first-order perturbation is included, the resulting formula is applicable to beams with relatively small slots, i.e., slots with a depth of less than 20% of the beam

TABLE II. The estimated slot characteristics of seven defective beams.

Number	Defective beams	Estimated ds/h	Estimated a/L	Actual ds/h	Actual a/L
1	Beam 1	~0.75	~0.27	0.35	0.28
2	Beam 2	~0.72	~0.27	0.5	0.28
3	Beam 3	~0.78–0.8	~0.5	0.35	0.5
4	Beam 7	~0.8–0.83	~0.4	0.625	0.4
5	Beam 8	~0.8–0.83	~0.4	0.625	0.5
6	Beam 9	~0.8–0.83	~0.35 or 0.65	0.625	0.36
7	Beam 11	~0.8–0.83	~0.42 or 0.58	0.375	0.42

height. Since we are more concerned about the ability to quantify small slots and the large slots are much easier to detect in practice, the inaccuracy of the model for large slot sizes should not be a problem.

A procedure was proposed for data collection and processing to quantify the slot parameters. Following this procedure, the slot location and depth were determined from the measured vibration signals. A test using 11 steel beams with various conditions was successful. The results of these tests showed that the slot can be inversely monitored by processing the vibration signals with the numerical results from the analytical models. The slot locations were determined with great accuracy, although the slot depths were estimated with large systematic error.

In the Introduction it was pointed out that there would be uncertainties caused by harmless conditions such as coatings, flexible end conditions, and wear, which might contribute to modal frequency changes in a structure. This paper has demonstrated that the method is robust in the face of the uncertainties present in this experimental setup (mounting and remounting, geometrical variations, etc). Some of these uncertainties could themselves be modeled and thus eliminated as sources of false alarms. How well the technique would perform in the field remains to be seen.

ACKNOWLEDGMENTS

The authors wish to thank the National Science Foundation (NSF Grant No. MSS-9024224) for support of this project.

APPENDIX

Substituting Eqs. (8) and (9) into (5) yields

$$\frac{\partial^2}{\partial x^2}\left[(I_0-I_1(x))\,\frac{\partial^2(V_{n0}(x)+V_{n1}(x))}{\partial x^2}\right] - \frac{\rho}{E}\,(A_0-A_1(x))(\omega_{n0}^2-\omega_{n1}^2)(V_{n0}(x)+V_{n1}(x))=0. \tag{A1}$$

Eliminating all the higher-order terms and subtracting Eq. (4) from Eq. (A1) gives

$$I_0\,\frac{\partial^4 V_{n1}(x)}{\partial x^4}-\frac{\partial^2}{\partial x^2}\left[I_1(x)\,\frac{\partial^2 V_{n0}(x)}{\partial x^2}\right] + \frac{\rho}{E}\,(A_0\omega_{n1}^2V_{n0}-A_0\omega_{n0}^2V_{n1}+A_1\omega_{n0}^2V_{n0})=0. \tag{A2}$$

Substituting Eq. (8) into Eq. (A2) yields

$$I_0\sum_{\substack{j=1,\\ j\neq n}}^{N}\epsilon_{nj}\,\frac{\partial^4 V_{j0}(x)}{\partial x^4}-\frac{\partial^2}{\partial x^2}\left[I_1(x)\,\frac{\partial^2 V_{n0}(x)}{\partial x^2}\right] + \frac{\rho}{E}\left(A_0\omega_{n1}^2V_{n0}-A_0\omega_{n0}^2\sum_{\substack{j=1,\\ j\neq n}}^{N}\epsilon_{nj}V_{j0}(x)+A_1\omega_{n0}^2V_{n0}\right) =0. \tag{A3}$$

Multiplying both sides of Eq. (A3) with $V_{m0}(x)$ and integrating along the beam gives

$$\frac{E}{\rho}\left[I_0\sum_{\substack{j=1,\\ j\neq n}}^{N}\epsilon_{nj}\int_0^l V_{m0}\,\frac{\partial^4 V_{j0}(x)}{\partial x^4}\,dx - \int_0^l V_{m0}\,\frac{\partial^2}{\partial x^2}\left[I_1(x)\,\frac{\partial^2 V_{n0}(x)}{\partial x^2}\right]dx + \left(A_0\omega_{n1}^2\int_0^l V_{m0}V_{n0}\,dx+\omega_{n0}^2\int_0^l A_1V_{m0}V_{n0}\,dx - A_0\omega_{n0}^2\sum_{\substack{j=1,\\ j\neq n}}^{N}\epsilon_{nj}\int_0^l V_{m0}V_{j0}(x)dx=0. \tag{A4}$$

Using Eq. (11) and

$$\frac{\partial^4 V_{n0}(x)}{\partial x^4}=\frac{\rho A_0\omega_{n0}^2}{EI_0}\,V_{n0}(x) \tag{A5}$$

to simplify Eq. (A4) yields

$$\sum_{\substack{j=1,\\ j\neq n}}^{N}\epsilon_{nj}\omega_{j0}^2N_{mj}\delta_{mj}-\frac{EI_0}{\rho A_0}\int_0^l V_{m0}\,\frac{\partial^2}{\partial x^2}\left[\frac{I_1(x)}{I_0}\,\frac{\partial^2 V_{n0}(x)}{\partial x^2}\right]dx + \left(\omega_{n1}^2N_{mn}\delta_{mn}+\omega_{n0}^2\int_0^l\frac{A_1}{A_0}\,V_{m0}V_{n0}(x)dx - \omega_{n0}^2\sum_{\substack{j=1,\\ j\neq n}}^{N}\epsilon_{nj}N_{mj}\delta_{mj}=0. \tag{A6}$$

Integrating by parts twice in the second term of Eq. (A6), we obtain

$$\frac{EI_0}{\rho A_0}\int_0^l V_{m0}\,\frac{\partial^2}{\partial x^2}\left[\frac{I_1(x)}{I_0}\,\frac{\partial^2 V_{n0}(x)}{\partial x^2}\right]dx =\frac{EI_0}{\rho A_0}\left[V_{m0}\,\frac{\partial}{\partial x}\left(\frac{I_1(x)}{I_0}\,\frac{\partial^2 V_{n0}(x)}{\partial x^2}\right)\right]_0^l - \frac{EI_0}{\rho A_0}\left[\frac{I_1(x)}{I_0}\,\frac{\partial^2 V_{n0}(x)}{\partial x^2}\,\frac{\partial V_{m0}}{\partial x}\right]_0^l + \frac{EI_0}{\rho A_0}\int_0^l\frac{I_1(x)}{I_0}\,\frac{\partial^2 V_{n0}(x)}{\partial x^2}\,\frac{\partial^2 V_{m0}}{\partial x^2}\,dx. \tag{A7}$$

The first two terms on the right-hand side of Eq. (A7) are zero because $I_1(x)$ is not zero only at the slot location, and thus we have

$$\frac{EI_0}{\rho A_0}\int_0^l V_{m0}\,\frac{\partial^2}{\partial x^2}\left[\frac{I_1(x)}{I_0}\,\frac{\partial^2 V_{n0}(x)}{\partial x^2}\right]dx =\frac{EI_0}{\rho A_0}\int_0^l\frac{I_1(x)}{I_0}\,\frac{\partial^2 V_{n0}(x)}{\partial x^2}\,\frac{\partial^2 V_{m0}}{\partial x^2}\,dx. \tag{A8}$$

Substituting Eq. (A8) into Eq. (A6) gives

$$\sum_{\substack{j=1,\\ j\neq n}}^{N} \epsilon_{nj}(\omega_{j0}^2-\omega_{n0}^2)N_{mj}\delta_{mj}$$

$$-\frac{EI_0}{\rho A_0}\int_0^l \frac{I_1(x)}{I_0}\frac{\partial^2 V_{n0}(x)}{\partial x^2}\frac{\partial^2 V_{m0}}{\partial x^2}\,dx$$

$$+\omega_{n0}^2\int_0^l \frac{A_1}{A_0}V_{m0}V_{n0}(x)dx+\omega_{n1}^2 N_{mn}\delta_{mn}=0. \qquad \text{(A9)}$$

Simplifying Eq. (A9) using Eqs. (12) and (13) yields Eq. (10).

[1] X. C. Man, L. McClure, Z. Wang, R. D. Finch, P. Robin, and B. Jansen, ''Slot Depth Resolution in Vibration Monitoring of Beams Using Frequency Shifts,'' J. Acoust. Soc. Am. **95**, 2029–2037 (1994).

[2] P. Robin, B. Jansen, X. C. Man, Z. Wang, and R. D. Finch, ''Vibration Monitoring of Steel Beams by Evaluation of Resonance Frequency Decay Rates,'' J. Acoust. Soc. Am. **96**, 867–873 (1994).

[3] D. J. Ewins, *Modal Testing: Theory and Practice* (Research Studies, Letchworth, England, 1984).

[4] S. P. Timoshenko, ''On the Correction for Shear of the Differential Equation for Transverse Vibrations of Prismatic Bars,'' Philos. Mag. **41**, 744–746 (1921).

[5] S. P. Timoshenko, ''On the Transverse Vibrations of Bars of Uniform Cross Section,'' Philos. Mag. **43**, 125–131 (1922).

[6] G. R. Cowper, ''The Shear Coefficient in Timoshenko's Beam Theory,'' J. Appl. Mech., 335–340 (June 1966).

A computational model of the cochlear nucleus octopus cell

Kenneth L. Levy and Daryl R. Kipke[a)]
Bioengineering Program, Arizona State University, Tempe, Arizona 85287-6006

(Received 5 March 1996; revised 17 February 1997; accepted 28 February 1997)

Cochlear nucleus octopus cells are characterized by a temporally precise response at the onset of tone bursts and other phasic stimuli. The objectives of this study were to develop a biologically plausible model of an octopus cell based on typical morphological and physiological properties, and to describe the model's ability to simulate responses of octopus cells and onset units. The compartmental model represents the basic morphology of octopus cells with a single passive, equivalent dendrite and a lumped, active soma. Independent, excitatory synaptic inputs are distributed on the dendrite and soma to represent inputs from 60 or 120 auditory-nerve fibers. The computed model responses were evaluated using simulated current injections, short-duration tone bursts, and several other types of stimuli. With biologically plausible values for the model parameters, the representation of 60 auditory-nerve inputs yields responses consistent with an O_L unit while the representation of 120 inputs yields responses consistent with an O_I unit. This study demonstrates that responses typical of O_L and O_I units can be produced with a relatively simple model of an octopus cell. It also suggests that the numbers of independent auditory-nerve fiber inputs to the cell can affect the onset response. © *1997 Acoustical Society of America.* [S0001-4966(97)00807-2]

PACS numbers: 43.64.Bt, 43.64.Qh [RDF]

INTRODUCTION

The cochlear nucleus complex (CN) stands as the gateway to the central auditory system. Auditory-nerve fibers terminate on CN principal cells, which, in turn, project to auditory areas in the brain stem and midbrain (Helfert *et al.*, 1991). One type of principal cell, the octopus cell, is localized to the caudal and medial region of the posteroventral cochlear nucleus (PVCN) and projects to the ventral nucleus of the lateral lemniscus and periolivary nuclei (Kane, 1973; Smith *et al.*, 1993). Octopus cells typically spike precisely at the onset of tone oursts over a broad frequency range (Godfrey *et al.*, 1975; Rhode *et al.*, 1983) indicating a trade-off of spectral selectivity for temporal precision (Winter and Palmer, 1995; Golding *et al.*, 1995).

Three types of onset units have been described in the CN (Godfrey *et al.*, 1975; Rhode *et al.*, 1983; Rhode and Smith, 1986; Rhode, 1991). Onset-*L* (O_L) units have one or two precisely timed spikes at the onset of a short-duration tone burst at their characteristic frequency (CF), followed by a low level ($\leqslant$200 spikes/s) of sustained activity [Fig. 1(A)]. Except for their relatively high peak-to-steady-state firing ratios, many of their descriptive parameters are similar to those of auditory-nerve fibers and primarylike units (Rhode and Smith, 1986): dynamic range (average of 26 dB) frequency selectivity (average $Q_{10} \approx 5$), and maximum firing rate (average of 186 spikes/s). Onset-*I* (O_I) units have a similar temporally precise response at stimulus onset, but with less sustained activity ($<$10 spikes/s) [Fig. 1(B)]. O_I units exhibit broader frequency selectivity and have a narrower dynamic range (i.e., they act more as a switch; dynamic range of 10–25 dB) relative to auditory-nerve fibers [Fig. 1(C)] (Godfrey *et al.*, 1975; Rhode and Smith, 1986). Onset-*C* (O_C) units exhibit several quasiperiodic responses after stimulus onset and elevated sustained activity (Rhode and Smith, 1986). For both O_I and O_L units, the latency of the first spike after the stimulus onset is 2–4 ms, and for an individual unit, the first-spike timing is precise with a standard deviation of 0.1–0.3 ms (Rhode and Smith, 1986; Winter and Palmer, 1995).

Several studies have associated octopus cells in PVCN with either an O_I response (Godfrey *et al.*, 1975; Rouiller and Ryugo, 1984; Feng *et al.*, 1994) or an O_L response (Godfrey *et al.*, 1975; Ritz and Brownell, 1982; Rhode *et al.*, 1983; Smith *et al.*, 1993). However, O_I and O_L units have also been recorded outside the octopus cell area of the PVCN (Rouiller and Ryugo, 1984; Rhode and Smith, 1986; Blackburn and Sachs, 1989; Frisina *et al.*, 1990; Winter and Palmer, 1995) demonstrating that octopus cells are not the exclusive basis for these response types. O_C units have been associated with stellate (multipolar) cells found throughout the ventral cochlear nucleus (Rhode *et al.*, 1983) and were not considered in the present study.

An octopus cell typically has a 25- to 30-μm-diam soma and several relatively large diameter (6–10 μm) and short (100–300 μm) primary dendrites which tend to be oriented across isofrequency laminas of the PVCN (Osen, 1969; Kane, 1973; Kane, 1977; Rhode *et al.*, 1983; Ostapoff *et al.*, 1994). Synaptic terminals cover an estimated 70% of the somatic and dendritic surface with the vast majority having characteristics of excitatory synapses (Kane, 1973) with glutamate as the putative neurotransmitter (Golding *et al.*, 1995). While intracellular recordings have not indicated inhibitory responses, there is evidence of terminals adjacent to octopus cells that immunolabel for the inhibitory transmitter GABA (Saint Marie *et al.*, 1989). While it is generally agreed that octopus cells receive convergent inputs from

a)Electronic mail: kipke@asu.edu

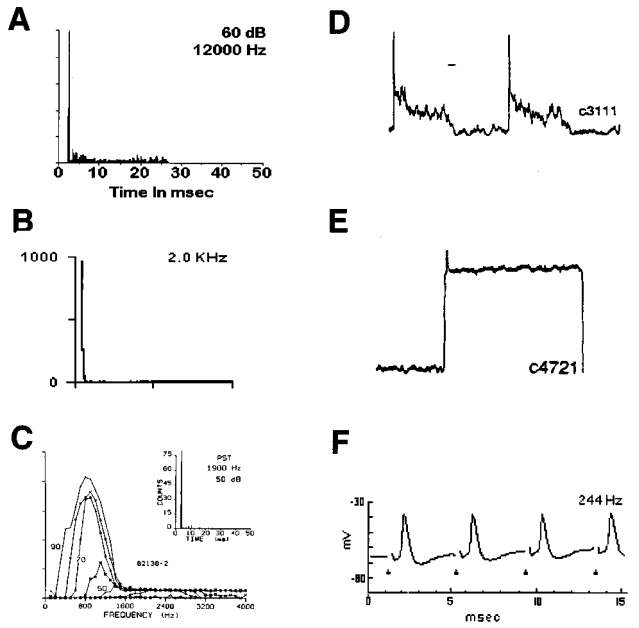

FIG. 1. Representative octopus cell responses from three experimental studies. (A) PSTH of an O_L unit. (B) PSTH of an O_I unit. (C) Response area of O_I unit with CF=2.2 kHz. (D) Intracellular recording in response to two CF tone bursts. (E) Intracellular recording in response to current injection. (F) Intracellular recording in response to strong shocks (10 V) of the auditory nerve at 244 Hz. Panel (A) reprinted with permission from Rhode (1983). Panels (B), (D), and (E) reprinted from Feng (1994). Panel (C) reprinted with permission from Rhode (1986). Panel (G) reprinted with permission from Golding (1995).

many auditory-nerve fibers (Liberman, 1993), it is very difficult to reliably measure the number of inputs distributed on the soma and dendrites. Using statistical arguments, Liberman (1993) estimates approximately 64 inputs per cell in the cat. The auditory-nerve fibers that terminate in the octopus cell area generally have intermediate to high CFs (Kane, 1973; Liberman, 1993) and tend to have high spontaneous rates (Liberman, 1993). A limited number of axon collaterals from octopus cells have been found to terminate in the octopus cell area (Golding *et al.*, 1995), which combined with the lack of inhibition, suggests recurrent connections among octopus cells.

Octopus cells typically have a membrane time constant of approximately 0.5 ms and an input resistance less than 10 MΩ, which is probably due to outward rectifier channels (Manis and Marx, 1991) during depolarization and mixed cation, inward rectifier channels during hyperpolarization (Golding *et al.*, 1995). *In-vivo* intracellular recordings in response to CF tone bursts exhibit single, precisely timed onset spikes (20–25 mV amplitude) followed by sustained depolarization with small amplitude fluctuations [Fig. 1(D)] (Feng *et al.*, 1994). Intracellular recordings with suprathreshold depolarizing current injections exhibit similar precisely timed spikes at the pulse onset followed by sustained depolarization with little or no amplitude fluctuations [Fig. 1(E)] (Romand, 1978; Feng *et al.*, 1994; Golding *et al.*, 1995).

Synaptic responses of octopus cells have been identified through the use of electrical shocks of the auditory nerve stump in a mouse brain-slice preparation (Golding *et al.*, 1995). Graded shocks elicited graded, time-varying somatic depolarization having a rise-time of around 0.5 ms. The typical short response latency was consistent with a monosynaptic connection to the auditory nerve, although a small number of responses exhibited larger latencies suggestive of an additional multisynaptic pathway. The response latencies were more variable to weak shocks than strong shocks and the cells were found to reliably synchronize to shocks at rates up to 244 Hz [Fig. 1(F)], which is near the upper range of auditory-nerve fiber average firing rates. At higher rates up to 700 Hz, the cells remained synchronized, but with more temporal variations. This ability of these cells to synchronize to high stimulus rates is also reflected by high degrees of synchronization by some O_L units to amplitude-modulated tones with modulation frequencies up to about 1000 Hz (Rhode and Greenberg, 1994) and to tone bursts with frequencies up to 1000 Hz (Rhode and Smith, 1986).

The experimental studies combine to provide a fairly rich composite picture of octopus cells based on morphological, electrophysiological, and unit response properties. However, links between these sets of data remain mostly descriptive rather than quantitative or predictive. For example, octopus cells receive many independent excitatory inputs from the auditory nerve and relatively few, if any, inhibitory inputs. Yet, their characteristic response involves precise timing at the stimulus onset and low sustained rates.

The objectives of this study were to develop a biologically plausible model of an octopus cell based on its typical morphological and physiological properties, and to describe the model's ability to simulate responses of octopus cells and onset units. Such a model provides a tool for investigating underlying mechanisms of octopus cells and aids in describing octopus cell processing. Some results of this study were previously presented in abstract form (Levy and Kipke, 1994a; Levy and Kipke, 1994b).

I. METHODS

A. Octopus cell model

The octopus cell model represents a typical octopus cell having properties consistent with, although not necessarily identical to, descriptions of individually identified octopus cells from several experimental studies (Osen, 1969; Kane, 1973; Kane, 1977; Rhode *et al.*, 1983; Ostapoff *et al.*, 1994). The representative octopus cell has four 7×150-μm cylindrical dendrites, a 25×25-μm cylindrical soma, a 5×15-μm axon hillock, and a 3×300-μm axon (Fig. 2). These dimensions are within the anatomically plausible range with the specific values chosen for numerical convenience. The specific membrane capacitance ($C_M = 1\ \mu\text{F/cm}^2$) and the specific axial resistance ($R_a = 150\ \Omega$ cm) are based on typical values for neural membranes (Rall, 1977). The specific membrane resistance ($R_m = 0.5\ \text{k}\Omega\ \text{cm}^2$) yields appropriate values for the membrane time constant ($\tau_m = 0.5$ ms) and the input impedance (R_{in}=3.5 MΩ). With these values, the dendritic characteristic length, $\lambda_d = 241\ \mu$m, and the dendritic electrotonic length, $L_d = 0.62$. The representative cell receives synaptic inputs from 60 independent auditory-nerve fibers ranging in CF from 4 to 1.4 kHz distributed on the dendrites and soma, with the higher frequency inputs proxi-

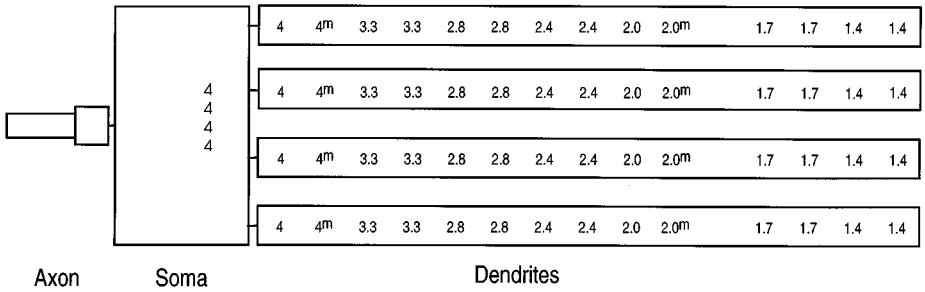

FIG. 2. The representative octopus cell consists of four identical cylindrical dendrites (7×150 μm), a cylindrical soma (25×25 μm), a cylindrical axon hillock (5×15 μm), and a cylindrical axonal segment (3×300 μm). The numbers in the dendrite and soma sections indicate the CF (in kHz) and distribution of the 60 independent auditory–nerve fiber inputs. The dendritic inputs are evenly spaced at 10-μm intervals. All inputs are from high spontaneous rate fibers except for those marked with a superscript, which are from medium spontaneous rate fibers.

mal and the lower frequencies distal to the soma; 56 inputs are divided equally among the four dendrites with the same tonotopic arrangement on each dendrite and four inputs are placed on the soma. The majority of inputs (52/60) are from high spontaneous rate nerve fibers and the remaining eight inputs are from medium spontaneous rate fibers all from a separate model of the auditory periphery. Available anatomical evidence suggests that low spontaneous rate fibers do not provide significant inputs to octopus cells (Liberman, 1993).

In implementing the model, the anatomical structure of the representative cell was simplified to increase computational efficiency. First, following Rall's 3/2 power law (Rall, 1989), the four dendrites were represented with a single equivalent 17.6×238-μm cylinder having the same electrotonic length. Second, the active axon was lumped into the soma. Using standard modeling procedures (Rall, 1989), the compartmental model was implemented with 15 equal-length (15.9 μm) dendritic compartments and two equal-length (12.5 μm) somatic compartments. The model parameters and equations are described in the Appendix.

The soma compartment opposite the dendrite contains the active channels. The active Hodgkin Huxley-like channels comprise the spike generator, with their equations based on a model of hippocampal CA3 neurons (Traub, 1982) with two modifications. First, the six rate equations for the three activation and inactivation parameters (m,h,n) were each doubled to decrease the spike duration such that it was more similar to the measured spike duration. Second, the synaptic densities of the active channels were set such that the computed spike amplitude is similar to measured spike amplitudes ($\overline{\mathbf{g}}_{\mathrm{Na}}=60$ mS/cm^2, $\overline{\mathbf{g}}_{\mathrm{K}}=120$ mS/cm^2). While it is problematic to set the synaptic densities in this way because of possible membrane damage caused by the intracellular electrodes, these data remain the best currently available. Voltage sensitive inward and outward rectifier channels found in octopus cells (Golding *et al.*, 1995) and other ventral cochlear nucleus cells (Manis and Marx, 1991) are not explicitly represented in the model. Rather, a primary effect of the outward rectifier channels at rest and during depolarization is to decrease R_{in}. This is represented by setting R_m to the relatively low, fixed value of 0.5 kΩ cm^2, which causes R_{in} to be 3.5 MΩ at the resting voltage of -65 mV.

The 56 dendritic inputs of the representative octopus cell are represented with 14 independent, time-varying synaptic conductances distributed uniformly on the equivalent dendrite, with one conductance in each of 14 dendrite compartments. Each synaptic conductance has a peak density of 1.2 mS/cm^2 relative to the compartment area and a rise time of 0.5 ms. The spike rate (probability) of the auditory-nerve input driving each conductance is increased by a factor of 4 and its refractory period is reduced by a factor of 4 (to 0.19 ms), relative to the outputs of the auditory periphery model (see below). The passive soma compartment received four independent conductances each with a peak density of 0.3 mS/cm^2. The synaptic transmission delay is represented by a constant 0.5 delay between the input spike and the onset of the postsynaptic conductance change. Although not strictly necessary, this input simplification scheme provided increased computational efficiency without degrading the spike-discharge properties of the model when using acoustic stimuli (Levy, 1996).

The octopus cell model was implemented using the GENESIS neurosimulator (Wilson *et al.*, 1989; Bower and Beeman, 1995) running on a Sun Sparc 20 workstation (Sun Microsystems, Inc.). The backward Euler method with a 15-μs time step was used for numerical integration. The model runs in approximately 0.04% real time ($3\frac{1}{2}$ hours of simulation for a 5 stimulus). The GENESIS implementation was verified by a custom program written in C.

B. Auditory periphery model

A separate model of the auditory periphery was implemented to transform the digital stimuli to simulated auditory-nerve fiber spiketrains, which were then used to drive the octopus cell model's synaptic inputs. This functional model consists of a filterbank (Holdsworth *et al.*, 1988; Slaney, 1993) combined with a model for neural transduction (Meddis, 1986; Meddis, 1988) that computes deterministic spike probability functions for an array of auditory-nerve fibers in response to arbitrary stimuli. For this study, the auditory periphery model has seven ''channels'' with each channel consisting of a bandpass gammatone filter driving two separate nonlinear neural transduction functions representing medium (16 spikes/s) and high spontaneous rate (64 spikes/s) auditory-nerve fibers. The filter bandwidth is based on the equivalent rectangular bandwidth (ERB) of a peripheral fil-

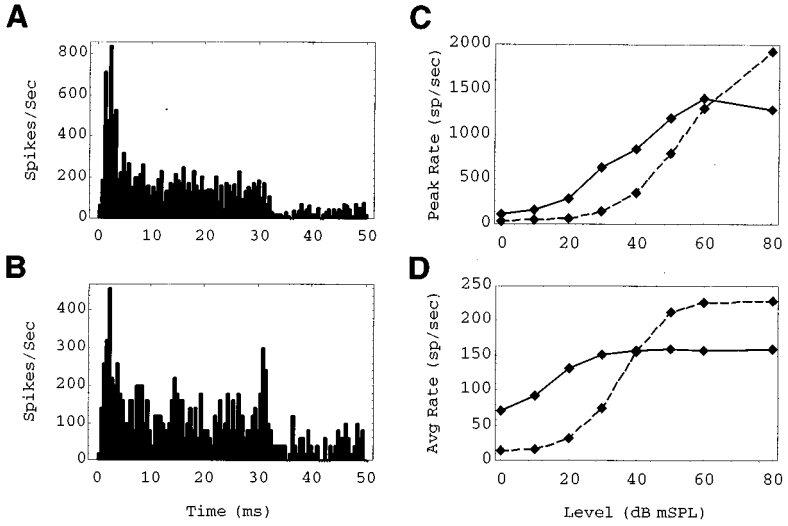

FIG. 3. Responses of the auditory periphery model to a 2.8-kHz, 30-ms tone burst presented 250 times at selected sound levels. (A) PSTH for a high spontaneous rate (HSR) fiber with CF=2.8 kHz, level=40 dB mSPL (B) PSTH for HSR fiber with CF=2.0 kHz, level=40 dB mSPL. Peak rate-intensity functions (C) and average rate-intensity functions (D) for a HSR fiber (solid) and a medium spontaneous rate fiber (dashed), each with CF=2.8 kHz.

ter, ERB $= (24.7)(4.37)(cf + l)$, where cf is the center frequency in kHz and the constants are set to provide a good fit to experimental data (Glasberg and Moore, 1990). From the frequency-dependent ERB, the filter bandwidth in radians is given by BW$=2\pi$ (1.019) ERB, where the scaling constant is that suggested by Patterson *et al.* (1992). The channel outputs are spike probability sequences.

The auditory periphery model was implemented as a C++ program using previously published parameter values for the filterbank (Holdsworth *et al.*, 1988) and neural transduction model (Meddis *et al.*, 1990). The stimulus gain was adjusted such that the rate-intensity curves for simulated high spontaneous rate fibers are similar to those recorded in cat (Sachs and Abbas, 1974). A model SPL (mSPL) was defined to correspond to sound level in SPL. With tone bursts presented over a 80-dB range, the simulated auditory-nerve fiber spiketrains exhibits reasonable PSTHs and rate-intensity functions (Fig. 3). The stimulus files have a resolution of 22 254 samples/s.

C. Simulations and data analysis

Simulations were run to facilitate comparison with published experimental results from octopus cells and onset units. The synthesized stimuli represent current injections, tone bursts at CF (duration: 30 ms; repeated every 50 ms), nerve shocks, amplitude-modulated (AM) tones (duration: 60 ms; carrier frequency: CF; depth: 1.0; variable modulation frequencies), frequency-modulated (FM) tones (duration: 167 ms; linear frequency sweep from 0 to 5 kHz or reversed), and pseudo-random white noise (bandwidth from dc to 10 kHz).

The computed responses were analyzed in terms of somatic potential, PSTH response pattern, first-spike latency (FSL), and sustained spike rate. Sustained depolarization was visually estimated as the average depolarization from the resting potential (reported to the nearest ± 5 mV) from 10 to 30 ms after stimulus onset with spikes ignored. Fourier-based or averaging algorithms were not used because they would be biased by spike activity. Also, this more qualitative assessment was found sufficient for the present analysis. Spikes were discriminated from the somatic potential with 15-μs resolution using a fixed amplitude threshold set at -35 mV except where otherwise noted. The threshold level was established by running the model interactively and finding the minimum threshold required to detect the small amplitude spikes and exclude subthreshold somatic potential fluctuations. During this process, spikes were unequivocally identified through monitoring active-channel conductances. With the fixed threshold, there may be a small number of spike detection errors, but these do not significantly affect the spike statistics. PSTHs were binned at 250 μs and constructed from 100 presentations of the stimulus. The FSL was calculated as the mean and standard deviation of the latency of the first spike, if it occurred, within 0.5 to 5 ms of stimulus onset for each presentation of the stimuli and was calculated using 15-μs resolution. The sustained rate was defined as the average firing rate from 10 to 30 ms after stimulus onset. For AM tone bursts, synchronization to the stimulus envelope was calculated as the vector strength (Goldberg and Brown, 1969) of the period histogram relative to the modulation period between 20- and 60-ms poststimulus onset. The spike analysis program was written in *Mathematica* (Wolfram, 1991) and C++.

II. RESULTS

During the model development process, selected parameters were adjusted within their biologically plausible range in order to achieve good similarity to experimental data. The verification process involved selecting one set of model parameters (described in Sec. I and the Appendix) and comparing simulated responses against responses of identified octopus cells for a diverse range of input conditions.

Simulated current injections verified that the model's subthreshold properties and spiking properties are consistent

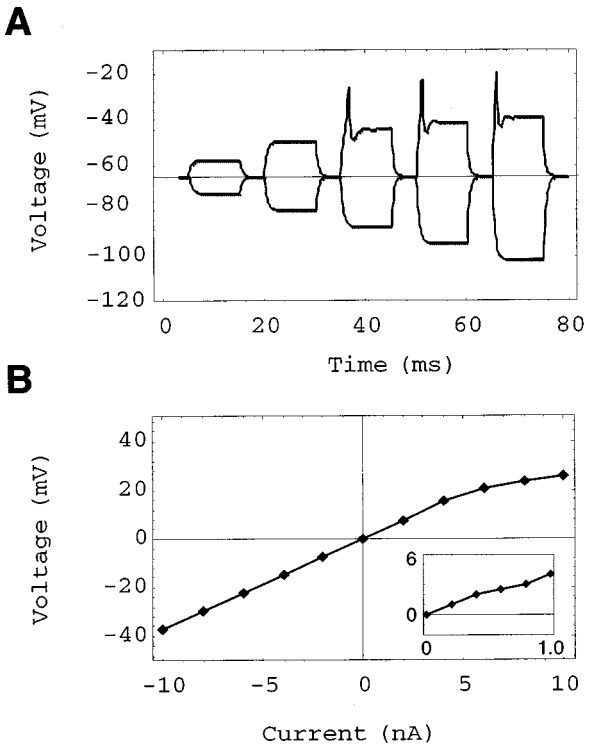

FIG. 4. Responses of the model to simulated current injections. (A) Somatic potential changes to 10 ms hyperpolarizing and depolarizing current steps at 2, 4, 6, 8, and 10 nA. (B) I-V curve constructed from the steady-state somatic potential; Inset: responses to depolarizing currents less than 1 nA. (C) V-I curve of an octopus cell in physiological solution (circles); reprinted with permission from Golding (1995).

with many of the octopus cell responses that have been observed in current-clamp experiments (Feng *et al.*, 1994; Golding *et al.*, 1995). Hyperpolarizing current pulses and depolarizing current pulses less than 6 nA evoke a quasilinear change in the somatic potential due to the passive membrane leakage conductance and largely inactivated sodium and potassium active conductances [Fig. 4(A) and 4(B)]. Depolarizing pulses of 6 nA or greater elicit a single spike at the pulse onset followed by sustained depolarization. Regular spiking was not observed even at the highest depolarizing current levels tested. The spike duration is approximately 0.7 ms and the spike amplitude is about 40 mV above the resting potential of -65 mV. R_{in} for the model can be estimated from the slope of the linear part of the I-V curve [Fig. 4(B)] and is found to be about 3.5 MΩ, which is within the range reported for octopus cells (Golding *et al.*, 1995). This estimated value of R_{in} is also consistent with the theoretical

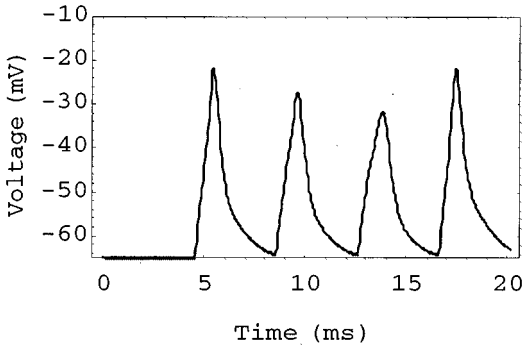

FIG. 5. Somatic potential variations of the model in response to simulated strong shocks of the auditory nerve at a rate of 250 Hz.

value of R_{in} calculated from passive membrane parameters (see Appendix). The model's I-V curve for depolarizing current pulses up to 1 nA [Fig. 4(B), inset] can be compared to that of one octopus cell [Fig. 4(C) open circles]. While these curves do not closely match, the relevant point for this study is that the model's R_{in} falls between that of this particular cell and the reported maximum of 10 MΩ for a set of 34 octopus cells (Golding *et al.*, 1995).

The model synchronizes to simulated 250-Hz shocks of the auditory nerve in a manner comparable to that reported for octopus cells [Fig. 5; compare to Fig. 1(F)] (Golding *et al.*, 1995). Additionally, synchronization remains up to shock rates of 750 Hz, which is consistent with experimental recordings (Golding *et al.*, 1995). The model's spikes are slightly larger and more variable than those recorded from the one octopus cell that Golding *et al.* (1995) report, but in this study, these discrepancies are secondary to the more favorable timing comparison. The synchronization of the model over a wide range of shock rates indicates that the model's passive membrane properties, active-channel conductances, and synaptic strengths interact in a manner that provides responses consistent with octopus cells. An auditory nerve shock was simulated by providing exactly coincident spikes across all of the auditory-nerve fibers at the specified shock rate. The peaks in somatic potential were verified to be spikes through examination of the active channel activation and inactivation parameters.

At a stimulus level of 20-dB mSPL, the onset response is well represented with precisely timed spikes at the stimulus onset and a low sustained rate [Fig. 6(A)]. At a stimulus level of 40 dB mSPL, the FSL decreases and becomes more precise, and the sustained rate increases slightly, which results in a PSTH that is similar to that of a typical O_L unit recorded in the PVCN [Fig. 6(B), compare to Fig. 1(A)]; thus, the model may be characterized as an O_L unit. At a level of 60 dB mSPL, the FSL becomes more precise, the peak rate increases, and the sustained rate decreases in comparison to the response at 40 dB mSPL [Fig. 6(C)]. At all three stimulus levels, the somatic potential exhibits sustained depolarization during the stimulus with subthreshold fluctuations and occasional spiking [Fig. 6(D)–(F)].

The model's response area [Fig. 7(A)] exhibits the broad frequency selectivity similar to that observed for one octopus

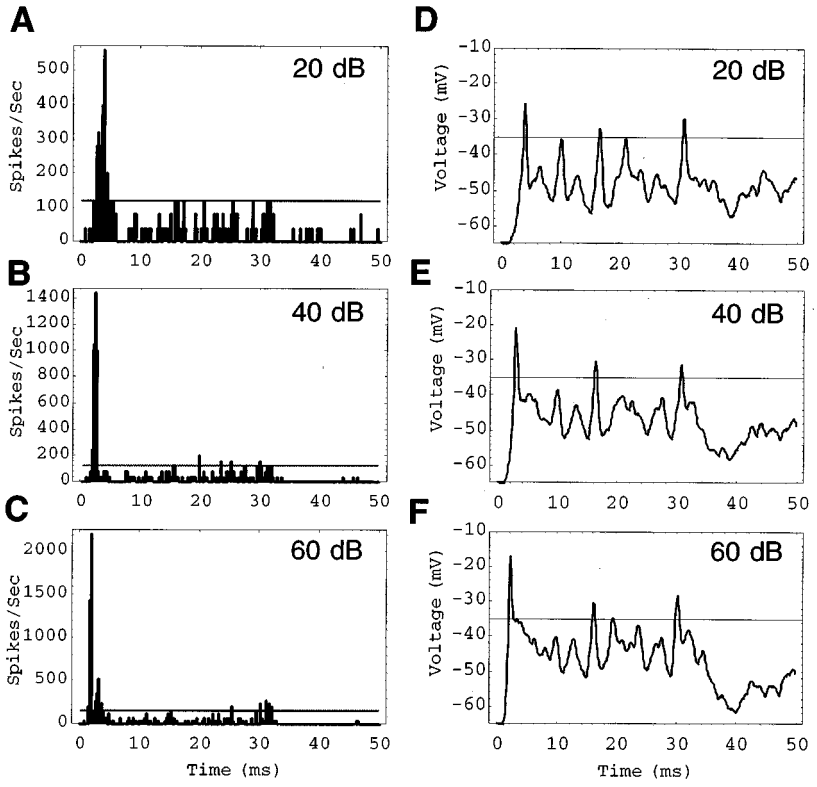

FIG. 6. Computed responses to CF tone bursts at three stimulus levels. (A)–(C): PSTHs using 100 stimulus trials. (D–F): somatic potentials for one stimulus trial. (A) FSL=3.4±0.8 ms, peak rate=560 spikes/s, sustained rate=33 spikes/s. (B) FSL=2.3±0.3 ms, peak rate=1450 spikes/s, sustained rate=42 spikes/s. (C) FSL=1.73±0.17 ms, peak rate=2200 spikes/s, sustained rate=37 spikes/s. (D) sustained depolarization=15 mV. [(E) and (F)] sustained depolarization=20 mV. In (A)–(C), the horizontal line indicates the upper 95% confidence interval for a Poisson process with the same average rate. In (D)–(F), the horizontal line at −35 mV indicates the spike discrimination threshold.

cell and several onset units [see, e.g., Fig. 1(C)] (Rhode *et al.*, 1983; Rhode and Smith, 1986). The response area was constructed from isointensity functions in response to ten tone bursts ranging from 500 Hz to 8 kHz at four stimulus levels. From responses to tone bursts at 0 dB mSPL, the CF of the model is estimated at 2.8 kHz. At 40 dB mSPL, the frequency selectivity is broader with approximately equal rate increases to stimuli ranging over one octave from 2 to 4 kHz. At 60 and 80 dB mSPL, the frequency selectivity continues to broaden, combined with relatively large response increases below 1 kHz due to entrainment by phase-locked auditory-nerve fiber inputs. The slightly elevated response at 4 kHz at the highest stimulus level is the result of an offset response of auditory-nerve fibers responding to the high levels of spectral blurring in the stimulus. The model has a sloping rate-level function with a dynamic range greater than 60 dB [Fig. 7(B)], which is somewhat higher than the average dynamic range of 26 dB for O_L units (Rhode and Smith, 1986).

The model's ability to simulate onset unit responses using stimuli other than tone bursts at CF was also investigated. The model strongly synchronizes (vector strength =0.74) to the stimulus envelope of an amplitude-modulated (AM) tone with modulation frequency of 125 Hz [Fig. 8(A)]. The somatic potential during one stimulus trial exhibits cycles of depolarization with spikes on the rising edge that

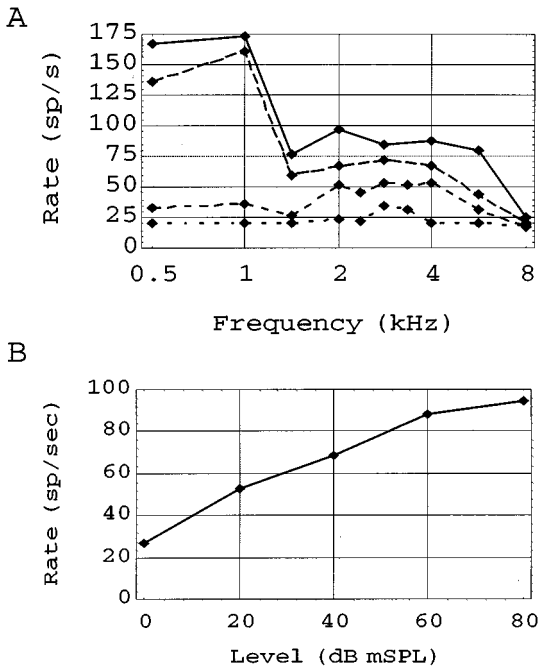

FIG. 7. (A) Response area (isointensity contours) of the model obtained using 30-ms tone bursts at four stimulus levels (0, 20, 40, and 60 dB mSPL) with 30 stimulus trials. (B) Rate-level function of the model using 2.8 kHz (CF) tone bursts.

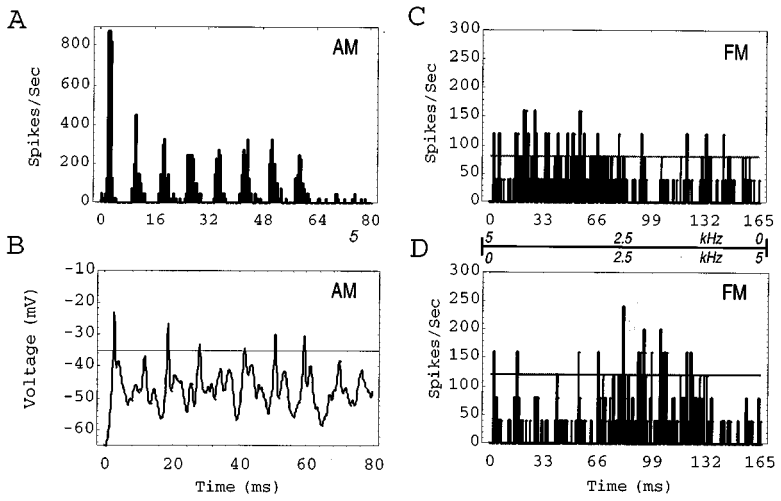

FIG. 8. Computed responses to AM and FM tone bursts. (A) PSTH to a 60-ms AM tone (40 dB mSPL, carrier frequency=CF; modulation frequency=125 Hz, modulation depth=1). Vector strength=0.74. (B) Somatic potential during one stimulus trial of simulation in *A*. (C) PSTH to a 167-ms FM tone (high-to-low linear frequency sweep: 5 to 0 kHz). (D) PSTH to reversed stimulus from *C*: (low-to-high linear frequency sweep: 0 to 5 kHz). The instantaneous frequency for both FM stimuli is shown on the axis between the *C* and *D*. Both FM stimuli were presented at 40 dB mSPL.

are synchronized to the stimulus envelope [Fig. 8(B)]. Simulations using AM tones with higher modulation frequencies result in much lower than expected vector strengths because the octopus cell model receives inadequate inputs due to insufficient synchronization in the auditory periphery model.

The model responds weakly to frequency-modulated (FM) tone bursts, although there is a small increase in the tendency to fire when the stimulus frequency is near the CF of 2.8 kHz [Fig. 8(C) and (D)]. While the peak firing rates for frequency sweeps in either direction are slightly above those expected for a Poisson process with the same average rate, they are well below the peak rates of 600 spikes/s or greater for other stimuli. However, it should be noted that the FM stimuli were presented continuously without a silent period; the inclusion of an intervening silent period elicits an onset response in addition to the responses that are shown.

The model exhibits an onset response to short-duration bursts of broadband noise presented at an intermediate stimulus level of 40 dB/Hz$^{1/2}$ [Fig. 9(A)]. Compared to CF tone-burst responses, the somatic potential exhibits a similar onset spike, but has a slightly larger sustained depolarization than that observed for CF tone bursts at the same level [Fig. 9(B)]. At a noise level of 20 dB/Hz$^{1/2}$, the onset response is greatly reduced, but the sustained rate is similar to the response at 40 dB [Fig. 9(C)]. At a noise level of 60 dB/Hz$^{1/2}$, the onset response is similar to that at 40 dB, with a slightly elevated sustained rate [Fig. 9(D)].

While octopus cells have been associated with both O_L and O_I units, many of the model's responses described thus far are largely consistent with O_L responses. By increasing only the number of excitatory inputs, a reasonable variation because this parameter has not been precisely estimated, the

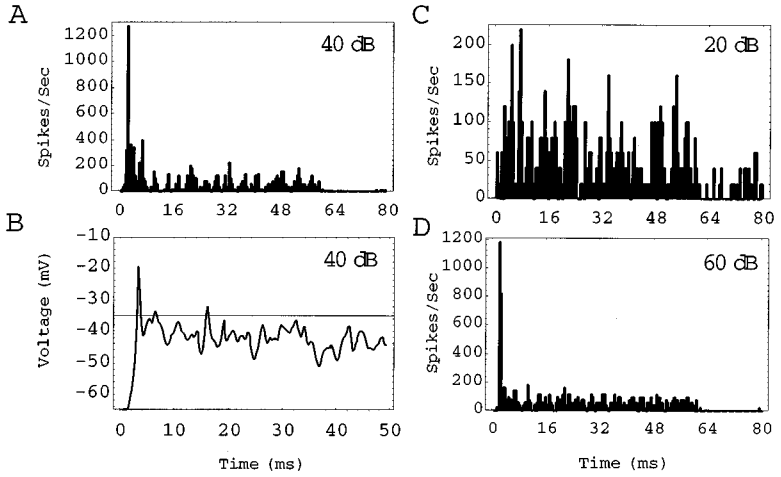

FIG. 9. Computed responses to noise bursts. (A) PSTH to 40 dB/Hz$^{1/2}$ noise: FSL=2.7±0.4, sustained rate=59 spikes/s. (B) Somatic potential to one stimulus trial: spike amplitude=20 mV, sustained depolarization=25 mV (40 dB/Hz$^{1/2}$ noise). (C) PSTH to 20 dB/Hz$^{1/2}$ noise: FSL=3.3±1.4, sustained rate=58 spikes/s. (D) PSTH to 60 dB/Hz$^{1/2}$ noise: FSL=2.0±0.17, sustained rate=67 spikes/s. The stimulus was uniformly distributed pseudorandom white noise with 60-ms duration presented with 30-ms silent periods.

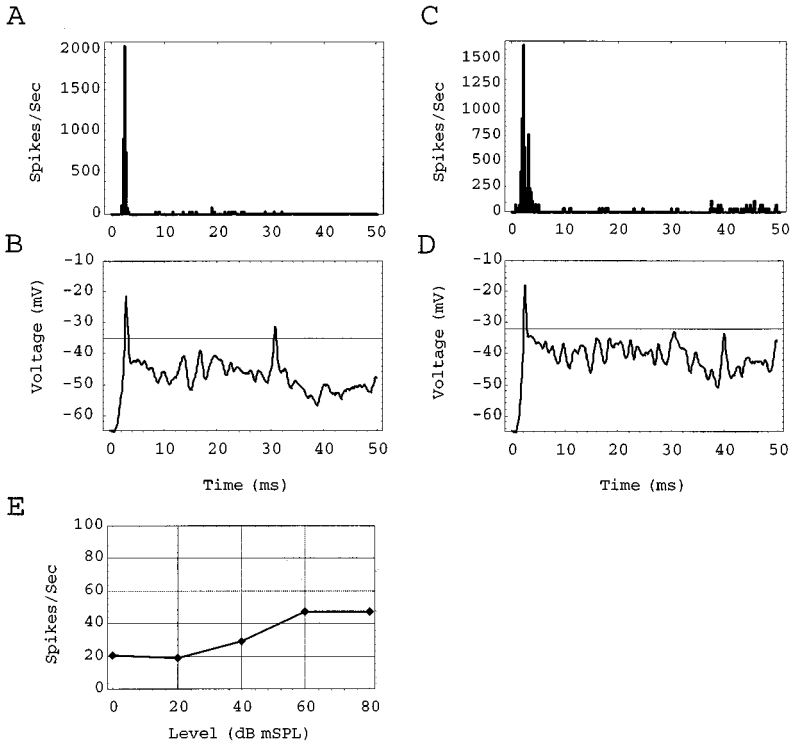

FIG. 10. Effects of increasing the number of represented independent inputs from 60 to 120. Synaptic conductance densities were either decreased by one-half [(A) and (B)] or unchanged [(C) and (D)]. (A) PSTH: FSL=2.4±0.2; sustained rate=8 spikes/s. (B) Somatic potential: sustained depolarization=20 mV. (C) PSTH:FSL=2.0±0.4; sustained rate=6 spikes/s. (D) Somatic potential: sustained depolarization=25 mV. The spike discrimination threshold was increased to −32 mV to compensate for the larger sustained depolarization. (E) Rate-level function for the model in (C) and (D). Stimulus was CF tone burst at 40 dB mSPL.

model's responses becomes more consistent with O_I responses. The number of inputs were increased not by adding additional synaptic conductances, but rather by increasing the instantaneous spike rate (probability) of the 15 existing synaptic conductances: Specifically, representing 120 inputs rather than 60 inputs required multiplying the original input spike rates by an additional factor of two. In the first set of simulations, the peak synaptic conductance for each input was reduced by one-half when the rate of each input was doubled such that, on average, the total synaptic conductance remained constant. The resulting response to a CF tone burst presented at 40 dB mSPL exhibits more O_I characteristics than the model with 60 inputs: the onset peak increases and becomes less variable with a lower sustained rate [Fig. 10(A)]. The somatic potential exhibits sustained depolarization of 20 mV with small subthreshold amplitude fluctuations [Fig. 10(B)].

In the second set of simulations, the peak synaptic conductances were not reduced when the input rates were doubled such that, in this case, the average total synaptic conductance was also doubled. The CF tone-burst response again exhibits O_I characteristics with a significant onset peak and a very low sustained rate [Fig. 10(C)]. The average latency of the first spike decreases by 0.3 ms with a small increase in standard deviation compared to the original model having 60 inputs. The somatic potential exhibits a sustained depolarization of 25 mV [Fig. 10(D)], which is larger than that of the original model. In this case, the spike detection threshold was increased to −32 mV (from −35 mV) to improve spike detection in lieu of the larger sustained depolarization. The rate-level function for this model configuration exhibits decreased dynamic range and response saturation at approximately one spike per stimulus trial.

III. DISCUSSION

In this study, a computational model of an octopus cell was developed using parameters estimated from anatomical and electrophysiological data. The objective was to simulate a representative octopus cell in order to better understand the anatomical and physiological properties that are important, or at least sufficient, for computing spike-discharge activity typical of O_I and O_L units. One of the principal findings is that a relatively simple model involving a single dendrite, a lumped, active soma, spike-related active channels, and many small excitatory inputs is able to account for many, but not all, of the major response properties attributed to octopus cells/onset units that have been reported in separate experimental studies. Specifically, the model exhibits a reasonable first-spike latency, which is one of the defining properties of onset units. At a second level of comparison, the frequency selectivity is representative of O_I units, but too broad for typical O_L units. The dynamic range is larger than both O_I and O_L units. Synchrony to AM tones compares well to both O_I and O_L units, within the limits of the auditory periphery model. The FM sweep preference compares to O_L units, but

not O_I units. The response to wideband noise stimuli is consistent for both O_I and O_L units. Increasing the number of (represented) independent inputs causes many response properties to become more similar to that of O_I units. We assert that rather than invalidating the model, the specific discrepancies between the model and experimental data serve to highlight areas that require additional investigation. This is a desired outcome of any investigative modeling study.

Developing the model was an iterative process, with its eventual form resulting from a compromise among sometimes contradictory data, interdependent parameters and qualitative parameter estimation. The model structure was established by abstracting anatomical features of octopus cells (e.g., cell size; distribution, number, and type of synaptic inputs). R_m and active channel parameters (rate constants and densities) were set such that the effects of current injection on the computed somatic potential were similar to intracellular recordings from octopus cells, for both *in situ* (Feng *et al.*, 1994) and brain-slice preparations (Golding *et al.*, 1995). Synaptic conductance densities were set such that computed somatic potentials and spike-discharge properties for simulated nerve shocks and CF tone bursts were similar to corresponding experimental observations (Golding *et al.*, 1995; Rhode *et al.*, 1983). In combining data from several species, an implicit assumption was made that the various observations related more to common features of a generalized octopus cell, rather than to unique features of octopus cells in a particular species. The compartmental modeling approach to mathematically representing these parameters is arguably the most accurate and plausible approach available, although the equations comprising the model do not reflect all of the known details of octopus cells.

Verification of the model rested on comparing computed responses to physiological responses of the few identified octopus that have been extensively characterized by Rhode *et al.* (1983), Golding *et al.* (1995), and Feng *et al.* (1994). Since there is inherent variability among these experimental descriptions due to the limited cell population, different experimental procedures, different species, and intrinsic variations among individual octopus cells, the model was evaluated in terms of whether the simulated average sustained somatic depolarization, peak and sustained firing rates and distributions of first-spike latencies were within biologically plausible ranges and whether they demonstrated appropriate response trends.

In current-clamp experiments, the model's sustained depolarization compares well to one of the octopus cells reported by Feng *et al.* (1994) at subthreshold and slightly suprathreshold current levels, although at much higher current levels, the model exhibits less sustained depolarization than the cell [compare Fig. 4(A) with Fig. 1(E)]. A simulated CF tone burst at 40 dB mSPL corresponds to the typical stimulus used to characterize onset units. For this stimulus, the model's peak rate is 2200 spike/s and the sustained rate is 37 spikes/s, yielding a peak-to-sustained ratio of 59, which is in the middle of the range of 10–100 found for both O_I and O_L units (Rhode and Smith, 1986), and which qualitatively compares well with the CF tone-burst response of the identified octopus cell (responding as an O_L unit) reported by Rhode *et al.* (1983). Because there are so few identified and characterized octopus cells, values for the distribution of first-spike latency were taken from pooled responses of O_I and O_L units recorded in PVCN. The experimental data show that CF tone bursts presented at moderate sound levels elicit first-spike latencies between 2 and 4 ms, with standard deviations of 0.1–0.3 ms (Rhode and Smith, 1986; Winter and Palmer, 1995). The latency tends to decrease with increased sound level (Winter and Palmer, 1995). For a comparable moderate-level stimulus, the model's mean first-spike latency is 2.3 ± 0.3 ms and it decreases with higher stimulus levels.

The ability of the octopus cell model to synchronize to AM tones compares favorably to the synchronization of O_I and O_L units within the limits of the auditory periphery model. The vector strength for the modeled response to a moderate-level AM tone with modulation frequency of 125 Hz is 0.73, which is consistent with the experimental data. The degree of AM synchronization is less than expected at higher modulation frequencies because the auditory periphery model has insufficient synchrony at the higher frequencies. In general, the auditory periphery model is less accurate for nontonal stimuli because, in part, it does not account for cochlear nonlinear frequency interactions and intensity related changes in peripheral filtering. O_I and O_L units typically synchronize to AM tones better than their auditory nerve inputs (Rhode and Greenberg, 1994; Frisina *et al.*, 1990). Using AM tones with carrier frequency set to the unit's CF, Rhode *et al.* (1994) reported a tendency of high-CF O_L units to exhibit low-pass or bandpass temporal modulation transfer functions (MTFs). The average cutoff frequency of the MTFs was 1100 Hz and the average maximum vector strength was 0.67 ± 0.12. The synchronization to AM tones was found to be largely insensitive to stimulus level. Frisina *et al.* (1990) also reported O_L units to synchronize strongly to AM tones, although these units were most likely VCN multipolar stellate cells rather than octopus cells. Direct comparison of modeled and experimental AM responses for O_I units is not possible because of the paucity of experimental data for these units.

The tendency to respond to FM sweeps in one direction preferentially has been described in responses of some, but not all onset units (Godfrey *et al.*, 1975; Rhode and Smith, 1986). Rhode and Smith (1986) reported that O_I units have the highest sweep preference, followed by O_I units with spontaneous rates less than 2 spikes/s. O_L units with higher spontaneous rates have little direction preference. The model does not exhibit a significant directional dependence although there is a slight increase in average firing rate at times when the stimulus' instantaneous frequency nears the CF of the model. This modeled response is more consistent with O_L units than O_I units.

Winter and Palmer (1995) found wideband noise and two-tone stimuli to generally facilitate responses of onset units. Modeled responses to simulated wideband noise bursts are generally consistent with these data. The sustained rate in response to a 40-dB/Hz$^{1/2}$ noise burst is 17 spikes/s (40%) higher than the sustained rate in response to a 40 dB mSPL

CF tone burst. The average first-spike latency also increases by 0.4 ms and is slightly more variable. Simulations using two-tone stimuli were not part of the present study.

While the argument that the model represents a set of sufficient, although perhaps not essential, parameters of octopus cells is strengthened by this robustness in simulating responses of onset units, the argument is tempered by the assumptions and simplifications of the model. Some of the simplifications are straightforward with easily measurable effects. For example, simplifying the input structure and removing the axon reduces the mean first-spike latency by 0.8 ms (25%) and the standard deviation by less than 10% compared to the more detailed model (Levy, 1996). As a second example, synaptic conductances, which include voltage-sensitive potassium channels that contribute to the fast synaptic potentials of octopus cells (Golding *et al.*, 1995), are described by a simple alpha-function with a 0.5-ms rise time (see Appendix).

However, other simplifications are more complex. Not implementing the axon of the representative octopus cell and placing the active channels directly on a soma compartment requires scaling $\overline{\mathbf{g}}_{\mathrm{Na}}$ and $\overline{\mathbf{g}}_{\mathrm{K}}$ by 1.7 because of the increased leakage conductance associated with the larger compartment. Additionally, the absolute values of these parameters are difficult to estimate because no direct experimental measures have been made. Setting these parameters to fit intracellularly recorded spike amplitudes and durations is problematic because of possible membrane damage by the electrode.

Feng *et al.* (1994) suggested that ''membrane properties,'' presumably including inward rectifier channels (Golding *et al.*, 1995), may play a critical role in the onset response. However, the present model cannot be used to investigate functional effects of inward rectifier channels because they are not explicitly represented. These channels activate under hyperpolarization and contribute to the cell's small R_{in} in this membrane state. Since the model does not include inhibitory inputs and there is very little hyperpolarization following a spike, the simulations (with the exception of hyperpolarizing current injections) do not involve conditions in which these channels would be activated. Beyond this issue, the modeled onset responses do suggest that both O_L and O_I responses can be generated by a cell with a relatively simple membrane that has only passive synaptic conductances and spike-related active conductances. While these simulations do not rule out the possibility that O_I and O_L units may correspond to octopus cells with different types of channels, or even to different cell types, they do offer an alternative explanation: Onset response variations may be the result of morphological or synaptic input variations within a population of otherwise similar octopus cells.

As a specific example, the model was used to investigate the effects of increasing the number of independent excitatory inputs. If O_I and O_L responses represent two extremes of an underlying response continuum involving the same morphological cell type (Rhode and Smith, 1986), then the number of inputs to a cell may be a factor in establishing that cell's position in the continuum. While several investigators have described the averaging of many weakly effective, near-coincident synaptic inputs as a contributing factor to the onset response of octopus cells (Rhode and Smith, 1986; Kim *et al.*, 1986; Golding *et al.*, 1995), there are few estimates of the numbers of inputs to these cells [see, e.g., Liberman (1993)] and these estimates are not precise.

Within the constraints of the model, the modeled responses indicate that increasing the number of inputs transforms an O_L unit to an O_I unit in terms of a smaller sustained rate and greater first-spike precision. This response change occurs both with and without compensatory adjustments in synaptic conductance density. In addition, the changes in the PSTH patterns from O_L to O_I are accompanied by changes in the dynamic range of the model that are also consistent with experimental findings. The response saturation of the model with 120 inputs simply reflects the model's inability to discharge more than once (on average) per stimulus trial.

In conclusion, this study contributes to the investigation of neuronal mechanisms underlying unit responses in the VCN and the functional implications of these responses on auditory processing. The relatively simple octopus cell model described here quantitatively predicts reasonable octopus cell/onset unit responses to typical experimental stimuli. While this study focused on describing the model's plausibility and accuracy, additional studies focus on the underlying response mechanisms (Kipke and Levy, 1997). More generally, computational models of this type promise to help bridge the chasms among electrophysiological and morphological observations, single-unit responses, and the complex, dynamic network-level neural computations that comprise auditory processing in the brain stem.

ACKNOWLEDGMENTS

This material is based upon work supported by the National Science Foundation under Grant No. BES-9409939 and by the Deafness Research Foundation. Three anonymous reviewers provided insightful comments that improved the paper.

APPENDIX

Table AI lists the model parameters. The following membrane equations describe the compartmental model solutions to the two-dimensional cable equations written for each section of the model. The membrane potential for dendrite compartment j $(j = 1,\ldots,15)$, $V_{dj}(t)$, is

$$c_m \frac{dV_{dj}}{dt} = -g_L(V_{dj}-E_r) - g_{\mathrm{syn}}(t)(V_{dj}-E_{\mathrm{syn}}) + \frac{1}{r_a}(V_{d(j+1)}-V_{dj}) - \frac{1}{r_a}(V_{dj}-V_{d(j-1)}). \tag{A1}$$

The potential of the passive somatic compartment $V_{s1}(t)$ is

TABLE AI. Model parameters.

Description	Symbol	Value
Dendrite		
Number of compartments		15
Diameter	d_d	17.6 μm
Length	l_d	238 μm
Peak synaptic conductance density	$\overline{\mathbf{g}}_{\text{syn}}$	1.2 mS/cm^2
Soma		
Number of compartments		2
Diameter	d_s	25 μm
Length	l_s	25 μm
Peak K^+ conductance density	$\overline{\mathbf{g}}_{\text{K}}$	120.0 mS/cm^2
Peak Na^{2+} conductance density	$\overline{g}_{\text{Na}}$	60.0 mS/cm^2
Specific membrane resistivity	R_m	0.5 kΩ cm^2
Specific axial resistivity	R_a	150 Ω cm
Specific membrane capacitance	C_m	1 μF/cm^2
Leakage conductance reversal potential	E_r	-65 mV
Synaptic input reversal potential	E_{syn}	45 mV
Na^{2+} reversal potential	E_{Na}	45 mV
K^+ reversal potential	E_{K}	-90 mV
Maximum synaptic conductance density	$\overline{\mathbf{g}}_{\text{syn}}$	0.3 mS/cm^2
Compartment membrane resistance	r_m	$R_m/\pi dl$ kΩ
Compartment axial resistance	r_a	$4R_a l/\pi d^2$ kΩ
Compartment capacitance	c_m	$C_m \pi dl$ μF
Dendritic characteristic length	λ_d	383 μm
Somatic characteristic length	λ_s	456 μm

$$c_m \frac{dV_{s1}}{dt} = -g_L(V_{s1}-E_r) - \left\{ (V_{s1}-E_{\text{syn}}) \sum_{j=1}^{4} g_{\text{syn}}(t)^{(j)} \right\} + \frac{1}{r_a}(V_{s2}-V_{s1}) - \frac{1}{r_a}(V_{s1}-V_{d1}). \quad \text{(A2)}$$

The potential of the active somatic compartment $V_{s2}(t)$ is

$$c_m \frac{dV_{s2}}{dt} = -g_L(V_{s2}-E_r) - g_{\text{Na}}(t)(V_{s2}-E_{\text{Na}}) - g_{\text{K}}(t) \times (V_{s2}-E_{\text{K}}) - \frac{1}{r_a}(V_{s2}-V_{s1}). \quad \text{(A3)}$$

$V_{s2}(t)$ is the variable described as the ''somatic potential'' in the text and figures.

1. Voltage-dependent conductances (active channels)

Sodium:

$$g_{\text{Na}}(V_m,t) = A_c \overline{g}_{\text{Na}} m^3 h,$$

with

$$dm/dt = \alpha_m(1-m) - \beta_m m,$$

$$\alpha_m(V_m) = \frac{-0.64(V_m-E_r-13)}{e^{-(V_m-E_r-13)/4}-1},$$

$$\beta_m(V_m) = \frac{0.56(V_m-E_r-40)}{e^{(V_m-E_r-40)/5}-1},$$

$$dh/dt = \alpha_h(1-h) - \beta_h h,$$

$$\alpha_h(V_m) = 0.256e^{-(V_m-E_r-17)/18},$$

$$\beta_h(V_m) = \frac{8.0}{e^{-(V_m-E_r-40)/5}+1},$$

Potassium:

$$g_{\text{K}}(V_m,t) = A_c \overline{g}_{\text{K}} n^4,$$

with

$$dn/dt = \alpha_n(1-n) - \beta_n n,$$

$$\alpha_n(V_m) = \frac{-0.064(V_m-E_r-15)}{e^{-(V_m-E_r-15)/5}-1},$$

$$\beta_n(V_m) = 1.0e^{-(V_m-E_r-10)/40}.$$

Time is specified in milliseconds, A_c is the membrane surface area of the compartment (cm^2) and V_m is the compartment membrane potential (mV). The rate equations for the activation and inactivation parameters are based on a previous modeling study which simulated hippocampal responses recorded at 37 °C (Traub, 1982), with slight modifications to better match available octopus cell data.

2. Synaptic conductance

With one input spike at $t = 0$, the synaptic conductance varies as an α function,

$$g_{\text{syn}}(t) = A_c \overline{g}_{\text{syn}} t/t_p e^{-t/t_p},$$

where $\overline{g}_{\text{syn}}$ is the maximum conductance density for either a soma or dendrite compartment, and t_p is the time to peak. This is implemented as the second-order differential equation

$$g''_{\text{syn}}(t) + \frac{2g'_{\text{syn}}}{t_p} + \frac{g_{\text{syn}}}{t_p^2} = \frac{e}{t_p} s(t),$$

where $s(t)$ is the input spiketrain,

$$s(t) = \delta(t-t_n),$$

with t_n, $n = 1,\ldots,N$ representing the times of the N spikes of the input auditory-nerve fiber.

Blackburn, C. C., and Sachs, M. B. (**1989**). ''Classification of unit types in the anteroventral cochlear nucleus: PST histograms and regularity analysis,'' J. Neurophysiol. **62,** 1303–1329.

Bower, J. M., and Beeman, D. (**1995**). *The Book of GENESIS* (Kluwer Academic, New York).

Feng, J. J., Kuwada, S., Ostapoff, E. M., Batra, R., and Morest, D. K. (**1994**). ''A physiological and structural study of neuron types in the cochlear nucleus. I. Intracellular responses to acoustic stimulation and current injection,'' J. Comp. Neurol. **346,** 1–18.

Frisina, R. D., Smith, R. L., and Chamberlain, S. C. (**1990**). ''Encoding of amplitude modulation in the gerbil cochlear nucleus: I. A hierarchy of enhancement,'' Hearing Res. **44,** 99–122.

Glasberg, B. R., and Moore, B. C. J. (**1990**). ''Derivation of auditory filter shapes from notched-noise data,'' Hearing Res. **47,** 103–18.

Godfrey, D. A., Kiang, N. Y. S., and Norris, B. E. (**1975**). ''Single unit activity in the posteroventral cochlear nucleus of the cat,'' J. Comp. Neurol. **162,** 247–268.

Goldberg, J. M., and Brown, P. B. (**1969**). ''Response of binaural neurons of dog superior olivary complex to dichotic tonal stimuli: Some physiological mechanisms of sound localization,'' J. Neurophysiol. **32,** 613–636.

Golding, N. L., Robertson, D., and Oertel, D. (**1995**). ''Recordings from slices indicate that octopus cells of the cochlear nucleus detect coincident firing of auditory nerve fibers with temporal precision,'' J. Neurosci. **15,** 3138–3153.

Helfert, R. H., Snead, C. R., and Altschuler, R. A. (**1991**). ''The ascending auditory system,'' in *Neurobiology of Hearing: The Central Auditory System*, edited by R. A. Altschuler, B. M. Clopton, and D. W. Hoffman (Raven, New York).

Holdsworth, J., Nimmo-Smith, I., Patterson, R. A., and Rice, P. (**1988**). ''Implementing a gammatone filter bank,'' MRC Applied Psychology Unit, Cambridge.

Kane, E. C. (**1973**). ''Octopus cells in the cochlear nucleus of the cat: Heterotypic synapses upon homeotypic neurons,'' Int. J. Neurosci. **5**, 251–279.

Kane, E. S. (**1977**). ''Descending inputs to the octopus cell area of the cat cochlear nucleus: An electron microscopic study,'' J. Comp. Neurol. **173,** 337–353.

Kim, D. O., Rhode, W. S., and Greenberg, S. R. (**1986**). ''Responses of cochlear nucleus neurones to speech signals: Neural encoding of pitch, intensity and other parameters,'' in *Auditory Frequency Selectivity*, edited by B. C. J. Moore and R. D. Patterson (Plenum, New York), pp. 281–288.

Kipke, D. R., and Levy, K. L. (**1997**). ''Sensitivity of the cochlear nucleus octopus cell to synaptic and membrane properties: A modeling study,'' J. Acoust. Soc. Am. **102,** 403–412.

Levy, K. L. (**1996**). ''The transformation of acoustic information by cochlear nucleus octopus cells: A modeling study,'' Arizona State University, Ph.D. dissertation.

Levy, K. L., and Kipke, D. R. (**1994a**). ''The importance of membrane properties and synaptic locations in octopus cells of the mammalian cochlear nucleus: A modeling study,'' in *The Neurobiology of Computation. Proceedings of the Third Annual Computation and Neural Systems Conference*, edited by F. H. Eckman and J. M. Bower (Kluwer Academic, Boston), pp. 93–98.

Levy, K. L., and Kipke, D. R. (**1994b**). ''The effects of dendritic and synaptic simplification in a compartmental model of a cochlear nucleus octopus cell,'' Ann. Biomed. Eng. **22:52**.

Liberman, M. C. (**1993**). ''Central projections of auditory nerve fibers of differing spontaneous rate, II: Posteroventral and dorsal cochlear nuclei,'' J. Comp. Neurol. **327,** 17–36.

Manis, P. B., and Marx, S. O. (**1991**). ''Outward currents in isolated ventral cochlear nucleus neurons,'' J. Neurosci. **11,** 2865–2880.

Meddis, R. (**1986**). ''Simulation of mechanical to neural transduction in the auditory receptor,'' J. Acoust. Soc. Am. **79,** 702–711.

Meddis, R. (**1988**). ''Simulation of auditory-neural transduction: Further studies,'' J. Acoust. Soc. Am. **83,** 1056–1063.

Meddis, R., Hewitt, M. J., and Shackleton, T. M. (**1990**). ''Implementation details of a computation model of the inner hair-cell/auditory nerve synapse,'' J. Acoust. Soc. Am. **87,** 1813–1816.

Osen, K. K. (**1969**). ''Cytoarchitecture of the cochlear nuclei in the cat,'' J. Comp. Neurol. **136,** 453–484.

Ostapoff, E. M., Feng, J. J., and Morest, D. K. (**1994**). ''A physiological and structural study of neuron types in the cochlear nucleus. II. Neuron types and their structural correlation with response properties,'' J. Comp. Neurol. **346,** 19–42.

Patterson, R. D., Robinson, K., Holdsworth, J., McKeown, D., Zhang, C., and Allerhand, M. H. (**1992**). ''Complex sounds and auditory images,'' in *Auditory Physiology and Perception*, edited by Y. Cazals, L. Demany, and L. Horner (Pergamon, London), pp. 429–443.

Rall, W. (**1977**). ''Core conductor theory and cable properties of neurons,'' in *Handbook of Physiology: The Nervous System, Cellular Biology of Neurons* (American Physiology Society, Washington, DC), pp. 39–97.

Rall, W. (**1989**). ''Cable theory for dendritic neurons,'' in *Methods in Neuronal Modeling*, edited by C. Koch and I. Segev (MIT, Cambridge, MA), pp. 9–62.

Rhode, W. S., Oertel, D., and Smith, P. H. (**1983**). ''Physiological response properties of cells labeled intracellularly with horseradish peroxidase in cat ventral cochlear nucleus,'' J. Comp. Neurol. **213,** 448–463.

Rhode, W. S. (**1991**). ''Physiological-morphological properties of the cochlear nucleus,'' in *Neurobiology of Hearing: The Central Auditory System*, edited by R. A. Altschuler, B. M. Clopton, and D. W. Hoffman (Raven, New York).

Rhode, W. S., and Greenberg, S. (**1994**). ''Encoding of amplitude modulation in the cochlear nucleus of the cat,'' J. Neurophysiol. **71,** 1797–1825.

Rhode, W. S., and Smith, P. H. (**1986**). ''Encoding time and intensity in the ventral cochlear nucleus of the cat,'' J. Neurophysiol. **56,** 262–286.

Ritz, L. A., and Brownell, W. E. (**1982**). ''Single unit analysis of the posteroventral cochlear nucleus of the decerebrate cat,'' Neurosci. **7**, 1995–2010.

Romand, R. (**1978**). ''Survey of intracellular recording in the cochlear nucleus of the cat,'' Brain Res. **148,** 43–65.

Rouiller, E. M., and Ryugo, D. K. (**1984**). ''Intracellular marking of physiologically characterized cells in the ventral cochlear nucleus of the cat,'' J. Comp. Neurol. **225,** 167–186.

Sachs, M. B., and Abbas, P. J. (**1974**). ''Rate versus level functions for auditory-nerve fibers in cats: Tone-burst stimuli,'' J. Acoust. Soc. Am. **56,** 1835–1847.

Saint Marie, R. L., Morest, D. K., and Brandon, C. J. (**1989**). ''The form and distribution of GABAergic synapses on the principal cell types of the ventral cochlear nucleus of the cat,'' Hearing Res. **42,** 97–112.

Slaney, M. (**1993**). An efficient implementation of the Patterson–Holdsworth auditory filter bank. Apple Computer, Inc.

Smith, P. H., Joris, P. X., Banks, M. I., and Yin, T. C. T. (**1993**). ''Responses of cochlear nucleus cells and projections of their axons,'' in *The Mammalian Cochlear Nuclei: Organization and Function*, edited by M. A. Merchan, J. M. Juiz, D. A. Godfrey, and E. Mugnaini (Plenum, New York), pp. 349–360.

Traub, R. D. (**1982**). ''Simulation of intrinsic bursting in CA3 Hippocampal neurons,'' Neurosci. **7**, 1233–1242.

Wilson, M. A., Bhalla, U. S., Uhley, J. D., and Bower, J. M. (**1989**). ''GENESIS: A system for simulating neural networks,'' in *Advances in Neural Information Processing Systems 1*, edited by D. S. Touretzky (Morgan Kaufmann, San Mateo, CA).

Winter, I. M., and Palmer, A. R. (**1995**). ''Level dependence of cochlear nucleus onset unit responses and facilitation by second tones or broadband noise,'' J. Neurophysiol. **73,** 141–159.

Wolfram, S. (**1991**). *Mathematica. A System for Doing Mathematics by Computer* (Addison-Wesley, California).

Sensitivity of the cochlear nucleus octopus cell to synaptic and membrane properties: A modeling study

Daryl R. Kipke[a] and Kenneth L. Levy
Bioengineering Program, Arizona State University, Tempe, Arizona 85287-6006

(Received 19 September 1996; revised 17 February 1997; accepted 28 February 1997)

Octopus cells of the posteroventral cochlear nucleus precisely fire at the onset of short-duration tone bursts, followed by little sustained activity. While this characteristic onset response has been described in experimental studies, its underlying mechanisms are not completely known. The objective of this study was to investigate these mechanisms through a sensitivity analysis of selected parameters of a compartmental model of the octopus cell. The parameters relate to cell morphology, passive electrical properties, synaptic inputs, and active channels. The modeled responses were used to evaluate the effects of four postulated mechanisms on the onset response: the cell's small membrane time constant, the cell's numerous weakly effective excitatory inputs, increases in spike threshold caused by sustained depolarization, and electrical loading of the soma by the dendrites. Simulations indicate that the model's onset response to tone bursts is an emergent property of multiple cell parameters that is best predicted by the ratio of synaptic conductance density to membrane leakage conductance density and by the level of sustained depolarization during the tone burst. © *1997 Acoustical Society of America.* [S0001-4966(97)00907-7]

PACS numbers: 43.64.Bt, 43.64.Qh [RDF]

INTRODUCTION

Octopus cells comprise one of the principal cell types in the posteroventral cochlear nucleus (PVCN). Each octopus cell receives afferent inputs from numerous auditory-nerve fibers that form excitatory synapses on its soma and its few short, relatively large dendrites (Osen, 1969; Kane, 1973; Rhode *et al.*, 1983). The dendrites extend along the tonotopic axis resulting, in part, in broad frequency selectivity. Octopus cells have been associated with either an O_I response (Godfrey *et al.*, 1975; Rouiller and Ryugo, 1984; Feng *et al.*, 1994) or an O_L response (Godfrey *et al.*, 1975; Ritz and Brownell, 1982; Rhode *et al.*, 1983; Smith *et al.*, 1993). The O_I response consists of one or two precisely timed spikes following the onset of the tone burst and no spikes during the duration of the stimulus. The O_L response consists of precisely timed onset spikes with sustained activity throughout the duration of the stimulus at rates up to 200 spikes/s (Godfrey *et al.*, 1975; Rhode and Smith, 1986). The tendency of these cells to respond at the onset of tone bursts suggests that octopus cells trade spectral resolution for temporal precision (Golding *et al.*, 1995) and that they may contribute to the encoding of temporal information, such as fundamental frequency (Kim *et al.*, 1986).

Various mechanisms of the octopus cells' onset response have been suggested. Based on observations of GABAergic terminals on octopus cells (Saint Marie *et al.*, 1989) and enhanced responses in PVCN onset units to GABA antagonists (Palombi and Caspary, 1992), inhibitory inputs have been suggested as a mechanism of reducing the sustained activity of octopus cells (Palombi and Caspary, 1992). However, inhibitory responses have not been observed in intracellular recordings of octopus cells (Golding *et al.*, 1995; Feng *et al.*, 1994). Separate from inhibitory effects, three mechanisms have been suggested to play a role in the onset response, including (1) a brief synaptic integration time that requires near coincidence of inputs for spiking (Golding *et al.*, 1995), (2) many weakly effective excitatory inputs that must temporally and spatially summate to be effective (Rhode and Smith, 1986; Golding *et al.*, 1995), and (3) increases in spike threshold related to increased depolarization (Ritz and Brownell, 1982; Feng *et al.*, 1994). In addition, previous modeling studies have shown that the electrical loading of the soma by dendrites can affect the measured membrane time constant (Rall, 1967), as well as the sustained firing rate (Baer and Tier, 1986).

In a previous study (Levy and Kipke, 1997), a biologically plausible computational model of a representative octupus cell was developed and verified as accurately simulating the types of responses that have been associated with octopus cells. This compartmental model has parameters based on many of the known morphological and physiological features of these cells, including excitatory synaptic inputs from simulated auditory-nerve fibers distributed on the dendrites and soma. The accuracy and robustness of the model was established by comparing computed responses with physiological responses for a wide range of stimuli, including current injections, characteristic frequency (CF) tone bursts, amplitude modulated tone bursts, frequency modulated tone bursts, and wideband noise. It was demonstrated that increasing the number of independent inputs from 60 to 120 resulted in the response changing from O_L to O_I. While this parameter variation is reasonable for octopus cells, it certainly is not a unique way of transforming the model to account for both O_I and O_L responses. The effects of additional model parameters should be investigated.

The objective of this study was to use the previously verified octopus cell model (Levy and Kipke, 1997) to inves-

[a]Electronic mail: kipke@asu.edu

tigate the mechanisms of the model's onset responses. The approach was to conduct a sensitivity analysis of model parameters to relate response variations to changes in summary parameters that correspond to the postulated mechanisms. This study provides increased insight into the mechanisms of the onset response. Additionally, this study suggests relationships between presumably normal variations in octopus cell properties and variations in onset responses, and it demonstrates the robustness of the model for simulating onset responses.

I. METHODS

A. Octopus cell model

The octopus cell model is fully described in a previous paper (Levy and Kipke, 1997) and will only be summarized in this section. The compartmental model represents a typical octopus cell having four 7×150-μm cylindrical dendrites and a 25×25-μm cylindrical lumped soma. The cell is specified to have dendritic and somatic synaptic inputs from 60 independent auditory-nerve fibers ranging in CF from 4 to 1.4 kHz, although these inputs are lumped and simplified in the model. The 56 dendritic inputs of the representative octopus cell are represented with 14 independent, time-varying synaptic conductances distributed uniformly on the equivalent dendrite (one conductance in each of 14 dendrite compartments), each with a peak density of 1.2 mS/cm^2 and a rise-time of 0.5 ms. The spike rate (probability) of the auditory-nerve input driving each conductance is increased by a factor of 4 and its refractory period is reduced by a factor of 4 (to 0.19 ms), relative to the outputs of the auditory periphery model. This input scaling scheme was found to accurately represent the 56 inputs and is addressed in a previous paper (Levy and Kipke, 1997). The passive soma compartment receives four independent synaptic conductances, each with a peak density of 0.3 mS/cm^2. The synaptic transmission delay is represented by a constant 0.5 delay between the input spike and the onset of the postsynaptic conductance change.

This model constitutes the ''reference model'' as described below. It has a characteristic frequency (CF) of 2.8 kHz and its responses are consistent with an O_L unit for CF tone bursts, current injections, nerve shocks amplitude-modulated tone bursts, and noise stimuli (Levy and Kipke, 1997). The model parameters most relevant to the results of this paper are listed in Table I, while the full mathematical description of the octopus cell model is provided in the companion paper (Levy and Kipke, 1997).

The model was implemented using the GENESIS neurosimulator (Bower and Beeman, 1995) running on a Sun Sparc 20 workstation (Sun Microsystems, Inc.). It is deterministic except for the pseudo-random spike generators. The simulations that involve the same number of independent inputs and stimulus use identical input spiketrains, i.e., these simulations share the set of auditory-nerve spike probabilities and random number seed for the spike generators.

TABLE I. Model parameters.

Description	Symbol	Value
Specific membrane capacitance	C_m	1 μF/cm^2
Specific membrane resistance	R_m	0.5 kΩ cm^2
Specific axial resistivity	R_a	150 Ω cm
Soma diameter	d_s	25 μm
Soma length	l_s	25 μm
Equivalent dendrite diameter	d_d	17.6 μm
Equivalent dendrite length	l_d	237 μm
Reversal potential for synaptic conductance	E_{exc}	45 mV
Reversal potential for leakage conductance	E_L	-65 mV
Synaptic conductance density	G_{exc}	1.2 mS/cm^2
Leakage conductance ($1/R_m$)	G_L	2 mS/cm^2
Potassium maximum conductance density	$\overline{\mathbf{g}}_{\text{K}}$	70 mS/cm^2
Sodium maximum conductance density	$\overline{\mathbf{g}}_{\text{Na}}$	35 mS/cm^2
Time constant of excitatory input	τ_{exc}	0.5 ms
Equivalent dendrite characteristic length	λ	383 μm
Equivalent dendrite electrotonic length	L	0.62

B. Auditory periphery model

Since auditory-nerve fibers provide synaptic inputs to octopus cells, a separate model of the auditory periphery is used to transform the digital stimuli to simulated spike activity in the auditory nerve. For this study, this model has seven channels, with each channel consisting of a peripheral bandpass (gammatone) filter (Holdsworth *et al.,* 1988) driving two nonlinear processes representing neural transduction (Meddis, 1986, 1988; Meddis *et al.,* 1990) for medium spontaneous rate (15 spikes/s) and high spontaneous rate (64 spikes/s) auditory-nerve fibers. The output of each channel is a numerical sequence representing the average spike probability of an auditory-nerve fiber having a CF equal to the center frequency of the peripheral filter.

C. Simulations and data analysis

The modeled responses were analyzed in terms of sustained somatic depolarization, first-spike latency (FSL), peak firing rate, and sustained firing rate. The sustained depolarization (SD) was estimated visually as the average depolarization from the resting potential (reported to the nearest ±5 mV) from 10 to 30 ms after stimulus onset with spikes ignored. Spikes were discriminated from the somatic potential with 15-μs resolution using a fixed amplitude threshold set at -35 mV. PSTHs were binned at 250 μs and were constructed from 100 presentations of the stimulus. The peak firing rate corresponded to the onset peak of the PSTH (a spike in the same bin for all trials corresponds to a peak rate of 4 000 spikes/s). The sustained rate was defined as the average rate over the interval from 10 to 30 ms after stimulus onset. The FSL was defined as the mean and standard deviation of the latency of the first spike within 0.5–5 ms of stimulus onset for each presentation of the tone bursts, and was calculated using 15-μs resolution.

The parameters selected for sensitivity analysis relate to cell morphology, passive electrical properties, synaptic in-

puts, and active channels, and were varied by a factor of two above and below the nominal values used for the reference model. For variations that altered the membrane area, the maximum synaptic conductance for a compartment was kept constant by compensating the synaptic density. In addition, the dendrite length was adjusted to maintain an electrotonic length of $0.6\,\lambda_d$ (keeping each compartment length $0.04\,\lambda_d$). For example, when the dendrite diameter was halved, the dendrite length was divided by $\sqrt{2}$ and the synaptic density was multiplied by $2\sqrt{2}$. These changes isolated the effects of the selected parameters by maintaining electrotonic equivalence and constant synaptic conductances between models. Parameter variations representing changes in the number of synaptic inputs and synaptic density were an exception. The number of inputs was varied by increasing input spike probabilities and reducing the synaptic density by the same amount such that, on average, the total number of input spikes remained the same. No compensatory changes were made when synaptic density was varied. All of the simulations used 30-ms tone bursts (1 ms rise–fall time) repeated at 20 Hz at the model's CF of 2.8 kHz.

To facilitate quantitative comparisons of effects among the parameter variations, three summary parameters were calculated from the model's low-level parameters. The first two summary parameters: (1) membrane time constant, $\tau_m = R_m C_m$, and (2) dendritic-to-somatic conductance ratio, $\rho = g_{\text{in},d}/g_{\text{in},s} = r_{\text{in},s}/r_{\text{in},d}$ are standard modeling quantities (Segev *et al.*, 1995). The third summary parameter, synaptic-to-leakage conductance density ratio, $S/L = G_{\text{exc}}/G_L$ was defined in this study as a means of succinctly representing the interaction between the synaptic conductance density, G_{exc}, and the specific leakage conductance, $G_L = 1/R_m$. In the expression for ρ, the dendritic input conductance, $g_{\text{in},d}$, is the inverse of the dendritic input impedance, $r_{\text{in},d} = R_m/\pi\lambda d_d \coth(L)$ (Rall, 1989). The somatic input conductance, $g_{\text{in},s}$, is the inverse of the somatic input impedance, $r_{\text{in},s} = (4R_a l_s/\pi d_s^2) + (R_m/\pi d_s l_s)$ for a single-compartment, cylindrical soma.

II. RESULTS

Responses to tone bursts and summary parameters of the reference octopus cell model and its variants are summarized in Table II. To facilitate describing the results, an onset response ''quality'' (ranging from O_I to O_L) is defined in terms of peak rate, FSL, and sustained rate. ''More O_I'' refers to a response having a smaller sustained rate, higher peak rate, and/or smaller FSL than a reference response. Likewise, ''more O_L'' refers to a response with the opposite trends. The responses resulting from each parameter variation are compared to the corresponding responses of the reference model.

A. Responses of the reference model

In response to a CF tone burst at 40 dB mSPL, the somatic potential and spiking properties of the reference model were qualitatively similar to typical O_L units and some octopus cells (Rhode *et al.*, 1983; Rhode and Smith, 1986; Rouiller and Ryugo, 1984; Godfrey *et al.*, 1975; Winter and Palmer, 1995). The PSTH exhibits the characteristic sharp onset peak followed by a low sustained rate that is characteristic of O_L units [Fig. 1(A)]. The soma remains depolarized throughout the stimulus period with small-amplitude spikes riding on a sustained depolarization [SD $=20$ mV; Fig. 1(B)]. The values of the summary parameters represent the reference state of the model; $\rho=6$, $\tau_m = 0.5$ ms, $S/L = 0.6$.

B. The effects of stimulus level

At 20 dB mSPL, the onset response persists, albeit with a smaller peak rate and a longer FSL (mean and standard deviation) [Fig. 2(A)]. At 60 dB mSPL, the peak rate increases and the FSL (mean and standard deviation) decreases relative to the 40 dB mSPL response [Fig. 2(B)]. At both 20 and 40 dB mSPL, the sustained rate is slightly smaller than that at 40 dB mSPL. However, the sustained depolarization is less at 20 dB mSPL than at the two higher stimulus levels [Fig. 2(C) and (D)]. The summary parameters (τ_m, ρ, and S/L) do not change with stimulus level.

C. The effects of cell morphology

The effects of cell morphology were investigated by separately varying the diameters of the dendrite and soma. Decreasing the dendrite diameter by one-half causes the response to become more O_L compared to the reference model. The PSTH exhibits a slightly smaller peak rate, a smaller mean FSL and a slightly larger FSL standard deviation [Fig. 3(A)]. The sustained rate increases from 42 to 225 spikes/s. Doubling the dendrite diameter causes the response to become more O_I with the PSTH containing only an onset peak and no sustained firing [Fig. 3(B)]. The peak rate decreases and the mean FSL increases, although the FSL standard deviation does not change. The sustained depolarization (SD$=20$ mV) does not change relative to the reference model when the dendrite diameter is decreased by one-half, but it does decrease slightly (s.d.$=15$ mV) when the dendrite diameter is doubled [Fig. 3(C) and (D)].

Changes in dendrite diameter cause significant response changes which are best summarized in terms of ρ and S/L, because, in this case, τ_m does not change and SD changes very little. With the smaller dendrite diameter, S/L increases and the dendrite loads the soma less (smaller ρ), leading to more of an O_L response. With the larger dendrite, S/L decreases and the dendritic load on the soma increases (larger ρ), leading to more of an O_I response.

In separate simulations, the synaptic conductance density rather than the total synaptic conductance was held constant as the dendrite diameter was varied. In this case, the sustained rate is intermediate to the reference model and the previously described one-half dendrite model, while the sustained depolarization decreases. By keeping the synaptic conductance density constant, a smaller dendrite diameter does not effect S/L, but it still decreases ρ. These simulations further indicated that both ρ and S/L affect the quality of the onset response.

Variations of the soma diameter (with $\overline{\mathbf{g}}_{\text{Na}}$ and $\overline{\mathbf{g}}_{\text{K}}$ held constant) do not significantly change the FSL, although SD decreases with both increases and decreases in soma diam-

TABLE II. Summary of parameter sensitivity. SD: sustained depolarization, ρ: dendritic-to-somatic conductance ratio, τ_m: membrane time constant, S/L: synaptic-to-leakage conductance density ratio.

Parameter	Peak rate (spikes/s)	Sustained rate (spikes/s)	FSL (ms)	SD (mV)	ρ	τ_m (ms)	S/L
Reference model							
40 dB mSPL	1440	42	2.3±0.3	20	6	0.5	0.6
Stimulus intensity							
20 dB mSPL	560	33	3.4±0.8	15	6	0.5	0.6
60 dB mSPL	2200	37	1.7±0.2	20	6	0.5	0.6
Dendrite diameter							
1/2	1200	225	1.5±0.7	20	2.1	0.5	1.7
2	560	0	3.4±0.3	15	16.9	0.5	0.2
Soma diameter							
1/2	1280	28	2.4±0.3	15	12	0.5	0.6
2	1200	119	2.3±0.3	15	3	0.5	0.6
Specific memb. resistivity, R_m							
1/2	880	0	3.3±0.4	10	4.2	0.25	0.4
2	1200	116	1.9±0.6	25	8.5	1	0.9
Specific memb. capacitance, C_m							
1/2	1920	102	2.1±0.4	15	6	0.25	0.6
2	1800	2	2.7±0.3	20	6	1	0.6
Specific axial resistivity, R_a							
1/2	1240	33	2.4±0.3	20	8.5	0.5	0.9
2	1320	76	2.3±0.3	20	4.3	0.5	0.4
Synaptic conduct. density, G_{exc}							
1/2	1160	0	3.7±0.4	10	6	0.5	0.3
2	1320	215	1.6±0.6	25	6	0.5	1.2
Number of synaptic inputs							
1/2	1080	103	2.3±0.5	15	6	0.5	1.2
2	2040	8	2.4±0.2	20	6	0.5	0.3
Inhibition							
	1560	31	2.6±0.3	10	6	0.5	0.6
No AN fiber adaptation							
	560	66	2.4±0.9	15	6	0.5	0.6
Max. Na^{2+} conduct., $\overline{\mathbf{g}}_{\text{Na}}$							
1/2	1240	5	2.6±0.3	20	6	0.5	0.6
2	1400	223	1.9±0.6	15	6	0.5	0.6
Max. K^+ conduct., $\overline{\mathbf{g}}_{\text{K}}$							
1/2	1300	93	2.3±0.3	20	6	0.5	0.6
2	1160	13	2.4±0.3	15	6	0.5	0.6
Max. K^+ and Na^{2+} conduct.							
1/2	1600	9	2.5±0.3	20	6	0.5	0.6
2	1360	168	2.1±0.4	15	6	0.5	0.6

eter, and the sustained rate increases when the diameter is doubled. These parameter variations change ρ, but do not change τ_m and S/L. When the soma diameter is halved, the dendritic load on the soma increases, which causes lower sustained depolarization and sustained rate. When the soma diameter is doubled, the dendritic load on the soma decreases and the responses change in the opposite direction. In these simulations, the sodium and potassium conductance densities were not changed from the reference model, although the somatic synaptic density was adjusted to maintain the same somatic synaptic conductance. When the sodium and potassium densities were adjusted to maintain constant total conductances (i.e., doubling them when the soma was halved), the response changes are similar to those resulting from changing the active channel densities without diameter changes (described below).

D. The effects of passive membrane parameters

The effects of passive membrane properties were evaluated by separately changing R_m, R_a, and C_m. When R_m is decreased by one-half, the response becomes more O_I com-

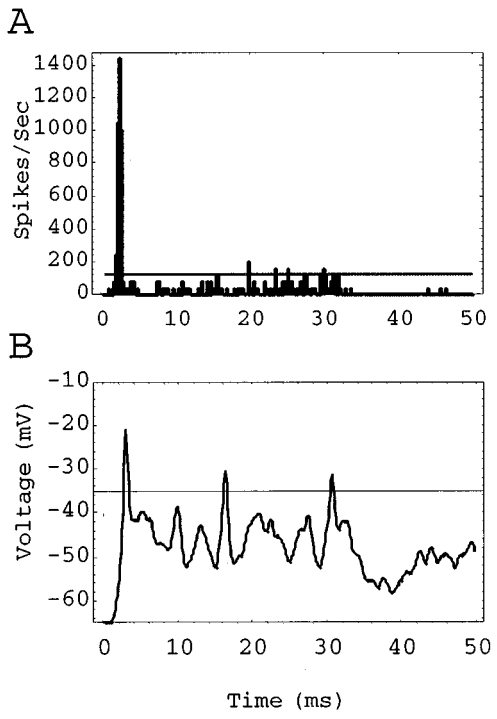

FIG. 1. Responses of the reference model to a 40 dB mSPL tone burst at CF. (A) PSTH. (B) Somatic potential. All of the PSTHs shown are constructed from 100 stimulus trials. The horizontal line in the somatic potential trace at −35 mV is the spike discrimination threshold (ρ=6, τ_m = 0.5 ms, S/L = 0.6, SD=20 mV).

pared to the reference model with the PSTH exhibiting a smaller peak rate, increased FSL (mean and standard deviation) and no sustained firing [Fig. 4(A)]. When R_m is doubled, the peak rate again decreases, but is now accompanied by a sharply increased sustained rate and a decreased mean FSL [Fig. 4(B)]. At the smaller R_m, the sustained depolarization decreases (SD=10 mV), while at the higher R_m, the sustained depolarization increases relative to the reference model [Fig. 4(C) and (D)].

Variations in R_m cause each of the summary parameters to change. At one-half R_m, τ_m, ρ, and S/L all decrease. When R_m is doubled, the summary parameters all increase. In this case, the larger SD is accompanied by an increase in sustained firing, which suggests that the spike threshold increases less than the increase in the size of the somatic potential fluctuations produced by the inputs.

Since $\tau_m = R_m C_m$, variations in C_m further isolate the effects of τ_m. Doubling C_m results in a decreased sustained rate and increased mean FSL; decreasing C_m by one-half results in an increased sustained rate and decreased mean FSL. It is notable that these responses are opposite to those resulting from changes in R_m (e.g., compare twice C_m and twice R_m). Moreover, these responses contradict the hypothesis that a smaller τ_m alone leads to more of an O_I response.

Variations in R_a further isolate the effects of S/L. Decreasing R_a by one-half does not significantly change the onset response, while doubling R_a causes the response to become more O_L. In these simulations, ρ varies inversely with R_a, τ_m does not depend on R_a, and S/L varies inversely with R_a. The relationship between S/L and R_a results from how the synaptic conductances were compensated with changes in the surface area of a dendrite compartment.

E. The effects of synaptic properties

The effects of synaptic properties on the onset response were evaluated in four ways: (1) changing the synaptic density, (2) changing the number of inputs, (3) using constant input spike probabilities, and (4) adding inhibitory inputs.

Decreasing the synaptic density by one-half causes the response to become more O_I with a small decrease in peak rate and no sustained activity. The mean FSL increases by 1.4 ms with a small increase (0.1 ms) in its standard deviation. Doubling the synaptic density makes the response more O_L with a small increase in peak rate and a large increase in sustained rate. The mean FSL decreases by 0.7 ms with a 0.2 ms increase in standard deviation. In this case, the sustained

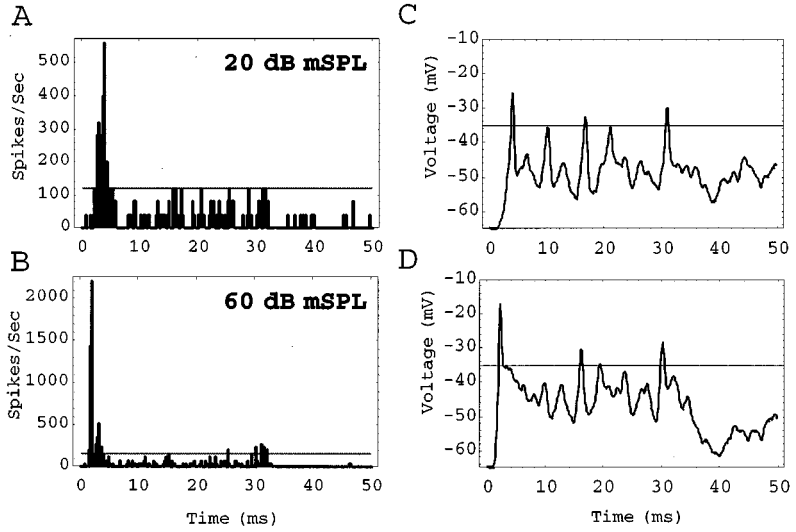

FIG. 2. Responses of the reference model to stimulus intensity variations. (A) and (C) PSTH and somatic potential to a 20 dB mSPL tone burst; SD=15 mV. (B) and (D) PSTH and somatic potential to a 60 dB mSPL tone burst; SD=20 mV (ρ=6, τ_m = 0.5 ms, S/L = 0.6).

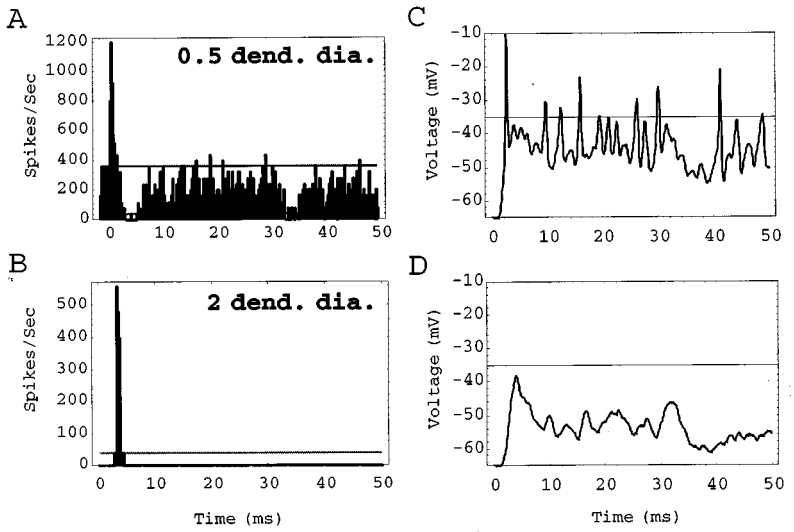

FIG. 3. Effects of dendrite diameter relative to the reference model. (A) and (C) PSTH and somatic potential with dendrite diameter decreased by one-half; ρ=2.1, τ_m = 0.5 ms, S/L = 1.7, SD=20 mV. (B) and (D) PSTH and somatic potential with dendrite diameter doubled; ρ=16.9, τ_m = 0.5 ms, S/L = 0.2, SD=15 mV.

depolarization increased to 25 mV as a result of temporal and spatial summation of larger synaptic potentials.

Changing the number of independent inputs was represented by changing input rates and synaptic densities. Specifically, doubling the number of inputs (from 60 to 120) was implemented by doubling the input rates and halving the synaptic densities such that, on average, the total number of input spikes times the conductance in a compartment remained constant. Doubling the number of independent inputs makes the responses more O_I [Fig. 5(A)]. The mean FSL does not change appreciably, but the standard deviation decreases. The sustained depolarization does not change from the reference model [Fig. 5(C)]. Halving the number of inputs was implemented by halving the input rates and doubling the synaptic densities, resulting in fewer, but stronger inputs. Decreasing the number of independent inputs by one-half makes the computed responses more O_L. The PSTH has a slightly broader peak occurring at the same latency and a higher sustained rate [Fig. 5(B)]. Sustained depolarization decreases from that of the reference model, although the synaptic potentials increase in amplitude [Fig. 5(D)].

The PSTH differences in these four cases are best explained in terms of S/L and SD since τ_m and ρ do not change with any of these parameter variations. S/L and SD varies directly with synaptic density and inversely to the number of inputs. A decreased S/L reflects smaller synaptic potentials that lead to an increase in the degree of coincidence required of the inputs to reliably elicit a response, and thus, more of an O_I response. Conversely, a larger S/L leads to more O_L responses. However, the FSL varied differently depending on how S/L is changed, either by varying synaptic density, or by changing the number of inputs. The mean FSL de-

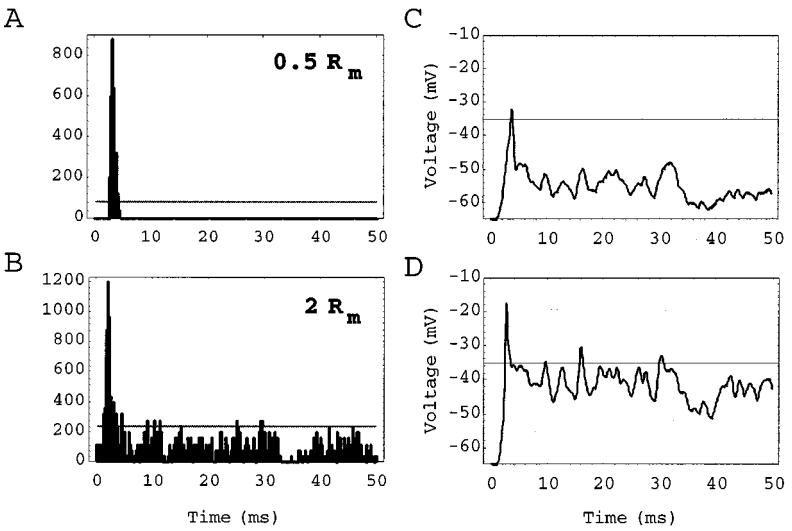

FIG. 4. Effects of variations in specific membrane resistance, R_m, relative to the reference model. (A) and (C) PSTH and somatic potential with R_m decreased by one-half; ρ=4.2, τ_m = 0.25 ms, S/L = 0.4, SD=10 mV. (B) and (D) PSTH and somatic potential with R_m doubled; ρ=8.5, τ_m = 1.0 ms, S/L = 0.9, SD=25 mV.

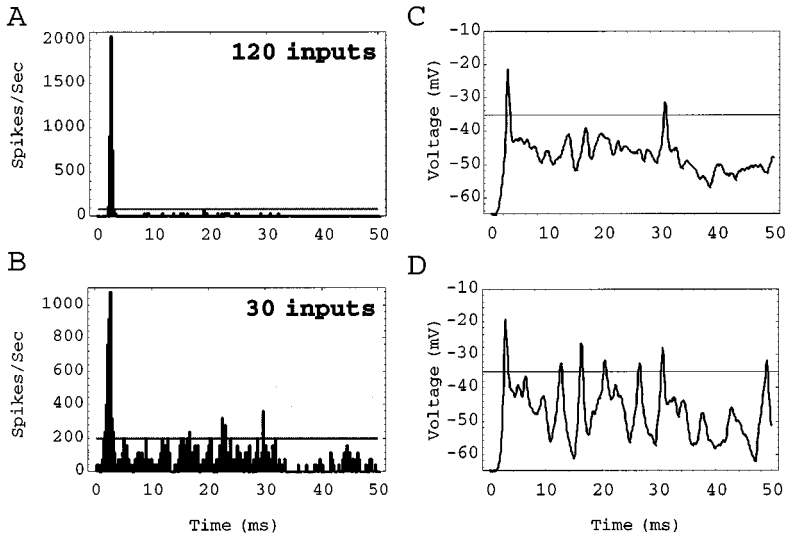

FIG. 5. Effects of variations in the number of inputs relative to the reference model. (A) and (C) PSTH and somatic potential with the number of inputs doubled; ρ=6, τ_m = 0.5 ms, S/L = 0.3, SD=20 mV. (B) and (D) PSTH and somatic potential with the number of inputs decreased by one-half; ρ=6, τ_m = 0.5 ms, S/L = 1.2, SD=15 mV. The synaptic conductance density was changed to compensate for the different numbers of inputs as described in the text.

creases and the standard deviation increases when the synaptic density (G_{exc}) is doubled because fewer input spikes are needed to bring the soma to threshold, with no change in the input rate. When the number of inputs is halved (and synaptic densities are doubled), the FSL becomes more widely distributed with no change in mean latency because again fewer input spikes are needed to elicit the first spike, but the input rate also effectively decreases by one-half.

The effects of auditory-nerve fiber spike rate adaptation on the onset response were evaluated by removing the normal adaptation from the auditory-nerve fiber inputs, i.e., by setting the fiber spike probabilities to a constant value throughout the stimulus. The onset response becomes more O_L in terms of a decreased peak rate and increased sustained rate. The mean FSL increases by 0.1 ms with a relatively large 0.6-ms increase in standard deviation. The sustained depolarization decreases (SD=15 mV). Removing adaptation from the inputs does not affect the three summary parameters.

The effects of delayed inhibition were investigated by adding inhibitory inputs on the distal dendrites. These inputs were driven by auditory-nerve inputs that were delayed an additional 0.5 ms relative to the excitatory inputs. The inhibitory inputs lead to more of an O_I response in terms of a larger peak rate and a smaller sustained rate. The mean FSL increases by 0.3 ms with no change in standard deviation. The sustained depolarization also decreases (SD=10 mV). The inhibitory inputs do not effect τ_m, ρ, and S/L.

F. The effects of active channel conductances

Changing the densities of the active potassium and sodium conductances, both separately and jointly, highlights active channel effects on the model's onset response. In these simulations, the channels' rate constants were not modified. Decreasing $\overline{\mathbf{g}}_{\text{Na}}$ by one-half makes the response more O_I with a slightly larger mean FSL, but with no change in standard deviation nor sustained depolarization. Doubling $\overline{\mathbf{g}}_{\text{Na}}$ makes the response more O_L with no appreciable change in peak rate, but with a larger sustained rate and decreased FSL (mean and standard deviation). Variations in $\overline{\mathbf{g}}_{\text{K}}$ do not affect the onset response to such a large degree. Decreasing $\overline{\mathbf{g}}_{\text{K}}$ by one-half causes the response to become more O_L, with slightly elevated sustained firing. Neither the FSL nor SD changes significantly. Doubling $\overline{\mathbf{g}}_{\text{K}}$ causes the response to become more O_I, but again, with little change in FSL and slightly decreased SD.

These results demonstrate that the effects of $\overline{\mathbf{g}}_{\text{K}}$ and $\overline{\mathbf{g}}_{\text{Na}}$ are opposite. However, when these parameters are changed in concert, the effects of $\overline{\mathbf{g}}_{\text{Na}}$ dominate the model's response. Specifically, when both $\overline{\mathbf{g}}_{\text{Na}}$ and $\overline{\mathbf{g}}_{\text{K}}$ are decreased by one-half, the model becomes more O_I [Fig. 6(A)], but with little change in sustained depolarization [Fig. 6(C)]. When $\overline{\mathbf{g}}_{\text{Na}}$ and $\overline{\mathbf{g}}_{\text{K}}$ are doubled, the model becomes more O_L [Fig. 6(B)]. The somatic potential exhibits decreased sustained depolarization [Fig. 6(D)].

The summary parameters, τ_m, ρ, and S/L do not depend on active channel densities and thus, are not useful for explaining these results. They can be explained in terms of changes in spike threshold. Increasing $\overline{\mathbf{g}}_{\text{Na}}$ leads to a larger inward sodium current and a concomitant decrease in spike threshold, the membrane potential at which the total inward current becomes greater than the outward potassium and leakage currents. Decreasing $\overline{\mathbf{g}}_{\text{Na}}$ reduces the sodium current, which increases the threshold and makes spiking less likely. The effects of $\overline{\mathbf{g}}_{\text{K}}$ are negligible because the active potassium conductance is not activated at subthreshold depolarizations. The small decrease in sustained depolarization when $\overline{\mathbf{g}}_{\text{Na}}$ and/or $\overline{\mathbf{g}}_{\text{K}}$ is doubled is probably due to repolarizing current from more and larger spikes.

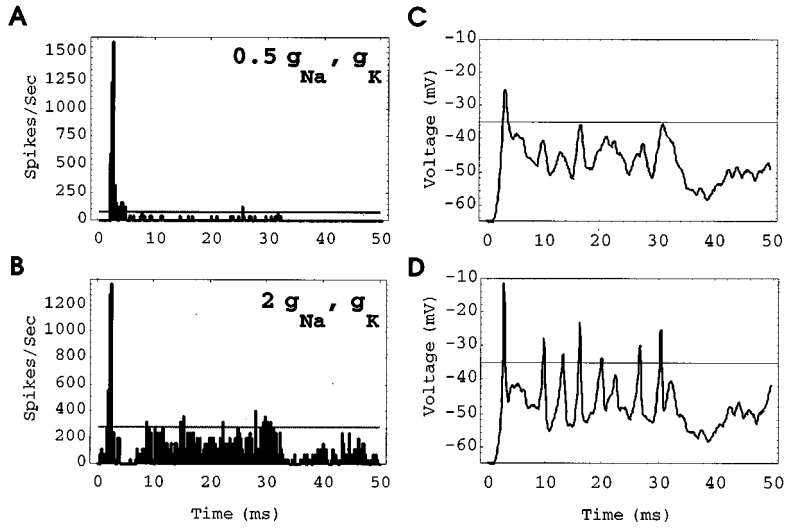

FIG. 6. Effects of variations in active channel densities relative to the reference model. (A) and (C) PSTH and somatic potential with $\overline{g}_{Na}$ and $\overline{g}_{K}$ both decreased by one-half; ρ=6, τ_m = 0.5 ms, S/L = 0.6, SD=20 mV. (B) and (D) PSTH and somatic potential with $\overline{g}_{Na}$ and $\overline{g}_{K}$ both doubled; ρ=6, τ_m = 0.5 ms, S/L = 0.6, SD=15 mV.

III. DISCUSSION

This study explores the response space of a compartmental model of the octopus cell by varying selected model parameters and observing their effects on the characteristic onset response of this cell type. The defining features of this response are the one or two spikes that occur with great precision shortly after the onset of each stimulus presentation and the low rate of sustained firing during the steady-state portion of the stimulus. Relating response variations to parameter variations helps to gain insight into the underlying mechanisms of the onset response. This approach is complicated by the fact that the octopus cell model is nonlinear. Effects of particular model parameters (trends toward O_I or O_L responses) are a nonlinear function of other parameters, and isolated parameter variations often affect more than one summary parameter. While each parameter variation in this study reflects a change from the same initial condition (i.e., the reference model), the general robustness of the model suggests that these results would remain consistent if alternative initial conditions were selected. However, in spite of these difficulties, it is possible to discern response trends related to general types of parameter variations, and from these trends, to begin to build a picture of the mechanisms.

The dendritic-to-somatic conductance ratio ρ quantifies the degree of loading on the soma by the dendrite(s). One working hypothesis is that a large ρ predicts more of an O_I response. However, the simulations demonstrate that while ρ predicts the effects of cell morphology, it does not predict the effects of other cell parameters. Specifically, when the dendrite diameter is doubled or the soma diameters are halved, ρ increases and the response becomes more O_I. This association between ρ and onset quality is expected under the hypothesis. However, when R_m is doubled, ρ increases, but the response becomes more O_L. Additionally, ρ does not change with some parameter variations that result in notable response changes (e.g., synaptic conductance density).

The membrane time constant, τ_m, relates to the effective temporal integration window of the model, i.e., the time frame during which near-coincident inputs summate to cause somatic depolarization. A second working hypothesis is that a smaller time constant requires more input coincidence and, thus, results in more of an O_I response. However, τ_m is found to be of limited use in predicting the onset response. For example, doubling either C_m or R_m causes a doubling of τ_m. When C_m is doubled, the FSL increases and the sustained rate decreases. However, when R_m is doubled, the FSL decreases and the sustained rate increases.

These opposite response changes reflect the different roles that C_m and R_m play in the onset response. Specifically as C_m increases, the membrane conductance decreases, whereas when R_m increases, the membrane conductance increases. Thus, combining these observations and the simulation results, one notices that the FSL is related to the membrane conductance and not the time constant. The effect of the membrane conductance is to increase the size of the synaptic potential, and thus, reducing the FSL. Additionally, while a smaller τ_m decreases the coincidence window for the inputs, it has little effect on the FSL because it is less than the rise-time of the synaptic conductance. These results concerning τ_m run counter to the notion that the octopus cell's fast membrane underlies its short-latency response.

For many of the parameter variations, the response changes can be explained in terms of changes in the synaptic density ratio S/L which is an indicator of how effective a synaptic input is in causing a somatic depolarization (termed ''synaptic effectiveness''). Specifically, for parameter variations where S/L increases, the synaptic effectiveness increases and the response becomes more O_L. Likewise, for variations when S/L decreases, the synaptic effectiveness decreases and the response becomes more O_I. The most direct method of changing S/L is by changing the synaptic conductance density, G_{exc}, but S/L also changes with variations in dendrite diameter, R_m, R_a, and the number of independent inputs. For these parameter variations, synaptic effectiveness

tends to dominate the effects of the other mechanisms and become the strongest predictor of the quality of the onset response. The most notable exceptions to this trend are with variations in soma diameter and active channel conductances in which there are significant response changes, although S/L does not change. However, these exceptions can be explained in terms of other mechanisms, including the effects of the active channels on the spike threshold.

Finally, a third working hypothesis for an onset response mechanism is that an increase in the somatic sustained depolarization decreases the sustained rate through an increase in spike threshold due to partial inactivation of the sodium channel (i.e., through depolarization block). However, the simulations indicate that the SD response parameter does not predict such changes in sustained rate. For example, the highest observed level of SD (from increasing G_{exc}) is accompanied by a relatively high sustained rate rather than a low rate as predicted. These results do not outright contradict the hypothesis unless depolarization-block is strictly defined as producing an unattainable threshold rather than just an increased threshold. These results do suggest that the threshold remains only slightly above the sustained depolarization.

In some simulations, a notch is evident in the PSTH immediately after the onset peak [for example, in Fig. 3(A)]. This brief silent period is associated with a relatively large amplitude spike. The large initial spike causes increased sodium channel inactivation which leads to an increased spike threshold and relative refractory period. Additionally, the model fires precisely on nearly every stimulus trial which effectively obviates any subsequent spikes for three to five milliseconds after the PSTH onset peak.

In summary, one of the results of this study is that the onset response is an emergent property of the model. The basic onset response results from the interactions of many parameters, each of which are assigned biologically plausible values. Halving or doubling the values of individual parameters affect the quality of the onset response, ranging from O_I to O_L, but is not sufficient for eliminating the response completely. Some parameters, such as R_m, cause more of a change than other parameters. This suggests that the onset response is a robust feature of the general structure of octopus cells and that relatively modest individual variations in morphological and physiological properties within a population of octopus cells are sufficient for generating responses ranging from O_I to O_L.

A second result is that the quality of the onset response cannot be predicted solely from any one of the four analysis parameters (membrane time constant, sustained depolarization, dendritic-to-somatic conductance ratio, and synaptic-to-leakage conductance ratio). These parameters are relatively simple summary measures of a subset of model parameters or responses, and are each related to a proposed mechanism of the octopus cell's onset response. This result suggests that any one of these proposed mechanisms alone is not sufficient for accounting for the quality of the octopus cell's onset response. Specifically, there is no obvious relationship between the time constant of the model or the level of sustained depolarization and the onset response. However, there is a strong relationship between the ratio of the synaptic conductance and the leakage conductance and the onset response. It is hypothesized that this ratio affects the synaptic potential size as well as the efficiency in which the synaptic potential is transmitted to the soma, i.e., it changes the synaptic effectiveness. In addition, the simulations demonstrate that an increased sustained somatic depolarization usually corresponds to an increased sustained firing rate, and that increasing the active-channel sodium conductance density increases the sustained firing rate. However, the sustained somatic depolarization does not entirely block spike activity. Thus, it is hypothesized that the sustained somatic depolarization affects the threshold and the onset response, but by a limited amount.

ACKNOWLEDGMENTS

This material is based upon work supported by the National Science Foundation under Grant No. BES-9409939 and the Deafness Research Foundation. Three anonymous reviewers provided insightful comments that improved the paper.

Baer, S. M., and Tier, C. (**1986**). ''An analysis of a dendritic neuron model with an active membrane site,'' J. Math. Biol. **23**, 137–161.

Bower, J. M., and Beeman, D. (**1995**). *The Book of GENESIS* (Kluwer Academic, New York).

Feng, J. J., Kuwada, S., Ostapoff, E. M., Batra, R., and Morest, D. K. (**1994**). ''A physiological and structural study of neuron types in the cochlear nucleus. I. Intracellular responses to acoustic stimulation and current injection,'' J. Comp. Neurol. **346,** 1–18.

Godfrey, D. A., Kiang, N. Y. S., and Norris, B. E. (**1975**). ''Single unit activity in the posteroventral cochlear nucleus of the cat,'' J. Comp. Neurol. **162,** 247–268.

Golding, N. L., Robertson, D., and Oertel, D. (**1995**). ''Recordings from slices indicate that octopus cells of the cochlear nucleus detect coincident firing of auditory nerve fibers with temporal precision,'' J. Neurosci. **15,** 3138–3153.

Holdsworth, J., Nimmo-Smith, I., Patterson, R. A., and Rice, P. (**1988**). Implementing a gammatone filter bank. MRC Applied Psychology Unit, Cambridge.

Kane, E. C. (**1973**). ''Octopus cells in the cochlear nucleus of the cat: Heterotypic synapses upon homeotypic neurons,'' Int. J. Neurosci. **5**, 251–279.

Kim, D. O., Rhode, W. S., and Greenberg, S. R. (**1986**). ''Responses of cochlear nucleus neurones to speech signals: Neural encoding of pitch, intensity and other parameters,'' in *Auditory Frequency Selectivity*, edited by B. C. J. Moore and R. D. Patterson (Plenum, New York), pp. 281–288.

Levy, K. L., and Kipke, D. R. (**1997**). ''A computational model of the cochlear nucleus octopus cell,'' J. Acoust. Soc. Am. **102**, 391–402.

Meddis, R. (**1986**). ''Simulation of mechanical to neural transduction in the auditory receptor,'' J. Acoust. Soc. Am. **79,** 702–711.

Meddis, R. (**1988**). ''Simulation of auditory-neural transduction: Further studies,'' J. Acoust. Soc. Am. **83,** 1056–1063.

Meddis, R., Hewitt, M. J., and Shackleton, T. M. (**1990**). ''Implementation details of a computation model of the inner hair-cell/auditory nerve synapse,'' J. Acoust. Soc. Am. **87,** 1813–1816.

Osen, K. K. (**1969**). ''Cytoarchitecture of the cochlear nuclei in the cat,'' J. Comp. Neurol. **136,** 453–484.

Palombi, P. S., and Caspary, D. M. (**1992**). ''$GABA_A$ receptor antagonist bicuculline alters response properties of posteroventral cochlear nucleus neurons,'' J. Neurophysiol. **67,** 738–746.

Rall, W. (**1967**). ''Distinguishing theoretical synaptic potentials computed for different somadendritic distributions of synaptic input,'' J. Neurophysiol. **30,** 1138–1168.

Rall, W. (**1989**). ''Cable theory for dendritic neurons,'' in *Methods in Neuronal Modeling*, edited by C. Koch and I. Segev (MIT, Cambridge, MA), pp. 9–62.

Rhode, W. S., Oertel, D., and Smith, P. H. (**1983**). ''Physiological response properties of cells labeled intracellularly with horseradish peroxidase in cat ventral cochlear nucleus,'' J. Comp. Neurol. **213,** 448–463.
Rhode, W. S., and Smith, P. H. (**1986**). ''Encoding time and intensity in the ventral cochlear nucleus of the cat,'' J. Neurophysiol. **56,** 262–286.
Ritz, L. A., and Brownell, W. E. (**1982**). ''Single unit analysis of the posteroventral cochlear nucleus of the decerebrate cat,'' Neurosci. **7**, 1995–2010.
Rouiller, E. M., and Ryugo, D. K. (**1984**). ''Intracellular marking of physiologically characterized cells in the ventral cochlear nucleus of the cat,'' J. Comp. Neurol. **225,** 167–186.
Saint Marie, R. L., Morest, D. K., and Brandon, C. J. (**1989**). ''The form and distribution of GABAergic synapses on the principal cell types of the ventral cochlear nucleus of the cat,'' Hearing Res. **42,** 97–112.
Segev, I., Rinzel, J., and Shepherd, G. M. (**1995**). *The Theoretical Foundation of Dendritic Function* (MIT, Cambridge, MA).
Smith, P. H., Joris, P. X., Banks, M. I., and Yin, T. C. T. (**1993**). ''Responses of cochlear nucleus cells and projections of their axons,'' in *The Mammalian Cochlear Nuclei: Organization and Function*, edited by M. A. Merchan, J. M. Juiz, D. A. Godfrey, and E. Mugnaini (Plenum, New York), pp. 349–360.
Winter, I. M., and Palmer, A. R. (**1995**). ''Level dependence of cochlear nucleus onset unit responses and facilitation by second tones or broadband noise,'' J. Neurophysiol. **73,** 141–159.

Interpretation of distortion product otoacoustic emission measurements. I. Two stimulus tones

David M. Mills[a)]
Virginia Merrill Bloedel Hearing Research Center, Department of Otolaryngology, Head and Neck Surgery, University of Washington, Box 357923, Seattle, Washington 98195-7923

(Received 10 October 1996; revised 27 January 1997; accepted 28 January 1997)

The interpretation of common but poorly understood observed characteristics of distortion product emissions is assisted by the development of a simple model. This model essentially includes only saturation of the cochlear amplifier, with emissions arising naturally from the same nonlinear processes which cause the saturation. The model provides useful physical explanations of emission behavior, particularly considered as a function of the stimulus intensities of the two primaries, i.e., behavior with fixed stimulus frequencies. It is assumed that emission generation consists of two main components which are always present in the total emission, but which most often have approximately opposite, i.e., canceling, phases. One component arises in a small region centered about the peak of the emission generation function, while the other arises from the region basal to this peak. At low stimulus levels with normal cochlear amplifier operation, the peak of the emission generation function is sharp, so the emission from the peak region dominates the total emission. This ''peak'' emission has typically been characterized as the ''active'' emission. At high stimulus levels where saturation is important, or at all levels when the gain of the cochlear amplifier is reduced, the summed ''basal'' component dominates the total emission. The characteristics of this basal emission are similar to, and continuous with, the characteristics of the truly ''passive'' emission, i.e., the emission observed when the cochlear amplifier gain is identically zero. Under circumstances when the emissions from the peak and basal components are approximately equal, there is seen a sharp ''notch'' characteristic of phase cancellation. The simple model produces emission distributions as a function of independent variation of the two stimulus amplitudes which are in good agreement with observation. It is shown that the furosemide assay provides a good estimate of cochlear amplifier gain when a correction factor of about 10 dB is added. However, when using two stimulus tones, neither absolute emission amplitudes, or emission input–output functions, or the furosemide assay can adequately distinguish between cases of moderate versus poor cochlear amplifier dysfunction when the cochlear amplifier gains are in the range from about half normal to zero. [S0001-4966(97)01006-0]

PACS numbers: 43.64.Jb, 43.64.Kc [RDF]

INTRODUCTION

Since their discovery (Kemp, 1978), otoacoustic emissions have become an increasingly important tool for the investigation of cochlear function. In particular, distortion product otoacoustic emissions have proven useful in both clinical and research settings. One reason is that these emissions are measurable both in humans and in many common laboratory animals. In contrast, other stimulus paradigms such as spontaneous, transient-evoked, and stimulus frequency emissions are relatively easy to measure in humans, but not as easily measured in most nonprimates (Avan *et al.*, 1990).

Distortion product otoacoustic emissions are produced when two tones (frequencies f_1 and f_2) are presented to the ear. Combination tones are emitted by the cochlea in response. The strongest emission is usually at the cubic distortion tone (CDT) frequency of $2f_1-f_2$. Distortion product emissions have some advantages and unique features which allow measurements to be made which probably cannot be made in any other way. These features provide their strengths and, simultaneously, of course, their potential weaknesses.

One such feature is that emissions are intrinsically a global response from the cochlea, representing the summed response at the ear canal from all parts of the basilar membrane. The available evidence is that the majority of the CDT emission energy originates in the region containing the peaks of the two traveling waves at f_1 and f_2, and is probably more closely associated with the f_2 peak (Brown and Kemp, 1984; Martin *et al.*, 1987). In any case, for emission measurements the two frequencies f_1 and f_2 are usually relatively close together, so that the emission originates in a relatively localized area of the cochlea. This suggests that, by simply changing the stimulus frequencies, the region in the cochlea which is being measured changes. This feature allows for great flexibility compared to eighth nerve or direct basilar membrane measurements. The disadvantage of the global aspect is that emissions coming from even slightly different regions in the cochlea can, depending on their relative phases at the point of summation, add or subtract from the summed emission. There are a number of complex phe-

a)Electronic mail: dmmills@u.washington.edu

nomena observed which might be attributed to such phase cancellation (e.g., Kössl, 1993; Lonsbury-Martin *et al.*, 1987; Mills *et al.*, 1993; Whitehead *et al.*, 1992a).

As another example, it is now well established that CDT emissions measured while presenting low-level stimuli are highly correlated with good cochlear amplifier function, and are similarly vulnerable to ototoxic insult (Brown *et al.*, 1989; Johnstone *et al.*, 1990; Rübsamen *et al.*, 1995; Whitehead *et al.*, 1992b). CDT emissions from high-level stimuli appear to be relatively invulnerable, and are at least potentially useful to determine the ''passive'' cochlear response (Mills *et al.*, 1993, 1994; Schmiedt and Adams, 1981). However, high and low are relative terms, and there is no *a priori* way to know how to interpret the emissions measured in many circumstances. For example, in developing animals, or in situations of moderate conductive hearing loss, high stimulus levels may be required to obtain measurable emissions. However, these high stimulus levels may correspond *in the cochlea* to low-level signals, physiologically. Such emissions actually may be indicative of the sensitive, vulnerable aspects of cochlear functioning (Mills *et al.*, 1994; Mills and Rubel, 1996). As will be shown, the presence of ''passive'' emissions also interferes with measurements to distinguish moderate and severe cochlear amplifier dysfunction, at least measurements restricted to two tone stimuli.

Another potential virtue of distortion product emissions is the large number of different stimulus parameters which may be specified. These provide a four-dimensional space over which to explore cochlear function, consisting of the frequencies and intensities of both stimuli, i.e., f_1, L_1, f_2, L_2 (Mills and Rubel, 1994). In practice, this aspect may have led to more confusion than understanding. When the stimulus frequency ratio is changed, for example, there are complex changes in CDT amplitude and phase responses (e.g., Brown and Gaskill, 1990; Brown *et al.*, 1992; Whitehead *et al.*, 1992a; Mills and Rubel, 1997). In general, the reasons for these changes are not well established. In terms of phase changes as a function of stimulus frequency ratio, attempts have been made to employ these to estimate traveling wave latencies, with moderate success (Brown *et al.*, 1992; Brown and Kemp, 1985; Kimberley *et al.*, 1993; Mahoney and Kemp, 1995). However, a number of recent measurements clearly show that emissions typically appear to be made up of two or more components, each associated with a *different* latency (Brown *et al.*, 1996; Moulin and Kemp, 1996a, b; Stover *et al.*, 1996; Wable *et al.*, 1996; Whitehead *et al.*, 1996).

There are also complex changes with fixed frequencies and with stimulus amplitude levels, L_1 and L_2, varied independently (Mills and Rubel, 1994). For example, the CDT emission amplitude is not symmetric, so that given the same L_1, higher CDT amplitudes can occur for $L_2 < L_1$ compared to $L_2 = L_1$. Recently, there has been an emerging consensus on recommendations for using L_1/L_2 ratios in the range 10–15 dB (Hauser and Probst, 1991; Mills *et al.*, 1993; Whitehead *et al.*, 1995a, b). However, the criteria used to decide upon the best stimulus amplitude ratio remains uncertain.

Clearly, many such issues can be resolved only through an adequate understanding of the relevant cochlear dynamics, i.e., those nonlinear dynamics which explain the generation of distortion product emissions. Such an understanding would presumably involve several stages. First would be the determination of a generally accepted linear dynamical model of cochlear functioning which would produce the observed sharpness of tuning for a single, low-intensity tone. Second would be the specification of the mechanism for the nonlinear response, including the process for generation of the distortion product emissions, and relevant calculations involving two-tone stimuli.

Unfortunately, for even the linear cochlear model there is no consensus. For example, while the basilar membrane deflection itself certainly appears to be actively amplified, it has been suggested that additional sharpness of tuning is provided by dynamics of a subsystem involving the tectorial membrane (e.g., Allen, 1980; Allen and Fahey, 1993; Brown *et al.*, 1992; Gummer *et al.*, 1996; Zwislocki, 1985). It is probably a considerable understatement to say that, for cochlear mechanics at the present time, there is simply not an adequate determination of the characteristics of the structures involved to construct a unique dynamical model.

In spite of this lack of consensus, it seems useful to attempt to develop a simple, pragmatic model which can assist with understanding some aspects of distortion product emissions. Given the current uncertainties, it seems prudent to take the most general view possible, and to use elements that are well established by observations without tying the model to particular mechanisms or dynamics. The basic model presented is therefore intended to be of the absolute minimum complexity required to plausibly provide the necessary nonlinear features, and to introduce the fewest possible free parameters. The goal is not to provide a tautologically ''correct'' model, but to employ a simple model as a way to further our physical understanding of some complex and confusing observations. In particular, the emission model leads to an improved physical understanding of the complex cochlear responses as a function of stimulus intensities. It further provides some useful guidance, and tentative quantitative results, connecting the actual cochlear amplifier gain with observed emission characteristics.

In this paper the model is applied to cases in which there are at most two stimulus tones present. Applications to situations in which there are three tones, especially emission ''suppression'' paradigms, are considered in Part II (Mills, 1997). In Part I, the model illustrates that the important features of the observed variation with the two stimulus intensities can be explained by simple saturation alone. On the other hand, the model results imply that saturation alone cannot provide an adequate explanation for the complex behavior observed when the stimulus frequency ratio is varied.

I. METHODS

For comparison with model predictions, results are presented for distortion product emission measurements from adult gerbils. All procedures and equipment used were as previously reported (Mills and Rubel, 1996, 1997). In addition, it may be noted that contour maps in this and previous reports (Mills *et al.*, 1994; Mills and Rubel, 1994) were gen-

erated using Systat 5.1 (Systat, Evanston, IL) with the line fit algorithm ''NEXPO.'' Model maps presented for comparison use the same stimulus level grid interval as the observed emission measurements. Contour lines in observed maps were omitted when the emission amplitudes were less than 10 dB from the noise floor. Contour lines in model maps were omitted at a corresponding level to make the comparisons clearer.

Procedures for the care and use of the animals used in this study were approved by the University of Washington Animal Care Committee (*re*: Grant No. NIH DC 00395, Ontogeny of sensory processes).

II. MODEL

The cochlear response will be approximated using a quasilinear approximation. The stimulus is generally assumed to consist of two sinusoidal inputs of different frequencies (f_1 and f_2). Except in the regions where either wave would be the appropriate frequency to be amplified by the cochlear amplifier, the total cochlear response is assumed to be linear and passive, consisting simply of the linear superposition of the two stimulus waves. In the regions where amplification occurs, the amplification of each individual wave is limited by the saturation of the force providing the amplification. The two traveling waves interact *only* through this saturation of the cochlear amplifier. That is, the amount of gain available will be assumed to depend on the instantaneous sum of the amplitudes of the two waves at any cochlear location. The amplitude of distortion produced will be assumed to be small compared to the typical amplitudes of the two primary waves, at least near and basal to their peaks.

To considerably simplify the calculations, the basic cochlear response will not be determined through the integration of a wave equation with the attendant necessity to choose relevant dynamical variables. Rather, the typical results from such calculations will be assumed, and parameters matched to observation. In choosing these parameters, there will be three main sources. Model parameters associated with the linear, active response will be based on the threshold cochlear responses along the basilar membrane derived from a transform of neural recordings (Allen and Fahey, 1993). Parameters associated with the passive cochlear response will be chosen to fit distributions summarized by Dallos (1973, Fig. 4.14). These cochlear responses were based on a comparison of observational data of basilar membrane motion and modifications of a model originally proposed by Zwislocki (1965), and represent essentially passive cochlear function. The general effects of saturation on the active response will be developed in accordance with the interpretation of basilar membrane measurements at different stimulus levels (Johnstone *et al.*, 1986). The generation of the emissions will be assumed to arise naturally from the *same* nonlinear process or processes that result in the observed saturation.

For the model, the usual assumptions are made for the frequency-place relationship (e.g., Tarnowski *et al.*, 1991). That is, the passive response of the basilar membrane is assumed to be fixed such that the positions of the resonant peaks are located at equal intervals with equal changes in the logarithm of the frequency. For convenience, distances from the base, x, are indicated by the *decrease* of frequency in octaves. That is, the location $x=3$ denotes a characteristic frequency $1/2^3=1/8$ of the characteristic frequency at the base ($x=0$). For any frequency, the place where the traveling wave begins to be amplified is assumed to be fixed on the basilar membrane, and this location is assumed to be independent of amplitude. This location is also assumed to be approximately the location at which a passive wave of the same frequency would peak, although this assumption is not essential. The distance over which the amplification force is present, w, is also assumed to be fixed and amplitude independent. At the same time that a wave becomes vulnerable to amplification by the cochlear amplifier, it is assumed that resistive losses also begin to be important. This assumption is justified partly by the observation that the amplification begins where the passive response would peak, which is the location where resistive losses become important for the passive wave. The resistive losses are presumed to increase sharply as the apical end of the cochlear amplifier gain region is reached, located at $x_f=x_w+w$. Thereafter, the resistive losses are assumed to remain large. A sketch of this model is shown in Fig. 1(A).

A typical ''threshold tuning curve'' for the model is shown in Fig. 1(B). This is obtained from the low-amplitude response of the model, i.e., operated in the linear regime, and results from the calculated response at a fixed location to a single tone varied in frequency. Possible effects of the middle ear are ignored in these presentations. The threshold shift associated with the sharp tip of the tuning curve, ΔT, is defined as shown, and is equal to 38 dB in this case.

As the stimulus level is increased above the linear regime, the effects of saturation must be taken into account. For any wave in its own active amplification zone, it is assumed that the available cochlear amplifier gain, g_a, will be reduced depending on the instantaneous amplitude of the total cochlear response at that point. That is, the degree of saturation of amplification of a given traveling wave is assumed to depend on the instantaneous amplitude of the sum of all waves at that point, including the amplitude of the traveling wave itself. This is a critical simplifying assumption. This suggestion is supported by measurements of two tone suppression (e.g., Cooper, 1996) and from experiments in which a high-intensity low-frequency tone was shown to modulate the cochlear amplifier gain for high-frequency tones (Patuzzi *et al.*, 1984). In the latter experiment, the maximum reduction in gain occurred during the maximum excursion portions of the low-frequency cycle. This result implies that the passive, high-amplitude responses in the cochlear base, caused by the intense low-frequency signal, transiently interferred with the amplification there according to the instantaneous amplitude.

The precise form for the reduction of gain due to saturation is derived in Fig. 1(C). Consider first a single wave at frequency f, which at any distance from the base, x, and at time, t, can be represented approximately by

$$y(x,t)=y_0(x)\sin 2\pi ft. \tag{1}$$

Note that the response $y(x,t)$ is taken to be that cochlear

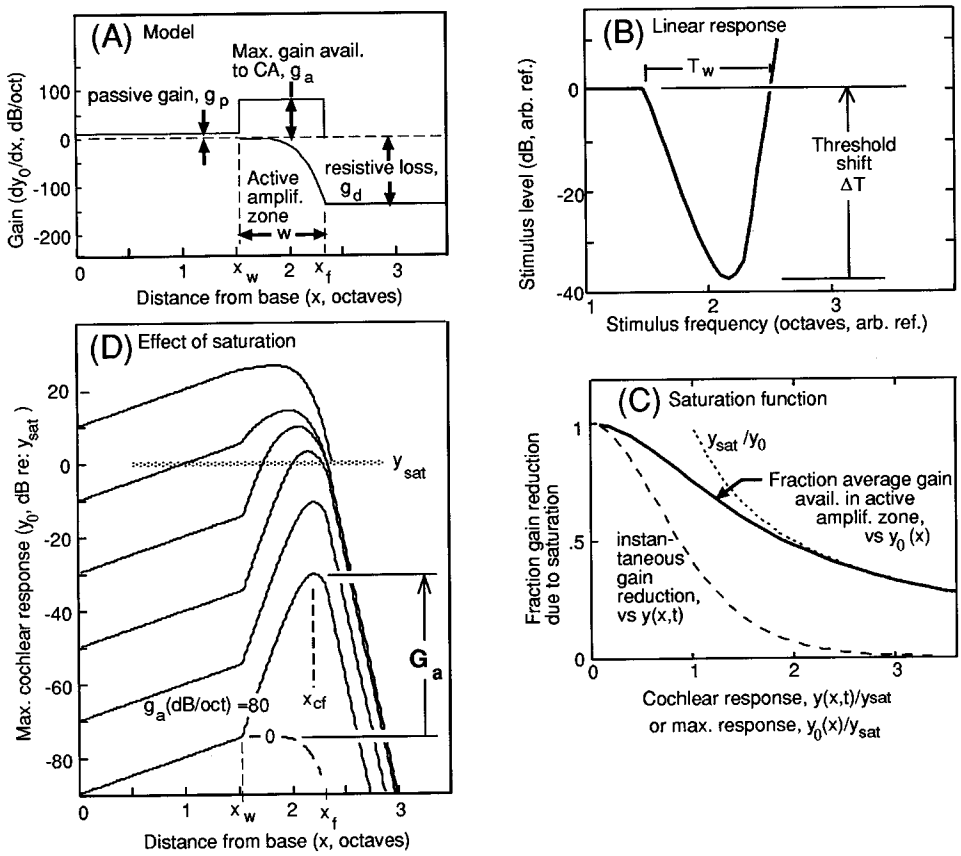

FIG. 1. Clockwise from upper left. (A) A sketch of the basic model. The distance from the base, x, represents the *decrease* in characteristic frequency in octaves from the base. For a given frequency, f, identified with the distance, x_f, the active amplification zone extends from the distance $(x_f - w)$ to x_f. The distances x_f are assumed spaced at equal logarithmic intervals in f. As the response at a given frequency, f, propagates in from the left, the traveling wave first benefits from a passive growth, g_p, here equal to 10 dB/octave. When the stimulus reaches the point $x = x_w = (x_f - w)$, active amplification of the traveling wave by the cochlear amplifier begins. A typical amplification rate of 80 dB/octave is illustrated, with the width of the active zone, $w = 0.8$ octaves. At the same time that amplification begins, resistive losses begin to become important. The resistive losses are assumed to increase rapidly as the end of the amplification region is approached, i.e., near x_f. For the model shown, the increase is proportional to the fourth power of the distance from the start of the amplification region. Following the amplification region, it is assumed that the resistive losses remain high, so that the traveling wave quickly decreases to negligible amplitude. The characteristic loss rate, g_d, illustrated is 140 dB/octave. (B) The linear, threshold tuning curve calculated for the model parameters above. It is assumed that the cochlear response is monitored at a fixed point x and that the stimulus frequency is varied. It is assumed that the distance x is large enough that the active zone, w, for all stimulus frequencies is located to the right of the base. The stimulus level required to reach a criterion response at this position is plotted on the vertical axis, with the stimulus frequency on the horizontal axis. (C) As stimulus levels are increased, the amplitude of the traveling wave reaches values at which the instantaneous gain of the cochlear amplifier is reduced due to saturation. The saturation is assumed to affect the growth rate of waves only when they are in their respective active amplification zones. The lower dashed line denotes the assumed instantaneous gain reduction (on the vertical axis) plotted against the instantaneous cochlear response amplitude $y(x,t)$ on the horizontal axis. The lower dashed line shown is $\{1 - \tanh^2(y(x,t)/y_{\text{sat}})\}$. The resulting *average* gain reduction for a sinusoidal signal with amplitude $y_0(x)$ is given by the solid line. The upper dashed line gives the curve (y_{sat}/y_0) for reference. Note that for this panel the axes are not logarithmic. (D) The variation of the cochlear response for single tones with stimulus level as a parameter, stepped at 20-dB intervals. At larger amplitudes, saturation of the cochlear amplifier becomes important, resulting in a reduction in the available gain at that point. The peak of the cochlear response shifts about 1/2 octave toward the base at large stimulus levels. At low stimulus levels, the difference, G_a, between the peak response with normal cochlear amplifier gain (solid line) and zero gain (dashed line) defines the intrinsic net gain of the cochlear amplifier. For this case, G_a is 43 dB. For low stimulus levels, the peak location is denoted x_{cf}, which is slightly less than x_f.

variable which best represents the cochlear sensitivity, and is not necessarily the basilar membrane deflection (Allen, 1980; Neely, 1993; Zwislocki and Cefaratti, 1989). For the moment, consider the situation of a hard saturation, such that the gain available to the traveling wave is equal to g_a when $|y(x,t)|$ is below y_{sat}, but zero when it is larger. For $|y_0| < y_{\text{sat}}$, saturation has no effect on the traveling wave. However, if the cochlear response $y(x,t)$ exceeds y_{sat} during any part of the cycle, there will be zero energy input during *that portion* of the cycle. We assume, however, that energy may still be fed into the wave for the *rest* of the cycle. On average, then, the gain will be reduced by the fraction (y_{sat}/y_0) when $y_0 \geqslant y_{\text{sat}}$, as shown by the upper dashed line in Fig. 1(C). This statement actually represents an approximation, correct within the factor $2/\pi$, to the solution of the relevant trigonometric equation. Although it is not essential for the model, it may be noted that if the equivalent ''Q'' is reasonably high, the cochlear response will remain approximately sinusoidal even if power is supplied only during part of each cycle (e.g., consider pushing a swing).

For the actual model computations, such an abrupt on–off saturation is not used. Instead, a physiologically realistic ''soft'' saturation function is employed, shown by the lower dashed curve in Fig. 1(C). The instantaneous gain reduction function plotted is equal to $\{1 - \tanh^2(y/y_{\text{sat}})\}$. This is, for example, a useful approximation for the saturation effects in

the outer hair cell voltage-displacement transfer function (e.g., Santos-Sacchi, 1989, 1991). After suitable convolution of this instantaneous response, the *average gain* available to the traveling wave of amplitude $y_0(x)$ is obtained, and illustrated by the solid line in Fig. 1(C). It can be seen that the average gain reduction is approximately y_{sat}/y_0 for y_0 greater than about $2y_{\text{sat}}$.

These calculations imply that for excursions with a peak value of $2y_{\text{sat}}$ or more, there is the same amount of power fed into the traveling wave over each cycle for either hard or soft saturation. Thus when the amplitude of the response is large compared to the characteristic saturation level, the precise form of the saturation matters little. Because energy can still be fed into the traveling wave at times near the zero crossings, there is some cochlear amplifier gain even at comparatively high signal levels. For signal levels 20 dB above the saturation level, for example, the gain is reduced to 10% of its normal level. This is still a significant amount of gain, both in terms of producing a modest amplification of the cochlear response and in terms of producing distortion products.

Because the gain is specified as a function of stimulus amplitude, the model results in a single nonlinear first-order differential equation for the case of a single tone stimulus. This is numerically integrated to obtain the responses shown in Fig. 1(D). Responses are illustrated for stimulus tones stepped at 20-dB intervals. To obtain these responses, the values for g_a and g_d were first chosen so that the low stimulus amplitude response of the model would approximately match the shapes of threshold cochlear responses at mid and basal regions of the cochlea in the cat (Allen and Fahey, 1993). Note that the typical total cochlear amplifier gains observed for the cat are somewhat larger than the responses in Fig. 1, which were chosen to be more typical of the gerbil. The value for the passive slope, g_p, was set at 10 dB/octave, based on the range of 7–12 dB/octave for both theory and observation of essentially passive basilar membrane responses (Dallos, 1973, Fig. 4-14).

A third requirement for the model is that it give reasonable responses as a function of stimulus intensity for single tone responses as inferred by Johnstone *et al.* (1986). This agreement includes a half-octave basal shift in the peak location as the stimulus level increases, which is also suggested by pure-tone damage studies (Cody and Johnstone, 1981). Note that, in this model, the peak shifts toward the base with increasing stimulus level because the loss rate is assumed to be independent of amplitude, but the gain is not. As the overall amplitude of the response increases, the saturation reduces the gain of the cochlear amplifier. The peak, which is located at the point where the cochlear amplifier gain and resistive losses are equal, therefore naturally moves toward the base.

By definition, the net effective gain of the cochlear amplifier is given by the difference between the response peak with normal and zero gain at low stimulus levels where the response is linear (Nuttal and Dolan, 1996). This is the value G_a shown in Fig. 1(D), which is 43 dB in this example. Note that the ''cochlear amplifier gain'' can refer to two different quantities: One is the underlying gain rate g_a in dB/octave which is a model parameter *input*; the other is the effective peak gain G_a, in dB, which is an *output* of the model. The context, or the use of the corresponding symbols, will make clear which is meant.

The value of G_a obtained should be compared with that found for the threshold shift, which was 5 dB less [Fig. 1(B)]. The difference is due to the assumption of a 10-dB/octave passive gain. If the passive growth is set to zero, both values are identically 43 dB. While only a small difference, this example illustrates the danger of assuming that the threshold shift and cochlear amplifier gain are *identical*. For similar reasons, a difference between these two measures can occur if the middle ear transfer is frequency dependent.

The shape of the cochlear response function at zero gain [lower, dashed curve in Fig. 1(D)] is identical to the shape when the cochlear amplifier gain is completely saturated, i.e., the response at the highest stimulus levels. Except for an amplitude scale factor, the results of peak broadening from *either* cause will have identical effects on the emissions from the cochlea, as will be shown in detail.

As the stimulus level increases, the effective gain of the cochlear amplifier decreases. At each stimulus level, responses such as those in Fig. 1(D) give the peak value reached. The peak values plotted against the stimulus levels give the corresponding input–output, or ''growth'' functions (Fig. 2). Also shown is the growth function for the zero gain case.

As in Fig. 1(D), the vertical difference between the peak amplitudes with normal and zero gain defines the cochlear amplifier gain at a given stimulus level. Note that, because the slope for the input–output function is 1:1 at low stimulus levels, the cochlear amplifier gain can be defined equally well as the horizontal shift as shown in Fig. 2. Although it is a trivial difference, it is often a conceptual advantage with a fixed noise floor to focus on the horizontal measurement, equivalent to measuring a threshold shift. In Fig. 2(B), the shift in location of the peak of the response is also shown.

Now consider the situation relevant to distortion product emissions when two primary tones (frequencies f_1 and f_2) are present simultaneously. Considering only the primaries, the cochlear response at any point, x, can be approximated by

$$y(x,t) \cong y_1(x)\sin(2\pi f_1 t) + y_2(x)\sin(2\pi f_2 t). \tag{2}$$

It is assumed that the gain available to the cochlear amplifier is reduced depending on the instantaneous amplitude $y(x,t)$ according to the gain function in Fig. 1(C) (the lower dashed curve). Equivalently, the *average* reduction (over one complete cycle) is indicated by the solid curve, as a function of the sum of the amplitudes $\{y_1(x)+y_2(x)\}$. As discussed above, the gain available is assumed to depend only on the instantaneous *magnitude* of the total cochlear response at any point, independent of how the traveling waves reach that response level. Saturation affects the f_1 or f_2 response only within each frequency's respective active amplification zones.

With two stimulus frequencies present, the model results in two coupled, nonlinear, first-order differential equations which can easily be numerically integrated to obtain the co-

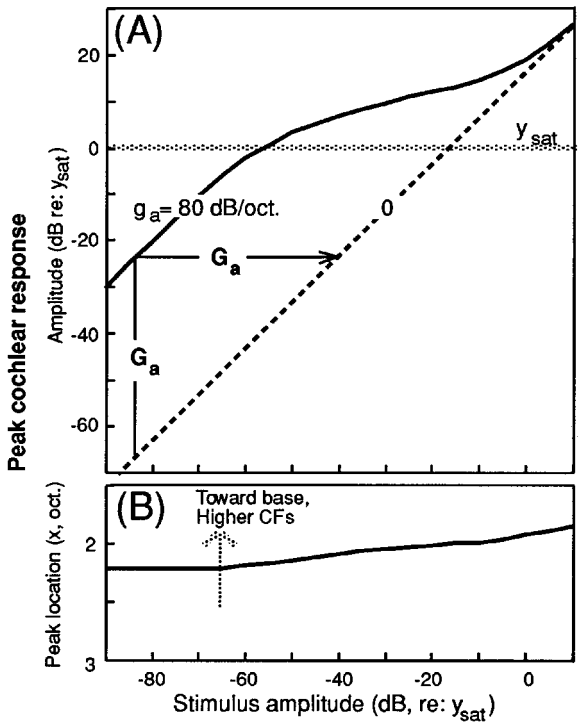

FIG. 2. Variation of the peak cochlear response with stimulus level for a single tone stimulus. (A) Amplitude response. The maximum responses are determined from cochlear response curves such as Fig. 1(D), and plotted versus stimulus level. The growth function for normal cochlear amplifier gain (80 dB/oct) is shown by the solid curve, while the growth function for zero gain is shown by the dashed line. At low stimulus levels, the difference is G_a, here 43 dB, as in Fig. 1(D). (B) Location of maximum cochlear response as a function of stimulus level. The peak location shifts about 1/2 octave toward the base with increasing stimulus level. Parameters same as Fig. 1.

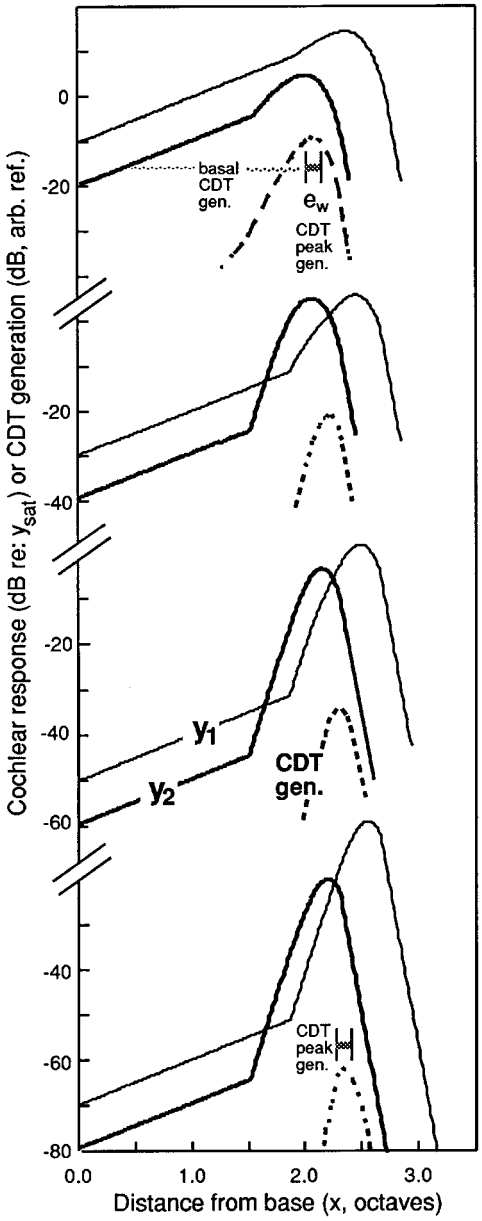

FIG. 3. The response of the cochlea with two tones. The stimulus frequency ratio is assumed to be $f_2/f_1=1.28$ and the level $y_1(0)$ to be 10 dB above $y_2(0)$, i.e., the cochlear responses measured at the base of the cochlea are 10 dB different. Because the middle ear is assumed to be transparent, these responses at the base may be directly identified with the stimulus levels, L_1 and L_2. Model parameters are the same as previous figures. The solid lines show the responses $y_1(x)$ and $y_2(x)$ at the primary frequencies, in dB *re*: the saturation level y_{sat}. The distribution of the cubic distortion tone (CDT) emission *generation* is shown by the dashed lines, in dB with an arbitrary reference. The CDT generation must be integrated to obtain the total emission seen in the ear canal. Two distinct areas of emission are denoted in the figure: the region of width e_w (here equal to 1/8 octave) centered on the peak of emission, and the region basal to this peak region. Other parameters are the same as previously described.

chlear response. Cochlear responses for parameters appropriate to distortion tone emissions are illustrated in Fig. 3. Unless otherwise noted, the stimulus frequency ratio is $f_2/f_1=1.28$, and the stimulus amplitude ratio is $L_1/L_2=10$ dB. The stimulus levels increase 20 dB between each pair of responses.

Inspection of the resulting curves leads to the following conclusions. Even with L_1 larger than L_2 at the base of the cochlea, for low stimulus levels the f_2 cochlear response increases sharply when it reaches its cochlear amplifier region, quickly becoming larger than the f_1 response. It is consequently much larger than the f_1 response when that frequency finally begins to be amplified. At moderate levels when saturation begins to be important, the f_2 response reduces the gain available to the f_1 response significantly compared to the single tone response. Only for stimulus levels much above the saturation level (top curves in Fig. 3) does the f_1 response dominate the f_2.

The generation of distortion products is assumed to be due to the same nonlinearity (or nonlinearities) that cause the saturation. To estimate the rate of generation of the emission from the primary response intensities, $y_1(x)$ and $y_2(x)$, note that an emission at a frequency of $2f_1-f_2$ will have an instantaneous generation rate proportional to $(y_1)^2y_2$ for small signal amplitudes, assuming only reasonable smoothness in the distortion mechanism (Schetzen, 1989). While the emission generation for the real cochlea will undoubtedly saturate at high stimulus levels, this assumption will be expected to give adequate results at lower signal levels that are correct for any reasonable, physiologically relevant saturation mechanisms (i.e., mechanisms without discontinuities in magnitude or slope). With this assumption, the distribution of the emission generated is shown in Fig. 3 by the dashed

lines. For low stimulus levels, the distribution of CDT generation is quite sharp, but it broadens (especially toward the base) as the stimulus intensity increases. This broadening results from the broadening of the peaks of the primary stimuli which is due to saturation. For later discussion, two specific regions for the cubic distortion tone generation are defined, as shown in the top panel of Fig. 3. One region is the area immediately around and including the peak of emission, of total width e_w. The other region is the area basal to this peak region.

In Fig. 4(A), the growth functions for both the f_1 and f_2 peak responses are summarized. For sufficiently low stimulus levels, even with two stimuli present the gains of the f_1 and f_2 peaks are the same as for the single tone case. The f_2 cochlear amplifier gain is illustrated in Fig. 4(A). The location of the maxima of the cochlear responses are shown in Fig. 4(B). It can be seen that the maximum CDT generation is always located between the two traveling wave peaks, but is closer to the f_2 peak location than to the f_1 peak.

To calculate the total CDT emission, generation functions such as those shown in Fig. 3 must be integrated along the x axis. Because of probable rapid phase changes in the traveling waves generating the emissions, it is likely that there will significant differences in the phases of emissions generated from different regions of the cochlea. This leads to the possibility of cancellation when out-of-phase emissions are summed at the stapes. For simplicity in the model calculations, it will be assumed that the CDT emissions effectively originate in three generation regions: (1) a small area around the location of the emission maximum from which, because of its small size, the emission adds in phase; (2) the area apical of this peak area, which sums to zero due to rapid phase changes; (3) the area basal to the peak, which sums to a nonzero contribution. It is further assumed that the sum for this third area, the net ''basal'' emission, may have a different phase than the summed emission from the peak region. The difference in phase angle, denoted Ψ, between the emissions from the two regions as well as the width of the peak coherence region, e_w, will be specified as model parameters. Note that it is not necessary to specify a size for the basal region, as the emission generation function falls off sufficiently rapidly toward the base to result in a finite integral.

These two emission generation regions are illustrated at the top of Fig. 3. Note that for small stimulus levels (lower sections of Fig. 3), the peak CDT emission will dominate the basal, unless the coherence area around the peak is assumed to be unrealistically small. As response levels reach saturation, however, the total emission from the area basal to the peak increases to dominate that from the peak region.

Figure 4(C) illustrates the emission growth functions which may be expected, for different angles, Ψ, between the summed emission from the peak area and that of the region basal to the peak. The width of the coherence region around the peak is taken to be $e_w = 1/8$ octave in all cases. For small stimulus levels and normal cochlear amplifier gains, the emission from the peak region dominates the basal region. However, for large stimulus levels, or for small cochlear amplifier gains, the basal emission dominates that from the peak region. This is to be expected, since the cochlear responses have quite broad distributions in both these circumstances.

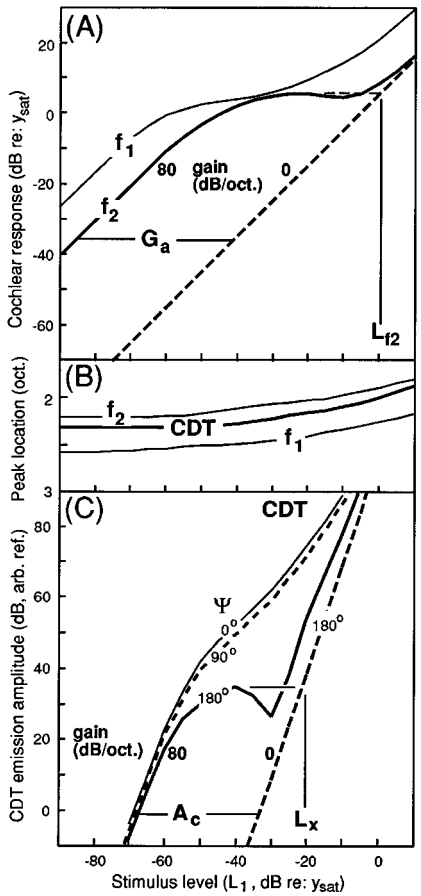

FIG. 4. Growth functions for cochlear responses for two-tone stimuli. (A) The peak responses at the primary frequencies f_1 and f_2 are illustrated, for a cochlear amplifier gain g_a of 80 dB/octave. Also shown is the f_2 response for zero gain. The difference at low stimulus levels is the net cochlear amplifier gain, G_a, as noted. The stimulus level, L_1, is defined to be the cochlear response at the base, i.e., $y_1(0)$. Note that the peak response for f_2 actually decreases with increasing stimulus levels near $L_1 = y_{sat}$. The reason is that the passive growth of f_1 significantly interferes with the cochlear amplifier gain in this region. The active–passive crossover level for the f_2 response, L_{f2}, is defined for later use. In this case, it is approximately equal to y_{sat}. (B) Shift in the location of the maximum responses with stimulus level. There is about a half-octave shift in the locations of all three peaks for this range of stimulus levels. (C) The response of the integrated cubic distortion tone (CDT) emission. For a gain g_a of 80 dB/octave, three different curves are shown. The parameter, Ψ, is the difference in phase angle between the emission originating in the peak coherence region (width $e_w = 1/8$ octave) and the emission from the region basal of this peak region. Only one CDT response is illustrated for a cochlear amplifier gain of zero; the other angles give nearly the same responses. At low stimulus levels, the shift in CDT ''threshold'' defines the difference A_c, between normal and zero gain as shown. For these parameters, $A_c = 33$ dB, compared to $G_a = 43$ dB. The characteristic crossover stimulus level, L_x, for the CDT emission is also defined. Here, it is 20 dB below y_{sat}, so that L_x is about 20 dB less than L_{f2} as defined in A. Same parameters as Fig. 3.

The overall responses with angles, Ψ, near 180° are quite similar to those most frequently observed, and will be generally used for later illustrations. An advantage of assuming that Ψ is approximately 180° is that it clearly divides the response into different areas, and makes it easy to unequivocally define the crossover stimulus level, L_x, noted in Fig. 4(C). However, it should be noted that observed emission functions for a small subset of the parameter space look more

like the model results for smaller relative angles, such as those for $\Psi = 0°$ and 90° illustrated in Fig. 4(C) (e.g., Mills *et al.*, 1994; Mills and Rubel, 1994, 1996).

In Fig. 4 is defined the distance, A_c, the threshold shift for the emission as the gain is decreased to zero. Note that the value of the shift does not depend significantly on the phase angle, Ψ. The threshold shift, A_c, corresponds to the distance G_a, but is *not* equal to it.

III. RESULTS

A. Choice of parameters for input-output functions

As stated earlier, an important task for those employing distortion product otoacoustic emissions is the selection of a subset of stimulus parameters. There is rarely time for a complete investigation of the entire four-dimensional parameter space associated with two stimulus tones (i.e., two frequencies and two intensities). Further, there is obviously great redundancy in the emission distribution. Therefore, such a complete exploration should not be required for the practical determination of most interesting aspects of cochlear function. The simple model presented here cannot assist with the choice of frequency ratio, as the observed frequency dependence is complex, and the reasons for this complexity are largely unknown. However, the model can and should assist with the determination of the best amplitude ratios at a given frequency ratio. Note that with the stimulus frequencies fixed, all observed changes with stimulus level must be due to nonlinear effects.

Figure 5 shows the amplitude responses calculated from the model for the L_1 and L_2 stimuli varied independently. Contour lines represent lines of constant CDT amplitude, at 10-dB intervals in all three maps. In Fig. 5(A), the emission amplitudes resulting from a cochlear amplifier gain g_a of 80 dB/octave are shown. Contours for the passive case, with a cochlear amplifier gain of zero, are shown in Fig. 5(B).

For determination of the cochlear amplifier gain from the emissions, one might argue that, instead of the absolute emission magnitude, it is the *difference* between the active and passive emissions at low stimulus levels that is important. The calculated ratios between these two emission amplitudes (difference of the amplitudes expressed in dB) are shown in Fig. 5(C). It can be seen that the difference tends to a constant value of about 100 dB over a relatively large area in the lower left side of the map. In this region, the ratio L_1/L_2 ranges from $+20$ to -10 dB. Because of the slope of 3:1 for the passive growth function, this difference corresponds to a CDT shift A_c of $100/3 = 33$ dB. The correct gain figure, A_c, can be accurately determined only using the low stimulus levels approximately bounded by the 100-dB contour in Fig. 5(C). Within this area, one should choose the stimulus ratios which give the highest absolute amplitudes for the case of normal gain, to obtain the best signal to noise ratios. Therefore, when using a single growth function for determination of the cochlear amplifier gain, the model supports the idea that the most efficient ratio is in the range $L_1/L_2 = +10$ to $+20$ dB. However, equal level primaries, or even ratios as low as $L_1/L_2 = -10$ dB, would not give incorrect results, *provided* that the active emissions could be followed to sufficiently low stimulus level, i.e., at or below the 100-dB contour in Fig. 5(C). For the remainder of this report, the preferred ratio of $L_1/L_2 = +10$ dB is used unless otherwise noted.

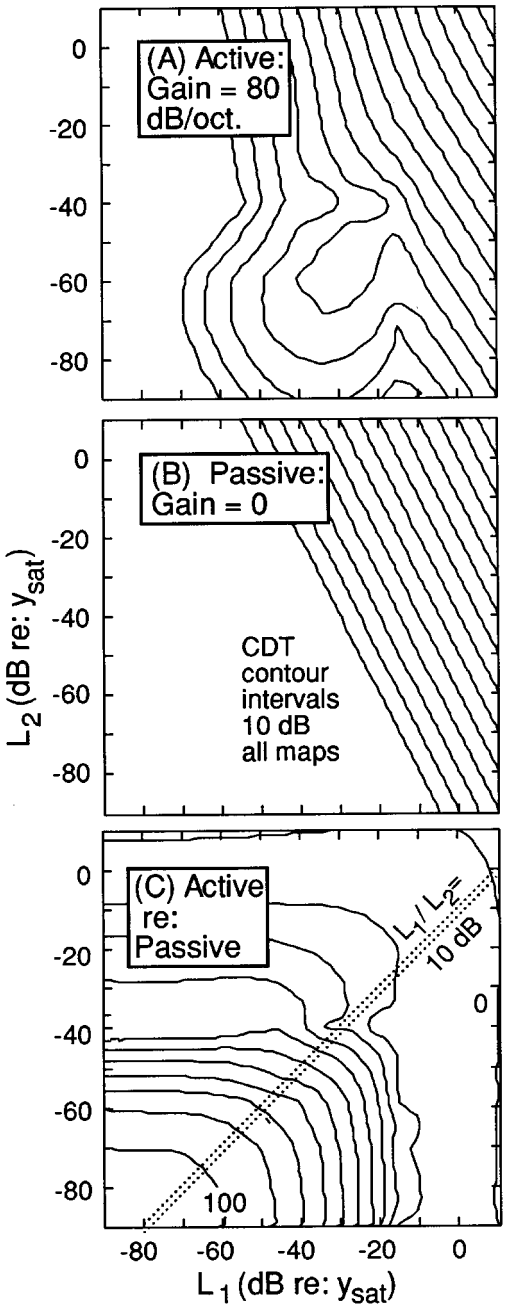

FIG. 5. Contour map showing the amplitude of the CDT emission as a function of the stimulus levels L_1 and L_2 varied independently. CDT emission amplitude contour lines are shown at 10-dB intervals, except that they are not shown below a specific level in (A) and (B) chosen to represent the typical noise floor. (A) Contour map for case with normal cochlear amplifier gain ($g_a = 80$ dB/octave) and other parameters as previous. The angle between the emission from the region around the peak and the basal region, Ψ, is assumed to be 180°. (B) A map with the same parameters as (A) except with zero cochlear amplifier gain. (C) The ratio of the normal versus passive emission amplitudes, or, equivalently, the difference in dB between emission amplitudes in maps (A) and (B). The line for the growth function for which L_1 is 10 dB above L_2 is shown for reference.

B. Distribution of amplitude and phase of normal emission

We repeat in Fig. 6(A) in more detail the contour map of the normal emission from Fig. 5. For comparison, in Fig. 6(B) is presented a map derived from measurements of the emissions from an adult gerbil, for $f_2 = 8$ kHz and for $f_2/f_1 = 1.28$, the same frequency ratio as the model. For this map, measurements were made at 5-dB intervals throughout the stimulus amplitude space $L_1 \times L_2$.

For the model contour map [Fig. 6(A)], the angle, Ψ, between the emission from the region containing the peak CDT amplitude, and the region basal to that, is assumed to be 180°. Typical phase directions are shown by the arrows. Note that while the zero phase reference for the map is arbitrary, the difference between the angles is not. Where the two emission amplitudes from the two areas are nearly equal, there is a sharp decrease in the summed emission amplitudes. The locations of these ''notches'' are seen in the sharp inward deflections in the contour lines, further identified by the shaded lines in Fig. 6. Note that the most prominent notch occurs across a region where the stimulus level L_1 is a constant, equal to 14 dB below y_{sat}. The notch is parallel to the right vertical axis. There is also a less obvious notch at $L_2 = -40$ dB *re*: y_{sat}, which occurs for a constant L_2, so that the notch is parallel to the horizontal axis.

Physically, these results from the model calculations can be understood as follows. Note first that the emissions in Fig. 6(A) are dominated by either peak or basal emissions, the areas being delineated by the lines where phase cancellation between these components occurs. Consider the horizontal cancellation line at about $L_2 = -40$ dB (*re*: y_{sat}). The traveling wave associated with f_2, i.e., $y_2(x,t)$ dominates the response $y_1(x,t)$ in this region of $L_1 x L_2$ parameter space. Whether or not there is phase cancellation then depends primarily on the relative degree of saturation of the y_2 response. That is, the proportion of peak versus basal emission depends only on the *shape* of the y_2 peak. As the L_2 level increases and the wave saturates more, the basal emission becomes dominant. Therefore, the phase cancellation occurs for the *same* L_2 level, independent of L_1. Similar reasoning explains the vertical notch for constant L_1. As noted earlier, it requires a much higher y_1 to dominate the response because y_2 peaks first. Once y_1 does dominate the response, however, the same argument holds, and the location of the phase cancellation depends only on the level of the L_1 amplitude.

Overall, the observed results in Fig. 6(B) agree very well with the model calculations. Consider the contours of constant CDT emission amplitude. The observed emission is asymmetrical with respect to L_1 and L_2, so that these emissions extend to much lower L_2 values, as do the emissions from the model. The slope of the observed CDT emission at these very low stimulus levels is approximately the same as that for the model, including a lower slope seen as a function of L_2 than as a function of L_1. The passive response also has the same general slope as the model. The most obvious difference between the two maps is that the observed response does not look like the model at the highest stimulus levels. This is presumably a result of saturation of the emission generation mechanism at these stimulus levels. As was noted earlier, the model emissions were calculated using a small signal approximation which was not expected to properly represent effects at high signal levels.

In comparing the observed phase response with that of the model, note that there is a prominent phase cancellation along the right vertical axis, for $L_1 = 70$ dB SPL. The phase angles change about 180° across this notch, as expected. As in the model, the observed phase cancellation occurs for a *constant* L_1, for L_2 up to about 45 dB SPL.

The observed phase angles in Fig. 6(B) through the entire ''basal'' emission areas [as identified in Fig. 6(A)] have all approximately the same, vertical direction (defined as 0°). The observed phase angles in the peak emission areas are not nearly as constant, however. Throughout the lower center of the map in Fig. 6(B), the phase angle decreases regularly as L_1 decreases, going from about 270° near the phase cancellation region, at $L_1 = 65$ dB SPL, to about 90° for $L_1 = 35$ dB SPL. This rotation is in the direction of increasing phase lag with decreasing stimulus level. This rotation is independent of L_2 up to $L_2 = 45$ dB SPL. Above this level in L_2, the phases are again approximately constant. The angles start at about 270° for $L_2 = 50$ dB SPL and rotate slowly with increasing $L2$, reaching about 0° at $L_2 = 85$ dB SPL. These transition regions at $L_1 = 70$ dB SPL and $L_2 = 45$ dB SPL are marked with shaded lines in Fig. 6(A). Note that in the observed map, as in the model, the transition level for L_1 is about 25 dB higher than for L_2. The phase cancellation seen in the model at $L_2 = -40$ dB *re*: y_{sat} is not as strong in the observed map, in contrast to the phase cancellation at fixed L_1. This appears to be due to the fact that the peak emissions are rotated as one travels across the map, so that there is not a 180° difference between the two ''components'' at $L_2 = 45$ dB SPL. The possibility of such phase rotation was not included in the model for simplicity. Note that the frequencies are fixed, so such phase rotations must be entirely due to nonlinear, stimulus amplitude dependent effects.

The map from the model in Figs. 5 and 6 should also be compared to other observed responses taken at a similar scale, with contours drawn by the same fitting function (Mills and Rubel, 1994, Fig. 1). There are obviously a variety of different contour shapes as the parameters are changed. With respect to the phase cancellation, the following points can be made. It is quite common to find a vertical notch in the lower half of the maps, near the right axis. That is, there is often a phase cancellation line for the *same* L_1 in the region where $L_2 \ll L_1$. In other maps (not usually the same ones) there are also seen horizontal notches at a constant L_2, in the region where L_2 is larger than the quantity $(L_1 - 25\ \text{dB})$. The emission contours also indicate that the L_1, L_2 asymmetry noted above changes slowly, but is present for a wide variation in stimulus parameters.

C. Relationship between cochlear amplifier gain and CDT shift

The shift for the CDT ''threshold,'' A_c is only about 33 dB for the case presented previously (Fig. 4). The quantity A_c is the shift in the stimulus level to reach a criterion CDT amplitude at a given amplitude for normal compared to zero

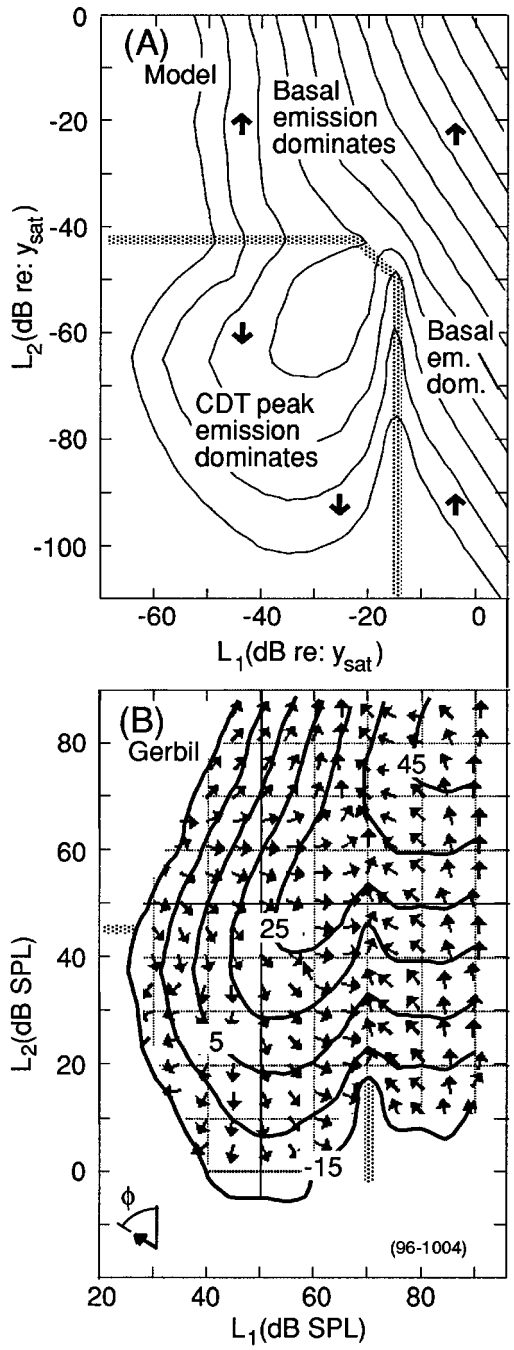

FIG. 6. Contour maps comparing model to observation. Lines of constant CDT emission amplitudes are shown as a function of the stimulus levels, plotted at 10-dB intervals in both maps. (A) Model. Contour map of the CDT emission amplitude, same parameters as Fig. 5. The phase cancellation lines (or notches, indicated by the broad shaded lines) naturally divide the $L_1 \times L_2$ space into regions where the emission from either the basal region or the peak region dominates. The relative phase angles of the two emissions are shown, the zero reference is arbitrary. Lower contour lines have been deleted to represent the noise floor. The CDT amplitude scale has an arbitrary reference level in the model calculations. (B) Adult gerbil. The stimulus frequencies were $f_1 = 6.25$ kHz and $f_2 = 8$ kHz ($f_2/f_1 = 1.28$). Stimulus levels were stepped at 5-dB intervals through the range $L_1 = 20-90$ dB SPL and $L_2 = -10-85$ dB SPL, CDT emission amplitudes are indicated, in dB SPL. Only contours 10 dB or more above the noise floor are shown. Arrows indicate relative direction of phase angle of emission. The end of the tail of the arrow is located at the position (L_1, L_2) of the stimulus producing the emission measured. As noted in the bottom left of the figure, relative phase lead is indicated by counterclockwise rotation. For example, as stimulus levels are moved to lower L_1 along the bottom of the map, the phase angles decrease, i.e., the relative phase lag increases.

gain, at low stimulus levels. In comparison, the shift in the peak amplitude, or cochlear amplifier gain, G_a, is 43 dB for the same model parameters [Fig. 1(D)]. For this case, therefore, an uncritical use of the CDT shift would lead to an underestimate of the cochlear amplifier gain by 10 dB. Because of the simplicity of the model, it is unlikely that model calculations will give the exact numerical relationship between the CDT shift and the true gain. However, this calculation is very helpful to demonstrate that there is *not* necessarily an equality between them. Further, the model suggests that the relationship is likely to become even more discordant when the gain is reduced below normal.

Model responses for cochlear amplifier gains from 0 to 80 dB/octave, at 20-dB intervals, are illustrated in Fig. 7. A cochlear amplifier operating at half-gain (40 dB/octave) gives a CDT growth function which is only slightly different than a completely inoperative cochlear amplifier [Fig. 7(C)]. At the same time, a cochlear amplifier gain g_a of 40 dB/octave produces an improvement in actual threshold of $G_a = 18$ dB [Fig. 7(A) and (B)]. Even this low gain would be of assistance in overall auditory function. These model results would predict that CDT shifts (or emission growth functions) may well distinguish cochleas with good hearing function on the one hand from those with moderate or profound cochlear dysfunction on the other. Unfortunately, these model results imply that distortion product emissions using two stimulus tones are likely to be comparatively unsuccessful at distinguishing cases of moderate from severe cochlear dysfunction. That is, a 20-dB hearing loss due to partial dysfunction of the cochlear amplifier (gain half-normal) could not be distinguished from that with a complete loss of cochlear amplifier function (gain equal zero) on the basis of emissions using two stimulus tones.

These model results imply that moderate versus severe cochlear amplifier dysfunction could not be securely distinguished with measurement of *either* the absolute value of the emissions or the decrease in emissions (A_c) when the cochlear amplifier operation is interrupted. However, the measurement of A_c, being a within-subject difference measurement, would always be more accurate than an absolute magnitude measurement.

Note also in Fig. 7(C) the sharp decrease in the response (the ''notch'') resulting from phase cancellation. For low stimulus levels the emission generated in the CDT peak region generally dominates, where at higher stimulus levels the CDT emission generated basal to the peak dominates. The notch, when observed, marks the dividing line between these two regions, and appears not to move at all as the cochlear amplifier gain is varied. However, a notch is not always observed. For the $g_a = 0$ and $g_a = 20$ dB/octave cases, for example, the emission distribution is so broad that the emission from the basal area dominates at *all* stimulus levels.

The crossover level, L_x, is defined as the intercept between the peak emission amplitude (before the notch) and the passive response [Fig. 4(C)]. Of course, L_x requires the existence of the cochlear amplifier for its determination, because if the cochlear amplifier gain is zero, the power law response of the resulting passive emissions gives no scale factor at all. However, there is only a weak dependence on

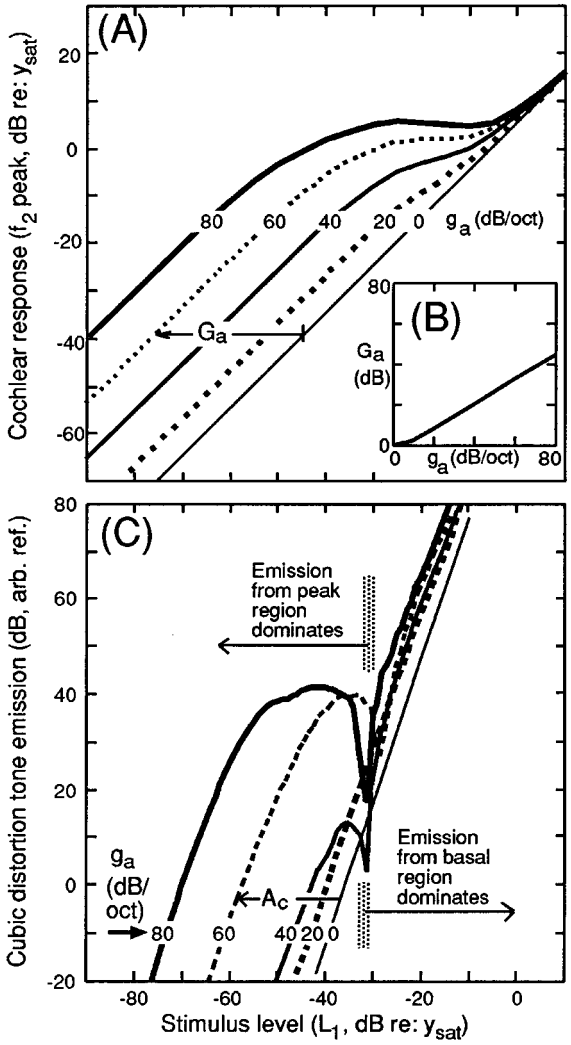

FIG. 7. (A) Peak cochlear responses versus stimulus level, with the gain of the cochlear amplifier, g_a, as a parameter. Only the f_2 response is shown. The stimulus frequency ratio is $f_2/f_1=1.28$ for all curves, and the stimulus level ratio is $L_1/L_2=10$ dB. Other model parameters are as previous. For a cochlear amplifier input gain of $g_a=60$ dB/octave, the resultant gain of the cochlear amplifier, G_a, is indicated. (B) There is a nonlinear relationship between g_a and G_a as shown. The relationship is nonlinear because resistive losses are assumed independent of either the cochlear amplifier gain or the cochlear response level, so that resistive losses affect the total cochlear amplifier gain (G_a) more when the gain rate, g_a, is small than when it is large. (C) CDT emissions as a function of stimulus level for the same conditions. The angle between the emission coming from the CDT peak region and that from the basal emission region is taken to be 180°. There is a notch at the stimulus level, $L_1 \cong -30$ dB *re*: y_{sat}, where the emissions from these two regions are equal. The CDT threshold shift, A_c, for a gain of 60 dB/octave is indicated. Because the emissions depend nonlinearly on the cochlear responses, the CDT emission shifts are nonlinearly dependent on the cochlear amplifier gain, g_a. That is, the CDT responses for $g_a=20$ and 40 dB/octave can be scarcely distinguished from the purely passive case for $g_a=0$. Note that the division into levels where the dominant emission comes from either the peak or basal regions is only approximate. For gains, g_a, of 0–20 dB/octave, there are *no* regions where the peak emission dominates that from the basal region.

the *value* of the cochlear amplifier gain. For a gain varying from 80 to 40 dB/octave, there is a decrease in L_x of less than 10 dB. This could be demonstrated in Fig. 7(C) (but is not) by plotting the intercept of the active emission maximum with the ''passive'' emission, as illustrated in Fig.

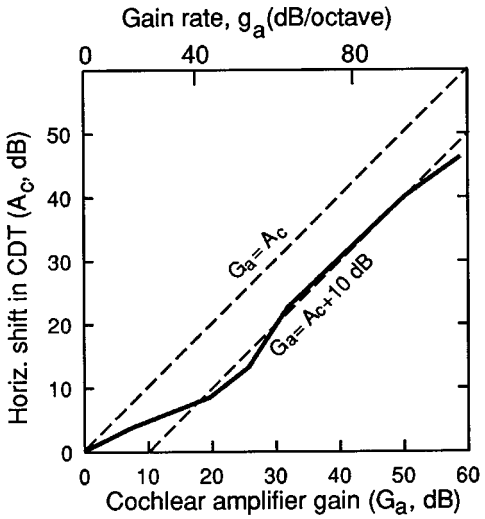

FIG. 8. The relationship for the model between the horizontal shift in the CDT emission (the threshold shift, A_c) and the actual gain of the cochlear amplifier, G_a. A sequence of model integrations with cochlear amplifier gains, g_a, from 0 to 100 dB/octave was used to generate this plot. Values of g_a are indicated at the top of this figure. As noted in Fig. 7(B), there is not a linear relationship between g_a and G_a. Same parameters as in Fig. 7. Dashed lines illustrate two approximate relationships between G_a and A_c.

4(C). The reason for the weak dependence appears to be that, as long as the saturation level itself (y_{sat}) does not vary with cochlear location, L_x is determined primarily by the *passive* properties of the cochlea. It is equivalent to a passive threshold measure which is determined by the input transmission conductance from the ear canal to the peak of the passive cochlear response. In the model, this location also marks the start of the active amplification of the wave. Therefore, one could say that L_x depends on the entire passive input conductance, i.e., from the ear canal to the point where active amplification begins (Mills *et al.*, 1994; Mills and Rubel, 1996).

A summary of the relationship between the horizontal shift in the CDT (the dimension A_c) and the corresponding cochlear amplifier gain (G_a) is presented in Fig. 8. The relationship fails of equality except for the trivial case of zero gain. For most of the range of gains, it would be an adequate correction to add 10 dB to the measured CDT shift A_c. However, the estimate of the correction factor derived using this simple model requires confirmation by experiment and/or more precise model calculations.

D. Emission response as a function of cochlear amplifier gain

Acute furosemide intoxication causes a rapid decrease in endocochlear potential (e.g., Kusakari *et al.*, 1978). For times shorter than the typical adaptation time of 15 min (Mills *et al.*, 1993), the decrease in endocochlear potential will result in a proportional decrease in cochlear amplifier gain. This allows a detailed comparison between observations and model. During furosemide intoxication, when one follows the emission response with a given stimulus pair, *none* of the stimulus parameters are changing. In terms of cochlear (not neural) function, the only change occurring

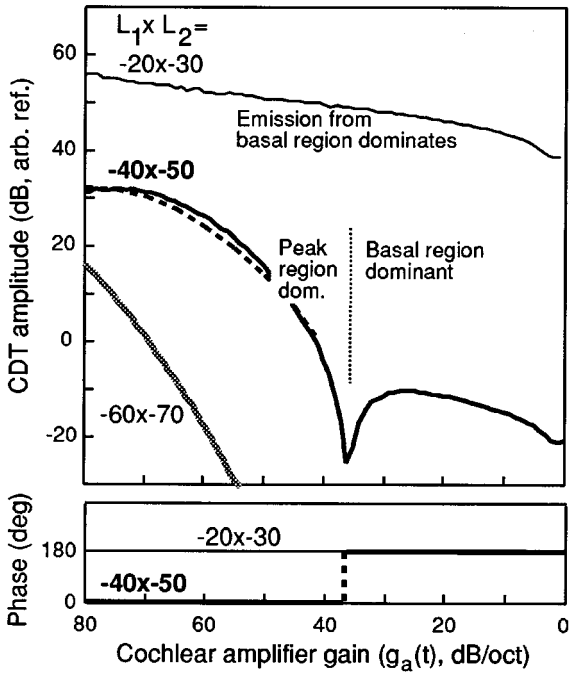

FIG. 9. Model results. The variation of the CDT emission as a function of the cochlear amplifier gain is shown for fixed stimulus frequencies and levels. The pre-injection growth function was the same as that shown in Fig. 7(C) for $g_a = 80$ dB/octave, which has a notch at $L_1 = -30$ dB *re*: y_{sat}. Stimulus levels were chosen which were 10 dB above this notch level, 10 dB below the notch level, and 20 dB below that. The upper panel displays the CDT amplitude response, the lower the phase angle response for the two stimulus levels indicated. Note the phase zero reference is arbitrary; the phase relationship between the two stimulus levels is not. There is a 180° phase shift for the emission for $L_1 \times L_2 - 40 \times -50$ following the phase cancellation at the gain $g_a = 37$ dB SPL. For lower gains, the phase angle of this emission is the same as that for higher stimulus levels. The phase angle for the -60×-70 emission is the same as the initial -40×-50 angle and is not shown. The dashed line in the upper panel summarizes empirical results from three gerbils where the endocochlear potential and emissions were monitored simultaneously. See text for details.

with acute furosemide intoxication appears to be the change in the gain of the cochlear amplifier (Mills *et al.*, 1993; Ruggero and Rich, 1991).

The model responses as a function of cochlear amplifier gain, $g_a(t)$, are illustrated in Fig. 9. Results are presented for three typical stimulus level pairs with the same basic parameter set as for Fig. 7 [for $g_a = 80$ dB/octave, denoted by the heavy line in Fig. 7(C)]. Stimulus level pairs are located 10 dB above the notch in the growth function seen in Fig. 7(C), 10 dB below the notch, and 20 dB below that.

For the highest level stimuli, in Fig. 7(C), the emission is dominated by the basal emission for all gains, g_a. The emission decreases monotonically about 15 dB as the cochlear amplifier gain goes to zero. This emission, which we previously referred to as ''passive,'' depends significantly on the cochlear amplifier gain. The ''passive'' emission is now understood not to be distinct from the ''active'' emission *in any way*, i.e., not in the mechanisms of generation, means of transmission out of the cochlea, etc. The passive emission originates in a region of the cochlea which (1) produces negligible emission relative to that from the peak when the emission distribution is sharp, but which (2) becomes dominant when the emission distribution becomes broader. The broadening may occur for any reason such as lack of gain or high stimulus levels. No matter the reason, the emission becomes truly passive *only* when the cochlear amplifier gain is precisely zero, or is completely negligible due to very high stimulus levels. The components which have been called ''active'' and ''passive'' might therefore be more correctly identified by their putative region of generation, i.e., as ''peak'' or ''basal'' emissions.

These distinctions become clearer when the emissions from below the notch area [Fig. 7(C)] are followed in detail. The middle curve of Fig. 9(A) shows the response for a stimulus level of -40×-50 dB *re:* y_{sat}. Comparing the contour maps from the model with an observed map (Fig. 6), it can be seen that this level is approximately equivalent to $L_1 \times L_2 = 50 \times 40$ dB SPL for these parameters in the gerbil. The normal emission for this stimulus level is located just below the notch. So, the emission from the peak region dominates at the normal gain. For stimulus levels about this magnitude, the CDT amplitude does not change much as the gain initially begins to decrease. For the particular parameters -40×-50, there is actually a slight *increase* in the emission amplitude as the gain begins to decrease from the normal level. This increase occurs because the basal emission component initially decreases faster with a decrease in g_a than does that from the peak region. That is, the decrease in gain moves the basal response down from a highly saturated location, while the peak response itself stays nearly as high. This result is related to the compressive nature of the saturation.

In general, for a stimulus level originally located so the CDT is near the notch, but below it (see Fig. 4), the summed emission is the difference of two nearly equal components. The total emission therefore can actually *increase* with the initial decline in gain, if the nondominant component initially decreases faster than the dominant one. The more general case is that, because of the compressive nature of the cochlear amplifier, there is very little decrease in emission amplitudes at these moderate stimulus levels as the gain initially decreases from normal.

As the cochlear amplifier gain continues to decrease, the peaks of the traveling waves decrease rapidly in total amplitude and become more rounded. The resulting distribution of emission changes, so that the total emission from the peak region begins to decline more rapidly than the emission from the basal region. Note that for zero gain, the basal region *always* dominates for these model parameters (i.e., $e_w \cong 1/8$ octave). Therefore, for emissions for which the peak region dominates at normal gain, there must come a point as the gain decreases where the emissions from the peak and base regions are equal. At this point, assuming $\Psi \cong 180°$, there will be a sharp notch. This is shown in Fig. 9 at a cochlear amplifier gain, g_a, of about 37 dB/octave. Below the notch, the net emission rebounds and then slowly declines. For all gains, g_a, below 37 dB/octave, therefore, the cochlear response is quite broad at all stimulus levels and the basal emission therefore dominates. The change in the associated phase angle is indicated in the bottom panel.

For the third stimulus level pair, with L_1 now 30 dB below the notch level, the emission from the peak region

drops rapidly with the initial decrease of g_a. The decline is so abrupt that, for any reasonable noise floor, the subsequent transition to a basal emission will never be observed. The model results suggest that such a transition must occur.

In simultaneous recordings of the endocochlear potential (EP) and emissions following furosemide injection in gerbils, the following empirical result was obtained (Mills *et al.*, 1993). For stimulus levels of $L_1 \times L_2 = 50 \times 40$ dB SPL, the observed change in the CDT amplitude, ΔCDT, during the initial decline was related to the observed change in EP, ΔEP, by the relationship

$$\Delta \mathrm{CDT} = -0.009(\Delta \mathrm{EP})^2, \tag{3}$$

where the CDT amplitude is expressed in dB and the EP in millivolts (mV). The EP change and $g_a(t)$ can be connected if the very reasonable assumption is made that the gain of the cochlear amplifier is linearly dependent on the voltage between the endolymph and the interior of the outer hair cell, at least during the initial, rapid decline of the EP. (That is, there is not time for adaptation, known to occur on a 15-min time scale, to affect the cochlear amplifier gain.) Equation (3) then becomes

$$\Delta \mathrm{CDT} = -0.009 * \{\mathrm{EP}_0 - V_0\}^2 \{1 - g_a(t)/g_{a0}\}^2, \tag{4}$$

where g_{a0} is the normal cochlear amplifier gain and the quantity $\{\mathrm{EP}_0 - V_0\}$ is the normal, preinjection potential difference between the endolymph and the interior of the outer hair cell, voltage V_0. The curve shown by the dashed line in Fig. 9(A) illustrates relationship (4) assuming the total preinjection voltage $\{\mathrm{EP}_0 - V_0\}$ is about 120 mV and the cochlear amplifier gain about 80 dB/octave. There is excellent agreement between the empirical results from observation and these model calculations.

Our previous interpretation of the form of these responses, particularly responses like those of Eq. (3), was that the cochlear amplifier was normally at a relative maximum in total gain as a function of the gain rate (Mills *et al.*, 1993). This hypothesis was offered at the time as an explanation for the zero slope of the emissions as a function of EP change, at moderate stimulus levels. This hypothesis is now thought to be unlikely because the present model results provide such a natural, detailed fit with the observations at all stimulus levels. The same physical mechanisms which give rise to emission growth functions exhibiting saturation with notches are seen to account for the observed behavior as the cochlear amplifier gain is decreased. Once the parameters (Ψ and e_w) are chosen which give model growth functions like those observed at normal cochlear amplifier gains, the behavior as the gain is decreased follows directly (Fig. 9).

The model response thus provides a natural explanation for the complex variation with time of emission amplitude observed following furosemide injection (Mills and Rubel, 1994). Figure 10 summarizes observed responses from an adult gerbil for direct comparison with the model results in Fig. 9. Figure 10(A) presents the growth function prior to injection, and about 8 min after injection. Figure 10(B) presents in detail the time course of the emission amplitudes following injection, at the three stimulus levels noted in Fig. 10(A). Note that the axis in Fig. 10(B) is time after injection with furosemide, not cochlear amplifier gain. The agreement with Fig. 9 is quite good nevertheless, and, in particular, there is good agreement between the model and observed responses in the *relationships* between the three curves. For the moderate stimulus response, this agreement includes a sharp minimum, followed by a ''plateau'' associated with a phase shift of about 180° [Fig. 10(C)]. In contrast, the amplitude of the higher level stimulus decreases moderately, while the phase angle changes very little. The emission with stimulus levels $L_1 \times L_2 = 40 \times 30$ dB SPL drops quickly to the noise floor and does not reappear.

Even with the large dosages of furosemide used in these studies, it seems unlikely that the EP would have ever been driven negative enough to force the cochlear amplifier gain completely to zero. Comparison with Fig. 9 suggest that the gains in Fig. 10 declined to about $g_a \cong 10-20$ dB/octave at the minimum. This view is reinforced by the observation that there was still an additional decrease in the emission amplitudes found post mortem, as indicated by the curve segments on the right hand side of Fig. 10(B). These measurements, taken 1-h post mortem, may truly represent a ''passive'' response.

Previous estimates of normal cochlear amplifier gains were made by comparing the preinjection CDT response with the emission after injection with furosemide, taken during the ''plateau'' observed at mid-stimulus amplitudes (Mills *et al.*, 1994; Mills and Rubel, 1996). The horizontal shift in the CDT at low stimulus levels, here denoted A_c, was taken as an estimate of the cochlear amplifier gain. It can now be appreciated that this procedure underestimates the true gain for two reasons. First, even if the gain of the cochlear amplifier had been interrupted completely, Fig. 8 suggests that A_c typically underestimates the true gain, G_c, by about 10 dB. Second, a comparison of the observed responses with the model calculation (Fig. 9) implies that the gain was probably not reduced completely to zero, but was probably about 10–20 dB/octave during most of the ''plateau.'' The gain could have been as high as 37 dB/octave, but not higher. The effect of this second potential error usually will be small, however. As shown in Fig. 7, the curves for $g_a = 40$ dB/octave and $g_a = 0$ are very similar, with a horizontal difference of about 5 dB. This adds a relatively small uncertainty when measuring gains in the normal range. However, when attempting to measure relatively small cochlear amplifier gains, this second effect would need to be taken into account.

IV. DISCUSSION

A. Possible conclusions from a simple model

One may quite legitimately object to the simple emission model employed here on a number of grounds. For example, it has not been derived through solutions to the traveling wave equation in the cochlea. In that sense, it certainly fails to represent the ''real'' cochlea. However, in its defense several points may be made.

First, although the model does not represent accurately the ''real'' cochlea, a cochlea with the qualities of the model could be *constructed*. Such a constructed cochlea would ac-

complish all the essential, known requirements for a cochlea. That is, it would provide a spatial frequency analyzer with signal compression, by providing amplification of low level, but not high level, signals. Such a constructed cochlea may be properly termed a *gedanken* cochlea, and employed for the same purposes as such thought experiments have traditionally been employed. For example, the model calculations here show that the threshold shift, A_c, is not equal to the gain of the cochlear amplifier, G_a. This demonstrates that there is not *necessarily* an equality between these two quantities in the real cochlea. This is actually a useful result, because at one time it seemed ''intuitively obvious'' that such an equality necessarily existed.

Because the model is so simple and calculations consequently easy, it leads itself to exploration of a number of previously confusing observations. Such exploration can lead to a better physical understanding of the possible mechanisms in the real cochlea. One example of this understanding is the explanation of the previously mysterious ''intimate relationship'' between active and passive emissions (Mills and Rubel, 1994), discussed in the next section.

There are several important observations for which this model does not provide such physical understanding. It does not explain at all the complex behavior observed as the stimulus frequency ratio is changed. This is not particularly distressing, however, because this behavior is outside the scope of the model, and this behavior may actually occur quite outside the cochlear amplifier region in the real cochlea. Perhaps more unfortunate is the fact that the model does not provide an explanation of the observation that the slope of the emission input–output function at low stimulus levels is typically about two, rather than three, in the normal gerbil cochlea (Mills *et al.*, 1994; Mills and Rubel, 1996). While it is possible to obtain such slopes with a model of this type, it requires somewhat artificial assumptions about the distribution of saturation elements, and such assumptions have been avoided to maintain simplicity in the model.

The assumption in the model that the emission can be considered to originate in two adjacent regions with opposite phases is not entirely arbitrary. For relatively smooth amplitude distributions, this behavior can arise quite naturally from consideration of the summation of emissions when the phase angle varies monotonically across the emitting region. As one proceeds from the stapes, consider the first area found to have significant emission, and define the region bounded by the variation of emission phase in this area over a total of 180°, from $+90°$ to $-90°$. The net emission from this first region would have a single phase angle somewhere near 0°. The phase over the next region to be defined would vary from $-90°$ to $-270°$, and the sum would have a net phase approximately opposite to the first region. The emissions summed from these two regions would, of course, partially cancel each other. The actual sums and resultant angles would, of course, depend on the actual amplitude distribution. For the model, the calculated amplitude distribution is employed together with the simplest approximation to the phase distribution, that there are only two regions of approximately opposite phase and that the boundaries of these two regions are fixed relative to the peak of the emission.

The model also does not consider the possible reflection of the $2f_1-f_2$ wave at its characteristic place (Stover *et al.*, 1996). It would be possible to account for such reflection effects with a model of this type but it would require additional assumptions to be made. In any event, the ''reemission'' at $2f_1-f_2$ becomes important only for small stimulus frequency ratios. So, the model results presented here are approximately correct for all frequency ratios $f_2/f_1>1.1$.

B. ''Active'' and ''passive'' emissions

The model calculations and their good comparison with observation (esp. Figs. 6, 9, and 10) lead to the following conclusions. There *is* a ''passive'' source of emissions, i.e., there are emissions when the cochlear amplifier gain is identically zero. Emissions that had been previously identified as passive emissions, however, generally can be seen now not to be strictly passive, or only approximately passive. These were the emissions at high stimulus levels, or at moderate stimulus levels when the cochlear amplifier gain was reduced. Now it is clear that this gain was probably not identically zero. Instead, it now seems obvious that these were generally situations in which the emissions from the region basal of the emission peak region dominated those from the peak region. These ''basal'' emissions are ''continuous'' with the truly passive emissions. *More precisely, it can now be appreciated that true passive emissions are a special case of basal emission dominance, occurring for zero cochlear amplifier gain.*

What was correct about the previous suggestions was that there were two different ''components,'' and that there was an ''intimate relationship'' between them (Mills and Rubel, 1994). The two ''components'' are generated by the same physical mechanisms in the cochlea, and are always present. They originate in slightly different areas relative to the traveling wave patterns (Lonsbury-Martin *et al.*, 1987). The shapes of the peaks of the traveling waves determine which one dominates. In most circumstances, at high stimulus levels the peaks broaden so that the emission from the basal area dominates and this emission has similar characteristics to the truly ''passive'' emission.

The presence in emissions of two nearly equal components which usually are 180° out of phase has important implications for distortion product measurements, and provides useful explanations for a number of previously confusing observations. These two ''components'' are always present in the emission because there is always some emission contribution from the peak region and from the region basal to it. The interesting consequences occur depending on the phase angle between the two components and their relative amplitudes, and because of the variation in these relationships with stimulus amplitudes or other parameters.

Further, while there is no requirement in the simple model that these two regions primarily give rise to out of phase emissions, typical observed growth functions and contour maps certainly give the impression that this is the case more often than not [Figs. 6, 10; and Mills and Rubel, 1994]. Certainly, while the relative angle, Ψ, may vary with parameters, it is *not* random. In nearly every normal adult gerbil

which has been measured at the same parameters as in Fig. 10(A), there was a notch observed in approximately the same location, with the same characteristics (Mills *et al.*, 1993, 1994; Mills and Rubel, 1994, 1996). The presence of observed notches does vary with stimulus parameters, of course, especially f_2/f_1 frequency ratio (Mills and Rubel, 1994). It seems probable that a detailed model of the generation of distortion product emissions will confirm that the phase relationship between these two ''regions'' is primarily a result of the phase relationships in the traveling waves which generate the emissions.

C. Phase cancellation effects and interpretation of emission measurements

In the model it has been shown that under most circumstances the emission consists of several components which partially subtract from each other. The consequences of this aspect of the model appear to be verified in observations of real cochleas (e.g., Figs. 6 and 10). The effects of these partial phase cancellations can confuse the interpretation of emission measurements. This is a particular problem for measurements in which only a small number of stimulus sets are employed. For example, unusual effects may be seen if measurement points are located near a region where the two ''components'' nearly cancel, i.e., near a ''notch'' in the input–output function, or if the experimental manipulation brings such a notch region into the measurement.

For example, consider attempts to measure the effect of the efferent system on cochlear mechanics, using distortion product emissions. In a typical paradigm, a single stimulus pair is presented to one ear. The CDT emission amplitude is monitored as a variety of manipulations are applied to the other ear and/or to the efferent system (Kirk and Johnstone, 1993; Kujawa *et al.*, 1992; Morgenstern *et al.*, 1995; Siegel and Kim, 1982; Williams and Brown, 1995). While most investigators have found a small decrease in magnitude of the CDT emission, in fact, the magnitude and sign of the distortion product emission change due to efferent effects apparently depend strongly on the amplitude and frequency ratios of the stimuli employed to obtain the emission. This result can easily be understood if the emission is assumed to consist of two or more components in partial phase cancellation, and if the efferent system affects one component more strongly than the others. Alternately, the efferent system could be simply changing the angle between the components slightly. While such measurements establish that the efferent system does affect cochlear mechanics in some way, the mechanisms and functional value of these efferent effects remain to be established. To establish the effect of efferents on the cochlear amplifier using emissions will require emission measurements to be made that actually lead to a determination of the cochlear amplifier gain and/or other important parameters.

D. Assessment of peripheral hearing function

It has been shown that emission growth functions using two stimulus tones can distinguish between cases of normal cochlear amplifier gain and cases with low or zero gain

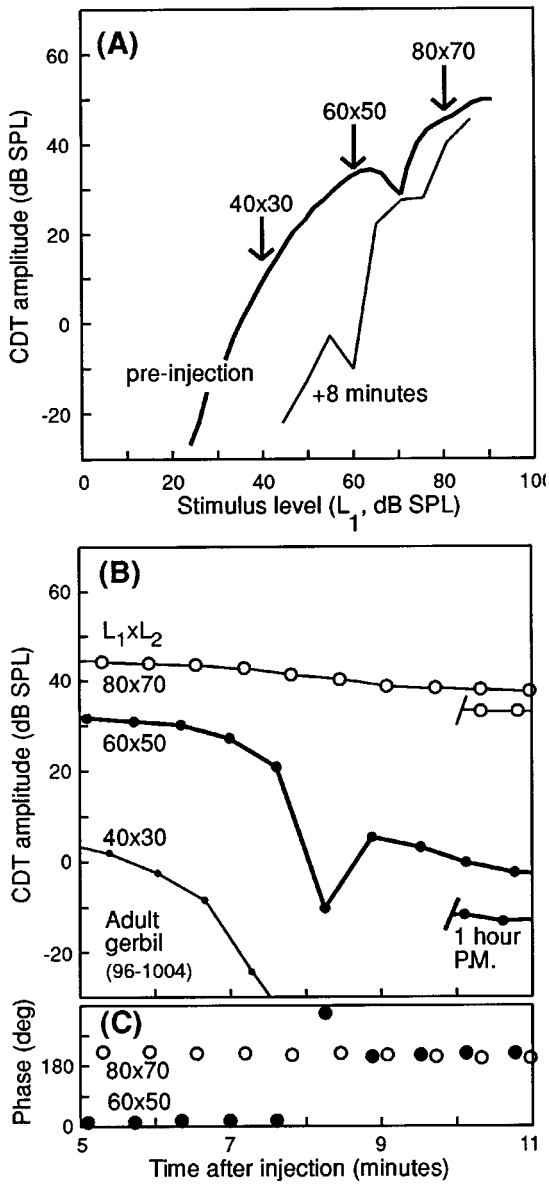

FIG. 10. Response of emissions with time following furosemide injection in adult gerbil, monitored at fixed stimulus frequencies $f_1=6.25$ and $f_2=8$ kHz ($f_2/f_1=1.28$). For all curves, stimulus level L_1 is 10 dB above L_2. (A) The pre-injection growth function is shown, stimulus levels were stepped at 2-dB intervals. The vertical arrows indicate the three stimulus levels that were followed at 40-s intervals after injection. The growth function at 8 min after injection is also shown, stimulus levels were stepped at 5-dB intervals. This was the time that there was an apparent phase cancellation in the emission for $L_1\times L_2=60\times 50$ dB SPL. (B) Amplitude versus time response for the emissions at three different stimulus levels. The short segments on the right side represent measurements made 1-h post mortem. (C) Phase response following furosemide injection for the two stimulus levels noted. The shift after the minimum in the response for $L_1\times L_2=60\times 50$ dB SPL was about $+190°$ or $-170°$.

(Figs. 5, 7, 8). The model confirms previous suggestions that the preferred stimulus ratio is $L_1/L_2\cong 10$ dB. However, the model calculations also imply that, as long as the amplitude of the emissions is large enough to be measured, the exact ratio is not critical (Fig. 5). It is the difference between the active and passive emissions which gives a measure of cochlear amplifier function.

The presence of the passive emission component in dis-

tortion product emissions is an advantage in one sense, as it allows for the determination of the passive input transmission conductance through the determination of the passive ''threshold'' measure, L_x, at least in experimental animals (Mills *et al.*, 1994; Mills and Rubel, 1996). However, the presence of the passive emissions has its negative consequence. For two tone stimuli, the presence of the passive emissions is one factor that makes the discrimination between moderate and poor cochlear amplifier function so difficult [Fig. 7(C)]. The other factor is that the total emission amplitudes fall off much more quickly than the peak cochlear response. So, the emission shift, A_c, is nonlinearly related to the cochlear amplifier gain (Fig. 8).

These model results imply that discrimination between these two clinically important states, moderate versus severe cochlear amplifier dysfunction, cannot be adequately made using distortion product emissions using two stimulus tones. The discrimination is poor on the basis of either absolute emission amplitude, emission growth functions, or the CDT shift using a furosemide assay. Of these three possible approaches, the last one offers some hope, in that it involves a within animal difference. Of course, this assay cannot be employed with humans.

This is not only a characteristic of the model, but is supported by the available data. Distortion product emissions using two stimulus tones have been demonstrated to be successful in distinguishing good from moderate cochlear dysfunction but fail to distinguish between moderate and severe cochlear dysfunction in humans (Gorga *et al.*, 1993, 1994; Lonsbury-Martin *et al.*, 1990a, b; Martin *et al.*, 1990; Whitehead *et al.*, 1995a, b). The model results in Fig. 7 illustrate why this should be the case.

Finally, in this paper only the effects of changing the cochlear amplifier gain (dB/octave) have been considered in detail. This parameter is almost certainly an important aspect of cochlear function, and, in addition, is easily manipulated experimentally with certain ototoxic drugs. However, given the complexity of the cochlear amplifier, it is quite likely that cochlear amplifier dysfunction is effectively multidimensional. Dysfunctions involving changes in other parameters may require different approaches.

ACKNOWLEDGMENTS

Thanks to R. Folsom, S. Norton, S. Woolley, and two anonymous reviewers for useful comments on earlier versions of this manuscript. Support was provided by Grant No. NIH CD 00395 from the National Institute on Deafness and Other Communication Disorders, National Institutes of Health.

Allen, J. B. (**1980**). ''Cochlear micromechanics—A physical model of transduction,'' J. Acoust. Soc. Am. **68,** 1660–1670.

Allen, J. B., and Fahey, P. F. (**1993**). ''A second cochlear-frequency map that correlates distortion product and neural tuning measurements,'' J. Acoust. Soc. Am. **94,** 809–816.

Avan, P., Loth, D., Menguy, C., and Teyssou, M. (**1990**). ''Evoked otoacoustic emissions in guinea pig: Basic characteristics,'' Hearing Res. **44,** 151–160.

Brown, A. M., and Gaskill, S. A. (**1990**). ''Measurement of acoustic distortion reveals underlying similarities between human and rodent mechanical responses,'' J. Acoust. Soc. Am. **88,** 840–849.

Brown, A. M., and Kemp, D. T. (**1984**). ''Suppressibility of the $2f_1-f_2$ stimulated acoustic emissions in gerbil and man,'' Hearing Res. **13,** 29–37.

Brown, A. M., and Kemp, D. T. (**1985**). ''Intermodulation distortion in the cochlea: Could basal vibration be the major cause of round window CM distortion?'' Hearing Res. **19,** 191–198.

Brown, A. M., Gaskill, S. A., and Williams, D. M. (**1992**). ''Mechanical filtering of sound in the inner ear,'' Proc. R. Soc. London Biol. **250**, 29–34.

Brown, A. M., Harris, F. P., and Beveridge, H. A. (**1996**). ''Two sources of acoustic distortion products from the human cochlea,'' J. Acoust. Soc. Am. **100,** 3260–3267.

Brown, A. M., McDowell, B., and Forge, A. (**1989**). ''Acoustic distortion products can be used to monitor the effects of chronic gentamicin treatment,'' Hearing Res. **42,** 143–156.

Cody, A. R., and Johnstone, B. M. (**1981**). ''Acoustic trauma: Single neuron basis for the 'half-octave shift,' '' J. Acoust. Soc. Am. **70,** 707–711.

Cooper, N. P. (**1996**). ''Two-tone suppression in cochlear mechanics,'' J. Acoust. Soc. Am. **99,** 3087–3098.

Dallos, P. (**1973**). *The Auditory Periphery: Biophysics and Physiology* (Academic, New York).

Gorga, M. P., Neely, S. T., Bergman, B., Beauchaine, K. L., Kaminski, J. R., Peters, J., and Jesteadt, W. (**1993**). ''Otoacoustic emissions from normal-hearing and hearing-impaired subjects: Distortion product responses,'' J. Acoust. Soc. Am. **93,** 2050–2060.

Gorga, M. P., Neely, S. T., Bergman, B. M., Beauchaine, K. L., Kaminski, J. R., and Liu, Z. (**1994**). ''Toward understanding the limits of distortion product otoacoustic emission measurements,'' J. Acoust. Soc. Am. **96,** 1494–1500.

Gummer, A. W., Hemmert, W., and Zenner, H.-P. (**1996**). ''Resonant tectorial membrane motion in the inner ear: Its crucial role in frequency tuning,'' Proc. Natl. Acad. Sci. USA **93,** 8727–8732.

Hauser, R., and Probst, R. (**1991**). ''The influence of systemic primary-tone level variation L_2-L_1 on the acoustic distortion product emission $2f_1-f_2$ in normal human ears,'' J. Acoust. Soc. Am. **89,** 280–286.

Johnstone, B. M., Gleich, B., Mavadat, N., McAlpine, D., and Kapadia, S. (**1990**). ''Some properties of the cubic distortion tone emission in the guinea pig,'' Adv. Audiol. **7**, 57–62.

Johnstone, B. M., Patuzzi, R., and Yates, G. K. (**1986**). ''Basilar membrane measurements and the traveling wave,'' Hearing Res. **22,** 147–153.

Kemp, D. T. (**1978**). ''Stimulated acoustic emissions from within the human auditory system,'' J. Acoust. Soc. Am. **64,** 1386–1391.

Kimberley, B. P., Brown, D. K., and Eggermont, J. J. (**1993**). ''Measuring human cochlear traveling wave delay using distortion product emission phase responses,'' J. Acoust. Soc. Am. **94,** 1343–1350.

Kirk, D. L., and Johnstone, B. M. (**1993**). ''Modulation of f_1-f_1: Evidence for a GABA-ergic efferent system in apical cochlea of the guinea pig,'' Hearing Res. **67,** 20–34.

Kössl, M. (**1993**). ''Evidence for a mechanical filter in the cochlea of the 'constant frequency' bats, *Rhinolophus rouxi* and *Pteronotus pamellii*,'' Hearing Res. **72,** 73–80.

Kujawa, S. G., Glattke, T. J., Fallon, M., and Bobbin, R. P. (**1992**). ''Intracochlear application of acetylcholine alters sound-induced mechanical events within the cochlear partition,'' Hearing Res. **61,** 106–116.

Kusakari, J., Ise, I., Comegys, T. H., Thalmann, I., and Thalmann, R. (**1978**). ''Effect of ethacrynic acid, furosemide, and ouabain upon the endolymphatic potential and upon high energy phosphates of the stria vascularis,'' Laryngoscope **88,** 12–37.

Lonsbury-Martin, B. L., Harris, F. P., Stagner, B. B., Hawkins, M. D., and Martin, G. K. (**1990a**). ''Distortion product emissions in humans. I. Basic properties in normally hearing subjects,'' Ann. Otol. Rhinol. Laryngol. Suppl. 147 **99,** 3–14.

Lonsbury-Martin, B. L., Harris, F. P., Stagner, B. B., Hawkins, M. D., and Martin, G. K. (**1990b**). ''Distortion product emissions in humans. II. Relations to acoustic immittance and stimulus frequency and spontaneous otoacoustic emissions in normally hearing subjects,'' Ann. Otol. Rhinol. Laryngol. Suppl. 147 **99,** 15–29.

Lonsbury-Martin, B. L., Martin, G. K., Probst, R., and Coats, A. C. (**1987**). ''Acoustic distortion products in rabbit ear canal. I. Basic features and physiological vulnerability,'' Hearing Res. **28,** 173–189.

Mahoney, C. F. O., and Kemp, D. T. (**1995**). ''Distortion product otoacoustic emission delay measurement in human ears,'' J. Acoust. Soc. Am. **97,** 3721–3735.

Martin, G. K., Lonsbury-Martin, B. L., Probst, R., Scheinin, S. A., and

Coats, A. C. (**1987**). ''Acoustic distortion products in rabbit ear canal. II. Sites of origin revealed by suppression contours and pure-tone exposures,'' Hearing Res. **28,** 191–208.
Martin, G. K., Ohlms, L. A., Franklin, D. J., Harris, F. P., and Lonsbury-Martin, B. L. (**1990**). ''Distortion product emissions in humans. III. Influence of sensorineural hearing loss,'' Ann. Otol. Rhinol. Laryngol. Suppl. 147 **99,** 30–42.
Mills, D. M. (**1997**). ''Interpretation of distortion product otoacoustic emission measurements. II. Estimating tuning characteristics using three stimulus tones,'' J. Acoust. Soc. Am. (submitted).
Mills, D. M., and Rubel, E. W. (**1994**). ''Variation of distortion product otoacoustic emissions with furosemide injection,'' Hearing Res. **77,** 183–199.
Mills, D. M., and Rubel, E. W. (**1996**). ''Development of the cochlear amplifier,'' J. Acoust. Soc. Am. **100,** 428–441.
Mills, D. M., and Rubel, E. W. (**1997**). ''Development of distortion product emissions in the gerbil: 'Filter' response and signal delay,'' J. Acoust. Soc. Am. **101,** 395–411.
Mills, D. M., Norton, S. J., and Rubel, E. W. (**1993**). ''Vulnerability and adaptation of distortion product otoacoustic emissions to endocochlear potential variation,'' J. Acoust. Soc. Am. **94,** 2108–2122.
Mills, D. M., Norton, S. J., and Rubel, E. W. (**1994**). ''Development of active and passive mechanics in the mammalian cochlea,'' Aud. Neurosci. **1**, 77–99.
Morgenstern, C., Biermann, E., and Zangemeister, W. H. (**1995**). ''The efferent innervation of outer hair cells in humans: Physiological investigations,'' Acta Oto-Laryngol. **115,** 206–210.
Moulin, A., and Kemp, D. T. (**1996a**). ''Multicomponent acoustic distortion product otoacoustic phase in humans. I. General characteristics,'' J. Acoust. Soc. Am. **100,** 1617–1639.
Moulin, A., and Kemp, D. T. (**1996b**). ''Multicomponent acoustic distortion product otoacoustic phase in humans. II. Implications for distortion product otoacoustic emissions generation,'' J. Acoust. Soc. Am. **100,** 1640–1662.
Neely, S. T. (**1993**). ''A model of cochlear mechanics with outer hair cell motility,'' J. Acoust. Soc. Am. **94,** 137–146.
Nuttall, A. L., and Dolan, D. F. (**1996**). ''Steady-state sinusoidal velocity responses of the basilar membrane in guinea pig,'' J. Acoust. Soc. Am. **99,** 1556–1565.
Patuzzi, R., Sellick, P. M., and Johnstone, B. M. (**1984**). ''The modulation of the sensitivity of the mammalian cochlea by low frequency tones. III. Basilar membrane motion,'' Hearing Res. **13,** 19–27.
Rübsamen, R., Mills, D. M., and Rubel, E. W. (**1995**). ''The effects of furosemide on distortion product otoacoustic emissions and on neuronal responses in the anteroventral cochlear nucleus,'' J. Neurophysiol. **74,** 1628–1638.
Ruggero, M. A., and Rich, N. C. (**1991**). ''Furosemide alters organ of Corti mechanics: Evidence for feedback of outer hair cells upon the basilar membrane,'' J. Neurosci. **11,** 1057–1067.
Santos-Sacchi, J. (**1989**). ''Asymmetry in voltage-dependent movements of isolated outer hair cells from the organ of Corti,'' J. Neurosci. **9,** 2954–2962.
Santos-Sacchi, J. (**1991**). ''Reversible inhibition of voltage-dependent outer hair cell motility and capacitance,'' J. Neurosci. **11,** 3096–3110.
Schetzen, M. (**1989**). *The Volterra and Wiener Theories of Nonlinear Systems* (Krieger, Malabar, FL).
Schmiedt, R. A., and Adams, J. C. (**1981**). ''Stimulated acoustic emissions in the ear canal of the gerbil,'' Hearing Res. **5,** 295–305.
Siegel, J. H., and Kim, D. O. (**1982**). ''Efferent neural control of cochlear mechanics? Olivocochlear bundle stimulation affects cochlear biomechanical nonlinearity,'' Hearing Res. **6,** 171–182.
Stover, L. J., Neely, S. T., and Gorga, M. P. (**1996**). ''Latency and multiple sources of distortion product otoacoustic emissions,'' J. Acoust. Soc. Am. **99,** 1016–1024.
Tarnowski, B. I., Schmiedt, R. A., Hellstrom, L. L., Lee, F. S., and Adams, J. C. (**1991**). ''Age-related changes in cochleas of mongolian gerbils,'' Hearing Res. **13,** 277–283.
Wable, J., Collet, L., and Chéry-Croze, S. (**1996**). ''Phase delay measurements of distortion product otoacoustic emissions at $2f_1-f_2$ and $2f_2-f_1$ in human ears,'' J. Acoust. Soc. Am. **100,** 2228–2235.
Whitehead, M. L., Lonsbury-Martin, B. L., and Martin, G. K. (**1992a**). ''Evidence for two discrete sources of $2f_1-f_2$ distortion-product otoacoustic emission in rabbit. I: Differential dependence on stimulus parameters,'' J. Acoust. Soc. Am. **91,** 1587–1607.
Whitehead, M. L., Lonsbury-Martin, B. L., and Martin, G. K. (**1992b**). ''Evidence for two discrete sources of $2f_1-f_2$ distortion product otoacoustic emission in rabbit. II: Differential physiological vulnerability,'' J. Acoust. Soc. Am. **92,** 2662–2682.
Whitehead, M. L., McCoy, M. J., Lonsbury-Martin, B. L., and Martin, G. K. (**1995a**). ''Dependence of distortion-product otoacoustic emissions on primary levels in normal and impaired ears. I. Effects of decreasing L_2 below L_1,'' J. Acoust. Soc. Am. **97,** 2346–2358.
Whitehead, M. L., Stagner, B. B., McCoy, M. J., Lonsbury-Martin, B. L., and Martin, G. K. (**1995b**). ''Dependence of distortion-product otoacoustic emissions on primary levels in normal and impaired ears. II. Asymmetry in L_1, L_2 space,'' J. Acoust. Soc. Am. **97,** 2359–2377.
Whitehead, M. L., Stagner, B. B., Martin, G. K., and Lonsbury-Martin, B. L. (**1996**). ''Visualization of the onset of distortion-product otoacoustic emissions, and measurement of their latency,'' J. Acoust. Soc. Am. **100,** 1663–1679.
Williams, D. M., and Brown, A. M. (**1995**). ''Contralateral and ipsilateral suppression of the $2f_1-f_2$ distortion product in human subjects,'' J. Acoust. Soc. Am. **97,** 1130–1140.
Zwislocki, J. (**1965**). ''Analysis of some auditory characteristics,'' in *Handbook of Mathematical Psychology*, edited by R. D. Luce, R. R. Bush, and E. Galanter (Wiley, New York), pp. 1–97.
Zwislocki, J. J. (**1985**). ''Are nonlinearities observed in firing rates of auditory-nerve afferents reflections of a nonlinear coupling between the tectorial membrane and the organ of Corti?'' Hearing Res. **22,** 217–221.
Zwislocki, J. J., and Cefaratti, L. K. (**1989**). ''Tectorial membrane II: Stiffness measurements *in vivo*,'' Hearing Res. **42,** 211–227.

Two-tone suppression of basilar membrane vibrations in the base of the guinea pig cochlea using "low-side" suppressors

C. Daniel Geisler
Department of Neurophysiology and of Electrical and Computer Engineering, University of Wisconsin-Madison, Madison, Wisconsin 53706-1532

Alfred L. Nuttall
Oregon Hearing Research Center, Oregon Health Sciences University, Portland, Oregon and Kresge Hearing Research Institute, University of Michigan, Ann Arbor, Michigan

(Received 26 September 1996; revised 31 March 1997; accepted 1 April 1997)

The responses of the basilar membrane (BM) in the basal section of the guinea pig cochlea were measured by laser interferometry. The stimuli were pairs of harmonically related tones, presented simultaneously. One tone, at the BM's characteristic frequency (CF) of about 17 kHz, was presented at a low intensity. The other tone, presented at various intensities, was a ''low-side'' suppressor, with a frequency of 0.2–8 kHz. As observed by many others, the suppressor tone, when presented at high enough intensity, reduced the magnitude of the CF component of BM displacement, sometimes dramatically. However, regardless of whether the CF component was suppressed or not, the sum of the displacement amplitudes of the CF and suppressor components was always greater than the displacement amplitude of the unsuppressed CF component. For suppressor frequencies up to 4 kHz, the suppression was both tonic and phasic, and synchronized to the suppressor period. For higher suppressor frequencies, principally tonic suppression was seen. [S0001-4966(97)06807-0]

PACS numbers: 43.64.Kc, 43.64.Nf, 43.64.Bt [RDF]

INTRODUCTION

For almost two decades, it has been known that the responses of a point on the mammalian basilar membrane (BM) which are evoked by a tone at or near the characteristic frequency (CF) can be reduced (suppressed) by the sounding of another tone (Rhode, 1977). This ''two-tone suppression'' seems to be a universal property of basilar-membrane vibrations, for it has been observed throughout the cochlea, both in its mid-basal turn (Rhode, 1977; Patuzzi *et al.*, 1984b; Ruggero *et al.*, 1992; Nuttall and Dolan, 1993), its extreme base (Cooper and Rhode, 1993; Rhode and Cooper, 1993; Cooper, 1996), and in its apex (Cooper and Rhode, 1993, 1995, 1996). It can be demonstrated with virtually any CF response obtained at physiological intensities, and the suppressor tone can have almost any frequency, up to a half-octave or more above CF, depending on the cochlear location.

That is not to say, however, that the frequency of the suppressor tone is not an important stimulus variable. It is, both in a quantitative and qualitative manner. For example, when the suppressor frequency is greater than CF, the strength of the suppression (termed ''high-side'') drops off rapidly with increasing separation of the two frequencies (Rhode, 1977; Cooper and Rhode, 1996). Yet, when the frequency of the suppressor is lower than CF (''low-side'' suppression), its value seems to be almost immaterial (Cooper and Rhode, 1996). Despite this difference, some theoretical studies (e.g., Geisler *et al.*, 1993) suggest that the same basic mechanism is at work in all cases of basilar-membrane suppression: namely, the saturation of the ''cochlear amplifier,''[1] the process in the living cochlea which enhances the responses of low-intensity sounds (for review, see Dallos, 1992).

By contrast, the amplifier-saturation theory (cf. Zwicker, 1979), *cannot* account for important aspects of the low-side suppression of the discharge rates of auditory-nerve (AN) fibers (Cai and Geisler, 1996c). In particular, it cannot account for the strong discharge-rate suppressions inflicted by low-side suppressors upon the class of AN fibers having ''lower'' rates ($<$20/s) of spontaneous discharge (Fahey and Allen, 1985; Cai and Geisler, 1996b).

In order to understand this discrepancy, it is necessary to distinguish between a total response (i.e., the complete output waveform) and particular frequency components of that response which are dissected out by Fourier analysis. For, while the common form of the amplifier-saturation theory produces strong suppression of the CF *component* with a low-side suppressor (Zwicker, 1979), with only rare exceptions does it permit the major peak of the *total* neural response to be suppressed below the level of the unsuppressed CF component (Cai and Geisler, 1996c). By contrast, the responses of lower spontaneous primary fibers as a rule *do* undergo strong attenuation of the total response with low-side suppressors. Indeed, the responses of these primary fibers can occasionally be completely shut off by low-side suppressors (Fahey and Allen, 1985; Cai and Geisler, 1996a).

Thus the major purpose of this study is to cast further light on the low-side suppressions which occur on the basilar membrane. In particular, we wanted to know which aspects of the suppressions can be accounted for by the amplifier-saturation theory, and which aspects match the demonstrated results of AN-fiber studies. Although low-side suppression

of basilar-membrane responses has been previously demonstrated by several different groups (Patuzzi *et al.*, 1984b; Ruggero *et al.*, 1992; Rhode and Cooper, 1993; Nuttall and Dolan, 1993), in only one study (Cooper, 1996) was enough information provided to case clear light upon this question. Cooper's results strongly support the theory, for in no case did he observe suppression of the total response, although a wide range of suppressor frequencies was used (0.25–24 kHz; CF was 26 kHz).

Here we report experiments which verify and extend Cooper's observations. In addition, we show new data on the *temporal* attributes of the cochlear amplifier's reactions to low-side suppressors. The complex interactions which we observed between the time-modulated amplitudes and phases of the cochlear amplifier's output case new light on its mechanisms. An abbreviated report of our results, illustrated with different data, has been given previously (Geisler and Nuttall, 1997).

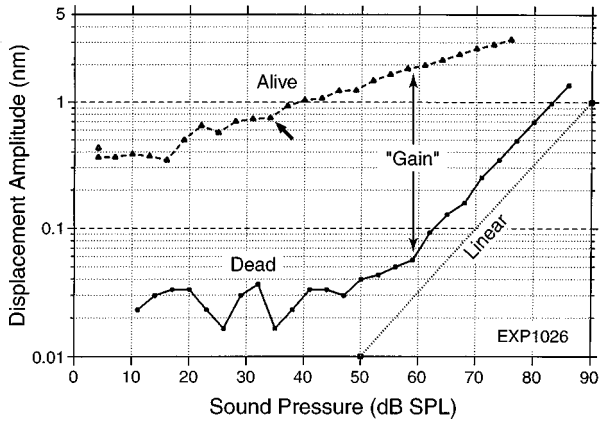

FIG. 1. Responses of the basilar membrane to near-CF tones before and after death. The level of the CF tone used in this experiment's suppression studies (34 dB SPL) is indicated by an arrow. EXP1026.

I. METHODS

The responses of the basilar membrane in the basal turn of the guinea pig cochlea were measured by a laser Doppler velocimeter (Polytec Corp. OFV 1102), according to a technique which has been well described previously (Nuttall *et al.*, 1991). Briefly, this technique involves carefully scraping a small hole in the wall of scala tympani and dropping small glass microbeads through that hole onto the basilar membrane, at about the 18-kHz place. The laser beam is then positioned such that a detectible reflection is obtained from one of the beads. The difference of the optical frequencies in the incident and reflected light beams (Doppler shift) can be used to determine the bead's instantaneous velocity, which was recorded by the computer at a 205-kHz sampling rate. This measuring technique is linear over a large range of velocities.

The data reported here were obtained from six different animals. For each of them, monitoring of the animal's compound action potential (CAP) indicated that the surgery and bead placement caused so little loss in basal cochlear sensitivity ($<$10 dB) that the cochlea was judged to be in nearly normal condition during measurements. Along with this relative CAP preservation, strong compression of the responses to CF tones was observed in each case. In two of the experiments, CF responses were obtained both before and after death. The data from one of these animals are shown in Fig. 1. Note that there was a sensitivity drop of at least 40 dB with death, a drop which we attribute to the loss of the cochlear amplifier. A similar cochlear-amplifier gain was seen in the other animal in which it was measured. These data argue that the cochleas of all six animals were in nearly normal local condition, with large cochlear-amplifier gains, on the order of 40 dB when measured.

In most of the experiments, the ''alive'' curve was linear at low intensities, becoming compressive only in the vicinity of 30 dB SPL. The curve of Fig. 1 is therefore unusual in our series as it did not become linear at low intensities. It is possible that some unknown source of noise was operative in that case, although compression at *very* low intensities (e.g., 0 dB SPL) is in fact seen in some cochleas, particularly those which appear to be in excellent condition (e.g., Ruggero, 1992; Nuttall and Dolan, 1996).

During the early stages of this project, data were also obtained from two additional animals. Due to a change in experimental protocols after those first two experiments, the data obtained from them are not directly comparable with those of the last six. Nothing in those early data, however, conflicts with the response behavior reported below.

The stimuli were pairs of harmonically related tones, digitally synthesized using a 12-bit A/D converter (two channels) with a total conversion rate of approximately 205 kHz. One of those tones, the ''CF tone,'' was fixed in both frequency (usually at 17 kHz) and level (on the order of 30 dB SPL, which was usually at the onset of single-tone compression; 34 dB SPL for the animal of Fig. 1). In one animal, several different CF intensities were used. The frequency of the other tone, the ''suppressor,'' was fixed at either 200 Hz, 500 Hz, or some integer multiple of 1 kHz (1–4 or 8), and it was presented in a sequence of intensities, starting at a low value and increasing in 10-dB steps. When the sequence of all intensities had been completed at one suppressor frequency, that frequency was changed and a new intensity sequence begun. In several cases, repeat sequences were taken. Reproducibility in all such cases was very good.

Each two-tone stimulus was presented continuously for about 20 s. The resulting 20-s response record was broken up into 1000 consecutive 20-ms segments, each time locked to the stimulus waveform. These segments then were combined together and further processed to form the average response for one period of the suppressor tone (or some integer multiple of that period). As our interferometer measured bead *velocity*, the period histograms were integrated to obtain basilar-membrane *displacement.*

Fourier analysis of the period histograms was used to separate out various frequency components. Plotting the waveform of a band of frequencies which bracketed CF (CF $\pm$some integer multiple of the suppressor frequency) was used to show amplitude and phase modulation of the response to the CF tone. When needed, automated peak-

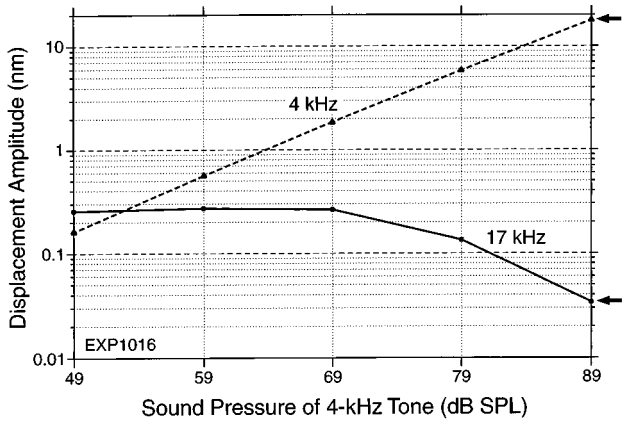

FIG. 2. The amplitudes of the CF (17 kHz) and suppressor (4 kHz) response components, plotted as functions of suppressor-tone sound pressure. The two points generated at 89 dB SPL, indicated by arrows, are melded into one point in Fig. 3. EXP1016.

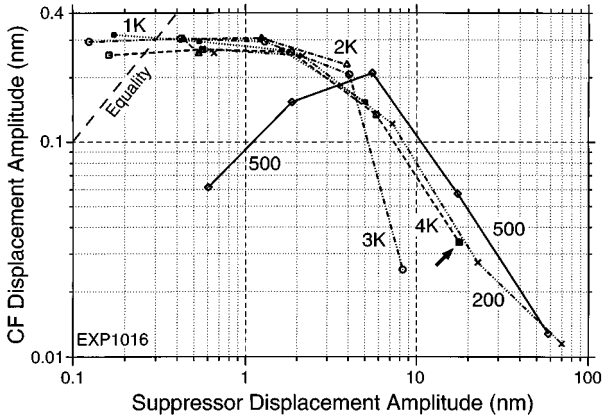

FIG. 3. The amplitudes of the CF response component, plotted as functions of the amplitude of the suppressor response component, for six different suppressor frequencies (0.2–0.4 kHz). The amplitudes of the two components are equal on the ''equality'' line. The single point generated from the two 89-dB points of Fig. 2 is indicated by an arrow. EXP1016.

picking routines were used to find the minima and maxima of the various waveforms.

II. RESULTS

A. Response amplitudes

Figure 2 plots the typical behavior of the principal response components (CF and suppressor frequency) produced with a suppressor of frequency 4 kHz. As the sound level of the suppressor tone (L_{SUP}) was raised, the response component at the suppressor frequency grew in a virtually linear manner. By contrast, the CF response component stayed virtually constant in amplitude until L_{SUP} reached a certain threshold level (70 dB SPL in this case), above which the CF component was monotonically suppressed. Note that this threshold of suppression was reached only after the amplitude of the suppressor component exceeded that of the unsuppressed CF component.

In order to compare the responses produced with suppressors of different frequencies, the amplitudes of the two principal response components were used as the axes of a summary figure. Thus the two data points which represented the principal response components produced by a single two-tone stimulus in Fig. 2 (e.g., those produced at a suppressor intensity of 89 db SPL, indicated by arrows) were merged into a single point (marked by an arrow) in Fig. 3, the summary figure for this experiment.

This figure, which contains the entire set of response amplitudes obtained in this experimental animal, using suppressors of six different frequencies, has a number of significant features. First and most important, suppression of the CF response component occurred only when the suppressor component of the response was greater in amplitude than that of the CF component (the ''equality'' line marks equal amplitudes of the two components). More precisely, the suppressor in this particular experiment, regardless of frequency, had to produce a suppressor response component whose amplitude was at least 2 nm, in order to suppress the CF component, in this case about 0.3 nm in amplitude when unsuppressed. More generally, we observed, without exception in our six experiments, that the low-side suppressor had to produce a displacement response at least as large as the single-tone CF component in order for suppression to occur, no matter what the suppressor frequency.

The consistency of the 2.0-nm suppression threshold in Fig. 3 argues strongly that the feature of the responses which produced low-side suppression was BM *displacement*, as opposed to *velocity*, since the thresholds of suppression would have varied by about 26 dB if they had been expressed in terms of velocity (velocity increases linearly with frequency and there was a 20-fold spread in suppressor frequencies used in this particular experiment).

A final feature of the data in Fig. 3 concerns the non-monotonic behavior of the CF component produced with the 500-Hz suppressor: At low suppressor levels, the CF response actually *increased* with increasing suppressor-component amplitudes. We attribute these increases in CF-component amplitude, which was heading toward the unsuppressed level, to unexpectedly slow recovery of the basilar membrane from the suppressions produced by the preceding suppressor (200 Hz), given just a short time before the lowest level suppression measurements made at 500 Hz. As can be seen in the figure, the 200-Hz tone at its greatest intensity produced strong CF suppression (almost 30 dB). Evidently, recovery of the cochlear partition from this suppression was not instantaneous, but took longer than 40 s, the time interval which elapsed between the end of the 200-Hz stimulation and the third level of 500-Hz stimulation. This attribution is supported by the fact that such clear CF recovery was seen only twice, each time during 500-Hz sequences that immediately followed a 200-Hz sequence that produced powerful suppression at its last intensity.

In one experiment, CF tones at three different intensities were used (36–56 dB SPL), each subjected to suppression by four different low-side tones having frequencies spaced at octave intervals (1–8 kHz). The amplitudes of the two principal components of the resulting responses are shown in Fig. 4, with all of the data points obtained at one CF intensity joined by a line. These data are illuminating. Most impor-

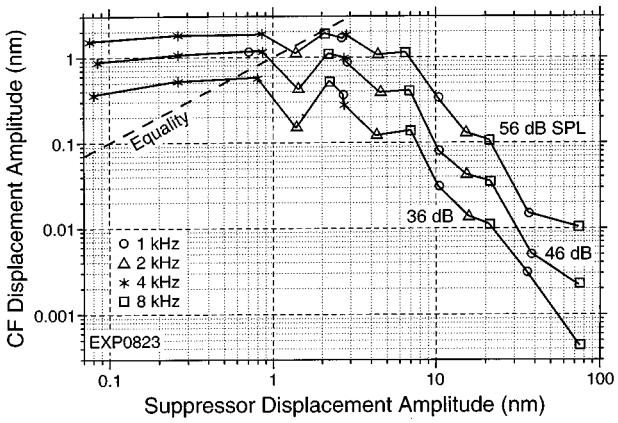

FIG. 4. The amplitudes of the CF response component, plotted as functions of the amplitude of the suppressor response component, for three different CF sound pressures (36–56 dB SPL). Points in each curve were generated with one of four different suppressor frequencies (at octave spacings from 1 to 8 kHz), each of which has a separate symbol. EXP0823.

tantly, they follow exactly the trends pointed out in Fig. 3, at all three CF intensities. Thus the behavior in that figure is not only repeated, it apparently can be extended to include other CF intensities as well. That is, in our hands CF suppression occurs only when the amplitude of the suppressor-components's *displacement* equals or exceeds that of the CF response, regardless of the suppressor's frequency or of the CF-component's amplitude.

Although the three curves in Fig. 4 vary slightly from each other, each one looks like it is plotting a single function. Since, in fact, each of those curves is a composite made up of points obtained with four different suppressors (each indicated with a separate symbol), the conjecture that *displacements* of basilar-membrane vibrations determine low-side suppression is supported in dramatic fashion. For if velocity or some other derivative were the suppressive agent, then surely such a combination of *displacement* data points would be much more variable.

Figure 4 has several other interesting features. For one, the amplitudes of the unsuppressed CF components in the three curves only differ by about 10 dB. Since the pressures of the CF tones themselves differed by 20 dB, strong compression of the CF responses occurred, consistent with our conclusion that the cochlea was in good shape during this experiment. A second significant feature of Fig. 4 is the near equality of the thresholds for CF suppression shown in the three curves (2–3 nm). This near coincidence argues that thresholds for the low-side suppression of a CF response are relatively insensitive to the magnitude of that response.

B. Temporal aspects of the responses

The low-side suppression of CF responses does not simply reduce the average level of those responses: it also affects them in a phasic manner. Figure 5 shows the waveforms of the CF responses obtained in one experiment with four successive levels of a 500-Hz suppressor. At the lowest level of the suppressor (56 dB SPL), the CF envelope is very slightly modulated at the suppressor frequency (panel A). With a 10-dB increase in suppressor level, this low-

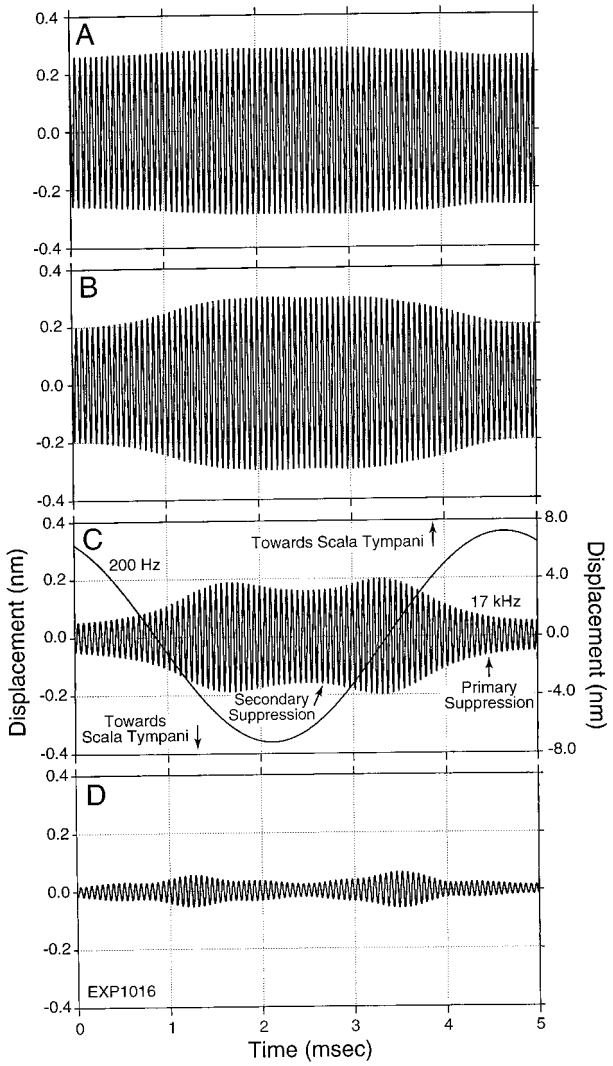

FIG. 5. CF responses obtained with a 200-Hz suppressor (left ordinate), for four different suppressor-tone sound pressures (56–86 dB SPL). Also shown in panel C is the suppressor response component (right ordinate). Directions and suppressions are indicated. EXP1016.

frequency modulation becomes clear (panel B). As will be shown explicitly in the next panel, the maximum amount of suppression occurred approximately when the basilar membrane had its greatest displacement toward scala tympani.

With yet another 10-dB increase (panel C), the depth of suppression increased. As in the previous panel, the maximum amount of suppression occurred almost simultaneously with the positive (scala tympani) peak of the suppressor response component, which is shown in this case (right ordinate). Several new features are also apparent in this response. First, another phase of suppression appeared in the CF response, approximately 180° out-of-phase with the primary phase. Second, at no time during the suppressor's period did the amplitude of the CF response get back to its unsuppressed level: It was now suppressed tonically as well as phasically.

At the highest level of the suppressor (86 dB SPL), the CF response was reduced further in amplitude but maintained its basic bi-lobed temporal structure (panel D).

When the frequency of the low-frequency tone is in-

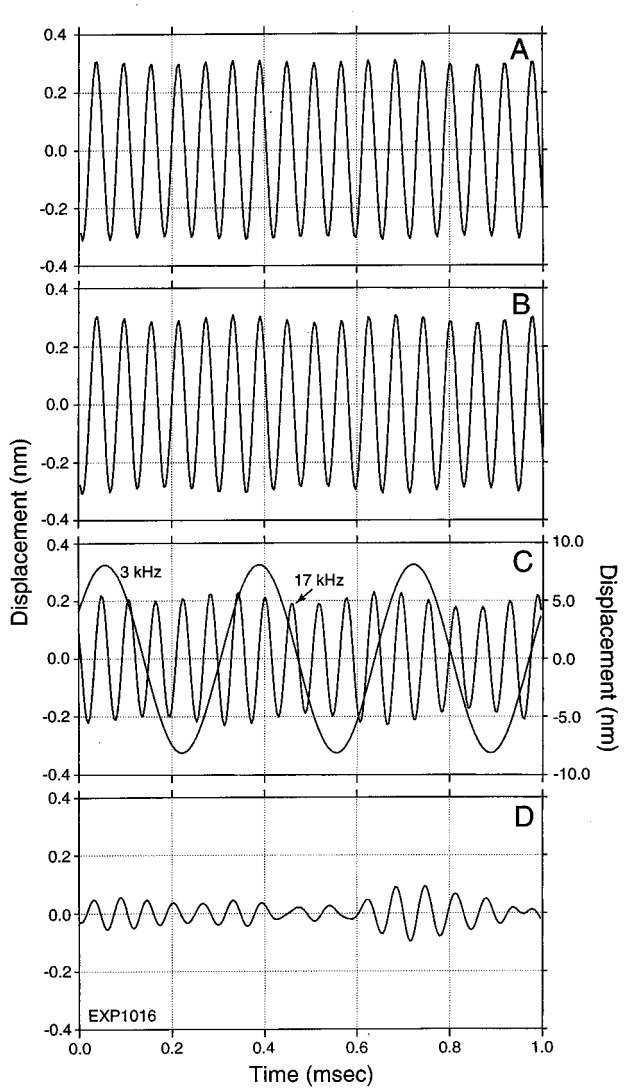

FIG. 6. CF responses obtained with a 3-kHz suppressor (left ordinates), for four different suppressor-tone sound pressures (58–88 dB SPL). Also shown in panel C is the suppressor response component (right ordinate). EXP1016.

creased to 3 kHz, a different temporal pattern of suppression is observed (Fig. 6). At the lowest suppressor level (58 dB SPL), no suppression of the CF response is evident (panel A). With a 10-dB increase in suppressor intensity, slight phasic suppression at 3 kHz is seen (panel B). Although slightly more 3-kHz phasic suppression is seen at the next suppressor level (panel C), the principal suppressive effect is tonic in nature. The response component at the suppressor frequency is also shown in this panel (right ordinate).

At the highest suppressor level (88 dB SPL), strong tonic suppression of the CF response occurred, accompanied by phasic suppression (panel D). However, the fundamental frequency of the latter is not 3 kHz, that of the suppressor, but 1 kHz instead! Evidently the processes responsible for maintaining the amplitude of the CF response could not keep pace with the rapid changes called for by the large 3-kHz vibrations, and so settled into the slower rhythm set by the fundamental frequency of the two-tone complex. This inability of the phasic suppression to follow the higher suppression frequencies was universal. Across all experiments, the upper

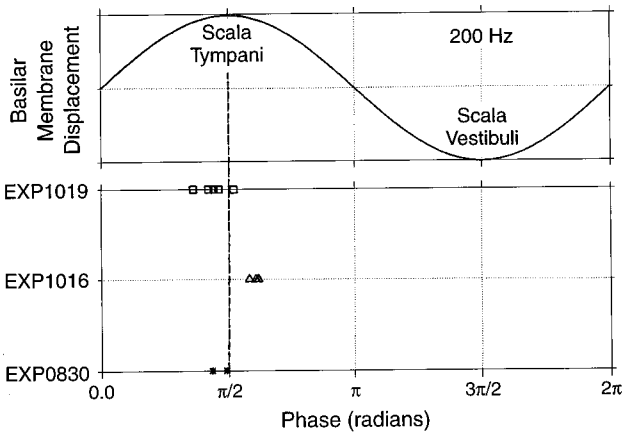

FIG. 7. The phases of maximum CF response suppressions, relative to the phase of the 200-Hz suppressor response component, at different suppressor intensities. All relevant experiments (3). Top panel shows suppressor response component. From Geisler and Nuttall (1997), with permission.

frequency of the suppressor was around 2 kHz.

As pointed out in Fig. 5(C), the phase of maximum suppression which occurred at our lowest suppressor frequency (200 Hz) nearly coincided with the maximum displacement of the basilar membrane toward scala tympani. This timing was invariant in the three experiments for which we have clear data at that frequency. The quantitative defense of this statement is given in the summary data of Fig. 7, which shows the phases of maximum CF suppression relative to the phase of the suppressor component (which was by far the largest and thus the dominant component in the response). In each experiment, all of the data points (each taken at a different suppressor level) cluster tightly around the instant of maximum scala-tympani displacement. In a fourth experiment, noise distortion of the 200-Hz response components prevented such phase determinations, but the equally strong 200-Hz phasic modulations of the CF response observed in that case had almost exactly the same phase relationships to the waveform of the 200-Hz *stimulating* tone as it did in the other three experiments.

The phases of maximum suppression of the CF response relative to the phases of the suppressor response component were also calculated for suppressors of 500 and 1000 Hz. Such data for one experiment are shown in Fig. 8. As suppressor frequency increased, a gradual increase is seen in the *phase* delay between the displacement peak and the point of maximum suppression, implying that there were short *time* delays involved in the activation of the suppression mechanisms and/or in the operation of the suppressor mechanisms themselves (see below for more evidence). These time delays appeared to have different values in the different experiments, leading to increasing disparities in the inter-animal comparisons made at the higher suppressor frequencies (not shown).

In addition to amplitude modulation of the CF response, a low-side suppressor also produces time-related phase modulation. This can be seen most clearly in Fig. 9, which contains the image of a suppressed CF response (solid line) superimposed upon that of an unsuppressed CF response (dotted line). Close attention to the zero crossings of the two

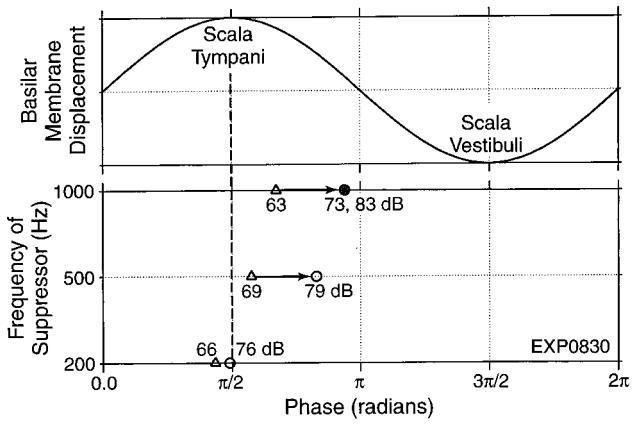

FIG. 8. The phases of maximum CF response suppressions, relative to the phase of the suppressor response component, for three different suppressor frequencies (200, 500, and 1000 Hz). Different data points were taken at different suppressor sound levels (indicated with different symbols). Note the increased phase delay with both increased suppressor frequency and intensity. Top panel shows suppressor response component. EXP0830.

images shows that the greater the amplitude suppression of the CF response, the greater also was its phase *lead*. This coupling of amplitude suppression with phase lead seems to be general feature of the phasic suppressions which we obtained.

Returning for a moment to Fig. 5, notice that all of the phasic suppressions, both primary and secondary, which were produced by the 200-Hz suppressor are more or less symmetrical in time. This symmetry, which generally characterized 200-Hz suppressions in all of our experiments, did not usually hold at the higher suppressor frequencies. For example, consider the CF-response waveform shown in Fig. 10. Obtained with a moderately strong 1-kHz suppressor tone (75 dB SPL), the suppression pattern exhibited at this higher frequency is very asymmetric, with neither the primary nor secondary suppressions being symmetrical about their midpoints. Possible neural counterparts of this asymmetry will be considered in Sec. III.

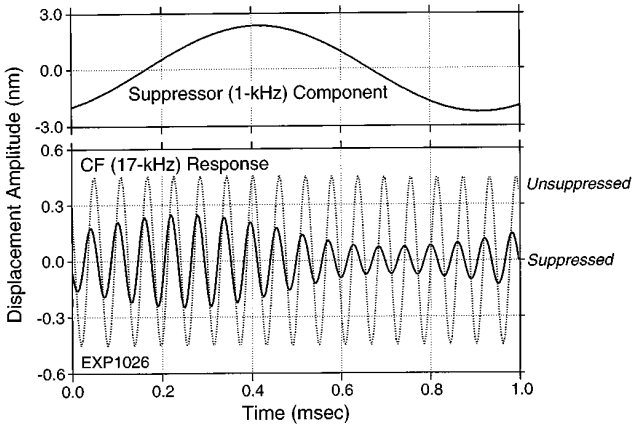

FIG. 9. Suppressed CF response (solid line) compared to an unsuppressed CF response (dotted line). Top panel shows suppressor response component generated simultaneously with the suppressed CF response. Suppressor was a 1-kHz tone presented at 83 dB SPL. EXP1026.

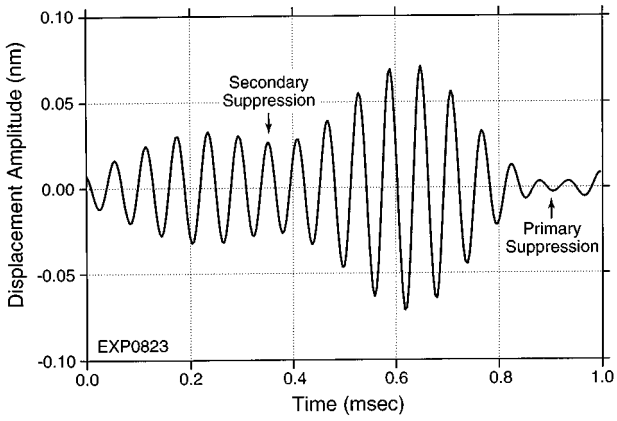

FIG. 10. Suppressed CF response generated with a 1-kHz suppressor (75 dB SPL). EXP0823.

C. A model

Many of the features of our suppression data can be mimicked with the ''saturating feedback'' type of model suggested more than a decade ago by Zwicker (1979). The major premises of this model are that the amplification of low-intensity responses in the cochlea is due to feedback forces, that the gain of the cochlear amplifier is controlled by the receptor currents flowing through the outer hair cells (OHC), and that these receptor currents (or the forces controlled by them) show compressively nonlinear behavior at higher intensities.

One version of this model is shown schematically in Fig. 11. In panel A is an idealized version of an outer hair cell's input/output (I/O) curve, showing the compressive characteristics at either extremity that are universally observed (e.g., Russell *et al.*, 1986; Dallos and Cheatham, 1992). An acous-

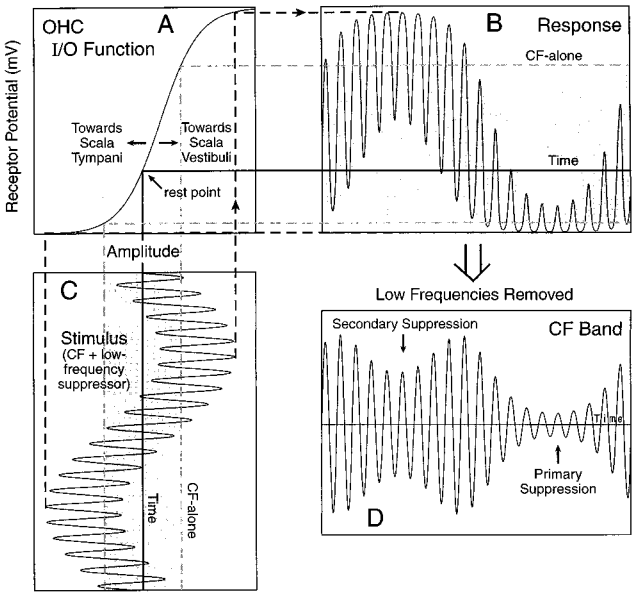

FIG. 11. Idealized sketch on an OHC's input/output curve (panel A), with two-tone input (panel C) and output (panel B). The envelopes for single-tone (CF) stimulation at the same level are shown with shading. The low-frequency components are removed from the output in panel D. From Geisler and Nuttall (1997), with permission.

tic signal (panel C) forms the input to the whole feedback system, and the resulting hair cell receptor potential (assuming no cell-membrane filtering) forms the hair cell's output (panel B).

When the input is a single CF tone (only its unvarying envelope is shown, by shading), the hair cell's output also has a fixed amplitude (that envelope is also shown by shading). To the extent that the I/O curve is linear, this output signal and the resulting cochlear-amplifier gain will also be linear. However, because this I/O curve is compressive, the hair cell's output signal will in fact be compressed when the input signal is large enough to push the resulting displacements into either of the compressive regions.

This type of compression is seen especially clearly in the waveforms produced by excitation with two simultaneous tones, one of them at CF and the other with a much lower frequency. At the moment that the lower frequency tone nears its peak, the two-tone input signal is greater in magnitude than the CF tone alone (i.e., moves above the shaded area) and so the outer cell is pushed further out along its I/O curve than it was for the single-tone case. The resulting output signal shows greatly compressed peaks (panel B). Identically the same processes operate at each trough of the low-frequency signal, where an even greater compression of response troughs occurs, due to the asymmetrically placed ''rest point'' of the OHC I/O function.

As a tone with frequency more than an octave below CF is not amplified in the base of the cochlea (cf. Rhode, 1978; Ruggero, 1992), the low-frequency component of the hair cell's output voltage obviously produces no self-amplification. Moreover, that low-frequency component presumably does not play a *direct* role in the amplification of the CF signal either, for, according to theory (cf. Patuzzi and Robertson, 1988; Hubbard and Mountain, 1990), only the CF response contained within the feedback signal affects CF amplification. Thus, since its only apparent role in cochlear amplification is its effect upon the OHC's CF response, we removed the low-frequency component from the receptor potential to allow better visualization of the CF response. The resulting hair cell waveform (panel D) is also approximately that of the CF response of the basilar membrane, should the OHC I/O function of Fig. 11(A) be inserted into most recent cochlear models (e.g., Cai and Geisler, 1996c).

D. Extrapolation of experimental data to estimate cochlear amplifier properties

The striking similarity of the model's output [Fig. 11(D)] with the experimental data [e.g., Fig. 5(C)] suggests that the model is a good representation of the processes involved in the cochlear amplifier. Assuming that is so, the modeling process outlined in Fig. 11 can be used in an inverse fashion with the experimental data to produce an estimate of the OHC's I/O characteristics. The reasoning is as follows.

Since the low-frequency component of the basilar-membrane responses is basically linear (cf. Fig. 2), it is just a scaled replica of the low-frequency component of the *input* signal and can be used in its stead. On the output side, the *envelope* of the CF response is a measure of the time-varying

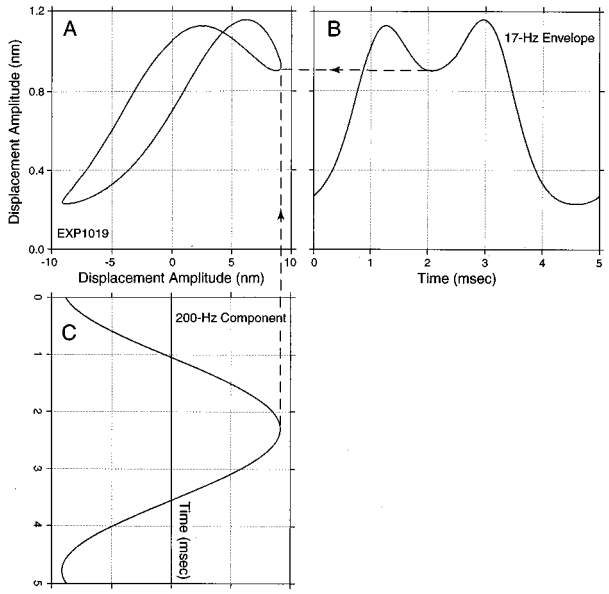

FIG. 12. Relationship between the 200-Hz suppressor response component (panel C) and the envelope of the resulting CF response (panel B), expressed as a suppressor-component/CF-envelope plot (panel A). EXP1019.

gain of the cochlear amplifier. Thus working forward from the low-frequency response (representing the acoustic input) and backward from the envelope of the CF component (reflecting the gain of the cochlear amplifier), an estimate of the relationship between the two can be established.

Such an estimate was formed (Fig. 12) by plotting the low-frequency response component on the x axis (panel C) and the CF response envelope (panel B) on the y axis. The result is the ''Lissajous figure'' shown in panel A. Somewhat disappointingly, this is not a single-valued curve. However, if the envelope waveform (the ''output'') is treated as having been delayed by 150 μs relative to the input and that delay is compensated (i.e., the envelope is *advanced* in time by 150 μs), the resulting curve does become nearly single valued, as shown in Fig. 13(B). One branch of this curve can thus be treated as an estimate of the cochlear amplifier's input/*gain* characteristic (panel D).

We can go even one step further. Reference to Fig. 11 shows that the gain of the cochlear amplifier is determined by the *slope* of the OHC's I/O curve: The flatter the curve (i.e., the smaller the slope), the lower the gain. Thus if we were to integrate this input/gain function we would obtain an (unscaled) estimate of the hair cell's I/O characteristic. This has been done [Fig. 13(C)], producing a curve which does indeed bear a close resemblance to the I/O curves measured in living outer hair cells (Russell *et al.*, 1986; Dallos and Cheatham, 1992).

The idea of repeating this process at different intensities of the low-frequency component in order to create a composite estimate of the entire I/O curve (and to check the consistency of the various estimates) has occurred to us. Unfortunately, strong phasic suppression is always accompanied by tonic suppression (cf. Figs. 5 and 9), which is a completely unknown process. Not knowing how to incorporate this tonic suppression into the model, at this time we cannot produce

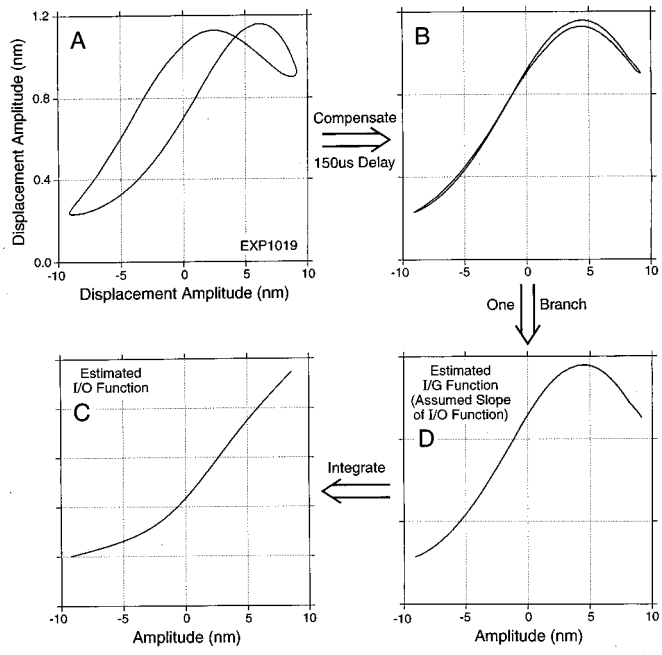

FIG. 13. Estimates (unscaled) of the cochlear amplifier's input/gain function (panel D) and the OHC's input/output function (panel C). The estimates were formed by advancing the CF envelope of Fig. 12(B) in time by 150 μs (panel B), taking one branch of the resulting curve (panel D), and then integrating (panel C). EXP1019.

an estimate of the entire I/O curve just from the phasic suppressions (see Sec. III).

III. DISCUSSION

A. Comparisons with previous data

Where comparable, the responses reported here are very similar to those reported in most other studies of the low-side suppression of basal basilar-membrane vibrations. Of importance, the phasic suppression of CF responses reported here, usually with both primary and secondary phases, has been universally observed in relevant studies (Patuzzi *et al.*, 1984b; Ruggero *et al.*, 1992; Rhode and Cooper, 1993; Cooper, 1996). With the lone exception of the study by Ruggero *et al.* (1992), all of the others also report that the moment of maximum suppression nearly coincides with the maximum displacement of the basilar membrane toward scala tympani. Moreover, the accuracy of this single exception has been challenged on technical grounds (Cooper, 1996).

Of particular importance, we report here that suppression of the CF response component was produced in our experiments only when the *displacement* of the suppressor response component was equal to or greater than that of the CF response component. Or stated more conservatively, the *sum* of the CF and the suppressor displacement components was always greater than that of the unsuppressed CF response component. This inequality, first demonstrated by Cooper (1996), appears to be an iron-clad rule in low-side suppression, never violated so far as we know. Although this inequality is not explicitly mentioned by the other investigators of low-side suppression, all examples given in their published data satisfy it. Nevertheless, until the entire parameter space available to the two tones is explored, it cannot be stated that this inequality invariably occurs in low-side suppressions.

The absolute values of the amplitudes which just produced suppression in our study seem small (e.g., thresholds about 2 nm in Fig. 4), but they fall within the 1- to 5-nm threshold range for suppression reported by Cooper (1996).

We often observed a delay between the moment of maximum CF suppression and the peak of basilar-membrane displacement (cf. Figs. 8 and 13). Such delays are also seen by others. For example, Rhode and Cooper gave an example of a similar (100-μs) delay in their 1993 paper.

The phase modulations seen in our data also seem to be a general feature of low-side suppressions. Cooper (1996) reported that low-side suppression produced phase leads in his CF response component that could reach *average* values as high as 0.1 cycle, although average phase leads of more than $\frac{1}{4}$ cycle could be achieved if the frequency of the high-frequency tone were set slightly higher than CF. The phase leads we observed routinely reached $\frac{1}{4}$ cycle in the time regions of maximum suppression (cf. Fig. 9); our average phase leads would of course have been smaller.

Finally, tonic suppression of the CF response has been observed in many of these low-side studies in the basal region (Ruggero *et al.*, 1992; Cooper, 1996; Cooper and Rhode, 1996). Moreover, even in those reports whose figures did not show tonic suppression, it was not specifically denied (Patuzzi *et al.*, 1984b; Rhode and Cooper, 1993; Cooper and Rhode, 1993). Thus tonic suppression might have been seen in those studies at higher suppressor intensities, but went unreported.

B. Implications regarding cochlear mechanisms

Among the many characteristics of the model schematized in Fig. 11, three stand out: (1) suppression can only occur when the peak (or trough) of the BM displacement (hence receptor potential) produced by the two-tone stimulus response waveform is appreciably greater in magnitude than that of the response produced by the CF tone alone; (2) When suppression does occur, its maximum phasic effect occurs at the moment of maximum displacement toward one or the other of the scalae, depending upon the position of the OHC's ''rest point'' [which is biased toward scala tympani in Fig. 11(A)]; (3) With intense enough stimulation, a secondary phase of suppression will occur, centered about the moment of maximum displacement toward the other scala, 180° out-of-phase with the primary suppression. Overlooking small time delays, these three characteristics were observed, without exception, in our experimental data. Thus the ''saturation feedback'' theory can be said to account fully for those aspects of our data, at least in a qualitative sense.

Tonic suppression is not an explicit feature of this model, although it is expected, as has been pointed out previously (Cai and Geisler, 1996c). For, according to the theory, the gain of the cochlear amplifier depends upon the slope of the OHC's input/output curve. Thus, with a suppressor of large amplitude, a strict application of the theory would predict that the gain of the cochlear amplifier would be expected to change from virtually normal (at the instants

when the suppressor's response component passed through zero) to virtually nil (at the suppressor component's peak and/or trough) at least once during each cycle of the suppressor.

However, a low-Q feedback circuit cannot be transformed into a high-Q circuit instantaneously. *Some* time-dependent processes must be involved, and hence there must be some suppressor frequency above which the system's gain would be unable to follow fully the waveform predicted from Fig. 11. The fact that we obtained strong tonic suppression with all of our suppressors, even the 200-Hz tones (Fig. 5), implies that some of the processes within the cochlear amplifier must have relatively slow processes. Moreover, the temporal processes of these suppressions are not constant, but seem closely tied to the depth of suppression. For instance, the cochlear amplifier seems to have been able to follow faithfully the substantial phasic suppressions generated by the 200-Hz suppressor at 66 dB SPL [Fig. 5(B)], because the peak of the CF response is unchanged from that of the unsuppressed case (panel A). However, at higher suppressor intensities (panels C and D), the cochlear amplifier never fully recovered its unsuppressed state at any time.

The subharmonic phasic suppressions which occur at high suppressor frequencies (Fig. 6) are another clear indication that time-dependent processes are involved in the cochlear amplifier. Unable to follow the rapid transitions demanded by those high frequencies (>2 kHz), the system synchronizes to a lower frequency, the basic periodicity of the two-tone complex. The phase modulations seen in the suppressed portions of the CF responses (cf. Fig. 9) are also marks of time-dependent processes within the cochlear amplifier.

The long recoveries from strong suppression which we have occasionally seen (e.g., the 500-Hz trace in Fig. 3) indicate that suppressive effects upon the basilar membrane's response may sometimes last much longer than previously recognized. Perhaps they are related to other long-term suppressive effects recently observed in cochlear recordings (Sridhar *et al.*, 1995; Cai and Geisler, 1996d), or to the mechanisms of temporary threshold shift. The total indifference of the suppressor response component to these recoveries, in fact to all aspects of CF suppression, argues that all suppressive effects, short or long, take place only within the mechanisms of the cochlear amplifier, not in the passive physical properties (e.g., stiffness) of the cochlear partition.

The very small basilar-membrane amplitudes at which CF suppression is initiated (ca. 2 nm) are very surprising in view of the much larger responses (nearly 100 nm) which are produced with strong low-frequency tones (e.g., Figs. 3 and 4). This small threshold can be accounted for with the feedback theory of cochlear amplification (cf. Zwicker, 1979). Suppose that in the frequency region near CF the feedback term can be described by the classic expression:

$$\text{gain} = A/(1 - A^*B), \tag{1}$$

where A is gain without feedback and B is the output of the feedback element. If now the term A^*B has value 0.99 (neglecting phase shifts), then the gain of the feedback circuit is 100 A. Now suppose that the gain of the feedback element is compressed just slightly (say 1%), then the term A^*B drops in value to 0.98 and the gain of the feedback circuit drops to 50 A (cf. Patuzzi *et al.*, 1989; Yates, 1990). Thus, since it does seem unreasonable to suppose that slight compressions in OHC generator potentials occurred at displacement amplitudes much smaller than those produced by intense sounds, large suppressions of the CF response at low displacements are not unexpected. The surprise is that, with such high estimated gains (ca. 55 dB), the cochlear amplifier behaves linearly at *any* sound level.

Our assumption that the OHC receptor potential is the controlling signal in the cochlear amplifier's feedback circuit is still controversial, for the electrical properties of the hair cell membrane presumably limit drastically the frequency range over which this potential could be of significance. However, indications are that more complete modeling of the OHCs, including their mechanical and electrical environments (e.g., Mountain and Hubbard, 1994; Dallos and Evans, 1995) will unravel this mystery.

C. Relationships between basilar-membrane suppression and auditory-nerve fiber suppression

A comprehensive study of the low-side suppression displayed by AN fibers has just been published (Cai and Geisler, 1996a,b,c). In one phase of that study, a saturating OHC input/output function similar to that of Fig. 11(A) was imbedded in a functioning feedback-circuit model, whose output was used to test the ability of the ''saturation feedback'' theory to account for those data (Cai and Geisler, 1996c).

The conclusion drawn in that study was that while the model could reproduce the phasic properties of the suppressions, it could not account for the great *tonic strength* of the low-side suppressions exhibited by the class of AN fibers having lower rates of spontaneous activity (<20/s). In fact, some of those fibers had their ''driven'' spike activity *totally* suppressed by the addition of the low-side tone! As the data presented in this paper are fully consistent with that model, it follows that the great tonic strength of low-side suppression exhibited by lower spontaneous AN fibers *cannot* be accounted for by the low-side suppression observed on the basilar membrane, at least in the base of the cochlea. Speaking roughly, low-side suppression of basal AN fibers behaves as if a high-pass filter were located somewhere between the basilar membrane and the primary neurons, a filter which sharply attenuates the low-frequency components of basilar-membrane vibrations during low-side suppression (cf. Pfeiffer, 1970). With a minor exception, no such filtering mechanism has ever been found. This single exception is the apparent velocity coupling between IHC cilia deflections and basilar-membrane vibrations at low frequencies. However, this high-pass filtering effect appears to be limited to suppressor frequencies below 1000 Hz (Patuzzi and Yates, 1987), and its calculated effect upon total suppression is very minor, even for very low suppressor frequencies (Cai and Geisler, 1996c). More importantly, such high-pass filtering is totally at odds with the virtual indifference of low-side suppression to the frequency of the suppressor tone (e.g., Schmiedt, 1982).

Relevant to the tonic suppression of the *CF responses* which is observed on the basilar membrane, it is interesting to note that the model used in the AN-fiber studies (Cai and Geisler, 1996c) had to incorporate a ''gain-smoothing'' (low-pass) filter within the cochlear-amplifier stage in order to obtain realistic phasic suppressions. The tonic suppressions reported here indicate that the use of a cochlear-amplifier filter in that model was fully justified. However, the complex temporal properties which characterize our data at high suppressor frequencies cannot be accounted for by a simple low-pass filter. Obviously some much more complicated time-dependent processes are involved.

In our data taken at multiple levels of the CF tone (Fig. 4), we noted that the suppressor-level threshold for low-side suppression was relatively insensitive to the level of the CF tone. This insensitivity to CF level of the basilar membrane's suppression threshold seems able to account for a similar indifference which is observed in the suppression thresholds of AN-fiber suppression (Schmiedt, 1982; Fahey and Allen, 1985; Cai and Geisler, 1996a).

Turning to the *phasic* suppressions, the temporal patterns of suppression observed in AN-fiber discharges are very similar to those which we observed on the basilar membrane. For example, the basilar-membrane suppression waveforms shown in Figs. 5 and 9 look much like those often observed in AN-fiber discharge patterns (e.g., Sachs and Hubbard, 1981; Sellick *et al.*, 1982; Patuzzi *et al.*, 1984a; Cai and Geisler, 1996a). One difference between the two types of studies is that two phases of suppression (called ''peak splitting'') were observed in the AN-fiber studies only at low suppressor frequencies ($\leqslant$500 Hz), while in this basilar-membrane study we clearly saw two phases of suppression with suppressor frequencies as high as 1 kHz.

Perhaps the asymmetry of the basilar-membrane suppression patterns observed with those high suppressor frequencies can account for the difference. The basilar-membrane displacement pattern in Fig. 10, for example, clearly shows two phases of suppression but it would most probably not produce two clear phases of suppression in a hair-cell/nerve-fiber model: the main peak would totally dominate the output of the model.

Another point of comparison between the basilar-membrane and AN-fiber suppression data concerns the absolute values of the suppression phases. In all of our relevant experiments, the moment of maximum suppression which occurred on the basilar membrane at our lowest suppressor frequency (200 Hz) nearly coincided with maximum displacement of the basilar membrane toward scala *tympani* (Fig. 7). In agreement with our observations, the moment of maximum neural suppression incurred by primary neurons in the first turn of the guinea pig cochlea, coincided, at a very low suppressor frequency (40 Hz), approximately with the maximum displacement of the basilar membrane toward scala tympani, as inferred from cochlear-microphonic recordings (Sellick *et al.*, 1982). However, in a recent study of cat AN fibers, the opposite polarity was observed: maximum neural suppression, at the lowest suppressor frequency used 950 Hz), occurred at about the moments of maximum displacement toward scala vestibuli, also inferred from CM recordings (Cai and Geisler, 1996a). A species difference in the operating point of the outer hair cell could explain these findings of opposite polarity, but there is no convincing evidence that such a variation of the operating point occurs.

D. Suggestions for further studies

The most obvious suggestion for future work is to identify the mysterious factor(s) which suppress(es) the responses of lower-spontaneous AN fibers so much more strongly than those of the basilar membrane during low-side suppression. Perhaps it is extra-cochlear potentials, a suggested by Hill *et al.* (1989). The time-dependent processes of the cochlear amplifier are also intriguing. Just how low must the frequency of a suppressor be in order to produce no tonic suppression? Why does the suppressor frequency of 2 kHz seem to be the upper limit for faithful following of the suppressor waveform by phasic suppression? Do these limiting frequencies vary with cochlear position? More fundamentally, what can knowledge about these various time-dependent processes tell us about the inner workings of the cochlear amplifier?

ACKNOWLEDGMENTS

This research was supported (in part) by research Grant Nos. NIDCD-DC00116 and -DC00141 from the National Institute on Deafness and Other Communication Disorders, National Institutes of Health. We thank Dr. Nigel Cooper for helpful discussions and for his critique of this manuscript.

[1]The still mysterious process by which the low-level responses of the basilar membrane are greatly enhanced in the living cochlea is often called the ''cochlear amplifier.'' For convenience (if not for conviction), we will also adopt that terminology. By ''gain'' of the cochlear amplifier, we mean the difference in the amplitudes of the CF responses obtained in the living and dead cochleas.

[2]It is recognized that the response to the CF component of a two-tone stimulus which is evoked on the (nonlinear) basilar membrane is not a fixed-amplitude sinusoid but rather one which is both amplitude modulated (Figs. 5, 9, and 10) and phase modulated (Fig. 9). Thus the contributions of a *band* of frequencies around CF are needed to represent the response *to* the CF tone. For the sake of verbal simplicity, this amplitude- and phase-modulated response waveform is simply called the ''CF response.'' For quantitative purposes, we measured within each CF response the amplitude of the single sinusoid whose frequency actually is CF. The term ''CF (response) component'' is used to identify that sinusoid. Likewise, by the term ''suppressor (response) component'' we mean the single sinusoid within a response whose frequency is that of the suppressor tone.

Cai, Y., and Geisler, C. D. (**1996a**). ''Suppression in auditory-nerve fibers of cats using low-side suppressors. I. Temporal aspects,'' Hearing Res. **96,** 94–112.

Cai, Y., and Geisler, C. D. (**1996b**). ''Suppression in auditory-nerve fibers of cats using low-side suppressors. II. Effect of spontaneous rates,'' Hearing Res. **96,** 113–125.

Cai, Y., and Geisler, C. D. (**1996c**). ''Suppression in auditory-nerve fibers of cats using low-side suppressors. III. Model results,'' Hearing Res. **96,** 126–140.

Cai, Y., and Geisler, C. D. (**1996d**). ''Long-term suppression of the responses of auditory nerve fibers to a characteristic-frequency tone by a low-frequency suppressor,'' Hearing Res. **96,** 141–150.

Cooper, N. P. (**1996**). ''Two-tone suppression in cochlear mechanics,'' J. Acoust. Soc. Am. **99,** 3087–3098.

Cooper, N. P., and Rhode, W. S. (**1993**). ''Nonlinear mechanics at the base and apex of the mammalian cochlea: *In vivo* observations using a

displacement-sensitive laser interferometer,'' in *Biophysics of Hair Cell Sensory Systems*, edited by H. Duifhuis, J. W. Horst, P. van Dijk, and S. M. van Netten (World Scientific, Singapore), pp. 249–256.
Cooper, N. P., and Rhode, W. S. (**1995**). ''Nonlinear mechanics at the apex of the guinea pig cochlea,'' Hearing Res. **82,** 225–243.
Cooper, N. P., and Rhode, W. S. (**1996**). ''Two-tone suppression in apical cochlear mechanics, '' Aud. Neurosci. **3**, 123–134.
Dallos, P. (**1992**). ''The active cochlea,'' J. Neurosci. **12,** 4575–4585.
Dallos, P., and Cheatham, M. A. (**1992**). ''Cochlear hair cell function reflected in intracellular recordings *in vivo*,'' in *Sensory Transduction*, edited by D. P. Corey and S. D. Roper (Rockefeller U. P., New York), pp. 371–393.
Dallos, P., and Evans, B. N. (**1995**). ''High-frequency motility of outer hair cells and the cochlear amplifier,'' Science **267,** 2006–2009.
Fahey, P. F., and Allen, J. B. (**1985**). ''Nonlinear phenomena as observed in the ear canal and at the auditory nerve,'' J. Acoust. Soc. Am. **77,** 599–612.
Geisler, C. D., Bendre, A., and Liotopoulos, F. K. (**1993**). ''Time-domain modeling of a nonlinear, active model of the cochlea,'' in *Biophysics of Hair Cell Sensory Systems*, edited by H. Duifhuis, J. W. Horst, P. van Dijk, and S. M. van Netten (World Scientific, Singapore), pp. 330–337.
Geisler, C. D., and Nuttall, A. L. (**1997**). ''Two-tone 'low-side' suppression in responses of basal basilar membrane,'' in *Diversity in Auditory Mechanics*, edited by E. R. Lewis (World Scientific, Singapore) (in press).
Hill, K. G., Stange, G., Gummer, A. W., and Mo, J. (**1989**). ''A model proposing synaptic and extra-synaptic influences on the responses of cochlear nerve fibers,'' Hearing Res. **39,** 75–90.
Hubbard, A. E., and Mountain, D. C. (**1990**). ''Haircell forward and reverse transduction: Differential suppression and enhancement,'' Hearing Res. **43,** 269–272.
Mountain, D. C., and Hubbard, A. E. (**1994**). ''A piezoelectric model of outer hair cell function,'' J. Acoust. Soc. Am. **95,** 350–354.
Nuttall, A. L., Dolan, D. F., and Avinash, G. (**1991**). ''Laser doppler velocimetry of basilar membrane vibration,'' Hearing Res. **51,** 203–214.
Nuttall, A. L., and Dolan, D. F. (**1993**). ''Two-tone suppression of inner hair cell and basilar membrane responses in the guinea pig,'' J. Acoust. Soc. Am. **93,** 390–400.
Nuttall, A. L., and Dolan, D. F. (**1996**). ''Steady-state sinusoidal velocity responses of the basilar membrane in guinea pig,'' J. Acoust. Soc. Am. **99,** 1556–1565.
Patuzzi, R., Sellick, P. M., and Johnstone, B. M. (**1984a**). ''The modulation of the sensitivity of the mammalian cochlea by low frequency tones. I. Primary afferent activity,'' Hearing Res. **13,** 1–8.
Patuzzi, R., Sellick, P. M., and Johnstone, B. M. (**1984b**). ''The modulation of the sensitivity of the mammalian cochlea by low frequency tones. III. Basilar membrane motion,'' Hearing Res. **13**, 19–27.
Patuzzi, R., and Yates, G. K. (**1987**). ''The low-frequency response of inner hair cells in the guinea pig cochlea: Implications for fluid coupling and resonance of the stereocilia,'' Hearing Res. **30,** 83–98.
Patuzzi, R., and Robertson, D. (**1988**). ''Tuning in the mammalian cochlea,'' Physiol. Rev. **68,** 1009–1082.
Patuzzi, R., Yates, G. K., and Johnstone, B. M. (**1989**). ''Outer hair cell receptor current and sensorineural hearing loss,'' Hearing Res. **42,** 47–72.
Pfeiffer, R. R. (**1970**). ''A model for two-tone inhibition of single cochlear-nerve fibers,'' J. Acoust. Soc. Am. **48,** 1373–1378.
Rhode, W. S. (**1978**). ''Some observations on cochlear mechanics,'' J. Acoust. Soc. Am. **64,** 158–176.
Rhode, W. S. (**1977**). ''Some observations of two-tone interactions measured using the Mössbauer effect,'' in *Psychophysics and Physiology of Hearing*, edited by E. F. Evans and J. P. Wilson (Academic, London), pp. 27–38.
Rhode, W. S., and Cooper, N. P. (**1993**). ''Two-tone suppression and distortion production on the basilar membrane in the hook region of cat and guinea pig cochleae,'' Hearing Res. **66,** 31–45.
Ruggero, M. A. (**1992**). ''Response to sound of the basilar membrane of the mammalian cochlea,'' Curr. Opin. Neurobiol. **2**, 449–456.
Ruggero, M. A., Robles, L., and Rich, N. C. (**1992**). ''Two-tone suppression in the basilar membrane of the cochlea; Mechanical basis of auditory-nerve rate suppression,'' J. Neurophysiol. **68,** 1087–1099.
Russell, I. J., Cody, A. R., and Richardson, G. P. (**1986**). ''The responses of inner and outer hair cells in the basal turn of the guinea pig cochlea and in the mouse cochlea grown *in vitro*,'' Hearing Res. **22,** 199–216.
Sachs, M. B., and Hubbard, A. E. (**1981**). ''Response of auditory-nerve fibers to characteristic-frequency tones and low-frequency suppressors,'' Hearing Res. **4,** 309–324.
Schmiedt, R. A. (**1982**). ''Boundaries of two-tone rate suppression of cochlear-nerve activity,'' Hearing Res. **7,** 335–351.
Sellick, P. M., Patuzzi, R., and Johnstone, B. M. (**1982**). ''Modulation of responses of spiral ganglion cells in the guinea pig cochlea to low frequency sound,'' Hearing Res. **7,** 199–221.
Sridhar, T. S., Liberman, M. C., Brown, M. C., and Sewell, W. F. (**1995**). ''A novel cholinergic 'slow effect' of efferent stimulation on cochlear potentials in the guinea pig,'' J. Neurosci. **15,** 3667–3678.
Yates, G. K. (**1990**). ''Basilar membrane nonlinearity and its influence on auditory nerve rate-intensity functions,'' Hearing Res. **50,** 145–162.
Zwicker, E. (**1979**). ''A model describing nonlinearities in hearing by active process with saturation at 40 dB,'' Biol. Cybern. **35,** 243–250.

Characterizing cochlear mechano-electric transduction in ears damaged with pure tones

Mark E. Chertoff,[a] Timothy C. Steele, and Lin Bian
Kansas University Medical Center, Department of Hearing and Speech, 39th and Rainbow Blvd., Kansas City, Kansas 66160

(Received 12 November 1996; revised 28 March 1997; accepted 29 March 1997)

Cochlear microphonics were recorded in response to Gaussian noise from the round window of Mongolian gerbils. A nonlinear systems identification procedure provided the frequency-domain parameters of a third-order polynomial equation describing cochlear mechano-electric transduction (MET). Exposure to an 8-kHz pure tone at 100 dB SPL for 20 min reduced the magnitude of the linear, quadratic, and cubic terms significantly. Animals exposed to a 1- or 4-kHz pure tone showed changes in the quadratic term. Differentiation of the polynomial equation and algebraic manipulations of the coefficients provided physiologic indices of MET. The sensitivity, saturation voltages, and sound pressures required to saturate MET were altered in animals exposed to an 8-kHz pure tone. Limited changes occurred in animals exposed to a 1- or 4-kHz pure tone. © *1997 Acoustical Society of America.* [S0001-4966(97)05607-5]

PACS numbers: 43.64.Nf, 43.64.Kc, 43.64.Wn [RDF]

INTRODUCTION

Cochlear mechano-electric transduction (MET) is a process in which cochlear partition displacement is converted into electrical events via deflection of hair-cell stereocilia. This process is reflected by the cochlear microphonic (Nieder and Nieder, 1971; Patuzzi *et al.*, 1989a), an electrical potential generated from the vector summation of outer hair-cell currents (Dallos *et al.*, 1972). In a previous study, Chertoff *et al.* (1996a) characterized MET in Mongolian gerbil by applying a nonlinear systems identification procedure (Bendat, 1990) to the cochlear microphonic (CM) recorded at the round window. The nonlinear systems identification procedure provided the frequency-domain parameters of a third-order polynomial equation characterizing MET. The third-order polynomial description accounted for 83%–92% of the MET for low and high frequencies, respectively.

In addition to providing a phenomenological description of MET, the frequency-domain parameters were used to gain insight into the physiologic mechanisms underlying MET. A physiologic interpretation was obtained by solving the equation for a range of input sound pressures. The solution yielded an asymmetric saturating function grossly similar to single hair-cell MET functions (Dallos, 1986; Hudspeth and Corey, 1977) and MET functions obtained with pure-tone modulation (Nieder and Nieder, 1971) and low-frequency pure-tone procedures (Patuzzi *et al.*, 1989b). The saturation and asymmetry in the function was related to the influence of transduction channel state on hair-cell receptor currents.

Exposure to a 4-kHz tone at 100 dB SPL for 20 min altered the parameters of the polynomial model and coherence functions (Chertoff *et al.*, 1996a). Although the change in coherence functions indicated that MET became more linear at about 4 kHz, the change in the polynomial parameters were variable and the limited number of animals ($n=4$) made it difficult to provide a physiologic description of the altered MET. The main purpose of this study was to characterize MET in animals with hearing loss produced by pure-tone stimulation and use indices derived from the coefficients of the polynomial model (see the Appendix) to describe physiologic changes in MET. Animals also were exposed to pure tones with different frequencies to evaluate the sensitivity of the indices to hearing loss associated with damage to different frequency regions of the cochlea.

I. GENERAL METHODS

The methods in this study are similar to that reported previously by Chertoff *et al.* (1996a); therefore, only a brief description is presented. More detail is provided where methods differed.

A. Animal preparation

Thirty-two Mongolian gerbils (45–76 g) with normal hearing were used as subjects. Normal hearing was defined as compound action potential (CAP) thresholds below 25 dB SPL for the frequencies 1, 2, 4, 8, and 16 kHz. Animals were anesthetized with pentobarbital (64 mg/kg) and subsequent injections of one-third the initial dose given as necessary. Body temperature was recorded by a rectal thermometer and maintained at 37 °C with a heating pad (Harvard). To gain access to the round window, the left pinna was removed and the postauricular aspect of the bulla exposed. The bulla was opened with a surgical drill and a silver ball electrode placed against the round window. The electrode was held against the round window with a cotton wick, which also kept the middle ear dry through capillary action. The bulla remained opened during the entire experiment.

[a]Author to whom all correspondence should be sent. Electronic mail: mchertof@kumc.wpo.ukans.edu

 0001-4966/97/102(1)/441/10/$10.00

B. Stimulus delivery and data acquisition

The signals and data acquisition procedures used in this study were similar to those described earlier (Chertoff *et al.*, 1996a). Tone bursts and Gaussian noise signals were created in an array processor (AP2, Tucker–Davis Technology) and digitized at 65.536 kHz (DA1, Tucker–Davis Technology). The output of the digital-to-analog converter connected to a headphone buffer (HB6, Tucker–Davis Technology) and to a shielded (Mu metal) headphone (Etymotic ER-2). The headphone was coupled to a tube and sealed to the external bony canal. Signal level and spectrum were monitored with a calibrated probe microphone (Etymotic ER7-C) placed approximately 5 mm from the umbo of the tympanic membrane.

Tone bursts, 2 ms in duration and windowed with a 1-ms $\cos^2$ ramp, were used to elicit compound action potentials (CAP). Cochlear microphonics were recorded in response to a frozen 250-ms sequence of Gaussian noise windowed with a 5-ms $\cos^2$ ramp. The signal was delivered at 88 dB SPL and the spectrum equalized between 100 and 10 240 Hz using an inverse filter routine developed by Chertoff and Chen (1996).

Electrical activity recorded from an electrode on the round window and a needle electrode inserted in the neck (ground) was filtered between 3 and 30 kHz and amplified 500 times by a low-noise amplifier (Stanford SR560). Subsequently, the signal was low-pass filtered at 16 kHz, amplified ten times (Stewart VBF 10M), and digitized at 65.536 kHz (AD2, Tucker–Davis Technology).

Threshold estimates were obtained by monitoring the CAP on a digital oscilloscope while attenuating signal level until 25 dB SPL. If a response was present at 25 dB SPL, the CAP was recorded and stored on disk. Ensuing CAPs were recorded at signal levels progressively attenuated by 5 dB until 0 dB SPL. One CAP response consisted of the average of 200 signal presentations.

For the nonlinear systems identification analysis of MET, both the input signal and the CM were recorded. A sequence of frozen Gaussian noise was delivered to the headphone and recorded by the microphone. The rms was computed and the attenuator adjusted by a feedback software routine to obtain the desired signal level. When the desired signal level was obtained, the noise was recorded by the microphone, digitized, averaged ten times, and stored on disk. Next, the same sequence of noise was delivered and the CM recorded, digitized, and stored on disk. One response was the average of ten signal presentations. This procedure was repeated for ten noise sequences that differed in phase resulting in a set of ten input and ten output records.

C. Experimental design

This study consisted of three successive experiments completed over eight months. In the first experiment 16 of the 32 animals were divided into a control group ($n=8$) and a group exposed to a 4-kHz pure tone ($n=8$). The results (Chertoff *et al.*, 1996b) showed that although the major hearing loss was at 8 kHz, changes in the polynomial parameters occurred at frequencies below and including 4 kHz. In a second experiment, eight additional animals were exposed to an 8-kHz pure tone in order to shift hearing loss to higher frequencies to determine if configuration of hearing loss influenced the indices derived from the polynomial parameters. For completeness, we conducted a third experiment in which eight final animals were exposed to a 1-kHz pure tone.

The control and exposure groups received the following procedure. CAP thresholds were obtained to tone bursts, followed by CM recordings to Gaussian noise. In the control group, a silent interval of 20 min elapsed and subsequent recordings of the CAP and CM obtained. In the experimental groups, the 20-min silent interval was replaced with either a 1-, 4-, or 8-kHz pure tone presented at 100 dB SPL (Mercer 9805). After exposure, CAP thresholds and CM recordings were repeated. In the 1- and 8-kHz exposure groups, the CM was recorded a second time after exposure (approximately 20 min later) to determine the reliability of the change in polynomial coefficients.

The harmonic distortion in the acoustic system was measured during a 1-kHz exposure in one animal to ensure that the level of the harmonics were not large enough to cause a hearing loss. The highest level of distortion was 45 dB SPL. A pure-tone signal at this level and frequency was presented to an additional animal for 20 min to determine if this exposure level created a hearing loss. The results showed that at this signal level and duration, no hearing loss could be measured. Therefore, the hearing loss produced in this study was due to the energy at the exposure frequency and not the harmonics.

D. Signal processing and nonlinear systems identification

Each input and output record was divided into 256 point subrecords. With a record length of 16 384 points, this yielded 64 subrecords per record. The total of 10 input/output responses resulted in 640 distinct subrecords from which spectral estimates were obtained. For the spectral estimates, leakage error was reduced with a Hanning window and overlap processing of 50% was used to recover energy lost by the Hanning window (Bendat and Piersol, 1986).

The magnitude and phase of the linear system frequency response functions were obtained from the ratio of the cross-spectral density functions and the input autospectral density functions. The magnitude and phase represent the voltage and phase of the CM relative to the sound pressure at the tympanic membrane. The magnitude and phase of the nonlinear frequency response functions of the third-order polynomial model of MET were obtained from uncorrelated spectral density functions computed from conditioned input records (Chertoff *et al.*, 1996a; Bendat and Piersol, 1986, 1993; Bendat and Palo, 1990). The magnitude and phase of these functions represent the gain and sign of a third-order polynomial equation relating input to output.

E. Statistics

The influence of hearing loss on the dependent variables (e.g., ''*A*'' coefficients, maximum, minimum, slope, and sound pressures at maximum and minimum saturation) was determined by subtracting the particular dependent variable

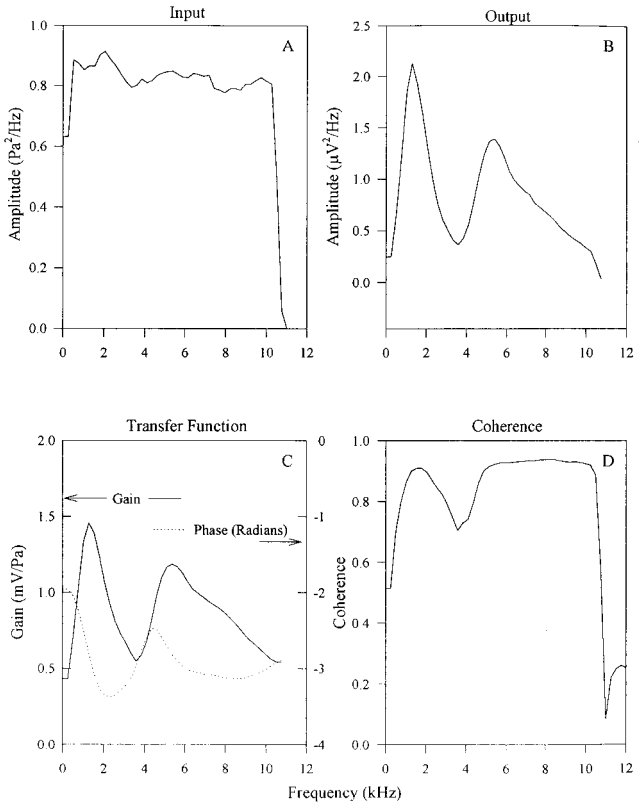

FIG. 1. Average ($n=32$ animals) input autospectral density function, output autospectral density function, transfer function (magnitude and phase), and coherence function. Spectral estimates were computed with 640 averages and a spectral resolution of 256 Hz.

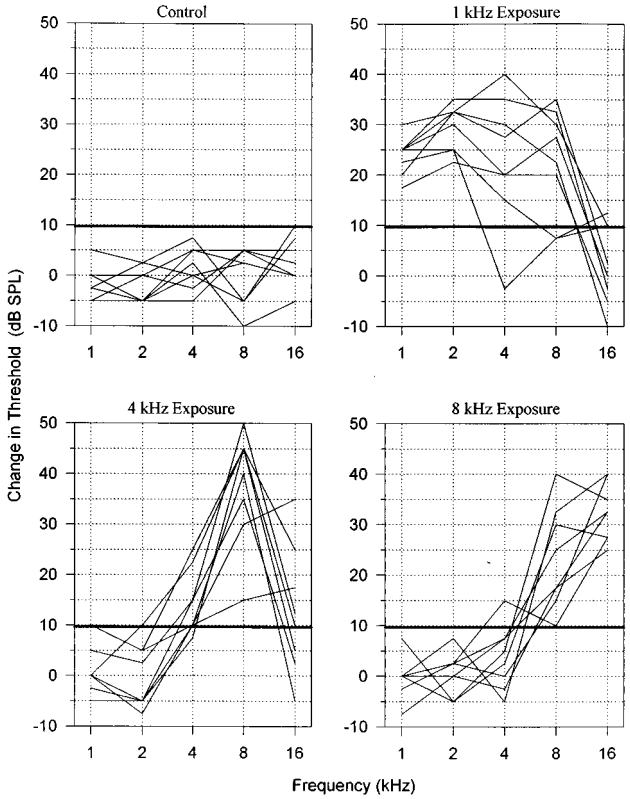

FIG. 2. Change in compound action potential threshold for control animals and animals exposed to either 1-, 4-, or 8-kHz pure tones. Exposure level was 100 dB SPL for 20 min. Dark solid line represents mean+2 s.d. change in threshold for the control animals averaged across all frequencies.

of interest before exposure from the dependent variable after exposure. The difference scores were submitted to a between group (control, 1-, 4-, and 8-kHz exposure groups) repeated measures analysis of variance (ANOVA). If a group effect was significant *post hoc* analysis was completed with the Newman–Keuls procedure. If a group by frequency interaction effect was significant each exposure group was compared to the control group with a between-group repeated measures analysis of variance. This determined if the change in the dependent variable across frequency differed between the exposure group and the control group. A probability of less than 0.05 was considered statistically significant. The major focus of this study was on group or group by frequency effects. The frequency effect alone was not of interest, only indicating that the dependent variable differed as a function of frequency. Any violations of symmetry or sphericity were controlled by adjusting the degrees of freedom with the Huyn–Feldt procedure (Maracuilo and Serlin, 1988). The adjusted degrees of freedom are reported when appropriate.

II. RESULTS

A. Input/output

The input spectrum, averaged across the 32 animals, is illustrated in Fig. 1(A). In general the energy was evenly distributed, although a slight increase was present in the low frequencies. The energy in the CM [Fig. 1(B)] reached a maximum at approximately 1.3 kHz, followed by a minimum at 3.6 kHz. Subsequently a second maximum occurred at 5.4 kHz, followed by steady decrease in energy. The magnitude of the transfer function [Fig. 1(C)] was similar in shape to the spectrum of the output. The average gain was 1.46 ± 0.32 s.d. mV/Pa at 1.3 kHz and 1.19 ± 0.34 s.d. mV/Pa at 5.4 kHz. The largest phase delay (-3.35 ± 0.33 s.d. rads) occurred at 2 kHz, followed by a phase transition between 4 kHz and 6 kHz. A delay of -3.12 ± 0.38 s.d. rads and -3.01 ± 0.38 s.d. rads occurred at 8 kHz and 10 kHz, respectively. The average linear coherence function [Fig. 1(D)], a measure of the correlation between input and output, was not unity for any frequency, indicating the presence of nonlinearity in these data. Coherence values were smaller for very low frequencies and frequencies centered around 4 kHz, as compared to higher frequencies.

B. Compound action potential thresholds

The influence of pure-tone exposure on CAP thresholds was obtained by subtracting CAP thresholds before exposure from CAP thresholds after exposure. Figure 2 illustrates the change in threshold for the control group and the 1-, 4-, and 8-kHz exposure groups, respectively. The dark solid line is the mean +2 s.d. (averaged across all frequencies) change in threshold for the control group and any elevation in threshold above this line was considered a hearing loss. In general, the 1-kHz exposure group had hearing loss which extended for a

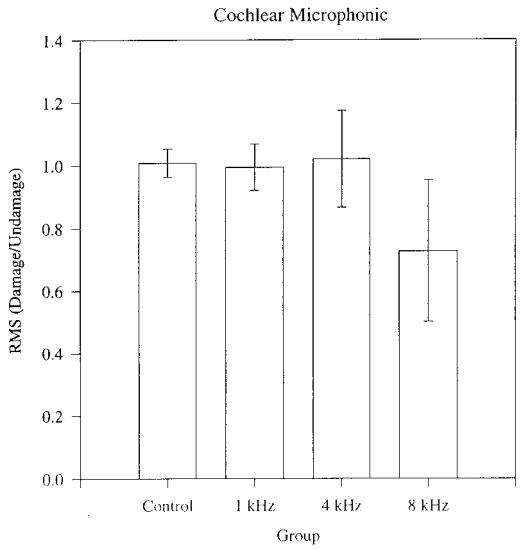

FIG. 3. Change in the rms amplitude of the cochlear microphonic for control and exposure groups. Error bars are ± 1 s.d.

broad range of frequencies. Hearing threshold remained unchanged at 16 kHz in five of the eight animals. The 4-kHz group had a small change in hearing at 4 kHz with the major change at 8 kHz. In some animals the hearing was elevated at 16 kHz whereas in others, hearing was normal. The hearing loss in the 8-kHz group started at 8 kHz and was more pronounced at 16 kHz. Considerable variability between animals in the extent of hearing loss occurred in each exposure group. For example, in the 1-kHz group threshold elevations at 4 kHz varied from 0 to 40 dB. Similarly, in the 8-kHz group some animals showed only a minimal change in hearing at 8 kHz, whereas one animal had a 40-dB elevation in hearing.

C. Cochlear microphonic

The root-mean-square (rms) of the CM in response to Gaussian noise was obtained from the square root of the area under the output autospectral density function. The average change in rms (after exposure/before exposure) for the control and exposure groups is illustrated in Fig. 3. Kruskal–Wallis ANOVA yielded a significant change in rms between groups ($H=14.78$, $p<0.05$). *Post hoc* contrasts indicated that the rms in the 8-kHz group was reduced compared to other groups. Further analysis on individual animals showed that some animals from the other groups also showed a reduced CM. These animals tended to have hearing loss in the high frequencies. A multiple regression analysis was completed to determine the relation between frequency at which hearing loss occurred and the reduction in CM. Results indicated that elevation of threshold at 16 kHz accounted for a major part of the variance, indicating that animals with hearing loss at 16 kHz tended to have a reduced CM independent of the exposure condition.

D. Nonlinear systems identification

1. 'A' coefficients

The influence of hearing loss on the frequency domain coefficients of the third-order polynomial equation characterizing mechano-electric transduction (MET) is illustrated in Fig. 4. Rows show the linear ($A1$), quadratic ($A2$), and cubic ($A3$) coefficients, respectively, whereas columns indi-

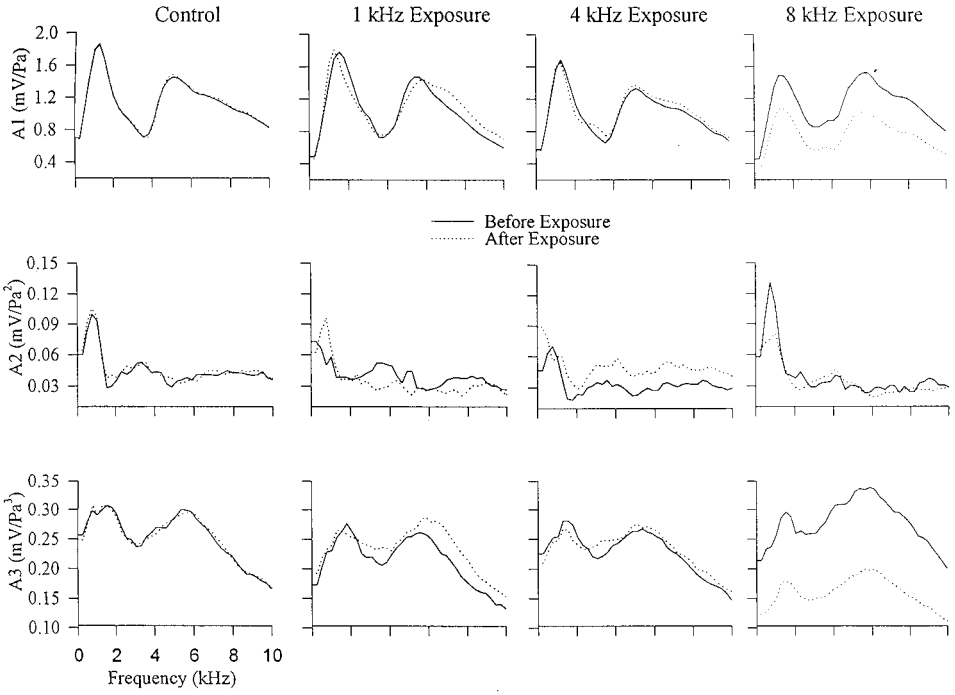

FIG. 4. Magnitude of the ''*A*'' coefficients before and after exposure for the control animals and exposed animals. The rows represents $A1$, $A2$, and $A3$, respectively, and the columns, the exposure condition. Solid lines represent the amplitude of the A coefficients before exposure and dotted lines, after exposure.

cate the exposure condition. Solid lines are results before exposure, dashed lines, after exposure. The change in A1 differed between the groups ($F_{3,38}=7.2$, $p<0.05$) and the change differed with frequency ($F_{114,1064}=2.26$, $p<0.05$). *Post hoc* analysis revealed that hearing loss caused by exposure to the 1-kHz or 4-kHz pure tones did not alter the $A1$ coefficient significantly. By contrast, exposure to the 8-kHz tone reduced the $A1$ coefficient. Exploring the interaction indicated that the reduction in $A1$ in the 8-kHz group was more pronounced around 1.2 kHz and 6 kHz ($F_{4,53}=3.40$, $p<0.05$).

$A2$, or the quadratic coefficient, was altered as a result of hearing loss. The change in A2 differed significantly between groups ($F_{3,28}=5.3$, $p<0.05$) and interacted with frequency ($F_{114,1064}=3.12$, $p<0.05$). Subsequent analysis showed that the $A2$ coefficient increased in animals exposed to the 4-kHz pure tone. The effect of hearing loss on $A2$ in the 1- and 8-kHz groups interacted with frequency (1 kHz, $F_{14,195}=2.44$, $p<0.05$; 8 kHz, $F_{6,87}=2.63$, $p<0.05$). Exposure to the 1-kHz tone increased $A2$ in the low frequencies and decreased $A2$ around 6 kHz. Exposure to 8 kHz resulted in a reduction of $A2$ in the low frequencies.

The bottom row shows the results for $A3$, the cubic coefficient. Similar to $A1$, the group and group by frequency interaction were significant ($F_{3,28}=7.71$, $p<0.05$; $F_{114,1064}=2.17$, $p<0.05$). Further analysis yielded no significant change in $A3$ for animals exposed to 1 kHz or 4 kHz when compared to the control group, whereas the $A3$ coefficient was reduced in the 8-kHz group. Neither the 1- or 4-kHz group showed any interaction with frequency. The 8-kHz exposure group had a significant interaction ($F_{7,93}=2.98$, $p<0.05$) and *post hoc* contrasts indicated that the reduction in $A3$ was more prominent around 6 kHz.

In addition to changes in the A coefficients, hearing loss influenced the ''fit'' of the polynomial model of MET. That is, the cumulative coherence function, a measure of the proportion of variability described by the of the third-order polynomial equation, was altered after exposure to pure tones. ANOVA indicated a significant group by frequency interaction ($F_{114,1064}=1.50$, $p<0.05$). After exposure the cumulative coherence increased for the 4-kHz group between 2.5 kHz and 3.8 kHz ($F_{3,43}=3.72$, $p<0.05$). The 8-kHz group yielded an increase in coherence through the center frequencies and a decrease at the lowest three frequencies ($F_{9,132}=2.00$, $p<0.05$). The increase in cumulative coherence was due mainly to the increase in the linear coherence, which increased approximately 5% for the 4-kHz group and 1.2% for the 8-kHz group.

2. ''A'' coefficient reliability

Pure-tone exposure increased the variability in the magnitude of the polynomial coefficients. Figure 5 illustrates the between-animal standard deviation of the difference scores in the control and exposure groups. In general, the between-animal variability was larger for the exposed animals than for the control animals. Moreover, the 8-kHz exposure group showed the largest variability, with the greatest variation in the $A1$ and $A3$ coefficients. A correlation between the second recording after exposure and the first recording after exposure was computed to determine the within-animal reliability. For the 1-kHz exposure group, the average correlation coefficients computed across all animals were 0.99, 0.85, and 0.94 for the $A1$, $A2$, and $A3$ coefficients, respectively. For the 8-kHz group, the average correlation coefficients were 0.99, 0.88, and 0.93 for the three A coefficients, respectively. ANOVA showed no significant effects between recordings one and two for either the 1-kHz or 8-kHz groups, indicating that the change in the coefficients was reliable.

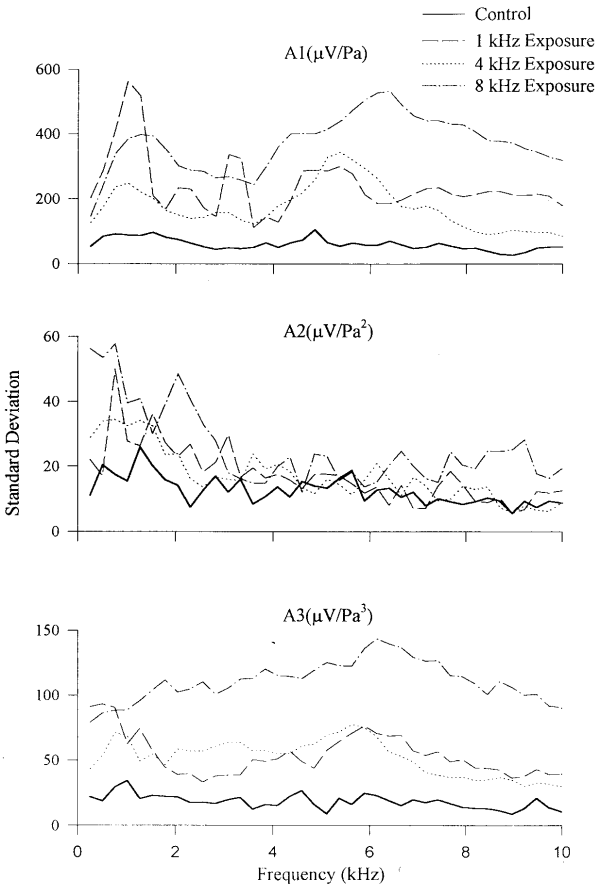

FIG. 5. Between-animal variability of the change in magnitude of the ''A'' coefficients. Each line represents the standard deviation of the difference score computed from subtracting the magnitude of the A coefficient obtained before exposure from the A coefficient after exposure.

3. Physiologic indices of MET

Figure 6 shows an example of a MET curve and associated physiologic indices. The curve was obtained by solving the polynomial equation for input pressures ranging from -1.5 Pa to 1.5 Pa and using the average ($n=8$) ''A'' coefficients at 1 kHz. The signs of the coefficients were obtained from their phase. The maximum and minimum voltages reflect the saturation of hair-cell currents when hair cell transduction channels are closed and open, respectively. The slope represents the sensitivity of MET, that is, the amount of current flow through hair cells for a given sound pressure. The sound pressure at which the maximum and minimum voltage occur reflects the amount of sound pressure (or indirectly, the amount of cochlear partition displacement) required to saturate hair-cell currents. These indices were ob-

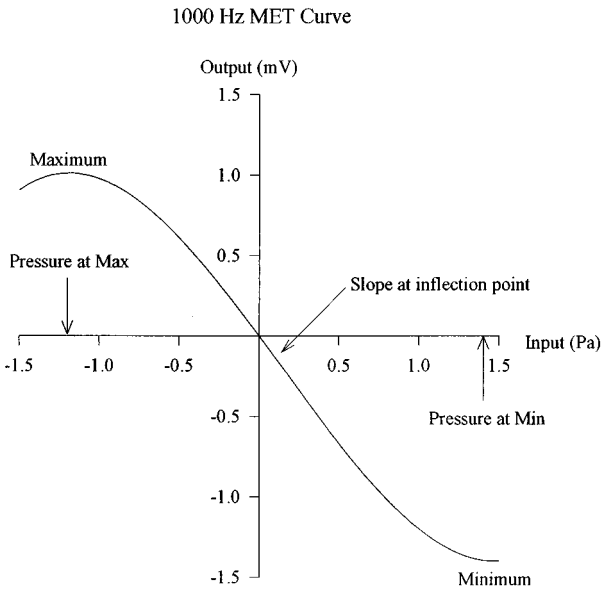

FIG. 6. Example of a mechano-electric transduction curve obtained from a polynomial equation using the average *A* coefficients at 1000 Hz in eight animals. The physiologic indices are illustrated: maximum voltage, minimum voltage, slope, and sound pressures at maximum and minimum voltages, respectively. Values obtained from equations in the Appendix.

tained from differentiation of the polynomial model of MET and algebraic manipulations of the '*A*' coefficients (see the Appendix).

The maximum and minimum voltages for the control and exposure groups before and after exposure are illustrated in Fig. 7. ANOVA yielded a significant change in both the maximum and minimum voltage (maximum: $F_{3,28}=6.92$, $p<0.05$; minimum: $F_{3,28}=6.61$, $p<0.05$) and a significant group by frequency interaction (maximum: $F_{117,1092}=2.02$, $p<0.05$; minimum: $F_{117,1092}=2.11$, $p<0.05$). *Post hoc* analysis indicated that the maximum and the absolute value of the minimum were significantly reduced in the 8-kHz group as compared to the control group. No significant change occurred for the 1- or 4-kHz exposure groups. The significant group by frequency interaction was associated with the maximum voltage in the 8-kHz group ($F_{5,75}=2.75$, $p<0.05$). Results indicated that the reduction in the maximum voltage was greater for frequencies around 1 kHz and 6 kHz.

Figure 8 illustrates the sound pressures required to reach the maximum and minimum of the transduction curves. In general, more sound pressure was required to reach the maximum or minimum for frequencies at about 1 to 2 kHz than for other frequencies in all groups. The amount of sound pressure required to saturate the transduction curves was altered significantly as a result of hearing loss (positive pressure: $F_{3,28}=4.22$, $p<0.05$; negative pressure: $F_{3,28}=6.66$, $p<0.05$) and the change in amount of sound pressure depended upon frequency (positive pressure: $F_{111,1092}=1.24$, $p<0.05$; negative pressure: $F_{111,1092}=1.62$, $p<0.05$). Further analysis indicated that more pressure (positive and negative) was required to saturate the transduction curves for animals in the 8-kHz exposure group compared to the control group. Moreover, the effect was more substantial for frequencies around 1.2 kHz and positive sound pressures ($F_{16,244}=2.01$, $p<0.05$). In the 4-kHz group, the pressure required to reach maximum saturation was reduced significantly at approximately 2–3 kHz ($F_{11,150}=1.92$, $p<0.05$).

The influence of hearing loss on the slope of the transduction curves is illustrated in Fig. 9. The solid lines indicate the slope before exposure and the dotted lines, after expo-

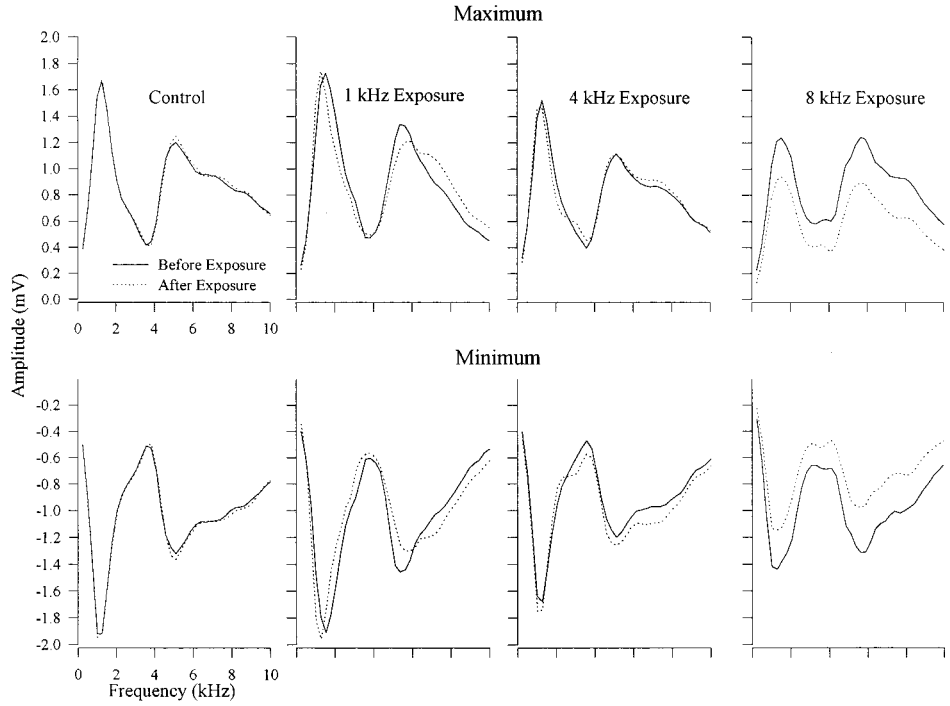

FIG. 7. Average maximum and minimum voltages of MET for the control and experimental animals. Top row indicates the maximum voltages and bottom row the minimum voltages, and columns indicate the exposure conditions. Solid lines represent voltages before exposure, and dotted lines after exposure.

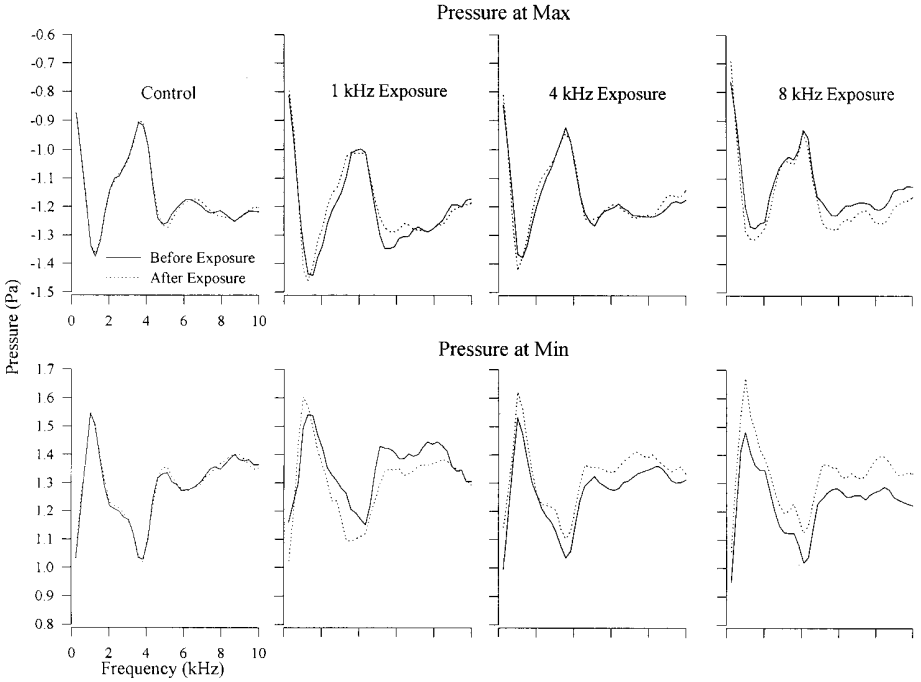

FIG. 8. Average sound pressures required to reach maximum (top row) and minimum (bottom row) voltages of MET, respectively. Top row indicates the pressures required to reach maximum voltage and bottom row the pressures required to reach minimum voltage. Columns indicate the exposure conditions. Solid lines represent sound pressures before exposure, and dotted lines, after exposure.

sure. The analysis indicated a significant group ($F_{3,28}=7.26$, $p<0.05$), and group by frequency interaction ($F_{117,1092}=2.26$, $p<0.05$). *Post hoc* analysis yielded no significant differences between the 1-kHz, 4-kHz, and control groups. In contrast, the slope in the 8-kHz group was reduced compared to the control group. Furthermore, a significant interaction indicated that the slope was reduced more for frequencies at 1.2 and 6 kHz ($F_{4,55}=3.53$, $p<0.05$) for the 8-kHz exposure group.

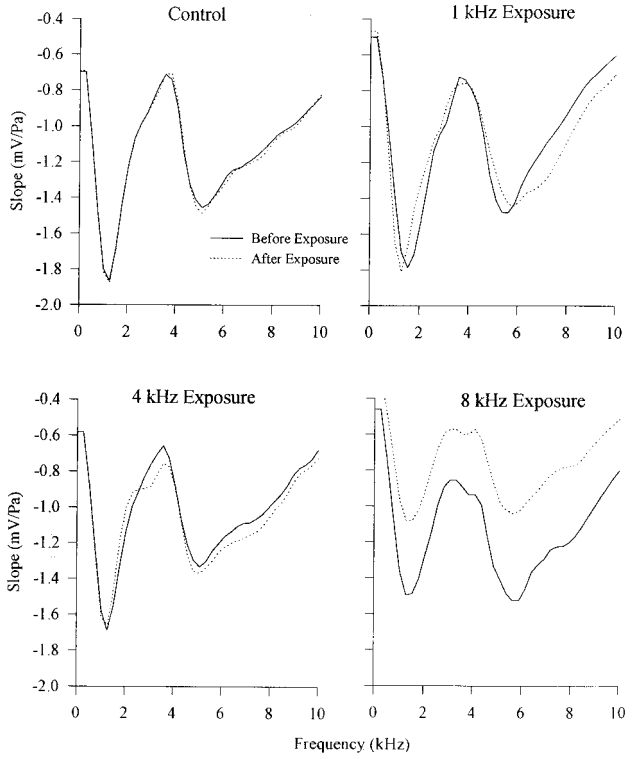

FIG. 9. Average slope of MET for control and experimental animals. Solid line represents the slope before exposure, and the dotted line, after exposure.

III. DISCUSSION

A. Comparison to previous study

The average transfer function relating cochlear microphonic amplitude and phase relative to the amplitude and phase of the sound pressure at the tympanic showed similar trends to Chertoff *et al.* (1996a). The magnitude increased for low frequencies reaching a peak at approximately 1 kHz and a notch at 4 kHz. Subsequently, the magnitude of the transfer function showed an increase in gain followed by a decrease in gain in the high frequencies. The phase illustrated a steep phase lag for low frequencies, a phase transition at the notch frequency, and finally a phase lag reaching a plateau in the high frequencies.

The magnitude of the A coefficients and phase of the transfer function, however, differed from the previous study. The magnitude of $A1$ in our previous study was 724.3 ± 214.4 μV/Pa at 8 kHz, whereas in this study the average value was 1056.2 ± 306.7 μV/Pa. Overall, larger linear coefficients occurred for five of the six frequencies reported previously. The magnitude of $A3$ became smaller for 0.5, 1, 2, and 4 kHz and for 8 and 10 kHz the values remained the same. The magnitude of $A2$ was reduced for the low frequencies (0.5, 1, and 2 kHz) and remained the same for the high frequencies (4, 8, and 10 kHz). The different magnitudes may be due to the different signal levels used in this

study. In this study we recorded the CM to a higher signal level (88 vs 85 dP SPL) because we felt that it would increase the nonlinearity in MET and enlarge the size of the nonlinear terms. This would be important when examining the effect of hearing loss on the coefficients. Larger coefficients would reduce the influence of a floor effect if hearing loss reduced the magnitude of the coefficients. Although the magnitude of the linear term increased, the size of the nonlinear terms decreased or remained the same.

The phase delay in this study was less than the phase delay reported in our previous work. This suggests that the location of the recorded CM moved within the base of the cochlea, perhaps due to the higher signal level. This is consistent with earlier work by Honrubia and Ward (1968) who showed that the maximum CM can shift basally up to 4 mm in the cochlea with increasing signal level. The mechanism of the shift was explained by Dallos (1973) as a result of the nonlinear input/output growth of the CM. That is, with increasing level the response of the base of the cochlea to a low-frequency tone grows linearly while the response at the apex saturates. Eventually the CM produced in the base would dominate, explaining the shift in the CM. More recently, however, changes in peak basilar membrane displacement to lower frequencies due to increasing signal level (Ruggero *et al.*, 1992), and the shift of the peak response of single hair cells to lower frequencies (Zhang and Zwislocki, 1996) suggests that the shift in the CM may reflect the migration in the peak of basilar membrane displacement.

Interestingly, the change in the coefficients with level provides information concerning the adequacy of a third-order polynomial description of MET. An appropriate model should be independent of input level (Bendat and Palo, 1990). This suggests that the third-order polynomial model is not the best model of MET because the magnitude of the coefficients changed with signal level. One solution is to obtain a mathematical function or model which characterizes MET more appropriately. Until this occurs, however, future studies may require polynomial functions obtained at multiple signal levels to characterize MET fully.

B. 8-kHz exposure

The most dramatic change in MET occurred in animals exposed to the 8-kHz pure tone. All of the animals had hearing loss at 16 kHz, which correlated with the reduction in the rms of the CM. Moreover, these animals had the largest change in the polynomial coefficients ($A1$ and $A3$), which lead to alterations in the physiologic indices describing MET. That is, the maximum, minimum, and slope of MET were reduced and the sound pressures required for saturation where elevated. These results are consistent with Patuzzi *et al.* (1989c) who showed changes in both the magnitude and shape of the cochlear microphonic transfer curves after pure-tone exposure lasting more than 150 s.

A reduction in the maximum, minimum, and slope indicate that the amount of current passing through outer hair cells was reduced as a result of pure-tone exposure. This could occur for many physiologic reasons. For example, the reduction in the endocochlear potential, blockage of transduction channels, alterations in the compliance of the basilar membrane, or changes in hair cell tectorial membrane coupling (Patuzzi, 1995) could alter these indices. In this study, a likely location of damage is at hair-cell transduction channels located in the stereocila (Hudspeth, 1982). Noise exposure alters hair-cell stereocilia through changes in stiffness, fusion with neighboring stereocilia, formation of giant stereocilia, splaying, breakage, and complete elimination (for review see Lim, 1986). One or any combination of these anatomic variants would change the mechanics of transduction channels and lead to permanent closure of transduction channels. Closure of hair-cell transduction channels would reduce hair-cell receptor currents (Patuzzi *et al.*, 1989c).

In addition to an overall reduction in the maximum, minimum, and slope, greater change occurred for frequencies around 1.2 and 6 kHz. One explanation is that pure-tone exposure altered the vector summation of hair-cell receptor currents, leading to frequency specific effects. Another possibility, however, is that reduction at different frequencies reflect alterations in different mechanisms involved in MET. For example, uncoupling outer hair-cell stereocilia from the tectorial membrane may lead to changes in MET at some frequencies whereas altering transduction channels directly could influence other frequencies. Future work using cochlear models and studies correlating anatomical changes with changes in the physiologic indices of MET, will be necessary to determine if frequency effects relate to modifications in specific mechanisms underlying MET.

Greater amounts of sound pressure were required to drive MET into saturation after exposure, indicating that larger cochlear partition displacements were required to saturate hair-cell receptor currents. This suggests that cochlear partition compliance was reduced after exposure. A reduction in compliance would require more sound pressure to displace stereocilia to get the maximum number of channels open. This may be the result of a direct physical change of the basilar membrane, or it could be due to changes in hair-cell stereocilia. Floppy stereocilia (Lim, 1986) would decrease the coupling between the organ of Corti and the tectorial membrane, altering cochlear partition vibration. Also, it is conceivable that floppy stereocilia are more difficult to displace than stiff stereocilia. Therefore, more cochlear partition displacement would be required to deflect stereocilia to the angle required to obtain the maximum number of open channels.

C. 1-kHz and 4-kHz exposure

Exposure to the 1- or 4-kHz pure tones had no effect on the rms of the CM and limited effects on the polynomial description of MET. One reason for the limited change in the 1- and 4-kHz groups is the relation between electrode location and site of damage. The round window electrode is sensitive to electrical potentials generated from outer hair-cell receptor currents in the base of the cochlea (Dallos, 1973). At high sound pressures, the cochlear partition at the base of the cochlea vibrates to low and high frequencies. Thus, assuming that normal hearing thresholds at 16 kHz indicate normal outer hair cells in the base of the cochlea, the CM at low and high frequencies generated from receptor currents in the base of the cochlea will be normal. This is consistent

with the results of Patuzzi *et al.* (1989a) who showed that damaging the first turn by ablation, streptomycin, current injection, and acoustic trauma had little effect on the amplitude of the CM generated from a low-frequency tone presented at high signal levels.

Another explanation for the apparent lack of change in the 1- and 4-kHz groups is the increase in between-animal variability after exposure limited the chance of finding a statistically significant result. This is first seen in the audiograms. Animals in the same exposure group could have threshold elevations that varied by 40 dB. Presently, the reason for the large between-animal variation is not known. Large between-animal variability in both threshold elevation and extent of cochlear damage is a common finding of many noise exposure studies (Cody and Robertson, 1983), the mechanisms of which have not been identified [see Henderson *et al.* (1993) for a review].

Although the 8-kHz group showed the largest variability, the magnitude of A1 and A3 was reduced in all animals in that group. This was not the case for the 4-kHz exposure group. The amount of change and direction differed between animals. For example, the mean data for the 4-kHz exposure group showed changes in the A1 coefficient, but not all animals showed this pattern. Two of the animals in the 4-kHz group, that had audiograms similar to the 8-kHz group (i.e., loss at 16 kHz), showed a reduction in A1 similar to the 8-kHz group. The other six animals showed an increase in the magnitude of A1 for high frequencies. It seems possible that cochlear MET in these animals was altered but the limited number of animals limited the power of the statistical analysis. Moreover, in the 1-kHz group, A3 appeared to increase after exposure. Examining individual animals showed that some animals had large changes after damage where as others did not. The high correlations between the two recordings after damage suggests that these changes were not due to random fluctuations. It is possible that MET was altered in animals exposed to the 1- or 4-kHz pure tones but the way in which MET changed differed between animals. Future studies with histology will be necessary to determine if these animals differed in extent or type of cochlear damage.

IV. SUMMARY AND CONCLUSIONS

A nonlinear systems identification procedure provided the frequency domain parameters of a third-order polynomial equation characterizing MET in normal animals and in animals with hearing loss. The coefficients of the equations were altered by hearing loss. One unique aspect of this study was that differentiation and algebraic manipulations of the parameters of the phenomenological model provided physiologic indices of MET. These indices revealed a change in the sensitivity as well as the saturation voltage and sound pressures to reach saturation of MET in animals exposed to an 8-kHz pure tone. These changes indicated a reduction in hair-cell current and alterations in cochlear partition displacement. Few statistically significant changes occurred in animals exposed to 1- or 4-kHz tones. This was attributed to the limited ''vision'' of the round window electrode to basal regions of the cochlea and/or the increase in animal variability after exposure decreasing the power of the statistical analysis.

ACKNOWLEDGMENTS

The authors thank Jeff Radel, Geetha Krishnan, Greg Ator, and Julius Bendat for their valuable comments on the manuscript. This research was supported in part by research Grant No. 1 R29 DC02117-01A2 from the National Institute on Deafness and other Communication Disorders, National Institutes of Health, and USPHS Grant No. HD02528 to the Smith Mental Retardation and Human Development Research Center.

APPENDIX

The physiologic indices characterizing MET were derived from the polynomial coefficients obtained from the nonlinear systems identification procedure in the following manner. The dependence on frequency was eliminated to simplify notation.

Let

$$y = A_1 x + A_2 x^2 + A_3 x^3, \tag{A1}$$

then

$$\frac{dy}{dx} = A_1 + 2A_2 x + 3A_3 x^2$$

and

$$\frac{d^2 y}{dx^2} = 2A_2 + 6A_3 x,$$

$$\frac{dy}{dx} = 0 \quad \text{when} \quad 3A_3 x^2 + 2A_2 x + A_1 = 0.$$

The solution to this quadratic equation yields the sound pressures at the maximum and minimum, respectively. Hence,

$$x = \frac{-A_2 \pm \sqrt{A_2^2 - 3A_1 A_3}}{3A_3}. \tag{A2}$$

From the x coordinates, the corresponding maximum and minimum are found by

$$y = A_1 x + A_2 x^2 + A_3 x^3$$

and letting

$$\Delta = A_2^2 - 3A_1 A_3,$$

yields

$$y = \frac{2A_2^3 - 9A_1 A_2 A_3 \pm 6A_1 A_3 \sqrt{\Delta} \mp 2A_2^2 \sqrt{\Delta}}{27A_3^2}. \tag{A3}$$

The inflection point is obtained by

$$\frac{d^2 y}{dx^2} = 0$$

when

$$2A_2+6A_3x=0, \text{ namely, } x=\frac{-A_2}{3A_3} \tag{A4}$$

at

$$x=\frac{-A_2}{3A_3}, \quad y=\frac{-9A_1A_2A_3+2A_2^3}{27A_3^2}. \tag{A5}$$

The slope at

$$x=\frac{-A_2}{3A_3}$$

is

$$\frac{dy}{dx}=A_1+2A_2x+3A_3x^2=\frac{3A_1A_3-A_2^2}{3A_3}. \tag{A6}$$

Bendat, J. S. (**1990**). *Nonlinear System Analysis and Identification from Random Data* (Wiley, New York).

Bendat, J. S., and Palo, P. (**1990**). ''Practical techniques for nonlinear system analysis/identification,'' Sound and Vibration, 28–33.

Bendat, J. S., and Piersol, A. G. (**1993**). *Engineering Applications of Correlation and Spectral Analysis* (Wiley, New York), 2nd ed.

Bendat, J. S., and Piersol, A. G. (**1986**). *Random Data: Analysis and Measurement Procedures* (Wiley, New York), 2nd ed.

Chertoff, M. E., and Chen, J. (**1996**). ''An *in situ* calibration routine for click stimuli,'' J. Am. Acad. Audiol. **7**, 130–136.

Chertoff, M. E., Steele, T. C., Ator, G. A., and Bian, L. (**1996a**). ''Characterizing cochlear mechano-electric transduction using a nonlinear systems identification procedure,'' J. Acoust. Soc. Am. **100,** 3741–3753.

Chertoff, M. E., Steele, T. C., Bian, L., and Ator, G. A. (**1996b**). ''Reliability and sensitivity of a third-order polynomial characterization of cochlear mechano-electric transduction in gerbils,'' Presented at the 19th meeting of the Association for Research in Otolaryngology, St. Petersburg Beach, FL.

Cody, A. R., and Robertson, D. (**1983**). ''Variability of noise-induced damage in the guinea pig cochlea: electrophysiological and morphological correlates after strictly controlled exposures,'' Hearing Res. **9,** 55–70.

Dallos, P. (**1973**). ''Cochlear potentials,'' in *The Auditory Periphery, Biophysics and Physiology*, edited by P. Dallos (Academic, New York), Chap. 5.

Dallos, P. (**1986**). ''Neurobiology of cochlear inner and outer hair cells: Intracellular recordings,'' Hearing Res. **22,** 185–198.

Dallos, P., Billone, M. C., Durrant, J. D., Wang, C. Y., and Raynor, S. (**1972**). ''Cochlear inner and outer hairs cells: Functional differences,'' Science **177,** 356–358.

Henderson, D., Subramaniam, M., and Boettcher, F. A. (**1993**). ''Individual susceptibility to noise-induced hearing loss: an old topic revisited,'' Ear Hear. **14**, 152–168.

Honrubia, V., and Ward, P. H. (**1968**). ''Longitudinal distribution of the cochlear microphonics inside the cochlear duct (guinea pig),'' J. Acoust. Soc. Am. **44,** 951–958.

Hudspeth, A. J. (**1982**). ''Extracellular current flow and the site of transduction by vertebrate hair cells,'' J. Neurosci. **2,** 1–10.

Hudspeth, A. J., and Corey, D. P. (**1977**). ''Sensitivity, polarity, and conductance change in the response of vertebrate hair cells to controlled mechanical stimuli,'' Proc. Natl. Acad. Sci. USA **74,** 2407–2411.

Lim, D. (**1986**). ''Effects of noise and ototoxic drugs at the cellular level in the cochlea: a review,'' Am. J. Otolaryngol. **7**, 73–99.

Marascuilo, L. A., and Serlin, R. C. (**1988**). *Statistical Methods for the Social and Behavioral Sciences* (Freeman, New York).

Nieder, P., and Nieder, I. (**1971**). ''Determination of microphonic generator transfer characteristic from modulation data,'' J. Acoust. Soc. Am. **49,** 478–492.

Patuzzi, R. B. (**1995**). ''Monitoring cochlear homeostasis with automatic analysis of the low-frequency cochlear microphonic,'' in *Active Hearing*, edited by A. Flock, D. Ottoson, and M. Ulfendahl (Pergamon, New York).

Patuzzi, R. B., Yates, G. K., and Johnstone, B. M. (**1989a**). ''The origin of the low-frequency microphonic in the first cochlear turn of guinea-pig,'' Hearing Res. **39,** 177–188.

Patuzzi, R. B., Yates, G. K., and Johnstone, B. M. (**1989b**). ''Outer hair cell current and sensorineural hearing loss,'' Hearing Res. **42,** 47–72.

Patuzzi, R. B., Yates, G. K., and Johnstone, B. M. (**1989c**). ''Changes in cochlear microphonic and neural sensitivity produced by acoustic trauma,'' Hearing Res. **39,** 189–202.

Ruggero, M. A., Robles, L., Rich, N. C., and Recio, A. (**1992**). ''Basilar membrane responses to two-tone and broadband stimuli,'' Philos. Trans. R. Soc. London, Ser. B **336,** 307–315.

Zhang, M., and Zwislocki, J. J. (**1996**). ''Intensity-dependent peak shift in cochlear transfer functions at the cellular level, its elimination by sound exposure, and its possible underlying mechanisms,'' Hearing Res. **96,** 46–58.

Absolute pitch and sex affect event-related potential activity for a melodic interval discrimination task

Edwin C. Hantz
Division of Otolaryngology, Department of Surgery, Box 8629, 601 Elmwood Avenue, University of Rochester Medical Center, Rochester, New York 14642 and Eastman School of Music, 26 Gibbs Street, Rochester, New York 14604

Kelley G. Kreilick
Division of Otolaryngology, Department of Surgery, Box 8629, 601 Elmwood Avenue, University of Rochester Medical Center, Rochester, New York 14642

Elizabeth W. Marvin
Eastman School of Music, 26 Gibbs Street, Rochester, New York 14604

Robert M. Chapman
Department of Brain and Cognitive Sciences, University of Rochester, Rochester, New York 14627

(Received 10 May 1996; revised 5 March 1997; accepted 6 March 1997)

Absolute pitch is a special ability which allows for special perceptual/cognitive strategies. Studies have shown differences in event-related scalp potentials between absolute-pitch (AP) and relative-pitch (RP) subjects of equal musical training. In this study, highly trained musicians (15 females/15 males) performed a melodic interval discrimination task, using intervals on-pitch in equal-tempered tuning (A4=440 Hz) and tuned a half-semitone sharp. Subjects identified target intervals (probability 0.2) in a series of 400 randomly transposed intervals. AP subjects were expected to perform differently across intonation conditions, whereas RP subjects were not. Event-related potentials (ERPs) were recorded from three midline sites and two lateral sites. ERPs were analyzed by principal component analysis and analysis of variance. Sex was also considered as an independent subject variable. Performance was not significantly different either by absolute pitch or sex. Reaction times did not reveal any significant interactions involving AP or sex, but showed a significant effect by response type (target/nontarget). Strong P3 activity appeared to the target melodic intervals regardless of subject group or intonation. PCA factors with maxima at 352, 511, and 709 ms were sensitive to task relevance. Males showed greater positivity than females along the midline. A significant intonation by response type by sex interaction indicated a greater spread of values for females than males, and greater similarity in response by sex for the sharp than the on-pitch intervals. AP subjects showed reduced P3 activity along the midline, but increased over lateral sites. In a difficult musical task, the ERPs were sensitive to the sex of the listeners, as well as to whether they had absolute pitch.
[S0001-4966(97)02807-5]

PACS numbers: 43.64.Ri, 43.75.Cd, 43.66.Hg [RDF]

INTRODUCTION

Although relatively little is known about the neural correlates of perceptual or cognitive processes active during music listening, the recording of event-related scalp potentials has proven to be a useful tool in gaining some insights into these processes.[1–17]

Event-related potential (ERP) recording involves sampling brain activity in synchrony with some repeating class of musical events. Although passive listening is sometimes measured as a control condition, subjects are usually required to perform specific tasks in which the individual stimuli are attended to and evaluated. By averaging the brain wave samples corresponding to the members of an event class, knowledge can be gained about the neural response to musical events of a particular event type.

The early components of the ERP waveforms, such as the typical negative trough at about 100 ms after stimulus onset (N1) and the positive peak at about 200 ms (P2) reflect the processing of the sensory attributes of the stimuli and are sensitive to their acoustic properties. Components after about 250 ms have been associated with cognitive processing. The best known of these, called the ''P3'' or ''P300,'' is a positive peak occurring between 300 and 700 ms from the onset of a task-relevant, infrequent, or surprising stimulus. The P3 has been linked to the use of working memory, that part of the memory system which transfers current sensory information from short-term to long-term memory, and conversely compares long-term memories to incoming information.[7,18–24]

The purpose of the current study is to investigate the neural processing of sequential (melodic) musical intervals as reflected by ERPs. Basic to the perception of music is the ability to discriminate differences in pitch and the perceived distance between them. Further, a small segment of the population possesses long-term memory for pitch, so-called ''absolute,'' or ''perfect'' pitch. Absolute pitch (AP) is usually manifested by the ability to name pitches without

prompting or the use of a reference pitch, or the ability to produce a given pitch on request. Although the musical value of absolute pitch is debatable,[25] a considerable number of professional musicians possess it.

There are clear behavioral differences between AP and non-AP listeners. AP possessors can with ease and certainty ''track'' the progression of tonalities (keys) in a musical composition, and determine (on the basis of pitch, and not timbral or other textural cues) when a musical idea is recalled in the original key. A listener without AP might be able to perform the same task, but with considerably more expenditure of effort. There are situations in which having AP is, however, a liability; e.g., dealing with transposed music, either within or outside standard tunings. Miyazaki[26–29] has extensively studied absolute pitch. In particular, AP possessors have been found to be slower and less accurate in identifying musical intervals relative to out-of-tune versus in-tune reference pitches than non-AP subjects. The non-AP subjects had to rely solely on relative pitch, and they showed no difference between the out-of-tune and in-tune conditions. The AP subjects also performed less well than non-AP subjects in the detection of altered transposed melodies. Benguerel and Westdal,[30] on the other hand, found that AP subjects could successfully abandon AP in favor of using a relative-pitch strategy in an interval naming task in which the use of AP led to naming errors. The manipulation of the use, or misuse, of AP is one of the goals of the current study.

It is important to note that AP musicians do not possess superior pitch discrimination or short-term memory for pitch relative to non-AP musicians of equal training. Siegel[31] found superior memory for pitch among AP subjects only when the pitch difference was 75¢ (0.75 semitone); when 10¢ (0.1 semitone) the AP subjects and non-AP controls did not differ ''in overall performance or rate of forgetting.'' ERP evidence of the equivalent pitch discrimination of AP and non-AP musicians has been presented by Tervaniemi *et al.*[32] in an investigation of mismatch negativity (MMN). MMN is a negative component (similar to, but not identical with N1) elicited by an acoustically deviant stimulus in a passive listening task, and has been positively correlated with pitch discrimination ability.[33] Tervaniemi *et al.* concluded:

> In summary, with AP and non-AP groups, which were matched with regard to musical training, differences were not found in auditory information processing reflected by the MMN component of the ERP. In the light of the earlier MMN results showing a close correlation between the MMN and pitch-discrimination accuracy, it might be concluded that pitch discrimination and identification are based on different brain mechanisms. (p. 314)

The categorical nature of pitch-naming ability is well documented.[25–27,34–36] Category boundaries are not sharply delineated, however, but are quite fuzzy. Miyazaki[26] found that for pitch increments of 20¢ (60 pitches per octave) naming judgments showed that the greatest agreement and shortest response times across AP subjects clustered around the central in-tune (with respect to the equal-tempered scale) pitch within each name category; as pitches approached the quarter-tone boundary between name categories, response times increased and there was considerable disagreement as to which category the boundary pitches belonged. In this respect, the naming of pitch seems to resemble the naming of visual colors.

From a neuroscience standpoint, absolute-pitch ability provides a unique opportunity to study variations in listening strategies and possible differences in brain function, as it provides one area of long-term memory use available only to a small segment of the general population. Further, there is emerging evidence of psyiological differences between AP possessors and musicians without absolute pitch; e.g., evoked oto-acoustic emissions from AP possessors are longer,[37] and AP possessors have a larger plenum temporale on the left side of the brain.[38]

More centrally, in active listening tasks, that is, those in which subjects are required to respond to certain stimuli designated as ''targets,'' differences in the late cognitive components of the ERP have been found between AP and non-AP subjects. Several studies have found reduced or absent P3s for AP subjects in tasks involving pitch, timbre, and sequential interval discrimination.[7,17,39,40] Surprisingly, when the AP subjects did produce reduced P3s, the peaks exhibited significantly shorter latency than those of the non-AP subjects. Evers *et al.*[41] have also found this shorter latency with AP subjects in a visual oddball task, suggesting that the speedier processing in AP subjects may extend to nonauditory modalities. In a pitch memory task, however, Hantz *et al.*[8] found that AP musicians could produce just as robust P3s as non-AP musicians, and did not have significantly shorter latencies. Hantz *et al.*[8] did, however, find differences at the sensory processing level between the two subject groups: AP musicians showed a greater sensitivity to piano tones versus white noise than the non-AP musicians. Barnea *et al.*[42] found differences in the scalp distribution of the P3 between AP and non-AP subjects for auditory stimuli but not for visual stimuli. In a target-detection task, the two subject groups produced equivalent P3s. When comparing piano tones to spoken note names (male voice), the results were mixed. AP subjects appeared to produce reduced P3s for piano tones in a memory probe task, but stronger P3s for piano tones in a pitch/name comparison task. Overall, the authors concluded that their ''results suggest that P300 amplitudes represent activities associated with verbal categorization.'' (p. 37)

The current study was designed to further investigate the neural correlates of the processing of pitch at both the sensory and cognitive ends of the ERP. To investigate the possible use of long-term versus working memory, two subject groups with equivalent musical training were used: absolute-pitch musicians (the ''AP'' group) and relative-pitch musicians (the ''RP'' group). It is assumed that differences in performance and ERPs across the subject groups will occur to the extent that the members of the AP group use an AP strategy. The decision to use only musically trained subjects was based on the difficulty of the task, which required a specialized knowledge of musical interval sizes.

To manipulate the possible use of an AP strategy, the stimulus series was constructed so that for some intervals the use of an AP strategy might be advantageous, whereas in others it would be detrimental.

In addition to absolute pitch, the sex of each subject was also considered as a subject variable. Although the investigation of sex differences in perceptual and cognitive behavioral data have been conducted for some time, consideration of such differences in ERP data is relatively recent. The inclusion of sex differences in a study primarily designed to study absolute pitch was motivated largely by our own earlier findings.[43]

Marvin[44] has discovered sex differences among trained musicians in the accuracy with which they discriminate among four forms of transformed melodies. Men and women discriminated equally well in the two conditions in which the melodies were played in their original temporal order, but men discriminated significantly better than women in the two conditions in which the melodies were played backward. This suggests that the men were better able to mentally manipulate the melodies as whole shapes, and that the women may have relied too heavily on a feature-recognition strategy, which was less effective due to patterns of retrograde or retrograde-inversional invariance in some melodies. The experiment appears to be a musical analog to the vector versus landmark sex differences found in navigational experiments. Marvin *et al.*[45] also found behavioral differences by sex among musicians in a melodic recognition task involving modulating melodies; i.e., melodies which changed key. The two sexes performed equally well on the task, but females responded significantly earlier than males, presumably responding to the earliest point of difference (a landmark strategy) rather than waiting for the completion of the melodies and comparing initial and final keys (a vector strategy). Melodic intervals might be considered the building blocks of longer melodies. To the extent that females show a greater sensitivity to melodic details, they might be expected to perform better on the current task and show enhanced ERP activity.

In other behavioral studies, Hassler[46] and McRoberts and Sanders[47] have explored hemispheric sex differences in musically trained subjects. McRoberts and Sanders asked subjects to discriminate among fundamental-frequency contours presented either binaurally or dichotically. Their results suggest that the male advantage found in the binaural condition reflects a sex difference in the coordination of the two hemispheres during conjoint processing of the same stimuli rather than a difference in the degree of males' hemispheric specialization for these stimuli. Hassler,[46] on the other hand, tested hemispheric lateralization using tests of spatial orientation, spatial visualization, tactile-visual discrimination, and verbal fluency. She found stronger lateralization in males than females in all subject groups except musicians.

Measuring ERPs during a task involving memory for missing and reordered timbres, Hantz *et al.*[43] found that even though the two sexes performed equally well on the task, males had significantly greater late positivity (at 675-ms poststimulus onset) than females. Females, on the other hand, had a greater anterior to posterior spread of amplitude values than males along the midline at 336 ms for the timbre task, but not for a control condition involving white noise bursts at two different intensity levels. For the white noise, females also showed greater differentiation between targets and nontargets, possibly suggesting a greater sensitivity to changes in intensity.

The current study investigated the use of absolute pitch, and possible sex differences, in a melodic interval discrimination task. Subjects were asked to detect target melodic intervals under two conditions: when the intervals were on-pitch in equal-tempered tuning, A4=440 Hz, and when the intervals had been transposed up a quarter-tone (50¢). The latter condition (''sharp'') placed the constituent pitches of the intervals on the quarter-tone boundaries between pitch name categories, leaving the relative pitches of the individual intervals internally ''in-tune.'' It was assumed that when the intervals were on-pitch, they could be identified either using relative or absolute pitch, but that when they were sharp, relative pitch alone would be the reliable identification strategy.

We expected the results to fall along the lines of the following hypotheses:

(1) Absolute-pitch subjects would show a performance advantage, either in accuracy or reaction time, for the on-pitch intervals, or alternatively a performance decrement for the sharp intervals.
(2) The late positive (P3) components of the ERP should distinguish between targets and nontargets; for the relative-pitch subjects, the components should not differ by tuning, but for the absolute-pitch subjects, the late components for the sharp intervals should be distinguishable from those for the on-pitch intervals.
(3) Absolute-pitch subjects should also show a differentiation in the early sensory-processing components of the ERP as a function of tuning.
(4) Males may show a greater late positivity than females; females may show a performance advantage on the task.

I. METHODS

A. Procedures

Interval discrimination was investigated by presenting a series of melodic intervals. A digitally sampled piano timbre was used since absolute pitch for piano tones has been shown to be stronger than for sine tones.[36,37] The sounds were provided by a Roland S-50 Sampling Keyboard, and were sampled at a rate of 30 kHz. The series, as described below, was generated and timed by a Yamaha QX1 digital sequencer via Musical Instrument Digital Interface (MIDI) to the digital sampler. The sounds were presented binaurally through AKG K-240 headphones. Subjects were seated in a reclining chair inside a sound-treated chamber throughout the experimental session. Subjects were instructed to keep their eyes open and to only blink between sounds. They were also told to relax, keep their head and neck still, not to swallow, clench their jaw, etc.

With setup and subject screening time, the brainwave recording session usually lasted approximately 1 h.

B. Subjects and screening procedures

Thirty paid volunteers were used in the study, 15 females and 15 males. Their musical backgrounds were assessed by their answers to a music survey. The survey determined the subjects' musical performance backgrounds, music listening habits, and degree of music academic training. All subjects were either enrolled in a professional music school or had a music degree. They had studied a musical instrument an average of 13.3 (females) and 12.3 (males) years. Subjects were from various musical disciplines, but all could be described as musical professionals.

All subjects were screened for hearing deficits, age, neurological disorders, and prescription medications. The mean subject age was 21.3 (females) and 22.9 (males) years. Ten of the subjects had absolute pitch (5 females, 5 males) as assessed by asking the subjects to name 12 isolated pitches without prompting or prior rehearsal. It was an abbreviated form of the test used in Hantz *et al.*[7] Each of the 12 chromatic pitches was played once in a random order, randomly distributed from F1 to G5. The timbre used in the absolute-pitch screening test was the same sampled piano sound used in the interval series. Each pitch lasted 2 s followed by a 6-s interstimulus interval in which to mark the letter name (e.g., D♭) of the pitch on an answer sheet. Octave placement of the pitches was ignored. In scoring the task, one point was given for exactly correct responses, and no points were given for any other answers; i.e., no points were awarded for near-hits (half-step errors). Chance level of performance was, therefore, a score of $1/12 = 8.5\%$.

All but one of the subjects were right-handed, although six had familial left-handedness. The lone left-hander was an AP female. The six subjects with familial left-handedness were distributed as follows: AP females (1 of 5), AP males (0 of 5), RP females (3 of 10), RP males (2 of 10).

C. Stimuli

The interval-discrimination series consisted of notes in sequential pairs, melodic intervals. Each trial consisted of one interval in one of three sizes: major 3rd (400¢), perfect 4th (500¢), or tritone (augmented 4th=600¢). The intervals were randomly ordered and randomly transposed to begin ± 15 semitones on either side of C4. All intervals appeared in both tuning conditions: on-pitch in equal temperament tuning with A4=440Hz, and transposed a quarter-tone sharp. Intervals appeared equally ascending/descending and above/below C4. Of the 400 trials, major thirds appeared with 0.2 probability, perfect fourths with 0.2 probability, and tritones with 0.6 probability. The perfect fourth was designated the ''target'' and subjects were instructed to press one of two buttons to each target trial and the other button to all nontargets. Prior to the test series, subjects heard five examples each of the targets and nontargets. None of the subjects had any trouble understanding the task, and none required a repetition of the examples.

The intonation was checked using a Korg multitemperament tuner (MT-1200). All sounds were of 250-ms duration, so each interval lasted 500 ms. There was a 1500-ms interstimulus time interval. An intensity level of 75 dB SPL as measured through a calibrated 6-cc coupler and measuring amplifier (B&K, 2130) was maintained.

D. Performance measure

In scoring the task, separate tallies were kept for on-pitch and sharp intervals. For each intonation category:

score=[(hits/40)-(false alarms/160)]*100;

that is, score=percent correctly identified targets minus percent misidentified nontargets. An overall score was computed as the mean of the on-pitch score and the sharp score.

E. ERP recording

The experiment involved placing tin surface electrodes on the subject's scalp using an electro-cap with active leads at Fz, Cz, Pz, and two custom lateral sites: LTP (left temporoparietal) and RTP (right temporo-parietal). The custom sites are at the centers of the squares formed by C3, P3, T5, and T3, and C4, P4, T6, and T4, respectively. Reference electrodes were at linked earlobes, and a ground electrode at the Gnd site (forehead) on the cap. Electrode impedance was maintained below 5.0 kΩ. Eye movements were monitored by additional electrodes placed at the supraorbital rim and at the lateral canthus of the left eye.

The amplifiers were calibrated at the beginning of each session. The high filter setting for data recording was 130 Hz and the low filter setting was at 0.3 Hz. The five brainwave channels, the eye channel, the button presses, and the music were all sent to a Data Translations DT2821 A/D board and sampled at 500 Hz. All data were stored in a 486 PC and transferred to optical disks for off-line analysis. Sampling began 100 ms before each stimulus and continued for 1500 ms after stimulus onset. In addition to the digital sampling, eye movements and subject responses were recorded and monitored on a strip chart recorder.

The button presses were tallied off-line. For each brainwave channel, four averages were computed corresponding to correct responses to the two stimulus conditions (on-pitch/sharp) and the two responses (target/nontarget). To make the averages, each trial was corrected to a baseline average derived from the 75 ms prior to stimulus onset. Trials containing artifacts in excess of 75 μV were tossed out. The overall averages were then filtered with a 10-Hz low-pass filter.

F. Data analysis

Principal component analysis (PCA) with varimax rotation was performed on 95 data points beginning at the onset of the second tone of each interval, the decision point for the behavioral response, and extending every 8 ms to 760 ms. PCA was chosen as the method of waveform analysis in preference to measuring peak amplitudes/latencies or mean areas of the late components because it recognizes and incorporates in the analysis the possibility of component overlap, and provides a purer set of measures.[48]

The PCA was computed on 600 waveforms. Only the six components with Eigenvalues above 1 were retained for further analysis. Five-way ANOVAS were run separately on the scores of each of the principal components, with sex and

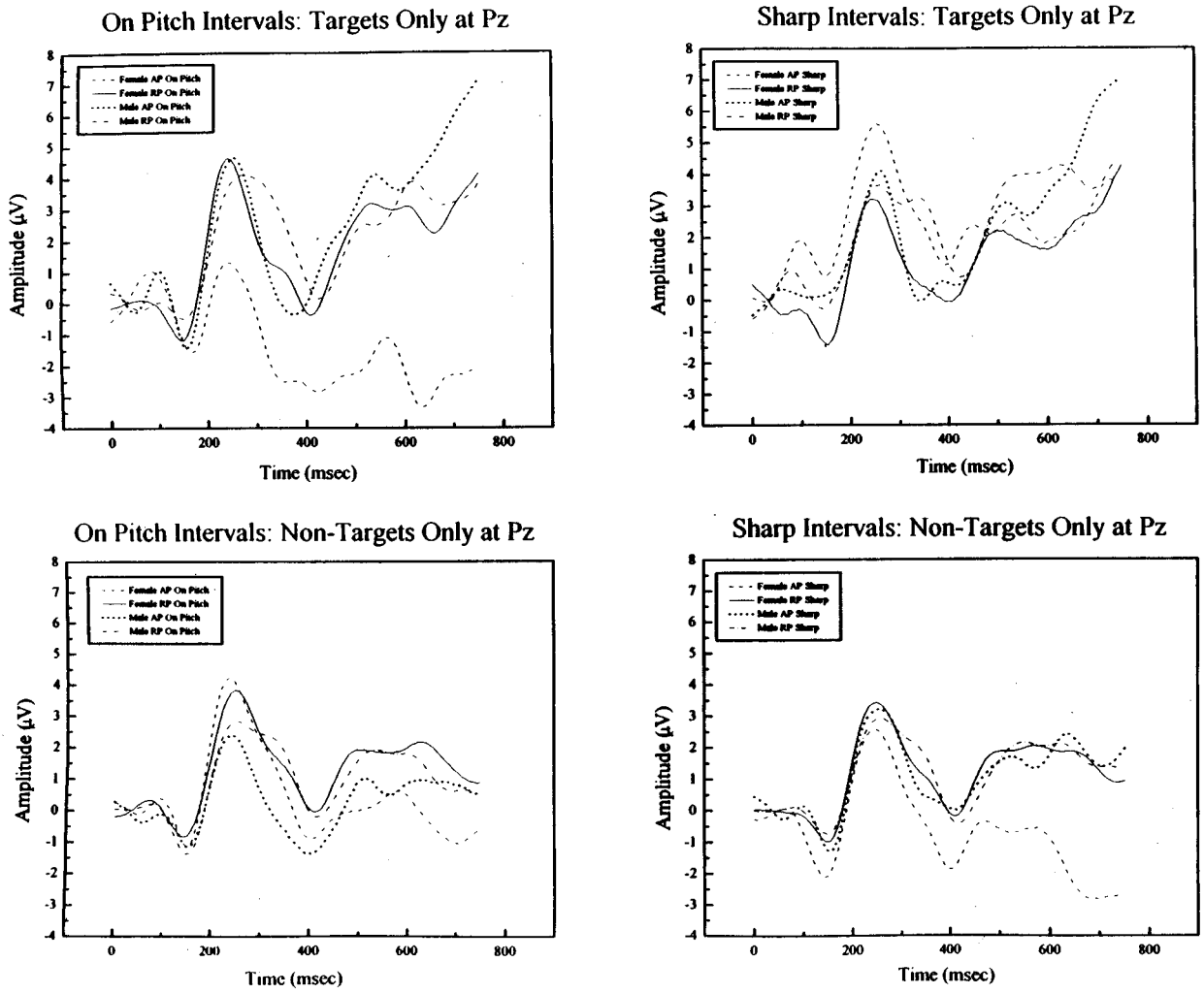

FIG. 1. Grand-averaged ERP waveforms by response type (target/nontarget) and intonation (on-pitch/sharp) for the four subject groups: absolute-pitch females ($N=5$), absolute-pitch males ($N=5$), relative-pitch females ($N=10$), and relative-pitch males ($N=10$). Only the waveforms at Pz are shown. The time line is measured from stimulus onset.

absolute/relative pitch as between subject group factors, and the five recording sites × two stimulus conditions (on-pitch/sharp) × two response conditions (target/nontarget) as repeated measures. The p values reported, unless otherwise indicated, are the result of univariate tests corrected for degree of freedom (Greenhouse-Geisser).

II. RESULTS

A. Subject group factors

Subjects were places into two groups on the basis of their scores on the absolute-pitch test: absolute pitch (AP, $N=10$) and relative pitch (RP, $N=20$). Mean percent correct for the absolute pitch group was 85.4 (s.d.=15.0, minimum=62.5, maximum=100.0); mean score for the relative pitch group was 20.6 (s.d.=14.5, minimum=0.0, maximum=41.7). The two nonoverlapping groups are highly statistically different: $F(1,29)=121.36$, $p<0.0001$. The RP group were expected to perform at chance level (1/12=8.5%). A possible explanation for the higher than chance scores in the RP group is that the subjects had a great deal of musical training. Some subjects may have had very good memory for certain pitches, e.g., A, and may have been able to use their excellent relative pitch to identify approximately 20% of the pitches. On the other hand, expecting perfect or near-perfect scores (12/12=100%) from the AP group, obtaining only about 85% scores may have been due to the use of a sampled piano timbre, an unfamiliar timbre to some subjects.

An equal number of each sex was in each group yielding: AP females (5), AP males (5), RP females (10), and RP males (10). Age was not statistically different for either absolute pitch or sex groups, but the AP musicians did have significantly [$F(1,29)=8.75$, $p<0.007$] more years training on their instruments: AP ($M=15.8$ yrs, s.d.=3.1), RP ($M=11.4$ yrs, s.d.=4.1). Since training has been shown to be a factor in both performance and ERP differences in musical tasks, it is possible that differences between the AP and RP groups may be, in part, attributable to increased training.

B. Performance

The mean performance accuracy scores were as follows: on-pitch intervals 58.7% (s.d.=28.5); sharp intervals 57.1%

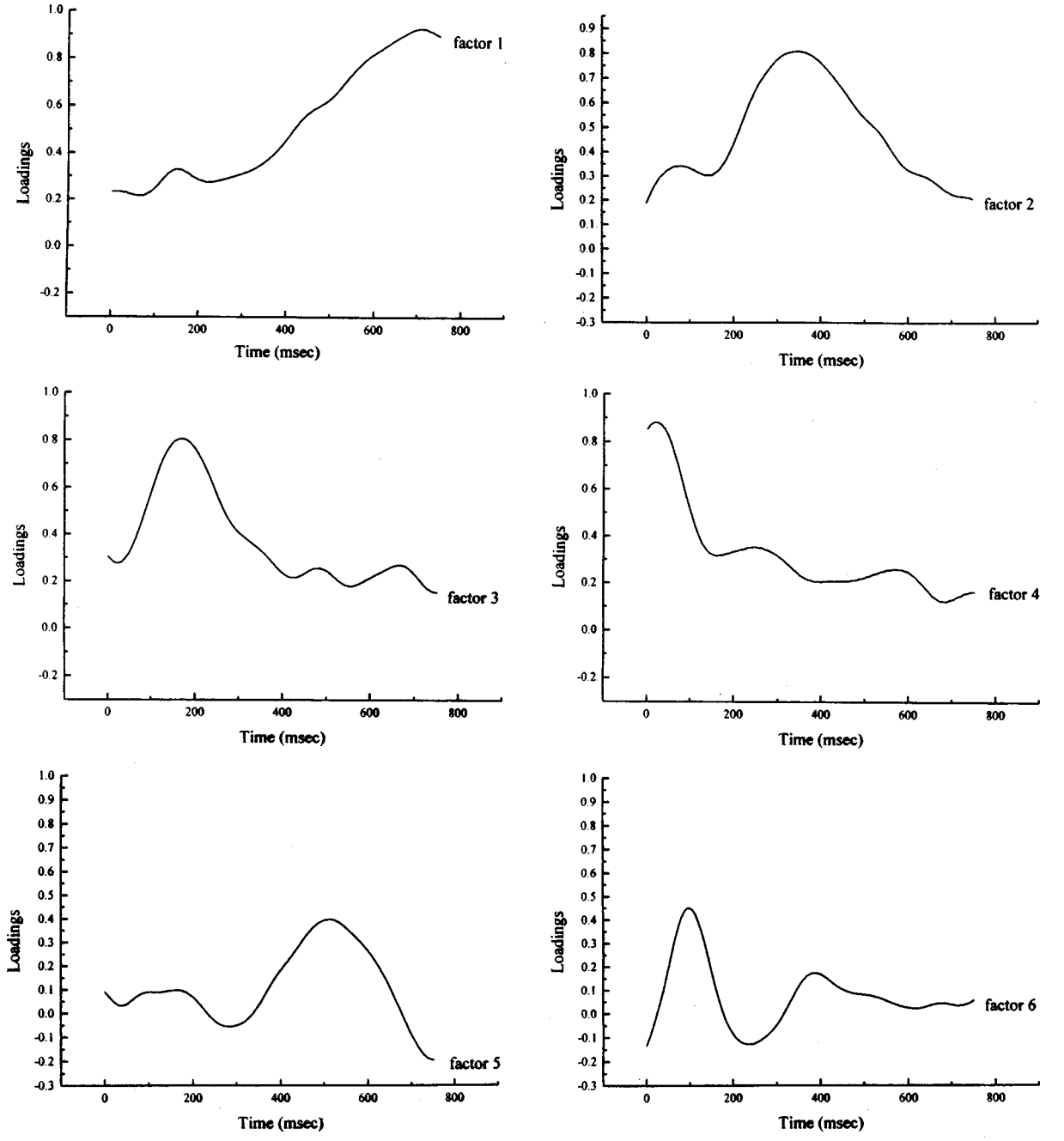

FIG. 2. The principal components (factors) from the principal components analysis. Factors are labeled ''factor 1'' through ''factor 6'' in decreasing amount of variance accounted for. The time line is measured from the second note of each interval; i.e., the decision point. See Table I for the time point of the maximum and the percent of the variance accounter for each factor.

(s.d.=28.1); overall score 57.9% (s.d.=28.1). These scores are well above chance, but indicate that the task was difficult. A three-way ANOVA was run on the performance scores with on-pitch/sharp, AP/RP, and sex as the factors. None of the performance scores were significantly different for either absolute pitch [$F(1,26)=0.03$, $p<0.862$] or sex [$F(1,26)=3.58$, $p<0.069$], nor was the interaction between AP/RP and sex significant [$F(1,26)=2.14$, $p<0.155$]. The nearly significant effect for sex was in the predicted direction: females ($M=59.6\%$, s.d.=29.3), males ($M=53.39$, s.d.=24.90). In particular it should be noted that the absolute-pitch subjects did not have more difficulty identifying the sharp intervals than the on-pitch intervals. Or, put the other way around, the AP subjects did not show an advantage over the RP subjects for the on-pitch intervals. The lack of significant behavioral differences by subject group or intonation means that differences in the brain waveforms may be due to processing differences apart from performance accuracy.

Analysis of reaction times for correct responses revealed a highly significant effect for stimulus type [$F(1,26)=22.7$, $p<0.0001$]. It took significantly longer to identify a target (1075 ms) than to reject a nontarget (1013 ms). A main effect for absolute pitch approached significance [$F(1,26)=3.46$, $p<0.07$], the AP subjects responding, overall, quicker (999 ms) than the RP subjects (1065 ms). The

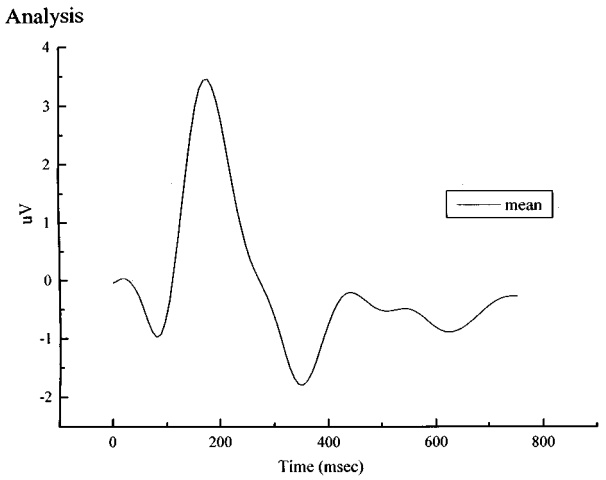

FIG. 3. The centroid (mean waveform) for the principal components analysis. Factor scores measure deviations from this grand mean. The time line is measured from the second note of each interval; i.e., the decision point.

interaction between absolute pitch and intonation was not significant for reaction time, nor was any interaction involving sex.

C. Waveforms

Figure 1 shows the grand-averaged waveforms for the pitch interval series by intonation (on-pitch/sharp), response (target/nontarget), and by subject group (absolute pitch/relative pitch; female/male). Only the waveforms at Pz are shown. In general, targets evoked much greater late positivity than did the nontargets. Other differences are discussed below.

D. Principal components analysis

The six components (factors) with Eigenvalues above 1 are shown in Fig. 2. Figure 3 presents the centroid (mean waveform) for the analysis. Time points represent elapsed time from the onset of the second tone in each interval, the decision tone, and not from the beginning of each trial, the onset of the first tone. When comparing Figs. 2 and 3 with Fig. 1, it should be kept in mind that time points in Figs. 2 and 3 are 250 ms later than those of Fig. 1. Factor scores measure deviations from the centroid, and not positive or negative fluctuations relative to baseline zero. Table I presents the six factors in descending order of amount of variance accounted for. Of the six factors, only factors 2, maximum at 352 ms, and factor 5, maximum at 511 ms, showed a main effect for response type (target/nontarget) [$F(1,26)=7.20$, $p<0.01$; and, $F(1,26)=5.62$, $p<0.02$, respectively]. These two factors account for 25.1% and 3.5% of the total variance, respectively. Together they represent the P3 activity antecedent to motoric expression of the decision to correctly press the ''target'' button rather than the ''nontarget'' button. Figure 4 shows the type by site interaction for factor 1. Although this factor, accounting for 30.6% of the total variance, is not significant for response type collapsed across sites, it is clear that the interaction is significant [$F(4,104)=12.74$, $p<0.0001$] and that the factor measures late P3 activity.

TABLE I. Principal components.

Factors	% of variance accounted for	Time of maximum value (ms)
1	30.62	709
2	25.10	352
3	16.73	168
4	14.36	20
5	3.54	511
6	2.33	98

Sum of 1–6: 92.68

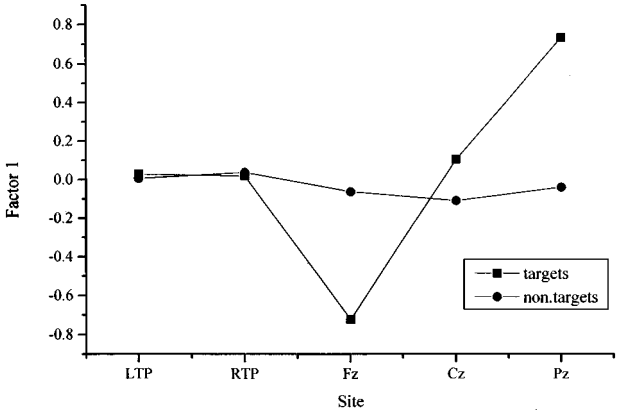

FIG. 4. The response type by recording site interaction for factor 1 (709 ms maximum) scores (means for all subjects).

All six factors showed main effects for recording site at the 0.0002 level or better. No factor was sensitive to the on-pitch/sharp condition, although factor 6, maximum at 98 ms, approached significance [$F(1,26)=3.78$, $p<0.06$]. Factor 6 accounted for only 2.3% of the total variance, however. The individual factors will be discussed in decreasing order of the amount of variance for which they account.

As noted above (Fig. 4), factor 1 shows the characteristics of late P3 activity. Factor 1 scores were fairly flat at all sites in response to the nontargets, but showed a strong negative to positive distribution from front to back (electrodes Fz to Pz) for the targets. Two interactions involving sex were

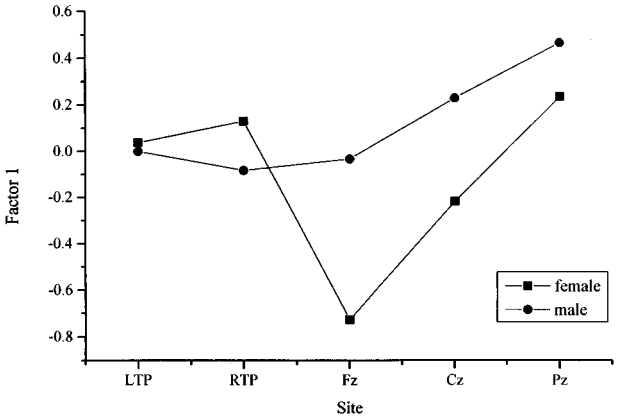

FIG. 5. The recording site by sex interaction for factor 1 scores.

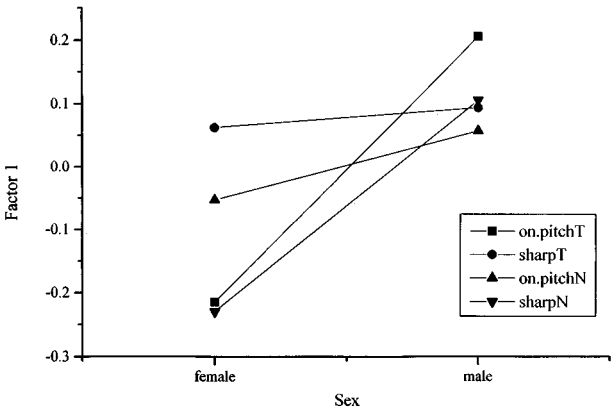

FIG. 6. The intonation (on-pitch/sharp) by response type (T=target/N=nontarget) by sex interaction for factor 1 scores.

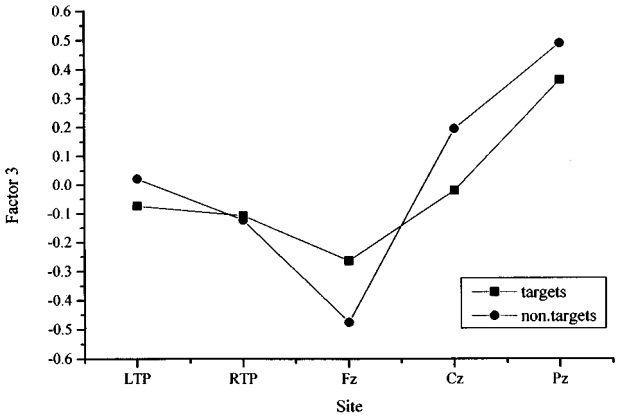

FIG. 8. The response type (targets/nontargets) by recording site interaction for factor 3 (168 ms maximum).

significant for factor 1: the site by sex interaction [Fig. 5, $F(4,104)=3.84$, $p<0.02$] and intonation by type by sex interaction [Fig. 6, $F(1,26)=5.00$, $p<0.03$]. The site by sex interaction (Fig. 5) indicates that males had greater positivity along the midline sites than did females. This greater late positivity, with a maximum near 700-ms post-stimulus onset, agrees with data reported by Hantz *et al.*[45] The intonation (on-pitch/sharp) by response type by sex interaction (Fig. 6) showed a greater spread of values by females than males, and that the two sexes had more similar values for the sharp intervals than the on-pitch intervals.

The intonation by response type by site interaction for factor 2, maximum at 352 ms, was not significant [$F(1,26)=0.01$, $p=0.92$]. The P3-like character of factor 2 is indicated in that all values for targets were more positive than those for nontargets at comparable sites. The interaction also indicates the lack of a significant difference between responses to the on-pitch versus sharp intervals. Figure 7 shows the significant [$F(4,104)=2.94$, $p<0.04$] site by absolute-pitch interaction for factor 2. The main source of the interaction was the difference between AP and RP musicians in the reversed relative scores along the midline versus the two lateral sites. Absolute-pitch subjects showed greater positivity at the temporal-parietal sites, whereas along the midline, AP subjects show consistently lower scores than RP subjects. The current study does not provide enough information for a detailed interpretation of this interesting interaction. Such differences might be due to different cognitive strategies employed by the two subject groups or to differences in arousal levels between the two groups. Further research is necessary to provide enough information for a detailed interpretation of this interaction. Factor 2 also yielded an almost-significant [$F(1,26)=3.49$, $p<0.07$] main effect for sex (females$=-0.154$, males$=0.165$).

Factor 3, maximum at 168 ms, accounted for 16.7% of the variance. Figure 8 shows the significant [$F(4,104)=3.60$, $p<0.02$] type by site interaction for factor 3. Nontargets exhibited a greater spread of scores than targets, and showed larger anterior–posterior distribution, similar to what factor 1 showed for targets. An almost-significant main effect for absolute pitch appeared with respect to factor 3 [$F(1,26)=3.64$, $p<0.06$]: AP$=-0.311$, RP$=0.140$.

Factor 4, maximum at 20 ms, had no significant effects other than by site.

Factor 5 (maximum at 511 ms), one of the P3 factors, is significant for response type [$F(1,26)=5.62$, $p<0.01$]. This can be seen in Fig. 9 in that all values for targets, either

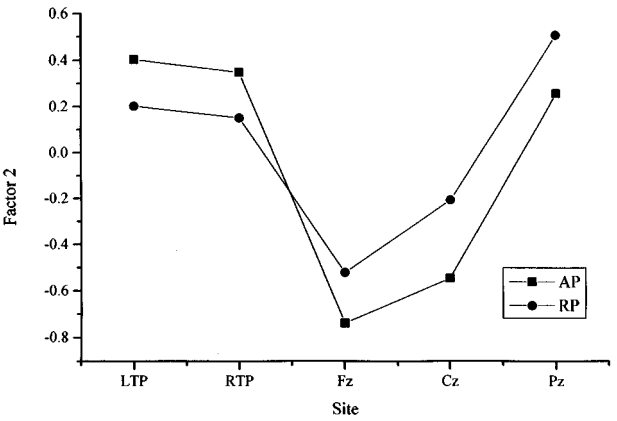

FIG. 7. The recording site by absolute pitch (AP=absolute pitch/RP=relative pitch) interaction for factor 2 (352 ms maximum).

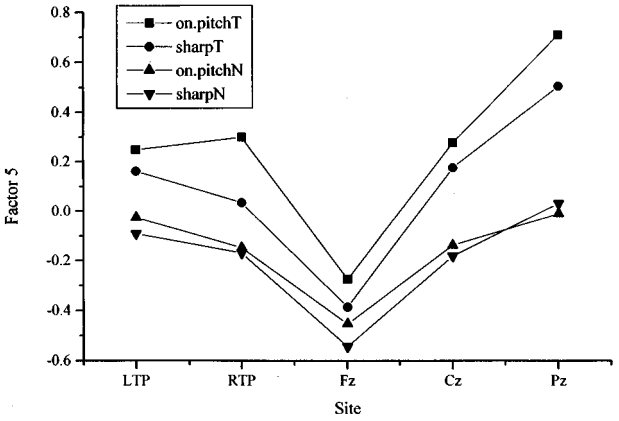

FIG. 9. The intonation (on-pitch/sharp) by response type (T=target/N=nontarget) by recording site interaction for factor 5 (511 ms maximum).

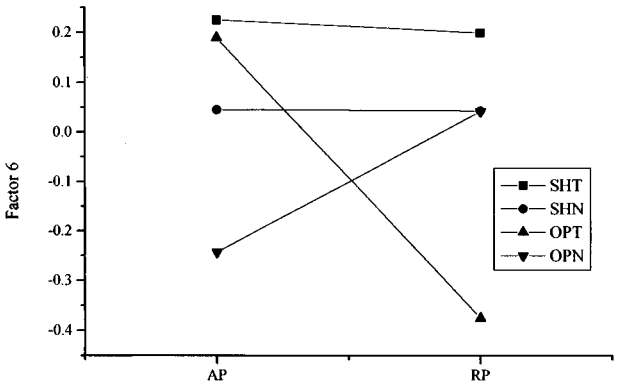

FIG. 10. The intonation (OP=on-pitch/SH=sharp) by response type (T=target/N=nontarget) by absolute pitch (AP=absolute pitch/RP =relative pitch) interaction for factor 6 (98 ms maximum).

on-pitch or sharp, are more positive than the corresponding values for nontargets.

The intonation (on-pitch/sharp) by absolute pitch interaction approached significance [$F(1,26)=3.08$, $p<0.08$]. Among the cognitive components, this was the only interaction between absolute pitch and intonation to approach significance. AP subjects showed a stronger (more positive) reaction to the sharp intervals than to the on-pitch intervals. What is surprising is that the RP subjects seem to have reacted the opposite. The type by sex by absolute-pitch interaction also approached significance [$F(1,26)=3.45$, $p<0.07$], mostly due to the response to the targets. Interactions between absolute pitch and sex need to be evaluated with caution, however, due to the low N caused by dividing the AP group by sex.

Factor 6, maximum at 98 ms, accounts for 2.3% of the total variance. The type by absolute-pitch interaction was significant [$F(1,26)=4.47$, $p<0.04$]. This result is contained in the intonation by type by absolute pitch interaction (Fig. 10), which is also significant [$F(1,26)=3.95$, $p<0.05$]. Figure 10 shows that the AP and RP subject groups responded very much the same to the sharp stimuli regardless of type, but differently to the on-pitch targets and nontargets.

III. SUMMARY AND DISCUSSION

The lack of an interaction between absolute pitch and intonation, either with respect to performance scores or reaction times, was unexpected. Absolute-pitch subjects performed equally well on the on-pitch and sharp intervals. Across all subjects, reaction times were significantly shorter for nontargets than targets, indicating that it was easier to reject a nontarget than identify a target.

All subject groups produced P3 activity to the targets in both intonation conditions. This activity can be measured by comparing scores on three of the PCA factors: factor 1 (at 709 ms), factor 2 (at 352 ms), and factor 5 (at 511 ms). With respect to factor 1, males showed greater positivity along the midline sites than females. This finding is in keeping with results reported elsewhere.[45] There was a significant intonation by response type by sex interaction for factor 1, with females exhibiting a greater spread of values than males, and greater similarity, by sex, for the sharp than the on-pitch intervals.

A clear difference in ERPs between absolute-pitch and relative-pitch musicians was obtained with respect to factor 2. Figure 7 suggests that absolute-pitch subjects showed lower values (less positivity) than relative-pitch subjects along the midline, but higher values (more positivity) at the temporal-parietal electrode sites. Component 2 had other typical P3 properties in its timing, midline distribution, and showing significantly more positivity to target intervals than to nontargets in this oddball task. This finding can be expressed as the two groups of musicians having different scalp distributions of this P3 component. This means that the two groups to some extent may have used different brain mechanisms while performing the pitch interval task. A decrease in P3 for absolute-pitch musicians has been taken to support a context updating interpretation of this ERP component.[39] The common account of the absolute-pitch ability suggested that these individuals have access to a set of internal standards that allows them to fetch the name of a tone without comparing the representation of the tone to a recently presented standard.[31] This suggested to Donchin and colleagues that context updating of tone pitches was not needed by such absolute-pitch listeners and led to their prediction that AP subjects would not use the mechanism manifested by the P3. The data reported here at the midline sites confirms their findings and extends them to a pitch-interval task. However, the present data add a new and different result from the lateral sites that went the opposite direction. To the extent that people with absolute pitch process melodic intervals while producting a P3, the present data do not support the context updating interpretation of P3. Whatever the P3 represents may not have ceased in absolute-pitch musicians, but rather gone to different brain mechanisms. For example, the greater P3 activity of AP subjects over lateral sites might be due to increased use of auditory and language cortex, an interesting idea that should be more carefully tested in future work.

The AP subjects also showed a stronger reaction to the sharp intervals at 511 ms (factor 5) than the on-pitch intervals.

The lack of a difference between the AP and RP subjects in performance may indicate that some of the AP subjects determined early on that an AP strategy was not going to be helpful on certain trials, and therefore abandoned the strategy overall. This may have also reduced the possible ERP effects. In future work, the problem might be overcome by presenting the in-tune and sharp intervals in blocks, thus allowing the AP subjects to settle into the use of an AP strategy for the appropriate blocks.

Several interactions involving both absolute pitch and sex reached near significance. Perhaps with a larger N, such interactions would become significant. The current study demonstrates that ERPs are sensitive to both absolute-pitch and sex differences in musical tasks.

ACKNOWLEDGMENTS

This work was supported by NIH/NIDCD Grant No. RO1-DC00674 and the International Center for Hearing and

Speech Research (R.I.C.H.S.) of the Rochester Institute of Technology. The authors also wish to thank John Chapman and John McCrary for help with this research.

[1] V. De Pascalis, F. C. Marucci, M. P. Penna, and D. Labbrozzi, ''Event-related potentials in musically sophisticated and unsophisticated subjects: A study in hemispheric specialization,'' Neuropsychologia **25**, 947–955 (1987).
[2] M. Besson and F. Macar, ''An event-related potential analysis of incongruity in music and other nonlinguistic contexts,'' Psychophysiology **24**, 14–25 (1987).
[3] D. Cohen and A. Erez, ''Event-related potential measurements of cognitive components in response to pitch patterns,'' Music Percept. **8**, 405–430 (1991).
[4] D. Cohen, R. Granot, H. Pratt, and A. Barneah, ''Cognitive meanings of musical elements as disclosed by event-related potential (ERP) and verbal experiments,'' Music Percept. **11**, 153–184 (1993).
[5] G. C. Crummer, E. Hantz, S. W. Chuang, J. Walton, and R. D. Frisina, ''Neural basis for music cognition: Initial experimental findings,'' Psychomusicology **7**, 117–126 (1988).
[6] G. C. Crummer, J. P. Walton, J. Wayman, E. C. Hantz, and R. D. Frisina, ''Neural processing of musical timbre by musicians, nonmusicians, and musicians possessing absolute pitch,'' J. Acoust. Soc. Am. **95**, 2720–2727 (1994).
[7] E. C. Hantz, G. C. Crummer, J. W. Wayman, J. P. Walton, and R. D. Frisina, ''Effects of musical training and absolute pitch on the neural processing of melodic intervals: A P3 even-related potential study,'' Music Percept. **10**, 25–42 (1992).
[8] E. C. Hantz, K. G. Kreilick, A. L. Braveman, and K. P. Swartz, ''Effects of musical training and absolute pitch on a pitch memory task: An event-related potential study,'' Psychomusicology **14**, 53–76.
[9] E. C. Hantz, K. G. Kreilick, and K. Karcich, ''Effects of musical training and absolute pitch on a pitch discrimination task: An event-related potential study,'' Aud. Neurosci. (submitted).
[10] E. C. Hantz, K. G. Kreilick, W. Kananen, and K. P. Swartz, ''The neural correlates of melodic and harmonic closure: An event-related potential study,'' Music Percept. (submitted).
[11] C. Levett and F. Martin, ''The relationship between complex music stimuli and the late components of the event-related potential,'' Psychomusicology **11**, 125–140 (1992).
[12] K. A. Paller, G. McCarthy, and C. C. Wood, ''Event-related potentials elicited by deviant endings to melodies,'' Psychophysiology **29**, 202–206 (1992).
[13] K. P. Swartz, E. C. Hantz, G. C. Crummer, J. P. Walton, and R. D. Frisina, ''Does the melody linger on? Music cognition in Alzheimer's disease,'' Sem. Neurol. **9**, 152–158 (1989).
[14] K. P. Swartz, J. P. Walton, G. C. Crummer, E. C. Hantz, and R. D. Frisina, ''P3 event-related potentials and performance of healthy older and Alzheimer's dementia subjects for music perception tasks,'' Psychomusicology **11**, 96–118 (1992).
[15] K. P. Swartz, J. P. Walton, E. C. Hantz, E. Goldhammer, G. C. Crummer, and R. D. Frisina, ''P3 event-related potentials and performance of young and old subjects for music perception tasks,'' Int. J. Neurosci. **78**, 223–239 (1994).
[16] R. Verleger, ''P3-evoking wrong notes: Unexpected, awaited, or arousing?'' Int. J. Neurosci. **55**, 171–179 (1990).
[17] J. W. Wayman, R. D. Frisina, J. P. Walton, E. C. Hantz, and G. C. Crummer, ''Effects of musical training and absolute pitch ability on event-related activity in response to sine tones,'' J. Acoust. Soc. Am. **91**, 3527–3531 (1992).
[18] R. M. Chapman and H. R. Bragdon, ''Evoked responses to numerical and non-numerical visual stimuli while problem solving,'' Nature (London) **203**, 1155–1157 (1964).
[19] R. M. Chapman, ''Dual thrust in interpreting P3 and memory,'' Behav. Brain Sci. **11**, 377–379 (1988).
[20] E. Donchin, ''Event-related potentials: A tool in the study of human information processing,'' in *Evoked Brain Potentials and Behavior*, edited by H. Begleiter (Plenum, New York, 1979).
[21] E. Donchin, W. Ritter, and W. C. McCallum, ''Cognitive psychophysiology: The endogenous components of the ERP,'' in *Event-Related Brain Potentials in Man*, edited by E. Callaway, P. Tueting, and S. H. Koslow (Academic, New York, 1978), pp. 349–411.
[22] E. Donchin, G. A. Miller, and L. A. Farwell, ''The endogenous components of the event-related potential—A diagnostic tool?'' in *Progress in Brain Research*, Vol. 70, edited by D. F. Swaab, E. Fliers, M. Mirmiran, W. A. Van Gool, and F. Van Haaren [Elsevier Science (Biomedical Division), Amsterdam, 1986], pp. 87–102.
[23] M. Fabiani, G. Gratton, D. Karis, and E. Donchin, ''Definition, identification, and reliability of measurement of the P300 component of the event-related brain potential,'' in *Advances in Psychophysiology*, Vol. 2, edited by P. K. Ackles, J. R. Jennings, and M. G. H. Coles (JAI Press, Greenwich, CT, 1987), pp. 1–78.
[24] R. D. Frisina, J. P. Walton, and G. C. Crummer, ''Neural basis for music cognition: Neurophysiological foundations,'' Psychomusicology **7**, 99–107 (1988).
[25] W. D. Ward and E. M. Burns, ''Absolute pitch,'' in *The Psychology of Music*, edited by D. Deutsch (Academic, New York, 1982), pp. 431–451.
[26] K. Miyazaki, ''Musical pitch identification by absolute pitch possessors,'' Percept. Psychophys. **44**, 501–512 (1988).
[27] K. Miyazaki, ''The speed of musical pitch identification by absolute-pitch possessors,'' Music Percept. **8**, 175–186 (1990).
[28] K. Miyazaki, ''Perception of musical intervals by absolute pitch possessors,'' Music Percept. **9**, 413–426 (1992).
[29] K. Miyazaki, ''Absolute pitch as an inability: Identification of musical intervals in a tonal context,'' Music Percept. **11**, 55–72 (1993).
[30] A.-P. Benguerel and C. Westdal, ''Absolute pitch and the perception of sequential musical intervals,'' Music Percept. **9**, 105–120 (1991).
[31] J. A. Siegel, ''Sensory and verbal coding strategies in subjects with absolute pitch,'' J. Exp. Psychol. **103**, 37–44 (1974).
[32] M. Tervaniemi, K. Alho, P. Paavilainen, M. Sams, and R. Näätänen, ''Absolute pitch and event-related brain potentials,'' Music Percept. **10**, 305–316 (1993).
[33] A. H. Lang, T. Nyrke, M. Ek, O. Aaltonen, and R. Näätänen, ''Pitch discrimination performance and auditive event-related potentials,'' in *Psychophysiological Brain Research*, Vol. 1, edited by C. H. M. Brunia, A. W. K. Gaillard, and A. Kok (Tilburg U. P., Tilburg, 1990), pp. 294–298.
[34] G. R. Lockhead and R. Byrd, ''Practically perfect pitch,'' J. Acoust. Soc. Am. **70**, 387–389 (1981).
[35] K. Miyazaki, ''Absolute pitch identification: Effects of timbre and pitch region,'' Music Percept. **7**, 1–14 (1989).
[36] R. J. Zatorre and C. Beckett, ''Multiple coding strategies in the retention of musical tones by possessors of absolute pitch,'' Mem. Cognit. **17**, 582–589 (1989).
[37] C. H. Chouard and R. Sposetti, ''Environmental and electrophysiological study of absolute pitch,'' Acta Oto-Laryngol. **111**, 225–230 (1991).
[38] G. Schlaug, L. Jeacke, Y. Huang, and H. Steiner, ''*In vivo* evidence of structural brain asymmetry in musicians,'' Science **267**, 669–671 (1995).
[39] M. Klein, M. G. H. Coles, and E. Donchin, ''People with absolute pitch process tones without producing a P300,'' Science **233**, 1306–1309 (1984).
[40] G. C. Crummer, J. P. Walton, J. Wayman, E. C. Hantz, and R. D. Frisina, ''Neural processing of musical timbre by musicians, nonmusicians, and musicians processing absolute pitch,'' J. Acoust. Soc. Am. **95**, 2720–2727 (1994).
[41] S. Evers, K.-H. Grotemeyer, and B. Suhr, ''Effect of absolute pitch ability on visual event-related potentials,'' Proceedings of the Third International Conference on Music Perception and Cognition, Liège, Belgium, pp. 429–430 (1994).
[42] A. Barnea, R. Granot, and H. Pratt, ''Absolute pitch—Electrophysiological evidence,'' Int. J. Psychophysiol. **16**, 29–38 (1994).
[43] E. C. Hantz, E. W. Marvin, K. G. Kreilick, and R. M. Chapman, ''Sex differences in memory for timbre: An event-related potential study,'' Int. J. Neurosci. **87**, 17–40.
[44] E. W. Marvin, ''The effect of sex differences on recognition of melodic transformations,'' Proceedings of the Third International Conference on Music Perception and Cognition, Liège, Belgium, pp. 449–450 (1994).
[45] E. W. Marvin, E. C. Hantz, K. G. Kreilick, and T. C. Bever, ''Sex differences in the perception of melodies,'' Music Percept. (submitted).
[46] M. Hassler, ''Functional cerebral asymmetries and cognitive abilities in musicians, painters, and controls,'' Brain Cognit. **13**, 1–17 (1990).
[47] G. W. McRoberts and B. Sanders, ''Sex differences in performance and hemispheric organization for a nonverbal auditory task,'' Percept. Psychophys. **51**, 118–122 (1992).
[48] R. M. Chapman and J. W. McCrary, ''EP component identification and measurement by principal components analysis,'' Brain Cognit. **27**, 228–310 (1995).

Forward-masked intensity discrimination: Duration effects and spectral effects[a)]

Robert S. Schlauch,[b)] Nicole Lanthier, and Joe Neve
University of Minnesota, Minneapolis, Minnesota 55455

(Received 12 September 1996; revised 17 March 1997; accepted 18 March 1997)

Three experiments were completed to examine the effect of masker duration and spectrum on forward-masked intensity discrimination. Four listeners participated in each experiment. Intensity discrimination was measured in quiet and in the presence of forward maskers using adaptive forced-choice procedures. The standard duration was either short (10 ms) or long (250 ms) in experiment 1 and short (10 ms) in experiment 2. The standard always occurred 100 ms after the offset of the masker. In the first experiment employing 1.0-kHz maskers and standards, a short duration masker (10 ms) produced more masking than a long duration masker (250 ms). A mid-level elevation of the Weber fraction was observed for all conditions. To ensure that the results of experiment 1 were not influenced by off-frequency listening, the second experiment employed a broadband noise masker. As before, a short duration (10 ms) masker produced more masking than a long duration masker (100 ms) and a mid-level elevation of Weber fractions was observed. This outcome is inconsistent with a peripheral sensory effect for which an increase in masker duration should result in a greater amount of adaptation, and, as a consequence, more masking. A third experiment employing a broadband noise masker and standard showed the greatest amount of masking for low-level standards, but only when the duration of the masker and standard was short. This result is similar to one seen for a single listener in the first experiment for short duration tonal maskers and standards. For this listener, a second tone presented at 4.133 kHz presented simultaneously with the 1.0-kHz masker reduced significantly the amount of masking for low-level standards, but the mid-level elevation of the Weber fraction remained. Taken together, these results suggest that perceptual similarity plays a role in forward-masked intensity discrimination but does not account entirely for the mid-level elevation of the Weber fraction. [S0001-4966(97)02907-X]

PACS numbers: 43.66.Ba, 43.66.Dc, 43.66.Fe [WJ]

INTRODUCTION

Zeng and Turner (1992) reported a marked deterioration in pure-tone intensity just-noticeable differences (jnd's) for mid-level standards when the jnd's were measured in the presence of a high-level masker presented 100 ms before the standard tone. The jnd's for low- and high-level standards were, for the most part, unaffected by the masker. They argue that elevated jnd's for mid-level standards are consistent with adaptation of low-spontaneous rate (SR) neurons which have a slower recovery time from stimulation than high-SR neurons (Relkin and Doucet, 1991). The elevation of jnds for mid-level standards for forward masking is attributed to saturation of high-SR units by the standard; low-SR units are presumed to operate in a suboptimal region of their response curve during recovery of adaptation from stimulation by the masker for mid-level standards.

If the mid-level elevation of jnd's in forward-masked *intensity discrimination* is caused by the failure of low-SR neurons to recover fully from adaptation by the time the standard is presented, then the duration of the masker should play an important role in the size of the intensity jnd for mid-level standards. Evidence from prior studies, both physiological and behavioral, supports the notion that masker duration is related to the amount of adaptation. In cat, Young and Sachs (1973) found that the time constant for recovery from adaptation in auditory nerve fibers increased as the duration of exposure to a masker increased. Harris and Dallos (1979) reported similar results for chinchilla. Behaviorally, Kidd and Feth (1982) demonstrated that the effects of forward masking on *detection* increased as the duration of the masker increased in a tonal detection task. Based on this analysis and Zeng's hypothesis (Zeng *et al.*, 1991; Zeng and Turner, 1992) that the mid-level elevation of jnd's is due to slow recovery from adaptation of low-SR neurons, one would predict that a long duration masker would result in more adaptation and a greater amount of masking than a short duration masker. The goal of our study was to investigate the role of masker duration in forward-masked intensity discrimination.

I. EXPERIMENT 1. FORWARD-MASKED JND'S: TONAL MASKERS

A. Subjects

Four young (22–30 years) adults with normal hearing served as subjects. Two subjects (1 and 2) had considerable

[a)]Portions of this paper were presented at the 129th meeting of the Acoustical Society of America in Washington, DC [Schlauch and Lanthier, J. Acoust. Soc. Am. **97**, 3276(A) (1995)].

[b)]Corresponding author address: Dept. of Communication Disorders, 115 Shevlin Hall, University of Minnesota, Minneapolis, MN 55455, Electronic mail: Schla001@maroon.tc.umn.edu

experience in psychoacoustic experiments. The other two subjects had never participated in a psychoacoustic experiment prior to this one. All listeners were given several hours of practice at the tasks in this study prior to data collection.

B. Stimuli

Maskers and standards were 1.0-kHz pure tones that were digitally generated at a sampling rate of 20 kHz by a custom-designed 16-bit digital-to-analog converter. Three channels were employed. The standard and increment were generated with separate channels that were mixed before being presented to the headphones. The increment was added in phase with the standard, but the resultant data in this experiment and subsequent experiments are plotted in terms of the orthogonal increment (Weber fractions). A third channel generated the masker tone.

The masker, which was always presented 100 ms prior to the standard, had a duration of either 10 or 250 ms. Standard and increment durations were also either 10 or 250 ms. All stimuli had 5-ms cosine-squared onset and offset ramps. The masker level was fixed at 90 dB SPL within a block of trials. The level of the standard tone varied over blocks of trials by steps of 10 dB, from 20 to 80 dB SPL.

C. Procedure

Intensity resolution performance was measured using a two-interval forced-choice (2IFC) adaptive task (Levitt, 1971). A decision rule was selected that targeted 79.4% correct performance. For every incorrect response, the level of the tone added in phase with the standard was increased by 3 dB. After three consecutive correct responses, the level was decreased by 3 dB. Subjects were given visual feedback regarding the accuracy of their responses following each trial. The Weber fraction for a single block was calculated based on the mean of reversals in stimulus level direction within that block. Average thresholds were based on a minimum of three 50-trial blocks. Time permitting, additional blocks were completed if the standard deviation of the first three blocks exceeded 3.5 dB.

Intensity resolution was measured in a quiet condition (no masker) and in the presence of a forward masker. In the masked condition, the masker and standard were presented in each observation interval. In the quiet condition, only the standard was presented. The masker and standard durations used in five conditions in experiment 1 are illustrated in Fig. 1. Figure 1 also illustrates the time course of masker and standard presentation for a single trial in the 2IFC task for each of the conditions. Note that the time between the offset of the standard tone in interval one and the onset of the standard tone in interval two was 850 ms for all conditions. Fixing this time was presumed to place similar demands on short-term memory across conditions.

D. Results

Figure 2 illustrates Weber fractions for conditions where the standard was 250 ms (with 250-ms masker and in quiet).

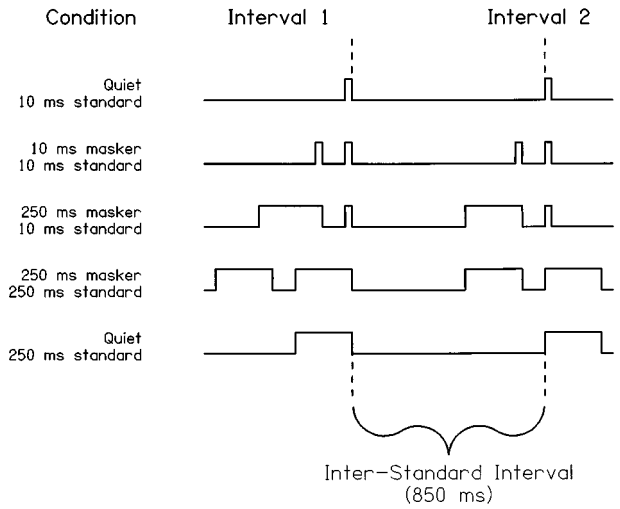

FIG. 1. The time sequence for a trial for the conditions in experiment 1.

All subjects show a mid-level elevation of their Weber fractions under the forward-masked condition compared with the quiet condition.

Figure 3 illustrates Weber fractions for each listener for conditions where the standard was 10 ms (with 10-ms masker, with 250-ms masker, and in quiet). For most masked conditions, a mid-level elevation of the Weber fraction is observed as compared to the unmasked condition consistent with Zeng *et al.* (1991) and Zeng and Turner (1992). A larger elevation of the Weber fraction is observed for the 10-ms masker condition than for the 250-ms masker condition.

Subject 4 in the 10-ms masker, 10-ms standard condition evidenced more masking than the other subjects and the pattern of masking was different than that for the other subjects. Her Weber fractions were elevated relative to the quiet condition for all levels with the greatest amount of masking occurring for low levels rather than for moderate levels of the standard. Within 20 dB of threshold, a 35- to 50-dB increment in the standard level $[10\log(\Delta I/I+1)]$ was re-

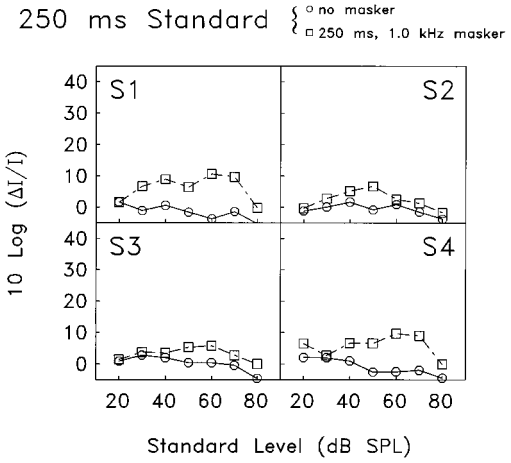

FIG. 2. Weber fractions (dB) as a function of level (dB SPL) for conditions with a 250-ms standard. Data are shown for 4 listeners (S1, S2, S3, S4) in quiet (circles) and in the presence of a 250-ms masker (squares). The masker and standard were 1.0-kHz tones.

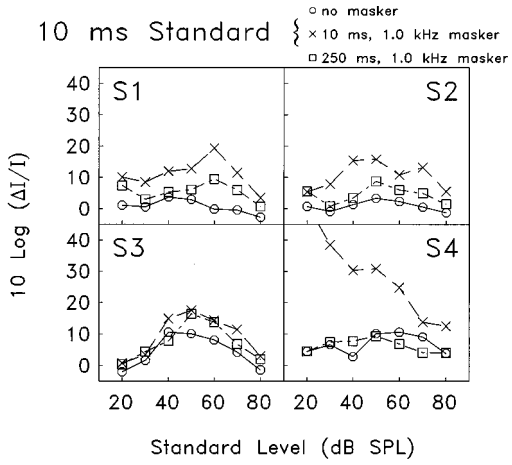

FIG. 3. Weber fractions (dB) as a function of level for conditions with a 10-ms standard. Data are shown for the same 4 listeners as in Fig. 2 for a quiet condition (circles) and for conditions with 250-ms maskers (squares) and 10-ms maskers (×). The masker and standard were 1.0-kHz tones.

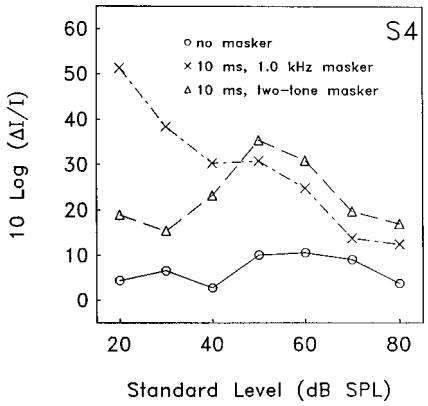

FIG. 4. Weber fractions (dB) as a function of level for subject 4 (S4) for some conditions employing 10-ms standards. Weber fractions are shown for a 1.0-kHz tone in quiet (circles) and for a 1.0-kHz tone in the presence of a 10-ms, 1.0-kHz masker (×). Also shown are Weber fractions for a 1.0-kHz tone in the presence of a two-tone complex (triangles), which included 1.0- and 4.133-kHz tone. The addition of the 4.133-kHz tone to the 1.0-kHz masker resulted in significantly smaller Weber fractions for the low-level standards.

quired to reach the criterion performance level for this task. A possible explanation for this poor performance at low sensation levels may be due to this subject's inability to distinguish between the offset of the masker and the onset of the standard for this condition with short duration stimuli. A consequence of this inability may have been a perceptual averaging of the magnitude of the masker and the standard, a result that would yield poor performance for low-level standards.

Moore and Glasberg (1982) reported that perceptual similarity of the masker and signal in a forward-masked *detection* task may play a role in the amount of masking observed. They demonstrated that the presentation of an auditory cue (in their experiment a noise band) with the masker reduced significantly the thresholds in a condition where the frequency of the masker and signal were identical. To examine the influence of this cognitive phenomenon in our study, a cue was added to the masker. The cue was a 90 dB SPL, 4.133-kHz tone presented simultaneously with the masker. Thus, for this condition, the masker interval contained a two-tone complex; the 1000-Hz masker and the 4.133-kHz cue. Based on our preliminary data and those of Zeng and Turner (1992), the frequency of the cue was assumed to be far enough away in frequency from the frequency of the standard so that it would not act as a masker or suppressor of the standard.[1] As seen in Fig. 4, the addition of this cue reduced significantly the amount of forward masking for low-level standards compared with the amount observed in the same condition without the cue.

Figure 5 illustrates the amount of forward masking for group-mean data for the conditions in experiment 1. Because subject 4 performed differently than the other subjects in the 10-ms masker, 10-ms standard condition, average data for this condition are shown with and without her data. In the panel that included data from subject 4, data from her *cued* condition were averaged with the data for the other subjects. This approach is justified by the finding that subject 4's data from the cued condition show the same pattern as that of the other subjects from the condition without a cue. The greatest amount of masking was observed in the 10-ms masker, 10-ms standard condition followed by the 250-ms masker, 250-ms standard condition. The least amount of masking was observed for the 250-ms masker, 10-ms standard condition.

E. Discussion

In experiment 1, a short duration masker yielded more masking than a long duration masker. At first glance, this finding seems inconsistent with Zeng's (Zeng *et al.*, 1991; Zeng and Turner, 1992) prediction that the elevation of jnd's for mid-level standards in forward masking are due to the slow recovery of adaptation of VIIIth-nerve neurons with low-SR, and high thresholds. In prior studies, lengthening the duration of an adapting stimulus increases the amount of

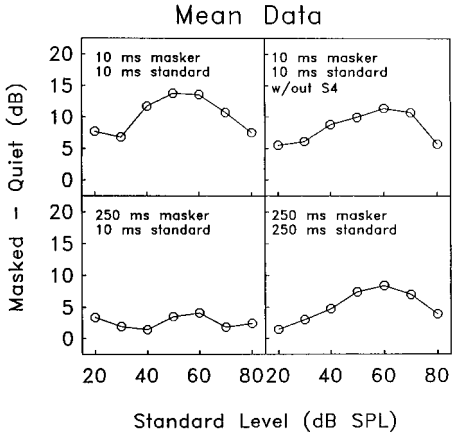

FIG. 5. This figure illustrates group mean differences between Weber fractions (dB) obtained for masked and quiet conditions for identical duration standards. The upper-right panel contains average data for S1, S2, and S3 who had similar Weber fractions for the 10-ms masker and 10-ms standard condition. The remaining panels contain average data for all four listeners. The data for S4 that were included in the group average in the upper-left panel are from her condition with a two-tone masker (1.0 kHz and 4.133 kHz). Note that identical masker and standard durations produced more masking than the condition where the masker was longer than the standard.

neural adaptation (Young and Sachs, 1973; Smith, 1977; Harris and Dallos, 1979) and increases the amount of masking seen in a forward-masked *detection* task (Kidd and Feth, 1982).

Two explanations come to mind to illustrate why increasing the duration of the masker in a forward-masked intensity discrimination task did not result in more masking. First, as mentioned earlier, Moore and Glasberg (1982) showed that perceptually similar sounds show a greater amount of masking than ones that are not perceptually similar in a forward-masked *detection* task. The finding that an auditory cue reduced the amount of masking in their study supports the notion that a cognitive mechanism mediates at least a portion of the masking in conditions where the masker and signal are perceptually similar (Moore and Glasberg, 1982). The same mechanism may apply to the present study. A second explanation involves off-frequency listening. Wright and Dai (1994) have shown, in a tonal detection-in-noise task, that duration plays an important role in attention and directly affects the width of the effective listening band. If the listening band is narrow for a long duration masker and wide for a short duration signal, as reported by Wright and Dai (1994), off-frequency listening could account for the reduction in masking seen for the long duration masker used in the present study. That is, listeners could attend to regions above and below the region adapted by the long duration masker to listen for an increment in the short duration standard. To isolate an explanation based on off-frequency listening from one based on perceptual similarity, additional forward-masked intensity discrimination data for tonal standards were collected in the presence of a broadband masker.

II. EXPERIMENT 2. BROADBAND NOISE MASKERS AND TONAL STANDARDS

A. Subjects

Four additional subjects, ages 25–27 years, were recruited for this study. Three of the subjects had hearing within normal limits bilaterally (thresholds better than 10 dB HL). One of the subjects had normal hearing through 3.0 kHz and a mild sensori-neural loss of 30–35 dB HL at 4.0 and 8.0 kHz.

B. Stimuli

The 1.0-kHz pure-tone standard and increment were generated in the same manner that was described for experiment 1. The masker was a broadband noise produced by a custom designed generator. The noise was low-pass filtered (Kemo, model VBF/25) at 10.0 kHz at 135 dB/oct. The noise was rectangularly gated.

The masker, which was always presented 100 ms prior to the standard, had a duration of either 10 or 100 ms. The standard and increment durations were 10 ms. The level of the noise masker was fixed at 98 dB SPL (58 dB/Hz). This overall level of the noise resulted in a level of 80 dB SPL within an assumed 160-Hz wide critical band centered at 1.0 kHz (Scharf, 1970). The level of the masker in the critical band was lower than the level of the tonal masker in Experiment 1 and its duration was shorter (100 ms vs 250 ms). These changes were made out of consideration for our listeners. The level of the standard tone varied over blocks of trials by steps of 10 dB, from 30 to 80 dB SPL.

TABLE I. Detection thresholds (dB SPL) for the 10-ms, 1.0-kHz tone used as a standard in experiment 2. Thresholds are shown for each of the experimental conditions [quiet and two durations of broadband noise (BBN)]. Standard deviations are shown in parentheses.

Subject	Quiet	10-ms BBN masker	100-ms BBN masker
5	25.5 (0.3)	31.2 (1.9)	31.0 (0.2)
6	20.3 (0.4)	28.7 (3.7)	23.5 (1.8)
7	20.0 (0.4)	20.6 (0.6)	27.7 (0.7)
8	19.9 (2.6)	20.1 (0.9)	24.9 (0.8)
Mean	21.4	25.2	26.8

C. Procedure

Detection thresholds for the tonal standard alone and for the tonal standard in the presence of the BBN masker were measured using a 2IFC adaptive procedure that converged on 79.4% correct detections (Levitt, 1971). The same 2IFC adaptive procedure was used to assess intensity discrimination performance in three conditions: (1) quiet (no masker) 10-ms standard; (2) 100-ms masker, 10-ms standard; and (3) 10-ms masker, 10-ms standard.

D. Results

Detection thresholds for the 1.0-kHz tone in quiet and for the 1.0-kHz tone in the presence of the BBN maskers are shown in Table I. The masker resulted in a slight (4–5 dB on average) elevation of the threshold for the standard tone. The trend was for the 100-ms BBN masker to result in a greater elevation of threshold than the 10-ms BBN masker, but the difference is small.

The results of experiment 2 are illustrated in Fig. 6. The results show that all subjects had elevated Weber fractions in

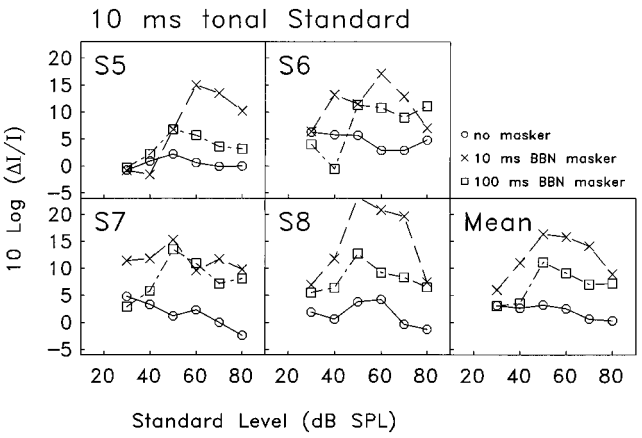

FIG. 6. Weber fractions (dB) as a function of level for subjects S5, S6, S7, and S8. Weber fractions are shown for a 10-ms, 1.0-kHz tone in quiet (circles) and for a 10-ms, 1.0-kHz tone in the presence of a 100-ms broadband noise masker (squares) and a 10-ms (×) broadband noise masker.

TABLE II. Detection thresholds (dB SPL) for the 10-ms, broadband noise (BBN) used as a standard in experiment 3. Thresholds are shown for each of the experimental conditions (quiet and two durations of BBN maskers). Standard deviations are shown in parentheses.

Subject	Quiet	10-ms BBN masker	100-ms BBN masker
5	33.9 (0.4)	37.5 (1.8)	40.5 (1.8)
6	20.1 (1.2)	19.9 (2.3)	21.2 (1.5)
7	23.7 (0.1)	25.7 (1.5)	26.7 (1.9)
8	11.9 (1.3)	10.0 (0.5)	13.9 (2.6)
Mean	22.3	23.3	25.6

forward-masked conditions, especially for mid-levels. The 10-ms broadband masker produced, on average, a greater amount of masking than the 100-ms masker.

III. EXPERIMENT 3: BROADBAND NOISE MASKERS AND STANDARDS

A. Procedure and method

The procedure and method are identical to those of experiment 2, except that the tonal standard and increment of experiment 2 was replaced with a 10-kHz wide noise band (identical to the masker). The noise standard and increment were added in phase by splitting the output of a single noise generator and routing the outputs to separate digital attenuators. The masker was set to 90 dB SPL. All stimuli were gated rectangularly. The same subjects that participated in experiment 2 participated in experiment 3.

Detection threshold for the BBN standard alone and for the BBN standard in the presence of the BBN masker were measured using a 2IFC procedure that converged on 79.4% correct detections.

B. Results

Detection threshold for the BBN standard alone and for the BBN standard in the presence of the BBN masker are shown in Table II. All of the thresholds for these conditions are within a few dB of each other indicating that the masker had little if any effect on detection thresholds. Note, though, that subject 5, who has a mild high-frequency sensori-neural hearing loss, has a threshold for the BBN in quiet of 37.5 dB SPL. His detection threshold for this condition is higher than the lowest level of the standard of 30 dB SPL employed in the intensity discrimination task. For this reason, average data for the intensity discrimination task discussed below will be examined with and without his data.

The results of experiment 3 are illustrated in Fig. 7. Weber's law was found to hold for BBN in quiet, a result consistent with that of Miller (1947). For the 100-ms masker, 3 of the 4 subjects (S6, S7, S8) showed elevated Weber fractions for the mid-level standards. For the 10-ms masker, the greatest elevation in the Weber fraction was observed for low sensation levels (SL). There was a decrease in the Weber fraction as SL increased for this condition with the 100-ms masker. The average data, both with and without the subject with the mild high-frequency hearing loss (subject 5), show this result.

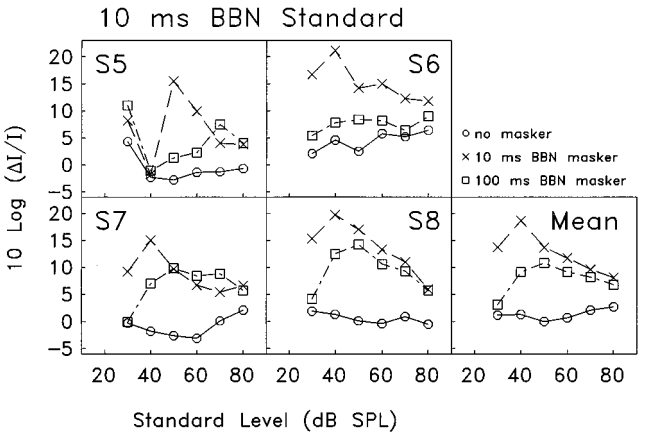

FIG. 7. Same as Fig. 6 except the standard and masker were broadband noise.

IV. GENERAL DISCUSSION

Zeng and Shannon (1995) performed a series of studies to attempt to isolate the source of the mid-level elevation of jnd's seen in forward masking. In electrical hearing, the mid-level elevation of jnd's was observed for listeners with cochlear implants but not for those listeners with cochlear nucleus implants. In additional measurements from listeners with acoustic hearing and thresholds within normal limits, a large elevation of jnd's was seen for ipsilateral maskers but only a small elevation was seen for contralateral maskers. They argue that the small elevation seen for contralateral maskers could be due to cross hearing. That is, the high levels of these maskers was believed to be sufficient to vibrate the skull and to elevate the Weber fraction in the ear with the standard. Taken together, the results of their studies of electrical and acoustical hearing support the idea that the mechanism responsible for the mid-level elevation of jnd's is located in the auditory nerve or the cochlear nucleus. This finding supports Zeng and his colleagues hypothesis (Zeng *et al.*, 1991; Zeng and Turner, 1992) that the mid-level elevation of jnd's in forward-masked intensity discrimination has a physiological correlate in the slower rate of recovery from adaptation of low-SR neurons in the auditory nerve. Despite this attractive link, evidence is accumulating that much of the masking seen in forward-masked intensity discrimination does not occur at the level of the auditory nerve.

First, the finding in our study that a long duration masker produced less masking than a short duration masker is inconsistent with the finding of physiological studies of adaptation measured in single fibers of the auditory nerve. Harris and Dallos (1979) found that the time required for units to recover from adaptation in forward masking increased with the duration of exposure of the adapting stimulus. Although data have not been reported for stimulus durations and interstimulus intervals identical to those used in the present experiment, the single finding to date is that adaptation increases with increased duration of an adapting stimulus for neurons in the auditory nerve (Young and Sachs, 1973; Smith, 1977; Harris and Dallos, 1979).

A possible explanation for the additional masking noted with short duration maskers than for longer duration ones is

confusion caused by a perceptually similar masker and standard. In the present study, a short duration masker produced more masking than a long duration masker when the duration of the standard was short. We found that perceptually similar stimuli (similar or identical in spectrum) result in a greater amount of masking than perceptually dissimilar stimuli, and the shape of the masking function may differ as well. A long duration broadband masker (100 ms) and short duration broadband standard (10 ms) yielded a masking function with the greatest amount of masking occurring for mid-level standards. By contrast, a broadband masker and standard with the same short duration (10 ms) produced a masking function with the greatest amount of masking for low-level standards and the amount of masking diminished as the standard level increased. The same result was observed for one of the participants in experiment 1, where tonal stimuli were used as the masker and standard. In a follow-up condition for this listener, an auditory cue, remote in frequency from the masker and standard, was presented simultaneously with the masker. The cue was only effective in reducing the amount of observed masking for low-level standards: The mid-level elevation of the Weber fraction remained. This result implies that confusion resulting from perceptual similarity has its greatest effects at low standard levels. In these conditions, the listener may integrate the energy in the masker and standard, which would have a much greater effect for low-level standards.

The idea that temporal integration of the masker and standard may play a role in forward-masked intensity discrimination was suggested by Zeng (1994) and Plack (1996). Consistent with this notion is their separate findings that elevated jnd's in forward-masked intensity discrimination occur at levels where loudness enhancement is observed. Applied to the present study, one would expect to see the greatest amount of loudness enhancement for perceptually similar stimuli. We did not measure loudness enhancement for our stimuli, but Zwislocki and Sokolich (1974) found that changing the duration of a masker burst from 10 to 50 ms had a negligible effect on the loudness of a 10-ms burst. Zwislocki and Sokolich's (1974) finding is inconsistent with the hypothesis that suggests tight coupling between loudness enhancement and the mid-level bump, but data from the same group of subjects using identical stimuli must be compared before any conclusions are drawn.

If the temporal integration hypothesis is invoked to account for elevated jnd's for low-level standards, why did the Weber fraction remain elevated for mid-level standards in the presence of the cue designed to signal the offset of the masker and the onset of the standard? The answer may be related to the absence of contextual cues in this task at moderate levels. Plack *et al.* (1995) reported a reduction in masking when a tone was presented along with the masker and standard in a forward-masked intensity discrimination task. A ''reference tone'' was placed between the masker and standard or immediately following the standard. This reference tone reduced the amount of masking produced by the masker alone when it was close in frequency to the standard, a result they argue is consistent with the listener making use of the proximal stimulus (the reference tone) to judge whether an increment was presented in one of the intervals in a 2IFC task. According to their explanation, which is based on the theory of intensity perception of Durlach and Braida (1969), the reference tone provides a context for judging whether an increment was added to the mid-level standards. At these mid-levels, listeners are supposedly unable to rely on natural perceptual anchors (i.e., detection threshold and the level considered uncomfortably loud) located at the extremes of the dynamic range of intensity.

The increase in the amount of forward masking seen for perceptually similar stimuli and the reduction in masking observed when a reference tone is placed in close proximity to the standard, particularly when the proximal stimulus occurs *after* the standard, are inconsistent with a peripheral sensory phenomenon (i.e., cochlea or auditory nerve). Also difficult to explain by a peripheral sensory mechanism is the finding that backward masking produces a mid-level elevation of the jnd as seen in forward masking (Plack and Viemeister, 1992). These results, combined with those of Zeng and Shannon (1995), who isolated the mid-level elevation of jnd's to the auditory nerve or cochlear nucleus, lead us to conclude that the cochlear nucleus or even higher centers of the brain are responsible for the elevation of jnd's observed in forward masking. Although adaptation of low-SR fibers in the auditory nerve show a long recovery from adaptation that is seemingly consistent with a mid-level elevation of jnd's, the remaining evidence does not support this theory, at least at the level of the auditory nerve.

On the other hand, the cochlear nucleus, with its complex interconnections, may provide a physiological correlate for a short duration masker producing more masking than long duration one. Shore (1995) examined recovery rates of several classes of cells in the ventral cochlear nucleus in forward masking and found that some classes of cells (i.e., primarylike, primarylike notch, and onset cells) have slower recovery in their onset responses to a short duration masker (50 ms) than to a longer duration masker (100 ms). The significance of this finding in the context of the our psychophysical findings is muddled somewhat by her observation that ''as may be expected from the results with auditory nerve (Harris and Dallos, 1979), the longer, 100-ms maskers produced greater rate decrements and slower recoveries than the 50-ms maskers for all unit types studied (Shore, 1995; pg. 39).'' Clearly, the role of the cochlear nucleus and higher levels of the auditory system in forward-masked intensity discrimination requires further study.

V. CONCLUSIONS

(1) Short duration maskers produced more masking than long duration maskers in a forward-masked intensity discrimination task. Broadband maskers as well as tonal maskers produced this effect which eliminates off-frequency listening as a possible explanation. This result is inconsistent with what is known about the effects of duration on adaptation in the auditory nerve which implies that the mechanism producing the masking effect is central to the auditory nerve.

(2) There is evidence that a portion of the masking is cognitive in origin. For one subject, a cue presented simultaneously with the masker reduced the Weber fractions for

low-level standards. This likely cognitive effect was seen only for short duration maskers and standards.

ACKNOWLEDGMENTS

Experiment 1 is based on experiment 1 in Nicole Lanthier's Master's thesis. Experiments 2 and 3 are based on experiments from Joe Neve's Master's thesis. These theses were submitted to the Graduate School of the University of Minnesota in partial fulfillment of the requirements for the Master of Arts degree in Communication Disorders. Dr.'s Fan-Gang Zeng and Chris Plack made useful comments during the review process. This work was supported by the Bryng Bryngelson Communication Disorders Research Fund and by NIDCD, Grant No. R29DC01542.

[1]Most authors find that suppressors have maximum effect when they are roughly 20% above the frequency of the stimulus they are intended to suppress (Shannon, 1974). We ran a few blocks of trials with this favorable ratio and found that thresholds did not improve for the first author (not one of the subjects) for a 10-ms, 50 dB SPL standard and a 10-ms tonal masker.

Durlach, N. I., and Braida, L. D. (**1969**). ''Intensity perception. I. Preliminary theory of intensity resolution,'' J. Acoust. Soc. Am. **46,** 372–383.

Harris, D. M., and Dallos, P. (**1979**). ''Forward masking of auditory nerve fiber responses,'' J. Neurophysiol. **42,** 1083–1107.

Kidd, G., and Feth, L. L. (**1982**). ''Effects of masker duration in pure-tone forward masking,'' J. Acoust. Soc. Am. **72,** 1384–1386.

Levitt, H. (**1971**). ''Transformed up–down methods in psychoacoustics,'' J. Acoust. Soc. Am. **49,** 467–477.

Miller, G. A. (**1947**). ''Sensitivity to changes in the intensity of white noise and its relation to masking and loudness,'' J. Acoust. Soc. Am. **19,** 609–619.

Moore, B. C. J., and Glasberg, B. R. (**1982**). ''Contralateral and ipsilateral cueing in forward masking,'' J. Acoust. Soc. Am. **71,** 942–945.

Plack, C. J. (**1996**). ''Loudness enhancement and intensity discrimination under forward and backward masking,'' J. Acoust. Soc. Am. **100,** 1024–1030.

Plack, C. J., and Viemeister, N. F. (**1992**). ''Intensity discrimination under backward masking,'' J. Acoust. Soc. Am. **92,** 3087–3101.

Plack, C. J., Carlyon, R. P., and Viemeister, N. F. (**1995**). ''Intensity discrimination under forward and backward masking: Role of referential coding,'' J. Acoust. Soc. Am. **97,** 1141–1149.

Relkin, E. M., and Doucet, J. R. (**1991**). ''Recovery from forward masking in the auditory nerve depends on spontaneous firing rate,'' Hearing Res. **55,** 215–222.

Scharf, B. (**1970**). ''Critical bands,'' in *Foundations of Modern Auditory Theory*, edited by J. V. Tobias (Academic, New York), Vol. 1, pp. 157–202.

Shannon, R. V. (**1974**). ''Two-tone unmasking and suppression in a forward-masking situation,'' J. Acoust. Soc. Am. **59,** 1460–1470.

Shore, S. E. (**1995**). ''Recovery of forward-masked responses in ventral cochlear nucleus neurons,'' Hearing Res. **82,** 31–43.

Smith, R. L. (**1977**). ''Short-term adaptation in single auditory nerve fibers: Some postimulatory effects,'' J. Neurophysiol. **40,** 1098–1112.

Wright, B. A., and Dai, H. (**1994**). ''Detection of unexpected tones with short and long durations,'' J. Acoust. Soc. Am. **95,** 931–937.

Young, E., and Sachs, M. B. (**1973**). ''Recovery from sound exposure in auditory nerve fibers,'' J. Acoust. Soc. Am. **54,** 1535–1543.

Zeng, F.-G. (**1994**). ''Loudness growth in forward masking: Relation to intensity discrimination,'' J. Acoust. Soc. Am. **96,** 2127–2132.

Zeng, F.-G., and Shannon, R. V. (**1995**). ''Possible origins of the non-monotonic intensity discrimination function in forward masking,'' Hearing Res. **82,** 216–224.

Zeng, F.-G., and Turner, C. W. (**1992**). ''Intensity discrimination in forward masking,'' J. Acoust. Soc. Am. **92,** 782–787.

Zeng, F.-G., Turner, C. W., and Relkin, E. M. (**1991**). ''Recovery from prior stimulation II. effects upon intensity discrimination,'' Hearing Res. **55,** 223–230.

Zwislocki, J. J., and Sokolich, W. G. (**1974**). ''On loudness enhancement of a tone burst by a preceding tone burst,'' Percept. Psychophys. **16,** 87–90.

Effects of modulator phase for comodulation masking release and modulation detection interference

Virginia M. Richards, Emily Buss, and Lijun Tian
Department of Psychology, 3815 Walnut Street, University of Pennsylvania, Philadelphia, Pennsylvania 19104

(Received 8 August 1996; accepted for publication 14 January 1997)

In an effort to evaluate the importance of across-frequency comparisons of envelope patterns in comodulation masking release (CMR) experiments and to compare joint effects of target–masker frequency separation for both CMR and modulation detection interference (MDI) tasks, thresholds were measured for three tasks. These tasks were: (a) the detection of sinusoidal amplitude modulation (SAM) of a tone, (b) the detection of a reduction in the modulation depth of a fully modulated SAM tone, and (c) the detection of a tone added to a narrow band of noise. Thresholds were obtained for the target alone and for the target presented with two maskers. For the detection of SAM, thresholds did not depend on whether the modulation patterns of the target and masker elements were the same or random. For the latter two tasks, modulator phase effects were apparent for target–masker frequency separations less than 1–2 oct. In contrast, past work has shown that observers can compare modulator envelope phases across frequency separations larger than 1–2 oct [Strickland *et al.*, J. Acoust. Soc. Am. **86**, 2160–2166 (1989); Yost and Sheft, J. Acoust. Soc. Am. **85**, 848–857 (1989)]. In a second experiment, thresholds for the detection of SAM were obtained after prolonged exposure to a fully modulated SAM tone. For four of the five observers, modulation-rate specific adaptation was obtained for test/adapting carrier-frequency separations approaching 2 oct below and 1 oct above the adaptor. © *1997 Acoustical Society of America.* [S0001-4966(97)00206-3]

PACS numbers: 43.66.Dc, 43.66.Mk [JWH]

INTRODUCTION

Modulation detection interference (MDI) experiments show that sensitivity to the presence of amplitude modulation at a target frequency is diminished by the addition of an amplitude-modulated masker at a remote frequency region (Yost and Sheft, 1989; Yost and Sheft, 1994). The resulting interference, the MDI, is largely independent of the frequency separation between the target and the off-frequency masker. Moreover, when sinusoidal amplitude modulation (SAM) is used, the magnitude of the MDI does not depend consistently on the relative phases of the modulators but does depend on the relative rates of the modulators. When the target and off-frequency masker do not share the same modulation rate, the magnitude of the MDI is diminished (Yost *et al.*, 1989).

In a recent survey of a large number of experiments, Yost and Sheft (1994) reported MDIs in the range of 10–15 dB [as 20 log(m), where m is modulation depth] across a number of target-masker frequency separations. However, substantial individual differences are apparent in the literature. For example, Hall and Grose (1991) reported that MDIs were not obtained for all observers, while others have reported observer-dependent effects of relative target-masker modulation phases for small target–masker frequency separations (Bacon and Konrad, 1993; Yost and Sheft, 1994).

In contrast to MDI experiments, comodulation masking release (CMR) experiments show that coherence of across-frequency envelope patterns allows enhanced detection for a tone added to a masker (Hall *et al.*, 1984). In a typical CMR experiment, thresholds are obtained in three conditions. In one condition, a single narrow-band masker is centered at the signal frequency. This condition will be referred to as the target-alone condition. For the other two conditions, two or more narrow-band maskers are present, one centered at the target frequency and the other(s) at disparate frequencies. When both the target and off-frequency maskers are present, the envelopes of the maskers are either identical or unrelated. These conditions will be referred to as in-phase and random-phase conditions, respectively. CMR has been defined in a variety of ways; here the term CMR will be used to denote the difference in thresholds obtained in the target-alone and the in-phase conditions.

Experiments indicate that thresholds are lowest in the in-phase condition, somewhat higher in the target-alone condition, and higher still in the random-phase condition. Schooneveldt and Moore (1987) and Cohen and Schubert (1987) found that when a single off-frequency masker was used, the magnitude of the threshold differences depended on the frequency separation between the target and off-frequency masker. For small target–masker frequency separations the CMR is largest, but the CMR falls as the target–masker frequency separation grows. Likewise, for small target–masker frequency separations, thresholds in the random-phase conditions are largest, falling with increases in target–masker frequency separations. Based on the pattern of thresholds obtained in an exhaustive study, Schooneveldt and Moore (1987) suggested that the large CMRs obtained for closely spaced maskers reflect ''within channel'' processing, i.e., interactions within single auditory filters. They attributed the CMR obtained for wider target-masker fre-

quency separations, a value that asymptoted at approximately 3 dB in their study, to across-channel, or across-frequency, processing. Thus the 3-dB effect was described as reflecting a ''true'' CMR. Based on their results, which included masker separations as large as an octave, Schooneveldt and Moore suggested that the ''true'' CMR was relatively independent of frequency separation. However, Cohen and Schubert (1987) found that for masker separations in excess of 3/4 of an octave, thresholds in the target-alone, the in-phase, and the random-phase conditions are essentially the same. Only Cohen (1991) has reported sizable effects of off-frequency envelope patterns (in-phase versus random-phase) for frequency separations in excess of an octave, with the largest effect being obtained when the target and maskers were of different levels.

The contrast between MDI and CMR results, then, is that for the former class of experiments modulated maskers *interfere* with detection of changes at the target frequency (presence of modulation), and for the latter class of experiments modulated maskers *enhance* the detection of changes at the target frequency (the addition of the signal). Both Yost and Sheft (1990) and Moore and Jorasz (1992) completed experiments in an effort to begin to understand differences in the mechanisms which underlie CMR and MDI results. Yost and Sheft (1990) examined both an MDI and a CMR-like task. The target frequency was 4000 Hz and the masker frequency 1000 Hz. For the MDI task, the stimulus at the target frequency was either a tone or a SAM tone, and the threshold modulation depth of the SAM was estimated. In one of the CMR-like tasks, the observer detected a decrement in the modulation depth at the target frequency: The target was either fully modulated or partially modulated. This parallels the typical CMR experiment in that a reduction in depth of modulation mimics the effect of adding a tone to a narrow band of noise—adding a tone to a narrow band of noise acts to flatten the slowly fluctuating envelope. For both the MDI and CMR-like tasks, when an off-frequency masker was present, it was either (a) a tone or (b) a fully modulated SAM tone modulated in phase with respect to the target SAM tone. Their results indicated MDI-like behavior for both tasks. That is, regardless of whether the signal to be detected was the presence of modulation or a change in depth of modulation, flanking SAM maskers generated higher thresholds than did flanking tonal maskers. Moore and Jorasz (1992), who used multiple maskers, did obtain a CMR-like result for the detection of reduction of SAM modulation depth when the target was fully modulated and its onset delayed relative to the maskers, but in other conditions obtained MDI-like results.

The failure of Yost and Sheft (1990) and Moore and Jorasz (1992) to obtain a CMR is of interest on several grounds. First, Grose and Hall (1989) and Moore *et al.* (1990) have shown that CMRs are obtained when a tone is added in-phase to the carrier of a SAM tone, a task equivalent to a modulation depth discrimination task. In both experiments, multiple off-frequency SAM tones that were fairly closely spaced in frequency were used. The multiplicity and nearness of the off-frequency makers may have encouraged a dominance of CMR over MDI (cf. Moore and Jorasz, 1992; Bacon and Moore, 1993).

A second reason that the failure to measure CMR for decrements in the modulation depth of SAM tones is notable is that Strickland *et al.* (1989) and Yost and Sheft (1989) have demonstrated that observers are able to make across-frequency comparisons of modulation patterns for SAM tones separated by more than an octave. In their studies, observers discriminated between two SAM tones with modulators that were either in-phase or phase-delayed with respect to one another. The just detectable phase delay was measured for a variety of carrier-frequency separations. The results indicate that thresholds increase with increasing carrier-frequency separations up to a separation of an octave or so, and then level off with further separations. Strickland *et al.* (1989) also demonstrated that for frequency separations of an octave and larger, sensitivity to differences in envelope phase did not depend on the addition of low- or high-pass noise, nor did sensitivity depend on the relative levels of the two SAM tones. Both groups of researchers interpreted their data as possibly indicating (a) diminished interactions in a single, possibly additive channel for carrier-frequency separations in excess of an octave, and (b) that under some conditions observers may compare modulator phases across frequency, as indicated by the fact that thresholds were reliably obtained even when large differences in carrier frequencies were tested.

These experiments suggest that sensitivity to differences in the modulation phase of simultaneously presented SAM tones may depend on cues present in a single channel when the SAM carriers are separated by less than an octave, but when the carriers are separated by an octave or more, sensitivity to differences in modulator phases appears to depend upon across-channel comparisons (Strickland *et al.*, 1989; Yost and Sheft, 1989). In contrast, CMRs are not measured for SAM target-maskers that are widely separated in frequency (Yost and Sheft, 1990; Moore and Jorasz, 1992). Comparisons between the CMR experiments and experiments that examine sensitivity to differences in modulator phase, however, should be guarded. Fantini (1991), who employed simulaneously presented SAM noise maskers, found that sensitivity to across-frequency differences in modulator phase did not predict thresholds for the addition of a tone. In contrast, her data suggest that across-frequency differences in modulation depth may facilitate the detection of a tone added to modulated noise maskers.

To summarize, the MDI is relatively independent of the target–masker frequency separation, and is relatively independent of relative target–masker modulator phases, two results that support the proposition that the MDI reflects across-frequency interference. In contrast, CMR depends both on target–masker frequency separation and on whether envelope patterns are the same or random across frequency, which suggests that CMR data are largely driven by single-channel processing. A second observation that suggests a large single-channel component of CMR is that in the random-phase condition, thresholds tend to fall with in-

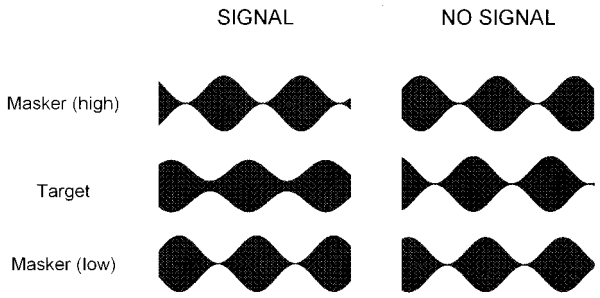

FIG. 1. Signal and no-signal stimuli (left and right columns, respectively) are depicted for the random-phase condition. The high- and low-frequency maskers are the top and bottom sketches, and the target element is in the center.

creases in target–masker frequency separation (Schooneveldt and Moore, 1987; Cohen and Schubert, 1987). If the target and maskers have envelope patterns that are randomly chosen on different trials, and if more than one element (target and one or more maskers) is passed by a single filter, then an added tone will lead to less consistent changes in the aggregate envelope, making the detection of the added tone more difficult.

In experiment I, a single crew of observers completed both MDI and CMR experiments. Two types of CMR experiments were tested; one using SAM tones as maskers and the other using narrow bands of noise as maskers. All three tasks used the same procedures and stimulus parameters. As a result, experiment I provides within-observer comparisons across two CMR tasks and an MDI task, and in particular, provides direct comparisons of the joint effects of target-masker frequency separation and relative modulator phases for these three tasks.

In experiment II, the degree of adaptation for the detection of sinusoidal amplitude modulation was measured. The experiment was somewhat atypical compared to most selective adaptation experiments because our goal was to determine the effect that adaptation to a SAM tone at one carrier frequency has on observers' ability to detect amplitude modulation at a different carrier frequency. This experiment is largely exploratory in nature and reflects an effort to provide an estimate of the ''bandwidth'' for interaction among carriers independent from that measured by Strickland *et al.* (1989) and Yost and Sheft (1989). As there is no accepted model of behavioral adaptation, any interpretation of the experimental results is guarded.

I. EXPERIMENT I: THE JOINT EFFECTS OF MODULATOR PHASE AND FREQUENCY SEPARATION ON CMR AND MDI

In this experiment, three tasks were tested. Observers detected (a) the sinusoidal amplitude modulation of a 1500-Hz tone, (b) the reduction in depth of modulation of a fully modulated 1500-Hz SAM tone, and (c) a 1500-Hz tone added to a narrow band of noise centered at 1500 Hz. The SAM tones were modulated at 16 Hz, and the narrow-band noise masker bandwidth was approximately 25-Hz-wide, providing an expected rate of envelope maxima of approximately 16 s.

Figure 1 shows an example of signal and no-signal stimuli (left and right columns, respectively) for the detection of reductions in modulation depth in the random-phase condition. The central element is the target, and it along with the two flanking maskers have randomly chosen starting modulator phases. For the in-phase conditions (not shown), the target and maskers have coincident modulation maxima and minima, and for the tonal maskers (not shown), the maskers are not modulated.

For each of the three tasks, thresholds were measured in four conditions. In one of the conditions, the target-alone condition, energy was present only in the region of 1500 Hz. For the other three conditions, two additional maskers were present. The maskers were equidistant from the 1500-Hz target frequency on a logarithmic scale, one above and one below the target frequency. The maskers were either tones or multitone complexes appropriate for the task (e.g., SAM tones or narrow bands of noise). When complex maskers were used, the maskers' envelope patterns were either identical or randomly related. The four conditions will be referred to as (a) target-alone, (b) tonal maskers, (c) in-phase maskers, and (d) random-phase maskers. Regardless of the change to be detected, digital scaling ensured that the level at the target frequency was the same for the signal and no-signal stimuli. As a result, across-frequency changes in level could not contribute to detection (e.g., profile analysis, Green, 1988). Finally, the target–masker frequency separation was systematically varied.

II. METHODS FOR EXPERIMENT I

A. Stimulus generation

The stimuli were digitally generated and presented using a sample rate of 25 000 samples/s. The target stimulus was presented via one channel of a two-channel digital-to-analog converter, and when the off-frequency maskers were present, they were presented simultaneously through the second channel. The stimulus duration was 400 ms, including 20-ms cosine-squared onset and offset ramps. The digital outputs were low-pass filtered at 8 kHz (KEMO VBF 8; attenuation skirts approx. 85 dB oct), summed using an analog adder, and presented diotically through two channels of Sennheiser HD410SL headphones.

For the tasks using SAM tone targets, the phases of the carriers were randomly chosen on each interval from a uniform distribution ranging from 0 to 2π rad. For the in-phase conditions, the starting phase of the target and masker modulator was randomly chosen from a uniform distribution ranging from 0 to 2π rad on each interval. For the random-phase conditions, the starting phase of the individual modulators were randomly chosen from a uniform distribution ranging from 0 to 2π rad.

The narrow bands of ''noise'' were formed by summing 33 equal-amplitude tones separated by 0.76 Hz (much smaller than the inverse of the stimulus duration). On each interval, the phases of the individual components of the tar-

get band were independently chosen from a uniform distribution with a range of 0 to 2π rad. For the in-phase condition, the same phase relations were used for all noise bands. In the random-phase conditions, different phases were randomly chosen for the different masker bands. The added signal tone had a frequency equal to the central component of the masker, but the phase was random with respect to the component to which it was added.

The target frequency was 1500 Hz. The off-frequency maskers were separated from the signal by approximately 0.33, 0.6, 0.88, 1.45, and 2 oct. Each stimulus element (i.e., target or masker) was presented at 65 dB SPL.

B. Procedures

A 2IFC procedure was used, with the signal interval being as likely to be the first as the second interval. The ''signal'' to be detected was the presence of SAM, the reduction in the depth of SAM, or the addition of the 1500-Hz tone. That is, the standard was a tone (0 percent modulation depth), a SAM tone (100 percent modulation depth), or a narrow band of noise, respectively.

Thresholds were estimated using a 2-down, 1-up staircase procedure which estimated the 71 percent correct performance level (Levitt, 1971). Each threshold estimate was generated using blocks of 50 trials and were based on the average of the last even number of reversals, excluding at least the first three. For detection of SAM, the initial step size was 4 dB (20 log(m)), which was reduced to 2 dB after three reversals. When the reduction in SAM depth was to be detected, the initial step size was 0.6 dB, which was reduced to 0.3 dB after three reversals. On occasion, the track was driven above 0 dB, a modulation depth greater than 1. On those occasions, step sizes were reduced to values more appropriate for the observer's sensitivity (e.g., step sizes of 0.3 and 0.15), and thresholds remeasured. Due to level equalization, there is some difficulty in describing the level of the added tone for the tone-in-noise task. Here, the added tone is described in terms of its amplitude relative to the amplitude of the component to which it was added—signal to component level, in dB. Note that this measure is appropriate only for the target element as only the target element was scaled to achieve level equalization. Also, this measure is typically used when the signal is added in phase to a component of the masker (Green, 1988), which was not the case in this experiment. Thus the signal level is denoted as ''sig re comp; rp''—signal relative to component, random phase. The level of the added tone was initially adjusted using a 4 dB step size, which was reduced to 2 dB after three reversals.

The different tasks were blocked, as were the different masker conditions (e.g., tonal maskers, target-alone, etc.) within each task. The order in which the blocks were tested was randomly determined for each observer. The reported thresholds are based on the final eight threshold estimates measured. Regardless of our efforts to reduce the influence of long-term practice and carry-over effects on the data,[1] shifts in sensitivity may be present in the data in some conditions. Unfortunately, there was not ample time to fully repeat the experiment. Only Obs 2 repeated one task (SAM detection), and for her the two data sets were remarkably similar. Her most recent data are presented.

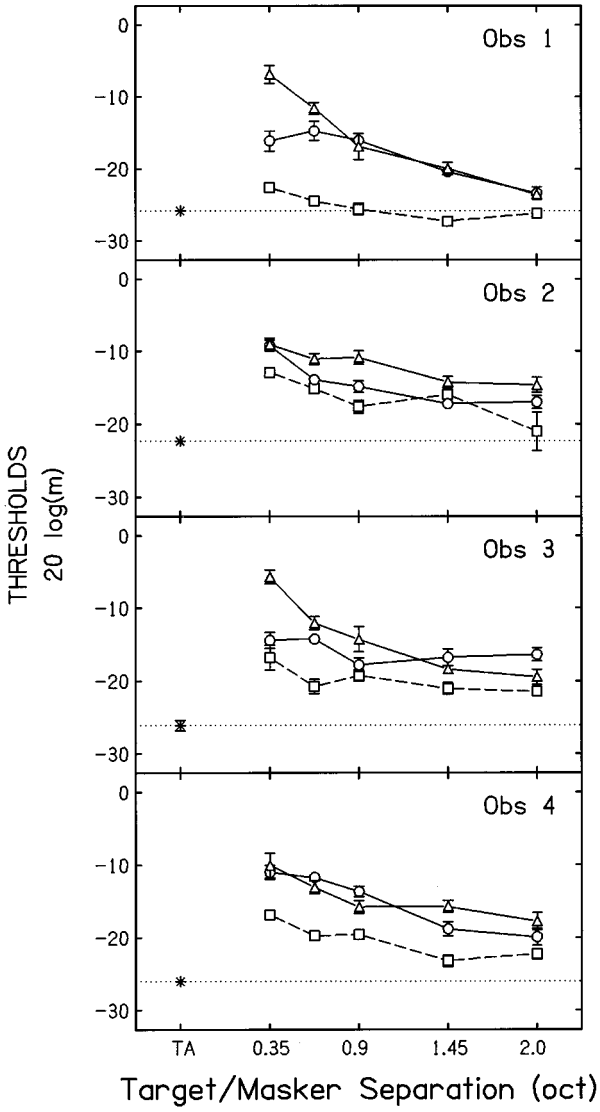

FIG. 2. Thresholds for modulation detection, 20 log(m), are plotted as a function of the frequency separation between the target and off-frequency maskers in octaves. Thresholds for the individual observers are plotted separately and error bars indicate the standard errors of the mean across replicate threshold estimates. The asterisk and dotted horizontal line indicate the target-alone thresholds. Squares, circles, and triangles indicate thresholds obtained for tonal maskers, in-phase, and random-phase SAM maskers, respectively.

Observer 1 participated as a partial requirement for an undergraduate course, Obs 2 is the second author, and Obs 3 and 4 were paid for participation. All observers had thresholds of 10 dB HL or better (for frequencies ranging from 500 to 8000 Hz) and ranged in age from 22 to 27 years. Results from two observers who began but did not finish the experiment are not included. Observers were tested in a double-walled sound-proof booth.

III. RESULTS AND DISCUSSION OF EXPERIMENT I

Figure 2 shows the results for the modulation detection task. The results for the different observers are plotted sepa-

rately. The abscissa indicates the target–masker frequency separation in octaves and the ordinate shows the threshold level in increments of 20 log(m).

Thresholds for the target-alone condition are indicated using asterisks and horizontal dotted lines. Squares connected with dashed line segments show thresholds obtained when tonal maskers were used, circles show thresholds obtained with in-phase SAM maskers, and triangles show thresholds obtained with random-phase SAM maskers. Error bars indicate the standard errors of the mean across eight replicate threshold estimates.

For all observers except Obs 1, thresholds obtained with tonal maskers (squares) are somewhat larger than thresholds in the target-alone condition (asterisk, horizontal line). Across all observers and frequency separations, thresholds in the target-alone condition are on average 4.6 dB lower than thresholds obtained with tonal maskers. With regard to effects of modulator phase randomization, averaging across target–masker frequency separations and observers, thresholds in the in-phase condition (circles) are 1.8 dB lower than thresholds in the random-phase condition (triangles). This difference is exaggerated for Obs 1 and 3 at the smaller target–masker frequency separations. Averaging thresholds obtained in the in- and random-phase conditions, thresholds are on average 5.5 dB lower for tonal maskers than for modulated maskers. This difference, the MDI, reaches significance in a paired comparisons ANOVA ($p<0.05$, modified Bonferroni test for multiple comparisons).

The results of this condition are in good agreement with past experiments, except that the MDI is somewhat more modest than typically reported (e.g., 10–15 dB; Yost and Sheft, 1994). As in past experiments, differences in target–masker frequency separation had little influence on the magnitude of the MDI (cf. Yost and Sheft, 1989; Yost and Sheft, 1994). The effects of modulator phase randomization were modest. Past work, which has employed a variety of different, but fixed, target–masker phase relations have likewise reported relatively small phase effects (e.g., Bacon and Konrad, 1993; Yost and Sheft, 1994). The small effect of phase randomization emphasizes the degree to which modulator phase does not interact with sensitivity in MDI experiments—even when phases are randomized, only a minimal effect of uncertainty appears to be introduced.

Figure 3 shows the results for the detection of reductions in modulation depth relative to a standard modulation depth of 1. The abscissa is target–masker separation in octaves, and the ordinate shows threshold modulation depth in terms of 20 log(m). Note that the y axis is reversed relative to that of Fig. 2, ensuring that ''poorer'' thresholds are plotted higher on the ordinate.

For Obs 2–4, thresholds obtained with tonal maskers (squares) are slightly elevated relative to thresholds in the target-alone condition (asterisk, dotted line). Only Obs 1 demonstrates appreciable ''energetic'' masking with tonal maskers, masking which lessens as the target–masker frequency separation grows.

Comparing thresholds in the in-phase and target-alone conditions (circles versus asterisks), in-phase modulation did not lead to thresholds lower than those measured without

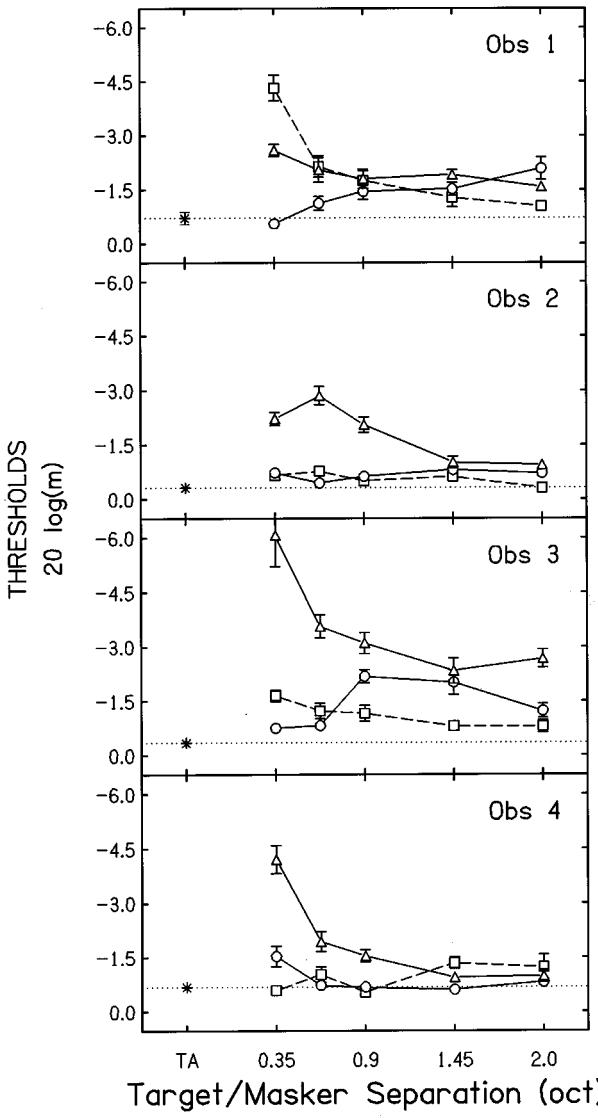

FIG. 3. As Fig. 2, except that thresholds are for the detection of reductions in modulation depth relative to a standard modulation depth of 1.

maskers. Thus no CMR was obtained. The absence of a CMR might reflect the absence of across-frequency level differences that are frequently present in CMR experiments (Green, 1988; Hall and Grose, 1988; Fantini and Moore, 1994). For small- and moderate-frequency separations, however, thresholds are consistently superior in the in-phase (circles) than random-phase (triangles) conditions. The effects of modulator phase randomization diminish as the target-masker frequency separations approach 1–1$\frac{1}{2}$ oct.

Because no CMR was obtained, there is no evidence that our observers employed across-frequency processing in order to reduce thresholds. Recall, however, that both Strickland *et al.* (1989) and Yost and Sheft (1989) found that sensitivity to differences in the modulator phases of two SAM tones decreased as the frequency separation between carriers increased, a result that may reflect interactions within a single processing channel. When the two carriers were separated by an octave or more, thresholds tended to be constant, possibly reflecting stable across-channel comparisons. In the current experiment, effects of phase randomization were not ob-

tained for target-masker frequency separations larger than 1–1½ oct. Following Strickland *et al.* (1989) and Yost and Sheft (1989), it seems reasonable to posit that phase randomization leads to poorer thresholds whenever the target and masker are passed through a single analysis channel.

More generally, given the gross similarity of the current data and the results of Strickland *et al.* (1989) and Yost and Sheft (1989), it seems plausible to conclude that observers depended only upon information available in a single channel, and that interactions within a single channel led to reduced sensitivity when the modulator phases were randomly chosen. For example, if SAM tones with randomly chosen phases are passed through a single filter, changing the modulation depth of one of the SAM tones will not always have the same effect on the congregate waveform. For sufficiently wide target–masker frequency separations, the target and masker will not interact, and the effects of phase randomization would approach zero. Alternatively, the contribution of across-frequency comparisons, while measurable when changes in modulator phases are tested (Strickland *et al.*, 1989; Yost and Sheft, 1989), may not be measurable in CMR tasks.

Another plausible explanation is that across-frequency comparisons were incorporated for all target–masker frequency separations tested but were of diminished usefulness as the target–masker frequency separation grew. For this explanation it would be assumed that for this task, across-frequency comparisons are not sufficiently strong to provide a measurable CMR but are sufficiently detrimental to generate reduced thresholds when modulator phases are randomized. In order to be consistent with the Strickland *et al.* (1989) and Yost and Sheft (1989) data, this explanation would require that observers are sensitive to differences in modulator phases for wide-frequency separations, but that the sensitivity is either too weak, or not incorporated into the decision, when reductions in modulation depth are to be detected.

The thresholds obtained for the detection of a tone added to narrow bands of noise are shown in Fig. 4. Thresholds are expressed as signal re component ratio in dB, with the caveat that the signal was added without respect to phase of the masker component to which it was added. Upward pointing arrows indicate that thresholds could not be reliably estimated. For all observers, thresholds obtained using tonal maskers (squares) were nearly the same as those measured in the target-alone condition (asterisk and dotted line). Only Obs 1 demonstrates a clear CMR; for modest target–masker frequency separations, thresholds in the in-phase conditions (circles) are lower than target-alone thresholds (asterisk, dotted line). In contrast, in the in-phase condition, both Obs 3 and 4 have the largest thresholds when the target–masker frequency separation is smallest. Observer 2 provides an intermediate result: Thresholds in the in-phase condition are relatively independent of target–masker frequency separation.

For the random-phase conditions (triangles), thresholds fall as the target–masker frequency separation increases, and thresholds are higher in the random-phase than the in-phase conditions for frequency separations less than 1–2 oct. Comparing the results obtained for the detection of a tone added to noise (Fig. 4) and for the detection of a decrement in modulation depth (Fig. 3), the pattern of results tends to be similar, and in particular, the individual differences obtained are generally consistent across the two tasks. The most striking difference in the pattern of results occurs for Obs 2. For Obs 2, phase effects occur for larger target–masker frequency separations in the tone-in-noise task than the SAM task. These data are consistent with the results of Fantini (1991), who found good correspondence between sensitivity to a tone added to one of two simultaneous SAM noise-band maskers and sensitivity to changes in the modulation depth of two SAM bands of noise.

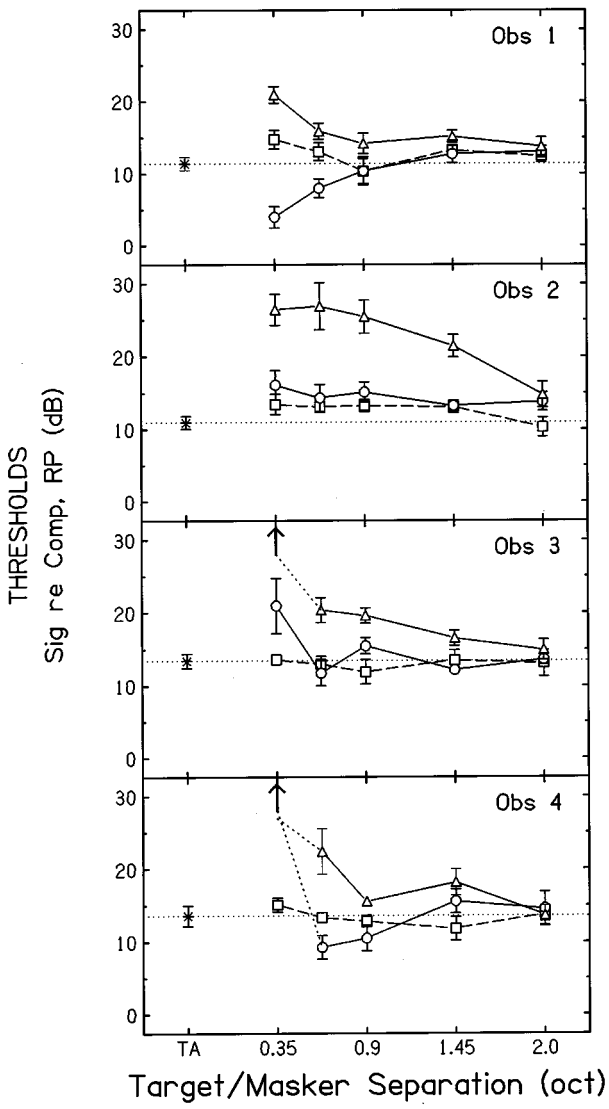

FIG. 4. As Figs. 2 and 3, except that thresholds are in terms of signal re component amplitude, in dB, with the signal being added without respect to the phase of the component to which it is added. Upward pointing arrows indicate that thresholds could not be reliably estimated.

To summarize the results of experiment I, the results for the detection of SAM are consistent with past reports in that the relative target–masker modulator phases did not have a strong impact on the magnitude of the MDI, even when random modulator phases were tested. For both the detection of

a reduction in the modulation depth of a SAM tone and the detection of a tone added to a narrow band of noise, the relative patterns of the target and masker envelopes did influence thresholds. A CMR was obtained for only one of the four observers, and only when noise maskers were used. The differential effects of masker phase randomization obtained in the MDI and CMR tasks suggest, but do not guarantee, that different mechanisms underlie the two tasks. One interpretation of the results is that for the CMR tasks, observers depend largely on information processed by a single channel, whereas for the MDI task, across-frequency integration leads to interference.

IV. EXPERIMENT II: ADAPTATION TO SINUSOIDAL AMPLITUDE MODULATION

In considering the results of experiment I, and in particular the results obtained when a reduction in the modulation depth of a SAM tone was to be detected, one possible interpretation was that observers base their decisions on stimulus interactions within a single channel, a channel which includes interactions across frequencies as distant as an octave. In an effort to provide an independent measure of the existence of such a channel, a selective adaptation experiment was completed. The experimental question was not the modulation rates for which adaptation to amplitude modulation occurs, but the range of carrier frequencies for which adaptation occurs. If the adaptation occurs for a relatively broad range of carrier frequencies, that result would suggest that there is some type of interaction across a wide frequency range. However, because little is agreed upon about the interpretation of behavioral adaptation studies (cf. Moody *et al.*, 1984; Wakefield and Viemeister, 1984), it is not obvious what such interactions would reflect—changes in strength of activity in a single channel, changes in perceptual anchors, or one of several alternative explanations.

The general methods and stimulus timing used were based on a study reported by Tansley and Suffield (1983). The adapting stimulus was a fully modulated SAM tone centered at 1500 Hz and modulated at either 16 or 56 Hz. The test stimulus was modulated at 16 Hz. The test sounds had carriers ranging from 375 to 6000 Hz, and the adaptor-test frequency separations were the same as the target–masker frequency separations used in experiment I. Pilot work suggested that sensitivity to changes from a fully modulated standard was relatively unaffected by a SAM adaptor, and so we chose to measure adaptation for the detection of amplitude modulation.

A. Procedures

The stimulus generation methods and the presentation levels were identical to those of experiment I. Thresholds were measured using a 2IFC procedure and a 2-down, 1-up staircase algorithm (Levitt, 1971). Unlike experiment I, threshold estimates are based on 45 rather than 50 trials. Both the adapting and test stimuli were presented at 65 dB SPL. Observers were seated in a double-walled sound-proof booth. Listeners first heard 10 min of the adapting sound. During this time, no effort was expended to ensure that observers were attending to the sounds, except that the headphones were kept in place. After the initial adaptation period and before the first trial, observers received a visual warning that trials were about to begin, followed by an additional 30 s of the adapting sound. After each trial, a minimum 1 s of additional exposure to the adapting sound was enforced. Moreover, after the 15th and 28th trial, an additional 30 s of the adapting sound was presented.

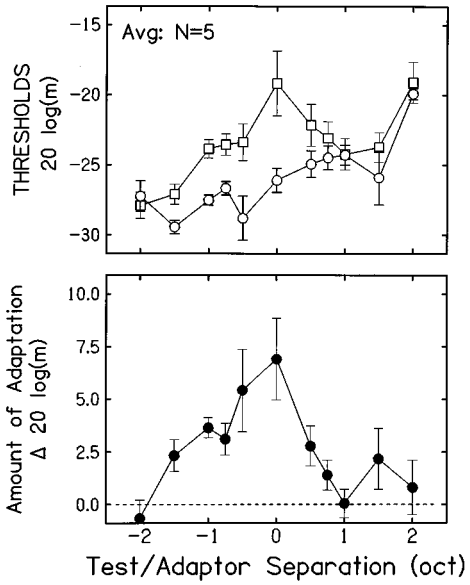

FIG. 5. The top panel shows the average thresholds for the detection of amplitude modulation following exposure to a fully modulated SAM tone centered at 1500 Hz and modulated at either 16 (squares) or 56 (circles) Hz. Error bars indicate the standard error of the mean across observers. The lower panel shows the difference in thresholds for the 16- and 56-Hz adaptors. Error bars indicate the standard error of the mean of the differences across observers.

The order in which the different test carrier frequencies and adaptor modulation rates were tested was random. For each test carrier frequency, four thresholds were measured one after another. Any time that elapsed between the completion of one threshold estimate and the beginning of the next was filled with the adapting sound. The final threshold estimate is the average of just those four threshold estimates. When data were collected for more than one test carrier in a session, 2 or 10 min of exposure to the adapting sound was enforced between blocks, depending on the duration of the observer's break. At the start of each day's session, one of the two adapting modulation rates was randomly chosen and used throughout the day's session. For one of the observers, different adaptor rates were used in a single day, but a break period of over an hour separated the sessions.

Two of the four observers who participated in Experiment I participated in this experiment—Obs 2 and 3. Three additional observers were recruited, all having thresholds in quiet within 10 dB HL for frequencies ranging from 500–8000 Hz. These observers ranged in age from 22 to 39 years. In order to assess the degree to which the 56-Hz adapting sound was a neutral adaptor, thresholds were also obtained for the target-alone condition of the SAM detection task as described in experiment I.

B. Results and Discussion of experiment II

The top panel of Fig. 5 shows the average results from five observers for adaptors with modulation rates of 16 (squares) and 56 (circles) Hz. Thresholds, in increments of 20 log(m), are plotted as a function of the carrier frequency of the test stimulus relative to the carrier frequency of the adaptor (1500 Hz). Error bars reflect the standard errors of the mean across the thresholds measured for the five observers. These averages are largely representative of individual results, with the key exception that Obs 3 demonstrated no consistent effect of the modulation rate of the adaptor (i.e., the squares were not elevated relative to the circles). Because the pattern of Obs 3's thresholds were like those of the other observers when the 56-Hz adaptor was tested, the effect of including his thresholds in the average is to reduce the separation between the 56- and 16-Hz functions. On average, when the adaptor was modulated at 56 Hz and the test sound was centered at 1500 Hz, thresholds were within 1 dB of thresholds obtained without an adaptor (not plotted). That is, the 56-Hz adapting sound appears to act as a reasonable neutral adaptor.

The bottom panel of Fig. 5 shows the magnitude of adaptation for each test carrier frequency. Differences in the thresholds obtained after adaptation to the 16- and 56-Hz SAM adaptors are plotted as a function of the test–adaptor carrier frequency separation. The amount of adaptation is maximal when the test and adapting sounds share the same carrier, and remains robust for test sounds centered between 2 oct below and 1 oct above the adaptor. These data indicate further reaching effects of modulation adaptation than one might conjecture based on the results reported by Kay and Matthews (1971), who concluded that adaptation to frequency modulation does not extend beyond a critical bandwidth. Because there is some consistency in the target–masker separations for which modulation phase effects were obtained (experiment I) and test–adaptor frequencies where adaptation effects were obtained (experiment II), the current data are not inconsistent with a single-channel account of the phase effects obtained experiment I's CMR tasks.

V. SUMMARY AND CONCLUSIONS

The results of experiment I confirm that the relative phases of target and masker modulators do not have a large effect on the detection of SAM, but do influence the detection of reductions in modulation depth of a fully modulated SAM tone and the detection of a tone added to a narrow band of noise. For the latter two tasks, however, no CMR was consistently obtained. Moreover, for the detection of reductions in modulation depth and the detection of a tone added to noise, the joint effects of envelope randomization and frequency separation are relatively consistent across observers, suggesting the actions of similar mechanisms in these two tasks. The impact of off-frequency maskers was limited to frequency separations of 1–2 oct, even though sensitivity to differences in envelope patterns has been measured for wider frequency separations (Strickland *et al.*, 1989). In experiment II, modulation rate-specific adaptation was obtained for the detection of amplitude modulation for four of the five observers tested. Adaptation was present for test carrier frequencies between 2 oct below and 1 oct above the adapting carrier frequency. The results of experiments I and II may be attributed to several types of interactions, and in particular, single-channel models of interactions cannot be discounted.

ACKNOWLEDGMENTS

This work was supported by grant RO1 DC 02012 from the National Institutes of Health and a grant from the University Research Foundation of the University of Pennsylvania. Shane Brant, Jennifer J. Lentz, and Peter Marvit provided helpful suggestions both for this experiment and pilot work that led to its completion. Dr. Jacob Nachmias pro--vided helpful suggestions on an earlier draft of this manuscript, as did two anonymous reviewers.

[1]Initial practice consisted of approximately 5 h experience in the two SAM tasks. Then, for whichever task the observer was to first complete, ten threshold estimates were measured for the target-alone condition. Next, one of the three different masker conditions was tested. Ten threshold estimates were obtained for each frequency separation, in random order. For each frequency separation, an additional five threshold estimates were measured if evidence of practice was apparent (one-tailed t test; $p<0.05$ criterion). Before moving on to the next masker condition, five threshold estimates were repeated for the first frequency separation encountered. If evidence of practice was obtained, five additional thresholds were obtained, yielding a new estimate of threshold. Then, five thresholds were obtained for the second frequency separation tested. This procedure continued until no practice effects were obtained. Before moving onto the next task, observers revisited the target-alone condition.

Bacon, S. P., and Konrad, D. L. (**1993**). ''Modulation detection interference under conditions favoring within- or across-channel processing,'' J. Acoust. Soc. Am. **93,** 1012–1022.

Bacon, S. P., and Moore, B. C. J. (**1993**). ''Modulation detection interference: Some spectral effects,'' J. Acoust. Soc. Am. **93,** 3442–3453.

Cohen, M. F. (**1991**). ''Comodulation masking release over a three octave range,'' J. Acoust. Soc. Am. **90,** 1381–1384.

Cohen, M. F., and Schubert, E. D. (**1987**). ''Influence of place synchrony on detection of a sinusoid,'' J. Acoust. Soc. Am. **81,** 452–458.

Fantini, D. A. (**1991**). ''The processing of envelope information in comodulation masking release (CMR) and envelope discrimination,'' J. Acoust. Soc. Am. **90,** 1876–1888.

Fantini, D. A., and Moore, B. C. J. (**1994**). ''A comparison of the effectiveness of across-channel cues available in comodulation masking release and profile analysis tasks,'' J. Acoust. Soc. Am. **96,** 3451–3462.

Green, D. M. (**1988**). *Profile Analysis: Auditory Intensity Discrimination* (Oxford U.P., New York).

Grose, J. H., and Hall III, J. W. (**1989**). ''Comodulation masking release using SAM tonal complex maskers: Effects of modulation depth and signal position,'' J. Acoust. Soc. Am. **85,** 1276–1284.

Hall III, J. W., and Grose, J. H. (**1988**). ''Comodulation masking release: Evidence for multiple cues,'' J. Acoust. Soc. Am. **84,** 1669–1675.

Hall III, J. W., and Grose, J. H. (**1991**). ''Some effects of auditory grouping factors on modulation detection interference (MDI),'' J. Acoust. Soc. Am. **90,** 3028–3035.

Hall, J. W., Haggard, M. P., and Fernandes, M. A. (**1984**). ''Detection in noise by spectro-temporal pattern analysis,'' J. Acoust. Soc. Am. **76,** 50–56.

Kay, R. H., and Matthews, D. R. (**1971**). ''On the existence in human auditory pathways of channels selectively tuned to the modulation present in frequency-modulated tones,'' J. Physical. **225**, 657–667.

Levitt, H. (**1971**). ''Transformed up-down methods in psychoacoustics,'' J. Acoust. Soc. Am. **49,** 167–177.

Moody, D. B., Cole, D., Davidson, L. M., and Stebbins, W. C. (**1984**). ''Evidence for a reappraisal of the psychophysical selective adaptation

paradigm,'' J. Acoust. Soc. Am. **76,** 1076–1079.

Moore, B. C. J., Glasberg, B. R., and Schooneveldt, G. P. (**1990**). ''Across-channel masking and comodulation masking release,'' J. Acoust. Soc. Am. **87,** 1683–1694.

Moore, B. C. J., and Jorasz, U. (**1992**). ''Detection of changes in modulation depth of a target sound in the presence of other modulated sounds,'' J. Acoust. Soc. Am. **91,** 1051–1061.

Schooneveldt, G. P., and Moore, B. C. J. (**1987**). ''Comodulation masking release (CMR): Effects of signal frequency, flanking-band frequency, masker bandwidth, flanking-band level, and monotic versus dichotic presentation of the flanking band,'' J. Acoust. Soc. Am. **82,** 1944–1956.

Strickland, E. A., Viemeister, N. F., Fantini, D. A., and Garrison, M. A. (**1989**). ''Within- versus cross-channel mechanism in detection of envelope phase disparity,'' J. Acoust. Soc. Am. **86,** 2160–2166.

Tansley, B. W., and Suffield, J. B. (**1983**). ''Time course of adaptation and recovery of channels selectively sensitive to frequency and amplitude modulation,'' J. Acoust. Soc. Am. **74,** 765–775.

Wakefield, G. W., and Viemeister, N. F. (**1984**). ''Selective adaptation to linear frequency-modulated sweeps: Evidence for direction specific FM channels?'' J. Acoust. Soc. Am. **75,** 1588–1592.

Yost, W. A., and Sheft, S. (**1989**). ''Across-critical-band processing of amplitude-modulated tones,'' J. Acoust. Soc. Am. **85,** 848–857.

Yost, W. A., and Sheft, S. (**1990**). ''A comparison among three measures of cross-spectral processing of amplitude modulation with tonal signals,'' J. Acoust. Soc. Am. **87,** 897–900.

Yost, W. A., and Sheft, S. (**1994**). ''Modulation detection interference:Across-frequency processing and auditory grouping,'' Hear. Res. **79**, 48–58.

Yost, W. A., Sheft, S., and Opie, J. (**1989**). ''Modulation interference in detection and discrimination of amplitude modulation,'' J. Acoust. Soc. Am. **86,** 2138–2147.

Profile analysis with an asynchronous target: Evidence for auditory grouping

Nicholas I. Hill[a] and Peter J. Bailey
Department of Psychology, University of York, York YO1 5DD, United Kingdom

(Received 13 November 1996; revised 17 March 1997; accepted 18 March 1997)

Green and Dai [in *Auditory Physiology and Perception*, edited by Y. Cazals, L. Demany, and K. Horner (Pergamon, Oxford, 1992)] reported a series of experiments which suggested that listeners' ability to perform simultaneous across-frequency comparisons of intensity is severely impaired when the target and flanking components begin or end at different times. The present experiment sought to replicate the effect of onset asynchrony and included an additional condition in which the leading portion of the asynchronous target component was accompanied by a pair of ''captor'' tones. The intended purpose of the captor tones was to promote a perceptual organization in which the leading and synchronous portions of the asynchronous target component were grouped with different auditory objects. For all six listeners an asynchrony of 320 ms raised thresholds substantially relative to the synchronous onset condition, the magnitude of the increase ranging between 6 and 16 dB. By contrast, the mean elevation of threshold in the presence of the captor was only 3 dB, although for all listeners thresholds were still greater than for the synchronous onset condition. The results support the view that the deleterious effect of onset asynchrony on profile analysis performance is due to the operation of auditory grouping principles. © *1997 Acoustical Society of America.* [S0001-4966(97)03907-6]

PACS numbers: 43.66.Fe, 43.66.Ba [WJ]

INTRODUCTION

The ability of listeners to perform simultaneous across-frequency comparisons of intensity has been the subject of considerable research in recent years (Green, 1988; Hall *et al.*, 1995). In a typical profile analysis task, a multicomponent stimulus is presented in each of two observation intervals, with listeners required to indicate the interval in which the relative level of one component was increased. To ensure that detection is based on a simultaneous across-channel comparison of intensity rather than a successive within-channel comparison, the overall level of the stimuli in each of the two observation intervals is randomized. The results from such studies indicate that listeners are highly sensitive to changes in spectral profile, with thresholds being comparable to those obtained in traditional intensity discrimination tasks. Moreover, thresholds are relatively unaffected by factors such as the duration of the interstimulus interval (Green *et al.*, 1983) and moderate within-trial randomization of pitch (Richards *et al.*, 1989).

Since profile analysis requires comparison of intensities across frequency, any manipulation that interferes with the integration of auditory information across frequency is likely to lead to a drop in performance. One such manipulation is ear of presentation. Usually in profile analysis experiments the stimuli are presented diotically; however, if the target and flanking components are presented to different ears, then signal threshold is increased markedly (Green and Kidd, 1983; Bernstein and Green, 1987). A plausible explanation for this result is that when the target component is presented to the opposite ear, its contribution to the timbre of the complex is reduced or eliminated thereby rendering a strategy based on a successive comparison of timbre less effective. Implicit in this account is the assumption that listeners are less good at judging the relative intensities of two concurrent but distinct auditory objects (in the above case, the signals at the two ears) than they are at discriminating spectral profiles.

A second factor that is believed to affect the across-frequency integration of information is relative onset time (Dannenbring and Bregman, 1978; Darwin and Ciocca, 1992; Grose and Hall, 1993; Hill and Darwin, 1996). For example, Darwin and Ciocca (1992) measured the contribution of a mistuned harmonic to the pitch of an otherwise harmonic complex as a function of the difference in onset time between the mistuned component and the rest of the complex. The pitch-matching data indicated a monotonic decrease in the contribution of the mistuned component with increasing onset asynchrony up to 320 ms, by which time its contribution had been entirely removed.

Evidence that differences in relative onset times may influence the across-frequency processing underlying profile analysis comes from a study reported by Green and Dai (1992). In one experiment they varied the amount by which the target component led the rest of the complex, all tones ending synchronously. An onset asynchrony of 50 ms resulted in an elevation in signal threshold of 10–15 dB. Further increases in onset asynchrony up to 500 ms resulted in a smaller but significant drop in performance, to the extent that listeners' thresholds were close to the value that could be achieved by simply selecting the interval in which the asynchronous component was loudest. In a different experiment from the same series, Green and Dai (1992) demonstrated that the dramatic drop in performance was only observed when the target component was gated asynchronously. Gat-

[a]Corresponding author, Electronic mail: nihl@york.ac.uk

 0001-4966/97/102(1)/477/5/$10.00

ing a nontarget component asynchronously had no significant effect on threshold.

In addition to replicating the effect of onset asynchrony observed by Green and Dai (1992), the present experiment sought to establish whether the impaired ability of listeners to perform across-frequency comparisons of intensity was due to perceptual segregation of the target and flanking components, or to some other factor such as adaptation. For example, adaptation caused by the leading portion of the asynchronous target will reduce the effective level of the synchronous portion relative to that of the flanking components. Green and Kidd (1983) found that for a 21-component complex a reduction of 6 dB in the relative level of the pedestal increased threshold by approximately 10 dB. Some evidence against adaptation as an explanation is provided by Green and Dai's finding of effects of offset asynchrony. That is, thresholds were also elevated when the target and flanking components began synchronously, but the target component continued for some time after the offset of the flanking components. However, for any given value of asynchrony, the magnitude of the offset effect was approximately half that observed for onset asynchrony, and it is therefore possible that adaptation was a contributory factor.

I. EXPERIMENT

A. General

The present experiment was a partial replication of the study by Green and Dai (1992). Three conditions were employed. In the synchronous onset condition, all components of the complex were gated on and off at the same time. In the asynchronous onset condition, the target component began 320 ms ahead of the flanking components. The choice of an asynchrony of 320 ms was based partly on the data of Darwin and Ciocca (1992), who found that such an asynchrony entirely removed the contribution of a mistuned harmonic to the pitch of the complex. Similarly, the data of Green and Dai (1992) suggest that increasing asynchrony beyond 250 ms has little if any effect on threshold. To assess whether any increase in signal threshold in the asynchronous onset condition was due to perceptual segregation of the target component, a ''captor'' condition was included in which the leading portion of the asynchronous target was accompanied by two captor tones. The simplest perceptual organization of the stimuli in the captor condition is one comprising two successive complex tones with the leading portion of the target component grouped with the captors, and the synchronous portion grouped with the flanking components. If the increase in threshold observed by Green and Dai (1992) was due to the mere presence of an onset asynchrony between the target and flanking components, then the presence of the captor tones would be expected to have little effect. However, if the effect of asynchrony resulted from perceptual segregation of the target and flanking components, then by reducing the tendency for segregation the presence of the captor tones should lead to an improvement in performance. The inclusion of the captor condition was motivated by the study of Darwin and Sutherland (1984) in which it was found that the presence of a captor tone could largely reverse the effect of onset asynchrony observed in vowel perception.

B. Listeners

The six listeners (4 male) were aged between 20 and 34. All listeners had normal pure-tone thresholds over the range of frequencies tested. No screening for profile discrimination performance was undertaken but all listeners received several hours of practice in profile tasks before data collection for the present experiment was begun. Listener NH was the first author. The remaining listeners were students at the university and received payment.

C. Stimuli and equipment

The basic stimulus comprised seven logarithmically spaced sinusoids at frequencies of 0.2, 0.342, 0.585, 1, 1.71, 2.924, and 5 kHz. In the synchronous onset condition, all components were gated on and off at the same time and had a duration of 200 ms. In the asynchronous onset condition the 1-kHz tone began 320 ms ahead of the remaining components, all components terminating synchronously. In the captor condition, the 1-kHz component also began 320 ms before the flanking components, but this time the leading portion of the 1-kHz component was spectrally flanked by a pair of captor tones. The captor tones began synchronously with the 1-kHz component and had a duration of 320 ms. The frequencies of these captor tones were 0.75 and 1.25 kHz. All durations included 10-ms $\cos^2$ onset and offset ramps. The overall level of the stimuli was selected randomly on each presentation from a uniform distribution spanning the range 40–70 dB SPL per component. The phase of each component was selected randomly on each presentation. In the synchronous and asynchronous conditions, the signal was an increment in the intensity of the 1000-Hz component. In the captor condition the signal was an increment in the intensities of both the 1000-Hz component and the two captor tones. Increasing the intensities of both the target and captor tones in the signal interval ensured that listeners were unable to use differences in the relative intensities of the target and captor tones as a cue. A schematic illustration of the stimuli used in the asynchronous and captor conditions is given in Fig. 1.

Stimuli were synthesized in real time at a sampling rate of 20 kHz using custom software running on an IBM-compatible PC. The resulting waveforms were converted to voltages using 16-bit DACs (TDT model DD1) and were low-pass filtered at 8 kHz (TDT model FT2). The overall level of the stimuli was controlled using a pair of attenuators (TDT model PA4). Stimuli were presented diotically over Sennheiser HD414 headphones. Listeners were run individually in a sound-attenuating enclosure.

D. Procedure

Thresholds were determined using a two-alternative, forced-choice, adaptive procedure which targeted the intensity increment corresponding to 79% correct responses (Levitt, 1971). In each session listeners completed 12 runs of a 60-trial adaptive procedure which lasted approximately 1 h.

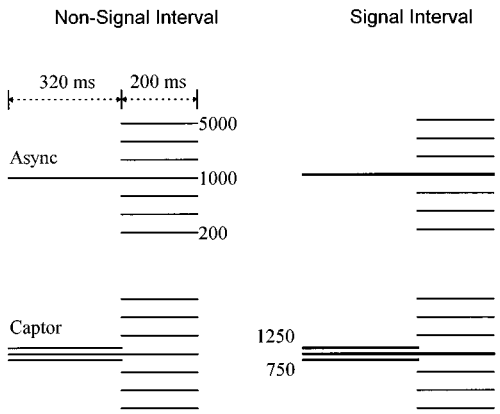

FIG. 1. Schematic illustration of the stimuli used in the asynchronous onset and captor conditions. The bold lines indicate relative increments in intensity.

Each run began with the size of the intensity increment set to 10 dB using the metric $10\log(1+\Delta I/I)$. During a run the magnitude of the intensity increment was varied logarithmically using an initial ratio of 0.7225. This ratio was increased to 0.85 following the first error so as to increase the resolution of the adaptive procedure near threshold.[1] The data corresponding to the first three or four reversals in each run were ignored, estimated threshold being based on the average intensity increment over the remaining even number of reversals. A typical threshold estimate was based on an average of 4–8 reversals.

The beginning of each trial was signaled by the presentation of a spot in the center of a computer screen for 200 ms. In the asynchronous and captor conditions, the first observation interval followed 500 ms after the disappearance of the spot, and the interstimulus interval was also 500 ms. In the synchronous onset condition, these intervals were increased to 820 ms so that the temporal position of the flanking components within a trial was fixed across all three conditions. Listeners were given an unlimited time in which to respond, immediately after which they were presented with feedback for 400 ms. The next trial began 1 s after the termination of feedback.

So far as was possible listeners participated on a daily basis. On any given session the same condition was presented on each of the 12 runs in order to minimize effects of uncertainty. All listeners were run first on the captor condition, then on the asynchronous onset condition, and finally on the synchronous onset condition. In each condition listeners were run until performance was stable which typically took between four and six sessions. The reported thresholds were derived from the last two sessions of data collection in each condition.[2] To facilitate comparisons between the present data and those reported by Green and Dai (1992), the threshold intensity increment obtained in each individual run was converted to the corresponding signal-to-standard ratio in decibels defined as $20\log(\Delta A/A)$. Runs in which the threshold was greater than two standard deviations from the mean were omitted. The number of runs excluded on the basis of this criterion ranged between zero and three for any one condition and listener.

E. Results

Table I shows the threshold signal-to-standard ratio in decibels and associated standard error for each listener and condition. The bottom row shows the mean and standard error across listeners. Also shown are the pairwise differences between performance in the three conditions. All listeners had higher thresholds in the asynchronous onset condition than the synchronous condition, the increase in threshold ranging from 5.68 dB for listener NH to 15.80 dB for listener RW. For a three-down, one-up adaptive procedure and a level variation of 30 dB, the expected threshold of a listener basing his/her decision only on sequential level comparisons between stimuli is 7.75 dB (Green, 1988). Therefore even listener MF with a relatively high threshold of 5.28 dB appears to have been making some use of within-interval, across-frequency cues. In addition to higher thresholds, the data for the asynchronous onset condition also displayed a marked increase in across-listener variability relative to the synchronous onset condition.

In comparing the thresholds obtained in the synchronous onset condition with the mean threshold across listeners reported by Green and Dai (1992), three factors need to be considered. First, in the study of Green and Dai the targeted threshold corresponded to 94% correct responses whereas in the present experiment it corresponded to 79% correct responses. The corresponding difference in signal level between these two points on the psychometric function is approximately 5 dB (Raney *et al.*, 1989). Second, Green and Dai (1992) employed a 21 component complex whereas the

TABLE I. Threshold signal level defined as $20\log(\Delta A/A)$ and associated standard error of the mean for each listener and condition. The bottom row shows the mean and standard error across listeners. Also shown are the pairwise differences between performance in the three conditions.

	Threshold (dB)						Difference (dB)		
Listener	Sync		Async		Captor		Async-Sync	Captor-Sync	Async-Captor
NH	−17.04	(0.47)	−11.39	(0.72)	−14.78	(0.50)	5.68	2.26	3.42
AC	−15.63	(0.45)	−6.31	(0.52)	−12.70	(0.70)	9.32	2.93	6.39
RW	−13.03	(0.59)	2.77	(0.57)	−10.84	(0.54)	15.80	2.19	13.61
AK	−12.50	(0.61)	−2.59	(0.52)	−7.77	(0.53)	9.91	4.73	5.18
KM	−10.94	(0.57)	−2.29	(0.34)	−8.82	(0.49)	8.65	2.12	6.53
MF	−10.05	(0.41)	5.28	(0.37)	−6.81	(0.52)	15.33	3.24	12.09
Mean	−13.20	(1.10)	−2.42	(2.46)	−10.29	(1.25)	10.78	2.91	7.87

complex used in the present experiment comprised only seven components, both complexes spanning the frequency range from 0.2 to 5 kHz. The data of Bernstein and Green (1987) suggest that thresholds for a signal added to the 1-kHz component of a 21 component complex are approximately 5 dB lower than those for a seven component complex spanning the same frequency range. Third, the present experiment employed an intensity rove of 30 dB between presentations whereas a rove of 20 dB was employed by Green and Dai (1992). Given these considerations, the fact that the thresholds in the present experiment are similar to those reported by Green and Dai suggests that there is little difference in sensitivity between the two sets of listeners.

For all listeners, the presence of the captor tones improved performance relative to that in the asynchronous onset condition. Those listeners who showed the greatest effect of onset asynchrony also showed the largest improvement in the captor condition. The across-listener variability in the captor condition was similar to that in the synchronous condition and substantially less than for the asynchronous condition. Despite the beneficial effect of the captor tones, all listeners had higher thresholds in the captor condition than in the synchronous onset condition. The mean difference between thresholds in the synchronous and captor conditions was approximately 3 dB.

When questioned about their perceptual experiences, all listeners reported that in the asynchronous onset condition the first sound was perceived as continuing into the second. However, in the captor condition two successive and distinct sounds were perceived.

F. Discussion

The fact that thresholds in the asynchronous onset condition were substantially higher than those obtained when all components began synchronously confirms Green and Dai's (1992) finding that the ability to perform simultaneous across-frequency comparisons of intensity is impaired when the onset of the target component precedes that of the flanking components. The magnitude of the effect observed in the present experiment is somewhat smaller than that reported in the Green and Dai study. There are several factors that may contribute towards this difference. These include the amount of listener training, differences in the number and duration of components used in the two studies, and differences in targeted threshold. Given the across-listener variability in performance in the asynchronous onset condition, the difference between experiments could also be due to individual differences in the two sets of listeners.

The reason for the large across-listener variability in thresholds for the asynchronous onset condition is unclear. One possibility is that the perceptual consequences of an increase in the level of the target component may have been less apparent in the asynchronous onset condition with the result that listeners were less likely to adopt a common strategy. For example, the increased salience of the target component may have encouraged some listeners to base their decision on an explicit comparison of the loudness of the target and flanking complex, whereas others may have based their decision on a characteristic change in the timbre of an auditory object comprising the flanking complex and the partially segregated target. The across-listener variability may simply reflect the fact that the strategies adopted by the listeners differed in their effectiveness, with those listeners relying on an explicit comparison of the loudness of the target and flanking complex likely to have the higher thresholds (cf. Dai and Green, 1992).

The fact that the presence of the two captor tones resulted in lower thresholds demonstrates that the mere presence of an asynchrony between the target and flanking components is not sufficient to produce the substantial increase in threshold reported by Green and Dai (1992).[3] Rather, the data, together with listener's subjective reports, are consistent with the idea that the deleterious effect of asynchrony was due to the target being perceptually segregated from the flanking components. In the present experiment the effect of perceptual segregation on threshold was relatively large. However, not all stimulus manipulations which promote perceptual segregation of the target and flanking components lead to such large effects. For example, Green and Nguyen (1988) investigated the effect of amplitude modulating the target component of a 21 component complex on profile discrimination performance. Although the modulation did increase thresholds somewhat, the effects were smaller than those found for onset asynchrony. Similarly, our own pilot data suggest that frequency modulating the target component at a rate of 10 Hz has little effect on threshold, provided the zero-to-peak modulation depth does not exceed 3% of center frequency. These latter two results, both derived from stimulus manipulations that facilitate ''hearing out'' of the target component, indicate that further work is needed on the relationship between objective and subjective measures of segregation.

The finding that a captor can reduce the effect of onset asynchrony in a profile analysis task is consistent with previous studies in which a captor has been utilized in an attempt to reverse the effect of onset asynchrony (Darwin and Sutherland, 1984; Ciocca and Darwin, 1993; Carlyon, 1994). For example, Carlyon (1994) investigated listeners' ability to detect a mistuning resulting from incoherently modulating the frequency of one component of an otherwise coherently modulated harmonic complex. When the incoherently modulated component was immediately preceded and followed by a pure tone, detection thresholds were elevated. Carlyon argued that the increase in threshold was due to the fact that the temporally flanking pure tone caused the incoherently modulated component to segregate from the rest of the complex. To test this hypothesis, Carlyon included conditions in which the pure tone was presented as one component of a multitone complex which preceded and followed the frequency modulated complex. In general, these conditions resulted in lower thresholds, suggesting that the tendency of the incoherently modulated component to segregate from the complex was reduced when the temporally flanking pure tone was provided with an alternative set of components with which to form a perceptual group.

In summary, the present experiment has confirmed Green and Dai's finding (Green and Dai, 1992) that listeners' ability to discriminate spectral profiles is impaired when the

target and flanking components begin at different times. The experiment also demonstrates that the increase in threshold resulting from gating the target component on ahead of the flanking components can be largely reversed by presenting a pair of captor tones for the duration of the asynchronous portion of the target. This latter result is consistent with the hypothesis that the deleterious effect of onset asynchrony results from perceptual segregation of the target and flanking components.

ACKNOWLEDGMENTS

The authors would like to thank Hedwig Gockel and Huanping Dai for constructive comments on an earlier version of this manuscript. Financial support was provided by the U.K. Medical Research Council through project Grant No. G9436832N.

[1]For example, if the first three responses in a run were correct, the level increment would be reduced to 7.225 dB (0.7225×10.0 dB). An error on the following trial would result in the increment being set to 8.50 dB (7.225 dB/0.85).

[2]Listener MF showed no evidence of learning in either the synchronous or asynchronous onset conditions. For this listener the reported threshold in these conditions was averaged over six sessions.

[3]The results of a study by Dai and Green (1992) suggest that it is unlikely that listeners were performing successive comparisons of intensity between one or other of the captor tones and the most proximal nonsignal component.

Bernstein, L. R., and Green, D. M. (**1987**). ''The profile-analysis bandwidth,'' J. Acoust. Soc. Am. **81,** 1888–1895.

Carlyon, R. P. (**1994**). ''Detecting mistuning in the presence of synchronous and asynchronous interfering sounds,'' J. Acoust. Soc. Am. **95,** 2622–2630.

Ciocca, V., and Darwin, C. J. (**1993**). ''Effects of onset asynchrony on pitch perception: Adaptation or grouping?'' J. Acoust. Soc. Am. **93,** 2870–2878.

Dai, H., and Green, D. M. (**1992**). ''Auditory intensity perception: Successive versus simultaneous, across-channel discriminations,'' J. Acoust. Soc. Am. **91,** 2845–2854.

Dannenbring, G. L., and Bregman, A. S. (**1978**). ''Streaming vs. fusion of sinusoidal components of complex tones,'' Percept. Psychophys. **24,** 369–376.

Darwin, C. J., and Ciocca, V. (**1992**). ''Grouping in pitch perception: Effects of onset asynchrony and ear of presentation,'' J. Acoust. Soc. Am. **91,** 3381–3390.

Darwin, C. J., and Sutherland, N. S. (**1984**). ''Grouping frequency components of vowels: When is a harmonic not a harmonic?'' Q. J. Exp. Psychol. **36A**, 193–208.

Green, D. M. (**1988**). *Profile Analysis: Auditory Intensity Discrimination* (Oxford University, Oxford).

Green, D. M., and Dai, H. (**1992**). ''Temporal relations in profile comparisons,'' in *Auditory Physiology and Perception*, edited by Y. Cazals, L. Demany, and K. Horner (Pergamon, Oxford), pp. 471–477.

Green, D. M., and Kidd, Jr., G. (**1983**). ''Further studies of auditory profile analysis,'' J. Acoust. Soc. Am. **73,** 1260–1265.

Green, D. M., Kidd, Jr., G., and Picardi, M. C. (**1983**). ''Successive versus simultaneous comparisons in auditory intensity discrimination,'' J. Acoust. Soc. Am. **73,** 639–643.

Green, D. M., and Nguyen, Q. T. (**1988**). ''Profile analysis: Detecting dynamic spectral changes,'' Hearing Res. **32,** 147–164.

Grose, J. H., and Hall, J. W. (**1993**). ''Comodulation masking release: Is comodulation sufficient?'' J. Acoust. Soc. Am. **93,** 2896–2902.

Hall, J. W., Grose, J. H., and Mendoza, L. (**1995**). ''Across-channel processes in masking,'' in *Hearing*, edited by B. C. J. Moore (Academic, San Diego), pp. 243–266.

Hill, N. I., and Darwin, C. J. (**1996**). ''Lateralization of a perturbed harmonic: Effects of onset asynchrony and mistuning,'' J. Acoust. Soc. Am. **100,** 2352–2364.

Levitt, H. (**1971**). ''Transformed up-down methods in psychoacoustics,'' J. Acoust. Soc. Am. **49,** 467–477.

Raney, J. J., Richards, V. M., Onsan, Z. A., and Green, D. M. (**1989**). ''Signal uncertainty and psychometric functions in profile analysis,'' J. Acoust. Soc. Am. **86,** 954–960.

Richards, V. M., Onsan, Z. A., and Green, D. M. (**1989**). ''Auditory profile analysis: Potential pitch cues,'' Hearing Res. **39,** 27–36.

Discrimination of temporal asymmetry in cochlear implantees

Christian Lorenzi
MRC, Applied Psychology Unit, 15 Chaucer Road, Cambridge CB2 2EF, United Kingdom and PCH Département de Psychologie Cognitive, Institut de Psychologie, Université Lumière Lyon II, 69676 Bron Cedex, France

Stéphane Gallégo
Laboratoire de Physiologie Sensorielle, ''Perception & Mécanismes Auditifs,'' UPRESA CNRS 5020, Pav. U. Hôpital E. Herriot, 69437 Lyon Cedex 03, France

Roy D. Patterson
MRC, Applied Psychology Unit, 15 Chaucer Road, Cambridge CB2 2EF, United Kingdom

(Received 1 February 1996; revised 2 January 1997; accepted 2 April 1997)

Several studies have recently demonstrated that normal-hearing listeners are sensitive to short-term temporal asymmetry in the envelopes of sinusoidal or noise carriers. This paper presents a study in which cochlear implantees were presented trains of current pulses with temporally asymmetric envelopes through one channel of an implant that stimulates the auditory nerve directly, thereby bypassing cochlear processes. When the level of the stimuli was adjusted to fit their audibility range, the implantees were able to discriminate temporal asymmetry over a much wider range than normal-hearing listeners. The results suggest that the perception of temporal asymmetry is limited by compression in the normal cochlea. © *1997 Acoustical Society of America.* [S0001-4966(97)06707-6]

PACS numbers: 43.66.Jh, 43.66.Mk, 43.66.Sr, 43.66.Ts [WJ]

INTRODUCTION

When a sound with an asymmetric temporal envelope is reversed in time, it often produces a marked change in the timbre of the sound. The effect is important because the power spectrum of a sound does not vary with the time reversal. Although the perceptual effect of the time reversal is well-known, it was largely ignored until recently, when Patterson (1994a, b) showed how the effects of the time reversal could be studied systematically using ''damped'' and ''ramped'' sinusoids. The term ''damped sinusoid'' refers to a segment of a sinusoid with a damped exponential envelope that is repeated cyclically to produce a sustained sound. The ''ramped sinusoid'' is simply the damped sinusoid reversed in time. The envelope ''damps'' down in the former case and ''ramps'' up in the latter case. Normal-hearing listeners can discriminate damped sinusoids from ramped sinusoids when the half-life of the envelope is in the range 1–50 ms. Compression in the cochlea of the normal-hearing listener reduces the dynamic range of damped and ramped sinusoids in the neural representations flowing from the cochlea. This led to the intriguing suggestion that cochlear implantees might exhibit even better asymmetry discrimination than normal-hearing listeners because the implant bypasses the cochlea and any compression it might impose. We assume, as argued by Shannon (1986), that sensitivity to level differences in the central auditory system of cochlear implantees is about the same as that for normals when presented at the same sensation level. It is also the case that with implantees, one can restrict the stimulation to a single electrode and thereby preclude spectral cues to a degree that is not possible with normal listeners. Thus cochlear implantees would appear to provide us with a unique opportunity to investigate the limits of retrocochlear processing of temporal asymmetry.

There have been several demonstrations that cochlear implantees can process temporal envelope information. Hochmair and Hochmair-Desoyer (1984) reported that implantees could distinguish among square, triangle, and sine waves for repetition frequencies up to 400 Hz. Shannon (1986) demonstrated near normal temporal integration, gap detection, and forward masking in two implantees, and more recently, Shannon (1992) reported that implantees could detect amplitude modulation at least as well as normal-hearing listeners. In these experiments, however, there is no manipulation of temporal asymmetry.

I. EXPERIMENT

Pairs of ramped and damped envelopes with the same half-life were presented to cochlear implantees to assess their discrimination of temporal asymmetry. The electrical signal was delivered directly to a single electrode of a Digisonic DX10 implant without going through the preprocessor to avoid the compression normally applied by the device.

A. Method

Five postlingually deaf listeners (SP, BM, LR, FJ, BR) participated in the experiment. Clinical information about these patients is presented in Table I. They were all implanted with a Digisonic DX10 device (MXM), which is a transcutaneous 15-channel cochlear implant with an intracochlear electrode array (Beliaeff *et al.*, 1994). Activation was limited to the most basal electrode which delivered biphasic current pulses; the remaining 14 electrodes in the array were connected together to serve as the return path for the current

TABLE I. Clinical data for the five cochlear implantees of the study.

Patient	Age (years)	Cause of deafness	Duration of implant use (months)	Pulse amplitude (V)	Min (μs/phase)	Max (μs/phase)
BM	64	head trauma	7	1.5	12	55
SP	44	head trauma	6	1.3	14.5	45
LR	60	unknown	3	1.3	10	45
FJ	45	head trauma	48	1.6	25	95
BR	36	progressive deafness	1	1.3	10	40

(''common ground'' mode of stimulation). X-ray photographs revealed that electrode positioning was roughly the same for all implantees. All stimuli were presented directly to the implanted electrode without going through the speech processor. For each implantee, the pulse amplitude was fixed and the pulse duration was adjusted from threshold (min) to comfort level (max); the pulse amplitude and the min and max values for each implantee are presented in Table I. All implantees were experienced in two-interval, two-alternative forced choice tasks (2I, 2AFC).

1. Stimuli

The stimuli were trains of biphasic current pulses of fixed amplitude. The pulse duration as a function of time was shaped by a ramped or damped function. Equation (1) shows the general form of a damped envelope:

$$\text{damp}(t) = \min + [\max - \min]\exp[ct/\text{hl}] \quad (0 < t < T), \tag{1}$$

hl is the half-life of the damped envelope, and c is a constant ($-0.693\,147$), that brings the envelope to $[\max - \min]/2$ in hl ms. T is the repetition period which is 50 ms. The pulse rate was 800 Hz, which was the maximum pulse rate provided by the device used to perform direct stimulation. The ramped envelopes were produced by reversing the damped envelopes in time. The envelopes were digitally generated on a PC by a 16-bit D/A converter at a sampling frequency of 44.1 kHz. The electrical stimuli were generated using a Digistim system (MXM) connected to the PC via a serial port. The duration of the stimuli was 500 ms; the silent interval between stimuli was 500 ms. The comfort level, max, was adjusted as the half-life was increased so that the stimuli were of approximately equal loudness. The loudness of the stimuli was equated by asking each implantee to adjust the level of each damped stimulus to that of a damped stimulus with a 8-ms half-life. Adjustment was performed using an initial step size of 5 μs/phase and a final step size of 0.5 μs/phase. Three estimates were collected and averaged. The average max values measured for each half-life and for each implantee are presented in Table II.

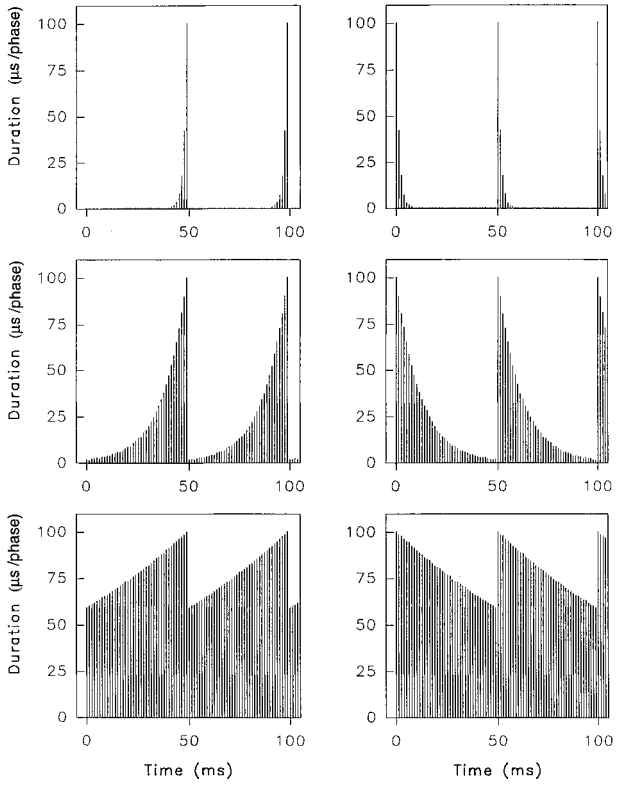

FIG. 1. Ramped (left column) and damped (right column) current pulse trains with a half-life of 1 ms (top section), 8 ms (middle section), and 64 ms (bottom section). The carrier frequency is 800 Hz. The repetition period is 50 ms.

Segments of the current pulse trains are presented in Fig. 1; the left and right panels show ramped and damped functions, respectively. The half-life of the exponential is 1 ms in the top section, 8 ms in the middle section, and 64 ms in the bottom section of Fig. 1. The trains of current pulses show that the Digistim system preserves the temporal envelope.

2. Procedure

Implantees sat in front of a keyboard connected to the computer controlling the experiment. The task was 2I, 2AFC. In a given trial, implantees were presented a ramped stimulus in one interval and a damped stimulus with the same half-life in the other interval, and asked to choose the interval with the ''more tonal quality.'' In each trial, inter-

TABLE II. Max values (in μs/phase) producing stimuli of equal loudness as the half-life is increased from 0.25 to 1024 ms. The data are presented for the five cochlear implantees of the study.

hl (ms)	0.25	0.5	1	2	4	16	32	64	128	256	512	1024
BM	65	60	60	60	55	55	50	45	40	40	37	40
SP	53	52.5	50	48	46.5	44	43	42	41	40	38	37.5
LR	38	40	41	43	45	45	45	45	40	37	35	35
FJ	80	86.5	90	90	95	95	85	77	71	65.5	67	65
BR	35	35	35	37	42.5	36	31.5	30	27.5	23	23	23

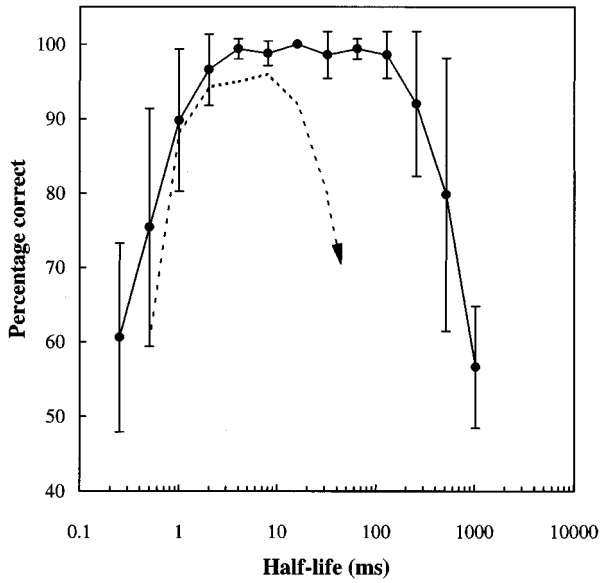

FIG. 2. Average psychometric function for the five cochlear implantees, showing performance as a function of hl. Error bars show one standard deviation about the mean performance of the five implantees. For comparison, the data are plotted along with the mean of the data obtained with normal-hearing listeners.

vals were presented in random order. A correct response corresponded to a ramped response. The half-life was fixed within a block and was varied from 0.25 to 1024 ms from block to block. Each block contained 30 trials. Implantees received visual feedback concerning the accuracy of their response after each trial. They received 15 min of preliminary training before participating in the experiment.

B. Results

The average psychometric function for the five implantees is presented by the solid line with filled circles in Fig. 2. The dotted line without symbols show the mean of the data obtained by Patterson (1994b) and Irino and Patterson (1996) with normal-hearing listeners, using a carrier frequency of 800 Hz and a repetition rate of 50 ms. The results show that implantees can discriminate ramped and damped envelopes better than normal-hearing listeners. Performance is above chance for half-lives as short as 0.5 ms and as long as 500 ms; the range for normal-hearing listeners is about 1–50 ms. The individual psychometric functions were very similar in shape to that of the average psychometric function. Table III presents estimates of the shortest and the longest just-discriminable half-lives for the individual psychometric functions, and it shows that the short and long thresholds covary. The number of doublings between the short and long threshold is presented in the right-hand column; it is close to ten for all of the implantees indicating that the size of the range where discrimination is possible is highly consistent across implantees.

TABLE III. Short threshold half-life and long threshold half-life for the five cochlear implantees. The number of doublings between the short and long thresholds half-lives is presented in the last column.

Patient	Shortest hl (ms)	Longest hl (ms)	Number of doublings
BM	0.57	610	10.06
SP	0.9	780	9.75
LR	0.2	300	10.55
FJ	0.69	860	10.28
BR	0.4	460	10.16

II. DISCUSSION AND CONCLUSIONS

When damped and ramped envelopes with the same half-life are presented to cochlear implantees at the optimum intensity and without compression, they can discriminate the temporal asymmetry over a much broader range of half-lives than normal-hearing listeners. The stimulation was restricted to a single electrode, thereby precluding the use of spectral cues. As stimuli were equated in loudness, it is also unlikely that loudness cues played a role in the discrimination task. Discrimination at the shortest half-lives may have been limited by the pulse rate of the Digistim device, 800 Hz, so envelopes with half-lives less than 1.25 ms would not be properly represented. However, extension of the discrimination range to shorter half-lives would only strengthen the conclusion.

The obvious explanation for the superior discrimination performance of the hearing-impaired listeners would appear to be that compression in the normal cochlea reduces sensitivity to level differences, and temporal asymmetry is encoded as differences in level differences. Without compression, and assuming the same level processing mechanism in the central auditory system, hearing-impaired listeners are operating on larger level differences and so do better, but of course, only within their much reduced dynamic range. This is consistent with Shannon's (1992) finding that implantees often exhibit greater sensitivity to amplitude modulation than normal-hearing listeners when the modulation rate is less than 300 Hz.

Implantees cannot discriminate temporal pitch above 300 Hz (Tong *et al.*, 1982). All the implantees who participated in the presented study labeled ramped stimuli as ''smooth,'' ''uniform,'' or ''continuous,'' and damped stimuli as ''interrupted'' or ''with a drum-like quality.'' This suggests that the ''tonal quality'' used to instruct listeners was interpreted by implantees as a ''smooth quality.''

Finally, the results indicate that it is important to ensure that hearing aids and cochlear implants do not restrict temporal asymmetry unduly when applying compression to control level. Asymmetry is a prominent property of speech sounds and hearing-impaired listeners are likely to make good use of it when it is available.

ACKNOWLEDGMENTS

The first author was supported by a post-doctoral grant from the FYSSEN Foundation. The second author was supported by a CIFRE doctoral grant from the MXM Company. We wish to thank two anonymous reviewers for extensive comments on earlier versions of the paper.

Beliaeff, M., Dubus, P., Leveau, J. M., Repetto, J. C., and Vincent, P. (**1994**). ''Sound processing and stimulation coding of DIGISONIC DX10 15-channel cochlear implant,'' in *Advances in Cochlear Implant*, edited by E. S. Hochmair (Vienna, Manz), pp. 198–203.

Hochmair, E. S., and Hochmair-Desoyer, I. J. (**1984**). ''Aspects of sound signal processing using the Vienna intra- and extracochlear implants,'' in *Cochlear Implants*, edited by R. A. Schindler and M. M. Merzenich (Raven, New York), pp. 101–110.

Irino, T., and Patterson, R. D. (**1996**). ''Temporal asymmetry in auditory perception and a ''delta-gamma'' theory of asymmetric intensity enhancement in the peripheral auditory system,'' J. Acoust. Soc. Am. **99,** 2316–2331.

Patterson, R. D. (**1994a**). ''The sound of a sinusoid: Spectral models,'' J. Acoust. Soc. Am. **96,** 1409–1418.

Patterson, R. D. (**1994b**). ''The sound of a sinusoid: Time-interval models,'' J. Acoust. Soc. Am. **96,** 1419–1428.

Shannon, R. (**1986**). ''Temporal processing in cochlear implants,'' in *Sensorineural Hearing Loss: Mechanisms, Diagnosis and Treatment*, edited by M. J. Collins, T. J. Glattke, and L. A. Harker (University of Iowa, Iowa City), pp. 349–368.

Shannon, R. (**1992**). ''Temporal modulation transfer functions in patients with cochlear implants,'' J. Acoust. Soc. Am. **91,** 2156–2164.

Tong, Y. C., Clark, G. M., Blamey, P. J., Busby, P. A., and Dowell, R. C. (**1982**). ''Psychophysical studies for 2 multiple-channel cochlear implant patients,'' J. Acoust. Soc. Am. **71,** 153–160.

Interference effects in short-term memory for timbre

Gary E. Starr[a] and Mark A. Pitt
Ohio State University, Columbus, Ohio 43210

(Received 3 May 1996; accepted for publication 13 March 1997)

Four experiments investigated memory for timbre using the interpolated-tone paradigm [Deutsch, Science **168**, 1604–1605 (1970)], in which participants discriminate pairs of tones (standard and comparison) separated by intervening (interpolated) tones. Interpolated tones varied from the standard tone in spectral similarity (within-dimensional variation), fundamental frequency (cross-dimensional variation), and repetition frequency. While the latter two variables had negligible effects on timbre memory, interference with timbre memory increased with the spectral similarity of the interpolated tones to the standard tone. The findings closely parallel those found for pitch memory, and suggest that memory interference depends on perceptual similarity in both cases.
 [S0001-4966(97)02507-1]

PACS numbers: 43.66.Jh, 43.66.Hg [JWH]

INTRODUCTION

An aim of research in auditory information processing is to understand how sound objects (e.g., speech, car horns, piano tones) are perceived and remembered. One experimental approach to investigating this issue has been to study how listeners perceive, both individually and in combinations, the auditory dimensions that make up sounds, such as pitch, timbre, and loudness (Melara and Marks, 1990a, 1990b). This paper continues in this tradition, focusing on memory for timbre and pitch.

Research on memory for pitch and timbre has examined whether memory for one dimension is affected by the other and how memory representations change over time (Krumhansl and Iverson, 1992; Melara and Marks, 1990a, 1990b; Pitt and Crowder, 1992). For example, Crowder (1989) had participants make speeded same/different pitch judgments to two tones separated by 500 ms. The judgments were faster and more accurate when the tones were played on the same instrument (i.e., had the same timbre) than when played on different instruments, suggesting timbre variation interfered with the memory for pitch. Melara and Marks (1990a, 1990b; Krumhansl and Iverson, 1992; Pitt, 1994) replicated and extended this cross-dimensional interference effect using a speeded classification paradigm (Garner, 1974). They also found the reverse effect: Pitch variation disrupted memory for timbre.

Cross-dimensional interference disappears, however, when memory for the standard tone is probed later in time. Using a same/different discrimination task, Deutsch (1970, 1982 for a review) and Semal and Demany (1991, 1993) obtained this result in experiments designed to elucidate the characteristics of pitch memory. A condition in which a five-second silent interval separated the standard and comparison tones provided a baseline measure of discrimination. Of interest was discrimination in other conditions, in which six tones were presented during the 5-s interval. These interpolated tones varied in pitch and timbre similarity to the standard tone.

For example, Semal and Demany (1991, experiment 1) had listeners discriminate the pitch of sine waves while interpolated tones were either close or far from the standard tone in pitch, timbre, or both dimensions. Timbre was varied by changing the harmonic complexity of the tones. Interpolated tones close in timbre were also sine waves, while tones far in timbre consisted of the first eight harmonics of a tone. Pitch was manipulated by varying the frequency range within which the interpolated tones could be selected. Interpolated tones close in pitch varied by no more than two semitones; tones far in pitch were at least two octaves different from the standard.

The primary finding was that pitch memory was disrupted by variation in the pitch of the interpolated tones (i.e., same-dimension interference), but not variation in timbre (cross-dimension interference). Relative to the baseline, discrimination was disrupted twice as much by interpolated tones close in pitch than tones far in pitch (error rates were 39% and 19%, respectively). Memory interference changed little when timbre varied, with error rates in the close and far timbre conditions not being reliably different (26% and 33%, respectively). Semal and Demany (1993) replicated this minimal effect of cross-dimensional interference in pitch memory with the dimension of loudness.

What emerges from these studies is that the representations of pitch and timbre are susceptible to cross-dimensional information when first encoded. Within 5 s cross-dimensional influences diminish to the point where intradimensional similarity is the primary source of interference. It appears as though dimensional representations solidify with time and, in so doing, lose their susceptibility to interference from other dimensions.

The latter claim is based primarily on evidence from pitch memory research. If these findings are indicative of general principles of auditory memory, then similar results should be found with other dimensions of sound. The purpose of the present study was to test this proposal by investigating short-term memory for timbre. We used the same

[a]Corresponding author address: Department of Psychology, Wingate University, Campus Box 5005, Wingate, NC 28174; Electronic mail: gstarr@wingate.edu

interpolated-tone paradigm as previous research (Deutsch, 1970, 1972, 1973). Participants discriminated tones that differed in timbre, and interpolated sequences varied in pitch and timbre similarity to the standard tone.

If timbre memory is similar to pitch memory, more interference should be found when the timbres of the interpolated tones are similar to the timbre of the standard tone than when they are not. Also, changes in the pitch of the interpolated tones should not interfere with timbre memory. Such an outcome would indicate that timbre is represented independently of pitch.

I. EXPERIMENT 1: TIMBRE INFLUENCES ON TIMBRE MEMORY

The aim of the first experiment was to determine if timbre similarity affects short-term memory for timbre. Four testing conditions were created. In the *baseline* condition, 5 s of silence occurred between the standard and comparison tones. In the three interpolated conditions, tones varying in timbre distance from the standard tone were presented during the 5-s retention interval. The only difference between the interpolated tones in the three conditions was the timbre distance of the tones to the standard tone.

A second aim of experiment 1 was to determine if musical training interacts with similarity effects in timbre memory. Past work on memory for timbre and pitch (Beal, 1985; Pechmann and Mohr, 1990; Pitt, 1994) found that musically untrained listeners show larger interference effects than trained listeners. Similar differences could be found with the current paradigm. This idea was explored by running the experiment with two groups of listeners. Untrained listeners were expected to show poorer discrimination in the interpolated conditions than the trained listeners.

A. Method

1. Participants

Thirty untrained listeners, with an average of 4 months playing a musical instrument, were recruited from the introductory psychology pool at Ohio State University. Twenty-five musicians were recruited from the same population; training on their primary instrument averaged 8 years. All participants reported normal hearing.

Discrimination accuracy in the baseline condition had to be at least 88% correct for a participant's data to be included in the analysis. The criterion was set *a priori* and in keeping with past work (Deutsch, 1970; Semal and Demany, 1991, 1993). This inclusion criterion was used because the aim of the project was to assess how interpolated tones disrupt memory. If participants cannot discriminate timbre in the absence of interpolated tones, the cause of poor and similar discrimination across conditions is difficult to interpret (see also footnote 1).

Fifteen nonmusicians and eleven musicians passed the inclusion criterion.[1] While this qualification rate (47%) may seem low, it is higher than that reported by Semal and Demany (1991, 38% in experiment 1) using the same paradigm.

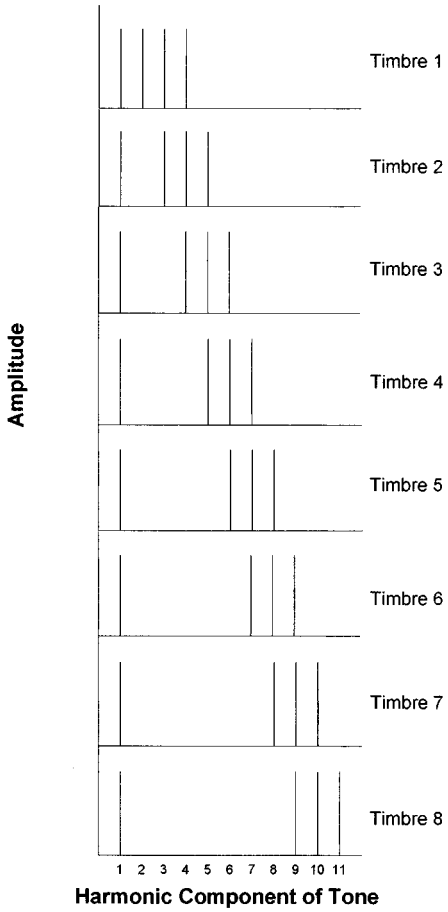

FIG. 1. Spectral composition of the eight timbres. The fundamental frequency (1) and harmonics 2–11 are plotted on the *x* axis. Amplitude is plotted on the *y* axis. The names of the timbres used in the text are printed next to the respective graphs.

2. Materials and apparatus

Timbre was manipulated by making incremental changes in the harmonic composition of a tone (i.e., spectral envelope). The complex tones comprised three immediately adjacent, equal-amplitude harmonics and their common fundamental frequency ($f1$). The fundamental frequency is the lowest perceived frequency component in a tone, and was always present in the eight timbres. Variation occurred only in the three contiguous harmonics, which moved as a group one harmonic step at a time farther in frequency from the fundamental (e.g., timbre $1 = f1 + f2 + f3 + f4$; timbre $2 = f1 + f3 + f4 + f5$, etc.). A total of eight timbres were digitally synthesized (using in-house software) in this manner, and are depicted in Fig. 1. These timbres sounded hollow, with perceived ''sharpness'' increasing from timbre 1 to timbre 8.

Timbre was varied using this method because the acoustics could be precisely and easily controlled while at the same time we were able to achieve a sufficiently wide range of variation in timbre. In addition, the procedure has been used successfully in related work (Semal and Demany, 1991; Singh, 1987). Although it is of minimal relevance to the question of immediate interest (timbre memory), one minor

drawback of using this method was that it does not permit conclusions to be drawn about which aspect of spectral envelope was responsible for any observed effects of timbre variation on timbre memory. This is because two acoustic characteristics of spectral envelope, centroid (average) frequency and frequency bandwidth, covaried across the timbres, being the smallest for timbre 1 and largest for timbre 8. Because the covariation does not compromise conclusions drawn about the question of interest (timbre memory), we felt the benefits of using the method outweighed the minor cost.

The eight timbres were synthesized at 37 fundamental frequencies (A2–A5, 110–880 Hz, in semitone steps), producing a pool of 296 tones. The duration of all tones was 300 ms, with onset and offset rise/fall times of 5 ms. All tones were judged to be of equal loudness by the first author and two listeners trained in psychoacoustic experimentation, and digitized onto computer hard-disk at the sampling rate of 10 kHz (low-pass filtered at 4.8 kHz) with a precision of 12 bits.

Stimulus presentation and response collection were controlled by a microcomputer. Participants sat in individual sound-attenuated booths and listened to stimuli through AKG K240 studio headphones (binaural presentation) at a comfortable listening level. A white-on-black computer monitor was located 24 in. in front of each participant.

a. Timbre similarity rating experiment. A rating experiment was conducted to validate our intuitions that the eight timbres varying in spectral envelope were sufficiently discriminable for the purposes of our experiment. This experiment was a necessary precondition for proceeding with Experiment 1. Ten listeners were presented a pair of tones, separated from each other by 500 ms, and then rated the similarity of their timbres on a seven-point scale (1 = most similar; 7 = least similar). All possible pairs were presented 2–3 times in a single randomized list. Results showed that timbres were rated as more different as spectral similarity decreased. Similarity ratings correlated strongly with the number of steps between timbres ($r = -0.64$, $p < 0.001$). The mean similarity rating was 1.1 when timbres differed by one step, 2.1 when they differed by three steps, and 3.5 when they differed by six steps. Thus, these stimuli satisfy the timbre-similarity requirements of the experiment.

3. Experimental conditions and design

The *baseline* condition, in which there was 5 s of silence between standard and comparison tones, was always run first to assess participants' ability to discriminate timbre. Three interpolated tone conditions were created that spanned most of the range of spectral variation in the preceding similarity rating experiment. In each, a single timbre was presented six times.[2] In the *one-step* condition, the interpolated timbre was one timbral step from the standard tone. In the *four-step* and *six-step* conditions, the interpolated timbre differed from the standard tone by four and six steps, respectively. Discrimination was expected to improve with increasing timbre distance between the standard and interpolated tones.

The fundamental frequencies of the standard and comparison tones were either 311 or 349 Hz, but always remained constant in a trial. In ''same'' trials, the identical stimulus was presented as standard and comparison. In ''different'' trials, the standard and comparison tones differed from each other by three timbre steps (e.g., standard=timbre 2, comparison=timbre 5, see Fig. 1).[3] There were 24 same and 24 different trials in each condition. Four of the timbres (timbres 2, 3, 7, and 8) were used as the standard tone in the one-step and four-step conditions (half of the time at each frequency). Because the set of timbres was limited to seven,[4] only timbres 2 and 8 could serve as standard tones in the six-step condition, reducing the set of possible standard and interpolated tone pairings by half. It is unlikely that this imbalance across conditions might affect discrimination because trial presentation was randomized (not blocked, see below) across interpolated conditions. Moreover, this problem was corrected in subsequent experiments, and the pattern of data did not change.

In ''different'' trials, direction of movement along the timbre continuum was counterbalanced across trials, with as many upward progressions (e.g., standard=timbre 2, comparison=timbre 5) as downward progressions (e.g., standard=timbre 5, comparison=timbre 2). The standard and comparison tones did not vary from each other in pitch. Because the set of timbres was limited to seven, there were only two possible standard/comparison pairs (timbres 2 and 5, and 8 and 5, respectively) in the six-step condition. Again, this imbalance was corrected in subsequent experiments.

4. Procedure

The experiment had two phases. In phase one (baseline condition), participants, who were tested in groups of four or fewer, were told that they would hear two tones separated by 5 s of silence, and were to determine if the tones were the same or different. They were to make a ''same'' response if the two tones were identical, and a ''different'' response if there was any difference between the tones. Responses were collected using two buttons on a four-button response board, one labeled ''same,'' the other labeled ''different.'' Participants used the left index finger to press the ''same'' button, the right index finger to press the ''different'' button. Feedback on the accuracy of responses was not provided.

Each trial started with the word ''READY'' printed on the computer screen in front of each listener. The phrase ''are the TONES the same or different'' was then printed on the screen, and 500 ms later the first tone was played. Five seconds later the second tone was presented, at which time participants responded. The next trial began once a response was collected or 3 s had elapsed. Prior to the baseline session, participants were given 12 practice baseline trials. All trials of the baseline condition were presented in a randomized list. The baseline session lasted approximately 10 min.

Phase two (interpolated conditions) was the same as phase one with the following exceptions. Participants were told that the 5-s interval would be filled with a sequence of tones. They were explicitly instructed to ignore the interpolated tones. Three hundred milliseconds of silence separated the standard tone from the first interpolated tone and the six interpolated tones from each other. There were 1400 ms of silence between the last interpolated tone and the comparison

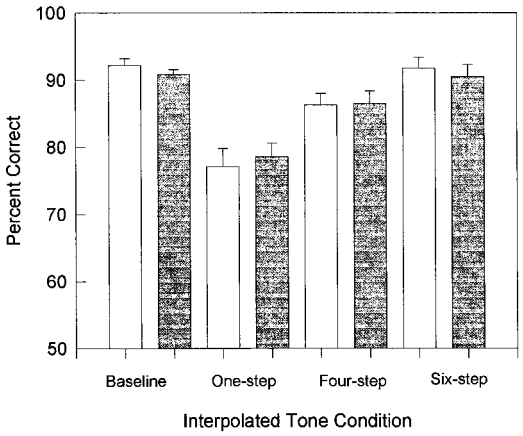

FIG. 2. Mean percent correct for musicians (clear bars) and nonmusicians (shaded bars) in the four conditions of experiment 1 (error bars are standard error of the mean).

tone. This extended silent interval demarcated the interpolated sequence from the comparison tone. After the last interpolated tone, the phrase ''get ready to respond'' was printed on the screen to alert participants that the comparison tone was about to be presented. The comparison tone was then played and participants had to respond. All interpolated trials were presented in a randomized list. Two short breaks were provided. Phase two lasted approximately 35 min.

B. Results and discussion

Figure 2 shows the mean proportion correct for the four conditions. The clear bars show results for the musically trained group and the shaded bars show results for the untrained group. Error bars represent the standard error of the mean.

As can be seen in the graph, accuracy was nearly identical for musicians and nonmusicians across all conditions. The largest difference between means was in the one-step condition (2%). No statistical comparisons between musicians and nonmusicians approached significance.

For both groups, accuracy steadily increased as timbre distance between the standard and repeating interpolated tones increased. An interpolated timbre that was one step removed from the standard tone resulted in a 13% drop in accuracy from the baseline. This drop was reduced to 7% in the four-step condition, and interference disappeared completely in the six-step condition.[5]

Based on the lack of difference between musically trained and untrained listeners, data in each of the four conditions were averaged across groups and submitted to a one-way analysis of variance, which yielded a reliable main effect $[F(3,75)=31.6,\ p<0.001]$. Paired comparisons revealed that all differences between conditions, with the exception of the baseline condition and the six-step condition, were statistically reliable ($p<0.05$).

The pattern of results is strikingly similar to that found with pitch (Semal Demany, 1991; see Deutsch, 1986 for similar results with tone duration). With respect to same-dimension interference, memory for both dimensions appears to be similar.

II. EXPERIMENT 2: CROSS-DIMENSIONAL INTERFERENCE IN TIMBRE MEMORY

Having demonstrated a timbre similarity effect, we turned to the question of cross-dimensional (i.e., pitch) interference in timbre memory. In experiment 1 pitch distance was held constant. In experiment 2, timbre distance and pitch distance were varied across six interpolated conditions. There were three pitch distances: same, close, and far. At each pitch distance there were two timbre distances: one-step and five-step. A timbre similarity effect should be found at each of the three pitch distances, with discrimination better in the five-step than one-step conditions.

How discrimination changes across pitch distance will reveal the nature of pitch influences. If timbre memory is affected more by tones similar in pitch, than accuracy should be lower in the close pitch conditions than the far pitch conditions. Whether it is uniformly lower at the two timbre distances will depend on whether timbre and pitch interference interact.

On the other hand, similar timbre discrimination across pitch distances would suggest timbre memory is not disrupted by pitch information.

A. Method

1. Participants

Twenty-four participants, unselected as to musical experience, were recruited from the same population as in experiment 1. Sixteen scored above the inclusion criterion. Participants had an average of 1.6 years of training on a single musical instrument. None had participated in the previous experiment.

2. Materials and design

The experiment was identical to experiment 1 in all respects except for the experimental design. In addition to the baseline condition, there were six interpolated conditions, which were created by crossing two levels of timbre distance (one-step and five-step) with three levels of pitch distance (same, close, and far). A five-step timbre distance was used so that the same four tones could serve as a standard in all conditions, rectifying the inconsistency across timbre distances in experiment 1. In the *same-pitch* conditions, pitch remained constant across all tones. In the *close-pitch* conditions, pitches of the interpolated tones were one semitone above or below the pitch of the standard tone. In the *far-pitch* condition, pitches of the interpolated tones were one octave plus one semitone above or below the pitch of the standard. As in experiment 1, the pitch and timbre of the interpolated tones remained constant within a trial.

B. Results and discussion

The results are shown in Fig. 3. Discrimination in the interpolated conditions dropped by an average of 16% from baseline $[F(6,90)=15.0,\ p<0.001]$. A two-way ANOVA with pitch distance and timbre distance as variables yielded a main effect of timbre distance $[F(1,15)=16.35,\ p<0.001]$, a main effect of pitch distance $[F(2,30)=4.91,\ p<0.05]$, and no significant interaction $[F(2,30)=0.52,\ p<0.56]$.

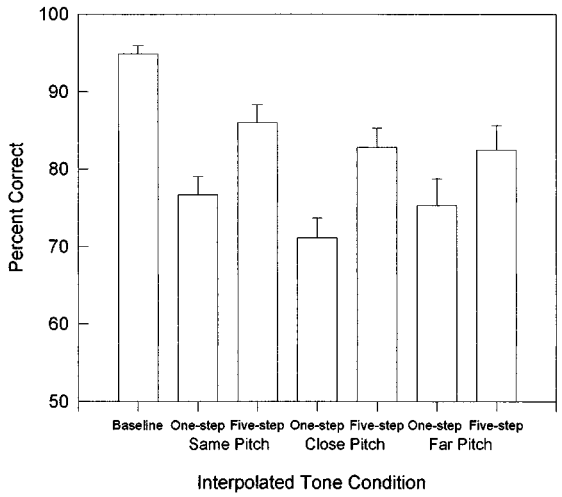

FIG. 3. Mean percent correct for the seven conditions of experiment 2.

Post hoc analyses indicated that at each pitch distance, discrimination in the one-step condition was significantly lower than in the five-step condition. Additionally, accuracy in the same-pitch condition was significantly higher than in the close-pitch condition. The close-pitch and far-pitch conditions did not differ reliably, nor did the same-pitch and far-pitch conditions.

The timbre similarity effect found in experiment 1 was replicated here, regardless of pitch distance. That there was a significant difference in accuracy between the five-step condition and the baseline condition, when one was not found between the six-step and baseline conditions of experiment 1, is not suprising. The five-step timbres are slightly closer perceptually than six-step timbres. If interference increases as perceptual similarity increases, then accuracy should be lower in the five-step condition compared to the six-step condition. However, based on this explanation, accuracy should have been lower in the four-step condition of experiment 1 than in the five-step condition of the present experiment, which was not the case. At present we have no explanation for this outcome and believe it is due to sampling variability.

Pitch interference effects were minimal overall, and they differed minimally as a function of timbre distance. In the five-step conditions, the effects of pitch distance were nonexistent, with accuracy being virtually identical in the close-pitch and far-pitch conditions. In the one-step conditions, there was a weak effect of pitch distance, with accuracy being 4% higher in the far-pitch than the close-pitch condition, but this difference did not approach significance ($F<1$). At best, these data suggest that pitch variation had a minimal effect on timbre memory.

Although the results of experiment 2 can be interpreted as suggesting that the dimensions of pitch and timbre are represented separately in memory, this conclusion is not meant to imply that the two dimensions are completely independent of each other. Variation in spectral envelope can influence perception of pitch as well as timbre (Singh and Hirsh, 1992; Terhardt, 1974; Terhardt *et al.*, 1982). Thus, for some stimuli, the two dimensions might not be easily separable.

If this were true for the current timbres, it might be argued that the results reflect memory for pitch. On the basis of such an argument, there should be a strong correlation between discrimination in this experiment and in an experiment in which listeners were explicitly told to discriminate tones varying in pitch. This possibility was tested in a follow-up experiment. Twenty-seven musically trained listeners were run through the baseline condition of experiment 2 and a comparable pitch-discrimination condition in which the same timbres were used, but the pitch varied instead of timbre. Although all listeners performed satisfactorily in the pitch discrimination task (75% or better), accuracy for these same listeners varied considerably in the timbre discrimination task, ranging from 30%–100%. Furthermore, there was no correlation between performance in the two discrimination tasks ($r=0.03$), suggesting that the results of experiments 1 and 2 do not reflect memory for pitch (i.e., fundamental frequency).

The aim of the final two experiments was to elucidate further the cause of interference in memory for timbre. The experiments focused on two variables in the interpolated sequence. Experiment 3 examined whether a single interpolated tone produces similar amounts of disruption as six presentations of that tone. Experiment 4 explored whether a single change in timbre within the interpolated sequence causes additional memory disruption.

III. EXPERIMENT 3: ADDITIVE TIMBRE INTERFERENCE EFFECTS

One question raised by the results of experiments 1 and 2 is whether there are additive interference effects from presenting the interpolated timbre six times, or whether a single presentation of that tone is sufficient to produce the demonstrated similarity effect. One study that did manipulate the number of interpolated tones found small additive effects (Massaro, 1970). In his experiment 1, participants discriminated pitches when there were one or two interpolated tones. Accuracy was 4% higher when a single interpolated tone was presented instead of two.

The purpose of experiment 3 was to determine if additive interference effects could be found for timbre memory. The experimental design was identical to experiment 1 except that a single interpolated tone was presented between the standard and comparison tones.

A. Method

1. Participants

Twenty-eight participants were recruited from the same population as experiment 1. Twenty-one scored above the inclusion criterion. None participated in the previous experiments. Musical training averaged 1.21 years.

2. Experimental design

The single interpolated tone occurred at the same time in a trial as the first interpolated tone in experiment 1. There was a 4300 ms ISI between the interpolated tone and the comparison tone.

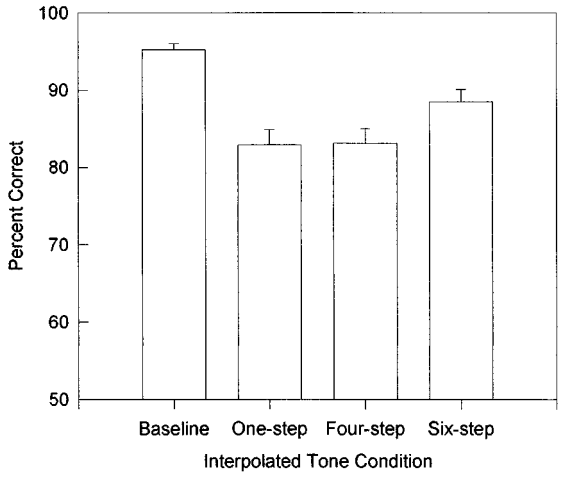

FIG. 4. Mean percent correct for the four conditions of experiment 3.

B. Results and discussion

Mean accuracy is plotted in Fig. 4. A timbre similarity effect is evident in the figure. Interpolated timbres more similar to the standard produced more interference than those less similar to the standard. The effects were highly reliable in a one-way ANOVA [$F(3,60)=20.4$, $p<0.0001$]. All comparisons between conditions were also significant, except that between the one-step and four-step conditions.

To determine whether one interpolated tone produced the same pattern of interference as six, a 2×3 (Experiment$\times$Interpolated Condition) ANOVA was performed on the data from experiments 1 and 3. The data were first normalized for variation in baseline discrimination across experiments by subtracting (for each listener) accuracy in each of the three interpolated conditions from baseline. These difference scores (small scores represent high accuracy, large scores low accuracy) were then submitted to the analysis. There was a reliable main effect of experiment [$F(1,45)=8.48$, $p<0.006$], with the surprising result that one interpolated tone produced more interference than six. The main effect of condition reached significance [$F(2,90)=31.46$, $p<0.001$], while the interaction of experiment with interpolated condition was marginally significant [$F(2,90)=3.01$, $p<0.06$].

One outcome that differs slightly from what was found in experiment 1 is the lack of an increase in accuracy between the one-step and four-step conditions. Comparison of the means (normalized relative to baseline performance) with their counterparts in experiment 1 revealed that accuracy in the one-step condition was slightly higher (1%, a smaller difference score) in the present experiment and accuracy in the four-step condition was 5% lower (a larger difference score). The variation could be due to the presentation of just a single interpolated tone. However, given that the variation is small and not consistent across interpolated conditions, we conclude for the time being that it is due to sampling variability.

At present, two possible explanations present themselves for why one interpolated tone produced more interference than six. First, differences in baseline discrimination across experiments may might account for why larger effects were found with one interpolated tone. Accuracy in the baseline condition of experiment 3 was 5% greater than that in experiment 1 (Figs. 2 and 4), whereas accuracy in the interpolated conditions differed minimally across conditions. The other explanation is that auditory grouping principles (Bregman, 1990) are responsible for the differences in discrimination. When an interpolated tone was presented six times, those tones might have grouped with each other, and apart from the standard tone, thereby disrupting memory for the standard tone only minimally. However, when only one interpolated tone was presented, it might have grouped with the standard tone and formed a single stream, causing more interference than when that same interpolated tone grouped with the other five interpolated tones (Bregman and Rudnicky, 1975; Jones *et al.*, 1987).

Although multiple presentations of the same interpolated timbre yielded no additive interference effects in timbre memory, additive effects might be found if timbre itself varied during the interpolated sequence. Massaro (1970; see also Deutsch, 1974), who found additive effects in pitch memory, used interpolated tones that differed in pitch. Although the cause of the memory decrement he found could have been due to the addition of a second interpolated tone rather than to a change in pitch of the second tone, the results of the current experiment suggest the former explanation is unlikely. The final experiment tested for additive interference when the interpolated tones changed in timbre.

IV. EXPERIMENT 4: ADDITIVE INTERFERENCE DUE TO TIMBRE VARIATION

Timbre variation within the interpolated sequence was limited to a single change, which occurred in the second interpolated tone. Timbre was held constant in tones 2–6. If interpolated tones beyond the first position do not disrupt memory for the standard, then the pattern of results should be predictable from knowing only the timbre distance between the first interpolated tone and the standard. In this case, the results should mirror those in experiment 1. On the other hand, if the second interpolated tone affects memory when its timbre differs from the first, then discrimination should differ compared to the case in which the first tone is simply repeated.

How discrimination differs was also investigated. One likely possibility is that interference caused by the second tone depends on the timbre distance between it and the standard, much like disruption caused by the first interpolated tone. Memory interference should decrease as timbre distance from the standard increases. If this effect held irrespective of the timbre distance between the first interpolated tone and the standard, interference effects would be additive across interpolated tones.

A. Method

1. Participants

Participants were from the same population as in past experiments. None had participated in any of the previous experiments, and all reported normal hearing. Thirty-four of forty-three met the inclusion criterion.

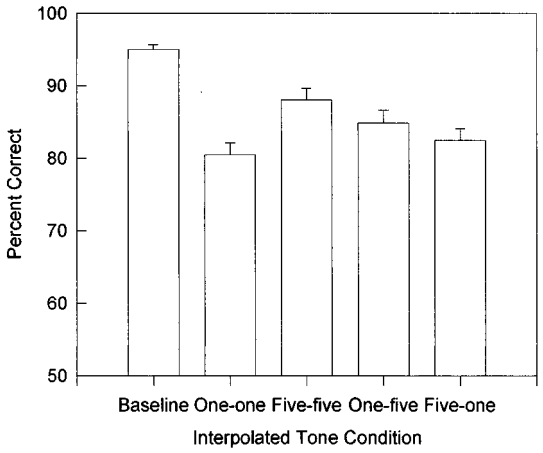

FIG. 5. Mean percent correct for the five conditions of experiment 4.

2. Experimental design

The *baseline* condition was identical to that in experiment 1. Four interpolated conditions were created, two *no-change* and two *change*. The no-change conditions were identical to the same-pitch conditions in experiment 2. The condition names were changed from one-step and five-step to *one-one* and *five-five* to convey the manipulations more clearly. Each word in the condition name denotes the timbre distance from the standard to the first and second interpolated tones, respectively.

The one-step and five-step intervals were also used in the change conditions. In the *one-five* condition, the first interpolated tone was one timbre step from the standard tone (e.g., standard=timbre 1, interpolated tone=timbre 2) and the next five interpolated tones were five timbre steps from the standard (e.g., timbre 6). In the *five-one* condition, this ordering was reversed, with the first interpolated tone five timbre steps from the standard (e.g., standard=timbre 1, interpolated tone=timbre 6), and the remaining five interpolated tones one timbre step from the standard (e.g., timbre 2).

The baseline condition was presented first, followed by the four interpolated conditions, which were presented together in one randomized list. The experiment was identical to Experiment 1 in all other respects.

B. Results and discussion

The results are graphed in Fig. 5. The by-now familiar timbre similarity effect is evident in the baseline and no-change conditions. Accuracy dropped 15% from baseline in the one-one condition and 7% in the five-five condition. All statistical comparisons between these conditions were reliable.

If the second interpolated tone had no effect on timbre memory, then the pattern of means in the no-change conditions should also be found in the change conditions. It is not. Instead, accuracy is slightly better in the one-five than five-one conditions. When each is compared with its no-change counterpart (same first timbre), an interesting outcome emerges. Accuracy in the one-five condition improved by 5% over that in the one-one condition. Accuracy in the five-one condition decreased by 6% compared with the five-five condition. The interaction across these conditions was reliable in a two-way ANOVA [$F(1,33)=16.99$, $p<0.001$], with timbre distance of the first tone (one-step and five-step) and timbre distance of the second tone (one-step and five-step) serving as variables. Accuracy in the five-one and one-five conditions did not differ reliably.

One interpretation of these results is that interference in the change conditions was an average of the effects of interpolated tones 1 and 2. Note that the means in both change conditions lie half-way between the no-change means. When the one-step timbre followed the five-step timbre, more interference was obtained than when the five-step was repeated, but not as much as that found in the one-one condition. When the five-step timbre followed the one-step timbre, a partial release from interference was found. Deutsch and Feroe (1975) found a similar release from interference in memory for pitch. Discrimination accuracy increased by approximately 8% when the fourth interpolated tone shared a specific pitch relationship with the second interpolated tone.

The present results clearly show that interpolated timbres beyond the first can affect memory for the standard. The form of the influence, disruption or release from interference, depends on the within-dimension similarity relationship among the interpolated tones and the standard. Net interference over tones appears to be an average of the effects observed when the tones are presented individually in the initial position of the interpolated sequence.

V. GENERAL DISCUSSION

Although a sizable amount of research has explored the acoustic and perceptual dimensions that define timbre (see Handel, 1989 for a review), relatively little work has been directed at identifying the characteristics of timbre memory *per se*. The current study sought to correct this state of affairs. Three characteristics of timbre memory were identified.

(1) Timbre memory is disrupted by irrelevant within-dimension variation. In eight conditions across the four experiments, interference increased as timbre distance decreased between the interpolated and standard tones. The range of dimensional variation within which interference occurs is limited for timbre, just as it is for pitch. Interference in timbre memory is found when the interpolated tones were fewer than six timbre steps from the standard. Interference in pitch memory is found when the interpolated tones were within $\frac{5}{6}$ of a whole tone (Deutsch, 1972) from the standard. Although the pitch and timbre scales are not directly comparable, the evidence does suggest that interference is caused by stimuli only within a certain proximity to the standard.

(2) Timbre memory is disrupted minimally by irrelevant pitch variation. Interference in timbre memory changed when pitch distance varied between standard and interpolated tones (experiment 2).

(3) Interference effects in timbre memory can be additive, but they depend on the composition of the interpolated sequence, emerging only when timbre varies. A single interpolated tone caused more interference than six repetitions of that tone (experiments 1 and 3). By simply

changing the timbre of the second interpolated tone, interference changed (experiment 4). How it changed (increased or decreased) depended on the timbre distance between the interpolated tones and the standard.

A similar additive interference effect has been found in suffix effect experiments using two suffixes (Crowder and Morton, 1969; Morton *et al.*, 1971). In a typical suffix effect experiment, participants hear a short list of items (e.g., eight) that must be recalled serially immediately after list presentation. An additional item, the suffix, is presented at the end of the list. Participants are often told to ignore the suffix or use it as a recall cue. Typical results are that inclusion of the suffix reduces recall of the last list item (Crowder and Morton, 1969). Presentation of a second suffix acoustically identical to the first leads to no additional drop in recall of the last item (Crowder, 1978; LeCompte and Watkins, 1995; Watkins and Sechler, 1989). However, when the second suffix is acoustically different from the first, recall drops. For example, LeCompte and Watkins (1995, experiment 1) found that recall of the last item was 8% better when two suffixes were presented in the same voice as the recall list than when the second of the two suffixes was in a different voice.

These findings are equivalent to what was found in the present study: Changes in the timbre of interpolated tones, not their repetition frequency, caused interference. The similarity of the results between the suffix-effect experiments and the present study suggest that findings using both tasks reflect the operation of the same process in auditory memory.

We began by noting similarities in how pitch and timbre are encoded during perception. Combined with the results of pitch memory experiments (e.g., Semal and Demany, 1991, 1993), our findings make it possible to extend this observation to a longer-term representation of the two dimensions of sound. Pitch and timbre are processed similarly within the first five seconds (Melara and Marks, 1990b). This conclusion must be confined to memory for the particular attributes of pitch and timbre compared thus far: fundamental frequency and spectral composition. Follow-up work will focus on determining if other attributes of both dimensions of sound yield similar findings.

ACKNOWLEDGMENTS

Some of the data reported here were presented at the 127th and the 131st meetings of the Acoustical Society of America. We thank Bruno Repp and an anonymous reviewer for helpful comments. Address correspondence to Gary Starr, Department of Psychology, Wingate University, Campus Box 5005, Wingate, NC, 28174.

[1]Accuracy for the nonqualified participants averaged approximately 65% correct in all the interpolated conditions and 81% correct in the baseline condition. Other than the decrease in accuracy in the interpolated conditions compared to baseline, no differences were found between the interpolated conditions, making interpretations of interference effects difficult.

[2]Readers familiar with the Deutsch paradigm will notice simplifications in our use of the procedure compared with its implementation by Deutsch (1970) and Semal and Demany (1991). For example, timbre of the interpolated tones was held constant. The results of pilot work, in which a range of other types of timbres was used, prompted these changes. Contact the authors for these data.

[3]A pilot experiment was conducted to identify an appropriate timbre distance for ''different'' trials. A distance needed to be found for which the timbres were different enough to be discriminated, yet similar enough to avoid ceiling effects. A three-step distance was chosen because accuracy scores and qualification rates in experiments identical to the baseline condition were similar to those reported by Semal and Demany (1991) in a comparable condition.

[4]Detailed analyses of the close-timbre rating data revealed that timbres 1 and 2 were rated significantly less similar than all other adjacent pairs. Mean rating was 3.2, with the rating for the next highest pair being 2.2. (Mean rating for all pairs except timbre1–timbre2 was 1.8.) This marked difference prompted us to use timbre 1 only as an interpolated tone, not as a standard or comparison tone. Therefore, only seven of the eight close timbres served as standard and comparison tones.

[5]A signal detection analysis was performed on the data to measure accuracy without the potentially contaminating effects of response bias. For each participant, *d*-primes, adjusted for data collected in the same/different paradigm (MacMillan and Creelman, 1991) was computed for each of the four conditions. In the baseline, one-step, four-step, and six-step conditions, mean *d*-primes were 1.97, 1.07, 1.73, and 1.91, respectively. As is evident, the results of the sensitivity analysis parallel those obtained using percent correct: Accuracy increased as timbre distance between the standard and interpolated tones increased. A similar outcome was found between the accuracy measures when the sensitivity analysis was applied to the other experiments.

Beal, A. L. (**1985**). ''The skill of recognizing musical structure,'' Mem. Cognit. **13**, 405–412.

Bregman, A. S. (**1990**). *Auditory Scene Analysis: The Perceptual Organization of Sound* (MIT, Cambridge, MA).

Bregman, A. S., and Rudnicky, A. I. (**1975**). ''Auditory segregation: Stream or streams?'' J. Exp. Psychol. Hum. Percept. Perform. **1,** 263–269.

Crowder, R. G. (**1978**). ''Mechanisms of auditory backward masking in the stimulus suffix effect,'' Psychol. Rev. **85,** 502–524.

Crowder, R. G. (**1989**). ''Imagery for musical timbre,'' J. Exp. Psychol. **15,** 472–478.

Crowder, R. G., and Morton, J. (**1969**). ''Precategorical acoustic storage (PAS),'' Percept. Psychophys. **5,** 365–373.

Deutsch, D. (**1970**). ''Tones and numbers: Specificity of interference in immediate memory,'' Science **168,** 1604–1605.

Deutsch, D. (**1972**). ''Mapping of interactions in the pitch memory store,'' Science **175,** 1020–1022.

Deutsch, D. (**1973**). ''Interference in memory between tones adjacent in the musical scale,'' J. Exp. Psychol. **100,** 228–231.

Deutsch, D. (Ed.) (**1974**). ''Generality of interference by tonal stimuli in recognition memory for pitch,'' Q. J. Exp. Psychol. **26**, 299–234.

Deutsch, D. (**1982**). *The Psychology of Music* (Academic, New York).

Deutsch, D. (**1986**). ''Recognition of durations embedded in temporal patterns,'' Percept. Psychophys. **39,** 179–186.

Deutsch, D., and Feroe, J. (**1975**). ''Disinhibition in pitch memory,'' Percept. Psychophys. **17,** 320–324.

Garner, W. R. (**1974**). *The Processing of Information and Structure* (Erlbaum, Potomac, MD).

Handel, S. (**1989**). *Listening: An Introduction to the Perception of Auditory Events* (MIT, Cambridge, MA).

Jones, M. R., Kidd, G., and Wetzel, R. (**1981**). ''Evidence for rhythmic attention,'' J. Exp. Psychol. Hum. Percept. Perform. **7,** 1059–1073.

Krumhansl, C. L., and Iverson, P. (**1992**). ''Perceptual interactions between musical pitch and timbre,'' J. Exp. Psychol. Hum. Percept. Perform. **18,** 739–751.

LeCompte, D. C., and Watkins, M. L. (**1995**). ''Grouping in primary memory: The case of the compound suffix,'' J. Exp. Psychol. Learn. Mem. Cognit. **21**, 96–102.

MacMillan, N. A., and Creelman, C. D. (**1991**). *Detection Theory: A User's Guide* (Cambridge U. P., London).

Massaro, D. W. (**1970**). ''Forgetting: Interference or decay?'' J. Exp. Psychol. **83,** 238–243.

Melara, R. D., and Marks, L. E. (**1990a**). ''HARD and SOFT interacting dimensions: Differential effects of dual context on classification,'' Percept. Psychophys. **47,** 307–325.

Melara, R. D., and Marks, L. E. (**1990b**). ''Interactions among auditory dimensions: Timbre, pitch, and loudness,'' Percept. Psychophys. **48,** 169–178.
Morton, J., Crowder, R. G., and Prussin, H. A. (**1971**). ''Experiments with the stimulus suffix effect,'' J. Exp. Psychol. **91,** 169–190.
Pechmann, T., and Mohr, G. (**1992**). ''Interference in memory for tonal pitch: Implications for a working memory model,'' Mem. Cognit. **20**, 314–320.
Pitt, M. A. (**1994**). ''Perception of pitch and timbre by musically trained and untrained listeners,'' J. Exp. Psychol. Hum. Percept. Perform. **20,** 976–986.
Pitt, M. A., and Crowder, R. G. (**1992**). ''The role of spectral and dynamic cues in imagery for musical timbre,'' J. Exp. Psychol. Hum. Percept. Perform. **18,** 728–738.
Risset, J. C., and Wessel, D. L. (**1982**). ''Exploration of timbre by analysis and synthesis,'' in *The Psychology of Music*, edited by D. Deutsch (Academic, New York), Chap. 2.
Semal, C., and Demany, L. (**1991**). ''Dissociation of pitch from timbre in auditory short-term memory,'' J. Acoust. Soc. Am. **89,** 2404–2410.
Semal, C., and Demany, L. (**1993**). ''Further evidence for an autonomous processing of pitch in auditory short-term memory,'' J. Acoust. Soc. Am. **94,** 1315–1322.
Singh, P. G. (**1987**). ''Perceptual organization of complex-tone sequences: A trade-off between pitch and timbre?'' J. Acoust. Soc. Am. **82,** 886–889.
Singh, P. G., and Hirsh, I. J. (**1992**). ''Influence of spectral locus and FO changes on the pitch and timbre of complex tones,'' J. Acoust. Soc. Am. **95,** 2650–2661.
Terhardt, E. (**1974**). ''Pitch, consonance, and harmony,'' J. Acoust. Soc. Am. **55,** 1061–1069.
Terhardt, E., Stoll, G., and Seewann, M. (**1982**). ''Pitch of complex tone signals according to virtual pitch theory: Tests, examples, and predictions,'' J. Acoust. Soc. Am. **71,** 679–688.
Watkins, M. J., and Sechler, E. S. (**1989**). ''Adapting to an irrelevant item in an immediate recall task,'' Mem. Cognit. **17**, 682–692.

Psychophysical studies with two binaural cochlear implant subjects[a)]

R. J. M. van Hoesel and G. M. Clark
The Bionic Ear Institute, Department of Otolaryngology, The University of Melbourne, 384-388 Albert Street, Melbourne 3002, Australia

(Received 1 March 1996; accepted for publication 30 January 1997)

Psychophysical studies have been completed with two binaural cochlear implant patients. In our earlier studies [van Hoesel *et al.*, J. Acoust. Soc. Am. **94**, 3178–3189 (1993); R. J. M. van Hoesel and G. M. Clark, Ann. Otol. Rhinol. Laryngol. Suppl. 106 **104**, 233–235 (1995)], lateralization experiments showed good sensitivity to interaural amplitudes but poor sensitivity to interaural time delays when compared with normal hearing subjects. In the studies presented here, both temporal and binaural intensity interactions were further explored. Interaural time delay (ITD) perception was investigated using direct measurement of the just-noticeable difference (jnd) in ITD. Both rate and place of stimulation were varied. Binaural rate discrimination was measured and compared with monaural rate perception. Binaural intensity interaction was explored for matched and unmatched place conditions by means of loudness summation and central masking studies. Results showed that ITDs for interaural time delays were large when compared to normal hearing, even when place of stimulation on each of the two sides was carefully matched. The jnds in ITD were similar for stimulation rates from 50 to 200 pps, and increased at 300 pps. Rate difference limens experiments showed similar results for diotic and monaural stimuli, but improved jnds for dichotic presentation at stimulation rates below 150–200 pps. Binaural intensity interactions showed loudness summation effects with both patients, for matched as well as unmatched place conditions. Central masking was also observed with both subjects, although it was not found to be place dependent. [S0001-4966(97)02506-X]

PACS numbers: 43.66.Pn, 43.66.Ts, 43.66.Ba, 43.64.Me [JWH]

INTRODUCTION

In order to investigate the percepts that arise from binaural electrical stimulation, psychopysical studies were conducted with two Nucleus Pty. Ltd. cochlear implant patients, who after a number of years of wearing a monaural implant, were implanted in the contralateral side with a second implant. It was considered ethical and prudent to postpone implanting further patients binaurally, until such a time that clear advantages were apparent from the data with these two patients. With normal hearing, the difference in time of arrival (phase, envelope, or both) at the two ears plays a key role in localizing a sound source (e.g., Sayers, 1964). The release from masking, also referred to as the masking level difference (MLD) has often been shown for diotic signals in dichotic noise or dichotic signals in diotic noise (Hirsh, 1948; Licklider, 1948). It shows the importance of the relative timing of stimulation in the two ears when distinguishing sounds from background noise. To investigate whether similar advantages may be obtained with binaural cochlear implant patients, it is important to examine how well binaural temporal and amplitude information is discerned by these patients. Our earlier reports described fusion and lateralization effects resulting from interaural time and amplitude differences (van Hoesel *et al.*, 1993; van Hoesel and Clark, 1995). Results for both patients showed diminished effects of time delays when compared to normal hearing.

The studies presented here are divided into those concerned with binaural temporal interaction (Sec. II) and binaural amplitude interaction (Sec. III). The first of three studies described in Sec. II, examined the effect of place on the jnd in ITD. It was not expected that the decreased sensitivity to interaural time delays observed previously was the result of stimulation at basal positions necessitated by the limited insertion depths with current electrode arrays. This is because good sensitivity to time delays has been demonstrated for high-frequency amplitude modulated signals which contain no low-frequency spectral components (Henning, 1974, 1980). It was, however, possible that in our earlier studies inaccurate place matching on the two sides may have affected ITD sensitivity. It was postulated that patients may only be sensitive to small delays between the two sides for well-matched places of stimulation, as has been observed acoustically (Nuetzel and Hafter, 1981).

In the second study in Sec. II, ITDs were measured for a number of rates of stimulation. Monaural rate difference limens with cochlear implant patients vary with rate of stimulation (Lim and Tong, 1989; Shannon, 1983), and typically show a low or bandpass curve with rate limens increasing rapidly above cutoff frequencies in the range 200–500 pps. It was hypothesized that interaural time delays with cochlear implants may not be well perceived for rates above those monaural cutoff rates. Since our earlier studies used a constant rate of 200 pulses per second (pps), in these studies the

[a)]Some of the data presented in this paper were presented at the 1994 International Cochlear Implant, Speech and Hearing Symposium in Melbourne, Australia.

ITD jnd was also measured for other rates between 50 and 300 pps with both patients.

In the third study concerned with interaural temporal interaction, binaural rate perception (diotic and dichotic) was compared with monaural rate perception to determine whether binaural rate information was better perceived than monaural rate information. This has been indicated by some binaural results with normal hearing (Jesteadt and Wier, 1977). In the dichotic case, with normal hearing, clear beating and roughness sensations are perceived for sinusoids of slightly differing frequencies in the two ears (Licklider *et al.*, 1950). It was postulated that some of these effects might also occur with differing rates of electrical stimulation on the two sides.

In Sec. III of the paper, binaural loudness and central masking studies are described. Binaural loudness perception was studied to determine if summation of loudness occurs for electrical stimulation as it does for normal hearing (e.g., Scharf, 1969). If large differences were found between the two cases, speech processing strategies may need to compensate for this. With normal hearing, elevated hearing thresholds in one ear result when a sound of similar spectral content is presented in the contralateral ear at the same time (Zwislocki, 1978). A central masking study was therefore also completed to determine whether the intensity threshold for detection of an electrical stimulus on one side increases in the presence of a contralateral masker and whether this is dependent on the place of stimulation of the masker. The combined results from the studies presented in this paper, along with our earlier results, will help determine whether binaural electrical stimulation strategies can be expected to offer advantages over monaural strategies for these patients, and if so, how to best combine information on the two sides for optimal binaural speech strategies.

I. PATIENTS AND STIMULI

The selection criteria, implant, and array details for the first binaural cochlear implant patient (P1) in Australia was described in van Hoesel *et al.* (1993). This patient was male, and had a profound hearing loss resulting from trauma in 1961. He was fitted with a 22 channel implant in 1984. He received his second implant in 1989. As described in the earlier study, improved binaural performance for this patient was observed using two independent processors, each with an $F0/F1/F2$ strategy (Blamey *et al.*, 1987). The $F0/F1/F2$ strategy, for each side, stimulated two places along the electrode array in accordance with $F1$ and $F2$ estimates, at a rate equal to the $F0$ (voicing) frequency. $F0$, $F1$, and $F2$ estimates were calculated independently for each side from the corresponding microphone signal. A second patient (P2) was subsequently implanted binaurally. This patient was also male, and had a profound hearing loss resulting from Meniere's disease from 1981 to 1985, when he was implanted in the right ear with his first Cl-1 implant. This implant is the current device marketed by Cochlear Ltd. and uses nonsimultaneous pulsatile stimulation on a 22-banded electrode array inserted into the scala tympani (Clark *et al.*, 1979). He was selected for binaural implantation according to similar criteria as P1, and was implanted with an additional Cl-1 device in the left ear in 1993. Further motivation for binaural implantation with this patient was the availability of only about half of the 22 electrodes with the earlier implant due to electrode shorts and uncomfortably high-pitched sensations from the most basal electrodes, presumably resulting from the fairly shallow insertion depth on this side. The limited number of electrodes available on the previously implanted side may limit possible binaural advantages with speech processing strategies for this patient. For the psychophysical studies presented here, however, we were always concerned with simple stimuli using single electrodes on each side. Given that the data obtained were generally similar for both patients, it may be reasonable to assume that smaller range of available matched places for P2 has not adversely affected these experiments.

Electrical stimulation, in the studies described, always employed biphasic current pulses on bipolar electrode pairs. Electrodes were numbered in an apical to basal direction so that the difference in insertion depths between the two sides could be determined directly from the electrode numbers on the two sides when place pitch percepts were matched, even when the arrays on the two sides had differing numbers of bands as is the case for P1 (van Hoesel *et al.*, 1993). Members of bipolar pairs were always separated by two electrodes (1.5 mm) and identified by the more apical member. To identify left or right sides, the letters ''L'' or ''R'' precede the bipolar pair number. For example, the notation of the *binaural* stimulus ''L(3)/R(5)'' implies bipolar pair (5,3) on the left side and pair (7,5) on the right side. Unless noted otherwise, pulse duration used in the experiments was always 100 μs per phase, repetition rate was 200 pps, and duration of the stimuli was 300 ms with zero rise–fall times. Stimuli were always delivered via custom built hardware directly to the patients' transmitter coils, so that all electrical stimulation parameters could be carefully controlled. This included ITDs, which could be accurately controlled to within less than 10 μs, which approximates the jnd for ITDs with click stimuli for normal hearing. Operation of the system was verified by monitoring current outputs from dummy implants with a 100-MHz storage oscilloscope.

II. BINAURAL TEMPORAL INTERACTION

A. Effect of place of stimulation on interaural time delay jnds

1. Rationale and method

It was hypothesized that inaccurate place matching on the two sides may have adversely affected interaural time delay perception in earlier studies. A place-pitch study was considered appropriate to determine insertion depths psychophysically. From a preliminary pilot study it became clear that neither of the subjects could repeatedly complete direct pitch comparisons between electrodes on the two sides. Only an average across a large number of experimental trials might be expected to give a good estimate of the overall insertion offset between the two sides. This meant that direct comparison of all (20×20) electrode pairs on both sides was not possible, particularly given that sessions with these subjects were restricted to one per week. As an alternative, the method of magnitude estimation (Stevens, 1975) was used to

determine the pitch of the electrodes on the two sides for each patient. Results were compared with x-ray scans. All electrodes on both sides, excepting any shorted bands, were first balanced for loudness at a medium loud level corresponding to a stimulation level of about 80% of the electrodes' respective dynamic ranges in terms of clinical current level (CL) units. The dynamic range was defined as the range of currents eliciting threshold through to maximal loudness level that the patient can tolerate before the sensation became uncomfortably loud. The level at 80% of the dynamic range will be referred to as ''80% DR,'' and was comparable to everyday conversation loudness level experienced by the patients with their speech processors. Loudness balancing was via a continual A/B/A, etc. comparison with a fixed reference electrode near the middle of the array on the right side, followed by sweeps across each array. The loudness balanced stimuli were combined into a stimulus block consisting of all possible monaural stimuli, which was then presented to the patients in random order, one stimulus at a time without a reference signal. The patients were required to assign a number to the pitch sensation experienced from each stimulus in a ratio metrically consistent manner. The patients were allowed to use any number range they preferred, but were specifically instructed to try to ignore numerical boundaries such as 1 or 100. The patients had two training sessions spaced one week apart, after which data were collected for three further consecutive weekly sessions. The stimulus block was presented once at the start of each data collection session to allow the patient to become familiar with the sounds. Data were collected from a total of 20 blocks and the averaged results were used to calculate the estimated relative offset in insertion depths between the two sides from simple correlations using both linear and logarithmic fits. The calculated offset between the two sides, in the linear case, corresponded to the offset for which the absolute value of the sum of differences in the pitch of paired electrodes on the two sides was minimized. In the logarithmic case, it was equal to the offset for which the average ratio of pitches assigned to the paired electrodes on the two sides best approached unity. Some electrodes were omitted from this analysis when they appeared to be located outside the round window as indicated by both the x rays and the observed pitch estimates. The results from the pitch study were compared with radiometric insertion depth estimates obtained from a 2-D computer model described by Cohen *et al.* (in press) derived from a modified Stenver's view (Marsh *et al.*, 1993). The relative alignment of the arrays on the two sides was estimated from both the psychophysical and radiometric data.

The estimated offset was used to explore the effects of place of stimulation on ITD perception. Two place experiments were conducted. In the first, a single fixed electrode on the right side, located near the middle of the array, was combined with most of the available electrodes on the contralateral side. For patient P1, the most basal electrodes on the left side were suspected to lie outside the round window, and were therefore omitted from the study. For patient P2, a slightly more apical place on the right side was chosen since the array on this side had a fairly shallow insertion depth compared to the left side. For this reason, the five most apical rings on the left side were omitted for this patient. Time restrictions with the patients allowed only about half of the possible binaural place combinations to be tested once within a single session. In each session therefore, half of the possible combinations were randomly selected for presentation in that session. The remaining half of the combinations were presented (in random order) in the following session. Results were collected over four consecutive sessions giving two measurements of the jnd for each left/right place combination.

Measurement of the jnd in ITD for each binaural combination (and all jnds described throughout this paper) used a three interval forced choice paradigm targeting 70.7% correct response level on the psychometric curve. The procedure used a modified fixed level, two-up/one-down paradigm (Levitt, 1971). The patients were simply instructed to determine which of the three stimuli was ''the odd one out.'' Each run was terminated after the tenth turning point. The step size was decreased to half the initial value after the first three turning points. The jnd was taken to be the average of the last six turning points.

In the second place experiment, three electrodes located in the apical, mid, and basal regions of the array on the right side were combined with four electrodes spaced evenly across the array on the left side, giving a total of 12 combinations. This number of combinations was found to be the maximum number of combinations that could comfortably be presented to each patient in a single session. The same forced choice procedure as in the first place experiment was used. Results from two consecutive sessions were combined to give two estimates of the jnd for each combination.

2. Results and discussion

The results from the pitch magnitude estimation study are shown for both patients in Fig. 1(A). Averaged pitch estimates for each electrode are displayed along the *y* axis, and electrode band number (numbered apical to basal) along the *x* axis. The two curves for each patient show averaged pitch estimates for left and right ears. The average horizontal offset between the left and right curves indicates the insertion depth offset between the two sides. Typical error bars indicating one standard deviation are shown for electrode 15 on each array. The large variation in pitch estimates for the electrodes is reflected in the size of these error bars as well as in the nonmonotonic nature of the curves. Nevertheless, given direct comparison across the two sides was not possible, a smooth fit through these curves was expected to indicate the average relative offset between the arrays. The offset was calculated as described in Sec. II A 1. Both linear and logarithmic fits showed offsets of 6 electrodes for patient P1, and 8.5 electrodes for patient P2.

The results from the 2-D computer model derived from the x-ray data are presented in Fig. 1(B)–(E). By comparing the left and right plots, the relative offset for each patient was determined by averaging the differences in angular insertion for corresponding electrodes on the two sides. In a temporal bone study using the same computer model (Cohen *et al.*, in press), the standard deviation of the mean error for the esti-

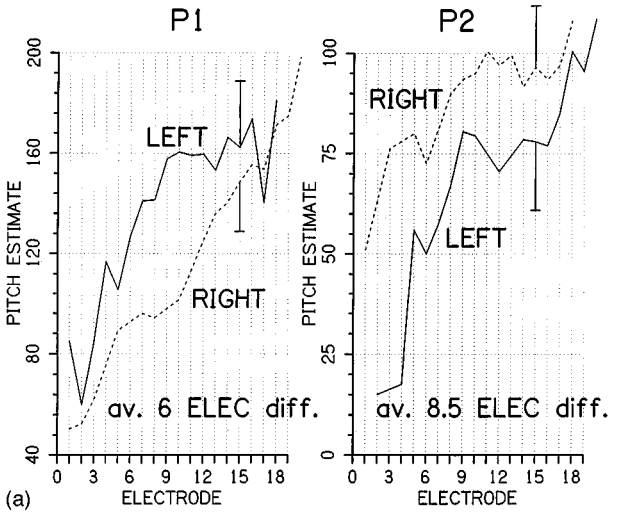

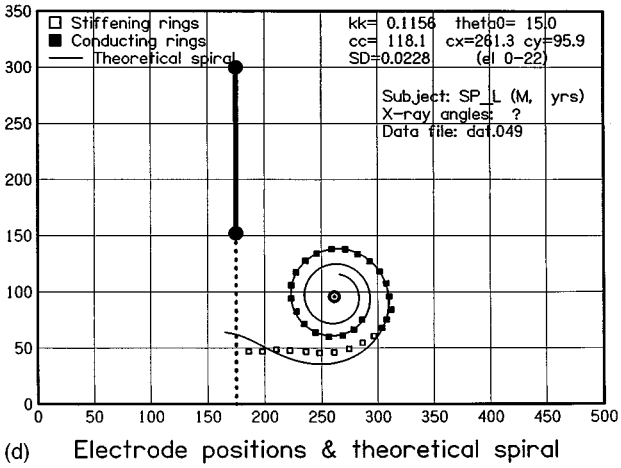

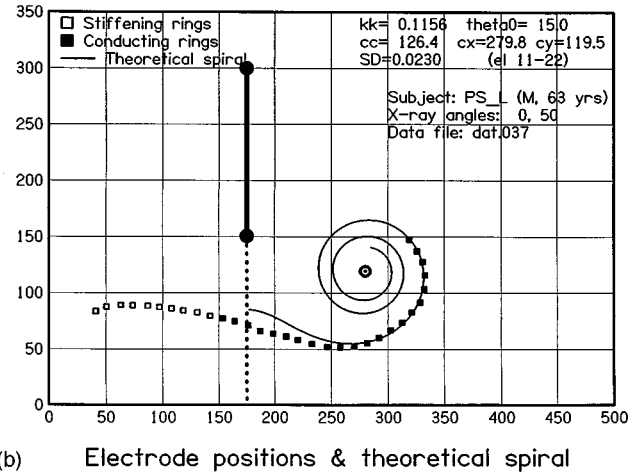

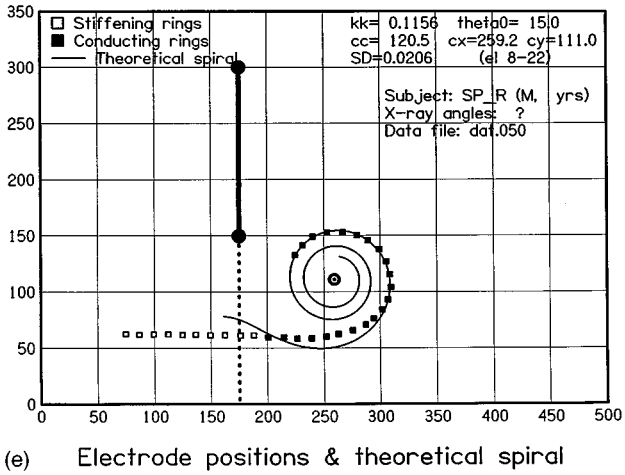

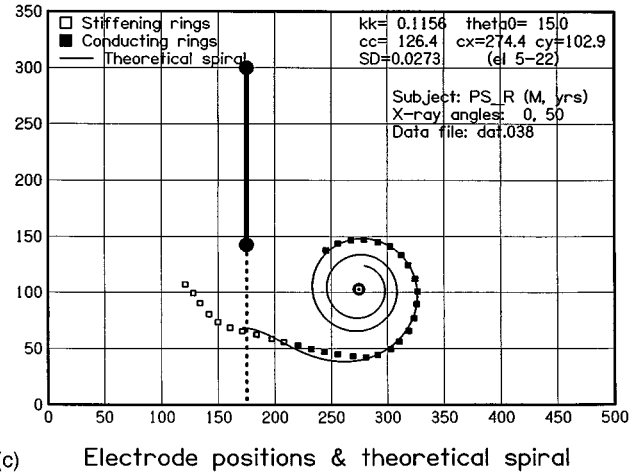

FIG. 1. Panel A shows pitch magnitude estimation results for left (dashed curve) and right (solid curve) sides for subjects P1 and P2. Results are the average of 20 presentations of each stimulus. Standard deviation for electrode 15 is indicated by the error bars for each curve, and is representative of the typical standard deviation of the pitch estimates for each of the stimuli used. The average horizontal displacement between the two curves was used to indicate the relative offset in insertion depth between the two sides (see text). Panels B/C and D/E show radiometric data (electrode positions and landmarks) and spiral fits to the data for left/right arrays for P1 and P2, respectively.

mated insertion angle was approximately 3.75° (personal communication) so that a reasonable upper bound for the error in relative insertion offset between two sides in a binaurally implanted subject was considered to be about 5°. This corresponds to less than 0.5 electrode places in the first turn of the cochlea. The offsets (rounded to the nearest half electrode place accuracy) were found to be 6 electrodes for P1 and 8.5 electrodes for P2. These offsets agreed (within the allowed half electrode place rounding) exactly with the averaged offsets calculated from the psychophysical data for each of the two patients, so that the psychophysical procedure and offset calculations derived therefrom appear to give a good estimate of the relative insertion depths.

The results from the jnd measurements for ITD for various place combinations are shown in Fig. 2. Results from the first and second place experiments are shown together. The three plots correspond to the three fixed places chosen on the right side for the second place experiment. Data from the second experiment are shown by the triangular symbols and solid lines. The unconnected circular symbols on the top plot

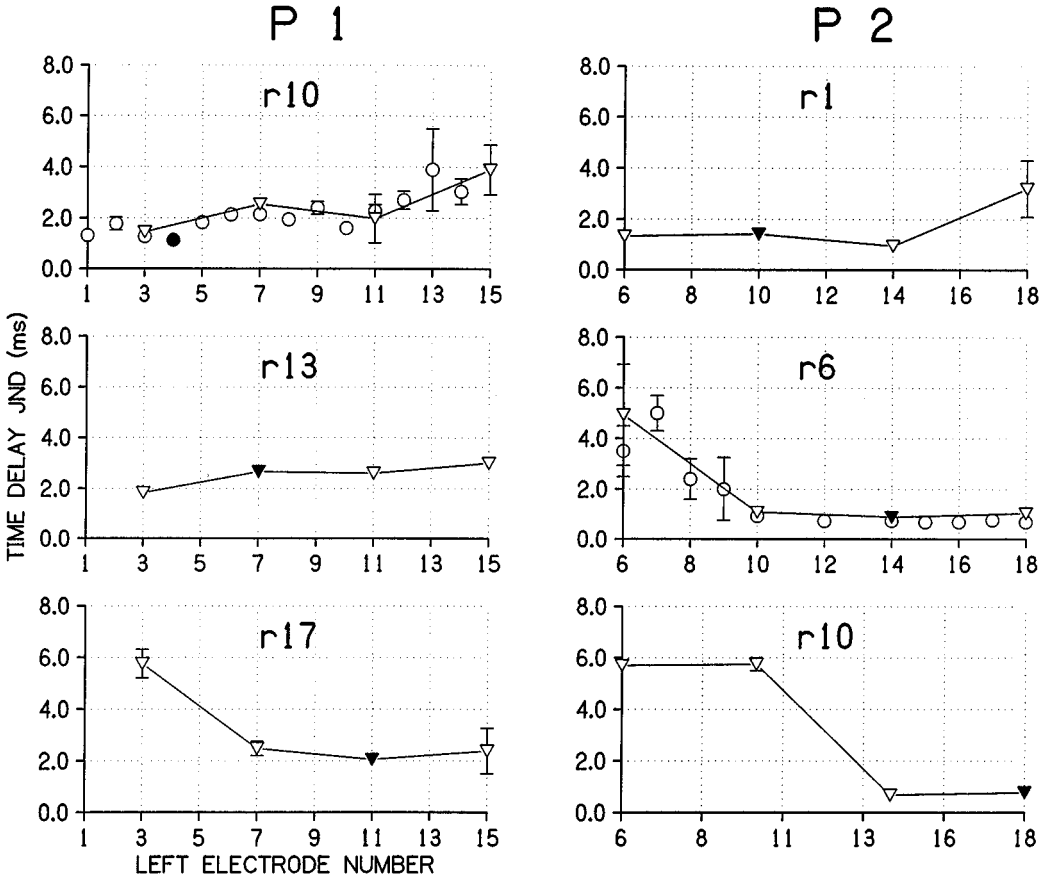

FIG. 2. Interaural time delay jnds as a function of place of stimulation on the left side with the place of stimulation held fixed on the right side. Each graph is for a fixed place on the right side. Graphs in the left column are for subject P1; those on the right are for P2. Solid symbols indicate binaural best matched place pair in accordance with results from Fig. 1. Circular symbols are data from the first place experiment (see text), triangular symbols are results from the second.

for patient P1 and the center plot for patient P2 show additional results of the first experiment for which the fixed electrode on the right side was combined with most of the available electrodes on the left side. The filled symbols in each plot indicate the nearest matched place combination according to the results in Fig. 1.

All the left/right place combinations tested showed jnd measurements for ITD of at least 0.5 to 1 ms for both patients. This value is very high compared to acoustic interaural jnds in ITD for normal hearing, which can be as low as 10 μs for appropriate stimuli (for a review see Durlach and Colburn, 1978). Given that data from only two binaural implant subjects is currently available, it may be premature to assume that ITDs cannot be well perceived with cochlear implants. On the other hand, large values for jnds in ITD perception have also been found in experiments with some hearing-impaired listeners (Gabriel *et al.*, 1992).

From the results it can be also be seen that, compared to the best matched place condition, the time delay jnd did not become appreciably larger until the offset between the two sides was more than about 4–8 electrodes (3–6 mm). This corresponds to the region for which in our previous fusion experiments (van Hoesel *et al.*, 1993; van Hoesel and Clark, 1995) multiple auditory images were perceived rather than just one fused image. It should be noted that the current spread resulting from stimulating a single bipolar pair with a spatial extent of 1.5 mm, which was the case for all stimuli used in these experiments, probably spans more than one electrode place (Tong *et al.*, 1989). Place mismatches smaller than about one electrode space should still stimulate matched regions on the two sides. In view of the findings of these experiments, it appears unlikely that the relatively poor ITD discrimination found was the result of stimulating unmatched places.

B. Effect of rate of stimulation on interaural time delay jnd

1. Method

The effect of rate on ITD sensitivity was explored over the range 50–300 pps. Two different fixed places were selected on the right side and each was combined with it's respectively matched place on the left side in accordance with the results in Fig. 1. The jnds in ITD were measured for each binaural combination at 50, 100, 200, and 300 pps. All stimulus components were loudness balanced against electrode R10 at 200 pps for P1, and R11 at 200 pps for P2. The current level of the components was set at about 80% DR. All rate and place combinations were presented, in random order, once within a session. After an initial training session, data were collected for two subsequent sessions spaced one

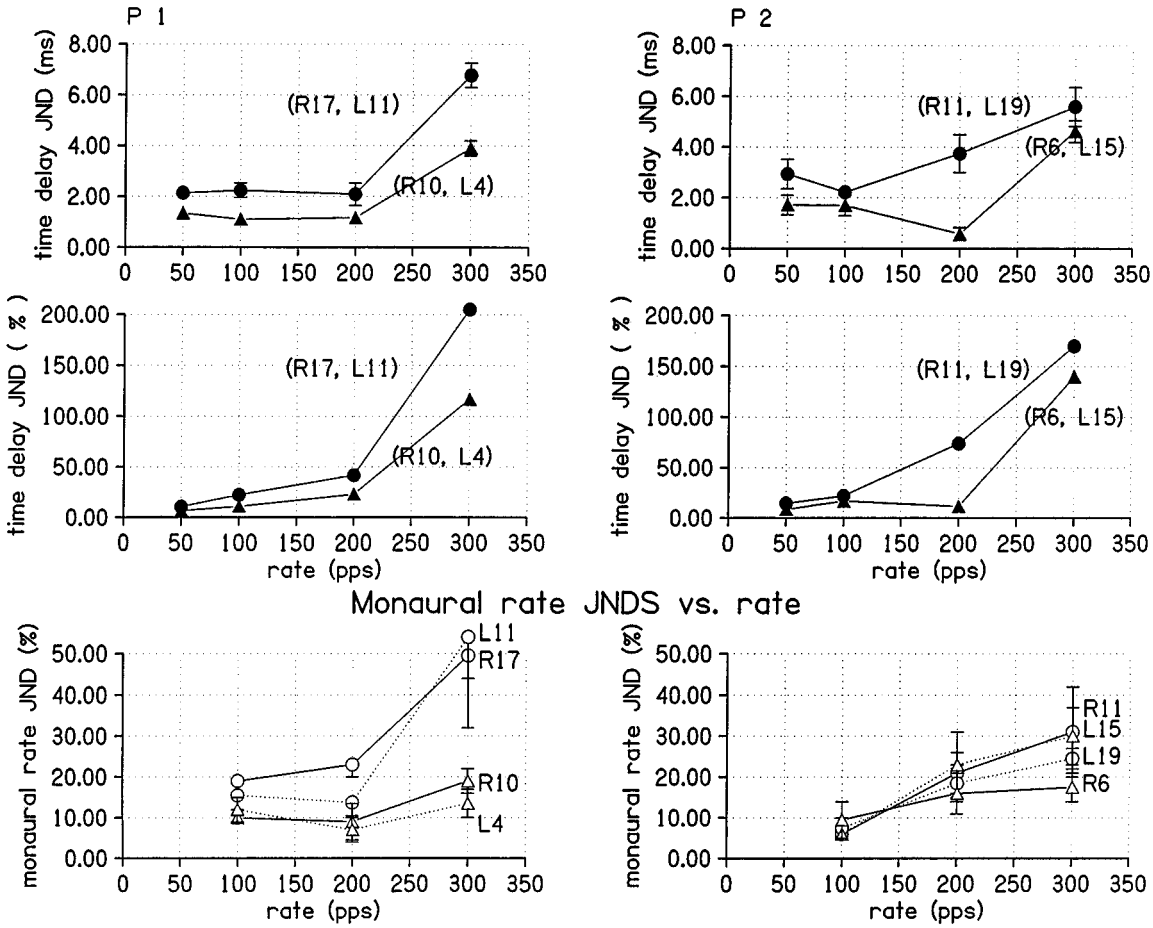

FIG. 3. Interaural time delay jnds as a function of rate of stimulation for two matched place pairs for each patient. The left column shows the results for P1; the right those for P2. The top plot shows jnds in ms; the middle plot the same data in terms of percentage of the stimulation rate. The lower plots show the monaural rate jnd data for the same electrodes for comparison.

week apart. The three interval forced choice procedure described in Sec. II A1 was again used to measure the jnds.

2. Results and discussion

The effect of rate on ITD perception is shown in Fig. 3. The left column consists of plots for patient P1, the right for P2. The top plot for each patient displays two curves, corresponding to two binaural place combinations. Each curve shows the measured jnds in ITD at four pulse rates. Each point shown on each of the curves is the average of two jnd measurements for that stimulus. The curves show no jnds less than around half a millisecond for any of the rates. For both patients, the just noticeable ITDs measured for 300 pps were larger than those measured for the lower rates. This is also the case for the monaural rate jnd curves for the electrodes in question, which have been included in the bottom plots of each column for reference. The monaural curves are typical for monaural rate perception with cochlear implant patients (e.g., Lim and Tong, 1989; Shannon, 1983) and demonstrate the ability of the auditory system to follow the stimulus period only up to 200–500 pps. It may be the case that if either side alone cannot track higher stimulus rates, the ongoing temporal information presented on the two sides will also be distorted, and ITD perception will be degraded, as is the case in the top plots for the higher rates. Furthermore, if the ITD jnd is dependent on unambiguous temporal cues from both envelope and ongoing fine structure of the stimulus (cf. van Hoesel *et al.*, 1993), a degradation in performance would be expected when these cues were in opposition as was the case when the time delay exceeded half the repetition interval. To illustrate this point, the middle plots in Fig. 3 show the ITD results replotted in terms of percentage of the stimulus interval rather than in milliseconds along the *y* axis. The point at which fine and envelope delays convey opposing temporal cues is the 50% line along the *y* axis. The data show a steepening of the jnd curves near this line. Further experiments are required to separate the effects of monaural rate jnds and opposing cues.

C. Binaural rate discrimination

1. Introduction

To complement the time delay jnd results obtained in Secs. II A and II B, the measurement of monaural and binaural rate discrimination was completed for binaural electrical stimulation. Binaural diotic rate jnds were compared with monaural rate jnds. These conditions were tested to determine if patients can combine information from the two sides to improve discrimination. This has been shown to be the case for some (e.g., Jestaedt *et al.*, 1977), but not all (e.g., Pickler and Harris, 1955) loudness and frequency dis-

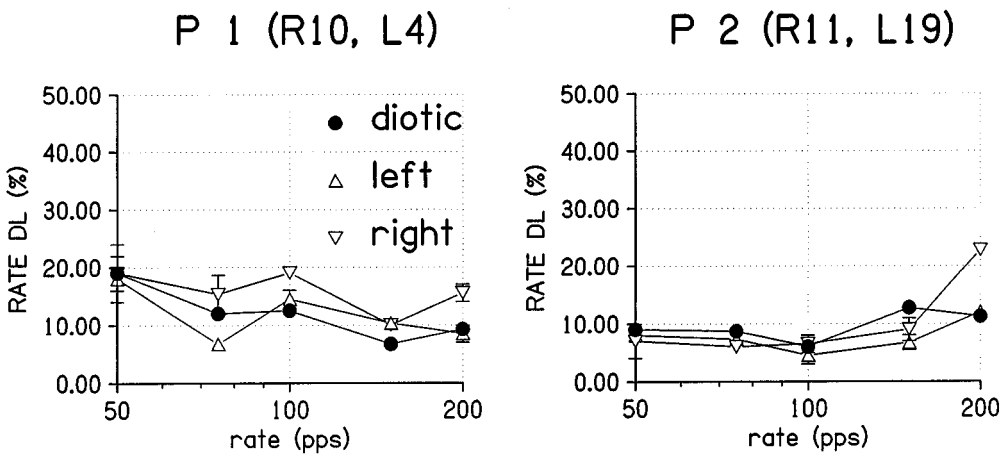

FIG. 4. Diotic and monaural rate jnds as a percentage of the stimulation rate for a fixed matched place pair for each subject.

crimination experiments reported for normal hearing subjects. A maximum ratiometric improvement of about 1.4 is expected if electrical binaural diotic stimulation is subject to information integration theory (Green and Swets, 1966). Rate jnds on each side were also measured in the presence of fixed rates on the contralateral side (dichotic stimulation). This was motivated by results from normal hearing subjects which indicate that, when sinusoids of slightly different frequencies are presented to the two ears, a binaural beating sensation is heard which increases in frequency as the difference between the two sides increases (Licklider *et al.*, 1950).

2. Method

For each patient, a single electrode was selected near the middle of the array on the right side. The current level was set to evoke a comfortably loud sensation, similar to levels experienced by the patients with their speech processors in everyday conversation, and corresponded to an intensity of around 80% DR. An electrode, matched in place according to the results from Sec. II A, was selected on the left side and balanced in loudness against the right electrode using a continuous A/B/A/etc. paradigm. For each of the two sides, the monaural rate jnd was measured at reference rates of 50, 75, 100, 150, and 200 pps, using the three interval forced choice procedure described in Sec. II A 1. This range was chosen so as to allow the auditory system to track the electrical pulse rate (Tong *et al.*, 1983). For the dichotic rate jnds, the monaural procedure was repeated at the five reference rates, but now an additional stimulus was presented on the contralateral side. Stimulation on the contralateral side was always fixed at a rate equal to the reference rate for both reference and probe stimuli, in each of the five cases. As an example, when measuring the rate DL at 100 pps on the left side, the dichotic condition corresponded to the case where the rate was varied near 100 pps on the left side in the presence of a fixed 100 pps stimulus on the right side. For the diotic condition, rates on both sides were always varied together. For the diotic rate case, loudness adjusted stimuli were also tested in a pilot study to determine whether the increase in overall loudness due to loudness summation across the two ears affected the rate jnds. Results indicated that this was not the case, however, so that loudness adjustments compensating for binaural summation were not applied to the stimuli in this experiment. To minimize any loudness cues resulting from rate variations, which might therefore allow patients to distinguish probes from reference stimuli more readily, approximately 10% of the dynamic range (in terms of Cochlear device ''current level'' units) random intensity jitter was applied to all stimuli.

3. Results and discussion

The data in Fig. 4 show similar rate jnds for both monaural and diotic listening conditions. No improvement resulted from integration across the two ears. It is possible that the more deterministic firing of nerves with binaural electrical stimulation is not subject to temporal integration in the same way as normal hearing (for which equal variances of signal and noise are often assumed). Given that interaural time delays are poorly perceived by these patients, it is perhaps not surprising that other temporal information from the two ears is also combined differently to normal hearing.

Figure 5 shows the measured monaural and dichotic rate jnds for right and left sides in the top and bottom graphs, respectively. Decreases in rate jnds are clearly evident for both patients for the dichotic condition at low pulse rates. For patient P1, the differences between dichotic and monaural jnds are clearly demonstrated below 150 pps. It is worth noting that although the measured monaural rate jnds for P1 are rather large and variable with rate, the dichotic jnd curve is nevertheless a much smooth function increasing monotonically with rate. For patient P2, the measured dichotic jnd was lower than the monaural rate jnd at all rates below 200 pps. Although neither of the patients reported binaural beats, the changes in percept when the contralateral stimulus was at a slightly different rate, were described by patient P1 as having added a ''buzzing'' quality. This is interesting when compared to the changes in roughness that are often described for normal hearing when a sinusoid on one side is held fixed on one side while, starting from a diotic condition, the frequency is progressively altered on the contralateral side (Licklider *et al.*, 1950).

The temporal interaction implied by these results is in contrast to both the diotic rate results of Fig. 4, as well as the poor ITD perception described in Secs. II A and II B. Al-

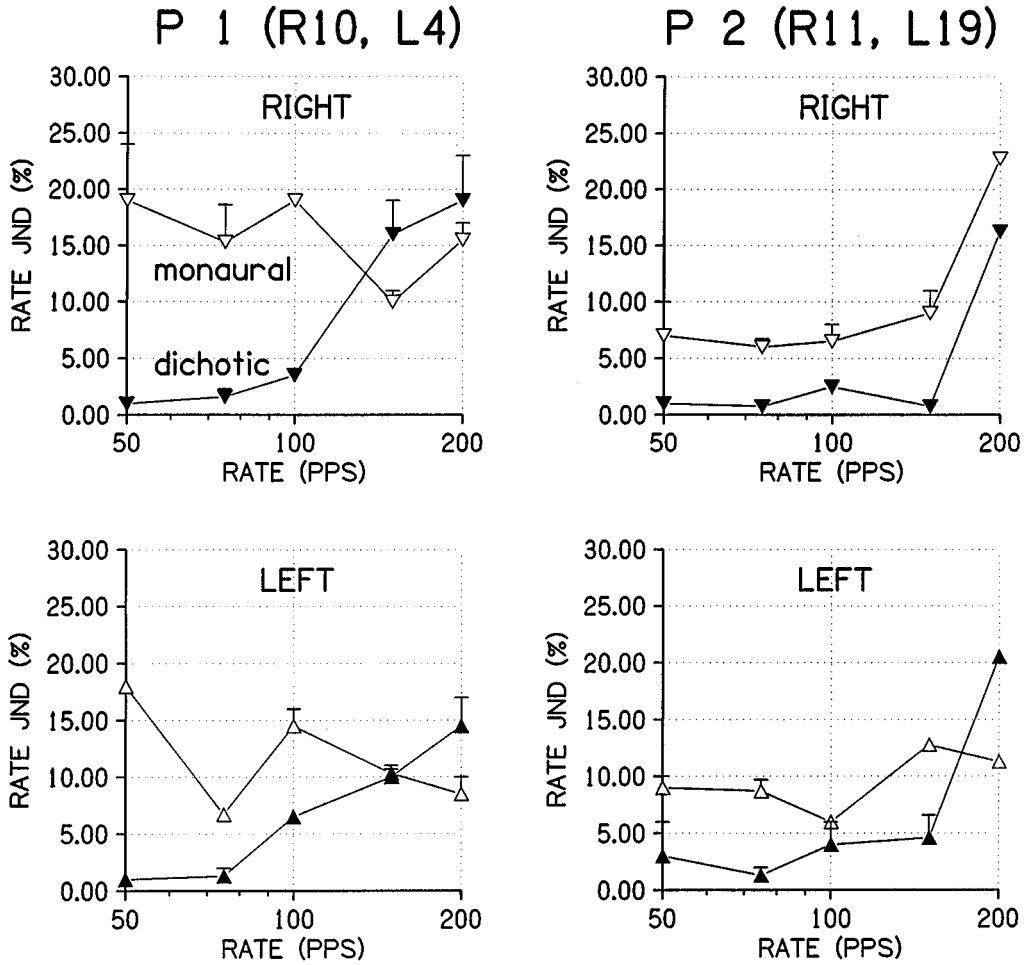

FIG. 5. Dichotic and monaural rate jnds as a percentage of the stimulation rate for a fixed matched place pair for each subject. Results on the left are for P1, those on the right are for P2. The top plot for each subject shows rate jnds with (dichotic), and without (monaural), contralateral fixed reference rate.

though our earlier studies imply that lateralization is only weakly affected by ITD, the results could be explained by lateralization cues if continually varying ITDs, such as those produced by applying different rates on the two sides, are much better perceived than static ITDs. This remains to be determined from further experiments. If this is not the case, a model capable of predicting this result would require a mechanism that is insensitive to interaural delays, shows no advantage in rate jnds for diotic stimulation compared to monaural stimulation, and yet is able to detect rate differences between the two sides that are considerably smaller than rate jnds on either side. The data presented here alone do not allow us to speculate about the details of such a model.

Informal tests with these patients showed that for large rate differences between the two sides (typically beyond about 20–50 pps for rates of 100 and 200 pps), the percepts split into two distinct pitches in the two ears. This is also the case for normal hearing with sinusoidal stimuli when the interaural frequency difference becomes large enough. In acoustic studies with sinusoidal stimuli, place and rate are simultaneously affected, so that the percept may split into two as a result of place differences falling outside a fairly narrow, well-matched characteristic frequency range. Our data suggest that even when the place of stimulation remains unaltered, the percept will split when temporal information on the two sides differs by a large enough amount.

III. BINAURAL INTENSITY INTERACTION

A. Binaural summation of loudness

1. Method

The summation of loudness from the two ears was investigated for electrical stimulation. For normal hearing, the loudness of a sound presented to both ears is generally greater than that of the same sound presented to just one ear. The bandwidth and intensity of the sound affect how much louder the binaural stimulus appears compared to the monaural case (Scharf, 1978; Durlach and Colburn, 1978). In a pilot study (van Hoesel *et al.*, 1991), loudness summation was studied by adjusting monaural electrical stimuli to match the loudness of binaural stimuli with patient P1. However, results from this study did not directly relate binaural loudness to stimulation currents on the two sides. Additional loudness growth curves were required to relate stimulation amplitudes to the magnitude of loudness. In the study presented here, loudness summation and growth were simultaneously characterized by using the method of magnitude estimation (Stevens, 1975) to estimate monaural and binaural

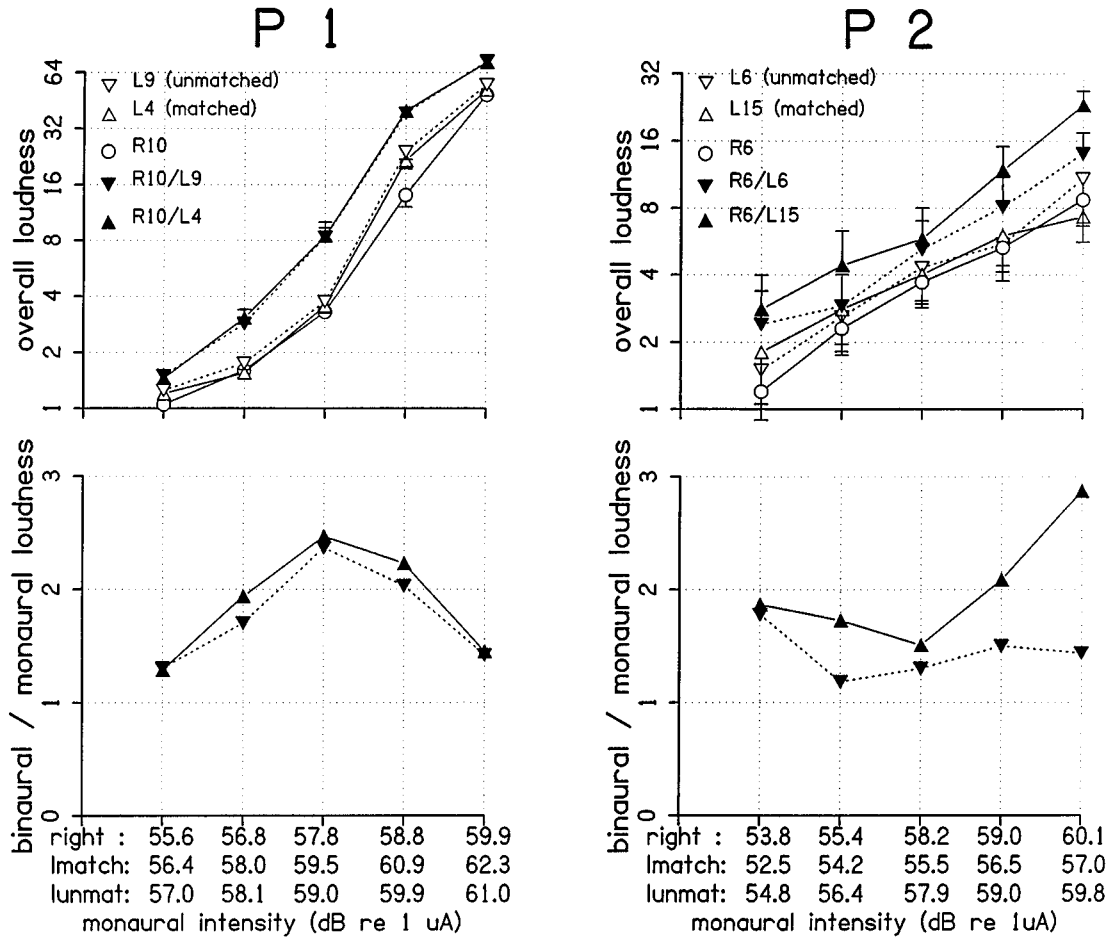

FIG. 6. Loudness summation results for matched and unmatched place conditions at five balanced left/right loudness pairs. Top plots show increased loudness for binaural stimuli (solid symbols) compared to loudness of monaural components (unfilled symbols). Lower plots show binaural/monaural loudness ratio. Current intensity is shown along the *x* axis for each subject: ''lmatch''=matched place on the left, ''lunmatched''=unmatched place on the left side with respect to the electrode selected on the right side.

loudness percepts for both patients. A fixed electrode place on the right side was selected such that for the matched place binaural stimulus, electrodes on both sides were not too close to either extreme of the electrode array. A deliberately mismatched place on the left side was also selected to test if a binaural mismatched place stimulus behaved differently to the matched stimulus. Five current intensity levels were chosen for the right electrode, spaced equidistantly on a logarithmic current scale and approximately spanning the electrode's dynamic range. The two electrodes on the left side were then balanced against the right electrode at each of the five levels. The loudness balancing was performed by adjusting the intensity of the left electrode in a continuously alternating left/right sequence of 300 ms bursts separated by 500 ms gaps, until the two sides appeared equally loud. The 15 resulting monaural stimuli were combined with the ten available L/R balanced loudness pairs to give a total stimulus block comprising 25 stimuli. The block was presented in random order, and after each monaural or binaural stimulus, the patients were asked to estimate the overall perceived loudness. In an initial session, all stimuli were balanced for loudness, and patients were trained in the magnitude estimation task. In a subsequent session, the data were collected from 20 presentations of the stimulus block. Since the total number of stimuli in a block was not large (25), the 20 data points for each stimulus configuration could be collected in a single session.

2. Results and discussion

The results of the loudness summation study are shown in Fig. 6. The top left and right graphs show average loudness estimates by P1 and P2, respectively, for both monaural and binaural stimuli. Unfilled symbols show loudness estimates for monaural stimuli, whereas binaural loudness is indicated by the filled symbols. The *y* axis displays assigned loudness values. The *x* axis shows the monaural current intensity used on each side. The lower diagrams in Fig. 6 show the ratio of binaural to monaural loudness, for matched loudness components on each side, calculated from upper figures. Since the average loudness estimates of left and right components of the binaural stimuli were usually not exactly equal, the ''monaural loudness'' for each point plotted was taken to be the average value of the left and right monaural loudness estimates.

The data for both patients show that with approximately loudness balanced stimuli in each ear, the overall loudness was approximately doubled when compared to stimulating

either side monaurally. Some differences are evident between the two patients' data. For patient P1, both matched and unmatched places showed similar trends in loudness summation. This agrees with results from the acoustic literature which show that for normal hearing, loudness summation with pure tones is independent of the frequency discrepancy between the two sides (Scharf, 1969). For P1, the ratio of binaural to monaural loudness ranged from almost 2.5 for stimuli eliciting midrange loudness percepts, to around 1.5 for very soft and very loud stimuli. It is possible, however, that this is due to numerical saturation effects at the more extreme levels, rather than any true level dependence of the summation. For the matched place condition, the increase in loudness due to binaural summation averaged across the five intensity levels was 1.93 for P1. Patient P2, in contrast to P1, showed more summation for the matched place condition than the unmatched condition. It is possible that this second patient, who was not yet as experienced in psychophysical tasks as P1, may have been listening to just one side or the other rather than to the overall loudness sensation for the unmatched place condition where two images rather than one fused image may have been heard (cf. van Hoesel *et al.*, 1993). This phenomenon is discussed in the literature for acoustic stimulation with normal hearing for example in Scharf (1969, p. 1202). For the matched place condition, the ratio of binaural to monaural loudness was in the range of 1.5–3, with most summation at the highest current intensities used. The averaged ratio of binaural to monaural loudness for the matched place, across the five level conditions, was 2.0 for this patient.

For both patients, the matched place data showed an average binaural-to-monaural loudness ratio of about 2. That is to say, the matched place binaural sound, with equal loudness components in each ear, was about twice as loud as the monaural sound in either ear. This is a useful ''rule of thumb'' result for initial binaural speech processor implementations. The differences in level dependence between the two patients, may either be due to different numerical biases, or else reflect different ''effective bandwidths'' of the electrical stimulation. For normal hearing the bandwidth determines how the amount of summation varies with intensity. The rise and fall of the summation curve with increasing intensity, with P1 for example, can also be seen in Scharf's data (Scharf, 1968) for octave band noise centered on 1 kHz, whereas the steady increase displayed by patient P2 is more like Scharf's data for broadband noise.

B. Central masking

1. Method

With normal hearing, elevated hearing thresholds in one ear result when a sound of similar spectral content is presented in the contralateral ear at the same time (Zwislocki, 1978). To investigate this phenomenon for electrical stimulation, a fixed place was selected on the right side. The threshold level for this place was measured using the 3 AFC procedure described in Sec. II A. Eight places on the contralateral side were then selected and all balanced for equal loudness at 80% DR. The threshold of the electrode on the right side was then measured again in the presence of each of the eight electrodes on the left side at their respective 80% DR levels. The increase in threshold compared to the monaural level measured was calculated as a percentage of the available dynamic range for the right side place. Duration of stimuli on both sides was 300 ms and both left and right electrodes were activated simultaneously. The procedure was repeated for two different fixed places on the right side for each patient. To determine how much central masking was found in our study in terms of loudness, loudness growth functions (LGFs) were obtained with both patients for the right ear electrodes used in this experiment. The method of magnitude estimation (Stevens, 1975) was used for this purpose. Approximately ten levels were chosen for each electrode, approximately evenly spaced on a logarithmic current scale to give rise to percepts ranging from just above threshold to just below uncomfortably loud.

2. Results and discussion

The central masking results for both patients are shown in Fig. 7, and display an increase in threshold of around 20%–40% of the dynamic range, but unlike acoustic results with normal hearing, show no place-dependent effects. Loudness growth functions (LGF) measured are shown on log/log scales in Fig. 8. The current intensity is plotted logarithmically in dB *re*: 1 μ A along the *x* axis. For patient P1, rather than being a simple power function (straight line) the slope of the LGF function is seen to decrease at low intensities. This means that the central masking effect of 20%–40% of the length spanned along the *x* axis, translates to about 7%–20% of the length spanned along the *y* axis. In other words, central masking amounts to a shift of about 7%–20% of the perceived loudness range for this patient. For patient P2 on the other hand, the LGF is well approximated by a straight line on log/log coordinates, so that 20%–40% of the length along the *x* axis corresponds to 20%–40% of the length along the *y* axis.

The location and mechanism of central masking with normal hearing is not yet well understood. Although the superior olive appears a likely candidate (Zwislocki, 1978), numerous binaural projections at higher centers cannot be excluded (for a review of binaural projections see, e.g., Moore, 1990). The sharp frequency selectivity demonstrated for central masking with normal hearing is in contrast to our result. It may be the case that aspects of central masking operate at more than just one site along the auditory pathway, or that neural functions at higher centers have been modified with the onset of deafness and subsequent prosthesis. Our results could be the result of a different interaction site, perhaps higher up in the auditory pathway, compared to the normal hearing case. This idea receives some support from a pilot study conducted with P1 in which interaural time delays up to 200 ms did not alter the amount of central masking. In the normal hearing case, central masking is strongly dependent on the interaural time delay. Some physiological data furthermore imply the involvement of the medial efferent system (Warren and Liberman, 1989) via the outer hair cells, which would not be activated with electrical stimulation. Alternatively, it is possible that our two patients

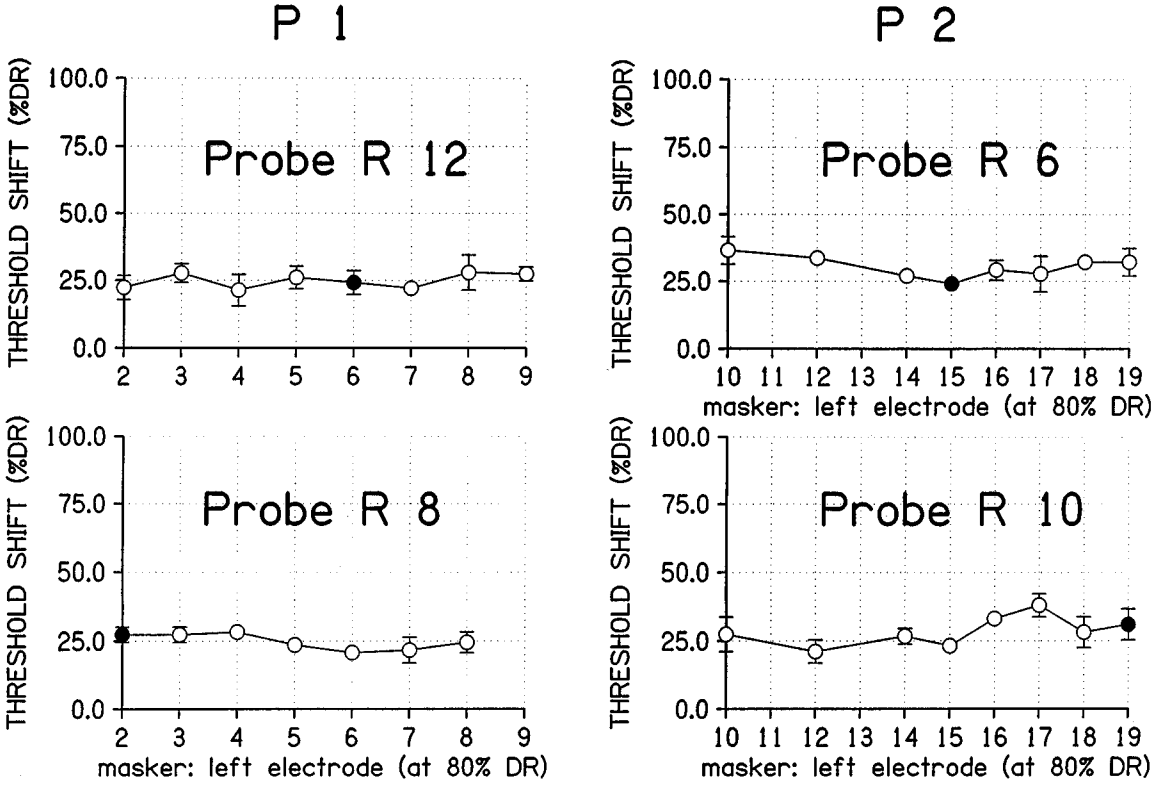

FIG. 7. Central masking results for two fixed places on the right as a function of the place of stimulation on the left. The *x* axis shows the electrode selected on the left side, the *y* axis shows the increase in threshold (% dynamic range) on the right side compared to monaural threshold. Solid symbols show the place of stimulation corresponding to ''best-matched place'' in agreement with Fig. 1.

were not able to learn the central masking task sufficiently well to be able to direct attention to the quiet test tone in the presence of the much louder contralateral masker. It seems unlikely, however, in that case, that the results for the different electrodes would have shown such a consistent degree of masking.

IV. SUMMARY AND DISCUSSION

Our psychophysical results to date with both binaural implant patients, have shown that percepts from binaural stimulation can be fused. Although interaural amplitudes are well perceived, interaural time delays are not, when compared to normal hearing. This has been confirmed in the experiments reported here using direct jnd measurements with both patients for rates from 50 to 300 pps and places of stimulation spanning the entire electrode arrays on both sides. Diotic rate perception results showed no improvement when compared to monaural jnds. However, dichotic presentation showed that under some conditions, binaural temporal interaction can lead to improved rate jnds. For place matched, loudness balanced single electrode pairs, binaural loudness was about twice as loud as either monaural side alone. Central masking gave rise to increased thresholds, but was not place dependent as is the case for normal hearing.

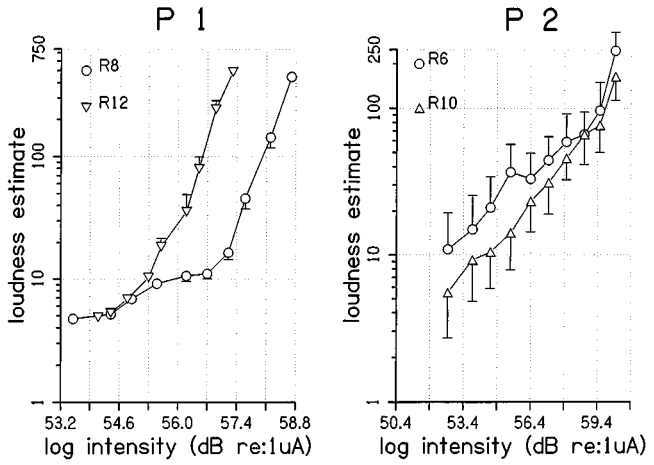

FIG. 8. Loudness growth functions for the probe electrodes used in the central masking experiment. Results are plotted as log current intensity versus log loudness estimates. These curves were used to determine how much the central masking effect shown in Fig. 7 amounted to in terms of loudness.

It is perhaps somewhat surprising that none of the electrical stimulus configurations tested have yielded good sensitivity to ITDs. Given the highly deterministic nature of electrical stimulation, one might expect improved ITD jnds compared to normal hearing. Two possible explanations may be contributing to this result. The first is that the neural circuitry required to accurately detect interaural delays in the normal hearing case has decayed in these patients. The second is that electrical stimulation with the present device is unable to reproduce neural excitation similar enough to the normal hearing case to allow interaural time delay mechanisms to unambiguously extract information (even for ''well-matched places'' on the two sides). As an example, the present implants cannot accurately stimulate parts of the neural population in accordance with normal hearing traveling

wave delays along the basilar membrane. This means that neural delays present to compensate for these delays in the normal hearing case might introduce unwanted delays in the electrical case, which might in turn adversely affect perception of ITDs.

When comparing with traditional models for binaural hearing to explain our electrical results, we note that a mechanism is required in which interaural amplitudes may affect lateralization percepts even when time delays have little or no effect. This means we must discount models which translate amplitude differences to time delays. The improved jnd for the dichotic case is interesting and in contrast to the decreased binaural temporal sensitivity generally observed with these two patients. Our earlier studies indicated only a weak dependence of lateralization on ITD, implying lateralization cues may not be responsible for the result obtained here. It is possible, however, that the continually changing ITDs introduced by the different rates on the two sides provide a noticeable ''dynamic lateralization'' effect. Lateralization studies with time-varying ITDs are required to test this hypothesis. If lateralization percepts are not responsible, we must assume some other rate comparison mechanism, perhaps again at a higher center and derived from the monaural channels. This mechanism must be capable of comparing rate data from each side independent of ITDs. A running autocorrelation on each monaural signal followed by a cross correlator comparing the two autocorrelated signals could achieve the desired function. Our central masking and binaural loudness summation results can be interpreted in terms of additive models. The lack of place dependence found for central masking with electrical stimulation, however, implies that these patients could not monitor loudness in individual ''binaural channels.'' This is also in opposition to results for normal hearing with acoustic stimuli, which show strong frequency selectivity for central masking, and lends further support to the suggestion that higher centers may be used by these patients to combine binaural information. Whether or not such higher centers function similarly in the normal hearing case, or whether they have adapted after prosthesis remains at this stage an open question.

The results obtained in these studies should be taken into consideration when attempting to develop successful speech processors for these first two binaural cochlear implant patients. From the data collected here, it seems likely that binaural intelligibility gains through unmasking will be absent from basic implementations of binaural cochlear implant strategies for these patients. The dichotic rate advantage found does not offer an obvious speech processing scheme that would benefit from this result. One possibility might be to use an intelligent preprocessor to separate multiple sound sources and present stimuli from these sources at separate rates to the binaural patient with an advanced implant system.

ACKNOWLEDGMENTS

This work was supported by the Australian Research Council's Human Communication Research and the Cooperative Research Centre for Cochlear Implant, Speech and Hearing Research. The authors wish to thank the two binaural patients for their participation in this research, and Lawrence Cohen for his help with the computer models to determine the insertion depths from the radiological data, and wish to acknowledge Fan-Gang Zeng and another anonymous reviewer for their useful comments on an earlier draft of this document.

Blamey, P. J., Dowel, R. C., Clark, G. M., and Seligman, P. M. (**1987**). ''Acoustic parameters measured by a formant estimating speech processor for a multiple channel cochlear implant,'' J. Acoust. Soc. Am. **82**, 48–57.

Clark, G. M., Patrick, J. F., and Bailey, Q. R. (**1979**). ''A cochlear implant round window array,'' J. Otolarynogol. Otol. **93**, 107–109.

Cohen, L. T., Xu, J. Xu, S. A., and Clark, G. M. (**in press**). ''Improved methods for specifying positions of the electrode bands of a cochlear implant array,'' J. Am. Otol. (in press).

Durlach, N. I., and Colburn, H. S. (**1978**). In *Handbook of Perception* (Academic, New York), Vol. IV, Chap. 10, pp. 373–406.

Gabriel, K. B., Koehnke, J., and Colburn, H. S. (**1992**). ''Frequency dependence of binaural performance in listeners with impaired binaural hearing,'' J. Acoust. Soc. Am. **91,** 336–347.

Green and Swets (**1966**). *Signal Detection Theory and Psychophysics* (Wiley, New York).

Henning, G. B. (**1974**). ''Detectability of interaural delay in high-frequency complex waveforms,'' J. Acoust. Soc. Am. **55,** 84–90.

Henning, G. B. (**1980**). ''Some observations on the lateralization of complex waveforms,'' J. Acoust. Soc. Am. **68,** 446–454.

Hirsh, I. J. (**1948**). ''The influence of interaural phase on interaural summation and inhibition,'' J. Acoust. Soc. Am. **20**, 536–544.

Jesteadt, W., and Wier, C. C. (**1977**). ''Comparison of binaural and monaural discrimination of intensity and frequency,'' J. Acoust. Soc. Am. **61,** 169–177.

Levitt, H. (**1971**). ''Transformed up-down methods in psychoacoustics,'' J. Acoust. Soc. Am. **49,** 467–477.

Licklider, J. C. R. (**1948**). ''The influence of interaural phase upon the masking of speech by white noise,'' J. Acoust. Soc. Am. **20,** 150–159.

Licklider, J. C. R., Webster, J. C., and Hedlun, J. M. (**1950**). ''On the frequency limits of binaural beats,'' J. Acoust. Soc. Am. **22,** 468–473.

Lim, H. H., and Tong, Y. C. (**1989**). ''Pitch scaling, difference limens, and identification of electrical pulse rate on multi-channel cochlear implant patients—implications on temporal speech processing,'' Proc. Ann. Int. Conf. IEEE Eng. Med. Biol. Soc. **11**, 1065–1066.

Marsh, M. A., Xu, J., Xu, S.-A., Blamey, P. J., Abonyi, J., and Clark, G. M. (**1993**). ''Radiological evaluation of multi channel intra cochlear implant insertion depth,'' Am. J. Otol. **14**(4), 386–391.

Moore, D. R. (**1991**). ''Anatomy and physiology of binaural hearing,'' Audiology **30**, 125–134.

Nuetzel, J. M., and Hafter, E. R. (**1981**). ''Discrimination of interaural delays in complex waveforms: spectral effects,'' J. Acoust. Soc. Am. **69,** 1112–1118.

Pickler, A. G., and Harris, J. D. (**1955**). ''Channels of reception in pitch discrimination,'' J. Acoust. Soc. Am. **27**, 124–131.

Sayers, B. M. (**1964**). ''Acoustic-image lateralization judgements with binaural tones,'' J. Acoust. Soc. Am. **36,** 923–926.

Scharf, B. (**1968**). ''Binaural loudness summation as a function of bandwidth,'' Reports of the Sixth International Congress on Acoustics, 25–28 (A-35).

Scharf, B. (**1969**). ''Dichotic summation of loudness,'' J. Acoust. Soc. Am. **45,** 1193–1205.

Scharf, B. (**1978**). *Handbook of Perception* (Academic, New York), Vol. IV, Chap. 6, pp. 217–218.

Shannon, R. V. (**1983**). ''Multichannel electrical stimulation of the auditory nerve in man. I. Basic psychophysics,'' Hear. Res. **11**, 157–189.

Stevens, S. S. (**1975**). *Psychophysics* (Wiley, New York).

Tong, Y. C., Blamey, P. J., Dowell, R. C., and Clark, G. M. (**1983**). ''Psychophysical studies evaluating the feasibility of a speech processing strategy for a multichannel cochlear implant,'' J. Acoust. Soc. Am. **74,** 73–80.

Tong, Y. C., and Clark, G. M. (**1986**). ''Loudness summation, masking and temporal interaction for sensations produced by electric stimulation of two sites in the human cochlea,'' J. Acoust. Soc. Am. **79,** 1958–1966.

Tong, Y. C., Clark, G. M., and Lim, H. H. (**1989**). ''Estimation of the effective spread of neural excitation produced by a bipolar pair of scala tympani electrodes,'' Ann. Otol. Rhinol. Laryngol. Suppl. **128,** 37–38.

van Hoesel, R. J. M., and Clark, G. M. (**1995**). ''Fusion and lateralization study with two binaural cochlear implant patients,'' Ann. Otol. Rhinol. Laryngol. Suppl. 166 **104**, Part 2, 233–235.

van Hoesel, R. J. M., Tong, Y. C., Hollow, R. D., and Clark, G. M. (**1993**). ''Psychophysical and speech perception studies: a case report on a bilateral cochlear implant subject,'' J. Acoust. Soc. Am. **94,** 3178–3189.

van Hoesel, R. J. M., Tong, Y. C., Hollow, R. D., Huigen, J. M., and Clark, G. M. (**1991**). ''Preliminary studies on a bilateral cochlear implant user,'' J. Acoust. Soc. Am. Suppl. 1 **88,** S193.

Warren III, E. H., and Liberman, M. C. (**1989**). ''Effects of contralateral sound on auditory-nerve responses. I. Contributions of cochlear efferents,'' Hearing Res. **37,** 89–104.

Zwislocki, J. J. (**1978**). ''Masking: Experimental and theoretical aspects of simultaneous, forward, backward, and central masking,'' in *Handbook of Perception* (Academic, New York), Vol. IV, Chap. 8, pp. 283–337.

Performance over time of adult patients using the Ineraid or Nucleus cochlear implant

Richard S. Tyler
Department of Otolaryngology–Head and Neck Surgery, Department of Speech Pathology and Audiology, The University of Iowa, Iowa City, Iowa 52242-1078

Aaron J. Parkinson
Department of Otolaryngology-Head and Neck Surgery, The University of Iowa, Iowa City, Iowa 52242-1078

George G. Woodworth
Department of Statistics and Actuarial Sciences, The University of Iowa, Iowa City, Iowa 52242-1078

Mary W. Lowder and Bruce J. Gantz
Department of Otolaryngology–Head and Neck Surgery, The University of Iowa, Iowa City, Iowa 52242-1078

(Received 18 March 1996; accepted for publication 6 March 1997)

This study examined the average and individual performance over time of 49 adult cochlear implant subjects. Subjects were randomly assigned to receive either the Ineraid cochlear implant, with analog processing, or the Nucleus cochlear implant, with feature-extraction processing. All subjects had postlingual profound bilateral sensorineural hearing loss and received no significant benefit from hearing aids before implantation. Group data were examined in two ways. First, only subjects who had complete data over the test period were examined. Second, an analysis of all available data was carried out by mixed linear-model analysis. In this analysis, to account for missed follow-ups at the planned intervals, data consisting of the observations closest in time to the planned test times were modeled by natural splines with knots at the planned follow-up times. Contrasts between all pairs of planned follow-up times for each device were tested, as were contrasts between devices at each planned follow-up time. Results indicated little difference between the performance of the Ineraid and Nucleus subjects in their level of performance or their rate of learning. Postimplantation performance was typically superior to preimplantation performance within 9 months, and continued to improve up to 18–30 months depending on the speech perception measure. In some subjects, improvements in speech perception measures were observed up to four or five years postimplantation. There was also evidence that three subjects had a decrement in overall speech perception performance, although their postimplantation scores were always higher than their preimplantation scores. In at least one subject this was likely a result of age-related cognition decrements. [S0001-4966(97)01507-5]

PACS numbers: 43.66.Sr, 43.66.Ts, 43.71.Ky, 43.64.Me [JWH]

INTRODUCTION

Considerable data are now available concerning the performance of cochlear implants for individuals with profound sensorineural hearing loss. Studies examining performance of cochlear implant recipients over time have indicated that most gains in performance with cochlear implants occur in the first 9–12 months of use. Considerable variation in the overall performance and rate of improvement over time among subjects has been reported (Cohen *et al.*, 1993; Dorman *et al.*, 1990; Spivak and Waltzman, 1990; Tye-Murray *et al.*, 1992). None of the studies cited had substantial data beyond two years, and few had directly compared different cochlear implant designs over time.

There is a general lack of longitudinal data concerning the development of auditory perception skills in cochlear implant recipients over time. Most studies have been concerned with documenting postimplantation speech perception abilities over preimplantation abilities. Brown *et al.* (1987), Dowell *et al.* (1986), and Waltzman *et al.* (1986) examined improvement in speech perception scores over time with Nucleus subjects. However, none of these studies went beyond 12 months and all had relatively small subject groups. Spivak and Waltzman (1990) compared the preoperative speech perception performance of 15 subjects, wearing hearing aids, to their postoperative performance at 3 months as well as at 1, 2, and 3 years using Nucleus cochlear implants. On average, subjects exhibited the greatest amount of improvement in the first 3 months of implant use. They also reported smaller, but significant, gains in the perception of segmental features and open-set recognition of word and sentence materials over the next 3 years. Improvement over this time was most evident in those subjects with open-set speech recognition at 3 months postimplantation. A problem with this study was related to the sample size available beyond 2 years. Spivak and Waltzman (1990) presented data on only 5 subjects at 3 years. Consequently, comparisons were made between time points with very unequal numbers in each group. For example, comparisons were made between 15

TABLE I. Biographical data for the Nucleus cochlear implant subjects (NA=not available).

Subject number	DOB	Duration of profound deafness (years)	Age at profound deafness (years)	Age at onset of hearing loss (years)	Experience with implant (months)	Number of channels active	Ear implanted
N1	4/26/17	4	65	32	41	20	right
N2	11/22/55	8	22	21	52	18	left
N3	3/30/24	1	61	37	53	20	left
N4	3/1/42	23	22	21	55	13	left
N5	12/5/57	19	10	2	55	16	right
N6	2/14/20	3	64	13	53	15	left
N7	4/14/35	22	30	8	55	13	right
N8	9/27/59	1	27	26	56	18	left
N9	6/17/64	10	13	2	0	NA	left
N10	9/19/45	30	12	5	55	14	left
N11	5/29/34	7	47	47	59	20	right
N12	1/24/38	7	43	26	50	19	left
N13	1/4/42	2	45	44	31	19	left
N14	7/13/58	1	29	28	54	16	left
N15	10/23/42	15	31	17	60	20	right
N16	8/18/49	5	34	6	60	19	left
N17	10/16/25	20	44	43	51	19	left
N18	6/19/45	10	34	15	54	18	left
N19	1/26/23	5	62	5	50	20	right
N20	5/5/66	15	8	7	13	20	left
N21	2/2/20	10	60	12	55	17	left
N22	11/10/46	31	12	13	55	19	right
N23	11/29/23	17	49	21	54	19	right
N24	11/28/35	28	27	20	49	20	right
N25	6/26/28	27	35	14	41	16	left

subjects at 3 months and 5 of the 15 subjects at 3 years postimplantation.

Dorman *et al.* (1990) reported on the spondee recognition in 27 Ineraid subjects over a 2-year period. They observed that the rate of ''reacquisition of spondee word recognition'' varied considerably in their group of subjects. The median score at 1 month postconnection was 10%, with the range of scores being 0%–84%. At 2 years (22–28 months),

TABLE II. Biographical data for the Ineraid cochlear implant subjects.

Subject number	DOB	Duration of profound deafness (years)	Age at profound deafness (years)	Age at onset of hearing loss (years)	Experience with implant (months)	Number of channels active	Ear implanted
I1	1/25/24	35	27	27	53	4	left
I2	7/10/18	3	65	13	53	4	left
I3	7/16/15	1	70	70	41	4	right
I4	11/27/19	8	59	51	54	4	right
I5	1/21/22	7	58	23	56	4	right
I6	1/14/22	44	21	20	54	4	right
I7	4/5/22	7	58	38	53	4	right
I8	10/14/28	2	57	31	53	4	right
I9	1/1/37	5	46	21	52	4	left
I10	8/5/24	17	47	26	17	4	left
I11	2/11/50	5	33	21	53	4	right
I12	8/15/55	1	32	6	58	4	left
I13	4/23/55	10	24	22	54	4	left
I14	6/26/27	22	40	16	52	4	right
I15	12/13/33	4	52	23	31	4	left
I16	6/22/38	47	4	3	54	4	left
I17	5/26/53	14	22	2	56	4	left
I18	3/5/21	10	59	15	57	4	right
I19	2/25/39	16	35	9	18	4	right
I20	10/19/64	1	24	0	53	4	left
I21	4/8/60	7	23	5	53	4	left
I22	2/23/21	19	50	48	55	4	left
I23	5/1/44	1.5	45	31	56	4	left
I24	12/25/17	25	48	39	52	4	left
I25	4/26/27	6	57	51	32	4	right

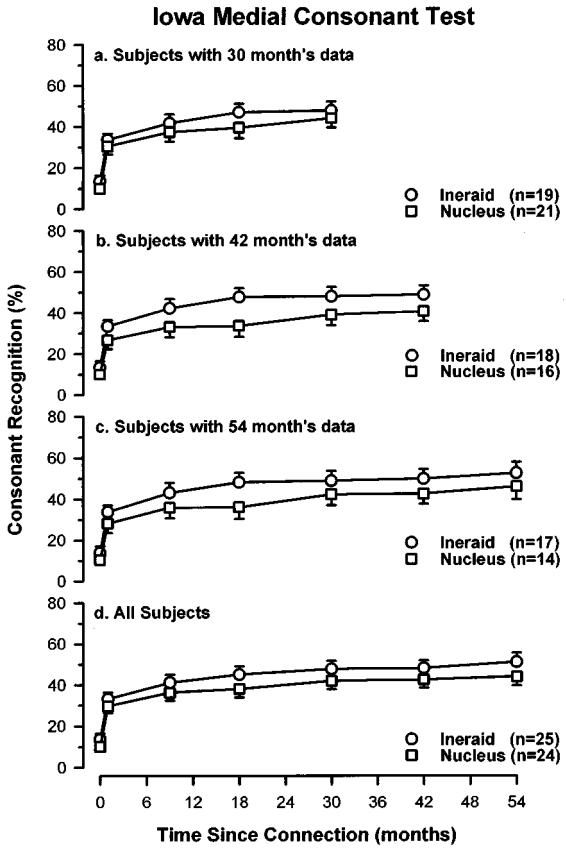

FIG. 1. Mean scores over time for the Iowa Medial Consonant Test. Top three panels show group data for the same subjects over the time periods indicated. Vertical bars represent standard errors of the means. The bottom panel shows estimated mean scores over time for all available data based on the mixed general model linear analysis. Vertical bars represent standard errors based on large sample approximations.

the median score was 56%, but scores still varied widely—0%–100%. Dorman *et al.*, contrary to the results of Spivak and Waltzman (1990), found that poor open-set speech recognition soon after device activation (0%–12% at 1 month) was not necessarily a prognosis of poor performance 1 or 2 years later. Out of the 14 subjects who scored 12% or less at 1 month, only 3 scored less than 28%, and 8 scored more than 50% after 22–28 months of experience. Dorman *et al.* found that some of the better subjects exhibited high performance very soon after connection, whereas others gradually improved over a 2-year period before reaching a high level of performance.

The University of Iowa Cochlear Implant Program has data for individuals using the Ineraid and the Nucleus cochlear implants for more than 5 years. In this study, we present data for two groups of adult multichannel implant subjects, the purpose being to examine mean and individual performance over time. Examining performance over time is important for a number of reasons. These reasons include the need to verify the long-term effects of electrical stimulation on the auditory system, being able to counsel potential subjects of the time course to be expected for improvement, and to plan rehabilitation strategies. We were interested in comparing the rate of improvement, as well as the overall performance of the two devices. Individual data were also of interest as it is possible that noteworthy trends in the performance of individuals were obscured by mean data. This is especially a concern when one considers the wide variation in performance evident among subjects in previous studies.

I. METHOD

A. Subjects

The subjects for this study were 49 adult (26 male, 23 female) cochlear implant subjects, 25 with the Ineraid device and 24 with the Nucleus device. Subjects were randomly assigned to receive either the Ineraid or the Nucleus cochlear implant. Biographical data for the Nucleus and Ineraid subjects are shown in Table I and Table II, respectively. All subjects had postlingual profound bilateral sensorineural hearing loss, and received no significant benefit from hearing aids before receiving a cochlear implant. Preoperatively, no subject scored more than 4% for the NU-6 Word Recognition Test (Tillman and Carhart, 1966), nor greater than 10% for the Iowa Sentence Test (Tyler *et al.*, 1986), both tested without visual clues. By the end of this study period (54 months) 4 subjects (2 from each implant group) were deceased. One Nucleus subject withdrew due to lack of benefit from implantation after 9 months of implant use. An additional Nucleus subject dropped out of the study soon after connection due to lack of benefit (i.e., our original Nucleus subject pool was 25). Data for this subject are therefore not presented in this manuscript.

Over the first 18 months, subjects were evaluated 1 month after implant connection and then at 9 and 18 months. Thereafter, they were evaluated at annual intervals—at 30, 42, and 54 months. At each evaluation, several open-set and closed-set speech tests were administered. The acoustic stimuli for the speech tests were presented via laser video disc in a sound field, under sound-treated conditions, with the loudspeaker placed at 45° azimuth on the side of the subject's implanted ear. The consonant test was presented in vision-alone and audition-plus-vision modes, in addition to audition-alone, allowing the calculation of consonant lipreading enhancement. Lipreading enhancement was expressed as the percentage of the possible enhancement over a subject's vision-alone score, and was defined by the formula:

$$\text{lipreading enhancement} = \frac{(A+V)-V}{100-V},$$

where $A+V$ was the audition-plus-vision score and V was the vision-only score (Tyler *et al.*, 1992). All the other speech tests were presented audition-alone. For all tests, the presentation level was about 70 dB SPL (65–75 dB SPL) and were administered and scored under computer control. Subjects were permitted to adjust their processors to their most comfortable listening level.

The speech test battery consisted of the Iowa Medial Consonant Test, the Iowa Medial Vowel Test (Tyler *et al.*, 1983), the Iowa Sentence Test, and the NU-6 Word Recognition Test. The Iowa Medial Consonant test was a 78-item (13 consonants repeated 6 times) closed-set test with the consonant stimulus presented in an ''/I/consonant/I/'' context. The Iowa Medial Vowel Test was a 54-item (9 vowels repeated 6 times) closed-set test with the vowel stimulus pre-

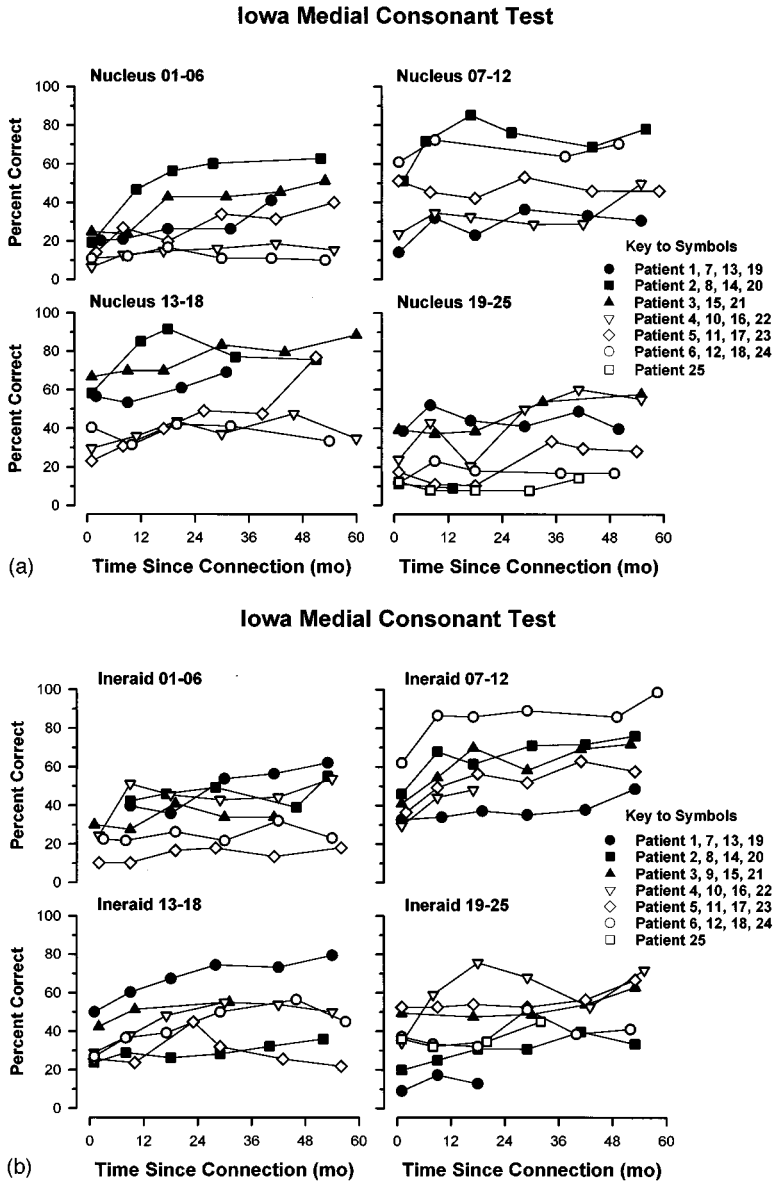

FIG. 2. (a) Individual scores over time for the Iowa Medial Consonant Test for the Nucleus implant group. (b) Individual scores over time for the Iowa Medial Consonant Test for the Ineraid implant group.

sented in an ''/h/vowel/d/'' context. The Iowa Sentence Test was an open-set test and consisted of five 20-item lists (one list presented randomly at each session), scored by number of key words correct (average of 85 words per list). The NU-6 Word Recognition Test was an Iowa recording of list one (50 words, 150 phonemes) of that test with the stimuli presented in a random order at each presentation.

B. Equipment and design

All the Nucleus subjects in this study used a 22-electrode feature-extraction processing strategy. Initially all were programmed with the $F0F1F2$ strategy. This produces pulsatile stimulation on a maximum of two channels (or electrodes) per stimulus cycle. This strategy extracts and codes first ($F1$) and second ($F2$) formant frequency and their amplitudes. Frequency values for $F1$ and $F2$ determine which electrodes are stimulated ($F1$ more apically and $F2$ more basally) and the amplitude of each formant determines the amount of current delivered by these electrodes. Fundamental frequency ($F0$) is coded as the rate of stimulation. During the investigation, 13 of the Nucleus subjects received an alternative feature-extraction processor, the Mini Speech Processor. This processor made available an additional processing strategy (Multipeak or MPEAK). We refer to this strategy as $F0F1F2B3B4B5$. It stimulates a maximum of four channels per stimulus cycle. In addition to $F0$, $F1$, and $F2$, three additional fixed electrodes ($B3$, $B4$, and $B5$) are stimulated when high-frequency information is present (default electrodes are 7, 4, and 1) (see Parkinson *et al.*, 1996).

Some subjects benefit from this more recent strategy, some prefer the $F0F1F2$ and many show no preference. Performance differences between the $F0F1F2$ and $F0F1F2B3B4B5$ strategies have been described by others (Kim *et al.*, 1992; Parkinson *et al.*, 1996; Skinner *et al.*,

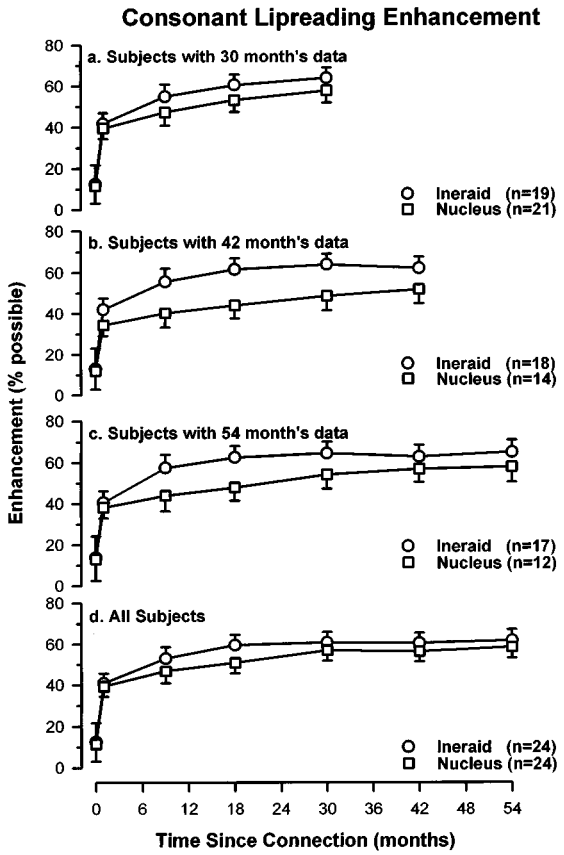

FIG. 3. Mean scores over time for Consonant Lipreading Enhancement. Top three panels show group data for the same subjects over the time periods indicated. Vertical bars represent standard errors of the means. The bottom panel shows estimated mean scores over time for all available data based on the mixed general model linear analysis. Vertical bars represent standard errors based on large sample approximations.

1991; Waltzman *et al.*, 1992). Our data suggest that performance differences between these two strategies generally are not large, on an individual or average basis (Parkinson *et al.*, 1996). Parkinson *et al.*, in an ABAB design, compared performance of the $F0F1F2$ and $F0F1F2B3B4B5$ speech processing strategies in a group of 17 subjects using the Nucleus Mini Speech Processor on a number of speech measures. For 13 of these subjects (N8, N10, N11, N12, N14, N16, N17, N18, N19, N21, N22, N23, and N25) this ''upgrade'' study coincided with the time period examined for the present ''over-time'' analysis. For periods during which the two studies coincided, only the speech scores obtained with the $F0F1F2$ processing strategy just prior to commencing the upgrade study (for 10 of the above subjects this was using the Nucleus Wearable Speech Processor III and for 3 subjects this was using the Nucleus Mini Speech Processor) and at the end of the upgrade study (at which time they were all using the $F0F1F2$ strategy in the Mini Speech Processor) were used. This allowed us to investigate any effect the study protocol or change in *processor* may have had on performance over time. Six of the 13 subjects (N16, N17, N19, N21, N22, and N23) used $F0F1F2B3B4B5$ for periods ranging from 1 to 2 years after completion of the Parkinson *et al.* study. Two subjects (N18 and N25) have data using $F0F1F2$ for 12 months beyond the end of the Parkinson *et al.* upgrade study. For the other 5 subjects, the end of the present study and the Parkinson *et al.* study coincided. All 13 subjects had at least 18 months of total implant experience before commencing the upgrade study and were therefore beyond the point in time during which most improvement in performance occurs (see results). The data for all 13 subjects were examined to investigate what effect the newer processing strategy and/or processor may have had on performance over time. In the present investigation, the data presented for the subjects who underwent the upgrade study represent the optimal of the two feature extraction alternatives for each individual after completion of the upgrade study. Data collected with each strategy were not treated separately for the group analyses.

The Ineraid device consists of a compressed analog four-channel (four electrodes) speech processor. This processor initially compresses the input signal to compensate for the reduced dynamic range of electrically evoked hearing. The output is bandpass filtered into four channels with the output of each channel presented simultaneously to each of the four electrodes. Speech is coded by the relative stimulus amplitudes across the four channels, and the temporal features of the waveforms within each channel. Detailed descriptions for both the Ineraid and Nucleus devices can be found in Eddington (1980), Parkinson *et al.* (1996), Skinner *et al.* (1991), Patrick and Clark (1991), and Wilson (1993).

II. RESULTS

Most of the subjects had such limited hearing preimplantation that they could not hear the test stimuli. Subjects who could not hear the test stimuli were assigned chance scores for the purpose of the following graphs. However, the statistical significance of the difference between mean score at zero months and other time points was not tested because of the unrealistically low variance (because many subjects were assigned chance) at the zero-month condition.

There were follow-up times where data for an individual were not available. Therefore, to represent a true picture of performance over time, unaffected by differences in the number of subjects available, two approaches were taken. First, graphs are presented where subjects were included only if they had data for all scheduled visits. That is, the average data represented by each point in the graph represent the same subject set across time. This was done for three time intervals; 30, 42, and 54 months. Thus subjects who had complete data over 54 months are also included in the other two graphs. Second, a mixed general linear model (SAS/STAT User's guide, 1989; Woodworth, 1995) was used to analyze all the available data from all subjects over a 54-month period. Because subjects did not always appear for follow-up visits at the planned intervals, we modeled the growth curves with interpolating splines with ''knots'' at the planned observation times. Contrasts among all pairs of planned follow-up times for each device (i.e., between sessions) were tested, as were contrasts between devices at each planned follow-up time (i.e., within sessions). Since there were 15 contrasts between follow-up times and 6 between devices, all tests were run at the $p<0.01$ significance level.

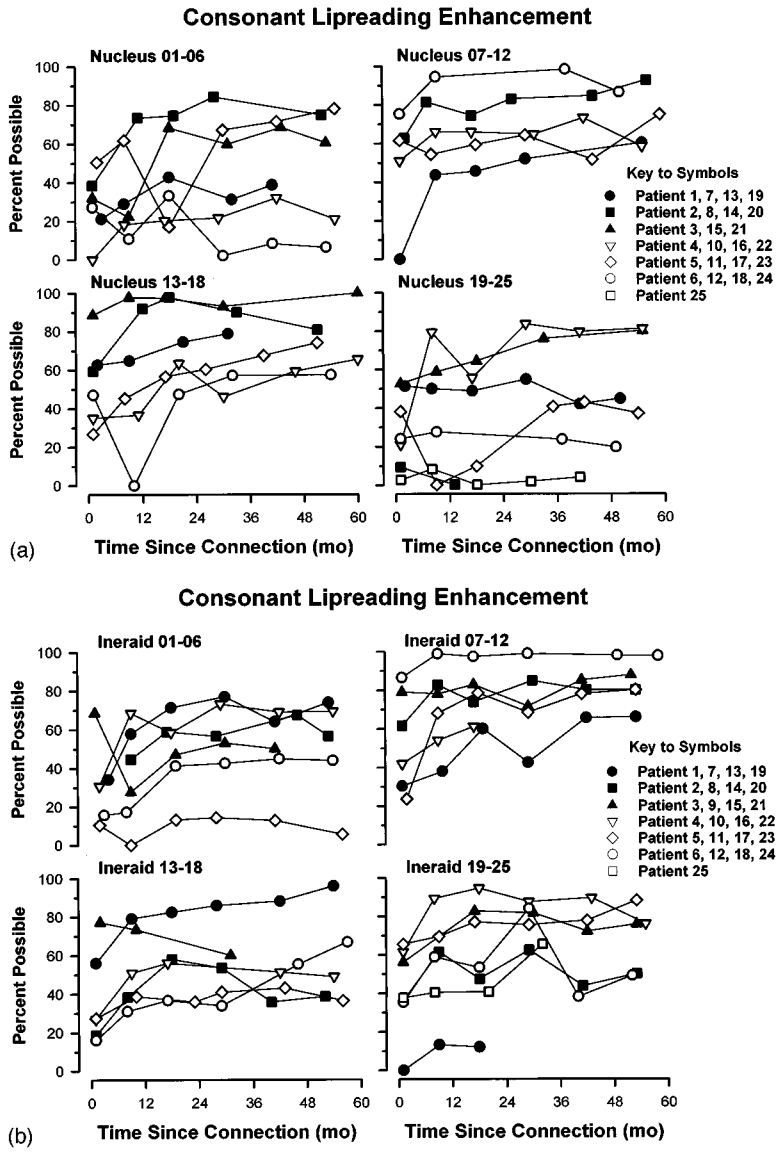

FIG. 4. (a) Individual scores over time for Consonant Lipreading Enhancement for the Nucleus implant group. (b) Individual scores over time for Consonant Lipreading Enhancement for the Ineraid implant group.

Figure 1 illustrates mean performance over time on the consonant test for the Nucleus and the Ineraid groups. The top three panels show subjects with complete data for 30, 42, and 54 months experience, respectively. In each panel, each data point represents the mean performance of the *same* group of subjects. In the bottom panel, estimated mean scores are shown for all subjects.

Between-device analyses of the mixed-model data indicated no significant difference between the two implant types over the 54-month period for the consonant test (see the Appendix). These results suggest that there were no differences in overall performance, and that there was no difference in the average rate of improvement for the two implant groups. All graphs representing the group data show an almost immediate improvement in consonant perception. By 1 month postimplantation, the subjects were scoring, on average, around 30% correct for consonant recognition. Although not all subjects were tested preimplantation (see Sec. I), most would have scored at chance levels (7.7%) prior to implantation as few had sufficient aided hearing to hear the stimulus. Testing of the mixed-model data indicated significant improvements in mean performance between 1 and 9 months ($t=3.63$, $p=0.0003$, Ineraid; $t=3.04$, $p=0.0026$, Nucleus) and between 9 and 30 months ($t=3.82$, $p=0.0002$, Ineraid; $t=3.24$, $p=0.0013$, Nucleus) for both implant groups. No significant improvement in mean score was noted after 30 months (i.e., $p>0.01$).

Figure 2(a) and (b) plots individual consonant test scores over time for the Nucleus and Ineraid groups. For clarity, the subjects are divided into four groups for each figure. The lack of significant intergroup differences is most likely related to the substantial variation in individual performance in both groups of implant subjects. There was also considerable variation in the rate of improvement among individuals. A number of subjects showed dramatic improvement in consonant recognition after only one month of implant experience. For example, subjects N8, N11, N12, N13, N14, N15, I12, I13, I21, and I23 scored between 50% and 60% correct at

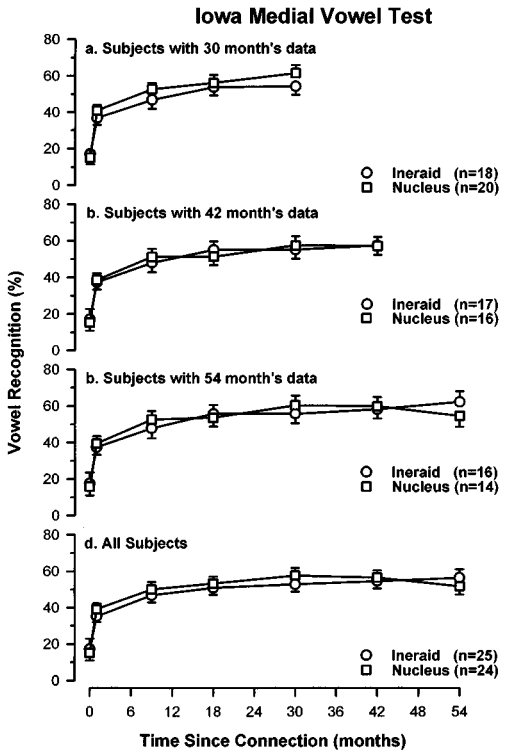

FIG. 5. Mean scores over time for the Iowa Medial Vowel Test. Top three panels show group data for the same subjects over the time periods indicated. Vertical bars represent standard errors of the means. The bottom panel shows estimated mean scores over time for all available data based on the mixed general model linear analysis. Vertical bars represent standard errors based on large sample approximations.

1-month postimplantation. Others reached similar levels of performance, but took longer (e.g., N2, N21, I1, I22). Performance for many subjects after 18-months experience appeared to become more stable, as the group data suggested. However, that is not to say that learning did not occur after this period. A number of subjects continued to show improvement after this time, although not as rapidly as in the first 12 months. Three Ineraid and seven Nucleus subjects showed a statistically significant (by the binomial theorem—Thornton and Raffin, 1978) improvement in consonant recognition when comparing their scores at 18 months (by which time most improvement had occurred) to their scores at 54 months. An additional Nucleus subject who had data to 42 months also showed a significant improvement in consonant score at 42 months over that obtained at 18 months. One Nucleus subject and 1 Ineraid subject showed significant decrements in performance between 18 and 54 months. Seventeen Ineraid and 13 Nucleus subjects did not exhibit significant changes after 18 months. Six subjects (2 Nucleus and 4 Ineraid) with data of less than 42 months were not considered in this analysis. While the poorer implant subjects tended to stay at similar levels through 54 months, there were some who eventually attained relatively high levels of consonant recognition (e.g., N5, N10, N23, I20).

It is important to note that some subjects (N14, I17, and I22) showed significant *decreases* in performance over time, even after showing initial improvement. In the case of I22, the decrease occurred between 18 and 42 months with some recovery evident at 54 months for the consonant test. However, as in the other two subjects, I22 showed similar deterioration in performance for some of the other speech measures. Subjects showing significant late long-term changes in performance across speech tests will be discussed in detail later.

Figure 3 shows the average consonant lipreading enhancement provided by the implants over time. Lipreading enhancement is the amount of enhancement provided by the implant to consonant perception, expressed as a percentage of the possible improvement over the score obtained by lipreading alone (see Tyler *et al.*, 1992). This metric allowed us to compare and combine performance across subjects. The spline analysis indicated no significant difference in mean scores between the Ineraid and Nucleus subjects at any time (see the Appendix). Scores improved significantly up to 18 months for the Ineraid group and for the Nucleus group. Mean performance for both implant groups improved between 1 and 9 months ($t=5.37$, $p=0.0000$, Ineraid; $t=5.74$, $p=0.0000$, Nucleus). Only the Nucleus group showed significant improvement after 9 months ($t=3.28$, $p=0.0012$, between 9 and 30 months), but not beyond 30 months ($p>0.01$).

Individual data for consonant enhancement are presented in Fig. 4(a) and (b). While many subjects appeared to have reached a reasonably stable level of performance beyond 18 to 30 months, there were others who demonstrated changes in consonant enhancement scores over time. Given that lipreading enhancement is in part derived from the subjects' consonant scores, it is not surprising that there was considerable variation in both overall performance and in rate of improvement as observed for the consonant test. Two Ineraid and 5 Nucleus subjects showed significant improvements in consonant lipreading enhancement when their scores at 18 months were compared to their scores at 54 months. One Nucleus and 2 Ineraid subjects had significantly decreased scores when their scores at 18 months were compared to 54 months. Seventeen Ineraid and 16 Nucleus subjects showed no significant differences between 18 and 42 or 54 months, and 6 other subjects (4 Ineraid and 2 Nucleus) only had data to 30 months or less.

As Fig. 5 shows, there was practically no difference in average vowel perception between the two implant groups (see the Appendix). Statistical testing of the spline data indicated that there was significant improvement in mean vowel scores for both the Ineraid and Nucleus groups between 1 and 9 months ($t=4.32$, $p=0.0000$, Ineraid; $t=4.05$, $p=0.0001$, Nucleus). Significant improvement was also evident for the Ineraid group between 9 and 42 months ($t=3.19$, $p=0.0016$) with no further improvement after 42 months. In the case of the Nucleus subjects, a significant increase in mean vowel score was noted between 9 and 30 months ($t=3.15$, $p=0.0019$) with a slight decrement in mean performance between 30 and 54 months ($t=-2.85$, $p=0.0047$).

Figure 6(a) and (b) shows the individual data and, again, there was considerable variation in the performance of individual subjects over time. Two Ineraid subjects and 1 Nucleus subject showed significant improvement in vowel

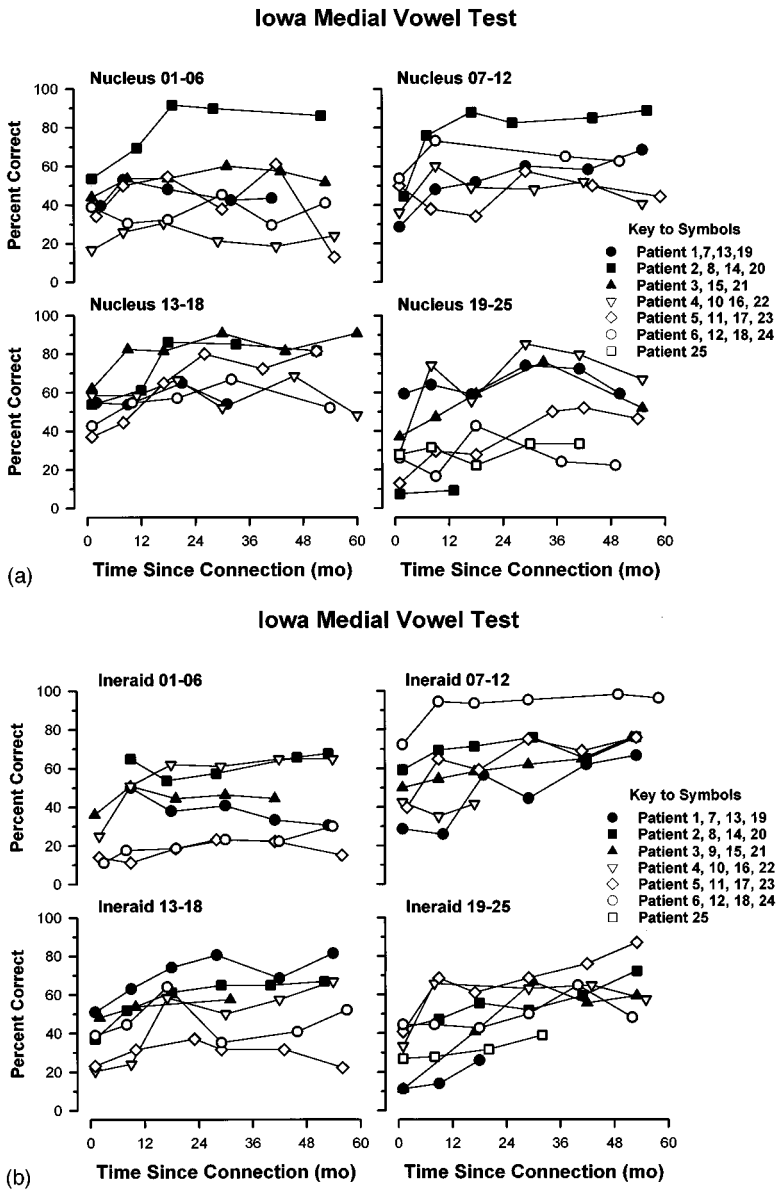

FIG. 6. (a) Individual scores over time for the Iowa Medial Vowel Test for the Nucleus implant group. (b) Individual scores over time for the Iowa Medial Vowel Test for the Ineraid implant group.

recognition when comparing their scores at 18 months to 54 months. Two Nucleus subjects showed a significant decrease in vowel scores between 18 and 54 months. Nineteen Ineraid and 19 Nucleus subjects showed no significant changes between their enhancement scores at 18 and 42 or 54 months. Six (4 Ineraid and 2 Nucleus) subjects did not have more than 42 months experience. Examining Fig. 6(a), the trend for some individuals' performance to decrease toward the end of the study period is evident. However, it was likely that N5 contributed most to the decrement in mean performance of the Nucleus subjects between 30 and 54 months. The test session at 54 months was the subject's first testing day with a new cochlear implant. This subject was reimplanted just prior to the 54-month test session due to internal device failure. This subject has been seen since the 54-month visit and performance for this test was similar to that prior to 54 months. Further, there was no consistent decrease in performance on other speech measures. When this subject's vowel score at 54 months was not considered in the data, no significant difference was evident between 30 and 54 months ($t=2.11$, $p=0.0357$). Figure 5, showing the mean vowel data, reflects the result with the data point for this subject not considered at 54 months.

Figures 7 and 8 show the average scores over time for NU-6 words and phonemes. The spline analysis indicated that average performance across devices was not significantly different for the NU-6 test scored by the number of words correct or phonemically (see the Appendix). The rate of improvement for NU-6 word recognition was different for each implant group. For the Nucleus group, there was a significant improvement in average score between 1 and 9 months ($t=3.13$, $p=0.0019$) and between 9 and 18 months ($t=3.63$, $p=0.0003$) with no further improvement after 18 months of experience ($p>0.01$). However, a significant difference in performance (at one month) was not found until 42 months of use for the Ineraid group, suggesting a slower

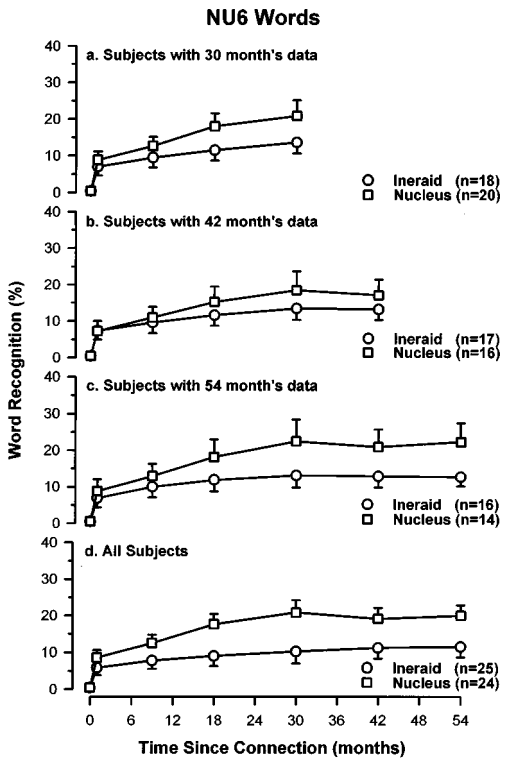

FIG. 7. Mean scores over time for the NU-6 Words Test. Top three panels show group data for the same subjects over the time periods indicated. Vertical bars represent standard errors of the means. The bottom panel shows estimated mean scores over time for all available data based on the mixed general model linear analysis. Vertical bars represent standard errors based on large sample approximations.

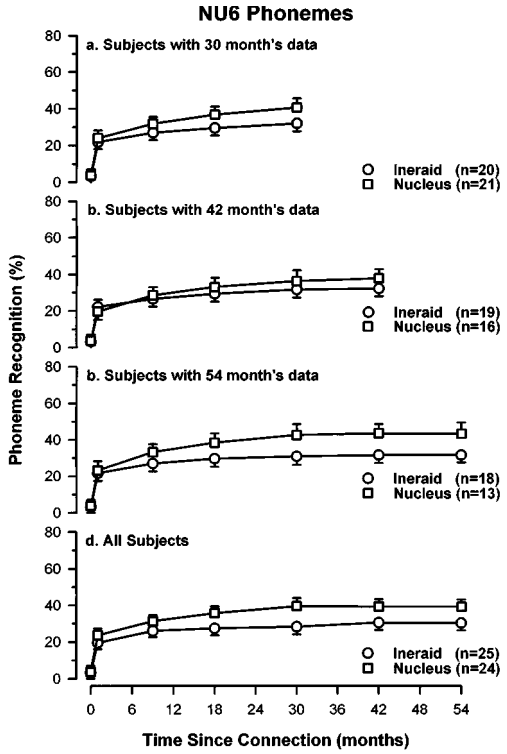

FIG. 8. Mean scores over time for the NU-6 Phoneme Test. Top three panels show group data for the same subjects over the time periods indicated. Vertical bars represent standard errors of the means. The bottom panel shows estimated mean scores over time for all available data based on the mixed general model linear analysis. Vertical bars represent standard errors based on large sample approximations.

rate of improvement ($t=2.96$, $p=0.0034$). A significant improvement was found for the Nucleus group when the NU-6 test was scored phonemically between 1 and 9 months ($t=3.38$, $p=0.0008$) and 9 and 18 months ($t=2.82$, $p=0.0052$), with no improvement observed after 18 months ($p>0.01$). The Ineraid group demonstrated a different rate of improvement for the NU-6 test scored phonemically as opposed to when scored by the number of words correct. A significant difference was noted between 1 and 9 months ($t=2.85$, $p=0.0047$) and between 9 and 18 months ($t=0.88$, $p=0.0025$), as with the Nucleus subjects. For both implant groups, the improvement observed in mean scores for the NU-6 test was not as dramatic as with the other tests, consistent with the clinical observation that the NU-6 test is more difficult than other tests for these subjects.

Figure 9(a) and (b) shows individual data over time for the NU-6 word test. These data indicate that a number of Nucleus subjects were scoring better on this test relative to the Ineraid subjects. This trend was also evident in the average data shown in Fig. 7. If our statistical requirement had not been as strict (i.e., $0.01<p<0.05$), significant differences in mean performance would have been evident at 18, 30, and 54 months, in favor of the Nucleus group (see the Appendix). Three Ineraid and 2 Nucleus subjects showed significant improvements in word recognition when comparing their scores at 18 months to 54 months. One Ineraid subject with data to 42 months showed a significant improvement in word score between 18 and 42 months. Seventeen Ineraid and 20 Nucleus subjects showed no significant changes. Six (4 Ineraid and 2 Nucleus) subjects did not have data beyond 30 months. Being a more difficult test, there was not as much variation in individual subject scores for the NU-6 test when compared to the other tests in the battery [Fig. 9(a) and (b)]. However, for those who scored above 20% words correct, the general trend was for gradual improvement over time, consistent with the group data. Two subjects, N15 and I9, showed a considerable decline in performance after reasonable amounts of experience. Subject N15 showed a consistent pattern of improvement up to around 30 months postimplantation, and then suffered a decline in performance at the 42 and 54 month visits. Fortunately, this pattern was not evident in the other speech measures. In fact, this subject, overall, had excellent speech perception scores [e.g., scored at or near 100% for the sentence test—see Fig. 12(a)]. Subject 19 scored more than 20% up to 9 months and then dropped below 10% for the rest of the study period. However, phoneme scores for the same subject remained quite good over the 54-month study period. This subject also did not display the same trend across the other speech measures. When scored phonemically, there were large differences in individual performance and learning rates for the NU-6 test, as there was with the other speech perception tests [Fig. 10(a) and (b)]. Four Ineraid and 5 Nucleus subjects showed a significant improvement in phoneme recognition when comparing their scores at 18 months to their score at 54 months. One Ineraid subject (as with their word score) and 1 Nucleus subject, with experience to 42 months, showed significant improvements in pho-

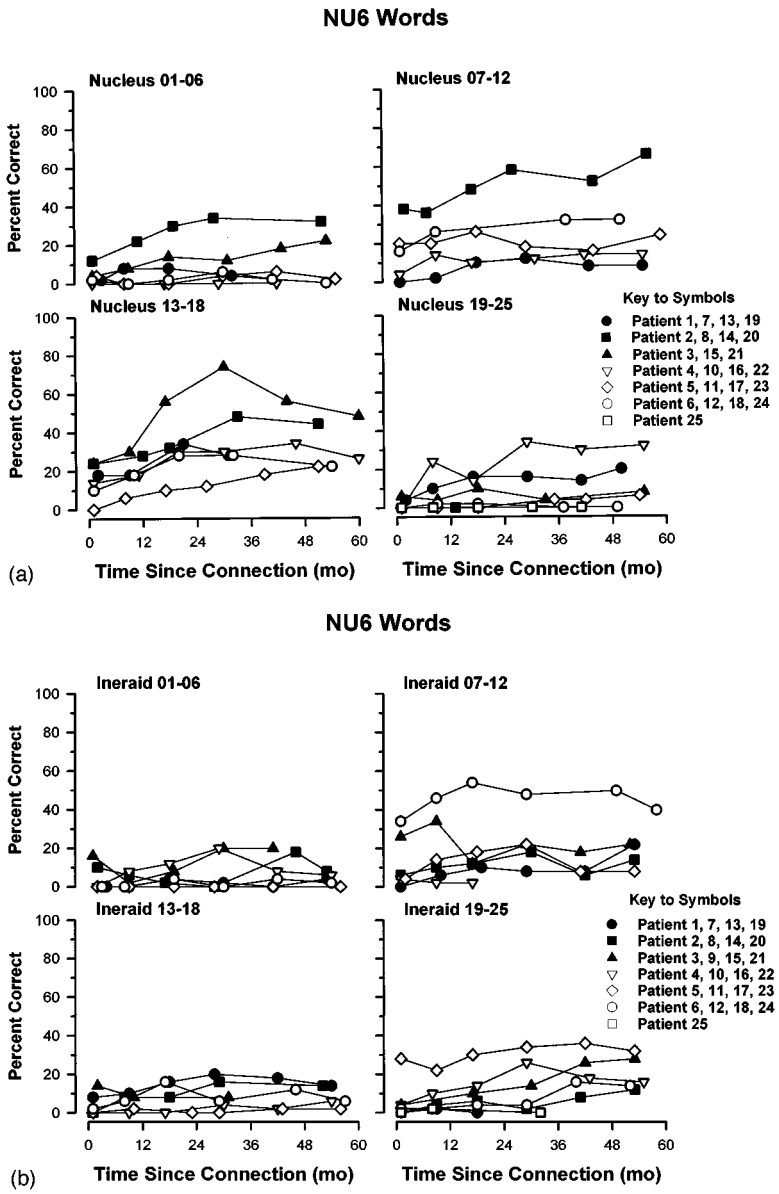

FIG. 9. (a) Individual scores over time for the NU-6 Words Test for the Nucleus implant group. (b) Individual scores over time for the NU-6 Words Test for the Ineraid implant group.

neme scores between 18 and 42 months. Two Nucleus and 3 Ineraid subjects showed significant decreases in NU-6 phoneme scores between 18 and 54 months. Thirteen Ineraid and 14 Nucleus subjects showed no significant changes. Four Ineraid and 2 Nucleus subjects did not have data beyond 30 months.

Figure 11 shows that mean scores for the sentence test also did not differ between the two implant groups at any time point (see the Appendix). For both the Ineraid and Nucleus subjects, a significant improvement was found for mean sentence scores between 1 and 9 months ($t=5.37$, $p=0.0000$, Ineraid; $t=5.74$, $p=0.0000$, Nucleus). However, the Nucleus group continued to show improvement with a significant difference found between 9 and 30 months ($t=3.28$, $p=0.0012$). As with the other tests, individual performance varied greatly as did learning over time [Fig. 12(a) and (b)]. Five Ineraid and 5 Nucleus subjects showed significant improvements in sentence scores when comparing performance at 18 months to 54 months. Two Nucleus subjects and 1 Ineraid subject showed a significant decrease in performance between 18 and 54 months. Fifteen Ineraid and 15 Nucleus subjects showed no significant changes between 18 and 42 or 54 months. Six (4 Ineraid and 2 Nucleus) subjects did not have more than 30 months experience.

It was of interest to see if late changes in long-term performance with individual subjects were reflected across speech tests. From the analyses described above, very few subjects showed changes across more than one or perhaps two of the speech tests. Therefore, as a conservative approach to evaluate long-term changes in overall performance, we defined significant change in overall performance when all the following criteria were met:

(i) First, a change in performance, in the same direction

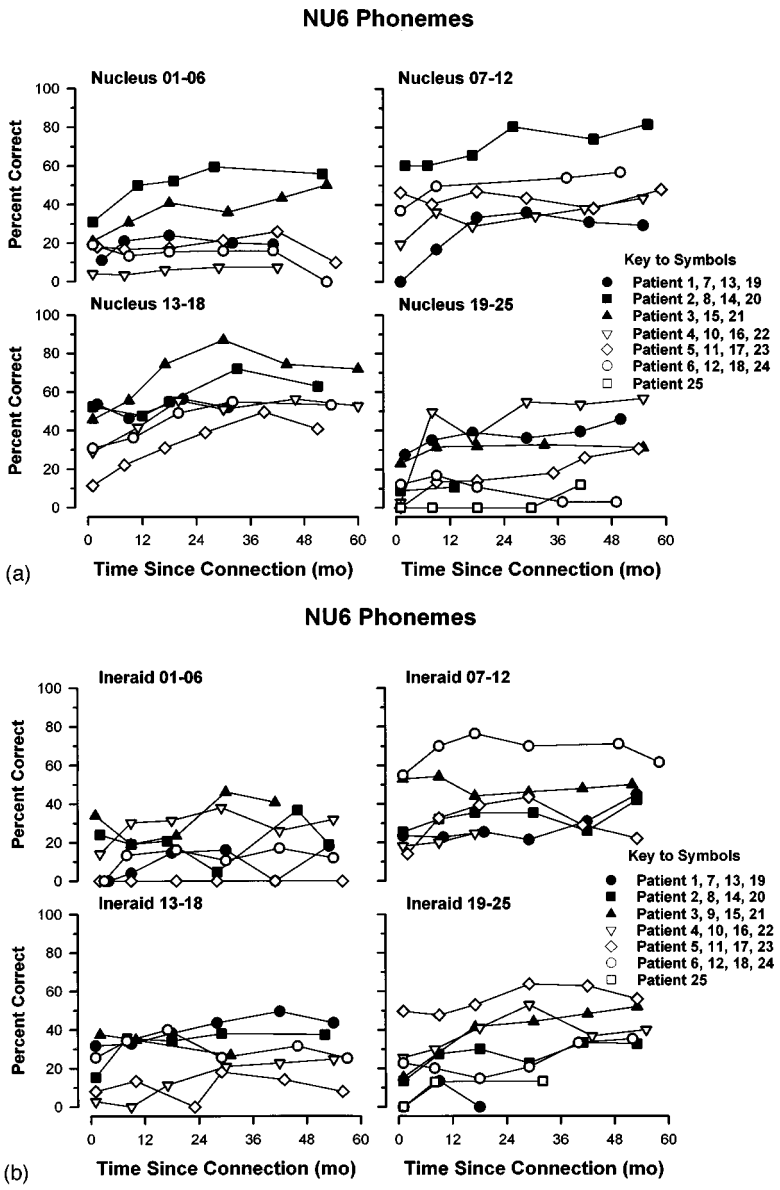

FIG. 10. (a) Individual scores over time for the NU-6 Phoneme Test for the Nucleus implant group. (b) Individual scores over time for the NU-6 Phoneme Test for the Ineraid implant group.

(either increasing or decreasing), was reflected over two or more consecutive data points for any of the speech perception measures. That is, performance either improved or decreased and did not return to previous levels.

(ii) Second, the overall change was statistically significant at the 0.05 level by the binomial theorem (Thornton and Raffin, 1978). That is, the score just prior to the period of change was significantly different from the score at the end of the period of change.

Using these two criteria, we found that 27 subjects experienced a significant change in performance on at least one of the speech measures. As a conservative approach, we further required that:

(iii) The change in performance was evident (not necessarily statistically significant), and in the same direction, over at least four of the six speech measures made. The four measures could not include NU-6 phonemes *and* words, nor consonant recognition *and* consonant lipreading enhancement. This is because these pairs of measurements are not independent.

Six subjects met all three criteria (Fig. 13). Two Ineraid subjects (I7 and I9) and one Nucleus subject (N17) showed improvement in overall performance (to the left of Fig. 13). Two Nucleus subjects (N14 and N18) and one Ineraid subject (I22) demonstrated decrement in performance over a number of speech measures (to the right of Fig. 13).

Subject I7 showed statistically significant improvement (t values all ≥ 2.35, p values ≤ 0.044), by the binomial theorem, for all tests except the consonant test between 30 and 54 months. Subject N17 was included in this group after demonstrating significant improvement between 18 and 54 months for the sentence test ($t=4.17$, $p=0.0000$) and for the consonant test ($t=4.84$, $p=0.0000$). In addition, apart from

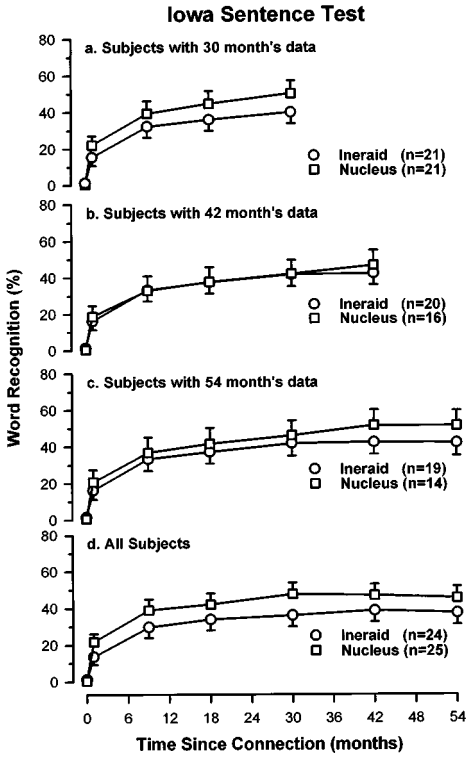

FIG. 11. Mean scores over time for the Iowa Sentence Test. Top three panels show group data for the same subjects over the time periods indicated. Vertical bars represent standard errors of the means. The bottom panel shows estimated mean scores over time for all available data based on the mixed general model linear analysis. Vertical bars represent standard errors based on a large sample approximations.

the score for NU-6 phonemes at 54 months, there was an overall upward trend in speech scores across all the test measures. Subject I9 showed significant improvement for consonant lipreading enhancement between 30 and 54 months ($t = 2.56$, $p = 0.0106$). While modest gains were observed there was consistent improvement across the other speech scores after 18 months.

Subject N14 was included in the group showing decline in performance over time as a significant difference was noted for the consonant test between 18 and 54 months ($t = -2.79$, $p = 0.0052$) (as well as consonant lipreading enhancement). In addition, there was decline in performance across the other speech tests between 42 and 54 months. Subject I22 demonstrated a significant drop in score between 18 and 54 months for consonant lipreading enhancement ($t = -3.43$, $p = 0.0006$), and for the sentence test ($t = -3.38$, $p = 0.0007$). There was also a general trend of decreasing performance for the other tests over the 18 to 54 month period, except for a recovery in performance for the consonant test at 54 months. Subject N18 also showed an overall decline in speech recognition between 18 and 54 months, statistically significant for the sentence test ($t = -2.17$, $p = 0.0304$).

During the course of the study 5 Nucleus patients (N5, N8, N10, and N19) and 1 Ineraid patient (I3) experienced internal device breakdowns. The Nucleus breakdowns were all due to internal device failure and the Ineraid due to trauma to the percutaneous pedestal. Scores for these patients were checked for significant changes, using the binomial theorem, before and after reimplantation for any effects on performance overtime. The Ineraid patient suffered a blow to the head which fractured the percutaneous pedestal, requiring full replacement of the internal receiver/stimulator at 15 months postimplantation. No significant effect was observed on this patient's speech scores when scores were compared before and after reimplantation. The Nucleus patients suffered internal device failures for varied reasons. Subject N18 experienced device failure immediately following the original surgery and so all data presented here are with that subject's second device. Subjects N10 and N19, who experienced failures at 51 and 8 months, respectively, showed small effects on overall performance. Specifically, N10 significantly improved on the consonant test but significantly decreased on the sentence test. Subject N19 significantly improved on the sentence test but for none of the other tests. It should be noted that reimplantation for this subject occurred within the first 9 months of implant use when most improvement was generally observed in these subjects. Subject N5 was reimplanted at 55 months postimplantation and showed significant decrements in scores for the vowel, sentence, and NU-6 phoneme tests, but performance recovered back to previous levels by the next annual test visit. Subject N8 showed significant gains after reimplantation for the consonant, vowel, and sentence tests. Like subject N19, subject N8 was reimplanted early (at three months) at a time when significant changes in performance generally occur under normal circumstances. As with most other subjects, both of these subjects improved up to around 18 months postimplantation before reaching a plateau in performance over time.

III. DISCUSSION

The primary observations of this investigation include:

(i) Postimplantation performance was superior to preimplantation performance;
(ii) Mean performance increased dramatically during the first 9 months and continued to improve, at a slower rate, up to around 18 to 30 months depending on the speech measure;
(iii) There was little difference between the Ineraid and Nucleus subjects in their level of performance or their rate of learning;
(iv) Improvements in speech perception for some speech measures were observed up to 3 or 4 years postimplantation in some subjects;
(v) There was evidence that a few subjects experienced a decrement in overall speech perception performances.

These observations are generally consistent with and extend those reviewed in the introduction (e.g., Tye-Murray *et al.*, 1992; Waltzman *et al.*, 1986). It is remarkable that most subjects show such rapid gains in speech understanding in the first 9 months after receiving their cochlear implants. Many continue to improve over the first $1\frac{1}{2}$–$2\frac{1}{2}$ years, and longer in some subjects. It is not known why some subjects continue to show improvements over several years and most others appear to stabilize. Possible factors include external (additional learning opportunities, aural rehabilitation pro-

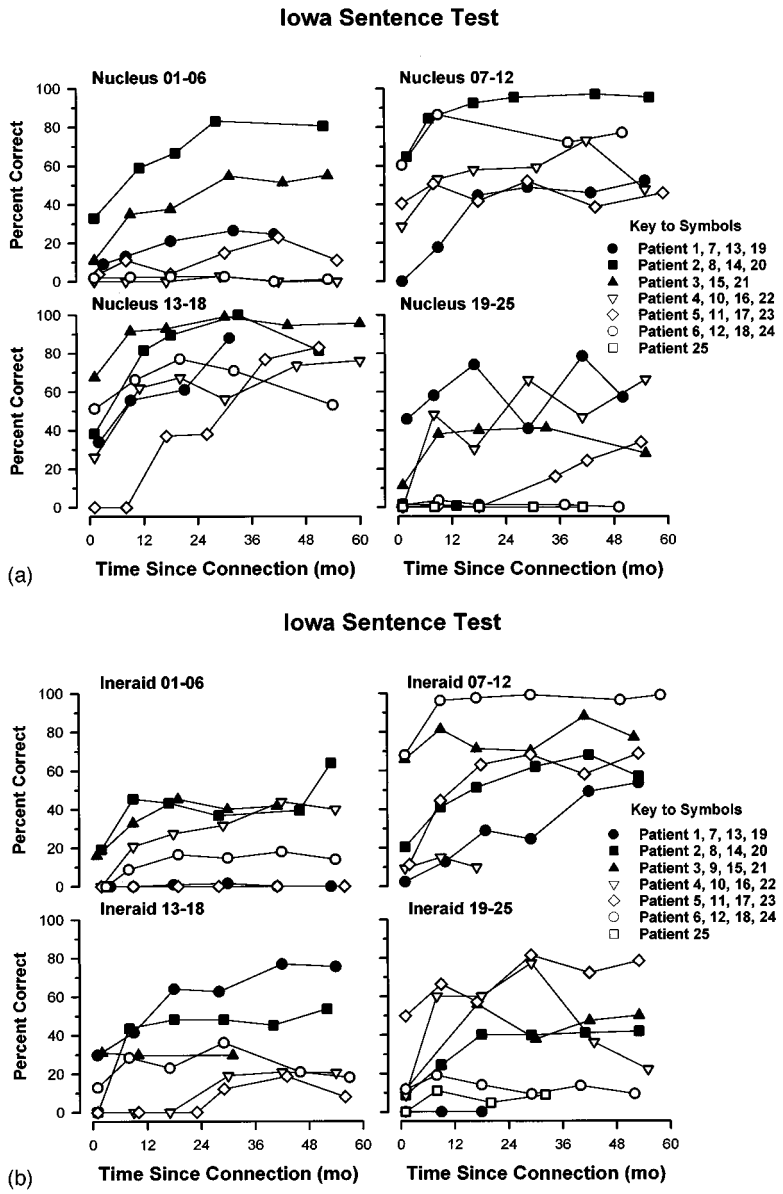

FIG. 12. (a) Individual scores over time on the Iowa Sentence Test for the Nucleus implant group. (b) Individual scores over time on the Iowa Sentence Test for the Ineraid implant group.

grams, processor adjustments or changes), and internal (reorganization of the central nervous system—see Tyler and Summerfield, 1996) factors.

It was troublesome to note that a few subjects showed a decrease in performance over time after having made substantial gains with the cochlear implant. It will be important to monitor these subjects for a longer period to see if the decrease in their performance over time continues. It is possible that electrical stimulation has had some deleterious effect on the nervous system for these subjects. However, measurements of electrical thresholds over time from implanted subjects do not show deterioration (Brown *et al.*, 1995; Dorman *et al.*, 1992). It might be expected that older subjects would have some deterioration of the central nervous system independent of their cochlear implant. Such cognitive losses in the elderly could result in poorer speech understanding, whether listening through a hearing aid or a cochlear implant (Schum, 1994). Indeed, the subject denoted as I22 in Fig. 13 is elderly and clinical observations made by the audiologist indicated definite age-related changes in the subject's cognitive and physical function. It is also possible that the disease producing the hearing loss has continued, or that a new disease process, unrelated to the cochlear implant, is affecting the auditory system.

It is difficult to be sure exactly how changing the Nucleus subjects to the ''upgraded'' processor might have affected performance over time. Four of the subjects (N18, 22, 23, and 25) had been implanted from 18 to 22 months before the upgrade study began. The other subjects had been implanted for much longer. Most of the improvement noted in the present study occurred by 18 months. Therefore, we suspect that any effects, if present, were small.

Only 13 of the 24 of the Nucleus patients reported in the present study participated in the upgrade study during the time period we are reporting. We examined these 13 subjects separately. Six of these subjects preferred and used the more

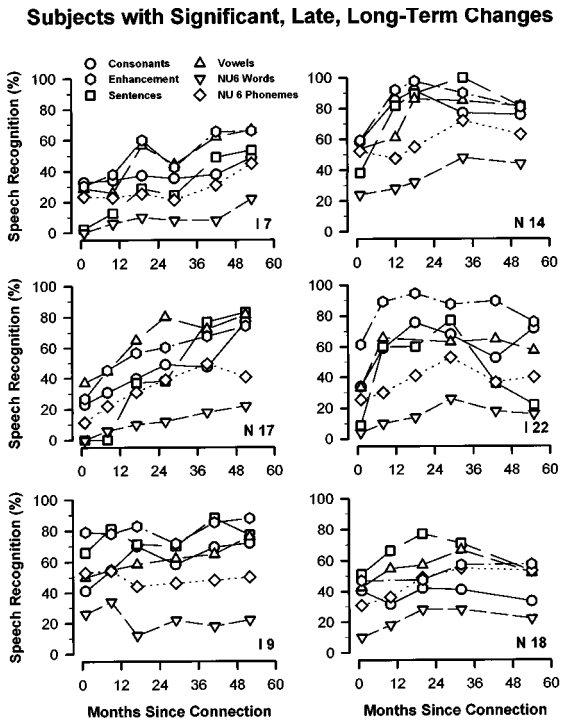

FIG. 13. Speech perception scores over time for individual subjects with significant late long-term changes in performance.

recent $F0F1F2B3B4B5$ speech processing strategy after the processor upgrade. In the upgrade study, Parkinson *et al.* (1996) found little difference between the two speech strategies, within or across test sessions, over the 12-month study period on an individual or group basis. To investigate individual effects for the 13 subjects involved in the upgrade study, speech scores using $F0F1F2$ (for most subjects in the Wearable Speech Processor) at the beginning of the study were compared to the scores with the same strategy in the Mini Speech Processor at the end of the 12-month study. A significant change in overall performance was determined to have taken place if a change was evident on three or more of the speech measures. As applied earlier with our subjects showing late long-term changes, the speech measures could not include both NU-6 words *and* phonemes nor consonant recognition *and* consonant lipreading enhancement. Examination of the individual data in this way showed that only two subjects improved their scores over three (N23) and four (N22) measures. One additional subject (N18) was one of those identified as showing a decrement in performance after long-term use of the cochlear implant over a period of time that corresponded to the upgrade study and one year beyond. With only three individuals (N18, N22, and N23) showing any evidence of a consistent change in performance during the upgrade study, it is likely that the ''true'' pattern of *average* performance overtime is as observed in the present study.

We should note that other processing strategies, with different versions of compressed analog, feature extraction, or other alternatives, might differ from the ones described here. For example, strategies that produce more normal speech should result in faster learning curves.

In summary, it is clear from these data that cochlear implantation in postlingually deafened adults provides significant benefits for speech perception. There is little difference in mean performance over time between Ineraid and Nucleus (with feature-extraction processing) implant users despite considerable differences in their speech processing schemes. These data likely reflect the large individual variation in performance among implant users and highlight the importance of within-subject comparisons of processing schemes in future studies. Processors are available which allow comparison of pulsatile and analog strategies within the same subjects. Although speech perception performance seems to stabilize for most subjects after 18–30 months of use, some subjects showed changes in performance even after considerable experience. Future study might be directed toward the investigation of the effect of altering or ''fine-tuning'' various fitting parameters with the aim being to further improve performance.

ACKNOWLEDGMENTS

Supported (in part) by research Grant No. 2 P50 DC 00242-11 from the National Institute on Deafness and Other Communication Disorders, National Institutes of Health; Grant No. RR00059 from the General Clinical Research Centers Program, Division of Research Resources, NIH; the Lions Clubs International Foundation; and the Iowa Lions Foundation.

APPENDIX

Between device statistics (t values) for the speech measures over time are given in Table AI, P values are shown in parentheses. Note: Degrees of freedom are large (251) because they are based on pooling the number of degrees of freedom (number of observations—1) per subject.

TABLE AI. Between device statistics.

Speech measure	Month 1	Month 9	Month 18	Month 30	Month 42	Month 54
Consonants	0.23 (0.8162)	0.77 (0.4415)	1.20 (0.2295)	0.55 (0.5845)	0.60 (0.5479)	0.44 (0.6614)
Enhancement	0.78 (0.4384)	0.88 (0.3797)	1.20 (0.2305)	1.01 (0.3112)	1.01 (0.3119)	1.11 (0.2677)
Vowels	0.90 (0.3676)	0.57 (0.5680)	0.42 (0.6750)	0.81 (0.4190)	0.34 (0.7350)	0.71 (0.4796)
NU-6 words	0.96 (0.3399)	1.51 (0.1332)	2.20 (0.0287)	2.27 (0.0243)	1.87 (0.0621)	2.10 (0.0366)
NU-6 phonemes	0.82 (0.4157)	1.10 (0.2707)	1.56 (0.1202)	1.84 (0.0668)	1.58 (0.1154)	1.56 (0.1205)
Sentences	1.31 (0.1913)	1.11 (0.2693)	0.97 (0.3344)	1.31 (0.1911)	0.96 (0.3382)	0.89 (0.3719)

Brown, A. M., Dowell, R. C., and Clark, G. M. (**1987**). ''Clinical results for postlingually deaf subjects implanted with multichannel cochlear prostheses,'' Ann. Otol. Rhinol. Laryngol. **96,** 127–128.

Brown, C. J., Abbas, P. J., Bertschy, M., Tyler, R. S., Lowder, M., Takahashi, G., Purdy, S., and Gantz, B. J. (**1995**). ''Longitudinal assessment of physiological and psychophysical measures in cochlear implant users,'' Ear Hear. **16**(5), 439–458.

Cohen, N. L., Waltzman, S., Fisher, S. G., and The Department of Veterans Affairs Cochlear Implant Study Group. (**1993**). ''A prospective, randomized study of cochlear implants,'' New England J. Med. **328**, 233–237.

Dorman, M. F., Dankowski, K., McCandless, G., Parkin, J. L., and Smith, L. (**1990**). ''Longitudinal changes in word recognition by subjects who use the Ineraid cochlear implant,'' Ear Hear. **11**, 455–459.

Dorman, M. F., Smith, L. M., Dankowski, K., McCandless, G. A., and Parkin, J. L. (**1992**). ''Long-term measures of electrode impedance and auditory thresholds for the Ineraid cochlear implant,'' J. Speech Hear. Res. **35**(5), 1126–1130.

Dowell, R. C., Mecklenburg, D. J., and Clark, G. M. (**1986**). ''Speech recognition for 40 subjects receiving multichannel cochlear implants,'' Arch. Otolaryngol. **112,** 1054–1059.

Eddington, D. K. (**1980**). ''Speech discrimination in deaf subjects with cochlear implants,'' J. Acoust. Soc. Am. **68,** 885–891.

Kim, H., Shim, Y. J., Kim, Y. M., Cho, G. J., and Moon, S. K. (**1992**). ''Comparison of speech recognition ability with different speech processing strategies by Korean cochlear implantees,'' Ann. Otol. Rhinol. Laryngol. **101,** 659–664.

Parkinson, A. J., Tyler, R. S., Woodworth, G. G., Lowder, M. W., and Gantz, B. J. (**1996**). ''A within-subject comparison of adult patients using the Nucleus *F0F1F2* and *F0F1F2B3B4B5* speech processing strategies,'' J. Speech Hear. Res. **39,** 261–277.

Patrick, J. F., and Clark, G. M. (**1991**). ''The Nucleus 22-channel cochlear implant system,'' Ear Hear. **12**(4), Suppl., 35–95.

SAS Institute, Inc. (**1989**). SAS/STAT User's Guide. Version 6, 4th ed., Vol. 2 (SAS Institute, Inc., Cary, NC).

Schum, D. (**1994**). ''Cognitive changes in the elderly,'' Paper presented at the Audiological Management of the Elderly Conference, Iowa City, IA.

Skinner, M. W., Holden, L. K., Holden, T. A., Dowell, R. C., Seligman, P. M., Brimacombe, J. A., and Beiter, A. L. (**1991**). ''Performance of postlinguistically deaf adults with the wearable speech processor (WSP III) and Mini Speech Processor (MSP) of the Nucleus multi-electrode cochlear implant,'' Ear Hear. **12**(1), 3–22.

Skinner, M. W., Clark, G. M., Whitford, L. A., Seligman, P. M., Staller, S. J., Shipp, D. B., Shallop, J. K., Everingham, C., Menapace, C. M., Arndt, P. L., Antogenelli, T., Brimacombe, J. A., Sipke, P., Daniels, P., George, C. R., McDermott, H. J., and Beiter, A. L. (**1994**). ''Evaluation of a new spectral peak coding strategy for the Nucleus 22 channel cochlear implant system,'' Am. J. Otol. **15**, Suppl. 2, 15–27.

Spivak, L. G., and Waltzman, S. B. (**1990**). ''Performance of cochlear implant subjects as a function of time,'' J. Speech Hear. Res. **33,** 511–519.

Thornton, A. R., and Raffin, M. J. M. (**1978**). ''Speech-discrimination scores modeled as a binomial variable,'' J. Speech Hear. Res. **21,** 507–518.

Tillman, T. W., and Carhart, R. (**1966**). ''An expanded test for speech discrimination utilizing CNC monosyllabic words,'' Northwestern University Auditory Test No 6 Technical report No SAM-TR-66-55 USAF School of Aerospace Medicine Brooks Air Force Base, Texas.

Tye-Murray, N., Tyler, R. S., Woodworth, G. G., and Gantz, B. J. (**1992**). ''Performance over time with a Nucleus or Ineraid cochlear implant,'' Ear Hear. **13**, 200–209.

Tyler, R. S., Preece, J. P., and Lowder, M. W. (**1983**). *The Iowa Cochlear Implant Test Battery* (University of Iowa, Iowa City, IA).

Tyler, R. S., Preece, J. P., and Tye-Murray, N. (**1986**). *The Iowa Phoneme and Sentence Tests* (The University of Iowa, Iowa City, IA).

Tyler, R. S., Opie, J. M., Fryauf-Bertschy, H., and Gantz, B. J. (**1992**). ''Future directions for cochlear implants,'' J. Speech-Language Pathol. Audiol. **16**, 151–164.

Tyler, R. S., and Summerfield, A. Q. (**1996**). ''Cochlear implantation: Relationships with research on auditory deprivation and acclimatization,'' Ear Hear. **17**(3), Suppl. 385–505.

Waltzman, S. B., Cohen, N. L., and Fischer, S. (**1992**). ''An experimental comparison of cochlear implant systems,'' Seminars in Hearing **13**(3), 195–207.

Waltzman, S. B., Cohen, N. L., and Shapiro, W. H. (**1986**). ''Long-term effects of multichannel cochlear implant usage,'' Laryngoscope **6**, 1083–1087.

Wilson, B. S. (**1993**). ''Signal processing,'' in *Cochlear Implants: Audiological Foundations*, edited by R. S. Tyler (Singular, San Diego, CA), pp. 35–85.

Woodworth, G. G. (**1995**). ''Using Delta Splines to analyze irregularly spaced longitudinal data with an application to the Iowa Cochlear Implant Project 1,'' (Technical Report) Department of Statistics and Actuarial Science and Department of Preventative Medicine, Division of Biostatistics, University of Iowa.

Articulatory control of phonological vowel length contrasts: Kinematic analysis of labial gestures

Ingo Hertrich[a] and Hermann Ackermann
Department of Neurology, University of Tübingen, D-72076 Tübingen, Germany

(Received 26 June 1996; accepted for publication 31 January 1997)

The present study investigated the articulatory control of the German vowel quantity contrast, i.e., the phonological difference between short and long vowels. By means of an optoelectronic system the excursions of the compound lower lip/jaw opening and closing gestures were measured during production of test sentences comprising the target sequence /pVp/ (V=/a/, /i/, /u/, /a:/, /i:/, /u:/). First, a highly linear relationship between peak velocity and movement amplitude emerged within each quantity class. Second, vowel quantity systematically influenced the scaling of velocity and amplitude during oral opening. Third, as compared to their short counterparts, long vowels showed an increased peakedness of the velocity profile. Finally, the velocity profiles of the long vowels were characterized by an asymmetric shape in terms of a prolonged deceleration phase of the opening and a lengthened acceleration interval of the closing movement. With respect to durational coarticulation patterns, the control of vowel quantity clearly differed from intrinsic, i.e., vowel type-induced, variability. The latter was partially compensated for at the level of word duration by shortening of the prevocalic consonant whereas vowel quantity turned out to be primarily due to the lengthening of the syllable /pV/. © *1997 Acoustical Society of America.* [S0001-4966(97)00806-0]

PACS numbers: 43.70.Aj, 43.70.Bk, 43.70.Fq [AL]

INTRODUCTION

Both orofacial and laryngeal articulatory gestures are characterized by a highly linear correlation between peak velocity and amplitude which is, to some extent, preserved even across variation of speaking rate (Ostry *et al.*, 1983; Ostry and Munhall, 1985). This relationship constrains the degrees of freedom during speech motor execution because an increase of displacement gives rise to higher peak velocity (Kelso *et al.*, 1985; Vatikiotis-Bateson and Kelso, 1993). The task dynamical systems approach suggests that mass-springs provide, within some limits, a model for articulatory gestures. On this basis, the linear correlation between amplitude and peak velocity can be considered to reflect invariant ''stiffness'' of the assumed mass-spring during movement execution. Conceivably, this measure represents an important control parameter of skilled motor processes because modification of stiffness allows one to produce predictable changes in the relationship between peak velocity and movement range (Gracco, 1994).

As concerns articulatory movements, stiffness, in terms of the ratio of peak velocity and amplitude, and movement time show an inverse interdependency. Ostry and Munhall (1985), therefore, proposed the following formula: [(peak velocity)/(movement amplitude)] (movement time) $=c$, where parameter c is a constant value. Within the framework of this model, movement time can be controlled solely by the adjustment of stiffness. Thus, at least for those segments of the acoustic signal which depend on the duration of single articulatory gestures, explicit representation of ''time'' is not necessarily required in order to produce phonetically relevant length modifications. Using a reiterant syllable substitution task, Kelso and coworkers were able to partially confirm these suggestions (Kelso *et al.*, 1985; Vatikiotis-Bateson and Kelso, 1993). As concerns the English language, these authors found a decrease of stiffness in parallel with the prolongation of stressed syllables. However, these durational changes were also associated with variation of movement amplitude: Accented syllables showed larger displacements than their unstressed counterparts. In French, the signaling of syllable stress even predominantly depends upon movement range. Obviously, therefore, various languages differ in the extent to which movement duration and stiffness contribute to the control of stress.

Besides the adjustment of single articulatory excursions, intergestural phasing might be relevant for phonetic timing as well. Edwards *et al.* (1991) and Harrington *et al.* (1995) found, e.g., that ''truncation'' of an articulatory gesture by the subsequent one contributes to the differentiation of accented and unaccented syllables. This kind of shortening gives rise to reduced movement amplitude concomitant with preserved peak velocity. Furthermore, vowel lengthening induced by the following voiced consonant has been shown to consist of a particular prolongation of the final portion of the vowel opening gesture. This finding has been interpreted to reflect the adjustment of intergestural timing in terms of a delayed initiation of the consonant closing gesture (DeJong, 1991).

The mass-spring model predicts invariant velocity profiles of articulatory gestures. In contrast, the control of intergestural phasing should compromise their shape in that truncation of an articulatory movement shortens while a delayed initiation of the subsequent movement lengthens the deceleration phase of the preceding gesture. Parameter c can be considered a measure of the shape of velocity profiles (Munhall *et al.*, 1985). In case of a triangular geometry, c

[a]Electronic mail: ingo.hertrich@uni-tuebingen.de

achieves a value of 2.0. Sinusoidal profiles are characterized by $c=\pi/2$, and rectangles by $c=1.0$. Whereas Ostry and Munhall (1985) conceived of parameter c as a constant, Adams *et al.* (1993) found a systematic variation of this measure with speaking rate during tongue tip movements. Slow gestures turned out to have larger values than faster ones. As a parameter of the velocity profile's peakedness, Adams *et al.* (1993) introduced the coefficient of kurtosis. However, the validity of this measure has been questioned because it yielded inconsistent results. Substitution of the term: (movement amplitude)/(movement time), by (average velocity) within the formula for parameter c leads to the following equation: $c=$ peak velocity/ average velocity (Hoole *et al.*, 1994). It is obvious that this interpretation of parameter c provides a simple measure of the peakedness of velocity profiles which may be more adequate than the coefficient of kurtosis. Thus, increased values of parameter c during reduced speech rate, as observed by Adams *et al.* (1993), indicate an enlarged peakedness of the velocity profiles. Besides parameter c, speech tempo influences the symmetry of the velocity profiles in terms of their skewness or the relative time to peak velocity (Adams *et al.*, 1993).

In some languages such as German, the distinction between long and short vowels represents an important aspect of the temporal organization of the acoustic signal which has to be adequately controlled. For example, German has minimal pairs exclusively differing in vowel length, e.g., ''Rate'' [ra:thə] (English ''installment'') versus ''Ratte'' [rathə] (English ''rat''). This component of phonetic timing has been labeled ''vowel quantity,'' e.g., /a/ versus /a:/, in contrast to ''vowel type,'' e.g., ''a,'' ''i,'' ''u'' which predominantly refers to the vocal tract configuration (MacNeilage, 1980). Vowel quantity can be considered a more feasible paradigm of speech timing—in terms of the articulatory encoding of phonological length contrasts—than stress-dependent adjustments of segment lengths or final lengthening effects. First, besides durational parameters other acoustic cues such as sound intensity also contribute to accent signaling. Stressed and unstressed segments have been suggested to vary along the hyper-hypoarticulation dimension rather than being two temporally specified categories, (DeJong, 1995; DeJong *et al.*, 1993). Second, phrase-final lengthening does not necessarily represent a specific phenomenon of speech timing, but might reflect a universal pattern in motor sequencing.

In some respect, the opposition of German short and long vowels resembles the English tense/lax distinction (Kohler, 1995). Accordingly, the high vowels /u/ and /i/ show a more open vocal tract configuration than their long counterparts /u:/ and /i:/ with respect to tongue position (Bohn *et al.*, 1991). Formant measurements revealed that, as a rule, short vowels are more centralized than their long cognates. In unstressed position this effect even may exceed the durational contrast (Jessen, 1993). On this basis it might be questioned that the phonological vowel length contrast represents a feasible model of phonetic timing. However, Jessen's study did not rely on strict minimal pairs. Therefore, coarticulation effects due to different phonetic environments cannot be ruled out. Using electromagnetic articulography, Hoole and Kühnert (1996), e.g., have shown significant interactions between vowel tenseness and surrounding consonant categories on the position of tongue and jaw during the production of high vowels.

Despite controversies about the nature of the German vowel system (see Becker, 1995), duration seems to be the strongest acoustic correlate of the distinction of short and long vowels, at least in stressed position (Jessen, 1993). It seems to be warranted, therefore, that the present study uses the term ''quantity'' for this phenomenon, assuming a particular mechanism of articulatory timing to be responsible for the implementation of this contrast. The findings of Hoole *et al.* (1994) indicate that the time course of movement velocity during the opening–closing cycle may shed light on this mechanism.

A few studies dealing with a similar durational contrast as the German vowel length effect are available for Swedish and Icelandic. As concerns the latter languages, the distinction between short and long vowels depends upon the durational ratio between the vowel and the succeeding consonant (Pind, 1995; Sock and Löfqvist, 1995) and has been called ''complementary quantity'' (Becker, 1995). However, standard German has not been classified as a language with complementary quantity effects (Becker, 1995). Thus, its durational features may be different. In contrast to other languages, vowel quantity in German has been assumed to represent a primarily prosodic feature, being linked to syllable structure of stressed syllables rather than to vocalic segments (Vennemann, 1991; Becker, 1995). First, short vowel categories do not occur in open syllables, and second, short vowels differ from long cognates with respect to the maximum possible number of following consonants.

The present investigation used a /pVp/ sequence, with short and long vowels in medial position, for the examination of the articulatory kinematics of the German vowel length effect. In consideration of the data obtained from durational stress adjustments, sentence-final lengthening effects, and kinematic changes with speech rate, the following hypotheses can be adduced with respect to the articulatory control of the distinction of short and long vowel.

(a) If labial opening and closing gestures predominantly account for the length contrast between short and long vowels in a /pVp/ context, a high correlation between the duration of the opening-closing cycle and vowel duration must be expected. As an alternative, the temporal coordination between the laryngeal devoicing/voicing gesture and the labial opening–closing cycle might account for the implementation of vowel quantity. In the latter case, long target vowels should be compensated for by the shortening of other segments.

(b) If the control of vowel quantity primarily depends upon the scaling of peak velocity and movement amplitude, short vocalic segments should be characterized by an increased stiffness of the lower lip gestures as compared to their long counterparts. As an alternative, intergestural phasing might be relevant in this regard as well. If so, systematic alterations of the velocity profile's symmetry must be expected.

(c) Assuming that long vowels can be understood in terms of a local reduction of speech rate, these segments

should have increased values of parameter *c* as compared to their short cognates.

Opening and closing movements seem to represent differentially controlled synergistic actions (Gracco, 1994). For example, the latter tend to be performed with higher peak velocity and shorter duration than their opening cognates (Adams *et al.*, 1993; Forrest *et al.*, 1989; Vatikiotis-Bateson and Kelso, 1993; Gracco, 1994). Moreover, opening gestures are more sensitive to variation of speech rate than closing movements (Adams *et al.*, 1993). Thus, opening and closing gestures may contribute in a differential way to the articulatory kinematics underlying the German vowel length effect.

Most conclusions with respect to the mass–spring analogy have been inferred from correlational data on movement amplitude and peak velocity. In order to obtain scattergrams which are prerequisite to this kind of analysis, sufficient variability of the respective parameters must be available. Kinematic data indicate that high vowels such as /i/ and /u/ are characterized by smaller lower lip movements than the low counterpart /a/. These various vowel types, thus, should elicit systematic changes in movement amplitude of the compound lower lip/jaw gestures. Articulatory excursions, therefore, were measured across different vocalic phonemes of the target word ''gepVpe.'' Admittedly, this procedure introduces a further dimension of durational variability since these three vowels are known to have different intrinsic lengths within a given quantity class (Antoniadis and Strube, 1984). For example, the length of /i:/ just amounts to about 60% of the duration of /a:/ (Hertrich and Ackermann, 1995). However, if quantity represents a separate dimension of phonetic control (Becker, 1995), different mechanisms of vowel quantity adjustment and intrinsic durational variability must be expected, e.g., in terms of durational coarticulatory compensation.

I. METHODS

A. Subjects

Six staff members (3 males, 3 females; age: 20–30 years) from the Department of Neurology, University of Tübingen, participated in the present study. These individuals never had suffered from any diseases of the central nervous system or the cranial nerves. All of them were native German speakers.

B. Speech material

Subjects had to produce German sentences of the type ''Ich habe gepVpe gelesen'' (''I have read gepVpe''; V=/a/, /a:/, /i/, /i:/, /u/, /u:/, /y/, or /y:/). The respective eight target words were visually presented eight times each in randomized order. Sixty-four sentences (8 vowels×8 repetitions) were thus recorded from each subject. In order to obtain sufficient variability of movement amplitude, the present study considered the three vowel types ''a'' (=/a/ or /a:/), ''i'' (=/i/ or /i:/), and ''u'' (=/u/ or /u:/). The sentence productions with vowel ''y'' were discarded from analysis since the respective bilabial gestures were quite similar to the ''u'' items. Furthermore, we wanted to avoid an over-representation of small-amplitude gestures. No instruction with respect to speech rate was given to the subjects.

C. Recording procedure

Tracking of labial movements relied on an optoelectronic system (ELITE; Bioengineering Technology & Systems, Italy; Ferrigno and Pedotti, 1985). In addition to kinematic measurements, the acoustic speech signal was recorded on a DAT tape (PCM 2000; Sony, Japan) by means of a head-mounted microphone (C 410/B; AKG, Austria), placed about 5 cm in front and 5 cm to the right of the mouth. Subjects were sitting on a chair throughout the experiment with reflecting markers (diameter=0.6 cm) attached to the nasion, upper and lower lips in the midsagittal plane and to the right and left corner of the mouth. Two cameras, both of them supplied with a corona of infrared light emitting diodes, were mounted 2 m in front and 1 m to the left and right, respectively, of the speaker's head. In order to achieve optimal spatial resolution, calibration was restricted to a volume of about $40\times40\times40$ cm, with the speaker's head at its center, by means of zoom objectives. Each camera system automatically detected the reflector locations at a sampling rate of 100 Hz within a two-dimensional representation of the calibrated space. The three-dimensional reconstruction of the respective trajectories was performed off-line under manual control for correct marker assignment. Under dynamic conditions the spatial resolution of the ELITE system amounts to about 0.2 mm (Borghese and Ferrigno, 1990). This degree of accuracy is similar to that achieved by other available optical systems (e.g., Munhall, 1993).

D. Data processing

Preliminary inspection of the data revealed that the lower lip predominantly contributes to the opening and closure of the vocal tract during production of the /pVp/ sequences (see Kuehn and Moll, 1976). Therefore, the upper lip was discarded from analysis. In order to exclude interferences of head movements with the kinematic recordings, the three-dimensional distance between the markers attached to the nasion and the lower lip, respectively, was considered the basic kinematic parameter. The opening and closing components of the lower lip movements during production of the /pVp/ sequences approximately occur in the nasion-lower lip direction. In contrast, the lip protrusion of rounded vowels can be expected to occur in a direction orthogonal to this line and thus can be neglected within the context of the present investigation. Both jaw movements as well as lower lip excursions relative to the jaw may contribute to the trajectory of the nasion-lower lip distance. The present study considered the compound movement of these two articulators since it represents the functionally releveant trajectory with respect to oral opening and closing. Prior to parameter extraction, the lower lip trajectories were slightly smoothed by means of a three-point averaging filter.

The velocity curve of the lower lip trajectory was computed using the three-point difference method: $vt=(xt+dt-xt-dt)/2dt$; vt=velocity at time t, xt=nasion-lower lip

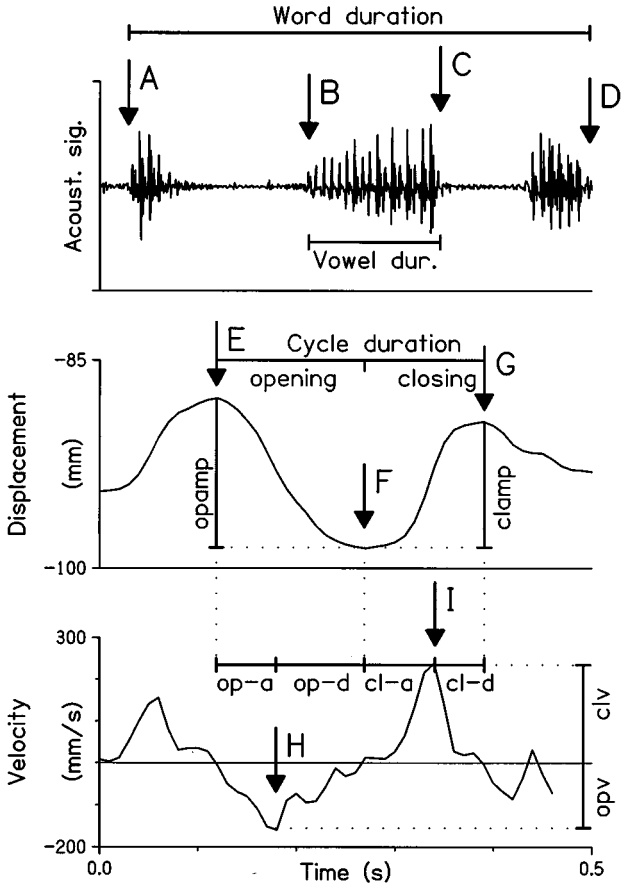

FIG. 1. Target word /gepa:pe/ produced by speaker *N*4: acoustic speech oscillogram (upper panel), three-point smoothed lower lip trajectory (mid panel), and the respective velocity trace (lower panel). A=target word onset, B=target vowel onset, C=target vowel offset, D=word end, E=pretarget closure, F=maximum opening, G=posttarget closure, H=peak velocity of opening gesture, I=peak velocity of closing gesture, opamp=amplitude of opening gesture, clamp=amplitude of closing gesture, op-a=opening acceleration time, op-d=opening deceleration time, cl-a=closing acceleration time, cl-d=closing deceleration time, opv=opening peak velocity, clv=closing peak velocity.

distance at time t, dt=time interval between two adjacent sample points. Comparison of unfiltered and low-pass filtered velocity curves revealed significantly reduced peaks and troughs, respectively, in the latter case. For example, three-point smoothing may gave rise to a decrease of measured absolute maximum velocity up to about 100 mm/s (Ackermann *et al.*, 1995). Since the present study aimed at the determination of peak values, the velocity data were derived from the unfiltered trajectories. Figure 1 provides an example of the acoustic signal, the lower lip displacement, and the respective velocity values. Although the time course of the velocity curve appears ''noisy,'' the peak values as well as their temporal locations could be more precisely determined at the unfiltered data than after smoothing.

E. Acoustic and kinematic parameters

The duration of the target word (''word duration''), as determined from vowel onset of the first (arrow A in Fig. 1) to vowel offset of the final syllable (arrow D), and the duration of the target vowel /V/ (''vowel duration''), i.e., the interval between its onset (arrow B) and the respective steep decline of signal amplitude (arrow C), were measured by means of a cursor at the acoustic signal (Hertrich and Ackermann, 1994).

In order to select the kinematic intervals of interest, the onset of both the first and the second schwa of the target word were manually marked at the simultaneously displayed lower lip trajectory. A peak-picking algorithm developed by the Motor Control Lab of the Department of Neurology, University of Tübingen, automatically determined the maximum nasion-lower lip distance within this time interval (i.e., maximum opening of the vocal tract during the production of the target sequence /pVp/; arrow F). Then the minimum nasion-lower lip distances during the interval between, first, onset of the first schwa and maximum opening and, second, maximum opening and onset of the second schwa were detected (arrows E and G). These two events represent the bilabial occlusions preceding and following the target vowel, respectively. On the basis of these measures, the amplitude of the opening and closing gesture (''opening amplitude,'' ''closing amplitude''), the respective durations (''opening time,'' ''closing time'') as well as ''cycle time,'' i.e., the sum of the opening and closing intervals, were calculated. The absolute maximum velocities during oral opening and closing were determined in the same way (arrows H and I).

As a measure of the coordination between labial articulation and the laryngeal adduction initiating the target vowel, the time interval from the beginning of the opening gesture (arrow E) to vowel onset (arrow B) was measured (''time to vowel onset'').

In order to characterize the dynamics of the two articulatory gestures considered, the linear regression functions of peak velocity on amplitude were computed separately for each quantity class across the three vowel types. Furthermore, parameter c(=[peak velocity/movement amplitude] $\times$movement time; Ostry and Munhall, 1985) as well as the relative duration of the acceleration phase (=time to peak velocity/movement time; Adams *et al.*, 1993) were calculated as measures of the velocity profile's peakedness and symmetry.

F. Statistical analysis

In order to test the effects of vowel quantity on the acoustic and kinematic measures considered, two-way analyses of variance (ANOVAs) including the independent factor variables quantity (long, short) and vowel type (''a,'' ''i,'' ''u'') were performed. When a differential behavior of the opening and closing gestures had to be expected, gesture was added as an intra-utterance factor within a repeated measures design. The evaluation of vowel quantity effects on the slopes and intercepts of the computed regression functions relied on an analysis of covariance with ''peak velocity'' as the dependent variable, ''amplitude'' as the covariate, and quantity as the independent factor.

TABLE I. Analysis of variance with vowel type and quantity as independent factors and vowel duration as the dependent variable: Table of individual F values.

		Subjects					
	d.f.	*N*1	*N*2	*N*3	*N*4	*N*5	*N*6
Vowel type	2,42	73.44	266.13	52.30	39.99	43.55	53.30
Quantity	1,42	406.93	349.14	90.01	137.80	156.71	97.18
Vowel type×quantity	2,42	14.41	39.94	12.14	20.76	9.76	7.77

All values are significant at $p<0.01$.

II. RESULTS

A. Analysis of durational parameters

In order to test hypothesis (a), vowel, word, and movement cycle lengths were analyzed.

1. Interactions of vowel quantity and vowel type with respect to segment durations

All speakers produced the expected quantity contrast, i.e., a significant difference in length between long and short vowel targets. Furthermore, statistical analysis revealed intrinsic durational variability of the vocalic segments as indicated by a main effect of vowel type (Table I). Prolongation of the low vowels (/a/, /a:/) as compared to their high counterparts (/i/, /i:/, /u/, /u:/) accounts for these findings (Table II). Finally, a significant quantity×vowel type interaction emerged (Table I) in that the absolute difference in length between /a/ and /a:/ exceeded that of the other two minimal pairs (Table II).

Port (1981) suggested that invariant durational ratios rather than constant absolute differences characterize the English tense/lax opposition. On the basis of this assumption, the quantity×vowel type interaction simply might reflect intrinsic durational variability. In order to assess ratios rather than the absolute differences, the ANOVA was repeated with the logarithmic values of vowel duration as the dependent variable. Whereas quantity and vowel type each yielded comparable main effects under these conditions, the two-way interaction failed significance in three of the six speakers ($p>0.05$). Thus, Port's suggestion could be, at least partially, confirmed. Although the quantity effect in absolute measures, i.e., in milliseconds, depends on vowel height, the same regularity seems to control the phonological durational contrast in low and high vocalic phonemes. It remains to be settled, however, whether this finding is restricted to the speech material of the present study or whether it represents a more general principle (see Gopal, 1990, 1996).

To some degree, intrinsic durational variability of vowels can be compensated for by the adjustment of neighboring segments (Hertrich and Ackermann, 1995). Accordingly, the average difference in duration between vowel types ''a,'' on the one hand, and ''i'' as well as ''u,'' on the other (mean difference across all speakers=30 ms, standard deviation (s.d.)=6 ms; long and short targets being pooled), exceeded the respective word length contrasts (16 ms, s.d.=16 ms). It is noteworthy, however, that vowel quantity had an inverse effect on word and vowel lengths (average durational difference between long and short vowels=32 ms, s.d.=9 ms, difference between the respective words=48 ms, s.d.=22 ms; data pooled across vowel types and speakers). The temporal domain of the quantity contrast, thus, extends beyond the respective vocalic segment.

2. Correlations between vowel duration and movement cycle time

The difference in mean movement cycle time between short and long vowels (data pooled across subjects and vowel types) was 47 ms (s.d.=12 ms). A similar value emerged for word durations (see above). Obviously, thus, an increase of the articulatory opening-closing cycle duration of the target sequence /pVp/, in the absence of any relevant

TABLE II. Individual means of vowel duration and movement cycle duration (standard deviation in parentheses).

	/a/		/a:/		/i/		/i:/		/u/		/u:/	
(A) Vowel duration [ms]												
*N*1	50	(*7*)	116	(*13*)	31	(*4*)	77	(*8*)	32	(*4*)	67	(*8*)
*N*2	65	(*5*)	116	(*8*)	42	(*5*)	68	(*6*)	39	(*5*)	55	(*5*)
*N*3	63	(*7*)	96	(*7*)	53	(*4*)	60	(*12*)	43	(*6*)	66	(*9*)
*N*4	51	(*6*)	105	(*11*)	43	(*4*)	71	(*15*)	44	(*3*)	56	(*10*)
*N*5	52	(*9*)	102	(*7*)	37	(*8*)	64	(*9*)	38	(*8*)	62	(*13*)
*N*6	70	(*8*)	113	(*14*)	53	(*5*)	69	(*7*)	48	(*10*)	73	(*12*)
(B) Cycle duration [ms]												
*N*1	189	(*10*)	261	(*21*)	181	(*19*)	213	(*27*)	171	(*16*)	225	(*29*)
*N*2	198	(*10*)	253	(*16*)	180	(*16*)	213	(*10*)	168	(*12*)	186	(*11*)
*N*3	214	(*7*)	263	(*5*)	185	(*9*)	246	(*14*)	208	(*18*)	278	(*7*)
*N*4	183	(*14*)	254	(*13*)	171	(*11*)	203	(*18*)	163	(*9*)	183	(*22*)
*N*5	200	(*11*)	271	(*27*)	189	(*12*)	247	(*11*)	204	(*18*)	256	(*17*)
*N*6	195	(*12*)	249	(*18*)	176	(*5*)	204	(*15*)	179	(*19*)	200	(*24*)

TABLE III. Table of correlation coefficients: Correlational patterns between (A) vowel duration and articulatory movement cycle time and (B) vowel duration and the interval from the beginning of the opening gesture to vowel onset at the acoustic signal (''time to vowel onset''). Columns 1 and 2 display data pooled across vowel types separately for each quantity class, the data in columns 3 to 5 were pooled across vowel quantity classes within each vowel type category.

(A) Correlations between vowel duration and cycle time					
	/a,i,u/	/a:,i:,u:/	/a,a:/	/i,i:/	/u,u:/
*N*1	0.16	0.57[a]	0.88[a]	0.48	0.81[a]
*N*2	0.76[a]	0.91[a]	0.96[a]	0.74[a]	0.77[a]
*N*3	0.15	0.22	0.92[a]	0.53	0.79[a]
*N*4	0.12	0.93[a]	0.94[a]	0.80[a]	0.70[a]
*N*5	0.02	0.41	0.80[a]	0.83[a]	0.72[a]
*N*6	0.66[a]	0.91[a]	0.93[a]	0.77[a]	0.84[a]
pooled	0.31[a]	0.52[a]	0.83[a]	0.50[a]	0.58[a]
(B) Correlations between vowel duration and ''time to vowel onset''					
	/a,i,u/	/a:,i:,u:/	/a,a:/	/i,i:/	/u,u:/
*N*1	−0.62[a]	−0.56[a]	0.08	0.08	0.73[a]
*N*2	−0.39	−0.03	0.40	0.20	0.07
*N*3	−0.59[a]	−0.67[a]	0.16	0.23	0.60
*N*4	−0.35	0.15	0.61	0.02	0.63[a]
*N*5	−0.66[a]	−0.49	0.30	0.60	0.30
*N*6	−0.68[a]	−0.18	0.50	0.24	0.77[a]
pooled	−0.45[a]	−0.32[a]	0.18	0.11	0.39[a]

[a]Significant at the level $p<0.01$.

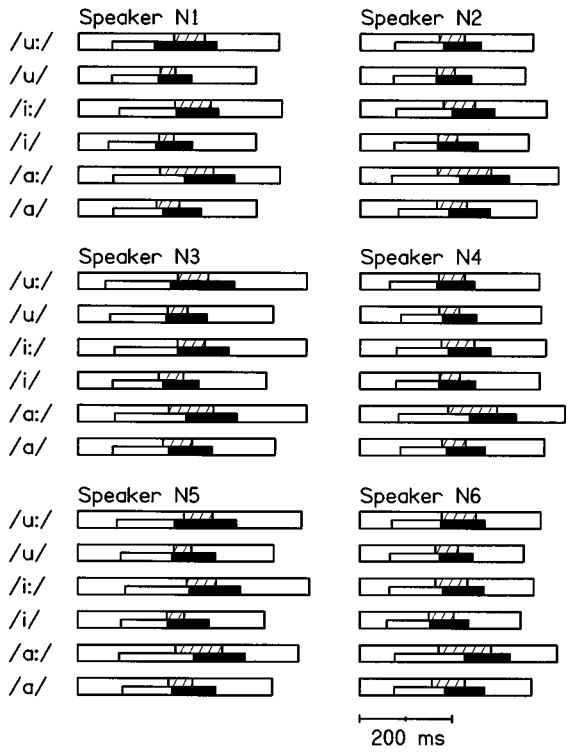

FIG. 2. Schematic display of the individual means, across the eight repetitions of each test sentence, of word duration (large rectangles), vowel duration (hatched rectangles in the upper half of the ''word rectangles''), and temporal extension of the opening (small unfilled rectangles) and the closing gesture (small filled rectangles).

compensation by neighboring segments, predominantly contributes to quantity-induced word prolongation.

As concerns the speech material of the present study, two different mechanisms, conceivably, influence the acoustic duration of the target vowels: The duration of the opening-closing cycle and the timing of laryngeal adduction as indicated by vowel onset at the acoustic speech signal. To differentiate between these two alternatives, Pearson's correlation coefficients were computed, first, between vowel duration and movement cycle time and, second, between vowel duration and the time interval extending from the beginning of the opening gesture to vowel onset (''time to vowel onset''). In case of positive correlations between movement cycle time and vowel duration, without negative correlations between vowel duration and ''time to vowel onset,'' vowel duration can be expected to primarily depend on the articulatory cycle. In contrast, negative correlations between ''time to vowel onset'' and vowel duration, concomitant with missing positive correlations between cycle duration and vowel duration, indicate that the coordination of orofacial and laryngeal gestures represents the essential factor underlying the observed variability of vowel duration. In order to determine whether the effects of quantity and type on vowel duration comprise different mechanisms, two series of correlation analyses were performed. First, quantity was discarded as a source of variability by a separate consideration of long- and short-vowel utterances (Table III, columns 1 and 2). Under these conditions, vowel type represents the only systematic source of variability underlying the computed correlations. Second, the three vowel types were considered separately (Table III, columns 3 to 5) with quantity being the main source of variability. As concerns the latter analysis, the computed correlation coefficients between movement cycle time and vowel duration consistently achieved high values (Table IIIA, columns 3–5). Furthermore, no negative correlations between ''time to vowel onset'' and vowel duration occurred under this condition (Table IIIB, columns 3–5). Since long and short vowels showed an even larger difference in cycle time than in vowel duration, these data indicate a strong relationship between vowel quantity and the articulatory opening-closing cycle.

When vowel type represented the source of variability, the computed correlation patterns were inconsistent across speakers and quantity categories (Table III, columns 1 and 2). At least in some speakers, intrinsic vowel lengths do not tightly depend upon the duration of the articulatory movement cycle. Furthermore, the observed negative correlations between vowel duration and ''time to vowel onset'' (Table IIIB, columns 1 and 2) suggest an association between the intrinsic durational variability of vowels and laryngeal-supralaryngeal coordination. Figure 2 illustrates this finding. As compared to ''a,'' vowel onset of the high vowels ''i'' and ''u'' was delayed with respect to the beginning of the articulatory opening-closing cycle. ANOVAs performed with ''time to vowel onset'' as the dependent variable revealed a significantly ($p<0.01$) shorter duration of this measure in the context of low (/a/ and /a:/) as compared to high vowels (/i/, /u/ and /i:/, /u:/, respectively) ($F[1,142]=8.82$ for short vowels and 10.72 for long vowels; data pooled across subjects).

TABLE IV. Analysis of variance with vowel type and quantity as independent factors and movement cycle time as the dependent variable: Table of individual F values (A) for the opening gesture, (B) for the closing gesture, and (C) for both gestures with gesture as an intra-utterance factor.

	d.f.	$N1$	$N2$	$N3$	$N4$	$N5$	$N6$
			(A) Opening gesture				
Type	2,42	13.94[a]	34.55[a]	8.33[a]	16.86[a]	4.19	7.79[a]
Quantity	1,42	13.49[a]	80.99[a]	93.70[a]	39.91[a]	47.50[a]	11.93[a]
Type×quantity	2,42	9.26[a]	5.48[a]	1.74	7.77[a]	5.46[a]	4.28
			(B) Closing gesture				
Type	2,42	4.08	23.41[a]	20.57[a]	5.42[a]	3.46	1.06
Quantity	1,42	40.58[a]	15.21[a]	182.11[a]	10.53[a]	27.94[a]	7.49[a]
Type×quantity	2,42	8.45[a]	3.83	15.57[a]	0.61	2.23	1.11
			(C) Repeated measures ANOVA with both gestures				
Type	2,42	8.79[a]	58.05[a]	27.81[a]	37.79[a]	4.17	20.08[a]
Quantity	1,42	71.98[a]	93.14[a]	361.07[a]	86.86[a]	144.10[a]	50.31[a]
Type×quantity	2,42	3.71	8.29[a]	3.81	12.60[a]	1.22	4.29
Gesture	1,42	18.95[a]	173.60[a]	168.52[a]	48.40[a]	19.31[a]	31.71[a]
Gesture×type	2,42	9.11[a]	4.28	5.75[a]	2.46	3.75	1.47
Gesture×quantity	1,42	2.83	22.67[a]	2.55	5.56	1.61	0.53
Gesture×type×quantity	2,42	11.63[a]	1.63	10.24[a]	1.94	4.97	2.68

[a]Significant at the level $p<0.01$.

3. Differential contribution of opening and closing gestures to the vowel quantity contrast

All subjects showed a significant main effect of quantity on the duration of both the opening and the closing gesture (Table IV). In consideration of previous studies which investigated the effects of stress and consonant categories on vowel production (Edwards *et al.*, 1991; DeJong, 1991; Gracco, 1994), it was expected that the opening gesture predominantly participates in the control of vowel quantity. Therefore, a repeated measures ANOVA was performed with the independent factors quantity, vowel type, and gesture, and with movement time as the dependent variable. A differential contribution of oral opening and closing to the quantity contrast should give rise to a significant gesture×quantity interaction. However, this relationship emerged in speaker $N2$ only ($p<0.01$). Two individuals ($N1$, $N3$) exhibited, instead, a significant three-way gesture×quantity×vowel type interaction. In these instances, the effect of quantity on the duration of the opening and closing gestures depends on vowel type (Fig. 2). Although all speakers showed a lengthened cycle duration of long as compared to short vowels, a fairly large variability across vowel types emerged with respect to the relative contribution of the opening and the closing gestures. In all individuals, modification of the opening gesture primarily accounted for the quantity distinction of vowel type ''a.'' By contrast, some speakers (e.g., $N1$ in Fig. 2) produced the long vowel /u:/ by means of a prolonged closing gesture.

B. Influence of vowel quantity on the dynamics of opening and closing gestures

In order to test hypothesis (b), the contribution of intragestural velocity/amplitude scaling to the quantity contrast was assessed. Given that ''a,'' ''i,'' and ''u'' differ in amplitude of lower lip excursions (Johnson, 1991) and assuming that these various vowel types are characterized by a common scaling mechanism, a strong linear relationship between peak velocity and amplitude across vowel types must be expected within each quantity category. By contrast, variation across short and long vowels should give rise to systematic alterations of the peak velocity/amplitude scaling. Figure 3 displays the individual peak velocity/amplitude plots separately for opening and closing gestures together with the respective linear regression lines for short and long vowel quantity. Significant correlations between peak velocity and amplitude emerged in all instances ($p<0.0001$) with coefficients ranging from 0.76 to 0.99. As a rule, closing gestures achieved higher values (all>0.93) than the opening movements. Apart from a few exceptions, the intercepts of the opening, but not the closing gestures significantly differed from zero. Since the spring model implies that the intercept of the linear velocity/amplitude regression equals zero, these findings are not compatible with a ''pure'' mass-spring model and point to additional mechanisms of temporal control such as intergestural timing (Edwards *et al.*, 1991).

In order to test for each speaker whether the slopes and intercepts obtained from short and long vowels exhibit significant differences, an analysis of covariance was performed with peak velocity as the dependent variable, amplitude as a covariate, and quantity as a categorical factor. As a rule, the slope for the opening gesture was steeper in short than in long vowels. Thus, short vocalic segments are characterized by an increased articulatory stiffness during the opening movement (Figs. 3 and 4). In speakers $N1$ and $N6$ this effect achieved significance ($p<0.01$), whereas the error bars of the slopes from speaker $N3$ almost completely overlap. With respect to the intercept of the opening gesture, none of the subjects showed a significant quantity difference.

As concerns oral closure, vowel quantity did not significantly influence the slopes (all $p>0.05$). With respect to the intercepts, a significant difference between short and long vowels emerged in speaker $N3$ ($p<0.01$), a respective tendency in subject $N5$ ($p=0.06$). Presumably, these findings reflect individual strategies of quantity-dependent modifica-

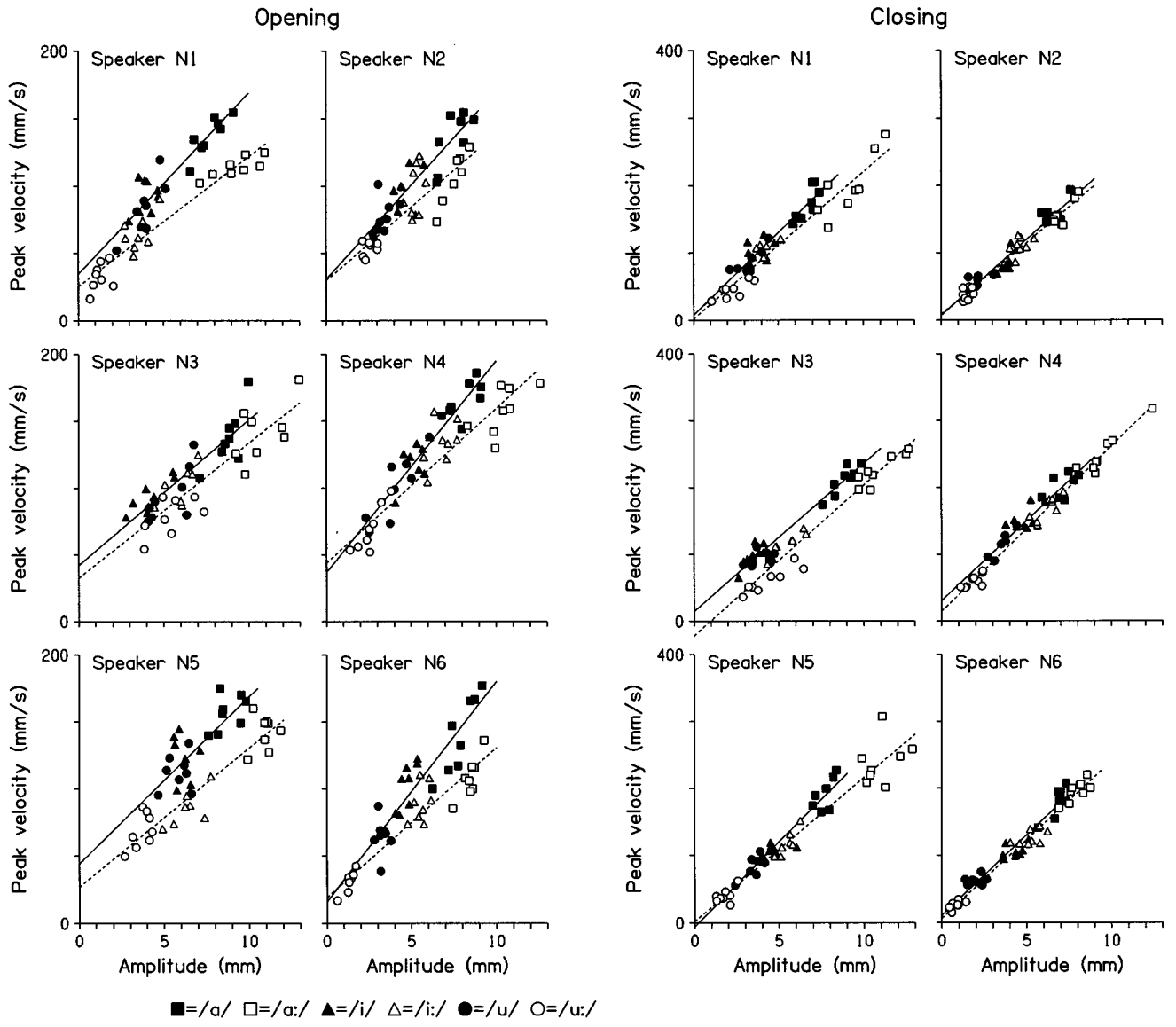

FIG. 3. Scatterplots of peak velocity and movement amplitude values as well as the calculated regression lines. Each symbol refers to a single sentence utterance: filled (unfilled) symbols=short (long) vowels, squares=''a'' targets, triangles=''i'' targets, circles=''u'' targets. Regression lines were computed across vowel types, separately for short (solid) and long vowels (dashed). Note the different scales for peak velocity of the opening and closing gestures.

tion of the closing gesture since both these individuals had the smallest quantity differences with respect to their slopes for the opening movement.

C. Influence of vowel quantity on velocity profile shapes

Besides the scaling of peak velocity and amplitude, adjustments of the shape of the velocity profiles might contribute to the control of speech timing (hypothesis *c*). Parameter *c* and the ratio between the acceleration phase and gesture duration were considered measures of peakedness and symmetry, respectively. Parameter *c* showed a tendency towards increased values in long vowels (Fig. 5). However, this effect was not consistent across vowel types and speakers, and a significant quantity main effect emerged in some cases only (Table V).

With respect to the velocity profiles' symmetry, all speakers exhibited a significant gesture×quantity interaction (Table VI). As concerns oral opening, the relative duration of the acceleration phase was shorter in long as compared to short vowels. The closing gestures showed an inverse relationship (Fig. 6). The factor vowel type yielded, in contrast, only inconsistent effects across subjects.

III. DISCUSSION

A. Relevance of the mass–spring model for the control of vowel quantity

The present study revealed a highly linear relationship between peak velocity and amplitude across vowel types within each quantity class for compound lower lip/jaw movements in a /pVp/ context. Obviously, thus, the ''amplitude instruction by vowel type'' paradigm represents a fea-

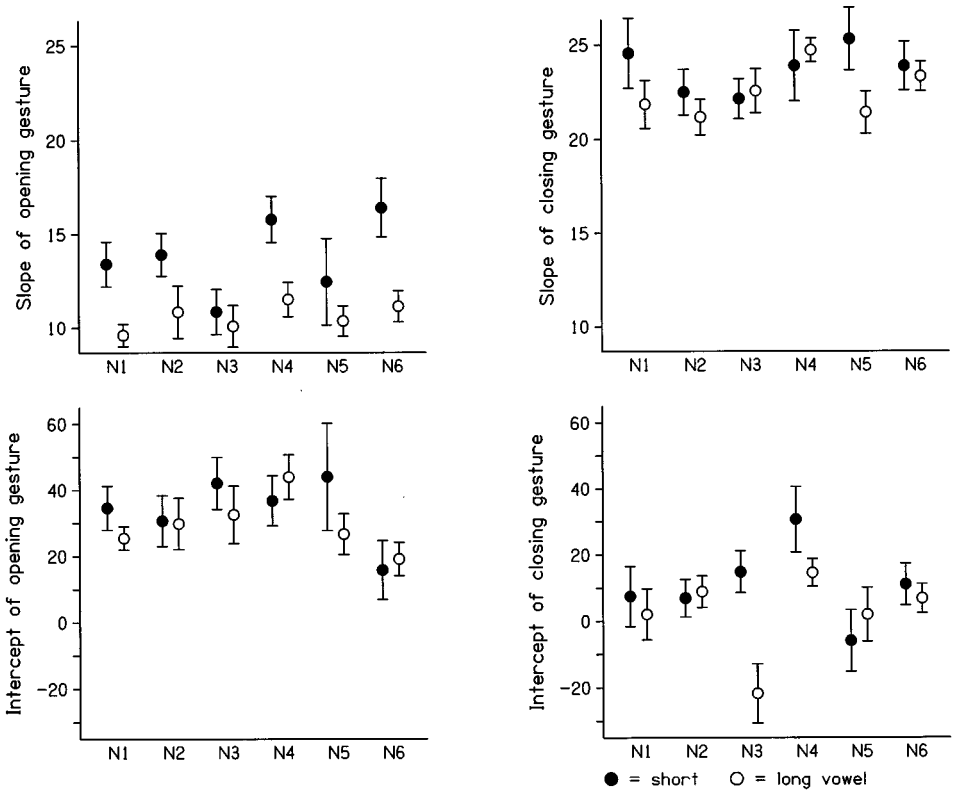

FIG. 4. Slope and intercept values with standard error bars as derived from the regression lines displayed in Fig. 3. Each regression refers to 3(vowel types)×8(repetitions)=24 sentence productions.

sible approach to elicit systematic variations of lower lip displacements. Moreover, the compound lower lip/jaw movements reflect the behavior of a mass-spring in terms of an automatic amplitude/velocity co-specification at a given stiffness of the system. As expected on the basis of this model, systematic changes of articulatory stiffness paralleled the adjustment of vowel duration: Short targets showed an increased slope of the peak velocity/amplitude scaling as compared to their long counterparts during oral opening. Since a significant correlation between vowel duration and movement cycle time emerged, these articulatory processes can be considered a relevant mechanism for the control of vowel quantity. In contrast to oral opening, the closing gesture was found to be less susceptible to the vowel length contrast. The latter finding corroborates recent studies which indicate rather rigid dynamic properties of the closing movements (e.g., Gracco, 1994).

Considering the equation provided by Ostry and Munhall (1985), invariant movement time across changes of amplitude must be expected in the presence of a given stiffness. However, previous investigations (e.g., Vatikiotis-Bateson and Kelso, 1993) revealed, to some degree, a larger range with longer gesture durations. Accordingly, the present study showed on average longer movement cycle durations in low (''a'') as compared to high vowels (''i,'' ''u''). These data, as well as the finding of several studies (e.g., Ostry and Munhall, 1985; Adams *et al.*, 1993) that parameter c consistently exceeds the theoretical value of $\pi/2$, are at variance with an ideal spring system which is characterized by amplitude-independent cycle durations and sinusoidal velocity curves. Therefore, Kelso and co-workers added a cubic stiffness component to the spring function (Kelso *et al.*, 1985; Vatikiotis-Bateson and Kelso, 1993). However, the acceleration values obtained at very small displacements from the equilibrium point indicate that even this modified version of a mass-spring (''soft spring'') cannot completely account for the amplitude dependency of movement time (Kelso *et al.*, 1985). In other words, the soft spring fails to provide a comprehensive and economical description of the observed variability of kinematic parameters, i.e., to predict, at least under certain conditions, the amplitude/velocity as well as the amplitude/time relationships by the adjustment of a single system parameter. In accordance with these previous findings, the present study revealed that articulatory stiffness, i.e., the linear scaling factor of peak velocity and amplitude, only partially accounts for the control of vowel duration.

B. Adjustments of the velocity profile geometry along with vowel quantity

Within the context of dynamical systems, the velocity profiles' shape is determined by the model function. A symmetrical and sinusoidal geometry must be expected in the case of a simple mass–spring system. Actual speech data, however, have revealed systematic alterations in this regard. For example, the tongue tip opening gesture examined by Adams *et al.* (1993) showed higher values of parameter c during slow as compared to fast speech. Furthermore, the

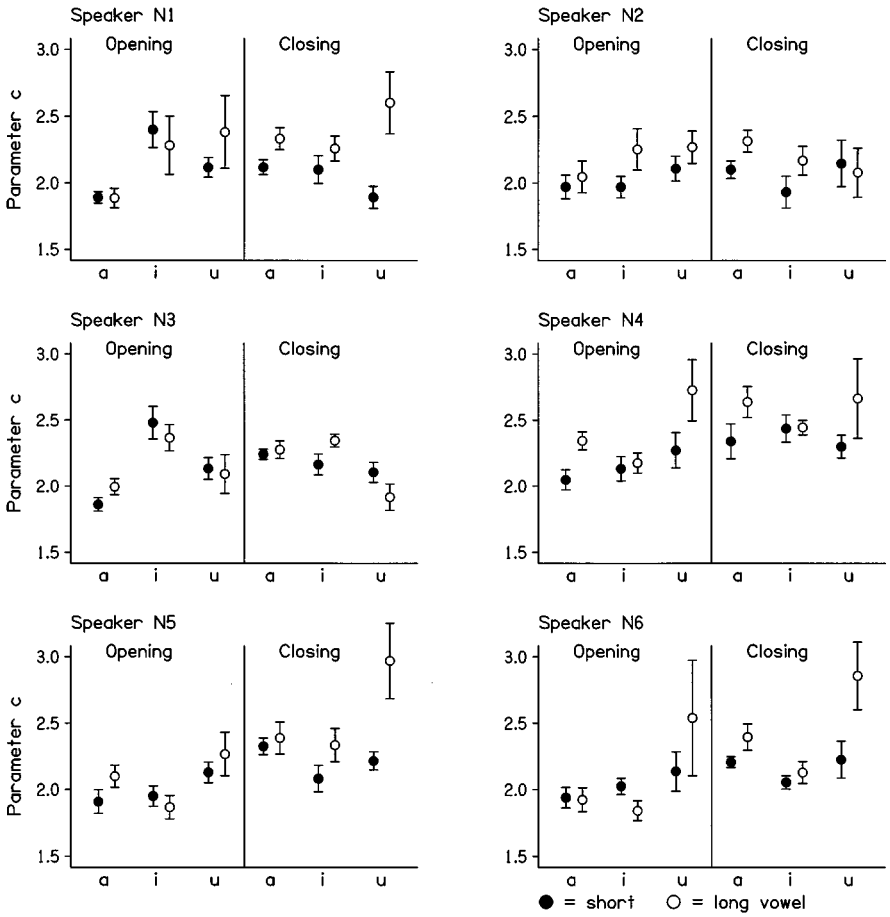

FIG. 5. Subject means with standard error bars of parameter *c*, a measure of velocity profile's peakedness, across eight repetitions of each test sentence.

relative length of the acceleration phase was inversely related to movement duration. The present study found similar relationships: (a) an increased value of parameter *c* in case of longer durations; (b) a longer deceleration phase of the opening and an increased acceleration interval of the closing movement in long as compared to short vowels. The investigation of the durational characteristics of English vowel categories yielded similar results (Johnson, 1991). The modification of the deceleration phase of the opening gesture can be interpreted in terms of intergestural timing mechanisms,

TABLE V. Analysis of variance with vowel type and quantity as independent factors and parameter *c* as the dependent variable: Table of individual *F* values (A) for the opening gesture, (B) for the closing gesture, and (C) for both gestures with gesture as an intra-utterance factor.

	d.f.	*N*1	*N*2	*N*3	*N*4	*N*5	*N*6
				(A) Opening gesture			
Type	2,42	4.50	1.28	12.55[a]	4.44	4.14	3.26
Quantity	1,42	0.13	3.53	0.01	6.58	0.96	0.21
Type×quantity	2,42	0.76	0.42	0.82	1.34	0.99	1.36
				(B) Closing gesture			
Type	2,42	0.16	0.74	8.02[a]	0.06	3.39	6.42[a]
Quantity	1,42	13.06[a]	1.43	0.03	3.14	8.64[a]	8.54[a]
Type×quantity	2,42	3.06	0.85	3.45	0.75	2.94	2.71
				(C) Repeated measures ANOVA with both gestures			
Type	2,42	3.36	0.30	12.74[a]	3.87	9.21[a]	13.74[a]
Quantity	1,42	8.05[a]	4.03	0.00	16.95[a]	11.45[a]	7.09
Type×quantity	2,42	3.99	0.68	1.49	3.68	3.13	6.14[a]
Gesture	1,42	0.40	0.10	0.16	3.59	18.41[a]	5.20
Gesture×type	2,42	2.60	1.85	9.44[a]	1.07	0.11	0.37
Gesture×quantity	1,42	2.96	0.12	0.03	0.04	2.84	1.16
Gesture×type×quantity	2,42	0.14	0.66	1.90	0.02	1.80	0.01

[a]Significant at the level $p<0.01$.

TABLE VI. Analysis of variance with vowel type and quantity as independent factors and relative acceleration time as the dependent variable: Table of individual F values (A) for the opening gesture, (B) for the closing gesture, and (C) for both gestures with gesture as an intra-utterance factor.

	d.f.	*N*1	*N*2	*N*3	*N*4	*N*5	*N*6
			(A) Opening gesture				
Type	2,42	0.77	1.61	5.75[a]	0.48	1.15	8.82[a]
Quantity	1,42	15.02[a]	10.59[a]	6.38	2.93	4.37	19.74[a]
Type×quantity	2,42	0.90	0.09	0.61	0.06	0.97	0.80
			(B) Closing gesture				
Type	2,42	6.41[a]	1.14	5.16[a]	1.51	5.54[a]	16.82[a]
Quantity	1,42	69.95[a]	4.68	18.34[a]	21.96[a]	19.15[a]	25.38[a]
Type×quantity	2,42	7.29[a]	1.54	13.00[a]	0.79	3.77	9.51[a]
			(C) Repeated measures ANOVA with both gestures				
Type	2,42	1.64	1.13	7.83[a]	0.67	4.40	1.13
Quantity	1,42	0.40	0.27	0.66	3.32	2.96	0.66
Type×quantity	2,42	3.30	0.71	7.29[a]	0.22	3.25	1.92
Gesture	1,42	11.01[a]	0.03	17.85[a]	0.42	51.96[a]	19.59[a]
Gesture×type	2,42	2.80	1.57	2.75	1.57	2.29	31.21[a]
Gesture×quantity	1,42	68.79[a]	14.68[a]	24.09[a]	28.47[a]	35.50[a]	62.48[a]
Gesture×type×quantity	2,42	1.11	1.12	4.04	0.79	1.22	6.43[a]

[a]Significant at the level $p<0.01$.

i.e., truncation of the opening movement in case of short vowels and delayed onset of the closing movement in case of long vowels (Edwards *et al.*, 1991). However, the lengthened relative acceleration time of the closing gesture in long vowels can neither be accounted for by a specification of stiffness nor by intergestural phasing. This effect might be due to intragestural timing processes in terms of a particularly slow performance during the initial phase of oral closure. A simi-

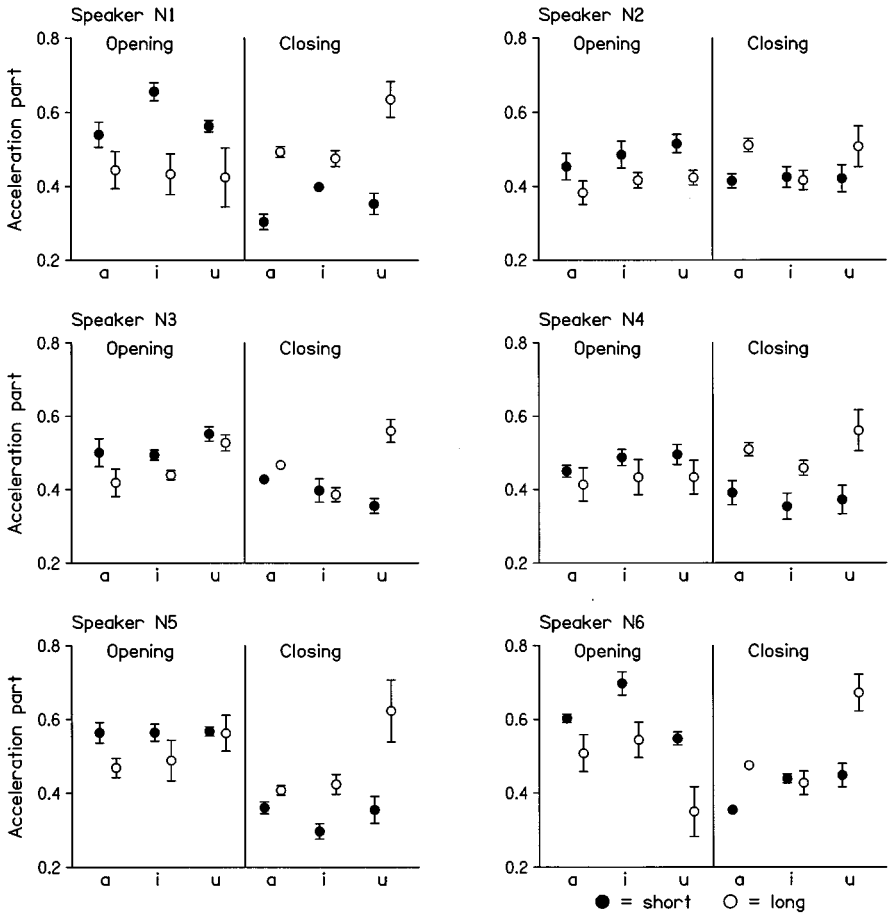

FIG. 6. Subject means with standard error bars of the relative duration of the acceleration part of each gesture, averaged across eight repetitions of each test sentence.

lar mechanism has been suggested by Edwards and coworkers with respect to phrase-final lengthening (Edwards and Beckman, 1988; Edwards *et al.*, 1991). Since the latter effect could not be explained by a specific control mechanism such as the adjustment of stiffness, an intermediate level of ''time'' representation was assumed by these authors. Conceivably, a differential behavior of the jaw and the lower lip is responsible for the prolonged initial part of the closing gesture: e.g., a slow jaw movement of early onset associated with a faster, but delayed labial gesture. However, the present investigation cannot clarify this issue since only the compound lower lip/jaw movements were recorded.

Within the context of the present study, the factor vowel type did not consistently influence the shape of the velocity profiles. Assuming that systematic alterations of the velocity profile's geometry reflect mechanisms of intergestural timing, this finding can be considered a further argument for the suggestion that intrinsic vowel length variability and quantity-induced durational patterns differ with respect to their control.

C. The differential control of opening and closing gestures

In accordance with previous studies (Adams *et al.*, 1993; Ackermann *et al.*, 1995), the closing gesture, as a rule, had a shorter duration than the preceding opening movement, showed a steeper regression line between peak velocity and amplitude, and apparently was less susceptible to temporal demands. Assuming a rather stereotypic nature of the closing gesture, a predominant contribution of the opening movement to the lengthening of long vowels must be expected. As concerns the scaling of peak velocity and amplitude, this hypothesis was confirmed. With respect to movement duration, however, a significant three-way interaction between gesture, quantity, and vowel type emerged in some speakers. A particular pattern of effects could be observed: A prolongation of the opening gesture gives rise to the lengthening of ''a'' whereas modulation of the initial part of the closing gesture predominantly accounts for the quantity distinction of the vowel ''u.'' These findings indicate that the control of quantity does not solely depend on the adjustment of single gestures. Lindblom (1963) suggested that vowel lengthening (''vowel undershoot hypothesis'') results from a continuous approximation to the respective target position. In the case of ''a,'' the target is characterized by a wide open position. Therefore, vowel prolongation should be associated with an increased duration of the opening gesture. In contrast, a well-articulated long German ''u'' is characterized by a rather narrow lip opening. Accurate durational control of such small movements might be difficult. It is conceivable, therefore, that the gesture towards the vowel target consists of a short and slightly overshooting opening phase and a succeeding approximation towards the intended /u:/ target. Under these conditions, the latter motor component represents the initial part of the closing gesture.

These suggestions have some implications for the relation between gestures and segments in general. Acoustic targets, i.e., segment rather than gesture durations, are the relevant entities conveying linguistic information (Johnson *et al.*, 1993; Ohala, 1993). Models of articulatory phonology, however, consider acoustic segments to be a function of underlying gestures (Browman and Goldstein, 1986). Admittedly, articulatory movements underly the acoustic signals in a causal sense and therefore a statistical relation between durations of articulatory movements and phonetic segments must exist. However, the relation between gestures and segments seems to be rather indirect and multifaceted when the former are defined in terms of kinematic events. In order to solve this problem, Fowler and Saltzman (1993) differentiated between ''phonetic gestures'' and ''articulatory movements.'' On this basis they defined ''gesture'' as ''a member of a family of functionally equivalent articulatory movement patterns that are actively controlled with reference to a given speech-relevant goal.'' In consideration of this suggestion, the observed differential contribution of opening and closing gestures to the quantity contrast depending on vowel type might reflect a discrepancy between articulatory movements defined in terms of oral opening and closing on the one hand, and in terms of target approximation on the other. Although the /pVp/ movement cycle can be subdivided into an opening and a closing phase, the phonetically relevant articulatory units may be different entities in that the movement cycle consists of two speech gestures, the first of which is directed towards the vowel target and the second of which is directed towards the succeeding consonant place of articulation.

The present study considered the compound lower lip/jaw gestures. However, the vowel ''u'' differs from ''a'' not only in amplitude but also in the feature of lip rounding. Although the kinematic aspect of lip protrusion in rounded vowels has been more or less discarded from analysis, differences between ''a'' and ''u'' in lip tension and in the relative timing of jaw and lower lip may still be present in addition to differences in amplitude. Conceivably, the biphasic pattern of the lower lip and jaw closing gesture in /u:/ is caused by a partial desynchchronization of the lower lip and the jaw.

D. Vowel quantity and intrinsic durational variability

As in earlier studies (Antoniadis and Strube, 1984; Hertrich and Ackermann, 1995; Ramers, 1988), low vowels were found to have longer durations than their high counterparts. This intrinsic temporal variability has been explained by different movement times of the jaw opening gesture in the various vowel contexts (Stevens *et al.*, 1966; Lehiste, 1970; Nooteboom, 1985). Assuming a high correlation between lower lip and jaw excursions (e.g., Gracco, 1994) and disregarding compensatory effects between these two articulators (Lindblom, 1990), the cycle time of lower lip and jaw movements as measured in the present study should be closely related to intrinsic vowel durations as well. However, the calculation of correlation coefficients did not reveal a consistently tight relationship between intrinsic vowel durations and movement cycle time. Furthermore, the intrinsic durational variability showed partial compensation at the word level and led to negative correlations between vowel duration and the time interval between the beginning of oral opening and vowel onset. At least partially, thus, intrinsic vowel durations seem to reflect differences in laryngeal-

supralaryngeal coordination rather than in movement execution time. These suggestions are in line with the observation that the voice onset time preceding /a/ is shorter than in case of /u/ or /i/ (Port and Rotunno, 1979). By contrast, the quantity effect on word length exceeded the difference between short- and long-vowel duration. Thus, vowel quantity seems to reflect a mechanism of syllable lengthening extending beyond the vocalic segment. These findings corroborate the suggestion of a prosodic nature of the German quantity contrast (Becker, 1995; Vennemann, 1991).

E. Subject variability

The most consistent finding across subjects was the differential quantity effect on the symmetry of velocity profiles of opening and closing gestures. With respect to the remaining parameters, the subjects showed a less consistent behavior. In some speakers, short-vowel quantity was associated with an increased slope of the scaling of peak velocity and amplitude of the opening gesture. It is noteworthy that subject *N*3 exhibited a significant quantity difference for the intercepts of the closing gesture in the absence of relevant slope differences in the opening gesture. This finding can be interpreted in terms of a biphasic movement pattern: Long vowels are characterized by a particularly slow initial part of the closing gesture which is excluded from amplitude/velocity scaling, leading to a negative intercept. With respect to parameter c, i.e., the peakedness of velocity profiles, high values in long vowels may arise in cases when the actual movement is performed in a relatively short time, preceded or followed by a phase of an approximate steady state. This mechanism of intergestural timing was observed in some cases only. These aspects of subject variability suggest that the control of vowel quantity cannot be assigned to a single mechanism but has to be considered as the result of target-directed behavior which, to some degree, comprises individual strategies.

IV. CONCLUSIONS

The relation between peak velocity and movement range was found to be highly linear across amplitude variability induced by the vowel types ''a,'' ''i,'' and ''u.'' Control of German vowel quantity was performed (1) by the adjustment of the peak velocity/amplitude scaling factor during oral opening, (2) by the modification of the velocity profiles' peakedness of both the opening and closing gestures, and, most consistently, (3) by a vowel-related asymmetry of the velocity profiles. The relative contribution of these effects varied across speakers reflecting individual strategies to achieve the acoustically relevant goal of durational adjustment. The differential contribution of opening and closing movements to quantity-induced vowel duration seems to depend on vowel type, indicating that the relation between phonetic segment durations and articulatory movement durations is quite complex and that measurable unidirectional articulatory gestures are not identical with phonetic target approximations. Furthermore, opening and closing gestures are controlled differently. The closing gesture can be regarded as a fast, ballistic movement, whereas the opening gesture is more sensitive to phonetic timing aspects. Analysis of compensatory timing features revealed that the control of quantity largely differs from the mechanism underlying intrinsic vowel durations. In the former case, consonant–vowel (CV) syllable lengthening rather than vowel prolongation seems to be the relevant principle, which might confirm the assumption of a prosodic nature of the German vowel quantity contrast.

Ackermann, H., Hertrich, I., and Scharf, G. (**1995**). ''Kinematic analysis of lower lip movements in ataxic dysarthria,'' J. Speech Hear. Res. **38,** 1252–1259.

Adams, S. G., Weismer, G., and Kent, R. D. (**1993**). ''Speaking rate and speech movement velocity profiles,'' J. Speech Hear. Res. **36,** 41–54.

Antoniadis, Z., and Strube, H. W. (**1984**). ''Untersuchungen zur spezifischen Dauer deutscher Vokale,'' Phonetica **41**, 72–87.

Becker, T. (**1995**). ''Das Vokalsystem der deutschen Standardsprache,'' Ph.D. thesis, University of Munich.

Bohn, O.-S., Flege, J. E., Dagenais, P. A., and Fletcher, S. G. (**1991**). ''Differenzierung und Variabilität der Zungenpositionen bei der Artikulation deutscher Vokale,'' Zeitschrift für Dialektologie und Linguistik, Beiheft, 1–26.

Borghese, N. A., and Ferrigno, G. (**1990**). ''An algorithm for 3-D automatic movement detection by means of standard TV cameras,'' IEEE Trans. Biomed. Eng. **37,** 1221–1225.

Browman, C. P., and Goldstein, L. M. (**1986**). ''Towards an articulatory phonology,'' Phonology Yearbook **3**, 219–252.

DeJong, K. (**1991**). ''An articulatory study of consonant-induced vowel duration changes in English,'' Phonetica **48**, 1–17.

DeJong, K. J. (**1995**). ''The supraglottal articulation of prominence in English: Linguistic stress as localized hyperarticulation,'' J. Acoust. Soc. Am. **97,** 491–504.

DeJong, K., Beckman, M. E., and Edwards, J. (**1993**). ''The interplay between prosodic structure and coarticulation,'' Lang. Speech **36**, 197–212.

Edwards, J., and Beckman, M. E. (**1988**). ''Articulatory timing and the prosodic interpretation of syllable duration,'' Phonetica **45**, 156–174.

Edwards, J., Beckman, M. E., and Fletcher, J. (**1991**). ''The articulatory kinematics of final lengthening,'' J. Acoust. Soc. Am. **89,** 369–382.

Ferrigno, G., and Pedotti, A. (**1985**). ''ELITE: A digital dedicated hardware system for movement analysis via real-time TV signal processing,'' IEEE Biomed. Eng. **32**, 943–950.

Forrest, K., Weismer, G., and Turner, G. S. (**1989**). ''Kinematic, acoustic, and perceptual analyses of connected speech produced by Parkinsonian and normal geriatric adults,'' J. Acoust. Soc. Am. **85,** 2608–2622.

Fowler, C. A., and Saltzman, E. (**1993**). ''Coordination and coarticulation in speech production,'' Lang. Speech **36**, 171–195.

Gopal, H. S. (**1990**). ''Effects of speaking rate on the behavior of tense and lax vowel durations,'' J. Phon. **18**, 497–518.

Gopal, H. S. (**1996**). ''Generalizability of current models of vowel duration,'' Phonetica **53**, 1–32.

Gracco, V. L. (**1994**). ''Some organizational characteristics of speech movement control,'' J. Speech Hear. Res. **37,** 4–27.

Harrington, J., Fletcher, J., and Roberts, C. (**1995**). ''Coarticulation and the accented/unaccented distinction: Evidence from jaw movement data,'' J. Phon. **23**, 305–322.

Hertrich, I., and Ackermann, H. (**1994**). ''Acoustic analysis of speech timing in Huntington's disease,'' Brain Lang. **47**, 182–196.

Hertrich, I., and Ackermann, H. (**1995**). ''Coarticulation in slow speech: Durational and spectral analysis,'' Lang. Speech **38**, 159–187.

Hoole, P., and Kühnert, B. (**1996**). ''Tongue-jaw coordination in German vowel production,'' Paper presented at the 4th Speech Production Seminar: Models and Data, Autrans, France, 20–24 May 1996.

Hoole, P., Mooshammer, C., and Tillmann, H. G. (**1994**). ''Kinematic analysis of vowel production in German,'' Proceedings ICSLP'94, Yokohama, Japan, pp. 53–56.

Jessen, M. (**1993**). ''Stress conditions on vowel quality and quantity in German,'' Working Papers of the Cornell Phonetics Laboratory **8**, 1–27.

Johnson, K. (**1991**). ''Dynamic aspects of English vowels in /bVb/ sequences,'' UCLA Working Papers in Phonetics **80**, 99–120.

Johnson, K., Ladefoged, P., and Lindau, M. (**1993**). ''Individual differences in vowel production,'' J. Acoust. Soc. Am. **94,** 701–714.

Kelso, J. A. S., Vatikiotis-Bateson, E., Saltzman, E. L., and Kay, B. (**1985**). ''A qualitative dynamic analysis of reiterant speech production: Phase portraits, kinematics, and dynamic modeling,'' J. Acoust. Soc. Am. **77,** 266–280.

Kohler, K. J. (**1995**). *Einführung in die Phonetik des Deutschen* (Schmidt, Berlin, Germany).

Keuhn, D. P., and Moll, K. L. (**1976**). ''A cineradiographic study of VC and CV articulatory velocities,'' J. Phon. **4**, 303–320.

Lehiste, I. (**1970**). *Suprasegmentals* (MIT, Cambridge, MA).

Lindblom, B. (**1963**). ''Spectrographic study of vowel reduction,'' J. Acoust. Soc. Am. **35,** 1773–1781.

Lindblom, B. (**1990**). ''Explaining phonetic variation: A sketch for the H & H theory,'' in *Speech Production and Speech Modelling*, edited by W. J. Hardcastle and A. Marchal (Kluwer, Dordrecht, The Netherlands), pp. 403–439.

MacNeilage, P. F. (**1980**). ''Distinctive properties of speech motor control,'' in *Tutorials in Motor Behavior*, edited by G. E. Stelmach and J. Requin (North-Holland, Amsterdam, The Netherlands), pp. 607–621.

Munhall, K. G. (**1993**). ''Kinematic analysis of speech using an optoelectronic measurement system,'' Forschungsberichte des Instituts für Phonetik und sprachliche Kommunikation der Universität München **31**, 163–168.

Munhall, K. G., Ostry, D. J., and Parush, A. (**1985**). ''Characteristics of velocity profiles of speech movements,'' J. Exp. Psychol. Hum. Percept. Perform. **11,** 457–474.

Nooteboom, S. G. (**1985**). ''A functional view of prosodic timing in speech,'' in *Time, Mind, and Behavior*, edited by J. A. Michon and J. L. Jackson (Springer- Verlag, Berlin, Germany), pp. 242–252.

Ohala, J. J. (**1993**). ''Coarticulation and phonology,'' Lang. Speech **36**, 155–170.

Ostry, D. J., Keller, E., and Parush, A. (**1983**). ''Similarities in the control of the speech articulators and the limbs: Kinematics of tongue dorsum movement in speech,'' J. Exp. Psychol. Hum. Percept. Perform. **9,** 622–636.

Ostry, D. J., and Munhall, K. G. (**1985**). ''Control of rate and duration of speech movements,'' J. Acoust. Soc. Am. **77,** 640–648.

Pind, J. (**1995**). ''Speaking rate, voice-onset-time, and quantity: The search for higher-order invariants for two Icelandic speech cues,'' Percept. Psychophys. **57,** 291–304.

Port, R. F. (**1981**). ''Linguistic timing factors in combination,'' J. Acoust. Soc. Am. **69,** 262–274.

Port, R. F., and Rotunno, R. (**1979**). ''Relation between voice-onset time and vowel duration,'' J. Acoust. Soc. Am. **66,** 654–662.

Ramers, K. H. (**1988**). *Vokalquantität und qualität im Deutschen* (Niemeyer, Tübingen, Germany).

Sock, R., and Löfqvist, A. (**1995**). ''Quantity contrast in Swedish kinematic and acoustic patterns,'' in *Proceedings of the 13th International Congress of Phonetic Sciences*, edited by K. Elenius and P. Branderud (KTH and Stockholm University, Stockholm, Sweden), Vol. 3, pp. 580–583.

Stevens, K. N., House, A. S., and Paul, A. P. (**1966**). ''Acoustical description of syllabic nuclei: An interpretation in terms of a dynamic model of articulation,'' J. Acoust. Soc. Am. **40,** 123–132.

Vatikiotis-Bateson, E., and Kelso, J. A. S. (**1993**). ''Rhythm type and articulatory dynamics in English, French and Japanese,'' J. Phon. **21**, 231–265.

Vennemann, T. (**1991**). ''Skizze der Deutschen Wortprosodie,'' Zeitschrift für Sprachwissenschaft **10**, 86–111.

Temporal and spectral estimations of harmonics-to-noise ratio in human voice signals

Yingyong Qi
Department of Speech and Hearing Sciences, University of Arizona, Tucson, Arizona 85721

Robert E. Hillman
Voice and Speech Laboratory, Massachusetts Eye and Ear Infirmary, Boston, Massachusetts 02215 and Department of Otology and Laryngology, Harvard Medical School, Cambridge, Massachusetts 02139 and Communication Science and Disorders, MGH-Institute of Health Professions, Boston, Massachusetts 02215

(Received 4 November 1996; accepted for publication 18 March 1997)

The quantity, harmonic-to-noise ratio (HNR), has been used to estimate the level of noise in human voice signals. HNR estimation can be accomplished in two ways: (1) on a time-domain basis, in which HNR is computed directly from the acoustic waveform; and (2) on a frequency-domain basis, in which HNR is computed from a transformed representation of the waveform. An algorithm for computing HNR in the frequency domain was modified and tested in the work described here. The modifications were designed to reduce the influence of spectral leakage in the computation of harmonic energy, and to remove the necessity of spectral baseline shifting prescribed in one existing algorithm [G. de Krom, J. Speech Hear. Res. **36**, 254–266 (1993)]. Frequency-domain estimations of HNR based on this existing algorithm and our modified algorithm were compared to time-domain estimations on synthetic signals and human pathological voice samples. Results indicated a highly significant, linear correlation between frequency- and time-domain estimations of HNR for our modified approach. [S0001-4966(97)03307-9]

PACS numbers: 43.70.Aj, 43.70.Gr [AL]

INTRODUCTION

A valid and reliable method for estimating levels of noise in the human voice would be expected to provide useful information for the evaluation and management of voice disorders. Current techniques for measuring noise in the human voice treat the acoustic signal as a sum of two parts: a harmonic and a noise component. Based on this assumption, estimates of the harmonic-to-noise ratio (HNR) have been calculated. HNR estimation can be accomplished in two ways: (1) on a time-domain basis, in which HNR is computed directly from the acoustic waveform; and (2) on a frequency-domain basis, in which HNR is computed from a transformed representation of the waveform.

The time and frequency representations of a signal are usually related through Fourier transformations. Thus measurements in the time domain should have their equivalence in the frequency domain. The equivalency between time- and frequency-domain measurements, however, is not always apparent unless the signal is strictly periodic. For example, there are two major factors that complicate the estimation of HNR in human voice signals. First, the spectrum of a recorded acoustic signal has to be computed using a limited (windowed) segment of the signal. The application of a window broadens the harmonics of a signal, the extent to which depends on the shape and length of the window. Second, human voice signals are not truly periodic. There are period-to-period variations in fundamental frequency ($F0$ perturbation), which also tend to broaden the harmonics. This effect is more apparent in some disordered voices in which there is an increase in $F0$ perturbation. Combined together, these sources of spectral broadening or spectral leakage make it difficult to obtain accurate estimates of HNR for human voice signals in the frequency domain (Cox *et al.*, 1989). For similar reasons, it is equally difficult to measure HNR in human voice signals in the time domain. Thus it is necessary to employ approximation techniques to obtain frequency- and time-domain-based estimations of HNR in human voices. One approach to evaluating these approximation techniques would be to determine the extent to which the resulting HNR estimations preserve time and frequency equivalency.

A representative, time-domain approach for calculating HNR was proposed by Yumoto *et al.* (1982). To calculate HNR, an ''average'' wave for a single period is determined as the mean of a succession of periods. The energy of this average defines the harmonic component. Each individual period is then compared to this average. The variance of the period ensemble (all periods used to compute the mean) is used to define the noise component (see Yumoto *et al.* for details). Zero padding is used to time-normalize periods prior to computation of the mean and variance. This simple time-normalization procedure is difficult to apply to disordered voices that exhibit relatively large $F0$ perturbation, in part, because the computed variance will be significantly inflated by such perturbation. An example period ensemble and the mean and standard deviation of this ensemble are shown in Fig. 1. Note that there is a noticeable increase in the variance around sample 60 where zero padding has been used.

Qi (1992) proposed a modification to the time-domain method of calculating HNR originally developed by Yumoto *et al.* In this modification, periods are time-normalized using dynamic time warping, a procedure that optimally aligns waveforms in time prior to computation. Qi and his col-

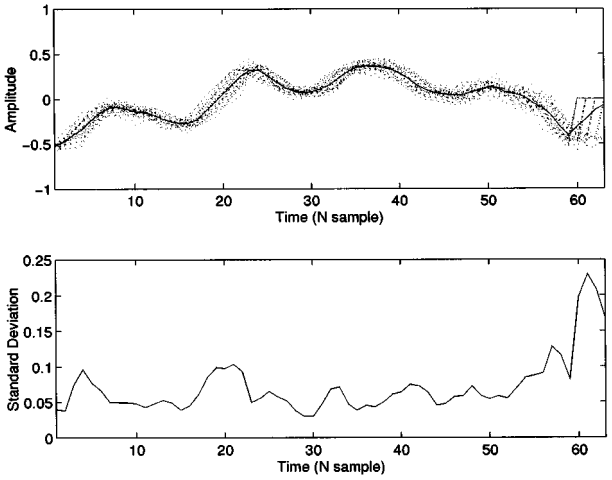

FIG. 1. An example period ensemble and its mean and standard deviation. Zero padding was used to time-normalize the period ensemble.

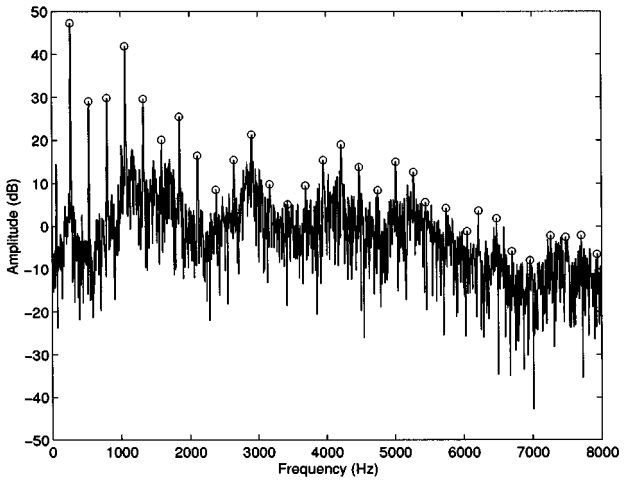

FIG. 3. The DFT spectrum of a signal with harmonic peaks marked.

leagues later demonstrated (Qi *et al.*, 1995b) that optimal time-normalization could also be accomplished using zero-phase transformations, and that an appropriate time-normalization minimizes the influence of $F0$ perturbation on the computation of HNR over a wide range of disturbances in voice signals. An example period ensemble after zero-phase transformation and its mean and standard deviation are shown in Fig. 2. Because the variances due to phase differences have been removed, the overall variance of the ensemble is reduced.

A number of techniques have been proposed for calculating HNR in the frequency domain (Kasuya *et al.*, 1986; Muta *et al.*, 1988; Cox *et al.*, 1989; Emanuel, 1991; de Krom, 1993). One recent, frequency-domain (or transformed-domain) approach to calculating HNR was proposed by de Krom (1993). In this method, the ''noise floor'' of a spectrum is estimated by cepstral liftering and spectral baseline shifting. Cepstral liftering is used to remove harmonic components in the spectrum, and baseline shifting is used to position the ''noise floor'' on a ''reasonable'' reference level. HNR is defined as the energy of the original spectrum relative to the energy of the cepstral-liftered and baseline-shifted spectrum. An example spectrum of a voice signal is shown in Fig. 3. The peaks of harmonics are marked. The cepstrum-liftered and baseline-shifted noise floor of the spectrum is shown in Fig. 4, together with the spectrum and its harmonic peaks.

HNR estimation in the frequency domain has a number of potential advantages over time-domain-based approaches. First, it is less difficult to estimate the mean $F0$ of a windowed signal segment required for the computation of HNR in the frequency domain than it is to identify individual period boundaries needed to compute HNR in the time domain. Second, HNR of different frequency ranges can be computed easily in the frequency domain. Finally, HNR in the frequency domain may be less sensitive to low-frequency am-

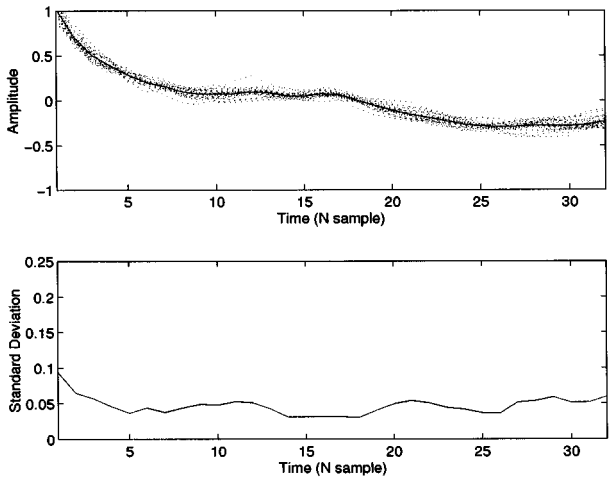

FIG. 2. The period ensemble of Fig. 1 after zero-phase transformation and its mean and standard deviation. Note that only half of the data points are shown. The other half is a mirror image of the first half.

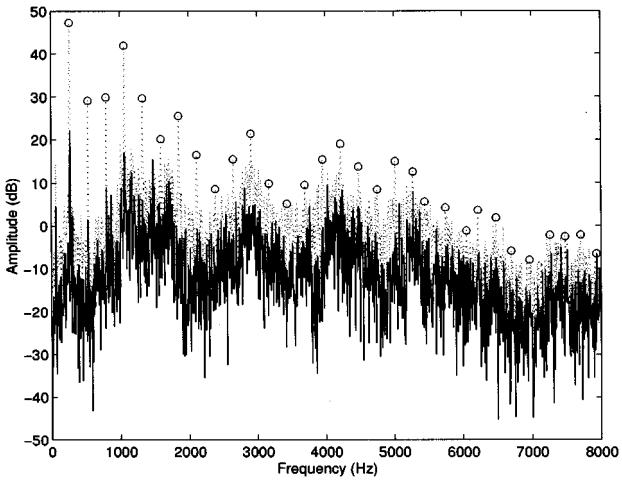

FIG. 4. The noise spectrum (solid line) obtained from comb cepstral liftering and baseline shifting. The original spectrum (dotted line) and its harmonic peaks are also shown.

plitude modulations. This advantage potentially could be useful in the analysis of voice signals from continuous discourse (Hillenbrand *et al.*, 1994).

Certain improvements/modifications, however, need to be made to the algorithm proposed by de Krom for computing HNR in the frequency domain. In the de Krom approach, it was implicitly assumed that all spectral components with amplitudes greater than a ''noise floor'' contribute to the energy of the harmonics. This assumption is not necessarily correct, in part, because of spectral leakages. In addition, the magnitude of baseline shift depends heavily on the estimation of spectral minima, which is strongly influenced by $F0$ and $F0$ perturbations. Because calculation of the magnitude of baseline shift is a crucial step in the computation of HNR, errors in baseline shift would introduce biases to the estimation of HNR. de Krom has, for example, pointed out that, ''Multiplication with a Hanning window increases the bandwidth of the harmonics. A consequence of this harmonic broadening is that we will obtain lower HNR values than could be expected... . In the spectra of signals with low fundamental frequencies, the harmonics are spaced close together, and the sidelobes of the smoothing window very much determine the minima to be reached in between harmonics.'' (page 261, de Krom, 1993)

The main purpose of the work to be described was to develop and test a modified algorithm for estimating HNR in the frequency domain. Specifically, procedures for estimating the levels of harmonics and ''noise floor'' were modified to reduce the influence of spectral leakage and to remove the necessity of calculating the magnitude of baseline shifting. Comparisons were made between this modified HNR estimation in the frequency domain and HNR estimation in the time domain.

I. METHOD

A. Estimation of HNR in the frequency domain

Estimation of HNR in the frequency domain requires computations of the magnitudes of harmonic and noise components. Numerically, both harmonic and noise components are estimated on the basis of discrete Fourier transform (DFT) of the signals. Further transformation of the signals, e.g., the cepstral transformation, may facilitate the separation of harmonic components from noise.

As explained previously, a major factor influencing estimation of the harmonic components in voice signals is the windowing effect. The DFT spectrum of a windowed signal segment is the convolution of the spectrum of the signal and the spectrum of the window. The resulting spectrum at any given frequency is a weighted sum of all spectral components of the signal, where the weighting is determined by the spectrum of the window function (Oppenhelm and Schafer, 1989). The spectrum of the window function is characterized by a main lobe and several side lobes. It is possible to balance the influence of the main lobe and the side lobes of the window function by manipulating the window shape. It is also possible to reduce the width of the main lobe by using a relatively long window. It is, however, practically impossible to eliminate the window effect (Oppenheim and Schafer, 1989).

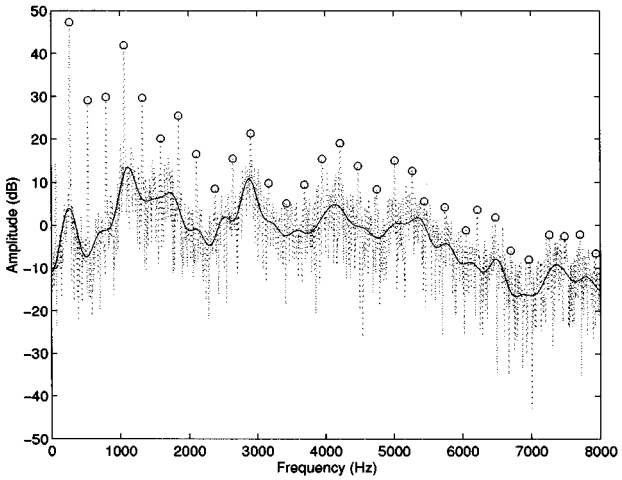

FIG. 5. The noise reference level (solid line) obtained from low-quefrency cepstral liftering. The original spectrum (dotted line) and its harmonic peaks are also shown.

Spectral leakage is inevitable and somewhat unpredictable. One way to estimate the energy of the harmonics is to sum all spectral components that exceed specified threshold levels as described by de Krom (1993). An alternative is to use the summation of only spectral peaks as an estimation of the harmonic energy. The latter approach has the following advantages:

(1) The window effect (spectral leakage) tends to introduce less error to the spectral peaks than to neighboring spectral components.
(2) The percentage of random magnitude fluctuations is usually smaller at the spectral peaks than at neighboring spectral components.
(3) The spectral peaks are relatively simple to measure.

Because of these advantages, the sum of spectral peaks was used as a measure of harmonics energy in our modified approach for estimating HNR in the frequency domain.

In de Krom's algorithm, the estimation of noise was obtained from the inverse transformation of the comb liftered cepstrum, followed by a heuristic baseline shift. The baseline shifting is complicated and is needed, in part, because all spectral energy above the noise floor is used to estimate HNR. In our modified algorithm, HNR is estimated as the energy of the spectral peaks that exceed a reference noise level. Thus rather than the whole noise spectrum, only a discrete set of noise reference levels at these peak frequencies need to be estimated. The average of this discrete set of noise reference levels can be estimated from the low-quefrency part of the cepstrum, thus the need for spectral baseline shifting is eliminated. An example of the low-quefrency, cepstrum-based estimation of the noise floor is shown in Fig. 5 together with the spectrum and its harmonic peaks.

B. Relationship between temporal and spectral estimations

Relationships between time-domain HNR and the level of added noise in synthetic signals has been extensively assessed in previous work (Qi, 1992; Qi *et al.*, 1995b). In the present work, the relationships between time- and frequency-domain estimations of HNR have been established using a limited set of synthetic signals and a relatively large set of human voice signals. We assumed that the establishment of highly significant, linear relationships between temporal and spectral estimations of HNR would help to confirm the equivalency (but not necessarily the validity) between time- and frequency-domain HNR measurements.

Obviously, a crucial factor in both time- and frequency-domain estimations of HNR is the size of the time window (signal length). The selection of window length is often made on the basis of a compromise between frequency versus time resolution. A short time window would introduce high spectral leakage, whereas a long time window would make it difficult to compute HNR for nonstationary voice signals (Qi and Shipp, 1992). Because our objective was to evaluate our modified approach for frequency-domain estimation of HNR relative to time-domain-based estimation, a fixed window size of 200 ms (3200 samples) was used.

1. Synthetic signals

The vowel /ɑ/ was synthesized using a formant synthesizer (Fant, 1960). The synthesizer was a five-pole, autoregressive digital filter whose coefficients were determined by five given pairs of formant frequencies and bandwidth. The unperturbed excitation source to the synthesizer was generated from a parametric model of glottal output proposed by Fant *et al.* (Fant *et al.*, 1985; Klatt and Klatt, 1990; Childers and Lee, 1991). This model (hereafter referred to as the LF model) specifies differentiated glottal flow using four independent parameters. In the present work, all temporal parameters of the LF model, t_p, t_e, and t_c, were defined as a constant proportion of the fundamental period. The amplitude of the negative flow derivative, Ee, was set to a level so that the intensity of the synthetic signal is around 65 dB (Qi and Bi, 1994). Specifically, t_p, was at 45% of the fundamental period. t_e was at 60% of the fundamental period. t_c was at 100% of the fundamental period. Ee was set to 50. The synthesis was made by convolving this excitation input with the impulse response of the autoregressive digital filter (Qi *et al.*, 1995a). The sampling frequency for the synthesizer was 16 kHz.

Noise was introduced by adding a Gaussian random noise to the excitation source. The level of noise was controlled by the standard deviation of the Gaussian distribution. Perturbations in fundamental frequency were introduced by adding a uniformly distributed random number to the interval of each period of the excitation input. The level of $F0$ perturbation, i.e., the variance of the random number generator, was set at 1% of the fundamental period. Fundamental frequency levels of 120 Hz and 240 Hz were used, respectively. The synthetic signal was informally presented to three experienced listeners and was judged to be an acceptable /ɑ/. It was perceived as a noisy /ɑ/ when relatively large noise perturbations were introduced.

2. Human voice signals

Human voice samples of 48 subjects (24 men and 24 women) diagnosed with a wide range of pathological conditions were obtained from the Voice and Speech Laboratory of Massachusetts Eye and Ear Infirmary (Diaz *et al.*, 1993; Kay-Elemetrics, 1994). Each subject was asked to sustain (at least 3 s long) the vowel /ɑ/ three times at comfortable fundamental frequency and intensity levels. Each vowel sample was recorded using a condenser microphone (Sennheiser) and a digital tape recorder (Tascom, DA-30) in a sound treated booth.

All recordings were low-pass filtered ($f_c = 7.5$ kHz) and digitized into a computer at a sampling rate of 16 kHz and 16-bit A/D resolution. One of the three /ɑ/ vowels for each subject was selected as the representative production for that subject. A 200-ms, stable segment from each voice sample was visually identified and selected using a waveform editor. These selected voice samples were subjected to the acoustic analyses of interest.

3. HNR computation in the time domain

The modified approach described by Qi *et al.* (1995b) was used to obtain estimates of HNR in the time domain. Zero-phase transformation was used to achieve time-normalization of period ensembles. Zero-phase transformation is preferable to dynamic programming, in part, because it is simpler to implement, faster to compute, and, thus is potentially easier to apply in voice research and clinical evaluation of voice disorders. In addition, zero-phase transformation has an accuracy equivalent to dynamic programming based time-normalization, when errors in fundamental period determination are small (Qi *et al.*, 1995b).

Period boundaries of synthetic signals were obtained from the synthesis program. Period boundaries of human voice samples were identified using a time-delayed, peak-picking algorithm. Time delay was introduced to ensure correct determination of global, rather than local, maximum (or minimum) within a given range. Visual inspection indicated that boundaries between fundamental period were determined reasonably accurately for all human voice samples.

The computation of the zero-phase transformation is fully described in a previous report (Qi *et al.*, 1995b). Briefly, zero-phase transformation consists of the following:

Identifying period boundaries of a voice segment.
Computing the period-synchronized, zero-padded fast Fourier transformation (FFT) for each period.
Computing the magnitude spectrum and setting the phase of all frequency components to zero.
Inversely transforming the zero-phased magnitude spectrum.

Finally, HNR was computed as the ratio between the energy of the average waveform and the energy of the variance of the time-normalized, period ensemble.

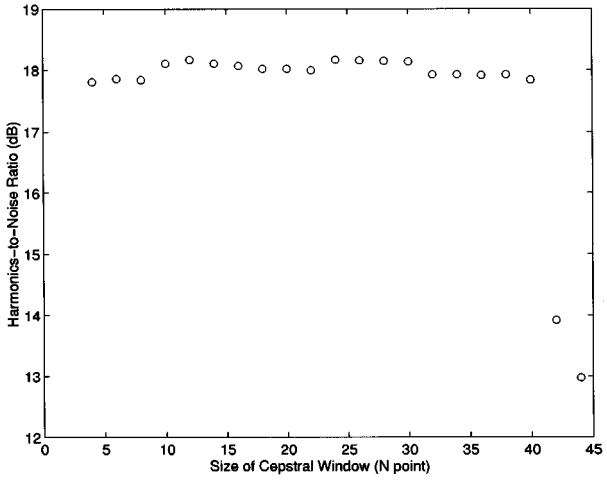

FIG. 6. The HNR as a function of cepstral window length.

4. HNR computation in the frequency domain

Computation of HNR in the frequency domain consists of the following:

Computing the DFT (3200 point) spectrum of a windowed signal segment.

Identifying the harmonic peaks using a frequency-delayed, peak-picking algorithm. The frequency delay was introduced to ensure that each peak located was global within a given frequency range of the spectrum.

Computing the cepstrum of the same signal segment.

Applying a cepstral window to lifter out the high-quefrency part of the cepstrum.

Inversely transforming the liftered cepstrum to obtain an estimation of the smoothed reference noise level.

Finally, HNR was computed as the mean difference between the harmonic peaks and the reference levels of noise at these peak frequencies.

An important parameter in this process is the size of the cepstral window, L. It determines the amount of high-quefrency components that are included in the estimation of reference noise levels. It should be large enough to adequately model the variations of the spectral envelope, but small enough to exclude cepstral peaks. Fortunately, it is relatively stable over a range of values. A constant $L=24$ (1.5 ms) was used in the present analysis. Examples of HNR estimates as a function of L are shown in Fig. 6 for a female voice sample ($F0=275$ Hz). This figure illustrates the relative stability of HNR estimates across a wide range of cepstral window sizes.

II. RESULTS

HNR estimations of the synthetic signals as a function of noise level are illustrated in Fig. 7(a) and (b). As shown, the time-domain estimates of HNR of synthetic signals appear to be more accurate than the frequency-domain HNR estimations of these synthetic signals. Frequency-domain HNR estimations are further away from the diagonal at low noise

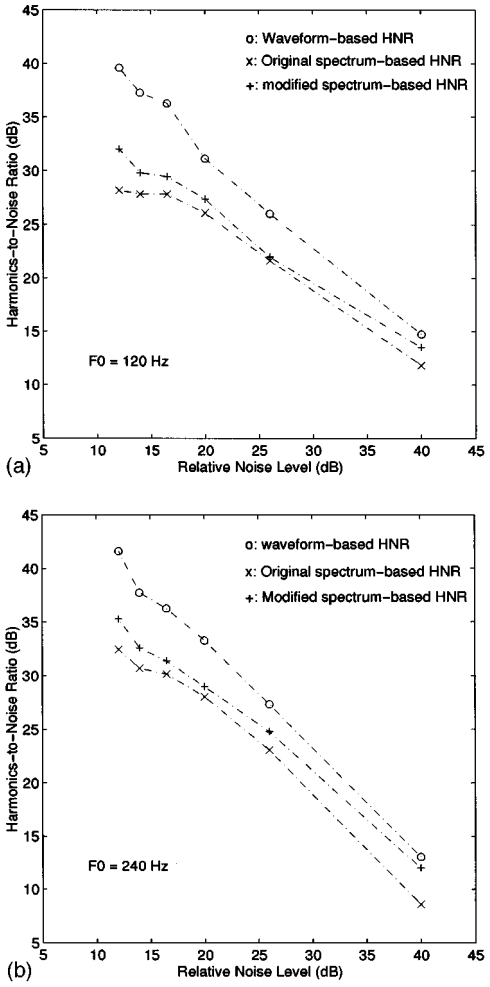

FIG. 7. The HNR as a function of noise level for synthetic signals.

levels than they are at high noise levels. Modified frequency-domain HNR estimation may be slightly better than the de Krom-based frequency-domain HNR estimation of these synthetic signals.

The HNRs of human voice signals that were computed using our modified algorithm in the frequency domain are shown as a function of HNRs computed using the zero-phase transformation based algorithm in the time domain (Qi *et al.*, 1995b) in Fig. 8. The dashed line in Fig. 8 is the least-square regression line. For comparison, the HNRs that were computed using the frequency-domain algorithm proposed by de Krom (a three-point bandwidth was used for liftering cepstral peaks) are plotted as a function of zero-phase transformation based time-domain estimates for the same set of human voice signals in Fig. 9.

Spearman correlational analyses of measurements of the human voice signals indicate that our modified frequency-domain-based estimates were significantly correlated with the time-domain-based estimates of HNR ($r=0.88$, $p<0.0001$). There was also a significant correlation between the frequency-domain estimate of HNR proposed by de Krom (1993) and the modified time-domain-based estimation ($r=0.57$, $p<0.0001$). It is obvious, however, that our modified frequency-domain approach yielded a much stronger correlation with the time-domain estimate of HNR than de Krom's (1993) method. Our method accounts for roughly

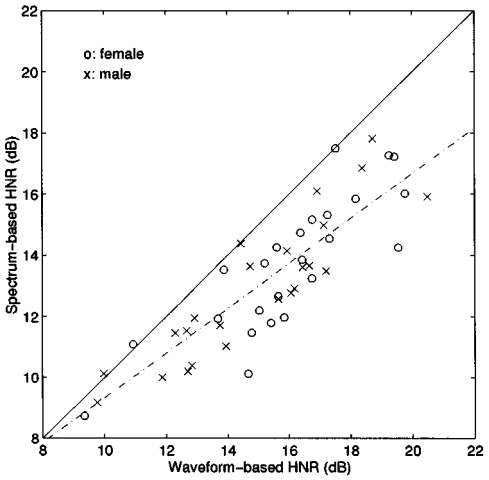

FIG. 8. The modified frequency-domain HNR as a function of the time-domain HNR for human voice signals.

77% of the variance ($r^2=0.77$) in the time-domain-based estimates, compared to 33% ($r^2=0.33$) accounted for by de Krom's approach. Finally, it should be noted that the slope of the least-square regression lines was smaller than unity in both sets of data (see Figs. 8 and 9), although it is closer to unity for our modified method than for de Krom's approach. Overall, estimates of HNR for the human voice signals in the frequency domain tend to be smaller than those in the time domain.

III. DISCUSSIONS AND CONCLUSIONS

A modified algorithm for computing HNR in the frequency domain was developed and tested. Modifications were aimed at reducing the influence of spectral leakage in the computation of harmonic energy and removing the necessity of spectral-baseline shifting prescribed in the existing algorithm (de Krom, 1993). The modified frequency-domain estimation of HNR was compared to time-domain estimation. A significant linear relationship between time and frequency estimations of HNR was established for human voice signals, suggesting equivalency between our modified time- and frequency-domain estimations of HNR. Because frequency-domain HNR has a number of advantages discussed previously, it may be preferable for many practical applications.

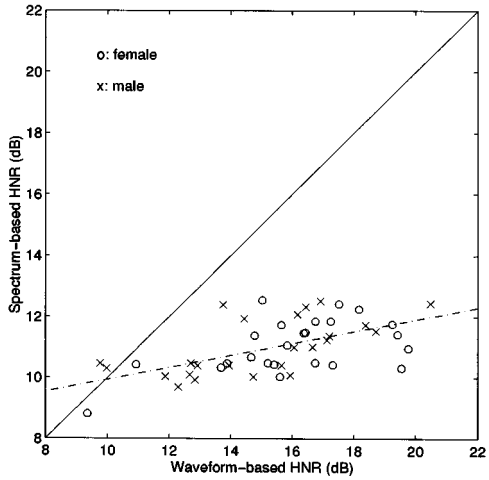

FIG. 9. The original frequency-domain HNR as a function of the time-domain HNR for human voice signals.

The correspondence between time- and frequency-domain estimation of HNR in human voice signals was not perfect, i.e., the slope of the regression line relating the two was not unity for human voice signals. Two factors may contribute to reducing the slope of the regression line between time- and frequency-domain estimates:

(1) Time-normalization of the period ensemble may have exaggerated the similarity between individual periods of the waveform, resulting in a slight overestimation of HNR in the time domain.
(2) Spectral leakage may have reduced the magnitude of harmonics in the process of estimating HNR in the frequency domain, resulting in a slight underestimation of HNR.

It is important to be aware of the differences between frequency- and time-based estimation of HNR and the possible origins of such differences.

The establishment of a highly significant, linear relationship between time- and frequency-domain estimations of HNR suggests to us that it should be productive to further explore the use of these measurements to define physical properties of human voice signals. Claims about the validity of these measurements are not warranted. Validation of these measurements depends on our ability to synthesize signals that are true representations of normal/pathological voices. This is difficult to accomplish because of our lack of complete understanding of normal/pathological voice production. For example, voice signals usually are synthesized using a linear, source-filter system that ignores the interactions between source and filter. Such synthetic signals are relatively simple to analyze, but are not complete representations of human voice signals. It is even more challenging to synthesize various pathological voices. Our aim was to demonstrate that the frequency-domain HNR measurement developed and tested here is in better compliance with the time and frequency equivalency principle of signal analysis than the existing frequency-domain approach.

ACKNOWLEDGMENTS

This work was supported, in part, by grants from the National Institute of Deafness and Other Communication Disorders: (1) DC01440, Analysis and Improvement of Alaryngeal Speech, and (2) DC00266, Objective Assessment of Vocal Hyperfunction.

Childers, D., and Lee, C. (**1991**). ''Vocal quality factors: Analysis, synthesis, and perception,'' J. Acoust. Soc. Am. **90,** 2394–2410.

Cox, N. B., Ito, M., and Morrison, M. D. (**1989**). ''Technical considerations in computation of spectral harmonics-to-noise ratios for sustained vowels,'' J. Speech Hear. Res. **32,** 203–218.

de Krom, G. (**1993**). ''A cepstrum-based techniques for determining a harmonics-to-noise ratio in speech signals,'' J. Speech Hear. Res. **36,** 254–266.

Diaz, J., Hillman, R., Gress, C., Bunting, G., and Doyle, P. (**1993**). ''Voicebase: A clinical and research database for voice disorders,'' ASHA **35**, 183.
Emanuel, F. (**1991**). ''Spectral noise,'' Sem. Speech Language **12**, 115–130.
Fant, G. (**1960**). *Acoustic Theory of Speech Production* (Mouton, S-Gravenhage).
Fant, G., Liljencrants, J., and Lin, Q. G. (**1985**). ''A four-parameter model of glottal flow,'' STL-QPSR **4**, 1–12.
Hillenbrand, J., Cleveland, R., and Erickson, R. (**1994**). ''Acoustic correlates of breathy vocal quality,'' J. Speech Hear. Res. **37,** 769–778.
Kasuya, H., Ogawa, S., Mashima, K., and Ebihara, S. (**1986**). ''Normalized noise energy as an acoustic measure to evaluate pathologic voice,'' J. Acoust. Soc. Am. **80,** 1329.
Kay-Elemetrics (**1994**). *Voice and Speech Laboratory—Massachusetts Eye and Ear Infirmary—Voice Disorders Database* (Kay Elemetrics, Lincoln Park, NJ).
Klatt, D., and Klatt, L. (**1990**). ''Analysis, synthesis, and perception of voice quality variations among female and male talkers,'' J. Acoust. Soc. Am. **87,** 820–857.
Muta, H., Baer, T., Kikuju, W., Tervo, M., and Fukuda, H. (**1988**). ''A pitch-synchronous analysis of hoarseness in running speech,'' J. Acoust. Soc. Am. **84,** 1292–1301.
Oppenheim, A., and Schafer, R. (**1989**). *Discrete-Time Signal Processing* (Prentice-Hall, Englewood Cliffs, NJ).
Qi, Y. (**1992**). ''Time-normalization in voice analysis,'' J. Acoust. Soc. Am. **92,** 2569–2576.
Qi, Y., and Bi, N. (**1994**). ''A simplified approximation of the four-parameter LF model of voice source,'' J. Acoust. Soc. Am. **96,** 1182–1185.
Qi, Y., and Shipp, T. (**1992**). ''An adaptive method for tracking voicing irregularities,'' J. Acoust. Soc. Am. **91,** 3471–3477.
Qi, Y., Weinberg, B., and Bi, N. (**1995a**). ''Enhancement of female esophageal and tracheoesophageal speech,'' J. Acoust. Soc. Am. **97,** 2461–2465.
Qi, Y., Weinberg, B., Bi, N., and Hess, W. J. (**1995b**). ''Minimizing the effect of period determination on the computation of amplitude perturbation in voice,'' J. Acoust. Soc. Am. **97,** 2525–2532.
Yumoto, E., Gould, W., and Baer, T. (**1982**). ''Harmonics-to-noise ratio as an index of the degree of hoarseness,'' J. Acoust. Soc. Am. **71,** 1544–1550.

A model of lingual coarticulation based on articulatory constraints

Daniel Recasens
Laboratori de Fonètica, Institut d'Estudis Catalans, c/Carme 47, Barcelona 08001, Spain and Universitat Autònoma de Barcelona, Bellaterra, Barcelona, Spain

Maria Dolors Pallarès and Jordi Fontdevila
Laboratori de Fonètica, Institut d'Estudis Catalans, c/Carme 47, Barcelona 08001, Spain

(Received 27 December 1995; accepted for publication 14 February 1997)

The magnitude and temporal extent of consonantal and vocalic coarticulation are reported for VCV sequences with two vowels (/i/, /a/) and seven consonants (/p/, /n/, dark /l/, /s/, /ʃ/, /ɲ/,/k/). Different degrees of articulatory constraint, or DAC values, are assigned to the consonants and vowels based on knowledge of their articulatory properties, in particular, the degree of involvement of the tongue dorsum in closure or constriction formation. Mean results on dorsopalatal contact and $F2$ frequency for five speakers of the Catalan language are presented. Predictions based on the DAC value for consonants and vowels account satisfactorily for the C-to-V effects (e.g., those for /ɲa/ are more prominent that those for /pi/); moreover, vowel-dependent effects tend to be negatively correlated with the DAC value for the consonant (e.g., they are more prominent when the intervocalic consonant is /p/ than when it is dark /l/). V-to-C effects are also conditioned by the tongue-dorsum position for the consonantal gesture. Coarticulatory directionality trends reveal that the extent to which the vowel-dependent tongue-dorsum activity may be anticipated is closely linked to the mechanico-inertial constraints associated with the tongue dorsum during consonantal production; this observation explains the salience of the vowel-dependent anticipatory effects in VCV sequences favoring C-to-V anticipation and of the vowel-dependent carryover effects in VCV sequences giving special weight to C-to-V carryover.
[S0001-4966(97)03106-8]

PACS numbers: 43.70.Aj, 43.70.Bk [AL]

INTRODUCTION

Two general principles of segmental overlap in a phonetic string have been proposed in the literature: The extent to which a vowel falls short of its target (i.e., the amount of undershoot) increases with the distance between the articulatory targets for the vowel and for the adjacent consonant (Stevens *et al.*, 1966), and coarticulation on consonants affects mostly those articulators which are not involved in closure or constriction formation (Öhman, 1966). There is, however, no model that predicts how much coarticulation is allowed by a given phonetic segment, or the extent to which a particular phonetic segment is likely to affect the surrounding segments in the speech chain. The aim of this paper is to present such a model by examining the relative salience of the C-to-V, V-to-C, and V-to-V coarticulatory effects in Catalan VCV sequences with several consonants (bilabial stop /p/, alveolar nasal /n/, dark alveolar lateral /l/, alveolar fricative /s/, alveolopalatal fricative /ʃ/, alveolopalatal nasal /ɲ/, velar stop /k/) and vowels (high front /i/, low back /a/). Our work is mostly concerned with tongue-dorsum activity[1] since two of the variables under investigation, i.e., dorsopalatal contact and $F2$, are known to be positively correlated.[2]

Spatiotemporal patterns of tongue-dorsum coarticulation should be of general interest for theories of articulatory control in speech production in so far as they have received less attention than those for more mobile articulators such as the lips or the velum (e.g., Krakow, 1989; Boyce, 1990) presumably because it was believed that labial and velar coarticulation would be more extensive than lingual coarticulation. In many respects the coarticulatory patterns presented in this paper ought to have a universal status (although some coarticulation aspects may differ across languages; Beddor and Yavuz, 1995) and may prove useful in predicting the frequency of occurrence of some assimilatory processes (i.e., it may turn out that phonetic segments more prone to undergo assimilations exhibit prominent coarticulatory effects along the relevant articulatory dimensions).

A. Articulatory constraint

In the present study phonetic segments are characterized in terms of articulatory gestures. An articulatory gesture is an actively controlled movement toward a presumed target configuration (e.g., lip rounding for rounded vowels, tongue-dorsum raising for palatal articulations) (Browman and Goldstein, 1986). Phonetic segments may be produced with one or two lingual gestures and thus with one or more lingual articulators (e.g., the tongue tip for /t/, the tongue tip and the tongue dorsum for dark /l/). The biomechanics of the lingual articulator(s) may cause some displacement on other tongue regions. Thus the strength of the coupling effects between the tongue tip or the tongue blade and the tongue dorsum should increase with an increase in the retraction and the

extent of the apicolaminal closure or constriction, for alveolopalatals versus alveolars and for laminoalveolars versus apicoalveolars.

These notions are clearly related to a core concept within our descriptive framework, i.e., degree of articulatory constraint (DAC).[3] The formulation of the concept DAC derives from assumptions about the degree of involvement of the speech articulators in the formation of a closure or constriction based on information obtained from experimental production data, e.g., data on articulatory displacement and linguopalatal contact. As shown below, the consonants and vowels of interest in this paper will be assigned different DAC values depending on the degree of tongue dorsum constraint during their production. The DAC scale proceeds from a DAC minimum of 1 to a DAC maximum of 3, where the number of levels could be any other than 3; the assignment process of DAC values to vowels does not differ from that used for consonants and implies that vowels may exhibit constriction locations along the vocal tract (Wood, 1979).

Dorsals, i.e., alveolopalatals /ʃ/ and /ɲ/, palatal /i/, velar /k/, and dark /l/, are maximally constrained and thus specified for a maximal DAC value (DAC=3). Considerable tongue-dorsum involvement in the production of all these consonants renders them highly constrained: Alveolopalatals and palatals are articulated with active tongue dorsum raising toward the palatal zone where they cause large amounts of contact (Recasens, 1990; Recasens and Romero, 1997) and dorsovelars share similar kinematic properties; the production of dark /l/ involves two lingual gestures, i.e., tongue tip raising for a primary apicoalveolar closure and active tongue postdorsum retraction for a secondary dorsopharyngeal constriction (Sproat and Fujimura, 1993).

Labial /p/ is minimally constrained and thus specified for a minimal DAC value (DAC=1). This is so since the tongue body may not be required to achieve an articulatory target. Its obvious correlate in the vowel class is /ə/ which appears to be more sensitive to contextual effects than other vowels (Dutch: Bergem, 1994; English: Kondo, 1994) although it has been reported to exhibit an articulatory target at a neutral tongue position (Browman and Goldstein, 1992).

An intermediate degree of tongue-dorsum constraint and thus an intermediate DAC value (DAC=2) can be tentatively assigned to phonetic segments for the production of which the tongue dorsum is not directly involved in closure or constriction formation but is subject to coupling effects with the primary articulator. This would be the case for alveolars /n/ and /s/ (in accordance with tongue blade raising for these consonants causing some tongue dorsum raising to occur; Kent and Moll, 1972; Lindblom, 1983) and for low back /a/ (in view of the tongue root retraction gesture for this vowel bringing about some concomitant tongue dorsum lowering).

In addition to the place of articulation and interarticulatory coupling, the manner of articulation may also affect the DAC specification for consonants. Thus, the precise formation of a medial groove for fricatives (e.g., Stone *et al.*, 1992) should render /s/ more constrained than nonfricative alveolars which would cause this consonant to exhibit a DAC value of 3 instead of 2.

To summarize, the DAC scale ranks phonetic sound categories from maximally to minimally constrained as follows: /ʃ/, /ɲ/, /i/, /k/, dark /l/, (/s/) (DAC=3)>/n/, /a/, (/s/) (DAC=2)>/p/, /ə/ (DAC=1). It needs to be emphasized that this is a preliminary DAC classification which could be improved with a more accurate formulation of the articulatory constraints for consonants and vowels.

B. Specific coarticulatory effects

1. C-to-V coarticulation

DAC values should have a bearing on the extent to which a given segment will influence adjacent segments, and the final outcome will also depend on the DAC value for the contextual segment and whether the constraints involved are compatible or opposing. Within this framework, a first goal of this study is to investigate the prominence of the consonant-to-vowel effects (C-to-V) in the three scenarios described below and to determine interactions between the magnitude and the temporal extent of C-to-V coarticulation (Sec. II A).

The first scenario is at work when C and V are produced with comparable articulatory trajectories, as for /ɲi/, /ni/, and /la/ since /ɲ/, /n/, and /i/ involve tongue-dorsum raising (as a consequence of coupling between the tongue tip and the tongue dorsum for /n/) and /l/ and /a/ are produced with tongue-dorsum lowering. Little C-to-V coarticulation is expected to occur for /ɲi/ and /ni/ since both phonetic segments are either specified for the same DAC value (i.e., DAC=3 for /ɲ/ and /i/ in the sequence /ɲi/) or the vowel is more constrained than the consonant (i.e., DAC=3 for /i/ and DAC=2 for /n/ in the sequence /ni/). Some C-to-V effects should occur when the consonant is more constrained than the vowel especially if highly constrained (i.e., DAC=3 for /l/ and DAC=2 for /a/ in the sequence /la/). An interesting research topic is to find out whether such effects will be more or less salient than those occurring in CV combinations of antagonistic phonetic segments exhibiting the same DAC relationship (as for /ɲa/ below).

C and V are produced with opposing articulatory trajectories in a second scenario, as for /ɲa/, /na/, and /li/ where /ɲ/, /n/, and /i/ involve tongue-dorsum raising and dark /l/ and /a/ involve tongue-dorsum lowering. The sequence /ɲa/ should show some C-to-V coarticulation since the DAC value for the consonant (DAC=3) exceeds that for the vowel (DAC=2). In principle, little C-to-V coarticulation is expected to occur if both segments are specified for the same DAC value, i.e., 2 in the sequence /na/ or 3 in the sequence /li/. It deserves to be seen, however, whether constriction requirements for consonants yield C-to-V effects in these circumstances and whether these effects increase with the degree of antagonism between C and V (i.e., for /li/ vs /na/).

One of the two adjacent phonetic segments is specified for DAC=1 in a third scenario, as for /pi/ where the consonant involves no tongue dorsum activation. This segmental combination should yield minimal C-to-V effects.

2. Vowel-dependent coarticulation

The coarticulatory analysis presented in this paper also examines the salience of the vowel-dependent effects as a function of the seven consonants of interest (Sec. II B). For that purpose, the magnitude of the effects from /i/ vs /a/ will be measured during the consonant (V-to-C), and their size and temporal extent as well as the interaction between the two will be computed along the fixed transconsonantal vowel /i/ or /a/ (V-to-V).[4]

Tongue-dorsum related data in the literature are in accordance with the prediction that coarticulatory sensitivity for consonants and vowels is inversely related to their DAC value. Using the same dataset as in the current study, V-to-C effects in symmetrical VCV sequences reported in Recasens *et al.* (1995) show that variability for consonants proceeds in the progression labials>dentoalveolars >alveolopalatals, dark /l/ and /s/; many other production studies reveal the same trend [see Recasens (in press) for a review]. On the other hand, the degree of coarticulatory sensitivity for vowels decreases for /ə/>/a/>/i/ (Kiritani *et al.*, 1977; Recasens, 1985, 1991a). More tongue-dorsum coarticulation for velars than other dorsal consonants is in agreement with their showing a palatovelar constriction in front vowel contexts and a velar one in back vowel contexts (Swedish: Öhman, 1966; American English: Kent and Moll, 1972). This finding does not run against consonantal segments specified for a high DAC value allowing little vowel coarticulation but appears to be due to the consonant and the vowel not being able to achieve adjacent tongue-dorsum targets unless the consonantal constriction moves toward that for the vowel (Wada *et al.*, 1970).

As indicated by data in the literature (Gay, 1974, 1977; Carney and Moll, 1971; Recasens, 1984, 1987, 1989), the relationship between coarticulatory sensitivity and DAC becomes more complex when V-to-V effects are accounted for. It appears that the occurrence of these effects is conditioned not only by the DAC specification for the intervocalic consonant but also by that of the fixed vowel. The prediction will be tested that consonant-dependent differences in V-to-V coarticulation (e.g., for effects across bilabials exceeding those across alveolopalatals) should occur when the fixed vowel is not highly constrained (e.g., /a/) but could be cancelled out if the fixed vowel is specified for a maximal DAC value (e.g., /i/).

While DAC is a potential predictor of coarticulatory sensitivity, the present study will also test for a large number of consonants whether articulatory position determines the articulatory dimension along which coarticulation occurs (Sec. II B 3). Preliminary data from the literature indicate that C-to-V effects on high vowels involve tongue lowering while those on low vowels cause the tongue dorsum to raise and that V-to-C effects are determined by the target lingual position for the consonant (Recasens, 1987, 1991a, b). Thus the fact that the production of /ɲ/ (also /k/) requires the achievement of a dorsal closure justifies why this consonant allows larger tongue-dorsum raising and fronting effects associated with V2=/i/ in the sequence /aɲi/ than tongue-dorsum lowering and backing effects associated with V2 =/a/ in the sequence /iɲa/; also, consonants produced with active tongue-dorsum lowering such as dark /l/ are more sensitive to lowering effects associated with following /a/ in the sequence /ila/ than to raising effects exerted by following /i/ in the sequence /ali/.

It will also be investigated whether there is an inverse correlation between the vocalic effects and the consonantal effects, and thus whether context-dependent sensitivity for a given phonetic segment varies inversely with coarticulatory aggression on the adjacent phonetic segments (Fowler and Saltzman, 1993).

C. Coarticulatory directionality

A novelty of the present investigation is to analyze the relative prominence of the anticipatory direction (right-to-left) and the carryover direction (left-to-right) for the consonantal and the vocalic effects in VCV production. This analysis will be carried out with reference to the DAC value for the phonetic segments involved and will evaluate whether coarticulatory direction is conditioned by the gestural demands for the intervocalic consonant (Sec. II C). There is some evidence in the literature in support of the notion that the prominence of the anticipatory and carryover component of consonantal coarticulation varies with the lingual requirements for the consonant and determines the directionality of the vocalic effects [see Recasens (in press) for a review]. Evidence on C-to-V coarticulation reveals that, among consonants specified for a high DAC value, some exert more prominent carryover than anticipatory effects (dorso-alveolopalatals, in line with tongue-dorsum activity proceeding more slowly at consonantal release than at consonantal onset) while others require a strong anticipatory component (dark /l/, in line with strong demands on the formation of a double lingual constriction). Within this framework the direction of the vocalic effects shows the following trends whose validity will be tested in the present paper: On the one hand, vowel-dependent carryover effects exceed vowel-dependent anticipatory effects across consonants exerting more prominent carryover than anticipatory C-to-V coarticulation; on the other hand, consonants requiring a strong anticipatory component allow more prominent vowel-dependent anticipatory than carryover effects or exhibit a significant reduction of the latter in comparison to the former. Special attention will be given to those consonants (bilabials, dentoalveolar stops, fricatives, clear /l/) which have been reported to favor either coarticulatory direction in previous studies.

I. METHOD

A. Articulatory and acoustic analysis procedure

*F*2 and linguopalatal contact data were collected for /iCi/, /aCa/, /iCa/, and /aCi/ with stress on the first syllable.[5] As indicated in the Introduction, the consonants were /p/, /n/, (dark) /l/, /s/, /ʃ/, /ɲ/, and /k/. Sequences were read five times each by five Catalan speakers (DR, JP, JS, DP, JC). In Catalan, unstressed /a/ (i.e., V2 in the sequences of the present study) is realized as [ə] systematically. Differences in quality

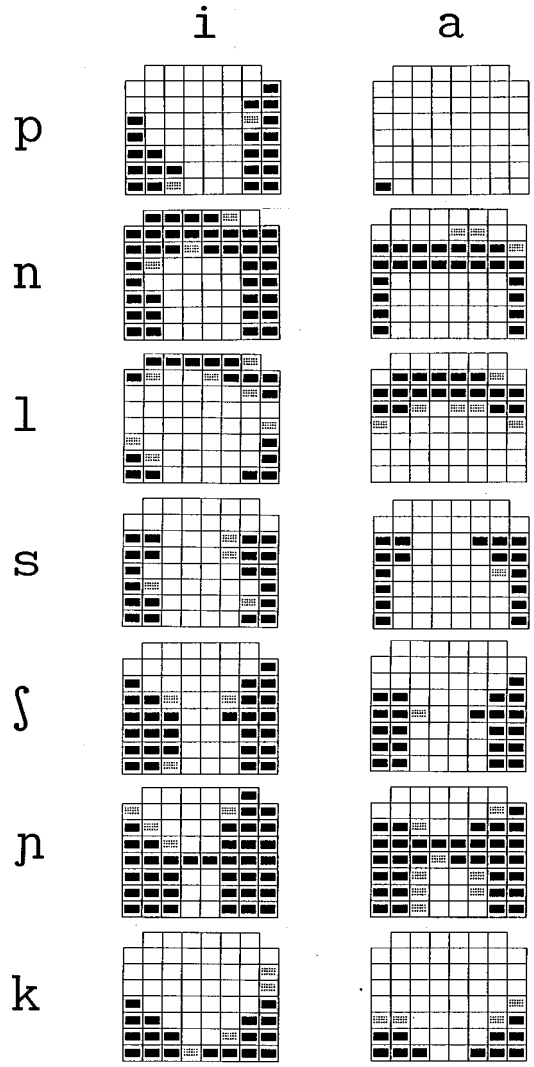

FIG. 1. Linguopalatal configurations at consonantal midpoint for different consonants in symmetrical VCV sequences (speaker DR). Data have been averaged across repetitions. Percentages of electrode activation: (black) 80%–100%; (dotted) 40%–80%; (white) less than 40%.

between V1 and V2 do not render the /aCa/ sequences fully symmetrical, although we will refer to them as such all throughout the paper.[6]

Linguopalatal contact was gathered every 10 ms using artificial palates equipped with 62 electrodes [Reading electropalatographic (EPG) system; Hardcastle *et al.*, 1989]. Figure 1 displays average linguopalatal configurations for each consonant. The four front rows at the top of each EPG display belong to the alveolar zone (extending from the teeth to the alveolar ridge) and the four back rows belong to the palatal zone (from the alveolar ridge back to the soft palate). The graphic representations in the figure do not capture the fact that the distance between adjacent rows is smaller at the former zone than at the latter.

The EPG data reported in this paper will be expressed in *Qp* values, where *Qp* stands for the percentage of contact activation over the palatal zone, i.e., number of activated palatal electrodes/total number of palatal electrodes. The *Qp* index has been computed using the four back rows of the artificial palate in the case of /l/ but the three back rows in the case of /n/, /s/, /ʃ/, and /ɲ/, since a central closure or constriction at the frontmost row of the palatal zone is generally absent for the alveolar lateral but frequently present for the two nasals and for the two fricatives.[7] The *Qp* index for /k/ and /p/ has also been calculated without taking into account the aforementioned row given that the contact pattern at the three back rows of the artificial palate provides an adequate and sufficient articulatory characterization of velars and bilabials in the context of /i/.

The acoustic data were recorded at a 20-kHz sampling rate. *F*2 values were obtained at the same temporal intervals as the EPG data using LPC (25-ms Hamming window, 12 coefficients) and visual inspection of spectrographic displays on a Kay CSL analysis system. The latter method was applied instead of the former when an unsatisfactory resolution was provided by the all-pole peak picking LPC method, i.e., at the VC boundary of VCV sequences with nasal consonants (because of the presence of spectral discontinuities associated with nasal poles and zeros) and during the consonantal period in VCV sequences with fricatives /s/ and /ʃ/ (because of the presence of frication noise at low spectral regions). *F*2 frequencies were measured using a cursor moving in 20-Hz steps after careful inspection of the spectrographic patterns by two experimenters.

An EPG criterion was used in order to determine the consonantal boundaries for /l/ and for /n/ and /ɲ/, i.e., from onset to offset of central alveolar contact for the lateral and of complete closure for the nasal stops. However, the segmentation of /s/, /ʃ/, /p/, and /k/ was performed on waveform and spectrographic displays, from onset to offset of the frication noise for the two fricatives (it was often hard to identify a well-defined period based on the degree of constriction narrowing on the linguopalatal contact patterns) and from offset of V1 formant structure to closure offset at the stop burst for the two stops (bilabial /p/ shows no lingual activity and complete closure /k/ was not visible when occurring behind the palatal zone).

B. Criteria for measuring coarticulatory effects

Coarticulatory effects were calculated in size (C-to-V, V-to-C, V-to-V) and temporal extent (C-to-V, V-to-V) according to the measurement criteria summarized next.

1. C-to-V coarticulation

C-to-V temporal effects were taken to occur during the period when a significant consonant-related acoustic or articulatory difference extends into the vowel. In order to obtain such effects, *Qp* and *F*2 frequency values were first computed for all repetitions of /iCi/ and /aCa/ for each speaker in 10-ms steps starting at the consonantal onset back to V1 onset and at the consonantal offset until V2 offset. No data were collected for *Qp* effects from /l/ on /a/ since little or no linguopalatal contact occurs along this vowel in this consonantal environment. The resulting values were then compared statistically (one-way ANOVAs, Scheffé; $df_{bg}=1$, $df_{wg}=4$) with a measure of steady-state V1 of the same symmetrical VCV sequence type for studying C-to-V1 an-

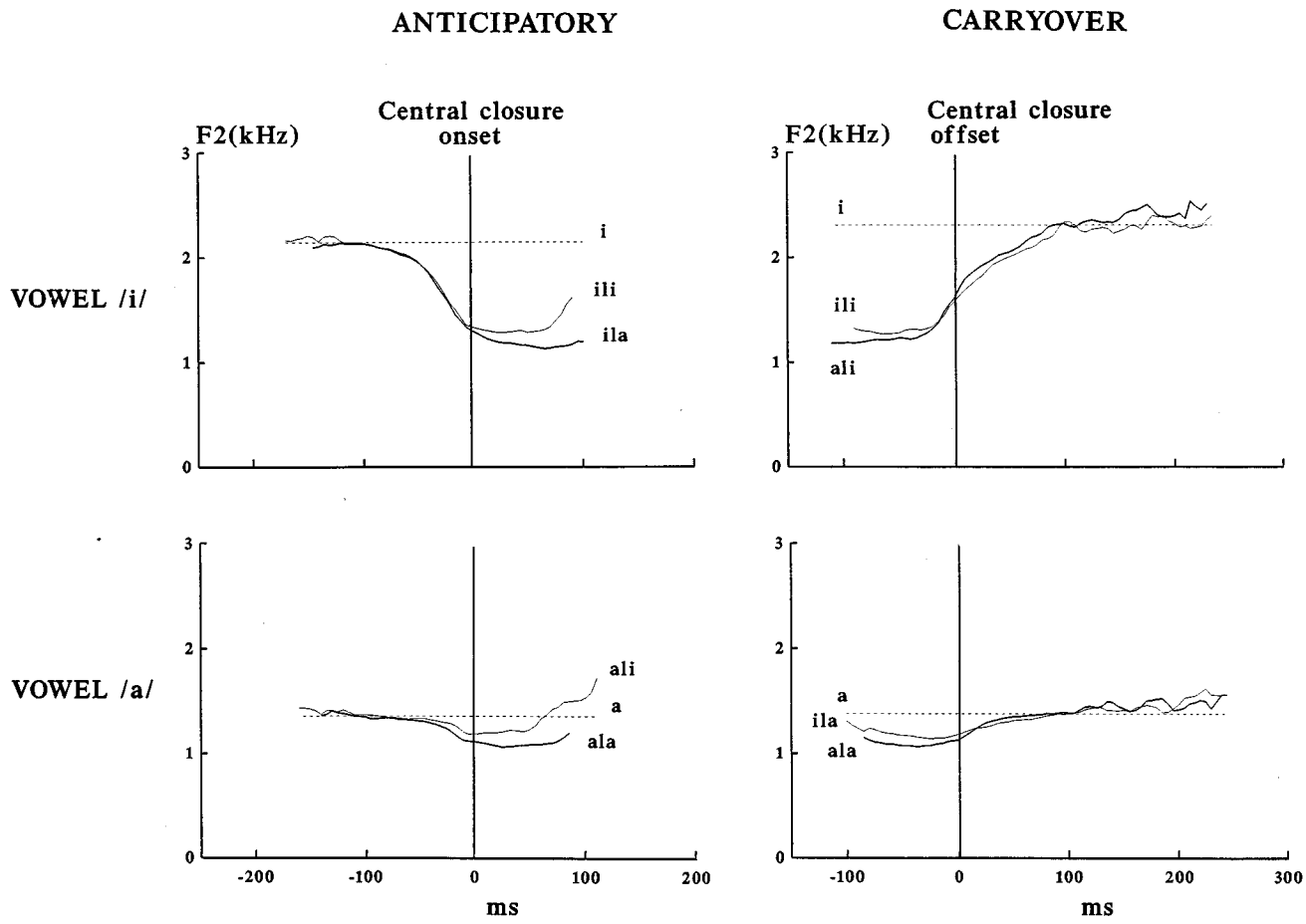

FIG. 2. *F*2 trajectories showing anticipatory effects (left) and carryover effects (right) in a single repetition of /VIV/ sequences with fixed /i/ (top) and fixed /a/ (bottom). Data correspond to speaker JP. The zero point on the *x* axis occurs at /l/ central closure onset for the anticipatory effects and at central closure offset for the carryover effects. See text for details.

ticipation and of steady-state V2 for studying C-to-V2 carryover. For each repetition of a given symmetrical VCV sequence, steady-state vowel values were established at the highest *Qp* and *F*2 for /i/ and at the lowest *Qp* and *F*2 for /a/, starting at the vowel midpoint backward in the case of V1 and at two-thirds of the vowel duration onward in the case of V2. Those maxima were found either at a single temporal frame or along a plateau lasting several frames; the selection of a different temporal criterion for V1 and V2 is justified by the fact that (sentence-final) V2 was longer than V1 and the V2 steady-state period was located further away from the consonantal period than the V1 steady-state period. The steady-state V1 and V2 values for each VCV sequence type represent the average across values for the individual repetitions of that sequence. The last significant difference obtained in the statistical analysis procedure ($p<0.05$) was taken to be the onset of C-to-V1 anticipatory coarticulation when the vowel being measured was V1 and the offset of C-to-V2 carryover coarticulation when the vowel subject to measurement was V2. Onsets and offsets of the C-to-V effects for each VCV sequence type were separately averaged across speakers; the resulting averages will be used as a measure of C-to-V temporal coarticulation in this paper.[8]

Figure 2 exemplifies the method of analysis of the C-to-V effects exerted by dark /l/ on /i/ (top) and on /a/ (bottom). A dotted line has been traced at the estimated *F*2 value for the steady-state portion of V1 and for that of V2. A statistical comparison between the steady-state value and all other *F*2 frequency values along V1=/i/ of the sequence /ili/ (top left) yields a significant difference starting at the 0 temporal point at central closure onset back to −80 ms. The application of the same procedure to V2=/i/ yields a 80-ms long C-to-V effect after the 0 temporal point at central closure offset (top, right). Anticipatory and carryover effects on /a/ (bottom) were found to last until −70 ms and 40 ms, respectively.

The largest *Qp* or *F*2 difference between V1 or V2 of a symmetrical VCV sequence and the steady-state vowel value is taken to be the (positive or negative) size of a C-to-V effect. This maximal size difference usually occurs near closure onset for the anticipatory C-to-V effects and near closure offset for the carryover C-to-V effects. C-to-V size effects reported in this paper correspond to average values across repetitions and speakers for each symmetrical VCV sequence. In Fig. 2 the size of the C-to-V anticipatory effect for V1=/i/ (i.e., the largest *F*2 difference between steady-state V1=/i/ and V1=/i/ of /ili/) amounts to 811 Hz, while that of the C-to-V carryover effect for V2=/i/ equals 736 Hz. As for the /a/ condition, C-to-V size effects measure 243 Hz (anticipatory) and 254 Hz (carryover).

2. V-to-C coarticulation

V-to-C effects were measured in Qp and $F2$ size at the midpoint of the consonantal period for all consonants except for /p/ and /k/ (since oral stops exhibit no formant structure during closure). Differences were obtained for the sequence pairs /iCi/–/iCa/ and /aCi/–/aCa/ (anticipatory coarticulation) and /iCi/–/aCi/ and /iCa/–/aCa/ (carryover coarticulation), and averaged across speakers and repetitions. This experimental setting allows studying the extent to which /a/ affects the consonant when /i/ stays constant (in the sequence pairs /iCi/-/iCa/ and /iCi/–/aCi/) and how much V-to-C coarticulation is exerted by /i/ when the fixed vowel is /a/ (in the sequence pairs /aCa/–/iCa/ and /aCa/–/aCi/). Differences (positive) were computed when /i/ caused a higher Qp or $F2$ than /a/ at the consonantal midpoint. V-to-C coarticulation values reported in this paper correspond to averages across differences for each speaker; negative values (i.e., when /a/ yielded a higher Qp or $F2$ than /i/) were equated to zero in this averaging procedure. Data for each type of VCV pair were submitted to one-way ANOVAs Scheffé ($df_{bg}=1$, $df_{wg}=4$) with vowel context as the independent variable and were considered to be significant at the $p<0.05$ significance level.

3. V-to-V coarticulation

V-to-V temporal effects occur during the period along which a significant vowel-dependent articulatory or acoustic difference extends into the transconsonantal vowel. In order to single out such effects, Qp and $F2$ frequency differences as a function of /i/ vs /a/ (for /i/>/a/) were calculated for the same VCV pairs given in Sec. I B 2 every 10 ms, starting at consonantal onset back to V1 onset and from consonantal offset until V2 offset. Essentially the sequence pairs with symmetrical /iCi/ allow studying the effect of /a/ along fixed /i/ and those with symmetrical /aCa/ allow measuring the effect of /i/ along fixed /a/. Those differences were submitted to one-way ANOVAs Scheffé ($df_{bg}=1$, $df_{wg}=4$) at each temporal point during fixed V1 for studying V-to-V anticipation and during fixed V2 for studying V-to-V carryover. The last significant difference ($p<0.05$) counting backward during V1 was taken to be the onset of a V2-to-V1 anticipatory effect and the last one counting onward during V2 was taken to be the offset of a V1-to-V2 carryover effect. Data on V-to-V temporal coarticulation presented in this paper refer to the mean onset and offset times of the V-to-V effects across speakers for each VCV sequence pair.

Figure 2 illustrates the procedure for measuring V-to-V coarticulation. V2-to-V1 anticipatory effects occur when a significant difference between the pairs of $F2$ trajectories /ili/–/ila/ (top left) and /ali/–/ala/ (bottom left) extends before the 0 temporal point at central closure onset; significant tests for these trajectories yielded 0 ms for the former sequence pair and -40 ms for the latter. On the other hand, V1-to-V2 carryover effects take place when a significant difference between the $F2$ trajectory pairs /ili/–/ali/ (top right) and /ila/–/ala/ (bottom right) extends after the 0 temporal point at central closure offset; significant effects for both pairs were nonexistent (0 ms).

Analogously to the C-to-V effects, the size of a V-to-V effect is taken to be the largest Qp or $F2$ frequency difference and usually occurs near closure onset for the anticipatory direction and near closure offset for the carryover direction. When this difference was not significant, the size of the V-to-V effect was taken at the first temporal frame showing the expected coarticulatory difference. V-to-V size effects reported in this paper correspond to averages across speakers and repetitions. In the data of Fig. 2, the size of V-to-V anticipation is 35 Hz (/ili/–/ila/) and 79 Hz (/ali/–/ala/), and that of V-to-V carryover amounts to 0 Hz (/ili/–/ali/) and to 54 Hz (/ila/–/ala/).

C. Other statistical analyses

The size and the temporal extent of the consonantal and vocalic effects for the different consonants across speakers were also submitted to one-way ANOVAs (Scheffé) in order to determine the existence of consonant-dependent significant differences ($df_{bw}=6$, $df_{wg}=28$; $p<0.05$). For that purpose, negative C-to-V size effects were transformed into positive values and separate tests were conducted for the anticipatory and for the carryover component in each vowel condition.

Four correlation analyses involving the consonantal effects or the vocalic effects were separately performed for each vowel condition and coarticulatory direction across consonants and speakers: between the size and the temporal extent of the C-to-V effects; between the size and the temporal extent of the V-to-V effects; between the size of the V-to-C effects and the size of the V-to-V effects; between the size of the V-to-C effects and the temporal extent of the V-to-V effects. The purpose of this analysis was to investigate whether an increase in magnitude for a given coarticulatory effect was matched by an increase in duration and, less importantly, if V-to-C and V-to-V effects were strongly correlated. Four other correlations were carried out between the consonantal effects and the vocalic effects which should bear on the issue of whether vocalic coarticulation varies inversely with the DAC value for the consonant: between C-to-V size and V-to-C size; between C-to-V size and V-to-V size; between C-to-V size and V-to-V time; between C-to-V time and V-to-V time. In this paper positive or negative correlations will be taken to occur when the r value is relatively low (equal or larger than 0.70, whether significant or not) so as to make sure that no meaningful interactions between coarticulatory effects are left out.

II. RESULTS

A. C-to-V coarticulatory effects

Figure 3(a) and (b) displays Qp and $F2$ data on C-to-V coarticulation for all seven consonants and the two vowels /i/ [Fig. 3(a)] and /a/ [Fig. 3(b)]. Effects are plotted separately for C-to-V size and temporal extent and for the anticipatory direction (A; stippled bars) and carryover direction (C; black bars). The height of the bars indicates whether C-to-V effects are larger/smaller (size effects) and longer/shorter (temporal effects).[9] For example, according to Fig. 3(a), the anticipatory and carryover effects in dorsopalatal contact (Qp) from

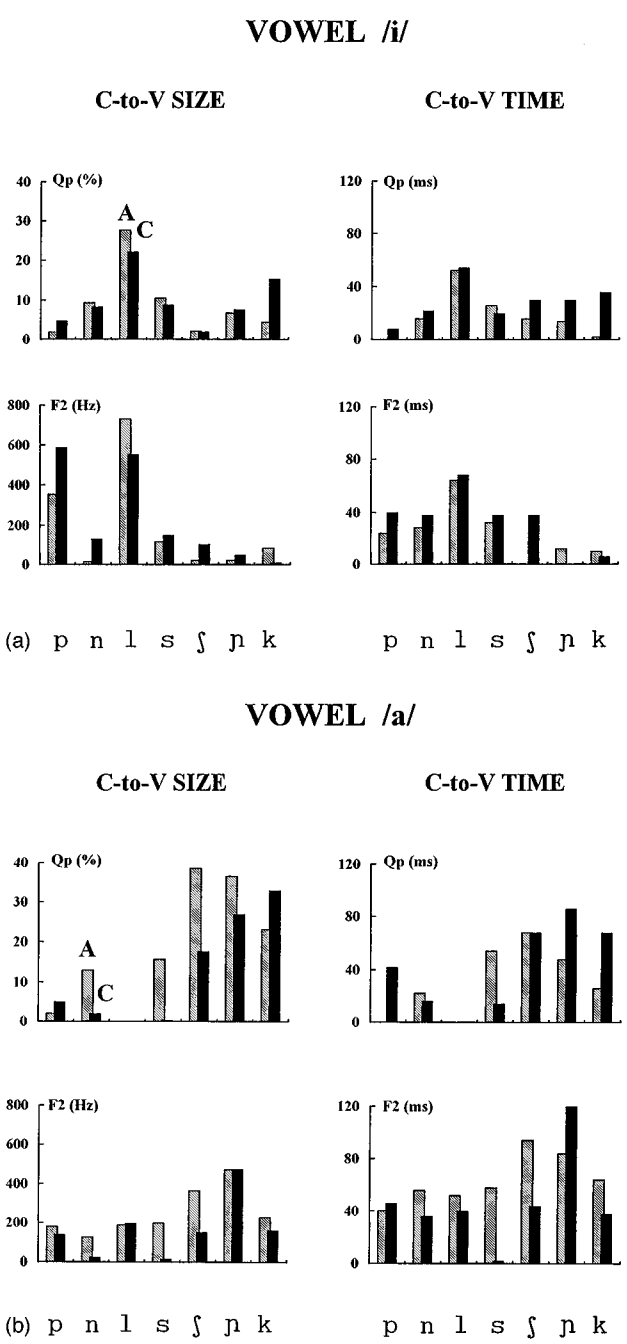

FIG. 3. (a) Mean C-to-V effects across repetitions and speakers for each consonant when the contextual vowel is /i/. Size effects in % of electrode activation and in Hz (left) and temporal effects in ms (right) are plotted separately for *Qp* (above) and *F*2 (below), and for each coarticulatory direction, i.e., anticipatory (stippled bars) and carryover (black bars). (b) Same representation as in (a) when the fixed vowel is /a/.

/l/ on /i/ are larger and longer than those exerted by other consonants and the situation for the *F*2 effects is essentially the same as that for the *Qp* effects referred to.

The numerical values for the coarticulatory effects represented in the figures are presented in Table I (means and standard errors). Size effects in the table are assigned a positive or a negative sign depending on whether the consonant causes an increase or a decrease in the *Qp* or *F*2 value for the vowel. Thus the table assigns a negative sign to the anticipatory and carryover size effects from /l/ on /i/ meaning that this consonant causes *Qp* and *F*2 to lower during V1 and V2.

1. /i/ context

According to the predictions in the Introduction section (see Sec. B 1), coarticulation should not be too prominent in sequences made of compatible consonants involving tongue-dorsum raising whether specified for the same DAC value as /i/ (i.e., 3 in the case of alveolopalatals and velars) or for a lower DAC value (i.e., 2 for alveolars excluding /l/). C-to-V effects in *Qp* and *F*2 in the figure are indeed small and short for alveolopalatals /ɲ/ and /ʃ/ and for velar /k/ although this trend is less clear for the carryover effects in *Qp* for reasons pointed out in Sec. II C 1 a.[10] According to Table I, these effects are positive (in *Qp*) and slightly positive or negative (in *F*2) which is in accordance with these consonants being articulated with a similar degree of tongue-dorsum height to that for /i/. Size and temporal effects in *Qp* and *F*2 for the alveolars /n/ and /s/ are often somewhat more prominent than those for alveolopalatals and velars which does not accord with the DAC value for alveolars being lower than that for /i/. The intermediate status of the C-to-V size effects for /n/ and /s/ is reflected by their being significantly different from those for other consonants in some cases. The negative sign of the C-to-V size effects in *Qp* and *F*2 for /n/ and /s/ (see Table I) may account for this finding: It appears that the production of these two consonants involves some lowering of the tongue predorsum (presumably because of manner requirements in the case of /s/ and of language-specific constraints in the case of /n/) which renders them not fully compatible with the tongue-dorsum raising gesture for /i/.[11]

Little C-to-V coarticulation was expected to occur as a function of /p/ since bilabials do not involve tongue-dorsum activity (DAC=1) and /i/ is specified for a maximum DAC value (3) (see Sec. B 1). *Qp* effects for bilabial /p/ in the figure are indeed small and short. C-to-V effects in *F*2 (also in *F*3) for /p/ were unexpectedly large and long; more specifically, size effects were found to be significantly larger than those for most other consonants. This outcome is probably unrelated to tongue-dorsum activity but to *F*2 and *F*3 of /i/ being highly sensitive to variations in lip rounding, i.e., to a protrusion of the lips, a decrease of their area or both (Fant, 1960). The negative sign of the *F*2 size effects in Table I is indeed related to lip closing for /p/; *Qp* size effects (which could be exclusively attributed to tongue predorsum lowering) are also negative but very small.

One scenario deserves special attention, i.e., the sequence /li/ with the participation of lingual gestures which are at the same time highly constrained (dark /l/ and /i/ are both specified for DAC=3) and antagonistic (the vowel is produced with tongue-dorsum raising and fronting and the consonant with tongue-dorsum lowering and backing) (see Sec. B 1). The figure reveals the existence of large and long C-to-V effects in this case with size effects being significantly larger than those for most other consonants. This coarticulatory outcome indicates that the requirements for a highly constrained consonant override those for a highly constrained vowel when the two phonetic segments are produced with antagonistic lingual gestures. The negative sign

TABLE I. Mean Qp and $F2$ coarticulation values across speakers and repetitions for different consonants when the fixed vowel is /i/. Data are separately displayed for the size and the temporal extent of the C-to-V, V-to-C, and V-to-V effects at the anticipatory and carryover level. Size effects are given in % of electrode activation (Qp) and in Hz ($F2$); temporal effects are given in ms. C-to-V size effects can be positive or negative (i.e., the consonant contributes to a raising or a lowering of the Qp or $F2$ frequency value for the vowel). An asterisk indicates the presence of significant V-to-C size effects ($p<0.05$). A variability measure (se=standard error) is also given.

			C to V				V to C		V to V			
			Anticipatory		Carryover		Anticipatory	Carryover	Anticipatory		Carryover	
	Vowel /i/		Size	Time	Size	Time	Size		Sice	Time	Size	Time
Qp	/p/	$\overline{X}$	−1.83	0.00	−4.83	8.00	26.67*	31.00*	3.00	0.00	11.67	70.00
		se	*1.52*	*0.00*	*1.78*	*5.83*	*1.99*	*1.43*	*1.07*	*0.00*	*1.73*	*16.43*
	/n/	X	−9.33	16.00	−8.33	22.00	13.33*	15.83*	5.50	10.00	5.00	30.00
		se	*2.73*	*10.30*	*3.11*	*10.68*	*1.86*	*1.92*	*1.20*	*10.00*	*1.21*	*20.00*
	/l/	X	−27.63	52.00	−22.13	54.00	13.38*	13.38*	6.50	14.00	4.13	2.00
		se	*0.64*	*3.74*	*3.71*	*12.49*	*3.40*	*3.39*	*2.86*	*14.00*	*2.18*	*2.00*
	/s/	X	−10.50	26.00	−8.83	20.00	8.83*	4.66	2.50	0.00	1.50	0.00
		se	*2.07*	*14.70*	*2.31*	*12.25*	*1.80*	*2.12*	*1.18*	*0.00*	*0.55*	*0.00*
	/ʃ/	X	2.17	16.00	2.00	30.00	4.00	6.83*	1.50	8.00	5.33	28.00
		se	*0.68*	*16.00*	*2.72*	*23.24*	*1.57*	*1.61*	*0.93*	*8.00*	*2.21*	*20.83*
	/ɲ/	X	6.83	14.00	7.67	30.00	0.17	12.83*	1.00	6.00	6.94	23.33
		se	*1.67*	*8.72*	*1.27*	*12.65*	*0.17*	*2.89*	*0.81*	*6.00*	*3.20*	*12.02*
	/k/	X	4.46	2.00	15.33	36.00	11.15*	4.50	3.75	6.00	1.00	0.00
		se	*2.94*	*2.00*	*4.11*	*9.27*	*2.80*	*2.00*	*2.07*	*4.00*	*0.49*	*0.00*
$F2$	/p/	$\overline{X}$	−353.00	24.00	−587.00	40.00	…	…	89.60	8.00	72.00	18.00
		se	*109.43*	*6.78*	*84.35*	*6.32*			*21.67*	*8.00*	*28.02*	*11.14*
	/n/	X	15.20	28.00	−130.40	38.00	632.13*	646.10*	309.20	26.00	415.60	46.00
		se	*85.40*	*11.58*	*38.15*	*15.30*	*68.32*	*74.20*	*56.94*	*6.78*	*58.52*	*18.60*
	/l/	X	−732.00	64.00	−552.40	68.00	193.32*	86.97*	118.64	12.00	77.96	10.00
		se	*31.29*	*6.00*	*98.84*	*8.60*	*22.34*	*13.81*	*36.49*	*5.83*	*50.44*	*10.00*
	/s/	X	−116.00	32.00	−149.60	38.00	99.20*	137.40*	41.60	2.00	52.80	12.00
		se	*51.74*	*22.67*	*43.90*	*13.56*	*33.11*	*37.26*	*24.68*	*2.00*	*8.62*	*9.70*
	/ʃ/	X	20.80	0.00	−104.00	38.00	104.00	116.40	48.80	0.00	74.00	0.00
		se	*12.99*	*0.00*	*42.01*	*20.35*	*43.67*	*54.59*	*15.56*	*0.00*	*39.28*	*0.00*
	/ɲ/	X	20.80	12.00	−48.80	0.00	22.40	105.48*	26.40	4.00	33.67	0.00
		se	*18.82*	*12.00*	*7.09*	*0.00*	*12.24*	*11.63*	*10.32*	*4.00*	*10.59*	*0.00*
	/k/	X	86.00	10.00	10.40	6.00	…	…	41.00	8.00	94.20	50.00
		se	*42.17*	*10.00*	*58.25*	*4.00*			*23.11*	*5.83*	*52.44*	*27.93*

of the C-to-V size effects in Qp and $F2$ from /l/ on /i/ (Table I) reveals that the consonant contributes to much tongue dorsum lowering during the vowel.

According to Table III, correlations between C-to-V size and C-to-V temporal extent, i.e., $CV_s \times CV_t$, yield high positive r values for Qp and $F2$ and for the anticipatory and for the carryover direction meaning that the duration of the consonantal effect varies with its magnitude in the /i/ context condition. A close correspondence between C-to-V size and temporal extent can be seen for fixed /i/ in Fig. 3(a). Larger effects are also longer (as those for /l/) and smaller effects are also shorter (as those for /p/ in Qp and for alveolopalatals and velars in $F2$).

2. /a/ context

According to predictions in Sec. B 1, prominent consonant-dependent effects on /a/ should occur in scenarios where the consonant and the vowel are produced with opposing articulatory trajectories and the DAC value for the consonant exceeds the DAC value of 2 for /a/. Figure 3(b) shows large and long C-to-V effects in Qp and $F2$ for consonants requiring tongue-dorsum raising and specified for a DAC maximum, i.e., alveolopalatals /ɲ/ and /ʃ/ and velar /k/. These effects are often significantly different from those for other consonants. They are positive (Table II) meaning that the consonant causes tongue dorsum raising to occur during the vowel.

In comparison to alveolopalatals and velars, the size and temporal effects in the figure are usually smaller and shorter for the alveolars /n/, /s/, and dark /l/ and for the bilabial /p/. This is the expected outcome for consonants such as /n/ and /s/ involving different articulatory trajectories from that for the vowel and specified for the same moderate DAC value (see Sec. B 1). In this case, C-to-V effects can be somewhat more prominent than predicted since the tongue-dorsum position for the consonant is higher than that for the vowel (as revealed by Qp and $F2$ effects for /na/ and /sa/ showing a positive sign; see Table II) and consonants tend to override vowels when the two phonetic segments are specified for the same DAC value and are antagonistic (as for /li/). C-to-V effects of little prominence for /p/ accord with this consonant exhibiting a minimal DAC value (see Sec. B 1). These effects often exhibit a negative sign due to lip closing and/or some tongue lowering (Table II). The existence of smaller C-to-V effects in $F2$ (also in $F3$) from /p/ on /a/ than on /i/ is in accordance with predictions in Fant's nomograms relat-

TABLE II. Same contents as in Table I when the fixed vowel is /a/.

			C to V				V to C		V to V			
			Anticipatory		Carryover		Anticipatory	Carryover	Anticipatory		Carryover	
Vowel /a/			Size	Time	Size	Time	Size		Size	Time	Size	Time
Qp	/p/	X	2.00	0.00	−5.00	42.00	17.17*	21.50*	3.67	30.00	2.83	6.00
		se	*0.50*	*0.00*	*1.97*	*28.00*	*2.91*	*2.89*	*1.87*	*30.00*	*1.76*	*4.00*
	/n/	X	13.00	22.00	2.00	16.00	9.67*	12.17*	1.83	6.00	1.50	2.00
		se	*0.86*	*2.00*	*1.41*	*16.00*	*3.28*	*1.59*	*0.81*	*4.00*	*1.30*	*2.00*
	/l/	X	…	…	…	…	5.50	4.75	1.28	22.00	2.97	10.00
		se					*1.62*	*1.85*	*0.86*	*22.00*	*1.34*	*7.75*
	/s/	X	15.67	54.00	−0.33	14.00	6.33*	2.67	2.33	8.00	1.50	0.00
		se	*1.43*	*6.00*	*3.15*	*8.72*	*1.57*	*1.63*	*1.27*	*8.00*	*0.93*	*0.00*
	/ʃ/	X	38.50	68.00	17.67	68.00	0.17	2.17	1.50	0.00	0.33	0.00
		se	*2.90*	*5.83*	*3.76*	*11.58*	*0.17*	*1.33*	*0.55*	*0.00*	*0.33*	*0.00*
	/ɲ/	X	36.50	48.00	26.83	86.00	3.17	14.83*	0.67	0.00	11.00	24.00
		se	*2.20*	*4.90*	*2.90*	*13.27*	*1.52*	*4.37*	*0.41*	*0.00*	*3.26*	*10.30*
	/k/	X	23.00	26.00	32.84	68.00	20.00*	12.83	10.67	6.00	6.50	6.00
		se	*5.76*	*7.48*	*3.91*	*12.00*	*2.06*	*4.76*	*3.24*	*4.00*	*3.37*	*6.00*
F2	[p]	X	−179.20	40.00	−137.00	46.00	…	…	151.20	78.00	81.40	18.00
		se	*27.67*	*4.47*	*34.00*	*15.68*			*29.81*	*15.94*	*18.62*	*8.00*
	[n]	X	124.00	56.00	22.40	36.00	158.94*	172.91*	124.44	92.00	112.56	50.00
		se	*31.62*	*14.35*	*28.86*	*20.64*	*45.74*	*38.49*	*14.68*	*13.19*	*30.75*	*22.14*
	[l]	X	−187.00	52.00	−196.00	40.00	197.27*	90.92*	99.39	52.00	29.09	6.00
		se	*40.72*	*13.93*	*31.21*	*3.16*	*21.66*	*21.08*	*13.02*	*17.44*	*13.21*	*6.00*
	[s]	X	198.40	58.00	14.40	2.00	83.50	123.30	58.40	2.00	67.20	66.00
		se	*59.82*	*12.81*	*23.45*	*2.00*	*28.84*	*49.23*	*21.45*	*2.00*	*23.10*	*29.26*
	[ʃ]	X	364.80	94.00	151.20	44.00	114.80*	117.20	132.80	44.00	60.00	25.00
		se	*25.66*	*5.10*	*30.92*	*19.13*	*27.62*	*44.36*	*27.05*	*15.03*	*16.57*	*16.58*
	[ɲ]	X	472.00	84.00	475.20	126.00	89.32	186.80*	76.00	24.00	131.20	22.00
		se	*29.31*	*5.10*	*115.89*	*18.06*	*43.83*	*34.53*	*43.89*	*17.49*	*40.86*	*7.35*
	[k]	X	228.00	64.00	160.80	38.00	…	…	148.00	42.00	87.00	30.00
		se	*9.38*	*6.00*	*86.69*	*17.15*			*39.27*	*18.81*	*53.86*	*18.97*

ing variations in lip rounding to changes in constriction location. As expected (Sec. B 1), dark /l/ exerts moderate $F2$ effects on /a/ in spite of the consonant being highly constrained since the two phonetic segments are produced with comparable articulatory trajectories and small differences in tongue-dorsum position. Thus for consonants specified for DAC=3, C-to-V effects appear to be less prominent when the consonant and the vowel gestures are compatible (as for /la/) than when they are antagonistic (as for /ɲa/). Negative C-to-V effects in $F2$ for dark /l/ (Table II) are consistent with this consonant requiring active tongue-dorsum lowering.

Analogously to the /i/ condition, C-to-V size effects and C-to-V temporal effects, i.e., $CV_s \times CV_t$, are highly correlated in the /a/ condition (see Table III). High positive r values were obtained both for Qp (anticipatory effects) and

TABLE III. Correlations for C-to-V, V-to-C, and V-to-V effects in Qp and $F2$ across data for seven consonants and five speakers; lowercase s and t indicate size and temporal effects, respectively. r values at and above 0.70 are given independently for the anticipatory and carryover direction and for each fixed vowel condition. An asterisk indicates the presence of significant correlations ($p<0.05$).

	Vowel /i/				Vowel /a/			
	Qp		*F2*		*Qp*		*F2*	
	Anticipatory	Carryover	Anticipatory	Carryover	Anticipatory	Carryover	Anticipatory	Carryover
C effects								
$CV_s \times CV_t$	0.94*	0.79	0.84	0.73	0.81		0.84	0.94*
V effects								
$VC_s \times VV_s$		0.91*	0.99*	0.99*	0.82			1.00*
$VC_s \times VV_t$		0.87	0.95	0.96			0.72	
$VV_s \times VV_t$		0.94*	0.95*			0.91*	0.71	
C effects×V effects								
$CV_s \times VC_s$								
$CV_s \times VV_s$	0.71					0.71		
$CV_s \times VV_t$					−0.85			
$CV_t \times VV_t$		−0.70			−0.79			

for $F2$ (anticipatory and carryover effects). A close match between the C-to-V effects in size and temporal extent is apparent across consonants in the graphs of Fig. 3(b).

B. Vocalic coarticulatory effects

1. Fixed /i/

Figure 4(a) displays the size and the temporal extent of vocalic coarticulation in the sequence pairs /iCi/–/iCa/ (anticipatory) and /iCi/–/aCi/ (carryover), i.e., the size of the vocalic effects at the consonantal midpoint (V-to-C) and their size and temporal extent during the fixed vowel /i/ (V-to-V). Effects are always positive and occur when the Qp or $F2$ value for /i/ exceeds that for /a/.

The data in Fig. 4(a) show that vowel-dependent effects in Qp and/or $F2$ tend to be larger and longer for consonants specified for lower DAC values (bilabial /p/, alveolar /n/) than for consonants requiring more active tongue-dorsum control (dark /l/, fricative /s/, alveolopalatals, velars). This finding is in accordance with the degree of coarticulatory resistance varying directly with the DAC value for the consonant and with the DAC value for /s/ being higher (3) than that for /n/ (2). The size effects for /p/ and /n/ are significantly different from those for other consonants; moreover the Qp effects are significantly larger for /p/ vs /n/ which accords with DAC differences between the two consonants.

Correlation data for the /i/ context condition in Table III often reveal high positive r values between the size of the V-to-C effects, and the size and the temporal extent of the V-to-V effects (i.e., $VC_s \times VV_s$, $VC_s \times VV_t$), and between the two latter magnitudes (i.e., $VV_s \times VV_t$). This trend occurs for $F2$ both at the anticipatory and carryover levels, and for Qp at the carryover level. Figure 4(a) reveals that consonants allowing large vocalic size effects are the same ones allowing long vocalic effects in temporal extent (/p/, /n/), while vocalic effects are usually small and short for another set of consonants (dark /l/, /s/, alveolopalatals, velars).

Negative correlation values between the consonantal and the vocalic effects should be taken as evidence that the latter vary inversely with respect to the former (see Sec. I C). As shown in Table III, only one high negative correlation (i.e., $CV_t \times VV_t$) was obtained out of 16 possibilities. Low correlation values occur since the degree of vocalic coarticulation is inversely related to the degree of C-to-V coarticulation in some cases (/l/) but not in others (alveolopalatals, velars). Thus while dark /l/ exerts maximal C-to-V coarticulation and allows vowel-dependent effects of little prominence, alveolopalatals and velars exhibit little C-to-V and vocalic coarticulation.

2. Fixed /a/

Vocalic coarticulatory effects for fixed /a/ are displayed in Fig. 4(b). $F2$ effects in temporal extent reveal the expected trend for consonants specified for higher DAC values to allow lesser vocalic coarticulation than consonants with lower DAC values. Indeed, dorsal /l/, /ɲ/, /ʃ/, and /k/ and fricative /s/ (which appears to be specified for a high DAC value) allow shorter V-to-V anticipatory temporal effects in $F2$ frequency than consonants /p/ and /n/ requiring lesser tongue-dorsum activation.

V-to-C size effects in Qp are also most prominent for consonants /p/ and /n/ (for /p/>/n/) specified for low DAC values, as well as for /k/ which may be due to vowel-related changes in velar closure fronting; these effects for /p/ and /k/ (also V-to-V size effects in Qp for /k/) are significantly larger than those for other consonants. V-to-C size effects in $F2$ are small and show a less coherent picture, with anticipatory size effects decreasing in the progression /l/>/n/, /ʃ/>/s/, /ɲ/ for most speakers. V-to-V size effects in Qp and $F2$ and V-to-V temporal effects in Qp are very small and short.

Correlation data for the /a/ context condition in Table III yield similar results to those for the /i/ condition. High positive r values occur at least once for correlations involving vocalic effects exclusively, i.e., $VC_s \times VV_s$, $VC_s \times VV_t$, $VV_s \times VV_t$, meaning that there is a good correspondence between vowel-dependent size and temporal coarticulation. An inverse correlation between vocalic coarticulation and consonantal coarticulation was found to hold just for 2 out of 16 correlation pairs (i.e., $CV_s \times VV_t$, $CV_t \times VV_t$). The absence of high negative correlations between the consonant-dependent and vowel-dependent effects appears to be mostly related to the high variability in the coarticulatory effects across consonants (given the considerable number of consonants included in the correlation analyses) and to /a/ exhibiting little dorsopalatal contact (Qp correlations only).

3. Articulatory dimension of the V-to-C effects

Data on V-to-C coarticulation in Tables I and II and those for the individual speakers reveal a trend for the vowel-dependent effects during the consonantal period to favor the target articulatory position for the consonant.

A comparison between V-to-C effects in the two tables reveals that consonants /ɲ/ and /k/ requiring a high tongue-dorsum position allow larger effects in tongue-dorsum raising (exerted by /i/ in the fixed /a/ context) than in tongue-dorsum lowering (exerted by /a/ in the fixed /i/ context). This is so for the coarticulatory effects in Qp (/ɲ/, /k/) and in $F2$ (/ɲ/). Thus for example, the size of the anticipatory and carryover effects in $F2$ for /ɲ/ is 89.32 Hz and 186.8 Hz in the fixed /a/ context but only 22.4 Hz and 105.48 Hz in the fixed /i/ context. $F2$ and dorsopalatal contact (Qp) trajectories for /ɲ/ in Fig. 5 suggest that the raising movement for /aɲi/ occurs earlier (it begins during V1 and ends about closure offset) than the lowering movement for /iɲa/ (it begins during closure or somewhat later and ends during the V2 period). It thus appears that the tongue dorsum early achieves a high position when /ɲ/ follows /a/ and holds this position as long as possible when /ɲ/ follows /i/.

Dark /l/, on the other hand, allows effects in tongue-dorsum lowering exerted by /a/ in the fixed /i/ context over those exerted by /i/ in the fixed /a/ condition which accords with this consonant involving active tongue-dorsum lowering. This trend is at work for the Qp data but not so for the $F2$ data (see Tables I and II). Qp and $F2$ data in Fig. 5 reveal indeed that the lowering trajectories for /ila/ begin

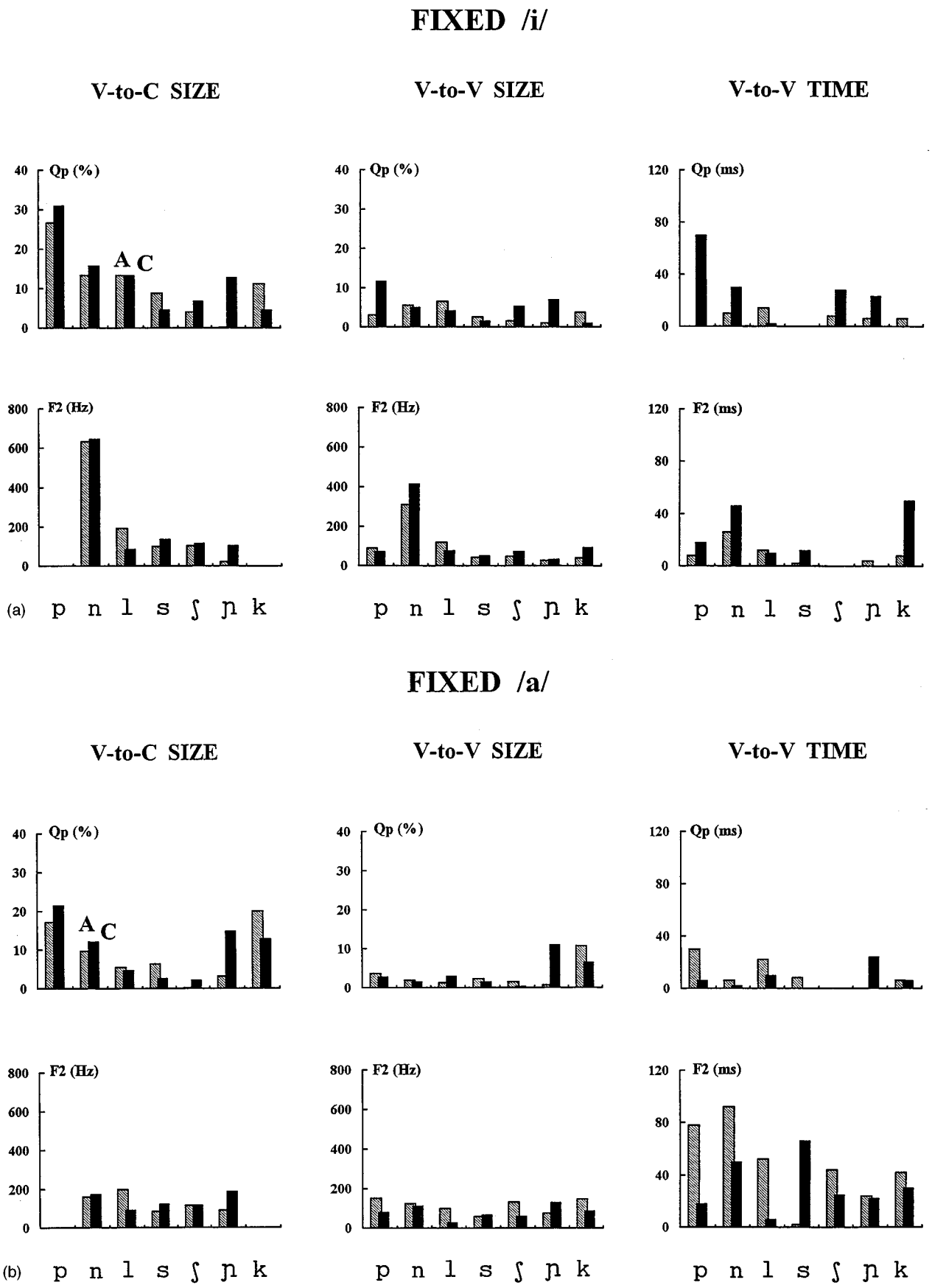

FIG. 4. (a) Mean V-to-C and V-to-V effects across repetitions and speakers for each consonant when the fixed vowel is /i/. Size effects in % of electrode activation and in Hz (left: V-to-C, middle: V-to-V) and temporal effects in ms (right: V-to-V) are plotted separately for *Qp* (above) and *F*2 (below), and for each coarticulatory direction, i.e., anticipatory (dotted bars) and carryover (black bars). (b) Same representation as in (a) when the fixed vowel is /a/.

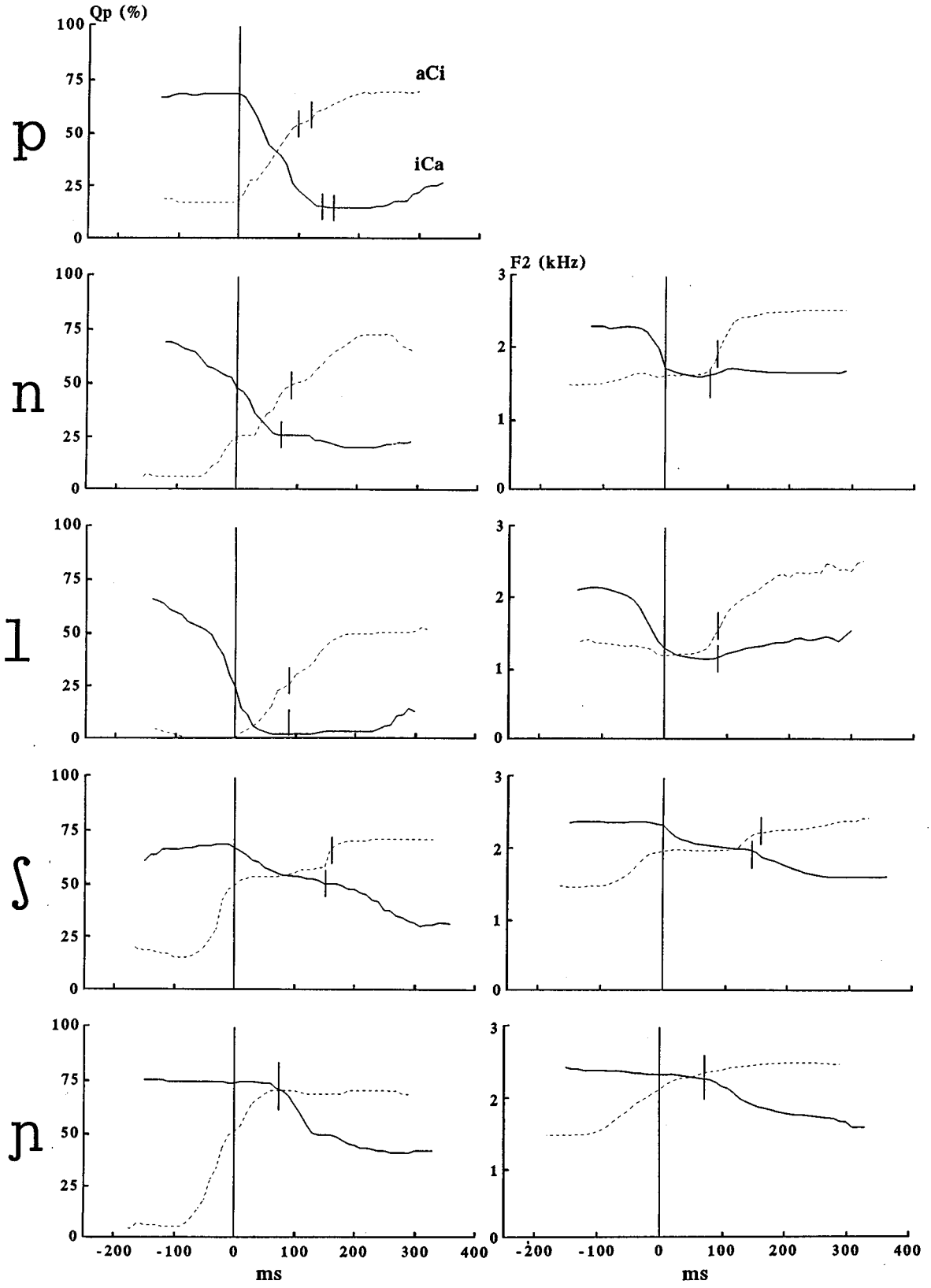

FIG. 5. *Qp* trajectories (left) and *F*2 trajectories (right) for the sequences /aCi/ (dashed lines) and /iCa/ (solid lines) lined up at the onset of the consonantal period (0-ms value along the temporal axis). Short vertical marks crossing the *F*2 and *Qp* trajectories have been inserted at the offset of the consonantal period. Data correspond to a single speaker, i.e., JP (/l/, /n/, /ɲ/) and DR (/ʃ/, /p/).Trajectories for /p/ have been displayed for *Qp* only (no formant structure is available during the closure period for this consonant); vertical marks have been indicated at closure offset and at burst offset in this case.

earlier (during V1) and achieve an earlier endpoint (during closure) than the raising trajectories for /ali/ (in this case raising onset occurs toward the end of V1 or during the central closure period and a raising maximum is not achieved until the V2 period). It is thus apparent that the tongue reaches and maintains a low target position for the production of dark /l/ which is more compatible with that for a low vowel than with that for a high vowel.

According to data in Tables I and II, bilabial /p/ (Qp) and dentoalveolar /n/ (Qp, $F2$) also allow more prominent effects from /a/ in the fixed /i/ condition than effects from /i/ in the fixed /a/ condition. Qp trajectories for bilabial /p/ in Fig. 5 show indeed that, although the increase in lingual contact for /api/ and the contact decrease for /ipa/ begin more or less at the same time (at V1 offset), the latter ends earlier (at closure offset) than the former (during V2). This finding suggests that bilabial /p/ is more sensitive to tongue-dorsum lowering effects than to tongue-dorsum raising effects, which is consistent with this lingual region exhibiting a low position at rest. Trajectories for /n/ in the figure show that, analogously to dark /l/, $F2$ lowering onset for /ina/ occurs earlier (during V1) than $F2$ raising onset for/ani/ (at the end of the closure period); the offset of these $F2$ trajectories also takes place much earlier after /i/ (at closure onset) than after /a/ (during V2). As for the Qp data, the lowering trajectory for /ina/ and the raising trajectory for /ani/ start more or less simultaneously during V1 while their endpoint is achieved earlier for the former (at closure offset) than for the latter (during V2). Predominance of the vowel-related lowering effects for /n/ is a quite unexpected outcome since the tongue dorsum should exhibit a high position during the production of this consonant if subject to coupling effects with the primary tongue tip articulator. This finding suggests that /n/ and perhaps other dentoalveolar consonants may differ with respect to tongue-dorsum height across languages (i.e., /n/ would be specified for a rather low tongue-dorsum position in Catalan) and that articulatory regions which are not involved in the closure or constriction making process may be actively controlled.

Data in Tables I and II reveal that fricatives /s/ and /ʃ/ also favor slightly the effects from /a/ over those from /i/ (for Qp and $F2$ in the case of /s/, and for Qp in the case of /ʃ/). The situation for fricatives is exemplified by the Qp and $F2$ trajectories for /ʃ/ in Fig. 5 (the /s/ trajectories show an analogous behavior to those for /ʃ/ in the figure). Table II indicates a slight predominance of the vowel-dependent lowering vs raising effects for these consonants (thus, for example, V-to-C effects for /s/ amount to 99.2 Hz and 137.4 Hz in the fixed /i/ context, and to 83.5 Hz and 123.3 Hz in the fixed /a/ context). These V-to-C data are not in agreement with the onset times of trajectory movement in Fig. 5 (since raising onset for /aʃi/ occurs earlier than lowering onset for /iʃa/) and may be related to Qp and $F2$ raising trajectories achieving a plateau while the corresponding lowering trajectories exhibit continuous motion.

C. Coarticulatory direction

In order to evaluate the relative salience of the two coarticulatory directions, values for the size and the temporal extent of the anticipatory component have been subtracted from those of the carryover component (see Tables I and II) and the resulting differences have been displayed in Fig. 6(a) and (b) (consonant-dependent effects) and in Fig. 7(a) and (b) (vowel-dependent effects). Differences in sign have not been taken into account in the subtraction procedure. Negative values in the figures indicate that anticipation prevails over carryover; positive values indicate the opposite relationship.

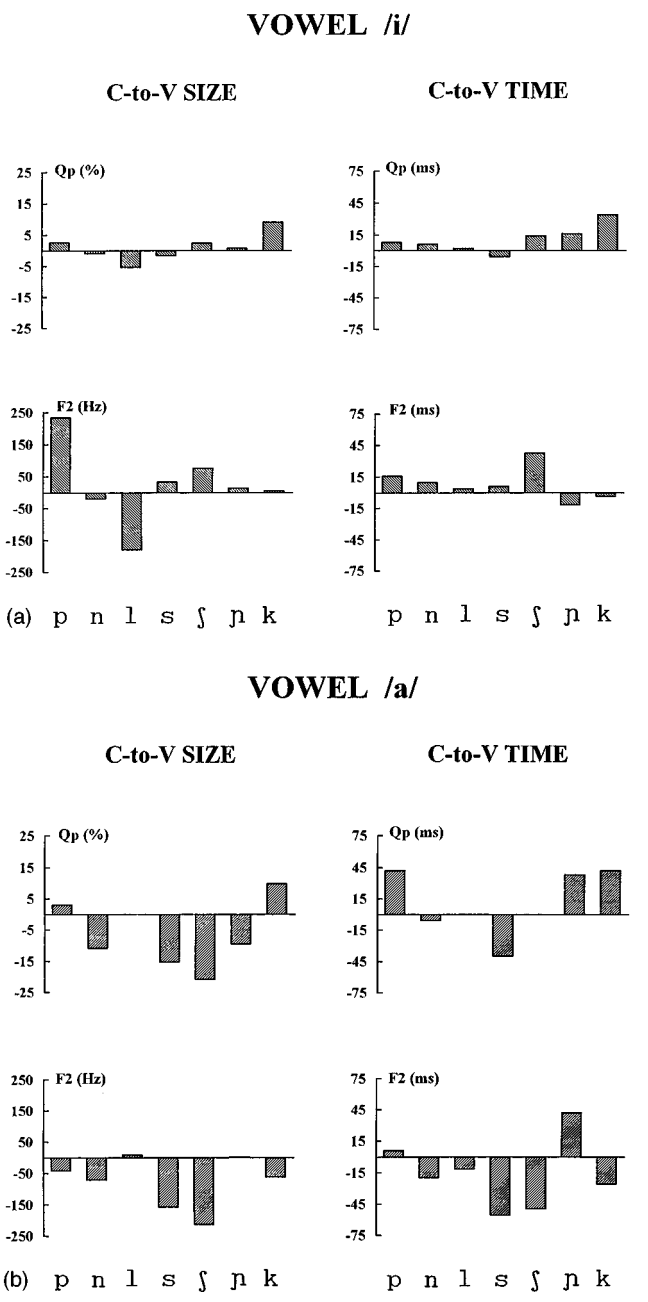

FIG. 6. (a) Differences in coarticulatory direction for the C-to-V effects for each consonant across repetitions and speakers when the contextual vowel is /i/. Predominance of the anticipatory component yields a negative value (below the 0 line); predominance of the carryover component yields a positive value (above the 0 line). Size effects in % of electrode activation and in Hz (left) and temporal effects in ms (right) are plotted separately for Qp (above) and $F2$ (below). (b) Same representation as in (a) when the fixed vowel is /a/.

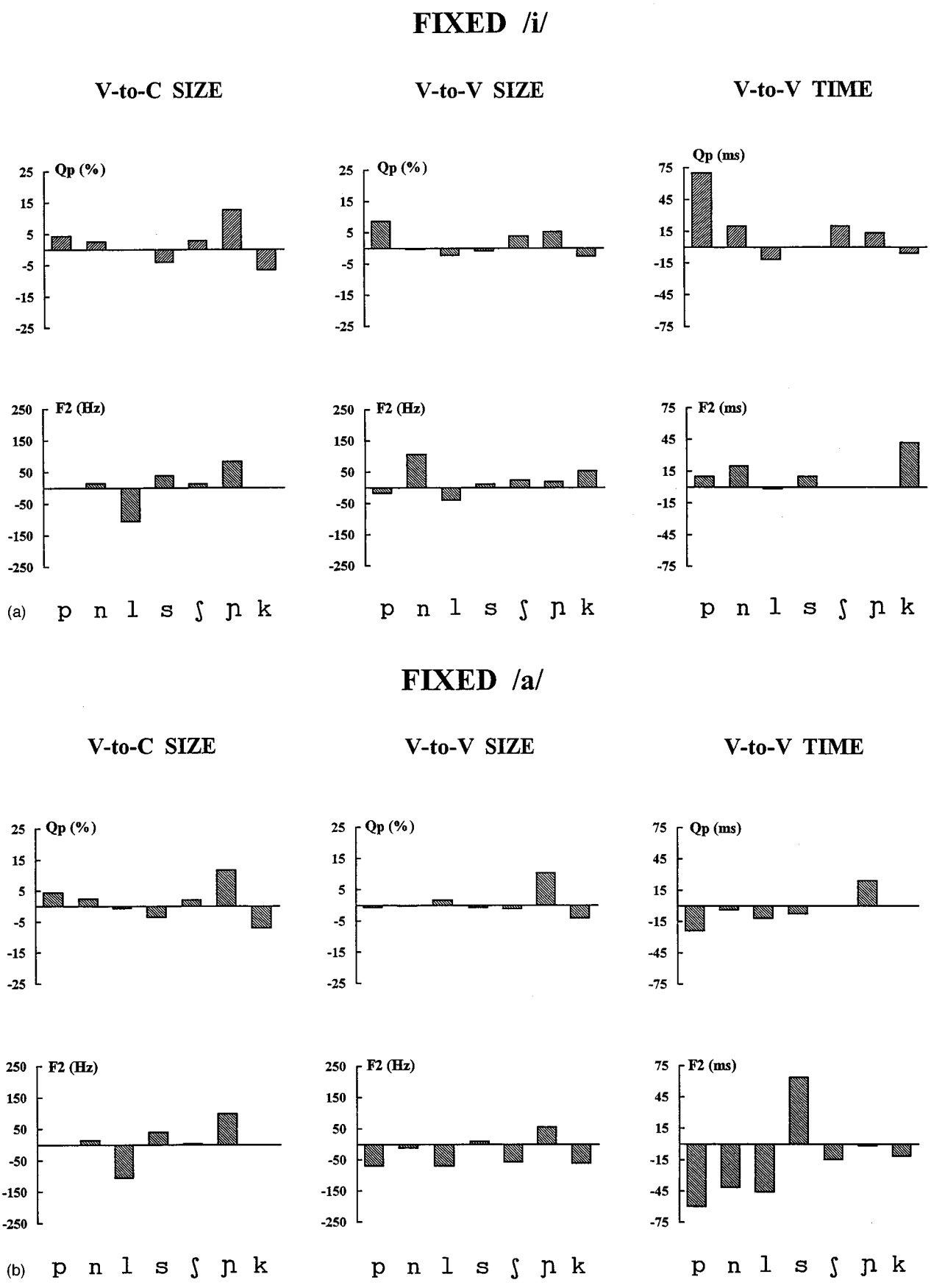

FIG. 7. (a) Differences in coarticulatory direction for the V-to-C and V-to-V effects for each consonant across repetitions and speakers when the fixed vowel is /i/. Predominance of the anticipatory component yields a negative value (below the 0 line); predominance of the carryover component yields a positive value (above the 0 line). Size effects in % of electrode activation and in Hz (left: V-to-C, middle: V-to-V) and temporal effects in ms (right: V-to-V) are plotted separately for *Qp* (above) and *F2* (below). (b) Same representation as in (a) when the fixed vowel is /a/.

1. C-dependent coarticulation

a. /i/ context. According to Fig. 6(a), C-to-V effects in Qp and $F2$ show some noticeable trends in coarticulatory direction. On the one hand, alveolopalatals and velars tend to favor carryover over anticipatory coarticulation in size and temporal extent; the absence of much C-to-V anticipation in a sequence made of two comparable highly constrained phonetic segments (such as /ʃ/, /ɲ/, or /k/ and the vowel /i/) may lead to the prevalence of the carryover component associated with the mechanico-inertial properties of the tongue-dorsum raising gesture. On the other hand, dark /l/ exerts larger (but not longer) anticipatory than carryover effects; the salience of the C-to-V anticipatory effects in this case appears to be linked to the performance of the highly constrained lingual gesture for the consonant when preceded by the antagonistic vowel /i/.

Speaker-dependent Qp and $F2$ data reveal no clear coarticulatory direction pattern for the alveolars /s/ and /n/ although most speakers favor the carryover direction in some instances. Size and temporal effects for the bilabial /p/ also show predominance of the carryover component which may be related to the influence of the bilabial release and, as for the other nondorsal consonants /n/ and /s/, to the inertial requirements associated with the raising of the tongue dorsum induced by the vowel /i/.

b. /a/ context. Qp and $F2$ data in Fig. 6(b) show that fricatives resemble other constrained consonants in exerting strong gestural anticipation: Size and temporal data reveal that /s/ and /ʃ/ often favor the C-to-V anticipatory component. To a lesser extent, predominance of anticipation over carryover is also at work for the alveolars /n/ (size and temporal coarticulation in Qp and $F2$) and /l/ (coarticulation in $F2$ temporal extent for four speakers). Overall, alveolars may give preference to the anticipatory component in line with the tongue dorsum being ruled by apical activity and not being subject to strong mechanico-inertial constraints during their production in the /a/ context; consonants subject to important manner requirements, i.e., fricatives, give particular emphasis to the anticipatory direction.

More retracted dorsal consonants exhibit a different behavior. Alveolopalatal /ɲ/ favors anticipatory size effects in Qp and also in $F2$ [for four speakers in spite of Fig. 6(b) not showing so since one speaker exhibits very large carryover effects], presumably because the articulatory manifestation of the dorsal gesture is more /j/-like at consonantal release than at consonantal formation; temporal effects in Qp and $F2$ for /ɲ/ are however longer at the carryover versus anticipatory level. Regarding velar /k/, C-to-V effects are larger and longer for the carryover vs anticipatory direction (Qp) and for the anticipatory versus carryover direction ($F2$). The finding of more prominent carryover than anticipatory effects for dorsals vs alveolars is in accordance with the mechanico-inertial properties associated with the tongue-dorsum raising gesture for the former consonantal class.

No clear coarticulatory direction holds for bilabial /p/ which favors anticipation in $F2$ size and perhaps carryover in Qp size (longer carryover vs anticipatory effects in Qp for this consonant are associated with two speakers only).

2. V-dependent coarticulation

a. Fixed /i/. According to Fig. 7(a) highly constrained dark /l/, which favors consonant-dependent anticipation, often gives priority to the anticipatory direction for the vocalic effects in size and temporal extent. On the other hand, consonants assigning more weight to carryover over anticipation for the C-to-V effects also allow more prominent vowel-dependent carryover than anticipation, i.e., /ɲ/ and /ʃ/ (in Qp and $F2$) and /k/ (in $F2$).

Consonants giving much less clear priority to a specific direction in consonant-dependent coarticulation favor no obvious direction when the vowel-dependent effects are taken into consideration. This is so for most speakers in the case of /p/ (which shows prevalence of the carryover direction in Qp and of the anticipatory direction in $F2$ size for four speakers) and of /s/ (which favors the anticipatory component for the Qp size effects and the carryover component for the $F2$ effects). While exhibiting a similar behavior to /p/ and /s/ in C-to-V directionality, alveolar /n/ gives some more weight to the carryover over the anticipatory component component for the vocalic effects.

b. Fixed /a/. Qp and $F2$ data in Fig. 7(b) reveal the existence of maximal vocalic anticipation for consonants (/p/, /n/, /l/) giving preference to no clear C-to-V coarticulatory direction (/p/) or to C-to-V anticipation (/n/, /l/). There is a trend to favor more prominent vocalic effects in $F2$ size and temporal extent and in Qp temporal extent at the anticipatory vs carryover level for /p/, /l/, and /n/; somehow V-to-C trends in Qp for /p/ and /n/ are larger at the carryover level. Velar /k/ also tends to favor the anticipatory component for the vocalic effects whether related to a more salient consonant-dependent carryover component (for Qp) or anticipatory component (for $F2$); preference for vocalic anticipation for /k/ in the fixed /a/ context condition follows from specific constraints in the production of velars (see Sec. III). Alveolopalatal /ɲ/, which exerts longer C-to-V effects at the carryover level than at the anticipatory level, is the only consonant clearly allowing more prominent vowel-dependent carryover vs anticipatory coarticulation. Fricatives, which clearly exert more prominent anticipatory versus carryover effects, may give more weight to either the vowel-dependent anticipatory or the carryover component: There is a trend for /s/ to favor Qp anticipation and $F2$ carryover; as for /ʃ/, vocalic size effects are quite small for Qp and may give priority to the anticipatory direction for $F2$.

III. GENERAL SUMMARY AND DISCUSSION

Data reported in Sec. II confirm the validity of the DAC model of coarticulation in many respects. Consonants and vowels were assigned different DAC values depending on the degree of tongue-dorsum constraint during their production, i.e., 3 to alveolopalatals, palatals, velars, and dark /l/, 1 to bilabials and the schwa, and 2 to those consonants and vowels the production of which involves some uncontrolled tongue-dorsum activity (/n/, /a/). It was also suggested that manner requirements could raise the DAC value (e.g., from 2

to 3 for /s/). As shown next, this DAC scale accounts to a large extent for the C-to-V, V-to-C, and V-to-V effects reported in the present study.

An important finding was that the prominence of the C-to-V effects depends both on the relative DAC specification for the two adjacent phonetic segments as well as on their articulatory trajectories being compatible or antagonistic. When the consonant and the vowel are specified for the same DAC value, C-to-V effects are negligible in a situation of gestural compatibility (e.g., /ɲi/) and become more prominent as the degree of gestural antagonism increases (e.g., for /li/ vs /na/, /sa/). When the consonant is specified for a higher DAC value than the vowel, C-to-V effects increase with the degree of gestural antagonism involved (e.g., for /ɲa/ vs /la/). Negligible C-to-V coarticulation occurs when the DAC value for the vowel exceeds that for the consonant (e.g., for /pi/, /pa/). More prominent C-to-V effects in tongue-dorsum lowering than expected for /si/ indicate that manner of articulation may modify the basic DAC value (from 2 to 3 in this case). It thus appears that gestural antagonism does not only prevent coarticulatory effects from occurring (as postulated by several coarticulation theories: Henke, 1966; Bell-Berti and Harris, 1981) but, on the contrary, may cause C-to-V coarticulation to increase. Our finding is consistent with differences in the production mechanisms of consonants and vowels: The formation of a closure or constriction requires consonants to be actualized during the adjacent vowel and such production requirements become especially relevant with the difficulty involved in the making of the vowel-to-consonant transition. It can be claimed that maximal antagonism results in maximal C-to-V coarticulation so as to ensure that the consonantal gesture is successfully realized and that, for a given DAC value, consonants are more constrained than vowels.

V-to-C coarticulation data reported in Sec. II are consistent with the notion that V-to-C sensitivity should vary inversely with the DAC value for the consonant, i.e., in the progression bilabials>dentoalveolars>alveolopalatals, velars, dark /l/, /s/ (which is in support of /s/ being specified for DAC=3). This progression was found to hold in both fixed vowel conditions in spite of the initial expectation that it should be at work when the fixed vowel is /a/ but not necessarily so when it is /i/ since a highly constrained fixed vowel could prevent much V-to-V coarticulation from occurring. However, there were very few high negative correlations between the vocalic effects and the consonantal effects in both vowel conditions, and thus no inverse relationship between the strength of the two coarticulatory types. This finding has been attributed to several factors often acting concomitantly such as the high number of consonants submitted to analysis or the coexistence of little consonantal and vocalic coarticulation in some scenarios (e.g., in sequences with alveolopalatal consonants and the vowel /i/).

High correlations were obtained between C-to-V effects in size and temporal extent meaning that larger effects are usually longer (e.g., for /li/, /ɲa/) while smaller effects are often shorter (e.g., for /p/, /n/, /l/, and /s/ with adjacent /a/). A similar relationship appears to hold for the vocalic effects, more so when the fixed vowel is /i/ than when it is /a/ (e.g., effects in the former vowel context are larger and longer for /p/ and /n/ and smaller and shorter for /s/ and dorsals including dark /l/). It thus appears that the extent of the consonant- and vowel-dependent effects along the time domain is related to their magnitude (see also Farnetani and Recasens, 1993).

The notion that the articulatory dimension of the C-to-V effects should depend on the target articulatory position for the consonant was also confirmed. Articulatory activity associated with the target tongue position often begins earlier and is held for a longer period than that for other tongue positions. Thus consonants requiring tongue-dorsum raising (alveolopalatals, velars) are more sensitive to effects from /i/ vs /a/ while those involving tongue-dorsum lowering favor effects from /a/ vs /i/ (bilabial /p/, alveolar /n/, dark /l/). Some justification for /p/ and /n/ involving tongue-dorsum lowering is needed: Tongue-dorsum relaxation for /p/ may occur concomitantly with lip closing (see Engstrand, 1988), while tongue-dorsum lowering for /n/ is possibly a language-specific characteristic (see Footnote 8 for other possible explanations). Fricatives /s/ and /ʃ/ were found not to clearly favor either tongue-dorsum raising effects or tongue-dorsum lowering effects associated with the adjacent vowel; this particular behavior may be related to fricatives requiring the formation of a precise medial groove which causes the tongue-dorsum surface to occupy an intermediate position between that for high and low consonantal articulations.

An important goal of this study was to test the implications of the DAC model with respect to coarticulatory directionality. C-to-V data presented in the paper confirm that, among consonants specified for a high DAC value, some favor the anticipatory component while others favor the carryover component. Prevalence of the anticipatory component for dark /l/ follows from this consonant involving the formation of two lingual constrictions; such anticipatory effects are especially salient when tongue-dorsum lowering and retraction for dark /l/ needs to be made during the preceeding antagonistic vowel /i/. Consonants produced with active tongue-dorsum raising, i.e., the alveolopalatal /ɲ/ and the velar /k/, favor the carryover over the anticipatory component due to the tongue dorsum being lowered more slowly at consonantal release than raised at consonantal onset, and thus in line with the tongue dorsum mechanico-inertial requirements for the consonant; moreover, this asymmetrical relationship becomes more obvious as the articulatory distance between the vowel and the consonant increases, i.e., for /ɲ/ and /k/ with adjacent /a/ vs /i/. Coarticulatory directionality for other consonants appears to depend on whether the vowel causes the tongue dorsum to be raised or not during the consonant. Prevalence of the anticipatory direction occurs in the context of /a/ when tongue-dorsum raising is absent, presumably in line with the flexibility of the apical articulator (for the alveolar /n/) and with lingual grooving associated with manner of articulation demands (for the fricatives /s/ and /ʃ/); tongue-dorsum raising for /n/, /s/, /ʃ/, and /p/ with adjacent /i/ contributes to an increase in the mechanico-inertial requirements which results in a more prominent dorsal release and a more salient carryover vs anticipatory component.

Our model predicts that the direction of the vocalic effects should conform to the directionality trends for consonantal coarticulation. Predominance of the V2-dependent anticipatory effects for /l/ occurs presumably since vowel anticipation is not much affected by the carryover component for this consonant; on the other hand, the salience of the vowel-dependent carryover effects in the case of /ɲ/ accords with the mechanico-inertial constraints associated with the tongue-dorsum raising gesture preventing much vowel-related anticipation from occurring. Vocalic anticipation is also blocked when fixed /i/ contributes to the raising of the tongue dorsum during the consonant; this would explain why consonantal and vocalic effects for /n/, /ʃ/, and perhaps /p/ are more prominent at the carryover level when adjacent to /i/ and at the anticipatory level when adjacent to /a/. The absence of a clear directionality pattern for the vocalic effects for /s/ in the two fixed vowel contexts may be attributed to the strong manner requirements for this consonant and perhaps to the mechanico-inertial requirements on the tongue dorsum in the /i/ context. Analogously to dorsal /ɲ/, dorsal /k/ favors the carryover component for the consonantal and vocalic effects in the /i/ condition; prevalence of vocalic anticipation in the /a/ context condition appears to be related to how the tongue dorsum is being controlled during velar closure.[12]

ACKNOWLEDGMENTS

This work was supported by ESPRIT Basic Research Action 6975 project from EC (''Speech Maps''), CS93-9.908 research grant of the Government of Catalonia, and project CE93-0020 of the Ministry of Education and Science of Spain. The authors would like to thank Anders Löfqvist and three anonymous reviewers for comments on a previous version of the manuscript.

[1]The term ''tongue dorsum'' is preferred to the term ''tongue body'' and refers to the upper surface of the tongue in front of the hard and soft palate where palatal and velar sounds are articulated (Catford, 1988).

[2]In a previous paper (Recasens *et al.*, 1995), the degree of dorsopalatal contact was correlated with *F*2 at the consonantal midpoint in the sequences /iCi/ and /aCa/ for the same consonants analyzed in the present study. High positive correlations were found across consonants and speakers as well as across consonants for a given speaker. This finding is consistent with data collected with vocal tract analogues indicating an increase in *F*2 frequency with a decrease in dorsopalatal constriction width (Stevens and House, 1955; Fant, 1960; Gay *et al.*, 1991).

[3]The DAC scale is not to be identified with the CR (coarticulatory resistance) scale proposed elsewhere (Bladon and Al-Bamerni, 1976). The CR scale assigns different values to phonetic segments depending on the degree of coarticulation allowed. The following CR values correspond to different allophones of English /l/: 1 to the least resistant allophone, i.e., clear /l/ in *leaf*; 2 to an allophone specified for an intermediate CR degree, i.e., dark /l/ in *feel*; 3 to the most resistant allophone, i.e., syllabic /l/ (*fiddle*). The DAC scale characterizes phonetic segments according to the types of articulatory constraints involved in their production and can be used as a predictor of coarticulatory resistance (see Sec. B 2).

[4]The term ''fixed vowel'' is applied to VCV pairs used to investigate vowel-dependent coarticulation. It refers to the vowel which is kept constant in a given VCV pair, e.g., V1=/a/ in the sequence pair /api/-/apa/ which allows studying right-to-left effects associated with V2=/i/ vs /a/ in this particular V1 condition.

[5]*F*3 and *F*1 coarticulatory effects were also measured for the same speech material. Results for *F*3 were highly similar to those for *F*2 which is in accordance with both formants being related to dorsopalatal constriction location and narrowing (Fant, 1960); they will be reported occasionally when deviating from those for *F*2 in some interesting way. *F*1 coarticulatory effects will not be commented in this paper since they differ from those for *F*2 in many respects presumably because of reflecting jaw opening variations in addition to changes in dorsopalatal constriction width.

[6]The following piece of evidence suggests that differences in phonetic realization between V1 and V2 in the /aCa/ sequences (i.e., V1 was realized as stressed [a] and V2 as unstressed [ə]) did not affect the analysis results significantly. Had this been the case, V-to-V carryover effects would have exceeded the corresponding anticipatory effects in /VpV/ sequences (where /p/ is specified for a minimal DAC value) since there are reasons to expect stressed vowels to exert more coarticulation than unstressed ones and non-reduced vowels to allow less coarticulation than reduced ones. V-to-V coarticulation data across /p/ on fixed /a/ reported in Sec. II reveal that the opposite in fact happened, i.e., anticipatory size and temporal effects were found to be more prominent than carryover effects. More carryover than anticipatory V-to-V coarticulation across /p/ in the fixed /i/ context is probably independent of the stress pattern since stressed and unstressed /i/ differ very slightly in Catalan.

[7]The exclusion of that row from the calculation of the *Qp* index for the latter four consonants is also advisable when their place of articulation is more front than usual since the dorsal contact at the front palatal zone in this case is presumably related to interarticulatory coupling effects with the tongue front rather than to tongue-dorsum activation.

[8]In a few instances, reinforcement of the tongue-dorsum raising gesture by the action of successive dorsopalatal V1 and C in the sequences /iɲV/ and /iʃV/ may cause articulatory overshoot, i.e., more dorsopalatal contact and frequency displacement than usual for a long period of time during V2. Carryover effects extending until vowel offset in these circumstances have been excluded from analysis.

[9]In this paper, a given coarticulatory effect will be often characterized in comparison to other effects as ''large'' or ''small'' (size) and ''long'' or ''short'' (temporal extent).

[10]C-to-V effects in *F*3 for dorsal /ɲ/ and /k/ are somewhat larger and longer than *F*2 effects. This finding is consistent with information provided by nomograms (Fant, 1960) showing that a considerable reduction of the constriction area for alveolopalatals causes more *F*3 than *F*2 raising as the constriction location moves forward from the mediopalate to the prepalate. It also accords with negative *F*3 effects if, as indicated by electropalatographic data (Recasens, 1991a), some constriction retraction for /i/ in this specific consonantal environment is accompanied by a decrease in lingual contact at the prepalate.

[11]Other explanations could account for the *Qp* and *F*2 lowering for /n/ and /s/. Apical consonants have been reported to be articulated with a somewhat concave tongue surface behind closure location and some postdorsum retraction resulting into a narrower pharyngeal passage than that exhibited by laminoalveolar articulations (Dart, 1991). Some tongue-dorsum relaxation could also be related to nasality and the resulting lack of pressure containment associated with it (Perkell, 1969).

[12]The salience of the anticipatory component for the vocalic effects is consistent with ultrasound data showing an early onset of V2 related tongue-dorsum movement during V1 (Parush *et al.*, 1983), and with electromagnetic midsagittal articulometry data showing V2 anticipation in /akV/ sequences during closure mostly for V2=/i/ but also for V2=/a/ (Mooshammer *et al.*, 1995). Our EPG data generally show more dorsopalatal contact during V1 for /aki/ than for /ika/ which is consistent with a strong V2-dependent forward movement in the former sequence already during V1. It is agreed that these anticipatory effects reflect passive forward tongue-dorsum movement associated with the large mass of the tongue body being controlled in a continuous fashion (Perkell, 1969). This forward movement does not occur to the same extent when V1=/i/ since the tongue dorsum is already located at a front location at closure onset in this case.

Beddor, P. S., and Yavuz, H. K. (**1995**). ''The relationship between vowel-to-vowel coarticulation and vowel harmony in Turkish,'' in *Proceedings of ICPhS95*, Vol. 2, edited by K. Elenius and P. Branderud (Arne Strömbergs Grafiska, Stockholm), pp. 44–51.

Bell-Berti, F., and Harris, K. S. (**1981**). ''A temporal model of speech production,'' Phonetica **38**, 9–20.

Bergem, D. R. van (**1994**). ''A model of coarticulatory effects on the schwa,'' Speech Commun. **14,** 143–162.

Bladon, R. A. W., and Al-Bamerni, A. (**1976**). ''Coarticulation resistance in English /l/,'' J. Phonetics **4**, 137–150.
Boyce, S. E. (**1990**). ''Coarticulatory organization for lip-rounding in Turkish and American English,'' J. Acoust. Soc. Am. **88,** 2584–2595.
Browman, C. P., and Goldstein, L. (**1986**). ''Towards an articulatory phonology,'' Phonology **3**, 219–252.
Browman, C. P., and Goldstein, L. (**1992**). '' 'Targetless' schwa: An articulatory analysis,'' in *Papers in Laboratory Phonology II. Gesture, Segment, Prosody*, edited by G. J. Docherty and R. Ladd (Cambridge U. P., Cambridge), pp. 26–56.
Carney, P. J., and Moll, K. L. (**1971**). ''A cinefluorographic investigation of fricative consonant-to-vowel coarticulation,'' Phonetica **23**, 193–202.
Catford, J. C. (**1988**). *A Practical Introduction to Phonetics* (Clarendon, Oxford).
Dart, S. N. (**1991**). ''Articulatory and acoustic properties of apical and laminal articulations,'' UCLA Working Papers in Phonetics **79**.
Engstrand, O. (**1988**). ''Articulatory correlates of stress and speaking rate in Swedish VCV utterances,'' J. Acoust. Soc. Am. **83,** 1863–1875.
Fant, G. (**1960**). *Acoustic Theory of Speech Production* (Mouton, The Hague).
Farnetani, E., and Recasens, D. (**1993**). ''Anticipatory consonant-to-vowel coarticulation in the production of VCV sequences in Italian,'' Language Speech **36**, 279–302.
Fowler, C. A., and Saltzman, E. (**1993**). ''Coordination and coarticulation in speech production,'' Language Speech **36**, 171–195.
Gay, T. (**1974**). ''A cinefluorographic study of vowel production,'' J. Phonetics **2**, 255–266.
Gay, T. (**1977**). ''Articulatory movements in VCV sequences,'' J. Acoust. Soc. Am. **62,** 183–193.
Gay, T., Boë, L. J., Perrier, P., Feng, G., and Swayne, E. (**1991**). ''The acoustic sensitivity of vocal tract constrictions: a preliminary report,'' J. Phonetics **19**, 445–452.
Hardcastle, W. J., Jones, W., Knight, C., Trudgeon, A., and Calder, G. (**1989**). ''New developments in electropalatography: A state-of-the-art report,'' Clin. Ling. Phon. **3**, 1–38.
Henke, W. L. (**1966**). ''Dynamic Articulatory Model of Speech Production using Computer Simulation,'' Ph.D. Dissertation, Massachussetts Institute of Technology.
Kent, R. D., and Moll, K. L. (**1972**). ''Cinefluorographic analyses of selected lingual consonants,'' J. Speech Hear. Res. **15,** 453–473.
Kiritani, S., Itoh, K., Hirose, H., and Sawashima, M. (**1977**). ''Coordination of the consonant and vowel articulations—X-ray microbeam study on Japanese and English,'' Ann. Bull. Res. Inst. Logopedics Phonatrics (University of Tokyo) **11**, 11–21.
Kondo, Y. (**1994**). ''Phonetic underspecification in schwa,'' in *ICSLP94*, Vol. 1 (The Acoustical Society of Japan), pp. 311–314.
Krakow, R. A. (**1989**). ''The Articulatory Organization of Syllables: A Kinematic Analysis of Labial and Velar Gestures,'' Ph.D. dissertation, Yale University.
Lindblom, B. (**1983**). ''Economy of speech gestures,'' in *The Production of Speech*, edited by P. F. MacNeilage (Springer-Verlag, New York), pp. 217–245.
Mooshammer, C., Hoole, P., and Kuhnert, B. (**1995**). ''On loops,'' J. Phonetics **23**, 3–22.
Öhman, S. (**1966**). ''Coarticulation in VCV sequences,'' J. Acoust. Soc. Am. **39,** 151–168.
Parush, A., Ostry, D. J., and Munhall, K. G. (**1983**). ''A kinematic study of lingual articulation in VCV sequences,'' J. Acoust. Soc. Am. **74,** 1115–1125.
Perkell, J. S. (**1969**). *Physiology of Speech Production:Results and Implications of a Quantitative Cineradiographic Study* (MIT, Cambridge).
Recasens, D. (**1984**). ''V-to-V coarticulation in Catalan VCV sequences,'' J. Acoust. Soc. Am. **76,** 1624–1635.
Recasens, D. (**1985**). ''Coarticulatory patterns and degrees of coarticulatory resistance in Catalan VCV sequences,'' Language Speech **28**, 97–114.
Recasens, D. (**1987**). ''An acoustic analysis of V-to-C and V-to-V coarticulatory effects in Catalan and Spanish VCV sequences,'' J. Phonetics **15**, 299–312.
Recasens, D. (**1989**). ''Long range coarticulatory effects for tongue dorsum contact in VCVCV sequences,'' Speech Commun. **8,** 299–312.
Recasens, D. (**1990**). ''The articulatory characteristics of palatal consonants,'' J. Phonetics **18**, 267–280.
Recasens, D. (**1991a**). ''An electropalatographic and acoustic study of consonant-to-vowel coarticulation,'' J. Phonetics **19**, 179–192.
Recasens, D. (**1991b**). ''Organización articulatoria durante la producción de algunas secuencias VCV del castellano,'' Rev. Argentina Lingü. **7**, 73–88.
Recasens, D. (**in press**). ''Lingual coarticulation,'' in *Coarticulation*, edited by W. J. Hardcastle (Cambridge U. P., Cambridge).
Recasens, D., Pallarès, M. D., and Fontdevila, J. (**1995**). ''Co-articulatory variability and articulatory-acoustic correlations for consonants,'' Eur. J. Disorders Commun. **30**, 203–212.
Recasens, D., and Romero, J. (**1997**). ''An EMMA study of segmental complexity in alveolopalatals and palatalized alveolars,'' Phonetica **54**, 43–58.
Sproat, R., and Fujimura, O. (**1993**). ''Allophone variation in English /l/ and its implications for phonetic implementation,'' J. Phonetics **21**, 291–312.
Stevens, K. N., House, A. S., and Paul, A. P. (**1966**). ''Acoustical description of syllabic nuclei: An interpretation in terms of a dynamic model of coarticulation,'' J. Acoust. Soc. Am. **40,** 123–132.
Stevens, K. N., and House, A. S. (**1955**). ''Development of a quantitative description of vowel articulation,'' J. Acoust. Soc. Am. **27,** 484–493.
Stone, M., Faber, A., Raphael, L. J., and Shawker, T. H. (**1992**). ''Cross-sectional tongue shape and linguopalatal contact patterns in [s], [ʃ], and [l],'' J. Phonetics **20**, 253–270.
Wada, T., Yasumoto, M., Iteoka, N., Fujiki, Y., and Yoshinaga, R. (**1970**). ''An approach to the cinefluorographic study of articulatory movements,'' Cleft Palate J. **7**, 506–522.
Wood, S. (**1979**). ''A radiographic analysis of constriction locations for vowels,'' J. Phonetics **7**, 25–43.

Tongue surface displacement during bilabial stops

Mario A. Svirsky,[a] Kenneth N. Stevens, Melanie L. Matthies, Joyce Manzella, Joseph S. Perkell, and Reiner Wilhelms-Tricarico

Speech Communication Group, Research Laboratory of Electronics, Massachusetts Institute of Technology, Cambridge, Massachusetts 02139

(Received 21 November 1995; accepted for publication 20 March 1997)

The goals of this study were to characterize tongue surface displacement during production of bilabial stops and to refine current estimates of vocal-tract wall impedance using direct measurements of displacement in the vocal tract during closure. In addition, evidence was obtained to test the competing claims of passive and active enlargement of the vocal tract during voicing. Tongue displacement was measured and tongue compliance was estimated in four subjects during production of /aba/ and /apa/. All subjects showed more tongue displacement during /aba/ than during /apa/, even though peak intraoral pressure is lower for /aba/. In consequence, compliance estimates were much higher for /aba/, ranging from 5.1 to 8.5×10^{-5} cm^3/dyn. Compliance values for /apa/ ranged from 0.8 to 2.3×10^{-5} cm^3/dyn for the tongue body, and 0.52×10^{-5} for the single tongue tip point that was measured. From combined analyses of tongue displacement and intraoral pressure waveforms for one subject, it was concluded that smaller tongue displacements for /p/ than for /b/ may be due to active stiffening of the tongue during /p/, or to intentional relaxation of tongue muscles during /b/ (in conjunction with active tongue displacement during /b/). © *1997 Acoustical Society of America.* [S0001-4966(97)03407-3]

PACS numbers: 43.70.Aj, 43.70.Bk [AL]

INTRODUCTION

What happens inside the vocal tract when an obstruent stop consonant is produced? Initially there is an increase in intraoral pressure, which can result in outward movement of the vocal-tract walls. All stop sounds require this pressure buildup to achieve a burst when they are released, but voiced and unvoiced stops require different articulatory adjustments. In particular, voiced stops require a transglottal pressure difference to sustain glottal vibration (although it may not always be sustained throughout closure). Two main mechanisms have been proposed that may be used by speakers to maintain this pressure difference: it may be done with *active* enlargement of the supraglottal vocal tract (Rothenberg, 1968; Kent and Moll, 1969; McGowan *et al.*, 1995), and/or with a relaxed state of supraglottal muscles (which results in *passive* deformation of the vocal tract; cf. Perkell, 1969). Bell-Berti (1974) proposed that pharyngeal cavity size may be controlled with predominantly passive or active mechanisms by different speakers. Westbury (1983) pointed out that while there was good reason to believe in an active component to facilitate voicing during a stop, the issue of active and passive contributions to vocal-tract enlargement would be difficult to settle on the basis of kinematic data alone.

At the end of a vowel preceding an unvoiced stop, glottal vibration may be stopped quickly by spreading the glottis, perhaps in combination with stiffening the vocal-tract walls. Following release of the consonant, the intraoral pressure decreases and the walls are hypothesized to move inward with a time constant that depends on their physical properties. Vocal-tract wall deformation has traditionally been analyzed using a lumped parameter model whose low-frequency equivalent is shown in Fig. 1. The model parameters are subglottal pressure P_s, transglottal impedance Z_g, and vocal-tract wall resistance R_w and compliance C_w. In this low-frequency approximation, valid below about 20 Hz, the mass of the vocal-tract walls is neglected. The parameters in this model are not fixed. For example, compliance values change greatly depending on whether articulatory muscles adopt a tense or lax state.

Accurate measurements of the parameters listed above are necessary to improve models for how long glottal vibration lasts during closure, and also to improve our models of the release of stop sounds. In particular, accurate estimates of vocal-tract compliance (i.e., the extent to which the vocal tract deforms in response to pressure) are important for designing articulatory models, because assuming rigid walls would lead to major errors in any model. Some existing estimates were obtained with indirect methods (Rothenberg, 1968) or using measurements made on surfaces outside the vocal tract (Ishizaka *et al.*, 1975; Wodicka *et al.*, 1993). The reason for such indirect approaches is that it is difficult to measure movement parameters inside the vocal tract, especially when the mouth and velum are closed. The goal of this study was to refine current estimates of vocal-tract impedance using direct measurements of tongue surface displacement during production of labial stops. In particular, we wanted to obtain evidence to test the competing claims of passive and active enlargement of the vocal tract during voicing. Our approach was made possible by the use of an electromagnetic midsagittal articulometer (EMMA; see Perkell *et al.*, 1992), which allowed us to gather sufficient quan-

[a]Currently at the Department of Otolaryngology—Head and Neck Surgery, Indiana University School of Medicine, Indianapolis, IN 46202-5200.

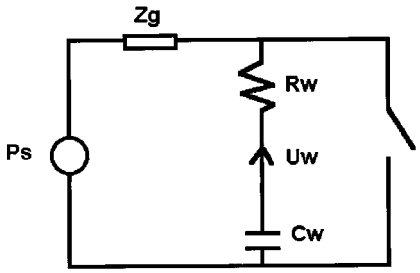

FIG. 1. Lumped parameter circuit model of the supraglottal cavity during a stop consonant. Z_g represents transglottal resistance; P_s is subglottal pressure; R_w and C_w are vocal-tract wall resistance and compliance; and U_w represents airflow. Vocal-tract wall mass is neglected at very low frequencies. Release of the stop is represented by the closure of the switch.

tities of kinematic data from vocal-tract structures during bilabial closure.

I. METHODS

The subjects were four young adult males. Two of them (S1 and S2) were native speakers of American English and the other two (S3 and S4) were native speakers of Ewe, an African language. Both English and Ewe voiced stops are typically produced with glottal vibration, at least at the beginning of the segment, when they are in intervocalic position. The productions from these four subjects were no exception, and the /b/ segments frequently showed glottal vibration throughout the entire closure. Subjects read at least ten repetitions each of three utterances: /apa/ and /aba/ (in which we were primarily interested), and /ama/ (included as a control condition). We expected to find minimal pressure-induced tongue surface displacement in the /ama/ control condition, because during the production of /m/ the velopharyngeal port is open so intraoral pressure remains low, precluding any passive tongue deformation. We used an electromagnetic midsagittal articulometer (EMMA: cf. Perkell *et al.*, 1992) to measure displacement of the tongue dorsum. A small transducer coil (4 mm by 4 mm base, 2.5 mm height) was fixed to the tongue surface (between 4 and 6 cm from the tongue tip) with a biocompatible cement. Alternating magnetic fields generated by a three-transmitter system induce an alternating voltage in the transducer coil. The transduced voltages from the tongue coil, as well as from two other coils placed on the upper incisors and the bridge of the nose for fixed reference points, were low-pass filtered at 100 Hz and digitized at 312.5 samples per s, (sps). Subject S4 had an additional transducer attached to the tongue blade, approximately 1 cm from the tip.

With subject S2, a Glottal Enterprises differential pressure transducer was used to simultaneously measure intraoral pressure (*re*: atmospheric pressure). The transducer was coupled to the oral cavity via a plastic (polyethylene) probe tube approximately 10 cm in length and with an inner diameter of 0.2 cm. The pressure measurements were calibrated using a U-tube manometer and were found to be linear over the pressure range of interest (0–24 cm H_2O).

The acoustic signal was recorded through a directional microphone, low-pass filtered at 4.8 kHz and sampled at 10 kHz. After digitizing the acoustic, movement, and (in S2's case) pressure data, the signals were demultiplexed into separate, time-aligned signal streams. The digitized movement data were then low-pass filtered with 71-tap FIR filters (cutoff frequency about 150 Hz), and converted to x,y coordinates with reference to an x axis which lies in the midsagittal plane, and is parallel to the subject's occlusal plane.

Figure 2 shows a display generated by the software used to extract movement data. The acoustic signal during an /apa/ utterance is shown in window 1, where T_b, T_r, and T_a indicate closure, release, and beginning of the second /a/, respectively. Window 2 shows the expanded acoustic signal around the time of release, T_r. Time-aligned movement data (the positions of a tongue transducer) are shown in window 3: The three traces are the x and y coordinates of the tongue transducer over time, and a measure of transducer misalignment (see Perkell *et al.*, 1992). Window 4 shows an x-y plot of the displacement data (the front of the vocal tract is to the right) and a reference circle of 1 mm radius. The trajectory of the tongue transducer is indicated by the dotted line, with dots representing samples taken at 3.2-ms intervals. The acoustic events were marked interactively for each utterance: the time of closure T_b, defined as the point in the acoustic time waveform just after the last full glottal cycle of the first /a/; the time of release, T_r, defined as the point in the acoustic waveform where there is a sudden increase in high-frequency noise amplitude at the end of the closure period; and T_a, defined as the point in the acoustic waveform just before the first full glottal cycle of the second /a/. A cursor, time-aligned across all the displays, was used to mark the events T_b, T_r, and T_a. The zoomed speech waveform with the cursor located at release time T_r, shown in window 2, was used to locate T_r more precisely. As the x-y data in window 4 show, beginning at the time of closure there is a downward displacement of the tongue, which is presumably due to increased intraoral pressure. At the time of release intraoral pressure is sharply reduced and the tongue moves back up.

Because the x-y data were rotated to make the occlusal plane horizontal, the y axis is the direction perpendicular to the occlusal plane. Mechanical compliance per unit area was calculated as the displacement perpendicular to the occlusal plane (i.e., along the y coordinate) that occurred between T_b and T_r, divided by the estimated peak intraoral pressure. This way of calculating compliance assumes that the tongue displacement perpendicular to the occlusal plane between T_b and T_r is due to increased intraoral pressure. Therefore, systematic movements perpendicular to the occlusal plane and unrelated to pressure would result in over- or underestimates in our compliance measurements. Peak intraoral pressure estimates were obtained from a study of pressure during VCV syllables in males, females, and children by Subtelny *et al.* (1966). We used the average male values from that study: 6.43 cm of H_2O for /p/ and 4.37 cm of H_2O for /b/. While this methodology is appropriate to obtain reasonable estimates of compliance, it may be refined in future studies by measuring intraoral pressure for all subjects. Another possible refinement would involve the simultaneous analysis of the locations of several pellets to separate the local reaction

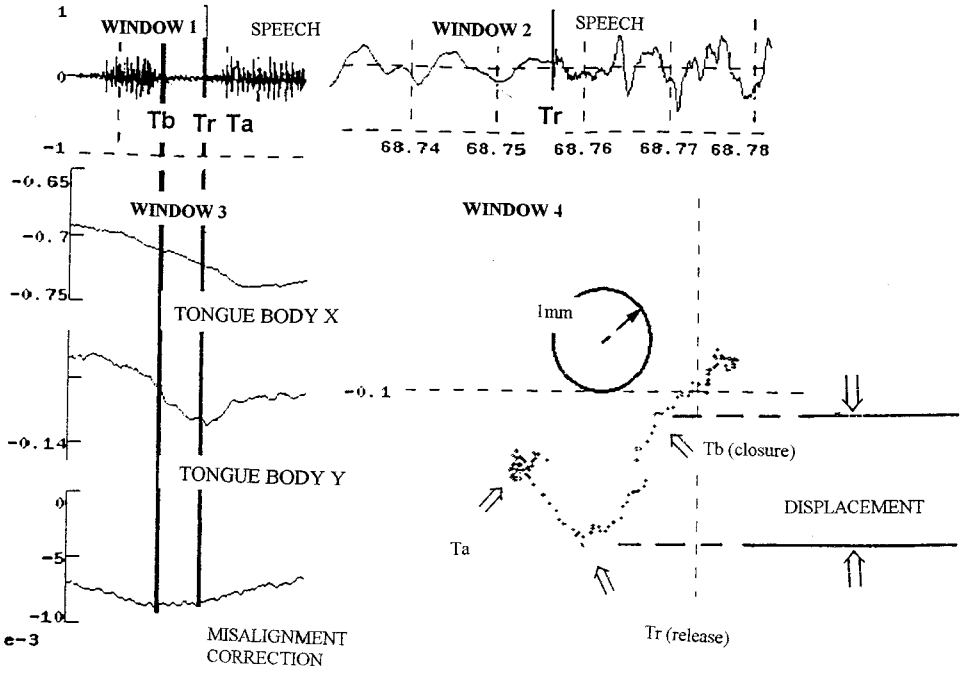

FIG. 2. Display used to extract movement data. Window 1 shows the speech signal for one /aba/ token. Three points are marked: T_b, the beginning of closure, defined as the point in the acoustic time waveform just after the last full glottal cycle of the first /a/; the time of release, T_r, defined as the point in the acoustic waveform where there is a sudden increase in high-frequency noise amplitude at the end of the closure period; and T_a defined as the point in the acoustic waveform just before the first full glottal cycle of the second /a/. Window 2 shows the expanded acoustic signal around T_r. Time axis values are in s. Note the weak periodicity before T_r and the release noise immediately following T_r. Time-aligned movement data are shown in window 3: x and y coordinates of the tongue transducer (in dm), and a measure of transducer misalignment correction (see Perkell *et al.*, 1992). Window 4 shows an x-y plot of the same data, with the occlusal plane being parallel to the x axis and the front of the vocal tract placed to the right. The tongue surface starts a more pronounced downward displacement at closure time T_b, it reverses its movement direction at release time T_r, and remains relatively steady after the second vowel starts at T_a. A 1-mm circle is displayed as a reference, and the two horizontal lines to the right of the x-y data indicate measured displacement for this token.

to pressure on the tongue surface from the global component of tongue deformation.

The pressure and movement signals obtained from subject S2 were used to assess the validity of a passive tongue displacement model. If tongue displacements during closure were mostly passive and driven by intraoral pressure, the displacement trace should lag pressure by a small time interval (determined by the impedance of the vocal-tract walls). On the other hand, if vocal-tract expansion was actively driven, displacement and pressure signals would not necessarily be time synchronized. We assessed the synchrony between pressure and displacement waveforms in two ways. First, we found the time difference corresponding to the maximum of the correlation function between each pair of pressure and displacement signals (holding one signal fixed and applying variable time shifts to the other signal). Second, we determined the relative positions of the most prominent peak in the (smoothed) first derivatives of each pressure and displacement signal. These peaks indicate the instants when each signal is changing at a maximum rate.

We also assessed the pressure-displacement relation by applying two kinds of mathematical models to the pressure-displacement data. First we used a second-order model of the form

$$\text{Pressure} = m\,\frac{d^2y}{dt^2} + b\,\frac{dy}{dt} + ky, \tag{1}$$

where y is vocal-tract displacement perpendicular to the occlusal plane and m, b, and k are constants representing mass, damping, and stiffness per unit area, respectively. Equation (1) can be discretized and rewritten as:

$$\text{Pressure}(n) = a_0 y(n) + a_1 y(n-1) + a_2 y(n-2) \tag{2}$$

for the purpose of fitting discrete-time signals. For each of the ten /aba/ and ten /apa/ tokens, a least-squares procedure was applied to obtain values of a_1, that minimized the difference between predicted and actual displacement. To the extent that tongue displacement is passive and the second-order model in Eq. (2) is accurate, this model should give a good prediction of displacement as a function of the driving pressure. The other model that we used incorporated a linear trend, in addition to the parameters of the first model:

$$\text{Pressure}(n) + a_3 n + a_4 = a_0 y(n) + a_1 y(n-1) + a_2 y(n-2). \tag{3}$$

The left side of the equation now includes, in addition to the measured intraoral pressure, a linear term that represents active expansion of the vocal tract (i.e., downward tongue displacement). If vocal-tract expansion was passive, Eq. (2) would give good predictions of tongue displacement, and Eq. (3) would not yield substantially better fits than Eq. (2). On the other hand, if vocal-tract expansion was at least partly active, Eq. (3) should provide better fits to the data than Eq. (2) and the estimated values of a_3 should be positive, indicating that downward (rather than upward) displacement of

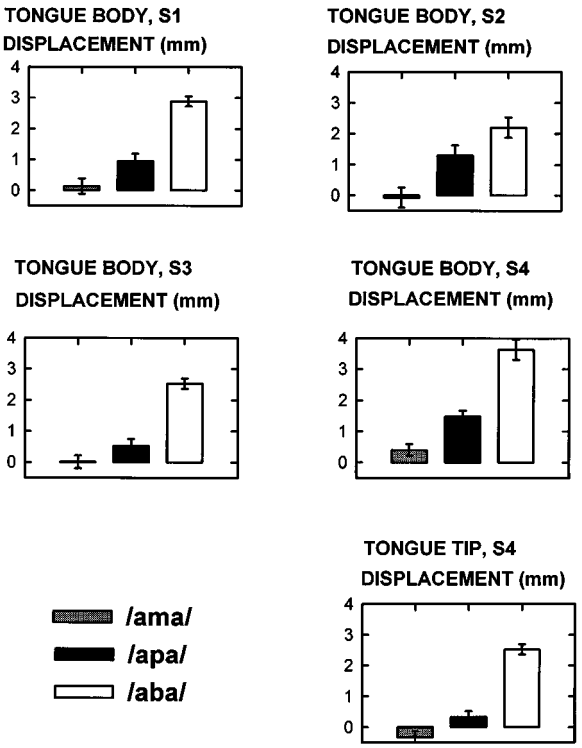

FIG. 3. Mean tongue displacement and standard errors for each category, subject, and (in S4's case) each tongue transducer. Transducers are in the tongue body for all subjects and, in S4's case, there is an additional transducer near the tongue tip.

the vocal tract is taking place and that this displacement is unrelated to intraoral pressure.

II. RESULTS

A. Tongue displacement and estimated compliance

Figure 3 shows plots of mean tongue displacement and standard error values for each token, subject, and (in S4's case) each tongue transducer. A series of *t*-tests revealed that in all cases, the magnitude of peak displacement for /aba/ (in the direction perpendicular to the occlusal plane) was significantly higher than for /apa/, and significantly higher for /apa/ than for /ama/. Displacements during /ama/ were not significantly different from zero. Table I shows average peak displacements and the compliances associated with them.

TABLE I. Average displacement perpendicular to the occlusal plane for each subject, token type and (for subject S4) transducer location. All numbers are the mean from ten measurements. The two bottom rows list compliance values calculated based on the displacements that appear in the first three rows.

		S1	S2	S3	S4 (tongue body)	S4 (tongue tip)
displacement (mm)	ama	0.13	−0.07	0.01	0.39	−0.32
	apa	0.95	1.30	0.52	1.48	0.33
	aba	2.89	2.20	2.53	3.64	2.53
Compliance (cm^3/dyn) (all numbers are $\times 10^{-5}$)	apa	1.51	2.06	0.82	2.35	0.52
	aba	6.74	5.13	5.90	8.49	5.90

B. Synchrony between intraoral pressure and tongue displacement

Figures 4 and 5 show intraoral pressure and displacement over time for S2, for /apa/ and /aba/ tokens, respectively. Intraoral pressure rises rapidly during /apa/, which is consistent with oral closure and the open glottal configuration necessary to stop voicing. Pressure during /aba/ rises more slowly, with lower values at the time of release. This result is consistent with the need to maintain a transglottal pressure difference that is compatible with continued glottal vibration (the pressure traces do indeed show fluctuations due to glottal vibration almost through the end of most /aba/ tokens). It is interesting to observe that the relatively sharp, fast downward tongue dorsum displacements during /apa/ or /aba/ were generally close to the rise in intraoral pressure. Consistent with this observation, maxima of the cross-correlation functions between pressure and displacement for all /apa/ tokens were obtained, with displacement lagging pressure by a mean of 1.3 ms and a standard error of 1.0 ms. In other words, the cross-correlation function is maximized when pressure is delayed by about 1.3 ms. Results for /aba/ were qualitatively similar, with a mean lag of 5.4 ms and a standard error of 1.9 ms.

We also compared the timing of the peaks of the first derivative for the pressure and displacement traces. This comparison indicates the timing between rapid changes in the two signals. The comparison was made both for the timing between pressure increase and downward tongue displacement, and for the timing between pressure release and the concomitant upward displacement of the tongue. For /apa/, the maximum of the first derivative of the pressure rise preceded the one for displacement by 10.0 ms (standard error: 1.2 ms) and the maximum for the pressure decrease preceded the one for displacement by 8.2 ms (standard error: 0.9 ms). First derivative maxima for displacement traces showed longer lags for /aba/: 18.2 ms for the pressure rise and 12.1 ms for the release (standard errors of 1.4 and 2.7 ms, respectively). Longer lags for /aba/ than for /apa/ are consistent with the greater compliance measured during the voiced stop, since (according to the model depicted in Fig. 1) the displacement time constants are the product of vocal-tract wall resistance and compliance.

C. Modeling tongue displacement

Figure 6 shows vertical tongue displacement for two representative /apa/ tokens, as well as the two model predictions for each token. Connected dots show actual data; dotted lines are the predictions made by the second-order model with no trend, and the solid lines are predictions made by the model that includes a linear trend. Visual examination of the top panel reveals that the model with a linear trend predicts displacement much better than the model with no trend, while both models provide similarly good predictions for the token in the bottom panel. One way to quantify this observation is to calculate the rms of the residuals (i.e., the rms of the difference between model predictions and actual displacement) for each token and each model. Residuals for the token in the top panel were 0.78 mm (model with no trend)

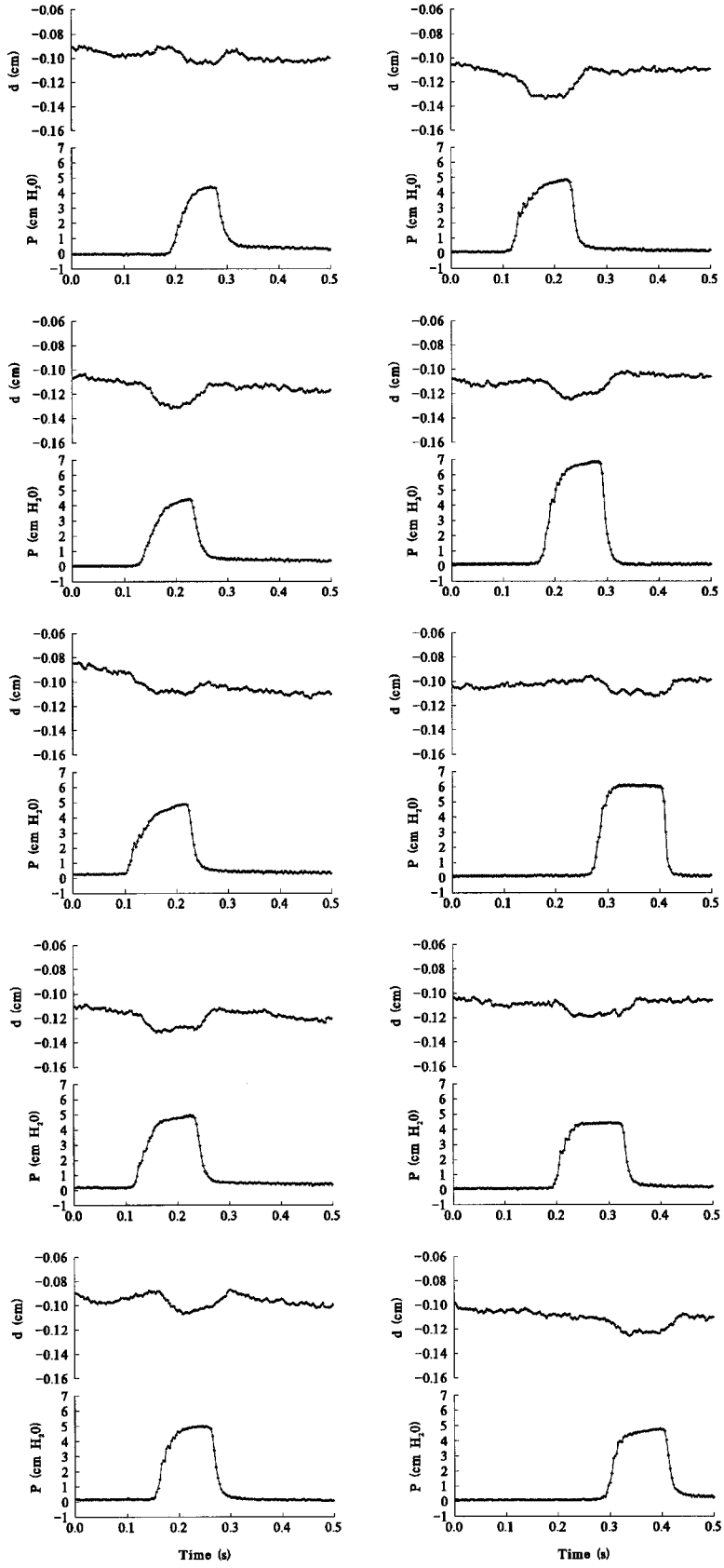

FIG. 4. Tongue displacement (perpendicular to the occlusal plane) and pressure waveforms for /apa/ utterances from subject S2. The top trace in each panel shows tongue displacement in the direction perpendicular to the occlusal plane (in dm), and the bottom trace shows pressure (in cm H_2O). The horizontal axis is time (s), and the plots span 500 ms.

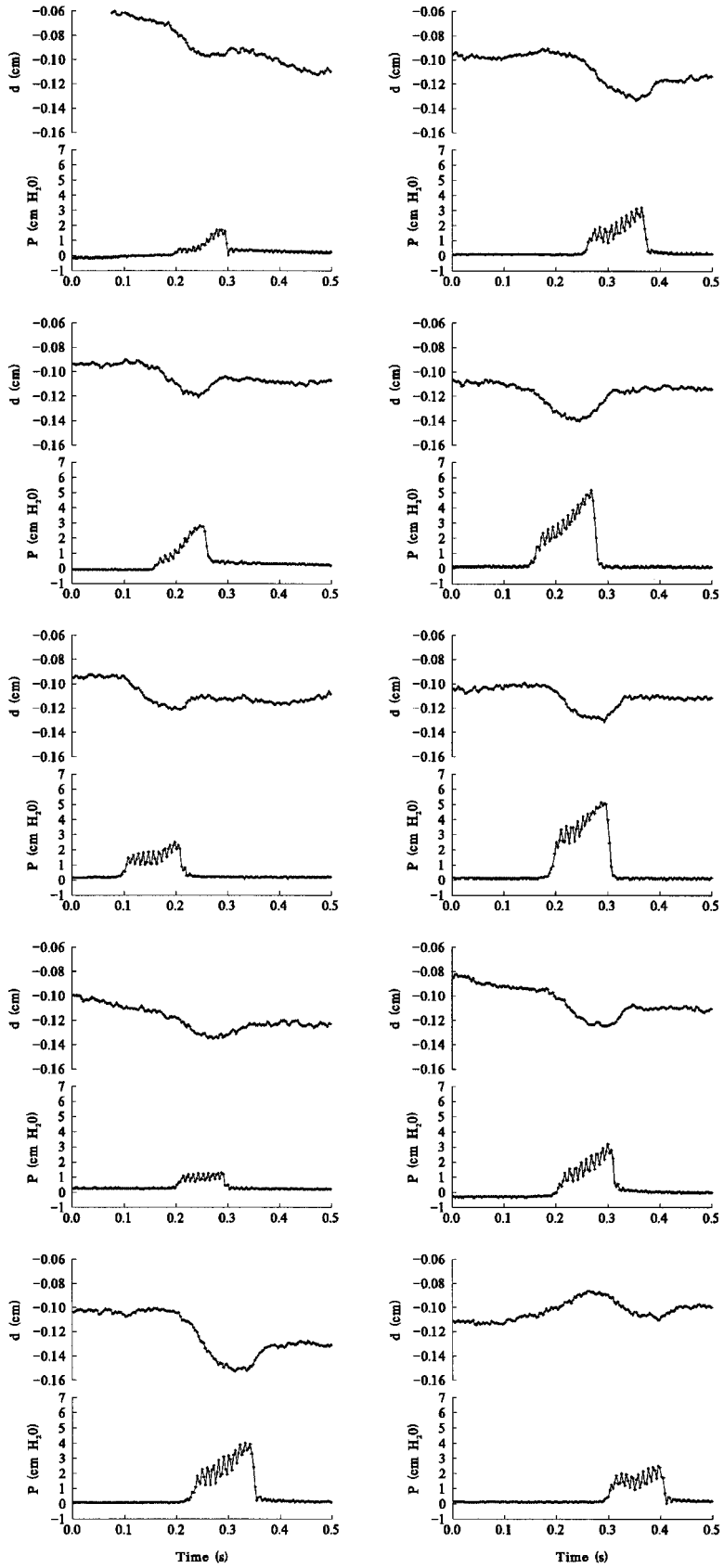

FIG. 5. Tongue displacement and pressure waveforms for /aba/ utterances, subject S2. The top trace in each panel shows tongue displacement in the direction perpendicular to the occlusal plane (in dm), and the bottom trace shows pressure (in cm H_2O). The horizontal axis is time (s), and the plots span 500 ms.

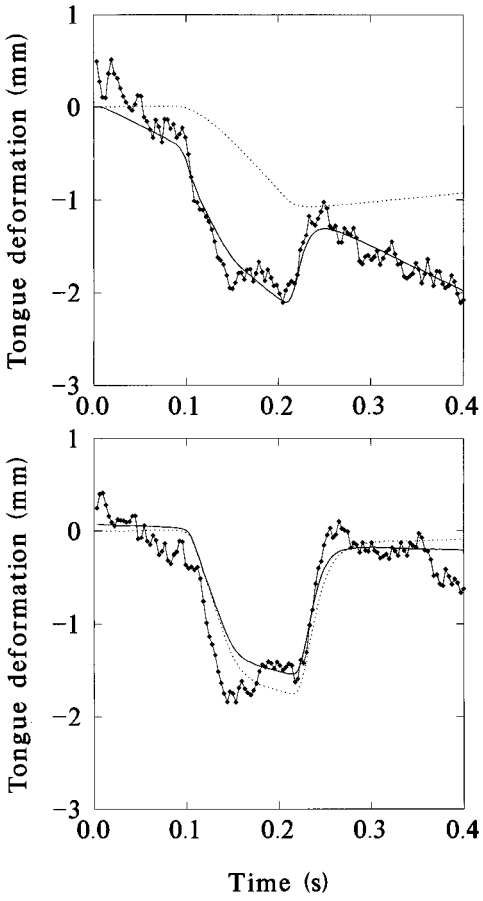

FIG. 6. Black dots show tongue deformation in the direction perpendicular to the occlusal plane (versus time) for two representative /apa/ tokens. The superimposed lines show model predictions for each token. Dotted lines correspond to a second-order model with no trend, which gave a poor fit for the token shown in the top panel (residual of 0.78 mm) and a good fit for the token in the bottom panel (residual was 0.28 mm). Predictions of the model with a linear trend are represented with solid lines. This model yielded good fits for both tokens, with residuals of 0.17 and 0.23 mm for the top and bottom panels, respectively (note how the solid lines seem to match the data relatively well).

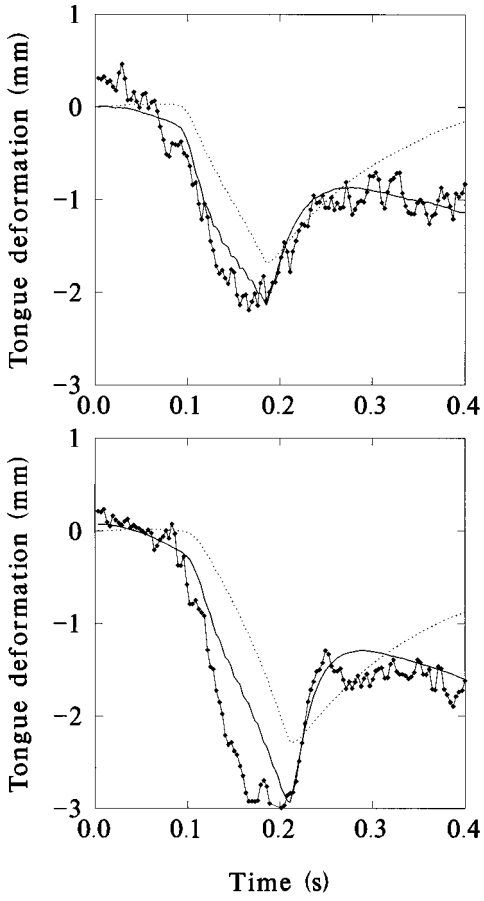

FIG. 7. Black dots show tongue deformation in the direction perpendicular to the occlusal plane for two representative /aba/ tokens, and the superimposed lines show model predictions for both tokens. Residuals were poor for the model with no trend (residuals of 0.52 and 0.75 mm, respectively) but were good for the model that included a linear trend (0.21 and 0.29 mm).

and 0.17 mm (model with linear trend); whereas for the token in the bottom panel residuals were 0.28 mm (model with no trend) and 0.23 mm (model with linear trend). Figure 7 shows two representative /aba/ tokens and model predictions. Residuals were poor for the model with no trend (residuals of 0.52 and 0.75 mm, respectively) but were good for the model that included a linear trend (0.21 and 0.29 mm).

Table II lists the rms residuals obtained for each /aba/ and /apa/ token using each model. To summarize the data, we may classify residuals in three categories: residuals smaller than 0.3 mm indicate a very good fit since measurement noise for the EMMA system we used is in the order of 0.2 mm; residuals greater than 0.5 mm are classified as ''poor'' and residuals between 0.3 and 0.5 mm are classified as ''intermediate.'' Although any classification scheme such as this one has to be somewhat arbitrary, other definitions of good, bad, and intermediate tokens would not change the conclusions we draw from the data.

The first column in Table II shows that the fit was quite poor for /aba/ tokens using the model with no trend: Eight tokens gave a poor fit, two were intermediate, and none were well fit by the model. The average residual (0.93 mm) was quite large. Results using the model with no trend were much better for /apa/ than for /aba/: Five tokens gave a good fit, only two gave a poor fit and three were intermediate. The

TABLE II. rms values of the difference between modeling results and actual tongue displacement (i.e., residuals) for each /aba/ and /apa/ token, for second-order models with and without a superimposed linear displacement trend. Estimates for the trends superimposed on each individual token are also shown.

	Model with no trend		Model with linear trend			
	aba	apa	aba		apa	
	residuals (mm)	residuals (mm)	resid (mm)	trend (mm/s)	resid (mm)	trend (mm/s)
1	2.53	0.41	0.47	11.0	0.29	1.5
2	0.74	0.34	0.27	4.1	0.19	1.3
3	0.53	0.78	0.21	5.4	0.17	4.9
4	0.52	0.28	0.21	2.8	0.23	0.7
5	1.54	0.42	0.67	7.1	0.40	0.5
6	1.05	0.27	0.36	6.1	0.27	0.0
7	0.68	0.69	0.63	0.5	0.23	−1.9
8	0.50	0.21	0.19	2.8	0.16	−0.7
9	0.75	0.27	0.29	4.4	0.14	−1.0
10	0.46	0.22	0.33	2.5	0.17	−0.5
Mean	0.93	0.39	0.36	4.7	0.22	0.48

average residual was 0.39 mm. Residuals for /aba/ were substantially better with the model that incorporated a linear trend than with the model with no trend: Five tokens were well fit by the model, only two were poorly fit, and three were intermediate, with a mean residual of 0.36 mm over all tokens. Addition of a linear trend to the model improved the fit to the /apa/ tokens as well (mean residual was 0.22 mm) but this improvement was less dramatic than for /aba/, mostly because the model without a linear trend was quite good for /apa/ tokens to begin with.

Table II also shows that the linear displacement trends obtained with the model were quite different for voiced and unvoiced tokens: /aba/ tokens required sizeable trends that were always positive, indicating a downward trend in tongue movement (4.8 mm/s on the average), while /apa/ tokens were best fit with rather small trends (mean of 0.48 mm/s) that were sometimes positive and sometimes negative. This result suggests that a significant downward tongue movement, unrelated to intraoral pressure, occurred during production of /aba/ but not during /apa/. However, this was not enough to influence initial compliance estimates significantly. Finally, the second-order coefficients were quite small, suggesting that the second-order model does not provide a substantially better description than the first-order model depicted in Fig. 1.

III. DISCUSSION

A. Values of tongue compliance

All subjects showed more tongue displacement during /aba/ than during /apa/ ($p<0.05$, two-tailed t-tests), even though peak intraoral pressure was lower for /aba/. In consequence, compliance estimates were much higher for /aba/, ranging from 5.1 to 8.5×10^{-5} cm^3/dyn. Compliance values for /apa/ ranged from 0.82 to 2.35×10^{-5} cm^3/dyn for the tongue body and 0.52×10^{-5} for the single tongue tip point that was measured. Tongue displacement values for /ama/ were not significantly different from zero, indicating that the tongue movement observed during the plosives was not simply a coarticulatory effect of bilabial closure.

To the extent that they can be compared, these values are consistent with the literature. Ishizaka *et al.* (1975) measured the compliance of the cheek and neck outer surfaces, finding cheek compliance values of 0.3×10^{-5} cm^3/dyn for a tense posture and 1.18×10^{-5} cm^3/dyn for a lax posture of the cheek, roughly equal to the values found by Wodicka *et al.* (1993) for the maternal abdomen. These values are 2–8 times smaller than the ones we found for the tongue, possibly reflecting an actual difference in compliance for tongue versus cheek surfaces. In another study, Rothenberg (1968) measured the average compliance of the vocal tract by measuring the change of pressure resulting from the introduction or removal of known quantities of air from the oral cavity. With the articulators positioned for a bilabial stop and assuming a lax posture, the measured value was 4×10^{-5} cm^3/dyn; when the cheeks and lips were tensed, the measured value was 0.68×10^{-5} cm^3/dyn. Assuming an alveolar closure position with lax vocal-tract walls, the compliance was 0.53×10^{-5} cm^3/dyn and with tense walls it was 0.38×10^{-5} cm^3/dyn. These values are somewhat lower than the ones we measured. This discrepancy may be due to the different nature of the measurements: Rothenberg measured average vocal-tract compliance while we measured compliance of the tongue dorsum and tip, which should be higher than average vocal-tract compliance (as discussed below).

It is important to note that the method we used for estimating compliance is correct only for pressure-driven movements (as tongue displacement during /p/ may have been during these experiments) but not for movements that are at least partly active. Assuming that the 4.7-mm/s linear displacement trend estimated for /b/ was the active part of the movement, and that the average time from closure to release was 100 ms, the average deformation due to active movement would be about 0.47 mm. If this estimate applied to all subjects in the study, the compliance estimates for /b/ would be 13%–21% too high, because the displacement due to pressure alone would be 0.47 mm less than the values listed in Table I. In addition to this systematic error, there is a ''random'' source of error in our measurements, arising from using values from the literature for intraoral pressure. Intersubject variability in intraoral pressure, as measured by the standard deviations in Subtelny and Worth's study, was 1.07-cm H_2O for /b/ and 1.42-cm H_2O for /p/. These standard deviations amount to 17% of the mean values for /p/ and 32% of the mean values for /b/. Since the relative accuracy of distance measurements obtained with EMMA is much lower than this 17%–32% range (Perkell *et al.*, 1992), the accuracy of our compliance estimates is limited by the accuracy of the intraoral pressure values that we used. Future studies should obtain simultaneous pressure and kinematic measures in a large number of subjects, and attempt to factor out the effect of active vocal tract movements.

B. Tongue compliance versus average vocal-tract compliance

In order to make a more informed comparison between our compliance measurements and those obtained by Rothenberg, we need to assess the possible range of average vocal-tract compliance. An indirect way of estimating average vocal-tract compliance during /aba/ is to estimate the volume of air passing into the vocal tract (during the closure for the voiced stop) and the average displacement of the subject's vocal-tract surface. The ratio of these two parameters is the average displacement of the vocal tract, and it can be used to estimate compliance. Since all our subjects are male, we used a vocal-tract surface area of 100 cm^2 for these calculations (the approximate area of a cylinder that has an average cross section of 3 cm^2 and a length of about 17 cm). Holmberg *et al.* (1988) measured average flow during production of a vowel in 25 male subjects, finding an average of 0.19 l/s and a standard deviation of 0.07 l/s. Average glottal flow during /b/ is less than during a vowel because transglottal pressure decreases during closure, as intraoral pressure rises. As a rough approximation, we estimate average flow during /b/ as 50% of the vowel flow. Average closure dura-

tion during /b/ was approximately 100 ms for our subjects. In consequence, the amount of air entering the vocal tract during /b/ is estimated as

$$\text{volume} = 0.19 \text{ l/s} \times 0.5 \times 0.1 \text{ s} = 0.0095 \text{ l} = 9.5 \text{ cm}^3.$$

In a vocal tract with 100-cm^2 surface, the average deformation would be 9.5 cm^3/100 cm^2=0.095 cm=0.95 mm.

Assuming a peak pressure of 5-cm H_2O for /b/, the resulting average compliance during /b/ is 1.94×10^{-5} cm^3/dyn, consistent with Rothenberg's values and between 2.6 and 4.4 times lower than our tongue compliance values. Even if we use very conservative values (0.3 l/s, the highest flow measured by Holmberg *et al.* among 25 subjects; /b/ duration of 150 instead of 100 ms), the resulting estimate of average vocal-tract compliance would be 4.6×10^{-5} cm^3/dyn, lower than any of our measured values for the tongue. We conclude that compliance of the tongue dorsum (at least during production of /b/) is quite probably higher than for the rest of the vocal tract.

C. Passive displacement or active expansion?

Cineradiographic studies have found that voiced stops are produced with a larger supraglottal volume than their voiceless cognates (Kent and Moll, 1969; Perkell, 1969). Perkell proposed that this difference may be due to passive expansion permitted by more lax vocal-tract walls during production of the voiced consonant (at least for alveolars). Kent and Moll preferred the explanation that the larger supraglottal volume during voiced stops was due to active expansion of the vocal tract. In a study that modeled the aerodynamic data obtained by Löfqvist *et al.* (1995), McGowan *et al.* (1995) found support for the hypothesis of active upper vocal-tract volume control. Rothenberg (1968) estimated that ''in bilabial and retroflexed closures the [supraglottal] cavity can be used to absorb the glottal air flow to maintain voicing during a reasonably long articulatory closure,'' but he thought this explanation was less plausible for some occurrences of voiced alveolar stops. Bell-Berti (1974) found that speakers use different mechanisms to allow pharyngeal expansion during utterance-medial voiced stops. It is indeed difficult to select one of the two explanations without access to appropriate experimental data. Westbury (1993) correctly indicated that ''it is at least difficult, if not impossible [...] to differentiate changes in vocal-tract dimensions resulting from vocal-tract expansion and cavity enlargement'' (i.e., passive or active expansion) using only kinematic data.

However, we believe our combined kinematic and aerodynamic data from subject S2 may help shed light on this issue, suggesting that tongue deformation may be passive and pressure driven for /apa/ and that active vocal-tract expansion is superimposed on the passive, pressure driven deformation for /aba/. The present data confirm that there is more vocal-tract expansion during /b/ than during /p/, but do not support the active expansion hypothesis as the *sole* explanation. Active expansion could conceivably start anytime around the beginning of the voiced stop. However, study of the synchrony between pressure and displacement data in subject S2 (see Figs. 4 and 5) shows that pressure increases are always followed a few milliseconds later by downward tongue displacements. This close synchrony is consistent with passive, pressure driven increase of supraglottal size but not with solely active expansion, unless we are willing to postulate that active tongue movements and pressure increases are synchronized so well that the lag between them has a standard deviation of 1–2 ms, a time interval about the same length as a single action potential. Thus the close synchrony favors a passive component. An active component is indicated by the modeling of tongue deformation for /aba/ tokens, which shows reasonably good results only when a linear trend is included in the model. The fitted slopes are positive (i.e., downward tongue displacement) for all ten /aba/ tokens and are quite substantial, averaging 4.7 mm/s. On the other hand, modeling /apa/ tokens shows that reasonably good fits can be obtained without a linear trend. When a linear trend is included in the voiceless data, the slopes are sometimes positive, sometimes negative, and they average only 0.48 mm/s. In summary, a presumably active, substantial, consistent linear displacement is superimposed on pressure driven tongue displacement during /aba/ but a similar case may not be made for /apa/, where tongue displacement can be reasonably explained by passive, pressure driven deformation only. However, these conclusions cannot be overgeneralized because they are based on few data: a single fleshpoint of a single talker. The relative contribution of pressure driven deformation and active movement during bilabial stops remains an open question that should be explored in future studies, to refine the estimates of tongue compliance.

IV. SUMMARY

We conclude that our kinematic data are consistent with the physical description provided in the Introduction, based on a simple lumped parameter model that includes vocal-tract resistance and compliance. Smaller tongue displacements for /p/ than for /b/ may be due to active stiffening of the tongue during /p/, and/or to intentional relaxation of tongue muscles during /b/ (in conjunction with active tongue displacement during /b/), in order to accommodate airflow into the oral cavity while maintaining a transglottal pressure differential that will allow vocal fold vibration. Finally, these data allow us to refine estimates of vocal-tract wall compliance obtained with indirect methods.

ACKNOWLEDGMENTS

This research was supported by NIDCD Grant Nos. DC00075, DC01925, and DC00423.

Bell-Berti, F. (**1975**). ''Control of pharyngeal cavity size for English voiced and voiceless stops,'' J. Acoust. Soc. Am. **57,** 456–461.

Holmberg, E., Hillman, R., and Perkell, J. (**1988**). ''Glottal airflow and transglottal air pressure measurements for male and female speakers in soft, normal and loud voice,'' J. Acoust. Soc. Am. **84,** 511–529.

Ishizaka, K., French, J. C., and Flanagan, J. L. (**1975**). ''Direct determination of vocal tract wall impedance,'' IEEE Trans. Acoust. Speech Signal Process. **4,** 370–373.

Kent, R. D., and Moll, K. L. (**1969**). ''Vocal tract characteristics of the stop cognates,'' J. Acoust. Soc. Am. **46,** 1549–1555.

Löfqvist, A., Koenig, L. L., and McGowan, R. S. (**1995**). ''Vocal tract aerodynamics in /aCa/ utterances: Measurements,'' Speech Commun. **16,** 49–66.
McGowan, R. S., Koenig, L. L., and Löfqvist, A. (**1995**). ''Vocal tract aerodynamics in /aCa/ utterances: Simulations,'' Speech Commun. **16,** 67–88.
Perkell, J. S. (**1969**). ''Physiology of speech production: Results and implications of a quantitative cineradiographic study,'' Research Monograph No. 53 (MIT, Cambridge, MA).
Perkell, J. S., Cohen, M. H., Svirsky, M. A., Matthies, M. L., Garabieta, I., and Jackson, M. T. T. (**1992**). ''Electro-magnetic midsagittal articulometer (EMMA) systems for transducing speech articulatory movements,'' J. Acoust. Soc. Am. **92,** 3078–3096.
Rothenberg, M. (**1968**). ''The breath-stream dynamics of simple-released-plosive production,'' *Bibliotheca Phonetica*, No. 6 (Karger, Basel).
Subtelny, J. D., Worth, J. H., and Sakuda, M. (**1966**). ''Intraoral pressure and rate of flow during speech,'' J. Speech Hear. Res. **9,** 498–518.
Westbury, J. (**1983**). ''Enlargement of the supraglottal cavity and its relation to stop consonant voicing,'' J. Acoust. Soc. Am. **73,** 1322–1336.
Wodicka, G. R., Lam, A. M., Bhargava, V., and Sunkel, D. (**1993**). ''Acoustic impedance of the maternal abdomen,'' J. Acoust. Soc. Am. **94,** 13–18.

Developmental weighting shifts for noise components of fricative-vowel syllables

Susan Nittrouer and Marnie E. Miller
Boys Town National Research Hospital, 555 North 30th Street, Omaha, Nebraska 68131

(Received 22 July 1996; revised 14 February 1997; accepted 19 March 1997)

Previous studies have convincingly shown that the weight assigned to vocalic formant transitions in decisions of fricative identity for fricative-vowel syllables decreases with development. Although these same studies suggested a developmental increase in the weight assigned to the noise spectrum, the role of the aperiodic-noise portions of the signals in these fricative decisions have not been as well-studied. The purpose of these experiments was to examine more closely developmental shifts in the weight assigned to the aperiodic-noise components of the signals in decisions of syllable-initial fricative identity. Two experiments used noises varying along continua from a clear /s/ percept to a clear /ʃ/ percept. In experiment 1, these noises were created by combining /s/ and /ʃ/ noises produced by a human vocal tract at different amplitude ratios, a process that resulted in stimuli differing primarily in the amplitude of a relatively low-frequency (roughly 2.2-kHz) peak. In experiment 2, noises that varied only in the amplitude of a similar low-frequency peak were created with a software synthesizer. Both experiments used synthetic /ɑ/ and /u/ portions, and efforts were made to minimize possible contributions of vocalic formant transitions to fricative labeling. Children and adults labeled the resulting stimuli as /s/ vowel or /ʃ/ vowel. Combined results of the two experiments showed that children's responses were less influenced than those of adults by the amplitude of the low-frequency peak of fricative noises. [S0001-4966(97)06307-8]

PACS numbers: 43.71.An, 41.71.Ft [WS]

INTRODUCTION

Previous work conducted in this laboratory has investigated developmental changes in the phonetic labeling of syllable-initial fricatives /s/–/ʃ/. The first studies (Nittrouer, 1992; Nittrouer and Studdert-Kennedy, 1987) examining these developmental changes followed from earlier work with adults on phonetic context effects in fricative labeling (Kunisaki and Fujisaki, 1977; Mann and Repp, 1980; Whalen, 1981). Those experiments with adults were designed largely to establish whether or not experienced listeners make use perceptually of changes in the spectra of fricative noises due to the quality of the following vowel; specifically, lip-rounding is thought to lower the overall spectral center of gravity. At the time of those experiments, attributes of vocalic syllable portions were considered secondary to the perception of syllable-initial fricatives in that, according to this view, they only indirectly influence perception through their acoustic effect on the primary cue. The fricative noise itself was considered to be the primary cue. To investigate these phonetic context effects, stimuli were constructed with fricative noises varying along a frequency continuum, and with vocalic portions appropriate for a rounded or unrounded vowel. The first studies of children's fricative labeling had the stated goal of examining whether or not children had sufficient experience to use these purported secondary properties of the vocalic portion in making decisions about fricative identity.

Since those first experiments with adults, prevailing views of speech perception have shifted in a subtle but significant way. Although details of the process have yet to be agreed upon, it is now generally accepted that phonetic category judgments depend upon the perceptual integration of multiple acoustic properties spread across the spectrum in time and/or frequency (e.g., Best *et al.*, 1989; Hodgson and Miller, 1992; Kluender *et al.*, 1988; Remez *et al.*, 1994). One finding from early studies of phonetic context effects that helped to effect this change in viewpoint was that formant transitions at voicing onset were found to influence decisions of fricative identify. Thus a direct consequence of fricative production found in a portion of the signal temporally separate from the acoustic fricative segment had clear perceptual consequences for fricative identification. This sort of influence of one signal portion on perceptual decisions about what had been considered to be a separate segment could not be viewed as a phonetic context effect. Furthermore, it was shown that children can use such temporally diverse properties in making phonetic decisions, at least as well as adults (Walley and Carrell, 1983).

In studies of fricative-vowel syllables, the relative weights assigned to characteristics of the aperiodic noise and to characteristics of the vocalic formants vary across listeners of different ages (Nittrouer, 1992, 1996; Nittrouer and Studdert-Kennedy, 1987). Children assign more weight than adults to characteristics of the vocalic formant transitions, but assign less weight to characteristics of the noise spectra. Our most recent work with the /s/–/ʃ/ distinction (Nittrouer and Miller, 1997) focused on refining our understanding of the developmental changes in the weighting of vocalic formant transitions. That work supported the general conclusion from earlier work (Nittrouer, 1992, 1996; Nittrouer and

Studdert-Kennedy, 1987) that there is a developmental decrease in the weight assigned to vocalic formant transitions for fricative decisions, and additionally showed that adults and children treat these vocalic formant transitions differently. Specifically, adults tend to attribute a large portion of the variance in formant frequencies at vocalic onset to vowel quality. Children attribute more of the frequency variance in these formant transitions to the fricative, and less to the vowel. Thus gains have been made in understanding developmental changes in the perceptual processing of formant transitions, but little has been done to improve our understanding of developmental changes in the perceptual processing of aperiodic noise. The purpose of the work described here was to examine specifically developmental changes in the weighting of noise characteristics in decisions of fricative identity.

I. EXPERIMENT 1: NATURAL NOISES

The purpose of this experiment was to examine potential developmental shifts in the weighting of fricative-noise spectra. We wished to conduct this investigation using natural fricative noises. Previous studies of fricative labeling have all used synthetic fricative noises, and so may have failed to incorporate some aspect of these noises that children require either to process them as speech (i.e., as produced by a human vocal tract) or to distinguish between places of constriction. To deal with these requirements, we added together the digitized waveforms of natural /s/ and /ʃ/ noises at different, but controlled, amplitudes to form a continuum. In that way we constructed noises that were disproportionately more like /s/ or /ʃ/, but were nonetheless produced by a human vocal tract. Upon completion, we found that the major difference among the resulting fricative spectra was in the amplitude of one low-frequency peak at roughly 2.2 kHz. This difference in fricative spectra can be traced to the frequencies of the first and second poles in natural /s/ and /ʃ/ noises. Heinz and Stevens (1961) found that /ʃ/ noises had a mean first-pole frequency of 2067 Hz and a mean second-pole frequency of 4983 Hz. They found a mean first-pole frequency for /s/ of 4850 Hz. Thus the second pole of /ʃ/ and the first pole of /s/ are similar in frequency. When these noises are added together at different amplitude ratios the primary difference below 5000 Hz would predictably be the amplitude of that low-frequency pole, which was the first pole of the /ʃ/ noise. Heinz and Stevens did not provide estimates of poles higher than the second, but our procedures did not produce noises differing significantly in the frequency range above 5000 Hz.

Experiment 1 effectively became a test of the extent to which fricative judgments by children and adults are related to the amplitude of this low-frequency peak. Previous experiments (Nittrouer, 1992, 1996; Nittrouer and Studdert-Kennedy, 1987) demonstrated that children did not weight the fricative-noise spectrum as much as adults in their decisions of fricative identity. Therefore, we reasoned, children probably would not notice differences in spectral morphology among the noises. The high-frequency components of the fricative noises were similarly shaped. Therefore, if children did not attend to differences among stimuli in the low-frequency peak, they should label all stimuli as beginning with the same fricative. Whether children would hear the stimuli as predominantly starting with /s/ or /ʃ/ could not be predicted before the experiment was done.

Another issue we had to address in stimulus construction was how to set the formant transitions so that their influence on fricative judgments would be minimized. Our goal was to examine developmental shifts in perceptual weighting of the noise spectrum. Differences between children and adults in the weighting of formant transitions have been documented (Nittrouer, 1992, 1996; Nittrouer and Miller, 1997; Nittrouer and Studdert-Kennedy, 1987), and we wished to prevent having these age-related difference influence listeners' judgments to such an extent that age-related differences in the weighting of the noise spectra would be obscured. However, minimizing the contribution of any one property is easier said than done. Phonetic decisions rely on the integration of several perceptually equivalent properties (Best *et al.*, 1981), such that the setting of any one property affects the settings of all other properties that support judgments of the categories being examined. Therefore, setting a parameter to be ''neutral'' in its influence is tricky because the influence (or lack of influence) changes with each setting (or combination of settings) of the other parameters. Pilot work demonstrated that flat formants were unacceptable because the perceived discontinuity in articulatory trajectories disrupted normal speech perception. One reasonable alternative was to use settings for formant transitions that were ''halfway'' (perceptually) between those appropriate for a preceding /s/ or /ʃ/. However, that plan was difficult to implement for the reason offered above: In multidimensional stimuli such as speech, changing the setting of any one parameter alters the setting for all other parameters that support judgments of the categories being examined. In a sense then, the halfway point between categories for any parameter is a moving target. Instead, we sought to minimize the contribution of formant transitions by allowing only one to vary. Thus the third formant ($F3$) transition, which normally differs for a preceding /s/ or /ʃ/, was set the same for all stimuli. Only the second formant ($F2$) transition was permitted to vary as appropriate for a preceding /s/ or /ʃ/.

In summary, this study was undertaken to examine developmental changes in the perceptual weighting of fricative-noise spectra, using natural fricative noises. Our prediction was that children would respond with predominantly one fricative label or the other, regardless of the amplitude of the low-frequency peak. Labeling functions for adults and children should be similarly steep in this experiment. Previous studies have shown that children's labeling functions are shallower than those of adults, a difference attributed to children not attending to the fricative-noise spectra as much as adults. By minimizing the information provided by the formant transitions, we hoped to direct children's attention to the noise spectra. Therefore, their labeling functions should be as steep as those of adults, but shifted to one side or the other.

A. Method

1. Subjects

Twenty-one children and 21 adults participated. The children were between 5 years 11 months and 7 years 11 months (mean=7 years 2 months). Younger children were not included because pilot work showed that they were unable to label accurately and reliably the best exemplars of each response category. In fact, five additional 6-year-olds started this experiment, but were dismissed because they were unable to meet this criterion. The adults were all between 20 and 40 years of age. Two additional adults started the experiment, but were dismissed because they failed to label accurately and reliably the best exemplars of each category during testing. Male/female ratios for this experiment were 5/16 for children and 7/14 for adults.

All subjects passed a hearing screening of the frequencies 0.5, 1.0, 2.0, 4.0, and 6.0 kHz presented to each ear separately at 25 dB HL (ANSI, 1989). None of the subjects had any history of speech or language problems. The children were given the Goldman–Fristoe Test of Articulation (Goldman and Fristoe, 1986), and the mean score was 93rd percentile, with individual scores ranging from the 33rd to the 99th percentiles. Adults were given the reading subtest of the Wide Range Achievement Test-Revised [WRAT-R (Jastak and Wilkinson, 1984)]. The mean score on this test was the 64th percentile, with a range from the 27th to the 87th percentiles.

2. Equipment

All testing took place in a soundproof booth. Hearing was screened with a Maico MA41 audiometer using TDH-39 headphones. Natural speech samples were digitized with an AKG C535 EB microphone, a Shure M268 preamplifier, a Frequency Devices 901F filter, and a Data Translation DT 2801A analog-to-digital converter. This system provided a linear frequency response. Presentation of stimuli and recording of responses was controlled by a computer. Stimuli were presented via a Data Translation 2801A digital-to-analog converter, a Frequency Devices 901F filter, a Crown D-75 amplifier, and AKG-K141 headphones. This system provided a linear frequency response for output. Reinforcement (for children only) consisted of cartoon pictures presented on a color-graphics monitor, and a bell ringing. Recorded stories (also for children only) were presented via a Nakamichi MR-2 audiocassette player with AKG-K141 headphones. Synthetic versions of the stories were generated with DEC talk (Digital Equipment Corporation, 1984).

3. Stimuli

The stimuli used in this experiment were hybrid stimuli consisting of natural noises and synthetic vocalic portions. All stimuli were created and presented at a 20-kHz sampling rate, with a 10-kHz high-frequency filter cut-off. The noises were taken from an adult, male speaker's production of /s/ and /ʃ/. The two noises selected for use were chosen from several tokens, were typical of all /s/ or /ʃ/ noises, and were similar in amplitude to each other. The /s/ and the /ʃ/ noises that were selected were both truncated to 100 ms. This duration allowed us to obtain waveform portions that were relatively constant in amplitude across time. Also, Jongman (1989) showed that this duration should be sufficiently long for speakers to recognize /s/ and /ʃ/. The rms amplitudes of the noises were then adjusted, and the waveforms of the noises added together, to make seven /s/-to-/ʃ/ amplitude ratios varying between 4/1 (most /s/-like) to 1/1 (most /ʃ/-like). Pilot work showed that the 1/1 ratio was sufficient to elicit 100% /ʃ/ responses from adult listeners. When /s/ and /ʃ/ noises were combined in this way, the major difference among the resulting stimuli was the amplitude of the low-frequency pole (at roughly 2.2 kHz) relative to the higher frequency components, as shown in Fig. 1. The relative amplitude of this peak was 12 dB lower for the most /s/-like noise than for the most /ʃ/-like noise.

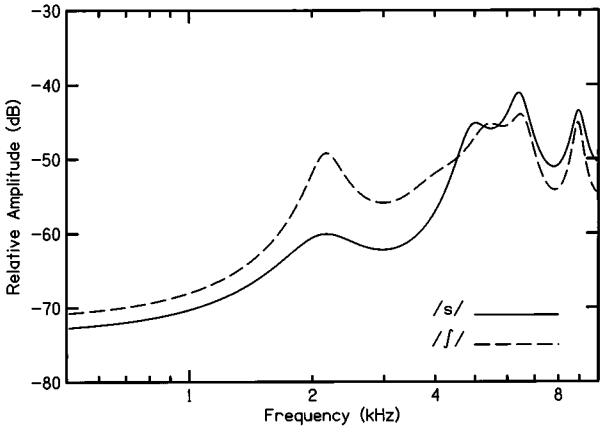

FIG. 1. Spectra for the most /ʃ/-like (dashed line) and the most /s/-like (solid line) noises from experiment 1, created by combining noises produced by a human vocal tract at various amplitude ratios.

Vocalic portions were synthetic and were the same as those used in experiment 2 of Nittrouer and Miller (1997). Each portion was 260 ms long. For all stimuli, F3 started at 2400 Hz, and fell over the first 50 ms to a steady-state frequency of 2100 Hz. This starting frequency was the midpoint of $F3$ frequency at voicing onset in natural tokens of /sɑ/, /ʃɑ/, /su/, and /ʃu/ (Nittrouer, 1996; Nittrouer and Miller, 1997). The steady-state frequency for $F3$ was taken from Whalen (1981). For $F2$, two settings were used for each vowel: one appropriate for a preceding /ʃ/ and one appropriate for a preceding /s/. For the /u/ portions, $F2$ fell through the entire portion to an ending frequency of 850 Hz. $F2$ onset for /(ʃ)u/ was 1800 Hz and $F2$ onset for /(s)u/ was 1480 Hz.[1] For the /ɑ/ portions, $F2$ fell over the first 100 ms to a steady-state frequency of 1130 Hz. For /(ʃ)ɑ/, $F2$ onset was 1570 Hz; for /(s)ɑ/, $F2$ onset was 1250 Hz. The fundamental frequency ($f0$) fell through the entire /u/ portion from 120 to 100 Hz, and $F1$ was constant at 250 Hz. The $f0$ fell through the entire /ɑ/ portion from 100 to 80 Hz. Fundamental frequency had to be slightly higher for /u/ than for /ɑ/ stimuli to maintain similar pitches across the two vowels, presumably due to the lower spectral center of gravity for /u/ than for /ɑ/. $F1$ started at 450 Hz in /ɑ/, rose over the first 50 ms to 650 Hz, and remained there for the remainder of the vocalic portion. Each of these four vocalic portions

[/(ʃ)ɑ/, /(s)ɑ/, /(ʃ)u/, and /(s)u/] were combined with each of the seven fricative noises, making a total of 28 stimuli.

4. Procedures

The screening tasks were presented first, followed by the labeling task. For the labeling task, stimuli from each vowel were presented separately. Half the subjects heard the /u/ stimuli first, and half heard the /ɑ/ stimuli first. For adults, stimuli with both vowels were presented in a single session. For children, stimuli with /ɑ/ and /u/ were presented on separate days, thus requiring two sessions.

In the labeling task, children were introduced to the response labels (''sa,'' ''sha,'' ''sue,'' or ''shoe'') with tape-recorded stories accompanied by pictures. Each story was presented twice: once with natural speech and once with synthetic speech. These stories served both to familiarize children with the response labels and to provide experience listening to synthetic speech. Ten practice items (five each of /sV/ and /ʃV/ were provided prior to the start of testing, using the best exemplars of each category. For example, the best exemplar of /su/ was the seventh noise on the fricative continuum combined with the /u/ portion with an $F2$ onset of 1480 Hz. Each listener had to identify nine of these ten stimuli correctly to proceed to testing.

Each stimulus was presented ten times across the test session, in randomized blocks of 14: each of the seven noises paired with a /(ʃ)V/ and a /(s)V/. Listeners indicated their responses by pointing to one of two pictures and saying the response label. The experimenter entered the responses into the computer. For a subject's data to be included in the final analysis, more than 80% accurate responses had to be given to the best exemplars during testing, thereby insuring that data were included only from subjects who maintained attention to the task.

Labeling data for each vocalic portion for each listener was transformed to probit scores (Finney, 1964). From each probit distribution, a mean (i.e., the point on the fricative-noise continuum at which 50% of responses were /ʃ/ and 50% were /s/ and a slope (change in probit units per step on the fricative-noise continuum) were derived. The probit analysis extrapolates beyond the physical continuum when necessary to obtain distribution means. We establish limits for these extrapolated means of 3.5 steps beyond the continuum in either direction (i.e., distribution means could not be less than −2.5 or greater than 10.5 steps). This procedure has been used previously (Nittrouer, 1992, 1996; Nittrouer and Miller, 1997), and does not compromise the integrity of the analysis. Truncating the range of possible distribution means in this way only decreases the probability of finding statistically significant age effects because, based on previous work, children are more likely than adults to show extreme distribution means. Distribution means were considered to be phoneme boundaries. Three-way analyses of variance (ANOVAs) were performed on phoneme boundaries and slopes, with ages as a between-subjects factor, and vowel (/ɑ/ or /u/) and transition (appropriate for /s/ or /ʃ/) as within-subjects factors.

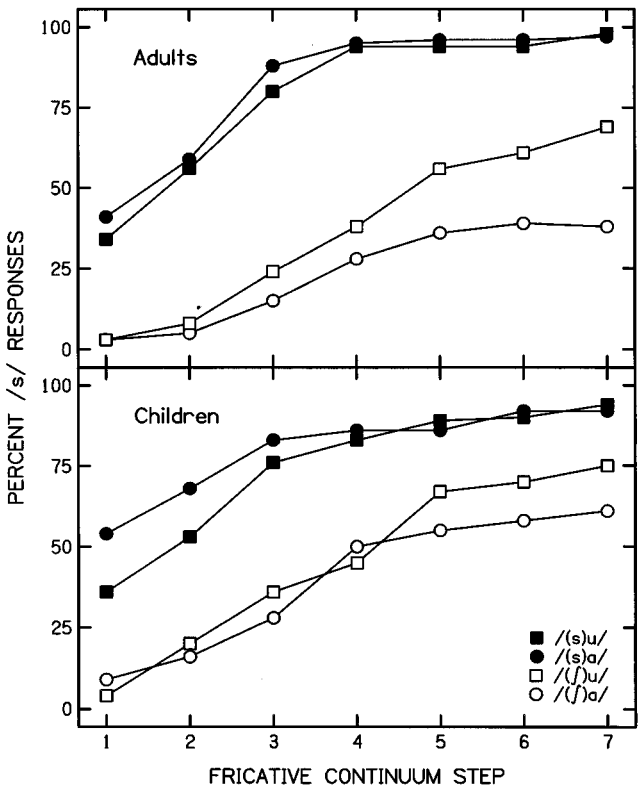

FIG. 2. Labeling functions from experiment 1 for adults (top) and children (bottom).

B. Results

1. Phoneme boundaries

Preliminary analysis showed no difference in response patterns for 6- and 7-year-olds, and so their data were combined, giving us two groups of equal sizes. Figure 2 shows labeling functions for adults and children. Table I lists phoneme boundaries on the top and means for each vowel across transition conditions on the bottom. Children generally gave more /s/ responses than adults, particularly for the /ɑ/ stimuli, as indicated by the fact that children's phoneme boundaries were at lower steps on the fricative-noise continuum. Among the significant results for the ANOVA were

TABLE I. Mean phoneme boundaries for experiment 1 in fricative-continuum steps (top). Mean for each vowel across transition condition (bottom). Standard deviations are in parentheses.

	Children	Adults
/(s)ɑ/	0.10	1.03
	(1.98)	(1.51)
/(ʃ)ɑ/	5.75	7.44
	(2.19)	(2.16)
/(s)u/	1.44	1.90
	(1.61)	(0.69)
/(ʃ)u/	5.09	5.46
	(2.11)	(1.74)
/ɑ/ mean	2.92	4.23
	(1.51)	(0.93)
/u/ mean	3.26	3.68
	(1.28)	(0.84)

TABLE II. Mean slopes for experiment 1, in probit units per fricative continuum step. Standard deviations are in parentheses.

	Children	Adults
/(s)ɑ/	0.374	0.596
	(0.323)	(0.327)
/(ʃ)ɑ/	0.337	0.283
	(0.234)	(0.127)
/(s)u/	0.531	0.752
	(0.361)	(0.268)
/(ʃ)u/	0.511	0.459
	(0.318)	(0.180)
/ɑ/ mean	0.356	0.440
	(0.257)	(0.189)
/u/ mean	0.521	0.605
	(0.312)	(0.185)

both the main effect of age, $F(1,40)=8.79$, $p=0.005$, and the interaction of age×vowel, $F(1,40)=4.41$, $p=0.042$. Given this interaction, we did a simple effects analysis for each vowel separately. The age effect was significant for /ɑ/ only, $F(1,40)=11.56$, $p=0.002$. Thus we may conclude that children had lower phoneme boundaries for stimuli with the /ɑ/ vowel. The only other significant results from the ANOVA were the main effect of transition, $F(1,40)=172.03$, $p<0.001$, and the interaction of vowel×transition, $F(1,40)=31.42$, $p<0.001$. Therefore we may conclude that phoneme boundaries were lower on the fricative-noise continuum when the formant transition was appropriate for a preceding /s/ rather than a preceding /ʃ/, and this transition effect was greater for /ɑ/ than for /u/. However, adults and children showed no differences in either the magnitude of the transition effect or in the interaction of this effect with vowel.

2. Slopes

Table II displays mean slopes for each vocalic portion (top) and for each vowel across transition conditions (bottom). Listeners in both groups had steeper functions for /u/ than for /ɑ/ stimuli, as indicated by a statistically significant vowel effect, $F(1,40)=18.77$, $p<0.001$. The transition effect was also significant, $F(1,40)=28.09$, $p<0.001$, which seems to be due entirely to adults, but not children, having steeper functions for stimuli with /s/ transitions than for those with /ʃ/ transitions. A significant age×transition interaction, $F(1,40)=19.29$, $p<0.001$, confirms this impression. As a further check on this last conclusion (that adults' responses completely accounted for the overall transition effect), we did a Simple Effects Analysis looking at the transition effect for adults and children separately. Only adults showed a significant transition effect, $F(1,40)=46.96$, $p<0.001$. Finally, we did a Simple Effects Analysis looking at the age for each transition condition separately. The age effect was significant for stimuli with /s/ transitions only, $F(1,35)=7.44$, $p=0.001$. Consequently, it may be concluded that adults had steeper functions than children for stimuli with /s/ transitions only.

C. Discussion

Our prediction was met in part: Children gave more responses of one phonetic category /s/ than adults, but only for stimuli with the vowel /ɑ/. For /u/, adults and children generally placed phoneme boundaries at the same points along the fricative-noise continuum. The reason for this lack of an age effect for /u/ may be explained at least partly by the formant transitions. We gave $F3$ the same frequency trajectories across all stimuli in hopes of minimizing the contributions of formant transitions to phonetic decisions. Instead we received a reminder of the fact that equal acoustic settings do not always produce equal phonetic effects across stimuli or listeners. $F3$ at voicing onset was 2400 Hz, which is the midpoint of $F3$ onsets that we found for natural tokens of /sɑ/, /ʃɑ/, /su/, and /ʃu/ (Nittrouer, 1996; Nittrouer and Miller, 1997). However, steady-state $F3$ was lower than in those natural tokens: 2100 Hz here for all vocalic portions; 2320 and 2365 Hz, for /u/ and /ɑ/, respectively, for the natural vocalic portions of those earlier studies. Therefore, $F3$ at voicing onset may have been high, relative to the steady-state frequency. Comparing across vowels, $F3$ onset is normally higher for fricative /ɑ/ than for fricative /u/. Comparing across fricatives, $F3$ onset is higher following /s/ than following /ʃ/. The results of Nittrouer and Miller (1997), which we were conducting at the same time as this study, showed that adults attribute more of the variance in $F3$-onset frequency to the vowel gesture and less to the fricative gesture than children. For these stimuli, $F3$ was consistently ''high'' at voicing onset. For /ɑ/ stimuli, adults would have attributed most of that ''high'' quality to the vowel, and so there was little, if any, left to be attributed to the fricative. For /ʃɑ/ in particular, there would have been no information in the formant transitions to indicate a syllable-initial /s/: $F2$ indicates a preceding /ʃ/ and, as suggested earlier, adults attribute the high $F3$-onset frequency to the vowel. Accordingly, adults' functions for /ʃɑ/ never crossed the 50% line toward /s/ responses. Children, on the other hand, would have attributed most of the high $F3$ onset for /ʃɑ/ to the fricative, and so would have been more inclined to respond ''s'' to these stimuli. In fact, we find the greatest age-related difference in placement of phoneme boundaries for the /ʃɑ/ stimuli. For /u/ stimuli, the high $F3$ frequency could not readily be attributed to the vowel. Therefore, adults had to attribute a large portion of its variance to the fricative as children normally do, and so adults' phoneme boundaries for /u/ were more similar to those of children.

Regarding the slopes of the labeling functions, adults' and children's functions were similarly steep for stimuli with /ʃ/ transitions only. For stimuli with /s/ transitions, adults' functions were steeper than both children's functions for stimuli with /s/ transitions and adults' functions for stimuli with /ʃ/ transitions. The reason for this finding is unclear, but whatever it is, we failed to draw listeners' perceptual attention equally to the noise spectrum across vocalic context and listener age, as we had hoped to do.

Finally, there was nothing in these data to support the contention that previously observed age differences in the extent to which fricative-noise spectra influenced fricative judgments were due to children, compared to adults, having

a greater bias against or more difficulty processing synthetic noises. If such an age-related difference was the source of previously observed age-related effects, then we would expect to find no age effect here when natural fricative noises were used. In fact, an age effect was found.

In summary, this experiment provides some evidence that children are less attentive to the structure of fricative noises than adults are. For stimuli with the vowel /ɑ/, children gave more /s/ responses than adults, regardless of the variation in the amplitude of the low-frequency noise peak. However, results were confounded because, in spite of our efforts, the settings for formant transitions at voicing onset may not have been neutral. Experiment 2 was designed to look more closely at how adults and children weight the fricative-noise spectrum by emphasizing differences between /s/ and /ʃ/ noises, and by again trying to render vocalic formant transitions neutral.

II. EXPERIMENT 2: SYNTHETIC NOISES

The purpose of this experiment was to examine more closely age-related differences in attention to fricative-noise structure, while holding the contributions of formant transitions to a minimum. Experiment 1 demonstrated that combining naturally produced fricative noises created noises that differed primarily in the amplitude of the low-frequency pole. In this experiment we used synthetic noises, which allowed us to specify precisely the amplitude of that low-frequency peak relative to both the other noises and to a higher frequency spectral peak. We emphasized this spectral difference by bandlimiting the fricative noises to frequencies below 5 kHz. As with experiment 1, our prediction was that children would largely assign one fricative label or the other. Because of the results of experiment 1, we predicted that the fricative label assigned to most stimuli would be ''s.''

Experiment 1 also taught us about how formant transitions should be adjusted if the effect they have on fricative decisions is to be minimized. Holding formant trajectories constant across stimuli produces uneven effects across those stimuli. Instead the settings for these formants should be as close to the halfway points between natural phonetic categories as possible.

A. Method

1. Subjects

With these stimuli, children as young as five years were able to identify the best examplars of each response category correctly. Consequently, 13 5-year-olds (mean=5 years 1 month; range=4 years 10 months to 5 years 5 months), 13 7-year-olds (mean=7 years 1 month; range=6 years 9 months to 7 years 5 months), and 12 adults participated. The male/female ratio was 7/6 for 5-year-olds, 8/5 for 7-year-olds, and 4/8 for adults. Subjects had to meet the same screening criteria for hearing and speech in this experiment as in experiment 1. Mean scores on the Goldman–Fristoe Test of Articulation were the 65th percentile (range from the 28th to the 99th) for 5-year-olds and the 85th percentile (range from the 81st to the 89th) for 7-year-olds. Mean score for adults on the reading subtest of the WRAT-R was the 74th percentile (range from the 39th to the 92nd percentiles).

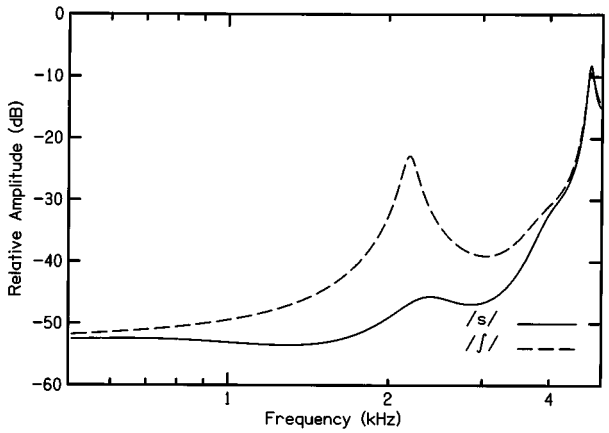

FIG. 3. Spectra for the most /ʃ/-like (dashed line) and the most /s/-like (solid line) noises from experiment 2, created by combining noises produced by a software synthesizer.

Five additional 5-year-olds started the experiment, but were dismissed: two failed to meet the training criterion and three failed to meet the testing criterion for best examplars. Three additional 7-year-olds and one adult also started the experiment, but were dismissed because they failed to meet the testing criterion.

2. Stimuli

Stimuli were created and presented at a 10-kHz sampling rate, with a high-frequency filter cutoff of 5 kHz. This frequency range was selected because the low-frequency peak found to distinguish /s/ and /ʃ/ noises was within this frequency range. We wished to emphasize this peak, and so did not include the higher spectral portions that were similar across stimuli in experiment 1. In this way, the spectral difference across stimuli should be more perceptually salient that in the first experiment. Therefore, finding evidence that children's responses were still not influenced by the noise spectra as much as adults' responses would provide stronger evidence of an age-related difference in perceptual weighting.

The duration of the fricative noise was the same as in the first experiment. The noises were synthetic, and had two poles: one at 2.2 kHz and one at 4.8 kHz. These noises were constructed to vary only in the amplitude of the low-frequency peak. Figure 3 shows spectra for the most /ʃ/-like and the most /s/-like noises, and shows that there is roughly a 22-dB difference in the amplitude of the low-frequency peak in these noises. The low-frequency peak for the most /ʃ/-like stimulus is 15 dB lower than the higher-frequency peak; the low-frequency peak for the most /s/-like stimulus was 37 dB lower than the higher-frequency peak. There were nine noises between these two end points that differed in the amplitude of the low-frequency peak in roughly 2.2-dB steps. Thus the fricative noises in this experiment highlighted the difference across stimuli in this low-frequency peak.

The duration and $f0$ settings of the vocalic portions were the same as in experiment 1, but $F2$ and $F3$ transitions differed. Onset frequencies for these transitions were selected based on the results of a pilot study in which we explored a range of $F2$ and $F3$ settings. In this experiment, we selected

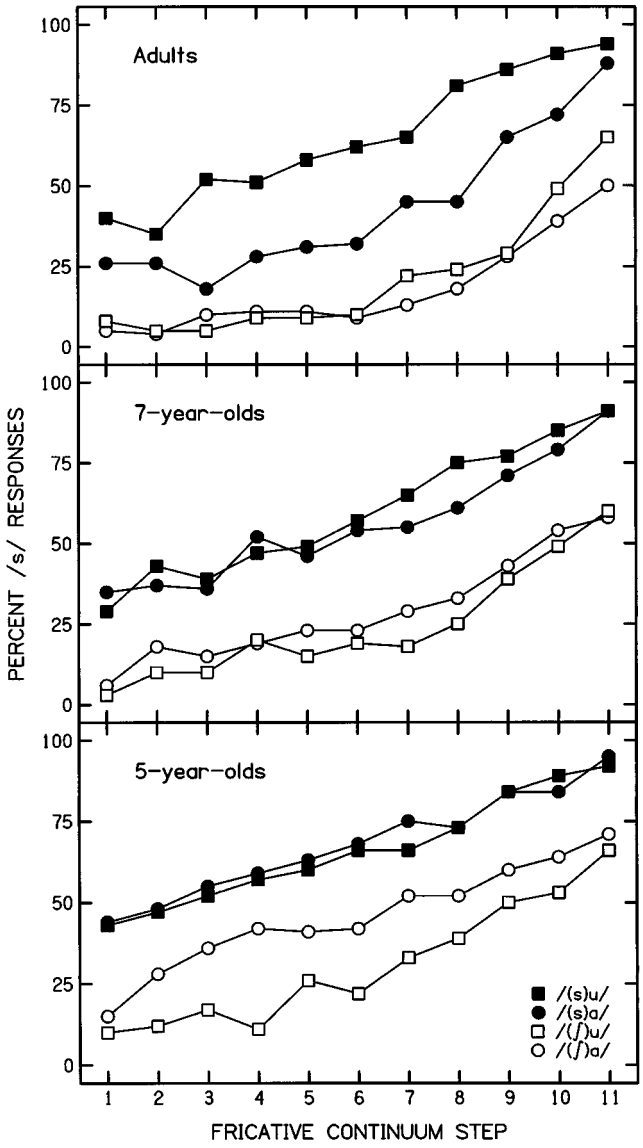

FIG. 4. Labeling functions from experiment 2 for adults (top), 7-year-olds (center), and 5-year-olds (bottom).

the two settings for each vowel that straddled by two steps in each direction the halfway point between the clearest settings from that study. As noted earlier, it is difficult to find a stable halfway point for parameter settings, and so we used two settings to increase the probability that we were at least in the general vicinity of that point. Onset frequencies of vocalic $F2$ were 1490 Hz for /(ʃ)ɑ/, 1330 Hz for /(s)ɑ/, 1720 Hz for /(ʃ)u/, and 1560 Hz for /(s)u/. Other aspects of the $F2$ trajectories were the same as in experiment 1. For the two /ɑ/ portions, $F3$ fell over the first 100 ms to a steady-state frequency of 2300 Hz. For /(ʃ)ɑ/, $F3$ onset was 2340 Hz; for /(s)ɑ/, $F3$ onset was a 2420 Hz. For the two /u/ portions, $F3$ fell over the first 130 ms to a steady-state frequency of 2100 Hz. For /(ʃ)u/, $F3$ onset was 2280 Hz; for /(s)u/, $F3$ onset was 2440 Hz. As in natural speech, $F3$-onset frequency varied more in the /u/ that in the /ɑ/ stimuli as a function of preceding fricative. Each of these vocalic portions was combined with each of the 11 noises, making 44 stimuli.

TABLE III. Mean phoneme boundaries for experiment 2 in fricative-continuum steps (top). Mean for each vowel across transition condition (bottom). Standard deviations are in parentheses.

	5-year-olds	7-year-olds	Adults
/(s)ɑ/	2.77	4.33	6.89
	(3.59)	(3.64)	(2.96)
/(ʃ)ɑ/	6.77	9.85	11.78
	(4.48)	(3.61)	(2.59)
/(s)u/	2.34	3.50	2.59
	(3.13)	(3.61)	(3.81)
/(ʃ)u/	8.94	10.50	11.05
	(1.29)	(2.20)	(2.39)
/ɑ/ mean	4.77	7.09	9.34
	(3.78)	(3.39)	(2.13)
/u/ mean	5.64	7.00	6.82
	(1.92)	(2.33)	(1.97)

3. Equipment and procedures

The equipment and the procedures were the same as those of experiment 1. Each stimulus was presented ten times, in randomized blocks of 22. One change was made in the statistical analysis from the last experiment: planned, orthogonal contrasts were used to examine potential group differences. The contrasts were adults versus all children and 7- versus 5-year-olds.

B. Results

1. Phoneme boundaries

Figure 4 shows labeling functions for adults, 7-year-olds, and 5-year-olds. Table III lists phoneme boundaries for each vocalic portion (top) and means for each vowel, across transition conditions (bottom). As with the first experiment, there was a developmental trend to fewer /s/ responses. Mean phoneme boundaries across vocalic portions were 5.20 for 5-year-olds, 7.05 for 7-year-olds, and 8.08 for adults. Reflecting this trend, we find a significant main effect of age, $F(2,35)=5.11$, $p=0.011$, and significant planned comparisons for adults versus all children, $F(1,35)=6.00$, $p=0.019$, and for 7- versus 5-year-olds, $F(1,35)=4.22$, $p=0.048$. This developmental trend appears to hold for all vocalic portions, except /(s)u/. In addition to this age effect, we found a significant age×vowel interaction, $F(2,35)=4.51$, $p=0.018$, and a significant adults versus all children planned comparison for the vowel effect, $F(1,35)=8.30$, $p=0.007$. This result reflects the finding that age-related differences are greater for /ɑ/ that for /u/. Finally, the main effect of transition was significant, $F(1,35)=172.17$, $p<0.001$, as was the vowel×transition interaction, $F(1,35)=14.77$, $p<0.001$.

For these stimuli, separate ANOVAs were done for each vocalic portion to test for significant age effects. Three of the four ANOVAs showed significant results: /(ʃ)ɑ/, $F(2,35)=5.98$, $p=0.006$; /(s)ɑ/, $F(2,35)=4.60$, $p=0.017$; and /(ʃ)u/, $F(2,35)=3.78$, $p=0.033$. Thus there was a developmental decrease in the probability of /s/ responses for all vocalic portions, except /(s)u/.

TABLE IV. Mean slopes for experiment 2, in change in probit unit per fricative-continuum step. Standard deviations are in parentheses.

	5-year-olds	7-year-olds	Adults
/(s)ɑ/	0.183	0.167	0.212
	(0.087)	(0.062)	(0.116)
/(ʃ)ɑ/	0.174	0.175	0.206
	(0.079)	(0.059)	(0.128)
/(s)u/	0.163	0.202	0.226
	(0.094)	(0.132)	(0.106)
/(ʃ)u/	0.252	0.230	0.289
	(0.198)	(0.174)	(0.171)
/ɑ/ mean	0.178	0.171	0.209
	(0.072)	(0.044)	(0.113)
/u/ mean	0.208	0.216	0.257
	(0.131)	(0.149)	(0.124)

2. Slopes

Table IV displays mean slopes for each group for each vocalic portion (top) and mean slopes for each vowel (bottom). Although children's slopes are slightly lower than those of adults, this difference is not statistically significant. The vowel effect only approached statistical significance, $F(1,35)=3.74$, $p=0.061$, whereas it had been significant in experiment 1. The only significant results observed in the ANOVA were the main effect of transition, $F(1,35)=5.38$, $p=0.026$, and the interaction of vowel×transition, $F(1,35)=5.70$, $p=0.023$. Therefore we may conclude only that functions were slightly steeper for /(ʃ)u/ than for /(s)u/.

C. Discussion

As predicted, children gave more /s/ responses than adults, but only for three of the four vocalic portions. As to why a similar age-related trend was not found for /(s)u/, it is possible that phoneme boundaries for /(s)u/ were placed where they were for different reasons for adults and children, as suggested for experiment 1. It appears that children simply gave a preponderance of /s/ responses: The formant transitions were not particularly informative, and children did not attend to the low-frequency peak in the fricative noise. Adults, on the other hand, attended to this low-frequency peak, and so were generally more likely than children to give /ʃ/ responses. We suggest that the similarity in placement of the labeling functions for the /(s)u/ stimuli was due to adults demonstrating the traditional vowel effect (i.e., more /s/ responses to /u/ than to /ɑ/ stimuli). Nittrouer and Miller (1997) found that the predicted vowel effect is observed for adults' responses to /(s)V/ stimuli only when $F3$ transitions differ between vocalic portions. In experiment 1, $F3$ was the same across all vocalic portions, and adults failed to show the traditional vowel effect for /(s)V/. The fact that adults showed this vowel effect in this experiment meant that their /(s)u/ phoneme boundaries were lower on the fricative-noise continuum, and so no age effect was found for this condition.

The slopes of the labeling functions were similar across listener groups, vocalic contexts, and transitions, Nonetheless, there were clear developmental trends to higher phoneme boundaries for three of the four vocalic portions. Therefore, results from this experiment generally support the hypothesis that children (5–7 years old) are less attentive to the structure of fricative noises than are adults.

III. GENERAL DISCUSSION

The combined results of these two experiments provide evidence that the role of aperiodic noise spectra in fricative decisions increases with increasing age. In fact, these experiments demonstrate two possibly related developmental trends. First, young children appear less sensitive to the structure of aperiodic noise, a result suggested by Allen and Wightman (1992). In addition, aperiodic noise structure provides less information for young children than for adults about place of consonant constriction, a result previously demonstrated by Parnell and Amerman (1978). Unfortunately, the present experiments do little to resolve the ''chicken and egg'' question: Are children unable to resolve details of noise structure, and so this acoustic parameter provides little information for children to use in phonetic decisions? Or, do children fail to assign strong weights to the details of noise structure in phonetic decisions, and so they pay little attention to this structure? Future work will need to address this important question.

These results have implications for the development of speech-production skills. Nittrouer (1995) and Nittrouer *et al.* (1989) found that children's /s/ and /ʃ/ noises were not as differentiated acoustically as those of adults. Specifically, children's fricative noises lacked the low-frequency peak evident in adults' noises (Appendix, Nittrouer, 1995). Theories of adult speech perception aside, surely there is information in the acoustic speech signal that directs a child in how to move her vocal tract. If children do not notice the low-frequency peak in fricative noise, it may explain why they fail to incorporate the articulatory maneuver that produces this peak in their own productions. Of course, it is possible that young children are simply unable to make the tongue configuration required to produce this low-frequency peak, but we find no evidence in this study that they are even aware of this peak. In either case, we find a relation between what children attend to in the speech of others and what they produce in their own speech.

In summary, these two studies provide evidence that children do not weight the information provided by the spectral structure of aperiodic noises in their fricative decisions as much as adults do. This developmental trend for speech perception corresponds with a trend observed in speech production: Children neither attend perceptually to the low-frequency peak found in the noises of palatal fricatives nor do they produce these low-frequency peaks in their own attempts at palatal fricatives.

ACKNOWLEDGMENTS

This work was supported by research Grant No. 4 R01 DC00633-09 from the National Institutes on Deafness and Other Communication Disorders, National Institutes of Health. We thank Kris Kalil for help testing subjects and Bob Fulkerson for programming help. Carol A. Fowler, Donna L. Neff, Stephen J. Neely, and Court S. Crowther provided comments on earlier drafts of this manuscript.

[1]The fricative in parentheses indicates that vocalic formant transitions were appropriate for that initial consonant.

Allen, P., and Wightman, F. (**1992**).''Spectral pattern discrimination by children,'' J. Speech Hear. Res. **35,** 222–233.

ANSI (**1989**). ANSI S3.6-1989, ''Specifications for audiometers'' (American National Standards Institute, New York).

Best, C. T., Morrongiello, B. A., and Robson, R. C. (**1981**). ''Perceptual equivalence of acoustic cues in speech and nonspeech perception,'' Percept. Psychophys. **29,** 191–211.

Best, C. T., Studdert-Kennedy, M., Manuel, S., and Rubin-Spitz, J. (**1989**). ''Discovering phonetic coherence in acoustic patterns,'' Percept. Psychophys. **45,** 237–250.

Digital Equipment Corporation (**1984**). *DECtalk v 2.0* (Maynard, MA).

Finney, D. J. (**1964**). *Probit Analysis* (Cambridge University, Cambridge, England).

Goldman, R., and Fristoe, M. (**1986**). *Goldman Fristoe Test of Articulation* (American Guidance Service, Circle Pines, MN).

Heinz, J. M., and Stevens, K. N. (**1961**). ''On the properties of fricative consonants,'' J. Acoust. Soc. Am. **33,** 589–593.

Hodgson, P., and Miller, J. L. (**1992**). ''Phonetic category structure depends on multiple acoustic properties: Evidence for within-category trading relations,'' J. Acoust. Soc. Am. **92,** 2464(A).

Jastak, S., and Wilkinson, G. S. (**1984**). *The Wide Range Achievement Test-Revised* (Jastak, Wilmington, DE).

Jongman, A. (**1989**).''Duration of frication noise required for identification of English fricatives,'' J. Acoust. Soc. Am. **85,** 1718–1725.

Kluender, K., Diehl, R., and Wright, B. (**1988**). ''Vowel-length differences before voiced and voiceless consonants: An auditory explanation,'' J. Phon. **16**, 153–169.

Kunisaki, O., and Fujisaki, H. (**1977**). ''On the influence of context upon perception of voiceless fricative consonants,'' Ann. Bull. RILP **13**, 85–91.

Mann, V. A., and Repp, B. H. (**1980**). ''Influence of vocalic context on perception of the [ʃ]-[s] distinction,'' Percept. Psychophys. **28,** 213–228.

Nittrouer, S. (**1992**). ''Age-related differences in perceptual effects of formant transitions within syllables and across syllable boundaries,'' J. Phon. **20**, 1–32.

Nittrouer, S. (**1995**). ''Children learn separate aspects of speech production at different rates: Evidence from spectral moments,'' J. Acoust. Soc. Am. **97,** 520–530.

Nittrouer, S. (**1996**). ''Discriminability and perceptual weighting of some acoustic cues to speech perception by 3-year-olds,'' J. Speech Hear. Res. **39,** 278–297.

Nittrouer, S., and Miller, M. E. (**1997**). ''Predicting developmental shifts in perceptual weighting schemes,'' J. Acoust. Soc. Am. **101,** 2253–2266.

Nittrouer, S., and Studdert-Kennedy, M. (**1987**). ''The role of coarticulatory effects in the perception of fricatives by children and adults,'' J. Speech Hear. Res. **30,** 319–329.

Nittrouer, S., Studdert-Kennedy, M., and McGowan, R. S. (**1989**). ''The emergence of phonetic segments: Evidence from the spectral structure of fricative-vowel syllables spoken by children and adults,'' J. Speech Hear. Res. **32,** 120–132.

Parnell, M. M., and Amerman, J. D. (**1978**). ''Maturational influences on perception of coarticulatory effects,'' J. Speech Hear. Res. **21,** 682–701.

Remez, R. E., Rubin, P. E., Berns, S. M., Pardo, J. S., and Lang, J. M. (**1994**). ''On the perceptual organization of speech,'' Psychol. Rev. **101,** 129–156.

Walley, A. C., and Carrell, T. D. (**1983**). ''Onset spectra and formant transitions in the adult's and child's perception of place of articulation in stop consonants,'' J. Acoust. Soc. Am. **73,** 1011–1022.

Whalen, D. H. (**1981**). ''Effects of vocalic transitions and vowel quality on the English /s/–/ʃ/ boundary,'' J. Acoust. Soc. Am. **69,** 275–282.

Mechanisms of vowel recognition for Ineraid patients fit with continuous interleaved sampling processors

Michael F. Dorman[a)]
Department of Speech and Hearing Science, Arizona State University, Tempe, Arizona 85287-0102 and Division of Otolaryngology/Head and Neck Surgery, University of Utah Health Sciences Center, Salt Lake City, Utah 84132

Philipos C. Loizou
Department of Applied Science, University of Arkansas at Little Rock, Little Rock, Arkansas 72204-1099

(Received 19 December 1995; revised 24 March 1997; accepted 16 April 1997)

Vowel recognition was assessed for eight, cochlear implant patients who use the Ineraid's six-electrode array. Recognition was tested in three conditions: with the Ineraid after years of experience; with a CIS processor at fitting of the processor; and with the CIS processor after 1 month's experience. At the time of fitting of the CIS processor, vowel recognition was not superior to that with the Ineraid. Recognition improved significantly over the period of a month. At 1 month, performance was significantly better with the CIS processor than with the Ineraid. This outcome is interpreted to mean that remapping of the vowel space is necessary following fitting with the CIS processor and some of the remapping occurs over a time period of days or weeks, rather than hours. Vowel errors at one month could be accounted for by two mechanisms. One is that patients attended to low-frequency channels at the expense of high-frequency channels, or could not use information in high-frequency channels. The second is that, for diphthongs, patients could not detect frequency change over the course of the utterance. © *1997 Acoustical Society of America.* [S0001-4966(97)07507-3]

PACS numbers: 43.71.Cq, 43.71.Ky [WS]

INTRODUCTION

The continuous interleaved sampling (CIS) processing strategy has been shown to improve the speech understanding abilities of patients fit with the Ineraid's six intracochlear electrodes and percutaneous pedestal (Wilson *et al.*, 1991; Boex *et al.*, 1994). Wilson *et al.* (1991) report a 28 percentage point improvement for scores on the Spondee Recognition Test, a 12 percentage point improvement for words in the CID sentences, a 39 percentage point improvement for words from the SPIN test, and a 20 percentage point improvement for NU-6 words. The improvement in performance also extends to segmental phonemes. Both Lawson *et al.* (1993) and Boex *et al.* (1994) report an improvement in transmitted information for consonants of about 17% percentage points. For the subjects in the present experiment, consonant scores increased from 50% correct with the Ineraid processor to 69% correct with a CIS processor. Each patient evidenced a higher score with a CIS processor than with the Ineraid.

The improvements in speech understanding can be rationalized by pointing to the increased number of electrodes accessed by the CIS processor (six versus four in the analogue version of the Ineraid) and to the reduction in current interaction, and thus increased channel independence, achieved by the use of the nonsimultaneous pulses. Increased channel independence, in turn, should result in increased spectral resolution.

In the context of improved sentence, word, and consonant recognition, it is curious that neither Wilson *et al.* (1990) nor Boex *et al.* (1994) report improvement in group-mean scores for vowel recognition. It is difficult to understand why a strategy which improves the resolution of consonant information would not also improve the resolution of vowel information. One possibility is that the improvement in consonant recognition is based solely on improvement in the resolution of temporal information, i.e., waveform or amplitude-envelope shape, and is not based on improvement in the resolution of spectral information. This does not seem to be the case, however, because place of articulation, which is not well conveyed by envelope shape, is better conveyed by CIS processors than by the analogue strategy of the Ineraid (Lawson *et al.*, 1993). Thus at least part of the improvement in performance with a CIS strategy must be due to better resolution of spectral information.

In order to better understand the processes underlying vowel recognition by Ineraid patients fit with CIS processors, patients were presented synthesized vowels in the /bVt/ format. Synthesized vowels of constant duration and pitch contour were used in order to require patients to rely on spectral information, and thus spectral resolution, for vowel identification. Identification accuracy was assessed in three conditions. In one condition vowel identification was assessed with the Ineraid's analogue strategy. In the second condition vowel identification was assessed within hours of fitting the patients with a CIS processor. The aim of these two conditions was to determine if the Wilson *et al.* (1991) and Boex *et al.* (1994) results could be replicated. In the third condition vowel identification was assessed after the patients had

[a)]Corresponding author address: Department of Speech and Hearing Science, Arizona State University, Tempe, AZ 85287-0102.

worn the CIS processor for approximately 1 month. The aim of this condition was to determine whether vowel identification would improve after experience with the signal processor. If vowel identification improves after experience with a processor, then the results for consonants and vowels could be accommodated under a single account—an improvement in spectral resolution—with the provision that it takes patients longer to remap the vowel space than to remap the consonant space. A longer period may be needed to remap the vowel space because vowels are compressed into a smaller frequency space than consonants, and have fewer cues in the time/amplitude domain to aid in identification.

The data collected at 1 month were subjected to a number of analyses in an effort to account for errors in vowel identification after the patients had accommodated to their signal processor. To perform these analyses the vowels were first processed through a software model of the CIS processor. The data of interest were the channel output levels of the processor's six channels because it is the pattern of these output levels which encodes vowel identity. In one analysis we assessed whether the errors in vowel identification were based on overall similarity of the output patterns across the six electrodes. In other analyses we assessed whether errors in identification could be understood in terms of selective attention to low-frequency channels at the expense of high-frequency channels (or an inability to use information in high-frequency channels) and/or an inability to detect spectral change over the time course of the vocalic portion of the signal.

I. METHOD

A. Subjects

The subjects were eight patients who had used the Ineraid processor for no less than 4 years, and who had used a CIS processor for a month. They ranged in age from 31 to 73 years.

B. Stimuli

The stimuli were the words ''beet, bit, bait, bet, bat, bought, but, boot, Bert, Bart, bout, bite, boat'' synthesized using the KLATT algorithm (see Dorman *et al.*, 1991). The vowels were realized as [i ɪ eᴵ ɛ æ ɔ ʌ u ɝ ɑr aᵘ aᴵ oᵘ]. Each stimulus was synthesized with five formants. Each stimulus was composed of a 5-ms /b/ burst, a 5-ms silent interval, 30-ms /b/ transitions, a 90-ms vocalic nucleus, 50-ms /t/ transitions, 80 ms of silence, and final /t/-burst aspiration of 50 ms. The $F0$ contour was the same for all signals. Formant frequencies are shown in Table I.

The 13 stimuli were blocked without replacement into groups of 13. The stimuli within the blocks were randomized. Each block was presented five times. The patients had been tested with the vowel set many times through their Ineraid processors before the current test administration.

C. Signal processors

The four-channel Ineraid processor has been described in Eddington (1980) (see also Wilson *et al.*, 1991). The CIS processor was an implementation of the Wilson *et al.* (1991) processor fabricated at the University of Innsbruck (Zierhofer *et al.*, 1994). The signal processor was a six-channel design with sixth-order bandpass filters, 400-Hz first-order smoother, and full wave rectification. Channel center frequencies were 393, 639, 1037, 1680, 2730, and 4440 Hz. The channels were of equal width on a logarithmic scale. Signals were preemphasized above 1200 Hz. Pulse duration and pulse rate were optimized for each patient.

TABLE I. Frequencies of $F1$, $F2$, and $F3$ during the vocalic portion of synthetic /bVt/ words. Double entries in a column indicate starting and ending frequencies of the formant in the vocalic portion of the word.

	$F1$	$F2$	$F3$
beet	313–200	2048	2695
bit	390–460	1765–1556	2460–2536
bet	546	1610	2539
bat	703	1562	2500
bought	625–650	859–910	2700–2730
but	625	1220	2539
boot	350	1054	2304
Bert	470–420	1270–1337	1540
boat	530–440	1088–900	2300
bout	684–420	1203–940	2538–2140
bite	660–400	1180–1880	2500–2524
bait	480–330	1720–2200	2520–2580
Bart	644–537	937–1220	2294–1542

D. Design

On the day before the patients were fit with a CIS processor, they were tested through their Ineraid processors with a variety of speech materials, including the vowel stimuli described above. On the day of fitting, and four to six weeks following the fitting, the patients were once again tested with the speech material.

E. Procedure

The test signals were delivered directly to the patients' signal processors via the auxiliary input jack. The patients were presented two practice lists (with correct answers) before the test sequence began. Responses were collected via a touch sensitive response pad.

II. RESULTS AND DISCUSSION

A. Ineraid versus CIS at fitting

The mean percent correct score for patients using the analogue processor was 35% correct. The mean percent correct score for the same patients using the CIS processor was 41% correct. Changes in individual scores are shown in Fig. 1. The group mean scores did not differ significantly (Wilcoxon $z=0.98$, $p=0.32$). However, five of the eight patients achieved higher scores with the CIS processor. The range of improvement was 2–28 percentage points. One patient scored the same in both conditions while two other patients scored 12 percentage points and 16 percentage points lower with the CIS processor. The absence of a significant improvement for the group mean data is consistent with Wilson *et al.* (1990) and Boex *et al.* (1994). However, the absence

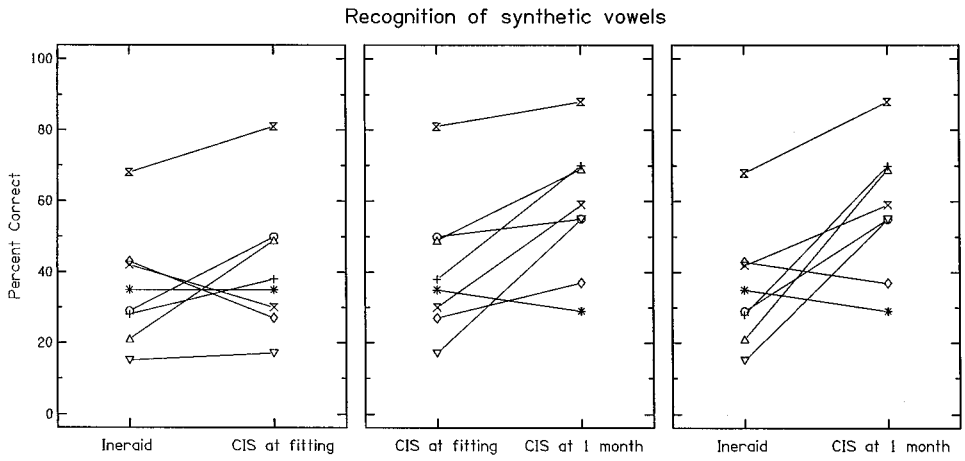

FIG. 1. Patients' scores as a function of time and type of processor.

of a significant group effect obscures the outcome that some of the patients achieved higher scores for vowels immediately upon fitting with the CIS processor.

B. CIS at fitting versus CIS after experience

After a month's experience with the signal processing scheme the mean vowel-recognition score was 58% correct. The mean score differed significantly from that at fitting (41% correct) (Wilcoxon $z=2.17$, $p=0.029$). As shown in Fig. 1 seven of the eight patients achieved a higher score at one month than at fitting. The range of improvement was from 5 to 38 percentage points. The score for one patient dropped 6 percentage points. We interpret this outcome to mean that remapping of the vowel space is necessary following fitting with the CIS processor and *some* of the remapping occurs over a time period of days or weeks, rather than hours. Of course, given our design, we cannot determine exactly the period over which the remapping takes place, but that period is within a month.

C. CIS after experience versus Ineraid

The mean score of 58% correct for the CIS processor at 1 month differed significantly from the 35% score for the Ineraid (Wilcoxon $z=2.03$, $p=0.04$). As shown in Fig. 1 six of the eight patients scored higher with the CIS processor. The range of improvement was 17–42 percentage points. The scores of two patients remained 6 percentage points lower than with the Ineraid. Thus after experience with the processing scheme, group-mean performance was better with the CIS processor than with the Ineraid. This outcome is fully in accord with the inference from studies of consonant recognition that, on average, spectral resolution improves when Ineraid patients are fit with CIS processors.

D. Analysis of vowel errors after experience with the CIS processor

The mean identification scores, expressed as percents, collected after the patients had worn the CIS processor for a month, are shown in Table II. The front vowels and diphthongs /i ɪ ɛ e^{I} æ/ and /ɝ/ were relatively well identified (range=65%–90% correct). The back vowels and diphthongs, and /ɑr/, were not well identified (range =22%–57% correct). Error responses were not widely distributed across vowels but rather were commonly limited to one or two vowels. For example, the dominant error response to ''bet'' was ''bit,'' the dominant error for ''but'' was ''bat,'' and the dominant error for ''bat'' was ''bet.'' In order to better understand why certain vowels were relatively well identified, while others were not, and to understand the factors contributing to the dominant error responses, the vowels were processed through a software simulation of the signal processor and the channel output levels were displayed.

Inspection of the output levels in Fig. 2 for the vowels [i ɪ ɛ æ] suggests an account for their relatively high level of recognition. Note, first, the levels of channels one and two as the first formants in this series rise from approximately 250 Hz to 700 Hz. The rise in $F1$ over this vowel set is encoded by the difference in outputs of channels 1 and 2. That is, channel 1 minus channel 2 is a large positive number for [i], and is a smaller positive number for [I]. Channel 1 minus channel 2 is a relatively small negative number for [ɛ] and a larger negative number for [æ]. Thus the magnitude and sign of channel 1 minus channel 2 change in a systematic manner with the rise in $F1$ frequency. Now, note the differences in output levels for channels 3 and 4 as an indication of the frequency of the second formant. In this instance the magnitude of the differences gives some information about $F2$. Moreover, the *average levels* of channels 3 and 4 change in a systematic manner with the fall in $F2$, i.e., the lowest overall level is for [i] and the highest is for [æ]. Given a good estimate of $F1$, and some information about $F2$, it is expected that front vowels would be relatively well identified (Dubno and Dorman, 1987).

The word ''bert'' was also well identified (mean score =90% correct). Inspection of the channel output pattern indicated a peak in energy in channel 4 and fall in energy thereafter. This pattern is the result of the low $F3$ throughout the vocalic portion of the signal and makes the channel output pattern distinct from all of the other vowels in the test set.

TABLE II. Stimulus-response matrix for words presented via a CIS processor. Scores are percentages pooled across subjects. Decimal values of 0.5 or less are rounded down.

	RESPONSE												
	beet	bit	bait	bet	bert	bat	but	bought	bout	boat	bite	boot	bart
beet	82	2	12	2									
bit		72	2	10	5							10	
bait	10	15	75										
bet		15	2	70	5	2					5		
bert					90		2	2		2	2		
bat				17		65	2	5	2	2	2		2
but			5	12	2	27	22	5	5		7		12
bought				7		5	17	50	10		2		5
bout				2	2		5		37	47			5
boat					12		10	22		47			7
bite			22	10	5					2	57		2
boot				5	32	2				10		50	
bart						5	10	55			5		25

If the account offered above is accurate, i.e., that front vowels are well identified because the outputs of channels 1, 2, and 3 are *dissimilar*, then it might be the case that vowels which have *similar* outputs of channels 1, 2, and 3 will be difficult to identify. This is, in fact, often the case. Consider the outcome that [ʌ] in ''but'' was the most common error response for [ɔ] in ''bought.'' The output patterns for the two vowels are shown at the top of Fig. 3. The pattern of outputs for channels 1, 2, and 3 of the two vowels is similar. The substitution of ''but'' for ''bought'' suggests that patients either attend inappropriately to the lower number channels and/or are not able to use differences in the output levels of the higher channels as an aid in identification. This account can also be extended to the error response of [æ] in ''bat'' when presented [ʌ] in ''but'' (Fig. 3, middle) and the error response of [ɛ] in ''bet'' when presented [æ] in ''bat'' (Fig. 3, bottom). Consider, now, the signal which was among

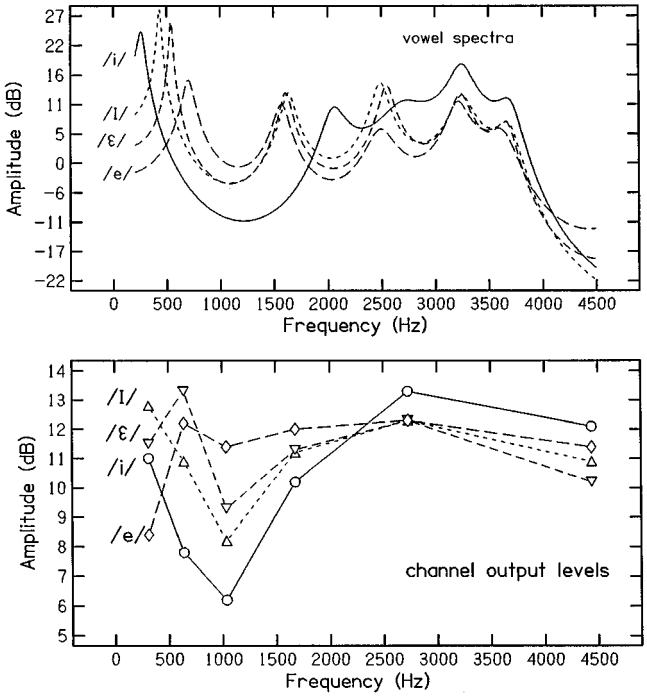

FIG. 2. (top) Spectra of the vowels in ''beet, bit, bet, bat'' derived from a 20-ms window, centered at the midpoint of the vowel, and 14 pole LPC analysis. (bottom) Output levels of the CIS processor for the vowels in ''beet, bit, bet, bat.'' Sequential points along each function represent the output levels of channels 1–6.

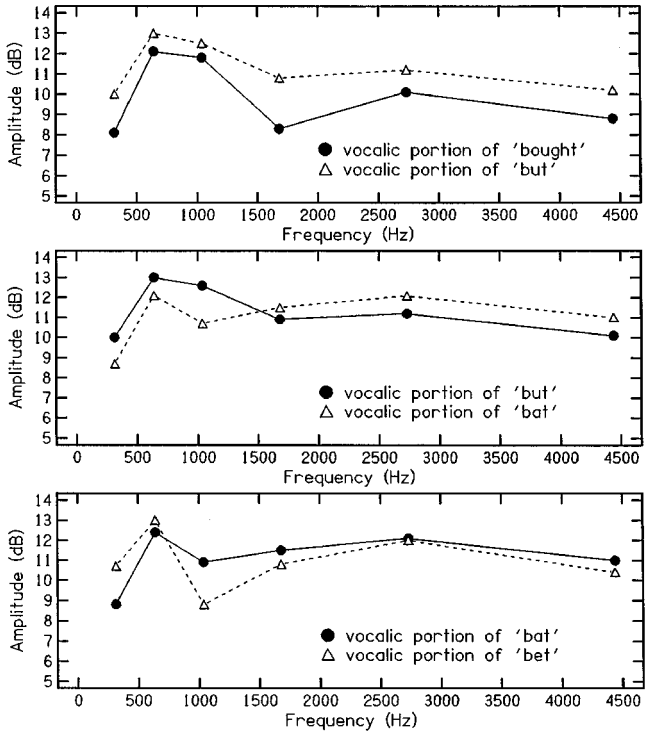

FIG. 3. Channel output levels for target vowels (solid functions) and the most common substitutions (dashed functions).

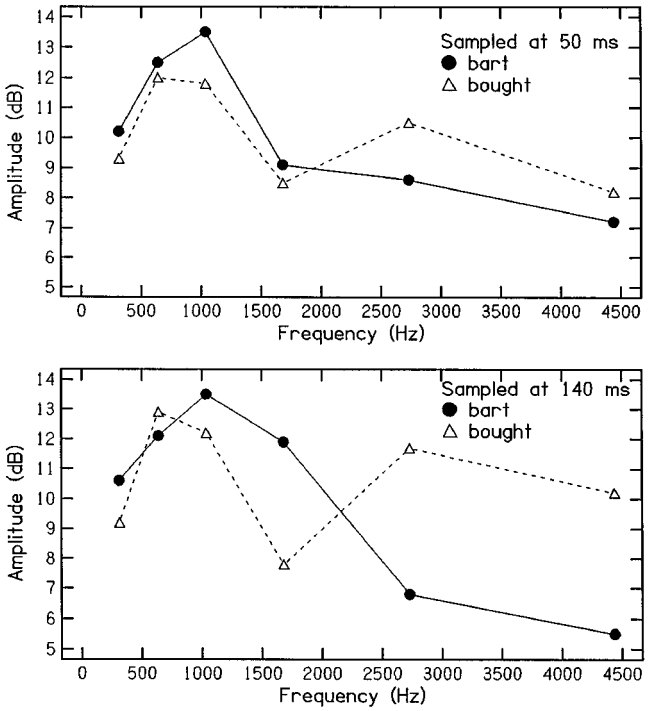

FIG. 4. Channel output levels sampled at 50 ms (top) and 140 ms (bottom) for the target vowel, in ''Bart,'' and the most common substitution, ''bought.''

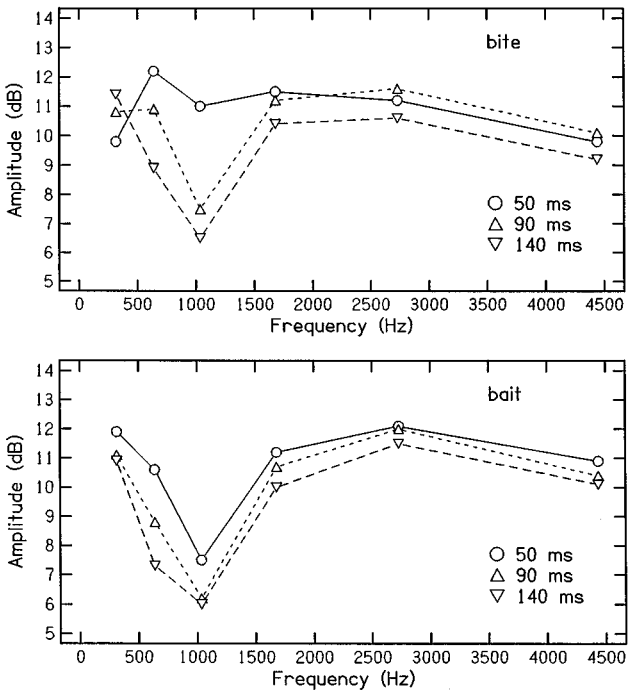

FIG. 5. Channel output levels sampled at three intervals during the diphthong in ''bite'' (top) and ''bait'' (bottom). The target was ''bite'' and the most common substitution was ''bait.''

the least well identified, the *r*-colored vowel in ''Bart,'' and the most common error response, ''bought.'' As shown at the top of Fig. 4, the output patterns of the two vowels are very similar, across channels 1–4, when sampled near the beginning of the words. However, when sampled near the end of the words, the patterns differ—mostly in the output of channels 3–4, and 4–5 (channel 4 increases about 3 dB for ''bart'') because of the fall in $F3$ characteristic of *r*-colored vowels. Once again it appears that the listeners did not attend to, or were not able to use, the changes in output levels of the higher channels as an aid in identification.

To account for the confusions of ''boat'' for ''bout'' (i.e., [o^{u}] for [a^{u}]), and ''bait'' for ''bite'' (i.e., [e^{I}] for [a^{I}]) another account—not detecting change—is reasonable. As shown in Fig. 5 when patients substituted ''bait'' for ''bite'' they substituted a vowel with a generally similar pattern of channel outputs as that of the target, but which changed less over time than the target. When ''boat'' was substituted for ''bout,'' the patients also substituted a vowel whose spectrum, and thus channel output levels, changed less over time than the target diphthong. The substitution of ''bought'' for ''Bart,'' discussed above as an example of not attending to information in the higher channels, also fits into an account of not detecting change in the pattern of channel outputs.

The discussion above was predicated on differences in mean scores for individual vowels averaged over the group of seven patients. Of course, the patients differed in their ability to identify vowels. Some patients were very poor, e.g., 29% correct, while others were very good, e.g., 88% correct. Individual differences in identification accuracy could be accounted for by assuming that patients differ in sensitivity to differences in channel output. That is, patients with poor overall identification accuracy could be patients who needed large differences in channel outputs to hear a difference in signal frequency. Patients with good identification accuracy could be those who need small differences in channel levels to hear a difference in signal frequency. Preliminary data on pure-tone frequency discrimination suggests that this may be the case (Dorman *et al.*, 1996).

E. Can a similarity metric based on the *overall* shape of channel outputs account for errors in identification?

In one account of errors in identification offered above, we suggested that patients inappropriately attend to the outputs of low-frequency channels, and/or cannot detect changes in higher-frequency channels. This account stresses attention to a portion of the channel outputs and not to the overall pattern of channel outputs. To determine if similarity in the *overall* pattern of channel outputs could provide a better account of errors in identification than the one offered above, we classified each vowel in a six-dimensional space, i.e., the channel output levels, and assessed the Euclidean distance among vowels. The metric and the distances between the channel vectors of the vowels are shown in the Appendix. According to the Euclidean distance metric, the smaller the distance between the channel vectors of two vowels, the more similar are the two vowels. For example, the distance between the channel vectors of the vowels in ''beet'' and ''Bert'' is 3.62, while that between the vowels in ''beet'' and ''bait'' is 0.94. This indicates that it is more

TABLE III. Percent error response and Euclidean distance associated with 15 stimulus–response pairs.

Stimulus and error response	Percent error response	Euclidian distance
bart–bought	70	1.3
but–bat	37	0.87
bout–boat	30	0.56
bought–but	23	0.86
bat–bet	23	1.23
bite–bait	20	1.27
beet–bait	20	0.94
boat–bought	20	0.97
boot–bert	17	1.76
bet–bit	17	1.14
bought–bout	17	1.09
bait–beet	13	0.94
boat–but	13	0.97
bart–but	13	1.33
boat–bart	13	1.15
	Spearman	$r=-0.27$

likely for patients to confuse ''bait'' with ''beet'' than ''Bert'' with ''beet.'' To simplify understanding of the predictions and the actual outcomes, 15 stimulus response pairs are shown in Table III along with the percent error response and the Euclidean distances. The Spearman rank order correlation between percent error response and Euclidean distance was not significant at -0.27. In addition, the metric does not capture asymmetries in response. In the distance metric, the distance $d(ij)$ is symmetric. This means that if vowel i is confused with vowel j, then vowel j will be confused with vowel i. This is not the case as shown in the confusion matrix in Table II. For example, [a^I] in ''bite'' was often heard as [e^I] in ''bait,'' but [e^I] was never heard as [a^I]. Thus the Euclidean distance metric fails to capture an important aspect of the data—asymmetries in response.

III. DISCUSSION

In the Introduction we pointed out that, when Ineraid patients are fit with a CIS processor, consonant and word scores improve but vowel scores, on average, do not. This outcome is difficult to understand if, in fact, the improvement in consonant and word recognition is based, even partially, on an improvement in spectral resolution. We hypothesized that vowels might not show improved scores at fitting if it were the case that the change from four-channel analogue to six-channel CIS processing greatly alters the representation of vowel space along the electrically stimulated cochlea. On this view, vowels might be recognized better after a period of accommodation to the pattern of electrical stimulation. The outcomes of significantly better performance at one month versus fitting, and of better performance at one month versus the Ineraid supports our hypothesis. These outcomes allow improvements in vowel recognition to be encompassed by the same explanatory concept as improvements in consonant recognition, i.e., an improvement in spectral resolution. However, this is not to say that all improvements in consonant recognition are derived from an improvement in spectral resolution. Improved resolution of amplitude envelopes plays a significant role in consonant recognition (Lawson *et al.*, 1993; Shannon *et al.*, 1995).

Our analyses of errors in identification suggests that patients either attend inappropriately to information in low-frequency channels of the processor, and/or are unable to use differences in higher-frequency channels. Our analyses also suggests that some errors, those for diphthongs, commonly involve not detecting change in channel outputs. To examine the adequacy of our analysis we have developed a classification algorithm for vowel recognition based on the concepts that patients attend to low-frequency channels at the expense of higher-frequency channels and that patients use the difference in outputs of adjacent channels to code the frequencies of vowel formants. Because only one token of each vowel was used in our experiment, we could not test the algorithm on novel vowel tokens. However, we could determine if the algorithm, when presented with the vowels from the current experiment, would make the same errors as patients and whether the errors would be asymmetric. The algorithm predicts seven of the eight most common errors and makes those errors in an asymmetric fashion. Thus there is reason to believe that the assumptions of attention to low-frequency channels, and use of adjacent channel output levels to code formant frequencies are reasonable ones.

ACKNOWLEDGMENT

This research was supported by Grant No. DC RO1 00654-5 from the National Institute on Deafness and Other Communication Disorders.

APPENDIX

For monothongs, channel vectors were taken in the steady-state portion of the vowel. Diphthongs were divided into segments (a and b) of equal duration, channel vectors were taken of each segment, and the channel vectors were then averaged. The distance $d(i,j)$ between vowels i and j is then defined as follows. Let $c_a(m)^{(i)}$ $(m=1,\ldots,6)$ be the average output level of channel m in segment ''a'' of vowel i, and $c_b(m)^{(j)}$ be the average output level of channel m in segment ''b'' of vowel j, then

$$d(i,j)=\frac{1}{2}\left[\frac{1}{6}\sqrt{\sum_{m=1}^{6}(c_a(m)^{(i)}-c_a(m)^{(j)})^2}+\frac{1}{6}\sqrt{\sum_{m=1}^{6}(c_b(m)^{(i)}-c_b(m)^{(j)})^2}\right].$$

The distances between the channel vectors of the vowels in the test set are shown in Table AI. Only the entries above the diagonal are shown since the matrix is symmetric.

TABLE AI.

	beet	bit	bait	bet	bert	bat	but	bought	bout	boat	bite	boot	bart
beet		1.14	0.94	1.97	3.62	2.35	2.61	2.93	2.71	2.75	1.84	2.45	3.38
bit			0.57	1.14	2.69	1.93	1.97	2.41	2.05	2.03	1.34	1.71	2.61
bait				1.31	2.91	1.92	2.13	2.59	2.34	2.31	1.27	2.03	2.79
bet					2.59	1.23	1.31	1.70	1.61	1.59	1.04	1.79	1.98
bert						2.89	2.27	2.71	2.42	2.06	2.36	1.76	1.68
bat							0.87	1.40	1.39	1.71	1.06	2.30	1.96
but								0.86	0.97	0.97	0.98	1.70	1.33
bought									1.09	0.97	1.57	1.78	1.30
bout										0.56	1.40	1.40	1.56
boat											1.36	1.04	1.15
bite												1.67	1.85
boot													1.63
bart													

Boex, C., Pelizzone, M., and Montandon, P. (**1994**). ''Improvements in speech recognition with the CIS strategy for the Ineraid multichannel intracochlear implant,'' in *Advances in Cochlear Implants*, edited by I. Hochmair-Desoyer and E. Hochmair (International Interscience Seminars, Mantz).

Dorman, M. F., Dankowski, K., Smith, L., and McCandless, G. (**1991**). ''Identification of synthetic vowels by patients using the Symbion multichannel cochlear implant,'' Ear Hear. **10**, 40–43.

Dorman, M., Smith, L., Smith, M., and Parkin, J. (**1996**). ''Frequency discrimination and speech recognition by patients who use the Ineraid and CIS cochlear-implant signal processors,'' J. Acoust. Soc. Am. **99,** 1174–1184.

Dubno, J., and Dorman, M. (**1987**). ''Effects of spectral flattening on vowel identification,'' J. Acoust. Soc. Am. **82,** 1503–1511.

Eddington, D. K. (**1980**). ''Speech discrimination in deaf subjects with cochlear implants,'' J. Acoust. Soc. Am. **68,** 885–891.

Lawson, D., Wilson, B., and Finley, C. (**1993**). ''New processing strategies for multichannel cochlear prostheses,'' in *Progress in Brain Research*, Vol. 97, edited by J. Allum, D. Allum-Mecklenburg, F. Harris, and R. Probst (Elsevier Science, New York).

Shannon, R., Zeng, F-G., Kamath, V., Wygonski, J., and Ekelid, M. (**1995**). ''Speech recognition with primarily temporal cues,'' Science **270,** 303–304.

Wilson, B. S., Lawson, D., and Finley, C. (**1990**). ''Speech processors for auditory prostheses,'' Fourth Quarterly Progress Report on NIH Project No. N01-DC-9-2401, 1–9.

Wilson, B. S., Finley, C., Lawson, D., Wolford, R., Eddington, D., and Rabinowitz, W. (**1991**). ''Better speech recognition with cochlear implants,'' Nature (London) **352,** 236–238.

Zierhofer, C., Peter, O., Bril, S., Pohl, P., Hochmair-Desoyer, I., and Hochmair, E. (**1994**). ''A multichannel cochlear implant system for high-rate pulsatile stimulation strategies,'' in *Advances in Cochlear Implants*, edited by I. Hochmair-Desoyer and E. Hochmair (International Interscience Seminars, Mantz).

Perception of the American English liquid /ra–la/ contrast by humans and monkeys

Joan M. Sinnott[a] and Charles H. Brown
Comparative Hearing Laboratory, Psychology Department, University of South Alabama, Mobile, Alabama 36688

(Received 13 February 1996; revised 14 February 1997; accepted 19 March 1997)

Human and monkey perception of the American English liquid /ra–la/ contrast was compared using various synthetic continua in which the normal spectral and temporal cues were either complete, partial, or altered in various ways. Two experiments compared human and monkey *discrimination* of the various continua using a low-uncertainty repeating-standard procedure. Results showed that, while human sensitivity was best at the human phoneme boundary, monkey sensitivity was best inside the /ra/ category. Also, while humans were more sensitive than monkeys to temporal variation in the stimuli, monkeys were more sensitive than humans to spectral variation, particularly for stimuli inside the /ra/ category. Two additional experiments compared human and monkey *identification* of the /ra–la/ continua using a higher-uncertainty go/nogo identification procedure. Monkeys performed as accurately as humans (including one native Spanish and one native Hindi listener) in identifying the stimuli. However, human and monkey ''phoneme boundaries'' were in different places, with monkey boundaries shifted more toward /ra/ than human boundaries. These results suggest that human boundaries may be based on some sort of specific linguistic knowledge. Despite these boundary differences, monkeys showed a trading relation comparable to that of humans, indicating that the /ra–la/ trading relation has a psychoacoustic basis and that linguistic knowledge is not a necessary prerequisite for it to occur. [S0001-4966(97)03107-X]

PACS numbers: 43.71.Es [WS]

INTRODUCTION

Over the past two decades, much research has been devoted to studying how animals perceive human speech sounds. These studies have revealed both differences and similarities in human and animal sensitivity. On the one hand, studies of differential sensitivity have found that animals are quantitatively less sensitive than humans to the acoustic cues underlying speech sounds (Sinnott *et al.*, 1976; Sinnott and Adams, 1987; Sinnott and Kreiter, 1991). Despite this, other studies have found that animals appear qualitatively similar to humans for more complex types of processing such as categorical perception of VOT and place-of-articulation contrasts (Kuhl and Miller, 1978; Kuhl, 1981; Kuhl and Padden, 1982, 1983), phonetic category formation for VOT and place-of-articulation contrasts (Kuhl and Miller, 1975; Kluender *et al.*, 1987), the VOT-$F1$ onset trading relation (Kluender, 1991; Kluender *et al.*, 1994), and ''speech mode processing'' for /ra–la/ (Dooling *et al.*, 1995). These studies indicate that human linguistic knowledge is not necessary for these complex effects to occur.

Previous studies of animal speech discrimination have used, for the most part, vowel contrasts, or VOT or place-of-articulation consonant contrasts (but see also Dooling *et al.*, 1995). Here we compare human and monkey discrimination and identification of the American English liquid /r–l/ contrast, which has attracted much attention because native Japanese speakers learning English have so much difficulty with it, particularly in the syllable-initial position (e.g., Miyawaki *et al.*, 1974; Strange and Dittmann, 1984; Underbakke *et al.*, 1988; Logan *et al.*, 1991). These results suggest that perhaps the acoustic cues underlying /r–l/ may not be psychoacoustically very salient, and may even require sensitization in early infancy (Eimas, 1975). The /r–l/ contrast is based primarily on two acoustic cues: a spectral cue in $F3$, and a temporal cue in $F1$ (Polka and Strange, 1985). It is interesting to note that the English continuant /r/ (phonetically, [ɹ]) is quite rare among the languages of the world; the trill [r] and flap [ɾ] are much more common (Maddieson, 1984). It is therefore of interest to determine how animal sensitivity to this contrast compares to the more universal contrasts that have been tested both with regard to differential sensitivity to the underlying acoustic cues, as well as with regard to more complex phenomena such as categorical perception and trading relations.

The present study consisted of five experiments designed to examine in detail both human versus monkey sensory-level processing as well as higher level phenomena that invoke categorization and memorial processes: (1) A conventional written identification (ID) procedure was used with humans to measure phoneme boundaries along various /ra–la/ continua; (2) A low-uncertainty discrimination procedure presented pairwise comparisons from the continua to compare perceptual boundaries in humans and monkeys; (3) A low-uncertainty discrimination procedure was used to compare human and monkey differential sensitivity to the acoustic cues underlying this contrast; (4) A higher-uncertainty go/nogo (GNG) ID procedure was used to com-

[a]Electronic mail: jsinnott@jaguari.usouthal.edu

pare identified perceptual boundaries in humans and monkeys; (5) The GNG ID procedure was used to compare the /r–l/ trading relation in humans and monkeys. The strength of the present series of experiments is that both humans and monkeys were tested under identical procedures (except for Experiment 1), thus precise quantitative as well as qualitative comparisons could be made between species.

There are both theoretical and practical reasons to examine the perception of human speech by animals. Theoretically, such comparisons will ultimately help to distinguish between theories of speech perception that invoke general auditory-perceptual processes (e.g., Jusczyk, 1982; Pisoni *et al.*, 1994) versus those that resort to some sort of special speech processing mechanism, typically based on articulatory-gestural capacities (e.g., Best, 1995; Liberman, 1996). Animals provide a nonarticulatory ''clean slate'' for human speech sound learning, and for them all speech sounds will be heard as nonspeech sounds. The animal experiments tell us what capacities we have inherited from mammalian ancestors that provide the basis for higher-level linguistic speech sound perception. Practically speaking, the development of animal models of human speech perception will allow us to investigate the physiological bases of speech perception (e.g., Sinex *et al.*, 1991).

I. GENERAL METHOD

A. Subjects

Subjects were six female humans: author JMS, BSR, ICL, JEM, RAK, and TLW; four male humans: DMB, KWM, TAC, and WAS, and four 6-year-old male Japanese macaque monkeys (*macaca fuscata*): Andy, Dart, Harry, and Port. All humans except JMS ranged from 25 to 35 years old, and were naive as to the purposes of the experiment at the time of testing. All humans were native speakers of American English except ICL and WAS, whose native languages were Spanish and Hindi, respectively. Both had learned English as teenagers, had been in America for about ten years, and spoke English with accents. RAK was a bilingual English-German speaker, exposed to both languages from birth, and had no accent in English, as judged by other members of the laboratory. All three bilingual subjects worked regularly in our laboratory, and it was very convenient to test them. All subjects except TAC had previously participated in various psychoacoustic and speech discrimination experiments.

B. Apparatus

The free-field test situation is described elsewhere in detail (Sinnott *et al.*, 1992). Briefly, all subjects were tested in the free-field inside a double-walled IAC booth (1.98 m$\times$1.82 m$\times$1.52 m) lined with sound-absorbing insulation (Sonex). Subjects responded on a custom-made contact-sensitive metal disk mounted over a cuelight embedded in Plexiglas. The stimulus system included a 12-bit D/A converter (Data Translation), a low-pass filter set at 4800 Hz (Frequency Devices), programmable attenuators (Data Translation), an amplifier (NAD 3240 PE), and loudspeaker (Polk 10). Stimuli were calibrated with a B&K sound-pressure level (SPL) meter and 0.5-in. condenser microphone placed in the position of the subject's head. Monkeys sat in primate chairs and received 190-mg banana-flavored pellets as rewards from an automatic feeder. All experimental contingencies were controlled by a Compaq computer.

C. Stimuli

Stimuli consisted of /ra–la/ continua in which the normal acoustic cues were either complete, partial, or altered in various ways. Stimuli were generated on the Klatt synthesizer in the Canadian Speech Research Environment (University of Western Ontario). Syllables were 220 ms in duration with a 10-ms rise–fall time. $F0$ fell linearly over the duration of the syllable from 125 to 80 Hz. Formant frequencies and bandwidths in Hz of the steady-state /a/ vowel were as follows: $F1=700$, $BW1=90$; $F2=1200$, $BW2=90$; $F3=2600$, $BW3=130$; $F4=3300$, $BW4=400$; $F5=3700$, $BW5=500$. Stimuli were synthesized and presented at a 10-kHz sampling rate, filtered at 4800 Hz, and presented in the free-field at 60 dB SPL (A). The specific continua used are described in Secs. II A and VI A (see below).

II. EXPERIMENT 1: WRITTEN IDENTIFICATION BY HUMANS

The purpose of this experiment was to obtain /ra–la/ ID data from American English speakers using a conventional written ID procedure, in order to assess where perceptual boundaries would occur along various /ra–la/ continua and provide a comparison with our later ID studies using the monkey GNG ID procedure (see Sec. V).

Normal /ra–la/ stimuli were constructed by varying both a spectral cue in the third formant ($F3$) and a temporal cue in the first formant ($F1$) (Polka and Strange, 1985). Along with normal /ra–la/ stimuli, we also included some stimuli in which either the spectral or temporal cue was eliminated; the purpose of this manipulation was to assess which of these cues was the most important for identification. An additional ''conflicting cues'' continuum was constructed to investigate an hypothesis according to which the two cues varying in opposite directions should cancel each other out and become less discriminable (Polka and Strange, 1985).

Finally, we included some ''nonspeech'' control stimuli that were constructed by reversing the cues across formants: The spectral cue was put into $F1$ instead of $F3$ and the temporal cue was put into $F3$ instead of $F1$. The purpose of this manipulation was to investigate the American English listeners' ability to identify stimuli in which a spectral and temporal cue were both present, but put into a context where they would not be perceived as English speech. Thus these stimuli should be much more difficult to identify compared to the normal /ra–la/ stimuli.

A. Method

Four of the stimulus continua used in experiment 1 are shown in Fig. 1. In these stimuli, the spectral cue occurred in $F3$ and the temporal cue in $F1$.

Figure 1(a) shows the *full cues* /ra–la/ continuum (RALA), which was constructed by varying both the spectral

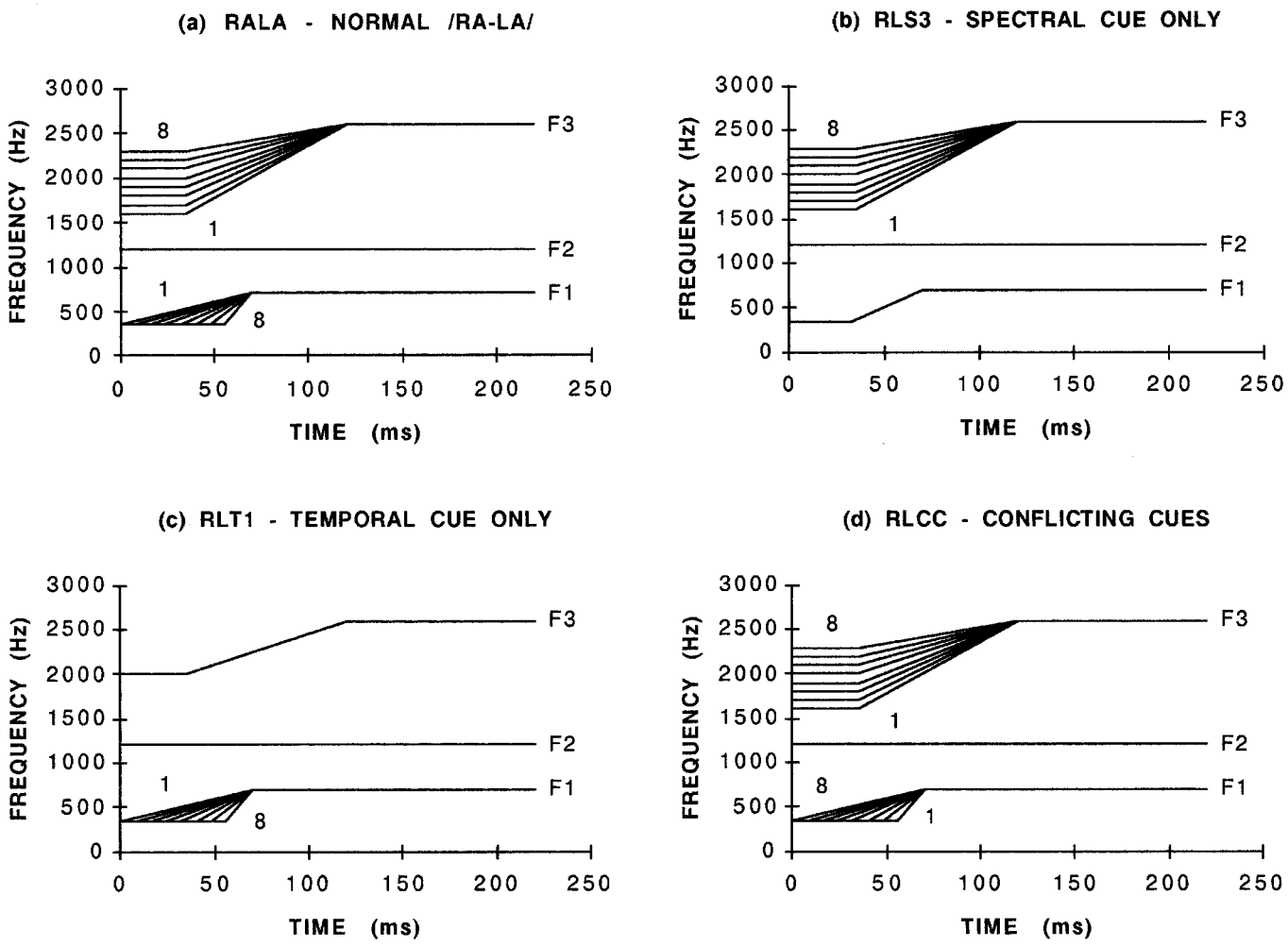

FIG. 1. (a)–(c) Schematized spectrographic patterns of the four stimulus continua used in experiment 1 in which the spectral cue occurred in $F3$ and the temporal cue in $F1$.

and temporal cue. The spectral cue consisted of varying the onset frequency of $F3$. For /ra/, stimulus 1 in the continuum, $F3$ began at 1600 Hz, remained flat for 35 ms, then rose linearly over the next 85 ms to 2500 Hz. For /la/, stimulus 8 in the continuum, $F3$ began at a higher frequency of 2300 Hz, and then followed the same temporal pattern as /ra/. The temporal cue consisted of delaying the onset of a transition in $F1$. For /ra/, $F1$ began at 350 Hz and moved linearly over the next 70 ms to 700 Hz. For /la/, $F1$ began at 350 Hz, remained flat for 56 ms, and then began an abrupt transition over the next 14 ms to 700 Hz. The eight-stimulus continuum was synthesized by increasing the $F3$ onset in 100-Hz steps, and the $F1$ delay in 8-ms steps.

Figure 1(b) shows the *spectral cue only* continuum (RLS3), which consisted of varying the normal $F3$ spectral cue, but holding the $F1$ temporal cue constant by setting the transition to begin at a middle value of 32 ms. Figure 1(c) shows the *temporal cue only* continuum (RLT1), which consisted of varying the normal $F1$ temporal cue, but holding the $F3$ spectral cue constant at a middle value of 2000 Hz; Fig. 1(d) shows the *conflicting cues* continuum (RLCC). This continuum consisted of varying the $F3$ spectral cue in the normal manner, but varying the $F1$ temporal cue in the opposite direction from normal. Thus the first ''/ra/'' stimulus contained the normal spectral cue for /ra/, but the normal temporal cue for /la/. The eighth ''/la/'' stimulus contained the normal spectral cue for /la/, but the normal temporal cue for /ra/.

Figure 2 shows the ''reversed'' continua in which the spectral cue occurred in $F1$ and the temporal cue in $F3$. Figure 2(a) shows the *reversed full cues* continuum (RLRV), which varied both cues as follows: For the first ''/ra/'' stimulus, $F1$ began at 350 Hz, remained flat for 35 ms, then rose linearly over the next 85 ms to 700 Hz. For the eighth ''/la/'' stimulus, $F1$ remained constant at 700 Hz. The temporal cue consisted of delaying the onset of a transition in $F3$. For ''/ra/,'' $F3$ began at 1600 Hz and moved linearly over the next 70 ms to 2600 Hz. For ''/la/,'' $F3$ began at 1600 Hz, remained flat for 56 ms, and then began an abrupt transition over the next 14 ms to 2600 Hz.

Figure 2(b) shows the *reversed spectral cue only* continuum (RVS1), which contained the varying spectral cue in $F1$, and the temporal cue in $F3$ set to a middle value of 32 ms. Figure 2(c) shows the *reversed temporal cue only* continuum (RVT3), which contained the varying temporal cue in $F3$, and the spectral cue in $F1$ set to a middle value of 550 Hz.

Six humans, JMS, DMB, TAC, RAK, JEM, and KWM,

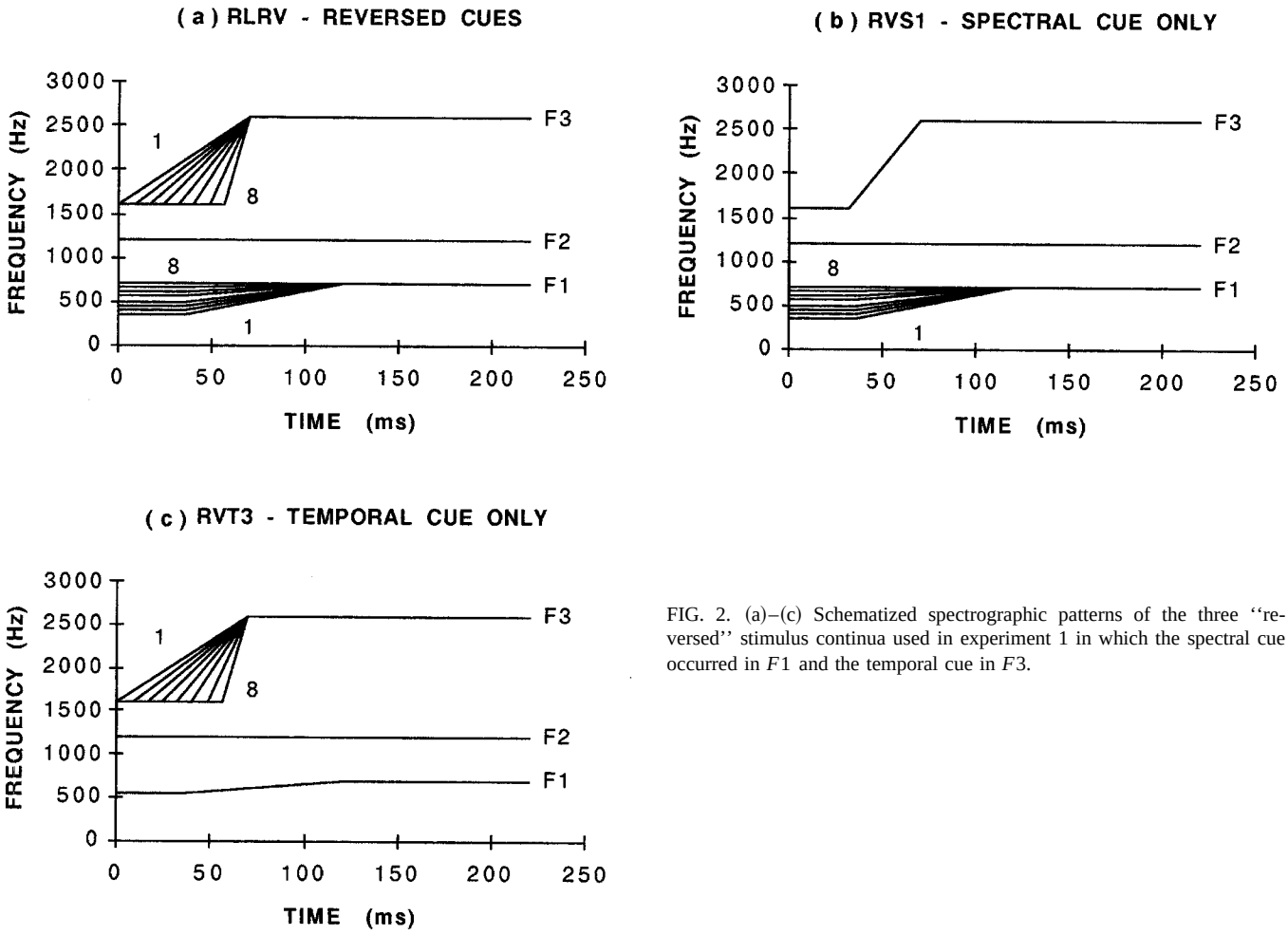

FIG. 2. (a)–(c) Schematized spectrographic patterns of the three ''reversed'' stimulus continua used in experiment 1 in which the spectral cue occurred in $F1$ and the temporal cue in $F3$.

were tested. DMB was not tested on RLRV, RVS1, and RVT3. Each subject sat inside the booth and worked at her/his own pace. A trial began when the subject contacted the response disk with the left hand, which caused a randomly chosen stimulus to be repeated at a rate of one per s until the subject released the disk. The subject wrote down with the right hand on a response sheet if the stimulus sounded more like /ra/ or /la/. Subjects were told to make a response in all cases, even if the stimuli did not sound like a normal /ra/ or /la/.

All subjects were tested first on RALA. After that, the order of testing the other six continua was counterbalanced among subjects, with a total of five sessions occurring for each continuum. Each session consisted of 80 trials representing 8 responses for each of the 10 stimuli, so the final data were based on 40 responses per stimulus.

B. Results and discussion

Figure 3 shows individual human ID functions for the four continua shown in Fig. 1. Boundaries between /ra/ and /la/ were calculated from the transition durations, interpolated if necessary, at which a stimulus was identified 50% of the time as one syllable 10 the other. (Probit analysis was not used to smooth the functions since all functions were highly monotonic.) For the sake of simplicity, graphs show the percent of stimuli identified as /la/.

Figure 3(a), (b), (c) shows boundaries for RALA, RLS3, and RLT1. Most subjects had clear boundaries between stimuli 4 and 6 on all these continua, except for DMB who heard most of the stimuli as /ra/ and had a boundary shifted toward /la/. Boundaries for all subjects are listed in Table I.

Figure 3(d) shows boundaries for RLCC, which had the conflicting cues. Interestingly, the two cues did not appear to cancel each other entirely. Instead, subjects seemed to tune into one cue or the other and ended up with reasonable ID functions, except that no boundaries occurred between stimuli 4 and 6, as in Fig. 3(a), (b), (c). Three subjects identified stimuli at the extreme end of the continuum as /la/, indicating that their perception followed the spectral cue, and had boundaries between stimuli 6 and 8. Two subjects identified stimuli at the beginning of the continuum as /la/, indicating that their perception followed the reversed temporal cue, and had boundaries between stimuli 2 and 4. Subject TAC heard stimuli at both ends of the continuum as /la/, and thus had a less orderly identification function.

Figure 4(a), (b), (c) shows functions for the reversed continua RLRV, RVS1, and RVT3. Boundaries for RLRV [Fig. 4(a)] indicated that subjects managed to hear /ra/ and /la/ in the stimuli, probably due to the forced-choice nature of the response procedure. However, most subjects heard stimuli in the beginning of the continuum as /la/, which is the opposite percept from the normal /ra–la/ continuum. Only

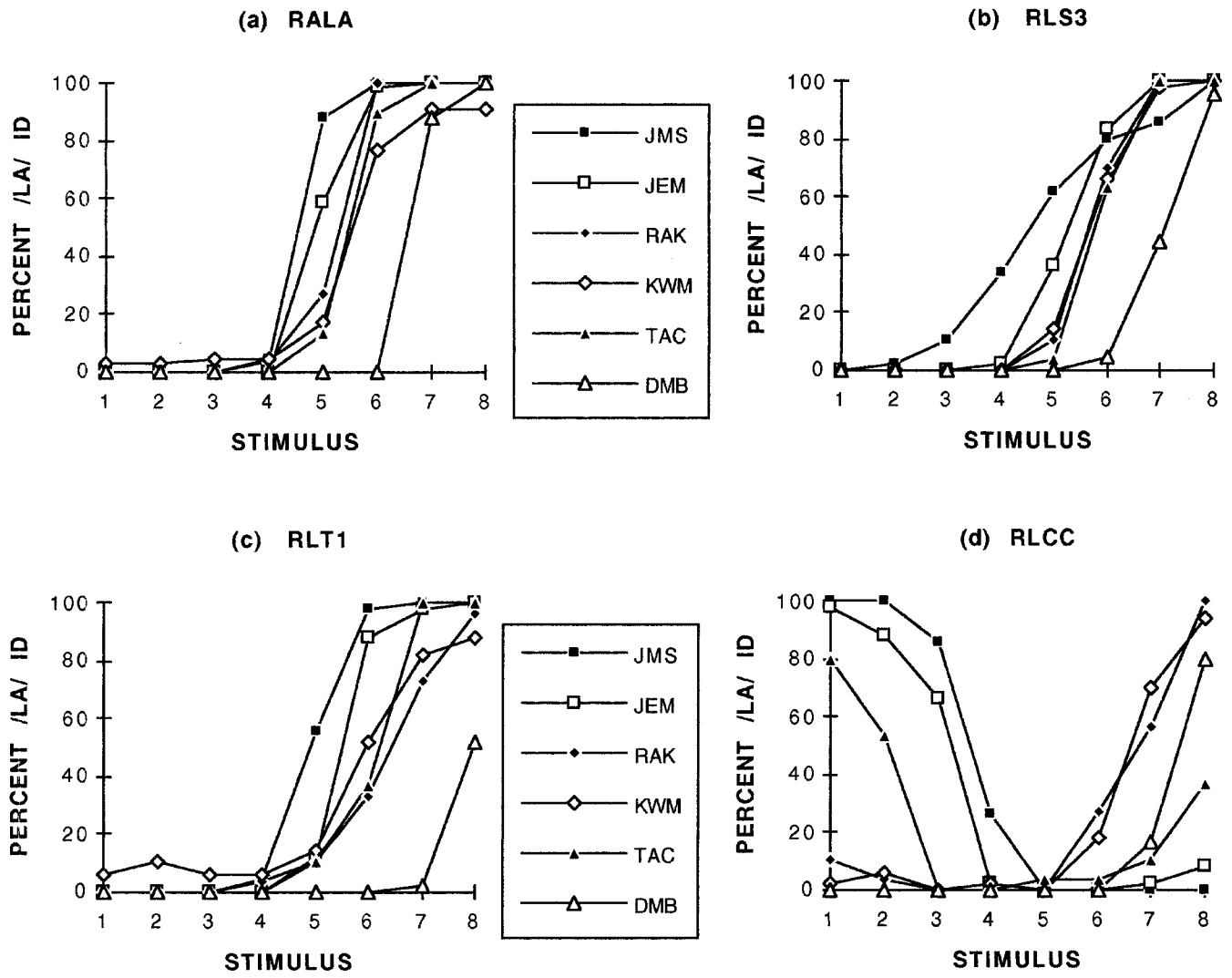

FIG. 3. (a)–(d) Written identification functions from human subjects for the four stimulus continua shown in Fig. 1. Percent of stimuli identified as /la/ are plotted as a function of stimulus number along each continuum.

one subject, TAC, heard /la/ stimuli at the end of the continuum. For the most part, these same strategies were carried over to RVS1 [Fig. 4(b)]. All subjects found the reversed temporal cue in RVT3 very hard to identify and boundaries were less orderly in this condition [Fig. 4(c)]. When queried as to what all these reversed stimuli sounded like, most subjects responded that they sounded vaguely like some sort of human speech, but did not resemble any English sounds.

TABLE I. Perceptual /ra–la/ boundaries (in terms of stimulus number along the continuum) for six humans as measured in experiment 1 (written identification). RALA=normal /ra–la/ continuum; RLS3=spectral cue only continuum; RLT1=temporal cue only continuum.

	RALA	RLS3	RLT1
JMS	4.5	4.5	4.9
JEM	4.8	5.5	5.5
RAK	5.3	5.8	6.5
KWM	5.6	5.9	6
TAC	5.5	5.9	6.2
DMB	6.5	7.2	8
Mean	5.37	5.8	6.18

III. EXPERIMENT 2: DISCRIMINATION OF PAIRWISE COMPARISONS

The purpose of this experiment was to compare perceptual boundaries in humans and monkeys by measuring their sensitivity to pairwise comparisons along the continua. Based on the results of experiment 1, we hypothesized that clear human peaks between stimuli 4 and 6 would emerge in RALA, RLS3, and RLT1. Some form of peak should also emerge in RLCC and RLRV, since humans did manage to categorize these continua, although the resulting boundaries did not occur at stimuli 4–6. For monkeys, it was an open question as to whether clear peaks would emerge. RVS1 and RVT3, because of their disorderly ID functions, were not used in this experiment.

A. Method

Stimuli were RALA, RLS3, RLT1, RLCC, and RLRV. Subjects were five humans, JMS, DMB, RAK, JEM, KWM, and two monkeys, Harry and Port. The pairwise testing was very time consuming, and all subjects were unable to complete all conditions, therefore some of the comparisons below were based on three or four humans.

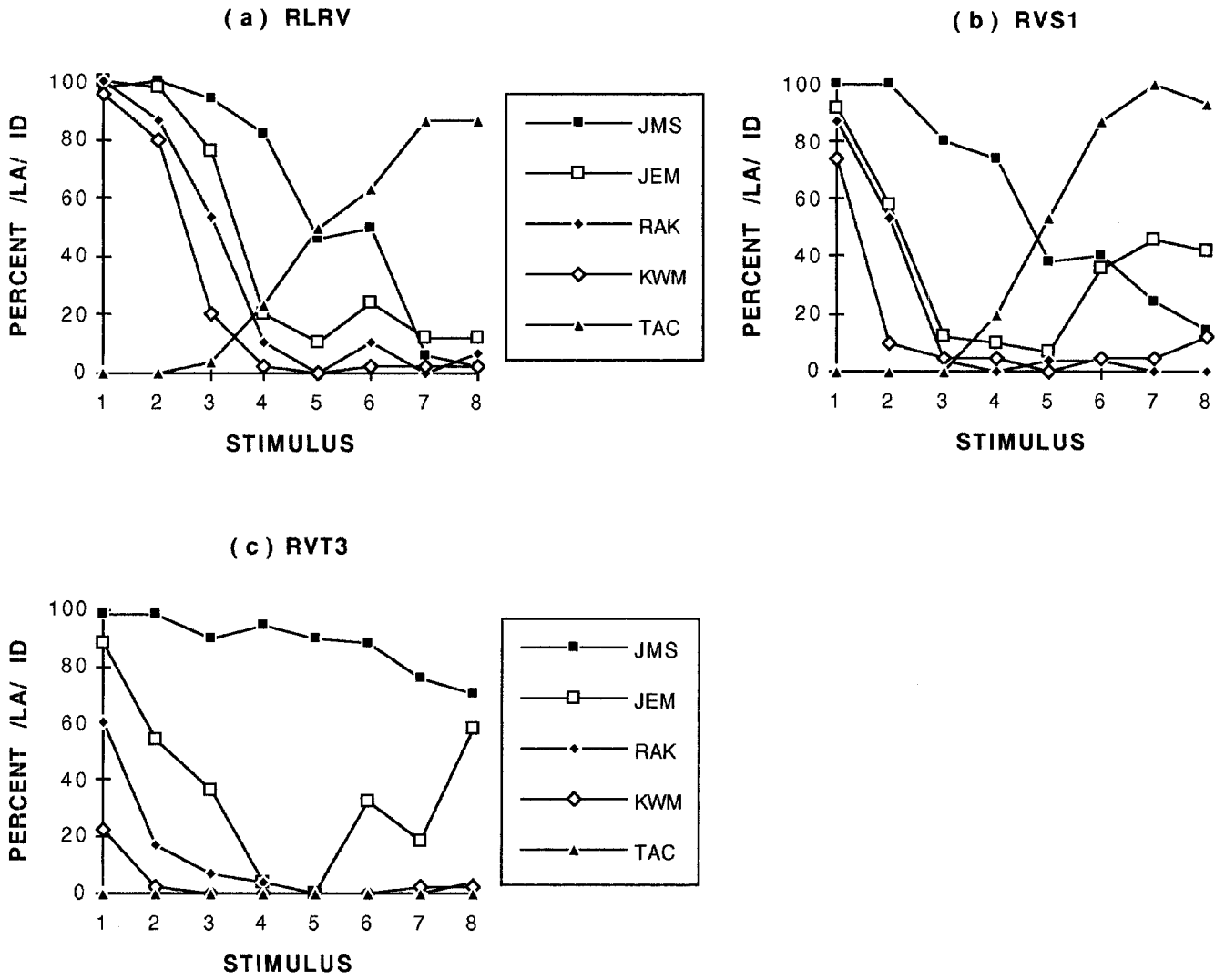

FIG. 4. (a)–(c) Written identification functions from human subjects for the three ''reversed'' stimulus continua shown in Fig. 2. Percent of stimuli identified as ''/la/'' are plotted as a function of stimulus number along each continuum.

All subjects were tested with a low-uncertainty repeating-standard same–different AX discrimination procedure that has been extensively used over the last 20 years in studies of animal psychoacoustics and speech discrimination (Sinnott, 1994, 1995). A trial began when the subject contacted the response disk during the flashing cuelight. At this time, the cuelight steadied and the standard stimulus began repeating at a rate of 1 per 800 ms. After a variable time period of 1600–6400 ms, two identical target stimuli occurred. The target stimuli always represented a two-step upward change along the continuum from the standard, e.g., if the standard was stimulus 1, the target was stimulus 3, etc.

A subject had a 1600-ms response interval, measured from the onset of the target, to release the disk in order to score a *hit*, which was immediately rewarded with a food pellet (monkeys) or the feeder click (humans). Following rewards, an intertrial interval (ITI) occurred, during which the cuelight extinguished and trials could not be initiated.

If the subject did not respond to the target during the response interval (*miss*), a 3-s ITI (timeout) occurred as feedback to the subject. On control trials, a target occurred that was identical to the standard. Responses to control trials (*false alarms*) and other premature releases were punished with 8-s timeouts. Control trials that were not responded to (*correct rejections*) were immediately followed by a two-step target stimulus that contained a highly salient +6-dB intensity cue, to which all subjects could easily respond. This ''suprathreshold'' stimulus was thus nearly always correctly discriminated and essentially rewarded the subject for correct rejecting the control trial, keeping false alarms to a minimum.

Only one stimulus pair was presented during a daily session. Because different pairs of stimuli differed in their discriminability, the proportion of test and control trials was adjusted to keep the density of reward constant at about 70 hits per 15-min session for humans, and about 140 hits per 35-min session for monkeys. Testing thus progressed through four stages: 1=20% test trials, and 80% control trials, which were followed by the suprathreshold stimulus; 2=40% test trials and 60% control trials; 3=60% test trials and 40% control trials; and 4, the final stage,=80% test trials and 20% control trials. As a subject's discrimination improved and her/his false alarm rate remained below 5%, s/he was moved to the next stage. If a subject's false alarm rate

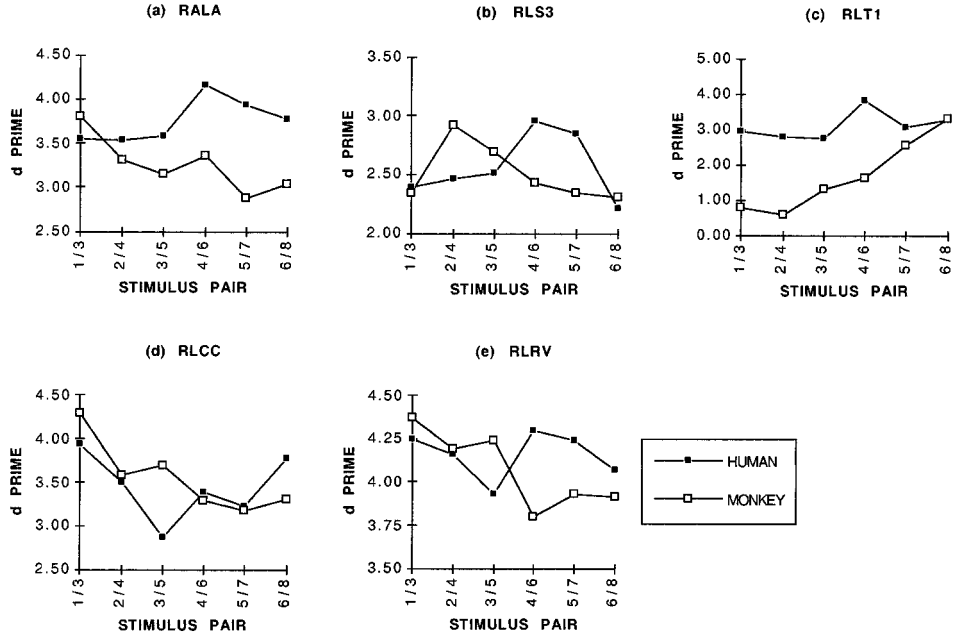

FIG. 5. (a)–(e) d' scores for humans and monkeys for pairs of stimuli along five stimulus continua, as measured in experiment 2.

increased to over 20%, s/he was moved back one stage. This procedure kept all subjects reward densities constant and their false alarm rates at approximately 3%–5%.

All subjects were tested first with RALA, after that presentation of the other continua was counterbalanced across subjects. For each continuum, subjects started with pair 1-3, moved in order to pair 6-8 over the next six sessions, and then back again. This sequence was repeated five times per continuum, resulting in ten sessions per pair. In total, human subjects were exposed to about 400 presentations for each pair, while monkeys were exposed to about 800, which allowed all subjects to reach asymptotic levels of performance for each stimulus pair. For each session, a subject's hit and false alarm rate were transformed into a d' score. Final data consisted of averaging d' over each subject's three best sessions with the highest d' scores, and with false alarm rates below 20%. Final data were based on about 150 presentations per pair for humans, and about 300 for monkeys.

B. Results and discussion

Figure 5 shows averaged discrimination functions for humans and monkeys for the five continua, plotted in terms of d'. Results for each continuum were analyzed separately with two-way repeated-measures ANOVAS, to examine the main effects of SPECIES and PAIR, and the interaction between these two factors.

Figure 5(a) shows data for RALA, based on five humans and two monkeys. The human data show a peak at pair 4/6, matching the boundaries identified in experiment 1 [see Fig. 3(a)], and better sensitivity for the last three pairs (4/6, 5/7, 6/8) than for the first three pairs (1/3, 2/4, 3/5) inside the /ra/ category. The monkey data show a different pattern: a smoother function, with best sensitivity inside the /ra/ category, and gradually decreasing sensitivity as the pairs increase. Note, however, a very small peak at pair 4/6. The SPECIES×PAIR interaction was significant [$F(5,25)=5.14$; $p<0.01$], indicating a differently shaped function for humans and monkeys. There were no main effects of SPECIES or PAIR.

Figure 5(b) shows data for RLS3, based on three humans and two monkeys. The humans show peaks at pairs 4/6 and 5/7, again matching the boundaries identified in Experiment 1 [see Fig. 3(b)], while the monkeys show a peak at pair 2/4, inside the /ra/ category. Here also, the SPECIES ×PAIR interaction was significant [$F(5,15)=4.36$; $p<0.05$]. The main effect of PAIR was also significant [$F(5,15)=3.62$; $p<0.05$), but there was no effect of SPECIES.

Figure 5(c) shows data for RLT1, based on three humans and two monkeys. The human data show a clear peak at pair 4-6, again matching the boundaries identified in experiment 1 [see Fig. 3(c)], while the monkey data show a function with very poor sensitivity for the early pairs inside the /ra/ category, and gradually increasing sensitivity for the later pairs. Here also, the SPECIES×PAIR interaction was significant [$F(5,15)=12.58$; $p<0.01$]. The main effect of PAIR was also significant [$F(5,15)=20.8$; $p<0.01$], but there was no effect of SPECIES.

Figure 5(d) shows data for RLCC, based on four humans and two monkeys. This function was the only one in which humans did not show a peak at pair 4/6, indeed they show a major ''dip'' at pair 3/5, supporting the hypothesis of Polka and Strange (1985) that the two cues should cancel each other out in the region of the phoneme boundary. Sensitivity seems to have shifted toward the ends of the continuum, matching more or less the boundaries indentified in experiment 1 [see Fig. 3(c)]. The monkeys show gradually decreasing sensitivity as pairs increase. Here again, the SPECIES ×PAIR interaction was significant [$F(5,20)=4.29$; $p<0.01$]. The main effect of PAIR was also significant

[$F(5,20)=9.44$; $p<0.05$], but there was no effect of SPECIES.

Figure 5(e) shows data for RLRV, based on three humans and two monkeys. Both functions show high discriminability, but the humans show slightly better sensitivity for the later pairs, while the monkeys show their usual smooth function with gradually decreasing sensitivity as pairs increase. Here again, the SPECIES×PAIR interaction was significant [$F(5,15)=5.14$; $p<0.05$]. There were no main effects of SPECIES or PAIR.

The present results indicate that perception of RALA, RLS3, and RLT1 was categorical-like for humans, since clear peaks emerged in their functions at pair 4/6, but continuous for monkeys, since no clear peaks emerged in their functions. Caution might be used in interpreting the statistics, because of the small number of subjects tested. Nevertheless, our primary interest was in the SPECIES×PAIR interaction, and since PAIR was a within-subject variable, each subject was her/his own control on this variable. Note also that there were no main effects of SPECIES in any of the analyses, indicating that humans and monkeys were well matched for overall sensitivity.

When spectral variation was involved (e.g., RALA, RLS3, RLCC, RLRV), monkeys showed gradually decreasing sensitivity as pairs increased. Monkey sensitivity appears to follow Weber's Law: The frequency DL is more or less a constant proportion of the standard, but on an absolute basis, the frequency DL increases with frequency. Therefore, as $F3$ increases in frequency moving from /ra/ to /la/ along the continuum, a constant change in Hz would become less discriminable. The human functions appear in violation of Weber's Law for these continua.

When temporal variation only was involved, as for RLT1, monkeys showed increasing sensitivity as pairs increased. However, this might also be explained by Weber's law: As pairs increase, the transitions become shorter, and thus in terms of the absolute difference in duration to be discriminated, sensitivity should be better with shorter transitions. Again, the human function appears in violation of Weber's law for this continuum.

Other comparative pairwise discrimination studies using English VOT and place-of-articulation continua have reported animals to exhibit boundaries in the same places as humans along the continua (Kuhl, 1981; Kuhl and Padden, 1982, 1983). For VOT, a true psychoacoustic or physiological discontinuity appears to exist (Sinex *et al.*, 1991). For place-of-articulation, the monkey boundary found by Kuhl and Padden (1983) may have been based on a physical attribute in the stimuli, since the F2 transition changed direction between the /b/, /d/, and /g/ categories (rising, flat, and falling, respectively). In contrast, in the present study, there was no physical discontinuity distinguishing the /ra/ and /la/ categories. For example, the onset frequency of $F3$ remained below that of the steady-state vowel along the entire continuum from /ra/ to /la/, so there was no change of direction of the $F3$ transition.

A recent study by Dooling *et al.* (1995) using a response latency measure has reported that birds perceived phonetic boundaries in a synthetic /ra–la/ continuum. As in the present study, there were no physical discontinuities in their /ra–la/ continuum that could account for the boundaries. The authors took the birds' boundaries to be similar to those of humans, although, since no humans were directly compared with the birds in that experiment, it is possible that the birds' boundaries were not identical to human boundaries. It is also important to note that Dooling *et al.* did not perform a d' analysis on their bird data, thus it is possible that changes in response criterion could have contributed to the birds' boundaries.

IV. EXPERIMENT 3: COMPARISONS OF DIFFERENTIAL SENSITIVITY TO ACOUSTIC CUES UNDERLYING /ra–la/

The purpose of this experiment was to compare human and monkey differential sensitivity to the acoustic cues underlying both normal and ''nonspeech'' /ra–la/ stimuli. Based on pure-tone DLs (difference limens), we would expect that humans and monkeys would perform more similarly for temporal than spectral cues, since monkey temporal DLs are about 2–3 times those of humans, while frequency DLs are about 10 times those of humans (Sinnott, 1994). However, comparison of both spectral and temporal DLs in other types of speech contrasts (vowels, VOT, and place-of-articulation) reveal monkey DLs about 2–3 times those of humans (Sinnott, 1994).

The reversed continua were included to compare human and monkey sensitivity to ''nonspeech'' control stimuli, and to compare sensitivity for similar cues in $F1$, the lower-frequency formant, versus $F3$, the higher-frequency formant. We hypothesized that human and monkey sensitivity would converge more for cues in $F3$, since data with vowels and pure tones indicate that monkey DLs tend to converge with those of humans as frequency increases (Sinnott and Kreiter, 1991; Sinnott *et al.*, 1992).

A. Method

Stimuli were RALA, RLS3, RLT1, RLRV, RVS1, and RVT3. Subjects were four humans, JMS, KWM, DMB, and TAC, and two monkeys, Harry and Port. The procedure was identical to that used in experiment 2, except that the standard stimulus was always either stimulus 1 or 8 from the continuum, and the target stimuli were any of the other seven stimuli from the continuum. Targets were presented using the method of constant stimuli.

Humans worked in 10–15 min daily sessions that terminated after 70 rewards, and monkeys worked in 30–35 min sessions that terminated after 140 rewards. Subjects were tested in three basic conditions with a total of nine different continua: RALA, RLS3, and RLT1 with both a /ra/ (stimulus 1) and a /la/ (stimulus 8) background (henceforth referred to as LARA, LRS3, and LRT1), and the reversed continua RLRV, RVS1, and RVT3, all with a stimulus 1 background. All subjects were tested first with the RALA or LARA continua, before being tested with the reversed continua. Humans were tested for a total of six sessions on each continuum, monkeys were tested for ten, which allowed all subjects to reach asymptotic levels of performance.

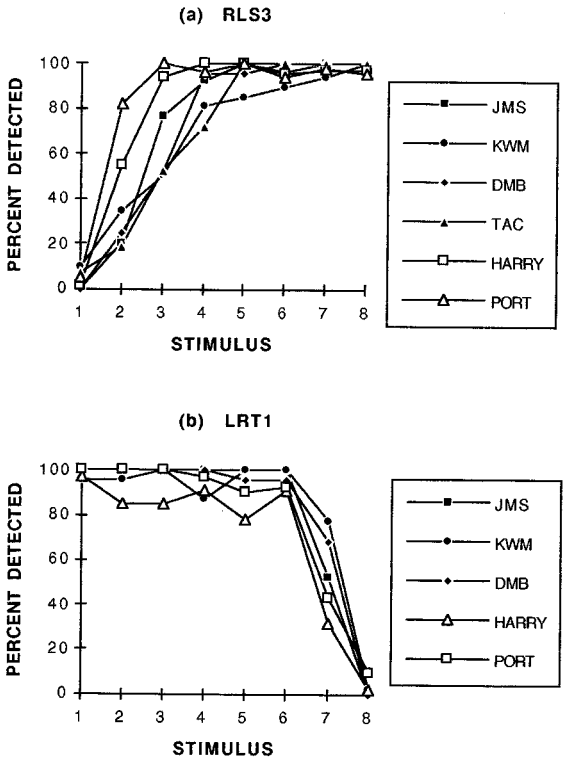

FIG. 6. Individual psychometric functions plotting percent detection as a function of stimulus number along continua RLS3 (a) and LRT1 (b), as measured in experiment 3.

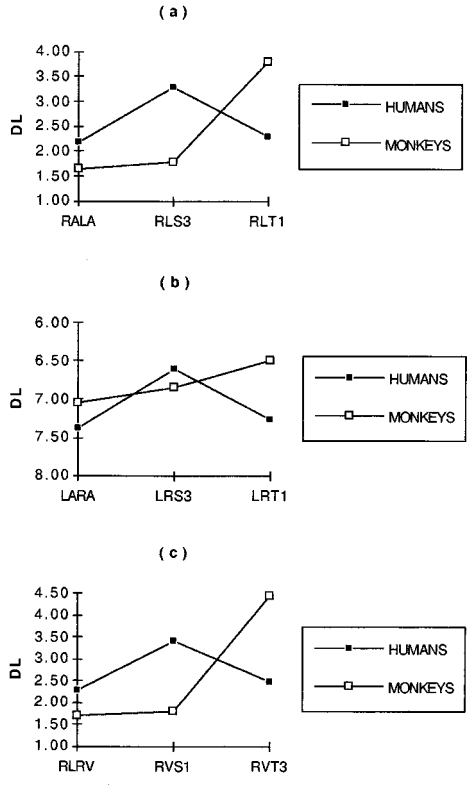

FIG. 7. (a)–(c) Averaged DLs for humans and monkeys for nine stimulus continua, as measured in experiment 3.

For each session, the total number of presentations (typically 8–15), hits and false alarms to each target were recorded, and d' scores were calculated for each target stimulus along the continuum. The DL was considered to be the stimulus number (interpolated if necessary) corresponding to a d' of 2.0. This measure equals a 50% hit rate on the psychometric function for a false alarm rate of 3%, but increases to a 65% hit rate, for example, for a false alarm rate of 8%. Final DLs were calculated by averaging each subject's three best sessions with the highest d' scores.

B. Results and discussion

Figure 6(a), (b) shows examples of individual psychometric functions for two continua. Figure 6(a) shows a condition in which both monkeys outperformed all humans: RLS3 with a /ra/ background. Figure 6(b) shows a condition in which all humans outperformed both monkeys: LRT1 with a /la/ background.

Figure 7 shows averaged DLs measured for all nine continua. ANOVAS were performed separately on each of the three basic conditions comparing the effects of SPECIES (human vs monkey) and CUES (full cue, spectral cue only, temporal cue only).

Figure 7(a) shows averaged DLs for RALA, RLS3, and RLT1, measured in terms of stimulus number along the continuum (1-8). In this condition, low numbers convey greater sensitivity. There were no main effects of SPECIES, but the effect of CUES was significant ($F[2,8]=14.64$; $p<0.01$), indicating that sensitivity was best for RALA, followed by RLS3, followed by RLT1. The SPECIES×CUES interaction was also significant ($F[2,8]=26.04$; $p<0.01$), indicating that, while humans were more sensitive to RLT1, monkeys were more sensitive to RALA and RLS3.

Figure 7(b) shows the averaged DLs for LARA, LRS3, and LRT1, where DLs are measured from stimulus 8, thus the y axis is reversed and higher numbers convey greater sensitivity. Here, the overall range of sensitivity is smaller, due to the lower DLs obtained using the /la/ background. In this condition, the main effect of SPECIES was significant ($F[1,3]=53.45$; $p<0.010$), indicating that humans were overall more sensitive than monkeys. The main effect of CUES was significant ($F[2,6]=9.84$; $p<0.05$), indicating that sensitivity was better for LARA than for LRS3 or LRT1. The SPECIES×CUES interaction was also significant ($F[2,6]=10.52$; $p<0.05$), indicating that, while humans were more sensitive to LARA and LRT1, monkeys were more sensitive to LRS3.

Figure 7(c) shows averaged DLs measured for RLRV, RVS1, and RVT3. In this condition, low numbers convey greater sensitivity. There were no main effects of SPECIES, but the main effect of CUES was significant ($F[2,6]=22.52$; $p<0.01$), indicating that sensitivity was best for RLRV, followed by RVS1, followed by RVT3. The SPECIES × CUES interaction was also significant ($F[2,6]=10.52$; $p<0.05$), indicating that, while humans were more sensitive to RVT3, monkeys were more sensitive to RLRV and RVS1.

The most striking result in this experiment was that monkeys were actually more sensitive than humans in all three cases where only the spectral cue varied (RLS3, LRS3, RVS1), and in two cases where all cues varied (RALA,

RLRV). On the other hand, humans were always more sensitive than monkeys when only the temporal cue varied (RLT1, LRT1, and RVT3).

If only the results for RALA and RLS3 are considered, it is unclear if the greater sensitivity of monkeys was due to better sensitivity to the spectral cue, or better sensitivity to the higher-frequency $F3$ itself. However, monkeys also outperformed humans for RLRV and RLS1, where the spectral cue occurred in the lower-frequency $F1$. These results indicate that the better sensitivity of monkeys in both cases was due to better sensitivity to spectral cues in general, and not simply due to better sensitivity to F3 itself than humans.

RLRV can also be viewed as a ''nonspeech'' control task to help determine if the poor spectral sensitivity of humans compared to monkeys for RALA was due to some strong form of categorical perception operating for humans, resulting in poor intraphonemic discrimination, particularly inside the /ra/ category. However, since the same results were obtained for the reversed continuum, the human–monkey differences cannot simply be explained by means of categorical perception, unless one assumes that categorical perception was also operating for humans in the reversed continuum.

These results, showing that monkeys were more sensitive than humans in conditions where the spectral cue varied, are very unusual. In over 20 years of comparing humans and monkeys on various psychoacoustic and speech discrimination tasks, we have never before found monkeys to outperform humans (Sinnott, 1994). Neither pure-tone DLs nor other speech DLs would predict the outcome of the present experiment. For discrimination of pure tones, monkey DLs are typically 5–10 times larger than those of humans, and for the place-of-articulation contrast based on a spectral cue, monkey DLs are about twice those of humans (Sinnott, 1994). At present, we have no explanation for why humans performed so poorly compared to monkeys in discrimination of these spectral cues in both $F1$ and $F3$. The important message of this experiment is that when experimenters carefully and rigorously apply modern methods of comparative psychoacoustics, animals can sometimes show exceptionally sensitive thresholds.

V. EXPERIMENT 4: IDENTIFICATION OF PERCEPTUAL BOUNDARIES

The purpose of this experiment was to compare perceptual boundaries in humans and monkeys for each continuum, using an ID procedure specifically designed for monkeys. One other ID study using VOT contrasts has reported animal boundaries in the same place as human boundaries (Kuhl and Miller, 1978; but see also Waters and Wilson, 1976). On the basis of these data, we might also expect that monkey /ra–la/ boundaries should coincide with those of humans. However, our discrimination data from experiment 2, which showed monkeys to be most sensitive to stimuli inside the /ra/ category, suggest that monkey boundaries might be shifted more toward /ra/ than human boundaries.

A. Method

Stimuli were RALA, RLS3, RLT1, and RLRV (see Figs. 1 and 2). Human subjects were JMS and KWM from Experiments 1–3 and three new humans, TLW, ICL, and WAS. Recall that ICL and WAS were non-native speakers of English. Monkey subjects were two from Experiments 2 and 3 (Harry and Port), and two new ones, Andy and Dart. The basic apparatus was the same as that used in the discrimination procedure and therefore monkeys transferred easily to the ID procedure.

The go/nogo identification (GNG ID) procedure was modeled after one previously developed by Kuhl and Miller (1978). As with the discrimination procedure, the trial sequence began with the flashing cuelight. After a variable silent interval of 2–4 s, two identical stimuli from the continuum were presented at 60 dB SPL (A), pulsed at a rate of 1 per s. For training stimuli, the two endpoint stimuli (1,8) from each continua were presented. If stimulus 1 was presented, the subject was rewarded for holding through the 2-s response interval, but punished with an 8-s timeout for releasing. If stimulus 8 was presented, the subject was rewarded for releasing the disk during the 2-s response interval, but punished with a 8-s timeout for holding through it. In order to prevent the development of response biases for either holding or releasing, a correction procedure operated such that, after errors, the same training stimulus was presented on successive trials until a correct response occurred. Correction procedure trials were not analyzed nor counted in the data analysis. Test stimuli consisted of stimuli 2, 3, 4, 5, 6, and 7 from each continuum. The subject was rewarded for any response, hold, or release when these test stimuli were presented.

Subjects passed through three training stages in which the proportion of training and test trials differed. Stage 1 consisted of 75% training trials but only 25% test trials; stage 2 consisted of 62.5% training trials and 37.5% test trials; stage 3, the final stage, consisted of 50% training trials and 50% test trials. For each session, a psychometric function was obtained plotting the subject's perception of the test stimuli as either more similar to training stimulus 1 or stimulus 8, depending on whether s/he held or released, respectively, to the test stimulus. The identified boundary was considered to be the level of detection on the function half-way between the false alarm rate and 100%. For example, a 0% false alarm rate would result in a boundary at exactly the 50% level of detection, but a 10% false alarm rate would result in a boundary at the 55% level.

All subjects were tested first with RALA; after that the order of the various continua was randomized among subjects. Humans were tested for five sessions at stage 3 on each continuum; monkeys were tested for ten sessions. Since 8 (human) or 15 (monkey) responses per stimulus were obtained per session, this resulted in a total of 40 responses per stimulus for humans and 150 for monkeys.

B. Results and discussion

Figure 8 shows examples of individual ID functions obtained for two continua. For RALA [Fig. 8(a)], the monkey

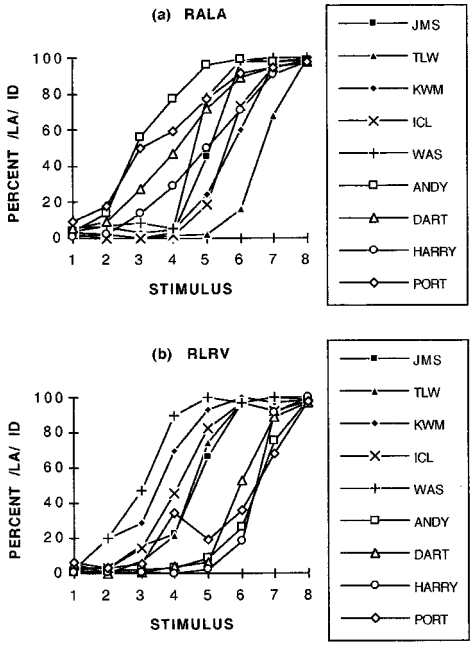

FIG. 8. Individual ID functions from five humans and four monkeys for continua RALA (a) and RLRV (b), plotting percent of stimuli identified as /la/, as measured in the GNG ID paradigm in experiment 4.

functions were shifted toward /ra/ relative to the humans': Human boundaries occurred between stimuli 4 and 6, monkey boundaries occurred between stimuli 3 and 5. For RLRV [Fig. 8(b)], all the monkey functions were shifted toward ''/la/'' relative to humans: Human boundaries occurred between stimuli 3 and 4.5; monkey boundaries occurred between stimuli 5.5 and 6.5. The boundaries of Spanish listener ICL were basically similar to those of the American English listeners, but Hindi listener WAS's boundaries were shifted more toward /ra/ compared to the other human boundaries.

TABLE II. Perceptual boundaries (in terms of stimulus number along the continuum) for five humans and four monkeys as measured in experiment 4. RALA=normal /ra–la/ continuum; RLS3=spectral cue only continuum; RLT1=temporal cue only continuum. RLRV=reversed cues continuum.

Humans	RALA	RLS3	RLT1	RLRV
JMS	5.1	4.8	5.1	4.6
KWM	5.7	5.7	5.6	3.5
TLW	6.7	6.5	6.2	4.5
ICL	5.6	5	4.8	4.1
WAS	4.6	5.1	4.5	3.1
Mean	5.54	5.42	5.24	3.96
Monkeys	RALA	RLS3	RLT1	RLRV
Andy	2.8	3.8	3.8	6.5
Dart	4.2	4.5	3.7	6
Harry	5	3.1	6.4	6.4
Port	3.5	4.5	4.7	6.5
Mean	3.88	3.98	4.65	6.35

Figure 9 shows averaged boundaries for all conditions tested. All boundaries are listed in Table II. Separate one-way ANOVAS were conducted on each condition to examine the effect of SPECIES on the boundaries. Significant differences occurred for RALA [$F(1,7)=19.426$; $p<0.01$], for RLS3 [$F(1,7)=23.01$; $p<0.01$] and for RLRV [$F(1,7)=111.25$; $p<0.01$]. For RLT1, the effect was not significant [$F(1,7)=1.92$; $p>0.10$].

Our results showing ID boundaries in different places for humans and monkeys contrast with those of Kuhl and Miller (1978), who showed that chinchillas had VOT boundaries in the same place as humans, and that their boundaries even shifted with place of articulation in the exact same manner as did human boundaries. On the other hand, Waters and Wilson (1976) have reported monkey VOT boundaries in different places from humans'.

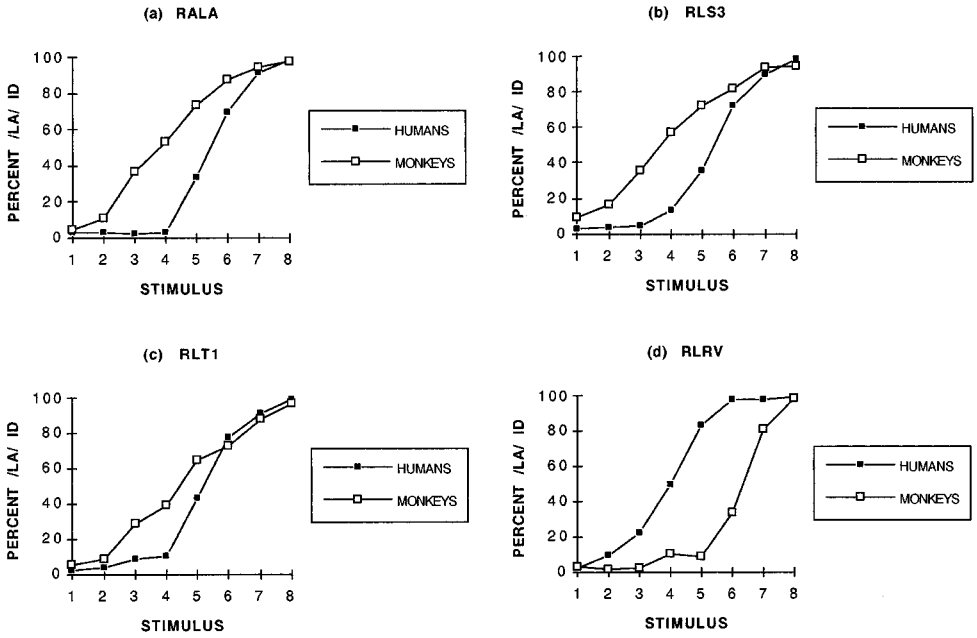

FIG. 9. (a)–(c) Averaged identification functions for humans and monkeys for four stimulus continua, plotting percent of stimuli identified as /la/, as measured in experiment 4.

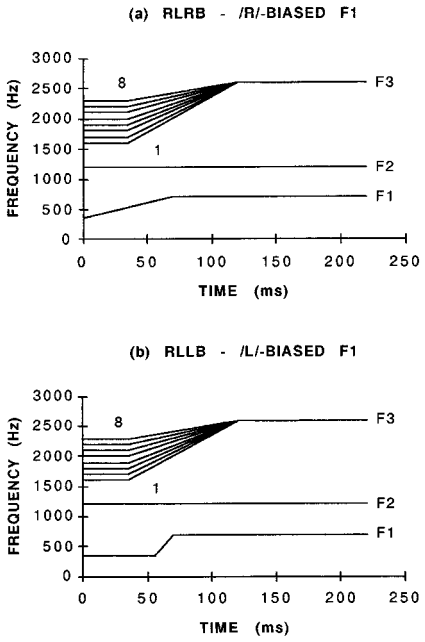

FIG. 10. Schematized spectrographic patterns of the (a) /ra/-biased and (b) /la/-biased stimulus continua used in experiment 5.

RLRV was included as a nonspeech control continuum, hopefully to show human and monkey boundaries in the same place. This was not the case: The monkeys performed significantly differently from humans on this continuum also, although the boundaries shifted in opposite directions for the two species. However, the RLRV data are informative because they show that the monkeys' /ra/-shifted RALA boundaries were not due to a bias for releasing in the ID procedure, nor were they directly dependent on better sensitivity to intraphonemic /ra/ than humans, since monkeys were also more sensitive to intraphonemic ''/ra/'' in RLRV, yet their boundary in this case shifted toward ''/la/.''

VI. EXPERIMENT 5: IDENTIFICATION OF TRADING RELATIONS

The purpose of this experiment was to test if monkeys would show a humanlike trading relation in the /ra–la/ stimuli. Trading relations are demonstrated by showing that a change in the value of one cue (e.g., the temporal cue in $F1$), which by itself causes a change in the phonetic percept, can be offset by an opposing change in the setting of another cue (e.g., the spectral cue in $F3$), in order to maintain the original phonetic percept (Polka and Strange, 1985). Thus if the temporal cue is set for /ra/, a larger change toward /la/ in the spectral cue is necessary in order to perceive /la/. Similarly, if the temporal cue is set for /la/, then a larger change toward /ra/ in the spectral cue is necessary to perceive /ra/.

A. Method

Two new stimulus continua, modeled after those of Polka and Strange (1985), were constructed for this experiment and are shown in Fig. 10.

Figure 10(a) shows the /ra/-biased continuum (RLRB), which varied the $F3$ spectral cue in the normal manner, but set the $F1$ temporal cue appropriate for /ra/, i.e., $F1$ began at 350 Hz and moved linearly, with a 0-ms delay, over the next 70 ms to 700 Hz. Figure 10(b) shows the /la/-biased continuum (RLLB), which varied the $F3$ spectral cue in the normal manner, but set the $F1$ temporal cue appropriate for /la/, i.e., $F1$ began at 350 Hz, remained flat for 56 ms, and then began an abrupt transition over the next 14 ms to 700 Hz. One additional continuum was used in this experiment for comparison to the two biased continua: RLS3, in which the spectral cue only varied and the temporal cue in $F1$ was held at a middle value of 32 ms [see Fig. 1(b)].

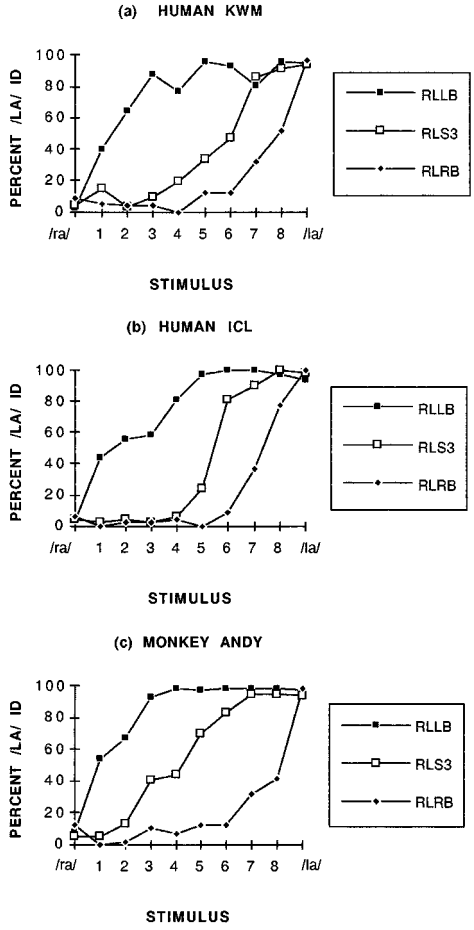

FIG. 11. (a)–(c) Individual identification functions for three subjects plotting the percent of stimuli identified as /la/ comparing the /ra/-biased and /la/-biased stimulus continua, as measured in experiment 5.

Human subjects were JMS, ICL, KWM, and TLW from experiment 4, and one new one, BSR. Monkey subjects were Andy, Dart, Harry, and Port from experiment 4. The ID procedure was identical to that used in experiment 4, except that training stimuli for each continuum were always stimuli 1 and 8 from the RLS3 continuum. This was necessary to provide all subjects with a clear reference for /ra/ and /la/, because, early on in the experiment, we found that some subjects perceived nearly all the stimuli on the /la/-biased continuum as /la/, even those with the most /ra/-like spectral cue.

B. Results and discussion

Figure 11 shows individual ID functions from a representative human subject [Fig. 11(a)], the native Spanish

TABLE III. Perceptual boundaries (in terms of stimulus number along the continuum) for five humans and four monkeys as measured in experiment 5. RLLB=/la/-biased continuum; RLS3=spectral cue only continuum; RLRB =/ra/-biased continuum.

Humans	RLLB	RLS3	RLRB
JMS	0.50	5.60	7.60
TLW	0.50	5.80	7.50
BSR	5.20	6.00	6.40
KWM	1.50	6.20	8.10
ICL	1.70	5.50	7.40
Mean	1.88	5.82	7.40
Monkeys	RLLB	RLS3	RLRB
Andy	1.00	4.30	8.20
Dart	0.80	4.30	8.20
Harry	3.20	4.30	5.50
Port	0.70	4.20	5.00
Mean	1.43	4.28	6.73

speaker [Fig. 11(b)], and a representative monkey subject [Fig. 11(c)]. Each subject's functions for RLS3 are similar to those for the same continuum in experiment 4. For all three subjects, the functions shift closer to /ra/ in RLLB, the /la/-biased continuum, and closer to /la/ in RLRB, the /ra/-biased continuum. These results are indicative of a trading relation between the temporal and spectral cues: As the temporal cue became appropriate for /la/ (/ra/), a value closer to /ra/ (/la/) on the spectral cue was necessary in order to maintain the boundary between these two percepts. Boundaries for all subjects are listed in Table III.

These individual results are verified in the averaged data shown in Fig. 12. A two-way ANOVA comparing the effects of SPECIES and CONTINUUM indicated that the effect of SPECIES was significant [$F(1,7)=13.32$; $p<0.01$], indicating that overall monkey boundaries were shifted more toward /ra/ than human boundaries. The effect of CONTINUUM was significant [$F(2,14)=91.16$; $p<0.01$], indicating that the three continua diverged for both humans and monkeys. Importantly, the SPECIES×CONTINUUM interaction was *not significant* [$F(2,14)=1.01$; $p>0.25$], indicating that the divergence between the three continua was similar for the two species.

Our results are similar to those of Kluender (1991), who found that Japanese quail showed the trading relation between VOT and $F1$ onset frequency in /ba–pa/ stimuli. As $F1$ onset became lower, a corresponding change toward longer VOTs was necessary to maintain the VOT boundary. It is important to note, however, that the quail were tested using a peck-rate procedure on which it was impossible to test humans, although Kluender's stimuli were tested on human subjects using human testing techniques. Nevertheless, the possibility cannot be ruled out that differences exist between quail and human boundaries that were not found in the Kluender study due to the nature of the animal testing techniques. The advantage of the present study is that humans and monkeys were tested with the same procedure that allowed precise comparisons to be made between the species.

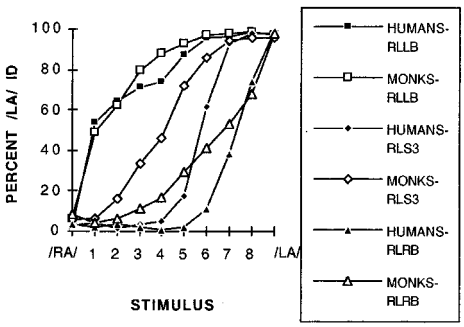

FIG. 12. Averaged identification functions based on five humans and four monkeys plotting the percent of stimuli identified as /la/ comparing the /ra/-biased and /la/-biased stimulus continua, as measured in experiment 5.

Kluender and Lotto (1994) went on to show that their quail showed the VOT trading relation without having been previously exposed to covarying cues in the contrast. Since in the present study, all subjects were pre-exposed to appropriately covarying spectral and temporal cues for /ra–la/ in experiment 4, we cannot conclude that the /ra–la/ trading relation was known *a priori* by monkeys and not learned by them somewhere along the line of the present series of experiments. However, it should be noted that two of the monkeys (Harry, Port) were also exposed to the *conflicting cues* continuum in experiment 2, in which the two cues did not vary in the appropriate fashion, yet these two monkeys showed a normal trading relation in experiment 5.

VII. GENERAL DISCUSSION

Our discrimination experiments 2 and 3 and the ID experiment 4 revealed some striking differences between human and monkey sensitivity to /ra–la/: Monkeys had better sensitivity within intraphonemic /ra/ than they did at the human category boundary, and their ID functions were shifted more toward /ra/ than human functions. If we assume that monkeys were responding to these stimuli of the basis of general auditory capacities, then the present human results suggest that the American English /ra–la/ boundary may result from some acquired linguistic experience. Until more animal data are available, testing the locations of identified category boundaries in other speech contrasts, it is too early to assume that animal boundaries will always be in the same places along speech continua as human boundaries.

Despite these boundary differences, monkeys in experiment 5 showed a humanlike trading relation in these stimuli, where the spectral and temporal cues interact. These results show that, despite psychoacoustic differences, monkeys show a complex trading relation between these two cues similar to that which operates in normal American English speech perception. Thus this trading relation appears to have a psychoacoustic basis and linguistic experience is not a necessary prerequisite for it to occur.

Let us return to the problem of non-native listeners of English /ra–la/. Although we did not test any Japanese listeners, we did test one native Hindi and one native Spanish listener. Neither had any trouble identifying the American English /ra–la/ boundary in experiment 4, and neither required any discrimination training from experiments 2 to 3 to

do so. Furthermore, our Spanish subject performed similarly to the American English subjects (and monkeys) on the /ra–la/ trading relation in experiment 5. It should be noted that both Spanish and Hindi have /r–l/ contrasts. Their /l/'s are similar to English /l/, but their /r/'s are trilled, unlike the English continuant (Principles of the International Phonetic Association, 1968). Most likely, our Spanish and Hindi subjects either assimilated English /r–l/ into learned English categories, or they assimilated /r–l/ into their own native contrasting categories, and thus their identification was very good (Best, 1994). Of course, our monkeys perceived /r–l/ as nonspeech sounds, thus their identification was also very good (Best, 1994).

On the other hand, there is a long history of research with native Japanese listeners showing that they have a hard time learning to differentiate the /r–l/ contrast (e.g., Miyawaki *et al.*, 1975; Strange and Dittmann, 1984; Underbakke *et al.*, 1988; Logan *et al.*, 1991), although some studies have found that performance could be improved with training. These results suggest that the problem that Japanese listeners have with /r–l/ processing is due to the fact that the Japanese do not have a contrast between liquids: Their /r/ is restricted to postvocalic environments and is realized phonetically as a flap, sometimes with retroflexing and sometimes with lateral release (Underbakke *et al.*, 1988). Thus they initially assimilate both English /r/ and /l/ into the same /r/ category, and discrimination is very difficult (Best, 1994).

Underbakke *et al.* (1988) also found that, while trained Japanese subjects exhibited a trading relation similar to those of native English speakers, no trading relation was exhibited before training. The authors concluded that the /r–l/ trading relation ''is not solely attributable to generalized auditory processing constraints, but rather also is a function of phonemic processes that can be modified in the course of learning a second language.'' Obviously, our monkey data suggest otherwise, that this trading relation *is* solely attributable to general auditory processes, unless one wants to assume that our monkeys, like trained Japanese, also developed some sort of phonemic processing while listening to synthetic /r–l/. If we do not want to assume this, then it appears that untrained Japanese listeners have actually lost (albeit not necessarily permanently) the ability to attend to certain acoustic cues that are, under normal circumstances, psychoacoustically very salient to the general mammalian auditory system.

Indeed, the picture can sometimes get more confusing as more speech perception data materialize from different experiments using different procedures. We have plans to directly compare native English, native Japanese, and monkey listeners in their abilities to identify natural tokens of /r/ vs /l/ under conditions of both low (e.g., in the simple context of the vowel /a/ as spoken by one talker) and high (e.g., in the context of several vowels as spoken by several talkers) contextual variability. It is likely that both Japanese and monkey listeners will perform similarly to native English listeners under conditions of low contextual variability. However, under conditions of higher contextual variability, the Japanese listeners may well start to ''break down,'' relative to native English listeners (e.g., see Logan *et al.*, 1991). Monkeys may also start to ''break down,'' although Kuhl and Miller (1975) report that chinchillas were able to maintain a VOT category identification (/ba/ vs /pa/) in the face of vowel and talker variation.

Comparisons between the Japanese and monkey listeners in identifying /ra/ vs /la/ under conditions of high acoustic variability should be particularly interesting. If the Japanese perform better than the monkeys, then this would suggest that verbal humans are able to form new phonetic categories for non-native speech sounds that are more robust than those of non-verbal subjects who can use only general auditory processes. If the Japanese and monkeys perform similarly, then this would suggest that Japanese listeners have neither ''lost'' nor ''gained'' anything, relative to what is available from the general auditory system. But if the monkeys perform better than the Japanese, then this would suggest that Japanese phonology indeed causes some sort of ''loss'' of the ability to attend to acoustic cues originally salient to the general auditory system.

In this way, animals will continue to provide psychoacoustically pure specimens with which to compare the performance of human infants, children, and native and non-native adult listeners. These types of direct comparisons should ultimately help to clarify theories of human speech perception and the relative roles of general auditory versus linguistic processes in language development and cross-language learning.

ACKNOWLEDGMENTS

This research was supported by RCDA award K04 DC 00042 and R01 DC 00541 to JMS. Portions of these data were presented at the 124th Meeting of the Acoustical Society of America, New Orleans, LA, 1992. We thank David Barnett, Troy Clifton, Regina Kressley, Irma Lopez, Waseem Malik, Jane Moore, Kelly Mosteller, Becky Roush, and Trina Williamson for participating as human subjects and for testing animals. We thank Winifred Strange, Terry Gottfried, and one anonymous reviewer for helpful comments during the preparation of this manuscript.

Best, C. (**1994**). ''The emergence of native-language phonological influences in infants: A perceptual assimilation model,'' in *The Development of Speech Perception*, edited by J. Goodman and H. Nusbaum (MIT, Cambridge, MA), pp. 167–224.

Best, C. (**1995**). ''A direct realist view of cross-language speech perception,'' in *Speech Perception and Linguistic Experience: Issues in Cross-language Research*, edited by W. Strange (York, Timonium, MD), pp. 171–204.

Dooling, R., Best, C., and Brown, S. (**1995**). ''Discrimination of synthetic full-formant and sinewave /ra–la/ continua by budgerigars and zebra finches,'' J. Acoust. Soc. Am. **97,** 1839–1846.

Eimas, P. (**1975**). ''Auditory and phonetic coding of the cues for speech: Discrimination of the /r–l/ distinction by young infants,'' Percept. Psychophys. **18,** 341–347.

Jusczyk, P. (**1982**). ''The processing of speech and nonspeech sounds by infants: Some implications,'' in *Development of Perception, Vol. 1*, edited by R. Aslin, J. Alberts, and M. Petersen (Academic, New York), pp. 191–216.

Kluender, K. (**1991**). ''Effects of first formant onset properties on voicing judgments result from processes not specific to humans,'' J. Acoust. Soc. Am. **90,** 83–96.

Kluender, K., Dielh, R., and Killeen, P. (**1987**). ''Japanese quail can learn phonetic categories,'' Science **237,** 1195–1197.

Kluender, K., and Lotto, A. (**1994**). ''Effects of first formant onset frequency on [-voice] judgments result from auditory processes not specific to humans,'' J. Acoust. Soc. Am. **95,** 1044–1052.
Kuhl, P. (**1981**). ''Discrimination of speech by nonhuman animals: Basic auditory sensitivities conducive to the perception of speech sound categories,'' J. Acoust. Soc. Am. **70,** 340–349.
Kuhl, P., and Miller, J. D. (**1975**). ''Speech perception by the chinchilla: Voicing distinction in alveolar plosive consonants,'' Science **190,** 69–72.
Kuhl, P., and Miller, J. D. (**1978**). ''Speech perception by the chinchilla: Identification functions for synthetic VOT stimuli,'' J. Acoust. Soc. Am. **63,** 905–917.
Kuhl, P., and Padden, D. (**1982**). ''Enhanced discriminability at the phonetic boundaries for the voicing feature in macaques,'' Percept. Psychophys. **32,** 542–550.
Kuhl, P., and Padden, D. (**1983**). ''Enhanced discriminability at the phonetic boundaries for the place feature in macaques,'' J. Acoust. Soc. Am. **73,** 1003–1010.
Liberman, A. (**1996**). *Speech: A Special Code* (MIT, Cambridge, MA).
Logan, J., Lively, S., and Pisoni, D. (**1991**). ''Training Japanese listeners to identify English /r/ and /l/. A first report,'' J. Acoust. Soc. Am. **89,** 874–886.
Maddieson, I. (**1984**). *Patterns of Sound* (Cambridge U. P., Cambridge, London).
Miyawaki, K., Strange, W., Verbrugge, R., Liberman, A., Jenkins, J., and Fulimura, O. (**1975**). ''An effect of linguistic experience: The discrimination of /r/ and /l/ by native speakers of Japanese and English,'' Percept. Psychophys. **18,** 331–340.
Pisoni, D., Lively, S., and Logan, J. (**1994**). ''Perceptual learning of nonnative speech contrasts: Implications for theories of speech perception,'' in *The Development of Speech Perception*, edited by J. Goodman and H. Nusbaum (MIT, Cambridge, MA), pp. 121–166.
Polka, L., and Strange, W. (**1985**). ''Perceptual equivalence of acoustic cues that differentiate /r/ and /l/,'' J. Acoust. Soc. Am. **78,** 1187–1197.
Principles of the International Phonetic Association (**1968**). Dept. of Phonetics, University College, London, England.
Sinex, D., McDonald, L., and Mott, J. (**1991**). ''Neural correlates of nonmonotonic temporal acuity for voice onset time,'' J. Acoust. Soc. Am. **90,** 2441–2449.
Sinnott, J. (**1994**). ''Comparisons of human and monkey differential sensitivity to speech, nonspeech and monkey speech sounds,'' in *Current Topics in Acoustic Research*, edited by J. Menon (Council for Scientific Research, Trivandrum, India), pp. 355–364.
Sinnott, J. (**1995**). ''Methods to assess the processing of speech sounds by animals,'' in *Methods in Comparative Psychoacoustics*, edited by G. Klump, R. Dooling, R. Fay, and W. Stebbins (Birkhauser Verlag, Basel, Switzerland), pp. 281–292.
Sinnott, J., and Adams, F. (**1987**). ''Differences in human and monkey sensitivity to acoustic cues underlying voicing contrasts,'' J. Acoust. Soc. Am. **82,** 1539–1547.
Sinnott, J., Brown, C., and Brown, F. (**1992**). ''Frequency and intensity discrimination in Mongolian gerbils, African monkeys, and humans,'' Hearing Res. **59,** 205–212.
Sinnott, J., and Kreiter, N. (**1991**). ''Differential sensitivity to vowel continua in Old World monkeys and humans,'' J. Acoust. Soc. Am. **89,** 2421–2429.
Sinnott, J., Beecher, M., Moody, D., and Stebbins, W. (**1976**). ''Speech sound discrimination by monkeys and humans,'' J. Acoust. Soc. Am. **60,** 687–695.
Strange, W., and Dittmann, S. (**1984**). ''Effects of discrimination training on the perception of /r–l/ by Japanese adults learning English,'' Percept. Psychophys. **36,** 131–145.
Underbakke, M., Polka, L., Gottfried, T., and Strange, W. (**1988**). ''Trading relations in the perception of /r/–/l/ by Japanese learners of English,'' J. Acoust. Soc. Am. **84,** 90–100.
Waters, R., and Wilson, W. (**1976**). ''Speech perception by rhesus monkeys: The voicing distinction in synthesized labial and velar stop consonants,'' Percept. Psychophys. **19,** 285–289.

Simulation of the effect of threshold elevation and loudness recruitment combined with reduced frequency selectivity on the intelligibility of speech in noise

Yoshito Nejime[a] and Brian C. J. Moore
Department of Experimental Psychology, University of Cambridge, Downing Street, Cambridge CB2 3EB, England

(Received 28 August 1996; revised 19 March 1997; accepted 19 March 1997)

The effect of loudness recruitment and threshold elevation together with reduced frequency selectivity have been simulated to examine the combined effect of the two major consequences of cochlear hearing loss on the intelligibility of speech in speech-shaped noise. In experiment 1, four conditions were simulated: a moderate flat loss with auditory filters broadened by a factor of three (B3R2); a moderate-to-severe sloping loss with auditory filters broadened by a constant factor of three (B3RX); and these conditions with linear amplification applied prior to the simulation processing (B3R2+, B3RX+). For conditions B3R2 and B3RX, performance was markedly worse than for a control condition (normal hearing, condition R1) tested in a previous study. For conditions B3R2+ and B3RX+, linear amplification improved performance considerably. However, performance remained below that for condition R1 by between 5% and 19%. In experiment 2 the broadening of the auditory filters was made more realistic by making it a function of the absolute threshold at the center frequency of the auditory filter. Three different hearing losses were simulated: a moderate-to-severe sloping loss with variable broadening of the auditory filters (BXRX); the same moderate-to-severe sloping loss with linear amplification (BXRX+); and the same broadening of the auditory filters but without the simulation of loudness recruitment and threshold elevation (BX). For condition BXRX, performance was markedly worse than in condition R1, while performance in condition BX was somewhat worse than for condition R1. For condition BXRX+, linear amplification according to the NAL procedure improved performance to a large extent but it remained worse than for condition R1. The results are consistent with previous evidence indicating that only part of the decrease of performance produced by actual cochlear hearing loss can be compensated by conventional linear hearing aids. [S0001-4966(97)02707-0]

PACS numbers: 43.71.Ky, 43.71.Gv [WS]

INTRODUCTION

People with cochlear hearing loss often have difficulty in understanding speech, especially when the speech is accompanied by interfering sounds. However, there is controversy over whether this is primarily due to reduced audibility of the speech signal (Humes *et al.*, 1987; Zurek and Delhorne, 1987) or to abnormalities in the perceptual analysis of the signal, even when it is well above the absolute threshold (Plomp, 1978, 1986; Dreschler and Plomp, 1980, 1985; Glasberg and Moore, 1989). It has been difficult to decide what factors are most important, since the elevation of absolute threshold that is the most obvious sign of hearing loss is usually associated with a variety of suprathreshold changes, such as reduced dynamic range (loudness recruitment) (Fowler, 1936; Steinberg and Gardner, 1937; Villchur, 1974), reduced temporal resolution for narrow-band fluctuating stimuli (Fitzgibbons and Wightman, 1982; Tyler *et al.*, 1982; Glasberg *et al.*, 1987; Glasberg and Moore, 1992), reduced ability to discriminate frequency differences in pure and complex tones (Glasberg and Moore, 1989; Moore and Peters, 1992), and reduced frequency selectivity (Pick *et al.*, 1977; Florentine *et al.*, 1980; Tyler *et al.*, 1984; Glasberg and Moore, 1986; Moore and Glasberg, 1986; Tyler, 1986). For a review, see Moore (1995).

Some of the methods for addressing this problem were reviewed in earlier publications (Baer and Moore, 1993, 1994; Moore and Glasberg, 1993; Moore *et al.*, 1995). These publications argued that an appropriate method was to process sounds so as to simulate the effect of one specific aspect of hearing impairment, and to present those sounds to normally hearing subjects for evaluation. Provided the simulation is accurate, this makes it possible to study the effect of that aspect in isolation. This has been applied to loudness recruitment (Villchur, 1974; Glasberg and Moore, 1992; Moore and Glasberg, 1993; Duchnowski and Zurek, 1995; Moore *et al.*, 1995) and to reduced frequency selectivity (Villchur, 1977; Summers and Al-Dabbagh, 1982; Celmer and Bienvenue, 1987; Gagné and Erber, 1987; Moore *et al.*, 1992; ter Keurs *et al.*, 1992; Baer and Moore, 1993, 1994).

Previous studies from our group have used a digital simulation of threshold elevation combined with loudness recruitment to examine the intelligibility of speech in quiet, against a background of a single competing talker (Moore and Glasberg, 1993) and against a background of noise

[a]Present address: Multimedia Systems Research Dept., Central Research Laboratory, Hitachi Ltd., Kokubunji, Tokyo 185, Japan.

(Moore *et al.*, 1995). Three different types of cochlear hearing loss were simulated, including moderate and severe flat losses and a sloping loss. For speech in quiet, simulation of hearing loss produced a reduction in the ability to understand low-level speech. However, speech at sufficiently high levels was highly intelligible in all conditions. Linear amplification according to the National Acoustics Laboratory (NAL) prescription (Byrne and Dillon, 1986), applied prior to the simulation, gave high intelligibility for speech at normal conversational levels. For speech presented at a fixed input level of 65 dB SPL, against a background of a single competing talker, simulation of hearing loss produced substantial decrements in performance. Linear amplification according to the NAL prescription improved performance markedly for the conditions simulating flat losses, but was less effective for the condition simulating a sloping loss. It was concluded that the loss of intelligibility for speech, in the presence of a single competing talker, is only partly compensated by linear amplification of the type typically used in hearing aids.

For speech presented at a fixed input level of 65 dB SPL, against a background of speech-shaped noise, simulation of threshold elevation and loudness recruitment showed much smaller decrements in performance than those obtained using a single competing talker. When linear amplification according to the NAL prescription was applied, performance improved markedly for conditions simulating a moderate hearing loss, and did not differ significantly from that for normal hearing (using unprocessed stimuli). It was concluded that loudness recruitment and threshold elevation have larger effects for a fluctuating background sound than for a steady background, and linear amplification is more effective in the latter case.

In an earlier study using a simulation of reduced frequency selectivity, Baer and Moore (1993) examined the intelligibility of speech in quiet and against a background of speech-shaped noise. They simulated reduced frequency selectivity using spectral smearing designed to evoke, in normally hearing subjects, auditory excitation patterns resembling those that would be evoked by the same stimuli in subjects with broadened auditory filters. It should be noted that this simulation does not mimic the changes in the time patterns at the outputs of the auditory filters produced by broadening of the filters. Essentially, the simulation mimics the consequences of reduced frequency selectivity for place coding, but not for time coding (Baer and Moore, 1993, 1994).

The signal processing was based on smearing of the short-term power spectrum, using broadened auditory filters defined in the frequency domain. The overlap-add technique (Allen, 1977) was used to perform the processing. They simulated the reduced frequency selectivity associated with several different amounts of broadening of the auditory filters: symmetrical broadening by factors of 3 and 6, and several degrees of asymmetrical broadening using different broadening factors for the upper branch and for the lower branch of the auditory filters. The results showed that spectral smearing using symmetrical broadening by a factor of 3 or 6 had little effect on the intelligibility of speech in quiet, but had a substantial effect on the intelligibility of speech in noise at speech-to-noise ratios of 0 and -3 dB. In a subsequent study, they examined the intelligibility of speech against a background of a single competing talker using the same broadening conditions (Baer and Moore, 1994). The results showed that reduced frequency selectivity had slightly larger effects for a fluctuating background than for a steady background.

The present study simulates the effect of threshold elevation and loudness recruitment *in combination with* reduced frequency selectivity on the ability to understand speech in a background of noise. Hereafter, we refer to this simulation as the ''combined simulation.'' The results of the earlier studies suggested that both loudness recruitment with threshold elevation and reduced frequency selectivity are sufficient to produce a substantial decrease in the ability to understand speech in the presence of background sounds. People with cochlear hearing loss usually have both loudness recruitment and reduced frequency selectivity. It remains unclear how the two effects combine, for example whether they are additive, whether one is dominant over the other, or whether the combined effect is greater than a simple sum of the individual effects, which might happen if each removes cues that are left unaffected by the other. The two simulations certainly change the perception of speech in noise differently; the simulation of loudness recruitment with threshold elevation changes the audibility of speech stimuli and their perceived dynamics, while the spectral smearing makes the speech appear ''fuzzy'' (less clear) and subjectively harder to separate from the background.

The specific questions addressed in this study are as follows:

(1) How much is the intelligibility of speech affected by simulating threshold elevation and loudness recruitment in combination with reduced frequency selectivity? This was assessed by using normally hearing subjects listening to signals processed via the combined simulation and comparing the results with those of earlier studies.
(2) To what extent can the deleterious effects of the combined factors be counteracted by linear amplification with appropriate frequency response shaping? To answer this question, speech intelligibility was measured using the combined simulation, but including frequency-dependent linear amplification according to the revised NAL procedure (Byrne and Dillon, 1986).

I. EXPERIMENT 1

A. Method of simulation

1. Rationale

Our method for combining the simulations is based on the concatenation of the two simulations which have been described in detail in earlier publications (Baer and Moore, 1993; Moore and Glasberg, 1993). A brief description of each simulation, and of how they were modified in order to combine them, is given next.

We assume that, in an impaired ear, reduced frequency selectivity can be characterized as a broadening of the auditory filters. This effect can be simulated by smearing the

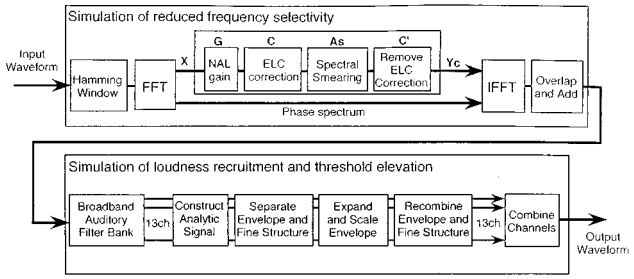

FIG. 1. A block diagram of the sequence of processing stages used in the combined simulation for experiment 1.

short-term power spectra of the stimuli in such a way that the excitation pattern produced in a normal ear, calculated over a short period of time, will resemble that found with unprocessed stimuli in an impaired ear.

In a normal cochlea, complex sounds are subjected to a limited-resolution frequency analysis followed by a compressive nonlinearity operating independently in different frequency regions. We assume that, in an impaired ear, the compression function is reduced or absent, and that this is the main cause of loudness recruitment (Moore, 1995; Moore and Glasberg, 1997). This effect can be simulated in normal listeners by filtering the stimuli into a number of frequency bands, and applying an expansive nonlinearity in each band independently.

To implement the combined simulation we first applied the simulation of reduced frequency selectivity and then applied the simulation of threshold elevation combined with loudness recruitment.

2. Implementation

Figure 1 shows the total processing flow of our combined simulation. The first half of the combined simulation is the simulation of reduced frequency selectivity (Baer and Moore, 1993). An overlap-add method (Allen, 1977) was used here, and the waveform of the input stimuli was processed frame by frame. For each of the analysis/synthesis frames, the short-term spectrum was calculated using a Hamming window and a fast Fourier transform (FFT). The length of the Hamming window was 128 samples at a sample rate of 16 kHz, corresponding to an input frame size of 8 ms. The windowed signals were padded with 64 zeros on each side and converted to the frequency domain with a 256-point FFT. The size of the FFT was chosen to be reasonably small so as to limit computational complexity, while still being sufficiently long to encompass a typical pitch period and give reasonable frequency resolution.

Spectral smearing was then performed, using a procedure described below, and the smeared spectrum was transformed back into the time domain using an inverse FFT. Waveforms obtained from overlapping frames were added to produce the output from this stage of the processing.

The spectral smearing was performed by replacing each component of the power spectrum with a weighted sum of the surrounding components. The weighting function was similar to the shape of the broadened auditory filter centered on the component, except for a ''correction'' to allow for the fact that the stimuli would pass through the normal auditory filters of the subjects used in the listening tests; see Baer and Moore (1993) for details. The auditory filter was assumed to have the form of the roex(p) filter suggested by Patterson *et al.* (1982):

$$W(g)=(1+pg)\exp(-pg), \tag{1}$$

where g is the deviation from the center frequency (f_c) of the filter divided by f_c, $W(g)$ is the intensity weighting function describing the filter shape, and p is a parameter determining the sharpness of the filter. In normally hearing subjects, the auditory filter shape is symmetrical at moderate sound levels, and the ERB of the filter is equal to $4f_c/p$. Thus, the value of p can be calculated using the equation for the ERB suggested by Glasberg and Moore (1990):

$$\mathrm{ERB}=24.7(0.00437f_c+1), \tag{2}$$

where the ERB and f_c are both specified in Hertz. The broadening of the filter is defined by dividing the value of p by the broadening factor that it is desired to simulate.

Mathematically, the basic idea of the spectral smearing procedure can be expressed by the equation

$$Y(n)=\sum_i A_w(n,i)X(i), \tag{3}$$

where $Y(n)$ is the magnitude of the nth component of the output power spectrum, $A_w(n,i)$ is the weighting function described above, and $X(i)$ is the ith component of the input power spectrum.

In some conditions, frequency-dependent linear amplification according to the NAL procedure (Byrne and Dillon, 1986) was applied. This was implemented in the spectral domain by modifying the short-term spectra of the input signal. Since the linear amplification was intended to resemble the function of a typical hearing aid, it was applied *prior* to the simulation. This was achieved by multiplying each component of the input $X(i)$ by the appropriate NAL gain. This allowed very accurate implementation of the NAL-prescribed gain (far better than would be achieved in a conventional hearing aid).

In addition, since the spectral smearing by broadened auditory filters occurs after transmission of the sound through the outer and middle ear, the transmission characteristic was taken into account in the simulation. This was achieved using the ''ECL correction'' proposed by Glasberg and Moore (1990), which is based on the 100-phon equal-loudness contour as specified in ISO recommendation R.226 (ISO 226, 1987). This was implemented in a similar way to the application of NAL-prescribed gain, by multiplying each component of the input spectrum (with NAL amplification where appropriate) by the appropriate gain of the ELC correction.

It should be remembered, however, that the final processed speech signal was to be presented to normally hearing subjects and had to pass through their outer and middle ear. Hence, the effect of the outer/middle ear correction was removed before the inverse FFT. This recorrection was

achieved by multiplying each component of the processed spectrum (after smearing) by the inverse of the corresponding ELC gain.

The overall effect of the spectral processing is expressed by

$$Y_c(n) = C'(n)\Sigma A_w(n,i)C(i)G(i)X(i), \quad (4)$$

where $C(i)$ is the ELC correction gain for the ith frequency component, $C'(i)$ is its inverse, and $G(i)$ is the NAL recommended gain for that component.

Segments of the processed waveform were created by inverse FFT (IFFT). The number of components in Eq. (4) was 128. This whole process was repeated for a series of overlapping frames, which were then added. The shift between frames was 64 samples, or $\frac{1}{4}$ the length of the frame. The phase of each component for the IFFT was unchanged from that in the original FFT, as was the case in the earlier studies using this method. This causes the harmonic structure to be preserved in the output. Even though the power spectrum within each frame is smeared, aspects of the temporal wave shape are preserved in the phase spectrum and are retained in the overlap-add procedure (Baer and Moore, 1993).

The second half of the combined simulation, the simulation of loudness recruitment with threshold elevation, is illustrated in the bottom half of Fig. 1. The input signal was filtered into a number of frequency bands, and the expansive nonlinearity was applied independently to the output of each band. The filters for the band splitting were chosen to have widths and shapes comparable to those of auditory filters measured in subjects with moderate to severe cochlear hearing loss (Glasberg and Moore, 1986). Specifically, they were chosen to have ERBs three times as great as typically found in normally hearing subjects (Glasberg and Moore, 1990). It should be emphasized that this use of relatively broad filters did not imply that we were repeating the simulation of the effect of reduced frequency selectivity. Rather, we were merely attempting to achieve a degree of independence between adjacent frequencies comparable to that which would occur in a typical case of cochlear hearing loss.

The filters were implemented digitally. Each filter was made up of four first-order ''gammatone'' filters in series (Patterson and Cutler, 1989; de Boer and Kruidenier, 1990; Stone, 1995). The resulting filter is very similar to a fourth-order gammatone filter, and its attenuation characteristic is very similar to that of the rounded-exponential filter [Eq. (1)] often used to describe psychoacoustical data (Patterson *et al.*, 1982; Glasberg and Moore, 1990). Thirteen filters were used. Their center frequencies and bandwidths were the same as in our earlier studies (Moore and Glasberg, 1993). An additional, shallow, high-pass filter was applied to reduce the effect of the ''tail'' of the low-frequency side of the filters with the four highest center frequencies. The outputs of the filters were time aligned so that, for a pulse input, the peaks in the responses all coincided. After this time alignment, if the outputs of the filters were mixed without any further processing, the output generally sounded almost identical to the (suitably band-limited) input.

To implement the expansive nonlinearity without introducing excessive spectral distortion, we processed the envelopes of the waveforms at the output of each filter. The envelope of the output of each channel was obtained using the Hilbert transform. The envelope was slightly smoothed by taking a running average of 160 successive samples (Moore and Glasberg, 1993). This is equivalent to lowpass filtering the envelope with a cutoff frequency of about 100 Hz.

In essence, the processing of the envelope for a given filter involved raising the envelope to a power N. When N has a value greater than 1, this has the effect of magnifying fluctuations in the envelope. We simulated ''complete'' loudness recruitment, assuming that loudness reaches its ''normal'' value at 100 dB SPL. If the envelope in a given frequency band is raised to the power N, then the level (in dB) of the processed stimulus in that band, L_p, is a linear function of the level of the unprocessed stimulus, L_u, with slope N:

$$L_p = NL_u + K, \quad (5)$$

where K is a constant. The overall levels were scaled so that $L_u = L_p$ when $L_p = M$ dB. In this experiment, M was fixed at 100 dB. Hence $K = (1-N)M = (1-N)100$ and

$$L_p = NL_u - (N-1)100. \quad (6)$$

For example, if $N = 2$, a value of L_u of 75 dB gives a value of L_p of 50 dB, and a value of L_u of 50 dB gives a value of L_p of 0 dB. A value of N of 2 simulates the recruitment typically found in cases of moderate to severe cochlear loss, where, for example, a 50-dB range of stimulus levels (from 50–100 dB) gives the same range of loudness as a 100-dB range of stimulus levels (from 0–100 dB) in a normal ear (Miskolczy-Fodor, 1960; Moore *et al.*, 1985; Moore and Glasberg, 1997). For levels of L_u and L_p above 100 dB, the value of L_p was set equal to the value of L_u.

All processing was performed digitally using a Silicon Graphics Indy. Input stimuli were lowpass filtered at 7 kHz (Kemo VBF8/04, 90 dB/oct slope) and sampled with 12-bit resolution (Masscomp EF12M) at a 16-kHz rate. After processing, the stimuli had 16-bit resolution and were converted to a 48-kHz sampling rate on the Indy using a standard UNIX program for sampling frequency conversion. They were then recorded digitally on digital audio tape.

B. Processing conditions

The processing conditions were chosen to be similar to those used in earlier studies (Baer and Moore, 1993, 1994; Moore and Glasberg, 1993; Moore *et al.*, 1995) which simulated just one aspect of cochlear hearing loss. The following conditions were used:

(1) Uniform processing across bands with a broadening factor of 3 and a slope for recruitment of $N = 2$. This simulates a flat moderate hearing loss (threshold about 50 dB HL). We refer to this as condition B3R2.
(2) Processing with more envelope expansion at high frequencies and with a constant broadening factor of 3 across bands, to simulate a hearing loss increasing with frequency. The value of N was 1.5 for frequencies up to 1.0 kHz. The power was then increased smoothly to 3.0 as frequency increased to 4.0 kHz, and remained at 3.0

TABLE I. Specification of condition B3RX showing the absolute threshold simulated at each audiometric frequency and the power to which the envelope was raised at that frequency.

Frequency (kHz)	0.25	0.5	0.75	1.0	1.5	2.0	3.0	4.0	5.0
Threshold (dB)	33	33	33	33	43	50	60	67	67
Power, *N*	1.5	1.5	1.5	1.5	1.75	2.0	2.5	3.0	3.0

above 4.0 kHz. The exact thresholds simulated and the envelope powers used are given in Table I. We refer to this as condition B3RX.

(3) Processing as in condition B3R2 with the frequency-dependent gain recommended by the NAL revised procedure which is shown in Table II. We refer to this as condition B3R2+.

(4) Processing as in condition B3RX with the frequency-dependent gain recommended by the NAL revised procedure which is shown in Table II. We refer to this as condition B3RX+.

The NAL procedure gave the gains only at each audiometric frequency for each of the hearing losses simulated by B3R2 and B3RX. To calculate the gains in the combined simulation at each frequency, n, each gain curve was interpolated with a spline function.

C. Experimental method

To allow comparison of the results of the present combined simulation with the results of previous studies (Baer and Moore, 1993; Moore *et al.*, 1995), the method was chosen to be similar to that of those studies. Here we give a brief outline of the method.

1. Stimuli

The speech materials used were the 12 audio-visual sentence lists (MacLeod and Summerfield, 1990); in this study audio-only presentation was used. Each list consists of 15 sentences, each of which contains three key words, spoken by a male talker of standard British English. The score for each list was always the percent of key words correct out of 45. The speech was presented, at the input to the simulation, at a root-mean-square (rms) level of 65 dB SPL. The speech-shaped noise was presented at levels of 68, 71, and 74 dB SPL for conditions B3R2, B3R2+, and B3RX+. For condition B3RX, the levels used were 65, 68, and 71 dB SPL since intelligibility was very low with the noise at 74 dB.

The sentences and noise were mixed prior to processing in each of the conditions, and recorded on digital audio tape with a 7-s interval between sentences, to allow for subject responses. The noise began approximately 0.5 s before each sentence and ended just after the sentence. A band of noise was recorded at the start of each tape for calibration of absolute levels.

Subjects were tested in a double-walled sound-attenuating chamber. They sat facing the loudspeaker, at a distance of about 1 m. The walls of the chamber were lined with 100 mm thick foam to reduce reflected sound. Sound levels were calibrated using a CEL 414/3 precision sound level meter (C-weighting), placed at the center of the position where the subject's head would be.

2. Subjects and design

All subjects were self-assessed as having normal hearing. None had any history of hearing disorder. They were paid for their services. Each of the four conditions was tested using three complete lists (one for each speech-to-noise ratio). The order of the lists was the same for each subject, but the order of the conditions was counterbalanced across subjects using a Latin Square design. Prior to formal testing of a given condition, one complete list processed with that condition was given as a practice list without noise. Testing for that condition then began, starting with the highest speech-to-noise ratio and ending with the lowest. Twelve subjects were tested, using two different Latin Squares.

3. Test procedure

Subjects were told that their task was to repeat back exactly what they had heard. They were informed that the stimuli were meaningful sentences presented at various loudness levels, some of which would make detection difficult. They were told that the speech might sound distorted. They were encouraged to enunciate their responses clearly, and to endeavor always to say something, even if it didn't seem to make sense. Subjects responded in the silent interval between sentences. If, during that silent interval, they wanted to revise their initial answer, they were allowed to do so; only the final answer was scored. A strict scoring criterion was used; for example, subjects had to state correctly the tenses of verbs and whether nouns were singular or plural.

D. Results

Figure 2 shows mean psychometric functions (percent correct as a function of speech-to-noise ratio) for all conditions. The results for a control condition using unprocessed stimuli (condition R1) are also shown. These results were obtained by Moore *et al.* (1995) under identical conditions to

TABLE II. The values of the gain in decibels for the linear amplification recommended by the NAL procedure, at each audiometric frequency.

Frequency (kHz)	0.25	0.5	0.75	1.0	1.5	2.0	3.0	4.0	5.0
Gain for B3R2+ (dB)	6	15	20	24	24	22	21	21	21
Gain for B3RX+ (dB)	−1	8	13	17	20	20	22	25	25

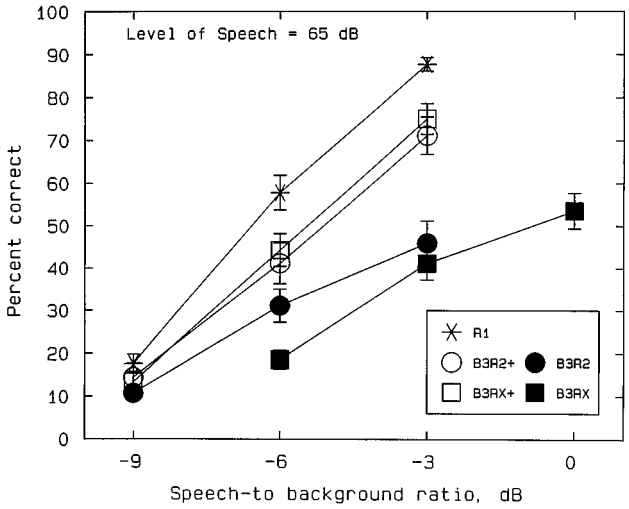

FIG. 2. Mean psychometric functions across the 12 subjects showing the percent correct as a function of speech-to-noise ratio for each condition. The results for a control condition using unprocessed stimuli (condition R1) were obtained by Moore *et al.* (1995). Error bars show ± one standard error across subjects.

those of the present study, so the results should be directly comparable. The combined simulation of threshold elevation, recruitment, and reduced frequency selectivity in conditions B3R2 and B3RX led to substantial degradations in performance compared to condition R1. Performance was poorest for condition B3RX. At the speech-to-background ratio of −3 dB, scores were only about 40% for the conditions with simulated hearing loss, compared to almost 90% for the control condition.

Amplification according to the NAL formula produced marked improvements in performance for speech-to-noise ratios of −6 dB and above. However, this improvement was not apparent at the ratio of −9 dB. Performance in conditions B3R2+ and B3RX+ remained below that for condition R1 at all three S/N ratios. This indicates that some aspect of the simulated hearing loss was not adequately compensated by linear amplification and contrasts with the results found previously using the simulation only of threshold elevation and loudness recruitment, where NAL amplification restored performance to normal (Moore *et al.*, 1995).

For further analysis and comparison with the results of previous studies, the psychometric functions for each subject were fitted using probit analysis (Finney, 1971). This procedure gives estimates of the slopes of the psychometric functions (in probit units) and of the 50% correct points. Table III gives the 50% points and the slopes for each subject in each condition and the mean value for each condition.

To assess the statistical significance of the effects seen in the data, an analysis of variance (ANOVA) was conducted on the 50% points with factors subject and condition. The variance associated with the two-way interaction was used to estimate the residual variance. The GENSTAT package used gave an estimate of the standard error of differences between means for the different conditions. This standard error was

TABLE III. Fifty per cent correct points (*P*) and slopes (*S*) of the probit functions for each subject and each condition in experiment 1.

Subject		B3R2	B3RX	B3R2+	B3RX+
DV	*P*	−6.20	−3.26	−7.89	−7.42
	S	0.242	0.339	0.350	0.213
BM	*P*	−2.29	−1.97	−4.02	−6.58
	S	0.186	0.145	0.430	0.329
AS	*P*	−1.14	+0.40	−4.15	−5.01
	S	0.295	0.101	0.190	0.263
PS	*P*	−4.45	−1.41	−6.03	−4.67
	S	0.230	0.160	0.370	0.273
HF	*P*	+10.05	2.15	−5.29	−5.72
	S	0.056	0.112	0.313	0.324
CO	*P*	+3.44	−2.28	−6.33	−4.81
	S	0.075	0.095	0.244	0.335
GM	*P*	−4.93	−0.84	−5.83	−5.97
	S	0.291	0.217	0.219	0.449
SJ	*P*	−3.31	+6.09	−2.71	−3.87
	S	0.279	0.067	0.240	0.257
CL	*P*	−3.08	−2.34	−5.26	−6.40
	S	0.256	0.210	0.275	0.283
LG	*P*	−0.48	+0.58	−3.94	−3.69
	S	0.118	0.332	0.462	0.319
JC	*P*	−2.47	−0.74	−6.05	−4.43
	S	0.157	0.182	0.255	0.335
OH	*P*	−2.15	−1.31	−3.74	−5.90
	S	0.171	0.149	0.329	0.407
Mean	*P*	−1.43	−0.41	−5.10	−5.37
SD	*P*	4.37	2.53	1.43	1.14
Mean	*S*	0.196	0.176	0.306	0.316
SD	*S*	0.083	0.087	0.085	0.065

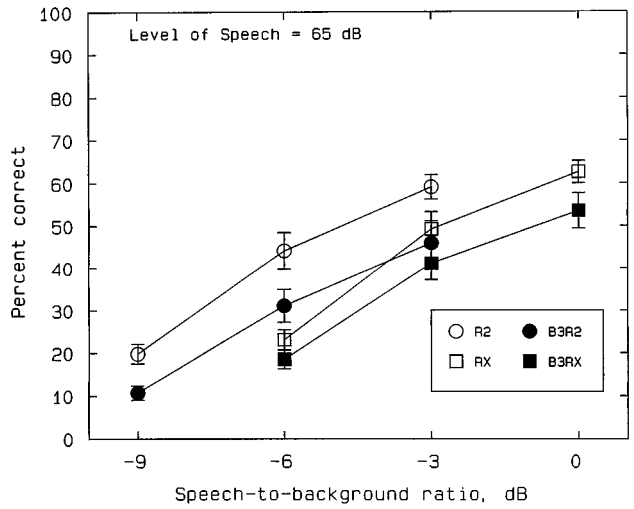

FIG. 3. Comparison of the mean results for the nonamplified conditions, B3R2 and B3RX, with the mean results of the simulation only of recruitment combined with the threshold elevation obtained by Moore *et al.* (1995) for the same loudness recruitment conditions (R2 and RX). Error bars show ± one standard error across subjects.

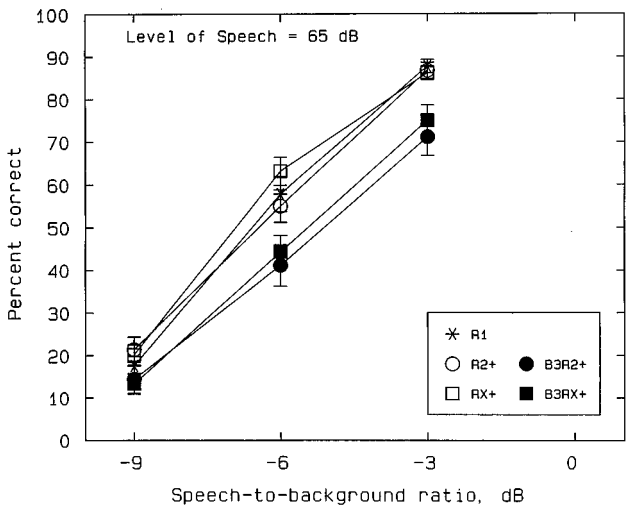

FIG. 4. Comparison of the mean results for the amplified conditions, B3R2+ and B3RX+, with the mean results of the simulation only of recruitment combined with threshold elevation obtained by Moore *et al.* (1995) for the same loudness recruitment conditions (R2+ and RX+) and for a control condition using unprocessed stimuli (condition R1). Error bars show ± one standard error across subjects.

used to assess the significance of the differences between means (Lane *et al.*, 1987, p. 110).

The effect of subjects was just significant [$F(11,33) = 2.10$, $p = 0.049$], indicating small differences in overall performance between subjects. The effect of condition was highly significant [$F(3,33) = 13.60$, $p < 0.001$], and accounted for most of the variance in the data. The 50% point for B3R2+ was significantly smaller than that for B3R2 ($p < 0.001$), and the 50% for B3RX+ was also significantly smaller than that for B3RX ($p < 0.001$), indicating a significant improvement produced by linear amplification. The 50% points for conditions B3R2+ and B3RX+ did not differ significantly, indicating that linear amplification restored performance to similar levels for both types of simulated hearing loss.

A similar ANOVA was conducted on the slope values shown in Table III. The effect of subjects was not significant [$F(11,33) = 0.94$, $p = 0.519$]. The effect of condition was highly significant [$F(3,33) = 9.65$, $p < 0.001$]. The slopes for conditions B3R2+ and B3RX+ did not differ significantly. The slopes for B3R2 and B3RX were significantly less than those for the conditions with linear amplification ($p < 0.001$), but did not differ significantly from each other.

Relative to performance in the control condition (R1), the degradation produced by the simulation in conditions B3R2 and B3RX was greater at higher performance levels. For example, the speech-to-noise ratio had to be about 6 dB higher in condition B3RX than in R1 to achieve 50% correct, while the difference was only about 3.5 dB at a 25% performance level. The same tendency was observed in previous work simulating only recruitment and threshold elevation (Moore *et al.*, 1995).

E. Discussion

Figure 3 compares the mean results for the nonamplified conditions, B3R2 and B3RX, with the mean results of the simulation only of recruitment and threshold elevation obtained by Moore *et al.* (1995) for the same loudness recruitment conditions (R2 and RX). Figure 4 shows the same comparison for the conditions with NAL linear amplification (B3R2+, B3RX+, R2+, and RX+). These figures show that the spectral smearing increased the amount of degradation in performance for all cases. The plots of performance for the combined simulation lie almost parallel to those for the recruitment-only simulation. As shown in Fig. 4, linear amplification according to the NAL formula did not restore performance for conditions B3R2 and B3RX as much as for the recruitment-only conditions R2 and RX. The linear amplification compensated for the decrease of audibility produced as part of the loudness recruitment simulation, but did not compensate for the distortion caused by the spectral smearing. Thus, the effect of the spectral smearing clearly appeared as a suprathreshold effect in the combined simulation.

To confirm the statistical significance of these effects, *t*-tests were conducted on the 50% correct points estimated by probit analysis for several pairs of conditions (R2 vs B3R2, RX vs B3RX, R2+ vs B3R2+ and RX+ vs B3RX+) using the data in Table III and data obtained by Moore *et al.* (1995). The differences were all significant: R2 vs B3R2, $p < 0.02$; RX vs B3RX, $p < 0.05$; R2+ vs B3R2+, $p < 0.01$; RX+ vs B3RX+, $p < 0.002$.

These significance levels vary across comparisons mainly because of individual differences in some conditions. For the conditions B3R2 and B3RX, the 50% points showed a large spread across subjects (Table III), possibly due to individual differences in absolute thresholds; in these two conditions the levels of the stimuli were rather low, especially at high frequencies. Also, for these conditions, some subjects showed very shallow psychometric functions (small slope values), and even at the highest S/N ratio, they scored less than 50%. In this case, the probit analysis gave high

values for the estimated 50% point (Subjects HF, CO, and SJ in Table III). The large distribution of 50% points across subjects caused the relatively low significance levels in comparisons involving conditions B3R2 and B3RX.

In an earlier study, Baer and Moore (1993) used a simulation of reduced frequency selectivity only. Their signal-processing method was similar to ours, and they used the same audio-visual sentence lists and speech-shaped noise. They showed that, for the symmetrical broadening condition with a broadening factor of 3, at a -3 dB S/N ratio, the mean performance was about 19% lower than performance without any smearing. In Fig. 3, at -3 dB S/N ratio, the difference in mean performance between conditions B2R2 and R2 is about 15%, while the difference between conditions B3RX and RX is 10%. In Fig. 4, at -3 dB S/N ratio, the difference between conditions B3R2+ and R2+ is 19%, while the difference between conditions B3RX+ and RX is 10%. These values are smaller than but comparable to the value of 19% found by Baer and Moore for smearing only. This finding suggests that the effect of spectral smearing is roughly additive with the effect of the loudness recruitment and threshold elevation; spectral smearing impairs performance by roughly the same amount regardless of the type of recruitment simulation used, and regardless of whether NAL amplification is applied.

II. EXPERIMENT 2: SIMULATION OF A SLOPING HEARING LOSS WITH VARIABLE BROADENING OF THE AUDITORY FILTERS

In experiment 1, the moderate-to-severe sloping loss was simulated using values for the absolute threshold that changed across frequency. However, the value for the broadening factor was kept at a constant value of 3. This was almost certainly unrealistic. In normally hearing subjects, the auditory filters become less sharply tuned on their low-frequency sides with increasing sound level (corresponding to the ''upward spread of masking''). In hearing-impaired subjects, the auditory filters are broader than normal, and the amount of broadening, on average, increases with increasing absolute threshold (Moore, 1995). However, changes in frequency selectivity with level are less pronounced in hearing-impaired than in normally hearing subjects (Stelmachowicz *et al.*, 1987; Murnane and Turner, 1991). Also, the broadening of the auditory filters with hearing loss at low frequencies seems to be somewhat less than occurs at higher frequencies (Faulkner *et al.*, 1990), possibly reflecting a reduced contribution of the active mechanism in the cochlea at low frequencies. Hence, to make the simulation more realistic, the broadening factor for each filter should be made to depend on the amount of hearing loss and on frequency.

In experiment 2 we simulated the effect of threshold elevation and loudness recruitment in combination with reduced frequency selectivity, using a more realistic degree of broadening of the auditory filters. In addition, the signal processing to take into account the frequency-dependent transfer function of the outer and middle ear was modified to make the simulation more realistic. The specific question addressed was: How does the intelligibility of speech in the more realistic combined simulation compare with that for normal hearing (unprocessed stimuli), for the simulation only of recruitment and threshold elevation, and for the combined simulation with uniform broadening of the auditory filters?

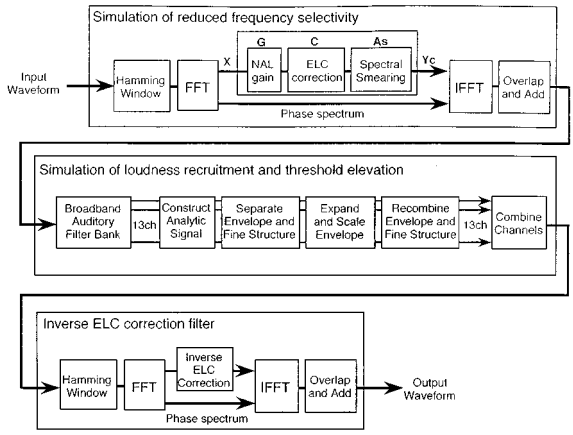

FIG. 5. A block diagram of the sequence of processing stages used in the modified combined simulation of experiment 2.

A. Method of simulation

Figure 5 shows the total processing flow of the modified combined simulation. The first part of the modified combined simulation was a simulation of reduced frequency selectivity similar to that used in experiment 1. As described earlier, symmetrical broadening of the auditory filter is defined by dividing the value of p for normal hearing by the broadening factor B [see Eq. (1)]. In experiment 1, the value of B was a fixed value of 3.

In the present simulation, the broadening factor; B, was made a function of the absolute threshold, TH, in dB HL at the center frequency of the auditory filter, in a manner similar to that described by Moore *et al.* (1996). We assumed that the auditory filter does not broaden at all for absolute thresholds less than 22 dB HL. For values of TH between 22 and 65 dB, and for center frequencies above 1 kHz, we assumed that the bandwidth of the auditory filter is broadened by a certain factor, B, relative to normal, where

$$B = 10^{0.01348(\mathrm{TH}-22)}. \tag{7}$$

For values of TH greater than 65 dB, the value of B was set to the value that would be obtained for TH=65 dB. This gives a maximum value for B of 3.8. To account for the somewhat reduced broadening that occurs at low frequencies, the term (TH$-$22) was divided by the factor $1 - 0.355 \log_{10} F$, where F is the center frequency in kHz, whenever F was less than 1. Apart from these changes in the value of B, and the method of implementing the ELC correction (see below), the simulation of spectral smearing was similar to that used in experiment 1.

The simulation of threshold elevation and loudness recruitment was also similar to that used in experiment 1. It would make the simulation more realistic if the bandwidths of the filters in this stage were varied according to the hearing loss, as in the spectral smearing stage. However, the exact filter bandwidths used in this stage are not critical.

TABLE IV. Specification of condition BXRX, showing the values of the broadening factor, B, at each audiometric frequency.

Frequency (kHz)	0.25	0.5	0.75	1.0	1.5	2.0	3.0	4.0	5.0
B	1.26	1.32	1.36	1.41	1.91	2.38	3.25	3.8	3.8

Also, changing the bandwidths would cause a change in overall level at the output of each band, which would make it difficult to compare the results to earlier results using the recruitment simulation. Hence, the filters for this stage were not changed.

Since the final processed speech signal goes through the subject's own outer/middle ear, the correction for the effect of the outer/middle ear provided by $C(i)$ in Eq. (4) should be removed (an inverse correction applied). In experiment 1, this inverse correction was performed by an additional multiplication in stage 1 [the term $C'(n)$ in Eq. (4)]. However, in principle it is more realistic to apply the inverse correction at the end of the combined simulation. In this way, all changes in the sound produced by the processing are applied before the inverse correction. In the present experiment, this was achieved by a third stage of processing (bottom of Fig. 5). This stage implemented a frequency shaping filter using the overlap-add technique, similar to that used in the first stage for spectral smearing. The third stage included a Hamming window, a FFT, power spectrum modification using the inverse gains of the ELC correction, and an inverse FFT (IFFT). The size of the Hamming window, FFT, and IFFT was 256, as in the first stage. The phase spectrum was not modified, thus preserving the temporal wave shape of the output from the second stage. To take this modification into account, the value of M for each band was slightly shifted from 100 dB, by an amount depending on the value of the 100-phon equal-loudness contour. For example, if the ELC correction (C) required an attenuation of 4 dB at a specific center frequency, then M was increased to 104 dB. This changed the absolute threshold for each band, but not the dynamic range between the threshold and the point at which loudness reached its ''normal'' value.

B. Processing conditions

The following processing conditions were used:

(1) A condition similar to condition B3RX of experiment 1, except that the broadening factor B was changed as a function of frequency and hearing loss in the way described above. The values of B at the each audiometric frequency are shown in Table IV. We refer to this condition as BXRX.
(2) Processing as in condition BXRX with the frequency-dependent gain recommended by the NAL revised procedure which is the same as for experiment 1. We refer to this as condition BXRX+.
(3) Processing only with the spectral smearing, without the loudness recruitment, using the same variable broadening factor across frequency as in the other two conditions. We refer to this as condition BX.

C. Experimental method

The method was the same as for experiment 1 except for the number of subjects and the number of sentence lists used. The speech was presented, at the input to the simulation, at a root-mean-square (rms) level of 65 dB SPL. The speech-shaped noise was presented at levels of 68, 71, and 74 dB SPL for conditions BX and BXRX+. For condition BXRX, the levels used were 65, 68, and 71 dB SPL since intelligibility was very low with the noise at 74 dB. The sentences and noise were mixed prior to processing in each of the conditions.

Six subjects were used, all self-assessed as having normal hearing. None had any history of hearing disorder. Each of the three conditions was tested using three complete sentence lists (one for each speech-to-noise ratio). The order of the lists was the same for each subject, but the order of the conditions was counterbalanced across subjects using a Latin Square design. Prior to formal testing of a given condition, one complete list processed with that condition was presented without noise for practice. Testing for that condition then began, starting with the highest speech-to-noise ratio and ending with the lowest.

D. Results

Figure 6 shows mean psychometric functions (percent correct as a function of speech-to-noise ratio) across the six subjects for all conditions. The results for the control condition (R1) taken from Moore *et al.* (1995) are also shown. Performance in condition BXRX was substantially worse

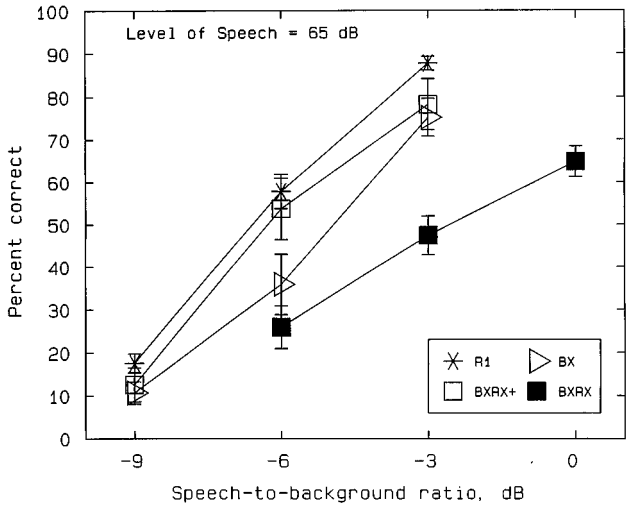

FIG. 6. Mean psychometric functions across the six subjects showing the percent correct as a function of speech-to-noise ratio for each condition of experiment 2. The results for a control condition using unprocessed stimuli (condition R1) were obtained by Moore *et al.* (1995). Error bars show ± one standard error across subjects.

TABLE V. Results of experiment 2 showing 50% correct points (P) and slopes (S) of the probit functions for each subject and each condition.

Subject		BXRX	BXRX+	BX
MJ	P	−4.18	−7.29	−6.11
	S	0.126	0.319	0.255
MH	P	−0.68	−5.42	−3.34
	S	0.152	0.302	0.478
CL	P	−1.69	−3.87	−5.09
	S	0.205	0.274	0.375
NB	P	−2.03	−6.40	−6.08
	S	0.277	0.336	0.408
AF	P	−2.13	−6.58	−4.78
	S	0.125	0.425	0.316
JS	P	−3.85	−4.94	−5.01
	S	0.176	0.386	0.308
Mean	P	−2.43	−5.75	−5.07
SD	P	1.34	1.25	1.01
Mean	S	0.177	0.340	0.357
SD	S	0.058	0.056	0.080

than in condition R1. At a speech-to-noise ratio of −3 dB, the score was only about 48% for condition BXRX, compared to almost 90% for condition R1.

Amplification according to the NAL formula produced marked improvements in performance at speech-to-noise ratios of −6, and −3 dB. However, performance in condition BXRX+ remained below that for condition R1 at all three S/N ratios. This indicates that linear amplification does not compensate fully for the deficits in performance produced by the combined simulation.

The mean performance in condition BX, which includes only the effect of reduced frequency selectivity with the variable broadening factor, was lower than that for condition BXRX+ at −6 dB S/N ratio, but almost the same at −3 and −9 dB S/N ratios. This indicates that linear amplification effectively compensates for the part of the combined simulation related to threshold elevation and loudness recruitment and is consistent with the conclusion reached in earlier studies (Moore *et al.*, 1995).

Table V gives the 50% points and the slopes of the psychometric functions for each subject in each condition and the mean value for each condition. An ANOVA was conducted on the 50% points with factors subject and condition. The effect of subjects was just significant [$F(5,10) = 3.54$, $p = 0.042$]. The effect of condition was highly significant [$F(2,10) = 23.36$, $p < 0.001$], and accounted for most of the variance in the data. The mean 50% point for condition BXRX+ was significantly lower (better) than that for condition BXRX ($p < 0.001$), indicating a large effect of linear amplification. The 50% points for conditions BX and BXRX+ did not differ significantly, indicating that the simulated loudness recruitment had little effect after NAL linear amplification. However, the effect of spectral smearing remained even after amplification.

A similar ANOVA was conducted on the slope values shown in Table V. The effect of subjects was not significant [$F(5,10) = 0.81$, $p = 0.567$]. The effect of condition was significant [$F(2,10) = 12.96$, $p = 0.002$]. The slopes for conditions BX and BXRX+ did not differ significantly. The mean slope for condition BXRX was significantly less than that for

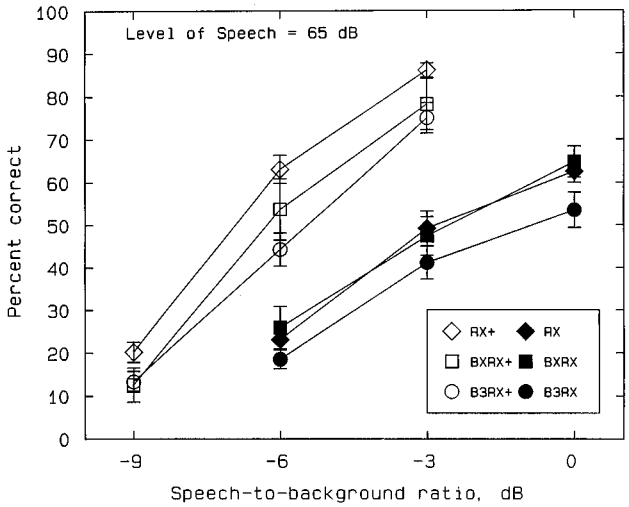

FIG. 7. Comparison of the mean results for conditions BXRX and BXRX+ with the mean results of the simulation only of recruitment combined with threshold elevation obtained by Moore *et al.* (1995) for the same loudness recruitment conditions (RX and RX+), and with the mean results of the simulation using a constant broadening factor of 3 for the same loudness recruitment conditions (B3RX and B3RX+) obtained in experiment 1. Error bars show ± one standard error across subjects.

condition BXRX+ ($p < 0.001$), indicating that the benefit of NAL amplification in condition BXRX+ was relatively greater at higher performance levels. For example, the speech-to-noise ratio was about 2.3 dB lower in condition BXRX+ than in condition BXRX at the 50% correct points, while the difference was only about 2 dB at the 25% points.

E. Discussion

Figure 7 compares mean results of conditions BXRX and BXRX+ from the present experiment with the mean results from experiment 1 and with the results of Moore *et al.* (1995). For the conditions without NAL amplification (filled symbols), performance for condition BXRX was close to that for condition RX, and both gave better performance than for condition B3RX. This suggests that the effects of the more realistic broadening used in experiment 2 were less deleterious than the effects of the constant broadening factor of 3 used in experiment 1. Indeed, without amplification, the realistic broadening used in experiment 2 gave a negligible extra effect compared to the simulation of threshold elevation and recruitment alone. It seems that in condition BXRX, reduced audibility was the main factor affecting performance.

A different pattern of results was observed when NAL amplification was applied. In this case, performance for condition BXRX+ was close to that for condition B3RX+, and both gave poorer performance than for condition RX+. Presumably, the linear amplification compensated effectively for reduced audibility, leaving reduced frequency selectivity as the main factor affecting performance.

To assess the statistical significance of these effects, t-tests for independent measures were conducted on the 50% correct points of each pair of conditions. For the conditions without NAL amplification, the difference between conditions RX and BXRX was not significant, but conditions

BXRX and RX both gave significantly lower 50% points than condition B3RX ($p<0.05$). For the conditions with NAL amplification, conditions B3RX+ and BXRX+ both gave significantly higher 50% points (i.e., poorer performance) than condition RX+ ($p<0.05$). However, the difference between conditions B3RX+ and BXRX+ was not significant.

The results of the *t*-tests support the idea that, without NAL amplification, performance for condition BXRX was similar to that for condition RX rather than to that for condition B3RX. However, when NAL amplification was applied, performance for condition BXRX+ became closer to that for condition B3RX+ and was significantly worse than that for condition RX+.

For the conditions without NAL linear amplification, performance was probably mainly limited by the audibility of the speech stimuli. Speech intelligibility depended mainly on the higher-level portions of the speech. These higher-level portions are often dominated by low-frequency components of speech. For condition BXRX, the broadening factor was less than 2.0 (i.e., less than the broadening used in condition B3RX) at frequencies below 1.0 kHz. Thus, the distortion of the most audible portions of the speech produced by the spectral smearing was relatively small. Therefore, for condition BXRX, performance was limited mainly by the effect of loudness recruitment and threshold elevation, and the effect of spectral smearing was small.

It is worth considering the possibility that the comparison of results across studies was affected by the slight change in the simulation procedure used; recall that in the earlier studies, and in experiment 1, the inverse ELC correction was applied at the end of the first stage (spectral smearing), while in experiment 2 it was applied as an extra stage after the simulation of threshold elevation and loudness recruitment. The change in procedure might have led to an overall level in condition BXRX that was slightly higher than that for condition B3RX. To check on this, the overall output level was compared for condition BXRX and for a modified stimulation of that same condition with the ELC inverse correction applied as in the earlier simulations. For an input of speech-shaped noise with a level of 65 dB SPL, the overall output from the simulation used in experiment 2 was 0.3 dB larger in rms value than that from a simulation program similar to that used in the earlier studies. This is a very small difference, but it should be remembered that audibility was a critical factor in the conditions without NAL amplification. If the overall level had been exactly the same for the different conditions, then we would expect this to shift the curve for condition BXRX slightly to the right relative to the curve for condition RX, i.e., performance would have been slightly worse for condition BXRX than for condition RX, indicating a deleterious effect of the spectral smearing. However, even with this ''correction,'' the effect of the spectral smearing would have been small.

When NAL linear amplification was applied, the decrease of audibility caused by the simulation of threshold elevation and loudness recruitment was largely compensated. In this case, the effect of spectral smearing was much more clear. Both condition BXRX+ and condition B3RX+ gave significantly higher 50% correct points than the condition RX+. However, the 50% points for conditions BXRX+ and B3RX+ did not differ significantly. The broadening factors for condition BXRX+ were smaller than those for condition B3RX+ at frequencies of 2 kHz and below, but larger for frequencies of 3 kHz and above. It is generally assumed that there is more speech information below 2 kHz than above 3 kHz (Pavlovic, 1987), so one might have expected poorer performance in condition B3RX+. The data show a small trend in the expected direction at -3 and -6 dB S/N ratios, but the 50% points were not significantly different for conditions BXRX+ and B3RX+. This suggests that, under conditions of simulated NAL amplification, where audibility is no longer a factor limiting performance, the high frequencies in the speech make an important contribution to intelligibility.

A similar conclusion can be reached by comparing the results of condition BX with the results of the study of Baer and Moore (1993) which used a constant broadening factor of 3 (condition B3). In both cases, the stimuli were not subjected to any simulation of threshold elevation and loudness recruitment, so audibility should not have been a factor limiting performance. Baer and Moore reported that, at a -3 dB S/N ratio, performance in condition B3 was 19% worse than in the control condition with no smearing. In our experiment, performance at the same ratio for condition BX was 13% worse than for condition R1. Hence, the deleterious effect of the spectral smearing was slightly greater in condition B3 than in condition BX, but not by very much. Again, this leads to the conclusion that the higher frequencies in the speech were making a substantial contribution to intelligibility.

III. CONCLUSIONS

We have simulated the effect of loudness recruitment and threshold elevation in combination with reduced frequency selectivity in order to examine the combined effect of the two major consequences of cochlear hearing loss on the intelligibility of speech in speech-shaped noise. In experiment 1, four different conditions were simulated: a moderate flat loss with auditory filters broadened by a constant factor of three (B3R2); a moderate-to-severe sloping loss with auditory filters broadened by a constant factor of three (B3RX); and these conditions with NAL linear amplification applied prior to the simulation processing (B3R2+, B3RX+).

For conditions B3R2 and B3RX, the mean performance across 12 subjects was markedly worse than for a control condition (normal hearing, condition R1) tested in a previous study. For conditions B3R2+ and B3RX+, linear amplification according to the NAL procedure improved performance considerably. However, performance with NAL amplification remained below that for normal hearing by between 5% and 19%. It should be noted that the NAL amplification used in this study was much more exact than would generally be achieved in a hearing aid. Therefore, the improvements that we found with NAL amplification might be larger than would typically be observed with real hearing aids set up to give the same nominal gain.

Comparison of the results with previous results using simulations only of recruitment and threshold elevation (R2, RX, R2+, RX+) showed significantly poorer performance for the combined simulation. This was true both without and with simulated NAL amplification. The results suggest that the reduced frequency selectivity simulated by spectral smearing is a suprathreshold factor that is relatively unaffected by amplification and which combines roughly additively with the effects of loudness recruitment and threshold elevation.

In experiment 2 the broadening of the auditory filters was made more realistic than in earlier experiments by making it a function of the absolute threshold at the center frequency of the auditory filter. Three different hearing losses were simulated: a moderate-to-severe sloping loss with variable broadening of the auditory filters (BXRX); the same moderate-to-severe sloping loss with NAL linear amplification (BXRX+); and the same broadening of the auditory filters but without the simulation of loudness recruitment and threshold elevation (BX).

For condition BXRX, the mean performance of six subjects was markedly worse than in condition R1. The mean performance in condition BX was somewhat worse than in condition R1. For condition BXRX+, linear amplification according to the NAL procedure improved performance to a large extent but it remained worse than for condition R1. This is consistent with previous evidence indicating that only part of the decrease of performance produced by actual cochlear hearing loss can be compensated by conventional linear hearing aids (Moore, 1995).

Performance for condition BXRX was significantly better than that for condition B3RX (experiment 1), which used a fixed broadening factor across all impaired auditory filters. Also, performance for condition BXRX was almost the same as for condition RX, which only simulated the effect of loudness recruitment and threshold elevation. It appears that, without amplification, the higher-frequency regions of the speech were largely inaudible, so the substantial spectral smearing in those regions in condition BXRX had little effect. In contrast, when NAL amplification was applied, performance for condition BXRX+ was close to that for condition B3RX+, and both gave significantly poorer performance than for condition Rx+. The NAL amplification restored the audibility of the higher frequencies, and in this case the effect of the spectral smearing became apparent.

ACKNOWLEDGMENTS

We thank Brian Glasberg, Thomas Baer, and Deborah Vickers for assistance with many aspects of this work and for very helpful comments on an earlier version of this paper. Richard Tyler, Winifred Strange, and an anonymous reviewer also provided helpful comments. This work was supported by the MRC (UK), The European Union (TIDE Project) and Hitachi Ltd. (Japan).

Allen, J. B. (**1977**). ''Short term spectral analysis, synthesis and modification by discrete Fourier transform,'' IEEE Trans. Acoust. Speech Signal Process. **ASSP-25,** 235–238.

Baer, T., and Moore, B. C. J. (**1993**). ''Effects of spectral smearing on the intelligibility of sentences in the presence of noise,'' J. Acoust. Soc. Am. **94,** 1229–1241.

Baer, T., and Moore, B. C. J. (**1994**). ''Effects of spectral smearing on the intelligibility of sentences in the presence of interfering speech,'' J. Acoust. Soc. Am. **95,** 2277–2280.

Byrne, D., and Dillon, H. (**1986**). ''The National Acoustic Laboratories' (NAL) new procedure for selecting the gain and frequency response of a hearing aid,'' Ear Hear. **7**, 257–265.

Celmer, R. D., and Bienvenue, G. R. (**1987**). ''Critical bands in the perception of speech signals by normal and sensorineural hearing loss listeners,'' in *The Psychophysics of Speech Perception*, edited by M. E. H. Schouten (Nijhoff, Dordrecht, The Netherlands).

de Boer, E., and Kruidenier, C. (**1990**). ''On ringing limits of the auditory periphery,'' Biol. Cybern. **63,** 433–442.

Dreschler, W. A., and Plomp, R. (**1980**). ''Relations between psychophysical data and speech perception for hearing-impaired subjects. I,'' J. Acoust. Soc. Am. **68,** 1608–1615.

Dreschler, W. A., and Plomp, R. (**1985**). ''Relations between psychophysical data and speech perception for hearing-impaired subjects. II,'' J. Acoust. Soc. Am. **78,** 1261–1270.

Duchnowski, P., and Zurek, P. M. (**1995**). ''Villchur revisited: Another look at automatic gain control simulation of hearing loss,'' J. Acoust. Soc. Am. **98,** 3170–3181.

Faulkner, A., Rosen, S., and Moore, B. C. J. (**1990**). ''Residual frequency selectivity in the profoundly hearing-impaired listener,'' Br. J. Audiol. **24**, 381–392.

Finney, D. J. (**1971**). *Probit Analysis* (Cambridge U. P., Cambridge).

Fitzgibbons, P. J., and Wightman, F. L. (**1982**). ''Gap detection in normal and hearing-impaired listeners,'' J. Acoust. Soc. Am. **72,** 761–765.

Florentine, M., Buus, S., Scharf, B., and Zwicker, E. (**1980**). ''Frequency selectivity in normally-hearing and hearing-impaired observers,'' J. Speech Hear. Res. **23,** 643–669.

Fowler, E. P. (**1936**). ''A method for the early detection of otosclerosis,'' Arch. Otolaryngol. **24,** 731–741.

Gagné, J. P., and Erber, N. P. (**1987**). ''Simulation of sensorineural hearing impairment,'' Ear Hear. **8**, 232–243.

Glasberg, B. R., and Moore, B. C. J. (**1986**). ''Auditory filter shapes in subjects with unilateral and bilateral cochlear impairments,'' J. Acoust. Soc. Am. **79,** 1020–1033.

Glasberg, B. R., and Moore, B. C. J. (**1989**). ''Psychoacoustic abilities of subjects with unilateral and bilateral cochlear impairments and their relationship to the ability to understand speech,'' Scand. Audiol. Suppl. **32,** 1–25.

Glasberg, B. R., and Moore, B. C. J. (**1990**). ''Derivation of auditory filter shapes from notched-noise data,'' Hearing Res. **47,** 103–138.

Glasberg, B. R., and Moore, B. C. J. (**1992**). ''Effects of envelope fluctuations on gap detection,'' Hearing Res. **64,** 81–92.

Glasberg, B. R., Moore, B. C. J., and Bacon, S. P. (**1987**). ''Gap detection and masking in hearing-impaired and normal-hearing subjects,'' J. Acoust. Soc. Am. **81,** 1546–1556.

Humes, L. E., Dirks, D. D., and Kincaid, G. E. (**1987**). ''Recognition of nonsense syllables by hearing-impaired listeners and by noise masked normal listeners,'' J. Acoust. Soc. Am. **81,** 765–773.

ISO 226 (**1987**). *Acoustics—Normal Equal-loudness Contours* (International Organization for Standardization, Geneva).

Lane, P., Galwey, N., and Alvey, N. (**1987**). *Genstat 5. An Introduction* (Clarendon, Oxford).

MacLeod, A., and Summerfield, Q. (**1990**). ''A procedure for measuring auditory and audiovisual speech-reception thresholds for sentences in noise: rationale, evaluation, and recommendations for use,'' Br. J. Audiol. **24**, 29–43.

Miskolczy-Fodor, F. (**1960**). ''Relation between loudness and duration of tonal pulses III. Response in cases of abnormal loudness function,'' J. Acoust. Soc. Am. **32,** 486–492.

Moore, B. C. J. (**1995**). *Perceptual Consequences of Cochlear Damage* (Oxford U. P., Oxford).

Moore, B. C. J., and Glasberg, B. R. (**1986**). ''Comparisons of frequency selectivity in simultaneous and forward masking for subjects with unilateral cochlear impairments,'' J. Acoust. Soc. Am. **80,** 93–107.

Moore, B. C. J., and Glasberg, B. R. (**1993**). ''Simulation of the effects of loudness recruitment and threshold elevation on the intelligibility of speech in quiet and in a background of speech,'' J. Acoust. Soc. Am. **94,** 2050–2062.

Moore, B. C. J., and Glasberg, B. R. (**1997**). ''A model of loudness perception applied to cochlear hearing loss,'' Auditory Neurosci. **3,** 289–311.
Moore, B. C. J., and Peters, R. W. (**1992**). ''Pitch discrimination and phase sensitivity in young and elderly subjects and its relationship to frequency selectivity,'' J. Acoust. Soc. Am. **91,** 2881–2893.
Moore, B. C. J., Glasberg, B. R., and Simpson, A. (**1992**). ''Evaluation of a method of simulating reduced frequency selectivity,'' J. Acoust. Soc. Am. **91,** 3402–3423.
Moore, B. C. J., Glasberg, B. R., and Vickers, D. A. (**1995**). ''Simulation of the effects of loudness recruitment on the intelligibility of speech in noise,'' Br. J. Audiol. **29**, 131–143.
Moore, B. C. J., Glasberg, B. R., and Vickers, D. A. (**1996**). ''Factors influencing loudness perception in people with cochlear hearing loss,'' in *Psychoacoustics, Speech and Hearing Aids*, edited by B. Kollmeier (World Scientific, Singapore).
Moore, B. C. J., Glasberg, B. R., Hess, R. F., and Birchall, J. P. (**1985**). ''Effects of flanking noise bands on the rate of growth of loudness of tones in normal and recruiting ears,'' J. Acoust. Soc. Am. **77,** 1505–1515.
Murnane, O., and Turner, C. W. (**1991**). ''Growth of masking in sensorineural hearing loss,'' Audiology **30**, 275–285.
Patterson, R. D., and Cutler, A. (**1989**). ''Auditory preprocessing and recognition of speech,'' in *Research Directions in Cognitive Science, Vol. I. Cognitive Psychology*, edited by A. D. Baddeley and N. O. Bernsen (Erlbaum, London).
Patterson, R. D., Nimmo-Smith, I., Weber, D. L., and Milroy, R. (**1982**). ''The deterioration of hearing with age: frequency selectivity, the critical ratio, the audiogram, and speech threshold,'' J. Acoust. Soc. Am. **72,** 1788–1803.
Pavlovic, C. (**1987**). ''Derivation of primary parameters and procedures for use in speech intelligibility predictions,'' J. Acoust. Soc. Am. **82,** 413–422.
Pick, G., Evans, E. F., and Wilson, J. P. (**1977**). ''Frequency resolution in patients with hearing loss of cochlear origin,'' in *Psychophysics and Physiology of Hearing*, edited by E. F. Evans and J. P. Wilson (Academic, London).
Plomp, R. (**1978**). ''Auditory handicap of hearing impairment and the limited benefit of hearing aids,'' J. Acoust. Soc. Am. **63,** 533–549.
Plomp, R. (**1986**). ''A signal-to-noise ratio model for the speech-reception threshold of the hearing impaired,'' J. Speech Hear. Res. **29,** 146–154.
Steinberg, J. C., and Gardner, M. B. (**1937**). ''The dependency of hearing impairment on sound intensity,'' J. Acoust. Soc. Am. **9,** 11–23.
Stelmachowicz, P. G., Lewis, D. E., Larson, L. L., and Jesteadt, W. (**1987**). ''Growth of masking as a measure of response growth in hearing-impaired listeners,'' J. Acoust. Soc. Am. **81,** 1881–1887.
Stone, M. A. (**1995**). ''Spectral enhancement for the hearing impaired,'' Ph.D. thesis, University of Cambridge.
Summers, I. R., and Al-Dabbagh, A. D. (**1982**). ''Simulated loss of frequency selectivity and its effects on speech perception,'' Acoust. Lett. **5,** 129–132.
ter Keurs, M., Festen, J. M., and Plomp, R. (**1992**). ''Effect of spectral envelope smearing on speech reception. I,'' J. Acoust. Soc. Am. **91,** 2872–2880.
Tyler, R. S. (**1986**). ''Frequency resolution in hearing-impaired listeners,'' in *Frequency Selectivity in Hearing*, edited by B. C. J. Moore (Academic, London).
Tyler, R. S., Summerfield, A. Q., Wood, E. J., and Fernandes, M. A. (**1982**). ''Psychoacoustic and phonetic temporal processing in normal and hearing-impaired listeners,'' J. Acoust. Soc. Am. **72,** 740–752.
Tyler, R. S., Hall, J. W., Glasberg, B. R., Moore, B. C. J., and Patterson, R. D. (**1984**). ''Auditory filter asymmetry in the hearing impaired,'' J. Acoust. Soc. Am. **76,** 1363–1368.
Villchur, E. (**1974**). ''Simulation of the effect of recruitment on loudness relationships in speech,'' J. Acoust. Soc. Am. **56,** 1601–1611.
Villchur, E. (**1977**). ''Electronic models to simulate the effect of sensory distortions on speech perception by the deaf,'' J. Acoust. Soc. Am. **62,** 665–674.
Zurek, P. M., and Delhorne, L. A. (**1987**). ''Consonant reception in noise by listeners with mild and moderate sensorineural hearing impairment,'' J. Acoust. Soc. Am. **82,** 1548–1559.

Vibrato extent and intonation in professional Western lyric singing

Eric Prame
Department of Speech, Music, and Hearing, Royal Institute of Technology (KTH), P.O. Box 700 14, S-100 44 Stockholm, Sweden

(Received 12 December 1996; revised 11 March 1997; accepted 14 March 1997)

Two important aspects of singers' $F0$ control have been investigated: vibrato extent and intonation. From ten commercially available compact disc recordings of F. Schubert's *Ave Maria*, 25 tones were selected for analysis. Fundamental frequency was determined by spectrograph analysis of a high overtone at each turning point of the vibrato undulations. It was found that the mean vibrato extent for individual tones ranged between ± 34 and ± 123 cent and that the mean across tones and singers amounted to ± 71 cent. Informal measurements on Verdi opera arias showed much higher figures. With regard to intonation substantial departures from equally tempered tuning were found for individual tones. A tone's vibrato extent was found to have a negative correlation with tone duration and a positive correlation with intonation. © *1997 Acoustical Society of America.* [S0001-4966(97)00707-8]

PACS numbers: 43.75.Bc [WJS]

INTRODUCTION

Vocal vibrato is an important aspect of professional opera and German ''lied'' singing in the Western cultures. Basically it corresponds to a frequency modulation of $F0$ characterized by its rate and extent. This modulation, in turn, causes amplitude modulations of the individual spectrum partials (see, e.g., Sundberg, 1987; Horii, 1989; Imaizumi *et al.*, 1994) which result in a modulation of the overall amplitude. This amplitude modulation may be both in phase and out of phase with the original frequency modulation.

A spectrogram of a sung tone shows a set of undulating wave patterns, of which the peaks and the troughs can be determined. Figure 1(A) shows one partial of such a tone. The fundamental frequency average can be seen to change slightly with time. In Fig. 1(B) the vibrato undulations have been isolated from the underlying gliding average shown in Fig. 1(C). This average, computed as a running one-vibrato-cycle mean of $F0$ represents the equivalent fundamental frequency of the tone (M. Metfessel in Seashore, 1932; Sundberg, 1978; Shonle and Horan, 1980; Brown, 1996). The departure of this mean from a target value reflects the intonation of the tone. Such departures can be measured as the deviation of the tone's running mean $F0$ from a target value, calculated according to equally tempered tuning, using the tuning of the accompaniment as the reference. Henceforth, this deviation, expressed in cent, will be referred to as $MF0$.

In the late 1920s and early 1930s, Carl E. Seashore and his co-workers explored in depth most aspects of vibrato thus establishing a platform for future studies in this field (Seashore, 1932, 1936, 1937, 1938). Although they designed and used instruments which were highly advanced for their time, accuracy and flexibility were limited as compared to present standards. After Seashore, many other studies dedicated to specific aspects of vibrato have been published (for reviews, see, e.g., Sundberg, 1987; Titze, 1994). However, it is sometimes difficult to compare results on vibrato extent from various studies, as it is often unclear what they relate to, amplitude or peak-to-peak, given in cent or as percentages of a tone or of a semitone. In the present investigation vibrato extent values refer to amplitude, preceded by ''$\pm$,'' and are given in cent.

In a previous investigation vibrato rate was studied (Prame, 1994). The aim of the present investigation was to examine two aspects of singers' $F0$ patterns. One is the variation of $MF0$, an almost unexplored field since the thirties, when Seashore (1937) published some articles on this topic (see, also, Sundberg, 1987; de Krom and Bloothooft, 1995). The other is vibrato extent, the description of which is still incomplete.

I. MEASUREMENTS

The same material was used for this study as in a previous investigation of vibrato rate, i.e., Franz Schubert's *Ave Maria*, D839 (Fig. 2), recorded on compact disc by ten prominent artists (Table I), all representing Western classical music tradition (Prame, 1994). The criteria for the selection of tones was the same in the present study as in the previous one, i.e., all tones should be long enough to provide reliable data. Thus the same 25 tones as before were selected for the analysis. The accompaniment was performed on different instruments. Of these, harp and piano did not interfere with the measurements of the solo voice while orchestra and choir occasionally caused minor difficulties.

Measurements were made on time spectrograms as displayed on a KAY DSP sonagraph, model 5500 (setup: frequency range: dc-4 kHz, analysis format: spectrographic display, transform size: 600 pts, analysis window: Hamming, and time axis: 400 or 800 ms). $F0$ was determined at all crests and troughs on the highest partial [U in Eq. (2)] that was distinctly displayed on the screen. As the frequency scale is linear, the obtainable resolution increases with the partial number. $F0$ values could not be adequately obtained

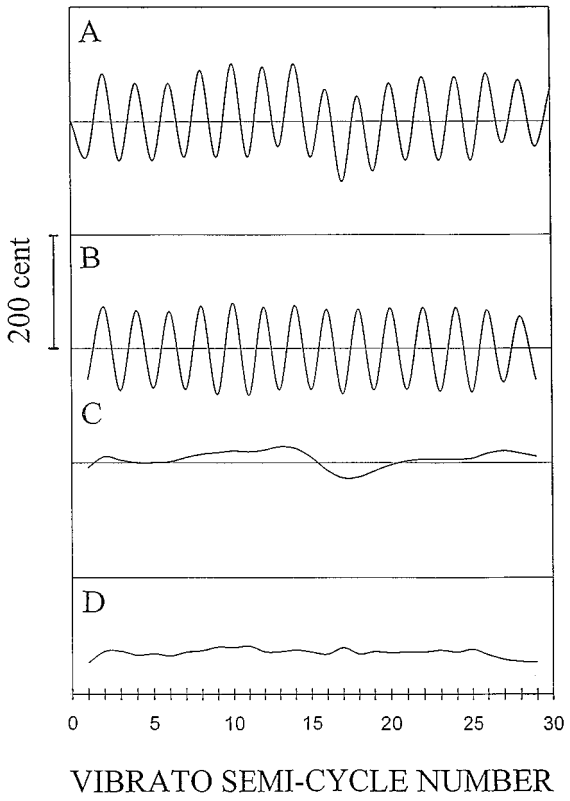

FIG. 1. Example of frequency modulation in a vibrato tone plotted in terms of $F0$ versus semicycle number. The original data is shown in panel (A). Panels (B) and (C) show the two components analyzed of the $F0$ variation, i.e., the vibrato modulation (B) and the running semicycle mean, $MF0$ (C). Panel (D) represents the envelope of the vibrato extent.

from 13 tones, mostly due to too low sound level. The total material thus included 237 tones.

The tuning of the accompaniment was determined by a listening experiment. The first bar of the accompaniment was repeatedly played over a loudspeaker. A professional violinist was asked to adjust the frequency of a complex tone so that it matched the pitch of the root of the chord. Three attempts were made for each recording, and the mean of the three readings was used as a measure of the tuning. The readings differed in average less than 1.4 cent from their respective means.

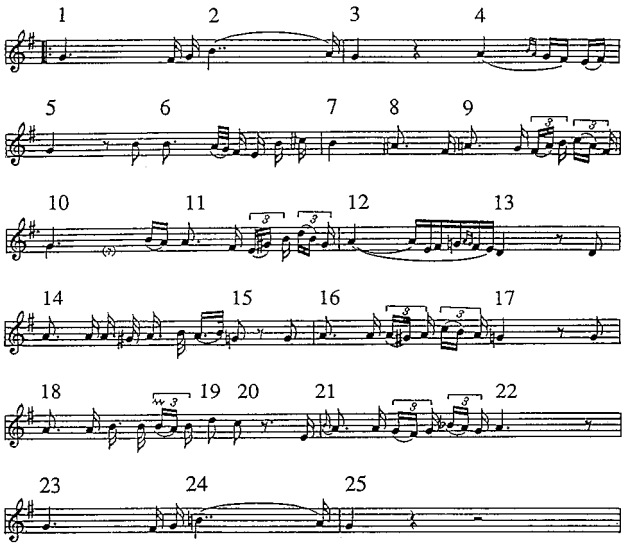

FIG. 2. Franz Schubert's song *Ave Maria* (D839) with the numbering of the 25 notes selected for analysis.

From $F0$ values of the type shown in Fig. 1(A) the vibrato extent (V) and the $MF0$ were calculated, see Fig. 1(B) and (C). The calculations for one vibrato cycle number n is found as the averages of two adjacent half-cycles, thus involving the three samples $n-1$, n, and $n+1$. Refer to Fig. 3 and the following formulas:

$$\nu_n = \left| \frac{[(-a_{n-1}+a_n)+(a_n-a_{n+1})]/(2\cdot 2)}{(a_{n-1}+2a_n+a_{n+1})/4} \right| = \left| \frac{a_{n-1}-2a_n+a_{n+1}}{a_{n-1}+2a_n+a_{n+1}} \right|, \quad (1a)$$

$$V_n = 1200 \log_2 \left[1 + \left| \frac{a_{n-1}-2a_n+a_{n+1}}{a_{n-1}2a_n+a_{n+1}} \right| \right] \text{ (cent)}; \quad (1b)$$

$$MF0_n = 1200 \log_2 \left[\frac{a_{n-1}+2a_n+a_{n+1}}{4\cdot W\cdot U} \right] \text{ (cent)}. \quad (2)$$

These operations are then repeated in unit steps of n, i.e., for each half cycle. Eq. (1a) defines the vibrato extent as a fraction and Eq. (1b) shows the vibrato extent expressed in cent. W in Eq. (2) is the target frequency according to the tempered scale, using the tuning of the accompaniment as the reference, and U is the partial number selected for measurement. Finally, the vibrato extent envelope curve [Fig. 1(D)] was derived by rectifying (i.e., taking the absolute values of the turning points) and smoothing the curve shown in Fig. 1(B).

The accuracy of the measurements can vary, particularly depending on the frequency of the partial selected. An experiment was carried out to estimate the accuracy obtained by this method. A professional mezzo-soprano was asked to sing the song with piano accompaniment. Her singing was recorded from an audio microphone and also by an electroglottograph that produced a signal reflecting the vocal fold contact area. This recording was analyzed in two ways. The audio recording was analyzed by the Sonagraph procedure described above. The electroglottograph recording was analyzed by means of the SWELL pitch tracking program using the double peak picking strategy (Ternström, 1991). The agreement between the two methods was high, the mean discrepancy being 2.5 cent with s.d. 2.7 cent.

Equations (1b) and (2) above, do not completely eliminate the influence of vibrato on $MF0$. However, as we shall mainly restrict our analysis to means computed over entire tones, the accuracy will be satisfactory for our purposes. As three values are needed for the calculation of each data point in Eqs. (1) and (2) the total number of calculated points will be two less than the number of measurements for each tone.

II. RESULTS

Figure 4 illustrates the variation of vibrato extent for all artists' performance of tones 1 and 23 as function of vibrato semicycle. As can be seen in Fig. 2 these tones occur in a

TABLE I. The ten artists singing *Ave Maria* by Schubert.

Artist	Voice classification	Key	Age of artist	Recording year	Language	Accompaniment	Tempo (s) (quarter note duration)
1	soprano	Bb4	37	1975	German	piano	1.95
2	soprano	Bb4	42	1990	German	orchestra	2.18
3	soprano	Bb4	41	1984	Latin	harp	1.80
4	soprano	Bb4	41	1988	German	piano	2.13
5	soprano	Bb4	26	1971	German	piano	2.10
6	mezzo	Ab4	34	1936	German	piano	3.00
7	alto	G4	38	1971	German	piano	2.33
8	tenor	C4	38	1979	German	orchestra	2.10
9	tenor	Bb3	35	1968	Latin	organ/choir	2.13
10	tenor	Bb3	52	1987	Latin	piano	2.53

similar musical context, although tone 23 is different in the sense that it is the second time this context appears in the piece. A certain similarity can be discerned between each individual artist's rendering of these two tones. For example, artist 3 shows an increase of the vibrato extent during the tone while artist 8 keeps a basically constant vibrato extent throughout the tone.

The vibrato extent normally increases in the beginning and decreases in the ending of the tone. This is illustrated in Fig. 5 which displays the mean and s.d. for vibrato extent across all artists and tones as a function of vibrato semitones. In calculating these means only tones with a length of at least eight vibrato periods were included. The two curves are rather smooth and arch shaped; the tones' vibrato extent starts and ends well above zero, at 42 and 55 cent, respectively.

Artists' mean vibrato extent, calculated for each tone and then averaged across all tones, is another relevant aspect. Table II lists these means together with associated extremes and standard deviations for each artist.

Interesting observations can be made in Table II. The mean vibrato extent for individual tones ranged between ± 34 and ± 123 cent and the artist means varied between ± 57 and ± 86 cent. The mean across tones and singers was ± 71 cent. The s.d. averaged across artists for intratone variation and intertone variation are similar.

Figure 6 shows the variation of the semicycle *MF*0 for all artists' performance of tones 1 and 23. For some artists the deviations from equally tempered tuning show similarities between the two tones. For example, singer 2 shows a somewhat falling/rising curve shape, singer 4 adheres to the equally tempered tuning, and singer 10 exhibits a slowly rising curve. It is also interesting to note that singers 2 and 8 both show a *MF*0 gesture that is synchronized with the chord change at two thirds of the duration of tone 1. These observations suggest that intonation was used as an expressive means at least by some of the singers.

Also in the case of *MF*0 it is interesting to study artists' mean *MF*0, calculated for each tone and then averaged across all tones. Table III lists these means together with associated scatter data for each artist. Also, the tuning of the accompaniment *re*: 440 Hz is given for each recording.

Table III shows that the mean difference across artists between sharpest and flattest intonation was 54 cent, the individual maximum amounting to 69 cent. Again, s.d. aver-

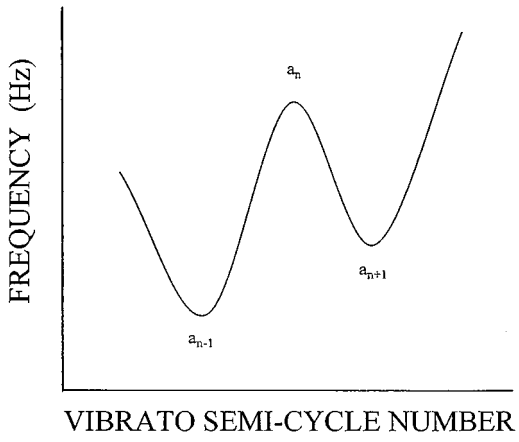

FIG. 3. Definition of the measuring points used in Eqs. (1) and (2).

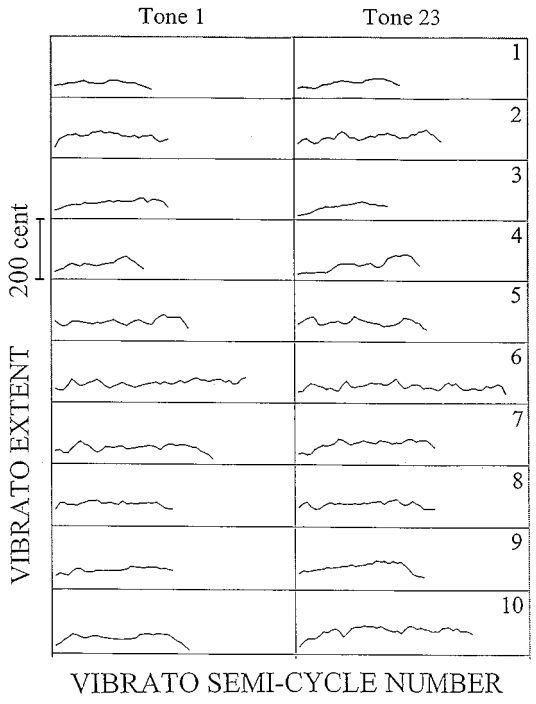

FIG. 4. All ten artists' vibrato extent envelope curves for tones 1 and 23 plotted as function of semicycle number.

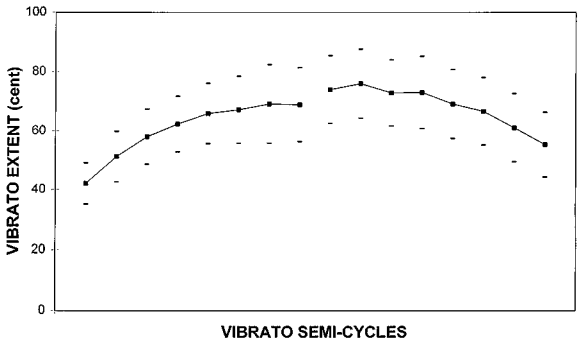

FIG. 5. Mean ± one s.d. for vibrato extent during the beginning and ending of tones, averaged across artists and tones, as function of vibrato semicycle. Only tones containing at least eight vibrato cycles are included.

aged across artists for intratone variation and intertone variation are similar. The artist mean deviation from the accompaniment varied between -20 and $+12$ cent.

A significant negative correlation between vibrato extent and tone duration was found for the 237 tones ($p<0.001$; $r=-0.44$); the longer the tone, the smaller the vibrato extent. Also, for the same 237 tones, a positive correlation was observed between mean vibrato extent and mean *MF*0 deviation ($p<0.001$; $r=+0.39$); the intonation of tones with great vibrato extent tended to be sharper. Note that as the number of measured tones is high (237), the significance levels can still be high ($p<0.001$) although the correlation coefficients (r) are rather low.

The above observations were based on measurements of sung performances of one single song, F. Schubert's *Ave Maria*. An interesting question is to what extent similar observations can be gathered from songs with different musical ambiance's. Vibrato extent was estimated from various tones in a set of performances of dramatic pieces, such as opera arias by G. Verdi and some dramatic passages from F. Schubert's *Erlkönig*. A typical variation range seemed to be ±50 to ±150 cent, approximately; thus, the vibrato extent was clearly wider than what was found for the *Ave Maria* song.

Informal measurements were carried out also on four violin performances of Schubert's song *Ave Maria*. The results indicated that the violinists had a much smaller vibrato extent than the singers, approximately half or less. Moreover, the violinists' variation of *MF*0 within tones was considerably smaller than that of the singers. Similar observations were previously reported by Meyer (1978).

III. DISCUSSION

Our investigation was based on commercially available recordings of ten singers of world fame, all performing one and the same German lied. Therefore our material should be representative of lied singing. As the frequency range of *Ave Maria* is no more than 13 semitones, each singer could be assumed to sing in a comfortable pitch range. Given the musical character of the piece, it could be further assumed that the same was true with regard to intensity and tempo. Thus, the data can be assumed not to be influenced by any extreme vocal conditions.

The present investigation concerned two distinct aspects of fundamental frequency control in singing, viz. vibrato extent and *MF*0, the tones' mean departures from equally tempered tuning. In the following, these two aspects will be discussed separately.

With regard to *vibrato extent* our results are in reasonable agreement with those previously published in comparable investigations. Our values are, however, higher than Seashore's commonly quoted average of ±50 cent with a typical variation range of ±30 to ±70 cent. Seashore also reported that extreme values can reach ±150 cent, which is similar to our findings.

How should a mean value for the vibrato extent of a tone be defined? In the present investigation we have applied a straightforward definition, the average of all calculated vibrato semicycles of a tone. In performances of Verdi's opera

TABLE II. Vibrato extent values for the ten artists. Column 1. Vibrato extent first averaged over all vibrato periods within each tone and then averaged across all 25 tones; Columns 2 and 3. Extreme values among the 25 tone means; Column 4. s.d. of the 25 tone means; Column 5. Mean s.d. across the 25 tones; Column 6. Mean vibrato rate (Hz) according to Prame (1994). In each column the extremes are marked with bold.

	Vibrato extent					
Artist:	Mean (cent)	Max (cent)	Min (cent)	Intertone s.d. (cent)	Intratone s.d. (cent)	Rate Mean (Hz)
1	72	106	38	**17**	14	5.6
2	84	105	59	12	**18**	6.5
3	71	99	42	16	13	6.3
4	73	102	50	16	13	6.0
5	64	85	36	13	10	5.9
6	**57**	**71**	44	**8**	10	**6.7**
7	72	88	51	9	10	5.9
8	**86**	**123**	**66**	15	14	**5.4**
9	60	80	**34**	11	**10**	5.6
10	70	111	48	14	12	5.8
Average	71	97	47	13	13	6.0
s.d.:	9	16	10	3	3	0.4

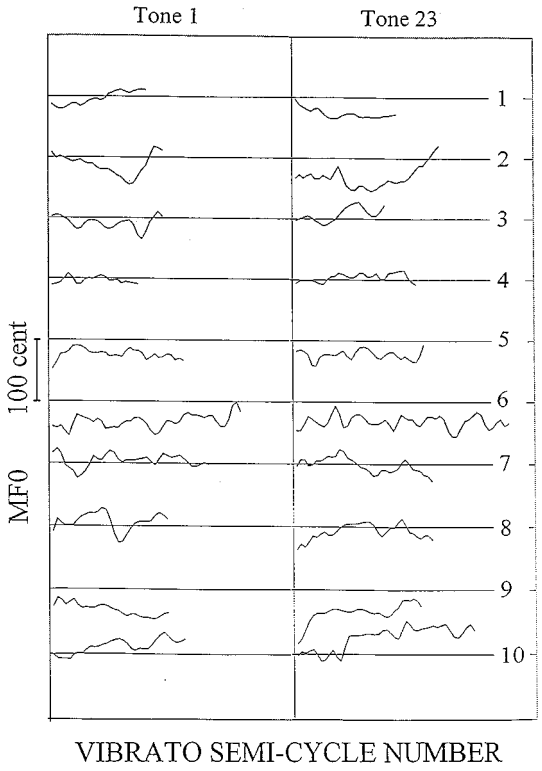

FIG. 6. All ten artists' $MF0$ curves for tones 1 and 23 plotted as function of semicycle number.

arias and in most recorded performances of the *Ave Maria*, the vibrato extent tends to start at a rather high value of the tone, as illustrated in Fig. 5. In performances of, e.g., early baroque music, the vibrato extent may be small or even close to zero during the first part of the tones. The means calculated from such tones cannot be compared with the values reported in the present investigation. Indeed, no one of our ten singers used the early music vibrato type.

The correlation between vibrato extent and tone duration was found to be negative. This is surprising, taking into account that the vibrato extent during onset and decay was typically smaller than in the middle of the tone. Hence, mean values for short tones could be expected to be small. Still the opposite was observed. This implies that the maximum extent value of a short tone is considerably greater than that of a long tone.

The maximum and minimum values of the individual singer's vibrato extent differed by a factor of 2 or more. Similar observations were made by Keidar *et al.* (1984). This suggests a substantial influence of a number of factors including musical context, tone length, and probably also musical expression (Sundberg *et al.*, 1995). In addition, musical and performance style also influence vibrato extent. For all these reasons, it is difficult to attribute a typical vibrato extent value to an individual singer, if the above mentioned factors are not taken into consideration. Vibrato rate, by contrast, is much less varying within as well as between singers (Prame, 1994).

The results regarding $MF0$ are interesting. The greatest tone mean departures from equally tempered tuning were $+42$ and -44 cent, and within a singer the greatest difference between sharpest and flattest tone mean was no less than 69 cent. Also some artists' $MF0$ tends to consistently depart from the accompaniment; for example, for artists 5 and 6, the mean deviation from the accompaniment was -20 cent and for artist 10 it was $+12$ cent. Taking into consideration that these values are means across 25 tones, the departures are remarkable. Indeed, some of these deviations exceed by an order of magnitude the just-noticeable difference for frequency discrimination (Wier *et al.*, 1977).

The $MF0$ is obviously highly relevant to whether or not a tone is perceived as in tune. This aspect has been examined in a different investigation (Sundberg *et al.*, 1996). The field of $MF0$ variation in sung performance seems to hide interesting and as yet unknown phenomena which invite further investigation.

TABLE III. Tuning data for the ten recordings analyzed. The accompaniment columns show means of accompaniment's departures from $A4=440$ Hz in cent and in Hz, respectively. The $MF0$ variation columns concern the singers intonation. The Deviation column shows mean deviation of $MF0$ from accompaniment, first averaged over all vibrato periods within each tone and then averaged across all 25 tones. The Max-min column lists the difference between sharpest and flattest tone mean. Intertone and intratone s.d. refer to the singer's deviation across and within the 25 tone. In each column the extremes are marked with bold.

	Accompaniment		$MF0$ variation			
Artist:	(cent)	(Hz)	Deviation (cent)	Max-min (cent)	Intertone s.d. (cent)	Intratone s.d. (cent)
1	15	+3.9	5	60	15	9
2	11	+2.8	7	66	**17**	11
3	9	+2.3	−7	45	12	11
4	3	+0.9	10	47	13	9
5	20	+5.1	**−20**	45	**10**	**8**
6	**−2**	**−0.4**	−20	57	13	8
7	10	+2.6	5	**42**	10	10
8	**34**	**+8.7**	9	**69**	16	**14**
9	1	+0.3	−14	52	14	9
10	8	+2.0	**12**	60	13	12
Average	11	+2.8	−1	54	13	10
s.d.:	10	2.6	13	9	2	2

IV. CONCLUSIONS

A great number of data on vibrato extent and $MF0$ was assembled from recordings of ten singers of world fame performing Schubert's *Ave Maria*. The mean vibrato extent for individual tones ranged between ± 34 and ± 123 cent. The artist means varied between ± 57 and ± 86 cent. The mean across tones and singers amounted to ± 71 cent. Informal measurements of opera arias by G. Verdi showed higher figures, ranging between ± 50 and ± 150 cent, approximately.

$MF0$ revealed remarkable departures from equally tempered tuning. The greatest tone mean departures from equally tempered tuning amounted to $+42$ and -44 cent, and within a singer the greatest difference between sharpest and flattest tone mean was 69 cent. The difference between the artist's mean intonation and the accompaniment ranged between -20 and $+12$ cent. A tone's vibrato extent was found to have a negative correlation with tone duration and a positive correlation with $MF0$.

ACKNOWLEDGMENTS

Johan Sundberg and Johan Liljencrants are gratefully acknowledged for their helpful and stimulating discussions, Johan Sundberg also for assistance in preparing this manuscript, and Lars Frydén for patiently and accurately determining the tuning of the accompaniment. Some of the above results have been presented at the 15th International Congress on Acoustics (ICA95) in Trondheim 1995.

Brown, J. C., and Vaughn, K. V. (**1996**). ''Pitch center of stringed instrument vibrato tones,'' J. Acoust. Soc. Am. **100,** 1728–1735.

de Krom, G., and Bloothooft, G. (**1995**). ''Timing and Accuracy of Fundamental Frequency Changes in Singing,'' in *Proceedings of the 13th International Congress of Phonetic Sciences* (ICPhS 95), Stockholm, edited by K. Elenius and P. Branderud (TMH at KTH, Stockholm), Vol. I, pp. 206–209.

Horii, Y. (**1989**). ''Acoustic analysis of vocal vibrato: a theoretical interpretation of data,'' J. Voice **3**, 36–43.

Imaizumi, S., Saida, H., Shimura, Y., and Hirose, H. (**1994**). ''Harmonic analysis of the singing voice:—Acoustic characteristics of vibrato,'' in *Proceedings of the Stockholm Music Acoustics Conference* (SMAC93) Royal Swedish Academy of Music, Stockholm, pp. 197–200.

Keidar, A., Titze, I., and Timberlake, C. (**1984**). ''Vibrato characteristics of tenors singing high C's,'' in *Transcripts of the 13th Symposium Care of the Professional Voice Part I,* edited by V. Laurence (The Voice Foundation, New York), pp. 105–110.

Meyer, J. (**1978**). *Physikalische Aspekte des Geigenspiels* (Verlag der Zeitschrift Instrumentenbau, Siegburg), pp. 59–70.

Prame, E. (**1994**). ''Measurements of the vibrato rate of ten singers,'' J. Acoust. Soc. Am. **96,** 1979–1984.

Seashore, C. E. (Ed.) (**1932**). ''The vibrato,'' in *University of Iowa Studies in the Psychology of Music* (Univ. of Iowa, Iowa City), Vol. I.

Seashore, C. E. (Ed.) (**1936**). ''Psychology of the vibrato in voice and instrument,'' in *University of Iowa Studies in the Psychology of Music* (Univ. of Iowa, Iowa City), Vol. III.

Seashore, C. E. (Ed.) (**1937**). ''Objective analysis of musical performance,'' in *University of Iowa Studies in the Psychology of Music* (Univ. of Iowa, Iowa City), Vol. IV.

Seashore, C. E. (**1938**). *Psychology of Music* (McGraw-Hill, New York).

Shonle, J. I., and Horan, K. E. (**1980**). ''The pitch of vibrato tones,'' J. Acoust. Soc. Am. **67,** 246–252.

Sundberg, J. (**1978**). ''Effects of the vibrato and the 'singing formant' on pitch,'' Musica Slovaca VI, 1978, Bratislava, 51–69; also J. Res. Singing **5**(2), 5–17.

Sundberg, J. (**1987**). *The Science of the Singing Voice* (Northern Illinois University, De Kalb, IL).

Sundberg, J., Iwarsson J., and Hagegård, H. (**1995**). ''A Singer's Expression of Emotions in Sung Performance,'' in *Vocal Fold Physiology,* edited by O. Fujimura and M. Hirano (Singular, San Diego).

Sundberg, J., Prame, E., and Iwarsson J. (**1996**). ''Replicability and Accuracy of Pitch Patterns in Professional Singers,'' in *Vocal Fold Physiology,* edited by P. J. Davis and N. H. Fletcher (Singular, San Diego).

Ternström, S. (**1991**). *Sound Swell Manual* (Sound Swell, Solna, Sweden).

Titze, I. R. (**1994**). *Principles of Voice Production* (Prentice-Hall, Englewood Cliffs, NJ).

Wier, C. C., Jesteadt, W., and Green, D. M. (**1977**). ''Frequency discrimination as a function of frequency and sensation level,'' J. Acoust. Soc. Am. **61,** 178–184.

The spatial inhomogeneity of pressure inside a violin at main air resonance

Guy Vandegrift
Department of Physics, The University of Texas at El Paso, El Paso, Texas 79968-0515

Eccles Wall
Greensboro College, Greensboro, North Carolina 27412

(Received 8 February 1996; revised 15 November 1996; accepted 27 March 1997)

The fluctuating pressure inside a violin is investigated at the $A0$ (main air) resonance, under the assumption that the walls are kept rigid. Three effects are shown to contribute to a reduction in the fluctuating pressure near the violin's f-holes. The strongest effect arises from a tendency to form a standing wave within the relatively long, thin shape of the upper bout. A second and smaller effect arises from the violin's nonuniform shape, and is modeled by treating the upper bout as an acoustical waveguide with nonuniform cross section. A third effect is associated with the Green's function of an acoustical radiator, and will significantly reduce the fluctuating pressure in the immediate vicinity of the violin's f-hole. Experimental verification of the theory is obtained by measuring the fluctuating pressure inside a rectangular box, with the resonance being driven by a small loudspeaker located outside the aperture. © *1997 Acoustical Society of America.* [S0001-4966(97)06107-9]

PACS numbers: 43.75.De [WJS]

INTRODUCTION

The violin's main air resonance ($A0$ mode) strongly resembles a Helmholtz resonator, which is characterized by a small aperture and uniform fluctuating pressure throughout the chamber.[1–5] However, the upper bout of the violin is sufficiently long and thin, and the f-hole sufficiently large, that the $A0$ mode also somewhat resembles the quarter wavelength mode of an open-ended resonator.[2,3,6,7] Other complications are:

(1) the violin's nonuniform shape;[6–9]
(2) the aperture acting as an acoustical radiator;[10,11]
(3) the flexibility of the walls (i.e., coupling to wood modes).[5]

This paper investigates the inhomogeneity in fluctuating pressure inside the violin at the $A0$ mode, under the simplifying assumption that the walls are rigid. However, the conclusions are relevant to the fact that the plates of a violin do flex. Cremer[5] describes a linear model that treats the violin as two or more rigid plates held by spring mechanisms. The air near an f-hole is treated simply as another mass with an associated spring constant caused by the compressibility of air.[4] The equations in this model resemble those of a discrete set of masses linked by harmonic springs. In its simplest version, only two masses are considered: one wall that moves as a piston, and one mass of air localized to a region near the f-hole. This yields two modes: the air ($A0$) mode, and a ''wood'' mode, taken to represent the $T1$ mode,[12–15] higher in frequency by a factor of approximately 1.5. Coupling between air and wood motion is shown[5] to lower the frequency of the air mode ω_0 to a value perhaps 5%–7% lower than the classical Helmholtz frequency ω_H [i.e., $\omega_H \approx c(L_f/V_T)^{1/2}$, where c is the speed of sound, V_T is the total volume of the violin, and L_f is the sum of the lengths of the two f-holes[4]].

Measurements of the violin's bridge admittance, $|v(\omega)/F(\omega)|$, exhibit several dips and peaks as the frequency ω is varied.[5,14,15] Cramer's simple two-mass model suggests an explanation for this as it predicts a bridge admittance which diverges at $\omega=\omega_O$ and vanishes at $\omega=\omega_H$. (Note that ω_O is the resonant frequency of the air mode after it has been shifted away from the ''Helmholtz'' frequency ω_H by wood-coupling effects. For the sake of simplicity, the two-mass model justifiably neglects any frequency shifts due to complications in air motion described later in this paper.)

Cremer refers to the region on the upper plate between the f-holes as the ''island,'' and argues that it plays an important role in the coupling of air and wood motion. This coupling depends on the mass and stiffness of the wood, as well as on the fluctuating air pressure, especially at locations of maximum plate motion. Holographic studies of the violin's motion at the $T1$ mode indicate that motion is indeed large near the f-holes, although not so large that the relatively small ''island'' completely dominates the production of sound.[5] In a demonstration not recommended on a good violin, one can see the wood flex and hear a change in tone by pressing hard on the instrument near the f-hole. While this change in tone may be due to changes in harmonics higher than the frequencies of interest, it suggests that the magnitude of fluctuating air pressure at the f-holes might be important. While not all investigations of pressure inside the violin at the $A0$ resonance have reported a reduction of pressure near the f-holes, our analysis clearly predicts that such a reduction should exist.[8,15]

A completely uniform fluctuating pressure is associated with an ideal Helmholtz resonator and occurs if the f-hole is sufficiently small. This can be understood as follows: If the size of the cavity, L, is kept constant, then a reduction in

aperture size reduces the resonance frequency $\omega = k/c$ to the pint where $kL \ll 1$, so that a sound wave would transit the cavity in a time much less than a period of oscillation. Thus the air comes to a sort of mechanical equilibrium with respect to sound vibrations at very low frequencies. Shaw[8] has modeled the $A0$ mode using acoustical impedances and concluded from both calculations and measurements that the pressure in the upper bout is 30%–40% higher than in the lower bout. This is due to inductances (kinetic energy of air) not associated with the f-holes. In a classical Helmholtz resonator, all the acoustical inductance is at the aperture, while the cavity provides all the acoustical capacitance (potential energy of compression). We have analyzed the acoustical circuit of Fig. 2(c) in Shaw's paper, taking the limit that the inductance L_f goes to infinity, which corresponds to a vanishingly small f-hole. As one would expect, the fluctuating pressures in the upper and lower bout are equal in this limit.

Standing waves in an acoustical waveguide arise from capacitance and inductance distributed equally along the waveguide. As the frequency of the mode is increased (by increasing aperture area), there is a tendency to form a standing wave inside the violin. We shall call this tendency the ''standing-wave'' effect, and it causes the fluctuating pressure to increase slightly as one moves away from the aperture. The distance from the middle of an f-hole to the top of the upper bout is about 18 cm, while a quarter wavelength for the main air resonance ($A0$ at 285 Hz) is 30 cm. The lower part of the violin is about 15 cm long, so that a smaller standing-wave effect would be expected in the lower bout. A highly simplistic model of the pressure difference between the upper and lower bouts is obtained by modeling two standing waves with pressures that match at the f-holes. Using the wavelengths and lengths listed above, one can obtain a crude estimate of the difference in pressure between the upper and lower bout by taking the pressure to be sinusoidal and assuming antinodes ($\partial p/\partial z = 0$) at the top and bottom. This simple estimate yields a 20% difference between the pressure at the top of the upper bout and the bottom of the lower bout. In this article, we shall focus on the upper bout because it should exhibit the stronger inhomogeneity in pressure fluctuations. However, the methods discussed can be applied to the lower bout as well.

Aside from the ''standing-wave'' effect, one must consider two other effects. The ''shape'' effect is due to the constriction near the center of the violin, apparently designed to allow room for the bow. It produces a discontinuous change in the slope of the pressure whenever the cross-sectional area changes abruptly, as shown schematically in Fig. 1. In the case of a violin, the ''shape'' effect enhances the ''standing-wave'' effect, although only slightly, as we shall see later. The ''source'' effect arises from the Green's function for an acoustical radiator inside a cavity.[10,11] It also causes a drop in pressure near the aperture, as sketched in Fig. 1. In contrast to the ''shape'' effect, which occurs only when the chamber is long and thin, the ''source'' effect is present in every Helmholtz resonator, provided one is sufficiently close to the aperture.

Our analysis indicates that the ''standing-wave'' effect is the dominant non-Helmholtz effect throughout the upper bout of the violin. However, both the ''shape'' and ''source'' effects should exert a small influence throughout most of the upper bout. And, we predict that the ''source'' effect will significantly reduce the fluctuating pressure at close proximity to the f-hole.

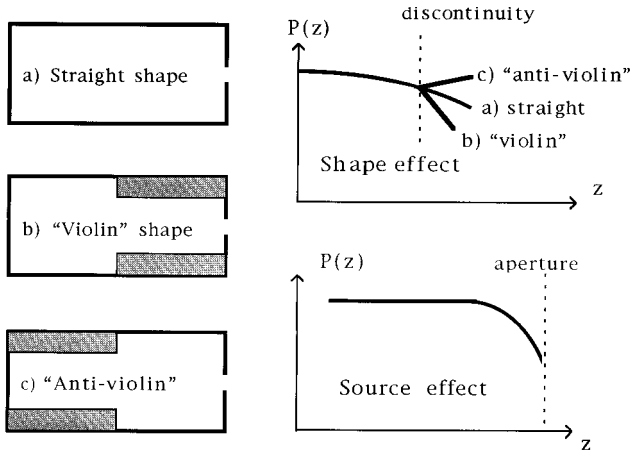

FIG. 1. The fluctuating pressure inside a rectangular cavity with irregular cross section depends on whether the shape is (a) ''straight,'' (b) ''violin-like,'' or (c) opposite that of the violin, i.e., ''antiviolin.'' The ''shape effect'' is shown for a discontinuity in the cross-sectional area of the chamber. The ''source'' effect is a sudden drop in pressure near the aperture.

I. THEORY

The source effect arises from the fact that the aperture radiates with phase opposite to the uniform pressure fluctuation associated with the Helmholtz resonance.[10,11] We start by integrating the Green's function over the surface of the aperture, noting that the first and larger term yields a constant, independent of position, which we denote as P_1:

$$p(\mathbf{r}) = \int\int \left\{ \frac{1}{k^2 V} - \frac{1}{4\pi} \frac{N}{|\mathbf{r}-\mathbf{r}'|} \right\} \sigma(\mathbf{r}')\, d^2\mathbf{r}' \approx \left[1 - \frac{Nk^2 V}{4\pi} \left\langle \frac{1}{s} \right\rangle \right] P_1, \tag{1}$$

where $\sigma = -j\omega(\mathbf{v}\cdot\mathbf{n})$ is proportional to the velocity fluctuation at the aperture, with the convention $\partial/\partial t = j\omega$. We denote $\langle 1/s \rangle$ to be the weighted average of the inverse of the distance $|\mathbf{r}-\mathbf{r}'|$ from the field point $\mathbf{r}$ to source points $\mathbf{r}'$ on the aperture. N is associated with image sources and depends on the location of the aperture:

$N = 2$ if near center of a wall;
$N = 4$ if at a corner between two walls;
$N = 8$ if at a corner between three walls.

The source effect appears to be unrelated to the Bernoulli principle ($2\,\delta P = -\rho\,\delta v^2$), which is nonlinear and therefore negligible at low amplitude. A physical appreciation of the source effect is obtained by considering a double Helmholtz resonator, formed by joining two identical resonators at the aperture. Since the two pressures in each chamber are out of phase, the aperture is an antinode in velocity and a node in pressure. In the case of a single resonator, we shall see that the fluctuating pressure at the aperture is reduced, but typically not to zero.

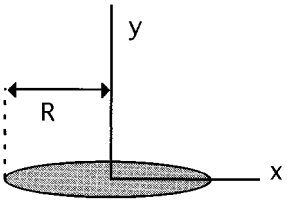

FIG. 2. The geometry used to deduce the pressure near a circular aperture or radius R.

For distances much greater than the size of the aperture, one may take $\langle 1/s \rangle$ to be the inverse distance to the center of the aperture. However, since the source effect is strong only near the aperture, it is best to find $\langle 1/s \rangle$ by integrating over the surface of the aperture. For thin walls and a small circular aperture, this integration is equivalent to calculating the potential of a charged disk.[1,5] Define x and y so that the distance to the center of the aperture of radius R is $s=(x^2+y^2)^{1/2}$, as shown in Fig. 2. From Ref. 16, one can deduce

$$\left\langle \frac{1}{s} \right\rangle = \frac{1}{R} \arctan\left(\frac{R}{y}\right) \text{ if } x=0,$$
$$\left\langle \frac{1}{s} \right\rangle = \frac{1}{R} \arcsin\left(\frac{R}{x}\right) \text{ if } y=0 \quad \text{and} \quad x \geqslant R, \tag{2}$$
$$\left\langle \frac{1}{s} \right\rangle = \frac{1}{R}\left\{\frac{\pi}{2}\right\} \text{ if } y=0 \quad \text{and} \quad x \leqslant R.$$

The case $y=0$ corresponds to a determination of pressure along a line in contact with the wall and entering the aperture at $x \leqslant R$. Using Eq. (1) and $k=(2R/V)^{1/2}$ for a small circular aperture, one obtains $\langle Nk^2V/4\pi s \rangle = 1/2$ on the surface of the aperture. Thus the fluctuating pressure at the aperture is half that within the chamber, if the aperture is not at a corner. In the Appendix, this is shown to be a general result for an ''ideal'' Helmholtz resonator (i.e., a resonator in which the ''shape'' and ''standing-wave'' effects are absent).

Next, we consider the shape effect, which in contrast to the source effect, is well known in that it is related to the joining of two acoustical waveguides of different areas.[2,3] Here, we show that the shape effect can also be obtained using Webster's horn equation[2,3,17,18] for a waveguide of nonuniform cross-sectional area $A=A(z)$:

$$k^2 p + \frac{1}{A}\frac{\partial}{\partial z}\left(A \frac{\partial p}{\partial z}\right) = 0, \tag{3}$$

where $p(z)$ is the fluctuating pressure. The boundary conditions are that $\partial p/\partial z$ vanishes at the end opposite the aperture, and that both p and $A\partial p/\partial z$ be continuous, the latter being proportional to the air flux ($\rho\ \partial v/\partial t = -\partial p/\partial z$). The boundary conditions are sufficient, provided ω is known. Let z be the distance to the end opposite the aperture, and let $z=a$ be the point where the area changes by a factor $1/\beta$. (For example, $A=1$ for $z<a$ and $A=1/\beta$ for z/a.) For $z<a$, we have

$$p(z) = P\ \cos(kz)\cos(\omega t), \tag{4}$$

and, for $z>a$,

$$p(z) = P[C_1\ \cos(kz) + C_2\ \sin(kz)]\cos(\omega t). \tag{5}$$

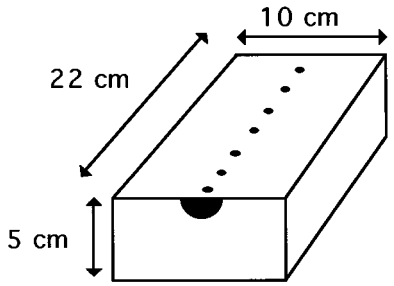

FIG. 3. A sketch of the resonant cavity. The shaded area is the aperture, and the line of black holes are plugged access holes for the microphone.

Using the continuity of $p(z)$ and $A\partial p/\partial z$ at $z=a$ yields

$$C_1 = \cos^2(ka) + \beta\ \sin^2(ka),$$
$$C_2 = (1-\beta)\cos(ka)\sin(ka). \tag{6}$$

A conventional analysis of the ''shape'' effect, obtained by joining acoustical waveguides of different area, yields the same result.[2,3]

Since the ''shape'' and ''source'' effects tend to be located at different locations, we shall combine them in an *ad hoc* fashion by multiplying Eqs. (4) and (5) by the factor in front of P_1 in Eq. (1).

II. EXPERIMENT

In order to eliminate complications caused by the exotic shape and plate flexibility associated with a real violin, w designed an experimental resonator that was not a simulation of a violin, but rather an effort to establish the correctness of our theory. Since the shape effect is small for an actual violin, we designed our resonant cavity in order to exaggerate this effect. The rectangular cavity shape allowed us to introduce large discontinuities in cross section by inserting blocks into the chamber.

The air resonance was driven by a small speaker placed approximately 1 cm from the aperture, as was previously done in an investigation of the main air resonance of a violin.[4] The resonant cavity was a plywood box of dimensions $22\times5\times10$ cm, with seven plugged holes located along the center of one wall, as shown in Fig. 3. The fluctuating pressure was measured at each plugged hole by replacing the plug by a small microphone[19] that fit into the hole flush with the inner wall of the box. A semicircular aperture of radius 1.5 cm was cut from an aluminum plate that formed the front face of the box. The aluminum plate was clamped to the box, and ''plastic wood'' was used at the holes so that the microphone and plugs would fit snugly. Two wooden blocks of length 11.4 cm were inserted into the chamber to reduce the cross-sectional area of the chamber by a factor of 0.424. In this manner, all three cavity shapes shown in Fig. 1 could be studied. The resonant frequencies for the ''straight,'' ''violin,'' and ''anti-violin'' shapes are 173, 172, and 210 Hz, respectively.

Since this aperture is at a corner between two walls, three image sources will also contribute to the Green's function, so that $N=4$ in Eq. (1). On the other hand, we can model the semicircular aperture as a full circle by pretending

the cavity had twice the volume V, with the aperture being located at the center of a wall ($N=2$). Since N and V enter as a product in Eq. (1), we see that both treatments yield identical values for magnitude of the source effect. The inverse distance $\langle 1/s \rangle$ is the same for both geometries, provided we always average over the source and all its images.

Figure 4 displays the experimentally measured pressure as well as theoretical curves showing the relative importance of the ''shape'' and ''source'' effects. The seven experimental data points exhibit both an apparent change in slope of pressure (shape effect) and a significant drop in pressure near the aperture (source effect). The solid line shows our theoretical prediction for each of the three shapes. In order to deduce the relative importance of the three effects, we have used dashed lines to plot versions of the theory that do not include certain effects. The dashed line for the straight shape is a simple model which takes the pressure variation to be $\cos(kz)$, thus incorporating only the ''standing-wave'' effect. The full model, incorporating all the effects, appears to give the best fit to the experimental data for all three shapes.

The curves in Fig. 4 do not show the pressure falling to the value $(1/2)P$, as discussed in the Appendix and following Eq. (2). This occurs because our resonator is not an ideal Helmholtz resonator, which is characterized by incompressible airflow confined to the region very close to a small aperture.

III. APPLICATION TO A VIOLIN

We shall now apply these ideas to the upper bout of an actual violin. For our calculation, we divide the chamber into four parts and consider one-fourth of a violin with half an f-hole. Picture the violin with the f-holes facing you and the fingerboard at the top. Bisect the violin with a vertical line along the corpus centerline. Then cut the violin into two pieces, top and bottom, near the center of the f-holes, so that we are left with a single cavity with an aperture that consists of half of one f-hole, located at the corner between two walls. The following parameters are used: $L=18$ cm, $\beta=1.2$, and $V=600$ cm^3 (one-fourth the actual volume). The discontinuity in area is taken to be 11 cm from the top of the upper bout.

A crude model of the f-hole is obtained by treating one f-hole as two closely spaced circles or radius 0.8 cm, centered 3.2 cm apart, with one hole being within our subdivided chamber, centered at $z_A=16.4$ cm. An estimate of frequency, using a circular aperture, yields $2\pi f \approx c(2R/V)^{1/2}=282$ Hz.[1–3] A compromise must be made between matching to the area of a typical f-hole (4–6 cm^2) or to the $A0$ frequency (275–295 Hz). Fortunately, the calculated pressure is not strongly sensitive to variations in these parameters. This insensitivity also suggests that we are justified in using a simple estimate of resonant frequency that neglects both shape effects and aperture images.

The solid line of Fig. 5 (labeled ''along to plate'') shows the prediction for points located on the top plate for a path starting from the uppermost region of the upper bout leading to contact with an aperture. Since the airflow resembles the electric field on a charged conducting disk, the fluctuating pressure should be uniform at the aperture, as shown in the figure. In order to make a graph with this uniform pressure, we have suppressed the variation associated with shape effects at the f-hole. In other words, for values of z located beyond the f-hole at z_A, Eq. (1) is multiplied by an appropriate constant instead of by Eq. (5). This difficulty in ob-

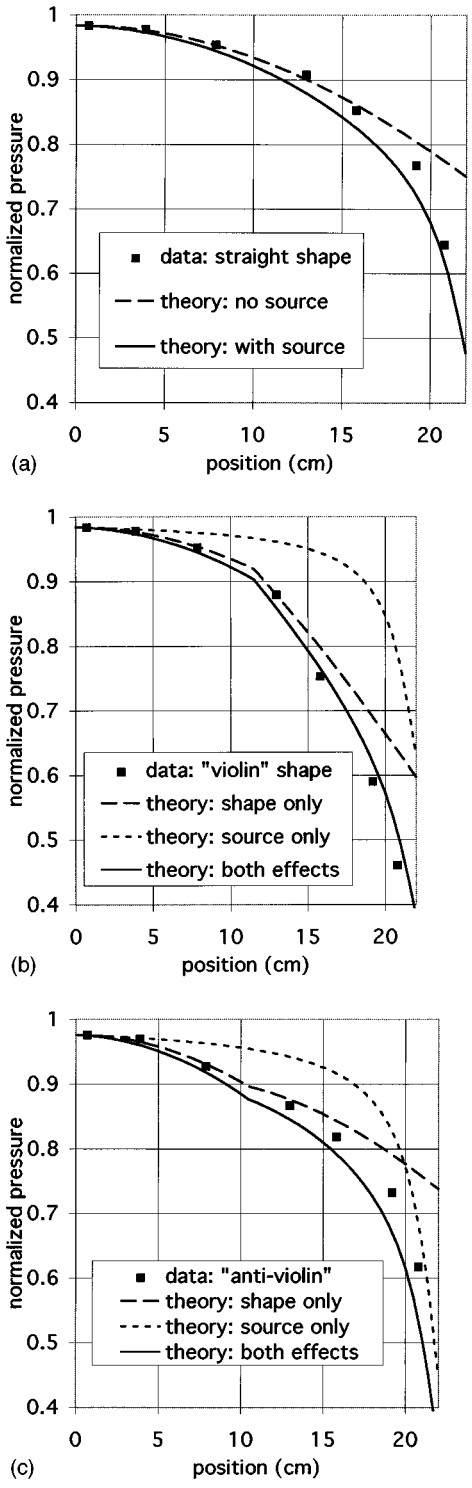

FIG. 4. Experimental data for the three configurations: (a) straight, (b) violin, (c) antiviolin. Squares show experimentally observed data. The solid lines are theoretical predictions which include all effects. The dashed lines show theoretical predictions when only the source or only the shape effects are included. The dashed line for the straight shape is a simple model which takes the pressure variation to be $\cos(kz)$.

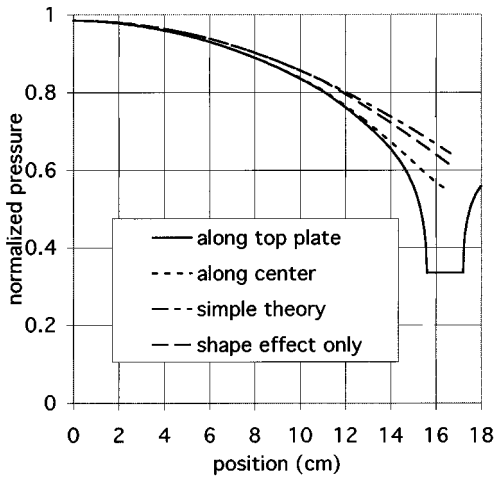

FIG. 5. A theoretical curve showing the pressure inside a violin. The solid line (along top plate) shows the prediction for points located on the top plate on a path starting from the uppermost region of the upper bout leading to contact with an f-hole, with the shape effect being suppressed only at the aperture. The three dashed lines calculate the pressure along a path located 2 cm below the top plate. The curve ''along center'' incorporates the full theory, incorporating both shape and source effects. ''Simple theory'' neglects both shape and source effects by assuming $pc\cos(kz)$. ''Shape effect only'' includes the shape effect, but neglects the source effect.

taining a uniform pressure at the surface of the aperture suggests that the *ad hoc* method of multiplying both effects may not be valid when both ''source'' and ''standing-wave'' effects are large.

The three dashed lines in Fig. 5 show calculated pressure at points 2 cm below the top plate, taking $\langle 1/s\rangle^{-1}$ to be $((z-z_A)^2+2^2)^{1/2}$. In order to establish the relative importance of the various effects, predictions of the full theory, as well as simplified versions are shown. The line marked ''along center'' represents our best estimate, incorporating the full theory including both shape and source effects. The curve labeled ''simple theory''neglects both the shape and source effects by assuming a pressure proportional to $\cos(kz)$. This ''simple'' theory models only the ''standing-wave'' effect, and is adequate for most of the upper bout, but fails somewhat near the f-holes. The curve marked ''shape effect only'' includes the shape effect, but neglects the source effect. This curve is almost identical to the ''simple theory,'' which suggests that the shape effect is relatively unimportant in modeling the pressure variation in a violin.

In conclusion, the fluctuating pressure inside a Helmholtz resonator is nonuniform for two reasons: First, the aperture acts as an acoustical source, causing the pressure to drop in the immediate vicinity of the aperture. Second, if the resonator is long and thin, there is a tendency to form a standing wave in the cavity, with the high pressure being located in the back of the chamber. This effect is enhanced if the chamber has a discontinuity in the cross-sectional area of the form found in the violin's upper bout. Both theoretical and experimental evidence indicates that the fluctuating pressure inside a violin is considerably lower near the f-holes than would be predicted by simply modeling the main air resonance as a classical Helmholtz resonator.

ACKNOWLEDGMENT

The authors are grateful to the University of North Carolina, Greensboro for the use of equipment and the purchase of the microphone.

APPENDIX: DERIVATION OF $\langle Nk2\,V/4\pi s\rangle = 1/2$ AT THE APERTURE FOR AN IDEAL HELMHOLTZ RESONATOR WITH $N=2$

Here, we show that for an ideal Helmholtz resonator, the fluctuating pressure at the aperture is exactly one-half of the fluctuating pressure throughout the rest of the chamber, provided that the aperture is not at a corner. In keeping with this assumption of an ideal Helmholtz resonator, we take the fluctuating pressure to have the uniform value P_1 throughout most of the chamber. Thus we assume a very small aperture, and, consequently, a low value of $k=\omega/c$, so that the ''shape'' and ''standing-wave'' effects are absent.

The simplest proof is based on the null in fluctuating pressure at the aperture for the double Helmholtz resonator described in Sec. I. One notes that, if an identical resonator is placed on the other side of the aperture, then symmetry dictates a pressure node at the aperture. Hence the factor $\langle Nk^2V/4\pi s\rangle$ in Eq. (1) must be unity for a double resonator. Next, we observe that the factor $\langle 1/s\rangle$ in Eq. (1) is independent of whether the resonator is single or double. However, $k=\omega/c$ decreases by a factor of $2^{1/2}$ for a single resonator because the ''mass'' of the air remains the same when the ''spring constant''[4] is halved in the process of converting a double resonator into a single one. Hence, $\langle Nk^2V/4\pi s\rangle$ is half as big for a single Helmholtz resonator as it is for a double resonator. Therefore, $\langle Nk^2/4\pi sV\rangle = 1/2$ on the surface of a single Helmholtz resonator.

A more detailed proof is based on an analog between air velocity and electrostatic field at low ω.[1] The maximum kinetic energy T and the potential energy U of a Helmholtz resonator are

$$T=\frac{\rho_0}{2}\int v^2\,d\tau, \quad U=\frac{c^2\rho_0}{2V}\left[\int \frac{\mathbf{v}\cdot d\mathbf{a}}{\omega}\right]^2,$$

where ρ_0 is the mass density of air. [This formula for potential energy can be obtained from Eq. (2) of Ref. 4, with the substitution of $\int \mathbf{v}\cdot\mathbf{da}$ for $\omega\xi(\pi R^2)$, where ξ is the displacement of the cylinder of air and K is the spring constant. Note that $U=(1/2)K\xi^2$ and $c^2=\gamma P_0/\rho_0$.] Setting $T=U$ yields

$$k^2V=\frac{[\int \mathbf{v}\cdot d\mathbf{a}]^2}{\int v^2 d\tau},$$

from which the resonant frequency of an ideal Helmholtz resonator can be deduced. Since the manipulations to follow are quite familiar in electrostatics, we use a notation that follows from viewing $\mathbf{v}=-\nabla\Phi^*$ as an electric field, where Φ^* is the analog to electrostatic potential at the aperture. Other analogs are E^*, Q^*, and ρ^*, representing energy, charge, charge density, and potential, respectively. From any good textbook on electrostatics,[16] we have (in cgs units):

$$E^* = \frac{1}{8\pi}\int v^2\, d\tau = \frac{1}{2}(Q^*)(\Phi^*),$$

$$\int v \cdot d\mathbf{a} = 2\pi Q^*,$$

$$\Phi^*(\mathbf{r}_A) = \int \frac{\rho^*}{|\mathbf{r}-\mathbf{r}'|}\, d\tau' \equiv Q^*\left\langle \frac{1}{s} \right\rangle,$$

provided **r** is somewhere on the surface of the aperture. (In contrast to electrostatic calculations, the surface integral of velocity here is taken over only one surface.) Algebraic manipulation of these equations gives our results:

$$\frac{k^2 V}{2\pi}\left\langle \frac{1}{s} \right\rangle = \frac{1}{2}.$$

Lest there by any doubt, a third proof is offered. The fluctuating pressure far outside the resonator is zero because the radiation field is small, owing to the low frequency and small aperture size. The line integral of **v** from far outside the resonator to deep inside is proportional to P_1 because $j\omega\rho\int \mathbf{v}\cdot d\mathbf{r} = P_1$ (recall that $\rho\ \partial\mathbf{v}/\partial t = j\omega\mathbf{v} = -\nabla p$). If the aperture is not near a corner, the air flow pattern is identical inside and outside the resonator. Therefore, by symmetry, the line integral representing pressure starts at 0 far outside the resonator, reaches $P_1/2$ at the aperture, and finally asymptotes to P_1 deep within the ideal Helmholtz resonator.

[1] Lord Rayleigh, *The Theory of Sound* (Macmillan, London, 1929), Chap. XVI, Art. 303-307, pp. 170–83.

[2] A. D. Pierce, *Acoustics* (McGraw-Hill, New York, 1981), Chap. 7.

[3] L. E. Kinsler and A. R. Frey, *Fundamentals of Acoustics* (Wiley, New York, 1982), 3rd ed., Chap. 10.

[4] G. Vandegrift, ''Experimental investigation of the Helmholtz resonance of a violin,'' Am. J. Phys. **61**, 415–421 (1993).

[5] L. Cremer, *The Physics of the Violin* (MIT, Cambridge, MA, 1984), Chaps. 10 and 13.

[6] B. Denardo and S. Alkov, ''Acoustic resonators with variable nonuniformity,'' Am. J. Phys. **62**, 315–321 (1994).

[7] B. Denardo and M. Bernard, ''Design and measurements of variably nonuniform acoustic resonators,'' Am. J. Phys. **64**, 745–751 (1996).

[8] E. A. Shaw, ''Cavity resonance in the violin: Network representation and the effect of damped and undamped ribholes,'' J. Acoust. Soc. Am. **87**, 398–410 (1990).

[9] E. V. Jansson, ''Acoustical properties of complex cavities. Prediction and measurements of resonance properties of violin-shaped and guitar-shaped cavities,'' Acustica **37**, 211–221 (1977).

[10] G. Vandegrift. ''A simple derivation of the Gren's function for a rectangular Helmholtz resonator at low frequency,'' J. Acoust. Soc. Am. **94**, 574–575 (1993).

[11] J. Van Bladel, ''Coupling through small apertures with an application to Helmholtz' resonator,'' J. Acoust. Soc. Am. **45**, 604–613 (1969).

[12] E. Jansson, I. Milin, and J. Meyer, ''Investigations into the acoustical properties of the violin,'' Acustica **62**, 1–15 (1986).

[13] K. Marshal, ''Modal analysis of a violin,'' J. Acoust. Soc. Am. **77**, 695–709 (1985).

[14] J. A. Moral and E. V. Jansson, ''Eigenmodes, input admittance, and the function of the violin,'' Acustica **50**, 329–337 (1982).

[15] I. M. Firth, ''Modal analysis of the air cavity of the violin,'' J. Catgut Acoust. Soc. **48**, 17–24 (1987).

[16] J. D. Jackson, *Classical Electrodynamics* (Wiley, New York, 1975), p. 92. [Note that Eq. 3.178 in this 1st edition is in error, and the entire calculation is absent from the 2nd edition.]

[17] E. Eisner, ''Complete solutions of the Webster horn equation,'' J. Acoust. Soc. Am. **41**, 1126–1146 (1967).

[18] A. H. Benade, ''The Physics of Brasses,'' Sci. Am. (July 1973). Reprinted in *The Physics Music* (Freeman, San Francisco, 1977).

[19] The microphone was a 0.75-cm-diam ''Tie-Pin'' microphone obtained from Radio Shack: Cat. No. 33-1063 (Cost ~$30).

Dependence of ultrasonic attenuation and absorption in dog soft tissues on temperature and thermal dose

Christakis A. Damianou,[a] Narendra T. Sanghvi, Francis J. Fry, and Roberto Maass-Moreno
Indiana University, Department of Physiology and Biophysics and Indianapolis Center for Advanced Research, Indianapolis, Indiana 46202

(Received 19 September 1995; accepted for publication 2 April 1997)

The effect of temperature and thermal dose (equivalent minutes at 43 °C) on ultrasonic attenuation in fresh dog muscle, liver, and kidney *in vitro*, was studied over a temperature range from room temperature to 70 °C. The effect of temperature on ultrasonic absorption in muscle was also studied. The attenuation experiments were performed at 4.32 MHz, and the absorption experiments at 4 MHz. Attenuation and absorption increased at temperatures higher than 50 °C, and eventually reached a maximum at 65 °C. The rate of change of tissue attenuation as a function of temperature was between 0.239 and 0.291 Np m^{-1} MHz^{-1} $°C^{-1}$ over the temperature range 50–65 °C. A change in attenuation and absorption was observed at thermal doses of 100–1000 min, where a doubling of these loss coefficients was observed over that measured at 37 °C, presumably the result of changes in tissue composition. The maximum attenuation or absorption was reached at thermal dosages on the order of 10^7 min. It was found that the rate at which the thermal dose was applied (i.e., thermal dose per min) plays a very important role in the total attenuation absorption. Lower thermal dose rates resulted in larger attenuation coefficients. Estimations of temperature-dependent absorption using a bioheat equation based thermal model predicted the experimental temperature within 2 °C.
 [S0001-4966(97)07107-5]

PACS numbers: 43.80.Cs [FD]

INTRODUCTION

The goal of high-intensity focused ultrasound (HIFU) surgery is to destroy pathological tissue without negatively affecting the surrounding normal tissue. Although the idea of using HIFU was proposed in the middle of this century by Lynn *et al.* (1942), clinical use is only now being established due to the recent developments of sophisticated systems (for example, Sanghvi *et al.*, 1991; Vallancien *et al.*, 1992; Chapelon *et al.*, 1993; Hynynen *et al.*, 1993, and a better understanding of ultrasound and its interaction with biological tissue due to the experience gained over these years.

One of the most important issues for HIFU surgery is the understanding and control of thermal exposure in tissue. When tissue temperature is maintained between 50 and 100 °C for a few seconds (<5 s), thermal lesions are created. Significant progress has been made in the understanding of how thermal lesions in some tissues (for example, brain and liver) may vary with the amount of acoustic power applied and the pulse duration. However, there is little information concerning the effect of heating on absorption (by tissues) which affects the size and shape of the thermal lesions. Absorption is an acoustic property which represents the rate at which energy in tissue is converted to heat. The absorption coefficient exhibited by soft tissue varies widely from tissue to tissue (Goss *et al.*, 1979) and as a function of temperature. For short pulses (<5 s), it is one of the primary factors contributing to the temperature elevation in tissue, because the effect of blood flow dissipation is minimal. Attenuation includes absorption, scattering, and reflection components, but when scattering and reflection are minimized, attenuation is largely comprised of losses due to absorption.

There are a number of studies on the effect of temperature on tissue attenuation or absorption. Dunn (1962) studied the effect of absorption at temperatures up to 30 °C in the spinal cord of mice, where an increase of absorption with temperature was reported. Dunn and Brady (1974) studied absorption as a function of temperature in mammalian central nervous tissue at different frequencies, and it was shown that absorption decreased at frequencies lower than 1 MHz and increased at frequencies higher than 1 MHz. Gammel *et al.* (1979) studied the effect of attenuation with temperature on excised porcine liver, kidney, back fat, and spleen, and for human liver. Measurements were made as the frequency was varied from 1.5 to 10 MHz at three different temperatures (4, 20, and 37 °C). It was found that above 5 MHz, the attenuation decreased with temperature for all tissues, including the human liver. Pressure absorption studies by Fry *et al.* (1991) in rat liver at 30, 37, and 41 °C revealed no statistically significant differences in absorption as a function of temperature.

To study tissue ablation, the attenuation at higher temperatures (50–100 °C) needs to be known. Robinson and Lele (1969) studied the changes in attenuation from 30 to 90 °C in cat brain, and showed that the attenuation stays essentially constant up to 50 °C, and then increases rapidly. Bamber and Hill (1979) studied the effect of temperature on attenuation over the range 5–65 °C on excised liver tissues. Attenuation of bovine liver decreased and then increased un-

[a]Author to whom all correspondence should be sent: I.C.F.A.R./Indiana University, Department of Physiology and Biophysics, VanNuys Medical Science Building 374, 635 Barnhill Dr., Indianapolis, IN 46202, Electronic mail: damianou@spidernet.com.cy

til it reached 65 °C, where it stayed constant. In human liver, the attenuation dropped with temperature, but for frequencies lower than 2 MHz, the change was insignificant.

While in past years some studies examined attenuation or absorption as a function of temperature (up to 37 °C) and some at higher temperatures, no study examined both attenuation and absorption as a function of temperature or as a function of thermal dose, particularly in the range used in HIFU surgery.

This paper reports on the effect of temperature and of thermal dose on attenuation in dog muscle, kidney, and liver *in vitro* for temperatures from room temperature up to 70 °C, and on absorption in dog muscle. Muscle was chosen because it is a commonly used tissue for ultrasound exposure studied, as it provides a relatively clear ultrasonic path (Hynynen *et al.*, 1993). Liver and kidney were chosen because of the clinical interest in the treatment of these organs with HIFU (see for example Frizzell, 1988; ter Haar *et al.*, 1989; Fry *et al.*, 1991; Yang *et al.*, 1992). Attenuation was measured using the transmission and reception method (Kossoff *et al.*, 1973), and absorption using the rate of heating method (Fry and Fry, 1954). The effects of changes in absorption and attenuation on the temperature elevation were demonstrated by temperature measurements and by simulations.

I. MATERIALS AND METHODS

A. Sample preparation

Tissue samples taken from mongrel dogs immediately after euthanasia were immersed in 0.9% saline at room temperature. The samples were placed in a small vacuum chamber until no air bubbles were released from the tissue as determined by visual inspection. This method has been proven successful in removing air inclusions in liver tissue (Bamber and Hill, 1985). The attenuation or absorption measurements were taken immediately after this procedure because some reports indicated changes in attenuation with time after excision (Frizzell *et al.*, 1979). When moving the tissue samples from the vacuum chamber to the water bath, they were kept submerged in degassed saline to minimize air exposure.

For attenuation or absorption measurements in muscle tissue, the muscle fibers were oriented perpendicular to the beam. In the case of kidney, the cortex was placed in the path of the two transducers, while for measurements in liver, care was taken to avoid any large vessels or cavities in the ultrasonic path.

B. Attenuation measurement system

The attenuation coefficient measured was based on the transmission and reception method described by Kossoff *et al.* (1973). Two unfocused circular transducers of 8 mm diameter were mounted on the arms of a caliper. This indicated the distance between them (or sample thickness). The transducers with the sample in-between were submerged in a degassed saline bath [Fig. 1(A)]. A controlled heat exchanger with adjustable temperature (Haake, model D1) was immersed in the bath to vary the tissue temperature and the

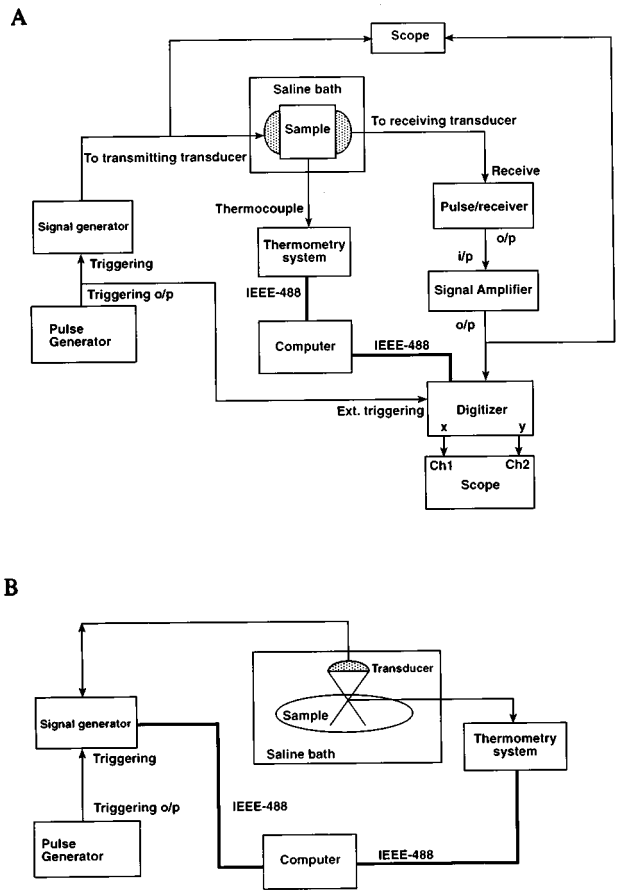

FIG. 1. (A) Block diagram of the setup used to measure the attenuation versus temperature or thermal dose using the transmission-reception method. (B) Block diagram of the setup used to measure the absorption versus temperature or thermal dose using the rate of heating method.

thermal dose. A needle-type thermocouple (Physitemp Instruments, NJ) was inserted in the tissue and temperature measured using an HP 7500 series B system and an HP 1326B multimeter. The emitting transducer was driven by a signal generator (Tektronix, model TM 5003). The applied voltage was typically between 10 and 20 V and the burst mode was used. The resonant frequency of this transducer was 4.32 MHz. Both the emitted and the received signals were monitored using a 150-MHz oscilloscope. The received signal was detected by a pulser/receiver (Panametrics 5050 PR) and channeled through a signal amplifier (Panametrics model 5601) to a digitizer (Tektronix RTD 710). The data were stored in a PC computer (Gateway 486/33 MHz). The received signal without and with the sample were captured, and based on the decrease of the signal strength, on the sample thickness, and on the frequency, the attenuation in $\mathrm{Np\,m^{-1}\,MHz^{-1}}$ was measured. A linear dependence of attenuation and frequency was assumed for all tissues based on the data reported by Hynynen (1990). The variation of this measurement in the same tissue site was less than 1%. Measurements at different sites in homogeneous tissues (where no ducts or other layers were present) showed a variation of about 10%.

Care was taken to ensure that high attenuation coefficients were not related to air bubbles or other undesired inclusions within the ultrasonic path.

C. Absorption measurement

The absorption was measured using the widely used rate of heating method (Fry and Fry, 1954). It relates temperature changes to the absorption of ultrasound by the following equation:

$$\alpha = \frac{\rho_t c_t (\partial T/\partial t)}{2I}, \tag{1}$$

where α is the absorption coefficient (Np m^{-1} MHz^{-1}), ρ_t is the density of the tissue, c_t is the specific heat of the tissue, t is the time, and T and I are, respectively, the temperature and the ultrasound intensity at a tissue location. By measuring the temperature close to the surface of the tissue, the exponential dependence of tissue as a function of depth can be neglected. The above equation assumes negligible thermal conduction. Therefore, to measure the absorption, one measures the rate of temperature rise at the focal point, placed a few mm from the tissue surface, while applying a short pulse of known intensity. In this study the pulse was of 1-s duration in continuous mode. The power chosen was such that the tissue temperature elevation was about 1–2 °C, thereby reducing the conduction effect. The rate of temperature change was measured using finite differences. The value used for density was 1100 kg/m^3, and the value for specific heat was 3770 J kg^{-1} °C.

The temperature was measured using a 50-μm-diam T-type, copper-constantan thermocouple (Physitemp). The accuracy of the thermocouple was checked by using a mercury thermometer of 0.1 °C resolution. The thermocouple was placed a few millimeters beneath the surface in the submerged tissue and the temperature was measured every 0.1 s using an HP 7500 series B system and an HP 1326B multimeter. To eliminate viscous heating, the rate of temperature change was measured 0.3 s after the ultrasound beam was turned on. After that interval the rate of temperature change was linear. Figure 1(B) shows the block diagram of the absorption measurement system. It consists of a signal generator (Tektronix, model TM 5003) and a power amplifier (ENI, 240L) to drive the focused transducer described below (used to elevate the tissue temperature) and the thermometry system.

The accuracy of measuring absorption depends on three factors: (a) correct measurement of the peak intensity at the thermocouple site; (b) correct measurement of the temperature derivative with respect to time; and (c) elimination of the effect of conduction which affects factor (b). The effect of spatial conduction was minimized by using a sufficiently wide beam relative to the size of the thermocouple. The pulse duration and applied power were chosen to produce small temperature elevations and thus eliminate the effect of conduction. This technique for measuring the absorption has been shown to be very accurate (Fry and Fry, 1954). The measurements obtained were similar to those obtained by other authors for similar tissues (for example, Fry *et al.*, 1991). Low absorption values may indicate that the measurement was affected by conduction, thus lowering the temperature gradient, or that the focus was not placed close enough to the thermocouple. Therefore, high absorption values were considered to be more reliable.

D. Focused ultrasonic transducer

A focused piezo-ceramic transducer with a 75-mm focal length (Etalon, Inc., Lebanon, IN) consisting of two concentric elements (one shaped as a disk and the other as an annulus of 15- and 40-mm o.d., respectively) was used for three purposes: (a) to produce temperature elevations in the tissue to measure absorption using a wide beam (15-mm o.d., transducer) and thus minimizing the conduction effect: (b) to elevate the tissue temperature so that absorption at different temperature could be measured (15-mm o.d. transducer); and (c) to elevate the tissue temperature with a sharply focused beam (40-mm o.d. transducer) in order to compare experimental and simulated temperature during a typical ultrasonic surgery protocol. Both elements were driven at 4 MHz.

E. Acoustic power calibration

In order to measure the absorption, the peak intensity at the focus was required. This was found by measuring the total acoustic power delivered and the half-intensity beam width of the focused transducer. The acoustic power delivered by the transducer was measured using the ultrasound power meter (Precision Advanced, Model UPM-DT-10) with the transducer driven by a rf-power amplifier (ENI, 240L) fed by a signal generator (Tektronix, TM 5003). The transducer was immersed in the water-filled power meter tank containing a force balance and an ultrasonic absorber placed 1–2 cm from the transducer surface. The measurement was taken a few seconds after the power was applied to the transducer and measurement stabilization was established. The force measured by the balance was converted to acoustic power in Watts.

F. Intensity field measurement

The intensity distribution of the focused transducer beam was estimated by measuring its output with a needle hydrophone having an active element diameter of 0.5 mm (Specialty Engineering Associates, San Jose, CA). The transducer under test was driven by the pulser output of a pulser/receiver (Panametrics 5050PR). The hydrophone was connected to the receiver input of the pulser/receiver. The resulting signal was further amplified (Panametrics 5601) and then digitized using a 10-bit digitizer (Sony-Tektronix, RTD 710) operating at 200 MHz. The three-dimensional intensity profile was obtained by moving the hydrophone laterally and axially using stepper motors (B&B Motor and Control Corp.) controlled with a stepper driver (Velmex, Inc. 8300 series). The average intensity at the focus was estimated from the ratio of power to area of the lateral half-intensity beam. For this transducer, the peak intensity was twice the average intensity (verified analytically and experimentally). The peak intensity was also measured directly using a calibrated PVDF ultrasonic hydrophone (GEC Marconi Research Center, Y-34-3598-02). Both methods measured the same peak intensity with a difference of less than 1%.

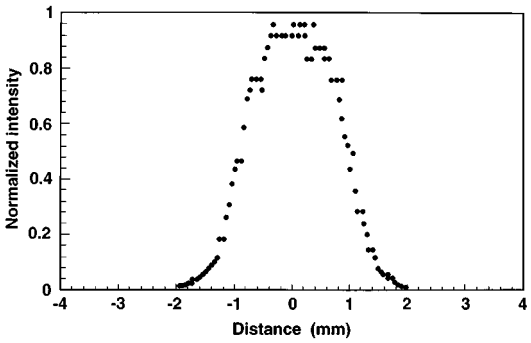

FIG. 2. Experimental normalized intensity profile for the transducer with 15-mm-diam, focal length of 75 mm and resonant frequency of 4 MHz.

G. Control of tissue temperature

The temperature of the tissue during absorption experiments was raised either ultrasonically using the focused transducer, or via water bath heating using the heater described in the methods for attenuation measurements. For ultrasonic heating, the transducer was driven by the signal generator and rf amplifier using a long duration pulse (typically 2–5 min) in the burst mode, and when steady state temperature was reached the generator mode was switched to continuous mode in order to measure absorption. The temperature of the tissue was varied by varying the number of bursts while keeping the voltage fixed. The tissue temperature elevation with water bath, or with ultrasound heating, was maintained constant during the measurements with variations smaller than 0.02 and 0.05 °C, respectively.

II. TEMPERATURE SIMULATION

A. Thermal dose calculation

Before the attenuation or absorption measurement was made, the tissue temperature and the total applied thermal dose (referenced at 43 °C) were measured. The thermal dose for changing temperature exposure was calculated using the technique suggested by Sapareto and Dewey (1984). Numerical integration was used to calculate the time that would yield an equivalent thermal dose at a reference temperature for different temperature profiles, as given by

$$t_{43} = \sum_{t=0}^{t=\text{final}} R^{(43-T_t)}\,\Delta t, \tag{2}$$

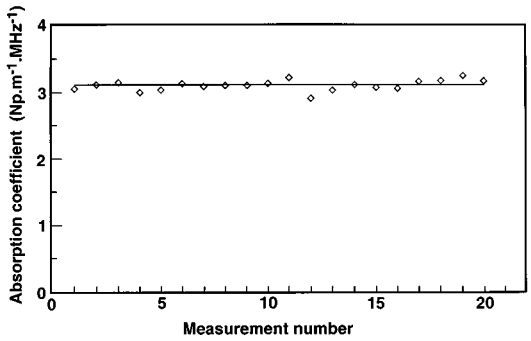

FIG. 3. Absorption coefficient measured 20 times at the same location in dog muscle *in vitro* at 37 °C (tissue temperature raised ultrasonically). Mean ±s.d. value is 3.09±0.08 Np m^{-1} MHz^{-1}.

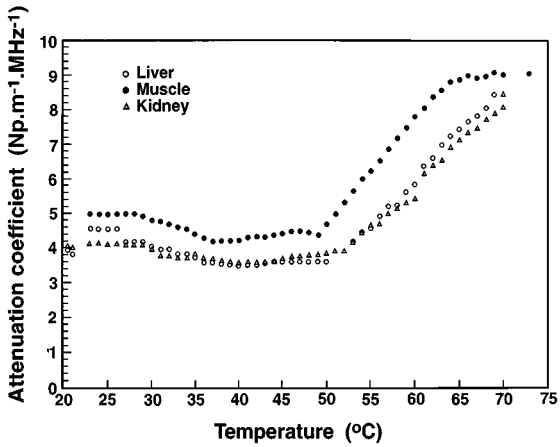

FIG. 4. Attenuation coefficient versus temperature for dog muscle, liver, and kidney *in vitro*.

where t_{43} is the equivalent time at 43 °C, and T_t is the average temperature during Δt. The value of R was 0.25 for temperatures lower than 43 °C and 0.5 for temperatures higher than 43 °C. These values were chosen because they are the most common values measured (Sapareto and Dewey, 1984). Because the rate at which the temperature was increased was low, the thermal dose was measured every 1 s. Equation (2) was also used to estimate the simulated thermal dose based on the temperature history.

B. Temperature estimation

Experimental temperature versus time profiles were obtained in dog muscle *in vitro* and then compared to the corresponding simulated profiles. The temperature was estimated from the bioheat equation by using finite difference techniques described in detail by Damianou and Hynynen (1993, 1994). The estimation of the temperature requires the power density profile for a specific transducer, power, and absorption, and was calculated by using the computer program described by Fan and Hynynen (1992).

III. RESULTS

Figure 2 shows the lateral intensity beam profile of the 15-mm transducer element measured in water. This beam width is adequate for the rate of heating method, as found by Goss *et al.* (1977) and by Parker (1983, 1988). These studies showed that for a half-intensity beam width smaller than 2 mm the conduction effect plays a very important role, and thus the pulse-decay technique should be used. Figure 3 shows the absorption of dog muscle *in vitro* at 37 °C measured 20 times at the same location. The variability of absorption gave a standard deviation of about 0.08 Np m^{-1} MHz^{-1}, showing that the measurements were repeatable.

Figure 4 shows the variation of attenuation with temperature in excised dog muscle, liver, and kidney *in vitro*. For each tissue type three different samples were used. The difference in attenuation at any temperature for a specific

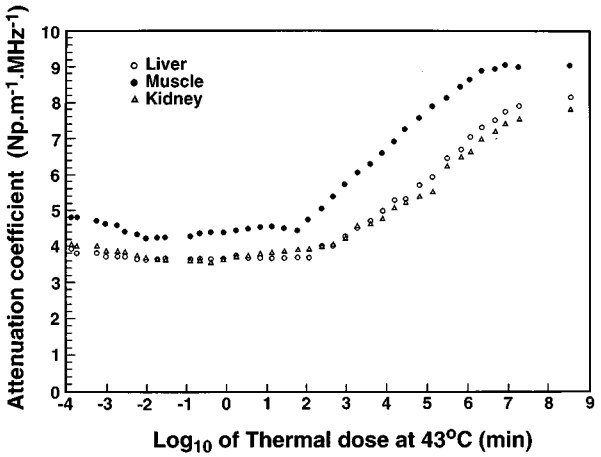

FIG. 5. Attenuation coefficient versus thermal dose at 43 °C for dog muscle, liver, and kidney *in vitro*. Same heating protocol as in Fig. 4.

tissue when three measurements were taken was smaller than 0.1 Np m^{-1} MHz^{-1}. At low temperatures (lower than 50 °C) the attenuation was constant, then it increased, and at temperatures higher than 65 °C it reached a maximum. The attenuation at temperatures higher than 65 °C was almost twice that at low temperatures. The slope in the increasing attenuation region (50–62 °C) found using linear regression (correlation coefficient 0.93–0.99) was 0.291, 0.259, and 0.239 Np m^{-1} MHz^{-1} $°C^{-1}$ for muscle, liver, and kidney, respectively. The measurement was terminated at 70 °C, in order to avoid gas evolution. Gas evolution results in a rapid increase of attenuation (Bamber and Nassiri, 1985). When the temperature was reduced from 70 °C to room temperature, the attenuation remained high, suggesting that the tissue had been permanently altered by the temperature changes.

Figure 5 shows the attenuation versus thermal dose at 43 °C for the heating results shown in Fig. 4. A significant increase of attenuation was seen at doses higher than 100–1000 min, with the maximum attenuation reached at 10^7 min. In the results of Fig. 6, dog muscle was immersed in a saline bath at constant temperature, and the thermal dose was varied by varying the time the sample was immersed in the bath. By varying the bath temperature, different rates of thermal dose delivery were achieved. For example, when the bath temperature was set at 46 °C, a 100-min dose at 43 °C was delivered in 11.11 min. Thus the dose rate was 9 min of

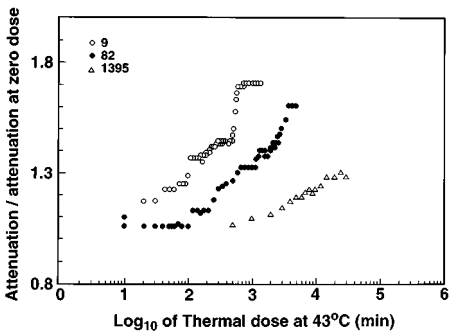

FIG. 6. Attenuation/attenuation at zero dose versus thermal dose at 43 °C for dog muscle *in vitro* with rates (applied dose per min) of 9, 82, and 1395 (min at 43 °C/min).

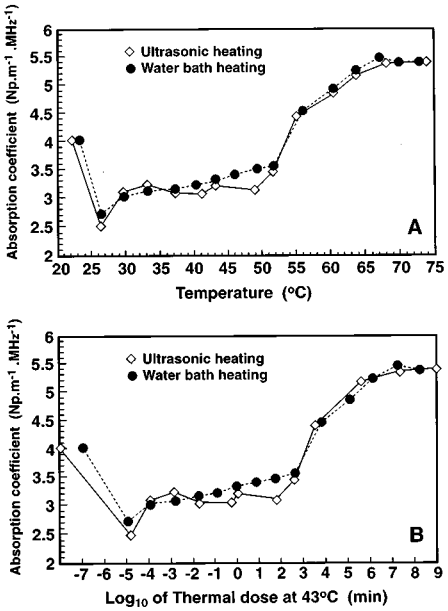

FIG. 7. (A) Absorption coefficient versus temperature (ultrasonically and water bath heated). Dog muscle *in vitro*. (B) Absorption coefficient versus thermal dose.

thermal dose at 43 °C per min. Because numerator and denominator are expressed in min, the dose rate is a dimensionless quantity. When the bath was set at 50 °C, the dose rate was 82, and at 54 °C it was 1395. Figure 6 shows the attenuation normalized to the attenuation at zero thermal dose plotted against the thermal dose at 43 °C for three different heating rates. A higher attenuation change was seen at lower heating rates. Also the dose where increasing attenuation occurred was lower for the lower heating rates.

Figure 7 shows the effect of temperature and thermal dose on absorption in one sample of dog muscle. In all, five samples were tested either by ultrasonic or by water bath heating. Differences in absorption seen at each temperature were less than 0.2 Np m^{-1} MHz^{-1}. The trend of absorption changes was similar to that observed in the attenuation measurements. Significant absorption changes occur at 50 °C, and at a thermal dose of 100 min. Maximum absorption was established at 65 °C and at doses higher than 10^7 min. The absorption at 65 °C was 1.7 times that measured at 37 °C.

Figure 8(A) shows experimental and simulated temperature changes as a function of time for dog muscle *in vitro*. The power applied was 4.26 W for 5 s. Since the temperature change was small, the absorption coefficient at 37 °C was used (3.2 Np m^{-1} MHz^{-1}). In the decaying portion a better agreement was obtained using a tissue conductivity value of 0.4 W m^{-1} $°C^{-1}$. However, due to the lower conduction effect, the simulated temperature at the end of the 5-s pulse was higher by 3 °C than the experimental temperature. The simulated temperature with a conductivity of 0.5 W m^{-1} $°C^{-1}$ is in good agreement with the measured temperature during the rising part. Figure 8(B) shows experimental and simulated temperature profiles for a 5-s pulse and an applied power of 14.15 W that resulted in temperature changes typical of ultrasonic surgery. When a constant absorption coefficient was assumed, the difference between the

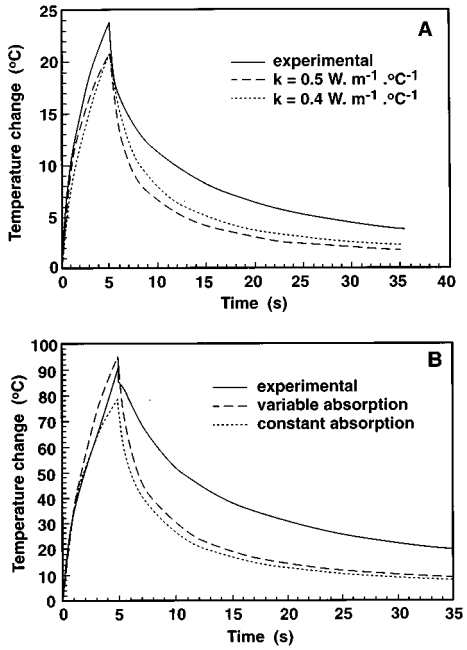

FIG. 8. (A) Experimental and simulated temperature change versus time. k=thermal conductivity (power=4.26 W, 5-s pulse, f = 4 MHz, focal distance=75 mm, diameter=40 mm, depth in tissue=15 mm). (B) Experimental and simulated temperature change versus time (power 14.15 W, 5-s pulse, f = 4 MHz, focal distance=75 mm, diameter=40 mm, depth in tissue=15 mm).

simulated and the experimental temperature profiles was 12 °C at the end of the 5-s pulse. The temperature was also simulated using a dose-dependent absorption based on the results of Fig. 6 (extrapolating for heating rate= 10^8), where a 2 °C difference between simulated and experimental temperature profiles was observed. This clearly shows the effect of the dose dependence of absorption on the estimated tissue temperature.

IV. DISCUSSION

The attenuation coefficient in liver observed in this study (4 Np m^{-1} MHz^{-1} at 37 °C) is comparable to the absorption or attenuation values published in the classical papers by Fry *et al.* (1991) for rat liver (4 Np m^{-1} MHz^{-1}), Parker (1983) in bovine liver (5.0 Np m^{-1} MHz^{-1}), Lin *et al.* (1988) for *in vitro* human liver (4.5 Np m^{-1} MHz^{-1}), Goss *et al.* (1979) for cat, mouse, pig, and beef liver (2.3 Np m^{-1} MHz^{-1}), Frizzell *et al.* (1979) for an 8-h postmortem beef liver (4.4 Np m^{-1} MHz^{-1}). The attenuation of kidney was also about 4 Np m^{-1} MHz^{-1} at 37 °C. In contrast, the corresponding value of muscle was 4.6 Np m^{-1} MHz^{-1}, which is comparable to 4.1 Np m^{-1} MHz^{-1} reported by Moros *et al.* (1991), confirming the view that muscle exhibits a higher absorption coefficient.

For low temperatures, the change in attenuation with temperature appeared to be insignificant. This information is important for hyperthermia applications, because it shows that variations in temperature in this range should not be attributed to variations in temperature-dependent attenuation. The attenuation of soft tissues above 50 °C showed an increase with temperature for all three tissue types studied. This increase was monotonic, and at about 65 °C, a maximum was reached. This maximum attenuation was almost twice the value seen at physiological temperatures (37 °C). The same trend of increasing absorption with temperature reported by Dunn and Brady (1974) for frequencies higher than 1 MHz was thus confirmed in the present study at 4 MHz. The attenuation versus temperature study alone does not explain the effect of heating. The time the temperature is maintained (estimated by using the thermal dose) gives more information on the physical changes occurring in tissue. The attenuation versus thermal dose trend shows that the attenuation in soft tissue begins to increase at dosages in the range of 100–1000 min (with the thermal dose referenced to 43 °C). This indicates that when the thermal dose reaches the threshold for necrosis, tissue attenuation increases as tissue becomes necrosed. For different tissue types there is literature on the thermal threshold of necrosis in minutes at different temperatures. Damianou *et al.* (1995) summarized threshold doses for the onset of such necrosis (in equivalent minutes referenced at 43 °C) for various tissues. Typically, the threshold for all important tissue types varies from 50 to 240 min. Eventually, when high doses are applied (typically 10^7 min) the tissue becomes totally necrosed and attenuation does not show further changes with temperature. Presumably this occurs because the physical properties of what remains of the tissue are less dependent on temperature. The irreversibility of the attenuation changes when the temperature was reduced from 70 °C to room temperature also support this view that past the threshold for necrosis, the attenuation changes were largely dependent on the state of the tissue, and not on temperature.

The effect of temperature on absorption was studied in muscle. Both ultrasonic and water (saline) bath heating showed similar trends. The advantage of ultrasonic heating is that it is faster and it can be used for *in vivo* experiments. The advantage of water bath heating is that the tissue and water are in the same temperature, and thus the effect of reflection due to a temperature-dependent, propagation velocity mismatch in the water–tissue interface is minimized. The absorption exhibited in muscle as a function of the temperature and the thermal dose showed behavior similar to that observed in the attenuation study. The attenuation changed from 4.4 Np m^{-1} MHz^{-1} from 37 °C, to about 9 Np m^{-1} MHz^{-1} at 65 °C. The corresponding change in absorption was from 3.2 Np m^{-1} MHz^{-1} to 5.5 Np m^{-1} MHz^{-1}. The value of absorption was 73% and 61% that of attenuation at 37 and 65 °C, respectively. Thus the change of attenuation with temperature was dominated by absorption processes. Scattering and reflection comprise the balance of the observed attenuation. However, the reflective coefficient due to propagation velocity mismatch that occurs in the water–muscle interface was calculated to be 2.6% in the central axis at 23 °C. This estimation was based on the propagation velocities reported by Nguyen and Faust (1992). Therefore the difference between absorption and attenuation in this case is largely attributable to scattering.

An important concept explored in this study was the effect that the rate at which a certain dose is applied has on

the tissue attenuation. In the experiments of Figs. 4 and 5, the rate at which the dose was delivered varied with temperature, with higher rates observed at higher temperatures. Although the rates were all derived in this study, the rate of 43 °C was about 2, and about 10^6 at 65 °C. The results shown in Fig. 6, where the rate was controlled, clearly show that the change in attenuation is greater for the lower dose administration rates. For the rate of 1395, the change in attenuation was about 30%. Typically, in ultrasonic surgery dosages of 10^7 min referenced at 43 °C are applied in 5 s ($\frac{1}{12}$ min) with resulting rates in the order of 10^8. In the near field where temperature elevation is slow during the treatment time, the change in absorption will be higher. The rate found by assuming an unwanted near-field dose of 900 min at 43 °C, maintained for 30 min (a typical treatment time during HIFU), is then 30. Based on the results of Fig. 6 the attenuation changes drastically, resulting in thermal enhancement in that region. This will increase the lesion size and, as the treatment progresses, the lesion will grow axially toward the transducer.

The temperature dependence of absorption has a large and definite impact on tissue temperature elevation. During the application of a short pulse of ultrasound, the temperature elevation depends primarily on the ultrasonic source parameters (intensity and pulse duration), and on tissue absorption. The ultrasonic source parameters can be accurately determined and controlled and so tissue absorption remains the key factor in the determination of tissue temperature. For high intensity applications, where the tissue temperature is typically 50–100 °C, the change in absorption with temperature can be the dominant factor for understanding temperature trends. In the thermal model the change of absorption used was chosen from the high rate (applied dose/per min) curve. The simulated temperature was in good agreement with the experimental during HIFU exposures only when the effect of temperature was taken into account. During the temperature decay period, the experimental temperature was higher than in the simulated curve. Here, conduction is the dominant factor for temperature changes. The difference between the experimental and simulated temperature may be attributable to uncertainty in the thermal conductivity. Figure 8(A) shows that, if a lower conductivity is used in the simulation, the difference between the experimental and simulated temperature narrows.

Bamber, J., and Hill, C. (**1979**). ''Ultrasonic attenuation and propagation speed in mammalian tissues as a function of temperature,'' Ultrasound Med. Biol. **5,** 149–157.

Bamber, J., and Nassiri, D. (**1985**). ''Effect of gaseous inclusions on the frequency dependence of ultrasonic attenuation in liver,'' Ultrasound Med. Biol. **11,** 293–298.

Chapelon, J., Gelet, A., Margonari, J., Gorry, F., Theillere, Y., and Cathignol, D. (**1993**). ''High intensity ultrasound ablation of anine prostate,'' Proceedings of the 14th Annual Internat. Conf. IEEE/EMBS, 29 Oct.–1 Nov., Paris, France, IEEE Catalog No. 92CH3207-8, 346–347.

Damianou, C., and Hynynen, K. (**1993**). ''Focal spacing and near-field heating during pulsed high temperature ultrasound therapy,'' Ultrasound Med. Biol. **19,** 777–787.

Damianou, C., and Hynynen, K. (**1994**). ''The effect of various physical parameters on the size and shape of necrosed tissue volume during ultrasound surgery,'' J. Acoust. Soc. Am. **95,** 1641–1649.

Damianou, C., Hynynen, K., and Fan, X. (**1995**). ''Evaluation of accuracy of a theoretical model for predicting the necrosed tissue volume during focused ultrasound surgery,'' IEEE Trans. Sonics Ultrason. **42**(2), 182–187.

Dunn, F. (**1962**). ''Temperature and amplitude dependence of acoustic absorption in tissue,'' J. Acoust. Soc. Am. **34,** 1545–1547.

Dunn, F., and Brady, J. (**1974**). ''Temperature and frequency dependence of ultrasonic absorption in tissue,'' in *Proceedings of the 8th International Congress of Acoustics*, p. 366.

Fan, X., and Hynynen, K. (**1992**). ''The effect of wave reflection and refraction at soft tissue interfaces during ultrasound hyperthermia treatments,'' J. Acoust. Soc. Am. **91,** 1727–1736.

Frizzell, L. (**1988**). ''Threshold dosages for damage to mammalian liver by high intensity focused ultrasound,'' IEEE Trans. Ultrason. Ferroelectr. Freq. Control **UFFC-35,** 578–581.

Frizzell, L., Cartensen, E., and Davis, D. (**1979**). ''Ultrasonic absorption in liver tissue,'' J. Acoust. Soc. Am. **65,** 1309–1312.

Fry, W., and Fry, R. (**1954**). ''Determination of absolute sound levels and acoustic absorption coefficients by thermocouple probes-theory,'' J. Acoust. Soc. Am. **26,** 294–310.

Fry, F., Reilly, C., Dines, K., Etchison, M., and Trauner, E. (**1991**). ''Absorption in liver at the focus of an ultrasonic shock wave field,'' Ultrasound Med. Biol. **17**(1), 65–69.

Gammell, P., Le Croissette, D., and Heyser, R. (**1979**). ''Temperature and frequency dependence of ultrasonic attenuation in selected tissues,'' Ultrasound Med. Biol. **5,** 269–277.

Goss, S., Cobb, J., and Frizzell, L. (**1977**). ''Effect of beam width hand thermocouple size on the measurement of ultrasonic absorption using the thermoelectric technique,'' Ultrasonic Symposium Proceedings, IEEE Catalog No. 77CH1264-ISU.

Goss, S., Johnston, R., and Dunn, F. (**1979**). ''Ultrasonic absorption and attenuation of high frequency sound in mammalian tissues,'' Ultrasound Med. Biol. **5,** 93–108.

Hynynen, K. (**1990**). ''Biophysics and technology of ultrasound hyperthermia,'' in *Methods of External Hyperthermic Heating* (Springer-Verlag, New York).

Hynynen, K., Darkazanli, A., Unger, E., and Schenck, J. (**1993**). ''MRI-guided non-invasive ultrasound surgery,'' Med. Phys. **20**(1), 107–115.

Kossoff, G., Kelly-Fry, E., and Jellins, J. (**1973**). ''Average velocity of ultrasound in the human female breast,'' J. Acoust. Soc. Am. **53,** 1730–1736.

Lynn, J., Zwemer, R., Chick, A., and Miller, A. (**1942**). ''A new method for generation and use of focused ultrasound in experimental biology,'' J. Gen. Physiol. **26,** 179–193.

Moros, E., Dutton, A., Roemer, R., Burton, M., and Hynynen, K. (**1993**). ''Experimental evaluation of two simple thermal models using hyperthermia in muscle *in vivo*,'' Int. J. Hyperthermia **9**, 581–598.

Parker, K. (**1983**). ''Ultrasonic attenuation and absorption in liver tissue,'' Ultrasound Med. Biol. **9**(4), 363–369.

Parker, K., Asztely, M., Lerner, R., Schenk, E., and Waag, R. (**1988**). ''*In vivo* measurements of ultrasound attenuation in normal or diseased liver,'' Ultrasound Med. Biol. **14**(2), 127–136.

Nguyen, M., and Faust, U. (**1992**). ''Possibilities and limitations of temperature monitoring using ultrasound techniques,'' Ultrasonics **30**(2), 128–131.

Robinson, T., and Lele, P. (**1969**). ''An analysis of lesion development in the brain and in plastics by high-intensity focused ultrasound at low-megahertz frequencies,'' J. Acoust. Soc. Am. **51,** 133–1351.

Sanghvi, N., Fry, F., Foster, R., Chua, R., Chua, G., Griffith, S., Birhle, R., Yang, R., Zing, J., and Hennige, L. (**1991**). ''System design and considerations for a high intensity focused ultrasound device for the treatment of tissue *in vivo*,'' Med. Biol. Eng. Comp. **29,** 48.

Sapareto, S., and Dewey, W. (**1984**). ''Thermal dose determination in cancer therapy,'' Int. J. Radiation Oncology Biol. Phys. **10**, 787–800.

ter Haar, G., Sinnett, D., and Rivens, I. (**1989**). ''High intensity focused ultrasound-A surgical technique for the treatment of discrete liver tumors,'' Philos. Mag. Lett. **34,** 1743–1750.

Yang, R., Reilly, C., Rescorla, F., Sanghvi, N., Fry, F., Franklin, T., and Grosfeld, J. (**1992**). ''Effects of high-intensity ultrasound in the treatment of experimental liver cancer,'' J. Pediatric Surg. **126**, 246–251.

Vallancien, G., Harouni, M., Veillon, B., Mombet, A., Prapotnich, D., Bisset, J., and Bouragan, J. (**1992**). ''Focused extracorporeal pyrotherapy: Feasibility study in man,'' J. Endourol. **6**, 173–180.

Statistical properties of estimates of signal-to-noise ratio and number of scatterers per resolution cell

Keith A. Wear, Robert F. Wagner, and David G. Brown
Food and Drug Administration, Center for Devices and Radiological Health, 12720 Twinbrook Parkway, Rockville, Maryland 20852

Michael F. Insana
Radiology Deptartment, University of Kansas Medical Center, Kansas City, Kansas 66160

(Received 19 April 1996; accepted for publication 14 February 1997)

Elementary theory underlying the relationship between the number of scatterers per resolution cell (N) and echo intensity signal-to-noise ratio (SNR) is reviewed. A relationship between the probability density functions for estimates of N and SNR^2 is derived. This relationship is validated using a computer simulation. Phantom and *in vitro* experiments are described. In one set of experiments on phantoms, empirical distributions of estimates of N and SNR^2 are measured and compared to theoretical predictions. The utility of SNR^2 for discrimination of phantoms with different values for N is assessed using receiver operating characteristic (ROC) analysis. In another set of experiments, the frequency dependence of the SNR^2 estimate is investigated for a two-component phantom and for excised dog kidney. It is shown that the frequency dependence of the SNR can help to identify the presence of two or more scattering components that are spatially mixed. With regard to kidney data, measurements performed both parallel and perpendicular to the predominant nephron orientation are reported. The observed anisotropy is compared to the anisotropy of backscatter coefficient encountered in previous investigations.
[S0001-4966(97)01107-7]

PACS numbers: 43.80.Qf, 43.80.Vj, 43.80.Gx [FD]

INTRODUCTION

Many fundamental problems in physics and astronomy can be analyzed in terms of the random walk. In particular, scattering of a radio-frequency (rf) wave from a random medium involves the random walk in two dimensions (the real and imaginary components of the rf signal). Much of this theory may be found in Middleton's analysis of rf communications[1] and Goodman's analysis of laser speckle.[2]

When the number of scatterers per resolution cell of a measurement system is large and the cell is sufficiently extended so that the phases of the scattered waves are uniformly distributed over $0-2\pi$, the central limit theorem applies and the resulting net scattered field obeys circular Gaussian statistics.[2–4] The net scattered field is *incoherent* and its appearance in an image is referred to as *fully developed speckle*. The first- and second-order statistics of this speckle are well understood.[1–4] If the scatterers are periodically organized or sufficiently dense such that there is little variation in the phases of the scattered waves, the net field is *coherent*.

When there are few scatterers per resolution cell, the central limit theorem does not apply. If their phases are still uniformly distributed over $0-2\pi$, the result is referred to as non-Gaussian speckle, which has statistical properties determined by the number of scatterers per resolution cell. This has been studied by Jakeman,[5] Pusey *et al.*,[6] Cardoso,[7] Wilhelmij and Denbigh,[8] Denbigh *et al.*,[9] and Sleefe and Lele.[10] Wagner *et al.*[11] reported peculiar aspects of the estimator of the number of scatterers per resolution cell and offered a theoretical explanation (presented in more detail below). Narayanan *et al.* have performed simulations and experiments which modeled conditions in which the backscatter coefficients of the scatterers vary throughout the scattering volume.[12] They studied how the statistics of the echo envelope changed as the ''effective'' number of scatterers per resolution cell varied. In their model, the echo envelope obeys a generalized K distribution[13] which approaches, in various limits, Rayleigh, Rician, Gaussian, and lognormal distributions. As the width of the distribution of scattering cross sections increases (and the effective number of scatterers per resolution cell decreases), the statistics of the echo envelope become increasingly non-Rayleigh.[12] Chen *et al.* have published a derivation of a method for determination of frequency-dependent effective scatterer number density. Their notion of effective scatterer number density is the actual number density multiplied by a frequency-dependent factor that depends on the differential scattering cross sections of the scatterers. They have validated their technique with experimental measurements[14] and explored statistical uncertainty in estimates of effective scatterer number density.[15]

In Sec. I of this paper a derivation of a formula which relates the number of scatterers per resolution cell to echo intensity signal-to-noise ratio (SNR) is presented. In Sec. II, the computer simulation and experimental methods are described. In Sec. III, simulated and empirical (based on phantom measurements) distributions of estimates of N and SNR^2 are compared with theory. Measurements of the frequency dependence of SNR^2 for a two-component phantom (model for kidney) and for excised dog kidney are reported. Finally, in Sec. IV, some concluding remarks are made.

I. THEORY

The probability density function (pdf) for the case of an *infinite* number of contributions, or steps in the two-dimensional random walk, was solved by Lord Rayleigh in 1880[16] in the context of the superposition of vibrations. Pearson posed the problem of finding the pdf for the *finite* case of the 2D random walk in 1905—motivated by his interest in the migration of birds and their ''random flights.''[17] Kluyver presented a formal solution within about two months.[18] Many details and bibliographical notes on this problem are presented at the end of Chandrasekhar's classic review.[19] Further contributions have been made by Pusey *et al.* (1974)[6] and Merzbacher *et al.* (1977).[20]

The process may be viewed as a random phasor sum. The received complex signal (such as the radio-frequency voltage output from an ultrasound transducer), E, is modeled as the sum of N complex signals, $a_i = |a_i| \exp(j\phi_i)$, from individual identical discrete scatterers:

$$E = \sum_{i=1}^{N} a_i . \tag{1}$$

N is the number of scatterers per resolution cell. The phases of the a_i are assumed to be statistically independent and uniformly distributed over the interval $(0, 2\pi)$. The *intensity* of the signal is given by $I = |E|^2$. It is well known that in the limit of large N, the *envelope*, $|E|$, obeys a *Rayleigh* distribution and the intensity obeys a *chi-squared* distribution with two degrees of freedom (i.e., an exponential distribution).[4] (Although a K distributed rather than constant backscatter coefficient may offer a more general model for tissue,[12,13] the simple model employed here is useful to produce insight into the problem and to predict the outcomes of the experiments described below.)

The correlation between one intensity measurement, I, and another measurement, I' (where the second measurement is obtained either by translating the transducer or changing the time delay between the transmitted burst and the moment of reception), may be expressed as

$$\langle II' \rangle = \sum_{i=1}^{N} \sum_{j=1}^{N} \sum_{k=1}^{N} \sum_{l=1}^{N} \langle a_i^* a_j a_k'^* a_l' \rangle. \tag{2}$$

Angular brackets denote expectation. Asterisks denote complex conjugation. Since the phases of the a_i are independent and uniformly distributed from 0 to 2π, it follows that $\langle a_i a_j \rangle = \langle a_i a_j' \rangle = \langle a_i a_j^* \rangle = \langle a_i a_j'^* \rangle = 0$ for $i \neq j$. Also, $\langle a_i \rangle = \langle a_i' \rangle = \langle a_i a_i' \rangle = 0$. (The last equality follows from the fact that the sum of two random phases which are uniformly distributed from 0 to 2π is also effectively uniformly distributed from 0 to 2π.) Equation (2) may now be rewritten

$$\langle II' \rangle = \sum_{i=1}^{N} \langle a_i^* a_i a_i'^* a_i' \rangle + \sum_{i=1}^{N} \sum_{j \neq i}^{N} \langle a_i^* a_i \rangle \langle a_j'^* a_j' \rangle + \sum_{i=1}^{N} \sum_{j \neq i}^{N} \langle a_i^* a_i' \rangle \langle a_j a_j'^* \rangle. \tag{3}$$

(Recall that if two random variables, r and s, are independent then they are also uncorrelated so that $\langle rs \rangle = \langle r \rangle \langle s \rangle$.) The terms in Eq. (3) may be simplified as follows:

$$\sum_{i=1}^{N} \langle a_i^* a_i a_i'^* a_i' \rangle = N \langle |a|^2 |a'|^2 \rangle,$$

$$\sum_{i=1}^{N} \sum_{j \neq i}^{N} \langle a_i^* a_i \rangle \langle a_j'^* a_j' \rangle = \langle I \rangle \langle I' \rangle \left(1 - \frac{1}{N} \right), \tag{4}$$

$$\sum_{i=1}^{N} \sum_{j \neq i}^{N} \langle a_i^* a_i' \rangle \langle a_j a_j'^* \rangle = |\langle E^* E' \rangle|^2 \left(1 - \frac{1}{N} \right),$$

where $\langle I \rangle = N \langle |a|^2 \rangle$. Now, Eq. (3) may be rewritten as

$$\langle II' \rangle = \left(1 - \frac{1}{N} \right) (\langle I \rangle \langle I' \rangle + |\langle E^* E' \rangle|^2) + N \langle |a^2| |a'^2| \rangle. \tag{5}$$

This equation is the same as Jakeman's equation (13) if all scatterers are assumed to be identical.[5] If N is now taken to be a random variable, then $\langle I \rangle = \langle N \rangle \langle |a|^2 \rangle$ and $(1 - N^{-1})$ is replaced by $\langle N(N-1) \rangle / \langle N \rangle^2$ above. The ratio of the first and second moments of I may be obtained by setting $I' = I$. If N is assumed to obey a Poisson probability density function [so that $\langle N(N-1) \rangle = \langle N \rangle^2$] then the following is obtained;

$$\frac{\langle I^2 \rangle}{\langle I \rangle^2} = 2 + \frac{1}{\langle N \rangle}, \tag{6}$$

which may be rewritten as

$$\langle N \rangle = \frac{\mathrm{SNR}^2}{1 - \mathrm{SNR}^2}, \tag{7}$$

where $\mathrm{SNR}^2 = \langle I \rangle^2 / (\langle I^2 \rangle - \langle I \rangle^2)$ is the so-called point signal-to-noise ratio. Thus $\langle N \rangle$ may be estimated from measurements of SNR^2. Difficulties arise however when estimates of SNR^2 equal one (estimate of $\langle N \rangle$ is infinite) or exceed one (estimate of $\langle N \rangle$ is negative!). As will be seen in Sec. III, estimates of SNR^2 greater than or equal to one may be commonly encountered in applications in medical ultrasound. In fact (as will also be seen), the probability density function for the estimate of SNR^2 may be reasonably modeled as a Gaussian centered at the true SNR^2. This Gaussian probability density function often has substantial area in the region of SNR^2 greater than or equal to one. Other approaches for estimation of $\langle N \rangle$ based on the statistical properties of the rf signal or envelope rather than the intensity are also plagued by singularities.[7,10,12]

The probability density function for the estimate of $\langle N \rangle$ may be obtained from the conservation of probability mass:

$$p(N) dN = p(\mathrm{SNR}^2) d\mathrm{SNR}^2. \tag{8}$$

The required derivative may be calculated from Eq. (7) to be $d\mathrm{SNR}^2/dN = 1/(1+N)^2$. The quantity $d\mathrm{SNR}^2/dN$ is also a measure of the sensitivity of SNR^2 to changes in N, which is relatively high for N less than or approximately equal to 1 and diminishes rapidly as N increases.

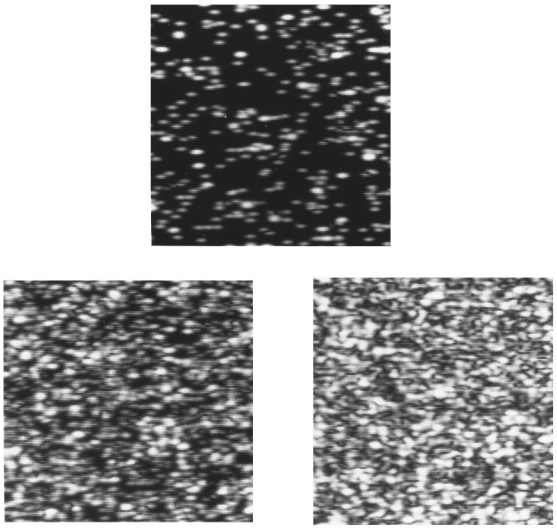

FIG. 1. Sample images generated by computer simulation. The top image corresponds to fewer than 1 scatterer per resolution volume. The lower left and right images correspond to 2 and 6 scatterers per resolution volume, respectively.

II. METHODS

A. Simulation

The theory was first tested using a computer simulation. Scatterers were Poisson distributed throughout a two-dimensional area. A uniform random number generator was used to obtain x and y coordinates for each scatterer. The complex phasor for each scatterer was taken to be $e^{j2\pi x/\lambda}$. The 2-D phasor distribution was then convolved with a 2-D Gaussian in order to simulate blurring by the system point spread function. Sample images are shown in Fig. 1 for three scatterer number densities (<1, 2, and 6).

Using the same simulation program, 4200 scatterers were Poisson distributed throughout a two-dimensional area. The total image area was equal to that of 200 speckle spots so that $N=4200/200=21$. The intensity was taken as the sum of the squares of the real and imaginary parts of the resultant two-dimensional complex function. This process was repeated 500 times. Intensity SNR^2 and N [from Eq. (7)] were estimated for each image. The histogram of values of SNR^2 was fit to a Gaussian. The probability distribution of the estimates of N was computed from this Gaussian using Eq. (8).

B. Single component experiments

In the first set of experiments, empirical distributions of estimates of N and SNR^2 were measured. An ATL Ultramark 8 with a 3.5-MHz annular array transducer was used. Data acquired with this system were digitized (11 bits) at 12 MHz. The -6-dB bandwidth was approximately 1.0 MHz. The resolution volume was approximately 1.2 mm^3.

Four phantoms were interrogated. They consisted of glass beads embedded in agar. The phantoms were constructed with scatterer number densities of 1.0, 2.0, 6.0, and 9.5 mm^{-3}. (With a resolution volume equal to 1.2 mm^3, this led to values of N equal to 1.2, 2.4, 7.2, and 11.4.) The scatterer size ranges were chosen to maintain the average backscatter coefficient approximately the same for all four phantoms. The sound speed for all phantoms was approximately 1556 m/s. The physical characteristics of the phantoms are summarized in Table I. Data were analyzed across regions approximately 1.65 cm deep and 2 cm wide. Differences in attenuation experienced by echoes from scatterers at the near and far edges of the region of interest were sufficiently small to sustain the validity of the equal echo amplitude assumption leading to Eq. (1). (Note: Substantial differences in attenuation across the region of interest would tend to increase estimates of intensity variance relative to the mean, decrease SNR, and deflate estimates of N.)

TABLE I. Physical characteristics for the four phantoms interrogated in the first set of experiments. The phantoms consisted of glass beads embedded in agar. SND (scatterer number density) refers to the number of scatterers per unit volume. N refers to the number of scatterers per system resolution cell of the ATL system at 3.5 MHz (approximately 1.2 mm^3). The sound speed for all phantoms was approximately 1556 m/s. Attenuation coefficients were measured in transmission substitution experiments over the range from 2 to 10 MHz. Power law fits are given in the table.

	Phantom characteristics I			
Phantom	Scatterer size range (μm)	SND (mm^{-3})	N (per res. cell)	Attenuation coefficient (cm^{-1})
A	75–90	9.5	11.4	$0.05f^{1.8}$
B	90–106	6.0	7.2	$0.05f^{1.9}$
C	180–212	2.0	2.4	$0.12f^{1.7}$
D	212–250	1.0	1.2	$0.12f^{1.6}$

Discriminability was assessed by area (A_z) under the receiver operating characteristic (ROC) curve. A_z was computed using the program LABROC developed at the University of Chicago. This program computes the maximum likelihood estimate of a binormal ROC curve and its associated parameters. It assumes that the data follow normal distributions after some (possibly unknown) monotonic transformation.[21]

The trade-off between region of interest (ROI) size and discriminability was investigated. As ROIs become smaller, measurements exhibit higher variability and discriminability decreases. ROI length was maintained at a constant value (1.65 cm) sufficiently long to ensure that estimates of SNR^2 were essentially unbiased. (At smaller gate lengths, less than or equal to about 1 cm, estimates of intensity *mean* remain unbiased but estimates of intensity *variance* become appreciably negatively biased so that estimates of SNR and SNR^2 become positively biased.[22]) ROI size was varied by altering the number of A lines contained within.

C. Multiple component experiments

In a second set of experiments, two single component phantoms, a two-component phantom, and a sample of dog kidney cortex were examined. Previous investigations have indicated that kidney may be modeled as a two-component structure.[22]

Data were acquired from the phantoms in the range from 1.0 to 7.5 MHz using three separate Panametrics transducers (center frequencies: 2.25 MHz, 3.5 MHz, and 5.0 MHz; -6-dB bandwidths: 87%, 89%, 69%; focal lengths: about 55 mm; diameters: 19 mm). A Panametrics 5052UA broadband

TABLE II. Physical characteristics for the four phantoms interrogated in the second set of experiments. The phantoms consisted of glass beads embedded in agar. SND (scatterer number density) refers to the number of scatterers per unit volume. N refers to the number of scatterers per system resolution cell for the three Panametrics transducers (see text). The sound speed for all phantoms was approximately 1534 m/s.

	Phantom characteristics II			
Phantom	Scatterer size range (μm)	SND (mm^{-3})	N (per res. cell 2.25, 3.5, 5.0 MHz)	Attenuation coefficient (cm^{-1})
large, sparse	125–175	0.1	0.2, 0.09, 0.04	$0.031f^{1.72}$
small, dense	40–80	18.7	13.0, 5.4, 2.6	$0.031f^{1.72}$

pulser/receiver and an 8-bit LeCroy TR8828D digitizer (25 MHz) were used.

SNR^2 was computed as a function of frequency. The rf data were filtered in software with a bank of Gaussian bandpass filters (full width half maximum=1.2 MHz) with center frequencies separated by 0.5 MHz. Thus the resolution cell lengths or the effective pulse lengths were determined both by the bandpass characteristics of the transducers and by bandwidths of the filters. SNR^2 was computed for each filtered waveform and the results were plotted as functions of center frequency. Analysis was performed throughout the -20-dB bandwidths of the transducers.

The two-component phantom consisted of a set of large (mostly between 125 μm and 175 μm in diameter) sparse (scatterer number density=0.1 mm^{-3}) scatterers and a set of small (mostly between 40 μm and 80 μm in diameter) dense (scatterer number density=18.7 mm^{-3}) scatterers. For purposes of comparison, two single component phantoms, one containing large sparse scatterers with the sizes and density listed above, and one containing small dense scatterers with the sizes and density listed above, were interrogated. The speed of sound was approximately 1534 m/s and the attenuation coefficient was 0.031 $f^{1.72}$ dB/cm for all three phantoms. The phantom properties are summarized in Table II.

An excised dog kidney was scanned in saline at 19 °C. The tissue data were obtained using a 10-MHz transducer (19-mm diameter, 53-mm focal length). Signals were digitized at 50 MHz. Strips of the renal cortex were cut such that the nephron orientation was well defined. Samples were cast in agar blocks so that they could be interrogated with the ultrasound beam either parallel or perpendicular to the nephron orientation.

III. RESULTS

In Fig. 2, histograms of estimates of SNR^2 (left column) and N (right column) are shown for the simulated data. It can be seen that the histogram for estimates of SNR^2 peaks somewhere just below 1.0. The distribution is sufficiently broad that estimates greater than 1.0 are numerous, leading to physically unrealizable (negative or infinite) estimates for N. The dashed line in the left panel is a Gaussian fit to the histogram. The dashed line in the right panel was obtained using the Gaussian pdf on the left and Eq. (8). The theoretical and experimental forms for the pdf of estimates of N are in very good agreement. The results of χ^2 goodness-of-fit tests are summarized in Table III.

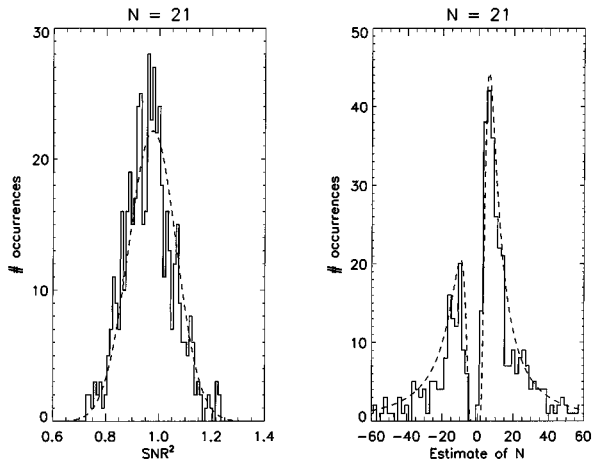

FIG. 2. Histograms of estimates of SNR (left) and N (right) for simulated data. The dashed line in the left panel is a Gaussian fit to the histogram. The dashed line in the right panel was obtained using the Gaussian pdf on the left and Eq. (8).

In Fig. 3, histograms of estimates of SNR^2 (left column) and N (right column) are shown for phantoms with $N=1.2$ (top row) and $N=11.4$ (bottom row). It can be seen that the histograms for estimates of SNR^2 may be reasonably modeled as Gaussians (dashed curves). Therefore, the binormal ROC analysis used to estimate A_z is justified. The dashed curves in the right column of Fig. 3 represent theoretical probability density functions for estimates of N based on the Gaussian fits for the histograms of estimates of SNR^2 and Eq. (7). The histograms for estimates of N are in excellent agreement with the theory presented above. The results of χ^2 goodness-of-fit tests are summarized in Table III.

The means and standard deviations of estimates of N derived from Gaussian fits for histograms SNR^2 were 1.1 ± 0.2, 2.2 ± 0.3, 3.3 ± 0.3, and 3.2 ± 0.3 corresponding to true values for N of 1.2, 2.4, 7.2, and 11.4. Evidently, as N increases and a higher fraction of SNR^2 measurements exceed 1, the task of estimation of N from SNR^2 measurements

TABLE III. Goodness-of-fit tests. Values of $X^2=\Sigma(o_i-e_i)^2/e_i$ (where o_i and e_i are observed and expected frequencies) computed for the empirical histograms. The number of degrees of freedom (the number of bins in histogram minus 3 for amplitude. mean, and standard deviation computed from data) is given in parentheses. The critical value for X^2 at the 0.05 level of significance is given to the right of the slash. In all cases, $X^2<X^2_{0.05}$ and the hypothesis that the observed variables obey the theoretical probability density functions is accepted.[25]

	Goodness-of-fit tests		
Source	N (per res. cell)	SNR^2 X^2(d.o.f.)/$X^2_{0.05}$	N X^2(d.o.f.)/$X^2_{0.05}$
Simulation	21	37.8(36)/51.0	35.0(33)/47.3
Phantom A	11.4	8.9(11)/19.7	13.1(15)/25.0
Phantom B	7.2	15.0(13)/22.4	21.8(16)/26.3
Phantom C	2.4	15.3(11)/19.7	8.8(10)/18.3
Phantom D	1.2	20.4(12)/21.0	11.3(8)/15.5

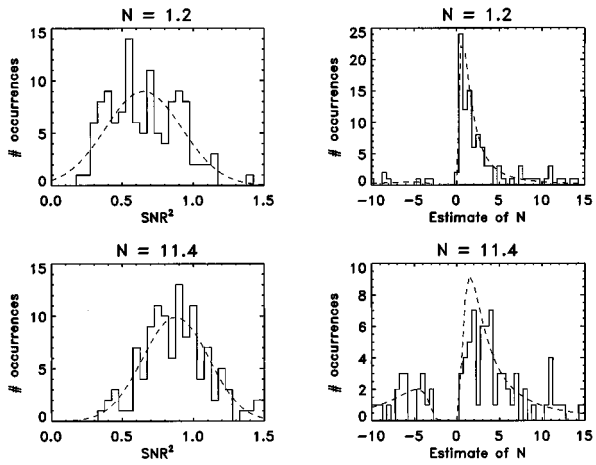

FIG. 3. Histograms of estimates of SNR (left column) and N (right column) for phantom data. $N=1.2$ for the top row and $N=11.4$ for the bottom row. The dashed curves correspond to functional fits to the data.

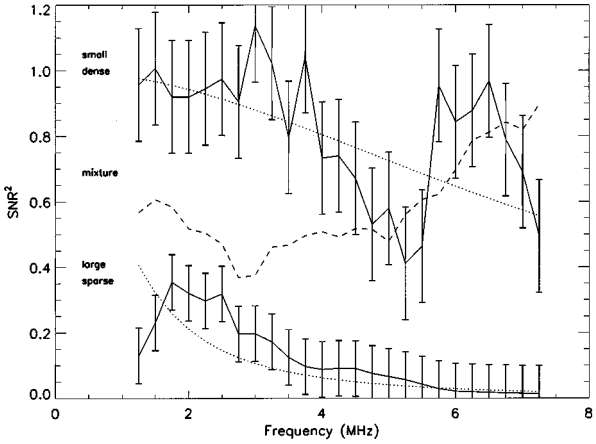

FIG. 5. SNR^2 as a function of frequency for the phantom containing small, dense scatterers (solid line), the phantom containing large, sparse scatterers (solid line), and the phantom containing both sets of scatterers (dashed line). The dotted lines represent functional fits to the data based on the frequency dependence of the resolution volume.

becomes more challenging and performance degrades. (See the discussion at the end of Sec. I.)

Figure 4 shows the area under the ROC curve, A_z, as a function of ROI area. As expected, there is a trade-off between spatial resolution and A_z. The phantoms with $N=7.2$ and $N=11.4$ were essentially undifferentiable, as evidenced by A_z approximately equal to 0.5. These phantoms are easily discriminated from the phantom with $N=1.2$, with A_z approaching 0.9 for the ROI area near 2.5 cm^2. The more subtle differentiation task of $N=1.2$ vs $N=2.4$ yielded A_z near 0.8 for the ROI area near 2.5 cm^2.

In Fig. 5, estimates of SNR^2 are plotted vs frequency for the two-component phantom and the two one-component phantoms. The measurements for the single component phantoms decrease steadily with frequency due to the frequency dependence of the size of the resolution cell. The dotted curves in Fig. 5 represent functional fits to the data of the form $SNR^2=N/(1+N)=1/(1+1/N)=1/(1+Cf^2)$, where C is determined by the scatterer number density (scatterers per unit volume) and the resolution cell size (which is assumed to vary inversely as frequency squared due to the frequency dependence of the transducer diffraction pattern). Recall that N in the expression above corresponds to scatterers per resolution cell, not scatterers per unit volume.

The SNR^2 for the two-component phantom exhibits a more complicated variation with frequency. The differential scattering cross section for the small scatterers increases more rapidly with frequency than that for the large scatterers. Consequently, the small dense scatterers dominate the backscatter at high frequencies. Hence SNR^2 for the mixture attains values comparable to that for the small, dense scattering phantom at high frequencies. At low frequencies, neither component dominates and the SNR^2 is determined by an *effective* number of scatterers per resolution cell which is somewhere in between N_{LS} and $N_{LS}+N_{SD}$ (where the subscript LS refers to large, sparse and the subscript SD refers to small dense).

SNR^2 is plotted as a function of frequency for the excised kidney specimen in Fig. 6. Measurements with ultrasonic beam orientation parallel and perpendicular to the pre-

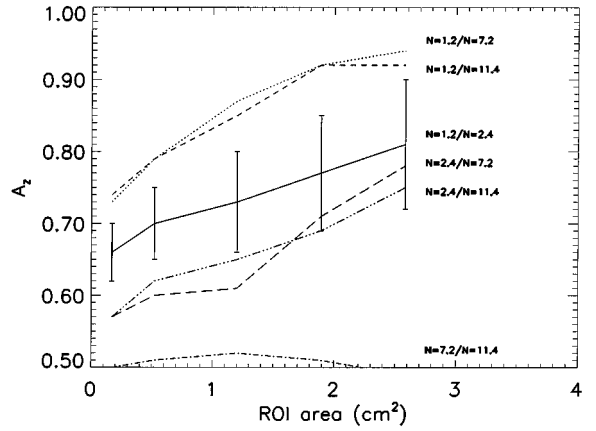

FIG. 4. Area under the ROC curve, A_z, as a function of ROI area for various phantom comparisons. The standard deviations of estimates of A_z for all the cases were similar to those drawn for the $N=1.2/N=2.4$ comparison.

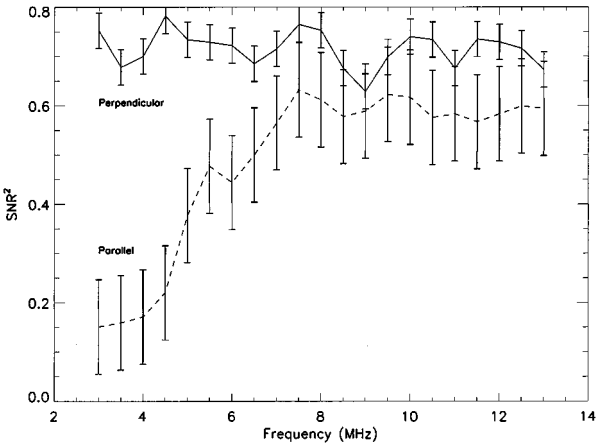

FIG. 6. SNR^2 as a function of frequency for the excised kidney specimen. Orientations both parallel (dashed line) and perpendicular (solid line) to the predominant nephron orientation were investigated.

dominant nephron orientation are shown. Since neither orientation is characterized by a simple $1/(1+Cf^2)$ frequency dependence, neither can be considered a simple single component entity.

IV. DISCUSSION

The number of scatterers per resolution cell (N) (or some related parameter) has been proposed by several authors as a potentially useful candidate for ultrasonic tissue characterization. It may be estimated from the first and second moments of echo intensity. However, because of the odd shape of the probability density function for the estimate of N, in many instances it may be preferable to work with SNR^2. This approach avoids physically unrealizable (negative or infinite) estimates of number of scatterers per resolution cell.

Measurements of SNR^2 are relatively sensitive in the range of N less than or approximately equal to 1 or 2. They may be useful for detection of subtle contractions or expansions of tissues for which N is normally in this range. For larger N, SNR^2 is less likely to be useful for assessing contraction or expansion (as evidenced by the lack of separability of phantoms with densities of 7.2 and 11.4). It may still be useful for detecting lesions which are characterized by a value of N that is dramatically different from that of the embedding tissue. The declining effectiveness of SNR^2 (for estimating number of scatterers per resolution cell) as N increases is consistent with the findings by Wagner *et al.*[11] and Chen *et al.*[15] that the variance of estimates of N increases dramatically as N increases beyond 1. This phenomenon represents a serious limitation to the potential utility of SNR or SNR^2 for tissue characterization. SNR imaging has been employed with a modest degree of success, for characterization of the liver.[26]

Measurements of SNR^2 may be used to investigate media which contain multiple components. Since the relative contributions of the two types of scatterers in the two-component phantom experiment varied with frequency, the *frequency dependence* of SNR^2 was useful. The frequency dependence of SNR^2 in kidney may be compared with published results regarding frequency-dependent measurements of the backscatter coefficient. Previous investigations have suggested that below about 5 MHz, the dominant scattering structure is the glomerulus (approximately 200 μm in size).[23] Above 5 MHz, renal tubules and arterioles dominate. The present data support that view. Glomeruli constitute a sparse distribution of large scatterers. When the beam is parallel to the nephron structure, backscattering from the small structures (tubules and blood vessels) is less. Therefore, below 5 MHz, the large, sparse structures are most apparent and the SNR^2 is low. Increasing frequency increases the SNR^2 as the smaller scatterers begin to dominate backscatter. However, at perpendicular incidence, more of the blood vessels and tubules contribute to the backscatter signal, apparently even at low frequencies. Consequently, the SNR^2 remains near one at all frequencies. This behavior is consistent with previous investigations based on integrated backscatter coefficient (IBC).[23] IBC varies with angle of incidence for the reasons listed above. However, the frequency dependence of backscatter (a signature of scatterer size) seems to be independent of angle.

Finally, the reader should be cautioned that sole reliance on first-order statistical properties such as SNR can lead to ambiguity when the second-order structure is significant. Nonstationarity, due to attenuation, inhomogeneity, or the presence of regularly spaced scatterers will tend to increase estimates of intensity variance relative to the mean, decrease SNR, and deflate estimates of N. Analysis of this case is given in Ref. 24.

ACKNOWLEDGMENTS

The authors wish to thank Tim Hall, University of Kansas, for constructing the phantoms used in this experiment. The authors also wish to thank Charles E. Metz and coworkers at the University of Chicago for providing software for ROC analysis. The mention of commercial products, their sources, or their use in connection with material reported herein is not to be construed as either an actual or implied endorsement of such products by the Food and Drug Administration. Partial support for one of the authors (MFI) was provided by a grant from the National Institutes of Health, RO1 DK43007.

[1] D. Middleton, *An Introduction to Statistical Communication Theory* (McGraw-Hill, New York, 1960), Chap. 9.

[2] J. W. Goodman, ''Statistical properties of laser speckle patterns,'' in *Laser Speckle and Related Phenomena*, edited by J. C. Dainty (Springer-Verlag, Berlin, 1984), pp. 9–75.

[3] C. B. Burckhardt, ''Speckle in ultrasound *B*-mode scans,'' IEEE Trans. Sonics Ultrason. **SU-25**, 1–6 (1978).

[4] R. F. Wagner, S. W. Smith, J. M. Sandrik, and H. Lopez, ''Statistics of speckle in ultrasound *B*-scans,'' IEEE Trans. Sonics Ultrason. **30**, 156–163 (1983).

[5] E. Jakeman, ''Speckle statistics with a small number of scatterers,'' Opt. Eng. **23**, 453–461 (1984).

[6] P. N. Pusey, D. W. Schaefer, and D. E. Koppell, ''Single-interval statistics of light scattered by identical independent scatterers,'' J. Phys. A: Math. Nucl. Gen. **7**, 530–540 (1974).

[7] J. F. Cardoso, ''3-D Ultrasonic speckle modeling: Below the Rayleigh limit,'' SPIE **768**, Int. Symp. Pattern Recog. Acoust. Imag. 207–214 (1987).

[8] P. Wilhelmij and P. Denbigh, ''A statistical approach to determining the number density of random scatterers from backscattered pulses,'' J. Acoust. Soc. Am. **76**, 1810–1818 (1984).

[9] P. Denbigh, Q. Smith, and I. Hampton, ''Determination of fish number density by a statistical analysis of backscattered sound,'' J. Acoust. Soc. Am. **90**, 457–469 (1991).

[10] G. E. Sleefe and P. P. Lele, ''Tissue characterization based on scatterer number density estimation,'' IEEE Trans. Ultrason. Ferroelectr. Freq. Control **35**, 749–757 (1988).

[11] R. F. Wagner, D. G. Brown, K. A. Wear, M. F. Insana, and T. J. Hall, ''Statistical properties of the scatterer number density estimator,'' Ultrason. Imaging **13**, 192 (1991).

[12] V. M. Narayanan, P. M. Shankar, and J. M. Reid, ''Non-Rayleigh statistics of ultrasonic backscattered signals,'' IEEE Trans. Ultrason. Ferroelectr. Freq. Control **41**, 845–852 (1994).

[13] L. Weng, J. M. Reid, P. M. Shankar, and K. Soetanto, ''Ultrasound speckle analysis based on the *K* distribution,'' J. Acoust. Soc. Am. **89**, 2992–2995 (1991).

[14] J.-F. Chen, E. L. Madsen, and J. A. Zagzebski, ''A method for determination of frequency-dependent effective scatterer number density,'' J. Acoust. Soc. Am. **95**, 77–85 (1994).

[15] J.-F. Chen, J. A. Zagzebski, and E. L. Madsen, ''Statistical uncertainty in estimates of an effective scatterer number density for ultrasound,'' J. Acoust. Soc. Am. **96**, 2556–2563 (1994).

[16] J. W. Strutt, later Baron Rayleigh, a.k.a. Lord Rayleigh, *Theory of Sound* (Macmillan, London, 1894).

[17] K. Pearson, *A Mathematical Theory of Random Migration*, Math. Contr.

Theory Evol., XV (Draper Co. Res. Mem., Biometric Ser. 3, London, 1906).
[18] J. C. Kluyver, Konink. Akad. Wetenschap Amsterdam **14**, 341 (1905).
[19] S. Chandrasekhar, ''Stochastic problems in physics and astronomy,'' Rev. Mod. Phys. **15**, 1 (1943).
[20] E. Merzbacher, J. M. Feagin, and T.-H. Wu, ''Superposition of the radiation from *N* independent sources and the problem of random flights,'' Am. J. Phys. **45**, 964–969 (1977).
[21] C. E. Metz, ''ROC methodology in radiologic imaging,'' Invest. Radiol. **21**, 720–733 (1986).
[22] K. A. Wear and R. L. Popp, ''Methods for estimation of statistical properties of envelopes of ultrasonic echoes from myocardium,'' IEEE Trans. Med. Imaging **MI-6**, 281–291 (1987).
[23] M. F. Insana, T. J. Hall, and J. L. Fishback, ''Identifying acoustic scattering sources in normal renal parenchyma from the anisotropy in acoustic properties,'' Ultrasound Med. Biol. **17**, 613–626 (1991).
[24] R. F. Wagner, M. F. Insana, and D. G. Brown, ''Statistical properties of radio-frequency and envelope-detected signals with applications to medical ultrasound,'' J. Opt. Soc. Am. A **4**, 910–922 (1987).
[25] J. S. Bendat and A. G. Piersol, *Random Data: Analysis and Measurement Procedures* (Wiley–Interscience, New York, 1971), Chap. 4, pp. 119–122.
[26] J. T. M. Verhoeven, J. M. Thijssen, and A. G. M. Teeuwes, ''Improvement of Lesion detection by echographic image processing: the signal-to-noise ratio imaging,'' Ultrason. Imag. **13**, 239–251 (1991).

LETTERS TO THE EDITOR

This Letters section is for publishing (a) brief acoustical research or applied acoustical reports, (b) comments on articles or letters previously published in this Journal, and (c) a reply by the article author to criticism by the Letter author in (b). Extensive reports should be submitted as articles, not in a letter series. Letters are peer-reviewed on the same basis as articles, but usually require less review time before acceptance. Letters cannot exceed four printed pages (approximately 3000–4000 words) including figures, tables, references, and a required abstract of about 100 words.

Using acoustic radiation force as a concentration method for erythrocytes

Kenji Yasuda,[a] Stephan Shuichi Haupt, and Shin-ichiro Umemura
Advanced Research Laboratory, Hitachi, Ltd., 2520 Akanuma, Hatoyama, Saitama 350-03, Japan

Toshiki Yagi
Zoological Institute, Faculty of Science, University of Tokyo, Hongo, Tokyo 113, Japan

Masaharu Nishida and Yasuhisa Shibata
Instrument Division, Hitachi, Ltd., 882 Ichige, Hitachinaka, Ibaraki 312, Japan

(Received 20 May 1996; accepted for publication 7 March 1997)

We investigated the potential damage inflicted on erythrocytes by acoustic radiation force when the cells are concentrated by a 500-kHz ultrasonic standing wave at the pressure node. The extent of the damage was estimated from the concentrations of potassium ions, iron complexes, and lactate dehydrogenase released from the cells. After 2 min of ultrasound irradiation at 12.8 mJ/m^3, the cells concentrated on the pressure node, with a cell distribution half-width of 138 μm; no significant release of intracellular components was detected, even after 15 min of irradiation. The results indicate that even small ions like potassium are not released as a result of ultrasound irradiation on cell membranes without cavitation, and they demonstrate the potential use of acoustic radiation force for concentrating living cells in biomedical applications. © *1997 Acoustical Society of America.* [S0001-4966(97)01407-0]

PACS numbers: 43.25.Uv, 43.25.Zx, 43.80.Vj [MAB]

INTRODUCTION

A method for noncontact concentration of erythrocytes in continuous mode could be incorporated in a fully automated analysis system providing contamination-free, real-time measurement. One noncontact force having several advantages for concentrating biomaterials is the ultrasonic radiation force. For example, it can be used to form a hyperbolic potential field with a span of a millimeter order, and has recently been applied for sedimentation of deoxyribonucleic acids (DNA),[1] hybridoma cells,[2,3] and erythrocytes.[4–6]

Early theoretical studies on ultrasonic radiation forces[7,8] pointed out that rigid and compressible spheres in a nonviscous fluid can be trapped in such a field. Feke and his colleagues used ultrasound to fractionate small particles in solution.[9–12] The efficacy of using an ultrasonic standing plane wave to concentrate small particles has been evaluated theoretically and experimentally,[13] and the effect of the Bjerknes attractive force on particles in liquid has been reported.[4] Such a concentration method could be used to separate different materials continuously by exploiting the competition between the acoustic radiation force and other external forces such as gravitational, or electrostatic forces.[5,6,14]

Before ultrasound irradiation finds a practical use in concentration or separation of biomaterials, its effects on them should be evaluated. There are reports that several types of living cells are damaged by ultrasound in the presence of cavitation,[15,16] and the viability of hybridoma cells subjected to ultrasound irradiation in the absence of cavitation has been investigated.[3] Damage to DNA concentrated by acoustic radiation force has also been studied.[1] While hybridoma cells and DNA were not affected by acoustic radiation force, the permeability of cell membranes may be a more suitable indicator of damage for more fragile specimens such as erythrocytes and should be evaluated.

In this paper we therefore investigated the release of intracellular components from erythrocytes subjected to acoustic radiation force.

I. MATERIALS AND METHODS

A. Apparatus and analysis system

The setup consisted of acousto-electronic and optical subsystems (see Fig. 1 in Ref. 13). In brief, the former con-

[a]Corresponding author address: Advanced Research Lab., Hitachi, Ltd. 2520 Akanuma, Hatoyama, Saitama 350-03, Japan; Electronic mail: yasuda@harl.hitachi.co.jp

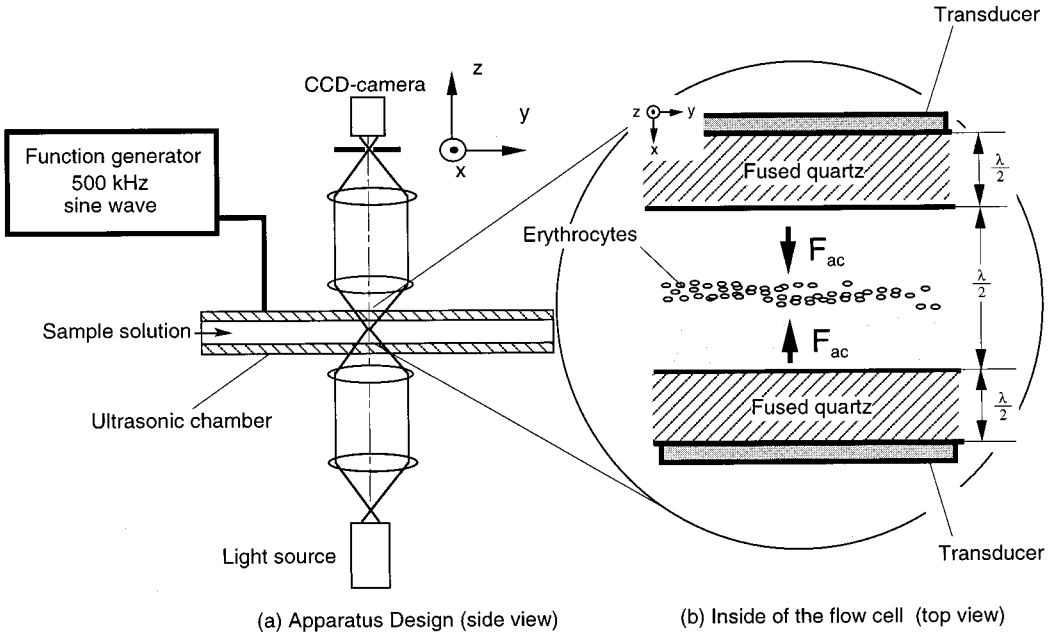

FIG. 1. Schematic diagram of the apparatus for concentration of erythrocytes.

sisted of an ultrasonic chamber (volume, 0.3 ml) with a pair of PZT ceramic transducers driven by a function generator providing a 500-kHz sine wave. An inverted phase-contrast microscope (20× PL obj.) served for optical observation. Images were recorded by a CCD camera and stored by a personal computer with video capture board (see Fig. 1).

B. Samples

We used erythrocytes obtained from guinea pigs. Five ml of blood containing 1%(w/v) heparin were centrifuged at $600\times g$ for 10 min at 4 °C to separate erythrocytes, which were then washed three times in physiological saline [0.9% NaCl, 20-mM Tris-HCl (pH 7.4)] by centrifugation at $3000\times g$ for 20 min at 4 °C. For the sample solutions, the washed erythrocytes were resuspended in physiological saline at a hematocrit of 3.3%.

C. Measurement of content release from erythrocytes under ultrasound application

Sample solutions were introduced into the ultrasonic chamber for ultrasound irradiation. The frequency, 500 kHz, was chosen to match the half-wavelength to the fluid width in the chamber. The amplitude and irradiation duration of ultrasound were adjusted according to the samples.

After ultrasound irradiation the sample solutions were removed from the chamber and the concentration of potassium ions in the sample solution was measured with an ion-selective electrode (6582-10c, Horiba, Ltd.) whereas the total iron concentration in the sample solution was measured by inductively coupled plasma spectroscopy (P-5200 ICP system, Hitachi, Ltd.). The enzymatic activity of lactate dehydrogenase [LDH (140 kDa)] was measured by a UV-rate method, based on oxidation of nicotinamide adenine dinucleotide.

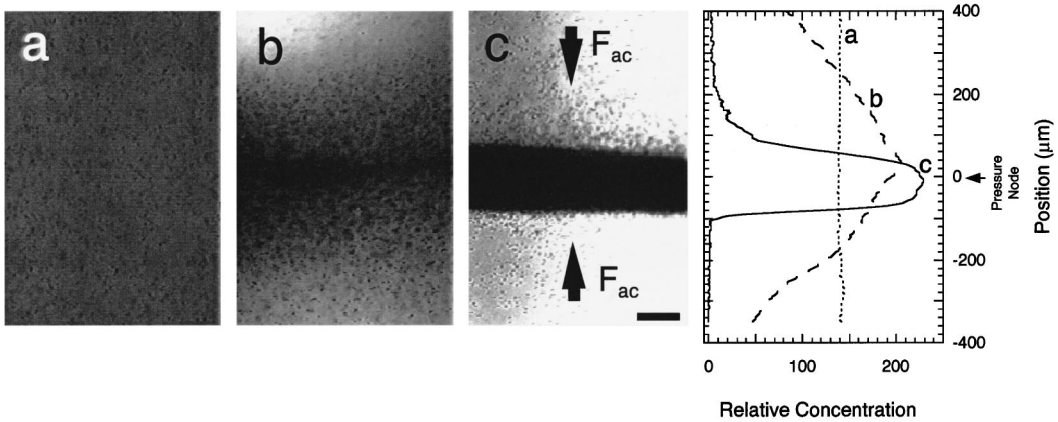

FIG. 2. Micrographs and intensity profiles of time change in the distribution of erythrocytes leading to an equilibrium state. Micrographs: (a) without ultrasonic irradiation; (b) with 12.8-mJ/m^3 ultrasonic irradiation for 1 min; (c) for 2 min. Graph: dashed line indicates the erythrocyte distribution as shown in (a); broken line, (b); and real line, (c); Y axis corresponds to darkness (in arb. units) in micrographs. The intensity profiles are plotted against the distance from the pressure node.

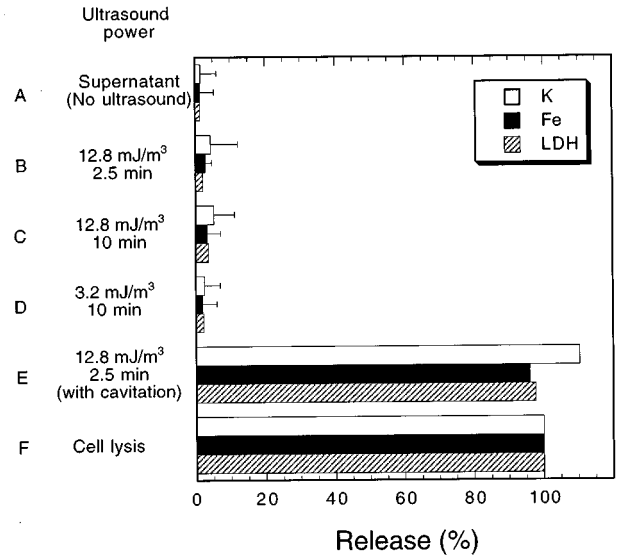

FIG. 3. Summary of the release of potassium ion (K^+), iron (Fe), and LDH. The values are the mean values for three samples. Error bars are the maximum values. The magnitude of ultrasound power was estimated from the halfwidth of the particle distribution.

II. RESULTS AND DISCUSSION

Figure 2 shows the time change in the erythrocyte distribution under the influence of a standing wave in the ultrasonic chamber. Initially cells were dispersed throughout the chamber [Fig. 2(a)]. When irradiated with 180-V_{pp} ultrasound they started migrating toward the pressure node of the ultrasonic standing wave. Figure 2(b) shows the spatial distribution of the cells in the chamber after 1-min ultrasound irradiation, and Fig. 2(c) shows the distribution after 2 min. The half-width of the particle distribution narrowed to 138 μm after 2 min and to 112 μm after 10 min (i.e., 76% of the erythrocytes were concentrated within 112-μm width).

The temperature rise caused by ultrasound irradiation was measured using a K-type thermocouple. After ultrasound irradiation started, the temperature of the sample solutions rose from 20 °C and stabilized at 35 °C within 8 min (data not shown).

The average value of ultrasonic energy density in the ultrasonic chamber was estimated from the half-width of the particle distribution by using Eq. (6) in Ref. 13 [in which the particle distribution was calculated from the balance between diffusion force and acoustic radiation force (see Sec. II A in Ref. 13)]:

$$E_{\mathrm{ac}}=\frac{3k_BT_A\ \ln(2)}{2\pi R^3A(1-\cos(kX_h))}, \tag{1}$$

where

$$A=\frac{5\rho-2\rho'}{2\rho+\rho'}-\frac{\gamma}{\gamma'}. \tag{2}$$

Here E_{ac} is the average acoustic energy density, R is the particle radius, k_B is the Boltzmann constant, T_A is the absolute temperature, ρ is the density of the particles, ρ' is the density of the medium, γ is the compressibility of the particles, γ' is the compressibility of the medium, k is the wave number of the ultrasound, and X_h is the half-width of particle distribution.

For $X_h=112\ \mu$m, $T_A=300$ K, ρ of erythrocytes $=1.099$,[5] and γ of erythrocytes $=3.4\times10^{-11}$ cm^2/dyn,[5] we have $E_{\mathrm{ac}}=12.8$ mJ/m^3 when 180 V_{pp} ultrasound is applied and the cells are idealized as spheres of $R=2.5\ \mu$m.

The release of intracellular components from erythrocytes was monitored under the above ultrasound field. Figure 3 shows the release of potassium ions, iron complex, and LDH into the supernatant of the sample solution (samples A–F). Sample (A) was the supernatant of the sample solution without ultrasound irradiation. Samples (B) and (C) were collected after 2.5 min and 10 min of 12.8-mJ/m^3 ultrasound irradiation, respectively, and (D) after 10 min of 3.2-mJ/m^3 ultrasound irradiation. The results indicate that the extent of release after ultrasound irradiation (samples B–D) was only a small fraction of the values obtained from complete cell lysis (sample F). Even after 15-min ultrasound irradiation, the values remained small percentages (data not shown). We also investigated the effect of cavitation. The cavitation threshold in our experiment estimated by direct observation of cavities, was 12.8 mJ/m^3, and 2.5-min application of 12.8-mJ/m^3 ultrasound, leading to cavitation (sample E) resulted in complete cell lysis.

The small release observed in samples (B)–(D) may be caused by unhealthy cells susceptible to damage by the acoustic pressure. In fact, the influence of acoustic radiation force is observed to be much stronger on the overall sample at the beginning of the irradiation because of the distribution and the nature of the potential field (data not shown). An amplitude modulation could be a remedy to such release.

Several reports on release from liposomes indicate that a rise in temperature affects the release of glucose.[17] Thus the above difference among samples (A)–(D) may be caused by the difference in solution temperatures. In fact, the release increased gradually with the temperature rise during ultrasound irradiation (data not shown).

III. CONCLUSION

The results presented here suggest that acoustic radiation force is effective for concentrating erythrocytes without notable damage under a cavitation-free condition. This method may also be useful for concentrating, collecting, and transporting other compartmented structures from cells to liposomes.

ACKNOWLEDGMENTS

We thank Dr. Hiroyuki Takei, Dr. Kazuo Takeda of Hitachi, Ltd., and Dr. Hideto Mitome of National Industrial Research Institute of Nagoya for their valuable suggestions and discussion, and Dr. Shojiro Asai of Hitachi, Ltd. for his support and continuous encouragement.

[1] K. Yasuda, M. Kiyama, S. Umemura, and K. Takeda, ''DNA concentration using acoustic radiation force,'' J. Acoust. Soc. Am. **99**, 1248–1251 (1996).

[2] F. Trampler, S. A. Sonderhoff, P. W. S. Pui, D. G. Kilbum, and J. M. Piret, ''Acoustic cell filter for high density perfusion culture of hybridoma cells,'' Bio. Technol. **12**, 281–284 (1994).

[3] P. W. S. Pui, F. Trampler, S. A. Sonderhoff, M. Groeschl, D. G. Kilburn, and J. M. Piert, ''Batch and semicontinuous aggregation and sedimentation of hybridoma cells by acoustic resonance fields,'' Biotechnol. Prog. **11**, 146–152 (1995).
[4] M. A. H. Weiser and R. E. Apfel, ''Interparticle forces on red blood cells in a standing wave field,'' Acustica **56**, 114–119 (1984).
[5] M. A. H. Weiser and R. E. Apfel, ''Extension of acoustic levitation to include the study of micro-size particles in a more compressible host liquid,'' J. Acoust. Soc. Am. **71**, 1261–1268 (1982).
[6] R. E. Apfel, ''Acoustic radiation pressure-principles and application to separation science,'' Proceedings of the DAGA Conference, pp. 19 ff (1990).
[7] L. V. King, ''On the acoustic radiation pressure on circular discs: Inertia and diffraction corrections,'' Proc. R. Soc. London, Ser. A **153**, 1–16 (1936).
[8] K. Yoshioka and Y. Kawashima, ''Acoustic radiation pressure on a compressible sphere,'' Acustica **5**, 167–173 (1955).
[9] T. L. Tolt and D. L. Feke, ''Separation devices based on forced coincidence response of fluid-filled pipes,'' J. Acoust. Soc. Am. **91**, 3152–3156 (1992).
[10] Z. I. Mandralis and D. L. Feke, ''Fractionation of suspensions using synchronized ultrasonic and flow fields,'' AIChE. J. **39**, 197–206 (1993).
[11] T. L. Tolt and D. L. Feke, ''Separation of dispersed phases from liquids in acoustically driven chambers,'' Chem. Eng. Sci. **48**, 527–540 (1993).
[12] Z. Mandralis, W. Bolek, W. Burger, E. Benes, and D. L. Feke, ''Enhanced synchronized ultrasonic and flowfield fractionation of suspensions,'' Ultrasonics **32**, 113–121 (1994).
[13] K. Yasuda, S. Umemura, and K. Takeda, ''Concentration and fractionation of small particles in liquid by ultrasound,'' Jpn. J. Appl. Phys. **34**, 2715–2720 (1995).
[14] K. Yasuda, S. Umemura, and K. Takeda, ''Particle separation using acoustic radiation force and electrostatic force,'' J. Acoust. Soc. Am. **99**, 1965–1970 (1996).
[15] D. E. Hughes and W. L. Nyborg, ''Cell disruption by ultrasound,'' Science **138**, 108–114 (1962).
[16] C. C. Church, H. G. Flynn, M. W. Miller, and P. G. Sacks, ''The exposure vessel as a factor in ultrasonically-induced mammalian cell lysis-II. An explanation of the need to rotate exposure tubes,'' Ultrasound Med. Biol. **8**, 299–309 (1982).
[17] K. Fukuzawa, H. Ikeno, A. Tokumura, and H. Tsukatani, ''Effect of α-tocopherol incorporation on glucose permeability and phase transition of lecithin liposomes,'' Chem. Phys. Lipids **23**, 13–22 (1979).

Use of the fast field program for predicting diffraction of sound by curved surfaces

James P. Chambers and Richard Raspet
National Center for Physical Acoustics, University of Mississippi, University, Mississippi 38677

Yves H. Berthelot
George W. Woodruff School of Mechanical Engineering, Georgia Institute of Technology, Atlanta, Georgia 30332

Michael J. White[a)]
U.S. Army Construction Engineering Research Laboratory, P.O. Box 9005, Champaign, Illinois 61826-9005

(Received 10 June 1996; revised 26 March 1997; accepted 27 March 1997)

The fast field program (FFP) is a powerful tool for solving outdoor sound propagation problems in stratified atmospheres. It is shown here to be equally powerful for solving for the propagation of sound over curved surfaces of finite impedance. Results from scale model experiments are in excellent agreement with the FFP calculation in the deep shadow, penumbra, and bright zone behind the surface. The results are also compared with Berry and Daigle's creeping wave series [J. Acoust. Soc. Am. **83**, 2047–2058 (1988)]. The FFP calculation and creeping wave series yield identical results in the deep shadow. In the penumbra and bright zone behind the curved surface the FFP is in slightly better agreement with the data than the creeping wave series, although the differences are typically 1 dB or less which is comparable to the experimental error. The improvement is due to the more accurate sound speed profile and coordinate mapping used rather than to any differences in the computational method. [S0001-4966(97)05207-7]

PACS numbers: 43.28.Fp, 43.20.Fn [LCS]

INTRODUCTION

It has been previously shown[1,2] that the FFP method is a useful tool to solve propagation problems in stratified atmospheres with complex boundary conditions. Simply put, the FFP method solves for the pressure using the Fourier–Bessel transform

$$p(r,z)=\frac{1}{2\pi}\int_0^\infty \hat{p}(z,z_s;k)J_0(kr)k\,dk, \tag{1}$$

the solution to which can be found in the above named references. In Eq. (1), z_s and z are the source and receiver heights, r is the horizontal distance, $\hat{p}$ is the height-dependent pressure, and k is the acoustic wave number in air. It has been shown that the diffraction of sound by a right circular cylinder with radius R_0 can be modeled[3] as propagation over a flat surface with an upward refracting sound speed profile given by $c=c_0e^{-z/R_0}$. Thus it is a logical extension to solve for the diffraction by the curved surface as refraction by a stratified atmosphere. The geometry of the diffraction problem is given in Fig. 1. The original coordinates for the problem are given in Fig. 1(a) as x and y. To use Eq. (1) these coordinates are transformed into the r,z coordinates of Fig. 1(b) as

$$r=R_0[\phi_0-\tan^{-1}(y/x)], \tag{2}$$

$$z=R_0\ \ln\left(\frac{\sqrt{x^2+y^2}}{R_0}\right). \tag{3}$$

Alternately, the diffraction problem can be solved using the creeping wave series of Berry and Daigle.[4] The creeping wave series was amended (empirically) by Berthelot[5] who defined the source–receiver distance as the shortest path between the two that does not intersect the surface rather than as the projected arc length along the surface. This modification has been incorporated in the present work. The creeping wave series assumes a sound-speed profile of the form

$$c(z)=\frac{c_0}{\sqrt{1+2z/R_0}}\approx c_0\left[1-\frac{z}{R_0}+\frac{3}{2}\frac{z^2}{{R_0}^2}\cdots\right], \tag{4}$$

which compares to

$$c(z)=c_0e^{-z/R_0}\approx c_0\left[1-\frac{z}{R_0}+\frac{1}{2}\frac{z^2}{{R_0}^2}\cdots\right] \tag{5}$$

for the exponential profile used in the FFP method. The power series expansion demonstrates that the two sound speeds are identical to first order in z/R_0 and should give identical results for the large radii of curvature typically found in outdoor sound problems. For the diffraction problem examined here, higher-order terms may affect the propagation. Near the surface in the deep shadow, the two solutions should show the closest agreement since the sound-speed profiles are nearly the same. However, as the source or receiver are removed from the surface, the solutions should diverge slightly as the assumed sound speed profiles differ. For the diffraction problem examined here, the radius of curvature, R_0, is 2.5 m so that for a receiver height of 0.35 m

[a)]Present address: Applied Research Associates, 5941 S. Middle Field Rd., Suite 100, Littleton, CO 80123.

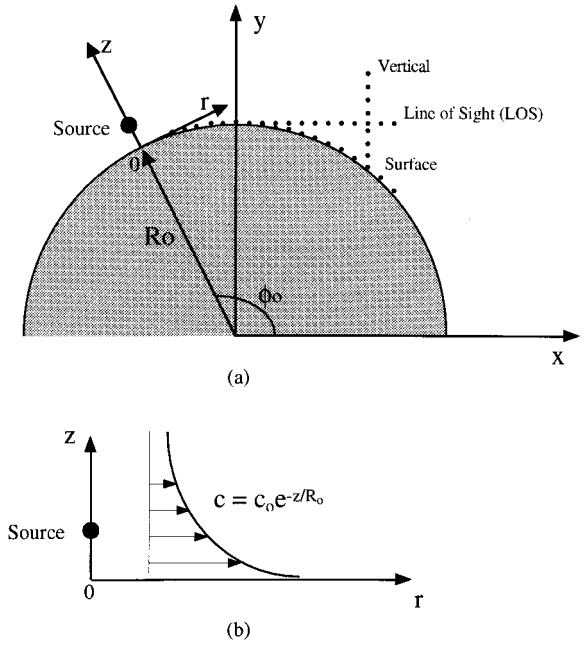

FIG. 1. Geometry of (a) original problem and (b) transformed problem.

the sound speed used in the creeping wave series is 1.7% greater than the sound speed used in the FFP method. At a height of 1.0 m the difference is 11%. The higher sound speeds calculated by Eq. (4) translate into a smaller sound-speed gradient which has the effect of decreasing insertion losses.

I. EXPERIMENT

Scale model experiments were conducted indoors. The diffracting surface was a section of plywood bent with a radius of curvature of 2.5 m. The source was located at the same vertical height y and 1.12 m away from the apex of the curved surface as illustrated in Fig. 1(a). The calculations are also compared to previously reported data on a carpet covered surface taken by Berthelot and Zhou.[6] For these measurements the diffracting surface described above was covered with a thin layer of industrial carpet. For the carpeted surface the source was 1.22 m away from the apex.

The Delany–Bazley relations[7] were used to estimate the surface impedance of both the bare plywood surface and of the carpeted surface.[8] For the bare plywood surface a flow resistivity of $\sigma = 75 \times 10^6$ N s m^{-4} was obtained while for the carpet covered surface a flow resistivity of $\sigma = 1.6 \times 10^6$ N s m^{-4} was obtained.

A. Rigid surface

Pressure measurements were taken along the surface, along the limiting ray or line of sight, and along a vertical line that crossed from the shadow through the penumbra and into the bright zone. These measurement locations are indicated in Fig. 1(a). The quantity of interest is the insertion loss, IL, which is, in decibels, the difference between the sound pressure level in a free field and the sound-pressure

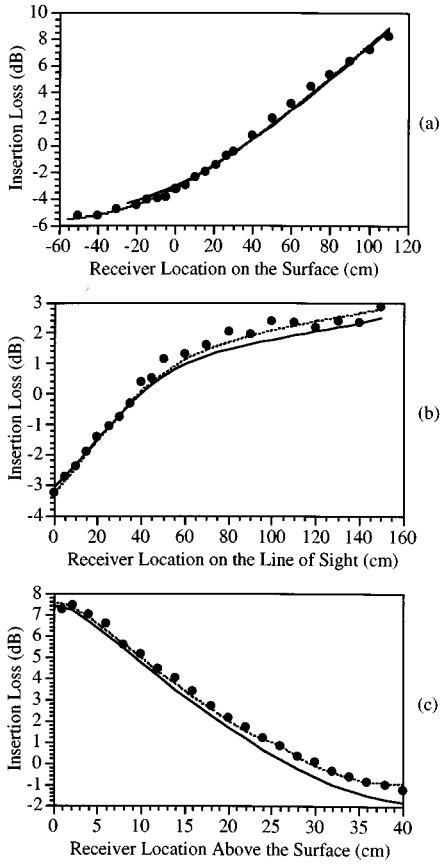

FIG. 2. Insertion loss in the vicinity of the plywood surface for the creeping wave series (—), FFP (---), and experimental data (●). The insertion loss is presented at 5 kHz as a function of distance (a) along the surface, (b) along the line of sight, and (c) above the surface along a vertical line. The ordinate has been auto scaled to show better resolution of the insertion loss.

level in the presence of the curved surface at the same location. Figure 2(a) shows the insertion loss as a function of distance along the surface at a frequency of 5 kHz. The apex is located at 0 cm. Negative values of distance indicate that the receiver is on the side of the surface that faces the source while positive values of distance indicate that the receiver is on the shadow side of the surface. The agreement between both calculations and the data is excellent.

Figure 2(b) shows the insertion loss along the line of sight or limiting ray as a function of distance away from the source where 0 cm represents the apex of the curved surface. The agreement between the FFP and the data is excellent. The creeping wave series predicts slightly lower insertion losses than the FFP although the difference is less than 1 dB. Without the correction by Berthelot,[5] the insertion loss predicted by the creeping wave series would be substantially lower for the given geometry.

Figure 2(c) shows the insertion loss along a vertical line that crosses the shadow and bright zones. The receiver begins in the shadow zone on the surface at an arc distance of 1.0 m from the apex. The receiver location proceeds vertically until it crosses the line of sight at a height of 20 cm and continues into the bright zone to a height of 40 cm. The

agreement between the FFP and the experimental data are once again excellent at all receiver locations. Near the surface at 0 cm, the FFP and the creeping wave series agree quite closely as they did in Fig. 2(a). In the bright zone at 40 cm, the creeping wave series under predicts the insertion loss by about 1 dB.

The improvement found using the FFP formulation is due to two factors related to the problem formulation: (1) the assumed sound-speed profile and (2) the mapping from x, y to r, z. While the coordinate mapping and the sound speed profile *are* physically linked, they do not have to be in a numerical implementation. For the insertion loss shown in Fig. 2(c) we compared the solutions from: (1) Berry and Daigle's original creeping wave series,[4] (2) the same creeping wave series with the empirical correction to the mapping given by Berthelot,[5] (3) the FFP method using the exponential sound-speed profile and coordinate mapping presented earlier [Eqs. (2), (3), and (5)], and (4) the same FFP method utilizing the quasi-linear profile [Eq. (4)] but keeping the exponential mapping from x, y to r, z for the source and receiver [Eqs. (2) and (3)]. Numbers 2 and 3 are currently shown in the manuscript. We found that the original creeping wave series (not shown) under predicted the insertion loss by about 2 dB which is consistent with Berry and Daigle's original work. The amended creeping wave series provides an improved result and under predicts the data by up to 1 dB. The FFP method presented provides the best agreement with the data. The FFP method with the quasilinear profile was better than the original creeping wave series but not as good as the amended one. Therefore, the exponential sound-speed profile is responsible for some improvement and the mapping is responsible for the rest. Thus the exponential sound-speed profile and its attendant mapping, which are an exact transform, provide the best result. The problem happens to be solved with the FFP method in this paper but could have just as easily been solved with some other numerical method such as a Parabolic Equation (PE) method.[3] The creeping wave series, as posed, is constrained to the use of the quasilinear profile in Eq. (4). It may be possible to reformulate an analytic solution using the exponential profile in Eq. (5) whose solution would be based on functions other than the Airy functions found in the creeping wave series. This procedure will be left to future work.

B. Finite impedance surface

Next the FFP was applied to previously reported data on a carpet-covered barrier.[6] In this experiment, data were recorded along the surface and the line of sight.

Figure 3(a) shows the insertion loss along the surface of the carpeted barrier. The insertion loss above this barrier is considerably higher than above the plywood barrier, as expected due to absorption by the carpet. Once again there is quite good agreement between both calculations and the experimental data.

Figure 3(b) illustrates the insertion loss along the line of sight behind the carpeted surface. Both calculations yield good agreement with the experimental data although the creeping wave series appears to be diverging from the data at the furthest distance examined in this data set.

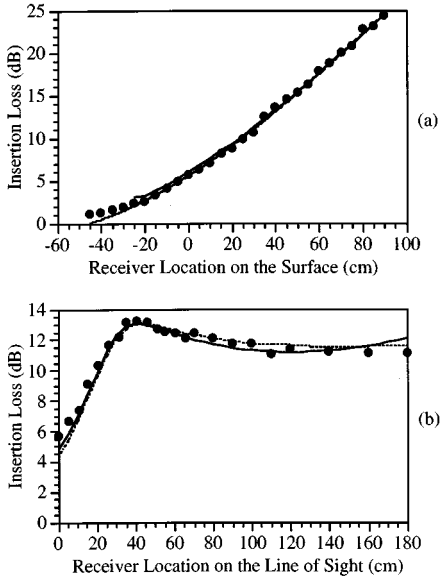

FIG. 3. Insertion loss in the vicinity of the carpeted surface for the creeping wave series (—), FFP (---), and experimental data (●). The insertion loss is presented at 10 kHz as a function of distance (a) along the surface and (b) along the line of sight. The ordinate has been auto scaled to show better resolution of the insertion loss.

II. CONCLUSIONS

The FFP method accurately predicts the sound field in the vicinity of a curved surface. In the deep shadow there is virtually no difference between the predictions from the FFP and the creeping wave series. At receiver locations away from the surface, the FFP yields slightly better agreement with observed data but the differences are typically 1 dB or less. The improvement is due to the more accurate sound-speed profile and coordinate mapping used. The sound-speed profiles examined here contain extremely large gradients in sound speed with respect to height when compared to those found in naturally occurring wind and temperature profiles outdoors. Thus the observed differences in the calculations would be negligible for naturally occurring refraction but the differences could be significant for barrier analysis. The FFP will be used in the future to investigate the effects of turbulence on barrier insertion loss.[9]

ACKNOWLEDGMENTS

The first author was supported by a Hertz Fellowship from the Fannie and John Hertz Foundation when a portion of this work was performed. The authors would also like to thank Lou Sutherland for his insightful comments.

[1] S. W. Lee, N. Bong, W. F. Richards, and R. Raspet, ''Impedance formulation of the fast field program for acoustic wave propagation in the atmosphere,'' J. Acoust. Soc. Am. **79**, 628–634 (1986).

[2] Y. L. Li and M. J. White, ''A note on using the fast field program,'' J. Acoust. Soc. Am. **95**, 3100–3102 (1994).

[3] X. Di and K. E. Gilbert, ''The effect of turbulence and irregular terrain on outdoor sound propagation,'' in *Proceedings of Sixth International Symposium on Long-Range Sound Propagation* (National Research Council, Ottawa, Canada, 1994), pp. 315–333.

[4] A. Berry and G. A. Daigle, ''Controlled experiments on the diffraction of sound by a curved surface,'' J. Acoust. Soc. Am. **83**, 2047–2058 (1988).

[5] Y. H. Berthelot, ''A note on the acoustic penumbra behind a curved surface,'' J. Acoust. Soc. Am. **99**, 2428–2429 (1996).
[6] Y. H. Berthelot and J. Zhou, ''Scale model experiments on the validity of the matched asymptotic expansions theory for sound diffraction by curved surfaces of finite impedance,'' J. Acoust. Soc. Am. **93**, 605–608 (1992).
[7] M. Delany and E. Bazley, ''Acoustical properties of fibrous materials,'' Appl. Acoust. **3**, 105–116 (1970).
[8] T. F. W. Embleton, J. E. Piercy, and G. A. Daigle, ''Effective flow resistivity of ground surfaces determined by acoustical measurements,'' J. Acoust. Soc. Am. **74**, 1239–1244 (1983).
[9] R. Raspet and W. Wu, ''Calculation of average turbulence effects on sound propagation based on the fast field program formulation,'' J. Acoust. Soc. Am. **97**, 147–153 (1985).

Variation of measured nitrogen sound speed with temperature and pressure

George S. K. Wong and Lixue Wu
Institute for National Measurement Standards, National Research Council, Ottawa, Ontario K1A 0R6, Canada

(Received 29 August 1996; accepted for publication 24 March 1997)

Based on nitrogen sound speeds measured by Younglove and McCarty in 1980 [J. Chem. Thermodynam. **12**, 1121–1128 (1980)], a multicolumn coefficient fitting method is used to derive an empirical equation for the computation of sound speed at temperatures from 150 to 330 K and pressures from 0.028 75 to 1.506 85 MPa. The maximum deviation between the measured sound speeds and those computed with the empirical equation is less than 380 ppm. [S0001-4966(97)03507-8]

PACS numbers: 43.58.Dj [SLE]

LIST OF SYMBOLS

$c(T,P)$ nitrogen sound speed as a function of temperature and pressure, m/s
$c(T_i)$ sound speeds as functions of temperatures T_i, m/s
P pressure, MPa
T_i thermodynamic temperatures $= 273.15 + t$, kelvin
$I = 1,2,3,\ldots$
$t(68)$ temperature (based on International Temperature Scale of 1968, ITS-68), degrees Celsius
$t(90)$ temperature (based on ITS-90), degrees Celsius
$T(68)$ temperature (based on ITS-68), kelvin
$T(90)$ temperature (based on ITS-90), kelvin
t temperature, degrees Celsius

Pressure coefficients:

$$A_0, A_1, A_2, ..., A_n;\ B_0, B_1, B_2, ..., B_n;$$
$$C_0, C_1, C_2, \ldots, C_n;\ D_0, D_1, D_2, \ldots, D_n$$

Temperature coefficients:

$$A, B, C, D;\ a_0 \cdots a_3;\ b_0 \cdots b_3;\ c_0 \cdots c_3;$$
$$d_0 \cdots d_3$$

INTRODUCTION

Sound speeds for gaseous nitrogen measured at temperatures from 80 to 350 K over a pressure range from 0.028 75 to 1.506 85 MPa were published.[1] The variations of the measured sound speeds with pressure for 16 temperature groups are shown in Fig. 1. The temperatures shown are based on $T(68)$ that has been redefined[2] in 1990. It is relatively difficult to obtain nitrogen sound speeds at other pressures and temperatures that do not coincide with those measured above. The aim here is to apply a multicolumn coefficient two-dimensional fitting procedure (for three parameters) that is based on curve fitting algorithm of Nelder and Mead[3] to the measured data, to derive an empirical equation that enables one to compute nitrogen sound speeds as functions of pressure and $T(90)$ temperature over a selected temperature range from 150 to 330 K.

I. THEORY OF MULTICOLUMN COEFFICIENT CURVE FITTING PROCEDURE

Sound speed c as a function of pressure P and temperature T is shown schematically in Fig. 2. At a particular temperature T_0, the sound speed is represented by

$$c(T_0) = A_0 + B_0 P + C_0 P^2 + D_0 P^3 + \cdots , \tag{1}$$

where A_0, B_0, C_0, and D_0 are pressure coefficients obtained by applying least-squares fit to data available for sound speeds at various pressures measured at temperature T_0. Similarly, equations can be obtained for sound speeds at other temperatures T_i:

$$c(T_i) = A_i + B_i P + C_i P^2 + D_i P^3 + \cdots , \tag{2}$$

where $i = 1,2,3,\ldots$.

By applying least-squares fit to the above column coefficients: A_0 and A_i; B_0 and B_i; C_0 and C_i; and D_0 and D_i, at temperatures T_0 and T_i, respectively, the following equations are obtained for temperature coefficients A, B, C, and D:

$$A = a_0 + a_1 T + a_2 T^2 + a_3 T^3 + \cdots , \tag{3}$$

$$B = b_0 + b_1 T + b_2 T^2 + b_3 T^3 + \cdots , \tag{4}$$

$$C = c_0 + c_1 T + c_2 T^2 + c_3 T^3 + \cdots , \tag{5}$$

$$D = d_0 + d_1 T + d_2 T^2 + d_3 T^3 + \cdots , \tag{6}$$

where $a_0, a_1, \ldots, a_n$; $b_0, b_1, \ldots, b_n$; $c_0, c_1, \ldots, c_n$; and $d_0, d_1, \ldots, d_n$ are temperature coefficients.

The final equation for sound speed as functions of T and P is

$$c(T,P) = A + BP + CP^2 + DP^3 + \cdots . \tag{7}$$

II. IMPLEMENTATION

The ten selected temperatures; 150, 170, 190, 210, 230, 250, 270, 290, 310, and 330 K (see Fig. 1), were converted to $t(90)$ temperatures with the eighth-order polynomial formula[2] published by the Bureau International des Poids et

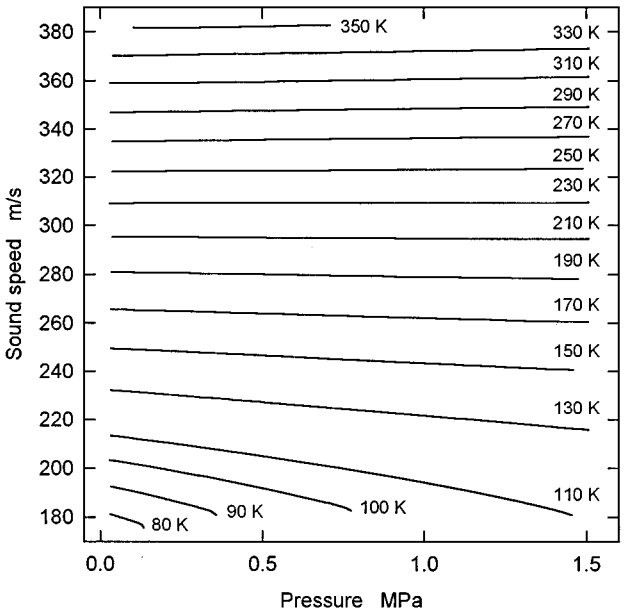

FIG. 1. Sound speeds measured by Younglove and McCarty (Ref. 1) over a pressure range from 0.028 75 to 1.506 85 MPa at various kelvin temperatures.

Measures [the relevant formula is Eq. (1.3) on p. 17 of the BIPM document]. For the above temperature conversion from $T(68)$ to $T(90)$, the maximum difference in temperature is less than 0.015 K. By applying the above multicolumn coefficient fit method (order 4) to the nitrogen sound speeds $c(T=150), c(T=170), \ldots, c(T=330)$ measured by Younglove and McCarty[1] at pressures from 0.028 75 to 1.506 85, a set of coefficients was obtained. These coefficients then served as the initial set of coefficients in the simplex search algorithm of Neder and Mead[3] to minimize the maximum deviation between the calculated sound speeds and the measured values. The final set of coefficients is given in the following empirical equation for the measured nitrogen sound speed:

$$c(T,P)=(a_0+a_1T+a_2T^2+a_3T^3+a_4T^4)+(b_0+b_1T+b_2T^2+b_3T^3+b_4T^4)P+(c_0+c_1T+c_2T^2+c_3T^3+c_4T^4)P^2+(d_0+d_1T+d_2T^2+d_3T^3+d_4T^4)P^3. \quad (8)$$

Numerical coefficients such as A, B, C, and D in Eqs. (3)–(6) for implementation of Eq. (8) are listed in Table I.

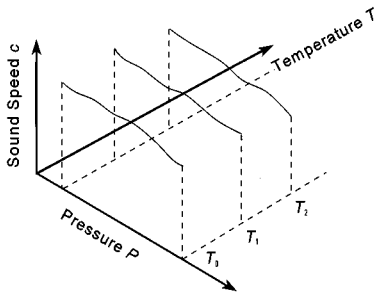

FIG. 2. Sound speed as a function of pressure and temperature.

TABLE I. Coefficients of the polynomial for calculating the measured sound speed in nitrogen.

Suffix x	Coefficients a_x	b_x
0	7.498807E+1	−4.995914E+1
1	1.637500E+0	4.304042E−1
2	−4.255792E−3	−7.509721E−4
3	8.418188E−6	−1.755359E−6
4	−7.103148E−9	4.620853E−9

Suffix x	Coefficients c_x	d_x
0	−3.471191E+1	3.674089E+0
1	7.230239E−1	−1.170882E−1
2	−5.529711E−3	1.172667E−3
3	1.784546E−5	−4.439198E−6
4	−2.050775E−8	5.642919E−9

By substituting pressures in MPa and $T(90)$ temperatures in kelvin into Eq. (8), the maximum deviation between the calculated sound speeds and the measured values[1] is less than 380 ppm. If all of the 16 temperature groups shown in Fig. 1 (i.e., 80–350 K instead of just 150–330 K) were selected, the corresponding maximum deviation is slightly more than 1000 ppm. At 1 atm, the theoretical nitrogen sound speeds calculated with known virial coefficients is in agreement with the measured nitrogen sound speeds[1] to approximately 600 ppm over the temperature range from − 3 °C to 50 °C.

It is interesting to note that over a temperature range from −10 to 40 °C, for a pressure change from 90 to 110 kPa, the maximum variation in nitrogen sound speed is less than 100 ppm (or approximately ±50 ppm from standard pressure). Since the above temperature range and pressure variations encompass a majority of environmental conditions for acoustical measurements in air that contains over 78% nitrogen, the effects of barometric pressure variations on the sound speed in air may be ignored.

III. CONCLUSIONS

Based on published experimental data[1] on the sound speed of gaseous nitrogen, an empirical equation is obtained to enable calculation of nitrogen sound speed based on measurement in terms of temperature over a temperature range from 150 to 330 K and pressure over a pressure range from 0.028 75 to 1.506 85 MPa. The uncertainty of the measured data is quoted[1] as 300 ppm. When the empirical equation is applied over the above temperature and pressure ranges, the maximum deviation of the computed sound speed from the measured data is less than 380 ppm.

[1] B. A. Younglove and R. D. McCarty, ''Speed-of-sound measurements for nitrogen gas at temperatures from 80 to 350 K and pressures to 1.5 MPa,'' J. Chem. Thermodynam. **12**, 1121–1128 (1980).

[2] *Supplementary Information for the International Temperature Scale of 1990*, edited by H. Preston-Thomas and T. J. Quinn (Bureau International des Poids et Mesures Sèvres, France, 1990); see also H. Preston-Thomas, ''The International Temperature Scale of 1990 (ITS-90),'' Metrologia **27**, 3–10 (1990).

[3] J. A. Nelder and R. Mead, ''A simplex method for function minimization,'' Comput. J. **7**, 308–313 (1965). See also, W. H. Press *et al.*, *Numerical Recipes* (Cambridge U. P., Cambridge, 1989).

Fractal dimension of sustained vowel productions in neurological dysphonias: An acoustic and electroglottographic analysis

Ingo Hertrich[a)]
Department of Neurology, University of Tübingen, D-72076 Tübingen, Germany

Werner Lutzenberger
Institut of Medical Psychology and Behavioral Neurobiology, University of Tübingen, D-72076 Tübingen, Germany

Sybille Spieker and Hermann Ackermann
Department of Neurology, University of Tübingen, D-72076 Tübingen, Germany

(Received 22 October 1996; accepted for publication 24 February 1997)

In order to investigate whether nonlinear methods of signal analysis provide a measure of phonatory irregularities in neurogenic voice disorders, the present study computed the fractal dimension (D) both of the electroglottographic (EGG) and the acoustic signal of sustained vowel productions obtained from patients with Parkinson's disease (PD) and cerebellar atrophy (CA). Compared with normal speakers, the female PD group as well as the male and female CA patients showed an increased dimension (D) of the EGG. The dimensional complexity of the acoustic signal largely depended on vowel type. Furthermore, the dimension of the acoustic signal was reduced in male PD patients as compared to the respective controls. © *1997 Acoustical Society of America.* [S0001-4966(97)04206-9]

PACS numbers: 43.70.Aj, 43.70.Dn, 43.70.Gr, 43.25.Rq [AL]

INTRODUCTION

Neurological dysphonias may give rise to rather abrupt changes of the spectral characteristics of the acoustic or electroglottographic (EGG) signal (Ramig, 1986; Hertrich and Ackermann, 1995a,b). Prevailing perturbation measures fail to provide a reliable quantitative account of these phenomena. First, sudden spectral shifts impede accurate pitch extraction which is a prerequisite to the computation of conventional voice parameters such as jitter, shimmer, and harmonics-to-noise ratio. Second, most perturbation measures suggest acoustic instabilities to reflect random alterations of an underlying periodic signal (Laver *et al.*, 1992). Nonlinear methods of signal analysis indicate, however, that this assumption might not hold true (Herzel and Wendler, 1991; Herzel *et al.*, 1995; Mende *et al.*, 1990).

The computed fractal dimension of a signal can be considered a quantitative estimate of its complexity (Narayanan and Alwan, 1995). Besides perturbation measures, nonlinear analysis, thus, may represent an alternative approach to the analysis of voice abnormalities. Using an algorithm developed for the estimation of the dimensional complexity of electroencephalographic signals (Lutzenberger *et al.*, 1995), the present study re-analyzed a corpus of voice recordings obtained in patients with Parkinson's disease or cerebellar atrophy (Hertrich and Ackermann, 1995a,b). Based on the results of these former studies, female Parkinsonian patients were expected to show a particularly high dimensionality of their laryngeal vibratory behavior.

In order to assess both the behavior of the laryngeal source as well as the effects of vocal tract filtering, the EGG and the acoustic signal of six different vowel categories were considered. For the sake of applicability of the algorithm, the present study assumed, irrespective of the nature of the actual voice signal, ''stationarity'' within vowel portions of a duration of 0.4 s. Thus voice instabilities within the analyzed signal portions increase dimensional complexity, whereas discontinuities between these signal portions should give rise to increased intrasubject variability.

I. METHODS

The present study included patients with Parkinson's disease (PD, 15 males, 9 females), cerebellar atrophy (CA, 5 males, 7 females), and a group of healthy volunteers (NC, 12 males, 13 females) (see Hertrich and Ackermann, 1995a,b). Both the EGG and the acoustic signal were simultaneously recorded in a sound-treated room onto a DAT recorder (PCM 2000; Sony) using a laryngograph (KAY Elemetrics) and a head-mounted microphone (C410/B; AKG). Subjects were asked to produce three repetitions of six German vowels for a duration of about 4 s each (order of stimulus presentation: [u,a,i,o,y,ɛ,o,i,ɛ,u,a,y,ɛ,u,i,a,y,o]). Using commercially available software (CSL 4300; KAY Elemetrics), the recorded signals were sampled at 5 kHz after anti-aliasing filtering. Computation of fractal dimension relied on 2-s intervals starting about 0.5 s after vowel onset.

The mathematical procedure used for the calculation of fractal dimensions has been described by Lutzenberger *et al.* (1995). The 2-s intervals of the acoustic and EGG signals were subdivided into seven overlapping segments of $N_0 = 2048$ samples each. In order to eliminate low-intensity random noise, a singular value decomposition was performed, based on a 32-dimensional parameter space of delay coordi-

a)Electronic mail: ingo.hertrich@uni-tuebingen.de

nates. The variance corresponding to all principal components with eigenvalues lower than twice the smallest of a total of 32 eigenvalues was removed from the data set. On average, 17 eigenvalues were above the threshold, accounting for 99% of total variance. Using the number of eigenvalues which accord to this criterion as the embedding dimension, the computation of the ''pointwise dimension'' (Farmer *et al.*, 1983) was based on the number $N(r)$ of signal points located at a distance smaller than r from a reference point. This calculation was performed for 32 equidistant reference points. For a given reference point, the number of samples $N(r)$ lying in a hypercube with radius r was determined. The various radii were selected in a data-driven manner. The distance between subsequent radii r_i was determined such that each enlargement of the radius increased the total count by an exponentially increasing number of points, i.e., $N(r_{i+1}) = 2N(r_i)$; $N_{r1} = N_0/20$. Using a double-logarithmic scale, the obtained counts were plotted against r. Whereas large values of $\log(r)$ lead to saturation parallel to the abscissa, $\log(N)$ increases monotonically with small values of $\log(r)$. The respective linear slopes represent an estimate of the pointwise dimension. In order to prevent the saturation decline from the computation of slopes, the points were successively removed from the right side until the right-most point did not have the largest vertical distance from the linear regression line. For each of the 32 reference points the slope of the corresponding function was calculated. The median across the 32 computed slopes provided a measure of dimensional complexity.

Since, as a rule, high-dimension values were associated with high variability, the dimension values were transformed to their natural logarithm $\log(D)$. The mean of $\log(D)$ across the 21 intervals obtained from each vowel (3 repetitions $\times$ 7 signal portions) was considered a measure of average dimensional complexity under a given condition. The respective standard deviation (s.d.) provided a measure of intrasubject instability of $\log(D)$.

Evaluation of the effects of signal type, vowel category, subject group, and gender on fractal dimensions relied on repeated measures analyses of variance (ANOVAs) with the between-subject factors group {NC,PD,CA} and sex {male, female} and the within-subject factors signal {acoustic, EGG} and vowel {a,ε,i,o,u,y}. Two overall ANOVAs were performed, one with $\log(D)$ and one with s.d. as the dependent variable. For intrasubject effects, computation of p values relied on the Greenhouse–Geisser epsilon adjustment.

In case of significant interactions, *post hoc* ANOVAs were performed in order to test for (1) differences between males and females within each subject group and (2) differences between the patient groups and the controls, separately for males and females.

II. RESULTS

Significant group×sex interactions emerged for both the fractal dimension $\log(D)$ and its standard deviation s.d. indicating gender-specific group effects on these measures (Table I). Since both between-subject factors interacted significantly with signal, *post hoc* analyses were performed separately for the acoustic and EGG signal. Apart from signal×vowel×group on $\log(D)$, all interactions between group and vowel failed significance, indicating a relative independence of the effects of vowel type from the ones of the neurological disorders. Therefore, the subject means of $\log(D)$ and its s.d. across the six vowel categories were used as dependent variables for testing the differential effects of group and sex. These *post hoc* analyses (Table II and Fig. 1) showed a prominent influence of sex on $\log(D)$ within the control group at the acoustic level. Male voices were characterized by higher dimension values than the female ones. The average acoustic dimension of the male PD patients ($D = 1.16$) was significantly reduced in comparison to the respective controls ($D = 1.72$). As expected, the EGG signal of the PD subjects showed a gender effect. In comparison with the respective controls (males: $D = 1.11$; females: $D = 1.10$), the two female patient groups (PD: $D = 1.29$; CA: $D = 1.32$) as well as, to a lesser degree, the male CA subjects ($D = 1.23$) achieved significantly increased dimension values. Both the female PD and the male CA subjects showed an increased s.d. of $\log(D)$ at the acoustic level when compared to the respective control groups. With respect to the variability of the EGG dimension, significant differences

TABLE I. Repeated measures ANOVA results with $\log(D)$ and s.d. as dependent variables, group and sex as intersubject, and vowel and signal as intrasubject factors. Significance: $* = p < 0.01$.

Source	df	F values for $\log(D)$	F values for s.d.
Group	2, 55	0.67	9.76*
Sex	1, 55	2.03	2.37
Group×sex	2, 55	7.03*	4.01
Signal	1, 55	53.35*	7.79*
Signal×group	2, 55	6.89*	5.72*
Signal×sex	1, 55	13.03*	16.12*
Signal×group×sex	2, 55	1.84	4.34
Vowel	5, 275	84.35*	13.91*
Vowel×group	10, 275	1.07	1.00
Vowel×sex	5, 275	3.77	1.73
Vowel×group×sex	10, 275	1.33	1.48
Signal×vowel	5, 275	51.80*	11.37*
Signal×vowel×group	10, 275	3.52	1.64
Signal×vowel×sex	5, 275	3.92	2.74
Signal×vowel×group×sex	10, 275	0.72	1.03

TABLE II. *Post hoc* ANOVAs with respect to gender and subject group effects (F values and significance). Significance: $* = p < 0.05$; $** = p < 0.01$.

	Acoustic signal		EGG	
	$\log(D)$	s.d. $\log(D)$	$\log(D)$	s.d. $\log(D)$
NC_{male}-NC_{female}	27.50**	0.72	0.04	0.0
PD_{male}-PD_{female}	0.10	4.11	5.27*	11.02**
CA_{male}-CA_{female}	2.00	3.08	0.48	1.0
PD_{male}-NC_{male}	10.73**	0.05	2.07	1.13
CA_{male}-NC_{male}	2.56	10.47**	5.61*	8.63**
PD_{female}-NC_{female}	2.41	5.26*	8.31**	11.39**
CA_{female}-NC_{female}	0.06	0.45	9.64**	13.06**

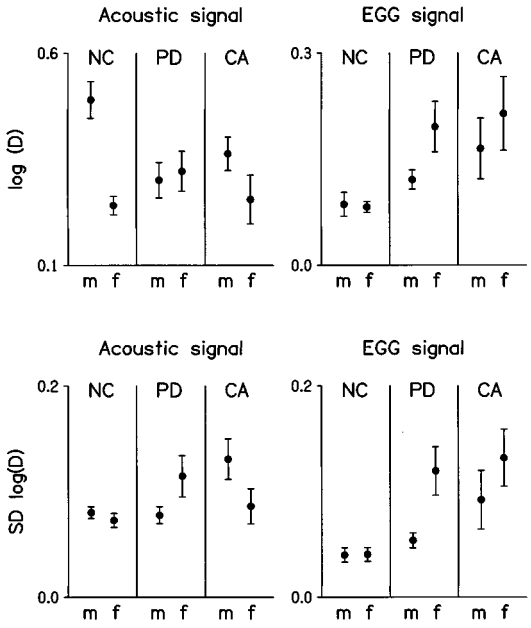

FIG. 1. Fractal dimension (upper panels) and respective intrasubject variability (lower panels) of the acoustic signal (left) and the EGG signal (right) from sustained vowel productions in male (m) and female (f) patients with Parkinson's disease (PD), cerebellar ataxia (CA), and healthy volunteers (NC): Group means with standard error bars.

emerged between the female controls and both female patient groups as well as between the CA males and the respective volunteers.

Overall ANOVA had revealed a strong main effect of the factor vowel. In order to avoid the influence of disease-dependent variability, *post hoc* analysis of vowel-specific effects on $\log(D)$ was restricted to the control group. Repeated measures ANOVAs with sex as the intersubject and vowel as the intrasubject factor were performed separately for the acoustic and EGG signal. As concerns the acoustic level, both main effects as well as their interaction achieved significance (sex: $F[1,23]=27.50$, $p<0.0001$; vowel: $F[5,115]=67.54$, $p<0.0001$; vowel×sex: $F[5,115]=5.15$, $p<0.01$). In both groups the vowel /a/ had the highest dimension value (males: $D=2.54$; females: $D=1.69$), whereas the high vowels /i/, /u/, and /y/ yielded lower values (see Fig. 2). With respect to the EGG signal, neither significant main effects of vowel and sex nor a significant vowel ×sex interaction emerged ($p>0.05$).

III. CONCLUSION

Calculation of fractal dimensions seems to provide a quantitative measure of at least some of the phonatory irregularities observed in Parkinsonian and cerebellar dysphonia. However, this parameter does not further specify the type of voice discontinuities. In contrast to the EGG, the acoustic signal revealed a strong influence of vowel category on the computed fractal dimension: low vowel /a/ yielded the largest values, whereas the high vowels were characterized by a lower dimension. This dependency on the vocal tract resonance function indicates that the dimensional complexity of the acoustic signal has only a limited relevance for the analysis of glottal source behavior.

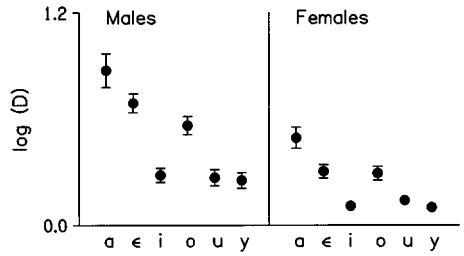

FIG. 2. Means with standard error bars of $\log(D)$ across the subjects of the control groups as derived from the acoustic signal of each vowel category.

ACKNOWLEDGMENTS

This study has been supported by a grant from the BMFT (Förderschwerpunkt: Morbus Parkinson und andere Basalganglienerkrankungen; Forschungsverbund München, 01KL9001/1) and the DFG (SFB 307/B10: Neurobiologische Aspekte des Verhaltens und seiner pathologischen Abweichungen). The authors would like to thank Werner Mende (Department of Geophysics, Freie Universität Berlin) and Kathleen Wermke (Institute of Anthropology, Humboldt-Universität Berlin) for important discussions during the early stages of the project.

Farmer, J. D., Ott, E., and Yorke, J. A. (**1983**). ''The dimension of chaotic attractors,'' Physica D **7,** 153–180.

Hertrich, I., and Ackermann, H. (**1995a**). ''Gender-specific vocal dysfunctions in Parkinson's disease: Electroglottographic and acoustic analyses,'' Ann. Otol. Rhinol. Laryngol. **104,** 197–202.

Hertrich, I., and Ackermann, H. (**1995b**). ''Electroglottographic assessment of vocal instabilities in patients with Parkinson's disease and cerebellar atrophy,'' in *Pathologies of Speech and Language: Contributions of Clinical Phonetics and Linguistics*, edited by T. W. Powell (International Clinical Phonetics and Linguistics Association, New Orleans), pp. 199–202.

Herzel, H., Berry, D., Titze, I., and Steinecke, I. (**1995**). ''Nonlinear dynamics of the voice: Signal analysis and biomechanical modeling,'' CHAOS **5,** 30–34.

Herzel, H., and Wendler, J. (**1991**). ''Evidence of chaos in phonatory samples,'' in *Eurospeech: Proceedings of the 2nd European Conference on Speech Communication and Technology*, Vol. I, Genova, Italy, 24–26 September 1991, pp. 263–266.

Laver, J., Hiller, S., and Mackenzie Beck, J. (**1992**). ''Acoustic waveform perturbations and voice disorders,'' J. Voice **6**, 115–126.

Lutzenberger, W., Preissl, H., and Pulvermüller, F. (**1995**). ''Fractal dimension of electroencephalographic time series and underlying brain processes,'' Biol. Cybern. **73,** 477–482.

Mende, W., Herzel, H., and Wermke, K. (**1990**). ''Bifurcations and chaos in newborn infant cries,'' Phys. Lett. A **145,** 418–424.

Narayanan, S. S., and Alwan, A. A. (**1995**). ''A nonlinear dynamical systems analysis of fricative consonants,'' J. Acoust. Soc. Am. **97,** 2511–2524.

Ramig, L. A. (**1986**). ''Acoustic analyses of phonation in patients with Huntington's disease: Preliminary report,'' Ann. Otol. Rhinol. Laryngol. **95,** 288–293.

Dialect variation and formant frequency: The American English vowels revisited

Robert Hagiwara
Waisman Center & Department of Communicative Disorders, University of Wisconsin-Madison, Madison, Wisconsin 53706

(Received 9 February 1996; accepted for publication 27 February 1997)

Vowel production data collected from 15 southern Californian English-speaking monolinguals is compared with data reported by Hillenbrand *et al.* [J. Acoust. Soc. Am. **97**, 3099–3111 (1995)] and Peterson and Barney [J. Acoust. Soc. Am. **24**, 175–184 (1952)]. Recordings were made of nine women and six men producing multiple repetitions of [i, ɪ, e, ɛ, æ, u, ʊ, o, ɑ, ʌ, ɹ̩] in three consonant contexts. The frequencies of the first three formants were measured by simultaneous comparison of wideband spectrograms, narrow-band FFT spectral slices, and LPC spectra taken at vowel center, or steady state where available. The Southern Californian data are seen to differ greatly from that described by Peterson and Barney (1952) and Hillenbrand *et al.* (1995). © *1997 Acoustical Society of America.* [S0001-4966(97)04906-0]

PACS numbers: 43.70.Fq, 43.70.Hs [AL]

Reference to formant frequency data from a wide variety of American English dialects is useful in forming and testing theories of vowel features, of the relation between speech production and perception, and the progress of (socio)linguistic change, as well as in providing adequate information for building speech technological applications in recognition and synthesis, and establishing dialect-appropriate norms in clinical speech therapy. However, there is a dearth of such data.

The purpose of this study is to illustrate the variability observed across American English dialects in the domain of steady-state formant frequency, and to provide, in the absence of more extensive data from Southern Californian English, a verifiable and testable set of formant frequency norms for adult men and women. Vowel data from college-aged southern Californian speakers will be seen to diverge from similar data reported for northern Midwesterners (Hillenbrand *et al.*, 1995), and from ''General American'' speakers (Peterson and Barney, 1952). This letter is also an appeal to other researchers to produce similar, ''local'' studies of American English, with a view to cooperatively producing an ''acoustic atlas'' of American English dialects as indicated by formant frequency.

The data in this study comprise a subset of the data reported in Hagiwara (1995), which contains a fuller description of the complete corpus than will be included in this letter. Undergraduate students at UCLA were asked to respond to a Speaker Survey Form if they were willing to participate in a phonetic study of /r/ in dialects of American English. Of the respondents to the survey, 15 were selected for their similarity in age (18–26), geographic background, and gross socioeconomic and educational indicators. They represent a relatively unmarked, middle-class, ''suburban'' population. They include Anglo-Americans, African Americans, and Asian Americans, but appear to represent as unified a speech community as can reasonably be studied without imposing predetermined sociometric boundaries on a target group of speakers. That is, to the degree that ''Southern California American English'' is a dialect within which a certain amount of ethno-social variation is to be expected, these 15 appear to represent the region. Each was compensated $10 U.S. for participating in the study.

Sixty-nine monosyllabic words were selected to illustrate the plain (nonrhoticized) vowels and three allophones of /r/ in southern California English. Thirty words illustrate plain vowels in three consonantal environments: /b_t/, /t_k/, and /h_d/. Three exemplify syllabic /ɹ̩/ in the same environments. These 33 words together form the database for the present study. Table I lists the words used. Only real English words and familiar proper nouns were used; where a word of the appropriate phonological shape did not exist, a word as close in shape as possible to the target was substituted, as with ''put.'' The word ''hoed'' was respelled as a proper noun (''Hode'') to avoid its relatively odd-looking spelling.

Each word was presented in the frame ''Cite__twice.'' This frame was selected to provide ''citation'' form pronunciations, but in a continuous speech stream. The symmetrical, nonflapping coronal environment was necessary for a simultaneous study conducted with the same speakers. Each word/frame was included three times in random order in a single recording script. Each speaker was recorded reading from the script in a sound-treated room on professional quality equipment.

The subjects' speech was digitized from the audio cassette tape of the recording session at 10 kHz using the Kay Elemetrics Computerized Speech Laboratory. Frequencies were measured for the first three formants (F_1, F_2, F_3) of each syllabic nucleus in the words illustrating syllabic [ɹ̩] and other vowels. Formant frequencies were determined by simultaneous evaluation of several transforms of the signal. These included wideband spectrograms and narrow-band FFT spectra averaged over a 30-ms window through the steady-state portion of the vowel, if there was one. If no steady state was present, the 30-ms window was placed in the center of the vowel. Bandwidths for spectrograms and narrow-band spectra were varied to achieve the best formant

TABLE I. Words illustrating the 11 vowels of Southern Californian English.

	/i/	/ɪ/	/e/	/ɛ/	/æ/	/u/	/ʊ/	/o/	/ɑ/	/ʌ/	/ɹ̩/
b_t	beat	bit	bate	bet	bat	boot	put	boat	bought	but	Bert
t_k	teak	tick	take	tech	tack	duke	took	toke	tock	tuck	Turk
h_d	heed	hid	hate	head	had	hoot	hood	Hode	hod	hut	herd

resolution for each token. Generally, bandwidths were 200 Hz (wideband) and 59 Hz (narrow band) for men, and 293/59 Hz for women. Also included were an LPC formant history superimposed over the spectrogram and/or an LPC slice taken in the center of the FFT window superimposed over the FFT spectrum. The number of LPC poles used varied between 10 and 14 depending on the sex of the speaker, the number of formants visible in the spectrogram, and whether or not more poles were needed to resolve two formants which were close together.

By using multiple views of the spectral properties of the signal, a certain degree of on-line checking was introduced during the measurement process, with the result of greater confidence in the state of the measurements. Moreover, well-known problems such as discerning low-frequency F_1's in higher pitched voices, or the apparent merger of close formants in LPC analysis, as well as the problem of locating formants in voices that exhibit consistent spectral ''eccentricities'' (unexpected zeroes, unusually strong harmonics, etc.) were more easily avoided. The results are summarized in Table II.

The southern Californian /u/ and /ʊ/ have higher F_2 values than /ɑ/. This is partly the result of the ''duke'' context, in which /u/ is accompanied by a front on-glide. However, even discounting the fronting influences of the ''duke'' context, the F_2 of /u/ still averages around 1500 Hz for women and 1300 Hz for men, still quite a bit higher than /o/ or /ɑ/.

The inclusion of the ''duke'' context, and to a lesser extent the ''boot'' context, to add breadth to the production database. In the near-citation forms produced in this study, speakers sometimes produced fully round allophones of back vowels. However, in casual speech, southern Californians rarely produce fully rounded vowels.

The combined centrality and unrounding observed in the southern Californian speakers result in a vowel space which resembles a parallelogram more than the traditional trapezoidal or triangular figures usually associated with vowel spaces. This is illustrated in Fig. 1.

While several American dialects have been studied in detail in their socio-historical contexts (see, for instance, Labov 1994, and references therein for some discussion), and these often make use of acoustic measurements, there are relatively few well-known studies of vowels formants in American English cited in the phonetics literature. Of these, the classic study by Peterson and Barney (1952) is probably the most cited. The recent paper by Hillenbrand *et al.* (1995), being paradigmatically similar to the Peterson and Barney study, although conducted over a much larger corpus in a different dialect, is also a very important work.

Peterson and Barney (1952, PB hereafter) was a study with the primary objective of showing that information obtained by spectrographic analysis of speech was useful in characterizing vowel quality. The vowels /i, ɪ, ɛ, æ, ɑ, ɔ, ʊ, u, ʌ, ɹ̩/ were included. Fundamental frequency, F_1, F_2, and F_3, were measured during steady-state portions of /h_d/ productions by 33 men, 28 women, and 15 children. In general, little can be said about the dialectal affiliations of the speakers involved, or of the dialectal homogeneity of the group as a whole. ''Two of the speakers were born outside the United States and a few others spoke a foreign language before learning English. Most of the women and children grew up in the Middle Atlantic speech area. The male speakers represented a much broader regional sampling of the United States, the majority of them spoke General American.'' (PB, p. 177).

The acoustic data were studied two ways; first by spectrographic analysis, to determine formant frequencies. Analysis of these data suggested that static formant frequencies were good at differentiating vowel quality. The data were then used in a listening test, where listeners were asked to identify the word uttered. For the most part, correct identification was achieved, despite the less than perfect listening

TABLE II. Formant averages for 15 southern Californian speakers of English. Units are Hz. Standard deviations are in parentheses.

	F_1		F_2		F_3		
	W	*M*	*W*	*M*	*W*	*M*	
i	362 (36)	291 (31)	2897 (176)	2338 (205)	3495 (239)	2920 (219)	i
ɪ	467 (62)	418 (36)	2400 (151)	1807 (85)	3187 (262)	2589 (117)	ɪ
e	440 (48)	403 (43)	2655 (187)	2059 (138)	3252 (277)	2690 (166)	e
ɛ	808 (167)	529 (68)	2163 (195)	1670 (67)	3065 (285)	2528 (143)	ɛ
æ	1017 (134)	685 (105)	1810 (131)	1601 (59)	2826 (231)	2524 (271)	æ
u	395 (48)	323 (31)	1700 (364)	1417 (215)	2866 (225)	2399 (248)	u
ʊ	486 (115)	441 (40)	1665 (166)	1366 (122)	2926 (261)	2446 (173)	ʊ
o	516 (130)	437 (37)	1391 (212)	1188 (118)	2904 (263)	2430 (216)	o
ɑ	997 (102)	710 (97)	1390 (99)	1221 (69)	2743 (201)	2405 (175)	ɑ
ʌ	847 (154)	574 (80)	1753 (140)	1415 (88)	2989 (264)	2496 (211)	ʌ
ɹ̩	477 (82)	429 (40)	1558 (170)	1362 (79)	1995 (347)	1679 (91)	ɹ̩

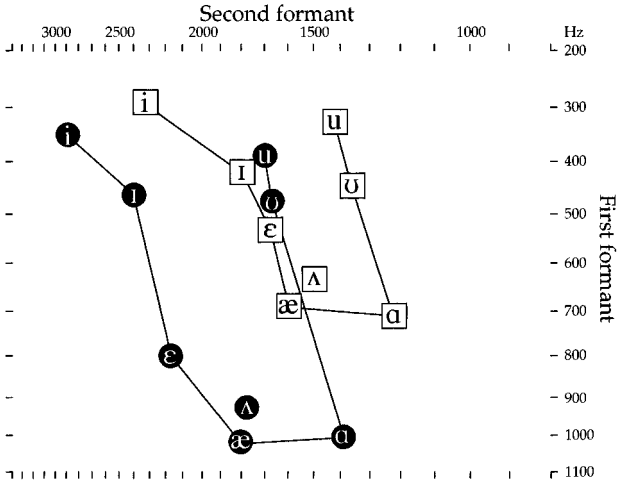

FIG. 1. Women's (filled circles) and men's (open squares) vowel centers from the present study. Vowels are joined by lines in order (starting at the upper right) /i, ɪ, ɛ, æ, ɑ, ʊ, u/. Not joined on the line is /ʌ/. Other vowels were eliminated for visual clarity and to facilitate comparison. Units are Hertz, plotted in a Bark scale.

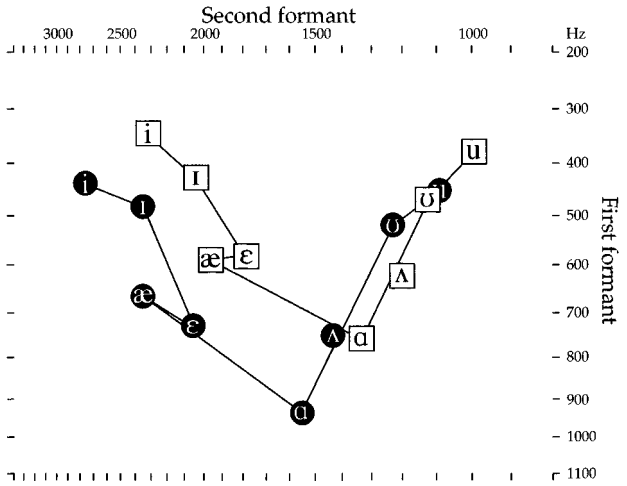

FIG. 3. Women's (filled circles) and men's (open squares) vowel centers from Hillenbrand *et al.* (1995), plotted in the same space as Fig. 1. Vowels are joined by lines in order (starting at the upper right) /i, ɪ, ɛ, æ, ɑ, ʊ, u/. In these data, /ʌ/ accidentally fell on the line between /ɑ/ and /ʊ/.

conditions. Where confusions occurred, they appeared to follow reasonable patterns (/ɑ-ɔ/ confusions, etc).

The PB vowel spaces are illustrated in Fig. 2, which presents the PB F_1 and F_2 averages (see PB, Table II, p. 183) plotted to the same scale as Fig. 1. The men's and women's productions are superimposed in the same plot. As in Fig. 1, the vowels represented are /i, ɪ, ɛ, æ, ɑ, ʊ, u/ (joined by the lines) and /ʌ/. Figure 2 illustrates the classic ''trapezoidal'' form of the ''General American'' vowel space defined by the point vowels.

Recognizing a number of limitations in the PB study, Hillenbrand *et al.* (1995; HGCW hereafter) collected a new corpus, using productions from 45 men, 48 women, and 46 children. These speakers were carefully screened for dialect; all were from the northern Midwest area. HGCW included F_4 measurements, as well as measurements from multiple points during the vowel. They also included /e/ and /o/ vowels, excluded from the PB study. LPC formant histories were superimposed over a wideband spectrogram, and adjustments made until the first four formants were adequately resolved by the LPC. Formant frequencies were then extracted from the LPC peaks. Listening tests were also performed with the data, and a variety of analyses offered.

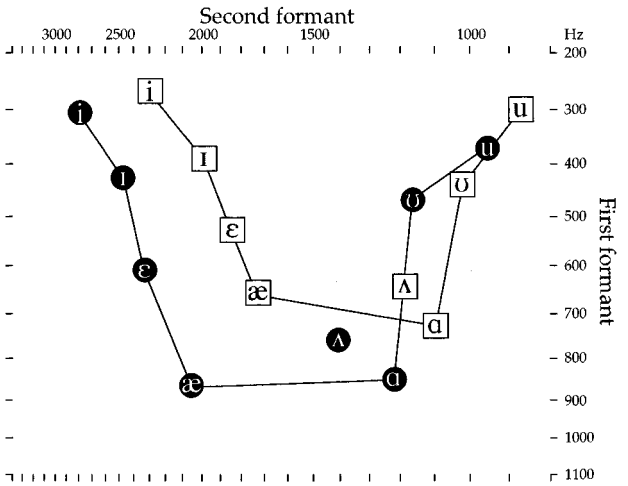

FIG. 2. Women's (filled circles) and men's (open squares) vowel centers from Peterson and Barney (1952), plotted in the same space as Fig. 1. Vowels are joined by lines in order (starting at the upper right) /i, ɪ, ɛ, æ, ɑ, ʊ, u/. Not joined on the line is /ʌ/.

The HGCW vowel centers (see HGCW, Table V, p. 3103) are plotted in Fig. 3. Note the extreme raising of /æ/ relative to its position in PB or the present study, and the centrality of /ɑ/. This configuration (along with the position of /ɔ/, not included in Fig. 3) is the result of a clockwise chain shift among the low vowels typical of the northern midwest (the Northern Cities Shift, as described in sum by Labov, 1994, and many sources therein). With the raising of /æ/ out of the ''low front corner'' of the space, and the low, central position of /ɑ/, this configuration of point vowels suggests a triangle, and is quite distinct, both in outline and in composition from either of the two previous figures.

Comparing the present study's data in Fig. 1 with the PB data in Fig. 2, the obvious differences are in the F_2 frequencies of the back and central vowels. As noted earlier, the canonical back vowels /u/ and /ʊ/ are typically unrounded in Californian speech. Thus they appear with F_2 frequencies more characteristic of the central space in the PB data in Fig. 2. Further, the canonical central vowel /ʌ/ has a much higher F_2 in the southern California data than in PB. The low vowels /ɑ/ and /æ/ are approximately 200 Hz higher in the Californian women than for PB's women speakers. The men have similar F_1 values for these vowels in the two studies.

The most obvious difference between the HGCW vowels in Fig. 3 and the PB ones is in the position of the vowels transcribed /æ/ and /ɑ/. /ɑ/ in the HGCW space has moved into a central position relative to its position in the PB space; the /æ/ vowel has been fronted and raised. The /ʌ/ vowel, in contrast, is almost identical in the two studies. (This is also true of /ɹ/, which was included in all studies under discussion, but not represented graphically in Figs. 1–3.) More

subtly, the /u/ and /ʊ/ vowels in the PB are extremely back (have extremely low F_2's). While still low the HGCW F_2 values for /u/ and /ʊ/ are slightly higher than in PB.

The configuration in Fig. 3 indicates a well-established ''Northern Cities Shift,'' such as described recently by Labov (1994, summarizing sources therein). The Northern Cities Shift dialects are characterized by a centralized reflex of /ɑ/ (more properly /a/), and a raised /æ/, among other changes, that have been observed to varying degrees in the cities of Detroit, Chicago, and Cleveland, as well as upstate New York. HGCW described their speakers as being raised in southern Michigan and other areas in the upper midwest. Thus it is fair to assume that, even if they are not speakers of Northern Cities Shift dialects, they are from areas heavily influenced by them. Thomas (1958) refers to the relative centrality of /ɑ/ in his ''Northern Central'' dialects, which include the northern midwest, the same region studied in HGCW.

The PB study, conducted at Bell Laboratories in New Jersey, used speakers from a variety of places, and even some who spoke other languages than English natively. However, the women speakers in that study are identified as primarily from the Middle Atlantic region. Thomas (1958) indicates that the Middle Atlantic region includes most of New Jersey, and specifically excludes upstate New York and the northern Midwest.

Comparing Figs. 1 and 3 reveals as many differences between HGCW's vowel space and the southern Californian space as between HGCW and PB. This clearly demonstrates considerable variation between contemporaneous regional variants of American English.

The purpose of this discussion is merely to demonstrate that ''American English'' is an amorphous entity at best, and that there are considerable regional (and also social) differences, particularly in urban centers (Labov, 1994). In discussions of vowel production, references to ''General American'' are not as informative as references to data from *specific* dialects.

Throughout this report, an effort has been made to characterize the southern Californian vowel space and the spaces reported in HGCW and PB without reference to an arbitrary standard. In their paper, HGCW point out that the PB results are often regarded as the definitive set of static formant frequencies describing the American English vowels, serving as a comparator with other languages and pathological speech, target values in speech synthesis, prototype values, etc. Such a view clearly misrepresents the intent of PB, and belies the reality of the whole of American English, even perhaps ''General American.'' At best, the PB results are a profile of a ''specific dialect at a specific time in the history of that dialect'' (HGCW, p. 3108).

Implicit in HGCW's discussion is the need for more such profiles. HGCW provide one, with the purpose not only of replicating the PB study but also determining the how dynamic information can be used to discriminate vowels. The data in the present study represent another profile of a different dialect. They were collected originally with the intention of providing baseline F_3 measurements against which lowered F_3 in American /r/ could be compared (Hagiwara, 1995). However, as this paper argues, the resulting information about the form of the southern Californian vowel space is interesting in its own right, particularly as it provides counterpoint to the view of the PB or the HGCW formant values as somehow representative of the state of American English as a whole.

As HGCW point out, large studies are consuming of time, money, and scholarly resources. Documentation of every American dialect on such a scale is obviously beyond the scope of any single researcher or research group, especially considering that in the best case it would include more than static formant frequency information. However, studies of a dozen or so speakers are well within the scope of most researchers, perhaps most students, and, in the absence of studies of large numbers of speakers, would be better than nothing. If the results of many such studies were combined, they would fill a significant void in objective descriptions of American English, and help pinpoint areas where the greater resources of larger, or more expansive studies may most profitably be employed.

Such investigations would not only lead to a better understanding of American English vowels, but also yield a database of general interest to phonetics, sociolinguistics, speech training, and speech technology.

ACKNOWLEDGMENTS

The author would like to thank Peter Ladefoged, James Hillenbrand, and two anonymous JASA reviewers for comments on earlier versions of this letter.

Hagiwara, R. (**1995**). ''Acoustic realizations of American /r/ as produced by women and men,'' UCLA Ph.D. dissertation. Also *UCLA Working Papers in Phonetics* **90**.

Hillenbrand, J., Getty, L. A., Clark, M. J., and Wheeler, K. (**1995**). ''Acoustic characteristics of American English vowels,'' J. Acoust. Soc. Am. **97,** 3099–3111.

Labov, W. (**1994**). *Principles of Linguistic Change, Volume 1: Internal Factors* (Blackwells, Cambridge).

Peterson, G. E., and Barney, H. L. (**1952**). ''Control methods used in a study of the vowels,'' J. Acoust. Soc. Am. **24,** 175–184.

Thomas, C. K. (**1958**). *An Introduction to the Phonetics of American English* (Ronald, New York), 2nd ed.

Piano strings and “phantom” partials

Harold A. Conklin, Jr.
Box 1915, Dunedin, Florida 34697

(Received 1 April 1991; revised 24 August 1994; accepted 27 September 1994)

Additional partials can occur in the radiated tone of pianos at frequencies other than those predicted by classical string equations. [S0001-4966(97)04007-1]

PACS numbers: 43.75.Mn, 43.40.Cw [DWM]

The tones of pianos can have spectral components not predicted by classical string equations. This is illustrated by Fig. 1, which shows a portion of the acoustical spectrum of the tone E_3 (Nominal Fundamental Frequency=164.81 Hz) from a mechano-acoustic piano. The span shown (2.1–2.9 kHz) contains normal transverse partials Nos. 13 through 17, which were found to occur at frequencies predictable from string data. Un-numbered partials, here termed ‘‘phantoms,’’ also appear in Fig. 1, the most prominent ones at frequencies slightly below the frequencies of the (numbered) normal partials. For phantoms to be distinguishable in a spectrogram from normal partials, the normal partials must be inharmonic, like those of real piano strings, and the spectrum analyzer must have sufficient resolution. As resolution is increased, phantoms may be seen to accompany normal partials of increasingly low number.

The phantom partials discussed here result from the presence of normal transverse partials, and may be classified as ‘‘even’’ or ‘‘odd.’’ An ‘‘even’’ phantom has a frequency exactly twice that of the single responsible normal partial. If a piano string vibrates transversely at a single frequency, with non-negligible displacement, a longitudinal force at twice the transverse frequency will be produced at each end of the string. When this force is translated to the soundboard by the soundboard bridge (on which the speaking length of the string has been terminated), a true second harmonic tone will be produced. The existence of such forces can be inferred by applying reciprocity to the result of Melde’s experiment as described by Rayleigh,[1] or by noting that the instantaneous displacement of a transversely vibrating string in *either* direction from its rest position will increase its instantaneous tension.

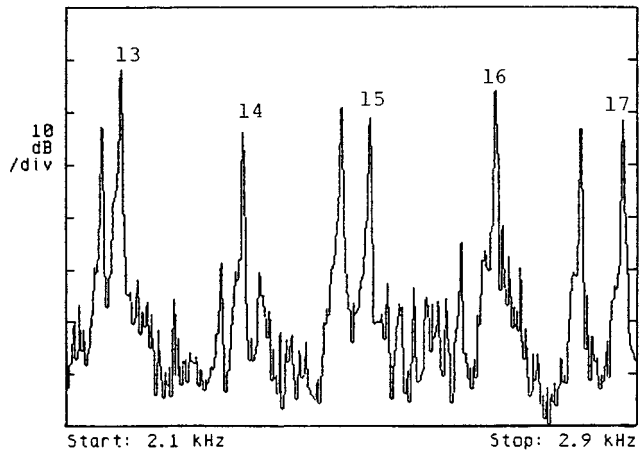

FIG. 1. Portion of acoustical spectrum (2.1–2.9 kHz) of the tone E_3 from a mechano-acoustic piano. Normal transverse partials 13–17 are numbered.

‘‘Odd’’ phantoms are those that have frequencies equal to the sum (or difference) of the frequencies of two normal partials.

Example: A phantom appearing just below the frequency of partial 13 may have a frequency equal to the sum of the frequencies of partials 6 and 7. While it has been found that the parent normal partials very often are numerically adjacent, as in the example above, other combinations (such as 5 plus 8) are common. In a few instances phantoms have been observed that appear to be at the difference frequency of two normal partials. To account for ‘‘odd’’ phantoms appears to require nonlinearity, of either the piano structure, the string, or the measuring equipment. In the findings reported here, nonlinearity of the measuring equipment was much too small to produce phantoms of the observed amplitudes. The responsible nonlinearity seems to reside with the vibrating string and its terminations. Phantoms have also been found in the acoustical output of a guitar and in the vibrations of strings mounted on a monochord.

Phantom partials in a piano tone usually are lower in level than their normal-partial neighbors, but this is not always the case, as shown by Fig. 1, in which the phantom just below normal partial 15 is slightly higher in level than partial 15, and in which partial 17 and the phantom just below it have almost the same level. The effect of phantom partials on the perceived tone quality of mechano-acoustic pianos is believed to be significant.

[1] J. W. S. Rayleigh, ‘‘On the Maintenance of Vibrations by Forces of Double Frequency, and On the Propagation of Waves Through a Medium Endowed with a Periodic Structure,’’ Scientific Papers, Vol. III, 1 (1887).

Erratum: "Prediction of SNR gain for passive higher-order correlation detection of energy transients" [J. Acoust. Soc. Am. 98, 248–260 (1995)]

Lisa A. Pflug
Naval Research Laboratory, Stennis Space Center, Mississippi 39529-5004

George E. Ioup and Juliette W. Ioup
Department of Physics, University of New Orleans, New Orleans, Louisiana 70148

Robert L. Field
Naval Research Laboratory, Stennis Space Center, Mississippi 39529-5004

(Received 25 February 1997; accepted for publication 3 March 1997)

PACS numbers: 43.60.Gk, 43.60.Cg, 43.10.Vx [JLK]

Appendices A and B contain typographical errors.

In Appendix A on page 258, assumption number 3 should read:

(3) The square of the distinct underlying noise process is uncorrelated across p realizations of the ensemble at any given time,

$$E\{n_1^2(t)n_2^2(t)\cdots n_p^2(t)\}=E\{n_1^2(t)\}E\{n_2^2(t)\}\cdots E\{n_p^2(t)\},\quad 1,2,\ldots,p \text{ distinct.}$$

In Appendix B on page 259, the first expression and following sentence should read: The qth-order ensemble moment of p zero-mean noise sequences, each of length N with $t_i=k_i\Delta t$, is

$$\begin{aligned}E\left\{\left[\sum_{k=0}^{N-1} n_1(t)n_2(t)\cdots n_p(t)\Delta t\right]^q\right\}&=(\Delta t)^q E\left\{\left[\sum_{k_1=0}^{N-1} n_1(t_1)n_2(t_1)\cdots n_p(t_1)\right]\right.\\&\quad\left.\times\left[\sum_{k_2=0}^{N-1} n_1(t_2)n_2(t_2)\cdots n_p(t_2)\right]\cdots\left[\sum_{k_q=0}^{N-1} n_1(t_q)n_2(t_q)\cdots n_p(t_q)\right]\right\}\\&=(\Delta t)^q E\left\{\sum_{k_1=0}^{N-1}\sum_{k_2=0}^{N-1}\cdots\sum_{k_q=0}^{N-1} n_1(t_1)n_1(t_2)\cdots n_1(t_q)n_2(t_1)n_2(t_2)\cdots n_2(t_q)\right.\\&\quad\left.\cdots n_p(t_1)n_p(t_2)\cdots n_p(t_q)\right\}.\end{aligned}$$

This expression is approximately zero when q is odd. It is only nonzero when q is even and times are equal in pairs.

 0001-4966/97/102(1)/660/1/$10.00